

**FUNKCIONÁLIS DISZPERZIÓK:  
A KOLLOIDSTABILITÁSTÓL AZ ANTIOXIDÁNS  
KOMPOZITOKIG**

**SZILÁGYI ISTVÁN**



SZEGEDI TUDOMÁNYEGYETEM  
Természettudományi és Informatikai Kar  
Fizikai Kémiai és Anyagtudományi Tanszék

Szeged  
2022

**TARTALOMJEGYZÉK**

RÖVIDÍTÉSEK JEGYZÉKE	3
1. BEVEZETÉS	4
2. IRODALMI ÁTTEKINTÉS	6
2.1. A kolloidok stabilitásáért felelős felületi erők	6
2.2. Ionspecifikus kölcsönhatások	9
2.3. Antioxidáns rendszerek	14
3. CÉLKITŰZÉSEK	17
4. KÍSÉRLETI MÓDSZEREK	18
4.1. Felhasznált anyagok	18
4.2. Mérési módszerek és a kísérleti adatok kiértékelése	18
4.3. Antioxidáns aktivitás felmérése	19
5. EREDMÉNYEK ÉS KÖVETKEZTETÉSEK	20
5.1. Ionspecifikus határfelületi kölcsönhatások	20
5.2. Részecske diszperziók ionos folyadékokban	26
5.3. Funkcionalizálás polielektrolitokkal	31
5.4. Enzimatis antioxizánsok immobilizálása	38
5.5. Molekuláris és mesterséges antioxizánsok rögzítése kompozitokban	43
6. ÖSSZEFOGLALÁS	50
7. AZ EREDMÉNYEK VÁRHATÓ ALKALMAZÁSAI	51
8. IRODALOMJEGYZÉK	52
9. AZ ÉRTEKEZÉS ALAPJÁT KÉPEZŐ KÖZLEMÉNYEK	58
10. KÖSZÖNETNYILVÁNÍTÁS	60

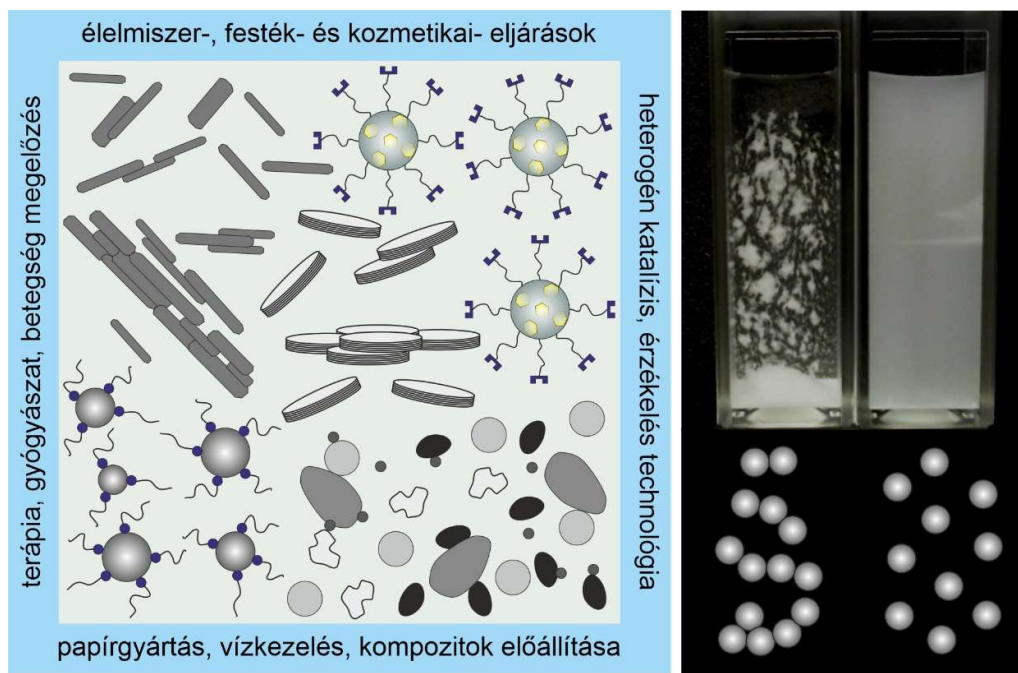


## RÖVIDÍTÉSEK JEGYZÉKE

ACA	Aszkorbinsav	IEP	Izoelektromos pont
AFM	Atomerő mikroszkóp	IL	Ionos folyadék
AL	Amidin latex	IP-2	Poliimidazólium polimer
ASP	Adszorpció telítési határ	IR	Infravörös
BMIM <sup>+</sup>	1-butyl-3-metil-imidazólium	LDH	Réteges kettős hidroxid
BMPiP <sup>+</sup>	1-butyl-1-metil-piperidínium	MIM <sup>+</sup>	Metil-imidazólium
BMPL <sup>+</sup>	1-butyl-3-metil-pirrolidínium	MnO <sub>2</sub> NP	Mangán(IV)-dioxid részecske
BMPY <sup>+</sup>	1-butyl-2-metil-piridínium	MOF	Fémorganikus vázszerkezet
Bpy	2,2'-Bipiridin	NBT	Nitro-kék tetrazólium
CAT	Kataláz	OMIM <sup>+</sup>	1-oktil-3-metil-imidazólium
Cit	Citrát	PAA	Poli(akrilát)
CCC	Kritikus koagulátó koncentráció	P(AA-BA)	Poli(akrilát-ko-butyl-akrilát)
CCIS	Kritikus koagulátó ionerősség	P(AAM-DADMAC)	Poli(akrilamid-ko-diallil dimetil ammónium klorid)
CN	Katechin	PAMAM	Poli(amido-amin)
CuHsm	Réz(II)-hisztamin (1:2) komplex	PB	Poisson-Boltzmann
CuBpy	Réz(II)-bipiridil (1:2) komplex	PBP	Berlini kék részecske
DCF	2',7'-diklorofluorescein	PDADMAC	Poli(diallil-dimetil-ammónium klorid)
DH	Debye-Hückel	PEI	Poli(etilén-imin)
DLS	Dinamikus fényszórás	PLL	Poli(L-lizin)
DLVO	Derjaguin-Vervej-Landau-Overbeek	PPN	Papain
DPPH	1,1-difenil-2-pikrilhidrazil	PSS	Poli(sztiroil-szulfonát)
EA	Ellagsav	PSP	Protamin-szulfát
EAN	Etil-ammónium nitrát	P(VP-MA)	Poli(vinilpiridin-metilakrilát)
ELS	Elektroforetikus fényszórás	PZC	Nulla töltéspont
EMIM <sup>+</sup>	1-etil-3-metil-imidazólium	QC	Kvercetin
ESR	Elektronspin rezonancia	ROS	Reaktív oxigén származékok
FeCit	Vas(III)-citrát (1:2) komplex	RNS	Reaktív nitrogén származékok
GA	Galluszsav	SEM	Pásztázó elektron mikroszkópia
GPX	Glutation peroxidáz	SL	Szulfát latex
H <sub>2</sub> DCF	2',7'-dikloro-dihidrofluorescein diacetát	SOD	Szuperoxid dizmutáz
HEP	Heparin	TEM	Transzmissziós elektron mikroszkópia
HMIM <sup>+</sup>	1-hexil-3-metil-imidazólium	TiONW	Titanát nanoszál
HNT	Halloizit nanocső	TNS	Titán-dioxid nanolap
HRP	Torma peroxidáz	UV-Vis	Ultraibolya-látható
Hsm	Hisztamin	XPS	Röntgen fotoelektron spektroszkópia
IC <sub>50</sub>	50% hatást kiváltó koncentráció	XRD	Röntgendiffraktometria

## 1. BEVEZETÉS

A nanométeres, illetve kolloid mérettartományba eső részecskék diszperziói széles körben nyernek felhasználást különféle ipari, környezeti és orvosi biológiai alkalmazásokban, így válva a mindennapjaink részévé [1-5]. Az ilyen típusú részecskék rendkívül változatos tulajdonságokkal rendelkeznek mind összetételüket, mind alakjukat tekintve és ezek hangolásával a felhasználási céloktól függően megfelelő szerkezetek állíthatók elő. Az alkalmazások során a diszperz rendszerek kolloidstabilitása az egyik legkritikusabb paraméter. A stabilis diszperziók egyenletesen elosztott egyedi részecskéket tartalmaznak, ezek aggregációja a minta destabilizálódásához vezet. Az aggregációs folyamat korai fázisában dimer részecskék képződnek, míg a későbbi szakaszban nagyobb klaszterek is kialakulhatnak, illetve összekapcsolódásukkal fázisszeparáció is lejátszódhat [6]. Ez a folyamat a részecskék és a közeg anyagi minőségétől függően szedimentációhoz vagy fölöződéshez vezet (1. ábra).



**1. ábra.** Bal oldal: Különböző összetételű és alakú részecskék felhasználási lehetőségei. Jobb oldal: Instabil (ülededő) és stabil diszperziók sematikus ábrázolása.

A különböző mérettartományba eső részecskék kolloidstabilitását, illetve a köztük létrejövő erőhatások minőségét és mértékét számos tényező befolyásolja [7]. Ilyen paraméter például a részecske mérete, anyagi összetétele és töltése. Az utóbbi esetben beszélhetünk szerkezeti töltésről, amikor a töltés csak az alkotó atomok és ionok sztöchiometriai viszonyaitól függ [8]. Emellett a felületi protonálódási és deprotonálódási folyamatok az oldat pH-jától függő töltés kialakulásához vezethetnek [9]. Szerkezeti és pH-függő töltés létrejöhet külön-külön és együttesen is, amint azt a későbbiekben példákkal is illusztrálni fogom. A következőkben néhány példát mutatok be részecske diszperziók stabilitásának fontosságára különféle alkalmazásokban.

A kereskedelmi forgalomban kapható festékek például fontos mindennapi termékek. Ezek olyan diszperz rendszerek, amelyeknél a megfelelő mértékű kolloidstabilitás kiemelt jelentőségű. Az utóbbi évtizedekben a legnagyobb áttörést ezen a területen a vízbázisú festékek kifejlesztése jelentette, amely lehetővé tette a környezeti és egészségügyi kockázattal járó, ezért rendkívül káros szerves oldószerek kiváltását. A vízbázisú festékek alkotóelemei a közegen kívül a szín-, töltő- és stabilizáló komponensek. Például, a titán-dioxid részecskék, magas törésmutatójuknak köszönhetően, rendkívül jó minőségű pigment anyagok fehér színű festékekben [10]. Polimer latex részecskéket szintén alkalmaznak fehér festékekben, mivel nagy a környezeti stabilitásuk és ezáltal felületi védőréteget is képeznek [11]. A természetben gyakran előforduló, vagy olcsó alapanyagokból „bottom-up” technikákkal nyerhető részecskék, mint például a mészkő, az agyagásványok vagy a homok, széleskörűen megtalálhatók festékekben, mint töltőanyagok, míg a színezék diszperziókat különféle polimerek és felületaktív anyagok stabilizálják.

Egy másik példa, ahol viszont éppen a diszpergált részecskék destabilizálása a cél, az a különféle ipari és kommunális szennyvizek tisztítása. A kolloidok és nanorészecskék növekvő felhasználása miatt koncentrációjuk jelentős mértékben megnőtt a szennyvizekben, eltávolításuk hagyományos szűrési eljárásokkal nem megoldható. Kivonásuk a szennyvízből azért is fontos az elsődleges szennyvíztisztítás során, mivel a felületükre adszorbeálódó baktériumoknak és vírusoknak védelmet nyújthatnak a fertőtlenítő eljárások során. A probléma megoldásának érdekében a részecskéket tartalmazó diszperz rendszert destabilizálják polielektrolitok [12] vagy többértékű fémionok segítségével [13], ami után a leülepedő szilárd anyag már viszonylag egyszerűen elválasztható a vizes fázistól, amely további kezelési folyamatokon esik át.

A nanorészecskék egyik fontos felhasználása orvosbiológiai eljárásokhoz köthető, ahol hordozóként [14] vagy pedig hatóanyagként [15] kerülhetnek alkalmazásra. A doktori dolgozatomban is tárgyalásra kerülő réteges kettős hidroxidok (LDH) [16], titán-dioxid nanolapok (TNS) [17] és haloizit nanocsövek (HNT) [18] hatékony hordozónak bizonyultak kis molekulájú gyógyszerhatóanyagok, vagy terápiás célú makromolekulák esetében is. A másik, ugyancsak a dolgozat anyagához kapcsolódó, rohamosan fejlődő terület az antioxidáns hatású részecske diszperziók alkalmazása betegség megelőzési, illetve terápiás céllal [19-21]. Megfelelő paraméterekkel rendelkező nanoszerkezetek felhasználásra kerültek többek között őssejtek élettartamának megnövelésére, csontszövet regenerációjára, gyulladással járó, neurodegeneratív és rákos megbetegedések kezelésére. Emellett optimalizált dózisban való mindennapi utánpótlásukkal a megnövekedett oxidatív stressz csökkenthető. A felsorolt alkalmazások többségében a részecskék folyadék közegben találhatóak, tehát a rendszer kolloidstabilitása kiemelt jelentőségű. A részecske aggregáció következtében a fajlagos felület csökkenése miatt lecsökken a hatékonyság és további komplikációk is felléphetnek, mint például a vérerek elzáródása a képződő aggregátumok hatására [22]. A részecskék stabilizálása céljából különféle biokompatibilis polimerekkel és kis molekulatömegű anyagokkal módosítják azok felületét [2, 23, 24].

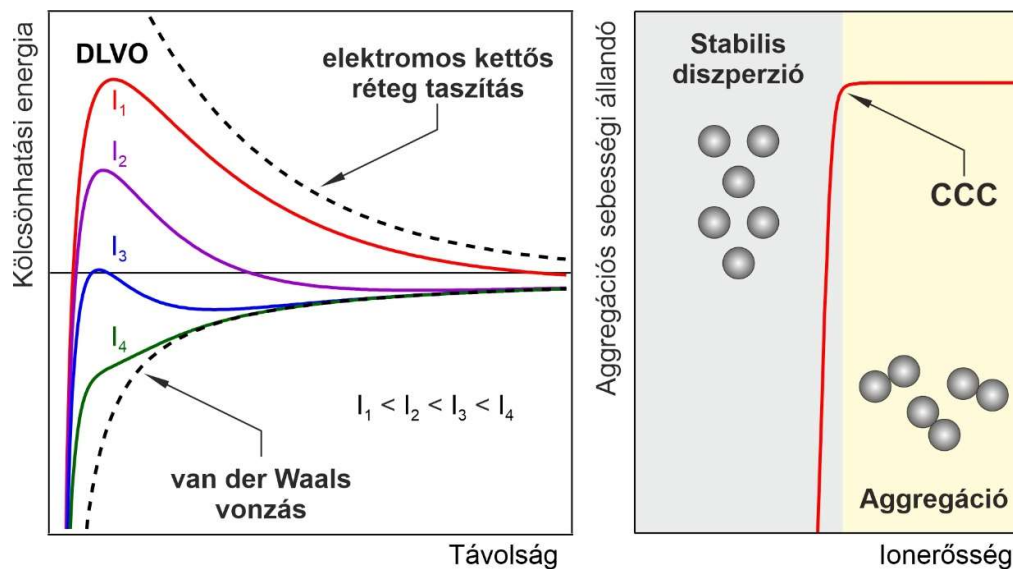
## 2. IRODALMI ÁTTEKINTÉS

### 2.1. A kolloidok stabilitásáért felelős felületi erők

Az előző fejezetben ismertetett gyakorlati példák is rámutatnak a részecskék kolloidstabilitásának fontosságára. Homogénean elosztatott részecskékből álló stabilis diszperziók előállítása elvárás például a festék-, élelmiszer- vagy kozmetikai termékek gyártása során, míg kolloid rendszerek destabilizálása szükséges a szennyvízkezelési és papírgyártási folyamatok során. A diszpergált részecskék stabilitása a közöttük létrejövő vonzó és taszító erőhatások egymáshoz való viszonyának következménye, ezeket tárgyaljuk a következőkben.

#### *Derjaguin-Landau-Verwey-Overbeek elmélet*

Töltéssel nem rendelkező részecskék folyadékban diszpergálva vonzzák egymást a közöttük fellépő van der Waals kölcsönhatásoknak köszönhetően, amelyek mindig jelen vannak, kivéve, ha a közeg és a részecske törésmutatója megegyezik [7]. A legtöbb nanométeres és kolloid mérettartományba eső anyag felületén azonban szerkezeti és/vagy pH-tól függő töltés alakul ki, illetve töltéssel rendelkező anyagok lehetséges adszorpciója is hozzájárul a felületi töltés kialakulásához. Oldott elektrolitok jelenléte az úgynevezett elektromos kettős réteg képződéséhez vezet [25], amelyek Coulomb-féle taszítást fejtenek ki két részecske közeledése során. Az eredő erőhatás a felsorolt vonzó és taszító kölcsönhatások egymáshoz viszonyított mértékétől függ. Ez a felismerés vezetett a Derjaguin-Landau-Verwey-Overbeek (DLVO) elmélet [26, 27] létrejöttéhez (2. ábra), ennek részletei monográfiákban elérhetőek [6, 7, 28].



**2. ábra.** Bal oldal: A kölcsönhatási energia távolság függése DLVO kölcsönhatások feltételezése esetén különböző ionerősségeknél ( $I$ ). Jobb oldal: részecske dimer képződés aggregációs sebességi állandójának változása az ionerősséggel a DLVO elméletből számolva.

Az eredő kölcsönhatási energia változása a felülettől való távolság ( $h$ ) függvényében ( $V(h)$ ) az 1. egyenlettel számítható azokkal a feltételekkel, hogy a vonzó kölcsönhatások ( $V_{vdW}(h)$ ) esetében a Derjaguin-féle megközelítést [7], míg a taszító potenciál energia esetében ( $V_{EDL}(h)$ ) a Debye-Hückel elméletet [29] alkalmazzuk.

$$V(h) = V_{vdW}(h) + W_{EDL}(h) = -\frac{RH}{12h} + 2\pi\epsilon\epsilon_0 R\psi_0^2 \exp(-\kappa h) \quad 1$$

ahol  $R$  a részecske sugara,  $H$  a Hamaker konstans,  $\epsilon$  a közeg relatív permittivitása,  $\epsilon_0$  a vákuum permittivitása,  $\psi_0$  a felületi potenciál és  $\kappa$  az inverz Debye paraméter, aminek értékét a 2. egyenlet adja meg.

$$\kappa = \sqrt{\frac{2N_A e^2 I}{\epsilon\epsilon_0 k_B T}} \quad 2$$

itt  $k_B$  a Boltzmann konstans,  $T$  a hőmérséklet,  $N_A$  az Avogadro szám,  $e$  az elemi töltés és  $I$  az ionerősség.

Ahogy az a fenti egyenletekből kitűnik,  $V_{vdW}(h)$  függ a részecskék méretétől és anyagi minőségétől, míg  $V_{EDL}(h)$  a méret mellett a felület töltésének mértékétől, illetve a közeg permittivitásától és az alkalmazott ionerősségtől. Diszpergált részecskék aggregációs sebességi állandója ( $k$ ) a módosított Fuchs elmélettel a 3. egyenlet szerint számítható [30].

$$k = \frac{4k_B T}{3\eta R} \left[ \int_0^\infty \frac{B(h)}{(2R+h)^2} \exp\left(\frac{V(h)}{k_B T}\right) dh \right]^{-1} \quad 3$$

ahol  $B(h)$  a hidrodinamikai ellenállási együttható és  $\eta$  a közeg viszkozitása. Az egyenlet az aggregáció korai szakaszában érvényes, ahol az egyedi részecskék mellett főként csak a dimer képződés játszódik le.

Kizárólag DLVO-típusú (van der Waals és elektromos kettősréteg eredetű) erőhatásokat figyelembe véve, a részecske aggregációs sebességi állandójának ionerősség függése a 2. ábra szerint változik. Eszerint meredeken nő, majd konstans értéket vesz fel a kritikus koaguláló koncentráció (CCC) felett. Ez a tendencia a 3. egyenlettel összhangban rávilágít arra, hogy mind a diszperzió elektrolittartalma, mind pedig a jelen lévő ionok vegyértékének növelése a taszító erők gyengüléséhez, illetve a részecskék aggregációjához vezet. Azonban a DLVO elmélet nem tesz különbséget az ionok anyagi minősége között, például egyértékű sók esetén ugyanazt a CCC értéket jósolja, függetlenül a sók kémiai összetételétől, illetve a kation és anion típusától. Ez a megállapítás kiemelt fontosságú a jelen doktori mű későbbi szakaszában ismertető eredmények tárgyalásánál.

#### *DLVO elméleten kívüli kölcsönhatások*

A mérési technikák fejlődésével lehetőség nyílt a szilárd felületek közötti kölcsönhatások, illetve az aggregációs állandók közvetlen mérésére. Ilyen módszerek az erőhatások meghatározására alkalmazott atomerő mikroszkóp (AFM) alapú kolloid próba [31, 32] és az aggregációs állandó közvetlen mérése időfüggő statikus vagy dinamikus fényszórással [33]. A kísérletileg és számításos módszerekkel meghatározott adatok közötti jelentős különbségek

rávilágítottak arra a tényre, hogy a diszperziók kolloidstabilitását nem lehet a van der Waals kölcsönhatások és az elektromos kettősrétegek révén kifejtett erőkkel leírni minden esetben. Ez különösen igaz a felülettől való kis távolságokra, ahol a fenti kölcsönhatásokra támaszkodó DLVO elmélet nem alkalmas a domináns erőhatások leírására. Itt fontos megjegyezni, hogy a felületi tulajdonságok megváltozása specifikusan adszorbeálódó molekulák hatására szintén a DLVO erőkötől eltérő eredetű részecske-részecske kölcsönhatások létrejöttéhez vezethetnek.

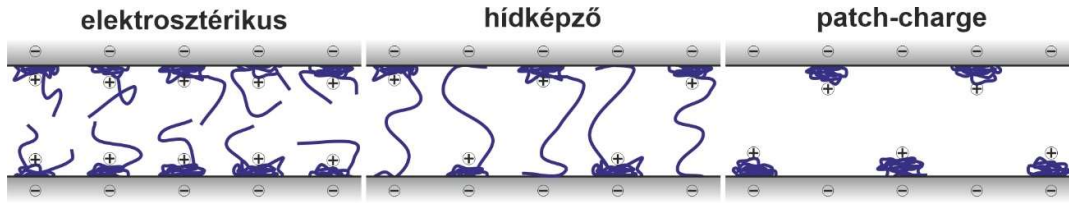
Ahogy az a fentiekben is említésre került, a DLVO elmélet nem képes kezelni a rövidtávú erőhatásokat, vagyis amikor a távolság a felülettől 1-2 nanométer körüli. Ilyen járulékos kölcsönhatás például a Born taszítás [7], amely a felületek érintkezésénél jön létre az anyagokat alkotó atomok vagy molekulák elektronhéjainak átfedése miatt. Habár számos empirikus potenciálfüggvényt bevezettek az elmúlt évek során a Born taszítás kvantitatív leírására, az erőhatás távolság függvényének pontos megadására alkalmas általános egyenletet mindeztáig nem került megalkotni.

A másik, szintén a felülettől kis távolságokra jelentkező erő a solvatációval hozható összefüggésbe. Mivel a jelen dolgozatban főleg vizes rendszereket tárgyalunk, ezért nevezzük ezeket itt hidratációs erőhatásoknak [34]. A vizes közegben diszpergált részecskék felülete eltérő mértékben tartalmazhat ionizált funkció csoportokat vagy állandó szerkezeti töltést, ezért hidratáció játszódik le, a tömbfázisban előforduló oldott ionokhoz hasonló módon. Két felület közvetlen kapcsolata esetén munkát kell befektetni a felületi vízmolekulák eltávolításához, ami a rendszer szabadenergia növekedéséhez vezet. A hidratációs erőhatások ezért mindig taszító jellegűek, kis távolságoknál jelentkeznek és jól megkülönböztethetőek az elektromos kettősrétegek átlapolásából származó taszító erőkötől. Közvetlen mérésük is lehetséges megfelelő műszer alkalmazásával [35, 36].

A távolsággal monoton csökkenő hidratációs taszítás mellett rövid hatótávolságú taszító oszcillációs erőhatások is megjelenhetnek megfelelő oldószerek jelenlétében, így például vízben [37], vagy a későbbiekben tárgyalásra kerülő kizárólag ionokat tartalmazó közegben [38]. Ezek periodicitása közel egy oldószersz molekulák dimenziójával egyezik meg és nehezen észlelhetőek olyan felületek esetében, ahol az érdesség kiterjedése összemérhető az oldószersz méretével. Olyan részecskék esetében, amelyek felülete nem tartalmaz töltéssel rendelkező csoportokat, jelentős mértékben jelentkeznek hidrofób kölcsönhatások a két felület találkozásakor. Újabban jelenlétüket feltételezték alacsony töltéssűrűséggel bíró felületek között is [39], így relevánssá válhatnak a doktori dolgozatban tárgyalásra kerülő részecskék esetében is. Ezek a hidrofób kölcsönhatások vonzó jellegűek, rövid hatótávolságúak és nagyságuk összemérhető a van der Waals kölcsönhatásokkal a felület anyagi minőségétől függően.

Fontos megemlíteni az adszorbeált polimer láncokhoz köthető erőhatásokat is. Mivel a dolgozatban tárgyalásra kerülő munka során töltéssel rendelkező makromolekulákat (más néven polielektrolitokat) alkalmaztunk, az ezek által lehetségesen indukált erőhatások tárgyalása is szükséges. Polielektrolitok adszorpciója ellentétes töltéssel rendelkező szilárd felületeken változatos konformáció kialakulásához vezethet, amelyek döntően befolyásolják a

létrejövő vonzó és taszító erőhatások mértékét [40-42]. Egyenletes felületi borítottság és erősen adszorbeálódó polielektrolit rétegek esetében a taszító kölcsönhatások főképp elektromos kettősréteg eredetűek, nagyságuk a polielektrolit töltésétől függ. Ha viszont a makromolekulák adszorpciójuk során kiterjedt konformációt vesznek fel, más szóval a lánc bizonyos részei eltávolodnak a felülettől, akkor ez a jelenség újabb taszító- és vonzó kölcsönhatások kialakulásához vezethet (3. ábra).



**3. ábra.** Polielektrolit adszorpció hatására kialakuló határfelületi taszító (elektrosztérikus) és vonzó (hídkepző és „patch-charge”) kölcsönhatások sematikus ábrázolása negatív töltésű felület és pozitívan töltött polielektrolit esetében.

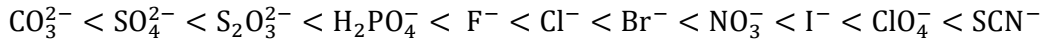
Két polielektrolittal borított részecske közeledése esetén a felületről lelógó láncok átlapolása ozmózis nyomás kialakulásához vezet, amely taszító kölcsönhatások formájában jelentkezik, ezt diszperziókban többféle mérési módszerrel is bizonyították [43-45]. A jelenséget a DLVO elméletbe foglalt elektromos kettősrétegek közötti kölcsönhatással együtt elektrosztérikus taszításnak nevezzük, amely a részecskék stabilitásának nagymértékű növekedésével járhat. Ezt a későbbiekben több példán keresztül is szemléltetni fogom. Alacsonyabb felületi borítottságú rendszerekben a következő kölcsönhatások alakulhatnak ki. A felületről lelógó polielektrolit lánc részletek egy másik részecske felületén található üres helyhez kapcsolódhatnak [6]. Ez a hídkepző tulajdonság, amit közvetlen mérésekkel is kimutattak [46, 47], és ami extra vonzási erők megjelenésével jár. Ezek hatótávolsága sokkal nagyobb lehet, mint a van der Waals kölcsönhatásoké. Rövidebb távolságoknál jelentkezik viszont a polielektrolitok szigetekben való adszorpciója során kialakuló „patch-charge” (folt-töltés) vonzó kölcsönhatás, amely során az adszorbeált polielektrolit folt Coulomb-féle vonzó hatást fejt ki a közeledő felület üres, ennél fogva ellentétes töltéssel rendelkező területére [48]. Ezek az erők jellemzően nagy lánc töltéssűrűséggel rendelkező polielektrolitok adszorpciója során és közepes borítottságnál hatnak a felülethez közel, és erősségük meghaladja a van der Waals vonzási kölcsönhatásokét [40].

## 2.2. Ionspecifikus kölcsönhatások

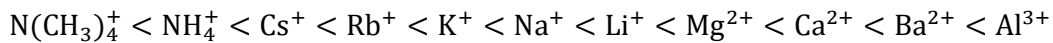
Az előző fejezetben tárgyalt szilárd részecskék között ható erők közül nagy fontosságú az elektromos kettősrétegek közötti taszítás, ami függ az ionerősségtől (1. és 2. egyenletek) [28]. Emellett a részecskékre adszorbeálódó polimerek konformációja szintén változik az oldott elektrolitok mennyiségétől [49]. Rendkívül fontos azonban kiemelni, hogy az oldott ionok koncentrációja mellett azok kémiai minősége és vegyértéke is jelentősen befolyásolja a határfelületi tulajdonságokat. Az alábbiakban ezt a jelenséget tárgyaljuk részletesebben.

### Hofmeister sorozat

A tojássárgájában megtalálható proteinek sóoldatokban való stabilitását először Franz Hofmeister vizsgálta több, mint száz évvel ezelőtt. Kísérleti eredményeire támaszkodva megalkotta a sóalkotó anionok alábbi sorrendjét a protein oldatok stabilizálására vonatkoztatva [50].

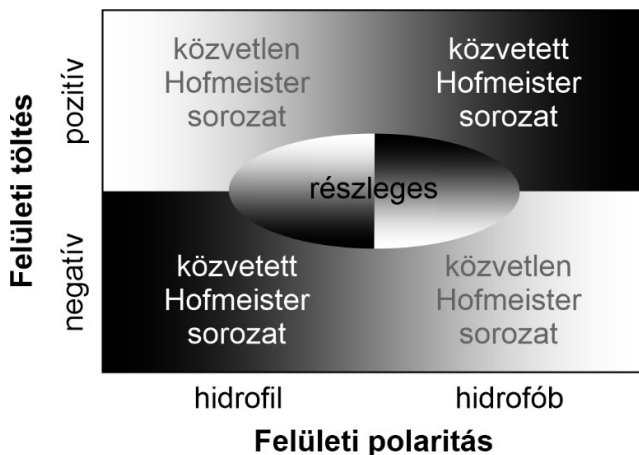


Eszerint a fenti sorozat jobb oldalán található ionok a fehérje oldatokat stabilizálják, míg a bal oldalon lévők kicsapódást okoznak ugyanabban a koncentráció tartományban. Ennek hatására széleskörű vizsgálatok indultak a Hofmeister sorozat alkalmazhatóságát tekintve különféle proteinek és elektrolitok alkalmazásával. E vizsgálatok eredményeként született meg az empirikus Hofmeister sorozat sóalkotó kationokra is [51].



Hasonlóan az anionokhoz, ebben az esetben is a jobb oldalon található ionok rendelkeznek a legjobb stabilizáló tulajdonsággal, a bal oldaliak már kisebb koncentrációnál is kisózzák a fehérjéket oldataikból. A proteinek stabilitására kifejtett hatáson kívül felismerték a fenti sorozatok teljes vagy részleges alkalmazhatóságát más rendszerekben is. Eszerint az oldott ionok kémiai minősége hatással van többek között sóoldatok felületi feszültségére [52] és viszkozitására [53], valamint adszorpciós folyamatokra [54], polielektrolitok töltésviszonyaira [55] és proteinek biológiai működésére is [56].

Ugyancsak felismerték, hogy a részecske diszperziók stabilitása, illetve a CCC értéke, is függ a jelenlévő oldott elektrolitok összetételétől [57-61]. Ez a jelenség nem magyarázható a DLVO elmélettel, amely pontszerű töltéseket feltételez és nem tesz különbséget az ugyanolyan vegyértékű, de különböző kémiai összetételű ionok között, tehát ezek jelenlétében ugyanakkora CCC-t várnánk (lásd 2.1 fejezet). Részletes kutatások eredményei arra is rámutattak, hogy az oldott ionok minősége mellett a részecskék felületének tulajdonságai is



**4. ábra.** Sematikus Hofmeister diagram a felületi töltés és polaritás függvényében a közvetlen és a közvetett sorozatok jelzésével.

befolyásolják a Hofmeister sorozatban szereplő ionok hatását a létrejövő erőhatásokra [62]. A felület töltésének előjele és hidrofobicitása szerint különbséget teszünk közvetlen (amikor az ionok sorrendje a fenti sorozatok szerint alakul, illetve a jobb oldalon található ionok rendelkeznek a legkisebb destabilizáló hatással) és közvetett (amikor a sorozatok jobb oldalán található ionok már kisebb ionerősségeknél aggregációt okoznak) Hofmeister sorozatok között (4. ábra) [63]. Ezek szerint a negatívan töltött



hidrofób részecskék a közvetlen Hofmeister sorozatot követik (a CCC értékek balról jobbra nőnek a fenti sorozatokban szereplő ionok esetében), míg a pozitív töltéssel rendelkező hidrofób részecskék esetében a CCC balról jobbra csökken, a közvetett Hofmeister sorozatnak megfelelően. Hidrofil karakterű részecskék diszperzióiban a tendencia megfordul és az ionok ezzel ellentétesen hatnak a CCC értékekre. Természetesen éles határt nem tudunk felállítani, ezért a sorozatok részlegesen átfedhetnek, amint az különböző nanorészecskék esetében a későbbiekben bemutatásra kerül.

Több tanulmány is arra a megállapításra jutott, hogy a különböző kémiai minőségű ionok a részecskék felületéhez való affinitásuk révén fejtik ki a CCC értékekre gyakorolt hatásukat [64-66]. Eszerint ellenionok adszorpciója a felületi töltéssűrűség csökkenéséhez és ennél fogva alacsony CCC értékekhez vezet az elektromos kettősrétegek közötti taszítás mértékének csökkenése miatt. Például anionok affinitása pozitív töltéssel rendelkező alumínium-oxid felülethez jó egyezést mutatott a közvetlen Hofmeister sorozattal [67], valamint hasonló tendenciát határoztak meg pozitív töltésű latex részecskék esetében is [59], ezáltal jelezve a felületek hidrofób karakterét. Negatív töltéssel rendelkező alumínium- [67] és vas-oxid [68] részecskék esetében kimutatták, hogy a kationok affinitása a közvetlen Hofmeister sorozatot követi. Negatívan töltött latex és agyagásvány részecskék esetében a diszperzió stabilitás a közvetlen Hofmeister sorozatnak megfelelően változott, pozitív töltésű latex, agyagásvány és fém-oxid CCC értéke pedig a közvetlen sorozatot követte [58, 59, 69-72]. Proteinnel módosított latex [60, 71] és kalcinált titán-dioxid [70] kolloid vizsgálata során megállapították, hogy a negatív töltésű hidrofil részecskékre jellemző sorrend érvényes a CCC adatokra.

A kép azonban ennél összetettebb, mivel a mérési eredmények más esetekben csak részleges egyezést mutattak a Hofmeister sorozatokkal, illetve a részecskék felületének feltételezett hidrofobicitása nem igazolta a közvetlen vagy közvetett sorozatok alkalmazhatóságát [73-75]. A fentiek tükrében meglepő, hogy bizonyos részecske diszperzióknál nem tapasztaltak eltérést a különböző minőségű elektrolitokban mért CCC értékek között [76, 77]. Hiányosság az adatokban, hogy mellék- és ellenionok hatásának kiterjedt vizsgálatára nem került sor ugyanazon, vagy nagyon hasonló tulajdonságú részecskék esetében. További probléma, hogy a többértékű ionok a protein precipitációban mutatott effektusuk miatt szerepelnek az eredeti sorozatokban, azonban ezeket a részecske aggregációra való hatásukat tekintve nem szerencsés együtt tárgyalni az egyértékű ionokkal, ahogyan azt a következő fejezetben bemutatásra kerülő adatokból is látni fogjuk. Továbbá az adatok vagy hiányosak, vagy nem léteznek a nanométeres dimenziójú anyagok többségére. Ezek alapján indokolt az ion specifikus hatások felmérése az egyes részecskék diszperzióinak további felhasználása előtt.

#### *Többértékű elektrolitok*

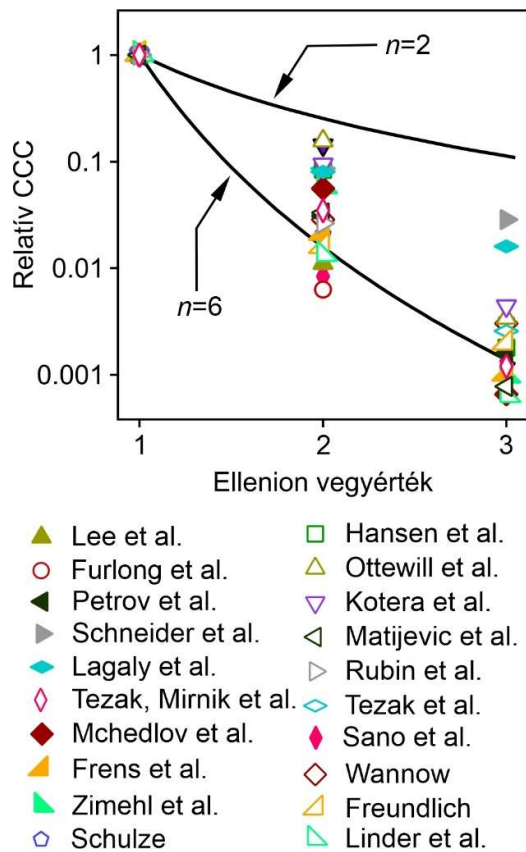
Az ugyanolyan vegyértékkel rendelkező elektrolitok által okozott CCC értékek közötti különbséget nem tudjuk a DLVO elmélettel magyarázni, viszont az oldott ionok töltése hatással van az elektromos kettősrétegek által okozott taszító erőkre [78]. Ez a hatás az ionerősségen, illetve a Debye paraméteren keresztül érvényesül, ahogyan azt már a 2.1 fejezetben tárgyaltuk. A növekvő vegyérték a CCC csökkenéséhez vezet a következő egyenlet szerint.

$$CCC \sim z^{-n}$$

4

ahol  $z$  az adott ion vegyértéke. A klasszikus szabály szerint  $n = 6$ , amelyet már jóval a DLVO elmélet előtt kísérleti adatok alapján feltételezett Schulze [79, 80] és Hardy [81], ez azonban az alább ismertetésre kerülő érvelés alapján nem érvényes korlátlanul.

Elméleti síkon levezetve a CCC vegyértékfüggését belátható, hogy a klasszikus szabály a DLVO elméletből csak rendkívül nagy töltéssel rendelkező részecskékre ( $\psi_0 > 100$  mV) bizonyítható, amely túlzó a természetben előforduló, vagy éppen laboratóriumi körülmények között előállított részecskékre nézve, főképp többértékű ionok jelenlétében [7]. Reális nagyságrendű felületi töltés esetében inkább az  $n = 2$  alkalmazható a 4. egyenletben. Ezen kívül a levezetés  $z: z$  típusú elektrolitokra érvényes, amelyekben az ellenionok és mellékionok vegyértéke megegyezik. Tudjuk azonban, hogy ilyen típusú sók viszonylag ritkán fordulnak elő valós rendszerekben, ahol sokkal inkább a  $1: z$  vagy  $z: 1$  típusú aszimmetrikus elektrolitok (amelyekben vagy az ellenionok, vagy pedig a mellékionok a többértékűek) találhatók meg, amelyek oldhatósága jóval nagyobb, mint a  $z: z$  típusúaké.



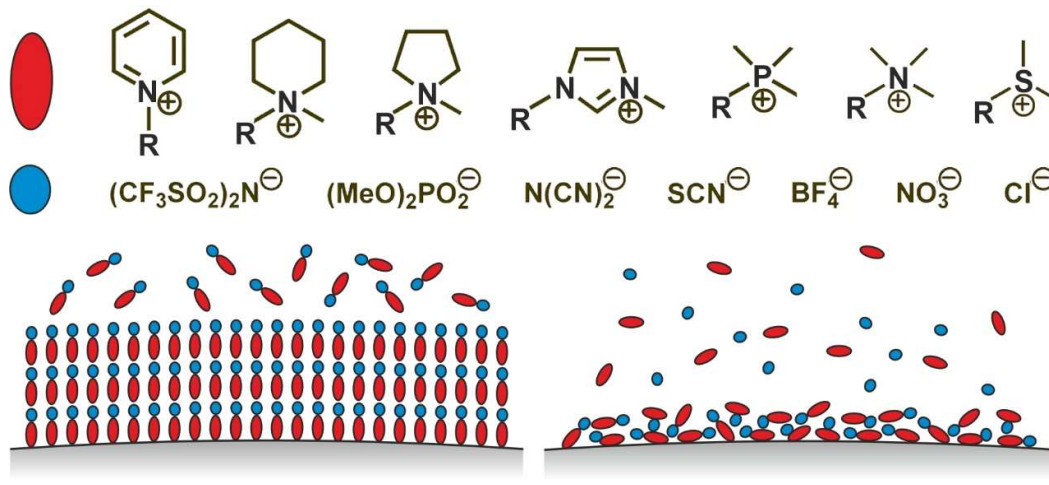
**5. ábra.** Relatív CCC adatok az ellenionok vegyértékének függvényében az egyértékű ionokra normalizálva. A folytonos vonalak a Schulze-Hardy szabályt jelzik magas ( $n = 6$ ) és alacsony ( $n = 2$ ) felületi töltés esetében.

Valóban, a CCC értékek egyre pontosabb meghatározásával, illetve újszerű részecske rendszerek vizsgálatával egyértelművé vált, hogy a hatodik hatvány szabály ( $n = 6$ ) nem alkalmazható általánosan minden diszperzióra [82-84]. Ezt szemlélteti az 5. ábra, miszerint a CCC csökkenése az ellenionok vegyértékével legtöbbször elmarad az  $n = 6$  kitevőtől, viszont néhány esetben meghaladja azt [57, 79, 85-102]. Ugyancsak látható az ábrán, hogy alacsonyabb töltést feltételezve a DLVO elméletből levezetett  $n = 2$  függésnél a CCC értékek minden esetben nagyobb mértékben csökkennek a vizsgált rendszerekben. A diszperziót destabilizáló hatás az ellenionok vegyértékével egyértelműen nő, azonban ennek számszerűsítése bonyolult feladat pusztán a DLVO elméletet alkalmazva. Az eddig közölt eredmények ismeretében az is látszik, hogy a részecskék kolloidstabilitását főképp többértékű ellenionok jelenlétében vizsgálták korábban. Viszont a mellékionok vegyértékének változtatása is hozzájárul az elektromos kettősrétegek közötti taszítás mértékéhez az ionerősségen, illetve a Debye paraméteren keresztül (lásd 1. és 2. egyenletek a 2.1 fejezetben).

A fenti információkból is kiderül, hogy a Schulze-Hardy szabály általánosan nem alkalmazható diszperziók esetében, és a 4. egyenlet kitevőjének számértéke nagyban függ az alkalmazott részecskék és a közeg fizikai-kémiai paramétereitől. Mivel a kolloid- és nanorészecskéket legtöbbször elektrolitok jelenlétében alkalmazzák, ezek hatását a kolloidstabilitásra minden esetben fel kell mérni az alkalmazás előtt.

### *Ionos folyadékok*

Az előzőekben tárgyalt szeretlen sókra vonatkozóan viszonylag nagyszámú kísérleti adat érhető el a kolloidstabilitás és a részecskék közötti erőhatások eredetét és nagyságát illetően vizes rendszerekben. Vannak azonban olyan újszerű oldószerek, illetve diszperzió közegek, amelyekről kevesebb információ áll rendelkezésünkre. Ilyenek például az ionos folyadékok (IL) [103-105], amelyek kizárólag ionokból állnak, olvadáspontjuk 100 °C alatti, jelentős részük folyékony halmazállapotú szobahőmérsékleten is, illetve aszimmetrikus összetételűek: általában egy nagyobb szerves kationból és kisebb anionból állnak (6. ábra), ezért nehezen kristályosodnak.



**6. ábra.** Fent: Néhány IL-okat alkotó kation és anion képlete. Lent: IL komponensek lehetséges határfelületi elrendeződése (lent balra: irányított elrendeződés a határfelületen és ionpárok jelenléte, lent jobbra: random felületi elrendeződés és részleges disszociáció).

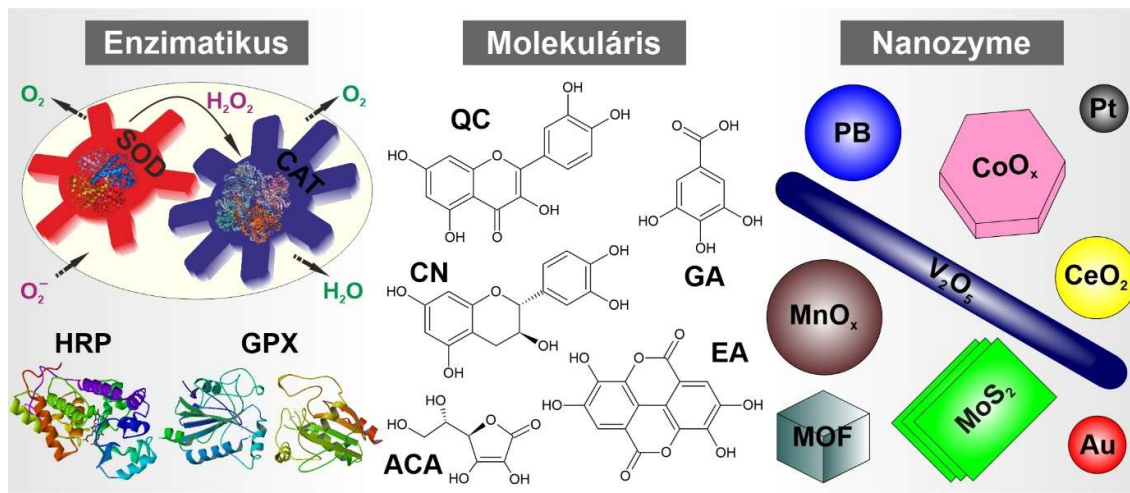
Előnyös tulajdonságaik közé tartozik például a rendkívül alacsony gőznyomás [106, 107], a jelentős elektrokémiai ellenálló képesség [108], vagy a kiemelkedő kémiai és hőstabilitás [109]. IL-ok előállítását, tisztítását és tulajdonságaikat tömbfázisban az elmúlt évtizedekben viszonylag széleskörűen vizsgálták már, azonban a határfelületi viselkedésük részletes feltárására irányuló kutatások csak a közelmúltban indultak el [110]. Különféle oxidokat [111-113], agyagásványokat [114, 115] és nemesfémeket [116, 117] diszpergáltak IL oldatokban, amelyek számos esetben a részecske szintézis közegeként is funkcionáltak [118, 119]. Megfigyelték, hogy a szilárd részecskék stabilis rendszert alkotnak megfelelő IL-okban [117, 120, 121], amely ellentmondásban van a DLVO elmélettel, mivel az instabilis diszperziók létezését jósolja magas elektrolit (ion) koncentrációknál. A nyilvánvaló ellentmondás

feloldására átfogó kutatások kezdődtek, amelyekben a lehetséges aggregáció mechanizmusát, illetve az uralkodó felületi erőhatások mértékét és eredetét vizsgálták számos IL-részecske rendszerben. Alapvetően kétféle típusú stabilizáló mechanizmust feltételeznek. Az első elmélet szerint, amely AFM alapú kolloid próba módszerével mért eredményekre támaszkodik [120], az IL komponensek szekvenciális határfelületi adszorpciójakor IL rétegződés alakul ki a felületen, ami taszító oszcillációs erőhatások megjelenésével és a részecske diszperziók stabilizálásával jár (6. ábra). A második elmélet szerint, amelyet makroszkopikus felületek közötti erőhatások közvetlen mérése során kapott eredmények alapján javasoltak [122], az IL-ok hasonlóan viselkednek az elektrolitok híg oldataihoz. A döntő többségük ionpárt alkot, viszont csak kis mennyiségben (<0,1%) disszociálnak, amely alacsony ionerősséghez és elektromos kettősréteg kialakulásához vezet. Ennélfogva a kettős rétegek között létrejövő taszítás felelős a részecskék stabilitásáért, hasonlóan a DLVO elméletéhez.

Habár nagyszámú rendszert vizsgáltak különféle mérési módszerek felhasználásával a közelmúltban [123-127], nem sikerült egyértelműen eldönteni, hogy a fenti elméletek közül melyik a helyes, illetve alkalmazható-e bármelyik is általánosságban [38]. Az elvégzett kísérletek eredményei azonban rávilágítottak arra, hogy az IL komponensek határfelületi elrendeződése döntő fontossággal bír a kialakuló erőhatások eredetét és mértékét illetően. A részecske diszperziók kolloidstabilitásának vizsgálata szükséges IL komponensek jelenlétében aggregációs állandók, felületi töltések és erők pontos meghatározása céljából.

### 2.3. Antioxidáns rendszerek

Az oxigén- (ROS) és nitrogéntartalmú (RNS) szabadgyökök intenzív termelődésével járó oxidatív stressz felelős számos megbetegedés kialakulásáért, illetve ipari termékek minőségének romlásáért [128-130]. Ennek csökkentését antioxidánsokkal érhetjük el [131-133], amelyek lehetnek természetes (enzimatis és molekuláris), illetve szintetikus (enzimutánszó fémkomplex és nanozyme) eredetűek is (7. ábra).



7. ábra. Különböző eredetű és típusú antioxidánsok. A rövidítések jelentése a 3. oldalon található. Nanozyme az enzimszerű működésre képes nanorészecske szinonimája.

*Enzimatisz antioxiánsok*

Antioxiáns hatású enzimek (endogén antioxiánsok) a leghatékonyabb védekező rendszerek az oxidatív stressz ellen [134]. Egymással együttműködve kaszkád reakcióban bontják le a szabadgyököket, mint ahogy az a 7. ábrán látható a szuperoxid dizmutáz (SOD) és kataláz (CAT) enzimek esetében szuperoxid gyök anionok ártalmatlanítása során. Ezeknek az antioxiánsoknak az utánpótlása, illetve felhasználása ipari folyamatokban nehézkes, mivel rendkívül érzékenyek a környezeti paraméterekre (például pH, hőmérséklet, nyomás, ionerősség vagy enzim inhibitorok jelenléte). Ennek kivédésére olyan kutatások indultak el, amelyek során az enzimeket szilárd hordozóra rögzítették. A hordozó feladata a biokatalitikus funkció megóvása nem ideális, a valóságoshoz közelebbi kísérleti körülmények között [135].

Antioxiáns enzimek immobilizálása során alkalmazott módszerek között megtaláljuk az olyan, általánosságban enzimek rögzítésére kifejlesztett eljárásokat, mint a hordozó felületére való adszorpciót vagy kovalens rögzítést, kompozitokba való beágyazást szol-gél folyamatokban vagy interkalálást réteges anyagokba [136]. SOD, CAT és egyéb peroxidáz enzimeket tartalmazó hibrid anyagok kerültek kifejlesztésre különféle egyfázisú (szén nanocső [137], TNS [138], polimer hidrogél [139], réz-foszfát [140], vas-oxid [141] és arany nanorészecske [142]) vagy hibrid ([143-146]) hordozókon, amelyekkel szemben a legfőbb elvárások a megfelelő kémiai ellenálló képesség, biokompatibilitás és méret voltak, amelyek kulcs paraméterek a sikeres felhasználás érdekében. Habár az előállított nanoszerkezetek többsége folyadék közegben került alkalmazásra, ezek aggregációs hajlamának és kolloidkémiai viselkedésének megismerésére nem fektettek megfelelő hangsúlyt.

Az egyféle enzimet tartalmazó nanokompozitok kifejlesztése mellett megfogalmazódott a többféle enzim együttes immobilizálásának az igénye is, amelyek a sejten belüli működésnek megfelelően kaszkád reakcióban bontanák le a szabadgyököket. Ezek során SOD és CAT enzimeket rögzítettek arany [147] és szilícium-dioxid [148] nanorészecskéken, valamint polimer alapú hordozón [149]. SOD és peroxidáz enzim párok együttes immobilizálására is történtek kísérletek polimer hordozóhoz kovalensen kötve [150], mesterséges peroxiszómába zárva [151], illetve mezopórusos szilícium-dioxid részecskébe [152] vagy nanogélbe ágyazva [153]. A természetes enzimek mellett történtek próbálkozások olyan fémkomplexek nanoszerkezetekbe történő rögzítésére, amelyek képesek utánozni antioxiáns enzimek működését redox tulajdonságú fémionok jelenléte és/vagy az aktív centrumhoz hasonló szerkezetük miatt. Ezekben az esetekben szilícium-dioxid [154], agyagásvány [155] vagy polimer [156] hordozókat alkalmaztak, illetve néhány esetben jelentős antioxiáns hatás elérését közölték [157].

A szintézis, szerkezeti jellemzés és antioxiáns hatás felmérése megtörtént ezekben a rendszerekben, viszont nem folytak átfogó vizsgálatok az adott diszperziók kolloidstabilitásának vizsgálatára. Összegezve, a fenti anyagokra mért jelentős antioxiáns hatás megkérdőjelezhető, mivel a kompozit részecskék aggregálódhattak alkalmazásuk során.

### *Molekuláris antioxidánsok*

Az exogén eredetű antioxidánsok közé tartoznak azok az enzimekhez képest kis molekulatömegű vegyületek, amelyek táplálékkal jutnak be az élő szervezetekbe [158]. Ebbe az úgynevezett molekuláris antioxidánsok csoportjába sorolhatók többek között a vitaminok (például C- vagy E-vitamin), a fenolos antioxidánsok (például klorogénsav és ellagsav (EA)), a karotinoidok (például  $\beta$ -karotin vagy likopin) és a flavonoidok (például kvercetin és rutin) is. Néhány molekuláris antioxidáns szerkezeti képlete látható a 7. ábrán. A C-vitamin főként a hidroxil-, alkoxil- és szuperoxid gyökökkel szemben lép fel, de a tokoferollal szinergizmusban részt vesz a lipid peroxidáció megakadályozásában is [159]. Az E-vitamin a sejtmembránban bekövetkező lipid peroxidációt akadályozza egy kisebb reaktivitású komponens létrehozásával, mely nem képes megtámadni a membránban található lipideket. A vitaminokhoz hasonlóan a többi exogén antioxidáns is fellép a lipid peroxidációval szemben vagy önállóan, vagy más antioxidánsokkal együttesen [132].

Az exogén antioxidánsok aktivitása elmarad az enzimatis eredetűektől, viszont még így is igen fontos szerepet töltenek be a különböző élettani és ipari folyamatokban. Számos esetben hátrányt jelent az alacsony vízoldhatóságuk (EA), vagy éppen limitált kémiai stabilitásuk (kurkumin), amely meggátolja terápiás vagy ipari célú alkalmazásukat [160, 161]. A hátrányok kiküszöbölésére megindult kutatások során nanokompozitokba való beépíthetőségüket is vizsgálták. Például kurkumin LDH-ba való interkalálásával megnövelték stabilitását, amelyet így fotodinámiai terápiaiban alkalmaztak rákos sejtek elpusztítására [162]. Az EA vízoldhatóságának növelésére többféle hordozót is alkalmaztak [163-165], illetve az előállított kompozitok antioxidáns hatását is egyértelműen bizonyították. HNT mint hordozó felhasználásával kvercetin molekuláris antioxidáns kontrollált kibocsátása is elérhetővé vált [166, 167].

Az előállított antioxidáns-nanorészecske kompozitok jelentős előrelépést mutattak főleg a vízoldhatóság és hőtűrő képesség javítása terén, viszont a rendszerek kolloidstabilitását ezekben az esetekben sem mérték fel, illetve ennek megfelelően nem is hangolhatták. A részecskék aggregációra való hajlamának részletes vizsgálata már csak azért is szükséges, mivel a legtöbb esetben oldatfázisban kerülnek felhasználásra.

### *Antioxidáns nanorészecskék*

Ahogy fentebb említésre került, az antioxidáns enzimek optimális reakciókörülmények mellett jól működnek, viszont nagyon érzékenyek a kísérleti körülményekre, így a hőmérséklet, nyomás, ionerősség vagy pH jelentős változása aktivitásuk elvesztéséhez vezethet [136]. Az előzőekben tárgyalt enzim immobilizálás, mint stabilizáló stratégia mellett a mesterséges enzimek területén az egyik ígéretes kutatási irány az enzimatis funkciójú nanorészecskék (az úgynevezett nanozyme-ok) fejlesztése, amelyek a természetes enzimek alternatívájaként alkalmazhatóak számos előnyös tulajdonságuk miatt [20]. Szintézisük az esetek többségében olcsó, a képződő anyagok szerkezete és összetétele változatos. Kémiai stabilitásuk a természetes enzimekhez képest sokkal nagyobb, ugyanakkor azokkal összemérhető antioxidáns aktivitással bírnak. Fizikai-kémiai sajátágaik igény szerint finomhangolhatók és

a számos esetben bizonyított biokompatibilitásuk miatt széles körben alkalmazhatóak orvosi, biológiai, ipari, kémiai és anyagtudományi területeken, elsősorban a ROS és RNS elleni védekezési eljárások során [19].

A szakirodalmi adatok szerint antioxidáns aktivitásúak egyes gömb alakú elemi fém nanorészecskék, mint a réz [168], az arany [169] vagy a platina [170], de akár a különböző vegyértékű fémionokat tartalmazó anyagok is, mint például a vanádium-pentoxid nanoszálak [171], négyzetes mangán-oxid részecskék [172], hexagonális vegyes kobalt-oxid [173] vagy különféle cérium-oxid nanoszerkezetek [174] és módosított származékjaik. Az utóbbi időben jelentős kutatói aktivitás mutatkozott berlini kék nanorészecskék (PBP) előállításának és antioxidáns tulajdonságainak vizsgálatában is [175]. Ezek az anyagok az oxidatív stresszt indukáló szabadgyökök iránt mutatott nagy affinitásuk miatt megfelelő hatékonysággal utánozzák a természetes enzimeket és sok esetben bizonyított alacsony toxicitásuk miatt biokompatibilisnek tekinthetők. Antioxidáns hatásuknak köszönhetően alkalmazzák őket gyulladáscsökkentőként, öregedésgátlóként, sebek gyógyításában, rákellenes terápiákban és idegrendszeri betegségek kezelésében is [20].

Az eddig publikált jelentős eredmények ellenére számos probléma még megoldásra vár ezen a kutatási területen. Például a vizsgált nanorészecskék szubsztrátum specifikussága messze elmarad a természetes enzimekétől. Továbbá a fentebb tárgyalt antioxidáns nanoszerkezetekhez hasonlóan a nanozyme-okat tartalmazó diszperziók kolloidkémiai viselkedését sem vizsgálták részletesen. Így például nem lehet tudni, hogy milyen kísérleti körülmények vezethetnek a részecskék aggregációjához, ami minden bizonnyal aktivitásuk csökkenéséhez vezetne alkalmazásukkor.

### 3. CÉLKITŰZÉSEK

Munkánk során szervetlen és szerves részecskék által alkotott diszperziók előállítását, kolloidstabilitását és felhasználásuk lehetőségeit tanulmányoztuk. Olyan kolloid- és ezen belül főleg nanorészecskék kerültek a vizsgálatok középpontjába, amelyek vagy potenciális jelöltek specifikus felhasználásokra (agyagásványok és titán-oxid szerkezetek), vagy pedig megfelelő modell részecskéként (polisztirol latex) alkalmazhatóak az alapvető határfelületi és aggregációs folyamatok megismerését célzó vizsgálatok során. A főbb célokat a következő pontok szerint csoportosíthatjuk.

- (i) Ionspecifikus kölcsönhatások tisztázása szervetlen elektrolitok és IL-ok jelenlétében, amelyek korábban nem kerültek vizsgálatra, illetve amelyekre vonatkozóan a szakirodalomban található adatok ellentmondásosak.
- (ii) Polielektrolitok adszorpciója során lejátszódó határfelületi jelenségek vizsgálata, amelyek hatással vannak az adott részecskék diszperzióinak formulálására és felhasználhatóságára.
- (iii) Antioxidáns aktivitású kompozitok diszperzióinak előállítása és vizsgálata az előző pontok eredményeinek ismeretében, illetve oxidatív stressz csökkentő hatásuk felmérése.

## 4. KÍSÉRLETI MÓDSZEREK

### 4.1. Felhasznált anyagok

A kísérleteknél alkalmazott kereskedelmi forgalomban elérhető vegyszerek mindegyike analitikai minőségű volt és további tisztítás nélkül került felhasználásra. A részecskéket illetően, a TNS [T1] hidrotermális eljárással került előállításra fluorozott köztiterméken keresztül egy korábban publikált módszer [176] módosításával. Az LDH [T2] esetében együttes lecsapásos szintézist [177] alkalmaztunk, amelyben a magnézium(II) és alumínium(III) sóoldatok megfelelő arányban történt elegyítése után a pH növelésével értük el az LDH kikristályosodását. A részecskeméret polidiszperzítésének csökkentése érdekében a nyersterméket hidrotermális eljárásnak [178] vetettük alá. Ezen kívül kereskedelmi forgalomban kapható felületi amidin (AL) vagy szulfát (SL) csoportokat tartalmazó polisztirol latex részecskéket [T3] használtunk. Az egydimenziós HNT [T4] esetében a megvásárolt anyag felületi hidroxil csoportjainak a számát, illetve felületi töltését, lúgos kezeléssel [179] növeltük meg. A titanát nanoszálak (TiONW) [T5] diszperzióit egy együttműködő partnertől szereztük be [180].

### 4.2. Mérési módszerek és a kísérleti adatok kiértékelése

A diszpergált részecskék töltését elektroforetikus fényszórás (ELS) módszerével határoztuk meg, ahol a Doppler effektus által kiváltott frekvencia-, illetve fáziseltolódás szolgált elsődleges kísérleti információként, amelyből a részecskék sebessége, elektroforetikus mobilitása, majd pedig a zéta (elektrokinetikai) potenciálja a Smoluchowski modell [181] alkalmazásával számítható volt az adott kísérleti körülmények között. A méréseket Malvern Zetasizer és Anton-Paar Litesizer készülékekkel végeztük.

A részecske aggregáció kvantitatív követése céljából hidrodinamikai sugarakat ( $R_h$ ) és aggregációs sebességi állandókat ( $k$ ) határoztunk meg dinamikus fényszórás mérés (DLS) módszerével. A diffúziós állandó számításához szükséges korrelációs függvények csökkenésének sebességét a másodrendű kumuláns expanzióval számítottuk, illetve a diffúziós állandó- $R_h$  konverziót a Stokes-Einstein egyenlettel végeztük [33]. A kolloidstabilitás leírására stabilitási arány ( $W$ ) értékeket használtunk, amelyeket idő ( $t$ ) függő DLS kísérletekben mértük a következők szerint.

$$W = \frac{k^{gyors}}{k} = \frac{(dR_h(t)/dt)_{t \rightarrow 0}^{gyors}}{(dR_h(t)/dt)_{t \rightarrow 0}} \quad 5$$

A *gyors* jelölés diffúzió kontrollált aggregációra utal, amit magas koncentrációjú sóoldatokban értünk el, ahol az elektrosztatikus taszító erők nem érzékelhetőek és ennél fogva a részecskék aggregációját kizárólag azok diffúziója határozza meg. Tehát  $W = 1$  érték gyors aggregációra és instabilis diszperziókra utal, míg magasabb értékek kisebb  $k$  adatokat és stabilisabb kolloid mintákat jeleznek. A méréseket ALV gyártmányú CGS-3 és NIBS/HPPS típusú berendezésekkel végeztük.



Az előállított anyagok szerkezetének vizsgálatára különféle spektroszkópai módszereket alkalmaztunk. Infravörös (IR) és Raman spektroszkópia (PerkinElmer Spectrum 100 és Bruker Senterra II berendezések) módszerével szilárd mintákat vizsgáltunk, melyekkel ki tudtuk mutatni az egyes komponensek jelenlétét a kompozit anyagokban. Katalitikus aktivitással rendelkező fémcentrumok lokális környezetének meghatározására elektronspin rezonancia (ESR) spektroszkópiát (Bruker EleXsys E500 készülék) használtunk szilárd és fagyaszott állapotú mintákban. Színváltozáson alapuló reakciók követésére és koncentráció meghatározásra ultraibolya-látható (UV-Vis) spektrofotometriát (Thermo Scientific Genesys 10S műszer) alkalmaztunk. A nanorészecskék összetételét röntgen fotoelektron spektroszkópia (XPS) segítségével határoztuk meg egy PHOIBOS 150 MCD 9 analizátorral felszerelt SPECS berendezést használva.

Az részecske szintézisek sikerességét, illetve réteges anyagok kristályszerkezetét porröntgen diffraktometria (XRD) segítségével határoztuk meg egy Bruker D8 Advanced készülékkel. Az előállított részecskék méretének és morfológiájának meghatározása során transzmissziós (TEM) és pásztázó (SEM) elektronmikroszkópiát használtunk (FEI Tecnai G2 és Hitachi S4700 berendezések). Az atomerő mikroszkópia (AFM) segítségével kétféle információhoz jutottunk: képalkotás módban (Digital Instruments Multimode Nanoscope IIIa) az anyagok átmérőjét és magassági profilját határoztuk meg, míg kolloid próba (Asylum Research MFP-3D) segítségével a részecskék közötti erőhatásokat közvetlenül is megmérhettük. Az oxidatív stressz sejten belüli felmérése céljából konfokális fluoreszcencia mikroszkóppal (Zeiss LSM 808) végeztünk méréseket.

### 4.3. Antioxidáns aktivitás felmérése

Az antioxidáns hatás vizsgálata érdekében kémiai tesztreakciókat alkalmaztunk megfelelő szubsztrátumok (szuperoxid gyök anion [182], hidrogén-peroxid [183], stabilis szerves gyökök [184] és redox aktív molekulák [185]) alkalmazásával. Az antioxidáns-szubsztrátum reakciók előrehaladásának közvetlen vagy közvetett felmérésére UV-Vis spektrofotometria segítségével került sor és az aktivitást a hatásos koncentráció (pontosabban az a koncentráció, ahol a maximális hatás 50%-át mértük,  $IC_{50}$ ) értékekben fejeztük ki. Ezen kívül a kifejlesztett biokatalizátor rendszerek funkciójának idő- és hőmérsékletfüggő változását is felmértük néhány esetben.

Az oxidatív stressz csökkentő hatást HeLa sejt kultúrákban indukált ROS termelése során teszteltük együttműködő partner bevonásával [T39]. Ebben az esetben olyan ROS érzékeny molekulákat alkalmaztunk indikátorként, amelyek a szabadgyökökkel való reakció során fluoreszkáló terméké alakulnak és a sejten belüli koncentrációjukat konfokális fluoreszcencia mikroszkóppal meghatározhatóak voltak. Továbbá megvizsgáltuk a nanokompozitok sejtekbe jutásának sikerességét a gvajakol (2-metoxifenol) teszt segítségével [186], illetve a lehetséges toxicitásukat a tradicionális apoptózis-nekrózis folyamatokon alapuló módszer felhasználásával mértük megfelelő inkubációs idők után.

## 5. EREDMÉNYEK ÉS KÖVETKEZTETÉSEK

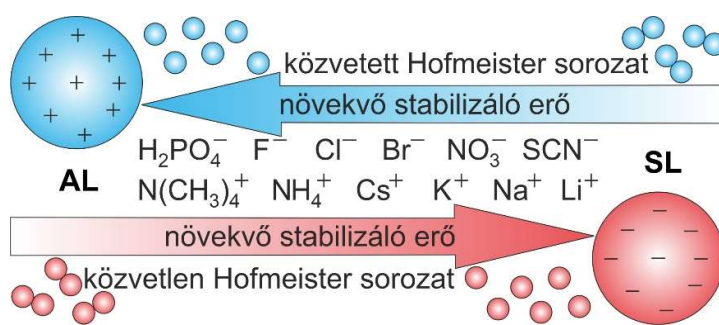
### 5.1. Ionspecifikus határfelületi kölcsönhatások

Különféle oldott sók hatása makromolekuláris oldatok vagy koloid diszperziók stabilitására egy igen intenzíven kutatott terület már azóta, hogy Hofmeister leírta az anionok liotróp sorozatát protein kicsapási kísérletekre alapozva [50], vagy éppen Schulze [79, 80] és Hardy [81] egymástól függetlenül publikálta a többértékű ionok diszperzió destabilizáló hatását. A koloid, illetve különösen a kisebb, a ma már nanonak nevezett részecskék fokozott felhasználásával egyértelművé vált, hogy ezek diszperzióinak stabilitása fontos szerepet játszik alkalmazásuk során. Homogén eloszlású és stabilis (aggregációnak ellenálló) részecskék szükségesek például gyógyszerhatóanyag molekulák szállítása során élő szervezetekben. Ugyanakkor az aggregáció kiváltása és az ezzel járó diszperzió destabilizálás például a papírgyártás egyik alaplépése. Az egyre növekvő számú részecske rendszerek, illetve a mérési technikák fejlődésének köszönhetően ionspecifikus határfelületi jelenségek vizsgálatával jó néhány kutatócsoport foglalkozik világszerte azért, hogy a korábban megalkotott szabályszerűségeket alkalmazhatóságát kiterjesszék, például új típusú nanorészecskékre. Ehhez az irányhoz csatlakozva a munkánk során használt latex, LDH, TNS és HNT részecskék töltés és aggregációs viszonyait határoztuk meg különféle elektrolit oldatokban.

#### *Egyértékű sók hatása*

Indifferens vagy felületekkel specifikus kölcsönhatás kialakítására képes oldott egyértékű ionokat tartalmazó részecske diszperziókban lejátszódó határfelületi kölcsönhatások vizsgálata során a közvetett és közvetlen Hofmeister sorozatok érvényességét tanulmányoztuk az ellen- és mellékionok koloidstabilitásra gyakorolt hatása alapján. Ezt az empirikus szabályt főként az egyes részecskékre meghatározott CCC értékekre alkalmaztuk, illetve vizsgáltuk a részecskék kémiai összetételének, felületük hidratáltságának és töltésviszonyainak hatását az alkalmazott kísérleti körülmények között.

Annak érdekében, hogy egyértelmű képet kapjunk a felületi töltés szerepéről, hidrofób jellegű pozitív AL és negatív SL részecskéket alkalmaztunk, illetve koloidstabilitásukat

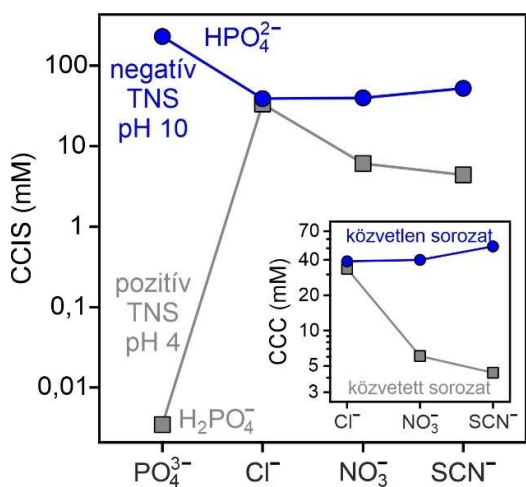


**8. ábra.** Egyértékű ionok hatása AL és SL részecskék aggregációjára, illetve CCC értékeire [T6]. Növekvő stabilizáló erő növekvő CCC adatokra utal.

vizsgáltuk különféle, a Hofmeister sorozatban szereplő egyértékű ionok jelenlétében [T6]. DLS méréseket végeztünk különböző időpontokban és a meghatározott stabilizációs tendenciák a 8. ábrán láthatóak. Megfigyelhető, hogy negatív felületi töltés esetén az ionok stabilizációra (illetve a CCC-re) gyakorolt hatása a közvetlen

Hofmeister sorozatot követi, míg pozitív töltés esetén a közvetett sorozat írja le a CCC értékek alakulását. Az egyes rendszerekben mért zéta potenciálokat különböző sókoncentrációknál meghatározva a hasadási síkhoz tartozó töltéssűrűségeket kiszámítottuk a Grahame egyenlet segítségével [28]. Ezekből az értékekből a Derjaguin megközelítést alkalmazva és feltételezve, hogy az aggregációt megakadályozó energiáját a CCC-nél eltűnik, a részecskék CCC adatait meghatároztuk minden egyes elektrolit rendszerben, a DLVO elmélet segítségével [187]. A mért és számított adatok összehasonlításából azt a következtetést vontuk le, hogy a DLVO elméletbe foglalt taszító és vonzó erők felelősek a részecske aggregáció mechanizmusáért, viszont a CCC értéke az ionok felülethez való affinitásától is függ, amely mértéke a 8. ábrán szereplő egyértékű ionok alkalmazásakor különböző.

TNS esetében megvizsgáltuk a diszperziók stabilitását ellen- és mellékionok jelenlétében pozitív és negatív töltésű részecskéket alkalmazva [T7]. A mért CCC, illetve kritikus koaguláltató ionerősség (CCIS) értékek alapján elmondhatjuk, hogy a foszfátionok protonált



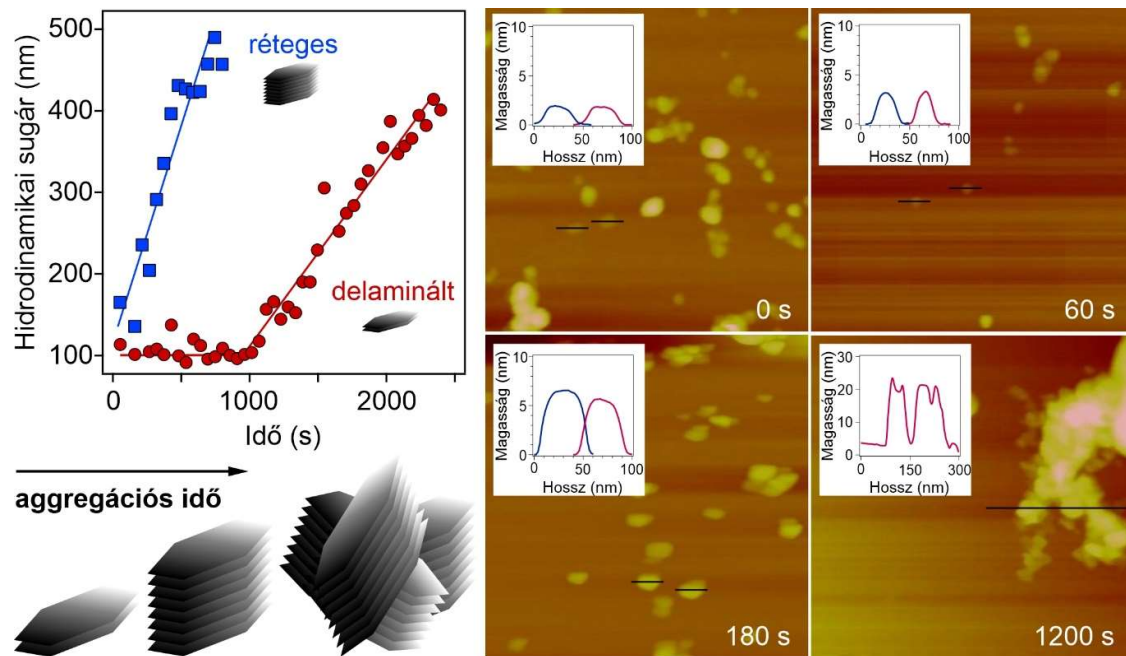
**9. ábra.** Pozitív (négyzetek) és negatív (körök) töltésű TNS részecskék CCIS és CCC értékei különböző elektrolitok jelenlétében [T7]. A beszűrt ábrán látható anionok sorrendje a Hofmeister sorozatot követi.

formái mind az izoelektromos pont (IEP) alatt, mind pedig felette erősen kemiszorbeálódnak a felületen, amelyet más titán-dioxid szerkezet esetében is bizonyítottak korábban kísérleti [188] és elméleti [189] módszerekkel egyaránt. Ez a jelenség a hagyományos Hofmeister sorozatoktól való eltérést okoz a koloidstabilitásban, ami nem várt CCC adatokban nyilvánult meg (9. ábra). A foszfátionoktól eltérően a klorid, nitrát és tiocianátionok hatása leírható a közvetett (ellenion, pozitív töltésű TNS), illetve a közvetlen (mellékion, negatív töltésű TNS) Hofmeister sorozattal. Bebizonyítottuk, hogy hasonlóan a fenti latex rendszereknél mért eredményekhez, amíg az eltérő destabilizáló hatásért az ionspecifikus adszorpció a felelős, addig a részecske aggregáció mechanizmusa a DLVO elmélettel jól leírható.

Negatív töltésű HNT részecskéket tartalmazó diszperziók esetében alkálifémionok oldataiban elvégzett ELS és DLS mérésekkel kimutattuk, hogy a nátrium(I), kálium(I) és cézium(I) ellenionok jelenléte eltérő felületi töltés és destabilizáló hatás kialakulásával jár [T8]. A kationokat változtatva a közvetlen Hofmeister sorozattal tudtuk leírni a CCC értékek változását. A kísérleti eredményeket elméleti számításokkal kiegészítve meghatároztuk a fémionok adszorpciójának hatását a részecskék töltéssűrűségére és megállapítottuk, hogy a CCC-k változása összhangban áll a kationok HNT felületekhez való affinitásával. Ilyen típusú szisztematikus vizsgálatokat korábban nem végeztek egydimenziós agyagásványok esetében.

Szintén fényszórás mérésekkel kimutattuk, hogy pozitív töltésű LDH részecskéknél a közvetett Hofmeister sorozat klorid-, nitrát- és tiocianát anionokra alkalmazható [T9]. A hidrogén-karbonát ionok besorolása azonban nem lehetséges a jelentős felületi kölcsönhatások, illetve felületi komplexek kialakulása miatt [75]. Az erős felületi adszorpció miatt az áttöltés jelenségét figyeltük meg megfelelően magas hidrogén-karbonát koncentrációknál. A mért CCC érték alacsonyabb volt, mint a fenti anionok esetében, ami ellentmond a közvetett Hofmeister sorozat által meghatározott sorrendnek. Mivel a gyakorlatban használt diszperziókban a széndioxid beoldódást nehéz elkerülni, ezért a fenti eredményeket mindenképpen figyelembe kellett vennünk elektrolitoldatokban diszpergált LDH részecskék esetében. Itt meg kell jegyezni, hogy a dihidrogén-foszfátionok jelenlétében is megállapítottuk, hogy a Hofmeister sorozattól való eltérést szintén a felületi komplexálódás miatt kialakuló erős adszorpció okozza.

További érdekesség, hogy a delaminált LDH részecskék egyértékű elektrolit által indukált aggregációja kétféle mechanizmus szerint játszódhat le. Rövid időintervallumokban és/vagy alacsony ionerősségeknél a réteges szerkezet újjáalakulása történik meg, míg a hosszabb időtartam és/vagy nagyobb ionerősség a képződő lamellás szerkezetű LDH részecskék random aggregációjának kedvez [T10]. Ezeket a megállapításokat időfüggő DLS, AFM és XRD mérésekkel igazoltuk, például a hidrodinamikai sugarak és magasságprofil mérése segítségével. Ezek szemléltetésére néhány eredményt a 10. ábrán mutatok be.



**10. ábra.** Bal oldal: Réteges és delaminált LDH részecskék instabilis diszperzióiban mért hidrodinamikai sugár értékek időbeli változása [T10]. A sematikus rajz az aggregáció mechanizmusát ábrázolja rétegződésen keresztül random klaszterek képződéséig. Jobb oldal: Különböző aggregációs időnél felvett AFM képek. A beszúrt ábrák a magasságprofilt ábrázolják a fekete vízszintes vonalak mentén.

Az eredmények alapján elmondhatjuk, hogy az általunk vizsgált nanorészecske rendszerek (TNS, HNT és LDH) közül a negatív töltéssel rendelkező HNT CCC értékeinek változása volt az egyetlen, amely megegyezett a Hofmeister sorozat által megjósolt tendenciával. A TNS és LDH diszperziókban a foszfátionok ionspecifikus adszorpciója jelentősen befolyásolja a CCC értékeket, míg az utóbbi részecskéknél ez a hidrogén-karbonátra is igaz volt. A munkánk során elért eredmények is alátámasztják az ionspecifikus hatások részletes vizsgálatának a szükségességét kolloid- és nanorészecskék egyértékű ionokat oldott állapotban tartalmazó diszperziókban. Mivel a gyakorlati alkalmazások során az elektrolitok jelenléte elkerülhetetlen, ezért a kutatásaink fontossága könnyen alátámasztható. Fontos megjegyezni, hogy a DLVO elmélet ugyanakkora CCC értékeket jósol különböző kémiai összetételű egyértékű sókra, ugyanis csak a vegyérték- és a koncentráció megváltozását veszi figyelembe (1. egyenlet), illetve az ionokat pontszerű töltéseként kezeli. Ez is indokolja a vizsgálataink fontosságát, ugyanis egyértékű sók oldataiban nem létezik általános, minden részecske és elektrolit típusra alkalmazható elmélet a CCC értékek megadására.

#### *Többértékű ionok hatása részecskék stabilitására*

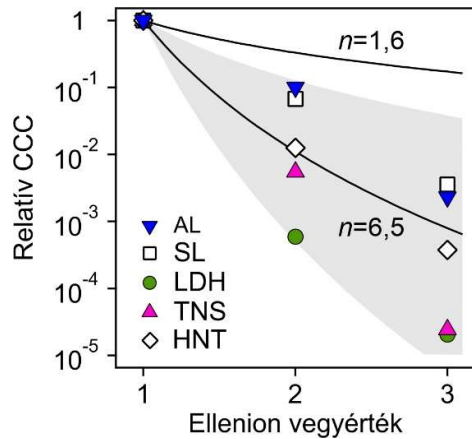
A többértékű ellenionok erősebb destabilizáló hatását már több mint 100 évvel ezelőtt felismerte Schulze [79] és Hardy [81]. Az ezt követően kidolgozott DLVO elmélet egyik nagy eredménye, hogy kvantitatívan leírja az oldott ionok vegyértékének hatását töltéssel rendelkező részecskék diszperzióinak stabilitására. Az 1. és 2. egyenletek szerint ez a vegyérték változás ionerősségre gyakorolt hatása miatt következik be. Számos korábbi kísérleti eredmény azt mutatta, hogy a CCC értékek az ellenionok vegyértékének hatodik hatványával csökkennek. Ezt hívjuk a klasszikus Schulze-Hardy szabálynak [78]. Azonban a hatodik hatvány szerinti összefüggés ( $n = 6$  a 4. egyenletben) nem vezethető le egyértelműen a DLVO elméletből, ennél jóval összetettebb a kép.

Mérési eredményeink szerint ugyanis LDH [T9], SL [T11], AL [17], TNS [T7] és HNT [T12] részecskék diszperzióinak stabilitása eltérő mértékben függ az oldatban megtalálható ellenionok vegyértékétől (11. ábra). A 4. egyenletben szereplő kitevő értéke  $3 < n < 11$  között változott. Általánosságban ezekről a rendszerekről elmondható, hogy a vegyértékfüggés negatív töltésű ellenionok jelenlétében több esetben is erősebben érvényesült, mint a kationok ellenionként való alkalmazásakor. Az eredmények alapján azt is megállapítottuk, hogy a CCC-vegyérték reláció nagyban összefügg a részecskék töltéssűrűségével, illetve az ellenionok felülethez való affinitásának mértékével, amely ionspecifikus kölcsönhatásokkal kialakuló funkciók csoportok létrejöttével járhat a felületen.

Habár az ionerősség és ezáltal a Debye paraméter (2. egyenlet), illetve az elektromos kettősrétegek átlapolása során fellépő taszító erők mértékének függése a mellékionok vegyértékétől egyértelmű, ez a terület kevésbé kutatott az ellenionokhoz képest. Abban a néhány közleményben [27, 190, 191], ami ebben a témában született eddig, hiányos és kvalitatív jellegű információk találhatóak meg. TNS [T7], AL és SL [T13] részecskék diszperziókban mért CCC értékek alapján megállapítottuk, hogy a vegyértékfüggés többértékű ellenionok jelenlétében az  $1 < n < 1,5$  kitevők (4. egyenlet) között helyezkedik el. Ez alapján

elmondhatjuk, hogy a rendszerben jelen lévő mellékionok hatását leíró inverz Schulze-Hardy szabály esetében a CCC vegyértékfüggése gyengébb a fentebb tárgyalt ellenionokéhoz képest, azonban nem elhanyagolható.

A korábban közölt levezetésekben a töltésfüggés számszerűsítésére törekedtek a DLVO elméletben szereplő erőhatások figyelembevételével [7]. Azonban ezekben szimmetrikus elektrolitokkal (a kation és az anion vegyértéke megegyezik) számoltak, amelyek oldhatósága

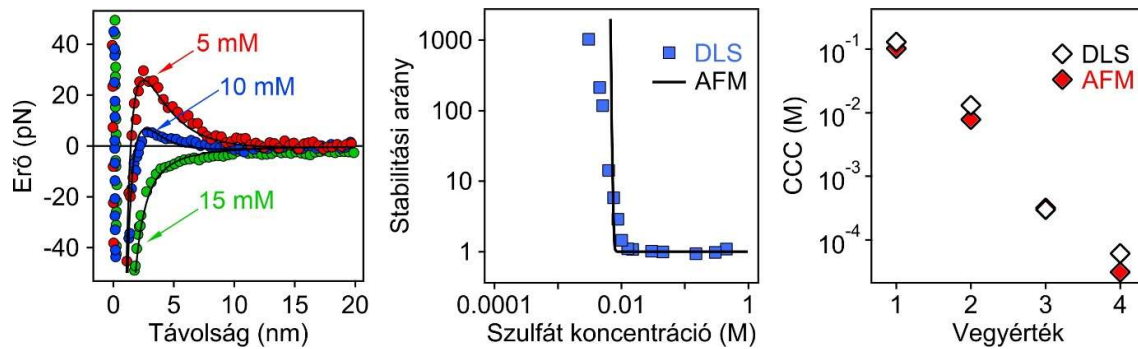


**11. ábra.** A CCC változása az ellenionok vegyértékével: mért (szimbólumok, üres: negatív, teli: pozitív részecske) és a DLVO elmélettel számolt (folytonos vonal) adatok. A beszűrt számértékek a 4. egyenletben szereplő hatványkitevő értékeit jelölik, míg a szürke terület a  $3 < n < 11$  függést.

nagyságrendekkel magasabb, mint a természetben, vagy az alap kutatások során előforduló részecskék töltése. A mellékionok esetében a PB elmélettel számított vegyértékfüggés  $n = 1$ , ami jó egyezést mutat a kísérletileg SL [T13] és TNS [T7] részecskékre meghatározott CCC értékekkel.

A 3. egyenletet felhasználva a részecskék aggregációs sebességi állandóját kiszámíthatjuk, ha ismerjük a felületek között fellépő potenciális energia nagyságát [30]. Az előbbi időfüggő DLS mérésekkel kísérletileg meghatározható [33], az utóbbi pedig a részecskék közötti vonzó és taszító erőhatások összegéből számítható [7], amely AFM alapú koloid próba segítségével mérhető, amennyiben mind a tartókaron, mind pedig a szubsztrátumon rögzítünk egy-egy részecskét a kérdéses diszperzióból [192]. Munkánk során ugyanazon AL részecskék aggregációs állandóit határoztuk meg ezeknek a módszereknek a segítségével különböző elektrolitokat tartalmazó diszperziókban, és az eredményül kapott stabilitási arányokat összehasonlítottuk [T17]. Meg kell jegyezni, hogy hasonló tanulmány (kétféle módszerrel, ugyanazon részecskékre meghatározott stabilitási arány értékek közlése) még nem született korábban. Néhány kiemelt eredményt a 12. ábrán mutatok be.





**12. ábra.** AL részecskék közötti kölcsönhatások jellemzése különböző vegyértékű ellenionok jelenlétében [T17]. Bal oldal: AFM-kolloid próba segítségével mért erőhatások (szimbólumok) különböző szulfát koncentrációknál. A folytonos vonalak a DLVO elmélettel számított erőhatásokat jelölik. Az elektromos kettősrétegek közötti taszító erők csökkenése, illetve eltűnése magasabb koncentrációknál jól megfigyelhető. Középső ábra: DLS módszerrel meghatározott stabilitási állandók (négyzetek) összehasonlítása az AFM mérések eredményeiből számított értékekkel (vonal). Jobb oldal: Mért (DLS) és számított (AFM) CCC értékek klorid, szulfát, ferri- és ferrocianid ellenionok jelenlétében.

A fenti ábrán bemutatott AFM mérési eredményekből is látható, hogy a meghatározott erők a DLVO elmélettel jól leírhatóak, tehát van der Waals és elektromos kettősréteg típusú kölcsönhatásokat feltételezve a mért és a számolt erők jó egyezést mutattak. A stabilitási állandók meghatározása (a mért erő átszámítása potenciális energiává és a 3. és 5. egyenletek használata) után megállapítottuk, hogy az adatok nagyon hasonlóan adódtak az időfüggő DLS mérésekben ugyanazon részecske diszperzió használatával kapott értékekhez. A 12. ábra alapján szintén elmondhatjuk, hogy a kísérleteket elvégezve klorid-, szulfát-, ferri- és ferrocianid ellenionokat tartalmazó közegekben a két módszerrel meghatározott CCC értékek nagyon hasonlóak voltak.

Felvetődik a kérdés, hogy vajon a CCC csökkenés az ellenion vegyértékkel milyen töltésszámig érvényes. A szakirodalmi adatok alapján elmondhatjuk, hogy a legtöbb esetben 1-3 vegyértékű ellenionokkal történtek vizsgálatok még napjainkban is [77, 82, 193]. Munkánk során egytől több ezerig változó töltésszámú poliamin és polikarboxilát homológ sorok alkalmazásával bebizonyítottuk, hogy AL és SL kolloid diszperziók stabilitásának érzékenysége az ellenionok vegyértékére csak bizonyos töltésszámig érvényes [T18]. Ezzel definiáltuk az úgynevezett polielektrolit szabályt, amely kimondja, hogy a CCC értékek 10-es töltésszám felett nem változnak, így ez tekinthető a Schulze-Hardy szabály alkalmazhatósági határának ezekben a rendszerekben.

A fejezet összefoglalásaként megállapíthatjuk, hogy a hagyományosan ellenionokra alkalmazott Schulze-Hardy (hatodik hatvány) szabály közvetlenül a DLVO elméletből nem vezethető le még szimmetrikus elektrolitokra sem, csak extrém magas felületi töltéssűrűség feltételezésével, amely a gyakorlatban található részecskékre nézve teljesen irreális. Viszont ehhez hasonló CCC vegyértékfüggést néhány esetben leírtak különféle módszerekkel meghatározott adatok alapján (lásd 5. ábra). Az egyéb részecske-elektrolit rendszerekben meghatározott CCC adatok azonban széles tartományban változtak,  $3 < n < 11$  között az

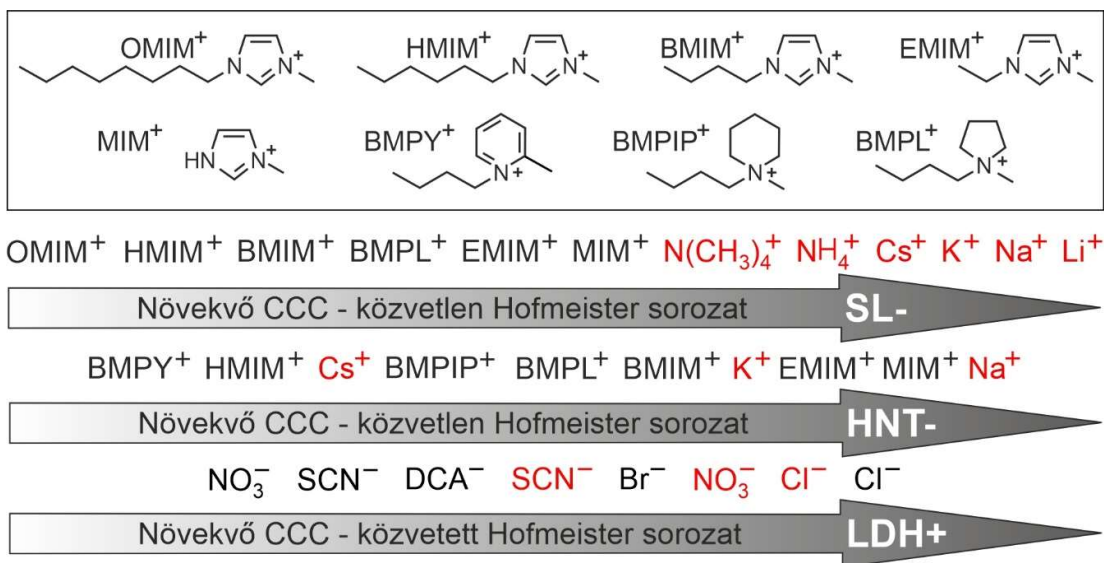
ellenionok töltésszámával  $z = 10$  értékig. Hasonlóan az egyértékű ionokhoz, a specifikus adszorpciónak itt is fontos szerepe van a felületek közötti erőhatások kialakításában. Többértékű ionok nagyobb mértékben adszorbeálódnak és feldúsulhatnak a részecskék felületén, amely az elektrosztatikus taszító erőket, és így a CCC-ket csökkenti [T15, T16]. Azonban az erőhatások közvetlen mérésével bebizonyítottuk, hogy például AL részecskék közötti kölcsönhatások a DLVO elmélettel jól leírhatóak. Ezek alapján megállapíthatjuk, hogy a vegyérték növelése a Debye paraméteren keresztül csökkenti az elektromos kettősrétegek közötti taszítást, viszont az ellenionok adszorpciója által okozott töltés semlegesítés miatt csökkenő felületi potenciál is hozzájárul a taszító erők csökkenéséhez (1. egyenlet). Ez a két hatás együttesen eredményezi a CCC vegyértékfüggését, amely mértéke nagyban függ az alkalmazott részecskék és elektrolitok kémiai minőségétől. Megállapíthatjuk tehát, hogy a hatodik hatvány szabály nem alkalmazható általánosságban, illetve újszerű (nano)részecskék esetében a többértékű ionok destabilizáló hatását megbízható módszerekkel szükséges meghatározni.

## 5.2. Részecske diszperziók ionos folyadékokban

Ahogy az már a 2.2 fejezetben tárgyaltuk, kolloid- és nanorészecskék stabilis diszperzióit sikeresen előállítottak IL rendszerekben [113, 116, 117, 120, 121], azonban a tudományos társadalomban nincs egységes álláspont a stabilizáló mechanizmust illetően [38]. Egyrészt az IL alkotók részleges disszociációja során kialakuló elektromos kettősrétegek közötti taszító erők jelenlétét feltételezik [122], másrészt pedig az IL komponensek felületi rétegződése során létrejövő oszcillációs erőket azonosították a stabilizáló kölcsönhatás okaként [120]. Abban teljes az egyetértés, hogy a rohamosan növekvő számú IL-részecske rendszerekben az aggregációs viszonyok döntően befolyásolják az adott minta felhasználhatóságát. Az eddig közölt eredmények alapján egyértelműen kijelenthető, hogy az IL alkotó komponensek határfelületi viselkedése jelentős hatással van a diszperziók stabilitására. Munkánk során ennek részletes vizsgálatát tűztük ki célul IL-részecske és IL-víz-részecske rendszerekben.

Vízzel elegyedő IL-ok híg oldataiban az alkotó komponensek nagymértékben disszociált állapotúak, majd mennyiségüket növelve egyre erőteljesebbé válik az ionpároképződés [194]. Ennél fogva alacsony koncentrációjú vizes oldataikban lehetőség nyílik az egyes alkotó ionok határfelületi viselkedésének a vizsgálatára. Részecske diszperziók kolloidstabilitása vizes IL oldatokban hasonló tendenciát mutat, mint szervesetlen elektrolitok esetében (lásd előző fejezet, egyértékű sók). Nevezetesen a CCC-hez tartozó koncentráció elérése után a diszperziók destabilizálódnak [120, 195, 196]. Ennél fogva DLS és ELS módszerek alkalmazásával meghatároztuk a kolloidstabilitást befolyásoló töltés- és aggregációs viszonyokat számos IL-részecske rendszerben, majd azokat összehasonlítottuk ugyanazon részecskék esetében szervesetlen elektrolit oldatokban mért értékekkel. Az alkalmazott IL kationokat, illetve a CCC értékekben megfigyelt tendenciákat a 13. ábra szemlélteti.





**13. ábra.** Felső rész: IL alkotó kationok szerkezeti képlete (a kémiai elnevezésekért lásd a rövidítések jegyzékét). Alsó rész: IL alkotó ionokkal kiegészített Hofmeister sorozatok SL [T19], HNT [T8, T12] és LDH [T9, T21] részecskékre. A piros színű ionok szervesetlen sókat, míg a fekete színnel szedettek IL alkotókat jelölnek.

SL részecskék diszperzióinak stabilitását vizsgáltuk különböző IL kationok oldataiban [T19]. Az alkalmazott mellékion klorid volt minden esetben. Bizonyítottuk, hogy az imidazólium kationok szerkezetében található alkylánc hossza döntően befolyásolja az adszorpció mértékét az ellentétesen töltött felületen. Eszerint rövidebb láncossznál töltés semlegesítés (MIM<sup>+</sup> és EMIM<sup>+</sup> jelenlétében), majd a BMIM<sup>+</sup>, HMIM<sup>+</sup> és OMIM<sup>+</sup> esetében áttöltődés játszódott le. Ez a viselkedés hasonló a változó szénatomszámú alkyláncot tartalmazó tenzid molekulák határfelületi viselkedéséhez [197]. Az adszorpciós folyamatok jelentősen befolyásolták a diszperziók kolloidstabilitását is. Míg a rövidebb alkyláncot tartalmazó IL kationok esetében a DLVO által leírt viselkedés volt megfigyelhető a változó IL koncentrációnál mért aggregációs sebességi állandókban, illetve jól definiált CCC értékeket figyeltünk meg a MIM<sup>+</sup>, EMIM<sup>+</sup> és BMIM<sup>+</sup> rendszerekben. Az OMIM<sup>+</sup> jelenlétében viszont az áttöltődés a részecskék stabilizációjával járt, ami az aggregációs sebességi állandók csökkenésében nyilvánult meg az IEP-nál magasabb IL koncentrációknál. Ez a jelenség a kialakuló pozitív felületi töltésnek, illetve az elektromos kettősrétegek és az ebből következő taszító erők megjelenésének köszönhető [197, 198].

A szakirodalomban a fentiekhez hasonló aggregációs viselkedést figyeltek meg pozitív felületi töltésű hematit [199] és titán-dioxid [197] részecskék esetében ellentétes töltést és változó alkyláncot tartalmazó felületaktív tenzid molekulák jelenlétében. A töltésviszonyokat és a CCC adatokat (13. ábra) tekintve szintén megegyező tendenciát kaptunk IL kationok HNT részecskéket tartalmazó oldataiban [T12]. Viszont ellenkező adszorpciós viselkedést tapasztaltunk TNS részecskék esetében lúgos közegben, ahol felületük negatív töltésű [T20]. Eszerint a MIM<sup>+</sup> és EMIM<sup>+</sup> oldataiban figyeltünk meg áttöltődést ELS mérések során, míg a BMIM<sup>+</sup> esetében csupán töltés semlegesítéshez vezetett az ellenion adszorpció a TNS

felületeken. Az adszorpciós trend meghatározta a diszperziók stabilitását, az erősebben adszorbeálódó ionok kisebb koncentrációnál destabilizálták a TNS részecskéket, ami a CCC értékekben is tükröződött.

Az egyes részecske rendszerekben tapasztalt eltérés oka a felületek hidrophil-hidrofób jellegéhez köthető. A TNS az alkalmazott kísérleti körülmények között (magas pH és alacsony ionerősség), főleg a deprotonált felületi hidroxid csoportok miatt, hidrophilebbnek tekinthető, mint a polisztirol alapú SL részecskék. A polaritásbeli különbségeket a titán-dioxid és a latex részecskék között korábban a szakirodalomban is már leírták [200, 201]. Ennél fogva a hosszabb szénláncot tartalmazó és ezáltal hidrofób karakterű IL kationok, mint a HMIM<sup>+</sup> és OMIM<sup>+</sup> nagyobb affinitást mutatnak az SL felülethez, míg a kisebb szénatomszámú, hidrophil jellegű MIM<sup>+</sup> ionok a TNS felületre adszorbeálódnak nagyobb mértékben. Fontos hangsúlyozni a felület polaritásának szerepét, illetve a polaritási viszonyok alapján kialakuló kölcsönhatásokat. Mivel egyértékű szerves ionokra általában nem jellemző ilyen mértékű áttöltés, mint az egyes IL kationok adszorpciója során, ezért a Coulomb-féle vonzás mellett az adszorpció egyik fontos hajtóereje a hidrophil-hidrophil és hidrofób-hidrofób kölcsönhatások kialakulása.

Ahogy a fentiekben említésre került, a részecske aggregáció mechanizmusa különböző IL koncentrációnál követi a töltésviszonyokban bekövetkező változásokat. Az IEP-nél, ahol az ellenionok adszorpciója töltés neutralizációt eredményez, gyors részecske aggregációt figyeltünk meg, ami a diszperziók destabilizációjával jár. Csökkentve az IL kation koncentrációját, az aggregáció sebessége csökken, majd stabilis kolloid mintákat kapunk. Ugyanezt tapasztaljuk számottevő áttöltés során. Ha az adszorpció után az IEP-nél magasabb koncentrációnál kialakuló pozitív töltés magas, akkor a részecskék nem aggregálódnak, illetve stabilis mintákat alkotnak. Ez a viselkedés összhangban van a DLVO elmélet által megjósolt kolloidstabilitással [26, 27]. Kellően nagy töltés esetében az elektromos kettősrétegek átlapolása során kialakuló taszító erők stabilizálják a diszperziókat, míg töltés semlegesítés során ezek gyengülnek, illetve eltűnnek, ami a van der Waals-féle vonzó erők dominanciájával és részecske aggregációval jár.

Az IL és szerves sók oldataiban mért CCC értékeket összehasonlítottuk, így létrehozva egy IL alkotó ionokkal kibővített Hofmeister sorozatot az SL [T19], a HNT [T8, T12] és az LDH [T9, T21] részecskékre. ELS és DLS méréseket alkalmazva egyértelműen bizonyítottuk, hogy az ionok hidratáltsága határozza meg azok affinitását a részecskék felületéhez, ami a CCC értékek változását eredményezi. A 13. ábrán látható tendenciák alapján elmondhatjuk, hogy az egyes részecske rendszerek között jelentős különbségeket tapasztaltunk attól függően, hogy szerves elektrolitokat vagy IL-okat oldottunk a diszperziókban, amely az oldott ionok közötti kölcsönhatást is előrevetíti.

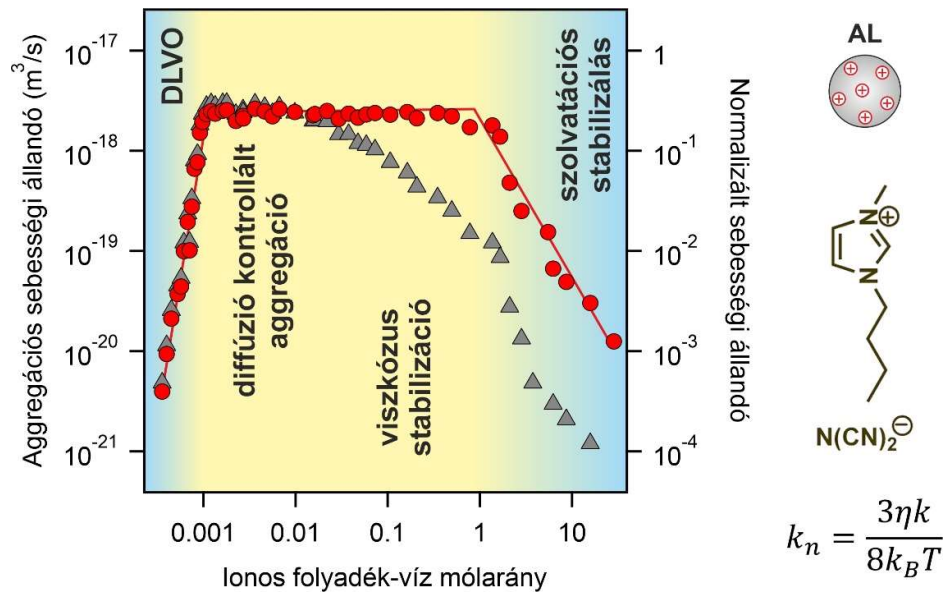
Az SL mintákban az IL kationok elkülönülnek az ammónium- és fémionoktól, jelenlétük lényegesen alacsonyabb CCC értékeket eredményez (13. ábra). Ez a fentebb tárgyalt szignifikáns hidrofób kölcsönhatásokkal magyarázható, amelyek erősítik a kationok adszorpcióját és az alkilcsoport hosszával arányosan nőnek. Ezzel magyarázható, hogy az OMIM<sup>+</sup>

kation esetében mértük a legkisebb CCC-t. Az SL-hez hasonlóan negatív töltésű HNT részecskékkel mért adatok szerint az IL kationok elkülönülése a fémionoktól megszűnt, a CCC-k alapján a tradicionális közvetlen Hofmeister sorozat kibővíthető IL kationokkal. Az SL részecskénél tapasztalt alkilánchossz függés továbbra is fennáll, illetve különbséget eredményez a MIM<sup>+</sup>, EMIM<sup>+</sup>, BMIM<sup>+</sup> és HMIM<sup>+</sup> molekulák határfelületi viselkedése között. Ugyanakkor a BMPY<sup>+</sup> jelenlétében mértük a legalacsonyabb CCC értéket. Ez arra utal, hogy a butillánc mellett a piridíniumgyűrű felülethez való affinitása is elősegíti az adszorpciót és ezáltal a töltés semlegesítést. Az ebből adódó diszperzió destabilizálás alacsonyabb kation koncentrációnál következik be.

LDH részecskéket és IL-okat tartalmazó mintákat fényszóráson alapuló technikákkal vizsgáltuk és ennek során kimutattuk, hogy a kolloidstabilitás IL-ok vizes oldataiban függ mind az ellenionok, mind pedig a mellékionok kémiai összetételétől [T21]. Megállapítottuk, hogy az aggregációs folyamatokat alapvetően DLVO-típusú erők irányítják, viszont az IL komponensek (például BMIM<sup>+</sup> vagy BMPL<sup>+</sup>) képesek számottevő adszorpcióra még mellékionként is. Az adszorpciós folyamatok döntően befolyásolják az elektrosztatikus eredetű részecske-részecske kölcsönhatások erősségét és így a CCC értékeket. További értékes megállapítások tehetők, ha összehasonlítjuk az IL és szervesetlen só alkotó anionok jelenlétében mért CCC-ket (13. ábra). A klorid, nitrát és tiocianát anionok esetében meghatározott CCC-k jelentősen eltérnek, ha BMIM<sup>+</sup> vagy kálium(I) kationok vannak jelen a rendszerben mellékionként [T9, T21]. Ez a nitrátionok esetében mutatkozik meg a legfeltűnőbbben, ugyanis BMIM-nitrát oldatokban mért CCC a legkisebb, holott ezt a BMIM-tiocianát rendszer esetében várnánk a közvetett Hofmeister sorozat alapján. A jelenség mögött az IL ionpárok eltérő mértékű képződése áll [202, 203], amely a BMIM-tiocianát rendszerben fokozottabban játszódik le és ennél fogva csökkenti a disszociált és adszorpcióra képes tiocianátionok koncentrációját, ami magasabb CCC értékekhez vezet.

Bebizonyítottuk, hogy a Hofmeister sorozatok IL alkotókkal bővíthetők, mind ellen-, mind pedig mellékionok esetében. A kérdéses rendszerek részletes vizsgálatára azonban szükség van minden esetben, mivel a specifikus ion-ion és ion-felület kölcsönhatások miatt a szervesetlen elektrolitokra érvényes megfontolások nem alkalmazhatók.

Az IL alkotó ionok határfelületi viselkedésének megismerése után vizsgáltuk a részecske stabilitásért felelős erőhatások eredetét AL és SL, valamint különféle IL-ok alkalmazásával [T22, T23]. Kationként BMIM<sup>+</sup>, BMPY<sup>+</sup>, BMPL<sup>+</sup> és etil-ammónium, míg anionként diciánamid, tiocianát, tetrafluoroborát és nitrát ionokat alkalmaztunk. Fontos megjegyezni, hogy ezek a IL-ok szobahőmérsékleten is folyékony halmazállapotúak, ezért lehetőségünk nyílt a kolloidstabilitás vizsgálatára híg vizes, majd töményebb IL oldatokban, végül pedig tiszta IL rendszerekben, amelyek csak nyomokban tartalmaztak vizet. Általánosságban nagyon hasonló eredményeket kaptunk a különböző IL összetételeknél, ezért itt az AL-BMIM-diciánamid rendszer és vizes oldataik DLS módszerrel [33] követett aggregációs folyamatait tárgyalom a meghatározott sebességi állandók bemutatásán keresztül (14. ábra).



**14. ábra.** Pozitív töltésű AL részecskék abszolút (háromszögek, bal oldali tengely) és normalizált (körök) aggregációs sebességi állandói az IL (BMIM-diciánamid, szerkezeti képlet az ábra bal oldalán látható) koncentráció függvényében híg vizes oldatoktól a tiszta IL alkalmazásáig bezárólag [T22]. Az egyenlet a Smoluchowski-féle összefüggéssel normalizált sebességi állandó (jobb oldali tengely) számítását mutatja be.

Az aggregációs sebességi állandó értékeket ( $k$ ) elemezve megállapítottuk, hogy latex kolloidok esetében a stabilitásért felelős erőhatások a DLVO elmélettel leírhatóak az IL-ok híg vizes oldataiban, ahol az ionpárképződés elhanyagolható. Ezek szerint az aggregáció sebessége addig növekszik, amíg el nem érjük a diffúzió kontrollált tartományt a CCC-nél. Növelve az IL-víz arányt, a sebességi állandók csökkenését figyeltük meg, majd vizet csak nyomokban tartalmazó IL esetében stabilis diszperziókat azonosítottunk. Ez ellentmond korábbi, kolloidstabilitást leíró elméleteknek, amelyek magas iontartalomnál a részecskék gyors aggregációját jósolják [6, 7, 28]. A stabilizáció mechanizmusának megértése érdekében a kapott állandókat normalizáltuk a Smoluchowski által, elméleti megfontolások alapján javasolt aggregációs állandóval [33]. Azonos hőmérsékletű és részecske koncentrációjú diszperziókban ennek értéke csupán a közeg viszkozitásától függ, amely mérésével számítani tudtuk a Smoluchowski-féle sebességi állandót minden egyes mérési pontra.

A számított normalizált sebességi állandók ( $k_n$ ) elemzése alapján egyértelművé vált, hogy a közbenső IL koncentrációknál tapasztalható csökkenés a sebességi állandókban a növekvő viszkozitásnak köszönhető, amely által a részecskék diffúziója lelassul a diszperziókban. Ettől eltekintve az aggregáció diffúzió kontrollált ebben a viszkozus stabilizációs tartományban. Vizet csak nyomokban tartalmazó tiszta IL rendszerekben viszont a normalizált sebességi állandók is stabilis mintákat jeleztek, mivel azok értéke csökkent az IL koncentrációval, illetve nem volt mérhető tiszta IL-okban. Az ebben a tartományban tapasztalt jelenséget neveztük el szolvatációs stabilizálásnak, mivel létrejött az IL, mint közeg jelenlétének köszönhető.

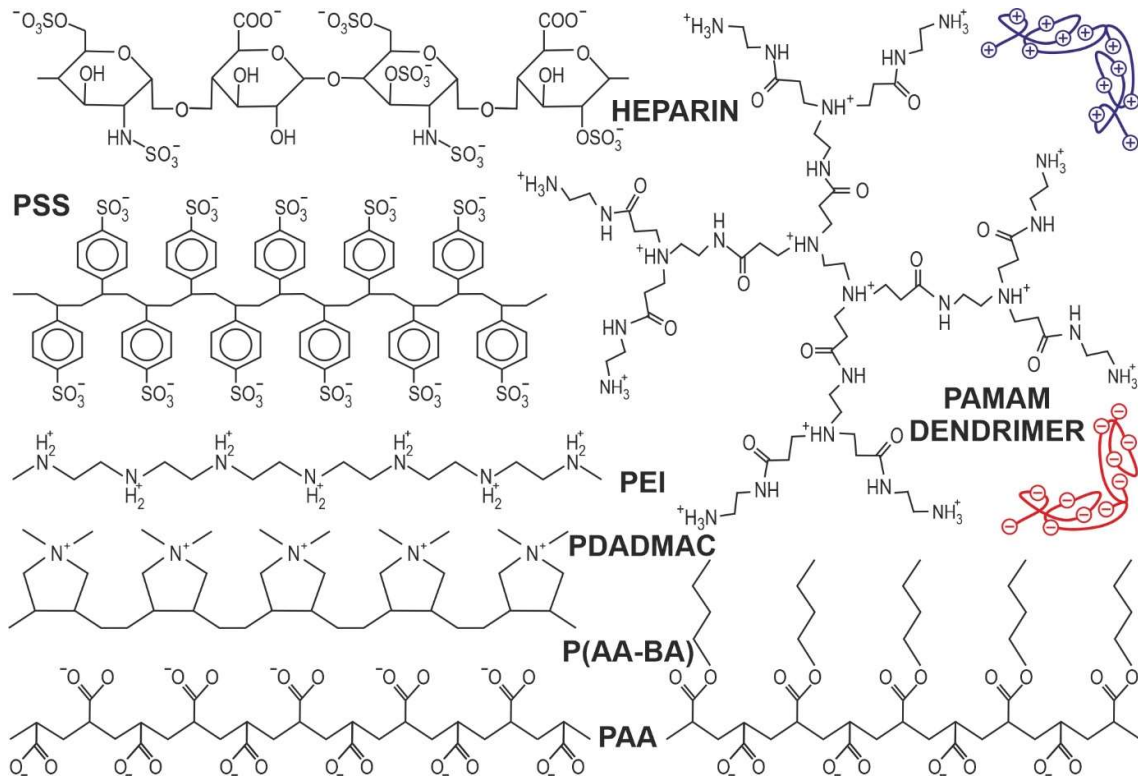
A fenti eredményekkel bizonyítottuk, hogy stabilis részecske-IL diszperziók hozhatók létre vízmentes (vagy vizet csak nyomokban tartalmazó) közegben. Ezek a kísérleti adatok azonban nem nyújtanak elegendő információt arra vonatkozóan, hogy a 6. ábrán, illetve a hozzá tartozó szövegben felvázolt kétféle (elektromos kettősréteg, vagy rendezett felületi adszorpció által kiváltott) stabilizáló mechanizmus közül melyik lehet a meghatározó az általunk vizsgált diszperziókban. Ennek eldöntésére fényszórás méréseket végeztünk a fentiekhez hasonlóan szisztematikus módon SL-etil-ammónium nitrát (EAN) és vízzel hígított rendszereiben [T23]. ELS kísérletek eredményei alapján bebizonyítottuk, hogy a részecskék töltését teljes mértékben árnyékolják az adszorbeálódó IL alkotó ionok és így elektromos térben nem mozognak. Tehát a stabilizációs erők nem lehetnek elektrosztatikus eredetűek. Ezáltal megállapítottuk, hogy a jelentkező taszító kölcsönhatások az IL komponensek határfelületi rétegződésének köszönhetőek, ami oszcillációs taszító erők kialakulásához és ennél fogva stabilis részecske diszperziók kialakulásához vezet tiszta IL-okban. Továbbá megvizsgáltuk a stabilizáció mechanizmusát  $\text{NaNO}_3$  hozzáadása után (az anion ugyanaz, mint az EAN esetében). Kimutattuk, hogy a hozzáadott nátrium ionok beépülnek a határfelületi IL rétegekbe és ezáltal változik a diszperziók stabilitása. Ez általánosságban igaz mindhárom (DLVO, viszkózus és szolvatációs stabilizációs) aggregációs tartományra.

Az IL oldatokra kapott eredményeink alátámasztják azokat a főként empirikus úton nyert korábbi megállapításokat, amelyek alapján stabilis diszperziókról számoltak be IL közegben különféle részecskékkel [113, 117, 121, 126, 204]. Azt a tényt is megerősítettük, hogy vízzel elegyedő IL-okban diszpergált részecskék aggregálódnak kellően magas IL koncentrációknál a DLVO elmélettel összhangban [120, 125, 195]. Ezáltal a kutatási eredményeink által elsőként mutattuk meg, hogy szisztematikusán változtatva a IL-részecske rendszerekben a víztartalmat, a stabilizációs mechanizmus alapján eredményeinket 3 tartományra oszthatjuk fel. Eszerint alacsony koncentrációnál elektromos kettősrétegek közötti taszítás, növelve az IL dózist a növekvő viszkozitás, míg tiszta IL-okban szolvatációs erőhatás felelős a stabilis diszperziók létrejöttéért. Továbbá elsőként szolgáltatunk kísérleti bizonyítékot arra, hogy a szolvatációs stabilitás a felületen önrendeződő IL alkotó ionok rétegződésének köszönhető és nem a korábban feltételezett [122] disszociációjuk során kialakuló elektromos kettősrétegek átlapolása miatt fellépő elektrosztatikus taszítás stabilizál.

### 5.3. Funkcionalizálás polielektrolitokkal

A potenciális alkalmazások szempontjából a diszpergált részecskék felületének funkcionálizálása két okból is nagy jelentőségű. Egyrészt az aggregációra való hajlamukat tudjuk így csökkenteni, másrészt az így létrejövő felületi funkciók csoportok lehetőséget adnak további komponensek immobilizálására, illetve ezáltal hibrid anyagok előállítására. Esetünkben a felületi funkcionálizálással az antioxidáns hatású anyagok kötődését és az adszorpció során kialakuló szerkezetét tudtuk optimalizálni. Ahogy azt a későbbiekben bemutatjuk, a megfelelő polielektrolitok kiválasztásával, illetve a kísérleti körülmények hangolásával mind a kolloidstabilitás, mind pedig a részecskék határfelületi tulajdonságai

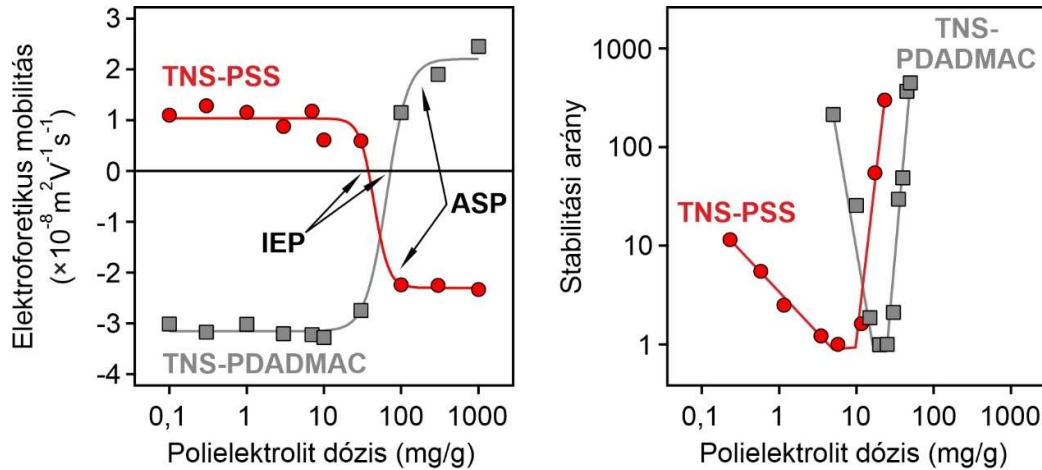
optimalizálhatóak. Itt a cél a legmagasabb antioxidáns aktivitás elérése. Néhány felhasznált polielektrolit szerkezeti képlete a 15. ábrán látható.



**15. ábra.** Polielektrolitok szerkezeti képletei ionizált formában (ahol a funkciós csoportok vagy a teljesen protonált (aminok), vagy a teljesen deprotonált (karboxilátok és szulfonátok) állapotban vannak). Az elnevezések a rövidítések jegyzékében találhatóak.

A polielektrolit adszorpciót, illetve annak hatását diszpergált részecskék töltés és aggregációs viszonyaira, ELS, DLS és AFM kolloid próba módszerekkel vizsgáltuk. Az első tárgyalásra kerülő rendszerben, kihasználva a TNS nanolapok pH-függő töltését, bebizonyítottuk, hogy felületük a PZC-nél alacsonyabb és magasabb pH értéken is módosítható, mégpedig olyan polielektrolitokkal, amelyek ellentétes töltésűek az alkalmazott kísérleti körülmények között [T24]. Ezeknek a megfontolásoknak megfelelően negatív töltésű PSS-t használtunk savas, míg pozitív töltésű PDADMAC-ot lúgos pH-jú mintákban. A mért elektroforetikus mobilitás és stabilitási arány értékek tendenciái megegyeztek a két rendszerben (természetesen figyelembe véve a töltésméretet, lásd 16. ábra). Ezek szerint mindkét minta esetében töltéskompensáció játszódott le az adszorbeált, ellentétesen töltött polielektrolitoknak köszönhetően az IEP értékeknek megfelelő dózisoknál. Az IEP dózis a TNS-PSS rendszerben alacsonyabb volt a TNS-PDADMAC-hoz képest, a pozitív töltésű TNS (savas pH tartomány, PZC alatt) kisebb felületi töltésének köszönhetően. Tovább növelve a polielektrolit koncentrációt, bekövetkezik a részecskék áttöltése. Ez az eredmény jó egyezést mutat más ellentétesen töltött részecskék/felületek esetében korábban közölt adatokkal [40, 205, 206]. Az áttöltődés hajtóerejét az adszorpció során fellépő entrópiaváltozással [207], ion-ion korrelációkból eredő vonzó erőkkel [208] és hidrofób kölcsönhatásokkal [209] magyarázhatjuk. A polielektrolit

megkötődés az adszorpciós telítési határ (ASP) értékekig folytatódott, a további hozzáadott polielektrolit molekulák az oldatfázisban maradnak a TNS felület telítődése miatt.



**16. ábra.** Bal oldal: Elektroforetikus mobilitás értékek állandó TNS (10 mg/L)) és változó polielektrolit koncentrációnál pH=4 (körök, pozitív töltésű TNS) és pH=10 (négyzetek, negatív TNS) esetében. Jobb oldal: az elektroforetikus mobilitás mérésekkel azonos kísérleti körülmények között mért stabilitási arány értékek. A mérési adatok közötti vonalak szemvezetőként szolgálnak.

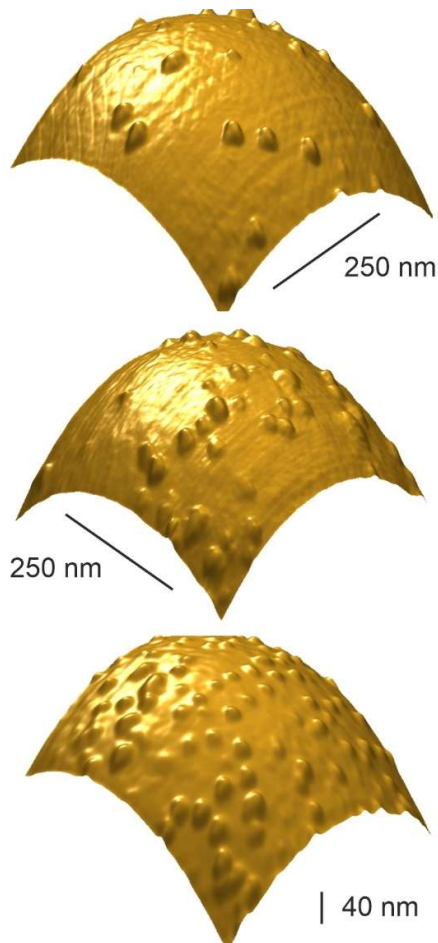
A polielektrolit dózis kolloidstabilitásra kifejtett hatásának vizsgálatára időfüggő DLS méréseket végeztünk az elektroforetikus kísérleteknél alkalmazott körülmények között. A stabilitási arányok V-alakú görbét vettek fel mindkét esetben (jóllehet, ez kissé torzult a TNS-PSS rendszerben, lásd 16. ábra). Ezzel kimutattuk, hogy a részecske diszperziók stabilitása az IEP-től távoli polielektrolit dózisoknál a legnagyobb (amit magas, vagy nem mérhető stabilitási arány értékek jeleznek). Töltés semlegesítés esetében az egyhez közeli stabilitási arány adatok diffúzió kontrollált aggregációra utalnak, ennek sebessége csökkent az IEP-től távolodva. Az eredmények alapvetően a DLVO elmélettel magyarázhatóak. Megfelelően nagy töltéssűrűség esetében (alacsony vagy magas polielektrolit dózisoknál) az elektromos kettősrétegek közötti taszítás stabilizálja a részecskéket, viszont ez a hatás töltés hiányában eltűnik az IEP érték közelében, ahol a vonzó van der Waals erők destabilizálják a diszperziókat. Egyéb polielektrolit indukált erőhatások jelenléte nem kizárható, viszont ezek nem változtatják meg lényegesen a stabilitási tartományokat. Ilyen nem-DLVO hatás lehet a „patch-charge” vonzás (3. ábra), amely jellemzően részleges felületei borítottságnál (az ASP-nál alacsonyabb dózisonál) jelentkezik és például a TNS-PSS rendszerben tapasztalt kisebb mértékű stabilitási arány csökkenést okozza az IEP előtt.

A fent tárgyalt töltésmérleghez és aggregációs viselkedéshez hasonló eredményeket kaptunk eltérő összetételű, de ellentétes töltéssel rendelkező polielektrolit-részecske rendszerekben is. Megállapítottuk, hogy TiONW részecskék pH-függő töltése alapján kolloidstabilitásuk hangolható megfelelő polielektrolitok (PSS [T5], PDADMAC [T25], PSP [T26] és PAMAM dendrimer [T27]) segítségével, az alkalmazott kísérleti körülmények változtatásával. A TNS és TiONW morfológiája és összetétele közötti különbség nem befolyásolta nagymértékben a



diszperziók paramétereit polielektrolitok jelenlétében [T26]. Megmutattuk, hogy LDH részecskéket kis molekulatömegű P(AA-BA) kopolimerekkel funkcionálizálva nagy stabilitású kompozit diszperziók állíthatók elő [T30], amelyeket felhasználtunk rendkívül előnyös mechanikai és szerkezeti tulajdonságokkal bíró latex-LDH hibrid anyagok szintézise során [210]. LDH részecskék töltés és aggregációs viszonyainak, illetve kolloidstabilitásuk optimalizálására HEP polielektrolitot is használtunk és bizonyítottuk, hogy a HEP dózistól függően stabilis vagy instabilis kolloidok állíthatók elő a felhasználási céloknak megfelelően [T31]. Ez a megállapítás ugyancsak igazolásra került HNT-PSP [T4] és HNT-IP-2 [T12] diszperziókban is, amelyek előállításánál során egydimenziós, funkcionizált hordozó nanorészecskéket kaptunk.

A fenti rendszerekben a polielektrolit dózis változtatásával mindenhol megfigyeltük az adszorpció következtében bekövetkező töltés semlegesítést, majd az azt követő áttöltést. Ezek a jelenségek a diszperziók destabilizálásával, illetve újra stabilizálásával jártak. A DLVO



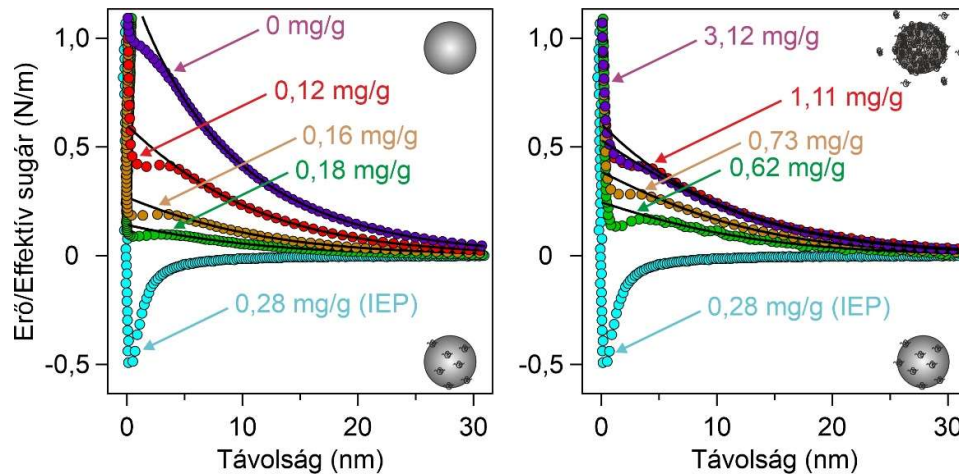
**17. ábra.** Háromdimenziós AFM topográfiai képek SL részecskék felületén adszorbeálódott PAMAM dendrimerekről. Az alkalmazott PAMAM dózis fentről lefelé nő.

eredetű részecskék közötti erőhatások minden rendszerben jelen voltak, emellett legtöbbször a vonzó „patch-charge” kölcsönhatások jelentkeztek, például az SL-PAMAM rendszerben [211], ahol a dendrimer adszorpció foltokban (patch) játszódtott le, és az ellentétesen töltött üres felületi helyekkel (charge) létesülő elektrosztatikus vonzás eredményeként alakult ki jelentősebb kölcsönhatás. A 17. ábrán bemutatott háromdimenziós AFM képeken jól látható, hogy ezeknek a foltoknak a felületi sűrűsége megnő a 10-es generációjú PAMAM dózisének növelésével, ami a „patch-charge” effektus eltűnésével jár az ASP érték körül, mivel kevesebb „charge” áll rendelkezésre. Kolloid próba mérésekkel bizonyítottuk, hogy az ilyen típusú kölcsönhatások dominanciája a PAMAM generációs számának, és ezáltal méretének (molekulatömegének) növekedésével erősödik. Más kutatók megállapították [212], hogy az SL-PAMAM rendszerekben a „patch-charge” vonzás csökken az ionerősség növelésével; ez szintén az effektus elektrosztatikus eredetére utal, ami nagyobb sókoncentrációknál árnyékolásra kerül.

SL részecskék esetében a töltés-aggregáció-erőhatás összefüggések tisztázására lehetőségünk nyílt a polielektrolit adszorpció következtében fellépő erőhatások közvetlen mérésére az AFM alapú kolloid próba segítségével, amit kiegészítettünk DLS és ELS mérésekkel. Ellentétesen töltött lineáris PEI-t



alkalmazva bebizonyítottuk, hogy az adszorpció által okozott töltés semlegesítés után bekövetkező áttöltés során lejátszódott a diszperziók újra stabilizálása [T3]. Tapasztalataink szerint mind a maximálisan adszorbeálódó, mind pedig a töltés semlegesítéshez szükséges polielektrolit mennyisége növekedett az ionerősség növelésével és a molekulatömeg nem befolyásolta ezeket a tendenciákat. A részecskék között ható erőket AFM koloid próba módszerrel meghatározva egyértelműen megállapítottuk, hogy a koloidstabilitás a DLVO elmélettel magyarázható [T28], ahogyan ez a 18. ábrán látható mért és számolt erővonalak egyezéséből ez jól látható.

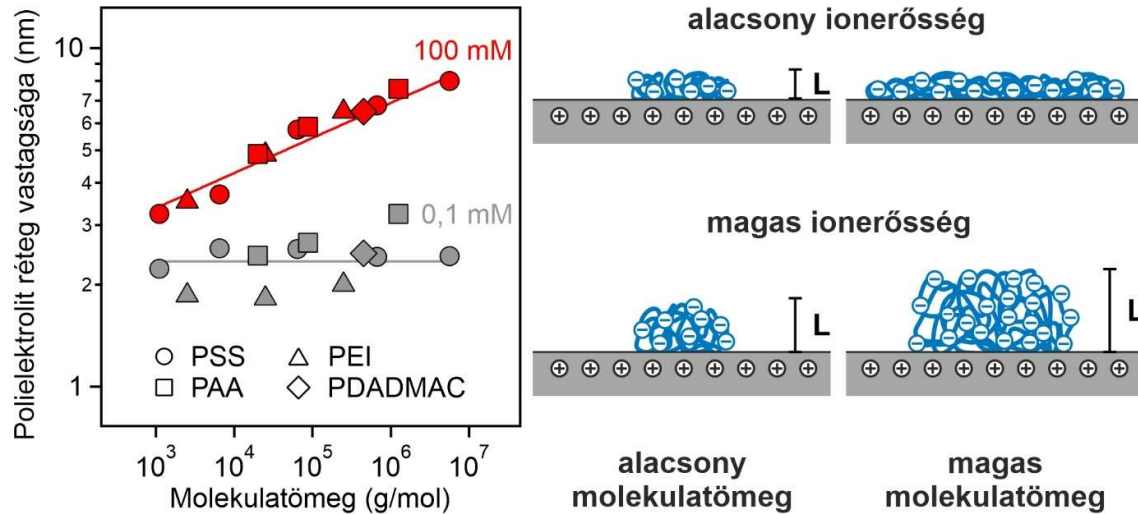


**18. ábra.** SL-PEI rendszerben különböző polielektrolit dózisoknál AFM koloid próba módszerével mért normalizált erők a felülettől való távolság függvényében [T28]. A folytonos vonalak a DLVO elmélettel számított erőket jelölik. A mérések során gyengén savas ( $\text{pH}=4$ ) közeget alkalmaztunk a funkcionális csoportok protonálása, illetve a polielektrolit ionizálása és a felületen való adszorpciója érdekében.

A felülettől pár nanométerre a módszer nem alkalmazható megbízhatóan, távolabb azonban a számolt és mért erővonalak közötti egyezés kielégítő. Ez abból adódik, hogy a gyengén savas közegben a parciálisan ionizált [213] lineáris PEI az adszorpció folyamán homogén réteget képez. Így nem alakulnak ki sem foltok, sem pedig a folyadékfázisba belógó polielektrolit lánc szegmensek. Ennél fogva az uralkodó kölcsönhatások a töltésviszonyoktól függően jól leírhatók (1. egyenlet) az elektromos kettősrétegek közötti taszítással és a van der Waals vonzásokkal. Eszerint megfelelően nagy töltés esetén (az IEP-től távol) a taszító erők, míg az IEP környezetében vonzó erők dominálnak. Az SL-PEI rendszer egyfajta kivételt képezett a vizsgált részecske diszperziók között, mivel szinte minden más esetben tapasztaltuk a nem DLVO típusú erőhatások jelenlétét. Ez valószínűleg a PEI egyenletes felületi eloszlásának köszönhető, illetve annak, hogy a szoros tapadás a felülethez megakadályozza az oldatfázisba belógó lánc szegmensek kialakulását és ezáltal például sztérikus erők megjelenését.

Meg kell jegyezni, hogy a fentiekhez hasonlóan homogén adszorbeált réteg jellemzően csak alacsony ionerősségnél (indifferens elektrolitra vonatkoztatva alacsonyabb, mint 10 mM) alakul ki latex-polielektrolit rendszerekben. Ugyanis DLS mérésekkel [214] változó

ionerősségnél és molekulatömegnél meghatározott adszorbeált polielektrolit rétegvastagság (ami a polielektrolittal borított és az eredeti részecskék hidrodinamikai sugarainak különbsége) adatok arra mutattak rá, hogy a kísérleti körülmények hatással vannak a láncok határfelületi konformációjára (19. ábra) [49, 215].

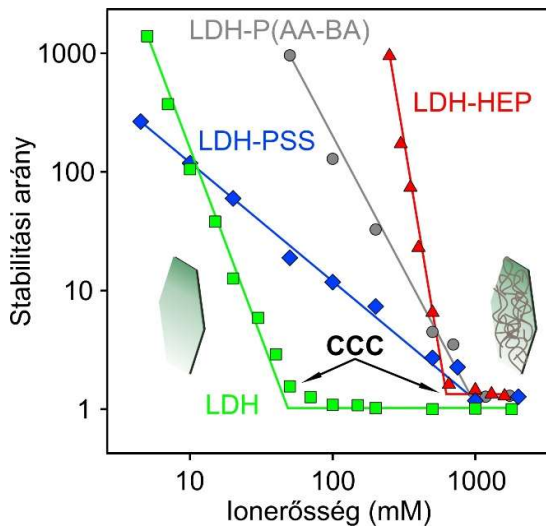


**19. ábra.** Bal oldal: Időfüggő DLS mérésekkel meghatározott latex részecskéken adszorbeálódott polielektrolit rétegek (AL-PSS, AL-PAA, SL-PEI és SL-PDADMAC, az ASP dózist alkalmazva mindegyik mintában) vastagsága (L) a molekulatömeg függvényében magas és alacsony ionerősségeknél. Jobb oldal: Az ionerősség és molekulatömeg variálásának hatására az adszorbeált polielektrolit láncok konformációjában bekövetkező változások sematikus ábrázolása ellentétes töltésű felületre tapadó polielektrolit feltételezése esetében.

A mérési eredmények alapján megállapítottuk, hogy egy adott molekulatömegű makromolekulát tartalmazó részecske-poliektrolit rendszerben általánosságban a rétegvastagság az ionerősséggel növekszik. Ez az oldott ionok töltésárnyékoló hatásának köszönhető azáltal, hogy csökkenti az intramolekuláris taszító erőket és ezáltal az adszorbeált polielektrolit láncok kiterjedt szerkezetet vehetnek fel, ami a részecskék hidrodinamikai méretének növekedését okozzák. Ez a növekedés lényegesen hangsúlyosabb nagyobb molekulatömegű polielektrolitok esetében (19. ábra). Viszont alacsony sókoncentráció alkalmazásakor a molekulatömeg nem befolyásolja jelentősen a rétegvastagságot, mivel egy kompaktabb, a felülethez erősebben tapadó polielektrolit réteg jön létre. Ezek a mért adatokban felismerhető tendenciák jó egyezést mutatnak más kutatók által elméleti számítások során kapott eredményekkel [216].

Az ASP dózisanak megfelelő mennyiségű polielektrolittal borított részecskék esetében három további fontos megállapítást is tehetünk. Először, a felületi funkcionizálás megnövekedett kolloidstabilitást eredményez, amely a CCC értékek növekedéséhez vezet az adszorbeált polielektrolitokat nem tartalmazó kolloidokhoz képest. Ennek mértéke eltérő volt az egyes rendszerekben. Például latex diszperziókban a stabilizáció mérsékelt volt [215, 217], viszont

szervetlen részecskék esetében számottevő eltolódást mértünk a CCC értékekben. Ezt illusztrálom a 20. ábrán P(AA-BA) [T15] és HEP [T31] makromolekulákkal borított LDH részecskék esetében. A CCC értékek növekedése jól illusztrálja, hogy a polielektrolit



**20. ábra.** LDH részecskék és az ASP-vel megegyező koncentrációban alkalmazott polielektrolitokkal módosított származékjai esetében mért stabilitási állandó értékek az ionerősség függvényében egyértékű elektrolitok oldatokban.

Harmadszor, bizonyítottuk, hogy megfelelő ASP dózisokat alkalmazva, ugyanazon részecskén két polielektrolit réteg is felépíthető. Ezt az LDH-PSS-PDADMAC rendszerben alkalmazott szekvenciális adszorpció módszerével [218] valósítottuk meg [T32]. Az egyes komponensek között fellépő elektrosztatikus és egyéb vonzó kölcsönhatásoknak köszönhetően rögzítettünk PSS és PDADMAC polielektrolitokat LDH felületen. A kísérleti körülmények optimalizálásával olyan hordozó rendszereket fejlesztettünk ki, amelyek alkalmasak egy vagy többféle kisebb molekula rögzítésére. Ezeket az eredményeket az 5.5 fejezetben mutatom be. Először bizonyítottuk, hogy két polielektrolit réteg felvitele rendkívüli mértékben megnöveli a diszperziók stabilitását és a képződött kolloidok destabilizálása még magas ionerősségnél sem lehetséges; a diffúzió kontrollált aggregáció állapotát nem értük el magas ionerősségnél sem.

Ahogy az a fentiekből kitűnik, nagyszámú ellentétesen töltött részecske-polielektrolit rendszert vizsgáltunk munkánk során. Az eredmények ismeretében a következő általános következtetéseket vonhatjuk le. A töltésviszonyok és a stabilitási tartományok korrelációja alapján, illetve széles sókoncentrációban elvégzett vizsgálatok eredményeit felhasználva azonosítottuk a polielektrolitok jelenlétében előforduló határfelületi erőhatások eredetét. Ennek alapján elmondhatjuk, hogy nagy töltéssűrűségű SL és AL részecskék alkalmazása során a kolloidstabilitás változása lineáris szerkezetű polielektrolitok (például PEI) jelenlétében a DLVO elmélettel viszonylag jól magyarázható. A kölcsönhatások természete és erőssége azonban jelentősen függ a molekulatölemtől és a diszperzióban oldott ionok

koncentrációjától. Komplexebb szerkezetű makromolekulák (például dendrimerek) használatkor a „patch-charge” eredetű vonzó erők lényegesen befolyásolták az erőhatások mérlegét. Ezek a polielektrolit inhomogén felületi adszorpciója miatt jelentkezhetnek gyengébben töltött (vagyis alacsonyabb elektrokinetikai potenciállal rendelkező) szervesen nanorészecskék (LDH, TNS, TiONW és HNT) esetében is. Megállapítottuk továbbá, hogy a DLVO elmélettel nem magyarázható sztérikus taszító erők megjelenésének is kedvez a mérsékelt felületi töltéssűrűség. Az adszorbeált polielektrolit láncok között így kialakuló elektrosztérikus taszítás (3. ábra) döntően hozzájárult a megnövekedett kolloidstabilitáshoz. Szintén a sztérikus taszító erők megjelenésének kedvez a semleges töltésű monomert is tartalmazó kopolimerek alkalmazása [T1, T30, T46], amelyek adszorpciójával rendkívül stabilis részecske diszperziók előállítása vált lehetségessé. A polielektrolit adszorpció által indukált részecskék közötti kölcsönhatásokat és azok kolloidstabilitásra gyakorolt hatásait összefoglaló cikkekben is publikáltuk [T15, T16, T33].

#### 5.4. Enzimatisz antioxiánsok immobilizálása

Az előzőekben tárgyalt hordozó részecskéket, illetve a módosított származékokat antioxiáns hatású kompozit diszperziók kifejlesztésében használtuk fel. Ennek során a főbb elvárások a megfelelően magas kolloid- és szerkezeti stabilitás, illetve antioxiáns hatás elérése voltak. A következő fejezetben enzimatisz antioxiánsok nanokompozitokba való beépíthetőségét tárgyaljuk a szekvenciális adszorpció módszerét használva [218]. Természetes enzimek immobilizálására elsősorban azok környezeti hatásokra (pH, ionerősség, hőmérséklet, stb.) való érzékenységének csökkentése érdekében van szükség [136]. Emellett az eredményül kapott kompozit anyagok rendelkeznek a heterogén katalizátorok minden előnyével, mint például a könnyebb elválaszthatóság a reakcióelegyeektől. A rögzítéssel járó változásokat az enzimek szerkezetében és ROS elbontó aktivitásában egyaránt teszteltük megfelelő mikroszkópiái, spektroszkópiái és fényszóráson alapuló kísérleti technikákkal, illetve a ROS elbontó képességet biokémiai reakciókban és sejt kultúrákon indukált oxidatív stressz csökkentése során mértük fel. Összességében bebizonyítottuk, hogy antioxiáns enzimek immobilizálása nanorészecske hordozókon nagymértékű aktivitás csökkenés nélkül lehetségessé. Ezen kívül rávilágítottunk, hogy a kifejlesztett biokatalizátor kompozitok elektrolitűző képessége a szintézis körülmények hangolásával növelhető. Az előállított biokatalizátorokat a következő oldalon az 1. táblázatban összegeztük.

Az antioxiáns enzimek közül az egyik legfontosabb a SOD, amely szuperoxid gyök anionokat dizmutál molekuláris oxigénre és hidrogén-peroxidra [130]. Az utóbbi ártalmas termék, amelyet a kataláz enzim bont el. Aktív centrumukban többféle fémiont tartalmazó SOD ismert, munkánk során a réz(II)-cink(II)-SOD enzimmal foglalkoztunk [219]. Rögzítése során sikeresen alkalmaztunk LDH-HEP [T34], TNS-PDADMAC [T35] és HNT-PSP [T4] funkcionális nanorészecskéket, az optimális enzim koncentráció a kompozitokban 10 mg/g volt. Fontos kihangsúlyozni, hogy az előállítás során alkalmazott kísérleti körülményeket (pH, ionerősség, polielektrolit dózis, stb.) minden esetben alapos és kiterjedt vizsgálatok (DLS,

ELS, SEM, TEM és IR) elvégzése után választottuk ki. Az eredmények alapján megállapítottuk, hogy a komponensek mennyiségének és minőségének optimalizálásával a fenti rendszerek mindegyikénél említésre méltó szerkezeti, diszperzió és funkcionális stabilitást jön létre az immobilizálás során. A leghatékonyabb rendszernek az LDH-HEP-SOD hibrid bizonyult [T34]. Egyrészt a polielektrolit adszorpció extrém magas sótűrő képességet eredményezett (989 mM CCC a 29 mM-al szemben, amit az LDH-SOD kompozitnál mértünk). Másrészt az IC<sub>50</sub> adatokkal (enzim koncentráció, amely szükséges a tesztreakcióban képződő szuperoxid gyök anionok koncentrációjának 50%-os csökkentéséhez [182]) kifejezett dizmutáló képesség is megközelítette (96 µg/l) a természetes SOD esetében hordozó nélkül mért értéket (69 µg/l). Habár SOD enzimek immobilizálásával kapcsolatos korábbi eredmények fellelhetőek a szakirodalomban [137-139, 143, 144], ezek között nem található olyan rendszer, amelyben mind a kolloid, mind pedig a funkcionális tulajdonságok hasonlóan kiemelkedőek lettek volna.

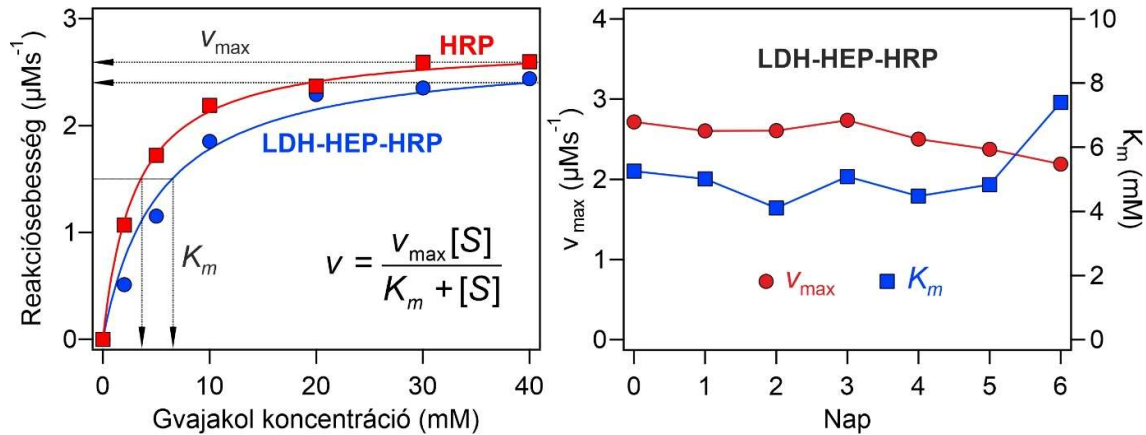
**1. táblázat.** A doktori dolgozatban tárgyalt immobilizált enzim rendszerek.

<b>hordozó</b>	<b>polielektrolit</b>	<b>enzim</b>	<b>összetétel<sup>a</sup></b>	<b>cikk</b>
LDH	HEP	SOD	LDH-SOD-HEP	[T34]
LDH	HEP	HRP	LDH-HEP-HRP	[T36]
LDH	HEP, PLL	SOD, HRP	LDH-HEP-HRP-PLL-SOD-HEP	[T39]
TNS	PDADMAC	SOD	TNS-PDADMAC-SOD	[T35]
TNS	PDADMAC	HRP	TNS-HRP-PDADMAC	[T37]
TNS	PDADMAC, PSS	SOD, HRP	TNS-PDADMAC-SOD-PSS-HRP TNS-HRP-PDADMAC-SOD-PSS	[T40]
HNT	PSP	SOD	HNT-PSP-SOD	[T4]
SL	HEP	HRP, PPN	SL-PPN-HEP-SOD	[T41]

<sup>a</sup>A komponensek sorrendje az elnevezésekben egyezik a szekvenciális adszorpció során alkalmazott sorrenddel.

A torma peroxidáz (HRP) egy olyan metalloenzim, mely aktív centrumában porfirin gyűrű nitrogén donoratomjai által koordinált vas(III)-ionokat tartalmaz [220]. Működése során különféle molekulák oxidációját katalizálja hidrogén-peroxid jelenlétében [221]. A biológiai jelentősége mellett fontos megemlíteni, hogy széles körben kerül felhasználásra számos iparágban, oxidációs folyamatokban alkalmazzák. Viszonylag magas IEP értéke miatt semleges közegben pozitív töltésű [222], ami viszonylag ritka a természetes enzimek között. Ennél fogva immobilizálásához negatív töltésű LDH-HEP [T36] és TNS-PDADMAC [T37] részecskéket alkalmaztunk. Mindkét rendszer megfelelő hordozónak bizonyult, az optimális enzimtartalom 10 mg/g-nak adódott, ugyanúgy, mint a fentiekben tárgyalt SOD esetében. Ez az enzimtartalom kellően magas a hatékony peroxidáz aktivitás eléréséhez, viszont kellően

alacsony ahhoz, hogy az enzim adszorpciója az ellentétesen töltött hordozók felületén ne okozzon olyan mértékű töltéscsökkenést, amely a részecskék destabilizációjával jár. Mind a TNS-HRP-PDADMAC, mind pedig a LDH-HEP-HRP esetében elmondhatjuk, hogy számottevő peroxidáz aktivitást mértünk a kompozitok esetében (lásd az LDH-HEP-HRP rendszerre vonatkozó grafikont a 21. ábrán).



**21. ábra.** Bal oldal: HRP és LDH-HEP-HRP aktivitása gvajakol szubsztrátum hidrogén-peroxid jelenlétében történő oxidációja során [T36]. A folytonos vonalak a Michaelis-Menten mechanizmus (beszúrt képlet, ahol  $v_{\max}$  a maximális reakciósebesség, míg  $K_m$  a Michaelis konstans) alkalmazásával számított értékeket ábrázolják. Jobb oldal: A peroxidáz aktivitás időfüggése a  $v_{\max}$  és  $K_m$  értékekkel kifejezve.

A számított és mért adatok összehasonlításával megállapítottuk, hogy a kompozitok működése a gvajakol szubsztrátum oxidációja során a Michaelis-Menten mechanizmust [223] követi. Amint az a 21. ábrán is látható az LDH-HEP-HRP rendszerre, az enzim kis mértékben vesztett az aktivitásából az immobilizálás során, viszont a maximális reakciósebesség és Michaelis konstans értékek nem változtak számottevően 6 napon keresztül. A TNS-HRP-PDADMAC peroxidáz aktivitásának mérése után eredményül azt kaptuk, hogy a kompozitban rögzített enzim működése szélesebb pH tartományban biztosított, mint a természetes enzim, vagy a TNS-HRP hibrid esetében [T37]. Ezekből az eredményekből is kiténik a polielektrolitok alkalmazásának fontossága, mivel azok nem kizárólag a kolloidstabilitás biztosítására szolgálnak, hanem a szerkezeti stabilitás kialakításához is hozzájárulhatnak. Összességében elmondhatjuk, hogy a HRP rögzítése sikeres volt, az előállított kompozitok rendelkeznek azokkal a tulajdonságokkal, amelyek alapján, további vizsgálatok elvégzése után, alkalmasak lehetnek ipari oxidáló-, vagy hidrogén-peroxid eltávolító szerként.

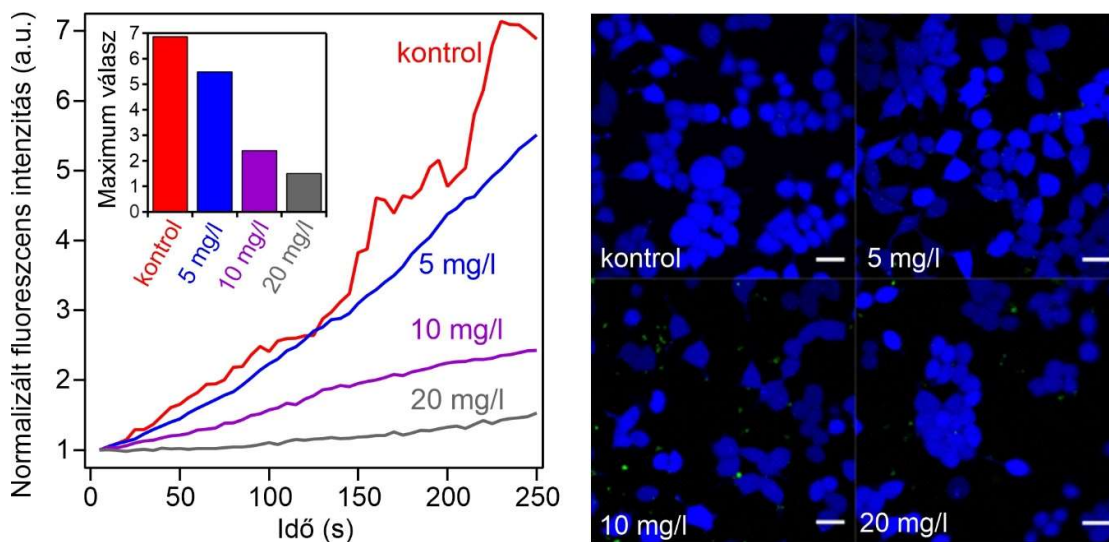
A munka következő fázisában biomimetikus megközelítést alkalmazva, elvégeztük SOD és HRP enzimek együttes immobilizálását. Ezzel a sejten belüli állapotokat utánoztuk, ahol többféle antioxidáns enzim tandem reakciókban végzi a ROS lebontást. A szintézishez használt szekvenciális adszorpció módszerét nagy kiterjedésű felületeket alkalmazva már felhasználták a korábbiakban [218], viszont az általunk publikált eredmények az elsők között vannak, amelyek során ezt a módszert lamellás nanorészecskéken enzimek együttes megkötésére alkalmazták.

LDH hordozóra rögzítettünk SOD és HRP enzimeket HEP és polilizin (PLL) polielektrolitok segítségével, az előállítás során az LDH-HEP-HRP-PLL-SOD-HEP sorrendet alkalmazva [T39]. Emellett szintetikus polielektrolitokat és TNS részecskéket használtunk fel HRP és SOD enzimek együttes immobilizálására kétféle szekvencia (TNS-PDADMAC-SOD-PSS-HRP és TNS-HRP-PDADMAC-SOD-PSS) szerint [T40]. Általánosságban mikroszkópiai (TEM), spektroszkópiai (UV-Vis) és fényszóráson (ELS és DLS) alapuló módszerekkel megállapítottuk, hogy az előállított kompozit részecskék homogén, nem aggregálódó, diszperziókat alkottak. Enzim kioldódást nem tapasztaltunk egyik esetben sem. Bebizonyítottuk, hogy a szekvenciális adszorpció során felhasznált komponensek sorrendjének változtatásával az antioxidáns aktivitás növelhető. Az előállítás során minden egyes lépésben meghatároztuk a töltés- és aggregációs viszonyokat, mivel a módszer alapvető feltétele, hogy a részlépések során ne lépjen fel részecske aggregáció, illetve, hogy kialakuljon a szükséges töltésmérleg a következő komponens beépítéséhez Coulomb-féle vonzó kölcsönhatások segítségével.

Biokémiai tesztreakciókkal bebizonyítottuk, hogy az előállított anyagok (LDH-HEP-HRP-PLL-SOD-HEP [T39], TNS-PDADMAC-SOD-PSS-HRP és TNS-HRP-PDADMAC-SOD-PSS [T40]) mind a szuperoxid gyök anionok dizmutációjában, mind pedig gvajakol szubsztrátum hidrogén-peroxid jelenlétében történő oxidációjában a natív enzimekhez hasonló aktivitással rendelkeznek. Fontos eredményünk, hogy ezáltal kétféle antioxidáns hatással (szuperoxid gyök anion dizmutáció és peroxidáz aktivitás) rendelkező rendszereket kaptunk. Például az LDH-HEP-HRP-PLL-SOD-HEP esetében a SOD aktivitást kifejező  $IC_{50}$  érték hasonló tartományba esett (78  $\mu\text{g/l}$ ), mint a természetes enzimnél mért érték (69  $\mu\text{g/l}$ ). A peroxidáz aktivitást kifejező Michaelis konstans (2,64 és 1,56 mM, a kompozitra és a HRP-re, egyenként) és maximális reakciósebesség (3,8 és 4,6  $\mu\text{M/s}$ ) értékekre hasonló megállapítások tehetők.

A következő lépésben az oxidatív stressz csökkentő képességet HeLa (méhnyakrák) sejt kultúrákon teszteltük az LDH-HEP-HRP-PLL-SOD-HEP esetében [T39]. Itt három kérdésre kerestünk választ: a kompozitok bejutnak-e a sejtbe, ott oxidatív stressz csökkentő hatást kifejtenek-e, illetve van-e mérhető toxicitásuk. Eredményeinkkel megmutattuk, hogy 1 órás inkubálási idő alkalmazása után a kompozit bejut a sejtekbe. A mérések során sejt lízist végeztünk, majd az oldhatatlan részeket centrifugálással eltávolítottuk és a gvajakol tesztet [186] alkalmazva megállapítottuk, hogy a sejt tartalmaz-e HRP enzimet. Ennek jelenléte egyértelműen jelzi a kompozit bejutását a sejtbe. Azt is megállapítottuk, hogy mesterségesen indukált oxidatív stressz nagymértékben csökkenthető a kompozit alkalmazásával. Ennek során a ROS-érzékeny  $\text{H}_2\text{DCF}$  (2',7'-dikloro-dihidrofluorescein diacetát) DCF (2',7'-diklorofluorescein) molekulákká való oxidációját követtük fluoreszcens mikroszkóp segítségével. A LDH-HEP-HRP-PLL-SOD-HEP hibridet különböző koncentrációban alkalmazva a mért fluoreszcens intenzitás értékek csökkenését tapasztaltuk és 20  $\text{mg/l}$  dózisonál az oxidatív stressz az optimális szintre csökkent (22. ábra).





**22. ábra.** Bal oldal: DCF jelenlétének köszönhető fluoreszcencia intenzitás időbeli változása különböző koncentrációjú LDH-HEP-HRP-PLL-SOD-HEP jelenlétében. A beszúrt ábrán a kísérlet végén mért intenzitások láthatóak. Jobb oldal: HeLa sejtkultúrák képei különböző kompozit koncentrációknál. Sejthalál esetén zöld (apoptózis) vagy piros (nekrózis) színeződés következne be, míg a kék szín egészséges sejtek jelenlétére utal [T39].

A fenti eredmények ismeretében felvetődik a kompozit citotoxicitásának kérdése. Ugyanis sejthalál esetén nem történik ROS termelés, és az eredmények azt sugallhatják, hogy az anyagunk elbontja a ROS molekulákat, holott azok nem is képződnek a menadion hatására. Bemutattuk, hogy a kompozitok sejtnövekedést gátló hatása elhanyagolható az alkalmazott kísérleti körülmények mellett. Ezeket a méréseket a sztenderd apoptózis-nekrózis teszttel végeztük. A 22. ábrán jól látható, hogy a sejtek elszíneződése nem volt észlelhető, illetve a kontrol kísérlethez hasonló tulajdonságú sejteket figyeltünk meg konfokális mikroszkóp segítségével különböző LDH-HEP-HRP-PLL-SOD-HEP koncentrációknál. Kimutattuk, hogy a kompozit 20 mg/l dóziséig nem mutat citotoxikus hatást. Az előzőek szerint ugyanennél a koncentrációnál optimális a kifejtett oxidatív stressz csökkentő hatás.

Habár antioxidáns enzimek együttes rögzítésével foglalkozó tanulmányok megtalálhatóak a szakirodalomban [148, 150, 151, 224, 225], az általunk előállított LDH és TNS alapú, SOD és HRP enzimeket tartalmazó kompozitok számos előnnyel rendelkeznek a korábban publikált rendszerekhez képest. Az egyik legfontosabb eredmény, hogy a szekvenciális adszorpció módszere nem igényli bonyolult kémiai reakciók lejátszódását, mivel az egyes lépésekben használt alkotó elemek főként fiziszorpcióval kapcsolódnak. Szintén fontos megemlíteni, hogy a hordozó nanorészecskék egyszerűen és olcsón előállíthatóak, akár nagyobb mennyiségben is, ami a kompozitok ipari felhasználása esetén lenne előnyös. A kifejlesztett hibridek lehetséges alkalmazása a legtöbb esetben folyadék közegben várható. Ennek ellenére a korábban publikált kaszkád rendszerek kolloidstabilitásának jellemzésére nem végeztek átfogó vizsgálatokat, ami felveti a részecske aggregáció esetén fellépő káros következmények problémáját. Az általunk előállított kettős enzimaktivitással rendelkező anyagok esetében viszont a kísérleti körülmények hangolásával időben stabilis diszperziókat kaptunk.



A papain (PPN) enzim antioxidáns hatása jól ismert [226], mégis hidrolitikus aktivitása az, ami miatt a PPN az egyik iparban legtöbbször használt enzim [227, 228]. ELS és DLS mérésekkel kimutattuk, hogy a PPN határfelületi viselkedése eltérő a fejezetben tárgyalt enzimekétől, mivel SL részecskék felületéhez való kötődése során töltés semlegesítés, illetve áttöltés játszódott le [T38]. Az aggregációs viszonyok is eszerint alakultak, instabil diszperziókat figyeltünk meg az IEP közelében, míg stabilisakat ettől kisebb és nagyobb PPN dózisoknál. Megállapítottuk, hogy a felületi töltés és aggregációs viszonyok ilyen jellegű összefüggése alapján a PPN a polielektrolitokhoz hasonlóan viselkedik az ellentétesen töltött részecskék felületén. Enzim aktivitás vizsgálatok eredményei alapján kimutattuk, hogy az előállított SL-PPN kompozit jelentős proteáz- és antioxidáns aktivitással is rendelkezik. A munka folytatásaként a szekvenciális adszorpció módszerét alkalmazva együttesen rögzítettünk PPN és HRP enzimeket SL hordozókon HEP polielektrolit segítségével [T41]. A PPN erős felületi adszorpciója miatt ebben az esetben csak egy polielektrolit alkalmazása volt indokolt. Az előállított SL-PPN-HEP-HRP kompozitban kötött enzimek kioldódását nem tapasztaltuk, illetve az anyag só indukált aggregációra való érzékenysége elhanyagolható volt. Bebizonyítottuk továbbá, hogy az SL-PPN-HEP-HRP mind hidrolitikus, mind pedig peroxidáz hatással rendelkezik, amely nem lenne lehetséges a PPN és HRP enzimek együttes oldatbeli alkalmazásával az előbbi fehérjebontó hatása miatt, amely a HRP enzim lebomlásához és aktivitásának elvesztéséhez vezet. Mivel mindkét enzim ipari felhasználása külön-külön igen jelentős, együttes alkalmazásuk lehetőséget biztosíthat költség- és/vagy időhatékony enzimatisztálási eljárásoknak főként az élelmiszeriparban [229, 230].

A fenti eredmények alapján megállapíthatjuk, hogy az enzimek rögzítése kompozitokban sikeres volt egy és több biokatalizátor immobilizálása esetében is. Az előállított rendszerek antioxidáns hatása jelentős, illetve rendelkeznek megfelelő kolloidstabilitással, avagy só indukált aggregációval szemben ellenállóak. Itt kell megjegyezni, hogy a szerkezeti és a termikus stabilitásuk még nem ideális, például az aktív centrum geometriája megváltozhat koordinációra képes molekulák jelenlétében vagy torzulhat magasabb hőmérsékleten, ami aktivitásvesztést jelent. A következő fejezetben tárgyalt molekuláris és mesterséges antioxidánsok alkalmazásával ezekre a problémákra is kerestük a megoldást.

## 5.5. Molekuláris és mesterséges antioxidánsok rögzítése kompozitokban

### *Exogén antioxidánsok*

Az enzimatisztálási antioxidánsok mellett fontos oxidatív stressz csökkentő hatóanyagok a molekuláris antioxidánsok [158]. Néhány ilyen típusú exogén antioxidáns szerkezeti képlete látható a 7. ábrán. Ezek ROS lebontó hatékonysága ugyan elmarad a korábban tárgyalt enzimekétől, viszont élelmiszerekben és egyéb növényi forrásokban viszonylag magas koncentrációban előfordulnak és ennél fogva utánpótlásuk megfelelő dózisban lehetséges [132]. A gyengébb hatékonysághoz hozzájárul, hogy szerkezetileg nem mindig stabilisak, illetve más esetben alacsony vízoldhatóságuk gátolja a terápiás alkalmazásukat élő szervezetekben.

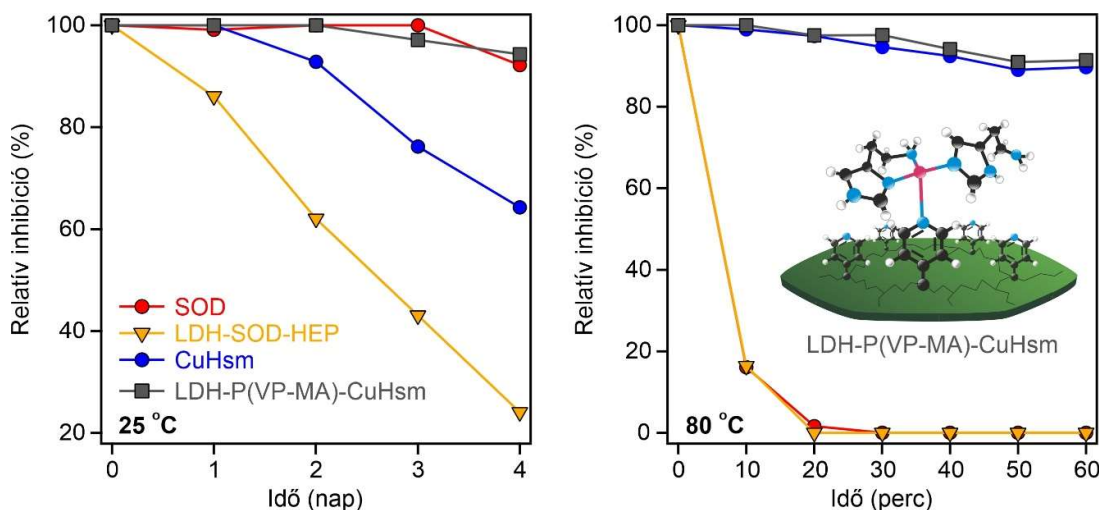
Munkánk során jellemeztük természetes forrásokból kivonható számos molekuláris antioxidáns aktivitását [T43]. Szobahőmérsékletű etanolos extrakciót alkalmazva 16, a Dél-Alföldön termesztett növényből vontunk ki hatóanyagokat, közöttük antioxidáns hatásúakat. Az extraktumokban fázisseparatoráció játszódott le. A szabadgyök elbontó tulajdonságokat egy jól ismert tesztreakcióban 1,1-difenil-2-pikrilhidrazil (DPPH) gyök alkalmazásával jellemeztük [184], majd a hatásos koncentrációkat ( $IC_{50}$ , ami a DPPH gyökök 50%-ának elbontásához szükséges antioxidáns mennyiség) összehasonlítottuk az aszkorbinsavra kapott értékekkel. Bizonyítottuk, hogy az extrakció során képződő fázisok (felső folyadék és alsó, szilárd növényi részeket is tartalmazó) antioxidáns hatást mutattak, illetve a legtöbb esetben a tiszta folyadék fázis aktivitása volt a magasabb a DPPH elbontás során. Az egyes növényekben megtalálható molekulák és az aktivitási eredmények összevetéséből megállapítottuk, hogy a közönséges dió magas polifenol- és peptidtartalma az aszkorbinsavhoz képest 44%-kal hatásosabb gyökfogó képességet eredményezett. Ez az extraktum bizonyult a legaktívabbnak a vizsgált növényi rendszerek közül.

A molekuláris antioxidánsok vízdoldhatósága gyakran alacsony, ezért is végeztünk etanol közegű extrakciót a fenti kísérleteknél. Az alacsony oldhatóság meggátolja nagy dózisz felhasználásukat, amelyek terápiás célok esetében előnyösek lennének [160]. Ez igaz például az ellagsavra (EA) is (7. ábra) [231]. Ezt a problémát az EA LDH rétegek közötti immobilizálásával oldottuk meg, illetve a szerkezeti és morfológiai tulajdonságokat szerves oldószerekkel való kezeléssel javítottuk [T44]. Kimutattuk, hogy az EA interkalálása a rétegek közé sikeres volt, viszont ez a folyamat gyűrűfelnyílást eredményezett, ami viszont nem befolyásolta döntően az aktivitást sem DPPH tesztreakciókban, sem pedig réz(II)-ion redukciós antioxidáns kapacitás (CuPRAC [232]) mérésekben. Bebizonyítottuk, hogy jelentős EA koncentráció alkalmazható vizes közegben az LDH-EA kompozitok diszpergálásával. Míg az EA vízdoldhatósága 10 mg/l [231], addig az LDH-EA diszperziókban 5 g/l koncentrációt is elértünk, ami figyelembe véve a kompozit EA tartalmát, közel 90-szeres koncentráció növekedést jelent vizes közegben. Az előállított LDH-EA kolloidstabilitását polielektrolitok segítségével optimalizáltuk [T45]. Kimagasló sótűrő képesség (1 M koncentrációnál magasabb CCC értékeket kaptunk egyértékű elektrolit oldataiban) alakult ki a PEI és P(AAM-DADMAC) polielektrolitokkal történő funkcionálizálása után. Ez az ASP-nek megfelelő dózisonál jelentkező erős elektrosztatikus taszító erőknek köszönhető. Viszont a PSP-vel való felületi kezelés után a kolloidstabilitás nem növekedett az etanollal kezelt LDH-EA részecskéhez képest. Az LDH-EA-PEI és LDH-EA-P(AAM-DADMAC) nanokompozitok antioxidáns hatását DPPH gyökök lebontásában és CuPRAC reakciókban tesztelve bebizonyítottuk, hogy az EA jelentősen nem veszített az aktivitásából az immobilizálás és a polielektrolittal való felületi funkcionálizálás során, illetve stabilis vizes diszperzióban az oldhatósági határának többszörösére növeltük a koncentrációját, amint azt a fentiekben említettük. Habár EA immobilizálás témában korábban is történtek kutatások [163-165], ezek egyik hiányossága a kolloidstabilitással kapcsolatos megfontolások figyelmen kívül hagyása volt, ami nagyban meggátolja az EA tartalmú kompozitok alkalmazását vizes közegben, illetve elektrolitok és egyéb aggregációt okozható vegyületek jelenlétében.

### Enzimutánzó fémkomplexek

Mivel az antioxidáns metalloenzimek (SOD, HRP, CAT, stb.) ROS lebontó képességéért az aktív centrumban található fémionok felelősek [219, 220, 233], enzimutánzó fémkomplexek [234-236], illetve hasonló tulajdonságú fémionokat tartalmazó úgynevezett nanozyme részecskék [20, 170, 174] alkalmazhatóak a biokatalizátorok szerkezeti és/vagy funkcionális utánzására. A nanozyme-ok alkalmazásával a környezeti hatásokra rendkívül érzékeny természetes enzimek kiválthatóak szélsőségesebb kísérleti körülmények között is működőképes antioxidáns hatású anyagokkal és molekulákkal. Saját és a korábbiakban közölt eredményeket a témában egy összefoglaló cikkben is ismertettük [T42].

Mivel a réz(II)-ionok felelősek alapvetően a SOD enzim működésért, bizonyítottan SOD aktivitással rendelkező 1:2 fém:ligandum arányban összemért réz(II)-hisztamin komplexet (CuHsm) rögzítettünk P(VP-MA) polielektrolittal módosított LDH nanorészecskéken [T46]. A polielektrolit szerepe összetett volt. Egyrészt a negatívan töltött metilakrilát csoportok biztosították az erős rögzítést a hordozóhoz, másrészt a piridin-nitrogének koordinálódtak a fémkomplexben található réz(II)-centrumhoz, így elsőrendű kötésen keresztül egy stabilis szerkezet alakult ki (sematikus ábrázolásért lásd 23. ábra), minek hatására nem tapasztaltuk a komplex kioldódását a kompozitból.



**23. ábra.** Időfüggő SOD aktivitás mérések eredményei a nitro-kék tetrazólium (NBT)-szuperoxid gyök anion reakció inhibíciójával kifejezve [T46]. Bal oldal: 25 °C-on 4 napon át kivitelezett mérések eredményei. Jobb oldal: 80 °C-on 1 órán át mért értékek. A beszúrt rajzon az LDH-P(VP-MA)-CuHsm kompozit sematikus szerkezete látható.

A réz(II)ion közvetlen környezetében kialakuló koordinációs geometriát ESR vizsgálatokkal határoztuk meg, míg a sikeres komplex immobilizálást IR spektroszkópiai mérésekkel is bizonyítottuk. Bemutattuk, hogy a polielektrolit dózis optimalizálásával, illetve az ASP dózissnál való alkalmazásával, nagy stabilitású kolloid rendszereket tudunk létrehozni. A sóoldatokban mért 610 mM CCC érték alapján elmondhatjuk, hogy az előállított LDH-P(VP-MA)-CuHsm kompozit elektrolit oldatokban is hatékonyan alkalmazható. Továbbá

bebizonyítottuk, hogy a komplex immobilizálás során nem veszített az aktivitásából, sőt az NBT-szuperoxid gyök tesztreakcióban [182] mért  $IC_{50}$  értéke  $0,260 \mu\text{M}$ -ról  $0,097 \mu\text{M}$ -ra csökkent, ami jelentős aktivitás növekedést jelent. Ezen kívül megfelelően magas koncentrációknál mindkét anyag esetében közel 100%-os inhibíciót értünk el.

A CuHsm, LDH-P(VP-MA)-CuHsm, SOD és LDH-SOD-HEP anyagok szuperoxid lebontó képességét teszteltük időfüggő mérésekben is (23. ábra). A  $25 \text{ }^\circ\text{C}$ -on végzett SOD aktivitás vizsgálatokkal kimutattuk, hogy az LDH-P(VP-MA)-CuHsm hatékonyságát négy napon keresztül megőrzi, hasonlóan a természetes enzimhez. Ezzel szemben az LDH-SOD-HEP kompozit aktivitása ez alatt az idő alatt közel 80%-kal csökken, míg a nem immobilizált CuHsm is jelentősen veszített dizmutáló képességéből. Szintén érdekes eredmények születtek a  $80 \text{ }^\circ\text{C}$ -on egy órán keresztül mért aktivitások elemzése során. Kimutattuk, hogy a natív SOD és immobilizált változata (LDH-HEP-SOD) ilyen körülmények között 20 perc alatt denaturálódik, viszont az általunk kifejlesztett nanokompozit megtartja aktivitását és hatékony antioxidáns marad a magas hőmérséklet ellenére is. Az idő- és hőmérsékletfüggő mérések eredményeit összegezve megállapíthatjuk, hogy a LDH-P(VP-MA)-CuHsm nanokompozit működési stabilitása jobb akár a természetes, akár az immobilizált SOD enzim esetében tapasztalttól. Amellett, hogy több napon keresztül és magasabb hőmérsékleten is megőrzi az aktivitását, rendelkezik a heterogén katalizátorokra jellemző olyan előnyökkel, mint például a könnyebb elválaszthatóság a reakcióelegytől, illetve az ipari folyamatokban való alkalmazás lehetősége a magas kolloidstabilitás miatt.

Hasonlóan az előző fejezetben tárgyalt antioxidáns enzim kaszkád rendszerekhez, a szekvenciális adszorpció módszerét alkalmazva enzimutánzó fémkomplexek együttes rögzítését is elvégeztük. A SOD utánzó réz(II)-bipiridil (CuBpy) és a HRP utánzó vas(III)-citrát (FeCit) tartalmú komplexeket LDH hordozón PSS és PDADMAC polielektrolitok segítségével immobilizáltuk [T47]. Az egyes komponensek felhasználandó dózisait ELS és DLS mérések eredményei alapján határoztuk meg, azt az elvet követve, hogy minden egyes részrendszernek megfelelő töltéssel rendelkező stabilis kolloidot kellett alkotnia. Az előállított LDH-PSS-CuBpy-PDADMAC-FeCit kompozit SOD és HRP utánzó képességét, illetve a DPPH és CuPRAC tesztekben mutatott aktivitását felmértük. Eredményeink alapján bizonyítottuk, hogy tömegkoncentrációban kifejezve a kompozit részecske közel azonos (sőt valamivel jobb) szuperoxid gyök lebontó képességgel rendelkezett ( $IC_{50}$  érték  $26 \mu\text{g/l}$ ), mint a SOD enzim ( $69 \mu\text{g/l}$ ). Ez jelentős eredmény, ugyanis a szakirodalmi adatok között immobilizált SOD utánzó fémkomplexek esetében nem található a természetes enzimhez hasonló aktivitás [154, 156, 157, 237].

ESR spektroszkópiai vizsgálatokkal bebizonyítottuk, hogy a kiemelkedő szuperoxid gyök dizmutáló tulajdonság az immobilizált fémkomplexek között kialakuló intermolekuláris kölcsönhatásnak köszönhető. Ez abban nyilvánul meg, hogy az immobilizálás során a Cit ligandum egyik donoratoma koordinációs kötést alakít ki a CuBpy komplexben található réz(II) ionnal, így megváltoztatva annak koordinációs geometriáját, illetve redox aktivitását. Ezt a megállapítást támasztja alá az a megfigyelésünk is, hogy a nem immobilizált komplexek

esetében annál a koncentrációnál, amelynél a LDH-PSS-CuBpy-PDADMAC-FeCit kompozit az NBT-szuperoxid gyök anion reakciót 100%-ban inhibálta, nem volt mérhető számottevő aktivitás. A további mérési eredményeink azt mutatták, hogy a kompozit szelektív SOD aktivitással rendelkezik, ugyanis a HRP és CuPRAC tesztreakciókban nem mutatott aktivitást, míg a DPPH teszt során csupán a gyökök 55%-ának elbontására volt képes elfogadható időn belül.

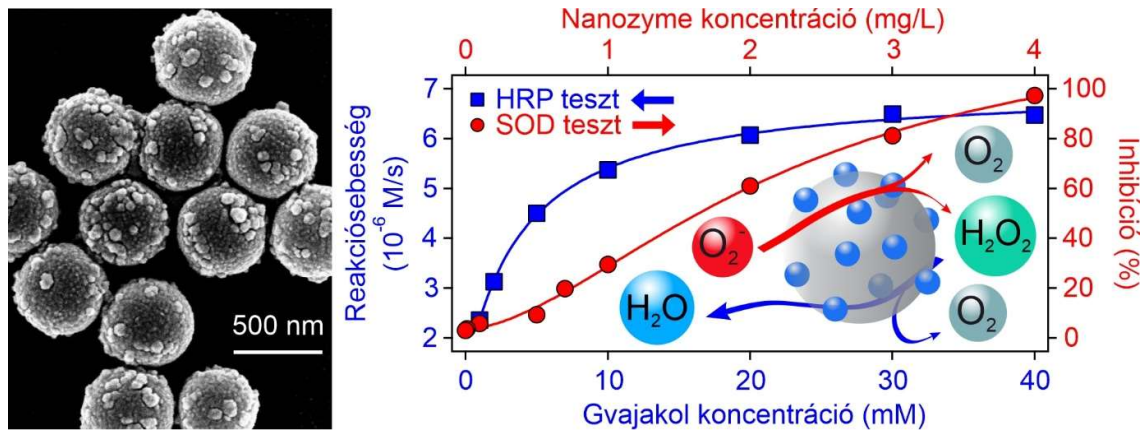
A fenti eredményekből is kitűnik, hogy lehetséges a drága, érzékeny és nehezen hozzáférhető természetes enzimek helyettesítése fémkomplexekkel. Munkánk során az előállított fémkomplex tartalmú kompozitok széleskörű vizsgálatára került sor. A szerkezetet érintő aspektusok mellett optimalizáltuk a kolloidstabilitást. A LDH-P(VP-MA)-CuHsm esetében jelentős funkcionális stabilitásról beszélhetünk mind időben, mind pedig a hőmérséklet függvényében. A LDH-PSS-CuBpy-PDADMAC-FeCit előállítása során olyan szerkezet jött létre, amely szelektíven dizmutálja a szuperoxid gyök anionokat. Mind a két eredmény jelentős előrelépést jelent, főleg az ipari folyamatokban felhasználható antioxidánsok fejlesztésének területén.

#### *Antioxidáns nanozyme-ok*

Ahogy az a 2. fejezetben is említésre került, az enzimutánzó anyagok fejlesztésének egyik újszerű iránya olyan nanoméretű nanozyme-ok előállítása, amelyek bár szerkezetileg teljesen különbözőek, az enzimek aktív centrumában található fémionokat tartalmaznak és így enzimszerű működéssel rendelkeznek [15]. Hangsúlyozni kell azonban, hogy ebben az esetben maga a jellemzően egyetlen fázist tartalmazó nanorészecske felelős a működésért, illetve katalitikus aktivitással rendelkező más komponens bevonása nem szükséges az előállítás során. Hasonló megfontolásokat követve, antioxidáns enzimek működését utánozni képes nanoanyagok előállítása viszonylag nagy figyelmet kapott a kutatói társadalomban [20]. Ennek során különféle összetételű és alakú nanorészecskéket [170-172, 238, 239], illetve kompozitjait [240-242] állították elő (7. ábra). A viszonylag nagyszámú publikáció ellenére két területen továbbra sem történt előrelépés az antioxidáns nanozyme anyagok fejlesztése során. Az első a részecskék formulázása (például inert hordozón való rögzítés), amely főként ipari folyamatokban szükséges ahhoz, hogy áramlásos üzemmódban használt reaktorokban váljanak használhatóvá. A második olyan nanozyme-ok kifejlesztése, amelyek az aggregációval szemben ellenállóak. Ez utóbbi rendkívül fontos bármely típusú felhasználás során, hiszen a részecskék aggregálódása során képződő klaszterek aktivitása kisebb a fajlagos felület csökkenése miatt, illetve a folyamat fázis szeparációt eredményezhet. Munkánk során ezeken a területeken kíséreltünk meg előre lépni enzimutánzó nanorészecskék polimer alapú hordozókra való rögzítésével.

Már egy ideje ismert, hogy a ferro- és ferricianidot is tartalmazó PBP anyagok ROS lebontó aktivitással rendelkeznek [175, 243]. Habár polimer funkcionizált PBP részecskéket korábban sikeresen előállítottak [244, 245], átfogó kolloidkémiai jellemzésük vizes diszperziókban nem történt meg. Munkánk során PBP mintákat együttes lecsapás módszerével állítottunk elő, a kialakult szerkezetről röntgen fotoelektron- (XPS) és UV-Vis spektroszkópia

segítségével kaptunk információkat, amelyek alapján megállapítottuk a sikeres PBP képződést [T48]. Ugyan limitált kolloidstabilitása miatt alkalmazása nagy dózisban nem lehetséges, latex részecskékre történő immobilizálásával ez lehetővé vált. A 42 nm hidrodinamikai sugarú PBP részecskéket nagyobb méretű (249 nm) AL hordozón rögzítettük elektrosztatikus eredetű vonzó erők segítségével heteroaggregáció módszerével, amely során stabilis, negatív töltésű PBP és pozitív AL részecskék diszperzióit elegyítettük különböző arányban. Kimutattuk, hogy 600 mg/g PBP dózissal elhanyagolható az AL-PBP kompozitok aggregációja a magas pozitív töltéssűrűség és az ebből következő jelentős elektromos kettősréteg tasztítás miatt. Megmutattuk, hogy a nanozyme-ok egyenletesen adszorbeálódnak a hordozó latex felületén ezen kísérleti körülmények mellett, amint az jól látható a 24. ábrán bemutatott SEM felvételen is.

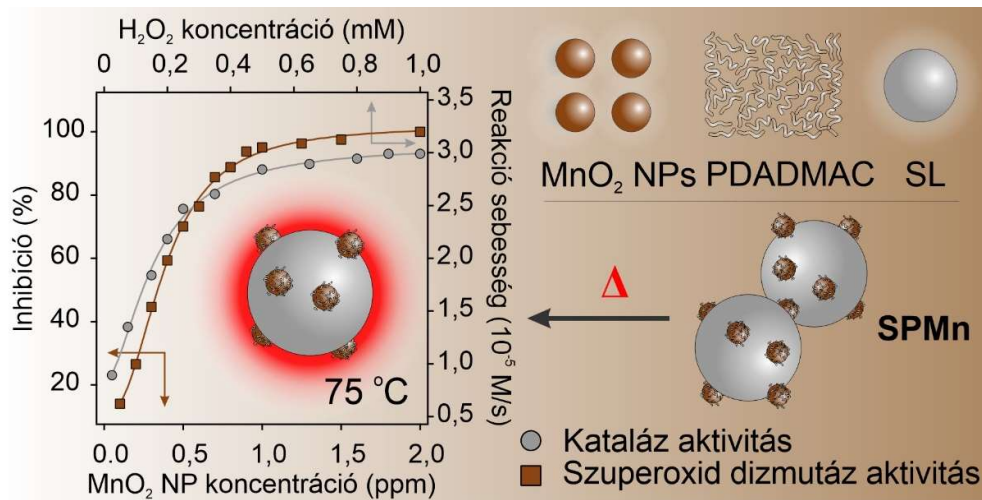


**24. ábra.** Bal oldal: Az SL-PBP kompozit SEM felvétele. Jobb oldal: a gvajakol oxidáció sebessége a szubsztrátum koncentrációjának függvényében (HRP aktivitás, bal oldali és alsó tengelyek, négyzet szimbólum), illetve NBT-szuperoxid gyök anion reakció inhibíciója a PB koncentráció függvényében (SOD aktivitás, jobb oldali és felső tengelyek, kör szimbólum) [T48]. A SOD aktivitás esetében a folytonos vonal az IC<sub>50</sub> érték meghatározására használt matematikai függvény, míg a HRP aktivitásnál a Michaelis-Menten mechanizmus alapján számolt adatokat jelöli. A beszúrt rajz a kettős enzimaktivitást szemlélteti.

Előállításuk után meghatároztuk antioxidáns aktivitásukat a SOD és HRP tesztreakciók segítségével. Megállapítottuk, hogy a PBP aktív mind a szuperoxid gyök anion dizmutálás, mind pedig a hidrogén-peroxid jelenlétében katalizált gvajakol oxidáció során is, tehát SOD és HRP aktivitással is rendelkezik. Az utóbbi esetben a mért reakciósebességek jó egyezést mutattak a Michaelis-Menten modellel [223] számolt értékekkel (24. ábra). Összességében egy olyan kompozit létrejöttét sikerült elérni, amely alkalmas a szuperoxid gyök anionok és hidrogén-peroxid együttes elbontására, tehát széles spektrumú antioxidáns hatással rendelkezik. A kifejlesztett AL-PBP rendszer jelentős időbeli kolloidstabilitást mutatott, mivel aggregációt, illetve ebből következő üledéket vagy fölözödést a diszperziókban több nap után sem tapasztaltunk.

A lehetséges antioxidáns hatású nanoméretű anyagokat tovább kutatva monodiszperz részecskeméret eloszlású mangán-dioxid (MnO<sub>2</sub> NP) nanozyme-okat állítottunk elő

hidrotermális eljárással [172]. A szerkezetüket és alakjukat XPS, SEM és TEM módszerekkel határoztuk meg és megállapítottuk, hogy a negatív töltésű nanorészecskék pelyhes szerkezetet vettek fel, illetve 10 mM elektrolit koncentrációnál és pH 9 érték alatt már aggregálódnak [T49]. Az  $\text{MnO}_2$  NP részecskéket PDADMAC polielektrolittal funkcionálisztuk annak érdekében, hogy SL hordozóra való rögzítés kivitelezhető legyen Coulomb-féle vonzó erők segítségével. A kísérleti körülmények optimalizálásával olyan SL-PDADMAC- $\text{MnO}_2$  NP (SPMn) kompozitot állítottunk elő, amely kiemelkedő szerkezeti stabilitással rendelkezik, továbbá egyidejűleg képes szuperoxid gyök anionok és hidrogén-peroxid lebontására, ezáltal utánozva a SOD és CAT enzimek működését (25. ábra).



**25. ábra.** SPMn kompozitok összetételének és 75 °C-on meghatározott antioxidáns aktivitásának sematikus ábrázolása [T49]. SOD aktivitás a kompozit különböző koncentrációinál mért NBT-szuperoxid gyök reakcióra gyakorolt inhibíciójával, míg a CAT aktivitás a hidrogén-peroxid bontásának sebességével került kifejezésre.

Bebizonyítottuk továbbá, hogy az SPMn hibrid antioxidáns hatását magasabb hőmérsékleteken (például 75 °C) is megtartja, ahol a természetes SOD és CAT enzimek denaturálódnak, vagyis teljesen elvesztik aktivitásukat. Meg kell jegyezni, hogy a nanozyme és a kompozit aktivitása is csökkent a hőmérséklet emelésével, azonban ez a csökkenés sokkal kisebb mértékű az SPMn esetében, mivel a melegítés hatására az  $\text{MnO}_2$  NP részecskék nagymértékű aggregálódása következik be. Ebből is jól látszik az SL-PDADMAC hordozó hatása, miszerint az aggregáció mértékét csökkenti, illetve a kolloidstabilitást növeli.

A fenti eredmények alapján megállapíthatjuk, hogy nanozyme részecskéket tartalmazó antioxidáns kompozitok heteroaggregációval előállíthatóak a kísérleti körülmények gondos megválasztásával. Esetünkben latex részecskék, vagy polielektrolittal funkcionáliszt származékjaik megfelelő hordozónak bizonyultak a diszperziók stabilitásának és az antioxidáns hatásnak a fenntartásához. Az ilyen jellegű kutatásaink során szerzett tapasztalatok alapján, heteroaggregációval előállított anyagok tulajdonságairól és felhasználásáról egy összefoglaló cikket is publikáltunk a terület egyik vezető szaklapjában [T50].



## 6. ÖSSZEFOGLALÁS

A doktori munkában bemutatott eredmények egy közel 10 éves, a Genfi Egyetemen és Szegedi Tudományegyetemen folytatott, felfedező kutatás során jöttek létre, amelyben alapvető kolloidkémiai folyamatok pontosabb megismerésével és antioxidáns diszperz rendszerek fejlesztésével foglalkoztam kolloid és nanoméretű részecskék (LDH, TNS, HNT, TiONW, SL és AL) alkalmazásával.

Egy- és többértékű elektrolitok jelenlétében vizsgáltuk a fenti részecskék só indukált aggregációval szemben mutatott ellenállását, szisztematikusan változtatva a mellék- és ellenionok vegyértékét, kémiai összetételét, illetve koncentrációját. Megállapítottuk, hogy a Hofmeister sorozat és a Schulze-Hardy-féle hatodik hatvány szabály csak néhány esetben alkalmazható a CCC értékek leírására. Határfelületi ion specifikus kölcsönhatások fontos szerepet játszanak a részecskék felületi töltésének és ezáltal a stabilizáló elektrosztatikus erők kialakításában. IL komponensek összetételének és koncentrációjának változtatásával hasonló következtetésekre jutottunk. Eszerint az alkotó ionok és a részecskék felületének hidratáltsága befolyásolja a specifikus ion adszorpció mértékét, amely ellenionok esetében csökkenő elektrosztatikus taszítással jár. Bebizonyítottuk, hogy míg a DLVO elméletben foglalt erőhatások fontos szerepet játszanak az aggregációs mechanizmus kialakításában, addig a CCC értékek meghatározásában fontos szerepe van az oldott ionok adszorpciójának.

Kimutattuk, hogy 10-es töltésszámnál nagyobb töltést hordozó többértékű poliamin és poliakrilát ionokra a polielektrolit szabály érvényes, vagyis ezután a CCC értéke nem változik a vegyértékkel. Az ellentétesen töltött polielektrolitok erős adszorpciója révén töltés semlegesítés és áttöltés játszódik le a részecskéken, amely döntően befolyásolja a diszperziók kolloidstabilitását. A felületi adszorbeált polielektrolit réteg szerkezetétől függően különféle vonzó és taszító kölcsönhatások jelenlétét azonosítottunk be, amelyek egy része a DLVO elmélettel leírható. A másik részük viszont az egyenetlen felületi borítottsággal hozható összefüggésbe, amely a részecskék és a polielektrolitok szerkezetének, összetételének és töltésviszonyainak következménye.

A fenti eredményekre támaszkodva antioxidáns diszperziókat állítottunk elő polielektrolitok felületmódosító hatását kihasználva enzimatis, molekuláris és enzimutánzó vegyületek immobilizálásával. Antioxidáns enzimek egyenként, illetve együttesen is rögzítésre kerültek kompozitokban. Biokémiai tesztrendszerekkel és sejt kultúrákon elvégzett mérésekkel igazoltuk a kifejlesztett hibrid anyagok oxidatív stressz csökkentő potenciálját. Molekuláris antioxidánsokat részecskékben rögzítettünk, így lehetővé téve nagy dózisban való alkalmazásukat, ami jelentős előrelépés a lehetséges alkalmazási területük bővítése során. Természetes enzimek működését utánozni képes fémkomplexek részecske-polielektrolit kompozitokban való immobilizálásával szélsőséges körülmények között is működő, szelektív antioxidánsokat hoztunk létre. Végül nanozyme részecskéket formulázva polimer alapú hordozókon magas hőmérsékleten is alkalmazható ROS-t elbontó kompozitokat fejlesztettünk ki. A fenti antioxidáns hibrid anyagok jelentős szerkezeti- és kolloidstabilitást mutattak.



## 7. AZ EREDMÉNYEK VÁRHATÓ ALKALMAZÁSAI

A dolgozatban ismertetett kutatások során alkalmazott kolloid- és nanorészecskék, illetve származékjaik felhasználása rohamosan növekszik számos területen a nanotechnológia előretörésének és a dinamikus fejlődő műszeres háttérnek köszönhetően. A doktori dolgozatban tárgyalt eredmények az alábbiak szerint járulhatnak hozzá ehhez a folyamathoz.

Az újszerű nanorészecskék előállításának optimalizálása és ionspecifikus kölcsönhatásaik részletes ismerete orvosbiológiai (például nanorészecske alapú gyógyszerhatóanyag szállítás) és ipari (például élelmiszer vagy kozmetikai ipari eljárások) alkalmazásokban is rendkívül fontos, mivel az ezek során alkalmazott nanorészecskéknek elektrolitokat is tartalmazó közegben kell kifejteni a hatásukat.

Az IL-részecske rendszerek növekvő számú alkalmazásai (például heterogén katalízis, vagy védőbevonatok készítése) során a stabilizációs tartományokat leíró eredményeinkre támaszkodhatnak a kutatók és fejlesztők. A létrehozott ismeretanyag mindenképpen hasznos lesz amennyiben részecskéket alkalmazunk IL közegben bármely területen, illetve továbbiakban felhasználható diszperziókat szeretnénk fejleszteni.

Polielektrolitok alkalmazása például a papírgyártásban, víztisztításban és a ruhaiparban is nélkülözhetetlen felületmódosító hatásuk miatt. A munkánk során kapott eredmények hozzájárulnak a polielektrolit-részecske diszperziókban lejátszódó alapfolyamatok megértéséhez, illetve az alkalmazott rendszerek működésének optimalizálásához. Ezen kívül a kifejlesztett részecske-polielektrolit rendszerek ígéretes jelöltek más típusú enzim vagy enzimutánzó anyagok hordozójaként.

Az antioxidánsok szerepe megkérdőjelezhetetlen mind élettani (oxidatív stressz hatására kialakuló betegségek), mind pedig ipari (élelmiszerek, kozmetikumok, petrokémiai termékek minősége és eltarthatósága) szempontból. Antioxidáns enzimek, illetve ezek együttes immobilizálásával olyan stabilis rendszereket állítottunk elő, amelyek alkalmasak a ROS sejten belüli lebontására, illetve lehetséges az élő szervezetbe juttatásuk. Az antioxidáns enzimeket együttesen tartalmazó részecskék alkalmazásának tesztelése gyulladósos bélbetegségek kezelésében már tervezés alatt áll, kivitelezésük hamarosan elkezdődik egy orvosbiológiai együttműködés keretein belül.

A magas kémiai és hőstabilitással rendelkező mesterséges antioxidánsok, mint például a fent ismertetett immobilizált fémkomplexek, ígéretes jelöltek a kőolaj vagy gumiipari folyamatok során alkalmazott eljárásokban ROS koncentráció optimalizálására, ahol az extrém körülmények (magas hőmérséklet és nyomás) nem teszik lehetővé az enzimátikus vagy molekuláris antioxidánsok alkalmazását.

Összefoglalva, a jelen tézisekben ismertetett eredmények számottevő érdeklődésre tarthatnak számot mind a felfedező, mind pedig az alkalmazott kutatással foglalkozó tudóstársadalomban. Ez a témához kapcsolódó publikációkra kapott hivatkozások növekvő számában, illetve ipari partnerek érdeklődésében is kifejeződik.

**8. IRODALOMJEGYZÉK**

- [1] P.G. de Gennes, *Nature* 412 (2001) 385-385.
- [2] T.L. Moore, L. Rodriguez-Lorenzo, V. Hirsch, S. Balog, D. Urban, C. Jud, B. Rothen-Rutishauser, M. Lattuada, A. Petri-Fink, *Chem. Soc. Rev.* 44 (2015) 6287-6305.
- [3] E. Dickinson, *Adv. Colloid Interface Sci.* 165 (2011) 7-13.
- [4] Z.Y. Cai, Z.W. Li, S. Ravaine, M.X. He, Y.L. Song, Y.D. Yin, H.B. Zheng, J.H. Teng, A.O. Zhang, *Chem. Soc. Rev.* 50 (2021) 5898-5951.
- [5] S. Shrestha, B. Wang, P. Dutta, *Adv. Colloid Interface Sci.* 279 (2020) 102162.
- [6] M. Elimelech, J. Gregory, X. Jia, R.A. Williams, *Particle deposition and aggregation: Measurement, modeling, and simulation*, Butterworth-Heinemann Ltd., Oxford, 1995.
- [7] J. Israelachvili, *Intermolecular and surface forces*, 3 ed., Academic Press, London, 2011.
- [8] R. Rojas Delgado, M. Arandigoyen Vidaurre, C.P. De Pauli, M.A. Ulibarri, M.J. Avena, *J. Colloid Interface Sci.* 280 (2004) 431-441.
- [9] G.A. Parks, *Chem. Rev.* 65 (1965) 177-198.
- [10] F. Tiarks, T. Frechen, S. Kirsch, J. Leuninger, M. Melan, A. Pfau, F. Richter, B. Schuler, C.L. Zhao, *Prog. Org. Coat.* 48 (2003) 140-152.
- [11] R.S. Jadhav, K.J. Patil, D.G. Hundiwale, P.P. Mahulikar, *Polym. Adv. Technol.* 22 (2011) 1620-1627.
- [12] B. Bolto, J. Gregory, *Water Res.* 41 (2007) 2301-2324.
- [13] R.J. Honda, V. Keene, L. Daniels, S.L. Walker, *Environ. Eng. Sci.* 31 (2014) 127-134.
- [14] L.X. Zhang, J. Hu, Y.B. Jia, R.T. Liu, T. Cai, Z.P. Xu, *Nanoscale* 13 (2021) 7533-7549.
- [15] J.J.X. Wu, X.Y. Wang, Q. Wang, Z.P. Lou, S.R. Li, Y.Y. Zhu, L. Qin, H. Wei, *Chem. Soc. Rev.* 48 (2019) 1004-1076.
- [16] Z.B. Cao, B. Li, L.Y. Sun, L. Li, Z.P. Xu, Z. Gu, *Small Methods* 4 (2019) 1900343.
- [17] F.U. Rehman, C. Zhao, H. Jiang, X. Wang, *Biomater. Sci.* 4 (2016) 40-54.
- [18] A.C. Santos, C. Ferreira, F. Veiga, A.J. Ribeiro, A. Panchal, Y. Lvov, A. Agarwal, *Adv. Colloid Interface Sci.* 257 (2018) 58-70.
- [19] L.Y. Wang, B.H. Zhu, Y.T. Deng, T.T. Li, Q.Y. Tian, Z.G. Yuan, L. Ma, C. Cheng, Q.Y. Guo, L. Qiu, *Adv. Funct. Mater.* 31 (2021) 2101804.
- [20] R.Z. Tian, J.Y. Xu, Q.A. Luo, C.X. Hou, J.Q. Liu, *Front. Chem.* 8 (2021) 831.
- [21] C.W. Li, L.L. Li, S. Chen, J.X. Zhang, W.L. Lu, *Front. Bioeng. Biotechnol.* 8 (2020).
- [22] A.M.E. Abdalla, L. Xiao, C.X. Ouyang, G. Yang, *Nanoscale* 6 (2014) 14141-14152.
- [23] E.W. Peng, E.S.G. Choo, P. Chandrasekharan, C.T. Yang, J. Ding, K.H. Chuang, J.M. Xue, *Small* 8 (2012) 3620-3630.
- [24] C. Vasti, D.A. Bedoya, R. Rojas, C.E. Giacomelli, *J. Mater. Chem. B* 4 (2016) 2008-2016.
- [25] A.V. Delgado, F. Gonzalez-Caballero, R.J. Hunter, L.K. Koopal, J. Lyklema, *J. Colloid Interface Sci.* 309 (2007) 194-224.
- [26] B. Derjaguin, L.D. Landau, *Acta Phys. Chim.* 14 (1941) 633-662.
- [27] E.J.W. Verwey, J.T.G. Overbeek, *Theory of stability of lyophobic colloids*, Elsevier, Amsterdam, 1948.
- [28] D.F. Evans, H. Wennerstrom, *The colloidal domain*, John Wiley, New York, 1999.
- [29] S.H. Behrens, D.I. Christl, R. Emmerzael, P. Schurtenberger, M. Borkovec, *Langmuir* 16 (2000) 2566-2575.
- [30] W.B. Russel, D.A. Saville, W.R. Schowalter, *Colloidal dispersions*, Cambridge University Press, Cambridge, 1989.
- [31] H.J. Butt, *Biophys. J.* 60 (1991) 1438-1444.
- [32] W.A. Ducker, T.J. Senden, R.M. Pashley, *Nature* 353 (1991) 239-241.
- [33] H. Holthoff, S.U. Egelhaaf, M. Borkovec, P. Schurtenberger, H. Sticher, *Langmuir* 12 (1996) 5541-5549.
- [34] S. Leikin, V.A. Parsegian, D.C. Rau, R.P. Rand, *Annu. Rev. Phys. Chem.* 44 (1993) 369-395.
- [35] R.M. Pashley, J.N. Israelachvili, *J. Colloid Interface Sci.* 97 (1984) 446-455.
- [36] Y.J. Diao, M.W. Han, J.A. Lopez-Berganza, L. Valentino, B. Marinas, R.M. Espinosa-Marzal, *Langmuir* 33 (2017) 8982-8992.
- [37] R.M. Pashley, J.N. Israelachvili, *J. Colloid Interface Sci.* 101 (1984) 511-523.
- [38] M.A. Gebbie, A.M. Smith, H.A. Dobbs, A.A. Lee, G.G. Warr, X. Banquy, M. Valtiner, M.W. Rutland, J.N. Israelachvili, S. Perkin, R. Atkin, *Chem. Commun.* 53 (2017) 1214-1224.

- [39] F.J. Montes Ruiz-Cabello, G. Trefalt, P. Maroni, M. Borkovec, *Langmuir* 30 (2014) 4551-4555.
- [40] M. Borkovec, G. Papastavrou, *Curr. Opin. Colloid Interface Sci.* 13 (2008) 429-437.
- [41] G. Decher, *Science* 277 (1997) 1232-1237.
- [42] L.L. Feng, M.C. Stuart, Y. Adachi, *Adv. Colloid Interface Sci.* 226 (2015) 101-114.
- [43] G. Fritz, V. Schadler, N. Willenbacher, N.J. Wagner, *Langmuir* 18 (2002) 6381-6390.
- [44] K.E. Bremmell, G.J. Jameson, S. Biggs, *Colloid Surf. A* 139 (1998) 199-211.
- [45] A. Hajdu, M. Szekeres, I.Y. Toth, R.A. Bauer, J. Mihaly, I. Zupko, E. Tombacz, *Colloid Surf. B* 94 (2012) 242-249.
- [46] F. Brunel, I. Pochard, S. Gauffine, M. Turesson, C. Labbez, *J. Phys. Chem. B* 120 (2016) 5777-5785.
- [47] G. Papastavrou, L.J. Kirwan, M. Borkovec, *Langmuir* 22 (2006) 10880-10884.
- [48] Y.K. Leong, *Colloid Polym. Sci.* 277 (1999) 299-305.
- [49] E. Seyrek, J. Hierrezuelo, A. Sadeghpour, I. Szilagy, M. Borkovec, *Phys. Chem. Chem. Phys.* 13 (2011) 12716-12719.
- [50] W. Kunz, J. Henle, B.W. Ninham, *Curr. Opin. Colloid Interface Sci.* 9 (2004) 19-37.
- [51] P. Lo Nostro, B.W. Ninham, *Chem. Rev.* 112 (2012) 2286-2322.
- [52] A. Diehl, A.P. dos Santos, Y. Levin, *J. Phys.-Condes. Matter* 24 (2012).
- [53] H.D.B. Jenkins, Y. Marcus, *Chem. Rev.* 95 (1995) 2695-2724.
- [54] J. Manna, N. Shilpa, A.K. Bandarapu, R.K. Rana, *ACS Appl. Nano Mater.* 2 (2019) 1525-1532.
- [55] J.C. Fu, J.B. Schlenoff, *J. Am. Chem. Soc.* 138 (2016) 980-990.
- [56] H.I. Okur, J. Hladilkova, K.B. Rembert, Y. Cho, J. Heyda, J. Dzubiella, P.S. Cremer, P. Jungwirth, *J. Phys. Chem. B* 121 (2017) 1997-2014.
- [57] B. Tezak, E. Matijevic, K.F. Schulz, *J. Phys. Chem.* 59 (1955) 769-773.
- [58] F. Dumont, A. Watillon, *Discuss. Farad. Soc.* 52 (1971) 352-380.
- [59] T. Lopez-Leon, J.L. Ortega-Vinuesa, D. Bastos-Gonzalez, *ChemPhysChem* 13 (2012) 2382-2391.
- [60] J.M. Peula-Garcia, J.L. Ortega-Vinuesa, D. Bastos-Gonzalez, *J. Phys. Chem. C* 114 (2010) 11133-11139.
- [61] R. Tian, G. Yang, H. Li, X.D. Gao, X.M. Liu, H.L. Zhu, Y. Tang, *Phys. Chem. Chem. Phys.* 16 (2014) 8828-8836.
- [62] N. Schwierz, D. Horinek, U. Sivan, R.R. Netz, *Curr. Opin. Colloid Interface Sci.* 23 (2016) 10-18.
- [63] N. Schwierz, D. Horinek, R.R. Netz, *Langmuir* 26 (2010) 7370-7379.
- [64] W.Y. Yu, N. Du, Y.T. Gu, J.G. Yan, W.G. Hou, *Langmuir* 36 (2020) 6557-6568.
- [65] R. Prathapan, R. Thapa, G. Garnier, R.F. Tabor, *Colloid Surf. A* 509 (2016) 11-18.
- [66] A. Salis, D.F. Parsons, M. Bostrom, L. Medda, B. Barse, B.W. Ninham, M. Monduzzi, *Langmuir* 26 (2010) 2484-2490.
- [67] R. Sprycha, *J. Colloid Interface Sci.* 127 (1989) 1-11.
- [68] A. Breeuwsma, J. Lyklema, *Discuss. Faraday Soc.* 52 (1971) 324-333.
- [69] T. Lopez-Leon, A.B. Jodar-Reyes, D. Bastos-Gonzalez, J.L. Ortega-Vinuesa, *J. Phys. Chem. B* 107 (2003) 5696-5708.
- [70] F. Dumont, J. Warlus, A. Watillon, *J. Colloid Interface Sci.* 138 (1990) 543-554.
- [71] T. Lopez-Leon, A.B. Jodar-Reyes, J.L. Ortega-Vinuesa, D. Bastos-Gonzalez, *J. Colloid Interface Sci.* 284 (2005) 139-148.
- [72] G. Lagaly, O. Mecking, D. Penner, *Colloid Polym. Sci.* 279 (2001) 1090-1096.
- [73] G.V. Franks, *J. Colloid Interface Sci.* 249 (2002) 44-51.
- [74] R.B. Leggat, S.A. Taylor, S.R. Taylor, *Colloid Surf. A* 210 (2002) 69-81.
- [75] Z.P. Xu, Y.G. Jin, S.M. Liu, Z.P. Hao, G.Q. Lu, *J. Colloid Interface Sci.* 326 (2008) 522-529.
- [76] T. Oncsik, G. Trefalt, Z. Csendes, I. Szilagy, M. Borkovec, *Langmuir* 30 (2014) 733-741.
- [77] T. Hegedüs, D. Takács, L. Vásárhelyi, I. Szilagy, Z. Kónya, *Langmuir* 37 (2021) 2466-2475.
- [78] J.T.G. Overbeek, *Pure Appl. Chem.* 52 (1980) 1151-1161.
- [79] H. Schulze, *J. Prakt. Chem.* 25 (1882) 431-452.
- [80] H. Schulze, *J. Prakt. Chem.* 27 (1883) 320-332.
- [81] W.B. Hardy, *J. Phys. Chem.* 4 (1900) 235-253.
- [82] A.K. Rakshit, B. Naskar, S.P. Moulik, *J. Dispersion Sci. Technol.* 42 (2021) 503-513.
- [83] C.Y. Chen, W.L. Huang, *Environ. Sci. Technol.* 51 (2017) 2077-2086.
- [84] K. Afshinnia, M. Sikder, B. Cai, M. Baalousha, *J. Colloid Interface Sci.* 487 (2017) 192-200.
- [85] C. Schneider, M. Hanisch, B. Wedel, A. Jusufi, M. Ballauff, *J. Colloid Interface Sci.* 358 (2011) 62-67.

- [86] G. Lagaly, S. Ziesmer, *Adv. Colloid Interface Sci.* 100 (2003) 105-128.
- [87] B. Tezak, E. Matijevic, K. Shulz, M. Mirnik, J. Herak, V.B. Vouk, M. Slunjski, S. Babic, J. Kratochvil, T. Palmar, *J. Phys. Chem.* 57 (1953) 301-307.
- [88] N.O. McHedlov-Petrossyan, V.K. Klochkov, G.V. Andrievsky, *J. Chem. Soc.-Faraday Trans.* 93 (1997) 4343-4346.
- [89] G. Frens, J.J.F.G. Heuts, *Colloids Surf.* 30 (1988) 295-305.
- [90] A. Kotera, K. Furusawa, K. Kudo, *Kolloid Z.* 240 (1970) 837-842.
- [91] E. Matijevic, M. Kerker, *J. Phys. Chem.* 62 (1958) 1271-1276.
- [92] A.J. Rubin, P.L. Hayden, G.P. Hanna, *Water Res.* 3 (1969) 843-852.
- [93] M. Sano, J. Okamura, S. Shinkai, *Langmuir* 17 (2001) 7172-7173.
- [94] H. Freundlich, *Z. Phys. Chem.* 57 (1907) 385-470.
- [95] H.A. Wannow, *Kolloidchem. Beih.* 50 (1939) 367-472.
- [96] S.E. Linder, H. Picton, *J. Chem. Soc.* 67 (1895) 63-74.
- [97] D.N. Furlong, A. Launikonis, W.H.F. Sasse, J.V. Sanders, 80 (1984) 571-588.
- [98] F.K. Hansen, E. Matijevic, 76 (1980) 1240-1262.
- [99] R. Lee, K. Stack, D. Richardson, T. Lewis, G. Garnier, *Colloid Surf. A-Physicochem. Eng. Asp.* 396 (2012) 106-114.
- [100] R.H. Ottewill, D.G. Rance, *Croat. Chem. Acta* 50 (1977) 65-75.
- [101] Y.Y. Petrov, S.Y. Avvakumova, M.P. Sidorova, L.E. Ermakova, V.V. Voitylov, A.V. Voitylov, *Colloid J.* 73 (2011) 834-840.
- [102] R. Zimehl, G. Lagaly, 22 (1987) 225-236.
- [103] R.D. Rogers, K.R. Seddon, *Science* 302 (2003) 792-793.
- [104] N.V. Plechkova, K.R. Seddon, *Chem. Soc. Rev.* 37 (2008) 123-150.
- [105] J.P. Hallett, T. Welton, *Chem. Rev.* 111 (2011) 3508-3576.
- [106] M.J. Earle, J. Esperanca, M.A. Gilea, J.N.C. Lopes, L.P.N. Rebelo, J.W. Magee, K.R. Seddon, J.A. Widegren, *Nature* 439 (2006) 831-834.
- [107] P. Wasserscheid, *Nature* 439 (2006) 797-797.
- [108] F. Endres, *ChemPhysChem* 3 (2002) 144-154.
- [109] H.L. Ngo, K. LeCompte, L. Hargens, A.B. McEwen, *Thermochim. Acta* 357 (2000) 97-102.
- [110] R. Hayes, G.G. Warr, R. Atkin, *Chem. Rev.* 115 (2015) 6357-6426.
- [111] R. Kanzaki, C. Guibert, J. Fresnais, V. Peyre, *J. Colloid Interface Sci.* 516 (2018) 248-253.
- [112] R. Bhandary, J.G. Alauzun, P. Hesemann, A. Stocco, M. In, P.H. Mutin, *Soft Matter* 13 (2017) 8023-8026.
- [113] J.S. Gao, R.S. Ndong, M.B. Shiflett, N.J. Wagner, *ACS Nano* 9 (2015) 3243-3253.
- [114] G.K. Dedzo, C. Detellier, *Adv. Funct. Mater.* 28 (2018) 1703845.
- [115] D. Brondani, C.W. Scheeren, J. Dupont, I.C. Vieira, *Analyst* 137 (2012) 3732-3739.
- [116] P.S. Campbell, C.C. Santini, D. Bouchu, B. Fenet, K. Philippot, B. Chaudret, A.A.H. Padua, Y. Chauvin, *Phys. Chem. Chem. Phys.* 12 (2010) 4217-4223.
- [117] E. Vanecht, K. Binnemans, S. Patskovsky, M. Meunier, J.W. Seo, L. Stappers, J. Fransaer, *Phys. Chem. Chem. Phys.* 14 (2012) 5662-5671.
- [118] J. Luczak, M. Paszkiewicz, A. Krukowska, A. Malankowska, A. Zaleska-Medynska, *Adv. Colloid Interface Sci.* 230 (2016) 13-28.
- [119] Y. Zhou, M. Antonietti, *J. Am. Chem. Soc.* 125 (2003) 14960-14961.
- [120] J.A. Smith, O. Werzer, G.B. Webber, G.G. Warr, R. Atkin, *J. Phys. Chem. Lett.* 1 (2010) 64-68.
- [121] K. Ueno, A. Inaba, M. Kondoh, M. Watanabe, *Langmuir* 24 (2008) 5253-5259.
- [122] M.A. Gebbie, M. Valtiner, X. Banquy, E.T. Fox, W.A. Henderson, J.N. Israelachvili, *Proc. Natl. Acad. Sci. U. S. A.* 110 (2013) 9674-9679.
- [123] M.W. Han, R.M. Espinosa-Marzal, *ACS Appl. Mater. Interfaces* 11 (2019) 33465-33477.
- [124] E. Bordes, B. Morcos, D. Bourgogne, J.M. Andanson, P.O. Bussiere, C.C. Santini, A. Benayad, M.C. Gomes, A.A.H. Padua, *Front. Chem.* 7 (2019).
- [125] V. Valmacco, G. Trefalt, P. Maroni, M. Borkovec, *Phys. Chem. Chem. Phys.* 17 (2015) 16553-16559.
- [126] M. Mamusa, J. Siriex-Plenet, F. Cousin, E. Dubois, V. Peyrea, *Soft Matter* 10 (2014) 1097-1101.
- [127] X. Zhang, Y.X. Zhong, J.W. Yan, Y.Z. Su, M. Zhang, B.W. Mao, *Chem. Commun.* 48 (2012) 582-584.
- [128] R.S. Sohal, R. Weindruch, *Science* 273 (1996) 59-63.

- [129] S.C. Lourenco, M. Moldao-Martins, V.D. Alves, *Molecules* 24 (2019) 4132.
- [130] H. Sies, *Exp. Physiol.* 82 (1997) 291-295.
- [131] M.T. Lin, M.F. Beal, *Nature* 443 (2006) 787-795.
- [132] A.M. Pisoschi, A. Pop, *Eur. J. Med. Chem.* 97 (2015) 55-74.
- [133] S. Choi, J. Han, J.H. Kim, A.R. Kim, S.H. Kim, W. Lee, M.Y. Yoon, G. Kim, Y.S. Kim, *J. Cosmet. Dermatol.* 19 (2020) 970-976.
- [134] M.A. El-Missiry, *Antioxidant enzyme*, InTech, Rijeka, 2012.
- [135] Y.H. Lin, Z.W. Chen, X.Y. Liu, *Trends Biotechnol.* 34 (2016) 303-315.
- [136] R.A. Sheldon, S. van Pelt, *Chem. Soc. Rev.* 42 (2013) 6223-6235.
- [137] S. Singh, V.K. Dubey, *Int. J. Pept. Res. Ther.* 22 (2016) 171-177.
- [138] K. Kamada, A. Yamada, N. Soh, *RSC Adv.* 5 (2015) 85511-85516.
- [139] S. Bobone, E. Miele, B. Cerroni, D. Roversi, A. Bocedi, E. Nicolai, A. Di Venere, E. Placidi, G. Ricci, N. Rosato, L. Stella, *Langmuir* 31 (2015) 7572-7580.
- [140] X.Y. Lang, L.L. Zhu, Y.N. Gao, I. Wheeldon, *Langmuir* 33 (2017) 9073-9080.
- [141] S.A. Mohamed, M.H. Al-Harbi, Y.Q. Almulaiky, I.H. Ibrahim, R.M. El-Shishtawy, *Electron. J. Biotechnol.* 27 (2017) 84-90.
- [142] A.T.E. Vilian, K. Giribabu, S.R. Choe, R. Muruganantham, H. Lee, C. Roh, Y.S. Huh, Y.K. Han, *Sens. Actuators, B* 251 (2017) 804-812.
- [143] Y.M. Fan, X.D. Cao, T. Hu, X.G. Lin, H. Dong, X.N. Zou, *J. Phys. Chem. C* 120 (2016) 3955-3963.
- [144] X. Zhu, X.H. Niu, H.L. Zhao, J. Tang, M.B. Lan, *Biosens. Bioelectron.* 67 (2015) 79-85.
- [145] I.K. Deshapriya, C.S. Kim, M.J. Novak, C.V. Kumar, *ACS Appl. Mater. Interfaces* 6 (2014) 9643-9653.
- [146] F.F. Zhou, J.Q. Luo, B.K. Qi, X.R. Chen, Y.H. Wan, *Ind. Eng. Chem. Res.* 58 (2019) 11710-11719.
- [147] A.M. Pudlartz, E. Czechowska, M.S. Karbownik, K. Ranoszek-Soliwoda, E. Tomaszewska, G. Celichowski, J. Grobelny, E. Chabielska, A. Gromotowicz-Poplawska, J. Szmraj, *Nanomedicine* 15 (2020) 23-39.
- [148] F.P. Chang, Y.P. Chen, C.Y. Mou, *Small* 10 (2014) 4785-4795.
- [149] I. Louzao, J.C.M. van Hest, *Biomacromolecules* 14 (2013) 2364-2372.
- [150] A. Grotzky, E. Atamura, J. Adamcik, P. Carrara, P. Stano, F. Mavelli, T. Nauser, R. Mezzenga, A.D. Schluter, P. Walde, *Langmuir* 29 (2013) 10831-10840.
- [151] P. Tanner, V. Balasubramanian, C.G. Palivan, *Nano Lett.* 13 (2013) 2875-2883.
- [152] Y.H. Lin, Y.P. Chen, T.P. Liu, F.C. Chien, C.M. Chou, C.T. Chen, C.Y. Mou, *ACS Appl. Mater. Interfaces* 8 (2016) 17944-17954.
- [153] Q. Wu, Z.G. He, X. Wang, Q. Zhang, Q.C. Wei, S.Q. Ma, C. Ma, J. Li, Q.G. Wang, *Nat. Commun.* 10 (2019) 240.
- [154] Y.C. Fang, H.C. Lin, I.J. Hsu, T.S. Lin, C.Y. Mou, *J. Phys. Chem. C* 115 (2011) 20639-20652.
- [155] I. Szilagyi, L. Horvath, I. Labadi, K. Hernadi, I. Palinko, T. Kiss, *Cent. Eur. J. Chem.* 4 (2006) 118-134.
- [156] Z. Csendes, C. Dudas, G. Varga, E.G. Bajnoczi, S.E. Canton, P. Sipos, I. Palinko, *J. Mol. Struct.* 1044 (2013) 39-45.
- [157] I. Szilagyi, I. Labadi, K. Hernadi, I. Palinko, I. Fekete, L. Korecz, A. Rockenbauer, T. Kiss, *New J. Chem.* 29 (2005) 740-745.
- [158] J. Bouayed, T. Bohn, *Oxidative Med. Cell. Longev.* 3 (2010) 228-237.
- [159] K. Biliska, N. Wojciechowska, S. Alipour, E.M. Kalemba, *Antioxidants* 8 (2019).
- [160] F.A. Moura, K.Q. de Andrade, J.C.F. dos Santos, O.R.P. Araujo, M.O.F. Goulart, *Redox Biol.* 6 (2015) 617-639.
- [161] F.C. Neto, L.T. Marton, S.V. de Marqui, T.A. Lima, S.M. Barbalho, *Crit. Rev. Food Sci. Nutr.* 59 (2019) 2136-2143.
- [162] K. Khorsandi, R. Hosseinzadeh, M. Fateh, *RSC Adv.* 5 (2015) 93987-93994.
- [163] S. Alfei, F. Turrini, S. Catena, P. Zunin, B. Parodi, G. Zuccari, A.M. Pittaluga, R. Boggia, *New J. Chem.* 43 (2019) 2438-2448.
- [164] M.Z. Hussein, S.H. Al Ali, Z. Zainal, M.N. Hakim, *Int. J. Nanomed.* 6 (2011) 1373-1383.
- [165] M.M. Shaik, M. Kowshik, *Int. J. Polym. Mater. Polym. Biomat.* 68 (2019) 208-215.
- [166] J. Hari, A. Gyurki, M. Sarkozi, E. Foldes, B. Pukanszky, *J. Colloid Interface Sci.* 462 (2016) 123-129.
- [167] J. Hari, P. Polyak, D. Mester, M. Micusik, M. Omastova, M. Kallay, B. Pukanszky, *Appl. Clay Sci.* 132 (2016) 167-174.

- [168] F. Dashtestani, H. Ghourchian, A. Najafi, *Bioorganic Chem.* 80 (2018) 621-630.
- [169] Y.H. Lin, J.S. Ren, X.G. Qu, *Adv. Mater.* 26 (2014) 4200-4217.
- [170] M. Moglianetti, E. De Luca, P.A. Deborah, R. Marotta, T. Catelani, B. Sartori, H. Amenitsch, S.F. Retta, P.P. Pompa, *Nanoscale* 8 (2016) 3739-3752.
- [171] A.A. Vernekar, D. Sinha, S. Srivastava, P.U. Paramasivam, P. D'Silva, G. Muges, *Nat. Commun.* 5 (2014) 5301.
- [172] N. Singh, M.A. Savanur, S. Srivastava, P. D'Silva, G. Muges, *Angew. Chem.-Int. Edit.* 56 (2017) 14267-14271.
- [173] T. Wang, P. Su, F.Y. Lin, Y. Yang, *Sens. Actuator B-Chem.* 254 (2018) 329-336.
- [174] A. Dhall, W. Self, *Antioxidants* 7 (2018) 97.
- [175] H. Oh, J.S. Lee, D. Sung, J.H. Lee, S.H. Moh, J.M. Lim, W.I. Choi, *Nanomedicine* 14 (2019) 2567-2578.
- [176] X.G. Han, Q. Kuang, M.S. Jin, Z.X. Xie, L.S. Zheng, *J. Am. Chem. Soc.* 131 (2009) 3152-3153.
- [177] J. He, M. Wei, B. Li, Y. Kang, D.G. Evans, X. Duan, Preparation of layered double hydroxides, in: X. Duan, D.G. Evans (Eds.), *Layered Double Hydroxides 2006*, pp. 89-119.
- [178] Z.P. Xu, G.S. Stevenson, C.Q. Lu, G.Q.M. Lu, P.F. Bartlett, P.P. Gray, *J. Am. Chem. Soc.* 128 (2006) 36-37.
- [179] P. Rouster, M. Dondelinger, M. Galleni, B. Nysten, A.M. Jonas, K. Glinel, *Colloid Surf. B* 178 (2019) 508-514.
- [180] E. Horvath, A. Kukovecz, Z. Konya, I. Kiricsi, *Chem. Mat.* 19 (2007) 927-931.
- [181] A.V. Delgado, E. Gonzalez-Caballero, R.J. Hunter, L.K. Koopal, J. Lyklema, *Pure Appl. Chem.* 77 (2005) 1753-1805.
- [182] C. Beaucham, I. Fridovich, *Anal. Biochem.* 44 (1971) 276-287.
- [183] A.C. Maehly, B. Chance, *Methods Biochem. Anal.* 1 (1954) 357-424.
- [184] W. Brand-Williams, M.E. Cuvelier, C. Berset, *Food Sci. Technol.-Lebensm.-Wiss. Technol.* 28 (1995) 25-30.
- [185] R. Apak, K. Guclu, M. Ozyurek, S.E. Karademir, *J. Agric. Food Chem.* 52 (2004) 7970-7981.
- [186] D.R. Doerge, R.L. Divi, M.I. Churchwell, *Anal. Biochem.* 250 (1997) 10-17.
- [187] G. Trefalt, I. Szilagyi, M. Borkovec, *J. Colloid Interface Sci.* 406 (2013) 111-120.
- [188] P.A. Connor, A.J. McQuillan, *Langmuir* 15 (1999) 2916-2921.
- [189] R. Luschtinetz, J. Frenzel, T. Milek, G. Seifert, *J. Phys. Chem. C* 113 (2009) 5730-5740.
- [190] H. Freundlich, *Z. Chemie Industrie Kolloide* 7 (1910) 193-195.
- [191] J.B. Rosenholm, J. Nylund, B. Stenlund, *Colloid Surf. A* 159 (1999) 209-218.
- [192] M. Borkovec, I. Szilagyi, I. Popa, M. Finessi, P. Sinha, P. Maroni, G. Papastavrou, *Adv. Colloid Interface Sci.* 179 (2012) 85-98.
- [193] X.Y. Wei, D.Q. Pan, Z. Xu, D.F. Xian, X.L. Li, Z.Y. Tan, C.L. Liu, W.S. Wu, *Sci. Total Environ.* 768 (2021) 144174.
- [194] M. Bester-Rogac, A. Stoppa, J. Hunger, G. Hefter, R. Buchner, *Phys. Chem. Chem. Phys.* 13 (2011) 17588-17598.
- [195] H. Sajjadi, A. Modaressi, P. Magri, U. Domanska, M. Sindt, J.L. Mieloszynski, F. Mutelet, M. Rogalski, *J. Mol. Liq.* 186 (2013) 1-6.
- [196] M. Galli, S. Saringer, I. Szilagyi, G. Trefalt, *Colloid Interfac.* 4 (2020) 20.
- [197] D.W. Fuerstenau, M. Colic, *Colloid Surf. A* 146 (1999) 33-47.
- [198] E. Ruckenstein, H. Huang, *Langmuir* 19 (2003) 3049-3055.
- [199] L. Liang, J.J. Morgan, *Aquat. Sci.* 52 (1990) 32-55.
- [200] A. Niecikowska, M. Krasowska, J. Ralston, K. Malysa, *J. Phys. Chem. C* 116 (2012) 3071-3078.
- [201] J.L. Trompette, J.F. Lahitte, *J. Phys. Chem. B* 123 (2019) 3859-3865.
- [202] H.K. Stassen, R. Ludwig, A. Wulf, J. Dupont, *Chem.-Eur. J.* 21 (2015) 8324-8335.
- [203] A. Stoppa, J. Hunger, G. Hefter, R. Buchner, *J. Phys. Chem. B* 116 (2012) 7509-7521.
- [204] L.Z. Ren, L.J. Meng, Q.H. Lu, Z.F. Fei, P.J. Dyson, *J. Colloid Interface Sci.* 323 (2008) 260-266.
- [205] R.R. Netz, J.F. Joanny, *Macromolecules* 32 (1999) 9013-9025.
- [206] J. Faraudo, A. Martin-Molina, *Curr. Opin. Colloid Interface Sci.* 18 (2013) 517-523.
- [207] S.Y. Park, R.F. Bruinsma, W.M. Gelbart, *Europhys. Lett.* 46 (1999) 454-460.
- [208] M. Quesada-Perez, E. Gonzalez-Tovar, A. Martin-Molina, M. Lozada-Cassou, R. Hidalgo-Alvarez, *ChemPhysChem* 4 (2003) 235-248.

- [209] J.Y. Carrillo, A.V. Dobrynin, *Langmuir* 23 (2007) 2472-2482.
- [210] S. Pearson, M. Pavlovic, T. Auge, V. Torregrossa, I. Szilagy, F. D'Agosto, M. Lansalot, E. Bourgeat-Lami, V. Prevot, *Macromolecules* 51 (2018) 3953-3966.
- [211] M. Finessi, I. Szilagy, P. Maroni, *J. Colloid Interface Sci.* 417 (2014) 346-355.
- [212] I. Popa, G. Papastavrou, M. Borkovec, *Phys. Chem. Chem. Phys.* 12 (2010) 4863-4871.
- [213] R.G. Smits, G.J.M. Koper, M. Mandel, *J. Phys. Chem.* 97 (1993) 5745-5751.
- [214] E. Seyrek, J. Hierrezuelo, I. Szilagy, A. Sadeghpour, M. Borkovec, *Chimia* 65 (2011) 439-439.
- [215] A. Sadeghpour, E. Seyrek, I. Szilagy, J. Hierrezuelo, M. Borkovec, *Langmuir* 27 (2011) 9270-9276.
- [216] C.Y. Kong, M. Muthukumar, *J. Chem. Phys.* 109 (1998) 1522-1527.
- [217] J. Hierrezuelo, A. Sadeghpour, I. Szilagy, A. Vaccaro, M. Borkovec, *Langmuir* 26 (2010) 15109-15111.
- [218] G. Decher, J.B. Schlenoff, *Multilayer thin films*, Wiley-VCH, Weinheim, 2002.
- [219] J.S. Richardson, K.A. Thomas, B.H. Rubin, D.C. Richardson, *Proc. Natl. Acad. Sci. U. S. A.* 72 (1975) 1349-1353.
- [220] M. Gajhede, D.J. Schuller, A. Henriksen, A.T. Smith, T.L. Poulos, *Nat. Struct. Biol.* 4 (1997) 1032-1038.
- [221] D.K. Bhattacharyya, U. Bandyopadhyay, R.K. Banerjee, *J. Biol. Chem.* 267 (1992) 9800-9804.
- [222] C.B. Lavery, M.C. MacInnis, M.J. MacDonald, J.B. Williams, C.A. Spencer, A.A. Burke, D.J.G. Irwin, G.B. D'Cunha, *J. Agric. Food Chem.* 58 (2010) 8471-8476.
- [223] K.A. Johnson, R.S. Goody, *Biochemistry* 50 (2011) 8264-8269.
- [224] P. Tanner, O. Onaca, V. Balasubramanian, W. Meier, C.G. Palivan, *Chem.-Eur. J.* 17 (2011) 4552-4560.
- [225] M. Iwasaki, M. Yoshimoto, *Langmuir* 37 (2021) 10624-10635.
- [226] M.C. Liu, S.J. Yang, D. Hong, J.P. Yang, M. Liu, Y. Lin, C.H. Huang, C.J. Wang, *Chem. Cent. J.* 10 (2016) 39.
- [227] J. Fernandez-Lucas, D. Castaneda, D. Hormigo, *Trends Food Sci. Technol.* 68 (2017) 91-101.
- [228] J. Drenth, J.N. Jansonius, R. Koekoek, H.M. Swen, B.G. Wolthers, *Nature* 218 (1968) 929-932.
- [229] S. Raveendran, B. Parameswaran, S.B. Ummalyma, A. Abraham, A.K. Mathew, A. Madhavan, S. Rebello, A. Pandey, *Food Technol. Biotechnol.* 56 (2018) 16-30.
- [230] H.J. Dai, S.Y. Ou, Z.J. Liu, H.H. Huang, *Carbohydr. Polym.* 169 (2017) 504-514.
- [231] I. Bala, V. Bhardwaj, S. Hariharan, M. Kumar, *J. Pharm. Biomed. Anal.* 40 (2006) 206-210.
- [232] M. Ozyurek, K. Guclu, E. Tutem, K.S. Baskan, E. Ercag, S.E. Celik, S. Baki, L. Yildiz, S. Karaman, R. Apak, *Anal. Methods* 3 (2011) 2439-2453.
- [233] I. Fita, M.G. Rossmann, *J. Mol. Biol.* 185 (1985) 21-37.
- [234] C. Belle, J.L. Pierre, *Eur. J. Inorg. Chem.* (2003) 4137-4146.
- [235] A.J. Wu, J.E. Penner-Hahn, V.L. Pecoraro, *Chem. Rev.* 104 (2004) 903-938.
- [236] I.N. Jakab, O. Lorincz, A. Jancso, T. Gajda, B. Gyurcsik, *Dalton Trans.* (2008) 6987-6995.
- [237] H. Ohtsu, Y. Shimazaki, A. Odani, O. Yamauchi, W. Mori, S. Itoh, S. Fukuzumi, *J. Am. Chem. Soc.* 122 (2000) 5733-5741.
- [238] Z. Liu, L.N. Xie, K.Q. Qiu, X.X. Liao, T.W. Rees, Z.Z. Zhao, L.N. Ji, H. Chao, *ACS Appl. Mater. Interfaces* 12 (2020) 31205-31216.
- [239] B. Bhushan, P. Gopinath, *J. Mat. Chem. B* 3 (2015) 4843-4852.
- [240] Y.Y. Huang, Z. Liu, C.Q. Liu, E.G. Ju, Y. Zhang, J.S. Ren, X.G. Qu, *Angew. Chem.-Int. Edit.* 55 (2016) 6646-6650.
- [241] Y.Y. Huang, C.Q. Liu, F. Pu, Z. Liu, J.S. Ren, X.G. Qu, *Chem. Commun.* 53 (2017) 3082-3085.
- [242] F.M. Wang, E.G. Ju, Y.J. Guan, J.S. Ren, X.G. Qu, *Small* 13 (2017) 1603051.
- [243] J. Estelrich, M.A. Busquets, *Int. J. Mol. Sci.* 22 (2021) 5993.
- [244] M. Shokouhimehr, E.S. Soehnen, J.H. Hao, M. Griswold, C. Flask, X.D. Fan, J.P. Babilion, S. Basu, S.P.D. Huang, *J. Mater. Chem.* 20 (2010) 5251-5259.
- [245] L. Cheng, H. Gong, W.W. Zhu, J.J. Liu, X.Y. Wang, G. Liu, Z. Liu, *Biomaterials* 35 (2014) 9844-9852.



## 9. AZ ÉRTEKEZÉS ALAPJÁT KÉPEZŐ KÖZLEMÉNYEK

- [T1] P. Rouster, M. Pavlovic, **I. Szilagyi**, Improving the stability of titania nanosheets by functionalization with polyelectrolytes, *RSC Adv.* 6 (2016) 97322-97330.
- [T2] G. Varga, Z. Somosi, A. Kukovecz, Z. Konya, I. Palinko, **I. Szilagyi**, A colloid chemistry route for the preparation of hierarchically ordered mesoporous layered double hydroxides using surfactants as sacrificial templates, *J. Colloid Interface Sci.* 581 (2021) 928-938.
- [T3] **I. Szilagyi**, D. Rosicka, J. Hierrezuelo, M. Borkovec, Charging and stability of anionic latex particles in the presence of linear poly(ethylene imine), *J. Colloid Interface Sci.* 360 (2011) 580-585.
- [T4] B. Katana, P. Rouster, G. Varga, S. Muráth, K. Glinel, A.M. Jonas, **I. Szilagyi**, Self-assembly of protamine biomacromolecule on halloysite nanotubes for immobilization of superoxide dismutase enzyme, *ACS Appl. Bio Mater.* 3 (2020) 522-530.
- [T5] E. Horvath, L. Grebikova, P. Maroni, T. Szabo, A. Magrez, L. Forro, **I. Szilagyi**, Dispersion characteristics and aggregation in titanate nanowire colloids, *ChemPlusChem* 79 (2014) 592-600.
- [T6] T. Oncsik, G. Trefalt, M. Borkovec, **I. Szilagyi**, Specific ion effects on particle aggregation induced by monovalent salts within the Hofmeister series, *Langmuir* 31 (2015) 3799-3807.
- [T7] P. Rouster, M. Pavlovic, **I. Szilagyi**, Destabilization of titania nanosheet suspensions by inorganic salts: Hofmeister series and Schulze-Hardy rule, *J. Phys. Chem. B* 121 (2017) 6749-6758.
- [T8] B. Katana, D. Takács, E. Csapo, T. Szabo, A. Jamnik, **I. Szilagyi**, Ion specific effects on the stability of halloysite nanotube colloids-inorganic salts versus ionic liquids, *J. Phys. Chem. B* 124 (2020) 9757-9765.
- [T9] M. Pavlovic, R. Huber, M. Adok-Sipiczki, C. Nardin, **I. Szilagyi**, Ion specific effects on the stability of layered double hydroxide colloids, *Soft Matter* 12 (2016) 4024-4033.
- [T10] A. Szerlauth, E. Balog, D. Takács, S. Sáringer, G. Varga, G. Schusztér, **I. Szilagyi**, Self-assembly of delaminated layered double hydroxide nanosheets for the recovery of lamellar structure, *Colloid Interface Sci. Commun.* 46 (2021) 100564.
- [T11] **I. Szilagyi**, A. Polomska, D. Citherlet, A. Sadeghpour, M. Borkovec, Charging and aggregation of negatively charged colloidal latex particles in the presence of multivalent oligoamine cations, *J. Colloid Interface Sci.* 392 (2013) 34-41.
- [T12] B. Katana, D. Takács, A. Szerlauth, S. Sáringer, G. Varga, A. Jamnik, F.D. Bobbink, P.J. Dyson, **I. Szilagyi**, Aggregation of halloysite nanotubes in the presence of multivalent ions and ionic liquids, *Langmuir* 37 (2021) 11869-11879.
- [T13] T. Cao, **I. Szilagyi**, T. Oncsik, M. Borkovec, G. Trefalt, Aggregation of colloidal particles in the presence of multivalent coions: The inverse Schulze-Hardy rule, *Langmuir* 31 (2015) 6610-6614.
- [T14] G. Trefalt, **I. Szilagyi**, G. Tellez, M. Borkovec, Colloidal stability in asymmetric electrolytes: Modifications of the Schulze-Hardy rule, *Langmuir* 33 (2017) 1695-1704.
- [T15] M. Pavlovic, P. Rouster, T. Oncsik, **I. Szilagyi**, Tuning colloidal stability of layered double hydroxides: from monovalent ions to polyelectrolytes, *ChemPlusChem* 82 (2017) 121-131.
- [T16] S. Muráth, S. Sáringer, Z. Somosi, **I. Szilagyi**, Effect of ionic compounds of different valences on the stability of titanium oxide colloids, *Colloid Interfac.* 2 (2018) 32.
- [T17] P. Sinha, **I. Szilagyi**, F.J.M. Ruiz-Cabello, P. Maroni, M. Borkovec, Attractive forces between charged colloidal particles induced by multivalent ions revealed by confronting aggregation and direct force measurements, *J. Phys. Chem. Lett.* 4 (2013) 648-652.
- [T18] **I. Szilagyi**, A. Sadeghpour, M. Borkovec, Destabilization of colloidal suspensions by multivalent ions and polyelectrolytes: From screening to overcharging, *Langmuir* 28 (2012) 6211-6215.
- [T19] T. Oncsik, A. Desert, G. Trefalt, M. Borkovec, **I. Szilagyi**, Charging and aggregation of latex particles in aqueous solutions of ionic liquids: Towards an extended Hofmeister series, *Phys. Chem. Chem. Phys.* 18 (2016) 7511-7520.
- [T20] P. Rouster, M. Pavlovic, T. Cao, B. Katana, **I. Szilagyi**, Stability of titania nanomaterials dispersed in aqueous solutions of ionic liquids of different alkyl chain lengths, *J. Phys. Chem. C* 123 (2019) 12966-12974.
- [T21] D. Takács, B. Katana, A. Szerlauth, D. Sebők, M. Tomšič, **I. Szilagyi**, Influence of adsorption of ionic liquid constituents on the stability of layered double hydroxide colloids, *Soft Matter* 17 (2021) 9116-9124.
- [T22] **I. Szilagyi**, T. Szabo, A. Desert, G. Trefalt, T. Oncsik, M. Borkovec, Particle aggregation mechanisms in ionic liquids, *Phys. Chem. Chem. Phys.* 16 (2014) 9515-9524.
- [T23] D. Takács, M. Tomsic, **I. Szilagyi**, Effect of water and salt on the colloidal stability of latex particles in ionic liquid solutions, *Colloid Interfac.* 6 (2022) 2.
- [T24] S. Sáringer, P. Rouster, **I. Szilagyi**, Regulation of the stability of titania nanosheet dispersions with oppositely and like-charged polyelectrolytes, *Langmuir* 35 (2019) 4986-4994.
- [T25] T. Szabo, V. Toth, E. Horvath, L. Forro, **I. Szilagyi**, Tuning the aggregation of titanate nanowires in aqueous dispersions, *Langmuir* 31 (2015) 42-49.

- [T26] P. Rouster, M. Pavlovic, E. Horvath, L. Forro, S.K. Dey, **I. Szilagyi**, Influence of protamine functionalization on the colloidal stability of 1D and 2D titanium oxide nanostructures, *Langmuir* 33 (2017) 9750-9758.
- [T27] M. Pavlovic, M. Adok-Sipiczki, E. Horvath, T. Szabo, L. Forro, **I. Szilagyi**, Dendrimer-stabilized titanate nanowire dispersions as potential nanocarriers, *J. Phys. Chem. C* 119 (2015) 24919-24926.
- [T28] M. Finessi, P. Sinha, **I. Szilagyi**, I. Popa, P. Maroni, M. Borkovec, Charge reversal of sulfate latex particles by adsorbed linear poly(ethylene imine) probed by multiparticle colloidal probe technique, *J. Phys. Chem. B* 115 (2011) 9098-9105.
- [T29] B. Katana, D. Takács, F.D. Bobbink, P.J. Dyson, N.B. Alsharif, M. Tomšič, **I. Szilagyi**, Masking specific effects of ionic liquid constituents at the solid-liquid interface by surface functionalization, *Phys. Chem. Chem. Phys.* 22 (2020) 24764-24770.
- [T30] M. Pavlovic, M. Adok-Sipiczki, C. Nardin, S. Pearson, E. Bourgeat-Lami, V. Prevot, **I. Szilagyi**, Effect of macroRAFT copolymer adsorption on the colloidal stability of layered double hydroxide nanoparticles, *Langmuir* 31 (2015) 12609-12617.
- [T31] M. Pavlovic, L. Li, F. Dits, Z. Gu, M. Adok-Sipiczki, **I. Szilagyi**, Aggregation of layered double hydroxide nanoparticles in the presence of HEP: Towards highly stable delivery systems, *RSC Adv.* 6 (2016) 16159-16167.
- [T32] Z. Somosi, M. Pavlovic, I. Palinko, **I. Szilagyi**, Effect of polyelectrolyte mono- and bilayer formation on the colloidal stability of layered double hydroxide nanoparticles, *Nanomaterials* 8 (2018) 986.
- [T33] **I. Szilagyi**, G. Trefalt, A. Tiraferri, P. Maroni, M. Borkovec, Polyelectrolyte adsorption, interparticle forces, and colloidal aggregation, *Soft Matter* 10 (2014) 2479-2502.
- [T34] M. Pavlovic, P. Rouster, **I. Szilagyi**, Synthesis and formulation of functional bionanomaterials with superoxide dismutase activity, *Nanoscale* 9 (2017) 369-379.
- [T35] P. Rouster, M. Pavlovic, **I. Szilagyi**, Immobilization of Superoxide Dismutase on polyelectrolyte functionalized titania nanosheets, *ChemBiochem* 19 (2018) 404-410.
- [T36] M. Pavlovic, P. Rouster, Z. Somosi, **I. Szilagyi**, Horseradish peroxidase-nanoclay hybrid particles of high functional and colloidal stability, *J. Colloid Interface Sci.* 524 (2018) 114-121.
- [T37] P. Rouster, M. Pavlovic, S. Saringer, **I. Szilagyi**, Functionalized titania nanosheet dispersions of peroxidase activity, *J. Phys. Chem. C* 122 (2018) 11455-11463.
- [T38] S. Saringer, R.A. Akula, A. Szerlauth, **I. Szilagyi**, Papain adsorption on latex particles: Charging, aggregation, and enzymatic activity, *J. Phys. Chem. B* 123 (2019) 9984-9991.
- [T39] M. Pavlovic, S. Murath, X. Katona, N.B. Alsharif, P. Rouster, J. Maleth, **I. Szilagyi**, Nanocomposite-based dual enzyme system for broad-spectrum scavenging of reactive oxygen species, *Sci. Rep.* 11 (2021) 4321.
- [T40] S. Saringer, P. Rouster, **I. Szilagyi**, Co-immobilization of antioxidant enzymes on titania nanosheets for reduction of oxidative stress in colloid systems, *J. Colloid Interface Sci.* 590 (2021) 28-37.
- [T41] S. Sáringer, T. Valtner, Á. Varga, J. Maléth, **I. Szilagyi**, Development of polymer-based multifunctional composite particles of protease and peroxidase activities, *J. Mat. Chem. B* (2022) 10.1039/D1TB01861B
- [T42] S. Murath, N.B. Alsharif, S. Saringer, B. Katana, Z. Somosi, **I. Szilagyi**, Antioxidant materials based on 2D nanostructures: A review on recent progresses, *Crystals* 10 (2020) 148.
- [T43] A. Szerlauth, S. Murath, S. Viski, **I. Szilagyi**, Radical scavenging activity of plant extracts from improved processing, *Heliyon* 5 (2019) e02763.
- [T44] S. Murath, S. Szerlauth, D. Sebok, **I. Szilagyi**, Layered double hydroxide nanoparticles to overcome the hydrophobicity of ellagic acid: An antioxidant hybrid material, *Antioxidants* 9 (2020) 153.
- [T45] A. Szerlauth, S. Murath, **I. Szilagyi**, Layered double hydroxide-based antioxidant dispersions with high colloidal and functional stability, *Soft Matter* 16 (2020) 10518-10527.
- [T46] M. Pavlovic, M. Nafradi, P. Rouster, S. Murath, **I. Szilagyi**, Highly stable enzyme-mimicking nanocomposite of antioxidant activity, *J. Colloid Interface Sci.* 543 (2019) 174-182.
- [T47] Z. Somosi, N.V. May, D. Sebok, I. Palinko, **I. Szilagyi**, Catalytic antioxidant nanocomposites based on sequential adsorption of redox active metal complexes and polyelectrolytes on nanoclay particles, *Dalton Trans.* 50 (2021) 2426-2435.
- [T48] N.B. Alsharif, G.F. Samu, S. Sáringer, S. Muráth, **I. Szilagyi**, A colloid approach to decorate latex particles with Prussian blue nanozymes, *J. Mol. Liq.* 309 (2020) 113066.
- [T49] N.B. Alsharif, K. Bere, S. Sáringer, G.F. Samu, D. Takács, V. Hornok, **I. Szilagyi**, Design of hybrid biocatalysts by controlled heteroaggregation of manganese oxide and sulfate latex particles to combat reactive oxygen species, *J. Mat. Chem. B* 9 (2021) 4929-4940.
- [T50] N.B. Alsharif, B. Katana, S. Murath, **I. Szilagyi**, Composite materials based on heteroaggregated particles: Fundamentals and applications, *Adv. Colloid Interface Sci.* 294 (2021) 102456.

## 10. KÖSZÖNETNYILVÁNÍTÁS

Azért, hogy ez a doktori dolgozat létrejöhesse Michal Borkovec professzort illeti az első köszönet, aki a Genfi Egyetemen eltöltött 8,5 év alatt a kezdeti időkben posztdoktori témavezetőként egyengette a karrieremet, majd független kutatóvá válásom után is sokat segített az akadémiai pálya minden területére kiterjedő rendkívül hasznos tanácsaival és támogatásával.

Nagyon sajnálom, hogy Pálinkó István professzor nem élhette meg ennek a dolgozatnak az elkészültét, aki a doktori tanulmányaim óta segítette kutatói pályám felépítését először, mint (társ)témavezető, majd később, mint barát és kutatásban együttműködő partner. Hálásan köszönöm Tóth Ágota professzor asszonynak, hogy lehetőséget adott a kutatócsoportom megalapítására az általa vezetett Fizikai Kémiai és Anyagtudományi Tanszéken. Köszönöm a segítséget és támogatást, amit kaptam (és azóta is kapok) Tőle a Svájcban való hazatelepülés óta eltelt időszakban.

A köszönetet érdemlők listáján mindenképpen helyet érdemel Meleg István középiskolai kémiatanárom, Dr. Labádi Imre, Prof. Dr. Kiss Tamás és Prof. Dr. Hernádi Klára doktori (társ)témavezetőim, akik a tanulmányaim alatt mind hozzájárultak, hogy a kutatói-oktatói pályán minél jobb esélyekkel indulhassak. Ausztráliai posztdoktori munkám témavezetőjének, Prof. Dr. Peter M. May-nek, hálásan köszönöm a szakmai és személyes tanácsait, főként arra vonatkozóan, hogyan kell egy kutatócsoportot menedzselni, vagy éppen hogyan kell az akadémiai és ipari szponzorok elvárásainak megfelelni.

Köszönetemet fejezem ki valamennyi végzett és jelenlegi PhD, diplomamunkás és szakdolgozó hallgatónak, valamint posztdoktori kutatóknak és egyéb munkatársamnak, akik a genfi és szegedi csoportjaimban tehetségükkel, hozzáállásukkal és munkájukkal nagyban hozzájárultak a dolgozatban tárgyalt eredmények létrejöttéhez. Szintén köszönöm a velem együttműködő számos hazai és külföldi kolléga munkáját, akikkel eredményes munkakapcsolatot sikerült kialakítani az elmúlt évtizedben.

Köszönöm a Svájci Kutatási Alap (150162, C15.0024), a Magyar Tudományos Akadémia (Lendület 96130), a Nemzeti Kutatási, Fejlesztési és Innovációs Hivatal (SNN131558), az Emberi Erőforrások Minisztériuma (20391-3/2018/FEKUSTRAT) és a Gazdaságfejlesztési és Innovációs Operatív Program (2.3.4-15-2020-0006) anyagi támogatását, amely nélkül a doktori műben tárgyalt eredmények nem jöhettek volna létre.

Hálával tartozok feleségemnek, Andreának, hogy 3 országon átívelő tudományos pályám során kitartott mellettem és olyan családi háttérrel biztosított, amely átsegített minden nehézségen. Köszönet illeti két fiamat, Zétényt és Bencét, akik nélkül nem az lennék, aki vagyok és akik remélhetőleg büszkék lesznek rám, ha majd fel tudják mérni, hogy mennyi munka volt ezen doktori mű megírásában és a benne ismertetett eredmények elérésében. Végezetül töretlen szeretetükért és határtalan támogatásukért nagyon hálás vagyok szüleimnek és testvéremnek.

Cite this: *RSC Adv.*, 2016, 6, 97322

## Improving the stability of titania nanosheets by functionalization with polyelectrolytes†

Paul Rouster, Marko Pavlovic and Istvan Szilagyi\*

Titania nanosheets (TNS) have been synthesized by the hydrothermal method and functionalized with poly(diallyldimethylammonium chloride) (PDADMAC) or poly(acrylamide-co-diallyldimethylammonium chloride) (P(AAm-co-DADMAC)) polyelectrolytes. The morphology and the composition of the materials were investigated by X-ray diffraction and microscopy techniques. The polyelectrolyte coating led to dramatic changes in the charging behavior and in the colloidal stability of the TNS in aqueous suspensions, as revealed by electrophoretic and light scattering measurements. The adsorption of PDADMAC and P(AAm-co-DADMAC) on the oppositely charged TNS surface gave rise to charge neutralization and charge reversal at appropriate polyelectrolyte doses and to unstable and stable suspensions, respectively. In the latter situation, the polyelectrolyte functionalized nanosheets were resistant against aggregation even at high ionic strengths where the bare TNS rapidly aggregated. Highly stable suspensions were obtained especially in the presence of P(AAm-co-DADMAC) layer on the TNS surface due to the repulsive interparticle forces originating from both electrostatic and steric interactions. The obtained suspensions of excellent colloidal stability are promising candidates as carrier systems for instance in biomedical treatments, where homogeneous distribution of primary particles is required for the delivery of biologically active molecules.

Received 23rd September 2016  
Accepted 5th October 2016

DOI: 10.1039/c6ra23707j

www.rsc.org/advances

### Introduction

Over the past decades, titania has been widely used in various applications, *e.g.*, in electrochemistry,<sup>1–5</sup> (photo)catalysis,<sup>6–14</sup> biomedical processes,<sup>15–18</sup> development of paints<sup>19,20</sup> and water treatment.<sup>21–23</sup> Depending on the synthesis conditions, titania and its composites of various shapes and compositions have been obtained.<sup>24,25</sup> Among them, spherical nanoparticles are the most commonly used structures, however, they may be overruled in the future due to the potential development and applications of other titania derivatives, such as nanotubes and nanosheets. They appear to exhibit, in some cases, improved mechanical and structural properties compared to the beads.

For instance, Wang *et al.*<sup>26</sup> showed that surface fluorinated anatase titania nanosheets (TNS) display higher photocatalytic activity than the commonly used P25 particles. However, the elimination of fluorine from the surface led to a decrease in the photocatalytic activity, whereas the formation of titanium(IV) oxydifluoride (TiOF<sub>2</sub>) is expected to weaken the activity due to the development of non-photoreactive TiOF<sub>2</sub> material. They assumed that the improved photocatalytic activity was owing to the efficient separation of the electrons and holes occurring on

the sheet-like geometry. The influence of the shape of the titania nanostructures on the catalytic activity was also studied by Yu *et al.*<sup>27</sup> A decrease in the photocatalytic activity under UV light irradiation was reported in the following order: nanosheets > nanotubes > nanoparticles.

Moreover, in bioapplications,<sup>15,18,28</sup> titania nanotubes and nanowires are receiving growing interest, while limited focus has been made on TNS so far. In most studies dealing with biomedical applications such as drug delivery, titania nanotubes are obtained from titania foils by various types of syntheses. Due to their biocompatibility, improved physico-chemical properties and ease of processability, various drugs have been intercalated in the structure and/or adsorbed on the outer surface of titanate derivatives.

One can easily realize that the colloidal stability of the above mentioned heterogeneous systems is a critical issue in these applications, since stable dispersion of primary particles is required for both the high catalytic activity and the successful delivery of biomolecules. However, only a moderate number of studies dealing with the functionalization and its effect on the colloidal stability of titania derivatives were published to date. Among these papers,<sup>29–34</sup> it was shown that the functionalization of titanate nanowires by polyelectrolytes or dendrimers led to an increase in the colloidal stability towards higher electrolyte concentrations. It was also found that the experimental conditions (*e.g.*, polyelectrolyte dose, ionic strength and pH) largely influence the charging and aggregation of the titanate

Department of Inorganic and Analytical Chemistry, University of Geneva, 30 Quai Ernest-Ansermet, CH-1205 Geneva, Switzerland. E-mail: istvan.szilagyi@unige.ch

† Electronic supplementary information (ESI) available. See DOI: 10.1039/c6ra23707j

compounds. The main message of these studies is that the functionalization of titania derivatives offers a unique way to tune the colloidal stability and to tailor the properties of the materials making them suitable for various applications in suspensions.

However, no systematic studies on the surface charge properties and colloidal stability of TNS have been published yet in the literature. Therefore, we report here on the synthetic routes for anatase TNS and their surface fluorinated form followed by their functionalization with two types of polyelectrolytes. The structural properties have been assessed by various techniques in solid state and in aqueous suspensions. The colloidal behavior and the interactions at the interface between the bare or coated TNS are studied and experimental conditions to obtain stable or aggregating suspensions are suggested. The present results provide unique information for those applying TNS derivatives in suspensions, where the aggregation and stability features must be well defined.

## Materials and methods

### Preparation of the precursor TiO<sub>2</sub> nanosheets

The synthesis of the TiO<sub>2</sub> precursor was based on the protocol of Han *et al.*<sup>35</sup> Briefly, 5 mL of tetrabutyl titanate (TiOBu<sub>4</sub>, reagent grade 97%, Sigma Aldrich) was mixed with 0.8 mL of hydrofluoric acid (HF, for analysis, 48–51% in water, Arcos Organics) under vigorous stirring in a Teflon-lined autoclave, which was then put in a stainless steel autoclave and sealed. During the hydrothermal treatment, the autoclave was placed in an oven at 200 °C for 24 h. At the end of the reaction, the autoclave was removed from the oven and allowed to cool down to room temperature. The solid material was collected by ultracentrifugation at a speed of 10 000 rpm for 10 min. In the washing process, the supernatant was removed and the concentrated suspension was diluted. This procedure was repeated three times using ultrapure water (Millipore, with a resistivity of 18.2 MΩ cm at 25 °C), two times with ethanol (analytical reagent grade, Fisher Scientific) and a last time again with ultrapure water, which was used for all the sample preparation throughout the experiments. Finally, the suspension was dried under vacuum at 50 °C. The powder was then collected and grinded in a mortar before undergoing a final drying step at 80 °C for 3 h.

### Conversion of the TiO<sub>2</sub> nanosheets to anatase nanosheets

The obtained powder (white-yellowish color) of TiO<sub>2</sub> nanosheets was converted to titania (TiO<sub>2</sub>) nanosheets (TNS) of anatase phase by washing at different sodium hydroxide (NaOH pellets, for analysis 98.5%, Arcos Organics) concentrations.<sup>26,36</sup> First, the powder was dispersed in 1 M NaOH and underwent a centrifugation step at 10 000 rpm for 5 min. The supernatant was then removed and the slurry was redispersed in 0.1 M NaOH prior to the next centrifugation step. The dispersion and centrifugation in 0.1 M NaOH was repeated twice. The final step consisted of removing the supernatant and diluting the concentrated suspension in water before the centrifugation

step. This was repeated until a pH of 7–8 was obtained. The supernatant was then removed and the powder (whitish color) was allowed to dry in an oven at 80 °C for 3 h.

### Functionalization of the TNS

The TNS were functionalized with two different polyelectrolytes, namely poly(diallyldimethylammonium chloride) (PDADMAC,  $M_w = 100\text{--}200\text{ kg mol}^{-1}$ , 20 wt% in water, Aldrich) and poly(acrylamide-*co*-diallyldimethylammonium chloride) (P(AAm-*co*-DADMAC),  $M_w = 250\text{ kg mol}^{-1}$ , 10 wt% in water, Aldrich). The copolymer contained 55 wt% acrylamide. The TNS were dispersed in pH 9 ± 0.1 (adjusted with NaOH) water at appropriate particle concentration. This pH was used in all of the experiments. Polyelectrolyte stock solutions (1000, 100, 10, 1, 0.1, 0.01 mg L<sup>-1</sup>) were obtained by dilution.

Samples of 10 mg L<sup>-1</sup> TNS functionalized with 200 mg g<sup>-1</sup> PDADMAC or 600 mg g<sup>-1</sup> P(AAm-*co*-DADMAC) were made prior to the stability studies. The mg g<sup>-1</sup> unit refers to mg polyelectrolyte per one gram of TNS. Accordingly, 10 mL of a 100 mg L<sup>-1</sup> stock suspension of bare TNS was added dropwise into solutions of 7.2 mL PDADMAC or 21.6 mL P(AAm-*co*-DADMAC) of 100 mg L<sup>-1</sup> concentration diluted to 90 mL with water. After allowing two hours reaction time, the suspensions were centrifuged at 10 000 rpm for 20 min to remove the excess polyelectrolytes that did not adsorb on the surface. After the removal of the supernatant, the obtained slurry was redispersed in water and the ionic strength was set to 5 ± 0.5 mM with sodium chloride (NaCl, puriss. p.a., ≥99.5%, Sigma Aldrich).

### Characterization of the bare and functionalized TNS

Powder X-ray diffraction (XRD) was performed on an Empyrean (PANalytical) X-ray diffractometer in the reflection geometry using the CuKα<sub>1</sub> radiation (Johansson type Ge monochromator). The powder was placed on a silicon zero background holder for the acquisition of the XRD patterns. The data were collected for two theta (2θ) ranging from 5° to 70° with a step of 0.0131° and for an exposure time of either 298 s or 798 s per step. The XRD pattern of the silicon zero background holder was also recorded and subtracted from the diffractogram of the material.

Transmission electron microscopy (TEM, Tecnai G2 Sphera microscope, FEI) images of the bare and coated particles were collected on a device equipped with a LaB6 cathode and operated at 120 kV. The carbon hexagonal mesh (CF200H-CU-UL, Electron Microscopy Sciences) was treated with plasma for twenty seconds prior to the deposition of the colloidal suspension on it in order to increase the hydrophilicity of the mesh surface. About 5 μL sample was deposited on the mesh. After 2 min, the excess solution was removed with filter paper. Finally, the coated mesh was placed on the specimen and mounted in the microscope for imaging.

Images were also recorded with an atomic force microscope (AFM) in the tapping mode using an AFM (MFP-3D, Asylum Research) mounted on an inverse optical microscope (Zeiss Axiovert 200). A silicon cantilever (AC160TS, Olympus Micro-Cantilever) with a spring constant of 26 N m<sup>-1</sup> was used. Height

dc 1931\_21

and phase images of the TNS deposited on PDADMAC coated mica (highest quality grade V1, Plano GmbH) were recorded simultaneously at a scan rate of 1 Hz and with a resolution of  $512 \times 512$  pixels.

Electrophoretic mobilities were measured with a Zetasizer Nano ZS from Malvern Instruments. For the determination of the mobilities, 5 mL solutions were prepared. Basically, 0.5 mL of the uncoated or coated TNS suspension was added to 4.5 mL solution composed of NaCl or polyelectrolyte at the appropriate concentration. The samples were allowed to rest overnight before measuring the electrophoretic mobilities, which were obtained by averaging the results of five individual measurements for several solutions under the same conditions.

Dynamic light scattering (DLS) measurements were performed with a compact goniometer system (ALV/CGS-3, ALV GmbH) using borosilicate glass cuvettes (Kimble Chase). The scattering angle was set to  $90^\circ$ , the correlation function was accumulated for 20 s (corresponding to the duration of one run) and a second order cumulant fit was used to determine the diffusion coefficient. The hydrodynamic radius ( $R_h$ ) was then calculated by using the Stokes–Einstein equation.<sup>37</sup> In the time-resolved aggregation experiments, about 50–300 runs were performed depending on the speed of aggregation. Based on these measurements, the colloidal stability was expressed in terms of stability ratio ( $W$ ), which was calculated from the initial increase in the size as follows:<sup>38,39</sup>

$$W = \frac{(dR_h(t)/dt)_{t \rightarrow 0, \text{fast}}}{(dR_h(t)/dt)_{t \rightarrow 0}} \quad (1)$$

where the fast condition corresponds to the fast aggregation of the TNS in a 1 M NaCl solution. Under this experimental condition, the aggregation of the particles is solely controlled by their diffusion, *i.e.*, each collision results in dimer formation.<sup>40–42</sup> Accordingly, stability ratios close to unity indicate fast aggregation and unstable samples, while higher values refer to slower aggregation and stable suspensions. The same particle concentration ( $1 \text{ mg L}^{-1}$ ) was used in all of the time-resolved experiments, whereas, the polyelectrolyte dose or the ionic strength was varied. Note that the sample preparation for the DLS was done in a similar manner as the one for the electrophoretic mobility measurements in order to link both results together and to make some correlations. The difference in sample preparation lies in the fact that 2 mL solutions were prepared for DLS and that the size measurements were performed directly after mixing the bare or coated TNS stock suspensions with the salt or the polyelectrolyte solutions.

## Results and discussion

### Characterization of the bare nanosheets

It is known from the literature that  $\text{TiOF}_2$  nanosheets can be synthesized *via* hydrothermal routes.<sup>26,43,44</sup> When synthesized in the form of nanosheets or nanocubes, one may use these compounds as precursor to obtain anatase nanosheets. Such a conversion can be achieved by calcination,<sup>44</sup> by washing the fluorinated material with alkaline solutions<sup>26,36</sup> or by

performing solvothermal or hydrothermal treatments.<sup>43,45</sup> Therefore, we have synthesized  $\text{TiOF}_2$  first for further conversion to TNS of anatase phase by alkali treatments. The synthesized precursor powder was characterized by XRD measurements. In Fig. 1, the XRD diffractograms of the precursor and of the final product are displayed with the expected ones for  $\text{TiOF}_2$  and for anatase  $\text{TiO}_2$ .

The XRD pattern of the precursor product shows two characteristic peaks, namely at  $2\theta = 23.4^\circ$  and at  $2\theta = 25.3^\circ$  corresponding to the (100) plane of  $\text{TiOF}_2$  and to the (101) plane of  $\text{TiO}_2$ , respectively. The broader peaks observed at these two  $2\theta$  values for the precursor product suggest a weak crystallization of the sample. This can originate from the action of the  $\text{F}^-$  ions on the titania lattice during the hydrothermal treatment.<sup>26</sup> Indeed, the  $\text{F}^-$  ions can induce a dissolution-recrystallization of the titania lattice due to their strong affinity to titanium(IV) leading to an inhibition of the extensive bridging of the Ti–O–Ti bonds and of their crystal growth. Therefore,  $\text{F}^-$  ions also act as a structure directing agent. However, the intensity of the  $\text{TiOF}_2$  peak at  $2\theta = 23.4^\circ$  is much lower compared to the one at  $2\theta = 25.3^\circ$  of anatase in the precursor product. This result tends to suggest that our material is essentially composed of anatase  $\text{TiO}_2$  and that some  $\text{F}^-$  ions may have been incorporated in its structure or on its surface.

Xiang *et al.*<sup>36</sup> reported that surface  $\text{F}^-$  could be removed by alkali treatment due to a ligand exchange reaction between the  $\text{F}^-$  present on the titania material and the  $\text{OH}^-$  ions in solution. Moreover, the XRD pattern of the final TNS product exhibits no more peaks related to  $\text{TiOF}_2$  indicating that all the  $\text{F}^-$  ions have been removed from the material during the NaOH treatment. No narrowing of any peaks took place suggesting that the crystal structure of the material was not altered by the treatment. Thus, it was speculated that the  $\text{F}^-$  ions were mainly located on the surface of the material, from where they were removed through the ligand exchange reaction between the  $\text{F}^-$  and  $\text{OH}^-$ .

TEM images showed that the morphology and the dimensions of the nanosheets were not modified by the exposure of

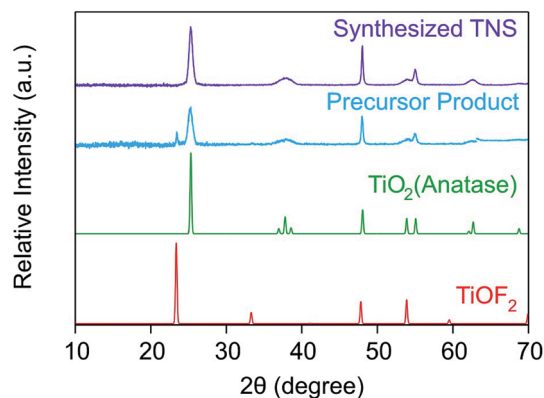


Fig. 1 XRD diffractogram of the precursor  $\text{TiOF}_2$  and of the final TNS product obtained by alkali treatment. The theoretical diffractograms for  $\text{TiOF}_2$  and anatase (obtained from the JCPDS sheets no. 04-007-8589 and no. 00-021-1272, respectively) are also shown for comparison.



dc\_1931\_21

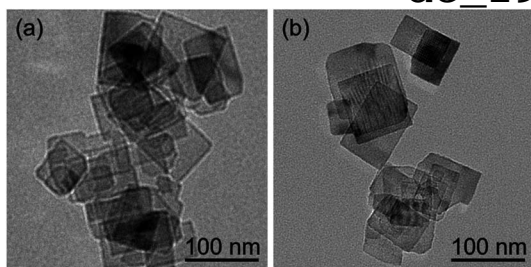


Fig. 2 TEM images of the nanosheets (a) before and (b) after the NaOH treatment.

the material to the alkali treatment (Fig. 2a and b). The length and width distributions of the nanosheets were similar for the precursor and for the final product (Fig. S1a and S1b in the ESI†). Moreover, the thickness of the NaOH treated nanosheets was determined by AFM (Fig. 3) and was found to be  $9 \pm 2$  nm. This value agreed quite well with the one measured by TEM ( $12 \pm 2$  nm) (Fig. S1c†). The slight difference between these values may result from the imprecise starting and ending point when using the TEM images for height measurements. Indeed, more precise values can be achieved by AFM imaging due to the sharper transition from the TNS surface to the substrate surface.

An important parameter to understand the charging behavior in aqueous TNS suspensions is the point of zero charge (PZC). We refer to the PZC as the value corresponding to charge neutralization of the material by the pH of the medium. Below the PZC, the material is positively charged, whereas above the PZC, it possesses negative charges. We found the charge inversion point at  $\text{pH } 5.2 \pm 0.2$  (Fig. S2†) meaning that the TNS are negatively charged at pH 9, where our experiments were

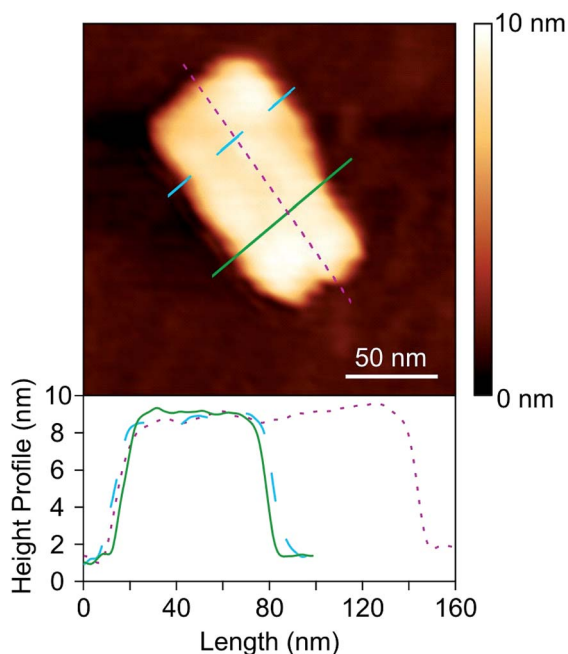


Fig. 3 AFM image of a single TNS with its corresponding height profile.

carried out. The obtained PZC is similar to the ones found for other titania compounds.<sup>33,46,47</sup>

To determine the surface charge density ( $\sigma$ ) of the TNS, the electrophoretic mobilities ( $u$ ) were measured at different ionic strengths and converted to electrokinetic potentials ( $\zeta$ ) using the Smoluchowski equation given as:<sup>48</sup>

$$\zeta = \frac{u\eta}{\varepsilon\varepsilon_0} \quad (2)$$

where  $\eta$  is the viscosity of water,  $\varepsilon_0$  is the permittivity of vacuum and  $\varepsilon$  is the dielectric constant. The potentials at different ionic strengths were then fitted with the Debye-Hückel model developed for the charge-potential relationship as follows:<sup>40</sup>

$$\sigma = \varepsilon\varepsilon_0\kappa\zeta \quad (3)$$

where  $\kappa$  is the inverse Debye length, which considers the contribution of all the ionic species present in the solution. The calculated surface charge density was  $-8 \text{ mC m}^{-2}$  (Fig. S3†).

DLS measurements in stable TNS suspensions yielded a hydrodynamic radius of 92 nm and a polydispersity index (PDI) of 0.36 (Table 1). Moreover, an average particle radius of 47 nm and a PDI of 0.30 were also determined by TEM. The PDI value is consistent with the one obtained by DLS, whereas a significant difference was found between the radii measured by DLS or TEM. Accordingly, the latter measurement yielded a much smaller value. Such a discrepancy originates from the polydispersity of the particles and from the presence of some aggregates, which are weighted more in the DLS measurements due to their higher contribution to the intensity of the scattered light.

### Charging and aggregation in the presence of polyelectrolytes

Two different polyelectrolytes were chosen to functionalize the titania nanosheets, namely PDADMAC and P(AAm-co-DADMAC). The molecular mass of PDADMAC was similar to the one of the copolymer, therefore, the difference between them lies mostly in their charge density. Accordingly, PDADMAC is fully charged due to the quaternary amines in its structure, while P(AAm-co-DADMAC) is of lower charge density due to the presence of the neutral acrylamide groups in the block

Table 1 Main characteristics of the bare TNS and of the PDADMAC and P(AAm-co-DADMAC) functionalized TNS determined in aqueous suspensions

Material	$\sigma^a$ ( $\text{mC m}^{-2}$ )	$R_h^b$ (nm)	PDI <sup>b</sup>	CCC <sup>c</sup> (mM)
Bare TNS	-8	92	0.36	19
TNS-PDADMAC	13	109	0.34	106
TNS-P(AAm-co-DADMAC)	2	99	0.41	— <sup>d</sup>

<sup>a</sup> Surface charge density obtained by electrophoresis. <sup>b</sup> Hydrodynamic radius and polydispersity index were determined in stable suspensions by DLS, where an uncertainty of about 5 nm was found for the size measurements. <sup>c</sup> Critical coagulation concentration (CCC) calculated from the stability ratio *versus* ionic strength plots. <sup>d</sup> The CCC was not reached within the salt concentration range studied.



dc\_1931\_21

copolymer (Fig. 4). The main goal of this part of the work was to clarify the effect of the acrylamide chain on the charging and aggregation processes.

The electrophoretic mobility and the stability ratio values of the TNS at different polyelectrolyte loading are shown in Fig. 4a and b, respectively. In general at low doses, the mobility values were negative due to the uncompensated charges of the TNS. The mobilities were slightly higher, but in the same range as the ones measured for the uncoated TNS at the corresponding ionic strength. By increasing the polyelectrolyte dose, the

electrophoretic mobilities of both systems increase until charge neutralization of the TNS takes place at the isoelectric point (IEP). Here, the IEP is defined as the dose, where charge neutralization of the particles occurs by polyelectrolyte adsorption. IEPs of  $2.5 \text{ mg g}^{-1}$  and of  $41.8 \text{ mg g}^{-1}$  were found for PDADMAC and P(AAm-co-DADMAC), respectively. The difference in the IEP values lies in the fact that the charge density of P(AAm-co-DADMAC) is lower than the one of PDADMAC meaning that a higher amount of P(AAm-co-DADMAC) is needed to compensate the surface charges of the TNS compared to PDADMAC.

Above the IEP, charge reversal of the coated particles occurs due to an increase of the adsorbed amount of the polyelectrolytes on the surface. Such charge inversion is caused by specific interactions (*e.g.*, hydrophobic forces, entropy gain or charge correlation effect) between the adsorbed polyelectrolyte chains.<sup>49–51</sup> The electrophoretic mobility values increase until reaching the onset of the adsorption saturation plateau (ASP). The ASP corresponds to the maximum amount of polyelectrolytes that can adsorb on the surface while the remaining polyelectrolytes stay dissolved in the bulk. In the PDADMAC system, the further increase of the electrophoretic mobility after the ASP is due to the measurement of both the coated TNS and of the bare PDADMAC in solution. Similar to the IEPs, the individual systems reach the ASP at different polyelectrolyte doses, around  $200 \text{ mg g}^{-1}$  and  $600 \text{ mg g}^{-1}$  for PDADMAC and P(AAm-co-DADMAC), respectively due to their different charge density and to possible hydrophobic intermolecular interactions in the case of the copolymer. Such charge neutralization and subsequent charge reversal have already been reported for other colloidal particles in the presence of oppositely charged polyelectrolytes.<sup>30–32,34,52–55</sup>

Moreover, the stability ratios of the TNS in the same polyelectrolyte concentration range were determined (Fig. 4b). For high polyelectrolyte doses, the suspensions are stable, as indicated by high stability ratio values. By decreasing the polyelectrolyte dose, the stability ratios decrease until reaching the fast aggregation regime around 9 and  $21 \text{ mg g}^{-1}$  for PDADMAC and P(AAm-co-DADMAC), respectively. The value of the stability ratios is equal or lower than unity at these doses, which are close to the IEPs determined by electrophoresis. The colloidal stability of the particles is limited at low doses as indicated by the moderate stability ratio values. Below a P(AAm-co-DADMAC) dose of  $2 \text{ mg g}^{-1}$ , a plateau is observed indicating electrostatic origin of the interparticle forces at low coverage.<sup>52</sup> Similar aggregation behavior was found for negatively charged colloidal particles in the presence of PDADMAC<sup>56</sup> or other positively charged polyelectrolytes.<sup>57</sup> In these studies, a significant influence of the ionic strength on the colloidal stability was reported, however, the effect of the molecular mass of the polyelectrolytes was not significant.

Let us now discuss the possible surface forces responsible for the above mentioned aggregation behavior. When the stability ratio is equal to one, the aggregation is diffusion controlled due to the lack of repulsive interactions between the particles. This situation can be explained with the theory developed by Derjaguin, Landau, Overbeek and Verwey (DLVO)

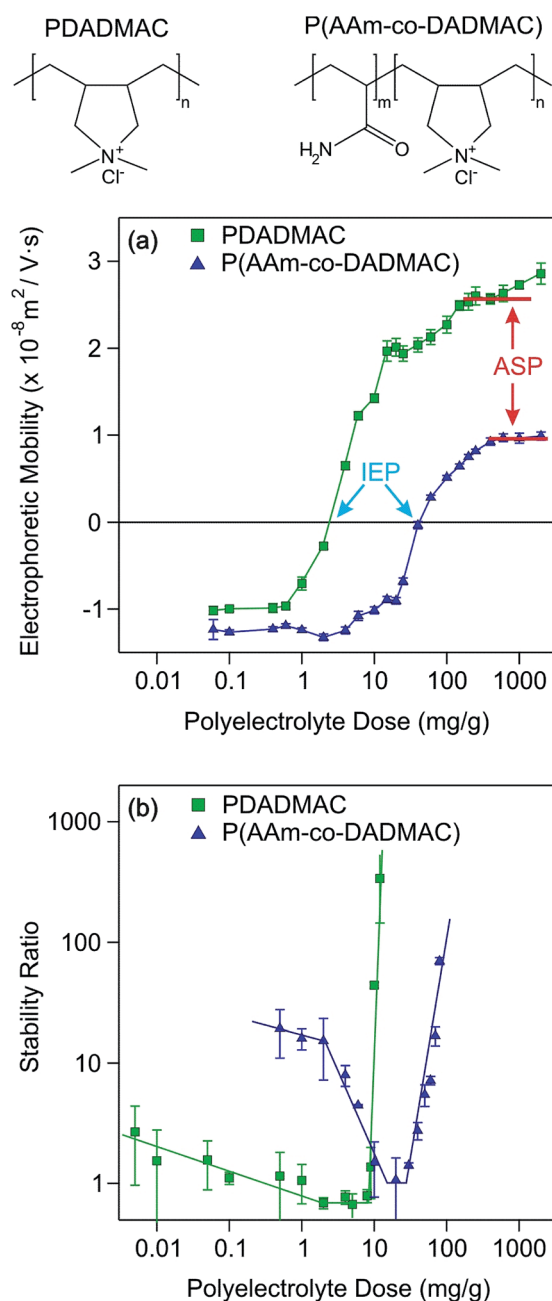


Fig. 4 Electrophoretic mobilities (a) and stability ratios (b) of TNS versus the PDADMAC or P(AAm-co-DADMAC) dose (milligrams of polyelectrolyte per gram of TNS) measured at 4.5 mM ionic strength. The chemical structures of the polyelectrolytes are shown on the top.

dc\_1931\_21

for the stability of charged colloids.<sup>40,41</sup> Accordingly, an electrical double layer forms around the particles giving rise to repulsive forces once they overlap. However, these interactions vanish upon charge neutralization by polyelectrolyte adsorption or charge screening by simple salts. On the other hand, DLVO also predicts the continuous presence of attractive van der Waals forces. The overall interparticle force is the superposition of these repulsive and attractive interactions.

Given the definition of the stability ratio in eqn (1), lower values than unity indicate the presence of an additional (non-DLVO) force corresponding to patch-charge interactions.<sup>58</sup> Such forces are due to the presence of positive polyelectrolyte islands adsorbed on the TNS, which interacts with the negative parts of the other partially coated TNS. Similar acceleration around the IEP has been reported in other particle-polyelectrolyte systems too.<sup>34,59,60</sup> However, such a patch-charge attraction is more pronounced for the PDADMAC system, while it was only slightly observed for the P(AAm-co-DADMAC) samples. This fact indicates that the highly charged PDADMAC tends to form islands on the surface and the copolymer with neutral monomer groups in its structure adsorbs partially under the form of islands with the PDADMAC part on the surface and with the P(AAm) block dangling into the solution.

Another effect of the patch-charge forces is the differences in the stability ratios at low doses. The values at the same polyelectrolyte loading are much smaller for the PDADMAC system than for the P(AAm-co-DADMAC) owing to the formation of polyelectrolyte patches on the surface and to a subsequent acceleration in the aggregation for the first case. These patch-charge interactions are present only when the particles are not fully coated (*i.e.*, when empty places are available on the surface) and disappear at high coverage leading to similar trend in the stability ratios in the present systems at high doses. Accordingly, highly stable suspensions were obtained for both the PDADMAC and the P(AAm-co-DADMAC) modified TNS at

polyelectrolyte concentrations higher than the onset of the ASP. The improvement in the colloidal stability compared to the moderately stable low dose region is striking once the stability ratio values are compared.

The tendency in the stability of the TNS-PDADMAC suspensions at different doses was verified by recording TEM images with the corresponding samples (Fig. 5). At low PDADMAC dose below the IEP, the particles are moderately stable and low order of aggregates are formed (Fig. 5a). We refer to order of aggregation as the number of particles aggregating together, *i.e.*, dimer, trimer *etc.* Around the IEP, the TNS form irregularly shaped clusters composed of high order of aggregates due to the unstable suspensions under these experimental conditions (Fig. 5b). It appears that during aggregation the TNS prefer to adopt a face-to-face orientation in the clusters. Similar structure has already been observed for titanate nanowires functionalized with polyelectrolytes.<sup>32,34</sup> Moreover, for a PDADMAC dose corresponding to the onset of the ASP, the images reveal the presence of single particles along with a few dimers (Fig. 5c), which have been formed during drying in the sample preparation process for TEM imaging.

#### Stability of bare and polyelectrolyte coated TNS

Knowing the colloidal behavior of the TNS during their coating process at different polyelectrolyte doses, the next step was to investigate the properties of the nanosheets of complete polyelectrolyte coverage at different salt concentrations. The main purpose was to determine whether the coated particles exhibit higher stability compared to the bare ones or not and that which of the obtained materials could be used under physiological conditions in bioapplications.

The charging of bare and coated TNS was first studied (Fig. 6a). The TNS were functionalized by adsorbing the polyelectrolytes at the onset of the ASP corresponding to doses of 200 mg g<sup>-1</sup> and 600 mg g<sup>-1</sup> for PDADMAC and P(AAm-co-

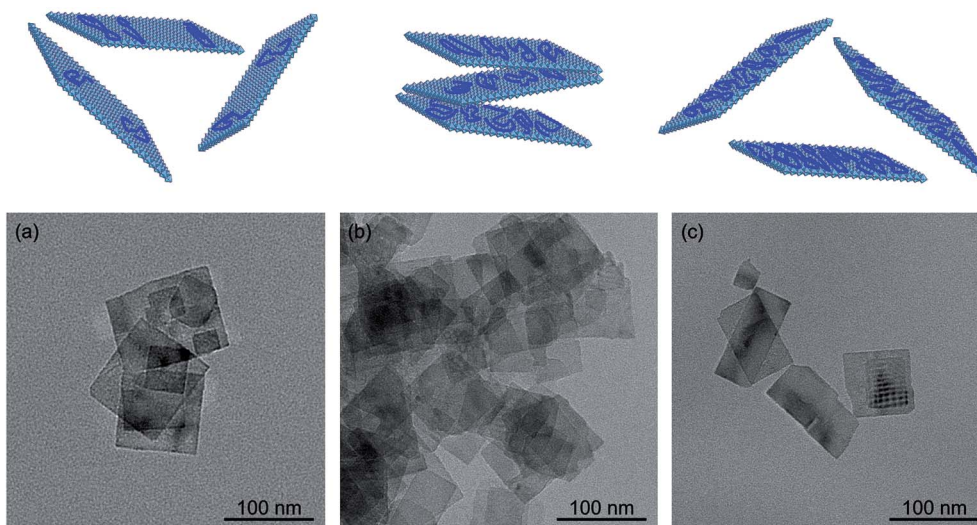


Fig. 5 TEM images and schemes of PDADMAC functionalized TNS at different doses (a) below the IEP at 0.1 mg g<sup>-1</sup>, (b) around the IEP at 3 mg g<sup>-1</sup> and (c) above the IEP at 200 mg g<sup>-1</sup> polyelectrolyte loading, which corresponds to the ASP.

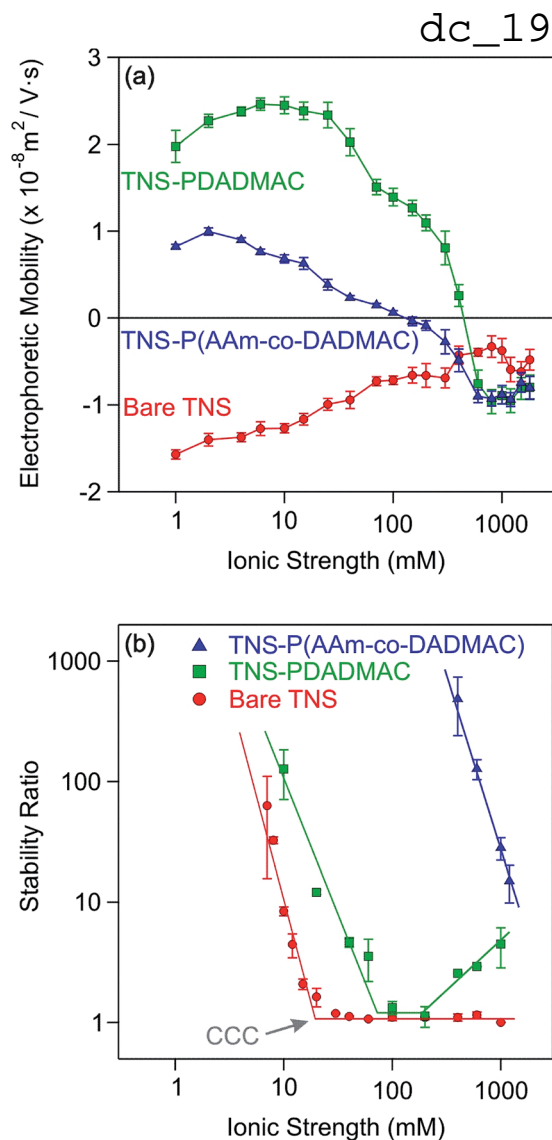


Fig. 6 (a) Electrophoretic mobility and (b) stability ratio of the bare TNS, TNS-PDADMAC and TNS-P(AAm-co-DADMAC) as a function of the ionic strength adjusted by NaCl.

DADMAC), respectively. From the electrophoretic mobilities, one can observe that the bare TNS possess negative charges in the entire NaCl concentration range investigated. An increase in the salt level leads to an increase in the electrophoretic mobility due to charge screening of the particle surface by the counterions.

When the TNS are coated with the polycations, they possess a positive interface at lower salt concentrations. However, the magnitude of the electrophoretic mobilities differs in this regime due to the difference in the charge density of the polyelectrolytes. The surface charge densities (Table 1 and Fig. S3†) of the coated TNS were determined from the electrophoretic results using eqn (2) and (3). For the PDADMAC coated TNS, it fell in the same range in magnitude as the one obtained for the bare TNS. However, a lower surface charge density in magnitude was found for the P(AAm-co-DADMAC) functionalized TNS compared to the uncoated TNS. Indeed, the PDADMAC block of

the copolymer is adsorbed on the surface neutralizing the TNS charges, while the presence of the P(AAm) block of the copolymer of neutral charge resulted in an overall low surface charge density of the coated TNS.

In addition, the hydrodynamic radii and PDI values measured in stable suspensions were very similar to the bare one indicating that the coating procedure did not cause any aggregation of the particles. In both systems, the mobilities show a maximum, which originates from the electrokinetic effect.<sup>61</sup> The decrease in the electrophoretic mobility value after the observed maximum is due to charge screening by the counterions present in the bulk.

For the PDADMAC coated TNS above the NaCl concentration of 450 mM, the electrophoretic mobility becomes negative and reaches a plateau around 600 mM, where the mobilities are comparable to the bare TNS at this ionic strength. The P(AAm-co-DADMAC) functionalized TNS exhibit a similar charging behavior, although the charge inversion occurred at a lower salt level, around 131 mM. The observed charge reversal process is quite surprising as it was expected that the charges would be screened by the salt ions leading to electrophoretic mobility values close to zero. The slightly negative charge in this region can originate from specific adsorption of the  $\text{Cl}^-$  ions, as reported for other monovalent anions adsorbing on particle surfaces of low charge density,<sup>62</sup> and/or from salt-induced desorption of the polyelectrolytes.<sup>63–65</sup>

The tendency in the stability ratios of the bare TNS indicates a slow aggregation range at low ionic strength and unstable suspensions at high salt concentrations (Fig. 6b). The sharp transition between these regimes occurs at a critical coagulation concentration (CCC) of 19 mM (Table 1). Similar CCCs were reported for other inorganic particles.<sup>31,34,62</sup> Such changes in the colloidal stability are in line with the DLVO theory. The particles repel each other due to the overlap of the electrical double layers, which overcomes the attractive van der Waals forces and it gives rise to stable suspensions at low ionic strengths. On the contrary, above the CCC, the system is unstable and diffusion controlled aggregation takes place due to charge screening and subsequent vanishing of the electrical double layers.

However, the situation with the TNS-PDADMAC system is more complicated. The CCC was observed at 106 mM, therefore, PDADMAC coating of the TNS resulted in an increase in the particle stability by a factor of five, if one compares this CCC to the one for the bare TNS. Below 106 mM, the stability ratios increase with decreasing the salt level meaning that the system is stable here. Nevertheless, the slope in this slow aggregation regime is smaller than for the bare TNS indicating the presence of patch-charge attractions induced by the heterogeneous adsorption of the polyelectrolytes. Whereas above 131 mM, a slight increase in the stability ratios was observed resulting in a moderate restabilization of the suspension for higher salt concentrations.

Interpreting the results obtained at high ionic strengths for the PDADMAC functionalized TNS by electrophoresis and DLS together, one can make some assumptions on the behavior of the system. As for salt concentrations above 450 mM, the restabilization of the suspensions cannot be solely explained by

the electrostatic repulsion caused by the charge reversal process, but with the involvement of conformational changes and partial desorption of the adsorbed PDADMAC chains. Indeed, an increase in the salt content may lead to a swelling of the polyelectrolyte layer as reported earlier<sup>66</sup> and thus to a breakage of some electrostatic bonds between the PDADMAC and the negatively charged TNS. Moreover, the partial desorption and swelling of the polyelectrolyte from the TNS surface may lead to the formation of a sort of brush-like conformation of the adsorbed layer due to the appearance of more tails and loops stretching out from the TNS surface leading to steric repulsion upon their overlap.<sup>53,54,67</sup> Such a significant effect of the salt level on the adsorption mechanism and conformation of the polyelectrolyte chains on the surface was also reported on the basis of computer simulations.<sup>68</sup> In addition, the same theoretical method was used to study the effect of ionic strength or chain length of polyelectrolytes on the adsorption in confined spaces.<sup>69</sup>

Furthermore, it was found that the TNS-P(AAm-co-DADMAC) suspensions are stable until very high ionic strengths (above 1000 mM) and no CCC value could be determined up to 3000 mM NaCl concentration. Therefore, the coating of the TNS by this copolymer resulted in a tremendous increase (over more than a factor of 50) in the stability compared to the bare particles. This enormous stabilizing effect originates from the electrostatic and steric repulsion between the adsorbed chains. The latter one is more pronounced for polyelectrolytes of low charge density or for neutral polymers. The presence of the non-charged P(AAm) part in the P(AAm-co-DADMAC) chain certainly enhances the strength of the steric repulsion compared to the highly charged PDADMAC. Such a brushy structure of the grafted P(AAm) has also been reported for silica surfaces.<sup>70</sup>

This finding indicates that the surface functionalized nanosheets are highly stable even at the physiological ionic strength in blood (about 160 mM) making the developed material suitable for biomedical delivery processes for instance.

## Conclusions

Titania nanosheets (TNS) of anatase phase were synthesized in a hydrothermal route followed by alkali treatments. The formation of the TNS was confirmed and their size and charge characteristics were determined in aqueous suspensions prior to their functionalization with two types of polyelectrolytes. The charge of the TNS was neutralized and reversed owing to the adsorption of PDADMAC or P(AAm-co-DADMAC) at appropriate doses, which vary for the different polyelectrolytes due to their dissimilar charge density. The colloidal stability was tuned by changing the polyelectrolyte loading and hence, stable or unstable dispersions could be designed. Full coverage of the nanosheet surface resulted in an improved resistance against aggregation. Accordingly, TNS-PDADMAC exhibited a 5 times increase in the stability in salt solutions compared to the bare particles. More interestingly, TNS-P(AAm-co-DADMAC) presented a tremendous increase in the colloidal stability and the suspensions were stable even at extremely high ionic strengths, where the bare and the PDADMAC coated nanosheets rapidly

aggregated. Similar origin of the interparticle forces was suggested for both polyelectrolyte systems. Repulsive double layer and steric forces were responsible for the stabilization, however, the strength of the latter ones were much larger for the TNS-P(AAm-co-DADMAC). Therefore, these functionalized TNS materials appear to be suitable candidates in the field of drug delivery by acting as nanocarriers. Indeed, as the stability of the bare TNS is quite limited, the reported increase in the stability upon functionalization could facilitate, open up and extend their use in various fields.

## Acknowledgements

This work was supported by the Swiss Secretariat for Education, Research and Innovation (C15.0024), COST Action CM1303, University of Geneva and Swiss National Science Foundation. The authors are grateful to Celine Besnard for the XRD measurements and to Michal Borkovec for providing access to the instruments in the Laboratory of Colloid and Surface Chemistry.

## References

- 1 L. Z. Wang and T. Sasaki, *Chem. Rev.*, 2014, **114**, 9455–9486.
- 2 Y. Bai, Z. Xing, H. Yu, Z. Li, R. Amal and L. Z. Wang, *ACS Appl. Mater. Interfaces*, 2013, **5**, 12058–12065.
- 3 C. Janaky, N. R. de Tacconi, W. Chanmanee and K. Rajeshwar, *J. Phys. Chem. C*, 2012, **116**, 19145–19155.
- 4 H. Haspel, G. Peintler and Á. Kukovecz, *Chem. Phys. Lett.*, 2014, **607**, 1–4.
- 5 E. F. Rodriguez, D. H. Chen, A. F. Hollenkamp, L. Cao and R. A. Caruso, *Nanoscale*, 2015, **7**, 17947–17956.
- 6 A. Veres, J. Menesi, C. Janaky, G. F. Samu, M. K. Scheyer, Q. S. Xu, F. Salahioglu, M. V. Garland, I. Dekany and Z. Y. Zhong, *RSC Adv.*, 2015, **5**, 2421–2428.
- 7 B. Reti, K. Mogyorosi, A. Dombi and K. Hernadi, *Appl. Catal., A*, 2014, **469**, 153–158.
- 8 R. Kun, M. Balazs and I. Dekany, *Colloids Surf., A*, 2005, **265**, 155–162.
- 9 A. L. Linsebigler, G. Q. Lu and J. T. Yates, *Chem. Rev.*, 1995, **95**, 735–758.
- 10 E. G. Bajnoczi, N. Balazs, K. Mogyorosi, D. F. Sranko, Z. Pap, Z. Ambrus, S. E. Canton, K. Noren, E. Kuzmann, A. Vertes, Z. Homonnay, A. Oszko, I. Palinko and P. Sipos, *Appl. Catal., B*, 2011, **103**, 232–239.
- 11 K. Kordás, M. Mohl, Z. Kónya and A. Kukovecz, *Transl. Mater. Res.*, 2015, **2**, 015003–015020.
- 12 G. Potari, D. Madarasz, L. Nagy, B. Laszlo, A. Sapi, A. Oszko, A. Kukovecz, A. Erdohelyi, Z. Konya and J. Kiss, *Langmuir*, 2013, **29**, 3061–3072.
- 13 D. Dontsova, V. Keller, N. Keller, P. Steffanut, O. Felix and G. Decher, *Macromol. Rapid Commun.*, 2011, **32**, 1145–1149.
- 14 X. T. Zhang, A. Fujishima, M. Jin, A. V. Emeline and T. Murakami, *J. Phys. Chem. B*, 2006, **110**, 25142–25148.
- 15 V. B. Damodaran, D. Bhatnagar, V. Leszczak and K. C. Popat, *RSC Adv.*, 2015, **5**, 37149–37171.
- 16 D. V. Bavykin and F. C. Walsh, *Eur. J. Inorg. Chem.*, 2009, 977–997.



dc 1931-21

- 17 K. Kamada, A. Yamada and N. Soh, *RSC Adv.*, 2015, **5**, 85511–85516.
- 18 A. L. Papa, L. Dumont, D. Vandroux and N. Millot, *Nanotoxicology*, 2013, **7**, 1131–1142.
- 19 F. Tiarks, T. Frechen, S. Kirsch, J. Leuninger, M. Melan, A. Pfau, F. Richter, B. Schuler and C. L. Zhao, *Prog. Org. Coat.*, 2003, **48**, 140–152.
- 20 S. Farrokhpay, *Adv. Colloid Interface Sci.*, 2009, **151**, 24–32.
- 21 Y. X. Tang, Z. L. Jiang, Q. L. Tay, J. Y. Deng, Y. K. Lai, D. G. Gong, Z. L. Dong and Z. Chen, *RSC Adv.*, 2012, **2**, 9406–9414.
- 22 R. J. Honda, V. Keene, L. Daniels and S. L. Walker, *Environ. Eng. Sci.*, 2014, **31**, 127–134.
- 23 J. Grzechulska, M. Hamerski and A. W. Morawski, *Water Res.*, 2000, **34**, 1638–1644.
- 24 Y. W. L. Lim, Y. X. Tang, Y. H. Cheng and Z. Chen, *Nanoscale*, 2010, **2**, 2751–2757.
- 25 H. Brahmi, G. Katwal, M. Khodadadi, S. Chen, M. Paulose, O. K. Varghese and A. Mavrokefalos, *Nanoscale*, 2015, **7**, 19004–19011.
- 26 Z. Y. Wang, K. L. Lv, G. H. Wang, K. J. Deng and D. G. Tang, *Appl. Catal., B*, 2010, **100**, 378–385.
- 27 Y. L. Yu, P. Zhang, L. M. Guo, Z. D. Chen, Q. Wu, Y. H. Ding, W. J. Zheng and Y. Cao, *J. Phys. Chem. C*, 2014, **118**, 12727–12733.
- 28 X. L. Ding, X. Q. Yang, L. Zhou, H. B. Lu, S. B. Li, Y. Gao, C. H. Lai and Y. Jiang, *Int. J. Nanomed.*, 2013, **8**, 569–579.
- 29 A. L. Papa, J. Boudon, V. Bellat, A. Loiseau, H. Bisht, F. Sallem, R. Chassagnon, V. Berard and N. Millot, *Dalton Trans.*, 2015, **44**, 739–746.
- 30 T. Szabo, V. Toth, E. Horvath and I. Szilagyi, *Chimia*, 2014, **68**, 454.
- 31 T. Szabo, V. Toth, E. Horvath, L. Forro and I. Szilagyi, *Langmuir*, 2015, **31**, 42–49.
- 32 M. Pavlovic, M. Adok-Sipiczki, E. Horvath, T. Szabo, L. Forro and I. Szilagyi, *J. Phys. Chem. C*, 2015, **119**, 24919–24926.
- 33 E. Horvath, I. Szilagyi, L. Forro and A. Magrez, *J. Colloid Interface Sci.*, 2014, **416**, 190–197.
- 34 E. Horvath, L. Grebikova, P. Maroni, T. Szabo, A. Magrez, L. Forro and I. Szilagyi, *ChemPlusChem*, 2014, **79**, 592–600.
- 35 X. G. Han, Q. Kuang, M. S. Jin, Z. X. Xie and L. S. Zheng, *J. Am. Chem. Soc.*, 2009, **131**, 3152–3153.
- 36 Q. J. Xiang, K. L. Lv and J. G. Yu, *Appl. Catal., B*, 2010, **96**, 557–564.
- 37 H. Holthoff, S. U. Egelhaaf, M. Borkovec, P. Schurtenberger and H. Sticher, *Langmuir*, 1996, **12**, 5541–5549.
- 38 K. L. Chen, S. E. Mylon and M. Elimelech, *Langmuir*, 2007, **23**, 5920–5928.
- 39 L. Ehrl, Z. Jia, H. Wu, M. Lattuada, M. Soos and M. Morbidelli, *Langmuir*, 2009, **25**, 2696–2702.
- 40 G. Trefalt, I. Szilagyi and M. Borkovec, *J. Colloid Interface Sci.*, 2013, **406**, 111–120.
- 41 B. Derjaguin, *Trans. Faraday Soc.*, 1940, **35**, 0203–0214.
- 42 C. Henry, K. K. Norrfors, M. Olejnik, M. Bouby, J. Luetzenkirchen, S. Wold and J. P. Minier, *Adsorption*, 2016, **22**, 503–515.
- 43 Z. A. Huang, Z. Y. Wang, K. L. Lv, Y. Zheng and K. J. Deng, *ACS Appl. Mater. Interfaces*, 2013, **5**, 8663–8669.
- 44 K. L. Lv, J. G. Yu, L. Z. Cui, S. L. Chen and M. Li, *J. Alloys Compd.*, 2011, **509**, 4557–4562.
- 45 Z. Y. Wang, B. B. Huang, Y. Dai, X. L. Zhu, Y. Y. Liu, X. Y. Zhang and X. Y. Qin, *CrystEngComm*, 2013, **15**, 3436–3441.
- 46 A. Niecikowska, M. Krasowska, J. Ralston and K. Malysa, *J. Phys. Chem. C*, 2012, **116**, 3071–3078.
- 47 M. Lorenzetti, E. Gongadze, M. Kulkarni, I. Junkar and A. Iglic, *Nanoscale Res. Lett.*, 2016, **11**, 378–390.
- 48 A. V. Delgado, F. Gonzalez-Caballero, R. J. Hunter, L. K. Koopal and J. Lyklema, *J. Colloid Interface Sci.*, 2007, **309**, 194–224.
- 49 J. Forsman, *Langmuir*, 2012, **28**, 5138–5150.
- 50 J. C. Fu and J. B. Schlenoff, *J. Am. Chem. Soc.*, 2016, **138**, 980–990.
- 51 M. Quesada-Perez, E. Gonzalez-Tovar, A. Martin-Molina, M. Lozada-Cassou and R. Hidalgo-Alvarez, *ChemPhysChem*, 2003, **4**, 235–248.
- 52 J. Hierrezuelo, A. Sadeghpour, I. Szilagyi, A. Vaccaro and M. Borkovec, *Langmuir*, 2010, **26**, 15109–15111.
- 53 E. Illes and E. Tombacz, *J. Colloid Interface Sci.*, 2006, **295**, 115–123.
- 54 F. Brunel, I. Pochard, S. Gauffine, M. Turesson and C. Labbez, *J. Phys. Chem. B*, 2016, **120**, 5777–5785.
- 55 E. D. E. Hyde, R. Moreno-Atanasio, P. A. Millner and F. Neville, *J. Phys. Chem. B*, 2015, **119**, 1726–1735.
- 56 A. Fuchs and E. Killmann, *Colloid Polym. Sci.*, 1998, **279**, 53–60.
- 57 I. Szilagyi, D. Rosicka, J. Hierrezuelo and M. Borkovec, *J. Colloid Interface Sci.*, 2011, **360**, 580–585.
- 58 Y. K. Leong, *Colloid Polym. Sci.*, 1999, **277**, 299–305.
- 59 S. Schwarz, S. Bratskaya, W. Jaeger and B. R. Paulke, *J. Appl. Polym. Sci.*, 2006, **101**, 3422–3429.
- 60 J. Hierrezuelo, A. Vaccaro and M. Borkovec, *J. Colloid Interface Sci.*, 2010, **347**, 202–208.
- 61 M. Borkovec, S. H. Behrens and M. Semmler, *Langmuir*, 2000, **16**, 5209–5212.
- 62 M. Pavlovic, R. Huber, M. Adok-Sipiczki, C. Nardin and I. Szilagyi, *Soft Matter*, 2016, **12**, 4024–4033.
- 63 S. T. Dubas and J. B. Schlenoff, *Macromolecules*, 2001, **34**, 3736–3740.
- 64 H. Mjehed, J. C. Voegel, B. Senger, A. Chassepot, A. Rameau, V. Ball, P. Schaaf and F. Boulmedais, *Soft Matter*, 2009, **5**, 2269–2276.
- 65 L. L. Han, Z. W. Mao, H. Wuliyasu, J. D. Wu, X. Gong, Y. G. Yang and C. Y. Gao, *Langmuir*, 2012, **28**, 193–199.
- 66 E. Seyrek, J. Hierrezuelo, A. Sadeghpour, I. Szilagyi and M. Borkovec, *Phys. Chem. Chem. Phys.*, 2011, **13**, 12716–12719.
- 67 R. Meszaros, I. Varga and T. Gilanyi, *Langmuir*, 2004, **20**, 5026–5029.
- 68 A. G. Cherstvy and R. G. Winkler, *J. Phys. Chem. B*, 2012, **116**, 9838–9845.
- 69 S. J. de Carvalho, R. Metzler and A. G. Cherstvy, *Soft Matter*, 2015, **11**, 4430–4443.
- 70 A. Li, S. N. Ramakrishna, E. S. Kooij, R. M. Espinosa-Marzal and N. D. Spencer, *Soft Matter*, 2012, **8**, 9092–9100.



Contents lists available at ScienceDirect

# Journal of Colloid and Interface Science

journal homepage: [www.elsevier.com/locate/jcis](http://www.elsevier.com/locate/jcis)



## Regular Article

# A colloid chemistry route for the preparation of hierarchically ordered mesoporous layered double hydroxides using surfactants as sacrificial templates



Gábor Varga<sup>a</sup>, Zoltán Somosi<sup>b</sup>, Zoltán Kónya<sup>c,d</sup>, Ákos Kukovecz<sup>d</sup>, István Pálinkó<sup>a</sup>, Istvan Szilagyí<sup>b,\*</sup>

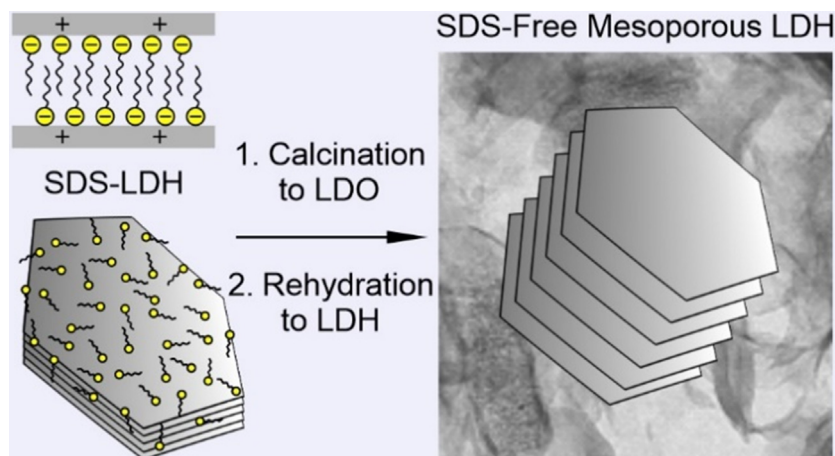
<sup>a</sup> Materials and Solution Structure Research Group, Department of Organic Chemistry, University of Szeged, H-6720 Szeged, Hungary

<sup>b</sup> MTA-SZTE Lendület Biocolloids Research Group, Interdisciplinary Excellence Center, Department of Physical Chemistry and Materials Science, University of Szeged, H-6720 Szeged, Hungary

<sup>c</sup> MTA-SZTE Reaction Kinetics and Surface Chemistry Research Group, H-6720 Szeged, Hungary

<sup>d</sup> Department of Applied and Environmental Chemistry, University of Szeged, H-6720 Szeged, Hungary

## GRAPHICAL ABSTRACT



## ARTICLE INFO

### Article history:

Received 16 July 2020

Revised 19 August 2020

Accepted 28 August 2020

Available online 9 September 2020

### Keywords:

Mesoporous layered double hydroxides

Sacrificial template

Colloid stability

Efficient anion removal

SDS-LDH precursor

## ABSTRACT

An efficient synthetic route was developed to prepare hierarchically ordered mesoporous layered double hydroxide (LDH) materials. Sodium dodecyl sulfate (SDS) was used as a sacrificial template to tune the interfacial properties of the LDH materials during the synthetic process. The SDS dose was optimized to obtain stable dispersions of the SDS-LDH composites, which were calcined, then rehydrated to prepare the desired LDH structures. Results of various characterization studies revealed a clear relationship between the colloidal stability of the SDS-LDH precursors and the structural features of the final materials, which was entirely SDS-free. A comparison to the reference LDH prepared by the traditional co-precipitation-calcination-rehydration method in the absence of SDS shed light on a remarkable increase in the specific surface area (one of the highest within the previously reported LDH materials) and pore volume as well as on the formation of a beneficial pore size distribution. As a proof of concept, the mesoporous LDH was applied as adsorbent for removal of nitrate and dichromate anions from aqueous samples, and excellent efficiency was observed in both sorption capacity and recyclability. These results

\* Corresponding author.

E-mail address: [szistvan@chem.u-szeged.hu](mailto:szistvan@chem.u-szeged.hu) (I. Szilagyí).

make the obtained LDH a promising candidate as adsorbent in various industrial and environmental processes, wherever the use of mesoporous and organic content-free materials is required.

© 2020 The Author(s). Published by Elsevier Inc. This is an open access article under the CC BY license (<http://creativecommons.org/licenses/by/4.0/>).

## 1. Introduction

Layered double hydroxide (LDH) materials, also named as hydrotalcites after their naturally occurring form, are lamellar anionic clays, i.e., they possess anion exchange capacity, which is extensively utilized in applications including drug delivery [1], catalysis [2] or environmental remediation [3]. In these processes, one of the critical steps is anion adsorption on the outer surface or in the interlayer space of the oppositely charged LDH layers. The origin of the positive charge can be exemplified by the substitution of magnesium(II) ions with aluminum(III) in the brucite ( $\text{Mg}(\text{OH})_2$ ) structure [4], notwithstanding that various divalent and trivalent metal ions were reported as layer forming constituents in LDH structures [5,6].

Towards development of efficient LDH-based anion exchangers of advantageous features for the target applications, several synthetic routes were recommended. The key parameters of such LDHs are the surface charge, specific surface area and pore size distribution, which determine the type of anions preferred for the adsorption/intercalation process. For example, LDH materials of lower surface charge density, but higher pore sizes are good candidates to immobilize and deliver larger biomolecules [7], while high surface charge and area are required for the most efficient anion absorbers in water decontamination [8]. In the latter case, significant effort was made to remove inorganic toxic anions including nitrate and chromate from aqueous environmental or industrial systems [3,9]. Unfortunately, the achieved sorption capacities of porous LDHs were only able to approach the efficiency of non-porous counterparts [9]. Despite the fact that numerous hard (e.g., solid particles) or soft (e.g., surfactants) template-based processes have been developed to build up porous LDHs, significant increase in the sorption capacity was not achieved. This tendency might be attributed to two issues. First, the templates were not removed from the final materials and thus, the availability of the ion-exchange sites were limited [9]. Second, the presence of macropores lead to formation of hollow spheres [10] around the template and this resulted in a significant decrease in the microporous surface area [11].

Surfactant-mediated preparation of porous LDHs attracted widespread attention in the scientific community in the recent past, since these amphiphilic molecules showed high affinity to LDH surfaces leading to their intercalation and subsequent increase in the distance between the lamellae [12–14]. Among surfactants, sodium dodecyl sulfate (SDS) was extensively used for this purpose [15–17]. Such a pillared structure facilitates the diffusion of the target ions into the interlayer gallery and thus, higher ion-exchange capacity can be achieved. Therefore, LDHs intercalated with SDS were widely used in environmental processes to remove ionic contaminants [16–20] and in the preparation of LDH-based functional materials by immobilization of small molecules of thermoresponsive [12], photoluminescent [21] or hydrophobic [22] properties. The more accessible space is also beneficial once the aim is to attach larger polymeric molecules between the layers [6,23–25].

In these studies, it was confirmed that SDS adsorbed strongly on the oppositely charged surface, and single-molecule adsorption occurred at low concentrations, SDS aggregates formed at higher coverage, while the LDH surface became saturated with the adsorbed SDS around the critical micelle concentration (CMC),

which was reported to be around 8 mM [26–28]. Adsorption of SDS at higher concentrations may also reverse the sign of LDH charge leading to the formation of negatively charged SDS-LDH composites [26,29,30]. For instance, the high surfactant affinity was utilized in SDS removal from wastewaters with LDH-titania composites, in which the role of the titania was the photocatalytic decomposition of SDS [31].

Most of the above applications of the SDS-LDH materials took place in dispersions, where possible aggregation of the particles may play an important role, since the aggregates often sediment and hence, the available surface area dramatically decreases. Moreover, surface charge and aggregation processes are strongly related properties of colloidal particles including LDHs [32], therefore, SDS adsorption significantly affects the colloidal stability of the samples. Despite the importance of this issue, systematic studies reporting surface charge densities and aggregation rates of SDS-modified LDHs cannot be found in the literature. The obtained pillared SDS-LDH composites usually possessed high surface area compared to the ones containing small inorganic anions [16,26,33]; however, the organic content of these materials prevents their use in certain applications, e.g., in biological systems. Therefore, SDS removal without sacrificing the high specific surface area would be beneficial, but this topic was rarely investigated in the past.

In the present work, a colloid approach was used to obtain fine dispersions of SDS-LDH composites followed by their calcination to layered double oxide (LDO) to eliminate the SDS content. The organic content-free LDH structure was reconstructed by rehydration of the LDO. The charging and aggregation processes in the SDS-LDH dispersions were optimized in electrophoretic and dynamic light scattering experiments, while the structural features were investigated by electron microscopy, X-ray diffraction, IR spectroscopy, specific surface area and pore size measurements. To demonstrate the sorption ability of the obtained mesoporous materials, the efficiency in removal of dichromate and nitrate anions from aqueous samples was assessed and the adsorption kinetics were analyzed by appropriate models.

## 2. Materials and method

### 2.1. Chemicals

All the AR-grade chemicals were purchased from Merck and Sigma-Aldrich and used as received without further purification. More specific data are given in the [Supplementary material \(SM\)](#).

### 2.2. Synthesis of the pristine $\text{MgAl-Cl-LDH}$

The co-precipitation method [34] was applied, in which 3.0 M NaOH solution was added to a vigorously stirred and  $\text{N}_2$ -blanketed solution of  $\text{MgCl}_2$  and  $\text{AlCl}_3$  of 3:1 M ratio at room temperature. The solid material formed was filtered, dried for 24 h at 60 °C and kept in a desiccator under  $\text{N}_2$  until its use in Method 1, as described below.

### 2.3. Preparation of mesoporous LDH

Method 1. 100.0 mL of 3.0/10.0/30.0 mM sodium dodecyl sulfate (SDS) aqueous solutions were prepared and added to the

MgAl–Cl–LDH dispersions containing 5 g solid material. The samples obtained after SDS adsorption are denoted as SDS<sub>3</sub>-MgAl–Cl–LDH, SDS<sub>10</sub>-MgAl–Cl–LDH and SDS<sub>30</sub>-MgAl–Cl–LDH, respectively. The slurries were stirred at pH ~ 8.5 (set by 0.015 M NaOH aqueous solution) and 60 °C for 12 h. The solid material was filtered off, washed with distilled water several times and dried at 60 °C overnight. The SDS content was removed by calcination at 510 °C for 12 h leading to the formation of LDO compounds (LDO<sub>3</sub>, LDO<sub>10</sub> and LDO<sub>30</sub>, respectively). The LDH structures were reconstructed by rehydration, in which the LDOs were dispersed in 100.0 cm<sup>3</sup> of 20.0 mM NaCl dissolved in mixtures of H<sub>2</sub>O/EtOH/0.015 M NaOH aqueous solution of 85:5:10 vol ratio under N<sub>2</sub> atmosphere. The slurries were stirred at 50 °C for 96 h followed by repeated filtration, washing (with water) and drying steps to obtain the LDH<sub>3</sub> (from SDS<sub>3</sub>-MgAl–Cl–LDH), LDH<sub>10</sub> (from SDS<sub>10</sub>-MgAl–Cl–LDH) and LDH<sub>30</sub> (from SDS<sub>30</sub>-MgAl–Cl–LDH) final products.

Method 2. During the co-precipitation of LDH in the presence of SDS, 100.0 mL of SDS solutions of 3.0/10.0/30.0 mM concentration were mixed with 50.0 cm<sup>3</sup> aqueous solutions containing 15.0 mM of MgCl<sub>2</sub> and 5.0 mM of AlCl<sub>3</sub>. The pH was kept at 10.5 by addition of 3 M NaOH. After 12 h stirring at 60 °C, the obtained solid materials were separated by filtration, washed with water several times and dried at 60 °C overnight. The solids formed are denoted as c-SDS<sub>3</sub>-MgAl–Cl–LDH, c-SDS<sub>10</sub>-MgAl–Cl–LDH and c-SDS<sub>30</sub>-MgAl–Cl–LDH and the numbers refer to the concentration of the surfactant during co-precipitation. Like in Method 1, the SDS content was removed by calcination at 510 °C for 12 h leading to LDO formation, which was again transformed to LDH by rehydration. The obtained final materials are denoted as c-LDH<sub>3</sub>, c-LDH<sub>10</sub> and c-LDH<sub>30</sub>, in respect to SDS dose used in the synthesis.

#### 2.4. Characterization techniques

Electrophoretic mobility was measured with a LiteSizer 500 (Anton Paar) device equipped with a 40 mW laser source operating at 658 nm wavelength. Disposable plastic omega-shaped capillary cells (Anton Paar) were used for the measurements. Conversion method of mobilities to zeta potentials and further data treatment are described in the SM.

Dynamic light scattering (DLS) was used to measure the hydrodynamic size of the dispersed particles. The measurements were carried out with the same LiteSizer device as above at 175° scattering angle in disposable plastic cuvettes (VWR). The cumulant method was used to fit the correlation functions, which were collected for 20 s to determine the hydrodynamic radii of the particles. To assess the colloidal stability of the dispersions, the apparent aggregation rates were measured and used to calculate stability ratios, as detailed elsewhere [35] and in the SM. Note that stability ratios close to unity indicate rapid particle aggregation and unstable dispersions, while higher values refer to more stable samples.

X-ray diffraction (XRD) patterns were recorded on a Rigaku XRD-MiniFlex II instrument applying Cu K $\alpha$  radiation of 0.15418 nm wavelength with 40 kV accelerating voltage at 30 mA.

The morphologies of the samples prepared were studied by scanning electron microscopy (SEM). The SEM images were recorded on a S-4700 electron microscope (Hitachi) with an accelerating voltage of 10–18 kV. More detailed images on the samples prepared were captured by transmission electron microscopy (TEM). For these measurements, a FEI Tecnai™ G2 20 X-Twin type instrument was used operating at acceleration voltage of 200 kV. The materials were imaged in dried stage by both techniques.

BET (Brunauer-Emmett-Teller) N<sub>2</sub>-sorption experiments were carried out on a NOVA3000 (Quantachrome) instrument. The samples were degassed with N<sub>2</sub> at 100 °C for 5 h under vacuum to clean

the surface of the adsorbent materials. The measurements were performed at the temperature of liquid N<sub>2</sub>.

IR spectra were measured on a BIO-RAD Digilab Division FTS-65A/896 apparatus, equipped with a diffuse reflectance spectroscopy (DRS) accessory. In a typical measurement, 256 scans were collected with 4 cm<sup>-1</sup> resolution in the 4000–600 cm<sup>-1</sup> wavenumber range.

#### 2.5. Assessment of sorption capacity

For the nitrate adsorption study, 50 mg of LDH samples were suspended in 10.0 mL solutions containing 5–625 mg/L nitrate anions at room temperature. The samples were continuously stirred at pH 7.0 for 120 h. After the reaction terminated, 1 mL aliquots were filtered with a 0.22  $\mu$ m membrane filter, and the concentration of nitrate ions in the filtrate was determined by UV-Vis spectrophotometry (Shimadzu UV-1650). For the dichromate adsorption, appropriate amount of K<sub>2</sub>Cr<sub>2</sub>O<sub>7</sub> was dissolved in 100.0 mL of water and the pH was adjusted to 5.0 by adding appropriate amount of NH<sub>4</sub>OH solution. Thereafter, 100.0 mg of LDH materials was added into the solution. The reaction time (5–240 min) and the initial concentration of dichromate ion (5–1400 mg/L) were altered. An aliquot of the sample was filtered after 120 h, and the concentration of the dichromate in the filtrate was measured by UV-Vis spectrometry (Shimadzu UV-1650). The error of these methods is about 3%.

The absorbents were regenerated by dispersing the used LDH compounds in 3 M NaCl aqueous solutions, which were vigorously stirred for 12 h. The slurry was then filtered by 0.45  $\mu$ m membrane filter, washed with water several times and dried at 65 °C overnight. See SM for more details of the evaluation of sorption capacity measurements.

### 3. Results and discussion

To prepare the mesoporous LDH materials, SDS<sub>3</sub>-MgAl–Cl–LDH, SDS<sub>10</sub>-MgAl–Cl–LDH and SDS<sub>30</sub>-MgAl–Cl–LDH composites were obtained with Method 1 at different surfactant-to-LDH ratios. Subsequently, they were calcined to the form of LDO and rehydrated to LDH<sub>3</sub>, LDH<sub>10</sub> and LDH<sub>30</sub>. Extensive structural characterization was performed to explore the correlation between the structure of the obtained materials and the reaction conditions, especially the colloid stability of the precursors. For comparison, c-LDH<sub>3</sub>, c-LDH<sub>10</sub> and c-LDH<sub>30</sub> materials were prepared by Method 2 using the standard co-precipitation technique. Finally, the adsorption efficiencies were probed by the removal of inorganic anions from aqueous samples.

#### 3.1. Stability of SDS<sub>x</sub>-MgAl–Cl–LDH dispersions

Surface charge density of +0.5 mC/m<sup>2</sup> was determined for the pristine MgAl–Cl–LDH on the basis of zeta potential measurements (Fig. S1), which were evaluated by the Debye-Hückel model [36] (see SM for the details of the calculation). Such a low charge was accompanied with low critical coagulation concentration of 7 mM, as determined in DLS measurements. These values are typical for LDH colloids containing small inorganic charge compensating anions [32].

Thereafter, in the colloidal approach applied to optimize the synthetic conditions of mesoporous LDHs, the optimal SDS concentrations were explored. Accordingly, the charging and aggregation processes of MgAl–Cl–LDH were followed at different SDS concentrations. Zeta potential measurements were carried out, and slightly positive values were recorded at low SDS doses due to the moderate positive structural charge of the particles (Fig. 1)



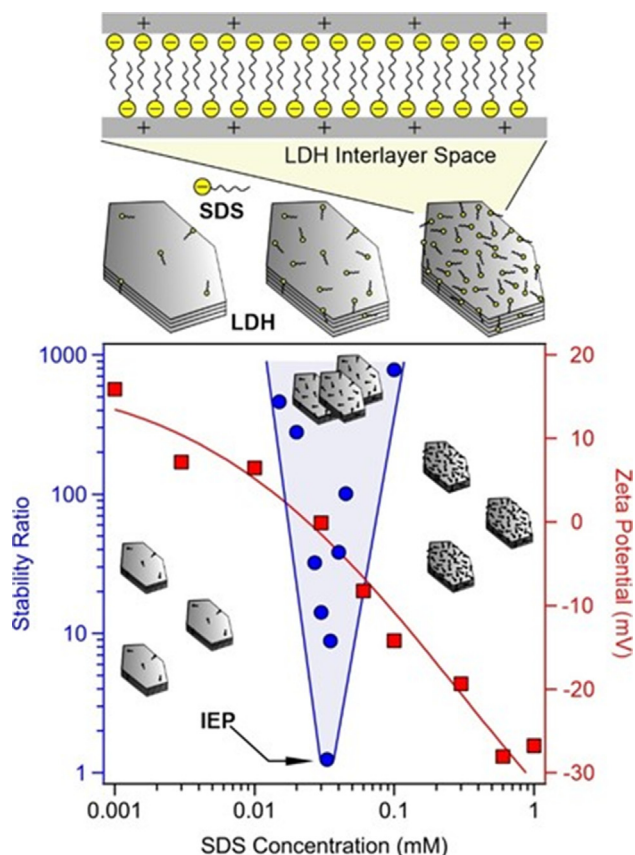


**Fig. 1.** Zeta potentials (squares, right axis) and stability ratios (circles, left axis) of MgAl-Cl-LDH particles as a function of the SDS concentration in aqueous dispersions at 10 mg/L particle concentration and pH 7. The solid lines are eye guides, and the upper scheme illustrates the SDS bilayer formation between the lamellae. Note that stability ratio close to unity refers to rapid particle aggregation and unstable dispersion.

[37]. Increasing the concentration of SDS, the mobilities decreased indicating surfactant adsorption on the oppositely charged MgAl-Cl-LDH surface. The adsorption process led to charge neutralization at the isoelectric point (IEP) and overcharging at higher doses. Such a reversal in the sign of the charge has been already reported for LDH materials in the presence of strongly adsorbing monovalent ions [38] including SDS [26,30]. The SDS adsorption continued until highly negative zeta potential values.

Colloidal stability was assessed in time resolved DLS measurements under the same experimental conditions as in the mobility study. In unstable samples, the hydrodynamic radii increased with time due to particle aggregation (Fig. S2). From these plots, stability ratios were calculated, as detailed in the SM.

Comparing the tendency in the charging and aggregation data shown in Fig. 1, it is obvious that the charging behavior significantly affects the speed of aggregation. The MgAl-Cl-LDH forms stable dispersion below the IEP, where it possesses significant positive charge due to the small amount of adsorbed SDS. Besides, at elevated SDS concentrations, at which the particles are highly negatively charged, the dispersions are stable again. In contrast, the samples are unstable once the overall charge of the particles is zero at the IEP. These results clearly indicate that the major interparticle forces are of electrostatic origin, in line with the classical theory by Derjaguin, Verwey, Landau and Overbeek [39,40]. Similar charge-aggregation relations were also observed in other nanoparticle systems [32,41].

During the synthesis by Method 1, the MgAl-Cl-LDH concentration was 100 times higher compared to the experiments shown in Fig. 1, therefore, SDS concentrations of 3.0/10.0/30.0 mM were

used leading to the formation of SDS<sub>3</sub>-MgAl-Cl-LDH, SDS<sub>10</sub>-MgAl-Cl-LDH and SDS<sub>30</sub>-MgAl-Cl-LDH composites. The first one forms an unstable dispersion, since the SDS dose is close to the IEP, the second one is just slightly above the CMC of SDS [26] and the final one is at high zeta potential (Fig. 1), where the surface of the MgAl-Cl-LDH is largely negatively charged due to SDS adsorption. In the latter case, the SDS<sub>30</sub>-MgAl-Cl-LDH forms highly stable colloid.

### 3.2. Structural features of SDS<sub>x</sub>-MgAl-Cl-LDH

The XRD patterns of the SDS<sub>3</sub>-MgAl-Cl-LDH, SDS<sub>10</sub>-MgAl-Cl-LDH and SDS<sub>30</sub>-MgAl-Cl-LDH and the unmodified MgAl-Cl-LDH are presented in Fig. 2. The resulting structure of the latter one is consistent with a rhombohedral unit cell, which is analogous to chloride-containing MgAl-LDHs (see JCPDS#51-1528 database) [42]. Similarly, (003) and (006) Bragg reflections were also observed for the SDS-treated composites. However, more pronounced staging effect was observed with increasing the SDS concentration indicating the presence of a new LDH phase. This is clearly confirmed by the appearance of (003') and (006') as well as by the disappearance of (003) bands on increasing the SDS concentration. This phenomenon was observed earlier in other SDS-LDH systems too [13,30]. A new peak appeared around 20° at higher SDS loadings, which originates from the joint effect of complex multiple staging and the different water content [43].

The interlayer distances were calculated with Bragg's equation [44] (see SM for details), and its value was 0.77 nm for the SDS<sub>3</sub>-MgAl-Cl-LDH, similarly to other chloride-containing LDHs [45]. Nevertheless, the coexistence of (003) and (003') peaks indicates two-phase materials of 0.77 and 2.52 nm distances in the case of SDS<sub>10</sub>-MgAl-Cl-LDH. Only the (003') diffraction with an interlayer distance of 2.76 nm could be detected for SDS<sub>30</sub>-MgAl-Cl-LDH. These data shed light on that SDS molecules tend to intercalate by increasing the dose. The internalization process could be rationalized with micelles, since the applied SDS concentrations are above the CMC during the synthesis of both SDS<sub>10</sub>-MgAl-Cl-LDH and SDS<sub>30</sub>-MgAl-Cl-LDH. However, as shown in the zeta

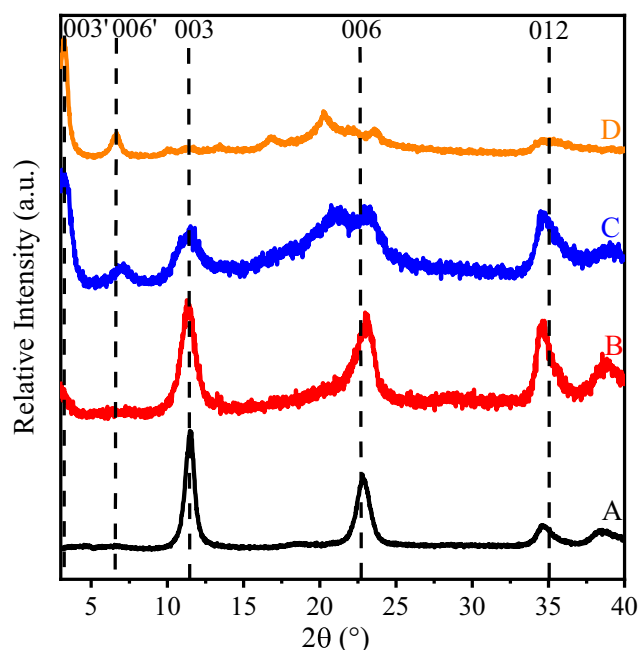


**Fig. 2.** XRD patterns of (A) MgAl-Cl-LDH, (B) SDS<sub>3</sub>-MgAl-Cl-LDH, (C) SDS<sub>10</sub>-MgAl-Cl-LDH and (D) SDS<sub>30</sub>-MgAl-Cl-LDH precursor composites prepared by Method 1.

potential study in the previous section, the surfactants are of high affinity to the LDH surface, therefore, DS bilayer formation (illustrated in Fig. 1) in the interlayer space [13] is more feasible.

Recall that the pillared  $\text{SDS}_{30}\text{-MgAl-Cl-LDH}$  is of high negative charge, it forms stable dispersions (Fig. 1), and DS most likely exchanged the majority of chloride ions in the structure. SEM images recorded in dried stage revealed that its morphology was non-defined (Fig. S3A), and it most likely consisted of aggregated particles due to the particle aggregation occurred during the drying process in the SEM measurement.

Besides, very similar XRD patterns were recorded for the materials obtained in the first step of Method 2 (Fig. S4), and they indicate single-phase and non-pillared LDHs. This observation confirmed that no DS intercalation occurred during coprecipitation in Method 2, which was verified by the very similar and small interlayer distances of 0.78, 0.75 and 0.79 nm for  $c\text{-SDS}_3\text{-MgAl-Cl-LDH}$ ,  $c\text{-SDS}_{10}\text{-MgAl-Cl-LDH}$  and  $c\text{-SDS}_{30}\text{-MgAl-Cl-LDH}$ , respectively.

Fig. 3 shows the IR spectra of the LDH composites prepared in the first step of by Method 1. All of the SDS modified samples exhibited characteristic bands of DS due to intercalation and adsorption on the outer surface of the  $\text{MgAl-Cl-LDH}$ . The following peaks were assigned to the DS content:  $\nu_{\text{as}}(\text{CH})$  ( $2922\text{ cm}^{-1}$ ),  $\nu_{\text{sym}}(\text{CH})$  ( $2855\text{ cm}^{-1}$ ),  $\delta(\text{CH})$  ( $1468/1366\text{ cm}^{-1}$ ),  $\nu_{\text{as}}(\text{S=O})$  ( $1220\text{ cm}^{-1}$ ) and  $\nu_{\text{sym}}(\text{S=O})$  ( $1071\text{ cm}^{-1}$ ) (Table S1) [13,33,46,47]. Apart from the vibrational peaks of DS, the bands of the  $\text{MgAl-Cl-LDH}$  material originating from the surface adsorbed carbonate ions and the water content were also identified.

The IR spectra of the  $c\text{-SDS}_3\text{-MgAl-Cl-LDH}$ ,  $c\text{-SDS}_{10}\text{-MgAl-Cl-LDH}$  and  $c\text{-SDS}_{30}\text{-MgAl-Cl-LDH}$  prepared by Method 2 contained the same vibrational bands (Fig. S5) due to the similar chemical composition of the materials. However, DS molecules adsorbed only on the outer surface, as discussed above. By comparing Fig. 3 and Fig. S5, one may realize that the materials prepared by Method 2 contained less carbonate in their structures. This is due to the fact that Method 1 is a more complex process with more time in contact with atmospheric carbon dioxide, which adsorbed in higher extent than during the shorter Method 2.

### 3.3. LDH-LDO-LDH conversion

In the next step, the  $\text{SDS-LDH}$  composites were calcined in both Methods 1 and 2 to obtain the corresponding LDO materials forming after the collapse of the LDH structure during the thermal treatment. Results of XRD experiments revealed that the long-range order of LDHs discontinued and amorphous mixed oxides were obtained (Fig. S6). Similar formation of LDO by LDH dehydration has already been reported in the literature [48–51].

To recover the LDH-like structures, the LDO compounds were rehydrated in water-ethanol- $\text{NaOH-NaCl}$  solutions in both Methods 1 and 2. The successful reconstruction was confirmed by XRD (Fig. 4 and Fig. S7) by detecting the characteristic pattern for LDH structures [37]. Indeed, single-phase LDHs of similar structures were obtained. On the basis of the interlayer distances, incorporation of chloride (from the rehydrating solution) and/or carbonate (from atmospheric carbon dioxide) anions were assumed.

To further study the structure of the LDH materials, especially the nature of the interlayer space, IR measurements were carried out. The same IR spectra were recorded within the experimental error for all LDHs (Fig. S8), irrespective to the preparation method applied. Two types of characteristic absorption bands were identified in these spectra. First, the ones centered at  $1426$  and  $992\text{ cm}^{-1}$  were assigned to  $\nu_3$  and  $\nu_2$  vibration modes of surface-adsorbed carbonate ions. Second, the peaks located at  $3535$  and  $1638\text{ cm}^{-1}$  were assigned to the  $\nu$  and  $\beta$  vibration modes of the water content. More importantly, not even trace amounts of organic compounds were detected. This result clearly confirms that the SDS template (i.e., intercalated DS anion) was completely eliminated during calcination leading to the formation of template-free LDH materials after rehydration.

Comparing the SEM images of the  $\text{SDS}_{30}\text{-MgAl-Cl-LDH}$  (Fig. S3A) and  $\text{LDH}_{30}$  (Fig. S3B) materials (i.e., LDH with adsorbed SDS at a dose of 30 mM and the one after rehydration without any SDS), the difference in the morphology is striking. The former one consists of aggregated particles of non-defined structure, while

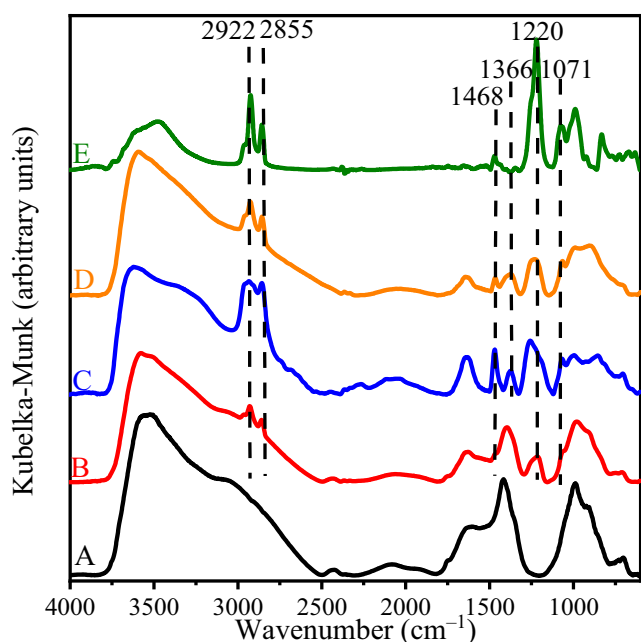


Fig. 3. IR-DRS spectra of (A)  $\text{MgAl-Cl-LDH}$ , (B)  $\text{SDS}_3\text{-MgAl-Cl-LDH}$ , (C)  $\text{SDS}_{10}\text{-MgAl-Cl-LDH}$ , (D)  $\text{SDS}_{30}\text{-MgAl-Cl-LDH}$  and (E) SDS.

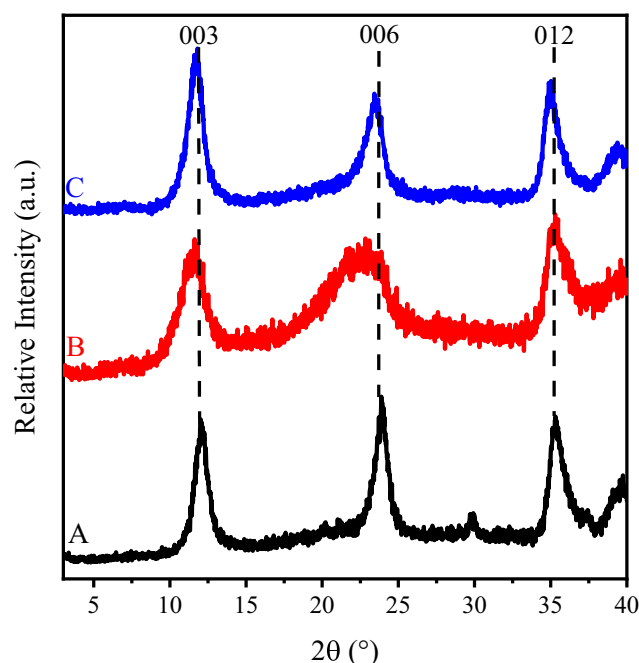


Fig. 4. XRD patterns of (A)  $\text{LDH}_3$ , (B)  $\text{LDH}_{10}$  and (C)  $\text{LDH}_{30}$  obtained after rehydration of  $\text{LDO}_3$ ,  $\text{LDO}_{10}$  and  $\text{LDO}_{30}$ , respectively, during Method 1.

the latter one composed of cauliflower-like morphology indicating a highly porous hierarchical structure.

Furthermore, mesoporous holes with different widths were observed on the TEM images of certain LDHs prepared by Method 1 (Fig. 5). Such a tendency to form mesopores was more pronounced by increasing the SDS dose during the synthesis. This issue will be further explored later in the specific surface area assessment. Another interesting finding is that LDH nanosheets stayed in vertically on the cavities suggesting the possible location of an LDH shell around the template before calcination. Nevertheless, similar mesoporous structure was not found in the TEM image of the LDH<sub>3</sub> (Fig. 5A) and of the other LDHs prepared by Method 2 (c-LDH<sub>3</sub>, c-LDH<sub>10</sub> and c-LDH<sub>30</sub> in Fig. S9A, Fig. S9B and Fig. S9C, respectively). In these cases, the obtained materials were identified

as ordinary LDH structures with particle aggregates, in which the sheets arranged vertically around a supposed nodule [52].

Indeed, hierarchical structure was already observed for LDH<sub>10</sub> (Fig. 5B), but it was the most pronounced for LDH<sub>30</sub> (Fig. 5C) indicating that the high colloidal stability of the precursor c-SDS<sub>30</sub>-MgAl-Cl-LDH plays important role in the formation of the materials in the calcination and rehydration steps. The successful application of the colloid chemistry-based design was justified by the advantageous structure of the LDH<sub>30</sub>.

### 3.4. Porosity assessment

To receive quantitative information on the porosity of the obtained LDHs, BET measurements were carried out. As the most

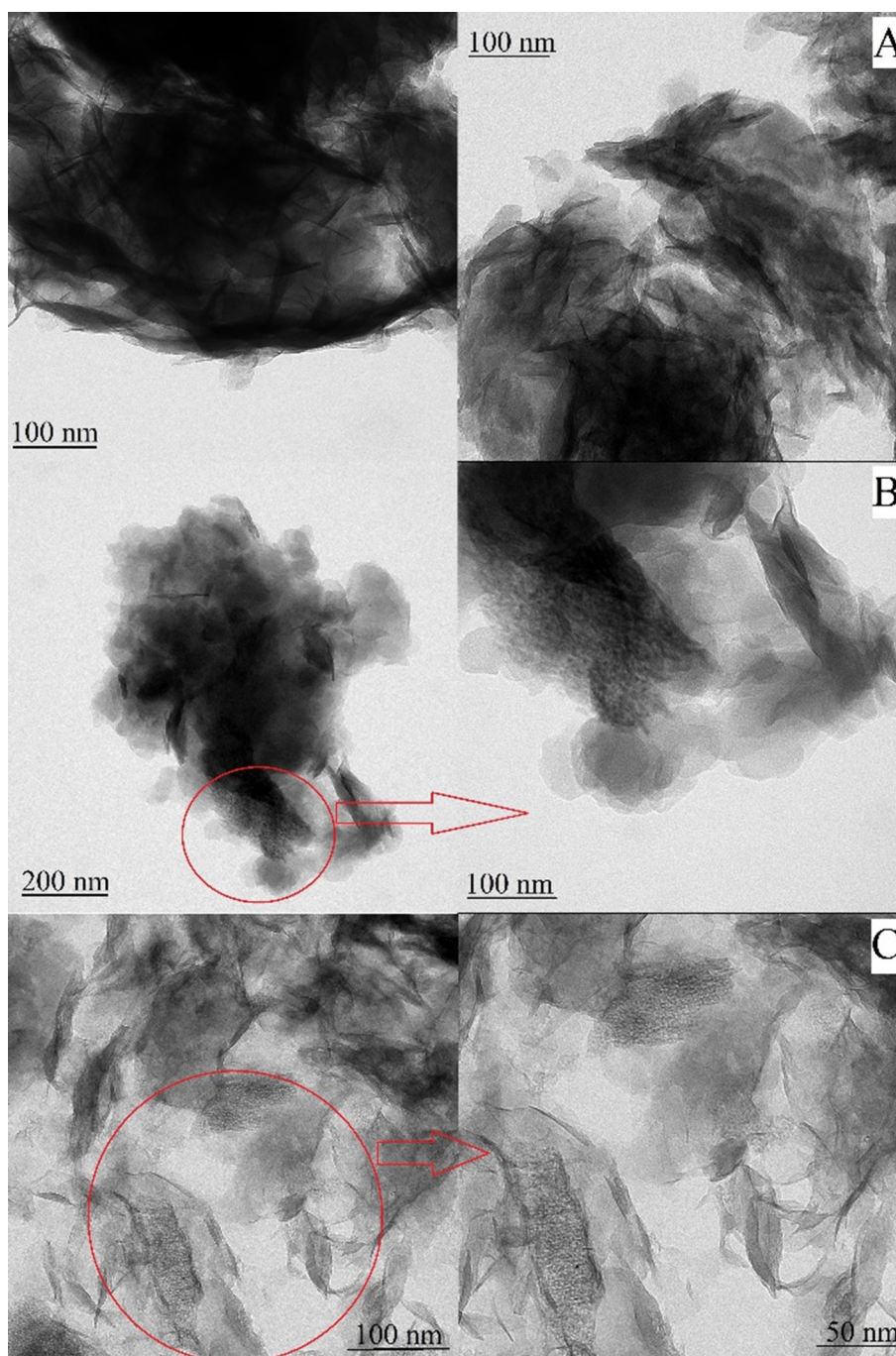


Fig. 5. TEM images of (A) LDH<sub>3</sub>, (B) LDH<sub>10</sub> and (C) LDH<sub>30</sub> prepared by Method 1.



important factors, specific surface area and pore diameter distribution were determined in  $N_2$ -adsorption/desorption measurements (Fig. 6 and Fig. S10A). It was found that almost all of the rehydrated structures exhibited type IV isotherm with  $H_3$  type hysteresis loop ( $p/p_0 > 0.4$ ) indicating the presence of mesopores [53]. However, this type of isotherm and hysteresis loop are typical for plate-like particles of slit shape pores [54]. This feature is usually related to particle aggregates.

On the other hand, rehydrated composites made by Method 1 with high amount of SDS ( $LDH_{30}$ ) or Method 2 with low amount of SDS ( $c-LDH_3$ ) exhibited much slower  $N_2$  desorption profile attributed to the presence of thinner nanoplatelets and more mesopores compared to chloride-containing LDHs [55]. For  $LDH_{30}$ , the detected hysteresis loop, grouped in  $H_2$  hysteresis, indicates desorption limitation, which is related to the appearance of pores of narrow size distributions and relatively uniform channel, similar to pores with facile pore connectivity [56,57].

Surface area and pore volume values significantly increased in the  $LDH_3 < LDH_{10} < LDH_{30}$  order (Fig. 7 and Table S2) indicating that increasing the SDS concentration during the synthesis in Method 1 gives rise to a more porous and hierarchical structure. An important note that the surface area and total pore volume was much higher for  $LDH_{30}$  than for  $c-LDH_{30}$ , which can be attributed to the significantly different morphology shown in the SEM images (Fig. 7 inset). Accordingly, the compact and aggregated structure for the latter one leads to lower porosity than for the cauliflower-like structure in the case of  $LDH_{30}$ .

If one compares the data for  $MgAl-Cl-LDH$  and  $LDH_{30}$ , 8-time and 48-time increases can be observed in the surface area and total pore volume, respectively. These results are in line with the SEM (Fig. S3B and Fig. 7) and TEM (Fig. 5C) images of  $LDH_{30}$ , in which, the highly ordered mesoporous structure is well presented. This result is remarkable, and the determined values are close or even higher than the ones ever reported for LDH materials after synthetic template removal (see a comprehensive set of previously published data in Table S3) [10,58,59].

Typically, the obtained LDH structures give a complete mesopore distribution in the range of 3.5–50.0 nm, depending on the

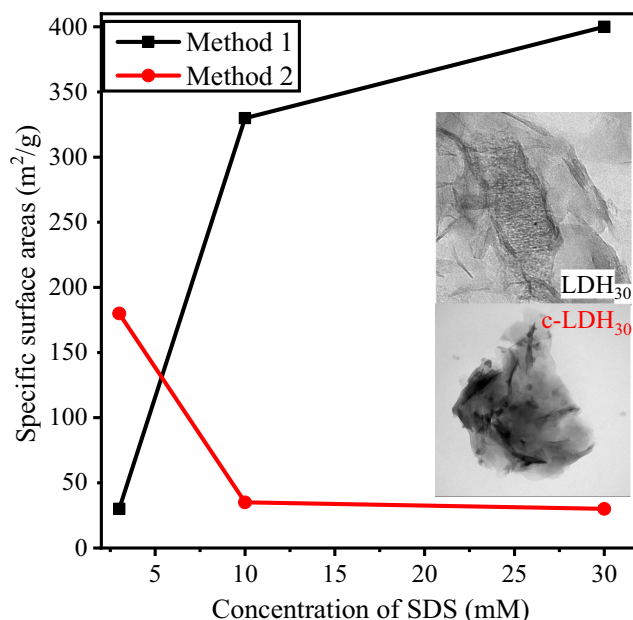


Fig. 7. Specific surface area values as a function of SDS concentration applied in Method 1 (squares) and Method 2 (circles). The TEM images  $LDH_{30}$  and  $c-LDH_{30}$  are shown in the inset. The lines serve to guide the eyes. The measurement error is typically 5%.

synthesis conditions. The main difference between the pore diameter repartition of LDH materials obtained with Method 1 (Fig. 8) and Method 2 (Fig. S10B) is that only pores of around 4 nm sizes were detected for  $c-LDH_3$ ,  $c-LDH_{10}$  and  $c-LDH_{30}$ , while additional pores up to 50 nm were observed for the materials prepared by Method 1 (Table S2). Note that pore diameters around 4.0 nm might be partially related to the tensile strength effect, which may distort this region of the pore size distribution. The

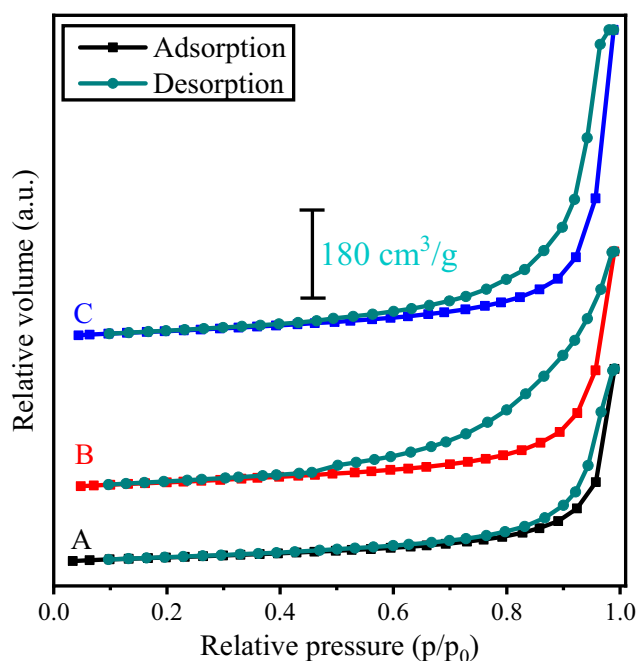


Fig. 6.  $N_2$  sorption isotherms of (A)  $LDH_3$ , (B)  $LDH_{10}$  and (C)  $LDH_{30}$  materials obtained by Method 1.

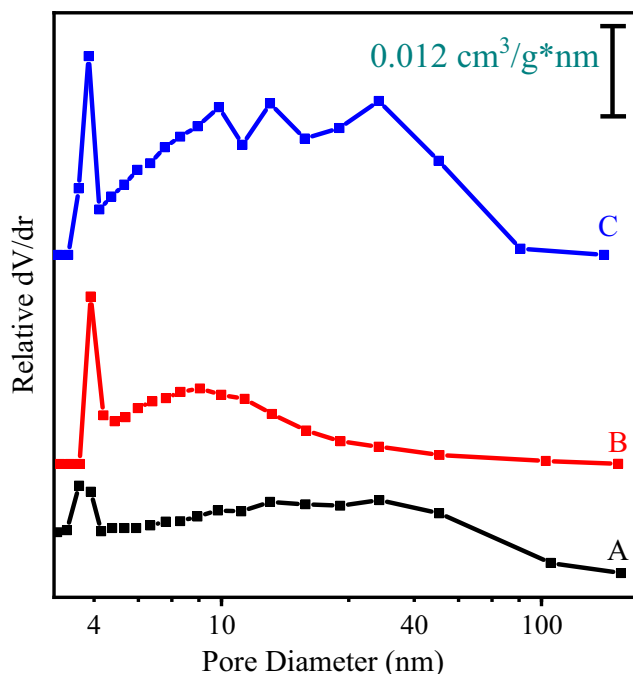


Fig. 8. Pore diameter distribution of (A)  $LDH_3$ , (B)  $LDH_{10}$  and (C)  $LDH_{30}$  materials obtained by Method 1. The data were calculated from the desorption part of the sorption isotherms.

highest value was determined for LDH<sub>30</sub> indicating that starting from highly charged and stable precursors is the best strategy to obtain such a mesoporous LDH (for comparative data, see Table S3). The obtained high  $dV/dr$  values for LDH<sub>3</sub>, LDH<sub>10</sub> and LDH<sub>30</sub> as well as c-LDH<sub>3</sub> illustrated the formation of hierarchically porous structures [60].

These findings shed light on the important role of SDS adsorption on the MgAl–Cl–LDH material through its effect on the surface charge properties and on the aggregation of the particles. In other words, more porous LDHs or wider pore size distribution can be obtained once the precursor materials (i.e., SDS-LDH hybrid before calcination) are made by adsorption/intercalation of SDS on pristine LDHs, like in Method 1. Moreover, the adsorbed amount and the colloidal stability of the SDS-LDH composites also affect the final structure. Once the feeding material for calcination and subsequent rehydration forms a stable dispersion, then the developed structure shows highly mesoporous and hierarchical features. Accordingly, the most advantageous properties of the final material were obtained, when the highest SDS dose was applied, which condition resulted in homogeneously distributed primary SDS<sub>30</sub>-MgAl–Cl–LDH particles of high negative charge. In contrast, SDS presence during co-precipitation in Method 2 did not lead to such an advanced feature. Another possible contribution of the intercalated SDS content to the high porosity of the final materials is that its gaseous thermal decomposition products (e.g., sulfur dioxide) carved well-defined pores and channels into the LDHs during calcination. Similar phenomenon was reported earlier in the literature [61–63].

### 3.5. Efficiency in contaminant removal from water

As a proof of concept, the obtained materials were tested in dichromate and nitrate adsorption experiments. Concerning the former ion, its removal is of great importance for the protection of natural waters from adverse effect of nitrification. On one hand, it is evident that the application of LDHs as anion exchangers should be an efficient solution to solve this problem. On the other hand, it was pointed out that nitrate ions do not attach strongly to the positively charged LDHs and thus, direct anion-exchange reactions were not very successful [64–66].

Therefore, it came as a bit of surprise that our materials showed notable nitrate adsorption (Fig. S11). Let us consider that the amounts of the adsorbed nitrate ions were independent of the applied adsorbent with different porous structure and surface area. Taking into account the relatively low hydrodynamic ionic radius of nitrate anion (2.62 Å), the more porous systems might contribute to faster stream of anions, this fact did not influence the adsorption capacity [67]. The amount of the removed ion increased with increase of the concentration of the nitrate ions up to 575 mg/L nitrate ion loading. The maximum amount of adsorbed nitrate was experienced at 104 mg/g LDH concentration.

Besides, the adsorption capacity could be determined by fitting the measured points with the Langmuir isotherm [68] (Fig. S11 and Table S4, see details of calculations in SM). Comparison to the literature data (Table S5), one may notice that the sorption capacity of 749.7 mg/g determined for LDH<sub>30</sub> is the highest within the single-phase LDH materials applied earlier for nitrate adsorption. To explore the possible intercalation process of nitrate during ion exchange, XRD patterns were recorded at various nitrate concentrations (Fig. S12), and they clearly indicated the staging effect and intercalation of the nitrate ions.

In the second part of the adsorption studies, the dichromate ion, a well-known carcinogenic contaminant, was used as model compound. Under the conditions applied,  $Cr_2O_7^{2-}$  was the predominant species in the samples [69]. The time-dependent measurements (Fig. S13) indicates different sorption capacities for LDH<sub>3</sub>, LDH<sub>10</sub>

and LDH<sub>30</sub>, which increased in this order, in line with their specific surface area. The sorption data indicate that the diffusion of dichromate anions could be enhanced by increasing the pore sizes in contrast to nitrate ions, where no differences were observed for LDH<sub>3</sub>, LDH<sub>10</sub> and LDH<sub>30</sub>. This is due to the higher hydrodynamic radius of dichromate, which prevents its diffusion into smaller pores. This effect led to efficient ion exchange especially for the LDH<sub>30</sub>.

The sorption isotherms were calculated to determine the capacity of the LDHs in dichromate adsorption. They could be interpreted by both the Langmuir (equation S8 and Fig. 9) and the Freundlich [70] model (equation S9 and Fig. S14). The first method fit slightly better to the experimental data. The parameters of the isotherms are given in Table 1. The determined sorption capacity of the non-modified LDH structure (19.8 mg/g) is in agreement with previously published data (21.0 mg/g) [71]. For the LDH<sub>3</sub>, LDH<sub>10</sub> and LDH<sub>30</sub> structures, the sorption capacity increased parallel with the surface area and/or total pore volume. Therefore, the LDH<sub>30</sub> was the most efficient and, to the best of our knowledge, the obtained value (388.5 mg/g) was the highest among the previously published single-phase LDH materials (Table S6) [9,72–74]. More importantly, the sorption capacity obtained for LDH<sub>30</sub> is also higher than those of the adsorbents usually used for dichromate removal in the industry (Table S7).

Recyclability of adsorbents is always an important parameter. To explore this issue, desorption of dichromate ions was carried out in concentrated (3 M) NaCl solutions. Thereafter, the adsorption isotherms were registered again with the regenerated (dichromate-free) materials. Fig. 10 shows the adsorption capacity values obtained during 5 cycles. Only slight decrease (about 8%) was observed after 5 cycles indicating excellent recyclability of LDH<sub>30</sub>. In comparison, it was reported for MgAl–CO<sub>3</sub>–LDH that only 65% of the ion-exchange capacity could be regenerated after five cycles [71].

The dichromate intercalation and the ion exchange during regeneration were investigated by XRD measurements (Fig. S15). The patterns clearly show that dichromate intercalation occurred during the adsorption reaction indicated by the increased inter-layer distances. Moreover, they decreased back to the original

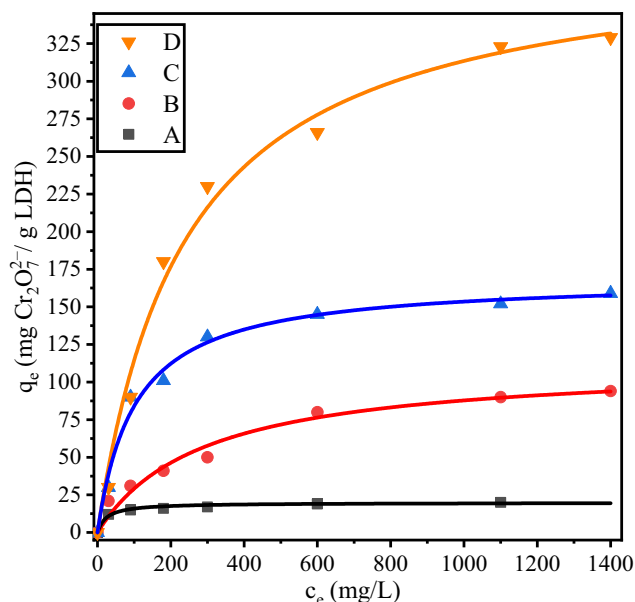
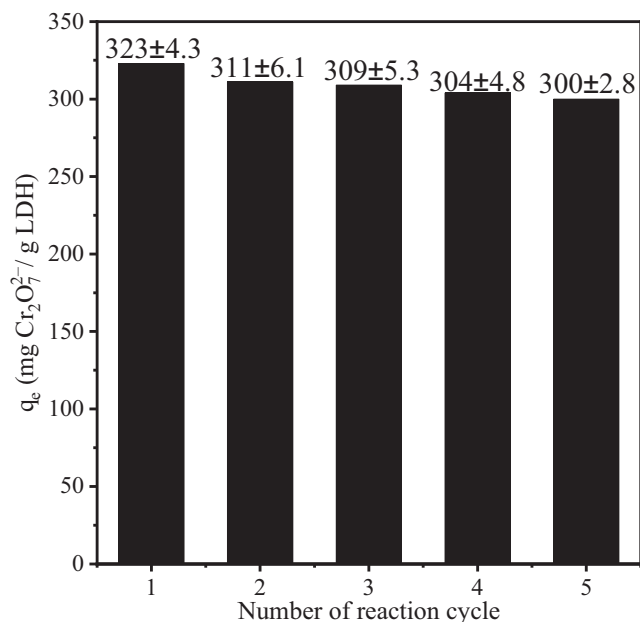


Fig. 9. Dichromate ion adsorption isotherm of (A) MgAl–Cl–LDH, (B) LDH<sub>3</sub>, (C) LDH<sub>10</sub> and (D) LDH<sub>30</sub>. The solid lines are fits using the Langmuir model.

**Table 1**  
Langmuir and Freundlich isotherm parameters for the adsorption of dichromate ion.

Adsorbent	Langmuir		Freundlich	
	$q_m$ (mg/g)	$K_L$ ( $\cdot 10^{-3}$ L/mg)	$n$	$K_F$ (L/g)
MgAl–Cl–LDH	19.8	41.0	2.5	2.0
LDH <sub>3</sub>	113.1	3.5	3.7	13.9
LDH <sub>10</sub>	169.0	9.9	4.8	24.0
LDH <sub>30</sub>	388.5	0.4	6.3	36.2



**Fig. 10.** Regeneration of LDH<sub>30</sub> adsorbent for 5 consecutive cycles indicated by the adsorption capacities.

value after the regeneration protocol was carried out in NaCl, which shed light on the successful elimination of dichromate.

An interesting information worth mentioning is that the inter-layer distance did not change after the anion-exchange reaction in dichromate solutions (Fig. S16). This observation is in contrast with data reported earlier underlining that dichromate (or chromate) intercalation always takes place into LDHs [9,71,75].

#### 4. Conclusions

The present study demonstrates that hierarchical LDH materials of mesoporous features can be obtained with the combined colloid approach. This method relies on the charging and stability assessments of the precursor materials composed of pristine LDH and adsorbed sacrificial SDS molecules on the outer surface and in the interlayer space. Light scattering experiments revealed that SDS adsorption led to charge neutralization and overcharging at appropriate amount of added surfactant. In the latter case, the SDS<sub>30</sub>–MgAl–Cl–LDH composites formed highly stable colloids. The SDS template was completely removed by calcination to LDO<sub>30</sub> and the characteristic LDH features were recovered by rehydration to LDH<sub>30</sub>. For this material, a hierarchical porous structure was obtained. More precisely, 8-time and 48-time increases were detected in the surface area and total pore volume, respectively, in comparison to the case, when template-free LDH material was calcined and rehydrated with the same method.

The LDH structures presented outstanding sorption capacities for both nitrate and dichromate anions with LDH<sub>30</sub> as the most efficient one. It was pointed out that the adsorbents developed were

able to remove nitrate and chromate anions in large quantities by intercalation. To the best of our knowledge, the adsorption capacity of the LDH<sub>30</sub> sample is the highest among the previously reported LDH materials and superior to several industrially used dichromate removing agents. Furthermore, LDH<sub>30</sub> showed excellent recyclability.

These advanced properties could be achieved only once the SDS dose is properly adjusted, i.e., the precursor SDS-LDH composite forms highly stable dispersions and surfactant intercalation takes place. Deviation from the optimal amount of SDS gives rise to lower surface area and total pore volumes as well as smaller pore diameters. The results clearly confirm that this novel colloid chemistry approach is a promising way to prepare mesoporous LDHs for applications, wherever organic content-free materials of highly hierarchical internal properties are required.

#### CRediT authorship contribution statement

**Gábor Varga:** Investigation, Formal analysis, Visualization. **Zoltán Somosi:** Investigation, Validation. **Zoltán Kónya:** Funding acquisition. **Ákos Kukovecz:** Funding acquisition. **István Pálínkó:** Supervision. **Istvan Szilagyi:** Conceptualization, Funding acquisition, Writing - original draft.

#### Declaration of Competing Interest

The authors declare that they have no known competing financial interests or personal relationships that could have appeared to influence the work reported in this paper.

#### Acknowledgements

Financial support by the Ministry of Human Capacities (20391-3/2018/FEKUSTRAT) and by the Hungarian National Research, Development and Innovation Office (SNN 131558) is gratefully acknowledged. G. Varga thanks for the postdoctoral fellowship under the grant PD 128189. The support from the University of Szeged Open Access Fund (4929) is gratefully acknowledged.

#### Appendix A. Supplementary material

Supplementary data to this article can be found online at <https://doi.org/10.1016/j.jcis.2020.08.118>.

#### References

- [1] Z.B. Cao, B. Li, L.Y. Sun, L. Li, Z.P. Xu, Z. Gu, 2D layered double hydroxide nanoparticles: recent progress toward preclinical/clinical nanomedicine, *Small Methods* (2019) 1900343.
- [2] F. Song, L.C. Bai, A. Moysiadou, S. Lee, C. Hu, L. Liardet, X.L. Hu, Transition metal oxides as electrocatalysts for the oxygen evolution reaction in alkaline solutions: an application-inspired renaissance, *J. Am. Chem. Soc.* 140 (2018) 7748–7759.
- [3] K.H. Goh, T.T. Lim, Z. Dong, Application of layered double hydroxides for removal of oxyanions: a review, *Water Res.* 42 (2008) 1343–1368.
- [4] P.J. Sideris, U.G. Nielsen, Z.H. Gan, C.P. Grey, Mg/Al ordering in layered double hydroxides revealed by multinuclear NMR spectroscopy, *Science* 321 (2008) 113–117.

- [5] Z. Gu, J.J. Atherton, Z.P. Xu, Hierarchical layered double hydroxide nanocomposites: structure, synthesis and applications, *Chem. Commun.* 51 (2015) 3024–3036.
- [6] F. Leroux, J.P. Besse, Polymer interleaved layered double hydroxide: a new emerging class of nanocomposites, *Chem. Mat.* 13 (2001) 3507–3515.
- [7] Z. Gu, A.C. Thomas, Z.P. Xu, J.H. Campbell, G.Q. Lu, In vitro sustained release of LMWH from MgAl-layered double hydroxide nanohybrids, *Chem. Mat.* 20 (2008) 3715–3722.
- [8] K.H. Goh, T.T. Lim, Z.L. Dong, Enhanced arsenic removal by hydrothermally treated nanocrystalline Mg/Al layered double hydroxide with nitrate intercalation, *Environ. Sci. Technol.* 43 (2009) 2537–2543.
- [9] H.P. Chao, Y.C. Wang, H.N. Tran, Removal of hexavalent chromium from groundwater by Mg/Al-layered double hydroxides using characteristics of in-situ synthesis, *Environ. Pollut.* 243 (2018) 620–629.
- [10] M.F. Shao, F.Y. Ning, Y.F. Zhao, J.W. Zhao, M. Wei, D.G. Evans, X. Duan, Core-shell layered double hydroxide microspheres with tunable interior architecture for supercapacitors, *Chem. Mat.* 24 (2012) 1192–1197.
- [11] H.S. Ji, W.H. Wu, F.H. Li, X.X. Yu, J.J. Fu, L.Y. Jia, Enhanced adsorption of bromate from aqueous solutions on ordered mesoporous Mg-Al layered double hydroxides (LDHs), *J. Hazard. Mater.* 334 (2017) 212–222.
- [12] G. Abellan, J.L. Jorda, P. Atienzar, M. Varela, M. Jaafar, J. Gomez-Herrero, F. Zamora, A. Ribera, H. Garcia, E. Coronado, Stimuli-responsive hybrid materials: breathing in magnetic layered double hydroxides induced by a thermoresponsive molecule, *Chem. Sci.* 6 (2015) 1949–1958.
- [13] P. Zhang, G.R. Qian, Z.P. Xu, H.S. Shi, X.X. Ruan, J. Yang, R.L. Frost, Effective adsorption of sodium dodecylsulfate (SDS) by hydrocalumite (CaAl-LDH-Cl) induced by self-dissolution and re-precipitation mechanism, *J. Colloid Interface Sci.* 367 (2012) 264–271.
- [14] J. Zhang, X.L. Xie, C.J. Li, H. Wang, L.J. Wang, The role of soft colloidal templates in the shape evolution of flower-like MgAl-LDH hierarchical microstructures, *RSC Adv.* 5 (2015) 29757–29765.
- [15] L. Fernandez, I. Ledezma, C. Borrás, L.A. Martínez, H. Carrero, Horseradish peroxidase modified electrode based on a film of Co-Al layered double hydroxide modified with sodium dodecylbenzenesulfonate for determination of 2-chlorophenol, *Sens. Actuator B-Chem.* 182 (2013) 625–632.
- [16] L. Deng, H.X. Zeng, Z. Shi, W. Zhang, J.M. Luo, Sodium dodecyl sulfate intercalated and acrylamide anchored layered double hydroxides: a multifunctional adsorbent for highly efficient removal of Congo red, *J. Colloid Interface Sci.* 521 (2018) 172–182.
- [17] Y. Kong, Y.R. Huang, C. Meng, Z. Zhang, Sodium dodecylsulfate-layered double hydroxide and its use in the adsorption of 17-estradiol in wastewater, *RSC Adv.* 8 (2018) 31440–31454.
- [18] H. Chen, G.R. Qian, X.X. Ruan, R.L. Frost, Removal process of nickel(II) by using dodecyl sulfate intercalated calcium aluminum layered double hydroxide, *Appl. Clay Sci.* 132 (2016) 419–424.
- [19] S.T. Lin, H.N. Tran, H.P. Chao, J.F. Lee, Layered double hydroxides intercalated with sulfur-containing organic solutes for efficient removal of cationic and oxyanionic metal ions, *Appl. Clay Sci.* 162 (2018) 443–453.
- [20] P. Zhang, S.D. Ouyang, P. Li, Y. Huang, R.L. Frost, Enhanced removal of ionic dyes by hierarchical organic three-dimensional layered double hydroxide prepared via soft-template synthesis with mechanism study, *Chem. Eng. J.* 360 (2019) 1137–1149.
- [21] J. Xu, D.P. Yan, S.D. Li, J. Lu, Controllable luminescence and electrochemical detection of Pb<sup>2+</sup> ion based on the 2,2'-Azino-bis(3-ethylthiazoline-6-sulfonate) dye and dodecanesulfonate co-intercalated layered double hydroxide, *Dyes Pigment.* 94 (2012) 74–80.
- [22] Q. Tao, H.P. He, R.L. Frost, P. Yuan, J.X. Zhu, Nanomaterials based upon silylated layered double hydroxides, *Appl. Surf. Sci.* 255 (2009) 4334–4340.
- [23] Q.Q. Chen, M.X. Nie, Y. Guo, Controlled synthesis and humidity sensing properties of CdS/polyaniline composite based on CdAl layered double hydroxide, *Sens. Actuator B-Chem.* 254 (2018) 30–35.
- [24] T. Wu, Q.H. Kong, H.K. Zhang, J.H. Zhang, Thermal stability and flame retardancy of polypropylene/NiAl layered double hydroxide nanocomposites, *J. Nanosci. Nanotechnol.* 18 (2018) 1051–1056.
- [25] Q.H. Kong, T. Wu, J.Q. Wang, H. Liu, J.H. Zhang, Improving the thermal stability and flame retardancy of PP/IFR composites by NiAl-layered double hydroxide, *J. Nanosci. Nanotechnol.* 18 (2018) 3660–3665.
- [26] P.C. Pavan, E.L. Crepaldi, G.D. Gomes, J.B. Valim, Adsorption of sodium dodecylsulfate on a hydrotalcite-like compound. Effect of temperature, pH and ionic strength, *Colloid Surf. A* 154 (1999) 399–410.
- [27] P. Zhang, M.X. Xiang, P. Li, S.D. Ouyang, T. He, Q. Deng, The enhancement roles of sulfate on the adsorption of sodium dodecylsulfate by calcium-based layered double hydroxide: microstructure and thermal behaviors, *Environ. Sci. Pollut. Res.* 26 (2019) 19320–19326.
- [28] P. Zhang, T. He, P. Li, X.Z. Zeng, Y. Huang, New insight into the hierarchical microsphere evolution of organic three-dimensional layer double hydroxide: the key role of the surfactant template, *Langmuir* 35 (2019) 13562–13569.
- [29] P. Zhang, S.D. Ouyang, P. Li, Z. Gu, Y.G. Huang, S. Deng, Effect of anion co-existence on ionic organic pollutants removal over Ca based layered double hydroxide, *J. Colloid Interface Sci.* 534 (2019) 440–446.
- [30] J. Wang, F. Yang, C.F. Li, S.Y. Liu, D.J. Sun, Double phase inversion of emulsions containing layered double hydroxide particles induced by adsorption of sodium dodecyl sulfate, *Langmuir* 24 (2008) 10054–10061.
- [31] F. Aoudjit, O. Cherifi, D. Halliche, Simultaneously efficient adsorption and photocatalytic degradation of sodium dodecyl sulfate surfactant by one-pot synthesized TiO<sub>2</sub>/layered double hydroxide materials, *Sep. Sci. Technol.* 54 (2019) 1095–1105.
- [32] M. Pavlovic, P. Rouster, T. Oncsik, I. Szilagy, Tuning colloidal stability of layered double hydroxides: from monovalent ions to polyelectrolytes, *ChemPlusChem* 82 (2017) 121–131.
- [33] J. He, B. Li, D.G. Evans, X. Duan, Synthesis of layered double hydroxides in an emulsion solution, *Colloid Surf. A* 251 (2004) 191–196.
- [34] J. He, M. Wei, B. Li, Y. Kang, D.G. Evans, X. Duan, Preparation of layered double hydroxides, in: X. Duan, D.G. Evans (eds.), *Layered Double Hydroxides*, 2006, pp. 89–119.
- [35] H. Holthoff, S.U. Egelhaaf, M. Borkovec, P. Schurtenberger, H. Sticher, Coagulation rate measurements of colloidal particles by simultaneous static and dynamic light scattering, *Langmuir* 12 (1996) 5541–5549.
- [36] G. Trefalt, I. Szilagy, M. Borkovec, Poisson-Boltzmann description of interaction forces and aggregation rates involving charged colloidal particles in asymmetric electrolytes, *J. Colloid Interface Sci.* 406 (2013) 111–120.
- [37] D.G. Evans, R.C.T. Slade, Structural aspects of layered double hydroxides, in: X. Duan, D.G. Evans (eds.), *Layered Double Hydroxides*, 2006, pp. 1–87.
- [38] M. Pavlovic, R. Huber, M. Adok-Sipiczki, C. Nardin, I. Szilagy, Ion specific effects on the stability of layered double hydroxide colloids, *Soft Matter* 12 (2016) 4024–4033.
- [39] B. Derjaguin, L.D. Landau, Theory of the stability of strongly charged lyophobic sols and of the adhesion of strongly charged particles in solutions of electrolytes, *Acta Phys. Chim.* 14 (1941) 633–662.
- [40] E.J.W. Verwey, J.T.G. Overbeek, *Theory of Stability of Lyophobic Colloids*, Elsevier, Amsterdam, 1948.
- [41] J. Song, Y.N. Tan, D. Janczewski, M.A. Hempenius, J.W. Xu, H.R. Tan, G.J. Vancso, Poly(ferrocenylsilane) electrolytes as a gold nanoparticle foundry: “two-in-one” redox synthesis and electrosteric stabilization, and sensing applications, *Nanoscale* 9 (2017) 19255–19262.
- [42] Y.S. Gao, J.W. Wu, Z. Zhang, R. Jin, X. Zhang, X.R. Yan, A. Umar, Z.H. Guo, Q. Wang, Synthesis of polypropylene/Mg<sub>3</sub>Al-X (X = CO<sub>3</sub><sup>2-</sup>, NO<sub>3</sub><sup>-</sup>, Cl<sup>-</sup>, SO<sub>4</sub><sup>2-</sup>) LDH nanocomposites using a solvent mixing method: thermal and melt rheological properties, *J. Mater. Chem. A* 1 (2013) 9928–9934.
- [43] S.P. Newman, S.J. Williams, P.V. Coveney, W. Jones, Interlayer arrangement of hydrated MgAl layered double hydroxides containing guest terephthalate anions: Comparison of simulation and measurement, *J. Phys. Chem. B* 102 (1998) 6710–6719.
- [44] W.H. Bragg, W.L. Bragg, The reflection of X-rays by crystals, *Proc. R. Soc. Lond. Ser. A-Contain. Pap. Math. Phys. Character* 88 (1913) 428–438.
- [45] N. Iyi, Y. Ebina, T. Sasaki, Water-swelling MgAl-LDH (layered double hydroxide) hybrids: synthesis, characterization, and film preparation, *Langmuir* 24 (2008) 5591–5598.
- [46] N. Iyi, T. Matsumoto, Y. Kaneko, K. Kitamura, Deintercalation of carbonate ions from a hydrotalcite-like compound: enhanced decarbonation using acid-salt mixed solution, *Chem. Mat.* 16 (2004) 2926–2932.
- [47] Y. Sun, Y. Zhou, X. Ye, J. Chen, Z. Wang, Fabrication and infrared emissivity study of hybrid materials based on immobilization of collagen onto exfoliated LDH, *Mater. Lett.* 62 (2008) 2943–2946.
- [48] Z.J. Yuan, S.M. Bak, P.S. Li, Y. Jia, L.R. Zheng, Y. Zhou, L. Bai, E.Y. Hu, X.Q. Yang, Z. Cai, Y.M. Sun, X.M. Sun, Activating layered double hydroxide with multivacancies by memory effect for energy-efficient hydrogen production at neutral pH, *ACS Energy Lett.* 4 (2019) 1412–1418.
- [49] S. Meszaros, J. Halasz, Z. Konya, P. Sipos, I. Palinko, Reconstruction of calcined MgAl- and NiMgAl-layered double hydroxides during glycerol dehydration and their recycling characteristics, *Appl. Clay Sci.* 80–81 (2013) 245–248.
- [50] T. Bujdoso, A. Patzko, Z. Galbacs, I. Dekany, Structural characterization of arsenate ion exchanged MgAl-layered double hydroxide, *Appl. Clay Sci.* 44 (2009) 75–82.
- [51] J.S. Valente, F. Figueras, M. Gravelle, P. Kumbhar, J. Lopez, J.P. Besse, Basic properties of the mixed oxides obtained by thermal decomposition of hydrotalcites containing different metallic compositions, *J. Catal.* 189 (2000) 370–381.
- [52] M.A. Ulibarri, F.M. Labajos, V. Rives, R. Trujillano, W. Kagunya, W. Jones, Comparative-study of the synthesis and properties of vanadate-exchanged layered double hydroxides, *Inorg. Chem.* 33 (1994) 2592–2599.
- [53] H.R. Suo, H.H. Duan, C.P. Chen, J.C. Buffet, D. O'Hare, Bifunctional acid-base mesoporous silica/aqueous miscible organic-layered double hydroxides, *RSC Adv.* 9 (2019) 3749–3754.
- [54] B. Li, Y.X. Zhang, X.B. Zhou, Z.L. Liu, Q.Z. Liu, X.H. Li, Different dye removal mechanisms between monodispersed and uniform hexagonal thin plate-like MgAl-CO<sub>3</sub>-LDH and its calcined product in efficient removal of Congo red from water, *J. Alloy. Compd.* 673 (2016) 265–271.
- [55] C.P. Chen, M.S. Yang, Q. Wang, J.C. Buffet, D. O'Hare, Synthesis and characterisation of aqueous miscible organic-layered double hydroxides, *J. Mater. Chem. A* 2 (2014) 15102–15110.
- [56] E. Mendioroz, J.A. Pajares, I. Benito, C. Pesquera, F. Gonzalez, C. Blanco, Texture evolution of montmorillonite under progressive acid treatment – change from H-3 to H-2 type of hysteresis, *Langmuir* 3 (1987) 676–681.
- [57] G.H. Zhang, B.Z. Lin, Y.Q. Qiu, L.W. He, Y.L. Chen, B.F. Gao, Highly efficient visible-light-driven photocatalytic hydrogen generation by immobilizing CdSe nanocrystals on ZnCr-layered double hydroxide nanosheets, *Int. J. Hydrog. Energy* 40 (2015) 4758–4765.
- [58] P. Gunawan, R. Xu, Direct assembly of anisotropic layered double hydroxide (LDH) nanocrystals on spherical template for fabrication of drug-LDH hollow nanospheres, *Chem. Mat.* 21 (2009) 781–783.



- [59] J. Li, N. Zhang, D.H.L. Ng, Synthesis of a 3D hierarchical structure of gamma-AlO(OH)/Mg-Al-LDH/C and its performance in organic dyes and antibiotics adsorption, *J. Mater. Chem. A* 3 (2015) 21106–21115.
- [60] R. Pourfaraj, S.J. Fatemi, S.Y. Kazemi, P. Biparva, Synthesis of hexagonal mesoporous MgAl LDH nanoplatelets adsorbent for the effective adsorption of Brilliant Yellow, *J. Colloid Interface Sci.* 508 (2017) 65–74.
- [61] J.M. Patterson, Z. Kortylewicz, W.T. Smith, Thermal-degradation of sodium dodecyl-sulfate, *J. Agric. Food Chem.* 32 (1984) 782–784.
- [62] D. Ramimoghadam, M.Z. Bin Hussein, Y.H. Taufiq-Yap, The effect of sodium dodecyl sulfate (SDS) and cetyltrimethylammonium bromide (CTAB) on the properties of ZnO synthesized by hydrothermal method, *Int. J. Mol. Sci.* 13 (2012) 13275–13293.
- [63] A. Malak-Polaczyk, C. Vix-Guterl, E. Frackowiak, Carbon/layered double hydroxide (LDH) composites for supercapacitor application, *Energy Fuels* 24 (2010) 3346–3351.
- [64] S. Miyata, Anion-exchange properties of hydrotalcite-like compounds, *Clay Clay Min.* 31 (1983) 305–311.
- [65] B.X. Li, J. He, D.G. Evans, X. Duan, Inorganic layered double hydroxides as a drug delivery system - intercalation and in vitro release of fenbufen, *Appl. Clay Sci.* 27 (2004) 199–207.
- [66] G. Varga, A. Kukovec, Z. Konya, L. Korecz, S. Murath, Z. Csendes, G. Peintler, S. Carlson, P. Sipos, I. Palinko, Mn(II)-amino acid complexes intercalated in CaAl-layered double hydroxide - well-characterized, highly efficient, recyclable oxidation catalysts, *J. Catal.* 335 (2016) 125–134.
- [67] S. Sugiharto, T.M. Lewis, A.J. Moorhouse, P.R. Schofield, P.H. Barry, Anion-cation permeability correlates with hydrated counterion size in glycine receptor channels, *Biophys. J.* 95 (2008) 4698–4715.
- [68] I. Langmuir, The adsorption of gases on plane surfaces of glass, mica and platinum, *J. Am. Chem. Soc.* 40 (1918) 1361–1403.
- [69] F. Brito, J. Ascanio, S. Mateo, C. Hernandez, L. Araujo, P. Gili, P. MartinZarza, S. Dominguez, A. Mederos, Equilibria of chromate(VI) species in acid medium and ab initio studies of these species, *Polyhedron* 16 (1997) 3835–3846.
- [70] H. Freundlich, Über die adsorption in lösungen, *Z. Phys. Chem.* 57 (1907) 385–470.
- [71] S. He, Y.F. Zhao, M. Wei, D.G. Evans, X. Duan, Fabrication of hierarchical layered double hydroxide framework on aluminum foam as a structured adsorbent for water treatment, *Ind. Eng. Chem. Res.* 51 (2012) 285–291.
- [72] N.N. Das, J. Konar, M.K. Mohanta, S.C. Srivastava, Adsorption of Cr(VI) and Se(IV) from their aqueous solutions onto Zr<sup>4+</sup>-substituted ZnAl/MgAl-layered double hydroxides: effect of Zr<sup>4+</sup> substitution in the layer, *J. Colloid Interface Sci.* 270 (2004) 1–8.
- [73] V.M. Boddu, K. Abburi, J.L. Talbott, E.D. Smith, Removal of hexavalent chromium from wastewater using a new composite chitosan biosorbent, *Environ. Sci. Technol.* 37 (2003) 4449–4456.
- [74] L. Zhu, Y. Liu, J. Chen, Synthesis of N-methylimidazolium functionalized strongly basic anion exchange resins for adsorption of Cr(VI), *Ind. Eng. Chem. Res.* 48 (2009) 3261–3267.
- [75] N. Tarutani, Y. Tokudome, M. Fukui, K. Nakanishi, M. Takahashi, Fabrication of hierarchically porous monolithic layered double hydroxide composites with tunable microcages for effective oxyanion adsorption, *RSC Adv.* 5 (2015) 57187–57192.



Contents lists available at ScienceDirect

# Journal of Colloid and Interface Science

www.elsevier.com/locate/jcis



## Charging and stability of anionic latex particles in the presence of linear poly(ethylene imine)

István Szilágyi, Dana Rosická<sup>1</sup>, José Hierrezuelo, Michal Borkovec\*

Department of Inorganic, Analytical, and Applied Chemistry, University of Geneva, Sciences II, 30, Quai Ernest-Ansermet, 1211 Geneva 4, Switzerland

### ARTICLE INFO

#### Article history:

Received 18 March 2011

Accepted 28 April 2011

Available online 4 May 2011

#### Keywords:

Polyethylenimine

Electrophoresis

Dynamic light scattering

Overcharging

Aggregation

Flocculation

Coagulation

### ABSTRACT

Charging properties and colloidal stability of negatively charged polystyrene latex particles were investigated in the presence of linear poly(ethylene imine) (LPEI) of different molecular masses by electrophoresis and dynamic light scattering (DLS). Electrophoretic mobility measurements illustrate that LPEI strongly adsorbs on these particles leading to charge neutralization at isoelectric point (IEP) and charge reversal. Time-resolved DLS experiments indicate that the aggregation of the latex particles is rapid near the IEP and slows down away from this point. Surprisingly, the colloidal stability does not depend on the molecular mass, which indicates that the adsorbed LPEI layer is rather homogeneous.

© 2011 Published by Elsevier Inc.

### 1. Introduction

Controlling stability and rheology of colloidal suspensions of charged particles by polyelectrolytes comes into renewed focus due to the importance of polyelectrolytes in several applications, such as waste-water treatment, papermaking, as well as formulation of foods, paints, or cosmetics [1–6]. Polyelectrolytes are further intensively investigated as drug or gene carriers in pharmaceutical and biomedical applications [7–9]. Finally, polyelectrolytes are widely used as building blocks in the layer-by-layer self-assembly process to fabricate surface coatings, hollow capsules, or free-standing membranes [10–15].

To improve the effectiveness of these processes on a rational basis, fundamental studies of polyelectrolyte adsorption, resulting interaction forces, as well as control of suspension stability and rheology comes into scrutiny from the experimental [3,16–23] and theoretical point of views [24–27]. Forces between surfaces with adsorbed polyelectrolytes were measured directly with the surface forces apparatus and with the colloidal probe technique based on the atomic force microscope (AFM) [28–34]. These studies have demonstrated that interaction forces are repulsive at high polyelectrolyte dose and that they are controlled by the surface charge in-

duced by the adsorbed polyelectrolyte and the resulting overlap between the diffuse parts of the electrical double-layer. At intermediate dose, the forces are controlled by van der Waals interactions and additional attractive forces originating from the inhomogeneous charge distribution within the adsorbed layer or correlation effects. The same pattern was confirmed by studies of colloidal stability [16–18,35,36] and suspension rheology [3,20,37]. Unstable suspensions and high yield stress is observed near the IEP due to attractive forces. Away from the IEP, suspensions become stable and flow more easily.

Many studies have focused on cationic polyelectrolytes due to the frequent appearance of negatively charged interfaces in nature [3–6]. Poly(ethylene imine) is an important polyelectrolyte within this class, and is known in two different forms [38,39]. Highly branched poly(ethylene imine) (BPEI) is obtained by ring-opening polymerization of ethylenimine and linear poly(ethylene imine) (LPEI) is synthesized by the hydrolysis of poly(2-oxazoline)s. These polyelectrolytes were investigated in substantial detail [31,38,40–44]. Being a weak polybase, the charging characteristics are determined by the ionization constants of the different amine groups present and the interactions between these groups. In particular, BPEI is never fully protonated in the accessible pH range, while LPEI is fully protonated only below pH 2. AFM imaging and layer thickness measurements revealed that BPEI flattens substantially upon adsorption [42]. BPEI is known to reverse the charge of negatively charged particles, and one knows that in the presence of BPEI, colloidal suspensions become unstable and have high-yield

\* Corresponding author.

E-mail address: [michal.borkovec@unige.ch](mailto:michal.borkovec@unige.ch) (M. Borkovec).

<sup>1</sup> Present address: Institute of New Technologies and Applied Informatics, Technical University of Liberec, 2, Studentská, 46117 Liberec 1, Czech Republic.

stress close to the IEP [19,20]. Repulsive forces due to diffuse layer overlap set in above the IEP as has been shown with the AFM-based colloidal probe technique [31].

Substantially less information is available on the interaction forces induced by LPEI. Therefore, here we report on the charging behavior and colloidal stability of negatively charged latex particles in the presence of LPEI. The charging and adsorption behavior was studied with electrophoretic mobility while colloidal stability was accessed by time-resolved dynamic light scattering (DLS). In analogy to other oppositely charged polyelectrolyte-particle systems, the present system is unstable near the isoelectric point (IEP) where the particle charge is neutralized by the adsorbed LPEI. Away from the IEP, the particles are stabilized due to the buildup of surface charge. Most surprisingly, however, no molecular mass dependence on the particle stability was found. This finding indicates that an adsorbed LPEI layer is much more homogenous than layers of many other polyelectrolytes adsorbed on oppositely charged substrates.

## 2. Materials and methods

### 2.1. Materials

Two samples of surfactant-free polystyrene latex particles were obtained from Interfacial Dynamics Corporation (Portland, USA). The sulfate latex (SL) has a radius of 135 nm, a polydispersity of 5.9% and a charge density of  $-0.011 \text{ C/m}^2$ . These quantities were determined by the manufacturer by transmission electron microscopy and conductometry, respectively. The carboxylate modified latex (CML) has a radius of 154 nm and a polydispersity of 4.2%, and surface charge density of  $-1.49 \text{ C/m}^2$  due to the brushy layer on the surface. The suspensions were purified by dialysis against Milli-Q water with a cellulose ester membrane with a molecular mass cutoff of 50 kg/mol (No. 131378, Spectrum, Rancho Dominguez, USA). The cleaning process was continued until the conductivity of the surrounding medium decreased to the value of Milli-Q water. The particle suspensions had concentrations in the range of 30–50 g/L. Hydrodynamic particle radii determined by dynamic light scattering in stable suspensions were 145 nm and 156 nm for the SL and CML, respectively. These values are somewhat larger than the diameters determined by TEM due to the finite polydispersity of the particles.

Samples of linear poly(ethylene imine) (LPEI) with weight averaged molar masses of about 2.5, 25, and 250 kg/mol were obtained from Polysciences (Eppenheim, Germany). The manufacturer reports polydispersity indices, which represent the ratio of between the mass weighted and number weighted molecular masses, of 1.6, 1.9, and 3.4, respectively. The high molecular mass sample was dissolved at a concentration of about 1 g/L in 0.08 M HCl and dialyzed with a cellulose ester membrane with a molecular mass cut-off of 10 kg/mol (No. 131270, Spectrum). In case of the two lower molecular mass samples, the hydrochloride salts were dissolved in Milli-Q water and dialyzed with a cellulose ester membrane with a molecular mass cut-off of 0.5 kg/mol (No. 131060, Spectrum). The final polymer concentrations were determined by total carbon and nitrogen analysis (TOCV, Shimadzu). The Staudinger indices were obtained by capillary viscosimetry at different polymer concentrations, and they were found to be 27, 40 and 137 mL/g for the molecular masses of 2.5, 25 and 250 kg/mol, respectively. These values agree reasonably well to earlier measurements on LPEI [40] and BPEI [41,45]. All solutions were prepared in Milli-Q water and pH 4.0 was adjusted with HCl. The desired ionic strength was obtained by adding KCl to the solutions. All solutions used in the experiments were always filtered by a 0.1  $\mu\text{m}$  filter prior to sample preparation. The measurements were carried out at a temperature of  $25.0 \pm 0.2 \text{ }^\circ\text{C}$ .

### 2.2. Electrophoretic mobility

Electrokinetic measurements were performed with a ZetaNano ZS (Malvern Instruments, Worcestershire, UK) at electric field strength of 4 kV/m. Samples were prepared by mixing a variable volume of water with 0.5 mL of stock KCl solutions to obtain the desired ionic strength. The polyelectrolyte stock solution and about 1.0 mL of the latex suspension were added subsequently. The final particle concentration was 5–15 mg/L and the sample volume was 5.0 mL. The mobility of the particles in these suspensions was measured and recorded after equilibrating the samples overnight at 25.0  $^\circ\text{C}$ . The experiments were carried out in plastic capillary cells (Malvern Instruments) cleaned by 2% Hellmanex solution. The samples were equilibrated for 1 min in the cell prior to the measurements and the results were obtained by taking the average of six individual runs.

### 2.3. Time-resolved dynamic light scattering

Time-resolved dynamic light scattering (DLS) measurements were performed on a compact goniometer system (ALV/CGS-3, Langen, Germany). The instrument uses a He/Ne laser operating at 633 nm as a light source and an avalanche photodiode as a detector. Each correlation function was accumulated for 30 s and this process was repeated typically during 30 min. The apparent hydrodynamic radius was evaluated with a second-order cumulant fit. The aggregation rate constants were calculated from the initial relative rate of increase of the hydrodynamic radius and are reported as the stability ratio [46,47]

$$W = \frac{k_{\text{fast}}}{k} \quad (1)$$

where  $k_{\text{fast}}$  is the fast aggregation rate coefficient in the excess of monovalent salt, and  $k$  is the actual aggregation rate coefficient. The absolute fast aggregation rate coefficient was obtained for the bare particles in 1.0 M KCl solutions with known estimates of the hydrodynamic and optical properties of the particles. The values of  $k_{\text{fast}}$  are  $(1.9 \pm 0.3) \times 10^{-18} \text{ m}^3/\text{s}$  for SL and  $(3.1 \pm 0.2) \times 10^{-18} \text{ m}^3/\text{s}$  for CML.

DLS measurements were carried out in round borosilicate glass cuvettes cleaned with boiling piranha solution consisting of concentrated  $\text{H}_2\text{SO}_4$  and 30%  $\text{H}_2\text{O}_2$  mixed at a volume ratio of 3:1 for 3 h. They were subsequently rinsed extensively with water and dried in a dust-free environment. The samples for particle aggregation measurements were prepared by mixing water and KCl solution in the cuvette resulting in a volume between 0.2 and 1.7 mL. Subsequently, 0.1–1.6 mL of the polyelectrolyte stock solution was added to obtain the desired dose. The experiment was started by adding 0.2 mL of the particle suspension into the cuvette and mixing with a vortex stirrer. The final particle concentration was 3–7 mg/L, which was sufficiently dilute such that the aggregation remained in its early stages and the contribution of higher order aggregates could be neglected. This aspect was verified by the fact that apparent hydrodynamic radius increased only by 10–20% in the course of the experiment. In order to get reliable results for highly stable suspensions, the particle concentration was increased about 10-fold with respect to the concentrations used for the other experiments.

## 3. Results and discussion

Charging behavior and colloidal stability of negatively charged latex particles in the presence of cationic linear poly(ethylene imine) (LPEI) were investigated. The experimental techniques involve measurements of the electrophoretic mobility and aggregation rate by

dynamic light scattering (DLS). Two types of latex particles were used, namely weakly charged sulfate latex (SL) and highly charged carboxylate modified latex (CML). All the experiments were carried out at pH 4.0, whereby about 65% of the secondary amino groups in the LPEI are charged [40].

### 3.1. Ionic strength dependence

Charging properties of SL particles were investigated in the presence of LPEI of a molecular mass of 250 kg/mol by measuring electrophoretic mobility (Fig. 1A). At low polymer dose, the mobilities are negative indicating the negative charge of bare SL particles. With increasing polyelectrolyte dose, the adsorbed amount increases leading to charge neutralization at the isoelectric point (IEP). The electrophoretic mobility shows that the adsorption of LPEI continues beyond the IEP leading to charge reversal or overcharging. At higher dose, the electrophoretic mobility curves reach an adsorption saturation plateau (ASP). This plateau indicates that the adsorbed amount has reached its maximum, and that any polymer further added to the system remains dissolved in solution. The fact that LPEI adsorbs quantitatively below the ASP has been verified by repeating the measurements at different particle concentrations and confirming that there is no dependence of the electrophoretic mobility on the particle concentration [47,48]. A very similar behavior was observed with the CML latex (Fig. 2A). Such charge reversals is characteristic for polyelectrolytes adsorbing to oppositely charged particles [17,18,47,49–52].

The electrophoretic mobility depends significantly on the ionic strength. The magnitude of the data decreases with increasing the ionic strength at low polymer doses due to the screening of counter ions of the bare particle surfaces. This point was confirmed by the good agreement with the electrophoretic data of the bare latexes. The electrophoretic mobility beyond the ASP shows similar trend for SL, as their values increase by decreasing ionic strength. Although a non-monotonic dependence of the plateau value of the mobility was observed for the CML latex, this trend is in good agreement with the prediction of the standard electrokinetic model developed by O'Brien and White [53].

The ionic strength has only a weak influence on the IEP (Fig. 3, Table 1). For the SL, the IEP increases with the ionic strength, indicating that the charge of the adsorbed polyelectrolyte is partially neutralized by bound chloride anions. For CML the IEP is approximately constant, suggesting that the role of co-adsorbing ions is weak. This trend is further exemplified by considering the charging ratio (CR). This parameter represents the number of elementary charges of the polyelectrolyte that are necessary to neutralize the charge on the particle, and is precisely unity when the adsorption is stoichiometric. For SL, the magnitude of the surface charge density is low and the CR lies between 5 and 7. This super-stoichiometric charge neutralization indicates that a substantial fraction of the polyelectrolyte charge is neutralized by anions from the inert salt, and has also been observed in other polyelectrolyte-particle systems [17,47]. For CML, the magnitude of the charge density is high due to the brushy surface layer and the CR is about 0.3. This

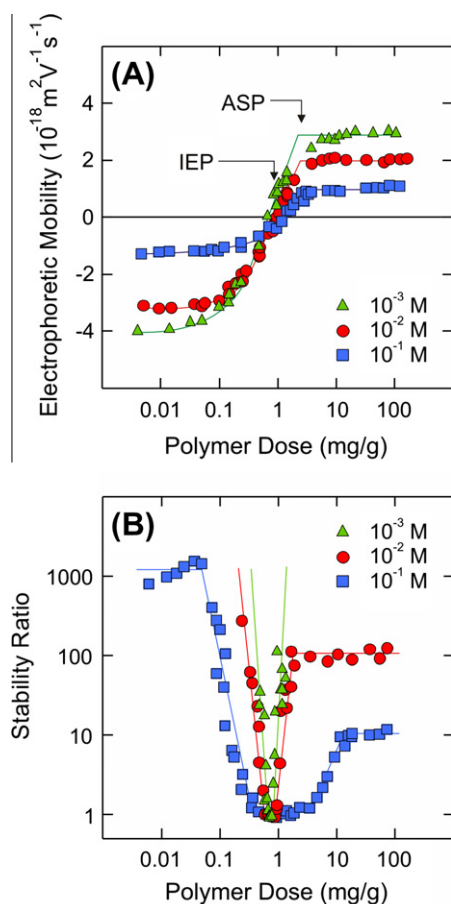


**Fig. 1.** Electrophoretic mobility (A) and stability ratio (B) of sulfate latex (SL) particles as a function of the dose of linear poly(ethylene imine) (LPEI) with molecular mass of 250 kg/mol at pH 4.0 for different ionic strengths. The isoelectric point (IEP) and adsorption saturation plateau (ASP) are indicated. The lines serve to guide the eye only.

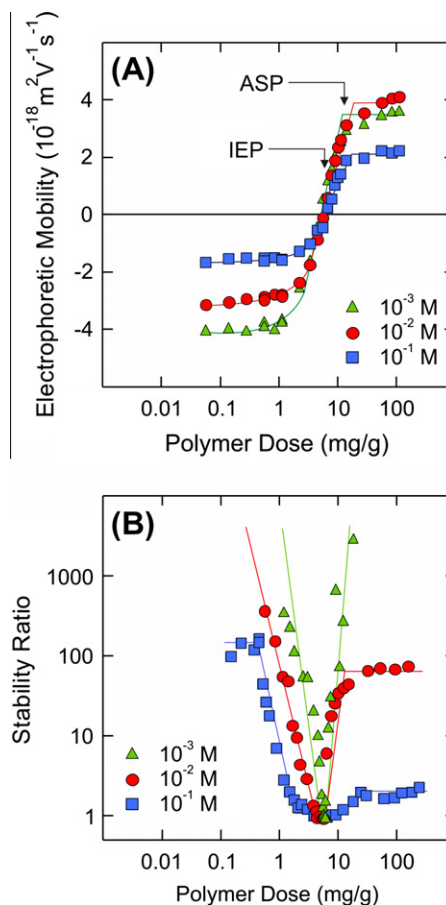


**Fig. 2.** Electrophoretic mobility (A) and stability ratio (B) of carboxylate modified latex (CML) particles as a function of the dose of linear poly(ethylene imine) (LPEI) with molecular mass of 250 kg/mol at pH 4.0 for different ionic strengths. The lines serve to guide the eye only.



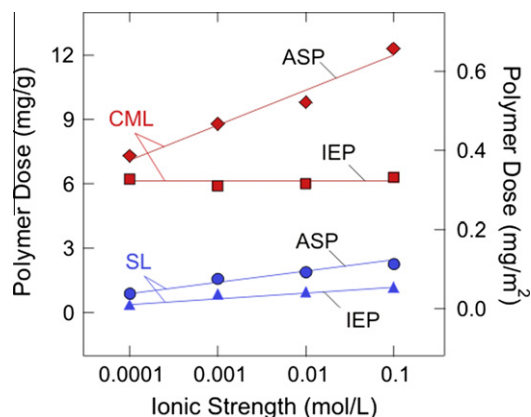


**Fig. 3.** Amount of LPEI with molecular mass of 250 kg/mol adsorbed on SL and CML particles at the saturation plateau (ASP) and isoelectric points (IEP) obtained from electrophoretic mobility measurements. The lines serve to guide the eye only.

**Table 1**  
Summary of adsorbed amount, charging ratio, and stability ratio for LPEI of 250 kg/mol.

Particle	Ionic strength (mol/L)	IEP <sup>a</sup> (mg/g)	ASP <sup>b</sup> (mg/g)	CR <sup>c</sup>	W <sup>d</sup>
SL	10 <sup>-4</sup>	0.3	0.9	1.88	0.94
SL	10 <sup>-3</sup>	0.8	1.6	5.01	0.99
SL	10 <sup>-2</sup>	0.9	1.9	5.64	1.01
SL	10 <sup>-1</sup>	1.1	2.3	6.89	1.03
CML	10 <sup>-4</sup>	6.2	7.3	0.33	0.98
CML	10 <sup>-3</sup>	5.9	8.8	0.31	0.96
CML	10 <sup>-2</sup>	6.0	9.8	0.32	0.95
CML	10 <sup>-1</sup>	6.3	12.3	0.33	1.01

<sup>a</sup> Amount adsorbed at IEP.  
<sup>b</sup> Amount adsorbed at saturation plateau.  
<sup>c</sup> Charging ratio at IEP.  
<sup>d</sup> Stability ratio at IEP.

value indicates that the polyelectrolyte charge is fully neutralized by the particle charge and moreover that a fraction of the surface charge is further neutralized by co-adsorbed cations.

The dose at the ASP represents the maximum amount of the adsorbed polyelectrolyte (Table 1 and Fig. 3). The CML adsorbs LPEI in much higher quantities than SL due to the higher magnitude of the surface charge density of the former. In both cases, however, the adsorbed amount of the polyelectrolyte increases with the ionic strength indicating that the ASP is governed by electrostatic forces and this increase can be explained with the reduced repulsion between the polyelectrolyte chains adsorbed on the surface. At low ionic strength, each adsorbed LPEI chain forms an extended diffuse layer, which leads to lateral repulsion, and small adsorbed amount. With increasing ionic strength, the repulsion weakens and the adsorbed amount increases.

Colloidal stability in the systems above was investigated by time-resolved DLS experiments. In these measurements, particle aggregation was characterized by aggregation rate constants determined from the rate of increase of the hydrodynamic radii and is expressed in the stability ratio *W*. Recall that *W* = 1 indicates fast aggregation in the presence of excess simple salt leading to an unstable system, while increasing *W* > 1 signals slow particle aggregation.

The stability ratios for SL and CML in the presence of LPEI of a molecular mass of 250 kg/mol are shown in Figs. 1B and 2B for different ionic strengths. In both cases, the aggregation is rapid near the IEP due to the attractive van der Waals forces, which represent the dominant force between neutral particles [46,54–56]. The stability ratio at IEP remains close to unity, even at low ionic strengths (Table 1). This feature is most unusual for such polyelectrolyte-particle systems of opposite charge, as normally an acceleration

of the fast aggregation rate at IEP is observed at low salt levels [16–18,47].

The stability ratio increases on both sides of the IEP. At polyelectrolyte doses below IEP, the negative charge of the particles is only partially compensated leading to the formation of a diffuse layer, which induces electrostatic repulsion between the particles. At doses above IEP, the particle is positively charged due to the charge reversal by the LPEI and the system is stabilized by electrostatic forces. At low and high polymer doses, the stability ratio reaches a plateau, which indicates similar aggregation mechanism in the case of bare and polyelectrolyte-coated particles.

The ionic strength influences the particle stability in two different ways. First, the fast aggregation regime is narrow at low ionic strengths and widens with increasing the concentration of the inert electrolyte. This dependence is due to the reduction of the electrostatic repulsion between the particles with increasing ionic strength. In the slow region, the stability ratio increases very rapidly away from the IEP, especially at low ionic strengths. Second, the plateau values in the stability ratio at high dose decreased with increasing ionic strength. This trend also indicates the importance of electrostatic repulsive forces, since the surface charge is progressively screened with increasing salt level. Similar trends were observed in other polyelectrolyte-particle systems [16–18,35,36,47,57,58].

### 3.2. Molecular mass dependence

LPEIs with molecular mass of 2.5, 25 and 250 kg/mol were used to study the effect of this parameter on the charging and aggregation of SL or CML particles. The corresponding electrophoretic mobility and stability measurements at varied molecular masses are shown in Figs. 4 and 5. The experiments were carried out at pH 4 and an ionic strength of 10 mM.

One observes a minor effect of the molecular mass on the electrophoretic mobility for the SL (Fig. 4A). The IEP and ASP shift towards lower doses with increasing molecular mass. This trend could be eventually explained by weaker binding of salt anions to the high molecular mass polymer. No dependence on the molecular mass was observed with the CML (Fig. 5A). This fact is probably related to the fact that the adsorption process is close to stoichiometric. No dependence of the IEP on the molecular mass was equally reported for anionic poly(styrene sulfonate) (PSS) adsorbed on cationic amidine latex particles, which also is a system featuring stoichiometric adsorption [17]. In the case of adsorption of poly(amido amine) (PAMAM) dendrimers on sulfate latex particles, the IEP shifts markedly towards higher doses [18]. This trend was rationalized by the increasing amount of bound counterions by the dendrimers with increasing molecular mass.

The colloidal stability follows the same trends as the electrophoretic mobility. For the SL particles, the stability curve shifts slightly towards higher dose with increasing molecular mass (Fig. 4B). For CML particles, no dependence was observed. More importantly, the shapes of the stability curves are independent on the molecular mass in both systems. The instability regions are narrow and in the slow aggregation region, the stability ratio increases very rapidly away from the IEP. This lack of dependence of the stability ratio on the molecular mass is most unusual in polyelectrolyte-particle systems. In all other systems, where the molecular mass dependence was studied, a marked acceleration of the aggregation rate with increasing molecular mass was found in the slow regime [16–18,35,57].

### 3.3. Absence of patch-charge interactions

Two characteristic effects were reported with respect of particle aggregation in the presence of oppositely charged polyelectrolytes.

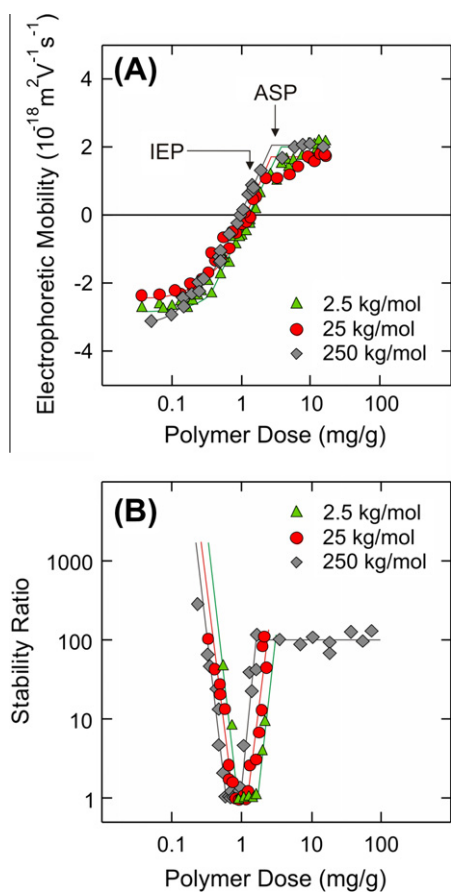


**Fig. 4.** Electrophoretic mobility (A) and stability ratio (B) of sulfate latex (SL) particles as a function of the dose of linear poly(ethylene imine) (LPEI) at an ionic strength of 10 mM and pH 4.0 for different molecular masses. The lines serve to guide the eye only.

First, the aggregation accelerates at the IEP with decreasing ionic strength and is faster than in rapidly aggregating system in the presence of a simple salt [16–18,47]. Second, the aggregation in the slow regime accelerates with increasing molecular mass, even at low ionic strength [16–18,35,57]. Both effects are absent in the presently investigated LPEI systems.

The acceleration of the aggregation rate was previously explained in terms of attractive patch-charge interactions as follows. The polyelectrolyte adsorbs in a loose laterally heterogeneous monolayer, where basically single highly charged polyelectrolyte globules are adsorbed on a surface of opposite charge. This heterogeneous distribution is well documented for positively charged PA-MAM dendrimers adsorbed on a negatively charged silica surface by atomic force microscopy (AFM) [59]. The surface charge density of such a patchy surface is highly heterogeneous, whereby the positively charged patches (i.e., dendrimers) are positioned on a negatively charged background (i.e., silica). When two particles with such heterogeneously charged surfaces approach each other, they will orient such that a positively charged patch faces a negatively charged one on the other surface. Oppositely charged patches will lead to an additional electrostatic attraction and to an acceleration of the aggregation rate [60]. The existence of such patch-charge interaction forces has been confirmed by the AFM-based colloidal probe technique [30,61]. Computer simulations have equally demonstrated that such attractive forces indeed lead to an acceleration of the particle aggregation as described above [24].

The present LPEI system behaves differently, and does not show any of the indicative trends of patch-charge attraction effects discussed above. Therefore, we conclude that the surface charge dis-

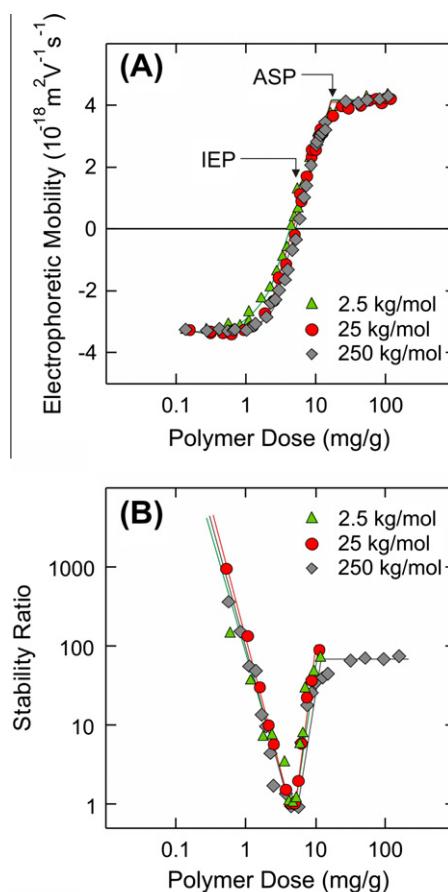


**Fig. 5.** Electrophoretic mobility (A) and stability ratio (B) of carboxylate modified latex (CML) particles as a function of the dose of linear poly(ethylene imine) (LPEI) at an ionic strength of 10 mM and pH 4.0 for different molecular masses. The lines serve to guide the eye only.

tribution induced by adsorbed LPEI has to be unusually homogeneous. The reasons could be the following. At the present experimental conditions, LPEI is rather weakly charged and therefore it will tend to adsorb in a more extended configuration. Moreover, the charges of LPEI are located on the backbone, which makes the polyelectrolyte more hydrophilic and less affected by dispersion or hydrophobic interactions.

The two situations probably resemble the dilute and semi-dilute 2-d Wigner liquid regimes discussed in the context of polyelectrolyte adsorption by Dobrynin et al. [25]. When patch-charge interactions are important, the adsorbed polyelectrolyte film is heterogeneous, and its structure is probably quite reminiscent to the dilute 2-d Wigner liquid. In this situation, the individual polyelectrolyte chains are well separated on the surface. In the absence of patch-charge interactions, as observed for LPEI here, adsorbed polyelectrolyte film is more homogeneous, and may well resemble the semi-dilute 2-d Wigner liquid. In this case, the individual chains are adsorbed in an extended configuration, but they cross frequently, which leads to a random network on the surface. While such a surface is still heterogeneous on length scales smaller than the mesh-size of this network, it appears homogeneous on larger length scales.

#### 4. Conclusion

The present study reports on charging behavior and colloidal stability of negatively charged latex particles in the presence of linear poly(ethylene imine) (LPEI). LPEI adsorbs strongly on the

oppositely charged colloidal particles leading to a charge reversal beyond the isoelectric point (IEP). The particles aggregate rapidly close to the IEP, but the aggregation slows down away from it. Basically no dependence of the aggregation rate on the molecular mass was found. From this observation we conclude that the adsorbed LPEI layer is laterally unusually homogeneous.

The absence of the molecular mass dependence is in sharp contrast to most of the other polyelectrolyte-particle systems, where the aggregation rate increases with increasing molecular mass. This acceleration was interpreted by attractive patch-charge interactions induced by the heterogeneous structure of the adsorbed layer. Such patch-charge interactions are absent in the present system.

### Acknowledgment

Financial support by the Swiss National Science Foundation and the University of Geneva as well as excellent technical support by Olivier Vassalli is gratefully acknowledged.

### References

- [1] P.G. de Gennes, *Nature* 412 (2001) 385.
- [2] R. Mezzenga, P. Schurtenberger, A. Burbidge, M. Michel, *Nat. Mater.* 4 (2005) 729–740.
- [3] A.M. Howe, R.D. Wesley, M. Bertrand, M. Cote, J. Leroy, *Langmuir* 22 (2006) 4518–4525.
- [4] D. Horn, F. Linhart, *Retention Aids*, Blackie Academic and Professional, London, 1996.
- [5] M. Borkovec, G. Papastavrou, *Curr. Opin. Colloid Interface Sci.* 13 (2008) 429–437.
- [6] B. Bolto, J. Gregory, *Water Res.* 41 (2007) 2301–2324.
- [7] D.J. Wells, *Gene Ther.* 11 (2004) 1363–1369.
- [8] M. Chittchang, H.H. Alur, A.K. Mitra, T.P. Johnston, *J. Pharm. Pharmacol.* 54 (2002) 315–323.
- [9] S. Yu, J. Hu, X. Pan, P. Yao, M. Jiang, *Langmuir* 22 (2006) 2754–2759.
- [10] G. Decher, *Science* 277 (1997) 1232–1237.
- [11] C.H. Porcel, A. Izquierdo, V. Ball, G. Decher, J.C. Voegel, P. Schaaf, *Langmuir* 21 (2005) 800–802.
- [12] F. Caruso, R.A. Caruso, H. Möhwald, *Science* 282 (1998) 1111–1114.
- [13] G.B. Sukhorukov, E. Donath, S. Davis, H. Lichtenfeld, F. Caruso, V.I. Popov, H. Möhwald, *Polym. Adv. Technol.* 9 (1998) 759–767.
- [14] A. Fery, F. Dubreuil, H. Möhwald, *New J. Phys.* 6 (2004) 18.
- [15] D. Sebok, T. Szabo, I. Dekany, *Appl. Surf. Sci.* 255 (2009) 6953–6962.
- [16] J. Gregory, *J. Colloid Interface Sci.* 42 (1973) 448–456.
- [17] G. Gillies, W. Lin, M. Borkovec, *J. Phys. Chem. B* 111 (2007) 8626–8633.
- [18] W. Lin, P. Galletto, M. Borkovec, *Langmuir* 20 (2004) 7465–7473.
- [19] F. Bouyer, A. Robben, W.L. Yu, M. Borkovec, *Langmuir* 17 (2001) 5225–5231.
- [20] B.C. Ong, Y.K. Leong, S.B. Chen, *J. Colloid Interface Sci.* 337 (2009) 24–31.
- [21] R. Meszaros, I. Varga, T. Gilanyi, *Langmuir* 20 (2004) 5026–5029.
- [22] E. Pal, D. Sebok, V. Hornok, I. Dekany, *J. Colloid Interface Sci.* 332 (2009) 173–182.
- [23] E. Illes, E. Tombacz, *Colloid Surf. A* 230 (2003) 99–109.
- [24] M. Trulsson, J. Forsman, T. Akesson, B. Jonsson, *Langmuir* 25 (2009) 6106–6112.
- [25] A.V. Dobrynin, A. Deshkovski, M. Rubinstein, *Macromolecules* 34 (2001) 3421–3436.
- [26] R.R. Netz, J.F. Joanny, *Macromolecules* 31 (1998) 5123–5141.
- [27] J. Ennis, L. Sjoström, T. Akesson, B. Jonsson, *Langmuir* 16 (2000) 7116–7125.
- [28] M.A.G. Dahlgren, A. Waltermo, E. Blomberg, P.M. Claesson, L. Sjoström, T. Akesson, B. Jonsson, *J. Phys. Chem.* 97 (1993) 11769–11775.
- [29] I. Popa, G. Gillies, G. Papastavrou, M. Borkovec, *J. Phys. Chem. B* 114 (2010) 3170–3177.
- [30] I. Popa, G. Papastavrou, M. Borkovec, *Phys. Chem. Chem. Phys.* 12 (2010) 4863–4871.
- [31] R. Pericet-Camara, G. Papastavrou, S.H. Behrens, C.A. Helm, M. Borkovec, *J. Colloid Interface Sci.* 296 (2006) 496–506.
- [32] S. Block, C.A. Helm, *Macromolecules* 42 (2009) 6733–6740.
- [33] E. Poptoshev, M.W. Rutland, P.M. Claesson, *Langmuir* 15 (1999) 7789–7794.
- [34] M.A. Plunkett, A. Feiler, M.W. Rutland, *Langmuir* 19 (2003) 4180–4187.
- [35] S. Schwarz, S. Bratskaya, W. Jaeger, B.R. Paulke, *J. Appl. Polym. Sci.* 101 (2006) 3422–3429.
- [36] D. Bauer, H. Buchhammer, A. Fuchs, W. Jaeger, E. Killmann, K. Lunkwitz, R. Rehm, S. Schwarz, *Colloids Surf. A* 156 (1999) 291–305.
- [37] Y.K. Leong, P.J. Scales, T.W. Healy, D.V. Boger, *Colloids Surf. A* 95 (1995) 43–52.
- [38] M. Borkovec, G.J.M. Koper, *Macromolecules* 30 (1997) 2151–2158.
- [39] H.M.L. Lambermont-Thijs, F.S. van der Woerd, A. Baumgaertel, L. Bonami, F.E. Du Prez, U.S. Schubert, R. Hoogenboom, *Macromolecules* 43 (2010) 927–933.
- [40] R.G. Smits, G.J.M. Koper, M. Mandel, *J. Phys. Chem.* 97 (1993) 5745–5751.
- [41] I.H. Park, E.J. Choi, *Polymer* 37 (1996) 313–319.
- [42] A. Pfau, W. Schrepp, D. Horn, *Langmuir* 15 (1999) 3219–3225.
- [43] J.D. Ziebarth, Y.M. Wang, *Biomacromolecules* 11 (2010) 29–38.
- [44] M. Borkovec, G.J.M. Koper, *J. Phys. Chem.* 98 (1994) 6038–6045.
- [45] A. von Harpe, H. Petersen, Y.X. Li, T. Kissel, *J. Controlled Release* 69 (2000) 309–322.
- [46] M. Kobayashi, M. Skarba, P. Galletto, D. Cakara, M. Borkovec, *J. Colloid Interface Sci.* 292 (2005) 139–147.
- [47] J. Kleimann, C. Gehin-Delval, H. Auweter, M. Borkovec, *Langmuir* 21 (2005) 3688–3698.
- [48] A. Mezei, R. Meszaros, *Langmuir* 22 (2006) 7148–7151.
- [49] H.W. Walker, S.B. Grant, *Colloids Surf. A* 119 (1996) 229–239.
- [50] M. Ashmore, J. Hearn, *Langmuir* 16 (2000) 4906–4911.
- [51] M. Ashmore, J. Hearn, F. Karpowicz, *Langmuir* 17 (2001) 1069–1073.
- [52] R. Rehm, E. Killmann, *Colloids Surf. A* 149 (1999) 323–328.
- [53] R.W. O'Brien, L.R. White, *J. Chem. Soc. Faraday Trans. II* 74 (1978) 1607–1626.
- [54] W. Lin, M. Kobayashi, M. Skarba, C. Mu, P. Galletto, M. Borkovec, *Langmuir* 22 (2006) 1038–1047.
- [55] L. Ehrl, Z. Jia, H. Wu, M. Lattuada, M. Soos, M. Morbidelli, *Langmuir* 25 (2009) 2696–2702.
- [56] K.L. Chen, M. Elimelech, *Environ. Sci. Technol.* 43 (2009) 7270–7276.
- [57] S. Schwarz, W. Jaeger, B.R. Paulke, S. Bratskaya, N. Smolka, J. Bohrisch, *J. Phys. Chem. B* 111 (2007) 8649–8654.
- [58] J. Hierrezuelo, A. Sadeghpour, I. Szilágyi, A. Vaccaro, M. Borkovec, *Langmuir* 26 (2010) 15109–15111.
- [59] B.P. Cahill, G. Papastavrou, G.J.M. Koper, M. Borkovec, *Langmuir* 24 (2008) 465–473.
- [60] S.J. Miklavic, D.Y.C. Chan, L.R. White, T.W. Healy, *J. Phys. Chem.* 98 (1994) 9022–9032.
- [61] I. Popa, G. Papastavrou, M. Borkovec, M. Trulsson, B. Jonsson, *Langmuir* 25 (2009) 12435–12438.



# Self-Assembly of Protamine Biomacromolecule on Halloysite Nanotubes for Immobilization of Superoxide Dismutase Enzyme

Bojana Katana,<sup>†</sup> Paul Rouster,<sup>‡</sup> Gábor Varga,<sup>§</sup> Szabolcs Muráth,<sup>†,||</sup> Karine Glinel,<sup>‡,||</sup> Alain M. Jonas,<sup>‡,||</sup> and Istvan Szilagy<sup>\*,†,||</sup>

<sup>†</sup>MTA-SZTE Lendület Biocolloids Research Group, University of Szeged, H-6720 Szeged, Hungary

<sup>‡</sup>Institute of Condensed Matter and Nanosciences - Bio and Soft Matter, Université catholique de Louvain, B-1348 Louvain-la-Neuve, Belgium

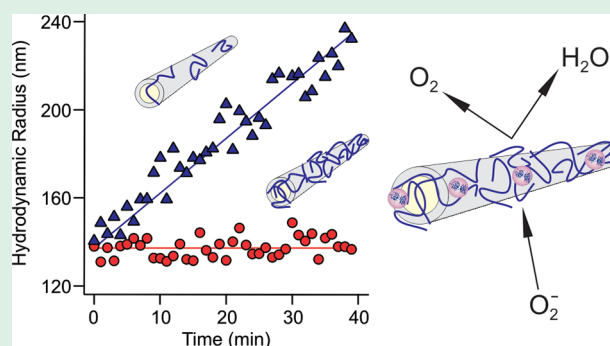
<sup>§</sup>Department of Organic Chemistry, University of Szeged, H-6720 Szeged, Hungary

<sup>||</sup>Interdisciplinary Excellence Center, Department of Physical Chemistry and Materials Science, University of Szeged, H-6720 Szeged, Hungary

## Supporting Information

**ABSTRACT:** An antioxidant material composed of halloysite nanotubes (HNTs), protamine sulfate polyelectrolyte (PSP), and superoxide dismutase (SOD) enzyme was prepared by self-assembly of the PSP and SOD biomacromolecules on the nanoparticulate support. The structural, colloidal and biocatalytic features were assessed. Adsorption of PSP on the oppositely charged HNT surface at appropriate loadings gave rise to charge neutralization and overcharging, which resulted in unstable and stable dispersions, respectively. The formation of a saturated PSP layer on the HNT led to the development of positive surface charge and to remarkable resistance against salt-induced aggregation making the obtained HNT-PSP hybrid suitable for immobilization of negatively charged SOD. No enzyme leakage was observed from the HNT-PSP-SOD composite indicating sufficient structural stability of this material due to electrostatic, hydrophobic, and hydrogen bonding interactions taking place between the particles and the biomacromolecules. Enzymatic assays revealed that SOD kept its functional integrity upon immobilization and showed high activity in superoxide radical dismutation. In this way, stable antioxidant bionanocomposite dispersions were obtained, which can be used as antioxidants in heterogeneous samples.

**KEYWORDS:** halloysite nanotubes, superoxide dismutase, protamine sulfate, colloidal stability, self-assembly



## INTRODUCTION

Antioxidant enzymes are the most efficient defense systems against reactive oxygen species (ROS), which are responsible for the development of several diseases including cancer due to their high reactivity against lipids and other cell constituent biomolecules.<sup>1</sup> On the other hand, their harmful effect leads to the damage of commercial products during chemical manufacturing processes in the food<sup>2</sup> and cosmetic<sup>3</sup> industries. Among them, superoxide radical anions are the most adverse ones, since they serve also as precursors to other ROS such as peroxides.<sup>4</sup> The natural defense systems developed during evolution against superoxide radicals are the so-called superoxide dismutase (SOD) enzymes.<sup>5</sup> They are able to effectively decompose superoxide radicals to molecular oxygen and hydrogen peroxide. The latter one is subsequently converted to oxygen and water by catalase and peroxidase enzymes in the cellular environment.<sup>6</sup>

Despite its great promise in biomedical and industrial applications as an antioxidant agent,<sup>7</sup> the supplementation of

SOD is complicated due to its high sensitivity to environmental conditions including pH, temperature, and the presence of enzyme inhibitor molecules. To overcome this problem, immobilization of SOD attracted considerable attention in the scientific community over the past decade.<sup>8–11</sup> The role of the solid support is (i) to defend the enzyme during the supplementation process and (ii) to deliver SOD to the desired location in the living organisms or in the industrial samples. For example, SOD enzyme was embedded in mesoporous silica and conjugation with a cell-penetrating protein led to excellent activity in reducing cellular oxidative stress.<sup>12</sup> In another approach, SOD was captured in polyacrylamide hydrogel nanoparticles and remained active upon immobilization.<sup>13</sup> Due to the tuned permeability of the carrier, the substrates and the products freely diffused in the

**Received:** October 16, 2019

**Accepted:** December 3, 2019

**Published:** December 3, 2019

system, while the enzyme was protected against denaturation by inhibitors. To avoid enzyme leakage, SOD was covalently attached to carbon nanoparticles and the obtained material maintained long-term superoxide radical scavenging activity and was found to be nontoxic.<sup>14</sup> The selection of the carrier nanomaterials is especially important, since denaturation of the enzyme may occur due to changes in its conformation upon adsorption on the surface of the solid support. Therefore, polyelectrolyte functionalization of the carrier clay<sup>9</sup> or titania<sup>10</sup> particles were performed to avoid enzyme degradation and to improve the colloid stability of the system. The latter issue is crucial, given the fact that the applications of the enzyme-nanoparticle conjugates are foreseen mostly in liquid medium, that is, in biofluids and in industrial liqueurs, where aggregation of the biocatalytic particles gives rise to loss of enzymatic activity.

Due to their advantageous properties such as biocompatibility, high aspect ratio, and availability in large scale,<sup>15–17</sup> halloysite nanotubes (HNTs) are promising candidates as solid supports in immobilization processes.<sup>18,19</sup> Moreover, their advantages over other clay particles include the relatively narrow size distribution and possible activation of the surface functional groups.<sup>20</sup> These features facilitate the formation of fine HNT dispersions in aqueous medium. Enzyme attachment on the outer surface or in the lumen, which are oppositely charged at physiological pH, attracted considerable contemporary interest in the scientific community. Accordingly, lactase,<sup>21</sup> lipase,<sup>22</sup> amylase,<sup>23</sup> lactamase,<sup>20</sup> urease,<sup>24</sup> and glucose oxidase<sup>25</sup> were immobilized in/on HNTs or their surface functionalized derivatives. The general conclusion was that HNT is a promising candidate for enzyme delivery processes; however, the substrate diffusion into the lumen and product release from it are often the limits of the HNT application as a carrier in enzyme immobilization. The HNTs have already proven to act as sufficient delivery agents for molecular antioxidants such as quercetin,<sup>26</sup> curcumin,<sup>27</sup> and resveratrol,<sup>28</sup> nevertheless, immobilization of antioxidant enzymes was not reported so far.

Besides, in many of the bioapplications of HNTs, surface functionalization with macromolecules is necessary to strengthen the adsorption of the guest molecules and to avoid unwanted aggregation processes. The interaction between HNTs and polyelectrolytes (heparin,<sup>29</sup> poly(ethylene imine),<sup>20</sup> poly(acrylamide-*co*-diallyldimethylammonium chloride),<sup>30</sup> poly(amido amine) dendrimers,<sup>31</sup> and chitosan<sup>32</sup>) was studied to some extent. Furthermore, immobilization of drug molecules among polyelectrolyte layers adsorbed on the surface of HNT was also carried out.<sup>33</sup> The general remarks were that polyelectrolyte adsorption onto HNTs significantly influences the surface features and that the adsorption process plays a major role in the aggregation mechanism of the nanotubes. Despite these works reported earlier, the fundamental understanding of the relation between the surface charge properties and the colloidal stability of polyelectrolyte decorated HNTs is missing.

The present study, therefore, aims at the development of stable colloids of a nanocomposite consisting of self-assembled biomacromolecules such as protamine sulfate polyelectrolyte (PSP) and SOD enzyme on the HNT, which served as solid support. The influence of the experimental conditions such as biomacromolecule dose, pH, and ionic strength on the colloidal and structural stability of HNT-PSP-SOD was explored by spectroscopy, microscopy, and light scattering

techniques, whereas the superoxide radical scavenging activity was probed in biochemical assays.

## EXPERIMENTAL SECTION

**Materials.** Biomacromolecules including PSP (from salmon sperm, molecular weight of 5000–10 000 g/mol), xanthine oxidase (from bovine milk, lyophilized powder, 0.4–1.0 units/mg protein), and SOD (from bovine liver, lyophilized powder,  $\geq 1500$  units/mg protein) were purchased from Sigma-Aldrich. Nitro blue tetrazolium (NBT), KCl, KBr, ethanol, and xanthine were bought from VWR. Coomassie Brilliant Blue (G-250) was purchased from Fisher Scientific. Ortho-phosphoric acid ( $\text{H}_3\text{PO}_4$ , 85%) was acquired from Carl Roth. All chemicals were used as received. The measurements were carried out at 25 °C and pH 7. High purity water from a VWR Purity TU+ device was used for all the sample preparations. Salt solutions and water applied for light scattering experiments were filtered through a 0.1  $\mu\text{m}$  syringe filter (Millex).

**Alkali Activation of HNTs.** The raw HNT powder was purchased from Sigma-Aldrich. To improve the surface properties, alkali activation was performed using a method reported earlier.<sup>20</sup> Briefly, the commercial (raw) HNT powder was dispersed at a concentration of 20 g/L in a 14.5 mM KOH solution under magnetic stirring for 24 h. The dispersion was centrifuged at 10 000 rpm for 10 min. The supernatant was removed and the slurry was redispersed in water. The centrifugation steps were repeated until the pH of the supernatant was around 7. Afterwards, the slurry was recovered and put in a glass container in an oven at 110 °C for 15 h to obtain a dry powder. The obtained hydroxylated HNTs were then dispersed in water at a concentration of 10 000 mg/L to be used as a stock dispersion for sample preparation. In the following, the term HNT will refer to the hydroxylated HNT unless mentioned otherwise. To compare the dispersion characteristics of the raw and activated HNT, the electrophoretic mobilities, hydrodynamic radii and polydispersity indices were determined in stable dispersions by light scattering. The mobilities were the same ( $-2.5 \times 10^{-8} \text{ m}^2/(\text{V s})$ ) for both samples within the experimental error, the radii were 146 and 225 nm, while the polydispersities were 20 and 25% for the activated and the raw HNT, respectively. These data clearly indicate the improvement of the particle size distribution after the alkaline treatment.

**Electrophoretic Mobility.** The electrophoretic light scattering measurements were performed with a Litesizer 500 instrument (Anton Paar). In a sample preparation process, 0.2 mL of stable HNT dispersion of 100 mg/L concentration was added to a 1.8 mL solution composed of PSP and/or KCl at appropriate concentrations. The samples were allowed to rest for 2 h at room temperature before measuring the electrophoretic mobility. An equilibration time of 1 min was also applied in the device prior the measurements that were performed in 350  $\mu\text{L}$  omega-shaped plastic cuvettes (Anton Paar). The average value of five individual measurements was reported.

The electrophoretic mobility of the bar HNT was found to be negative in a wide range of pH due to the abundance of the deprotonated silanol groups on the outer surface (SI Figure S1). Electrophoresis can only detect the net charge of the particles; therefore, the contribution of the positively charged protonated Al–O–H groups<sup>34</sup> of the inner surface of the HNT could not be assessed by this technique. A steep decrease in the values was observed in the pH 4–6 regime, since the  $\text{pK}_a$  of the silanol groups falls in this range and the mobility was almost constant above pH 7.

**Dynamic Light Scattering.** To assess the possible aggregation processes in the samples, time-resolved dynamic light scattering (DLS) measurements were carried out with a Litesizer 500 instrument (Anton Paar) equipped with a 40 mW semiconductor laser (658 nm wavelength) operating in the backscattering mode at a scattering angle of 175°. To determine the hydrodynamic radii, the correlation functions were collected for 20 s, and the decay rate constants were calculated using the cumulant analysis. The diffusion coefficients were converted to hydrodynamic radius with the Stokes–Einstein equation.<sup>35</sup> The particle concentration was kept constant (10

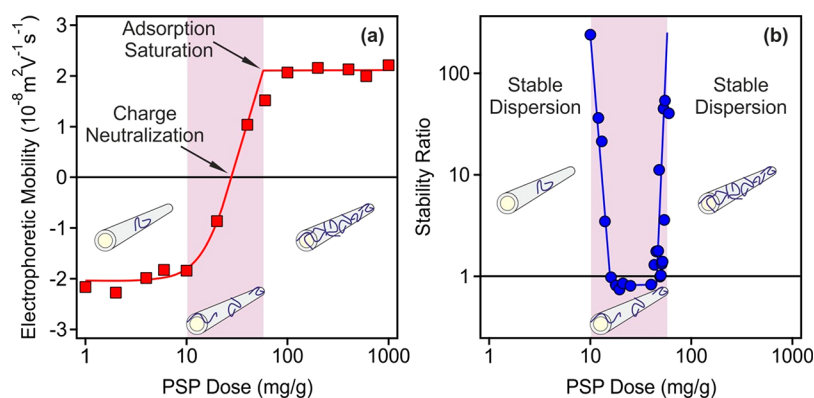


**Figure 1.** (a) Variation of the electrophoretic mobility and (b) stability ratio of HNT as a function of the PSP dose. The measurements were performed at pH 7, 1 mM ionic strength adjusted by KCl and 10 mg/L HNT concentration. The mg/g unit on the *x*-axis refers to mg of PSP per one gram of HNT. The PSP dose range corresponding to the aggregation regime is shaded. The lines serve to guide the eyes.

mg/L), and the PSP and/or KCl concentration was varied. Otherwise, the sample preparation procedure was the same as in the electrophoretic studies with the exception that the DLS measurements were acquired immediately after adding the HNT stock dispersion and vortexing the sample for 25 s. The samples were equilibrated for 30 s in the instrument before data collection was started. The colloidal stability was expressed in terms of stability ratio.<sup>9,10,36–38</sup> Its value is unity in the case of unstable dispersions, where the particle aggregation is controlled solely by their diffusion, whereas higher stability ratios refer to slower aggregation and thus, to more stable samples.

**IR Spectroscopy.** FT-IR spectroscopy was applied to determine the presence of the PSP and SOD in the composites. A BIO-RAD Digilab Division FTS-65A/896 device was used to record the spectra, for which 256 scans were performed with 4  $\text{cm}^{-1}$  resolution in the 4000–600  $\text{cm}^{-1}$  wavenumber range. The spectrum of each sample was taken in the diffuse reflectance mode (DRS) fixing the incident angle in the 45° position. To prepare the samples, 30 mg of the solid material measured with analytical accuracy was mixed with 300 mg of KBr.

**Electron Microscopy.** Morphological studies were carried out using scanning electron microscopy (SEM, Hitachi S-4700) and transmission electron microscopy (TEM, FEI TECNAI G<sup>2</sup>20 X-TWIN). For SEM, 10 kV accelerating voltage was applied on the nanotubes mounted on a double sided carbon tape. Before measurements, the samples were coated with gold via physical vapor deposition using a Quorum Technologies SC7620 device. For TEM measurements, the dispersions of the particles were dried on copper–carbon mesh grid, and 200 kV accelerating voltage was used for imaging in the bright field mode.

**Thermal Gravimetric Analysis.** To test the thermal decomposition of the bare and functionalized HNTs, thermal gravimetric analysis (TGA) was carried out on a Mettler Toledo TGA/SDTA851e instrument under nitrogen atmosphere. The samples were allowed to equilibrate for 5 min at 30 °C in the instrument before being submitted to a heating rate of 10 °C/min up to 700 °C. For the TGA experiments, solid samples were obtained by centrifugation of the dispersions and subsequent drying in a desiccator at room temperature.

**Bradford Test.** The amount of SOD adsorbed on the PSP-modified HNT (HNT-PSP) was quantified by the Bradford test.<sup>39</sup> The Bradford reagent was prepared in a 250 mL volumetric flask by dissolving 25 mg of Coomassie Brilliant Blue in 12.5 mL of ethanol followed by the addition of 25 mL of phosphoric acid. Then, the solution was completed to 250 mL with ultrapure water. A calibration curve was obtained by using standard SOD solutions with concentrations in the range from 1 to 100 mg/L. These solutions were prepared by mixing 400  $\mu\text{L}$  of a SOD solution at a given concentration with 1.6 mL of the Bradford reagent. The mixture was then allowed to equilibrate during 5 min prior to the acquisition of the

UV–vis spectrum, which was recorded with a Genesys 10S spectrophotometer (Thermo Scientific). The absorbance bands centered at 465 and 595 nm corresponding to the free dye and to both the SOD–dye complex and free dye, respectively, were monitored. To quantify the amount of SOD adsorbed on the HNT-PSP particles, dispersions were prepared by mixing 10 mg of SOD per gram of HNT-PSP to obtain a final SOD concentration of 50 mg/L. Then, these dispersions were centrifuged and the supernatant was recovered and filtered through a syringe filter of 0.1  $\mu\text{m}$  pore size to remove any HNT-PSP-SOD that may still be present in order to only assess the amount of free SOD that did not adsorb on the HNT-PSP particles. Finally, 400  $\mu\text{L}$  of this supernatant was mixed with 1.6 mL of the Bradford reagent. The difference between the absorbance values recorded at 595 and 465 nm wavelengths were used to obtain the amount of free SOD present after removing the HNT-PSP-SOD from the system.

**SOD Activity.** To determine the SOD activity of the developed material (HNT-PSP-SOD), the Fridovich method<sup>40</sup> was applied. However, the enzymatic assay protocol had to be slightly modified to adapt to the light scattering events resulting from the dispersed particles. Each sample was composed of xanthine (3 mM, 0.2 mL), NBT (3 mM, 0.1 mL), xanthine oxidase (3 mg/mL, 0.3 mL), and the stock solution containing the catalyst (free or immobilized SOD with various concentrations) in phosphate buffer to reach a final volume of 3 mL. The phosphate buffer concentration in the samples was 1 mM and the pH was set to 7. Once all the reagents were mixed together, the samples were left to equilibrate for 1 min prior to monitoring the increase of the absorbance band at 565 nm for 5 min. Such an increase of the absorbance, caused by the increasing concentration of the blue colored product resulting from the NBT-superoxide radical reaction, was determined for several SOD concentrations in the sample. Furthermore, due to the scattering of the HNT particles, the corresponding HNT-PSP samples devoid of SOD were used as references. The inhibition of the NBT-superoxide radical reaction was then calculated and the activity in dismutation of the radicals by the enzyme was expressed in  $\text{IC}_{50}$  values, which correspond to the SOD concentration needed to decompose 50% of the radicals formed in the probe reaction. The average error of the method is about 5%.

## RESULTS AND DISCUSSION

**Self-Assembly of PSP on HNT.** As a natural polyelectrolyte, PSP was used to functionalize the surface of HNT. The aim of such a functionalization was (i) to obtain biocompatible nanotubes for further enzyme immobilization, (ii) to enhance the strength of attractive enzyme–particle interactions, and (iii) to tune the colloidal stability of the HNT. The PSP possesses positive charge at physiological pH due to the high occurrence of the arginine amino acids of positively charged side chain groups.<sup>41</sup> PSP has proven to strongly adsorb on oppositely



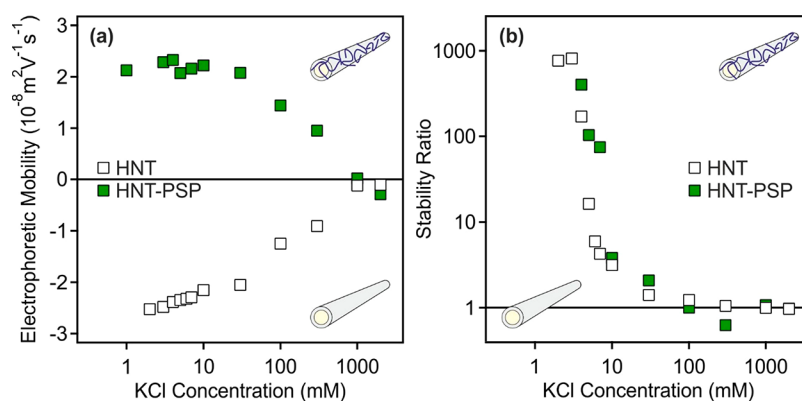


**Figure 2.** (a) Electrophoretic mobility and (b) stability ratio of HNT (empty symbols) and HNT-PSP (filled symbols) versus KCl concentration. The measurements were performed at neutral pH and 10 mg/L particle concentration. The HNT-PSP particles were prepared with a PSP dose of 100 mg/g.

charged particles leading to their overcharging and thus, to their charge inversion.<sup>38</sup>

The electrophoretic mobility was first measured at different PSP doses, where the particle concentration, ionic strength, and pH were kept constant. As shown in Figure 1a, negative electrophoretic mobilities of about  $-2.0 \times 10^{-8} \text{ m}^2/(\text{V s})$  were recorded at low PSP loadings. This value is similar to the mobility of the bare HNT at the selected ionic strength (1 mM). For PSP doses higher than 10 mg/g, a sharp increase of the electrophoretic mobility was observed, which indicates the adsorption of PSP chains onto the oppositely charged surface of HNT.

Such an adsorption led to charge neutralization and overcharging at appropriate polyelectrolyte doses. At PSP concentrations higher than 100 mg/g, the mobility remained constant around  $2.0 \times 10^{-8} \text{ m}^2/(\text{V s})$  due to the formation of a saturated PSP layer on the HNT surface. Further added polyelectrolyte did not adsorb and remained dissolved in the bulk solution. The magnitude of the mobilities of the bare and PSP-coated HNT is the same within the experimental error, indicating very similar magnitude of the surface charge in both cases. Similar results were reported with other inorganic particles in the presence of oppositely charged polyelectrolytes.<sup>42–46</sup>

Aggregation of the PSP-modified HNT was investigated at different PSP doses by time-resolved DLS (SI Figure S2). The hydrodynamic radius was constant within the experimental error at a PSP dose of 10 mg/g, and a slight increase was detected at a dose of 50 mg/g; however, a significant increase of the hydrodynamic size of the particles was observed at a dose of 20 mg/g. Comparing with the electrophoretic mobility measurements discussed above, these three doses are below, above, and at the charge neutralization point, respectively. The trend in the stability ratio followed a U-shape curve with a minimum reached for the PSP dose corresponding to the charge neutralization point (Figure 1b).

The aggregation was rapid, i.e., the stability ratio was close to one, at the minimum, while the dispersions were stable before and after this regime, where the particles possessed sufficiently high surface charge. These results can be qualitatively described by the DLVO (Derjaguin, Landau, Verwey, and Overbeek) theory.<sup>47</sup> Accordingly, repulsive electrical double layer forces do not exist at charge neutralization owing to the lack of surface charge, therefore, van der Waals attractions destabilize the dispersions due to

particle aggregation. The bottom line of these results is that HNT modified with a PSP layer adsorbed at saturation (HNT-PSP, obtained for a PSP dose of 100 mg/g) form stable colloidal samples consisting of homogeneously distributed primary particles of high surface area. On the basis of these results and due to the fact that SOD is negatively charged at neutral pH, enzyme adsorption is expected to occur on these HNT-PSP hybrid particles.

#### Effect of Surface Functionalization on the Resistance against Salt-Induced Aggregation.

To further assess the colloidal stability of the HNT-PSP particles (prepared with a PSP dose of 100 mg/g), the charging and aggregation processes were investigated in KCl solutions of different concentrations by electrophoresis and DLS. The effect of the adsorbed PSP layer on the stability of the HNT-PSP dispersions was explored by comparing the obtained data with the ones observed with the bare HNT (Figure 2). The tendencies observed for the variation of the electrophoretic mobility and the stability ratio data with increasing KCl concentration were similar in both cases. The magnitude of the mobility decreased with the KCl concentration increasing due to charge screening by the salt constituents and remained close to zero at high KCl concentration (Figure 2a).

Aggregation of bare and PSP-coated HNT was investigated in the same KCl concentration range by time-resolved DLS, and it was found that the speed of aggregation increased with KCl concentration. The hydrodynamic radius was constant within the experimental error at low ionic strength, while it increased with time once the KCl concentration was higher than 3 mM. The slopes of the hydrodynamic radius versus time plots increased with the increase of the ionic strength up to a threshold value of 30 mM (SI Figure S3), where they remained constant above it. Stability ratios were determined at several KCl concentrations and the slow and fast aggregation regimes were defined (Figure 2b).

In general, the stability ratios decreased until 30 mM in both systems and remained constant for higher KCl concentrations. Therefore, this value is the so-called critical coagulation concentration (CCC). Such a sharp transition between the fast and slow aggregation regime indicates the presence of DLVO-type forces reported earlier for charged colloidal particles dispersed in electrolyte solutions.<sup>9,10,37,38,44</sup> The CCC value of the HNT-PSP was very similar to the one determined for the HNT. Due to the fact that similar surface charge was assumed for the bare and coated HNT from the electrophoretic

mobility measurements, the identical CCC values confirm that the stabilizing forces originate from the overlap of the electrical double layers, as predicted by the DLVO model.

Despite the opposite sign of charge of the particles, one can conclude that the dispersion characteristics of HNT and HNT-PSP are very similar, and both nanotubes form stable dispersions below 30 mM KCl. However, HNT-PSP was selected for the SOD immobilization process as stronger enzyme adsorption is expected on their positively charged surface than in the case of negatively charged bare HNT.

**Immobilization of SOD.** Based on our previous experiences with enzyme immobilization on polyelectrolyte-functionalized particles,<sup>9,10</sup> the HNT-PSP-SOD bionanocomposite was prepared by adsorbing the SOD on the HNT-PSP prepared with a SOD dose of 10 mg/g. Accordingly, the obtained HNT-PSP-SOD nanotubes contained 100 mg of PSP and 10 mg of SOD together with 1 g of HNT. The isoelectric point of the enzyme is at pH 4.95,<sup>48</sup> therefore it is negatively charged at neutral pH, the condition, under which the experiments were carried out. It is expected that the enzyme strongly adsorbs on the oppositely charged material. However, further confirmation of the successful immobilization was necessary.

Therefore, the adsorption process was quantified by using the Bradford method<sup>39</sup> to determine the SOD concentration in the solution after removing the HNT-PSP-SOD particles by centrifugation. In other words, if SOD partitioning takes place between the solution phase and the particle surface, its presence should be detected by the Bradford test after removing the HNT-PSP-SOD from the sample. Applying such a test, potential enzyme leakage from the composite can be probed. The results, together with four reference measurements performed on SOD solutions of different concentrations, are shown in SI Figure S4. The absorbance decreases at 465 nm and increases at 595 nm when increasing the enzyme concentration. These variations of the intensity of absorption bands result from the binding of the dye to the SOD. The analysis of the spectra revealed that the spectrum measured for the supernatant obtained after SOD adsorption on HNT-PSP was similar to the one of the reference sample devoid of SOD molecules. This finding clearly shows that the enzyme quantitatively adsorbed on the HNT-PSP, and that no partitioning between the bulk and surface occurred, when an enzyme loading of 10 mg/g is applied. The fact that SOD was not detected after removing the HNT-PSP-SOD hybrid from the dispersions indicates negligible enzyme leakage from the composite. It was assumed that the strong attractive forces between the SOD molecules and the solid support were achieved through electrostatic and hydrophobic interactions as well as by hydrogen bonding.

To further prove the adsorption of the enzyme on the HNT-PSP, the FT-IR spectrum of the HNT-PSP-SOD composite was measured and compared to the spectra of the bare HNT and HNT-PSP (Figure 3).

The FT-IR spectrum of HNT exhibits two different Al–OH stretching bands at about 3702 and 3615  $\text{cm}^{-1}$ .<sup>49</sup> The intense peak at 1089  $\text{cm}^{-1}$  is associated with the stretching vibration mode of apical Si–O, while the absorption band at 1021  $\text{cm}^{-1}$  is assigned to the stretching vibration of Si–O–Si.<sup>50</sup> In addition, the intense peak around 900  $\text{cm}^{-1}$  can be identified as a single Al–OH bending vibration.<sup>51</sup> Moreover, in the FT-IR spectra of the HNT-PSP and HNT-PSP-SOD composite, the absorption bands at approximately 1677 and 1541  $\text{cm}^{-1}$ ,

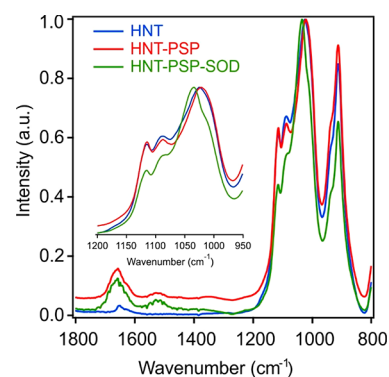


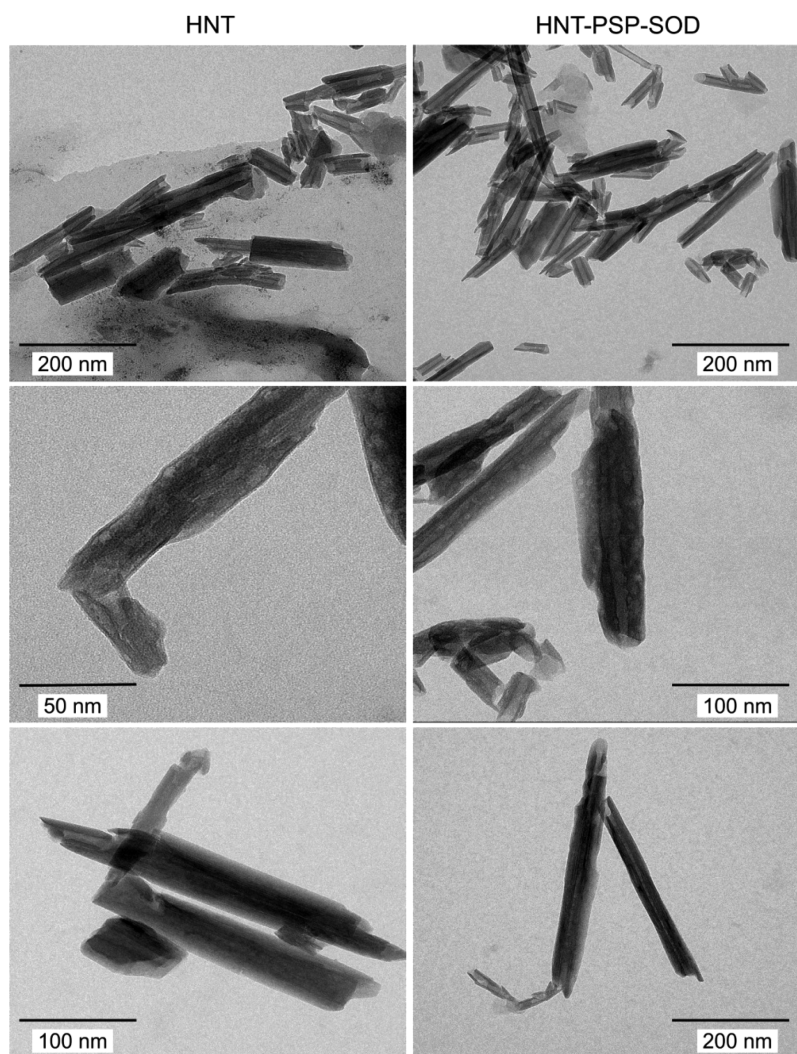
**Figure 3.** Diffuse reflectance FT-IR spectra of bare HNT, HNT-PSP, and HNT-PSP-SOD in solid state.

which are related to the shifted amide I and amide II vibrations, are attributed to the presence of PSP.<sup>52</sup> In the case of the HNT-PSP-SOD hybrid, the peak at 1035  $\text{cm}^{-1}$  is assigned to the shifted C–O stretching vibration of the histidine unit of the SOD enzyme.<sup>53</sup> The observed shifts of the characteristic bands indicate the strong interaction between HNT and PSP and SOD.

The possible changes in the nanoparticle morphology after surface modification were assessed by TEM and SEM. Due to the fact that the images were recorded after drying the sample, nanotube aggregates were observed. However, the typical morphological features of the bare and modified nanotubes can be identified. The tubular morphology of both HNT and HNT-PSP-SOD particles is clearly visible on the SEM micrographs (SI Figure S5). Furthermore, TEM images revealed the intrinsic layered-tubular structural motifs of the nanotubes (Figure 4). The length of the particles typically fell between 200 and 500 nm with ca. 50–60 nm of outer and 10 nm inner diameter, and the samples were moderately polydisperse in the lateral dimension. These features were unaltered after coating the tubes with PSP polyelectrolyte and SOD enzyme, thus the surface modification did not change the morphology of the carrier.

In addition, TGA measurements were carried out with the HNT, HNT-PSP, and HNT-PSP-SOD samples to study the thermal decomposition of the materials (SI Figure S6). For all samples, the dehydration occurred between 30 and 200 °C, which is typical for HNT derivatives.<sup>54</sup> Thereafter, the partial degradation of the organic compounds took place in the range of 200–400 °C. The decomposition of the organic content continued between 400 and 700 °C, and this process was accompanied by the dehydroxylation of the HNT<sup>55</sup> in this temperature range. The TGA curves were identical within the experimental error for the HNT-PSP and HNT-PSP-SOD due to the low amount (10 mg/g) of the enzyme present in the latter composite. However, a significant difference was observed between the thermal decomposition of HNT and HNT-PSP evidencing the presence of the PSP macromolecules on the HNT surface.

A remarkable stability of the HNT-PSP composite in aqueous dispersion was concluded in the previous chapter. Moreover, the effect of SOD adsorption on the electrophoretic mobilities and stability ratios was also studied to assess the charging and aggregation processes of the HNT-PSP-SOD containing 10 mg/g enzyme. Therefore, electrophoretic mobilities and hydrodynamic radii of HNT-PSP were measured in the 0–30 mg/g SOD concentration range (SI



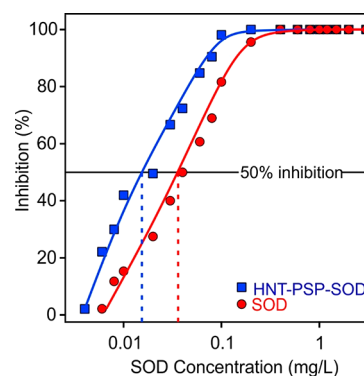
**Figure 4.** TEM micrographs of the bare HNT (left column) and HNT-PSP-SOD (right column) materials. The images were taken after drying 10 mg/L dispersions.

Figure S7). The mobilities were the same ( $2.3 \times 10^{-8} \text{ m}^2/(\text{V s})$ ) within the experimental error and they were very similar to the value determined for HNT-PSP ( $2.0 \times 10^{-8} \text{ m}^2/(\text{V s})$ ) indicating that enzyme adsorption at such low doses did not affect the surface charge of HNT-PSP. Besides, no particle aggregation was detected under the above experimental conditions, and the hydrodynamic radii were about 182 nm in the 0–30 mg/g dose range. In other words, the remarkable stability of the HNT-PSP remained unchanged upon SOD adsorption. Similar observations were published earlier<sup>10</sup> with composites containing SOD immobilized on particle-polyelectrolyte systems.

**Superoxide Radical Scavenging Activity.** The native and the immobilized SOD enzymes were tested in the dismutation of superoxide radicals performed in biochemical test reactions.<sup>40</sup> In these assays, superoxide radicals are produced during oxidation of xanthine to uric acid by xanthine oxidase. The forming radicals reduce NBT to formazan, and this reaction is accompanied by a color change from yellow to blue, which is followed by spectrophotometry. Indeed, when SOD is present in the system, it captures the radicals, that is, inhibits their reaction with NBT. The enzyme activity was expressed in terms of  $\text{IC}_{50}$ , which is the SOD concentration required for 50% inhibition or to capture 50% of the

superoxide radicals forming in the assay. The obtained reaction inhibition values as a function of the SOD concentration are presented in Figure 5.

The shape of the inhibition curves was very similar for both SOD and HNT-PSP-SOD indicating that the enzyme kept its



**Figure 5.** Inhibition of the reaction between NBT and superoxide radicals by SOD (circles) and HNT-PSP-SOD (squares). The solid lines are fits used to calculate the  $\text{IC}_{50}$  values. The average measurement error is about 5%.



functional integrity upon immobilization on the PSP-modified HNT. Complete inhibition (100%) was reached in both cases. The  $IC_{50}$  value was found to be slightly smaller for HNT-PSP-SOD (0.02 mg/L) than for native SOD (0.04 mg/L). This increase in the activity most likely originates from the electrostatic interactions between the HNT-PSP-SOD material and the substrate molecules. In other words, the negatively charged superoxide radicals are certainly attracted to the positively charged protamine chains on the surface so that they are available for the immobilized SOD in larger amounts. Considering the fact that enzyme immobilization often leads to significant loss of the enzyme activity,<sup>9,56</sup> the above results are remarkable.

Thus, the obtained HNT-PSP-SOD hybrid is a promising antioxidant candidate due to its high scavenging activity. In addition, it possesses remarkable colloidal and structural stability, which makes the composite an advantageous biocatalyst in applications. One of its potential utilizations can be in antioxidant therapy for inflammatory bowel diseases.<sup>57</sup> In such biomedical applications, the formation of a protein corona on the particle surface usually further improves the colloidal stability of the nanocomposites.<sup>58,59</sup>

## CONCLUSIONS

An antioxidant nanocomposite consisting of HNT with self-assembled PSP and SOD biomacromolecules on the outer surface was developed. The PSP showed high affinity to the oppositely charged nanotubes giving rise to significant changes in the surface charge properties by increasing the polyelectrolyte loading. The aggregation of the particles was tuned by varying the PSP dose, and stable dispersions were observed once the amount of the PSP biomacromolecule was high enough to cover the entire outer surface of the HNTs. The SOD adsorption on the PSP-coated nanotubes was confirmed by spectroscopic techniques, and the results indicated not only successful immobilization of SOD, but excellent structural stability of the hybrid system. The immobilization procedure did not affect the nanoscale morphology of the nanotubes. Enzymatic assays revealed that SOD kept its structural and functional integrity upon immobilization, since the HNT-PSP-SOD material showed SOD-like activity very similar to the one determined for the support-free enzyme. The slight increase in the dismutation ability was attributed to the advantageous electrostatic interaction between the composite surface and the substrate molecules. These results indicate that the obtained HNT-PSP-SOD dispersion can be considered as a highly active antioxidant with the benefits of the heterogenization process, for example, easier separation from the reaction mixture.

## ASSOCIATED CONTENT

### Supporting Information

The Supporting Information is available free of charge at <https://pubs.acs.org/doi/10.1021/acsabm.9b00953>.

pH and SOD dose-dependent electrophoretic mobilities, SEM images, results of DLS and TGA measurements (PDF)

## AUTHOR INFORMATION

### Corresponding Author

\*E-mail: [szistvan@chem.u-szeged.hu](mailto:szistvan@chem.u-szeged.hu).

### ORCID

Karine Glinel: 0000-0002-2000-0169

Alain M. Jonas: 0000-0002-4083-0688

Istvan Szilagyi: 0000-0001-7289-0979

### Notes

The authors declare no competing financial interest.

## ACKNOWLEDGMENTS

This research was financially supported by the Lendület program of the Hungarian Academy of Sciences (96130) and by the Ministry of Human Capacities, Hungary (20391-3/2018/FEKUSTRAT). K.G. is a Senior Research Associate of the F.R.S.-FNRS. The support from the University of Szeged Open Access Fund (4502) is gratefully acknowledged.

## REFERENCES

- (1) Winterbourn, C. C. Reconciling the chemistry and biology of reactive oxygen species. *Nat. Chem. Biol.* **2008**, *4*, 278–286.
- (2) Finley, J. W.; Kong, A. N.; Hintze, K. J.; Jeffery, E. H.; Ji, L. L.; Lei, X. G. Antioxidants in foods: State of the science important to the food industry. *J. Agric. Food Chem.* **2011**, *59*, 6837–6846.
- (3) Morsella, M.; d'Alessandro, N.; Lanterna, A. E.; Scaiano, J. C. Improving the sunscreen properties of  $TiO_2$  through an understanding of its catalytic properties. *ACS Omega* **2016**, *1*, 464–469.
- (4) Alfadda, A. A.; Sallam, R. M. Reactive oxygen species in health and disease. *J. Biomed. Biotechnol.* **2012**, *2012*, 936486.
- (5) Tainer, J. A.; Getzoff, E. D.; Richardson, J. S.; Richardson, D. C. Structure and mechanism of copper, zinc superoxide-dismutase. *Nature* **1983**, *306*, 284–287.
- (6) Hernandez-Ruiz, J.; Arnao, M. B.; Hiner, A. N. P.; Garcia-Canovas, F.; Acosta, M. Catalase-like activity of horseradish peroxidase: relationship to enzyme inactivation by  $H_2O_2$ . *Biochem. J.* **2001**, *354*, 107–114.
- (7) Bafana, A.; Dutt, S.; Kumar, S.; Ahuja, P. S. Superoxide dismutase: an industrial perspective. *Crit. Rev. Biotechnol.* **2011**, *31*, 65–76.
- (8) Zhu, X.; Niu, X. H.; Zhao, H. L.; Tang, J.; Lan, M. B. Immobilization of superoxide dismutase on Pt-Pd/MWCNTs hybrid modified electrode surface for superoxide anion detection. *Biosens. Bioelectron.* **2015**, *67*, 79–85.
- (9) Pavlovic, M.; Rouster, P.; Szilagyi, I. Synthesis and formulation of functional bionanomaterials with superoxide dismutase activity. *Nanoscale* **2017**, *9*, 369–379.
- (10) Rouster, P.; Pavlovic, M.; Szilagyi, I. Immobilization of Superoxide Dismutase on polyelectrolyte functionalized titania nanosheets. *ChemBioChem* **2018**, *19*, 404–410.
- (11) Li, Z.; Wang, F.; Roy, S.; Sen, C. K.; Guan, J. J. Injectable, highly flexible, and thermosensitive hydrogels capable of delivering superoxide dismutase. *Biomacromolecules* **2009**, *10*, 3306–3316.
- (12) Chen, Y. P.; Chen, C. T.; Hung, Y.; Chou, C. M.; Liu, T. P.; Liang, M. R.; Mou, C. Y. A new strategy for intracellular delivery of enzyme using mesoporous silica nanoparticles: Superoxide Dismutase. *J. Am. Chem. Soc.* **2013**, *135*, 1516–1523.
- (13) Bobone, S.; Miele, E.; Cerroni, B.; Roversi, D.; Bocedi, A.; Nicolai, E.; Di Venere, A.; Placidi, E.; Ricci, G.; Rosato, N.; Stella, L. Liposome-Templated Hydrogel Nanoparticles as Vehicles for Enzyme-Based Therapies. *Langmuir* **2015**, *31*, 7572–7580.
- (14) Singh, S.; Dubey, V. K. Multiwalled carbon nanotube-superoxide dismutase conjugate towards alleviating induced oxidative stress. *Int. J. Pept. Res. Ther.* **2016**, *22*, 171–177.
- (15) Zhang, Y.; Tang, A. D.; Yang, H. M.; Ouyang, J. Applications and interfaces of halloysite nanocomposites. *Appl. Clay Sci.* **2016**, *119*, 8–17.
- (16) Yuan, P.; Tan, D. Y.; Annabi-Bergaya, F. Properties and applications of halloysite nanotubes: recent research advances and future prospects. *Appl. Clay Sci.* **2015**, *112*, 75–93.
- (17) Vergaro, V.; Abdullayev, E.; Lvov, Y. M.; Zeitoun, A.; Cingolani, R.; Rinaldi, R.; Leporatti, S. Cytocompatibility and uptake of halloysite clay nanotubes. *Biomacromolecules* **2010**, *11*, 820–826.



- (18) Santos, A. C.; Ferreira, C.; Veiga, F.; Ribeiro, A. J.; Panchal, A.; Lvov, Y.; Agarwal, A. Halloysite clay nanotubes for life sciences applications: From drug encapsulation to bioscaffold. *Adv. Colloid Interface Sci.* **2018**, *257*, 58–70.
- (19) Lvov, Y.; Wang, W. C.; Zhang, L. Q.; Fakhrullin, R. Halloysite clay nanotubes for loading and sustained release of functional compounds. *Adv. Mater.* **2016**, *28*, 1227–1250.
- (20) Rouster, P.; Dondelinger, M.; Galleni, M.; Nysten, B.; Jonas, A. M.; Glinel, K. Layer-by-layer assembly of enzyme-loaded halloysite nanotubes for the fabrication of highly active coatings. *Colloids Surf., B* **2019**, *178*, 508–514.
- (21) Chao, C.; Liu, J. D.; Wang, J. T.; Zhang, Y. W.; Zhang, B.; Zhang, Y. T.; Xiang, X.; Chen, R. F. Surface modification of halloysite nanotubes with dopamine for enzyme immobilization. *ACS Appl. Mater. Interfaces* **2013**, *5*, 10559–10564.
- (22) Tully, J.; Yendluri, R.; Lvov, Y. Halloysite clay nanotubes for enzyme immobilization. *Biomacromolecules* **2016**, *17*, 615–621.
- (23) Zhai, R.; Zhang, B.; Liu, L.; Xie, Y. D.; Zhang, H. Q.; Liu, J. D. Immobilization of enzyme biocatalyst on natural halloysite nanotubes. *Catal. Commun.* **2010**, *12*, 259–263.
- (24) Shchukin, D. G.; Sukhorukov, G. B.; Price, R. R.; Lvov, Y. M. Halloysite nanotubes as biomimetic nanoreactors. *Small* **2005**, *1*, 510–513.
- (25) Kumar-Krishnan, S.; Hernandez-Rangel, A.; Pal, U.; Ceballos-Sanchez, O.; Flores-Ruiz, F. J.; Prokhorov, E.; de Fuentes, O. A.; Esparza, R.; Meyyappan, M. Surface functionalized halloysite nanotubes decorated with silver nanoparticles for enzyme immobilization and biosensing. *J. Mater. Chem. B* **2016**, *4*, 2553–2560.
- (26) Hari, J.; Sarkozi, M.; Foldes, E.; Pukanszky, B. Long term stabilization of PE by the controlled release of a natural antioxidant from halloysite nanotubes. *Polym. Degrad. Stab.* **2018**, *147*, 229–236.
- (27) Massaro, M.; Amorati, R.; Cavallaro, G.; Guernelli, S.; Lazzara, G.; Milioto, S.; Noto, R.; Poma, P.; RIELA, S. Direct chemical grafted curcumin on halloysite nanotubes as dual-responsive prodrug for pharmacological applications. *Colloids Surf., B* **2016**, *140*, 505–513.
- (28) Vergaro, V.; Lvov, Y. M.; Leporatti, S. Halloysite clay nanotubes for resveratrol delivery to cancer cells. *Macromol. Biosci.* **2012**, *12*, 1265–1271.
- (29) Eskandarloo, H.; Arshadi, M.; Enayati, M.; Abbaspourrad, A. Highly efficient recovery of heparin using a green and low-cost quaternary ammonium functionalized halloysite nanotube. *ACS Sustainable Chem. Eng.* **2018**, *6*, 15349–15360.
- (30) Tao, D.; Higaki, Y.; Ma, W.; Takahara, A. Halloysite nanotube/polyelectrolyte hybrids as adsorbents for the quick removal of dyes from aqueous solution. *Chem. Lett.* **2015**, *44*, 1572–1574.
- (31) Bahri-Laleh, N.; Sadjadi, S.; Poater, A. Pd immobilized on dendrimer decorated halloysite clay: Computational and experimental study on the effect of dendrimer generation, Pd valence and incorporation of terminal functionality on the catalytic activity. *J. Colloid Interface Sci.* **2018**, *531*, 421–432.
- (32) Li, H.; Zhu, X. H.; Xu, J. F.; Peng, W.; Zhong, S. A.; Wang, Y. The combination of adsorption by functionalized halloysite nanotubes and encapsulation by polyelectrolyte coatings for sustained drug delivery. *RSC Adv.* **2016**, *6*, 54463–54470.
- (33) Veerabadran, N. G.; Mongayt, D.; Torchilin, V.; Price, R. R.; Lvov, Y. M. Organized shells on clay nanotubes for controlled release of macromolecules. *Macromol. Rapid Commun.* **2009**, *30*, 99–103.
- (34) Mitra, G. B.; Bhattacharjee, S. Structure of halloysite. *Acta Crystallogr., Sect. B: Struct. Crystallogr. Cryst. Chem.* **1975**, *31*, 2851–2857.
- (35) Hassan, P. A.; Rana, S.; Verma, G. Making sense of Brownian motion: Colloid characterization by dynamic light scattering. *Langmuir* **2015**, *31*, 3–12.
- (36) Zaccone, A.; Wu, H.; Lattuada, M.; Morbidelli, M. Correlation between colloidal stability and surfactant adsorption/association phenomena studied by light scattering. *J. Phys. Chem. B* **2008**, *112*, 1976–1986.
- (37) Kobayashi, M.; Skarba, M.; Galletto, P.; Cakara, D.; Borkovec, M. Effects of heat treatment on the aggregation and charging of Stöber-type silica. *J. Colloid Interface Sci.* **2005**, *292*, 139–147.
- (38) Rouster, P.; Pavlovic, M.; Horvath, E.; Forro, L.; Dey, S. K.; Szilagyi, I. Influence of protamine functionalization on the colloidal stability of 1D and 2D titanium oxide nanostructures. *Langmuir* **2017**, *33*, 9750–9758.
- (39) Bradford, M. M. Rapid and sensitive method for quantitation of microgram quantities of protein utilizing principle of protein-dye binding. *Anal. Biochem.* **1976**, *72*, 248–254.
- (40) Beaucham, C.; Fridovich, I. Superoxide dismutase - improved assays and an assay applicable to acrylamide gels. *Anal. Biochem.* **1971**, *44*, 276–287.
- (41) Byun, Y.; Chang, L. C.; Lee, L. M.; Han, I. S.; Singh, V. K.; Yang, V. C. Low molecular weight protamine: A potent but nontoxic antagonist to heparin/low molecular weight protamine. *ASAIO J.* **2000**, *46*, 435–439.
- (42) Bauer, D.; Killmann, E.; Jaeger, W. Flocculation and stabilization of colloidal silica by the adsorption of poly-diallyl-dimethyl-ammoniumchloride (PDADMAC) and of copolymers of DADMAC with N-methyl-N-vinyl acetamide (NMVA). *Colloid Polym. Sci.* **1998**, *276*, 698–708.
- (43) Hyde, E. D. E.; Moreno-Atanasio, R.; Millner, P. A.; Neville, F. Surface charge control through the reversible adsorption of a biomimetic polymer on silica particles. *J. Phys. Chem. B* **2015**, *119*, 1726–1735.
- (44) Hajdu, A.; Szekeres, M.; Toth, I. Y.; Bauer, R. A.; Mihaly, J.; Zupko, I.; Tombacz, E. Enhanced stability of polyacrylate-coated magnetite nanoparticles in biorelevant media. *Colloids Surf., B* **2012**, *94*, 242–249.
- (45) Feng, L. L.; Stuart, M. C.; Adachi, Y. Dynamics of polyelectrolyte adsorption and colloidal flocculation upon mixing studied using mono-dispersed polystyrene latex particles. *Adv. Colloid Interface Sci.* **2015**, *226*, 101–114.
- (46) Yi, P.; Pignatello, J. J.; Uchimiya, M.; White, J. C. Heteroaggregation of cerium oxide nanoparticles and nanoparticles of pyrolyzed biomass. *Environ. Sci. Technol.* **2015**, *49*, 13294–13303.
- (47) Derjaguin, B.; Landau, L. D. Theory of the stability of strongly charged lyophobic sols and of the adhesion of strongly charged particles in solutions of electrolytes. *Acta Phys. Chim.* **1941**, *14*, 633–662.
- (48) Bannister, J.; Bannister, W.; Wood, E. Bovine erythrocyte cupro-zinc protein 1. Isolation and general characterization. *Eur. J. Biochem.* **1971**, *18*, 178–186.
- (49) Farmer, V. C.; Russel, J. D. The infra-red spectra of layer silicates. *Spectrosc. Acta* **1964**, *20*, 1149–1173.
- (50) Frost, R. L. Fourier-transform Raman-spectroscopy of kaolinite, dickite and halloysite. *Clays Clay Miner.* **1995**, *43*, 191–195.
- (51) Mei, D. D.; Zhang, B.; Liu, R. C.; Zhang, Y. T.; Liu, J. D. Preparation of capric acid/halloysite nanotube composite as form-stable phase change material for thermal energy storage. *Sol. Energy Mater. Sol. Cells* **2011**, *95*, 2772–2777.
- (52) Wang, Y. Y.; Qiu, W. Y.; Wang, Z. B.; Ma, H. L.; Yan, J. K. Extraction and characterization of anti-oxidative polysaccharide-protein complexes from *Corbicula fluminea* through three-phase partitioning. *RSC Adv.* **2017**, *7*, 11067–11075.
- (53) Szilagyi, I.; Berkesi, O.; Sipiczki, M.; Korecz, L.; Rockenbauer, A.; Palinko, I. Preparation, characterization and catalytic activities of immobilized enzyme mimics. *Catal. Lett.* **2009**, *127*, 239–247.
- (54) Fakhrullina, G.; Khakimova, E.; Akhatova, F.; Lazzara, G.; Parisi, F.; Fakhrullin, R. Selective antimicrobial effects of curcumin@halloysite nanoformulation: A *Caenorhabditis elegans* study. *ACS Appl. Mater. Interfaces* **2019**, *11*, 23050–23064.
- (55) Zhang, Y. M.; Li, Y. Q.; Zhang, Y. F.; Ding, D. Q.; Wang, L.; Liu, M.; Zhang, F. C. Thermal behavior and kinetic analysis of halloysite-stearic acid complex. *J. Therm. Anal. Calorim.* **2019**, *135*, 2429–2436.

(56) Sheldon, R. A.; van Pelt, S. Enzyme immobilisation in biocatalysis: why, what and how. *Chem. Soc. Rev.* **2013**, *42*, 6223–6235.

(57) Moura, F. A.; de Andrade, K. Q.; dos Santos, J. C. F.; Araujo, O. R. P.; Goulart, M. O. F. Antioxidant therapy for treatment of inflammatory bowel disease: Does it work? *Redox Biol.* **2015**, *6*, 617–639.

(58) Moore, T. L.; Rodriguez-Lorenzo, L.; Hirsch, V.; Balog, S.; Urban, D.; Jud, C.; Rothen-Rutishauser, B.; Lattuada, M.; Petri-Fink, A. Nanoparticle colloidal stability in cell culture media and impact on cellular interactions. *Chem. Soc. Rev.* **2015**, *44*, 6287–6305.

(59) Vasti, C.; Bedoya, D. A.; Rojas, R.; Giacomelli, C. E. Effect of the protein corona on the colloidal stability and reactivity of LDH-based nanocarriers. *J. Mater. Chem. B* **2016**, *4*, 2008–2016.



# Dispersion Characteristics and Aggregation in Titanate Nanowire Colloids

Endre Horváth,<sup>[a]</sup> Lucie Grebikova,<sup>[b]</sup> Plinio Maroni,<sup>[b]</sup> Tamás Szabó,<sup>[b, c]</sup> Arnaud Magrez,<sup>[a]</sup> László Forró,<sup>[a]</sup> and Istvan Szilagyi<sup>\*[b]</sup>

Titanate nanowires (TiONWs) are synthesized through the hydrothermal method and characterized in acidic aqueous dispersions by using electrophoresis, dynamic light scattering, and atomic force microscopy. The TiONWs have a rodlike shape with an average length of about 600 nm and a thickness of 35 nm. They are positively charged under the conditions used. Their surface charge properties and aggregation are investigated in the presence of oppositely charged poly(styrene sulfonate) (PSS) polyelectrolyte. Charge neutralization followed by a subsequent charge reversal process is observed, which is attributed to the adsorption of PSS. The colloids are unstable near the charge neutralization point and stable at lower and higher PSS doses, in good qualitative agreement with the

theory developed by Derjaguin, Landau, Verwey, and Overbeek (DLVO). The nanowires prefer to align along the walls, leading to “spaghetti-like” oriented aggregates. The aggregation processes of bare and PSS-coated TiONWs are monitored at different concentrations of an inert electrolyte; slow aggregation is found at low salt levels, whereas aggregation is rapid beyond the critical coagulation concentration, as predicted by the DLVO theory, which describes the colloid stability of the TiONWs adequately in all the systems investigated. Coating of the nanowires with the polyelectrolyte leads to a critical coagulation concentration 75 times higher than that of the bare titanates, indicating the enormous stabilizing effect of PSS.

## Introduction

Titanate derivatives with anisotropic particle shape are attracting great interest owing to their growing importance in numerous applications, for example, in solar cells,<sup>[1–3]</sup> sensorics,<sup>[4]</sup> polymer composites,<sup>[5]</sup> as sources for the synthesis of novel materials,<sup>[6–8]</sup> and in photocatalytic water treatment.<sup>[9–13]</sup> In the latter application, their photocatalytic activity is exploited, and titanate compounds such as spherical particles, wires, platelets, and their composites with other materials are used as aqueous colloid systems.<sup>[14,15]</sup> Major challenges in these processes include the provision of a stable dispersion during the catalytic run and the post-treatment removal of the suspended catalyst from the effluent stream of purified water. The catalyst recovery can be achieved through aggregation and subsequent sedimentation followed by filtration of the titanate compounds, or

through their deposition on appropriate materials.<sup>[16]</sup> The type of liquid-phase aggregation of the nanoparticles has a significant effect on the textural properties such as the porosity, pore-size distribution, and mechanical stability of different solution casts, for example, dip-coated, screen-printed, and doctor-bladed functional coatings.<sup>[3]</sup> Importantly, the nano- and micron-scale structure of the aggregates greatly influences their level of toxicity, and hence, their potential impact on human health and the environment.<sup>[17]</sup> Therefore, detailed study of the colloidal behaviour of these catalysts and other nanomaterials suspended in liquid media is necessary.<sup>[18–20]</sup>

The stability of aqueous titanate dispersions has been the focus of many research groups worldwide, with investigations on the charging, surface forces, and aggregation processes of titanate nanoparticles,<sup>[21–23]</sup> nanotubes,<sup>[24]</sup> and nanosheets.<sup>[25,26]</sup> For instance, direct measurements of surface forces by the colloidal probe technique based on atomic force microscopy (AFM) revealed that the interaction between titanium dioxide surfaces across electrolyte solutions can be described well with the classical theory for the stability of aqueous colloidal dispersions developed by Derjaguin, Landau, Verwey, and Overbeek (DLVO).<sup>[27,28]</sup> Accordingly, the dispersions are stable at low electrolyte concentrations at which repulsive forces originating from the overlap of the electrical double layers predominate, whereas aggregation occurs at high salt levels at which the surface charges are screened and attractive van der Waals forces drive the interactions between the particles.

Although numerous titanate derivatives have been prepared and applied in aqueous systems, the aggregation processes

[a] Dr. E. Horváth, Dr. A. Magrez, Prof. L. Forró  
Laboratory of Physics of Complex Matter  
École Polytechnique Fédérale de Lausanne  
CH-1015 Lausanne (Switzerland)

[b] L. Grebikova, Dr. P. Maroni, Dr. T. Szabó, Dr. I. Szilagyi  
Laboratory of Colloid and Surface Chemistry  
University of Geneva  
CH-1205 Geneva (Switzerland)  
Fax: (+41) 22 379 6069  
E-mail: istvan.szilagyi@unige.ch

[c] Dr. T. Szabó  
Department of Physical Chemistry and Materials Science  
University of Szeged  
6720 Szeged (Hungary)



This article is part of the “Early Career Series”. To view the complete series, visit: <http://chempluschem.org/earlycareer>.

had to be controlled with an appropriate stabilizer or aggregation agent to obtain the desired colloidal properties.<sup>[29–31]</sup> One of the most effective classes of compounds for this purpose is the polyelectrolytes, which are used widely to tune the colloid stability of dispersions. Polyelectrolytes are charged polymers, and because of their high affinity with oppositely charged surfaces, they can be very effective flocculating or stabilizing agents, depending on the aim of the application.<sup>[32,33]</sup>

For this very reason, the interaction between titanate compounds and polyelectrolytes has been investigated recently. The research included the preparation of titanate–polyelectrolyte composite materials,<sup>[34,35]</sup> the adsorption of polyelectrolytes on the titanate surface, and investigation of their effect on the colloid stability and rheological properties.<sup>[36–38]</sup> In these studies, both negative<sup>[24,36,39–41]</sup> and positive<sup>[42]</sup> molecules were used, because the sign and magnitude of the surface charge density of titanates depends on the solution conditions (e.g., pH and ionic strength). The stabilization of titanate dispersions by polyelectrolytes was studied by using several techniques including AFM,<sup>[36]</sup> light scattering,<sup>[37,41]</sup> viscometry,<sup>[39]</sup> and surface potential measurements.<sup>[24,40]</sup> For example, the results of aggregation and sedimentation studies indicated that dispersions of titanate nanotubes can be stabilized by humic acid adsorption, and both steric and electrosteric interactions induced by the adsorbed polyelectrolyte chains were found to be responsible for the colloid stability of the systems.<sup>[24]</sup> Whereas DLVO forces predominated in the interparticle interactions in the case of bare titanate dispersions, the addition of polyelectrolytes to the samples usually gave rise to steric interactions and consequent stabilization.<sup>[39–41]</sup>

Nevertheless, these studies focused on the characterization of surface charges as well as the sizes and shapes of higher generations of aggregates, but lacked systematic quantitative investigations of the aggregation rates of titanate materials based on time-resolved coagulation kinetic measurements. However, the stabilization mechanism of colloidal particles in the presence of polyelectrolytes can be identified readily through time-resolved dynamic light scattering (DLS) and colloidal probe measurements, as proven for polystyrene latexes.<sup>[43–45]</sup>

Herein, we focus on the charging and aggregation processes of titanate nanowires (TiONWs) in the presence of an inert electrolyte (KCl) and oppositely charged poly(styrene sulfonate) (PSS) to clarify the governing interactions through DLS and electrophoresis measurements. Although the studied nanowires and precursor nanotubes have already been investigated extensively in the solid state,<sup>[46–48]</sup> very little information is available on the nanostructures of particles in aqueous dispersions; therefore, the sizes and shapes of the primary particles and their aggregates in TiONW dispersions were studied in detail through AFM.

## Results and Discussion

### Characterization of titanate nanowires in aqueous dispersions

After their preparation, the TiONWs were transferred into water and characterized in detail in the dispersions. The size of the nanowires was investigated through two independent techniques under the same experimental conditions. AFM images were recorded with TiONWs deposited on oppositely charged mica surface in suspensions at pH 3.0 (Figure 1 a), and

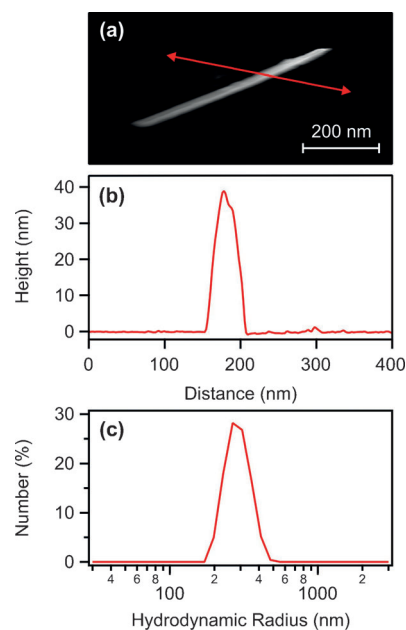


**Figure 1.** a) AFM image of a TiONW deposited on a mica surface from an acidic suspension. b) Height profile of TiONW measured along the red line in the above AFM image. c) Number-averaged size distribution in the TiONW dispersions as measured by DLS.

their length was found to be about 600 nm. The height profile of the image yielded a thickness of 35 nm (Figure 1 b) for the rodlike TiONWs. DLS measurements were performed in the same suspensions as used for the AFM experiments, and a z-averaged value of 662 nm was determined for the hydrodynamic diameter (Table 1) with a relatively low polydispersity

**Table 1.** Characteristic size and charge values for aqueous TiONW dispersions at pH 3.0.

Size [nm] <sup>[a]</sup>	Polydispersity index	Electrophoretic mobility [m <sup>2</sup> V <sup>-1</sup> s <sup>-1</sup> ]	ζ-potential [mV]	Surface charge [mC m <sup>-2</sup> ] <sup>[b]</sup>
662	0.19	1.69 × 10 <sup>-8</sup>	21.6	7.0

[a] Size expressed in hydrodynamic diameter measured in DLS experiments. [b] Surface charge density was obtained from the Gouy–Chapman fit to the ζ-potential data recorded at different ionic strengths, as detailed elsewhere.<sup>[49]</sup>

index of 0.19, indicating a narrow particle size distribution (Figure 1c). The dispersions were stable under these conditions for a few months: neither dissolution nor a change in shape or charge was detected during this period.

The electrophoretic mobilities recorded in the pH range from 3 to 11 revealed that the nanowires possessed positive charge at low pH values, whereas their charge was reversed with increasing pH.<sup>[49]</sup> The transition occurs at pH 4.1, which is similar to the point of zero charge of other titanate materials.<sup>[21,24,50,51]</sup> In the present work, we focus on positively charged TIONWs, so the samples were adjusted to pH 3.0 throughout the experiments. As shown in Table 1, the nanowire dispersions have a positive electrophoretic mobility under these conditions, corresponding to a  $\zeta$ -potential of 21.6 mV obtained by conversion of the mobility value to potential by using the classical Smoluchowski theory.<sup>[52]</sup> The surface charge density was determined from the ionic-strength dependence of the potential values by applying the Gouy–Chapman equation (based on the Poisson–Boltzmann theory developed for the description of the electrical double layer),<sup>[52]</sup> and a low surface charge value of  $7 \text{ mC m}^{-2}$  was found by fitting the experimental data. The low surface charge density and potential data imply a limited stability of the bare colloid in the presence of an aggregating agent.

#### Interaction between titanate nanowires and poly(styrene sulfonate)

PSS has already been proven to be a powerful aggregating agent in various systems,<sup>[43,53–55]</sup> but its interaction with titanate derivatives has only been investigated for the preparation of composite materials.<sup>[10,35]</sup> PSS can adsorb strongly on oppositely charged surfaces, leading to the formation of a thin adsorbed layer with a thickness of 2–10 nm depending on the molecular weight and the ionic strength applied.<sup>[56]</sup> Nevertheless, there is a lack of comprehensive characterization data for aggregation processes in titanate dispersions in the presence of PSS. The goal of this section is to describe the aggregation processes in systems containing TIONWs and PSS in acidic conditions (pH 3.0) under which the nanowires are positively charged and the PSS is negative (because the sulfonate groups are fully ionized at this pH value).

The electrophoretic mobilities were measured in dispersions containing TIONWs and PSS (Figure 2). The concentration of the nanowire suspension was kept constant in each series of experiments, and the dose of PSS was increased at a constant pH of 3.0 and ionic strength of 1 mM adjusted by the pH. At low PSS doses, a positive mobility was measured close to the value determined for the bare TIONWs under the same acidic conditions, which indicates a positive surface charge originating from the protonation of the hydroxyl groups on the surface. The electrophoretic mobilities decreased with increasing PSS dose owing to the adsorption of polyelectrolytes on the oppositely charged surface, and reached the isoelectric point (IEP) at a dose of 11.6 mg PSS per gram of TIONWs (denoted as  $\text{mg g}^{-1}$  in the following). This dose refers to the adsorbed

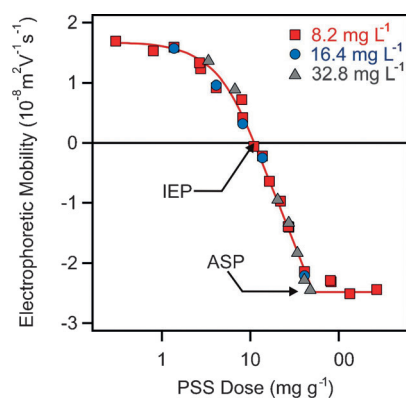


**Figure 2.** Electrophoretic mobility values of TIONW dispersions in the presence of PSS at pH 3.0, which provides an ionic strength of 1 mM. Three series of experiments were performed at different TIONW concentrations of 8.2, 16.4, and 32.8  $\text{mg L}^{-1}$ . The unit of the PSS dose refers to milligrams of polyelectrolyte normalized to one gram of TIONW. The isoelectric point (IEP) and the adsorption saturation plateau (ASP) are indicated by arrows; the solid line is provided as a guide for the eye.

amount of PSS appropriate for the neutralization of the charge of the nanowires to give an overall charge of zero.

Upon further increasing the PSS dose, the TIONW charges were reversed and the electrophoretic mobilities became negative. The charge-reversal process is typical for polyelectrolytes in the presence of oppositely charged surfaces.<sup>[24,43,57–59]</sup> This phenomenon originates from the adsorption of PSS on oppositely charged islands on the surface and from hydrophobic interactions between the polyelectrolyte chains. The surface was saturated at the adsorption saturation plateau (ASP) at  $51.4 \text{ mg g}^{-1}$ , which corresponds to the maximum amount of PSS that could be adsorbed on the TIONW surface. The mobility values were constant thereafter, and any further PSS added remained dissolved in the bulk. The electrophoretic measurements were repeated at different nanowire concentrations, as indicated by the different symbols in Figure 2, but the electrophoretic mobility values remained very similar in the same range of polyelectrolyte dose. In the case of significant partitioning of PSS between the surface and the bulk, one would expect a shift in the mobility curves measured at different nanowire concentrations for the same PSS dose.<sup>[60,61]</sup> Therefore, the overlapping of the curves of mobility versus PSS dose at different TIONW concentrations indicates the strong and irreversible adsorption of PSS on the surface. In general, the charge-reversal process resulted in higher absolute values of the electrophoretic mobility at the ASP compared with the data measured for bare TIONWs. The higher charge is expected to have a significant effect on the colloid stability of the dispersions.

The colloid stability was investigated in time-resolved DLS measurements by following the apparent hydrodynamic radius as a function of time at different PSS concentrations. The experimental conditions (TIONW concentration, PSS dose, pH, ionic strength, etc.) were exactly the same as for the electrophoretic study, which allowed us to compare the surface charge behavior and aggregation processes directly. The col-



loid stability was expressed in terms of the stability ratio, which is related to the diffusion-controlled aggregation of the bare TiONWs in an excess of an inert electrolyte. Note that fast (diffusion-controlled) aggregation occurs in the dispersions if the stability ratio is close to unity, whereas increased stability ratio values indicate more stable samples.<sup>[62]</sup> The colloid stability graph of the system containing the nanowires and the polyelectrolyte is shown in Figure 3.

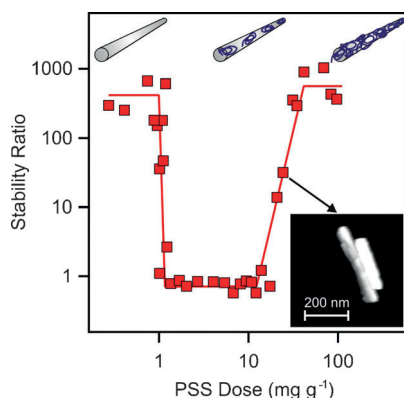


**Figure 3.** Colloid stability of TiONW dispersions in the presence of PSS expressed in stability ratio as a function of PSS dose at a nanowire concentration of  $8.2 \text{ mg L}^{-1}$  and at pH 3.0 (ionic strength of  $1 \text{ mM}$ ). The solid line is a guide for the eye, and the inset shows an AFM image of an aggregate recorded at a PSS dose of  $20 \text{ mg g}^{-1}$ .

The stability ratio was high at low PSS doses, indicating stable samples similar to the original TiONW suspensions in water. The aggregation became faster, that is, the stability ratio decreased, with increasing PSS dose, because of the adsorption of the polyelectrolyte on the surface and subsequent charge neutralization. Fast aggregation and unstable systems were observed near the IEP, at which the charges of the nanowires are neutralized by the adsorbed PSS. The transition between the slow and fast aggregation regimes was sharp. Interestingly, the region of instability was rather broad compared with those of other systems containing particles and oppositely charged polyelectrolytes at similar ionic strengths.<sup>[44,54]</sup> The stability ratio values increased again after the IEP; the charge reversal process occurred and a stable dispersion was obtained at appropriately high PSS concentrations. The plateaus in the stability graph (shown in Figure 3) at low and high polyelectrolyte doses correspond to the stabilities of the bare and PSS-coated TiONWs.

The colloid stability of the dispersions containing TiONWs and PSS follows a trend that can be predicted by DLVO theory.<sup>[27,28,52]</sup> Accordingly, the samples were stable at low PSS doses at which the nanowires possess positive charges owing to incomplete surface neutralization by PSS adsorption, and unstable near the IEP, at which the overall charge of the TiONWs is close to zero. In addition, the charge-reversal process at higher PSS concentrations resulted in slow aggregation of TiONWs and stable samples. The overlapping electrical double layers provide a repulsive interaction force that is responsible for the stabilization of the dispersions far from the

IEP, whereas the attractive van der Waals forces in the absence of the electrical double layers destabilize the dispersions for doses at which the net surface charge of the nanowires is close to zero. In summary, the colloid stability of the system is governed by the superposition of the repulsive double layer and attractive van der Waals forces, which are related to the presence or absence of surface charge. Similar aggregation behaviors and U-shaped stability curves have been reported for other polyelectrolyte-particle systems.<sup>[33,43,44,54]</sup> In addition, the stability ratio values in the fast aggregation regime were slightly lower than unity. The normalized slopes were related to the diffusion-controlled aggregation occurring in solutions of high KCl concentration, in which the interactions between the nanowires are governed only by van der Waals forces. Stability ratios lower than unity indicated an additional attraction, which was certainly not a DLVO-type force. We assume that this acceleration is caused by the formation of islands of adsorbed PSS on the surface, which gives rise to an additional attraction between these islands and the oppositely charged bare surfaces of other TiONWs. Similar types of patch-charge interactions have been discovered in other systems containing PSS and oppositely charged surfaces.<sup>[54,55]</sup> It is important to mention that the surface is partially covered at these doses close to the IEP, and hence, the formation of patches is feasible.

The orientation of the TiONWs in the aggregates was observed by taking AFM images of the same dispersions as used for the DLS study. As shown in the inset of Figure 3, the nanowires exhibited a preferential parallel alignment along the walls, resulting in a "spaghetti-like" structure of the aggregates. As discussed in more detail below, the above orientation of the TiONWs in the aggregates was typical in our systems, and no evidence was found for other structures, for example, house-of-card-type<sup>[24]</sup> or end-to-end aggregates,<sup>[49]</sup> which have been observed previously in the dried state. Note that to characterize the aggregation rates, we always stayed in the early stages of aggregation, during which the initial hydrodynamic radius increased by a maximum of up to 50% even in the case of unstable samples, so the structure of higher-generation aggregates was not considered.

### Colloid stability of bare (TiONW) and polyelectrolyte-coated (TiONW-PSS) nanowires

To clarify the stabilization mechanism in dispersions containing TiONWs and PSS, we investigated the surface charge properties and colloid stability of polyelectrolyte-coated nanowires, and compared them to the corresponding properties of the bare TiONW samples. The coated nanowires (denoted herein as TiONW-PSS) were prepared by adsorbing PSS at a dose of  $80 \text{ mg g}^{-1}$ , which was beyond the ASP value, so the TiONWs were fully covered with the polyelectrolyte. To probe the origin of the predominating forces between the nanowires, we varied the concentration of an inert electrolyte (KCl) systematically. Surface forces and the resulting aggregation processes are usually sensitive to the variation of the salt level in the case of electrostatic origin, but steric and other intermolecular



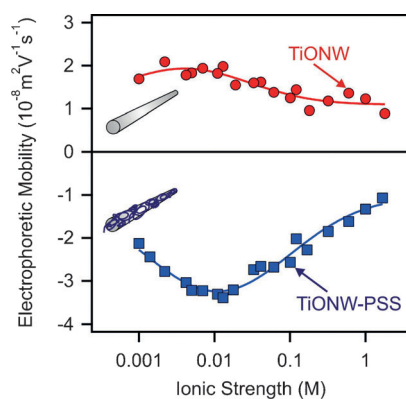


**Figure 4.** Electrophoretic mobility values of bare (TiONW) and PSS-coated (TiONW-PSS) nanowire dispersions as a function of the ionic strength adjusted with KCl at pH 3.0 and a PSS dose of  $80 \text{ mg g}^{-1}$  in the TiONW-PSS case. The nanowire concentrations were  $8.2 \text{ mg L}^{-1}$  in both cases. The solid lines are guides for the eye.

interactions show less response to these types of changes under such experimental conditions.<sup>[43,45,55]</sup> Accordingly, electrophoretic measurements were performed first with TiONW and TiONW-PSS suspensions at different KCl concentrations (Figure 4), with the pH and both the nanowire and polyelectrolyte concentrations kept constant throughout the experiments.

For the bare TiONW dispersions, the positive electrophoretic mobility values decreased slightly with increasing KCl concentration owing to the screening effect of the electrolyte on the surface charges. However, a maximum in the mobility plot was observed at lower salt concentrations, which can be also predicted with the standard electrokinetic model.<sup>[63,64]</sup> The mobilities remained positive over the entire concentration range studied. The TiONW-PSS nanowires possessed a negative charge because of charge reversal at this polyelectrolyte dose, and a minimum in the electrophoretic mobility data was again found at low salt levels for the same reasons as for the maximum in the bare TiONW case. Although this minimum was more pronounced, the general behavior was very similar. The electrophoretic mobility values decreased with increasing KCl concentration above  $10 \text{ mM}$  because of the screening effect of the potassium ions, which are the counterions in the TiONW-PSS system. It is also important to note that the coated nanowires had higher absolute surface charge values than the bare ones.

The colloid stabilities of the systems containing the bare or coated nanowires were investigated through time-resolved DLS experiments, and are represented as the stability ratio versus the ionic strength (Figure 5). Note that the same experimental conditions were applied as for the mobility experiments, so the surface charge properties could be correlated directly with the aggregation behavior. Similar shapes of the stability curves were observed for the TiONW and TiONW-PSS nanowires. Accordingly, the aggregation was slow at low salt levels and accelerated with increasing KCl concentration, leading to fast aggregation, that is, unstable systems, at concentrations higher than the critical coagulation concentration (CCC), which separates the slow and fast aggregation regimes.

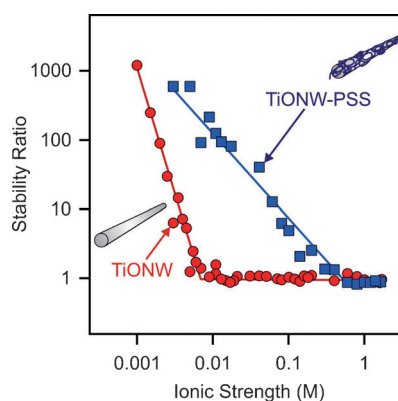


**Figure 5.** Colloid stability of bare (TiONW) and PSS-coated (TiONW-PSS) nanowire dispersions as a function of the ionic strength adjusted with KCl at pH 3.0 and a PSS dose of  $80 \text{ mg g}^{-1}$  in the TiONW-PSS case. The nanowire concentrations were  $8.2 \text{ mg L}^{-1}$  in both cases. The solid lines are guides for the eye.

Two main differences can be observed from Figure 5. On one hand, the CCC values were found to be  $8$  and  $600 \text{ mM}$  for TiONW and TiONW-PSS respectively, which implies that a significantly higher salt concentration was necessary to destabilize the coated nanowires than the bare ones. Consequently, upon coating the TiONWs with PSS, the aggregation processes slowed down by a factor of 75, resulting in a more stable dispersion. On the other hand, the slopes in the slow aggregation regimes were dissimilar, and a steeper transition between the fast and slow aggregation regimes was observed in the case of bare TiONWs. The DLVO theory also predicts steeper slopes, so the shallower transition for the TiONW-PSS system must originate from additional non-DLVO attractive forces. We assume that the extra attraction originates from the patch-charge interactions discussed above. These are not included in the DLVO theory, which considers a homogeneous surface charge distribution,<sup>[52]</sup> but have been observed in other systems containing PSS and oppositely charged colloidal particles.<sup>[54,55]</sup>

In general, the interaction forces responsible for the aggregation properties in both the bare and coated nanowire dispersions had an electrostatic origin. Pure DLVO-type forces were found in the TiONW samples, whereas both DLVO and patch-charge interactions were responsible for the colloid stability in the case of TiONW-PSS owing to the heterogeneous adsorption of the PSS molecules on the TiONW surfaces. Evidence of steric interactions, which would lead to additional stabilization effects especially in the fast aggregation regime, was not observed in these systems.

AFM images were recorded in aggregating suspensions to obtain information on the structure of the aggregates and the alignment of the nanowires upon aggregation (Figure 6). The bare nanowire aggregates were deposited on mica; for the TiONW-PSS, the surface of the mica was functionalized with 3-(ethoxydimethylsilyl)propylamine to create a positive surface because of the protonation of the primary amino groups under the acidic conditions used. The aggregates were imaged in the early stages of the aggregation (similarly to the time-resolved DLS experiments), so the formation of higher-genera-

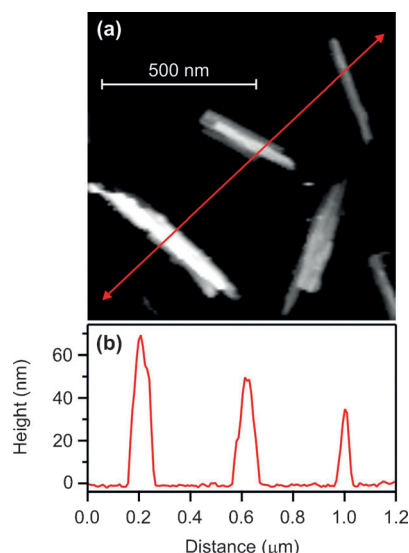


**Figure 6.** a) Bare TiONW aggregates of different populations adsorbed on mica and imaged by AFM in 20 mM KCl electrolyte at pH 3.0. b) Height profile of TiONWs measured along the red line in the above AFM image.

tion aggregates could be disregarded. Thanks to these carefully chosen experimental conditions, we were able to image monomers, dimers, and trimers in the same sample, as shown in Figure 6a. The TiONWs preferred a lateral side-by-side orientation upon aggregation, resulting in a “spaghetti-like” aggregate structure. This orientation led to a limited increase in the hydrodynamic radius in the time-resolved DLS measurements.

The height profile of the AFM image (Figure 6b) confirmed this orientation, and the height of the aggregates increased from the right to the left side of the image, indicating the presence of aggregated TiONWs of different generations. Similar information was obtained for the TiONW–PSS system (Figure 3), and aggregates with the house-of-card structure or with end-to-end connections were not observed in the AFM images, probably because we were observing the early stages of the aggregation process in the present case.

## Conclusion

In summary, TiONWs were synthesized in aqueous dispersions through the hydrothermal method from an anatase precursor, and their size, morphology, and surface charge were characterized under acidic conditions. The TiONWs had a rodlike shape with a length of 662 nm and a thickness of about 35 nm, and they were positively charged with a density of  $7 \text{ mCm}^{-2}$  at pH 3.0.

The charging and aggregation of the TiONW dispersions were also investigated in the presence of an inert electrolyte and PSS polyelectrolyte by using electrophoresis, DLS, and AFM measurements. The anionic polyelectrolyte was found to adsorb strongly on the oppositely charged TiONWs, leading to charge neutralization at the IEP and subsequent charge reversal continuing up to the ASP value, which corresponds to the maximum amount of PSS that could be adsorbed on the

TiONWs. The dispersions were unstable close to the IEP; however, slow aggregation and stable samples were observed below and after this point if the nanowires possessed sufficient charge density. This behavior is in good qualitative agreement with the DLVO theory. Nevertheless, similarly to other systems containing PSS, an additional patch–charge interaction also played a role in the colloid stability of the TiONWs, especially in the fast aggregation regime, leading to faster aggregation than for the diffusion-controlled process. AFM images recorded in the same dispersions indicated that the TiONWs preferred a wall–wall interaction upon aggregation, leading to a “spaghetti-like” aggregate structure in the early stages of the aggregation process. The salt-induced aggregation of bare and PSS-coated nanowires resulted in stability graphs of similar shape, with some differences in the slow aggregation regime owing to the patch–charge interactions. In addition, the CCC in the TiONW–PSS system was almost two orders of magnitude higher than that for the uncoated TiONWs, indicating an enormous stabilization effect of the adsorbed PSS layer.

The latter information is extremely useful for the scientific and technological communities interested in the stabilization or destabilization of positively charged titanate materials in aqueous dispersions for the design of TiONW systems with desired aggregation properties through application of the appropriate PSS dose and inert electrolyte concentration. This issue is especially important in applications such as water treatment and catalysis, for which stable and unstable dispersions are required in different steps of the processes.

## Experimental Section

### Materials

Poly(styrene sulfonate) sodium salt (PSS) was purchased from Polymer Standards Service GmbH (Mainz, Germany). The manufacturer reported a weight-average molecular mass of  $666 \text{ kg mol}^{-1}$  and a polydispersity index below 1.20. The polyelectrolyte was used without further purification. All the samples were prepared with Milli-Q water (Millipore, Molsheim, France) adjusted to pH 3.0 with HCl (Merck, Darmstadt, Germany), and the ionic strength was set through the addition of KCl (Acros Organics, Geel, Belgium). Other chemicals such as  $\text{TiO}_2$ , NaOH, KOH,  $\text{NH}_4\text{OH}$ , 3-(ethoxydimethylsilyl)propylamine (Sigma–Aldrich, Steinheim, Germany),  $\text{H}_2\text{O}_2$  (Reactolab, Servion, Switzerland),  $\text{H}_2\text{SO}_4$  (Carlo Erba Reagents, Balerna, Switzerland) were used as received. For general cleaning procedures, Hellmanex (Hellma GmbH & Co. KG, Müllheim, Germany) was used. All solutions were filtered with  $0.1 \mu\text{m}$  syringe filters (Millipore, Cork, Ireland) to remove dust particles. The measurements were performed at a temperature of  $25^\circ\text{C}$ .

### Preparation of titanate nanowires (TiONWs)

The protonated titanate nanowires (TiONWs) were prepared through a two-step hydrothermal process.<sup>[65]</sup>  $\text{TiO}_2$  (3.7 g, 99.7% anatase) was mixed with NaOH solution (35 mL, 10 M). The mixture was put into a Teflon-lined stainless steel autoclave (Parr Instrument Company, Moline, USA) and heated continuously at  $130^\circ\text{C}$  for 36 h. After the reaction, the autoclave was cooled down to room temperature at a rate of  $1^\circ\text{C min}^{-1}$ . The white intermediate product was decanted from the supernatant. In the second step of

the synthesis, KOH solution (35 mL, 15 M) was added to the solid material; the temperature was increased gently ( $3^{\circ}\text{Cmin}^{-1}$ ) to  $200^{\circ}\text{C}$ , and this temperature was maintained for 24 h. Thereafter, the system was cooled to  $150^{\circ}\text{C}$  at a rate of  $1^{\circ}\text{Cmin}^{-1}$  and then kept at  $150^{\circ}\text{C}$  for 12 h. The autoclave was then left to cool down to room temperature. The white product was collected, filtered, and washed several times with Milli-Q water. The alkaline sample was neutralized with the appropriate amount of 0.1 M HCl solution. It was then washed extensively with deionized water of  $80^{\circ}\text{C}$  to remove any remaining traces of NaCl and KCl from the sample. In the final step, the white powder was dried at  $100^{\circ}\text{C}$  for 6 h in air; this was followed by the final heat treatment at  $250^{\circ}\text{C}$  for 4 h. The sample was cooled in a desiccator under vacuum to complete the drying process. The resulting TiONW powder was suspended in water, and the pH of the dispersion was adjusted to 3.0 with HCl for further investigations and experiments. The mass concentration was determined by thermogravimetry: the dispersions (10 mL) were dried by heating up to  $150^{\circ}\text{C}$  for 24 h, and the concentration of the TiONWs was calculated from the amount of the water evaporated from the sample.

### Electrophoretic mobility and dynamic light scattering (DLS) measurements

Both electrophoretic mobility and hydrodynamic radius measurements were performed with a ZetaNano ZS (Malvern Instruments, Worcestershire, UK) instrument equipped with a He/Ne laser operating at 633 nm as a light source and an avalanche photodiode as a detector. The device applies an electric field strength of  $4\text{ kVm}^{-1}$  in the electrophoretic mode. Size measurements were made in the DLS mode of the same instrument at a scattering angle of  $173^{\circ}$ . The hydrodynamic radius was determined by using a second-order cumulant fit for the correlation function, which was accumulated for 30 s. For the electrophoretic measurements, a calculated amount of PSS solution was mixed with water and KCl stock solution to obtain the desired ionic strength. The pH of all these solutions was adjusted to 3.0 with HCl, which provided a background ionic strength of 1 mM. Finally, the TiONW dispersion ( $0.5\text{ mL}$ ,  $82\text{ mgL}^{-1}$ ) was added to the samples in a plastic vial. Accordingly, the final particle concentration was always  $8.2\text{ mgL}^{-1}$  and the total sample volume was  $5.0\text{ mL}$ . The mobilities of the TiONW dispersions were measured after equilibration of the samples overnight at room temperature. The measurements were performed in plastic capillary cells (Malvern Instruments, Worcestershire, UK) that were first cleaned with 2% Hellmanex solution and rinsed extensively with Milli-Q water. The samples were equilibrated for 1 min at  $25^{\circ}\text{C}$  in the instrument before the measurements were taken. The final electrophoretic mobility ( $\mu$ ) of the samples was calculated from the average of five individual measurements, and can be related to the  $\zeta$ -potential as shown in Equation (1), in which  $v$  is the velocity of the TiONWs,  $E$  is the electric field strength,  $\varepsilon_0\varepsilon$  is the permittivity of the water, and  $\eta$  is the viscosity of the medium.<sup>[52]</sup>

$$\mu = \frac{v}{E} = \frac{\varepsilon_0\varepsilon\zeta}{1.5\eta} \quad (1)$$

The hydrodynamic radii were measured in 1 cm square plastic cuvettes (Malvern Instruments, Worcestershire, UK) cleaned with 2% Hellmanex solution. In the time-resolved DLS experiments, 50 runs were usually performed, and the samples were prepared by mixing the appropriate volumes of PSS, water, and KCl stock solutions, each adjusted to pH 3.0. The aggregation experiment was initiated by injecting 0.2 mL of the TiONW dispersion. The final particle con-

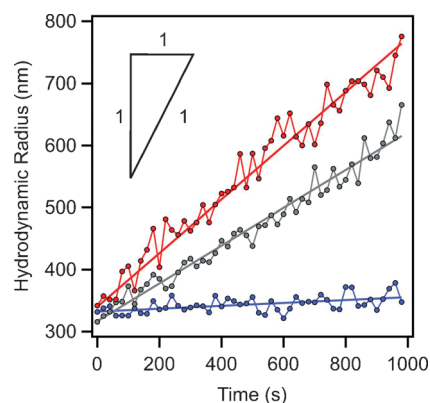


**Figure 7.** Hydrodynamic radius as a function of measurement time in time-resolved DLS experiments at a constant TiONW concentration of  $8.2\text{ mgL}^{-1}$  but different PSS doses at pH 3.0 in stable and aggregating dispersions. The slopes of the curves were used to quantify the colloid stabilities of the systems.

centration was  $8.2\text{ mgL}^{-1}$  in the samples, and the total volume was 2 mL. The dispersions were mixed with vortex and the DLS measurements were started immediately afterwards. The slopes of the curves of apparent hydrodynamic radius versus time (Figure 7) were calculated and divided by the mass concentration to obtain the normalized slopes ( $S$ ), as shown in Equation (2), in which  $dr_h/dt$  is the slope,  $V$  is the total volume, and  $m$  is the mass of TiONWs in the sample.

$$S = \frac{V}{m} \left. \frac{dr_h}{dt} \right|_{t=0} \quad (2)$$

The colloid stability is expressed in terms of the stability ratio ( $W$ ), as given in Equation (3), in which  $S_{fast}$  is the normalized slope for the diffusion-controlled aggregation determined in 1 M KCl solution, and  $S$  is the normalized slope in the actual experiment.

$$W = \frac{S_{fast}}{S} \quad (3)$$

Note that the aggregation is fast for a stability ratio close to unity, and higher values imply slower coagulation and more stable systems.

### Atomic force microscopy (AFM)

AFM imaging was performed in dispersions in amplitude modulation mode with a Cypher AFM (Asylum Research, Santa Barbara, USA) instrument. Biolever mini cantilevers (BL-AC40TS, Olympus, Japan) with a nominal tip radius smaller than 9 nm and a resonance frequency of 25–36 kHz in water were used. Prior to the experiments, the cantilevers were ozone-cleaned with a UV-ozone cleaner (PSD Pro, Novascan, Ames, USA) in an oxygen-enriched atmosphere for 20 min. Images were acquired at pH 3.0 at a scan rate of 0.8 Hz, velocity range of  $8\text{--}16\text{ }\mu\text{ms}^{-1}$ , free oscillation amplitude of about 23 nm, and a set point corresponding to about 70% of the free oscillation amplitude. The cantilever spring constants were in the range  $0.12\text{--}0.15\text{ Nm}^{-1}$ , as measured through thermal fluctuations in air. For the deposition of the TiONWs, two types of surfaces were used depending on the composition of the samples. The bare, positively charged TiONWs were deposited on oppositely charged mica, whereas the negative PSS-coated TiONWs (TiONW-

PSS) were deposited on positive aminofunctionalized mica (AF-Mica). High-grade mica was obtained from Plano (Wetzlar, Germany) and was freshly cleaved in air with scotch tape prior to use. The AF-Mica surface was obtained through vacuum silanization, that is, by placing freshly cleaved mica next to a 30  $\mu\text{L}$  drop of 3-(ethoxydimethylsilyl)propylamine for 12 h in an evacuated glass desiccator. The surfaces were immersed in TiONW dispersions for 5 min and then rinsed with electrolyte solution. For the bare TiONWs, the sample contained 8.2  $\text{mgL}^{-1}$  of solid in a 20 mm KCl solution, which is higher than the CCC and corresponds to the fast aggregation regime. In the case of TiONW-PSS, the same TiONW concentration was used, and the dispersion also contained 20  $\text{mg g}^{-1}$  PSS without added KCl at pH 3.0. The samples were prepared 30 min before starting the AFM imaging. The results were analyzed by using software provided by Asylum Research (Santa Barbara, USA).

## Acknowledgements

Financial support from the Swiss National Science Foundation (200021 150162, IZ73Z0\_128037/1), Swiss Contribution (SH/7/2/20), Swiss Scientific Exchange Program (12029) and the University of Geneva is gratefully acknowledged. Special thanks are extended to Olivier Vassalli for technical support and the careful performance of the experiments.

**Keywords:** adsorption · aggregation · colloids · polyelectrolyte · titanates

- [1] B. O'Regan, M. Grätzel, *Nature* **1991**, 353, 737–740.
- [2] N. K. Subbainan, C. A. Wijesinghe, F. D'Souza, *J. Am. Chem. Soc.* **2009**, 131, 14646–14647.
- [3] N. Tétreault, E. Horváth, T. Moehl, J. Brillat, R. Smajda, S. Bungener, N. Cai, P. Wang, S. M. Zakeeruddin, L. Forró, A. Magrez, M. Grätzel, *ACS Nano* **2010**, 4, 7644–7650.
- [4] E. Horváth, P. R. Ribic, F. Hashemi, L. Forró, A. Magrez, *J. Mater. Chem.* **2012**, 22, 8778–8784.
- [5] M. T. Byrne, J. E. McCarthy, M. Bent, R. Blake, Y. K. Gun'ko, E. Horvath, Z. Konya, A. Kukovec, I. Kiricsi, J. N. Coleman, *J. Mater. Chem.* **2007**, 17, 2351–2358.
- [6] J. G. Yu, Q. Li, S. W. Liu, M. Jaroniec, *Chem. Eur. J.* **2013**, 19, 2433–2441.
- [7] B. H. Park, B. S. Kang, S. D. Bu, T. W. Noh, J. Lee, W. Jo, *Nature* **1999**, 401, 682–684.
- [8] R. Kun, M. Balazs, I. Dekany, *Colloids Surf. A* **2005**, 265, 155–162.
- [9] M. Hodos, E. Horvath, H. Haspel, A. Kukovec, Z. Konya, I. Kiricsi, *Chem. Phys. Lett.* **2004**, 399, 512–515.
- [10] D. N. Priya, J. M. Modak, A. M. Raichur, *ACS Appl. Mater. Interfaces* **2009**, 1, 2684–2693.
- [11] E. G. Bajnóczy, N. Balázs, K. Mogyorósi, D. F. Srankó, Z. Pap, Z. Ambrus, S. E. Canton, K. Norén, E. Kuzmann, A. Vértes, Z. Homonnay, A. Oszkó, I. Pálkó, P. Sáros, *Appl. Catal. B* **2011**, 103, 232–239.
- [12] R. Asahi, T. Morikawa, T. Ohwaki, K. Aoki, Y. Taga, *Science* **2001**, 293, 269–271.
- [13] Z. H. Lin, P. Roy, Z. Y. Shih, C. M. Ou, H. T. Chang, *ChemPlusChem* **2013**, 78, 302–309.
- [14] M. R. Hoffmann, S. T. Martin, W. Y. Choi, D. W. Bahnemann, *Chem. Rev.* **1995**, 95, 69–96.
- [15] F. T. Chen, Z. Liu, Y. Liu, P. F. Fang, Y. Q. Dai, *Chem. Eng. J.* **2013**, 221, 283–291.
- [16] T. Szabó, A. Veres, E. Cho, J. Khim, N. Varga, I. Dékány, *Colloids Surf. A* **2013**, 433, 230–239.
- [17] A. Magrez, L. Horvath, R. Smajda, V. Salicó, N. Pasquier, L. Forro, B. Schwaller, *ACS Nano* **2009**, 3, 2274–2280.
- [18] M. Halma, K. Castro, C. Taviot-Gueho, V. Prevot, C. Forano, F. Wypych, S. Nakagaki, *J. Catal.* **2008**, 257, 233–243.
- [19] B. Hu, X. Cao, P. Zhang, *ChemPlusChem* **2013**, 78, 506–514.
- [20] I. Biondi, V. Laporte, P. J. Dyson, *ChemPlusChem* **2012**, 77, 721–726.
- [21] D. Kuscer, G. Stavber, G. Trefalt, M. Kosec, *J. Am. Ceram. Soc.* **2012**, 95, 487–493.
- [22] I. Sameut Bouhaik, P. Leroy, P. Ollivier, M. Azaroual, L. Mercury, *J. Colloid Interface Sci.* **2013**, 406, 75–85.
- [23] A. Feiler, P. Jenkins, J. Ralston, *Phys. Chem. Chem. Phys.* **2000**, 2, 5678–5683.
- [24] W. Liu, W. L. Sun, A. G. L. Borthwick, J. R. Ni, *Colloids Surf. A* **2013**, 434, 319–328.
- [25] R. Z. Ma, T. Sasaki, *Adv. Mater.* **2010**, 22, 5082–5104.
- [26] A. Matsuda, H. Sakamoto, M. A. B. Nor, G. Kawamura, H. Muto, *J. Phys. Chem. B* **2013**, 117, 1724–1730.
- [27] E. J. W. Verwey, J. T. G. Overbeek, *Theory of Stability of Lyophobic Colloids*, Elsevier, Amsterdam, **1948**.
- [28] B. Derjaguin, *Prog. Surf. Sci.* **1993**, 43, 1–14.
- [29] S. Farrokhpay, *Adv. Colloid Interface Sci.* **2009**, 151, 24–32.
- [30] K. Katagiri, H. Inami, K. Koumoto, K. Inumaru, K. Tomita, M. Kobayashi, M. Kakihana, *Eur. J. Inorg. Chem.* **2012**, 3267–3272.
- [31] K. Nakamura, Y. Oaki, H. Imai, *J. Am. Chem. Soc.* **2013**, 135, 4501–4508.
- [32] B. Bolto, J. Gregory, *Water Res.* **2007**, 41, 2301–2324.
- [33] M. Borkovec, G. Papastavrou, *Curr. Opin. Colloid Interface Sci.* **2008**, 13, 429–437.
- [34] J. X. Wang, W. X. Liu, G. H. Yin, H. D. Li, H. Liu, W. J. Zhou, H. L. Wang, Z. Wang, *Colloids Surf. A* **2012**, 414, 9–16.
- [35] R. E. Schaak, T. E. Mallouk, *Chem. Mater.* **2000**, 12, 3427–3434.
- [36] N. S. Bell, J. Sindel, F. Aldinger, W. M. Sigmund, *J. Colloid Interface Sci.* **2002**, 254, 296–305.
- [37] G. H. Kirby, D. J. Harris, Q. Li, J. A. Lewis, *J. Am. Ceram. Soc.* **2004**, 87, 181–186.
- [38] D. Khastgir, K. Adachi, *Polymer* **2000**, 41, 6403–6413.
- [39] C. D. Munro, K. P. Plucknett, *J. Am. Ceram. Soc.* **2009**, 92, 2537–2543.
- [40] K. R. Ratinaç, O. C. Standard, P. J. Bryant, *J. Colloid Interface Sci.* **2004**, 273, 442–454.
- [41] M. B. Romanello, M. M. F. de Cortalezzi, *Water Res.* **2013**, 47, 3887–3898.
- [42] F. Ogawa, T. Ban, Y. Ohya, *Thin Solid Films* **2008**, 516, 4863–4867.
- [43] J. Hierrezuelo, A. Sadeghpour, I. Szilágyi, A. Vaccaro, M. Borkovec, *Langmuir* **2010**, 26, 15109–15111.
- [44] I. Szilágyi, D. Rosická, J. Hierrezuelo, M. Borkovec, *J. Colloid Interface Sci.* **2011**, 360, 580–585.
- [45] M. Finessi, P. Sinha, I. Szilágyi, I. Popa, P. Maroni, M. Borkovec, *J. Phys. Chem. B* **2011**, 115, 9098–9105.
- [46] A. Kukovec, M. Hodos, E. Horvath, G. Radnoczi, Z. Konya, I. Kiricsi, *J. Phys. Chem. B* **2005**, 109, 17781–17783.
- [47] E. Horváth, A. Kukovec, Z. Kónya, I. Kiricsi, *Chem. Mater.* **2007**, 19, 927–931.
- [48] P. Szirmai, E. Horvath, B. Nafradi, Z. Mickovic, R. Smajda, D. M. Djokic, K. Schenk, L. Forro, A. Magrez, *J. Phys. Chem. C* **2013**, 117, 697–702.
- [49] E. Horváth, I. Szilágyi, L. Forró, A. Magrez, *J. Colloid Interface Sci.* **2014**, 416, 190–197.
- [50] A. Niecikowska, M. Krasowska, J. Ralston, K. Malysa, *J. Phys. Chem. C* **2012**, 116, 3071–3078.
- [51] Y. X. Tang, Z. L. Jiang, Q. L. Tay, J. Y. Deng, Y. K. Lai, D. G. Gong, Z. L. Dong, Z. Chen, *RSC Adv.* **2012**, 2, 9406–9414.
- [52] W. B. Russel, D. A. Saville, W. R. Schowalter, *Colloidal Dispersions*, Cambridge University Press, Cambridge, **1989**.
- [53] A. Gromer, M. Rawiso, M. Maaloum, *Langmuir* **2008**, 24, 8950–8953.
- [54] G. Gillies, W. Lin, M. Borkovec, *J. Phys. Chem. B* **2007**, 111, 8626–8633.
- [55] I. Popa, G. Gillies, G. Papastavrou, M. Borkovec, *J. Phys. Chem. B* **2010**, 114, 3170–3177.
- [56] E. Seyrek, J. Hierrezuelo, A. Sadeghpour, I. Szilágyi, M. Borkovec, *Phys. Chem. Chem. Phys.* **2011**, 13, 12716–12719.
- [57] R. R. Netz, J. F. Joanny, *Macromolecules* **1999**, 32, 9013–9025.
- [58] E. Illés, E. Tombácz, *J. Colloid Interface Sci.* **2006**, 295, 115–123.
- [59] R. Mészáros, I. Varga, T. Gilányi, *Langmuir* **2004**, 20, 5026–5029.
- [60] I. Szilágyi, A. Polomska, D. Citherlet, A. Sadeghpour, M. Borkovec, *J. Colloid Interface Sci.* **2013**, 392, 34–41.
- [61] A. Mezei, R. Meszaros, *Langmuir* **2006**, 22, 7148–7151.
- [62] H. Holthoff, S. U. Egelhaaf, M. Borkovec, P. Schurtenberger, H. Sticher, *Langmuir* **1996**, 12, 5541–5549.

- [63] R. W. O'Brien, L. R. White, *J. Chem. Soc. Faraday Trans. 2* **1978**, *74*, 1607–1626.
- [64] M. Borkovec, S. H. Behrens, M. Semmler, *Langmuir* **2000**, *16*, 5209–5212.

- [65] T. Kasuga, M. Hiramatsu, A. Hoson, T. Sekino, K. Niihara, *Adv. Mater.* **1999**, *11*, 1307–1311.

---

Received: December 17, 2013

Published online on February 24, 2014



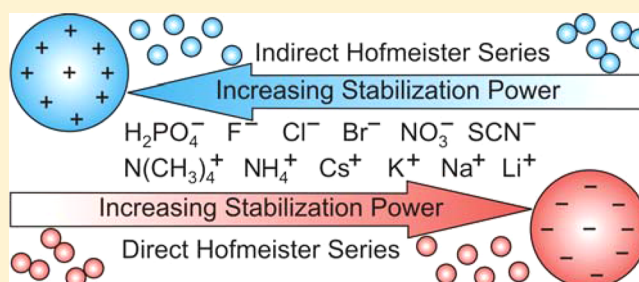
# Specific Ion Effects on Particle Aggregation Induced by Monovalent Salts within the Hofmeister Series

Tamas Oncsik, Gregor Trefalt, Michal Borkovec, and Istvan Szilagyi\*

Department of Inorganic and Analytical Chemistry, University of Geneva, 30 Quai Ernest-Ansermet, 1205 Geneva, Switzerland

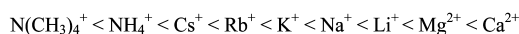
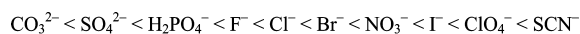
## Supporting Information

**ABSTRACT:** Ion specific effects of monovalent salts on charging and aggregation for two types of polystyrene latex particles were investigated by electrophoresis and time-resolved light scattering. The chemical composition of the electrolytes was systematically varied in the experiments. Accordingly,  $\text{NaH}_2\text{PO}_4$ ,  $\text{NaF}$ ,  $\text{NaCl}$ ,  $\text{NaBr}$ ,  $\text{NaNO}_3$ , and  $\text{NaSCN}$  were used to vary the anions and  $\text{N}(\text{CH}_3)_4\text{Cl}$ ,  $\text{NH}_4\text{Cl}$ ,  $\text{CsCl}$ ,  $\text{KCl}$ ,  $\text{NaCl}$ , and  $\text{LiCl}$  for the cations. The salt concentration dependence of the electrophoretic mobilities indicates that the surface charge was screened by the counterions when their concentrations increased. For the  $\text{SCN}^-$  ions, adsorption on positively charged particles leads to charge reversal. The aggregation rates are small at low electrolyte concentrations indicating stable dispersions under these conditions, and they increase with the salt concentration. When viscosity corrections are taken into account, no ion specific effects in the fast aggregation regime can be established. The slow and fast aggregation regimes are separated by the critical coagulation concentration (CCC). Within the experimental error, the CCCs are the same in systems containing different co-ions but the same counterions, with the exception of ammonium salts. However, the variation of counterions leads to different CCC values due to specific interaction of the counterions with the surface. These values follow the Hofmeister series for negatively charged sulfate latex particles, while the reversed order was observed for positively charged amidine latex. Comparison between experimental CCCs and those calculated by the theory of Derjaguin, Landau, Verwey, and Owerbeek reveals that variations in the surface charge due to ionic adsorption are mainly responsible for the ion specific effects in the aggregation process.



## INTRODUCTION

While the Hofmeister series has been known for more than a century, the molecular mechanisms governing this characteristic sequence in the ionic specificities are still not fully clarified.<sup>1–3</sup> The Hofmeister series was discovered in protein precipitation experiments, and this series classifies ions according to their increasing stabilization power of protein solutions, namely,



This sequence states that solutions of negatively charged proteins remain stable even at high salt concentrations in solutions containing the ions appearing in the right, while they precipitate already at lower salt concentrations containing the ions appearing on the left. Numerous other phenomena can be ordered according to the same sequence, for example, surface tension or viscosities of electrolyte solutions, dissolution heats of salts, binding of ligands, and charging of proteins or polyelectrolytes.<sup>2–13</sup>

Here, we focus on the relation between the Hofmeister series and colloidal particle aggregation.<sup>14–27</sup> This question has also been pursued for quite some time, whereby that community rather used the term *lyotropic series*. Particle aggregation is

known to be fast at high salt concentrations or for weakly charged particles, while it slows down at low salt concentrations or highly charged particles.<sup>15,28</sup> The transition between these two regimes is denoted as the critical coagulation concentration (CCC). The ionic valence induces an important dependence, which is referred to as the Schulze–Hardy rule.<sup>15,25,26,29</sup> This rule states that the CCC strongly decreases with an increase in the valence of the counterions. Thereby, multivalent cations are relevant for negatively charged particles, while multivalent anions, for positively charged ones.

However, even ions of the same valence may lead to different CCCs.<sup>17–25</sup> The respective shifts can be normally classified according to the Hofmeister series. Negatively charged particles typically follow the *direct Hofmeister series* quoted earlier. Thereby, the ions on the left induce lower CCCs, while the ions on the right, higher ones. On the other hand, positively charged particles follow the *indirect Hofmeister series*. The latter series maintains the same sequence of ions, but ions on the left induce higher CCCs, while the ions on the right, a lower one. However, ions of higher valence quoted within the Hofmeister

Received: January 20, 2015

Revised: March 15, 2015

Published: March 16, 2015



series should be excluded from this reasoning, since they primarily follow the Schulze–Hardy rule. Therefore, we only focus on monovalent ions here.

The classical theory of Derjaguin, Landau, Verwey, and Overbeek (DLVO) of colloidal aggregation surmises that the interactions between particles are described by a superposition of attractive van der Waals forces and repulsive double layer forces across an indifferent electrolyte solution.<sup>15,28</sup> The fast aggregation regime is governed by an attractive interaction potential, while the slow regime is characterized by a thermally activated energy barrier crossing. The DLVO theory suggests that the CCC is a sharp transition between these two regimes. A strong decrease of the CCC with ionic valence is equally predicted, in accordance to the Schulze–Hardy rule. Aggregation rates calculated with DLVO theory show reasonable agreement with experimental data, especially for weakly charged particles.<sup>30–32</sup>

However, this classical theory cannot directly rationalize any trends in particle aggregation rates within the Hofmeister series, as it considers no other ionic properties than the valence. Ionic specificity can be introduced into DLVO theory by assuming that ions are no longer indifferent. This picture supposes that ions adsorb specifically to the particle surfaces, thereby modifying the surface charge and thus the double layer force.<sup>33–38</sup> This simple approach qualitatively rationalizes the observed dependencies of the CCC.<sup>3,39,40</sup> The Hofmeister series also reflects the size and hydration of ions. Small and strongly hydrated anions, such as  $F^-$  and  $Cl^-$ , appear on the left, while large and poorly hydrated ones, such as  $SCN^-$  and  $I^-$ , on the right. The cations are arranged in the opposite way. On the left, one finds large and poorly hydrated cations, such as  $N(CH_3)_4^+$  and  $Cs^+$ , while strongly hydrated ones, such as  $Na^+$  and  $Li^+$ , are situated on the right. Suppose that the particle surface is hydrophobic and poorly hydrated. Poorly hydrated ions will adsorb to such surfaces more strongly than well hydrated ones (i.e., like-seeks-like). Binding of cations to a negatively charged surface will neutralize the surface charge and thus leads to a decrease of the CCC. Adsorption of anions will increase the magnitude of the surface charge and lead to a larger CCC. Analogous reasoning applies to positively charged particles. Adsorption of anions will neutralize the surface, while adsorption of cations will lead to increase of surface charge. Therefore, negatively charged hydrophobic particles follow the direct Hofmeister series, while positively charged ones, the indirect series. Similar arguments can be put forward for particles with a hydrophilic or well hydrated surface. Well hydrated ions will adsorb more strongly on such a hydrated substrate than poorly hydrated ions, and the situation is reversed. Stability of negatively charged hydrophilic particles should rather follow the indirect Hofmeister series, while positively charged ones, the direct series. This picture may be further complicated by additional forces induced by the adsorbed ions. Such short-ranged forces are normally not included in the DLVO theory. These forces are typically introduced into a modified treatment of the electric double layer where one introduces additional ion–substrate interactions (e.g., hydration, van der Waals, and image charges).<sup>40–42</sup> While such additional forces may modify the sequences within the series, the qualitative picture remains similar.

Particle surface charge density has often been found to vary systematically with the type of ions, as one would expect for a hydrophobic surface. The charge of positively charged alumina

decreased in the  $Cl^- > Br^- > I^-$  order following the indirect Hofmeister series.<sup>33</sup> The same trend was reported for positively charged latex particles as revealed by electrophoresis.<sup>17,19,20,43</sup>

The charge density of negatively charged alumina particles would decrease from  $Cs^+$  to  $Na^+$  with the direct Hofmeister series.<sup>33</sup> Similar trends were observed for negatively charged hematite, titania, and silica.<sup>36,44,45</sup> However, the behavior of the mentioned silica sample seems atypical, since other authors reported the charge density of silica to follow the indirect Hofmeister series as one would expect for a hydrophilic substrate.<sup>34,35,46</sup> Analogous behavior was reported for silver halide.<sup>47</sup>

Many trends in the observed CCCs are also consistent with the fact that surfaces of colloidal particles are hydrophobic. Negatively charged polystyrene and clay mineral particles follow the direct Hofmeister series, while positively charged metal oxides and polystyrene particles follow the indirect one.<sup>17,19–21,23,24</sup> While the same trend was observed for negatively charged silver halide particles,<sup>25</sup> the behavior of this system seems atypical, since the surface charge densities follow the reverse trend.<sup>47</sup> For polystyrene particles, however, only a few cations were investigated so far. The opposite dependence was observed for protein-coated latex or calcined titania, as one would expect for hydrophilic surfaces.<sup>18,19,21–23</sup> However, ion specific effects on particle aggregation were absent for weakly charged iron oxide, titania, and carboxylated latex particles.<sup>21,23,26</sup>

A transition between the direct and indirect Hofmeister series was observed for CCCs of titania after a heat treatment.<sup>21</sup> The native particles followed the indirect series in basic conditions, as one would expect for a hydrophilic surface. After heat treatment, the surface becomes hydrophobic, and the direct series is observed. A similar transition between the direct and indirect Hofmeister series was also evidenced for the water–silica interface upon pH variations through electric surface potentials obtained from direct force measurements.<sup>38</sup> In acidic conditions, the silica surface is more hydrophobic and thus follows the direct series. In basic conditions, the surface becomes more hydrophilic due to the ionization of the silanol groups and, therefore, reflects the indirect Hofmeister series. The observations that the charge density of silica may follow the direct<sup>45</sup> or the indirect<sup>34,35,46</sup> Hofmeister series could also be related to this hydrophobic to hydrophilic transition. In some situations, partial reversal of Hofmeister series was equally reported,<sup>21,23,34,48</sup> and this possibility was confirmed by computer simulations.<sup>39</sup>

The present work investigates how the position of monovalent ions within the Hofmeister series affects the aggregation of negatively and positively charged polystyrene latex particles. Absolute aggregation rate coefficients were measured by combining time-resolved static light scattering (SLS) and dynamic light scattering (DLS). Similar light scattering techniques were used to study particle aggregation earlier.<sup>27,49–52</sup> The surface charging properties were investigated by electrophoresis. The present study explores a larger number of ions than the previous investigations, especially cations. Moreover, the use of the indifferent chloride allows addressing the specific effect of different cations unequivocally. In addition, the variation of the absolute aggregation rate constant in the fast aggregation regime with the type of salt and particles is studied for the first time.

## EXPERIMENTAL SECTION

**Materials.** Polystyrene latex particles that were functionalized with amidine or sulfate groups on their surface were purchased from Invitrogen Corp. The particle size and the surface charge density of the particles were determined by the manufacturer by transmission electron microscopy (TEM) and conductometric titration. The sulfate latex has a mean radius of 265 nm, a polydispersity expressed as a coefficient of variation (CV) of 2.0%, and a surface charge density of  $-77 \text{ mC/m}^2$ . In the case of the amidine latex, the corresponding quantities are 110 nm, 4.3%, and  $+132 \text{ mC/m}^2$ . The same particles were used by us in a previous publication,<sup>53</sup> and their size was determined by SLS and DLS in stable suspensions. SLS measurements were analyzed using the Mie theory for spheres<sup>54</sup> and yield the mean radius of 263 nm for the sulfate latex and 110 nm for the amidine latex. The measured polydispersity expressed as the CV were 3.8% and 7.1%. All of these values obtained by SLS are in very good agreement with TEM. DLS yields slightly larger average radii, namely, 278 and 117 nm, probably due to polydispersity and hydration effects. The sulfate latex particles were dialyzed with cellulose ester membrane against pure water until the conductivity value was less than  $8 \times 10^{-5} \text{ S/m}$ , while for the amidine particles a polyvinylidene fluoride membrane was used. The particle concentrations of the dialyzed stock suspensions were determined by static light scattering by calibrating the scattering intensity with the original particle suspension of known concentration. The concentration of the sulfate latex stock suspension was 65 g/L, while the one of amidine latex, around 7 g/L. Analytical grade NaCl, KCl, CsCl,  $\text{NH}_4\text{Cl}$ , NaSCN (Sigma-Aldrich), LiCl,  $\text{NaH}_2\text{PO}_4$  (Acros Organics), NaF, NaBr,  $\text{NaNO}_3$ , and  $\text{N}(\text{CH}_3)_4\text{Cl}$  (Fluka) were dissolved in pure water, adjusted to pH 4.0 with HCl and filtered with a  $0.1 \mu\text{m}$  syringe filter (Millipore). All experiments were performed in a thermostated environment at a temperature of  $25.0 \pm 0.2 \text{ }^\circ\text{C}$ . Milli-Q water (Millipore) was used throughout.

**Electrophoretic Mobility.** ZetaSizer Nano ZS (Malvern) equipped with a He/Ne laser operating at 633 nm as a light source and an avalanche photodiode as a detector was used to measure the electrophoretic mobility of the particles in an electric field of 4 kV/m. The suspensions needed for the measurements were prepared by mixing the appropriate salt solutions with a particle stock suspension, with final particle concentration of 50 mg/L for the sulfate latex and 5 mg/L for the amidine latex. The suspensions were equilibrated for 1 min prior to the measurements. Five runs were performed for each sample, and averaged.

**Aggregation Rates by Light Scattering.** Absolute aggregation rates were determined in 1.0 M KCl by combined time-resolved SLS and DLS on the multiangle goniometer (ALV/CGS-8F). This goniometer uses eight fiber-optic detectors and solid state laser of a wavelength of 532 nm. Quartz cuvettes were first cleaned in piranha solution, which is a mixture of concentrated  $\text{H}_2\text{SO}_4$  and 30%  $\text{H}_2\text{O}_2$  at a volume ratio of 3:1, then rinsed with water, and dried in a dust-free oven at  $60 \text{ }^\circ\text{C}$ . The particle concentration was 4 mg/L ( $4.9 \times 10^{13} \text{ m}^{-3}$ ) for the sulfate latex, and 1 mg/L ( $1.7 \times 10^{14} \text{ m}^{-3}$ ) for the amidine latex. The stable particle stock suspension was injected into the salt solution in the cuvette, mixed, and immediately monitored by light scattering. The intensity and the correlation function were accumulated for 20 s, and the apparent hydrodynamic radius was calculated from the second order cumulant fit. This quantity was recorded as a function of time until the initial radius increased by about 40%. To determine the absolute aggregation rate coefficient, the SLS intensity  $I(q,t)$  and the apparent hydrodynamic radius  $r_h(q,t)$  were followed with time,  $t$ , at different magnitudes of the scattering vector,  $q$ . For short times, relative change of the scattering intensity can be written as<sup>55</sup>

$$\Sigma = \frac{1}{I(q, 0)} \left. \frac{dI(q, t)}{dt} \right|_{t \rightarrow 0} = kN_0 \left( \frac{I_2(q)}{2I_1(q)} - 1 \right) \quad (1)$$

where  $k$  is the aggregation rate coefficient and  $N_0$  is the initial particle number concentration while  $I_1(q)$  and  $I_2(q)$  are the scattering intensities of the monomers and dimers, respectively. The

corresponding expression for the relative rate of change of the hydrodynamic radius is<sup>55</sup>

$$\Delta = \frac{1}{r_h(q, 0)} \left. \frac{dr_h(q, t)}{dt} \right|_{t \rightarrow 0} = kN_0 \left( 1 - \frac{1}{\alpha} \right) \frac{I_2(q)}{2I_1(q)} \quad (2)$$

where  $\alpha = r_{h,2}/r_{h,1}$  with  $r_{h,1}$  and  $r_{h,2}$  being the hydrodynamic radii of the monomer and the dimer. Combining eqs 1 and 2, one obtains

$$\Sigma = \left( 1 - \frac{1}{\alpha} \right)^{-1} \Delta - kN_0 \quad (3)$$

A scatter plot of the relative rates  $\Sigma$  and  $\Delta$  gives a straight line, whereby the slope yields the hydrodynamic factor  $\alpha$  and the absolute aggregation rate coefficient follows from the intercept. The respective experimental results obtained in 1.0 M KCl solutions are shown in Figure 1. The aggregation rate coefficient for the sulfate latex was  $(3.3$

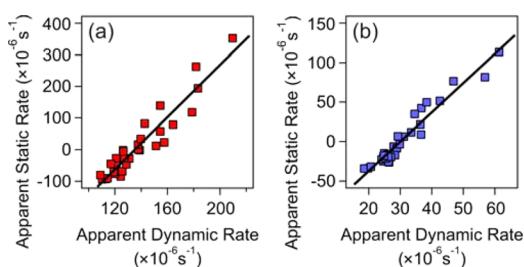


**Figure 1.** Scatter plot of the apparent static and dynamic rates for different latex particles for determination of the absolute rate coefficients in 1 M KCl solution: (a) sulfate latex and (b) amidine latex.

$\pm 0.2) \times 10^{-18} \text{ m}^3/\text{s}$  and for the amidine latex  $(3.0 \pm 0.2) \times 10^{-18} \text{ m}^3/\text{s}$ . These aggregation rate coefficients agree within experimental error with our previous measurements with time-resolved SLS for the same particles at pH 5.0 in 1.0 M KCl.<sup>53</sup> The hydrodynamic factors  $\alpha$  were for the sulfate latex  $1.37 \pm 0.02$  and for the amidine  $1.31 \pm 0.02$ . These values compare reasonably well with the theoretical value of 1.39, which can be calculated from low Reynolds number hydrodynamics.<sup>56</sup>

For other conditions, the aggregation rate was measured by time-resolved DLS with the compact single-angle goniometer (ALV/CGS-3) with a He/Ne laser of a wavelength of 633 nm. The hydrodynamic radius was monitored at a scattering angle of  $90^\circ$  in the same fashion as described previously. The particle concentration was chosen in the range of 50–200 mg/L for the sulfate latex and in the range of 2–10 mg/L for the amidine latex. The relative rate coefficient was obtained from the relative increase of the hydrodynamic radius. Absolute rate coefficients were obtained by dividing the apparent rate coefficient by the apparent rate coefficient in 1.0 M KCl at the same particle concentration and by multiplying this ratio by the absolute aggregation rate coefficient in 1.0 M KCl.

## RESULTS

Charging and aggregation of negatively charged sulfate latex particles and positively charged amidine particles were investigated in monovalent electrolyte solutions at pH 4.0 by electrophoresis and time-resolved DLS. The solution composition was systematically varied, whereby  $\text{N}(\text{CH}_3)_4\text{Cl}$ ,  $\text{NH}_4\text{Cl}$ , CsCl, KCl, NaCl, and LiCl were used to vary cations, while the anions were investigated with  $\text{NaH}_2\text{PO}_4$ , NaF, NaCl, NaBr,  $\text{NaNO}_3$ , and NaSCN. In this way, the influence of both counter- and co-ions could be addressed. Since these ions are situated within the Hofmeister series, the relation between particle aggregation rates and the position within this series will be clarified.

**General Trends.** The electrophoretic mobility of the particles is shown versus the salt concentration for the sulfate particle in Figures 2a and 3a, while for the amidine particles, in

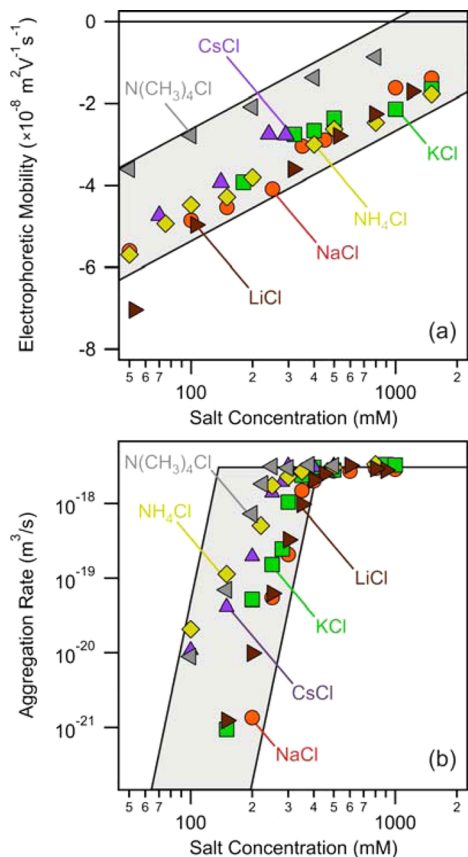


**Figure 2.** Charging and aggregation of negatively charged sulfate latex particles as a function of the concentration of various monovalent chloride salts of different cations: (a) electrophoretic mobilities and (b) aggregation rate coefficients. The gray region represents an envelope of all experimental data points.

Figures 4a and 5a. The magnitude of electrophoretic mobility typically decreases with the salt concentration due to screening of the surface charge. At low salt concentrations, negative and positive mobilities were observed for the sulfate and amidine latex particles, respectively. This sign reflects the charge of the ionized surface functional groups at pH 4.0. The actual values of the electrophoretic mobilities depend on the type of ions, and these trends will be discussed later.

Absolute particle aggregation rate coefficients are shown versus the salt concentration for the sulfate particle in Figures 2b and 3b and for the amidine particles in Figures 4b and 5b. At low salt concentration, the absolute aggregation rates are small. This behavior is referred to as the slow or reaction controlled regime, and the rate coefficients increase with the salt concentration strongly. At higher salt concentrations, the aggregation rate coefficients become large. Here, one has the fast or diffusion controlled regime, and the rate coefficients are almost independent of the salt level. The critical coagulation concentration was identified as the transition point between the slow and fast aggregation regimes. While the CCC depends sensitively on the type of ion present, no systematic trends concerning the aggregation rates in the slow regime could be established.

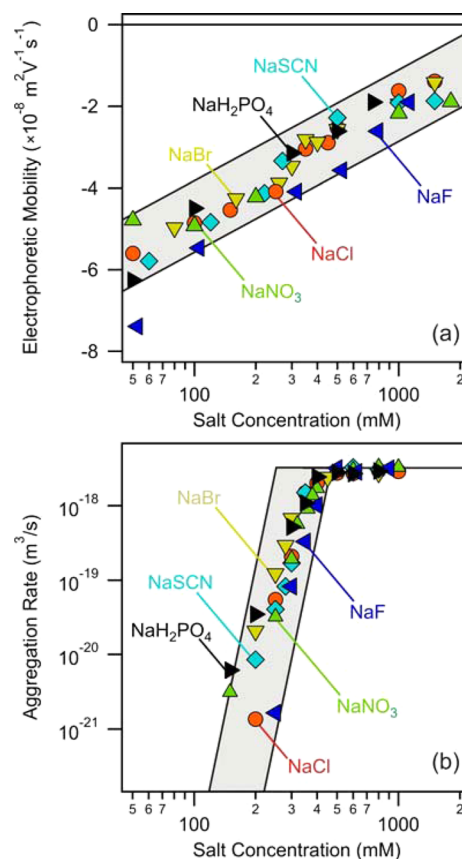


**Figure 3.** Charging and aggregation of negatively charged sulfate latex particles as a function of the concentration of various monovalent sodium salts of different anions: (a) electrophoretic mobilities and (b) aggregation rate coefficients. The gray region represents an envelope of all experimental data points.

**Fast Aggregation Regime.** When investigating eventual ion specific effects on aggregation rates at high electrolyte concentrations, one must realize that viscosities of concentrated electrolyte solution may significantly deviate from the one of pure water. The rate coefficients in the diffusion controlled regime may therefore vary, since the diffusion coefficient of the particles depends on the solution viscosity. In order to take this effect into account, known dynamic viscosities,  $\eta$ , of the salt solutions investigated here were considered.<sup>57,58</sup> To simplify the data analysis, the experimental viscosity data were represented with the relation<sup>10</sup>

$$\eta/\eta_0 = 1 + A\sqrt{c} + Bc + Dc^2 \quad (4)$$

where  $\eta_0 = 8.90 \times 10^{-4}$  Pa·s is the dynamic viscosity of water at 25 °C while  $A$ ,  $B$ , and  $D$  are constants. The constant  $A$  was calculated from the Debye–Hückel theory,<sup>10</sup> while  $B$  and  $D$  were obtained by least-squares fits to the experimental viscosity data. The resulting constants are reported in Supporting Information Table S1. To compare the experimental aggregation rates, the aggregation rate coefficients were normalized with the diffusion controlled aggregation rate coefficient,  $k_s$ , obtained from Smoluchowski's theory<sup>15,28</sup>

$$k_s = \frac{8k_B T}{3\eta} = 1.23 \times 10^{-17} \text{ m}^3/\text{s} \quad (5)$$

where  $k_B$  is the Boltzmann constant,  $T$  is the absolute temperature, and the numerical value refers to water at 25 °C.



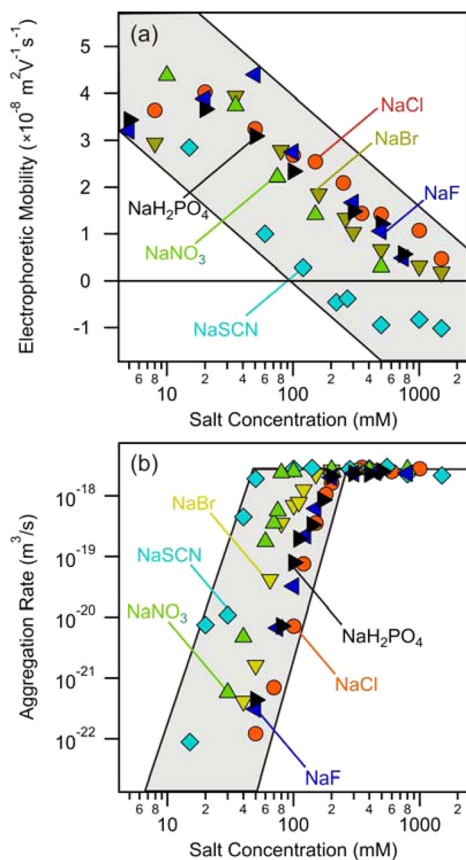


**Figure 4.** Charging and aggregation of positively charged amidine latex particles as a function of the concentration of various monovalent sodium salts of different anions: (a) electrophoretic mobilities and (b) aggregation rate coefficients. The gray region represents an envelope of all experimental data points.

The averaged normalized rate coefficients  $k/k_s$  above the CCC are shown in Figure 6a. These normalized rates are independent of the type of ions within the experimental error. Moreover, these normalized coefficients are very similar for the two types of particles used, namely,  $0.26 \pm 0.01$  for the sulfate latex and  $0.23 \pm 0.01$  for the amidine latex. However, this normalized coefficient may depend on the type of particle used. This point was established by reanalyzing fast aggregation rates of latex particles in nine different salt solutions, which include multivalent ions, which were published earlier by us.<sup>26</sup> These data include carboxyl and sulfate latex particles. The latter sulfate latex particles are different from the one used here. When the aggregation rate coefficients are normalized by Smoluchowski's rates including the correct viscosities, we find again no dependence on the type of ions present. However, the normalized rate coefficients differ from the values reported earlier. For the carboxyl latex particles, one finds  $0.16 \pm 0.01$ , while for the latter sulfate particles  $0.29 \pm 0.01$ . The fact that the normalized aggregation rates vary with the particle type somewhat is probably related to their variable polymeric compositions, which originates from the differing conditions during synthesis. Differences in surface roughness may equally contribute.<sup>59</sup> However, when the same type of particles is considered, the normalized fast aggregation rate coefficients are independent of the type of salt. This observation suggests that attractive forces acting in the fast aggregation regime are not influenced by the nature of the ions present. These

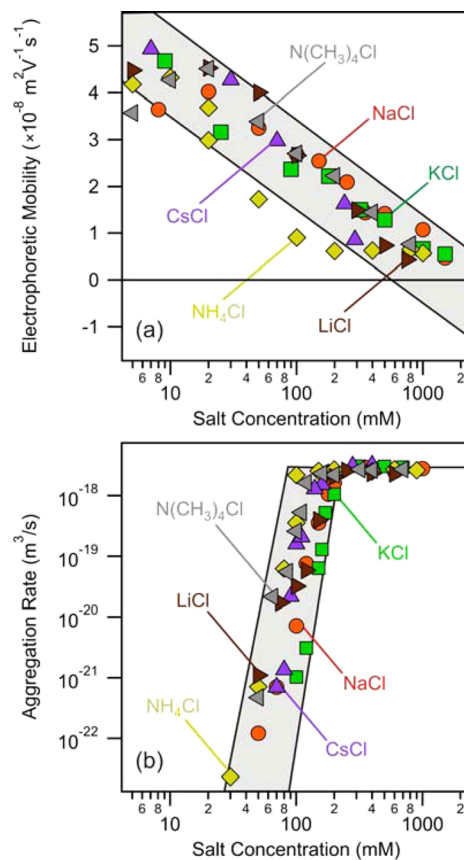


**Figure 5.** Charging and aggregation of positively charged amidine latex particles as a function of the concentration of various monovalent chloride salts of different cations: (a) electrophoretic mobilities and (b) aggregation rate coefficients. The gray region represents an envelope of all experimental data points.

experimental results should be contrasted with earlier reports, where a modest variation of the fast aggregation rate on the type of salt was reported.<sup>17,51</sup> In our view, however, these results are hardly conclusive, since viscosity corrections were not considered in these studies.

**Specific Ion Effects on Negatively Charged Sulfate Latex.** The electrophoretic mobility at given salt concentrations decreases with the type of cation from  $N(CH_3)_4^+$  to  $Li^+$ . This sequence reflects the expected direct Hofmeister series; namely,  $N(CH_3)_4^+ < NH_4^+ < Cs^+ < K^+ < Na^+ < Li^+$  (Figure 2a). This trend in the electrophoretic mobility reflects the affinity of the different cations to the surface. Therefore, poorly hydrated  $N(CH_3)_4^+$  ion adsorbs most strongly to the hydrophobic latex particle surface and, hence, reduces the magnitude of the surface charge and of the mobility. The strongly hydrated  $Li^+$  ion adsorbs weakly on the particle surface, or not at all, and the magnitudes of the surface charge and of the mobility are therefore the largest.

The CCC, which reflects the transition between the fast and slow regime, systematically varies with the type of cation (Figure 2b). The CCC shifts from low to high values following the direct Hofmeister series; namely,  $N(CH_3)_4^+ < NH_4^+ < Cs^+ < K^+ < Na^+ < Li^+$  (Figure 6b). This trend is expected for a negatively charged hydrophobic surface. The poorly hydrated  $N(CH_3)_4^+$  ion adsorbs strongly to the surface, thereby reducing the magnitude of surface charge, and therefore the CCC. On the other hand, well hydrated  $Li^+$  ion induces the highest CCC,

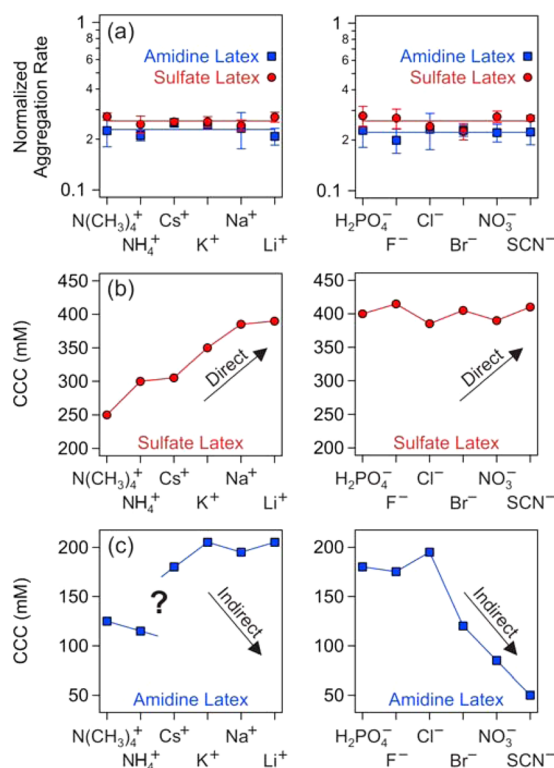


**Figure 6.** Characteristics of the latex particle aggregation versus the position in the Hofmeister series. The effect of cations is shown in the left column, while of the anions, in the right column. (a) Aggregation rate coefficients in the fast regime normalized by the Smoluchowski value. The error bars represent three times the standard deviation. CCCs for (b) sulfate particles and (c) amidine particles. The arrows indicate the expected trends from direct or indirect Hofmeister series. The lines serve to guide the eye only.

since the surface charge is high due to weak adsorption of this ion. These results are in agreement with molecular dynamic simulations at hydrophobic surfaces.<sup>40</sup> One further observes that the CCCs for  $Li^+$  and  $Na^+$  are almost identical, suggesting that these two ions do not adsorb to the surface at all. Similar trends in the CCCs following the direct Hofmeister series as typical for a negatively charged hydrophobic substrate were previously reported for various systems, including montmorillonite, silver iodide, and heat-treated titania.<sup>21,24,25</sup> The same trend was also documented for negatively charged polystyrene latex, but with  $Na^+$  and  $NH_4^+$  ions only.<sup>18,20</sup> When the particles are weakly charged, there are no ion specific effects on the charging and aggregation behavior in the presence of  $Na^+$ ,  $K^+$ , and  $Cs^+$  for iron oxide, titania, and carboxylate latex.<sup>21,23,26</sup> In this situation, the cations do not interact with the surface specifically.

Co-ions have no effect on the charging and aggregation of the sulfate latex particles (Figure 3). The electrophoretic mobilities are similar for all ions investigated, with the exception of  $F^-$ , which induces somewhat lower mobilities. The CCCs are identical within experimental error, and they have the value of  $400 \pm 10$  mM (Figure 6b). One might expect that the CCCs also follow the direct Hofmeister series  $H_2PO_4^-$ ,  $F^-$ ,  $Cl^-$ ,  $Br^-$ ,  $NO_3^-$ , and  $SCN^-$ . The poorly hydrated anions, such as  $NO_3^-$  and  $SCN^-$ , should adsorb more strongly to the negatively charged hydrophobic latex surface and induce an even higher magnitude of charge. However, such dependencies can be evidenced neither from the electrophoresis nor from the

CCC. Therefore, we conclude that these anions do not adsorb on the particle surface, due to its high negative surface charge. The present observations are similar to earlier studies, where only a weak dependence of the CCC of sulfate latex particles with the type of anion was found.<sup>17,18,20</sup>

To investigate ion specific effects on charging and aggregation of negatively charged particles, an indifferent anion must be chosen. As will become obvious in the next section, such an anion is the chosen  $Cl^-$ . Anions that are strongly interacting with the particle surface, such as  $NO_3^-$ , make the interpretation more difficult.<sup>18</sup>

**Specific Ion Effects on Positively Charged Amidine Latex.** At sufficiently low salt concentration, the electrophoretic mobility at given concentration decreases approximately in the sequence  $H_2PO_4^- > F^- > Cl^- > Br^- > NO_3^- > SCN^-$ , reflecting the indirect Hofmeister series (Figure 4a). This trend in the electrophoretic mobility was also found for other positively charged latex particles<sup>17,19,20</sup> and reflects the affinity of the different anions to the surface. Strongly hydrated anions, such as  $H_2PO_4^-$  or  $F^-$ , interact weakly with the hydrophobic latex particle surface. The poorly hydrated anions, such as  $NO_3^-$  or  $SCN^-$ , interact more strongly with the surface, and their adsorption reduces the surface charge. The adsorption of  $SCN^-$  is so pronounced that a charge reversal is induced. Such charge reversal has been observed for highly charged multivalent ions<sup>60,61</sup> but also for other strongly adsorbing monovalent ions.<sup>19,43</sup>

The CCCs decrease in the same sequence reflecting the expected indirect Hofmeister series (Figures 4b and 6c). However, a pronounced decrease of the CCC is only observed in the series  $Cl^- > Br^- > NO_3^- > SCN^-$ , while in the presence of  $H_2PO_4^-$ ,  $F^-$ , and  $Cl^-$  the CCC remains practically constant. This constancy indicates that the latter ions are basically indifferent and do not adsorb on the particle surface. Similar specificities involving  $Cl^-$ ,  $NO_3^-$ , and  $SCN^-$  ions were also reported for the CCCs for sulfate latex particles earlier.<sup>17,18,20</sup> However, the indifference for the other ions was not reported for latex so far, but only for weakly charged titania.<sup>21</sup> The observed trends in the CCCs agree with the ones predicted theoretically based on the ionic polarizability, except that the positions of  $Br^-$  and  $NO_3^-$  are reversed.<sup>41</sup>

In the presence of various co-ions, namely,  $Cs^+$ ,  $K^+$ ,  $Na^+$ , and  $Li^+$ , the measured electrophoretic mobilities and CCCs were very similar (Figures 5 and 6c). Since the affinity of these ions toward the surface decreases in the same sequence, one would expect that the CCCs follow the indirect Hofmeister series. However, no systematic dependence could be established, and the CCC remains constant at  $200 \pm 10$  mM. We suspect that these ions interact with the highly positively charged surface too weakly. Nitrogen-containing ions, namely,  $N(CH_3)_4^+$  and  $NH_4^+$ , behave irregularly. The indirect Hofmeister series would suggest higher CCCs, but the measured values are substantially lower than for the remaining cations within the series. This discrepancy could be probably related to a specific interaction between the amidine groups on the particle surfaces and the nitrogen-containing ions (e.g., hydrogen bonding). These findings are similar to previous measurements of the CCCs for positively charged latex particles, where small shifts between  $Na^+$  and  $NH_4^+$  were reported.<sup>18,20</sup>

**Origin of Interparticle Forces.** A simplified form of DLVO theory was used to clarify ion specific effects on the CCCs. Electrophoretic mobilities,  $u$ , were converted to diffuse layer potentials,  $\psi_D$ , with the Smoluchowski equation<sup>15</sup>



$$u = \frac{\epsilon\epsilon_0}{\eta} \psi_D \quad (6)$$

where  $\epsilon_0$  is the permittivity of vacuum and  $\epsilon$  is the dielectric constant. We have  $\epsilon = 80$  for water at room temperature. The accuracy of the Smoluchowski equation was checked with the standard electrokinetic model.<sup>62</sup> For the particles and concentration range considered, both models agreed within 3%. The surface charge density  $\sigma$  was determined by fitting  $\psi_D$  at different salt levels with the Debye–Hückel charge-potential relationship<sup>15,28</sup>

$$\sigma = \epsilon\epsilon_0\kappa\psi_D \quad (7)$$

where  $\kappa$  is the inverse Debye length defined by

$$\kappa^2 = \frac{2N_A e^2 c}{\epsilon\epsilon_0 k_B T} \quad (8)$$

where  $c$  is the molar concentration of the monovalent electrolyte,  $N_A$  the Avogadro number, and  $e$  the elementary charge. While the resulting charge densities reflect the extent of the ion adsorption, an eventual influence of the variation of the position of the shear plane with the type of ions is neglected.<sup>28,63</sup> The CCC was estimated from DLVO theory, which assumes that the total interaction energy can be written as a superposition of electrostatic double layer energy,  $V_{dl}$ , and the van der Waals energy,  $V_{vdw}$ ; namely,

$$V = V_{dl} + V_{vdw} \quad (9)$$

By invoking the Derjaguin and superposition approximations, one has<sup>15,28</sup>

$$V_{dl} = 2\pi r \epsilon\epsilon_0 \psi_D^2 \exp(-\kappa h) \quad (10)$$

where  $r$  is the particle radius and  $h$  is the separation distance between particle surfaces. The van der Waals interaction energy is approximated with the nonretarded expression

$$V_{vdw} = -\frac{Hr}{12h} \quad (11)$$

where  $H$  is the Hamaker constant. The CCC can be located by assuming that the energy barrier just vanishes<sup>15</sup>

$$V(h_{\max}) = 0 \quad \text{and} \quad \left. \frac{dV}{dh} \right|_{h=h_{\max}} = 0 \quad (12)$$

where  $h_{\max}$  is the separation at the energy barrier. Combining eqs 9–12, one can express the CCC as<sup>18,29</sup>

$$\text{CCC} = \frac{0.365}{N_A L_B} (H\epsilon\epsilon_0)^{-2/3} \sigma^{4/3} \quad (13)$$

where  $L_B = e^2/(4\pi\epsilon\epsilon_0 k_B T)$  is the Bjerrum length, which is 0.72 nm at room temperature in water. Note that the preceding relation is only approximate, since accurate DLVO calculations show that the energy barrier does not quite vanish at CCC.<sup>29</sup>

The calculated and experimental data given in Supporting Information Table S2 and Figure 7 show indeed a good correlation between the CCCs and the surface charge density. The straight line obtained from DLVO theory agrees with the experimental data reasonably well with the exception of the  $\text{NH}_4^+$  ion which is probably influenced by specific interactions with the amidine groups on the particle surface. By fitting eq 13 to the data, a Hamaker constant of  $H = 1.2 \times 10^{-20}$  J is found. The charge density for the sulfate latex measured by conductometric titration is  $-77 \text{ mC/m}^2$  and agrees quite well

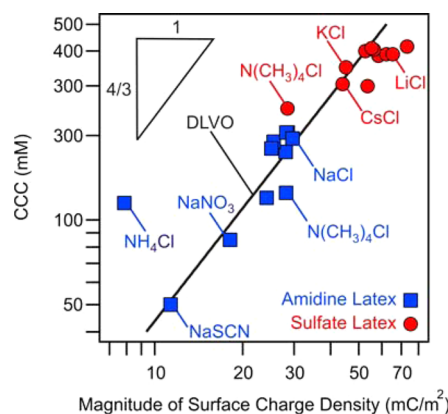


**Figure 7.** Comparison of experimental CCC values for the sulfate and amidine latex particles with DLVO theory. The data are plotted versus the magnitude of surface charge density, which was estimated from the electrophoretic mobility. The DLVO theory uses the superposition approximation to calculate the double layer interactions.

in magnitude with the highest charge densities reported in Figure 7, which refer to indifferent ions. On the other hand, the titrated charge of the amidine latex of  $+132 \text{ mC/m}^2$  reported by the manufacturer is probably too high, since Figure 7 rather suggests a charge density around  $+30 \text{ mC/m}^2$ .

The relatively good agreement between experimental data and DLVO theory indicates that the main reason for the ionic specificity is the modification of the surface charge through adsorption of these ions. Poorly hydrated counterions adsorb strongly on the hydrophobic latex particle surface, thereby decrease the magnitude of the surface charge and the CCC. Well hydrated counterions adsorb weakly, or not at all, and they hardly influence the surface charge and typically lead to high CCCs. The co-ions do not adsorb, and they influence the surface charge and the CCC only slightly. Similar trends were observed for charging of oxide particles,<sup>33,36</sup> while the reverse trends were obtained for silica at high pH.<sup>34,35,38</sup>

The fitted Hamaker constant  $H = 1.2 \times 10^{-20}$  J is in good agreement with the value of  $1.0 \times 10^{-20}$  J that is obtained from the full Lifshitz calculation.<sup>59,64</sup> However, these values are factors of 3–5 larger than the Hamaker constants of similar latex particles that were actually measured with the colloidal probe technique.<sup>59</sup> The reduction of these values is probably due to surface roughness. When one assumes that the presently used latex particles have comparably smaller Hamaker constants, the observed values of the CCCs indicate the presence of additional attractive non-DLVO forces. The substantial scatter of the data points in Figure 7 also points toward possible variation of the distance of the shear plane with the nature of the ion, or the importance of additional forces, which are most probably of hydrophobic nature.<sup>65</sup>

## CONCLUSION

Surface charge and aggregation of anionic and cationic polystyrene latex particles were investigated in the presence of various monovalent electrolytes by electrophoresis and time-resolved light scattering. Sodium salts of  $\text{H}_2\text{PO}_4^-$ ,  $\text{F}^-$ ,  $\text{Cl}^-$ ,  $\text{Br}^-$ ,  $\text{NO}_3^-$ , and  $\text{SCN}^-$  were used to probe the effect of anions, while with chloride salts of  $\text{N}(\text{CH}_3)_4^+$ ,  $\text{NH}_4^+$ ,  $\text{Cs}^+$ ,  $\text{K}^+$ ,  $\text{Na}^+$ , and  $\text{Li}^+$  the cations were varied. These ions interact with oppositely charged particle surfaces specifically. They normally adsorb, and thereby modify, the surface charge and the CCC. Poorly hydrated counterions, such as  $\text{N}(\text{CH}_3)_4^+$  and  $\text{SCN}^-$ , adsorb to

the oppositely charged surfaces more strongly, and they lower the magnitude of the surface charge and the CCC substantially. Strongly hydrated counterions, such as  $\text{Li}^+$  or  $\text{F}^-$ , do not adsorb, and lead to high magnitudes of the surface charge and high CCCs. For some well hydrated counterions, the CCC remains independent of the type of ion. In this regime, we suspect that these ions do not adsorb to the particle surface at all. On the other hand, these ions interact only weakly with equally charged surfaces, and the CCCs are basically independent of the nature of the co-ion. Moreover, we have demonstrated that the aggregation rate in the fast regime does not depend on the type of ions present but only on the type of particles.

DLVO theory can be used to confirm that the principal mechanism responsible for the shifts of the CCCs originates from modification of the surface charge. The dependence of the CCC on the surface charge density obtained from electrophoresis agrees well with DLVO theory. However, the Hamaker constant obtained by fitting the experimental CCC data is probably somewhat high, indicating the presence of additional non-DLVO forces.

## ■ ASSOCIATED CONTENT

### ● Supporting Information

Tables S1 and S2 with viscosity coefficients and experimental CCCs. This material is available free of charge via the Internet at <http://pubs.acs.org>.

## ■ AUTHOR INFORMATION

### Corresponding Author

\*E-mail: [istvan.szilagyi@unige.ch](mailto:istvan.szilagyi@unige.ch).

### Notes

The authors declare no competing financial interest.

## ■ ACKNOWLEDGMENTS

This research was supported by the Swiss National Science Foundation, the University of Geneva and the COST Action MP1106.

## ■ REFERENCES

- (1) Jungwirth, P.; Cremer, P. S. Beyond Hofmeister. *Nat. Chem.* **2014**, *6*, 261–263.
- (2) Zhang, Y. J.; Cremer, P. S. Chemistry of Hofmeister anions and osmolytes. *Annu. Rev. Phys. Chem.* **2010**, *61*, 63–83.
- (3) Lo Nostro, P.; Ninham, B. W. Hofmeister phenomena: An update on ion specificity in biology. *Chem. Rev.* **2012**, *112*, 2286–2322.
- (4) Weissenborn, P. K.; Pugh, R. J. Surface tension of aqueous solutions of electrolytes: Relationship with ion hydration, oxygen solubility, and bubble coalescence. *J. Colloid Interface Sci.* **1996**, *184*, 550–563.
- (5) Matubayasi, N.; Yamamoto, K.; Yamaguchi, S. I.; Matsuo, H.; Ikeda, N. Thermodynamic quantities of surface formation of aqueous electrolyte solutions—III. Aqueous solutions of alkali metal chloride. *J. Colloid Interface Sci.* **1999**, *214*, 101–105.
- (6) Diehl, A.; dos Santos, A. P.; Levin, Y. Surface tension of an electrolyte-air interface: A Monte Carlo study. *J. Phys.: Condens. Matter* **2012**, *24*.
- (7) Nihonyanagi, S.; Yamaguchi, S.; Tahara, T. Counterion effect on interfacial water at charged interfaces and its relevance to the Hofmeister series. *J. Am. Chem. Soc.* **2014**, *136*, 6155–6158.
- (8) Pozar, J.; Bohinc, K.; Vlachy, V.; Kovacevic, D. Ion-specific and charge effects in counterion binding to poly(styrene sulfonate) anions. *Phys. Chem. Chem. Phys.* **2011**, *13*, 15610–15618.
- (9) Salomaki, M.; Tervasmaki, P.; Areva, S.; Kankare, J. The Hofmeister anion effect and the growth of polyelectrolyte multilayers. *Langmuir* **2004**, *20*, 3679–3683.
- (10) Jenkins, H. D. B.; Marcus, Y. Viscosity B-coefficients of ions in solution. *Chem. Rev.* **1995**, *95*, 2695–2724.
- (11) dos Santos, A. P.; Diehl, A.; Levin, Y. Surface tensions, surface potentials, and the Hofmeister series of electrolyte solutions. *Langmuir* **2010**, *26*, 10778–10783.
- (12) Sowmiya, M.; Tiwari, A. K.; Sonu, Eranna, G.; Sharma, A. K.; Saha, S. K. Study of the binding interactions of a hemicyanine dye with nanotubes of beta-cyclodextrin and effect of a Hofmeister series of potassium salts. *J. Phys. Chem. C* **2014**, *118*, 2735–2748.
- (13) Medda, L.; Barse, B.; Cugia, F.; Bostrom, M.; Parsons, D. F.; Ninham, B. W.; Monduzzi, M.; Salis, A. Hofmeister challenges: Ion binding and charge of the BSA protein as explicit examples. *Langmuir* **2012**, *28*, 16355–16363.
- (14) Merk, V.; Rehbock, C.; Becker, F.; Hagemann, U.; Nienhaus, H.; Barcikowski, S. In situ non-DLVO stabilization of surfactant-free plasmonic gold nanoparticles: Effect of Hofmeister's anions. *Langmuir* **2014**, *30*, 4213–4222.
- (15) Evans, D. F.; Wennerstrom, H. *The Colloidal Domain*; John Wiley: New York, 1999.
- (16) Wang, D. W.; Tejerina, B.; Lagzi, I.; Kowalczyk, B.; Grzybowski, B. A. Bridging interactions and selective nanoparticle aggregation mediated by monovalent cations. *ACS Nano* **2011**, *5*, 530–536.
- (17) Lopez-Leon, T.; Ortega-Vinuesa, J. L.; Bastos-Gonzalez, D. Ion-specific aggregation of hydrophobic particles. *ChemPhysChem* **2012**, *13*, 2382–2391.
- (18) Lopez-Leon, T.; Santander-Ortega, M. J.; Ortega-Vinuesa, J. L.; Bastos-Gonzalez, D. Hofmeister effects in colloidal systems: Influence of the surface nature. *J. Phys. Chem. C* **2008**, *112*, 16060–16069.
- (19) Lopez-Leon, T.; Jodar-Reyes, A. B.; Ortega-Vinuesa, J. L.; Bastos-Gonzalez, D. Hofmeister effects on the colloidal stability of an IgG-coated polystyrene latex. *J. Colloid Interface Sci.* **2005**, *284*, 139–148.
- (20) Lopez-Leon, T.; Jodar-Reyes, A. B.; Bastos-Gonzalez, D.; Ortega-Vinuesa, J. L. Hofmeister effects in the stability and electrophoretic mobility of polystyrene latex particles. *J. Phys. Chem. B* **2003**, *107*, 5696–5708.
- (21) Dumont, F.; Warlus, J.; Watillon, A. Influence of the point of zero charge of titanium-dioxide hydrosols on the ionic adsorption sequences. *J. Colloid Interface Sci.* **1990**, *138*, 543–554.
- (22) Peula-Garcia, J. M.; Ortega-Vinuesa, J. L.; Bastos-Gonzalez, D. Inversion of Hofmeister series by changing the surface of colloidal particles from hydrophobic to hydrophilic. *J. Phys. Chem. C* **2010**, *114*, 11133–11139.
- (23) Dumont, F.; Watillon, A. Stability of ferric oxide hydrosols. *Discuss. Faraday Soc.* **1971**, *52*, 352–380.
- (24) Tian, R.; Yang, G.; Li, H.; Gao, X. D.; Liu, X. M.; Zhu, H. L.; Tang, Y. Activation energies of colloidal particle aggregation: Towards a quantitative characterization of specific ion effects. *Phys. Chem. Chem. Phys.* **2014**, *16*, 8828–8836.
- (25) Tezak, B.; Matijevic, E.; Schulz, K. F. Coagulation of hydrophobic sols in statu nascendi. III. The influence of the ionic size and valency of the counterion. *J. Phys. Chem.* **1955**, *59*, 769–773.
- (26) Oncsik, T.; Trefalt, G.; Csendes, Z.; Szilagyi, I.; Borkovec, M. Aggregation of negatively charged colloidal particles in the presence of multivalent cations. *Langmuir* **2014**, *30*, 733–741.
- (27) Schneider, C.; Hanisch, M.; Wedel, B.; Jusufi, A.; Ballauff, M. Experimental study of electrostatically stabilized colloidal particles: Colloidal stability and charge reversal. *J. Colloid Interface Sci.* **2011**, *358*, 62–67.
- (28) Elimelech, M.; Gregory, J.; Jia, X.; Williams, R. A. *Particle Deposition and Aggregation: Measurement, Modeling, and Simulation*; Butterworth-Heinemann: Oxford, U.K., 1995.
- (29) Trefalt, G.; Szilagyi, I.; Borkovec, M. Poisson-Boltzmann description of interaction forces and aggregation rates involving charged colloidal particles in asymmetric electrolytes. *J. Colloid Interface Sci.* **2013**, *406*, 111–120.

- (30) Behrens, S. H.; Borkovec, M.; Schurtenberger, P. Aggregation in charge-stabilized colloidal suspensions revisited. *Langmuir* **1998**, *14*, 1951–1954.
- (31) Lin, W.; Galletto, P.; Borkovec, M. Charging and aggregation of latex particles by oppositely charged dendrimers. *Langmuir* **2004**, *20*, 7465–7473.
- (32) Kobayashi, M.; Skarba, M.; Galletto, P.; Cakara, D.; Borkovec, M. Effects of heat treatment on the aggregation and charging of Stöber-type silica. *J. Colloid Interface Sci.* **2005**, *292*, 139–147.
- (33) Spryca, R. Electrical double-layer at alumina electrolyte interface 1. Surface-charge and zeta potential. *J. Colloid Interface Sci.* **1989**, *127*, 1–11.
- (34) Tadros, T. F.; Lyklema, J. Adsorption of potential determining ions at silica-aqueous electrolyte interface and role of some cations. *J. Electroanal. Chem.* **1968**, *17*, 267–275.
- (35) Abendroth, R. P. Behavior of a pyrogenic silica in simple electrolytes. *J. Colloid Interface Sci.* **1970**, *34*, 591–596.
- (36) Breeuwsma, A.; Lyklema, J. Interfacial electrochemistry of hematite ( $\alpha$ -Fe<sub>2</sub>O<sub>3</sub>). *Discuss. Faraday Soc.* **1971**, *52*, 324–333.
- (37) Dishon, M.; Zohar, O.; Sivan, U. From repulsion to attraction and back to repulsion: The effect of NaCl, KCl, and CsCl on the force between silica surfaces in aqueous solution. *Langmuir* **2009**, *25*, 2831–2836.
- (38) Morag, J.; Dishon, M.; Sivan, U. The governing role of surface hydration in ion specific adsorption to silica: An AFM-based account of the Hofmeister universality and its reversal. *Langmuir* **2013**, *29*, 6317–6322.
- (39) Schwierz, N.; Horinek, D.; Netz, R. R. Reversed anionic Hofmeister series: The interplay of surface charge and surface polarity. *Langmuir* **2010**, *26*, 7370–7379.
- (40) Schwierz, N.; Horinek, D.; Netz, R. R. Anionic and cationic Hofmeister effects on hydrophobic and hydrophilic surfaces. *Langmuir* **2013**, *29*, 2602–2614.
- (41) dos Santos, A. P.; Levin, Y. Ion specificity and the theory of stability of colloidal suspensions. *Phys. Rev. Lett.* **2011**, *106*.
- (42) Huang, H. H.; Ruckenstein, E. Effect of hydration of ions on double-layer repulsion and the Hofmeister series. *J. Phys. Chem. Lett.* **2013**, *4*, 3725–3727.
- (43) Calero, C.; Farauto, J.; Bastos-Gonzalez, D. Interaction of monovalent ions with hydrophobic and hydrophilic colloids: Charge inversion and ionic specificity. *J. Am. Chem. Soc.* **2011**, *133*, 15025–15035.
- (44) Yates, D. E.; Healy, T. W. Titanium-dioxide electrolyte interface 2. Surface-charge (titration) studies. *J. Chem. Soc., Faraday Trans. 1* **1980**, *76*, 9–18.
- (45) Franks, G. V. Zeta potentials and yield stresses of silica suspensions in concentrated monovalent electrolytes: Isoelectric point shift and additional attraction. *J. Colloid Interface Sci.* **2002**, *249*, 44–51.
- (46) Dove, P. M.; Craven, C. M. Surface charge density on silica in alkali and alkaline earth chloride electrolyte solutions. *Geochim. Cosmochim. Acta* **2005**, *69*, 4963–4970.
- (47) Bijsterbosch, B. H.; Lyklema, J. Interfacial electrochemistry of silver iodide. *Adv. Colloid Interface Sci.* **1978**, *9*, 147–251.
- (48) Yang, Z.; Li, Q. F.; Chou, K. C. Structures of water molecules at the interfaces of aqueous salt solutions and silica: Cation effects. *J. Phys. Chem. C* **2009**, *113*, 8201–8205.
- (49) Abe, T.; Kobayashi, S.; Kobayashi, M. Aggregation of colloidal silica particles in the presence of fulvic acid, humic, acid or alginate: Effects of ionic composition. *Colloids Surf., A* **2011**, *379*, 21–26.
- (50) Chen, K. L.; Mylon, S. E.; Elimelech, M. Enhanced aggregation of alginate-coated iron oxide (hematite) nanoparticles in the presence of calcium, strontium and barium cations. *Langmuir* **2007**, *23*, 5920–5928.
- (51) Holthoff, H.; Egelhaaf, S. U.; Borkovec, M.; Schurtenberger, P.; Sticher, H. Coagulation rate measurements of colloidal particles by simultaneous static and dynamic light scattering. *Langmuir* **1996**, *12*, 5541–5549.
- (52) Sandkuhler, P.; Lattuada, M.; Wu, H.; Sefcik, J.; Morbidelli, M. Further insights into the universality of colloidal aggregation. *Adv. Colloid Interface Sci.* **2005**, *113*, 65–83.
- (53) Szilagyi, I.; Szabo, T.; Desert, A.; Trefalt, G.; Oncsik, T.; Borkovec, M. Particle aggregation mechanisms in ionic liquids. *Phys. Chem. Chem. Phys.* **2014**, *16*, 9515–9524.
- (54) Mishchenko, M. I.; Travis, L. D.; Lacis, A. A. *Scattering, Absorption, and Emission of Light by Small Particles*; University Press: Cambridge, U.K., 2002.
- (55) Lin, W.; Kobayashi, M.; Skarba, M.; Mu, C.; Galletto, P.; Borkovec, M. Heteroaggregation in binary mixtures of oppositely charged colloidal particles. *Langmuir* **2006**, *22*, 1038–1047.
- (56) Yu, W. L.; Matijevic, E.; Borkovec, M. Absolute heteroaggregation rate constants by multiangle static and dynamic light scattering. *Langmuir* **2002**, *18*, 7853–7860.
- (57) Desnoyers, J. E.; Perron, G. The viscosity of aqueous solutions of alkali and tetraalkylammonium halides at 25 degrees C. *J. Solution Chem.* **1972**, *1*, 199–212.
- (58) Weast, R. C.; Astle, M. J. *CRC Handbook of Chemistry and Physics*, 60th ed.; CRC Press: New York, 1980.
- (59) Elzbiaciak-Wodka, M.; Popescu, M.; Montes Ruiz-Cabello, F. J.; Trefalt, G.; Maroni, P.; Borkovec, M. Measurements of dispersion forces between colloidal latex particles with the atomic force microscope and comparison with Lifshitz theory. *J. Chem. Phys.* **2014**, *140*, No. 104906.
- (60) Sadeghpour, A.; Szilagyi, I.; Borkovec, M. Charging and aggregation of positively charged colloidal latex particles in presence of multivalent polycarboxylate anions. *Z. Phys. Chem.* **2012**, *226*, 597–612.
- (61) Sinha, P.; Szilagyi, I.; Montes Ruiz-Cabello, F. J.; Maroni, P.; Borkovec, M. Attractive forces between charged colloidal particles induced by multivalent ions revealed by confronting aggregation and direct force measurements. *J. Phys. Chem. Lett.* **2013**, *4*, 648–652.
- (62) O'Brien, R. W.; White, L. R. Electrophoretic mobility of a spherical colloidal particle. *J. Chem. Soc., Faraday Trans. 2* **1978**, *74*, 1607–1626.
- (63) Diehl, A.; Levin, Y. Smoluchowski equation and the colloidal charge reversal. *J. Chem. Phys.* **2006**, *125*, No. 054902.
- (64) Bevan, M. A.; Prieve, D. C. Direct measurement of retarded van der Waals attraction. *Langmuir* **1999**, *15*, 7925–7936.
- (65) Montes Ruiz-Cabello, F. J.; Trefalt, G.; Csendes, Z.; Sinha, P.; Oncsik, T.; Szilagyi, I.; Maroni, P.; Borkovec, M. Predicting aggregation rates of colloidal particles from direct force measurements. *J. Phys. Chem. B* **2013**, *117*, 11853–11862.

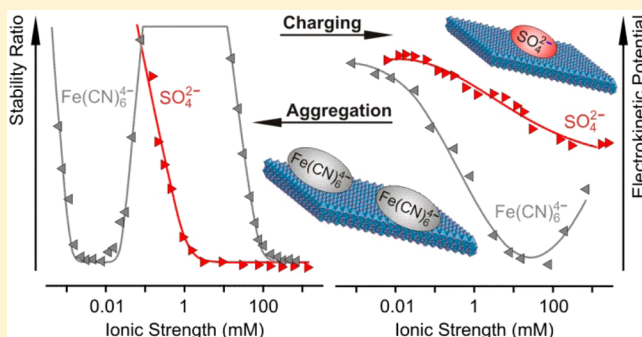


# Destabilization of Titania Nanosheet Suspensions by Inorganic Salts: Hofmeister Series and Schulze-Hardy Rule

Paul Rouster, Marko Pavlovic, and Istvan Szilagyi\*<sup>ID</sup>

Department of Inorganic and Analytical Chemistry, University of Geneva, CH-1205 Geneva, Switzerland

**ABSTRACT:** Ion specific effects on colloidal stability of titania nanosheets (TNS) were investigated in aqueous suspensions. The charge of the particles was varied by the pH of the solutions, therefore, the influence of mono- and multivalent anions on the charging and aggregation behavior could be studied when they were present either as counter or co-ions in the systems. The aggregation processes in the presence of inorganic salts were mainly driven by interparticle forces of electrostatic origin, however, chemical interactions between more complex ions and the surface led to additional attractive forces. The adsorption of anions significantly changed the surface charge properties and hence, the resistance of the TNS against salt-induced aggregation. On the basis of their ability in destabilization of the dispersions, the monovalent ions could be ordered according to the Hofmeister series in acidic solutions, where they act as counterions. However, the behavior of the biphosphate anion was atypical and its adsorption induced charge reversal of the particles. The multivalent anions destabilized the oppositely charged TNS more effectively and the aggregation processes followed the Schulze-Hardy rule. Only weak or negligible interactions were observed between the anions and the particles in alkaline suspensions, where the TNS possessed negative charge.

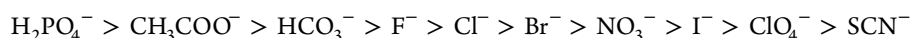


## INTRODUCTION

The influence of type and valence of dissolved salt constituents on fundamental phenomena such as conformation of polypeptides,<sup>1</sup> interaction forces between surfaces,<sup>2</sup> diffusion of proteins,<sup>3</sup> orientation of water molecules around ions,<sup>4</sup> aggregation of particles,<sup>5</sup> surface tension,<sup>6</sup> and charging<sup>7</sup> or association<sup>8</sup> of polyelectrolytes has been reported by numerous research groups in the past decades. Besides, the large number of recent reviews<sup>9–14</sup> also indicates widespread contemporary interest in the topic of ion specificity. Concerning the colloidal stability of particle suspensions in the presence of electrolytes, two major theories have been developed, namely, the Hofmeister series<sup>15</sup> and the Schulze-Hardy rule.<sup>16</sup>

As predicted by the classical theory developed by Derjaguin, Landau, Verwey, and Overbeek (DLVO),<sup>17–19</sup> charged

colloidal particles suspended in monovalent salt (i.e., cations and anions are in 1:1 molar ratio) solutions are stable at low ionic strengths, while they rapidly aggregate at higher electrolyte concentrations. The transition between such slow and fast aggregation regimes occurs at the critical coagulation concentration (CCC). The DLVO theory predicts the same CCC for the particles irrespectively of the type or composition of the monovalent salts. However, aggregation studies revealed that the CCC shifts upon variation of the chemical composition of these electrolytes.<sup>5,20–23</sup> Although this phenomenon cannot be explained by the DLVO theory, the order of CCCs for different ions usually follows the Hofmeister series.<sup>10</sup> For monovalent anions, the sequence can be given as



To apply this tendency to colloidal stability of suspensions, the sign of the charge and hydrophobicity of the particles have to be considered.<sup>10,12</sup> Accordingly, positively charged hydrophobic particles (e.g., layered double hydroxides<sup>22</sup>) follow the reversed Hofmeister series and the less hydrated anions on the right-hand side of the series induce lower CCC. Moreover, the ions on the left side destabilize hydrophilic particles (e.g., chitosan nanocapsules<sup>24</sup>) at lower concentrations indicating the direct Hofmeister series. For negatively charged particles, however, the tendency is the opposite and the trend in the

CCC of the hydrophobic particles (e.g., sulfonated latexes<sup>24</sup>) can be predicted by the direct series. The hydrophilic ones (e.g., protein-coated polystyrene particles<sup>24</sup>) follow the reserved order and hence, lower CCCs can be found in the presence of anions on the right-hand side. The effect of anions is

**Received:** May 5, 2017  
**Revised:** June 14, 2017  
**Published:** June 15, 2017

remarkable with negatively charged particles of lower surface charge, however, ion specificity was absent for highly charged particles of negative surface charge.<sup>20,21,25</sup>

Although certain multivalent anions (e.g.,  $\text{CO}_3^{2-}$  or  $\text{HPO}_4^{2-}$ ) have also been included in the traditional Hofmeister series, the effect of valence on particle aggregation has to be treated differently. The so-called Schulze-Hardy rule<sup>16,26</sup> states that the CCC strongly depends on the valence ( $z$ ) of the dissolved ions and the dependence can be quantified as

$$\text{CCC} \propto z^{-n} \quad (1)$$

The variation of the CCC by the valence can also be derived from the DLVO theory, however, the charge of the particles as well as the sign of the charge of the ions has to be considered. For asymmetric electrolytes containing multivalent counterions (i.e., ions of opposite sign of charge as the surface), the dependence can be quantified with  $n = 1.6$  in eq 1 for particles of low surface charge, while a stronger dependence of  $n = 6.5$  can be obtained for highly charged surfaces.<sup>25,27</sup> A weak influence ( $n = 1$ ) of the CCC by the valence of co-ions (i.e., ions of the same sign of charge as the surface) has also been reported.<sup>28,29</sup> Aggregation experiments carried out with latex,<sup>27,30,31</sup> carbon derivative,<sup>32</sup> clay,<sup>22</sup> and metal<sup>33</sup> particles confirmed the significant shift of the CCCs toward lower concentrations by increasing the valence.

Given their importance in consumer products<sup>34</sup> as well as in biomedical<sup>35</sup> and catalytic<sup>36</sup> applications, colloidal stability of titania particles in different ionic environments has been in the focus of several research groups in the past. For instance, photocatalytic activity of titania nanoparticles has been assessed in various salt solutions.<sup>37</sup> It was found that monovalent anions induced particle aggregation, while multivalent ions stabilized the particle dispersions via specific surface interactions. Such an adsorption process resulted in a competition for the active sites with contaminants and hydroxyl radicals and thus, significantly affected the catalytic activity of titania. Besides, ion specific effect on the structural properties of titania prepared by the sol-gel process has been reported.<sup>38</sup> Accordingly, variation of the type of monovalent salts in the reaction mixture led to different surface area due to the control of the ionic medium on the oxide network growth during the synthesis.

Moreover, the fundamental phenomena behind the aggregation of titania particles in the presence of mono or multivalent anions have been explored by various techniques. The charge of the particles was tuned by the pH, that is, positively charged titania was studied below the point of zero charge (PZC) and negatively charged ones above the PZC. In the latter case, comparison of results from light scattering experiments and theoretical calculations revealed that aggregation processes in synthetic titania suspensions can be well-described by the DLVO theory.<sup>39</sup> Besides, the CCC of positively charged titania particles was measured on the basis of the turbidity of the samples in the presence of different monovalent anions.<sup>40</sup> The sequence in the CCCs of the as-prepared particles followed the reversed Hofmeister series recommended for hydrophobic particles, however, most of the ion specific effect disappeared upon calcination of the titania due to the significant loss in the magnitude of the surface charge. In addition, the effect of monovalent and multivalent counterions on the stability of titania suspensions was studied above the PZC by photon correlation spectroscopy.<sup>41</sup> It was found that the CCC decreased with increasing the valence in agreement with the Schulze-Hardy rule. Apart from these studies, no systematic

investigation on the colloidal stability of titania in the presence of mono and multivalent anions (present as either counter or co-ions) has been published. More importantly, there is a lack of quantitative literature data on the aggregation rates and CCCs of titania particles of elongated structure such as rods, wires, or sheets. The growing number of applications of the titania materials of nonspherical shape calls for comprehensive investigation of their suspension stability in different ionic environments.

In the present work, charging and aggregation of synthetic titania nanosheets (TNS, structure is shown in Figure 1) were

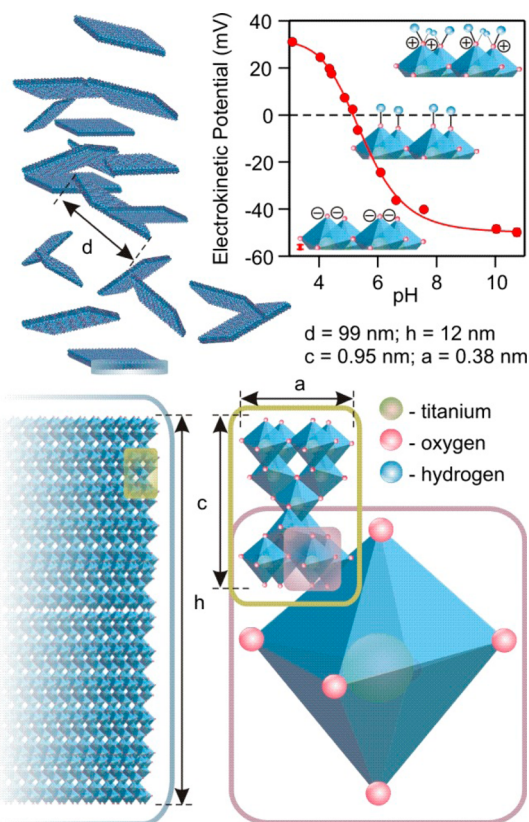


**Figure 1.** Schematic illustration of the structure of the TNS. The charging behavior is also presented by the electrokinetic potentials measured by electrophoresis in aqueous suspensions at different pHs and 1 mM ionic strength. Parameters  $d$  and  $h$  were measured by DLS and electron microscopy, respectively, whereas  $c$  and  $a$  were taken from the literature.<sup>65</sup>

studied in the presence of various mono and multivalent anions by electrophoresis and light scattering. The charge of the particles was tuned by the pH. Accordingly, positively charged TNS were investigated in the presence of different counterions below the PZC, while the influence of the co-ions was probed in alkaline suspensions above the PZC. The results were interpreted by means of the DLVO theory in principle, however, the tendencies in the destabilization power of the different anions were compared with the ones predicted by the Hofmeister series for the monovalent and the Schulze-Hardy rule for multivalent ions.

## EXPERIMENTAL METHODS

**Materials.** TNS was synthesized hydrothermally through a fluorinated intermediate product, as detailed elsewhere.<sup>42</sup> Analytical grade salts including KCl (Acros),  $\text{KNO}_3$  (Sigma),



KSCN (Acros),  $\text{KH}_2\text{PO}_4$  (Acros),  $\text{K}_2\text{SO}_4$  (Fluka),  $\text{K}_2\text{HPO}_4$  (Acros),  $\text{K}_3\text{Fe}(\text{CN})_6$  (Sigma), and  $\text{K}_4\text{Fe}(\text{CN})_6$  (Sigma) were used without further purification. The pH of the suspensions was adjusted by HCl (Sigma) and KOH (Sigma) and the measurements were carried out at 25 °C. High purity water (Millipore) was used for preparation of the samples in which TNS concentration was always kept at 1 mg/L.

**Methods.** Electrophoretic measurements were performed with a Zetasizer Nano ZS (Malvern) device to determine the electrophoretic mobilities ( $u$ ), which were converted to electrokinetic potentials ( $\zeta$ ) using Smoluchowski's model as<sup>43</sup>

$$\zeta = \frac{u\eta}{\epsilon_0\epsilon} \quad (2)$$

where  $\epsilon_0$  is the dielectric permittivity of the vacuum,  $\eta$  is the dynamic viscosity and  $\epsilon$  is the dielectric constant. The values of the two latter parameters in water at the temperature applied are  $8.9 \times 10^{-4}$  Pas and 78.5, respectively.

The hydrodynamic radius ( $R_h$ ) was obtained by dynamic light scattering (DLS) using a CGS-3 goniometer (ALV) at 90° scattering angle. Time-resolved measurements were carried out to determine the apparent aggregation rate coefficients ( $k_{\text{app}}$ ) as<sup>44</sup>

$$k_{\text{app}} = \frac{1}{R_h(0)} \left( \frac{dR_h(t)}{dt} \right)_{t \rightarrow 0} \quad (3)$$

where  $t$  is the time of the experiment and  $R_h(0)$  is the hydrodynamic radius of TNS measured in stable suspensions. The measurements were run for 20–60 min depending on the speed of aggregation.

## RESULTS

Similar to other titania compounds,<sup>37,39,45–49</sup> the TNS possess pH-dependent charge with a PZC of 5.2, as determined by electrophoresis (Figure 1).<sup>42</sup> Therefore, the effect of mono- and multivalent anions on the colloidal stability was investigated with positively and negatively charged nanosheets at pH 4 and 10, respectively. Surface charge properties were assessed by electrophoresis, while the aggregation processes were followed in time-resolved DLS experiments. Note that the experimental conditions (e.g., pH, salt, and TNS concentration) in a given suspension were exactly the same in both types of measurements. The competitive adsorption of ions on titania surfaces has previously been reported<sup>45,46,50</sup> and is expected in the present systems too. The influence of such processes on the colloidal stability will be clarified.

**Positively Charged TNS.** The ionization constants of the anions used in the study are given in Table 1. Accordingly at pH 4, monovalent anions include  $\text{Cl}^-$ ,  $\text{NO}_3^-$ ,  $\text{SCN}^-$ , and  $\text{H}_2\text{PO}_4^-$ , while  $\text{SO}_4^{2-}$  is divalent and  $\text{Fe}(\text{CN})_6^{3-}$  is trivalent. Note that 62% of the  $\text{Fe}(\text{CN})_6^{4-}$  ions are protonated at the respective pH.<sup>51</sup> Note also that the anions are the counterions, because the TNS is positively charged under this experimental condition.

Electrokinetic potentials measured at different ionic strengths are shown in Figure 2a. The shape of the plots was similar in the presence of  $\text{Cl}^-$ ,  $\text{NO}_3^-$ , and  $\text{SCN}^-$  anions and the potentials decrease with increasing the ionic strength. The values were the same within the experimental error for the first two anions, while slightly lower potentials were measured in the presence of the latter ion. Furthermore, the fact that the electrokinetic potentials turned to negative at high  $\text{SCN}^-$  concentrations

**Table 1. Ionization of the Inorganic Anions in Acidic and Alkaline Solutions**

anions <sup>a</sup>	$\text{pK}_1^b$	$\text{pK}_2^b$	$\text{pK}_3^b$	valence <sup>c</sup>	
				pH 4	pH 10
$\text{Cl}^-$	−0.71			1.00	1.00
$\text{NO}_3^-$	−1.40			1.00	1.00
$\text{SCN}^-$	−2.10			1.00	1.00
$\text{SO}_4^{2-}$	1.98	−2.00		1.99	2.00
$\text{PO}_4^{3-}$	12.35	7.21	2.14	0.99	2.00
$\text{Fe}(\text{CN})_6^{3-}$				3.00	3.00
$\text{Fe}(\text{CN})_6^{4-}$	4.20	2.00	−1.00	3.38 <sup>d</sup>	4.00

<sup>a</sup>Composition of anions shown in the fully ionized stage. <sup>b</sup>The protonation constants were taken from the Joint Expert Speciation System.<sup>51</sup> <sup>c</sup>Average valence calculated from the ionization equilibria at the respective pH. <sup>d</sup>The solution contains 38% of  $\text{Fe}(\text{CN})_6^{4-}$  and 62% of  $\text{HFe}(\text{CN})_6^{3-}$  at pH 4.

indicates significant adsorption of these anions on the oppositely charged TNS surfaces. The isoelectric point (IEP) is defined as the ionic strength, where the particles do not move in an electric field owing to the fact that their overall charge is zero.

Therefore, one can conclude that the decreasing charge with increasing electrolyte level is due to two effects, namely, charge screening by the salt and anion adsorption. The first one is present in all three systems, while the second phenomenon is more pronounced for  $\text{SCN}^-$  and exists in less extent in the other cases. Similar charging behavior was reported for positively charged titania particles in the presence of  $\text{Cl}^-$  and  $\text{NO}_3^-$  anions,<sup>37,52</sup> although comparison is difficult with previous results obtained with  $\text{SCN}^-$  due to the lack of systematic literature data with titania in the presence of this ion. However, adsorption of  $\text{SCN}^-$  on positively charged latex<sup>10,21</sup> or clay<sup>22</sup> particles and subsequent charge inversion was confirmed by electrophoresis.

The charging behavior of the TNS was found to be completely different in the presence of  $\text{H}_2\text{PO}_4^-$  counterions. The pK values of the  $\text{PO}_4^{3-}$  (Table 1) indicate the presence of solely monovalent anions in the suspensions at pH 4, nevertheless,  $\text{H}_2\text{PO}_4^-$  adsorption led to remarkable charge reversal of the particles, which showed the highest extent around 10 mM ionic strength. The potentials increased after this minimum due to the charge screening by the salt on the negatively charged nanosheets.

Such a characteristic charge neutralization and inversion was also observed with spherical titania particles at low pH in the presence of  $\text{H}_2\text{PO}_4^-$  ions.<sup>37,53</sup> Experimental<sup>54</sup> and theoretical<sup>55</sup> studies carried out with titania surfaces revealed that  $\text{H}_2\text{PO}_4^-$  binds as a bidental ligand to the titania surface atoms, that is, through two oxygens coordinated by the titanium(IV) ions of the solid. This binding mode results in extremely strong adsorption on the TNS particles and in accumulation of negative charges on the surfaces.

The tendencies of electrokinetic potentials in the biphosphate case were very similar to the ones in the presence of multivalent anions (Figure 2a). Namely, their adsorption decreased the TNS charge giving rise to charge neutralization at the IEP and subsequent charge reversal at higher ionic strengths. Toward very high salt concentrations, the potentials decreased, because the elevated level of the  $\text{K}^+$  counterions screen the surface charge and thus, the TNS move slower in the electric field. Comparing the potential data measured for the

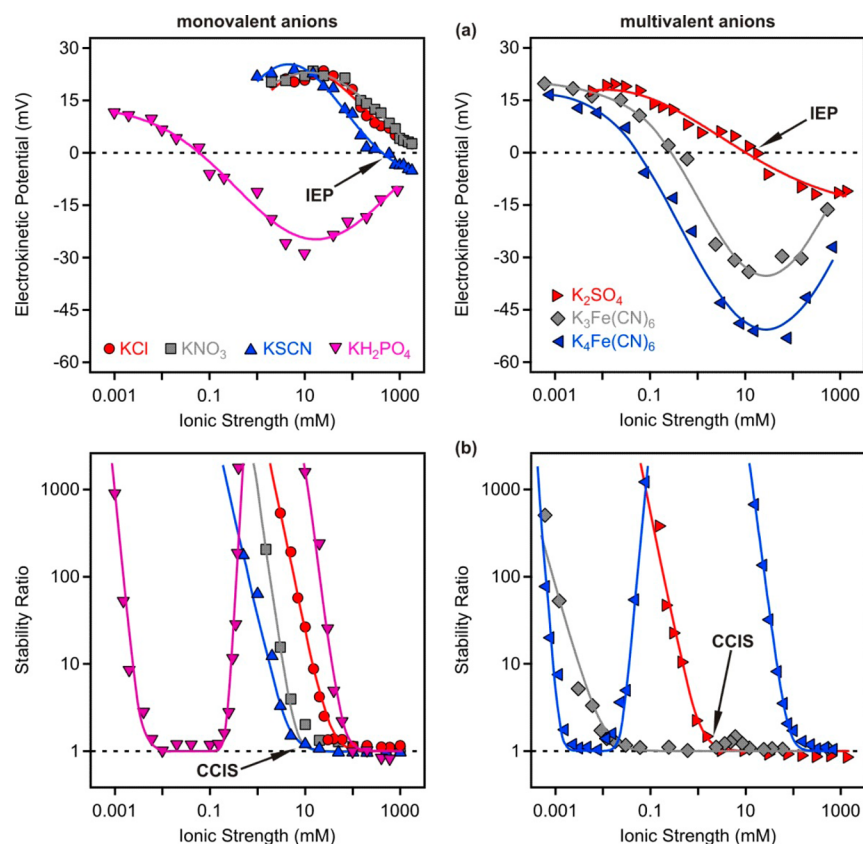


**Figure 2.** Electrokinetic potentials (a) and stability ratios (b) of TNS in the presence of monovalent (left column) and multivalent (right column) anions. The measurements were performed at pH 4 (positively charged particles) and 1 mg/L particle concentration. The solid lines in (a) serve to guide the eyes whereas in (b) show the results of calculations using eq 6.

positively charged nanosheets in solutions of  $\text{SO}_4^{2-}$ ,  $\text{Fe}(\text{CN})_6^{3-}$ , and  $\text{Fe}(\text{CN})_6^{4-}$  ions, two main features can be identified. First, the location of the IEP was shifted toward lower concentration by increasing the valence of the anions. Second, the extent of the charge reversal, that is, the magnitude of the potentials at the maximum charge inversion, also increased with the valence of the counterions. These phenomena are due to the increasing affinity of the anions to the positively charged surface by increasing their valence. Similar correlation between the surface charge and the valence of the adsorbing counterions was discovered on the basis of electrophoretic measurements performed with colloidal particles<sup>22,25,30,31</sup> including titania.<sup>46</sup> In addition, Monte Carlo calculations were carried out to describe the distribution of multivalent ions around and on charged colloidal particles<sup>56</sup> and planar surfaces.<sup>57</sup> These results and others<sup>58–60</sup> from model calculations also revealed that the strength of the counterion adsorption increases with the valence leading to a decreased effective charge and to charge reversal of the surfaces.

Comparing the electrokinetic potentials in the presence of  $\text{Fe}(\text{CN})_6^{3-}$  and  $\text{Fe}(\text{CN})_6^{4-}$ , the higher affinity of the latter anion to the TNS is clearly visible. However, the ionization equilibria (Table 1) shows that only 38% of the ions are present in the  $\text{Fe}(\text{CN})_6^{4-}$  form. The remaining part is protonated and the majority of the species is trivalent.<sup>51,61</sup> Given the significant difference of the charging properties of TNS in the presence of  $\text{Fe}(\text{CN})_6^{3-}$  and  $\text{Fe}(\text{CN})_6^{4-}$ , one can conclude that most of the ions close to the surface are tetravalent. Furthermore, the similar charging behavior of positively charged TNS in the presence of monovalent  $\text{H}_2\text{PO}_4^-$  and multivalent  $\text{Fe}(\text{CN})_6^{3-}$  or

$\text{Fe}(\text{CN})_6^{4-}$  ions is owing to the specific adsorption of the  $\text{H}_2\text{PO}_4^-$  via bidentate coordination to the surface, which resulted in high surface density of the  $\text{H}_2\text{PO}_4^-$  molecules and in a pronounced charge inversion. Deprotonation of these anions upon adsorption can also be feasible, however, no experimental evidence were obtained for this feature.

The colloidal stability of the suspensions was assessed in time-resolved DLS measurements. The apparent rate constants (eq 3) were measured and the speed of aggregation was expressed in terms of stability ratio ( $W$ ) as<sup>44</sup>

$$W = \frac{k_{\text{app}}(\text{fast})}{k_{\text{app}}} \quad (4)$$

where fast refers to fast or diffusion controlled aggregation of the particles. One can easily realize that  $W = 1$  in the case of unstable suspensions and higher values indicate slower aggregation and thus, more stable samples. Stability ratios for positively charged TNS in the presence of mono and multivalent anions are presented in Figure 2b. Note that the experimental conditions (e.g., pH, ionic strength range and TNS concentration) were the same as in the electrophoretic studies, therefore, the corresponding charging and aggregation features will be discussed together later.

For  $\text{Cl}^-$ ,  $\text{NO}_3^-$ , and  $\text{SCN}^-$  ions, the shapes of the stability ratio versus ionic strength curves were very similar and the trend followed the prediction by the DLVO theory.<sup>19</sup> Accordingly, slow aggregation and stable samples were observed at low salt levels, while stability ratios close to unity indicated rapidly aggregating particles and unstable suspensions

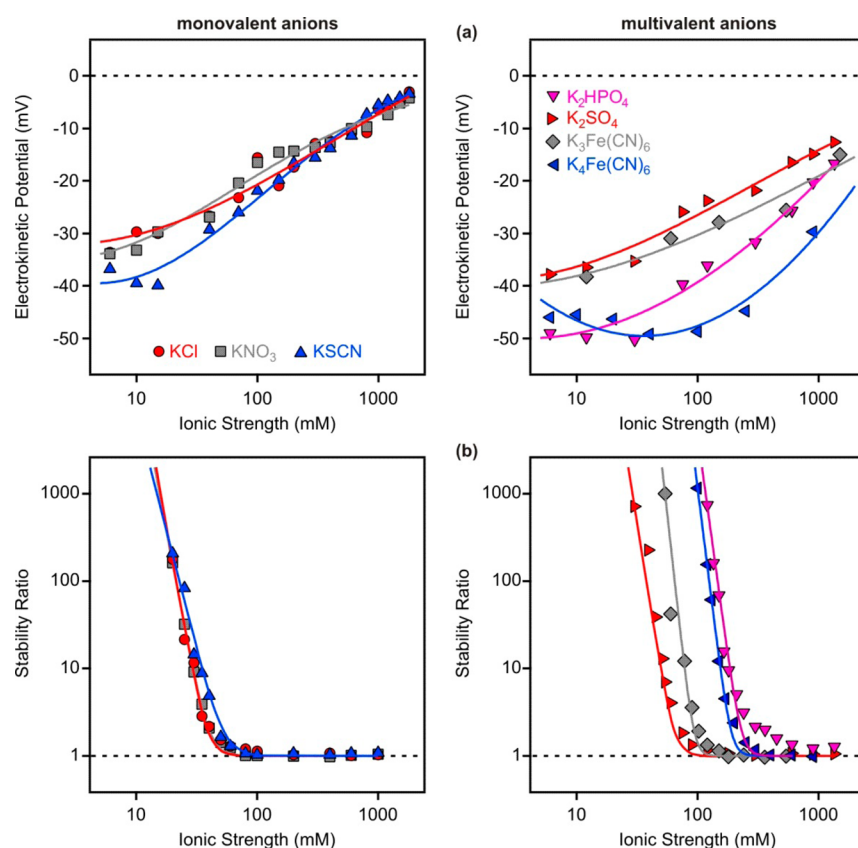


**Figure 3.** Electrokinetic potentials (a) and stability ratios (b) of TNS in the presence of monovalent (left column) and multivalent (right column) anions. The measurements were performed at pH 10 (negatively charged particles) and 1 mg/L particle concentration. The solid lines in (a) serve to guide the eyes whereas in (b) show the results of calculations using eq 6.

at high electrolyte concentrations. These regions are separated by the critical coagulation ionic strength (CCIS), which can be converted from the CCC using the ionic strength ( $I$ ) as

$$I = \frac{1}{2} \sum c_i z_i^2 \quad (5)$$

where  $c_i$  is the molar concentration of ion  $i$  with valence  $z_i$ . It is obvious that CCC and CCIS are identical for monovalent salts, while CCIS is always higher than the CCC for multivalent electrolytes. In the case of  $\text{Cl}^-$ ,  $\text{NO}_3^-$ , and  $\text{SCN}^-$  ions and positively charged TNS, the destabilization occurred due to charge screening, which led to the weakening of the repulsive double layer forces and the predominance of the attractive van der Waals interactions. Similar aggregation behavior was reported for spherical<sup>39</sup> or elongated<sup>62</sup> titania particles below the PZC in the presence of monovalent salts.

The trend in the stability ratios changed remarkably once the nanosheets were suspended in the  $\text{H}_2\text{PO}_4^-$  solutions. The stability ratios decreased by increasing the ionic strength at low concentrations and the fast aggregation regime was reached. A further increase of the electrolyte level resulted in restabilization of the suspensions giving rise to extremely high or not even measurable stability ratios in this intermediate concentration regime. Finally, the dispersions were destabilized at higher ionic strengths and the stability ratios decreased to one and remained constant thereafter. Interpreting these data with the help of the results obtained by electrophoresis, one can easily see that the first fast aggregation regime is located around the IEP and hence, the destabilization is due to the lack of charge and repulsive double layer forces. Besides, the

restabilization of TNS is the strongest near the minimum in the electrokinetic potentials indicating that the charge inversion resulted in the formation of an electrical double layer around the negatively charged particles, which was sufficiently strong to overcome the attractive forces giving rise to stable suspensions. Moreover, the destabilization at high ionic strengths is due to the screening of the surface charge by the  $\text{K}^+$  ions, which is also indicated by the decrease in the potentials in this concentration regime. The fact that the trend in the electrokinetic potentials is in good correlation with the stability ratios indicates that the major interparticle forces are of DLVO origin, while the adsorption process changes the extent of the repulsive double layer forces and hence, tunes the colloidal stability of the samples. Such a complex aggregation behavior of titania particles have not been published yet. However,  $\text{HPO}_4^{2-}$  adsorption led to similar ionic strength dependent colloidal stability for layered double hydroxide particles for instance.<sup>22</sup>

Regarding the multivalent ions, the shapes of the stability ratio versus ionic strength plots obtained in the presence of  $\text{SO}_4^{2-}$  and  $\text{Fe(CN)}_6^{3-}$  are similar to the ones measured for the  $\text{Cl}^-$ ,  $\text{NO}_3^-$ , and  $\text{SCN}^-$  ions, however, the CCIS values decrease with increasing the valence. For the  $\text{Fe(CN)}_6^{4-}$ , the tendency in the colloidal stability by varying the ionic strength is similar to the one discussed with the  $\text{H}_2\text{PO}_4^-$  and significant restabilization was observed owing to the charge reversal phenomenon. Nevertheless, it is surprising that such a restabilization was not induced by  $\text{Fe(CN)}_6^{3-}$  adsorption, albeit, the magnitude of the potentials in the charge inversion region are similar to the ones determined in the  $\text{H}_2\text{PO}_4^-$  system. This fact indicates that the TNS stabilization occurred



in the latter samples not solely by the electrical double layers. Indeed, measurements of interaction forces by the colloidal probe technique revealed that the accumulation of the  $\text{H}_2\text{PO}_4^-$  anions on titania surface leads to an anionic layer of 3–4 nm thickness, which induces an additional short-ranged repulsion giving rise to an improved colloidal stability.<sup>48</sup> On the other hand, this layer most likely does not form in the presence of the trivalent ions and the strength of the double layer forces is not high enough to overcome the van der Waals attraction and to slow down the TNS aggregation in the intermediate concentration regime.

**Negatively Charged TNS.** In contrast to the above situation in acidic solutions, the deprotonation processes resulted in the formation of divalent  $\text{HPO}_4^{2-}$  and tetravalent  $\text{Fe}(\text{CN})_6^{4-}$  ions at pH 10. The other anions kept the same valence as at pH 4 (Table 1). The TNS possess negative surface charge in alkaline suspensions (Figure 1), therefore, the anions are the co-ions in this case.

In general, the electrokinetic potentials increased with the ionic strength in each case and remained negative in the overall salt concentration regime investigated (Figure 3a). The values measured for the  $\text{Cl}^-$ ,  $\text{NO}_3^-$ , and  $\text{SCN}^-$  ions were identical for the first two anions and slightly smaller for the last one especially at low concentration. Such a similarity for the data measured with  $\text{Cl}^-$  and  $\text{NO}_3^-$  was also reported for spherical titania particles.<sup>52</sup>

For the multivalent ions, the magnitude of the potentials measured at the same ionic strength increased in the  $\text{SO}_4^{2-} < \text{Fe}(\text{CN})_6^{3-} < \text{HPO}_4^{2-} < \text{Fe}(\text{CN})_6^{4-}$  order indicating different affinity to the TNS surface of the same sign of charge. Similar ion specific adsorption of multivalent anions on like-charged titania surfaces was published earlier.<sup>37,46,53</sup> The surface charge increased with the valence of the anions, with the exception of the  $\text{HPO}_4^{2-}$ , which induced a more negative charge than the trivalent  $\text{Fe}(\text{CN})_6^{3-}$ . The stronger adsorption of the former ions is owing to the formation of the coordinative bonds<sup>54,55</sup> between the  $\text{HPO}_4^{2-}$  and the surface titanium(IV) ions leading to a more enhanced adsorption and to an increase in the magnitude of the surface charge density. For the other anions, the extent of the adsorption increased by increasing the valence, however, the driving force in the adsorption process is most likely the hydration level of the ions. Accordingly, the level of hydration decreases in the  $\text{SO}_4^{2-} > \text{Fe}(\text{CN})_6^{3-} > \text{Fe}(\text{CN})_6^{4-}$  sequence and hence, the tetravalent anion tend to adsorb on the hydrophobic particle surface stronger than the more hydrated divalent one. Similar relation between the hydration of multivalent ions and the extent of their adsorption was also discovered with other ionic compounds and particles.<sup>25,30,31</sup>

The stability ratios of TNS measured in the presence of different anions at pH 10 are shown as a function of the ionic strength in Figure 3b. The tendencies can be well-described by the DLVO theory in each cases,<sup>17–19</sup> and slow aggregation was observed at low concentrations and fast aggregation at high ionic strength. These regions were separated by the CCIS. Although these results indicate similar aggregation mechanism for all of the systems, the destabilization power of the mono and multivalent salts is different, as discussed later.

## DISCUSSION

Let us now interpret the above detailed experimental results concerning the influence of salt composition and valence of the anions on the colloidal stability of positively or negatively charged TNS. The most appropriate parameter to describe the

suspension stability is the CCIS, therefore, its tendencies by variation of the type of electrolytes will be discussed and compared to the ones predicted by the Hofmeister series for anions and the Schulze-Hardy rule.

**Hofmeister Series.** The effect of monovalent anions on the location of the CCIS is presented in Figure 4. The CCIS values

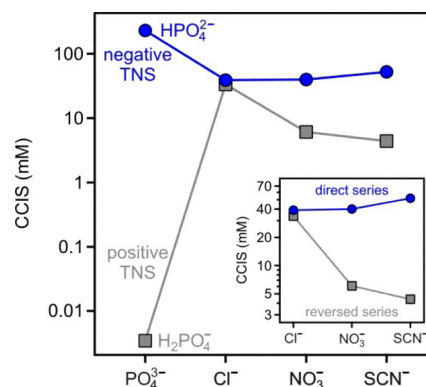


**Figure 4.** CCIS values of TNS as a function of anions ordered in the Hofmeister series. Positively charged particles with different monovalent counterions (squares) were measured at pH 4, while TNS of negative charge with co-ions (circles) at pH 10. The results with the KCl,  $\text{KNO}_3$ , and KSCN samples are enlarged in the inset. The solid lines are to guide the eyes.

were determined from the stability ratio versus ionic strength plots using the following formula<sup>63</sup>

$$W = 1 + \left( \frac{\text{CCIS}}{I} \right)^{-\beta} \quad (6)$$

where  $\beta$  can be calculated from the dependence of the stability ratios on the ionic strength in the slow aggregation regime as

$$\beta = \frac{d \log W}{dI} \quad (7)$$

In the case of positively charged particles studied at pH 4, the CCIS values decreased in the  $\text{Cl}^- > \text{NO}_3^- > \text{SCN}^- > \text{H}_2\text{PO}_4^-$  order. For the first three ions, the sequence is in agreement with the reversed Hofmeister series recommended for positively charged hydrophobic surfaces.<sup>12</sup> Such a trend can be explained by the fact that these anions adsorb on the oppositely charged TNS in different extent. Accordingly, less hydrated  $\text{SCN}^-$  shows the highest affinity to the surface and the adsorption decreases the charge density leading to weaker double layer forces and thus, to lower salt concentration necessary to destabilize the dispersion. On the other hand, the well-hydrated  $\text{Cl}^-$  prefers to stay in the bulk, therefore, the adsorption is not significant and the surface charge density of the particles remains high giving rise to stronger repulsion by the electrical double layers and to high CCIS. The same tendency was reported for the CCC of positively charged latex<sup>10,20,21</sup> and layered double hydroxide<sup>22</sup> particles as well as for titania spheres with  $\text{Cl}^-$  and  $\text{NO}_3^-$  anions.<sup>40</sup>

Furthermore, the situation is more complicated in the  $\text{H}_2\text{PO}_4^-$  samples. As discussed earlier, this anion adsorbs strongly on the positively charged nanosheets leading to charge neutralization and inversion. Such a high affinity led to the lowest CCIS among the monovalent salts under these experimental conditions. However, the reversed Hofmeister series predicts the highest CCIS for the  $\text{H}_2\text{PO}_4^-$  ion. This

atypical behavior is caused by the specific interaction between the anion and the TNS surface due to the bidental binding of the  $\text{H}_2\text{PO}_4^-$  through coordinative bonds.<sup>37,54,55</sup> Such a surface modification results in charge neutralization and the CCIS corresponds to this phenomenon rather than to the charge screening by the surrounding salt constituents. Similar charging and aggregation behavior and discrepancy from the Hofmeister series were also published with anionic clays.<sup>22</sup>

Let us now discuss the trend in the CCIS values measured with negatively charged TNS in the presence of the same anions at pH 10. Note that the  $\text{H}_2\text{PO}_4^-$  deprotonates at this pH<sup>51</sup> and the  $\text{HPO}_4^{2-}$  is the major species in the samples (Table 1). As shown in Figure 4, the CCIS increases in the  $\text{Cl}^- < \text{NO}_3^- < \text{SCN}^- < \text{HPO}_4^{2-}$  order. The position of the last anion is atypical because the traditional Hofmeister series predicts the lowest CCIS for this molecule, while the trend with first three ones agrees well with the sequence predicted by the direct series for negatively charged hydrophobic particles. The discrepancy with the  $\text{HPO}_4^{2-}$  is again owing to the formation of the surface complexes, which leads to significant anion adsorption on the like-charged TNS and hence, to higher surface charge density and to the highest CCIS among the ions investigated.

For the other ions, the poorly hydrated  $\text{SCN}^-$  tends to adsorb on the hydrophobic nanosheets giving rise to higher surface charge and stronger double layer repulsions. On the contrary, the well-hydrated  $\text{Cl}^-$  does not adsorb in considerable extent, therefore, the TNS are of smaller surface charge magnitude and thus, a lower CCIS was measured. Similar observations were reported for hydrophobic latexes of negative charge,<sup>23</sup> however, such a co-ion effect was not detected for highly charged polymeric particles.<sup>20</sup>

These results show that the colloidal stability and corresponding sequence in the CCIS of TNS particles in the presence of KCl,  $\text{KNO}_3$ , and  $\text{KSCN}$  salts can be predicted adequately with the direct or reversed Hofmeister series depending on the charge of the nanosheets. The dependence is stronger, when the anions are the counterions. Besides, the strong affinity of the  $\text{H}_2\text{PO}_4^-$  or  $\text{HPO}_4^{2-}$  anions to the TNS surface results in unusually low and high CCIS values under acidic or alkaline conditions, respectively.

**Schulze-Hardy Rule.** The effect of anion valence on the CCIS of the nanosheets is illustrated in Figure 5. It was shown regarding eq 1 that the trend in the CCC depends on the sign and the extent of the surface charge, therefore, the influence of co- and counterions should be treated differently. Concerning the latter case, the relation of the CCIS of strongly charged particles with the valence of anions of asymmetric salts can be described by the DLVO theory as

$$\text{CCIS} \propto z^{-4.9} \quad (8)$$

For particles of low surface charge, the location of the CCIS does not depend on counterion valence.<sup>27</sup> The CCIS data of positively charged TNS scatter for the monovalent anions due to ion specificity, as discussed in the previous section. Moreover, they decrease with the valence in general, but the dependence predicted by eq 8 was observed quantitatively only for the  $\text{SO}_4^{2-}$  ions. For the tri- and tetravalent anions, however, the experimental results show stronger dependence than the calculated one indicating that these ions interact with the oppositely charged surface specifically, most likely through chemical bonds, similarly to the case of  $\text{H}_2\text{PO}_4^-$ . For the tetravalent case, 38% of the ions are present in the  $\text{Fe}(\text{CN})_6^{4-}$

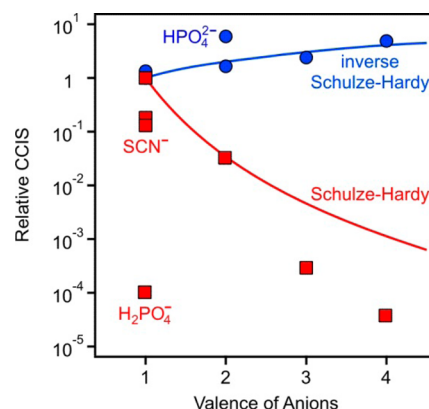


**Figure 5.** Relative CCIS values (normalized to the CCIS obtained in the presence of KCl in acidic suspension) as a function of valence of anions. Positively charged particles with different counterions (squares) were measured at pH 4 while TNS of negative charge with co-ions (circles) at pH 10. The solid lines indicate the traditional (eq 8) and the inverse (eq 9) Schulze-Hardy rule. Note that only 38% of the  $\text{Fe}(\text{CN})_6^{4-}$  ions at pH 4 are in the tetravalent form (Table 1) but these are the major anionic components close to the oppositely charged surface.

form (Table 1), however, most likely these anions are located in the vicinity of the surface and hence, responsible for the charging properties. Therefore, we have presented  $\text{Fe}(\text{CN})_6^{4-}$  as tetravalent in Figure 5. Such an interaction results in nanosheets of somewhat different surface properties (e.g., charge heterogeneity and hydrophobicity) than in the case of other ions. Similar dependence in the CCC of functionalized polystyrene particles has already been reported in the presence of  $\text{SO}_4^{2-}$ ,  $\text{Fe}(\text{CN})_6^{3-}$ , and  $\text{Fe}(\text{CN})_6^{4-}$  anions.<sup>31</sup>

Once the multivalent ions represent the co-ions (e.g., negatively charged TNS suspended in solutions of multivalent anions), the dependence given by the DLVO theory is<sup>29</sup>

$$\text{CCIS} \propto z + 1 \quad (9)$$

As shown in Figure 5, this relation led to an increase of the CCIS of the negatively charged TNS by increasing the valence of the anions. Excellent agreement was found between the experimental and calculated CCIS values for the  $\text{K}_2\text{SO}_4$ ,  $\text{K}_3\text{Fe}(\text{CN})_6$ , and  $\text{K}_4\text{Fe}(\text{CN})_6$  salts whereas the results with  $\text{K}_2\text{HPO}_4$  showed stronger dependence as the predicted one. This is again due to the formation of surface complexes with the latter anions, as discussed before. This so-called inverse Schulze-Hardy rule (eq 9) has already been observed for both cationic and anionic latexes,<sup>29,64</sup> however, no literature data are available for inorganic colloids including titania particles.

To further explore the origin of the interparticle forces responsible for the colloidal stability of the suspensions, the DLVO theory was used to calculate the CCIS from the electrokinetic potentials measured at the destabilization point as

$$\text{CCIS} = \frac{72\pi}{e^2 L_B} \left( \frac{\epsilon_0 \epsilon \zeta^2}{H} \right)^2 \quad (10)$$

where  $e$  is the base of the natural logarithm,  $L_B$  is the Bjerrum length, and  $H$  is the Hamaker coefficient. Their values used in the calculations were 2.72, 0.71 nm and  $2.70 \times 10^{-20}$  J, respectively.

The experimental CCIS data agree with the calculated ones relatively well with the exception of the  $\text{H}_2\text{PO}_4^-$ ,  $\text{Fe}(\text{CN})_6^{3-}$ ,



and  $\text{Fe}(\text{CN})_6^{4-}$  anions interacting with positively charged nanosheets (Figure 6). This finding indicates that the TNS

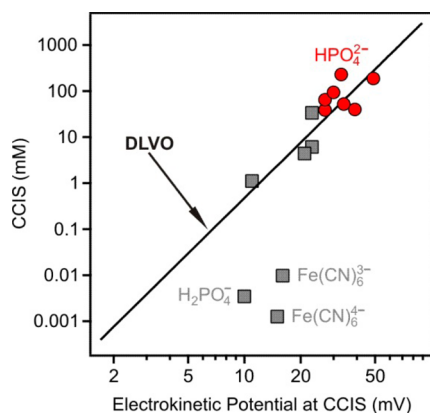


**Figure 6.** CCIS values as a function of the electrokinetic potentials measured at the CCIS. Positively charged particles with different counterions (squares) were measured at pH 4, whereas TNS of negative charge with co-ions (circles) at pH 10. The solid line indicates the results of calculations using the DLVO theory (eq 10).

aggregation is driven by DLVO type forces in the majority of the systems, however, the CCIS values vary with the potential owing to the adsorption of the ions especially in the case of positively charged nanosheets. Such an adsorption can change the charge densities in some extent but the overall interparticle force remains the sum of the repulsive double layer and attractive van der Waals forces. Similar results were reported with latex particles on the basis of aggregation<sup>20</sup> and colloidal probe<sup>2</sup> measurements.

Besides, in the presence of  $\text{H}_2\text{PO}_4^-$ ,  $\text{Fe}(\text{CN})_6^{3-}$ , and  $\text{Fe}(\text{CN})_6^{4-}$  anions, additional forces also act between the particles giving rise to significant deviation between the measured and the calculated CCIS. Because these ions interact strongly with the particle surfaces, such additional forces may originate from patch-charge interactions. Namely, the anions adsorb in the form of islands on the particle surfaces and the electrostatic attraction between those islands (patch) with the empty and oppositely charged place (charge) of the surface of another TNS leads to the rising of an additional attractive force. CCIS values lower than the calculated ones also confirm the presence of additional attractive forces, which were discovered also with positively charged latexes in the presence of  $\text{Fe}(\text{CN})_6^{3-}$  and  $\text{Fe}(\text{CN})_6^{4-}$  anions.<sup>31</sup> In addition, for the  $\text{H}_2\text{PO}_4^-$  system, the ionic layer forming upon anion adsorption<sup>48</sup> may induce bridging interaction between the particles and thus, the presence of these attractive forces leads to lower CCIS than the one calculated by the DLVO theory. In the absence of chemical interaction between the anions and the surface and subsequent additional forces, however, the aggregation processes are mainly driven by DLVO-type double layer and van der Waals interactions, as in the case of the majority of the anions investigated in the present study.

## CONCLUSIONS

Ion specific effects on charging and aggregation of TNS were investigated in aqueous suspensions. Electrophoretic and light scattering experiments were performed in the presence of various mono and multivalent anions with either positively or

negatively charged particles below or above the PZC, respectively.

The majority of the monovalent ions destabilized the suspensions by charge screening, however, their different extent of adsorption led to variations in the CCIS values, which separate slow and fast aggregation regimes. The sequence in the CCIS was in good agreement with the direct or reversed Hofmeister series for anions depending on the charge of the TNS. Nevertheless, the CCIS in the presence of  $\text{H}_2\text{PO}_4^-$  and  $\text{HPO}_4^{2-}$  anions does not follow the trend predicted by the Hofmeister series and this atypical behavior is owing to the bidental coordination of these species to the TNS and subsequent accumulation of negative charges on the surface, which also leads to charge inversion of the nanosheets when used below their PZC.

For positively charged TNS, the CCIS values decreased with the valence of the anions and pronounced charge reversal was reported for the di-, tri-, and tetravalent ones due to their significant adsorption on the nanosheets. In the latter case, this phenomenon induced a restabilization of the particles due to the sufficiently high surface charge density upon anion adsorption. The CCIS values qualitatively followed the Schulze-Hardy rule by varying the valence of the anions, however, specific interactions with the surface gave rise to a stronger dependence for the  $\text{Fe}(\text{CN})_6^{3-}$  and  $\text{Fe}(\text{CN})_6^{4-}$  ions. For negatively charged particles, the inverse Schulze-Hardy rule applies to describe the change in the CCIS by the valence of the anions.

Comparison of the experimental results with the ones obtained by calculations based on the DLVO theory revealed that repulsive electrical double layer and attractive van der Waals forces were responsible for particle aggregation in the majority of the systems, however, the CCIS values depended on the composition and the valence of the salts due to the different affinity of the anions to the surfaces. The presence of forces of non-DLVO origin were discovered only with anions ( $\text{H}_2\text{PO}_4^-$ ,  $\text{HPO}_4^{2-}$ ,  $\text{Fe}(\text{CN})_6^{3-}$ , and  $\text{Fe}(\text{CN})_6^{4-}$ ), which are in strong interaction (e.g., through primary chemical bonds) with the nanosheets.

The present results shed light on the importance of ion specificity on colloidal stability of TNS dispersions. Because only limited data are available for spherical titania materials and no information was published with titania of elongated structure, these findings are of special importance for scientists working with titania nanowire, nanosheet, or nanorod suspensions in the presence of mono- or multivalent electrolytes or in their mixtures.

## AUTHOR INFORMATION

### Corresponding Author

\*E-mail: [istvan.szilagyi@unige.ch](mailto:istvan.szilagyi@unige.ch). Phone: +41 22 3796031.

### ORCID

Istvan Szilagyi: 0000-0001-7289-0979

### Notes

The authors declare no competing financial interest.

## ACKNOWLEDGMENTS

Financial support by the Swiss Secretariat for Education, Research and Innovation (C15.0024), Swiss National Science Foundation (150162), COST Action CM1303 and University of Geneva is gratefully acknowledged. Special thanks to

Professor Michal Borkovec for the possibility to use the facilities in his laboratory.

## REFERENCES

- (1) Heyda, J.; Okur, H. I.; Hladilkova, J.; Rembert, K. B.; Hunn, W.; Yang, T. L.; Dzubielka, J.; Jungwirth, P.; Cremer, P. S. Guanidinium can both cause and prevent the hydrophobic collapse of biomacromolecules. *J. Am. Chem. Soc.* **2017**, *139*, 863–870.
- (2) Ruiz-Cabello, F. J. M.; Oncsik, T.; Rodriguez-Valverde, M. A.; Maroni, P.; Cabrerizo-Vilchez, M. Specific ion effects and pH dependence on the interaction forces between polystyrene particles. *Langmuir* **2016**, *32*, 11918–11927.
- (3) Rubin, J.; San Miguel, A.; Bommarius, A. S.; Behrens, S. H. Correlating aggregation kinetics and stationary diffusion in protein-sodium salt systems observed with dynamic light scattering. *J. Phys. Chem. B* **2010**, *114*, 4383–4387.
- (4) Tielrooij, K. J.; van der Post, S. T.; Hunger, J.; Bonn, M.; Bakker, H. J. Anisotropic water reorientation around ions. *J. Phys. Chem. B* **2011**, *115*, 12638–12647.
- (5) dos Santos, A. P.; Levin, Y. Ion specificity and the theory of stability of colloidal suspensions. *Phys. Rev. Lett.* **2011**, *106*, 167801.
- (6) Diehl, A.; dos Santos, A. P.; Levin, Y. Surface tension of an electrolyte-air interface: a Monte Carlo study. *J. Phys.: Condens. Matter* **2012**, *24*, 284115.
- (7) Malikova, N.; Rollet, A. L.; Cebasek, S.; Tomsic, M.; Vlachy, V. On the crossroads of current polyelectrolyte theory and counterion-specific effects. *Phys. Chem. Chem. Phys.* **2015**, *17*, 5650–5658.
- (8) Wei, S. H.; Chen, M. M.; Wei, C. S.; Huang, N. D.; Li, L. B. Opposite counter-ion effects on condensed bundles of highly charged supramolecular nanotubes in water. *Soft Matter* **2016**, *12*, 6285–6292.
- (9) Okur, H. I.; Hladilkova, J.; Rembert, K. B.; Cho, Y.; Heyda, J.; Dzubielka, J.; Cremer, P. S.; Jungwirth, P. Beyond the Hofmeister series: Ion-specific effects on proteins and their biological functions. *J. Phys. Chem. B* **2017**, *121*, 1997–2014.
- (10) Bastos-Gonzalez, D.; Perez-Fuentes, L.; Drummond, C.; Faraudo, J. Ions at interfaces: the central role of hydration and hydrophobicity. *Curr. Opin. Colloid Interface Sci.* **2016**, *23*, 19–28.
- (11) Mazzini, V.; Craig, V. S. J. Specific-ion effects in non-aqueous systems. *Curr. Opin. Colloid Interface Sci.* **2016**, *23*, 82–93.
- (12) Schwierz, N.; Horinek, D.; Sivan, U.; Netz, R. R. Reversed Hofmeister series-The rule rather than the exception. *Curr. Opin. Colloid Interface Sci.* **2016**, *23*, 10–18.
- (13) Lo Nostro, P.; Ninham, B. W. Hofmeister phenomena: An update on ion specificity in biology. *Chem. Rev.* **2012**, *112*, 2286–2322.
- (14) Parsons, D. F.; Bostrom, M.; Lo Nostro, P.; Ninham, B. W. Hofmeister effects: Interplay of hydration nonelectrostatic potentials and ion size. *Phys. Chem. Chem. Phys.* **2011**, *13*, 12352–12367.
- (15) Kunz, W.; Henle, J.; Ninham, B. W. 'Zur lehre von der wirkung der salze' (about the science of the effect of salts): Franz Hofmeister's historical papers. *Curr. Opin. Colloid Interface Sci.* **2004**, *9*, 19–37.
- (16) Overbeek, J. T. G. The rule of Schulze and Hardy. *Pure Appl. Chem.* **1980**, *52*, 1151–1161.
- (17) Derjaguin, B. A theory of interaction of particles in presence of electric double-layers and the stability of lyophobic colloids and disperse systems. *Prog. Surf. Sci.* **1993**, *43*, 1–14.
- (18) Derjaguin, B. On the repulsive forces between charged colloid particles and on the theory of slow coagulation and stability of lyophobic sols. *Trans. Faraday Soc.* **1940**, *35*, 203–214.
- (19) Behrens, S. H.; Borkovec, M.; Schurtenberger, P. Aggregation in charge-stabilized colloidal suspensions revisited. *Langmuir* **1998**, *14*, 1951–1954.
- (20) Oncsik, T.; Trefalt, G.; Borkovec, M.; Szilagy, I. Specific ion effects on particle aggregation induced by monovalent salts within the Hofmeister series. *Langmuir* **2015**, *31*, 3799–3807.
- (21) Oncsik, T.; Desert, A.; Trefalt, G.; Borkovec, M.; Szilagy, I. Charging and aggregation of latex particles in aqueous solutions of ionic liquids: Towards an extended Hofmeister series. *Phys. Chem. Chem. Phys.* **2016**, *18*, 7511–7520.
- (22) Pavlovic, M.; Huber, R.; Adok-Sipiczki, M.; Nardin, C.; Szilagy, I. Ion specific effects on the stability of layered double hydroxide colloids. *Soft Matter* **2016**, *12*, 4024–4033.
- (23) Lopez-Leon, T.; Jodar-Reyes, A. B.; Bastos-Gonzalez, D.; Ortega-Vinuesa, J. L. Hofmeister effects in the stability and electrophoretic mobility of polystyrene latex particles. *J. Phys. Chem. B* **2003**, *107*, 5696–5708.
- (24) Peula-Garcia, J. M.; Ortega-Vinuesa, J. L.; Bastos-Gonzalez, D. Inversion of Hofmeister series by changing the surface of colloidal particles from hydrophobic to hydrophilic. *J. Phys. Chem. C* **2010**, *114*, 11133–11139.
- (25) Oncsik, T.; Trefalt, G.; Csendes, Z.; Szilagy, I.; Borkovec, M. Aggregation of negatively charged colloidal particles in the presence of multivalent cations. *Langmuir* **2014**, *30*, 733–741.
- (26) Lyklema, J. Coagulation by multivalent counterions and the Schulze-Hardy rule. *J. Colloid Interface Sci.* **2013**, *392*, 102–104.
- (27) Trefalt, G.; Szilagy, I.; Tellez, G.; Borkovec, M. Colloidal stability in asymmetric electrolytes: Modifications of the Schulze-Hardy rule. *Langmuir* **2017**, *33*, 1695–1704.
- (28) Trefalt, G. Derivation of the inverse Schulze-Hardy rule. *Phys. Rev. E: Stat. Phys., Plasmas, Fluids, Relat. Interdiscip. Top.* **2016**, *93*, 032612.
- (29) Cao, T.; Szilagy, I.; Oncsik, T.; Borkovec, M.; Trefalt, G. Aggregation of colloidal particles in the presence of multivalent colons: The inverse Schulze-Hardy rule. *Langmuir* **2015**, *31*, 6610–6614.
- (30) Szilagy, I.; Polomska, A.; Citherlet, D.; Sadeghpour, A.; Borkovec, M. Charging and aggregation of negatively charged colloidal latex particles in the presence of multivalent oligoamine cations. *J. Colloid Interface Sci.* **2013**, *392*, 34–41.
- (31) Sinha, P.; Szilagy, I.; Ruiz-Cabello, F. J. M.; Maroni, P.; Borkovec, M. Attractive forces between charged colloidal particles induced by multivalent ions revealed by confronting aggregation and direct force measurements. *J. Phys. Chem. Lett.* **2013**, *4*, 648–652.
- (32) Chen, C. Y.; Huang, W. L. Aggregation kinetics of diesel soot nanoparticles in wet environments. *Environ. Sci. Technol.* **2017**, *51*, 2077–2086.
- (33) Afshinnia, K.; Sikder, M.; Cai, B.; Baalousha, M. Effect of nanomaterial and media physicochemical properties on Ag NM aggregation kinetics. *J. Colloid Interface Sci.* **2017**, *487*, 192–200.
- (34) Tiarks, F.; Frechen, T.; Kirsch, S.; Leuninger, J.; Melan, M.; Pfau, A.; Richter, F.; Schuler, B.; Zhao, C. L. Formulation effects on the distribution of pigment particles in paints. *Prog. Org. Coat.* **2003**, *48*, 140–152.
- (35) Damodaran, V. B.; Bhatnagar, D.; Leszczak, V.; Papat, K. C. Titania nanostructures: a biomedical perspective. *RSC Adv.* **2015**, *5*, 37149–37171.
- (36) Bajnoczi, E. G.; Balazs, N.; Mogyorosi, K.; Sranko, D. F.; Pap, Z.; Ambrus, Z.; Canton, S. E.; Noren, K.; Kuzmann, E.; Vertes, A.; et al. The influence of the local structure of Fe(III) on the photocatalytic activity of doped TiO<sub>2</sub> photocatalysts-An EXAFS, XPS and Mossbauer spectroscopic study. *Appl. Catal., B* **2011**, *103*, 232–239.
- (37) Budarz, J. F.; Turolla, A.; Piasecki, A. F.; Bottero, J. Y.; Antonelli, M.; Wiesner, M. R. Influence of aqueous inorganic anions on the reactivity of nanoparticles in TiO<sub>2</sub> photocatalysis. *Langmuir* **2017**, *33*, 2770–2779.
- (38) Nistico, R.; Magnacca, G. The hypersaline synthesis of titania: from powders to aerogels. *RSC Adv.* **2015**, *5*, 14333–14340.
- (39) Snoswell, D. R. E.; Duan, J. M.; Fornasiero, D.; Ralston, J. Colloid stability of synthetic titania and the influence of surface roughness. *J. Colloid Interface Sci.* **2005**, *286*, 526–535.
- (40) Dumont, F.; Warlus, J.; Watillon, A. Influence of the point of zero charge of titanium-dioxide hydrosols on the ionic adsorption sequences. *J. Colloid Interface Sci.* **1990**, *138*, 543–554.
- (41) Shih, Y. H.; Zhuang, C. M.; Tso, C. P.; Lin, C. H. The effect of electrolytes on the aggregation kinetics of titanium dioxide nanoparticle aggregates. *J. Nanopart. Res.* **2012**, *14*, 924.

- (42) Rouster, P.; Pavlovic, M.; Szilagy, I. Improving the stability of titania nanosheets by functionalization with polyelectrolytes. *RSC Adv.* **2016**, *6*, 97322–97330.
- (43) Delgado, A. V.; Gonzalez-Caballero, F.; Hunter, R. J.; Koopal, L. K.; Lyklema, J. Measurement and interpretation of electrokinetic phenomena. *J. Colloid Interface Sci.* **2007**, *309*, 194–224.
- (44) Holthoff, H.; Egelhaaf, S. U.; Borkovec, M.; Schurtenberger, P.; Sticher, H. Coagulation rate measurements of colloidal particles by simultaneous static and dynamic light scattering. *Langmuir* **1996**, *12*, 5541–5549.
- (45) Kosmulski, M.; Rosenholm, J. B. Electroacoustic study of adsorption of ions on anatase and zirconia from very concentrated electrolytes. *J. Phys. Chem.* **1996**, *100*, 11681–11687.
- (46) Velikovska, P.; Mikulasek, P. The influence of Cl<sup>-</sup>, SO<sub>4</sub><sup>2-</sup> and PO<sub>4</sub><sup>3-</sup> ions on the zeta-potential and microfiltration of titanium dioxide dispersions. *Sep. Purif. Technol.* **2007**, *58*, 295–298.
- (47) Lorenzetti, M.; Gongadze, E.; Kulkarni, M.; Junkar, I.; Iglc, A. Electrokinetic properties of TiO<sub>2</sub> nanotubular surfaces. *Nanoscale Res. Lett.* **2016**, *11*, 378–390.
- (48) Feiler, A.; Jenkins, P.; Ralston, J. Metal oxide surfaces separated by aqueous solutions of linear polyphosphates: DLVO and non-DLVO interaction forces. *Phys. Chem. Chem. Phys.* **2000**, *2*, 5678–5683.
- (49) Horvath, E.; Szilagy, I.; Forro, L.; Magrez, A. Probing titanate nanowire surface acidity through methylene blue adsorption in colloidal suspension and on thin films. *J. Colloid Interface Sci.* **2014**, *416*, 190–197.
- (50) Parsons, D. F.; Salis, A. The impact of the competitive adsorption of ions at surface sites on surface free energies and surface forces. *J. Chem. Phys.* **2015**, *142*, 134707.
- (51) May, P. M.; Rowland, D.; Konigsberger, E.; Hefter, G. JESS, a Joint Expert Speciation System - IV: A large database of aqueous solution physicochemical properties with an automatic means of achieving thermodynamic consistency. *Talanta* **2010**, *81*, 142–148.
- (52) Kosmulski, M.; Durand-Vidal, S.; Gustafsson, J.; Rosenholm, J. B. Charge interactions in semi-concentrated titania suspensions at very high ionic strengths. *Colloids Surf., A* **1999**, *157*, 245–259.
- (53) Rosenholm, J. B.; Kosmulski, M. Peculiar charging effects on titania in aqueous 1:1, 2:1, 1:2 and mixed electrolyte suspensions. *Adv. Colloid Interface Sci.* **2012**, *179-182*, 51–67.
- (54) Connor, P. A.; McQuillan, A. J. Phosphate adsorption onto TiO<sub>2</sub> from aqueous solutions: An in situ internal reflection infrared spectroscopic study. *Langmuir* **1999**, *15*, 2916–2921.
- (55) Luschtinetz, R.; Frenzel, J.; Milek, T.; Seifert, G. Adsorption of phosphonic acid at the TiO<sub>2</sub> anatase (101) and rutile (110) surfaces. *J. Phys. Chem. C* **2009**, *113*, 5730–5740.
- (56) Clavier, A.; Carnal, F.; Stoll, S. Effect of surface and salt properties on the ion distribution around spherical nanoparticles: Monte Carlo simulations. *J. Phys. Chem. B* **2016**, *120*, 7988–7997.
- (57) Torrie, G. M.; Valleau, J. P. Electrical double-layers 0.4. Limitations of the Gouy-Chapman theory. *J. Phys. Chem.* **1982**, *86*, 3251–3257.
- (58) Greberg, H.; Kjellander, R. Charge inversion in electric double layers and effects of different sizes for counterions and coions. *J. Chem. Phys.* **1998**, *108*, 2940–2953.
- (59) Patra, C. N. Structure of spherical electric double layers with fully asymmetric electrolytes: A systematic study by Monte Carlo simulations and density functional theory. *J. Chem. Phys.* **2014**, *141*, 184702.
- (60) Guerrero-Garcia, G. I.; Gonzalez-Tovar, E.; Quesada-Perez, M.; Martin-Molina, A. The non-dominance of counterions in charge-asymmetric electrolytes: non-monotonic precedence of electrostatic screening and local inversion of the electric field by multivalent coions. *Phys. Chem. Chem. Phys.* **2016**, *18*, 21852–21864.
- (61) Jordan, J.; Ewing, G. J. Protonation of hexacyanoferrates. *Inorg. Chem.* **1962**, *1*, 587–591.
- (62) Horvath, E.; Grebikova, L.; Maroni, P.; Szabo, T.; Magrez, A.; Forro, L.; Szilagy, I. Dispersion characteristics and aggregation in titanate nanowire colloids. *ChemPlusChem* **2014**, *79*, 592–600.
- (63) Grolimund, D.; Elimelech, M.; Borkovec, M. Aggregation and deposition kinetics of mobile colloidal particles in natural porous media. *Colloids Surf., A* **2001**, *191*, 179–188.
- (64) Rosenholm, J. B.; Nylund, J.; Stenlund, B. Synthesis and characterization of cationized latexes in dilute suspensions. *Colloids Surf., A* **1999**, *159*, 209–218.
- (65) Hanaor, D. A. H.; Sorrell, C. C. Review of the anatase to rutile phase transformation. *J. Mater. Sci.* **2011**, *46*, 855–874.



# Ion Specific Effects on the Stability of Halloysite Nanotube Colloids—Inorganic Salts versus Ionic Liquids

Bojana Katana, Dóra Takács, Edit Csapó, Tamás Szabó, Andrej Jamnik, and Istvan Szilagyi\*

Cite This: *J. Phys. Chem. B* 2020, 124, 9757–9765

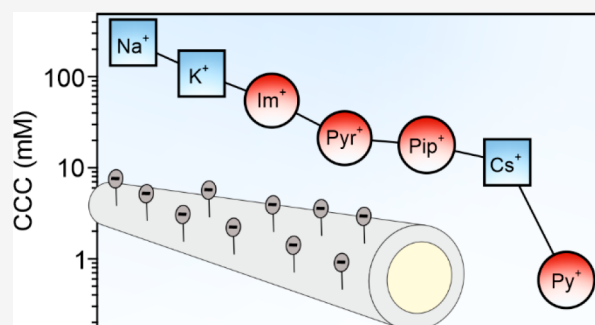
Read Online

ACCESS |

Metrics & More

Article Recommendations

**ABSTRACT:** Charging and aggregation processes were studied in aqueous dispersions of halloysite nanotubes (HNTs) in the presence of monovalent inorganic electrolytes and ionic liquid (IL) constituents. The same type of co-ion (same sign of charge as HNT) was used in all systems, while the type of counterions (opposite sign of charge as HNT) was systematically varied. The affinity of the inorganic cations to the HNT surface influenced their destabilizing power leading to an increase in the critical coagulation concentration (CCC) of HNT dispersions in the  $\text{Cs}^+ < \text{K}^+ < \text{Na}^+$  order. This trend agrees with the classical Hofmeister series for negatively charged hydrophobic surfaces. For the IL cations, the CCCs increased in the order  $\text{BMPY}^+ < \text{BMPIP}^+ < \text{BMPYR}^+ < \text{BMIM}^+$ . An unexpectedly strong adsorption of  $\text{BMPY}^+$  cations on the HNT surface was observed giving rise to charge neutralization and reversal of the oppositely charged outer surface of HNT. The direct Hofmeister series was extended with these IL cations. The main aggregation mechanism was rationalized within the classical theory developed by Derjaguin, Landau, Verwey, and Overbeek, while ion specific effects resulted in remarkable variation in the CCC values. The results unambiguously proved that the hydration level of the surface and the counterions plays a crucial role in the formation of the ionic composition at the solid–liquid interface and consequently, in the colloidal stability of the HNT particles in both inorganic salt and IL solutions.

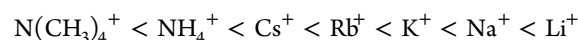
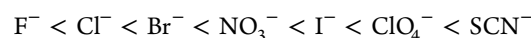


## INTRODUCTION

Halloysite nanotubes (HNTs) represent an interesting class of materials due to their advantageous properties such as biocompatibility, abundant surface functional groups, and availability in large scale, which are exploited in various applications.<sup>1–3</sup> HNTs are aluminosilicates of tubular structure with two different surface charge states.<sup>4</sup> The outer surface is negatively charged due to the presence of the deprotonated silanol groups, while the protonation of the aluminol groups results in a positively charged inner surface.<sup>5</sup> Recent reviews indicate a widespread contemporary interest in HNTs and their composites.<sup>6–10</sup> Despite the fact that numerous applications take place in liquid medium,<sup>11–14</sup> the main focus was made on the structural properties in the solid state, and less attention was paid to the colloidal features. In the handful of papers released on this topic,<sup>2,15–18</sup> low colloidal stability of the commercially available HNTs was reported, which leads to aggregation and subsequent sedimentation of the HNT materials. In some studies, the aggregation was suppressed by surface modification with polyelectrolytes.<sup>15,17,18</sup>

Ion specific effects particularly influence charging and aggregation of colloidal particles in aqueous samples;<sup>19–23</sup> however, this issue was not explored for HNT dispersions so far. Accordingly, ions of dissolved salts are able to interact specifically with surfaces, thereby modifying the charge density

to different extents.<sup>24–26</sup> Such a variation in the surface charge affects the aggregation processes and, thus, the colloidal stability of the samples. These phenomena prompted the establishment of the Hofmeister series of cations and anions to order their effect on particle aggregation processes. This theory was originally developed for the destabilization of protein solutions by inorganic salts,<sup>27</sup> but it has also proven to be a powerful tool to predict the stability of particle dispersions on the basis of the type of co- and counterions.<sup>19–21,28–32</sup> The original Hofmeister series were established as follows:



Note that only monovalent ions are presented in the above series, since the Schulze–Hardy rule<sup>33</sup> has to be applied once the effects of the multivalent ions are discussed. The above

Received: August 29, 2020  
Revised: October 9, 2020  
Published: October 20, 2020



sequences for anions and cations indicate that negatively charged colloidal particles form stable aqueous dispersions even in the presence of a high concentration of ions located on the right-hand side of the series, while the ions from the left-hand side induce their aggregation at lower concentrations. This is the so-called direct Hofmeister series. For positively charged surfaces, the reversed Hofmeister series applies, since the effect of ions on the colloidal stability of dispersions is just the opposite; i.e., the ions from the right side of the series destabilize the dispersions at low concentrations, while they are more stable in solutions of salt constituents located on the left side. The charge density and hydrophobicity of the colloidal particle also play an important role in determining the order of ions in this series. Accordingly, the above rules are valid only for hydrophobic particles, while the order is reversed for hydrophilic surfaces.<sup>31,34,35</sup>

However, there are cases in which water is not a suitable continuous medium in colloidal dispersions. Instead, ionic liquids (ILs)<sup>36,37</sup> are organic salts of low melting point with many advantageous properties including wide electrochemical window, low vapor pressure, and high chemical stability.<sup>36,38</sup> An important class of systems is particle suspensions in ILs, as they are relevant in many applications.<sup>39–42</sup> Among them, HNT-IL systems were studied and applied as catalysts,<sup>43</sup> anticorrosion agents,<sup>44</sup> supercapacitors,<sup>45</sup> sensors,<sup>46</sup> and building blocks in batteries.<sup>47</sup> Despite the considerable interest in studying colloid–IL systems, studies concerning particle aggregation in ILs have begun only recently.<sup>48–54</sup> It was soon realized that the interfacial assembly of the IL constituents greatly influences the interparticle forces<sup>55–57</sup> and, hence, the stability of colloidal dispersions. This issue can be adequately addressed in diluted IL solutions by investigating the effect of the interfacial properties on the forces between the particles. Therefore, interparticle forces and the subsequent particle aggregation mechanism in samples containing aqueous solutions of IL constituents were explored by different experimental techniques.<sup>49,56,58–60</sup> For diluted IL solutions, the measured trends in colloidal stability resembled the one described by the theory of Derjaguin, Landau, Verwey, and Overbeek (DLVO),<sup>61</sup> implying that ILs dissociate in the solutions causing charge screening and subsequent destabilization of the dispersion at high IL concentrations. Nevertheless, ILs of different compositions destabilized the particle dispersions at different concentrations, which contrasts with the DLVO theory. Such an ion specific effect in IL solutions is analogous to the one discussed for simple ions previously. In this way, a Hofmeister series can be established for IL cations and anions as well.<sup>62–64</sup> However, only a limited number of quantitative data are available for particle dispersions,<sup>59,60</sup> and such investigations for HNT-IL systems have not been performed so far.

In the present study, therefore, the colloidal stability of HNTs was investigated in the presence of different monovalent inorganic electrolytes (KCl, NaCl, and CsCl) and aqueous solutions of ILs (1-butyl-3-methylimidazolium chloride (BMIMCl), 1-butyl-2-methylpyridinium chloride (BMPYCl), 1-butyl-1-methylpyrrolidinium (BMPYRCl), and 1-butyl-1-methylpiperidinium chloride (BMPIPCl)). Based on the results, an extended Hofmeister series was proposed for the nanotubes, and the aggregation mechanism was compared to the predictions of existing theories.

## METHODS

**Materials.** The ILs (BMIMCl,  $\geq 99\%$ , BMPYCl,  $>98\%$ , BMPYRCl,  $99\%$ , and BMPIPCl,  $99\%$ , see Figure 1 for the

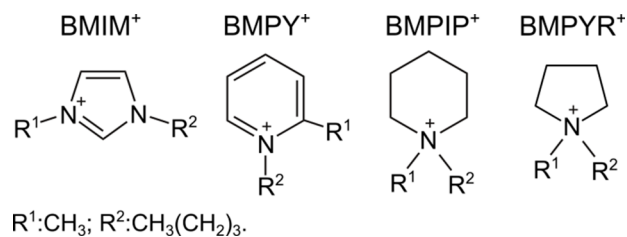


**Figure 1.** Chemical structure of IL constituent cations used in the present study (BMIM<sup>+</sup>, 1-butyl-3-methylimidazolium; BMPY<sup>+</sup>, 1-butyl-2-methylpyridinium; BMPIP<sup>+</sup>, 1-butyl-1-methylpiperidinium; BMPYR<sup>+</sup>, 1-butyl-1-methylpyrrolidinium; chloride was used as the anion).

structure of the cations) were purchased from Iolitec GmbH. Inorganic salts such as potassium chloride (KCl), sodium chloride (NaCl), and cesium chloride (CsCl) were bought from VWR. The raw HNT powder was purchased from Sigma-Aldrich. High purity water from a VWR Purity TU+ device was used for all the sample preparations. The measurements were carried out at 25 °C, and the HNT concentration was set to 10 mg/L. The water, salt, and IL solutions were filtered with a 0.1  $\mu\text{m}$  syringe filter (Millex) prior to the sample preparation to avoid dust contamination.

**Alkaline Treatment of HNTs.** Before use, the raw HNTs were treated with an alkaline solution in order to improve their surface properties and polydispersity.<sup>18</sup> Briefly, the HNTs were dispersed at a concentration of 20 g/L in a 14.5 mM KOH solution under magnetic stirring for 24 h. The hydroxylated HNTs were then washed several times with ultrapure water by centrifugation at 10 000 rpm for 10 min. The supernatant was removed, and the slurry was dried in an oven at 110 °C for 15 h. The dry powder was redispersed into water to obtain the HNT stock dispersions (denoted as h-HNT thereafter) at a concentration of 10 g/L.

**Electrophoresis.** The electrophoretic measurements were performed with a Litesizer 500 instrument (Anton Paar) equipped with a 40 mW semiconductor laser (658 nm wavelength). The samples were prepared by the following procedure. IL solutions of 1.8 mL volume and of calculated concentration were mixed with 0.2 mL of h-HNT of 10 mg/L. The suspensions were prepared by mixing the required amounts of water, salt, or IL solutions and the particle suspension to get the desired concentrations. The sample was allowed to rest overnight before performing the electrophoretic mobility measurements, which were carried out in an Univette (Anton Paar) accessory. The obtained electrophoretic mobility ( $\mu$ ) values were converted to zeta potentials ( $\zeta$ ) with the Smoluchowski equation:<sup>65</sup>

$$\zeta = \mu\eta/\epsilon_0\epsilon \quad (1)$$

where  $\eta$  is the viscosity,  $\epsilon$  is the dielectric constant of the medium, and  $\epsilon_0$  is the permittivity of the vacuum. Note that the Henry equation could be used below 1 mM ionic strengths in the BMPYCl system. However, the difference between the zeta potentials calculated by the two methods is comparable to the accuracy of our measurements. Therefore, the Smoluchowski equation was applied for all electrophoretic mobility–



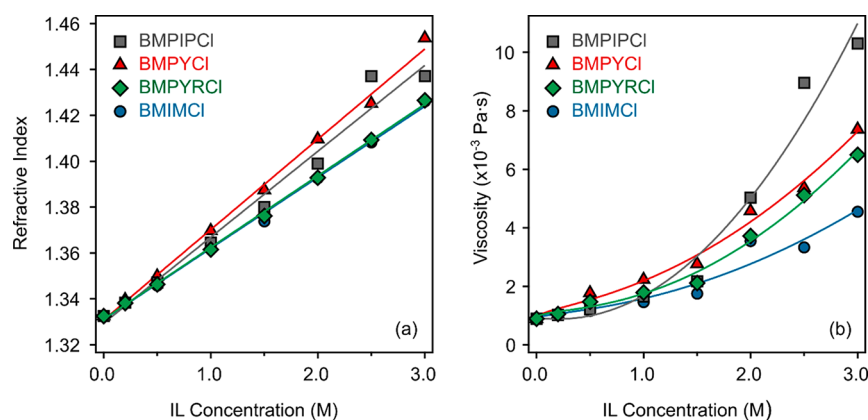


**Figure 2.** Refractive indices (a) and viscosities (b) of aqueous IL (BMIMCl, BMPYCl, BMPYRCI, and BMIPICl) solutions at different concentrations. The solid lines are fits using eqs 5 (a) and 6(b) applied for data interpolation.

**Table 1.** Fitting Parameters Used to Interpolate the Refractive Indices and Viscosities of the IL Solutions

composition	refractive index <sup>a</sup>		viscosity <sup>b</sup>		
	<i>a</i> (M <sup>-1</sup> )	<i>b</i>	<i>A</i> (M <sup>-1/2</sup> )	<i>B</i> (M <sup>-1</sup> )	<i>D</i> (M <sup>-2</sup> )
BMIMCl	3.10 × 10 <sup>-2</sup>	1.3310	0.3774	2.87 × 10 <sup>-4</sup>	0.3894
BMPYCl	3.94 × 10 <sup>-2</sup>	1.3308	0.7738	3.47 × 10 <sup>-2</sup>	0.6350
BMIPICl	3.74 × 10 <sup>-2</sup>	1.3294	0.1724	-7.70 × 10 <sup>-1</sup>	1.4782
BMPYRCI	3.12 × 10 <sup>-2</sup>	1.3311	0.7915	-5.95 × 10 <sup>-1</sup>	0.7591

<sup>a</sup>Fitting parameters of eq 5. <sup>b</sup>Fitting parameters of eq 6.

zeta potential conversions because of simplicity reasons. The concentration dependence of the  $\eta$  values is known for the inorganic salts<sup>19,66</sup> and was measured for the aqueous IL solutions, as detailed below. The average error of the zeta potentials determined in the electrophoretic measurements is about 5%.

**Dynamic Light Scattering.** Dynamic light scattering (DLS) was used to determine the hydrodynamic radius ( $R_h$ ) of the particles. The experiments were carried out with a Litesizer 500 instrument (Anton Paar) at a scattering angle of 175°. The correlation function was fitted with the cumulant method to obtain the decay rate constant ( $\Gamma$ ). The diffusion coefficient ( $D$ ) was calculated as follows:<sup>67</sup>

$$D = \Gamma/q^2 \quad (2)$$

where  $q$  is the scattering vector, which can be calculated using the parameters of the experimental setup:

$$q = (4\pi n/\lambda)\sin(\Theta/2) \quad (3)$$

where  $n$  is the refractive index of the medium,  $\lambda$  is the wavelength of the laser beam, and  $\Theta$  is the scattering angle. The refractive indices of the IL solutions were determined, as detailed later. The  $R_h$  was then calculated by the Stokes–Einstein equation:

$$R_h = k_B T / 6\eta\pi D \quad (4)$$

where  $k_B$  is the Boltzmann constant and  $T$  is the absolute temperature. The sample preparation procedure was the same as in the electrophoretic studies with the exception that the DLS measurements were started immediately after adding the h-HNTs stock suspension and mixing for 25 s. The samples were equilibrated for 30 s in the instrument before data collection began.

**Refractive Index.** The  $n$  values of the IL solutions were measured with an Abbat 3200 automatic one-wavelength

refractometer (Anton Paar) at 589 nm. The data used in eq 3 were interpolated with a linear fit on the  $n$  versus IL concentration values (Figure 2a):

$$n = c_{IL}a + b \quad (5)$$

where  $C_{IL}$  is the molar concentration of the ILs, while  $a$  and  $b$  are the fitting parameters given in Table 1.

**Viscosity.** The  $\eta$  data of the IL solutions were measured in a cone–plate geometry (CPE-40 cone) with a LVDV-II+ ProC/P viscometer (Brookfield). The  $\eta$  of the different IL–water mixtures was obtained by fitting the shear stress versus shear rate data with the Casson model.<sup>68</sup> The measured  $\eta$  values were then plotted against  $C_{IL}$  and fitted with the following equation<sup>66</sup>

$$\eta/\eta_0 = 1 + A\sqrt{c_{IL}} + Bc_{IL} + Dc_{IL}^2 \quad (6)$$

where  $\eta_0$  is the viscosity of water, while  $A$ ,  $B$ , and  $D$  constants are listed in Table 1. The above relation was applied for interpolation of  $\eta$  used in eqs 1 and 4. The experimental data determined in the IL concentration regimes applied and the fits with eq 6 are shown together in Figure 2b.

**Electron Microscopy.** Morphology studies of bare h-HNTs were carried out using transmission electron microscopy (TEM, FEI TECNAI G<sup>2</sup>20 X-TWIN). For the TEM measurements, the dispersions of the particles were dried on copper–carbon mesh grids, and 200 kV accelerating voltage was used for imaging in the bright field mode.

## RESULTS

Surface charge and aggregation rates of negatively charged halloysite nanotubes (h-HNTs) were investigated in the presence of inorganic electrolytes and ILs by electrophoresis and DLS. The principal aim of these experiments was to assess the affinities of the cations (which act as counterions) to the h-HNT surface and their effects on the stability of colloidal

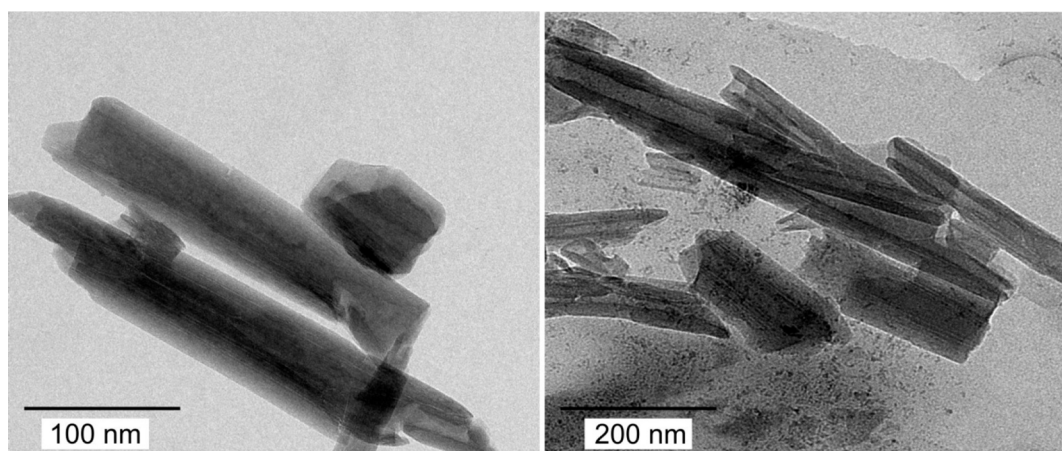


Figure 3. TEM micrographs of the bare h-HNTs. The images were taken after drying the dispersions.

dispersions. Based on these results, the validity of the Hofmeister series will be clarified for simple ions, and the series will be extended with IL cations.

**Characterization of the h-HNT.** The morphology of the h-HNTs was studied with TEM (Figure 3), and the elongated structure was confirmed. The outer diameter and length of the h-HNTs vary in the range of 50–60 and 200–500 nm, respectively, indicating moderate polydispersity in both dimensions.

The pH-dependent charge and size of h-HNT were investigated in the 3–11 pH regime. The zeta potentials were negative under the conditions applied due to the abundance of the deprotonated silanol groups on the outer surface (Figure 4). Although positive zeta potentials were

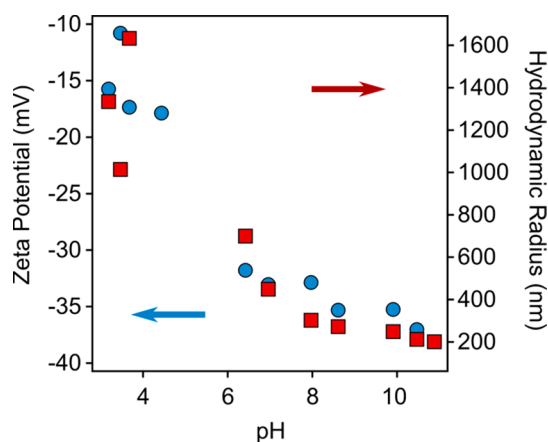


Figure 4. Zeta potentials (circles, left axis) and hydrodynamic radii (squares, right axis) of h-HNT as a function of the pH. The measurements were performed at 1 mM ionic strength.

reported earlier with a point of zero charge of 2,<sup>16</sup> this condition is out of the pH range studied here. The overall negative charge originates from the higher number of deprotonated silanol groups compared to the protonated aluminol groups.<sup>5</sup> However, one cannot determine this relation quantitatively on the basis of the zeta potential results. A significant decrease was observed in the pH range of 4–6, as the  $pK_a$  of the silanol groups falls in this range. Subsequently, the zeta potentials of h-HNT indicate a relatively high magnitude of surface charge over a wide pH range in the alkaline regime. The further colloidal stability studies were

carried out at pH 7. At this condition the particles possess considerable negative charge ( $-33$  mV zeta potential), while the pH is low enough to avoid possible carbon dioxide absorption into the samples, which would be a significant error source in the ion specificity studies.

The trend in the pH-dependent size of h-HNTs is analogous to the above-discussed zeta potential tendency. The hydrodynamic size decreased with the pH due to the increase of the surface charge and, consequently, the lowering of the tendency of the particles toward aggregation. The presence of some aggregates at lower pHs is due to the weaker double layer repulsion between the particles giving rise to higher average hydrodynamic radii in these samples. At pH 7 the hydrodynamic radius was obtained as 442 nm, and the polydispersity index was 0.15. These data indicate that the h-HNT dispersions are suitable for time-resolved DLS measurements, discussed later.

**Surface Charge Properties.** First, the charging features of h-HNT particles were investigated in the presence of NaCl, KCl, and CsCl, as no literature data were reported for these systems so far. In general, the magnitude of the zeta potentials decreased with the salt concentration, and they remained negative in the entire regime investigated (Figure 5a). However, at a given ionic strength, the measured potentials are system specific. An increase in magnitude can be observed in the  $Cs^+ < K^+ < Na^+$  order indicating ion specific interactions with the surface of h-HNT particles.

Subsequently, the effect of the IL cations on the charging conditions of h-HNT was investigated by measuring the zeta potential in a wide range of IL concentrations (Figure 5b). It was assumed that ILs completely dissociate to hydrated anions and cations under these experimental conditions.<sup>50,56,58</sup> It is obvious from the measured data that the system containing BMPY<sup>+</sup> cations behaved rather differently from the other systems. Accordingly, charge neutralization and reversal behavior of the h-HNT particles were observed, indicating high affinity of BMPY<sup>+</sup> cations to adsorb on the surface of the colloidal particles. A similar phenomenon has been already reported with some other IL cations with both hydrophilic<sup>59</sup> and hydrophobic<sup>60</sup> surfaces; however, it is rather exceptional behavior within monovalent counterions. For the BMIMCl, BMPYRCl, and BMPIPCl solutions, the absolute value of the zeta potential decreased with increasing the IL concentration, and the values remained in the negative regime even at high IL levels. Looking at the zeta potential at the same IL

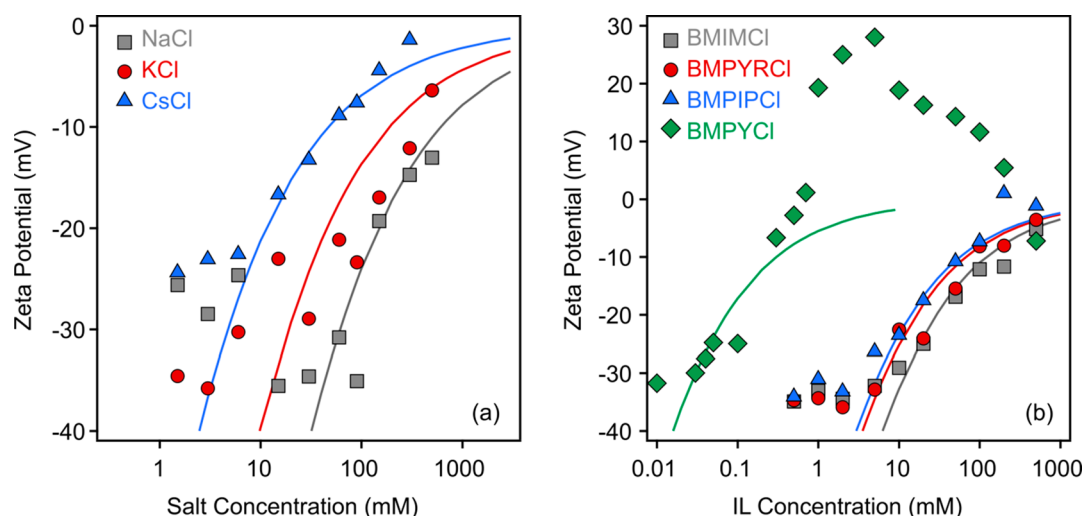


**Figure 5.** Zeta potentials of negatively charged h-HNTs at different concentrations of monovalent salts (a) and IL solutions (b). The lines are the results of calculations using eq 9.

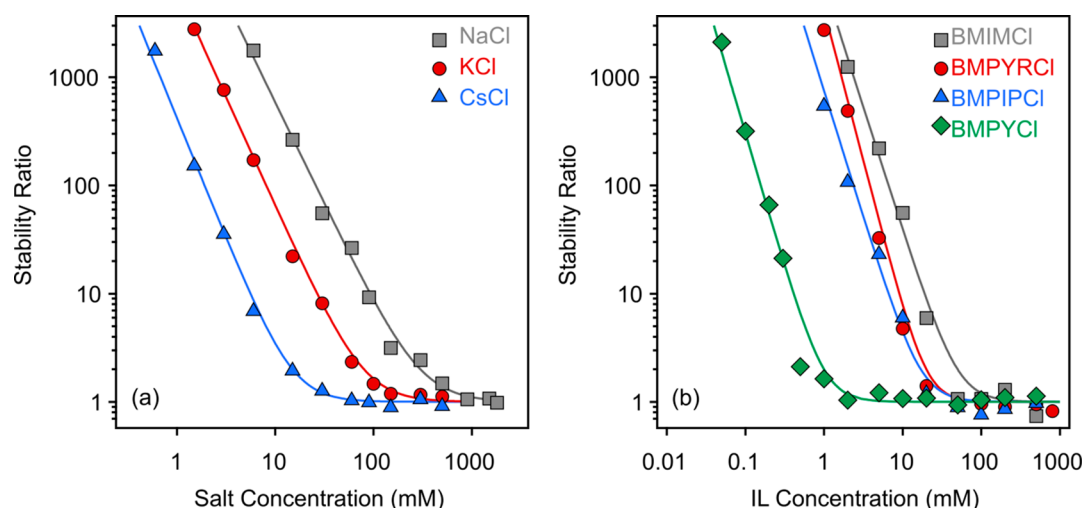


**Figure 6.** Stability ratios of h-HNTs at different concentrations of monovalent salt (a) and IL solutions (b). The lines are the results of calculations using eq 8.

concentrations, their magnitude followed the  $\text{BMPY}^+ < \text{BMPIP}^+ < \text{BMPYR}^+ < \text{BMIM}^+$  order indicating a decreasing adsorption tendency of the cations to the surface in this sequence. Note that  $\text{BMPY}^+$  is the only cation in which the methyl group is connected to a carbon atom (and to nitrogen in all other ILs). This fact may explain the different affinity to the surface; however, no unambiguous experimental evidence exists to underline this implication.

**Particle Aggregation.** The aggregation properties of systems containing h-HNT particles were investigated by time-resolved DLS experiments by following the change in the hydrodynamic radius under the same experimental conditions (pH, particle concentration, and ionic strength range) as for zeta potential measurements. The rate of aggregation was expressed in terms of stability ratio ( $W$ ), which was calculated as follows:<sup>69</sup>

$$W = \Delta_{\text{fast}} / \Delta \quad (7)$$

where  $\Delta$  is the apparent aggregation rate constant calculated from the initial increase in the hydrodynamic radii and  $\Delta_{\text{fast}}$  is the rate constant determined in 1 M KCl solutions, in which

fast aggregation of the particles occurs. Thus, stability ratios close to unity indicate unstable samples, and higher values refer to more stable dispersion and slower particle aggregation.

In general, the trends in the stability ratio values were the same for both inorganic salts and ILs (Figure 6a and Figure 6b, respectively). Accordingly, slow aggregation was observed at low ionic strengths, which is illustrated by the high stability ratio values. Then, in parallel with the increase in ionic strength, the stability ratio decreases until it reaches a unit value and remains constant within the experimental error at higher concentrations. This behavior resembles the one predicted by the DLVO theory,<sup>70</sup> which states that the overlap of the electrical double layers around the charged particles leads to the rise of repulsive electrostatic forces at low salt concentrations, which are stronger than the attractive van der Waals forces. This situation results in stable dispersions. Besides, the double layer forces weaken progressively with increasing the electrolyte level due to the surface charge screening, and thus van der Waals forces become predominant at high electrolyte concentrations leading to aggregation of the particles. These observations are generic for all colloidal

Table 2. Characteristic Aggregation and Charging Data of h-HNTs Particles Measured in Monovalent Salt and IL Solutions

salt/IL	NaCl	KCl	CsCl	BMIMCl	BMPYRCl	BMPIPCl	BMPYCl
CCC (mM) <sup>a</sup>	300	80	15	50	20	17	1
$\sigma$ (mC/m <sup>2</sup> ) <sup>b</sup>	-16	-10	-5	-8	-6	-5	-1
$\zeta$ (mV) <sup>c</sup>	-13	-15	-17	-15	-20	-19	-6

<sup>a</sup>Critical coagulation concentration calculated by eq 8. <sup>b</sup>Charge density determined with eq 9. <sup>c</sup>Zeta potential at the CCC.

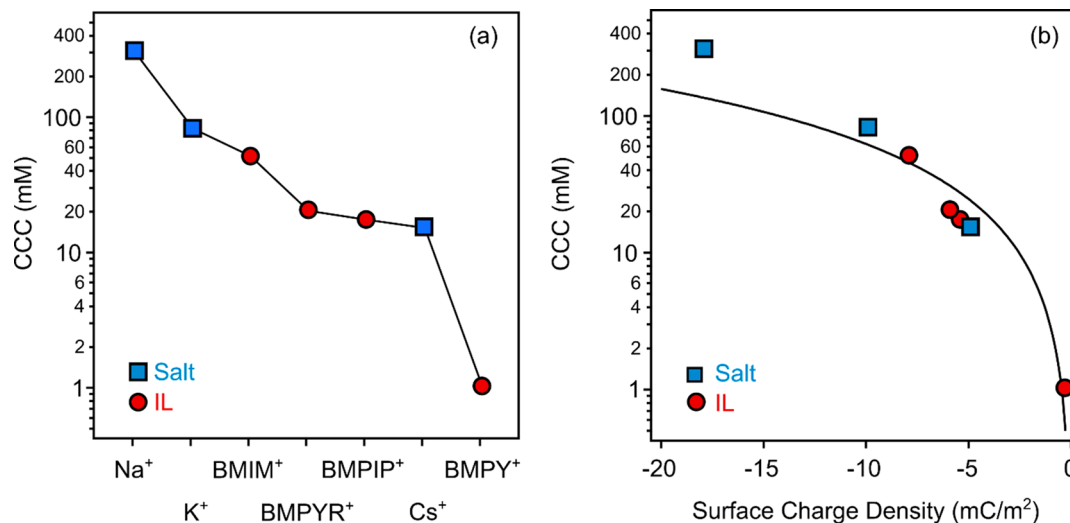


Figure 7. CCC values of h-HNT particles determined in the presence of monovalent salts and ILs (a). CCC versus the charge density data (b). The experimental CCCs and charge densities were calculated with eqs 8 and 9, respectively. The lines in (a) are just to guide the eyes, while in (b), it was calculated by eq 10.

systems, but the actual values of the stability ratios vary by changing the composition of the electrolytes. Such an influence of the type of electrolyte on the colloidal stability is not included in the DLVO theory.

Note that the charge reversal process may cause restabilization of the particles in certain systems;<sup>60</sup> however, this was not observed with the h-HNT-BMPYCl samples. This is due to the joint effect of the relatively low magnitude of the zeta potentials and charge screening by the nonadsorbed IL constituents. Similar results were also reported with titania particles dispersed in aqueous IL solutions.<sup>59</sup>

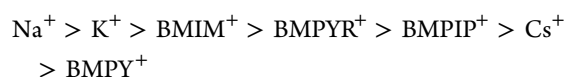
## DISCUSSION

**Ion Specific Effects.** To quantify the deviations in the aggregation tendencies for the different systems, the critical coagulation concentration (CCC) values were calculated from the stability ratio versus ionic strength plots with the following equation:<sup>69</sup>

$$W = 1 + (CCC/c)^{-\beta} \quad (8)$$

where  $c$  is the molar concentration and the exponent  $\beta$  was calculated from the slope of the stability ratios in the slow aggregation regime. Note that CCC defines the electrolyte concentration, at which the transition between the slow and fast aggregation regimes occurs.<sup>70</sup> The fitted curves are shown in Figure 6a and 6b, while the obtained CCCs are shown in Table 2 and Figure 7a.

The fitted CCC values for the h-HNTs in inorganic salt and IL solutions decrease in the following order:



Considering only the inorganic cations, the sequence corresponds to the direct Hofmeister series for negatively charged hydrophobic surfaces.<sup>19</sup> Once the IL cations are included, the presence of BMPY<sup>+</sup> leads to the lowest CCC. This remarkable effect stems from the strong adsorption of BMPY<sup>+</sup> to the surface of h-HNT resulting in charge neutralization and reversal, as discussed before. The CCCs in the case of other IL cations are located between K<sup>+</sup> and Cs<sup>+</sup> in the above order, which is considered as the Hofmeister series for h-HNT particles extended with IL cations.

**Charge–Aggregation Relation.** Earlier studies carried out with different colloid particle dispersions shed light on the importance of ion adsorption in the stability of colloids.<sup>19–21</sup> Therefore, this issue was explored by calculating the charge density ( $\sigma$ ) values from the zeta potential versus concentration plots using the Debye–Hückel model:<sup>70</sup>

$$\sigma = \epsilon \epsilon_0 \kappa \zeta \quad (9)$$

where  $\kappa$  is the inverse Debye length, which contains the contribution of the ionic species to the electrical double layer.<sup>65</sup> Note that this model is valid in the case of moderate zeta potentials, and thus deviation between the experimental and calculated values occurs at low ionic strength. The results of the calculations are shown in Figures 5, and the determined charge densities are given in Table 2. One can notice that they follow the same order as the CCCs discussed above. Accordingly, the lowest charge was determined for BMPY<sup>+</sup> and the highest for Na<sup>+</sup>.

Plotting the CCC values against the charge densities (Figure 7b), the charge–aggregation relation is unambiguous. The strength of cation adsorption is the highest for BMPY<sup>+</sup> and the lowest for Na<sup>+</sup>. The repulsive electrical double layer forces are the weakest in the former case due to the higher extent of



charge compensation upon adsorption; hence, destabilization takes place at a low CCC. The situation in the case of  $\text{Na}^+$  is the opposite. Weak adsorption on the oppositely charged surface does not significantly decrease the charge of h-HNT leading to strong double layer forces, which can be screened only at higher salt concentrations giving rise to a higher CCC value. In summary, the extent of the ion specific adsorption determines the location of the CCCs in the individual systems.

As discussed above, such a dependence of the CCC on the type of ions is not predicted by the DLVO theory, once the same particles are dispersed in different monovalent salt solutions. However, in the case of ion specific adsorption, the surface charge of the particle changes; thus, one cannot consider the properties of h-HNT to be the same in all systems. In other words, the significant adsorption of  $\text{BMPY}^+$  leads to different charging properties and strength of double layer forces than in the case of  $\text{Na}^+$ , where the charge is close to that of the bare h-HNT. The origin of the interparticle interactions can be further investigated by the relation derived from the DLVO theory, which allows the calculation of CCC values from the charge densities:<sup>70</sup>

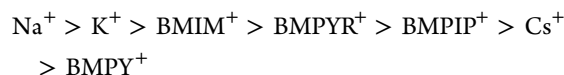
$$\text{CCC} = 0.365/N_A L_B (H\epsilon\epsilon_0)^{-2/3} \sigma^{4/3} \quad (10)$$

where  $N_A$  is Avogadro's number,  $H$  is the Hamaker constant, and  $L_B$  is the Bjerrum length, which is equal to 0.72 nm for monovalent electrolytes in water.<sup>19</sup> To obtain the best fit to the experimental data, a Hamaker constant of  $7.0 \times 10^{-21}$  J was used in eq 10.

Based on the relatively good agreement between the experimental and calculated CCCs (Figure 7b), one can conclude that DLVO theory predicts the CCC values rather well, once the appropriate charge densities are entered in eq 10. Such an agreement indicates that the aggregation mechanism, i.e., the origin of major interparticle forces, can be derived from the DLVO model. Nevertheless, the locations of the CCCs are system specific, and they are determined by the affinity of the counterions to the surface, which affects the strength of the double layer repulsion. Such a synergistic influence of DLVO forces and ion specific adsorption on the colloidal stability led to different CCCs and the establishment of the Hofmeister series of cations for the h-HNT particles.

## CONCLUSIONS

The effect of simple monovalent electrolytes ( $\text{NaCl}$ ,  $\text{KCl}$ , and  $\text{CsCl}$ ) and water-soluble ILs ( $\text{BMIMCl}$ ,  $\text{BMPYCl}$ ,  $\text{BMPYRCl}$ , and  $\text{BMPIPCl}$ ) on the surface charge and aggregation of h-HNT particles in dilute aqueous solutions was investigated by light scattering techniques. Very similar generic trends were observed in zeta potentials and stability ratios determined at different ionic strengths except for the  $\text{BMPY}^+$  cation. In that case, the unexpectedly strong adsorption gave rise to charge neutralization and reversal behavior of the negatively charged h-HNT. For the other systems, the magnitudes of both zeta potentials and stability ratios decreased with increasing the ionic strength leading to rapidly aggregating particles beyond the CCCs, whose order was determined as follows:



This sequence corresponds to the direct Hofmeister series suggested for cations in the presence of negatively charged hydrophobic surfaces. However, this is the first time when such

a series is established for HNTs and extended with IL cations. Comparison of the CCCs determined by the experiments and those calculated by the DLVO theory sheds light on the origin of the interparticle forces. It was found that the aggregation mechanism is controlled by the interplay between the repulsive electrical double layer and attractive van der Waals forces, which is in line with the DLVO theory. In addition, the variation of the CCC in different salt solutions results from the different extent of counterion adsorption on the h-HNT surface, which follows the opposite order than the CCC data shown above. These findings bring considerable new knowledge useful for designing the processable h-HNT dispersions in electrolyte solutions or in their mixtures. The interfacial assembly of IL constituents is of paramount importance to tune and predict the stability of colloidal systems including dispersions of HNT or other inorganic particles in ILs.

## AUTHOR INFORMATION

### Corresponding Author

Istvan Szilagyi – MTA-SZTE Lendület Biocolloids Research Group and Interdisciplinary Excellence Center, Department of Physical Chemistry and Materials Science, University of Szeged, H-6720 Szeged, Hungary; [orcid.org/0000-0001-7289-0979](https://orcid.org/0000-0001-7289-0979); Email: [szistvan@chem.u-szeged.hu](mailto:szistvan@chem.u-szeged.hu)

### Authors

Bojana Katana – MTA-SZTE Lendület Biocolloids Research Group and Interdisciplinary Excellence Center, Department of Physical Chemistry and Materials Science, University of Szeged, H-6720 Szeged, Hungary

Dóra Takács – MTA-SZTE Lendület Biocolloids Research Group and Interdisciplinary Excellence Center, Department of Physical Chemistry and Materials Science, University of Szeged, H-6720 Szeged, Hungary

Édit Csapó – Interdisciplinary Excellence Center, Department of Physical Chemistry and Materials Science, University of Szeged, H-6720 Szeged, Hungary; [orcid.org/0000-0001-8182-640X](https://orcid.org/0000-0001-8182-640X)

Tamás Szabó – Interdisciplinary Excellence Center, Department of Physical Chemistry and Materials Science, University of Szeged, H-6720 Szeged, Hungary; [orcid.org/0000-0002-6980-9524](https://orcid.org/0000-0002-6980-9524)

Andrej Jamnik – Faculty of Chemistry and Chemical Technology, University of Ljubljana, SI-1000 Ljubljana, Slovenia

Complete contact information is available at: <https://pubs.acs.org/10.1021/acs.jpbc.0c07885>

### Notes

The authors declare no competing financial interest.

## ACKNOWLEDGMENTS

The authors acknowledge financial support from the Hungarian National Research, Development and Innovation Office (SNN131558), the Slovenian Research Agency (research core funding No. P1-0201 and the project No. N1-0139 “Delamination of Layered Materials and Structure-Dynamics Relationship in Green Solvents”), and the Ministry of Human Capacities of Hungary (20391-3/2018/FEKUS-TRAT). T.S. also acknowledges the support by the János Bolyai Research Scholarship of the Hungarian Academy of Sciences (No. BO/00131/19/7) and the support from the ÚNKP-20-5 New National Excellence Program of the Ministry



for Innovation and Technology. The support from the University of Szeged Open Access Fund (5008) is gratefully acknowledged.

## REFERENCES

- (1) Santos, A. C.; Ferreira, C.; Veiga, F.; Ribeiro, A. J.; Panchal, A.; Lvov, Y.; Agarwal, A. Halloysite clay nanotubes for life sciences applications: From drug encapsulation to bioscaffold. *Adv. Colloid Interface Sci.* **2018**, *257*, 58–70.
- (2) Lazzara, G.; Cavallaro, G.; Panchal, A.; Fakhrullin, R.; Stavitskaya, A.; Vinokurov, V.; Lvov, Y. An assembly of organic-inorganic composites using halloysite clay nanotubes. *Curr. Opin. Colloid Interface Sci.* **2018**, *35*, 42–50.
- (3) Massaro, M.; Lazzara, G.; Milioto, S.; Noto, R.; Riela, S. Covalently modified halloysite clay nanotubes: synthesis, properties, biological and medical applications. *J. Mater. Chem. B* **2017**, *5*, 2867–2882.
- (4) Vergaro, V.; Abdullayev, E.; Lvov, Y. M.; Zeitoun, A.; Cingolani, R.; Rinaldi, R.; Leporatti, S. Cytocompatibility and uptake of halloysite clay nanotubes. *Biomacromolecules* **2010**, *11*, 820–826.
- (5) Mitra, G. B.; Bhattacharjee, S. Structure of halloysite. *Acta Crystallogr., Sect. B: Struct. Crystallogr. Cryst. Chem.* **1975**, *31*, 2851–2857.
- (6) Horky, P.; Skalickova, S.; Baholet, D.; Skladanka, J. Nanoparticles as a solution for eliminating the risk of mycotoxins. *Nanomaterials* **2018**, *8*, 727.
- (7) Fizir, M.; Dramou, P.; Dahiru, N. S.; Ruya, W.; Huang, T.; He, H. Halloysite nanotubes in analytical sciences and in drug delivery: A review. *Microchim. Acta* **2018**, *185*, 389.
- (8) Zahidah, K. A.; Kakooei, S.; Ismail, M. C.; Raja, P. B. Halloysite nanotubes as nanocontainer for smart coating application: A review. *Prog. Org. Coat.* **2017**, *111*, 175–185.
- (9) Zhang, Y.; Tang, A. D.; Yang, H. M.; Ouyang, J. Applications and interfaces of halloysite nanocomposites. *Appl. Clay Sci.* **2016**, *119*, 8–17.
- (10) Lvov, Y.; Wang, W. C.; Zhang, L. Q.; Fakhrullin, R. Halloysite clay nanotubes for loading and sustained release of functional compounds. *Adv. Mater.* **2016**, *28*, 1227–1250.
- (11) Hari, J.; Gyurki, A.; Sarkozi, M.; Földes, E.; Pukanszky, B. Competitive interactions and controlled release of a natural antioxidant from halloysite nanotubes. *J. Colloid Interface Sci.* **2016**, *462*, 123–129.
- (12) Yang, Y. T.; Chen, Y.; Leng, F.; Huang, L.; Wang, Z. J.; Tian, W. Q. Recent advances on surface modification of halloysite nanotubes for multifunctional applications. *Appl. Sci.* **2017**, *7*, 1215.
- (13) Lvov, Y. M.; Shchukin, D. G.; Mohwald, H.; Price, R. R. Halloysite clay nanotubes for controlled release of protective agents. *ACS Nano* **2008**, *2*, 814–820.
- (14) Matusik, J.; Hyla, J.; Maziarz, P.; Rybka, K.; Leiviska, T. Performance of halloysite-Mg/Al LDH materials for aqueous As(V) and Cr(VI) removal. *Materials* **2019**, *12*, 3569.
- (15) Kim, J.; Ryu, J.; Shin, J.; Lee, H.; Kim, I. S.; Sohn, D. Interactions between halloysite nanotubes and poly(styrene sulfonate) in solution. *Bull. Korean Chem. Soc.* **2017**, *38*, 107–111.
- (16) Joo, Y.; Sim, J. H.; Jeon, Y.; Lee, S. U.; Sohn, D. Opening and blocking the inner-pores of halloysite. *Chem. Commun.* **2013**, *49*, 4519–4521.
- (17) Katana, B.; Rouster, P.; Varga, G.; Muráth, S.; Glinel, K.; Jonas, A. M.; Szilagy, I. Self-assembly of protamine biomacromolecule on halloysite nanotubes for immobilization of superoxide dismutase enzyme. *ACS Appl. Bio Mater.* **2020**, *3*, 522–530.
- (18) Rouster, P.; Dondelinger, M.; Galleni, M.; Nysten, B.; Jonas, A. M.; Glinel, K. Layer-by-layer assembly of enzyme-loaded halloysite nanotubes for the fabrication of highly active coatings. *Colloids Surf., B* **2019**, *178*, 508–514.
- (19) Oncsik, T.; Trefalt, G.; Borkovec, M.; Szilagy, I. Specific ion effects on particle aggregation induced by monovalent salts within the Hofmeister series. *Langmuir* **2015**, *31*, 3799–3807.
- (20) Pavlovic, M.; Huber, R.; Adok-Sipiczki, M.; Nardin, C.; Szilagy, I. Ion specific effects on the stability of layered double hydroxide colloids. *Soft Matter* **2016**, *12*, 4024–4033.
- (21) Rouster, P.; Pavlovic, M.; Szilagy, I. Destabilization of titania nanosheet suspensions by inorganic salts: Hofmeister series and Schulze-Hardy rule. *J. Phys. Chem. B* **2017**, *121*, 6749–6758.
- (22) Higashitani, K.; Nakamura, K.; Fukasawa, T.; Tsuchiya, K.; Mori, Y. Ionic specificity in rapid coagulation of silica nanoparticles. *Langmuir* **2018**, *34*, 2505–2510.
- (23) Kang, B. B.; Tang, H. C.; Zhao, Z. D.; Song, S. S. Hofmeister series: Insights of ion specificity from amphiphilic assembly and interface property. *ACS Omega* **2020**, *5*, 6229–6239.
- (24) Lima, E. R. A.; Horinek, D.; Netz, R. R.; Biscaia, E. C.; Tavares, F. W.; Kunz, W.; Bostrom, M. Specific ion adsorption and surface forces in colloid science. *J. Phys. Chem. B* **2008**, *112*, 1580–1585.
- (25) Calero, C.; Farauto, J.; Bastos-Gonzalez, D. Interaction of monovalent ions with hydrophobic and hydrophilic colloids: Charge inversion and ionic specificity. *J. Am. Chem. Soc.* **2011**, *133*, 15025–15035.
- (26) Parsons, D. F.; Salis, A. Hofmeister effects at low salt concentration due to surface charge transfer. *Curr. Opin. Colloid Interface Sci.* **2016**, *23*, 41–49.
- (27) Kunz, W.; Henle, J.; Ninham, B. W. ‘Zur lehre von der wirkung der salze’ (about the science of the effect of salts): Franz Hofmeister’s historical papers. *Curr. Opin. Colloid Interface Sci.* **2004**, *9*, 19–37.
- (28) Yu, W. Y.; Du, N.; Gu, Y. T.; Yan, J. G.; Hou, W. G. Specific ion effects on the colloidal stability of layered double hydroxide single-layer nanosheets. *Langmuir* **2020**, *36*, 6557–6568.
- (29) Trompette, J. L.; Lahitte, J. F. Influence of the counterion nature on the stability sequence of hydrophobic latex particles. *J. Phys. Chem. B* **2019**, *123*, 3859–3865.
- (30) Merk, V.; Rehbock, C.; Becker, F.; Hagemann, U.; Nienhaus, H.; Barcikowski, S. In situ non-DLVO stabilization of surfactant-free plasmonic gold nanoparticles: Effect of Hofmeister’s anions. *Langmuir* **2014**, *30*, 4213–4222.
- (31) Lopez-Leon, T.; Santander-Ortega, M. J.; Ortega-Vinuesa, J. L.; Bastos-Gonzalez, D. Hofmeister effects in colloidal systems: Influence of the surface nature. *J. Phys. Chem. C* **2008**, *112*, 16060–16069.
- (32) Lopez-Leon, T.; Jodar-Reyes, A. B.; Bastos-Gonzalez, D.; Ortega-Vinuesa, J. L. Hofmeister effects in the stability and electrophoretic mobility of polystyrene latex particles. *J. Phys. Chem. B* **2003**, *107*, 5696–5708.
- (33) Trefalt, G.; Szilagy, I.; Tellez, G.; Borkovec, M. Colloidal stability in asymmetric electrolytes: Modifications of the Schulze-Hardy rule. *Langmuir* **2017**, *33*, 1695–1704.
- (34) Schwier, N.; Horinek, D.; Netz, R. R. Reversed anionic Hofmeister series: The interplay of surface charge and surface polarity. *Langmuir* **2010**, *26*, 7370–7379.
- (35) Schwier, N.; Horinek, D.; Sivan, U.; Netz, R. R. Reversed Hofmeister series-The rule rather than the exception. *Curr. Opin. Colloid Interface Sci.* **2016**, *23*, 10–18.
- (36) Hayes, R.; Warr, G. G.; Atkin, R. Structure and nanostructure in ionic liquids. *Chem. Rev.* **2015**, *115*, 6357–6426.
- (37) Zheng, Z. P.; Fan, W. H.; Roy, S.; Mazur, K.; Nazet, A.; Buchner, R.; Bonn, M.; Hunger, J. Ionic liquids: Not only structurally but also dynamically heterogeneous. *Angew. Chem., Int. Ed.* **2014**, *54*, 687–690.
- (38) Armand, M.; Endres, F.; MacFarlane, D. R.; Ohno, H.; Scrosati, B. Ionic-liquid materials for the electrochemical challenges of the future. *Nat. Mater.* **2009**, *8*, 621–629.
- (39) He, Z. Q.; Alexandridis, P. Nanoparticles in ionic liquids: interactions and organization. *Phys. Chem. Chem. Phys.* **2015**, *17*, 18238–18261.
- (40) Podgorssek, A.; Pensado, A. S.; Santini, C. C.; Gomes, M. F. C.; Padua, A. A. H. Interaction energies of ionic liquids with metallic nanoparticles: Solvation and stabilization effects. *J. Phys. Chem. C* **2013**, *117*, 3537–3547.
- (41) Campbell, P. S.; Santini, C. C.; Bouchu, D.; Fenet, B.; Philippot, K.; Chaudret, B.; Padua, A. A. H.; Chauvin, Y. A novel

stabilisation model for ruthenium nanoparticles in imidazolium ionic liquids: in situ spectroscopic and labelling evidence. *Phys. Chem. Chem. Phys.* **2010**, *12*, 4217–4223.

(42) Huang, Z. J.; Uranga, J. G.; Zhou, S. L.; Jia, H. Y.; Fei, Z. F.; Wang, Y. F.; Bobbink, F. D.; Lu, Q. H.; Dyson, P. J. Ionic liquid containing electron-rich, porous polyphosphazene nanoreactors catalyze the transformation of CO<sub>2</sub> to carbonates. *J. Mater. Chem. A* **2018**, *6*, 20916–20925.

(43) Sadjadi, S.; Akbari, M.; Heravi, M. M. Palladated nano-composite of halloysite-nitrogen-doped porous carbon prepared from a novel cyano-/nitrile-free task specific ionic liquid: An efficient catalyst for hydrogenation. *ACS Omega* **2019**, *4*, 19442–19451.

(44) Yang, Y. J.; Yaakob, S. M.; Rabat, N. E.; Shamsuddin, M. R.; Man, Z. Release kinetics study and anti-corrosion behaviour of a pH-responsive ionic liquid-loaded halloysite nanotube-doped epoxy coating. *RSC Adv.* **2020**, *10*, 13174–13184.

(45) Guo, S. F.; Zhao, K.; Feng, Z. Q.; Hou, Y. D.; Li, H.; Zhao, J.; Tian, Y. L.; Song, H. Z. High performance liquid crystalline bionanocomposite ionogels prepared by in situ crosslinking of cellulose/halloysite nanotubes/ionic liquid dispersions and its application in supercapacitors. *Appl. Surf. Sci.* **2018**, *455*, 599–607.

(46) Brondani, D.; Scheeren, C. W.; Dupont, J.; Vieira, I. C. Halloysite clay nanotubes and platinum nanoparticles dispersed in ionic liquid applied in the development of a catecholamine biosensor. *Analyst* **2012**, *137*, 3732–3739.

(47) Dedzo, G. K.; Detellier, C. Clay minerals-ionic liquids, nanoarchitectures, and applications. *Adv. Funct. Mater.* **2018**, *28*, 1703845.

(48) Guibert, C.; Dupuis, V.; Fresnais, J.; Peyre, V. Controlling nanoparticles dispersion in ionic liquids by tuning the pH. *J. Colloid Interface Sci.* **2015**, *454*, 105–111.

(49) Smith, J. A.; Werzer, O.; Webber, G. B.; Warr, G. G.; Atkin, R. Surprising particle stability and rapid sedimentation rates in an ionic liquid. *J. Phys. Chem. Lett.* **2010**, *1*, 64–68.

(50) Szilagy, I.; Szabo, T.; Desert, A.; Trefalt, G.; Oncsik, T.; Borkovec, M. Particle aggregation mechanisms in ionic liquids. *Phys. Chem. Chem. Phys.* **2014**, *16*, 9515–9524.

(51) Ueno, K.; Inaba, A.; Kondoh, M.; Watanabe, M. Colloidal stability of bare and polymer-grafted silica nanoparticles in ionic liquids. *Langmuir* **2008**, *24*, 5253–5259.

(52) Nordstrom, J.; Aguilera, L.; Matic, A. Effect of lithium salt on the stability of dispersions of fumed silica in the ionic liquid BMImBF<sub>4</sub>. *Langmuir* **2012**, *28*, 4080–4085.

(53) Mamusa, M.; Siritex-Plenet, J.; Cousin, F.; Dubois, E.; Peyre, V. Tuning the colloidal stability in ionic liquids by controlling the nanoparticles/liquid interface. *Soft Matter* **2014**, *10*, 1097–1101.

(54) Vanecht, E.; Binnemans, K.; Patskovsky, S.; Meunier, M.; Seo, J. W.; Stappers, L.; Fransaer, J. Stability of sputter-deposited gold nanoparticles in imidazolium ionic liquids. *Phys. Chem. Chem. Phys.* **2012**, *14*, 5662–5671.

(55) Sheehan, A.; Jurado, L. A.; Ramakrishna, S. N.; Arcifa, A.; Rossi, A.; Spencer, N. D.; Espinosa-Marzal, R. M. Layering of ionic liquids on rough surfaces. *Nanoscale* **2016**, *8*, 4094–4106.

(56) Valmacco, V.; Trefalt, G.; Maroni, P.; Borkovec, M. Direct force measurements between silica particles in aqueous solutions of ionic liquids containing 1-butyl-3-methylimidazolium (BMIM). *Phys. Chem. Chem. Phys.* **2015**, *17*, 16553–16559.

(57) Beattie, D. A.; Espinosa-Marzal, R. M.; Ho, T. T. M.; Popescu, M. N.; Ralston, J.; Richard, C. J. E.; Sellapperumage, P. M. F.; Krasowska, M. Molecularly-thin precursor films of imidazolium-based ionic liquids on mica. *J. Phys. Chem. C* **2013**, *117*, 23676–23684.

(58) Sajjadi, H.; Modaressi, A.; Magri, P.; Domanska, U.; Sindt, M.; Mieloszynski, J. L.; Mutelet, F.; Rogalski, M. Aggregation of nanoparticles in aqueous solutions of ionic liquids. *J. Mol. Liq.* **2013**, *186*, 1–6.

(59) Rouster, P.; Pavlovic, M.; Cao, T.; Katana, B.; Szilagy, I. Stability of titania nanomaterials dispersed in aqueous solutions of ionic liquids of different alkyl chain lengths. *J. Phys. Chem. C* **2019**, *123*, 12966–12974.

(60) Oncsik, T.; Desert, A.; Trefalt, G.; Borkovec, M.; Szilagy, I. Charging and aggregation of latex particles in aqueous solutions of ionic liquids: Towards an extended Hofmeister series. *Phys. Chem. Chem. Phys.* **2016**, *18*, 7511–7520.

(61) Israelachvili, J. *Intermolecular and surface forces*, 3rd ed.; Academic Press: London, 2011.

(62) Constantinescu, D.; Weingartner, H.; Herrmann, C. Protein denaturation by ionic liquids and the Hofmeister series: A case study of aqueous solutions of ribonuclease A. *Angew. Chem., Int. Ed.* **2007**, *46*, 8887–8889.

(63) Debeljuh, N.; Barrow, C. J.; Byrne, N. The impact of ionic liquids on amyloid fibrilization of A beta 16–22: tuning the rate of fibrilization using a reverse Hofmeister strategy. *Phys. Chem. Chem. Phys.* **2011**, *13*, 16534–16536.

(64) Tietze, A. A.; Bordusa, F.; Giernoth, R.; Imhof, D.; Lenzer, T.; Maass, A.; Mrestani-Klaus, C.; Neundorff, I.; Oum, K.; Reith, D.; Stark, A. On the nature of interactions between ionic liquids and small amino-acid-based biomolecules. *ChemPhysChem* **2013**, *14*, 4044–4064.

(65) Delgado, A. V.; Gonzalez-Caballero, E.; Hunter, R. J.; Koopal, L. K.; Lyklema, J. Measurement and interpretation of electrokinetic phenomena - (IUPAC technical report). *Pure Appl. Chem.* **2005**, *77*, 1753–1805.

(66) Jenkins, H. D. B.; Marcus, Y. Viscosity B-coefficients of ions in solution. *Chem. Rev.* **1995**, *95*, 2695–2724.

(67) Pusey, P. N. Dynamic light scattering. In *Neutrons, X-Rays and Light*; Lindner, P., Zemb, T., Eds.; Elsevier Science B.V.: Amsterdam, 2002; pp 203–220.

(68) Joye, D. D. Shear rate and viscosity corrections for a Casson fluid in cylindrical (Couette) geometries. *J. Colloid Interface Sci.* **2003**, *267*, 204–210.

(69) Grolimund, D.; Elimelech, M.; Borkovec, M. Aggregation and deposition kinetics of mobile colloidal particles in natural porous media. *Colloids Surf., A* **2001**, *191*, 179–188.

(70) Evans, D. F.; Wennerstrom, H. *The colloidal domain*; John Wiley: New York, 1999.



Cite this: *Soft Matter*, 2016,  
12, 4024

## Ion specific effects on the stability of layered double hydroxide colloids

Marko Pavlovic,<sup>a</sup> Robin Huber,<sup>a</sup> Monika Adok-Sipiczki,<sup>a</sup> Corinne Nardin<sup>ab</sup> and Istvan Szilagyi<sup>\*a</sup>

Positively charged layered double hydroxide particles composed of Mg<sup>2+</sup> and Al<sup>3+</sup> layer-forming cations and NO<sub>3</sub><sup>-</sup> charge compensating anions (MgAl-NO<sub>3</sub>-LDH) were synthesized and the colloidal stability of their aqueous suspensions was investigated in the presence of inorganic anions of different charges. The formation of the layered structure was confirmed by X-ray diffraction, while the charging and aggregation properties were explored by electrophoresis and light scattering. The monovalent anions adsorb on the oppositely charged surface to a different extent according to their hydration state leading to the Cl<sup>-</sup> > NO<sub>3</sub><sup>-</sup> > SCN<sup>-</sup> > HCO<sub>3</sub><sup>-</sup> order in surface charge densities. The ions on the right side of the series induce the aggregation of MgAl-NO<sub>3</sub>-LDH particles at lower concentrations, whereas in the presence of the left ones, the suspensions are stable even at higher salt levels. The adsorption of multivalent anions gave rise to charge neutralization and charge reversal at appropriate concentrations. For some di, tri and tetravalent ions, charge reversal resulted in restabilization of the suspensions in the intermediate salt concentration regime. Stable samples were also observed at low salt levels. Particle aggregation was fast near the charge neutralization point and at high concentrations. These results, which evidence the colloidal stability of MgAl-NO<sub>3</sub>-LDH in the presence of various anions, are of prime fundamental interest. These are also critical for applications to develop stable suspensions of primary particles for water purification processes, with the aim of the removal of similar anions by ion exchange.

Received 14th December 2015,  
Accepted 7th March 2016

DOI: 10.1039/c5sm03023d

www.rsc.org/softmatter

### Introduction

Layered double hydroxides (LDHs) are anionic clays composed of mixed positively charged lamellar hydroxides of divalent (*e.g.*, Mg<sup>2+</sup>, Zn<sup>2+</sup> or Ca<sup>2+</sup>) and trivalent (*e.g.*, Al<sup>3+</sup>, Fe<sup>3+</sup> or Cr<sup>3+</sup>) metal ions with charge compensating anions between the layers.<sup>1</sup> LDH particles and their composite materials are widely used in energy storage,<sup>2,3</sup> medical treatments,<sup>4-6</sup> coating,<sup>7</sup> catalysis<sup>8-10</sup> and the removal of water pollutants.<sup>11-13</sup> For the latter application, their relatively high anion exchange capacity is utilized to capture various types of anions (*e.g.*, NO<sub>3</sub><sup>-</sup>, SO<sub>4</sub><sup>2-</sup>, SeO<sub>4</sub><sup>2-</sup>, PO<sub>4</sub><sup>3-</sup> and AsO<sub>4</sub><sup>3-</sup>) during water purification processes. Ion exchange can take place by intercalation between the layers and also by adsorption on the particle surface. To achieve high efficiencies of these procedures, stable LDH suspensions containing primary particles are required during the ion exchange process. In addition, the particles have to be aggregated at a

later stage for their facile removal from the reaction mixture. The effect of anions on the colloidal stability thus needs to be comprehensively understood to control particle aggregation.

The classical theory developed for aqueous suspensions of charged colloidal particles by Derjaguin, Landau, Verwey and Overbeek (DLVO) has proven to be suitable to predict colloidal stability in the presence of electrolytes.<sup>14,15</sup> It states that the acting interparticle force is the superposition of the repulsive double layer and attractive van der Waals forces. The first one originates from the overlap of electrical double layers forming around the charged particles dispersed in a salt solution. Its magnitude decreases with an increase in the ionic strength due to the screening effect of the counterions on the surface charge. The attractive van der Waals forces are independent of the electrolyte concentration and only depend on the size and composition of the particles. Accordingly, aqueous colloids are stable at low ionic strength and unstable at higher electrolyte concentrations, while these stability regimes are separated by the critical coagulation concentration (CCC).<sup>16</sup>

The presence of simple salts of different compositions can lead to different CCCs. This ion specificity on particle aggregation usually follows the tendency described by the Hofmeister series<sup>17-19</sup> for anions and cations as

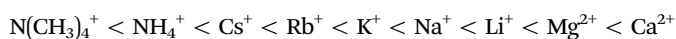
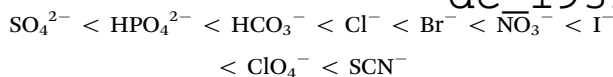
<sup>a</sup> Department of Inorganic and Analytical Chemistry, University of Geneva,  
30 Quai Ernest-Ansermet, CH-1205 Geneva, Switzerland.

E-mail: istvan.szilagyi@unige.ch; Tel: +41 22 3796031

<sup>b</sup> Institut des Sciences Analytiques et de Physicochimie pour l'Environnement et les Matériaux, Université de Pau et des Pays de l'Adour, 2 Avenue du Président Angot, F-64053 Pau, France



dc\_1931\_21



For the correct interpretation of this order, one has to consider the charge and the hydrophobicity of the particle surface. Accordingly, ions located on the right side of the series (e.g.,  $\text{SCN}^-$  and  $\text{Ca}^{2+}$ ) stabilize negatively charged, hydrophobic particles in aqueous suspensions leading to a higher CCC, while the ions on the left side (e.g.,  $\text{SO}_4^{2-}$  and  $\text{N}(\text{CH}_3)_4^+$ ) aggregate the particles at lower concentrations (direct Hofmeister series). The order is reversed (indirect Hofmeister series) for negatively charged, hydrophilic particles. These tendencies were established by aggregation studies with negatively charged latex,<sup>20,21</sup> clay,<sup>22,23</sup> silver iodide<sup>24</sup> and titania.<sup>25</sup> For positively charged, hydrophobic particles, the indirect Hofmeister series has to be considered, i.e., ions on the right side of the series induce aggregation at low concentrations, whereas the ones on the left side are able to destabilize suspensions only at high CCC. The order is reversed and the direct Hofmeister series is valid for positively charged, hydrophilic particles. The interaction of latex,<sup>20,26,27</sup> peptide<sup>28</sup> and gold<sup>29</sup> particles of positive charge with ions from the Hofmeister series followed the rule.

The effects of sodium salts of different anions ( $\text{SCN}^-$ ,  $\text{Br}^-$ ,  $\text{Cl}^-$ ,  $\text{SO}_4^{2-}$ ,  $\text{HPO}_4^{2-}$  and  $\text{CO}_3^{2-}$ ) within the Hofmeister series on the aggregation of weakly charged LDHs have been also investigated.<sup>30</sup> The reported CCC values showed good agreement with the tendency predicted by the indirect Hofmeister series for positively charged, hydrophobic particles. However, only a weak dependence on the type of salt was discovered for monovalent ions. The presence of multivalent anions decreased the CCCs significantly. This fact indicates the importance of the counterion valence on the colloidal stability of the particles, which has to be treated differently from the monovalent case.

Although the DLVO theory takes the valence of ions into account through the ionic strength, the type of salt (i.e., ion specificity) is not considered. Accordingly, electrical double layer forces decrease with the valence of counterions at the same salt concentrations and such a decrease leads to a dependence of the CCCs on the valence ( $z$ ) as

$$\text{CCC} \propto \frac{1}{z^n} \quad (1)$$

This is the so-called Schulze–Hardy rule<sup>31,32</sup> and  $n$  can vary between 2 and 6 depending on the surface charge density of the particles.<sup>33–35</sup> The aggregation of latex,<sup>35–39</sup> iron oxide,<sup>40,41</sup> clay,<sup>22,30,42</sup> and carbon derivative<sup>43,44</sup> particles was investigated in the presence of multivalent ions and a similar decrease in the CCCs was observed indicating the effectiveness of multivalent ions in the destabilization of aqueous colloids. It was pointed out in these studies that the adsorption of multivalent ions decreases the surface charge density more effectively, and hence, the CCCs were shifted towards lower concentrations since less salt is needed to screen repulsive double layer forces.

For LDH particles, interactions with multivalent anions (e.g.,  $\text{CO}_3^{2-}$ ,  $\text{SO}_4^{2-}$ ,  $\text{CrO}_4^{2-}$ ,  $\text{PO}_4^{3-}$  and  $\text{AsO}_4^{3-}$ ) have been extensively investigated to determine the adsorbed amount and to clarify the adsorption mechanism.<sup>45–51</sup> In spite of the large number of such studies, no comprehensive investigation on the effect of anion adsorption on aggregation kinetics and related colloidal stability has been published yet.

In the present research, we aimed at investigating the surface charge properties and aggregation of LDH particles composed of  $\text{Mg}^{2+}$  and  $\text{Al}^{3+}$  metal ions and  $\text{NO}_3^-$  interlayer anions (denoted as  $\text{MgAl-NO}_3\text{-LDH}$ ) in the presence of the  $\text{K}^+$  salts of various mono- and multivalent anions. The  $\text{NO}_3^-$  intercalated LDHs are widely applied, since other anions can be easily intercalated between the layers by ion exchange. Electrophoretic and dynamic light scattering experiments were performed in aqueous suspensions to explore possible ion specific effects on the colloidal stability of the samples over a wide range of electrolyte concentrations. On the basis of the measured CCCs, we have clarified the Hofmeister series and the Schulze–Hardy rule for LDH particles.

## Experimental section

### Materials

Analytical grade KCl, KSCN,  $\text{K}_2\text{HPO}_4$  (Acros Organics),  $\text{KHCO}_3$  (Alfa Aesar),  $\text{KNO}_3$ ,  $\text{K}_2\text{SO}_4$ ,  $\text{K}_2\text{HASO}_4$ ,  $\text{K}_3\text{Fe}(\text{CN})_6$  and  $\text{K}_4\text{Fe}(\text{CN})_6 \cdot 3\text{H}_2\text{O}$  (Sigma-Aldrich) were used. The salt solutions were prepared by dissolving the calculated amount of solid in ultrapure water (Millipore) and the pH was adjusted to 9 with 0.1 M KOH (Sigma-Aldrich) solution. This pH was also maintained in all stock suspensions and water was used for sample preparation throughout the experiments. The protonation constants ( $\text{p}K$ ) of inorganic anions together with their actual charge at pH 9 are presented in Table 1. All stock solutions were filtered using a 0.1  $\mu\text{m}$  pore-size filter (Millipore) prior to sample preparation and the measurements were carried out at 25 °C.

The  $\text{MgAl-NO}_3\text{-LDH}$  particles were prepared using the coprecipitation method.<sup>52–55</sup> The solutions of  $\text{Mg}(\text{NO}_3)_2$  and  $\text{Al}(\text{NO}_3)_3$  (Sigma-Aldrich) were added dropwise under vigorous stirring to  $\text{N}_2$ -blanketed 1.0 M NaOH (Acros Organics) until the final pH reached 10. The resulting suspension was subjected to

**Table 1** Protonation constants and calculated actual charges of the inorganic anions used in the present study

Anions <sup>a</sup>	$\text{p}K_1^b$	$\text{p}K_2^b$	$\text{p}K_3^b$	Valence at pH 9 <sup>c</sup>
$\text{Cl}^-$	−0.71	—	—	1.00
$\text{NO}_3^-$	−1.40	—	—	1.00
$\text{SCN}^-$	−2.10	—	—	1.00
$\text{CO}_3^{2-}$	10.33	6.35	—	1.04
$\text{SO}_4^{2-}$	1.98	−2.00	—	2.00
$\text{AsO}_4^{3-}$	11.50	6.94	2.19	1.99
$\text{PO}_4^{3-}$	12.35	7.21	2.14	1.98
$\text{Fe}(\text{CN})_6^{3-}$	—	—	—	3.00
$\text{Fe}(\text{CN})_6^{4-}$	4.20	2.00	−1.00	4.00

<sup>a</sup> Chemical formula in the deprotonated form. <sup>b</sup> The  $\text{p}K$  values were obtained from the JESS (Joint Expert Speciation System) database<sup>75</sup> at infinite dilution and 25 °C. <sup>c</sup> The valence was calculated on the basis of the protonation equilibria at pH 9 using the reported  $\text{p}K$  values.

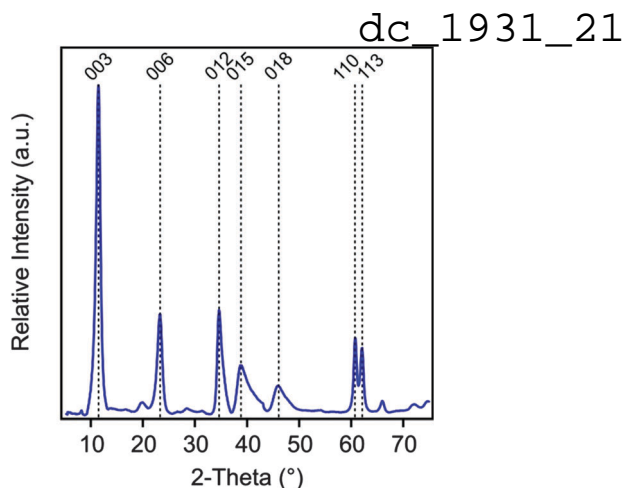


Fig. 1 Powder XRD pattern of the MgAl-NO<sub>3</sub>-LDH particles synthesized by coprecipitation and subjected to hydrothermal treatment.

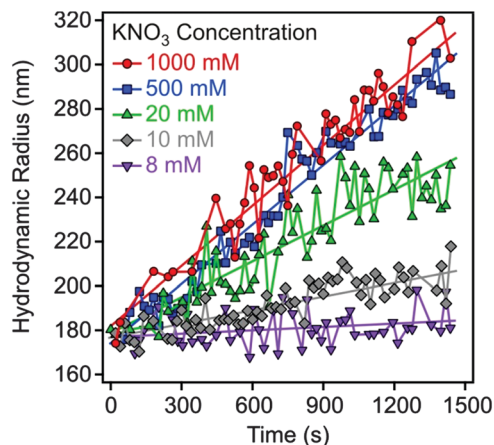


Fig. 2 Hydrodynamic radius of MgAl-NO<sub>3</sub>-LDH particles (5 mg L<sup>-1</sup>) as a function of time of the experiment measured at different KNO<sub>3</sub> concentrations.

hydrothermal treatment at 120 °C for 16 h in a teflon chamber embedded in a high-pressure steel reactor (Columbia International). The solid materials was rapidly filtered using a caustic resistant vacuum filter unit (Nalgene) equipped with a 0.45 μm membrane (Versapor) and washed thoroughly with ultrapure water. MgAl-NO<sub>3</sub>-LDH was then redispersed in pH 9 water resulting in a stock suspension of 10 g L<sup>-1</sup>, which was later diluted to reach the suitable particle concentration for the experiments. The X-ray diffraction (XRD) patterns, recorded on a STADI-P transmission powder diffractometer system (Stoe), unambiguously confirmed the LDH formation (Fig. 1). Accordingly, all patterns can be indexed to a 3R<sub>1</sub> polytype where 3 is the number of layers stacked along the *c*-axis of the elementary cell, *R* refers to the rhombohedral symmetry and 1 indicates the trigonal prismatic assembly of the hydroxyl groups in the neighboring layers. This information was derived from the (012), (015) and (018) reflections. Such a polytype form is commonly used for the description of LDH structures.<sup>56</sup> The lattice parameters were calculated from the observed peaks. An *a* dimension of 0.3 nm, which represents the shortest distance between two cations in the LDH layer, was calculated as twice the position of the (110) reflection.<sup>56</sup> A *c* parameter of 2.4 nm was obtained from the (003) reflection and it represents the thickness of three layers plus the interlayer space between them. The average thickness of the particles (*ν*) was calculated using the Scherrer equation as

$$\nu = K\lambda/\beta \cos\theta_B \quad (2)$$

where *K* is the shape factor, *λ* is the wavelength of the laser and *β* is the line broadening at the full width at half maximum. We found that *ν* = 17.4 nm.

### Electrophoretic mobility and stability ratio measurements

Electrophoretic mobilities were measured using a ZetaNano ZS (Malvern) device. The experiments were performed in plastic capillary cells (Malvern). For sample preparation, the calculated amount of electrolyte stock solution was mixed with ultrapure water to obtain the desired salt concentration. In the last step, the particle stock suspension was added. The final volume

(5 mL) and the MgAl-NO<sub>3</sub>-LDH concentration (5 mg L<sup>-1</sup>) were kept constant in the experiments. The suspensions were equilibrated overnight at room temperature and the electrophoretic mobilities were measured five times and the average values were reported. The standard deviation was always below 5%.

Dynamic light scattering (DLS) measurements were performed using a compact goniometer system (ALV/CGS-3) at 90° scattering angle and borosilicate glass cuvettes (Kimble Chase). A hydrodynamic radius of 168 nm and a polydispersity index of 0.39 were obtained for the MgAl-NO<sub>3</sub>-LDH particles in stable aqueous suspensions. Time-resolved DLS experiments were carried out to explore particle aggregation. Fig. 2 shows some typical measurements, in which the hydrodynamic radius (*R<sub>h</sub>*) was measured for 24 min under different experimental conditions. The initial increase in size was used to calculate the apparent aggregation rate (*Δ*) as

$$\Delta = \left. \frac{dR_h(t)}{dt} \right|_{t \rightarrow 0} \quad (3)$$

where *t* is the time of the experiment. The colloidal stability was expressed in terms of the stability ratio (*W*) via the following equation:<sup>57–59</sup>

$$W = \frac{\Delta_{\text{fast}}}{\Delta} \quad (4)$$

where fast refers to diffusion controlled aggregation, which was achieved in 1 M KCl solutions. The final sample volume was always 2 mL prepared by mixing calculated amount of salt solutions with the MgAl-NO<sub>3</sub>-LDH stock suspension to get a final particle concentration of 5 mg L<sup>-1</sup>. The salt concentration range and particle dose were the same for both the electrophoretic and the DLS experiments, while the pH was kept at 9 and checked before and after the measurements.

## Results and discussion

The surface charge properties and aggregation of positively charged MgAl-NO<sub>3</sub>-LDH particles were studied by electrophoresis and DLS



dc\_1931\_21

to investigate the suspension stability in the presence of simple inorganic electrolytes over a wide range of concentrations. The type and the charge of anions were systematically varied to explore ion specific effects on the colloidal stability of the samples. The anions are the counterions, whereas the  $K^+$  cation was used throughout all experiments. Monovalent anions within the Hofmeister series<sup>17</sup> were investigated first, followed by di, tri and tetravalent ones to establish the validity of the Schulze–Hardy rule<sup>31</sup> for anions interacting with the  $MgAl-NO_3-LDH$  particles.

### Effect of monovalent anions

Electrophoretic mobilities of the  $MgAl-NO_3-LDH$  particles were measured in the presence of  $K^+$  salts of different monovalent anions such as  $Cl^-$ ,  $NO_3^-$ ,  $SCN^-$  and  $HCO_3^-$  (Fig. 3A). The shape of the curves was similar for the first three anions. The mobilities were positive at low concentrations due to the structural charge of the particles and passed through a maximum, which can be predicted by the standard electrokinetic model.<sup>60</sup> Upon further increasing the salt concentration, the electrophoretic mobilities decreased and were

close to zero at high electrolyte levels due to the screening effect on the surface charge and the adsorption of the anions on the oppositely charged surface. The latter effect gave rise to slightly negative mobilities in the case of  $SCN^-$  at high electrolyte levels. Such a charge reversal has already been observed with this anion and other colloidal particles.<sup>20,21</sup> The electrophoretic mobilities also decreased at the same concentration in the  $Cl^- > NO_3^- > SCN^-$  order indicating specific adsorption of the ions. However, the surface charge properties of the particles are significantly different in the presence of the  $HCO_3^-$  anion. Its adsorption led to charge neutralization at the isoelectric point (IEP) and subsequent charge reversal at higher concentrations. The latter phenomenon was the most significant in this case among the monovalent anions due to the high affinity of  $HCO_3^-$  to the  $MgAl-NO_3-LDH$  surface. The strong interaction between carbonate or carboxylate containing anions and LDH particles is well known and has also been reported in other systems.<sup>2,51,61</sup> Finally, the mobilities start decreasing in magnitude at higher salt levels due to the screening effect of the  $K^+$  ions on the negative surface charge.

Light scattering has been proved to be a suitable method to follow aggregation processes;<sup>62–66</sup> therefore, DLS was used to determine stability ratios in the above systems under the same experimental conditions (Fig. 3B). In general, high stability ratios and stable suspensions were observed at low salt concentrations, whereas fast aggregation and unstable suspensions at high electrolyte levels were witnessed. These two regimes were separated by the CCC, which is the concentration at which the sharp transition between slow and fast aggregation occurs. The aggregation remains rapid after the CCC irrespectively of the types of anions used. The shape of the stability ratio *versus* salt concentration curves was very similar in the presence of  $Cl^-$ ,  $NO_3^-$  and  $SCN^-$ , whereas the slope in the slow aggregation regime was higher for  $HCO_3^-$  due to its strong adsorption which modified the  $MgAl-NO_3-LDH$  surface significantly.

The observed tendency is qualitatively in good agreement with the classical DLVO theory.<sup>14</sup> Accordingly, the overlap of the electrical double layers surrounding the particles leads to repulsive forces at low salt concentrations, which transcend the attractive van der Waals forces giving rise to stable suspensions. The double layer forces weaken progressively with the increasing electrolyte level due to surface charge screening by the salts. In addition, anion adsorption on the positively charged  $MgAl-NO_3-LDH$  surface leads to reduced surface charge density, and hence, to weaker double layer forces. Therefore, attractive van der Waals forces become predominant at high salt concentrations leading to aggregation of the particles and the formation of unstable samples.

The CCC values were determined from the stability plots and they decrease in the  $Cl^- > NO_3^- > SCN^- > HCO_3^-$  order (Fig. 4A and Table 2). The tendency for the first three ions agrees adequately with the indirect Hofmeister series for positively charged, hydrophobic particles.<sup>20</sup> The poorly hydrated  $SCN^-$  anions adsorb on the hydrophobic particles leading to lower surface charge, weaker repulsive forces and the lowest CCC. The well-hydrated  $Cl^-$  anions prefer to stay in the bulk and hardly adsorb on  $MgAl-NO_3-LDH$

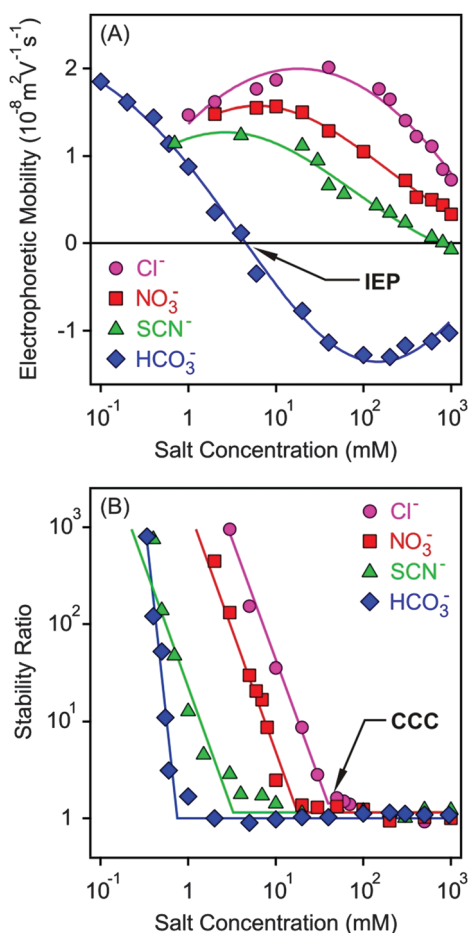


Fig. 3 Electrophoretic mobility (A) and stability ratio (B) values for  $MgAl-NO_3-LDH$  particles at different concentrations of monovalent anions. Stability ratios close to unity indicate rapid particle aggregation, while higher values refer to more stable suspensions. The lines are just to guide the eyes.

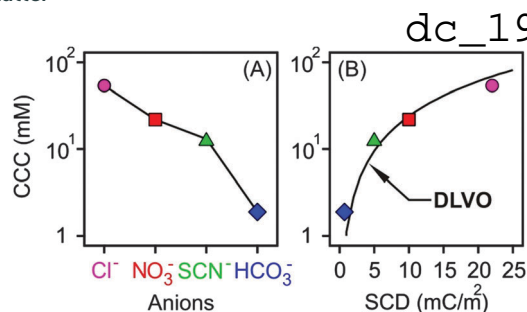


Fig. 4 CCC values of positively charged MgAl-NO<sub>3</sub>-LDH particles in the presence of different monovalent anions (A) and as a function of the surface charge density (B). The solid line in (A) serves to guide the eyes, while in (B) it shows the DLVO prediction calculated by eqn (7).

Table 2 CCC values of the MgAl-NO<sub>3</sub>-LDH particles in the presence of K<sup>+</sup> salts of various anions<sup>a</sup>

Anions <sup>b</sup>	First CCC (M)	Second CCC (M)	Third CCC (M)
Cl <sup>-</sup>	$5.4 \times 10^{-2}$	—	—
NO <sub>3</sub> <sup>-</sup>	$2.2 \times 10^{-2}$	—	—
SCN <sup>-</sup>	$1.3 \times 10^{-2}$	—	—
CO <sub>3</sub> <sup>2-</sup>	$1.9 \times 10^{-3}$	—	—
SO <sub>4</sub> <sup>2-</sup>	$3.2 \times 10^{-5}$	—	—
AsO <sub>4</sub> <sup>3-</sup>	$4.0 \times 10^{-5}$	—	—
PO <sub>4</sub> <sup>3-</sup>	$2.0 \times 10^{-7}$	$3.1 \times 10^{-6}$	$5.2 \times 10^{-1}$
Fe(CN) <sub>6</sub> <sup>3-</sup>	$1.1 \times 10^{-6}$	$3.0 \times 10^{-5}$	$6.0 \times 10^{-2}$
Fe(CN) <sub>6</sub> <sup>4-</sup>	$1.0 \times 10^{-13}$	$2.5 \times 10^{-13}$	$2.5 \times 10^{-1}$

<sup>a</sup> The CCCs were determined from the stability ratio *versus* salt concentration plots. The method has an error of about 10%. <sup>b</sup> Chemical formula in the deprotonated form.

giving rise to higher surface charge and the highest CCC within the anions investigated. A similar tendency was observed in other systems containing these anions and positively charged colloidal particles.<sup>18,20,21,27</sup> The situation in the HCO<sub>3</sub><sup>-</sup> case is more complicated. Considering the indirect Hofmeister series, one would expect the highest CCC in the presence of this anion. However, it is the opposite, the lowest CCC was measured. This is due to the specific affinity of the HCO<sub>3</sub><sup>-</sup> ions to the MgAl-NO<sub>3</sub>-LDH surface of alkaline nature leading to strong adsorption on the oppositely charged particles. This adsorption induced a significant charge reversal as shown in the mobility curve (Fig. 3A). The strong interaction is due to electrostatic attraction and hydrogen bonding between the HCO<sub>3</sub><sup>-</sup> anions and the hydroxyl groups of the surface.<sup>56</sup>

The anionic exchange capacity (AEC) of LDHs is typically in the range of 1–5 meq g<sup>-1</sup>.<sup>47,67,68</sup> Given the low particle concentration (5 mg L<sup>-1</sup>) in our experiments, only a small fraction (always below 1.5%) of monovalent anions are involved in the ion exchange process. In addition, the AEC includes both intercalation and adsorption on the outer surface, but we are not able to distinguish these processes in our experiments. However, we believe that charging and aggregation of MgAl-NO<sub>3</sub>-LDH platelets are mostly sensitive to adsorption and the tendencies obtained are related to this process rather than to anion intercalation.

To further clarify the aggregation mechanism, surface charge densities of the MgAl-NO<sub>3</sub>-LDH particles were determined and their relation to the CCCs was examined. For this, electrophoretic

mobility ( $u$ ) was converted to the electrokinetic potential using the Smoluchowski equation as<sup>14</sup>

$$\zeta = \frac{u\eta}{\varepsilon\varepsilon_0} \quad (5)$$

where  $\eta$  is the viscosity of water,  $\varepsilon_0$  is the permittivity of vacuum and  $\varepsilon$  is the dielectric constant. The surface charge density ( $\sigma$ ) was determined by fitting the potentials at different ionic strengths using the Debye-Hückel model developed for the charge-potential relationship as follows<sup>14</sup>

$$\sigma = \varepsilon\varepsilon_0\kappa\zeta \quad (6)$$

where  $\kappa$  is the inverse Debye length, which describes the contribution of all ionic species. The CCC was estimated from the DLVO theory as<sup>14,33</sup>

$$\text{CCC} = \frac{0.365}{N_A L_B} (H\varepsilon\varepsilon_0)^{-2/3} \sigma^{4/3} \quad (7)$$

where  $N_A$  is the Avogadro number,  $H$  is the Hamaker constant and  $H_B$  is the Bjerrum length, which is 0.72 nm for monovalent electrolytes in water. By fitting the experimental data with eqn 7, a Hamaker constant of  $H = 4.0 \times 10^{-20}$  J was found.

The calculated surface charge densities varied between +1 and +22 mC m<sup>-2</sup> for different monovalent anions (Fig. 4B). This range is similar to that reported for LDHs of various compositions.<sup>61,69–72</sup> The obtained sequence in the surface charge densities was Cl<sup>-</sup> > NO<sub>3</sub><sup>-</sup> > SCN<sup>-</sup> > HCO<sub>3</sub><sup>-</sup> which follows the indirect Hofmeister series with the exception of HCO<sub>3</sub><sup>-</sup>. As discussed above, this anion has high affinity to the MgAl-NO<sub>3</sub>-LDH surface leading to significant adsorption and reduced surface charge.

Excellent agreement was found between the experimental CCCs and the calculated ones. This fact confirms that the predominating interparticle forces are of DLVO origin and ion specificity plays an important role in the adsorption mechanism. Accordingly, well-hydrated anions such as Cl<sup>-</sup> do not or only weakly adsorb on the MgAl-NO<sub>3</sub>-LDH particles and the surface charge density as well as the CCC is high in the presence of this anion. For poorly hydrated ions such as SCN<sup>-</sup>, stronger adsorption leads to low surface charge density and CCC. In the case of HCO<sub>3</sub><sup>-</sup>, adsorption is further enhanced with specific interaction between the anion and the surface hydroxyl groups through mainly hydrogen bonds giving rise to the lowest CCC among the anions investigated. Although the adsorption processes resulted in different surface charge densities, the interparticle forces are still of DLVO origin as one can realize it from the excellent agreement between the experimental and calculated CCCs (Fig. 4B). A similar observation was also made on the basis of direct force and aggregation rate measurements for positively charged latex particles in the presence of similar anions.<sup>26</sup>

### Effect of divalent anions

Charging and aggregation of the MgAl-NO<sub>3</sub>-LDH particles were also studied in the presence of divalent anions such as SO<sub>4</sub><sup>2-</sup>, HAsO<sub>4</sub><sup>2-</sup> and HPO<sub>4</sub><sup>2-</sup> with the K<sup>+</sup> cation. Although LDHs of

dc\_1931\_21

different compositions are widely used to capture these anions in water purification processes,<sup>12,13</sup> their effect on colloidal stability has not been studied in detail to date.

Electrophoretic mobilities were positive at low salt concentrations due to the positive structural charge of the particles (Fig. 5A). Upon increasing the dose of divalent anions, the mobilities decreased rapidly and reached the IEP in each case. Pronounced charge reversal occurred with all of the anions indicating their large affinity to the surface. Such a charge reversal has already been reported for other LDHs in the presence of divalent anions.<sup>30,47,51</sup> However, the adsorption of  $\text{HPO}_4^{2-}$  led to the most negative electrophoretic mobilities, while very similar values were measured for  $\text{SO}_4^{2-}$  and  $\text{HAsO}_4^{2-}$ . A previously reported competitive adsorption study also confirmed that  $\text{HPO}_4^{2-}$  has greater affinity to the LDH surface than the  $\text{HAsO}_4^{2-}$  ions.<sup>45</sup> Upon further increasing the salt concentration, the mobilities increased due to the screening effect of the  $\text{K}^+$  cations on the surface charge. Note that  $\text{K}^+$  is the counterion of the negatively charged particles in this concentration regime.

The tendency in the stability ratios was very similar to the monovalent case for  $\text{SO}_4^{2-}$  and  $\text{HAsO}_4^{2-}$  anions (Fig. 5B), which

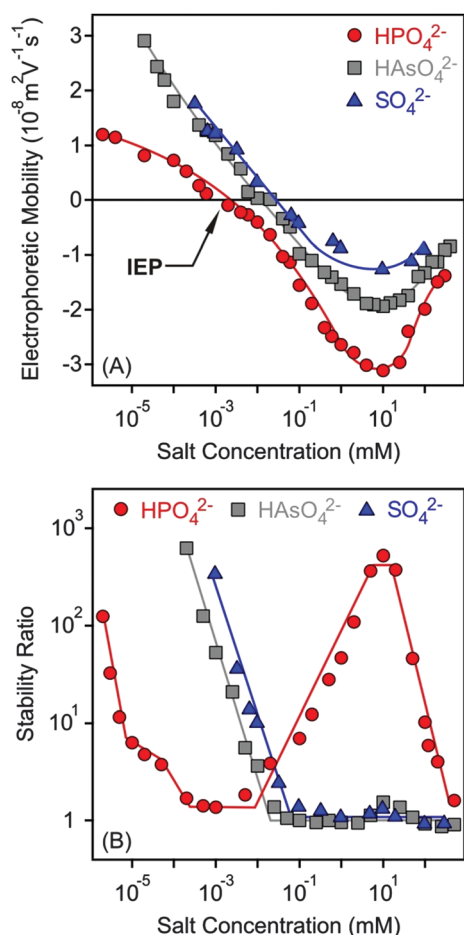


Fig. 5 Electrophoretic mobility (A) and stability ratio (B) values of MgAl-NO<sub>3</sub>-LDH as a function of the salt concentration using  $\text{K}^+$  salts of divalent anions. The lines are just to guide the eyes.

behaved alike in the aggregation experiments. Slow and fast aggregation regimes were separated by well-defined CCCs, which were lower compared to the monovalent anions (Table 2). This aggregation behaviour can be explained by the DLVO theory. Nevertheless, the stability curve was found to be very different for the  $\text{HPO}_4^{2-}$  anions, as one would expect from the results of the electrophoretic mobility measurements performed with the same systems. Three CCC values were obtained. Accordingly, stable MgAl-NO<sub>3</sub>-LDH suspensions were observed at low salt concentrations and aggregation became fast at a higher  $\text{HPO}_4^{2-}$  level (first CCC). The stability ratios increased (second CCC) in the intermediate regime and reached a plateau. At higher concentrations, the aggregation rates increased and fast aggregation occurred again (third CCC). Such a restabilization effect is typically induced by polyelectrolytes and multivalent ions in the presence of oppositely charged colloidal particles<sup>15,38,39,61,73</sup> and can be explained as follows. The high stability at a low salt level is due to sufficiently strong repulsive double layer forces, which weaken with increasing salt concentration, since the adsorption of anions reduces the surface charge. The double layer forces vanish at the IEP and the particles rapidly aggregate after the first CCC due to the attractive van der Waals forces. The aggregation slows down after the second CCC where the charge reversal phenomenon occurs and the high negative charge induces the formation of electrical double layers, which leads to repulsive interparticle forces. Upon further increasing the salt concentration, the aggregation becomes faster and unstable suspensions can be observed after the third CCC due to the screening effect of the  $\text{K}^+$  ions on the negative surface charge. For the  $\text{SO}_4^{2-}$  and  $\text{HAsO}_4^{2-}$  anions, the charge reversal did not result in sufficiently high surface charge density (as one can see in Fig. 5A); therefore, restabilization did not occur.

### Effect of multivalent anions

The surface charge and colloidal stability of the MgAl-NO<sub>3</sub>-LDH particles were studied in the presence of  $\text{Fe}(\text{CN})_6^{3-}$  and  $\text{Fe}(\text{CN})_6^{4-}$ , as tri- and tetravalent anions. The effect of these anions on the electrophoretic mobilities was similar to the divalent case. Accordingly, the particles were positively charged at low salt concentrations, while strong adsorption of the multivalent ions led to charge neutralization at the IEP and subsequent charge reversal at appropriately high electrolyte levels (Fig. 6A). The extremely low IEP and the large extent of charge reversal indicated higher affinity of  $\text{Fe}(\text{CN})_6^{4-}$  for the surface, while the behaviour of  $\text{Fe}(\text{CN})_6^{3-}$  was very similar to  $\text{HPO}_4^{2-}$ . For tetravalent anions, the magnitude of electrophoretic mobilities was more than twice higher than for bare MgAl-NO<sub>3</sub>-LDH particles, similar to the case of adsorption of polyelectrolytes on oppositely charged surfaces.<sup>15,51,61</sup> The mobilities started to increase after the minimum at higher concentrations due to the screening effect of counterions which are  $\text{K}^+$  for the negatively charged particles.

Similar to  $\text{HPO}_4^{2-}$ , three CCCs were observed for tri- and tetravalent ions (Fig. 6B and Table 2). The first CCC occurred due to charge neutralization, the second CCC originated from charge reversal induced restabilization, while the third CCC is

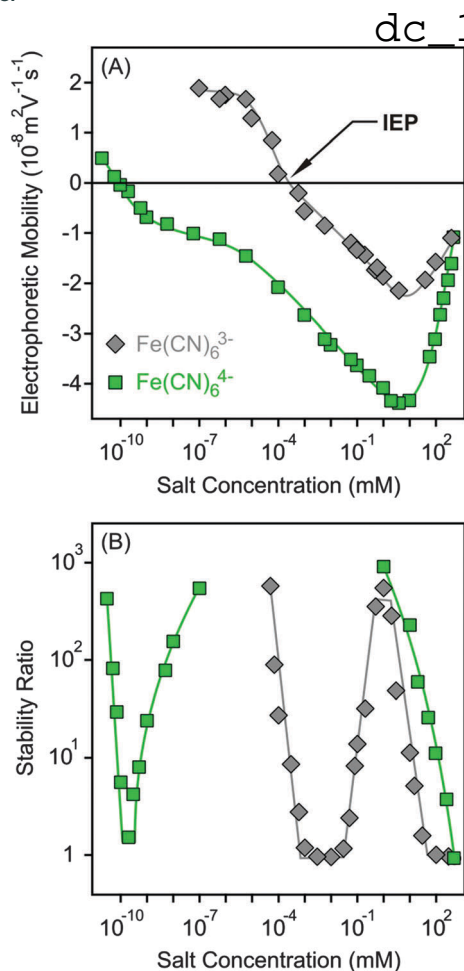


Fig. 6 Electrophoretic mobility (A) and stability ratio (B) values of MgAl-NO<sub>3</sub>-LDH particles versus the salt concentration for K<sup>+</sup> salts of tri and tetravalent anions. The lines serve to guide the eyes.

the result of the screening effect on the negative surface charge by the K<sup>+</sup> cations. The behaviour of Fe(CN)<sub>6</sub><sup>3-</sup> is so analogous to HPO<sub>4</sub><sup>2-</sup> in both electrophoretic and aggregation experiments that one could assume that the HPO<sub>4</sub><sup>2-</sup> anions deprotonate upon adsorption and show characteristic surface charge features for a trivalent anion. However, no unambiguous experimental evidence confirms this assumption. For the Fe(CN)<sub>6</sub><sup>4-</sup> anions, the particles were highly negative due to the overcharging process in the intermediate concentration regime, which resulted in highly stable samples, such that stability ratios could not be measured. Therefore, the stability ratios after the second CCC are not connected to the ones before the third CCC in Fig. 6B, since the expected maximum is above the detection limit of the experiment. Accordingly, Fe(CN)<sub>6</sub><sup>4-</sup> anions are powerful aggregating agents for LDHs and suspensions can be stabilized or destabilized by varying the salt concentration. The first CCC is much below the typical AEC value for LDHs; therefore, we assume that the adsorption of tetravalent anions on the outer particle surface plays the key role in the charging and aggregation processes of MgAl-NO<sub>3</sub>-LDH platelets, while intercalation between the layers can hardly take place due to short experiment time.

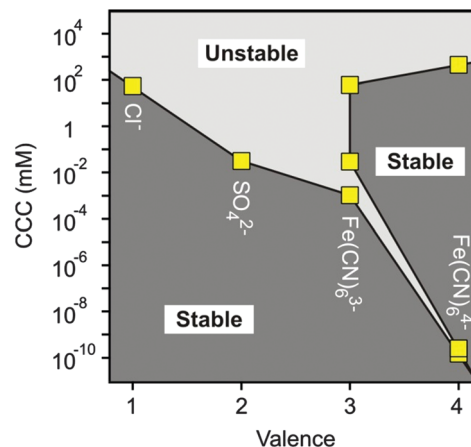


Fig. 7 Stability map of MgAl-NO<sub>3</sub>-LDH suspensions in the presence of anions of different valences. The stability of the different regions is also indicated. The CCCs were obtained from the aggregation versus salt concentration plots.

Let us now compare the CCCs in the presence of anions of different valences, such as Cl<sup>-</sup>, SO<sub>4</sub><sup>2-</sup>, Fe(CN)<sub>6</sub><sup>3-</sup> and Fe(CN)<sub>6</sub><sup>4-</sup> (Fig. 7). For the first two anions, only one CCC was observed since restabilization did not occur (Fig. 3B and 5B), while three CCCs were determined for the tri- and tetravalent ones. The first CCC decreases with the valence due to the increasing affinity and stronger adsorption on the MgAl-NO<sub>3</sub>-LDH surface. The second CCCs for Fe(CN)<sub>6</sub><sup>3-</sup> and Fe(CN)<sub>6</sub><sup>4-</sup> also decrease with valence. However, a higher third CCC was determined for the tetravalent ion than for the trivalent one. This behaviour can be correlated with the extent of charge reversal. The adsorption of Fe(CN)<sub>6</sub><sup>4-</sup> induced a much larger charge reversal and particles of highly negative charge were formed. Therefore, more K<sup>+</sup> counterions are needed to screen the surface charge leading to a higher third CCC in the case of Fe(CN)<sub>6</sub><sup>4-</sup> than for the Fe(CN)<sub>6</sub><sup>3-</sup> anions. The stability map shows that the suspensions are stable in the low concentration region and unstable at high salt levels for all valences. The peninsula on the right side indicates another stable regime due to restabilization at intermediate concentrations induced by the strong adsorption of tri- and tetravalent ions. Similar stability maps were reported for charged latex particles in the presence of multivalent ions.<sup>38,39,73</sup>

As discussed above, multivalent ions are more powerful in the destabilization of MgAl-NO<sub>3</sub>-LDH suspensions. Fig. 8 shows the relative CCCs normalized for the Cl<sup>-</sup> case for all the anions investigated in the present study together with some data from the literature<sup>39,41,73,74</sup> and with expected CCCs from the Schulze-Hardy rule.<sup>31,32</sup> The CCC values from the present work are systematically lower than the ones predicted by  $z^{-6}$  dependence. The difference is the most significant for HPO<sub>4</sub><sup>2-</sup> and Fe(CN)<sub>6</sub><sup>4-</sup>, for which extremely low CCCs were observed indicating high affinity of these ions to the surface. Some of the literature data (*e.g.*, for the hematite and latex particles) are also below the line predicted by the Schulze-Hardy rule. Such tendency is a bit surprising, since the  $z^{-6}$  dependence can be derived from the DLVO theory only for highly charged particles,



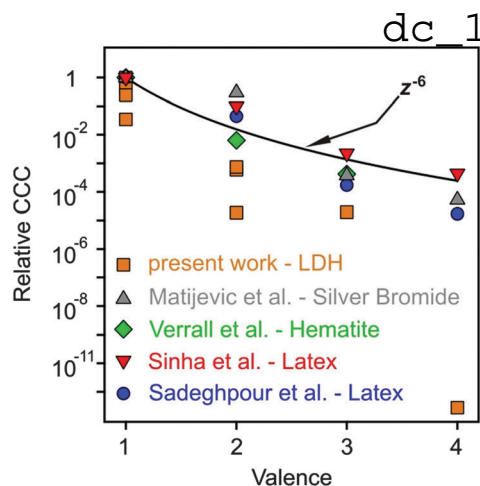


Fig. 8 Relative CCCs, normalized to its value for  $\text{Cl}^-$  ion in the present system and for the monovalent case in the others reported in the literature, as a function of the valence (actual charge under the experimental conditions applied). The solid line shows the dependence expected from the Schulze–Hardy rule (eqn (1)). Literature data include positively charged silver bromide,<sup>74</sup> hematite<sup>41</sup> and amidine functionalized polystyrene latex<sup>39,73</sup> particles in the presence of various anions.

whereas for surfaces of low surface charge density and surface potential (e.g.,  $\text{MgAl-NO}_3\text{-LDH}$  in our system), the DLVO theory predicts  $z^{-2}$  dependence.<sup>33–35</sup> On the other hand, direct measurements of surface forces and aggregation rates with colloidal latex particles revealed that although some additional forces are also present, the DLVO theory can describe the interparticle forces relatively well, even in the case of multivalent ions.<sup>36,73</sup> These facts indicate specific interaction between the anions and the particles surface, which enhances the adsorption and hence, decreases the surface charge density leading to lower CCCs. Therefore, the observed deviation from the expected dependence of the CCC on the valence is due to the high affinity of anions to  $\text{MgAl-NO}_3\text{-LDH}$ , while the interparticle forces are still of DLVO origin. One of the reasons for the high affinity is the strong hydrogen bonding network between the anions and the hydroxyl groups of the surface, which can be different for ions of different abilities (e.g., electronegativity) to form hydrogen bonds. Besides, the hydration state of the anions plays also a crucial role. Poorly hydrated anions tend to more strongly adsorb on the hydrophobic surfaces leading to lower CCCs, whereas well-hydrated ones adsorb only weakly and remain in solution giving rise to higher CCCs. The knowledge generated by these results can be certainly applied wherever LDH particles are used as adsorbents for anion capture in aqueous samples, since the colloidal stability of suspensions can be predicted and tuned according to the desired goals.

## Conclusions

Ion specific effects on charging and aggregation of positively charged  $\text{MgAl-NO}_3\text{-LDH}$  particles were investigated. The types of monovalent anions significantly affects the surface charge density and also the CCCs, both of which decrease in the  $\text{Cl}^- > \text{NO}_3^- > \text{SCN}^- > \text{HCO}_3^-$  order. This tendency agrees with the

indirect Hofmeister series only in part, since the  $\text{HCO}_3^-$  ion should be located on the left side. This deviation is due to the high affinity of  $\text{HCO}_3^-$  for the particle surface, which leads to strong adsorption and charge reversal at appropriately high salt concentrations. The extent of adsorption weakens towards the left side of the series due to the hydration level, which increases in this direction, and hence, well-hydrated ions such as  $\text{Cl}^-$  adsorb only weakly and prefer to stay in the solution, giving rise to the highest CCC.

Multivalent ions were found to be powerful destabilizing agents. Their adsorption led to charge neutralization and significant charge reversal in each case and restabilization of suspensions also occurred for  $\text{HPO}_4^{2-}$ ,  $\text{Fe}(\text{CN})_6^{3-}$  and  $\text{Fe}(\text{CN})_6^{4-}$  in the intermediate concentration regimes. The CCCs decreased with valence even more significantly than the ones predicted by the Schulze–Hardy rule. The present results indicate that multivalent inorganic anions show strong affinity for the  $\text{MgAl-NO}_3\text{-LDH}$  surface through electrostatic attraction, hydrophobic interactions and hydrogen bonds forming between the anions and the hydroxyl groups of the surface. However, the predominant interparticle forces can be well described by the DLVO theory.

In conclusion, effective LDH-based adsorbent systems can be proposed for water treatment processes, considering that the colloidal stability of aqueous suspensions can be controlled with the valence (or actual charge under the pH applied) and the concentration of the ions.

## Acknowledgements

This research was supported by the Swiss National Science Foundation (150162), Swiss Secretariat for Education, Research and Innovation (C15.0024) and COST Actions CM1303 and MP1106. The authors thank Professor Michal Borkovec for providing access to the light scattering instruments in his laboratory.

## References

- 1 C. Forano, U. Costantino, V. Prevot and C. Taviot Gueho, in *Handbook of Clay Science*, ed. F. Bergaya and G. Lagaly, Elsevier, Amsterdam, 2013, vol. 5A, pp. 745–782.
- 2 Z. Gu, J. J. Atherton and Z. P. Xu, *Chem. Commun.*, 2015, **51**, 3024–3036.
- 3 Y. G. Li, M. Gong, Y. Y. Liang, J. Feng, J. E. Kim, H. L. Wang, G. S. Hong, B. Zhang and H. J. Dai, *Nat. Commun.*, 2013, **4**, 1805.
- 4 A. Deak, L. Janovak, S. P. Tallosy, T. Bito, D. Sebok, N. Buzas, I. Palinko and I. Dekany, *Langmuir*, 2015, **31**, 2019–2027.
- 5 K. Ladewig, Z. P. Xu and G. Q. Lu, *Expert Opin. Drug Delivery*, 2009, **6**, 907–922.
- 6 G. Choi, O. J. Kwon, Y. Oh, C. O. Yun and J. H. Choy, *Sci. Rep.*, 2014, **4**, 4430.
- 7 A. L. Troutier-Thuilliez, H. Hintze-Bruening, C. Taviot-Gueho, V. Verney and F. Leroux, *Soft Matter*, 2011, **7**, 4242–4251.
- 8 S. Pausova, J. Krysa, J. Jirkovsky, C. Forano, G. Mailhot and V. Prevot, *Appl. Catal., B*, 2015, **170**, 25–33.



dc 1931 21

- 9 H. F. Liang, F. Meng, M. Caban-Acevedo, L. S. Li, A. Forticaux, L. C. Xiu, Z. C. Wang and S. Jin, *Nano Lett.*, 2015, **15**, 1421–1427.
- 10 S. Meszaros, J. Halasz, Z. Konya, P. Sipos and I. Palinko, *Appl. Clay Sci.*, 2013, **80–81**, 245–248.
- 11 S. L. Ma, L. Huang, L. J. Ma, Y. Shim, S. M. Islam, P. L. Wang, L. D. Zhao, S. C. Wang, G. B. Sun, X. J. Yang and M. G. Kanatzidis, *J. Am. Chem. Soc.*, 2015, **137**, 3670–3677.
- 12 F. L. Theiss, S. J. Couperthwaite, G. A. Ayoko and R. L. Frost, *J. Colloid Interface Sci.*, 2014, **417**, 356–368.
- 13 K. H. Goh, T. T. Lim and Z. Dong, *Water Res.*, 2008, **42**, 1343–1368.
- 14 D. F. Evans and H. Wennerstrom, *The Colloidal Domain*, John Wiley, New York, 1999.
- 15 I. Szilagyi, G. Trefalt, A. Tiraferri, P. Maroni and M. Borkovec, *Soft Matter*, 2014, **10**, 2479–2502.
- 16 M. Elimelech, J. Gregory, X. Jia and R. A. Williams, *Particle Deposition and Aggregation: Measurement, Modeling, and Simulation*, Butterworth-Heinemann Ltd, Oxford, 1995.
- 17 D. F. Parsons, M. Bostrom, P. Lo Nostro and B. W. Ninham, *Phys. Chem. Chem. Phys.*, 2011, **13**, 12352–12367.
- 18 J. M. Peula-Garcia, J. L. Ortega-Vinuesa and D. Bastos-Gonzalez, *J. Phys. Chem. C*, 2010, **114**, 11133–11139.
- 19 N. Schwierz, D. Horinek and R. R. Netz, *Langmuir*, 2010, **26**, 7370–7379.
- 20 T. Oncsik, G. Trefalt, M. Borkovec and I. Szilagyi, *Langmuir*, 2015, **31**, 3799–3807.
- 21 T. Lopez-Leon, J. L. Ortega-Vinuesa and D. Bastos-Gonzalez, *ChemPhysChem*, 2012, **13**, 2382–2391.
- 22 G. Lagaly and S. Ziesmer, *Adv. Colloid Interface Sci.*, 2003, **100**, 105–128.
- 23 R. Tian, G. Yang, H. Li, X. D. Gao, X. M. Liu, H. L. Zhu and Y. Tang, *Phys. Chem. Chem. Phys.*, 2014, **16**, 8828–8836.
- 24 B. H. Bijsterbosch and J. Lyklema, *Adv. Colloid Interface Sci.*, 1978, **9**, 147–251.
- 25 F. Dumont, J. Warlus and A. Watillon, *J. Colloid Interface Sci.*, 1990, **138**, 543–554.
- 26 F. J. M. Ruiz-Cabello, G. Trefalt, T. Oncsik, I. Szilagyi, P. Maroni and M. Borkovec, *J. Phys. Chem. B*, 2015, **119**, 8184–8193.
- 27 T. Lopez-Leon, J. M. Lopez-Lopez, G. Odriozola, D. Bastos-Gonzalez and J. L. Ortega-Vinuesa, *Soft Matter*, 2010, **6**, 1114–1116.
- 28 T. B. Schuster, D. D. Ouboter, E. Bordignon, G. Jeschke and W. Meier, *Soft Matter*, 2010, **6**, 5596–5604.
- 29 V. Merk, C. Rehbock, F. Becker, U. Hagemann, H. Nienhaus and S. Barcikowski, *Langmuir*, 2014, **30**, 4213–4222.
- 30 G. Lagaly, O. Mecking and D. Penner, *Colloid Polym. Sci.*, 2001, **279**, 1090–1096.
- 31 J. T. G. Overbeek, *Pure Appl. Chem.*, 1980, **52**, 1151–1161.
- 32 J. Lyklema, *J. Colloid Interface Sci.*, 2013, **392**, 102–104.
- 33 G. Trefalt, I. Szilagyi and M. Borkovec, *J. Colloid Interface Sci.*, 2013, **406**, 111–120.
- 34 G. Trefalt, F. J. Montes Ruiz-Cabello and M. Borkovec, *J. Phys. Chem. B*, 2014, **118**, 6346–6355.
- 35 T. Oncsik, G. Trefalt, Z. Csendes, I. Szilagyi and M. Borkovec, *Langmuir*, 2014, **30**, 733–741.
- 36 F. J. M. Ruiz-Cabello, G. Trefalt, Z. Csendes, P. Sinha, T. Oncsik, I. Szilagyi, P. Maroni and M. Borkovec, *J. Phys. Chem. B*, 2013, **117**, 11853–11862.
- 37 C. Schneider, M. Hanisch, B. Wedel, A. Jusufi and M. Ballauff, *J. Colloid Interface Sci.*, 2011, **358**, 62–67.
- 38 I. Szilagyi, A. Polomska, D. Citherlet, A. Sadeghpour and M. Borkovec, *J. Colloid Interface Sci.*, 2013, **392**, 34–41.
- 39 A. Sadeghpour, I. Szilagyi and M. Borkovec, *Z. Phys. Chem.*, 2012, **226**, 597–612.
- 40 K. L. Chen, S. E. Mylon and M. Elimelech, *Langmuir*, 2007, **23**, 5920–5928.
- 41 K. E. Verrall, P. Warwick and A. J. Fairhurst, *Colloids Surf., A*, 1999, **150**, 261–273.
- 42 Y. Mori, K. Togashi and K. Nakamura, *Adv. Powder Technol.*, 2001, **12**, 45–59.
- 43 L. Wu, L. Liu, B. Gao, R. Munoz-Carpena, M. Zhang, H. Chen, Z. H. Zhou and H. Wang, *Langmuir*, 2013, **29**, 15174–15181.
- 44 M. Sano, J. Okamura and S. Shinkai, *Langmuir*, 2001, **17**, 7172–7173.
- 45 A. Violante, M. Pucci, V. Cozzolino, J. Zhu and M. Pigna, *J. Colloid Interface Sci.*, 2009, **333**, 63–70.
- 46 R. L. Frost, A. W. Musumeci, J. T. Klopogge, M. O. Adebajo and W. N. Martens, *J. Raman Spectrosc.*, 2006, **37**, 733–741.
- 47 M. Jobbagy and A. E. Regazzoni, *J. Colloid Interface Sci.*, 2013, **393**, 314–318.
- 48 J. Hong, Z. L. Zhu, H. T. Lu and Y. L. Qiu, *RSC Adv.*, 2014, **4**, 5156–5164.
- 49 T. Bujdosó, A. Patzko, Z. Galbacs and I. Dekany, *Appl. Clay Sci.*, 2009, **44**, 75–82.
- 50 K. Kuzawa, Y. J. Jung, Y. Kiso, T. Yamada, M. Nagai and T. G. Lee, *Chemosphere*, 2006, **62**, 45–52.
- 51 Z. P. Xu, Y. G. Jin, S. M. Liu, Z. P. Hao and G. Q. Lu, *J. Colloid Interface Sci.*, 2008, **326**, 522–529.
- 52 J. He, M. Wei, B. Li, Y. Kang, D. G. Evans and X. Duan, in *Layered Double Hydroxides*, ed. X. Duan and D. G. Evans, 2006, vol. 119, p. 89–119.
- 53 D. Sranko, A. Pallagi, E. Kuzmann, S. E. Canton, M. Walczak, A. Sapi, A. Kukovec, Z. Konya, P. Sipos and I. Palinko, *Appl. Clay Sci.*, 2010, **48**, 214–217.
- 54 Q. Wang and D. O'Hare, *Chem. Rev.*, 2012, **112**, 4124–4155.
- 55 X. D. Sun and S. K. Dey, *J. Colloid Interface Sci.*, 2015, **458**, 160–168.
- 56 D. G. Evans and R. C. T. Slade, in *Layered Double Hydroxides*, ed. X. Duan and D. G. Evans, 2006, vol. 119, p. 1–87.
- 57 H. Holthoff, S. U. Egelhaaf, M. Borkovec, P. Schurtenberger and H. Sticher, *Langmuir*, 1996, **12**, 5541–5549.
- 58 M. Owczarz, A. C. Motta, M. Morbidelli and P. Arosio, *Langmuir*, 2015, **31**, 7590–7600.
- 59 E. Tombacz and M. Szekeres, *Appl. Clay Sci.*, 2004, **27**, 75–94.
- 60 M. Borkovec, S. H. Behrens and M. Semmler, *Langmuir*, 2000, **16**, 5209–5212.
- 61 M. Pavlovic, M. Adok-Sipiczki, C. Nardin, S. Pearson, E. Bourgeat-Lami, V. Prevot and I. Szilagyi, *Langmuir*, 2015, **31**, 12609–12617.
- 62 K. K. Norrfors, M. Bouby, S. Heck, N. Finck, R. Marsac, T. Schafer, H. Geckeis and S. Wold, *Appl. Clay Sci.*, 2015, **114**, 179–189.

dc 1931\_21

- 63 A. Zaccone, H. Wu, M. Lattuada and M. Morbidelli, *J. Phys. Chem. B*, 2008, **112**, 1976–1986.
- 64 R. Ferretti, S. Stoll, J. W. Zhang and J. Buffle, *J. Colloid Interface Sci.*, 2003, **266**, 328–338.
- 65 A. Zaccone, J. J. Crassous, B. Beri and M. Ballauff, *Phys. Rev. Lett.*, 2011, **107**, 168303.
- 66 E. Tombacz, C. Csanaky and E. Illes, *Colloid Polym. Sci.*, 2001, **279**, 484–492.
- 67 J. H. Choy, M. Park and J. M. Oh, *Curr. Nanosci.*, 2006, **2**, 275–281.
- 68 S. Vial, V. Prevot, F. Leroux and C. Forano, *Microporous Mesoporous Mater.*, 2008, **107**, 190–201.
- 69 M. Pavlovic, L. Li, F. Dits, Z. Gu, M. Adok-Sipiczki and I. Szilagyi, *RSC Adv.*, 2016, **6**, 16159–16167.
- 70 R. Rojas Delgado, M. Arandigoyen Vidaurre, C. P. De Pauli, M. A. Ulibarri and M. J. Avena, *J. Colloid Interface Sci.*, 2004, **280**, 431–441.
- 71 R. Rojas Delgado, C. P. De Pauli, C. B. Carrasco and M. J. Avena, *Appl. Clay Sci.*, 2008, **40**, 27–37.
- 72 R. B. Leggat, S. A. Taylor and S. R. Taylor, *Colloids Surf., A*, 2002, **210**, 69–81.
- 73 P. Sinha, I. Szilagyi, F. J. M. Ruiz-Cabello, P. Maroni and M. Borkovec, *J. Phys. Chem. Lett.*, 2013, **4**, 648–652.
- 74 E. Matijevic and M. Kerker, *J. Phys. Chem.*, 1958, **62**, 1271–1276.
- 75 P. M. May, D. Rowland, E. Konigsberger and G. Hefter, *Talanta*, 2010, **81**, 142–148.



Contents lists available at ScienceDirect

## Colloid and Interface Science Communications

journal homepage: [www.elsevier.com/locate/colcom](http://www.elsevier.com/locate/colcom)

Rapid Communication

## Self-assembly of delaminated layered double hydroxide nanosheets for the recovery of lamellar structure

Adél Szerlauth<sup>a,b</sup>, Edina Balog<sup>b</sup>, Dóra Takács<sup>a,b</sup>, Szilárd Sáringér<sup>a,b</sup>, Gábor Varga<sup>b,c</sup>, Gábor Schusztér<sup>b,\*</sup>, István Szilágyi<sup>a,b,\*</sup><sup>a</sup> MTA-SZTE Lendület Biocolloids Research Group, University of Szeged, H-6720 Szeged, Hungary<sup>b</sup> Department of Physical Chemistry and Materials Science, University of Szeged, H-6720 Szeged, Hungary<sup>c</sup> Material and Solution Structure Research Group, University of Szeged, H-6720 Szeged, Hungary

## ARTICLE INFO

## Keywords:

Layered double hydroxide  
Nanosheet  
Ordered restacking  
Self-assembly

## ABSTRACT

The aggregation mechanism of delaminated layered double hydroxide (dLDH) to form lamellar or even more complex nanostructures is revealed. It is found that dLDH nanosheets undergo ordered restacking via self-assembly upon salt induced aggregation within a short period of time. This first step is followed on longer term by the formation of house-of-cards-type aggregated clusters.

Lamellar inorganic nanostructures attracted widespread contemporary interest in liquid phase delamination processes as they are potential sources of unilamellar nanosheets and 2-dimensional graphene analogues [1–4]. Among them, layered double hydroxides (LDHs) represent an important class of materials with a general formula of  $[M_{1-x}^{2+}M_x^{3+}(\text{OH})_2]^{x+}[A_{x/n}^{n-}] \cdot m\text{H}_2\text{O}$ , where  $M^{2+}$  and  $M^{3+}$  stand for di- and trivalent metal ions, respectively, and  $A^{n-}$  can be a variety of intercalated charge compensating anions [5–7].

To enlarge their potential exploitation in the field of catalysis and materials science, the synthesis of porous and highly dispersed LDHs has become a priority [8]. Efforts were made to minimize the mass transfer limitations as well as to maximize the accessibility of the active sites on the surface of LDHs. However, conventionally synthesized, stone-like hydroxaltes cannot be used because of their well-known hydrophilic nature, high affinity to aggregation, and high surface charge density [8,9]. To address these drawbacks, the long-range order of the stone-like LDHs have been systematically broken producing single layers of LDHs (dLDHs), i.e., positively charged platelets with a thickness of 1 – 2 nm during delamination processes [8,10]. Various polar solvents such as DMF [8], alcohols [11], and acrylates [12] are commercially applied as delamination medium. Regardless of the noticeably advances obtained, these methods were as of yet strongly limited to the significant product losses and their non-ecofriendly features. Moreover, these methods cannot ensure that dLDHs still remain exfoliated after drying. Accordingly, water- and aqueous-miscible solvent-based strategies have been

designed and developed. These methods facilitate the existence of exfoliated hydroxaltes layers in solid phase, however, they are two-step synthesis procedures and still involve the application of non-ecofriendly organic additives [13,14]. Recently, direct syntheses of dLDHs have already become possible without the solidification of stone-like LDH phase [15]. Such dLDHs were applied as building blocks of catalysts [16], photodetectors [17], anion adsorbers [14], and electrodes [18], and for the preparation of ultrathin films [19]. Therefore, the self-assembly-driven restacking mechanism of dLDHs either into ordered or random morphologies is extensively studied.

LDHs of various compositions were delaminated either in alcohols or in the presence of surfactants and restacked by the evaporation or polarity change of the solvent [20]. The investigation of the recovered solid LDH particles revealed that the evaporation conditions determine the product morphology [21]. In general, restacking can be achieved by the addition of multivalent anions [11,22]. However, borate modified dLDHs remained delaminated upon drying after an appropriate aqueous miscible organic solvent treatment [9]. Such a dLDH powder can be a promising source for large scale production of unilamellar nanosheets.

Despite the above delamination–restacking studies, in which the products were characterized mainly in solid state, there is a lack of comprehensive investigation on such processes in colloid systems. Given the fact that application of dLDHs usually takes place in liquid media, aggregation mechanism and corresponding dispersion stability are major issues, which were explored, to the best of our knowledge, only in

\* Corresponding authors at: Department of Physical Chemistry and Materials Science, University of Szeged, H-6720 Szeged, Hungary.

E-mail addresses: [schuszt@chem.u-szeged.hu](mailto:schuszt@chem.u-szeged.hu) (G. Schusztér), [szistvan@chem.u-szeged.hu](mailto:szistvan@chem.u-szeged.hu) (I. Szilágyi).

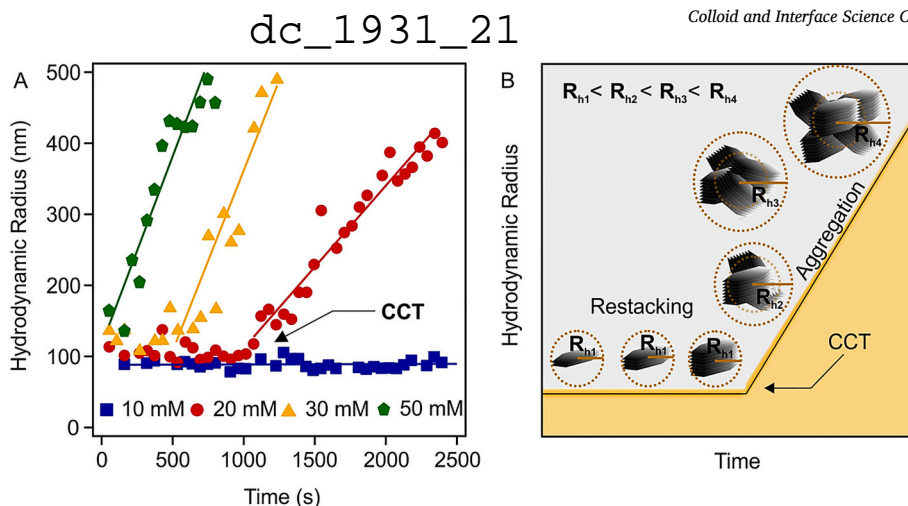


Fig. 1. Part A: Hydrodynamic radii of dLDH particles versus time measured by DLS at 10 mg/L particle concentration and different ionic strengths. Part B: The schematics of the restacking and aggregation mechanism.

one report so far [23]. It was concluded that with increasing salt concentration, the surface charge of the dLDHs decreases which causes particle aggregation. Furthermore, the critical coagulation concentration (CCC) drops with the increasing valence of the anions. Apart from this study on the aggregation of dLDHs, the orientation of the nanosheets and the morphology of the aggregates upon destabilization of dLDHs were not investigated in colloid dispersions to date.

Therefore, the aim of the present study is to explore the salt induced aggregation of dLDHs in dispersions produced via a simple aqueous synthetic route (see SI for the experimental procedure of dLDH dispersion preparation) [15]. The colloidal behaviour is assessed in light scattering, turbidity, and zeta potential measurements, while the structure of the primary particles and their aggregates are revealed by X-ray diffractometry (XRD), atomic force (AFM) and transmission electron microscopy (TEM). The experimental details of the synthesis method and characterization protocols are given in SI. The effect of salt concentration and reaction time on the morphology of the aggregates is clarified for the first time in aqueous dispersions.

The delaminated structure of dLDHs is confirmed by XRD measurements (see Fig. S1). No characteristic diffraction peak is detected in  $2\theta = 5 - 50^\circ$  range indicating that the dispersion does not contain lamellar LDHs. Indeed, the reflections at  $2\theta \approx 61^\circ$  with Miller indices of (110) and (113) prove the formation of unilamellar dLDHs [11]. Calculated unit cell parameters are presented in SI.

To probe the mechanism of salt induced restacking and aggregation self-assembly, time resolved dynamic light scattering (DLS) measurements are carried out, in which the dLDH concentration is kept constant while that of NaCl is systematically varied. The results indicate that the time evolution of the average hydrodynamic radius strongly depends on the salt concentration (see Fig. 1A). At low ionic strength, the dispersion is stable, i.e., the average hydrodynamic radius is constant over time within experimental error. By increasing the electrolyte concentration beyond a system-dependent threshold, the time evolution of the hydrodynamic radius can be divided in two distinct regimes. First, no change is observed within a short period whose length decreases with increasing electrolyte concentration. Second, the radius increases steeply after a threshold time denoted as critical coagulation time (CCT). The change in the second phase after CCT is in line with the theory by Derjaguin, Landau, Verwey and Overbeek (DLVO) [24,25], which states that an increasing electrolyte concentration leads to the weakening of electrical double layer repulsion and to subsequent particle aggregation due to predominating van der Waals attraction. The slopes of the radii versus time plots beyond CCT first increase in conjunction with the increasing ionic strength and then become constant above a certain electrolyte concentration, which is also predicted by this theory.

However, no sensible explanation can be found in the literature for the existence of the first regime, i.e., the lag phase, before the CCTs. To understand the striking fact that, although aggregation must have already started by the addition of electrolyte, no size growth is detected by DLS, let us consider the following. DLS is appropriate for measuring only the hydrodynamic radii, i.e., the largest dimension of the scattering objects [26]. Therefore, in accordance with the measured data, no significant change should be detected upon restacking the nanosheets in an ordered fashion, since such a plate-plate orientation increases only the thickness, but does not contribute significantly to the lateral dimension (see the schematics in Fig. 1B). In aqueous solutions, the plate-plate restacking is driven by the solvent water molecules which bind the metal hydroxide nanosheets together via hydrogen bonds [9]. After the recovery of their lamellar structure, i.e., after the CCTs, the LDHs randomly aggregate which leads to the prominent increase of the average hydrodynamic radius [27]. By increasing the ionic strength, the initial lag phase becomes shorter and completely disappears beyond 50 mM NaCl concentration.

The two distinct regimes with well-defined breakpoints are also observed when dLDH aggregation is studied via turbidity measurement (see Fig. S3), which has been proven earlier as a suitable tool to explore particle aggregation processes [28] and even to study the kinetics and mechanism of chemical precipitation [29,30]. After the initial steeply increasing part, a slighter change is detected in the turbidity at longer periods. Unlike DLS, turbidity measurement is sensitive to changes both in particle concentration and size even for not spherical objects. However, if the particle size is small, higher colloid concentration is required to detect the cloudiness. Since the initial dLDH colloid dispersion is somewhat transparent due to the small size and concentration of the platelets, the initial turbidity increase upon adding the electrolyte is caused by the growing thickness and thus stronger light scattering of LDHs. The less steep turbidity increase in the second regime might originate from the formation of larger aggregates of house-of-cards structures. The situation is similar to that when chemical precipitation occurs in a highly supersaturated solution. In such scenario, nucleation is predominant until the reactant concentration drops and crystal growth becomes advanced. In this analogy, dLDHs are thought as reactants to self-assemble to nuclei, i.e., LDHs, which then aggregate similarly to polynuclear crystal growth mechanism. Therefore, it is assumed that the two distinct regimes correspond to the oriented stacking and random aggregation, respectively. The threshold time separating the two regimes is denoted as CCT here as well. Similarly to the DLS results, the initial phase before the CCT becomes shorter at higher ionic strengths (see Fig. S3).

To highlight the synergy of turbidity and DLS results and to



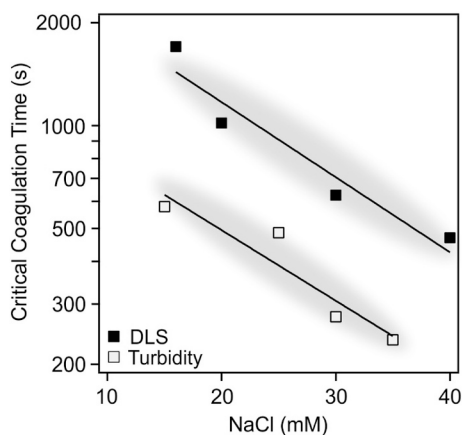


Fig. 2. CCTs as a function of NaCl concentration determined via DLS and turbidity measurements. The vertical scale is logarithmic.

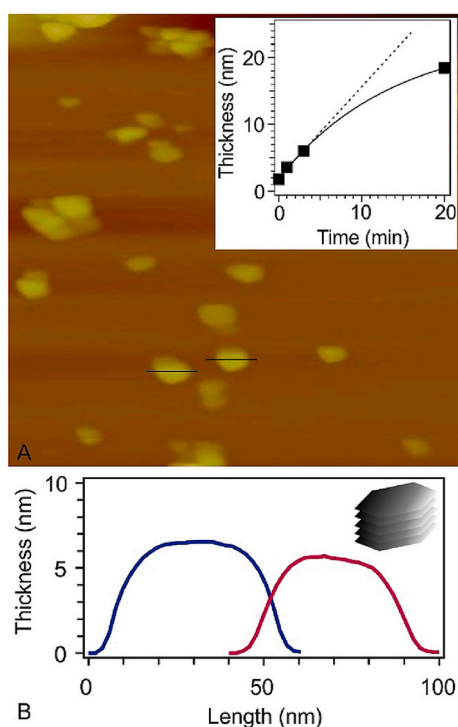


Fig. 3. AFM image of dLDHs 3 min after maintaining 30 mM NaCl concentration (A) and the height profiles related to the labelled particles (B). The inset shows the change in particle thickness as a function of reaction time based on the height profiles presented in Fig. S4.

strengthen their interpretation, the trends obtained for CCTs by the two different methods are compared (see Fig. 2). Note, however, that the absolute CCTs are somewhat different. This might be because the turbidity measurement is less sensitive than DLS thus such experiments must have been performed at 200-times higher dLDH concentration. Although aggregation could be expected at this high concentration, we recall that XRD measurements carried out with the same conditions indicated the absence of lamellar LDHs (Fig. S1). Nevertheless, CCTs determined by either method depict the same descending tendency at elevated ionic strengths, i.e., the exponents of the fitted exponential functions overlap within experimental error ( $-0.051 \pm 0.004$  for DLS and  $-0.048 \pm 0.003$  for turbidity). Such a result indicates similar aggregation mechanism in the dLDH dispersions.

To further confirm the above scenario, i.e., dLDHs first restack in an

ordered manner to form lamellar LDHs and then they aggregate, height profile assessment of the particles is carried out with AFM in a time resolved fashion. The dLDH suspension is sampled at selected times by dipping and then drying the AFM sample holder under ambient conditions. To obtain reliable data, the height of 15 particles is determined for each individual time step. In the absence of electrolyte, i.e., before the onset of stacking / aggregation, an average thickness of  $(1.75 \pm 0.25)$  nm is measured (Fig. S4A), which indicates that the particles consist of 1 – 2 layers only [15,16,31]. Once the electrolyte is added (30 mM NaCl), restacking starts which results in growing nanosheet thickness over time (see Fig. S4). As an example, Fig. 3A shows the AFM record of particles 3 min after the addition of NaCl solution; the corresponding height profiles are presented in Fig. 3B. It is found that the nanosheet thickness reaches  $(6.02 \pm 0.75)$  nm over this short period, i.e., it triples, while the lateral dimensions barely change (Fig. S4). Again, this observation coincides with the DLS results presenting no significant change of the hydrodynamic radius during the first regime. In addition to that, the increase in LDH thickness at different reaction times is shown in the inset of Fig. 3A. The tendency obtained for the average height of the particles at selected times is linear within a short time interval, while the curve saturates at longer runs (see SI–S2.3 for more data). These results further prove our hypothesis, that is, the nanosheets first recover the lamellar structure of the conventional LDHs while restacking layer-by-layer upon salt induced aggregation. Thereafter, during the second regime, large aggregates appear as a result of random aggregation and subsequent formation of house-of-cards structures of dimensions up to  $(18.42 \pm 5.21)$  nm, as represented in Fig. S4D. Note that the onset time of aggregation, taking place after ordered restacking, determined either by DLS (Fig. 1A, yellow markers) or AFM (Fig. 3A) measurements is very similar, although significantly different parameters are followed.

The thickness of dLDHs determined by TEM imaging is in good agreement with the AFM measurements. The average TEM thickness of the nanosheets shown in Fig. S5 is  $(1.75 \pm 0.33)$  nm, while the lateral dimension is in the range of  $(130 \pm 30)$  nm. The TEM image of randomly aggregated LDHs recorded after 20 min reaction time depicts the presence of flower-like motives (Fig. S6), which is similar to organic solvent treated LDHs reported elsewhere [32].

XRD measurements are also carried out at different time intervals with aggregating samples to confirm the formation of lamellar LDHs upon salt induced restacking of dLDHs. Considering the results (compare Fig. S1 and S2), no significant difference can be observed between the diffractograms of dLDHs recovered from a suspension containing no electrolyte and those obtained after 3 min aggregation time, since the small number of consecutive layers does not allow detecting any LDH-like reflections. However, after 10 and 20 min, the reflections corresponding to the lamellar LDH structure appear and the common LDH is recognized. Furthermore, the specific surface area obtained from BET analysis performed on nitrogen gas adsorption measurements decreases ( $210$ -,  $45$ - and  $30$   $\text{m}^2/\text{g}$  after 3-, 10- and 20 min reaction time, respectively; see SI for details) during the aggregation process in agreement with the literature [32]. Clearly, the specific surface area is in correlation with the number of separated nanosheets. Free dLDHs represent high specific surface area, while their restacking into consecutive layers and later on the aggregation of LDHs shrink such value. Accordingly, nitrogen gas adsorption results are also in good agreement with the turbidity, DLS and AFM results discussed above. Each method approves the existence of a two-step mechanism, i.e., a layer-by-layer restacking is followed by and somewhat separated from the aggregation of lamellar structures. As mentioned above, increasing the ionic strength leads to shorter lag phase. At 50 mM NaCl concentration, no such initial stage is detected either by DLS or turbidity measurements which logically means that no dLDHs should be present in the dispersion. Indeed, XRD pattern recorded with such electrolyte concentration right after the initiation of the experiment shows clear LDH reflections (Fig. S2–D).

The colloidal stability of dLDH dispersions is also assessed by investigating the charging and aggregation behaviour of the particles in



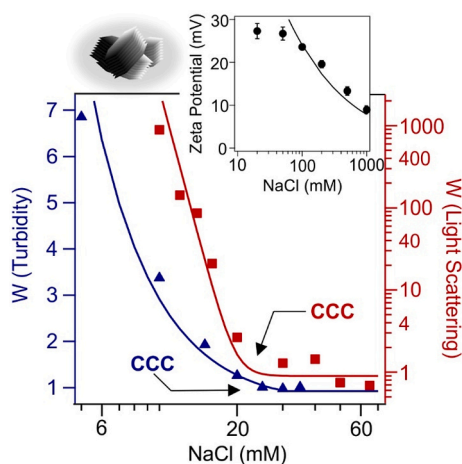


**Fig. 4.** Zeta potential (top right corner) and stability ratio ( $W$ ) of dLDHs. The latter one is determined in DLS (red square, right axis) and turbidity (blue triangle, left axis) measurements. The solid line in the zeta potential graph shows the potential values predicted by the Gouy–Chapman equation, while they are only eye guides in the stability ratio plots. (For interpretation of the references to colour in this figure legend, the reader is referred to the web version of this article.)

a wide range of electrolyte concentration. The zeta potential decreases by increasing the ionic strength due to the screening effect of the dissolved salt constituents. However, it remains positive in the entire NaCl concentration regime investigated (see the inset of Fig. 4). The zeta potential values are fitted with the Gouy–Chapman model [33] which was developed for the description of the change in potentials in the electrical double layer at different ionic strengths (see SI for details). This theory gives reliable estimate of the surface charge density at higher ionic strength, where friction forces are suppressed in electrokinetic experiments. According to the fit, a surface charge density of  $18 \text{ mC/m}^2$  is determined for dLDHs. This finding is in line with literature data obtained for LDHs in different electrolyte solutions [23,27,34] and further confirms that the restacking process leads to the formation of conventional LDH structures.

Finally, to assess the resistance of dLDH colloids against salt induced aggregation, time resolved DLS and turbidity measurements are performed. Stability ratio, the inverse of whose is equal to the fraction of particle collisions which results in aggregation (see SI for details), determined at different ionic strengths using the two methods show very similar trends (see Fig. 4). At low electrolyte concentrations, stable colloids form. Beyond the CCC, the dispersion becomes unstable indicated by stability ratios close to one. In this case the aggregation is controlled solely by the diffusion of particles. The CCCs determined in turbidity (16 mM) and DLS (20 mM) measurements are in good agreement. Such a tendency in the colloidal stability of the dLDH–NaCl samples is in qualitative agreement with the predictions of the DLVO theory implying the presence of interparticle forces of electrostatic origin similar to other LDH–electrolyte systems [23,27,34]. Note that non-DLVO interactions such as short-ranged forces originating from the hydration and the roughness of the surfaces may be present [35], however, we do not have experimental evidence to underpin this assumption.

In conclusion, the salt induced self-assembly-driven restacking and aggregation mechanism of dLDHs is investigated in aqueous dispersions. At low electrolyte concentration and for a short period of time, dLDHs stack together in plate–plate orientation giving rise to the recovery of conventional LDH nanostructure, while particle thickness linearly scales with time. Once the lamellar structure is formed, the LDHs aggregate and house-of-cards structures grow. The initial stacking regime becomes shorter upon increasing the electrolyte concentration and even disappears at high enough ionic strength. The results of morphological and

structural studies are in good agreement with the findings obtained in colloidal dispersions. Overall, the restacking mechanism of unilamellar dLDHs is explored in aqueous dispersions for the first time. We also highlight the possibility that a commercial UV–Vis photometer can be used to reliably determine some properties of colloid dispersions (e.g., critical coagulation time and stability ratio).

## Declaration of Competing Interest

There are no conflicts to declare.

## Acknowledgment

This work was supported by the Hungarian National Research, Development and Innovation Office through the grant SNN131558.

## Appendix A. Supplementary data

Supplementary data to this article can be found online at <https://doi.org/10.1016/j.colcom.2021.100564>.

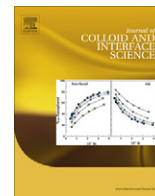
## References

- [1] J.N. Coleman, M. Lotya, A. O'Neill, S.D. Bergin, P.J. King, U. Khan, K. Young, A. Gaucher, S. De, R.J. Smith, I.V. Shvets, S.K. Arora, G. Stanton, H.Y. Kim, K. Lee, G.T. Kim, G.S. Duesberg, T. Hallam, J.J. Boland, J.J. Wang, J.F. Donegan, J. C. Grunlan, G. Moriarty, A. Shmeliov, R.J. Nicholls, J.M. Perkins, E.M. Grievson, K. Theuwissen, D.W. McComb, P.D. Nellist, V. Nicolosi, *Science* 331 (2011) 568–871.
- [2] K. Varoon, X.Y. Zhang, B. Elyassi, D.D. Brewer, M. Gettel, S. Kumar, J.A. Lee, S. Maheshwari, A. Mittal, C.Y. Sung, M. Cococcioni, L.F. Francis, A.V. McCormick, K.A. Mkhoyan, M. Tsapatsis, *Science* 333 (2011) 72–75.
- [3] S.L. Zhang, Q.F. Liu, Y.J. Yang, H. Zhang, J.J. Liu, S.S. Zeng, A.M. LaChance, A. T. Barrett, L.Y. Sun, *Chem. Commun.* 57 (2021) 789–792.
- [4] V. Dudko, K. Ottermann, S. Rosenfeldt, G. Papastavrou, J. Breu, *Langmuir* 37 (2021) 461–468.
- [5] P.J. Sideris, U.G. Nielsen, Z.H. Gan, C.P. Grey, *Science* 321 (2008) 113–117.
- [6] Z.B. Cao, B. Li, L.Y. Sun, L. Li, Z.P. Xu, Z. Gu, *Small Methods* 4 (2019) 1900343.
- [7] S. Livi, V. Bugatti, L. Estevez, J. Duchet-Rumeau, E.P. Giannelis, *J. Colloid Interface Sci.* 388 (2012) 123–129.
- [8] J.F. Yu, Q. Wang, D. O'Hare, L.Y. Sun, *Chem. Soc. Rev.* 46 (2017) 5950–5974.
- [9] Q. Wang, D. O'Hare, *Chem. Commun.* 49 (2013) 6301–6303.
- [10] Y.Y. Wang, C. Xie, Z.Y. Zhang, D.D. Liu, R. Chen, S.Y. Wang, *Adv. Funct. Mater.* 28 (2018) 1703363.
- [11] Q.L. Wu, A. Olafsen, O.B. Vistad, J. Roots, P. Norby, *J. Mater. Chem.* 15 (2005) 4695–4700.
- [12] S. O'Leary, D. O'Hare, G. Seeley, *Chem. Commun.* (2002) 1506–1507.
- [13] T. Hibino, *Chem. Mater.* 16 (2004) 5482–5488.
- [14] C.A. Antonyraj, P. Koilraj, S. Kannan, *Chem. Commun.* 46 (2010) 1902–1904.
- [15] Y.P. Zhang, H.P. Li, N. Du, R.J. Zhang, W.G. Hou, *Colloid Surf. A-Physicochem. Eng. Asp.* 501 (2016) 49–54.
- [16] F. Song, X.L. Hu, *Nat. Commun.* 5 (2014) 4477.
- [17] T.K.N. Nguyen, N. Dumait, F. Grasset, S. Cordier, D. Berthebaud, Y. Matsui, N. Ohashi, T. Uchikoshi, *ACS Appl. Mater. Interfaces* 12 (2020) 40495–40509.
- [18] Z.J. Yuan, S.M. Bak, P.S. Li, Y. Jia, L.R. Zheng, Y. Zhou, L. Bai, E.Y. Hu, X.Q. Yang, Z. Cai, Y.M. Sun, X.M. Sun, *ACS Energy Lett.* 4 (2019) 1412–1418.
- [19] L. Li, R.Z. Ma, Y. Ebina, N. Iyi, T. Sasaki, *Chem. Mater.* 17 (2005) 4386–4391.
- [20] J.T. Rajamathi, N. Ravishankar, M. Rajamathi, *Solid State Sci.* 7 (2005) 195–199.
- [21] F. Leroux, M. Adachi-Pagano, M. Intissar, S. Chauviere, C. Forano, J.P. Besse, *J. Mater. Chem.* 11 (2001) 105–112.
- [22] S. Murath, Z. Somosi, I.Y. Toth, E. Tombacz, P. Sipos, I. Palinko, *J. Mol. Struct.* 1140 (2017) 77–82.
- [23] W.Y. Yu, N. Du, Y.T. Gu, J.G. Yan, W.G. Hou, *Langmuir* 36 (2020) 6557–6568.
- [24] B. Derjaguin, L.D. Landau, *Acta Phys. Chim.* 14 (1941) 633–662.
- [25] F.J.M. Ruiz-Cabello, G. Trefalt, Z. Csendes, P. Sinha, T. Oncsik, I. Szilagy, P. Maroni, M. Borkovec, *J. Phys. Chem. B* 117 (2013) 11853–11862.
- [26] P.A. Hassan, S. Rana, G. Verma, *Langmuir* 31 (2015) 3–12.
- [27] M. Pavlovic, P. Rouster, T. Oncsik, I. Szilagy, *ChemPlusChem* 82 (2017) 121–131.
- [28] M. Kobayashi, D. Ishibashi, *Colloid Polym. Sci.* 289 (2011) 831–836.
- [29] N.P. Das, B. Müller, Á. Tóth, D. Horváth, G. Schusztzer, *Phys. Chem. Chem. Phys.* 20 (2018) 19768–19775.
- [30] N.P. Das, R. Zahorón, L. Janovák, Á. Deák, Á. Tóth, D. Horváth, G. Schusztzer, *Cryst. Growth Des.* 20 (2020) 7392–7398.
- [31] L. Li, Z. Gu, W.Y. Gu, Z.P. Xu, *RSC Adv.* 6 (2016) 95518–95526.
- [32] C.P. Chen, A. Wangriya, J.C. Buffet, D. O'Hare, *Dalton Trans.* 44 (2015) 16392–16398.

[33] G. Trefalt, I. Szilagy, M. Borkovec, J. Colloid Interface Sci. 406 (2013) 111–120.

[34] M. Pavlovic, R. Huber, M. Adok-Sipiczki, C. Nardin, I. Szilagy, Soft Matter 12 (2016) 4024–4033.

[35] Y. Diao, M. Han, J.A. Lopez-Berganza, L. Valentino, B. Marinas, R.M. Espinosa-Marzal, Langmuir 33 (2017) 8982–8992.



## Charging and aggregation of negatively charged colloidal latex particles in the presence of multivalent oligoamine cations

Istvan Szilagyi<sup>\*</sup>, Anna Polomska<sup>1</sup>, Damian Citherlet, Amin Sadeghpour<sup>2</sup>, Michal Borkovec

Department of Inorganic and Analytical Chemistry, University of Geneva, 30 Quai Ernest-Ansermet, 1211 Geneva, Switzerland

### ARTICLE INFO

#### Article history:

Available online 8 October 2012

#### Keywords:

Coagulation  
Latex  
Overcharging  
Dynamic light scattering  
Electrophoresis  
Oligoamine  
DLVO

### ABSTRACT

Charging and aggregation of negatively charged carboxyl latex particles in the presence of positively charged linear oligoamines containing 1–6 amine groups were investigated by electrophoretic mobility and dynamic light scattering. The oligoamines of low valence resemble simple inert salts and stabilize the suspensions by screening their charge. The oligoamines of higher valence induce overcharging at low concentrations, whereby destabilization is triggered by charge neutralization. At higher concentrations, destabilization is also induced by screening. The onset of first fast aggregation regime scales with the inverse six power of the valence in agreement with the Schulze–Hardy rule. Aggregation rates can be relatively well described by the DLVO theory which indicates that interactions are governed by van der Waals and electrostatic double layer forces.

© 2012 Elsevier Inc. All rights reserved.

### 1. Introduction

Multivalent ions are widely used to destabilize colloidal suspensions, especially in water-treatment. Since particles suspended in freshwaters and wastewaters are mostly negatively charged, good flocculants are positively charged. Trivalent iron or aluminum ions are most popular, mainly due to their low costs and biocompatibility. The fact that ions of high valence represent powerful flocculants has been inferred from the Schulze–Hardy rule already about one century ago [1–4]. This rule states that the salt concentration needed to destabilize a colloidal suspension scales as the inverse six power of the valence of the counterions of the particles involved. The approximate validity of this rule has been established for a wide range of metal cations [1,4–6].

The Schulze–Hardy rule was rationalized in the forties by Derjaguin, Landau, Verwey, and Overbeek (DLVO) [2,3,7,8]. The DLVO theory assumes that forces between colloidal particles are mainly governed by a superposition of attractive van der Waals forces and repulsive electrical double-layer forces. When double-layer forces dominate, a colloidal suspension is stable. When inter-particle forces are dictated only by van der Waals forces, the suspension becomes unstable. Thereby, particle aggregation is rapid as it is controlled by diffusion, and one refers to the fast aggregation

regime. When the strength of the van der Waals and double layer forces become comparable, the suspension is still unstable, but aggregation proceeds more slowly. In this slow aggregation regime, the interaction profile features an energy barrier, which is only occasionally overcome. The transition between the slow and fast regime can be induced by adding an appropriate additive referred to as the coagulant, which will be here salts of multivalent ions. As this transition occurs quite suddenly at a particular concentration of the coagulant, one refers to this point as the critical coagulation concentration (CCC).

Destabilization of a colloidal suspension by weakening of the double layer forces can be achieved by two principal mechanisms, namely screening and charge neutralization [2,3,9,10]. Screening occurs when the concentration of indifferent ions is being increased to the point that the interaction range of the double layer forces becomes so small that van der Waals forces will dominate [11]. Charge neutralization can only occur if an ion has a sufficiently large affinity to the oppositely charged particle surface. In that case, adsorption of oppositely charged ions will reduce the overall surface charge. This reduction will in turn weaken the magnitude of the double layer forces and at one point the van der Waals forces become dominant. These two mechanisms were first clearly established with various multivalent metal cations in the late fifties by Matijevic and coworkers [1,12]. However, it was equally recognized that hydrolysis and precipitation of metal hydroxo complexes complicates the picture substantially [13,14].

More recently it was shown that the Poisson–Boltzmann theory, which is commonly used within DLVO theory to estimate the double-layer interactions, may fail for multivalent ions due to the neglect of ion–ion correlations [15–18]. More accurate treatment of

<sup>\*</sup> Corresponding author. Fax: +41 22 379 6069.

E-mail address: [istvan.szilagyi@unige.ch](mailto:istvan.szilagyi@unige.ch) (I. Szilagyi).

<sup>1</sup> Present address: Department of Chemistry and Applied Biosciences, Swiss Federal Institute of Technology Zurich, 10 Wolfgang-Pauli-Strasse, 8093 Zurich, Switzerland.

<sup>2</sup> Present address: Physical Chemistry, Karl-Franzens University, 28 Heinrichstrasse, 8010 Graz, Austria.

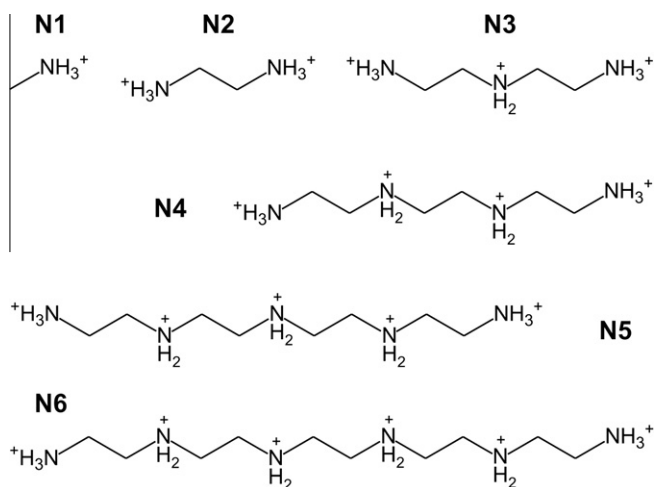


**Fig. 1.** Structure of linear aliphatic oligoamines in the fully ionized form used in this work. Methylamine (N1), ethylenediamine (N2), diethylenetriamine (N3), triethylenetetramine (N4), tetraethylenepentamine (N5), and pentaethylenhexamine (N6).

electrostatic interactions suggests that the presence of multivalent ions may not only lead to charge neutralization but equally to charge reversal or overcharging. Additional attractive interactions may occur in such situations as well. Such ion–ion correlation effects were suggested to be relevant for phenomena as diverse as in the cohesion of cement paste [19–21], charging of water–oxide interfaces [22–24], or compaction of DNA [25–27]. However, the importance of ion–ion correlations was not addressed in colloid stability so far. Charge reversal was reported in various systems containing multivalent metal ions previously [28,29], but this phenomenon was interpreted in terms of specific ion adsorption and surface precipitation of hydroxides.

The present study addresses the role of multivalent cations in colloidal stability anew. However, by working with organic multivalent cations we exclude any effects of hydrolysis or precipitation. The model systems studied are negatively charged carboxyl latex particles in the presence of various linear oligoamines (see Fig. 1). The relevant charging characteristics are studied with electrophoresis, while the colloidal stability is quantified in terms of aggregation rate constants measured by time-resolved dynamic light scattering. DLVO theory is used to predict the aggregation rates, and provided surface potentials are estimated from electrophoresis one finds a relatively good agreement with experiment.

## 2. Materials and methods

### 2.1. Materials

Negatively charged surfactant-free carboxylate-modified latex was obtained from Interfacial Dynamics Corporation (Portland, USA). The manufacturer has determined the mean particle radius as 154 nm and a polydispersity of 4.2% by transmission electron microscopy and a surface charge density of  $-1.49 \text{ C/m}^2$  by conductometry. The latter value is so substantial due to the dense polycarboxylate layer on the particle surface. The hydrodynamic radius of the latex particles determined by dynamic light scattering in stable suspension was 156 nm, which is larger than the radius determined by transmission electron microscopy due to the finite polydispersity. The particle stock suspension was purified by dialysis against Milli-Q water using a cellulose ester membrane with a molecular mass cut-off of 50 kg/mol (No. 131378, Spectrum Rancho, Dominguez, USA). The dialysis was performed until the

conductivity of the surrounding medium reached the value of the Milli-Q water.

Linear aliphatic oligoamines containing 1–6 amino groups were used (Table 1 and Fig. 1). The monomer (methylamine hydrochloride, N1), tetramer (triethylenetetramine tetrahydrochloride, N4), pentamer (tetraethylenepentamine pentahydrochloride, N5) and hexamer (pentaethylenhexamine, N6) were purchased from Aldrich (St. Louis, USA). The dimer (ethylenediamine dihydrochloride) whereas the trimer (diethylenetriamine, N3) was purchased from Acros Organics (New Jersey, USA). The hydrochloride salts (N1, N2, N4 and N5) were dissolved or the liquids (N3 and N6) were diluted. The final concentrations were determined by total carbon and nitrogen measurements (TOCV, Shimadzu). The distribution of the charged species and the degree of ionization was calculated from the tabulated ionization constants of the oligomers [30]. The protonation is complete at pH 4.0 for small oligomers up to N4, while about 70% of the amino groups are ionized in the case of the larger ones (N5, N6) similarly to linear poly(ethylene imine) of high molecular mass [31].

All solutions were prepared with Milli-Q water (Millipore, Molsheim, France) adjusted to pH 4.0 with HCl (Merck, Darmstadt, Germany) and KOH (Sigma–Aldrich, Steinheim, Switzerland). The ionic strength was adjusted by adding KCl (Acros, Geel, Belgium). Prior to sample preparation, all solutions were filtered by 0.1  $\mu\text{m}$  syringe filters (Millipore, Cork, Ireland). The measurements were performed at a temperature of  $25 \pm 0.2 \text{ }^\circ\text{C}$ .

### 2.2. Electrophoretic mobility

Charging properties of the particle suspensions were investigated by electrophoresis. The experiments were carried out with a laser velocimetry setup ZetaNano ZS (Malvern Instruments, Worcestershire, UK) at electric field strength of 4 kV/m. The samples were prepared in plastic containers by mixing first water with KCl stock solutions adjusted to pH 4.0 to obtain the desired ionic strength. Subsequently, oligomer stock solutions were added and the sample preparation was completed by adding 0.5 mL of particle stock suspension. The final particle concentration was about 11 mg/L and the total volume was 5 mL. The suspensions were shaken and equilibrated overnight. The aggregation state of the suspensions had no observable effects on the measured electrophoretic mobilities. The measurements were carried out in plastic capillary cells rinsed with Milli-Q water. Prior to the measurement, each sample was equilibrated in the cell placed in the instrument for 1 min. The final mobility value was obtained by taking the average of six individual runs.

Partitioning of the oligomers between the adsorbed and dissolved state was estimated by comparing the total oligomer concentrations  $c_{t,1}$  and  $c_{t,2}$  at two different particle concentrations  $c_{p,1}$  and  $c_{p,2}$ . The latter two concentrations were chosen around 20 mg/L and 200 mg/L. By assuming adsorption equilibrium and that the electrophoretic mobility is only a function of the adsorbed amount  $\Gamma$ , which itself only depends on the concentration of dissolved oligomers  $c_d$  in solution, one obtains [32]

$$\Gamma = \frac{c_{t,1} - c_d}{c_{p,1}} = \frac{c_{t,2} - c_d}{c_{p,2}} \quad (1)$$

By applying this equation at IEP for the two different particle concentrations, one finds the corresponding solution concentration, from which the adsorbed amount can be determined. By assuming that the adsorbed amount is independent of the particle concentration, the free concentration was determined at the particle concentration of 11 mg/L. From the adsorbed amount and the free concentration one can obtain the partitioning between the adsorbed and dissolved state.

**Table 1**  
Properties of linear oligoamines used in this work.

Name	Symbol	Ionization constants <sup>a</sup>	Degree of ionization <sup>b</sup>	IEP (mg/L) <sup>c</sup>	Partitioning (%) <sup>d</sup>
Methylamine	N1	10.63	1.00	–	>99
Ethylenediamine	N2	9.93, 6.85	1.00	–	>99
Diethylenetriamine	N3	9.80, 8.75, 3.73	0.89	1680	>99
Triethylenetetramine	N4	9.73, 8.86, 6.12, 2.60	0.79	80.7	97
Tetraethylenepentamine	N5	9.75, 9.11, 7.67, 3.99, 2.13	0.69	8.6	92
Pentaethylenehexamine	N6	9.89, 9.06, 6.03, 5.77, 2.96, 1.28	0.68	1.4	95

<sup>a</sup> Ionization constants at vanishing ionic strength taken from Ref. [30].

<sup>b</sup> Calculated degree of ionization at pH 4.0.

<sup>c</sup> Dose of oligoamines needed to reach the IEP with carboxylic latex particles.

<sup>d</sup> Fraction of oligoamines in solution for a carboxylic latex particle concentration of 11 mg/L.

### 2.3. Particle aggregation by dynamic light scattering

Time-resolved dynamic light scattering measurements at 90° were carried out with a compact goniometer (ALV/CGS-3, Langen, Germany) equipped with a He/Ne laser of a wavelength of 633 nm and an avalanche photodiode detector. The correlation functions were accumulated for 30 s and typically 70–120 runs were performed for each time-resolved experiment. The hydrodynamic radius was determined with a second-order cumulant fit of the correlation function. The aggregation rate coefficient  $k$  was calculated from the initial rate of change of the apparent hydrodynamic radius  $r_h$  as a function of time from the following relation [33,34]

$$\frac{1}{r_{h,0}} \left. \frac{dr_h}{dt} \right|_{t=0} = \left[ 1 + \frac{\sin(2qr)}{2qr} \right] \left( 1 - \frac{r_{h,1}}{r_{h,2}} \right) kn_0 \quad (2)$$

where  $r_{h,0}$  is the initial hydrodynamic radius,  $q$  the magnitude of the scattering vector,  $r$  is the particle radius,  $r_{h,2}/r_{h,1} = 1.38$  the ratio of the hydrodynamic radii of the dimer and the monomer, and  $n_0$  the initial particle number concentration. Eq. (2) assumes the validity of the Rayleigh–Gans–Debye (RGD) approximation, which was demonstrated to be applicable to similarly sized latex particles earlier [33,34]. The aggregation rate constant  $k$  was expressed as the stability ratio [33]

$$W = \frac{k_{\text{fast}}}{k} \quad (3)$$

where  $k_{\text{fast}}$  is the fast aggregation rate coefficient in excess salt. For the particles studied here, fast aggregation is reached in 0.5 M KCl electrolyte. Under these conditions, the fast aggregation rate constant was found to be  $k_{\text{fast}} = 3.1 \times 10^{-18} \text{ m}^3/\text{s}$ . The stability ratio was determined from the change of the apparent hydrodynamic radius with time.

Dynamic light scattering measurements were performed in round borosilicate glass cuvettes (Kimble Chase, Vineland, USA). The cuvettes were cleaned with boiling mixture of concentrated  $\text{H}_2\text{SO}_4$  and  $\text{H}_2\text{O}_2$  mixed at a volume ratio of 3:1 for 3 h and afterwards rinsed thoroughly with Milli-Q water and dried in dust-free environment. The samples were prepared by mixing in the cuvette varying volumes of water with KCl stock solutions to obtain the appropriate ionic strength. An appropriate amount of oligomer stock solution was then added and the aggregation experiment was started by injecting 0.2 mL of the particle suspension. The final particle concentration in the samples was about 11 mg/L and the total volume was 2 mL. The suspensions were mixed with vortex and the aggregation rate measurements were started immediately afterwards.

### 2.4. DLVO calculations

The stability ratio of a suspension with particles of radius  $r$  was calculated from the aggregation rate coefficient [35]

$$k = \frac{4}{3\beta\eta r} \left[ \int_0^\infty \frac{B(h/r)}{(2r+h)^2} \exp[\beta V(h)] dh \right]^{-1} \quad (4)$$

where  $h$  is the separation between the particles,  $\eta$  the viscosity of water,  $\beta$  the inverse thermal energy, and  $V(h)$  the total interaction energy. The hydrodynamic resistance function  $B(x)$  can be approximated by

$$B(x) = \frac{6x^2 + 13x + 2}{6x^2 + 4x} \quad (5)$$

where  $x = h/r$ . Within DLVO theory, the interaction energy is expressed as

$$V(h) = V_{\text{vdW}}(h) + V_{\text{dl}}(h) \quad (6)$$

where  $V_{\text{vdW}}(h)$  is the van der Waals and  $V_{\text{dl}}(h)$  the electrostatic interaction energy. Van der Waals interaction energy can be obtained from [2]

$$V_{\text{vdW}}(h) = -\frac{Ar}{12h} \quad (7)$$

where  $A$  is the Hamaker constant. The repulsive electrostatic interaction energy was calculated within the Derjaguin approximation and the Debye–Hückel theory with regulation [36]. Constant potential (CP) and constant surface charge (CC) boundary conditions were used. The ionic strength of the solution was estimated by calculating the concentrations of the various species originating from the partial ionization of the oligomers with the known ionization constants and applying the Davies correction for finite ionic strength [37]. Electrical surface potentials ( $\zeta$ -potentials) were obtained from the electrophoretic mobility with the Henry equation [2]. These potentials refer to the position of the slip plane, and lead to surface charge densities that are typically smaller than the ones obtained by conductometry.

## 3. Results and discussion

Charging and stability of aqueous suspensions of colloidal carboxylic latex particles were studied in the presence of multivalent linear oligoamines from N1 through N6 as shown in Fig. 1. Charging properties were probed by electrophoretic mobility measurements while suspension stability was investigated by time-resolved dynamic light scattering. The experimental results were compared to predictions of DLVO theory.

### 3.1. Charging properties

Electrophoretic mobilities of latex particles in the presence of multivalent oligoamines from N1 to N6 are shown in Fig. 2. They were investigated in solutions of pH 4.0 and with 1 mM KCl electrolyte added. The mobility increases with the concentration of N1 and N2 and remains negative as typical for indifferent monovalent or



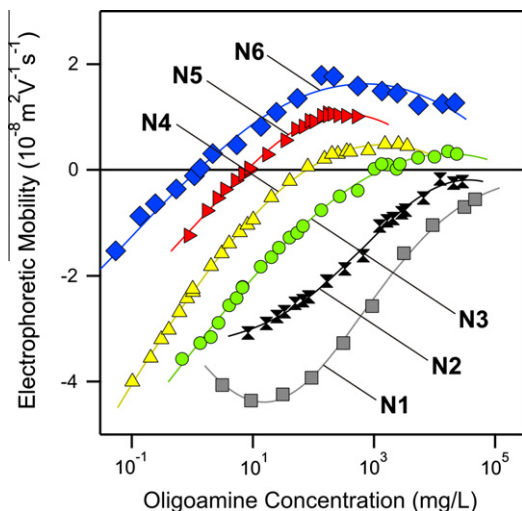


**Fig. 2.** Electrophoretic mobility of carboxyl latex particles as a function of oligoamine concentrations at pH 4.0 and with 1 mM KCl electrolyte added for different oligoamines. The solid lines are empirical functions that approximate the experimental data.

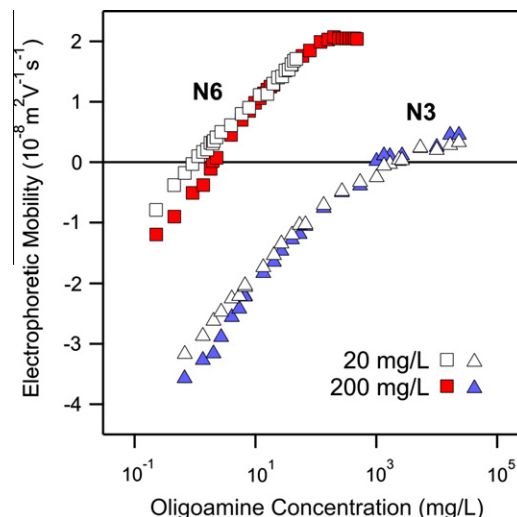


**Fig. 3.** Electrophoretic mobility of carboxyl latex particles as a function of the oligoamine concentration at pH 4.0 and with 1 mM KCl electrolyte added. The data are shown for N3 and N6 for two different particle concentrations.

divalent salts [38]. Oligoamines of higher valence lead to charge neutralization at the isoelectric point (IEP) and subsequent charge reversal. The charge reversal becomes more pronounced with increasing valence of the oligomers, and at the same time the IEP shift towards lower concentrations.

These results indicate that neither N1 nor N2 adsorb appreciably to the particle surface and that the increase in electrophoretic mobility with increasing concentration is solely due to screening. Since the charge reversal becomes more pronounced with increasing valence, the adsorption of the oligoamines becomes increasingly important too. The shift in the IEP with increasing valence is induced by the increasing affinity of the oligoamines to the oppositely charged surface. At higher concentrations, a significant contribution to the ionic strength and to the screening originates from the non-adsorbed oligoamines.

Partitioning between the adsorbed and dissolved state was studied by electrophoretic mobility measurements at different particle concentrations [32]. This method assumes that the electrophoretic mobility is only a function of the adsorbed amount and that the latter quantity only depends on the solution concentration but is independent on the particle concentration. Typical data are shown in Fig. 3.

The overlap of the curves measured at different particle concentrations shows that the total oligoamine concentration corresponds to the concentration in solution. In this case, the amount dissolved is much larger than the amount adsorbed, and the partitioning is such that the oligoamines are principally dissolved in the solution. The results of the quantitative analysis of similar experiments at IEP are summarized in Table 1. The partitioning into solution of oligoamines of lower valence is basically quantitative (>99%), while for the higher valence the partitioning between dissolved and adsorbed state becomes measurable (92–97%). Nevertheless, one can safely assume that the solution concentration of all oligoamines investigated can be well approximated by their total concentration.

The electrophoretic mobility of the particles in the presence of N6 was investigated at different salt levels and the results are shown in Fig. 4. The IEP shifts towards lower oligomer concentrations with increasing the salt level indicating that a competition for adsorption sites between the multivalent N6 and monovalent potassium ions takes place. Above the IEP, the electrophoretic

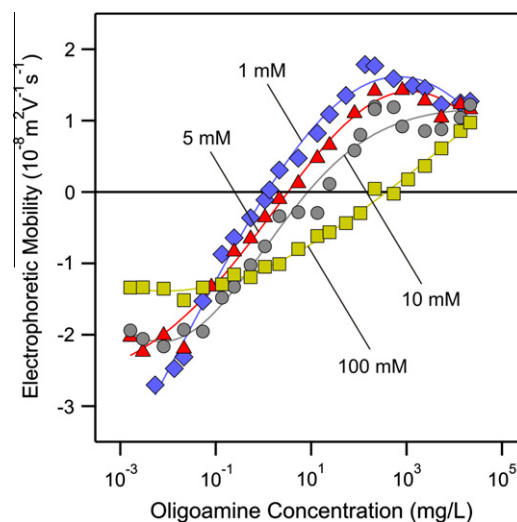


**Fig. 4.** Electrophoretic mobility of carboxyl latex particles as a function of the N6 concentration at pH 4.0 for different concentration of KCl electrolyte added. The solid lines are empirical functions that approximate the experimental data.

mobility decreases with increasing concentration of the monovalent salt. The addition of this salt reduces the surface potential and thus the mobility. The different mobilities at very low oligoamine concentrations originate from the ionic strength dependence of the mobility of the bare particles.

Fig. 5 summarizes the salt dependence of the electrophoretic mobilities of bare latex particles and the same particles in the presence of N6 at a concentration of 135 mg/L. At this concentration the particles have attained their highest mobility at low ionic strength. The mobility curve of the bare latex shows the typical minimum as a function of monovalent salt. This minimum characteristic for strongly negatively charged particles and is a direct consequence of the standard electrokinetic model [34,39]. In the presence of N6, the particles bear a positive charge and they show a similar salt dependence to the bare latex. However, the fact that the mobilities are lower in magnitude indicates a lower surface charge density. In the presence of N6, the mobility becomes negative at high salt concentrations and coincides with the mobility of

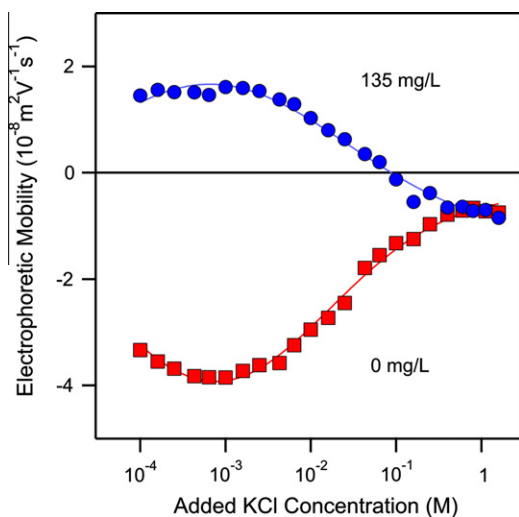


**Fig. 5.** Electrophoretic mobility of carboxyl latex particles as a function of the added KCl electrolyte at pH 4.0. Bare latex is compared with the same system in the presence of N6 at a concentration of 135 mg/L. The solid lines are empirical functions that approximate the experimental data.

the bare particles, indicating that the potassium ions fully displace N6 from the surface.

### 3.2. Particle aggregation

Time-resolved dynamic light scattering was used to investigate early-stage aggregation of the carboxylated latex particles in the presence of oligoamines at pH 4.0 and with 1.0 mM added KCl electrolyte. Stability ratios are shown as a function of the oligoamine concentration in Fig. 6. Recall that the stability ratio is about unity in the rapid aggregation regime, while in the slow aggregation regime its value becomes larger. Oligoamines of lower valence N1, N2, and N3 are in the slow aggregation regime at low concentrations, while at higher concentrations they attain the fast regime. The transition region between these two regimes is referred to as the critical coagulation concentration (CCC). Oligoamines of higher valence N4, N5, and N6 show more complicated behavior featuring two fast aggregation regimes. When the concentration of the oligoamine is increased, the stability ratio decreases at first and reaches unity in the first fast regime. When the concentration is increased further, the aggregation slows down. The stability ratio passes through a maximum and decreases again until the second fast regime is reached.

A stability map shown in Fig. 7 (top) summarizes the experimental CCC values obtained from Fig. 6. The onset of the first fast aggregation regime reminds of a coastline near the diagonal. The intermediate stabilization corresponds to the region resembling a peninsula on the right. The narrow channel between the peninsula and the coastline corresponds to the first fast regime, in which the IEP is located. The upper coastline of the peninsula reflects the onset of the second fast aggregation regime. The dependence of the CCC on the valence as expected from the Schulze–Hardy rule [3] is also indicated. Note that this rule states that the CCC is inversely proportional to the six power of the valence.

These stability experiments can be qualitatively interpreted with the electrophoresis results (see Fig. 2). Oligoamines of low valence N1, N2, and N3 do not adsorb to the particle surface significantly and the particles remain negative. An increase in the oligoamine concentration leads to an increase in the ionic strength and to a destabilization through screening of the particle charge. Oligoamines of higher valence N4, N5, and N6 adsorb more strongly

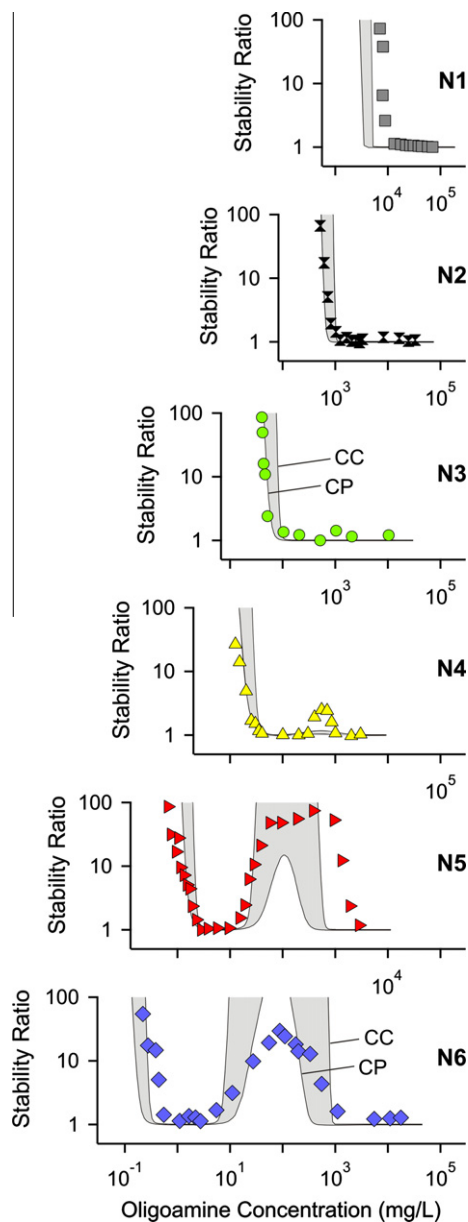


**Fig. 6.** Stability ratios of carboxyl latex particles as a function of the oligoamine concentrations at pH 4.0 and with 1 mM KCl electrolyte added for different oligoamines. The solid lines are calculations based on DLVO theory with constant charge (CC) and constant potential (CP) boundary conditions.

to the particle surface, leading to charge neutralization at IEP and to subsequent charge reversal. Therefore, the first fast aggregation regime is located near the IEP. At higher concentrations, the particles are stabilized by adsorption of the oligoamines, which induce a positive charge. At very high concentrations, one enters the second fast aggregation regime. The positively charged particles are destabilized by screening with chloride ions, which represent the counterions of the oligoamines. The transition between these two different regimes occurs at N3. While a minor charge reversal is observed by electrophoresis, hardly any corresponding stabilization of the suspension is evidenced.

The role of monovalent salt on aggregation processes was investigated with N6 in more detail. The stability ratio of the latex particles versus the N6 concentration is shown for different concentrations of added KCl electrolyte in Fig. 8. While the two fast aggregation regimes are well separated at low salt concentrations

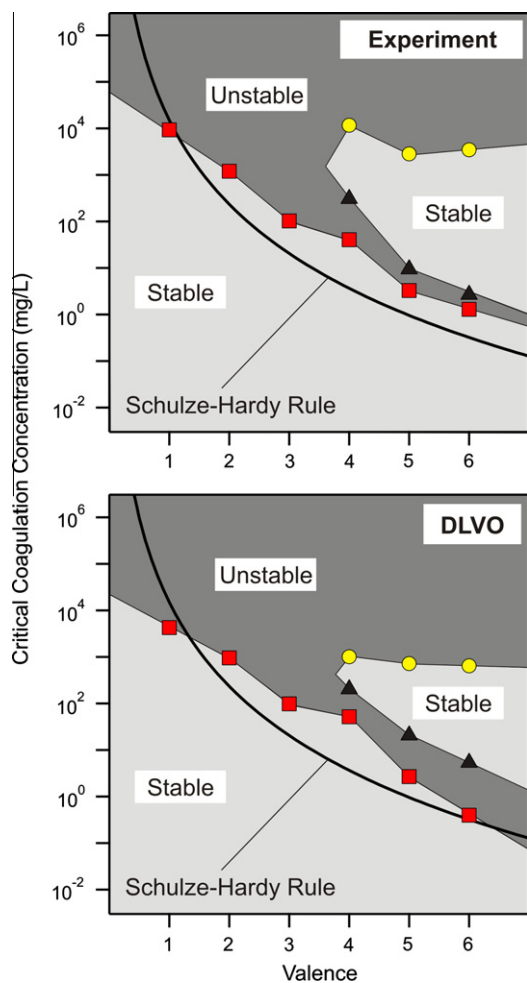


**Fig. 7.** Stability maps of carboxyl latex particles in the presence of oligoamines. The critical coagulation concentrations (CCCs) are shown as a function of the valence of the oligoamines at pH 4.0 and with 1 mM KCl electrolyte added. Experimental results (top) are compared to the DLVO predictions with constant charge boundary conditions (bottom). The solid line shows the expected dependence from the Schulze–Hardy rule. The representation assumes full ionization of the oligoamines for simplicity.

by an intermediate stability region, this region disappears at higher salt concentrations. With increasing KCl concentration, the height of the intermediate maximum in the stability ratio decreases and vanishes somewhere between 10 mM and 100 mM.

In order to locate this boundary more precisely, the stability was studied as a function of the concentration of the added KCl electrolyte at a concentration of N6 of 135 mg/L. These results are shown in Fig. 9, where the stability ratio of the bare latex is also shown. The stability plot of the bare latex in KCl is very similar to the one with N1 shown in Fig. 6 indicating that both cations are indifferent.

For both systems, the aggregation is rapid at high KCl concentrations, while it slows down at lower concentrations. The CCC is located near 20 mM in the presence of N6, while for the bare particles it is located around 300 mM. This difference in the CCCs indicates that the magnitude of the surface charge is much higher for the bare particles than for the particles with adsorbed N6. The qualitative similarity between the stability plots for the bare particles and the particles in the presence of N6 indicates that the stability is dictated by the same type of forces, namely van der Waals attraction and double layer repulsion. However, the stability ratio in the slow regime depends much more weakly on the concentration

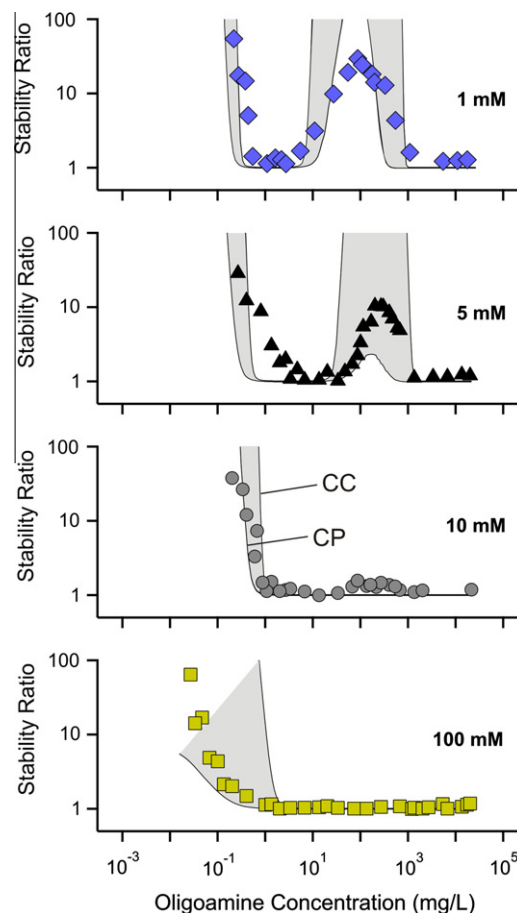


**Fig. 8.** Stability ratios of carboxyl latex particles as a function of the oligoamine concentrations at pH 4.0 and at different concentrations of KCl electrolyte added. The solid lines are calculations based on DLVO theory with constant charge (CC) and constant potential (CP) boundary conditions.

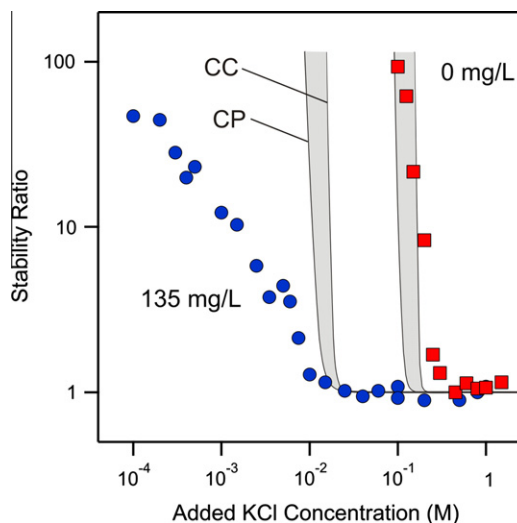


**Fig. 9.** Stability ratio of carboxyl latex particles as a function of the added KCl electrolyte at pH 4.0. Bare latex is compared with the same system in the presence of N6 at a concentration of 135 mg/L. The solid lines are calculations based on DLVO theory with constant charge (CC) and constant potential (CP) boundary conditions.

in the presence of N6 than for the bare particles. This weak dependence probably indicates that the charge distribution within the

adsorbed N6 film is much more heterogeneous than for the bare particle surface [28,40]. These heterogeneities may originate from lateral surface imperfections of the latex particles and could be amplified by the adsorption of the oligoamines. Another possible explanation for this phenomenon might be that ion–ion correlation forces are more important in the N6 system.

The overall stability behavior is further illustrated in the stability map shown in Fig. 10 (top), where the CCC is represented versus the added KCl electrolyte concentration. The lower coastline indicates the onset of the fast aggregation region at low oligoamine concentration. The peninsula on the left hand side shows the intermediate stabilization regime of positively charged particles. The upper horizontal coastline of the peninsula indicates the transition to the second fast aggregation region. The IEP is located within the channel between the coast and the peninsula.

These observations are again in line with the electrophoresis results (see Fig. 4). At low salt level, the electrophoretic mobility strongly increases through the IEP from negative to positive values. As a consequence, the suspension passes through the first fast aggregation regime and restabilizes at higher oligoamine concentrations. At higher concentrations, the mobility decreases again since the positive surface charge is screened by the increasing concentration of the oligoamine. The fact that the charge for the bare particles is higher in magnitude than for the particles with adsorbed N6 was also revealed by electrophoresis.

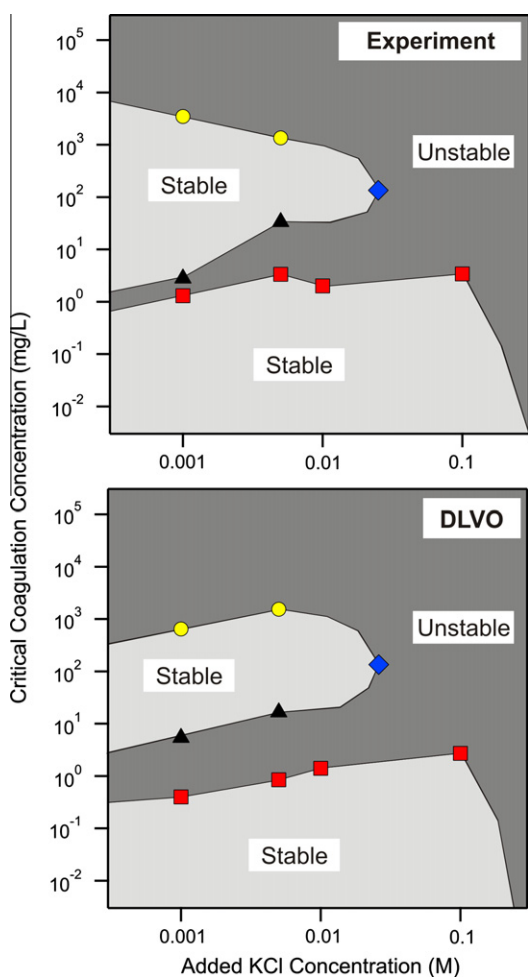


**Fig. 10.** Stability maps of carboxyl latex particles in the presence of N6. The critical coagulation concentrations (CCCs) are shown as a function of the added KCl electrolyte concentration at pH 4.0. Experimental results (top) are compared to the DLVO predictions with constant charge boundary conditions (bottom).

### 3.3. Predictions by DLVO theory

The stability ratio was further calculated with DLVO theory and the results are shown as solid lines in Figs. 6, 8 and 9. Van der Waals attraction was quantified with the known Hamaker constant  $A = 9.0 \times 10^{-21}$  J for polystyrene [41]. Surface potentials were calculated from interpolated electrophoretic mobility values shown in Figs. 2, 4 and 5 using the Henry model [2]. These potentials were used to obtain the electrostatic double layer potential energy within the Debye–Hückel approximation for constant charge (CC) and for constant potential (CP) as the boundary conditions. The ionic strength was calculated by considering the ionization of the individual oligoamines and the added KCl concentration. Thereby, the species distribution was determined at pH 4.0. The protonation constants given in Table 1 were corrected for the finite ionic strength by applying the Davies formula. Note that for the calculated stability ratios shown in the figures, the magnitude of the electric potentials was always below 30 mV. This condition must be satisfied in order that the Henry model and the Debye–Hückel theory remain good approximations. The stability maps were also obtained from DLVO theory, whereby the CCC was inferred from the calculated curves as the ones shown in Figs. 6, 8 and 9. The calculated maps are shown in Figs. 7 (bottom) and 10 (bottom).

The dependence of the stability ratio on the oligoamine concentration as shown in Fig. 6 is captured relatively well. The success of the classical DLVO theory may come somewhat as a surprise since ion–ion correlations were shown to modify the structure of the electrical double layer substantially [17,18]. However, it was also suggested that these correlations are only important close to the surface and that the classical mean-field Debye–Hückel theory is only valid at larger distances [17]. The surface potentials determined from electrophoretic mobilities reflect the charge reversal and therefore they probably take into account effects of ion–ion correlations close to the surface in an approximate fashion.

However, disagreements with DLVO theory are observed as well. In particular, the width of the intermediate restabilization region is always predicted as too small. This deficiency can be also seen in Fig. 7 as the calculated restabilization peninsula is substantially narrower than the experimental one. The dependence of the stability ratio on the oligoamine concentration in the slow aggregation regime is predicted to be larger than measured experimentally. This feature is particularly pronounced in the restabilization region after IEP, where monovalent chloride anions represent the counterions of the positively charged particles. When monovalent ions act as counterions, the barrier in the interaction potential is located at sub-nanometer separation distances, and at these distances one does no longer expect the DLVO theory to remain accurate [6,40,42]. The corresponding separation distances become larger, which suggests that DLVO theory should become more accurate. On the other hand, ion–ion correlation effects will also become more important and may influence the interaction profile [6].

Fig. 8 illustrates that DLVO theory predicts the dependence on the added KCl concentration relatively well. The stability concentrations at low oligoamine concentrations are predicted correctly, with the exception of the 5 mM salt level. When one compares the stability of the bare latex particles with the one in the presence of N6, one observes that DLVO rationalizes the CCC very well (Fig. 9). For the bare particles, the large slope of the stability plot observed experimentally is predicted by DLVO theory too. On the other hand, the DLVO theory suggests a large slope also in the presence of N6, but one observes a much smaller slope experimentally. We interpret this disagreement as originating from lateral charge heterogeneities within the adsorbed N6 film. Similar discrepancies between experimental stability data and DLVO theory were reported earlier and interpreted in a similar fashion [28,40].



Overall, the experimental stability data are relatively well described by DLVO theory. The predictions are good at low oligoamine concentrations, especially for the ones of higher valence. However, the theory predicts the restabilization regions after IEP as too narrow as the experimentally observed ones. In this regime, the predicted dependence on the oligoamine concentration is stronger than the one observed experimentally.

#### 4. Conclusions

Charging and aggregation rates of carboxyl latex particles in the presence of multivalent oligoamines were investigated by electrophoretic mobility and time-resolved dynamic light scattering. Oligoamines of low valence destabilize the colloidal suspension by screening similarly to simple ions. Oligoamines of higher valence lead to destabilization by charge neutralization, but is followed by subsequent restabilization due to overcharging. The charge-reversed particles are destabilized again at higher oligoamine concentrations due to screening by the oligoamine counterions. The latter effect was confirmed by experiments performed at different salt levels. Colloidal stability can be predicted with DLVO theory from electrophoretic mobilities relatively well. However, discrepancies are present especially in the intermediate restabilization region. These discrepancies could originate from nanometer scale charge heterogeneities within the adsorbed oligoamine films or ion–ion correlations.

The charge reversal observed for the oligoamines of higher valence strongly resembles the behavior in the presence of the linear poly(ethylene imine) [43,44] or other cationic polyelectrolytes [45–49]. The main difference between the present systems and the ones in the presence of polyelectrolytes is that the oligoamines up to N6 partition into solution while the polyelectrolytes adsorb quantitatively. This partitioning leads to the characteristic second fast aggregation regime observed for the oligoamines. This regime seems to be absent for polyelectrolytes. More details on the transition between the behavior for multivalent ions and polyelectrolytes can be found elsewhere [50]. The trends in the salt dependence of the mobility and stability for bare and oligomer-coated particles as shown in Figs. 5 and 9 are also similar to polyelectrolyte systems [38]. These findings indicate that even in this regime the suspensions are mainly stabilized by electrostatic double-layer interactions.

#### Acknowledgments

This article is dedicated to Egon Matijevic on the occasion of his 90th anniversary. We thank Robert Meszaros, Imre Varga and Robert Pugh for helpful discussions. This research was supported by the Swiss National Science Foundation and the University of Geneva.

#### References

[1] E. Matijevic, D. Broadhurst, M. Kerker, *J. Phys. Chem.* 63 (1959) 1552–1557.  
 [2] W.B. Russel, D.A. Saville, W.R. Schowalter, *Colloidal Dispersions*, Cambridge University Press, Cambridge, 1989.

[3] D.F. Evans, H. Wennerstrom, *The Colloidal Domain*, John Wiley, New York, 1999.  
 [4] I.M. Metcalfe, T.W. Healy, *Faraday Discuss.* (1990) 335–344.  
 [5] D. Grolimund, M. Elimelech, M. Borkovec, *Colloids Surf. A* 191 (2001) 179–188.  
 [6] C. Schneider, M. Hanisch, B. Wedel, A. Jusufi, M. Ballauff, *J. Colloid Interface Sci.* 358 (2011) 62–67.  
 [7] B. Derjaguin, L.D. Landau, *Acta Phys. Chim.* 14 (1941) 633–662.  
 [8] E.J.W. Verwey, J.T.G. Overbeek, *Theory of Stability of Lyophobic Colloids*, Elsevier, Amsterdam, 1948.  
 [9] O.G. Jones, S. Handschin, J. Adamcik, L. Harnau, S. Bolisetty, R. Mezzenga, *Biomacromolecules* 12 (2011) 3056–3065.  
 [10] A. Mezei, R. Meszaros, I. Varga, T. Gilanyi, *Langmuir* 23 (2007) 4237–4247.  
 [11] E. Tombacz, I. Abraham, M. Gilde, F. Szanto, *Colloids Surf.* 49 (1990) 71–80.  
 [12] E. Matijevic, L.H. Allen, *Environ. Sci. Technol.* 3 (1969) 264–268.  
 [13] B. Tezak, E. Matijevic, K.F. Schulz, *J. Phys. Chem.* 59 (1955) 769–773.  
 [14] L.J. Stryker, E. Matijevic, *J. Phys. Chem.* 73 (1969) 1484–1487.  
 [15] L. Guldbbrand, B. Jonsson, H. Wennerstrom, P. Linse, *J. Chem. Phys.* 80 (1984) 2221–2228.  
 [16] R. Kjellander, S. Marcelja, *J. Chem. Phys.* 82 (1985) 2122–2135.  
 [17] J. Ennis, S. Marcelja, R. Kjellander, *Electrochim. Acta* 41 (1996) 2115–2124.  
 [18] A.Y. Grosberg, T.T. Nguyen, B.I. Shklovskii, *Rev. Mod. Phys.* 74 (2002) 329–345.  
 [19] B. Jonsson, A. Nonat, C. Labbez, B. Cabane, H. Wennerstrom, *Langmuir* 21 (2005) 9211–9221.  
 [20] C. Labbez, A. Nonat, I. Pochard, B. Jonsson, *J. Colloid Interface Sci.* 309 (2007) 303–307.  
 [21] I. Pochard, C. Labbez, A. Nonat, H. Vija, B. Jonsson, *Cem. Concr. Res.* 40 (2010) 1488–1494.  
 [22] C. Labbez, B. Jonsson, M. Skarba, M. Borkovec, *Langmuir* 25 (2009) 7209–7213.  
 [23] M. Porus, C. Labbez, P. Maroni, M. Borkovec, *J. Chem. Phys.* 135 (2011) 064701.  
 [24] E. Wernersson, R. Kjellander, J. Lyklema, *J. Phys. Chem. C* 114 (2010) 1849–1866.  
 [25] S.M. Mel'nikov, M.O. Khan, B. Lindman, B. Jonsson, *J. Am. Chem. Soc.* 121 (1999) 1130–1136.  
 [26] M.O. Khan, S.M. Mel'nikov, B. Jonsson, *Macromolecules* 32 (1999) 8836–8840.  
 [27] K. Besteman, K. Van Eijk, S.G. Lemay, *Nat. Phys.* 3 (2007) 641–644.  
 [28] M. Schudel, S.H. Behrens, H. Holthoff, R. Kretzschmar, M. Borkovec, *J. Colloid Interface Sci.* 196 (1997) 241–253.  
 [29] R.O. James, T.W. Healy, *J. Colloid Interface Sci.* 40 (1972) 53–64.  
 [30] A.E. Martell, R.M. Smith, *Critical Stability Constants*, Plenum Press, New York, 1982.  
 [31] R.G. Smits, G.J.M. Koper, M. Mandel, *J. Phys. Chem.* 97 (1993) 5745–5751.  
 [32] A. Mezei, R. Meszaros, *Langmuir* 22 (2006) 7148–7151.  
 [33] H. Holthoff, S.U. Egelhaaf, M. Borkovec, P. Schurtenberger, H. Sticher, *Langmuir* 12 (1996) 5541–5549.  
 [34] W. Lin, M. Kobayashi, M. Skarba, C. Mu, P. Galletto, M. Borkovec, *Langmuir* 22 (2006) 1038–1047.  
 [35] M. Kobayashi, F. Juillerat, P. Galletto, P. Bowen, M. Borkovec, *Langmuir* 21 (2005) 5761–5769.  
 [36] S.L. Carnie, D.Y.C. Chan, *J. Colloid Interface Sci.* 161 (1993) 260–264.  
 [37] A. Sadeghpour, A. Vaccaro, S. Rentsch, M. Borkovec, *Polymer* 50 (2009) 3950–3954.  
 [38] J. Hierrezuelo, A. Sadeghpour, I. Szilagyí, A. Vaccaro, M. Borkovec, *Langmuir* 26 (2010) 15109–15111.  
 [39] M. Borkovec, S.H. Behrens, M. Semmler, *Langmuir* 16 (2000) 5209–5212.  
 [40] S.H. Behrens, M. Borkovec, P. Schurtenberger, *Langmuir* 14 (1998) 1951–1954.  
 [41] M.A. Bevan, D.C. Prieve, *Langmuir* 15 (1999) 7925–7936.  
 [42] L. Ehrl, Z. Jia, H. Wu, M. Lattuada, M. Soos, M. Morbidelli, *Langmuir* 25 (2009) 2696–2702.  
 [43] M. Finessi, P. Sinha, I. Szilagyí, I. Popa, P. Maroni, M. Borkovec, *J. Phys. Chem. B* 115 (2011) 9098–9105.  
 [44] I. Szilagyí, D. Rosicka, J. Hierrezuelo, M. Borkovec, *J. Colloid Interface Sci.* 360 (2011) 580–585.  
 [45] J. Hierrezuelo, A. Vaccaro, M. Borkovec, *J. Colloid Interface Sci.* 347 (2010) 202–208.  
 [46] J. Kleimann, C. Gehin-Delval, H. Auweter, M. Borkovec, *Langmuir* 21 (2005) 3688–3698.  
 [47] F. Bouyer, A. Robben, W.L. Yu, M. Borkovec, *Langmuir* 17 (2001) 5225–5231.  
 [48] W.L. Yu, F. Bouyer, M. Borkovec, *J. Colloid Interface Sci.* 241 (2001) 392–399.  
 [49] W. Lin, P. Galletto, M. Borkovec, *Langmuir* 20 (2004) 7465–7473.  
 [50] I. Szilagyí, A. Sadeghpour, M. Borkovec, *Langmuir* 28 (2012) 6211–6215.



# Aggregation of Halloysite Nanotubes in the Presence of Multivalent Ions and Ionic Liquids

Bojana Katana, Dóra Takács, Adél Szerlauth, Szilárd Sáring, Gábor Varga, Andrej Jamnik, Felix D. Bobbink, Paul J. Dyson, and Istvan Szilagy<sup>\*</sup>



Cite This: *Langmuir* 2021, 37, 11869–11879



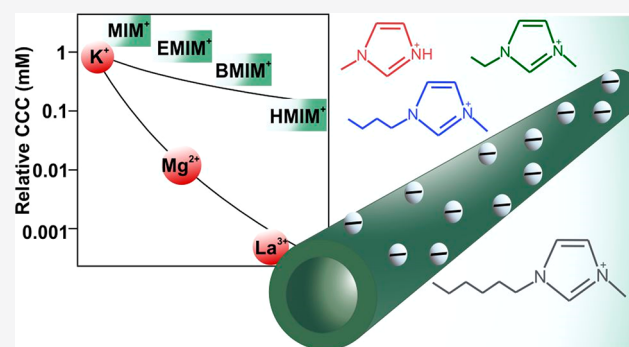
Read Online

ACCESS |

Metrics & More

Article Recommendations

**ABSTRACT:** Colloidal stability was investigated in two types of particle systems, namely, with bare (h-HNT) and polyimidazolium-functionalized (h-HNT-IP-2) alkali-treated halloysite nanotubes in solutions of metal salts and ionic liquids (ILs). The valence of the metal ions and the number of carbon atoms in the hydrocarbon chain of the IL cations (1-methylimidazolium (MIM<sup>+</sup>), 1-ethyl-3-methylimidazolium (EMIM<sup>+</sup>), 1-butyl-3-methylimidazolium (BMIM<sup>+</sup>), and 1-hexyl-3-methylimidazolium (HMIM<sup>+</sup>)) were altered in the measurements. For the bare h-HNT with a negative surface charge, multivalent counterions destabilized the dispersions at low values of critical coagulation concentration (CCC) in line with the Schulze–Hardy rule. In the presence of ILs, significant adsorption of HMIM<sup>+</sup> took place on the h-HNT surface, leading to charge neutralization and overcharging at appropriate concentrations. A weaker affinity was observed for MIM<sup>+</sup>, EMIM<sup>+</sup>, and BMIM<sup>+</sup>, while they adsorbed on the particles to different extents. The order HMIM<sup>+</sup> < BMIM<sup>+</sup> < EMIM<sup>+</sup> < MIM<sup>+</sup> was obtained for the CCCs of h-HNT, indicating that HMIM<sup>+</sup> was the most effective in the destabilization of the colloids. For h-HNT-IP-2 with a positive surface charge, no specific interaction was observed between the salt and the IL constituent cations and the particles, i.e., the determined charge and aggregation parameters were the same within experimental error, irrespective of the type of co-ions. These results clearly indicate the relevance of ion adsorption in the colloidal stability of the nanotubes and thus provide useful information for further design of processable h-HNT dispersions.



## INTRODUCTION

Halloysite nanotubes (HNT)<sup>1–3</sup> are layered aluminosilicates (Al<sub>2</sub>Si<sub>2</sub>O<sub>5</sub>(OH)<sub>4</sub>·*n*H<sub>2</sub>O) with hollow tubular structure possessing opposite signs of charges on the outer surface and inside the lumen.<sup>4</sup> The outer surface is negatively charged in aqueous dispersions at intermediate pH values due to the presence of deprotonated silanol groups, whereas the inner lumen is positively charged due to the ionized aluminol groups.<sup>5</sup> This dual charge nature combined with biocompatibility and large-scale accessibility make HNTs a promising candidate in a variety of applications, such as in biomedical and environmental sciences, wastewater treatment, nanoelectronics, and catalytic processes.<sup>6–11</sup> HNTs have been extensively characterized in the solid state with microscopy, spectroscopy, and scattering techniques. The outer diameter of the tubes is about 40–70 nm, the inner diameter is 10–20 nm, and their length is typically 500–1500 nm.<sup>12</sup> Unfortunately, the colloidal stability of commercially available HNTs is limited in aqueous environments, i.e., their dispersions can be easily destabilized by electrolyte-induced aggregation and subsequent sedimentation.<sup>13,14</sup> However, alkaline treatment of HNTs (results in h-

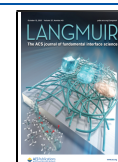
HNTs) increases the number of surface silanol groups, leading to improved colloidal stability.<sup>15</sup> In addition, aggregation processes of HNTs (and h-HNTs) can be also tuned by surface modification with appropriate polyelectrolytes.<sup>15–18</sup>

Since HNT particles may be dispersed in liquid media, usually in aqueous electrolyte solutions for many applications, a comprehensive understanding of their colloidal stability is necessary prior to applying them in such media. In general, the aggregation features of dispersed particles in dielectric media such as salt solutions can be adequately described with the Derjaguin, Landau, Verwey, and Overbeek (DLVO) theory at different ionic strengths.<sup>19,20</sup> It interprets the dispersion stability by considering van der Waals attractions between the particles and the repulsions as a result of the overlap of the

Received: July 22, 2021

Revised: September 16, 2021

Published: October 4, 2021



electrical double layers. Stable dispersions are predicted at low electrolyte concentrations, i.e., at low ionic strengths, while particles tend to aggregate with increasing levels of dissolved salts. These two regimes (reported as slow and fast aggregation regimes) are typically separated by the critical coagulation concentration (CCC).<sup>21</sup> The DLVO theory considers point-like charges in dielectric media; therefore, ions of the same valences are considered equally in the model, and thus, the same CCC is predicted irrespective of the type of ions present in the system. Nevertheless, many experimental results pointed out that the CCC changes once the chemical composition of the co-ions or counterions of the same valence is varied.<sup>22–26</sup> This deviation from DLVO theory was often interpreted that ions of different chemical compositions adsorb to surfaces to a different extent due to specific interactions between the ion and the surface. This issue can be resolved with the Hofmeister series of ions, which orders the salt constituent ions by their power in destabilization of dispersions, while surface properties such as hydrophobicity and type of functional group should also be taken into account.<sup>27–29</sup> However, for the multivalent ions, DLVO theory takes the valence of ions into account and predicts a decrease of the CCC with increasing valency through the Schulze–Hardy rule.<sup>30–32</sup> Furthermore, the extent of this decrease is different for co-ions<sup>33</sup> and counterions<sup>34</sup> as well as depending on the magnitude of the surface charge.<sup>35</sup> Hence, the ions of higher valences are more effective in destabilization of the colloidal dispersions. In this way, numerous studies have been published with systems containing nanoparticles and electrolytes of different valences and compositions, in which the aggregation mechanism and predominating interparticle forces were identified;<sup>36–41</sup> nevertheless, very limited information is available in the literature for HNT materials in this respect.<sup>13,14</sup>

In addition to the aqueous media discussed above, novel solvents come into play in the applications of HNT materials. For instance, systems composed of HNT particles and ionic liquids (ILs) have attracted considerable contemporary interest in applications<sup>42</sup> as anticorrosion agents,<sup>43</sup> catalysts,<sup>44</sup> or highly conductive materials.<sup>45</sup> ILs are organic salts of low melting point and possess several favorable features including a wide electrochemical window, low vapor pressure, high chemical stability, and advantageous interfacial properties.<sup>46–51</sup> Nanoparticles dispersed in ILs are widely used systems in various applications. However, the aggregation processes and relevant colloidal stability must be considered since stable dispersions containing well-dispersed particles are required in catalysis<sup>52</sup> for instance, whereas controlled particle aggregation in ILs can be the basis of the preparation of novel materials.<sup>53,54</sup> To explore the fundamental charging and aggregation features, the affinity of IL cations and anions to particle surfaces was studied. Findings with polystyrene,<sup>23</sup> melamine,<sup>55</sup> and silica<sup>56</sup> particles shed light on the importance of ion-specific adsorption from aqueous IL solution, which governed the surface charge properties, while the slightly modified DLVO theory was able to describe the origin of the interparticle forces. The original Hofmeister series was also extended with IL cations and anions based on the nature of their interactions with various surfaces and macromolecules.<sup>14,23,57,58</sup> Nevertheless, to the best of our knowledge, the colloidal stability of HNTs in IL solutions has been reported only once in the past.<sup>14</sup>

Therefore, in the present study, the charging and aggregation properties of bare and polyelectrolyte-coated h-

HNT particles were studied in the presence of electrolytes of different valences and in aqueous solutions containing imidazolium-based ILs with different alkyl chain lengths. The influence of the electrolyte and IL cations on the colloidal stability was systematically studied, which were present in the samples either as co-ions or counterions.

## EXPERIMENTAL METHODS

**Materials.** ILs, 1-methylimidazolium chloride (MIMCl, >95%), 1-ethyl-3-methylimidazolium chloride (EMIMCl, >98%), 1-butyl-3-methylimidazolium chloride (BMIMCl, >99%), and 1-hexyl-3-methylimidazolium chloride (HMIMCl, >98%) were purchased from Iolitec GmbH. Analytical-grade salts such as potassium chloride (KCl) and magnesium chloride (MgCl<sub>2</sub>) were bought from VWR, and lanthanum chloride (LaCl<sub>3</sub>) was obtained from Alfa Aesar. The raw HNT powder was purchased from Sigma-Aldrich and subjected to alkaline activation treatment before use.<sup>15</sup> For sample preparation, ultrapure water (resistivity of 18.2 mΩ·cm) was obtained from a VWR Purity TU+ instrument. The experiments were performed at 25 °C, and the h-HNT concentration was adjusted to 10 mg/L. The water, salt, and IL solutions were filtered with a 0.1 μm syringe filter (Millex). No unexpected or unusually high safety hazards were encountered.

The synthesis of the polyimidazolium-based polyelectrolyte (IP-2) has been reported earlier.<sup>59</sup> Accordingly, a solution containing 1,4-bis(chloromethyl)benzene and 1-(trimethylsilyl)imidazole in a 1:1 molar ratio was prepared in acetonitrile in a Schlenk flask, and it was refluxed for 48 h. The white-colored solid product was filtered, washed with acetonitrile and diethyl ether, and dried under vacuum for 24 h. The chemicals used for the above synthetic process were purchased from Sigma-Aldrich.

The IP-2-modified h-HNT stock dispersion (denoted as h-HNT–IP-2 thereafter) was prepared by simply mixing calculated volumes of a 1 g/L IP-2 solution and 10 g/L h-HNT dispersion followed by appropriate dilution with water. The h-HNT–IP-2 contained 200 mg of IP-2 per 1 g of h-HNT. This preparation was carried out at neutral pH; however, the charge balance remains the same in the pH range 3–7, so the above protocol can be applied at different pHs too.

**Raman Spectroscopy.** Raman measurements were performed with a Bruker Senterra II Raman microscope at an excitation wavelength of 765 nm applying 100 mW laser power and averaging 128 spectra with an exposition time of 6 s.

**Electron Microscopy.** Morphology studies of bare and IP-2-modified h-HNTs were carried out using transmission electron microscopy (TEM) with a FEI Tecnai G<sup>2</sup>-20 X-Twin microscope. The h-HNT and h-HNT–IP-2 dispersions of 10 mg/L concentration were dried on copper mesh grids with carbon support (CF200-Cu, Electron Microscopy Sciences), and the images in bright-field mode were obtained at a 200 kV acceleration voltage using a LaB<sub>6</sub> cathode.

**Electrophoresis.** The electrophoretic light-scattering measurements were performed on a Litesizer 500 device (Anton Paar) using a 40 mW semiconductor laser operating at a 658 nm wavelength. The samples were prepared via the following procedure. A 1.8 mL amount of IL solutions of various concentrations was mixed with 0.2 mL of h-HNT dispersion of 100 mg/L particle dose. The samples were allowed to rest for 2 h at room temperature before measuring the electrophoretic mobilities, which occurred after a 1 min equilibration time in the device. The measurements were performed in 700 μL omega-shaped plastic cuvettes (Anton Paar). The reported data are the average of the results of five individual measurements. In all cases, the obtained electrophoretic mobility (*u*) data were converted to zeta potentials ( $\zeta$ ) with the Smoluchowski equation<sup>60</sup>

$$\zeta = \frac{\eta u}{\epsilon_0 \epsilon} \quad (1)$$

where  $\eta$  is the dynamic viscosity,  $\epsilon$  is the dielectric constant of the medium, and  $\epsilon_0$  is the permittivity of the vacuum. The charge density of the particles ( $\sigma$ ) at the slip plane was determined with the Debye–Hückel model<sup>61</sup>

$$\sigma = \epsilon \epsilon_0 \kappa \zeta \quad (2)$$

where  $\kappa$  is the inverse Debye length.<sup>60</sup>

**Dynamic Light Scattering.** Dynamic light scattering (DLS) was used to measure the hydrodynamic radius ( $R_h$ ) of the particles. The experiments were carried out with the same Litesizer 500 instrument as used during electrophoresis at a scattering angle of 175°. The correlation function was fitted with the cumulant method to obtain the decay rate constant ( $\Gamma$ ). The translational diffusion coefficient ( $D$ ) was calculated as follows<sup>62</sup>

$$D = \frac{\Gamma}{q^2} \quad (3)$$

where  $q$  is the scattering vector, which can be calculated using the parameters of the experimental setup as

$$q = \left( \frac{4\pi n}{\lambda} \right) \sin\left(\frac{\Theta}{2}\right) \quad (4)$$

where  $n$  is the refractive index of the medium,  $\lambda$  is the wavelength of the laser beam, and  $\Theta$  is the scattering angle.  $R_h$  was then calculated by the Stokes–Einstein equation<sup>63</sup>

$$R_h = \frac{k_B T}{6\eta\pi D} \quad (5)$$

where  $k_B$  is the Boltzmann constant and  $T$  is the temperature. The same sample preparation procedure was applied as in the electrophoretic measurements; however, the DLS experiments were started after adding the particle stock dispersion and mixing for 25 s. The samples were equilibrated for 30 s in the device prior to data collection. From time-resolved DLS experiments, the stability ratio ( $W$ ) values were calculated as follows<sup>62,64</sup>

$$W = \frac{k^{\text{fast}}}{k} = \frac{\ln R_h(t)/dt_{t \rightarrow 0}^{\text{fast}}}{\ln R_h(t)/dt_{t \rightarrow 0}} \quad (6)$$

where  $k$  is the apparent aggregation rate constant calculated from the increase in the  $R_h$  data and  $k^{\text{fast}}$  is the rate constant determined in 1 M KCl solutions, in which diffusion-controlled particle aggregation occurs. Hence, the stability ratio is one in the case of unstable samples, and higher values indicate slower particle aggregation. The transition between the fast and the slow aggregation regimes is located at the CCC, whose value was determined as follows<sup>64</sup>

$$W = 1 + \left( \frac{\text{CCC}}{c} \right)^{-\beta} \quad (7)$$

where  $c$  is the molar concentration and  $\beta$  is calculated from the slope of the stability ratios before the CCC as

$$\beta = \frac{d \log \frac{1}{W}}{d \log c} \quad (8)$$

## RESULTS AND DISCUSSION

First, the h-HNT particles were functionalized with IP-2 polymer, and both systems, bare and IP-2-modified h-HNTs, were characterized by different techniques to verify the successful adsorption of IP-2 on the h-HNT particles. In addition, the colloidal stability of both systems was studied in the presence of metal salts and ionic liquid constituents by light-scattering techniques. The experimental conditions were kept constant in both types of measurements.

**Functionalization of h-HNT with IP-2.** To obtain the h-HNT–IP-2 particles, h-HNT was functionalized with IP-2 through adsorption of the polyelectrolyte on the oppositely charged surface. Such an adsorption process was followed, and the IP-2 dose needed to coat the h-HNT was determined in the zeta potential measurements performed at different IP-2

doses. As shown in Figure 1, negative zeta potentials were recorded at low IP-2 loadings, and they increased as the

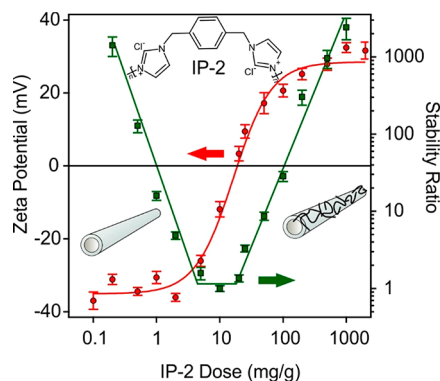


**Figure 1.** Zeta potentials (circles, left axis) and stability ratios (squares, right axis) of h-HNT particles versus the IP-2 dose at pH 7 and 10 mM ionic strength adjusted by KCl. Unit mg/g refers to milligrams of IP-2 per gram of h-HNT. Lines (red for the zeta potentials and green for the stability ratios) are eye guides. Structure presented at the top refers to IP-2. Two inset pictures represent the bare h-HNT (left) and h-HNT–IP-2 (right).

amount of added polyelectrolyte was increased, indicating the adsorption process on the oppositely charged surface. Such adsorption led to charge neutralization and overcharging at appropriate polymer doses, similar to other systems containing polyelectrolytes and oppositely charged surfaces.<sup>15,22,65</sup> At IP-2 doses higher than 200 mg/g, the zeta potentials remained constant due to the formation of a saturated IP-2 layer on the h-HNT surface, which provided a relatively high positive charge for the particles.

Aggregation of the IP-2-modified h-HNT particles was investigated at different IP-2 doses by time-resolved DLS (Figure 2). The hydrodynamic radius changed slightly at an IP-2 dose of 1 mg/g, where the h-HNT surface is partially neutralized with IP-2. A more significant increase was observed at a dose of 25 mg/g, at which the particles are positively charged. The largest increase was recorded at 10 mg/g IP-2 loading. Comparing with the zeta potential data, these doses

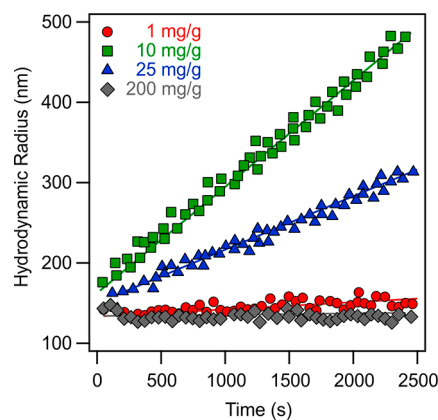


**Figure 2.** Hydrodynamic radii versus time at different doses of IP-2 measured in time-resolved DLS experiments. Experiments were performed at pH 7, 10 mM ionic strength adjusted by KCl and 10 mg/L h-HNT concentration. Unit mg/g refers to milligrams of IP-2 per gram of h-HNT, and lines are linear fits used for calculation of the stability ratios by eq 6.



are located below, above, and at the charge neutralization point, respectively. In addition, no aggregation was detected at a 200 mg/g dose, where the zeta potential measurements indicate the formation of a saturated IP-2 layer on the h-HNT. The aggregation tendencies were further assessed by determining the stability ratio values under the same experimental conditions as those used for the electrophoretic measurements.

Accordingly, fast particle aggregation occurred near the charge neutralization point (Figure 1), while the stability ratios increased away from this point, indicating stabilization of the dispersions. Such a U-shaped curve is typical for systems containing oppositely charged polyelectrolytes and particles including HNTs.<sup>15,17,22,66</sup> Referring to the data sets shown in Figure 2, stable samples were observed at 1 and 200 mg/g, moderate stability was observed at 25 mg/g, while rapid particle aggregation occurred at 10 mg/g. These findings are in qualitative agreement with the prediction of DLVO theory, since attractive forces destabilize the samples at charge neutralization (10 mg/g) while sufficiently charged particles (1 and 200 mg/g) are stable due to repulsion between the electrical double layers.

Considering the electrophoretic and DLS results, a dose of 200 mg/g was chosen for further measurements, because the h-HNT surface is completely coated with IP-2 and a stable dispersion is formed at this dose. Therefore, h-HNT-IP-2 refers to the composite of 200 mg/g polyelectrolyte content.

**Particle Characterization in Solid State.** To reveal the structural features of h-HNT-IP-2, its Raman spectrum was measured and compared to the spectra of h-HNTs and IP-2. The spectra are presented in Figure 3, and the full assignment of the Raman bands is listed in Table 1.

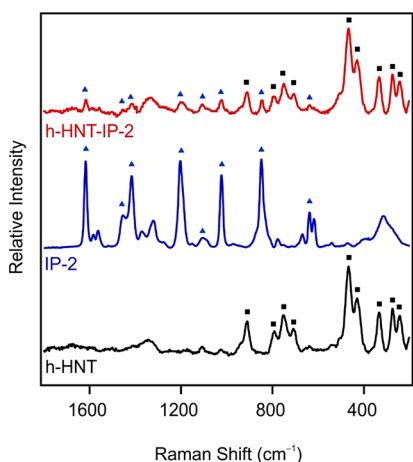


**Figure 3.** Raman spectra of h-HNT, IP-2, and h-HNT-IP-2. Characteristic vibrational bands of h-HNTs and IP-2 are indicated by squares and triangles, respectively.

The bands around 243 and 274  $\text{cm}^{-1}$  are due to the symmetric and asymmetric stretching modes of the triangular M-OH group. The intense peak at 333  $\text{cm}^{-1}$  is assigned to the H-bonded M-OH function. The other intense band at 468  $\text{cm}^{-1}$  is related to the Si-O bending vibration. Raman bands with medium intensity associated with the Al-OH translation modes were detected at 708, 750, and 792  $\text{cm}^{-1}$ . The associated vibration mode of the inner Al-OH groups was observed as a single band at 909  $\text{cm}^{-1}$ .<sup>67</sup>

**Table 1.** Observed Raman Bands and Their Assignments to the Components of the h-HNT-IP-2 Hybrid Material<sup>a</sup>

wavenumber ( $\text{cm}^{-1}$ )	assignment	compound
243	$\nu_{\text{sym}}(\text{M-OH})$	h-HNT, h-HNT-IP-2
274	$\nu_{\text{asym}}(\text{M-OH})$	h-HNT, h-HNT-IP-2
333	$\delta(\text{M-OH}\cdots\text{OH})$	h-HNT, h-HNT-IP-2
430	$\nu(\text{Al-O})$	h-HNT, h-HNT-IP-2
468	$\delta(\text{Si-O})$	h-HNT, h-HNT-IP-2
708, 750, 792	$\Gamma_{(\text{T})}(\text{Al-OH})$	h-HNT, h-HNT-IP-2
909	$\Gamma_{(\text{T}')}(\text{Al-OH})$	h-HNT, h-HNT-IP-2
618,669	$\tau_{\text{ring}}$	IP-2
637	$\rho_{\text{ring}}$	IP-2, h-HNT-IP-2
849	$\delta(\text{N-C})$	IP-2, h-HNT-IP-2
1023, 1105	$\delta_{\text{sym}}(\text{aromatic ring}), \delta_{\text{asym}}(\text{aromatic ring})$	IP-2, h-HNT-IP-2
1203	$\nu(\text{C}^{(+)}-\text{N})$	IP-2, h-HNT-IP-2
1321	$\nu_{\text{sym}}(\text{heteroaromatic ring})$	IP-2
1416	$\nu_{\text{sym}}(\text{aromatic ring})$	IP-2, h-HNT-IP-2
1455	$\nu_{\text{asym}}(\text{aromatic ring})$	IP-2, h-HNT-IP-2
1563	$\nu_{\text{asym}}(\text{heteroaromatic ring})$	IP-2
1583	$\nu_{\text{asym}}(\text{aromatic ring})$	IP-2
1617	$\nu(\text{C}=\text{N})$	IP-2, h-HNT-IP-2

<sup>a</sup> $\nu$  = stretching vibration; sym = symmetric; asym = asymmetric;  $\delta$  = bending vibration;  $\Gamma_{(\text{T})}$  = translation mode;  $\tau$  = twisting vibration;  $\rho$  = rocking vibration; M = metal.

In the case of IP-2 polymer, characteristic peaks at 618, 637, and 669  $\text{cm}^{-1}$  were identified as different deformation mode bands of the aromatic rings.<sup>68</sup> In addition, further deformation bands of the aromatic rings were observed at 1023 and 1105  $\text{cm}^{-1}$ . Furthermore, additional stretching mode vibration bands of this organic moiety were observed in the region 1321–1583  $\text{cm}^{-1}$ . Besides, one of the most intense peaks at 849  $\text{cm}^{-1}$  could be attributed to the N-C bending vibration.<sup>69</sup> Furthermore, the band at 1203  $\text{cm}^{-1}$  could be assigned to the  $\text{C}^{(+)}-\text{N}$  vibration.<sup>70</sup> The stretching mode vibration of the  $\text{C}=\text{N}$  moiety was also found at 1617  $\text{cm}^{-1}$ .

On the basis of the peak assignment, the presence of the polymer and particles was confirmed in h-HNT-IP-2. Note that the intensity of the IP-2 peaks decreased in the spectrum of the composite due to the higher sensitivity of the technique to h-HNT at the excitation wavelength used.<sup>71,72</sup>

The morphology of bare h-HNTs and h-HNT-IP-2 was studied with TEM (Figure 4). The outer diameter and length of h-HNT and h-HNT-IP-2 vary in the range of 50–60 nm and 200–1500 nm, respectively, indicating reasonable polydispersity in these dimensions. The elongated structure of the particles was confirmed for both systems, i.e., the morphology of the nanotubes did not change upon polyelectrolyte adsorption. From the h-HNT-IP-2 images, a shadow-like thin layer around the particles was observed, which may correspond to the adsorbed IP-2 layer on the h-HNT surface.

**Colloidal Stability in the Presence of Monovalent and Multivalent Metal Ions.** The charging and aggregation properties were investigated in the presence of monovalent (KCl) and multivalent ( $\text{MgCl}_2$  and  $\text{LaCl}_3$ ) salts. The zeta

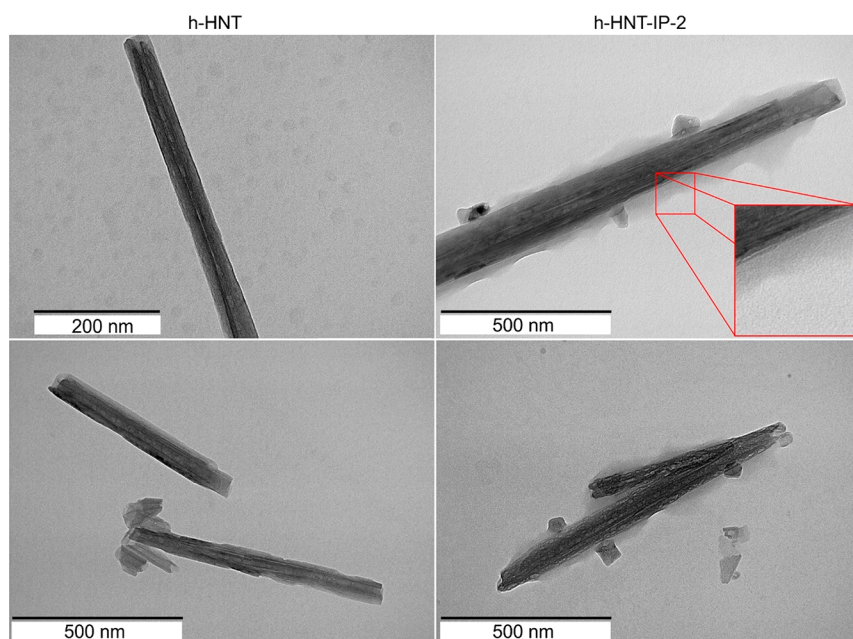


**Figure 4.** TEM images of the bare h-HNT (left column) and h-HNT-IP-2 (right column) materials. Images were taken after drying 10 mg/L dispersions on a copper-carbon mesh.

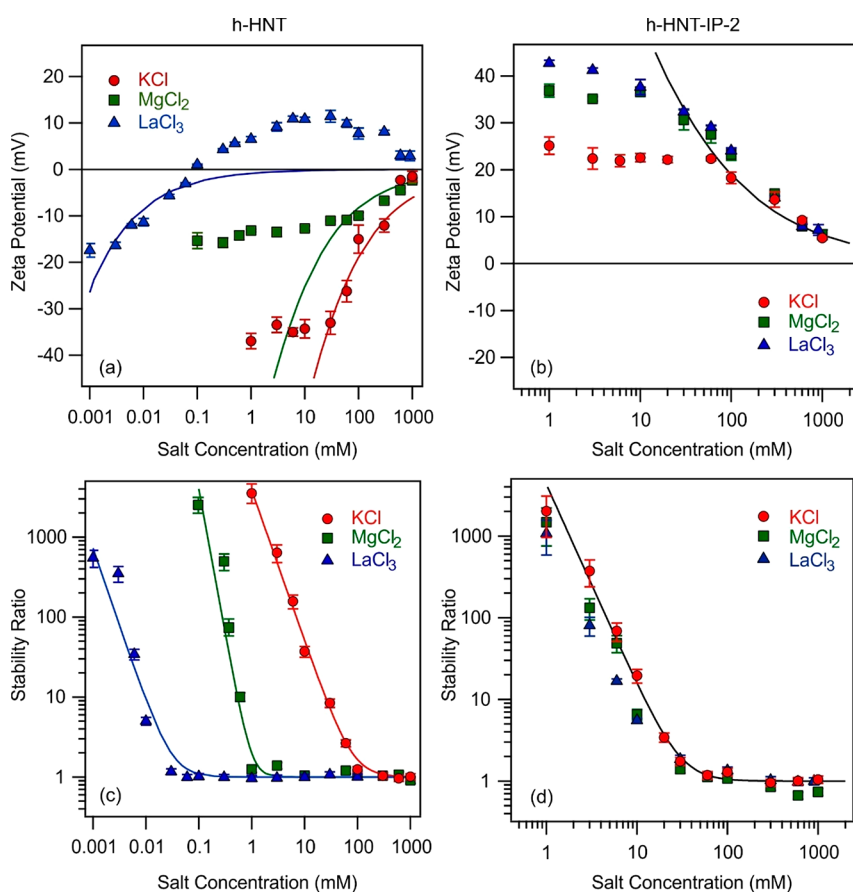


**Figure 5.** Zeta potentials (h-HNT (a) and h-HNT-IP-2 (b)) as well as stability ratios (h-HNTs (c) and h-HNT-IP-2 (d)) as a function of salt concentration at pH 7. Lines in a and b were calculated by eq 2 and in c and d by eq 7.

potentials measured for h-HNT and h-HNT-IP-2 are presented in Figure 5a and 5b, respectively.

For bare h-HNTs, the monovalent ( $K^+$ ) and multivalent ( $Mg^{2+}$  and  $La^{3+}$ ) ions are present as the counterions (for the h-

HNT-IP-2 particles, they act as co-ions), i.e., they are of the same sign of charge as the surface. In general, zeta potential data were negative at low ionic strengths and increased with the salt concentrations in all systems. For  $K^+$  and  $Mg^{2+}$ , the



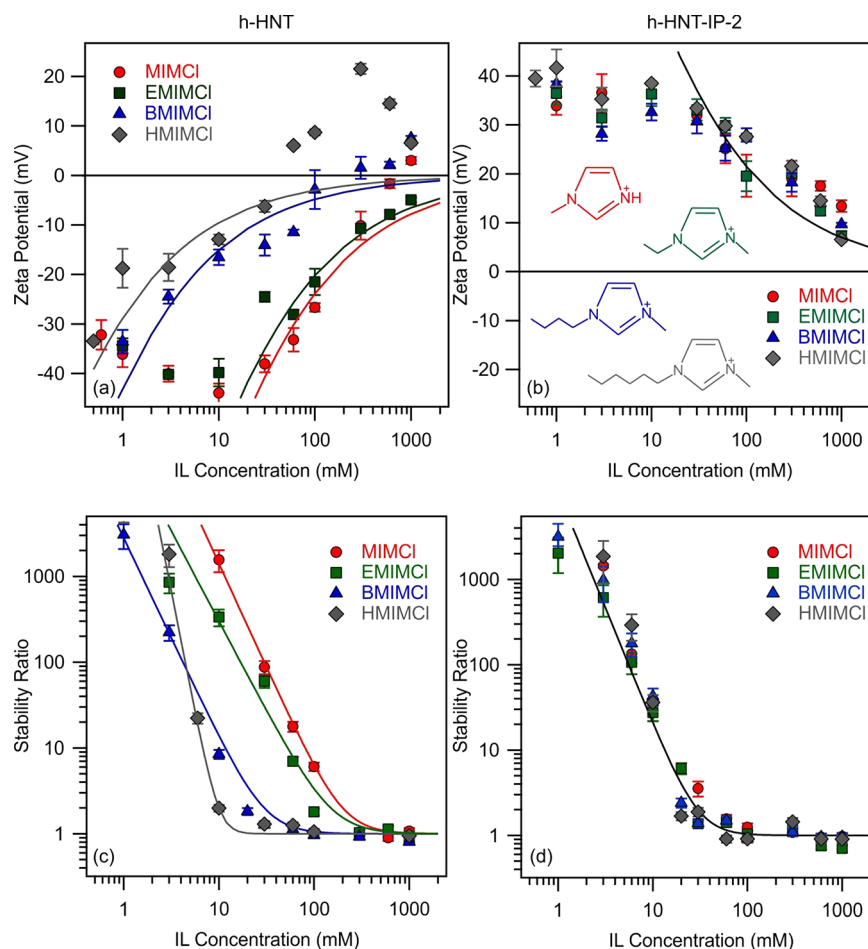


**Figure 6.** Zeta potentials (h-HNTs (a) and h-HNT-IP-2 (b)) as well as stability ratios (h-HNTs (c) and h-HNT-IP-2 (d)) as a function of IL concentration. Lines in a and b were calculated by eq 2 and in c and d by eq 7. Structure of IL cations is shown in the inset of b.

zeta potentials were close to zero at high-salt concentrations, while for  $\text{La}^{3+}$ , adsorption of the trivalent cation caused charge neutralization and overcharging at sufficiently high concentrations. The data clearly show that the affinity of the cations to the surface increased by increasing the valence.

One of the most important parameters, which can be estimated from the electrolyte concentration dependence of the zeta potentials, is the charge density at the slip plane. This calculation is possible within the Debye–Hückel model, which is valid only for indifferent ions, whose adsorption on the surface is negligible.<sup>61</sup> In addition, note that significant deviations between the experimental and the calculated zeta potential values occur at lower ionic strengths due to the electrokinetic effect.<sup>73</sup> The calculated surface charge density values for the bare h-HNTs in the presence of  $\text{K}^+$ ,  $\text{Mg}^{2+}$ , and  $\text{La}^{3+}$  are  $-1.4 \times 10^{-2}$ ,  $-6.0 \times 10^{-3}$ , and  $-6.2 \times 10^{-3}$  C/m<sup>2</sup>, respectively. Comparing the calculated and the experimental zeta potential data for the latter two, one can notice that these values are rather inaccurate, since the model described by eq 2 does not include specific ion adsorption, which can be clearly seen from the deviation between the measured and the calculated potential values.

On the other hand, for the h-HNT-IP-2 system, the zeta potential values were the same within the experimental error above 30 mM concentration, while differences were observed at lower salt concentrations (Figure 5b). With increasing electrolyte concentration, the zeta potential decreased after an

intermediate small maximum due to the electrokinetic effect<sup>73</sup> and remained positive in the entire concentration regime investigated. The obtained charge density values were the same within the measurement error ( $1.4 \times 10^{-2}$  C/m<sup>2</sup>) irrespective of the type of metal salt, indicating the absence of specific adsorption of the co-ions. These results indicate that the adsorption of salt constituents on the h-HNT-IP-2 surface is negligible and that the decrease in the potentials with increasing ionic strength is due to electrostatic screening of the surface charge.

The stability ratios measured at different salt or IL concentrations are presented in Figure 5c and 5d, respectively. The general trends in the stability ratios were the same in all cases. They decreased with increasing the ionic strength and remained close to unity at high concentrations. Accordingly, slow aggregation was observed at low salt concentrations, as in this region the stability ratio values are high while the particles undergo rapid aggregation above the CCC. This behavior is in line with the qualitative prediction of DLVO theory,<sup>20,74</sup> which states that the overlapping electrical double layers induce strong repulsion at low ionic strengths, giving rise to stabilized dispersions. Besides, at high salt concentrations, the extent of electrostatic repulsion decreases due to the screening effect of the salts and fast particle aggregation takes place owing to the presence of attractive forces. Such attractive forces originate from van der Waals interactions, and data of direct force measurements<sup>75–77</sup> shed light on the fact that other non-

DLVO attractive forces are also present at small surface separations. They result from ion correlations and surface heterogeneities.

For the monovalent salt, the stability ratio curve was identical within the experimental error with that reported earlier for the bare h-HNTs.<sup>14</sup> The onset of the fast particle aggregation was located at the same CCC, namely, at 80 mM. The stability curves for the multivalent counterions contain the slow and fast aggregation regions, i.e., the tendencies in the data were like in the monovalent case. However, for the di- and trivalent ions, the CCCs were substantially lower compared to that determined for K<sup>+</sup>. The CCC for the divalent (Mg<sup>2+</sup>) counterion was found to be 1 mM, and for the trivalent (La<sup>3+</sup>) counterion it was located at 0.03 mM salt concentration. Therefore, the CCC data decrease with increasing valence, in good agreement with the Schulze–Hardy rule<sup>31,78</sup> discussed later.

Nevertheless, the measured stability ratio values for the h-HNT–IP-2 dispersions were about the same for KCl, MgCl<sub>2</sub>, and LaCl<sub>3</sub> (Figure 5d), and hence, an identical CCC value (30 mM) was determined for all systems. In general, a dependence of the CCC on the valence of the co-ions is predicted by the inverse Schulze–Hardy rule.<sup>33,79</sup> However, there is no sign for such a decrease in the CCC by increasing the valency of the co-ions. This behavior indicates the powerful masking effects of the IP-2 polymer used for the functionalization of the h-HNT surface. In other words, the IP-2 coating gave rise to the formation of indifferent surfaces, which are insensitive for ion-specific effects. This conclusion is further confirmed by the very similar zeta potentials measured in the same systems. Such a masking phenomenon was already reported earlier in the case of polymeric latex particles functionalized with IP-2.<sup>66</sup>

**Colloidal Stability in IL Solutions.** Zeta potentials were measured for bare h-HNT in the presence of MIMCl, EMIMCl, BMIMCl, and HMIMCl (Figure 6a) at different concentrations, the different IL cations being the counterions and chloride ions the co-ions. In all cases, the zeta potential increases with increasing the IL concentration. For MIM<sup>+</sup>, EMIM<sup>+</sup>, and BMIM<sup>+</sup>, the particles were negatively charged over the entire IL dose range studied. The increase is primarily owing to the screening effect of the ions by the IL constituents, but adsorption of ions of different affinities to the surface also leads to such an increase in the zeta potentials. Accordingly, the data indicate that BMIM<sup>+</sup> has the highest affinity to the surface compared to MIM<sup>+</sup> and EMIM<sup>+</sup>. Adsorption of the counterions becomes more pronounced for those with longer aliphatic chains, leading to a significant charge reversal for HMIM<sup>+</sup>. At higher concentrations, the zeta potentials decrease in this system due to charge screening. A similar behavior was reported earlier with these ILs<sup>23</sup> as well as with aliphatic amines<sup>80</sup> adsorbed on latex particles.

The surface charge density values were calculated for the h-HNTs in the presence of MIM<sup>+</sup>, EMIM<sup>+</sup>, BMIM<sup>+</sup>, and HMIM<sup>+</sup>, and they were estimated to be  $-1.8 \times 10^{-2}$ ,  $-1.5 \times 10^{-2}$ ,  $-4.0 \times 10^{-3}$ , and  $-2.0 \times 10^{-3}$  C/m<sup>2</sup>, respectively. However, the striking deviation between the calculated and the measured zeta potential data for BMIM<sup>+</sup> and HMIM<sup>+</sup> indicates that the use of the Debye–Hückel model is not appropriate in these cases due to the strong counterion adsorption on the surface. For the h-HNT–IP-2 system, the addition of different IL co-ions (MIM<sup>+</sup>, EMIM<sup>+</sup>, BMIM<sup>+</sup>, and HMIM<sup>+</sup>) led to the same zeta potentials within the experimental error (Figure 6b), similar to results with h-HNT in salt solutions discussed above.

Moreover, after an initial maximum,<sup>73</sup> the zeta potential data decreased with increasing level of ILs for all systems, and the very similar potentials indicated that no specific adsorption of the IL cations occurred.

The stability ratios were determined for bare h-HNT in solutions of MIMCl, EMIMCl, BMIMCl, and HMIMCl (Figure 6c). The experimental conditions (e.g., pH, particle loading, and IL concentration range) were the same as those used in the zeta potential study in order to correlate the results. The bare h-HNT particles aggregated in a similar fashion in the IL solutions, and they followed DLVO-type behavior, namely, slow aggregation at low IL concentrations and rapid aggregation after the CCC. The only difference in the tendency of the stability ratios was observed for the HMIM<sup>+</sup>, where the slope in the slow aggregation regime was appreciably higher than that for the other systems. It was assumed that this is due to the strong adsorption of HMIM<sup>+</sup> giving rise to somewhat different surface properties compared to the other systems, where counterion adsorption takes place to a smaller extent. Although the trend in the stability ratios was qualitatively in line with DLVO theory, the CCC values were different, which is in contrast with this model since DLVO theory predicts the same CCC for all monovalent salts irrespective of the type of ions. The CCC in the presence of the MIM<sup>+</sup> was 200 mM IL and for EMIM<sup>+</sup> was 150 mM. In addition, in the presence of BMIM<sup>+</sup> and HMIM<sup>+</sup> cations, the CCCs were found to be 30 and 10 mM, respectively. The CCC values followed the MIM<sup>+</sup> > EMIM<sup>+</sup> > BMIM<sup>+</sup> > HMIM<sup>+</sup> order, in accordance with the trend in the zeta potential data discussed above.

Once the number of carbon atoms was increased in the hydrocarbon chains of IL cations, no differences were detected in the colloidal behavior of the h-HNT–IP-2 particles. The measured stability ratio values were identical within experimental error for MIMCl, EMIMCl, BMIMCl, and HMIMCl (Figure 6d), and thus, the onset of the rapid particle aggregation is located at the same CCC of 30 mM IL concentration for all systems. Considering that the IL cations are the co-ions in these dispersions, one can conclude that the ILs simply destabilize h-HNT–IP-2 by charge screening and no specific interaction took place between the ILs and the IP-2-modified h-HNTs. As in the presence of inorganic salts discussed above and in line with results reported earlier,<sup>66</sup> IP-2 functionalization prevented any ion-specific effects on the colloidal stability of the particles.

**CCC Dependence on the Valence and Alkyl Chain Length.** The dispersion destabilizing power of the ionic valence was derived from the DLVO-based Schulze–Hardy rule, which indicates that the CCC decreases with the valence ( $z$ ) of dissolved ions as follows<sup>61,78</sup>

$$\text{CCC} \propto \frac{1}{z^n} \quad (9)$$

where  $n$  changes between 1.6 and 6.5. This value is determined by the surface charge and related hydrophobicity of the particles. Accordingly, the exponent for weakly charged particles is  $n = 16$  in eq 9, while for particles of high surface charge, the dependence is  $n = 6.5$  if one considers asymmetric electrolytes.<sup>35</sup> However, the latter number can only be derived from DLVO theory for surfaces with extremely high magnitude of charge, around 1 C/m<sup>2</sup>, while the surface charge density for inorganic particles, such as HNTs, is typically much less than this value. Figure 7 shows the relative CCCs normalized to the

CCC obtained for KCl and the CCC values expected from the Schulze–Hardy rule (eq 9) with the above-mentioned limits.

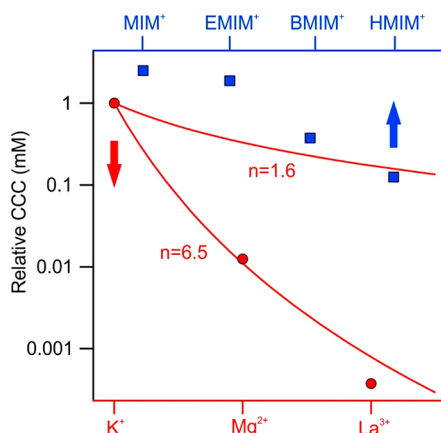


**Figure 7.** Relative CCC values (normalized to the CCC obtained in the presence of KCl) of bare h-HNTs for cations of either different valences (circles) or different alkyl chain lengths (squares). Solid lines indicate the direct (for  $n = 1.6$  and  $6.5$  in eq 9) Schulze–Hardy rule.

The CCCs decreased with increasing valence in the order  $K^+ > Mg^{2+} > La^{3+}$ , as expected, and the decrease shows good quantitative agreement with the  $n = 6.5$  dependence in eq 9. However, as discussed above, such a strong dependence can only be derived from DLVO theory for highly charged surfaces (above  $1 \text{ C/m}^2$  charge density), while the magnitude of the surface charge density determined for h-HNTs in KCl solutions was much smaller ( $1.4 \times 10^{-2} \text{ C/m}^2$  for KCl, for instance). It was assumed that the affinity of the cations, i.e., the strength of their adsorption to the oppositely charged h-HNTs, plays a major role in the aggregation processes. This is why multivalent ions adsorb to a larger extent and reduce the surface charge more significantly. This is in line with the results of the zeta potential measurements, as illustrated in Figure 5a. Once the surface charge density is reduced due to adsorption of counterions, a lower salt concentration is needed to destabilize the colloids and thus the CCC is lower. Therefore, the  $n = 6.5$  dependence of the CCC on the valence is the common result of ion adsorption and prediction of DLVO theory, as they are very sensitive to the valence of counterions.

The relative CCCs determined in the presence of IL cations are also shown in Figure 7. Concerning the tendency, the values decrease in the sequence  $MIMCl > EMIMCl > BMIMCl > HMIMCl$ . This trend reflects that the interfacial processes are tuned by the alkyl chain length.<sup>24</sup> Indeed, more hydrophobic cations of longer alkyl chains are located on the right-hand side, and they adsorb stronger to the particles, leading to lower CCCs, while the ones on the left-hand side are of more hydrophilic character due to shorter hydrocarbon chains. These counterions adsorb more weakly, giving rise to higher CCCs. The surface charge–CCC relation can be explained in a similar way to that discussed above with the multivalent ions. The above tendencies in the CCC are in good agreement with the findings reported earlier with colloidal particles dispersed in different metal salt or IL solutions.<sup>34,36,37,41,80</sup>

Another interesting finding, which deserves further discussion, is the higher CCCs for  $MIM^+$  and  $EMIM^+$  compared to that determined for KCl (Figure 7). It is suspected that this phenomenon is due to ion pair formation of ILs both on the

surface and in the bulk. The latter has been already reported earlier,<sup>51</sup> and such an association of the IL constituents in aqueous solution decreases the ionic strength. Thus, the repulsion between electrical double layers become stronger, leading to a higher CCC. On the other hand, adsorbed IL cations may attract chloride anions from the liquid phase and form ion pairs on the surface. This process results in a weaker charge neutralization, i.e., the surface charge is more negative, and it gives rise to a higher CCC than in the case of completely dissociated KCl. Once the cation adsorption is more pronounced, such as the  $BMIM^+$  and  $HMIM^+$ , the influence of ion pair formation on the surface charges and corresponding interparticle forces becomes negligible.

## CONCLUSIONS

The charging and aggregation properties of clay nanotubes, i.e., bare (h-HNTs) and polyimidazolium-functionalized (h-HNT–IP-2), were investigated in the presence of metal salt and IL solutions. In the case of h-HNTs, increasing the valence and alkyl chain length of the IL cations increased the affinity of the counterions to the surface, as revealed by zeta potential measurements, and subsequently affected the surface charge density of the particles. Colloidal stability studies revealed that the particle aggregation mechanism in each system qualitatively followed the prediction of DLVO theory irrespective of the type of counterions. However, significant differences were observed in the obtained CCC values, whose order was determined as  $MIM^+ > EMIM^+ > K^+ > BMIM^+ > HMIM^+ > Mg^{2+} > La^{3+}$ . The sequence agrees adequately with the Schulze–Hardy rule for the metal ions as a joint result of specific ion adsorption and valence dependence of the electrical double layer forces predicted by DLVO theory. The trend in the CCCs for IL cations originates from the hydrophobic nature of the counterions, which became more pronounced with increasing alkyl chain length on the imidazolium ring. Accordingly, the  $HMIM^+$  cations exhibited the greatest affinity to the particle surface, giving rise to charge neutralization and overcharging, while such a significant adsorption gave rise to weaker surface charge and consequently to the lowest CCC within the IL cations. The  $MIM^+$  adsorption was the weakest, and thus, the highest CCC was determined for this IL constituent.

For the h-HNT–IP-2 particles, where the metal and IL cations were the co-ions, ion-specific effects were not observed in either salt or IL solutions. In other words, both the zeta potentials and the stability ratios were the same within the experimental error in the presence of different metal salts and ILs. Therefore, the same surface charge density was determined in the presence of the mono- and multivalent salt constituents as well as the IL cations. On the other hand, the aggregation mechanism was realized within DLVO theory in all systems investigated. These results are consistent with the previously reported conclusions that the saturated IP-2 layer on the particles masks ion-specific effects and the colloidal stability of h-HNT–IP-2 depends only on the ionic strength applied in the dispersions.

Given the growing interest in HNT materials suspended in electrolyte or IL solutions, the present results provide important quantitative information on the interfacial properties and subsequently on the aggregation of the particles. Such a comprehensive study on the colloidal stability of HNT particles for various salts and ILs has not been reported so far. Therefore, the results are expected to be used in the design



of fine HNT dispersions in which the particle aggregation can be tuned by the ionic valence or by the length of the hydrocarbon chain of the IL constituent ions.

## AUTHOR INFORMATION

### Corresponding Author

Istvan Szilagyí – MTA-SZTE Lendület Biocolloids Research Group, Interdisciplinary Excellence Center, Department of Physical Chemistry and Materials Science, University of Szeged, H-6720 Szeged, Hungary; [orcid.org/0000-0001-7289-0979](https://orcid.org/0000-0001-7289-0979); Email: [szistvan@chem.u-szeged.hu](mailto:szistvan@chem.u-szeged.hu)

### Authors

Bojana Katana – MTA-SZTE Lendület Biocolloids Research Group, Interdisciplinary Excellence Center, Department of Physical Chemistry and Materials Science, University of Szeged, H-6720 Szeged, Hungary

Dóra Takács – MTA-SZTE Lendület Biocolloids Research Group, Interdisciplinary Excellence Center, Department of Physical Chemistry and Materials Science, University of Szeged, H-6720 Szeged, Hungary

Adél Szerlauth – MTA-SZTE Lendület Biocolloids Research Group, Interdisciplinary Excellence Center, Department of Physical Chemistry and Materials Science, University of Szeged, H-6720 Szeged, Hungary

Szilárd Sáringér – MTA-SZTE Lendület Biocolloids Research Group, Interdisciplinary Excellence Center, Department of Physical Chemistry and Materials Science, University of Szeged, H-6720 Szeged, Hungary

Gábor Varga – Material and Solution Structure Research Group, Department of Organic Chemistry, University of Szeged, H-6720 Szeged, Hungary; [orcid.org/0000-0002-7131-1629](https://orcid.org/0000-0002-7131-1629)

Andrej Jamnik – Faculty of Chemistry and Chemical Technology, University of Ljubljana, SI-1000 Ljubljana, Slovenia

Felix D. Bobbink – Institute of Chemical Sciences and Engineering, École Polytechnique Fédérale de Lausanne (EPFL), CH-1015 Lausanne, Switzerland; [orcid.org/0000-0001-7283-853X](https://orcid.org/0000-0001-7283-853X)

Paul J. Dyson – Institute of Chemical Sciences and Engineering, École Polytechnique Fédérale de Lausanne (EPFL), CH-1015 Lausanne, Switzerland; [orcid.org/0000-0003-3117-3249](https://orcid.org/0000-0003-3117-3249)

Complete contact information is available at:  
<https://pubs.acs.org/10.1021/acs.langmuir.1c01949>

### Notes

The authors declare no competing financial interest.

## ACKNOWLEDGMENTS

This research was sponsored by the Hungarian National Research, Development and Innovation Office (SNN131558), the Slovenian Research Agency (research core funding no. P1-0201 and project no. N1-0139 “Delamination of Layered Materials and Structure-Dynamics Relationship in Green Solvents”), and the Ministry of Human Capacities of Hungary (20391-3/2018/FEKUSTRAT). Support from the University of Szeged Open Access Fund (5481) is gratefully acknowledged.

## REFERENCES

- (1) Lvov, Y. M.; Shchukin, D. G.; Mohwald, H.; Price, R. R. Halloysite clay nanotubes for controlled release of protective agents. *ACS Nano* **2008**, *2*, 814–820.
- (2) Santos, A. C.; Ferreira, C.; Veiga, F.; Ribeiro, A. J.; Panchal, A.; Lvov, Y.; Agarwal, A. Halloysite clay nanotubes for life sciences applications: From drug encapsulation to bioscaffold. *Adv. Colloid Interface Sci.* **2018**, *257*, 58–70.
- (3) Lazzara, G.; Cavallaro, G.; Panchal, A.; Fakhruddin, R.; Stavitskaya, A.; Vinokurov, V.; Lvov, Y. An assembly of organic-inorganic composites using halloysite clay nanotubes. *Curr. Opin. Colloid Interface Sci.* **2018**, *35*, 42–50.
- (4) Vergaro, V.; Abdullayev, E.; Lvov, Y. M.; Zeitoun, A.; Cingolani, R.; Rinaldi, R.; Leporatti, S. Cytocompatibility and uptake of halloysite clay nanotubes. *Biomacromolecules* **2010**, *11*, 820–826.
- (5) Mitra, G. B.; Bhattacharjee, S. Structure of halloysite. *Acta Crystallogr., Sect. B: Struct. Crystallogr. Cryst. Chem.* **1975**, *31*, 2851–2857.
- (6) Dionisi, C.; Hanafy, N.; Nobile, C.; De Giorgi, M. L.; Rinaldi, R.; Casciaro, S.; Lvov, Y. M.; Leporatti, S. Halloysite Clay Nanotubes as Carriers for Curcumin: Characterization and Application. *IEEE Trans. Nanotechnol.* **2016**, *15*, 720–724.
- (7) Horky, P.; Skalickova, S.; Baholet, D.; Skladanka, J. Nanoparticles as a solution for eliminating the risk of mycotoxins. *Nanomaterials* **2018**, *8*, 727.
- (8) Fizar, M.; Dramou, P.; Dahiru, N. S.; Ruya, W.; Huang, T.; He, H. Halloysite nanotubes in analytical sciences and in drug delivery: A review. *Microchim. Acta* **2018**, *185*, 389.
- (9) Zhang, Y.; Tang, A. D.; Yang, H. M.; Ouyang, J. Applications and interfaces of halloysite nanocomposites. *Appl. Clay Sci.* **2016**, *119*, 8–17.
- (10) Lvov, Y.; Wang, W. C.; Zhang, L. Q.; Fakhruddin, R. Halloysite clay nanotubes for loading and sustained release of functional compounds. *Adv. Mater.* **2016**, *28*, 1227–1250.
- (11) Lvov, Y.; Aerov, A.; Fakhruddin, R. Clay nanotube encapsulation for functional biocomposites. *Adv. Colloid Interface Sci.* **2014**, *207*, 189–198.
- (12) Shchukin, D. G.; Sukhorukov, G. B.; Price, R. R.; Lvov, Y. M. Halloysite nanotubes as biomimetic nanoreactors. *Small* **2005**, *1*, 510–513.
- (13) Lisuzzo, L.; Cavallaro, G.; Parisi, F.; Milioto, S.; Lazzara, G. Colloidal stability of halloysite clay nanotubes. *Ceram. Int.* **2019**, *45*, 2858–2865.
- (14) Katana, B.; Takacs, D.; Csapo, E.; Szabo, T.; Jamnik, A.; Szilagyí, I. Ion specific effects on the stability of halloysite nanotube colloids-inorganic salts versus ionic liquids. *J. Phys. Chem. B* **2020**, *124*, 9757–9765.
- (15) Rouster, P.; Dondelinger, M.; Galleni, M.; Nysten, B.; Jonas, A. M.; Glinel, K. Layer-by-layer assembly of enzyme-loaded halloysite nanotubes for the fabrication of highly active coatings. *Colloids Surf., B* **2019**, *178*, 508–514.
- (16) Kim, J.; Ryu, J.; Shin, J.; Lee, H.; Kim, I. S.; Sohn, D. Interactions between halloysite nanotubes and poly(styrene sulfonate) in solution. *Bull. Korean Chem. Soc.* **2017**, *38*, 107–111.
- (17) Katana, B.; Rouster, P.; Varga, G.; Muráth, S.; Glinel, K.; Jonas, A. M.; Szilagyí, I. Self-assembly of protamine biomacromolecule on halloysite nanotubes for immobilization of superoxide dismutase enzyme. *ACS Appl. Bio Mater.* **2020**, *3*, 522–530.
- (18) Sadeghpour, A.; Vaccaro, A.; Rentsch, S.; Borkovec, M. Influence of alkali metal counterions on the charging behavior of poly(acrylic acid). *Polymer* **2009**, *50*, 3950–3954.
- (19) Derjaguin, B. On the repulsive forces between charged colloid particles and on the theory of slow coagulation and stability of lyophobic sols. *Trans. Faraday Soc.* **1940**, *35*, 203–214.
- (20) Verwey, E. J. W.; Overbeek, J. T. G. *Theory of stability of lyophobic colloids*; Elsevier: Amsterdam, 1948; pp 135–185.
- (21) Behrens, S. H.; Borkovec, M.; Schurtenberger, P. Aggregation in charge-stabilized colloidal suspensions revisited. *Langmuir* **1998**, *14*, 1951–1954.

- (22) Pavlovic, M.; Rouster, P.; Oncsik, T.; Szilagy, I. Tuning colloidal stability of layered double hydroxides: from monovalent ions to polyelectrolytes. *ChemPlusChem* **2017**, *2*, 121–131.
- (23) Oncsik, T.; Desert, A.; Trefalt, G.; Borkovec, M.; Szilagy, I. Charging and aggregation of latex particles in aqueous solutions of ionic liquids: Towards an extended Hofmeister series. *Phys. Chem. Chem. Phys.* **2016**, *18*, 7511–7520.
- (24) Bastos-Gonzalez, D.; Perez-Fuentes, L.; Drummond, C.; Faraudo, J. Ions at interfaces: the central role of hydration and hydrophobicity. *Curr. Opin. Colloid Interface Sci.* **2016**, *23*, 19–28.
- (25) Lopez-Leon, T.; Ortega-Vinuesa, J. L.; Bastos-Gonzalez, D. Ion-specific aggregation of hydrophobic particles. *ChemPhysChem* **2012**, *13*, 2382–2391.
- (26) Montes Ruiz-Cabello, F. J.; Oncsik, T.; Rodriguez-Valverde, M. A.; Maroni, P.; Cabrerizo-Vilchez, M. Specific ion effects and pH dependence on the interaction forces between polystyrene particles. *Langmuir* **2016**, *32*, 11918–11927.
- (27) Schwierz, N.; Horinek, D.; Sivan, U.; Netz, R. R. Reversed Hofmeister series-The rule rather than the exception. *Curr. Opin. Colloid Interface Sci.* **2016**, *23*, 10–18.
- (28) Parsons, D. F.; Salis, A. Hofmeister effects at low salt concentration due to surface charge transfer. *Curr. Opin. Colloid Interface Sci.* **2016**, *23*, 41–49.
- (29) Kunz, W.; Henle, J.; Ninham, B. W. 'Zur lehre von der wirkung der salze' (about the science of the effect of salts): Franz Hofmeister's historical papers. *Curr. Opin. Colloid Interface Sci.* **2004**, *9*, 19–37.
- (30) Hall, S. B.; Duffield, J. R.; Williams, D. R. A reassessment of the applicability of the DLVO theory as an explanation for the Schulze-Hardy rule for colloid aggregation. *J. Colloid Interface Sci.* **1991**, *143*, 411–415.
- (31) Lyklema, J. Coagulation by multivalent counterions and the Schulze-Hardy rule. *J. Colloid Interface Sci.* **2013**, *392*, 102–104.
- (32) Overbeek, J. T. G. The rule of Schulze and Hardy. *Pure Appl. Chem.* **1980**, *52*, 1151–1161.
- (33) Trefalt, G. Derivation of the inverse Schulze-Hardy rule. *Phys. Rev. E: Stat. Phys., Plasmas, Fluids, Relat. Interdiscip. Top.* **2016**, *93*, 032612.
- (34) Oncsik, T.; Trefalt, G.; Csendes, Z.; Szilagy, I.; Borkovec, M. Aggregation of negatively charged colloidal particles in the presence of multivalent cations. *Langmuir* **2014**, *30*, 733–741.
- (35) Trefalt, G.; Szilagy, I.; Tellez, G.; Borkovec, M. Colloidal stability in asymmetric electrolytes: Modifications of the Schulze-Hardy rule. *Langmuir* **2017**, *33*, 1695–1704.
- (36) Pavlovic, M.; Huber, R.; Adok-Sipiczki, M.; Nardin, C.; Szilagy, I. Ion specific effects on the stability of layered double hydroxide colloids. *Soft Matter* **2016**, *12*, 4024–4033.
- (37) Rouster, P.; Pavlovic, M.; Szilagy, I. Destabilization of titania nanosheet suspensions by inorganic salts: Hofmeister series and Schulze-Hardy rule. *J. Phys. Chem. B* **2017**, *121*, 6749–6758.
- (38) Higashitani, K.; Nakamura, K.; Fukasawa, T.; Tsuchiya, K.; Mori, Y. Ionic specificity in rapid coagulation of silica nanoparticles. *Langmuir* **2018**, *34*, 2505–2510.
- (39) Farner Budarz, J.; Turolla, A.; Piasecki, A. F.; Bottero, J.-Y.; Antonelli, M.; Wiesner, M. R. Influence of aqueous inorganic anions on the reactivity of nanoparticles in TiO<sub>2</sub> photocatalysis. *Langmuir* **2017**, *33*, 2770–2779.
- (40) Yu, W. Y.; Du, N.; Gu, Y. T.; Yan, J. G.; Hou, W. G. Specific ion effects on the colloidal stability of layered double hydroxide single-layer nanosheets. *Langmuir* **2020**, *36*, 6557–6568.
- (41) Hegedus, T.; Takacs, D.; Vasarhelyi, L.; Szilagy, I.; Konya, Z. Specific ion effects on aggregation and charging properties of boron nitride nanospheres. *Langmuir* **2021**, *37*, 2466–2475.
- (42) Dedzo, G. K.; Detellier, C. Clay minerals-ionic liquids, nanoarchitectures, and applications. *Adv. Funct. Mater.* **2018**, *28*, 1703845.
- (43) Yang, Y. J.; Mat Yaakob, S.; Rabat, N. E.; Shamsuddin, M. R.; Man, Z. Release kinetics study and anti-corrosion behaviour of a pH-responsive ionic liquid-loaded halloysite nanotube-doped epoxy coating. *RSC Adv.* **2020**, *10*, 13174–13184.
- (44) Sadjadi, S.; Akbari, M.; Heravi, M. M. Palladated nano-composite of halloysite-nitrogen-doped porous carbon prepared from a novel cyano-/nitrile-free task specific ionic liquid: An efficient catalyst for hydrogenation. *ACS Omega* **2019**, *4*, 19442–19451.
- (45) Li, H.; Feng, Z. Q.; Zhao, K.; Wang, Z. H.; Liu, J. H.; Liu, J.; Song, H. Z. Chemically crosslinked liquid crystalline poly(ionic liquid)s/halloysite nanotubes nanocomposite ionogels with superior ionic conductivity, high anisotropic conductivity and a high modulus. *Nanoscale* **2019**, *11*, 3689–3700.
- (46) Rogers, R. D.; Seddon, K. R. Ionic liquids - Solvents of the future? *Science* **2003**, *302*, 792–793.
- (47) Earle, M. J.; Esperanca, J. M.S.S.; Gilea, M. A.; Canongia Lopes, J. N.; Rebelo, L. P.N.; Magee, J. W.; Seddon, K. R.; Widegren, J. A. The distillation and volatility of ionic liquids. *Nature* **2006**, *439*, 831–834.
- (48) Wasserscheid, P. Chemistry - Volatile times for ionic liquids. *Nature* **2006**, *439*, 797–797.
- (49) Dozic, S.; Zec, N.; Tot, A.; Papovic, S.; Pavlovic, K.; Gadzuric, S.; Vranes, M. Does the variation of the alkyl chain length on N1 and N3 of imidazole ring affect physicochemical features of ionic liquids in the same way? *J. Chem. Thermodyn.* **2016**, *93*, 52–59.
- (50) Sheehan, A.; Jurado, L. A.; Ramakrishna, S. N.; Arcifa, A.; Rossi, A.; Spencer, N. D.; Espinosa-Marzal, R. M. Layering of ionic liquids on rough surfaces. *Nanoscale* **2016**, *8*, 4094–4106.
- (51) Hayes, R.; Warr, G. G.; Atkin, R. Structure and nanostructure in ionic liquids. *Chem. Rev.* **2015**, *115*, 6357–6426.
- (52) Yang, X.; Fei, Z. F.; Zhao, D. B.; Ang, W. H.; Li, Y. D.; Dyson, P. J. Palladium nanoparticles stabilized by an ionic polymer and ionic liquid: A versatile system for C-C cross-coupling reactions. *Inorg. Chem.* **2008**, *47*, 3292–3297.
- (53) Gopakumar, A.; Fei, Z. F.; Paunescu, E.; Auzelyte, V.; Brugger, J.; Dyson, P. J. UV-imprint resists generated from polymerizable ionic liquids and titania nanoparticles. *J. Phys. Chem. C* **2014**, *118*, 16743–16748.
- (54) Zhou, Y.; Antonietti, M. Synthesis of very small TiO<sub>2</sub> nanocrystals in a room-temperature ionic liquid and their self-assembly toward mesoporous spherical aggregates. *J. Am. Chem. Soc.* **2003**, *125*, 14960–14961.
- (55) Elmahdy, M. M.; Gutsche, C.; Kremer, F. Forces within single pairs of charged colloids in aqueous solutions of ionic liquids as studied by optical tweezers. *J. Phys. Chem. C* **2010**, *114*, 19452–19458.
- (56) Valmacco, V.; Trefalt, G.; Maroni, P.; Borkovec, M. Direct force measurements between silica particles in aqueous solutions of ionic liquids containing 1-butyl-3-methylimidazolium (BMIM). *Phys. Chem. Chem. Phys.* **2015**, *17*, 16553–16559.
- (57) Tietze, A. A.; Bordusa, F.; Giernoth, R.; Imhof, D.; Lenzer, T.; Maass, A.; Mrestani-Klaus, C.; Neundorff, I.; Oum, K.; Reith, D.; Stark, A. On the nature of interactions between ionic liquids and small amino-acid-based biomolecules. *ChemPhysChem* **2013**, *14*, 4044–4064.
- (58) Yang, Z. Hofmeister effects: an explanation for the impact of ionic liquids on biocatalysis. *J. Biotechnol.* **2009**, *144*, 12–22.
- (59) Zhong, W.; Bobbink, F. D.; Fei, Z. F.; Dyson, P. J. Polyimidazolium salts: Robust catalysts for the cycloaddition of carbon dioxide into carbonates in solvent-free conditions. *ChemSusChem* **2017**, *10*, 2728–2735.
- (60) Delgado, A. V.; Gonzalez-Caballero, E.; Hunter, R. J.; Koopal, L. K.; Lyklema, J. Measurement and interpretation of electrokinetic phenomena - (IUPAC technical report). *Pure Appl. Chem.* **2005**, *77*, 1753–1805.
- (61) Trefalt, G.; Szilagy, I.; Borkovec, M. Poisson-Boltzmann description of interaction forces and aggregation rates involving charged colloidal particles in asymmetric electrolytes. *J. Colloid Interface Sci.* **2013**, *406*, 111–120.
- (62) Holthoff, H.; Egelhaaf, S. U.; Borkovec, M.; Schurtenberger, P.; Sticher, H. Coagulation rate measurements of colloidal particles by simultaneous static and dynamic light scattering. *Langmuir* **1996**, *12*, 5541–5549.



(63) Hassan, P. A.; Rana, S.; Verma, G. Making sense of Brownian motion: Colloid characterization by dynamic light scattering. *Langmuir* **2015**, *31*, 3–12.

(64) Grolimund, D.; Elimelech, M.; Borkovec, M. Aggregation and deposition kinetics of mobile colloidal particles in natural porous media. *Colloids Surf., A* **2001**, *191*, 179–188.

(65) Klacic, T.; Sadzak, A.; Jukic, J.; Preocanin, T.; Kovacevic, D. Surface potential study of ceria/poly(sodium 4-styrenesulfonate) aqueous solution interface. *Colloids Surf., A* **2019**, *570*, 32–38.

(66) Katana, B.; Takács, D.; Bobbink, F. D.; Dyson, P. J.; Alsharif, N. B.; Tomšič, M.; Szilagyi, I. Masking specific effects of ionic liquid constituents at the solid–liquid interface by surface functionalization. *Phys. Chem. Chem. Phys.* **2020**, *22*, 24764–24770.

(67) Klopogge, J. T.; Frost, R. L. Raman microprobe spectroscopy of hydrated halloysite from a neogene cryptokarst from southern Belgium. *J. Raman Spectrosc.* **1999**, *30*, 1079–1085.

(68) Loo, B. H.; Tse, Y.; Parsons, K.; Adelman, C.; El-Hage, A.; Lee, Y. G. Surface-enhanced Raman spectroscopy of imidazole adsorbed on electrode and colloidal surfaces of Cu, Ag, and Au. *J. Raman Spectrosc.* **2006**, *37*, 299–304.

(69) Moumene, T.; Belarbi, E. H.; Haddad, B.; Villemin, D.; Abbas, O.; Khelifa, B.; Bresson, S. Study of imidazolium dicationic ionic liquids by Raman and FTIR spectroscopies: The effect of the nature of the anion. *J. Mol. Struct.* **2015**, *1083*, 179–186.

(70) Markham, L. M.; Mayne, L. C.; Hudson, B. S.; Zgierski, M. Z. Resonance Raman studies of imidazole, imidazolium, and their derivatives - The effect of deuterium substitution. *J. Phys. Chem.* **1993**, *97*, 10319–10325.

(71) Gonchar, K. A.; Kondakova, A. V.; Jana, S.; Timoshenko, V. Y.; Vasiliev, A. N. Investigation of halloysite nanotubes with deposited silver nanoparticles by methods of optical spectroscopy. *Phys. Solid State* **2016**, *58*, 601–605.

(72) Maksym, P.; Tarnacka, M.; Dzienia, A.; Erfurt, K.; Chrobok, A.; Zieba, A.; Wolnica, K.; Kaminski, K.; Paluch, M. A facile route to well-defined imidazolium-based poly(ionic liquid)s of enhanced conductivity via RAFT. *Polym. Chem.* **2017**, *8*, 5433–5443.

(73) Borkovec, M.; Behrens, S. H.; Semmler, M. Observation of the mobility maximum predicted by the standard electrokinetic model for highly charged amidine latex particles. *Langmuir* **2000**, *16*, 5209–5212.

(74) Derjaguin, B.; Landau, L. D. Theory of the stability of strongly charged lyophobic sols and of the adhesion of strongly charged particles in solutions of electrolytes. *Prog. Surf. Sci.* **1993**, *43*, 30–59.

(75) Sinha, P.; Szilagyi, I.; Montes Ruiz-Cabello, F. J.; Maroni, P.; Borkovec, M. Attractive forces between charged colloidal particles induced by multivalent ions revealed by confronting aggregation and direct force measurements. *J. Phys. Chem. Lett.* **2013**, *4*, 648–652.

(76) Montes Ruiz-Cabello, F. J.; Trefalt, G.; Maroni, P.; Borkovec, M. Accurate predictions of forces in the presence of multivalent ions by Poisson-Boltzmann theory. *Langmuir* **2014**, *30*, 4551–4555.

(77) Moazzami-Gudarzi, M.; Adam, P.; Smith, A. M.; Trefalt, G.; Szilagyi, I.; Maroni, P.; Borkovec, M. Interactions between similar and dissimilar charged interfaces in the presence of multivalent anions. *Phys. Chem. Chem. Phys.* **2018**, *20*, 9436–9448.

(78) Trefalt, G.; Szilagyi, I.; Borkovec, M. Schulze-Hardy rule revisited. *Colloid Polym. Sci.* **2020**, *298*, 961–967.

(79) Cao, T.; Szilagyi, I.; Oncsik, T.; Borkovec, M.; Trefalt, G. Aggregation of colloidal particles in the presence of multivalent cations: The inverse Schulze-Hardy rule. *Langmuir* **2015**, *31*, 6610–6614.

(80) Szilagyi, I.; Polomska, A.; Citherlet, D.; Sadeghpour, A.; Borkovec, M. Charging and aggregation of negatively charged colloidal latex particles in the presence of multivalent oligoamine cations. *J. Colloid Interface Sci.* **2013**, *392*, 34–41.

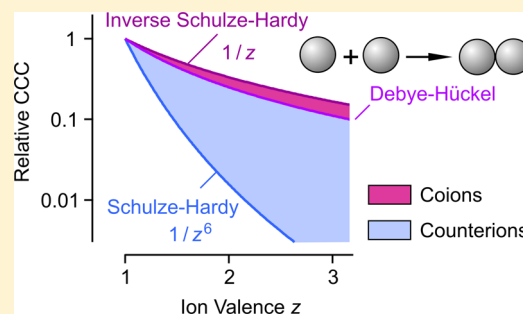
# Aggregation of Colloidal Particles in the Presence of Multivalent Coions: The Inverse Schulze–Hardy Rule

Tianchi Cao, Istvan Szilagyi, Tamas Oncsik, Michal Borkovec,\* and Gregor Trefalt\*

Department of Inorganic and Analytical Chemistry, University of Geneva, Sciences II, 30 Quai Ernest-Ansermet, 1205 Geneva, Switzerland

## Supporting Information

**ABSTRACT:** Shifts of the critical coagulation concentration (CCC) in particle suspensions in salt solutions containing multivalent co-ions and monovalent counterions are rationalized. One observes that the CCC is inversely proportional to the valence, and this behavior is referred to as the inverse Schulze–Hardy. This dependence is established by means of measurements of the stability ratio for positively and negatively charged latex particles with time-resolved light scattering. The same dependence is equally suggested by calculations of the CCC with the Derjaguin, Landau, Verwey, and Overbeek (DLVO) theory, whereby the full Poisson–Boltzmann equation for the asymmetric electrolytes has to be used. The latter aspect is essential, since in the case of multivalent co-ions the surface charge is principally neutralized by monovalent counterions. This rule complements the classical Schulze–Hardy rule, which applies in the case of multivalent counterions, and states that the CCC is inversely proportional to the sixth power of the valence.



## INTRODUCTION

More than a century ago, Schulze and Hardy discovered that multivalent ions destabilize colloidal suspensions much more effectively than monovalent ones.<sup>1,2</sup> Half a century later, Derjaguin, Landau, Verwey, and Overbeek (DLVO) explained this behavior by assuming that interactions between particles are governed by superposition of van der Waals forces and double layer forces.<sup>3,4</sup> Based on these assumptions, one finds—in agreement with experiment—that colloidal suspensions are stable at low salt concentrations, while they are unstable at higher ones. The abrupt transition between these two regimes is referred to as the critical coagulation concentration (CCC). For highly charged particles and symmetric  $z:z$  electrolytes, the DLVO theory predicts that<sup>5–7</sup>

$$\text{CCC} \propto \frac{1}{z^6} \quad (\text{Schulze–Hardy}) \quad (1)$$

where  $z$  is the ionic valence. This dependence was suggested on experimental grounds earlier, and is nowadays referred to as the *Schulze–Hardy rule*.

Multivalent, symmetric  $z:z$  electrolytes are hardly soluble, and whenever this rule is compared to experiment, one uses soluble asymmetric  $z:1$  or  $1:z$  electrolytes. Curiously, researchers have always studied systems where the multivalent ions represent the *counterions*, meaning that negatively charged particles can be more effectively coagulated by multivalent cations, while positively charged particles with multivalent anions. The CCCs in such systems often follow the Schulze–Hardy rule.<sup>8–15</sup>

To the best of our knowledge, however, the situation where multivalent ions represent the *co-ions* was not investigated so far. We therefore focus on this situation here, and investigate effects of multivalent anions on the aggregation of negatively charged particles or multivalent cations on positively charged ones. We argue that an analogous *inverse Schulze–Hardy rule* can be formulated in this situation, namely

$$\text{CCC} \propto \frac{1}{z} \quad (\text{inverse Schulze–Hardy}) \quad (2)$$

This dependence on the valence is weaker, but characteristic for the present situation of multivalent co-ions.

## EXPERIMENTAL SECTION

Two batches of polystyrene latex particles with a diameter of about 300 nm were used. In one batch, the particle surface was functionalized with amidine groups, while for the second one with sulfate groups. The particles were suspended in various salt solutions at a concentration of 10 mg/L, and the rate constants of doublet formation were measured in the early stages of the aggregation by time-resolved dynamic light scattering.<sup>10,16–19</sup> The stability ratio  $W$  was obtained from the relative rate of increase of the hydrodynamic radius normalized to its value at high salt conditions. The stability ratio is defined as  $W = k_{\text{fast}}/k$  where  $k_{\text{fast}}$  is the aggregation rate in the fast aggregation regime and  $k$  is the actual rate constant in question. The experiments were carried out at pH 4.0 and 25 °C. More details on the experimental procedures are

Received: May 5, 2015

Revised: June 1, 2015

Published: June 3, 2015

presented in the Supporting Information, and they are similar to the ones used previously.<sup>10</sup>

## RESULTS

We have investigated colloidal stability of negatively charged sulfate latex particles suspended in solutions of KCl, K<sub>2</sub>SO<sub>4</sub>, and K<sub>3</sub>Fe(CN)<sub>6</sub> electrolytes, and of positively charged amidine latex particles in solutions of KCl, MgCl<sub>2</sub>, and LaCl<sub>3</sub>. Figure 1 shows

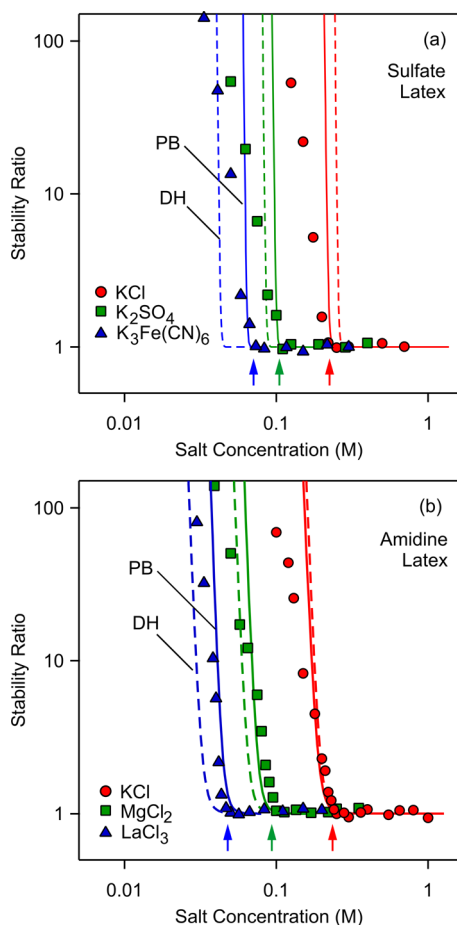


**Figure 1.** Comparison of experimental and calculated stability ratios in charged latex particle suspension versus the concentration of salts containing multivalent co-ions and monovalent counterions. The arrows indicate the experimental CCCs. DLVO calculations compare the Poisson–Boltzmann (PB) and Debye–Hückel (DH) models for double layer interactions. (a) Negatively charged sulfate latex particles in the presence of Cl<sup>−</sup>, SO<sub>4</sub><sup>2−</sup>, and Fe(CN)<sub>6</sub><sup>3−</sup> co-ions. (b) Positively charged amidine latex particles in the presence of K<sup>+</sup>, Mg<sup>2+</sup>, and La<sup>3+</sup> co-ions.

the measured stability ratios plotted versus the electrolyte concentration. The CCC can be identified from the break point in the stability curve (arrows in Figure 1). One observes that the CCC shifts toward lower salt concentrations with increasing valence of the co-ion. The dependence on the valence of the co-ion can be seen more clearly in Figure 2a, where we plot the CCC normalized to its value in the monovalent electrolyte. Indeed, one observes characteristic decrease of the normalized CCC with the ionic valence for both types of particles, namely for positively as well as negatively charged ones. Especially the behavior of the SL particles closely follows the 1/*z* dependence given in eq 2. These shifts may seem surprising, since the

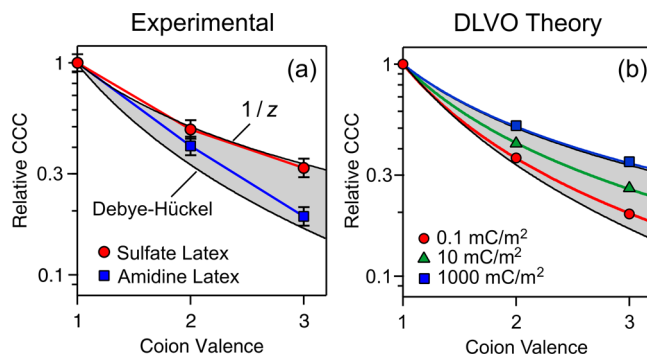


**Figure 2.** CCC normalized to its value in the monovalent electrolyte versus the valence of the co-ions in the salt solutions used. The shaded area lies between the Debye–Hückel result and the inverse Schulze–Hardy rule. (a) The present experimental data. (b) Calculations with DLVO theory with the surface charge densities indicated.

multivalent ions bear the *same* sign of charge as the particles, and therefore are hardly expected to adsorb to the particle surface.

To investigate this situation further, we have calculated the CCCs with DLVO theory. This theory surmises that the interaction energy potential between two particles  $V(h)$ , which is a function of the surface separation  $h$ , can be obtained as

$$V(h) = V_{\text{vdW}}(h) + V_{\text{dl}}(h) \quad (3)$$

where  $V_{\text{vdW}}(h)$  and  $V_{\text{dl}}(h)$  are contributions from van der Waals interactions and double layer overlap, respectively. By invoking the Derjaguin approximation and neglecting retardation effects, one has  $V_{\text{vdW}}(h) = -HR/(12h)$ , where  $H$  is the Hamaker constant and  $R$  is the particle radius. To calculate the contribution of the double layer, it is essential to solve the full Poisson–Boltzmann (PB) equation between two charged plates in the asymmetric  $z:1$  or  $1:z$  electrolytes. The electric potential profile  $\psi(x)$  can be obtained from<sup>7</sup>

$$\frac{d^2\psi}{dx^2} = -\frac{q}{\epsilon_0\epsilon} \sum_i z_i c_i e^{-z_i q\psi/k_B T} \quad (4)$$

where  $z_i$  is the ionic valence,  $c_i$  is the number concentration, and  $i$  runs over all ions in solution. The additional constants entering eq 4 include the elementary charge  $q$ , the dielectric permittivity of vacuum  $\epsilon_0$ , the dielectric constant of water  $\epsilon$ , the absolute temperature  $T$ , and the Boltzmann constant  $k_B$ . Once the electric potential profile  $\psi(x)$  is known, the pressure between the plates can be calculated from its value at the midplane, and the energy profile  $V_{\text{dl}}(h)$  can be then obtained by integrating the pressure twice. When the full energy profile  $V(h)$  is known, the aggregation rate coefficient  $k$  can be evaluated from the solution of the forced diffusion equation under steady-state conditions.<sup>5,7</sup> The stability ratio is then obtained by appropriate normalization of the rate coefficient. All these calculations are performed numerically. For weakly charged particles, the PB equation can be linearized, and the Debye–Hückel approximation can be used instead. In this case, the electrolyte composition enters through the Debye length, which depends on the ionic strength only. Further details on these calculations can be found in the Supporting Information, and they are similar to the ones presented elsewhere.<sup>7</sup>

Results of such DLVO calculations for asymmetric  $z:1$  or  $1:z$  electrolytes where the multivalent ions are co-ions for the charged particles are compared with the experimental data in

Figure 1. The corresponding results obtained with the Debye–Hückel theory are equally shown. A charge regulation parameter of 0.5 is chosen throughout. For sulfate latex, we use a surface charge density of  $-35 \text{ mC/m}^2$  and a Hamaker constant of  $1.0 \times 10^{-20} \text{ J}$ . The latter value is close to the theoretical value for smooth polystyrene in water.<sup>20,21</sup> Once these parameters are fixed, the DLVO theory predicts the valence dependence without further parameter adjustment. For amidine latex particles, we use a surface charge density of  $+14 \text{ mC/m}^2$  and a Hamaker constant of  $2.0 \times 10^{-21} \text{ J}$ . The resulting diffuse layer potentials at CCC are given in the Supporting Information (Table S1). These values are approximately independent of the valence, and they are around  $-30 \text{ mV}$  for the sulfate particles and about  $+10 \text{ mV}$  for the amidine particles.

The smaller value of the fitted Hamaker constant for the amidine particles could be due to their larger surface roughness. Such reduction of the Hamaker constant by roughness was recently demonstrated for larger polystyrene latex particles by direct force measurements.<sup>21</sup> Another explanation of the discrepancy between the fitted Hamaker constants could be related to a larger hydrophobicity of the sulfate particles, which would result in stronger attraction, and would be in turn interpreted as a larger apparent Hamaker constant. Van der Waals and hydrophobic attraction have very similar effects on aggregation rates, and cannot be disentangled without direct force measurements. Possibly, the two types of particles may have different roughness as well as hydrophobicity.

One observes that the PB theory rationalizes the shape of the stability curve and the respective shift with the valence quite well. Not surprisingly, the results of PB and Debye–Hückel theories are similar for the more weakly charged amidine particles, while the differences between these two theories become substantial for the more highly charged sulfate particles. In both cases, however, the use of the PB theory is essential in order to accurately rationalize the trends with the valence.

Further insight can be obtained by analyzing the dependence of the CCC on the valence. For weakly charged particles, the Debye–Hückel theory predicts that<sup>7</sup>

$$\text{CCC} \propto \frac{1}{z(z+1)} \quad (\text{Debye–Hückel}) \quad (5)$$

One obtains this dependence, since only the ionic strength enters this theory. For asymmetric  $z:1$  or  $1:z$  electrolytes, the ionic strength  $I$  can be expressed in terms of the salt concentration  $c$  as  $I = z(z+1)c/2$ . This dependence is similar to the frequently quoted<sup>5,7</sup> dependence on  $1/z^2$ , which applies for a symmetric  $z:z$  electrolyte, where  $I = z^2c/2$ . The derivation of these relations is given in the supplement.<sup>3,9</sup> The dependencies of the CCC on the valence predicted by eqs 2 and 5 are compared with the experimental data in Figure 2a. The amidine system follows more closely the Debye–Hückel dependence due to its weaker charge density, while the sulfate system follows the  $1/z$  dependence rather well. We have also carried out DLVO calculations of the CCCs within the PB theory for different charge densities, whereby a particle diameter of  $300 \text{ nm}$  and a Hamaker constant of  $1.0 \times 10^{-20} \text{ J}$  were used. These results are shown in Figure 2b. For low charge densities, the Debye–Hückel dependence is recovered. For high charge densities, one empirically finds an  $1/z$  dependence. This dependence suggests that the monovalent ions, whose concentration for  $z:1$  or  $1:z$  electrolytes is

proportional to the valence  $z$ , control the CCC by neutralization of the surface charge. This picture is consistent with the fact that for multivalent co-ions, the surface charge is largely neutralized by the monovalent counterions.<sup>22</sup> Currently, however, we have failed to derive the  $1/z$  dependence analytically, since the double layer forces in the presence of multivalent co-ions cannot be approximated by a simple exponential.<sup>22</sup> While these forces can be described by the PB equation in the salt-free region at short distances, this dependence is inaccurate at larger distances, and does not reproduce the expected dependence of the CCC. For this reason, we rely on the numerical solution of the PB equation.

Let us now compare this situation with the commonly investigated case of multivalent counterions. A selection of experimental CCCs in the classical situation of multivalent counterions<sup>10,19,23,24</sup> is shown in Figure 3a. Similar depend-

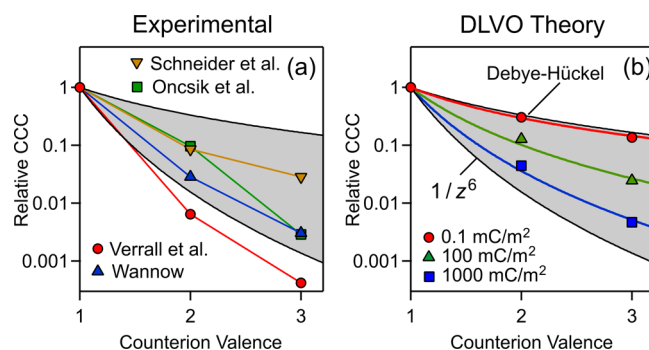


**Figure 3.** CCC normalized to its value in the monovalent electrolyte versus the valence of the counterions in the salt solutions used. The shaded area lies between the Debye–Hückel result and the Schulze–Hardy rule. (a) Experimental literature data refer to negatively charged sulfate latex by Oncsik et al.<sup>10</sup> and Schneider et al.,<sup>19</sup> positively charged hematite by Verrall et al.,<sup>23</sup> and negatively charged arsenic sulfide by Wannow.<sup>24</sup> (b) Calculations with DLVO theory with the surface charge densities indicated.

encies were established experimentally in other systems and wider ranges of valence.<sup>8–12</sup> The results of analogous DLVO calculations are summarized in Figure 3b. The calculations show that the dependence of the CCC on the valence becomes more pronounced with increasing surface charge density. However, even for surface charge densities as high as  $1000 \text{ mC/m}^2$ , one does not yet reach the  $1/z^6$  dependence, which is implied by the Schulze–Hardy rule. As shown in the supplement, this dependence is only obtained in the mathematical limit of  $\psi_D \rightarrow \infty$  for symmetric  $z:z$  electrolytes. A similar dependence is obtained approximately for asymmetric electrolytes for multivalent counterions.<sup>7,25</sup> The experimental CCCs typically show a dependence on the valence, which situates between the Debye–Hückel and  $1/z^6$  dependencies. While the magnitude of surface potential is generally low in these systems, its magnitude is further reduced by adsorption of multivalent counterions. For such low surface charge densities, the Debye–Hückel theory is applicable, and one rather expects the weaker  $1/z^2$  or  $1/[z(z+1)]$  dependencies for the CCC. With increasing valence, however, the multivalent ions adsorb more strongly, and they progressively reduce the surface charge density. This reduction leads to a further decrease of the CCC with valence. When both effects are combined, one sometimes observes—accidentally—the  $1/z^6$  dependence. While this mechanism was already advocated in the past,<sup>8,9</sup> the details



are far from being understood, especially quantitatively. The situation could be further complicated by the breakdown of the PB theory, which relies on a mean-field approximation, and neglects ion–ion correlations.<sup>26</sup> Such correlation effects have been shown to be relevant for multivalent counterions.

The present situation of multivalent co-ions is actually much simpler, since these highly charged ions will hardly adsorb on charged surfaces of the same sign.<sup>22</sup> In this case, the surface charge density remains independent of valence. Furthermore, the PB theory is expected to be valid, since this theory accurately captures experimental force curves.<sup>22</sup> While this fact may seem surprising, one must realize that the multivalent co-ions are strongly repelled from the charged surfaces, and that the surface charge is mainly neutralized by monovalent counterions. In this situation, the PB theory has been repeatedly shown to work correctly.<sup>21,26</sup> By the same token, effects of finite ionic size and of image charges are equally negligible.<sup>26,27</sup>

To understand why we refer to the  $1/z$  dependence as the *inverse* Schulze–Hardy rule, one must convert the salt concentration to the ionic strength, and consider the dependence of the corresponding critical coagulation ionic strength (CCIS) on the valence. In the Debye–Hückel regime, the CCIS is independent of valence. In the classical case of multivalent counterions, as given by eq 1, the CCIS scales approximately as  $1/z^4$ , and therefore the CCIS decreases with increasing valence. In the present case of multivalent co-ions, as given in eq 2, the CCIS scales approximately with  $z$ , and therefore the CCIS increases with the valence. When comparing these two situations, the dependence of the CCIS for the co-ions is *inversed* with respect to the ones of the counterions.

## CONCLUSION

We report on a characteristic dependence of the aggregation rates of charged colloidal particles with multivalent co-ions. The corresponding CCC decreases with valence, but the shift is much smaller than the one expected from the classical Schulze–Hardy rule, which is normally used in the opposite case of multivalent counterions. In the present case of multivalent co-ions, the CCC approximately scales as the inverse of the valence. We refer to this dependence as the *inverse* Schulze–Hardy rule.

## ASSOCIATED CONTENT

### Supporting Information

Details on materials, particle aggregation experiments, and DLVO calculations. The Supporting Information is available free of charge on the ACS Publications website at DOI: 10.1021/acs.langmuir.5b01649.

## AUTHOR INFORMATION

### Corresponding Authors

\*E-mail: [michal.borkovec@unige.ch](mailto:michal.borkovec@unige.ch).

\*E-mail: [gregor.trefalt@unige.ch](mailto:gregor.trefalt@unige.ch).

### Notes

The authors declare no competing financial interest.

## ACKNOWLEDGMENTS

This research was supported by the Swiss National Science Foundation and the University of Geneva.

## REFERENCES

- (1) Schulze, H. Schwefelarsen in wässriger Lösung. *J. Prakt. Chem.* **1882**, *25*, 431–452.
- (2) Hardy, W. B. A preliminary investigation of the conditions which determine the stability of irreversible hydrosols. *Proc. R. Soc. London* **1900**, *66*, 110–125.
- (3) Derjaguin, B.; Landau, L. D. Theory of the stability of strongly charged lyophobic sols and of the adhesion of strongly charged particles in solutions of electrolytes. *Acta Phys. Chim.* **1941**, *14*, 633–662.
- (4) Verwey, E. J. W.; Overbeek, J. T. G. *Theory of Stability of Lyophobic Colloids*; Elsevier: Amsterdam, 1948.
- (5) Russel, W. B.; Saville, D. A.; Schowalter, W. R. *Colloidal Dispersions*; Cambridge University Press: Cambridge, 1989.
- (6) Elimelech, M.; Gregory, J.; Jia, X.; Williams, R. A. *Particle Deposition and Aggregation: Measurement, Modeling, and Simulation*; Butterworth-Heinemann Ltd.: Oxford, 1995.
- (7) Trefalt, G.; Szilagy, I.; Borkovec, M. Poisson-Boltzmann description of interaction forces and aggregation rates involving charged colloidal particles in asymmetric electrolytes. *J. Colloid Interface Sci.* **2013**, *406*, 111–120.
- (8) Frens, G.; Heuts, J. J. F. G. The double layer potential as a rate determining factor in the coagulation of electrostatic colloids. *Colloids Surf.* **1988**, *30*, 295–305.
- (9) Overbeek, J. T. G. The rule of Schulze and Hardy. *Pure Appl. Chem.* **1980**, *52*, 1151–1161.
- (10) Oncsik, T.; Trefalt, G.; Csendes, Z.; Szilagy, I.; Borkovec, M. Aggregation of negatively charged colloidal particles in the presence of multivalent cations. *Langmuir* **2014**, *30*, 733–741.
- (11) Matijevic, E.; Kerker, M. The charge of some heteropoly anions in aqueous solutions as determined by coagulation effects. *J. Phys. Chem.* **1958**, *62*, 1271–1276.
- (12) Rubin, A. J.; Hayden, P. L.; Hanna, G. P. Coagulation of *Escherichia coli* by neutral salts. *Water Res.* **1969**, *3*, 843–852.
- (13) Tezak, B.; Matijevic, E.; Shulz, K.; Mirnik, M.; Herak, J.; Vouk, V. B.; Slunjski, M.; Babic, S.; Kratochvil, J.; Palmar, T. The mechanism of coagulation of lyophobic sols as revealed through investigations of silver halide sols in statu nascendi. *J. Phys. Chem.* **1953**, *57*, 301–307.
- (14) Sano, M.; Okamura, J.; Shinkai, S. Colloidal nature of single-walled carbon nanotubes in electrolyte solution: The Schulze–Hardy rule. *Langmuir* **2001**, *17*, 7172–7173.
- (15) Petrov, Y. Y.; Avvakumova, S. Y.; Sidorova, M. P.; Ermakova, L. E.; Voitylov, V. V.; Voitylov, A. V. Stability of tungsten(VI) oxide dispersions in electrolyte solutions. *Colloid J.* **2011**, *73*, 834–840.
- (16) Holthoff, H.; Egelhaaf, S. U.; Borkovec, M.; Schurtenberger, P.; Sticher, H. Coagulation rate measurements of colloidal particles by simultaneous static and dynamic light scattering. *Langmuir* **1996**, *12*, 5541–5549.
- (17) Sandkuhler, P.; Lattuada, M.; Wu, H.; Sefcik, J.; Morbidelli, M. Further insights into the universality of colloidal aggregation. *Adv. Colloid Interface Sci.* **2005**, *113*, 65–83.
- (18) Chen, K. L.; Mylon, S. E.; Elimelech, M. Enhanced aggregation of alginate-coated iron oxide (hematite) nanoparticles in the presence of calcium, strontium and barium cations. *Langmuir* **2007**, *23*, 5920–5928.
- (19) Schneider, C.; Hanisch, M.; Wedel, B.; Jusufi, A.; Ballauff, M. Experimental study of electrostatically stabilized colloidal particles: Colloidal stability and charge reversal. *J. Colloid Interface Sci.* **2011**, *358*, 62–67.
- (20) Bevan, M. A.; Prieve, D. C. Direct measurement of retarded van der Waals attraction. *Langmuir* **1999**, *15*, 7925–7936.
- (21) Elzbiaciak-Wodka, M.; Popescu, M.; Montes Ruiz-Cabello, F. J.; Trefalt, G.; Maroni, P.; Borkovec, M. Measurements of dispersion forces between colloidal latex particles with the atomic force microscope and comparison with Lifshitz theory. *J. Chem. Phys.* **2014**, *140*, 104906.
- (22) Montes Ruiz-Cabello, F. J.; Moazzami-Gudarzi, M.; Elzbiaciak-Wodka, M.; Maroni, P.; Labbez, C.; Borkovec, M.; Trefalt, G. Long-

ranged and soft interactions between charged colloidal particles induced by multivalent coions. *Soft Matter* **2015**, *11*, 1562–1571.

(23) Verrall, K. E.; Warwick, P.; Fairhurst, A. J. Application of the Schulze-Hardy rule to haematite and haematite/humate colloid stability. *Colloids Surf, A* **1999**, *150*, 261–273.

(24) Wannow, H. A. Über eine neue Methode zur quantitativen Koagulationsmessung. *Kolloidchem. Beih.* **1939**, *50*, 367–472.

(25) Hsu, J. P.; Kuo, Y. C. An extension of the Schulze-Hardy rule to asymmetric electrolytes. *J. Colloid Interface Sci.* **1995**, *171*, 254–255.

(26) Naji, A.; Kanduc, M.; Forsman, J.; Podgornik, R. Perspective: Coulomb fluids - weak coupling, strong coupling, in between and beyond. *J. Chem. Phys.* **2013**, 139.

(27) Hatlo, M. M.; Lue, L. The role of image charges in the interactions between colloidal particles. *Soft Matter* **2008**, *4*, 1582–1596.

# Colloidal Stability in Asymmetric Electrolytes: Modifications of the Schulze–Hardy Rule

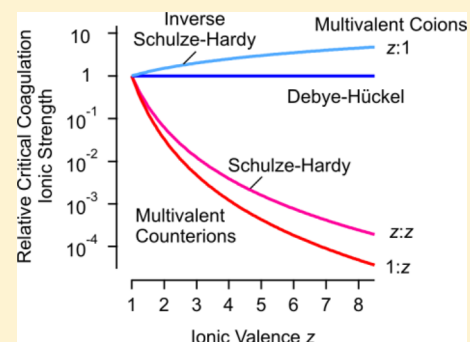
Gregor Trefalt,<sup>†</sup> Istvan Szilagyi,<sup>†</sup> Gabriel Téllez,<sup>‡</sup> and Michal Borkovec<sup>\*,†</sup>

<sup>†</sup>Department of Inorganic and Analytical Chemistry, University of Geneva, Sciences II, 30 Quai Ernest-Ansermet, 1205 Geneva, Switzerland

<sup>‡</sup>Departamento de Física, Universidad de los Andes, AA 4976, Bogotá, Colombia

## Supporting Information

**ABSTRACT:** The Schulze–Hardy rule suggests a strong dependence of the critical coagulation concentration (CCC) on the ionic valence. This rule is addressed theoretically and confronted with recent experimental results. The commonly presented derivation of this rule assumes symmetric electrolytes and highly charged particles. Both assumptions are incorrect. Symmetric electrolytes containing multivalent ions are hardly soluble, and experiments are normally carried out with the well-soluble salts of asymmetric electrolytes containing monovalent and multivalent ions. In this situation, however, the behavior is completely different whether the multivalent ions represent the counterions or co-ions. When these ions represent the counterions, meaning that the multivalent ions have the opposite sign than the charge of the particle, they adsorb strongly to the particles. Thereby, they progressively reduce the magnitude of the surface charge with increasing valence. In fact, this dependence of the charge density on the counterion valence is mainly responsible for the decrease of the CCC with the valence. In the co-ion case, where the multivalent ions have the same sign as the charge of the particle, the multivalent ions are repelled from the particles, and the surfaces remain highly charged. In this case, the inverse Schulze–Hardy rule normally applies, whereby the CCC varies inversely proportional to the co-ion valence.



## INTRODUCTION

Colloid scientists consider the derivation of the Schulze–Hardy rule from the Derjaguin, Landau, Verwey, and Overbeek (DLVO) theory as one of the major intellectual breakthroughs in the field during the past century.<sup>1–6</sup> This rule was established earlier by Schulze<sup>7</sup> and Hardy<sup>8</sup> and states that aqueous colloidal suspensions are destabilized by multivalent ions much more effectively than by monovalent ones. By assuming that interactions are dominated by dispersion and double layer forces, DLVO theory predicts that destabilization of a colloidal suspension is controlled by the onset of fast particle aggregation. Particle aggregation is governed by two mechanisms, namely fast and slow aggregation. Fast aggregation is diffusion controlled and is typically observed at high salt concentrations. Slow aggregation is controlled by thermal activation and normally occurs at low salt concentrations. The demarcation between these two regimes occurs at a rather well-defined salt concentration, which is referred to as the critical coagulation concentration (CCC). In particular, the Schulze–Hardy rule states that

$$\text{CCC} \propto \frac{1}{z^6} \quad (1)$$

where  $z$  is the ionic valence. This relation was suggested on experimental grounds and was also derived from DLVO theory.<sup>1–4</sup>

However, the assumptions made in the derivation of this relation are questionable. First, the derivation assumes a symmetric  $z:z$  electrolyte, but symmetric electrolytes containing ions with valences higher than two are insoluble. Contrarily, the experiments are typically carried out with asymmetric  $z:1$  or  $1:z$  electrolytes. These salts have often good solubility, and they can be chosen such that the multivalent ion is the counterion, meaning that the charge of this ion is opposite to the one of the particle. Second, the assumption is being made that the particles are highly charged, but electrokinetic measurements suggest rather low magnitudes of surface charge densities.<sup>3,9,10</sup> A compilation of available experimental results shows that the dependence of the CCC on the valence is often weaker than predicted by eq 1 but sometimes even stronger.<sup>11,12</sup> Finally, rather different behavior was recently reported for salts containing multivalent co-ions, meaning that the multivalent ion has the same sign of charge as the particle.<sup>13,14</sup> Here one also observes an increased destabilization power with increasing valence of the multivalent co-ions, but the dependence is weak and scales as

**Received:** December 13, 2016

**Revised:** January 26, 2017

**Published:** January 27, 2017

$$\text{CCC} \propto \frac{1}{z} \quad (2)$$

This dependence was referred to as the inverse Schulze–Hardy rule.<sup>14</sup>

The rationale behind this name originates from the consideration of the critical coagulation ionic strength (CCIS). As we shall argue in the following, it is helpful to consider the CCIS instead of the CCC, since the trivial dependence of the ionic strength on the concentration is removed. When considering the CCIS, this quantity decreases with the valence for the counterions, but it increases for the co-ions. Therefore, the dependence for the co-ions is inverse to the one of the counterions.

The above discussion illustrates that the numerous aspects concerning the dependence of the CCC on the valence of multivalent ions are still poorly understood. Moreover, the potential importance of ion correlations has been stressed in systems containing multivalent ions,<sup>15–18</sup> and this aspect was hardly addressed in the context of particle aggregation. These questions call for clarifications, and we will attempt to provide those in the present article.

## THEORY

The basic assumption of the DLVO theory is that the interaction energy  $V$  of two spherical colloidal particles has two main contributions

$$V = V_{\text{dis}} + V_{\text{dl}} \quad (3)$$

where  $V_{\text{dis}}$  and  $V_{\text{dl}}$  are the interaction energies due to dispersion forces and double layer overlap, respectively. The dispersion or van der Waals interaction energy can be accurately estimated within the Derjaguin approximation by the nonretarded contribution<sup>4,19</sup>

$$V_{\text{dis}} = -\frac{HR}{12h} \quad (4)$$

where  $H$  is the Hamaker constant,  $R$  the particle radius, and  $h$  the smallest surface separation distance.

**Double Layer Interaction Energies.** The repulsion between electrical double layers is responsible for stabilization of colloidal suspensions, and the respective interaction energy profile can be calculated by solving the Poisson–Boltzmann (PB) equation between two identical plates. In an electrolyte solution containing ions of valence  $z_i$  and number concentration  $c_i$ , the electrostatic potential  $\psi$  versus the position  $x$  satisfies<sup>4,20</sup>

$$\frac{d^2\psi}{dx^2} = -\frac{q}{\epsilon_0\epsilon} \sum_i z_i c_i e^{-z_i q\psi/(kT)} \quad (5)$$

where  $q$  is the elementary charge,  $\epsilon_0$  is the dielectric permittivity of vacuum,  $\epsilon$  is the dielectric constant,  $T$  is the absolute temperature,  $k$  the Boltzmann constant, and the index  $i$  runs over all the ions in solution. In the following, we always refer to room temperature of 25 °C and a dielectric constant of 79 as applicable for water. The solution of eq 5 is obtained subject to the boundary conditions  $\psi(\pm h/2) = \psi_{\text{dl}}$ , where  $h$  is the surface separation and  $\psi_{\text{dl}}$  is the double layer potential. This procedure implies the constant potential boundary condition, but for the symmetric system considered here, effects of charge regulation are minor.<sup>20</sup> The interaction potential can be obtained from the

swelling pressure, which can be calculated from the potential at the midplane  $\psi_M = (0)$  from the relation

$$\Pi = kT \sum_i c_i (e^{-z_i q\psi_M/(kT)} - 1) \quad (6)$$

Within the Derjaguin approximation, the force between the particles can be evaluated by integration

$$F = \pi R \int_h^\infty \Pi(h') dh' \quad (7)$$

and a second integration yields the interaction energy

$$V_{\text{dl}} = \int_h^\infty F(h') dh' \quad (8)$$

These interaction energies can be obtained from the numerical solution of the PB equation.<sup>20</sup>

In some situations, the interaction energies can also be calculated analytically. The simplest situation is described by the Debye–Hückel (DH) approximation, which assumes that the electrostatic potential is low. In this case, the PB equation simplifies to<sup>4</sup>

$$\frac{d^2\psi}{dx^2} = \kappa^2\psi \quad (9)$$

where  $\kappa^{-1}$  is the Debye screening length given by

$$\kappa^2 = \frac{2q^2 I}{kT\epsilon_0\epsilon} \quad (10)$$

where  $I$  is ionic strength and is given by

$$I = \frac{1}{2} \sum_i z_i^2 c_i \quad (11)$$

At sufficiently large distances, the osmotic pressure can be expressed as<sup>4</sup>

$$\Pi = 2\epsilon_0\epsilon\kappa^2\psi_{\text{dl}}^2 e^{-\kappa h} \quad (12)$$

A double integration of this result leads to the exponential DH interaction potential

$$V_{\text{dl}} = 2\pi R\epsilon_0\epsilon\psi_{\text{dl}}^2 e^{-\kappa h} \quad (13)$$

The DH approximation is strictly valid when

$$|\psi| \ll \frac{kT}{zq} \quad (14)$$

However, this approximation is rather robust and applies even when both sides of the inequality are still comparable.

The interaction potential given in eq 13 also remains correct for the PB equation at large distances, but the double layer potential  $\psi_{\text{dl}}$  must be replaced by an effective potential  $\psi_{\text{eff}}$ . This situation is also referred to as charge renormalization.<sup>21</sup> In the case of a symmetric  $z:z$  electrolyte, this effective potential can be expressed as

$$\psi_{\text{eff}} = \frac{4kT}{zq} \tanh\left(\frac{zq\psi_{\text{dl}}}{4kT}\right) \quad (15)$$

This relation illustrates a general property of the PB equation, namely, that the effective potential saturates and becomes independent of the surface charge, provided the surface is sufficiently highly charged ( $\psi_{\text{dl}} \rightarrow \infty$ ). We shall use the



dimensionless parameter  $\alpha$  to express the limiting magnitude of the effective potential

$$\psi_{\text{eff}}^{(\infty)} = \alpha \frac{kT}{q} \quad (16)$$

where  $kT/q = 25.7$  mV in water at room temperature. For the symmetric  $z:z$  electrolyte, eq 15 leads to  $\alpha = 4/z$ . As illustrated in Table 1, the effective saturation potentials decrease with valence.

**Table 1. Dimensionless Effective Saturation Potential  $\alpha^a$**

$z$	$z:z$	$1:z$	$z:1$
1	4	4	4
2	2	1.6077	6
3	1.3333	0.9939	8.7070
4	1	0.7174	12.3141
5	0.8	0.5608	17.0583 <sup>b</sup>
6	0.6667	0.4601	23.2283
7	0.5714	0.3901	31.1745
8	0.5	0.3385	41.3192

<sup>a</sup>For water at room temperature, the actual electric potentials are obtained by multiplying these values by 25.7 mV. Some of these numbers were reported earlier.<sup>21</sup> <sup>b</sup>This entry corrects the erroneous decimals of this number reported earlier<sup>21</sup> and cited elsewhere.<sup>24</sup>

The diffuse layer potential is related to the surface charge density. For an isolated plate in an arbitrary electrolyte, the PB model predicts that

$$\sigma = \pm [2kT\epsilon_0\epsilon \sum_i c_i (e^{-z_i q\psi_{\text{dl}}/(kT)} - 1)]^{1/2} \quad (17)$$

where the + sign refers to a positively charge surface and the – sign to a negatively charged one. Within the DH approximation, this relation simplifies to

$$\sigma = \epsilon_0\epsilon\kappa\psi_{\text{dl}} \quad (18)$$

This surface charge density represents the compensating charge of the diffuse layer and thus reflects the charge of the bare surface together with the layer of tightly adsorbed ions.

Let us now focus on the interaction profiles in asymmetric electrolytes. For the sake of illustration, assume that the particles are positively charged. The commonly discussed case is the asymmetric  $1:z$  electrolyte, where the multivalent ions correspond to the counterions. In this case, eq 13 remains a good approximation, but the corresponding expressions for the effective potentials are not known analytically. However, closed analytical forms for the effective saturation potentials have been derived recently, and they can be obtained numerically from the principal part of an integral expression.<sup>21</sup> These calculations lead to the values given in Table 1. The effective saturation potentials again decrease with the valence, but more strongly than in the symmetric case. Numerical solutions of the PB equation shown in Figure 1 illustrate again that the far-field approximation given by eq 13 can be used with confidence to rather small distances.

The less frequently discussed situation is the one of  $z:1$  electrolyte, where the multivalent ions correspond to the co-ions. At large distances, the far-field approximation given by eq 13 again remains valid, but with two important differences. The exponential decay only sets in when the surfaces are very far apart, and the effective saturation potentials increase with increasing valence as shown in Table 1. As illustrated in Figure

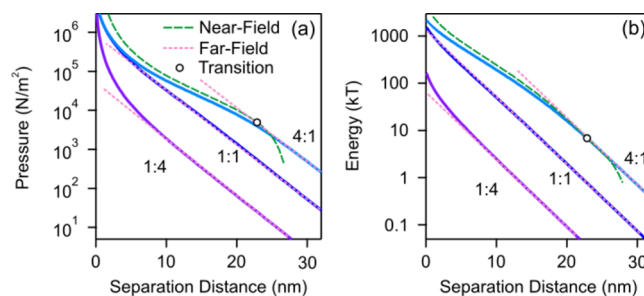


**Figure 1.** Numerical calculation of the double layer interaction between two positively charged surfaces in the presence of 4:1, 1:1, and 1:4 electrolytes. The ionic strength is 10 mM, and the surface charge density is 50 mC/m<sup>2</sup>. The far-field solutions are also indicated and for 4:1 electrolyte the near-field solution and the transition at distance  $h_t$ . (a) Swelling pressure and (b) interaction free energy between particles with a radius of 250 nm.

1, the interaction profile cannot be approximated with an exponential decay, except at very large distances. The reason for these marked deviations is that the highly charged multivalent co-ions are excluded from the proximity of the interface, and only monovalent counterions are enclosed in the gap. This situation resembles a salt-free system, which has been treated in the literature earlier.<sup>19,22–24</sup> At moderate surface separations and high surface charge densities, the swelling pressure can be expressed as<sup>25</sup>

$$\Pi = \frac{\pi kT}{2\lambda_B} \frac{1}{h^2} - kT(z+1)c \quad (19)$$

where  $\lambda_B$  is the Bjerrum length defined as

$$\lambda_B = \frac{q^2}{4\pi kT\epsilon_0\epsilon} \quad (20)$$

The first term in eq 19 corresponds to the pressure between two charged plates in the salt-free system as obtained first by Langmuir,<sup>26</sup> while the second term is an osmotic correction due to co-ion exclusion. Since this relation is a good approximation at smaller distances, it is also referred to as the near-field limit.

The entire interaction energy profile can be estimated by introducing a transition distance  $h_t$ , whereby eq 12 must be used for  $h > h_t$  while eq 19 for  $h \leq h_t$ . The resulting double integration can then be carried out analytically. The transition distance  $h_t$  is found by setting the energy of the multivalent ion to be  $2kT$  at the midplane. The respective calculation yields the result<sup>25</sup>

$$\kappa h_t = 2\pi \sqrt{\frac{z+1}{2}} e^{-1/z} \quad (21)$$

The interaction energy profiles estimated in this fashion are in good agreement with the numerical solution of the PB equation (see Figure 1). Indeed, the far-field exponential decay is only observed at very large distances, and the near-field behavior given by eq 19 dominates the profile. The deviations between the near-field expression and the numerical solution, which are especially evident in Figure 1a, originate from the fact that the numerical solution was obtained for a finite surface charge density of 50 mC/m<sup>2</sup>. On the other hand, the near-field expression given in eq 19 is only valid in the limit of high charge density.

The PB equation is based on a mean-field approximation and neglects effects of ion correlations. To estimate the validity of

this approximation, one can consider a dimensionless coupling parameter<sup>17,27,28</sup>

$$\Xi = 2\pi z^3 \lambda_B^2 |\sigma| / q \quad (22)$$

where  $z$  is the highest counterion valence. The mean-field PB theory is valid, and ion correlations are negligible when  $\Xi \ll 1$ . Typically, effects of ion correlations are potentially relevant close to the charged interface, especially within the adsorbed layer of multivalent counterions. However, as one moves away from the interface the potentials decay, and the mean-field PB theory becomes applicable.<sup>29–32</sup> Experimentally, one finds that these conditions are satisfied already at few nanometers away from the interface.<sup>33,34</sup>

**Colloidal Stability.** The aggregation rate of colloidal particles can be calculated from the steady state solution of the diffusion equation involving the respective energy profile.<sup>4</sup> This approach leads to the two expected regimes of slow and fast aggregation and can be used to predict the CCC. One may also consider the respective ionic strength, and in this case we refer to the CCIS. Derjaguin and Landau proposed a much simpler approach to estimate the CCC (or the CCIS) directly from the energy profile.<sup>1</sup> They assumed that the energy barrier is located at a vanishing energy, namely

$$V = 0 \quad \text{and} \quad \frac{dV}{dh} = 0 \quad (23)$$

This criterion is only valid in an approximate fashion, as it overestimates the actual values of the CCC.<sup>20</sup> However, it remains rather accurate when relative CCCs are considered. By choosing the appropriate double layer interaction potential, one can thus estimate the CCC by inserting eqs 3, 4, and 13 into eq 23.

Consider first the situation for the DH model. Since the salt concentration enters solely through the ionic strength, it is useful to consider the CCIS. With the double layer interaction within the DH and superposition approximation given in eq 13 one finds that<sup>4,5</sup>

$$\text{CCIS} = \frac{72\pi}{e^2} \frac{1}{\lambda_B} \left( \frac{\epsilon_0 \epsilon \psi_{dl}^2}{H} \right)^2 \quad (24)$$

This relation is equivalent to  $\psi_{dl}^2 / \kappa = \text{constant}$ . The latter condition was discussed in the context of colloid stability earlier.<sup>3,9</sup> Invoking the charge-potential relationship given by eq 18 leads to an alternative relation<sup>35</sup>

$$\text{CCIS} = \left( \frac{9}{8\pi e^2} \right)^{1/3} \frac{1}{\lambda_B} \left( \frac{\sigma^2}{\epsilon_0 \epsilon H} \right)^{2/3} \quad (25)$$

When one only considers the actual dependence on surface properties, one has

$$\text{CCIS} \propto \psi_{dl}^4 \propto \sigma^{4/3} \quad (26)$$

Thus, the CCIS is independent of the valence but depends strongly on the diffuse layer potential or the surface charge density. When one considers the relation between the salt concentration and the ionic strength, one can evaluate the CCC from eq 24 or 25. For a symmetric  $z:z$  electrolyte of concentration  $c$  one has  $I = z^2 c$ , and therefore

$$\text{CCC} \propto \frac{\psi_{dl}^4}{z^2} \propto \frac{\sigma^{4/3}}{z^2} \quad (27)$$

For the asymmetric  $1:z$  (or  $z:1$ ) electrolyte one has  $I = z(z+1)c/2$ , and thus

$$\text{CCC} \propto \frac{\psi_{dl}^4}{z(z+1)} \propto \frac{\sigma^{4/3}}{z(z+1)} \quad (28)$$

These dependencies are illustrated as relative CCC or CCIS in Figure 2. Provided the diffuse layer potential or the surface

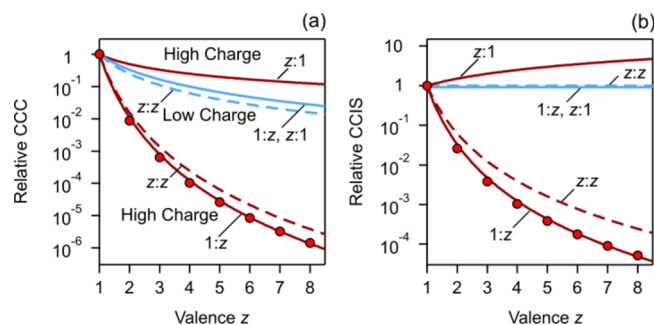


**Figure 2.** Theoretical colloidal stability limits for positively charged particles versus ionic valence. Comparison of asymmetric  $z:1$  and  $1:z$  (full lines) and symmetric  $z:z$  (dashed lines) electrolytes for particles of low charge density within DH theory and highly charged particles in the PB saturation limit. The points are exact numerical results obtained by inserting into eq 24 the respective saturation potentials given in Table 1, and the solid lines are the relations given in eqs 30 and 31. Dependence on the co-ion valence of (a) CCC and (b) CCIS normalized to the values in monovalent salt solution.

charge density remains constant, the CCC will decrease with increasing valence. However, this dependence is only induced through the trivial dependence of the ionic strength and the salt concentration. Therefore, the consideration of the CCIS is simpler, as this quantity is independent of the valence within the DH approximation.

Let us now consider very highly charged particles. Recall first the classical case of the symmetric  $z:z$  electrolyte. This limit follows by replacing  $\psi_{dl}$  in the respective DH expression given in eq 24 for the CCC by the effective saturation potential, and one obtains

$$\text{CCIS} \propto \frac{1}{z^4} \quad (29)$$

or, alternatively, the relation for the CCC given in eq 1. The derivation of the latter relation was considered as one of the major achievements of DLVO theory and is nowadays referred to as the Schulze–Hardy rule.

The same argument can be put forward for highly charged particles in an asymmetric  $1:z$  electrolyte, where the multivalent ions correspond to the counterions. In this situation, one can rely on the same argument as the one used to arrive at eqs 1 and 29. One must only insert the appropriate effective saturation potentials given in Table 1 into eq 24. While the resulting relation cannot be expressed analytically, the numerical data can be well fitted to the empirical relation

$$\text{CCIS} \propto \frac{1}{z^{4.9}} \quad (30)$$

or

$$\text{CCC} \propto \frac{1}{z^{6.5}} \quad (31)$$

These dependencies are shown in Figure 2 together with the exact numerical results. While the dependence of the CCIS (or CCC) is more pronounced for the asymmetric electrolyte than for the symmetric one, the latter result indeed provides a reasonable estimate of the actual dependence in the asymmetric situation. The dependencies for the asymmetric electrolyte reported here are stronger than earlier estimates based on series expansions,<sup>36</sup> suggesting that these expansions are inaccurate.

Let us now focus on the less frequently considered case of the  $z:1$  electrolyte, where the multivalent ions correspond to the co-ions. One now has to insert the interaction energy obtained from eqs 4, 12, and 19 into eq 23. While calculation is lengthy,<sup>25</sup> the final result is simple, namely

$$\text{CCIS} \propto z + 1 \quad (32)$$

or the relation for the CCC given in eq 2. This result again applies for highly charged particles. The above relation was proposed recently and was referred to as the inverse Schulze–Hardy rule.<sup>14,25</sup>

These dependencies are shown in Figure 2. By inspecting this figure, one observes the major advantage considering the CCIS. This quantity increases with the valence for multivalent co-ions, while it decreases for multivalent counterions. For the DH case, the CCIS is constant.

One should realize that the inverse Schulze–Hardy rule was already anticipated long time ago by Freundlich, and this aspect is also mentioned in the classical book by Verwey and Overbeek.<sup>2,37</sup> Freundlich argued that the CCC is solely determined by the adsorption of counterions. In the case of the  $z:1$  salt, the concentration of the monovalent counterions is  $z$  times larger than the salt concentration, which directly leads to eq 2. However, this argument overlooks that this dependence even occurs for entirely indifferent ions, and the presence of the co-ions is essential to induce screening, which leads to the existence of a CCC.

## ■ COMPARISON WITH EXPERIMENT

Let us now confront these relations with experimental results reported in the literature. In particular, numerous data sets were reported recently, and their availability makes such a comparison particularly useful. We will first discuss the frequently discussed case of multivalent counterions and address the rarely studied case of multivalent co-ions later.

**Multivalent Counterions.** Figure 3 shows experimentally measured stability ratios of charged colloidal particles versus the salt concentration in the presence of multivalent counterions by Sinha et al.<sup>10</sup> The stability ratio represents the inverse aggregation rate normalized to the one at high salt conditions. Thus, the stability ratio is large in the regime of slow aggregation and becomes unity in the fast aggregation regime. The transition between these two regimes marks the CCC or CCIS.

The data shown involve positively charged surfactant-free amidine latex particles in the presence of potassium salts of different anions, namely  $\text{Cl}^-$ ,  $\text{SO}_4^{2-}$ ,  $\text{Fe}(\text{CN})_6^{3-}$ , and  $\text{Fe}(\text{CN})_6^{4-}$ . For ions of low valence, the stability ratio decreases monotonously to the fast aggregation plateau. For the ions of higher valence, the stability ratio decreases at first but goes through an intermediate maximum at higher concentrations. This maximum is caused by the reversal of the surface charge that is induced by the adsorption of the multivalent counterions. For this reason, the relevant CCC or CCIS is located just after the initial decrease. The subsequent charge

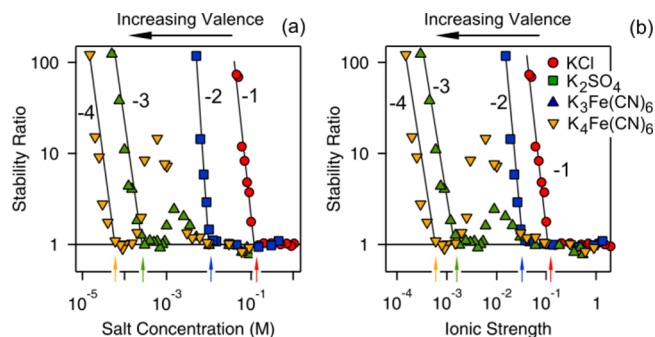


**Figure 3.** Aggregation of positively charged amidine particles in solutions of potassium salts of different multivalent anions by Sinha et al.<sup>10</sup> Stability ratios are plotted versus the (a) salt concentration and (b) ionic strength. The relevant CCCs or CCISs are indicated with arrows, and the respective valence is shown. Solid lines serve to guide the eye. Note the same trend with valence in both subfigures.

reversal will not be further discussed here, but its presence clearly indicates the strong tendency of multivalent ions to adsorb to oppositely charged surfaces and to modify their surface charge.

Relative CCCs or CCISs are plotted versus the valence of the counterions in Figure 4. The figure further summarizes similar

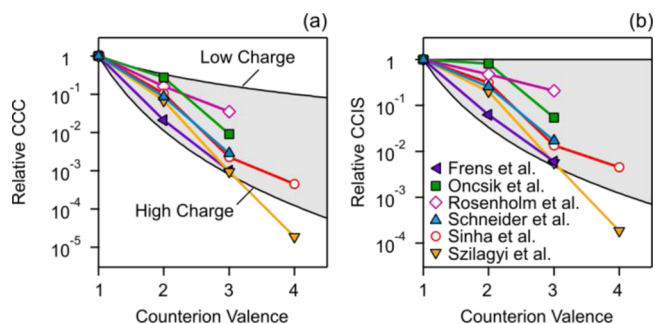


**Figure 4.** Colloidal stability limits in monovalent salt solution versus the valence of the counterions. Solid lines limiting the grey area show the dependencies in  $1:z$  or  $z:1$  electrolytes for low and high charge densities. Experimental data shown include multivalent anions and positively charged particles (open symbols) and multivalent cations and negatively charged particles (full symbols). The straight lines help to guide eyes. The different systems are detailed in Table 2. Dependence on the counterion valence of the (a) CCC and (b) CCIS normalized to the value in monovalent salt solution.

data reported in the literature for positively charged particles in the presence of multivalent anions<sup>10,13</sup> and negatively charged particles in the presence of multivalent cations.<sup>9,12,38,39</sup> While additional measurements of CCCs are available in the literature, we have selected the present systems since the electrokinetic potential ( $\zeta$ -potential) has also been measured at CCC. Table 2 provides further details on these systems. Besides the study by Frens et al.,<sup>9</sup> these data sets are relatively recent and have not yet been analyzed in the context of the Schulze–Hardy rule. The electrokinetic potential represents a good estimate of the double layer potential, which determines the strength of the double layer force.<sup>4,10,40</sup> In some situations, direct force measurements were also used to measure the diffuse layer potential, but in the presence of multivalent ions, these estimates were normally in good agreement.<sup>10,40,41</sup> While some disagreements were reported for monovalent systems,<sup>40</sup> we focus on electrokinetic potentials for simplicity here.



**Table 2. Particle Suspensions in the Presence of Multivalent Counterions**

particles <sup>a</sup>	salt	ref
silver iodide (−)	KNO <sub>3</sub> , Ba(NO <sub>3</sub> ) <sub>2</sub> , La(NO <sub>3</sub> ) <sub>3</sub>	9
sulfate latex (−)	KCl, MgCl <sub>2</sub> , LaCl <sub>3</sub>	12
amine latex <sup>b</sup> (+)	NaNO <sub>3</sub> , Na <sub>2</sub> SO <sub>4</sub> , Na <sub>3</sub> PO <sub>4</sub>	13 (latex 2)
sulfate latex (−)	KCl, MgCl <sub>2</sub> , LaCl <sub>3</sub>	38
amidine latex (+)	KCl, K <sub>2</sub> SO <sub>4</sub> , K <sub>3</sub> Fe(CN) <sub>6</sub> , K <sub>4</sub> Fe(CN) <sub>6</sub>	10
carboxyl latex (−)	N1, N2, N4, N6 <sup>c</sup>	39

<sup>a</sup>The sign of the particle charge is indicated in parentheses. <sup>b</sup>The latex is used where the electrokinetic potentials are reported. <sup>c</sup>The symbols denote aliphatic polyamines with different number of amine groups. The charges of N4 and N6 are taken to be +3 and +4, respectively.<sup>39</sup>

Figure 4 further shows the expected dependencies for weakly and highly charged particles, namely eqs 28 and 31. Numerical PB calculations suggest that the limiting behavior for highly charged particles is only attained for extremely high charge densities, which are unrealistic.<sup>20</sup> Nevertheless, the experimental data often roughly agree with the theoretical high charge density limit. This agreement is accidental, however, since the magnitudes of the surface charge densities and the respective diffuse layer potentials at the CCC are low. This point was already suggested earlier.<sup>3,9</sup> However, these conjectures were based on limited data sets. Recently, however, simultaneous measurements of stability ratios and electrophoretic mobilities in the presence of multivalent counterions became available (see Table 2). We have thus extracted the magnitudes of the respective surface charge densities and diffuse layer potentials from the electrophoretic mobilities at CCC reported in the corresponding publications with the standard electrokinetic model.<sup>4,42</sup> The results are summarized in Figure 5, and the numerical values are given in Table S1.

Let us first focus on the top row of Figure 5, where the dependencies involving the magnitude of the surface charge density at CCC are shown. Figure 5a demonstrates that the magnitude of the surface charge density strongly decreases with increasing valence. This trend is easily understood. Multivalent ions are attracted to an oppositely charged interface, and this interaction promotes adsorption of these ions. The nature of electrostatic interactions makes this trend progressively important with increasing valence, and the presence of this adsorbed layer leads to a decrease of the surface charge.

Since the surface charge decreases with increasing valence, this dependence has a major influence on the CCC. Since the magnitudes of charge densities are relatively low, one expects the DH approximation leading to eq 26 to be valid. Figure 5b demonstrates that this approximation is actually quite good. The experimental CCIS follow the expected power law behavior with the correct exponent of 4/3. Moreover, one observes the expected shift with the Hamaker constant for the two types of particles shown. The scatter in the data points is actually largest for the highest charge densities, which correspond to monovalent ions. Under these conditions, the DH approximation starts to break down. But in the presence of multivalent ions, the charge densities are low and the DH approximation becomes excellent. Figure 5b thus demonstrates unequivocally that variations in the CCISs are entirely due to variation in the surface charge density. A similar power-law dependence of the CCCs on the charge density was established for monovalent counterions of different affinities to the particle surface depending on their position in the Hofmeister series.<sup>43</sup>

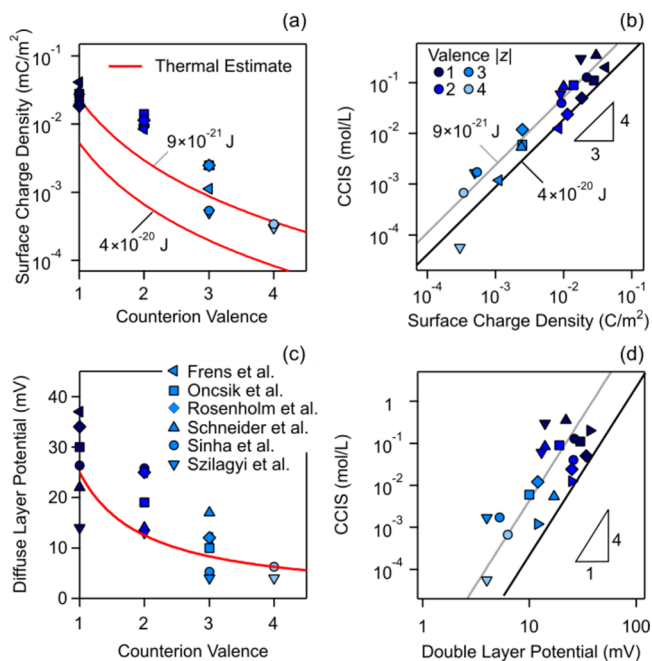


**Figure 5.** Comparison of the magnitudes of (a, b) surface charge density and of (c, d) diffuse layer potential at CCC for systems detailed in Table 2. (a, c) Dependence on the valence of the counterion. (b, d) CCIS versus the charge density or diffuse layer potential. The solid lines in (b, d) are the expected relationships from DH theory for two different Hamaker constants, namely  $9 \times 10^{-21}$  J for latex<sup>49</sup> and  $4 \times 10^{-20}$  J for silver iodide.<sup>50</sup> The solid lines in (a, c) denote the thermal estimate given by eq 33.

Let us now discuss the magnitudes of the diffuse layer potential at CCC, which are shown in the bottom row of Figure 5. The adsorption of multivalent ions is accompanied by a decrease in the magnitude of the diffuse layer potentials. Let us suppose that this potential at CCC can be roughly estimated by assuming that the adsorption energy of a multivalent ion is given by its thermal energy, namely

$$|\psi_{dl}| = \frac{kT}{zq} \approx \frac{25.7 \text{ mV}}{z} \quad (33)$$

This relation is the same as the limit of validity of DH theory given in eq 14 and is shown as the thermal estimate in Figure 5c. The respective thermal estimate for the charge density shown in Figure 5a further makes use of eqs 24 and 25. The thermal estimates in fact approximate the observed trends reasonably well. The CCIS also roughly depends on the diffuse layer potential as predicted by eq 26, and they roughly follow the expected exponent of 4. The substantial scatter in the diffuse layer potentials originates from the fact that the range of the potentials is much smaller than the one of the surface charge densities and that the potentials are more sensitive to the details of the adsorption process. The frequently cited rule that the CCC occurs for a diffuse layer potential around 25 mV directly follows from eq 33 but applies to monovalent salt solutions only.<sup>5,44</sup> In the presence of multivalent counterions, the respective potentials are much lower.

These arguments rely on the assumption that DH theory is applicable. Let us now provide evidence that this assumption is correct. We observe first that none of the potentials substantially exceed the values given in eqs 14 and 33, thus confirming the applicability of DH theory. Second, one should



also address whether the mean-field PB theory is applicable and ion correlations negligible. We have evaluated the parameter given in eq 22 with the surface charge densities and valences shown in Figure 5a. One finds that the coupling parameter  $\Xi$  always remains of the order of unity, suggesting that ion correlation effects are minor. While effects of ion correlations could be relevant close to the surface, especially within the adsorbed layer of multivalent counterions, such effects will be unimportant further away from the interface.<sup>29,32–34</sup> Colloidal stability is governed by the energy profile at distances of at least few nanometers, and in the presence of multivalent counterions these distances become even larger.<sup>20</sup> At this point, the electric potential has decayed sufficiently such that the mean-field DH theory becomes valid. These observations confirm that DH theory is a good approximation in these systems and that consideration of the PB model or theories involving ion correlations is not necessary.

The dependencies suggested by the PB model for highly charged surfaces given in eq 31 are unrelated to the experimentally observed trends in the CCIS. The surfaces in question are weakly charged, and the dependence in the CCIS solely originates from variations in the surface charge density. The resemblance of the dependencies on the valence observed experimentally and the ones predicted by the classical Schulze–Hardy rule given by eq 1 or 29 is related to the fact that the diffuse layer potentials approximately follow eq 33. Indeed, inserting eq 33 into eq 24 also leads also to the Schulze–Hardy rule given in eq 1. A similar argument was already proposed by Frens et al.,<sup>9</sup> and it is certainly more sensible than the one presented in textbooks, which assumes that the surface charge density is high. However, the data shown in Figure 4 indicate that the experimentally observed dependencies can be different as well. These deviations reflect variations in the diffuse layer potentials, which results from the different adsorption affinities of the multivalent ions to the particle surface. A more comprehensive theory of the CCC would involve a detailed model of the adsorption of the multivalent ions to the oppositely charged particle surface. Such models to predict the CCCs have been proposed in the past, but they were either limited to monovalent ions or too crude to capture the charging behavior correctly.<sup>3,11,45,46</sup> These models should involve the different ion-specific affinities to the surfaces, for example, as known for different monovalent ions within the lyotropic or Hofmeister series.<sup>43,47,48</sup> Further development of surface complexation models would be necessary to obtain realistic estimates of the diffuse layer potentials in the presence of multivalent counterions and to understand why the thermal estimate of the diffuse layer potential given in eq 33 is actually quite reasonable. The main current obstacle is the lack of detailed experimental data on adsorption and electrophoresis for the multivalent ions in question, which prohibits proper validation of such models.

**Multivalent Co-ions.** Figure 6 shows experimental stability ratios of charged colloidal particles versus the salt concentration in the presence of multivalent co-ions.<sup>14</sup> The system involves negatively charged surfactant-free sulfate latex particles in the presence of potassium salts of the same anions as discussed above. The stability curves shift to the left when plotted versus the salt concentration and to the right when plotted versus the ionic strength. This behavior is characteristic for multivalent co-ions and has been referred to as the inverse Schulze–Hardy rule.<sup>14</sup> This scenario differs substantially from the one of multivalent counterions (see Figure 3).

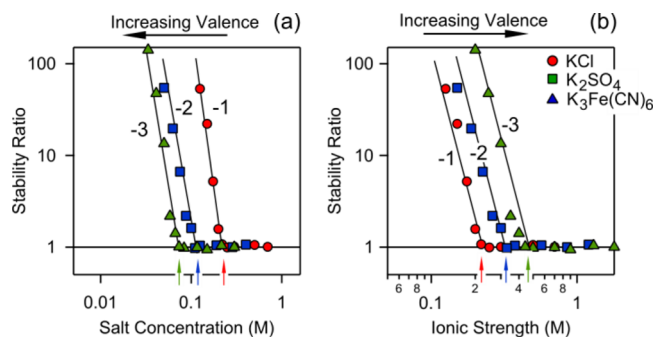


**Figure 6.** Aggregation of negatively charged sulfate latex particles in solutions of potassium salts of different multivalent anions by Cao et al.<sup>14</sup> Stability ratios versus the (a) salt concentration and (b) ionic strength. The relevant CCCs or CCISs are indicated with arrows and respective valence is shown. Solid lines serve to guide the eye. Note the opposite trend with valence in the two subfigures.

These trends are summarized more clearly in Figure 7, where the corresponding CCC and CCIS are plotted versus the

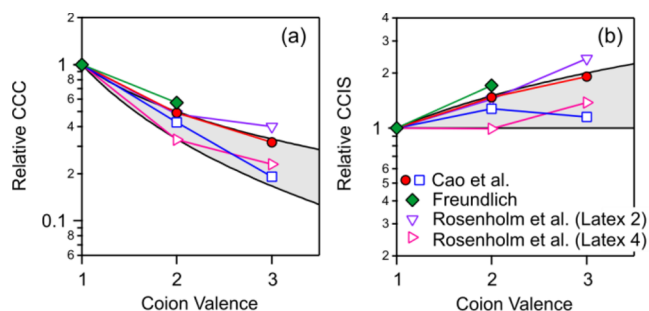


**Figure 7.** Colloidal stability limits versus the valence of the co-ions. Solid lines limiting the grey area show the dependencies in 1:z or z:1 electrolytes for low charge densities given by eqs 26 and 28 and high charge densities given by eqs 2 and 32. Experimental data shown include multivalent cations and positively charged particles (open symbols) and multivalent anions and negatively charged particles (full symbols). The straight lines help to guide eyes. The different systems are detailed in Table 3. Dependence on the co-ion valence of (a) CCC and (b) CCIS normalized to the value in monovalent salt solution.

valence of the co-ions. In the presence of multivalent co-ions, the CCC was so far determined for a handful of systems only. We are only aware of the two experimental studies by Rosenholm et al.<sup>13</sup> and Cao et al.<sup>14</sup> More details on the respective systems are given in Table 3. The actual numerical values can be found in Table S2. One indeed observes that the CCC decreases with valence, while it increases with the CCIS. Surprisingly, the study of Rosenholm et al.<sup>13</sup> does not remark this characteristic trend. Freundlich reported this effect in the

**Table 3. Particle Suspensions in the Presence of Multivalent Co-Ions**

particles <sup>a</sup>	salt	ref
sulfate latex (–)	KCl, K <sub>2</sub> SO <sub>4</sub> , K <sub>3</sub> Fe(CN) <sub>6</sub>	14
amidine latex (+)	KCl, MgCl <sub>2</sub> , LaCl <sub>3</sub>	14
arsenic sulfide (–)	NH <sub>4</sub> Cl, (NH <sub>4</sub> ) <sub>2</sub> SO <sub>4</sub>	37
amine latex (+)	NaNO <sub>3</sub> , Mg(NO <sub>3</sub> ) <sub>2</sub> , Al(NO <sub>3</sub> ) <sub>3</sub>	13 (latex 2)
amine latex <sup>b</sup> (+)	NaNO <sub>3</sub> , Mg(NO <sub>3</sub> ) <sub>2</sub> , Al(NO <sub>3</sub> ) <sub>3</sub>	13 (latex 4)

<sup>a</sup>The sign of the particle charge is indicated in parentheses. <sup>b</sup>The latex is used where the electrokinetic potentials are reported.

presence of divalent co-ions long time ago, and this aspect is briefly mentioned in the classical book by Verwey and Overbeek.<sup>2,37</sup> At that time, however, no data were available for co-ions of valence higher than two.

Figure 7 also shows the expected dependencies based on DH theory, which is applicable for low charge densities, together with the limiting behavior for high charge densities given by eqs 2 and 32. The limiting high charge behavior is reached rather quickly and already at moderate charge densities. This situation is in contrast to the case of multivalent counterions, where the limiting behavior is attained slowly and only for extremely high charge densities.<sup>20</sup> In this case, effects of ion correlations are also negligible, and the mean-field PB theory will remain a good approximation even for the higher charge densities in question. This statement can be verified by realizing that multivalent co-ions are excluded from the vicinity of the interface and the counterions are monovalent. Therefore, the coupling parameter given by eq 22 remains small.

Only few measurements of surface charge densities in the presence of multivalent co-ions are available.<sup>13,24</sup> Both studies report that the charge densities remain high in magnitude, even at elevated concentrations of co-ions of higher valence. This finding is reasonable since the strength of the electrostatic repulsion between the multivalent co-ions and the surface will increase with increasing valence, making their adsorption increasingly difficult. Therefore, we suspect that the transition between the limiting laws actually reflects the different surface charge densities of the particles investigated. However, the observations by Rosenholm et al.<sup>13</sup> for their sample denoted as “latex 4” appear inconsistent. In the presence of multivalent co-ions, they report high surface charge densities around  $17 \pm 3$  mC/m<sup>2</sup>, which suggests the applicability of the inverse Schulze–Hardy rule. However, the respective CCISs are almost independent of the valence of the co-ions, which rather indicates low surface charge densities. Therefore, additional measurements of surface charge densities at CCC in the presence of multivalent co-ions would be needed to make more definitive conclusions concerning the validity of the inverse Schulze–Hardy rule.

## CONCLUSIONS

We have revisited the applicability of the classical Schulze–Hardy rule given in eq 1. The commonly presented derivation of this rule from DLVO theory assumes symmetric  $z:z$  electrolytes and that the particles are highly charged. These assumptions are incorrect. First, salts of symmetric  $z:z$  electrolytes are insoluble for ions with valence higher than two. Experiments are normally carried out with the well soluble salts of asymmetric  $1:z$  or  $z:1$  electrolytes. Such electrolytes behave very differently whether the multivalent ions represent the counterions or co-ions. In the counterion case, where the multivalent ions have the opposite sign of charge as the particle, these ions adsorb to the particle surfaces. Thereby, they strongly reduce the magnitude of the surface charge. In the co-ion case, where the multivalent ions have the same sign of charge as the particle, these ions are repelled from the particles, and the surface charge remains high.

The commonly discussed situation is when the multivalent ions represent the counterions. While one can indeed argue that this situation can be approximated with a symmetric electrolyte, one cannot defend that the charge densities are high in magnitude. Electrophoretic mobility and direct force measurements show unambiguously that their values are so

low that the DH theory is applicable. In this regime, the dependence of the CCC on the valence is weak, but the CCC strongly depends on the surface charge density. This dependence is actually responsible for the experimentally observed dependence on the valence, since multivalent ions of higher valence adsorb more strongly to the particle surface and thus progressively reduce the magnitude of the surface charge density. The observed dependence of the CCC on valence thus results from a combination of a weak dependence of the ionic strength on the concentration and a stronger dependence of the surface charge density. While the diffuse layer potentials at CCC appear compatible with a thermal estimate, a more complete description would call for a detailed model capable to predict the variations of the surface charge due to adsorption of the multivalent ions to the oppositely charged particle surfaces.<sup>3,11</sup> The combination of these effects often leads to a similar trend as suggested by the classical Schulze–Hardy rule. While ionization and hydrolysis reactions in solutions may equally modify the observed behavior,<sup>6</sup> the presently discussed effects of valence were established in systems, where such reactions only play a minor role.

The less discussed situation is when the multivalent ions represent the co-ions. In this situation, the co-ions do not adsorb to the particles, which may indeed maintain a high surface charge. The assumption of highly charged surfaces is now justified. However, the interaction potential strongly deviates from the simple exponential law, and this aspect must be considered when deriving the dependence of the CCC on the valence. The resulting dependence given by eq 2 is weak and has been referred to as the inverse Schulze–Hardy rule. While one may argue that this dependence would be trivially obtained when only monovalent counterions would be relevant, this argument cannot be maintained as the co-ions are essential to introduce screening, which finally leads to the presence of the CCC. The scarce experimental data scatter between the limits of low and high charge densities, and currently hardly any information concerning the actual charge densities at CCC is available. More experimental and theoretical work is necessary to clarify the situation of the role of co-ions.

## ASSOCIATED CONTENT

### Supporting Information

The Supporting Information is available free of charge on the ACS Publications website at DOI: 10.1021/acs.langmuir.6b04464.

Tables with CCCs and electrokinetic potentials (PDF)

## AUTHOR INFORMATION

### Corresponding Author

\*E-mail [michal.borkovec@unige.ch](mailto:michal.borkovec@unige.ch) (M.B.).

### ORCID

Michal Borkovec: 0000-0002-1114-4865

### Notes

The authors declare no competing financial interest.

## ACKNOWLEDGMENTS

This work was supported by the Swiss National Science Foundation through Awards 140327 and 159874 and the University of Geneva.

## ■ REFERENCES

- (1) Derjaguin, B.; Landau, L. D. Theory of the Stability of Strongly Charged Lyophobic Sols and of the Adhesion of Strongly Charged Particles in Solutions of Electrolytes. *Acta Phys. Chim.* **1941**, *14*, 633–662.
- (2) Verwey, E. J. W.; Overbeek, J. T. G. *Theory of Stability of Lyophobic Colloids*; Elsevier: Amsterdam, 1948.
- (3) Overbeek, J. T. G. The Rule of Schulze and Hardy. *Pure Appl. Chem.* **1980**, *52*, 1151–1161.
- (4) Russel, W. B.; Saville, D. A.; Schowalter, W. R. *Colloidal Dispersions*; Cambridge University Press: Cambridge, 1989.
- (5) Evans, D. F.; Wennerstrom, H. *The Colloidal Domain*; John Wiley: New York, 1999.
- (6) Lyklema, J. Coagulation by Multivalent Counterions and the Schulze-Hardy Rule. *J. Colloid Interface Sci.* **2013**, *392*, 102–104.
- (7) Schulze, H. Schwefelarsen in wässriger Lösung. *J. Prakt. Chem.* **1882**, *25*, 431–452.
- (8) Hardy, W. B. A Preliminary Investigation of the Conditions Which Determine the Stability of Irreversible Hydrosols. *Proc. R. Soc. London* **1899**, *66*, 110–125.
- (9) Frens, G.; Heuts, J. J. F. G. The Double Layer Potential as a Rate Determining Factor in the Coagulation of Electrostatic Colloids. *Colloids Surf.* **1988**, *30*, 295–305.
- (10) Sinha, P.; Szilagyi, I.; Montes Ruiz-Cabello, F. J.; Maroni, P.; Borkovec, M. Attractive Forces between Charged Colloidal Particles Induced by Multivalent Ions Revealed by Confronting Aggregation and Direct Force Measurements. *J. Phys. Chem. Lett.* **2013**, *4*, 648–652.
- (11) Metcalfe, I. M.; Healy, T. W. Charge Regulation Modeling of the Schulze-Hardy rule and Related Coagulation Effects. *Faraday Discuss. Chem. Soc.* **1990**, *90*, 335–344.
- (12) Oncsik, T.; Trefalt, G.; Csendes, Z.; Szilagyi, I.; Borkovec, M. Aggregation of Negatively Charged Colloidal Particles in the Presence Of Multivalent Cations. *Langmuir* **2014**, *30*, 733–741.
- (13) Rosenholm, J. B.; Nylund, J.; Stenlund, B. Synthesis and Characterization of Cationized Latexes in Dilute Suspensions. *Colloids Surf., A* **1999**, *159*, 209–218.
- (14) Cao, T.; Szilagyi, I.; Oncsik, T.; Borkovec, M.; Trefalt, G. Aggregation of Colloidal Particles in the Presence of Multivalent Cations: The Inverse Schulze–Hardy Rule. *Langmuir* **2015**, *31*, 6610–6614.
- (15) Guldbbrand, L.; Jonsson, B.; Wennerstrom, H.; Linse, P. Electrical Double-Layer Forces: A Monte-Carlo Study. *J. Chem. Phys.* **1984**, *80*, 2221–2228.
- (16) Kjellander, R. Intricate Coupling between Ion-Ion and Ion-Surface Correlations in Double Layers as Illustrated by Charge Inversion-Combined Effects of Strong Coulomb Correlations and Excluded Volume. *J. Phys.: Condens. Matter* **2009**, *21*, 424101.
- (17) Naji, A.; Kanduc, M.; Forsman, J.; Podgornik, R. Perspective: Coulomb Fluids - Weak Coupling, Strong Coupling, in between and Beyond. *J. Chem. Phys.* **2013**, *139*, 150901.
- (18) Farauto, J.; Travasset, A. The Many Origins of Charge Inversion in Electrolyte Solutions: Effects of Discrete Interfacial Charges. *J. Phys. Chem. C* **2007**, *111*, 987–994.
- (19) Israelachvili, J. *Intermolecular and Surface Forces*, 2nd ed.; Academic Press: London, 1992.
- (20) Trefalt, G.; Szilagyi, I.; Borkovec, M. Poisson-Boltzmann Description of Interaction Forces and Aggregation Rates Involving Charged Colloidal Particles in Asymmetric Electrolytes. *J. Colloid Interface Sci.* **2013**, *406*, 111–120.
- (21) Tellez, G. Nonlinear Screening of Charged Macromolecules. *Philos. Trans. R. Soc., A* **2011**, *369*, 322–334.
- (22) Briscoe, W. H.; Attard, P. Counterion-Only Electrical Double Layer: A Constrained Entropy Approach. *J. Chem. Phys.* **2002**, *117*, 5452–5464.
- (23) Cowley, A. C.; Fuller, N. L.; Rand, R. P.; Parsegian, V. A. Measurement of Repulsive Forces between Charged Phospholipid Bilayers. *Biochemistry* **1978**, *17*, 3163–3168.
- (24) Montes Ruiz-Cabello, F. J.; Moazzami-Gudarzi, M.; Elzbiaciak-Wodka, M.; Maroni, P.; Labbez, C.; Borkovec, M.; Trefalt, G. Long-ranged and Soft Interactions Between Charged Colloidal Particles Induced by Multivalent Coions. *Soft Matter* **2015**, *11*, 1562–1571.
- (25) Trefalt, G. Derivation of the Inverse Schulze-Hardy Rule. *Phys. Rev. E: Stat. Phys., Plasmas, Fluids, Relat. Interdiscip. Top.* **2016**, *93*, 032612.
- (26) Langmuir, I. The Role of Attractive and Repulsive Forces in the Formation of Tactoids, Thixotropic, Gels Protein Crystals and Coacervates. *J. Chem. Phys.* **1938**, *6*, 873–896.
- (27) Moreira, A. G.; Netz, R. R. Binding of Similarly Charged Plates with Counterions Only. *Phys. Rev. Lett.* **2001**, *87*, 078301.
- (28) Netz, R. R. Electrostatics of Counter-Ions at and between Planar Charged Walls: From Poisson-Boltzmann to the Strong-Coupling Theory. *Eur. Phys. J. E: Soft Matter Biol. Phys.* **2001**, *5*, 557–574.
- (29) Hatlo, M. M.; Lue, L. A Field Theory for Ions Near Charged Surfaces Valid from Weak to Strong Couplings. *Soft Matter* **2009**, *5*, 125–133.
- (30) Samaj, L. Renormalization of a Hard-Core Guest Charge Immersed in a Two-Dimensional Electrolyte. *J. Stat. Phys.* **2006**, *124*, 1179–1206.
- (31) Tellez, G. Charge Inversion of Colloids in an Exactly Solvable Model. *Europhys. Lett.* **2006**, *76*, 1186–1192.
- (32) Gonzalez-Mozuelos, P.; Guerrero-Garcia, G. I.; Olvera de la Cruz, M. O. An Exact Method to Obtain Effective Electrostatic Interactions from Computer Simulations: The Case of Effective Charge Amplification. *J. Chem. Phys.* **2013**, *139*, 064709.
- (33) Montes Ruiz-Cabello, F. J.; Trefalt, G.; Maroni, P.; Borkovec, M. Accurate Predictions of Forces in the Presence of Multivalent Ions by Poisson-Boltzmann theory. *Langmuir* **2014**, *30*, 4551–4555.
- (34) Ebeling, D.; van den Ende, D.; Mugele, F. Electrostatic Interaction Forces in Aqueous Salt Solutions of Variable Concentration and Valency. *Nanotechnology* **2011**, *22*, 305706.
- (35) Hall, S. B.; Duffield, J. R.; Williams, D. R. A Reassessment of the Applicability of the DLVO theory as an Explanation for the Schulze-Hardy rule for Colloid Aggregation. *J. Colloid Interface Sci.* **1991**, *143*, 411–415.
- (36) Hsu, J. P.; Kuo, Y. C. The Critical Coagulation Concentration of Counterions: Spherical Particles in Asymmetric Electrolyte Solutions. *J. Colloid Interface Sci.* **1997**, *185*, 530–537.
- (37) Freundlich, H. Die Bedeutung der Adsorption bei der Fällung der Suspensionskolloide. *Z. Chem. Ind. Kolloide* **1910**, *7*, 193–195.
- (38) Schneider, C.; Hanisch, M.; Wedel, B.; Jusufi, A.; Ballauff, M. Experimental Study of Electrostatically Stabilized Colloidal Particles: Colloidal Stability and Charge Reversal. *J. Colloid Interface Sci.* **2011**, *358*, 62–67.
- (39) Szilagyi, I.; Polomska, A.; Citherlet, D.; Sadeghpour, A.; Borkovec, M. Charging and Aggregation of Negatively Charged Colloidal Latex Particles in Presence of Multivalent Polyamine Cations. *J. Colloid Interface Sci.* **2013**, *392*, 34–41.
- (40) Montes Ruiz-Cabello, F. J.; Trefalt, G.; Csendes, Z.; Sinha, P.; Oncsik, T.; Szilagyi, I.; Maroni, P.; Borkovec, M. Predicting Aggregation Rates of Colloidal Particles from Direct Force Measurements. *J. Phys. Chem. B* **2013**, *117*, 11853–11862.
- (41) Hartley, P. G.; Larson, I.; Scales, P. J. Electrokinetic and Direct Force Measurements between Silica and Mica Surfaces in Dilute Electrolyte Solutions. *Langmuir* **1997**, *13*, 2207–2214.
- (42) O'Brien, R. W.; White, L. R. Electrophoretic Mobility of a Spherical Colloidal Particle. *J. Chem. Soc., Faraday Trans. 2* **1978**, *74*, 1607–1626.
- (43) Oncsik, T.; Trefalt, G.; Borkovec, M.; Szilagyi, I. Specific Ion Effects on Particle Aggregation Induced by Monovalent Salts within the Hofmeister Series. *Langmuir* **2015**, *31*, 3799–3807.
- (44) Vallar, S.; Houivet, D.; El Fallah, J.; Kervadec, D.; Haussonne, J. M. Oxide Slurries Stability and Powders Dispersion: Optimization with Zeta Potential and Rheological Measurements. *J. Eur. Ceram. Soc.* **1999**, *19*, 1017–1021.

(45) Ehrl, L.; Jia, Z.; Wu, H.; Lattuada, M.; Soos, M.; Morbidelli, M. Role of Counterion Association in Colloidal Stability. *Langmuir* **2009**, *25*, 2696–2702.

(46) Sverjensky, D. A. Prediction of the Speciation of Alkaline Earths Adsorbed on Mineral Surfaces in Salt Solutions. *Geochim. Cosmochim. Acta* **2006**, *70*, 2427–2453.

(47) Dumont, F.; Watillon, A. Stability of Ferric Oxide Hydrosols. *Discuss. Faraday Soc.* **1971**, *52*, 352–380.

(48) Lopez-Leon, T.; Jodar-Reyes, A. B.; Bastos-Gonzalez, D.; Ortega-Vinuesa, J. L. Hofmeister Effects in the Stability and Electrophoretic Mobility of Polystyrene Latex Particles. *J. Phys. Chem. B* **2003**, *107*, 5696–5708.

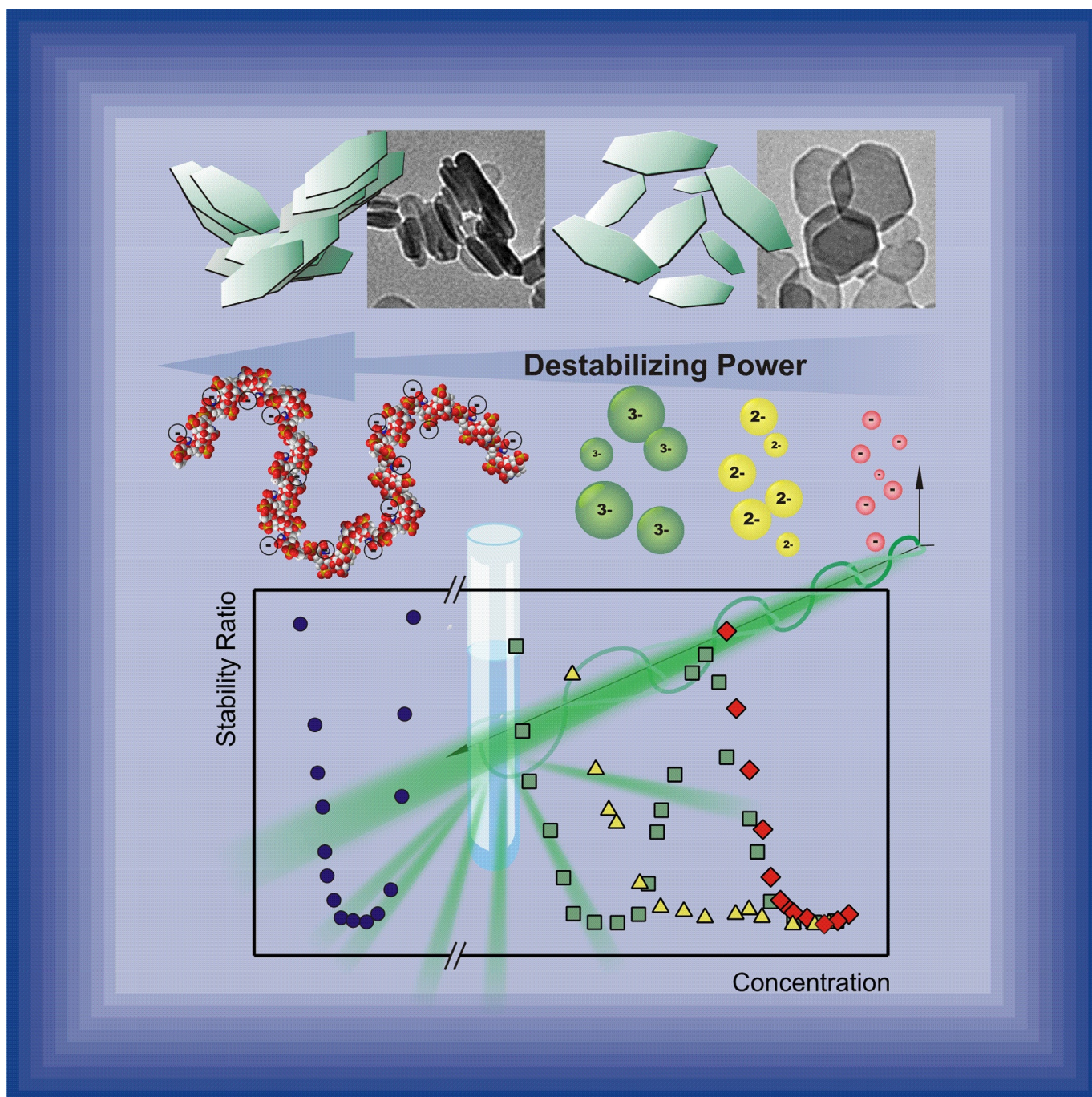
(49) Bevan, M. A.; Prieve, D. C. Direct Measurement of Retarded Van der Waals attraction. *Langmuir* **1999**, *15*, 7925–7936.

(50) Visser, J. On Hamaker constants: A Comparison between Hamaker Constants and Lifshitz - Van der Waals Constants. *Adv. Colloid Interface Sci.* **1972**, *3*, 331–363.



SPECIAL  
ISSUE

# Tuning Colloidal Stability of Layered Double Hydroxides: From Monovalent Ions to Polyelectrolytes

Marko Pavlovic, Paul Rouster, Tamas Oncsik, and Istvan Szilagy<sup>\*,[a]</sup>



The growing number of applications of layered double hydroxide (LDH) colloids demands for detailed understanding of particle aggregation processes in such samples. Tuning the colloidal stability in aqueous suspensions is essential to design stable systems or to induce controlled aggregation of these elongated particles. In this review, recent progress in this field is summarized; in particular, the charging and aggregation of LDHs of various compositions and sizes in the presence of different aggregating agents are discussed. The review focuses

on the effect of monovalent salts, multivalent ions, and polyelectrolytes on the suspension stability of LDHs. The provided information will help to better understand the origin of interparticle forces responsible for the colloidal stability and to design highly stable or aggregating LDH colloids according to the desired goals in certain applications. Moreover, potential future research directions to obtain a broader picture of LDH aggregation are also suggested.

## Introduction

Solid particles suspended in a liquid represent an important class of materials, which can be found in many everyday systems, such as paints, foods, and cosmetics and also in biomedical and other manufacturing processes.<sup>[1–8]</sup> The sizes of the particles vary from a few nanometers (nanoparticles) to the micrometer range (colloidal particles). Various compositions and shapes exist, for example, metals,<sup>[9–11]</sup> polymers,<sup>[12–16]</sup> and oxides<sup>[17–22]</sup> have been synthesized or can be found in nature. They are usually charged, the sign and magnitude of the charge depend on the environmental or experimental conditions (pH, type of solvent, adsorbed molecules, etc.). In general, when dealing with the stability of suspensions, stable samples refer to homogenous distribution of primary particles in the liquid medium, whereas rapid aggregation (the terms flocculation or coagulation are also used for this process) of the particles occurs in unstable systems and often leads to irreversible formation of dimers first and larger, irregularly shaped clusters at longer times.<sup>[23]</sup> In the late stages of aggregation, creaming, sedimentation, or formation of colloidal gels can be observed depending on the material properties and on the concentration of the particles.<sup>[24]</sup>

Suspensions containing inorganic particles of elongated structures are important systems in many applications. Among them, layered double hydroxides (LDHs) attract widespread contemporary interest owing to their advantageous properties such as considerable ion exchange capacity, biocompatibility, and chemical stability. LDHs are hydroxalite-type anionic clays containing lamellar mixed hydroxides with exchangeable anions between the layers (Figure 1).<sup>[25–29]</sup> The structure of the lamellar LDHs is based on brucite ( $\text{Mg}(\text{OH})_2$ ) with octahedral coordination around the metal ions. The divalent metal ions ( $\text{M}^{2+}$ ) can be substituted with trivalent ones ( $\text{M}^{3+}$ ) of similar coordination properties. This isomorphous substitution results in positively charged sheets, which are electrically neutralized by interlayer anions ( $\text{A}^{n-}$ ). Water molecules also exist between

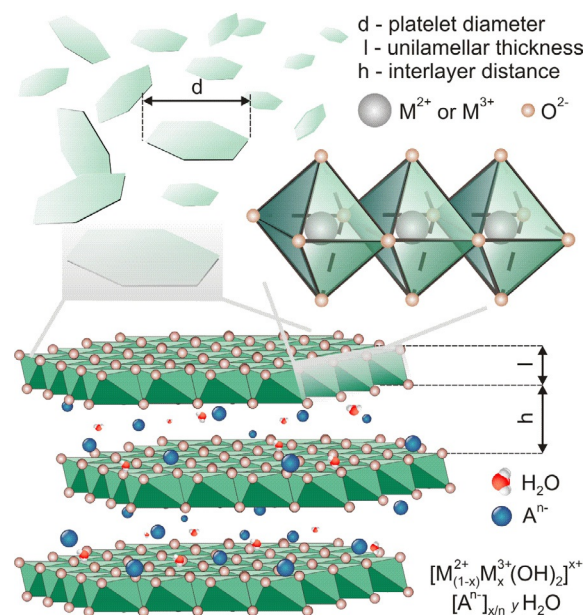


**Figure 1.** Schematic representation of the structure of LDHs. The general elemental composition is also indicated.

the layers, therefore, a general formula for LDHs can be suggested as  $[\text{M}_{(1-x)}^{2+}\text{M}_x^{3+}(\text{OH})_2]^{x+}[\text{A}^{n-}]_{x/n} \cdot y \text{H}_2\text{O}$ .<sup>[30,31]</sup>

Although LDHs can be found as hydroxalite in nature and also form in small amounts during some manufacturing processes,<sup>[32,33]</sup> they can also be easily synthesized. Co-precipitation is the most common method to prepare these anionic clays in large amounts, however, other processes (for example, anion exchange, rehydration, and hydrothermal methods) are also known and used.<sup>[27,34–36]</sup> The physicochemical properties of LDHs can be tuned by varying the experimental conditions during the synthesis.

Intercalation of negatively charged molecules (metal complexes, enzymes, various types of organic and inorganic anions, etc.) into the LDH layers has been widely studied over the past few decades.<sup>[32,37–40]</sup> In addition, core-shell structures or other novel composites with inorganic nanomaterials have also been prepared.<sup>[41,42]</sup> Recent reviews<sup>[36–38,43–47]</sup> and other contributions<sup>[48–59]</sup> indicate the importance of LDHs and their nanocomposites in several fields including catalysis, sensing, coating, capture of greenhouse gases, water treatment, and drug delivery.

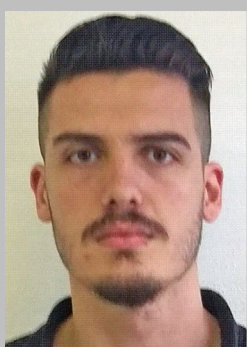
[a] M. Pavlovic, Dr. P. Rouster, T. Oncsik, Dr. I. Szilagy  
Department of Inorganic and Analytical Chemistry  
University of Geneva  
30 Quai Ernest-Ansermet, 1205 Geneva (Switzerland)  
E-mail: istvan.szilagy@unige.ch



This article is part of a Special Issue celebrating the 5th Anniversary of ChemPlusChem. To view the complete issue, visit:  
<http://dx.doi.org/10.1002/cplu.v82.1>.

Tuning colloidal stability, that is, controlling LDH aggregation, is essential especially in the two latter applications. Accordingly, stable suspensions of primary particles are required during the removal of unwanted anions in water treatment processes, whereas the particles can be eliminated by aggregation and subsequent sedimentation from the system.<sup>[60,61]</sup> In drug or gene delivery, the negatively charged biomolecules are

Marko Pavlovic received his MSc degree in chemistry from the University of Novi Sad, Serbia, in 2014 and started his PhD studies thereafter at the University of Geneva. His research is concerned with layered double hydroxides including their preparation, surface functionalization, and controlling their aggregation in suspensions.



Paul Rouster is a postdoctoral research associate at the University of Geneva. His PhD was awarded in physical chemistry and materials science at the University of Strasbourg, France. His research interests include polyelectrolytes, surface modification, synthesis and functionalization of nanomaterials.



Tamas Oncsik finished his undergraduate studies in chemistry at the University of Szeged, Hungary, in 2012. He is currently a PhD student at the University of Geneva. His research mainly focuses on ion-specific interactions in particle aggregation and the stability of nanoparticle dispersions in ionic liquids.



Istvan Szilagyi obtained his PhD in chemistry at the University of Szeged, Hungary. After completing a postdoctoral position at Murdoch University, Australia, he moved to the University of Geneva in 2009 where he holds a senior lecturer position. His research focuses on synthesis, modification, and formulation of layered nanomaterials.



immobilized between the LDH layers and on the outer surface, however, aggregation of the carrier particles in biofluids leads to the formation of irregularly shaped clusters, which impedes the successful delivery of the drug or gene molecules.<sup>[36,37,57,62–64]</sup> Therefore, the use of powerful stabilizing agents is crucial to achieve homogeneous distribution of the carrier LDH particles in living systems.<sup>[5,65,66]</sup> Aggregation can be prevented by coating with biomacromolecules, which are electrostatically or covalently bound to the particle surface.<sup>[5,67]</sup>

The above examples shed light on the importance of colloidal stability of LDH particles in applications where the aggregation processes have to be well-controlled. In the present review, we summarize the current understanding of the charging and aggregation in aqueous LDH colloids in the presence of various compounds including mono- or multivalent ions and polyelectrolytes. However, we do not focus on the preparation of LDH nanocomposites, on the results obtained by solid-state characterization techniques, or on the delamination strategies.

### Charging and Aggregation in Monovalent Salt Solutions

As mentioned before, the positive structural charge of the LDHs originates from the isomorphous substitution of the divalent metal ions by trivalent ones in the layers, similar to the replacement of  $Mg^{2+}$  by  $Al^{3+}$  in the naturally occurring hydro-talcite.<sup>[30]</sup> This structural charge is pH-independent above approximately pH 6, however, significant dissolution of the basic materials takes place in more acidic solutions. Such charge can be tuned by varying the divalent-to-trivalent metal ion ratio, which can also lead to different morphologies of the platelets.<sup>[42]</sup> In addition, LDHs contain considerable amounts of hydroxyl groups on the surface, which can deprotonate at high pH, leading to the development of pH-dependent negative surface charges. Nevertheless, the overall net charge, that is, the sum of the structural and pH-dependent charges, is always positive below approximately pH 11, but specifically adsorbing anions decrease the charge and related surface potential.<sup>[41,49]</sup> This issue will be discussed in detail later.

The magnitude of the surface charge density was determined for some systems. Potentiometric titrations were performed for a LDH composed of  $Zn^{2+}$  and  $Cr^{3+}$  layer forming metal ions of 2:1 molar ratio and  $Cl^{-}$  interlayer anions (Zn/Cr-Cl-LDH) between pH 6 and 12 at different ionic strengths adjusted with NaCl.<sup>[68]</sup> The data indicated a hydroxide ion consumption corresponding to  $250 \text{ mCm}^{-2}$  in surface charge until the high pH limit. The hydroxide ions both compensated for the positive charge by adsorption on the oppositely charged surface and induced the deprotonation of the surface hydroxyl groups at higher pH. Therefore, it is difficult to distinguish structural and pH-dependent charge from these results. Similar findings were obtained with Zn/Al-Cl-LDHs of different metal ion ratios.<sup>[69]</sup> In addition, potentiometric titration results with a Mg/Al- $NO_3$ -LDH sample in  $NaNO_3$  electrolyte showed a decrease in the surface charge density from pH 6 to 11, resulting in a point of zero charge (PZC) at the latter pH.<sup>[70]</sup> The location

of the PZC was also confirmed by electrophoretic measurements. Note that we refer to the PZC only if charge neutralization occurs by changing the pH, whereas neutralization by specific anion adsorption is located at the isoelectric point (IEP).

In other studies, surface charge densities were estimated from the ionic strength dependence of the electrokinetic potential by using the Debye–Hückel model.<sup>[71]</sup> Surface charge densities of 10 and 11  $\text{mCm}^{-2}$  were reported for two Mg/Al- $\text{NO}_3$ -LDHs at pH 9 in the presence of  $\text{NaNO}_3$  electrolyte.<sup>[72,73]</sup> A slightly higher value (15  $\text{mCm}^{-2}$ ) was determined for two Mg/Al- $\text{CO}_3$ -LDHs of the same composition, but with different lateral dimensions, indicating that the surface charge density mostly depends on the composition and only weakly on the size of the particles.<sup>[65]</sup> These results are in good agreement with the ones obtained from the above-mentioned potentiometric titration experiments, which were performed in the same pH range.

Monovalent ions are often considered as indifferent, that is, they adsorb only weakly or not at all on charged surfaces such as LDH. However, electrophoretic mobility measurements carried out with LDHs in the presence of monovalent electrolytes of various compositions yielded different results. The mobilities of Mg/Al- $\text{NO}_3$ -LDH particles were determined in aqueous solutions of NaCl and NaSCN at pH 7.<sup>[74]</sup> The values decreased with the salt concentration in both cases, but the decrease was more pronounced for the  $\text{SCN}^-$  counterions, leading to charge neutralization and to a slight charge reversal at higher salt levels. For the  $\text{Cl}^-$ , the mobilities remained positive in the entire concentration range investigated. The decrease in the electrophoretic mobilities can be rationalized by the charge screening effect and specific adsorption of the anions. The latter process was much stronger for the  $\text{SCN}^-$  ions and, hence, it induced an inversion of the surface charge.

Similar results were obtained with another Mg/Al- $\text{NO}_3$ -LDH in solutions of KCl,  $\text{KNO}_3$ , KSCN, and  $\text{KHCO}_3$  at pH 9.<sup>[73]</sup> As shown in Figure 2a, the adsorption of the  $\text{SCN}^-$  ions led to charge neutralization at the IEP and to subsequent charge reversal at higher salt levels in this system too. In addition, the electrophoretic mobilities decreased at the same concentration in the order  $\text{Cl}^- > \text{NO}_3^- > \text{SCN}^-$ , indicating the different extent of ion adsorption. The charging behavior of the particles is sig-

nificantly different in the presence of  $\text{HCO}_3^-$  anions. Similarly to  $\text{SCN}^-$ , the adsorption gave rise to charge neutralization at the IEP, but it is located at much lower concentration. The charge reversal resulted in more negative mobility values than for  $\text{SCN}^-$ . The strong interaction between carbonate- or carboxylate-containing anions and LDH particles is well-known and has also been reported for other systems.<sup>[36,75]</sup> Such a strong affinity is due to the Coulombic attraction between the opposite charges and to specific interactions of the  $\text{HCO}_3^-$  with the surface hydroxyl groups through mainly hydrogen bonds.

Aggregation of Mg/Al- $\text{NO}_3$ -LDH particles was followed by time-resolved dynamic light scattering (DLS) measurements.<sup>[73]</sup> The colloidal stability was expressed in terms of stability ratio, which is close to one for rapidly aggregating particles (unstable systems), whereas higher values indicate slower aggregation and more stable suspensions.<sup>[76]</sup> In general, high stability ratios were obtained at low salt levels and they decreased progressively with the electrolyte concentration until they reached the value of unity (Figure 2b). The stability ratios remained constant thereafter in the entire concentration range studied. The sharp transition between the slow and fast aggregation regimes is defined as the critical coagulation concentration (CCC). Such tendency of the stability ratios was explained by the theory developed by Derjaguin, Landau, Verwey, and Overbeek (DLVO) for charged colloids suspended in an electrolyte solution.<sup>[23,24,71]</sup> This theory states that the overall interparticle force is the sum of the repulsive electrical double layer and the attractive van der Waals forces. The first one decreases with increasing ionic strength due to charge screening by the dissolved ions and vanishes at high salt concentration. The latter one is always present, but becomes predominant once the repulsive forces weaken close to the CCC. After the CCC, only the van der Waals forces are present and the aggregation is entirely controlled by the diffusion of the particles, which can also lead to a significant increase in the suspension viscosity.<sup>[77]</sup> Transmission electron microscopy (TEM) and atomic force microscopy (AFM) images taken in dried stage or in suspensions, respectively, revealed that LDH particles prefer a face-to-face orientation in the aggregates regardless of the type of ions (Figure 3).<sup>[73,78]</sup>

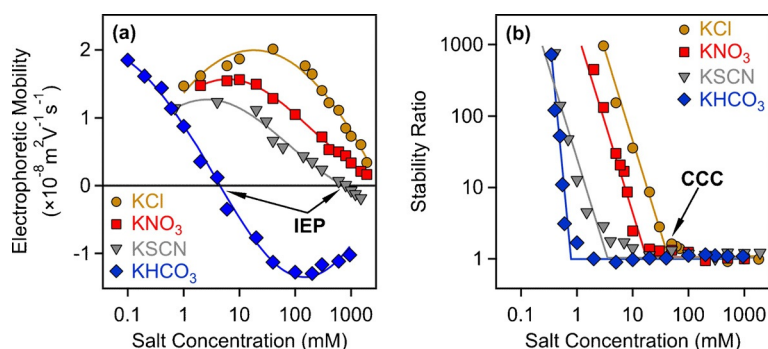


**Figure 2.** Electrophoretic mobility (a) and stability ratio (b) values for Mg/Al- $\text{NO}_3$ -LDH particles in various monovalent salt solutions at different concentrations and at pH 9. In (b), stability ratios close to one indicate rapid particle aggregation, whereas higher values refer to more stable systems. The lines are just to guide the eyes. Reproduced from Ref. [73] with permission from The Royal Society of Chemistry.



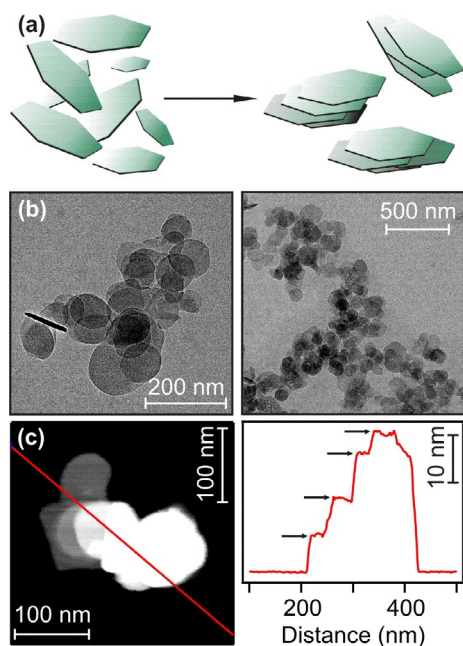


**Figure 3.** Schematic representation of the aggregation of LDH platelets (a). TEM (b) and AFM (c) images of Mg/Al-NO<sub>3</sub>-LDH particles aggregated in monovalent salt solutions at a concentration above the CCC. In (c), the height profile of the cluster along the red line in the AFM image is also shown. Reprinted with permission from Ref. [72]. Copyright 2016 American Chemical Society.

Ion-specific adsorption on the Mg/Al-NO<sub>3</sub>-LDH platelets led to different CCCs in the presence of KCl, KNO<sub>3</sub>, KSCN, and KHCO<sub>3</sub> salts (Figure 2b).<sup>[73]</sup> The CCCs decreased in the order Cl<sup>-</sup> > NO<sub>3</sub><sup>-</sup> > SCN<sup>-</sup> > HCO<sub>3</sub><sup>-</sup>, in the same way as the electrophoretic mobilities at the same concentration (Figure 2a). Such a sequence agrees only partially with the indirect Hofmeister series suggested for aggregation of positively charged, hydrophobic particles in monovalent salt solutions.<sup>[79–81]</sup> Accordingly, significant amounts of the poorly hydrated SCN<sup>-</sup> ions adsorb on the particle surface and, hence, the surface charge decreases, giving rise to weaker repulsive forces and to a lower CCC. Conversely, the well-hydrated Cl<sup>-</sup> anions adsorb only weakly and destabilize the suspension at the highest CCC. For the HCO<sub>3</sub><sup>-</sup>, the classical Hofmeister series predicts the highest CCC, however, the lowest one was measured. This variance is due to the enormously high affinity of the HCO<sub>3</sub><sup>-</sup> to the Mg/Al-NO<sub>3</sub>-LDH surface, as discussed above.

In addition, CCCs were determined by visual inspection during test tube experiments with another Mg/Al-NO<sub>3</sub>-LDH in the presence of different monovalent salts.<sup>[74]</sup> The CCCs decreased in the order Cl<sup>-</sup> > Br<sup>-</sup> > SCN<sup>-</sup> in agreement with the indirect Hofmeister series.

To sum up, tendencies in charging and aggregation of positively charged LDH particles in the presence of different monovalent salts usually follow the order described by the indirect Hofmeister series, with the exception of the HCO<sub>3</sub><sup>-</sup>. This anion shows great affinity and adsorbs strongly to LDH surfaces, leading to charge reversal of the particles. The observed dependence of the CCCs on the surface charge densities was re-

ported to be in excellent agreement with the ones suggested by the DLVO theory.<sup>[73]</sup> On the basis of these findings, one can conclude that adsorption of monovalent counterions reduces the surface charge and weakens the repulsive interaction, however, the aggregation is still governed by DLVO-type forces.

### Stability in the Presence of Multivalent Ions

Adsorption of di-, tri-, and tetravalent anions on LDH particles results in charge reversal, as shown in electrophoretic experiments performed in aqueous LDH suspensions in the presence of CO<sub>3</sub><sup>2-</sup>,<sup>[70,74,75]</sup> CrO<sub>4</sub><sup>2-</sup>,<sup>[82]</sup> SO<sub>4</sub><sup>2-</sup>,<sup>[73,74]</sup> HAsO<sub>4</sub><sup>2-</sup>,<sup>[73,82]</sup> HPO<sub>4</sub><sup>2-</sup>,<sup>[73,74]</sup> Fe(CN)<sub>6</sub><sup>3-</sup>,<sup>[73]</sup> Fe(CN)<sub>6</sub><sup>4-</sup>,<sup>[73]</sup> and citrate<sup>[75]</sup> ions. The extent of the charge inversion can be different depending on the composition and on the surface charge density of the particles as well as on the physicochemical properties of the multivalent ions. In spite of the similar solution speciation of the HPO<sub>4</sub><sup>2-</sup> and HAsO<sub>4</sub><sup>2-</sup> ions, the latter ones adsorb weaker on the Mg/Al-NO<sub>3</sub>-LDH, Mg/Al-Cl-LDH, and Mg/Al-CO<sub>3</sub>-LDH platelets than the HPO<sub>4</sub><sup>2-</sup> anions, as revealed by comparative adsorption studies<sup>[83]</sup> and electrophoretic mobility measurements.<sup>[73]</sup> Such a difference may originate from specific interactions between the anions and the particles (for example, hydrogen bonding or anion coordination to surface metal ions), however, no unambiguous evidence has been reported yet. In addition, it is difficult to distinguish the intercalated anions from the ones adsorbed on the outer surface of the particles. Intercalation of Fe(CN)<sub>6</sub><sup>3-</sup> ions between the lamellae of Mg/Al-Cl-LDH was reported,<sup>[84]</sup> but direct evidence for such a process was not found for Mg/Al-NO<sub>3</sub>-LDH platelets.<sup>[73]</sup> It is clearly difficult to directly compare these results owing to the different experimental conditions (for example, pH, composition of LDH, concentration of salt and particles), which certainly affect the intercalation process.

Let us now discuss the electrophoretic mobilities determined with Mg/Al-NO<sub>3</sub>-LDH in KCl, K<sub>2</sub>SO<sub>4</sub>, and K<sub>3</sub>Fe(CN)<sub>6</sub> solutions (Figure 4a).<sup>[73]</sup> For KCl, the mobilities pass through a maximum owing to the electrokinetic effect<sup>[85]</sup> and charge screening results in a continuous decrease at higher concentrations. Charge reversal occurs with di- and trivalent anions owing to their adsorption and the position of the IEP is shifted towards lower salt concentrations. Such a shift indicates an increase in the counterion affinity to the surface with increasing valence. The mobilities increase at high concentration owing to the screening effect of the counterions on the negatively charged particles. Note that the counterions are K<sup>+</sup> in this regime. Comparing the magnitude of the mobilities around the 30 mM salt level, one can realize that the extent of charge reversal increases with the valence, that is, anions of higher valence induce higher negative charge on the Mg/Al-NO<sub>3</sub>-LDH.

Figure 4b shows the corresponding stability ratio data determined by DLS in the same systems.<sup>[73]</sup> The effect of KCl has already been discussed. A similar shape of the stability curve was obtained in the K<sub>2</sub>SO<sub>4</sub> system, however, the CCC is markedly shifted towards lower concentration. The first finding indicates the presence of DLVO-type forces. Concerning the lower CCC, the divalent ions reduce the surface charge and the salt

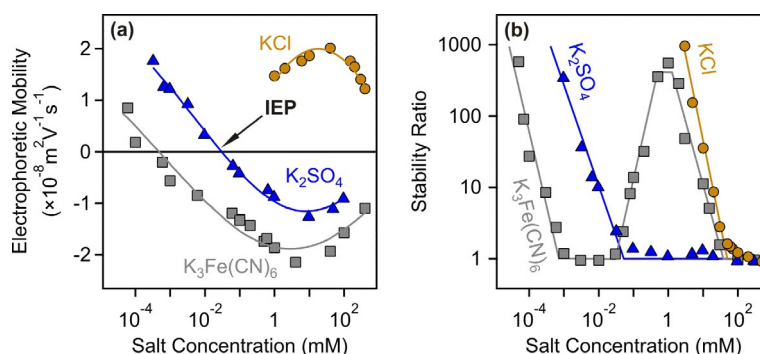


**Figure 4.** Electrophoretic mobility (a) and stability ratio (b) values for Mg/Al-NO<sub>3</sub>-LDH particles measured at different concentrations of KCl, K<sub>2</sub>SO<sub>4</sub>, and K<sub>3</sub>Fe(CN)<sub>6</sub> salts at pH 9. The lines are just to guide the eyes. Reproduced from Ref. [73] with permission from The Royal Society of Chemistry.

amount needed to screen the electrical double layer is smaller and, hence, the CCC is located at lower electrolyte concentrations.

The picture is more complicated for the trivalent case, where three CCC values were obtained. As the DLVO theory would predict, stable suspensions were observed at low salt concentrations, whereas aggregation became fast at higher salt levels and these regimes were separated by the first CCC. However, the stability ratios started to increase at the second CCC. After reaching an intermediate plateau, the aggregation accelerates and fast aggregation occurred again at high salt concentrations, resulting in a third CCC. Similar results have been published for Mg/Al-NO<sub>3</sub>-LDH with HPO<sub>4</sub><sup>2-</sup> and Fe(CN)<sub>6</sub><sup>4-</sup>[73] as well as for other colloidal particles in the presence of multivalent ions.<sup>[86–88]</sup> The first CCC was rationalized by charge neutralization at the IEP, the second one by electrostatic stabilization owing to the charge reversal process, whereas the third CCC at high concentration is the result of the screening effect of the cations on the oppositely charged surface. Such a destabilization–restabilization–destabilization phenomenon was observed only in the case of strong anion adsorption and significant charge reversal, whereas a smaller extent of charge inversion (for example, in the presence of SO<sub>4</sub><sup>2-</sup>) did not induce restabilization in the intermediate concentration regime.

Figure 5 compares the first CCCs reported for Mg/Al-NO<sub>3</sub>-LDH platelets of different sizes in the presence of various mono-, di-, and trivalent anions.<sup>[73,74]</sup> In general, the CCCs decrease with increasing valence. Such a tendency can be qualitatively predicted by the classical Schulze–Hardy rule, which states that the location of the CCCs is inversely proportional to the sixth power of the counterion valence.<sup>[89–91]</sup> Although the effect of multivalent co-ions on the CCC can also be derived from DLVO theory,<sup>[92]</sup> this situation has not been studied for LDHs yet.

For the counterion dependence, the smaller Mg/Al-NO<sub>3</sub>-LDH particles show an excellent agreement with this rule. On the other hand, the CCCs are systematically lower for the bigger ones, probably owing to stronger van der Waals attraction between the particles.<sup>[71]</sup> The scatter in the CCCs for anions with the same valence indicates the ion-specific effects on particle aggregation, as discussed earlier for the monovalent case.

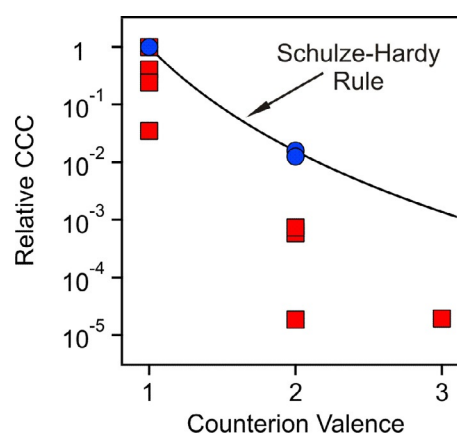


**Figure 5.** Relative CCCs (normalized to the monovalent case) of Mg/Al-NO<sub>3</sub>-LDHs with diameters of 70 nm (circles)<sup>[74]</sup> and of 336 nm (squares)<sup>[73]</sup> as a function of the valence of the counterions. The solid line shows the sixth power decrease suggested by the Schulze–Hardy rule.

Unlike specific ion adsorption, the Schulze–Hardy rule can be derived from DLVO theory, but only for highly charged surfaces.<sup>[93]</sup> However, LDHs are usually weakly charged. Thus, it was suggested that the stronger adsorption with increasing valence neutralizes the surface at lower concentrations and, therefore, smaller amounts of electrolyte are needed to destabilize the sample. In other words, ion adsorption is in principle responsible for the decrease in the CCCs, but the governing interparticle forces are of DLVO origin.<sup>[73,87,94]</sup>

## Stabilization by Polymeric Compounds

Polymeric materials are widely used to tune the colloidal stability of LDHs or other particles in suspensions. Among them, polyelectrolytes have proved to be powerful stabilizing agents owing to their strong affinity for oppositely charged surfaces.<sup>[95]</sup> Their adsorption usually leads to charge reversal at a high extent. Polyelectrolytes are charged polymers containing ionized or ionizable groups. They can be classified in different ways: linear or branched owing to their structure, natural or synthetic based on their origin, as well as strong or weak according to the possible dependence of the ionization of their functional groups on the pH of the medium.

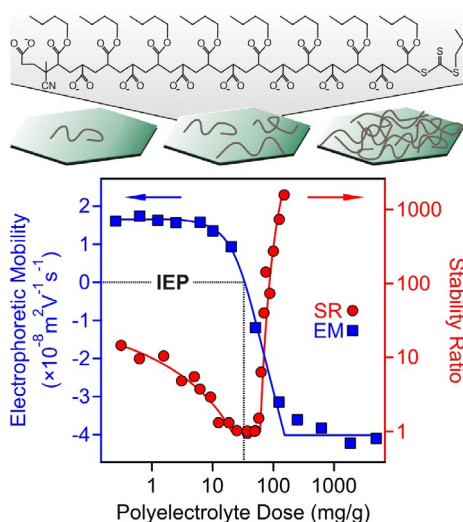


**Figure 6.** Top: Schematic representation of the adsorption of P(AA<sub>7.5</sub>-stat-BA<sub>7.5</sub>)-CTPPA polyelectrolyte (structure is also shown) on Mg/Al-NO<sub>3</sub>-LDH particles. Bottom: Electrophoretic mobility (EM, squares) and stability ratio (SR, circles) of Mg/Al-NO<sub>3</sub>-LDHs as a function of the P(AA<sub>7.5</sub>-stat-BA<sub>7.5</sub>)-CTPPA dose. The units on the x-axis refers to mg of polyelectrolyte per gram of particle. The lines just serve to guide the eyes. Data were taken from Ref. [72].

To assess the colloidal stability of Mg/Al-NO<sub>3</sub>-LDH platelets in the presence of oppositely charged P(AA<sub>7.5</sub>-stat-BA<sub>7.5</sub>)-CTPPA (AA: acrylic acid, BA: butyl acrylate, CTPPA: 4-cyano-4-thiopropylsulfanyl pentanoic acid, see Figure 6 for the chemical structure) copolymer, systematic electrophoretic and DLS experiments have been carried out.<sup>[72]</sup> The aim of this study was to find the optimal experimental conditions where highly stable suspensions form and where LDH-polymer nanocomposites can be synthesized in further polymerization steps. Figure 6 shows some electrophoretic mobility and stability ratio data measured at pH 9 and at 10 mM ionic strength. It was found that the surface charge is progressively neutralized owing to the adsorption of the P(AA<sub>7.5</sub>-stat-BA<sub>7.5</sub>)-CTPPA on the oppositely charged platelets. Well-defined IEP and charge reversal have been reported; however, the latter process resulted in negatively charged particles of much higher charge than in the

case of multivalent ions. The saturation plateau in the mobility curve indicates the limit of polyelectrolyte adsorption, that is, its onset corresponds to the maximum amount of P(AA<sub>7.5</sub>-stat-BA<sub>7.5</sub>)-CTPPA adsorbed on the Mg/Al-NO<sub>3</sub>-LDH.

Time-resolved DLS measurements revealed that the suspensions had limited stability at low doses as indicated by stability ratios around 10. Rapid particle aggregation occurred near the IEP, whereas highly stable samples were formed at high P(AA<sub>7.5</sub>-stat-BA<sub>7.5</sub>)-CTPPA concentrations. Similar to the case of simple salts (Figure 3), the polyelectrolyte-induced aggregation led to face-to-face orientation of the platelets in the clusters. The authors interpreted these results with DLVO theory. Accordingly, the lack of charge around the IEP gave rise to aggregation by van der Waals forces. The samples were stable at low and high doses, where the platelets possessed significant charge, owing to the presence of the repulsive electrical double layer forces.

Qualitatively similar results have been published with Mg/Al-CO<sub>3</sub>-LDH in the presence of heparin, which is a natural biocompatible polyelectrolyte from the glycosaminoglycan family. It has the highest negative line charge density among the known biological molecules<sup>[65]</sup> and it is extensively used as a stabilizer for drug or gene carrier LDHs.<sup>[96]</sup> Therefore, the effect of adsorption on particle aggregation is extremely important to prevent the formation of LDH clusters in living systems. In addition, experimental<sup>[97]</sup> and theoretical<sup>[98]</sup> studies pointed out that low molecular weight heparin can be intercalated between the Mg/Al-CO<sub>3</sub>-LDH and Mg/Al-Cl-LDH layers and such nanocomposites were used as efficient anti-restenotic drugs for clinical applications.<sup>[99]</sup> Similar to the previously discussed P(AA<sub>7.5</sub>-stat-BA<sub>7.5</sub>)-CTPPA system, charge neutralization and reversal as well as face-to-face aggregation of the platelets have been reported with Mg/Al-CO<sub>3</sub>-LDH particles in the presence of heparin, however, intercalation was not unambiguously confirmed.

To compare the colloidal stability of two bare and two polyelectrolyte-coated (with P(AA<sub>7.5</sub>-stat-BA<sub>7.5</sub>)-CTPPA and heparin) LDHs, electrophoretic mobilities (Figure 7a) and stability ratios (Figure 7b) are presented over a wide range of ionic strengths adjusted by monovalent salts. In the coating process, doses at

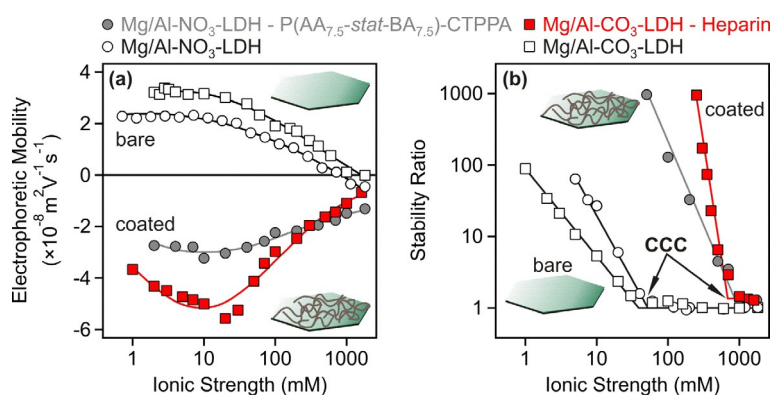


**Figure 7.** Electrophoretic mobility (a) and stability ratio (b) values of bare (empty symbols) and polyelectrolyte-coated (filled symbols) particles (Mg/Al-NO<sub>3</sub>-LDH: circles, Mg/Al-CO<sub>3</sub>-LDH: squares) as a function of the ionic strength. The solid lines serve only to guide the eyes. The Mg/Al-CO<sub>3</sub>-LDH data were taken from Ref. [65].



the adsorption saturation limit were applied, therefore, highly negative mobilities were measured for both P(AA<sub>7.5</sub>-stat-BA<sub>7.5</sub>)-CTPPA and heparin covered Mg/Al-NO<sub>3</sub>-LDH and Mg/Al-CO<sub>3</sub>-LDH, respectively. The bare particles were positively charged and the magnitude of the mobilities decreased with the ionic strength owing to charge screening by the salt. The main advantage of such coating is best illustrated by the stability curves, where much higher CCCs were observed for the polyelectrolyte covered platelets than for the bare ones. It was assumed that this enormous stabilization is a mutual effect of DLVO-type electrostatic and steric repulsion.<sup>[65]</sup> Although small differences can be observed owing to system specificity, the overall behavior of these LDHs in the presence of P(AA<sub>7.5</sub>-stat-BA<sub>7.5</sub>)-CTPPA and heparin polyelectrolytes were found to be analogous.

Similar charge neutralization and charge reversal have been published with other systems containing Mg/Al-CO<sub>3</sub>-LDH and Mg/Al-Cl-LDH particles together with poly(acrylic acid) (PAA).<sup>[75]</sup> The locations of the IEPs were almost the same regardless of the composition of the platelets. In addition, highly stable Mg/Al-Cl-LDH colloids have been synthesized in the presence of negatively charged PAA-*b*-PAM (AM: acryl amide) hydrophilic block copolymers.<sup>[100]</sup> The particles were prepared directly in the system through the formation of a polyelectrolyte-metal ion hybrid micelle and the Mg/Al-Cl-LDH size was tuned by changing the AA-to-metal ion ratio in the reaction mixture. The obtained composite materials were recommended for drug or gene delivery applications owing to their high resistance to aggregation.

To achieve such resistance and high stability for carrier LDHs, significant effort has been made to find other suitable stabilizers. The main requirements include biocompatibility, strong affinity to the surface, and enhanced cellular uptake of the coated particles. The effect of serum albumin adsorption on colloidal stability of drug-intercalated LDH platelets has been extensively investigated. In a recent contribution, Mg/Al-Cl-LDH was synthesized by the co-precipitation method and coated with bovine serum albumin (BSA).<sup>[5]</sup> BSA is a negatively charged protein and an animal variant of serum albumin, which is the most abundant protein in blood plasma. BSA adsorption on Mg/Al-Cl-LDH resulted in charge reversal. The colloidal stability of BSA-modified platelets was tested in phosphate buffer saline and in cell culture medium. It was found that several factors (for example, sequence of reagent addition, size and type of interlayer anion) influence the colloidal stability, however, particles can be prevented from aggregation by choosing a sufficient pre-coating strategy. In addition, such coating also enhanced the cellular uptake of the Mg/Al-Cl-LDH. In a follow-up article from the same research group, the particle stability was further improved by crosslinking the adsorbed BSA molecules with glutaraldehyde.<sup>[101]</sup> The crosslinking of BSA on the Mg/Al-Cl-LDH surface led to excellent redispersibility and affected neither the cytotoxicity nor the cellular uptake.

Charging and aggregation of Mg/Al-Cl-LDH, Mg/Al-CO<sub>3</sub>-LDH, and Mg/Al-DS-LDH (DS: dodecylsulfate) platelets were investigated in simulated biological fluids at high ionic strength and

in the presence of BSA.<sup>[66]</sup> DLS and zeta potential analyses explicitly confirmed the formation of a BSA corona on the particles owing to the strong adsorption of the protein, which led to the typical charge reversal of the positively charged LDHs. The build-up of the interfacial BSA layer improved the colloidal stability owing to steric repulsion and prevented the platelets from dissolution at lower pH, where the bare particles are chemically not stable. It was also found that the interlayer anions strongly influenced these properties and the use of Mg/Al-Cl-LDH and Mg/Al-CO<sub>3</sub>-LDH as drug carriers was recommended rather than Mg/Al-DS-LDH.

Alginate has also been used to stabilize Mg/Al-NO<sub>3</sub>-LDH suspensions to produce a matrix for membrane preparation purposes.<sup>[102]</sup> This macromolecule is a polysaccharide with numerous hydroxyl and carboxyl groups in its chain, which make alginate a negatively charged polyelectrolyte after deprotonation at sufficiently high pH. Mg/Al-NO<sub>3</sub>-LDH delaminated in formamide was mixed with alginate and the solvent was eliminated by washing thoroughly with water. Alginate adsorption on the platelets resulted in highly stable colloids and prevented the restacking of the unilamellar nanosheets, which occurred in the absence of the polyelectrolyte. The coated Mg/Al-NO<sub>3</sub>-LDH was easily redispersed after drying and the composite showed excellent thermal stability compared with the pure alginate.

We have reviewed so far the effects of oppositely charged polyelectrolytes on the colloidal stability of LDHs, nevertheless, charging and aggregation have also been investigated in the presence of neutral polymers.<sup>[103]</sup> Significant adsorption of non-charged polyethylene oxide-polypropylene oxide-polyethylene oxide block copolymer (EPE1100) was reported on the outer surface of Mg/Al-Cl-LDH. The polymer molecules formed an aggregated structure upon adsorption, which also changed the particle morphology. Solution depletion experiments showed that the surface saturated around the critical micelle concentration of the EPE1100 owing to the competition between surface aggregation and micelle formation processes. The adsorbed polymer layer shielded the surface charge, that is, the zeta potential, which was highly positive for the bare Mg/Al-Cl-LDH, continuously decreased with the polymer dose. Stable suspensions were obtained at sufficiently high EPE1100 dose even at high concentrations of an indifferent electrolyte where the bare particles rapidly aggregated. The authors inferred that hydration and steric repulsive forces were responsible for the improved particle stability.

In addition, surface charge properties of Mg/Al-Cl-LDH in the presence of cationic starch have also been studied.<sup>[104]</sup> Starch is a polysaccharide, the positive charges are generated by its chemical modification with quaternary amino groups. One would expect for this situation that adsorption is prevented by electrostatic repulsion between the particles and the polymers of the same sign of charge. However, a low-affinity Langmuir-type isotherm is obtained from batch experiments, which clearly indicated polyelectrolyte adsorption on the Mg/Al-Cl-LDH. Such an adsorption process did not change the zeta potential significantly and took place on the outer surface of the platelets, that is, starch intercalation into the lamellar structure



was not observed. It was assumed that the driving forces, which induced the adsorption, were hydrogen bonding between the surface hydroxyl groups and the polyelectrolyte as well as the entropic gain resulting from the release of solvent molecules upon adsorption. Addition of a monovalent electrolyte increased the adsorbed amount owing to charge screening; this effect was more pronounced with multivalent metal cations owing to the formation of negatively charged metal-hydroxo complexes, which can act as a bridge between the Mg/Al-Cl-LDH and the starch. A similar tendency in the adsorbed amount was documented for other systems containing multivalent ions, polyelectrolytes, and surfaces of the same sign of charge.<sup>[105]</sup> In addition, an increase in the pH or temperature also enhanced starch adsorption on the platelets. No aggregation experiments were carried out to assess the colloidal stability of the suspensions in this case.

## Summary and Outlook

In the present review, we have summarized the behavior of various types of LDH suspensions in the presence of mono- and multivalent salts as well as polymeric compounds. Results obtained from different experimental techniques were compared to make generic conclusions on charging and aggregation of LDH particles in these complex systems.

Monovalent anions adsorb on the positively charged particle surface to different extents, which can be classified by the indirect Hofmeister series of the ions. Deviation from this sequence is reported only for the  $\text{HCO}_3^-$  ions owing to their high affinity for LDH materials. The presence of DLVO-type interparticle forces were suggested, that is, slow and fast aggregation regimes were separated by well-defined CCCs. Ion adsorption modified the surface charge density, however, aggregation was still governed by repulsive double layer and attractive van der Waals forces. To control the suspension stability, such ion-specific effects have to be taken into account once LDHs are suspended in aqueous monovalent salt solutions.

Multivalent anions show high affinity for the LDH surfaces, leading to charge neutralization and to charge reversal at sufficiently high salt concentrations. The latter phenomenon is more pronounced on increasing the valence of anions and results in platelets of significant negative charge. Charge neutralization led to rapid particle aggregation at the CCC owing to the lack of repulsive double layer forces, whereas the LDHs of reversed charge were stable in the presence of tri- and tetravalent anions at intermediate concentrations. The CCCs decreased with the valence in good agreement with the Schulze-Hardy rule. On the basis of this information, efficient LDH-based ion-exchange systems can be designed for environmental applications.

Oppositely charged synthetic and natural polyelectrolytes are excellent stabilizing agents for LDHs, however, controlled aggregation can also be achieved by adjusting their dose in the suspensions. They strongly adsorb on the surface, giving rise to charge neutralization at intermediate and to charge reversal at high doses. Unstable suspensions were reported near the charge neutralization point, whereas highly stable suspen-

sions, in which the LDH platelets were stabilized by electrostatic and steric repulsions, were obtained once the particle surface was fully coated with the polyelectrolytes. In addition, neutral polymers can also stabilize LDH suspensions and positively charged polyelectrolytes are able to adsorb on the platelets of the same sign of charge. Highly stable LDH-polymer systems have been reported in numerous cases even at high ionic strengths where the bare particles rapidly aggregate. The enormous stabilizing effect of the polymeric materials has been utilized several times in delivery processes where it is essential to prevent the drug- or gene-intercalated particles from aggregation in biological fluids such as in blood. In addition, the negatively charged LDHs obtained as a result of the charge reversal process were used to prepare composite materials with other positively charged particles.

In spite of the good number of papers released on this topic, we are still not at the level of understanding nor of predicting the suspension behavior only from the composition, that is, the type of LDH and aggregating agents, of the systems. To further clarify the picture, several unclear issues have to be addressed in future investigations. For instance, only a limited number of quantitative data (for example, surface charge density, adsorption isotherm, and CCC) are available in the literature, where colloidal stability was only characterized qualitatively in the majority of the published articles. This point is especially important in designing delivery systems where the dose of the stabilizing polyelectrolytes has to be unambiguously known with good precision.

Although the origin of the interparticle forces was suggested in certain systems, these suggestions were made mainly on the basis of speculations. This topic should be further pursued by directly measuring the forces, for example, with the atomic force microscope (AFM)-based colloidal probe technique between a flat LDH surface and a LDH-modified tip. As discussed above, several articles have been published with LDHs in the presence of oppositely charged mono- or multivalent ions and polyelectrolytes; however, there is a lack of investigations dealing with co-ions. To assess the effect of organic and inorganic cations as well as positively charged polyelectrolytes on colloidal stability, determination of aggregation rates and adsorption isotherms is necessary in such systems.

On the basis of the results obtained in the binary (for example, LDH-polyelectrolyte) systems, promising stabilizing agents were recommended for LDHs; however, no studies on aggregation and charging have been performed yet in more complex fluids such as in blood plasma or in others where LDHs are present in multicomponent suspensions. These systems are especially relevant for the synthesis of composite materials where heteroaggregation between LDHs and other novel nanoparticles (for example, cationic clays, titanate, or nanometals) takes place in the preparation process and determines the material properties such as porosity and grain boundary. Such heteroaggregation has not been investigated yet in detail. In addition, theoretical studies on the effect of surface roughness and hydrophobicity of LDHs on the ion adsorption and related interparticle forces would be especially useful to interpret particle aggregation in a more quantitative fashion.

Hopefully these issues will be addressed in the future by combining experimental and theoretical techniques. The results of such investigations should definitely lead to a more detailed picture of the predominating interactions involved in LDH aggregation processes. With this knowledge in our hands, reliable predictive tools could be developed and used to design optimal LDH systems for the processes in question.

## Acknowledgments

Financial support from the Swiss National Science Foundation (150162), Swiss Secretariat for Education, Research and Innovation (C15.0024), COST Action (CM1303), and the University of Geneva are gratefully acknowledged. We thank Vanessa Prevot, Mónika Sipiczki-Ádok, Zhi Ping Xu, Sandwip Dey, István Pálinkó, Michal Borkovec, and Pál Sipos for fruitful discussions.

**Keywords:** aggregation · layered double hydroxides · multivalent ions · polyelectrolytes · surface charge

- [1] P. G. de Gennes, *Nature* **2001**, *412*, 385–385.
- [2] F. Tiarks, T. Frechen, S. Kirsch, J. Leuninger, M. Melan, A. Pfau, F. Richter, B. Schuler, C. L. Zhao, *Prog. Org. Coat.* **2003**, *48*, 140–152.
- [3] B. Bolto, J. Gregory, *Water Res.* **2007**, *41*, 2301–2324.
- [4] M. S. Nasser, F. A. Twaiq, S. A. Onaizi, *Sep. Purif. Technol.* **2013**, *103*, 43–52.
- [5] Z. Gu, H. L. Zuo, L. Li, A. H. Wu, Z. P. Xu, *J. Mater. Chem. B* **2015**, *3*, 3331–3339.
- [6] P. Saint-Cricq, S. Deshayes, J. I. Zink, A. M. Kasko, *Nanoscale* **2015**, *7*, 13168–13172.
- [7] P. Hervés, M. Perez-Lorenzo, L. M. Liz-Marzan, J. Dzubiella, Y. Lu, M. Bal-lauff, *Chem. Soc. Rev.* **2012**, *41*, 5577–5587.
- [8] B. Delalat, V. C. Sheppard, S. Rasi Ghaemi, S. Rao, C. A. Prestidge, G. McPhee, M. L. Rogers, J. F. Donoghue, V. Pillay, T. G. Johns, N. Kroger, N. H. Voelcker, *Nat. Commun.* **2015**, *6*, 8791.
- [9] K. A. Huynh, K. L. Chen, *Environ. Sci. Technol.* **2011**, *45*, 5564–5571.
- [10] B. Hu, X. Cao, P. Zhang, *ChemPlusChem* **2013**, *78*, 506–514.
- [11] I. Biondi, V. Laporte, P. J. Dyson, *ChemPlusChem* **2012**, *77*, 721–726.
- [12] A. Zacccone, H. Wu, M. Lattuada, M. Morbidelli, *J. Phys. Chem. B* **2008**, *112*, 1976–1986.
- [13] X. M. Zhu, T. G. Mason, *J. Colloid Interface Sci.* **2014**, *435*, 67–74.
- [14] T. López-León, J. L. Ortega-Vinuesa, D. Bastos-Gonzalez, *ChemPhys-Chem* **2012**, *13*, 2382–2391.
- [15] J. Ramos, J. Forcada, R. Hidalgo-Alvarez, *Chem. Rev.* **2014**, *114*, 367–428.
- [16] Y. Adachi, L. L. Feng, M. Kobayashi, *Colloids Surf. A* **2015**, *471*, 38–44.
- [17] J. Smith, G. B. Webber, G. G. Warr, R. Atkin, *Langmuir* **2014**, *30*, 1506–1513.
- [18] M. Schudel, S. H. Behrens, H. Holthoff, R. Kretschmar, M. Borkovec, *J. Colloid Interface Sci.* **1997**, *196*, 241–253.
- [19] T. Szabó, E. Tombacz, E. Illes, I. Dekany, *Carbon* **2006**, *44*, 537–545.
- [20] E. Horváth, L. Grebikova, P. Maroni, T. Szabo, A. Magrez, L. Forro, I. Szilagy, *ChemPlusChem* **2014**, *79*, 592–600.
- [21] L. Avadiar, Y. K. Leong, *Colloid Polym. Sci.* **2011**, *289*, 237–245.
- [22] Z. H. Lin, P. Roy, Z. Y. Shih, C. M. Ou, H. T. Chang, *ChemPlusChem* **2013**, *78*, 302–309.
- [23] M. Elimelech, J. Gregory, X. Jia, R. A. Williams, *Particle Deposition and Aggregation: Measurement, Modeling, and Simulation*, Butterworth-Heinemann Ltd., Oxford, **1995**.
- [24] W. B. Russel, D. A. Saville, W. R. Schowalter, *Colloidal Dispersions*, Cambridge University Press, Cambridge, **1989**.
- [25] C. Forano, U. Costantino, V. Prevot, C. Taviot Gueho, in *Handbook of Clay Science Vol. 5A* (Eds.: F. Bergaya, G. Lagaly), Elsevier, Amsterdam, **2013**, pp. 745–782.
- [26] V. Rives, *Layered Double Hydroxides: Present and Future*, Nova Science Publishers, Inc., New York, **2001**.
- [27] Q. Wang, D. O'Hare, *Chem. Rev.* **2012**, *112*, 4124–4155.
- [28] P. J. Sideris, U. G. Nielsen, Z. H. Gan, C. P. Grey, *Science* **2008**, *321*, 113–117.
- [29] P. Nalawade, B. Aware, V. J. Kadam, R. S. Hirlekar, *J. Sci. Ind. Res.* **2009**, *68*, 267–272.
- [30] D. G. Evans, R. C. T. Slade in *Layered Double Hydroxides, Vol. 119* (Eds.: X. Duan, D. G. Evans), Springer, Berlin, **2006**, pp. 1–87.
- [31] V. Bugris, H. Haspel, A. Kukovecz, Z. Konya, M. Sipiczki, P. Sipos, I. Palinko, *Langmuir* **2013**, *29*, 13315–13321.
- [32] S. J. Palmer, R. L. Frost, T. Nguyen, *Coord. Chem. Rev.* **2009**, *253*, 250–267.
- [33] A. M. Scheidegger, E. Wieland, A. C. Scheinost, R. Dahn, P. Spieler, *Environ. Sci. Technol.* **2000**, *34*, 4545–4548.
- [34] X. D. Sun, E. Neuperger, S. K. Dey, *J. Colloid Interface Sci.* **2015**, *459*, 264–272.
- [35] J. He, M. Wei, B. Li, Y. Kang, D. G. Evans, X. Duan in *Layered Double Hydroxides, Vol. 119* (Eds.: X. Duan, D. G. Evans), Springer, Berlin, **2006**, pp. 89–119.
- [36] Z. Gu, J. J. Atherton, Z. P. Xu, *Chem. Commun.* **2015**, *51*, 3024–3036.
- [37] V. Rives, M. del Arco, C. Martin, *Appl. Clay Sci.* **2014**, *88–89*, 239–269.
- [38] S. Omwoma, W. Chen, R. Tsunashima, Y. F. Song, *Coord. Chem. Rev.* **2014**, *258*, 58–71.
- [39] F. Leroux, C. Taviot-Gueho, *J. Mater. Chem.* **2005**, *15*, 3628–3642.
- [40] S. P. Newman, W. Jones, *New J. Chem.* **1998**, *22*, 105–115.
- [41] A. Deák, L. Janovak, S. P. Tallosy, T. Bitó, D. Sebok, N. Buzas, I. Palinko, I. Dekany, *Langmuir* **2015**, *31*, 2019–2027.
- [42] C. P. Chen, R. Felton, J. C. Buffet, D. O'Hare, *Chem. Commun.* **2015**, *51*, 3462–3465.
- [43] L. Wang, F. S. Xiao, *Green Chem.* **2015**, *17*, 24–39.
- [44] G. L. Fan, F. Li, D. G. Evans, X. Duan, *Chem. Soc. Rev.* **2014**, *43*, 7040–7066.
- [45] D. Tonelli, E. Scavetta, M. Giorgetti, *Anal. Bioanal. Chem.* **2013**, *405*, 603–614.
- [46] H. G. Wei, Y. R. Wang, J. Guo, N. Z. Shen, D. W. Jiang, X. Zhang, X. R. Yan, J. H. Zhu, Q. Wang, L. Shao, H. F. Lin, S. Y. Wei, Z. H. Guo, *J. Mater. Chem. A* **2015**, *3*, 469–480.
- [47] B. Zümreoglu-Karan, A. N. Ay, *Chem. Pap.* **2012**, *66*, 1–10.
- [48] L. L. Fu, G. G. Qi, O. Shekhah, Y. Belmabkhout, L. Estevez, M. Eddaoudi, E. P. Giannelis, *ChemSusChem* **2014**, *7*, 1035–1039.
- [49] V. J. Nagaraj, X. Sun, J. Mehta, M. Martin, T. Ngo, S. K. Dey, *J. Nanotech.* **2015**, *2015*, 350370.
- [50] J. H. Choy, M. Park, J. M. Oh, *Curr. Nanosci.* **2006**, *2*, 275–281.
- [51] G. Varga, A. Kukovecz, Z. Konya, L. Korecz, S. Murath, Z. Csendes, G. Peintler, S. Carlson, P. Sipos, I. Palinko, *J. Catal.* **2016**, *335*, 125–134.
- [52] T. Bujdosó, A. Patzko, Z. Galbacs, I. Dekany, *Appl. Clay Sci.* **2009**, *44*, 75–82.
- [53] M. Sipiczki, D. F. Sranco, G. Szollosi, A. Kukovecz, Z. Konya, P. Sipos, I. Palinko, *Top. Catal.* **2012**, *55*, 858–864.
- [54] F. L. Theiss, S. J. Couperthwaite, G. A. Ayoko, R. L. Frost, *J. Colloid Interface Sci.* **2014**, *417*, 356–368.
- [55] C. Mousty, V. Prevot, *Anal. Bioanal. Chem.* **2013**, *405*, 3513–3523.
- [56] S. He, Z. An, M. Wei, D. G. Evans, X. Duan, *Chem. Commun.* **2013**, *49*, 5912–5920.
- [57] K. Ladewig, Z. P. Xu, G. Q. Lu, *Expert Opin. Drug Delivery* **2009**, *6*, 907–922.
- [58] D. G. Evans, D. A. Xue, *Chem. Commun.* **2006**, 485–496.
- [59] F. Leroux, J. P. Besse, *Chem. Mater.* **2001**, *13*, 3507–3515.
- [60] K. H. Goh, T. T. Lim, Z. Dong, *Water Res.* **2008**, *42*, 1343–1368.
- [61] J. Hong, Z. L. Zhu, H. T. Lu, Y. L. Qiu, *RSC Adv.* **2014**, *4*, 5156–5164.
- [62] G. Choi, O. J. Kwon, Y. Oh, C. O. Yun, J. H. Choy, *Sci. Rep.* **2014**, *51*, 4430.
- [63] C. Del Hoyo, *Appl. Clay Sci.* **2007**, *22*, 103–121.
- [64] Z. P. Xu, Q. H. Zeng, G. Q. Lu, A. B. Yu, *Chem. Eng. Sci.* **2006**, *61*, 1027–1040.
- [65] M. Pavlovic, L. Li, F. Dits, Z. Gu, M. Adok-Sipiczki, I. Szilagy, *RSC Adv.* **2016**, *6*, 16159–16167.
- [66] C. Vasti, D. A. Bedoya, R. Rojas, C. E. Giacomelli, *J. Mater. Chem. B* **2016**, *4*, 2008–2016.

- [67] A. L. Papa, J. Boudon, V. Bellat, A. Loiseau, H. Bisht, F. Sallem, R. Chasagnon, V. Berard, N. Millot, *Dalton Trans.* **2015**, 44, 739–746.
- [68] R. Rojas Delgado, M. Arandigoyen Vidaurre, C. P. De Pauli, M. A. Ulibarri, M. J. Avena, *J. Colloid Interface Sci.* **2004**, 280, 431–441.
- [69] R. Rojas Delgado, C. P. De Pauli, C. B. Carrasco, M. J. Avena, *Appl. Clay Sci.* **2008**, 40, 27–37.
- [70] R. B. Leggat, S. A. Taylor, S. R. Taylor, *Colloids Surf. A* **2002**, 210, 69–81.
- [71] D. F. Evans, H. Wennerstrom, *The Colloidal Domain*, John Wiley, New York, **1999**.
- [72] M. Pavlovic, M. Adok-Sipiczki, C. Nardin, S. Pearson, E. Bourgeat-Lami, V. Prevot, I. Szilagyi, *Langmuir* **2015**, 31, 12609–12617.
- [73] M. Pavlovic, R. Huber, M. Adok-Sipiczki, C. Nardin, I. Szilagyi, *Soft Matter* **2016**, 12, 4024–4033.
- [74] G. Lagaly, O. Mecking, D. Penner, *Colloid Polym. Sci.* **2001**, 279, 1090–1096.
- [75] Z. P. Xu, Y. G. Jin, S. M. Liu, Z. P. Hao, G. Q. Lu, *J. Colloid Interface Sci.* **2008**, 326, 522–529.
- [76] H. Holthoff, S. U. Egelhaaf, M. Borkovec, P. Schurtenberger, H. Sticher, *Langmuir* **1996**, 12, 5541–5549.
- [77] L. Albiston, K. R. Franklin, E. Lee, J. Smeulders, *J. Mater. Chem.* **1996**, 6, 871–877.
- [78] J. A. Gursky, S. D. Blough, C. Luna, C. Gomez, A. N. Luevano, E. A. Gardner, *J. Am. Chem. Soc.* **2006**, 128, 8376–8377.
- [79] T. Oncsik, G. Trefalt, M. Borkovec, I. Szilagyi, *Langmuir* **2015**, 31, 3799–3807.
- [80] N. Schwierz, D. Horinek, R. R. Netz, *Langmuir* **2010**, 26, 7370–7379.
- [81] W. Kunz, J. Henle, B. W. Ninham, *Curr. Opin. Colloid Interface Sci.* **2004**, 9, 19–37.
- [82] M. Jobbágy, A. E. Regazzoni, *J. Colloid Interface Sci.* **2013**, 393, 314–318.
- [83] A. Violante, M. Pucci, V. Cozzolino, J. Zhu, M. Pigna, *J. Colloid Interface Sci.* **2009**, 333, 63–70.
- [84] M. Jobbágy, A. E. Regazzoni, *J. Phys. Chem. B* **2005**, 109, 389–393.
- [85] M. Borkovec, S. H. Behrens, M. Semmler, *Langmuir* **2000**, 16, 5209–5212.
- [86] I. Szilagyi, A. Polomska, D. Citherlet, A. Sadeghpour, M. Borkovec, *J. Colloid Interface Sci.* **2013**, 392, 34–41.
- [87] P. Sinha, I. Szilagyi, F. J. M. Ruiz-Cabello, P. Maroni, M. Borkovec, *J. Phys. Chem. Lett.* **2013**, 4, 648–652.
- [88] I. Szilagyi, A. Sadeghpour, M. Borkovec, *Langmuir* **2012**, 28, 6211–6215.
- [89] J. Lyklema, *J. Colloid Interface Sci.* **2013**, 392, 102–104.
- [90] J. T. G. Overbeek, *Pure Appl. Chem.* **1980**, 52, 1151–1161.
- [91] T. Oncsik, G. Trefalt, Z. Csendes, I. Szilagyi, M. Borkovec, *Langmuir* **2014**, 30, 733–741.
- [92] G. Trefalt, *Phys. Rev. E* **2016**, 93, 032612.
- [93] G. Trefalt, I. Szilagyi, M. Borkovec, *J. Colloid Interface Sci.* **2013**, 406, 111–120.
- [94] F. J. M. Ruiz-Cabello, G. Trefalt, Z. Csendes, P. Sinha, T. Oncsik, I. Szilagyi, P. Maroni, M. Borkovec, *J. Phys. Chem. B* **2013**, 117, 11853–11862.
- [95] I. Szilagyi, G. Trefalt, A. Tiraferri, P. Maroni, M. Borkovec, *Soft Matter* **2014**, 10, 2479–2502.
- [96] L. J. Wang, H. Y. Xing, S. J. Zhang, Q. G. Ren, L. M. Pan, K. Zhang, W. B. Bu, X. P. Zheng, L. P. Zhou, W. J. Peng, Y. Q. Hua, J. L. Shi, *Biomaterials* **2013**, 34, 3390–3401.
- [97] Z. Gu, A. C. Thomas, Z. P. Xu, J. H. Campbell, G. Q. Lu, *Chem. Mater.* **2008**, 20, 3715–3722.
- [98] H. Zhang, Z. P. Xu, G. Q. Lu, S. C. Smith, *J. Phys. Chem. C* **2010**, 114, 12618–12629.
- [99] Z. Gu, B. E. Rolfe, Z. P. Xu, A. C. Thomas, J. H. Campbell, G. Q. M. Lu, *Biomaterials* **2010**, 31, 5455–5462.
- [100] G. Layrac, M. Destarac, C. Gerardin, D. Tichit, *Langmuir* **2014**, 30, 9663–9671.
- [101] H. Zuo, Z. Gu, H. Cooper, Z. P. Xu, *J. Colloid Interface Sci.* **2015**, 459, 10–16.
- [102] H. L. Kang, Y. Shu, Z. Li, B. Guan, S. J. Peng, Y. Huang, R. G. Liu, *Carbohydr. Polym.* **2014**, 100, 158–165.
- [103] X. J. Wang, D. J. Sun, S. Y. Liu, R. Wang, *J. Colloid Interface Sci.* **2005**, 289, 410–418.
- [104] Y. Li, W. G. Hou, W. Q. Zhu, *Colloids Surf. A* **2007**, 303, 166–172.
- [105] A. Tiraferri, P. Maroni, M. Borkovec, *Phys. Chem. Chem. Phys.* **2015**, 17, 10348–10352.

Manuscript received: June 6, 2016


Revised: July 18, 2016

Accepted Article published: July 19, 2016

Final Article published: August 12, 2016

Review

# Effect of Ionic Compounds of Different Valences on the Stability of Titanium Oxide Colloids

Szabolcs Muráth, Szilárd Sáringer, Zoltán Somosi and István Szilágyi \* 

MTA-SZTE Lendület Biocolloids Research Group, Department of Physical Chemistry and Materials Science, University of Szeged, 1 Rerrich Béla tér, H-6720 Szeged, Hungary; muratsz@chem.u-szeged.hu (S.M.); saringer.szilard@chem.u-szeged.hu (S.S.); somosiz@chem.u-szeged.hu (Z.S.)

\* Correspondence: szistvan@chem.u-szeged.hu; Tel.: +36-62-343255

Received: 12 July 2018; Accepted: 12 August 2018; Published: 15 August 2018



**Abstract:** Titanium oxide particles of various morphologies have been prepared for applications of scientific or industrial interest in recent decades. Besides development of novel synthetic routes and solid-state characterization of the obtained particles, colloidal stability of titanium oxide dispersions was the focus of numerous research groups due to the high importance of this topic in applications in heterogeneous systems. The influence of dissolved ionic compounds, including monovalent salts, multivalent ions and polyelectrolytes, on the charging and aggregation behaviour of titanium oxide materials of spherical and elongated structures will be discussed in the present review.

**Keywords:** titanium oxide; colloidal stability; aggregation; surface charge; polyelectrolyte

## 1. Introduction

Titanium oxide is one of the most frequently studied inorganic materials due to the advantageous structural and chemical features utilized in a large number of applications. Recent reviews indicate a widespread contemporary interest in this compound and its derivatives [1–4]. For instance, the high refractive index makes it excellent pigment in white paints [5], where primary particles are homogeneously dispersed in the liquid medium. Biocompatibility is a key property in bioapplications, including delivery of bioactive molecules [6,7], tissue engineering [8], development of biosensors [9], biomimetic [10] and antibacterial materials [11]. Since the discovery of the photoelectric effect in titania [12], enormous effort has been made to develop photocatalytic systems composed of titanium oxide nanostructures or their composites [13–17]. It was also discovered that the shape [18] of the titania particles and the ionic environment [19] influences the photocatalytic activity. Moreover, novel titanium oxide-based substances were applied in solar cells [20], electrode materials [21], supercapacitors [22], inks [23] and electronics [24].

Large number of these applications relies on titanium oxides or their surface modified derivatives dispersed in a liquid medium, most frequently in aqueous solutions. Such dispersions can be directly used for example as delivery agents [6,7] or applied in synthetic processes for preparation of hybrid materials [25–27]. Colloidal stability of the particles is a key issue in photocatalytic applications, where stable dispersions of primary particles are required during the catalytic process, while aggregation, that is, destabilization of the dispersions, can be induced to eliminate the solid material by subsequent sedimentation and filtration [16,28,29]. To tune the stability of the heterogeneous systems, numerous stabilizing or destabilizing agents including simple salts or polymeric compounds have been already applied and comprehensive studies were published to describe the influence of the additives on the colloidal stability of the titanium oxide materials [5,30–33].

The aim of the present contribution is to clarify the charging and aggregation processes in such systems. Accordingly, dispersions containing titanium oxide particles of various shapes and ionic



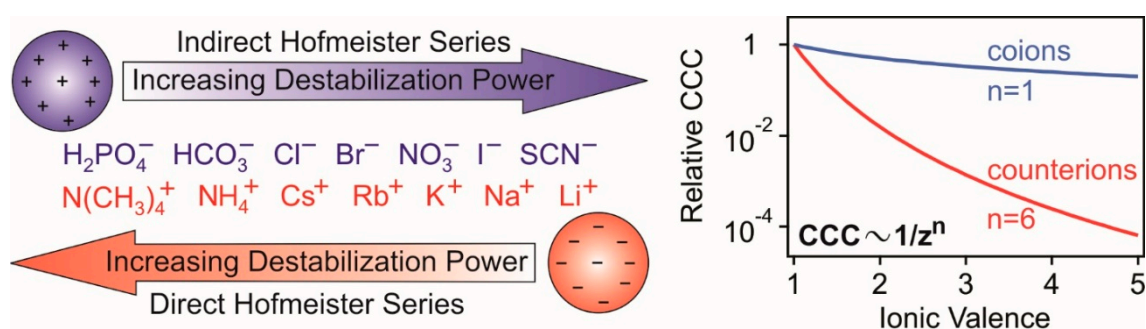
species from monovalent through multivalent ions to polyelectrolytes will be discussed and the relationship between the surface processes and the predominant interparticle forces will be ascertained. The main focus will be made on dispersed particle systems, studies performed with planar surfaces will not be discussed.

## 2. Stability of Titanium Oxide Particles in Electrolyte Solutions

### 2.1. General Considerations

In general, stable particle dispersions refer to homogeneously distributed primary particles in liquid medium, while in unstable dispersions particle aggregation occurs leading to the formation of dimers, trimers and higher ranked aggregates. The colloidal stability of charged particles dispersed in electrolyte solutions can be predicted by the classical theory developed by Derjaguin, Landau, Verwey and Overbeek (DLVO) [34,35]. This model interprets the overall interparticle forces acting between the particles in the presence of dissolved ions as the superposition of the repulsive electrical double layer forces and the attractive van der Waals forces. The first ones weaken with increasing the ionic strength, while the latter ones are always present independently of the solution composition [36]. Therefore, stable dispersions are predicted at low ionic strengths and rapid aggregation of the particles leading to unstable systems occurs at high electrolyte concentrations. These two regimes are typically separated by the critical coagulation concentration (CCC) or in other words by the critical coagulation ionic strength (CCIS). The value of these quantities is identical for monovalent salts, where the coions are of the same sign of charge as the surfaces and the counterions are oppositely charged.

Due to the fact that DLVO considers only the valence and the concentration of the ions in solution, it predicts equal CCC for the same particles dispersed in different monovalent salt solutions. However, large number of experimental literature data shows that the CCC is sensitive to the type or chemical composition of coions and counterions present in the systems [37–41]. Such a deviation from the theoretical prediction was explained by the different affinity of the ions and thus, different extent of adsorption of the surrounding anions and cations to the surfaces. This issue can be addressed by the Hofmeister series of ions (Scheme 1, left), which predicts the destabilization power of a given anion or cation considering the charge and the hydrophobicity of the particle surfaces [42–44].



**Scheme 1.** **Left:** Hofmeister series of anions and cations for hydrophobic colloidal particles. **Right:** representation of the Schulze-Hardy rule for counter and coions with the dependence of the CCC on the ionic valence ( $z$ ).

For multivalent ions, however, DLVO takes the valence of ions into account and predicts a decrease of the CCC with increasing the valence through the Schulze-Hardy rule [45–47]. Moreover, the extent of this decrease is different for coions [48] and counterions [49] (Scheme 1, right) as well as it also depends on the magnitude of the surface charge [50]. Therefore, the ions of higher valences are more effective in destabilization of the colloid dispersions. In the next section, the colloidal stability of titanium oxide particles will be discussed on the basis of these considerations.

## 2.2. Effect of pH on Charging and Aggregation

It is well known that titanium oxide surfaces possess pH dependent charge due to the protonation-deprotonation equilibria of the surface hydroxyl groups [51]. Accordingly, they are positively charged under acidic conditions and negatively charged at higher pH [52]. These regimes are separated by the point of zero charge (PZC), which corresponds to the pH, where the overall charge of the particle is zero. The PZC values of numerous titanium oxide particles were determined with various techniques in the past decades [23,31,53–58] and they were found to be in the range of 4–7 [51]. In addition, adsorption of ionic species may also change the charge and the position of the PZC of the titanium oxide materials [19,59]. To demonstrate this feature, the pH profile of the electrokinetic potentials (equal to zeta potential) of titanate nanowires and titania nanosheets are shown in Figure 1 [56,59].

The surface charge is sensitive for the ionic strength applied due to the screening effect of the ions present in the solution. In general, the magnitude of the surface charge density decreases with increasing the salt level, as pointed out in potentiometric experiments with spherical titania particles [57]. However, this observation is only valid for indifferent electrolytes, that is, adsorption of ions is negligible, which do not change the position of the PZC. The presence of anions or cations with significant affinity towards the surface may induce different changes in the surface charge density and the corresponding surface potential [59].

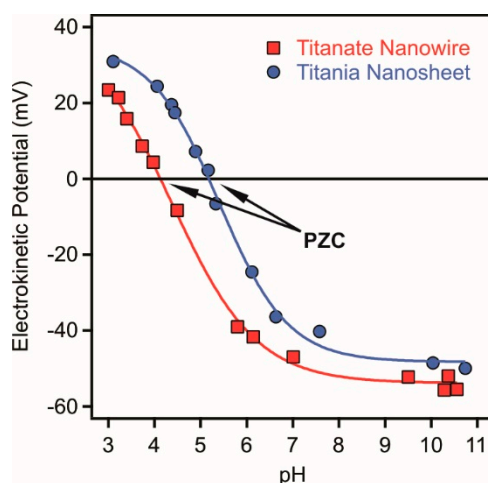


**Figure 1.** Electrokinetic potentials of titanate nanowires (squares, PZC 4.1) and titania nanosheets (circles, PZC 5.2) as a function of the pH at 1 mM ionic strength. The data were taken from References [56,59].

Aggregation of bare titanium oxide particles is usually governed by DLVO-type forces, therefore, the magnitude of the surface potential and the surface charge determines the strength of the repulsive forces originating from the overlapping electrical double layers formed around the particles. Colloidal stability of titania spheres of 200 nm in radius was investigated in time-resolved dynamic light scattering measurements [57], where the stability ratio values were determined to express the rate of aggregation in the dispersions (Figure 2). In the calculation of the stability ratios, the aggregation rates are normalized to the one measured in unstable dispersions, where the aggregation is controlled only by the diffusion of the particles [40,60–63]. Therefore, note that stability ratio values close to one indicate unstable dispersions, while higher values refer to more stable samples. It is clear from the stability ratio versus pH plot that the titania dispersions were stable at low and high pH indicated by large or not even measurable stability ratio values. In the intermediate pH regime, near the PZC, the stability ratios reached a minimum referring to rapid aggregation of the particles and to unstable dispersions.

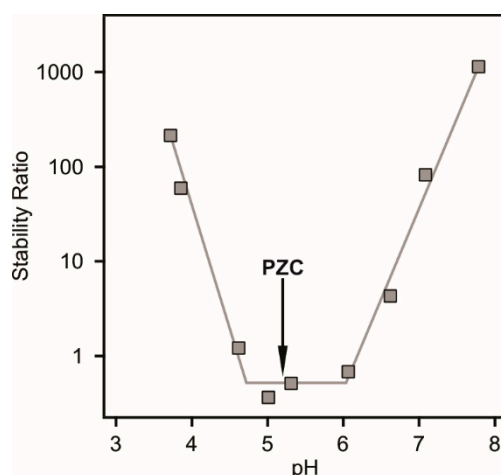


**Figure 2.** Stability ratio data of spherical titania particles measured at different pH at 7.5 mM ionic strength set by KCl. The particles have a PZC of 5.2 indicated with an arrow. Note that stability ratio values of one indicate that the particle aggregation is controlled solely by the diffusion of the particles, that is, each collision leads to dimer formation. Higher values are signals for slower aggregation rates. The data were taken from Reference [57].

An interesting feature in the stability ratio plot is that the values are slightly lower than one in the fast aggregation regime. This acceleration in the aggregation rates most likely originates from the interaction of the surface hydroxyl groups of different protonation stage. Although the overall charge of the particles is close to zero near the PZC, the surface may contain protonated and deprotonated groups, which can induce additional attractive electrostatic forces among the van der Waals interactions.

### 2.3. Colloidal Stability in the Presence of Monovalent Electrolytes

Salt-induced aggregation of titanium oxide materials was investigated by several authors and CCC values between 1–100 mM [7,59,62–66] were determined by various methods. For instance, a colloid stability study performed on spherical titania particles was carried out at different pH in KCl solutions by following particle aggregation with light scattering technique [67]. The position of the CCC varied with the pH due to the different surface charge densities and they were the lowest at pH close to the PZC. Theoretical calculations revealed that the aggregation mechanism can be adequately described by the DLVO theory, however, the roughness of the surface of the titania particles has to be taken into account.

A comprehensive study was carried out to investigate the specific effect of anions and cations on the colloidal stability of titania hydrosols [68]. The absorbance of the dispersions was measured with a spectrophotometer and stability ratios were calculated to determine the CCC. These quantities were then measured at different pH and in the presence of different monovalent anions and cations to order these ions in the Hofmeister series (Scheme 1) [44]. The CCC of titania decreased in the  $\text{Cs}^+ > \text{K}^+ > \text{Na}^+ > \text{Li}^+$  order above the PZC, which is consistent with the prediction by the indirect Hofmeister series for negatively charged hydrophilic particles [69].

Similar sequence was found for surface charge densities of titania particles in the presence of  $\text{K}^+$  and  $\text{Li}^+$  ions indicating that the ion-surface interaction is responsible for the charging and aggregation processes in these systems [70]. However, this sequence was reversed once titania particles were heat treated indicating that the surface became hydrophobic during calcination and the CCC follows the direct Hofmeister series for negatively charged hydrophobic particles. The same order was found for commercial titania particles pointing to the hydrophobic nature of their surfaces [71]. Nevertheless, it was also found that ion specific effects for positively charged titania below the PZC are not significant once the surface underwent calcination [68].

Electrokinetic potentials and stability ratios were determined with titania nanosheets under acidic and alkaline conditions, that is, with negatively and positively charged surfaces, in the presence of various monovalent anions by light scattering methods [59]. Therefore, the anions were applied as counterions below the PZC, which was reported to be 5.2 [31] and as coions above it. As shown in Figure 3 (left column), ion specific effects led to significantly different electrokinetic potentials and stability ratios once the pH was acidic, that is, positively charged nanosheets were present.

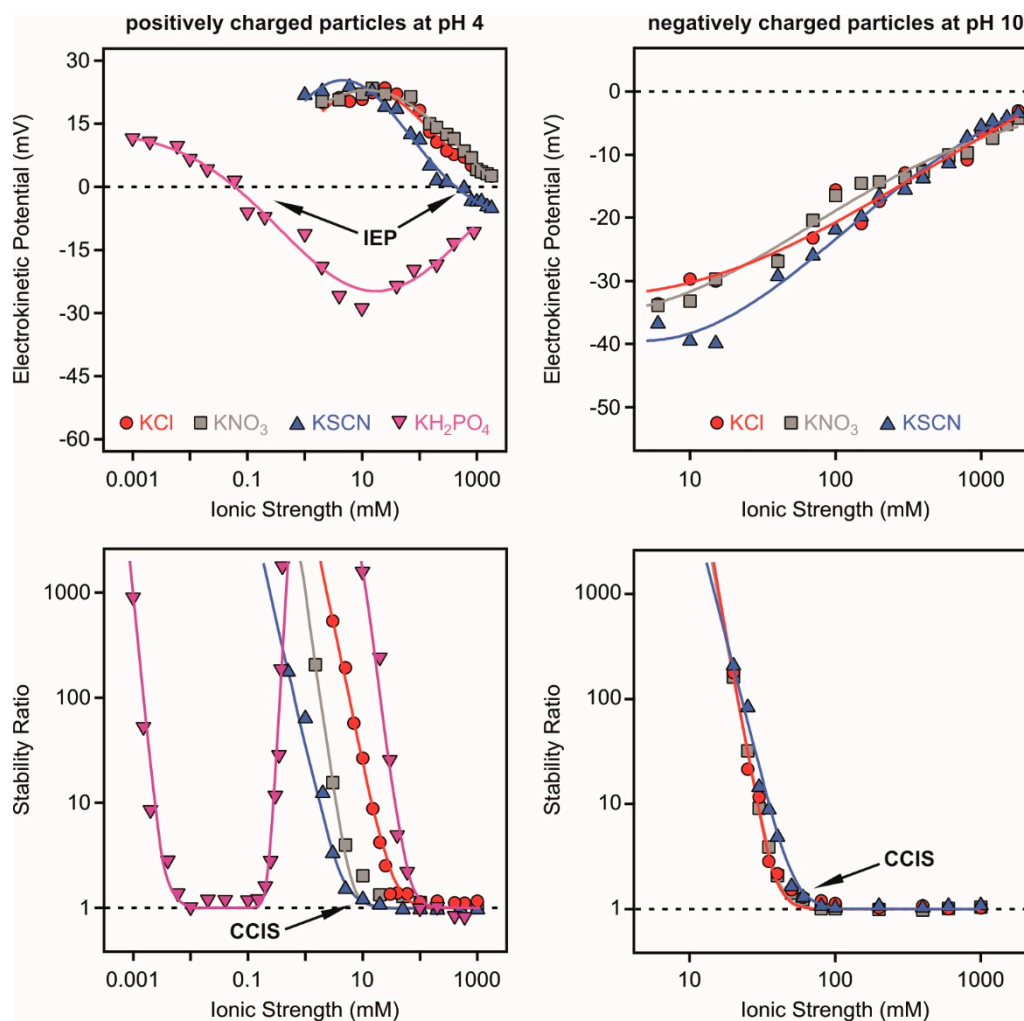


**Figure 3.** Electrokinetic potentials (**top row**) and stability ratios (**bottom row**) of titania nanosheets as a function of the ionic strength set by different monovalent electrolytes below the PZC at pH 4 (**left column**) and above the PZC at pH 10 (**right column**), where the nanosheets are positively or negatively charged, respectively. The particle concentration was 1 mg/L. Reprinted with permission from Reference [59]. Copyright (2017) American Chemical Society.

The affinity of the anions to the oppositely charged surface followed the  $\text{H}_2\text{PO}_4^- > \text{SCN}^- > \text{NO}_3^- > \text{Cl}^-$  order and thus, the charge of the particles increases in the same sequence at the same ionic strength. The adsorption of the  $\text{SCN}^-$  ions led to charge neutralization at the isoelectric point (IEP), which refers to the concentration of the adsorbent necessary to neutralize the surface charge. Further addition of the anions gave rise to slight reversal of the sign of the charge of the nanosheets. The charge reversal was more pronounced for the  $\text{H}_2\text{PO}_4^-$  system and highly charged titania of negative charge were observed at elevated salt concentrations. Such a high extent of charge reversal is rare for systems containing monovalent electrolytes and charged colloids but rather typical for multivalent ions [37]



and polyelectrolytes [72] in the presence of oppositely charged surfaces. This issue will be discussed later in detail.

The corresponding stability ratio values measured in the same systems correlate well with the electrokinetic potential data (Figure 3, left). Accordingly, the CCIS followed the  $\text{H}_2\text{PO}_4^- < \text{SCN}^- < \text{NO}_3^- < \text{Cl}^-$  sequence meaning that the lowest CCIS was found for the strongly adsorbing  $\text{H}_2\text{PO}_4^-$  and the highest for the weakly adsorbing  $\text{Cl}^-$  ions, as indicated by the measured potentials. These results clearly indicated that adsorption of ions led to different surface charge and hence, to different CCIS. The  $\text{SCN}^- < \text{NO}_3^- < \text{Cl}^-$  sequence followed the indirect Hofmeister series for positively charged hydrophobic particles [37,38,40,42,69], however, the position of the  $\text{H}_2\text{PO}_4^-$  is atypical, since its presence should lead to the highest CCIS (Scheme 1). Note that the numerical value of the CCIS and CCC are the same for monovalent salts.

The shape of the stability ratio plot in the case of the  $\text{H}_2\text{PO}_4^-$  ions can be described as follows. The dispersions were stable at low salt levels and turned to be unstable at the CCIS. However, the strong charge reversal process resulted in a high magnitude of the surface charge, giving rise to a restabilization process indicated by high, or not even measurable, stability ratios in the intermediate concentration regime. Such a restabilization phenomenon was due to the strong repulsive electrical double layer forces between the negatively charged nanosheets. The dispersions became unstable again at high ionic strength, since charge screening by the salt constituents occurred.

The specific interaction between phosphate anions of different valences and titania particle surfaces has already been observed in other systems too [73–76]. On the basis of results from experimental (infrared (IR) spectroscopy) and theoretical (efficient density-functional-based tight-binding calculations) methods, it was suggested that a primary chemical bond was established between the metal ions on the surface and the oxygen atom of the phosphate ions and this interaction gives rise to the accumulation of negative charges on the particle surface.

The trend for the negatively charged particles above the PZC is simpler (Figure 3, right). For the  $\text{NO}_3^-$  and  $\text{Cl}^-$  systems, both electrokinetic potentials and stability ratios were the same within the experimental error. In the case of  $\text{SCN}^-$  ions, slight increase in the magnitude of the potentials at the same ionic strength and in the CCIS was observed. This was in agreement with the direct Hofmeister series for negatively charged hydrophobic particles in the presence of monovalent coions. However, the effect of the coions was much weaker than the influence of counterions in the case of positively charged nanosheets and the same anions.

In systems containing titanium oxide particles and monovalent electrolytes, the generic conclusions can be summarized as follows. Regardless of the surface charge and the type of ions, the major interparticle interactions were the repulsive double layer and attractive van der Waals forces. Nevertheless, the different affinity of the counterions led to different charge density of the surfaces and hence, the double layer forces weakened once the counterion adsorption was stronger. Such a decrease in the extent of the repulsive interaction led to a decrease in the CCC or CCIS. The effect of coions is less pronounced. Summarily, specific ion adsorption determines the charging properties of the particles, while the aggregation mechanism and the predominant interparticle forces can be described within the DLVO theory.

#### 2.4. Multivalent Ion-Induced Aggregation

Similar studies were carried out with the same titania nanosheets as discussed above but in the presence of multivalent inorganic anions [59]. Accordingly, electrokinetic potential and stability ratio measurements were performed below and above the PZC, which was 5.2 [31], with positively or negatively charged nanosheets, respectively, in dispersions containing  $\text{H}_2\text{PO}_4^{2-}$ ,  $\text{SO}_4^{2-}$ ,  $\text{Fe}(\text{CN})_6^{3-}$  and  $\text{Fe}(\text{CN})_6^{4-}$  ions. The results are presented in Figure 4.

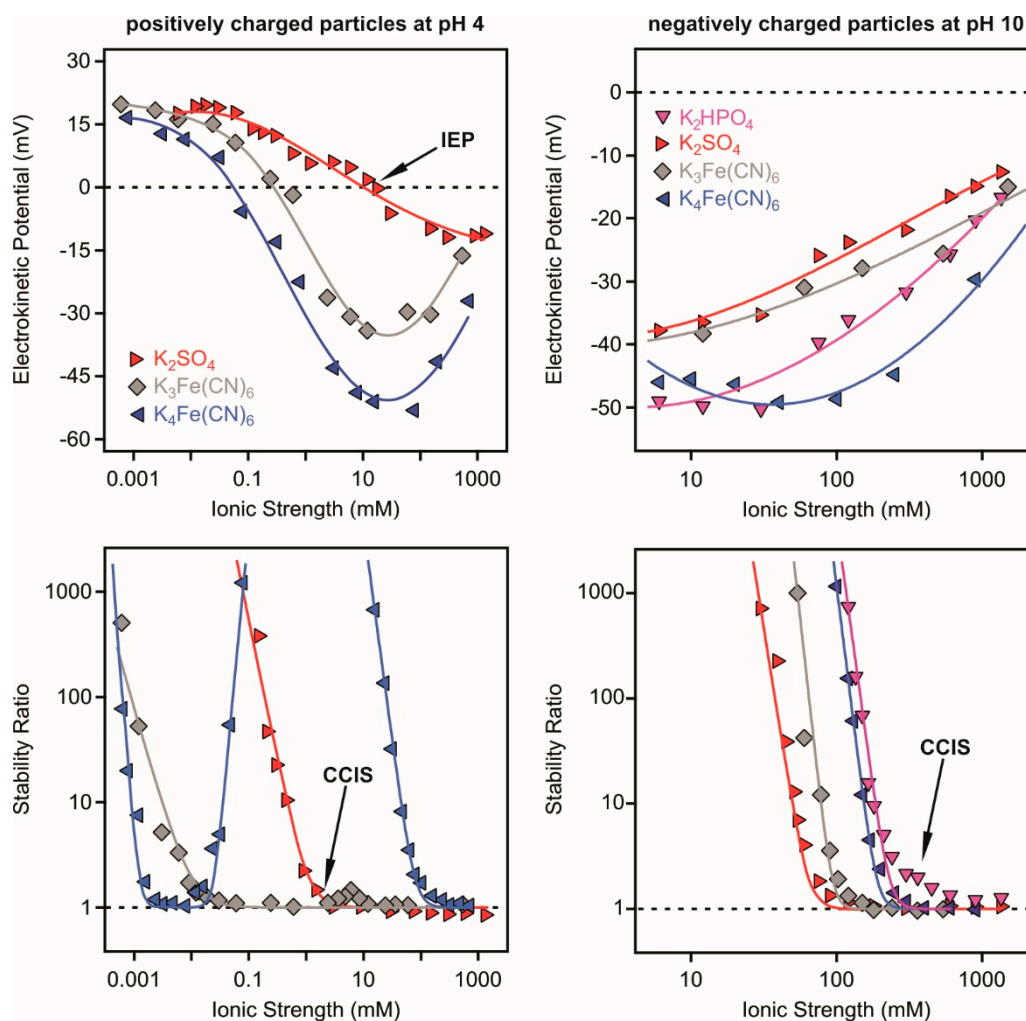


**Figure 4.** Electrokinetic potentials (**top row**) and stability ratios (**bottom row**) of titania nanosheets as a function of the ionic strength set by different multivalent electrolytes below the PZC at pH 4 (**left column**) and above the PZC at pH 10 (**right column**), where the nanosheets were positively or negatively charged, respectively. The concentration of the particles was kept constant at 1 mg/L. Reprinted with permission from Reference [59]. Copyright (2017) American Chemical Society.

For positively charged particles (Figure 4, left), well-defined IEP values indicated the adsorption of the anions on the oppositely charged surface. Such a charge neutralization was followed by charge reversal at higher ionic strengths and the extent of this phenomenon followed the  $SO_4^{2-} < Fe(CN)_6^{3-} < Fe(CN)_6^{4-}$  order. The location of the IEP decreased in this sequence. On the basis of the measured stability ratios, one can observe slow aggregation regime at low electrolyte concentrations and fast aggregation at high salt levels separated by the CCIS values. The CCIS decreased in the  $SO_4^{2-} > Fe(CN)_6^{3-} > Fe(CN)_6^{4-}$  sequence in qualitative agreement with the Schulze-Hardy rule [46,47,50] and in good correlation with the IEP values. It was concluded that multivalent ions of higher valences adsorbed stronger on the oppositely charged surface and thus, the reduced surface charge led to lower CCIS.

In addition, the tendency in the stability ratios for the  $Fe(CN)_6^{4-}$  dispersions was similar to the one for the  $H_2PO_4^-$  system discussed in the previous chapter. Restabilization of the nanosheets occurred in the intermediate salt concentration regime and three CCIS values could be observed. The first one is at lower ionic strength, the second one is when the restabilization started and the third one is at high salt level once the charge of the negative particles was screened by the salt constituent

ions. Such a behaviour has already been described in other oppositely charged particle-multivalent ion systems too [61].

For the negatively charged nanosheets above the PZC (Figure 4, right), the anions were the coions. The electrokinetic potentials increased in magnitude by increasing the valence of the anions indicating their adsorption on the like-charged surface. The adsorption of the  $\text{H}_2\text{PO}_4^{2-}$  was much stronger compared to the  $\text{SO}_4^{2-}$  of the same valence due to the specific interaction with the surface metal ions through primary chemical bonds [73–76]. The stability ratio plots contained slow and fast aggregation regimes separated by the CCIS values, which increased in the  $\text{SO}_4^{2-} < \text{Fe}(\text{CN})_6^{3-} < \text{Fe}(\text{CN})_6^{4-} < \text{H}_2\text{PO}_4^{2-}$  order. The position of the latter anion was atypical, owing to its above-mentioned accumulation on the surface but the  $\text{SO}_4^{2-} < \text{Fe}(\text{CN})_6^{3-} < \text{Fe}(\text{CN})_6^{4-}$  sequence followed adequately the inverse Schulze-Hardy rule (Scheme 1) developed for the colloidal stability of charged particles in the presence of multivalent coions [48,50]. Note that this order is the opposite if one considers the CCC values in the same systems. Both direct and inverse Schulze-Hardy rules can be derived within the DLVO theory, therefore, the major interparticle forces between both positively and negatively charged titania nanosheets were originated from the electrical double layer repulsion and van der Waals attraction [59].

Results from aggregation kinetic and zeta potential measurements performed with commercial titania particles of spherical shape and mono or multivalent cations showed similar dependence in the charging and aggregation processes [71]. The particles were slightly negatively charged, therefore, the metal ions acted as counterions. The zeta potential data showed that adsorption of the divalent ions caused significant charge reversal (Figure 5, left). Moreover, the adsorption of the monovalent ions also resulted in charge reversal but in a smaller extent. This behaviour is rather unusual for monovalent ions; it likely occurred because the pH was close to the PZC, that is, the particle charge was close to zero and a small number of adsorbed cations could reverse the charge of the titania surface. The CCIS values determined in light scattering experiments was substantially smaller for  $\text{Ca}^{2+}$  ions than for the  $\text{Na}^+$  salt (Figure 5, right) in agreement with the Schulze-Hardy rule. This tendency agreed well with calculations used to elucidate the compression of the electrical double layer at different ionic strengths.

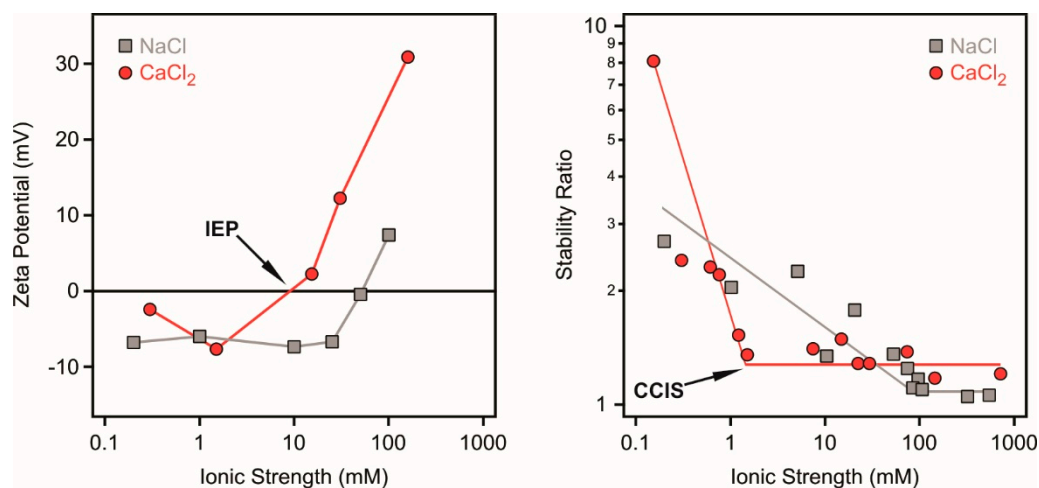


**Figure 5.** Zeta potential (**left**) and stability ratios (**right**) of titania particles as a function of the ionic strength adjusted by NaCl or CaCl<sub>2</sub>. The data were reproduced from Reference [71].

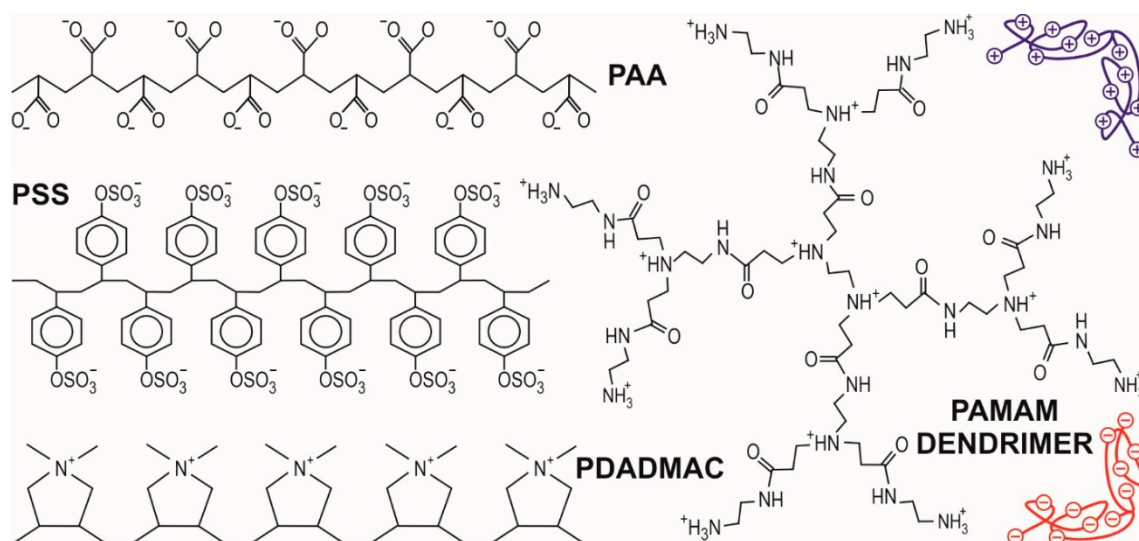
Similar charge reversal was observed with negatively charged titania spheres in the presence of  $\text{Ba}^{2+}$  ions, however, the electrokinetic potentials remained negative up to high ionic strengths for  $\text{K}^+$  ions [57]. The stability ratios were measured with photon correlation spectroscopy and the calculated CCC shifted in the  $\text{K}^+ > \text{Ba}^{2+}$  direction, as predicted by the Schulze-Hardy rule.

From the above discussed results, it is clear that multivalent counterions are more effective in destabilizing colloidal dispersions of titanium oxide materials. Their adsorption often leads to charge neutralization and charge reversal at appropriate concentrations. However, ion specific effects result in different affinity of the ions to the surface giving rise to different extent of charge reversal and to different CCIS within the ions of the same valences [59]. The CCC or CCIS values qualitatively follow the Schulze-Hardy rule but the quantitative description has to be clarified, since it depends on the magnitude of the surface charge and the stoichiometry of the electrolytes [50]. Recent data [59] indicates that effect of multivalent cations on the colloidal stability of titanium oxide particles is important and the inverse Schulze-Hardy rule [48] can be used to describe that phenomenon. However, systematic studies with variation of surface charge density and salt compositions as well as combining different techniques are needed to further pursue this issue.

### 3. Charging and Aggregation of Titanium Oxide Materials in the Presence of Polymers

#### 3.1. General Remarks

Polymers and their charged derivatives, the so-called polyelectrolytes, are often used to tune the stability of colloidal particles [72,77,78]. Polyelectrolytes (Scheme 2) are especially suitable as stabilizing or destabilizing agents, since they adsorb strongly and irreversibly on oppositely charged particles and thus, change the surface charge properties leading to variation of the interparticle forces and to different colloidal stability.



**Scheme 2.** The structure of some polyelectrolytes (PAA—poly(acrylic acid), PSS—poly(styrene sulfonate), PDADMAC—poly(diallyldimethyl ammonium) and PAMAM—poly(amido amine) dendrimer) used to tune colloidal stability of titanium oxide particles. The polyelectrolytes are shown in their ionized forms.

Adsorption of polyelectrolytes on particles of the same sign of charge was also reported with or without addition of bridging ions between the surface and the polymers [32,33,79]. Titanium oxide surfaces were modified by polymeric species either to tune their charging and aggregation behaviour or to functionalize them to prepare hybrid materials [30,80–82] or to enhance the adsorption capacity of the particles [26,83,84]. It was shown that polymer coating improves the cellular uptake of the particles in biomedical applications [6]. Furthermore, polyelectrolytes were used to eliminate titanium oxide materials from dispersions [85]. These applications rely on the nature of polymer-particle and particle-particle interaction; therefore, these phenomena have to be understood in detail. The following section will summarize the efforts made by several research groups in the field from the point of



view of charging and aggregation and corresponding colloid stability of polyelectrolyte functionalized titanium oxide materials.

### 3.2. Oppositely Charged Particle-Polyelectrolyte Systems

As the first example, Figure 6 illustrates the influence of PDADMAC adsorption on negatively charged titania nanosheets [31] and titanate nanowires [63]. The polyelectrolyte possesses permanent positive charge due to the quaternary amino groups in the chain.

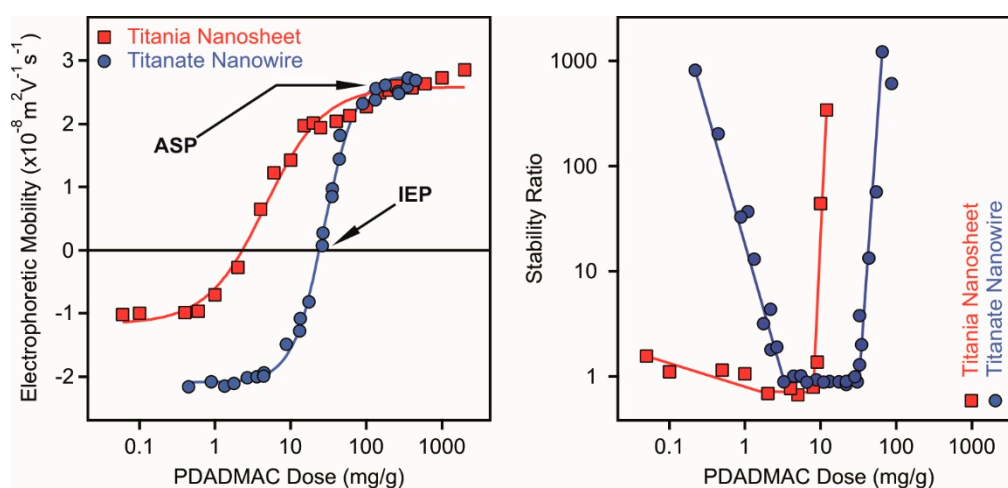


**Figure 6.** Electrophoretic mobilities (**left**) and stability ratios (**right**) of titania nanosheets (squares) and titanate nanowires (circles) at different doses of PDADMAC polyelectrolyte at 4.5 mM and 1 mM ionic strengths, respectively. The mg/g unit refers to mg PDADMAC per one gram of particle. The data were taken from References [31,63].

Concerning the electrophoretic mobility data (Figure 6, left), the values of both series with increasing polyelectrolyte dose showed a trend typical for oppositely charged polyelectrolyte-particle systems [37,72,78,86,87]. Accordingly, the mobilities are negative at low PDADMAC doses and correspond to the electrophoretic mobilities of the bare particles at the corresponding pH and ionic strength. Polyelectrolyte adsorption gave rise to increase in the mobilities and to charge neutralization of the particles at the IEP. The adsorption process continued beyond the IEP and charge reversal occurred. Such an inversion in the sign of the surface charge can be originated from hydrophobic interaction between the polyelectrolyte chains [88], from entropic effect due to the release of solvent molecules and counterions of the highly charged PDADMAC upon adsorption [89] and from ion-ion correlations [90]. The surface of the titanium oxides saturated with the polyelectrolyte at the adsorption saturation point (ASP), that is, further added PDADMAC remained dissolved in the solution. The mobilities were constant within the experimental error after the dose of the ASP.

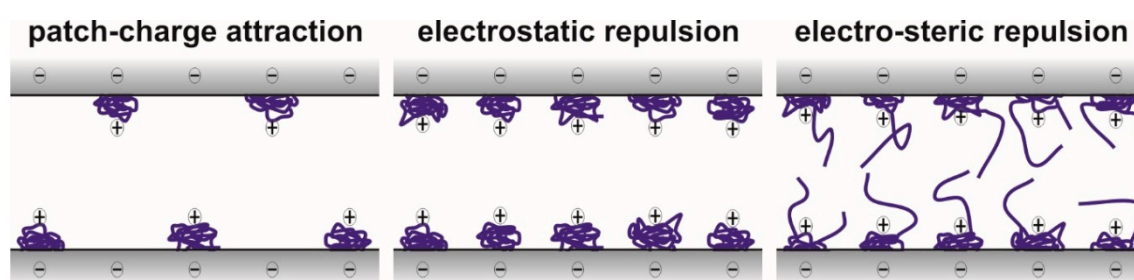
For the titanate nanowire system, the ASP values were determined at different ionic strengths and they increased with the salt level [63]. It was assumed that the electrostatic interaction between the adsorbed PDADMAC chains was responsible for such a tendency. At low electrolyte concentration, the adsorbed amount was limited, since the polyelectrolytes repelled each other on the surface. Once the ionic strength was increased, screening of the polyelectrolyte charge took place and thus, the reduced repulsion between the polyelectrolytes adsorbed on the surface led to higher adsorbed amount and to higher ASP. A decrease in the IEP data with increasing the ionic strength was also reported in the same system and the tendency was explained also with the electrostatic interaction between the adsorbed PDADMAC chains. The locations of the IEP and ASP values are system specific and depend on the surface charge densities of the titanium oxide materials, however, the above tendencies are generic in the individual systems.

The stability ratio data measured in the titania nanosheet and titanate nanowire systems (Figure 6, right) correspond well with the trend in the electrophoretic mobilities discussed above. Rapid particle aggregation and unstable dispersions were observed at doses close to the IEP, while the dispersions were more stable away from these polyelectrolyte loadings. For the nanowire particles, the samples were highly stable at low and high PDADMAC doses [63]. The stability ratio data resembled a U-shape curve, which has been already reported in other particle-polyelectrolyte systems too [37,60,72,91].

The titania nanosheets possessed limited stability at low doses indicated by lower stability ratios in this regime [31]. However, the formation of the saturated PDADMAC layer at the ASP led to stable dispersions and high or not even measurable stability ratio values were determined. Furthermore, the above observations were confirmed by imaging the particles with transmission electron microscopy at different polyelectrolyte doses. Accordingly, individual particles were imaged at low and high PDADMAC concentrations, while aggregated samples were found at doses close to the IEP.

Charging and aggregation of titania nanowires were studied in the presence of PSS (Scheme 2) below the PZC, where the nanowires are positively charged and the polyelectrolyte is of negative charge due to the deprotonation of the sulfonate functional groups [92]. The strong adsorption of the PSS on the oppositely charged surface was confirmed by electrophoretic measurements performed at different particle concentrations. The adsorption process led to charge neutralization and reversal similar to the above discussed systems, while the charge balance was the opposite due to the positively charged nanowires. Moreover, on the basis of the stability ratio data, unstable dispersions were observed near the IEP and stable ones at low and high doses. Similar results were published with titania nanosheets and titanate nanowires in the presence of protamine [62], poly(acrylamide-co-diallyldimethylammonium) chloride [31] and PAMAM dendrimers of different generations [66].

Although the overall tendencies were similar in these systems, different types of interparticle forces were observed. In general, repulsive electrical double layer and attractive van der Waals forces were always present. The latter ones were predominant close to doses of the IEP, while sufficiently charged particles were stabilized by the double layers at low and high polyelectrolyte doses. However, stability ratios lower than unity shed light on the presence of additional attractive forces especially near the IEP, at partial surface coverage [31,63,66]. It was assumed that patch-charge interaction [77,78,93] originating from electrostatic attraction between adsorbed polyelectrolyte islands and empty spaces of the partially covered surfaces was responsible for this additional attraction, which occurred with polyelectrolytes of high line charge density (Scheme 3).



**Scheme 3.** Illustration of different interaction forces between negatively charged particle surfaces with adsorbed polyelectrolytes of positive charge.

As discussed above, electrostatic repulsion between the polyelectrolyte coated surfaces is always present but the overlap of the adsorbed polyelectrolyte chains may give rise to the appearance of repulsive steric forces [94–96]. Such a steric stabilization can occur if the polyelectrolytes adsorb in an extended conformation and form tails on the surface, as illustrated in Scheme 3. The overlap of these tails leads to the rise of osmotic pressure, which causes repulsive interaction. These two effects (double layer and steric interaction) are often called an electrosteric stabilization mechanism [31,66,92]. One can

realize from these results that the nature of the adsorption process and the chemical composition of the polyelectrolytes and particles determine the strength of the interparticle forces of non-DLVO origin.

The stabilizing forces rose after polyelectrolyte adsorption can be demonstrated if one compares the charging and aggregation behaviour of bare and polyelectrolyte-coated titanium oxide materials. Polyelectrolyte coating refers to adsorption on the surface at a dose corresponding to the ASP, that is, the particles possess a saturated polyelectrolyte layer on their surface. Such a layer can be 2–10 nm thick depending on the experimental conditions applied [97]. Electrophoretic mobilities and stability ratios of bare and polyelectrolyte-coated titanate nanowires are shown in Figure 7.

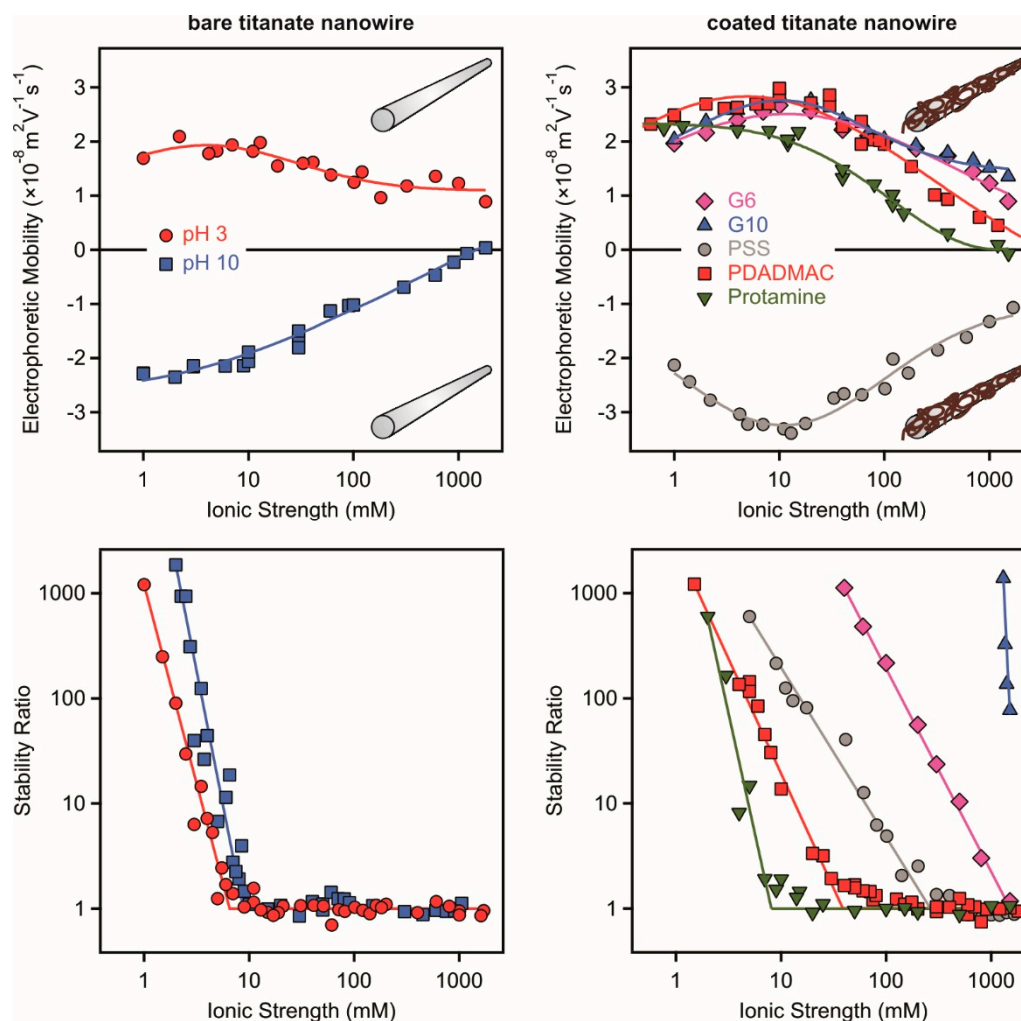


**Figure 7.** Charging and aggregation of bare (left column) and polyelectrolyte-coated (PAMAM dendrimers of generation 6 and 10, PSS, PDADMAC and protamine, right column) titanate nanowires. Electrophoretic mobilities (top row) and stability ratios (bottom row) as a function of the ionic strength adjusted by KCl. In the nanowire-PSS system pH 3 was set, while in the others pH 9, corresponding to positively and negatively charged particles, respectively. The data were taken from references [62,63,66,92].

The PZC of the bare nanowires is 4.1, therefore, they are positively charged at pH 3 and negatively at pH 9 (Figure 7, left). The magnitude of the electrophoretic mobilities decreases with increasing the ionic strength due to charge screening by the dissolved electrolyte constituents. Very similar CCC of about 8 mM was determined independently of the pH and the charge of the bare particles.

However, polyelectrolyte coating led to significant differences in both mobilities and stability ratios (Figure 7, right). This fact shed light on that the adsorption processes and interparticle forces

vary once different type of polyelectrolytes are used for the surface functionalization. Note that the coated particles are of the opposite charge to the bare particles, due to the charge reversal process. Although the electrophoretic mobility data also show some system specificity, the differences in the aggregation curves are more striking. Protamine coating did not give rise to significant change in the shape of the stability ratio plot or in the CCC, because this polyelectrolyte forms a homogeneous and thin layer on the nanowire surfaces and no additional (e.g., steric or patch-charge) forces were present between the functionalized particles [62].

The PDADMAC [63] and PSS [92] adsorption on the negatively and positively charged particles, respectively, resulted in remarkable increase in the CCC values (32 mM for PDADMAC and 600 mM for PSS) indicating the presence of steric stabilization among the electrical double layer repulsion. Moreover, the effect of PAMAM dendrimer layers on the colloidal stability of the titanate nanowires is the most significant compared to the other polyelectrolyte systems. The adsorption of the G6 led to a CCC of about 1500 mM, while the G10 stabilized the dispersions such that the CCC could not be determined, since it was higher than the solubility limit of KCl used to adjust the ionic strength [66]. These highly stable dispersions of primary particles are stabilized by electrosteric forces [94–96] and they are promising candidates in applications, wherever the nanowires should be resistant against salt-induced aggregation up to high ionic strengths.

### 3.3. Effect of Like-Charged Polyelectrolytes on the Stability of Titanium Oxide Dispersions

In this situation, the polyelectrolytes possess the same sign of charge as the particle surface and electrostatic repulsion is expected to hinder the adsorption process. However, as shown in the following examples, interaction between the like-charged polyelectrolytes and the titanium oxide particles can be promoted to tune colloid stability of the dispersions.

Adsorption of negatively charged polymethacrylate (PMA) on commercial titania spheres was reported above the PZC in the presence of  $Mn^{2+}$  ions [33]. On the basis of adsorption isotherms and results from electron paramagnetic spectroscopy experiments, it was suggested that the divalent metal ions induced the PMA adsorption and the  $Mn^{2+}$  ions adsorb directly on the titania-water interface and act as bridges between the surface and the polyelectrolyte. The formation of the titania- $Mn^{2+}$ -PMA complex improved the colloidal stability of the dispersions significantly. Such an adsorption process of like-charged polyelectrolytes was also reported in other particle systems either in the presence [98] or in the absence [32] of multivalent bridging ions.

In another contribution, interaction of  $BaTiO_3$  particles with PAA (Scheme 3) and PAA-poly(ethylene oxide) (PAA-PEO) copolymer was investigated at different ionic strengths adjusted by KCl or  $BaCl_2$  salts [99]. Adsorption of both polymeric species was confirmed on the titanate surface of the same charge using total organic carbon analysis performed on the solution phase to determine the possible concentration of the non-adsorbed polymers. Addition of divalent cations caused aggregation at lower concentrations compared to the monovalent ones in the  $BaTiO_3$ -PAA dispersions. The PAA-PEO macromolecules proved as excellent stabilizing agents, that is, stable samples were observed in the entire pH and salt concentration range investigated. It was suggested that the ionisable PAA part of the copolymer is adsorbed on the surface and it was shielded by the PEO chains from ion-bridging interaction, which would cause aggregation of the particles especially in the presence of multivalent ions. The PEO part also keeps the conformation of the adsorbed copolymer the same upon changes in the pH or ionic strengths, which results in stabilization of the dispersions under wide range of experimental conditions. Steric forces induced by the PEO segments played a major role in the improvement of the stability of the particle dispersions.

Titania nanoparticles were stabilized with the addition of PAA and titania-treated cotton fabric materials were prepared and investigated by light scattering, electron microscopy and in self-cleaning experiments [84]. The particles were negatively charged in a wide range of pH and no clear PZC was observed even at low pH, once PAA was present in the systems. This fact clearly indicated the adsorption of the polyelectrolyte on the like-charged surface and subsequent stabilization of the



dispersions. The distribution of the PAA modified particles on the cotton fibre surfaces was visualized on scanning electron microscopy (SEM) images.

Colloidal stability of titania spheres, nanotubes and their composites was studied in the presence of humic acid (HA) as well as mono and multivalent cations [79]. Zeta potential measurements revealed that the like-charged polyelectrolyte adsorbs on the titania surfaces. This result was also confirmed with IR spectroscopy by identifying the characteristic vibrational bands of the particles and polyelectrolytes in the spectrum recorded after HA adsorption. However, the presence of  $\text{Ca}^{2+}$  ions led to lower magnitude of the surface charge density likely due to the co-adsorption of the HA and the cations. Comparing the different titania structures, it was found that higher amount of polyelectrolyte adsorbed on the elongated materials and this finding was attributed to the higher specific surface area. The presence of HA inhibited the aggregation of the titania particles irrespectively of their shape, however, the stability was lower once  $\text{Ca}^{2+}$  and HA co-existed in the samples due to bridging effects.

To mimic the effect of natural organic matter on the charging and aggregation of spherical titania particles, the colloidal stability was investigated in the presence of HA and tannic acid (TA) [100]. Moreover, environmentally relevant cations were added to the dispersions to simulate the experimental conditions present in natural waters. Stabilizing effect of both HA and TA was reported and DLVO-type interaction qualitatively described the major interparticle forces. Polyelectrolyte adsorption led to an increase in the magnitude of zeta potentials and this phenomenon significantly contributed to the high stability through the increase in the strength of the electrical double layer forces. Adsorption of the divalent metal ions on the polyelectrolyte modified particles led to a decrease in the zeta potentials and to lower stability. However, aggregation was observed only in the presence of  $\text{Ca}^{2+}$  ions and not with the  $\text{Mg}^{2+}$  ions due to the formation of  $\text{Ca}^{2+}$  bridges between the polyelectrolyte chains adsorbed on the particle surfaces. The validity of size measurements carried out with light scattering was confirmed by SEM imaging, where similar sizes of the primary particles and aggregates were determined.

#### 4. Conclusions

The colloidal stability of titanium oxide particles of various shapes and compositions in the presence of numerous charged species was summarized in the present review. First, it can be concluded that specific adsorption of monovalent ions on the titanium oxide surfaces determines the surface charge properties leading to different magnitude of the surface potentials. The major interparticle forces are of DLVO origin in these systems, however, the different charging behaviour due to specific ion adsorption gives rise to variation in the strength of the electrical double layer forces and thus, to different CCC values. The sequence of the CCC can usually be predicted by the Hofmeister series of ions once the charge and the hydrophobicity of the particles are correctly considered.

Second, multivalent ions are able to reverse the sign of charge of oppositely charged particles by adsorbing on their surfaces. Restabilization of the dispersions often occurs at electrolyte concentrations corresponding to the highest extent of the charge reversal. The CCC or CCIS values decrease with the valence of the counterions according to the Schulze-Hardy rule, which can be derived from the DLVO theory. Slight dependence of the CCIS on the valence can also be observed for coions, as described by the inverse Schulze-Hardy rule.

Third, polyelectrolytes can be successfully applied as stabilizing or destabilizing agents for titanium oxides. In the oppositely charged particle-polyelectrolyte systems, charge neutralization induced by polyelectrolyte adsorption destabilizes the dispersions due to the lack of repulsive electrostatic forces. Moreover, the highest stability of the samples containing primary particles was observed once a saturated polyelectrolyte layer forms on the titanium oxide materials causing charge reversal. Additional patch-charge and steric interactions also play major roles in the aggregation processes. Adsorption of like-charged polyelectrolytes is feasible with or without the help of multivalent ions, which may act as bridging agent between the polyelectrolyte chain and the surface.

Considering the results reported to date, the major future challenges in the field can be summarized as follows. Although, the influence of simple salts on the colloidal stability of titanium

oxide materials was extensively studied in the past in case of mono or multivalent counterions, there is a lack comprehensive investigation on the effect of coions of different valences. Given the widespread use of titanium oxide particles in electrolyte mixtures in environmental, biomedical or industrial applications, this issue deserves more attention. In addition, quantitative description of the aggregation processes has to be performed, since the classical theories, for example, Schulze-Hardy rule, usually gives only a qualitative prediction for the aggregation processes. Polyelectrolyte-particle systems represent an important class of materials in various fields, however, it is still not possible to quantitatively predict adsorption or aggregation processes by considering only the chemical composition of the polymers and the particles. The understanding of the contribution of different interparticle forces to the colloidal stability of such dispersions is also far from complete. To deal with these challenges, combined studies using state-of-the-art experimental and theoretical techniques should be carried out. Finally, the efficiency of the titanium oxide dispersions in various applications can be improved once researchers from different fields collaborate to understand each aspects of the process and the features of the involved materials.

**Author Contributions:** The authors contributed equally to the writing of the present manuscript.

**Funding:** The authors are thankful for the financial support of the Hungarian Academy of Sciences through the Lendület project 96130.

**Conflicts of Interest:** The authors declare no conflict of interest.

## References

1. Wang, L.Z.; Sasaki, T. Titanium Oxide Nanosheets: Graphene Analogues with Versatile Functionalities. *Chem. Rev.* **2014**, *114*, 9455–9486. [[CrossRef](#)] [[PubMed](#)]
2. Kment, S.; Riboni, F.; Pausova, S.; Wang, L.; Wang, L.Y.; Han, H.; Hubicka, Z.; Krysa, J.; Schmuiki, P.; Zboril, R. Photoanodes Based on TiO<sub>2</sub> and Alpha-Fe<sub>2</sub>O<sub>3</sub> for Solar Water Splitting—Superior Role of 1d Nanoarchitectures and of Combined Heterostructures. *Chem. Soc. Rev.* **2017**, *46*, 3716–3769. [[CrossRef](#)] [[PubMed](#)]
3. YazdanYar, A.; Aschauer, U.; Bowen, P. Interaction of Biologically Relevant Ions and Organic Molecules with Titanium Oxide (Rutile) Surfaces: A Review on Molecular Dynamics Studies. *Colloid Surf. B* **2018**, *161*, 563–577. [[CrossRef](#)] [[PubMed](#)]
4. Kukovecz, A.; Kordas, K.; Kiss, J.; Konya, Z. Atomic Scale Characterization and Surface Chemistry of Metal Modified Titanate Nanotubes and Nanowires. *Surf. Sci. Rep.* **2016**, *71*, 473–546. [[CrossRef](#)]
5. Farrokhpay, S. A Review of Polymeric Dispersant Stabilisation of Titania Pigment. *Adv. Colloid Interface Sci.* **2009**, *151*, 24–32. [[CrossRef](#)] [[PubMed](#)]
6. Dempsey, C.; Lee, I.; Cowan, K.R.; Suh, J. Coating Barium Titanate Nanoparticles with Polyethylenimine Improves Cellular Uptake and Allows for Coupled Imaging and Gene Delivery. *Colloid Surf. B* **2013**, *112*, 108–112. [[CrossRef](#)] [[PubMed](#)]
7. Rouster, P.; Pavlovic, M.; Saringer, S.; Szilagyi, I. Functionalized Titania Nanosheet Dispersions of Peroxidase Activity. *J. Phys. Chem. C* **2018**, *122*, 11455–11463. [[CrossRef](#)]
8. Beke, S.; Korosi, L.; Scarpellini, A.; Anjum, F.; Brandi, F. Titanate Nanotube Coatings on Biodegradable Photopolymer Scaffolds. *Mater. Sci. Eng. C* **2013**, *33*, 2460–2463. [[CrossRef](#)] [[PubMed](#)]
9. Liu, H.; Duan, C.Y.; Su, X.; Dong, X.N.; Huang, Z.; Shen, W.Q.; Zhu, Z.F. A Hemoglobin Encapsulated Titania Nanosheet Modified Reduced Graphene Oxide Nanocomposite as a Mediator-Free Biosensor. *Sens. Actuators B Chem.* **2014**, *203*, 303–310. [[CrossRef](#)]
10. Yan, Y.; Wang, D.; Schaaf, P. Fabrication of N-Doped TiO<sub>2</sub> Coatings on Nanoporous Si Nanopillar Arrays through Biomimetic Layer by Layer Mineralization. *Dalton Trans.* **2014**, *43*, 8480–8485. [[CrossRef](#)] [[PubMed](#)]
11. Luckarift, H.R.; Dickerson, M.B.; Sandhage, K.H.; Spain, J.C. Rapid, Room-Temperature Synthesis of Antibacterial Bionanocomposites of Lysozyme with Amorphous Silica or Titania. *Small* **2006**, *2*, 640–643. [[CrossRef](#)] [[PubMed](#)]
12. Fujishima, A.; Honda, K. Electrochemical Photolysis of Water at a Semiconductor Electrode. *Nature* **1972**, *238*, 37–38. [[CrossRef](#)] [[PubMed](#)]

13. Linsebigler, A.L.; Lu, G.Q.; Yates, J.T. Photocatalysis on TiO<sub>2</sub> Surfaces—Principles, Mechanisms, and Selected Results. *Chem. Rev.* **1995**, *95*, 735–758. [[CrossRef](#)]
14. Reti, B.; Mogyorosi, K.; Dombi, A.; Hernadi, K. Substrate Dependent Photocatalytic Performance of TiO<sub>2</sub>/Mwcnt Photocatalysts. *Appl. Catal. A* **2014**, *469*, 153–158. [[CrossRef](#)]
15. Bajnoczi, E.G.; Balazs, N.; Mogyorosi, K.; Sranko, D.F.; Pap, Z.; Ambrus, Z.; Canton, S.E.; Noren, K.; Kuzmann, E.; Vertes, A.; et al. The Influence of the Local Structure of Fe(III) on the Photocatalytic Activity of Doped TiO<sub>2</sub> Photocatalysts-an Exafs, Xps and Mossbauer Spectroscopic Study. *Appl. Catal. B* **2011**, *103*, 232–239. [[CrossRef](#)]
16. Grzechulska, J.; Hamerski, M.; Morawski, A.W. Photocatalytic Decomposition of Oil in Water. *Water Res.* **2000**, *34*, 1638–1644. [[CrossRef](#)]
17. Veres, A.; Menesi, J.; Janaky, C.; Samu, G.F.; Scheyer, M.K.; Xu, Q.S.; Salahioğlu, F.; Garland, M.V.; Dekany, I.; Zhong, Z.Y. New Insights into the Relationship between Structure and Photocatalytic Properties of TiO<sub>2</sub> Catalysts. *RSC Adv.* **2015**, *5*, 2421–2428. [[CrossRef](#)]
18. Yu, Y.L.; Zhang, P.; Guo, L.M.; Chen, Z.D.; Wu, Q.; Ding, Y.H.; Zheng, W.J.; Cao, Y. The Design of TiO<sub>2</sub> Nanostructures (Nanoparticle, Nanotube, and Nanosheet) and Their Photocatalytic Activity. *J. Phys. Chem. C* **2014**, *118*, 12727–12733. [[CrossRef](#)]
19. Budarz, J.F.; Turolla, A.; Piasecki, A.F.; Bottero, J.Y.; Antonelli, M.; Wiesner, M.R. Influence of Aqueous Inorganic Anions on the Reactivity of Nanoparticles in TiO<sub>2</sub> Photocatalysis. *Langmuir* **2017**, *33*, 2770–2779. [[CrossRef](#)] [[PubMed](#)]
20. Tetreault, N.; Horvath, E.; Moehl, T.; Brillet, J.; Smajda, R.; Bungener, S.; Cai, N.; Wang, P.; Zakeeruddin, S.M.; Forro, L.; et al. High-Efficiency Solid-State Dye-Sensitized Solar Cells: Fast Charge Extraction through Self-Assembled 3d Fibrous Network of Crystalline TiO<sub>2</sub> Nanowires. *ACS Nano* **2010**, *4*, 7644–7650. [[CrossRef](#)] [[PubMed](#)]
21. Rodriguez, E.F.; Chen, D.H.; Hollenkamp, A.F.; Cao, L.; Caruso, R.A. Monodisperse Mesoporous Anatase Beads as High Performance and Safer Anodes for Lithium Ion Batteries. *Nanoscale* **2015**, *7*, 17947–17956. [[CrossRef](#)] [[PubMed](#)]
22. Zhou, W.J.; Liu, X.J.; Sang, Y.H.; Zhao, Z.H.; Zhou, K.; Liu, H.; Chen, S.W. Enhanced Performance of Layered Titanate Nanowire-Based Supercapacitor Electrodes by Nickel Ion Exchange. *ACS Appl. Mater. Interfaces* **2014**, *6*, 4578–4586. [[CrossRef](#)] [[PubMed](#)]
23. Kuscer, D.; Stavber, G.; Trefalt, G.; Kosec, M. Formulation of an Aqueous Titania Suspension and Its Patterning with Ink-Jet Printing Technology. *J. Am. Ceram. Soc.* **2012**, *95*, 487–493. [[CrossRef](#)]
24. Osada, M.; Sasaki, T. Exfoliated Oxide Nanosheets: New Solution to Nanoelectronics. *J. Mater. Chem.* **2009**, *19*, 2503–2511. [[CrossRef](#)]
25. Zheng, X.T.; He, H.L.; Li, C.M. Multifunctional Graphene Quantum Dots-Conjugated Titanate Nanoflowers for Fluorescence-Trackable Targeted Drug Delivery. *RSC Adv.* **2013**, *3*, 24853–24857. [[CrossRef](#)]
26. Papa, A.L.; Maurizi, L.; Vandroux, D.; Walker, P.; Millot, N. Synthesis of Titanate Nanotubes Directly Coated with Uspio in Hydrothermal Conditions: A New Detectable Nanocarrier. *J. Phys. Chem. C* **2011**, *115*, 19012–19017. [[CrossRef](#)]
27. Matsuda, A.; Sakamoto, H.; Nor, M.A.B.; Kawamura, G.; Muto, H. Characterization and Film Properties of Electrophoretically Deposited Nanosheets of Anionic Titanate and Cationic MgAl-Layered Double Hydroxide. *J. Phys. Chem. B* **2013**, *117*, 1724–1730. [[CrossRef](#)] [[PubMed](#)]
28. Sastre, F.; Bouizi, Y.; Fornes, V.; Garcia, H. Visible-Light Hydrogen Generation Using as Photocatalysts Layered Titanates Incorporating in the Intergallery Space Ruthenium Tris(Bipyridyl) and Methyl Viologen. *J. Colloid Interface Sci.* **2010**, *346*, 172–177. [[CrossRef](#)] [[PubMed](#)]
29. Xiong, L.; Sun, W.L.; Yang, Y.; Chen, C.; Ni, J.R. Heterogeneous Photocatalysis of Methylene Blue over Titanate Nanotubes: Effect of Adsorption. *J. Colloid Interface Sci.* **2011**, *356*, 211–216. [[CrossRef](#)] [[PubMed](#)]
30. Mullner, M.; Lunkenbein, T.; Miyajima, N.; Brey, J.; Müller, A.H.E. A Facile Polymer Templating Route toward High-Aspect-Ratio Crystalline Titania Nanostructures. *Small* **2012**, *8*, 2636–2640. [[CrossRef](#)] [[PubMed](#)]
31. Rouster, P.; Pavlovic, M.; Szilagy, I. Improving the Stability of Titania Nanosheets by Functionalization with Polyelectrolytes. *RSC Adv.* **2016**, *6*, 97322–97330. [[CrossRef](#)]
32. Fazio, S.; Guzman, J.; Colomer, M.; Salomoni, A.; Moreno, R. Colloidal Stability of Nanosized Titania Aqueous Suspensions. *J. Eur. Ceram. Soc.* **2008**, *28*, 2171–2176. [[CrossRef](#)]

33. Burlamacchi, L.; Ottaviani, M.F.; Ceresa, E.M.; Visca, M. Stability of Colloidal TiO<sub>2</sub> in the Presence of Polyelectrolytes and Divalent Metal Ions. *Colloids Surf.* **1983**, *7*, 165–182. [[CrossRef](#)]
34. Derjaguin, B. On the Repulsive Forces between Charged Colloid Particles and on the Theory of Slow Coagulation and Stability of Lyophobic Sols. *Trans. Faraday Soc.* **1940**, *35*, 0203–0214. [[CrossRef](#)]
35. Verwey, E.J.W.; Overbeek, J.T.G. *Theory of Stability of Lyophobic Colloids*; Elsevier: Amsterdam, The Netherlands, 1948.
36. Trefalt, G.; Szilagy, I.; Borkovec, M. Poisson-Boltzmann Description of Interaction Forces and Aggregation Rates Involving Charged Colloidal Particles in Asymmetric Electrolytes. *J. Colloid Interface Sci.* **2013**, *406*, 111–120. [[CrossRef](#)] [[PubMed](#)]
37. Pavlovic, M.; Rouster, P.; Oncsik, T.; Szilagy, I. Tuning Colloidal Stability of Layered Double Hydroxides: From Monovalent Ions to Polyelectrolytes. *Chempluschem* **2017**, *82*, 121–131. [[CrossRef](#)]
38. Oncsik, T.; Desert, A.; Trefalt, G.; Borkovec, M.; Szilagy, I. Charging and Aggregation of Latex Particles in Aqueous Solutions of Ionic Liquids: Towards an Extended Hofmeister Series. *Phys. Chem. Chem. Phys.* **2016**, *18*, 7511–7520. [[CrossRef](#)] [[PubMed](#)]
39. Bastos-Gonzalez, D.; Perez-Fuentes, L.; Drummond, C.; Faraudo, J. Ions at Interfaces: The Central Role of Hydration and Hydrophobicity. *Curr. Opin. Colloid Interface Sci.* **2016**, *23*, 19–28. [[CrossRef](#)]
40. Oncsik, T.; Trefalt, G.; Borkovec, M.; Szilagy, I. Specific Ion Effects on Particle Aggregation Induced by Monovalent Salts within the Hofmeister Series. *Langmuir* **2015**, *31*, 3799–3807. [[CrossRef](#)] [[PubMed](#)]
41. Lopez-Leon, T.; Ortega-Vinuesa, J.L.; Bastos-Gonzalez, D. Ion-Specific Aggregation of Hydrophobic Particles. *Chemphyschem* **2012**, *13*, 2382–2391. [[CrossRef](#)] [[PubMed](#)]
42. Schwierz, N.; Horinek, D.; Sivan, U.; Netz, R.R. Reversed Hofmeister Series—the Rule Rather Than the Exception. *Curr. Opin. Colloid Interface Sci.* **2016**, *23*, 10–18. [[CrossRef](#)]
43. Parsons, D.F.; Salis, A. Hofmeister Effects at Low Salt Concentration Due to Surface Charge Transfer. *Curr. Opin. Colloid Interface Sci.* **2016**, *23*, 41–49. [[CrossRef](#)]
44. Kunz, W.; Henle, J.; Ninham, B.W. ‘Zur Lehre Von Der Wirkung Der Salze’ (About the Science of the Effect of Salts): Franz Hofmeister’s Historical Papers. *Curr. Opin. Colloid Interface Sci.* **2004**, *9*, 19–37. [[CrossRef](#)]
45. Hall, S.B.; Duffield, J.R.; Williams, D.R. A Reassessment of the Applicability of the DLVO Theory as an Explanation for the Schulze-Hardy Rule for Colloid Aggregation. *J. Colloid Interface Sci.* **1991**, *143*, 411–415. [[CrossRef](#)]
46. Lyklema, J. Coagulation by Multivalent Counterions and the Schulze-Hardy Rule. *J. Colloid Interface Sci.* **2013**, *392*, 102–104. [[CrossRef](#)] [[PubMed](#)]
47. Overbeek, J.T.G. The Rule of Schulze and Hardy. *Pure Appl. Chem.* **1980**, *52*, 1151–1161. [[CrossRef](#)]
48. Trefalt, G. Derivation of the Inverse Schulze-Hardy Rule. *Phys. Rev. E* **2016**, *93*, 032612. [[CrossRef](#)] [[PubMed](#)]
49. Oncsik, T.; Trefalt, G.; Csendes, Z.; Szilagy, I.; Borkovec, M. Aggregation of Negatively Charged Colloidal Particles in the Presence of Multivalent Cations. *Langmuir* **2014**, *30*, 733–741. [[CrossRef](#)] [[PubMed](#)]
50. Trefalt, G.; Szilagy, I.; Tellez, G.; Borkovec, M. Colloidal Stability in Asymmetric Electrolytes: Modifications of the Schulze-Hardy Rule. *Langmuir* **2017**, *33*, 1695–1704. [[CrossRef](#)] [[PubMed](#)]
51. Kosmulski, M. The PH Dependent Surface Charging and Points of Zero Charge. Vii. Update. *Adv. Colloid Interface Sci.* **2018**, *251*, 115–138. [[CrossRef](#)] [[PubMed](#)]
52. Parks, G.A. The Isoelectric Points of Solid Oxides, Solid Hydroxides, and Aqueous Hydroxo Complex Systems. *Chem. Rev.* **1965**, *65*, 177–198. [[CrossRef](#)]
53. Kosmulski, M.; Rosenholm, J.B. Electroacoustic Study of Adsorption of Ions on Anatase and Zirconia from Very Concentrated Electrolytes. *J. Phys. Chem.* **1996**, *100*, 11681–11687. [[CrossRef](#)]
54. Liao, D.L.; Wu, G.S.; Liao, B.Q. Zeta Potential of Shape-Controlled TiO<sub>2</sub> Nanoparticles with Surfactants. *Colloid Surf. A* **2009**, *348*, 270–275. [[CrossRef](#)]
55. Niecikowska, A.; Krasowska, M.; Ralston, J.; Malysa, K. Role of Surface Charge and Hydrophobicity in the Three-Phase Contact Formation and Wetting Film Stability under Dynamic Conditions. *J. Phys. Chem. C* **2012**, *116*, 3071–3078. [[CrossRef](#)]
56. Horvath, E.; Szilagy, I.; Forro, L.; Magrez, A. Probing Titanate Nanowire Surface Acidity through Methylene Blue Adsorption in Colloidal Suspension and on Thin Films. *J. Colloid Interface Sci.* **2014**, *416*, 190–197. [[CrossRef](#)] [[PubMed](#)]
57. Barringer, E.A.; Bowen, H.K. High-Purity, Monodisperse TiO<sub>2</sub> Powders by Hydrolysis of Titanium Tetraethoxide 2. Aqueous Interfacial Electrochemistry and Dispersion Stability. *Langmuir* **1985**, *1*, 420–428. [[CrossRef](#)]



58. Szabo, T.; Veres, A.; Cho, E.; Khim, J.; Varga, N.; Dekany, I. Photocatalyst Separation from Aqueous Dispersion Using Graphene Oxide/TiO<sub>2</sub> Nanocomposites. *Colloid Surf. A* **2013**, *433*, 230–239. [[CrossRef](#)]
59. Rouster, P.; Pavlovic, M.; Szilagyi, I. Destabilization of Titania Nanosheet Suspensions by Inorganic Salts: Hofmeister Series and Schulze-Hardy Rule. *J. Phys. Chem. B* **2017**, *121*, 6749–6758. [[CrossRef](#)] [[PubMed](#)]
60. Hierrezuelo, J.; Vaccaro, A.; Borkovec, M. Stability of Negatively Charged Latex Particles in the Presence of a Strong Cationic Polyelectrolyte at Elevated Ionic Strengths. *J. Colloid Interface Sci.* **2010**, *347*, 202–208. [[CrossRef](#)] [[PubMed](#)]
61. Pavlovic, M.; Huber, R.; Adok-Sipiczki, M.; Nardin, C.; Szilagyi, I. Ion Specific Effects on the Stability of Layered Double Hydroxide Colloids. *Soft Matter* **2016**, *12*, 4024–4033. [[CrossRef](#)] [[PubMed](#)]
62. Rouster, P.; Pavlovic, M.; Horvath, E.; Forro, L.; Dey, S.K.; Szilagyi, I. Influence of Protamine Functionalization on the Colloidal Stability of 1d and 2d Titanium Oxide Nanostructures. *Langmuir* **2017**, *33*, 9750–9758. [[CrossRef](#)] [[PubMed](#)]
63. Szabo, T.; Toth, V.; Horvath, E.; Forro, L.; Szilagyi, I. Tuning the Aggregation of Titanate Nanowires in Aqueous Dispersions. *Langmuir* **2015**, *31*, 42–49. [[CrossRef](#)] [[PubMed](#)]
64. Zhou, D.X.; Ji, Z.X.; Jiang, X.M.; Dunphy, D.R.; Brinker, J.; Keller, A.A. Influence of Material Properties on TiO<sub>2</sub> Nanoparticle Agglomeration. *PLoS ONE* **2013**, *8*, e81239. [[CrossRef](#)] [[PubMed](#)]
65. Shih, C.J.; Lin, S.C.; Strano, M.S.; Blankschtein, D. Understanding the Stabilization of Liquid-Phase-Exfoliated Graphene in Polar Solvents: Molecular Dynamics Simulations and Kinetic Theory of Colloid Aggregation. *J. Am. Chem. Soc.* **2010**, *132*, 14638–14648. [[CrossRef](#)] [[PubMed](#)]
66. Pavlovic, M.; Adok-Sipiczki, M.; Horvath, E.; Szabo, T.; Forro, L.; Szilagyi, I. Dendrimer-Stabilized Titanate Nanowire Dispersions as Potential Nanocarriers. *J. Phys. Chem. C* **2015**, *119*, 24919–24926. [[CrossRef](#)]
67. Snoswell, D.R.E.; Duan, J.M.; Fornasiero, D.; Ralston, J. Colloid Stability of Synthetic Titania and the Influence of Surface Roughness. *J. Colloid Interface Sci.* **2005**, *286*, 526–535. [[CrossRef](#)] [[PubMed](#)]
68. Dumont, F.; Warlus, J.; Watillon, A. Influence of the Point of Zero Charge of Titanium-Dioxide Hydrosols on the Ionic Adsorption Sequences. *J. Colloid Interface Sci.* **1990**, *138*, 543–554. [[CrossRef](#)]
69. Schwierz, N.; Horinek, D.; Netz, R.R. Reversed Anionic Hofmeister Series: The Interplay of Surface Charge and Surface Polarity. *Langmuir* **2010**, *26*, 7370–7379. [[CrossRef](#)] [[PubMed](#)]
70. Yates, D.E.; Healy, T.W. Titanium-Dioxide Electrolyte Interface 2. Surface-Charge (Titration) Studies. *J. Chem. Soc. Faraday Trans.* **1980**, *76*, 9–18. [[CrossRef](#)]
71. Shih, Y.H.; Zhuang, C.M.; Tso, C.P.; Lin, C.H. The Effect of Electrolytes on the Aggregation Kinetics of Titanium Dioxide Nanoparticle Aggregates. *J. Nanopart. Res.* **2012**, *14*, 924. [[CrossRef](#)]
72. Szilagyi, I.; Trefalt, G.; Tiraferri, A.; Maroni, P.; Borkovec, M. Polyelectrolyte Adsorption, Interparticle Forces, and Colloidal Aggregation. *Soft Matter* **2014**, *10*, 2479–2502. [[CrossRef](#)] [[PubMed](#)]
73. Connor, P.A.; McQuillan, A.J. Phosphate Adsorption onto TiO<sub>2</sub> from Aqueous Solutions: An in Situ Internal Reflection Infrared Spectroscopic Study. *Langmuir* **1999**, *15*, 2916–2921. [[CrossRef](#)]
74. Feiler, A.; Jenkins, P.; Ralston, J. Metal Oxide Surfaces Separated by Aqueous Solutions of Linear Polyphosphates: DLVO and Non-DLVO Interaction Forces. *Phys. Chem. Chem. Phys.* **2000**, *2*, 5678–5683. [[CrossRef](#)]
75. Luschtinetz, R.; Frenzel, J.; Milek, T.; Seifert, G. Adsorption of Phosphonic Acid at the TiO<sub>2</sub> Anatase (101) and Rutile (110) Surfaces. *J. Phys. Chem. C* **2009**, *113*, 5730–5740. [[CrossRef](#)]
76. Rosenholm, J.B.; Kosmulski, M. Peculiar Charging Effects on Titania in Aqueous 1:1, 2:1, 1:2 and Mixed Electrolyte Suspensions. *Adv. Colloid Interface Sci.* **2012**, *179*, 51–67. [[CrossRef](#)] [[PubMed](#)]
77. Borkovec, M.; Papastavrou, G. Interactions between Solid Surfaces with Adsorbed Polyelectrolytes of Opposite Charge. *Curr. Opin. Colloid Interface Sci.* **2008**, *13*, 429–437. [[CrossRef](#)]
78. Borkovec, M.; Szilagyi, I.; Popa, I.; Finessi, M.; Sinha, P.; Maroni, P.; Papastavrou, G. Investigating Forces between Charged Particles in the Presence of Oppositely Charged Polyelectrolytes with the Multi-Particle Colloidal Probe Technique. *Adv. Colloid Interface Sci.* **2012**, *179*, 85–98. [[CrossRef](#)] [[PubMed](#)]
79. Liu, W.; Sun, W.L.; Borthwick, A.G.L.; Ni, J.R. Comparison on Aggregation and Sedimentation of Titanium Dioxide, Titanate Nanotubes and Titanate Nanotubes- TiO<sub>2</sub>: Influence of Ph, Ionic Strength and Natural Organic Matter. *Colloid Surf. A* **2013**, *434*, 319–328. [[CrossRef](#)]
80. Liu, M.J.; Ishida, Y.; Ebina, Y.; Sasaki, T.; Hikima, T.; Takata, M.; Aida, T. An Anisotropic Hydrogel with Electrostatic Repulsion between Cofacially Aligned Nanosheets. *Nature* **2015**, *517*, 68–72. [[CrossRef](#)] [[PubMed](#)]

81. Jiang, Y.J.; Yang, D.; Zhang, L.; Sun, Q.Y.; Sun, X.H.; Li, J.; Jiang, Z.Y. Preparation of Protamine-Titania Microcapsules through Synergy between Layer-by-Layer Assembly and Biomimetic Mineralization. *Adv. Funct. Mater.* **2009**, *19*, 150–156. [[CrossRef](#)]
82. Sasaki, T. Fabrication of Nanostructured Functional Materials Using Exfoliated Nanosheets as a Building Block. *J. Ceram. Soc. Jpn.* **2007**, *115*, 9–16. [[CrossRef](#)]
83. Rouster, P.; Pavlovic, M.; Szilagyi, I. Immobilization of Superoxide Dismutase on Polyelectrolyte Functionalized Titania Nanosheets. *Chembiochem* **2018**, *19*, 404–410. [[CrossRef](#)] [[PubMed](#)]
84. Goyal, N.; Rastogi, D.; Jassal, M.; Agrawal, A.K. Dispersion Stabilization of Titania Nanoparticles for Textile: Aggregation Behavior and Self-Cleaning Activity. *J. Dispers. Sci. Technol.* **2013**, *34*, 611–622. [[CrossRef](#)]
85. Ghimici, L.; Nichifor, M. Separation of TiO<sub>2</sub> Particles from Water and Water/Methanol Mixtures by Cationic Dextran Derivatives. *Carbohydr. Polym.* **2013**, *98*, 1637–1643. [[CrossRef](#)] [[PubMed](#)]
86. Vasti, C.; Borgiallo, A.; Giacomelli, C.E.; Rojas, R. Layered Double Hydroxide Nanoparticles Customization by Polyelectrolyte Adsorption: Mechanism and Effect on Particle Aggregation. *Colloid Surf. A* **2017**, *533*, 316–322. [[CrossRef](#)]
87. Hyde, E.D.E.; Moreno-Atanasio, R.; Millner, P.A.; Neville, F. Surface Charge Control through the Reversible Adsorption of a Biomimetic Polymer on Silica Particles. *J. Phys. Chem. B* **2015**, *119*, 1726–1735. [[CrossRef](#)] [[PubMed](#)]
88. Carrillo, J.Y.; Dobrynin, A.V. Molecular Dynamics Simulations of Polyelectrolyte Adsorption. *Langmuir* **2007**, *23*, 2472–2482. [[CrossRef](#)] [[PubMed](#)]
89. Park, S.Y.; Bruinsma, R.F.; Gelbart, W.M. Spontaneous Overcharging of Macro-Ion Complexes. *Europhys. Lett.* **1999**, *46*, 454–460. [[CrossRef](#)]
90. Quesada-Perez, M.; Gonzalez-Tovar, E.; Martin-Molina, A.; Lozada-Cassou, M.; Hidalgo-Alvarez, R. Overcharging in Colloids: Beyond the Poisson-Boltzmann Approach. *ChemPhysChem* **2003**, *4*, 235–248. [[CrossRef](#)] [[PubMed](#)]
91. Iselau, F.; Xuan, T.P.; Trefalt, G.; Matic, A.; Holmberg, K.; Bordes, R. Formation and Relaxation Kinetics of Starch-Particle Complexes. *Soft Matter* **2016**, *12*, 9509–9519. [[CrossRef](#)] [[PubMed](#)]
92. Horvath, E.; Grebikova, L.; Maroni, P.; Szabo, T.; Magrez, A.; Forro, L.; Szilagyi, I. Dispersion Characteristics and Aggregation in Titanate Nanowire Colloids. *ChemPlusChem* **2014**, *79*, 592–600. [[CrossRef](#)]
93. Leong, Y.K. Interparticle Forces Arising from an Adsorbed Strong Polyelectrolyte in Colloidal Dispersions: Charged Patch Attraction. *Colloid Polym. Sci.* **1999**, *277*, 299–305. [[CrossRef](#)]
94. Einarson, M.B.; Berg, J.C. Electrosteric Stabilization of Colloidal Latex Dispersions. *J. Colloid Interface Sci.* **1993**, *155*, 165–172. [[CrossRef](#)]
95. Fuchs, A.; Killmann, E. Adsorption of Polyelectrolytes on Colloidal Latex Particles, Electrostatic Interactions and Stability Behaviour. *Colloid Polym. Sci.* **1998**, *279*, 53–60. [[CrossRef](#)]
96. Fritz, G.; Schadler, V.; Willenbacher, N.; Wagner, N.J. Electrosteric Stabilization of Colloidal Dispersions. *Langmuir* **2002**, *18*, 6381–6390. [[CrossRef](#)]
97. Hierrezuelo, J.; Szilagyi, I.; Vaccaro, A.; Borkovec, M. Probing Nanometer-Thick Polyelectrolyte Layers Adsorbed on Oppositely Charged Particles by Dynamic Light Scattering. *Macromolecules* **2010**, *43*, 9108–9116. [[CrossRef](#)]
98. Tiraferri, A.; Maroni, P.; Borkovec, M. Adsorption of Polyelectrolytes to Like-Charged Substrates Induced by Multivalent Counterions as Exemplified by Poly(Styrene Sulfonate) and Silica. *Phys. Chem. Chem. Phys.* **2015**, *17*, 10348–10352. [[CrossRef](#)] [[PubMed](#)]
99. Kirby, G.H.; Harris, D.J.; Li, Q.; Lewis, J.A. Poly(Acrylic Acid)-Poly(Ethylene Oxide) Comb Polymer Effects on Batio3 Nanoparticle Suspension Stability. *J. Am. Ceram. Soc.* **2004**, *87*, 181–186. [[CrossRef](#)]
100. Romanello, M.B.; de Cortalezzi, M.M.F. An Experimental Study on the Aggregation of TiO<sub>2</sub> Nanoparticles under Environmentally Relevant Conditions. *Water Res.* **2013**, *47*, 3887–3898. [[CrossRef](#)] [[PubMed](#)]



# Attractive Forces between Charged Colloidal Particles Induced by Multivalent Ions Revealed by Confronting Aggregation and Direct Force Measurements

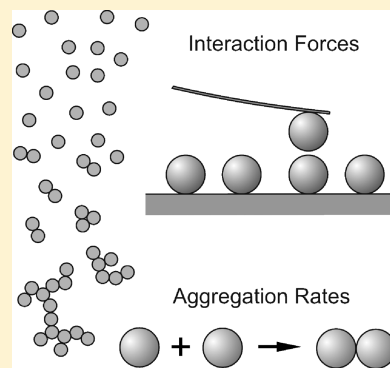
Prashant Sinha, Istvan Szilagyi, F. Javier Montes Ruiz-Cabello, Plinio Maroni, and Michal Borkovec\*

Department of Inorganic and Analytical Chemistry, University of Geneva, Sciences II, Quai Ernest-Ansermet 30, 1205 Geneva, Switzerland

**S** Supporting Information

**ABSTRACT:** Interactions involving charged particles in the presence of multivalent ions are relevant in wide-range of phenomena, including condensation of nucleic acids, cement hardening, or water treatment. Here, we study such interactions by combining direct force measurements with atomic force microscopy (AFM) and aggregation studies with time-resolved light scattering for particles originating from the same colloidal suspension for the first time. Classical DLVO theory is found to be only applicable for monovalent and divalent ions. For ions of higher valence, charge inversion and additional non-DLVO attractive forces are observed. These attractive forces can be attributed to surface charge heterogeneities, which leads to stability ratios that are calculated from direct force measurements to be higher than the experimental ones. Ion–ion correlations are equally important as they induce the charge inversion in the presence of trivalent or tetravalent ions, and they enhance the surface charge heterogeneities. Such heterogeneities therefore play an essential role in controlling interactions in particle suspensions containing multivalent ions.

**SECTION:** Glasses, Colloids, Polymers, and Soft Matter



Interaction forces involving macromolecules, nanoparticles, or water–solid interfaces are strongly modified by multivalent ions, and such effects are essential in the condensation of nucleic acids, crystal growth, cement hardening, or water treatment.<sup>1–3</sup> The recent focus on multivalent ions was triggered by the discovery that the Poisson–Boltzmann (PB) approximation describing electrical double-layers may fail in their presence due to neglect of ion–ion correlations.<sup>3–7</sup> As a consequence, one ought to question the Derjaguin, Landau, Verwey, and Overbeek (DLVO) theory that postulates that such forces are dominated by a superposition of attractive van der Waals forces and repulsive double-layer forces, the latter being precisely obtained from the doubtful PB approximation.<sup>8,9</sup> Still, the DLVO theory triumphed with the derivation of the classical Schulze–Hardy rule, which captures the influence of multivalent ions on the stability of colloidal suspensions.<sup>9–11</sup> This rule states that the critical coagulation concentration (CCC) defining the onset of fast aggregation scales as  $z^{-6}$  where  $z$  is the counterion valence. While this relation has been confirmed experimentally, eventual importance of surface charge heterogeneities was equally put forward.<sup>12–15</sup> It is probably fair to say that no consensus concerning the forces acting between colloidal particles in the presence of multivalent ions has been reached so far.

Precise measurements of aggregation rate constants between colloidal particles, which now can be routinely achieved with time-resolved light scattering or single particle counting techniques, do not help to disentangle these questions

either.<sup>2,11,16–19</sup> A clearer picture would emerge if such measurements could be complemented by direct force measurements involving the same particles, but this task is out of reach for many techniques available. The surface forces apparatus (SFA) can only measure forces between macroscopic mica sheets,<sup>8,20</sup> total internal reflection microscopy is restricted to the sphere–plane geometry,<sup>21</sup> and video-microscopy techniques require particles that are too large for reliable aggregation measurements.<sup>15,22,23</sup> The colloidal probe technique based on the atomic force microscope (AFM) is normally used to probe forces in the sphere–plane geometry,<sup>24,25</sup> but has been extended to measure forces between an AFM-tip and deposited particles<sup>26</sup> as well as between pairs of individual particles.<sup>27,28</sup>

Here we measure forces and aggregation rates involving particles from the same colloidal suspension for the first time. These measurements became possible since forces between pairs of particles of 1.0  $\mu\text{m}$  in diameter could be measured by the multiparticle colloidal probe technique (Figure 1a). These particles are sufficiently small to be used for aggregation studies whereby sedimentation and multiple-scattering effects become negligible. By combining these techniques, new information

**Received:** January 9, 2013

**Accepted:** February 5, 2013

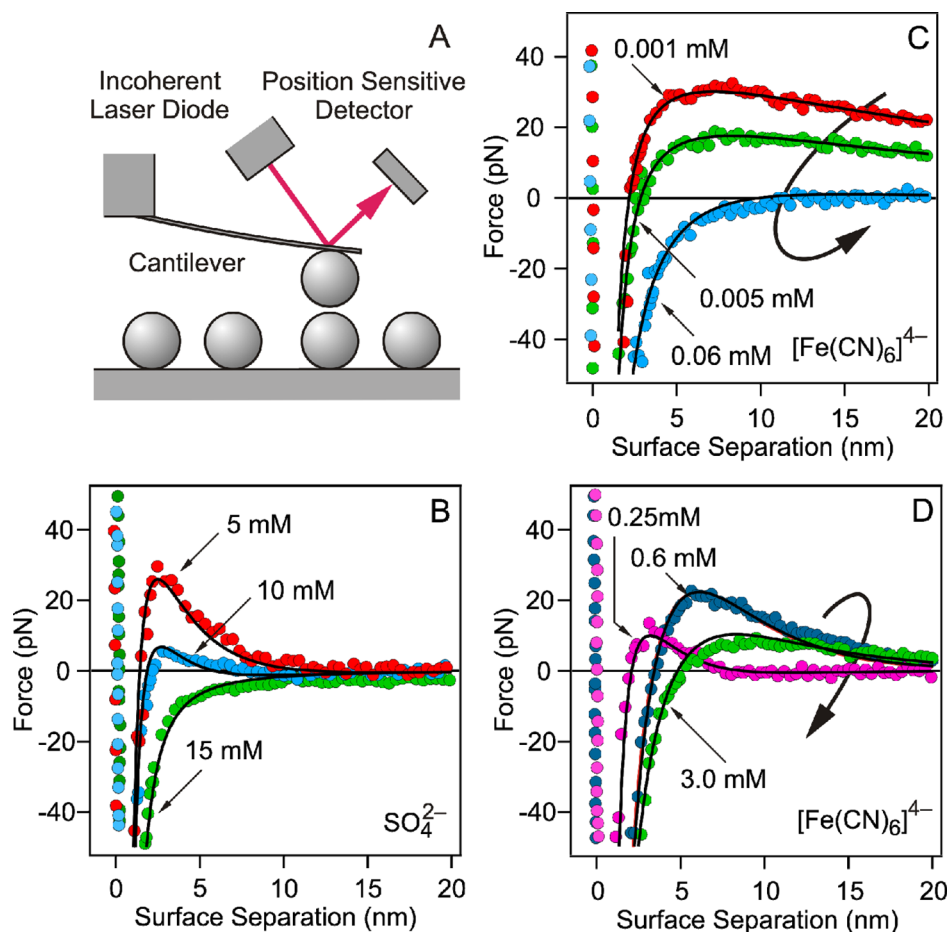


**Figure 1.** Forces measured by the colloidal probe technique. (A) Scheme of the experimental setup. (B) Forces in the presence of a divalent anion  $\text{SO}_4^{2-}$ , where repulsive forces weaken with increasing salt concentration and finally become attractive. Solid lines are best fits with DLVO theory. Reentrant forces in the presence of a tetravalent anion  $[\text{Fe}(\text{CN})_6]^{4-}$  at (C) low and (D) high concentrations.

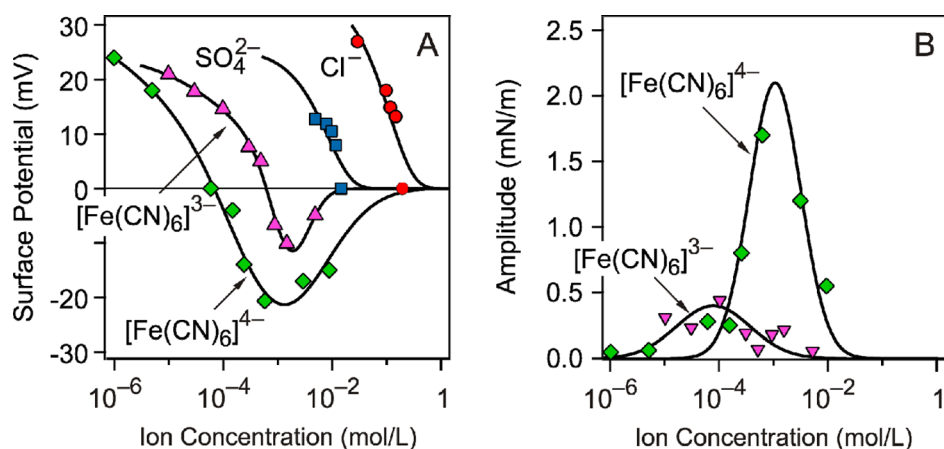


**Figure 2.** Parameters extracted from measured force profiles. Solid lines are empirical functions used for calculation of the aggregation rate constants. (A) Electric surface potentials whose sign has been inferred from electrophoretic mobility. (B) Amplitude of the attractive exponential non-DLVO contribution.

concerning the interactions between charged colloidal particles in the presence of multivalent ions is obtained.

Measured force profiles between positively charged amidine polystyrene latex particles in the presence of divalent and tetravalent anions are shown in Figure 1. Forces involving divalent ions could be fitted with the classical DLVO theory with a Hamaker constant of  $4.0 \times 10^{-21}$  J remarkably well (see

Supporting Information). The fitted surface potentials are shown in Figure 2a, and they decrease with increasing salt concentration as electrostatic screening suggests. The force profiles for tetravalent ions cannot be reconciled with the simple DLVO picture due to their reentrant nature and presence of additional attractions (Figure 1c,d). The reentrance can be explained by charge inversion as confirmed by



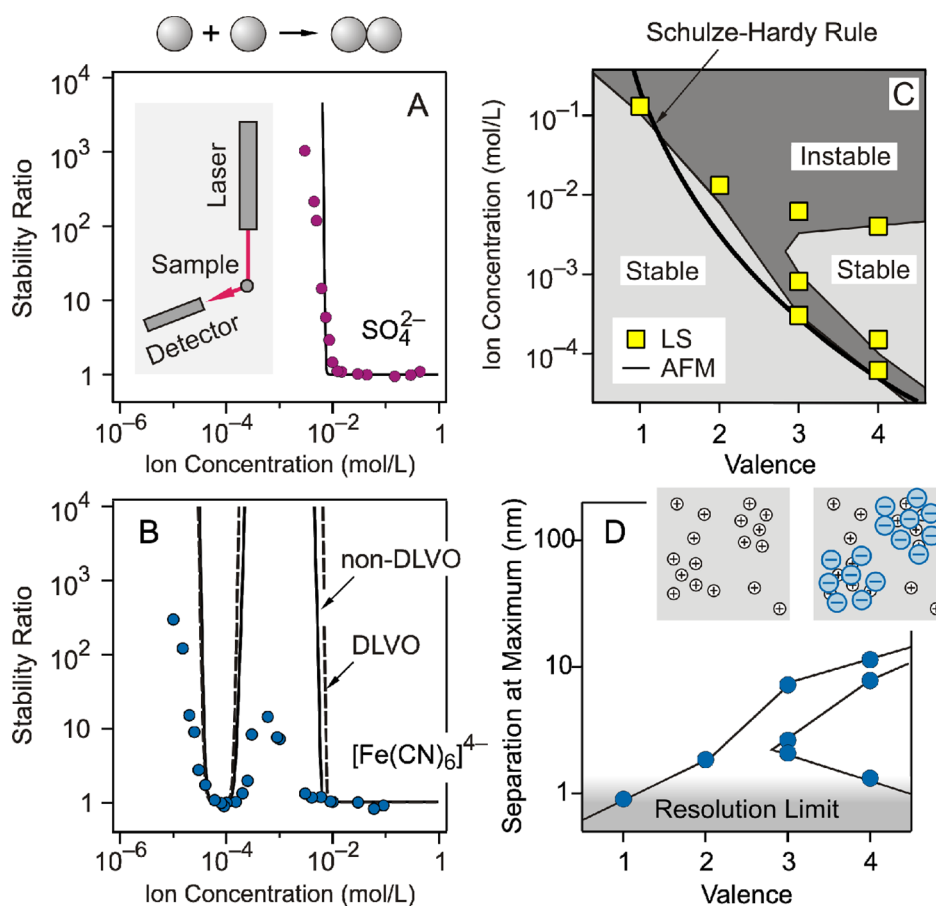


**Figure 3.** Experimental stability ratios of amidine latex particles (points) versus the counterion concentration compared with calculations based on direct force measurements (solid lines) for (A)  $\text{SO}_4^{2-}$  and (B)  $[\text{Fe}(\text{CN})_6]^{4-}$ . Schemes in A show the elementary aggregation process of the doublet formation and the light scattering setup used to measure the aggregation rate in the early stages. Solid lines in B include the non-DLVO contribution, while the dashed lines show contribution of DLVO forces only. (C) The stability map compares the valence of the counterion with the location of the CCC obtained from light scattering experiments (LS, points) and from estimates based on direct force measurements (AFM, lines). The thick line indicates the Schulze–Hardy rule. (D) Surface separation for the energy barrier at CCC for different valence. The insets in D provide a pictorial representation of the enhancement of surface charge heterogeneities by adsorption of multivalent counterions.

electrophoresis. Similar overcharging phenomena are documented in other systems.<sup>11,18</sup> With increasing concentration, the potential passes through the isoelectric point (IEP) and becomes negative. After going through a minimum, it finally decreases in magnitude due to screening. The attractive forces close to IEP are substantially stronger than for divalent counterions, and they are inconsistent with the corresponding Hamaker constant.

We interpret this additional non-DLVO attraction as originating from surface charge heterogeneities.<sup>12</sup> When such heterogeneities are arranged in a square lattice, the attraction is known to be exponential, and its inverse decay length is given by  $(\kappa^2 + (2\pi/a)^2)^{1/2}$  where  $\kappa^{-1}$  is the Debye length and  $a$  is the lattice spacing (see Supporting Information). When this additional force is added to the DLVO profiles, the observed forces can be reconciled with  $a = 15 \pm 5$  nm. The fitted surface potentials and amplitudes of the non-DLVO force are shown in Figure 2.

Early stage aggregation rates were measured in suspensions of the same particles as used for the force measurements by time-resolved light scattering.<sup>11,19</sup> Figure 3 shows these results as stability ratios, which is defined as  $W = k_{\text{fast}}/k$ , where  $k_{\text{fast}}$  is the fast aggregation rate coefficient measured at high salt concentrations and  $k$  is the aggregation rate coefficient at the

conditions investigated. Divalent counterions induce the classical salt dependence featuring the slow aggregation regime at low salt concentrations and fast aggregation at high concentrations. For tetravalent counterions, the stability ratio features an intermediate maximum due to charge inversion. The CCCs separating these regimes are summarized in a stability map for all counterions (Figure 3c).

Since force profiles and aggregation rates are available for exactly the same particles, the experimental aggregation rates can be compared with the ones calculated from the forces (Figure 3). These calculations involve no adjustable parameters. The map indicates that the CCCs are reproduced quite well for all types of ions, and that the Schulze–Hardy rule indeed reflects the shift of the lowest CCC. For divalent counterions, the experimental stability ratios are predicted well. The experimental fast aggregation rate  $k_{\text{fast}} = 3.8 \times 10^{-18}$  m<sup>3</sup>/s agrees with DLVO theory, which yields  $6.5 \times 10^{-18}$  m<sup>3</sup>/s. However, the agreement is only semiquantitative for tetravalent counterions, and the disagreement becomes especially important near the intermediate maximum. Including attractive non-DLVO forces improves the agreement with experiment somewhat, but substantial discrepancies remain.

These discrepancies originate most likely from lateral charge heterogeneities. Relevant interactions occur at distances of

several nanometers (Figure 3d). The energy barrier at CCC moves to larger distances with increasing valence, which excludes eventual contributions from ion–ion correlation forces, hydration forces, or roughness.<sup>5,18,19</sup> In particular, forces induced by ion–ion correlations have a subnanometer range,<sup>6,7</sup> which is substantially smaller than the one relevant here. We have already argued that for trivalent and tetravalent counterions, the additional non-DLVO attractive forces are consistent with lateral surface charge heterogeneities. Two additional observations support this picture further. (i) The rate calculations assume a radially symmetric force field, which is incorrect for heterogeneous surfaces. Aggregating particles will explore their rotational degrees of freedom to find the lowest free energy path, which results in faster aggregation. In the force measurements, however, particles have little freedom to adjust their mutual orientations. (ii) Variation between the measured force profiles involving different pairs of particles could be sometimes observed (see Supporting Information). Such differences are expected for heterogeneous surfaces since different particles will expose different patches. On the basis of these arguments, lateral charge heterogeneities emerge as the most likely explanation for the observed discrepancies between calculated and experimental stability ratios for tetravalent counterions. While the direct force measurements suggest a characteristic size of these heterogeneities of about 15 nm, their distribution could be wide and include substantially larger patches (i.e., charge polydispersity).

Trivalent counterions resemble tetravalent ones, even though the deviations from DLVO theory are less pronounced than in the tetravalent case. The results for monovalent counterions are similar to the divalent ones. For monovalent counterions, however, the energy barrier at CCC is located at subnanometer distances, which is comparable to the distance resolution in the force measurements (Figure 3d). In this case, the force profiles are probably no longer accurate in the relevant distance regime, and contributions from additional short-range interactions cannot be excluded.

Effects of ion–ion correlations seem evidenced in the progressive importance of the charge reversal observed in the presence of multivalent ions. However, the resulting surface potentials of these adsorbed layers remain small, and DLVO theory can be still used to describe the force profiles at larger distances. While ion–ion correlations induce attractive forces with a substantially smaller range than the one observed,<sup>6,7</sup> these forces could be modified by surface roughness, lateral charge heterogeneities, counterion bridging, or superstructures formed by multivalent ions.<sup>5</sup> While the observed attractive non-DLVO forces are likely induced by surface charge heterogeneities, the fact that these forces become more relevant in the presence of multivalent ions suggests the importance of ion–ion correlations. While the importance of such heterogeneities has also been suggested earlier,<sup>13,15</sup> the present results indicate that multivalent ions magnify these heterogeneities.

For the first time, we were able to combine direct force measurements and aggregation studies involving particles from the same suspension. These techniques reveal that DLVO theory is only applicable in the presence of monovalent and divalent counterions. For ions of higher valence, charge inversion and additional non-DLVO attractive forces are observed. These attractive forces can be attributed to surface charge heterogeneities, which lead to stability ratios calculated from direct force measurements to exceed the experimental ones. However, ion–ion correlation effects are equally relevant

as they induce charge inversion in the presence of ions of higher valence and enhance surface charge heterogeneities. This approach involving the multiparticle colloidal probe technique could also be confronted with other bulk characteristics (e.g., structure factor, osmotic pressure), and thus has the potential to become indispensable tool in our technical repertoire to study colloidal interactions.

## MATERIALS AND METHODS

Positively charged amidine polystyrene latex particles of 1.0  $\mu\text{m}$  in diameter suspended in ultrapure water adjusted to pH 4.0 were mixed with solutions of potassium salts of  $\text{Cl}^-$ ,  $\text{SO}_4^{2-}$ ,  $[\text{Fe}(\text{CN})_6]^{3-}$ , and  $[\text{Fe}(\text{CN})_6]^{4-}$ . Forces between particles were measured with an AFM mounted on an inverse optical microscope. The particle suspension was injected into the AFM fluid cell sealed with a silanized glass plate to which the particles attach spontaneously. A particle was picked up with a silanized tip-less cantilever in the cell and centered above another particle on the substrate. This multiparticle colloidal probe technique features a large internal surface area and thus allows the control of the amount of multivalent ions added precisely. The technique is also less sensitive to impurities. About 100 approach–retraction cycles were recorded per pair of particles, and the noise was reduced by averaging all forces curves and by down sampling to 3 pN. Force profiles between at least three pairs of particles were averaged. Absolute particle aggregation rates were determined in the same suspensions by time-resolved simultaneous static and dynamic light scattering. Stability ratios were obtained by dynamic light scattering at a scattering angle of  $90^\circ$ . The steady-state solution of the diffusion equation was used to calculate the aggregation rate from the interaction potential and the mutual diffusion coefficient. The interaction potential is obtained by integrating the fitted force profiles, whereby the concentration dependence of the parameters is quantified with empirical fits shown in Figure 2. The mutual diffusion coefficient was calculated from the diffusion coefficient of the individual particles measured by dynamic light scattering and by including hydrodynamic interactions between the particles. Further details are given in the Supporting Information.

## ASSOCIATED CONTENT

### Supporting Information

Additional information is provided concerning materials, methods, experimental data on monovalent and trivalent ions, and references. This material is available free of charge via the Internet <http://pubs.acs.org>.

## AUTHOR INFORMATION

### Corresponding Author

\*Phone: + 41 22 379 6405; E-mail: [michal.borkovec@unige.ch](mailto:michal.borkovec@unige.ch).

### Notes

The authors declare no competing financial interest.

## ACKNOWLEDGMENTS

This work was supported by the Swiss National Science Foundation and the University of Geneva.

## REFERENCES

- (1) Besteman, K.; Van Eijk, K.; Lemay, S. G. Charge Inversion Accompanies DNA Condensation by Multivalent Ions. *Nat. Phys.* 2007, 3, 641–644.

- (2) Chen, K. L.; Mylon, S. E.; Elimelech, M. Aggregation Kinetics of Alginate-Coated Hematite Nanoparticles in Monovalent and Divalent Electrolytes. *Environ. Sci. Technol.* **2006**, *40*, 1516–1523.
- (3) Jonsson, B.; Wennerstrom, H.; Nonat, A.; Cabane, B. Onset of Cohesion in Cement Paste. *Langmuir* **2004**, *20*, 6702–6709.
- (4) Kjellander, R.; Marcelja, S. Correlation and Image Charge Effects in Electric Double-Layers. *Chem. Phys. Lett.* **1984**, *112*, 49–53.
- (5) Nguyen, T. T.; Grosberg, A. Y.; Shklovskii, B. I. Macroions in Salty Water with Multivalent Ions: Giant Inversion of Charge. *Phys. Rev. Lett.* **2000**, *85*, 1568–1571.
- (6) Bohinc, K.; Grime, J. M. A.; Lue, L. The Interactions between Charged Colloids with Rod-Like Counterions. *Soft Matter* **2012**, *8*, 5679–5686.
- (7) Forsman, J. A Simple Correlation-Corrected Poisson–Boltzmann Theory. *J. Phys. Chem. B* **2004**, *108*, 9236–9245.
- (8) Israelachvili, J. *Intermolecular and Surface Forces*; Academic Press: London, 1992.
- (9) Russel, W. B.; Saville, D. A.; Schowalter, W. R. *Colloidal Dispersions*; Cambridge University Press: Cambridge, 1989.
- (10) Matijevic, E.; Broadhurst, D.; Kerker, M. On Coagulation Effects of Highly Charged Counterions. *J. Phys. Chem.* **1959**, *63*, 1552–1557.
- (11) Szilagyi, I.; Sadeghpour, A.; Borkovec, M. Destabilization of Colloidal Suspensions by Multivalent Ions and Polyelectrolytes: From Screening to Overcharging. *Langmuir* **2012**, *28*, 6211–6215.
- (12) Miklavic, S. J.; Chan, D. Y. C.; White, L. R.; Healy, T. W. Double Layer Forces between Heterogeneous Charged Surfaces. *J. Phys. Chem.* **1994**, *98*, 9022–9032.
- (13) Feick, J. D.; Velegol, D. Measurements of Charge Non-uniformity on Polystyrene Latex Particles. *Langmuir* **2002**, *18*, 3454–3458.
- (14) Perkin, S.; Kampf, N.; Klein, J. Long-Range Attraction between Charge-Mosaic Surfaces across Water. *Phys. Rev. Lett.* **2006**, *96*, 038301.
- (15) Park, B. J.; Vermant, J.; Furst, E. M. Heterogeneity of the Electrostatic Repulsion between Colloids at the Oil–Water Interface. *Soft Matter* **2010**, *6*, 5327–5333.
- (16) Xu, S. H.; Sun, Z. W. Progress in Coagulation Rate Measurements of Colloidal Dispersions. *Soft Matter* **2011**, *7*, 11298–11308.
- (17) Ehl, L.; Jia, Z.; Wu, H.; Lattuada, M.; Soos, M.; Morbidelli, M. Role of Counterion Association in Colloidal Stability. *Langmuir* **2009**, *25*, 2696–2702.
- (18) Schneider, C.; Hanisch, M.; Wedel, B.; Jusufi, A.; Ballauff, M. Experimental Study of Electrostatically Stabilized Colloidal Particles: Colloidal Stability and Charge Reversal. *J. Colloid Interface Sci.* **2011**, *358*, 62–67.
- (19) Behrens, S. H.; Borkovec, M.; Schurtenberger, P. Aggregation in Charge-Stabilized Colloidal Suspensions Revisited. *Langmuir* **1998**, *14*, 1951–1954.
- (20) Heuberger, M.; Zach, M.; Spencer, N. D. Density Fluctuations under Confinement: When Is a Fluid not a Fluid? *Science* **2001**, *292*, 905–908.
- (21) Bevan, M. A.; Prieve, D. C. Direct Measurement of Retarded van der Waals Attraction. *Langmuir* **1999**, *15*, 7925–7936.
- (22) Crocker, J. C.; Grier, D. G. Microscopic Measurement of the Pair Interaction Potential of Charge-Stabilized Colloid. *Phys. Rev. Lett.* **1994**, *73*, 352–355.
- (23) Gutsche, C.; Keyser, U. F.; Kegler, K.; Kremer, F. Forces between Single Pairs of Charged Colloids in Aqueous Salt Solutions. *Phys. Rev. E* **2007**, *76*, 031403.
- (24) Ducker, W. A.; Senden, T. J.; Pashley, R. M. Direct Measurement of Colloidal Forces Using an Atomic Force Microscope. *Nature* **1991**, *353*, 239–241.
- (25) Butt, H. J.; Cappella, B.; Kappl, M. Force Measurements with the Atomic Force Microscope: Technique, Interpretation and Applications. *Surf. Sci. Rep.* **2005**, *59*, 1–152.
- (26) Drelich, J.; Long, J.; Xu, Z.; Masliyeh, J.; White, C. L. Probing Colloidal Forces between a Si<sub>3</sub>N<sub>4</sub> AFM Tip and Single Nanoparticles of Silica and Alumina. *J. Colloid Interface Sci.* **2006**, *303*, 627–638.
- (27) Toikka, G.; Hayes, R. A.; Ralston, J. Surface Forces between Spherical ZnS Particles in Aqueous Electrolyte. *Langmuir* **1996**, *12*, 3783–3788.
- (28) Larson, I.; Drummond, C. J.; Chan, D. Y. C.; Grieser, F. Direct Force Measurements between Dissimilar Metal Oxides. *J. Phys. Chem.* **1995**, *99*, 2114–2118.

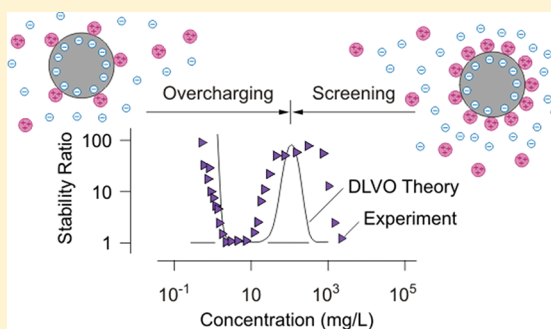
# Destabilization of Colloidal Suspensions by Multivalent Ions and Polyelectrolytes: From Screening to Overcharging

Istvan Szilagyi, Amin Sadeghpour, and Michal Borkovec\*

Department of Inorganic, Analytical, and Applied Chemistry, University of Geneva, Sciences II, 30 Quai Ernest-Ansermet, 1205 Geneva, Switzerland

## Supporting Information

**ABSTRACT:** The destabilization of charged colloidal suspensions is studied in the presence of polyelectrolytes and the corresponding oligomers. Two different systems are investigated, namely, negatively charged particles in the presence of polyamines and positively charged ones in the presence of polycarboxylates. Multivalent oligomers of low valence destabilize the particles by screening according to the Schulze–Hardy rule. Polyelectrolytes induce destabilization by overcharging. Both regimes can be observed for oligomers of intermediate valence. The stability data of any valence can be rather well described by the theory of Derjaguin, Landau, Verwey, and Overbeek (DLVO), indicating that the interactions are mainly governed by van der Waals and electrostatic double-layer forces.



## INTRODUCTION

The great achievement of the theory developed by Derjaguin, Landau, Verwey, and Overbeek (DLVO) was to derive the Schulze–Hardy rule from first principles.<sup>1–4</sup> This rule states that the critical coagulation concentration (CCC) scales as  $z^{-6}$ , where  $z$  is the valence of the counterion.<sup>5–7</sup> DLVO theory accounts for the sharp transition between slow and rapid aggregation regimes located at the CCC by stipulating that interparticle forces are dominated by the van der Waals attraction and electrostatic double-layer repulsion.<sup>8–10</sup> The latter forces have been deduced from Poisson–Boltzmann (PB) theory, which predicts a weakening of these forces due to increased screening at larger valence. This picture remained uncontested for almost half a century until theoretical evidence emerged that PB theory fails for multivalent ions because of ion–ion correlations.<sup>11–13</sup> For multivalent ions, such correlation effects predict a charge reversal and additional attractive forces that are not captured within the classical DLVO framework. These effects were suggested to be responsible for the collapse of polyelectrolyte brushes<sup>14</sup> or multilayers,<sup>15</sup> but their role in colloidal stability has hardly been addressed so far.<sup>7,16</sup>

Recently, the role of oppositely charged polyelectrolytes in the stability of colloidal suspensions has been investigated.<sup>17–21</sup> Suspensions aggregate rapidly near the isoelectric point (IEP), whereas aggregation slows down away from this point. This characteristic behavior can be explained by a charge reversal induced by the adsorbed polyelectrolyte, which initially leads to charge neutralization at the IEP and subsequent overcharging. Such overcharging was attributed to ion–ion correlation effects or the presence of dispersion or hydrophobic forces.<sup>12</sup> In these systems, the aggregation is further accelerated by additional

attractive non-DLVO forces, which originate from the patchy distribution of the surface charge.<sup>17,18,22</sup> However, the position of the IEP is typically independent of the valence (or the molecular mass) of the polyelectrolyte, which is in sharp contrast to the Schulze–Hardy rule.<sup>17,18,20,21</sup>

Here, we clarify the nature of the transition between the Schulze–Hardy and polyelectrolyte regimes by studying particle aggregation induced by polyelectrolyte oligomers. By comparing negatively charged carboxylated latex particles in the presence of cationic linear poly(ethylene imine) (LPEI) oligomers and positively charged amidine latex particles in the presence of anionic poly(acrylic acid) (PAA) oligomers, we find that this transition is governed by a competition between screening and overcharging effects. We further show that the experimental data can be well rationalized within classical DLVO theory.

## EXPERIMENTAL SECTION

Negatively charged carboxylated polystyrene latex particles with a diameter of 307 nm and positively charged amidine latex with a diameter of 220 nm were obtained from Interfacial Dynamic Corporation. Linear poly(ethylene imine) (LPEI) was purchased from Polysciences, and the respective oligomers were purchased from Sigma-Aldrich. Poly(acrylic acid) and its oligomers originate from Polymer Source Incorporation. Time-resolved dynamic light scattering was used to measure the particle aggregation rates. Each correlation function was repeatedly accumulated at a scattering angle of 90° with a compact goniometer system (ALV/CGS-3, Langen, Germany) for 20 s, and the apparent hydrodynamic radii were obtained through a

Received: February 6, 2012

Revised: March 23, 2012

Published: April 2, 2012



cumulant fit. The stability ratio  $W$  was evaluated by normalizing the inverse rate of the increase in the hydrodynamic radius with respect to fast aggregation conditions in excess KCl at a particle concentration of about 11 mg/L.<sup>3,18</sup> The electrophoretic mobility of the suspensions was measured by laser Doppler velocimetry with a Zetasizer Nano ZS (Malvern Instruments, Worcestershire, U.K.) under the same conditions as used for the stability experiments. Electrophoresis experiments were then used to estimate the partitioning between adsorbed and dissolved oligomers and polyelectrolytes by recording the mobility at two different particle concentrations.<sup>23</sup> Further details on materials and experimental methods are given in the Supporting Information.

## RESULTS AND DISCUSSION

Let us first discuss the experimental results for the stability of negatively charged particles in the presence of cationic polyelectrolytes or its oligomers. Figure 1a shows the stability ratio  $W$  of carboxylated latex particles in 1 mM KCl electrolyte at pH 4.0 in the presence of methylamine (N1), diethylenetriamine (N3), tetraethylenepentamine (N5), and LPEI with molecular masses of 2.5 kg/mol (N58) and 250 kg/mol (N5800). Sequence N1 and N3 illustrates the classical Schulze–Hardy rule. The particles aggregate slowly at low salt concentration, and the aggregation becomes rapid at higher concentrations. The CCC separates these two regimes, and its value shifts to substantially lower concentrations when N1 ( $1 \times 10^4$  mg/L) is replaced by N3 (30 mg/L).

Re-entrant fast aggregation behavior is observed with N5, however. At low concentration, the aggregation is slow but reaches a first fast aggregation regime at concentrations above 2 mg/L. The aggregation slows down again around 10 mg/L. The stability ratio remains at an intermediate plateau with  $W \approx 80$  and decreases near  $2 \times 10^3$  mg/L to reach the second fast aggregation regime. The first fast regime is induced by overcharging due to adsorbing N5, as can be confirmed by electrophoresis (Figure 1b). The electrophoretic mobility indeed reverses its sign at 5 mg/L, and this IEP lies within the first fast regime. The onset of the second fast regime is dictated by screening by the monovalent chloride anions because the particles are now positively charged. The stability in the presence of the polyelectrolytes is dominated by the overcharging, and the aggregation rate goes from slow to fast and back to slow. Indeed, the regime of fast aggregation coincides well with the position of the IEP observed by electrophoresis, and its position is independent of the molecular mass.

One encounters an entirely analogous situation for positively charged particles in the presence of an anionic polyelectrolyte and its oligomers. Figure 2 summarizes the results with amidine latex particles in 1 mM KCl electrolyte at pH 5.8 in the presence of acetic acid (C1), glutaric acid (C2), 1-(2-methylbutyl)heptane-1,3,5,7-tetracarboxylic acid (C4) and PAA with molecular masses of 5.7 kg/mol (C88) and 88 kg/mol (C1200). One observes very similar trends as for the oligomeric amines discussed above. Simple screening behavior is observed for C1, whereas C2 shows a small intermediate plateau due to overcharging. The overcharging effect is very pronounced for C4, whereby the intermediate plateau is no longer measurable. The first aggregation regime is located near the IEP around 1 mg/L, and the onset of the second fast aggregation regime is shifted to  $8 \times 10^4$  mg/L. Under these conditions, the particles are negatively charged and the counterions are now the monovalent potassium cations. The PAA analogs adsorb more strongly to the oppositely charged

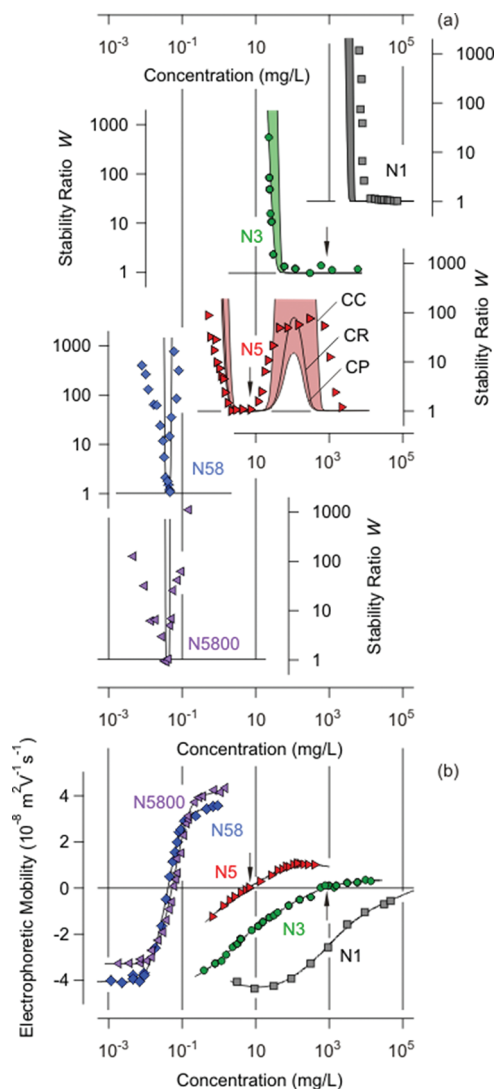


**Figure 1.** Properties of suspensions of carboxylated latex particles in the presence linear aliphatic amines at pH 4 and an ionic strength of 1.0 mM. Comparison of (a) colloidal stability and (b) electrophoretic mobility versus the oligomer or polyelectrolyte concentration. Solid lines are interpolations in b, and calculations are based on DLVO theory in a. Boundary conditions are the constant charge (CC), constant potential (CP), and constant regulation (CR). Isoelectric points (IEPs) induced by the oligomers are indicated by arrows. Horizontal grid lines indicate  $W = 1$ , and the vertical ones indicate the same concentrations.

latex particles than do the polyamines, which could be related to weaker dispersion or hydrophobic interactions in the latter system. The polyelectrolytes are dominated by overcharging only, and the position of the IEP is again independent of the molecular mass.

Because these two oppositely charged systems behave entirely analogously, we suspect that the observed trends are generic and that particle interactions are dominated by electrostatics. Screening dominates the destabilization in the presence of counterions of low valence. As the concentration of the salt is increased, the dissolved ions screen the electrostatic double-layer repulsion. With increasing valence, screening becomes more effective, and the CCC decreases. At the same time, however, a larger valence leads to an increasingly strong adsorption to the surface and to overcharging. This over-

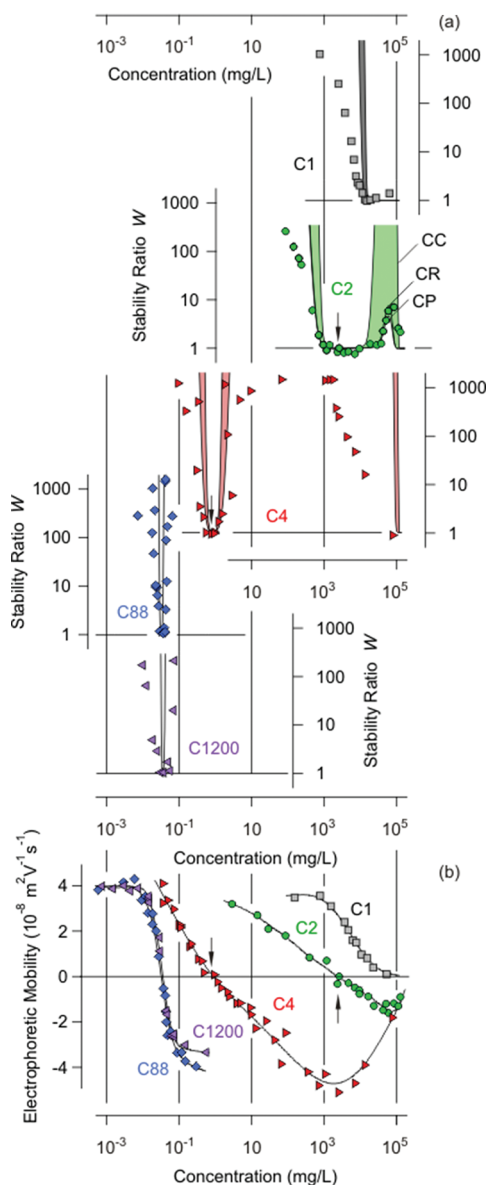


**Figure 2.** Properties of suspensions of amidine latex particles in the presence linear carboxylates at pH 5.8 and an ionic strength of 1.0 mM. Comparison of (a) colloidal stability and (b) electrophoretic mobility vs the oligomer or polyelectrolyte concentration. Solid lines are interpolations in b and predictions of linearized DLVO theory in a. Boundary conditions are the constant charge (CC), constant potential (CP), and constant regulation (CR). Isoelectric points (IEPs) induced by the oligomers are indicated by arrows. Horizontal grid lines indicate  $W = 1$ , and vertical ones indicate the same concentrations.

charging is responsible for the intermediate first aggregation regime, which finally entirely dominates the stability in the presence of polyelectrolytes. Under these circumstances, the valence of the polyelectrolyte no longer influences the position of the IEP. This “polyelectrolyte rule” has been previously reported for LPEI,<sup>20</sup> PAA,<sup>21</sup> and other polyelectrolytes.<sup>17,18,24</sup> In the latter case, polyelectrolytes adsorb quantitatively and screening originates only from the salt ions dissolved in solution, which is KCl in the present case. For the oligomers investigated, however, they partition principally into solution and screening is determined by the dissolved multivalent ions. As detailed in the Supporting Information, this characteristic

partitioning behavior has been confirmed by studying the electrophoretic mobility at different particle concentrations.<sup>23</sup>

The solid lines shown in Figures 1a and 2a refer to modeling results based on DLVO theory within the Derjaguin approximation. The concentration dependence of the electrophoretic mobility was interpolated and converted to surface potentials ( $\zeta$  potential) with Henry’s model.<sup>3</sup> The resulting electrostatic potentials were used to estimate the double-layer interaction on the Debye–Hückel level by invoking the boundary conditions of constant charge (CC) and constant potential (CP). For the oligomers, the ionic strength was calculated by taking the partial dissociation of the oligomers into account. The stability ratios were obtained by considering the hydrodynamic interactions and van der Waals forces. The latter were quantified with a Hamaker constant of  $9.0 \times 10^{-21}$  J for the carboxylated latex particles and  $2.0 \times 10^{-21}$  J for amidine particles. One should note that for the calculated stability ratios shown in Figures 1 and 2 the magnitude of the surface potential obtained from the mobility experiments is always below 25 mV, which is a condition that must be satisfied such that Henry’s and Debye–Hückel theory are applicable. Further details on the DLVO calculations are given in the Supporting Information.

One observes that results of such DLVO calculations agree with the experimental data rather well. Because the plateau value in the stability ratio for NS is very sensitive to the boundary conditions, we found that the data can be rationalized with a charge regulation (CR) model with a regulation parameter of 0.3. A similar situation arises with C2, and the observed peak in the stability ratio can be well described with a regulation parameter of 0.1.

A substantial discrepancy between the experimental data and DLVO calculations can be observed for C4 at higher concentrations. In this case, the experimentally observed dependence of the stability ratio on the concentration is much weaker than modeled by DLVO theory. This discrepancy is probably related to the fact that monovalent potassium cations are responsible for the screening and the barrier in the interaction potential lies at small separation distances, in fact, below 1 nm.<sup>8,9</sup> When multivalent ions act as counterions, the barrier shifts toward larger separations, making DLVO theory more accurate.<sup>7</sup> Similar effects may be responsible for analogous but less important discrepancies for C1 and C2. One also observes that suspensions are less stable in the presence of polyelectrolytes than DLVO theory suggests. This decrease in stability is probably related to the presence of electrostatic patch–charge attractions, which originate from the heterogeneous charge distribution within adsorbed polyelectrolyte layers.<sup>18,21,22</sup>

The overall good agreement between experimental stability data and DLVO calculations indicate that forces operating between the particles are well approximated within DLVO theory and that the  $\zeta$  potential provides a good estimate of the strength of the electrostatic double-layer interactions. This aspect may seem surprising from the point of view of modern theories of the electrical double layer, which predict additional attractive forces due to ion correlations.<sup>11,12</sup> Such attractions seem not to play a dominant role in the systems investigated here. A possible explanation of this inconsistency might be that ion correlations remain relevant for the adsorption process and the resulting extent of overcharging within the compact layer but that they are of minor importance within the diffuse layer, which appears to be well described by classical DLVO theory.

However, such forces could well represent the origin of the discrepancies observed for C1, C2, and, in particular, C4.

We conclude that the destabilization of charged colloidal suspensions occurs by screening in the case of small ions and by overcharging in the case of polyelectrolytes. With increasing counterion valence, the CCC corresponding to the first fast aggregation regime shifts toward lower concentrations according to the Schulze–Hardy rule. However, the position of the IEP is independent of the valence or the molecular mass of the polyelectrolyte, which is in line with the polyelectrolyte rule. Figure 3 illustrates this trend with additional data for oligomers

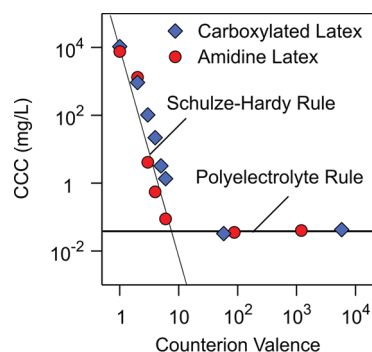


**Figure 3.** Variation of the critical coagulation concentration (CCC) of the first fast aggregation regime with the valence for carboxylated latex particles in the presence of linear aliphatic amines and for amidine latex particles in the presence of linear carboxylates. Full dissociation is assumed for simplicity. The solid lines show the dependencies expected from the Schulze–Hardy and the polyelectrolyte rules.

obtained at different valences. The transition between these two regimes occurs at a valence of about 10. The intermediate regime situated between valences 3–6 is characterized by two fast aggregation regimes. The first regime is located near the IEP and is governed by overcharging, and the second one is induced by the screening of the overcharged particle by the oligomer counterions. The fact that the suspension stability can be well described with DLVO theory has two main implications. First, non-DLVO forces are of minor importance in colloidal stability. Second, DLVO theory can be used to assess the suspension stability in systems containing multivalent ions and/or polyelectrolytes rather well. The latter finding could be of substantial importance for the design of novel flocculating agents that rely on mixtures of multivalent ions and polyelectrolytes.

## ■ ASSOCIATED CONTENT

### Supporting Information

Details on experimental protocols and calculations. This material is available free of charge via the Internet at <http://pubs.acs.org>.

## ■ AUTHOR INFORMATION

### Corresponding Author

\*Phone: +41 22 379 6405. Fax: +41 22 379 6069. E-mail: [michal.borkovec@unige.ch](mailto:michal.borkovec@unige.ch).

### Notes

The authors declare no competing financial interest.

## ■ ACKNOWLEDGMENTS

This research was supported by the Swiss National Science Foundation and the University of Geneva. Helpful discussions with Robert Meszaros, Imre Varga, and Robert Pugh are gratefully acknowledged.

## ■ REFERENCES

- (1) Derjaguin, B.; Landau, L. D. Theory of the stability of strongly charged lyophobic sols and of the adhesion of strongly charged particles in solutions of electrolytes. *Acta Phys. Chim.* **1941**, *14*, 633–662.
- (2) Verwey, E. J. W.; Overbeek, J. T. G. *Theory of Stability of Lyophobic Colloids*; Elsevier: Amsterdam, 1948.
- (3) Russel, W. B.; Saville, D. A.; Schowalter, W. R. *Colloidal Dispersions*; Cambridge University Press: Cambridge, U.K., 1989.
- (4) Elimelech, M.; Gregory, J.; Jia, X.; Williams, R. A., *Particle Deposition and Aggregation: Measurement, Modeling, and Simulation*. Butterworth-Heinemann: Oxford, U.K., 1995.
- (5) Matijevic, E.; Broadhurst, D.; Kerker, M. On coagulation effects of highly charged counterions. *J. Phys. Chem.* **1959**, *63*, 1552–1557.
- (6) Metcalfe, I. M.; Healy, T. W. Charge regulation modeling of the Schulze–Hardy rule and related coagulation effects. *Faraday Discuss.* **1990**, 335–344.
- (7) Schneider, C.; Hanisch, M.; Wedel, B.; Jusufi, A.; Ballauff, M. Experimental study of electrostatically stabilized colloidal particles: colloidal stability and charge reversal. *J. Colloid Interface Sci.* **2011**, *358*, 62–67.
- (8) Ehl, L.; Jia, Z.; Wu, H.; Lattuada, M.; Soos, M.; Morbidelli, M. Role of counterion association in colloidal stability. *Langmuir* **2009**, *25*, 2696–2702.
- (9) Behrens, S. H.; Borkovec, M.; Schurtenberger, P. Aggregation in charge-stabilized colloidal suspensions revisited. *Langmuir* **1998**, *14*, 1951–1954.
- (10) Chen, K. L.; Elimelech, M. Relating colloidal stability of fullerene (C-60) nanoparticles to nanoparticle charge and electrokinetic properties. *Environ. Sci. Technol.* **2009**, *43*, 7270–7276.
- (11) Kjellander, R.; Akesson, T.; Jonsson, B.; Marcelja, S. Double layer interactions in mono- and divalent electrolytes: A comparison of the anisotropic HNC theory and Monte Carlo simulations. *J. Chem. Phys.* **1992**, *97*, 1424–1431.
- (12) Nguyen, T. T.; Grosberg, A. Y.; Shklovskii, B. I. Macroions in salty water with multivalent ions: giant inversion of charge. *Phys. Rev. Lett.* **2000**, *85*, 1568–1571.
- (13) Quesada-Perez, M.; Gonzalez-Tovar, E.; Martin-Molina, A.; Lozada-Cassou, M.; Hidalgo-Alvarez, R. Overcharging in colloids: beyond the Poisson-Boltzmann approach. *ChemPhysChem* **2003**, *4*, 235–248.
- (14) Mei, Y.; Lauterbach, K.; Hoffmann, M.; Borisov, O. V.; Ballauff, M.; Jusufi, A. Collapse of spherical polyelectrolyte brushes in the presence of multivalent counterions. *Phys. Rev. Lett.* **2006**, *97*, 158301.
- (15) Ball, V.; Hubsch, E.; Schweiss, R.; Voegel, J. C.; Schaaf, P.; Knoll, W. Interactions between multivalent ions and exponentially growing multilayers: dissolution and exchange processes. *Langmuir* **2005**, *21*, 8526–8531.
- (16) Nguyen, T. T.; Shklovskii, B. I. Kinetics of macroion coagulation induced by multivalent counterions. *Phys. Rev. E* **2002**, *65*, 031409.
- (17) Gregory, J. Rates of flocculation of latex particles by cationic polymers. *J. Colloid Interface Sci.* **1973**, *42*, 448–456.
- (18) Gillies, G.; Lin, W.; Borkovec, M. Charging and aggregation of positively charged latex particles in the presence of anionic polyelectrolytes. *J. Phys. Chem. B* **2007**, *111*, 8626–8633.
- (19) Schwarz, S.; Jaeger, W.; Paulke, B. R.; Bratskaya, S.; Smolka, N.; Bohrisch, J. Cationic flocculants carrying hydrophobic functionalities: applications for solid/liquid separation. *J. Phys. Chem. B* **2007**, *111*, 8649–8654.
- (20) Szilagy, L.; Rosicka, D.; Hierrezuelo, J.; Borkovec, M. Charging and stability of anionic latex particles in the presence of linear poly(ethylene imine). *J. Colloid Interface Sci.* **2011**, *360*, 580–585.

(21) Sadeghpour, A.; Seyrek, E.; Szilagyi, I.; Hierrezuelo, J.; Borkovec, M. Influence of the ionization degree and molecular mass of weak polyelectrolytes on charging and stability behavior of oppositely charged colloidal particles. *Langmuir* **2011**, *27*, 9270–9276.

(22) Popa, I.; Gillies, G.; Papastavrou, G.; Borkovec, M. Attractive electrostatic forces between identical colloidal particles induced by adsorbed polyelectrolytes. *J. Phys. Chem. B* **2009**, *113*, 8458–8461.

(23) Mezei, A.; Meszaros, R. Novel method for the estimation of the binding isotherms of ionic surfactants on oppositely charged polyelectrolytes. *Langmuir* **2006**, *22*, 7148–7151.

(24) Walker, H. W.; Grant, S. B. Factors influencing the flocculation of colloidal particles by a model anionic polyelectrolyte. *Colloids Surf., A* **1996**, *119*, 229–239.





Cite this: *Phys. Chem. Chem. Phys.*, 2016, 18, 7511

# Charging and aggregation of latex particles in aqueous solutions of ionic liquids: towards an extended Hofmeister series

Tamas Oncsik, Anthony Desert,<sup>†</sup> Gregor Trefalt, Michal Borkovec and Istvan Szilagy<sup>i\*</sup>

The effect of ionic liquid (IL) constituents and other monovalent salts on the stability of polystyrene latex particles was studied by electrophoresis and light scattering in dilute aqueous suspensions. The surface charge and the aggregation rate were both sensitive to the type of ion leading to different critical coagulation concentration (CCC) values. Systematic variation of the type of IL cation and anion allows us to place these ions within the Hofmeister series. We find that the dicyanoamide anion should be placed between iodide and thiocyanate, while all 1-alkyl-3-methylimidazolium cations can be positioned to the left of the tetramethylammonium and ammonium ions. The hydrophobicity of the 1-butyl-1-methylpyrrolidinium (BMPL<sup>+</sup>) ion is intermediate between 1-ethyl-3-methylimidazolium (EMIM<sup>+</sup>) and 1-butyl-3-methylimidazolium (BMIM<sup>+</sup>). With increasing alkyl chain length, the 1-alkyl-3-methylimidazolium cations adsorb on the latex particles very strongly, and 1-hexyl-3-methylimidazolium (HMIM<sup>+</sup>) and 1-octyl-3-methylimidazolium (OMIM<sup>+</sup>) lead to pronounced charge reversal and to an intermediate restabilization region.

Received 24th November 2015,  
Accepted 7th February 2016

DOI: 10.1039/c5cp07238g

www.rsc.org/pccp

## 1. Introduction

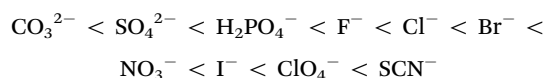
Ionic liquids (ILs) consist entirely of cations and anions, and these systems became the focus of intense research recently, mainly due to their uncommon properties, such as low vapour pressure or wide electrochemical window.<sup>1–3</sup> These aspects make ILs promising media in material science applications, including energy storage, extraction of minerals or biomolecules and electrodeposition.<sup>2–8</sup> An important class of materials in these applications are particle suspensions in ILs, as they are relevant in nanoparticle synthesis, catalysis, solar cells, or printing inks.<sup>9–13</sup> For example, numerous researchers have synthesized novel metal nanoparticles in ILs and they could relate the stability of these suspensions to their catalytic activity.<sup>11,14–17</sup> In this context, the stability of these suspensions plays a key role, and therefore particle aggregation in ILs was investigated recently.<sup>18–23</sup>

Such particle aggregation studies also focused on IL–water mixtures, and it was quickly realized that on the water-rich side the IL fully dissociates into ions, and that aqueous solutions

of ILs closely resemble simple electrolytes.<sup>19,20,24</sup> A good understanding of the influence of the presence of water in ILs is further important, since most ILs contain water to a certain extent.

Studies of colloidal particle aggregation in simple electrolyte solutions have a long history, including the landmark development of the Derjaguin, Landau, Verwey, and Overbeek (DLVO) theory.<sup>25</sup> This theory predicts, in agreement with experiment, that the aggregation of charged colloidal particles is slow at low salt concentrations, while at higher concentrations it becomes rapid. The sharp transition between these two regimes occurs at the so-called critical coagulation concentration (CCC). The CCC represents an important characteristic concerning the destabilization power of a given salt, or more precisely of the constituent ions. A major achievement of the DLVO theory was to rationalize the Schulze–Hardy rule, which states that multivalent counterions strongly lower the CCC.<sup>25–27</sup>

However, the CCC can be also influenced by other ionic properties than their valence. A well-studied aspect represents the Hofmeister series, which orders ions according to their hydrophobicity.<sup>28</sup> This series was originally developed to account for the stabilization power of protein solutions, namely

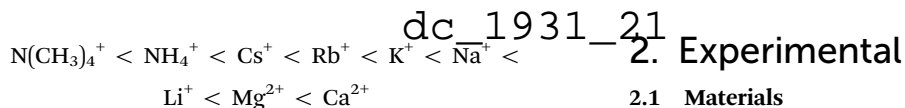


*Department of Inorganic and Analytical Chemistry, University of Geneva, 30 Quai Ernest-Ansermet, CH-1205 Geneva, Switzerland.*

*E-mail: istvan.szilagy@unige.ch; Tel: +41 22 3796031*

<sup>†</sup> Present address: École normale supérieure de Lyon, CNRS, Université de Lyon 1, Laboratoire de Chimie (UMR 5182), 46 Allée d'Italie, F-69364 Lyon, France.





The series indicates that negatively charged proteins form stable solutions even in the presence of high concentration of ions located on the right hand side, while the ions of the left hand side induce their precipitation already at low concentrations. Typically, particle aggregation follows the same series.<sup>29–33</sup> In particular, negatively charged particles follow the (above) direct Hofmeister series, whereby the ions on the left induce lower CCCs, while the ones on the right, higher ones. On the other hand, positively charged particles follow the (reversed) indirect Hofmeister series. Thereby, the ions on the left lead to higher CCCs, while the ones on the right, to lower ones. The role of divalent ions is more complicated, since their effect on particle aggregation is greatly influenced by the increased valence as described by the Schulze–Hardy rule.<sup>25–27</sup> Therefore, divalent ions are not considered here.

The position of an ion in the Hofmeister series can be qualitatively correlated with its hydrophobicity or its degree of solvation.<sup>34,35</sup> Hydrophilic and well-solvated anions, such as  $\text{F}^-$  or  $\text{Cl}^-$ , appear on the left, while hydrophobic and poorly hydrated anions, such as  $\text{I}^-$  or  $\text{SCN}^-$ , on the right. The cations are arranged in the opposite way. The hydrophilic cations, such as  $\text{Li}^+$  or  $\text{Na}^+$ , appear on the right, while the hydrophobic ones, such as  $\text{N(CH}_3)_4^+$  or  $\text{NH}_4^+$ , on the left. Many colloidal particles have a hydrophobic surface (e.g., polystyrene latex) and the hydrophobic ions will adsorb more strongly to these surfaces than the hydrophilic ones. Therefore, CCC will be lower in the presence of hydrophobic counterions than in the presence of hydrophilic ones. Conversely, the CCC will be higher in the presence of hydrophobic coions than in the presence of hydrophilic ones. In the latter situation, however, electrostatic repulsion between the coions and the charged particle may lead to very weak adsorption, and these effects may not be noticeable. In general, the CCCs will decrease with increasing hydrophobicity of cations for negatively charged hydrophobic particles (direct Hofmeister series), while they will also decrease with decreasing hydrophobicity of cations for positively charged particles (indirect Hofmeister series). The reverse argumentation applies to hydrophilic particles (e.g., silica). These trends have been confirmed by CCC measurements in numerous systems experimentally.<sup>29,31,32,36–38</sup>

In the present study, we investigate charging and aggregation of polystyrene latex particles in aqueous solutions of ILs. From the concentration dependence of the aggregation rate, one can extract the CCC, and the observed sequences in these quantities can be used to place the IL constituents into the Hofmeister series. The present investigation is related to an earlier study published by us, which focused on simple monovalent ions only.<sup>29</sup> That study used the same particles as the present one, thus facilitating a direct comparison of both. While ion specific effects on protein solubilisation and enzymatic activity in aqueous solutions of ILs were studied with a similar aim,<sup>39–43</sup> we believe that the determination of the CCC for uniform particles provides a reliable measure concerning the position of IL constituents within the Hofmeister series.

## 2. Experimental

### 2.1 Materials

Sulfate and amidine functionalized polystyrene latex particles were purchased from Invitrogen Corporation. The size and polydispersity of the particles were determined by interpreting static light scattering (SLS) data in stable suspensions using Mie theory.<sup>44</sup> Very good agreement was found with the values obtained in transmission electron microscopy (TEM) measurements by the manufacturer (Table 1). Dynamic light scattering (DLS) yielded slightly higher hydrodynamic radii, probably due to sample polydispersity. The same particles were used in our previous study,<sup>29</sup> where further properties of these particles are given. Prior to the experiments, the particles were dialyzed against ultrapure water until the conductivity remained constant and below  $0.8 \mu\text{S cm}^{-1}$ . For the dialysis, cellulose ester and polyvinylidene fluoride membranes (Spectrum Rancho) were used for the sulfate and amidine modified latex suspensions, respectively. The particle concentrations in the dialyzed stock suspensions were determined by SLS, whereby a calibration curve of the scattering intensity obtained with the original particle suspensions of known concentration was used. Typical concentrations in these stock suspensions were 65 and 7  $\text{g L}^{-1}$  for sulfate and amidine particles, respectively. Ultrapure Milli-Q water (Millipore) was used throughout.

ILs used in this study were purchased from IoLiTech and they include 1-butyl-3-methylimidazolium as a cation with chloride (BMIM–Cl), bromide (BMIM–Br), dicyanoamide (BMIM–N(CN)<sub>2</sub>) and thiocyanate (BMIM–SCN) ions, 1-butyl-1-methylpyrrolidinium ILs as the same anions (BMPL–Cl, BMPL–Br, BMPL–N(CN)<sub>2</sub> and BMPL–SCN) and the chloride salts of 3-methylimidazolium (MIM–Cl), 1-ethyl-3-methylimidazolium (EMIM–Cl), 1-hexyl-3-methylimidazolium (HMIM–Cl) and 1-octyl-3-methylimidazolium cations (OMIM–Cl) (Fig. 1). The ILs were dried under vacuum at 50 °C for one day and Karl-Fischer titration (Metrohm) was performed to determine their final water content, which was always below 1  $\text{g L}^{-1}$ . The dried ILs were handled in a glove box. In some cases, mixing the ILs with water resulted in the formation of precipitates due to the presence of impurities, which could be detected by light scattering. These precipitates were removed by allowing the aqueous solutions to stand overnight and filtering with a 0.1  $\mu\text{m}$  syringe filter (Millipore). Inorganic salts of analytical grade were purchased from Sigma Aldrich (NaCl, NaN(CN)<sub>2</sub> and NaSCN) and Fluka (NaBr). Their solutions were prepared by mixing the calculated amount of solid salt with ultrapure water. All stock solutions and water

Table 1 Characteristic size values of the sulfate and amidine functionalized polystyrene latex particles used in the present study

Latex particles	Average radius (nm)			Polydispersity <sup>c</sup> (%)	
	TEM <sup>a</sup>	SLS <sup>b</sup>	DLS <sup>b</sup>	TEM <sup>a</sup>	SLS <sup>b</sup>
Sulfate	265	263	278	2.0	3.8
Amidine	110	110	117	4.3	7.1

<sup>a</sup> Measured by the manufacturer. <sup>b</sup> Determined in stable suspensions. <sup>c</sup> Coefficient of variation.



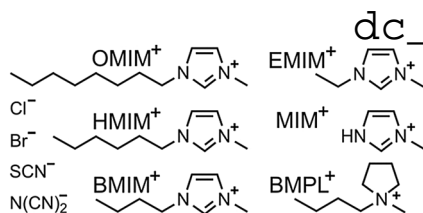


Fig. 1 Chemical structure of IL constituents used in the present study. The anions include chloride, bromide, thiocyanide and dicyanoamide with methylimidazolium, 1-alkyl-3-methylimidazolium and 1-butyl-1-methylpyrrolidinium as cations.

were adjusted to pH 4.0 with HCl and filtered prior to sample preparation. The measurements were carried out at a temperature of  $25.0 \pm 0.2$  °C.

## 2.2 Electrophoresis

A ZetaSizer Nano ZS (Malvern) instrument was used to determine the electrophoretic mobility of the particles. During sample preparation, water was mixed with the appropriate volume of stock electrolyte or IL solutions to reach the desired concentration. The particles were then added from the concentrated stock suspension to get final particle concentrations of  $5 \text{ mg L}^{-1}$  in the case of amidine and  $50 \text{ mg L}^{-1}$  for the sulfate latex. The samples were equilibrated for one minute in the instrument prior to the measurements. Five repetitions were performed and averaged.

## 2.3 Particle aggregation

Time-resolved DLS was used to follow the aggregation process in aqueous particle suspensions. This technique has proved to be most suitable to determine aggregation rates of colloidal particles.<sup>45–47</sup> The instrument used was an ALV/CGS-3 goniometer (ALV) system, equipped with a He/Ne laser of a wavelength of 633 nm and an avalanche photodiode as a detector. Samples were prepared in borosilicate glass cuvettes (Kimble Chase). Before the measurements, the cuvettes were cleaned in piranha solution, which is a mixture of concentrated  $\text{H}_2\text{SO}_4$  (Carlo Erba) and 30%  $\text{H}_2\text{O}_2$  (Reactolab) in a volume ratio of 3 : 1. Subsequently, they were washed with water and dried in a dust-free oven at 60 °C. The particle concentrations were varied in the range of  $2\text{--}10 \text{ mg L}^{-1}$  for the amidine latex and  $50\text{--}200 \text{ mg L}^{-1}$  for the sulfate latex, which corresponds to the number concentration range of  $(0.3\text{--}2.0) \times 10^{15} \text{ m}^{-3}$ . To start the aggregation experiment, the particle stock suspension was injected into a cuvette containing the respective salt solution, and the sample was mixed and inserted in the light scattering system. The correlation function was recorded for 20 seconds at a scattering angle of  $90^\circ$  and the second-order cumulant fit was used to determine the hydrodynamic radius. The change in this quantity was followed in 50–100 subsequent runs. To probe the early stages of the aggregation, the hydrodynamic radius values never increased more than 40% in these experiments. This increase is an adequate compromise between good measurement accuracy and minor interferences of higher aggregates.<sup>45,48</sup> The apparent dynamic aggregation rate coefficient  $\Delta$  was determined from the initial rate of increase

$$\Delta = \frac{1}{R_h(0)} \cdot \left. \frac{dR_h}{dt} \right|_{t \rightarrow 0} \quad (1)$$

where  $R_h$  is the hydrodynamic radius and  $t$  is the time. The measured apparent rates were then converted to absolute aggregation rate coefficients  $k$  by means of the relation

$$k = \frac{\Delta}{\Delta_{\text{fast}}} \cdot k_{\text{fast}} \quad (2)$$

where  $\Delta_{\text{fast}}$  is the apparent dynamic aggregation rate coefficient in 1.0 M KCl solution, where the aggregation is in the fast regime. The absolute aggregation rate coefficient  $k_{\text{fast}}$  was previously determined using time-resolved simultaneous static and dynamic light scattering in 1.0 M KCl solutions. In these measurements, the apparent static rate coefficients were obtained from the initial change of the scattered intensity at several scattering angles and plotted against the apparent dynamic aggregation rates. A linear fit was performed on the data and the absolute aggregation rate coefficient was calculated from the intercept.<sup>45</sup> The resulting values were  $k_{\text{fast}} = (3.3 \pm 0.2) \times 10^{-18} \text{ m}^3 \text{ s}^{-1}$  for the sulfate latex and  $(3.0 \pm 0.2) \times 10^{-18} \text{ m}^3 \text{ s}^{-1}$  for the amidine latex.<sup>29</sup> The CCCs were determined from plots of the rate coefficient  $k$  versus the salt concentration, whereby straight lines were fitted to the experimental points in the slow and fast aggregation regimes. The uncertainty of the CCC determined by this method is about 10%.

## 2.4 Viscosity

A DV-II Pro viscometer (Brookfield) was used to measure the dynamic viscosities of the IL solutions. The concentration ranges of the monovalent electrolytes were chosen according to the concentrations investigated in the mobility and aggregation measurements, usually up to 1.0 M. In this range, the viscosities varied linearly with the concentration, and the values for the individual samples were obtained from a linear fit of the data.

# 3. Results and discussion

Surface charge and aggregation rates of sulfate and amidine modified polystyrene latex particles were investigated in the presence of ILs and monovalent electrolytes by electrophoresis and DLS. The principal aim of these experiments was to place some common IL constituents (Fig. 1) into the Hofmeister series. In addition, the influence of the alkyl chain length within the 1-alkyl-3-methylimidazolium series was investigated.

## 3.1 General trends

Electrophoretic mobilities and aggregation rates of sulfate and amidine latex particles were measured in different ionic environments. Initially, we investigated the effect of anions, namely  $\text{Cl}^-$ ,  $\text{Br}^-$ ,  $\text{N}(\text{CN})_2^-$  and  $\text{SCN}^-$ , in the presence of  $\text{Na}^+$  as the cation (Fig. 2). Subsequently, the same anions were investigated in the presence of  $\text{BMIM}^+$  (Fig. 3) and  $\text{BMPL}^+$  (Fig. 4) as cations. In all systems, the electrophoretic mobility increases with the salt concentration for the sulfate particles and decreases for the amidine particles, sometimes resulting in an isoelectric point (IEP) and a subsequent weak charge reversal. These trends are mainly caused by the progressive screening through the



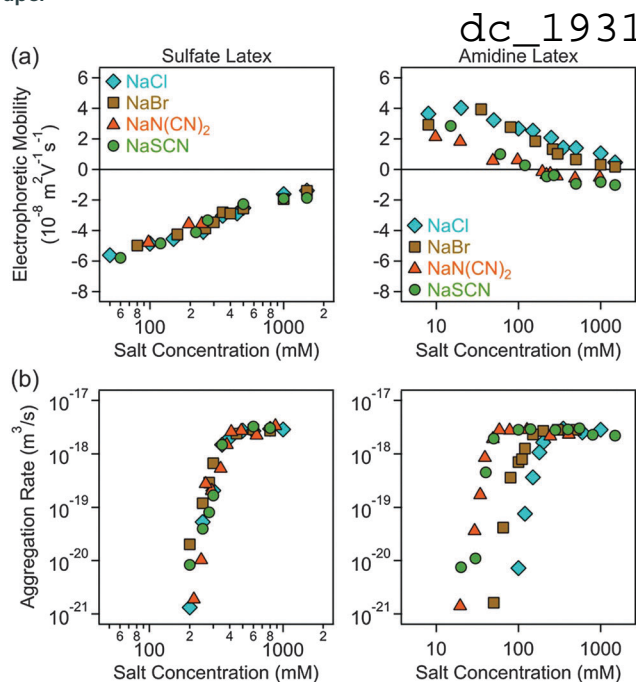


Fig. 2 Electrophoretic mobility (a) and absolute aggregation rate (b) for sulfate (left column) and amidine (right column) latex particles as a function of the salt concentration for different monovalent electrolytes of the sodium cation. The results with the  $\text{Cl}^-$ ,  $\text{Br}^-$  and  $\text{SCN}^-$  ions have been already published earlier.<sup>29</sup>

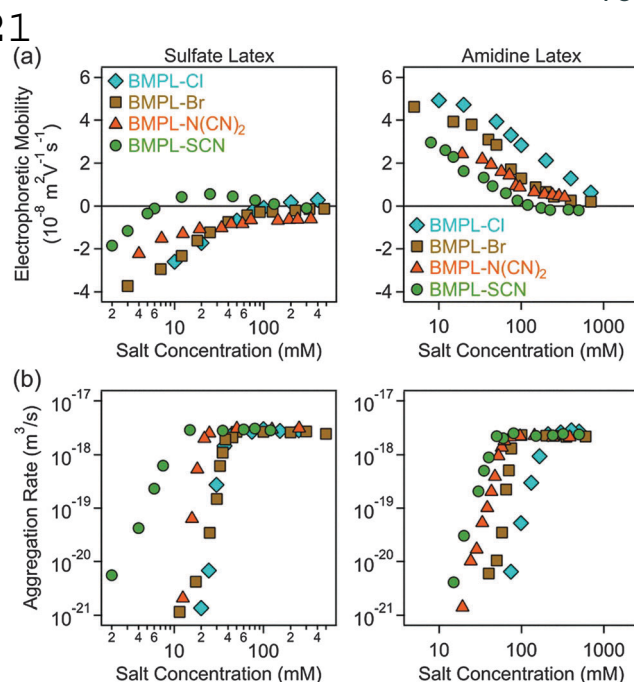


Fig. 4 Electrophoretic mobility (a) and absolute aggregation rate (b) values of sulfate (left column) and amidine (right column) latex particles as a function of the salt concentration for different ILs of the  $\text{BMPL}^+$  cation.

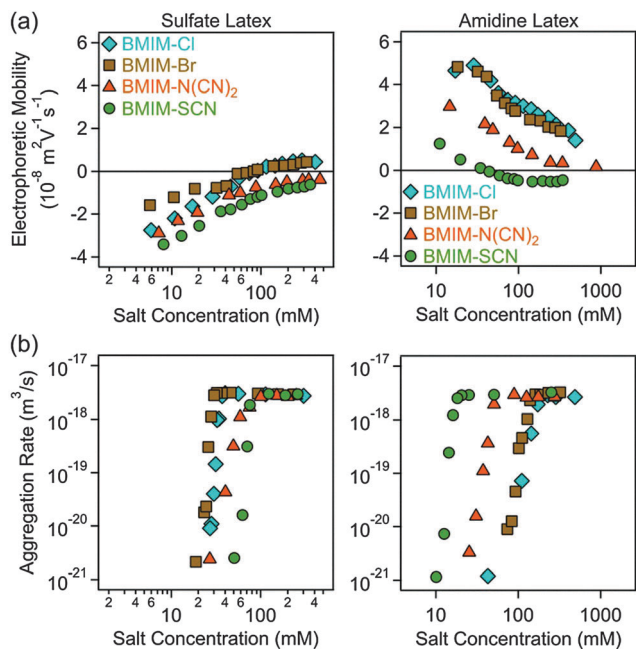


Fig. 3 Electrophoretic mobility (a) and absolute aggregation rate (b) values of sulfate (left column) and amidine (right column) latex particles as a function of the salt concentration in aqueous solutions of different ILs of the  $\text{BMIM}^+$  cation.

electrolyte and simultaneous adsorption of the counterions. The particle aggregation rates increase rapidly with increasing salt concentration in the slow aggregation regime, and reach a

constant value at higher concentrations in the fast aggregation regime. The CCC is located in the narrow transition zone between these two regimes. This behaviour is typical for charged colloidal particles dispersed in electrolyte solutions and can be predicted by the DLVO theory,<sup>25</sup> in some situations even quantitatively.<sup>49,50</sup> The characteristic influence of the type of ion present on the CCCs will be detailed below. No clear trends were observed in the dependencies of the aggregation rates on the salt concentration in the slow aggregation regimes.

### 3.2 Fast aggregation regime

The possible influence of the ion type on the fast aggregation rate coefficients measured above the CCCs was addressed. The ions investigated include  $\text{Cl}^-$ ,  $\text{Br}^-$ ,  $\text{N}(\text{CN})_2^-$  and  $\text{SCN}^-$  anions, and  $\text{Na}^+$ ,  $\text{BMIM}^+$  and  $\text{BMPL}^+$  cations. As one must consider viscosity effects, the absolute rate coefficients in the fast aggregation regime were normalized by Smoluchowski's rate coefficient for diffusion controlled aggregation<sup>51</sup>

$$k_S = \frac{8k_B T}{3\eta} \quad (3)$$

where  $k_B$  is the Boltzmann constant,  $T$  is the temperature, and  $\eta$  is the dynamic viscosity of the electrolyte solution. The latter value was measured for the respective salt or IL solutions within the appropriate concentration range. No dependence of the normalized fast aggregation rate coefficients on the type of ion is observed, and one finds very similar normalized coefficients for both types of particles (Fig. 5a). Their values were  $k_{\text{fast}}/k_S = 0.24 \pm 0.01$  and  $0.24 \pm 0.02$  for the sulfate and amidine particles, respectively. These values are comparable to the ones reported earlier for the same particles in the presence of





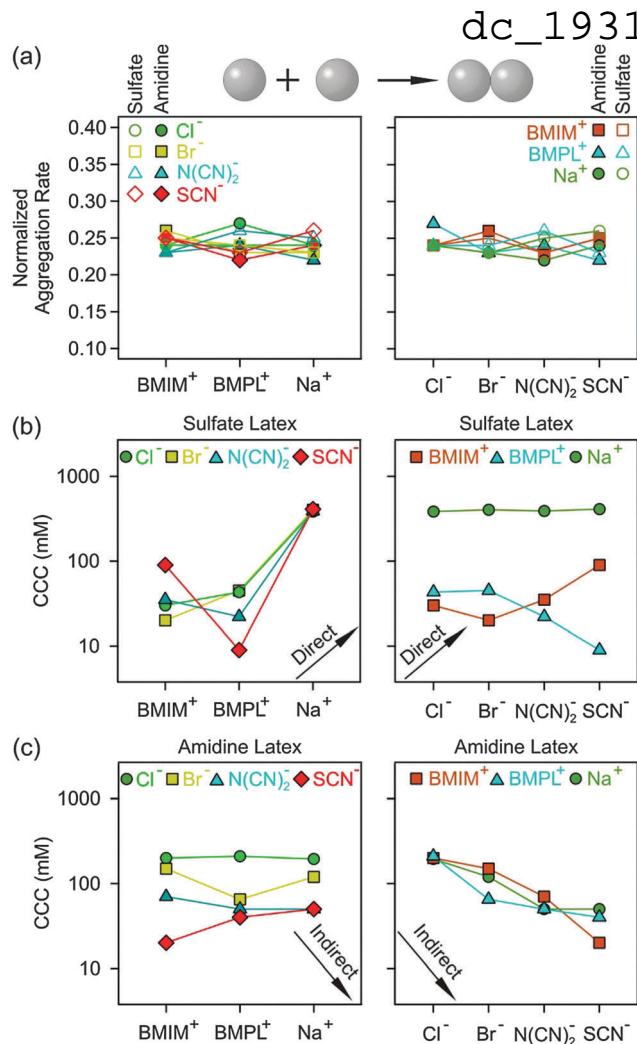


Fig. 5 Normalized fast aggregation rate coefficients (a) and CCC values for sulfate (b) and amidine (c) latex particles in the presence of different cations (left) and anions (right). The arrows indicate the expected trends according to the direct or indirect Hofmeister series. The lines are a guide to the eye.

several simple monovalent electrolytes, which were  $0.26 \pm 0.01$  and  $0.23 \pm 0.01$  for the sulfate and amidine latex, respectively.<sup>29</sup> These findings suggest that the attractive forces (*i.e.*, van der Waals and hydrophobic forces), which determine the fast aggregation rates, do not strongly depend on the type of ion present.

### 3.3 Ion specific effects

For negatively charged sulfate latex particles, there were no specific effects of the coions, provided Na<sup>+</sup> was used as the counterion. All the anions used, namely Cl<sup>-</sup>, Br<sup>-</sup>, N(CN)<sub>2</sub><sup>-</sup> and SCN<sup>-</sup>, adsorb to the particle surface only weakly, and therefore the electrophoretic mobility (Fig. 2a), aggregation rates (Fig. 2b) and CCCs (Fig. 5b) remain the same within the experimental error. With the exception of the N(CN)<sub>2</sub><sup>-</sup> anion, the same observation was already reported earlier.<sup>29</sup> For the amidine latexes, the electrophoretic mobilities decrease with the salt level and their values at the same concentration decrease within the series Cl<sup>-</sup>, Br<sup>-</sup>, N(CN)<sub>2</sub><sup>-</sup>, and SCN<sup>-</sup> (Fig. 2a). The adsorption of N(CN)<sub>2</sub><sup>-</sup>

and SCN<sup>-</sup> ions results in an IEP and a charge reversal, suggesting that these ions are rather hydrophobic and that they adsorb on these particles strongly. Similar charge reversal has been observed with other less solvated monovalent ions.<sup>29,34,52</sup>

The trend in the mobilities is also reflected in the CCCs (Fig. 2b and 5c). One observes that the CCC decreases in the same sequence as stated above, namely for Cl<sup>-</sup> being the highest and for N(CN)<sub>2</sub><sup>-</sup> and SCN<sup>-</sup> the lowest. This order can be explained as follows. The hydrophobic counterions, such as N(CN)<sub>2</sub><sup>-</sup> and SCN<sup>-</sup>, adsorb strongly on the hydrophobic particle surface, leading to a decrease of the surface charge and to lower CCCs. On the other hand, the hydrophilic Cl<sup>-</sup> counterion adsorbs weakly leading to highly charged particles, which also have higher CCCs. The observed sequence Cl<sup>-</sup> > Br<sup>-</sup> > SCN<sup>-</sup> reflects the expected indirect Hofmeister series, as reported before.<sup>29</sup> The new finding here is that N(CN)<sub>2</sub><sup>-</sup> behaves similar to SCN<sup>-</sup>. This observation agrees with earlier protein precipitation experiments.<sup>42</sup>

When the BMIM<sup>+</sup> counterion was used, electrophoretic mobilities and aggregation rates of the negatively charged sulfate latex particles were strongly influenced by the type of coion (Fig. 3a and b). The magnitude of the mobility and of the CCCs (Fig. 5b) was significantly lower in the presence of BMIM<sup>+</sup> than for Na<sup>+</sup>, confirming the considerable adsorption of the BMIM<sup>+</sup> counterions to the oppositely charged surface. In these systems, the mobilities and CCCs were sensitive to the type of coion, whereby the CCCs increase in the sequence Br<sup>-</sup> < N(CN)<sub>2</sub><sup>-</sup> < SCN<sup>-</sup>. With the exception of the Cl<sup>-</sup> ion, this trend reflects the expected direct Hofmeister series for negatively charged hydrophobic surfaces.<sup>33</sup> This finding is in line with recent colloidal probe experiments with hydrophilic silica particles in the presence of the BMIM<sup>+</sup> counterions, which reports the strength of the short-range attraction to increase in the sequence Cl<sup>-</sup> < N(CN)<sub>2</sub><sup>-</sup> < SCN<sup>-</sup>.<sup>24</sup> Such attraction was significant at salt levels close to the CCCs, and therefore the CCC is expected to decrease in the same sequence as stated above in agreement with the indirect Hofmeister series for negatively charged hydrophilic particles.

A similar sequence of counterions was observed for the amidine particles as in the presence of Na<sup>+</sup>. The mobilities (Fig. 3a) and the CCCs (Fig. 5c) decreased again in the sequence Cl<sup>-</sup> > Br<sup>-</sup> > N(CN)<sub>2</sub><sup>-</sup> > SCN<sup>-</sup> in agreement with the indirect Hofmeister series for positively charged hydrophobic surfaces.<sup>33</sup> The electrophoretic mobilities remain positive for weakly adsorbing Cl<sup>-</sup> and Br<sup>-</sup> counterions, while the strongly adsorbing SCN<sup>-</sup> ions induce a charge reversal. However, the IEP is situated at much lower concentration than for the Na<sup>+</sup> ions, which suggests that the hydrophobic BMIM<sup>+</sup> coion adsorbs to the particle surface, which in turn induces a stronger co-adsorption of SCN<sup>-</sup> ions due to ion pair formation on the surface. The formation of ion pairs between cations and anions has been reported in various ILs.<sup>53–57</sup> The IL constituent ions adsorbed on the particle surface may also form ion pairs with the oppositely charged ions. The formation of such surface ion pairs will then influence the surface charge and also the CCC. For the N(CN)<sub>2</sub><sup>-</sup> anion, charge neutralization occurs as well, but the adsorption is not strong enough to reverse the particle charge.

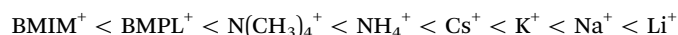


dc\_1931\_21

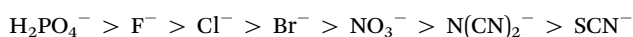
For the  $\text{BMPL}^+$  counterion, specific effects of coions were equally observed for sulfate latex particles. Similar electrophoretic mobilities were measured for  $\text{Cl}^-$  and  $\text{Br}^-$ , however, the presence of  $\text{N}(\text{CN})_2^-$  and  $\text{SCN}^-$  ions led to higher mobilities (Fig. 4a) and lower CCCs (Fig. 4b and 5b). This trend is opposite to the one observed for  $\text{BMIM}^+$ , and does not follow the anticipated direct Hofmeister series. This reversal of the Hofmeister series could be related to the counterion affinity to the oppositely charged particles and the extent of ion pairing on the surface. The observed trends in the CCCs indicate stronger ion pairing in the  $\text{BMIM-SCN}$  system than for  $\text{BMPL-SCN}$ . For the amidine particles, a weak charge reversal is again observed for the  $\text{SCN}^-$  ions, but the electrophoretic mobilities remain positive for the other counterions (Fig. 4a). The charge reversal occurred at higher concentration than in the  $\text{BMIM}^+$  system, which may indicate either weaker  $\text{BMPL}^+$  adsorption on the particle surface or weaker ion pair interactions between  $\text{BMPL}^+$  and  $\text{SCN}^-$  ions. Nevertheless, the trends in both the charging and aggregation properties of the amidine particles in the presence of  $\text{BMPL}^+$  and  $\text{BMIM}^+$  counterions are similar. Accordingly, the mobilities at the same concentration as well as the CCCs follow  $\text{Cl}^- > \text{Br}^- > \text{N}(\text{CN})_2^- > \text{SCN}^-$  (Fig. 4a and 5c). This order is in agreement with the indirect Hofmeister series expected for positively charged hydrophobic particles.<sup>31,33</sup>

The observed trends for the cation dependence are summarized in Fig. 5b and c. For the sulfate latex, the presence of the  $\text{BMIM}^+$  counterion leads to lower CCCs than  $\text{BMPL}^+$  in the presence of simple anions, while the trend is reversed in the presence of hydrophobic  $\text{N}(\text{CN})_2^-$  and  $\text{SCN}^-$  anions. This reversal is probably related to the variable extent of ion pair formation in these systems. No trend with CCCs was observed for amidine latex particles when the coions were varied.

Let us now compare the present results with the ones of an earlier study, which investigated the CCCs of exactly the same particles.<sup>29</sup> In particular, various anions in the presence of  $\text{Na}^+$  and various cations in the presence of  $\text{Cl}^-$  were investigated. Combining the present results with the ones from that study<sup>29</sup> enables us to place the IL constituents into the established Hofmeister series (Fig. 6). For sulfate latex particles, the extended Hofmeister series becomes



where the hydrophilic  $\text{Na}^+$  ions typically lead to the highest CCC, while the hydrophobic IL constituents to lower CCC.  $\text{BMIM}^+$  and  $\text{BMPL}^+$  have to be positioned on the left hand side of the series, indicating that they are even more hydrophobic than the  $\text{N}(\text{CH}_3)_4^+$  counterion. The sulfate particles show no effects of coions. The CCCs of amidine latex particles in the presence of different counterions decrease according to the indirect Hofmeister series as



The  $\text{N}(\text{CN})_2^-$  counterion has to be placed between  $\text{NO}_3^-$  and  $\text{SCN}^-$ . The  $\text{BMIM}^+$  and  $\text{BMPL}^+$  coions have again no influence on the CCC of the amidine particles. However, the  $\text{N}(\text{CH}_3)_4^+$  and  $\text{NH}_4^+$  coions lead to systematically lower CCCs, probably, due to specific interactions with the amidine groups.

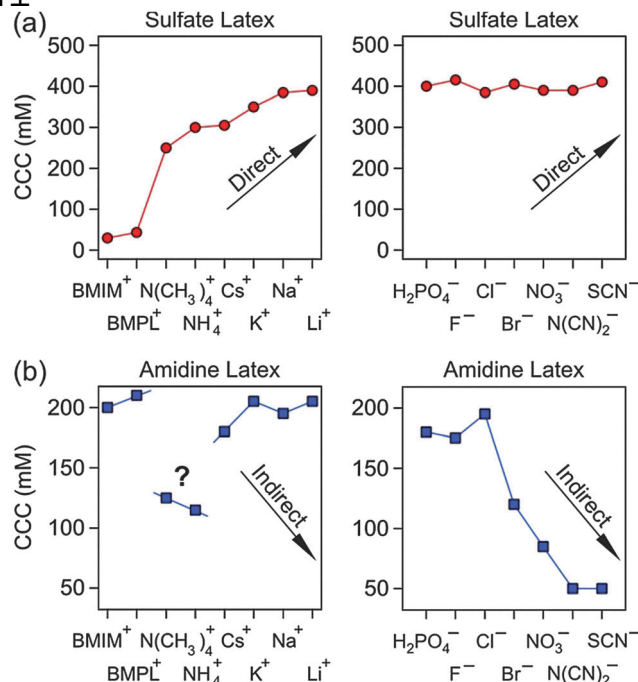


Fig. 6 CCC values for sulfate (a) and amidine (b) latex particles in the presence of different cations (left) and anions (right). The arrows indicate the expected trends according to the direct or indirect Hofmeister series. The lines are a guide to the eye.

### 3.4 Effect of the alkyl chain length

As shown in the previous section, the hydrophobic  $\text{BMIM}^+$  counterions strongly adsorb on the negatively charged sulfate latex particles and thus modify the particle charge and their CCCs (Fig. 3a and 5b). To further investigate the effects of cation hydrophobicity on charging and aggregation of these particles, we have studied electrophoretic mobilities and aggregation rates of sulfate latex particles in the presence of 1-alkyl-3-methylimidazolium counterions, namely for  $\text{MIM}^+$ ,  $\text{EMIM}^+$ ,  $\text{BMIM}^+$ ,  $\text{HMIM}^+$  and  $\text{OMIM}^+$ . Their hydrophobicity increases from the left to the right due to the increasing length of the alkyl chains (Fig. 1). In all cases, the  $\text{Cl}^-$  coion was used.

At sufficiently low concentrations, the electrophoretic mobilities increase with the concentration (Fig. 7a). In the presence of  $\text{MIM}^+$  and  $\text{EMIM}^+$ , the particles remained negatively charged within the entire range investigated. This increase is primarily due to screening by the increasing salt level, but the adsorption of these ions to the particle surface also contributes to this trend. However, adsorption of these counterions becomes more pronounced for longer aliphatic chains and leads to slight charge reversal for  $\text{BMIM}^+$ . The adsorption of  $\text{HMIM}^+$  and  $\text{OMIM}^+$  counterions becomes even more important and induces charge neutralization and a significant charge reversal. At higher concentrations, the mobilities decrease due to screening, as particularly evident in the presence of the  $\text{OMIM}^+$  cation. A similar charge reversal was already reported for negatively charged kaolinite particles in  $\text{OMIM-Cl}$  solutions.<sup>58</sup>

The charging behaviour is well-reflected in the respective aggregation rates. For the  $\text{BMIM}^+$ ,  $\text{EMIM}^+$  and  $\text{MIM}^+$  cations



dc\_1931\_21

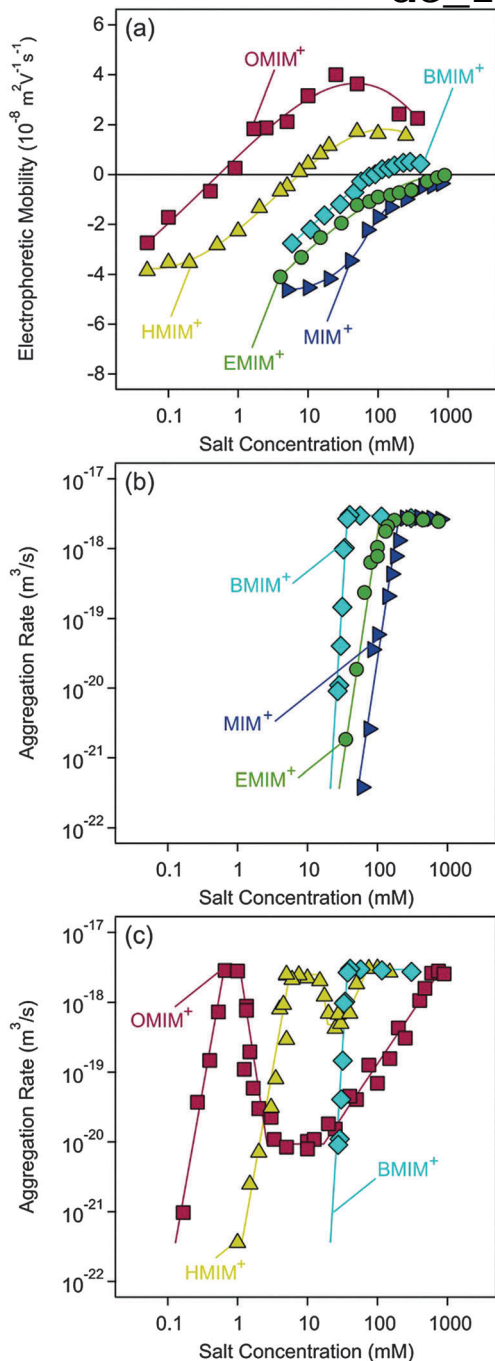


Fig. 7 Electrophoretic mobilities (a) and aggregation rate coefficients (b and c) of sulfate latex particles in the presence of ILs composed of the chloride anion and the 1-alkyl-3-methylimidazolium cation of different alkyl chains. The lines are a guide to the eye.

with short alkyl chains, the aggregation rates (Fig. 7b) show the classical behaviour of slow aggregation at low concentrations and rapid aggregation at high concentrations, with a CCC in between these two regimes. This situation is similar to the systems discussed above. The CCCs decrease systematically with increasing alkyl chain length, which is caused by the increasing adsorption strength due to increasing length of the alkyl chain.

However, the dependence of the aggregation rate on the IL concentration is notably different in the presence of the OMIM<sup>+</sup> counterion (Fig. 7c). The aggregation rates are small at low IL concentrations, and they go through a maximum near the IEP. The rate constant at the maximum corresponds to its value in the fast aggregation regime. Upon increasing the IL concentration further, one observes a decrease of the aggregation rate. The rate passes through a minimum and increases again to reach the value in the fast aggregation regime. A similar dependence is observed for the HMIM<sup>+</sup> counterion, albeit the intermediate minimum is much less pronounced. This shallower minimum is due to the weaker charge reversal of HMIM<sup>+</sup> as revealed by the electrophoresis. Clearly, OMIM<sup>+</sup> adsorbs most strongly, and the adsorption strength decreases with decreasing chain length.

One might suspect that the formation of micelles could be relevant in these systems, especially for the cations with a longer apolar alkyl chain. The CMC of OMIM-Cl was reported to be 220 mM and for HMIM-Cl 900 mM.<sup>59,60</sup> The latter value is at the end of the concentration range used in the present study. Therefore, the formation of micelles does not play any role in the adsorption and particle aggregation mechanism in the HMIM-Cl system. For the OMIM-Cl system, the CMC falls into the upper range of the destabilization due to charge screening by the chloride counterions. Again, micellization plays a minor role.

The observed dependence of the aggregation rate on the concentration of 1-alkyl-3-methylimidazolium can be interpreted in terms of a succession of three CCCs. The first CCC occurs at low concentration during the transition from the slow to fast regime. The second CCC is located after the maximum in the IL concentration, whereby the system undergoes a transition from the fast to slow regime. The third CCC is situated at the highest concentrations after the minimum in the aggregation rate, when the aggregation becomes fast again. Comparing the location of the CCCs with the electrophoretic mobilities in the same concentration ranges, one can realize that the first CCC is caused by charge neutralization, the second is connected with the charge reversal process, while the third CCC is due to the screening effect of the counterions on the surface charge.

A stability map of the CCCs *versus* the type of counterion of different chain lengths summarizes this characteristic behaviour well (Fig. 8). Three CCCs are observed for HMIM<sup>+</sup> and OMIM<sup>+</sup> counterions, while only one CCC is found for MIM<sup>+</sup>, EMIM<sup>+</sup> and BMIM<sup>+</sup>. Therefore, this map shows two regions where the dispersions are stable, meaning that the particle aggregation is significantly slower than that in the case of fast aggregation. That region is indicated as unstable. The first stability region in the lower left corner corresponds to the regular stabilization due to the negative charge of the latex particles. The second region on the right hand side corresponds to the positively charged particles after charge reversal, which is induced by the strong adsorption of the less solvated IL cations. The unstable region in the upper part of the map is due to destabilization and screening at the IEP. The narrow unstable channel in the lower right part of the map is due to the destabilization and charge neutralization at the IEP. The first CCC values at low IL concentration in the presence of 1-alkyl-3-methylimidazolium counterions





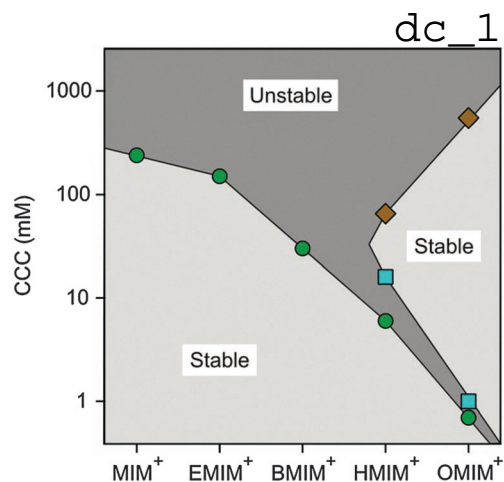


Fig. 8 Stability map including CCC values for sulfate latex particles in the presence of the 1-alkyl-3-methylimidazolium cation based ILs of different alkyl chain lengths with the chloride anion. The circles indicate the first CCC, squares show the second CCC and diamonds refer to the third CCC.

reflect the decreasing chain length and increasing hydrophilicity within the series



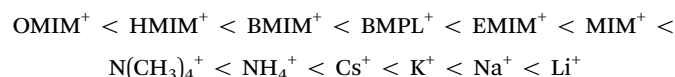
On the left hand side of the series, one finds the hydrophobic cations with a longer alkyl chain. They adsorb more strongly to the particle surface, and induce lower CCCs. Those on the right hand side are more hydrophilic and feature a shorter alkyl chain. The latter counterions adsorb more weakly, and lead to higher CCCs. This trend is reminiscent to previous findings for oxide and silver halide particles in the presence of ionic surfactants of variable chain lengths, whereby the IEP or the first CCC shifts towards smaller concentrations with increasing alkyl chain length.<sup>61–64</sup> In addition, the restabilization occurred in all systems containing surfactants with an octyl chain or longer. A subsequent destabilization at high concentrations was also observed, quite in analogy to OMIM<sup>+</sup>.<sup>64</sup> Enzymatic activity reflects the same order, namely, the proteins lose their activity in the presence of HMIM<sup>+</sup> at lower concentration than for EMIM<sup>+</sup>.<sup>39,40</sup>

Similar stability behaviour was reported for the aggregation of latex particles in the presence of multivalent ions or short-chain oligoamines.<sup>65,66</sup> In particular, the similarity to the system with the oligoamines is striking, and deserves further discussion.<sup>66</sup> These authors have studied electrophoresis and particle aggregation rates for negatively charged sulfate latex particles in the presence of aliphatic oligoamines with the structural formula H<sub>2</sub>NCH<sub>2</sub>CH<sub>2</sub>(NHCH<sub>2</sub>CH<sub>2</sub>)<sub>n</sub>NH<sub>2</sub> for n = 0, 1, 2, and 4. Under the mildly acidic conditions used, these oligoamines form multivalent cations. The concentration dependence of electrophoretic mobilities and of the aggregation rate was very similar to the one shown in Fig. 7, and shows an analogous trend with the increasing chain length. Moreover, the stability map of the CCCs versus the chain length looks surprisingly similar to Fig. 8. Due to these analogies, one might suspect in these two systems that the underlying mechanisms leading to charge reversal and destabilization are similar. The hydrophobic interaction will become

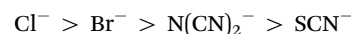
more important with increasing chain length and this aspect might be responsible in both systems for the increased extent of adsorption, which would then induce similar patterns in the charging behaviour and aggregation rates. Moreover, these oligoamines are only partially ionized and their charge could be further reduced by complexation of counterions and ion condensation effects. The interesting consequence of this hypothesis is that the multivalent nature of the longer-chain oligoamines becomes secondary and their increasing hydrophobicity determines the adsorption of these molecules and as a consequence, the aggregation of these particles.

## 4. Conclusions

The effect of simple monovalent ions and water-miscible ILs on the surface charge and aggregation of polystyrene latex particles was investigated by electrophoresis and time-resolved light scattering in dilute aqueous solutions. From studies performed on negatively charged sulfate latex particles, the Hofmeister series for the cations may be extended as



The hydrophobic ions shown on the left hand side lead to the lowest CCCs. The most hydrophobic ones, such as OMIM<sup>+</sup> and HMIM<sup>+</sup>, show more pronounced charge reversal and a subsequent restabilization. The left hand side of the series reflects the known trend of decreasing hydrophilicity with increasing chain length in surfactant solutions. For amidine latex particles, we conclude that the Hofmeister series for the anions should be extended as



whereby the hydrophobic ions are shown on the right hand side and they lead to the lowest CCCs.

## Acknowledgements

The present research was supported by the Swiss National Science Foundation, the University of Geneva and the COST Action CM1206.

## References

- 1 J. P. Hallett and T. Welton, *Chem. Rev.*, 2011, **111**, 3508–3576.
- 2 A. P. Abbott and K. J. McKenzie, *Phys. Chem. Chem. Phys.*, 2006, **8**, 4265–4279.
- 3 M. Armand, F. Endres, D. R. MacFarlane, H. Ohno and B. Scrosati, *Nat. Mater.*, 2009, **8**, 621–629.
- 4 A. Izgorodin, R. Hocking, O. Winther-Jensen, M. Hilder, B. Winther-Jensen and D. R. MacFarlane, *Catal. Today*, 2013, **200**, 36–40.
- 5 N. V. Plechkova and K. R. Seddon, *Chem. Soc. Rev.*, 2008, **37**, 123–150.





dc\_1931\_21

- 6 E. G. Garcia, A. K. Ressmann, P. Gaertner, R. Zirbs, R. L. Mach, R. Krska, K. Bica and K. Brunner, *Anal. Bioanal. Chem.*, 2014, **406**, 7773–7784.
- 7 R. Zirbs, K. Strassl, P. Gaertner, C. Schroder and K. Bica, *RSC Adv.*, 2013, **3**, 26010–26016.
- 8 R. Hayes, G. G. Warr and R. Atkin, *Chem. Rev.*, 2015, **115**, 6357–6426.
- 9 A. Podgorsek, A. S. Pensado, C. C. Santini, M. F. C. Gomes and A. A. H. Padua, *J. Phys. Chem. C*, 2013, **117**, 3537–3547.
- 10 P. S. Campbell, C. C. Santini, D. Bouchu, B. Fenet, K. Philippot, B. Chaudret, A. A. H. Padua and Y. Chauvin, *Phys. Chem. Chem. Phys.*, 2010, **12**, 4217–4223.
- 11 M. Anouti and J. Jacquemin, *Colloids Surf., A*, 2014, **445**, 1–11.
- 12 P. Wang, S. M. Zakeeruddin, P. Comte, I. Exnar and M. Gratzel, *J. Am. Chem. Soc.*, 2003, **125**, 1166–1167.
- 13 Z. Zolek-Tryznowska, J. Izdebska and M. Golazbek, *Color. Technol.*, 2014, **130**, 314–318.
- 14 E. Vanecht, K. Binnemans, S. Patskovsky, M. Meunier, J. W. Seo, L. Stappers and J. Fransaer, *Phys. Chem. Chem. Phys.*, 2012, **14**, 5662–5671.
- 15 K. Richter, A. Birkner and A. V. Mudring, *Phys. Chem. Chem. Phys.*, 2011, **13**, 7136–7141.
- 16 L. L. Lazarus, C. T. Riche, N. Malmstadt and R. L. Brutchey, *Langmuir*, 2012, **28**, 15987–15993.
- 17 G. Salas, A. Podgorsek, P. S. Campbell, C. C. Santini, A. A. H. Padua, M. F. C. Gomes, K. Philippot, B. Chaudret and M. Turmine, *Phys. Chem. Chem. Phys.*, 2011, **13**, 13527–13536.
- 18 C. Guibert, V. Dupuis, J. Fresnais and V. Peyre, *J. Colloid Interface Sci.*, 2015, **454**, 105–111.
- 19 J. A. Smith, O. Werzer, G. B. Webber, G. G. Warr and R. Atkin, *J. Phys. Chem. Lett.*, 2010, **1**, 64–68.
- 20 I. Szilagyi, T. Szabo, A. Desert, G. Trefalt, T. Oncsik and M. Borkovec, *Phys. Chem. Chem. Phys.*, 2014, **16**, 9515–9524.
- 21 K. Ueno, A. Inaba, M. Kondoh and M. Watanabe, *Langmuir*, 2008, **24**, 5253–5259.
- 22 J. Nordstrom, L. Aguilera and A. Matic, *Langmuir*, 2012, **28**, 4080–4085.
- 23 M. Mamusa, J. Siriex-Plenet, F. Cousin, E. Dubois and V. Peyrea, *Soft Matter*, 2014, **10**, 1097–1101.
- 24 V. Valmacco, G. Trefalt, P. Maroni and M. Borkovec, *Phys. Chem. Chem. Phys.*, 2015, **17**, 16553–16559.
- 25 D. F. Evans and H. Wennerstrom, *The Colloidal Domain*, John Wiley, New York, 1999.
- 26 T. Oncsik, G. Trefalt, Z. Csendes, I. Szilagyi and M. Borkovec, *Langmuir*, 2014, **30**, 733–741.
- 27 C. Schneider, M. Hanisch, B. Wedel, A. Jusufi and M. Ballauff, *J. Colloid Interface Sci.*, 2011, **358**, 62–67.
- 28 P. Lo Nostro and B. W. Ninham, *Chem. Rev.*, 2012, **112**, 2286–2322.
- 29 T. Oncsik, G. Trefalt, M. Borkovec and I. Szilagyi, *Langmuir*, 2015, **31**, 3799–3807.
- 30 D. F. Parsons, M. Bostrom, P. Lo Nostro and B. W. Ninham, *Phys. Chem. Chem. Phys.*, 2011, **13**, 12352–12367.
- 31 T. Lopez-Leon, M. J. Santander-Ortega, J. L. Ortega-Vinuesa and D. Bastos-Gonzalez, *J. Phys. Chem. C*, 2008, **112**, 16060–16069.
- 32 J. M. Peula-Garcia, J. L. Ortega-Vinuesa and D. Bastos-Gonzalez, *J. Phys. Chem. C*, 2010, **114**, 11133–11139.
- 33 N. Schwierz, D. Horinek and R. R. Netz, *Langmuir*, 2010, **26**, 7370–7379.
- 34 C. Calero, J. Faraudo and D. Bastos-Gonzalez, *J. Am. Chem. Soc.*, 2011, **133**, 15025–15035.
- 35 M. Lund, R. Vacha and P. Jungwirth, *Langmuir*, 2008, **24**, 3387–3391.
- 36 F. J. M. Ruiz-Cabello, G. Trefalt, T. Oncsik, I. Szilagyi, P. Maroni and M. Borkovec, *J. Phys. Chem. B*, 2015, **119**, 8184–8193.
- 37 F. Dumont, J. Warlus and A. Watillon, *J. Colloid Interface Sci.*, 1990, **138**, 543–554.
- 38 R. Tian, G. Yang, H. Li, X. D. Gao, X. M. Liu, H. L. Zhu and Y. Tang, *Phys. Chem. Chem. Phys.*, 2014, **16**, 8828–8836.
- 39 C. Lange, G. Patil and R. Rudolph, *Protein Sci.*, 2005, **14**, 2693–2701.
- 40 Z. Yang, *J. Biotechnol.*, 2009, **144**, 12–22.
- 41 C. Sanfilippo, N. D'Antona and G. Nicolosi, *Biotechnol. Lett.*, 2004, **26**, 1815–1819.
- 42 D. Constantinescu, H. Weingartner and C. Herrmann, *Angew. Chem., Int. Ed.*, 2007, **46**, 8887–8889.
- 43 K. Fujita, D. R. MacFarlane and M. Forsyth, *Chem. Commun.*, 2005, 4804–4806.
- 44 M. I. Mishchenko, L. D. Travis and A. A. Lacis, *Scattering, Absorption, and Emission of Light by Small Particles*, University Press, Cambridge, 2002.
- 45 H. Holthoff, S. U. Egelhaaf, M. Borkovec, P. Schurtenberger and H. Sticher, *Langmuir*, 1996, **12**, 5541–5549.
- 46 K. L. Chen, S. E. Mylon and M. Elimelech, *Langmuir*, 2007, **23**, 5920–5928.
- 47 A. Zaccone, H. Wu, M. Lattuada and M. Morbidelli, *J. Phys. Chem. B*, 2008, **112**, 1976–1986.
- 48 M. Schudel, S. H. Behrens, H. Holthoff, R. Kretzschmar and M. Borkovec, *J. Colloid Interface Sci.*, 1997, **196**, 241–253.
- 49 S. H. Behrens, M. Borkovec and P. Schurtenberger, *Langmuir*, 1998, **14**, 1951–1954.
- 50 M. Kobayashi, M. Skarba, P. Galletto, D. Cakara and M. Borkovec, *J. Colloid Interface Sci.*, 2005, **292**, 139–147.
- 51 M. Elimelech, J. Gregory, X. Jia and R. A. Williams, *Particle Deposition and Aggregation: Measurement, Modeling, and Simulation*, Butterworth-Heinemann Ltd., Oxford, 1995.
- 52 T. Lopez-Leon, J. L. Ortega-Vinuesa and D. Bastos-Gonzalez, *ChemPhysChem*, 2012, **13**, 2382–2391.
- 53 A. Stoppa, J. Hunger, G. Hefter and R. Buchner, *J. Phys. Chem. B*, 2012, **116**, 7509–7521.
- 54 R. Sadeghi and N. Ebrahimi, *J. Phys. Chem. B*, 2011, **115**, 13227–13240.
- 55 M. Bester-Rogac, A. Stoppa, J. Hunger, G. Hefter and R. Buchner, *Phys. Chem. Chem. Phys.*, 2011, **13**, 17588–17598.
- 56 M. Bester-Rogac, J. Hunger, A. Stoppa and R. Buchner, *J. Chem. Eng. Data*, 2011, **56**, 1261–1267.
- 57 H. K. Stassen, R. Ludwig, A. Wulf and J. Dupont, *Chem. – Eur. J.*, 2015, **21**, 8324–8335.



dc\_1931\_21

- 58 M. Markiewicz, W. Mroziak, K. Rezwan, J. Thoming, J. Hupka and C. Jungnickel, *Chemosphere*, 2013, **90**, 706–712.
- 59 U. Preiss, C. Jungnickel, J. Thoming, I. Krossing, J. Luczak, M. Diedenhofen and A. Klamt, *Chem. – Eur. J.*, 2009, **15**, 8880–8885.
- 60 J. Luczak, J. Hupka, J. Thoming and C. Jungnickel, *Colloids Surf., A*, 2008, **329**, 125–133.
- 61 D. W. Fuerstenau and M. Colic, *Colloids Surf., A*, 1999, **146**, 33–47.
- 62 A. Watanabe, *Bull. Inst. Chem. Res., Kyoto Univ.*, 1960, **38**, 179–215.
- 63 L. Liang and J. J. Morgan, *Aquat. Sci.*, 1990, **52**, 32–55.
- 64 R. H. Ottewill and M. C. Rastogi, *Trans. Faraday Soc.*, 1960, **56**, 866.
- 65 P. Sinha, I. Szilagyi, F. J. M. Ruiz-Cabello, P. Maroni and M. Borkovec, *J. Phys. Chem. Lett.*, 2013, **4**, 648–652.
- 66 I. Szilagyi, A. Polomska, D. Citherlet, A. Sadeghpour and M. Borkovec, *J. Colloid Interface Sci.*, 2013, **392**, 34–41.



# Stability of Titania Nanomaterials Dispersed in Aqueous Solutions of Ionic Liquids of Different Alkyl Chain Lengths

Paul Rouster,<sup>†</sup> Marko Pavlovic,<sup>‡</sup> Tianchi Cao,<sup>§</sup> Bojana Katana,<sup>‡</sup> and Istvan Szilagy<sup>\*,‡,||</sup>

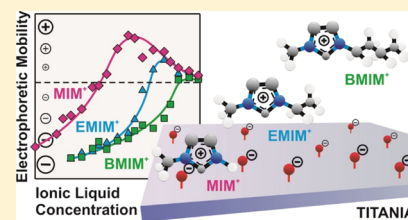
<sup>†</sup>Institute of Condensed Matter and Nanosciences–Bio and Soft Matter, Université Catholique de Louvain, Louvain-la-Neuve B-1348, Belgium

<sup>‡</sup>MTA-SZTE Lendület Biocolloids Research Group and <sup>||</sup>Interdisciplinary Excellence Center, Department of Physical Chemistry and Materials Science, University of Szeged, Szeged H-6720, Hungary

<sup>§</sup>Department of Inorganic and Analytical Chemistry, University of Geneva, Geneva CH-1205, Switzerland

## Supporting Information

**ABSTRACT:** Charging and aggregation of titania nanosheets (TNS) and spherical titania nanoparticles (TNP) were studied in aqueous solutions of ionic liquids. The pH and the length of the alkyl chain of the IL cations [1-methylimidazolium (MIM<sup>+</sup>), 1-ethyl-3-methylimidazolium (EMIM<sup>+</sup>), and 1-butyl-3-methylimidazolium (BMIM<sup>+</sup>)] were systematically varied in the experiments. No detectable interaction was observed between the IL cations and the positively charged TNS or TNP surfaces at low pH, where the imidazolium derivatives are the co-ions. For the negatively charged titania nano-objects, significant adsorption of MIM<sup>+</sup> and EMIM<sup>+</sup> took place, leading to charge neutralization and overcharging at appropriate concentrations. The BMIM<sup>+</sup> behaved like a simple salt constituent causing charge screening. For both TNS and TNP, the MIM<sup>+</sup> < EMIM<sup>+</sup> < BMIM<sup>+</sup> counterion order was obtained in the critical coagulation concentrations, indicating that MIM<sup>+</sup> was the most effective in destabilization of the dispersions. The major interparticle forces were of electrostatic origin; however, viscous stabilization was also observed at high IL concentrations. The same aggregation mechanism and charging behavior were found for the titania nano-objects irrespective of their shape. The results shed light on the hydrophilic nature of the surface of the TNS and TNP of negative charge, in contrast to earlier findings with hydrophobic colloidal particles, where the increasing alkyl chain length gave rise to higher destabilization power. The charging properties were governed by specific adsorption of the IL constituents, while the major interparticle forces were qualitatively well-predicted by the Derjaguin, Landau, Verwey, and Overbeek theory.



## INTRODUCTION

Nanomaterials in ionic liquids (ILs) represent novel and versatile systems, which are used in applications ranging from energy storage through biomolecule processing to catalysis.<sup>1–6</sup> ILs are defined as organic salts of low melting point. They possess several advantageous features including wide electrochemical window, low vapor pressure, and high chemical stability.<sup>7–11</sup> During the development processes of IL materials, nanoparticles are often dispersed in ILs, leading to the formation of colloidal dispersions, glasses, and gels depending on the composition of the samples and on the experimental conditions.<sup>12–16</sup> Apart from ILs, stable colloids were also obtained in molten inorganic salts because of the charge density oscillations around the dispersed particles.<sup>17</sup>

Once nanoparticle dispersions in ILs are involved in the application processes, the colloidal stability of the samples is a key point, as homogeneously distributed primary particles are required in certain cases such as in catalysis,<sup>18</sup> but particle aggregates in others, where materials are prepared by self-assembly of nanoparticles for instance.<sup>19,20</sup> Therefore, the charging and aggregation processes in ILs have recently become an important topic, which was not extensively studied in the past.<sup>14</sup> Accordingly, stability of iron oxide,<sup>21,22</sup> gold,<sup>23</sup>

ruthenium,<sup>24</sup> latex,<sup>25</sup> or silica<sup>26–29</sup> particles was investigated in room-temperature ILs with various methods.

Furthermore, the governing surface forces acting across ILs were explored and two types of stabilization mechanism were suggested on the basis of the results obtained with planar alumina and silica surfaces. It was assumed that repulsive interaction originates from the ordered interfacial layering of the IL constituents and subsequent appearance of oscillatory forces.<sup>30,31</sup> The thickness of the IL ion pairs can be of several nanometers depending on the size of the anions and cations. On the other hand, formation of a diffuse double layer comprising dissociated IL ions around charged surfaces was suggested and the presence of this layer leads to strong repulsive forces.<sup>32</sup> The latter mechanism relies on an interpretation, which is similar to the one suggested by the theory of Derjaguin, Landau, Verwey, and Overbeek (DLVO).<sup>33–35</sup> This model was developed for charged surfaces immersed in electrolyte solutions and it states that the overall interparticle forces are the sum of the repulsive electrical double layer and attractive van der Waals forces. The quantitative description of this theory is given in the

Received: April 28, 2019

Published: May 2, 2019

**Supporting Information.** The consensus view holds that long-ranged repulsive forces are present between surfaces across ILs; however, their origin still remains an open question.<sup>36</sup>

To further clarify the nature of the interaction forces in ILs, the interfacial behavior of the IL constituents has to be well-understood. Therefore, to explore the fundamental charging and aggregation processes, the affinity of IL cations and anions to particle surfaces was investigated. For example, results with polystyrene,<sup>37</sup> melamine,<sup>38</sup> and silica<sup>39</sup> particles revealed that ion-specific adsorption of the IL constituents from aqueous solutions determined the surface charge properties, whereas the major interparticle forces were described by the DLVO theory. On the basis of their interaction with particle surfaces or macromolecules, the traditional Hofmeister series was also extended to the IL cations and anions.<sup>37,40,41</sup> Concerning the quantitative description of the particle aggregation processes in diluted IL solutions, only a limited number of studies are available.<sup>23,25,37</sup> Therefore, precise measurements of aggregation rates are needed in order to probe the effect of the IL constituents on the colloidal stability of particle dispersions.

In the present study, charging and aggregation of titania nanosheets (TNS) and spherical titania nanoparticles (TNP) were investigated in aqueous solutions of imidazolium-based ILs of different alkyl chain lengths. Because of the pH-tunable charge of the titania nano-objects, the influence of the IL cations on the colloidal stability was studied, when they are present as either co-ions or counterions in the samples. Although IL-assisted synthesis of titania-based nanomaterials was reported in the past,<sup>42–44</sup> no systematic studies were published concerning the quantitative description of the surface charge behavior and aggregation mechanism of titania particles in aqueous IL solutions.

## ■ EXPERIMENTAL SECTION

**Materials.** The detailed synthesis of TNS has already been reported earlier.<sup>45</sup> TNP (P25), hydrochloric acid (HCl), sulfuric acid (H<sub>2</sub>SO<sub>4</sub>), hydrogen peroxide (H<sub>2</sub>O<sub>2</sub>), and potassium hydroxide (KOH) were purchased from Sigma-Aldrich. Analytical grade potassium chloride (KCl) was acquired from Acros Organics. The ILs such as 1-methylimidazolium chloride (MIMCl, 98%), 1-ethyl-3-methylimidazolium chloride (EMIMCl, >98%), and 1-butyl-3-methylimidazolium chloride (BMIMCl, 99%) were purchased from Iolitec GmbH. These ILs are solid at room temperature and their melting points are 86,<sup>46</sup> 89,<sup>47</sup> and 70 °C,<sup>48</sup> respectively. Ultrapure water (Millipore) was used and the pH of the dispersions were adjusted to 4 or 10 with HCl or KOH, respectively. The experiments were carried out at 25 °C and the particle concentration was 1 mg/L. The water, KCl, and IL solutions were filtered with a 0.1 μm syringe filter (Millex) prior to sample preparation.

**Electrophoresis.** The electrophoretic measurements were carried out on a ZetaSizer Nano ZS (Malvern) device. The samples were prepared according to the following procedure. IL solutions of 4.5 mL volume and of a calculated concentration were mixed with 0.5 mL of TNS or TNP at a concentration of 10 mg/L. The sample was allowed to rest overnight before performing the electrophoretic mobility measurements, which were carried out in plastic capillary cells (Malvern). In some cases, the obtained electrophoretic mobility (μ) values were converted to electrokinetic potentials (ζ) with the Smoluchowski equation<sup>49</sup>

$$\zeta = \frac{\mu\eta}{\epsilon_0\epsilon} \quad (1)$$

where η is the viscosity, ε is the dielectric constant of the medium, and ε<sub>0</sub> is the permittivity of vacuum. The η values of the aqueous IL solutions were determined as detailed later.

**Dynamic Light Scattering.** Dynamic light scattering (DLS) was used to measure the hydrodynamic radius (R<sub>h</sub>) of the particles. The experiments were carried out on an ALV/CGS-3 goniometer (ALV GmbH) at a scattering angle (θ) of 90°. The correlation function was fitted with the cumulant method to obtain the decay rate constant (Γ).<sup>50</sup> The diffusion coefficient (D) was calculated as follows

$$D = \frac{\Gamma}{q^2} \quad (2)$$

where q is the scattering vector, which can be calculated using the parameters of the experimental setup

$$q = \frac{4\pi n}{\lambda} \sin \frac{\theta}{2} \quad (3)$$

where n is the refractive index of the medium and λ is the wavelength of the laser beam. The refractive indices of the IL solutions were determined as detailed later. The R<sub>h</sub> was then calculated by the Stokes–Einstein equation

$$R_h = \frac{k_B T}{6\eta\pi D} \quad (4)$$

where k<sub>B</sub> is the Boltzmann constant and T is the absolute temperature. The DLS measurements were carried out in borosilicate glass cuvettes (Kimble Chase) cleaned with a mixture of concentrated H<sub>2</sub>SO<sub>4</sub> and H<sub>2</sub>O<sub>2</sub> in a 3:1 volume ratio. Thereafter, the cuvettes were rinsed with water and dried in a dust-free oven. For sample preparation, 0.2 mL of 10 mg/L TNS stock dispersion was added to 1.8 mL of IL solution of known concentrations and the DLS measurements were started after vortexing the samples for a few seconds.

**Refractive Index.** The n values of the IL solutions were measured with an Abbemat-WR/MW automatic multi-wavelength refractometer (Anton Paar) at a λ of 632 nm, which corresponds to the λ of the light scattering instrument. The n values used in eq 3 were interpolated with a linear fit on the n versus IL concentration data (Figure S1). The fitting parameters are given in Table S1.

**Viscosity.** The η data of the IL solutions were measured in a cone-plate geometry (CPE-40 cone) with an LVDV-II+ ProC/P viscometer (Brookfield) at pH 4 and 10. The η of the different IL–water mixtures was obtained by fitting the shear stress versus shear rate data with the Casson model.<sup>51</sup> The measured η values were then plotted against the IL concentration (c<sub>IL</sub>) and fitted with the following equation<sup>52</sup>

$$\frac{\eta}{\eta_0} = 1 + A\sqrt{c_{IL}} + Bc_{IL} + Dc_{IL}^2 \quad (5)$$

where η<sub>0</sub> is the viscosity of water, whereas A, B, and D constants are listed in Table S1. The above relation was applied for interpolation of η used in eqs 1 and 4. The experimental data determined in the IL concentration regimes applied and the fits with eq 5 are shown together in Figure 1.

**Transmission Electron Microscopy.** The morphology of the materials was explored by transmission electron microscopy (TEM). The TEM images were recorded on a Tecnai G2



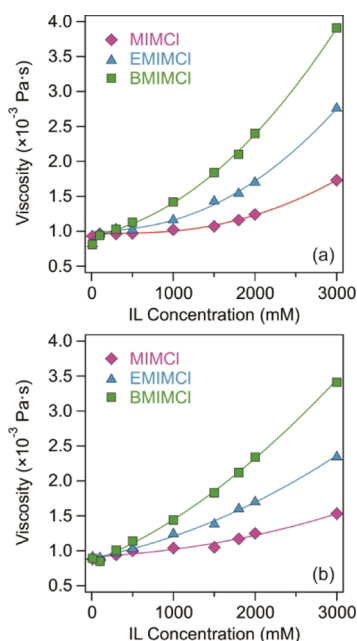


**Figure 1.** Viscosities of aqueous IL [MIMCl (diamond), EMIMCl (triangles), and BMIMCl (squares)] solutions measured at pH 4 (a) and 10 (b). The solid lines are the fits obtained with eq 5 used for the interpolation of the data.

Sphera microscope (FEI) at an acceleration voltage of 120 kV using a LaB6 cathode. The samples were prepared by placing 5  $\mu$ L of solution on the plasma-treated carbon mesh and by removing the excess liquid after 2 min. The obtained mesh with the material was installed on the sample holder and placed in an electron microscope.

## RESULTS

The charging properties of the titania particles were investigated by measuring the electrophoretic mobilities in aqueous dispersions containing dissolved KCl or ILs. On the basis of these results, a model for specific ion adsorption on the TNS and TNP surfaces was established and related to the aggregation mechanism of the titania nano-objects. The origin of the major interparticle forces was interpreted by the DLVO theory.

**Dispersion Properties of TNS and TNP in Salt Solutions.** It is well-known that the charge of titania particles can be tuned with the pH because of the protonation equilibria of the surface hydroxyl groups.<sup>53</sup> Accordingly, positively charged particles are present at low pH and negatively charged ones at high pH. The transition between the negative and positive regimes occurs at the point of zero charge (PZC), which usually falls in the pH range of 4.5–6.5 for titania materials.<sup>54,55</sup>

The results of the electrophoretic measurements performed at pH 4 and 10 confirmed that the TNS and TNP are positively and negatively charged, respectively, under these experimental conditions (Table S2). The electrophoretic mobilities were recorded at different KCl concentrations to probe the influence of the ionic strength on the surface charge properties (Figure S2). No significant differences were observed between the data determined with TNS and TNP at either pH 4 or 10. Although the values are system-specific, the trends in the magnitudes are very similar. They decrease by increasing the ionic strength because of the charge screening

by the salt constituents. The minimum or maximum in the mobilities is due to the electrokinetic effect, which is typical for charged particles moving in an electric field.<sup>56</sup> The mobilities were converted to electrokinetic potentials with eq 1 and the surface charge densities ( $\sigma$ ) were calculated using the Debye–Hückel relation<sup>35</sup>

$$\sigma = \epsilon_0 \epsilon \kappa \zeta \quad (6)$$

where  $\kappa$  is the inverse Debye length. The  $\sigma$  values of TNS and TNP were very similar at both pH 4 and 10 (Table S2), indicating that the protonation equilibria of the surface hydroxyl groups are identical irrespective of the shape of the titania nanostructures.

The aggregation processes were investigated in time-resolved DLS experiments by following the change in  $R_h$  at different ionic strengths. The speed of aggregation was expressed in terms of the stability ratio ( $W$ ), which was calculated as follows<sup>57</sup>

$$W = \frac{k_{\text{fast}}}{k} = \frac{\text{d}R_h/\text{d}t|_{t \rightarrow 0}^{\text{fast}}}{\text{d}R_h/\text{d}t|_{t \rightarrow 0}} \quad (7)$$

where  $t$  is the experiment time,  $k$  is the apparent aggregation rate coefficient, and fast refers to fast particle aggregation, a condition where each particle collision leads to dimer formation. This was achieved in 1 M KCl solutions. Note that  $W = 1$  indicates unstable colloids, whereas higher values are signals for slower particle aggregation and more stable dispersions. The interpretation of the stability ratio within the DLVO theory is given in the Supporting Information.

The stability ratios followed the same tendency at both pHs for TNS and TNP (Figure S2). They decreased with increasing the KCl concentration and remained close to unity at high ionic strengths. The sharp transition between the slow and fast aggregation regimes is located at the critical coagulation concentration (CCC), which was calculated as follows<sup>58</sup>

$$W = 1 + \left( \frac{\text{CCC}}{c} \right)^\alpha \quad (8)$$

where  $c$  is the molar concentration of a monovalent salt and  $\alpha$  was calculated from the slope of the stability ratios in the slow aggregation regime as

$$\alpha = \frac{\text{dlog } 1/W}{\text{dlog } c} \quad (9)$$

The trend in the stability ratio versus KCl concentration data and the value of the CCC in the different systems (Table S2) are in line with the DLVO theory.<sup>35</sup> As predicted by this theory, the magnitude of the repulsive electrostatic double layer forces weakens by increasing the ionic strength (see eqs S7 and S8 in the Supporting Information) because of charge screening and they vanish at the CCC. Such a charge screening effect can also be assumed from the tendency of the electrophoretic mobilities by changing the ionic strength, as discussed before. The particles rapidly aggregate at KCl concentrations above the CCC owing to the attractive van der Waals forces, which are supposed to be present irrespective of the salt level.

These results indicate that the charge of both TNS and TNP can be adequately tuned by the pH and positively charged particles are present at pH 4 and negative ones at pH 10. No significant differences in the surface charge behavior or

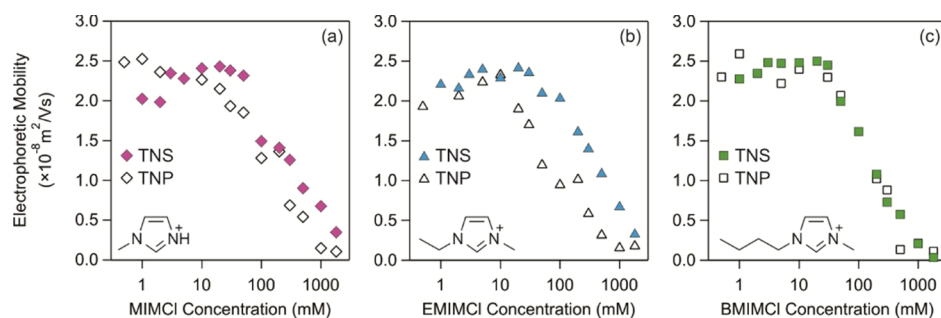


**Figure 2.** Electrophoretic mobilities of TNS (filled symbols) and TNP (empty symbols) as a function of MIMCl (a), EMIMCl (b), and BMIMCl (c) concentration at pH 4 and 1 mg/L particle concentration. The structures of the IL cations are presented in the inset.

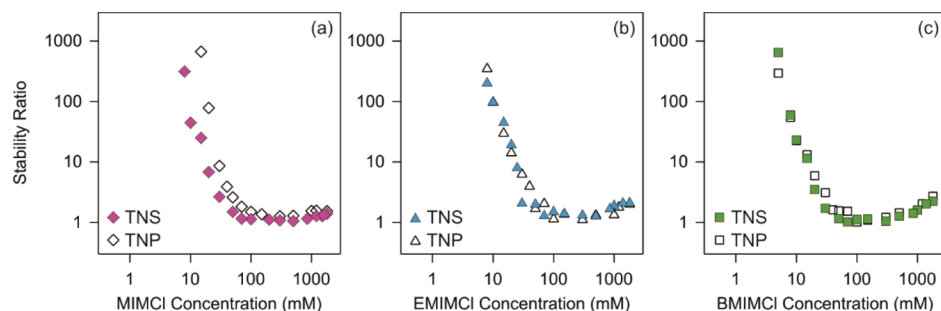


**Figure 3.** Stability ratios of TNS (filled symbols) and TNP (empty symbols) as a function of MIMCl (a), EMIMCl (b), and BMIMCl (c) concentration at pH 4 and 1 mg/L particle concentration.

aggregation mechanism were observed for the titania nano-objects of different shapes.

**Effect of ILs on the Colloidal Stability of Positively Charged Titania Particles.** Electrophoretic mobilities were measured with TNS and TNP in aqueous solutions of MIMCl (Figure 2a), EMIMCl (Figure 2b), and BMIMCl (Figure 2c) of different concentrations at pH 4, where the IL cations are the co-ions, that is, they are of the same sign of charge as the surface.

For the EMIMCl system, the values are shifted toward lower concentrations in the case of TNP; however, no clear difference was observed between TNS and TNP in the other two systems. In general, the trend in the mobilities resembled the one observed with KCl under these experimental conditions, as discussed in the previous chapter. The values decreased after a small maximum with increasing the IL dose and remained positive in the entire concentration regime investigated. No remarkable changes in the electrophoretic mobilities were detected by varying the alkyl chain length of the imidazolium ring (Figure S3a). The results indicate that adsorption of the positively charged IL constituents are negligible on the like-charged surface and that the decrease in the mobilities with increasing IL concentration is due to surface charge screening by the counterions.

The stability ratios were determined for TNS and TNP in solutions of MIMCl (Figure 3a), EMIMCl (Figure 3b), and BMIMCl (Figure 3c). The experimental conditions (e.g., pH, particle concentration, and IL concentration ranges) were the same as in the mobility study in order to relate the results. The TNS and TNP particles aggregated similarly in the IL solutions and the location of the stability regimes suggests DLVO-type behavior, namely, slow aggregation at low IL doses and rapid aggregation above the CCC. Similar to the mobility results, no clear dependence of the stability ratios on the alkyl chain length was detected (Figure S3b), indicating that the

dispersions were destabilized by the ILs because of the screening of the double layers and subsequent weakening of the electrostatic repulsion between the particles. In addition, weak adsorption of simple IL constituent anions on oppositely charged surfaces was reported earlier.<sup>59,60</sup> Therefore, this phenomenon may also contribute to the destabilization of the particles in the present systems. Because adsorption of the IL cations was negligible on both TNS and TNP, the strength of the repulsive interaction was regulated solely by the ionic strength. The DLVO theory predicts the same magnitude of the electrical double layer forces at the same ionic strength (eq S7) irrespective of the type of particles, and indeed, similar stability ratios were determined for TNS and TNP in the presence of given ILs.

Moreover, an increase in the stability ratios was detected in each system at the highest IL concentrations. This increase followed the MIMCl < EMIMCl < BMIMCl order and it originates from the increasing viscosity of the IL solutions in this regime. The aggregation rate coefficient described by Smoluchowski for diffusion-controlled particle aggregation is defined as<sup>57</sup>

$$k = \frac{8k_B T}{3\eta} \quad (10)$$

The above equation shows that an increase in the viscosity of the dispersion medium leads to a decrease in the rate of aggregation and to an increase of the stability ratios (see eq 7). The viscosities of the IL solutions were measured (Figure 1) and indeed, they increase with the IL concentration, leading to slower diffusion of TNS and TNP and to higher stability ratios. Such an effect of the viscosity on the aggregation rates of colloidal particles is the co-called viscous stabilization and it has already been reported in other particle systems containing inorganic salts<sup>61,62</sup> or ILs.<sup>23,25,37</sup>

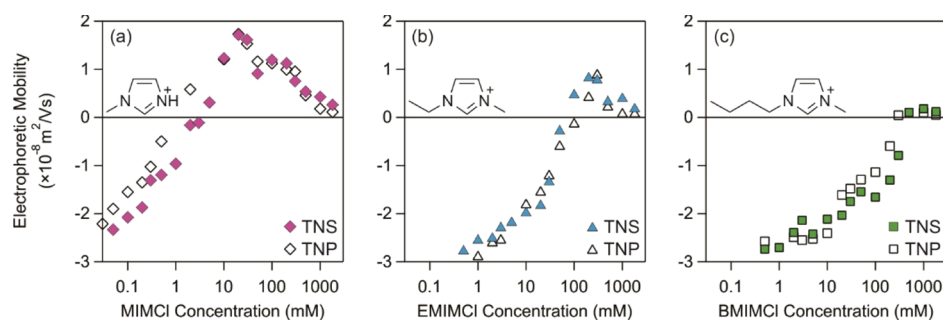


**Figure 4.** Electrophoretic mobilities of TNS (filled symbols) and TNP (empty symbols) as a function of MIMCI (a), EMIMCI (b), and BMIMCI (c) concentration at pH 10. The structures of the IL cations are presented in the inset.

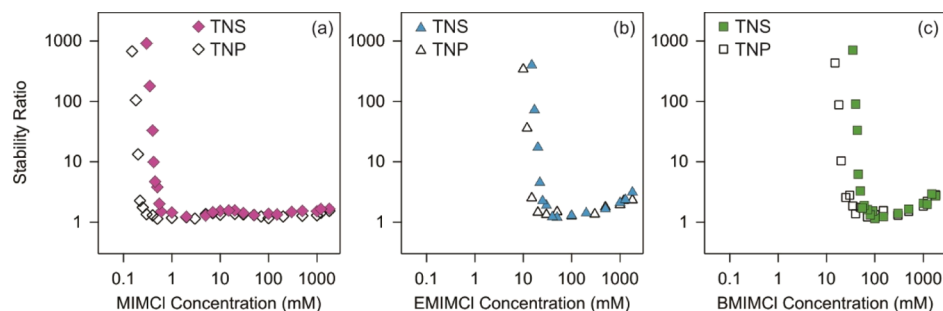


**Figure 5.** Stability ratios of TNS (filled symbols) and TNP (empty symbols) as a function of the MIMCI (a), EMIMCI (b), and BMIMCI (c) concentration at pH 10.

**Effect of ILs on the Colloidal Stability of Negatively Charged Titania Particles.** The charging and aggregation properties of the TNS and TNP were also assessed at pH 10, where the particles are negatively charged and thus, the IL cations are the counterions. Electrophoretic mobilities were measured first in the presence of MIMCI (Figure 4a), EMIMCI (Figure 4b), and BMIMCI (Figure 4c).

In general, no significant differences were observed between TNS and TNP in the individual systems. The mobilities were negative at low concentrations and they increased with the IL dose in each case. For the BMIMCI, the values were close to zero at high concentrations, whereas for MIMCI and EMIMCI, charge neutralization and subsequent overcharging occurred at appropriately high IL concentrations. This observation clearly indicates that a significant amount of MIM<sup>+</sup> and EMIM<sup>+</sup> cations was adsorbed on the oppositely charged particle surfaces. Monovalent counterion-induced charge reversal was reported earlier with TNS<sup>45</sup> and other colloidal particles<sup>62,63</sup> in certain solutions of inorganic salts. Comparing the mobility curves (Figure S4a), one can assume that the extent of the adsorption increased with decreasing the length of the alkyl chains of the imidazolium ring.

The stability ratios of TNS and TNP were determined by DLS in the MIMCI (Figure 5a), EMIMCI (Figure 5b), and BMIMCI (Figure 5c) systems. The tendencies in the data indicated the presence of DLVO-type forces. Stable dispersions were observed at low IL concentrations, where repulsive double layer forces are strong and unstable ones at high IL doses because of weak repulsion and predominating van der Waals attractive forces. Similar to the systems measured at pH 4, an increase in the stability ratios can be observed above the CCC and its extent increases in the MIMCI < EMIMCI < BMIMCI order. This slight re-stabilization, that is, slowdown in the rate of aggregation, of the particles is due to the effect of the higher viscosity in this regime. The data measured for TNP

were slightly shifted toward lower IL concentrations compared to the ones determined for TNS. In addition, a significant shift toward lower IL doses was also observed in the stability ratios by decreasing the alkyl chain length of the IL cations (Figure S4b). This finding is important and it will be further discussed in the next section.

## DISCUSSION

The effect of the alkyl chain length on the colloidal stability of the particles dispersed in aqueous IL solutions was further explored by comparing the tendencies in the electrophoretic mobilities and stability ratios determined for TNS and TNP at pH 4 and 10. The CCC values were calculated from the stability ratio versus IL concentration plots with eq 8. The data for all the systems are presented in Figure 6.

The CCC values of the TNP were slightly higher than the ones for the TNS at pH 4, whereas they were lower at pH 10. This observation is also valid for the KCl systems (Table S2).

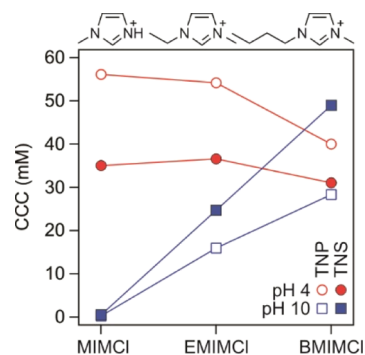


**Figure 6.** CCC values of TNS (filled symbols) and TNP (empty symbols) determined in the presence of ILs. The measurements were carried out at pH 4 (circles) and pH 10 (squares).



To explain these phenomena, the size and the morphology of the titania nano-objects were studied by recording TEM images with stable dispersions at low KCl and BMIMCl concentrations below the CCC (Figure 7).

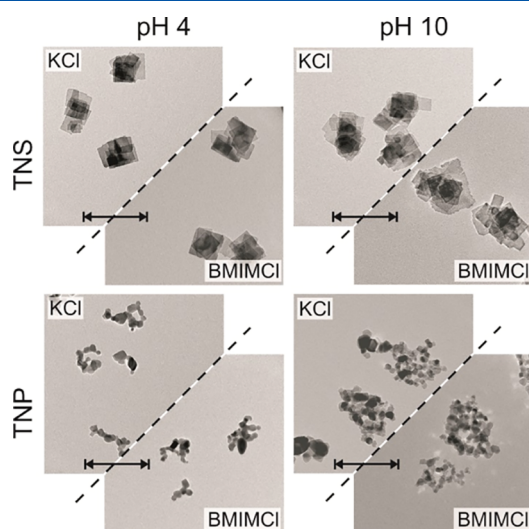


**Figure 7.** TEM images of TNS (top row) and TNP (bottom row) recorded with stable dispersions in KCl and BMIMCl solutions at pH 4 (left column) and pH 10 (right column). The scale bars indicate 200 nm distances.

The size of the TNS was about the same irrespective of the pH and type of ILs present in the samples. However, the TNP particles are present as small aggregates even in stable dispersions at low KCl or BMIMCl concentrations. The size of these TNP aggregates is smaller and larger than the size of the TNS at pH 4 and 10, respectively. As the strength of the attractive van der Waals forces increases with the size of the dispersed materials of the same composition (eq S6),<sup>35</sup> it is assumed that they are weaker for TNP at pH 4 and stronger at pH 10 than the ones acting between the nanosheets under these experimental conditions. Subsequently, the TNP aggregate at higher salt concentrations at pH 4 than at pH 10 because of the smaller size in the former case. Such a size-strength of attractive force relation is also responsible for the higher CCC of TNP at pH 4 and lower at pH 10 compared to the TNS. The general quantitative description of the size dependence of the strength of the attractive van der Waals forces is given in eq S6 and it can be assumed that this fact is responsible for the above trends in the CCC of TNS and TNP at the same IL concentrations.

Concerning the tendencies of the CCC by changing the alkyl chain length of the imidazolium group, no significant effect was detected at pH 4, when the particles are positively charged. Because the IL cations are the co-ions in these systems, one can conclude that the ILs destabilize the titania nano-objects solely by charge screening and no specific interaction took place between the IL cations and the TNP or TNS surface.

Besides, the CCC values increased in the sequence of MIMCl < EMIMCl < BMIMCl for both types of titania at pH 10, a condition where the IL cations are the counterions. On the basis of this fact, it can be assumed that the interfacial assembly of the cations and the colloidal stability are tuned by the alkyl chain length. Comparing the above tendency with the

electrophoretic mobility data (Figures 4 and S4), a correlation between the charging behavior and the aggregation processes can be established. In the case of MIMCl, the CCC falls in the concentration regime, where charge neutralization occurred. Therefore, the destabilization is due to such a charge compensation and lack of repulsive double layer forces. The same scenario also applies for the dispersions containing EMIMCl. However, the aggregation mechanism is governed by charge screening for BMIMCl, as the CCC is located at a lower IL concentration than the charge neutralization point. These assumptions are based on the qualitative evaluation of the data by the DLVO theory.

The above tendency in the CCC is in contrast with the findings reported earlier with polystyrene latex particles and imidazolium-based ILs of different lengths of the alkyl chains, where the opposite order was found with the same ILs.<sup>37</sup> The electrophoretic mobilities were also different and overcharging was found only with the BMIMCl. These results indicate a significant difference between the hydrophobicity of the titania and the polystyrene latex surfaces. Titania is considered as hydrophilic above the PZC;<sup>64</sup> therefore, the adsorption of well-hydrated MIM<sup>+</sup> is favorable. In addition, hydrogen bonding between the MIM<sup>+</sup> and the functional groups of the surface may also play a role and enhance the adsorption. The hydration level decreases with increasing the alkyl chain length and therefore, the BMIM<sup>+</sup> does not adsorb on the hydrophilic titania surfaces. For the hydrophobic latex particles, the above tendency is the opposite and more hydrophobic BMIM<sup>+</sup> adsorbs in the highest extent. It was also reported earlier that increasing the organic content in soils, that is, increasing the hydrophobicity, leads to stronger adsorption of ILs of longer alkyl chains.<sup>65</sup>

It is assumed that the adsorption of more hydrophobic ILs such as BMIM<sup>+</sup> on the TNS and TNP particles at pH 10, where the hydroxyl groups are deprotonated, giving rise to a highly ionic and hydrophilic nature of the surface, does not take place in a significant extent, whereas the hydrophilic MIM<sup>+</sup> shows high affinity, leading to the overcharging effect. These interfacial phenomena determined the aggregation processes and thus, MIMCl destabilizes the dispersions at lower concentrations, leading to a lower CCC. The above assumptions are fully supported by the electrophoretic mobility and stability ratio data determined for the titania particles dispersed in the aqueous IL solutions.

## CONCLUSIONS

The colloidal stability of titania nano-objects of sheet-like and spherical morphology was investigated in dispersions containing IL cations differing in their alkyl chain lengths. The charge of the TNS and TNP was tuned by the pH. No significant adsorption of the positively charged IL constituents was observed on the TNS or TNP surfaces of the same sign of charge. The aggregation behavior showed good qualitative agreement with the prediction by the DLVO theory (see the Supporting Information for more details on the DLVO model). However, a slowdown in the aggregation process was detected at high IL concentrations because of viscous stabilization.

Specific effects were observed with negatively charged titania dispersed in MIMCl, EMIMCl, and BMIMCl solutions. Because of the hydrophilic nature of the TNS and TNP above the PZC, the MIM<sup>+</sup> cations showed the highest affinity to the particle surfaces, leading to charge neutralization and



overcharging. The extent of the cation adsorption followed the  $\text{MIM}^+ > \text{EMIM}^+ > \text{BMIM}^+$  sequence. The samples were destabilized by the ILs because of charge neutralization in the first two cases, whereas BMIMCl constituent ions screened the surface charge at high concentrations. On the basis of the experimental data, it was assumed that the major interparticle forces originated from repulsive double layer and attractive van der Waals interaction together with viscous stabilization at high IL doses.

The CCC values of the TNS and TNP in the same IL solutions were different because of the size-strength of the van der Waals force relationship and smaller particles aggregated at higher IL concentrations. The colloidal stability of the positively charged titania nano-objects was insensitive to the alkyl chain length. For the negatively charged ones, the CCC changed in the  $\text{MIMCl} < \text{EMIMCl} < \text{BMIMCl}$  order, which correlates well with the charging properties. More hydrated  $\text{MIM}^+$  cations adsorb strongly on the hydrophilic surfaces and destabilize the dispersions by charge neutralization at a relatively low IL concentration. Adsorption of more hydrophobic  $\text{BMIM}^+$  is not favorable and thus, the titania samples are destabilized by charge screening at a higher IL dose. These findings are in contrast with the ones reported earlier on colloidal stability of latex particles in the presence of the same ILs. The deviation is owing to the different experimental conditions applied and to the more hydrophobic nature of the latex surface compared to titania.

Given the growing interest in IL-nanoparticle dispersions used for various applications, the present results bring important quantitative information about the interfacial properties of IL constituents on the surface of titania particles. The dependence of the alkyl chain length on the colloidal stability of hydrophilic titania particles was not studied in the past. Therefore, the findings will be especially helpful in designing processable particle dispersions in ILs, where the aggregation features can be controlled by the alkyl chain length of the IL cations or by other task-specific ILs of different hydration levels.

## ■ ASSOCIATED CONTENT

### ● Supporting Information

The Supporting Information is available free of charge on the ACS Publications website at DOI: [10.1021/acs.jpcc.9b03983](https://doi.org/10.1021/acs.jpcc.9b03983).

Description of the DLVO theory, physico-chemical data for ILs, TNS, and TNP, refractive indices of IL solutions, and electrophoretic mobility and stability ratio data for the TNS-IL and TNP-IL systems (PDF)

## ■ AUTHOR INFORMATION

### Corresponding Author

\*E-mail: [szistvan@chem.u-szeged.hu](mailto:szistvan@chem.u-szeged.hu).

### ORCID

Istvan Szilagyi: [0000-0001-7289-0979](https://orcid.org/0000-0001-7289-0979)

### Author Contributions

The paper was written through the contributions of all the authors. All the authors have given approval to the final version of the paper.

### Notes

The authors declare no competing financial interest.

## ■ ACKNOWLEDGMENTS

This research was financially supported by the Lendület program of the Hungarian Academy of Sciences (project 96130) and by the Ministry of Human Capacities, Hungary, through grant 20391-3/2018/FEKUSTRAT. The authors thank Professor Michal Borkovec for the access to the instruments in the Laboratory of Colloid and Surface Chemistry.

## ■ REFERENCES

- (1) Armand, M.; Endres, F.; MacFarlane, D. R.; Ohno, H.; Scrosati, B. Ionic-liquid materials for the electrochemical challenges of the future. *Nat. Mater.* **2009**, *8*, 621–629.
- (2) Hayes, R.; Warr, G. G.; Atkin, R. Structure and nanostructure in ionic liquids. *Chem. Rev.* **2015**, *115*, 6357–6426.
- (3) Antonietti, M.; Kuang, D.; Smarsly, B.; Zhou, Y. Ionic liquids for the convenient synthesis of functional nanoparticles and other inorganic nanostructures. *Angew. Chem., Int. Ed.* **2004**, *43*, 4988–4992.
- (4) Fernandes, N. J.; Wallin, T. J.; Vaia, R. A.; Koerner, H.; Giannelis, E. P. Nanoscale ionic materials. *Chem. Mater.* **2014**, *26*, 84–96.
- (5) Le Bideau, J.; Viau, L.; Vioux, A.; Ionogels. Ionogels, ionic liquid based hybrid materials. *Chem. Soc. Rev.* **2011**, *40*, 907–925.
- (6) Taskin, M.; Cognigni, A.; Zirbs, R.; Reimhult, E.; Bica, K. Surface-active ionic liquids for palladium-catalysed cross coupling in water: Effect of ionic liquid concentration on the catalytically active species. *RSC Adv.* **2017**, *7*, 41144–41151.
- (7) Rogers, R. D.; Seddon, K. R. CHEMISTRY: Ionic Liquids—Solvents of the Future? *Science* **2003**, *302*, 792–793.
- (8) Earle, M. J.; Esperança, J. M. S. S.; Gilea, M. A.; Canongia Lopes, J. N.; Rebelo, L. P. N.; Magee, J. W.; Seddon, K. R.; Widegren, J. A. The distillation and volatility of ionic liquids. *Nature* **2006**, *439*, 831–834.
- (9) Wasserscheid, P. Volatile times for ionic liquids. *Nature* **2006**, *439*, 797.
- (10) Zheng, Z. P.; Fan, W. H.; Roy, S.; Mazur, K.; Nazet, A.; Buchner, R.; Bonn, M.; Hunger, J. Ionic liquids: not only structurally but also dynamically heterogeneous. *Angew. Chem., Int. Ed.* **2015**, *54*, 687–690.
- (11) Dožić, S.; Zec, N.; Tot, A.; Papovic, S.; Pavlovic, K.; Gadzuric, S.; Vranes, M. Does the variation of the alkyl chain length on N1 and N3 of imidazole ring affect physicochemical features of ionic liquids in the same way? *J. Chem. Thermodyn.* **2016**, *93*, 52–59.
- (12) He, Z.; Alexandridis, P. Nanoparticles in ionic liquids: Interactions and organization. *Phys. Chem. Chem. Phys.* **2015**, *17*, 18238–18261.
- (13) Łuczak, J.; Paszkiewicz, M.; Krukowska, A.; Malankowska, A.; Zaleska-Medynska, A. Ionic liquids for nano- and microstructures preparation. Part 1: Properties and multifunctional role. *Adv. Colloid Interface Sci.* **2016**, *230*, 13–28.
- (14) Ueno, K.; Watanabe, M. From colloidal stability in ionic liquids to advanced soft materials using unique media. *Langmuir* **2011**, *27*, 9105–9115.
- (15) Vollmer, C.; Janiak, C. Naked metal nanoparticles from metal carbonyls in ionic liquids: Easy synthesis and stabilization. *Coord. Chem. Rev.* **2011**, *255*, 2039–2057.
- (16) Arquillière, P. P.; Helgadottir, I. S.; Santini, C. C.; Haumesser, P.-H.; Aouine, M.; Massin, L.; Rousset, J.-L. Bimetallic Ru-Cu nanoparticles synthesized in ionic liquids: Kinetically controlled size and structure. *Top. Catal.* **2013**, *56*, 1192–1198.
- (17) Zhang, H.; Dasbiswas, K.; Ludwig, N. B.; Han, G.; Lee, B.; Vaikuntanathan, S.; Talapin, D. V. Stable colloids in molten inorganic salts. *Nature* **2017**, *542*, 328–331.
- (18) Yang, X.; Fei, Z.; Zhao, D.; Ang, W. H.; Li, Y.; Dyson, P. J. Palladium Nanoparticles Stabilized by an Ionic Polymer and Ionic Liquid: A Versatile System for C–C Cross-Coupling Reactions. *Inorg. Chem.* **2008**, *47*, 3292–3297.

- (19) Gopakumar, A.; Fei, Z.; Păunescu, E.; Auzelyte, V.; Brugger, J.; Dyson, P. J. UV-imprint resists generated from polymerizable ionic liquids and titania nanoparticles. *J. Phys. Chem. C* **2014**, *118*, 16743–16748.
- (20) Zhou, Y.; Antonietti, M. Synthesis of Very Small TiO<sub>2</sub>Nanocrystals in a Room-Temperature Ionic Liquid and Their Self-Assembly toward Mesoporous Spherical Aggregates. *J. Am. Chem. Soc.* **2003**, *125*, 14960–14961.
- (21) Mamusa, M.; Siriex-Plénet, J.; Cousin, F.; Dubois, E.; Peyre, V. Tuning the colloidal stability in ionic liquids by controlling the nanoparticles/liquid interface. *Soft Matter* **2014**, *10*, 1097–1101.
- (22) Kanzaki, R.; Guibert, C.; Fresnais, J.; Peyre, V. Dispersion mechanism of polyacrylic acid-coated nanoparticle in protic ionic liquid, N,N-diethylethanolammonium trifluoromethanesulfonate. *J. Colloid Interface Sci.* **2018**, *516*, 248–253.
- (23) Vanecht, E.; Binnemans, K.; Patskovsky, S.; Meunier, M.; Seo, J. W.; Stappers, L.; Fransaer, J. Stability of sputter-deposited gold nanoparticles in imidazolium ionic liquids. *Phys. Chem. Chem. Phys.* **2012**, *14*, 5662–5671.
- (24) Podgoršek, A.; Pensado, A. S.; Santini, C. C.; Gomes, M. F. C.; Padua, A. A. H. Interaction energies of ionic liquids with metallic nanoparticles: Solvation and stabilization effects. *J. Phys. Chem. C* **2013**, *117*, 3537–3547.
- (25) Szilagy, I.; Szabo, T.; Desert, A.; Trefalt, G.; Oncsik, T.; Borkovec, M. Particle aggregation mechanisms in ionic liquids. *Phys. Chem. Chem. Phys.* **2014**, *16*, 9515–9524.
- (26) Smith, J.; Webber, G. B.; Warr, G. G.; Atkin, R. Silica particle stability and settling in protic ionic liquids. *Langmuir* **2014**, *30*, 1506–1513.
- (27) Ueno, K.; Inaba, A.; Kondoh, M.; Watanabe, M. Colloidal stability of bare and polymer-grafted silica nanoparticles in ionic liquids. *Langmuir* **2008**, *24*, 5253–5259.
- (28) Wittmar, A.; Ruiz-Abad, D.; Ulbricht, M. Dispersions of silica nanoparticles in ionic liquids investigated with advanced rheology. *J. Nanopart. Res.* **2012**, *14*, 65101–65110.
- (29) Gao, J.; Ndong, R. S.; Shiflett, M. B.; Wagner, N. J. Creating Nanoparticle Stability in Ionic Liquid [C4mim][BF<sub>4</sub>] by Inducing Solvation Layering. *ACS Nano* **2015**, *9*, 3243–3253.
- (30) Mezger, M.; Schroder, H.; Reichert, H.; Schramm, S.; Okasinski, J. S.; Schoder, S.; Honkimaki, V.; Deutsch, M.; Ocko, B. M.; Ralston, J.; et al. Molecular layering of fluorinated ionic liquids at a charged sapphire (0001) surface. *Science* **2008**, *322*, 424–428.
- (31) Sheehan, A.; Jurado, L. A.; Ramakrishna, S. N.; Arcifa, A.; Rossi, A.; Spencer, N. D.; Espinosa-Marzal, R. M. Layering of ionic liquids on rough surfaces. *Nanoscale* **2016**, *8*, 4094–4106.
- (32) Gebbie, M. A.; Valtiner, M.; Banquy, X.; Fox, E. T.; Henderson, W. A.; Israelachvili, J. N. Ionic liquids behave as dilute electrolyte solutions. *Proc. Natl. Acad. Sci. U.S.A.* **2013**, *110*, 9674–9679.
- (33) Derjaguin, B. A theory of interaction of particles in presence of electric double layers and the stability of lyophobic colloids and disperse systems. *Prog. Surf. Sci.* **1993**, *43*, 1–14.
- (34) Derjaguin, B. On the repulsive forces between charged colloid particles and on the theory of slow coagulation and stability of lyophobic sols. *Trans. Faraday Soc.* **1940**, *35*, 203–214.
- (35) Trefalt, G.; Szilagy, I.; Borkovec, M. Poisson-Boltzmann description of interaction forces and aggregation rates involving charged colloidal particles in asymmetric electrolytes. *J. Colloid Interface Sci.* **2013**, *406*, 111–120.
- (36) Gebbie, M. A.; Smith, A. M.; Dobbs, H. A.; Lee, A. A.; Warr, G. G.; Banquy, X.; Valtiner, M.; Rutland, M. W.; Israelachvili, J. N.; Perkin, S.; et al. Long range electrostatic forces in ionic liquids. *Chem. Commun.* **2017**, *53*, 1214–1224.
- (37) Oncsik, T.; Desert, A.; Trefalt, G.; Borkovec, M.; Szilagy, I. Charging and aggregation of latex particles in aqueous solutions of ionic liquids: Towards an extended Hofmeister series. *Phys. Chem. Chem. Phys.* **2016**, *18*, 7511–7520.
- (38) Elmahdy, M. M.; Gutsche, C.; Kremer, F. Forces within single pairs of charged colloids in aqueous solutions of ionic liquids as studied by optical tweezers. *J. Phys. Chem. C* **2010**, *114*, 19452–19458.
- (39) Valmacco, V.; Trefalt, G.; Maroni, P.; Borkovec, M. Direct force measurements between silica particles in aqueous solutions of ionic liquids containing 1-butyl-3-methylimidazolium (BMIM). *Phys. Chem. Chem. Phys.* **2015**, *17*, 16553–16559.
- (40) Tietze, A. A.; Bordusa, F.; Giernoth, R.; Imhof, D.; Lenzer, T.; Maass, A.; Mrestani-Klaus, C.; Neundorff, I.; Oum, K.; Reith, D.; et al. On the nature of interactions between ionic liquids and small amino-acid-based biomolecules. *ChemPhysChem* **2013**, *14*, 4044–4064.
- (41) Yang, Z. Hofmeister effects: An explanation for the impact of ionic liquids on biocatalysis. *J. Biotechnol.* **2009**, *144*, 12–22.
- (42) Ding, K.; Miao, Z.; Liu, Z.; Zhang, Z.; Han, B.; An, G.; Miao, S.; Xie, Y. Facile Synthesis of High Quality TiO<sub>2</sub>Nanocrystals in Ionic Liquid via a Microwave-Assisted Process. *J. Am. Chem. Soc.* **2007**, *129*, 6362–6363.
- (43) Bhandary, R.; Alauzun, J. G.; Hesemann, P.; Stocco, A.; In, M.; Mutin, P. H. Phase transfer of TiO<sub>2</sub> nanoparticles from water to ionic liquid triggered by phosphonic acid grafting. *Soft Matter* **2017**, *13*, 8023–8026.
- (44) Wang, P.; Yi, Q.; Xing, M.; Zhang, J. Selective synthesis of TiO<sub>2</sub> single nanocrystals and titanate nanotubes: a controllable atomic arrangement approach via NH<sub>4</sub>TiOF<sub>3</sub> mesocrystals. *Phys. Chem. Chem. Phys.* **2015**, *17*, 21982–21987.
- (45) Rouster, P.; Pavlovic, M.; Szilagy, I. Improving the stability of titania nanosheets by functionalization with polyelectrolytes. *RSC Adv.* **2016**, *6*, 97322–97330.
- (46) Sahandzhieva, K.; Naydenov, D.; Pérez-Salado Kamps, A.; Bart, H.-J.; Maurer, G. Liquid-Liquid Equilibrium in Systems with an Ionic Liquid: Experimental Data for an Example of the Biphasic Acid Scavenging Utilizing Ionic Liquids Process. *J. Chem. Eng. Data* **2010**, *55*, 4903–4906.
- (47) Ngo, H. L.; LeCompte, K.; Hargens, L.; McEwen, A. B. Thermal properties of imidazolium ionic liquids. *Thermochim. Acta* **2000**, *357*–358, 97–102.
- (48) Kick, M.; Keil, P.; König, A. Solid-liquid phase diagram of the two Ionic Liquids EMIMCl and BMIMCl. *Fluid Phase Equilib.* **2013**, *338*, 172–178.
- (49) Delgado, A. V.; González-Caballero, F.; Hunter, R. J.; Koopal, L. K.; Lyklema, J. Measurement and Interpretation of Electrokinetic Phenomena (IUPAC Technical Report). *Pure Appl. Chem.* **2005**, *77*, 1753–1805.
- (50) Hassan, P. A.; Rana, S.; Verma, G. Making sense of Brownian motion: Colloid characterization by dynamic light scattering. *Langmuir* **2015**, *31*, 3–12.
- (51) Joye, D. D. Shear rate and viscosity corrections for a Casson fluid in cylindrical (Couette) geometries. *J. Colloid Interface Sci.* **2003**, *267*, 204–210.
- (52) Jenkins, H. D. B.; Marcus, Y. Viscosity B-coefficients of ions in solution. *Chem. Rev.* **1995**, *95*, 2695–2724.
- (53) Parks, G. A. The isoelectric points of solid oxides, solid hydroxides, and aqueous hydroxo complex systems. *Chem. Rev.* **1965**, *65*, 177–198.
- (54) Kosmulski, M. The pH dependent surface charging and points of zero charge. VII. Update. *Adv. Colloid Interface Sci.* **2018**, *251*, 115–138.
- (55) Niecikowska, A.; Krasowska, M.; Ralston, J.; Malysa, K. Role of surface charge and hydrophobicity in the three-phase contact formation and wetting film stability under dynamic conditions. *J. Phys. Chem. C* **2012**, *116*, 3071–3078.
- (56) Borkovec, M.; Behrens, S. H.; Semmler, M. Observation of the mobility maximum predicted by the standard electrokinetic model for highly charged amidine latex particles. *Langmuir* **2000**, *16*, 5209–5212.
- (57) Holthoff, H.; Egelhaaf, S. U.; Borkovec, M.; Schurtenberger, P.; Sticher, H. Coagulation rate measurements of colloidal particles by simultaneous static and dynamic light scattering. *Langmuir* **1996**, *12*, 5541–5549.

(58) Grolimund, D.; Elimelech, M.; Borkovec, M. Aggregation and deposition kinetics of mobile colloidal particles in natural porous media. *Colloids Surf.* **2001**, *191*, 179–188.

(59) Elbourne, A.; McDonald, S.; Voïchovsky, K.; Endres, F.; Warr, G. G.; Atkin, R. Nanostructure of the ionic liquid-graphite Stern layer. *ACS Nano* **2015**, *9*, 7608–7620.

(60) Elbourne, A.; Voïchovsky, K.; Warr, G. G.; Atkin, R. Ion structure controls ionic liquid near-surface and interfacial nanostructure. *Chem. Sci.* **2015**, *6*, 527–536.

(61) Oncsik, T.; Trefalt, G.; Csendes, Z.; Szilagyi, I.; Borkovec, M. Aggregation of negatively charged colloidal particles in the presence of multivalent cations. *Langmuir* **2014**, *30*, 733–741.

(62) Oncsik, T.; Trefalt, G.; Borkovec, M.; Szilagyi, I. Specific ion effects on particle aggregation induced by monovalent salts within the Hofmeister series. *Langmuir* **2015**, *31*, 3799–3807.

(63) Lagaly, G.; Mecking, O.; Penner, D. Colloidal magnesium aluminum hydroxide and heterocoagulation with a clay mineral. I. Properties of colloidal magnesium aluminum hydroxide. *Colloid Polym. Sci.* **2001**, *279*, 1090–1096.

(64) Parkinson, L.; Ralston, J. The interaction between a very small rising bubble and a hydrophilic titania surface. *J. Phys. Chem. C* **2010**, *114*, 2273–2281.

(65) Studzińska, S.; Sprynskyy, M.; Buszewski, B. Study of sorption kinetics of some ionic liquids on different soil types. *Chemosphere* **2008**, *71*, 2121–2128.



Cite this: *Soft Matter*, 2021, 17, 9116

## Influence of adsorption of ionic liquid constituents on the stability of layered double hydroxide colloids

Dóra Takács,<sup>a</sup> Bojana Katana,<sup>a</sup> Adél Szerlauth,<sup>a</sup> Dániel Sebők,<sup>b</sup> Matija Tomšič<sup>id</sup><sup>c</sup> and István Szilágyi<sup>id</sup><sup>\*a</sup>

The influence of ionic liquid (IL) anions and cations on the charging and aggregation properties of layered double hydroxide (LDH) nanoparticles was systematically studied. Surface charge characteristics were explored using zeta potential measurements, while aggregation processes were followed in dynamic light scattering experiments in aqueous IL solutions. The results revealed that the aggregation rates of LDHs were sensitive to the composition of ILs leading to IL-dependent critical coagulation concentration (CCC) values being obtained. The origin of the interparticle forces was found to be electrostatic, in line with the classical Derjaguin–Landau–Verwey–Overbeek (DLVO) theory, as the experimental aggregation kinetics were in good agreement with the predicted data. The ion specific adsorption of IL anions led to different surface charge densities for LDHs, which decreased in the order  $\text{Cl}^- > \text{Br}^- > \text{DCA}^- > \text{SCN}^- > \text{NO}_3^-$  for counterions and  $\text{BMIM}^+ > \text{BMPYR}^+ > \text{BMPY}^+ > \text{BMPIP}^+$  in the case of coions resulting in weaker electrical double layer repulsion in these sequences. Since van der Waals forces are always present and their strength does not depend significantly on the ionic strength, the CCC values decreased in the above order. The present results shed light on the importance of the interfacial arrangement of the IL constituent ions on the colloidal stability of particle dispersions and provide important information on the design of stable or unstable particle-ionic liquid systems.

Received 22nd July 2021,  
Accepted 7th September 2021

DOI: 10.1039/d1sm01074c

rsc.li/soft-matter-journal

### 1. Introduction

Layered double hydroxides (LDHs) represent a class of inorganic layered materials consisting of positively charged hydroxide sheets of divalent (*e.g.*,  $\text{Mg}^{2+}$ ,  $\text{Zn}^{2+}$  or  $\text{Ca}^{2+}$ ) and trivalent (*e.g.*,  $\text{Al}^{3+}$ ,  $\text{Fe}^{3+}$  or  $\text{Cr}^{3+}$ ) metal ions coordinated by hydroxide groups, as well as interlayer water and anions compensating the charge on the layers.<sup>1</sup> The most common group of LDHs can be described by the general formula of  $[\text{M}(\text{II})_{1-x}\text{M}(\text{III})_x(\text{OH})_2][\text{A}^{n-} \cdot m\text{H}_2\text{O}]$ , where  $\text{M}(\text{II})$  and  $\text{M}(\text{III})$  are the divalent and trivalent metal ions and  $\text{A}^{n-} \cdot m\text{H}_2\text{O}$  is the interlamellar charge-neutralizing anion in the hydrated state.<sup>2</sup> The exploitation of the anion exchange capacity and lamellar structure – which are important properties of LDHs – is still a fascinating research topic, as these properties allow the direct intercalation of inorganic and organic anions.<sup>3–5</sup>

Numerous LDH applications based on the intercalation or exchange of specific guest molecules have been comprehensively studied in the past decades. For example, polyoxometalate intercalated LDHs proved to be efficient catalysts in dehydrogenation, esterification and oxidation reactions.<sup>6</sup> Anti-inflammatory, anti-cardiovascular and anti-cancer drugs were successfully immobilized in LDH supports and the obtained hybrids were used for biomedical therapies.<sup>7,8</sup> Besides, the intercalation phenomenon was utilized in the removal of dye contaminants from the aqueous environment.<sup>9</sup>

However, strong attraction between the highly charged hydroxide layers and the interlayer anions hinders the access to the interlayer space in many cases. Delamination of LDHs into single layers is a possible way to obtain LDH systems for immobilization of guest molecules regardless of their size,<sup>10</sup> but the delamination process is not straightforward in conventional media due to the high charge density, small interlayer distance and strong hydrophilicity.

One of the most promising candidates for the liquid phase delamination of LDHs is the ionic liquids (ILs), since they can be obtained using the desired molecular structures and physico-chemical properties.<sup>11–13</sup> ILs can be considered as molten salts and are generally composed of a bulky organic cation with an

<sup>a</sup> MTA-SZTE Lendület Biocolloids Research Group, Department of Physical Chemistry and Materials Science, University of Szeged, 1 Rerrich Béla tér H-6720 Szeged, Hungary. E-mail: szistvan@chem.u-szeged.hu

<sup>b</sup> Department of Applied and Environmental Chemistry, University of Szeged, 1 Rerrich Béla tér, H-6720 Szeged, Hungary

<sup>c</sup> Faculty of Chemistry and Chemical Technology, University of Ljubljana, Večna pot 113, SI-1000 Ljubljana, Slovenia

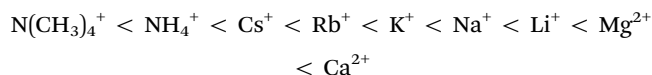
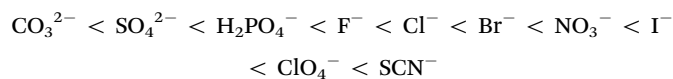


inorganic or organic anion. Their high chemical and thermal stability and extremely low vapor pressure generally make ILs less hazardous than organic solvents used in various applications.<sup>14,15</sup> It is known that ILs are able to reduce the strength of attractive forces between charged surfaces due to the possible combined effect of their interfacial assembly or partial dissociation.<sup>16–18</sup> Furthermore, the shielding of attractive interactions between the layers should also lead to the collapse of stacked structures and for instance, to the delamination of LDHs into unilamellar nanosheets. Although direct delamination of LDHs in ILs has not been reported yet, single layer nanosheets have been prepared in water-IL reversed emulsion<sup>19</sup> as well as by intercalating IL constituents and performing subsequent *in situ* polymerization within the layers.<sup>20</sup> The stabilization of the resulting delaminated LDH materials is a key point, which has not been explored in detail.

There is growing contemporary interest in application of LDH-IL systems. Accordingly, LDH supported palladium particles showed remarkable catalytic activity in nonaqueous ILs.<sup>21</sup> IL impregnated LDH was synthesized and used as a solid electrolyte in batteries for advanced energy storage applications.<sup>22</sup> IL assisted LDH synthesis led to the formation of particles of high specific surface area used for phosphate removal in water treatment processes.<sup>19</sup> Finally, it was pointed out that LDH-IL systems can be applied in the preparation of ionogels<sup>23</sup> or composite materials,<sup>24</sup> since the combination of the features of the inorganic matrix and specific ILs may lead to synergistic effects in property selection and tuning. The above examples indicate a need for a comprehensive investigation of LDH-IL interactions and subsequently, on the interparticle forces across ILs. Nevertheless, only a handful of studies can be found in the literature that are focusing on particle aggregation in ILs<sup>25–29</sup> and, to the best of our knowledge, no data are yet available for LDH-IL systems. Therefore, a systematic investigation on dispersion stability in such systems is required for a better understanding of the behavior of these complicated systems.

In this way, the first step is to gain knowledge of the interfacial assembly of IL constituents, since such a process is likely to play a crucial role in the stability of LDH particles in ionic media. Previous studies<sup>30–34</sup> on other particle-IL systems pointed out that ion specific effects, similar to inorganic electrolytes,<sup>35–37</sup> are important in the presence of IL constituents since they govern the adsorption of ions from solutions. Moreover, IL cations and anions can be arranged in sequences based on their adsorption affinity to a given surface.<sup>31,32,34</sup>

For standard inorganic salts, the extent of ion specific adsorption and its effect on the stability can be ordered in the Hofmeister series of anions and cations. This theory was originally developed to describe the influence of salt constituents on the stability of protein solutions as follows.<sup>38</sup>



Accordingly, negatively charged proteins were found to be stable at higher concentrations in salts containing the ions on the right side of the above series, while the ones on the left side induced protein precipitation already at low concentrations. Since the discovery of this effect, numerous experimental and theoretical studies were carried out to explain the ion adsorption mechanism and the subsequent change in the structure and stability of various biological systems, where proteins are important components.<sup>39–44</sup>

In the past decades, a large number of papers reported on the applicability of such order in other phenomena. For instance, ion specific effects on the assembly of amphiphilic molecules were comprehensively studied.<sup>45</sup> In addition, surface adsorption of cations followed the above order and the results of calculations revealed that the hydration of both the surface and the ions played a major role in the adsorption mechanism.<sup>46</sup> Particle aggregation studies<sup>31,34–37,47,48</sup> shed light on the fact that the critical coagulation concentration (CCC) data determined using the same particles in different electrolyte solutions can be ordered in the Hofmeister series too. However, the DLVO (Derjaguin, Landau, Verwey and Overbeek) theory,<sup>49</sup> which describes the surface forces in the presence of salt constituents, failed to predict the dependence of such forces on the type of salt present and consequently, the trends in CCC values measured in various salt solutions.<sup>31,47,50–52</sup>

Besides, the CCC of particles in IL solutions were also found to be sensitive to the type of ion.<sup>31,32,34</sup> Therefore, the traditional Hofmeister series of ions developed for the destabilization effect of ionic species in particle dispersions can be extended by using IL constituents. This issue can be adequately addressed in aqueous IL solutions by investigating the charging characteristics and aggregation properties of the colloidal particles.<sup>31,32,34</sup> Nevertheless, no similar investigations have been performed with LDH particles yet.

The aim of the present study was to provide insight into the effect of the interfacial properties of IL constituents on the interparticle forces in LDH dispersions. Therefore, the basic charging and aggregation processes for positively charged LDH particles in diluted aqueous IL solutions were investigated. The type of IL anion ( $\text{Cl}^-$ ,  $\text{Br}^-$ ,  $\text{DCA}^-$ ,  $\text{SCN}^-$ , and  $\text{NO}_3^-$ ) and cations ( $\text{BMIM}^+$ ,  $\text{BMPiP}^+$ ,  $\text{BMPYR}^+$ , and  $\text{BMPY}^+$ ) was systematically varied and thus, the specific effect of counter- and coions was studied. The surface charge properties were investigated using zeta (electrokinetic) potential measurements, while the aggregation features were assessed in time-resolved light scattering experiments. The aim was to discuss the generic dependence of the aggregation rates on the IL concentration and to address system specificities in the presence of different IL compounds.

## 2. Experimental

### 2.1. Materials

The ILs such as 1-butyl-3-methylimidazolium chloride (BMIMCl), 1-butyl-2-methylpyridinium chloride (BMPYCl), 1-butyl-1-methylpiperidinium chloride (BMPiPCl) and 1-butyl-1-methylpyrrolidinium chloride (BMPYRCl) were bought from IoLiTec GmbH,

while 1-butyl-3-methylimidazolium bromide (BMIMBr), 1-butyl-3-methylimidazolium nitrate (BMIMNO<sub>3</sub>) and 1-butyl-3-methylimidazolium thiocyanate (BMIMSCN) were purchased from Sigma-Aldrich and 1-butyl-3-methylimidazolium dicyanamide (BMIMDCA) was obtained from Merck. Ultrapure water was used during the sample preparation from a VWR Purity TU+ device. All stock solutions and the water were adjusted to pH 9.0 with NaOH (AnalR NORMAPUR) and they were filtered prior to sample preparation using 0.1 μm syringe filters (Millex) to avoid dust contamination. The experiments were carried out at 25 °C. The particle concentration was kept at 10 mg L<sup>-1</sup>.

The LDH particles used in the present work were prepared using the flash co-precipitation method followed by hydrothermal treatment.<sup>10,53</sup> Briefly, a mixed metal ion solution was prepared by dissolving the salts in water (0.2 M Mg(NO<sub>3</sub>)<sub>2</sub> and 0.1 M Al(NO<sub>3</sub>)<sub>3</sub>). The pH was set to 10 with 4.0 M NaOH solution. The alkali and salt solutions were mixed under an N<sub>2</sub> atmosphere. After stirring vigorously for 30 minutes, the sample was centrifuged and washed with water. The slurry was redispersed and the resulting dispersion was transferred to an autoclave and treated in an oven at 120 °C for 24 hours. After cooling to ambient temperature, the sample was separated and dried at 50 °C overnight. To prove the successful synthesis of the LDH, powder X-ray diffraction (XRD) measurements were performed on a Bruker D8 Advanced diffractometer with Cu Kα (0.1542 nm) as a radiation source in the 2θ range from 5° to 80° with the 0.02° step. The distinctive XRD pattern of the pristine LDH is shown in Fig. 1. The diffraction patterns show the reflections reported earlier for LDH-based materials.<sup>53</sup> The obtained LDH particles were then re-suspended in pH 9 water resulting in a stock dispersion of 5 g L<sup>-1</sup> concentration, which was later diluted to reach the suitable particle concentration for the experiments.

## 2.2. Electrophoretic light scattering

A Litesizer 500 instrument (Anton Paar) equipped with a 40 mW semiconductor laser (658 nm wavelength) was used to measure the electrophoretic mobility of the particles in aqueous solutions of ILs. The samples were prepared by mixing the appropriate amount of ILs and water to obtain the desired concentration. The LDH particles were then added by the appropriate addition of the stock dispersion to obtain the final particle concentration. Prior to measurements, the samples were left to rest for 2 hours at room temperature, and then they were equilibrated for 1 additional minute in the instrument. The electrophoretic mobility (*u*) of each sample was measured five times, averaged and converted to zeta potential ( $\zeta$ ) value using the Smoluchowski equation<sup>54</sup> as

$$\zeta = \frac{u\eta}{\epsilon_0\epsilon} \quad (1)$$

where  $\epsilon_0$  is the dielectric permittivity of a vacuum,  $\epsilon$  is the dielectric constant of the medium and  $\eta$  is the viscosity.

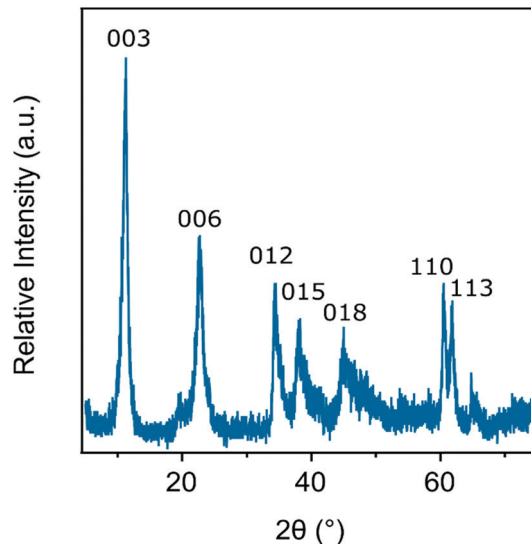


Fig. 1 Powder XRD pattern of the LDH particles synthesized by flash coprecipitation and subjected to hydrothermal treatment. The Miller indices are indicated.

## 2.3. Dynamic light scattering

To explore particle aggregation, time-resolved dynamic light scattering (DLS) measurements were performed using Litesizer 500 instrument (Anton Paar) at a scattering angle of 175°. The same sample preparation procedure as in the electrophoretic mobility studies was followed, with the exception that the DLS measurements started immediately after addition of the desired volume of LDH stock dispersion. The total volume of each sample was 2.0 mL and the experiments were carried out in disposable polystyrene cuvettes.

The hydrodynamic radius ( $R_h$ ) of the particles was calculated by the Stokes–Einstein equation from the diffusion coefficient ( $D$ ), which was extracted from the correlation function using the cumulant method.<sup>55</sup> Time-resolved measurements were carried out to determine the apparent aggregation rate coefficients ( $k_{app}$ ) as follows:<sup>56</sup>

$$k_{app} = \frac{1}{R_h(0)} \left( \frac{dR_h(t)}{dt} \right)_{t \rightarrow 0} \quad (2)$$

where  $R_h(0)$  is the hydrodynamic radius of LDH measured in a stable dispersion and  $t$  is the time of the experiment. The colloidal stability of the samples was expressed in terms of the stability ratio ( $W$ ):

$$W = \frac{k_{app(fast)}}{k_{app}} \quad (3)$$

where the fast subscript indicates fast or diffusion-controlled aggregation of the particles. The  $k_{app(fast)}$  value was determined separately for each system in the fast aggregation regime above the CCC. Note that the stability ratio close to unity indicates that the particles undergo rapid aggregation and formation of unstable dispersions. While higher stability ratio values are signals for slower aggregation and thus, more stable samples.

Accordingly, in a non-aggregating particle dispersion, stability ratios cannot be determined.

#### 2.4. Refractometry

The refractive index ( $n$ ) measurements were carried out on an Abbemat 3200 automatic one-wavelength refractometer (Anton Paar) at a wavelength of 589 nm. For the evaluation of the light scattering data, the  $n$  values were interpolated using a linear fit according to the following relation:

$$n = a \cdot c_{\text{IL}} + b \quad (4)$$

where  $c_{\text{IL}}$  is the molar concentration of the ILs, while  $a$  and  $b$  are the fitting parameters given in Table 1. The respective dependencies and the fits with eqn (4) are shown in Fig. 2a and b.

#### 2.5. Viscosimetry

A LVDV-II+ ProC/P viscometer (Brookfield) was used to measure the dynamic viscosities of the IL solutions in a cone-plate geometry (CPE-40 cone). The  $\eta$  of the different IL-water mixtures was determined by fitting shear stress *versus* shear rate data with the Casson model.<sup>57</sup> The experimental  $\eta$  values were fitted as follows:<sup>58</sup>

$$\frac{\eta}{\eta_0} = 1 + A\sqrt{c_{\text{IL}}} + B \cdot c_{\text{IL}} + D \cdot c_{\text{IL}}^2 \quad (5)$$

where  $\eta_0$  is the viscosity of water ( $8.90 \times 10^{-4}$  Pa s at 25 °C), while  $A$ ,  $B$  and  $D$  are constants summarized in Table 1. The respective dependencies and the fits with eqn (5) are shown in Fig. 2c and d.

### 3. Results and discussion

The surface charge properties and colloidal stability of positively charged LDH particles were investigated in the presence of aqueous IL solutions by electrophoresis and DLS, respectively. The IL composition, *i.e.*, the type of anions and cations, were systematically varied in the samples. Accordingly, BMIMCl, BMIMBr, BMIMNO<sub>3</sub>, BMIMSCN and BMIMDCA ILs were used to vary anions, while the influence of cations was investigated in the presence of BMIMCl, BMPYCl, BMPiPcI and BMPYRcI. Note that the anions are the counterions, while cations act as coions. Therefore, the effect of both counter and coions on the charging and aggregation features was assessed.

Ion pair formation in ILs is an important phenomenon in aqueous solutions, which influence the ionic strength significantly.

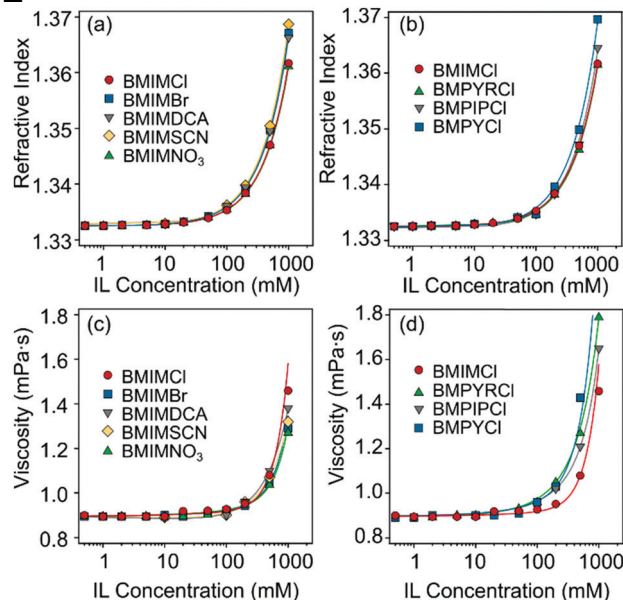


Fig. 2 (a and b) Refractive indices and (c and d) viscosities of aqueous IL (BMIMCl, BMIMBr, BMIMNO<sub>3</sub>, BMIMSCN, BMIMDCA, BMPYCl, BMPiPcI, and BMPYRcI) solutions at different concentrations. The solid lines represent the fits obtained with eqn (4) (a and b) and (5) (c and d).

Accordingly, in dilute aqueous solutions of ILs, the ion association is generally weak and ILs tend to fully dissociate. However, as the concentration of ILs increases, ions may start to associate and form ion pairs.<sup>27,59</sup> However, as it was pointed out earlier for BMIMCl,<sup>60</sup> such ion pair formation is negligible in the concentration range used in our study. It was assumed that the situation is the same (*i.e.*, no ion pairing) with the other ILs studied and the constituents are fully dissociated in solution. However, this can be different at the interface and the oppositely charged ions may form ion pairs with the IL components adsorbed on the particle surface. A similar effect was observed in particle aggregation studies earlier;<sup>31</sup> however, no consensus view exists in this topic in the scientific community yet.

#### 3.1. Effect of IL anions

First, the effect of IL anions on the surface charge properties and on the colloidal stability of LDHs was investigated in aqueous solutions of ILs at pH 9. Hence, the composition of ILs was systematically varied so that the ILs contained different anions (Cl<sup>-</sup>, Br<sup>-</sup>, DCA<sup>-</sup>, SCN<sup>-</sup>, and NO<sub>3</sub><sup>-</sup>) and the BMIM<sup>+</sup>

Table 1 Fitting parameters used to interpolate the refractive indices and viscosities of the diluted IL solutions

IL	Refractive index parameters		Viscosity parameters		
	$a$ (M <sup>-1</sup> )	$b$	$A$ (M <sup>-1/2</sup> )	$B$ (M <sup>-1</sup> )	$D$ (M <sup>-2</sup> )
BMIMCl	$2.92 \times 10^{-2}$	1.3325	$3.77 \times 10^{-1}$	$2.87 \times 10^{-4}$	$3.89 \times 10^{-1}$
BMIMBr	$3.46 \times 10^{-5}$	1.3325	$2.93 \times 10^{-3}$	$-3.30 \times 10^{-10}$	$4.17 \times 10^{-7}$
BMIMNO <sub>3</sub>	$2.26 \times 10^{-5}$	1.3325	$2.94 \times 10^{-3}$	$-3.40 \times 10^{-10}$	$3.66 \times 10^{-7}$
BMIMSCN	$3.61 \times 10^{-2}$	1.3325	$-1.08 \times 10^{-1}$	$5.29 \times 10^{-1}$	$5.52 \times 10^{-2}$
BMIMDCA	$3.37 \times 10^{-2}$	1.3326	$-1.63 \times 10^{-1}$	$6.86 \times 10^{-1}$	$2.06 \times 10^{-2}$
BMPYRcI	$2.89 \times 10^{-2}$	1.3323	$5.52 \times 10^{-2}$	$4.44 \times 10^{-1}$	1.54
BMPiPcI	$3.21 \times 10^{-2}$	1.3320	$1.43 \times 10^{-1}$	$3.08 \times 10^{-1}$	$3.95 \times 10^{-1}$
BMPYCl	$3.72 \times 10^{-2}$	1.3321	$-2.88 \times 10^{-2}$	$4.38 \times 10^{-2}$	3.92

dc\_1931\_21

cation. Note that under these experimental conditions the anions were the counterions. Therefore, they had the opposite sign of charge as the particle surface. The results on the zeta potentials are shown in Fig. 3a, which indicate that although the zeta potential values are system specific, the trend in their concentration dependence is very similar in all cases. Accordingly, they decrease by increasing the IL concentration (*i.e.*, the ionic strength) due to the surface charge screening by the IL constituents and remained very close to zero at higher ionic strength. One observes that the potential values remained positive in the entire regime investigated due to the structural charge of the particles. The maximum in the trend of the measured zeta potential in the range of low concentrations is due to the electrokinetic effect, which is a typical observation for charged particles moving in an electric field.<sup>61</sup> The magnitude of the zeta potential values at the same IL concentration decreases in the order  $\text{Cl}^- > \text{Br}^- > \text{DCA}^- > \text{SCN}^- > \text{NO}_3^-$  (Fig. 3a).

This tendency is also illustrated by the sequence of the surface charge densities ( $\sigma$ ) shown in Table 2, which can be estimated from the ionic strength dependence of the potentials by the Debye–Hückel model:<sup>49,62</sup>

$$\sigma = \epsilon \epsilon_0 \kappa \zeta \quad (6)$$

where  $\kappa$  is the inverse Debye length, which describes the distribution of the ionic species in the electrical double layer.<sup>54</sup>

The values of the stability ratio were determined in the dispersions by time-resolved DLS measurements under identical experimental conditions (*e.g.*, particle concentration, pH and IL concentration range) as the ones used in the electrophoretic studies, in order to allow a direct comparison of the tendencies in the measured zeta potential and stability ratio data. As shown in Fig. 3b, the general tendency was the same regardless of the type of the IL anions. Accordingly, slow aggregation and stable samples were observed at low IL concentrations, then the dispersions became unstable at high ionic strength as indicated by stability ratio values close to one. This behavior is typical for systems, in which the main interparticle forces originate from DLVO-type interactions, *i.e.*, the

superposition of the attractive van der Waals and the repulsive electrical double layer forces determines the colloidal stability of the dispersions. The observed slow and fast aggregation regimes are separated by the well-defined CCC values, which can be calculated from the stability ratio *versus* IL concentration plots as<sup>63</sup>

$$W = 1 + \left( \frac{\text{CCC}}{c_{\text{IL}}} \right)^{-\beta} \quad (7)$$

where  $\beta$  was obtained from the slope of the stability ratios in the slow aggregation regime before the CCC as

$$\beta = \frac{d \log 1/W}{d \log c_{\text{IL}}} \quad (8)$$

The CCC data were used to compare the destabilization power of the ILs. The CCC systematically varies with the type of anions and it shifts from high to low values (Table 2) following the order of  $\text{Cl}^- > \text{Br}^- > \text{DCA}^- > \text{SCN}^- > \text{NO}_3^-$ . The tendency of the first four ions agrees with the indirect Hofmeister series for positively charged hydrophobic particles determined in simple inorganic salts.<sup>31</sup> Accordingly, the poorly hydrated  $\text{SCN}^-$  ions adsorb strongly on the particle surface leading to a partial charge compensation and thus, a lower surface charge, together with a lower CCC value. Nevertheless, the well hydrated  $\text{Cl}^-$  ions prefer to stay in the bulk and induces the highest CCC, since they hardly adsorb on the hydrophobic LDH particles and the resulting surface charge is higher than for the other anions used. Once the CCC data are compared with literature values reported for LDH particles in the presence of standard dissolved salts containing the same anions,<sup>48</sup> one can easily notice that the CCCs determined in the present work are significantly different indicating the importance of the type of cations (potassium or  $\text{BMIM}^+$ ) in the system.

However, in the case of  $\text{NO}_3^-$  ions, the situation is more complicated because the surface charge and the CCC values indicated atypical behavior. If one considers the indirect Hofmeister series for positively charged hydrophobic LDH surfaces, these values should be higher than for the  $\text{SCN}^-$  anion, as it was observed in the presence of standard inorganic

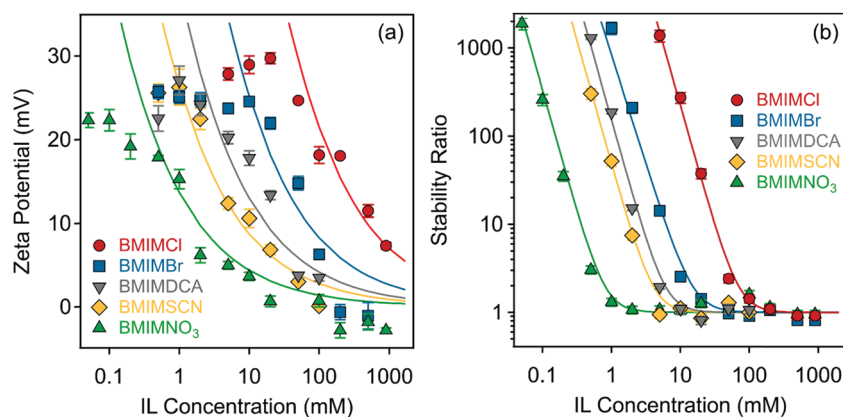


Fig. 3 (a) Zeta potentials and (b) stability ratios of LDH particles in the presence of ILs composed of different anions ( $\text{Cl}^-$ ,  $\text{Br}^-$ ,  $\text{DCA}^-$ ,  $\text{SCN}^-$  and  $\text{NO}_3^-$ ) and the  $\text{BMIM}^+$  cation. The solid lines are the fits obtained with eqn (6) (a) and (7) (b).



Table 2 Characteristic charging and aggregation data of LDH particles measured in diluted IL solutions

IL cations	BMIM <sup>+</sup>	BMIM <sup>+</sup>	BMIM <sup>+</sup>	BMIM <sup>+</sup>	BMIM <sup>+</sup>	BMPYR <sup>+</sup>	BMPY <sup>+</sup>	BMPIP <sup>+</sup>
IL anions	Cl <sup>-</sup>	Br <sup>-</sup>	DCA <sup>-</sup>	SCN <sup>-</sup>	NO <sub>3</sub> <sup>-</sup>	Cl <sup>-</sup>	Cl <sup>-</sup>	Cl <sup>-</sup>
$\sigma^a$ (mC m <sup>-2</sup> )	16	6	3	2	1	14	8	4
CCC <sup>b</sup> (mM)	70	15	6	4	0.8	50	30	10
$k_{app(fast)}^c$ ( $\times 10^{-3}$ s <sup>-1</sup> )	1.07	0.93	0.79	1.04	0.76	0.97	0.98	1.06

<sup>a</sup> Surface charge density determined with eqn (6). <sup>b</sup> Critical coagulation concentration calculated by eqn (7). <sup>c</sup> Apparent aggregation rate coefficient in the fast aggregation regime obtained by eqn (2).

electrolytes indicating the effect of the IL cation.<sup>37,48</sup> Nevertheless, the lowest CCC was measured for this ion. Such a discrepancy from the traditional series is probably due to the different counterion affinity to the oppositely charged particles and the different extent of IL ion pair formation on the surface. It is known that the ions may associate in the bulk in various ILs.<sup>64,65</sup> However, the IL constituents may also form ion pairs with the oppositely charged ions, while they are adsorbed on the particle surface.<sup>31</sup> Accordingly, BMIM<sup>+</sup> cations may adsorb on the LDH surface, which can induce a stronger co-adsorption of NO<sub>3</sub><sup>-</sup> ions owing to associated IL molecules on the surface. Such a phenomenon then influences the surface charge and thus, the CCC as well. The adsorption of BMIM<sup>+</sup> on the like-charged LDH surfaces will be further discussed later.

Looking at the zeta potential data before the CCC in the above system, one observes that they change only slightly (within 5 mV) before the CCC (0.8 mM); however, the decrease in the stability ratios is large in this regime. This is due to the low potential (around 20 mV) at limited IL concentrations.<sup>66</sup> Such a low zeta potential is at the limit, where colloid particles are usually stable and thus, very small changes in the zeta potentials may give rise to sudden increase in the apparent

aggregation rates and consequently, to a decrease in the stability ratios.

### 3.2. Effect of IL cations

Subsequently, the effect of the IL cations on the charging characteristics and aggregation features of LDH particles was also investigated. Zeta potentials and aggregation rates of positively charged particles were strongly influenced by the type of IL cations (BMIM<sup>+</sup>, BMPYR<sup>+</sup>, BMPY<sup>+</sup>, and BMPIP<sup>+</sup>) when the same (Cl<sup>-</sup>) counterion was used. Such a systematic experimental setup allows addressing the specific effect of different IL cations unequivocally. Fig. 4a indicates that the generic trend for the zeta potential values was similar to the one discussed in the previous section, *i.e.*, the zeta potential values decreased as the concentration of the ILs increased due to charge screening.

Also, the shape of the stability plots (Fig. 4b) was identical to those presented for varying anions (Fig. 3b). Accordingly, slow aggregation occurs at low IL concentrations and with increasing concentration, the stability ratio decreases until it reaches unity and subsequently settles at that value within the experimental error. Nevertheless, these observations are generic for colloidal systems containing charged particles in electrolyte solutions, but the actual values of the potentials and stability ratios vary by

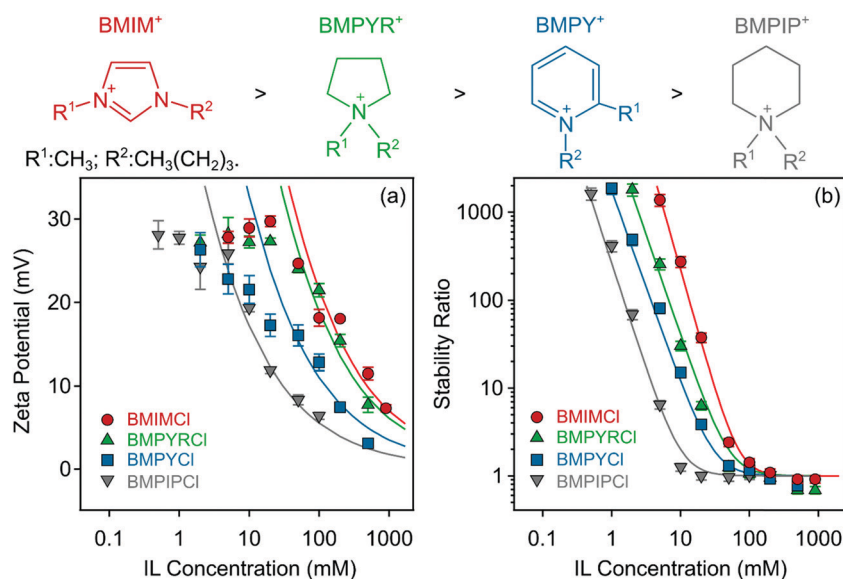


Fig. 4 Zeta potentials (a) and stability ratios (b) of LDH particles in the presence of ILs composed of different cations (BMIM<sup>+</sup>, BMPYR<sup>+</sup>, BMPY<sup>+</sup>, and BMPIP<sup>+</sup>) and the Cl<sup>-</sup> anion. The solid lines are the fits obtained with eqn (6) (a) and (7) (b). The structures of the IL cations are presented on the top in the order of decreasing CCC from left to right.

dc\_1931\_21

changing the composition of the ILs. An increase in these values can be observed in the  $\text{BMPIP}^+ < \text{BMPY}^+ < \text{BMPYR}^+ < \text{BMIM}^+$  order at the same IL concentration indicating ion specific interactions with the like-charged surface of LDH particles. CCC values reported earlier for colloidal particles in the presence of various monovalent inorganic coions showed no clear dependence on the type of coion.<sup>47,67</sup> However, when ILs were involved in the systematic study, the aggregation features were sensitive to the type of coion,<sup>31</sup> due to short-range attraction between the IL constituents, as revealed in direct force measurements.<sup>30</sup>

### 3.3. Specificities in the fast aggregation regime

Ion specific effects on the aggregation rates in the fast aggregation regime, *i.e.*, above the CCCs, were studied at high IL concentrations, where the viscosity of concentrated IL solutions can differ significantly from that of pure water.<sup>27</sup> However, the viscosities of the studied IL solutions were the same within the experimental error in the investigated concentration range (Fig. 2c and d) and thus, the apparent aggregation rates (eqn (2)) were used for comparison with the experimental values to clarify system specificities. Fig. 5 shows that although the CCC depends sensitively on the type of the counter- and coion present, the fast aggregation rate coefficients obtained were almost identical regardless of the nature of the IL constituents.

These observations indicate that the origin of the attractive forces (*i.e.*, van der Waals and possible hydrophobic interactions) is similar regardless of the type of ions. Similar findings were reported earlier for the latex particles in the presence of various monovalent electrolytes and ILs.<sup>31</sup> Moreover, the highest value of the CCC in the case of  $\text{BMIM}^+$  clearly indicates the adsorption of these coions on the LDH surface, as was assumed already in the study of the IL anion effects in these systems. Such adsorption leads to somewhat higher surface charge density and subsequently, to stronger electrical double layer forces and to higher CCC.

The difference between the effect of anions and cations on the CCC values also deserves a discussion. As shown in Fig. 5, the CCCs vary within two orders of magnitudes for the anions being the highest for  $\text{Cl}^-$  and the lowest for  $\text{NO}_3^-$ . Nevertheless,

the changes in the cation series were moderate, and decreased by about an order of magnitude. This difference can be explained as follows. The counterions adsorb usually stronger to surfaces and ion specificity is more pronounced.<sup>68</sup> Hence, modification in the surface charge upon counterion adsorption is larger, leading to a wider range of CCCs due to the strong relation between surface charge and aggregation features.<sup>47</sup> Similar differences were observed in the surface charge density and CCC data once IL constituents were present as counter- or coions in latex<sup>31</sup> and titania<sup>32</sup> particle dispersions.

### 3.4. Prevailing interparticle forces

To further elucidate the origin of the interparticle forces between the LDH particles dispersed in aqueous IL solutions, the DLVO theory was used because it can quantitatively predict the CCC for given colloidal particles from the determined surface charge density values as<sup>49,66</sup>

$$\text{CCC} = \frac{0.365}{N_A L_B} (H \epsilon \epsilon_0)^{-2/3} \sigma^{4/3} \quad (9)$$

where  $N_A$  is the Avogadro number,  $H$  is the Hamaker constant and  $L_B$  is the Bjerrum length, which corresponds to the distance, where the electrostatic interaction between two charges is comparable in magnitude to the thermal energy and its value is equal to 0.72 nm in water at room temperature. A Hamaker constant of  $1.4 \times 10^{-20}$  J was applied in eqn (9) to achieve the best fit to the experimental data. This value is in agreement with the one previously obtained for LDH particles.<sup>66</sup> It is important to mention that this relation is only approximate, as it is only accurate when the energy barrier completely disappears at the CCC.<sup>62</sup>

The calculated and experimental data are shown in Fig. 6 and they indicate that the experimental CCCs could be well-predicted by DLVO theory. These findings further confirmed that the predominant interparticle forces are of a similar origin regardless of the type of IL ions. However, the CCC values are governed by the modification of the surface charge by adsorbing IL constituents, whose affinity is different leading to variation in the strength of the stabilizing electrical double layer forces.

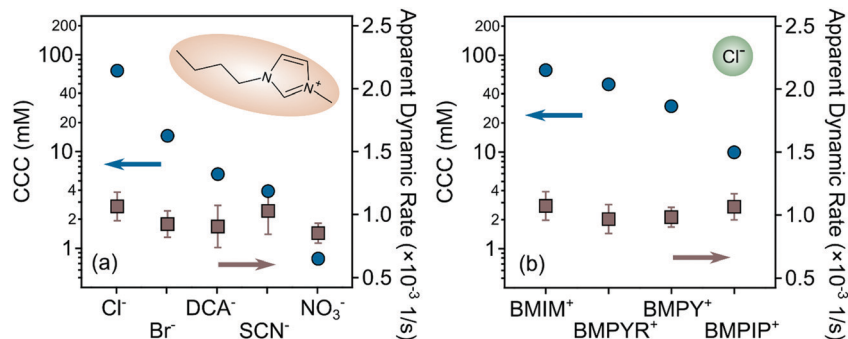


Fig. 5 CCCs (left axis) and apparent fast aggregation rate coefficients (right axis) for LDH particles in the presence of (a) different IL anions and (b) cations. The rates were determined by averaging the aggregation rates obtained above the CCC in each system.

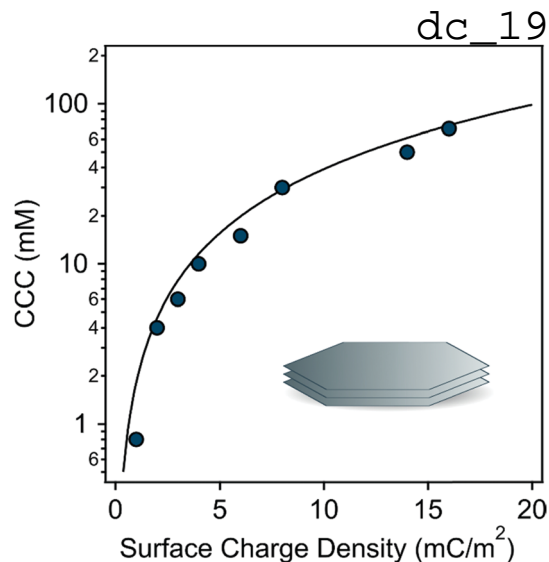


Fig. 6 The experimentally obtained CCCs of LDH particles (symbols) versus surface charge densities. The solid line shows the DLVO prediction, which was calculated by eqn (9).

## 4. Conclusions

The surface charge characteristics and aggregation kinetics of LDH particles were assessed in the presence of various ILs by light scattering techniques. ILs were composed of  $\text{Cl}^-$ ,  $\text{Br}^-$ ,  $\text{DCA}^-$ ,  $\text{SCN}^-$  and  $\text{NO}_3^-$  anions as well as  $\text{BMIM}^+$  cations, while ILs containing  $\text{Cl}^-$  anions with  $\text{BMIM}^+$ ,  $\text{BMPYR}^+$ ,  $\text{BMPY}^+$  and  $\text{BMPIP}^+$  cations were used to probe the effect of anions and cations, respectively. The deviation between the zeta potential and stability ratio data by varying the IL composition indicated specific ion adsorption on the particle surface in both situations. The trend in the obtained surface charge density values corresponds to the order of the CCCs, which partly follows the indirect Hofmeister series. It was also demonstrated that the aggregation rate in the fast aggregation regime does not depend on the type of IL constituent present in the system. This observation suggests that attractive forces acting in the fast aggregation regime are not influenced by the nature of the ions present. Moreover, it was found that the dependence of CCCs on the surface charge densities agrees well with DLVO theory. Although the origin of the interparticle forces was very similar in all systems regardless of the ILs present, ion specific effects were found to be important for the adsorption processes of the ILs on the surface. This observation shed light on the fact that IL ions interact strongly and specifically with the particle surface. Accordingly, the charging and aggregation properties were predominantly determined by the composition of the ILs, as they can modify the surface charge to different extents due to the different adsorption affinity of the IL constituents. The presented information provides useful insights for the scientific community working with LDH-IL dispersions developed for various purposes.

## Conflicts of interest

There are no conflicts to declare.

## dc\_1931\_21 Acknowledgements

The authors acknowledge financial support from the Hungarian National Research, Development and Innovation Office (SNN131558) and the Slovenian Research Agency (research core funding No. P1-0201 and the project No. N1-0139 'Delamination of Layered Materials and Structure-Dynamics Relationship in Green Solvents'). T. D. is sponsored by the ELTE Márton Áron Special College. The support from the University of Szeged Open Access Fund (5463) is gratefully acknowledged.

## References

- P. J. Sideris, U. G. Nielsen, Z. H. Gan and C. P. Grey, *Science*, 2008, **321**, 113–117.
- Z. B. Cao, B. Li, L. Y. Sun, L. Li, Z. P. Xu and Z. Gu, *Small Methods*, 2019, **4**, 1900343.
- J. Li, H. Z. Cui, X. J. Song, G. S. Zhang, X. Z. Wang, Q. Song, N. Wei and J. Tian, *RSC Adv.*, 2016, **6**, 92402–92410.
- F. L. Theiss, S. J. Couperthwaite, G. A. Ayoko and R. L. Frost, *J. Colloid Interface Sci.*, 2014, **417**, 356–368.
- G. Mishra, B. Dash and S. Pandey, *Appl. Clay Sci.*, 2018, **153**, 172–186.
- S. Omwoma, W. Chen, R. Tsunashima and Y. F. Song, *Coord. Chem. Rev.*, 2014, **258**, 58–71.
- Z. Gu, J. J. Atherton and Z. P. Xu, *Chem. Commun.*, 2015, **51**, 3024–3036.
- V. Rives, M. del Arco and C. Martin, *Appl. Clay Sci.*, 2014, **88–89**, 239–269.
- M. N. Pahalagedara, M. Samaraweera, S. Dharmarathna, C. H. Kuo, L. R. Pahalagedara, J. A. Gascon and S. L. Suib, *J. Phys. Chem. C*, 2014, **118**, 17801–17809.
- Q. Wang and D. O'Hare, *Chem. Rev.*, 2012, **112**, 4124–4155.
- R. D. Rogers and K. R. Seddon, *Science*, 2003, **302**, 792–793.
- R. Hayes, G. G. Warr and R. Atkin, *Chem. Rev.*, 2015, **115**, 6357–6426.
- Z. P. Zheng, W. H. Fan, S. Roy, K. Mazur, A. Nazet, R. Buchner, M. Bonn and J. Hunger, *Angew. Chem., Int. Ed.*, 2015, **54**, 687–690.
- R. Zirbs, K. Strassl, P. Gaertner, C. Schroder and K. Bica, *RSC Adv.*, 2013, **3**, 26010–26016.
- N. V. Plechkova and K. R. Seddon, *Chem. Soc. Rev.*, 2008, **37**, 123–150.
- M. A. Gebbie, A. M. Smith, H. A. Dobbs, A. A. Lee, G. G. Warr, X. Banquy, M. Valtiner, M. W. Rutland, J. N. Israelachvili, S. Perkin and R. Atkin, *Chem. Commun.*, 2017, **53**, 1214–1224.
- D. A. Beattie, R. M. Espinosa-Marzal, T. T. M. Ho, M. N. Popescu, J. Ralston, C. J. E. Richard, P. M. F. Sellapperumage and M. Krasowska, *J. Phys. Chem. C*, 2013, **117**, 23676–23684.
- A. Sheehan, L. A. Jurado, S. N. Ramakrishna, A. Arcifa, A. Rossi, N. D. Spencer and R. M. Espinosa-Marzal, *Nanoscale*, 2016, **8**, 4094–4106.
- T. R. Zhan, Y. M. Zhang, Q. Yang, H. H. Deng, J. Xu and W. G. Hou, *Chem. Eng. J.*, 2016, **302**, 459–465.

dc\_1931\_21

- 20 H. Benes, J. Kredatusova, J. Peter, S. Livi, S. Bujok, E. Pavlova, J. Hodan, S. Abbrent, M. Konefal and P. Ecorchard, *Nanomaterials*, 2019, **9**, 618.
- 21 B. M. Choudary, S. Madhi, N. S. Chowdari, M. L. Kantam and B. Sreedhar, *J. Am. Chem. Soc.*, 2002, **124**, 14127–14136.
- 22 Z. J. Wu, Z. K. Xie, J. Wang, T. Yu, Z. D. Wang, X. G. Hao, A. Abudula and G. Q. Guan, *ACS Sustainable Chem. Eng.*, 2020, **8**, 12378–12387.
- 23 E. Delahaye, Z. L. Xie, A. Schaefer, L. Douce, G. Rogez, P. Rabu, C. Gunter, J. S. Gutmann and A. Taubert, *Dalton Trans.*, 2011, **40**, 9977–9988.
- 24 F. Seidi, M. Jouyandeh, S. M. R. Paran, A. Esmaeili, Z. Karami, S. Livi, S. Habibzadeh, H. Vahabi, M. R. Ganjali and M. R. Saeb, *Colloids Surf., A*, 2021, **611**, 125826.
- 25 E. Vanecht, K. Binnemans, S. Patskovsky, M. Meunier, J. W. Seo, L. Stappers and J. Fransaer, *Phys. Chem. Chem. Phys.*, 2012, **14**, 5662–5671.
- 26 M. Mamusa, J. Siriex-Plenet, F. Cousin, E. Dubois and V. Peyrea, *Soft Matter*, 2014, **10**, 1097–1101.
- 27 I. Szilagyi, T. Szabo, A. Desert, G. Trefalt, T. Oncsik and M. Borkovec, *Phys. Chem. Chem. Phys.*, 2014, **16**, 9515–9524.
- 28 C. Guibert, V. Dupuis, J. Fresnais and V. Peyre, *J. Colloid Interface Sci.*, 2015, **454**, 105–111.
- 29 Z. Q. He and P. Alexandridis, *Phys. Chem. Chem. Phys.*, 2015, **17**, 18238–18261.
- 30 V. Valmacco, G. Trefalt, P. Maroni and M. Borkovec, *Phys. Chem. Chem. Phys.*, 2015, **17**, 16553–16559.
- 31 T. Oncsik, A. Desert, G. Trefalt, M. Borkovec and I. Szilagyi, *Phys. Chem. Chem. Phys.*, 2016, **18**, 7511–7520.
- 32 P. Rouster, M. Pavlovic, T. Cao, B. Katana and I. Szilagyi, *J. Phys. Chem. C*, 2019, **123**, 12966–12974.
- 33 B. Katana, D. Takács, F. D. Bobbink, P. J. Dyson, N. B. Alsharif, M. Tomšič and I. Szilagyi, *Phys. Chem. Chem. Phys.*, 2020, **22**, 24764–24770.
- 34 B. Katana, D. Takacs, E. Csapo, T. Szabo, A. Jamnik and I. Szilagyi, *J. Phys. Chem. B*, 2020, **124**, 9757–9765.
- 35 K. Higashitani, K. Nakamura, T. Fukasawa, K. Tsuchiya and Y. Mori, *Langmuir*, 2018, **34**, 2505–2510.
- 36 J. L. Trompette and J. F. Lahitte, *J. Phys. Chem. B*, 2019, **123**, 3859–3865.
- 37 W. Y. Yu, N. Du, Y. T. Gu, J. G. Yan and W. G. Hou, *Langmuir*, 2020, **36**, 6557–6568.
- 38 W. Kunz, J. Henle and B. W. Ninham, *Curr. Opin. Colloid Interface Sci.*, 2004, **9**, 19–37.
- 39 L. Medda, C. Carucci, D. F. Parsons, B. W. Ninham, M. Monduzzi and A. Salis, *Langmuir*, 2013, **29**, 15350–15358.
- 40 D. Constantinescu, H. Weingartner and C. Herrmann, *Angew. Chem., Int. Ed.*, 2007, **46**, 8887–8889.
- 41 A. Salis and B. W. Ninham, *Chem. Soc. Rev.*, 2014, **43**, 7358–7377.
- 42 H. I. Okur, J. Hladilkova, K. B. Rembert, Y. Cho, J. Heyda, J. Dzubiella, P. S. Cremer and P. Jungwirth, *J. Phys. Chem. B*, 2017, **121**, 1997–2014.
- 43 J. Rubin, A. San Miguel, A. S. Bommarius and S. H. Behrens, *J. Phys. Chem. B*, 2010, **114**, 4383–4387.
- 44 P. Lo Nostro and B. W. Ninham, *Chem. Rev.*, 2012, **112**, 2286–2322.
- 45 B. B. Kang, H. C. Tang, Z. D. Zhao and S. S. Song, *ACS Omega*, 2020, **5**, 6229–6239.
- 46 D. F. Parsons and B. W. Ninham, *Langmuir*, 2010, **26**, 6430–6436.
- 47 T. Oncsik, G. Trefalt, M. Borkovec and I. Szilagyi, *Langmuir*, 2015, **31**, 3799–3807.
- 48 M. Pavlovic, R. Huber, M. Adok-Sipiczki, C. Nardin and I. Szilagyi, *Soft Matter*, 2016, **12**, 4024–4033.
- 49 D. F. Evans and H. Wennerstrom, *The colloidal domain*, John Wiley, New York, 1999.
- 50 D. F. Parsons, M. Bostrom, P. Lo Nostro and B. W. Ninham, *Phys. Chem. Chem. Phys.*, 2011, **13**, 12352–12367.
- 51 J. M. Peula-Garcia, J. L. Ortega-Vinuesa and D. Bastos-Gonzalez, *J. Phys. Chem. C*, 2010, **114**, 11133–11139.
- 52 T. Lopez-Leon, J. L. Ortega-Vinuesa and D. Bastos-Gonzalez, *ChemPhysChem*, 2012, **13**, 2382–2391.
- 53 D. G. Evans and R. C. T. Slade, in *Layered Double Hydroxides*, ed. X. Duan and D. G. Evans, 2006, vol. 119, pp. 1–87.
- 54 A. V. Delgado, F. Gonzalez-Caballero, R. J. Hunter, L. K. Koopal and J. Lyklema, *J. Colloid Interface Sci.*, 2007, **309**, 194–224.
- 55 P. A. Hassan, S. Rana and G. Verma, *Langmuir*, 2015, **31**, 3–12.
- 56 H. Holthoff, S. U. Egelhaaf, M. Borkovec, P. Schurtenberger and H. Sticher, *Langmuir*, 1996, **12**, 5541–5549.
- 57 D. D. Joye, *J. Colloid Interface Sci.*, 2003, **267**, 204–210.
- 58 H. D. B. Jenkins and Y. Marcus, *Chem. Rev.*, 1995, **95**, 2695–2724.
- 59 M. Bester-Rogac, J. Hunger, A. Stoppa and R. Buchner, *J. Chem. Eng. Data*, 2011, **56**, 1261–1267.
- 60 M. Bester-Rogac, A. Stoppa, J. Hunger, G. Hefter and R. Buchner, *Phys. Chem. Chem. Phys.*, 2011, **13**, 17588–17598.
- 61 M. Borkovec, S. H. Behrens and M. Semmler, *Langmuir*, 2000, **16**, 5209–5212.
- 62 G. Trefalt, I. Szilagyi and M. Borkovec, *J. Colloid Interface Sci.*, 2013, **406**, 111–120.
- 63 D. Grolimund, M. Elimelech and M. Borkovec, *Colloids Surf., A*, 2001, **191**, 179–188.
- 64 A. Stoppa, J. Hunger, G. Hefter and R. Buchner, *J. Phys. Chem. B*, 2012, **116**, 7509–7521.
- 65 H. K. Stassen, R. Ludwig, A. Wulf and J. Dupont, *Chem. – Eur. J.*, 2015, **21**, 8324–8335.
- 66 M. Galli, S. Saringer, I. Szilagyi and G. Trefalt, *Colloids Interfaces*, 2020, **4**, 20.
- 67 T. Hegedus, D. Takacs, L. Vasarhelyi, I. Szilagyi and Z. Konya, *Langmuir*, 2021, **37**, 2466–2475.
- 68 T. Sugimoto, T. C. Cao, I. Szilagyi, M. Borkovec and G. Trefalt, *J. Colloid Interface Sci.*, 2018, **524**, 456–464.



## Particle aggregation mechanisms in ionic liquids†

Istvan Szilagyi, Tamas Szabo, Anthony Desert, Gregor Trefalt, Tamas Oncsik and Michal Borkovec\*

Cite this: *Phys. Chem. Chem. Phys.*, 2014, **16**, 9515

Aggregation of sub-micron and nano-sized polystyrene latex particles was studied in room temperature ionic liquids (ILs) and in their water mixtures by time-resolved light scattering. The aggregation rates were found to vary with the IL-to-water molar ratio in a systematic way. At the water side, the aggregation rate is initially small, but increases rapidly with increasing IL content, and reaches a plateau value. This behaviour resembles simple salts, and can be rationalized by the competition of double-layer and van der Waals forces as surmised by the classical theory of Derjaguin, Landau, Verwey, and Overbeek (DLVO). At the IL side, aggregation slows down again. Two generic mechanisms could be identified to be responsible for the stabilization in ILs, namely viscous stabilization and solvation stabilization. Viscous stabilization is important in highly viscous ILs, as it originates from the slowdown of the diffusion controlled aggregation due to the hindrance of the diffusion in a viscous liquid. The solvation stabilization mechanism is system specific, but can lead to a dramatic slowdown of the aggregation rate in ILs. This mechanism is related to repulsive solvation forces that are operational in ILs due to the layering of the ILs close to the surfaces. These two stabilization mechanisms are suspected to be generic, as they both occur in different ILs, and for particles differing in surface functionalities and size.

Received 24th February 2014,  
Accepted 4th April 2014

DOI: 10.1039/c4cp00804a

www.rsc.org/pccp

## Introduction

Ionic liquids (ILs) have unusual properties, including high chemical stability, low vapour pressure, and a wide electrochemical window.<sup>1–3</sup> Their properties can also be systematically varied through the nature of their ionic constituents. Due to these unique aspects, ILs are developing into promising media for material science applications.<sup>4–6</sup> Among those, particle suspensions in ILs represent an important class of media, as they are relevant in catalysis,<sup>7–11</sup> solar cell development,<sup>12</sup> and mirror design.<sup>13</sup> Such suspensions are also obtained during the synthesis of metal,<sup>14–16</sup> oxide,<sup>17,18</sup> or latex<sup>19</sup> particles in ILs. The stability of such suspensions, or their aggregation state, can be decisive. The presence of aggregates further determines the suspension rheology and controls the formation of particle assemblies, colloidal glasses, and gels.<sup>20–22</sup> Various reports indicate that the nature of ILs and of the particles affects their aggregation state strongly. Silica particles were reported to be unstable in imidazolium-based ILs, while their stabilization could be achieved by surface functionalization.<sup>23</sup> Metal and silica particles were reported to be stable in dry ILs, while small

amounts of water induced aggregation.<sup>15,16,24</sup> The presence of alkali metal cations was shown to stabilize particles in ILs.<sup>25</sup> However, this knowledge remains sketchy, and a mechanistic picture of particle aggregation in ILs is lacking.

The Derjaguin, Landau, Verwey, and Overbeek (DLVO) theory was developed to explain the stability of aqueous particle suspensions.<sup>21,23,26,27</sup> This theory represents the interaction potential as a superposition of van der Waals and electric double-layer forces, and explains why aqueous suspensions are stable at low salt levels, and unstable at higher salt levels. At low salt levels, the repulsive double-layer forces dominate and lead to slow aggregation. At higher salt levels, double-layer forces are screened, and the attractive van der Waals forces induce fast aggregation. While this behaviour is well-documented for simple salts,<sup>28–32</sup> a similar scenario might apply to dilute aqueous solutions of ILs.<sup>24</sup> The aggregation remains fast in aqueous suspensions at higher salt levels, since the diffusion is rapid due to the low viscosity of aqueous solutions. On the other hand, the high viscosity of ILs will substantially slow down the diffusion process. This effect will reduce the aggregation rate, and this mechanism will be referred to as *viscous stabilization*. The existence of highly stable particle suspensions in pure ILs contradicts DLVO theory, since the ILs should screen the double-layer forces fully.<sup>23</sup> Stabilization in ILs was attributed to solvation forces originating from their structuring near interfaces.<sup>21,23,24</sup> These forces were measured using the atomic force microscope and they were found to be oscillatory,

Department of Inorganic and Analytical Chemistry, University of Geneva,  
30 Quai Ernest-Ansermet, 1205 Geneva, Switzerland.

E-mail: [michal.borkovec@unige.ch](mailto:michal.borkovec@unige.ch); Tel: +41 22 379 6405

† Electronic supplementary information (ESI) available. See DOI: 10.1039/c4cp00804a



but overall repulsive.<sup>24,33</sup> This stabilization mechanism will be referred to as *solvation stabilization*.

Here we demonstrate that solvation and viscous stabilization controls the aggregation of particles in ILs. This assertion will be based on detailed measurements of aggregation rates of colloidal particles in IL–water mixtures with time-resolved light scattering. The present article provides the first systematic study of this kind, and shows that these techniques can be used to clarify the mechanisms of particle aggregation processes in ILs.

## Methods

The following section summarizes the essential methods and concepts needed to analyse particle aggregation kinetics by time-resolved light scattering. The supplement provides details concerning the materials and experimental protocols used.

### Particle aggregation kinetics

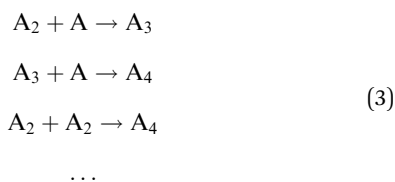
Particles suspended in a liquid diffuse due to thermal motion, and attractive van der Waals forces make them stick upon contact. When the suspension is initially composed of isolated particle monomers, they will form aggregates, initially dimers, according to the scheme



The kinetics of this process can be described using the rate equation

$$-\frac{dN_1}{dt} = 2 \cdot \frac{dN_2}{dt} = kN_1^2 \quad (2)$$

where  $N_1$  and  $N_2$  are the number concentrations of the monomers and dimers, respectively,  $t$  is the time, and  $k$  is the aggregation rate coefficient. Eqn (2) describing aggregation of colloidal particles is exactly the same as in chemical reaction kinetics, except in that field one defines the rate coefficient half as large. The other important difference from the chemical kinetics is that colloidal particles readily form higher order aggregates, such as trimers, tetramers, namely



Therefore, aggregates keep growing, until they sediment, cream, or interlink to form a gel. By assuming that each of these elementary kinetic steps proceeds with the same rate coefficient  $k$ , Smoluchowski has shown that in a suspension initially composed of monomers only, the total number of particles or aggregates  $N = N_1 + N_2 + N_3 + \dots$  decreases as<sup>26,27</sup>

$$N = \frac{N_0}{1 + t/T_{1/2}} \quad (4)$$

where  $N_0$  is the total (or initial) particle concentration  $N_0 = N_1 + 2N_2 + 3N_3 + \dots$  and

$$T_{1/2} = \frac{2}{kN_0} \quad (5)$$

is the half-time of aggregation. This half-time represents the characteristic time, after which the total number of aggregates is reduced by a factor of two. When only monomers and dimers are present, eqn (2) would lead to the same expression for  $T_{1/2}$  as eqn (5) up to the factor of 2.

The van der Waals attraction close to contact is normally very strong, which makes the aggregation process irreversible, meaning that aggregated particles do not detach from each other. For weaker attraction forces, as for example, in the case of depletion interactions or critical Casimir forces, the aggregation process may become reversible and lead to equilibrium phase separation.<sup>34–36</sup> Currently, we have no indications that such a situation might be encountered in ILs. Therefore, the irreversible aggregation process always leads to destabilization of a colloidal suspension, whereby the half-time given by eqn (5) sets the corresponding time scale. Depending on the system, however, this half-time may differ by orders of magnitude. When this half-time is large, the suspension is stable, while when it is small, it is unstable. For a half-time that is comparable to the experimental time window, the aggregation process can be followed by various techniques in real time. Initially, particle dimers form, while higher order aggregates occur later (Fig. 1). Correspondingly, one refers to *early stages* and *late stages* of the aggregation. Since the formation of doublets in eqn (1) is a second order kinetic process, the half-time does not only depend on the aggregation rate coefficient  $k$ , but also on the particle number concentration  $N_0$ . Thus, a suspension can be stabilized by adjusting the conditions such that aggregation rate coefficient is small, by appropriate dilution, or both.

In the case of fast aggregation, one assumes that the diffusing particles do not interact but they stick to each other at every encounter.<sup>26</sup> This model is equivalent to diffusion controlled reaction kinetics or, in colloid language, to a fast aggregation process. Smoluchowski has further shown that the corresponding rate coefficient is given by<sup>26,27</sup>

$$k_S = 16\pi D_1 R_1 = \frac{8k_B T}{3\eta} = 1.23 \times 10^{-17} \text{ m}^3 \text{ s}^{-1} \quad (6)$$

where by  $D_1$  and  $R_1$  denote the diffusion coefficient and the radius of the aggregating particles. The second equality sign in eqn (6) follows from the Stokes–Einstein relation, which relates the former quantities as<sup>26</sup>

$$D_1 = \frac{k_B T}{6\pi\eta R_1} \quad (7)$$

where  $\eta$  is the shear viscosity of the dispersing liquid,  $T$  is the absolute temperature, and  $k_B$  is the Boltzmann constant. The numerical value given in eqn (6) refers to water at 25 °C, while for ILs this value can be substantially smaller.



dc\_1931\_21

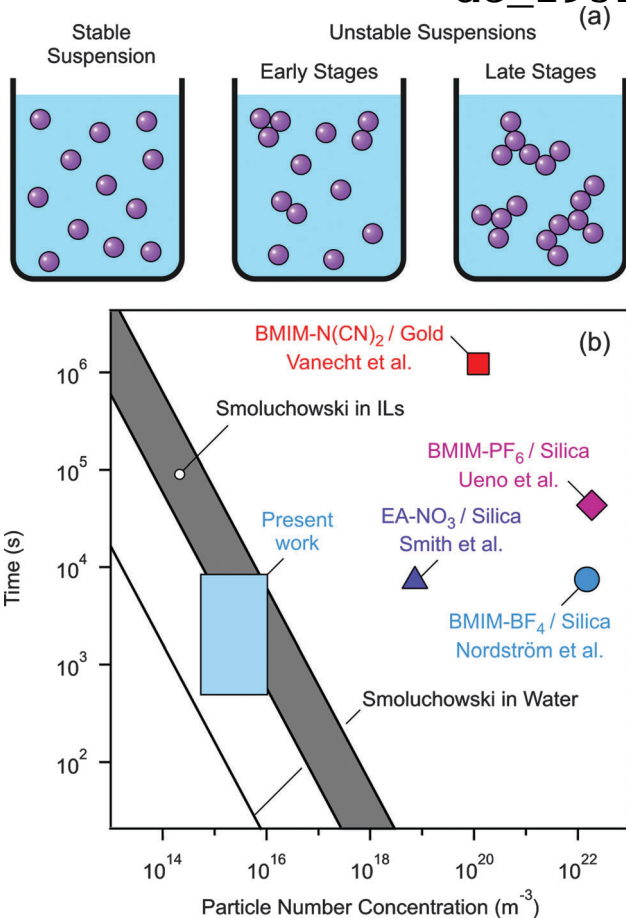


**Fig. 1** Particle aggregation in ILs. (a) Schemes depicting the structure of a stable suspension and of unstable suspensions at early and late stages of the aggregation. (b) Aggregation time scale versus the particle number concentration. Half-times are calculated using eqn (5) and Smoluchowski's eqn (6) in water (solid line) and in the ILs used in the present study (shaded area). The blue region indicates the conditions of the present experiments. Data points refer to experimental time windows reported by Nordström *et al.*,<sup>25</sup> Smith *et al.*,<sup>24</sup> involving ethylammonium ions (EA<sup>+</sup>), Vanecht *et al.*,<sup>16</sup> and Ueno *et al.*<sup>23</sup> The other acronyms are defined in Fig. 2 and further details are given in Table S6 (ESI†).

Eqn (5) and (6) can be used to distinguish stable and unstable colloidal particle suspensions in aqueous salt solutions (Fig. 1b). Since viscosities of ILs can be substantially larger than the ones of aqueous solutions,<sup>5,6</sup> the respective boundary is displaced to the right. The stability time windows and the corresponding particle concentrations for stable particle suspensions in ILs reported in the literature are also shown.<sup>16,23–25</sup> The fact that these points cluster above the grey region suggests the importance of solvation stabilization. When the interaction potential acting between the particles is known, aggregation rates could be estimated more accurately.<sup>26,37</sup> We shall not pursue this aspect here, since the information concerning the interaction potentials between particles in ILs is currently incomplete.

### Light scattering

Particle suspensions are being routinely characterized by static light scattering (SLS) and dynamic light scattering (DLS).<sup>26,38</sup>

When these techniques are employed in a time-resolved fashion, they allow probing particle aggregation processes in detail.<sup>39–42</sup>

SLS measures the light scattering intensity  $I$  versus the scattering angle  $\theta$ , which is commonly expressed in terms of the magnitude of the scattering vector

$$q = \frac{4\pi n}{\lambda_0} \sin \frac{\theta}{2} \quad (8)$$

where  $n$  is the refractive index of the medium and  $\lambda_0$  is the wavelength of the incident light in vacuum. The scattering intensity  $I(q)$  from a stable and dilute suspension of colloidal particles can be used to evaluate the particle size accurately. For small particles and weak contrast, the angular dependence of the scattering intensity can be calculated within the Rayleigh, Gans, and Debye (RGD) approximation. The contrast is characterized by the difference between the refractive indices of the particles and the dispersing liquid. In the general case, the exact Mie theory for spheres must be used.<sup>43</sup> For quantitative analysis, particle polydispersity and back-reflection correction have to be included.

The scattering intensity from an aggregating suspension varies with time. For a dilute suspension, this quantity can be expressed as

$$I(q, t) = I_1(q)N_1(t) + I_2(q)N_2(t) + \dots \quad (9)$$

where  $I_1(q)$  and  $I_2(q)$  are the scattering intensities of the monomer and dimer, respectively. For early stages of aggregation, one can measure the initial apparent static rate  $\Sigma$ , which reflects the rate of change of the scattering intensity normalized by the initial intensity. This quantity can be obtained from eqn (2) and (9) and reads<sup>40</sup>

$$\Sigma = \frac{1}{I(q, 0)} \cdot \left. \frac{dI(q, t)}{dt} \right|_{t=0} = kN_0 \left( \frac{I_2(q)}{2I_1(q)} - 1 \right) \quad (10)$$

In order to evaluate the aggregation rate coefficient, the optical factor must be known. Within the RGD approximation, this factor is given by<sup>26,40</sup>

$$\frac{I_2(q)}{2I_1(q)} = 1 + \frac{\sin(2qR_1)}{2qR_1} \quad (11)$$

In the general case, the T-matrix theory must be used to evaluate the ratio of scattering intensities.<sup>37,43</sup> At low scattering angles ( $q \rightarrow 0$ ), the apparent static rate is always positive, meaning that the scattering intensity increases with time. At larger angles, this quantity can also become negative, which reflects the fact that the scattering intensity may also decrease with time.

DLS measures the intensity autocorrelation function, and from its decay constant one can extract the apparent diffusion coefficient  $D$ . In a stable suspension, the particle radius can be directly evaluated from this quantity using the Stokes–Einstein equation (eqn (7)). When a dilute suspension aggregates, the apparent diffusion coefficient can be expressed as<sup>40</sup>

$$D(q, t) = \frac{D_1 I_1(q) N_1(t) + D_2 I_2(q) N_2(t) + \dots}{I_1(q) N_1(t) + I_2(q) N_2(t) + \dots} \quad (12)$$



where  $D_1$  and  $D_2$  correspond to the diffusion coefficients of the monomers and dimers, respectively. We prefer to report the apparent hydrodynamic radius  $R(q,t)$  that is obtained from the apparent diffusion coefficient  $D(q,t)$  using eqn (7). In the early stages of aggregation one can measure the apparent dynamic rate  $\Delta$ , which corresponds to the initial relative rate of change of the apparent hydrodynamic radius normalized to the initial radius. Following similar arguments as above, this rate can be expressed as<sup>40</sup>

$$\Delta = \frac{1}{R(q,0)} \cdot \left. \frac{dR(q,t)}{dt} \right|_{t \rightarrow 0} = kN_0 \left( 1 - \frac{1}{\alpha} \right) \frac{I_2(q)}{2I_1(q)} \quad (13)$$

where  $\alpha = D_1/D_2 = R_2/R_1 \approx 1.39$  is the hydrodynamic factor. The respective hydrodynamic radii of the monomer and the dimer are denoted as  $R_1$  and  $R_2$ . The numerical value of this factor  $\alpha$  can be estimated from low Reynolds number hydrodynamics.<sup>44</sup> This apparent dynamic rate is always positive, meaning that the hydrodynamic radius always increases with time, as one would intuitively expect. As will be shown in the next section, these light scattering techniques are a powerful means to investigate particle aggregation processes in ILs.

## Results and discussion

Aggregation of sub-micron sulphate and amidine latex particles, as well as nano-sized sulphate latex particles, was studied in various ILs and their mixtures with water (Fig. 2a). Many ILs are hygroscopic, and may contain substantial amounts of water.<sup>45</sup> We have therefore systematically studied particle suspensions over a wide range of IL-to-water molar ratios, from dilute solution of ILs in water (water side) to ILs containing small amounts of water (IL side). We have analysed ILs containing the anions tetrafluoroborate,  $\text{BF}_4^-$ , dicyanamide,  $\text{N}(\text{CN})_2^-$ , and thiocyanate,  $\text{SCN}^-$ , with 1-butyl-3-methylimidazolium,  $\text{BMIM}^+$ , as the cation. We have further investigated ILs with  $\text{N}(\text{CN})_2^-$  as

the anion, and  $\text{BMIM}^+$ , 1-butyl-3-methylpyridinium dicyanamide,  $\text{BMPY}^+$ , and 1-butyl-1-methylpyrrolidinium,  $\text{BMPL}^+$  as cations. Comparison experiments were carried out with 1-butylpyridinium tetrafluoroborate,  $\text{BPY-BF}_4$ , and simple KCl electrolyte solutions. Viscosities, refractive indices, and densities of the IL-water mixtures were determined by standard techniques (Fig. 2b and Fig. S1, ESI<sup>†</sup>). The viscosities of pure ILs used are 30–150 times larger than the one of water. Refractive indices and densities can be accurately described by ideal mixing laws. We will first summarize how light scattering can be used to characterize these particles and their aggregation kinetics. Subsequently, we will discuss the generic dependence of the aggregation rates on the IL-to-water molar ratio, and finally address system specificities.

### Particle characterization by light scattering

We study spherical polystyrene latex particles as model particles. Most experiments were carried out with sub-micron particles having amidine surface modification and a radius of 110 nm and with sulphate surface modification and a radius of 265 nm. Fig. 3a shows measured form factors of the particles in water and in  $\text{BMIM-SCN}$  whereby the scattering intensity originating from pure ILs was subtracted. This residual scattering can be up to 10 times larger than the one for toluene, probably due to the presence of nm-sized transient clusters that are spontaneously forming in the ILs.<sup>46</sup> However, this residual scattering is still sufficiently small such that the excess scattering from the particles can be easily measured. The form factors are compared with best fits with Mie theory, whereby the refractive index of 1.59 was used for polystyrene.<sup>47</sup> Analogous results of the simpler RGD calculations are also shown. One observes that

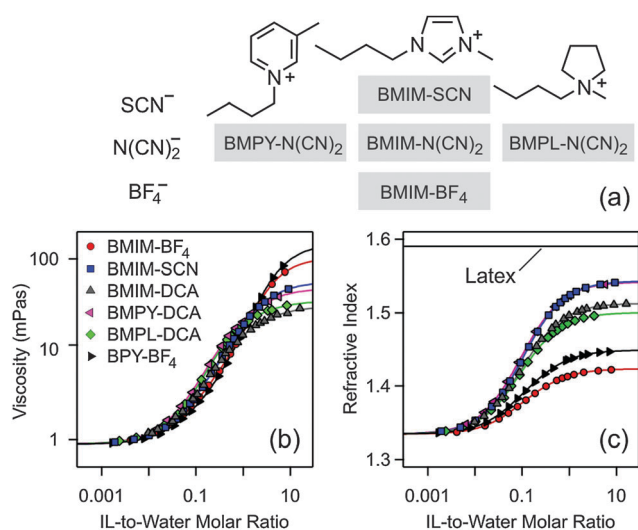


Fig. 2 Properties of ILs used and of their mixtures with water. (a) Structures and abbreviations, (b) shear viscosity, (c) and refractive index measured at 533 nm. The refractive index of the latex particles is also indicated.

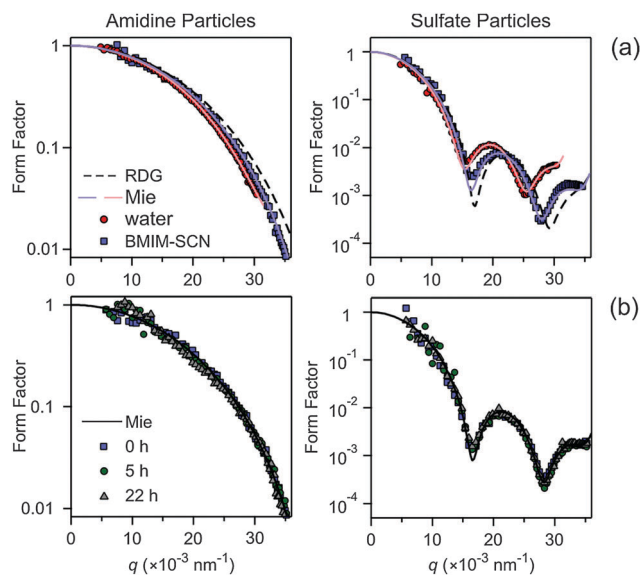


Fig. 3 Monomer form factors  $P(q)$  versus the magnitude of the scattering vector  $q$  of amidine latex particles of 110 nm in radius (left) and sulphate latex of 265 nm (right). (a) The experimental points in water and in pure  $\text{BMIM-SCN}$  are compared with Mie and RGD theory from which the particle radius can be extracted. (b) No dependence with time of the form factors is observed in  $\text{BMIM-SCN}$ .





dc\_1931\_21

the RGD theory is applicable in ILs, while deviations from this theory are apparent in water, especially for the larger sulphate particles. Mie theory must be used in that case. The fitted particle radii and polydispersities are in excellent agreement with the values obtained by electron microscopy (Table S1, ESI†). RGD theory works well in the IL since the contrast is smaller, meaning that the refractive index of the latex particle is closer to the one of the IL than the one of water (Fig. 2c). Fig. 3b further illustrates that the form factor of the latex particles remains the same over long times. The constancy of this scattering profile confirms that the particles remain stable in the IL and that they neither swell nor dissolve. Hydrodynamic radii were also measured by DLS in these suspensions and they are about 6% larger than the ones obtained by SLS (Table S1, ESI†). This slight increase in radius is probably caused by polydispersity effects or solvation of the surface layer. The absolute scattering intensity remains constant within the experimental error of about 5% over the entire experimental time period, which further demonstrates that sedimentation or creaming effects are negligible in these systems.

### Aggregation rates by time-resolved light scattering

The scattering intensity from an aggregating suspension may increase or decrease with time (Fig. 4a). The initial slope of this intensity trace reflects the apparent static rate  $\Sigma$  given in eqn (10) and this quantity can be determined by fitting a straight line to the initial part of the time-dependent scattering intensities. When the scattering intensity decreases with time, this quantity becomes negative. The measured dependence of the apparent static rate  $\Sigma$  on the magnitude of the scattering vector  $q$  is compared in Fig. 5a with predictions of RGD theory. This relation agrees well with the experiment for the amidine particles, but the more accurate T-matrix theory must be used for sulphate latex. The deviations are more important in water than in the IL due to larger contrast. The remaining discrepancies are probably related to slight particle asphericity. The respective aggregation rates are obtained by least-squares fit (Table 1). One observes that the aggregation rates in ILs are substantially smaller than the ones in water.

In an aggregating suspension, the apparent hydrodynamic radius always increases with time (Fig. 4b). The apparent dynamic rate  $\Delta$  can be obtained by fitting straight lines to the initial portion of the hydrodynamic radius trace. The dependence of the apparent dynamic rate  $\Delta$  on the magnitude of the scattering vector  $q$  can be fitted well with eqn (13) whereby the optical factor can be determined by RGD or T-matrix theory (Fig. 5b). When one uses the aggregation rate coefficients obtained from static light scattering, one obtains the hydrodynamic factors. They are summarized in Table 1 and they agree well with the theoretical value of  $\alpha = 1.39$ . The data points scatter more strongly in the IL due to weaker contrast.

When the optical and hydrodynamic factors are known, the aggregation rate coefficients can also be obtained from the measurement of the apparent dynamic rate at a specific scattering angle. The typical procedure is to perform time-resolved single-angle DLS experiments at various compositions and determine the apparent dynamic rates from the initial slope (Fig. 4c and d).

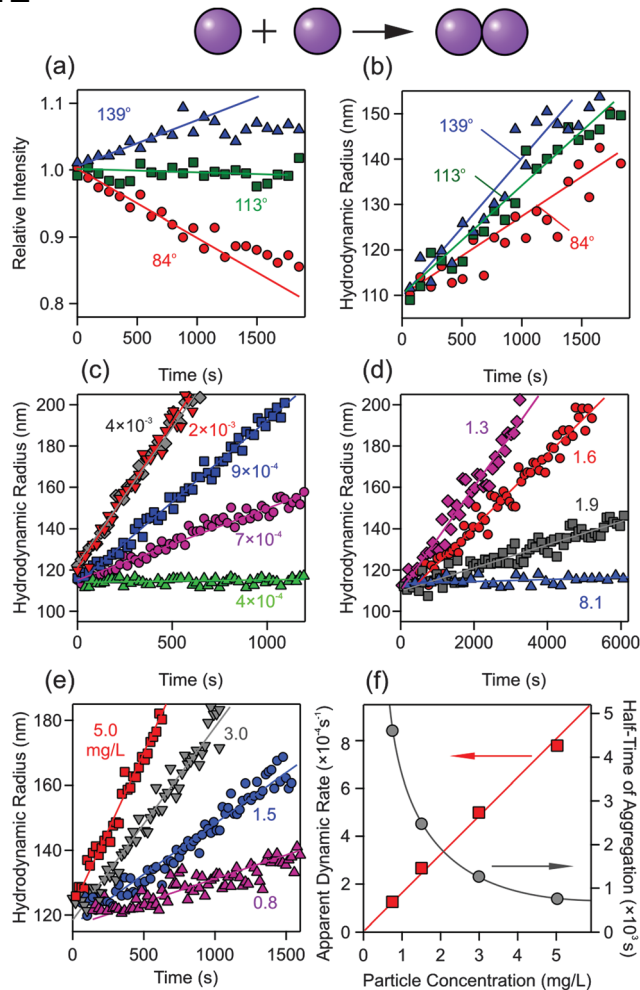


Fig. 4 Time-dependence of the light scattering signal in aggregating particle suspensions in ILs. Amidine latex particles measured at different scattering angles in BMIM-SCN of 0.092 IL-to-water molar ratio with (a) SLS and (b) DLS. Hydrodynamic radius measured using DLS for amidine latex particles in BPY-BF<sub>4</sub>-water mixtures at different IL-to-water molar ratios (c) on the water side and (d) on the IL side. Particle concentration dependence for amidine latex particles in BPY-BF<sub>4</sub> on the (e) hydrodynamic radius and (f) the apparent dynamic rate (left axis) and half-time of aggregation (right axis).

The rate coefficients can be extracted from eqn (13) by inserting the known values of the optical and hydrodynamic factors. This single-angle DLS technique was used to measure the rate coefficients in the various IL-water mixtures, and the resulting aggregation rates are in excellent agreement with multi-angle SLS (Table 1).

In order to probe the doublet formation rate, the experiment must be carried out in the early stages of aggregation. This condition can be ensured with time-resolved DLS by satisfying two criteria. First, the initial apparent hydrodynamic radius should agree within experimental error with the corresponding radius in a stable suspension. Second, the relative increase of the apparent radius should be not more than 20–30% of its initial value. Such conditions are best found by varying the particle concentration (Fig. 4e). This figure also indicates that



dc\_1931\_21

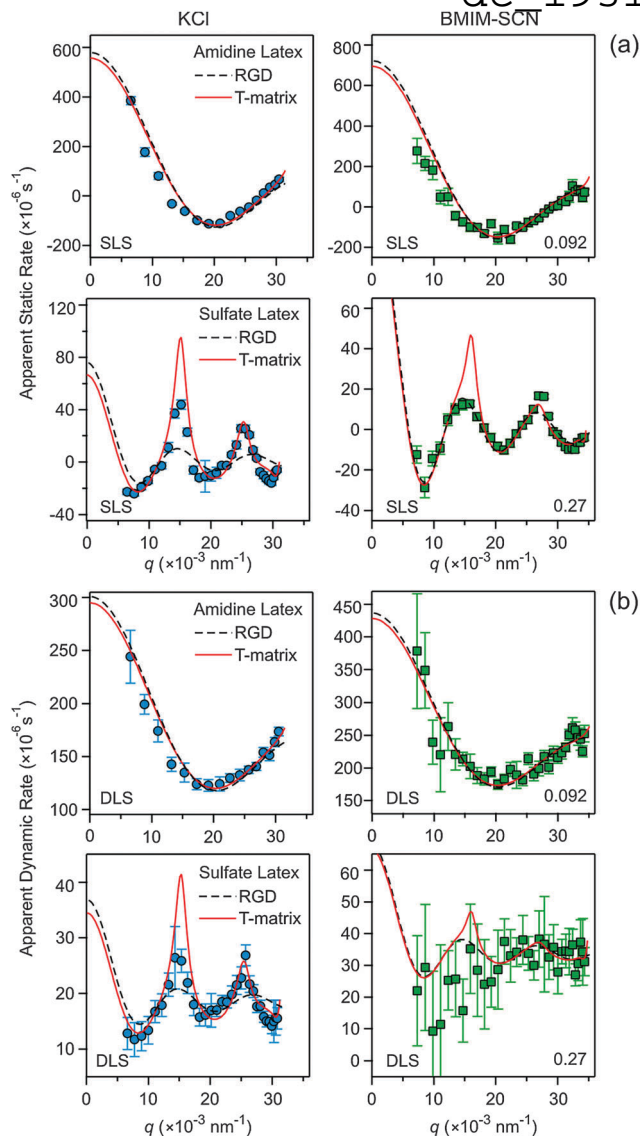


Fig. 5 Apparent aggregation rates versus the magnitude of the scattering vector  $q$  of amidine and sulphate latex particles measured in 1.0 M KCl (left column) and in BMIM-SCN water mixtures of the IL-to-water molar ratios indicated (right column). Experimental data are compared with RGD (dashed line) and T-matrix (solid line) calculations. The resulting aggregation rates and hydrodynamic factors are given in Table 1. (a) SLS and (b) DLS.

the apparent rate of aggregation is proportional to the particle concentration (Fig. 4f), as stipulated by eqn (13).

Another way to ensure that one focuses on the early stages of the aggregation process is to evaluate the half-time of the aggregation (Fig. 4f). These half-times are also shown in Fig. 1. Since our aim is to measure aggregation rates, we situate ourselves near the unstable region. The appropriate experimental window must be substantially shorter than the half-times, in practice by about a factor 3–5. To estimate the half-time properly, the actual aggregation rate coefficient must be known. However, this quantity is only accessible when the respective light scattering measurements have been completed and not when the experiment is initiated. From this point of view, the criteria concerning the relative increase of the hydrodynamic radius are more practical.

### Generic features

Fig. 6a shows the measured aggregation rates for the different latex particles in various ILs and in their water mixtures. The striking aspect is that all systems studied behave similarly. Three main aggregation regimes can be identified. (i) At low IL-to-water ratios, one recovers the classical DLVO regime. In this regime, the aggregation rate increases strongly with the IL content first, and then saturates at a plateau value. The increase in the rate corresponds to slow aggregation, which results from progressive screening of the double-layer repulsion. The plateau reflects fast aggregation, where particle encounters are only limited by their rapid diffusion in water. (ii) At higher IL-to-water ratios, the aggregation rate decreases gradually. This decrease originates from the increasing viscosity, even though the aggregation process remains diffusion controlled. In the systems studied, this mechanism can slow down the aggregation process by almost two orders of magnitude. This regime is referred to as *viscous stabilization*. (iii) At high IL-to-water ratios, which correspond to ILs containing small amounts of water, the aggregation rate decreases rapidly with increasing IL content. This regime reflects stabilization that is specific to the type of the IL, and will be referred to as *solvation stabilization*.

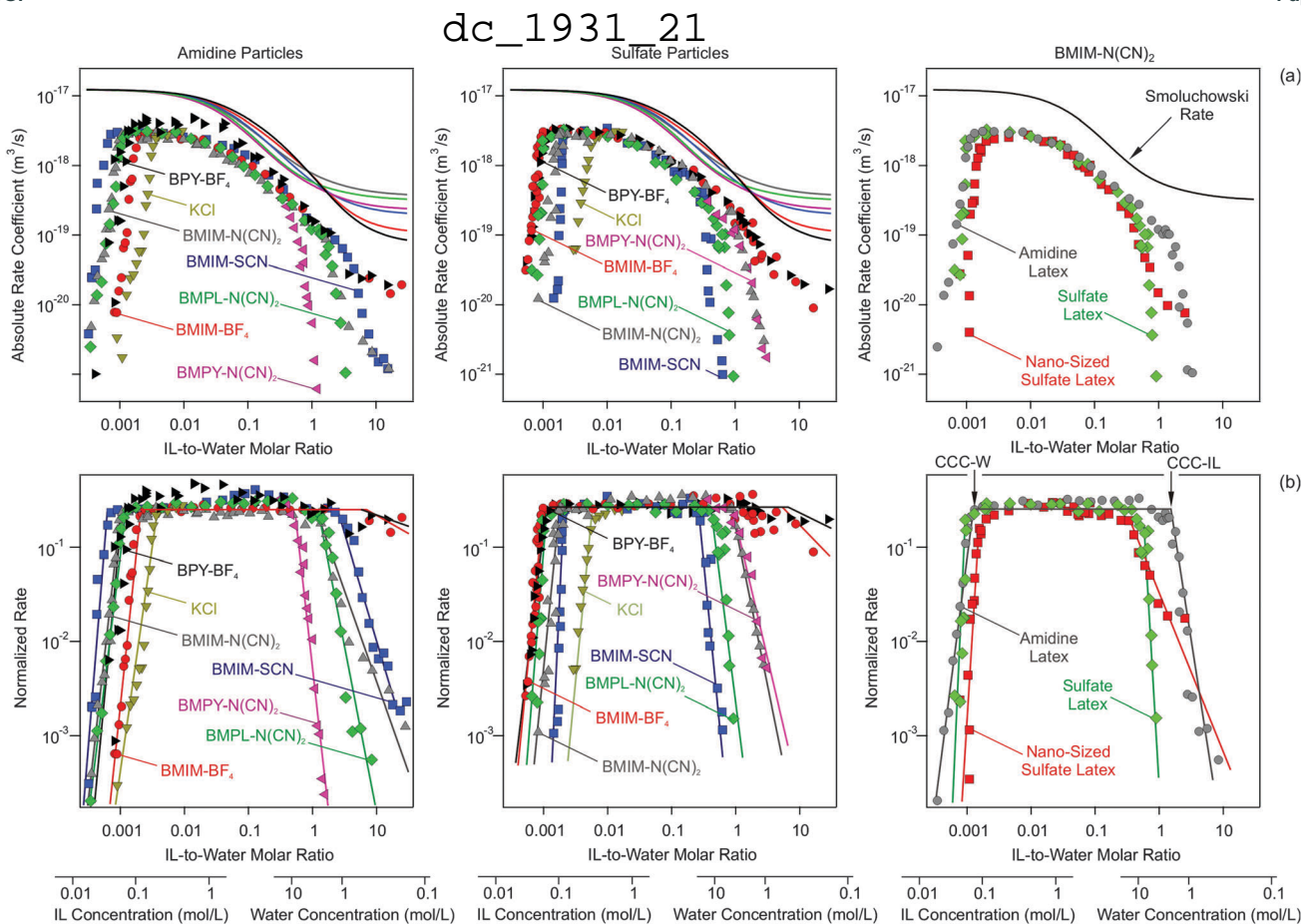
The DLVO regime (i) on the water-rich side is very similar to simple, monovalent salts, like KCl. This fact is not surprising since ILs normally dissociate in water like simple, strong electrolytes.<sup>48</sup> The effect of simple salts on the aggregation of colloidal particles is well documented.<sup>30–32</sup> The transition between slow and fast aggregation can be described by DLVO theory for weakly charged particles.<sup>30,31</sup> Slow aggregation for highly charged particles is often more rapid than predicted

Table 1 Aggregation rates and hydrodynamic factors of sub-micron latex particles measured using time-resolved light scattering

Method	Amidaine latex <sup>a</sup>		Sulphate latex <sup>b</sup>	
	KCl <sup>c</sup>	BMIM-SCN <sup>d</sup>	KCl <sup>c</sup>	BMIM-SCN <sup>d</sup>
Multi-angle SLS <sup>e</sup>	$(2.9 \pm 0.1) \times 10^{-18}$	$(8.5 \pm 0.5) \times 10^{-19}$	$(3.3 \pm 0.1) \times 10^{-18}$	$(4.5 \pm 0.9) \times 10^{-19}$
Multi-angle DLS <sup>f</sup>	$1.35 \pm 0.02$	$1.43 \pm 0.02$	$1.32 \pm 0.02$	$1.35 \pm 0.02$
Single-angle DLS <sup>e</sup>	$(3.1 \pm 0.3) \times 10^{-18}$	$(8.3 \pm 0.8) \times 10^{-19}$	$(3.2 \pm 0.2) \times 10^{-18}$	$(3.0 \pm 0.4) \times 10^{-19}$

<sup>a</sup> Amidaine latex of 110 nm in radius. <sup>b</sup> Sulphate latex of 265 nm in radius. <sup>c</sup> Measurements were carried out in 1.0 M KCl solutions. <sup>d</sup> IL-to-water molar ratios of 0.092 and 0.27 were used for amidaine and sulphate latexes, respectively. <sup>e</sup> Aggregation rate coefficients  $k$  in  $\text{m}^3 \text{s}^{-1}$ . <sup>f</sup> Measured hydrodynamic factor  $\alpha$ .





**Fig. 6** Aggregation rates of sub-micron latex particles versus the IL-to-water molar ratio in various ILs. Molar IL and water concentrations are indicated on separate axes. Amidine (left column) and sulphate latex (middle column) in different ILs, and different particles in BMPL-N(CN)<sub>2</sub> with the CCCs indicated for the amidine particles. (a) Aggregation rate coefficient  $k$  and (b) the same quantity normalized to the Smoluchowski rate coefficient  $k_s$ . Solid lines in (a) correspond to the Smoluchowski rate, while in (b) they serve to guide the eye.

by DLVO theory, which is typically caused by surface charge heterogeneities.<sup>30,32,49</sup>

The importance of viscous stabilization in regime (ii) can be confirmed by comparing the aggregation rate coefficients to the Smoluchowski's value  $k_s$  given in eqn (6). Viscosities of the IL-water mixtures increase strongly with increasing IL content (Fig. 2b), and thus the Smoluchowski's rate decreases (Fig. 6a). This point can be better illustrated by plotting the aggregation rate coefficients normalized with the Smoluchowski's value  $k/k_s$  (Fig. 6b). The normalized rate coefficient remains constant throughout the entire intermediate concentration regime (ii) within experimental error, which confirms that the aggregation is diffusion controlled. However, the rate coefficient is about a factor of 2–4 smaller than the Smoluchowski's value. Similar discrepancies were reported in aqueous suspensions of latex, silica, or metal oxide particles.<sup>49–52</sup> They can be partly explained by including van der Waals and hydrodynamic interactions in the calculation of the aggregation rate, which results in aggregation rates that are about a factor of two smaller than the Smoluchowski's value. While the Hamaker constant, which defines the strength of the van der Waals force, could vary with the type of IL and its water content, the actual value of the aggregation rate depends only weakly on

this constant.<sup>27</sup> The remaining discrepancies probably originate from inaccuracies in the hydrodynamic resistance function at small distances.<sup>52</sup>

The onset of solvation stabilization can be best localized through the abrupt decrease of the normalized rate coefficient at high IL content (Fig. 6b). Solvation stabilization occurring in regime (iii) on the IL-rich side is probably caused by repulsive forces generated by the structuring of the ILs near solid surfaces. This structuring was observed by X-ray reflectivity,<sup>53</sup> and the respective forces could be measured using the surface forces apparatus<sup>54</sup> and the atomic force microscope.<sup>24,33,55</sup> While such solvation forces are oscillatory, they are overall repulsive, and probably responsible for the stabilization of colloidal particles in ILs as suggested earlier.<sup>21</sup> Since we lack reliable models of the interaction potential acting between the particles in IL-water mixtures, we shall not attempt to evaluate the aggregation rates in this regime quantitatively.

The transition between slow and fast aggregation within the DLVO regime at the water rich side occurs in a narrow concentration range, referred to as the critical coagulation concentration (CCC). A similar critical concentration can be identified at the IL rich side, which signals the transition between the solvation and viscous stabilization regime. We distinguish





these two CCCs by referring to CCC-W on the water-rich side, and by CCC-IL on the IL-side. To remain in line with the customary definition of CCC in water, we will express CCC-W as molar concentration of the IL. In analogy, CCC-IL will be expressed as molar concentration of water. The respective molar concentration axes are indicated in Fig. 6. Fig. S2–S4 (ESI†) facilitate conversions to these and other concentration units. The respective CCCs can be inferred from Fig. 6 and they are summarized in Table S5 (ESI†).

### Sub-micron amidine latex particles

CCC-W is lower for the ILs than for the simple salts, such as KCl. Charged particles suspended in simple, monovalent salt solutions have CCCs in the range of 0.1–0.5 M.<sup>28,29,56</sup> The corresponding values induced by ILs are consistently lower, around 0.03–0.1 M. This shift is probably related to a stronger affinity of the IL anions to the particle surface than with  $\text{Cl}^-$ . One further observes that CCC-W increases in the sequence of  $\text{SCN}^-$ ,  $\text{N}(\text{CN})_2^-$ , and  $\text{BF}_4^-$ , suggesting that the affinity of the surface for these anions decreases in the same way. The effect of the cations on CCC-W is less pronounced.

The CCC-IL can be clearly observed for all ILs studied, except in the presence of the  $\text{BF}_4^-$  anion. Typical values observed reflect water concentrations of 2–7 M. The ILs containing the  $\text{BF}_4^-$  anion seem to induce only minor solvation stabilization for the water contents studied, eventually setting in below 1.0 M. This hypothesis seems to be consistent with the absence of aggregation of gold particles in very dry BMIM- $\text{BF}_4$  over time periods that were substantially larger than the half-times estimated using the Smoluchowski relation (Fig. 1b).<sup>16</sup> Silica suspensions were also found to be unstable in BMIM- $\text{BF}_4$ .<sup>23</sup> Adopting this hypothesis, CCC-IL increases in the sequence of  $\text{BF}_4^-$ ,  $\text{SCN}^-$ , and  $\text{N}(\text{CN})_2^-$ . The effect of cations seems to be more important for CCC-IL, since BMPY<sup>+</sup> yields the highest value, while BMIM<sup>+</sup> and BMPL<sup>+</sup> behave similarly.

### Sub-micron sulphate latex particles

The values of CCC-W for the sulphate particles are very similar to the values for the amidine particles. This fact can be understood since the magnitudes of the charge densities of both types of particles are comparable (Table S1, ESI†). However, the effects of anions are different. With the BMIM<sup>+</sup> cation, one observes the reverse sequence to the amidine particle. The CCC-W thus increases through the anions  $\text{BF}_4^-$ ,  $\text{N}(\text{CN})_2^-$ , and  $\text{SCN}^-$ . This trend suggests that the affinity of the surface for these anions decreases in the same sequence, and is thus opposite to the one for amidine particles. This reversed trend is probably related to the negative charge of these particles. The effect of cations on CCC-W is again minor, and these values are similar for BMIM<sup>+</sup>, BMPL<sup>+</sup>, and BPY<sup>+</sup>.

The CCC-IL for the sulphate particles situates in the range 3–13 M, which is somewhat larger than for the amidine particles. As for the amidine particles, the ILs containing the  $\text{BF}_4^-$  anions lead only to minor suspension stabilization at low water concentrations, around 0.4 M. The CCC-IL increases with  $\text{BF}_4^-$ ,  $\text{N}(\text{CN})_2^-$ , and  $\text{SCN}^-$ , which reflects the same sequences

observed at the water side. The role of cations is less important, one still observes the sequence BMPY<sup>+</sup>, BMIM<sup>+</sup>, and BMPL<sup>+</sup>. These findings suggest again that cations interact with the particle surfaces more weakly than anions.

### Nano-sized sulphate latex particles

To address the applicability of our findings to smaller particles, aggregation rates of nano-sized sulphate latex particles with 50 nm radius in BMPL-N(CN)<sub>2</sub> and its water mixtures were measured (Table S1, ESI†). Due to the weak scattering power of these particles, the respective measurements are more difficult, especially in ILs. While the overall trends are similar, the present data suggest that the nano-sized particles aggregate more slowly than the sub-micron sized ones on the IL side. This point is in agreement with the observation that suspensions of nano-sized silica particles were more stable than suspensions of larger ones.<sup>21</sup> However, such differences could also be related to different particle concentrations of the samples.

The present scenario is consistent with visual observations of silica particle suspensions in mixtures of ethylammonium nitrate and water by Smith *et al.*<sup>24</sup> These suspensions were stable in pure water and the pure IL, but unstable in the mixtures. Fig. 1 reveals that solvation stabilization must be the relevant stabilization mechanism in that system too. We thus estimate CCC-W to be around 0.1 M and CCC-IL to be around 2 M in that system.

## Conclusions

Our light scattering studies demonstrate that colloidal particles suspended in ILs and their water mixtures form aggregates. However, the time scale of this process strongly depends on the particle concentration and on the value of the aggregation rate coefficient. The rate coefficients vary characteristically. At the water side, ILs behave like simple, monovalent salts and the data are in line with the DLVO theory. In this DLVO regime, one observes slow aggregation at low IL content. With increasing IL content, the aggregation rate increases and finally reaches the plateau reflecting fast aggregation. At the IL side, aggregation may proceed again very slowly. Two mechanisms are responsible for this stabilization. The *viscous stabilization* mechanism is important in viscous ILs, and originates from the slowdown of the diffusion process in a viscous liquid. The *solvation stabilization* mechanism is system specific, but can lead to a dramatic slowdown of the aggregation rate. This mechanism is probably related to repulsive solvation forces that are operational in ILs due to strong layering close to surfaces. These two stabilization mechanisms are suspected to be generic, as they are operational in different ILs and for particles with different surface functionalities and of different size. We further suspect that in ILs containing  $\text{BF}_4^-$  anions the principal mechanism is viscous stabilization, and solvation stabilization is unimportant, unless the IL is extremely dry. On the other hand, ILs containing  $\text{N}(\text{CN})_2^-$  or  $\text{SCN}^-$  anions tend to stabilize suspensions by both mechanisms, and solvation stabilization can be even operational in ILs containing 10% of water by mass.





# Acknowledgements

Financial support by the Swiss National Science Foundation, Swiss Scientific Exchange Program and the University of Geneva is gratefully acknowledged.

# References

- 1 A. P. Abbott and K. J. McKenzie, *Phys. Chem. Chem. Phys.*, 2006, **8**, 4265–4279.
- 2 M. Armand, F. Endres, D. R. MacFarlane, H. Ohno and B. Scrosati, *Nat. Mater.*, 2009, **8**, 621–629.
- 3 F. Endres and S. Z. El Abedin, *Phys. Chem. Chem. Phys.*, 2006, **8**, 2101–2116.
- 4 N. V. Plechkova and K. R. Seddon, *Chem. Soc. Rev.*, 2008, **37**, 123–150.
- 5 H. Tokuda, K. Hayamizu, K. Ishii, M. Abu Bin Hasan Susan and M. Watanabe, *J. Phys. Chem. B*, 2004, **108**, 16593–16600.
- 6 H. Tokuda, K. Hayamizu, K. Ishii, M. A. B. H. Susan and M. Watanabe, *J. Phys. Chem. B*, 2005, **109**, 6103–6110.
- 7 M. Ruta, G. Laurenczy, P. J. Dyson and L. Kiwi-Minsker, *J. Phys. Chem. C*, 2008, **112**, 17814–17819.
- 8 J. D. Scholten, B. C. Leal and J. Dupont, *ACS Catal.*, 2012, **2**, 184–200.
- 9 F. T. Li, X. J. Wang, Y. Zhao, J. X. Liu, Y. J. Hao, R. H. Liu and D. S. Zhao, *Appl. Catal., B*, 2014, **144**, 442–453.
- 10 X. Yang, Z. F. Fei, D. B. Zhao, W. H. Ang, Y. D. Li and P. J. Dyson, *Inorg. Chem.*, 2008, **47**, 3292–3297.
- 11 S. Shylesh, D. Hanna, S. Werner and A. T. Bell, *ACS Catal.*, 2012, **2**, 487–493.
- 12 P. Wang, S. M. Zakeeruddin, P. Comte, I. Exnar and M. Gratzel, *J. Am. Chem. Soc.*, 2003, **125**, 1166–1167.
- 13 E. F. Borra, O. Seddiki, R. Angel, D. Eisenstein, P. Hickson, K. R. Seddon and S. P. Worden, *Nature*, 2007, **447**, 979–981.
- 14 H. Itoh, K. Naka and Y. Chujo, *J. Am. Chem. Soc.*, 2004, **126**, 3026–3027.
- 15 L. L. Lazarus, C. T. Riche, N. Malmstadt and R. L. Brutchey, *Langmuir*, 2012, **28**, 15987–15993.
- 16 E. Vanecht, K. Binnemans, S. Patskovsky, M. Meunier, J. W. Seo, L. Stappers and J. Fransaer, *Phys. Chem. Chem. Phys.*, 2012, **14**, 5662–5671.
- 17 Y. Zhou and M. Antonietti, *J. Am. Chem. Soc.*, 2003, **125**, 14960–14961.
- 18 M. Ramalakshmi, P. Shakkthivel, M. Sundrarajan and S. M. Chen, *Mater. Res. Bull.*, 2013, **48**, 2758–2765.
- 19 H. Minami, K. Yoshida and M. Okubo, *Macromol. Rapid Commun.*, 2008, **29**, 567–572.
- 20 Q. M. Ji, S. Acharya, G. J. Richards, S. L. Zhang, J. Vieaud, J. P. Hill and K. Ariga, *Langmuir*, 2013, **29**, 7186–7194.
- 21 K. Ueno and M. Watanabe, *Langmuir*, 2011, **27**, 9105–9115.
- 22 S. S. Moganty, S. Srivastava, Y. Y. Lu, J. L. Schaefer, S. A. Rizvi and L. A. Archer, *Chem. Mater.*, 2012, **24**, 1386–1392.
- 23 K. Ueno, A. Inaba, M. Kondoh and M. Watanabe, *Langmuir*, 2008, **24**, 5253–5259.
- 24 J. A. Smith, O. Werzer, G. B. Webber, G. G. Warr and R. Atkin, *J. Phys. Chem. Lett.*, 2010, **1**, 64–68.
- 25 J. Nordström, L. Aguilera and A. Matic, *Langmuir*, 2012, **28**, 4080–4085.
- 26 W. B. Russel, D. A. Saville and W. R. Schowalter, *Colloidal Dispersions*, Cambridge University Press, Cambridge, 1989.
- 27 M. Elimelech, J. Gregory, X. Jia and R. A. Williams, *Particle Deposition and Aggregation: Measurement, Modeling, and Simulation*, Butterworth-Heinemann Ltd., Oxford, 1995.
- 28 T. Lopez-Leon, A. B. Jodar-Reyes, D. Bastos-Gonzalez and J. L. Ortega-Vinuesa, *J. Phys. Chem. B*, 2003, **107**, 5696–5708.
- 29 D. N. Furlong, A. Launikonis, W. H. F. Sasse and J. V. Sanders, *J. Chem. Soc., Faraday Trans. 1*, 1984, **80**, 571–588.
- 30 S. H. Behrens, M. Borkovec and P. Schurtenberger, *Langmuir*, 1998, **14**, 1951–1954.
- 31 M. Kobayashi, M. Skarba, P. Galletto, D. Cakara and M. Borkovec, *J. Colloid Interface Sci.*, 2005, **292**, 139–147.
- 32 N. Ryde and E. Matijevic, *J. Chem. Soc., Faraday Trans.*, 1994, **90**, 167–171.
- 33 R. Hayes, G. G. Warr and R. Atkin, *Phys. Chem. Chem. Phys.*, 2010, **12**, 1709–1723.
- 34 V. J. Anderson and H. N. W. Lekkerkerker, *Nature*, 2002, **416**, 811–815.
- 35 A. Zaccone, J. J. Crassous and M. Ballauff, *J. Chem. Phys.*, 2013, **138**, 104908.
- 36 D. Bonn, J. Otwinowski, S. Sacanna, H. Guo, G. Wegdam and P. Schall, *Phys. Rev. Lett.*, 2009, **103**, 156101.
- 37 W. Lin, M. Kobayashi, M. Skarba, C. Mu, P. Galletto and M. Borkovec, *Langmuir*, 2006, **22**, 1038–1047.
- 38 B. J. Berne and R. Pecora, *Dynamic Light Scattering*, Robert E. Krieger Publishing, Malabar, 1990.
- 39 D. A. Weitz, J. S. Huang, M. Y. Lin and J. Sung, *Phys. Rev. Lett.*, 1984, **53**, 1657–1660.
- 40 H. Holthoff, S. U. Egelhaaf, M. Borkovec, P. Schurtenberger and H. Sticher, *Langmuir*, 1996, **12**, 5541–5549.
- 41 S. H. Xu and Z. W. Sun, *Soft Matter*, 2011, **7**, 11298–11308.
- 42 P. Sandkuhler, M. Lattuada, H. Wu, J. Sefcik and M. Morbidelli, *Adv. Colloid Interface Sci.*, 2005, **113**, 65–83.
- 43 M. I. Mishchenko, L. D. Travis and A. A. Lacis, *Scattering, Absorption, and Emission of Light by Small Particles*, University Press, Cambridge, 2002.
- 44 W. L. Yu, E. Matijevic and M. Borkovec, *Langmuir*, 2002, **18**, 7853–7860.
- 45 E. J. Gonzalez, A. Dominguez and E. A. Macedo, *J. Chem. Eng. Data*, 2012, **57**, 2165–2176.
- 46 S. Chen, S. Zhang, X. M. Liu, J. Wang, J. Wang, K. Dong, J. L. Sun and B. Xu, *Phys. Chem. Chem. Phys.*, 2013, **16**, 5893–5906.
- 47 X. Y. Ma, J. Q. Lu, R. S. Brock, K. M. Jacobs, P. Yang and X. H. Hu, *Phys. Med. Biol.*, 2003, **48**, 4165–4172.
- 48 M. Bester-Rogac, A. Stoppa, J. Hunger, G. Hefter and R. Buchner, *Phys. Chem. Chem. Phys.*, 2011, **13**, 17588–17598.
- 49 M. Schudel, S. H. Behrens, H. Holthoff, R. Kretzschmar and M. Borkovec, *J. Colloid Interface Sci.*, 1997, **196**, 241–253.



dc 1931\_21

- 50 S. H. Behrens, D. I. Christl, R. Emmerzael, P. Schurtenberger and M. Borkovec, *Langmuir*, 2000, **16**, 2566–2575.
- 51 M. Kobayashi, F. Juillerat, P. Galletto, P. Bowen and M. Borkovec, *Langmuir*, 2005, **21**, 5761–5769.
- 52 P. Sinha, I. Szilagyi, F. J. Montes Ruiz-Cabello, P. Maroni and M. Borkovec, *J. Phys. Chem. Lett.*, 2013, **4**, 648–652.
- 53 M. Mezger, H. Schroder, H. Reichert, S. Schramm, J. S. Okasinski, S. Schoder, V. Honkimaki, M. Deutsch, B. M. Ocko, J. Ralston, M. Rohwerder, M. Stratmann and H. Dosch, *Science*, 2008, **322**, 424–428.
- 54 R. G. Horn, D. F. Evans and B. W. Ninham, *J. Phys. Chem.*, 1988, **92**, 3531–3537.
- 55 J. J. Segura, A. Elbourne, E. J. Wanless, G. G. Warr, K. Voitchovsky and R. Atkin, *Phys. Chem. Chem. Phys.*, 2013, **15**, 3320–3328.
- 56 W. Lin, P. Galletto and M. Borkovec, *Langmuir*, 2004, **20**, 7465–7473.



## Article

# Effect of Water and Salt on the Colloidal Stability of Latex Particles in Ionic Liquid Solutions

Dóra Takács <sup>1</sup>, Matija Tomšič <sup>2</sup> and Istvan Szilagyí <sup>1,\*</sup>

<sup>1</sup> MTA-SZTE Lendület Biocolloids Research Group, Department of Physical Chemistry and Materials Science, University of Szeged, Rerrich Béla tér 1, H-6720 Szeged, Hungary; takacs.dora@szte.hu

<sup>2</sup> Faculty of Chemistry and Chemical Technology, University of Ljubljana, Večna pot 113, 1000 Ljubljana, Slovenia; Matija.Tomsic@fkkt.uni-lj.si

\* Correspondence: szistvan@chem.u-szeged.hu

**Abstract:** The colloidal stability of sulfate (SL) and polyimidazolium-modified sulfate (SL-IP-2) latex particles was studied in an ionic liquid (IL) of ethylammonium nitrate (EAN) and its water mixtures. Aggregation rates were found to vary systematically as a function of the IL-to-water ratio. Repulsive electrostatic interactions between particles dominated at low IL concentrations, while they were significantly screened at intermediate IL concentrations, leading to destabilization of the dispersions. When the IL concentration was further increased, the aggregation of latex particles slowed down due to the increased viscosity and finally, a striking stabilization was observed in the IL-rich regime close to the pure IL solvent. The latter stabilization is due to the formation of IL layers at the interface between particles and IL, which induce repulsive oscillatory forces. The presence of the added salt in the system affected differently the structure of the interfaces around SL and SL-IP-2 particles. The sign of the charge and the composition of the particle surfaces were found to be the most important parameters affecting the colloidal stability. The nature of the counterions also plays an important role in the interfacial properties due to their influence on the structure of the IL surface layers. No evidence was observed for the presence of long-range electrostatic interactions between the particles in pure ILs. The results indicate that the presence of even low concentrations of water and salt in the system (as undesirable impurities) can strongly alter the interfacial structure and thus, the aggregation mechanism in particle IL dispersions.

**Keywords:** ionic liquid; aggregation; latex particle; light scattering; colloidal stability



**Citation:** Takács, D.; Tomšič, M.; Szilagyí, I. Effect of Water and Salt on the Colloidal Stability of Latex Particles in Ionic Liquid Solutions. *Colloids Interfaces* **2022**, *6*, 2. <https://doi.org/10.3390/colloids6010002>

Academic Editor: habil. Reinhard Miller

Received: 26 November 2021

Accepted: 29 December 2021

Published: 31 December 2021

**Publisher's Note:** MDPI stays neutral with regard to jurisdictional claims in published maps and institutional affiliations.



**Copyright:** © 2021 by the authors. Licensee MDPI, Basel, Switzerland. This article is an open access article distributed under the terms and conditions of the Creative Commons Attribution (CC BY) license (<https://creativecommons.org/licenses/by/4.0/>).

## 1. Introduction

Room temperature ionic liquids (ILs) are a class of tunable and extraordinarily versatile solvents composed solely of ions and hence, they possess a variety of properties making them interesting for numerous applications [1,2]. For instance, they have advantageous characteristics such as negligible vapor tension, nonflammability, wide electrochemical window, high boiling, and low freezing points. Therefore, their operational range is quite imposing. In addition, they possess interesting solvation and interfacial properties. Thus, developing particle dispersions in ILs is a continuously evolving field since the physicochemical properties of the IL-(nano)particle dispersions can be superior compared to the ones of the one phase counterparts [3]. This improvement strongly depends on the balance of bulky and interfacial interactions between ILs and the particles [4,5]. Applications of IL-particle dispersed systems include producing functional nanomaterials [6,7], catalytic reactions [8–10] and various electrochemical processes [1,11], to name a few. Since the importance of these utilizations has begun to grow, the fundamental research must focus on the understanding of the mechanisms behind the stabilization of (nano)particles in ILs. While the properties of bulk ILs often define the solvent physicochemical parameters, when used as the solvent, these properties may be altered at the solid–IL interface due to the denser ion structuration near to the charged surface [12–14].

In general, the stability of colloidal systems is known to be governed by a balance of attractive and repulsive forces, which are well described for aqueous dispersions by the classical Derjaguin, Landau, Verwey, and Overbeek (DLVO) theory [15–17]. To prevent the particle aggregation in these colloids, the surface of the particles can be tailored to enhance the strength of the repulsive forces enough to overcome the van der Waals attraction and keep the particles separated [16]. This repulsion can be obtained either electrostatically or sterically or it can result from the combination of these two effects (electrosteric) [16]. Such stabilization can be achieved by modifying the surface of the particles with polymeric substances [15,18]. Nevertheless, ILs are fundamentally different in relation to the solvent properties of the polar liquids, since the electrostatic stabilization is typical for the polar molecular liquids is unlikely to occur in them, as their strong ionic character prevents the manifestation of the classical long-range repulsive interparticle interactions due to their strong charge screening [19,20]. Therefore, the proposed stabilizing mechanism in ILs is the so-called solvation force. In this situation, a solvation layer of IL ions forms around the particles resulting in repulsive interparticle interactions [6,21,22].

Experiments have recently demonstrated that the nanoscale features of ILs may be useful for controlling the stability of particle dispersions. The scattering measurements and molecular dynamic simulations revealed that many ILs are nanostructured in bulk [23–25] and the surface force measurements have demonstrated that this structuring manifests as layering, when ILs get in contact with solid surfaces [14,26,27]. Therefore, it is evident that the interfacial assembly of the IL ions around the particles has an important stabilization role in the particle suspension, since it greatly influences the interactions between the surfaces [18,28]. Besides, the IL constituents have distinct affinity to a given surface, so they can modify the surface charge in different extent, which affects the aggregation process in the media applied [22,29–31]. Therefore, to possibly tune the colloidal stability of an IL based dispersion, the parameters, which affect the strength on interactions between IL constituents and the solid surface, should be explored and optimized.

The properties of the solid–liquid interfaces are determined by the features of both the surface and the liquid. However, the surface composition can be further altered by introducing external influences, such as changes in ionic strength, temperature, or pH. In addition, many applications of ILs require homogeneously dispersed (nano)particles across a broad range of conditions [4,5,32]. Therefore, the consequences caused by the undesirable presence of water and/or salt impurities in such systems must be clarified. It is assumed that these components can strongly alter the interfacial structure of the solid–IL interface, since the IL solvation layering is disrupted in their presence [33–35]. Despite the absence of the aforementioned long-range electrostatic interactions in ILs, the charge of the surface and of the ions present determines the composition and structure of the adsorbed interfacial layer. Unfortunately, only a limited number of studies have been performed investigating the effect of added salt on the stability of IL based colloidal systems. For example, it has been shown, that the presence of  $\text{Li}^+$  in a silica–IL colloidal dispersion modifies the microstructure of the system and has a strong influence on the structuring of the interface [33]. Nevertheless, there is a lack of extensive research studies performed on IL-based colloidal dispersions containing additionally dissolved salts.

The scope of this work is to contribute to the fundamental understanding of the structuring features of solid–IL interface by focusing on its response to external influences, as the addition of water and  $\text{Na}^+$  salt to the colloidal system. Both the dispersed phase, in a form of the dispersed latex particles, and the IL solvent phase, represented by the pure ethylammonium nitrate (EAN), have been individually studied before, but their mixed system provides an excellent platform to explore fundamental charging and aggregation processes in such dispersions. EAN was chosen as it possesses some properties (e.g., relatively moderate viscosity and refractive index, low melting point), which makes it suitable for light scattering based studies as the present one. While latex particles have proved to be appropriate model particles to study fundamental aggregation processes. Therefore, this paper provides an improved understanding of how the above-mentioned factors govern the



interfacial composition, as the presented findings offer tools for tuning and optimizing the stability of IL-particle dispersions for specific applications. Note that surface charges and aggregation rates were also explored by our group in other particle-IL systems, but those studies concentrated on particles dispersed in diluted aqueous IL solutions [30,31,36,37]. The present work focuses on a much wider range of IL concentration (up to pure EAN) and on the effect of both water and salt content on the colloidal stability of the dispersions.

## 2. Materials and Methods

### 2.1. Materials

Spherical sulfate functionalized polystyrene latex particles (SL) were purchased from Thermo Fischer Scientific. The particles have a mean radius of 215 nm, a polydispersity of 1.8% expressed as coefficient of variation and a charge density of 12 mC/m<sup>2</sup>. These quantities were determined by the manufacturer using transmission electron microscopy (TEM) and conductometric titration, respectively. Dynamic light scattering (DLS) yielded slightly higher hydrodynamic radii (257 nm) in stable suspensions, due to the finite polydispersity of the original samples, since the particles of higher size contribute much more to the scattered intensity in the DLS measurements, than the smaller ones. Note that the negative charge of the particles is compensated with K<sup>+</sup> counterions.

The polyimidazolium-based polymer (IP-2) with Cl<sup>−</sup> counterions was synthesized according to the protocol described elsewhere [38]. The immobilization of the IP-2 polymer onto the surface of SL particles (denoted as SL-IP-2 thereafter) was achieved by simple mixing of proper volumes of ultrapure water, IP-2 and SL particle samples. The stock suspensions were subsequently diluted to 20 mg/L for light scattering measurements and set to pH 4 by HCl (VWR). During sample preparation, ultrapure water was obtained from Puranity TU+ (VWR) apparatus. Prior to use, the water and the electrolyte solutions were filtered with 0.1 μm syringe filters (Millex) to prevent dust contamination.

Ethylammonium nitrate (EAN) was purchased from IoLiTech GmbH (Heilbronn, Germany). It belongs to the class of room-temperature ILs, and it is completely miscible with water in all concentration ratios. For analysis of DLS measurements, the viscosity and refractive index data for EAN–water mixtures were taken from the literature [39]. The concentration of pure EAN is 11.6 mol/L, while the water content was below 3 g/L (which corresponds to 0.17 M), as determined by Karl-Fischer coulometric titrations using a KEM MKC-710 Karl Fischer Moisture Titrator. Sodium nitrate (NaNO<sub>3</sub>) used as background electrolyte was purchased from AnalR NORMAPUR.

### 2.2. Dynamic Light Scattering

Time-resolved DLS was applied to follow the possible aggregation processes in the samples. The measurements were performed using a NIBS High-Performance Particle Sizer (ALV GmbH) equipped with a 3 mW He-Ne laser of 633 nm wavelength and the scattering angle was 173°. The samples were prepared by mixing the appropriate amount of water with EAN and salt solutions to achieve the desired IL and NaNO<sub>3</sub> concentrations. The experiments were initiated by adding the aqueous particle suspension to the IL–water mixture in the cuvette, followed by rapid mixing. The final particle concentration was 20 mg/L, which was sufficiently low that the particle aggregation endured in its early stages and the contribution of the higher order aggregates could be neglected. This method limited the lowest achievable water content to about 3 g/L.

DLS probes the fluctuations of the scattered light and evaluates the dependence of the intensity correlation function with time. Each correlation function was recorded for 20 s and it was fitted with cumulant method to obtain the decay rate constant ( $\Gamma$ ) [40]. From this constant, one can extract the translational diffusion coefficient ( $D$ ), which is converted to hydrodynamic radius ( $R_h$ ) by means of the Stokes–Einstein relation [41]

$$D = \frac{\Gamma}{q^2} = \frac{k_B T}{6\pi\eta R_h} \quad (1)$$

where  $\eta$  is the viscosity of the media,  $T$  is the absolute temperature,  $k_B$  is the Boltzmann constant, and  $q$  is the magnitude of the scattering vector. The apparent dynamic rate constant ( $\Delta$ ), which describes the initial increase of  $R_h$ , is given as [40,42]

$$\Delta = \frac{1}{R_h(q,0)} \cdot \left( \frac{dR_h(q,t)}{dt} \right)_{t \rightarrow 0} = kN_0 \left( 1 - \frac{1}{\alpha} \right) \frac{I_2(q)}{2I_1(q)} \quad (2)$$

where  $t$  is the experimental measurement time,  $N_0$  is the initial number concentration of the particles ( $4.55 \times 10^{14}$  L/m<sup>3</sup>),  $k$  is the absolute aggregation rate coefficient (in m<sup>3</sup>/s unit), and  $\alpha$  is the hydrodynamic factor. This factor represents the ratio between the diffusion coefficients of the monomer ( $D_1$ ) and the dimer ( $D_2$ ) and its numerical value can be estimated from calculation of the friction coefficient of a dimer under laminar flow conditions ( $\alpha = D_1/D_2 = 1.39$ ) [43]. The contribution of the form factors of the monomer  $I_1(q)$  and the dimer  $I_2(q)$  to the scattered intensity was predicted by the Rayleigh–Gans–Debye approximation as  $I_2(q)/2I_1(q) = 1 + (\sin(2qR_1)/2qR_1)$ , where  $R_1$  is the radius of the particle [17,40]. In the early stages of aggregation, only a dimer formation is assumed, until the  $R_h$  does not increase more than 40% in these measurements. The value of  $\Delta$  can be obtained from the initial slope of the apparent  $R_h$  versus time, as shown in the Figure 1. Note that  $R_h$  always increases with time in an aggregating suspension, as one would intuitively expect. The standard error of the obtained  $\Delta$  values was about 8%.

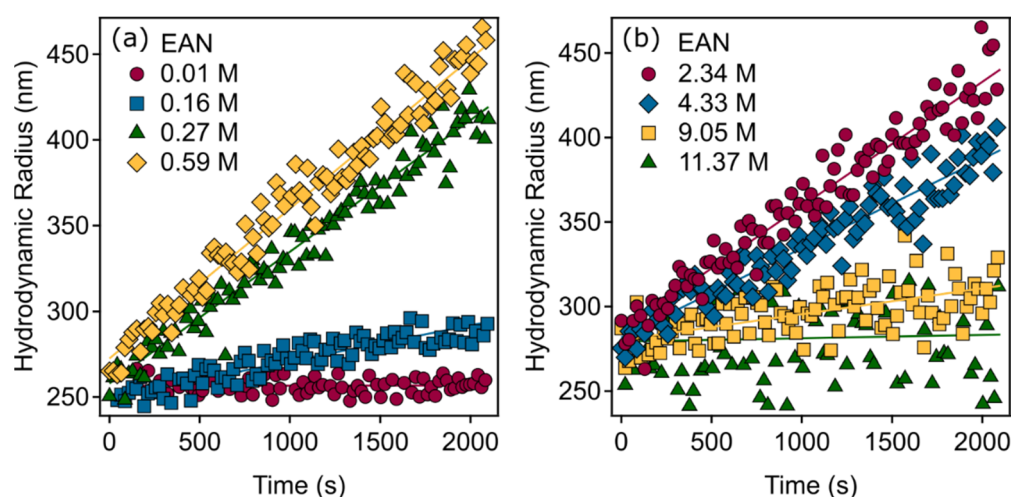


**Figure 1.** Time-dependence of the hydrodynamic radii measured by DLS for SL particles in EAN–water mixtures at different EAN concentrations on the water-rich side (a) and on the IL-rich side (b). The solid lines present the linear fits to the data used to calculate the aggregation rate constants according to Equation (2).

### 2.3. Phase Analysis Light Scattering

Continuously monitored phase analysis light scattering (cmPALS) measurements were performed with a Litesizer 500 instrument (Anton Paar) at a scattering angle of 175° to determine the electrophoretic mobility of the particles in IL–water mixtures. The applied voltage during the measurements was 200 V. In operation, the light source is producing coherent primary light beam, which is split by a beam splitter. One part is sent to the oscillating modulator and the other part is used in the light scattering experiment. The scattered light is then combined with the modulated reference beam from the modulator and detected on the primary scattering detector. Additionally, also a smaller part of the modulated reference beam from the modulator is monitored continuously by a secondary detector and used for the corrections of possible instabilities in modulator frequency. The resulting monitor trace represents the reference beam, while the detector trace shows the interference (modulation) between the scattered light from the sample and the modulated reference beam. The obtained phase plot shows the phase difference between the detector

and the monitor traces due to the Doppler effect on the scattered light by moving scattering particles and the fit of the cmpALS to the data, from which the electrophoretic mobility values were determined. This parameter quantifies the ratio between the travel velocity of the particle relative to the applied electric field. The sample preparation was identical as in the DLS measurements with the exception that the samples were allowed to rest for 2 h at room temperature before the measurements, which occurred after 1 min equilibration time in capillary cuvettes or with the Univette accessory (Anton Paar). The latter measuring cell is recommended for high conductivity samples; therefore, it was used to measure samples containing ILs. Five runs were performed and averaged.

### 3. Results and Discussion

The aggregation kinetics and charging characteristics of bare and IP-2 functionalized SL particles dispersed in IL–water mixtures in the concentration range from dilute solution of EAN in water to neat EAN containing only a small amount of water were investigated by light scattering measurements. The effect of added  $\text{NaNO}_3$  salt on the colloidal stability of these systems was also assessed. The principal aim of these experiments determining the electrophoretic mobilities and aggregation rates was to clarify the behavior of EAN at the solid–liquid interface and to study the sensitivity of the surface compositions to external influences, such as addition of water or salt.

#### 3.1. IP-2 Functionalization of SL

Commercially available SL particles were functionalized with oppositely charged IP-2 polymer. The aim was to find the optimal experimental conditions for stable dispersion of SL-IP-2 particles coated with the polymer. The pH of the samples was kept at 4.0, and the dispersions contained 10 mM KCl as a background electrolyte. Electrophoretic mobility measurements were performed to follow the adsorption of the polymer on the particle surface and the resulting data recorded at various IP-2 doses are shown in Figure 2.

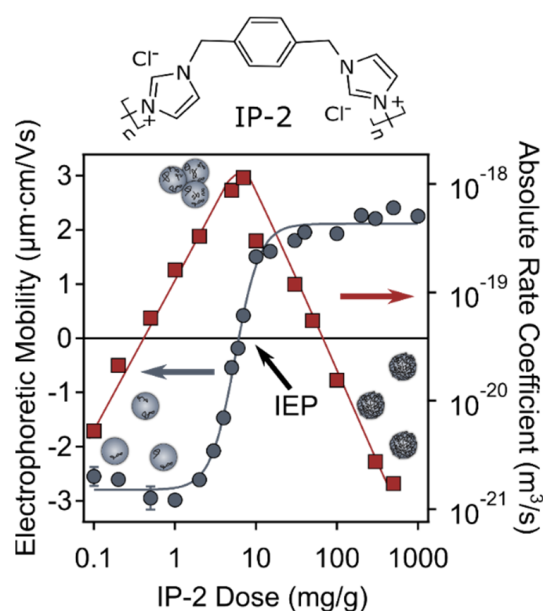


**Figure 2.** Electrophoretic mobility (circles, left axis) and absolute rate coefficient (squares, right axis) values of SL particles as a function of the IP-2 dose. The measurements were performed in aqueous dispersions at pH 4 and 10 mM ionic strength adjusted by KCl. The unit mg/g refers to mg IP-2 per one gram of SL. The arrows indicate the axis, to which mobility (blue arrow) and aggregation rate (red arrow) data points belong. The lines serve to guide the eye. The upper part of the figure shows the structure of IP-2 polymer.

In general, the mobilities changed from negative to positive by increasing the added amount of IP-2 polymer, indicating its strong affinity to the oppositely charged particle surface. The mobility values were negative at low doses, since the polymer was able to only partially compensate the surface charge of the particles at these conditions. A further increase in the IP-2 dose led to the charge neutralization at the isoelectric point (IEP), where the particles have zero net charge. The adsorption process continued at higher doses and subsequent charge reversal of the particles occurred leading to positive net charge on the particles. At the highest doses applied, the mobility values reached a plateau with an onset around a 200 mg/g dose. Note that the coated particles possess significantly lower magnitude of mobility at the plateau than the bare particles indicating a lower surface charge density in the former case.

Furthermore, the absolute aggregation rate coefficients were determined by time-resolved DLS measurements under the same experimental conditions as the electrophoretic mobilities to explore particle aggregation processes in the dispersions. Figure 2 indicates that the gradual decrease in the mobility values is in line with the changes in the absolute aggregation rates. Accordingly, when the particles possess high electrophoretic mobility values (either negative or positive), the aggregation rate values are low indicating the stable dispersions or slow aggregation. However, at IP-2 doses near to the IEP, the rate values increase indicating a rapid particle aggregation and hence, unstable samples. Such a charging and aggregation behaviors resemble the one observed earlier in oppositely charged polyelectrolyte–particle systems [31,36,44,45] and are in qualitative agreement with the DLVO theory, which predicts the stable dispersions in case, when the surface charge is high and the corresponding repulsive double layer forces prevail the attractive van der Waals interactions [46].

Based on these results, the particles prepared at a dose of 500 mg/g (sample denoted as SL-IP-2) were used for the further studies. At this composition, the SL particle surface is fully coated with the polymer, while the high positive charge and very low aggregation rate ensure appreciable colloidal stability of the SL-IP-2 sample. Therefore, in the following, the negatively charged particles are referred to as SL and positive ones as SL-IP-2 particles.

### 3.2. Generic Trend in Aggregation Kinetics

First, the aggregation characteristics of the SL and SL-IP-2 particles in EAN and in its water mixture systems were explored. Figure 3 indicates that in general, three main aggregation regimes were identified in both cases. Namely, at the water-rich side, i.e., up to 1.0 M EAN concentration, the aggregation rates were initially low, but they increased rapidly with increasing IL contents until they reached the plateau values. This tendency is consistent with the DLVO theory predictions and hence, it was named as DLVO regime. Accordingly, the initial increase of the aggregation rate values corresponds to the slow aggregation region, in which the trend is mainly governed by the progressive charge screening by the EAN ions and simultaneous surface adsorption of the counterions. Note that for the negatively charged SL particles ethylammonium cations, while for the positively charged SL-IP-2 nitrate anions were the counterions. The plateau at higher concentrations of EAN refers to the fast aggregation region, where the percentage of particle collisions, which lead to dimer formation only depends on the rate of their diffusion in the given media. The obtained absolute aggregation rates in this fast aggregation regime ( $k_{fast}$ ) were found to be  $2.63 \times 10^{-18} \text{ m}^3/\text{s}$  and  $5.12 \times 10^{-18} \text{ m}^3/\text{s}$  for the SL and SL-IP-2 particles, respectively.



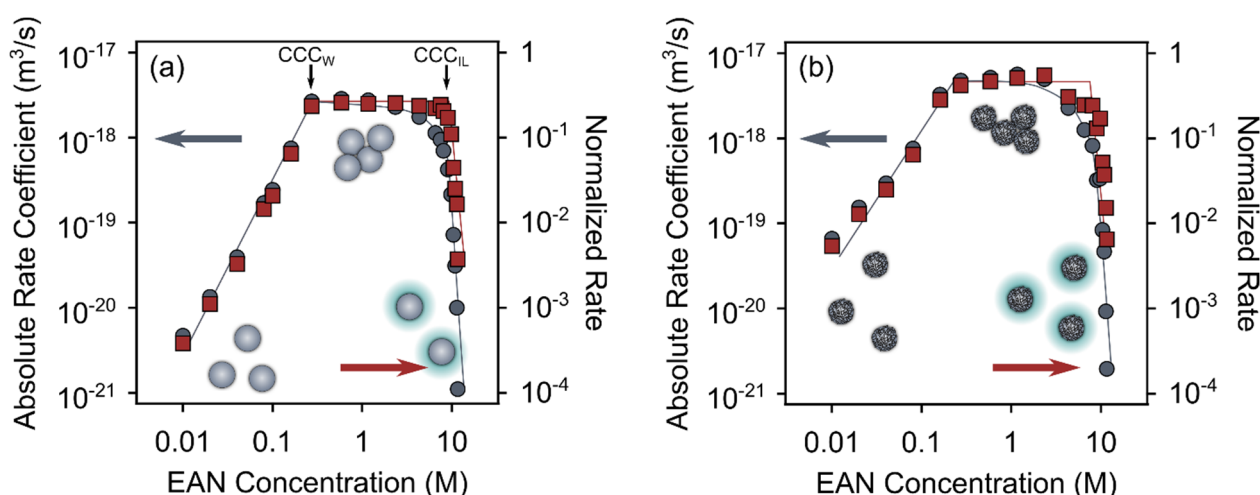


**Figure 3.** Absolute aggregation rate coefficients (circles, left axes) and normalized aggregation rate coefficients (squares, right axes) for SL (a) and SL-IP-2 (b) particles in water. In (a) the  $CCC_S$  corresponding to the water-rich ( $CCC_W$ ) and EAN-rich ( $CCC_{IL}$ ) concentration regimes are indicated. The solid lines serve to guide the eye.

This scenario is similar to the one induced by the simple inorganic salts [30,47,48], since the ILs tend to fully dissociate and hydrate in dilute aqueous solutions, similar as observed for the inorganic electrolytes [21,30,49]. The sharp transition between the reported fast and slow aggregation regimes is located at the so-called critical coagulation concentration (CCC). Therefore, this parameter can quantify the destabilization power of the given solvent medium. The obtained CCC values in the water-rich regime ( $CCC_W$ ) are expressed as molar concentrations of EAN (Table 1), but those in the IL-rich regime ( $CCC_{IL}$ ) are expressed as molar concentration of water. They were determined from the data presented in Figure 3 and are gathered in Table 1. The presented findings are generic for both SL (see Figure 3a) and SL-IP-2 particles (see Figure 3b).

**Table 1.** Characteristic aggregation data of the particles measured in EAN–water mixtures.

	SL		SL-IP-2	
	$CCC_W^a$	$CCC_{IL}^b$	$CCC_W^a$	$CCC_{IL}^b$
EAN	0.23	7.1	0.15	15.0
EAN—0.001 M $NaNO_3$	0.16	8.5	0.15	12.6
EAN—0.01 M $NaNO_3$	0.15	7.3	0.14	16.2
EAN—0.1 M $NaNO_3$	0.05	7.8	0.05	14.8

<sup>a</sup> Concentration of EAN in M. <sup>b</sup> Concentration of water in M. The accuracy of the CCC determination method is about 10%.

In the second regime, i.e., at intermediate EAN concentrations above 1.0 M, the decrease in the aggregation rates was gradual. This trend arises due to the increasing viscosity of the mixture. Nevertheless, the aggregation remains diffusion controlled. Therefore, this regime was designated to exhibit the viscous stabilization. To consider such a stabilization mechanism the aggregation rates were normalized by the Smoluchowski rate ( $k_S$ ), which takes into account the dynamic viscosity of the solution for diffusion-controlled aggregation as follows [22]

$$k_S = \frac{8k_B T}{3\eta} \quad (3)$$

Since the viscosities of the mixtures strongly increase with increasing IL concentration, in parallel the Smoluchowski's value decreases. Therefore, the normalized rate coefficient ( $k/k_S$ ) remains constant in the entire viscous stabilization regime, which proves that the gradual slowdown in the aggregation is caused by the increased viscosity of the media and

that the aggregation is diffusion controlled [48]. Note that the experimentally obtained aggregation rate coefficients ( $k$ ) were smaller than the calculated values ( $k_S$ ) by a factor around 2–3 in the fast aggregation regime. This discrepancy is because absolute rate constants are influenced by hydrodynamic and van der Waals interactions, while Smoluchowski's theory neglects them. Similar phenomena were observed in aqueous dispersion of other colloidal particles [50,51].

Finally, in the last regime, upon further increasing the IL concentration, one observes a rapid decrease of the aggregation rates. This phenomenon was denoted as solvation stabilization. In this regime, the samples contained only a small concentration of water. Since the stabilizing mechanism in IL media lies on the formation of solvation layers (which will be further discussed later), the water present in the samples can disrupt the layering of IL constituents at the particles surface. Similar interfering role of water at the interface was reported in other works as well [22,52,53]. The onset of the third characteristic regime is identified by the sudden decrease of the normalized aggregation rates at high IL concentration. Here, a similar critical coagulation concentration ( $CCC_{IL}$ ) can be identified as in the case of DLVO regime. Therefore,  $CCC_{IL}$  represents the transition between the viscous and solvation stabilization regimes and is expressed in molar concentration of water.

The obtained  $CCC_{IL}$  values (see Table 1) indicate that for the destabilization of the particles in the EAN-rich regime, the higher concentration of water is needed in the case of SL-IP-2 particles. This most probably originates from the fact that EAN is a good solvent for the coating polymer and creates a solvation sphere with polymer tails and loops around the SL particle, which manifests itself as an additional stabilizing contribution of steric origin acting between the adsorbed IP-2 layers [54].

In addition, one also observes that the magnitude of the aggregation rate coefficients in the intermediate regime for the SL-IP-2 particles is much higher than for the SL particles. This difference occurs due to the significantly higher surface charge of the bare SL particles (see Figure 2), which results in somewhat stronger electrostatic repulsion between the particles, i.e., in slower aggregation.

### 3.3. Charging Characteristics

To further investigate the behavior of ILs upon interaction with charged particles, the electrophoretic mobility values for both particles in the whole range of EAN–water mixtures were determined. It should be noted that the acidity conditions before the particle transfer to the IL–water mixtures are of great importance, because they determine the initial surface charge of the particles that is crucial from the aspect of the colloidal stability, i.e., charging feature affect the aggregation processes in terms of the nature or origin of interparticle forces [32]. Under the given experimental conditions (pH 4) the SL particles have negative charge, but the SL-IP-2 particles are positively charged.

Figure 4a shows that although the electrophoretic mobility values are specific to the given particles, the trends in the magnitudes are very similar in both cases. Accordingly, their absolute value initially decreases with increasing the EAN concentration due to the surface charge screening and eventually settles very close to zero at higher EAN concentrations. This behavior is typical for charged colloids suspended in monovalent salt solutions and can be well-explained with the traditional theories developed for the description of the electrical double layer [30,55]. In addition, the phase plots shown in Figure 4b provide information about the motion of the particles in the given media. One can observe that in the water-rich regime the charged particles tend to move towards the electrode of opposite polarity. However, on the IL side, where solvation stabilization occurs, no particle movement could be detected by applying the electric field during the cMPALS measurements.

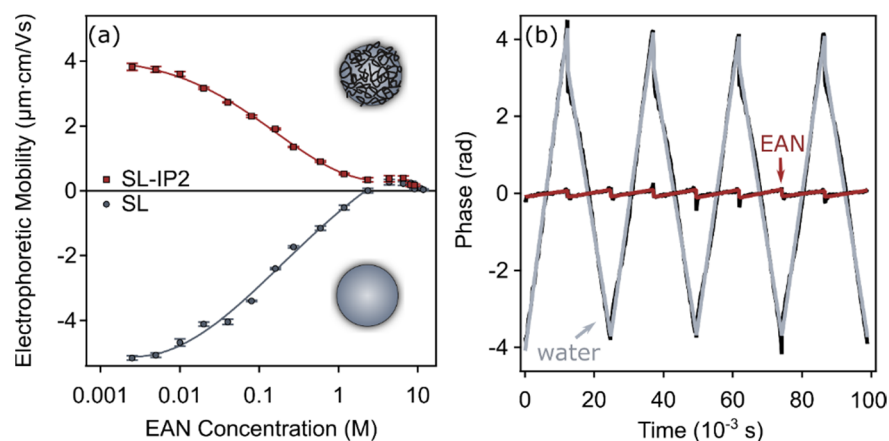


**Figure 4.** Charging characteristics of polystyrene latex particles in EAN–water mixtures. Electrophoretic mobility values of SL and SL-IP-2 particles at different EAN concentrations (a) and the obtained phase plots in the presence of SL particles on the water-rich side (2.5 mM EAN concentration) and IL-rich side (0.17 M water concentration) (b). Phase plots showing the phase difference between the detector trace and the monitor trace (black lines), while the grey (water) and red (EAN) lines indicate the cmPALS fit to the data. The solid lines in (a) represent the interpolation according to Equation (4).

The repulsive interactions that exist between nanoparticles in common solvents are generally electrostatic or steric in nature [16]. However, these observations suggest that if nanoparticles are successfully stabilized in EAN, electrostatic interparticle interactions may not be expressed because they are assumed to be quenched by the overwhelming ionic environment of the medium. Even though the particle surfaces are charged, conventional models of electrostatic repulsion in water cannot be successfully used in this case, since they are unable to account for such high ionic strengths as in ILs. In such cases, the origin of colloidal stabilization is most likely related to the formation of IL layers at the nanoparticles surface. Nonetheless, electrostatic interactions exist between all the charged species present in the system (anions, cations, and the particle surface charge), and are responsible for the nanoscopic structural organization. As shown in several experimental studies [6,21,26,33,56] and numerical simulations [57,58], such interactions originate from the structuration of IL layers near surfaces.

Furthermore, using the measured electrophoretic mobility values on the water-rich side  $CCC_W$  values can be calculated based on the DLVO theory [59]. Since the mobility data correlate with the electrokinetic potentials [17,60], the following equation can be used.

$$CCC_W = \frac{1}{8\pi l_B} \left( \frac{24\pi}{He\epsilon\epsilon_0} \right)^{2/3} \sigma^{4/3} \quad (4)$$

where  $l_B$  is the Bjerrum length,  $H$  is the Hamaker constant,  $e$  is the base of the natural logarithm,  $\epsilon$  is the dielectric constant,  $\epsilon_0$  is the vacuum permittivity, and  $\sigma$  is the surface charge density of the particle at the slip plane, which can be determined with the Debye-Hückel model [46]. The Hamaker constants used for the calculations was  $9 \times 10^{-21}$  J [29]. The obtained  $CCC_W$  values for the SL and SL-IP-2 particles were 0.25 M and 0.14 M, respectively, which are in a good agreement with the experimentally determined ones (see Table 1). The results imply that DLVO forces acted between particles in both systems in the water-rich regime (DLVO regime) and that the magnitude of the surface charge determines the  $CCC_W$ , which is higher for SL than for SL-IP-2 (see the mobility magnitudes in Figure 2 at low and high IP-2 doses).

### 3.4. Effect of Added Salt

Subsequently, the effect of the addition of  $NaNO_3$  on the aggregation processes in the particle-EAN systems was studied. It is expected that  $Na^+$  ion shows stronger influence on the interfacial features, since  $NO_3^-$  ions were already present in the mixtures as a component of EAN (i.e.,  $NO_3^-$  was chosen because no additional anions are introduced into the systems in this way). Note that, for the SL particle,  $Na^+$  was the counterion, while for the SL-IP-2, it acts as coion. Figure 5 shows the obtained aggregation rate trends for both studied latex particle types in the EAN–water mixtures at different concentrations of  $NaNO_3$

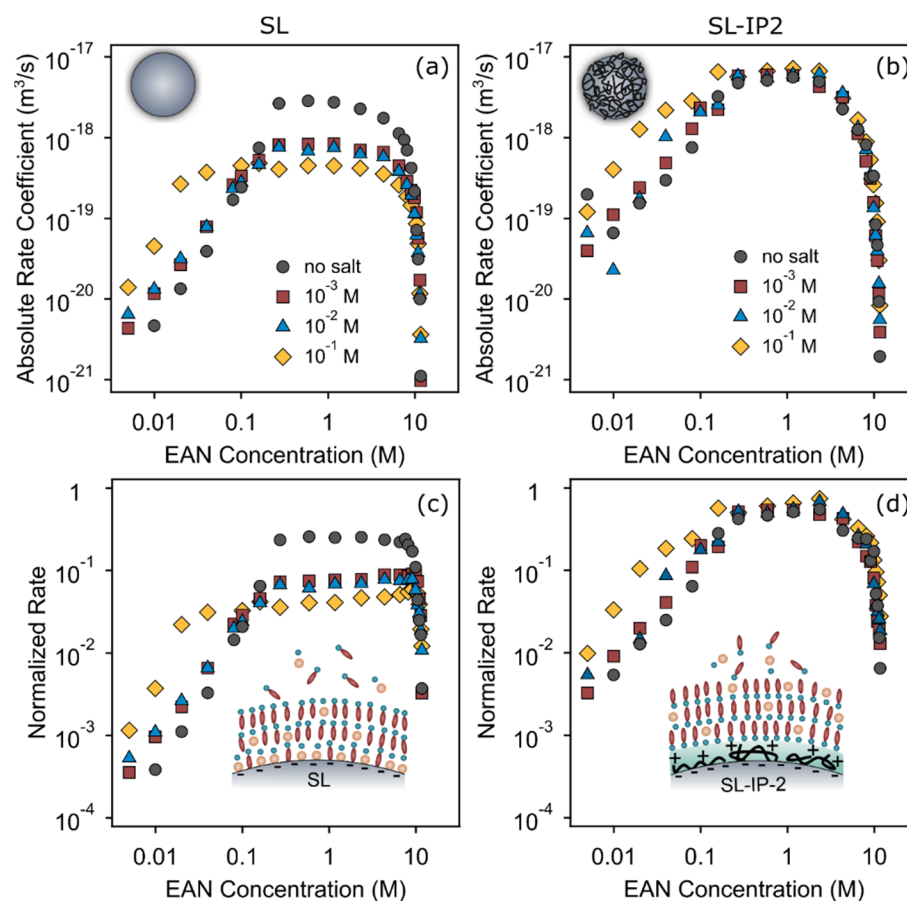


**Figure 5.** Absolute aggregation rate coefficients (a,b) and the same quantities normalized to the Smoluchowski rate coefficients (c,d) of SL (left column) and SL-IP-2 particles (right column) versus the EAN concentration in EAN–water mixtures with different concentrations of  $NaNO_3$  background electrolyte. The pH value of the aqueous stock solutions was set to 4.

The  $CCC_W$  values tend to decrease for both type of particles with increasing the concentration of  $NaNO_3$ , in the system (see Table 1). Accordingly, the smallest  $CCC_W$  can be observed in the presence of 0.1 M  $NaNO_3$ , due to the more significant charge screening from the increased amount of counterions, which agrees with the DLVO theory prediction.

Nevertheless, the  $CCC_{IL}$  value, which was determined at the IL-rich side, tend to be independent from the presence of  $NaNO_3$  for both type of particles, i.e., the obtained values were identical within the experimental error as in previously investigated systems with no salt added. However, the values significantly differ for the two particle types, probably due to the presence of additional steric interactions between the adsorbed IP-2 layers in case of SL-IP-2 particles. Such an additional repulsion led to increased resistance against water induced aggregation. The  $CCC$  values deduced from Figure 5c,d for SL and SL-IP-2 particles are summarized in Table 1.



Besides, Figure 5a further indicates that the presence of the  $Na^+$  ions seems to stabilize the SL dispersions in the intermediate concentration regime in EAN–water system, where the viscous stabilization occurs, since the aggregation rates in the presence of salt ions tend to be almost one order of magnitude smaller than in the case when the simple electrolyte is not present. Another noteworthy observation is that this stabilization is more pronounced with increasing amount of  $Na^+$  ions, e.g., the aggregation rates were the lowest at the presence of 0.1 M  $NaNO_3$ . This trend can be partly explained by the accumulation of  $Na^+$  ions on the negatively charged SL particle surface and thus, they are most probably involved in the development of the initial cationic layer, which compensates the negative charge of the SL. As  $Na^+$  ions can interact with the EAN components at the interface, they contribute to the formation of ordered solvation layers around the particle and consequently, also to the development of more stable particles. Similar scenario was observed for different solid/IL interfaces in the presence of inorganic ions [33,61]. In general, the influence of added ions can be attributed to their affinity with cations, anions, and the particle surface, to their size compared to that of the components of the IL and to their interaction with water.

Nevertheless, the generic trend in the aggregation rate coefficients in the case of SL-IP-2 particles, where the  $Na^+$  ions have the same sign of charge as the polymer-coated particles, was very similar in all cases, i.e., the above-mentioned  $NaNO_3$  concentration dependence on  $k$  could not be observed. This fact indicates that the electrostatic repulsion between the co-ions and the charged particle may lead to very weak adsorption, therefore  $Na^+$  ions interact only slightly with the particles of the same sign of charge and hence, their influence on the particle surface charge is negligible. As a result, the aggregation features of the SL-IP-2 particles are basically independent of the presence of the background salt and the obtained fast aggregation rates remain unchanged within the experimental uncertainty regardless of the  $NaNO_3$  concentration.

#### 4. Conclusions

Results of time-resolved light scattering measurements performed in aqueous EAN solutions revealed that the aggregation of bare and polymer functionalized latex particles is governed by electrostatic forces in the diluted IL samples, where dissociated and hydrated IL ions are present. The particle aggregation slows down at higher IL concentrations due to the increased viscosity of the medium. Besides, the particles were highly stable in pure ILs, where only a small amount of water was present. Under the latter experimental conditions, no significant change in the particle movement could be detected with applying an electric field in electrophoretic experiments. This indicates that the prevailing nature of colloidal stability of these systems is not electrostatic as in diluted IL solutions and that the dispersions are stable, rather due to repulsive oscillatory forces resulting from the layered assembly of the IL constituents on the particle surface. These results shed light on the origin of the main interparticle forces responsible for the colloidal stability of the particles in both pure ILs and in their aqueous solutions.

Furthermore, the effect of added  $NaNO_3$  to the system was also studied. The results indicate that the  $Na^+$  ions change the interfacial assembly of IL ions in the studied system and influence the stability of the colloidal dispersions. Such influence may be more or less significant, depending on the nature of the added ions (size, affinity to the surface and the solvation level of the ions) and the surface charge of the particles. In conclusion, the organization of the IL constituents at the particle surface as well as the interparticle forces can be altered by adding the appropriate type and amount of salt, which is particularly important once particle–IL dispersions are designed for certain applications. Knowing the physico-chemical parameters of the particles and ILs applied, the stability regimes can be qualitatively predicted based on the present findings.

**Author Contributions:** Conceptualization, I.S. and M.T.; methodology, D.T., I.S. and M.T.; software, I.S. and M.T.; validation, D.T., I.S. and M.T.; formal analysis, D.T., I.S. and M.T.; investigation, D.T., I.S. and M.T.; data curation, D.T., I.S. and M.T.; writing—original draft preparation, D.T.; writing—review and editing, I.S. and M.T.; visualization, D.T., I.S. and M.T.; supervision, I.S.; project administration, I.S. and M.T.; funding acquisition, I.S. and M.T. All authors have read and agreed to the published version of the manuscript.

**Funding:** The project was financed by the Hungarian National Research, Development and Innovation Office (SNN131558) and the Slovenian Research Agency (research core funding No. P1-0201 and project No. N1-0139 “Delamination of Layered Materials and Structure-Dynamics Relationship in Green Solvents”). D. T. was supported by the ÚNKP-21-3-SZTE-413 New National Excellence Program of the Ministry for Innovation and Technology from the source of the National Research, Development and Innovation Fund.

**Institutional Review Board Statement:** Not relevant.

**Informed Consent Statement:** Not relevant.

**Data Availability Statement:** Not relevant.

**Conflicts of Interest:** The authors declare no conflict of interest.

## References

1. Armand, M.; Endres, F.; MacFarlane, D.R.; Ohno, H.; Scrosati, B. Ionic-liquid materials for the electrochemical challenges of the future. *Nat. Mater.* **2009**, *8*, 621–629. [[CrossRef](#)] [[PubMed](#)]
2. Donato, K.Z.; Matejka, L.; Mauler, R.S.; Donato, R.K. Recent applications of ionic liquids in the sol-gel process for polymer–silica nanocomposites with ionic interfaces. *Colloids Interfaces* **2017**, *1*, 5. [[CrossRef](#)]
3. Franca, J.M.P.; Vieira, S.I.C.; Lourenco, M.J.V.; Murshed, S.M.S.; de Castro, C.A.N. Thermal conductivity of C<sub>4</sub>mim (CF<sub>3</sub>SO<sub>2</sub>)<sub>2</sub>N and C<sub>2</sub>mim EtSO<sub>4</sub> and their ionanofluids with carbon nanotubes: Experiment and theory. *J. Chem. Eng. Data* **2013**, *58*, 467–476. [[CrossRef](#)]
4. Minea, M.A.; Murshed, S.M.S. Ionic liquids-based nanocolloids—A review of progress and prospects in convective heat transfer applications. *Nanomaterials* **2021**, *11*, 1039. [[CrossRef](#)] [[PubMed](#)]
5. He, Z.Q.; Alexandridis, P. Ionic liquid and nanoparticle hybrid systems: Emerging applications. *Adv. Colloid Interface Sci.* **2017**, *244*, 54–70. [[CrossRef](#)]
6. Ueno, K.; Watanabe, M. From colloidal stability in ionic liquids to advanced soft materials using unique media. *Langmuir* **2011**, *27*, 9105–9115. [[CrossRef](#)]
7. Tunckol, M.; Durand, J.; Serp, P. Carbon nanomaterial-ionic liquid hybrids. *Carbon* **2012**, *50*, 4303–4334. [[CrossRef](#)]
8. Parvulescu, V.I.; Hardacre, C. Catalysis in ionic liquids. *Chem. Rev.* **2007**, *107*, 2615–2665. [[CrossRef](#)]
9. Hallett, J.P.; Welton, T. Room-temperature ionic liquids: Solvents for synthesis and catalysis. 2. *Chem. Rev.* **2011**, *111*, 3508–3576. [[CrossRef](#)]
10. Taskin, M.; Cognigni, A.; Zirbs, R.; Reimhult, E.; Bica, K. Surface-active ionic liquids for palladium-catalysed cross coupling in water: Effect of ionic liquid concentration on the catalytically active species. *RSC Adv.* **2017**, *7*, 41144–41151. [[CrossRef](#)]
11. Le Bideau, J.; Viau, L.; Vioux, A. Ionogels, ionic liquid based hybrid materials. *Chem. Soc. Rev.* **2011**, *40*, 907–925. [[CrossRef](#)] [[PubMed](#)]
12. Silvester, D.S.; Jamil, R.; Doblinger, S.; Zhang, Y.X.; Atkin, R.; Li, H. Electrical double layer structure in ionic liquids and its importance for supercapacitor, battery, sensing, and lubrication applications. *J. Phys. Chem. C* **2021**, *125*, 13707–13720. [[CrossRef](#)]
13. Beattie, D.A.; Espinosa-Marzal, R.M.; Ho, T.T.M.; Popescu, M.N.; Ralston, J.; Richard, C.J.E.; Sellapperumage, P.M.F.; Krasowska, M. Molecularly-thin precursor films of imidazolium-based ionic liquids on mica. *J. Phys. Chem. C* **2013**, *117*, 23676–23684. [[CrossRef](#)]
14. Mezger, M.; Schroder, H.; Reichert, H.; Schramm, S.; Okasinski, J.S.; Schoder, S.; Honkimaki, V.; Deutsch, M.; Ocko, B.M.; Ralston, J.; et al. Molecular layering of fluorinated ionic liquids at a charged sapphire (0001) surface. *Science* **2008**, *322*, 424–428. [[CrossRef](#)] [[PubMed](#)]
15. Elimelech, M.; Gregory, J.; Jia, X.; Williams, R.A. *Particle Deposition and Aggregation: Measurement, Modeling, and Simulation*; Butterworth-Heinemann Ltd.: Oxford, UK, 1995.
16. Israelachvili, J. *Intermolecular and Surface Forces*, 3rd ed.; Academic Press: London, UK, 2011.
17. Russel, W.B.; Saville, D.A.; Schowalter, W.R. *Colloidal Dispersions*; Cambridge University Press: Cambridge, UK, 1989.
18. Ueno, K.; Inaba, A.; Kondoh, M.; Watanabe, M. Colloidal stability of bare and polymer-grafted silica nanoparticles in ionic liquids. *Langmuir* **2008**, *24*, 5253–5259. [[CrossRef](#)] [[PubMed](#)]
19. Asencio, R.A.; Cranston, E.D.; Atkin, R.; Rutland, M.W. Ionic liquid nanotribology: Stiction suppression and surface induced shear thinning. *Langmuir* **2012**, *28*, 9967–9976. [[CrossRef](#)]

20. Hjalmarsson, N.; Atkin, R.; Rutland, M.W. Is the boundary layer of an ionic liquid equally lubricating at higher temperature? *Phys. Chem. Chem. Phys.* **2016**, *18*, 9232–9239. [[CrossRef](#)]
21. Smith, J.A.; Werzer, O.; Webber, G.B.; Warr, G.G.; Atkin, R. Surprising particle stability and rapid sedimentation rates in an ionic liquid. *J. Phys. Chem. Lett.* **2010**, *1*, 64–68. [[CrossRef](#)]
22. Szilagyi, I.; Szabo, T.; Desert, A.; Trefalt, G.; Oncsik, T.; Borkovec, M. Particle aggregation mechanisms in ionic liquids. *Phys. Chem. Chem. Phys.* **2014**, *16*, 9515–9524. [[CrossRef](#)] [[PubMed](#)]
23. Hayes, R.; Warr, G.G.; Atkin, R. Structure and nanostructure in ionic liquids. *Chem. Rev.* **2015**, *115*, 6357–6426. [[CrossRef](#)]
24. Hayes, R.; Imberti, S.; Warr, G.G.; Atkin, R. The nature of hydrogen bonding in protic ionic liquids. *Angew. Chem. Int. Ed.* **2013**, *52*, 4623–4627. [[CrossRef](#)]
25. Hao, J.C.; Zemb, T. Self-assembled structures and chemical reactions in room-temperature ionic liquids. *Curr. Opin. Colloid Interface Sci.* **2007**, *12*, 129–137. [[CrossRef](#)]
26. Werzer, O.; Cranston, E.D.; Warr, G.G.; Atkin, R.; Rutland, M.W. Ionic liquid nanotribology: Mica-silica interactions in ethylammonium nitrate. *Phys. Chem. Chem. Phys.* **2012**, *14*, 5147–5152. [[CrossRef](#)] [[PubMed](#)]
27. Elbourne, A.; Voitchovsky, K.; Warr, G.G.; Atkin, R. Ion structure controls ionic liquid near-surface and interfacial nanostructure. *Chem. Sci.* **2015**, *6*, 527–536. [[CrossRef](#)]
28. Sheehan, A.; Jurado, L.A.; Ramakrishna, S.N.; Arcifa, A.; Rossi, A.; Spencer, N.D.; Espinosa-Marzal, R.M. Layering of ionic liquids on rough surfaces. *Nanoscale* **2016**, *8*, 4094–4106. [[CrossRef](#)] [[PubMed](#)]
29. Oncsik, T.; Desert, A.; Trefalt, G.; Borkovec, M.; Szilagyi, I. Charging and aggregation of latex particles in aqueous solutions of ionic liquids: Towards an extended Hofmeister series. *Phys. Chem. Chem. Phys.* **2016**, *18*, 7511–7520. [[CrossRef](#)] [[PubMed](#)]
30. Katana, B.; Takács, D.; Csapo, E.; Szabo, T.; Jamnik, A.; Szilagyi, I. Ion specific effects on the stability of halloysite nanotube colloids—Inorganic salts versus ionic liquids. *J. Phys. Chem. B* **2020**, *124*, 9757–9765. [[CrossRef](#)]
31. Katana, B.; Takács, D.; Szerlauth, A.; Sáring, S.; Varga, G.; Jamnik, A.; Bobbink, F.D.; Dyson, P.J.; Szilagyi, I. Aggregation of halloysite nanotubes in the presence of multivalent ions and ionic liquids. *Langmuir* **2021**, *37*, 11869–11879. [[CrossRef](#)] [[PubMed](#)]
32. Riedl, J.C.; Kazemi, M.A.A.; Cousin, F.; Dubois, E.; Fantini, S.; Lois, S.; Perzynski, R.; Peyre, V. Colloidal dispersions of oxide nanoparticles in ionic liquids: Elucidating the key parameters. *Nanoscale Adv.* **2020**, *2*, 1560–1572. [[CrossRef](#)]
33. Nordstrom, J.; Aguilera, L.; Matic, A. Effect of lithium salt on the stability of dispersions of fumed silica in the ionic liquid BMImBF<sub>4</sub>. *Langmuir* **2012**, *28*, 4080–4085. [[CrossRef](#)] [[PubMed](#)]
34. Han, M.W.; Espinosa-Marzal, R.M. Influence of water on structure, dynamics, and electrostatics of hydrophilic and hydrophobic ionic liquids in charged and hydrophilic confinement between mica surfaces. *ACS Appl. Mater. Interfaces* **2019**, *11*, 33465–33477. [[CrossRef](#)]
35. Hayes, R.; Borisenko, N.; Corr, B.; Webber, G.B.; Endres, F.; Atkin, R. Effect of dissolved LiCl on the ionic liquid–Au(111) electrical double layer structure. *Chem. Commun.* **2012**, *48*, 10246–10248. [[CrossRef](#)]
36. Katana, B.; Takács, D.; Bobbink, F.D.; Dyson, P.J.; Alsharif, N.B.; Tomšič, M.; Szilagyi, I. Masking specific effects of ionic liquid constituents at the solid–liquid interface by surface functionalization. *Phys. Chem. Chem. Phys.* **2020**, *22*, 24764–24770. [[CrossRef](#)]
37. Takács, D.; Katana, B.; Szerlauth, A.; Sebők, D.; Tomšič, M.; Szilagyi, I. Influence of adsorption of ionic liquid constituents on the stability of layered double hydroxide colloids. *Soft Matter* **2021**, *17*, 9116–9124. [[CrossRef](#)] [[PubMed](#)]
38. Zhong, W.; Bobbink, F.D.; Fei, Z.F.; Dyson, P.J. Polyimidazolium salts: Robust catalysts for the cycloaddition of carbon dioxide into carbonates in solvent-free conditions. *ChemSusChem* **2017**, *10*, 2728–2735. [[CrossRef](#)] [[PubMed](#)]
39. Zarrougui, R.; Dhahbi, M.; Lemordant, D. Transport and thermodynamic properties of ethylammonium nitrate–water binary mixtures: Effect of temperature and composition. *J. Solut. Chem.* **2015**, *44*, 686–702. [[CrossRef](#)]
40. Holthoff, H.; Egelhaaf, S.U.; Borkovec, M.; Schurtenberger, P.; Sticher, H. Coagulation rate measurements of colloidal particles by simultaneous static and dynamic light scattering. *Langmuir* **1996**, *12*, 5541–5549. [[CrossRef](#)]
41. Berne, B.J.; Pecora, R. *Dynamic Light Scattering*; Robert E. Krieger Publishing: Malabar, FL, USA, 1990.
42. Cao, T.C.; Borkovec, M.; Trefalt, G. Heteroaggregation and homoaggregation of latex particles in the presence of alkyl sulfate surfactants. *Colloids Interfaces* **2020**, *4*, 52. [[CrossRef](#)]
43. Yu, W.L.; Matijevic, E.; Borkovec, M. Absolute heteroaggregation rate constants by multiangle static and dynamic light scattering. *Langmuir* **2002**, *18*, 7853–7860. [[CrossRef](#)]
44. Hierrezuelo, J.; Vaccaro, A.; Borkovec, M. Stability of negatively charged latex particles in the presence of a strong cationic polyelectrolyte at elevated ionic strengths. *J. Colloid Interface Sci.* **2010**, *347*, 202–208. [[CrossRef](#)]
45. Rouster, P.; Dondelinger, M.; Galleni, M.; Nysten, B.; Jonas, A.M.; Glinel, K. Layer-by-layer assembly of enzyme-loaded halloysite nanotubes for the fabrication of highly active coatings. *Colloid Surf. B* **2019**, *178*, 508–514. [[CrossRef](#)]
46. Trefalt, G.; Szilagyi, I.; Borkovec, M. Poisson-Boltzmann description of interaction forces and aggregation rates involving charged colloidal particles in asymmetric electrolytes. *J. Colloid Interface Sci.* **2013**, *406*, 111–120. [[CrossRef](#)] [[PubMed](#)]
47. Oncsik, T.; Trefalt, G.; Borkovec, M.; Szilagyi, I. Specific ion effects on particle aggregation induced by monovalent salts within the Hofmeister series. *Langmuir* **2015**, *31*, 3799–3807. [[CrossRef](#)] [[PubMed](#)]
48. Oncsik, T.; Trefalt, G.; Csendes, Z.; Szilagyi, I.; Borkovec, M. Aggregation of negatively charged colloidal particles in the presence of multivalent cations. *Langmuir* **2014**, *30*, 733–741. [[CrossRef](#)] [[PubMed](#)]
49. Valmacco, V.; Trefalt, G.; Maroni, P.; Borkovec, M. Direct force measurements between silica particles in aqueous solutions of ionic liquids containing 1-butyl-3-methylimidazolium (BMIM). *Phys. Chem. Chem. Phys.* **2015**, *17*, 16553–16559. [[CrossRef](#)]

50. Sinha, P.; Szilagyi, I.; Ruiz-Cabello, F.J.M.; Maroni, P.; Borkovec, M. Attractive forces between charged colloidal particles induced by multivalent ions revealed by confronting aggregation and direct force measurements. *J. Phys. Chem. Lett.* **2013**, *4*, 648–652. [[CrossRef](#)]
51. Kobayashi, M.; Juillerat, F.; Galletto, P.; Bowen, P.; Borkovec, M. Aggregation and charging of colloidal silica particles: Effect of particle size. *Langmuir* **2005**, *21*, 5761–5769. [[CrossRef](#)]
52. Vanecht, E.; Binnemans, K.; Patskovsky, S.; Meunier, M.; Seo, J.W.; Stappers, L.; Fransaer, J. Stability of sputter-deposited gold nanoparticles in imidazolium ionic liquids. *Phys. Chem. Chem. Phys.* **2012**, *14*, 5662–5671. [[CrossRef](#)]
53. Rubim, J.C.; Trindade, F.A.; Gelesky, M.A.; Aroca, R.F.; Dupont, J. Surface-enhanced vibrational spectroscopy of tetrafluoroborate 1-n-butyl-3-methylimidazolium (BMIBF<sub>4</sub>) ionic liquid on silver surfaces. *J. Phys. Chem. C* **2008**, *112*, 19670–19675. [[CrossRef](#)]
54. Guibert, C.; Dupuis, V.; Fresnais, J.; Peyre, V. Controlling nanoparticles dispersion in ionic liquids by tuning the pH. *J. Colloid Interface Sci.* **2015**, *454*, 105–111. [[CrossRef](#)]
55. Lopez-Leon, T.; Jodar-Reyes, A.B.; Bastos-Gonzalez, D.; Ortega-Vinuesa, J.L. Hofmeister effects in the stability and electrophoretic mobility of polystyrene latex particles. *J. Phys. Chem. B* **2003**, *107*, 5696–5708. [[CrossRef](#)]
56. Hayes, R.; Warr, G.G.; Atkin, R. At the interface: Solvation and designing ionic liquids. *Phys. Chem. Chem. Phys.* **2010**, *12*, 1709–1723. [[CrossRef](#)]
57. Canova, F.F.; Matsubara, H.; Mizukami, M.; Kurihara, K.; Shluger, A.L. Shear dynamics of nanoconfined ionic liquids. *Phys. Chem. Chem. Phys.* **2014**, *16*, 8247–8256. [[CrossRef](#)]
58. Feng, G.A.; Qiao, R.; Huang, J.S.; Dai, S.; Sumpter, B.G.; Meunier, V. The importance of ion size and electrode curvature on electrical double layers in ionic liquids. *Phys. Chem. Chem. Phys.* **2011**, *13*, 1152–1161. [[CrossRef](#)] [[PubMed](#)]
59. Galli, M.; Saringer, S.; Szilagyi, I.; Trefalt, G. A simple method to determine critical coagulation concentration from electrophoretic mobility. *Colloids Interfaces* **2020**, *4*, 20. [[CrossRef](#)]
60. Delgado, A.V.; Gonzalez-Caballero, F.; Hunter, R.J.; Koopal, L.K.; Lyklema, J. Measurement and interpretation of electrokinetic phenomena. *J. Colloid Interface Sci.* **2007**, *309*, 194–224. [[CrossRef](#)] [[PubMed](#)]
61. Mamusa, M.; Siriex-Plenet, J.; Cousin, F.; Dubois, E.; Peyrea, V. Tuning the colloidal stability in ionic liquids by controlling the nanoparticles/liquid interface. *Soft Matter* **2014**, *10*, 1097–1101. [[CrossRef](#)] [[PubMed](#)]



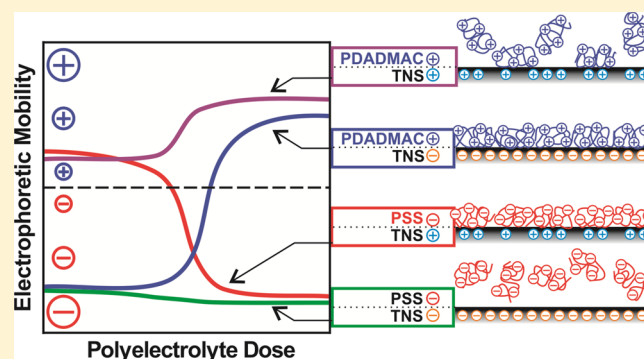
# Regulation of the Stability of Titania Nanosheet Dispersions with Oppositely and Like-Charged Polyelectrolytes

Szilárd Sáringer,<sup>†,‡</sup> Paul Rouster,<sup>§</sup> and István Szilágyi<sup>\*,†,‡,§</sup>

<sup>†</sup>MTA-SZTE Lendület Biocolloids Research Group and <sup>‡</sup>Interdisciplinary Excellence Center, Department of Physical Chemistry and Materials Science, University of Szeged, H-6720 Szeged, Hungary

<sup>§</sup>Institute of Condensed Matter and Nanosciences—Bio and Soft Matter, Université Catholique de Louvain, B-1348 Louvain-la-Neuve, Belgium

**ABSTRACT:** Charging and aggregation processes of titania nanosheets (TNS) were extensively studied in the presence of oppositely charged or like-charged polyelectrolytes in aqueous dispersions. The surface charge of the TNS was systematically varied by the pH; therefore, positive nanosheets were obtained at pH 4 and negative ones at pH 10. Strong adsorption of poly(styrene sulfonate) (PSS) of high negative line charge density on the TNS was observed at pH 4, leading to charge neutralization and reversal of the original sign of charge of the nanosheets. The adsorption of like-charged poly(diallyldimethylammonium chloride) (PDADMAC) was also feasible through a hydrophobic interaction. The predominating interparticle forces were mainly of the DLVO-type, but additional patch–charge attraction also took place in the case of PSS at low surface coverage. The TNS was found to be hydrophilic at pH 10 and no adsorption of like-charged PSS was possible because of strong electrostatic repulsion between the polyelectrolyte and the surface. The PDADMAC showed high affinity to the oppositely charged TNS surface in alkaline dispersions, giving rise to neutral and positively charged nanosheets at appropriate polyelectrolyte doses. Formation of a saturated PDADMAC layer on the TNS led to high resistance against salt-induced aggregation through the electrosteric stabilization mechanism. These results shed light on the importance of polyelectrolyte concentration, ionic strength, and charge balance on the colloidal stability of TNS, which is especially important in applications, where the nanosheets are dispersed in complex solution containing polymeric compounds and electrolytes.



## 1. INTRODUCTION

Inorganic nanomaterials are widely used in numerous applications in chemistry, biology, and materials science because of their high reactivity, increased surface area, lower melting point, ductility, and possible biocompatibility.<sup>1–3</sup> Among them, nanosized titanium oxides and their derivatives are applied as catalysts,<sup>4–6</sup> food additives,<sup>7</sup> sunscreen ingredients,<sup>8</sup> parts of photovoltaic devices,<sup>9–11</sup> environmental purification agents,<sup>12–16</sup> and carriers in delivery processes.<sup>17–20</sup> Despite the extensive use of titanium oxide nanomaterials in other fields, their history in medical, biological, or pharmaceutical science is relatively short.<sup>21</sup> For instance, the photodynamic therapeutic properties of titanate particles were recently utilized against cancer cells.<sup>22</sup> Another bio-related field, where titanium oxides are used in large extent, is drug delivery. Apart from biocompatibility, improved physicochemical properties and ease of processability allow relatively facile immobilization of various drugs or other biologically active molecules in their structures.<sup>17,18</sup>

Depending on the synthesis conditions, titanium oxides of various shapes and compositions have been prepared. Among them, spherical nanoparticles are the most commonly used

structures,<sup>23</sup> however, they may be overruled in the future because of the potential development and applications of other titanium oxide morphologies, such as nanotubes,<sup>24</sup> nanowires,<sup>25</sup> and nanosheets.<sup>26</sup> For example, titania nanosheets (TNS) possess well-defined layered or unilamellar structures associated with high surface area, good thermal stability, pH-tunable properties, biocompatibility, and versatile surface modification possibilities, which make these two-dimensional materials, for instance, very advantageous in bio-related applications.

It is obvious that the colloidal stability of the dispersed systems is a critical issue once the titania nanoparticles are applied in heterogeneous systems such as in blood, aqueous environmental samples, or industrial manufacturing processes.<sup>2</sup> In these applications, stable dispersions of primary particles are required once they are used either as catalysts or delivery agents. Experimental conditions like ionic strength, temperature, and pH significantly influence the charging and the

**Received:** January 25, 2019

**Revised:** March 18, 2019

**Published:** March 19, 2019

aggregation processes and hence, the colloidal stability of the titanium oxide compounds.<sup>27</sup> Although numerous articles can be found in the literature, which deal with functionalization of titania nanostructures by various compounds, only a limited number of studies was concerned with the effect of such a functionalization on the colloidal stability of the particles.<sup>28–32</sup>

Polyelectrolytes have proved to be efficient aggregation or stabilization agents for nanoparticles dispersed in an aqueous medium.<sup>33</sup> Furthermore, charging and aggregation processes of titanium oxide particles of various shapes and compositions were studied in the presence of polyelectrolytes.<sup>27</sup> In these studies, the particles were usually negatively charged because of the relatively low point of zero charge (PZC) of the titanium oxide compounds.<sup>34–36</sup> In this way, oppositely (positively) charged polyelectrolytes such as poly-(diallyldimethylammonium chloride) (PDADMAC)<sup>26</sup> or poly-(amido amine) dendrimers<sup>31</sup> were applied to tune the colloidal stability of the dispersions. Besides, the effect of like-charged (negative) polyelectrolytes [e.g., poly(acrylic acid)<sup>37</sup> or humic acid<sup>38</sup>] on the charging and aggregation of titanium oxide nano-objects was also investigated but in a much less extent than the oppositely charged systems. Nevertheless, no systematic studies were performed with samples, where the same polyelectrolytes were used as oppositely charged and like-charged by changing the sign of the charge of titanium oxide particles by the pH.

Accordingly, positively charged particles can be obtained at low pH and negative ones are present at higher pH, below and above the PZC, respectively.<sup>39</sup> On the other hand, the possible protonation of the polyelectrolytes has to be precisely known because variation in the pH often leads to significant changes in the line charge densities.<sup>40,41</sup> By considering these issues, the charge balance can be tuned by varying the surface charge of the titanium oxide material from positive to negative by the pH, while keeping the charge of the polyelectrolyte the same, that is, no changes in the charge density occur in that pH range.

Therefore, in the present study, systematic electrophoretic and dynamic light scattering (DLS) measurements were performed to assess the surface charge properties and aggregation processes of the TNS in the presence of PDADMAC and poly(styrene sulfonate) (PSS) polyelectrolytes. The measurements were performed at pH values below or above the PZC. In this way, both polyelectrolytes were probed as like-charged or oppositely charged substances. The results shed light on the adsorption mechanism of the PDADMAC or PSS on TNS and on the origin of the major interparticle forces induced by polyelectrolyte adsorption.

## 2. EXPERIMENTAL SECTION

**2.1. Materials.** The synthesis of TNS together with the structural characterization is detailed elsewhere.<sup>26</sup> Ionic strength and pH were adjusted by analytical grade NaCl, HCl, and NaOH, which were bought from VWR. Positively charged PDADMAC, (20 wt % aqueous solution with an average molecular mass of 275 kg/mol) and negatively charged PSS, (sodium salt, 10.6 kg/mol molar mass) were purchased from Sigma-Aldrich. All the measurements were carried out at 25 °C. High-purity water (VWR Purity TU+) was used for all the sample preparations. Water as well as the NaCl, HCl, and NaOH solutions were filtered with a 0.1 μm syringe filter (Millex).

**2.2. Methods.** Electrophoretic mobility and DLS measurements were performed with a Litesizer 500 instrument (Anton Paar) equipped with a 40 mW semiconductor laser (658 nm wavelength) operating in the backscattering mode at a scattering angle of 175°.

For the determination of the mobilities, 5 mL solutions were prepared. In brief, 0.5 mL dispersion of the uncoated or coated TNS of 10 mg/L concentration was added to 4.5 mL solution composed of the polyelectrolyte and/or NaCl at appropriate concentrations. The samples were allowed to rest 2 h at room temperature before measuring the electrophoretic mobilities after 1 min equilibration time in the device. The reported values are the average of five individual measurements. The experiments were performed in 350 μL volume omega-shaped plastic cuvettes (Anton Paar).

Time-resolved DLS measurements were carried out to determine the apparent aggregation rate coefficients ( $k_{app}$ ) of particle dimer formation as<sup>42</sup>

$$k_{app} = \frac{1}{R_h(0)} \frac{dR_h(t)}{dt} \quad (1)$$

where  $R_h$  is the hydrodynamic radius,  $t$  is the time of the experiment and  $R_h(0)$  is the  $R_h$  of TNS determined in stable dispersion. The measurements were run for 40–120 min depending on the speed of aggregation. The same particle concentration (1 mg/L) was used in all of the time-resolved measurements. In order to compare the tendencies, the sample preparation for the DLS was done in a similar manner as the one described above for electrophoresis. The only difference in the sample preparation was that the total volume was 2 mL for DLS and that after adding the particles to the solutions of polyelectrolyte and/or NaCl, the samples were stirred with a Vortex (VWR) for 25 s. Furthermore, the samples were equilibrated for 30 s in the instrument before starting the time-resolved measurements. The colloidal stability was expressed in terms of stability ratio ( $W$ ), which was calculated from the  $k_{app}$  values as follows<sup>42–45</sup>

$$W = \frac{k_{app}^{fast}}{k_{app}} \quad (2)$$

where the fast condition corresponds to the diffusion-controlled aggregation of the particles achieved in 1 M NaCl solution. One can realize that  $W = 1$  is associated to unstable dispersions, where all the particle collisions result in dimer formation.

## 3. RESULTS AND DISCUSSION

The detailed structural characterization of the bare TNS can be found elsewhere.<sup>26</sup> In brief, transmission electron microscopy analysis yielded 94 nm in lateral dimension with a polydispersity of 0.3, while the average height of the TNS was found to be 9 nm by atomic force microscopy. These data result in an aspect ratio of 10.4 for the nanosheets. The PZC of the TNS was reported to be at pH 5.2 in our earlier study.<sup>26</sup> Therefore, electrophoretic and DLS measurements were carried out at pH 4 and 10 to investigate the effect of oppositely charged or like-charged polyelectrolytes on the positively and negatively charged nanosheets, respectively.

**3.1. Charging and Aggregation of Positively Charged TNS.** Electrophoretic mobilities and stability ratios of TNS were determined at pH 4 in the presence of PSS and PDADMAC. In this situation, the former polyelectrolyte is oppositely charged, while the latter one possesses the same sign of charge as TNS. The nanosheets were of positive charge at low polyelectrolyte doses as indicated by the positive mobility values under these experimental conditions. However, the trend in the electrophoretic mobilities was different once PSS or PDADMAC was applied (Figure 1a).

PSS adsorption was indicated by the decrease of the mobilities by increasing the PSS concentration. Such an adsorption process led to charge neutralization at the isoelectric point (IEP) and charge reversal at higher doses. The main governing forces responsible for the latter phenomenon are the entropy gain due to the release of the

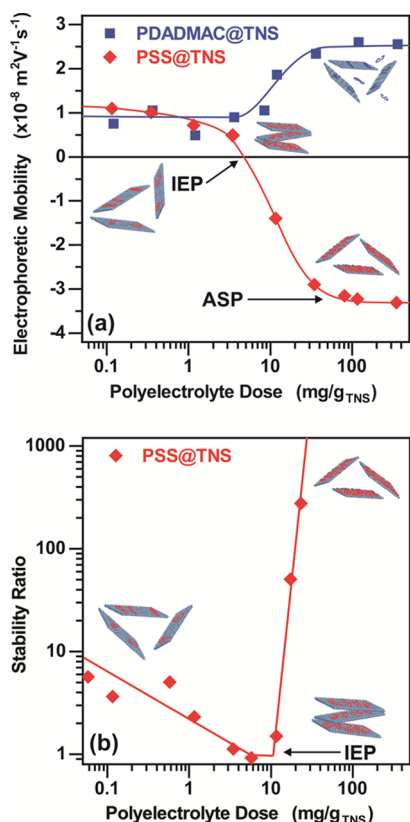


**Figure 1.** Electrophoretic mobility (a) and stability ratio (b) of TNS as a function of the polyelectrolyte dose at pH 4. The ionic strength and the TNS concentration were set to 1 mM and 1 mg/L, respectively. The PDADMAC@TNS dispersions were stable in the entire polyelectrolyte range, that is, no stability ratios could be measured. The unit in the  $x$ -axis indicates mg of polyelectrolyte per 1 g of TNS. The lines serve to guide the eyes.

solvent molecules upon polyelectrolyte adsorption<sup>46</sup> and the electrostatic attraction between the PSS and the empty places on the oppositely charged TNS surface. The adsorption continued until the mobilities reached a plateau at high PSS concentration. The onset of this plateau (ASP) corresponds to the polyelectrolyte dose, at which a saturated PSS layer forms on the surface of the oppositely charged TNS. Similar charging behavior has been previously reported with titanium oxide particles in the presence of oppositely charged polyelectrolytes.<sup>27,28,47,48</sup>

In the case of PDADMAC, however, the mobilities remained constant up to a dose of about 10 mg/g and then slightly increased at higher concentrations. This result indicates that adsorption of like-charged PDADMAC may occur, even on the positively charged TNS, at high polyelectrolyte loading. Similar adsorption process of like-charged polyelectrolytes was observed for negatively charged titanium oxides above the PZC,<sup>37,38,49</sup> but to the best of our knowledge, this is the first time, when adsorption of positively charged polyelectrolyte is reported on titanium oxide compounds of the same sign of charge.

Stability ratios were determined under the identical experimental conditions as in the mobility study (Figure 1b). By varying the PSS dose, significant changes in the colloidal stability of the nanosheets were observed. This was clearly demonstrated by the results of the time-resolved DLS measurements, where the increase in  $R_h$  was remarkably

different by increasing the polyelectrolyte dose (Figure 2). Dispersions possessing a limited stability were observed at low

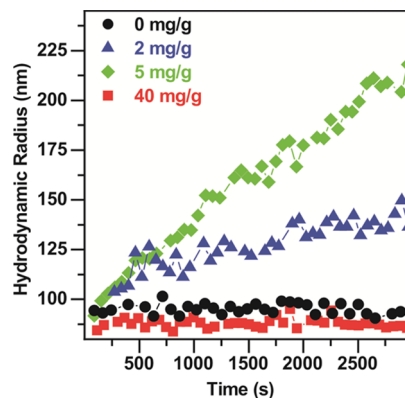


**Figure 2.** Hydrodynamic radii of TNS as a function of the experiment time at different PSS doses indicated in the inset. The measurements were carried out at 1 mM ionic strength, 1 mg/L TNS concentration and at pH 4.

polyelectrolyte concentrations as indicated by the fairly low stability ratio values determined in this regime. By increasing the amount of PSS, the stability ratio values decreased and reached a minimum followed by an increase at high PSS doses, where stable samples were obtained. Similar destabilization–restabilization mechanism has already been reported for titanium-oxide compounds in the presence of oppositely charged polyelectrolytes,<sup>26,27,30,31,47</sup> also with the same charge balance using nanowires and PSS.<sup>29</sup>

Comparing the trend in the mobilities and stability ratios, one can easily realize that the minimum in the latter values is located near the IEP. Therefore, the aggregation features of TNS at different PSS doses resembles to the one predicted by the classical theory developed by Derjaguin, Landau, Verwey, and Overbeek (DLVO).<sup>50,51</sup> Indeed, the nanosheets rapidly aggregate once the surface charges are neutralized at the IEP, where the repulsive electrical double layer interaction is absent and the attractive van der Waals force predominates. More stable dispersions were observed at low and high PSS doses, where the double layer forces overcome the attractive ones due to the sufficient charge of the nanosheets.

On the other hand, the difference in the slopes in the stability ratios in the slow aggregation regimes at low and high doses indicates the presence of additional (non-DLVO) attractive forces. This difference originates from the so-called patch-charge effect,<sup>52,53</sup> which is often induced by adsorption of strong polyelectrolytes on oppositely charged particles.<sup>54–56</sup> In the present situation, PSS tends to form islands (patch) on the surface upon adsorption, while empty positive places (charge) are still available on the TNS surface at low polyelectrolyte coverage. The patches are electrostatically attracted by the charges giving rise to the evolution of an attractive interaction in addition to the already existing van der Waals attractive forces. The patch–charge interaction leads to faster aggregation of the nanosheets and thus, to lower stability ratios and to a smaller slope in the slow aggregation regime at low surface coverage. Nevertheless, such an additional attraction is not pronounced at higher doses above the IEP, where the PSS coverage on the TNS surface is high. This is because of the insufficient number of positive charges on the surface, which prevents the electrostatic attraction with the



PSS patches. Although, bridging interaction between PSS-functionalized particles was reported earlier,<sup>33,54</sup> no evidence was found for this phenomenon in the present system most likely because of the low molecular mass of the PSS and the low ionic strength applied in the experiments.

Besides, no stability ratios could be determined for positively charged TNS in the presence of PDADMAC. As indicated by the results of the mobility measurements, PDADMAC adsorbs on the like-charged surface giving rise to an increase of the surface charge and hence, to stronger electrical double layer repulsion. Due to the fact that the bare particles were stable (see details later) at pH 4 and 1 mM ionic strength and that the presence of PDADMAC further enhanced the stabilizing electrostatic forces, the nanosheets formed stable dispersions in the entire PDADMAC concentration regime investigated. Therefore, stability ratio measurements were not possible under these experimental conditions.

**3.2. Charging and Aggregation of Negatively Charged TNS.** Electrophoretic and time-resolved DLS experiments were also carried out at pH 10 above the PZC of the TNS in a similar fashion than with the positively charged particles. Because the charge of the PSS and PDADMAC is pH-independent, the former one is of the same sign of charge as the nanosheets, while the latter one is oppositely charged. All other experimental conditions were the same as in the measurements discussed in the previous section. The electrophoretic mobility values are shown in Figure 3a.

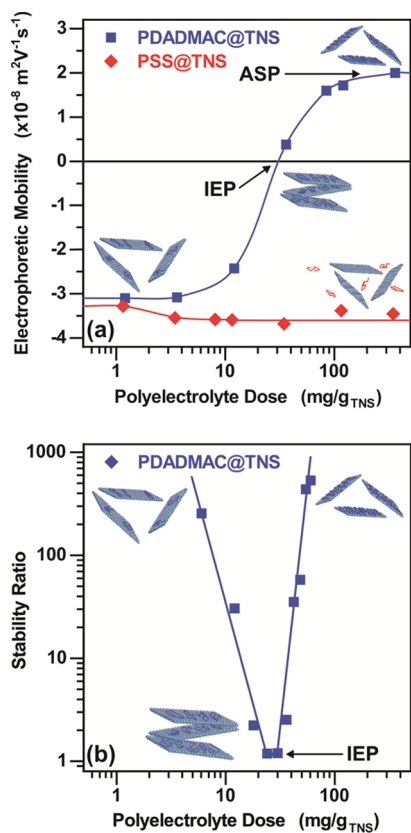


**Figure 3.** Electrophoretic mobility (a) and stability ratio (b) of TNS as a function of the polyelectrolyte dose at pH 10. The ionic strength and the TNS concentration were set to 1 mM and 1 mg/L, respectively. The PSS@TNS dispersions were stable in the entire polyelectrolyte range, that is, no stability ratios could be measured.

In the case of PSS, the mobilities remained negative and constant within the experimental error in the concentration regime investigated. This fact indicates negligible adsorption on the like-charged surface. This result is somewhat surprising because like-charged PDADMAC adsorbed on the TNS at low pH and adsorption of other like-charged polyelectrolytes has already been reported for negatively charged titanium oxide materials.<sup>27,37,38</sup> One can assume that the negatively charged TNS is more hydrophilic than the positive one and hence, the involvement of hydrophobic interaction is not feasible with the PSS, which remains dissolved in the solution. Besides, such a hydrophobic character is rather typical for PSS of significantly higher molar masses than the one used in the present study. Another possible explanation for the negligible adsorption is that because of the lower molar mass of the PSS, the release of solvent molecules upon adsorption and subsequent entropy gain<sup>46</sup> could not overcome the electrostatic repulsion between the polyelectrolyte and the surface.

In the other system, PDADMAC adsorbed strongly on the oppositely charged nanosheets and charge neutralization occurred at the IEP. The adsorption continued after the IEP, leading to charge reversal and to the formation of a saturated polyelectrolyte layer on the TNS at the ASP. The trend in the magnitude of the electrophoretic mobilities resembled to the one discussed in the PSS@TNS system at pH 4 in the previous chapter because the main interactions between the polyelectrolytes and the surfaces are the same irrespective of the charge balance in the oppositely charged systems.

No stability ratios could be determined in the samples containing PSS and negatively charged nanosheets because of the sufficiently high negative charge and the strong electrical double layer forces, which stabilize the dispersions under the experimental conditions applied. The tendency in the stability ratios in the PDADMAC system resembles a U-shape curve, which is typical for charged particles in the presence of oppositely charged polyelectrolytes.<sup>27,33,56</sup> Similar trend was found with the PSS systems at pH 4. As discussed earlier, such a destabilization–restabilization mechanism can be qualitatively described by the DLVO theory,<sup>51</sup> which states that particles of a neutralized surface charge at the IEP rapidly aggregate because of the absence of double layer repulsion and the presence of van der Waals attraction. On the other hand, nanosheets of sufficiently high charge below or above the IEP are stabilized by electrical double layer repulsion.

Comparing the behavior of the negatively and positively charged TNS discussed so far, the following conclusions can be taken. First, like-charged polyelectrolyte was adsorbed only on the positive nanosheets at low pH. This is most likely because of the different hydrophobicities of the nanosheets under acidic and alkaline conditions as well as the different molar masses of polyelectrolytes. Second, patch–charge attraction was detected at pH 4 in the PSS system at low surface coverage, nevertheless, this type of interaction was absent in the PDADMAC samples at pH 10 because very similar slopes were measured in the stability ratios in the slow aggregation regimes at low and high polyelectrolyte doses in the latter case. This result shed light on the fact that PDADMAC adsorbs in a more extended conformation on the TNS and hence, no polyelectrolyte patches are formed on the surface.

**3.3. Resistance Against Salt-Induced Aggregation of the Bare and Polyelectrolyte-Functionalized TNS.** The nature of the interparticle forces was further explored by systematically changing the ionic strength in the dispersions



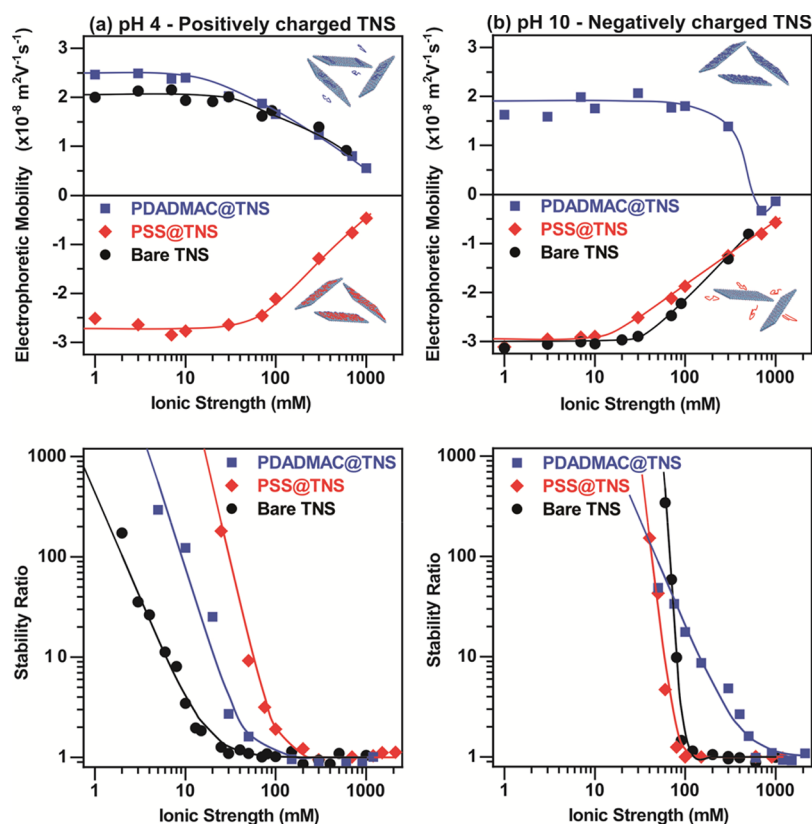


**Figure 4.** Electrophoretic mobility (top row) and stability ratio (bottom row) of TNS and its polyelectrolyte-functionalized derivatives as a function of the ionic strength at pH 4 (a) and pH 10 (b). The solid lines presented with the mobilities are just to guide the eyes, while the ones with the stability ratios are the results of calculations using eq 5.

containing bare TNS, TNS and PSS, and TNS and PDADMAC at both pH 4 and 10. The doses of the polyelectrolytes were set at the ASP determined earlier in the oppositely charged systems. Electrophoretic mobilities and stability ratios are presented in Figure 4.

In general, the tendencies in the absolute mobilities were very similar independent of the charge balance. Although the values were system specific, the magnitude of the mobilities decreased by increasing the ionic strength because of the screening effect of the dissolved salt constituents on the surface charges.<sup>33</sup>

Concerning the stability ratios, slow and fast aggregation regimes were separated by the critical coagulation concentration (CCC) values in each cases. This behavior is in line with the DLVO theory. At low-salt level, accordingly, the electrical double layers are strong and stabilize the dispersions, while these repulsive forces are weak or even vanish at higher ionic strengths due to charge screening by the salt constituent ions. Similar DLVO-type interparticle forces were also reported for titanium oxide particles of various shapes in different ionic environments.<sup>27,57,58</sup> Although the tendencies were similar in both mobility and stability curves obtained at different pHs by changing the ionic strength, the values showed remarkable system specificities.

Looking at the results obtained at pH 4, the magnitude of the mobilities followed the TNS < PDADMAC@TNS  $\approx$  PSS@TNS order at low doses (Figure 4a and Table 1). To assess the charge density ( $\sigma$ ) of the bare and functionalized nanosheets, electrophoretic mobilities ( $\mu$ ) were converted to zeta potentials ( $\zeta$ ) with the Smoluchowski model as<sup>59</sup>

**Table 1.** Characteristic Composition, Size, Polydispersity, Charging and Aggregation Data for TNS in the Bare and in the Polyelectrolyte-Functionalized Forms

	bare TNS		PDADMAC@TNS		PSS@TNS	
	pH 4	pH 10	pH 4	pH 10	pH 4	pH 10
$\mu$ ( $\text{m}^2/\text{Vs}$ ) <sup>a</sup>	2.0	-3.1	2.5	1.6	-2.5	-3.1
$\sigma$ ( $\text{mC}/\text{m}^2$ ) <sup>b</sup>	16	-18	16	19	-18	-17
CCC (mM) <sup>c</sup>	17	100	45	400	100	80
$\zeta_{\text{CCC}}$ (mV) <sup>d</sup>	24.6	-28.6	25.0	17.7	-27.0	-27.0

<sup>a</sup>Measured at 1 mM ionic strength. <sup>b</sup>Calculated with eq 4. <sup>c</sup>Determined from the stability ratio versus ionic strength plots using eq 5. <sup>d</sup>Zeta potentials at the CCC.

$$\zeta = \frac{\eta\mu}{\epsilon_0\epsilon} \quad (3)$$

where  $\eta$  is the viscosity of the medium ( $8.9 \times 10^{-4} \text{ Pa s}$ ),  $\epsilon$  is the dielectric constant of water (78.5), and  $\epsilon_0$  is the dielectric permittivity of vacuum ( $8.9 \times 10^{-12} \text{ F/m}$ ). Thereafter, the surface charge densities were calculated with the Grahame equation as<sup>50</sup>

$$\sigma = \frac{2k_B T \epsilon_0 \epsilon \kappa}{q} \sinh \left[ \frac{q\zeta}{2k_B T} \right] \quad (4)$$

where  $k_B$  is the Boltzmann constant,  $T$  is the temperature,  $q$  is the elementary charge, and  $\kappa$  is the inverse Debye length, which represents the contribution of all the ionic species present in the dispersion to the quantitative description of the electrical double layer.<sup>59</sup> One can conclude from the  $\sigma$  values

(Table 1) that the absolute charge determined at the slip plane (i.e., zeta potentials were used in eq 4) is higher for the PSS@TNS system and about the same for the PDADMAC@TNS and bare TNS.

A clear sequence of TNS < PDADMAC@TNS < PSS@TNS was observed in the CCC values at pH 4 (Table 1), which were calculated as follows<sup>60</sup>

$$W = 1 + \left[ \frac{CCC}{c_{\text{NaCl}}} \right]^\beta \quad (5)$$

where  $c_{\text{NaCl}}$  is the NaCl molar concentration and  $\beta$  was obtained from the stability ratios in the slow aggregation regime before the CCC as

$$\beta = \frac{d \log 1/W}{d \log c_{\text{NaCl}}} \quad (6)$$

Due to the fact that the shapes of the stability ratio versus ionic strength plots are very similar and only the CCC changes in the individual systems at pH 4, one can conclude that the aggregation mechanism is the same irrespective of the type of polyelectrolytes applied. The differences in the CCC are due to the different magnitude of charge, which is the highest for PSS@TNS and lowest for the bare TNS. Therefore, the electrical double layer forces are the strongest for PSS@TNS, leading to the highest CCC because an elevated salt concentration is needed to screen the repulsive double layer interaction and to destabilize the dispersions.

For the negatively charged TNS at pH 10, the electrophoretic mobilities, stability ratios, and the corresponding CCC were about the same for the bare TNS and PSS@TNS, indicating negligible adsorption of the like-charged polyelectrolyte on the nanosheets (Figure 4b). However, a large increase was observed in the CCC (Table 1), once the TNS surface was saturated with a self-assembled PDADMAC layer. This finding is a clear signal for the presence of a remarkable stabilizing effect of the polyelectrolyte layer. In addition, the slope in the slow aggregation regime was also different compared to the bare TNS or to the PSS@TNS systems. Due to the fact that the charge density of PDADMAC@TNS was only slightly higher than the one determined for the bare nanosheets (Table 1), the stabilization mechanism cannot be explained within the DLVO theory but is clearly related to the adsorbed PDADMAC chains. Similar shifts in the CCC have already been observed for negatively charged particles with a saturated PDADMAC layer on their surface.<sup>26,30,61</sup> This is most likely due to the steric stabilization mechanism,<sup>62</sup> which originates from the overlap of the adsorbed polyelectrolyte chains upon the approach of two particles. Once the chains overlap, an osmotic pressure evolves, which gives rise to repulsive interaction and to the formation of stable dispersions. Obviously, electrical double layer forces are also present and thus, the joint effect is the so-called electrosteric stabilization.<sup>27,62,63</sup>

To unambiguously confirm the origin of the interparticle forces in the dispersions of the bare and functionalized TNS, the theoretical CCC values were calculated within the DLVO model as<sup>50</sup>

$$CCC = \frac{72\pi}{e^2 L_B} \left[ \frac{\epsilon_0 \epsilon_r \zeta_{CCC}^2}{H} \right]^2 \quad (7)$$

where  $e$  is the base of the natural logarithm,  $L_B$  is the Bjerrum length, and  $H$  is the Hamaker constant. The values applied in the calculations were 2.72, 0.71 nm, and  $1.60 \times 10^{-20}$  J. The  $\zeta_{CCC}$  is the zeta potential at the CCC (Table 1) in this case. The calculated and measured data are shown in Figure 5.

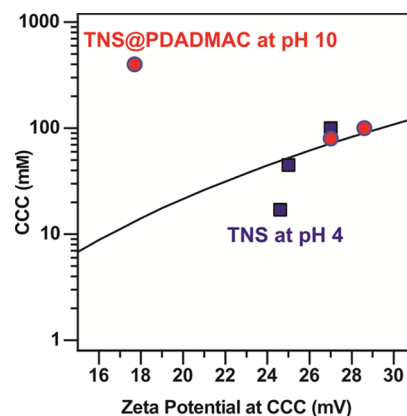


**Figure 5.** CCC values of bare and polyelectrolyte-functionalized TNS as a function of the zeta potentials at the CCC. Values determined at pH 4 are indicated by squares, while the ones at pH 10 are presented with circles. The solid line indicates the results of calculations using the DLVO theory (eq 7).

The experimental data agree well with the results of the theoretical calculation in four systems indicating the presence of DLVO forces as the major interparticle interaction. Nevertheless, two systems behaved somehow differently and hence, the presence of non-DLVO forces can be assumed. Although the deviation is small, the CCC of the positively charged bare TNS is lower than the predicted one, which is a clear sign for the presence of additional attractive forces. Because the pH in these samples is close to the PZC, the hydroxyl groups can be in different protonated stages<sup>39</sup> and they may interact through electrostatic attraction or via hydrogen bonding. These interaction leads to additional (non-van der Waals) attraction and to a lower CCC value.

On the other hand, the CCC of the PDADMAC@TNS system at pH 10 was significantly higher than the one calculated with the DLVO theory. The higher CCC is a clear signal for the operation of strong repulsive interparticle forces of the non-DLVO origin. As discussed above, this repulsion originates from the steric interaction between the adsorbed polyelectrolyte chains. The joint effect of steric and electrical double layer repulsions results in the formation of highly stable PDADMAC@TNS dispersions owing to the electrosteric stabilization mechanism.<sup>62</sup>

#### 4. CONCLUSIONS

The charging behavior and colloidal stability of TNS was investigated at different pHs in the presence of polyelectrolytes. The interactions between the polyelectrolytes and titania surface involved electrostatic, entropy, and hydrophobic effects irrespective of the charge balance. In the systems containing positively charged TNS at pH 4, the electrophoretic mobilities showed that adsorption of like-charged PDADMAC as well as oppositely charged PSS takes place, however, the extent of the adsorption is much higher in the latter case leading to charge neutralization and charge reversal. Time-resolved DLS measurements revealed that the TNS aggrega-

tion processes are sensitive to the PSS dose applied and the stability regimes correlate well with the charging behavior. Accordingly, charge neutralization induced rapid particle aggregation, while the dispersions were restabilized upon charge reversal. The major interparticle forces were of DLVO origin, however, patch-charge effects were observed at low surface coverage by the PSS.

Once the pH was shifted to 10, the negatively charged TNS did not interact with the like-charged PSS due to the hydrophilic character of the surface and to the low molar mass of the polyelectrolyte. The oppositely charged PDADMAC adsorbed strongly and the charge of the nanosheets changed from negative to zero and to positive by increasing the PDADMAC concentration. A saturated polyelectrolyte layer formed on the surface of the nanosheets at high polyelectrolyte loadings. Such a behavior again resulted in a destabilization–restabilization phenomenon, which showed a good qualitative agreement with the DLVO theory.

The resistance of the bare and polyelectrolyte-functionalized TNS against salt-induced aggregation was different in the individual systems and the TNS of saturated PDADMAC layer on the surface at pH 10 formed the most stable dispersion. The CCC values were also calculated within the DLVO model. Comparison with the experimental data revealed that the interparticle forces are of DLVO origin in the majority of the systems, however, additional attraction and repulsion was detected for the positively charged bare TNS and for the PDADMAC-coated TNS at pH 10, respectively. In the latter case, the joint effect of steric and double layer repulsions gave rise to highly stable dispersions, which could be destabilized only at high ionic strengths.

The results shed light on the importance of the interfacial processes of titanium-oxide particles in the presence of like-charged or oppositely charged polyelectrolytes. Such processes are responsible for the aggregation mechanism and subsequent colloidal stability of the samples. Once the nature of the interparticle forces is known, the colloidal stability can be predicted. Therefore, fundamental studies similar to the present one are needed in order to build comprehensive models to predict dispersion stability relevant in applications of titanium oxide particles, where polyelectrolytes of the same or opposite sign of charge are present.

## AUTHOR INFORMATION

### Corresponding Author

\*E-mail: szistvan@chem.u-szeged.hu.

### ORCID

István Szilágyi: 0000-0001-7289-0979

### Notes

The authors declare no competing financial interest.

## ACKNOWLEDGMENTS

This research was supported by the Lendület program of the Hungarian Academy of Sciences (grant number: 96130) and by the Ministry of Human Capacities, Hungary through the project 20391-3/2018/FEKUSTRAT.

## REFERENCES

(1) Patzke, G. R.; Zhou, Y.; Kontic, R.; Conrad, F. Oxide nanomaterials: Synthetic developments, mechanistic studies, and technological innovations. *Angew. Chem., Int. Ed.* **2011**, *50*, 826–859.

(2) Moore, T. L.; Rodriguez-Lorenzo, L.; Hirsch, V.; Balog, S.; Urban, D.; Jud, C.; Rothen-Rutishauser, B.; Lattuada, M.; Petri-Fink, A. Nanoparticle colloidal stability in cell culture media and impact on cellular interactions. *Chem. Soc. Rev.* **2015**, *44*, 6287–6305.

(3) Chen, G.; Roy, I.; Yang, C.; Prasad, P. N. Nanochemistry and nanomedicine for nanoparticle-based diagnostics and therapy. *Chem. Rev.* **2016**, *116*, 2826–2885.

(4) Li, X. Z.; Liu, H.; Cheng, L. F.; Tong, H. J. Photocatalytic oxidation using a new catalyst - TiO<sub>2</sub> microsphere - for water and wastewater treatment. *Environ. Sci. Technol.* **2003**, *37*, 3989–3994.

(5) Huang, Y.; Lu, Y.; Lin, Y.; Mao, Y.; Ouyang, G.; Liu, H.; Zhang, S.; Tong, Y. Cerium-based hybrid nanorods for synergistic photo-thermocatalytic degradation of organic pollutants. *J. Mater. Chem. A* **2018**, *6*, 24740–24747.

(6) Liu, H.; Li, X. Z.; Leng, Y. J.; Li, W. Z. An alternative approach to ascertain the rate-determining steps of TiO<sub>2</sub> photoelectrocatalytic reaction by electrochemical impedance spectroscopy. *J. Phys. Chem. B* **2003**, *107*, 8988–8996.

(7) Weir, A.; Westerhoff, P.; Fabricius, L.; Hristovski, K.; von Goetz, N. Titanium dioxide nanoparticles in food and personal care products. *Environ. Sci. Technol.* **2012**, *46*, 2242–2250.

(8) Morsella, M.; d'Alessandro, N.; Lanterna, A. E.; Scaiano, J. C. Improving the sunscreen properties of TiO<sub>2</sub> through an understanding of its catalytic properties. *ACS Omega* **2016**, *1*, 464–469.

(9) Tétreault, N.; Horváth, E.; Moehl, T.; Brillet, J.; Smajda, R.; Bungener, S.; Cai, N.; Wang, P.; Zakeeruddin, S. M.; Forró, L.; Magrez, A.; Grätzel, M. High-efficiency solid-state dye-sensitized solar cells: Fast charge extraction through self-assembled 3D fibrous network of crystalline TiO<sub>2</sub> nanowires. *ACS Nano* **2010**, *4*, 7644–7650.

(10) Rodriguez, E. F.; Chen, D.; Hollenkamp, A. F.; Cao, L.; Caruso, R. A. Monodisperse mesoporous anatase beads as high performance and safer anodes for lithium ion batteries. *Nanoscale* **2015**, *7*, 17947–17956.

(11) Osada, M.; Sasaki, T. Exfoliated oxide nanosheets: new solution to nanoelectronics. *J. Mater. Chem.* **2009**, *19*, 2503–2511.

(12) Tang, Y.; Jiang, Z.; Tay, Q.; Deng, J.; Lai, Y.; Gong, D.; Dong, Z.; Chen, Z. Visible-light plasmonic photocatalyst anchored on titanate nanotubes: a novel nanohybrid with synergistic effects of adsorption and degradation. *RSC Adv.* **2012**, *2*, 9406–9414.

(13) Honda, R. J.; Keene, V.; Daniels, L.; Walker, S. L. Removal of TiO<sub>2</sub> nanoparticles during primary water treatment: Role of coagulant type, dose, and nanoparticle concentration. *Environ. Eng. Sci.* **2014**, *31*, 127–134.

(14) Grzechulska, J.; Hamerski, M.; Morawski, A. W. Photocatalytic decomposition of oil in water. *Water Res.* **2000**, *34*, 1638–1644.

(15) Veres, Á.; Ménesi, J.; Janáky, C.; Samu, G. F.; Scheyer, M. K.; Xu, Q.; Salahioglu, F.; Garland, M. V.; Dékány, I.; Zhong, Z. New insights into the relationship between structure and photocatalytic properties of TiO<sub>2</sub> catalysts. *RSC Adv.* **2015**, *5*, 2421–2428.

(16) Bajnóczi, É. G.; Balázs, N.; Mogyorósi, K.; Srankó, D. F.; Pap, Z.; Ambrus, Z.; Canton, S. E.; Norén, K.; Kuzmann, E.; Vértess, A.; Homonnay, Z.; Oszkó, A.; Pálkó, L.; Sipos, P. The influence of the local structure of Fe(III) on the photocatalytic activity of doped TiO<sub>2</sub> photocatalysts—An EXAFS, XPS and Mossbauer spectroscopic study. *Appl. Catal., B* **2011**, *103*, 232–239.

(17) Dempsey, C.; Lee, I.; Cowan, K. R.; Suh, J. Coating barium titanate nanoparticles with polyethylenimine improves cellular uptake and allows for coupled imaging and gene delivery. *Colloids Surf., B* **2013**, *112*, 108–112.

(18) Rouster, P.; Pavlovic, M.; Sáring, S.; Szilágyi, I. Functionalized titania nanosheet dispersions of peroxidase activity. *J. Phys. Chem. C* **2018**, *122*, 11455–11463.

(19) Beke, S.; Kőrösi, L.; Scarpellini, A.; Anjum, F.; Brandi, F. Titanate nanotube coatings on biodegradable photopolymer scaffolds. *Mater. Sci. Eng., C* **2013**, *33*, 2460–2463.

(20) Liu, H.; Duan, C.; Su, X.; Dong, X.; Huang, Z.; Shen, W.; Zhu, Z. A hemoglobin encapsulated titania nanosheet modified reduced



graphene oxide nanocomposite as a mediator-free biosensor. *Sens. Actuators, B* **2014**, *203*, 303–310.

(21) Damodaran, V. B.; Bhatnagar, D.; Leszczak, V.; Papat, K. C. Titania nanostructures: a biomedical perspective. *RSC Adv.* **2015**, *5*, 37149–37171.

(22) Rehman, F. U.; Zhao, C.; Jiang, H.; Wang, X. Biomedical applications of nano-titania in theranostics and photodynamic therapy. *Biomater. Sci.* **2016**, *4*, 40–54.

(23) Katagiri, K.; Inami, H.; Koumoto, K.; Inumaru, K.; Tomita, K.; Kobayashi, M.; Kakihana, M. Preparation of hollow TiO<sub>2</sub> spheres of the desired polymorphs by layer-by-layer assembly of a water-soluble titanium complex and hydrothermal treatment. *Eur. J. Inorg. Chem.* **2012**, *2012*, 3267–3272.

(24) Wang, G. M.; Feng, H. Q.; Hu, L. S.; Jin, W. H.; Hao, Q.; Gao, A.; Peng, X.; Li, W.; Wong, K. Y.; Wang, H. Y.; Li, Z.; Chu, P. K. An antibacterial platform based on capacitive carbon-doped TiO<sub>2</sub> nanotubes after direct or alternating current charging. *Nat. Commun.* **2018**, *9*, 2055.

(25) Horváth, E.; Kukovec, Á.; Kónya, Z.; Kiricsi, I. Hydrothermal conversion of self-assembled titanate nanotubes into nanowires in a revolving autoclave. *Chem. Mater.* **2007**, *19*, 927–931.

(26) Rouster, P.; Pavlovic, M.; Szilágyi, I. Improving the stability of titania nanosheets by functionalization with polyelectrolytes. *RSC Adv.* **2016**, *6*, 97322–97330.

(27) Muráth, S.; Sáringer, S.; Somosi, Z.; Szilágyi, I. Effect of ionic compounds of different valences on the stability of titanium oxide colloids. *Colloids Interfaces* **2018**, *2*, 32.

(28) Papa, A.-L.; Boudon, J.; Bellat, V.; Loiseau, A.; Bisht, H.; Sallem, F.; Chassagnon, R.; Bérard, V.; Millot, N. Dispersion of titanate nanotubes for nanomedicine: comparison of PEI and PEG nanohybrids. *Dalton Trans.* **2015**, *44*, 739–746.

(29) Horváth, E.; Grebikova, L.; Maroni, P.; Szabó, T.; Magrez, A.; Forró, L.; Szilágyi, I. Dispersion characteristics and aggregation in titanate nanowire colloids. *ChemPlusChem* **2014**, *79*, 592–600.

(30) Szabó, T.; Tóth, V.; Horváth, E.; Forró, L.; Szilágyi, I. Tuning the aggregation of titanate nanowires in aqueous dispersions. *Langmuir* **2015**, *31*, 42–49.

(31) Pavlovic, M.; Adok-Sipiczki, M.; Horváth, E.; Szabó, T.; Forró, L.; Szilágyi, I. Dendrimer-stabilized titanate nanowire dispersions as potential nanocarriers. *J. Phys. Chem. C* **2015**, *119*, 24919–24926.

(32) Horváth, E.; Szilágyi, I.; Forró, L.; Magrez, A. Probing titanate nanowire surface acidity through methylene blue adsorption in colloidal suspension and on thin films. *J. Colloid Interface Sci.* **2014**, *416*, 190–197.

(33) Szilágyi, I.; Trefalt, G.; Tiraferri, A.; Maroni, P.; Borkovec, M. Polyelectrolyte adsorption, interparticle forces, and colloidal aggregation. *Soft Matter* **2014**, *10*, 2479–2502.

(34) Niecikowska, A.; Krasowska, M.; Ralston, J.; Malysa, K. Role of surface charge and hydrophobicity in the three-phase contact formation and wetting film stability under dynamic conditions. *J. Phys. Chem. C* **2012**, *116*, 3071–3078.

(35) Kuscer, D.; Stavber, G.; Trefalt, G.; Kosec, M. Formulation of an aqueous titania suspension and its patterning with ink-jet printing technology. *J. Am. Ceram. Soc.* **2012**, *95*, 487–493.

(36) Snoswell, D. R. E.; Duan, J.; Fornasiero, D.; Ralston, J. Colloid stability of synthetic titania and the influence of surface roughness. *J. Colloid Interface Sci.* **2005**, *286*, 526–535.

(37) Kirby, G. H.; Harris, D. J.; Li, Q.; Lewis, J. A. Poly(acrylic acid)-poly(ethylene oxide) comb polymer effects on BaTiO<sub>3</sub> nanoparticle suspension stability. *J. Am. Ceram. Soc.* **2004**, *87*, 181–186.

(38) Liu, W.; Sun, W.; Borthwick, A. G. L.; Ni, J. Comparison on aggregation and sedimentation of titanium dioxide, titanate nanotubes and titanate nanotubes-TiO<sub>2</sub>: Influence of pH, ionic strength and natural organic matter. *Colloids Surf., A* **2013**, *434*, 319–328.

(39) Parks, G. A. The isoelectric points of solid oxides, solid hydroxides, and aqueous hydroxo complex systems. *Chem. Rev.* **1965**, *65*, 177–198.

(40) Cakara, D.; Kleimann, J.; Borkovec, M. Microscopic protonation equilibria of poly(amidoamine) dendrimers from macroscopic titrations. *Macromolecules* **2003**, *36*, 4201–4207.

(41) Smits, R. G.; Koper, G. J. M.; Mandel, M. The influence of nearest-neighbor and next-nearest-neighbor interactions on the potentiometric titration of linear poly(ethylenimine). *J. Phys. Chem.* **1993**, *97*, 5745–5751.

(42) Holthoff, H.; Egelhaaf, S. U.; Borkovec, M.; Schurtenberger, P.; Sticher, H. Coagulation rate measurements of colloidal particles by simultaneous static and dynamic light scattering. *Langmuir* **1996**, *12*, 5541–5549.

(43) Chen, K. L.; Mylon, S. E.; Elimelech, M. Enhanced aggregation of alginate-coated iron oxide (hematite) nanoparticles in the presence of calcium, strontium and barium cations. *Langmuir* **2007**, *23*, 5920–5928.

(44) Ehrl, L.; Jia, Z.; Wu, H.; Lattuada, M.; Soos, M.; Morbidelli, M. Role of counterion association in colloidal stability. *Langmuir* **2009**, *25*, 2696–2702.

(45) Elimelech, M.; Gregory, J.; Jia, X.; Williams, R. A. *Particle Deposition and Aggregation: Measurement, Modeling, and Simulation*; Butterworth-Heinemann Ltd.: Oxford, 1995.

(46) Park, S. Y.; Bruinsma, R. F.; Gelbart, W. M. Spontaneous overcharging of macro-ion complexes. *Europhys. Lett.* **1999**, *46*, 454–460.

(47) Rouster, P.; Pavlovic, M.; Horváth, E.; Forró, L.; Dey, S. K.; Szilágyi, I. Influence of protamine functionalization on the colloidal stability of 1D and 2D titanium oxide nanostructures. *Langmuir* **2017**, *33*, 9750–9758.

(48) Ghimici, L.; Nichifor, M. Separation of TiO<sub>2</sub> particles from water and water/methanol mixtures by cationic dextran derivatives. *Carbohydr. Polym.* **2013**, *98*, 1637–1643.

(49) Fazio, S.; Guzmán, J.; Colomer, M. T.; Salomoni, A.; Moreno, R. Colloidal stability of nanosized titania aqueous suspensions. *J. Eur. Ceram. Soc.* **2008**, *28*, 2171–2176.

(50) Evans, D. F.; Wennerstrom, H. *The Colloidal Domain*; John Wiley: New York, 1999.

(51) Verwey, E. J. W.; Overbeek, J. T. G. *Theory of Stability of Lyophobic Colloids*; Elsevier: Amsterdam, 1948.

(52) Feick, J. D.; Velegol, D. Measurements of charge nonuniformity on polystyrene latex particles. *Langmuir* **2002**, *18*, 3454–3458.

(53) Miklavic, S. J.; Chan, D. Y. C.; White, L. R.; Healy, T. W. Double layer forces between heterogeneous charged surfaces. *J. Phys. Chem.* **1994**, *98*, 9022–9032.

(54) Leong, Y. K. Interparticle forces arising from an adsorbed strong polyelectrolyte in colloidal dispersions: charged patch attraction. *Colloid Polym. Sci.* **1999**, *277*, 299–305.

(55) Popa, I.; Papastavrou, G.; Borkovec, M. Charge regulation effects on electrostatic patch-charge attraction induced by adsorbed dendrimers. *Phys. Chem. Chem. Phys.* **2010**, *12*, 4863–4871.

(56) Gillies, G.; Lin, W.; Borkovec, M. Charging and aggregation of positively charged latex particles in the presence of anionic polyelectrolytes. *J. Phys. Chem. B* **2007**, *111*, 8626–8633.

(57) Wiese, G. R.; Healy, T. W. Coagulation and electrokinetic behavior of TiO<sub>2</sub> and Al<sub>2</sub>O<sub>3</sub> colloidal dispersions. *J. Colloid Interface Sci.* **1975**, *51*, 427–433.

(58) Rouster, P.; Pavlovic, M.; Szilágyi, I. Destabilization of titania nanosheet suspensions by inorganic salts: Hofmeister series and Schulze-Hardy rule. *J. Phys. Chem. B* **2017**, *121*, 6749–6758.

(59) Delgado, A. V.; González-Caballero, F.; Hunter, R. J.; Koopal, L. K.; Lyklema, J. Measurement and interpretation of electrokinetic phenomena. *J. Colloid Interface Sci.* **2007**, *309*, 194–224.

(60) Grolimund, D.; Elimelech, M.; Borkovec, M. Aggregation and deposition kinetics of mobile colloidal particles in natural porous media. *Colloids Surf., A* **2001**, *191*, 179–188.

(61) Somosi, Z.; Pavlovic, M.; Pálincó, I.; Szilágyi, I. Effect of polyelectrolyte mono- and bilayer formation on the colloidal stability of layered double hydroxide nanoparticles. *Nanomaterials* **2018**, *8*, 986.



(62) Fritz, G.; Schädler, V.; Willenbacher, N.; Wagner, N. J. Electrosteric stabilization of colloidal dispersions. *Langmuir* **2002**, *18*, 6381–6390.

(63) Illés, E.; Tombácz, E. The effect of humic acid adsorption on pH-dependent surface charging and aggregation of magnetite nanoparticles. *J. Colloid Interface Sci.* **2006**, *295*, 115–123.

# Tuning the Aggregation of Titanate Nanowires in Aqueous Dispersions

Tamás Szabó,<sup>†,‡</sup> Viktor Tóth,<sup>†</sup> Endre Horváth,<sup>§</sup> László Forró,<sup>§</sup> and Istvan Szilagyi<sup>\*,†</sup>

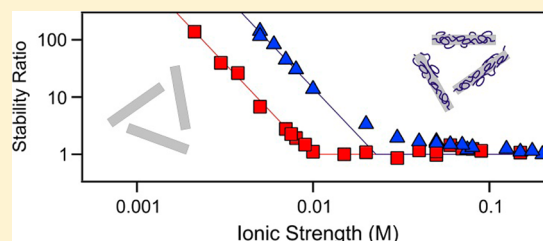
<sup>†</sup>Department of Inorganic and Analytical Chemistry, University of Geneva, 1205 Geneva, Switzerland

<sup>‡</sup>Department of Physical Chemistry and Materials Science, University of Szeged, 6720 Szeged, Hungary

<sup>§</sup>Laboratory of Physics of Complex Matter, École Polytechnique Fédérale de Lausanne, 1015 Lausanne, Switzerland

## Supporting Information

**ABSTRACT:** Electrophoretic and dynamic light scattering (DLS) measurements revealed that aggregation in aqueous dispersion of titanate nanowires (TiONWs) can be tuned by poly-(diallyldimethylammonium) chloride (PDADMAC) polyelectrolyte. The nanowires possessed negative charge under alkaline conditions which was compensated by the oppositely charged PDADMAC adsorbed on the surface. Such adsorption led to charge neutralization and subsequent charge reversal at the appropriate polyelectrolyte doses. The dispersions were stable at low PDADMAC concentration where the TiONWs possessed negative charge. However, fast aggregation of the nanowires occurred close to the charge neutralization point where the overall charge of the particles was zero. Charge inversion at high polyelectrolyte doses gave rise to restabilization of the samples and slow aggregation of the TiONWs even at higher ionic strengths where the original bare TiONW dispersions were unstable. The colloid stability of the bare nanowires can be explained well qualitatively by the Derjaguin, Landau, Verwey, and Overbeek (DLVO) theory; however, polyelectrolyte adsorption led to additional patch-charge attractions and osmotic repulsion between the particles. On the basis of the knowledge generated by the present work, experimental conditions (e.g., salt level, polyelectrolyte, and particle concentrations) can be adjusted in order to design stable and processable aqueous dispersions of TiONWs for further applications.



## INTRODUCTION

One of the most frequently investigated titanate derivatives nowadays are the titanate nanowires (TiONWs) due to the growing number of their applications for instance in sensing as materials for high-sensitivity accelerometer<sup>1</sup> or humidity sensor,<sup>2</sup> in electrochemistry as electrode constituents,<sup>3,4</sup> in solar cells as photoanode, and in catalysis. For the latter, similarly to other titanium(IV) compounds,<sup>5–7</sup> they have been used as catalysts in photocatalytic decomposition of various organic molecules<sup>8,9</sup> as well as catalyst support in hydrogenation reactions.<sup>10</sup> Many of their unique properties (e.g., metal-induced transformation into another form at high temperature<sup>11</sup> and surface conductance changes due to adsorption of small molecules<sup>12</sup>) related to these applications have been investigated in detail, but the majority of these studies contained investigations regarding their behavior only in the solid state. However, aqueous colloid dispersions of TiONWs are widely used during synthesis processes for these applications, and their colloid stability has to be tuned to obtain the desired dispersion properties. Accordingly, suspended TiONWs can be removed from the liquid medium by aggregation, subsequent sedimentation, and/or filtration, whereas a long-term kinetic stability of ultrafine dispersions of primary particles representing a high specific surface area can be achieved by preventing the aggregation with a stabilizing agent. In spite of the importance of the stability of these

disperse systems, only a limited number of related studies are available, and there is a lack of quantitative description of the charging and aggregation processes of titanate nanowires in the literature.<sup>13,14</sup>

It is well-known that charged polymers or so-called polyelectrolytes adsorb strongly on oppositely charged surfaces,<sup>15–17</sup> and they have been widely used to adjust aggregation processes in dispersions of charged particles.<sup>18–22</sup> Adsorption properties have been also utilized to construct hybrid materials containing titanium(IV) compounds and polyelectrolytes<sup>23,24</sup> as well as to control aggregation in aqueous dispersions of barium titanates,<sup>25,26</sup> lead zirconate titanates,<sup>27</sup> titanate nanotubes,<sup>28</sup> and titania nanoparticles.<sup>29</sup> Among the polyelectrolytes, poly(diallyldimethylammonium) chloride (PDADMAC) has been applied for surface treatment or as coagulating agent in various systems and coating agent to create bifunctionalized nanoparticles for therapeutic applications.<sup>30</sup> Accordingly, careful investigations performed with surface sensitive techniques such as reflectometry, ellipsometry, and atomic force microscopy as well as theoretical predictions revealed that PDADMAC adsorbs strongly on an oppositely charged surface, but the adsorption rate and amount greatly

Received: August 7, 2014

Revised: December 18, 2014

Published: December 19, 2014

depend on the experimental conditions (e.g., concentration of the polyelectrolyte, ionic strength, and pH).<sup>31,32</sup> Electrophoretic mobility (EPM), streaming potential, and light scattering measurements revealed that PDADMAC adsorption results in charge neutralization and also charge reversal of an oppositely charged surface at appropriately high concentrations due to hydrophobic interactions, entropic effect, or ion–ion correlation forces.<sup>33–36</sup> Such change in the sign of the surface charge is due to the formation of a polyelectrolyte layer with a thickness of a few nanometers depending on the experimental conditions applied.<sup>22,37,38</sup> Dynamic light scattering (DLS) studies pointed out that the hydrodynamic thickness of the PDADMAC layer adsorbed on colloidal latex particles increases with the ionic strength due to conformational changes of the adsorbed polyelectrolyte chains. At high salt levels, the electrostatic interactions between the adsorbed molecules and the electrolyte led to the formation of tails and loops extending away from the surface and hence to higher layer thickness values.<sup>33</sup> Surface charge neutralization of colloidal particles with the oppositely charged PDADMAC gave rise to fast aggregation of the particles while the charge reversal phenomenon enabled stabilization of the system.<sup>34</sup> Coating these particles with the polyelectrolyte significantly increased the stability of the dispersions.<sup>22</sup> Although, to the best of our knowledge, no studies have been reported on the interaction between TiONWs and PDADMAC, this polyelectrolyte was widely used in systems containing other titanate derivatives. Accordingly, titanate nanosheets were adsorbed on a PDADMAC modified surface to form perovskite-type thin films,<sup>39</sup> multilayer films were obtained by the layer-by-layer technique using PDADMAC as a “glue” to strongly bind adjacent titania or titanate nanotubes,<sup>40,41</sup> and a piezoelectric paper was fabricated by adsorbing barium titanate on wood cellulose fibers after surface modification with PDADMAC.<sup>42</sup>

Since TiONWs possess negative charge at pH values higher than their point of zero charge (PZC),<sup>13</sup> the positively charged PDADMAC is a promising candidate to tune the colloid stability of the nanowire dispersions. The polyelectrolyte adsorption is expected to change the surface charge properties of the particles, and hence, aggregation processes can be adjusted by the addition of the PDADMAC. Accordingly, charging and aggregation of TiONWs in the presence of PDADMAC have been investigated by electrophoresis and DLS in the present work. The effects of PDADMAC dose, ionic strength, and TiONW concentration on the EPMs and speed of particle aggregation were clarified. The TiONWs have been characterized in the solid state by various experimental techniques previously;<sup>2,13,43</sup> therefore, our study focused only on the dispersion properties. These findings will be the basis to design stable and processable biocompatible aqueous dispersions of TiONWs for further targeted applications such as thermal cancer therapy or drug delivery.

## EXPERIMENTAL SECTION

**Electrophoretic Mobility Measurements.** The electrophoretic mobility (EPM) and time-resolved dynamic light scattering (DLS) measurements were performed with a ZetaNano ZS (Malvern Instruments) device equipped with a He/Ne laser operating at 633 nm as a light source and an avalanche photodiode as a detector. A scattering angle of 173° was applied. The device applies an electric field strength of 4 kV/m in the electrophoretic mode.

The EPM measurements were carried out in plastic capillary cells (Malvern Instruments) cleaned with 2 wt % Hellmanex solution (Hellma) and rinsed extensively with Milli-Q water. For sample

preparation, a calculated amount of PDADMAC solution was mixed with water and KCl stock solution to obtain 4.5 mL sample with the desired polyelectrolyte concentration and ionic strength. Thereafter, the procedure was finalized by adding 0.5 mL of about 70 mg/L TiONW dispersion to the samples in a plastic vial. Accordingly, the final particle concentration was always around 7 mg/L, and the total sample volume was 5.0 mL. The pH of the stock solutions was adjusted to 9 before mixing them. The EPMs were measured after equilibrating the dispersions overnight at room temperature and also for 1 min in the instrument prior to the measurement. The EPM ( $\mu$ ) of the samples was calculated by averaging five individual measurements. The surface charge density ( $\sigma$ ) of the bare and polyelectrolyte coated particles was determined by fitting the surface potential values at different ionic strengths with the linear charge–potential relation within the Debye–Hückel approximation<sup>44</sup>

$$\sigma = \epsilon\epsilon_0\kappa\psi_D \quad (1)$$

where  $\epsilon\epsilon_0$  is the permittivity of the water,  $\psi_D$  is the diffuse layer potential, and  $\kappa$  is the inverse Debye length which can be calculated by taking the presence of the ionic species into account (see Supporting Information for more details). The  $\psi_D$  data were converted from the  $\mu$  values using the Henry equation<sup>45</sup>

$$\mu = f(x) \frac{\epsilon\epsilon_0}{\eta} \psi_D \quad (2)$$

where  $f(x)$  is the Henry function which takes the Debye length and the size of the particles into consideration and  $\eta$  is the viscosity of water.

**Light Scattering.** In the time-resolved DLS experiments, the apparent hydrodynamic radii ( $r_h$ ) were determined using a second-order cumulant fit for the correlation function which was accumulated for 30 s using the same device as for electrophoretic experiments. The measurements were carried out in 1 cm square plastic cuvettes (Malvern Instruments) cleaned by 2 wt % Hellmanex solution. In the time-resolved DLS experiments, typically 50 runs were performed over 25 min, and the samples were prepared as follows. Appropriate volumes of water, PDADMAC, and KCl stock solutions were mixed, which resulted in 1.8 mL solution with the desired polyelectrolyte concentration and ionic strength. The aggregation experiment was initiated by injecting 0.2 mL of the TiONW stock dispersion (which was previously subjected to ultrasonic treatment to minimize the initial aggregation) into the solutions. The final particle concentration was about 7 mg/L, the total volume was 2 mL, and the pH of all stock solutions was adjusted to 9. Such low particle concentration allowed us to avoid multiple scattering events (Figure S1) and to remain in the early stages of the aggregation process indicated by single-exponential decays of the correlation function even at the end of the experiments (Figure S2). The slopes of the apparent hydrodynamic radii versus time curves were calculated in the linear regimes and normalized by the mass concentrations ( $w$ ). The colloid stability of the systems was expressed in terms of the stability ratio ( $W$ ) as

$$W = \frac{S_{\text{fast}}w}{Sw_{\text{fast}}} \quad (3)$$

where  $S_{\text{fast}}$  and  $S$  are the slopes in the presence of an excess of indifferent electrolyte (1 M KCl, fast aggregation occurs) and for the actual measurements, respectively, and  $w_{\text{fast}}$  and  $w$  are the mass concentrations of the TiONW in the dispersions for fast aggregation (1 M KCl) and for the actual experiment, respectively. The aggregation of TiONWs was controlled only by the diffusion of the nanowires in the *fast* case in 1 M KCl solutions; therefore, stability ratios close to unity correspond to unstable systems while higher values refer to more stable samples.

In addition, combined static light scattering and DLS experiments performed on a multiangle goniometer revealed that the decay constants of the autocorrelation functions showed linear dependence of a zero intercept with the square of the scattering vector (Figure S3), indicating the translational origin of the diffusion coefficient and the absence of the contribution from the rotational diffusion coefficient to the correlation function. The translational diffusion coefficient was

then used to calculate the hydrodynamic radii applying the Stokes–Einstein relation (for more details see Supporting Information).

## RESULTS

We studied the charging and aggregation of TiONWs, which were synthesized by the hydrothermal process as detailed elsewhere,<sup>43,46</sup> in the presence of an inert salt as well as a polyelectrolyte by electrophoresis and DLS to clarify the stability of the dispersions under different experimental conditions. We have recently published two studies<sup>13,14</sup> on the dispersion characteristics of aqueous TiONW dispersions, and those results were considered when the experiments were planned, performed, and evaluated in the present work.

**Aggregation of Bare Nanowires.** As published earlier,<sup>13</sup> the TiONWs change their charge with the pH, and they are positively charged at low pHs, below the PZC, while their charge becomes negative at higher pHs. This phenomenon is typical for metal oxides including titanium(IV) oxide derivatives due to the protonation–deprotonation equilibrium of the different hydroxyl groups on the surface, and it can be detected by surface potential or EPM measurements.<sup>47–51</sup> Such charge transition occurred at pH 4.1 in the present system; therefore, the TiONWs were negatively charged in our experiments where the pH was always set to 9.0. A hydrodynamic radius of 188 nm was measured by DLS in stable dispersions together with a polydispersity index (PDI, determined by the cumulant analysis in the DLS measurements) of 0.26, which indicates a relatively narrow particle size distribution (Table 1).

**Table 1. Characteristic Dispersion Properties of Bare (TiONW) and Polyelectrolyte Coated (TiONW–PDADMAC) Nanowires<sup>a</sup>**

sample	$R_h$ (nm) <sup>b</sup>	PDI <sup>b</sup>	CCC (M)	$\sigma^c$ (mC/m <sup>2</sup> )	$\mu^d$ (m <sup>2</sup> /(V s))
TiONW	188	0.26	0.008	−8.2	−2.3
TiONW– PDADMAC <sup>c</sup>	202	0.34	0.032	+15.3	+2.5

<sup>a</sup>The parameters were determined at pH 9.0 and 25 °C. <sup>b</sup>Hydrodynamic radius ( $R_h$ ) and polydispersity index (PDI) were determined by DLS in stable dispersions, and the uncertainties of the size measurements were about 5 nm. <sup>c</sup>Surface charge density ( $\sigma$ ) was calculated by eq 1. <sup>d</sup>Electrophoretic mobility ( $\mu$ ) measured at 0.001 M ionic strength. <sup>e</sup>Polyelectrolyte dose of 300 mg/g was used to coat the TiONWs.

DLS measurements revealed that the dispersions were stable at low ionic strengths, but the TiONWs rapidly aggregated at higher electrolyte concentrations. In the latter case at an ionic strength of 0.1 M, the increase in the hydrodynamic radius depended on the particle concentration as shown in Figure 1a. Accordingly, the apparent size increased linearly at low concentrations and short time intervals while higher concentration of the nanowires led to saturation-type curves due to the formation of higher generation aggregates. If one compares the slopes obtained at experiment times where the increment was linear in each case, a linear relation can be found with the TiONW concentration (Figure 1a, inset). However, our main goal was to investigate the early stages of the aggregation; therefore, an intermediate concentration of 7 mg/L TiONW was chosen for further investigations. Variation of the ionic strength at the same particle concentration gave rise to different slopes in the apparent hydrodynamic radius versus time plots (Figure 1b). No increase in size was found below 0.001 M KCl

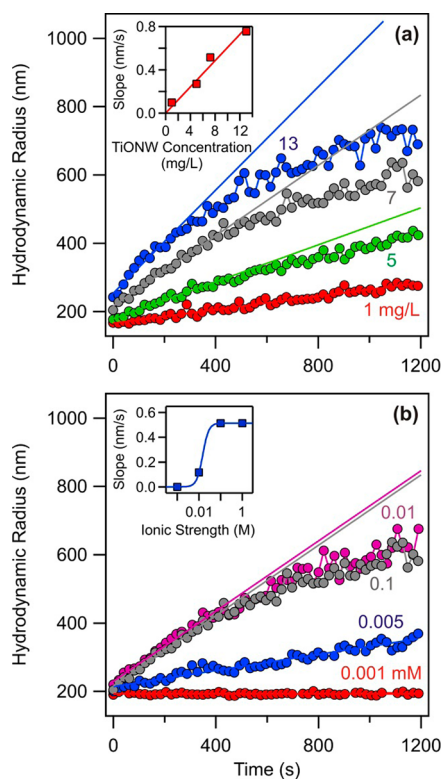


**Figure 1.** Apparent hydrodynamic radii of TiONWs in time-resolved DLS experiments. (a) Different concentrations of TiONW at 0.1 M ionic strength adjusted by KCl. The inset shows the initial slopes obtained from linear fits at different TiONW concentrations. (b) Aggregation of TiONWs in 7 mg/L dispersion at different ionic strengths. The initial slopes are presented in the inset as a function of the ionic strength. The experiments were carried out at 25 °C and pH 9.0.

concentration, indicating stable dispersions while the slopes increased with the concentration of the electrolyte above this dose, and they remained constant at high ionic strength (Figure 1b, inset). Note that only the initial linear regime was considered at high ionic strengths where the aggregation was fast (e.g., at 0.01 M KCl in Figure 1b), while the whole set of experimental points was used to obtain the slopes at lower salt levels (e.g., 0.005 M KCl) during the evaluation of the data.

The stability of the dispersions at different ionic strengths was expressed in terms of the stability ratio (Figure 2).<sup>14</sup> High stability ratios indicate slow aggregation, i.e., quasi-stable dispersions, while values close to unity correspond to rapidly aggregating, highly unstable samples where the aggregation is exclusively controlled by the diffusion of the particles. Accordingly, the nanowires were stable at low KCl concentrations and the stability ratios decreased by increasing the ionic strength up to the critical coagulation concentration (CCC) which separates the slow and fast aggregation regimes. The stability ratio values were unity and remained constant at higher electrolyte doses. Linear fits to the two aggregation regimes resulted in a CCC of 0.008 M. The EPMS, determined under the same experimental conditions as in the DLS study, increased with the ionic strength but remained negative in the entire concentration range investigated. This result can be explained by the screening effect of the potassium counterions on the surface charge. Moreover, the overall behavior of TiONWs followed the prediction of the theory developed by



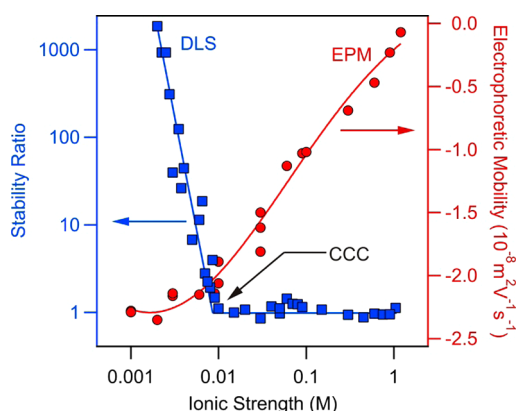


**Figure 2.** Stability ratio (DLS, squares) and EPM (circles) of TiONWs (7 mg/L) as a function of the ionic strength adjusted by KCl at 25 °C and pH 9.0. The CCC indicates the position of the critical coagulation concentration, and the lines serve just to guide the eyes.

Derjaguin, Landau, Verwey, and Overbeek (DLVO) for charged colloidal particles in an aqueous electrolyte solution.<sup>44</sup> Accordingly, the aggregation of the nanowires is governed by the superposition of the repulsive double layer and the attractive van der Waals forces. The electric double layer vanishes at high electrolyte concentrations where the surface charges are completely screened by the counterions leading to the predominance of the attractive van der Waals forces and hence to rapid aggregation of the TiONWs. Similar behavior of the particles was found in other systems containing titanate derivatives and electrolytes.<sup>48,49</sup> In our previous study,<sup>14</sup> we have shown by atomic force microscopic images recorded in dispersions that the TiONWs aggregated in a side-by-side orientation leading to a “spaghetti-like” structure of the aggregates. Since the slopes in the fast or so-called diffusion controlled aggregation regime as well as the CCC values were very similar to the values determined for the present system, we assume that the orientation of the TiONWs in the aggregates is the same in both cases.

#### Tuning the Colloid Stability by Polyelectrolyte.

PDADMAC is known as highly charged polyelectrolyte containing quaternary amino groups which are positively

charged in water in the entire pH range. Because of its strong affinity to oppositely charged surfaces, it has been used for modification of negatively charged substrates as well as to tune the aggregation process in aqueous dispersions of colloidal particles.<sup>31,34,38</sup> In our study, interaction between PDADMAC and the negatively charged TiONW was investigated by following the changes in the EPMs and in the speed of aggregation at different polyelectrolyte doses and ionic strengths.

Figure 3 shows the EPMs in the TiONW–PDADMAC system. In general, the surface charge was constant at very low polyelectrolyte doses, and the initial EPM values were in good agreement with the ones measured in the bare TiONW system at the corresponding ionic strengths. The mobilities increased with increasing the PDADMAC dose due to the strong adsorption of the positively charged polyelectrolyte. Such adsorption led to charge neutralization at the isoelectric point (IEP) where the overall charge of the particles was zero. Upon further addition of PDADMAC to the system, the nanowires reversed their charge, and positively charged particles were obtained beyond the IEP. Such a charge reversal phenomenon is typical in systems containing polyelectrolytes and oppositely charged surfaces<sup>21,22,34</sup> and can be originated from hydrophobic interactions between the polyelectrolyte chains,<sup>52</sup> from entropic effect due to the release of solvent and counterions of the highly charged PDADMAC<sup>53</sup> during its adsorption, and from ion–ion correlations.<sup>54,55</sup> The dose at the adsorption saturation plateau (ASP) was the limit of the adsorption at high PDADMAC concentrations. At this dose, the surface is not able to adsorb more PDADMAC under the experimental conditions applied and further added polyelectrolytes remained dissolved in the bulk. The EPMs were constant above the dose corresponding to the ASP, but their values on the plateau depended on the ionic strength.

The dependence of the stability ratios on the PDADMAC dose (Figure 3) was found to be similar at lower ionic strengths. Accordingly, the dispersions were stable at low polyelectrolyte concentrations, and the stability ratios decreased until the fast aggregation regime was reached near the IEP. The samples became stable again with increasing the dose after the IEP. These types of colloid stability curves are very typical for

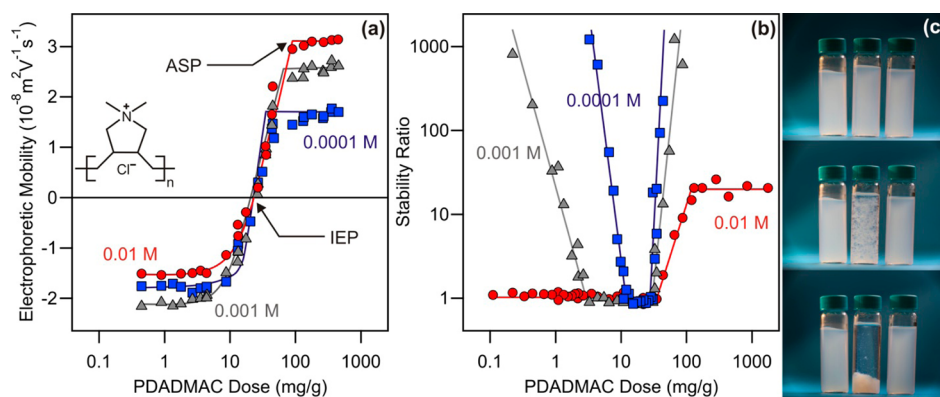


**Figure 3.** EPM (a) and stability ratio (b) of TiONWs as a function of the PDADMAC dose at different ionic strengths adjusted by KCl at 25 °C, pH 9.0, and TiONW concentration of 7 mg/L. The unit on the *x*-axis denotes mg of PDADMAC normalized to 1 g of TiONW. The adsorption saturation plateau (ASP) and the isoelectric point (IEP) are indicated by arrows while the other lines are just to guide the eyes. The chemical structure of PDADMAC is shown in the inset of graph (a). Schematic representation of the colloid stability of TiONW–PDADMAC systems (c). The PDADMAC concentration increased from left to right, while the pictures were taken with freshly mixed samples (top), after 15 min (middle) and 30 min (bottom). Note that the particle concentration was significantly higher than in the case of aggregation experiments in order to visualize the colloid stability of the systems.

systems containing colloidal particles and polyelectrolytes,<sup>22,33,34</sup> and they are in line with the DLVO theory. The TiONWs possessed negative charge at low PDADMAC doses where their charge is only partially neutralized. Such negative charge led to the formation of an electric double layer around the particles and hence repulsive forces between them. Since the nanowires had an overall charge of zero near the IEP, the electric double layer vanished and the attractive van der Waals forces predominated in the dispersion, giving rise to rapid aggregation of the TiONWs and to unstable dispersions. At high doses, the nanowires underwent the charge reversal process due to the PDADMAC adsorption, and the positive charge generated by this phenomenon led to the formation of an electric double layer and to the slowdown of the aggregation due to the overlap of the double layers.

Another interesting issue is the ionic strength dependence of the stability and mobility curves, since we described the interaction forces as of electrostatic origin in the explanation above. If this is the case, change in the concentration of an inert electrolyte, like KCl in the present case, should have significant effect on the aggregation even in the presence of a polyelectrolyte.<sup>21,22</sup> Indeed, the shape of the stability ratio versus PDADMAC dose curve at 0.01 M KCl concentration is different from those measured at lower ionic strengths which were discussed above (Figure 3b). The TiONWs rapidly aggregated at low PDADMAC doses at 0.01 M ionic strength since this salt level is above the CCC value of the bare nanowires (Table 1). However, the aggregation slowed down when the dose around the ASP was approached as indicated by the increase in the stability ratio values which had a plateau at high PDADMAC concentrations, showing the limited stability of the system at this ionic strength.

One can also recognize that the slopes in the stability ratio versus polyelectrolyte dose curves in the slow aggregation regimes were also different at different ionic strengths. Higher KCl concentration led to less steep curves in this region. We assume that these discrepancies originate from additional, non-DLVO attractions. They are weaker than the DLVO-type forces and can be derived from patch-charge interactions resulting from the lateral heterogeneity of the adsorbed PDADMAC layer.<sup>14,22</sup> Accordingly, the TiONW surfaces contain negatively charged, uncoated parts at coverage lower than the ASP dose, and they may interact with oppositely charged patches from the adsorbed polyelectrolytes on the surface of another particle. Such patch-charge attraction could contribute to the acceleration of the aggregation of TiONWs and give rise to faster aggregation of the particles, i.e., lower stability ratios, and hence smaller slopes in the slow aggregation regimes which were more sensitive to this additional attraction than the diffusion-limited regime. Since these patch-charge attractions occur at low distances from the surface, they are more pronounced at higher ionic strengths where the Debye length was small and the electric double layers were thin, leading to the emergence of short-range interactions. Another possible interparticle force which was observed in other systems and could be present here as well is the repulsive force due to the osmotic repulsion of the adsorbed PDADMAC chains.<sup>35,36,56</sup> These forces were found to be repulsive and increased with the ionic strength in the case of monovalent salts. Since in our systems the increase of ionic strength always led to less stable dispersions at the same PDADMAC dose (Figure 3b), the effect of such repulsive interactions should be minor compared to the electrostatic forces (DLVO and patch charge); otherwise, we should have

obtained highly stable dispersions at high ionic strength and polyelectrolyte doses.

Additional EPM measurements in the ionic strength range of 0.000 01–0.1 M were carried out to study the effect of the inert electrolyte on the IEP and ASP. As shown in Figure 4, the IEP

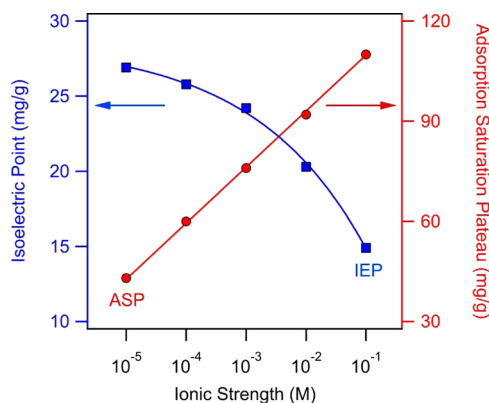


**Figure 4.** PDADMAC dose at the isoelectric point (IEP, squares) and at the adsorption saturation plateau (ASP, circles). The data were determined from the EPM versus PDADMAC dose curves at different ionic strengths. The measurements were performed at 25 °C, pH 9.0 and at a TiONW concentration of 7 mg/L. The solid lines serve only to guide the eyes. The presented values were obtained from linear fits to the experimental data and this method results in an average error of about 5%.

values decreased and the ASP values increased with the ionic strength, indicating that these parameters strongly depend on the KCl concentration applied. Their magnitudes were similar to those reported in polyelectrolyte adsorption studies previously, and such an increase in the adsorbed amount has been already reported in other systems containing polyelectrolytes and oppositely charged particles.<sup>22,57</sup> Both phenomena can be explained by the electrostatic interactions between the PDADMAC chains on the surface. Accordingly, the adsorption of the polyelectrolytes was hindered by the electrostatic repulsion between the PDADMAC molecules of the same charge. The increase in the ionic strength, i.e., in the KCl concentration, led to a screening effect of the polyelectrolyte charge by the chloride ions and also to reduced repulsion between the polyelectrolytes adsorbed on the surface. The TiONWs then were able to adsorb more PDADMAC at higher ionic strength which gave rise to higher ASP and lower IEP values since the polyelectrolyte adsorption is less hindered at higher salt levels.

**Aggregation of Polyelectrolyte Coated Nanowires.** As discussed earlier, the maximum adsorbed amount of the polyelectrolytes at a certain ionic strength can be expressed with the dose of the ASP, and such adsorption led to an oppositely charged nanowire (TiONW–PDADMAC). Let us discuss now the charging and aggregation of PDADMAC coated TiONWs and compare it to the similar properties of the bare nanowires.

To probe the surface charge and aggregation behavior of the particles and to identify the predominating interparticle forces, the EPMS and stability ratios were measured in dispersions containing TiONWs and PDADMAC at a dose of 300 mg of polyelectrolyte per 1 g of nanowire (which was higher than the ASP value even at high salt levels) at different ionic strengths (Figure 5). The mobilities of the TiONW–PDADMAC were

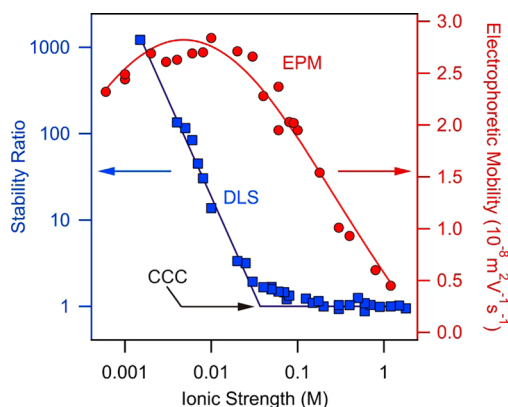


**Figure 5.** Stability ratio (DLS, squares) and EPM (circles) of TiONW–PDADMAC nanowires (TiONW was coated with PDADMAC at a dose of 300 mg/g) as a function of the ionic strength adjusted by KCl at 25 °C and pH 9.0. The TiONW concentration was 7 mg/L. CCC indicates the position of the critical coagulation concentration, and the solid lines serve only to guide the eyes.

positive in the entire ionic strength range investigated. They increased at low electrolyte concentrations and reached a maximum around 0.006 M KCl concentration. Such maximum was also observed in other systems containing charged colloidal particles and can be originated from ion–ion correlations<sup>58</sup> and the standard electrokinetic model.<sup>59</sup> After this maximum, the EPMs decreased with the ionic strength due to the screening effect of the counterions (chloride ions in this case) on the surface. Moreover, the stability ratio values were found to be high at low electrolyte concentrations (Figure 5), indicating the formation of stable dispersions. They decrease with increasing the KCl concentration until reaching the CCC. Fast aggregation occurred after the CCC and the stability ratios were around unity within the experimental error.

The size of the bare and the coated nanowires determined by DLS in stable dispersions at low ionic strength were close to each other (Table 1), and the small difference can be explained as follows. Upon the preparation of the TiONW–PDADMAC dispersion, the TiONW particles passed through an intermediate stage of polymer adsorption which produced nanowires of zero charge for a very short time interval. During this short period, a part of the TiONWs could aggregate, and hence the apparent hydrodynamic radius slightly increased. This phenomenon was observed in other polyelectrolyte–particle systems,<sup>33</sup> and the higher PDI value for TiONW–PDADMAC also confirmed this explanation.

Comparing the EPM, diffuse layer potential and stability ratio data obtained in the TiONW and TiONW–PDADMAC systems (Figures 2 and 5, Figures S4 and S5), the following conclusions can be made. The mobility data show the same trend but have the opposite sign due to the charge reversal process. The calculated  $\sigma$  data showed that TiONW–PDADMAC was almost twice as more charged as the bare TiONWs because the adsorption of the PDADMAC of high line charge density resulted in more charges located at the liquid/solid interface (Table 1). This deviation in  $\sigma$  resulted in a significant difference between the CCC values of the bare and coated nanowires. Accordingly, the CCC shifted from 0.008 to 0.032 M after polyelectrolyte coating which gave rise to more stable nanowire dispersions than the original ones without added PDADMAC (Table 1). This is important information and indicates that in the case of polyelectrolyte coating the

TiONW colloids can remain stable at ionic strengths up to 4 times higher than the bare ones for simple monovalent salts.

To further explore the origin of the interparticle forces in the above systems, theoretical calculations were performed to estimate the trend of the stability ratios by the DLVO theory using diffuse layer potentials calculated from the EPMs (Figure S4 and see Supporting Information for more details). The calculations predict also a shift in the CCC values due to the higher surface charge density of the TiONW–PDADMAC particles (Figure S5). The estimated slopes in the slow aggregation regime were very steep and agreed reasonable well with the experimental data for the bare TiONWs, but significant difference was observed in the case of TiONW–PDADMAC particles. At very low KCl concentrations, before the CCC of the theoretical curve, the measured stability ratio values were always much lower than the calculated ones, indicating the presence of additional attractive forces which were not predicted by the DLVO theory. We assume that the previously mentioned patch-charge interactions were responsible for the additional attraction at low ionic strength. Since they are induced by the adsorption of PDADMAC, these forces could not be present in the bare TiONW system; therefore, the agreement between experimental and calculated data was better in that case. However, the transition between the slow and fast aggregation regimes around the CCC was not sharp in the case of TiONW–PDADMAC compared to the bare TiONW. This deviation could originate from the fact that the adsorbed polyelectrolyte layers usually swell in this ionic strength range,<sup>22,33,57</sup> resulting in thicker and more hydrated PDADMAC layer on the surface which could lead to steric stabilization of the nanowires due to the osmotic repulsion between the adsorbed polyelectrolyte chains. Such repulsive forces were detected in polyelectrolyte–particle systems at high ionic strength,<sup>35,36,56</sup> and their effect on the structure of polymer brushes was also described.<sup>60</sup> Since the stability ratio values were only slightly higher than unity in this regime (Figure S5) and such an effect disappeared at higher ionic strength, where this phenomenon should be more pronounced, we assume that the strength of the osmotic repulsion was small compared to the forces of electrostatic origin.

## CONCLUSIONS

We have studied the surface charge and aggregation of TiONWs in aqueous dispersions in the bare form as well as in the presence of the PDADMAC polyelectrolyte. The bare nanowire dispersions were stable only at low ionic strength at millimolar salt levels. Higher concentration of a monovalent electrolyte led to fast aggregation of the TiONWs and to unstable systems. PDADMAC adsorbed strongly on the oppositely charged TiONW surface, and its adsorption gave rise to charge neutralization at the IEP and subsequent charge reversal at higher polyelectrolyte doses. The adsorption continued until the ASP where the maximum amount of PDADMAC was adsorbed on the surface and further added polyelectrolytes remained dissolved in the solution. Time-resolved DLS measurements performed at different polyelectrolyte doses revealed that the dispersions were unstable near the IEP and stable far before and after it. Adding PDADMAC to the TiONW sample at the dose of ASP resulted in polyelectrolyte coated nanowires. Similar trends were observed in the mobilities and stabilities in the case of both bare and polyelectrolyte coated TiONWs when the ionic strength was varied in these systems. These facts tend to show that the



aggregation processes were governed by interactions of DLVO origin mainly; however, the presence of attractive patch-charge and repulsive osmotic interactions was also detected especially in the TiONW-PDADMAC system. A highly significant advantage of the nanowire coating with polyelectrolyte was that the PDADMAC coverage resulted in a higher CCC value. In summary, the present study provides quantitative information which allows for designing stable or aggregating dispersions of TiONWs using a polyelectrolyte. Accordingly, the dose of polyelectrolyte, particle concentration, and salt level can be precisely adjusted to tune the dispersion stability in accordance with the desired goals.

## ■ ASSOCIATED CONTENT

### ● Supporting Information

Detailed experimental section including materials, light scattering, and DLVO calculations as well as results of static and dynamic light scattering measurements and theoretical calculations. This material is available free of charge via the Internet at <http://pubs.acs.org>.

## ■ AUTHOR INFORMATION

### Corresponding Author

\*E-mail: [istvan.szilagyi@unige.ch](mailto:istvan.szilagyi@unige.ch) (I.S.).

### Notes

The authors declare no competing financial interest.

## ■ ACKNOWLEDGMENTS

Financial support from the Swiss National Science Foundation (150162), Swiss Scientific Exchange Program (12029), Swiss Contribution (SH/7/2/20) and the University of Geneva is gratefully acknowledged. T.S., V.T., and I.S. are grateful to Prof. Michal Borkovec for providing access to the light scattering instruments in his laboratory.

## ■ REFERENCES

- (1) Koka, A.; Sodano, H. A. High-sensitivity accelerometer composed of ultra-long vertically aligned barium titanate nanowire arrays. *Nat. Commun.* **2013**, *4*, 2682–2682.
- (2) Horvath, E.; Ribic, P. R.; Hashemi, F.; Forro, L.; Magrez, A. Dye metachromasy on titanate nanowires: sensing humidity with reversible molecular dimerization. *J. Mater. Chem.* **2012**, *22*, 8778–8784.
- (3) Zhou, W. J.; Liu, X. J.; Sang, Y. H.; Zhao, Z. H.; Zhou, K.; Liu, H.; Chen, S. W. Enhanced performance of layered titanate nanowire-based supercapacitor electrodes by nickel ion exchange. *ACS Appl. Mater. Interfaces* **2014**, *6*, 4578–4586.
- (4) Hong, Z. S.; Wei, M. D. Layered titanate nanostructures and their derivatives as negative electrode materials for lithium-ion batteries. *J. Mater. Chem. A* **2013**, *1*, 4403–4414.
- (5) Kun, R.; Balazs, M.; Dekany, I. Photooxidation of organic dye molecules on TiO<sub>2</sub> and zinc-aluminum layered double hydroxide ultrathin multilayers. *Colloids Surf., A* **2005**, *265*, 155–162.
- (6) Bajnoczi, E. G.; Balazs, N.; Mogyorosi, K.; Sranko, D. F.; Pap, Z.; Ambrus, Z.; Canton, S. E.; Noren, K.; Kuzmann, E.; Vertes, A.; Homonnay, Z.; Oszko, A.; Palinko, L.; Sipos, P. The influence of the local structure of Fe(III) on the photocatalytic activity of doped TiO<sub>2</sub> photocatalysts—An EXAFS, XPS and Mossbauer spectroscopic study. *Appl. Catal., B* **2011**, *103*, 232–239.
- (7) Reti, B.; Mogyorosi, K.; Dombi, A.; Hernadi, K. Substrate dependent photocatalytic performance of TiO<sub>2</sub>/MWCNT photocatalysts. *Appl. Catal., A* **2014**, *469*, 153–158.
- (8) Huang, J. Q.; Cao, Y. G.; Liu, Z. G.; Deng, Z. H.; Wang, W. C. Application of titanate nanoflowers for dye removal: A comparative study with titanate nanotubes and nanowires. *Chem. Eng. J.* **2012**, *191*, 38–44.
- (9) Tang, Y. X.; Subramaniam, V. P.; Lau, T. H.; Lai, Y. K.; Gong, D. G.; Kanhere, P. D.; Cheng, Y. H.; Chen, Z.; Dong, Z. L. In situ formation of large-scale Ag/AgCl nanoparticles on layered titanate honeycomb by gas phase reaction for visible light degradation of phenol solution. *Appl. Catal., B* **2011**, *106*, 577–585.
- (10) Toth, M.; Kiss, J.; Oszko, A.; Potari, G.; Laszlo, B.; Erdohelyi, A. Hydrogenation of carbon dioxide on Rh, Au and Au-Rh bimetallic clusters supported on titanate nanotubes, nanowires and TiO<sub>2</sub>. *Top. Catal.* **2012**, *55*, 747–756.
- (11) Potari, G.; Madarasz, D.; Nagy, L.; Laszlo, B.; Sapi, A.; Oszko, A.; Kukovec, A.; Erdohelyi, A.; Konya, Z.; Kiss, J. Rh-induced support transformation phenomena in titanate nanowire and nanotube catalysts. *Langmuir* **2013**, *29*, 3061–3072.
- (12) Haspel, H.; Peintler, G.; Kukovec, Á. Dynamic origin of the surface conduction response in adsorption-induced electrical processes. *Chem. Phys. Lett.* **2014**, *607*, 1–4.
- (13) Horvath, E.; Szilagyi, I.; Forro, L.; Magrez, A. Probing titanate nanowire surface acidity through methylene blue adsorption in colloidal suspension and on thin films. *J. Colloid Interface Sci.* **2014**, *416*, 190–197.
- (14) Horváth, E.; Grebikova, L.; Maroni, P.; Szabó, T.; Magrez, A.; Forró, L.; Szilagyi, I. Dispersion characteristics and aggregation in titanate nanowire colloids. *ChemPlusChem* **2014**, *79*, 592–600.
- (15) Turesson, M.; Nonat, A.; Labbez, C. Stability of negatively charged platelets in calcium-rich anionic copolymer solutions. *Langmuir* **2014**, *30*, 6713–6720.
- (16) Faraudo, J.; Martin-Molina, A. Competing forces in the interaction of polyelectrolytes with charged interfaces. *Curr. Opin. Colloid Interface Sci.* **2013**, *18*, 517–523.
- (17) Meszaros, R.; Varga, L.; Gilanyi, T. Adsorption of poly(ethyleneimine) on silica surfaces: Effect of pH on the reversibility of adsorption. *Langmuir* **2004**, *20*, 5026–5029.
- (18) Koupanou, E.; Ahualli, S.; Glatter, O.; Delgado, A.; Krumeich, F.; Leontidis, E. Stabilization of lead sulfide nanoparticles by polyamines in aqueous solutions. A structural study of the dispersions. *Langmuir* **2010**, *26*, 16909–16920.
- (19) Bagaria, H. G.; Yoon, K. Y.; Neilson, B. M.; Cheng, V.; Lee, J. H.; Worthen, A. J.; Xue, Z.; Huh, C.; Bryant, S. L.; Bielawski, C. W.; Johnston, K. P. Stabilization of iron oxide nanoparticles in high sodium and calcium brine at high temperatures with adsorbed sulfonated copolymers. *Langmuir* **2013**, *29*, 3195–3206.
- (20) Chen, K. L.; Mylon, S. E.; Elimelech, M. Enhanced aggregation of alginate-coated iron oxide (hematite) nanoparticles in the presence of calcium, strontium and barium cations. *Langmuir* **2007**, *23*, 5920–5928.
- (21) Illes, E.; Tombacz, E. The effect of humic acid adsorption on pH-dependent surface charging and aggregation of magnetite nanoparticles. *J. Colloid Interface Sci.* **2006**, *295*, 115–123.
- (22) Szilagyi, I.; Trefalt, G.; Tiraferri, A.; Maroni, P.; Borkovec, M. Polyelectrolyte adsorption, interparticle forces, and colloidal aggregation. *Soft Matter* **2014**, *10*, 2479–2502.
- (23) Logar, M.; Bracko, I.; Potocnik, A.; Jancar, B. Cu and CuO/titanate nanobelt based network assemblies for enhanced visible light photocatalysis. *Langmuir* **2014**, *30*, 4852–4862.
- (24) Janaky, C.; de Tacconi, N. R.; Chanmanee, W.; Rajeshwar, K. Bringing conjugated polymers and oxide nanoarchitectures into intimate contact: Light-induced electrodeposition of polypyrrole and polyaniline on nanoporous WO<sub>3</sub> or TiO<sub>2</sub> nanotube array. *J. Phys. Chem. C* **2012**, *116*, 19145–19155.
- (25) Munro, C. D.; Plucknett, K. P. Aqueous colloidal characterization and forming of multimodal barium titanate powders. *J. Am. Ceram. Soc.* **2009**, *92*, 2537–2543.
- (26) Kirby, G. H.; Harris, D. J.; Li, Q.; Lewis, J. A. Poly(acrylic acid)-poly(ethylene oxide) comb polymer effects on BaTiO<sub>3</sub> nanoparticle suspension stability. *J. Am. Ceram. Soc.* **2004**, *87*, 181–186.
- (27) Ratinaç, K. R.; Standard, O. C.; Bryant, P. J. Lignosulfonate adsorption on and stabilization of lead zirconate titanate in aqueous suspension. *J. Colloid Interface Sci.* **2004**, *273*, 442–454.



- (28) Liu, W.; Sun, W. L.; Borthwick, A. G. L.; Ni, J. R. Comparison on aggregation and sedimentation of titanium dioxide, titanate nanotubes and titanate nanotubes-TiO<sub>2</sub>: Influence of pH, ionic strength and natural organic matter. *Colloids Surf., A* **2013**, *434*, 319–328.
- (29) Goyal, N.; Rastogi, D.; Jassal, M.; Agrawal, A. K. Dispersion stabilization of titania nanoparticles for textile: Aggregation behavior and self-cleaning activity. *J. Dispersion Sci. Technol.* **2013**, *34*, 611–622.
- (30) Hauck, T. S.; Ghazani, A. A.; Chan, W. C. W. Assessing the effect of surface chemistry on gold nanorod uptake, toxicity, and gene expression in mammalian cells. *Small* **2008**, *4*, 153–159.
- (31) Popa, I.; Cahill, B. P.; Maroni, P.; Papastavrou, G.; Borkovec, M. Thin adsorbed films of a strong cationic polyelectrolyte on silica substrates. *J. Colloid Interface Sci.* **2007**, *309*, 28–35.
- (32) Xie, F.; Nylander, T.; Piculell, L.; Utsel, S.; Wagberg, L.; Akesson, T.; Forsman, J. Polyelectrolyte adsorption on solid surfaces: Theoretical predictions and experimental measurements. *Langmuir* **2013**, *29*, 12421–12431.
- (33) Hierrezuelo, J.; Szilagyi, I.; Vaccaro, A.; Borkovec, M. Probing nanometer-thick polyelectrolyte layers adsorbed on oppositely charged particles by dynamic light scattering. *Macromolecules* **2010**, *43*, 9108–9116.
- (34) Hierrezuelo, J.; Vaccaro, A.; Borkovec, M. Stability of negatively charged latex particles in the presence of a strong cationic polyelectrolyte at elevated ionic strengths. *J. Colloid Interface Sci.* **2010**, *347*, 202–208.
- (35) Bauer, D.; Killmann, E.; Jaeger, W. Flocculation and stabilization of colloidal silica by the adsorption of poly-diallyl-dimethyl-ammoniumchloride (PDADMAC) and of copolymers of DADMAC with N-methyl-N-vinyl acetamide (NMVA). *Colloid Polym. Sci.* **1998**, *276*, 698–708.
- (36) Bauer, D.; Buchhammer, H.; Fuchs, A.; Jaeger, W.; Killmann, E.; Lunkwitz, K.; Rehm, R.; Schwarz, S. Stability of colloidal silica, sikron and polystyrene latex influenced by the adsorption of polycations of different charge density. *Colloids Surf., A* **1999**, *156*, 291–305.
- (37) Morga, M.; Adamczyk, Z. Monolayers of cationic polyelectrolytes on mica: Electrokinetic studies. *J. Colloid Interface Sci.* **2013**, *407*, 196–204.
- (38) Vaccaro, A.; Hierrezuelo, J.; Skarba, M.; Galletto, P.; Kleimann, J.; Borkovec, M. Structure of an adsorbed polyelectrolyte monolayer on oppositely charged colloidal particles. *Langmuir* **2009**, *25*, 4864–4867.
- (39) Schaak, R. E.; Mallouk, T. E. Prying apart Ruddlesden-Popper phases: Exfoliation into sheets and nanotubes for assembly of perovskite thin films. *Chem. Mater.* **2000**, *12*, 3427–3434.
- (40) Zhang, X. T.; Fujishima, A.; Jin, M.; Emeline, A. V.; Murakami, T. Double-layered TiO<sub>2</sub>-SiO<sub>2</sub> nanostructured films with self-cleaning and antireflective properties. *J. Phys. Chem. B* **2006**, *110*, 25142–25148.
- (41) Ma, R. Z.; Sasaki, T.; Bando, Y. Layer-by-layer assembled multilayer films of titanate nanotubes, Ag- or Au-loaded nanotubes, and nanotubes/nanosheets with polycations. *J. Am. Chem. Soc.* **2004**, *126*, 10382–10388.
- (42) Mahadeva, S. K.; Walus, K.; Stoeber, B. Piezoelectric paper fabricated via nanostructured barium titanate functionalization of wood cellulose fibers. *ACS Appl. Mater. Interfaces* **2014**, *6*, 7547–7553.
- (43) Horvath, E.; Kukovec, A.; Konya, Z.; Kiricsi, I. Hydrothermal conversion of self-assembled titanate nanotubes into nanowires in a revolving autoclave. *Chem. Mater.* **2007**, *19*, 927–931.
- (44) Trefalt, G.; Szilagyi, I.; Borkovec, M. Poisson-Boltzmann description of interaction forces and aggregation rates involving charged colloidal particles in asymmetric electrolytes. *J. Colloid Interface Sci.* **2013**, *406*, 111–120.
- (45) Deshiikan, S. R.; Papadopoulos, K. D. Modified Booth equation for the calculation of zeta potential. *Colloid Polym. Sci.* **1998**, *276*, 117–124.
- (46) Kasuga, T.; Hiramatsu, M.; Hoson, A.; Sekino, T.; Niihara, K. Titania nanotubes prepared by chemical processing. *Adv. Mater.* **1999**, *11*, 1307–1311.
- (47) Walsh, R. B.; Nelson, A.; Skinner, W. M.; Parsons, D.; Craig, V. S. J. Direct measurement of van der Waals and diffuse double-layer forces between titanium dioxide surfaces produced by atomic layer deposition. *J. Phys. Chem. C* **2012**, *116*, 7838–7847.
- (48) Snoswell, D. R. E.; Duan, J. M.; Fornasiero, D.; Ralston, J. Colloid stability of synthetic titania and the influence of surface roughness. *J. Colloid Interface Sci.* **2005**, *286*, 526–535.
- (49) Barringer, E. A.; Bowen, H. K. High-purity, monodisperse TiO<sub>2</sub> powders by hydrolysis of titanium tetraethoxide 2. Aqueous interfacial electrochemistry and dispersion stability. *Langmuir* **1985**, *1*, 420–428.
- (50) Kuscer, D.; Stavber, G.; Trefalt, G.; Kosec, M. Formulation of an aqueous titania suspension and its patterning with ink-jet printing technology. *J. Am. Ceram. Soc.* **2012**, *95*, 487–493.
- (51) Niecikowska, A.; Krasowska, M.; Ralston, J.; Malysa, K. Role of surface charge and hydrophobicity in the three-phase contact formation and wetting film stability under dynamic conditions. *J. Phys. Chem. C* **2012**, *116*, 3071–3078.
- (52) Carrillo, J. Y.; Dobrynin, A. V. Molecular dynamics simulations of polyelectrolyte adsorption. *Langmuir* **2007**, *23*, 2472–2482.
- (53) Park, S. Y.; Bruinsma, R. F.; Gelbart, W. M. Spontaneous overcharging of macro-ion complexes. *Europhys. Lett.* **1999**, *46*, 454–460.
- (54) Lyklema, J. Overcharging, charge reversal: Chemistry or physics? *Colloids Surf., A* **2006**, *291*, 3–12.
- (55) Quesada-Perez, M.; Gonzalez-Tovar, E.; Martin-Molina, A.; Lozada-Cassou, M.; Hidalgo-Alvarez, R. Overcharging in colloids: Beyond the Poisson-Boltzmann approach. *ChemPhysChem* **2003**, *4*, 235–248.
- (56) Fuchs, A.; Killmann, E. Adsorption of polyelectrolytes on colloidal latex particles, electrostatic interactions and stability behaviour. *Colloid Polym. Sci.* **1998**, *279*, 53–60.
- (57) Seyrek, E.; Hierrezuelo, J.; Sadeghpour, A.; Szilagyi, I.; Borkovec, M. Molecular mass dependence of adsorbed amount and hydrodynamic thickness of polyelectrolyte layers. *Phys. Chem. Chem. Phys.* **2011**, *13*, 12716–12719.
- (58) Grosberg, A. Y.; Nguyen, T. T.; Shklovskii, B. I. Colloquium: The physics of charge inversion in chemical and biological systems. *Rev. Mod. Phys.* **2002**, *74*, 329–345.
- (59) Borkovec, M.; Behrens, S. H.; Semmler, M. Observation of the mobility maximum predicted by the standard electrokinetic model for highly charged amidine latex particles. *Langmuir* **2000**, *16*, 5209–5212.
- (60) Jusufi, A.; Borisov, O.; Ballauff, M. Structure formation in polyelectrolytes induced by multivalent ions. *Polymer* **2013**, *54*, 2028–2035.

# Influence of Protamine Functionalization on the Colloidal Stability of 1D and 2D Titanium Oxide Nanostructures

Paul Rouster,<sup>†</sup> Marko Pavlovic,<sup>†</sup> Endre Horváth,<sup>‡</sup> László Forró,<sup>‡</sup> Sandwip K. Dey,<sup>§</sup> and Istvan Szilagyi<sup>\*,†</sup>

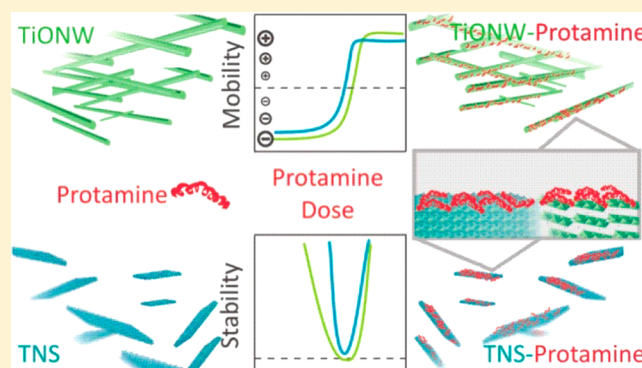
<sup>†</sup>School of Chemistry and Biochemistry, University of Geneva, CH-1205 Geneva, Switzerland

<sup>‡</sup>School of Basic Sciences, École Polytechnique Fédérale de Lausanne, CH-1015 Lausanne, Switzerland

<sup>§</sup>Materials Program, School for Engineering of Matter, Transport and Energy, Arizona State University, Tempe, Arizona 85287, United States

## S Supporting Information

**ABSTRACT:** The colloidal stability of titanium oxide nanosheets (TNS) and nanowires (TiONW) was studied in the presence of protamine (natural polyelectrolyte) in aqueous dispersions, where the nanostructures possessed negative net charge, and the protamine was positively charged. Regardless of their shape, similar charging and aggregation behaviors were observed for both TNS and TiONW. Electrophoretic experiments performed at different protamine loadings revealed that the adsorption of protamine led to charge neutralization and charge inversion depending on the polyelectrolyte dose applied. Light scattering measurements indicated unstable dispersions once the surface charge was close to zero or slow aggregation below and above the charge neutralization point with negatively or positively charged nanostructures, respectively. These stability regimes were confirmed by the electron microscopy images taken at different polyelectrolyte loadings. The protamine dose and salt-dependent colloidal stability confirmed the presence of DLVO-type interparticle forces, and no experimental evidence was found for additional interactions (e.g., patch-charge, hydrophobic, or steric forces), which are usually present in similar polyelectrolyte–particle systems. These findings indicate that the polyelectrolyte adsorbs on the TNS and TiONW surfaces in a flat and extended conformation giving rise to the absence of surface heterogeneities. Therefore, protamine is an excellent biocompatible candidate to form smooth surfaces, for instance in multilayers composed of polyelectrolytes and particles to be used in biomedical applications.



## INTRODUCTION

Titanium oxide and its derivatives are commonly used materials in catalysis, paint fabrication, water purification, novel device development and biomedical treatments.<sup>1–3</sup> Nanostructures of various phases, chemical compositions, and shapes are obtained depending on the experimental synthesis conditions applied.<sup>4,5</sup> Although spherical titanium oxide nanoparticles have attracted most of the interest to date, recent studies have indicated that 1D (i.e., nanowires or TiONW) and 2D (i.e., nanosheets or TNS) nanostructures may possess additional attributes with respect to photovoltaic, chemical, biochemical, and mechanical properties.<sup>1,4,6,7</sup> Chief among them is the potential application of TiONW and TNS for biomedical processes.<sup>8–10</sup>

Despite their potential and importance for their use in living systems, the various interactions between functionalized TiONW and/or TNS and biomacromolecules have not been revealed yet. For example, biocompatible protamine, a weak polyelectrolyte mainly composed of amino acid arginine, is commonly used in postsurgery medicines due to its ability to

reverse the anticoagulant effect of heparin.<sup>11</sup> Since protamine gives rise to a pI value of 12<sup>12</sup> and thus carries a net positive charge under physiological conditions and exhibits considerable affinity for oppositely charged surfaces, it has been used for the biomimetic mineralization of titania particles as well as a template for preparing titania–protamine composites with advantageous properties for enzyme immobilization.<sup>13,14</sup> The latter study demonstrated that the embedded biocatalytic proteins usually kept their functional integrity and exhibited higher thermal and recycling stability than the bare enzymes.

Protamine has been sometimes applied as a building block in polyelectrolyte or polyelectrolyte–particle multilayers in order to create novel structures of biomedical relevance. In one study, the core of the composite was dissolved to generate hollow structures, where bioactive molecules could be loaded and

Received: May 31, 2017

Revised: July 28, 2017

Published: August 22, 2017

released under specific conditions owing to their interactions with protamine.<sup>15</sup> In another study,<sup>16</sup> a similar layer-by-layer technique was used to prepare an alumina–titania composite in the presence of protamine. The dissolution of the alumina template and pyrolysis of the polyelectrolyte resulted in the formation of a continuous network of titania nanotube arrays. Also, multilayered ultrathin clay-protamine films have been demonstrated.<sup>17</sup> Moreover, protamine-assisted titania coating of silicon nanopillars was achieved in a layer-by-layer process to show the advantages with respect to solar absorption for the nanocomposites.<sup>18</sup> In the aforementioned studies, the high affinity of protamine to oppositely charged particle surfaces and subsequent charge inversion upon adsorption were always concluded on the basis of zeta potential measurements.

Protamine has also been used in various other biomedical applications, where its role was mostly to form biocompatible surfaces with advantageous charging properties. For instance, selective membranes containing protamine were developed for biosensor applications.<sup>19</sup> Drug nanoparticles were formulated with protamine-coated clay platelets to improve their applicability in living systems.<sup>20</sup> It has been shown that saturated protamine layers on inorganic carriers enhance the efficiency of DNA delivery processes into cells.<sup>21</sup> In addition, protamine–nucleic acid complexes have been prepared and adsorbed on functionalized gold nanoparticles in order to formulate a system for gene delivery applications.<sup>22</sup>

These examples clearly indicate the importance of protamine interactions with dispersed colloids or nanoparticles; however, the effects of protamine adsorption on charging and aggregation properties of such particles have not yet been comprehensively investigated. The colloidal stability of these systems is indeed the central question since aggregation of the nanostructures may prevent their *in vivo* applications.

In the present study, the colloidal stability of protamine-functionalized TNS and TiONW was investigated. Specifically, the charging properties were assessed by electrophoresis, while particle aggregation was followed using time-resolved light scattering experiments. Additionally, the structure of aggregated clusters was probed by electron microscopy. These studies allowed clarification of the mechanism of protamine adsorption and its effect on the stability of colloidal dispersions of protamine-functionalized TNS and TiONW.

## EXPERIMENTAL SECTION

**Materials.** High purity chemicals, protamine sulfate, and KOH from Sigma-Aldrich and KCl from Acros Organics were purchased and used for the experiments as received. Ultrapure water (Millipore) was used for sample preparation, and the measurements were performed at 25 °C and pH 9 adjusted by KOH. This pH value provides a slightly alkaline environment and also allows maintaining the acid–base processes in the samples.

The TNS and TiONW were prepared hydrothermally, and detailed synthetic procedures and results of solid state characterizations are given elsewhere.<sup>7,23</sup> The formation of the titanium oxide materials was unambiguously confirmed by recording and analyzing the X-ray diffraction patterns shown in Figures S1 and S2 for TNS and TiONW, respectively. Briefly, the main properties of the nanostructured particles can be summarized as follows. For TNS, the point of zero charge (PZC) and calculated geometrical surface area were 5.2 and 73 m<sup>2</sup>/g, respectively.<sup>23</sup> For TiONW, the corresponding numbers were 4.1 and 186 m<sup>2</sup>/g.<sup>24</sup> Note that the significant difference in surface areas is due to the layered structure (i.e., the inner porosity) of the latter material. However, since intercalation of larger molecules is not feasible in the interlayer space of TiONW, the effective outer surface area exposed to the adsorption processes of macromolecules was

calculated to be 30 m<sup>2</sup>/g. The calculations of the outer surface area are detailed in the Supporting Information. The PZC values of TiONW and TNS are similar to the ones reported for other titanium oxide derivatives.<sup>25–27</sup>

**Electrophoresis.** Electrophoretic mobility experiments were performed using a Zetasizer Nano ZS (Malvern Instruments) device. During sample preparation, 0.5 mL of bare TNS or TiONW of 10 mg/L and 36 mg/L concentration, respectively, was added to 4.5 mL of solution containing precise amounts of protamine and KCl. The concentration range was 0.1–100 mg/L for protamine and 1–2000 mM for KCl in the dispersions. The samples were then allowed to rest overnight before performing the mobility experiments. This time interval was long enough to complete the protamine adsorption processes, even in the case of saturated polyelectrolyte layers formed on the particles. Here, the average of five individual measurements on a sample is reported with an error of 5% for such an experimental procedure.

For isolated particles with low zeta potential, as in the case of TiONW and TNS, the electrophoretic mobility ( $u$ ) was converted to zeta potential ( $\zeta$ ) using the model developed by von Smoluchowski:<sup>28</sup>

$$\zeta = \frac{u\eta}{\epsilon_0\epsilon} \quad (1)$$

where  $\eta$  is the viscosity of the medium,  $\epsilon_0$  is the dielectric permittivity of the vacuum, and  $\epsilon$  is the relative dielectric constant of water at the respective temperature.

The low potential of the bare and protamine-functionalized TNS and TiONW also allowed the estimation of the surface charge density ( $\sigma$ ) using the Debye–Hückel theory that relates the change of the double layer potential ( $\psi_{DL}$ ) with the inverse Debye length ( $\kappa$ ) as<sup>29</sup>

$$\sigma = \epsilon\epsilon_0\kappa\psi_{DL} \quad (2)$$

Since a very thin hydrodynamically stagnant layer around the charged particles was assumed, the zeta potentials measured by electrophoresis were used in eq 2. Additionally, knowing the solution composition (and concentration of the background electrolyte), the magnitude of  $\kappa$  was calculated using

$$\kappa = \sqrt{\frac{2N_A e^2 I}{\epsilon\epsilon_0 k_B T}} \quad (3)$$

where  $N_A$  is Avogadro's number,  $e$  is the elementary charge,  $k_B$  is Boltzmann's constant,  $T$  is the absolute temperature, and  $I$  is the ionic strength defined as

$$I = \frac{1}{2} \sum_i z_i^2 c_i \quad (4)$$

where  $z_i$  is the valence, and  $c_i$  is the molar concentration of ion  $i$ .

**Light Scattering.** Dynamic light scattering (DLS) measurements were performed using an ALV/CGS-3 goniometer (ALV GmbH). The sample preparation procedure in the DLS experiments was very similar to the one described above for electrophoresis. The only difference is that the final volume was 2 mL for DLS, and the measurements were started immediately after the addition of the particles to the solutions containing protamine and KCl of known concentrations. The scattering angle was set at 90°, and the correlation function was accumulated for 20 s. The translational diffusion coefficient ( $D$ ) of the particles was determined by using a second order cumulant fit. The hydrodynamic radius ( $R_h$ ) was then calculated with the Stokes–Einstein equation:<sup>30</sup>

$$R_h = \frac{k_B T}{6\pi\eta D} \quad (5)$$

Time-resolved DLS experiments were carried out to assess the stability of the dispersions and expressed in terms of the stability ratio ( $W$ ) as<sup>30–34</sup>



$$W = \frac{\left. \frac{1}{R_h(0)} \frac{dR_h(t)}{dt} \right|_{t \rightarrow 0(\text{fast})}}{\left. \frac{1}{R_h(0)} \frac{dR_h(t)}{dt} \right|_{t \rightarrow 0}} \quad (6)$$

where “fast” indicates experimental conditions, under which aggregation is entirely controlled by the diffusion of TNS and TiONW. Such a condition was achieved in 1 M KCl solutions, where the electrostatic repulsion was screened by the salt and particle collisions resulting in the formation of aggregates. In essence, stability ratios close to unity indicate rapidly aggregating systems (i.e., unstable dispersions), while higher values refer to slower aggregation (i.e., more stable dispersions). The hydrodynamic radius of the primary particles ( $R_h(0)$ ) was found to be 99 and 225 nm for TNS and TiONW, respectively (Table 1).

**Table 1. Dispersion Characteristics of the Bare and Protamine-Coated TNS and TiONW**

	$R_h$ (nm) <sup>a</sup>	PDI <sup>a</sup>	CCC (mM) <sup>b</sup>	$\sigma$ (mC/m <sup>2</sup> ) <sup>c</sup>	ASP (mg/m <sup>2</sup> ) <sup>d</sup>
TNS	99	0.38	8.5	−8.3	
TNS-protamine	98	0.38	25.6	7.9	13.6
TiONW	225	0.34	7.3	−8.2	
TiONW-protamine	232	0.31	12.4	8.0	11.9

<sup>a</sup>Hydrodynamic radius and polydispersity index were measured by DLS in stable dispersions. The standard deviation of the size measurements is about  $\pm 5$  nm. <sup>b</sup>The CCC values were determined from the stability ratio versus ionic strength plots, and their accuracy is 5%. <sup>c</sup>The surface charge densities were estimated with the Debye–Hückel model (eq 2) with an average error of 10%. <sup>d</sup>The onsets of the adsorption saturation plateaus were obtained experimentally from the electrophoretic measurements performed at 1 mM ionic strength.

**Microscopy.** Transmission electron microscopy (TEM) images were recorded using a Tecnai G2 Sphera device (FEI). The microscope was equipped with a LaB6 cathode and operated with an acceleration voltage of 120 kV. Prior to the imaging of the samples, CF200H-CU-UL carbon hexagonal meshes (Electron Microscopy Sciences) were treated with plasma for 20 s. Thereafter, about 5  $\mu$ L of colloidal dispersion was drop-cast on the mesh and allowed to adsorb for 2 min followed by the removal of the excess of solution with a filter paper. The coated mesh was then placed on the holder, which was mounted on to the microscope for imaging.

## RESULTS AND DISCUSSION

Charging and aggregation properties of bare and protamine-functionalized TNS and TiONW were assessed in electrophoretic and time-resolved DLS experiments, respectively. In addition, the structure and orientation of nanostructured 1D and 2D particles forming aggregated clusters were determined by TEM. The effect of protamine dose, ionic strength, and dimensionality of the particles on the mechanism of protamine adsorption and colloidal stability was clarified.

**Colloidal Stability in the Presence of Protamine.** The influence of protamine-functionalized TNS and TiONW on the stability of colloidal dispersions was studied at 1 mM ionic strength and pH 9. Under these experimental conditions, protamine is positively charged due to its high pI of about 12,<sup>12</sup> while negative surface charges have been reported for titanium oxide nanoparticles due to their lower PZC.<sup>23,35</sup>

The electrophoretic mobilities were measured first, and they were negative at low protamine doses (Figure 1a). At very low protamine loadings, below 70 mg/g (i.e., 70 mg of protamine per gram of titanium oxide) and 17 mg/g for TNS and

TiONW, respectively, the mobility values were similar to that exhibited by the bare particles when measured under identical experimental conditions.<sup>23,35</sup> The mobilities increased with increasing the protamine dose, which can be explained by the adsorption of these macromolecules on the oppositely charged titanium oxide surfaces, followed by charge neutralization of the surfaces occurring at the isoelectric point (IEP) observed at 256 mg/g and 61 mg/g for TNS and TiONW, respectively. With further addition of protamine, beyond the dose corresponding to the IEPs, the charge on TNS and TiONW surfaces reversed to positive, and the electrophoretic mobility values increased. Such an overcharging phenomenon is typical in systems containing polyelectrolytes and oppositely charged surfaces<sup>36–42</sup> and is driven by entropy gain upon adsorption<sup>43</sup> and hydrophobic interactions between the polyelectrolyte chains<sup>44</sup> and ion correlation effects.<sup>45</sup> Moreover, on the basis of zeta potential measurements for silica surfaces,<sup>15</sup> clay platelets<sup>20</sup> as well as for titania nanotubes<sup>16</sup> and spherical particles,<sup>14</sup> similar charge reversal upon protamine adsorption has also been reported.

Continued adsorption and increasing electrophoretic mobilities eventually led to the onset of the adsorption saturation plateau (ASP), which was located at 988 mg/g and 359 mg/g for TNS and TiONW, respectively. For TNS, the value is significantly higher than what was reported in the presence of PDADMAC polyelectrolytes of high linear charge density.<sup>23</sup> This deviation is most likely due to the lower charge of protamine, which is due to the moderate repulsion between the polyelectrolyte chains on the surface, allowing for adsorption in a more compact conformation. In contrast, a lower loading value of 200 mg/g was reported to form a saturated protamine layer on a montmorillonite platelet.<sup>20</sup> Given the fact that those experiments were carried out at lower pH, the possession of higher protamine charge and repulsion between the protamine macromolecules resulted in a lower amount of adsorption on the clay surface. Note, above the ASP, further adsorption of protamine is prohibited, and the excess remains dissolved in the bulk state. To make sure that the surface is saturated with the polyelectrolyte, the electrophoretic mobilities were measured at different time intervals at the onset of the ASPs. It was found that the changes in the values for both TNS and TiONW were within the experimental error after a few minutes of equilibration time. Therefore, the applied protocol that the dispersions were left resting overnight before the electrophoretic measurements indeed allowed enough time for the formation of the saturated protamine layer on the surfaces.

If one converts the protamine dose from mg/g to mg/m<sup>2</sup> (corresponding to the surface coverage of the nanostructures) units, trends in the mobilities with varying the protamine dose are similar in this alternate representation (Figure 1a). However, the location of the charge neutralization points and the adsorption saturation plateaus occur at significantly lower value when depicted with respect to the surface area. Indeed, the IEP appears to be between 2 and 4 mg/m<sup>2</sup>, and the onsets of the ASP are located in the range of 8–14 mg/m<sup>2</sup> for both TNS and TiONW. Given the accuracy of the electrophoretic measurements, the values in these regimes can be considered as similar within experimental error. Such a collapse of the mobility curves upon conversion of the units can be explained by the fact that TNS possesses a higher outer surface area compared to the TiONW and that thus the adsorbed amount shifts toward lower values. These results clearly indicate that the shape (either 1D or 2D) of the titanium oxide



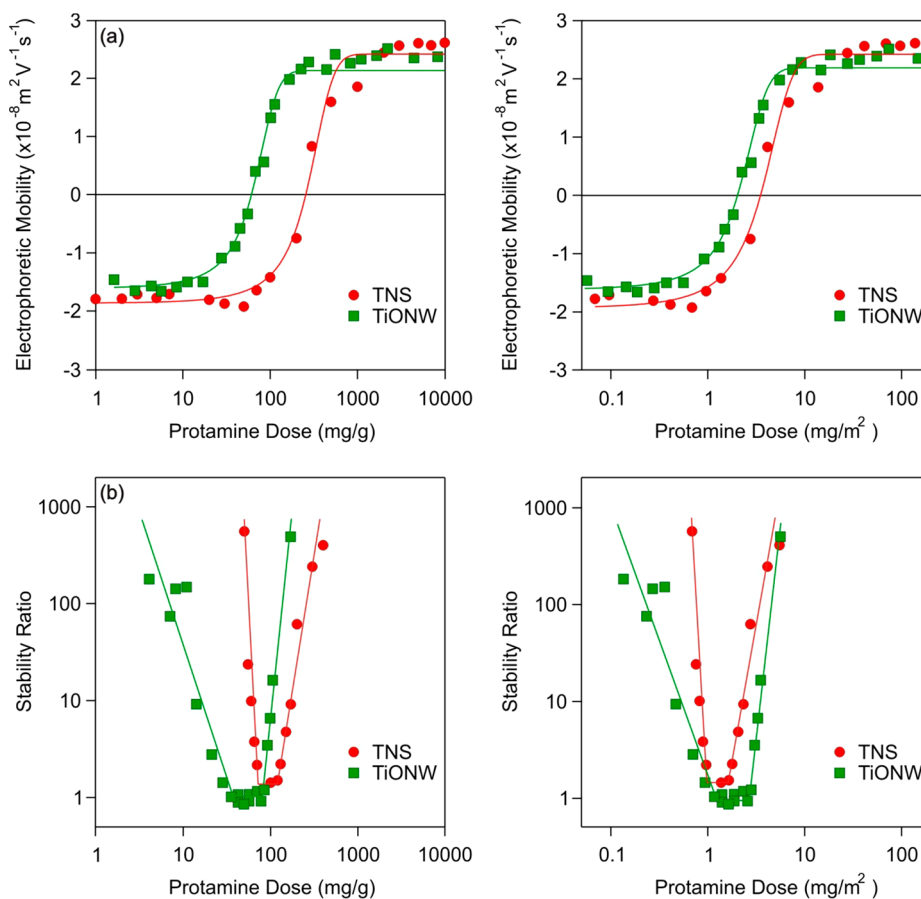


**Figure 1.** Electrophoretic mobilities (a) and stability ratios (b) of TNS and TiONW at different protamine doses in mg/g (left column) and in mg/m<sup>2</sup> (right column) measured at 1 mM KCl concentration and pH 9. The lines are to guide the eyes.

nanostructures has no significant influence on the amount of adsorbed protamine and on the corresponding charging behavior. In addition, the very similar adsorption behavior of the polyelectrolyte on both TNS and TiONW shows that the surface density of the oxygen atoms, which can enhance the adsorption of the protamine on the particles, is similar and that hence the facets of the different nanostructures are of similar composition and surface energy.

The aggregation studies for TNS and TiONW were conducted under exactly the same experimental conditions (i.e., polyelectrolyte dose, pH, and ionic strength) used in the electrophoretic studies above. As explained in the [Experimental Section](#), the colloidal stability was expressed in terms of the stability ratio. Note that in the case of reaction limited aggregation, the inverse of the stability ratio is equal to the fraction of collisions, which leads to dimer formation. On the other hand, when the aggregation is controlled solely by the diffusion of the particles, all collisions are successful, which leads to a stability ratio of unity.

Typical U-shaped stability ratio versus protamine dose curves were obtained with both titanium oxide nanostructures ([Figure 1b](#)), which are similar to other dispersions containing polyelectrolytes and oppositely charged colloidal particles.<sup>24,35,36,46,47</sup> However, the one measured for TNS appears to be narrower compared to the one for TiONW. For protamine doses around the IEPs, stability ratios close to unity were obtained indicating the instability of the systems due to rapid aggregation of the particles. Such protamine-induced destabilization was also reported for gold particles.<sup>48</sup> Further

away from this region (i.e., at low and high protamine loadings), the stability ratios were higher or not even measurable indicating stable dispersions. Although the tendency was the same in both mg/g and mg/m<sup>2</sup> representations of the applied loading, the shift in the fast aggregation regime disappeared, and the plots overlapped once the doses were converted from mg/g to mg/m<sup>2</sup>. This again is due to the higher surface area of TNS. Similar to protamine adsorption and charging behavior, no significant differences between the colloidal stability of TNS and TiONW in the presence of protamine were observed.

In general, such a trend of polyelectrolyte concentration-dependent stability ratios correlates well with the results of electrophoretic measurements and can be interpreted in terms of the Derjaguin, Landau, Verwey, and Overbeek (DLVO) theory.<sup>28,29,49</sup> This model was developed to predict the colloidal stability of charged particles in electrolyte solutions and states that the overall interparticle force is the sum of the repulsive double layer and attractive van der Waals forces. The strength of the former depends on the electric potential of the particles, whereas the attractive component is always present, and its extent is the same for the same type of materials.<sup>28</sup>

For the aggregation of TNS and TiONW particles at different protamine doses, one can readily observe that the lack of surface charge around the IEP and vanishing of the double layer repulsion, coupled with the predominance of the attractive van der Waals forces, led to fast aggregation. At low protamine doses, however, the charge of the bare TNS and TiONW is only partially compensated by the adsorbed polyelectrolytes,

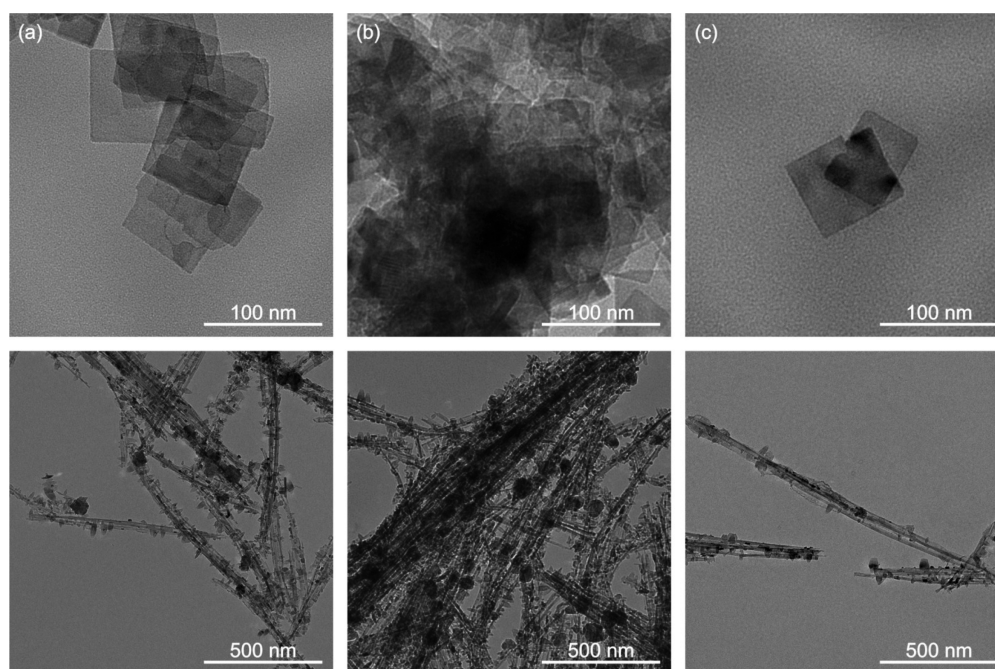


**Figure 2.** TEM images of TNS (top) and TiONW (bottom) in the presence of protamine below (a), around (b), and above (c) the isoelectric point. The images were taken with the same samples as those used in the DLS measurements.

and therefore, the repulsive forces induced by the overlapping electrical double layers overcome the attractive interactions, which led to an electrostatic stabilization of the system. A similar scenario prevails at high protamine doses above the IEP, where the charge of the particles is reversed. Here, a double layer forms around the positively charged protamine-functionalized TNS and TiONW giving rise to the restabilization of the dispersions due to electrostatic repulsion. The same types of interparticle forces were found irrespective of the shape or dimension of the titanium oxide nanostructures. Although the importance of additional forces of non-DLVO origin due to surface charge heterogeneities<sup>24,50,51</sup> and interactions between adsorbed polyelectrolyte chains<sup>23,52,53</sup> have been reported in other particle–polyelectrolyte systems, evidence of such forces was not found in the current study.

To confirm the results of the aggregation measurements, TEM images of both TNS and TiONW were taken at different protamine doses, namely, below, above, and in the vicinity of the IEP. At low protamine doses, stable dispersions were observed in the DLS measurements, and indeed, separated particles could be seen in the images (Figure 2a). Note that the drying process during the sample preparation for the TEM experiments could cause the formation of some particle dimers or trimers. However, the images are significantly different for both TNS and TiONW at the IEP (Figure 2b). Aggregation clearly occurred leading to the formation of clusters of larger sizes, and no individual particles or lower ranked aggregates could be found at these intermediate doses indicating unstable dispersions. Although it was found earlier that the TNS and TiONW nanostructures tend to aggregate in a face-to-face orientation in the presence of polyelectrolytes,<sup>23</sup> dendrimers,<sup>24</sup> or simple salts,<sup>36</sup> this conclusion cannot be unambiguously taken from the present results. Furthermore, stable dispersions were observed above the IEP, as indicated by the presence of individual nanostructures or slightly aggregated particles (Figure 2c). On the basis of the TEM analysis, one can conclude that irrespective of the shape of the titanium oxide

nanostructures, stable dispersions were obtained below and above the IEP, whereas unstable dispersions and aggregation were observed in the vicinity of the IEP. These results are in good agreement with the colloidal stability studies discussed earlier.

**Effect of Ionic Strength.** The influence of the background electrolyte concentration (adjusted by KCl) on the colloidal stability of the titanium oxide nanostructures at different protamine doses was also studied. Therefore, the data obtained from electrophoretic and time-resolved DLS measurements shown in Figure 1 were repeated at 10 mM KCl concentration. This ionic strength is slightly above the critical coagulation concentration (CCC) measured earlier for both TNS<sup>23</sup> and TiONW<sup>35</sup> at pH 9 (Table 1).

The electrophoretic mobilities were first determined (Figure 3a). At low polyelectrolyte coverage below 0.7 mg/m<sup>2</sup> and 0.6 mg/m<sup>2</sup> for TNS and TiONW, respectively, negative mobility values were obtained. In this regime, the magnitude of the mobilities was lower for both types of dispersions than the ones for bare particles in 10 mM KCl solutions. This difference is due to the low amount of adsorbed polyelectrolyte on the surface, which neutralizes a small fraction of the surface charge of the titanium oxide nanostructures. By further increasing the protamine coverage, charge neutralization of the particles appeared around 3.9 mg/m<sup>2</sup> and 1.8 mg/m<sup>2</sup> for the TNS and TiONW, respectively. However, charge reversal was observed at higher protamine doses, and the onsets of the ASPs fell in a similar range for both particles around 20 mg/m<sup>2</sup>.

Although the trend of the protamine dose-dependent mobilities was the same as that at 1 mM ionic strength, an important effect of KCl concentration on the surface charge properties was revealed. Specifically, the onset of the ASP values clearly increased with increasing salt concentration levels. This is attributed to the reduced repulsion between the adsorbed protamine chains at higher ionic strengths. Such a charge screening effect gives rise to a more compact conformation of the macromolecules on the surface and thus

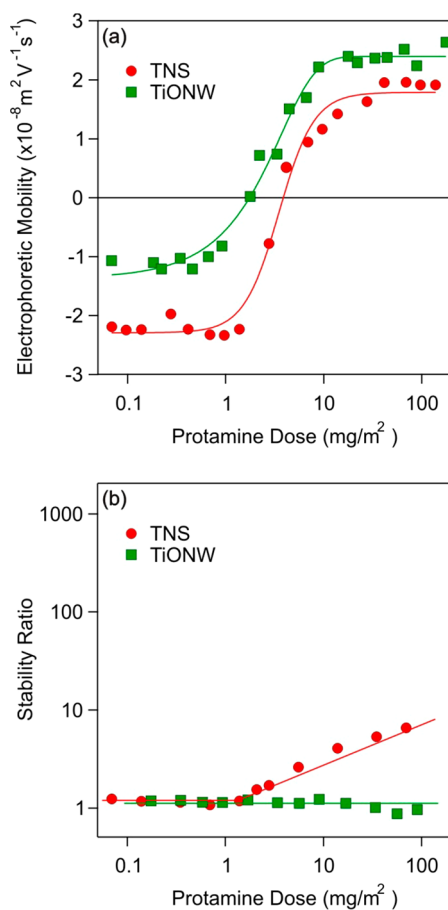


**Figure 3.** Electrophoretic mobility (a) and stability ratio (b) values of TNS and TiONW nanostructures measured at different protamine coverages at pH 9 and 10 mM KCl concentration. The lines are to guide the eyes.

to a higher adsorbed amount. Similar results have also been reported in other particle-oppositely charged polyelectrolyte systems.<sup>54</sup> Also compared to the 1 mM KCl case, the IEPs were similar and independent of the ionic strengths and shape of the particles, the latter due to the very similar surface charge densities of the bare TNS and TiONW (Table 1).

The increase of the electrolyte concentration, however, induced a more striking change in the aggregation behavior of both titanium oxide nanostructures. From the plot of the stability ratio versus protamine dose (Figure 3b), TNS were found to be unstable below the IEP; this is due to the fact that the salt concentration was higher than the CCC value of bare particles. The stability ratios being close to unity in this regime indicate that the aggregation was controlled solely by the diffusion of TNS. Above the IEP, however, a slight restabilization of the system occurred as indicated by an increase in the stability ratio values. Nevertheless, the colloidal stability of the functionalized TNS is rather limited, and the stability ratio values are lower than 10 in this regime. Note that a stability ratio of 10 means that 10% of particle collisions result in dimer formation.<sup>30</sup>

In contrast, irrespective of the protamine dose used, no stable dispersions were found at 10 mM ionic strength for the TiONW system. As a consequence, one can presume that the surface charges of the bare or functionalized nanowires are very similar and are screened by the salt at 10 mM ionic strength, which leads to fast particle aggregation. The observed trends in

colloidal stability with varying KCl concentrations are consistent with the DLVO theory. Clearly, interparticle forces of electrostatic origin are assumed to be operative between the polyelectrolyte-modified nanostructures. Similar observations have been reported in other systems, where charged colloidal particles were dispersed together with oppositely charged polyelectrolytes in aqueous solutions.<sup>23,24,35,36</sup>

The protamine dose at the onset of the ASP results in the full coverage of the outer surface of the titanium oxide nanostructures. Therefore, comparisons of the hydrodynamic radii and polydispersity index (PDI) of bare and protamine-functionalized TNS and TiONW (Table 1) showed very similar values (before and after the coating processes). This indicates that aggregation did not occur upon the formation of a saturated protamine layer.

**Colloidal Stability of Bare and Protamine-Coated TNS and TiONW.** The charging behavior and resistance against salt-induced aggregation of the protamine-coated particles, in a wide range of ionic strength, were explored using electrophoretic and DLS measurements. The mobilities of the coated particles are shown in Figure 4a. The corresponding values

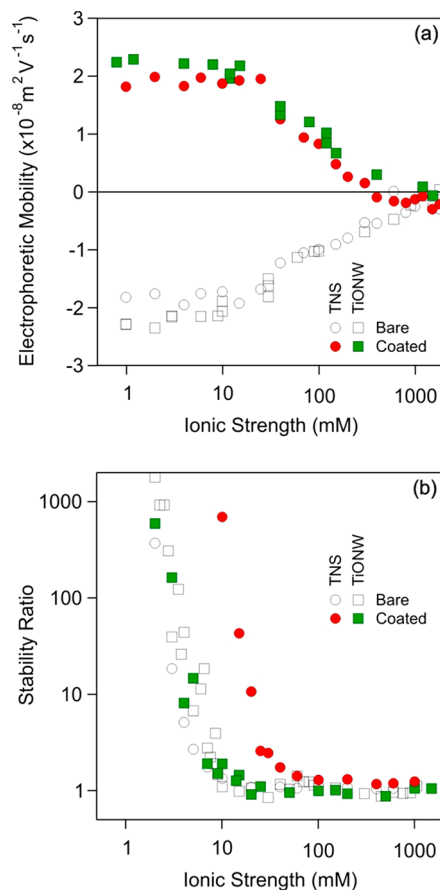


**Figure 4.** Electrophoretic mobility (a) and stability ratio (b) of bare and protamine-coated TNS (circle) and TiONW (square) as a function of the ionic strength set by KCl at pH 9.

measured for the bare TNS and TiONW are also presented for comparison. Obviously, the originally negative nanostructures became positively charged after the protamine coating procedure due to the overcharging phenomenon discussed previously.



In general, the magnitudes of the electrophoretic mobilities of both bare and coated titanium oxide materials are the same within experimental error. However, a decrease in the magnitude of the mobilities is observed with increasing KCl concentration. Note that values are close to zero at the highest ionic strengths. This observation can be explained by the progressive screening of the surface charges of the particles by the salt constituents and the subsequent thinning of the electrical double layer with increasing KCl concentration. On the basis of these results, one can conclude that the mobility values for both the bare or protamine-coated particles are similar in magnitude for a given ionic strength, again indicating that the shape of the nanostructures does not play a significant role in the charging properties. This finding also suggests that the intercalation of  $K^+$  ions into the layered structure of the TiONW is negligible.

The stability ratios determined under identical experimental conditions as applied in the mobility studies are presented in Figure 4b. The tendencies are the same for both bare and coated particles. Stable dispersions with high stability ratio values are observed at low ionic strengths, whereas unstable dispersions were found at high salt concentrations. The sharp transition between the stable and unstable regimes occurred at the CCC. Such an aggregation behavior is similar to other colloidal dispersions in electrolytic solutions<sup>30,33,55,56</sup> and can be explained in terms of the DLVO theory.<sup>28,29,49</sup> Indeed, as the ionic strength increases, more ions are available to screen the surface charges of the particles leading to a decrease in the repulsive strength of the electrical double layer, which vanishes around the CCC. After this point, the attractive van der Waals forces become predominant, which gives rise to diffusion controlled aggregation of the particles.

For both bare TNS and TiONW, the CCC was around 8 mM. Protamine coating of the TNS led to a slightly higher CCC value, which indicates that the polyelectrolyte coating enhances the colloidal stability of the particles to a small extent. However, the presence of the protamine layer on the TiONW did not marginally influence the stability of the dispersions.

Generally, polyelectrolyte coatings on inorganic particles often lead to an improved colloidal stability in comparison to the bare ones.<sup>23,24</sup> However, in the present systems, a significant stabilization effect of the protamine layer could not be concluded. This behavior is most likely due to the flat conformation of the adsorbed protamine on the TNS or TiONW surfaces, which solely gives rise to electrostatic stabilization via overlapping double layers. The improved particle stability upon polyelectrolyte coating is usually due to the joint effect of repulsive electrostatic and steric forces.<sup>23,52,53</sup> The latter interaction is especially important once the adsorbed polyelectrolytes form tails and loops on the surface, and hence, their overlap with other adsorbed polyelectrolytes on another particle leads to the rise of osmotic pressure, which induces repulsion between the colloids or nanostructures.<sup>57,58</sup> In the current context, the flat structure of the protamine layer on the surfaces does not allow any steric interactions, and therefore, the TNS and TiONW possess only limited colloidal stability after covering them with the polyelectrolyte.

The surface charge density of the protamine-coated particles was determined from the ionic strength dependence of the electrophoretic mobilities (eq 2). Data illustrated in Table 1 indicate that protamine-coated TNS and TiONW possess very similar surface charges and that their magnitude is identical to the ones measured for the bare titanium oxide nanostructures.

This fact also confirms that the stabilization forces are of electrostatic (DLVO) origin, since the very similar surface charge densities were accompanied by almost the same CCCs, as discussed before.

The effect of protamine coating on the colloidal stability of titanium oxide is rather unusual since polyelectrolyte adsorption often leads to the rise of interparticle forces of non-DLVO origin such as attractive patch-charge, bridging interactions, and repulsive steric forces. The present results clearly suggest that protamine forms a flat and homogeneous layer on the TNS and TiONW surfaces and that thus the aggregation mechanism is driven solely by DLVO-type (double layer and van der Waals) forces, which are the major interactions in the case of homogeneous surface charge distribution. In addition, these observations are generic and irrespective of the shape of the nanostructures. On the basis of these results, wherever smooth polyelectrolyte layers are required on negatively charged substrates, protamine can be suggested as a coating agent. For instance, this information is especially important, when polyelectrolyte–particle multilayers are to be built.<sup>17,59,60</sup> The protamine layer could therefore provide a smooth base for the stacking of building blocks. In addition, biomimetic mineralization of particle surfaces with protamine may be a promising route to obtain biocompatible delivery systems.

## CONCLUSIONS

A comparison of the colloidal behavior of titanium oxide nanosheets and nanowires was made in the presence of protamine on the basis of results from electrophoretic, light scattering, and electron microscopy studies. It was found that on both types of nanostructured surfaces, the oppositely charged polyelectrolyte adsorbed giving rise to charge neutralization and overcharging at appropriate protamine loadings. Aggregation studies revealed that the dispersions are stable at low and high protamine doses, while diffusion controlled aggregation resulted in unstable samples around the charge neutralization point. Such charging and aggregation behaviors were generic and irrespective of the shape of the titanium oxide nanostructures. Once the measured data are presented as a function of the protamine dose normalized to the surface area, the stability regimes were quantitatively identical. The major interparticle forces were interpreted in terms of the DLVO theory, i.e., repulsive double layer and attractive van der Waals forces are responsible for the aggregation processes in the presence of protamine of different concentrations. This finding is rather atypical since forces of non-DLVO origin have been reported earlier in several particle–polyelectrolyte systems. It was also observed that protamine adsorbed in a flat conformation on the nanostructures leading to the lack of surface heterogeneities and hence to conditions unfavorable for the emergence of patch-charge or steric interactions between the polyelectrolyte-functionalized TNS or TiONW. For scientists working on the development of particle–polyelectrolyte composites in dispersions or on thin films, these results are especially important since the homogeneous surface produced upon protamine adsorption provides an excellent basis for facile future steps during the preparation of such composite materials.



## ■ ASSOCIATED CONTENT

### Supporting Information

The Supporting Information is available free of charge on the ACS Publications website at DOI: [10.1021/acs.langmuir.7b01815](https://doi.org/10.1021/acs.langmuir.7b01815).

Powder XRD spectra of the materials and details of surface area calculation (PDF)

## ■ AUTHOR INFORMATION

### Corresponding Author

\*E-mail: [istvan.szilagyi@unige.ch](mailto:istvan.szilagyi@unige.ch).

### ORCID

Endre Horváth: [0000-0001-7562-2267](https://orcid.org/0000-0001-7562-2267)

Istvan Szilagyi: [0000-0001-7289-0979](https://orcid.org/0000-0001-7289-0979)

### Notes

The authors declare no competing financial interest.

## ■ ACKNOWLEDGMENTS

This research was supported by the Swiss Secretariat for Education, Research and Innovation (C15.0024), Swiss National Science Foundation (150162), and COST Action CM1303. We thank Professor Michal Borkovec for the access to the light scattering instruments in the Laboratory of Colloid and Surface Chemistry. The technical help of Mr. Olivier Vassalli during the time-resolved measurements is gratefully acknowledged.

## ■ REFERENCES

- (1) Wang, L. Z.; Sasaki, T. Titanium Oxide Nanosheets: Graphene Analogues with Versatile Functionalities. *Chem. Rev.* **2014**, *114*, 9455–9486.
- (2) Kordás, K.; Mohl, M.; Kónya, Z.; Kukovec, A. Layered titanate nanostructures: perspectives for industrial exploitation. *Transl. Mater. Res.* **2015**, *2*, 015003–015020.
- (3) Bajnoczi, E. G.; Balazs, N.; Mogyorosi, K.; Sranko, D. F.; Pap, Z.; Ambrus, Z.; Canton, S. E.; Noren, K.; Kuzmann, E.; Vertes, A.; Homonnay, Z.; Oszko, A.; Palinko, I.; Sipos, P. The influence of the local structure of Fe(III) on the photocatalytic activity of doped TiO<sub>2</sub> photocatalysts—An EXAFS, XPS and Mossbauer spectroscopic study. *Appl. Catal., B* **2011**, *103*, 232–239.
- (4) Yu, Y. L.; Zhang, P.; Guo, L. M.; Chen, Z. D.; Wu, Q.; Ding, Y. H.; Zheng, W. J.; Cao, Y. The Design of TiO<sub>2</sub> Nanostructures (Nanoparticle, Nanotube, and Nanosheet) and Their Photocatalytic Activity. *J. Phys. Chem. C* **2014**, *118*, 12727–12733.
- (5) Sasaki, T. Fabrication of nanostructured functional materials using exfoliated nanosheets as a building block. *J. Ceram. Soc. Jpn.* **2007**, *115*, 9–16.
- (6) Subramanian, V. R.; Sarker, S.; Yu, B. W.; Kar, A.; Sun, X. D.; Dey, S. K. TiO<sub>2</sub> nanotubes and its composites: Photocatalytic and other photo-driven applications. *J. Mater. Res.* **2013**, *28*, 280–293.
- (7) Horvath, E.; Kukovec, A.; Konya, Z.; Kiricsi, I. Hydrothermal conversion of self-assembled titanate nanotubes into nanowires in a revolving autoclave. *Chem. Mater.* **2007**, *19*, 927–931.
- (8) Zheng, X. T.; He, H. L.; Li, C. M. Multifunctional graphene quantum dots-conjugated titanate nanoflowers for fluorescence-trackable targeted drug delivery. *RSC Adv.* **2013**, *3*, 24853–24857.
- (9) Ding, X. L.; Yang, X. Q.; Zhou, L.; Lu, H. B.; Li, S. B.; Gao, Y.; Lai, C. H.; Jiang, Y. Titanate nanowire scaffolds decorated with anatase nanocrystals show good protein adsorption and low cell adhesion capacity. *Int. J. Nanomed.* **2013**, *8*, 569–579.
- (10) Papa, A. L.; Boudon, J.; Bellat, V.; Loiseau, A.; Bisht, H.; Sallem, F.; Chassagnon, R.; Berard, V.; Millot, N. Dispersion of titanate nanotubes for nanomedicine: comparison of PEI and PEG nanohybrids. *Dalton Trans.* **2015**, *44*, 739–746.
- (11) Byun, Y.; Chang, L. C.; Lee, L. M.; Han, I. S.; Singh, V. K.; Yang, V. C. Low molecular weight protamine: A potent but nontoxic antagonist to heparin/low molecular weight protamine. *ASAIO J.* **2000**, *46*, 435–439.
- (12) Jiang, Y. J.; Yang, D.; Zhang, L.; Li, L.; Sun, Q. Y.; Zhang, Y. F.; Li, J.; Jiang, Z. Y. Biomimetic synthesis of titania nanoparticles induced by protamine. *Dalton Trans.* **2008**, 4165–4171.
- (13) Jiang, Y. J.; Sun, Q. Y.; Jiang, Z. Y.; Zhang, L.; Li, J.; Li, L.; Sun, X. H. The improved stability of enzyme encapsulated in biomimetic titania particles. *Mater. Sci. Eng., C* **2009**, *29*, 328–334.
- (14) Wang, X. L.; Shi, J. F.; Zhang, S. H.; Wu, H.; Jiang, Z. Y.; Yang, C.; Wang, Y. X.; Tang, L.; Yan, A. F. MOF-templated rough, ultrathin inorganic microcapsules for enzyme immobilization. *J. Mater. Chem. B* **2015**, *3*, 6587–6598.
- (15) Haase, N. R.; Shian, S.; Sandhage, K. H.; Kroger, N. Biocatalytic Nanoscale Coatings Through Biomimetic Layer-by-Layer Mineralization. *Adv. Funct. Mater.* **2011**, *21*, 4243–4251.
- (16) Berrigan, J. D.; Kang, T. S.; Cai, Y.; Deneault, J. R.; Durstock, M. F.; Sandhage, K. H. Protein-Enabled Layer-by-Layer Syntheses of Aligned, Porous-Wall, High-Aspect-Ratio TiO<sub>2</sub> Nanotube Arrays. *Adv. Funct. Mater.* **2011**, *21*, 1693–1700.
- (17) Szabo, T.; Szekeres, M.; Dekany, I.; Jackers, C.; De Feyter, S.; Johnston, C. T.; Schoonheydt, R. A. Layer-by-layer construction of ultrathin hybrid films with proteins and clay minerals. *J. Phys. Chem. C* **2007**, *111*, 12730–12740.
- (18) Yan, Y.; Wang, D.; Schaaf, P. Fabrication of N-doped TiO<sub>2</sub> coatings on nanoporous Si nanopillar arrays through biomimetic layer by layer mineralization. *Dalton Trans.* **2014**, *43*, 8480–8485.
- (19) Crespo, G. A.; Afshar, M. G.; Bakker, E. Reversible Sensing of the Anticoagulant Heparin with Protamine Permeable Membranes. *Angew. Chem., Int. Ed.* **2012**, *51*, 12575–12578.
- (20) Tierney, T.; Bodnar, K.; Rasmuson, A.; Hudson, S. Carrier particle design for stabilization and isolation of drug nanoparticles. *Int. J. Pharm.* **2017**, *518*, 111–118.
- (21) Liu, Y. C.; Wang, T.; He, F. L.; Liu, Q. A.; Zhang, D. X.; Xiang, S. L.; Su, S. P.; Zhang, J. A. An efficient calcium phosphate nanoparticle-based nonviral vector for gene delivery. *Int. J. Nanomed.* **2011**, *6*, 721–727.
- (22) Rahme, K.; Guo, J. F.; Holmes, J. D.; O'Driscoll, C. M. Evaluation of the physicochemical properties and the biocompatibility of polyethylene glycol-conjugated gold nanoparticles: A formulation strategy for siRNA delivery. *Colloids Surf., B* **2015**, *135*, 604–612.
- (23) Rouster, P.; Pavlovic, M.; Szilagyi, I. Improving the stability of titania nanosheets by functionalization with polyelectrolytes. *RSC Adv.* **2016**, *6*, 97322–97330.
- (24) Pavlovic, M.; Adok-Sipiczki, M.; Horvath, E.; Szabo, T.; Forro, L.; Szilagyi, I. Dendrimer-Stabilized Titanate Nanowire Dispersions as Potential Nanocarriers. *J. Phys. Chem. C* **2015**, *119*, 24919–24926.
- (25) Kuscer, D.; Stavber, G.; Trefalt, G.; Kosec, M. Formulation of an Aqueous Titania Suspension and its Patterning with Ink-Jet Printing Technology. *J. Am. Ceram. Soc.* **2012**, *95*, 487–493.
- (26) Niecikowska, A.; Krasowska, M.; Ralston, J.; Malysa, K. Role of surface charge and hydrophobicity in the three-phase contact formation and wetting film stability under dynamic conditions. *J. Phys. Chem. C* **2012**, *116*, 3071–3078.
- (27) Lorenzetti, M.; Gongadze, E.; Kulkarni, M.; Junkar, I.; Igljic, A. Electrokinetic Properties of TiO<sub>2</sub> Nanotubular Surfaces. *Nanoscale Res. Lett.* **2016**, *11*, 378–390.
- (28) Evans, D. F.; Wennerstrom, H. *The Colloidal Domain*; John Wiley: New York, 1999.
- (29) Russel, W. B.; Saville, D. A.; Schowalter, W. R. *Colloidal Dispersions*; Cambridge University Press: Cambridge, U.K., 1989.
- (30) Holthoff, H.; Egelhaaf, S. U.; Borkovec, M.; Schurtenberger, P.; Sticher, H. Coagulation rate measurements of colloidal particles by simultaneous static and dynamic light scattering. *Langmuir* **1996**, *12*, 5541–5549.
- (31) Kobayashi, M.; Yuki, S.; Adachi, Y. Effect of anionic surfactants on the stability ratio and electrophoretic mobility of colloidal hematite particles. *Colloids Surf., A* **2016**, *510*, 190–197.

- (32) Chen, K. L.; Mylon, S. E.; Elimelech, M. Enhanced aggregation of alginate-coated iron oxide (hematite) nanoparticles in the presence of calcium, strontium and barium cations. *Langmuir* **2007**, *23*, 5920–5928.
- (33) Schneider, C.; Hanisch, M.; Wedel, B.; Jusufi, A.; Ballauff, M. Experimental study of electrostatically stabilized colloidal particles: Colloidal stability and charge reversal. *J. Colloid Interface Sci.* **2011**, *358*, 62–67.
- (34) Ehrl, L.; Jia, Z.; Wu, H.; Lattuada, M.; Soos, M.; Morbidelli, M. Role of counterion association in colloidal stability. *Langmuir* **2009**, *25*, 2696–2702.
- (35) Szabo, T.; Toth, V.; Horvath, E.; Forro, L.; Szilagyi, I. Tuning the aggregation of titanate nanowires in aqueous dispersions. *Langmuir* **2015**, *31*, 42–49.
- (36) Horvath, E.; Grebikova, L.; Maroni, P.; Szabo, T.; Magrez, A.; Forro, L.; Szilagyi, I. Dispersion Characteristics and Aggregation in Titanate Nanowire Colloids. *ChemPlusChem* **2014**, *79*, 592–600.
- (37) Hyde, E. D. E.; Moreno-Atanasio, R.; Millner, P. A.; Neville, F. Surface Charge Control through the Reversible Adsorption of a Biomimetic Polymer on Silica Particles. *J. Phys. Chem. B* **2015**, *119*, 1726–1735.
- (38) Brunel, F.; Pochard, I.; Gauffinet, S.; Turesson, M.; Labbez, C. Structure and Yielding of Colloidal Silica Gels Varying the Range of Interparticle Interactions. *J. Phys. Chem. B* **2016**, *120*, 5777–5785.
- (39) Lyklema, J. Overcharging, charge reversal: Chemistry or physics? *Colloids Surf., A* **2006**, *291*, 3–12.
- (40) Avadiar, L.; Leong, Y. K. Interactions of PEI (polyethylenimine)-silica particles with citric acid in dispersions. *Colloid Polym. Sci.* **2011**, *289*, 237–245.
- (41) Cherstvy, A. G.; Winkler, R. G. Simple model for overcharging of a sphere by a wrapped oppositely charged asymmetrically neutralized polyelectrolyte: Possible effects of helical charge distribution. *J. Phys. Chem. B* **2005**, *109*, 2962–2969.
- (42) Iselau, F.; Xuan, T. P.; Trefalt, G.; Matic, A.; Holmberg, K.; Bordes, R. Formation and relaxation kinetics of starch-particle complexes. *Soft Matter* **2016**, *12*, 9509–9519.
- (43) Park, S. Y.; Bruinsma, R. F.; Gelbart, W. M. Spontaneous overcharging of macro-ion complexes. *Europhys. Lett.* **1999**, *46*, 454–460.
- (44) Carrillo, J. Y.; Dobrynin, A. V. Molecular dynamics simulations of polyelectrolyte adsorption. *Langmuir* **2007**, *23*, 2472–2482.
- (45) Quesada-Perez, M.; Gonzalez-Tovar, E.; Martin-Molina, A.; Lozada-Cassou, M.; Hidalgo-Alvarez, R. Overcharging in colloids: Beyond the Poisson-Boltzmann approach. *ChemPhysChem* **2003**, *4*, 234–248.
- (46) Bauer, D.; Buchhammer, H.; Fuchs, A.; Jaeger, W.; Killmann, E.; Lunkwitz, K.; Rehm, R.; Schwarz, S. Stability of colloidal silica, sikron and polystyrene latex influenced by the adsorption of polycations of different charge density. *Colloids Surf., A* **1999**, *156*, 291–305.
- (47) Hierrezuelo, J.; Vaccaro, A.; Borkovec, M. Stability of negatively charged latex particles in the presence of a strong cationic polyelectrolyte at elevated ionic strengths. *J. Colloid Interface Sci.* **2010**, *347*, 202–208.
- (48) Vasimalai, N.; John, S. A. Aggregation and de-aggregation of gold nanoparticles induced by polyionic drugs: spectrofluorimetric determination of picogram amounts of protamine and heparin drugs in the presence of 1000-fold concentration of major interferences. *J. Mater. Chem. B* **2013**, *1*, 5620–5627.
- (49) Verwey, E. J. W.; Overbeek, J. T. G. *Theory of Stability of Lyophobic Colloids*; Elsevier: Amsterdam, The Netherlands, 1948.
- (50) Gillies, G.; Lin, W.; Borkovec, M. Charging and aggregation of positively charged latex particles in the presence of anionic polyelectrolytes. *J. Phys. Chem. B* **2007**, *111*, 8626–8633.
- (51) Leong, Y. K. Interparticle forces arising from an adsorbed strong polyelectrolyte in colloidal dispersions: charged patch attraction. *Colloid Polym. Sci.* **1999**, *277*, 299–305.
- (52) Meng, Z. Y.; Hashmi, S. M.; Elimelech, M. Aggregation rate and fractal dimension of fullerene nanoparticles via simultaneous multi-angle static and dynamic light scattering measurement. *J. Colloid Interface Sci.* **2013**, *392*, 27–33.
- (53) Bagaria, H. G.; Yoon, K. Y.; Neilson, B. M.; Cheng, V.; Lee, J. H.; Worthen, A. J.; Xue, Z.; Huh, C.; Bryant, S. L.; Bielawski, C. W.; Johnston, K. P. Stabilization of iron oxide nanoparticles in high sodium and calcium brine at high temperatures with adsorbed sulfonated copolymers. *Langmuir* **2013**, *29*, 3195–3206.
- (54) Seyrek, E.; Hierrezuelo, J.; Sadehpour, A.; Szilagyi, I.; Borkovec, M. Molecular mass dependence of adsorbed amount and hydrodynamic thickness of polyelectrolyte layers. *Phys. Chem. Chem. Phys.* **2011**, *13*, 12716–12719.
- (55) Szilagyi, I.; Trefalt, G.; Tiraferri, A.; Maroni, P.; Borkovec, M. Polyelectrolyte adsorption, interparticle forces, and colloidal aggregation. *Soft Matter* **2014**, *10*, 2479–2502.
- (56) Kobayashi, M.; Juillerat, F.; Galletto, P.; Bowen, P.; Borkovec, M. Aggregation and charging of colloidal silica particles: Effect of particle size. *Langmuir* **2005**, *21*, 5761–5769.
- (57) Einarson, M. B.; Berg, J. C. Electrosteric stabilization of colloidal latex dispersions. *J. Colloid Interface Sci.* **1993**, *155*, 165–172.
- (58) Fritz, G.; Schädler, V.; Willenbacher, N.; Wagner, N. J. Electrosteric stabilization of colloidal dispersions. *Langmuir* **2002**, *18*, 6381–6390.
- (59) Dontsova, D.; Keller, V.; Keller, N.; Steffanut, P.; Felix, O.; Decher, G. Photocatalytically Active Polyelectrolyte/Nanoparticle Films for the Elimination of a Model Odorous Gas. *Macromol. Rapid Commun.* **2011**, *32*, 1145–1149.
- (60) Kotov, N. A.; Haraszti, T.; Turi, L.; Zavala, G.; Geer, R. E.; Dekany, I.; Fendler, J. H. Mechanism of and defect formation in the self-assembly of polymeric polycation-montmorillonite ultrathin films. *J. Am. Chem. Soc.* **1997**, *119*, 6821–6832.

# Dendrimer-Stabilized Titanate Nanowire Dispersions as Potential Nanocarriers

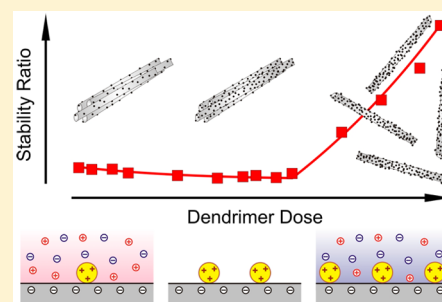
Marko Pavlovic,<sup>†</sup> Monika Adok-Sipiczki,<sup>†</sup> Endre Horváth,<sup>‡</sup> Tamás Szabó,<sup>§</sup> László Forró,<sup>‡</sup> and Istvan Szilagyfi<sup>\*,†</sup>

<sup>†</sup>Department of Inorganic and Analytical Chemistry, University of Geneva, 30 Quai Ernest-Ansermet, CH-1205 Geneva, Switzerland

<sup>‡</sup>Laboratory of Physics of Complex Matter, École Polytechnique Fédérale de Lausanne, CH-1015 Lausanne, Switzerland

<sup>§</sup>Department of Physical Chemistry and Materials Science, University of Szeged, H-6720 Szeged, Hungary

**ABSTRACT:** The effect of poly(amido amine) (PAMAM) dendrimers of generations G2, G6, and G10 on the dispersion stability of titanate nanowires (TiONWs) as potential nanocarriers was clarified in order to develop biocompatible delivery systems. The PAMAMs adsorbed strongly on the oppositely charged TiONWs even under slightly alkaline conditions where the macromolecules possess low amounts of charged groups and they were able to reverse the charge of the particles. This process resulted in unstable dispersions near the dose where the charge reversal occurred, while stable samples were observed away from it. No generation dependence was found on the aggregation and charging behavior at low ionic strengths. Although heterogeneous adsorption of the dendrimers led to attractive patch-charge interactions at intermediate doses, interparticle forces of electrostatic origin described by Derjaguin and Landau, Verwey, and Overbeek (DLVO) played the major role in colloidal stability. The nanowires were found to adopt a face-to-face orientation within the aggregates, giving rise to the formation of well-defined bundles. Highly stable dispersions were observed once the TiONWs were coated with PAMAM dendrimers of higher generations even at elevated ionic strengths.



## INTRODUCTION

Layered materials have anisotropic structure, and they have recently attracted widespread interest due to their advantageous structural and mechanical properties as well as their potential application as a source of unilamellar nanosheets.<sup>1,2</sup> Among such lamellar compounds, elongated titanate derivatives represent a new class of materials which are widely used as building blocks in sensors, nanocarriers, and potential catalysts.<sup>3–9</sup> Accordingly, nanocomposites consisting of layered titanates and hemoglobin showed high biocatalytic activity even in nonaqueous media<sup>10</sup> and reduced graphite oxide supported by layered titanate was developed and used as a mediator-free biosensor.<sup>11</sup> In addition, immobilization of horseradish peroxidase enzyme on layered titanate afforded a catalyst of good recyclability.<sup>12</sup> More recently, other titanate derivatives such as nanowires,<sup>13</sup> nanotubes,<sup>14</sup> and nanoflowers<sup>15</sup> were applied in drug delivery systems. The titanate nanowires (TiONWs) decorated with anatase crystals showed high loading ability for protein-based drugs, while nanotubes entered into cells successfully by endocytosis.

Most of the biomedical applications require functionalization of the titanate surfaces in order to prevent the aggregation of the particles in the living systems and to achieve well-controlled drug release. Moreover, titanate-based nanofilaments were found to be cytotoxic and thus their surface must be modified with biocompatible compounds.<sup>16</sup> To deal with these challenges, titanate nanotubes were coated with polyelectrolytes,<sup>17</sup> biodegradable polymers,<sup>18</sup> or inorganic nanoparticles.<sup>19</sup>

For instance, poly(ethylene imine)-coated particles showed better dispersion properties as the surface charge of the nanocarrier could be tuned easily by the pH.<sup>17</sup> The dispersion stability of TiONWs was also investigated by aggregation kinetic measurements in the presence of polyelectrolytes below and above the point of zero charge.<sup>20–22</sup> They revealed that the colloidal stability of the samples can be appropriately tuned by varying the concentration of the polyelectrolyte, pH, or ionic strength and that full polyelectrolyte coating resulted in highly stable aqueous dispersions.

Although these studies report polyelectrolytes as appropriate stabilizing agents, further research has to be performed in order to clarify their toxicity and to find specific ones for targeted drug delivery processes. Promising candidates to meet such requirements are the dendrimers. For instance, poly(amido amine) (PAMAM) dendrimers are widely used in biomedical applications.<sup>23–26</sup> Enzyme mimicking catalytic systems were also developed using PAMAMs,<sup>27</sup> and their composite materials were successfully applied as gene delivery vectors.<sup>25</sup>

PAMAM dendrimers are monodisperse, symmetrically branched macromolecules containing an ethylenediamine core and primary amines on the outer spheres. They are connected with oligoamide chains, and they double their molecular weight approximately by increasing the number of generations.<sup>26</sup> The

**Received:** September 8, 2015

**Revised:** October 6, 2015

**Published:** October 16, 2015



primary and tertiary amines can be protonated at appropriately low pH where the dendrimers become positively charged. Their protonation under different experimental conditions,<sup>28</sup> along with other fundamental properties such as self-diffusion<sup>29</sup> and their reversible swelling process,<sup>30</sup> was also investigated in detail. Toxicity of PAMAMs depends on the generation number and their concentration in the living systems;<sup>23,26</sup> however, they were found to be biocompatible both in the bare stage<sup>31</sup> and in composites.<sup>25,32</sup>

PAMAM dendrimers are ideal building blocks for a wide range of composite materials; therefore, their interaction with nanomaterials was extensively studied.<sup>33</sup> Accordingly, intercalation in layered clays,<sup>34</sup> their association with other macromolecules to form interpolyelectrolyte complexes,<sup>35</sup> and their ability to stabilize transition metal nanoclusters<sup>36</sup> have been reported. Adsorption experiments were also carried out on silica,<sup>37,38</sup> graphite,<sup>39</sup> and gold<sup>40</sup> surfaces using reflectometry, atomic force microscopy (AFM), and quartz crystal microbalance, respectively. For silica, it was found that low molecular weight PAMAMs at low pH and high ionic strength adsorb reversibly on the surface, while the adsorption of high generation ones at high pH and low ionic strength is completely irreversible.

Interaction of PAMAM dendrimers with colloidal particles was also widely studied to tune interparticle forces and related dispersion stability of the samples. For instance, silver nanoparticles were synthesized and protected against aggregation by adsorbed PAMAM dendrimers.<sup>41</sup> Detailed investigations were performed on systems containing sulfate modified polystyrene latex particles and PAMAM dendrimers in aqueous dispersions. Electrophoretic and time-resolved dynamic light scattering (DLS) experiments revealed that the molecules strongly adsorb on oppositely charged latexes leading to charge neutralization and subsequent charge reversal at appropriate doses.<sup>42</sup> The latter process was found to be superstoichiometric since it involves coadsorption of the dendrimer counterions. Unstable dispersions were reported near the charge neutralization point, while the samples were stable far from that dendrimer dose. Two types of interparticle forces were discovered, namely, classical forces described by Derjaguin and Landau, Verwey, and Overbeek (DLVO) and attractive patch-charge interactions due to the heterogeneous surfaces created by the incomplete coverage by the adsorbed PAMAM molecules. Such forces were identified by both the AFM colloidal probe technique and computer simulations using similar latex particles of higher size.<sup>43,44</sup> More recently, aggregation rate coefficients of these polystyrene particles were determined in the presence of PAMAM dendrimers by AFM and DLS and both experiments yielded very similar values especially for PAMAM of lower generation.<sup>45</sup>

Apart from these results concerning monodisperse spheres as model colloidal particles, no systematic aggregation studies have been published with systems containing titanate nanoparticles of anisotropic structure and PAMAM dendrimers. Given the facts that titanate derivatives are becoming popular nanocarriers in biomedical processes and controlling their aggregation with macromolecules has not been investigated yet in detail, we aimed to study the charging and aggregation of TiONWs in the presence of PAMAM dendrimers to characterize the colloidal stability of this potentially biocompatible delivery system. We were particularly interested in clarifying the effect of molecular weight and ionic strength on the colloidal

stability and structure of aggregates using electrophoresis, DLS, and transmission electron microscopy (TEM).

## EXPERIMENTAL SECTION

**Materials.** The TiONWs were synthesized by a two-step hydrothermal method from anatase (Sigma-Aldrich) which was reacted with concentrated NaOH (Sigma-Aldrich) solution at 130 °C. In the next step, the intermediate product was treated with concentrated KOH (Sigma-Aldrich) solution followed by heating at 200 °C for 1 day. The latter post-treatment process should enhance the stability in morphology and result in a better crystallinity which leads to an excellent long-term reproducibility in the scattering parameters of the nanowires. The white product was then filtered off and washed extensively with ultrapure water produced by a Milli-Q device (Millipore). The TiONWs were dried and suspended in water. The TiONWs have a specific surface area of 186 m<sup>2</sup>/g as determined by nitrogen adsorption experiments using the BET method. For more details, see our previous publications.<sup>20,22</sup> Similar to other titanium(IV) oxides,<sup>46,47</sup> the charge of TiONWs strongly depends on the pH. They are negatively charged under alkaline conditions with a surface charge density of -8.2 mC/m<sup>2</sup> at pH 9 as reported earlier.<sup>22</sup>

PAMAM dendrimers (Dendritech) were purchased in aqueous solutions and used without further purification. The characteristic size values for all generations used are shown in Table 1. The degree of protonation varies only slightly with the generation at pH 9 which was used throughout the experiments.<sup>28</sup>

**Table 1. Characteristic Structural Data of the PAMAM Dendrimers Used in the Present Work<sup>a</sup>**

generation	mol wt (kg/mol)	diam <sup>b</sup> (nm)	no. primary amine groups
G2	3.3	2.9	16
G6	58.0	6.7	256
G10	934.7	13.5	4096

<sup>a</sup>The values were reported by Dendritech. <sup>b</sup>Determined by DLS.

The temperature was kept at 25 °C in the measurements. Glassware, plastic vials, and cuvettes used in the experiments were cleaned with Hellmanex (Hellma) solution and washed thoroughly with ultrapure water.

**Methods.** The electrophoretic mobilities were measured with a ZetaNano ZS (Malvern) device using plastic capillary cells (Malvern). For sample preparation, PAMAM and KCl (Sigma-Aldrich) stock solutions were mixed with water to obtain the desired concentration and ionic strength followed by the addition of the TiONW stock to the samples. The procedure resulted in a final sample volume of 5.0 mL and particle concentration of about 7 mg/L. The electrophoretic mobilities were measured after overnight equilibration of the samples at room temperature. The mobility of each sample was measured five times and averaged.

For determination of the apparent size in time-resolved DLS measurements, the ZetaNano ZS (Malvern) instrument equipped with a He/Ne laser and an avalanche photodiode as a detector was used at 173° scattering angle. The hydrodynamic radii were determined using the cumulant method to fit the correlation function which was accumulated for 30 s.<sup>48</sup> Square plastic cuvettes (Malvern) of 1 cm path length were used for the measurements. Regarding sample preparation, dendrimer, KCl solutions, and ultrapure water



were mixed to adjust the desired polyelectrolyte dose and ionic strength. The aggregation experiments were initiated by injecting the TiONW stock dispersion which was previously subjected to ultrasonic treatment to mechanically disaggregate the small fraction of agglomerates that may have formed upon aging of the sample. Similar to the electrophoretic measurements, the final particle concentration was about 7 mg/L. This experimental setup allowed us to avoid multiple scattering events and to measure only the translational diffusion coefficient as detailed elsewhere.<sup>22</sup> In both electrophoretic and aggregation studies, the pH of stock solutions of dendrimers, KCl, and TiONW as well as water was adjusted to 9 by KOH and HCl (Sigma-Aldrich) prior to mixing them together.

The samples were imaged by TEM using a Tecnai G2 electron microscope (FEI) operating at 120 kV. In a typical experiment, a 3  $\mu$ L sample containing approximately 7 mg/L TiONW, calculated amount of the dendrimers, and KCl was deposited on a carbon coated 400-mesh copper grid. After 30 s, which was needed for the adsorption of the particles, the liquid phase was blotted off with a filter paper by holding it vertically. The images were then immediately taken from the sample without staining.

## RESULTS

**Effects of Dendrimer Generation.** Electrophoretic mobilities of TiONWs were measured in the presence of PAMAM dendrimers of generations G2, G6, and G10 (Figure 1a). These macromolecules can be considered as weak polyelectrolytes and thus bear a positive charge at pH 9, since only about 30% of the amino groups are protonated under this experimental condition.<sup>28</sup>

In general, the positively charged PAMAMs adsorb on the oppositely charged TiONWs and this is reflected in the increasing mobility values with the dendrimer dose. The adsorption led to charge neutralization at the isoelectric point (IEP) where the overall charge of the TiONW–PAMAM particles is zero. To quantify the contribution of the protonated groups of the dendrimers to the charge balance, one should note that these macromolecules tend to adsorb together with condensed counterions within the structure and, hence, a significant part of the positive PAMAM charge is neutralized by the chloride ions.<sup>42</sup> Therefore, the effective charge of the macromolecules is lower than the one that can be calculated on the basis of the chemical structure and the protonation equilibria. No trend can be observed with the generation; the IEP values fall within the experimental error. Although a clear dependence was reported on the IEPs earlier in other PAMAM systems, those investigations were carried out with latex particles and under acidic conditions where the PAMAMs are highly charged and significant counterion condensation takes place.<sup>42</sup>

Adding further dendrimers into the samples led to charge reversal which was previously discovered in several particle–polyelectrolyte systems.<sup>20–22,42,44,45,49–51</sup> The adsorption continues up to the dose at the onset of the adsorption saturation plateau (ASP) which correlates with the establishment of the maximum amount of dendrimers that can adsorb on the particle surface under these experimental conditions. The ASP values fell around 500 mg/g for all generations within the experimental error. This is much higher than the ASPs determined for other polyelectrolytes adsorbed on TiONWs (50–100 mg/g).<sup>20,22</sup> Those macromolecules were highly

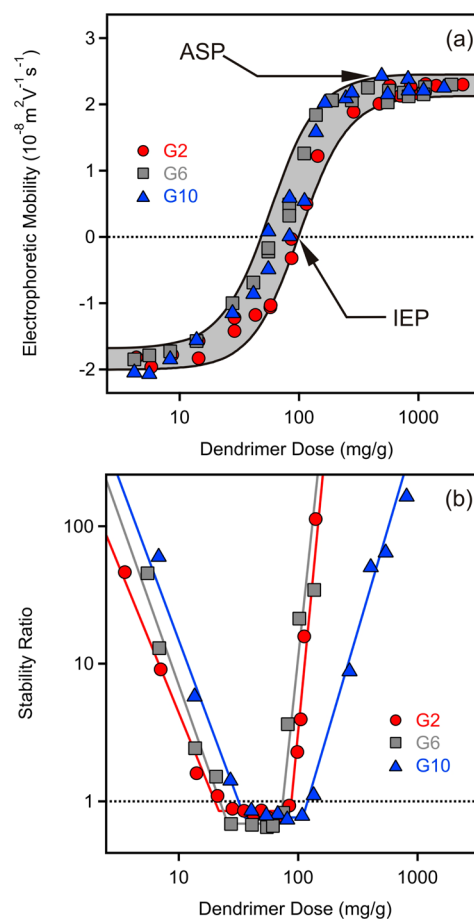


**Figure 1.** Electrophoretic mobility (a) and stability ratio (b) values as a function of the dendrimer dose measured in dispersions of 7 mg/L TiONW at 1.0 mM ionic strength for three generations (G2, G6, and G10) of PAMAM. The dose corresponds to milligrams of dendrimer per gram of nanowires. The lines are just to guide the eye.

charged, while the PAMAMs in our systems are only partially protonated and, therefore, the electrostatic repulsion between the adsorbed dendrimers is notably less and a higher amount can be adsorbed on the surface. Another possible explanation for the higher ASPs could be the formation of PAMAM multilayers on the surface, but we do not have unambiguous evidence for such a process. These phenomena are considered generic for all generations of the PAMAMs investigated, because no molecular mass dependence on the charging behavior was observed.

Light scattering has been proved as a suitable tool to follow particle aggregation in dispersions by measuring the apparent hydrodynamic radius under different experimental conditions in a time-resolved experiment.<sup>52–54</sup> Therefore, time-resolved DLS measurements were carried out to describe the colloidal stability of the systems under the same experimental conditions as in the mobility studies (Figure 1b). Constant values of hydrodynamic radii indicated stable dispersions, while their increase with time was an unambiguous signal for particle aggregation (Figure 2). A linear fit can be performed on the size versus time data, and the slope is proportional to the aggregation rate. Finally, the dispersion stability was expressed in terms of the stability ratio, which is the slope in the case of diffusion controlled aggregation divided by the slope yielded from the actual experiment at the same particle concentration.<sup>55</sup>

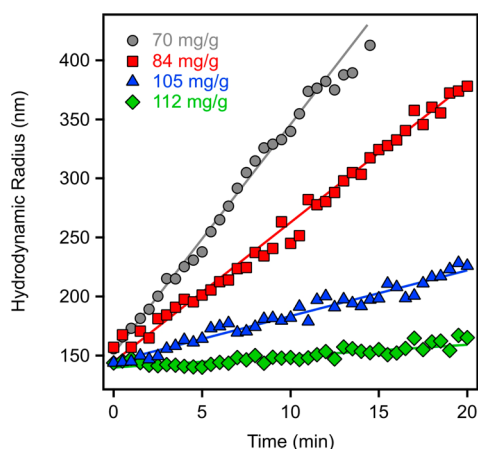


**Figure 2.** Change in hydrodynamic radius with time in some typical time-resolved DLS experiments with samples containing 7 mg/L TiONW and different doses of G2 PAMAM dendrimer at 1.0 mM ionic strength. The indicated doses refer to milligrams of dendrimer per gram of nanowires.

The diffusion controlled condition was achieved at 1.0 M KCl concentration where the surface charges are screened and the particles aggregate rapidly due to attractive van der Waals forces.<sup>56</sup> Accordingly, stability ratio values close to unity indicate unstable, rapidly aggregating samples, while higher values refer to more stable dispersions.

Figure 1b shows the stability ratios for different generations of PAMAMs at low ionic strength. The stability plots for G2 and G6 are almost identical, while it is somewhat different for G10. In all cases, stable dispersions were observed at low dendrimer doses and the stability ratios decreased with

increasing concentration. Fast aggregation and unstable systems were discovered near the dose corresponding to the IEP, while the aggregation slowed down at higher PAMAM concentrations. Considering the results of the electrophoretic measurements, such behavior can be explained by the classical DLVO theory developed for charged particles in aqueous dispersions.<sup>56</sup> Accordingly, the particles are negatively and positively charged at low and high PAMAM doses, respectively (Figure 1a). The surface charge is accompanied by the formation of electric double layers around the particles, and their overlap upon approach gives rise to repulsive interaction forces which can stabilize the sample. However, the TiONWs have an overall charge close to zero around the IEP and the electric double layers vanish, and hence the particles will rapidly aggregate due to the predominating attractive van der Waals forces. A similar origin of interparticle forces was discovered in other particle–polyelectrolyte systems confirmed by direct force measurements using the AFM-based colloidal probe technique.<sup>43–45,57</sup>

However, two phenomena require further clarification. First, the stability ratios in the fast aggregation regimes are systematically lower than 1. This fact indicates the presence of an additional attractive force which is absent in the reference system (TiONW in 1.0 M KCl). This force must be induced by the adsorbed PAMAM molecules, and it is of non-DLVO origin. This additional attraction can be explained by patch-charge interactions as follows. The dendrimers adsorb in a heterogeneous fashion on the surface and form positively charged patches. These patches can interact with a negatively charged part of another particle leading to Coulombic attraction and increased aggregation rate. Such patch-charge forces have already been discovered for dendrimers and also for

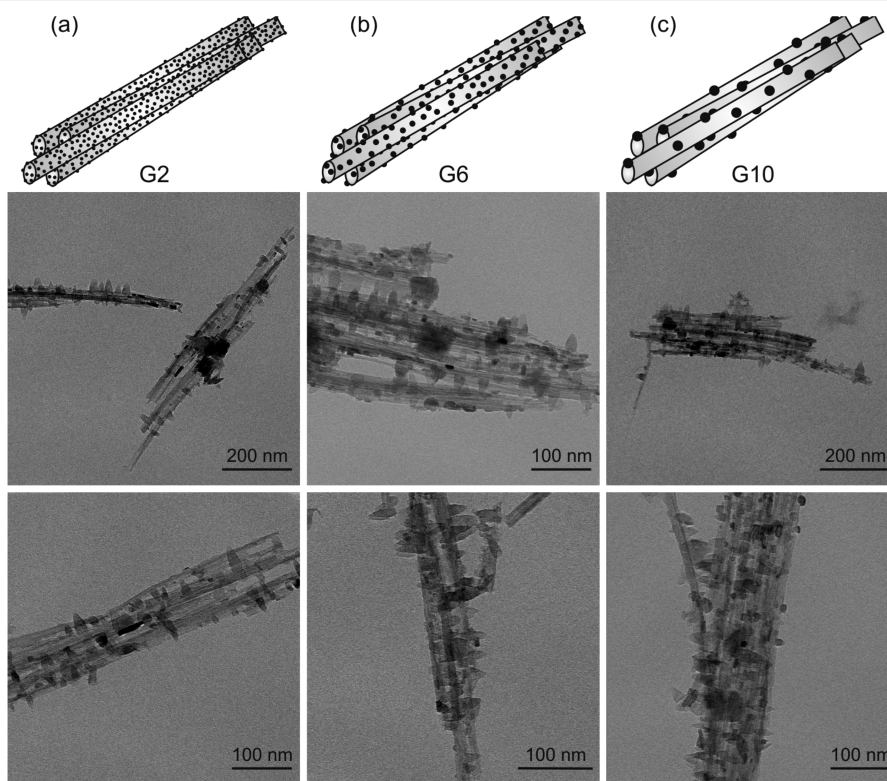


**Figure 3.** TEM images recorded for systems containing TiONWs and different generations of PAMAMs around the IEP. Dendrimer doses of 57, 55, and 55 mg/g were applied for G2 (a), G6 (b), and G10 (c), respectively.

other polyelectrolytes adsorbed on oppositely charged surfaces.<sup>20,42,44,57,58</sup> Second, the fast aggregation regime is slightly shifted to higher PAMAM doses in the case of G10 dendrimers. A similar finding was reported with latex particles with an even more significant shift.<sup>42</sup> This effect may originate from the counterion condensation, since higher generation dendrimers bring a considerable amount of negatively charged counterions to the surface and, hence, a part of the PAMAM's charge is already neutralized and a higher amount of dendrimer is required for reaching the IEP. Interestingly, this effect could not be detected in the electrophoretic mobility measurements (Figure 1a), most probably due to the lower sensitivity of that method. Obviously the shift is small and it would be more pronounced if the PAMAM molecules were highly charged (e.g., at low pH) and more counterions would be entrapped into their structure.

The orientation of the nanowires in the aggregates was also investigated near the IEPs by recording TEM images on samples prepared in the same way as for the mobility and scattering experiments (Figure 3). Accordingly, aggregating TiONW samples were imaged in the presence of G2 (Figure 3a), G6 (Figure 3b), and G10 (Figure 3c) dendrimers. It can be clearly seen that the nanowires prefer face-to-face orientation in the aggregates which leads to the formation of bundles or "spaghetti-like" structure regardless of the molecular weight and generation of the PAMAMs. The same orientation of the TiONWs was observed in AFM images during aggregation induced by inert salts or other type of polyelectrolytes.<sup>20</sup> The dark spots on the TEM images may originate from the presence of anatase nanocrystals grown on the nanowires, but the resolution of our instrument did not allow us to confirm this unambiguously.

**Effects of Ionic Strength.** Charging and aggregation were studied at different ionic strengths in the TiONW–G6 system first. Although the electrophoretic mobilities follow the general trend as described in the previous section, change in the ionic strength affects the shape of the curves significantly (Figure 4a). At low dendrimer dose, the mobility values are constant and refer to the electrophoretic mobility of the bare particles at the corresponding ionic strength (Figure 5a). Such values are very similar at lower salt levels (1 and 10 mM), while they decreased in magnitude at higher ionic strength (100 mM) due to the screening effect of the counterions on the particle surface charge. A similar phenomenon was observed at high doses where the particles are positively charged due to the charge reversal process. Accordingly, the mobility values are smaller at the ASP at high ionic strength, but the change is less significant compared to the low dendrimer dose case. Furthermore, the PAMAM doses at the IEP shift toward higher concentrations, indicating a counterion condensation into the adsorbed dendrimer structure. The same shift was also experienced with other weakly charged polyelectrolytes during their adsorption of oppositely charged particles.<sup>59</sup>

The ionic strength had a huge influence on the aggregation of the TiONWs in the presence of the G6 dendrimers (Figure 4b). As discussed earlier, the stability ratios at 1 mM KCl concentration indicate stable dispersions at low and high PAMAM doses, while fast aggregation occurs in the intermediate regime near the IEP. The shape of the stability ratio versus dose curves changed dramatically at higher ionic strengths (10 and 100 mM). The TiONWs aggregate rapidly in the entire range at and below the IEP. This fact is not surprising since the critical coagulation concentration (CCC, which

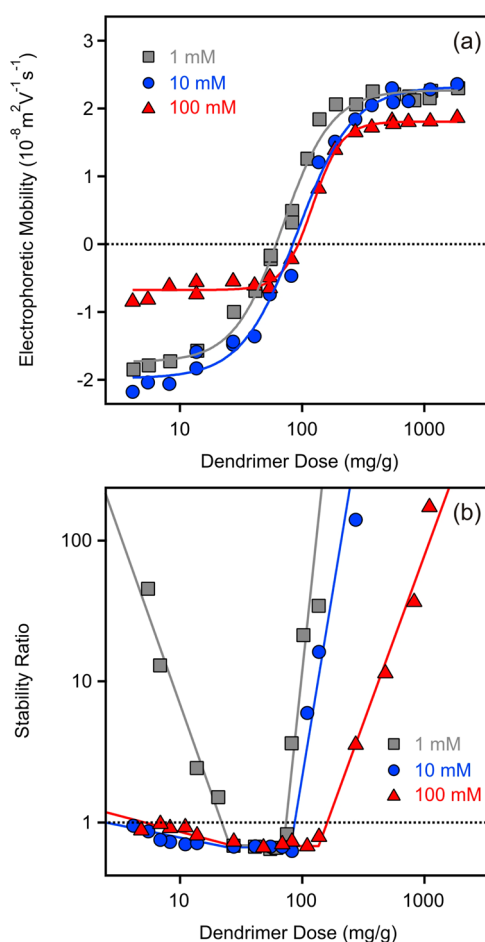


**Figure 4.** Electrophoretic mobility (a) and stability ratio (b) values as a function of the dendrimer dose measured in dispersions of 7 mg/L TiONW and G6 at different ionic strengths adjusted by KCl. The lines are just to guide the eye.

separates fast and slow aggregation regimes) was determined as 8 mM for the bare nanowires.<sup>22</sup> Accordingly, only a small amount of PAMAM is adsorbed on the TiONWs at low doses and, hence, the aggregation rate corresponds to the value of the bare particles (Figure 5b). However, stable dispersions and slow aggregation were observed at high dendrimer concentration where the charge reversal resulted in nanowires of positive charge. The slopes at higher dose are also sensitive to the ionic strength due to the screening effect of the counterions on the surface. In these cases, the counterions are the negative chloride ions and such a screening effect was also discovered in the electrophoretic mobility measurements (Figure 4a) as discussed above. The stability ratios are below 1 at all ionic strengths around the IEP. The lack of the effect of salt level on the responsible patch-charge interaction indicates that the adsorbed amount and the structure of the dendrimer layers on the surface are not affected by the KCl concentration; therefore, the ionic strength dependence of the stability curves is only due to the electrostatic screening of the counterions on the particle surfaces especially at higher doses. This set of data shed light on the stabilization of the dispersions by PAMAM adsorption even at higher ionic strengths where the bare particles rapidly aggregate indicated by their low CCC values.

To further explore this issue, surface charges and aggregation were studied with nanowires coated with dendrimers of different generations. Accordingly, a PAMAM dose higher



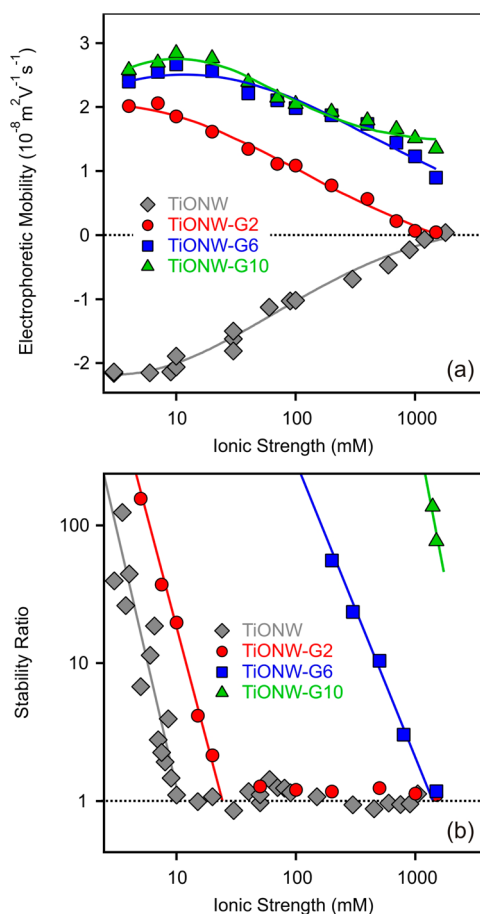


**Figure 5.** Electrophoretic mobility (a) and stability ratio (b) values of bare (TiONW) and PAMAM dendrimer-coated nanowires using different generations of PAMAM (TiONW-G2, TiONW-G6, and TiONW-G10) as a function of the ionic strength adjusted by KCl at pH 9. For the coated particles, about 1000 mg/g dendrimer doses were used to cover the TiONWs. The solid lines are to guide the eye.

than the onset of the ASP was applied in order to completely cover the TiONW surfaces and to obtain positively charged TiONW-G2, TiONW-G6, and TiONW-G10 particles. Figure 5a shows the electrophoretic mobilities of such nanowires together with the bare TiONW over a wide range of ionic strengths. The trends observed with the bare and TiONW-G2 particles are very similar, but of opposite sign of the charge due to the charge reversal process. The magnitude of the mobilities decreased with increasing the ionic strength and met around zero at high electrolyte concentration. This fact indicates that both bare and G2-coated nanowires has the same charge at an elevated KCl level, shedding light on the desorption of the G2 dendrimers from the particle surface. Such reversible adsorption has already been observed with low generation dendrimers<sup>38,42</sup> and also with other multivalent ions.<sup>60</sup> The electrophoretic mobilities of TiONW-G6 and TiONW-G10 nanowires were found to be very similar to slightly higher values in the latter case. Accordingly, the positive mobility values were recorded in the entire ionic strength range investigated and they decreased with increasing electrolyte concentration. The electrophoretic mobilities remained significantly positive even at high KCl concentrations where the mobility of the TiONW-G2 has already reached zero. The decrease of mobilities in the case of higher generation systems

is most likely due to the screening effect of the chloride anions on the positive surface charge.

On the basis of these results, we have tested the aggregation processes (Figure 5b) under the same experimental conditions (pH, ionic strength range, TiONW concentration, and dendrimer dose). The TiONW and TiONW-G2 systems showed similar behavior with a small shift in the CCC. As one could predict applying the DLVO theory, the particles were stable at low ionic strength due to the repulsive forces originating from the overlap of the electric double layers. By increasing the salt level, the surface charges are screened and such double layer repulsion disappears leading to the predominance of the attractive van der Waals forces and to rapidly aggregating samples. The mobility results (Figure 5a) indicate that this screening process is accompanied by desorption of the G2 molecules. Since the CCCs are slightly different, desorption of the dendrimers is incomplete at the ionic strength corresponding to the range of the CCCs.

In addition, the stability curves of TiONW-G6 and TiONW-G10 nanowires were also sensitive to the KCl concentration: stability ratios decreased with increasing salt level (Figure 5b). For the first system, a CCC of about 1500 mM was found, indicating an enormous stabilizing effect of the dendrimer coating compared to the 8 mM value determined for the bare particles. Moreover, the stabilization effect was even higher in the case of TiONW-G10, where only slow aggregation was observed at high salt levels and we were not able to reach the CCC due to the solubility limit of KCl. If one compares these data to the lower generation TiONW-G2 system, the following conclusions can be made. First, all coated systems are stable at very low ionic strengths regardless of the generation of the PAMAMs. Second, increasing the ionic strength led to desorption of G2 which is most likely not favorable for G6 and G10 even at high KCl concentrations. These facts clearly indicate that higher generation dendrimers can be used as dispersing agents even at high ionic strength; however, G2 most likely desorbs under these experimental conditions. For instance, in drug or gene delivery systems where the ionic strength is over 100 mM and hence aggregation of the bare nanowires would certainly occur, PAMAM dendrimer coating prevents such aggregation and provides highly stable dispersions suitable for the delivery and release processes.

## CONCLUSIONS

Electrophoretic, time-resolved DLS, and TEM experiments were carried out to clarify the effect of PAMAM dendrimers of different generations on the colloidal stability of TiONW dispersions. Our study on charging revealed that PAMAMs strongly adsorbed on the oppositely charged particles and charge neutralization as well as reversal occurred. These phenomena were independent of the molecular weight of the macromolecules. The dispersions were stable at low and high dendrimer doses at low ionic strength where the particles possessed sufficiently high negative or positive charge, respectively. Rapid aggregation and unstable systems were obtained near the dose of the charge reversal point. The predominating interparticle forces were mainly of DLVO origin; nevertheless, additional attraction due to patch-charge interactions was also discovered. The orientation of the nanowires in the aggregates resulted in the formation of bundles or "spaghetti-like" structures regardless of the generation of the dendrimers. The ionic strength dependence



of the aggregation rates pointed out an enormous stabilization effect of the PAMAM macromolecules of higher generations since the coated TiONW dispersions were stable even at salt levels where the bare particles undergo rapid aggregation due to their low CCC value. In conclusion, a potential nanocarrier (TiONW) to be used in biomedical applications can be stabilized by PAMAM macromolecules of higher generations and, on the basis of our results, appropriate doses can be calculated to obtain highly stable dispersions to be further investigated as biocompatible delivery systems. Accordingly, TiONWs coated with higher generation dendrimers are potential candidates in delivery processes as carriers where unwanted aggregation is prevented by the PAMAM layer even under extremely high ionic strengths.

## AUTHOR INFORMATION

### Corresponding Author

\*E-mail: [istvan.szilagyi@unige.ch](mailto:istvan.szilagyi@unige.ch)

### Author Contributions

The manuscript was written through contributions of all authors. All authors have given approval to the final version of the manuscript.

### Notes

The authors declare no competing financial interest.

## ACKNOWLEDGMENTS

Financial support from the Swiss National Science Foundation (150162), Swiss Scientific Exchange Program (14033), University of Geneva, Swiss Contribution (SH/7/2/20), Swiss Secretariat for Education, Research and Innovation (C15.0024), and COST Actions MP1106 and CM1303 is gratefully acknowledged. M.P. and I.S. are grateful to Prof. Michal Borkovec for providing access to the light scattering instruments in his laboratory. The authors also thank Mr. Olivier Vassalli for the technical support during the DLS experiments.

## REFERENCES

- (1) Nicolosi, V.; Chhowalla, M.; Kanatzidis, M. G.; Strano, M. S.; Coleman, J. N. Liquid Exfoliation of Layered Materials. *Science* **2013**, *340*, 1226419.
- (2) Bai, Y.; Xing, Z.; Yu, H.; Li, Z.; Amal, R.; Wang, L. Z. Porous Titania Nanosheet/Nanoparticle Hybrids as Photoanodes for Dye-Sensitized Solar Cells. *ACS Appl. Mater. Interfaces* **2013**, *5*, 12058–12065.
- (3) Pusztai, P.; Puskas, R.; Varga, E.; Erdohelyi, A.; Kukovec, A.; Konya, Z.; Kiss, J. Influence of Gold Additives on the Stability and Phase Transformation of Titanate Nanostructures. *Phys. Chem. Chem. Phys.* **2014**, *16*, 26786–26797.
- (4) Potari, G.; Madarasz, D.; Nagy, L.; Laszlo, B.; Sapi, A.; Oszko, A.; Kukovec, A.; Erdohelyi, A.; Konya, Z.; Kiss, J. Rh-Induced Support Transformation Phenomena in Titanate Nanowire and Nanotube Catalysts. *Langmuir* **2013**, *29*, 3061–3072.
- (5) Madarasz, D.; Potari, G.; Sapi, A.; Laszlo, B.; Csudai, C.; Oszko, A.; Kukovec, A.; Erdohelyi, A.; Konya, Z.; Kiss, J. Metal Loading Determines the Stabilization Pathway for  $\text{Co}^{2+}$  in Titanate Nanowires: Ion Exchange vs. Cluster Formation. *Phys. Chem. Chem. Phys.* **2013**, *15*, 15917–15925.
- (6) Osada, M.; Sasaki, T. Two-Dimensional Dielectric Nanosheets: Novel Nanoelectronics From Nanocrystal Building Blocks. *Adv. Mater.* **2012**, *24*, 210–228.
- (7) Koka, A.; Sodano, H. A. High-sensitivity Accelerometer Composed of Ultra-long Vertically Aligned Barium Titanate Nanowire Arrays. *Nat. Commun.* **2013**, *4*, 2682.
- (8) Bavykin, D. V.; Walsh, F. C. Elongated Titanate Nanostructures and Their Applications. *Eur. J. Inorg. Chem.* **2009**, *2009*, 977–997.
- (9) Zhou, W. J.; Liu, X. J.; Sang, Y. H.; Zhao, Z. H.; Zhou, K.; Liu, H.; Chen, S. W. Enhanced Performance of Layered Titanate Nanowire-Based Supercapacitor Electrodes by Nickel Ion Exchange. *ACS Appl. Mater. Interfaces* **2014**, *6*, 4578–4586.
- (10) Wang, Q. G.; Gao, Q. M.; Shi, J. L. Enhanced Catalytic Activity of Hemoglobin in Organic Solvents by Layered Titanate Immobilization. *J. Am. Chem. Soc.* **2004**, *126*, 14346–14347.
- (11) Liu, H.; Duan, C. Y.; Su, X.; Dong, X. N.; Huang, Z.; Shen, W. Q.; Zhu, Z. F. A Hemoglobin Encapsulated Titania Nanosheet Modified Reduced Graphene Oxide Nanocomposite as a Mediator-free Biosensor. *Sens. Actuators, B* **2014**, *203*, 303–310.
- (12) Soh, N.; Kaneko, S.; Uozumi, K.; Ueda, T.; Kamada, K. Preparation of an Enzyme/inorganic Nanosheet/magnetic Bead Complex and its Enzymatic Activity. *J. Mater. Sci.* **2014**, *49*, 8010–8015.
- (13) Ding, X. L.; Yang, X. Q.; Zhou, L.; Lu, H. B.; Li, S. B.; Gao, Y.; Lai, C. H.; Jiang, Y. Titanate Nanowire Scaffolds Decorated with Anatase Nanocrystals Show Good Protein Adsorption and Low Cell Adhesion Capacity. *Int. J. Nanomed.* **2013**, *8*, 569–579.
- (14) Papa, A. L.; Dumont, L.; Vandroux, D.; Millot, N. Titanate Nanotubes: Towards a Novel and Safer Nanovector for Cardiomyocytes. *Nanotoxicology* **2013**, *7*, 1131–1142.
- (15) Zheng, X. T.; He, H. L.; Li, C. M. Multifunctional Graphene Quantum Dots-conjugated Titanate Nanoflowers for Fluorescence-trackable Targeted Drug Delivery. *RSC Adv.* **2013**, *3*, 24853–24857.
- (16) Magrez, A.; Horvath, L.; Smajda, R.; Salicio, V.; Pasquier, N.; Forro, L.; Schwaller, B. Cellular Toxicity of  $\text{TiO}_2$ -Based Nanofilaments. *ACS Nano* **2009**, *3*, 2274–2280.
- (17) Papa, A. L.; Boudon, J.; Bellat, V.; Loiseau, A.; Bisht, H.; Sallem, F.; Chassagnon, R.; Berard, V.; Millot, N. Dispersion of Titanate Nanotubes for Nanomedicine: Comparison of PEI and PEG Nanohybrids. *Dalton Trans.* **2015**, *44*, 739–746.
- (18) Beke, S.; Korosi, L.; Scarpellini, A.; Anjum, F.; Brandi, F. Titanate Nanotube Coatings on Biodegradable Photopolymer Scaffolds. *Mater. Sci. Eng., C* **2013**, *33*, 2460–2463.
- (19) Papa, A. L.; Maurizi, L.; Vandroux, D.; Walker, P.; Millot, N. Synthesis of Titanate Nanotubes Directly Coated with USPIO in Hydrothermal Conditions: A New Detectable Nanocarrier. *J. Phys. Chem. C* **2011**, *115*, 19012–19017.
- (20) Horváth, E.; Grebikova, L.; Maroni, P.; Szabó, T.; Magrez, A.; Forró, L.; Szilagyi, I. Dispersion Characteristics and Aggregation in Titanate Nanowire Colloids. *ChemPlusChem* **2014**, *79*, 592–600.
- (21) Szabo, T.; Toth, V.; Horvath, E.; Szilagyi, I. Formulation of Multifunctional Material Dispersions. *Chimia* **2014**, *68*, 454–454.
- (22) Szabo, T.; Toth, V.; Horvath, E.; Forro, L.; Szilagyi, I. Tuning the Aggregation of Titanate Nanowires in Aqueous Dispersions. *Langmuir* **2015**, *31*, 42–49.
- (23) Parimi, S.; Barnes, T. J.; Callen, D. F.; Prestidge, C. A. Mechanistic Insight into Cell Growth, Internalization, and Cytotoxicity of PAMAM Dendrimers. *Biomacromolecules* **2010**, *11*, 382–389.
- (24) Astruc, D.; Boisselier, E.; Ornelas, C. Dendrimers Designed for Functions: From Physical, Photophysical and Supramolecular Properties to Applications in Sensing, Catalysis, Molecular Electronics, Photonics, and Nanomedicine. *Chem. Rev.* **2010**, *110*, 1857–1959.
- (25) Liu, X. H.; Ma, D. M.; Tang, H.; Tan, L.; Xie, Q. J.; Zhang, Y. Y.; Ma, M.; Yao, S. Z. Polyamidoamine Dendrimer and Oleic Acid-Functionalized Graphene as Biocompatible and Efficient Gene Delivery Vectors. *ACS Appl. Mater. Interfaces* **2014**, *6*, 8173–8183.
- (26) Frechet, J. M. J.; Tomalia, D. A. *Dendrimers and Other Dendritic Polymers*; John Wiley: New York, 2001.
- (27) Kirkorian, K.; Ellis, A.; Twyman, L. J. Catalytic Hyperbranched Polymers as Enzyme Mimics; Exploiting the Principles of Encapsulation and Supramolecular Chemistry. *Chem. Soc. Rev.* **2012**, *41*, 6138–6159.
- (28) Cakara, D.; Kleimann, J.; Borkovec, M. Microscopic Protonation Equilibria of Poly(amidoamine) Dendrimers from Macroscopic Titrations. *Macromolecules* **2003**, *36*, 4201–4207.

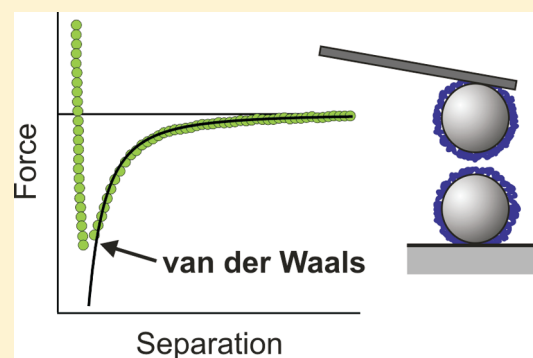
- (29) Banyai, I.; Keri, M.; Nagy, Z.; Berka, M.; Balogh, L. P. Self-diffusion of Water and Poly(amidoamine) Dendrimers in Dilute Aqueous Solutions. *Soft Matter* **2013**, *9*, 1645–1655.
- (30) Jachimska, B.; Lapczynska, M.; Zapotoczny, S. Reversible Swelling Process of Sixth-generation Poly(amido amine) Dendrimers Molecule as Determined by Quartz Crystal Microbalance Technique. *J. Phys. Chem. C* **2013**, *117*, 1136–1145.
- (31) Cheng, Y. Y.; Qu, H.; Ma, M. L.; Xu, Z. H.; Xu, P.; Fang, Y. J.; Xu, T. W. Polyamidoamine (PAMAM) Dendrimers as Biocompatible Carriers of Quinolone Antimicrobials: An in vitro study. *Eur. J. Med. Chem.* **2007**, *42*, 1032–1038.
- (32) Luo, D.; Haverstick, K.; Belcheva, N.; Han, E.; Saltzman, W. M. Poly(ethylene glycol)-Conjugated PAMAM Dendrimer for Biocompatible, High-efficiency DNA Delivery. *Macromolecules* **2002**, *35*, 3456–3462.
- (33) Tully, D. C.; Frechet, J. M. J. Dendrimers at Surfaces and Interfaces: Chemistry and Applications. *Chem. Commun.* **2001**, 1229–1239.
- (34) dos Reis, M. J.; Prevot, V.; Leroux, F.; Silverio, F.; Valim, J. B. Dendrimer Intercalation in Layered Double Hydroxides. *J. Porous Mater.* **2010**, *17*, 443–451.
- (35) Leisner, D.; Imae, T. Structural Evolution of an Interpolyelectrolyte Complex of Charged Dendrimers Interacting with Poly(L-glutamate). *J. Phys. Chem. B* **2004**, *108*, 1798–1804.
- (36) Ott, L. S.; Finke, R. G. Transition-metal Nanocluster Stabilization for Catalysis: A Critical Review of Ranking Methods and Putative Stabilizers. *Coord. Chem. Rev.* **2007**, *251*, 1075–1100.
- (37) Muresan, L.; Maroni, P.; Popa, I.; Porus, M.; Longtin, R.; Papastavrou, G.; Borkovec, M. Probing Conformational Changes of Polyamidoamine (PAMAM) Dendrimers Adsorbed on Silica Substrates. *Macromolecules* **2011**, *44*, 5069–5071.
- (38) Longtin, R.; Maroni, P.; Borkovec, M. Transition from Completely Reversible to Irreversible Adsorption of Poly(amido amine) Dendrimers on Silica. *Langmuir* **2009**, *25*, 2928–2934.
- (39) Muller, T.; Yablon, D. G.; Karchner, R.; Knapp, D.; Kleinman, M. H.; Fang, H.; Durning, C. J.; Tomalia, D. A.; Turro, N. J.; Flynn, G. W. AFM Studies of High-generation PAMAM Dendrimers at the Liquid/solid Interface. *Langmuir* **2002**, *18*, 7452–7455.
- (40) Rahman, K. M. A.; Durning, C. J.; Turro, N. J.; Tomalia, D. A. Adsorption of Poly(amidoamine) Dendrimers on Gold. *Langmuir* **2000**, *16*, 10154–10160.
- (41) Zheng, J.; Stevenson, M. S.; Hikida, R. S.; Van Patten, P. G. Influence of pH on Dendrimer-protected Nanoparticles. *J. Phys. Chem. B* **2002**, *106*, 1252–1255.
- (42) Lin, W.; Galletto, P.; Borkovec, M. Charging and Aggregation of Latex Particles by Oppositely Charged Dendrimers. *Langmuir* **2004**, *20*, 7465–7473.
- (43) Popa, I.; Papastavrou, G.; Borkovec, M. Charge Regulation Effects on Electrostatic Patch-charge Attraction Induced by Adsorbed Dendrimers. *Phys. Chem. Chem. Phys.* **2010**, *12*, 4863–4871.
- (44) Popa, I.; Papastavrou, G.; Borkovec, M.; Trulsson, M.; Jonsson, B. Long-ranged Attractive Forces Induced by Adsorbed Dendrimers: Direct Force Measurements and Computer Simulations. *Langmuir* **2009**, *25*, 12435–12438.
- (45) Finessi, M.; Szilagy, I.; Maroni, P. Dendrimer Induced Interaction Forces Between Colloidal Particles Revealed by Direct Force and Aggregation Measurements. *J. Colloid Interface Sci.* **2014**, *417*, 346–355.
- (46) Niecikowska, A.; Krasowska, M.; Ralston, J.; Malysa, K. Role of Surface Charge and Hydrophobicity in the Three-phase Contact Formation and Wetting Film Stability under Dynamic Conditions. *J. Phys. Chem. C* **2012**, *116*, 3071–3078.
- (47) Kuscer, D.; Stavber, G.; Trefalt, G.; Kosec, M. Formulation of an Aqueous Titania Suspension and its Patterning with Ink-Jet Printing Technology. *J. Am. Ceram. Soc.* **2012**, *95*, 487–493.
- (48) Hassan, P. A.; Rana, S.; Verma, G. Making Sense of Brownian Motion: Colloid Characterization by Dynamic Light Scattering. *Langmuir* **2015**, *31*, 3–12.
- (49) Quesada-Perez, M.; Gonzalez-Tovar, E.; Martin-Molina, A.; Lozada-Cassou, M.; Hidalgo-Alvarez, R. Overcharging in Colloids: Beyond the Poisson-Boltzmann Approach. *ChemPhysChem* **2003**, *4*, 234–248.
- (50) Lyklema, J. Overcharging, Charge Reversal: Chemistry or Physics? *Colloids Surf., A* **2006**, *291*, 3–12.
- (51) Faraudo, J.; Martin-Molina, A. Competing Forces in the Interaction of Polyelectrolytes with Charged Interfaces. *Curr. Opin. Colloid Interface Sci.* **2013**, *18*, 517–523.
- (52) Schneider, C.; Hanisch, M.; Wedel, B.; Jusufi, A.; Ballauff, M. Experimental Study of Electrostatically Stabilized Colloidal Particles: Colloidal Stability and Charge Reversal. *J. Colloid Interface Sci.* **2011**, *358*, 62–67.
- (53) Zaccone, A.; Wu, H.; Lattuada, M.; Morbidelli, M. Correlation Between Colloidal Stability and Surfactant Adsorption/association Phenomena Studied by Light Scattering. *J. Phys. Chem. B* **2008**, *112*, 1976–1986.
- (54) Chen, K. L.; Mylon, S. E.; Elimelech, M. Enhanced Aggregation of Alginate-coated Iron Oxide (Hematite) Nanoparticles in the Presence of, Calcium, Strontium and Barium Cations. *Langmuir* **2007**, *23*, 5920–5928.
- (55) Elimelech, M.; Gregory, J.; Jia, X.; Williams, R. A. *Particle Deposition and Aggregation: Measurement, Modeling, and Simulation*; Butterworth-Heinemann Ltd.: Oxford, U.K., 1995.
- (56) Evans, D. F.; Wennerstrom, H. *The Colloidal Domain*; John Wiley: New York, 1999.
- (57) Szilagy, I.; Trefalt, G.; Tiraferri, A.; Maroni, P.; Borkovec, M. Polyelectrolyte Adsorption, Interparticle Forces, and Colloidal Aggregation. *Soft Matter* **2014**, *10*, 2479–2502.
- (58) Leong, Y. K. Interparticle Forces Arising from an Adsorbed Strong Polyelectrolyte in Colloidal Dispersions: Charged Patch Attraction. *Colloid Polym. Sci.* **1999**, *277*, 299–305.
- (59) Szilagy, I.; Rosicka, D.; Hierrezuelo, J.; Borkovec, M. Charging and Stability of Anionic Latex Particles in the Presence of Linear Poly(ethylene imine). *J. Colloid Interface Sci.* **2011**, *360*, 580–585.
- (60) Szilagy, I.; Polomska, A.; Citherlet, D.; Sadehpour, A.; Borkovec, M. Charging and Aggregation of Negatively Charged Colloidal Latex Particles in the Presence of Multivalent Oligoamine Cations. *J. Colloid Interface Sci.* **2013**, *392*, 34–41.

# Charge Reversal of Sulfate Latex Particles by Adsorbed Linear Poly(ethylene imine) Probed by Multiparticle Colloidal Probe Technique

Marco Finessi, Prashant Sinha, István Szilágyi, Ionel Popa,<sup>†</sup> Plinio Maroni, and Michal Borkovec\*

Department of Inorganic, Analytical, and Applied Chemistry, University of Geneva, Sciences II, 30, Quai Ernest-Ansermet, 1211 Geneva 4, Switzerland

**ABSTRACT:** Interactions between negatively charged latex particles in the presence of cationic linear poly(ethylene imine) (LPEI) were studied with atomic force microscopy (AFM) and electrophoresis. Forces were measured directly with the recently developed multiparticle colloidal probe technique, which permits colloidal particles to attach to the cantilever in aqueous dispersions in situ and ensures a large surface area during experiment. It was observed that the forces vary from repulsive to attractive and back to repulsive with increasing polymer dose. The repulsive forces are due to overlap of the diffuse layers around charged surfaces. The attractive forces are independent of the ionic strength and the molecular mass of the polymer and can be rationalized in terms of classical van der Waals interactions. Additional electrostatic attractive forces due to patch-charge heterogeneities observed in other particle–polyelectrolyte systems are absent here. Their absence indicates that the adsorbed layer of LPEI has a high lateral homogeneity.



## INTRODUCTION

Polyelectrolytes adsorb strongly on oppositely charged particles, and thereby they modify the interparticle forces. For this reason, they are widely used as additives to control the stability and rheology of colloidal suspensions.<sup>1–6</sup> Important applications include papermaking, wastewater treatment, preparation of ceramic materials, or food processing.<sup>1,7–10</sup> More recently, it was realized that polyelectrolytes represent essential building blocks of functional multilayered structures.<sup>11–14</sup> Many of these applications were developed empirically, and we still only have rudimentary understanding of the mechanisms of how interaction forces are influenced by adsorbed polyelectrolytes.

Information on the interparticle forces induced by adsorbed polyelectrolytes was frequently obtained from studies of particle stability. Gregory suggested that adsorbed polyelectrolytes modify particle stability in two ways.<sup>2</sup> First, the adsorption of polyelectrolytes leads to charge neutralization at the isoelectric point (IEP) and subsequent charge reversal. Near IEP, the forces are attractive as they are dominated by van der Waals attraction, and the suspension is unstable. Away from the IEP, the surface charge induces an electrical double layer, which leads to repulsive forces, and a stable suspension. Second, the polyelectrolyte adsorbs in a laterally heterogeneous fashion, which leads to additional electrostatic patch-charge attractions. These attractions manifest themselves in an acceleration of the aggregation near the IEP, and they become stronger with increasing molecular mass of the polyelectrolyte. This effect can be understood since larger polyelectrolytes lead to larger patches on the surface and thus to stronger attractions. The correctness of this mechanism was confirmed

in subsequent and more detailed stability studies for various systems in the presence of oppositely charged polyelectrolytes as discussed elsewhere.<sup>3,4,8,15–19</sup> At higher polyelectrolyte doses, the adsorbed layer saturates and any excess polyelectrolyte remains dissolved in solution.<sup>4,18</sup> In this regime, the particle stability becomes independent of the polymer dose and is determined by repulsive electrical double-layer forces.<sup>20,21</sup>

Since the information on interparticle forces obtained from such stability studies is relatively indirect, researchers attempted to measure the resulting interaction forces directly. Popular techniques involve the surface forces apparatus (SFA) and variants thereof,<sup>22–24</sup> total internal reflection microscopy (TIRM),<sup>25</sup> and the colloidal probe technique based on atomic force microscopy (AFM).<sup>26–28</sup> Most of these studies were carried out when the polyelectrolyte was in excess, and therefore the measured forces were strongly repulsive and governed by electrical double-layer repulsion.<sup>22–24,26–31</sup> Measurements of interaction forces between surfaces whose charge neutralized by adsorbed polyelectrolytes are scarce. Such conditions have been achieved with the SFA or related techniques by exploiting the kinetics of the adsorption process<sup>22,24</sup> or with the colloidal probe technique by tuning the charge by means of solution pH.<sup>26</sup> Nevertheless, studies of the interaction forces of surfaces partially covered by polyelectrolytes are rare due to the difficulties to control the polyelectrolyte dose precisely.

Received: April 15, 2011

Revised: June 17, 2011

Published: June 20, 2011



Such measurements are now substantially facilitated by the recently developed AFM-based multiparticle colloidal probe technique whereby forces between a pair of colloidal particles are studied.<sup>32,33</sup> The advantages of this technique are 2-fold. First, the particles are attached to the cantilever and the substrate in solution, thereby avoiding the usual drying–rewetting process, which often leads to the formation of nanosized bubbles. Second, the experiments are carried out in a particle suspension, which offers a large surface area, and facilitates the precise control of the polyelectrolyte dose. With this technique it was possible to obtain detailed information on the forces induced by oppositely charged polyelectrolytes. In the two systems studied in detail, namely involving linear poly(styrene sulfonate) (PSS)<sup>32</sup> and dendritic poly(amido amine) (PAMAM),<sup>33</sup> the generic picture discussed above could be confirmed. The forces are dominated by electrostatic forces, namely by repulsive double-layer forces and by attractive patch-charge forces.

In the present study, this technique is being used to study the interaction forces between sulfate latex particles in the presence of linear poly(ethylene imine) (LPEI). While some studies have been devoted to interactions induced by branched poly(ethylene imine) (BPEI),<sup>23,27,34</sup> to the best of our knowledge no studies have been carried out with LPEI. Nevertheless, this polymer has some interesting properties, for example, LPEI is less toxic than BPEI.<sup>35</sup> Therefore, we investigated the resulting forces in this system in detail. We observe for the first time that interactions between adsorbed polyelectrolyte are dominated by repulsive electrical double-layer and attractive van der Waals interactions only and that patch-charge interactions are absent.

## EXPERIMENTAL SECTION

**Materials.** Sulfate functionalized polystyrene latex particles were obtained from Interfacial Dynamics Corporation (Portland, USA). The mean diameter of 3.1  $\mu\text{m}$  and polydispersity of 5.6% was determined with transmission electron microscopy by the manufacturer. They equally report a surface charge density of  $-67 \text{ mC/m}^2$  measured with conductometry. The sulfate latex particles were dialyzed against pure water with a cellulose membrane with a cutoff of 50 kg/mol molecular mass (Spectrum, No. 131378). The same latex particles were earlier used in related studies.<sup>33,36</sup>

Two samples of linear poly(ethylene imine) (LPEI) with molecular mass of 2.5 kg/mol and 250 kg/mol from Polysciences (Eppenheim, Germany) were used. The polydispersity indices were 1.6 and 3.4, respectively. The polymers were dissolved in 1 M HCl in an ultrasonic bath at a temperature of 60 °C overnight and subsequently dialyzed against pure water with a cellulose ester membrane with a molecular mass cutoff of 10 kg/mol for the high molecular mass polymer and of 0.5 kg/mol for the low molecular mass. The polymer concentration was measured by total organic carbon and nitrogen analysis (TOC-V, Shimadzu). The concentration of stock solutions was about 1 mg/L. The Staudinger indices for both LPEI samples were obtained by capillary viscosimetry, and found to be 27 and 137 mL/g for the molecular masses of 2.5 and 250 kg/mol, respectively. These values agree reasonably well with earlier measurements on LPEI<sup>37</sup> and BPEI.<sup>38,39</sup> The same LPEI samples were used in a related study focusing on colloidal stability.<sup>40</sup>

All solutions were prepared with Milli-Q water adjusted to pH 4 with HCl and to the desired ionic strength by eventually adding KCl. The samples were prepared by mixing 2 mL of a stock

suspension of latex particles of a concentration of about 0.1 g/L. The ionic strength is then adjusted with a KCl solution, and finally 0.01–2 mL of LPEI of concentrations in the range 0.01–1 mg/L is added to obtain a final volume of 2–8 mL. Prior to measurements, the sample was equilibrated overnight. The same sample was used to carry out the electrophoresis and direct force measurements. All measurements were performed at room temperature.

**Electrophoresis.** The electrophoretic mobility of the latex particles were carried out with ZetaNano ZS (Malvern Instruments, UK) and a ZetaCompact (CAD Instrumentation, Les Essarts le Roi, France). The electric fields were about 4–15 kV/m. The suspension was directly injected into the measurement cell. Both techniques yielded the same electrophoretic mobilities within 15%. Electrokinetic surface potentials, or  $\zeta$ -potentials, were calculated with the standard electrokinetic model developed by O'Brien and White.<sup>41</sup>

**Force Measurements.** Interaction forces between two sulfate latex particles were measured with a closed-loop AFM (MFP-3D, Asylum Research, Santa Barbara, USA) mounted on an inverted optical microscope (IX70, Olympus). A glass plate fitting the fluid cell was cleaned for 2–3 h in boiling piranha solution, which consists of a mixture of  $\text{H}_2\text{SO}_4$  (98%) and  $\text{H}_2\text{O}_2$  (30%) in a ratio of 3:1. After rinsing with Milli-Q water and drying with nitrogen, the plate was cleaned for 20 min in air plasma (PDC-32G, Harrick, New York) and finally silanized overnight in vacuum with 3-(ethoxydimethylsilyl)propylamine (Sigma-Aldrich). The silanization was verified by measuring the contact angle of water with a drop of water, which was approximately 36°. Tip-less AFM cantilevers ( $\mu\text{Masch}$ , Tallin, Estonia) were similarly cleaned in air-plasma and silanized. Prior to the experiment, the AFM fluid cell was rinsed with an electrolyte solution of the same pH and ionic strength of the sample to be investigated, which was previously degassed with a Gasstor degasser for 3 h. The particle suspension was injected into the AFM fluid cell and left overnight such that the particles would adhere to the substrate. To remove particles that did not stick to the substrate, the cell was flushed with a degassed electrolyte solution of the same ionic strength and pH as the suspension used. Subsequently, a colloidal spherical particle was picked up with the cantilever. This particle was centered above another particle on the substrate through the interference fringes observed with the optical microscope. The precision of this lateral centering is about 0.2  $\mu\text{m}$ . The zero separation was obtained from the onset of the constant compliance region with a precision of about 0.3 nm. The cantilever deflection was converted into a force by applying the Hooke's law and force constant of the cantilever in the range of 0.01–0.3 N/m. Softer cantilevers were used to detect single molecule pulling events, while with the more rigid ones, the jump-in instabilities during the measurement of the attractive force profiles upon approach can be avoided. The force constants were obtained from the average of three independent methods,<sup>42–44</sup> and these results agreed within 15%. The forces were mostly normalized to the effective radius defined as

$$R_{\text{eff}} = \frac{R_1 R_2}{R_1 + R_2} \quad (1)$$

where  $R_1$  and  $R_2$  are the radii of the interacting particles. The radii were obtained with the optical microscope with a precision of 0.2  $\mu\text{m}$ . In a typical experiment, about 100 force curves were measured. The interaction forces were obtained by averaging



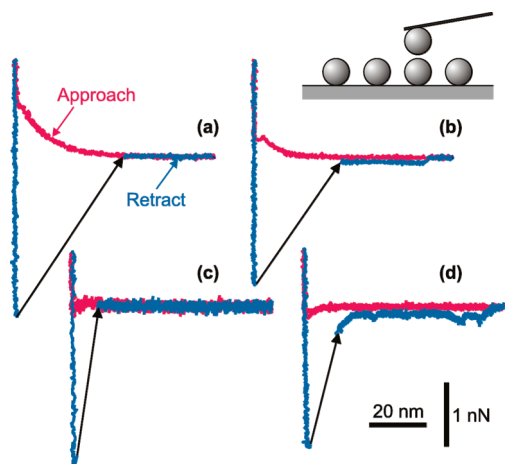


**Figure 1.** Typical individual approach-retract force curves between two sulfate latex particles with adsorbed LPEI of 250 kg/mol at pH 4. The jump-out instabilities are indicated with arrows. (a) Repulsive approach curve and short-range adhesion at a dose of 1.1 mg/g and an ionic strength of 1.1 mM. (b) Repulsive approach curve and peeling retraction event at a dose of 1.1 mg/g and an ionic strength of 3 mM. (c) Attractive approach curve and short-range adhesion at a dose of 0.28 mg/g and an ionic strength of 1.1 mM. (d) Attractive approach curve and multiple-chain retraction events at a dose of 0.28 mg/g and an ionic strength of 0.3 mM.

the approach profiles. The retraction part was analyzed for the presence of eventual single molecule pulling events. Forces were measured for 3–6 different pairs of particles.

Since the interaction forces near the IEP are extremely sensitive to minute variations in the polymer dose, the measured force profiles have often featured a minor repulsive part caused by a small but nonvanishing particle charge. These repulsive forces were subtracted by fitting the force profile at larger distances with the expected van der Waals and electrostatic force due to a diffuse layer overlap. The resulting force profiles were well reproducible for different strengths of the repulsive component and were in good agreement with the purely attractive forces observed. A similar approach was used to correct for the presence of such minor repulsive forces earlier.<sup>32,33,36,45–47</sup>

## RESULTS AND DISCUSSION

The multiparticle colloidal probe technique was used to measure interaction forces between pairs of sulfate latex particles with a diameter of 3.1  $\mu\text{m}$  in the presence of linear poly(ethylene imine) (LPEI). This cationic polyelectrolyte strongly adsorbs on the negatively charged particles and induces a charge reversal. This reversal manifests itself through weakening of the repulsive forces with increasing polymer dose up to the isoelectric point (IEP) and its subsequent strengthening beyond that point. The experiments were carried out at pH 4.0, whereby about 65% of the secondary amino groups in the LPEI are charged in solution.<sup>37</sup> The ionic strength was adjusted by adding KCl.

Figure 1 shows illustrative force profiles measured upon approach and retraction as a function of the separation distance for LPEI coated particles. At high LPEI dose, the forces are repulsive upon approach. Upon retraction, the profiles mostly show short-range adhesion and a jump-out of the cantilever, see Figure 1a. Rather infrequently, some single molecule events are observed, such as a peeling event characterized by a force plateau, see Figure 1b. At lower LPEI doses, the forces can be attractive

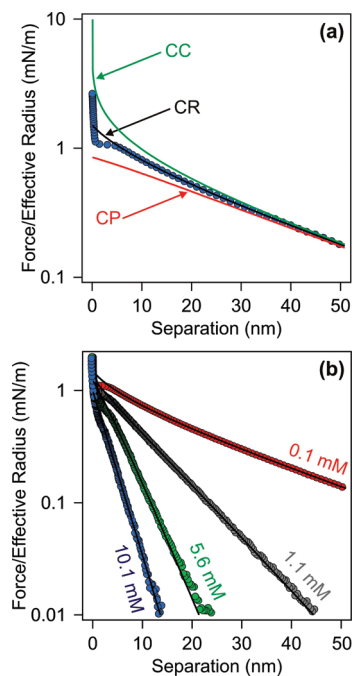


**Figure 2.** Interaction forces between sulfate latex particles as a function of the separation distance measured in KCl electrolyte solution of pH 4 with AFM. The forces have been fitted with PB theory. (a) Forces at an ionic strength of 0.1 mM compared with PB model with constant charge (CC), constant regulation (CR), and constant potential (CP) boundary conditions. (b) Different ionic strengths compared to the constant regulation boundary condition.

upon approach, and again mostly show short-ranged adhesion, see Figure 1c. In some cases, single molecule events reappear, including multiple chain events, see Figure 1d.

The short-range adhesion upon retraction is about 5 mN/m when the forces are repulsive, and this value is somewhat larger when the forces are attractive. Single molecule events are rare, and mostly consist of peeling events characterized by plateau forces in the range of 80–200 pN. Such events were observed only in <2% of all force profiles. Due to the few events observed, trends with the salt level or the polymer dose could not be established. Nevertheless, this finding clearly suggests that bridging forces are unimportant in this system.

The forces upon approach were analyzed in more detail. To improve the signal-to-noise ratio, few hundred of such force curves were recorded and averaged. The forces were further normalized to the effective radius of both particles.

**Repulsive Forces.** Forces between the bare sulfate latex particles are strongly repulsive and they are shown in Figure 2. One observes that the forces are nearly exponential, and that their range decreases with increasing ionic strength. These observations indicate that these forces originate from the overlap between the diffuse parts of the electric double layer. Indeed, the measured forces can be interpreted within Poisson–Boltzmann (PB) theory. This theory predicts that the force decays exponentially at larger distances, whereby its amplitude is related to the diffuse layer potential  $\psi_d$  while its range is given by the Debye length  $\kappa^{-1}$ . The latter quantity is related to the ionic strength  $I$  as<sup>48</sup>

$$\kappa^2 = \frac{2e^2 N_A I}{kT \epsilon \epsilon_0} \quad (2)$$

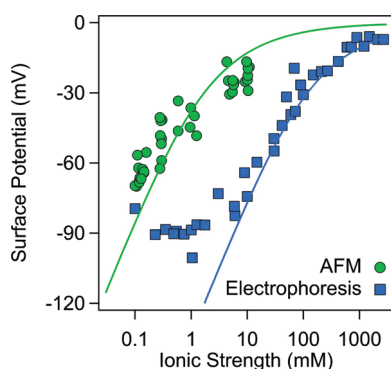


**Figure 3.** Surface potentials as a function of the ionic strength for the bare sulfate latex particles at pH 4. The solid lines are fits by PB theory. Potentials obtained by AFM are fitted with a charge of  $-3 \text{ mC/m}^2$  and the electrophoresis data with  $-25 \text{ mC/m}^2$ .

where  $e$  is the elementary charge,  $N_A$  Avogadro's number,  $I$  the ionic strength,  $k$  Boltzmann constant,  $T$  the absolute temperature, and  $\epsilon\epsilon_0$  is the permittivity of water. At shorter distances, these forces are sensitive to the boundary conditions. While the classical boundary conditions of constant charge (CC) and constant potential (CP) are insufficient to account for the detailed distance dependence, a quantitative fit can be obtained by introducing the constant regulation (CR) approximation.<sup>49</sup> This approximation introduces the so-called regulation parameter  $p$  ( $-\infty < p \leq 1$ ), and includes as special cases the classical boundary conditions of CC ( $p = 1$ ) and CP ( $p = 0$ ). Note that the regulation parameter can become negative as CP boundary condition does not represent a lower bound to the force.<sup>50</sup>

The best fit of the force at an ionic strength of 0.1 mM is shown in Figure 2a. The decay length extracted from the force curve is  $29.4 \pm 0.2 \text{ nm}$  and the diffuse layer potential is  $-70.0 \pm 0.3 \text{ mV}$ . The negative sign can be inferred from the presence of the sulfate groups on the surface of the latex particle. The regulation parameter is  $0.51 \pm 0.01$ , which indicates that the surface charge regulates strongly upon approach.

When the decay length was converted to the ionic strength with eq 2, the values always agreed within 20% with the known value from the solution composition. Larger deviations were only observed at the lowest ionic strengths, probably due to traces of dissolved carbon dioxide. The regulation parameters were about  $0.34 \pm 0.08$  and were roughly independent of the ionic strength.

The diffuse layer potential obtained from the force curves is shown in Figure 3. One observes that the magnitude of the potential decreases with increasing ionic strength as suggested by PB theory. The diffuse layer potential is expected to follow the Gouy–Chapman equation<sup>48</sup>

$$\psi_d = \frac{2kT}{e} \operatorname{asinh}\left(\frac{e\sigma}{2kT\epsilon\epsilon_0\kappa}\right) \quad (3)$$

where  $\sigma$  is the surface charge density. The diffuse layer potential yields a charge density of about  $-3.0 \text{ mC/m}^2$ . The magnitude of this value is substantially smaller than the one of the charge  $-67 \text{ mC/m}^2$  obtained by conductometry. The difference is probably due to specific adsorption of potassium ions to the particle surface.

The electrophoretic mobility of these particles was also measured, and the data confirm clearly that the particles are negatively charged. The surface potential can be extracted from

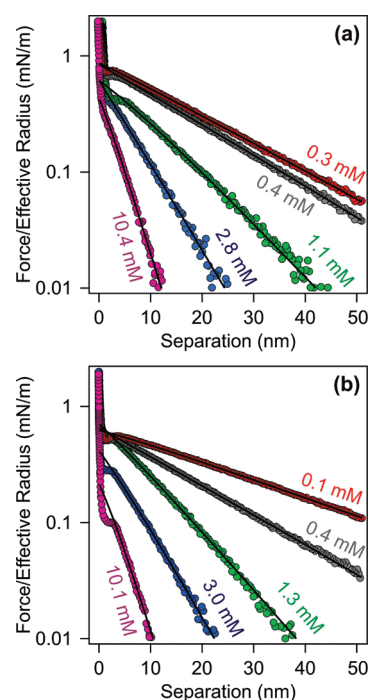


**Figure 4.** Interaction forces between sulfate latex particles as a function of the separation distance in the presence of LPEI at a dose of 1.1 mg/g measured at different ionic strengths at pH 4 with AFM. The forces have been fitted with PB theory with constant regulation (CR) approximation. Molecular mass of (a) 250 and (b) 2.5 kg/mol.

the mobilities with the standard electrokinetic model introduced by O'Brien and White.<sup>41</sup> The resulting potentials are also shown in Figure 3. While the overall trend of the surface potentials obtained from direct force measurements and electrophoresis is similar, the magnitudes of the surface potentials obtained by electrophoresis are substantially higher. At higher ionic strengths, they can be fitted with a surface charge of  $-25 \text{ mC/m}^2$ . This observation is at odds with the notion that an immobile layer at the particle surface shifts the plane of origin of the electrokinetic potential away from the one of the diffuse layer, and therefore the magnitude of the electrokinetic potential ( $\zeta$ -potential) should be smaller than of the diffuse layer potential. We suspect that the discrepancy originates from existing surface charge heterogeneities on the surface of the latex particles.<sup>51</sup> Such heterogeneities induce additional rotational motion of the particles in an external electric field and will result in electrophoretic mobilities that are higher than the ones predicted by the standard electrokinetic model.

At doses of 1.1 mg/g of LPEI or higher, the forces become again highly repulsive and they depend no longer on the polymer dose. Typical results are shown in Figure 4. The range of the forces depends strongly on the ionic strength, suggesting that they originate from double layer overlap. The forces are somewhat weaker for LPEI of the lower molecular mass than for the higher one. The forces can be quantitatively interpreted with PB theory. The best fits with the CR approximation are shown in Figure 4. The resulting Debye lengths agree within 15% with the expected value based on the ionic strength. The regulation parameters are  $0.3 \pm 0.1$ .

The resulting diffuse layer potentials are shown in Figure 5, and they decrease with increasing ionic strength. The positive

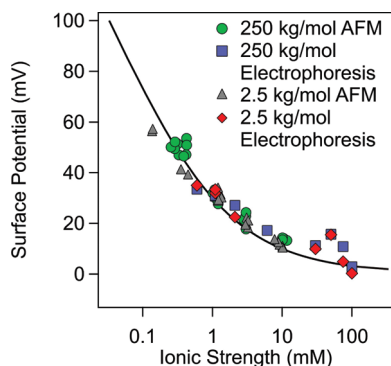


**Figure 5.** Surface potentials as a function of the ionic strength of the sulfate latex particles in the presence of LPEIs with a molecular mass of 2.5 and 250 kg/mol at a concentration of 1.1 mg/g and pH 4. Comparison between potentials obtained by AFM and electrophoresis. The solid line is the result of the PB theory.

sign of the potential can be inferred from the fact that the adsorbed LPEI is a cationic polyelectrolyte. One observes that the diffuse layer potentials are the same within experimental error for both molecular masses of LPEI. The ionic strength dependence can be again rationalized with eq 3. Best fit of the data yields a surface charge density of  $2.3 \text{ mC/m}^2$ . This value is identical to the surface charge density found by direct force measurements for saturated BPEI layers adsorbed on silica.<sup>27</sup>

In spite of some scatter in the experimental data points, the potentials obtained from electrophoretic mobilities agree very well with the ones obtained from direct force measurements. The reason for the good agreement between these two data sets can be rationalized by the fact that the adsorbed LPEI layer is laterally homogeneous, and for that reason the standard electrokinetic model is valid. Similarly good agreement between surface potentials obtained from electrokinetics and direct force measurements was found for saturated PSS layers adsorbed on amidine latex particles.<sup>47</sup>

**Charge Reversal and Attractive Forces.** Although the measurements of the forces in the absence and excess of LPEI could have also been carried out with the classical two-particle colloidal probe technique, the use of the multiparticle technique becomes essential for measurements at intermediate LPEI doses. Under these conditions, the added LPEI adsorbs quantitatively and the adsorbed amount can be only controlled with sufficient precision when the available surface area is sufficiently high. Although the control of this quantity is basically impossible with two particles of a surface area of few  $\mu\text{m}^2$ , this quantity can be accurately tuned when working in a suspension, where the surface exceeds several  $\text{m}^2$ .

Figure 6 shows the force profiles for different doses of LPEI with a molecular mass of 250 kg/mol. In the absence of LPEI, the particles are negatively charged and their force is strongly repulsive due to diffuse layer overlap, see Figure 6a. With increasing LPEI dose, the negative surface charge is progressively neutralized by the positively charged adsorbed LPEI, which reduces the magnitude of the surface potential and the strength of the repulsive force. As this strength is being reduced, an attractive force becomes apparent at short distances. At a dose of 0.28 mg/g, the repulsive force disappears and the force is now purely attractive, and the adsorbed polyelectrolyte precisely neutralizes the surface of the particle and a diffuse layer is no longer present. At this point, about 3 charges on the LPEI

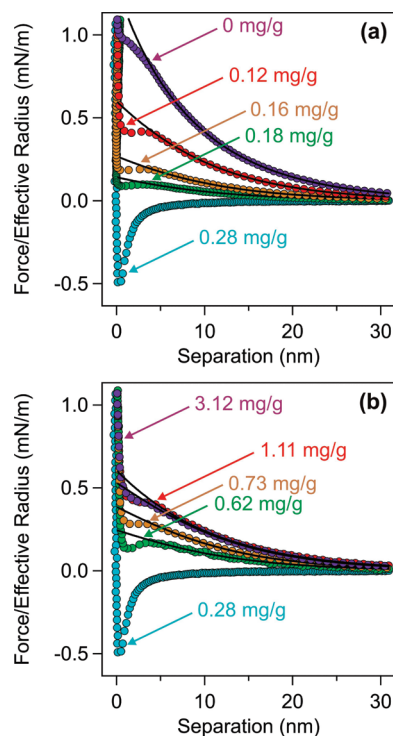


**Figure 6.** Interaction forces between sulfate latex particles as a function of the separation distance for various doses of LPEI of a molecular mass of 250 kg/mol at an ionic strength of 1.1 mM and pH 4. The forces are fitted with PB theory with constant regulation (CR) approximation. Polymer dose (a) below and at IEP and (b) at IEP and above.

neutralize one charge on the particle surface. Such superstoichiometric charging ratio indicates that during the adsorption of LPEI coadsorption of anions occurs.<sup>18</sup> The short-range attractive forces are equally apparent in Figure 2, but they are masked by the strongly repulsive double-layer forces and jump-in instabilities.

When the dose is increased beyond 0.28 mg/g, the forces become again repulsive due to diffuse layer overlap, see Figure 6b. In this regime, the LPEI continues to adsorb to the surface beyond the charge neutralization point due to electrostatic correlation forces and attractive hydrophobic interactions. As a consequence, a charge reversal takes place and the surface now becomes positively charged. A diffuse layer builds up again near such a charged surface and its presence manifests itself by repulsive forces due to diffuse layer overlap.

As the LPEI dose is increased further, the adsorption process saturates, and a maximum adsorbed amount is reached. When LPEI is added beyond this dose, the adsorbed amount does not increase any further and excess polymer remains dissolved in solution. Due to the constant adsorbed amount, the surface charge density remains constant as well, and thus the forces no longer vary with increasing the polymer dose. This aspect is illustrated in Figure 6b as the forces remain constant beyond a LPEI dose of 1.1 mg/g. The short-range attractive forces remain visible in the force profiles all the way up to saturation, but they are probably blurred by jump-in instabilities, see also Figure 4.

The repulsive part of these forces was fitted with the solution of PB equation within the CR approximation as discussed above. The fitted decay lengths agreed with the expected one based on the ionic strength within 10%. The regulation parameters were in



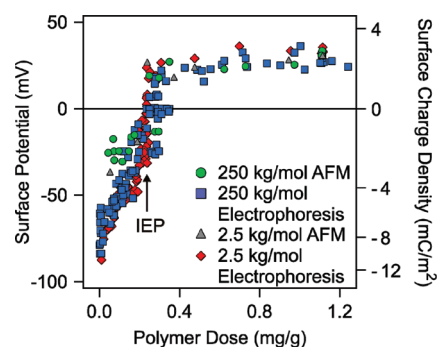


**Figure 7.** Surface potentials of sulfate latex particles as a function of polymer dose at an ionic strength of 1.1 mM and pH 4 obtained by AFM and electrophoresis. The surface charge density obtained from PB theory is indicated on the left axis in a nonlinear scale.

the range of  $0.3 \pm 0.1$ . The resulting diffuse layer potentials are compared with the electrokinetic potentials in Figure 7. One observes that the surface potentials obtained by the different techniques give very similar results. In particular, the dose needed to reach the IEP, at which the electrophoretic mobility is zero, coincides perfectly well with the dose at which repulsive diffuse layer overlap force vanishes. The only disagreement between the surface potentials obtained from direct force measurements and electrophoresis occurs at low LPEI dose. Recall that a similar disagreement was observed for the bare latex particles in the absence of any added LPEI, and interpreted in terms of surface charge heterogeneities. When the dose of LPEI remains low, these charge heterogeneities are not completely covered up by adsorbed LPEI, and the discrepancies persist up to a dose of about 0.1 mg/g. When the adsorbed amount increases beyond this point, the adsorbed LPEI generates a relatively homogeneous surface and good agreement between the surface potentials obtained from force measurements and electrophoresis is found. On the basis of the electrophoresis results, one observes that surface potential increases slowly with the polymer dose, and near the IEP makes a sudden transition up to the plateau. Similar behavior was observed during the charge reversal of amidine latex particles with PSS and of sulfate latex with PAMAM dendrimers.<sup>47,52</sup> This effect was interpreted by the lateral overlap of the diffuse layers around the individual polyelectrolyte chains.

Figure 8 shows the attractive forces at IEP. The maximal attractive force observed at short distances is lower when the surface charge is neutralized with the high molecular mass LPEI than for the low molecular mass. At larger distances, however, the distance dependence of these forces is remarkably independent of the ionic strength and the molecular mass. The latter behavior suggests that the attractive force is due to van der Waals dispersion interactions. Neglecting retardation effects, attractive dispersion force can be written as<sup>48</sup>

$$\frac{F}{R_{\text{eff}}} = -\frac{H}{6} \frac{1}{(h + \delta)^2} \quad (4)$$

where  $H$  is the Hamaker constant and  $\delta$  an eventual shift of the plane of origin of the van der Waals force with respect to the contact plane. The observed forces are fitted with  $H \approx 9.0 \times 10^{-21}$  J as was predicted from the dielectric spectra of polystyrene and water.<sup>53</sup> To obtain good agreement with the observed force profiles, a shift of  $\delta \approx 0.85$  nm must be chosen. This shift is likely to be related to surface roughness, whose root-mean-

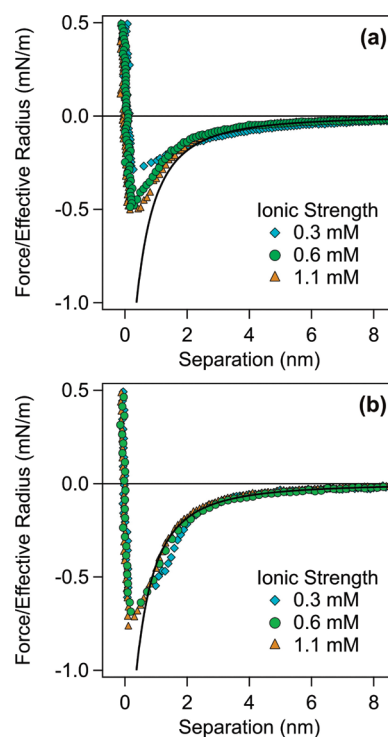


**Figure 8.** Interaction forces between sulfate latex particles as a function of the separation distance at different KCl concentrations at a LPEI dose of 0.28 mg/g (IEP) and pH 4. The solid line is the best fit with van der Waals theory. Molecular mass of (a) 250 and (b) 2.5 kg/mol.

square variation is about 1.3 nm as estimated from AFM topographic images.<sup>36</sup> The attractive force can be equally rationalized without a shift ( $\delta = 0$ ) but with a Hamaker constant of about a factor of 3–4 smaller. Therefore, the attractive forces are governed by van der Waals forces and there is no evidence of any additional attractive forces due to adsorbed LPEI. When the van der Waals force is determined in this way, one can also rationalize the short-ranged attractive part in the force profiles away from IEP in an approximate way.

The insensitivity of the attractive force to the ionic strength and molecular mass of the polyelectrolyte is in marked contrast to previous measurements of attractive forces between charged latex particles and oppositely charged polyelectrolytes at IEP.<sup>32,33,36,47</sup> These studies have focused on sulfate latex particles in the presence of PAMAM dendrimers and amidine latex particles in the presence of PSS. Both systems revealed substantially stronger attractive forces than the ones observed here, especially for high molecular mass polyelectrolytes at low ionic strength. The additional attractions were interpreted by lateral patch charge heterogeneities induced by the charged adsorbed polymers on the oppositely charged particle surface. These patch-charge heterogeneities were most pronounced for high molecular mass adsorbed PAMAM dendrimers. This regime is probably reminiscent to the dilute 2-d Wigner regime proposed by Dobrynin et al.<sup>54</sup> In this regime, the adsorbed layer consists of individual polyelectrolyte chains with minimal overlap.

From this point of view, the present results suggest that the layer of adsorbed LPEI is relatively homogeneous. Therefore, the LPEI molecules have to adsorb in an extended state. This regime could be similar to the semidilute 2-d Wigner regime introduced by Dobrynin et al.<sup>54</sup> Thereby, the individual chains lie flat on the



surface and they cross many times, which leads to denser network of adsorbed polyelectrolyte chains. Such a network would be much less laterally heterogeneous than the dilute 2-d Wigner regime, and could be the reason why no forces due to patch-charge attraction are observed. The polydispersity of LPEI could represent another reason for this behavior, at least partially. This novel observation is in contrast with previous reports that attractive forces between adsorbed polyelectrolyte layers exceed van der Waals forces substantially.<sup>24,33,47</sup>

## CONCLUSIONS

Direct force measurement between negatively charged latex particles in the presence of cationic linear poly(ethylene imine) (LPEI) were carried out with the AFM-based multiparticle colloidal probe technique. With increasing polymer dose, the forces vary from repulsive to attractive and back to repulsive. The remarkable point is that the attractive forces are independent of the ionic strength and the molecular mass of the polymer, and they are well described with classical van der Waals interactions. This behavior has not been described before and is in contrast with earlier reports in similar systems where additional electrostatic attractive forces due to patch-charge heterogeneities were observed.<sup>36,47</sup> Stability studies in a very similar system involving LPEI confirm the absence of patch-charge interactions independently.<sup>40</sup> The fact that these forces are unimportant in the present system indicates that the adsorbed layer of LPEI is unusually homogeneous and probably resembles the semidilute 2-d Wigner regime.

## AUTHOR INFORMATION

### Corresponding Author

\*Phone: +41 22 379 6053. Fax: +41 22 379 6069. E-mail: michal.borkovec@unige.ch.

### Present Addresses

<sup>†</sup>Department of Biological Sciences, Columbia University, New York, 10027 New York, United States.

## ACKNOWLEDGMENT

This work was supported by the COST Action D43, State Secretariat for Education and Research, Swiss National Science Foundation, and the University of Geneva. We thank Mihail Popescu to pointing out the role of surface charge heterogeneities on electrokinetic effects.

## REFERENCES

- (1) Bolto, B.; Gregory, J. *Water Res.* **2007**, *41*, 2301–2324.
- (2) Gregory, J. *J. Colloid Interface Sci.* **1973**, *42*, 448–456.
- (3) Borkovec, M.; Papastavrou, G. *Curr. Opin. Colloid Interface Sci.* **2008**, *13*, 429–437.
- (4) Bauer, D.; Buchhammer, H.; Fuchs, A.; Jaeger, W.; Killmann, E.; Lunkwitz, K.; Rehmet, R.; Schwarz, S. *Colloids Surf. A* **1999**, *156*, 291–305.
- (5) Howe, A. M.; Wesley, R. D.; Bertrand, M.; Cote, M.; Leroy, J. *Langmuir* **2006**, *22*, 4518–4525.
- (6) Chen, K. L.; Elimelech, M. *Environ. Sci. Technol.* **2008**, *42*, 7607–7614.
- (7) Horn, D., Polyethylenimine: Physicochemical properties and applications. In *Polymeric amines and ammonium salts*; Goethals, E. J., Ed.; Pergamon Press: New York, 1980; pp 333–355.
- (8) Schwarz, S.; Jaeger, W.; Paulke, B. R.; Bratskaya, S.; Smolka, N.; Bohrisch, J. *J. Phys. Chem. B* **2007**, *111*, 8649–8654.
- (9) Lewis, J. A.; Matsuyama, H.; Kirby, G.; Morissette, S.; Young, J. F. *J. Am. Ceram. Soc.* **2000**, *83*, 1905–1913.
- (10) Mezzenga, R.; Schurtenberger, P.; Burbidge, A.; Michel, M. *Nat. Mater.* **2005**, *4*, 729–740.
- (11) Decher, G. *Science* **1997**, *277*, 1232–1237.
- (12) Shchukin, D. G.; Sukhorukov, G. B.; Möhwald, H. *Angew. Chem., Int. Ed.* **2003**, *42*, 4472–4475.
- (13) Schlenoff, J. B. *Langmuir* **2009**, *25*, 14007–14010.
- (14) Block, S.; Helm, C. A. *Macromolecules* **2009**, *42*, 6733–6740.
- (15) Ashmore, M.; Hearn, J. *Langmuir* **2000**, *16*, 4906–4911.
- (16) Gillies, G.; Lin, W.; Borkovec, M. *J. Phys. Chem. B* **2007**, *111*, 8626–8633.
- (17) Yu, W. L.; Bouyer, F.; Borkovec, M. *J. Colloid Interface Sci.* **2001**, *241*, 392–399.
- (18) Kleimann, J.; Gehin-Delval, C.; Auweter, H.; Borkovec, M. *Langmuir* **2005**, *21*, 3688–3698.
- (19) Walker, H. W.; Grant, S. B. *Colloids Surf. A* **1996**, *119*, 229–239.
- (20) Hierrezuelo, J.; Sadeghpour, A.; Szilagyi, I.; Vaccaro, A.; Borkovec, M. *Langmuir* **2010**, *26*, 15109–15111.
- (21) Hierrezuelo, J.; Vaccaro, A.; Borkovec, M. *J. Colloid Interface Sci.* **2010**, *347*, 202–208.
- (22) Dahlgren, M. A. G.; Waltermo, A.; Blomberg, E.; Claesson, P. M.; Sjöstrom, L.; Akesson, T.; Jonsson, B. *J. Phys. Chem.* **1993**, *97*, 11769–11775.
- (23) Poptoshev, E.; Claesson, P. M. *Langmuir* **2002**, *18*, 2590–2594.
- (24) Poptoshev, E.; Rutland, M. W.; Claesson, P. M. *Langmuir* **1999**, *15*, 7789–7794.
- (25) Biggs, S.; Dagastine, R. R.; Prieve, D. C. *J. Phys. Chem. B* **2002**, *106*, 11557–11564.
- (26) Hartley, P. G.; Scales, P. J. *Langmuir* **1998**, *14*, 6948–6955.
- (27) Pericet-Camara, R.; Papastavrou, G.; Behrens, S. H.; Helm, C. A.; Borkovec, M. *J. Colloid Interface Sci.* **2006**, *296*, 496–506.
- (28) Kirwan, L. J.; Maroni, P.; Behrens, S. H.; Papastavrou, G.; Borkovec, M. *J. Phys. Chem. B* **2008**, *112*, 14609–14619.
- (29) Nnebe, I. M.; Tilton, R. D.; Schneider, J. W. *J. Colloid Interface Sci.* **2004**, *276*, 306–316.
- (30) Ruths, M.; Sukhishvili, S. A.; Granick, S. *J. Phys. Chem. B* **2001**, *105*, 6202–6210.
- (31) Maurice, G.; Meagher, L.; Ennis, J.; Gee, M. L. *Langmuir* **2001**, *34*, 4151–4158.
- (32) Popa, I.; Gillies, G.; Papastavrou, G.; Borkovec, M. *J. Phys. Chem. B* **2009**, *113*, 8458–8461.
- (33) Popa, I.; Papastavrou, G.; Borkovec, M.; Trulsson, M.; Jonsson, B. *Langmuir* **2009**, *25*, 12435–12438.
- (34) Bouyer, F.; Robben, A.; Yu, W. L.; Borkovec, M. *Langmuir* **2001**, *17*, 5225–5231.
- (35) Wightman, L.; Kircheis, R.; Rossler, V.; Carotta, S.; Ruzicka, R.; Kurs, M.; Wagner, E. *J. Gene. Med.* **2001**, *3*, 362–372.
- (36) Popa, I.; Papastavrou, G.; Borkovec, M. *Phys. Chem. Chem. Phys.* **2010**, *12*, 4863–4871.
- (37) Smits, R. G.; Koper, G. J. M.; Mandel, M. *J. Phys. Chem.* **1993**, *97*, 5745–5751.
- (38) Park, I. H.; Choi, E. J. *Polymer* **1996**, *37*, 313–319.
- (39) von Harpe, A.; Petersen, H.; Li, Y. X.; Kissel, T. *J. Controlled Release* **2000**, *69*, 309–322.
- (40) Szilagyi, I.; Rosicka, D.; Hierrezuelo, J.; Borkovec, M. *J. Colloid Interface Sci.* **2011**, *360*, 580–585.
- (41) O'Brien, R. W.; White, L. R. *J. Chem. Soc. Farad. Trans. 2* **1978**, *74*, 1607–1626.
- (42) Sader, J. E.; Larson, I.; Mulvaney, P.; White, L. R. *Rev. Sci. Instrum.* **1995**, *66*, 3789–3798.
- (43) Cleveland, J. P.; Manne, S.; Bocek, D.; Hansma, P. K. *Rev. Sci. Instrum.* **1993**, *64*, 403–405.
- (44) Hutter, J. L.; Bechhoefer, J. *Rev. Sci. Instrum.* **1993**, *64*, 1868–1873.
- (45) Lokar, W. J.; Ducker, W. A. *Langmuir* **2004**, *20*, 378–388.

- (46) Zohar, O.; Leizeron, I.; Sivan, U. *Phys. Rev. Lett.* **2006**, *96*, 177802.
- (47) Popa, I.; Gillies, G.; Papastavrou, G.; Borkovec, M. *J. Phys. Chem. B* **2010**, *114*, 3170–3177.
- (48) Russel, W. B.; Saville, D. A.; Schowalter, W. R. *Colloidal Dispersions*; Cambridge University Press: Cambridge, U.K., 1989.
- (49) Pericet-Camara, R.; Papastavrou, G.; Behrens, S. H.; Borkovec, M. *J. Phys. Chem. B* **2004**, *108*, 19467–19475.
- (50) Borkovec, M.; Behrens, S. H. *J. Phys. Chem. B* **2008**, *112*, 10795–10799.
- (51) Anderson, J. L. *J. Colloid Interface Sci.* **1985**, *105*, 45–54.
- (52) Popa, I.; Papastavrou, G.; Borkovec, M. *Macromolecules* **2010**, *43*, 1129–1136.
- (53) Bevan, M. A.; Prieve, D. C. *Langmuir* **1999**, *15*, 7925–7936.
- (54) Dobrynin, A. V.; Deshkovski, A.; Rubinstein, M. *Macromolecules* **2001**, *34*, 3421–3436.

## PAPER



Cite this: *Phys. Chem. Chem. Phys.*,  
2020, 22, 24764

## Masking specific effects of ionic liquid constituents at the solid–liquid interface by surface functionalization†

Bojana Katana,<sup>‡a</sup> Dóra Takács,<sup>‡a</sup> Felix D. Bobbink,<sup>id b</sup> Paul J. Dyson,<sup>id b</sup>  
Nizar B. Alsharif,<sup>a</sup> Matija Tomšič<sup>id c</sup> and Istvan Szilagyi<sup>id \*a</sup>

Ion specific effects of ionic liquid (IL) constituents on the surface charge and aggregation properties of two types of particles (positively charged amidine (AL) and polyimidazolium-functionalized sulfate (SL-IP-2) latexes) were investigated in IL solutions containing different anions and the 1-butyl-3-methylimidazolium cation. For the AL systems, the affinity of IL anions to the particle surface followed the sequence chloride < bromide < nitrate < acetate. The critical coagulation concentration values decreased in the same order indicating that ion specific adsorption determines the surface charge density and the extent of the repulsive interparticle forces. In contrast, no tendencies were observed for the SL-IP-2 particles, *i.e.*, both charge and aggregation features were insensitive to the type of anions. This surprising behavior sheds light on that surface functionalization with the polyimidazolium compound effectively masks interfacial ion specific effects. These results indicate new possible routes to the design of processable particle dispersions in ILs irrespective of their composition.

Received 24th May 2020,  
Accepted 16th October 2020

DOI: 10.1039/d0cp02805c

rsc.li/pccp

## 1 Introduction

Ionic liquids (ILs) continue to attract widespread interest due to their advantageous properties such as low vapor pressure, wide electrochemical window and their capacity to be structurally tuned for specific tasks such as for the functionalization of surfaces.<sup>1–3</sup> The assembly of the IL cations and anions at solid–liquid interfaces has been extensively studied, since ion specific effects play a major role in the physico-chemical properties of surfaces immersed in ILs or in their solutions.<sup>4–6</sup> The interfacial structure is responsible for reduced friction between surfaces,<sup>7</sup> exfoliation of layered materials<sup>8</sup> and stabilization of various particles in ILs.<sup>9–13</sup> In addition, specific interactions of IL ions with synthetic and natural macromolecules influence the stability of enzymes,<sup>14</sup> the rate of amyloid fibrillation<sup>15</sup> and phase transition behavior<sup>16</sup> through tailoring the inter and intramolecular forces.

The origin of ion specific effects on surface forces has been systematically explored by optical tweezer,<sup>17</sup> atomic force microscope<sup>18</sup> and surface force apparatus<sup>19</sup> in aqueous solutions of ILs and one of the main conclusions was that different affinity of the cations and anions for the surface may cause significant variation in the charge density upon ion adsorption. Consequently, this variation results in different extents of electrostatic repulsions between surfaces. Similar hypotheses were also reported on the basis of particle aggregation experiments in IL–water mixtures.<sup>9,20,21</sup> Moreover, theoretical studies shed light on the fact that the interfacial assembly of IL ions mainly depends on the composition of the surface, concentration and structure of the ILs.<sup>10,22</sup>

The IL cations and anions may be arranged in series based on their effects on the surface charge and interaction forces, similar to the Hofmeister series of ions, which was originally constructed for protein destabilization by simple salts.<sup>21,23,24</sup> Despite the fact that understanding the interfacial assembly of ILs is of huge importance during development of advanced materials in energy storage,<sup>25–27</sup> electrochemistry<sup>28</sup> and the preparation of novel catalysts,<sup>29</sup> only a few studies dealt with the systematic assessment of the effect of IL constituents on the charge and aggregation features of particles.<sup>9,20,21</sup> Another important aspect is that ion specific effects often hinder the application of IL mixtures to disperse and stabilize particles successfully. For instance, different affinity of the ions to the surfaces leads to asymmetric arrangement of the IL constituents near the surface, which may induce destabilization of the dispersions. Therefore, the possibility

<sup>a</sup> MTA-SZTE Lendület Biocolloids Research Group, Interdisciplinary Excellence Centre, Department of Physical Chemistry and Materials Science, University of Szeged, H-6720 Szeged, Hungary. E-mail: szistvan@chem.u-szeged.hu; Tel: +36 62 343255

<sup>b</sup> Institute of Chemical Sciences and Engineering, École Polytechnique Fédérale de Lausanne (EPFL), CH-1015 Lausanne, Switzerland

<sup>c</sup> Faculty of Chemistry and Chemical Technology, University of Ljubljana, Večna pot 113, SI-1000 Ljubljana, Slovenia

† Electronic supplementary information (ESI) available. See DOI: 10.1039/d0cp02805c

‡ These authors contributed equally to the work.

of masking interfacial ion specific effects would be beneficial in terms of gaining the stability of numerous systems. Nevertheless, to the best of our knowledge, no papers have been published on this topic yet.

In the present study, surface charges and colloidal stability of polymeric particles were investigated in the presence of aqueous IL solutions containing chloride ( $\text{Cl}^-$ ), bromide ( $\text{Br}^-$ ), nitrate ( $\text{NO}_3^-$ ) or acetate ( $\text{Ac}^-$ ) anions and the 1-butyl-3-methylimidazolium ( $\text{BMIM}^+$ ) cation. Two types of positively charged particles were studied, namely, polystyrene-based amidine latex (AL) and SL-IP-2 consisting of a sulfate latex (SL) functionalized with an imidazolium-based polymer (IP-2). In this way, ion specificity was explored with polymeric particles of the same sign of charge, but with different surface functionalities.

## 2 Experimental

### 2.1 Materials

Spherical polystyrene latex particles functionalized with sulfate (SL) or amidine (AL) groups were purchased from Thermo Fischer Scientific. The particle size and the charge density of the bare surfaces were determined by the manufacturer using transmission electron microscopy (TEM) and conductometric titration, respectively. The SL has a mean diameter of 430 nm, a polydispersity expressed as coefficient of variation of 1.8%, solid content of 8.1% (w/v%), specific surface area of  $1.3 \times 10^5 \text{ cm}^2 \text{ g}^{-1}$  and a charge density of  $-12 \text{ mC m}^{-2}$ . In the case of the AL, the corresponding quantities are 510 nm, 4.6%, 4.1%,  $1.1 \times 10^5 \text{ cm}^2 \text{ g}^{-1}$  and  $+197 \text{ mC m}^{-2}$ .

The polyimidazolium-based polymer (IP-2) was synthesized using a literature protocol.<sup>30</sup> Briefly, 1,4-bis(chloromethyl)benzene and 1-(trimethylsilyl)imidazole were dissolved in acetonitrile in 1 : 1 molar ratio in a Schlenk-flask. The mixture was heated to reflux for 48 h. The white solid product was removed by filtration, washed with acetonitrile and diethyl ether followed by drying under vacuum for 24 h. All chemicals used for the synthesis are from Sigma-Aldrich. The successful synthesis was confirmed with FT-IR spectroscopy by identifying the characteristic vibration peaks of IP-2 at 1150, 1560 and  $1625 \text{ cm}^{-1}$  (for the spectrum see Fig. S1 in the ESI†).<sup>30</sup>

Analytical grade potassium chloride (KCl) was purchased from VWR. The ILs, 1-butyl-3-methylimidazolium nitrate ( $\text{BMIMNO}_3$ ,  $\geq 95\%$ ), 1-butyl-3-methylimidazolium chloride ( $\text{BMIMCl}$ ,  $\geq 98\%$ ), 1-butyl-3-methylimidazolium acetate ( $\text{BMIMAc}$ ,  $\geq 95\%$ ) and 1-butyl-3-methylimidazolium bromide ( $\text{BMIMBr}$ ,  $> 97\%$ ) were purchased from Sigma-Aldrich. During sample preparation, ultrapure water was obtained from a Puranity TU+ (VWR) apparatus. The water and the salt solutions were filtered with  $0.1 \mu\text{m}$  syringe filters (Millex) to avoid dust contamination. All measurements were carried out at  $25 \text{ }^\circ\text{C}$  and pH value of 4 set by HCl (VWR) stock solutions.

The IP-2-modified SL stock dispersion (denoted as SL-IP-2 thereafter) was prepared by simple mixing of proper volumes of IP-2 of  $100 \text{ mg L}^{-1}$  concentration, SL particle stock solution of  $10 \text{ g L}^{-1}$  and ultrapure water.

### 2.2 Characterization of IP-2 and the ILs

The FT-IR spectrum was recorded on a JASCO FT-IR-4700 spectrometer equipped with a DTGS detector in attenuated total reflectance mode. Spectral resolution was  $4 \text{ cm}^{-1}$  with 256 scans collected for the spectrum, which was recorded in the wavenumber range of  $1800\text{--}1000 \text{ cm}^{-1}$ .

Refractive index and viscosity measurements were carried out with an Anton Paar Abbemat 3200 refractometer and a capillary viscometer, respectively. These data were used for the analysis of the light scattering measurements. For the data treatment, see Fig. S2a, b and Table S1 in the ESI.†

### 2.3 Electrophoresis

Electrophoretic mobility was measured with a Litesizer 500 instrument (Anton Paar) equipped with a 40 mW semiconductor laser of 658 nm wavelength operating in the backscattering mode at a scattering angle of  $175^\circ$ . For the determination of the electrophoretic mobilities, 2.0 mL samples were prepared. In brief, 0.4 mL particle dispersions of  $80 \text{ mg L}^{-1}$  or 0.2 mL of  $100 \text{ mg L}^{-1}$  concentration for AL and SL-IP-2, respectively, was added to 1.6 mL or 1.8 mL of solutions composed of ILs or KCl at appropriate concentrations. The samples were left to rest for 2 h at room temperature before measuring the electrophoretic mobilities, which occurred after 1 min equilibration time in the device. The reported values were the average of five individual measurements with a maximum standard deviation of  $\pm 5 \text{ mV}$ . The experiments were performed in  $350 \mu\text{L}$  volume  $\Omega$ -shaped plastic cuvettes or with the Univette (Anton Paar) accessory.

The measured electrophoretic mobility ( $u$ ) was converted to zeta potential ( $\zeta$ ) with the Smoluchowski equation as follows<sup>31</sup>

$$\zeta = u\eta/\varepsilon_0\varepsilon \quad (1)$$

where  $\varepsilon_0$  is the dielectric permittivity of vacuum and  $\varepsilon$  is the dielectric constant of water, with values of  $8.854 \times 10^{-12} \text{ F m}^{-1}$  and 78.5, respectively. The charge density at the slip plane ( $\sigma$ ) was calculated according to the Debye–Hückel model<sup>32</sup> as

$$\sigma = \varepsilon\varepsilon_0\kappa\zeta \quad (2)$$

where  $\kappa$  is the inverse Debye length, which contains the contribution of the ionic species to the electrical double layer and can be calculated for the IL solutions as<sup>31</sup>

$$\kappa = \sqrt{2N_A e^2 c_{\text{IL}} / \varepsilon_0 \varepsilon k_B T} \quad (3)$$

where  $N_A$  is Avogadro's number,  $e$  is the elementary charge,  $k_B$  is the Boltzmann constant and  $T$  is the absolute temperature.

### 2.4 Dynamic light scattering

The hydrodynamic radius ( $R_h$ ) of the particles was measured by dynamic light scattering (DLS) using a NIBS High-Performance Particle Sizer (ALV) equipped with a 3 mW He–Ne laser of 633 nm wavelength. The scattering angle was  $173^\circ$ , the correlation function was collected for 20 s and was fitted with the cumulant method<sup>33</sup> to obtain the decay rate constant ( $\Gamma$ ). The diffusion coefficient ( $D$ ) was calculated as



$$D = \Gamma/q^2 \quad (4)$$

where  $q$  is the scattering vector, which can be estimated using the parameters of the experimental setup as follows

$$q = (4\pi n/\lambda)\sin(\Theta/2) \quad (5)$$

where  $n$  is the refractive index of the medium,  $\lambda$  is the wavelength of the laser beam and  $\Theta$  is the scattering angle. The refractive indices of the IL solutions were determined and eqn (S1) (ESI†) was used for data interpolation. The  $R_h$  was then calculated with Stokes–Einstein equation<sup>34</sup> as

$$R_h = k_B T / 6\eta\pi D \quad (6)$$

The viscosity data points were interpolated using eqn (S2) (ESI†). Time-resolved DLS measurements were carried out to assess the possible aggregation processes in the samples. Typical results of these measurements, where 100–250 runs were performed depending on the speed of aggregation, are shown in Fig. S3 (ESI†). During sample preparation, 2 mL dispersions were prepared. The ionic strength or IL dose was adjusted by mixing appropriate amounts of stock solutions and the time-resolved DLS measurements were initiated by adding the desired volume of particle stock dispersions to the solutions containing all other components. The particle concentration was 16 mg L<sup>-1</sup> ( $2.18 \times 10^{14}$  m<sup>-3</sup>) for AL and 10 mg L<sup>-1</sup> ( $2.28 \times 10^{14}$  m<sup>-3</sup>) for SL-IP-2. These particle doses were good compromises to avoid the formation of higher ranked aggregates and to maintain sufficient scattered intensity for the light scattering experiments. The aggregation rate coefficient ( $k$ ) was calculated from the time dependent  $R_h$  values as<sup>33</sup>

$$(1/R_h^1)(dR_h/dt) = (I_2/2I_1)(1 - (R_h^1/R_h^2))kN_0 \quad (7)$$

where  $t$  is the experiment time,  $N_0$  is the number concentration of the particles,  $R_h^1$  and  $R_h^2$  are the hydrodynamic radius of the monomer and dimer, respectively. Note that only dimer formation is assumed until 40% increase in the hydrodynamic radius.<sup>33</sup> The contribution of the form factors of the monomer ( $I_1$ ) and dimer ( $I_2$ ) to the scattered intensity was calculated with the theory developed by Rayleigh, Debye and Gans<sup>33</sup>

$$I_2/2I_1 = 1 + (\sin(2Rq)/2Rq) \quad (8)$$

where  $R$  is the geometric radius of the particle. The colloidal stability of the samples was expressed in terms of stability ratio ( $W$ ), which can be calculated as

$$W = k_{\text{fast}}/k \quad (9)$$

where the  $k_{\text{fast}}$  was determined in 1 M KCl solutions, in which the repulsive double layer forces vanish and the particles undergo rapid aggregation, as predicted by the theory of Derjaguin, Landau, Verwey and Overbeek (DLVO).<sup>32,35</sup> The  $k_{\text{fast}}$  values were found to be  $5.70 \times 10^{-18}$  m<sup>3</sup> s<sup>-1</sup> and  $3.33 \times 10^{-18}$  m<sup>3</sup> s<sup>-1</sup> for the AL and SL-IP-2 particles, respectively. These data are similar to the ones obtained for latex particles earlier in the presence of monovalent electrolytes.<sup>21,36</sup> Note that the stability ratio is one in case of unstable dispersions, *i.e.*, all particle collisions lead to dimer formation. Higher values, on the other hand, refer to slower

aggregation and thus, to more stable samples. The standard error of stability ratio measurement is about 10%.

The critical coagulation concentration (CCC) values were calculated from the  $W$  versus  $c_{\text{IL}}$  plots with the following equation<sup>37</sup>

$$1/W = 1/(1 + CCC/c_{\text{IL}})^\beta \quad (10)$$

where  $\beta$  can be obtained from the slow aggregation regime (*i.e.*, before the CCC) of the  $W$  versus  $c_{\text{IL}}$  graphs as

$$\beta = d\log(1/W)/d\log c_{\text{IL}} \quad (11)$$

To compare experimental and theoretical CCC data, DLVO theory, which assumes that the total interaction energy can be considered as a superposition of the repulsive electrostatic double layer potential energy and the attractive van der Waals potential energy, was used to estimate the CCC as follows<sup>36</sup>

$$CCC = (0.365/N_A L_B)(H\epsilon_0\epsilon)^{-2/3}\sigma^{4/3} \quad (12)$$

where  $H$  is the Hamaker constant ( $1.00 \times 10^{-21}$  J was used for both AL and SL-IP-2 particles) and  $L_B$  is the Bjerrum length, which was calculated as

$$L_B = e^2/4\pi\epsilon_0\epsilon k_B T \quad (13)$$

Using the model above, it was assumed that the energy barrier vanishes at the CCC and attractive interparticle forces predominate beyond this concentration.

## 3. Results and discussion

### 3.1 Functionalization of SL with IP-2

The AL particles are commercially available, whereas SL-IP-2 particles were prepared by adsorbing a saturated IP-2 layer on the oppositely charged SL. To determine the polymer dose necessary to fully coat the SL surface, the zeta potential values were determined at different IP-2 doses (Fig. 1).

The SL particles are negatively charged at low IP-2 doses due to the presence of ionized sulfate functional groups. Increasing the amount of IP-2 led to charge neutralization and subsequent overcharging of the SL particles. The zeta potential values remain constant at high IP-2 doses, at which the surface of the particles contains a saturated IP-2 layer. These results resemble to other systems, where polyelectrolytes were adsorbed on oppositely charged latex particles.<sup>38–40</sup>

The aggregation tendencies were assessed by determining stability ratio values under the same experimental conditions as used for the potential measurements. Note that the stability ratio of unity refers to diffusion controlled rapid particle aggregation, while higher values indicate a decrease in the aggregation rates. The data shown in Fig. 1 suggest that rapid particle aggregation occurred near the charge neutralization point, while stable dispersions were observed far from it. Most importantly, particle aggregation is negligible at high doses.

Very similar observations were taken in systems containing oppositely charged latexes and polyelectrolytes,<sup>38–40</sup> but this is the first report, which involves a polyimidazolium compound.

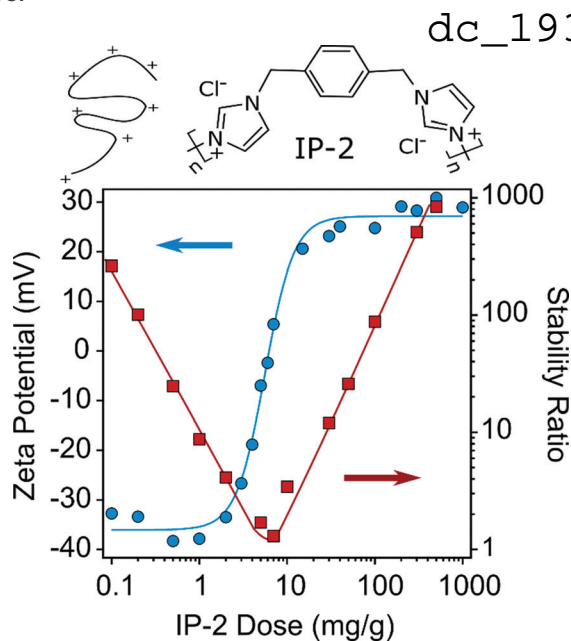


Fig. 1 Zeta potential (circles, left axis) and stability ratio (squares, right axis) values of SL particles as a function of the IP-2 dose at pH 4 and 10 mM ionic strength adjusted by KCl. Note that the inverse of the stability ratio is equal to the fraction of particle collisions, which results in dimer formation. The mg/g unit refers to mg IP-2 per one gram of SL. The lines serve to guide the eye. The arrows indicate the axis, to which potential (blue arrow) and stability ratio (red arrow) data points belong. The upper part shows the structure of IP-2.

Based on the above results, a dose of  $500 \text{ mg g}^{-1}$  was chosen (SL-IP-2) for the further studies, since under this condition the particle surface was saturated with IP-2 and stable dispersion was formed.

### 3.2 Charge and aggregation features of AL and SL-IP-2 particles in the presence of ILs

To investigate the specific interfacial effects of IL constituents, the zeta potentials of AL particles were measured first in aqueous solutions of BMIMAc, BMIMNO<sub>3</sub>, BMIMBr and BMIMCl in a wide range of IL concentrations. The results are shown in Fig. 2a. Note that the anions are the counterions and the BMIM<sup>+</sup> cation acts as co-ion in respect to the positively charged particles. In general, the zeta potential values decreased with the IL concentrations, similar to the case of indifferent KCl electrolyte (Fig. S4a, ESI<sup>†</sup>).

The surface charge densities were calculated from the salt concentration-dependent potential data using the Debye-Hückel model (eqn (2)).<sup>41</sup> The values (Table S2, ESI<sup>†</sup>) decreased in the order  $\text{Cl}^- > \text{Br}^- > \text{NO}_3^- > \text{Ac}^-$  indicating specific adsorption of the ions. Note that these charge densities were measured at the slip plane, therefore their magnitudes are much lower than the charge density of the bare surface determined in conductometric measurements by the manufacturer. Such a sequence agrees well with the reversed Hofmeister series, which classifies anions by their affinity towards positively charged hydrophobic surfaces.<sup>42</sup> Accordingly, the adsorption of the well-hydrated  $\text{Cl}^-$  is negligible, while  $\text{Ac}^-$  adsorbs strongly on the oppositely charged surface.

For the SL-IP-2 system, nevertheless, the zeta potentials were the same within the experimental error (Fig. 2b). After an intermediate maximum due to the electrokinetic effect,<sup>43</sup> the potentials decreased with increasing the IL concentrations in all cases, but no specific adsorption of the IL anions was detected. This result is in a striking contrast to the findings for the AL systems. In addition, specific anion adsorption on positively charged bare latexes<sup>21,36</sup> and the ones functionalized with positively charged polyelectrolytes<sup>39</sup> was reported in the past. Therefore, the insensitivity of the surface charge to the chemical composition of the surrounding anions in the SL-IP-2 systems is rather surprising. The different affinity of the anions to cationic surfaces was explained by their different level of hydration, *i.e.*, less hydrated anions tend to adsorb on hydrophobic surfaces, while this effect was not observed with the SL-IP-2 particles, most likely due to the less hydrophobic nature of their surface.

The stability ratios were determined by DLS to assess the particle aggregation processes in the IL solutions. The experimental conditions (*e.g.*, pH value, particle and IL concentration range) were the same as in the zeta potential study in order to allow the direct comparison of the results. For the AL systems, the stability ratios follow the same generic trend as a function of the IL concentration, *i.e.*, their values were high (slow aggregation) at low salt levels and decreased with increasing the IL loading and became unity (fast aggregation) at high IL concentrations (Fig. 2c). The threshold value, which separates the slow and fast aggregation regimes, is the so-called CCC, which was calculated by eqn (10).

These results are similar to the ones reported earlier for latex particle dispersions in simple inorganic salt solutions (see the case of KCl in Fig. S4b, ESI<sup>†</sup>) and they are in line with the prediction of the DLVO theory.<sup>35,44</sup> Accordingly, the overall forces acting between charged particles are the sum of the repulsive electrical double layer and the attractive van der Waals forces. Increasing the salt concentration leads to the weakening of the electrostatic repulsion by salt screening and thus, the particles rapidly aggregate after the CCC due to the predominating attractive forces. This explanation is also evident from the very low zeta potential values measured at the CCC (Table S2, ESI<sup>†</sup>).

Although the generic trend in the stability ratios was very similar in all systems containing AL particles, the CCC values were different (Fig. 3a). This result cannot be explained by the DLVO theory since it predicts the same CCC, once a particle is dispersed in different types of monovalent salt solutions. The CCC values follow the order  $\text{Cl}^- > \text{Br}^- > \text{NO}_3^- > \text{Ac}^-$ , in accordance with the surface charge density data determined in the same systems. Again, this order is in line with the suggestion of the reversed Hofmeister series for positively charged hydrophobic particles.<sup>36,42</sup>

For the SL-IP-2 particles, nevertheless, the measured stability ratio values were identical within the experimental error for BMIMAc, BMIMNO<sub>3</sub>, BMIMBr and BMIMCl (Fig. 2d) and thus, the onset of rapid particle aggregation was located at the same CCC for all systems. This finding is in striking contrast to earlier results with latex particles functionalized with a positively charged natural polyelectrolyte, where the presence of different inorganic salts led to different CCC values.<sup>39</sup> More importantly, we are not

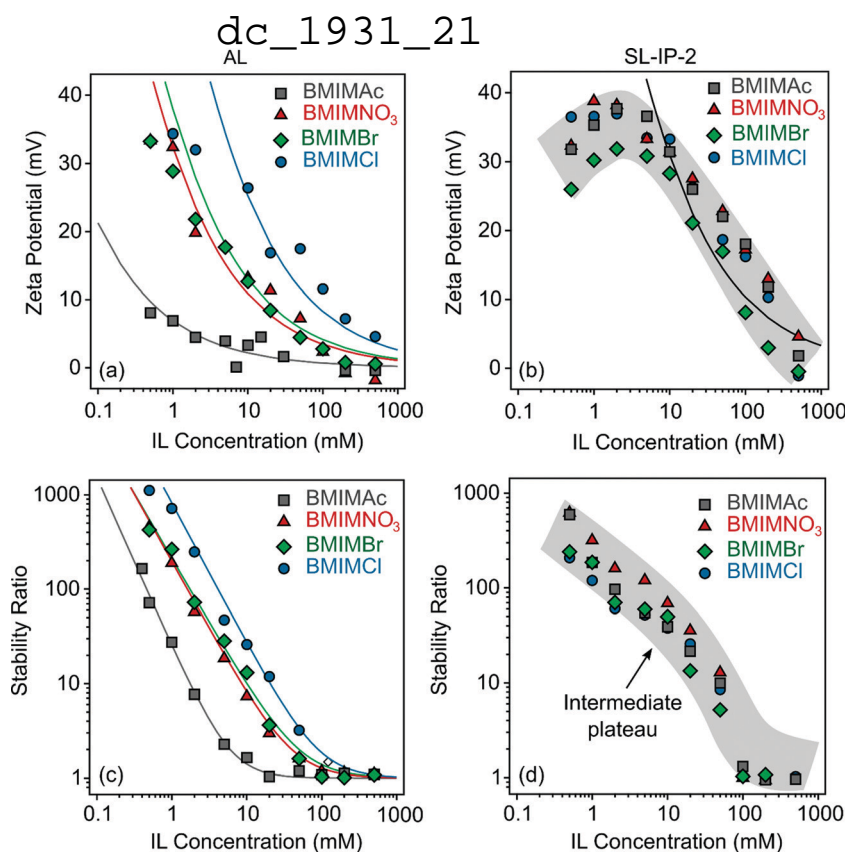


Fig. 2 Zeta potentials (AL (a) and SL-IP-2 (b)) as well as stability ratios (AL (c) and SL-IP-2 (d)) as a function of IL concentration at pH 4. The functions represented by lines in (a) and (b) were calculated using eqn (2) and in (c) with eqn (10).

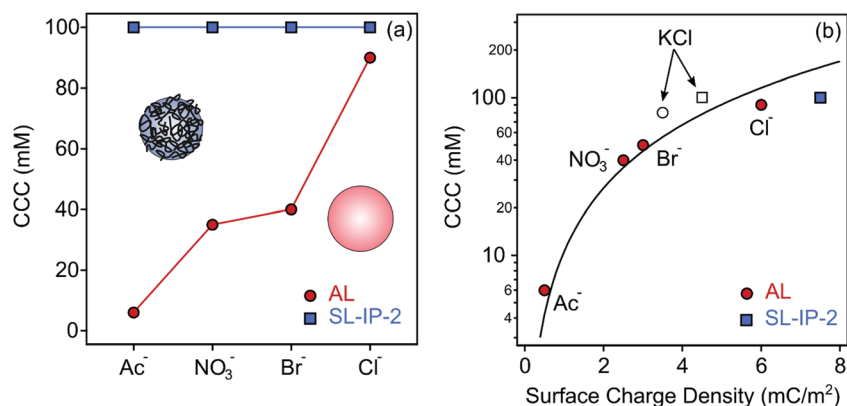


Fig. 3 CCC values of AL (red circles) and SL-IP-2 (blue square) determined in the presence of ILs (a) and CCC versus the charge density data (b). The empty symbols indicate the data measured with KCl. The lines in (a) were added merely to guide the eyes, while in (b), it was calculated using eqn (12).

aware of findings similar to the present one, which demonstrate that polyelectrolyte coating can be used to abolish ion specific effects on particle aggregation.

Besides, the tendency in the stability ratios was remarkably different from the AL samples and intermediate plateaus were discovered around 10 mM IL concentrations. The term “plateau” refers to the fact that the decrease of the stability ratios was not linear, but curved in the slow aggregation regime. This is rather unusual for latex particles and most likely originates from the swelling of the adsorbed IP-2 layer, which is indeed predicted in

the same ionic strength range as the location of the plateaus.<sup>45</sup> Such a swelling gives rise to the formation of polyelectrolyte tails and loops on the surface and subsequently, to the rise of stabilizing steric forces<sup>12</sup> to a minor extent (the main interparticle forces are still of DLVO origin). The increment in the stability ratios in this concentration range is due to the presence of these additional stabilization forces. An important note is that the height and the location of these plateaus are the same for all IL solutions. Notably, no ion specific effects could be detected for the aggregation of SL-IP-2 particles.

### 3.3 Origin of interparticle forces

Given the very similar surface charge density and CCC values for the AL and SL-IP-2 particles in inert KCl electrolyte, the striking contrast in the charge and aggregation features in IL solutions is very surprising. Note that deviations in the zeta potentials (Fig. S5a–d, ESI†) and stability ratios (Fig. S6a–d, ESI†) measured in the same IL solution for AL and SL-IP-2 particles are larger in the sequence  $\text{Cl}^- > \text{Br}^- > \text{NO}_3^- > \text{Ac}^-$ . These results show that ion specific effects can be abolished by surface functionalization of polyimidazolium.

To further clarify the origin of the interparticle forces for both AL and SL-IP-2 particles dispersed in IL solutions, the experimental CCC values were plotted against the surface charge density data and compared to the CCC calculated using the DLVO theory (eqn (12)).<sup>36</sup> The data shown in Fig. 3b indicate that the calculated and experimental CCC values are in good agreement, which indicates the presence of DLVO-type forces. However, the ion specific adsorption led to different surface charge densities for AL, which decrease in the order  $\text{Cl}^- > \text{Br}^- > \text{NO}_3^- > \text{Ac}^-$  leading to weaker electrical double layer repulsion. Since the van der Waals forces are always present and their strength does not depend on the ionic strength, the CCC values decrease in the above order due to the weakening of the repulsive double layer forces. In other words, DLVO forces govern the aggregation mechanism, while the CCC is determined by specific ion adsorption.

However, such a specific ion effect is absent for SL-IP-2 particles. The basic phenomenon behind this result most probably originates from the hydration level of the surface and the counterions. It was reported in other latex systems that weakly hydrated ions are of higher affinity to hydrophobic surfaces, *i.e.*, they adsorb stronger on hydrophobic latexes,<sup>21</sup> similar to the AL particles in the present study. Since the same counterions were applied with the SL-IP-2 particles, the lack of ion specific effects implies that the hydrophobic character of SL weakened upon surface functionalization by IP-2 and thus, the hydration level-based affinity of the counterions is not pronounced. The reason for the decreased hydrophobicity can be that stacking interaction took place between the imidazolium groups of BMIM<sup>+</sup> and IP-2 leading to an accumulation of the BMIM<sup>+</sup> molecules on the surface and to the formation of a more ionic interfacial environment. Such a stacking interaction was reported earlier based on electronic structure analysis.<sup>46</sup>

Although the present study focuses on polymeric particles, similar coating can be also possible on other surfaces used in ILs.<sup>6,11,13,26,27</sup> This would be a promising strategy to develop ionophobic surfaces, however, the experimental conditions (*e.g.*, pH, polymer concentration and ionic strength) must be precisely optimized before the coating procedure.

## 4 Conclusions

To conclude, it was successfully demonstrated that anion specific effects on the surface charge and aggregation of AL particles are important and that the tendency can be predicted

by the reversed Hofmeister series of anions for positively charged hydrophobic surfaces. The ion specific adsorption led to a decrease in the surface charge density and thus, lower CCC values were measured for strongly adsorbing anions such as  $\text{Ac}^-$ . The ion specificity plays an important role in the adsorption process, while the aggregation mechanism and the major interparticle forces could be described with the DLVO theory. These ion specific interactions, however, can be masked by functionalization of the surface with polyimidazolium, after which the anions behave like indifferent salt constituents giving rise to the same colloidal stability of the SL-IP-2 particles in different ILs. These results are especially important for the design of particle-IL dispersion of desired surface charge and aggregation characteristics.

## Conflicts of interest

There are no conflicts to declare.

## Acknowledgements

The authors acknowledge financial support from the Hungarian National Research, Development and Innovation Office (SNN131558), the Slovenian Research Agency (research core funding No. P1-0201 and the project No. N1-0139 'Delamination of Layered Materials and Structure-Dynamics Relationship in Green Solvents') and the Ministry of Human Capacities of Hungary (20391-3/2018/FEKUSTRAT). The support from the University of Szeged Open Access Fund (5019) is gratefully acknowledged.

## References

- 1 R. Hayes, G. G. Warr and R. Atkin, *Chem. Rev.*, 2015, **115**, 6357–6426.
- 2 Z. P. Zheng, W. H. Fan, S. Roy, K. Mazur, A. Nazet, R. Buchner, M. Bonn and J. Hunger, *Angew. Chem., Int. Ed.*, 2015, **54**, 687–690.
- 3 R. D. Rogers and K. R. Seddon, *Science*, 2003, **302**, 792–793.
- 4 M. Taskin, A. Cognigni, R. Zirbs, E. Reimhult and K. Bica, *RSC Adv.*, 2017, **7**, 41144–41151.
- 5 K. Z. Donato, L. Matejka, R. S. Mauler and R. K. Donato, *Colloids Interfaces*, 2017, **1**, 5.
- 6 D. A. Beattie, R. M. Espinosa-Marzal, T. T. M. Ho, M. N. Popescu, J. Ralston, C. J. E. Richard, P. M. F. Sellapperumage and M. Krasowska, *J. Phys. Chem. C*, 2013, **117**, 23676–23684.
- 7 R. M. Espinosa-Marzal, A. Arcifa, A. Rossi and N. D. Spencer, *J. Phys. Chem. Lett.*, 2014, **5**, 179–184.
- 8 A. Elbourne, B. McLean, K. Voitchovsky, G. G. Warr and R. Atkin, *J. Phys. Chem. Lett.*, 2016, **7**, 3118–3122.
- 9 I. Szilagyí, T. Szabo, A. Desert, G. Trefalt, T. Oncsik and M. Borkovec, *Phys. Chem. Chem. Phys.*, 2014, **16**, 9515–9524.
- 10 A. Podgorsek, A. S. Pensado, C. C. Santini, M. F. C. Gomes and A. A. H. Padua, *J. Phys. Chem. C*, 2013, **117**, 3537–3547.
- 11 E. Vanecht, K. Binnemans, S. Patskovsky, M. Meunier, J. W. Seo, L. Stappers and J. Fransaer, *Phys. Chem. Chem. Phys.*, 2012, **14**, 5662–5671.



dc 1931\_21

- 12 K. Ueno, A. Inaba, M. Kondoh and M. Watanabe, *Langmuir*, 2008, **24**, 5253–5259.
- 13 P. P. Arquilliere, I. S. Helgadottir, C. C. Santini, P. H. Haumesser, M. Aouine, L. Massin and J. L. Rousset, *Top. Catal.*, 2013, **56**, 1192–1198.
- 14 D. Constantinescu, H. Weingartner and C. Herrmann, *Angew. Chem., Int. Ed.*, 2007, **46**, 8887–8889.
- 15 N. Debeljuh, C. J. Barrow and N. Byrne, *Phys. Chem. Chem. Phys.*, 2011, **13**, 16534–16536.
- 16 W. L. Li and P. Y. Wu, *Polym. Chem.*, 2014, **5**, 761–770.
- 17 M. M. Elmahdy, C. Gutsche and F. Kremer, *J. Phys. Chem. C*, 2010, **114**, 19452–19458.
- 18 V. Valmacco, G. Trefalt, P. Maroni and M. Borkovec, *Phys. Chem. Chem. Phys.*, 2015, **17**, 16553–16559.
- 19 M. W. Han and R. M. Espinosa-Marzal, *ACS Appl. Mater. Interfaces*, 2019, **11**, 33465–33477.
- 20 P. Rouster, M. Pavlovic, T. Cao, B. Katana and I. Szilagyi, *J. Phys. Chem. C*, 2019, **123**, 12966–12974.
- 21 T. Oncsik, A. Desert, G. Trefalt, M. Borkovec and I. Szilagyi, *Phys. Chem. Chem. Phys.*, 2016, **18**, 7511–7520.
- 22 T. Kobayashi, A. Kemna, M. Fyta, B. Braunschweig and J. Smiatek, *J. Phys. Chem. C*, 2019, **123**, 13795–13803.
- 23 W. Kunz, J. Henle and B. W. Ninham, *Curr. Opin. Colloid Interface Sci.*, 2004, **9**, 19–37.
- 24 A. A. Tietze, F. Bordusa, R. Giernoth, D. Imhof, T. Lenzer, A. Maass, C. Mrestani-Klaus, I. Neundorf, K. Oum, D. Reith and A. Stark, *ChemPhysChem*, 2013, **14**, 4044–4064.
- 25 D. R. MacFarlane, M. Forsyth, P. C. Howlett, M. Kar, S. Passerini, J. M. Pringle, H. Ohno, M. Watanabe, F. Yan, W. J. Zheng, S. G. Zhang and J. Zhang, *Nat. Rev. Mater.*, 2016, **1**, 15005.
- 26 S. Kondrat and A. A. Kornyshev, *Nanoscale Horiz.*, 2016, **1**, 45–52.
- 27 S. Kondrat, P. Wu, R. Qiao and A. A. Kornyshev, *Nat. Mater.*, 2014, **13**, 387–393.
- 28 X. W. Mao, P. Brown, C. Cervinka, G. Hazell, H. Li, Y. Y. Ren, D. Chen, R. Atkin, J. Eastoe, I. Grillo, A. A. H. Padua, M. F. C. Gomes and T. A. Hatton, *Nat. Mater.*, 2019, **18**, 1350–1357.
- 29 X. Xu, Y. Li, Y. T. Gong, P. F. Zhang, H. R. Li and Y. Wang, *J. Am. Chem. Soc.*, 2012, **134**, 16987–16990.
- 30 W. Zhong, F. D. Bobbink, Z. F. Fei and P. J. Dyson, *ChemSusChem*, 2017, **10**, 2728–2735.
- 31 A. V. Delgado, F. Gonzalez-Caballero, R. J. Hunter, L. K. Koopal and J. Lyklema, *J. Colloid Interface Sci.*, 2007, **309**, 194–224.
- 32 G. Trefalt, I. Szilagyi and M. Borkovec, *J. Colloid Interface Sci.*, 2013, **406**, 111–120.
- 33 H. Holthoff, S. U. Egelhaaf, M. Borkovec, P. Schurtenberger and H. Sticher, *Langmuir*, 1996, **12**, 5541–5549.
- 34 P. A. Hassan, S. Rana and G. Verma, *Langmuir*, 2015, **31**, 3–12.
- 35 B. Derjaguin and L. D. Landau, *Acta Phys. Chim.*, 1941, **14**, 633–662.
- 36 T. Oncsik, G. Trefalt, M. Borkovec and I. Szilagyi, *Langmuir*, 2015, **31**, 3799–3807.
- 37 D. Grolimund, M. Elimelech and M. Borkovec, *Colloids Surf., A*, 2001, **191**, 179–188.
- 38 I. Szilagyi, G. Trefalt, A. Tiraferri, P. Maroni and M. Borkovec, *Soft Matter*, 2014, **10**, 2479–2502.
- 39 T. Lopez-Leon, A. B. Jodar-Reyes, J. L. Ortega-Vinuesa and D. Bastos-Gonzalez, *J. Colloid Interface Sci.*, 2005, **284**, 139–148.
- 40 J. Hierrezuelo, A. Vaccaro and M. Borkovec, *J. Colloid Interface Sci.*, 2010, **347**, 202–208.
- 41 W. B. Russel, D. A. Saville and W. R. Schowalter, *Colloidal dispersions*, Cambridge University Press, Cambridge, 1989.
- 42 N. Schwierz, D. Horinek and R. R. Netz, *Langmuir*, 2010, **26**, 7370–7379.
- 43 M. Borkovec, S. H. Behrens and M. Semmler, *Langmuir*, 2000, **16**, 5209–5212.
- 44 E. J. W. Verwey and J. T. G. Overbeek, *Theory of stability of lyophobic colloids*, Elsevier, Amsterdam, 1948.
- 45 J. Hierrezuelo, I. Szilagyi, A. Vaccaro and M. Borkovec, *Macromolecules*, 2010, **43**, 9108–9116.
- 46 R. P. Matthews, T. Welton and P. A. Hunt, *Phys. Chem. Chem. Phys.*, 2015, **17**, 14437–14453.

# Effect of MacroRAFT Copolymer Adsorption on the Colloidal Stability of Layered Double Hydroxide Nanoparticles

Marko Pavlovic,<sup>†</sup> Monika Adok-Sipiczki,<sup>†</sup> Corinne Nardin,<sup>†,‡</sup> Samuel Pearson,<sup>§,⊥</sup> Elodie Bourgeat-Lami,<sup>§</sup> Vanessa Prevot,<sup>\*,⊥,#</sup> and Istvan Szilagyi<sup>\*,†</sup>

<sup>†</sup>Department of Inorganic and Analytical Chemistry, University of Geneva, 30 Quai Ernest-Ansermet, CH-1205 Geneva, Switzerland

<sup>‡</sup>Institut des Sciences Analytiques et de Physicochimie pour l'Environnement et les Matériaux, Université de Pau et des Pays de l'Adour, 2 Avenue du Président Angot, F-64000 Pau, France

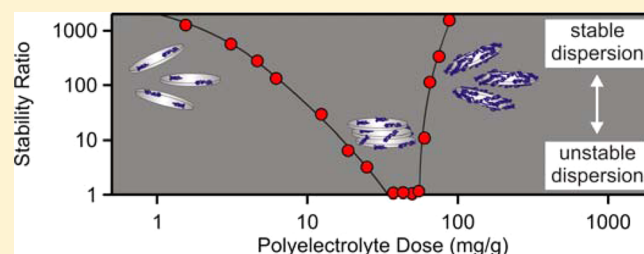
<sup>§</sup>University of Lyon, Univ. Lyon 1, CPE Lyon, CNRS, UMR 5265, Laboratoire de Chimie, Catalyse, Polymères et Procédés (C2P2), LCPP group, 43, Blvd du 11 Novembre 1918, F-69616 Villeurbanne, France

<sup>⊥</sup>Université Clermont Auvergne, Université Blaise Pascal, Institut de Chimie de Clermont-Ferrand, BP 10446, F-63000 Clermont-Ferrand, France

<sup>#</sup>CNRS, UMR 6296, F-63178 Aubière, France

## S Supporting Information

**ABSTRACT:** The colloidal behavior of layered double hydroxide nanoparticles containing Mg<sup>2+</sup> and Al<sup>3+</sup> ions as intralayer cations and nitrates as counterions (MgAl-NO<sub>3</sub>-LDH) was studied in the presence of a short statistical copolymer of acrylic acid (AA) and butyl acrylate (BA) terminated with 4-cyano-4-thiothiopropylsulfanyl pentanoic acid (CTPPA) (P(AA<sub>7.5</sub>-stat-BA<sub>7.5</sub>)-CTPPA) synthesized by reversible addition–fragmentation chain-transfer (RAFT) polymerization. Surface charge properties and aggregation of the particles were investigated by electrophoresis and dynamic light scattering (DLS), respectively. The negatively charged P(AA<sub>7.5</sub>-stat-BA<sub>7.5</sub>)-CTPPA adsorbed strongly on the oppositely charged particles, leading to charge neutralization at the isoelectric point (IEP) and charge reversal at higher copolymer concentrations. The dispersions were unstable, i.e., fast aggregation of the MgAl-NO<sub>3</sub>-LDH occurred near the IEP while high stability was achieved at higher P(AA<sub>7.5</sub>-stat-BA<sub>7.5</sub>)-CTPPA concentrations. Atomic force (AFM) and transmission electron (TEM) microscopy imaging revealed that the platelets preferentially adopted a face-to-face orientation in the aggregates. While the stability of the bare particles was very sensitive to ionic strength, the P(AA<sub>7.5</sub>-stat-BA<sub>7.5</sub>)-CTPPA copolymer-coated particles were extremely stable even at high salt levels. Accordingly, the limited colloidal stability of bare MgAl-NO<sub>3</sub>-LDH dispersions was significantly improved by adding an appropriate amount of P(AA<sub>7.5</sub>-stat-BA<sub>7.5</sub>)-CTPPA to the suspension.



## INTRODUCTION

Layered double hydroxides (LDHs) are hydrotalcite-type anionic clay materials<sup>1,2</sup> that have attracted an enormous amount of attention in recent years due to their tunable properties, ease of synthesis, and promise in extensive applications<sup>2,3</sup> including drug delivery,<sup>4</sup> catalysis,<sup>5,6</sup> wastewater treatment,<sup>7</sup> carbon dioxide capture,<sup>8</sup> and polymer nanocomposites.<sup>9,10</sup> Each layer in the LDH structure is composed of repeating octahedral units of a central metal ion (a mixture of M<sup>2+</sup> and M<sup>3+</sup>) coordinated by hydroxide ions, with anions in the interlayer galleries compensating for the net positive charge arising from the M<sup>3+</sup> species. LDH particles are typically in the nanometer size range with a high aspect ratio. Great compositional diversity is accessible in LDHs by altering the nature and the ratio of M<sup>2+</sup> and M<sup>3+</sup> as well as the type of the intercalating anion(s), and extensive studies have been performed to characterize the resulting structures in the solid state.<sup>6,11–13</sup> In contrast, colloidal properties such as surface

charge, stability, and aggregation behavior in aqueous solution have received much less attention, which is surprising given the relatively large number of contributions dealing with surface modification and the colloidal stability of cationic clays,<sup>14–16</sup> of which LDHs are considered to be the anionic counterpart. Both the lack of detailed understanding and the importance of colloidal stability for the synthesis and application of LDH-based materials motivated the conducted research.

The incorporation of LDH nanoparticles into polymer–inorganic nanocomposites is a thriving area of research due to the enhanced mechanical, thermal, and flammability properties displayed by the resulting materials.<sup>9,10</sup> While polymer–inorganic nanocomposites are accessible through a variety of strategies, the relatively new macroRAFT-assisted encapsulating

Received: September 7, 2015

Revised: November 3, 2015

Published: November 3, 2015

emulsion polymerization (REEP) technique, first developed by the Hawket group to encapsulate titanium dioxide pigments<sup>17</sup> and gibbsite clay platelets<sup>18</sup> in polymer latexes, and recently employed to encapsulate cerium dioxide nanoparticles,<sup>19</sup> shows great promise for synthesizing polymer–inorganic hybrid latexes containing charged inorganic particles. In the REEP approach, short charged polymers synthesized by RAFT polymerization (referred to as macroRAFT agents) are first adsorbed on the oppositely charged inorganic particle surface, and then emulsion polymerization is conducted under starve–feed conditions to grow a hydrophobic polymer shell around the inorganic particle. In addition to its stabilizing role, the adsorbed macroRAFT agent also enables emulsion polymerization to commence from the particle surface courtesy of the reactivatable RAFT function, thereby generating a uniform polymer shell. Controlling the initial dispersion state of the macroRAFT-modified inorganic particles is crucial to designing composite materials with controlled morphologies, but to date, this topic has not been thoroughly investigated. Because of their relevance to the REEP process, negatively charged macroRAFT agents are prime candidates for investigating polyelectrolyte–LDH interactions and colloidal stability relative to bare LDH.

Existing literature reports on the colloidal stability of bare LDHs have revealed that surface charge properties and therefore aggregation behavior are sensitive to the ionic environment. Colloidal stability can be lost through a reduction in the positive surface charge induced by high-pH conditions<sup>20,21</sup> or the specific adsorption of anions.<sup>22–24</sup> In the latter case, the isoelectric point (IEP) indicates the anion concentration at which the surface charge crosses from positive to negative<sup>25</sup> and can vary considerably depending on the nature of the anion.<sup>23</sup> To reduce this sensitivity to the ions in solution, polyelectrolytes have been widely used to stabilize charged nanoparticles through strong adsorption on the oppositely charged surfaces,<sup>26–31</sup> but the few reports on polyelectrolyte-stabilized LDH nanocomposites do not comprehensively describe the polyelectrolyte effect on stability and aggregation behavior.<sup>32–35</sup> Although the colloidal stability of a similar system containing gibbsite particles and macroRAFT polyelectrolytes has already been published,<sup>18</sup> the adsorption of macroRAFT agents on LDH particles and its influence on the dispersion stability have not been reported in the literature so far.

The present work aims to provide insights into the surface charge properties, colloidal stability, and aggregation propensity of macroRAFT-adsorbed LDH and bare LDH using electrophoretic mobility, light scattering, and microscopy imaging. A nitrate-intercalated Mg<sup>2+</sup>–Al<sup>3+</sup> LDH (denoted as MgAl-NO<sub>3</sub>-LDH) was chosen, since LDHs of such metal ion compositions are the most frequently studied<sup>36</sup> and therefore the most relevant for investigating fundamental colloidal properties. The macroRAFT agent (which will also be referred to as the polyelectrolyte) is a short statistical copolymer of acrylic acid (AA) and butyl acrylate (BA) denoted as P(AA<sub>7.5</sub>-stat-BA<sub>7.5</sub>)-CTPPA (where CTPPA is an abbreviation for the 4-cyano-4-thiothiopropylsulfanyl pentanoic acid RAFT function) and is representative of macroRAFT agents typically employed in the REEP process. This systematic study provides relevant insights into the dispersion properties of LDHs which are of further interest in many LDH applications.

## EXPERIMENTAL SECTION

All chemicals were purchased from Sigma-Aldrich and used as received unless otherwise specified. RAFT agent CTPPA was synthesized following a protocol previously reported in the literature.<sup>37</sup>

**Preparation of MgAl-NO<sub>3</sub>-LDH Nanoparticles.** LDHs containing Mg<sup>2+</sup> and Al<sup>3+</sup> cations and nitrate interlayer anions were prepared by flash coprecipitation followed by hydrothermal treatment.<sup>38,39</sup> Typically, a metallic nitrate solution (with a Mg<sup>2+</sup>/Al<sup>3+</sup> molar ratio of 2 and a total metal ion concentration of 0.3 M) was rapidly added to a NaOH (0.185 M) solution at 0 °C. The pH of the resulting solution was adjusted to 9.5, and the sample was transferred to an autoclave and held at 150 °C for 4 h. The resulting particles were collected by centrifugation, and the obtained gel was washed twice with deionized water. Redispersion was achieved by ultrasonication between each washing step. After the final wash, nanoparticles were again redispersed in deionized water and stored as a colloidal suspension of about 10 wt % at room temperature.

**Synthesis of the P(AA<sub>7.5</sub>-stat-BA<sub>7.5</sub>)-CTPPA MacroRAFT Copolymer.** In a round-bottomed flask, acrylic acid (AA) and butyl acrylate (BA) as monomers, CTPPA as the RAFT agent, 4,4'-azobis(4-cyanopentanoic acid) (ACPA) as the initiator, and 1,3,5-trioxane as the internal standard for nuclear magnetic resonance spectroscopy (NMR) analysis were dissolved in dioxane in a molar ratio of [monomer]/[RAFT]/[initiator] = 20:1:0.1 and a monomer concentration of 6 M. The solution was degassed with nitrogen for 30 min and placed in an oil bath at 80 °C. Samples were taken periodically using a nitrogen-purged syringe to determine conversion by NMR spectroscopy. After 5 h, corresponding to a degree of polymerization of 7.5 for both AA and BA, the solution was quenched in an ice bath. The resulting polymer was purified by three precipitation steps in cold diethyl ether, with redissolution in acetone between each precipitation. The final product was dried overnight in a vacuum oven, resulting in a gel-like yellow material which was analyzed by NMR spectroscopy and size exclusion chromatography (SEC) ( $M_{n,theor} = 1800$  g/mol,  $M_{n,SEC} = 1800$ , and a dispersity ( $\bar{D}$ ) of 1.1, where  $M_{n,SEC}$  and  $\bar{D}$  were obtained after methylation).

**Powder X-ray Diffraction.** Powder X-ray diffraction patterns were recorded on an X'Pert Pro Philips diffractometer with a diffracted beam graphite monochromator and a Cu K $\alpha$  radiation source in the  $2\theta$  range of 5–70° with a step of 0.013° and a counting time per step of 20 s.

**Electrophoresis.** Electrophoretic mobility measurements were performed with a ZetaNano ZS (Malvern Instruments) device under an electric field of 4 kV/m. The experiments were carried out in plastic capillary cells (Malvern Instruments) cleaned with 2 wt % Hellmanex solution (Hellma) and rinsed with Milli-Q water (Millipore) between each experiment. A stock solution of P(AA<sub>7.5</sub>-stat-BA<sub>7.5</sub>)-CTPPA was first prepared by dissolving the polymer in water using KOH to deprotonate the AA units and attain a pH value of 9. Appropriate volume aliquots of this stock solution were then taken to prepare the polymer solutions of different concentrations. The desired ionic strength was attained using KNO<sub>3</sub> stock solutions (also adjusted to pH 9) and water to give a final volume of 4.5 mL in each case. To these, 0.5 mL of a 100 mg/L MgAl-NO<sub>3</sub>-LDH stock dispersion was added, and each solution was left overnight to equilibrate. The samples were also equilibrated at 25 °C in the instrument for 1 min prior to the measurement. The electrophoretic mobility of each sample was measured five times and averaged.

**Light Scattering.** Dynamic light scattering (DLS) measurements were carried out using the ZetaNano ZS (Malvern Instruments) at a 173° scattering angle. This device is equipped with a He/Ne laser operating at 633 nm as a light source and an avalanche photodiode as a detector. The hydrodynamic radius was determined by accumulating the correlation function for 30 s and then applying a second-order cumulant fit.<sup>40</sup> The measurements were performed at 25 °C in 1 cm square plastic cuvettes (Malvern Instruments) cleaned with 2 wt % Hellmanex solution. In the time-resolved DLS experiments, typically 50 runs were performed over 25 min. Samples were prepared by mixing P(AA<sub>7.5</sub>-stat-BA<sub>7.5</sub>)-CTPPA and KNO<sub>3</sub> stock solutions with



Milli-Q water to give the desired polyelectrolyte concentrations and ionic strengths and a total volume of 1.8 mL. The aggregation experiment was initiated by injecting 0.2 mL of the MgAl-NO<sub>3</sub>-LDH stock dispersion, which was previously subjected to ultrasound treatment to minimize the initial aggregation. The final particle concentration was 10 mg/L, and the pH value was kept at 9. Such a low particle concentration allowed us to avoid multiple scattering events. In addition, combined static and DLS experiments performed on a multiangle goniometer (ALV/CGS-8, equipped with eight photomultiplier detectors and a solid-state laser (Coherent) operating at a wavelength of 532 nm) revealed that the decay constants of the autocorrelation functions show the typical linear dependence of a zero intercept with the square of the scattering vector. This fact confirms the translational origin of the diffusion coefficient. More details on the light-scattering technique can be found in the [Supporting Information](#) (Figures S1 and S2).

**Microscopy.** Transmission electron microscopy (TEM) images were recorded on a Tecnai G2 electron microscope (FEI) operating at 120 kV. Samples were prepared by placing 3  $\mu$ L of the particle dispersions at 10 mg/L LDH on carbon-coated 400-mesh copper grids, leaving them for 30 s, and then draining off the excess liquid with filter paper and allowing them to dry.

Atomic force microscopy (AFM) was used to image the particles in solution, in the amplitude modulation mode with a Cypher (Asylum Research) instrument. Biolever minicantilevers (Olympus) with a nominal tip radius smaller than 9 nm and a resonance frequency of 25–36 kHz in water were used. Images were acquired at a scan rate of 0.8 Hz. The positively charged MgAl-NO<sub>3</sub>-LDH particles were deposited on oppositely charged mica (Plano) which was freshly cleaved in air with scotch tape prior to use. Specifically, the mica surfaces were immersed in an MgAl-NO<sub>3</sub>-LDH suspension (10 mg/L particle and 100 mM KNO<sub>3</sub> concentration) for 5 min. Applying this salt concentration, the particles undergo fast aggregation, and hence the structure of the aggregates can be investigated. The samples were prepared 30 min before performing the AFM analysis.

## RESULTS AND DISCUSSION

Detailed studies were performed on the particle behavior in two colloidal systems. First, the surface charge properties and aggregation behavior of bare LDH (i.e., LDH in the absence of copolymer) were investigated as a function of ionic strength. Second, the colloidal stability of LDH particles in the presence of oppositely charged P(AA<sub>7.5</sub>-stat-BA<sub>7.5</sub>)-CTPPA was explored under similar conditions.

**Structure and Colloidal Stability of Bare LDH Particles.** The MgAl-NO<sub>3</sub>-LDH nanoparticles were first characterized in the solid state by X-ray diffraction (XRD) analysis to provide insight into their crystalline structure. The XRD pattern ([Figure 1](#)) displays the typical LDH structure reflections which can be indexed with a hexagonal lattice and  $R\bar{3}m$  symmetry, confirming the formation of the layered morphology with (i) sharp and intense basal 00 $l$  reflections in the low-angle region ( $2\theta < 25^\circ$ ), (ii) broad 0 $kl$  reflections in the middle-angle region ( $2\theta = 30\text{--}50^\circ$ ), and (iii)  $hk0$  and  $hkl$  reflections in the high-angle region ( $2\theta = 55\text{--}65^\circ$ ). The 003 and 006 diffraction lines at 10.2 and 20.3°, respectively, correspond to an interlamellar distance of 0.87 nm and are in good agreement with literature values for the nitrate-intercalated LDH phase.<sup>1</sup> The very minor peak observed at 14.5° corresponds to the formation of a small amount of Mg(OH)<sub>2</sub> side phase formed in the flash coprecipitation process due to minor deviation from the ideal pH value of 10 during the initial moment of mixing.

The size of the MgAl-NO<sub>3</sub>-LDH nanoparticles was measured by both TEM and DLS. Applying a Gaussian fit to the size distribution ([Figure 2a](#)) obtained by direct counting of the

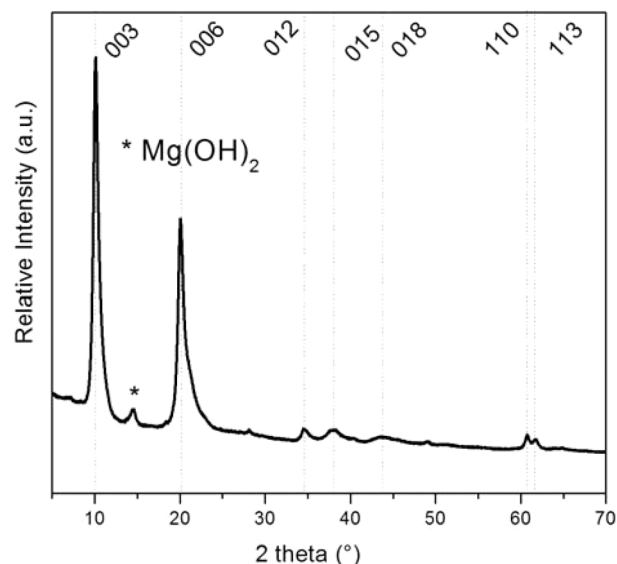


**Figure 1.** Powder XRD pattern of MgAl-NO<sub>3</sub>-LDH synthesized by flash coprecipitation.

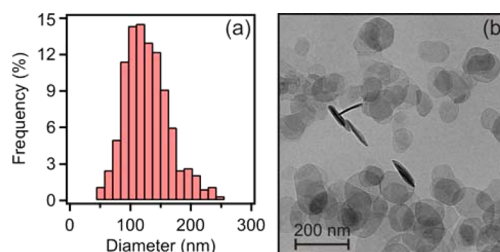


**Figure 2.** (a) Size distribution of MgAl-NO<sub>3</sub>-LDH particles measured by TEM in the solid state. (b) Typical TEM image of a MgAl-NO<sub>3</sub>-LDH sample.

particles on the TEM images ([Figure 2b](#)), an average particle diameter of  $112 \pm 5$  nm was obtained, while DLS yielded a mean hydrodynamic diameter of  $180 \pm 6$  nm with a relatively narrow size distribution indicated by a polydispersity index of 0.15. The uncertainties reported with the size values refer to standard deviations which were obtained from the Gaussian fit to the TEM data and the averaging process from individual DLS measurements, respectively. While these particle size values are not directly comparable (TEM is measured in the dry state, whereas DLS encompasses the solvating layer around the particles and overestimates the contribution from larger particles), the analyses are complementary in assessing the presence of well-dispersed particles with a relatively narrow particle size distribution. Such deviation in particle sizes determined in the dried state and dispersion is frequent.<sup>41,42</sup> Since the stability studies were predominantly performed in solution, we consider the hydrodynamic diameter measured by DLS to be more relevant.

After confirming the nitrate-intercalated crystal structure and the formation of well-dispersed and relatively uniform particles in solution, surface charge properties of the bare particles were probed by electrophoretic measurements at different ionic strengths ([Figure 3a](#)). KNO<sub>3</sub> was chosen to adjust the ionic strength to avoid any displacement of the intercalated nitrate counterions in the LDH. The positive electrophoretic mobility observed at low electrolyte concentration decreased with increasing salt concentration and crossed to slightly negative



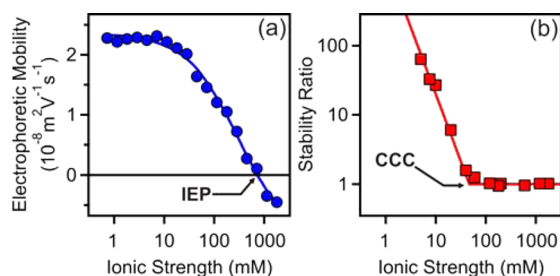


**Figure 3.** (a) Electrophoretic mobility and (b) stability ratio values of MgAl-NO<sub>3</sub>-LDH as a function of the ionic strength adjusted with KNO<sub>3</sub>. The solid lines are only to guide the eyes, and IEP refers to the isoelectric point while CCC is the critical coagulation concentration.

values beyond a KNO<sub>3</sub> concentration of approximately 0.7 M, indicating that the nitrate anions adsorb on the LDH surface. Such monovalent counterion-induced charge reversal has already been reported in the literature for LDH<sup>23</sup> and other colloidal particles.<sup>43,44</sup> Note that a slight charge reversal such as this at high electrolyte concentrations indicates that only a minor fraction of the nitrate anions was adsorbed on the surface and the majority was dissolved in the bulk solution. The screening of the positive LDH surface charge by the anions in solution was therefore the predominant factor contributing to the decreasing electrophoretic mobility with increasing ionic strength, with adsorption having a negligible effect.

The screening phenomenon could therefore be further explored by converting the mobilities to potentials ( $\zeta$ ) followed by comparison with theoretical models to extract the surface charge density ( $\sigma$ ). The electrokinetic potentials were obtained from the electrophoretic mobilities using the Smoluchowski equation.<sup>45</sup> The theoretical dependence of the potentials on the ionic strength was calculated by the Debye–Hückel model as<sup>45</sup>

$$\zeta = \frac{\sigma}{\epsilon\epsilon_0\kappa} \quad (1)$$

where  $\epsilon_0$  is the permittivity of vacuum,  $\epsilon$  is the dielectric constant of water and  $\kappa$  is the inverse Debye length which contains the contribution of all ionic species in the solution.

By fitting the theoretical potential values to the experimental ones (Figure S3),  $\sigma$  was found to be +0.011 C/m<sup>2</sup>. The fitting process was also repeated on the basis of the more accurate Poisson–Boltzmann theory,<sup>45</sup> and the same  $\sigma$  was obtained within the experimental error, which is similar to previously reported values (0.005–0.015 C/m<sup>2</sup>) for LDH particles measured in potentiometric titrations.<sup>20</sup> A reliable knowledge of  $\sigma$  can be important for other researchers dealing with the theoretical modeling of surface charges and adsorption processes in the presence of electrolytes.

The decreasing mobility with increasing ionic strength was accompanied by a decline in the colloidal stability of the particles. Light-scattering techniques have proven to be powerful tools for investigating particle aggregation in dispersions;<sup>30,41,46,47</sup> therefore, time-resolved DLS experiments were performed to further understand the aggregation process in this system. A fixed quantity of LDH dispersion was added to different KNO<sub>3</sub> solutions of identical volume but increasing ionic strength. DLS measurements of the particle size commenced immediately after LDH addition. The hydrodynamic radius ( $R_h$ ) was measured at different time intervals, and the colloidal stability of the dispersions was expressed as a stability ratio ( $W$ ) defined as<sup>48</sup>

$$W = \frac{\Delta_{\text{fast}}}{\Delta} \quad (2)$$

where  $\Delta_{\text{fast}}$  and  $\Delta$  are the initial aggregation rates in 1 M KNO<sub>3</sub> solution and in the aforementioned samples, respectively. The initial aggregation rates were calculated from the rate of increase of  $R_h$  as

$$\Delta = \left. \frac{1}{w} \frac{dR_h(t)}{dt} \right|_{t \rightarrow 0} \quad (3)$$

where  $w$  is the particle mass concentration and  $t$  is the time of the experiment. Since  $\Delta_{\text{fast}}$  was measured for a large excess of KNO<sub>3</sub>, where the aggregation is controlled only by the diffusion of the particles, stability ratios close to unity correspond to unstable systems while higher values indicate slower aggregation and therefore greater stability.

Figure 3b shows the stability ratios of MgAl-NO<sub>3</sub>-LDHs measured at different ionic strengths. Stable dispersions (indicated by high stability ratios) were observed at low electrolyte concentrations, but stability ratios decreased steadily with increasing ionic strength. At a certain ionic strength, defined as the critical coagulation concentration (CCC), the stability ratio reached a value of unity, corresponding to a maximal aggregation rate. In this system, the CCC occurs at  $62 \pm 5$  mM, which is comparable to values reported for other LDHs in the presence of monovalent electrolytes.<sup>23</sup> This aggregation behavior can be explained by the classical theory developed by Derjaguin, Landau, Verwey, and Overbeek (DLVO),<sup>45</sup> which states that the interparticle forces in aqueous dispersions containing charged colloidal particles and electrolytes are the superposition of repulsive electric double-layer forces and attractive van der Waals forces. Accordingly, the suspensions are stable at low electrolyte concentration due to the overlap of the double layers and the resulting repulsive forces, while the double layers are screened and such forces therefore vanish at sufficiently high ionic strengths. In the latter case, attractive van der Waals forces predominate in the system, leading to rapid aggregation of the particles. The aggregation of MgAl-NO<sub>3</sub>-LDH remains fast even at concentrations beyond the IEP (Figure 3a) at which restabilization of the dispersions could be envisaged, as has indeed been reported in other related systems.<sup>30</sup>

TEM images were recorded to identify the particle–particle orientation in the aggregates (Figure 4a,b). The samples were prepared at 50 mM ionic strength (close to the CCC), and the aggregated samples were imaged in order to obtain information on the structure of MgAl-NO<sub>3</sub>-LDH aggregates. In general, face-to-face orientation was observed; however, aggregation induced by the drying process during grid preparation could not be excluded. To circumvent the drying effect and gain a representative view of the aggregate structures in solution, the samples were imaged by AFM in the wet state. These results in fact confirmed the TEM observation of primarily face-to-face particle orientation as shown for a representative cluster of four aggregated particles in Figure 4c. The corresponding height profile (Figure 4d) confirms the proposed stacking orientation and shows that the height of the individual particles was about 7 nm. Although edge-to-face aggregation has been reported for negatively charged clay platelets<sup>14,15</sup> (and is therefore conceivable in our system), we saw no evidence of such structures. Indeed, a preference for face-to-face aggregation has also been observed in LDHs of other compositions.<sup>49</sup>

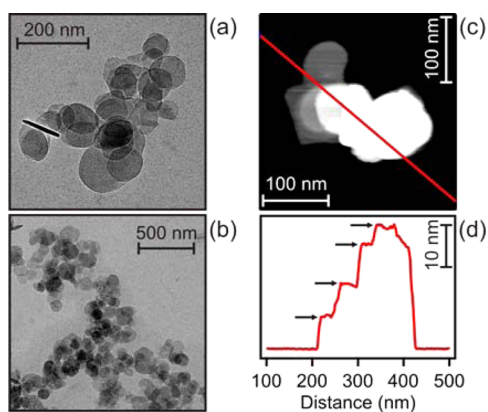


**Figure 4.** (a, b) TEM images of MgAl-NO<sub>3</sub>-LDH recorded with aggregated samples. (c) AFM image of an aggregate of four MgAl-NO<sub>3</sub>-LDH platelets in 100 mM KNO<sub>3</sub> electrolyte. (d) Height profile of the aggregate measured along the red line in the AFM image.

**LDH–Polyelectrolyte Interactions.** With this detailed understanding of bare LDH stability as a function of ionic strength, the influence of adsorbed P(AA<sub>7.5</sub>-stat-BA<sub>7.5</sub>)-CTPPA on LDH colloidal stability was then investigated. P(AA<sub>7.5</sub>-stat-BA<sub>7.5</sub>)-CTPPA was synthesized by RAFT (co)polymerization of acrylic acid (AA) and butyl acrylate (BA) using CTPPA as a RAFT agent to achieve a well-defined polymer of narrow molecular weight distribution (dispersity of 1.1) and an average of 7.5 units of each monomer per chain (Figure 5a). Because of the very similar reactivity ratios of the two monomers, they were incorporated statistically with negligible composition drift. After dissolution at pH 9, each copolymer chain possessed on average 8.5 negative charges due to the deprotonation of the 7.5 AA units plus the carboxylic acid end group of CTPPA.

First, three series of electrophoretic mobility measurements were performed. In each series, the concentration of MgAl-NO<sub>3</sub>-LDH particles (10 mg/L) and the ionic strength (either 1, 10, or 100 mM) were fixed, and the concentration of P(AA<sub>7.5</sub>-stat-BA<sub>7.5</sub>)-CTPPA was varied over more than 4 orders of magnitude (Figure 5b). The scattering intensity (44.9 kcps) of the copolymer solution at 3 mg/L concentration (the highest dose used in our study) was very similar to that measured in pure water (29.4 kcps); therefore, micelle or other aggregate formation is considered to be negligible under the experimental conditions applied in the present work.

At very low polyelectrolyte concentrations, the electrophoretic mobilities were positive and close to the values obtained for the bare LDH (Figure 3a) because the polyelectrolytes could only partially neutralize the opposite surface charge at these low doses. The mobility values decreased with increasing polyelectrolyte concentration as more copolymer was adsorbed on the oppositely charged platelets. Well-defined IEP values (i.e., polyelectrolyte doses at which electrophoretic mobility reached zero) were observed for all three series. Higher ionic strength reduced the IEP value since IEPs of 36, 32, and 16 mg/g were obtained for ionic strengths of 1, 10, and 100 mM, respectively.

Beyond the IEP, charge reversal occurred upon further addition of P(AA<sub>7.5</sub>-stat-BA<sub>7.5</sub>)-CTPPA. Such a charge reversal phenomenon has already been reported in the literature for similar particle–polyelectrolyte systems,<sup>28–31</sup> including RAFT polymers with platelet-type particles,<sup>18</sup> and can be attributed to several factors.<sup>25</sup> Although the overall net charge of the particles is zero at the IEP, the surface still contains empty places which

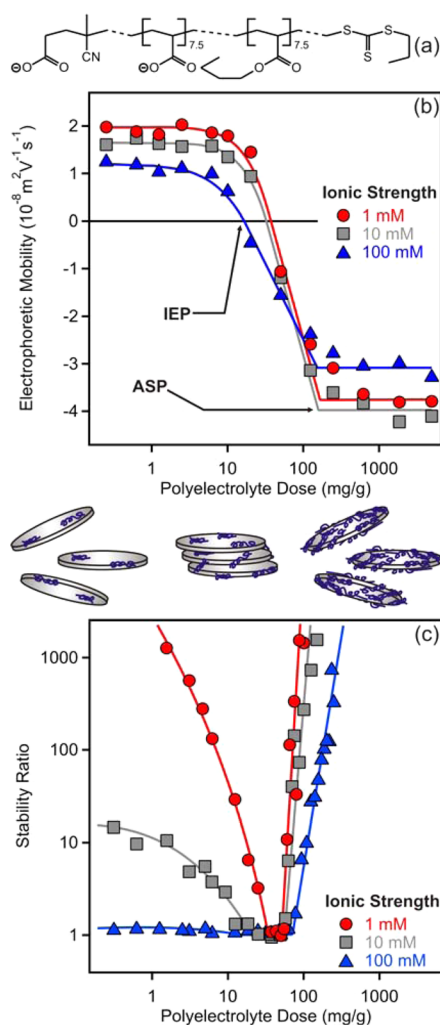


**Figure 5.** (a) Chemical structure of the P(AA<sub>7.5</sub>-stat-BA<sub>7.5</sub>)-CTPPA macroRAFT copolymer. (b) Electrophoretic mobilities and (c) stability ratios of MgAl-NO<sub>3</sub>-LDH in the presence of P(AA<sub>7.5</sub>-stat-BA<sub>7.5</sub>)-CTPPA polyelectrolyte at different ionic strengths adjusted by KNO<sub>3</sub>. The mg/g unit of the polyelectrolyte dose refers to milligrams of macroRAFT per gram of MgAl-NO<sub>3</sub>-LDH.

can be filled in further with polyelectrolyte molecules. Hydrophobic interactions between the chains<sup>50</sup> and entropic effects<sup>51</sup> such as solvent and counterion release from the charged P(AA<sub>7.5</sub>-stat-BA<sub>7.5</sub>)-CTPPA also drive adsorption beyond the IEP.

Polyelectrolyte adsorption continued until the onset of the adsorption saturation plateau (ASP), which corresponds to the point where no more macroRAFT can be adsorbed on the surface under the given experimental conditions. An ASP was observed for all ionic strengths used. Beyond this point, electrophoretic mobilities were essentially constant with increasing P(AA<sub>7.5</sub>-stat-BA<sub>7.5</sub>)-CTPPA concentration, indicating that additional polyelectrolytes remained dissolved in solution. The electrophoretic mobility absolute values at the plateau did, however, show some ionic strength dependence. Although similar profiles are observed for the 1 and 10 mM systems, the plateau in the 100 mM system corresponds to a significantly lower absolute mobility value due to the more pronounced screening of the negative surface charges by the potassium counterions.

To understand the dynamics of aggregation in the polyelectrolyte system, time-resolved DLS measurements were conducted to determine stability ratios in a manner similar to that used in the bare LDH experiments. The experimental conditions (pH, temperature, ionic strength, particle concentration, and macroRAFT concentration range) were identical to those used for the electrophoretic mobility study reported above in order to directly relate the aggregation to the surface charging behavior. Figure 5c shows these three series of stability ratio measurements as a function of polyelectrolyte concentration, with each series corresponding to an ionic strength of 1, 10, or 100 mM.

At very low polyelectrolyte doses, where only a small fraction of the positive charges on the particles were compensated for by adsorbed macromolecules, the stability of the dispersions was very sensitive to the ionic strength. The 1 mM  $\text{KNO}_3$  series has very high stability ratios ( $>1000$ ) at low polyelectrolyte concentration (i.e., below 1 mg/g). For the ionic strength of 100 mM, stability ratios close to unity were determined for polyelectrolyte doses lower than 100 mg/g, as can be expected when one considers the behavior of the bare particles. The 10 mM system shows intermediate stability ratios (around 15 at a polyelectrolyte concentration of 1 mg/g). With increasing P(AA<sub>7.5</sub>-stat-BA<sub>7.5</sub>)-CTPPA concentration, the stability ratios in the 1 and 10 mM systems then decline steadily to reach a value of unity at polyelectrolyte doses close to the previously determined IEP values. The stability ratios in all three systems sharply increased upon further increasing the polyelectrolyte concentration to give highly stable dispersions at high doses. The slopes of the stability ratio versus polyelectrolyte dose curves slightly changed with the salt level in this regime, with steeper slopes obtained at lower ionic strength.

These stability results highlight important features of the LDH–macroRAFT system. The aggregation behavior at very low doses is in agreement with the stability of the bare particles for similar ionic strengths (Figure 3b). Accordingly, the dispersions are stable in the low salt range (1 mM) due to the predominance of repulsive electric double-layer forces, while at high  $\text{KNO}_3$  concentrations these forces vanish due to the screening effect of the counterions, and hence attractive van der Waals forces cause fast aggregation as predicted by the DLVO theory. The decrease in the stability ratios at higher copolymer doses can also be explained by the weakening of the double-layer forces because the positive surface charge of MgAl- $\text{NO}_3$ -LDHs decreases as more negative macroRAFT agent is adsorbed (Figure 5b). Similar to other polyelectrolyte–particle systems,<sup>18,28–31</sup> the suspensions were unstable near the IEPs at which the overall charge of the particles was zero. The stability ratios were close to unity in this regime, indicating diffusion-controlled aggregation of the macroRAFT-functionalized platelets. Further increasing polyelectrolyte doses beyond the ASP generated highly stable particles in all three systems due to the reestablishment of the repulsive double-layer forces between the negatively charged surfaces. Qualitatively similar results were also reported with gibbsite platelets in the presence of anionic macroRAFT agents,<sup>18</sup> but quantitative comparison to our results is difficult due to the different composition of the particles and polyelectrolytes.

The sensitivity of the polyelectrolyte-coated particles to ionic strength was further explored at even higher ionic strength, and was compared to the behavior of the bare particles. Figure 6 shows time-resolved DLS measurements carried out with bare and P(AA<sub>7.5</sub>-stat-BA<sub>7.5</sub>)-CTPPA-coated particles at elevated

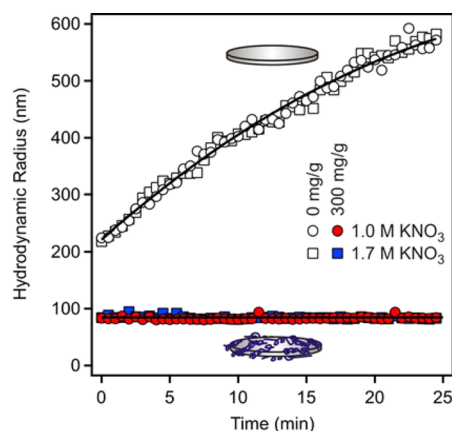


**Figure 6.** Time-resolved DLS measurements with bare (empty symbols) and P(AA<sub>7.5</sub>-stat-BA<sub>7.5</sub>)-CTPPA-coated MgAl- $\text{NO}_3$ -LDH (at a polyelectrolyte dose of 300 mg/g, filled symbols) for two ionic strengths (1.0 and 1.7 M adjusted by  $\text{KNO}_3$ ). Note that the different intercepts are due to the fast aggregation of bare MgAl- $\text{NO}_3$ -LDH in the short time period between when the samples were prepared and when the DLS measurements were started.

$\text{KNO}_3$  concentrations (1.0 and 1.7 M) at which one would expect unstable dispersions. It is clearly evident that the bare particles rapidly aggregated at these ionic strengths, which were higher than their CCC value, while the hydrodynamic radius of the macroRAFT-coated platelets remained unchanged throughout the measurement period. An average hydrodynamic radius of  $85 \pm 3$  nm was obtained from the experiment carried out at 1.7 M, which is in good agreement with the hydrodynamic radius of the bare particles ( $90 \pm 5$  nm) in stable samples. The remarkable stability of the macroRAFT-coated LDH even at extremely high ionic strengths contrasts with that of other polyelectrolyte-stabilized systems, which have been reported to undergo fast aggregation under similar conditions.<sup>28</sup> The enhanced stability can be rationalized by considering the polyelectrolyte adsorption characteristics. A dose of 300 mg/g (i.e., milligrams of polyelectrolyte per gram of LDH particles) applied to coat the MgAl- $\text{NO}_3$ -LDHs roughly corresponds to a polyelectrolyte surface density of 1.7 mg/m<sup>2</sup> (calculations in the Supporting Information). While lower than the grafting density of polymer brushes (10–20 mg/m<sup>2</sup>),<sup>52</sup> this value is higher than those reported in the literature for the adsorption of oppositely charged polyelectrolytes on latex,<sup>53</sup> magnetite,<sup>54</sup> or silica<sup>31</sup> particles. Such a higher adsorbed amount compared to that for simple polyelectrolytes is most likely enabled by the copolymer structure (Figure 5a), in which the randomly distributed butyl chains enhance adsorption by promoting hydrophobic affinity with previously adsorbed copolymer chains. To further probe the effect of butyl chains on the adsorption process, the onset of the ASP was compared with the value for pure PAA of the same molecular mass under identical conditions (Figure S4). It can be clearly seen that in the presence of butyl chains, the onset of the ASP is significantly shifted toward higher polyelectrolyte doses compared to those for the PAA samples. This result unambiguously confirms that the butyl groups enhance the adsorption most probably due to hydrophobic interactions between the adsorbed P(AA<sub>7.5</sub>-stat-BA<sub>7.5</sub>)-CTPPA chains. Even if a part of the macroRAFT agent may have been intercalated in the LDH structure, we suspect that most of the polyelectrolyte was adsorbed on the outer surface of the particles, leading to a



huge charge reversal (more than 100% in magnitude) at appropriately high doses.

TEM analysis was performed on two of the samples from the 1 mM  $\text{KNO}_3$  series (Figure 5c) to visualize the aggregates formed in the polyelectrolyte system. Only low-ionic-strength samples were suitable for analysis by TEM because higher levels of  $\text{KNO}_3$  led to its crystallization during the drying of the TEM grids, which prevented clear observation of the LDH aggregates (Figure S5). Polyelectrolyte loading of 50 mg/g (Figure 7a)

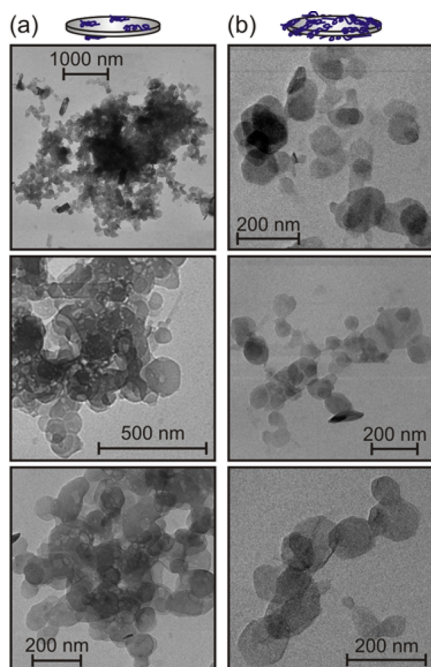


**Figure 7.** TEM images of  $\text{MgAl-NO}_3\text{-LDH}$  recorded with (a) aggregated and (b) stable samples in the presence of  $\text{P(AA}_{7.5}\text{-stat-BA}_{7.5})\text{-CTPPA}$  copolymer of 50 and 300 mg/g. The first dose (a) corresponds to the IEP, while the latter one (b) is close to the ASP where the particles are coated with the polyelectrolyte.

was compared to 300 mg/g (Figure 7b). Two key features are evident from these TEM images. First, aggregation was clearly promoted at the lower polyelectrolyte concentration. Second, the structure of the aggregates, i.e., the orientation of the platelets in the clusters, was the same as for bare particles (Figure 4) under the experimental conditions used.

On the basis of the stability studies presented in this work, the interparticle forces involved in the aggregation of LDH can be assumed to be DLVO-type both in the absence and in the presence of polyelectrolytes. The marked influence of ionic strength on the gradient of the Figure 5c curves (depicting the stability ratio versus the polyelectrolyte dose) indicates such a DLVO-type stabilization. These findings are in good agreement with those for polyelectrolyte-stabilized latex particle systems.<sup>27</sup> No evidence was found for other non-DLVO interparticle forces such as steric repulsion<sup>15,31,54</sup> or patch-charge attraction,<sup>29,55</sup> which have also been reported to occur in certain polyelectrolyte-particle systems. It can therefore be concluded that the surface charge distribution is uniform for bare and polyelectrolyte-adsorbed LDH and that the adsorption induces a higher surface charge density in magnitude and hence a higher stabilization effect of electrostatic origin.

## CONCLUSIONS

The surface charge properties and aggregation behavior of  $\text{MgAl-NO}_3\text{-LDH}$  nanoparticles as a function of ionic strength were studied in both the absence and the presence of an oppositely charged  $\text{P(AA}_{7.5}\text{-stat-BA}_{7.5})\text{-CTPPA}$  polyelectrolyte using electrophoresis, light scattering, and microscopy analysis. The colloidal stability of the bare particles could be explained by classical DLVO theory, with the specific adsorption of nitrate counterions also observed. The macroRAFT copolymer adsorbed on the oppositely charged  $\text{MgAl-NO}_3\text{-LDH}$  surface led to charge neutralization at the IEP and subsequent charge reversal at higher doses. The speed of aggregation depended strongly on the ionic strength at low doses, while unstable systems were observed near the IEPs at all salt levels investigated. Highly stable dispersions were obtained at elevated macroRAFT concentrations at which the particles were coated with the copolymers. No aggregation could be detected even at high ionic strength in such samples, indicating a high surface density of the molecules whose adsorption was enhanced by the butyl groups of the copolymers which have a high affinity for previously adsorbed chains on the LDH surface. Face-to-face orientation of the  $\text{MgAl-NO}_3\text{-LDH}$  platelets was found in the aggregates in both cases, i.e., in the absence or presence of copolymer at low doses. In conclusion, the  $\text{P(AA}_{7.5}\text{-stat-BA}_{7.5})\text{-CTPPA}$  macroRAFT copolymer was found to be a powerful agent for tuning the colloidal stability of the  $\text{MgAl-NO}_3\text{-LDH}$  dispersions and can be applied to formulate similar LDH samples for further applications wherever highly stable dispersions are desirable.

## ASSOCIATED CONTENT

### Supporting Information

The Supporting Information is available free of charge on the ACS Publications website at DOI: 10.1021/acs.langmuir.5b03372.

Detailed information and results of light scattering, electrophoretic and TEM measurements (PDF)

## AUTHOR INFORMATION

### Corresponding Authors

\*E-mail: [vanessa.prevot@univ-bpclermont.fr](mailto:vanessa.prevot@univ-bpclermont.fr).

\*E-mail: [istvan.szilagyi@unige.ch](mailto:istvan.szilagyi@unige.ch).

### Author Contributions

The manuscript was written through the contributions of all authors. All authors have given approval to the final version of the manuscript.

### Notes

The authors declare no competing financial interest.

## ACKNOWLEDGMENTS

Financial support from the Swiss National Science Foundation (150162), the Swiss Scientific Exchange Program (SCIEX-14033), the Swiss Secretariat for Education, Research and Innovation (C15.0024), and COST Actions MP1106 and CM1303 is gratefully acknowledged. M.P. and I.S. are grateful to Professor Michal Borkovec for access to the instruments in his laboratory. We also thank Mr. Olivier Vassalli for technical support during the DLS experiments. S.P., E.B.-L. and V.P. acknowledge financial support from ANR-11-JS08-0013.



## REFERENCES

- (1) Forano, C.; Costantino, U.; Prevot, V.; Taviot Gueho, C. Layered Double Hydroxides (LDH). In *Handbook of Clay Science*; Bergaya, F., Lagaly, G., Eds.; Elsevier: Amsterdam, 2013; Vol. 5A, pp 745–782.
- (2) Wang, Q.; O'Hare, D. Recent advances in the synthesis and application of layered double hydroxide (LDH) nanosheets. *Chem. Rev.* **2012**, *112*, 4124–4155.
- (3) Costantino, U.; Leroux, F.; Nocchetti, M.; Mousty, C. LDH in Physical, Chemical, Bio-chemical and Life Science. In *Handbook of Clay Science*; Bergaya, F., Lagaly, G., Eds.; Elsevier: Amsterdam, 2013; Vol. 5B, pp 765–791.
- (4) Choi, G.; Kwon, O. J.; Oh, Y.; Yun, C. O.; Choy, J. H. Inorganic nanovehicle targets tumor in an orthotopic breast cancer model. *Sci. Rep.* **2014**, *4*, 4430–4436.
- (5) He, S.; An, Z.; Wei, M.; Evans, D. G.; Duan, X. Layered double hydroxide-based catalysts: nanostructure design and catalytic performance. *Chem. Commun.* **2013**, *49*, 5912–5920.
- (6) Liang, H. F.; Meng, F.; Caban-Acevedo, M.; Li, L. S.; Forticaux, A.; Xiu, L. C.; Wang, Z. C.; Jin, S. Hydrothermal continuous flow synthesis and exfoliation of NiCo layered double hydroxide nanosheets for enhanced oxygen evolution catalysis. *Nano Lett.* **2015**, *15*, 1421–1427.
- (7) Ma, S. L.; Huang, L.; Ma, L. J.; Shim, Y.; Islam, S. M.; Wang, P. L.; Zhao, L. D.; Wang, S. C.; Sun, G. B.; Yang, X. J.; Kanatzidis, M. G. Efficient uranium capture by polysulfide/layered double hydroxide composites. *J. Am. Chem. Soc.* **2015**, *137*, 3670–3677.
- (8) Fu, L. L.; Qi, G. G.; Shekhah, O.; Belmabkhout, Y.; Estevez, L.; Eddaoudi, M.; Giannelis, E. P. Synthesis and carbon dioxide sorption of layered double hydroxide/silica foam nanocomposites with hierarchical mesostructure. *ChemSusChem* **2014**, *7*, 1035–1039.
- (9) Matusinovic, Z.; Wilkie, C. A. Fire retardancy and morphology of layered double hydroxide nanocomposites: a review. *J. Mater. Chem.* **2012**, *22*, 18701–18704.
- (10) Leroux, F.; Besse, J. P. Polymer interleaved layered double hydroxide: A new emerging class of nanocomposites. *Chem. Mater.* **2001**, *13*, 3507–3515.
- (11) Mignani, A.; Ballarin, B.; Giorgetti, M.; Scavetta, E.; Tonelli, D.; Boanini, E.; Prevot, V.; Mousty, C.; Iadecola, A. Heterostructure of Au nanoparticles-NiAl layered double hydroxide: Electrosynthesis, characterization, and electrocatalytic properties. *J. Phys. Chem. C* **2013**, *117*, 16221–16230.
- (12) Kun, R.; Balazs, M.; Dekany, I. Photooxidation of organic dye molecules on TiO<sub>2</sub> and zinc-aluminum layered double hydroxide ultrathin multilayers. *Colloids Surf., A* **2005**, *265*, 155–162.
- (13) Sranko, D.; Pallagi, A.; Kuzmann, E.; Canton, S. E.; Walczak, M.; Sapi, A.; Kukovec, A.; Konya, Z.; Sipos, P.; Palinko, I. Synthesis and properties of novel Ba(II)/Fe(III) layered double hydroxides. *Appl. Clay Sci.* **2010**, *48*, 214–217.
- (14) Tombacz, E.; Szekeres, M. Colloidal behavior of aqueous montmorillonite suspensions: the specific role of pH in the presence of indifferent electrolytes. *Appl. Clay Sci.* **2004**, *27*, 75–94.
- (15) Lagaly, G.; Ziesmer, S. Colloid chemistry of clay minerals: the coagulation of montmorillonite dispersions. *Adv. Colloid Interface Sci.* **2003**, *100-102*, 105–128.
- (16) Szabo, T. S.; Szekeres, M.; Dekany, I.; Jackers, C.; De Feyter, S.; Johnston, C. T.; Schoonheydt, R. A. Layer-by-layer construction of ultrathin hybrid films with proteins and clay minerals. *J. Phys. Chem. C* **2007**, *111*, 12730–12740.
- (17) Nguyen, D.; Zondanos, H. S.; Farrugia, J. M.; Serelis, A. K.; Such, C. H.; Hawket, B. S. Pigment encapsulation by emulsion polymerization using macro-RAFT copolymers. *Langmuir* **2008**, *24*, 2140–2150.
- (18) Ali, S. I.; Heuts, J. P. A.; Hawket, B. S.; van Herk, A. M. Polymer encapsulated gibbsite nanoparticles: Efficient preparation of anisotropic composite latex particles by RAFT-based starved feed emulsion polymerization. *Langmuir* **2009**, *25*, 10523–10533.
- (19) Zgheib, N.; Putaux, J. L.; Thill, A.; Bourgeat-Lami, E.; D'Agosto, F.; Lansalot, M. Cerium oxide encapsulation by emulsion polymerization using hydrophilic macroRAFT agents. *Polym. Chem.* **2013**, *4*, 607–614.
- (20) Rojas Delgado, R.; De Pauli, C. P.; Carrasco, C. B.; Avena, M. J. Influence of MII/MIII ratio in surface-charging behavior of Zn–Al layered double hydroxides. *Appl. Clay Sci.* **2008**, *40*, 27–37.
- (21) Leggat, R. B.; Taylor, S. A.; Taylor, S. R. Adhesion of epoxy to hydrotalcite conversion coatings: I. Correlation with wettability and electrokinetic measurements. *Colloids Surf., A* **2002**, *210*, 69–81.
- (22) Jobbagy, M.; Regazzoni, A. E. Complexation at the edges of hydrotalcite: The cases of arsenate and chromate. *J. Colloid Interface Sci.* **2013**, *393*, 314–318.
- (23) Lagaly, G.; Mecking, O.; Penner, D. Colloidal magnesium aluminum hydroxide and heterocoagulation with a clay mineral. I. Properties of colloidal magnesium aluminum hydroxide. *Colloid Polym. Sci.* **2001**, *279*, 1090–1096.
- (24) Rojas Delgado, R.; Arandigoyen Vidaurre, M.; De Pauli, C. P.; Ulibarri, M. A.; Avena, M. J. Surface-charging behavior of Zn–Cr layered double hydroxide. *J. Colloid Interface Sci.* **2004**, *280*, 431–441.
- (25) Lyklema, J. Overcharging, charge reversal: Chemistry or physics? *Colloids Surf., A* **2006**, *291*, 3–12.
- (26) Cherstvy, A. G.; Winkler, R. G. Polyelectrolyte adsorption onto oppositely charged interfaces: Image-charge repulsion and surface curvature. *J. Phys. Chem. B* **2012**, *116*, 9838–9845.
- (27) Szilagy, I.; Trefalt, G.; Tiraferri, A.; Maroni, P.; Borkovec, M. Polyelectrolyte adsorption, interparticle forces, and colloidal aggregation. *Soft Matter* **2014**, *10*, 2479–2502.
- (28) Szabo, T.; Toth, V.; Horvath, E.; Forro, L.; Szilagy, I. Tuning the aggregation of titanate nanowires in aqueous dispersions. *Langmuir* **2015**, *31*, 42–49.
- (29) Gillies, G.; Lin, W.; Borkovec, M. Charging and aggregation of positively charged latex particles in the presence of anionic polyelectrolytes. *J. Phys. Chem. B* **2007**, *111*, 8626–8633.
- (30) Szilagy, I.; Sadeghpour, A.; Borkovec, M. Destabilization of colloidal suspensions by multivalent ions and polyelectrolytes: From screening to overcharging. *Langmuir* **2012**, *28*, 6211–6215.
- (31) Bauer, D.; Buchhammer, H.; Fuchs, A.; Jaeger, W.; Killmann, E.; Lunckwitz, K.; Rehm, R.; Schwarz, S. Stability of colloidal silica, sikron and polystyrene latex influenced by the adsorption of polycations of different charge density. *Colloids Surf., A* **1999**, *156*, 291–305.
- (32) Zuo, H.; Gu, Z.; Cooper, H.; Xu, Z. P. Crosslinking to enhance colloidal stability and redispersibility of layered double hydroxide nanoparticles. *J. Colloid Interface Sci.* **2015**, *459*, 10–16.
- (33) Hornok, V.; Erdohelyi, A.; Dekany, I. Preparation of ultrathin membranes by layer-by-layer deposition of layered double hydroxide (LDH) and polystyrene sulfonate (PSS). *Colloid Polym. Sci.* **2005**, *283*, 1050–1055.
- (34) Hennous, M.; Derriche, Z.; Privas, E.; Navard, P.; Verney, V.; Leroux, F. Lignosulfonate interleaved layered double hydroxide: A novel green organoclay for bio-related polymer. *Appl. Clay Sci.* **2013**, *71*, 42–48.
- (35) Huang, S.; Cen, X.; Peng, H. D.; Guo, S. Z.; Wang, W. Z.; Liu, T. X. Heterogeneous ultrathin films of Poly(vinyl alcohol)/layered double hydroxide and montmorillonite nanosheets via layer-by-layer assembly. *J. Phys. Chem. B* **2009**, *113*, 15225–15230.
- (36) Sideris, P. J.; Nielsen, U. G.; Gan, Z. H.; Grey, C. P. Mg/Al ordering in layered double hydroxides revealed by multinuclear NMR spectroscopy. *Science* **2008**, *321*, 113–117.
- (37) Boursier, T.; Chaduc, I.; Rieger, J.; D'Agosto, F.; Lansalot, M.; Charleux, B. Controlled radical polymerization of styrene in miniemulsion mediated by PEO-based trithiocarbonate macromolecular RAFT agents. *Polym. Chem.* **2011**, *2*, 355–362.
- (38) Xu, Z. P.; Stevenson, G.; Lu, C. Q.; Lu, G. Q. Dispersion and size control of layered double hydroxide nanoparticles in aqueous solutions. *J. Phys. Chem. B* **2006**, *110*, 16923–16929.
- (39) Xu, Z. P.; Stevenson, G. S.; Lu, C. Q.; Lu, G. Q. M.; Bartlett, P. F.; Gray, P. P. Stable suspension of layered double hydroxide nanoparticles in aqueous solution. *J. Am. Chem. Soc.* **2006**, *128*, 36–37.

(40) Hassan, P. A.; Rana, S.; Verma, G. Making sense of Brownian motion: Colloid characterization by dynamic light scattering. *Langmuir* **2015**, *31*, 3–12.

(41) Chen, K. L.; Elimelech, M. Aggregation and deposition kinetics of fullerene (C<sub>60</sub>) nanoparticles. *Langmuir* **2006**, *22*, 10994–11001.

(42) Wu, L.; Liu, L.; Gao, B.; Munoz-Carpena, R.; Zhang, M.; Chen, H.; Zhou, Z. H.; Wang, H. Aggregation kinetics of graphene oxides in aqueous solutions: experiments, mechanisms and modeling. *Langmuir* **2013**, *29*, 15174–15181.

(43) Lopez-Leon, T.; Ortega-Vinuesa, J. L.; Bastos-Gonzalez, D. Ion-specific aggregation of hydrophobic particles. *ChemPhysChem* **2012**, *13*, 2382–2391.

(44) Calero, C.; Faraudo, J.; Bastos-Gonzalez, D. Interaction of monovalent ions with hydrophobic and hydrophilic colloids: Charge inversion and ionic specificity. *J. Am. Chem. Soc.* **2011**, *133*, 15025–15035.

(45) Evans, D. F.; Wennerstrom, H. *The Colloidal Domain*; John Wiley: New York, 1999.

(46) Abe, T.; Kobayashi, S.; Kobayashi, M. Aggregation of colloidal silica particles in the presence of fulvic acid, humic acid or alginate: Effects of ionic composition. *Colloids Surf., A* **2011**, *379*, 21–26.

(47) Zaccone, A.; Wu, H.; Lattuada, M.; Morbidelli, M. Correlation between colloidal stability and surfactant adsorption/association phenomena studied by light scattering. *J. Phys. Chem. B* **2008**, *112*, 1976–1986.

(48) Holthoff, H.; Egelhaaf, S. U.; Borkovec, M.; Schurtenberger, P.; Sticher, H. Coagulation rate measurements of colloidal particles by simultaneous static and dynamic light scattering. *Langmuir* **1996**, *12*, 5541–5549.

(49) Gursky, J. A.; Blough, S. D.; Luna, C.; Gomez, C.; Luevano, A. N.; Gardner, E. A. Particle-particle interactions between layered double hydroxide nanoparticles. *J. Am. Chem. Soc.* **2006**, *128*, 8376–8377.

(50) Carrillo, J. Y.; Dobrynin, A. V. Molecular dynamics simulations of polyelectrolyte adsorption. *Langmuir* **2007**, *23*, 2472–2482.

(51) Park, S. Y.; Bruinsma, R. F.; Gelbart, W. M. Spontaneous overcharging of macro-ion complexes. *Europhys. Lett.* **1999**, *46*, 454–460.

(52) Polzer, F.; Heigl, J.; Schneider, C.; Ballauff, M.; Borisov, O. V. Synthesis and analysis of zwitterionic spherical polyelectrolyte brushes in aqueous solution. *Macromolecules* **2011**, *44*, 1654–1660.

(53) Seyrek, E.; Hierrezuelo, J.; Sadeghpour, A.; Szilagyi, I.; Borkovec, M. Molecular mass dependence of adsorbed amount and hydrodynamic thickness of polyelectrolyte layers. *Phys. Chem. Chem. Phys.* **2011**, *13*, 12716–12719.

(54) Illes, E.; Tombacz, E. The effect of humic acid adsorption on pH-dependent surface charging and aggregation of magnetite nanoparticles. *J. Colloid Interface Sci.* **2006**, *295*, 115–123.

(55) Leong, Y. K. Interparticle forces arising from an adsorbed strong polyelectrolyte in colloidal dispersions: charged patch attraction. *Colloid Polym. Sci.* **1999**, *277*, 299–305.


 CrossMark  
 click for updates

 Cite this: *RSC Adv.*, 2016, 6, 16159

## Aggregation of layered double hydroxide nanoparticles in the presence of heparin: towards highly stable delivery systems†

 Marko Pavlovic,<sup>a</sup> Li Li,<sup>b</sup> Francois Dits,<sup>a</sup> Zi Gu,<sup>b</sup> Monika Adok-Spiczki<sup>a</sup> and Istvan Szilagyi<sup>\*a</sup>

The effect of heparin adsorption on the colloidal stability of layered double hydroxide particles as potential drug delivery agents was studied in aqueous suspensions. The lamellar structures were prepared by the co-precipitation method and composed of magnesium(II) and aluminium(III) mixed hydroxide as the layers and carbonate anions between the layers. Stable and positively charged particles were observed at low heparin concentrations and low ionic strengths where the surface charge was only partially neutralized by the oppositely charged natural polyelectrolyte adsorbed on the surface. Increasing the heparin dose resulted in charge neutralization and subsequent charge reversal at appropriate doses. The particles aggregated rapidly in the absence of sufficient surface charge, however, remarkably stable dispersions were obtained when the particles were completely covered by heparin. The latter coating process gave rise to two-times higher surface charge density in magnitude and about 20-times higher critical coagulation concentration than for the bare particles. The significant stabilization effect due to the heparin-coating resulted from repulsive interparticle forces of electrostatic and steric origin. On the basis of these findings, efficient delivery systems can be designed where the colloid stability of the carrier particles is enhanced by coating with a biocompatible polyelectrolyte.

 Received 7th December 2015  
 Accepted 2nd February 2016

DOI: 10.1039/c5ra26072h

[www.rsc.org/advances](http://www.rsc.org/advances)

### Introduction

Inorganic nanoparticles have been widely used as efficient gene and drug delivery agents.<sup>1–5</sup> Among them, layered double hydroxides (LDHs) are popular nanocarriers due to their ionic exchange property which allows intercalation of negatively charged bioactive substances between the layers as well as adsorption on the surface.<sup>3,6–11</sup> LDHs can be readily synthesized<sup>12,13</sup> and their size can be tuned to achieve the desired cellular uptake and drug release in the delivery process.<sup>14–17</sup> Similarly to other nanoparticles used in biomedical processes,<sup>18</sup> the colloidal stability of LDH-based carriers is a critical issue, since aggregation of the particles can prevent the successful delivery of the target molecules. Despite its importance, stabilization of LDH particles in aqueous dispersions has not been yet investigated in detail and the first systems describing highly stable protein or polymer modified platelets have been reported only recently.<sup>19–21</sup>

Polyelectrolytes have been proved as effective stabilizing agents for nanoparticles to be used in biochemical

processes.<sup>22–24</sup> In particular, low molecular weight heparin, a biocompatible sulfated polysaccharide which can be considered as natural polyelectrolyte, is a powerful injectable anticoagulant for numerous biomedical applications, because of its highest negative line charge density among the known biological molecules.<sup>25</sup> The effect of heparin adsorption on stability of nanoparticles has been investigated in certain systems. For instance, aggregation of gold nanoparticles was found to be sensitive to the heparin concentration.<sup>26</sup> This discovery led to the development of optical sensor to determine the concentration of the macromolecules based on the different visible spectra of the gold aggregates of different size.<sup>27,28</sup> Aggregation of drug nanocapsules was also prevented by using heparin during synthesis,<sup>29</sup> and nanogels composed of heparin and positively charged polyelectrolytes were used successfully in gene delivery for cancer treatment.<sup>30</sup> Apart from the applications as stabilizing agent or building block for carrier nanomaterials, heparin was also delivered as drug in biomedical treatments.<sup>31,32</sup>

Loading LDH with heparin has been studied mainly from the point of view of intercalation between the LDH layers. This type of composite materials can be used as drugs for clinical applications.<sup>33</sup> Such immobilization and the resulted structure of the nanocomposite have been investigated by both experimental<sup>34</sup> and theoretical<sup>35</sup> methods. Accordingly, successful intercalation was reported among the layers if heparin was present together

<sup>a</sup>Department of Inorganic and Analytical Chemistry, University of Geneva, Geneva, CH-1205, Switzerland. E-mail: istvan.szilagyi@unige.ch; Tel: +41 22 3796031

<sup>b</sup>Australian Institute for Bioengineering and Nanotechnology, The University of Queensland, Brisbane, QLD-4072, Australia

† Electronic supplementary information (ESI) available. See DOI: 10.1039/c5ra26072h

dc\_1931\_21

with the chloride salts of magnesium(II) and aluminium(III) ions in the co-precipitation process where the pH was increased to form heparin-LDH lamellar material.<sup>34</sup> A computational modelling study revealed that attractive electrostatic forces were responsible for the adsorption and strong immobilization on the lamellae and the heparin helices were oriented in parallel with the LDH layers due to structural deformation of the polyelectrolytes upon intercalation.<sup>35</sup> Self-diffusion of water and heparin and kinetics of drug release were also addressed in these papers. In addition, ultrathin biomimetic film composed of delaminated LDH nanosheets and heparin layers was prepared by the layer-by-layer method utilizing the high affinity of the heparin to the oppositely charged platelets.<sup>36</sup> The obtained film showed enhanced strength and good blood biocompatibility which can be beneficial in certain medical applications. Apart from these papers, studies on colloid stability of LDH particles in the presence of heparin have not been reported so far.

Therefore, in this research we carried out the investigation on the effect of heparin adsorption on aggregation of LDH particles of different sizes in detail. First of all, charging and stability of LDH particles, composed of magnesium(II) and aluminium(III) hydroxide and carbonate anions in the gallery, were studied in aqueous dispersions without and with heparin. The lamellar structure of the particles was determined by X-ray diffraction (XRD) and the colloidal properties were explored in electrophoretic and time-resolved dynamic light scattering (DLS) experiments. The orientation of the particles in stable and aggregated samples was finally examined by transmission electron microscopy (TEM). The results of the present work revealed that the speed of particle aggregation and related dispersion stability of the LDH-heparin colloids can be tuned by changing the experimental conditions such as polyelectrolyte dose, particle concentration and ionic strength. In this way, highly stable samples can be designed and applied as biocompatible carrier systems in further biomedical applications, especially in drug and gene delivery processes.

## Experimental section

### Materials

Low molecular weight sodium heparin was purchased from Acros Organics and used for sample preparation without further purification. The manufacturer reported an average molecular weight of about  $13.5 \text{ kg mol}^{-1}$ . Other chemicals such as  $\text{MgCl}_2$ ,  $\text{AlCl}_3$ ,  $\text{Na}_2\text{CO}_3$ ,  $\text{NaOH}$ ,  $\text{HCl}$  and  $\text{NaCl}$  (all from Sigma-Aldrich) used in the experiments were analytical grade or higher quality. Ultrapure water (Millipore) was used for solution preparations which were adjusted to pH ( $7.0 \pm 0.5$ ) for all stock solutions and dispersions before mixing them together. The experiments were carried out at a temperature of ( $25 \pm 0.2$ ) °C.

LDH particles were prepared by the co-precipitation method followed by hydrothermal treatment.<sup>37–40</sup> Briefly, a mixture of 0.6 M  $\text{MgCl}_2$  and 0.2 M  $\text{AlCl}_3$  solution (10 mL) was quickly added to 40 mL of mixed solution containing 0.40 M  $\text{NaOH}$  and 0.04 M

$\text{Na}_2\text{CO}_3$  under vigorous stirring. After mixing for 10 min, the LDH slurry was collected and washed twice. Then the particles were manually re-suspended in 40 mL deionized water. The inhomogeneous suspension was transferred to an autoclave (stainless steel with Teflon lining) and heated in an oven at 100 °C for 16 h (sample LDH1) or at 150 °C for 16 h (LDH2). After this hydrothermal treatment, a transparent and homogenous LDH suspension was obtained with the mass concentrations of 9.3 and 8.0  $\text{g L}^{-1}$  for LDH1 and LDH2, respectively. To completely cover the nanoparticles with heparin, 100 mg macromolecule was adsorbed on 1 g of LDH under the desired experimental conditions, as detailed later.

### Electrophoresis

The electrokinetic potential was converted from the electrophoretic mobility which was measured with a ZetaNano ZS (Malvern) device using an electric field of  $4 \text{ kV m}^{-1}$ . The experiments were performed in plastic capillary cells (Malvern) cleaned with 2% Hellmanex (Hellma) solution and rinsed with ultrapure water. In each measurement, 5 mL dispersion was prepared as follows. A calculated amount of heparin stock solution was mixed with NaCl solution and water to obtain the desired polyelectrolyte dose and ionic strength. The sample preparation was finalized by adding 0.5 mL of the particle stock dispersion of about 93 and 80  $\text{mg L}^{-1}$  (diluted from the original suspensions) for samples LDH1 and LDH2, respectively. The suspensions were equilibrated overnight at room temperature and their electrophoretic mobility was measured five times and the averaged. The method of conversion to electrokinetic potential is detailed in the ESI.†

### Light scattering

The aggregation of the LDH particles was followed in time-resolved DLS experiments which were carried out with a compact goniometer system (ALV/CGS-3) at 90° scattering angle. The instrument was equipped with a He/Ne laser operating at 633 nm as a light source and an avalanche photodiode as a detector. To determine the hydrodynamic radius ( $R_h$ ) of the LDH particles, the correlation function was accumulated for 20 seconds and a second cumulant fit was used.<sup>41</sup> The  $R_h$  measured for the platelet-like LDH particles is equal to the radius of an equivalent sphere. As shown in Fig. 1 for some examples, the  $R_h$  values were recorded in time-resolved measurements for 15–20 minutes depending on the speed of the aggregation. The increase in  $R_h$  was always linear in these experiments, indicating early stages of the aggregation. The slopes in the  $R_h$  versus time plots were used to calculate the stability ratio ( $W$ ) via the following equation:<sup>42–44</sup>

$$W = \frac{\left. \frac{dR_h(t)}{dt} \right|_{t \rightarrow 0, \text{fast}}}{\left. \frac{dR_h(t)}{dt} \right|_{t \rightarrow 0}} \quad (1)$$

where fast refers to rapid aggregation in the sample which was achieved in 1 M NaCl solutions where the particles undergo diffusion controlled aggregation. Note that  $W$  is close to unity in



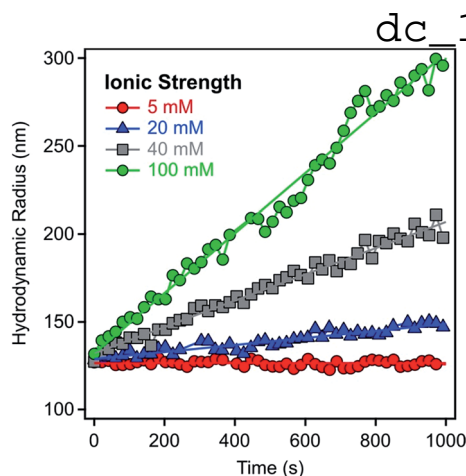


Fig. 1 Hydrodynamic radii of LDH1 particles versus time measured in time-resolved DLS experiments at  $9.3 \text{ mg L}^{-1}$  particle concentration and different ionic strengths adjusted with NaCl.

case of fast aggregation, but a higher value points to a slower aggregation and a more stable dispersion. The sample preparation was very similar to the electrophoretic measurements, *i.e.*, the dose of heparin, ionic strength and particle concentration were the same in both studies, but the total volume was 2 mL for the aggregation measurement. The time-resolved DLS experiments were initiated by injecting the LDH stock dispersion which was previously subjected to ultrasound treatment to minimize the initial aggregation. Such experimental conditions allowed us to directly compare surface charge properties with aggregation behaviour of the LDH particles under identical experimental conditions. The light scattering measurements were performed in borosilicate glass cuvettes (Kimble Chase) cleaned with the mixture of concentrated  $\text{H}_2\text{SO}_4$  (Carlo Erba) and 30%  $\text{H}_2\text{O}_2$  (Reactolab) at a volume ratio of 3 : 1 and washed with water followed by drying in a dust-free oven. Further information on the DLS measurements can be found in the ESI.†

### X-ray diffraction

Powder XRD patterns of solid LDH samples were registered in the 2-theta range of  $3\text{--}80^\circ$  on a Stadi-P (Stoe) instrument. This device uses  $\text{CuK}\alpha$  ( $\lambda = 0.15406 \text{ nm}$ ) radiation in Bragg–Brentano geometry. Positions of the peaks and full widths at half maximum (FWHM) were determined by applying Gaussian fits. More details about the interpretation of the XRD spectra are provided in the ESI.†

### Transmission electron microscopy

TEM imaging was carried out with a Tecnai G2 electron microscope (FEI) operating at 120 kV. During sample preparation,  $3 \mu\text{L}$  of the particle dispersion was placed on carbon coated 400-mesh copper grids, left for 30 seconds and drained off the excess liquid with filter paper and dried. The same experimental conditions (*e.g.*, particle concentration, pH and heparin dose) were applied for the original TEM samples as those used in electrophoretic and aggregation studies.

## dc\_1931\_21 Results and discussion

### Particle characteristics

We observed seven different peaks in the XRD pattern of both LDH1 and LDH2 (Fig. 2). Comparing them to the diffraction pattern of other carbonate LDHs,<sup>45–47</sup> we can unambiguously confirm the formation of the lamellar structure typical for this kind of LDHs. However, the minor peaks observed at  $19^\circ$  indicates the presence of a small amount of  $\text{Mg}(\text{OH})_2$  side phase. We could assign Miller indexes to each peak and use some of them to calculate lattice parameters which are necessary to describe a unit cell (Table 1). From the position of the first peak 003, a  $d_{003}$  parameter of 0.77 nm was calculated for both LDH particles. This value represents the thickness of one hydroxide layer and one interlayer spacing together. From the  $d_{003}$  value, the unit cell ( $c = 2.31 \text{ nm}$ ) was calculated for LDH1 and LDH2. Another important lattice parameter is the shortest distance between two cations in one hydroxide layer expressed by parameter  $a$ , which can be calculated as twice the  $d$ -spacing of the 110 reflection. The same  $a$  value (0.31 nm) was obtained for both particles. In addition, the average thickness of the particles ( $v$ ) along the  $c$  axis was found to be 18.2 and 17.3 nm for LDH1 and LDH2, respectively. This implies that the particles were constituted by about 20–25 brucite-like hydroxide layers. DLS measurements yielded hydrodynamic radii of 136.1 and 316.2 nm in stable dispersions for LDH1 and LDH2, respectively. The particles were slightly polydisperse, as indicated by their polydispersity index (PDI) values determined in the DLS experiments (Table 1).

### Charging of LDH in the presence of heparin

Surface charge of LDH1 was investigated first with electrophoresis. The particles possessed positive charges (electrokinetic potential was about 40 mV in aqueous dispersion without added polyelectrolyte at low ionic strength) due to their structural properties while the heparin is negatively charged at the

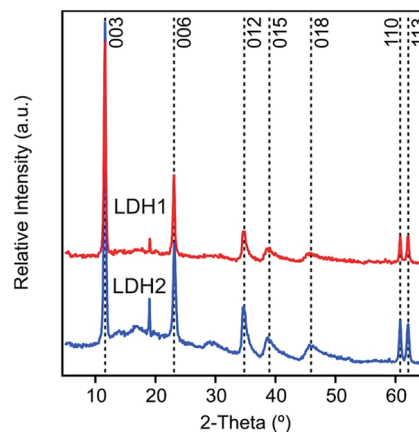


Fig. 2 Powder XRD pattern of the LDH particles, composed of magnesium(II) and aluminium(III) cations and carbonate interlayer anions, synthesized by co-precipitation. The peak at  $19^\circ$  could be due to the 001 peak of  $\text{Mg}(\text{OH})_2$  that was formed from soluble magnesium(II) and hydroxide ions after drying.

dc 1931-21

**Table 1** Characteristic structural and size data of the LDHs determined by XRD in solid state and by DLS in dispersion

	Peak position <sup>a</sup> (°)		Calculated parameters (nm)					Size <sup>b</sup>	
	003	110	$d_{003}$ <sup>c</sup>	$d_{110}$ <sup>c</sup>	$a$ <sup>d</sup>	$c$ <sup>e</sup>	$\nu$ <sup>f</sup>	$R_h$ (nm)	PDI
LDH1	11.6	60.8	0.77	0.15	0.31	2.31	18.2	136.1	0.274
LDH2	11.6	60.8	0.77	0.15	0.31	2.31	17.3	316.2	0.265

<sup>a</sup> Obtained from the XRD spectra. <sup>b</sup> Hydrodynamic radius and polydispersity index were measured by DLS. <sup>c</sup> Calculated with eqn (S8) (see ESI). <sup>d</sup> Shortest distance between two cations in the layer and  $a = 2d_{110}$ . <sup>e</sup> The width of a unit cell and  $c = 3d_{003}$ . <sup>f</sup> Average particle thickness, calculated with eqn (S9) (see ESI).

pH used ( $7.0 \pm 0.5$ ). In the individual experiments, particle concentration, ionic strength and pH were kept constant while the heparin concentration was varied. Such measurements were repeated at different ionic strength (1, 10 and 100 mM adjusted by NaCl) to explore the adsorption mechanism.

In general, the electrokinetic potentials were positive at low polyelectrolyte concentrations ( $0\text{--}1 \text{ mg g}^{-1}$ , and the  $\text{mg g}^{-1}$  unit

refers to mg heparin per one gram of particle) indicating the positive charge of the bare platelets (Fig. 3a). Increasing the heparin dose, the potential values decreased due to the heparin adsorption on the oppositely charged surface. This process gave rise to charge neutralization at the isoelectric point (IEP) when the heparin concentration reached the range of  $12\text{--}26 \text{ mg g}^{-1}$  depending on the ionic strength applied. The IEP corresponds to the dose where the overall charge of the particle is zero. Further adding heparin to the samples, charge reversal<sup>48–50</sup> occurred, indicating the continuous adsorption of heparin on the LDH1 platelet surface.<sup>51</sup> Similar charge reversal has been already observed in several dispersions containing colloidal particles and polyelectrolytes<sup>21,22,52–55</sup> or multivalent ions<sup>56–58</sup> and also in other systems of similar charge balance.<sup>29,59</sup> Monovalent anions can also cause such charge reversal of LDHs, but in a much smaller extent indicating the significantly higher affinity of the negatively charged polyelectrolytes (*e.g.*, heparin) to the oppositely charged particle surface.

The potential *versus* heparin dose curves saturated at high concentrations indicating full coverage of the LDH particle surface with the polyelectrolyte under these experimental conditions. Additional heparin molecules remained dissolved in solution after this concentration. Such saturation took place around  $100 \text{ mg g}^{-1}$  polyelectrolyte dose regardless of the ionic strength. However, the magnitude of the electrokinetic potential was sensitive to the ionic strength. At low heparin concentrations ( $0\text{--}3 \text{ mg g}^{-1}$ ), where the positive charge of the particles was only partially compensated by the adsorbed molecules of opposite charge, the potential values decreased at higher salt level (100 mM) due to the screening effect of the counterions on the surface charge. Once the heparin dose was high enough ( $100\text{--}300 \text{ mg g}^{-1}$ ), the ionic strength dependence of the potentials reflected the surface charge characteristics of the coated LDH1 at different salt levels as discussed later. Multivalent organic anions containing carboxylate groups showed similar adsorption properties on carbonate and chloride LDHs.<sup>51</sup> Accordingly, charge neutralization and subsequent charge reversal were reported on the basis of zeta potential measurements, but such processes took place in a much higher concentration range in those measurements due to the higher particle concentrations applied.

### Aggregation in the presence of heparin

Time-resolved DLS experiments were performed to follow the aggregation processes under the same experimental conditions as in the charge investigation above. At a low ionic strength (1 mM), stability ratios close to unity indicated unstable dispersions near the dose corresponding to the IEP (Fig. 3b). The aggregation slowed down, *i.e.*, the stability ratios increased, at low and high heparin doses. This behaviour can be well-explained by the classical theory developed by Derjaguin, Landau, Verwey and Overbeek (DLVO).<sup>60</sup> Accordingly, the repulsive electrical double layer forces between the particles vanish in the absence of surface charge and the attractive van der Waals forces will destabilize the particle colloids at the IEP. Significantly below or above this dose, the particles have

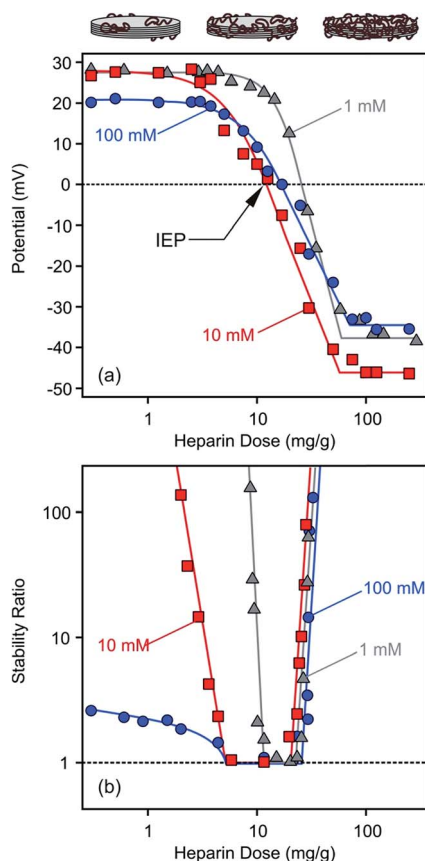


**Fig. 3** Electrokinetic potential (a) and stability ratio (b) values for LDH1 in the presence of heparin at different ionic strengths. Stability ratios close to unity indicate rapid particle aggregation while higher values point to more stable dispersions. The  $\text{mg g}^{-1}$  unit refer to mg heparin per gram of LDH. The lines are just to guide the eyes.

dc\_1931\_21

sufficient charge (Fig. 3a) and hence, electrical double layers form around the LDH, giving rise to repulsive forces and more stable dispersions. Such U-shaped curves are typical for polyelectrolyte-induced particle aggregation and found earlier in case of latex,<sup>61</sup> titanate<sup>21,62,63</sup> or silica<sup>64,65</sup> colloids in the presence of oppositely charged macromolecules.

The effect of ionic strength on particle aggregation was more pronounced at low heparin doses. The relatively narrow stability ratio *versus* dose curve at 1 mM salt level became larger at 10 mM. The dispersions possessed only limited stability at 100 mM NaCl, as indicated by stability ratios less than 3 (meaning that each third collision of the particles results in dimer formation) at very low heparin concentrations. The stability ratio values overlap within the experimental error at high doses and the transition between slow and fast aggregation was very abrupt (*i.e.*, the slopes were very steep) in this regime indicating that the charge reversal-induced restabilization of the dispersions is not very sensitive to the ionic strength. The dependence of the aggregation rates on the salt level is in line with the DLVO theory and can be explained with screening the surface charge with the counterions, which leads to smaller Debye lengths and weaker repulsive double layer forces at high salt levels. However, the heparin coated LDH1 was stable even at high ionic strengths, indicating an extremely high surface charge density or the presence of additional repulsive forces of non-DLVO origin.<sup>66–68</sup> This issue will be further explored shortly.

The stability of the dispersions and the structure of aggregates were studied by recording TEM images with the same samples used for the electrophoretic and time-resolved DLS experiments. Such images were taken at the low heparin dose (Fig. 4a), near the IEP (Fig. 4b) and at the high polyelectrolyte concentration (Fig. 4c). In the last case, the LDH1 particles should be completely covered by heparin. Note that the samples were dried during the TEM images, which could also induce some aggregation. Nevertheless, well-separated particles were observed at the low heparin dose indicating stable samples. Aggregation was observed close to the IEP, in good agreement with the stability study. Similar to other LDH systems,<sup>69,70</sup> the platelets prefer face-to-face orientation in the aggregates. Other types of orientation such as face-to-edge<sup>71</sup> or edge-to-edge<sup>72,73</sup> were not observed in the TEM images. Stable samples and separated particles were imaged at the high heparin dose where

the aggregation was prevented by the adsorbed polyelectrolyte layer.

### Effect of particle size

The changing trend in potentials (Fig. 5a) and stability ratios (Fig. 5b) was found to be similar for LDH2 particles of larger size by increasing the heparin concentration, indicating similar adsorption mechanism and interparticle forces as for the LDH1 of smaller size. However, differences can still be observed if one interprets the ionic strength dependence. At 100 mM NaCl concentration, the charge of the particles was close to zero at low heparin doses due to the enhanced screening effect of the counterions on the surface charge. Such low potentials led to unstable samples, indicated by stability ratios close to one in this regime. Similarly to the LDH1 system, the aggregation rates were sensitive to the electrolyte concentration mostly at low heparin doses, while stable dispersions were obtained at higher polyelectrolyte concentrations irrespectively from the ionic strength. TEM images, recorded with stable and unstable samples, confirm these findings (see Fig. S1 in ESI†). Accordingly, primary particles were found at low ( $1 \text{ mg g}^{-1}$ ) and high ( $30 \text{ mg g}^{-1}$ ) doses, while aggregates were imaged near the IEP ( $5 \text{ mg g}^{-1}$ ). The LDH2 platelets also show face-to-face orientation in the aggregates.

Although intercalation of heparin between the layers of certain LDHs has been published earlier,<sup>34</sup> we did not find any evidences for such process in our experiments. This is most likely due to the different conditions used in the reported study and our systems. The heparin is immobilized between the lamellae through the competition with chloride anions in the co-precipitation process in the report (where heparin has much higher affinity for LDH than chloride). However, the intercalation could occur only through exchange with carbonate (with high affinity for LDH) in our samples where it is also unlikely to introduce bulky macromolecules into the lamellar structure.

### Stability of bare and coated particles

The effect of heparin coating on colloidal stability was explored by comparing charging and aggregation of bare and fully covered particles at different salt levels. To achieve such coating, a heparin dose of  $100 \text{ mg g}^{-1}$  was applied for both

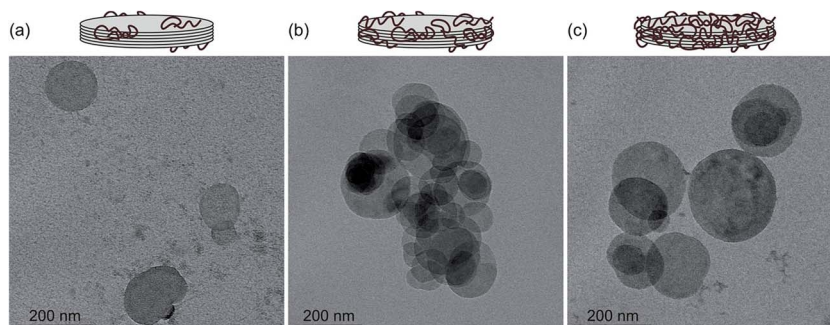


Fig. 4 TEM images of LDH1 particles at different heparin doses:  $1 \text{ mg g}^{-1}$  which refers to low dose and stable samples (a),  $15 \text{ mg g}^{-1}$  near the IEP with aggregated samples (b) and  $30 \text{ mg g}^{-1}$  where the particles reversed their charge and form stable dispersion (c).

dc\_1931\_21

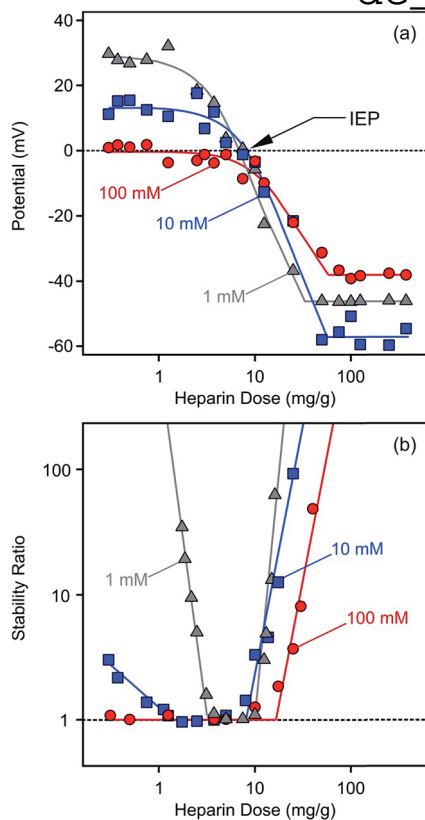


Fig. 5 Electrokinetic potential (a) and stability ratio (b) values for LDH2 in the presence of heparin at different ionic strengths. The  $\text{mg g}^{-1}$  unit refer to  $\text{mg heparin per gram of LDH}$ . The lines are just to guide the eyes.

particles, since this concentration was slightly above the saturation limit observed in the electrophoretic mobility curves (Fig. 3a and 5a). The ionic strength dependence on the electrokinetic potentials and stability ratios were determined over a wide range of NaCl concentration (Fig. 6).

Slightly different potentials were obtained at low ionic strengths for the bare LDH1 and LDH2 particles, but they were the same within the experimental error at higher salt levels (Fig. 6a). The electrokinetic potentials decreased with the ionic strength due to the screening effect of the counterions on the particle surface and remained positive, although very close to zero at the higher electrolyte concentrations, in the entire concentration range investigated. This finding is in line with the results of our other study, in which we found that  $\text{Cl}^-$  ions adsorb only weakly on LDHs, while more hydrophobic monovalent anions showed higher affinity and stronger adsorption on the surface.<sup>74</sup>

Heparin adsorption at the dose of  $100 \text{ mg g}^{-1}$  resulted in negatively charged particles as predicted by the results of the previous section. Similarly to the bare LDHs, the potentials of the coated ones deviated at low salt levels, while they showed good agreement at higher NaCl concentrations where the screening effect on the surface charges became important. Note that the sodium ions were the counterions in these systems. The effect of ionic strength on the potentials was similar again,

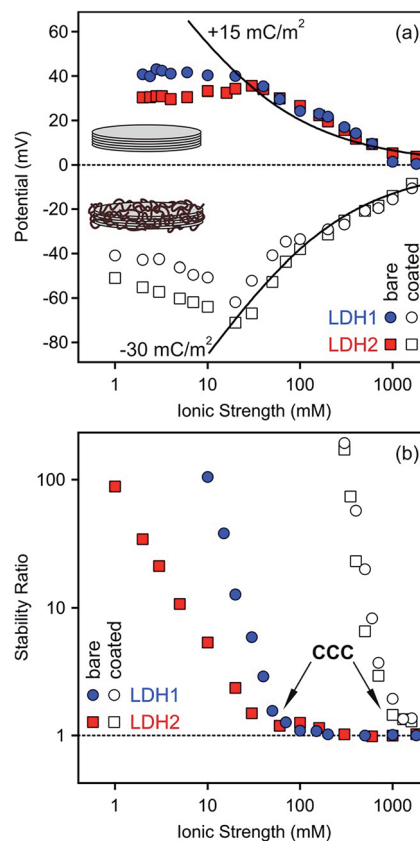


Fig. 6 Electrokinetic potential (a) and stability ratio (b) values for the bare (filled symbols) and heparin coated (empty symbols, at a dose of  $100 \text{ mg g}^{-1}$ ) LDH1 and LDH2 particles at different ionic strengths. The solid lines in (a) indicates the potentials calculated using the Debye-Hückel model. The surface charge densities are also indicated.

namely, they decreased with increasing the salt concentration, but remained negative even at high electrolyte levels. Such change in the potential or related electrophoretic mobility is typical for bare or polyelectrolyte coated colloidal particles of significant charge.<sup>62,75</sup> Theoretical potentials were calculated using the Debye-Hückel approximation (eqn (S2) in ESI†).<sup>60,62</sup> This theory is valid at high ionic strengths and significant differences can be observed at lower salt levels. The best fit to the experimental values was found with  $+15$  and  $-30 \text{ mC m}^{-2}$  surface charge densities for the bare and heparin coated particles, respectively. These data indicate that the polyelectrolyte coverage resulted in two-time higher surface charge in magnitude compared to the LDH1 and LDH2 bare particles.

Stability ratios determined at different ionic strengths for the bare and coated particles showed similar trend in general (Fig. 6b). Accordingly, the dispersions were stable at low NaCl levels, while stability ratios close to one indicated rapidly aggregating dispersions at higher ionic strengths. The slow and fast aggregation regimes were separated by the well-defined critical coagulation concentration (CCC) value. Such behaviour is typical for charged colloidal particles and can be explained by the DLVO theory. The interparticle forces are the superposition of attractive van der Waals and repulsive double layer forces and the latter ones decrease with the ionic strength



due to the progressively screened electrical double layer around the particles, leading to unstable particle dispersions at high salt levels.

Some differences can be observed in the stability ratio *versus* ionic strength curves for the bare particles. The CCC values fell in the same range, but slightly deviated (60 and 39 mM for LDH1 and LDH2, respectively). Such values are similar to those determined for LDH particles in the presence of simple monovalent anions (*e.g.*, Cl<sup>-</sup> and NO<sub>3</sub><sup>-</sup>), which are the counterions in these systems. However, complex and more hydrophobic anions (*e.g.*, SCN<sup>-</sup>) tend to adsorb stronger on the particles and shift the CCC towards lower concentrations.<sup>74</sup> In addition, the slopes in the slow aggregation regime are significantly different. For larger LDH2 particles, the stability ratios were smaller at the same NaCl concentrations, leading to smaller slopes at low ionic strengths compared to LDH1. Such deviation can be originated from the different sizes, since the attractive van der Waals forces are proportional to the Hamaker constant and the size of the particles.<sup>52,56,60</sup> The Hamaker constant is related to the composition of the materials and hence, should be the same for both particles. However, the size dependence on the strength of the attractive van der Waals forces results in a stronger attraction for larger particles, leading to a lower CCC and a lower stability ratio before the CCC, in good agreement with the present results obtained with the bare systems.

For the heparin coated particles, the stability curves agreed within the experimental error and a common CCC around 1100 mM ionic strength was determined. Note that the sodium ions are the counterions in this system and they are responsible for the destabilization by electrostatic screening of the surface charge. The effect of monovalent cations on aggregation of colloidal particles is usually very small or negligible.<sup>76</sup> This value is about 20-time larger than that for the bare LDHs, indicating an enormous stabilization effect of the heparin layer adsorbed on the platelets. Such polyelectrolyte-induced stabilization has been reported earlier for LDH<sup>20,21</sup> and other colloidal particles.<sup>24,75,77,78</sup> Since the size of the coated LDH1 particles is smaller than the LDH2 covered by heparin, different van der Waals forces can be expected and they should lead to different CCCs and slopes in the slow aggregation regime, similar to the bare particles discussed above. Nevertheless, the situation here is obviously different. The shape of the stability curves definitely indicates the presence of DLVO-type forces, but the extremely high CCC and the lack of differences in the stability ratios at lower ionic strength should be the sign of other types of repulsive interparticle forces. Polyelectrolyte layers adsorbed on oppositely charged surfaces are typically flat at low salt levels, but they are swollen at higher electrolyte concentrations.<sup>79</sup> The swelling leads to the formation of polyelectrolyte tails and loops around the particles and steric repulsion between the hairy particles can become important.<sup>66,68,80</sup> Our results can also be explained with the presence of repulsive steric forces between the adsorbed polyelectrolyte chains which are the most pronounced at high ionic strength due to the extended heparin layer around the platelets. As a result, these interparticle forces give rise to highly stable dispersions, which are potential

candidates as carriers in delivery processes even at high salt levels where the bare particles would rapidly aggregate. In particular, the polyelectrolyte covered particles are stable at the physiological ionic strength (150 mM in blood), which is higher than the CCCs of the bare particles. Accordingly, intercalation of the lamellar particles with a desired drug molecule and coating with the appropriate dose of heparin will certainly result in delivery systems which can pass the critical part of living organisms without any unwanted aggregation of the carrier nanoplatelets.

## Conclusions

Electrophoretic experiments revealed that heparin adsorption on oppositely charged LDH particles led to charge neutralization at the IEP and subsequent charge reversal at appropriate polyelectrolyte concentrations. The latter process led to two-time higher surface charge density in magnitude compared to the bare platelets. The electrokinetic potentials were sensitive to the ionic strength especially at low heparin doses due to the screening effect of the counterions on the LDH surface. Results of time-resolved DLS experiments showed that the samples were moderately stable at low polyelectrolyte concentrations. However, increasing the ionic strength gave rise to unstable dispersions in this regime and also near the IEP regardless of the salt level. Face-to-face orientation of the particles was found in TEM images recorded for the aggregated samples. Further increasing the heparin dose, the particles were restabilized where they possessed sufficiently high negative charge due to the charge reversal process. Highly stable LDH dispersions were obtained by completely covering their surface with the heparin macromolecules. Such stabilizing effect led to about 20-time increase in the CCC of the coated particles, indicating a significant resistance against aggregation even at higher electrolyte concentrations. These results allow designing efficient delivery systems where aggregation of nanocarrier LDH platelets can be tuned with biocompatible heparin macromolecules.

## Acknowledgements

The present research was supported by the Swiss National Science Foundation (150162), Swiss Scientific Exchange Program (SCIEX-14033), Swiss Secretariat for Education, Research and Innovation (C15.0024) as well as COST Action CM1303. The authors are grateful to Professor Michal Borkovec for providing access to the light scattering instruments in the Laboratory of Colloid and Surface Chemistry at the University of Geneva. Financial support to Z. G. was also provided by the National Health and Medical Research Council of Australia (NHMRC) Early Career Fellowship (APP1073591). We thank Professor Zhi Ping Xu for his useful comments on the manuscript.

## References

- 1 B. Delalat, V. C. Sheppard, S. Rasi Ghaemi, S. Rao, C. A. Prestidge, G. McPhee, M. L. Rogers, J. F. Donoghue,

- V. Pillay, T. G. Johns, N. Kroger and N. H. Voelcker, *Nat. Commun.*, 2015, **6**, 8791.
- 2 Z. P. Xu, Q. H. Zeng, G. Q. Lu and A. B. Yu, *Chem. Eng. Sci.*, 2006, **61**, 1027–1040.
- 3 J. H. Choy, S. Y. Kwak, Y. J. Jeong and J. S. Park, *Angew. Chem., Int. Ed.*, 2000, **39**, 4042–4045.
- 4 V. Brunetti, L. M. Bouchet and M. C. Strumia, *Nanoscale*, 2015, **7**, 3808–3816.
- 5 H. F. Bao, J. P. Yang, Y. Huang, Z. P. Xu, N. Hao, Z. X. Wu, G. Q. Lu and D. Y. Zhao, *Nanoscale*, 2011, **3**, 4069–4073.
- 6 M. Halma, C. Mousty, C. Forano, M. Sancelme, P. Besse-Hoggan and V. Prevot, *Colloids Surf., B*, 2015, **126**, 344–350.
- 7 N. K. Singh, Q. V. Nguyen, B. S. Kim and D. S. Lee, *Nanoscale*, 2015, **7**, 3043–3054.
- 8 Z. Gu, J. J. Atherton and Z. P. Xu, *Chem. Commun.*, 2015, **51**, 3024–3036.
- 9 L. Perioli and C. Pagano, *Expert Opin. Drug Delivery*, 2012, **9**, 1559–1572.
- 10 S. Vial, V. Prevot, F. Leroux and C. Forano, *Microporous Mesoporous Mater.*, 2008, **107**, 190–201.
- 11 Z. Gu, B. E. Rolfe, Z. P. Xu, J. H. Campbell, G. Q. Lu and A. C. Thomas, *Adv. Healthcare Mater.*, 2012, **1**, 669–673.
- 12 C. H. Zhou, Z. F. Shen, L. H. Liu and S. M. Liu, *J. Mater. Chem.*, 2011, **21**, 15132–15153.
- 13 Z. Ferencz, A. Kukovecz, Z. Konya, P. Sipos and I. Palinko, *Appl. Clay Sci.*, 2015, **112**, 94–99.
- 14 C. P. Chen, L. K. Yee, H. Gong, Y. Zhang and R. Xu, *Nanoscale*, 2013, **5**, 4314–4320.
- 15 M. Chen, H. M. Cooper, J. Z. Zhou, P. F. Bartlett and Z. P. Xu, *J. Colloid Interface Sci.*, 2013, **390**, 275–281.
- 16 H. Y. Dong, H. S. Parekh and Z. Ping, *J. Colloid Interface Sci.*, 2015, **437**, 10–16.
- 17 S. D. Li, J. H. Li, C. J. Wang, Q. Wang, M. Z. Cader, J. Lu, D. G. Evans, X. Duan and D. O'Hare, *J. Mater. Chem. B*, 2013, **1**, 61–68.
- 18 T. L. Moore, L. Rodriguez-Lorenzo, V. Hirsch, S. Balog, D. Urban, C. Jud, B. Rothen-Rutishauser, M. Lattuada and A. Petri-Fink, *Chem. Soc. Rev.*, 2015, **44**, 6287–6305.
- 19 H. Hu, K. M. Xiu, S. L. Xu, W. T. Yang and F. J. Xu, *Bioconjugate Chem.*, 2013, **24**, 968–978.
- 20 H. Zuo, Z. Gu, H. Cooper and Z. P. Xu, *J. Colloid Interface Sci.*, 2015, **459**, 10–16.
- 21 M. Pavlovic, M. Adok-Sipiczki, C. Nardin, S. Pearson, E. Bourgeat-Lami, V. Prevot and I. Szilagyi, *Langmuir*, 2015, **31**, 12609–12617.
- 22 E. D. E. Hyde, R. Moreno-Atanasio, P. A. Millner and F. Neville, *J. Phys. Chem. B*, 2015, **119**, 1726–1735.
- 23 M. A. Cohen Stuart, W. T. S. Huck, J. Genzer, M. Muller, C. Ober, M. Stamm, G. B. Sukhorukov, I. Szleifer, V. V. Tsukruk, M. Urban, F. Winnik, S. Zauscher, I. Luzinov and S. Minko, *Nat. Mater.*, 2010, **9**, 101–113.
- 24 A. L. Papa, J. Boudon, V. Bellat, A. Loiseau, H. Bisht, F. Sallem, R. Chassagnon, V. Berard and N. Millot, *Dalton Trans.*, 2015, **44**, 739–746.
- 25 B. Casu, A. Naggi and G. Torri, *Carbohydr. Res.*, 2015, **403**, 60–68.
- 26 H. Z. Huang and X. R. Yang, *Carbohydr. Res.*, 2004, **339**, 2627–2631.
- 27 B. K. Jena and C. R. Raj, *Biosens. Bioelectron.*, 2008, **23**, 1285–1290.
- 28 R. Cao and B. X. Li, *Chem. Commun.*, 2011, **47**, 2865–2867.
- 29 T. G. Shutava, P. P. Pattekari, K. A. Arapov, V. P. Torchilin and Y. M. Lvov, *Soft Matter*, 2012, **8**, 9418–9427.
- 30 J. Ramos, J. Forcada and R. Hidalgo-Alvarez, *Chem. Rev.*, 2014, **114**, 367–428.
- 31 A. M. E. Abdalla, L. Xiao, C. X. Ouyang and G. Yang, *Nanoscale*, 2014, **6**, 14141–14152.
- 32 S. R. Hwang and Y. Byun, *Expert Opin. Drug Delivery*, 2014, **11**, 1955–1967.
- 33 Z. Gu, B. E. Rolfe, Z. P. Xu, A. C. Thomas, J. H. Campbell and G. Q. M. Lu, *Biomaterials*, 2010, **31**, 5455–5462.
- 34 Z. Gu, A. C. Thomas, Z. P. Xu, J. H. Campbell and G. Q. Lu, *Chem. Mater.*, 2008, **20**, 3715–3722.
- 35 H. Zhang, Z. P. Xu, G. Q. Lu and S. C. Smith, *J. Phys. Chem. C*, 2010, **114**, 12618–12629.
- 36 Y. Q. Shu, P. G. Yin, B. L. Liang, S. S. Wang, L. C. Gao, H. Wang and L. Guo, *J. Mater. Chem.*, 2012, **22**, 21667–21672.
- 37 X. D. Sun and S. K. Dey, *J. Colloid Interface Sci.*, 2015, **458**, 160–168.
- 38 E. Geraud, V. Prevot, J. Ghanbaja and F. Leroux, *Chem. Mater.*, 2006, **18**, 238–240.
- 39 D. Sranko, A. Pallagi, E. Kuzmann, S. E. Canton, M. Walczak, A. Sapi, A. Kukovecz, Z. Konya, P. Sipos and I. Palinko, *Appl. Clay Sci.*, 2010, **48**, 214–217.
- 40 Z. P. Xu, G. Stevenson, C. Q. Lu and G. Q. Lu, *J. Phys. Chem. B*, 2006, **110**, 16923–16929.
- 41 P. A. Hassan, S. Rana and G. Verma, *Langmuir*, 2015, **31**, 3–12.
- 42 H. Holthoff, S. U. Egelhaaf, M. Borkovec, P. Schurtenberger and H. Sticher, *Langmuir*, 1996, **12**, 5541–5549.
- 43 M. Owczarz, A. C. Motta, M. Morbidelli and P. Arosio, *Langmuir*, 2015, **31**, 7590–7600.
- 44 K. L. Chen and M. Elimelech, *Langmuir*, 2006, **22**, 10994–11001.
- 45 G. Stoica, M. Santiago, S. Abello and J. Perez-Ramirez, *Solid State Sci.*, 2010, **12**, 1822–1830.
- 46 T. Bujdoso, A. Patzko, Z. Galbacs and I. Dekany, *Appl. Clay Sci.*, 2009, **44**, 75–82.
- 47 J. Hong, Z. L. Zhu, H. T. Lu and Y. L. Qiu, *RSC Adv.*, 2014, **4**, 5156–5164.
- 48 J. Faraudo and A. Martin-Molina, *Curr. Opin. Colloid Interface Sci.*, 2013, **18**, 517–523.
- 49 J. Lyklema, *Colloids Surf., A*, 2006, **291**, 3–12.
- 50 M. Quesada-Perez, E. Gonzalez-Tovar, A. Martin-Molina, M. Lozada-Cassou and R. Hidalgo-Alvarez, *ChemPhysChem*, 2003, **4**, 235–248.
- 51 Z. P. Xu, Y. G. Jin, S. M. Liu, Z. P. Hao and G. Q. Lu, *J. Colloid Interface Sci.*, 2008, **326**, 522–529.
- 52 I. Szilagyi, G. Trefalt, A. Tiraferri, P. Maroni and M. Borkovec, *Soft Matter*, 2014, **10**, 2479–2502.
- 53 Y. Adachi, L. L. Feng and M. Kobayashi, *Colloids Surf., A*, 2015, **471**, 38–44.

dc 1931 21

- 54 J. Sabin, C. Vazquez-Vazquez, G. Prieto, F. Bordini and F. Sarmiento, *Langmuir*, 2012, **28**, 10534–10542.
- 55 I. Popa, G. Gillies, G. Papastavrou and M. Borkovec, *J. Phys. Chem. B*, 2010, **114**, 3170–3177.
- 56 C. Schneider, M. Hanisch, B. Wedel, A. Jusufi and M. Ballauff, *J. Colloid Interface Sci.*, 2011, **358**, 62–67.
- 57 M. Jobbagy and A. E. Regazzoni, *J. Colloid Interface Sci.*, 2013, **393**, 314–318.
- 58 A. Jusufi, O. Borisov and M. Ballauff, *Polymer*, 2013, **54**, 2028–2035.
- 59 A. Abraham, A. Mezei and R. Meszaros, *Soft Matter*, 2009, **5**, 3718–3726.
- 60 D. F. Evans and H. Wennerstrom, *The Colloidal Domain*, John Wiley, New York, 1999.
- 61 G. Gillies, W. Lin and M. Borkovec, *J. Phys. Chem. B*, 2007, **111**, 8626–8633.
- 62 T. Szabo, V. Toth, E. Horvath, L. Forro and I. Szilagyi, *Langmuir*, 2015, **31**, 42–49.
- 63 L. Ghimici and M. Nichifor, *Carbohydr. Polym.*, 2013, **98**, 1637–1643.
- 64 D. Bauer, E. Killmann and W. Jaeger, *Colloid Polym. Sci.*, 1998, **276**, 698–708.
- 65 S. Schwarz, S. Bratskaya, W. Jaeger and B. R. Paulke, *J. Appl. Polym. Sci.*, 2006, **101**, 3422–3429.
- 66 G. Fritz, V. Schadler, N. Willenbacher and N. J. Wagner, *Langmuir*, 2002, **18**, 6381–6390.
- 67 K. A. Huynh and K. L. Chen, *Environ. Sci. Technol.*, 2011, **45**, 5564–5571.
- 68 Z. Y. Meng, S. M. Hashmi and M. Elimelech, *J. Colloid Interface Sci.*, 2013, **392**, 27–33.
- 69 J. A. Gursky, S. D. Blough, C. Luna, C. Gomez, A. N. Luevano and E. A. Gardner, *J. Am. Chem. Soc.*, 2006, **128**, 8376–8377.
- 70 G. P. Liu, S. Y. Liu, X. Q. Dong, F. Yang and D. J. Sun, *J. Colloid Interface Sci.*, 2010, **345**, 302–306.
- 71 E. Tombacz and M. Szekeres, *Appl. Clay Sci.*, 2004, **27**, 75–94.
- 72 L. Wu, L. Liu, B. Gao, R. Munoz-Carpena, M. Zhang, H. Chen, Z. H. Zhou and H. Wang, *Langmuir*, 2013, **29**, 15174–15181.
- 73 C.-W. Chiu and J.-J. Lin, *Prog. Polym. Sci.*, 2012, **37**, 406–444.
- 74 M. Pavlovic, R. Huber, M. Adok-Sipiczki, C. Nardin and I. Szilagyi, *Soft Matter*, submitted.
- 75 E. Horváth, L. Grebikova, P. Maroni, T. Szabó, A. Magrez, L. Forró and I. Szilagyi, *ChemPlusChem*, 2014, **79**, 592–600.
- 76 T. Oncsik, G. Trefalt, M. Borkovec and I. Szilagyi, *Langmuir*, 2015, **31**, 3799–3807.
- 77 M. Pavlovic, M. Adok-Sipiczki, E. Horvath, T. Szabo, L. Forro and I. Szilagyi, *J. Phys. Chem. C*, 2015, **119**, 24919–24926.
- 78 H. G. Bagaria, K. Y. Yoon, B. M. Neilson, V. Cheng, J. H. Lee, A. J. Worthen, Z. Xue, C. Huh, S. L. Bryant, C. W. Bielawski and K. P. Johnston, *Langmuir*, 2013, **29**, 3195–3206.
- 79 E. Seyrek, J. Hierrezuelo, A. Sadeghpour, I. Szilagyi and M. Borkovec, *Phys. Chem. Chem. Phys.*, 2011, **13**, 12716–12719.
- 80 H. G. Bagaria, Z. Xue, B. M. Neilson, A. J. Worthen, K. Y. Yoon, S. Nayak, V. Cheng, J. H. Lee, C. W. Bielawski and K. P. Johnston, *ACS Appl. Mater. Interfaces*, 2013, **5**, 3329–3339.



Article

# Effect of Polyelectrolyte Mono- and Bilayer Formation on the Colloidal Stability of Layered Double Hydroxide Nanoparticles

Zoltán Somosi<sup>1,2</sup>, Marko Pavlovic<sup>1</sup>, István Pálincó<sup>3</sup>  and István Szilágyi<sup>1,2,\*</sup> 

<sup>1</sup> MTA-SZTE Lendület Biocolloids Research Group, Department of Physical Chemistry and Materials Science, University of Szeged, H-6720 Szeged, Hungary; somosiz@chem.u-szeged.hu (Z.S.); mmpavlovic90@gmail.com (M.P.)

<sup>2</sup> Interdisciplinary Excellence Centre, Department of Physical Chemistry and Materials Science, University of Szeged, H-6720 Szeged, Hungary

<sup>3</sup> Material and Solution Structure Research Group, Department of Organic Chemistry, University of Szeged, H-6720 Szeged, Hungary; palinko@chem.u-szeged.hu

\* Correspondence: szistvan@chem.u-szeged.hu

Received: 25 October 2018; Accepted: 26 November 2018; Published: 28 November 2018



**Abstract:** Sequential adsorption of polyelectrolytes on nanoparticles is a popular method to obtain thin films after deposition. However, the effect of polyelectrolyte multilayer formation on the colloidal stability of the nanoparticles has not been studied in detail. In the present work, layered double hydroxides (LDH) were synthesized and interaction with oppositely and like-charged polyelectrolytes was investigated. Electrophoretic and light scattering measurements revealed that colloidal stability of LDH can be tuned by adsorption of poly(styrene sulfonate) (PSS) on the oppositely charged LDH surface in appropriate doses and thus, unstable or stable dispersions can be designed. Negatively charged LDH of adsorbed PSS monolayer was obtained and a poly(diallyldimethyl ammonium chloride) (PDADMAC) second layer was systematically built on the particles. The obtained polyelectrolyte bilayer provided high colloidal stability for the LDH-PSS-PDADMAC dispersions due to the presence of repulsive interparticle forces of electrostatic and steric origin. The results provide crucial quantitative information on designing highly stable particle-polyelectrolyte systems for the preparation of thin films or immobilization of guest substances between the layers for delivery processes.

**Keywords:** layered double hydroxide; polyelectrolyte layer; colloidal stability

## 1. Introduction

Self-assembled multilayers have been in the focus of many research groups due to their widespread applications in electrochemical devices, sensors, membranes, smart coatings and biotechnological procedures [1]. In the preparation processes, the sequential adsorption technique is applied, in which polyelectrolytes [2], nanoparticles [3], metal complexes [4], enzymes [5] and other suitable compounds [6–9] were used in the individual adsorption steps. Different substrates were applied as base for the multilayer formation including both planar surfaces [10] and colloidal particles [11]. In the latter case, once polyelectrolytes are applied as building blocks, the choice of the appropriate dose is critical, since polyelectrolyte adsorption on oppositely charged particles may lead to charge neutralization and unstable particle dispersions containing large aggregates, which are insufficient for further applications [12–14]. At higher polyelectrolyte loadings, however, stable dispersions of primary polyelectrolyte coated particles are formed and these samples can be processed well.



Among various nanomaterials, layered double hydroxides (LDH) [15–17] are excellent candidates as building blocks in sequential adsorption processes [18–20]. LDH are multifunctional materials, therefore, they are widely used in numerous fields including sensing [21], drug delivery [22], catalysis [23,24], electrochemistry [25,26] and environmental processes [27,28]. Due to the positive structural charge of LDH, they were applied together with negatively charged polyelectrolytes such as poly(styrene sulfonate) (PSS) in multilayered compounds. For instance, unilamellar LDH nanosheets were prepared by delamination of the layered structure and assembled layer-by-layer with PSS on glass substrate to obtain composite films of interesting magneto-optical properties [29]. Embedding ruthenium(III) complexes between the LDH-PSS layers led to the development of electrochemiluminescence sensors [4]. Polymer-modified LDH-PSS multilayered films showed excellent oxygen barrier performance with self-healing ability [30]. LDH films were prepared in a hydrothermal process and modified with PSS to achieve higher drug loading ability [31]. The drug release could be smartly controlled from the obtained hybrid materials. In addition, an LDH-PSS-based nanocontainer was synthesized to deliver corrosion inhibitors, which were either embedded in the polyelectrolyte layer or intercalated within the interlayer space of LDH [32].

The applications mentioned above clearly shed light on the importance of the interaction between the LDH particles and the polyelectrolytes. Accordingly, the surface charge properties and aggregation of LDH particles in the presence of oppositely charged polyelectrolytes such as PSS is a key issue to design stable colloids for the preparation of hybrid materials. Apart from its importance, systematic colloid stability studies involving LDH and negatively charged polyelectrolytes were rarely published in the past. As one of the few examples of such studies, adsorption of poly(acrylic acid) on LDH nanosheets led to charge neutralization and to rapid particle aggregation at intermediate doses [33]. Increasing the polyelectrolyte loading in the same system gave rise to the reversal of the sign of particle charge and to stable dispersions. Similar observations were also reported with LDH in the presence of oppositely charged heparin polyelectrolyte [34] and acrylate-based copolymer [35]. However, no results were published concerning the influence of PSS on the charging and aggregation of LDH particles in the corresponding literature.

In the present study, therefore, we report a systematic investigation on the colloidal stability of LDH in the presence of PSS and poly(diallyldimethyl ammonium chloride) (PDADMAC) polyelectrolytes. The LDH-PSS systems were prepared by electrostatic adsorption of the polyelectrolyte on the oppositely charged particles, while the LDH-PSS-PDADMAC samples were obtained by adsorbing PDADMAC on the LDH particles of a saturated PSS layer on the surfaces. The effect of polyelectrolyte dose on the colloidal stability and the resistance against salt-induced aggregation were investigated in electrophoretic and light scattering measurements.

## 2. Results and Discussion

### 2.1. Characterization of LDH

The sheet-like LDH particles composed of magnesium(II) and aluminium(III) layer forming metal ions and chloride intercalated anions were prepared by the flash co-precipitation method followed by hydrothermal treatment to narrow the particle size distribution. The synthetic process is detailed later (see Materials and Methods section). The formation of the lamellar structure was verified by X-ray diffraction (XRD). The diffractogram is shown in Figure 1.

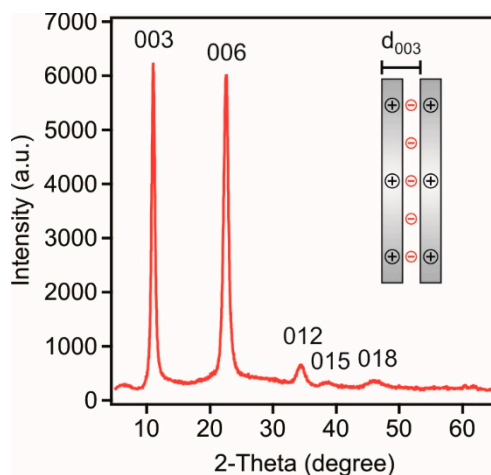


**Figure 1.** Powder XRD pattern of the LDH particles composed of magnesium(II) and aluminium(III) cations and chloride interlayer anions. The inset illustrates the meaning of the  $d_{003}$  value calculated from the (003) reflection.

Indeed, the diffraction pattern unambiguously confirmed the formation of the LDH, since the typical Miller indices for LDH could be assigned to the obtained material [20,34,36]. The sharp (003) and (006) reflections indicate the good crystallinity of the lamellar compound. To quantitatively analyze the XRD peaks, the Bragg equation [37] was used to calculate the  $d$ -spacing values as

$$n\lambda = 2d \sin \theta_B \quad (1)$$

where  $n$  is an integer (in general it is 1),  $\lambda$  is the wavelength of the incident wave,  $d$  is the lattice spacing and  $\theta_B$  is the Bragg angle. Using the position of the (003) peak, the  $d_{003}$  parameter, which represents the distance of one layer together with the interlayer space (see Figure 1 inset), was found to be 0.8 nm. The average size of the ordered domain ( $v$ ) was also calculated from the (003) peak with the Scherrer's equation [38] as

$$v = K\lambda / \beta \cos \theta_B \quad (2)$$

where  $K$  is the shape factor (0.89 was used in the calculation) and  $\beta$  is the line broadening at the full widths at half of the intensity. The thickness of the particle was calculated as about 30 nm meaning that the LDH is composed of about 38 layers.

The hydrodynamic radius of the LDH was determined in stable dispersions by dynamic light scattering (DLS) and the measurements yielded  $(167 \pm 6)$  nm and polydispersity index of  $(0.23 \pm 0.03)$ . Electrophoretic mobility of the particles was measured in the same sample and was found to be  $(1.0 \pm 0.5) \times 10^{-8}$  m<sup>2</sup>/Vs. These values indicate relatively narrow particle size distribution and low surface charge and they are similar to those reported for LDH materials earlier [13,34,35].

## 2.2. Colloidal Stability of LDH in the Presence of PSS

Surface charge properties of the LDH particles in the presence of PSS were assessed in electrophoretic mobility (EPM) measurements. Similarly to other LDH-polyelectrolyte systems [13], the adsorption of PSS is expected to occur on the outer surface of the particles, since intercalation is not feasible due to the narrow interlayer spacing. In the first experiment, the polyelectrolyte concentration was varied in a wide range at constant particle concentration and ionic strength (Figure 2).

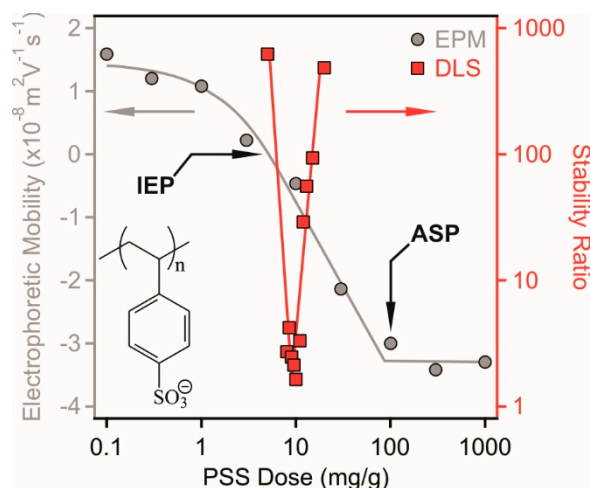


**Figure 2.** Electrophoretic mobility (circles, left axis) and stability ratio (squares, right axis) values of LDH particles in the presence of PSS polyelectrolyte. The measurements were carried out at 10 mg/L particle concentration and 10 mM NaCl was used as background electrolyte to adjust the ionic strength. The mg/g unit on the x-axis refers to mg PSS per one gram of LDH. The structure of PSS is shown in the inset.

Positive EPM values were measured at low PSS doses due to the structural charge of the particles. The data decreased with increasing the polyelectrolyte dose indicating the PSS adsorption on the oppositely charged surface. Such an adsorption process led to charge neutralization at the isoelectric point (IEP), where the overall charge of the particles is zero. Further addition of the polyelectrolytes gave rise to charge reversal and the adsorption continued until the onset of the adsorption saturation plateau (ASP), which corresponds to the dose at surface saturation. The value of ASP was calculated from the intercept of the linear fits on the plateau and in the decreasing mobility regime. This dose was found to be 100 mg/g and the EPM data were constant after this value. In other words, the onset of ASP refers to the maximum amount of PSS, which is able to adsorb on the LDH and further added polyelectrolytes remain dissolved in the solution. Similar charge neutralization and reversal processes were reported in oppositely charged particle-polyelectrolyte systems [12,39,40] including LDH-containing dispersions [13].

The EPM values were measured at different ionic strengths in a wide PSS concentration range (Figure S1) to probe the effect of the ionic environment on the charging properties of the LDH. Similar tendencies were observed at all salt concentrations (1 mM, 10 mM and 100 mM) as discussed above, i.e., charge neutralization at the IEP followed by charge reversal and the adsorption continued until the ASP. However, no clear dependence of the EPM was detected on the salt concentration under these conditions, i.e., the data scattered within the experimental error. It was assumed that such an insensitivity to the ionic strength is due to the counterion condensation into the adsorbed polyelectrolyte chains [41], which prevented efficient screening of the surface charge.

To assess the colloidal stability of the dispersions under the same experimental conditions as applied in the EPM study, stability ratios were determined as follows. Since light scattering techniques have proved as excellent tools to investigate the size of particles and corresponding stability of the dispersions [35,39,40,42,43], time-resolved DLS measurements were carried out, in which the hydrodynamic radius ( $R_h$ ) was measured at different time intervals (Figure 3).

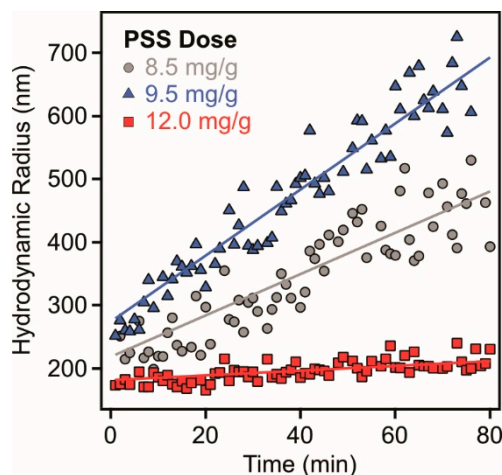


**Figure 3.** Hydrodynamic radii of LDH particles as a function of the measurement time in the presence of 8.5 mg/g (triangles), 9.5 mg/g (circles) and 12.0 mg/g (squares) PSS. The solid lines are linear fits used to calculate the apparent rates according to Equation (3).

In aggregating dispersions, the  $R_h$  data increased linearly with time ( $t$ ) indicating that the aggregation processes are in early stages. From the  $R_h$  versus time plots, the apparent rate ( $k_{app}$ ) of the particle aggregation was calculated and the colloidal stability was expressed in terms of stability ratio ( $W$ ) as [34,40,42]

$$W = \frac{k_{app}^{fast}}{k_{app}} = \frac{dR_h(t)/dt|_{t \rightarrow 0}^{fast}}{dR_h(t)/dt|_{t \rightarrow 0}} \quad (3)$$

where *fast* refers to diffusion controlled aggregation, which was achieved in 1 M NaCl solutions. From Equation (3), one can realize that stability ratio value of one indicates rapid particle aggregation and unstable dispersions, while higher values are signals for slower aggregation processes and more stable samples.

The time dependent  $R_h$  data (Figure 3) recorded at the IEP (9.5 mg/g) as well as below (8.5 mg/g) and above (12.0 mg/g) the IEP indicate that the speed of the aggregation is sensitive to the PSS dose. Indeed, high or not even measurable stability ratios were measured at low and high polyelectrolyte concentrations, where the particles possess positive and negative charge, respectively (Figure 2). Moreover, rapid aggregation of the LDH was experienced at doses close to the IEP indicating unstable dispersions in this regime. However, the location of the fast aggregation regime is slightly shifted comparing to the dose at the IEP due the low charge and the subsequent small velocity of the particles in the electric field in this regime, which leads to uncertainty of the EPM data close to the IEP.

Such a destabilization-restabilization behavior with increasing polyelectrolyte dose was reported for other LDH-polyelectrolyte systems too [13,33–35,44] and it can be qualitatively explained by the classical theory of Derjaguin, Landau, Verwey and Overbeek (DLVO) [45,46]. Accordingly, charged particles below and above the IEP dose are stabilized by the repulsion induced by the overlap of the electrical double layers of the particles. At the IEP, however, the LDH possess no charge, i.e., electrical double layer repulsion vanishes and attractive van der Waals forces predominate. Such an attraction causes rapid aggregation of the particles leading to unstable dispersions.

### 2.3. Effect of Polyelectrolyte Bilayer Formation on the Colloidal Stability

As shown above, a saturated PSS monolayer was formed on the LDH at a dose corresponding to the onset of the ASP (denoted as LDH-PSS later) and stable dispersion was observed under this experimental condition. In the next step, a second polyelectrolyte layer was systematically built by adsorbing positively charged PDADMAC polyelectrolyte on the LDH-PSS (100 mg/g of PSS dose, which is equal to the ASP) hybrids at 10 mM ionic strength. Electrophoretic mobilities and stability



ratios (Figure 4) were determined first to probe the influence of the PDADMAC concentration on the charging and aggregation properties of the LDH-PSS particles.

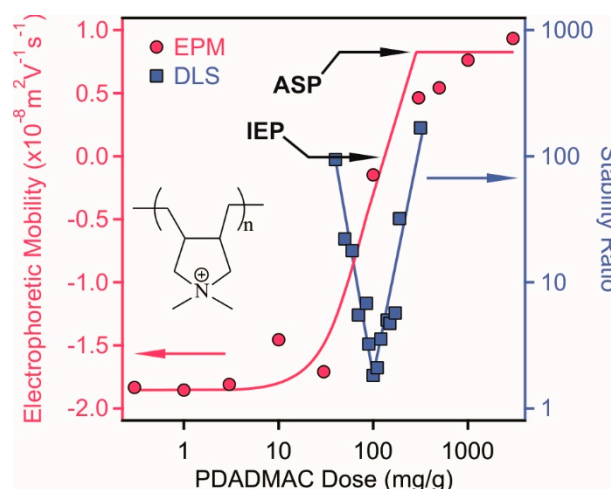


**Figure 4.** Electrophoretic mobilities (red circles, left axis) and stability ratios (blue squares, right axis) of LDH-PSS (100 mg PSS per one gram of LDH, which corresponds to the dose of the onset of the adsorption saturation plateau (ASP)) as a function of the poly(diallyldimethyl ammonium chloride) (PDADMAC) concentration. The measurements were performed at 10 mg/L particle concentration and 10 mM ionic strength adjusted by NaCl. The structure of PDADMAC is shown in the inset.

Both EPM and stability ratio data followed very similar trend as discussed before with the system containing only LDH and PSS (Figure 3). Namely, charge neutralization and reversal occurred due to the adsorption of PDADMAC on the LDH-PSS. However, the extent of charge reversal is smaller compared to the previous system and the ASP dose was determined as 300 mg/g. The EPM data were measured also at different ionic strengths (1 mM, 10 mM and 100 mM shown in Figure S2) and the EPM values at the ASP decreased with increasing the NaCl concentration due to charge screening. The IEP data were very similar indicating the same adsorption mechanism at different ionic strengths.

The stability ratios could be predicted by the DLVO theory, i.e., fast aggregation near the IEP and stable samples below and above the IEP owing to the presence of repulsive electrical double layer and attractive van der Waals forces. Such a behavior was reported for bare colloidal particles in the presence of PDADMAC [47–51]. To our best knowledge, however, this is the first time, when PDADMAC-induced destabilization-restabilization of polyelectrolyte-functionalized LDH particles is reported. Although comprehensive fundamental studies dealing PSS-PDADMAC multilayers have been published earlier [52–54], no information on the stability of colloidal particles functionalized with these polyelectrolytes has been reported.

The hydrodynamic radii of LDH, LDH-PSS and LDH-PSS-PDADMAC were determined in stable dispersions at low ionic strength by DLS (Figure S3) and their values were 167 nm, 216 nm and 352 nm, respectively. The rise in size reflects the formation of the polyelectrolyte layers on the surface. Furthermore, the significant increase for the LDH-PSS and LDH-PSS-PDADMAC compared to bare LDH indicates the presence of an extended polyelectrolyte mono- and bilayer, respectively. The increase is especially large upon adsorption of PDADMAC on LDH-PSS due to the high molecular mass of PDADMAC. In addition, the dispersions are stable before and after the polyelectrolyte addition, but the system passes through the IEP in a transient-like fashion during the adsorption process and becomes unstable for a very short time interval. This small period is long enough for the formation of some aggregates, which leads to certain increase in the hydrodynamic radius [55]. This increment in the size also contributes to the higher hydrodynamic radii for LDH-PSS and LDH-PSS-PDADMAC hybrids.

#### 2.4. Resistance against Salt-Induced Aggregation

One of the limitations of the use of LDH particles in applications taking place in dispersions is their low resistance against aggregation induced by electrolytes, which are present in the majority of the application processes [36]. In general, LDH dispersions are stable at very low ionic strengths, but small amount of salts may cause particle aggregation [13,34,56]. The critical salt level, which separates the stable and unstable regimes, is the so-called critical coagulation concentration (CCC). Polyelectrolyte functionalization has proved to be powerful tool to improve the stability of LDH or other colloidal particles [13,14,35,57,58]. In other words, particles coated with a saturated polyelectrolyte layer possessed higher CCC values than the bare ones. However, systematic studies dealing with polyelectrolyte bilayer-functionalized particles are missing. Therefore, we measured EPM and stability ratio values of LDH-PSS and LDH-PSS-PDADMAC particles (the doses of PSS and PDADMAC in the composites were equal to the onset of the ASP in the individual systems) at different ionic strengths and compared them to the data obtained in the bare LDH system (Figure 5). In this way, the effect of polyelectrolyte layer formation on the resistance against salt-induced aggregation was probed. Note that in these experiments, the polyelectrolyte-modified particles were prepared first in salt-free environment and added to NaCl solutions to obtain the desired ionic strength.

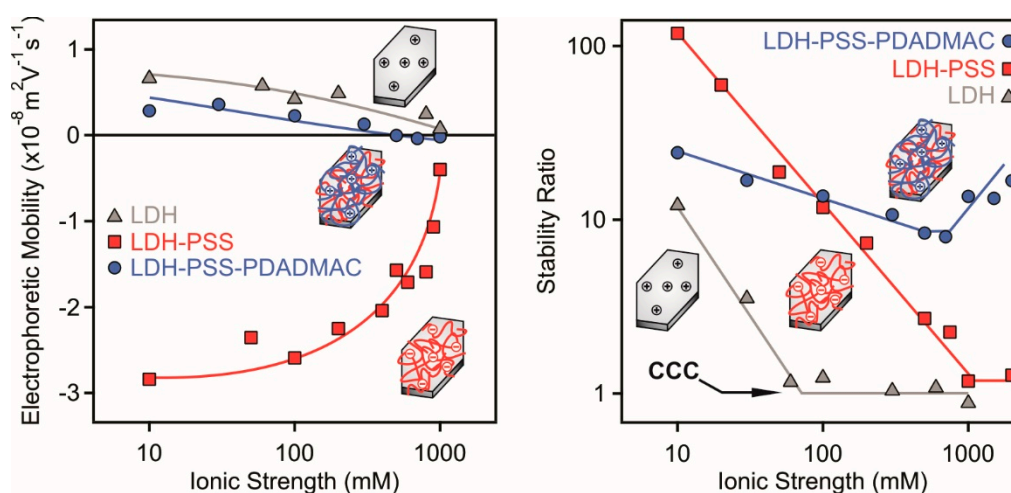


**Figure 5.** Electrophoretic mobility (left) and stability ratio (right) of bare LDH (triangles), LDH-PSS (squares) and LDH-PSS-PDADMAC (circles) particles versus the ionic strength adjusted by NaCl. A PSS dose of 100 mg/g and PDADMAC of 300 mg/g was applied in the composite particles. These doses correspond to the onsets of the ASP. The insets illustrate an LDH particle and its polyelectrolyte-functionalized derivatives.

The magnitude of the EPM data decreased with increasing the ionic strength in all cases due to the screening effect of the salt constituent ions on the surface charges (Figure 5, left). Another observation is that the LDH-PSS possessed the highest surface charge indicated by the highly negative EPM values at low salt concentrations. The LDH and LDH-PSS-PDADMAC particles were weakly charged and the mobilities were close to zero at high NaCl concentrations.

The stability ratios of LDH-PSS followed a tendency predicted by the DLVO theory [46] and reported for other polyelectrolyte coated LDH particles earlier [34,35,59]. Accordingly, stable dispersions were observed at low salt levels and stability ratios close to unity indicated rapid aggregation and unstable samples at high ionic strengths. These two regimes are separated by a well-defined CCC (Figure 5, right) at 1000 mM NaCl concentration. Given the low CCC of 50 mM for the bare particles, one can realize that the PSS coating led to an improved resistance against salt-induced aggregation. Such a high CCC cannot be explained by the DLVO theory and an additional stabilizing force should be included in the interpretation. It was assumed that repulsive electrical double layer forces are escorted with steric interactions [33,57,58,60,61], which are also of repulsive

nature and originate from the overlapping polyelectrolyte chains on the particle surfaces. Once two particles approach each other, an osmotic pressure is raised leading to repulsive forces. The LDH-PSS dispersions are stable until high ionic strengths, therefore, they can be used in applications taking place in electrolyte solutions.

The behavior of the LDH-PSS-PDADMAC is rather atypical. The stability ratios slightly decrease first with increasing the salt concentration reaching a minimum at around 1000 mM followed by an increase at higher ionic strengths. The stability ratio data are always significantly higher than unity, therefore, the aggregation is slower than in case of the diffusion controlled process. Given the fact that LDH of polyelectrolyte monolayer on the surface can always be destabilized at high ionic strength, the present finding is rather unusual. Moreover, EPM data showed that the particles were moderately charged in the salt concentration regime investigated, therefore, the electrical double layer forces are weak and most probably vanish at high salt levels, where the EPM values are close to zero. The stabilizing forces then must be steric and originate from the adsorbed PSS and PDADMAC chains.

Indeed, it was earlier reported that polyelectrolyte layers on particles swell under certain experimental conditions giving rise to the formation of tails and loops on the surfaces [12,50,55]. This is especially true once the ionic strength is increased in the samples, a condition which leads to thicker polyelectrolyte layers [52,53]. Note that this fact applies for electrostatically adsorbed polyelectrolyte layers, but the opposite trend was reported for polyelectrolyte brushes covalently grafted on surfaces [62,63]. Such a conformation of the polyelectrolytes enhances the development of steric forces due to the overlap between the chains on the approaching particles. Moreover, the hydrodynamic radii in stable dispersions increase significantly with the PSS mono- and PSS-PDADMAC bilayer adsorption (Figure S3) indicating an extended polyelectrolyte layer and bilayer formation on the surface of LDH-PSS and LDH-PSS-PDADMAC particles. Such an extended polyelectrolyte layer enhances the rise of repulsive steric interparticle forces.

### 3. Materials and Methods

#### 3.1. Chemicals

The inorganic compounds ( $\text{MgCl}_2 \cdot 6\text{H}_2\text{O}$  (VWR, Debrecen, Hungary),  $\text{AlCl}_3 \cdot 6\text{H}_2\text{O}$  (Alfa Aesar, Karlsruhe, Germany), NaOH (VWR) and NaCl (VWR)) were of analytical grade. Sodium salt of PSS (molecular mass of 10 kg/mol) and 20 weight % aqueous PDADMAC (average molecular mass of 275 kg/mol) solution were purchased from Sigma-Aldrich (Budapest, Hungary). All chemicals were used without further purification. Ultrapure water produced by a Puranility TU 3 UV/UF+ (VWR) device was used for all sample preparation and measurements. Insoluble impurities from the ultrapure water and from the NaCl solutions were eliminated with a Millex syringe filter of 0.1  $\mu\text{m}$  pore size (Sigma-Aldrich).

#### 3.2. LDH Synthesis

The LDH particles containing magnesium(II) and aluminium(III) ions in a 2:1 molar ratio and chloride charge compensating interlayer anions were prepared by the flash co-precipitation method followed by hydrothermal treatment [64]. In the synthetic process, 15 mL of mixed salt solution of magnesium(II) (3.0 mmol) and aluminium(III) (1.5 mmol) chloride was rapidly added into 60 mL of 0.15 M NaOH solution and the mixture was vigorously stirred for 30 min under nitrogen gas atmosphere. The just formed LDH slurry was separated by centrifugation and washed five times with water. The obtained material was then redispersed in 50 mL water. The sample was sonicated for 10 min in an ultrasonic bath and transferred into a stainless steel autoclave with a Teflon lining (Col-Int Tech, Irmo, SC, USA). The autoclave was placed in a preheated oven for a post hydrothermal treatment for 24 h at 120 °C. Thereafter, the autoclave was cooled to room temperature and the LDH dispersion was centrifuged and washed again with water. The LDH was filtered and dried to powder, which was

redispersed to obtain a stock dispersion of 10,000 mg/L particle concentration. Some of the powder was kept for XRD characterization.

### 3.3. Light Scattering

Electrophoretic mobility and  $R_h$  values were measured with a LiteSizer 500 (Anton Paar, Graz, Austria) light scattering device equipped with a 40 mW laser source operating at 658 nm wavelength. All experiments were conducted at 175° scattering angle and at 25 °C. The measurement cells were cleaned with 2 weight % Hellmanex III (Hellma Analytics, Müllheim, Germany) solutions, rinsed with water and dried in a dust-free oven.

Omega-shaped plastic capillary cuvettes (Anton Paar) were used for the electrophoretic experiments. In a typical sample preparation process, calculated amount of ultrapure water, polyelectrolyte and NaCl stock solutions were mixed to adjust the polyelectrolyte concentration and the ionic strength. The total volume of these mixtures was always 1.8 mL. The sample preparation process was finalized by adding 0.2 mL of 100 mg/L LDH stock dispersion. The samples were then left equilibrating for 3 h at room temperature. The capillary cuvettes were flushed with the majority of the dispersions and the last 0.35 mL was used for the actual measurement. The samples were equilibrated for 1 min in the device. The reported electrophoretic mobility values are the average of five individual measurements.

For the DLS experiments, the correlation functions were collected for 20 min and due to the monomodal size distribution of the particles, the Cumulant fit was applied to determine the decay rate constant and the diffusion coefficient [65]. The  $R_h$  was calculated from the diffusion coefficient using the Stokes-Einstein equation [46]. To determine stability ratios, time-resolved DLS experiments were carried out in plastic cuvettes (Hellma Analytics). The  $R_h$  values were recorded in different time intervals for 30–60 min depending on the speed of the aggregation. The sample preparation procedure was the same as in the electrophoretic measurements, but the experiments started immediately after adding the particle stock dispersions to the mixed solutions of NaCl and polyelectrolytes.

### 3.4. XRD Measurements

The formation of the layered structure was confirmed by XRD using a PW 1830 diffractometer (Philips, Amsterdam, The Netherlands), which applies Cu-K $\alpha$  radiation ( $L = 0.1542$  nm) and operates in Bragg-Brentano geometry with Ni filter at a voltage of 40 kV and a current of 30 mA. The diffractograms were recorded in the 4–80° 2-Theta range with a step size of 0.02°. The powder samples were placed on a glass zero background holder for the acquisition of the XRD patterns.

## 4. Conclusions

The present study reports a systematic assessment of the colloidal stability of positively charged LDH particles in the presence of PSS and PDADMAC polyelectrolytes of negative and positive charges, respectively. PSS adsorption led to charge neutralization and subsequent charge reversal at appropriate polyelectrolyte doses and these processes gave rise to destabilization and restabilization of the originally stable dispersions. The aggregation mechanism qualitatively followed the prediction of the classical DLVO theory indicating the presence of interparticle forces of electrostatic origin.

LDH-PSS particles of saturated polyelectrolyte layer on the surface were modified with PDADMAC at different loadings. Increasing the PDADMAC dose resulted in particles of zero overall charge at the IEP and of positive charge at the ASP, where a saturated polyelectrolyte bilayer composed of PSS and PDADMAC was formed on the LDH. The stability of both LDH-PSS and LDH-PSS-PDADMAC particles was investigated in a wide range of ionic strength and it was found that polyelectrolyte functionalization led to an improved colloidal stability of the LDH particles due to repulsion by the electrical double layers and steric interactions between the adsorbed polyelectrolyte chains. The latter effect is stronger, once a PSS-PDADMAC bilayer is formed on the particles.



The results indicate that the use of the LDH can be extended to applications carried out in dispersions containing higher level of electrolytes once the particles are coated with one or two polyelectrolyte layers. The presented sequential adsorption method allows embedding guest molecules between the polyelectrolyte layers in stable dispersions of high specific surface area, since the aggregation and subsequent sedimentation of the LDH is prevented by strong repulsive forces. In addition, the stable LDH-PSS and LDH-PSS-PDADMAC dispersions are excellent candidates as feeding materials in preparation of thin films on appropriate substrates.

**Supplementary Materials:** The following are available online at <http://www.mdpi.com/2079-4991/8/12/986/s1>, Figure S1: Electrophoretic mobility data of LDH in the presence of PSS measured at different ionic strengths; Figure S2: Electrophoretic mobility data of LDH-PSS in the presence of PDADMAC measured at different salt concentrations; Figure S3: Hydrodynamic radii of bare and polyelectrolyte-functionalized LDH.

**Author Contributions:** Z.S. performed most of the measurements and analyzed the primary experimental results with the assistance of M.P. I.P. corrected the manuscript. I.S. designed the experiments, supervised the research and wrote up the manuscript, which was read and approved by all of the authors.

**Funding:** This research was financially supported by the Lendület program of the Hungarian Academy of Sciences (project 96130) and by the Ministry of Human Capacities, Hungary through grant 20391-3/2018/FEKUSTRAT.

**Conflicts of Interest:** The authors declare no conflict of interest.

## References

1. Decher, G.; Schlenoff, J.B. *Multilayer Thin Films*; Wiley-VCH: Weinheim, Germany, 2002.
2. Ho, T.T.M.; Bremmell, K.E.; Krasowska, M.; MacWilliams, S.V.; Richard, C.J.E.; Stringer, D.N.; Beattie, D.A. In Situ ATR-FTIR Spectroscopic Study of the Formation and Hydration of a Fucoidan/Chitosan Polyelectrolyte Multilayer. *Langmuir* **2015**, *31*, 11249–11259. [[CrossRef](#)] [[PubMed](#)]
3. Kotov, N.A.; Haraszti, T.; Turi, L.; Zavala, G.; Geer, R.E.; Dekany, I.; Fendler, J.H. Mechanism of and Defect Formation in the Self-Assembly of Polymeric Polycation-Montmorillonite Ultrathin Films. *J. Am. Chem. Soc.* **1997**, *119*, 6821–6832. [[CrossRef](#)]
4. Zhang, B.; Shi, S.X.; Shi, W.Y.; Sun, Z.Y.; Kong, X.G.; Wei, M.; Duan, X. Assembly of Ruthenium(II) Complex/Layered Double Hydroxide Ultrathin Film and Its Application as an Ultrasensitive Electrochemiluminescence Sensor. *Electrochim. Acta* **2012**, *67*, 133–139. [[CrossRef](#)]
5. Caruso, F.; Schuler, C. Enzyme Multilayers on Colloid Particles: Assembly, Stability, and Enzymatic Activity. *Langmuir* **2000**, *16*, 9595–9603. [[CrossRef](#)]
6. Szabo, T.; Szekeres, M.; Dekany, I.; Jackers, C.; De Feyter, S.; Johnston, C.T.; Schoonheydt, R.A. Layer-by-Layer Construction of Ultrathin Hybrid Films with Proteins and Clay Minerals. *J. Phys. Chem. C* **2007**, *111*, 12730–12740. [[CrossRef](#)]
7. Tian, D.Y.; Wang, W.Y.; Li, S.P.; Li, X.D.; Sha, Z.L. A Novel Platform Designed by Au Core/Inorganic Shell Structure Conjugated onto Mtx/Ldh for Chemo-Photothermal Therapy. *Int. J. Pharm.* **2016**, *505*, 96–106. [[CrossRef](#)] [[PubMed](#)]
8. Han, J.B.; Xu, X.Y.; Rao, X.Y.; Wei, M.; Evans, D.G.; Duan, X. Layer-by-Layer Assembly of Layered Double Hydroxide/Cobalt Phthalocyanine Ultrathin Film and Its Application for Sensors. *J. Mater. Chem.* **2011**, *21*, 2126–2130. [[CrossRef](#)]
9. Szabo, T.; Peter, Z.; Illes, E.; Janovak, L.; Talyzin, A. Stability and Dye Inclusion of Graphene Oxide/Polyelectrolyte Layer-by-Layer Self-Assembled Films in Saline, Acidic and Basic Aqueous Solutions. *Carbon* **2017**, *111*, 350–357. [[CrossRef](#)]
10. Decher, G. Fuzzy Nanoassemblies: Toward Layered Polymeric Multicomposites. *Science* **1997**, *277*, 1232–1237. [[CrossRef](#)]
11. Caruso, F.; Caruso, R.A.; Mohwald, H. Nanoengineering of Inorganic and Hybrid Hollow Spheres by Colloidal Templating. *Science* **1998**, *282*, 1111–1114. [[CrossRef](#)] [[PubMed](#)]
12. Szilagy, I.; Trefalt, G.; Tiraferri, A.; Maroni, P.; Borkovec, M. Polyelectrolyte Adsorption, Interparticle Forces, and Colloidal Aggregation. *Soft Matter* **2014**, *10*, 2479–2502. [[CrossRef](#)] [[PubMed](#)]
13. Pavlovic, M.; Rouster, P.; Oncsik, T.; Szilagy, I. Tuning Colloidal Stability of Layered Double Hydroxides: From Monovalent Ions to Polyelectrolytes. *ChemPlusChem* **2017**, *82*, 121–131. [[CrossRef](#)]

14. Muráth, S.; Sáringer, S.; Somosi, Z.; Szilagyi, I. Effect of Ionic Compounds of Different Valences on the Stability of Titanium Oxide Colloids. *Colloids Interfaces* **2018**, *2*, 32. [[CrossRef](#)]
15. Sideris, P.J.; Nielsen, U.G.; Gan, Z.H.; Grey, C.P. Mg/Al Ordering in Layered Double Hydroxides Revealed by Multinuclear NMR Spectroscopy. *Science* **2008**, *321*, 113–117. [[CrossRef](#)] [[PubMed](#)]
16. Yu, J.F.; Wang, Q.; O'Hare, D.; Sun, L.Y. Preparation of Two Dimensional Layered Double Hydroxide Nanosheets and Their Applications. *Chem. Soc. Rev.* **2017**, *46*, 5950–5974. [[CrossRef](#)] [[PubMed](#)]
17. Gu, Z.; Atherton, J.J.; Xu, Z.P. Hierarchical Layered Double Hydroxide Nanocomposites: Structure, Synthesis and Applications. *Chem. Commun.* **2015**, *51*, 3024–3036. [[CrossRef](#)] [[PubMed](#)]
18. Zhao, J.W.; Xu, S.M.; Tschulik, K.; Compton, R.G.; Wei, M.; O'Hare, D.; Evans, D.G.; Duan, X. Molecular-Scale Hybridization of Clay Monolayers and Conducting Polymer for Thin-Film Supercapacitors. *Adv. Funct. Mater.* **2015**, *25*, 2745–2753. [[CrossRef](#)]
19. Hornok, V.; Erdohelyi, A.; Dekany, I. Preparation of Ultrathin Membranes by Layer-by-Layer Deposition of Layered Double Hydroxide (LDH) and Polystyrene Sulfonate (PSS). *Colloid Polym. Sci.* **2005**, *283*, 1050–1055. [[CrossRef](#)]
20. Wang, Q.; O'Hare, D. Recent Advances in the Synthesis and Application of Layered Double Hydroxide (LDH) Nanosheets. *Chem. Rev.* **2012**, *112*, 4124–4155. [[CrossRef](#)] [[PubMed](#)]
21. Mousty, C.; Prevot, V. Hybrid and Biohybrid Layered Double Hydroxides for Electrochemical Analysis. *Anal. Bioanal. Chem.* **2013**, *405*, 3513–3523. [[CrossRef](#)] [[PubMed](#)]
22. Choi, G.; Piao, H.; Kim, M.H.; Choy, J.H. Enabling Nanohybrid Drug Discovery through the Soft Chemistry Telescope. *Ind. Eng. Chem. Res.* **2016**, *55*, 11211–11224. [[CrossRef](#)]
23. Varga, G.; Timar, Z.; Murath, S.; Konya, Z.; Kukovecz, A.; Carlson, S.; Sipos, P.; Palinko, I. Ni-Amino Acid-Ca-Al-Layered Double Hydroxide Composites: Construction, Characterization and Catalytic Properties in Oxidative Transformations. *Top. Catal.* **2017**, *60*, 1429–1438. [[CrossRef](#)]
24. He, S.; An, Z.; Wei, M.; Evans, D.G.; Duan, X. Layered Double Hydroxide-Based Catalysts: Nanostructure Design and Catalytic Performance. *Chem. Commun.* **2013**, *49*, 5912–5920. [[CrossRef](#)] [[PubMed](#)]
25. Zhao, M.M.; Zhao, Q.X.; Li, B.; Xue, H.G.; Pang, H.; Chen, C.Y. Recent Progress in Layered Double Hydroxide Based Materials for Electrochemical Capacitors: Design, Synthesis and Performance. *Nanoscale* **2017**, *9*, 15206–15225. [[CrossRef](#)] [[PubMed](#)]
26. Vialat, P.; Mousty, C.; Taviot-Gueho, C.; Renaudin, G.; Martinez, H.; Dupin, J.C.; Elkaim, E.; Leroux, F. High-Performing Monometallic Cobalt Layered Double Hydroxide Supercapacitor with Defined Local Structure. *Adv. Funct. Mater.* **2014**, *24*, 4831–4842. [[CrossRef](#)]
27. Gwak, G.H.; Kim, M.K.; Oh, J.M. Composites of Quasi-Colloidal Layered Double Hydroxide Nanoparticles and Agarose Hydrogels for Chromate Removal. *Nanomaterials* **2016**, *6*, 25. [[CrossRef](#)] [[PubMed](#)]
28. Goh, K.H.; Lim, T.T.; Dong, Z. Application of Layered Double Hydroxides for Removal of Oxyanions: A Review. *Water Res.* **2008**, *42*, 1343–1368. [[CrossRef](#)] [[PubMed](#)]
29. Liu, Z.P.; Ma, R.Z.; Osada, M.; Iyi, N.; Ebina, Y.; Takada, K.; Sasaki, T. Synthesis, Anion Exchange, and Delamination of Co-Al Layered Double Hydroxide: Assembly of the Exfoliated Nanosheet/Polyanion Composite Films and Magneto-Optical Studies. *J. Am. Chem. Soc.* **2006**, *128*, 4872–4880. [[CrossRef](#)] [[PubMed](#)]
30. Dou, Y.B.; Zhou, A.; Pan, T.; Han, J.B.; Wei, M.; Evans, D.G.; Duan, X. Humidity-Triggered Self-Healing Films with Excellent Oxygen Barrier Performance. *Chem. Commun.* **2014**, *50*, 7136–7138. [[CrossRef](#)] [[PubMed](#)]
31. Ge, N.J.; Wang, D.H.; Peng, F.; Li, J.H.; Qiao, Y.Q.; Liu, X.Y. Poly(Styrenesulfonate)-Modified Ni-Ti Layered Double Hydroxide Film: A Smart Drug-Eluting Platform. *ACS Appl. Mater. Interfaces* **2016**, *8*, 24491–24501. [[CrossRef](#)] [[PubMed](#)]
32. Carneiro, J.; Caetano, A.F.; Kuznetsova, A.; Maia, F.; Salak, A.N.; Tedim, J.; Scharnagl, N.; Zheludkevich, M.L.; Ferreira, M.G.S. Polyelectrolyte-Modified Layered Double Hydroxide Nanocontainers as Vehicles for Combined Inhibitors. *RSC Adv.* **2015**, *5*, 39916–39929. [[CrossRef](#)]
33. Vasti, C.; Borgiallo, A.; Giacomelli, C.E.; Rojas, R. Layered Double Hydroxide Nanoparticles Customization by Polyelectrolyte Adsorption: Mechanism and Effect on Particle Aggregation. *Colloid Surf. A* **2017**, *533*, 316–322. [[CrossRef](#)]
34. Pavlovic, M.; Li, L.; Dits, F.; Gu, Z.; Adok-Sipiczki, M.; Szilagyi, I. Aggregation of Layered Double Hydroxide Nanoparticles in the Presence of Heparin: Towards Highly Stable Delivery Systems. *RSC Adv.* **2016**, *6*, 16159–16167. [[CrossRef](#)]

35. Pavlovic, M.; Adok-Sipiczki, M.; Nardin, C.; Pearson, S.; Bourgeat-Lami, E.; Prevot, V.; Szilagyi, I. Effect of Macroraft Copolymer Adsorption on the Colloidal Stability of Layered Double Hydroxide Nanoparticles. *Langmuir* **2015**, *31*, 12609–12617. [[PubMed](#)]
36. Pavlovic, M.; Huber, R.; Adok-Sipiczki, M.; Nardin, C.; Szilagyi, I. Ion Specific Effects on the Stability of Layered Double Hydroxide Colloids. *Soft Matter* **2016**, *12*, 4024–4033. [[PubMed](#)]
37. Bragg, W.H.; Bragg, W.L. The Reflection of X-Rays by Crystals. Proc. R. soc. Lond. Ser. A-Contain. *Pap. Math. Phys. Character* **1913**, *88*, 428–438.
38. Drits, V.; Srodon, J.; Eberl, D.D. XRD Measurement of Mean Crystalline Thickness of Illite and Illite/Smectite: Reappraisal of the Kubler Index and the Scherrer Equation. *Clay Clay Min.* **1997**, *45*, 461–475.
39. Iselau, F.; Xuan, T.P.; Trefalt, G.; Matic, A.; Holmberg, K.; Bordes, R. Formation and Relaxation Kinetics of Starch-Particle Complexes. *Soft Matter* **2016**, *12*, 9509–9519. [[CrossRef](#)] [[PubMed](#)]
40. Kobayashi, M.; Yuki, S.; Adachi, Y. Effect of Anionic Surfactants on the Stability Ratio and Electrophoretic Mobility of Colloidal Hematite Particles. *Colloid Surf. A* **2016**, *510*, 190–197. [[CrossRef](#)]
41. Manning, G.S. Limiting Laws and Counterion Condensation in Polyelectrolyte Solutions 1. Colligative Properties. *J. Chem. Phys.* **1969**, *51*, 924–933.
42. Trefalt, G.; Szilagyi, I.; Oncsik, T.; Sadeghpour, A.; Borkovec, M. Probing Colloidal Particle Aggregation by Light Scattering. *Chimia* **2013**, *67*, 772–776. [[CrossRef](#)] [[PubMed](#)]
43. Kumar, A.; Aerry, S.; Goia, D.V. Preparation of Concentrated Stable Dispersions of Uniform Ag Nanoparticles Using Resorcinol as Reductant. *J. Colloid Interface Sci.* **2016**, *470*, 196–203. [[CrossRef](#)] [[PubMed](#)]
44. Pavlovic, M.; Rouster, P.; Szilagyi, I. Synthesis and Formulation of Functional Bionanomaterials with Superoxide Dismutase Activity. *Nanoscale* **2017**, *9*, 369–379. [[CrossRef](#)] [[PubMed](#)]
45. Verwey, E.J.W.; Overbeek, J.T.G. *Theory of Stability of Lyophobic Colloids*; Elsevier: Amsterdam, The Netherlands, 1948.
46. Evans, D.F.; Wennerstrom, H. *The Colloidal Domain*; John Wiley: New York, NY, USA, 1999.
47. Bauer, D.; Killmann, E.; Jaeger, W. Flocculation and Stabilization of Colloidal Silica by the Adsorption of Poly-Diallyl-Dimethyl-Ammoniumchloride (PDADMAC) and of Copolymers of Dadmac with *N*-Methyl-*N*-Vinyl Acetamide (NMVA). *Colloid Polym. Sci.* **1998**, *276*, 698–708. [[CrossRef](#)]
48. Rouster, P.; Pavlovic, M.; Saringer, S.; Szilagyi, I. Functionalized Titania Nanosheet Dispersions of Peroxidase Activity. *J. Phys. Chem. C* **2018**, *122*, 11455–11463. [[CrossRef](#)]
49. Szabo, T.; Toth, V.; Horvath, E.; Forro, L.; Szilagyi, I. Tuning the Aggregation of Titanate Nanowires in Aqueous Dispersions. *Langmuir* **2015**, *31*, 42–49. [[CrossRef](#)] [[PubMed](#)]
50. Hierrezuelo, J.; Vaccaro, A.; Borkovec, M. Stability of Negatively Charged Latex Particles in the Presence of a Strong Cationic Polyelectrolyte at Elevated Ionic Strengths. *J. Colloid Interface Sci.* **2010**, *347*, 202–208. [[CrossRef](#)] [[PubMed](#)]
51. Fuchs, A.; Killmann, E. Adsorption of Polyelectrolytes on Colloidal Latex Particles, Electrostatic Interactions and Stability Behaviour. *Colloid Polym. Sci.* **1998**, *279*, 53–60. [[CrossRef](#)]
52. Piccinini, E.; Alberti, S.; Longo, G.S.; Berninger, T.; Breu, J.; Dostalek, J.; Azzaroni, O.; Knoll, W. Pushing the Boundaries of Interfacial Sensitivity in Graphene Fet Sensors: Polyelectrolyte Multilayers Strongly Increase the Debye Screening Length. *J. Phys. Chem. C* **2018**, *122*, 10181–10188. [[CrossRef](#)]
53. Dubas, S.T.; Schlenoff, J.B. Factors Controlling the Growth of Polyelectrolyte Multilayers. *Macromolecules* **1999**, *32*, 8153–8160. [[CrossRef](#)]
54. Lohmann, O.; Zerball, M.; von Klitzing, R. Water Uptake of Polyelectrolyte Multilayers Including Water Condensation in Voids. *Langmuir* **2018**, *34*, 11518–11525. [[CrossRef](#)] [[PubMed](#)]
55. Hierrezuelo, J.; Szilagyi, I.; Vaccaro, A.; Borkovec, M. Probing Nanometer-Thick Polyelectrolyte Layers Adsorbed on Oppositely Charged Particles by Dynamic Light Scattering. *Macromolecules* **2010**, *43*, 9108–9116. [[CrossRef](#)]
56. Lagaly, G.; Mecking, O.; Penner, D. Colloidal Magnesium Aluminum Hydroxide and Heterocoagulation with a Clay Mineral. I. Properties of Colloidal Magnesium Aluminum Hydroxide. *Colloid Polym. Sci.* **2001**, *279*, 1090–1096. [[CrossRef](#)]
57. Meng, Z.Y.; Hashmi, S.M.; Elimelech, M. Aggregation Rate and Fractal Dimension of Fullerene Nanoparticles Via Simultaneous Multiangle Static and Dynamic Light Scattering Measurement. *J. Colloid Interface Sci.* **2013**, *392*, 27–33. [[CrossRef](#)] [[PubMed](#)]

58. Toth, I.Y.; Nesztor, D.; Novak, L.; Illes, E.; Szekeres, M.; Szabo, T.; Tombacz, E. Clustering of Carboxylated Magnetite Nanoparticles through Polyethylenimine: Covalent Versus Electrostatic Approach. *J. Magn. Mater.* **2017**, *427*, 280–288. [[CrossRef](#)]
59. Pavlovic, M.; Rouster, P.; Somosi, Z.; Szilagyi, I. Horseradish Peroxidase-Nanoclay Hybrid Particles of High Functional and Colloidal Stability. *J. Colloid Interface Sci.* **2018**, *524*, 114–121. [[CrossRef](#)] [[PubMed](#)]
60. Fritz, G.; Schadler, V.; Willenbacher, N.; Wagner, N.J. Electrosteric Stabilization of Colloidal Dispersions. *Langmuir* **2002**, *18*, 6381–6390. [[CrossRef](#)]
61. Tiraferri, A.; Hernandez, L.A.S.; Bianco, C.; Tosco, T.; Sethi, R. Colloidal Behavior of Goethite Nanoparticles Modified with Humic Acid and Implications for Aquifer Reclamation. *J. Nanopart. Res.* **2017**, *19*, 107. [[CrossRef](#)]
62. Ballauff, M. Spherical Polyelectrolyte Brushes. *Prog. Polym. Sci.* **2007**, *32*, 1135–1151. [[CrossRef](#)]
63. Ahrens, H.; Forster, S.; Helm, C.A. Charged Polymer Brushes: Counterion Incorporation and Scaling Relations. *Phys. Rev. Lett.* **1998**, *81*, 4172–4175. [[CrossRef](#)]
64. Xu, Z.P.; Stevenson, G.; Lu, C.Q.; Lu, G.Q. Dispersion and Size Control of Layered Double Hydroxide Nanoparticles in Aqueous Solutions. *J. Phys. Chem. B* **2006**, *110*, 16923–16929. [[CrossRef](#)] [[PubMed](#)]
65. Hassan, P.A.; Rana, S.; Verma, G. Making Sense of Brownian Motion: Colloid Characterization by Dynamic Light Scattering. *Langmuir* **2015**, *31*, 3–12. [[CrossRef](#)] [[PubMed](#)]



© 2018 by the authors. Licensee MDPI, Basel, Switzerland. This article is an open access article distributed under the terms and conditions of the Creative Commons Attribution (CC BY) license (<http://creativecommons.org/licenses/by/4.0/>).



# Polyelectrolyte adsorption, interparticle forces, and colloidal aggregation

Cite this: *Soft Matter*, 2014, 10, 2479

Istvan Szilagy, Gregor Trefalt, Alberto Tiraferri, Plinio Maroni and Michal Borkovec\*

This review summarizes the current understanding of adsorption of polyelectrolytes to oppositely charged solid substrates, the resulting interaction forces between such substrates, and consequences for colloidal particle aggregation. The following conclusions can be reached based on experimental findings. Polyelectrolytes adsorb to oppositely charged solid substrates irreversibly up to saturation, whereby loose and thin monolayers are formed. The adsorbed polyelectrolytes normally carry a substantial amount of charge, which leads to a charge reversal. Frequently, the adsorbed films are laterally heterogeneous. With increasing salt levels, the adsorbed mass increases leading to thicker and more homogeneous films. Interaction forces between surfaces coated with saturated polyelectrolyte layers are governed at low salt levels by repulsive electric double layer interactions, and particle suspensions are stable under these conditions. At appropriately high salt levels, the forces become attractive, principally due to van der Waals interactions, but eventually also through other forces, and suspensions become unstable. This situation can be rationalized with the classical theory of Derjaguin, Landau, Verwey, and Overbeek (DLVO). Due to the irreversible nature of the adsorption process, stable unsaturated layers form in colloidal particle suspensions at lower polyelectrolyte doses. An unsaturated polyelectrolyte layer can neutralize the overall particle surface charge. Away from the charge reversal point, electric double layer forces are dominant and particle suspensions are stable. As the charge reversal point is approached, attractive van der Waals forces become important, and particle suspensions become unstable. This behaviour is again in line with the DLVO theory, which may even apply quantitatively, provided the polyelectrolyte films are sufficiently laterally homogeneous. For heterogeneous films, additional attractive patch–charge interactions may become important. Depletion interactions may also lead to attractive forces and suspension destabilization, but such interactions become important only at high polyelectrolyte concentrations.

Received 8th August 2013  
Accepted 15th January 2014

DOI: 10.1039/c3sm52132j

[www.rsc.org/softmatter](http://www.rsc.org/softmatter)

Department of Inorganic and Analytical Chemistry, University of Geneva, Sciences II, Quai Ernest-Ansermet 30, 1205 Geneva, Switzerland. E-mail: [michal.borkovec@unige.ch](mailto:michal.borkovec@unige.ch)

## 1 Introduction

Charged polymers or polyelectrolytes (PEs) are widely employed to modify properties of surfaces or of colloidal particle suspensions. They are industrially used in water purification,



*Istvan Szilagy is a senior lecturer at the University of Geneva since 2009. He got his PhD in inorganic chemistry at the University of Szeged, Hungary, in 2006. He was then a postdoctoral researcher at the Murdoch University, Perth, Australia. His research focuses on inorganic and colloid chemistry and the development of novel functional materials.*



*Gregor Trefalt is a postdoctoral researcher at the University of Geneva. He studied chemistry at the University of Ljubljana, Slovenia. He stayed in Ljubljana to obtain his PhD in 2012 at Jožef Stefan Institute to carry out research in the area of colloidal processing of ceramic materials. He now focuses on colloidal interactions, particle aggregation, and light scattering.*

dc\_1931\_21

papermaking, mineral separation, or to control flow properties of particle slurries.<sup>1–6</sup> Emerging industrial applications of PEs include, for example, stabilization of metallic iron particles for environmental remediation, use as additives in the chemical–mechanical polishing process, or in biomedical applications.<sup>7–11</sup> PEs are further employed to create protective or functional surface coatings, whereby important approaches include adsorption of PE monolayers,<sup>7,12–14</sup> fabrication of multilayers of oppositely charged PEs,<sup>13,15–18</sup> or the preparation of PE brushes by grafting or by adsorption of block copolymers.<sup>19–21</sup> Such coatings may be used to control surface properties, including wetting, lubrication, adhesion, or biological resistance.<sup>22,23</sup> Certain PEs offer the possibility to tune these properties through external stimuli, such as temperature or solution composition.<sup>24,25</sup>

PEs interact strongly with solid substrates, and in turn, they may substantially alter the respective surface characteristics. Thereby, the interaction forces between such surfaces can be modified, and as a consequence, properties of particle suspensions can be controlled. Understanding of the relationship between PE adsorption, particle interactions, and the stability of the resulting suspensions is critical for further

development of functional PE additives. The present review attempts to draw a systematic picture of these processes for the relevant situation when PEs adsorb onto oppositely charged solid substrates.

PE adsorption to solid substrates and the resulting charging behaviour were investigated by numerous experimental techniques. Planar substrates were probed with optical reflectivity, ellipsometry, quartz crystal microbalance, and streaming potential techniques,<sup>26–28</sup> while particle suspensions were characterized by means of classical batch depletion techniques, light, X-ray and neutron scattering, and electrophoresis.<sup>29–32</sup> This review will focus on linear or branched homopolymers, including dendrimers, in monovalent electrolyte solutions. We will further investigate properties of PE films in the same electrolyte solution as that used for the adsorption process and discuss the influence of salt concentration and effects of charge densities of the PEs and of the substrate. PE adsorption will be mainly interpreted in terms of the random sequential adsorption (RSA) model and its variants,<sup>33,34</sup> while the self-consistent field approach and computer simulation studies will be addressed only briefly.<sup>35–41</sup>

Adsorbed PEs modify interaction forces acting between substrates, and for this reason, they are frequently used as additives to control the stability of colloidal suspensions or to tune their rheological properties.<sup>1–4,7</sup> The resulting interaction forces between surfaces or particles in the presence of PEs were investigated with the surface forces apparatus (SFA),<sup>42,43</sup> total internal reflection microscope,<sup>44–46</sup> or the colloidal probe technique based on the atomic force microscope (AFM).<sup>47,48</sup> Particle aggregation phenomena were investigated with turbidity measurements, time-resolved light scattering, or rheology.<sup>4,49–51</sup> We only focus on interactions in symmetric systems involving the same type of interfaces or particles, and correspondingly on homoaggregation processes.

An interpretation of the underlying mechanisms of the adsorption process, interaction forces, and particle aggregation will be put forward. We explore to what extent interaction forces can be rationalized in terms of the classical theory of Derjaguin, Landau, Verwey, and Overbeek (DLVO).<sup>52–54</sup> The role of specific



*Alberto Tiraferrì is a Marie Curie postdoctoral fellow at the University of Geneva. He studied environmental engineering at the Politecnico di Torino, Italy, and received his PhD in 2012 at Yale University, New Haven, USA, in the area of membrane-based separation processes for water treatment. His current project explores the adsorption of macromolecules to surfaces and implication of these processes to membrane fouling and environmental remediation.*



*Plinio Maroni works as a senior scientist at the University of Geneva. He studied physics at the University of Pisa, Italy and he got his PhD in 2005 at the Swiss Federal Institute of Technology, Lausanne, in the area of molecular reactivity of molecules adsorbed on surfaces. His current research interests center around surface spectroscopy, surface sensitive optical and acoustic techniques, and local probe microscopy.*



*Michal Borkovec is a full professor of chemistry at the University of Geneva and a member of the Swiss National Research Council. He received his PhD in 1986 at Columbia University, New York, USA, and then worked as a lecturer at the Swiss Federal Institute of Technology, Zürich. Later, he became an associate professor at Clarkson University, Potsdam, USA, and in 2001 he accepted his current position at Geneva. His research interests include physical chemistry of colloids, interfaces, and polyelectrolytes.*

dc\_1931\_21

forces induced by PEs, in particular, steric, bridging, and depletion interactions will be equally discussed.<sup>54</sup> The relevance of these forces in controlling the suspension stability in the presence of PEs was proposed early on.<sup>55</sup> We will further discuss the patch-charge interactions resulting from the lateral heterogeneity of the adsorbed PE layers.<sup>56</sup> Simple models will be used to clarify the mechanisms of the interactions involved.

There are various important topics involving PE adsorption that will not be addressed in this review. We shall skip the interesting aspects related to adsorption of comb polymers, such as bottlebrush and dendronized polymers<sup>57–59</sup> or copolymers, such as block copolymers and proteins.<sup>60–66</sup> The response of adsorbed PE films when exposed to solutions of variable compositions or containing multivalent ions will not be addressed either.<sup>67–75</sup> We will not discuss mixed adsorbed PE films, which are especially important for multilayers prepared by the layer-by-layer deposition process,<sup>13,15–18,24,76,77</sup> as well as the adsorption of neutral polymers or PEs with the same sign of charge as the substrate.<sup>35,73,75,78</sup> Neither the adsorption of PEs to interfaces under applied external electric potential, nor to instable or fluid interfaces (*e.g.*, air–water and oil–water) will be addressed.<sup>79–82</sup> We also skip the discussion of interaction forces in asymmetric systems involving different types of surfaces, heteroaggregation, particle deposition, or growth of particle–PE multilayers.<sup>83–87</sup> Finally, we make no attempt to provide a detailed review of the numerous theoretical developments and computer simulations addressing PE adsorption and the resulting interaction forces. For these topics, we refer the interested reader to the appropriate literature.<sup>36–38,88</sup>

The present review is organized as follows. Section 2 summarizes the current understanding of the PE adsorption phenomena and the underlying charging process, whereby planar substrates as well as colloidal particles are discussed. Interaction forces between the same type of interfaces, either involving planar substrates, colloidal particles, or both, are addressed in Section 3. Particle aggregation phenomena involving the same type of particles are addressed in Section 4, whereby the main focus is on early stages of the homoaggregation process. An outlook highlighting open questions and possible research directions concludes the review.

## 2 Polyelectrolyte adsorption

This section focuses on adsorption of polyelectrolytes (PEs) to oppositely charged water–solid interfaces. These interfaces might be realized by means of a planar substrate or through the internal surface in a colloidal particle suspension. PEs normally have a linear architecture and some examples are summarized in Fig. 1. PEs can also be branched and corresponding examples include dendritic poly(amido amine) (PAMAM) or branched poly(ethylene imine) (BPEI). One refers to anionic and cationic PEs when they are negatively and positively charged, respectively. PEs with a permanent charge are called strong PEs, and they include sodium poly(styrene sulfonate) (PSS) and poly(diallyldimethyl ammonium) (PDDA). The charge of weak PEs varies with solution pH and ionic strength, and examples include poly(vinyl amine) (PVA), poly(L-lysine) (PLL), poly(acrylic

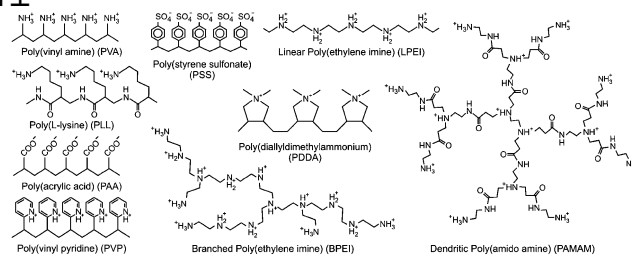


Fig. 1 Structural formulae of various fully ionized PEs discussed in this review. The names and acronyms refer to the ionized forms of the strong PEs, while to the neutral forms of the weak PEs.

acid) (PAA), linear poly(ethylene imine) (LPEI) or PAMAM. Their degree of ionization can be measured by potentiometric titrations and modelled with mean field or site binding models.<sup>89</sup> In monovalent electrolyte solutions, the gyration radius  $R_g$  of linear PEs obeys the classical scaling law<sup>90</sup>

$$R_g \propto M^\alpha \quad (1)$$

where  $M$  is the molecular mass and  $\alpha$  is the Flory exponent in the range 0.5–0.6. The hydrodynamic radius that is related to the diffusion coefficient of the PE chain is typically a factor of 1.5–2.0 smaller.<sup>90</sup> Adsorption of PEs will be discussed in the following.

### 2.1 Irreversible nature of the adsorption process

Highly charged PEs adsorb strongly to oppositely charged interfaces. This affinity is primarily caused by attractive electrostatic forces acting between the oppositely charged PE and substrate. Since the PE backbone is hydrophobic, however, attractive van der Waals and hydration forces are important as well. This subsection will compare adsorption to planar substrates and in colloidal suspensions and rationalize this process with simple models.

**Adsorption of PEs to planar substrates.** Numerous optical techniques are available to study the adsorption of PEs to planar solid substrates in real time.<sup>27,79,91–94</sup> Let us illustrate the adsorption process of PEs to oppositely charged substrates with reflectivity experiments as displayed in Fig. 2a, which allows monitoring of the change in the adsorbed mass per unit area. The example shown refers to strong cationic PDDA of molecular mass of about  $450 \text{ kg mol}^{-1}$  adsorbing to a negatively charged silica substrate.<sup>91</sup> The substrate is initially rinsed with a pure electrolyte solution adjusted to pH 4.0, and then the solution is changed to a PE solution in the same electrolyte and of the same pH. The adsorbed mass of the PE increases linearly with time at first. This increase reflects the rapid adsorption of the PE to the surface. Later, the adsorbed mass reaches a plateau. This plateau indicates that the PE film is saturated, and in spite of the presence of PE in the solution, no further adsorption occurs. When the surface is rinsed with the pure electrolyte solution, no desorption is observed. This feature suggests that the adsorption process is irreversible. If this process would be reversible, the PE would desorb from the surface, and the desorption could



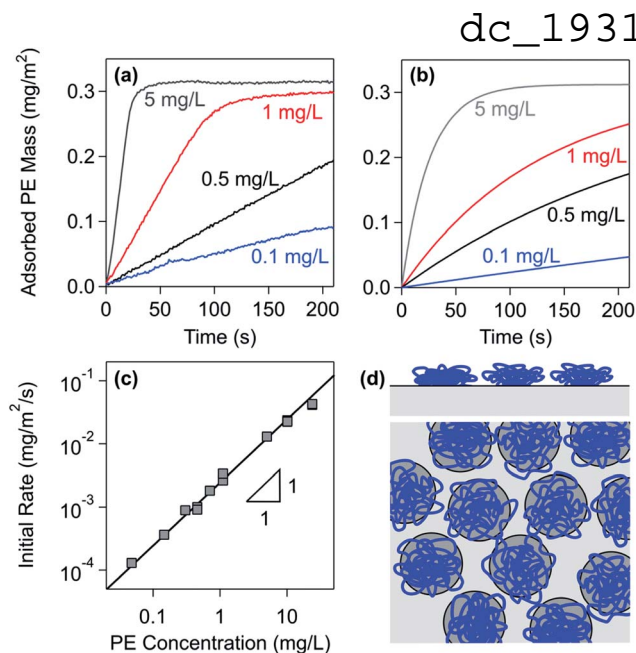


Fig. 2 Adsorption kinetics of PDDA to the silica surface in a solution of 50 mM monovalent salt at pH 4. (a) Measurements with optical reflectivity at different PE concentrations.<sup>91</sup> (b) Results of the simple irreversible adsorption model with the Langmuir blocking function. (c) Initial adsorption rate *versus* different PE concentrations. (d) Graphical illustration of the RSA model.

be evidenced in the reflectivity trace. The fact that adsorbed PE layers do not desorb in the PE-free electrolyte solution has been demonstrated in numerous systems.<sup>27,34,82,91,95–98</sup>

Partial desorption could be only demonstrated for PEs in special circumstances, for example, for PEs of very low molecular mass, typically below  $10 \text{ kg mol}^{-1}$ .<sup>27,95</sup> Desorption of PEs of higher molecular mass has been reported to be induced by changes in the solution composition or by exchange with other PEs.<sup>27,58,99</sup> However, the adsorption process is irreversible provided the composition of the electrolyte solution is not changed during the experiment.

With increasing concentration of the PE, the initial adsorption rate increases.<sup>91</sup> The rate law can be identified by plotting the initial rate *versus* the PE concentration as shown in Fig. 2c. Since this rate is proportional to the PE concentration, the adsorption process follows a first-order rate law in the PE concentration. Similar dependencies were observed with other PEs.<sup>34,97,100</sup>

Converting the data shown in Fig. 2c into the adsorbed number density, one finds an adsorption rate coefficient of  $k_a = 2.5 \times 10^{-6} \text{ m s}^{-1}$ . This rate coefficient can also be calculated from the cell geometry by assuming laminar flow and perfect sink conditions.<sup>34,101</sup> Based on the known flow rate and the hydrodynamic radius of PDDA of about 26 nm as estimated from light scattering experiments,<sup>90,102</sup> the perfect sink model predicts a rate coefficient of  $k_a = 4.9 \times 10^{-6} \text{ m s}^{-1}$ . This value is only about a factor two larger than the one observed experimentally. The remaining discrepancy could be related to forces acting between the PE and the substrate and to hydrodynamic interactions. A similar agreement between experimental and

calculated adsorption rate coefficients was reported in other PE systems.<sup>34,97,100</sup>

The plateau value is independent of the PE concentration to good approximation. However, this value may increase with increasing PE concentration somewhat. This increase can be rationalized by the finite relaxation time of the polymer chains.<sup>28,76,91</sup> With increasing PE concentration, the lateral relaxation of the individual adsorbing PEs is increasingly hindered by the rapidly arriving neighbouring PEs. A similar relaxation mechanism was also suggested to be present for protein adsorption.<sup>103</sup>

**Classical RSA model.** This model describes irreversible adsorption processes of colloidal particles, proteins, and PEs.<sup>104–106</sup> The particles are modeled as circular disks, and they are assumed to adsorb to a planar surface sequentially at random locations. Such a disk can only adsorb on an empty surface and an overlap with a previously deposited disk is not allowed; see Fig. 2d. The maximum coverage or the so-called jamming limit is<sup>104,105</sup>

$$\theta_{\text{jam}} \approx 0.55 \quad (2)$$

which is substantially smaller than the regular hexagonal packing with a coverage of 0.91. The surface coverage  $\theta$  can be related to the number density of adsorbed PE molecules  $\Gamma$  per unit area by

$$\theta = \pi a^2 \Gamma \quad (3)$$

where  $a$  is the disk radius, which is comparable to the gyration radius of the PE. The kinetics of the adsorption process can be approximated by relating the rate of change of the adsorbed number density with time  $t$  to the number concentration  $c$  of the PE in solution as

$$\frac{d\Gamma}{dt} = k_a c B(\Gamma) \quad (4)$$

where  $k_a$  is the adsorption rate coefficient of the PE and  $B(\Gamma)$  is the blocking (or available surface area) function. The Langmuir adsorption model suggests that

$$B(\Gamma) = \begin{cases} 1 - \Gamma/\Gamma_0 & \text{for } \Gamma < \Gamma_0 \\ 0 & \text{for } \Gamma \geq \Gamma_0 \end{cases} \quad (5)$$

where  $\Gamma_0$  is the adsorbed number density at saturation, which corresponds to the jamming limit within the RSA model. The predictions of this kinetic model are shown in Fig. 2b. The adsorbed mass per unit area is obtained by multiplying the adsorbed number density  $\Gamma$  with the mass of the PE. The model results agree with the experiment semi-quantitatively.

However, the model predicts a too gradual transition from the initial stages to saturation. An analysis of the RSA model leads to a blocking function, which suggests an even slower approach to saturation. Alternative blocking functions have been proposed to remedy this problem.<sup>66,105,106</sup> However, they were mainly used to describe irreversible adsorption of particles and proteins and have not been applied to model PE adsorption so far.



dc\_1931\_21

**Adsorption of PEs to colloidal particles.** When PEs are dissolved in a suspension of colloidal particles, they will also adsorb to their surface irreversibly. In this situation, one should distinguish two cases as illustrated in Fig. 3. When the total PE concentration is high, the PEs will adsorb to the particle surface until a saturated layer is formed. The excess PE will remain dissolved in solution. When the total PE concentration is low, the PE will adsorb to the particle surface until no PE is left in solution. In this case, we refer to an unsaturated layer. When performing such experiments in colloidal suspensions, larger concentration gradients during mixing must be avoided, otherwise the PE may distribute among the particles unevenly.

The irreversible nature of the adsorption can be confirmed experimentally with batch adsorption experiments as well.<sup>31,107</sup> Fig. 3c shows results of adsorption of dendritic PAMAM to sulfate latex particles, where the adsorbed amount was obtained by counting the adsorbed single molecules with the AFM.<sup>108</sup> The adsorbed mass is plotted *versus* the PE dose, which reflects the mass of PE relative to the mass of the particles ( $\text{mg g}^{-1}$ ).

At high PE doses, the adsorbed mass is constant due to saturation. The fact that the total adsorbed mass is independent of the solution concentrations was also experimentally confirmed with PVA and PDDA adsorbing to latex particles.<sup>30,31,107</sup> At low doses, the entire quantity of PE added is adsorbed, but is insufficient to achieve saturation, meaning that the plateau is not reached. The PE dose can be also expressed as the mass of the PE per unit particle surface area ( $\text{mg m}^{-2}$ ). These units are useful in the unsaturated regime, where the dose simply reflects the adsorbed mass. The fact that adsorption in the unsaturated regime is quantitative can be also demonstrated by electrophoresis, and this technique will be discussed in Section 2.3.

Deviations from this idealized picture occur due to the kinetics of the adsorption process. This process can be particularly slow when the PE concentration is close to the one needed to reach saturation. The simple model summarized in eqn (4) and (5) can be also used to model adsorption in suspensions, and the corresponding results are illustrated in Fig. 3d. When the adsorption time is too short such that adsorption cannot be completed, the plot of the adsorbed mass *versus* the PE concentration will be rounded. Such dependencies might be wrongly interpreted by an equilibrium adsorption isotherm.

When a substrate is continuously flushed with PE solution in a flow-through cell, one always obtains a saturated layer due to a sufficient supply of PEs. Unsaturated layers can be formed in a flow-through cell too. In that case, however, the PE feed solution must be changed to a pure electrolyte solution before the saturation plateau is reached.

## 2.2 Properties of adsorbed polyelectrolyte layers

Let us now discuss the main characteristics of saturated PE layers, particularly, the adsorbed mass, their thickness, water content, and lateral heterogeneity. Not much is known concerning the unsaturated layers, but we will also comment on those. The RSA model will be further generalized to introduce effects of electrostatic interactions.

**Absorbed mass.** Fig. 2a illustrates that the adsorbed mass at saturation for PDDA on silica in 50 mM salt solution is about  $0.3 \text{ mg m}^{-2}$ . These are small amounts, since an atomic monolayer corresponds to about  $1\text{--}2 \text{ mg m}^{-2}$ . Let us rationalize with the RSA model on why such a small amount corresponds already to saturation. Taking the hydrodynamic radius of about 26 nm for PDDA<sup>91</sup> and the maximum coverage given by eqn (2), one finds an adsorbed mass of  $0.1 \text{ mg m}^{-2}$ . The RSA model provides indeed a reasonable estimate, which supports the picture that the adsorbed film corresponds to a monolayer of adsorbed PE chains. In general, the mass adsorbed for saturated PE layers adsorbed to oppositely charged substrates can be even lower and typically is  $0.01\text{--}1 \text{ mg m}^{-2}$ .<sup>34,91,98,109–112</sup>

The mass of adsorbed PE depends on several factors related to the characteristics of the PE, those of the substrates, and the solution composition. Here, we discuss effects of the molecular mass, salt concentration, as well as the influence of the charge density of the PE and the substrate. These findings will be then explained in terms of a modified RSA model that includes electrostatic interactions between adsorbed molecules.

The adsorbed mass at saturation depends only weakly on the molecular mass for linear PEs.<sup>28,32</sup> This observation can be also rationalized with the RSA model. Based on eqn (1) and (3), this model suggests that the adsorbed number density scales as

$$\Gamma \propto M^{-2\alpha} \quad (6)$$

with the molecular mass  $M$ . From this relationship one finds that the adsorbed mass scales as  $\propto M^{1-2\alpha}$ . For typical values of the exponent  $\alpha$ , this relationship leads to an extremely weak dependence. On the other hand, for dendritic or branched PEs, the adsorbed mass increases with the molecular mass more

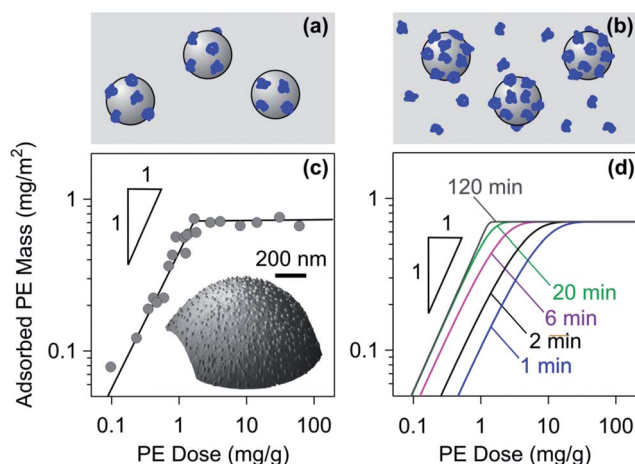


Fig. 3 Adsorption of PEs in a colloidal suspension of oppositely charged particles. Schematic representation of (a) the unsaturated layer that depletes the solution of the free PE and (b) the saturated layer with excess PE in solution. (c) Overnight adsorption of dendritic PAMAM of  $935 \text{ kg mol}^{-1}$  to sulfate latex particles of diameter  $3.1 \mu\text{m}$  in a colloidal suspension of pH 4.0 without salt added. The adsorbed amount was obtained by counting the adsorbed single molecules shown in the inset.<sup>108</sup> The solid line represents the expected adsorbed amount given the saturation value. (d) Representative results with the kinetic RSA model where the effect of finite adsorption time is indicated.

dc\_1931\_21

strongly, since the exponent  $\alpha$  is much smaller than that for linear PEs.<sup>34,95,113</sup>

The adsorbed mass normally increases with increasing concentration of the added monovalent electrolyte. Fig. 4 illustrates this trend for various PEs and substrates. This increase has been observed for a wide range of cationic and anionic PEs adsorbed on oppositely charged substrates, and typically results in an increase by a factor 2–4 when the salt concentration is increased by 4 orders of magnitude.<sup>28,32,34,91,97,98,110,112,114–116</sup> This salt dependence only reverses for very weakly charged PEs and high salt concentrations, whereby the adsorbed mass goes through a maximum, and finally decreases.<sup>97,98,117–119</sup>

Trends concerning the variation of the charge densities are less clearly established. The charge density of PEs can be varied by studying copolymers involving charged and neutral monomers, but other properties of the PEs may change at the same time (*e.g.*, hydrophobicity).<sup>31,111</sup> The charge density of the substrates has been sometimes varied by investigating different oxides, but other characteristics of these substrates are altered in this fashion as well.<sup>26,27</sup> A good way to tune the charge density of PEs and of the substrates is through weak ionizable groups and the respective pH adjustments. Nevertheless, the charges of the isolated components may not correspond to the ones in the adsorbed state, since ionization may occur upon adsorption.<sup>117,120,121</sup> The adsorbed mass normally increases with increasing charge density of the substrate and with decreasing charge density of the PE.<sup>29,34,91,111</sup> With decreasing PE charge density, the adsorbed mass may go through a maximum at very low charge densities.<sup>29,111,119,122</sup>

**Electrostatic RSA model.** The increase of the adsorbed mass with the salt concentration can be understood by considering the repulsion of the electric double layers formed around adsorbing PE coils. When the salt level is decreased, the repulsion becomes increasingly long ranged, which leads to saturation of the surface at lower adsorbed amounts.

This situation can be captured by a simple modification of the RSA model.<sup>106,123,124</sup> Since the adsorbing polymers repel each other due to overlapping electric double layers, one can model this phenomenon as an increase in the radius of the adsorbing disks to an effective radius  $a_{\text{eff}}$ , which now also includes the range of the repulsion of the surrounding diffuse layer. The situation is schematically depicted in Fig. 4d. The resulting surface coverage is now given by

$$\theta = \theta_{\text{jam}} \left( \frac{a}{a_{\text{eff}}} \right)^2 \quad (7)$$

The effective radius  $a_{\text{eff}}$  can be estimated by assuming that the interaction energy of two neighbouring PE chains will be comparable to the thermal energy, namely

$$u(2a_{\text{eff}}) \approx k_{\text{B}}T \quad (8)$$

where  $u(r)$  is the interaction potential between two adsorbing PEs at a center-to-center distance  $r$  and  $k_{\text{B}}T$  is the thermal energy with  $k_{\text{B}}$  being the Boltzmann constant and  $T$  being the absolute temperature. The screened Coulombic interaction can be used to model the interaction between two charged spheres in solution<sup>106,123,124</sup>

$$u(r) = k_{\text{B}}TL_{\text{B}}Z_{\text{eff}}^2 \left( \frac{e^{\kappa a}}{1 + \kappa a} \right)^2 \frac{e^{-\kappa r}}{r} \quad (9)$$

where  $Z_{\text{eff}}$  is the effective charge in units of the elementary charge  $q$ , and the Bjerrum length is abbreviated as

$$L_{\text{B}} = \frac{q^2}{4\pi k_{\text{B}}T\epsilon_0\epsilon} \approx 0.72 \text{ nm} \quad (10)$$

where  $\epsilon_0$  is the permittivity of vacuum and  $\epsilon$  is the dielectric constant of the liquid. The Debye length  $\kappa^{-1}$  in a monovalent electrolyte is given by

$$\kappa^2 = 8\pi L_{\text{B}}N_{\text{A}}c_{\text{S}} \quad \text{or} \quad \kappa^{-1} \approx \frac{0.30 \text{ nm}}{\sqrt{c_{\text{S}}}} \quad (11)$$

where  $c_{\text{S}}$  is the molar concentration of the electrolyte and  $N_{\text{A}}$  is the Avogadro's number. The numerical values refer to water at room temperature and the salt concentration is expressed in  $\text{mol L}^{-1}$ . For weakly charged objects, the effective charge  $Z_{\text{eff}}$  simply corresponds to the bare charge  $Z$ . For objects of higher charge, the effective charge will be lower than the bare charge due to adsorption of counterions. Poisson–Boltzmann theory suggests that the effective charge is constant for highly charged objects and is given by<sup>124</sup>

$$Z_{\text{eff}} = \frac{a}{L_{\text{B}}} (4\kappa a + 6) \quad (12)$$

The effective radius  $a_{\text{eff}}$  can be now estimated from eqn (8) and (9), and the adsorbed number density follows from eqn (3) and (7).

Results obtained from this modified RSA model are shown in Fig. 4a. One observes that this model predicts very similar dependencies to the ones observed for the adsorption of PDDA and dendritic PAMAM.<sup>34,91</sup> Fig. 4b shows a dimensionless representation of the surface coverage  $\theta$  versus the screening parameter  $\kappa a$  where the curves almost collapse on a master curve.<sup>124,125</sup> This model can qualitatively explain the characteristic increase of the adsorbed mass with decreasing charge density of the PE. In this case, decreasing the effective charge  $Z_{\text{eff}}$  will lead to smaller effective radii  $a_{\text{eff}}$  and therefore to larger adsorbed mass.

The RSA model can be further extended to rationalize the increase of the adsorbed mass with increasing charge density of the substrate.<sup>34</sup> At charged water–solid interfaces, electrical double layers form, and the diffuse layer contains a higher concentration of counterions than the one in the bulk. When two PE chains interact close to the interface, the higher concentration of counterions close to the interface will enhance the screening of the electrostatic interaction. Therefore, the electrostatic repulsion between the adsorbing chains will be weaker and result in a larger adsorbed mass. This effect can be included into the RSA model, and the modified model can explain the increase of the adsorbed amount of dendritic PAMAM with the solution pH quite well.<sup>34</sup> The more substantial adsorbed amounts of PAMAM compared to other PEs at very low salt concentrations shown in Fig. 4c can be probably rationalized through the same mechanism. The spirit of the electrostatic RSA model is similar to the treatment of the dilute 2-d

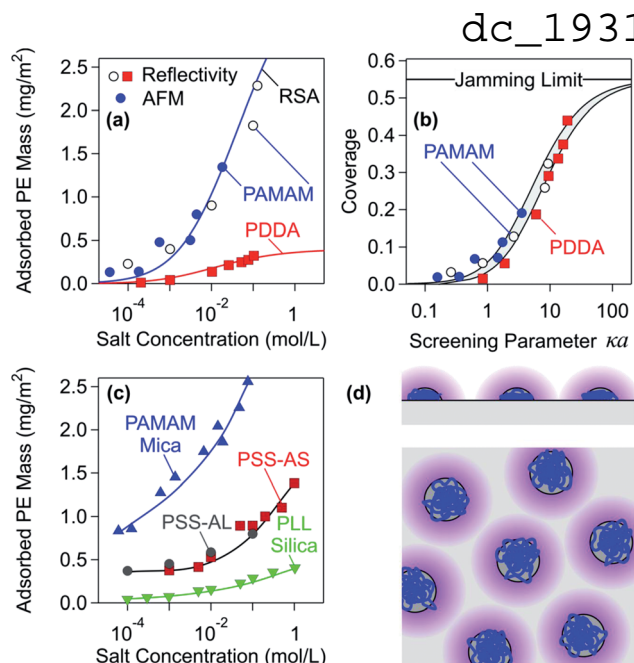


Fig. 4 Adsorbed mass of PEs on oppositely charged substrates versus salt concentration at saturation. (a) Adsorbed mass versus the salt concentration for dendritic PAMAM and linear PDDA on silica measured by reflectivity and AFM and comparison with the RSA model (solid lines).<sup>34,91</sup> (b) Dimensionless representation of the coverage  $\theta$  versus screening parameter  $\kappa a$  of the same data as shown in (a). The grey region corresponds to radii between 5 and 50 nm. (c) Further experimental results obtained with different substrates, namely mica, silica, amino-functionalized silica (AS), and amidine latex (AL). The solid lines serve as a guide to the eye. (d) Schematic representation of the electrostatic RSA model. The diffuse layer is indicated in purple.

Wigner regime, which makes the assumption that PEs adsorb individually and that their mutual interactions are dominated by diffuse layer repulsion.<sup>126</sup>

The RSA model is unable to predict the adsorption maximum that is observed for weakly charged PEs and high salt concentrations.<sup>97,117,118</sup> This maximum is related to the fact that PEs will not adsorb to oppositely charged substrates beyond a critical salt concentration threshold, if solely electrostatic forces are present.<sup>39,119,127</sup> At high salt levels, a weakly charged PE will be strongly screened. Therefore, attractive electrostatic forces acting between the PE and the substrate will be not sufficient to overcome the thermal motion, and the PE will no longer adsorb. Since the adsorbed amount increases with increasing salt levels, but vanishes above the salt threshold, a sharp maximum in the adsorbed amount results. In reality, however, additional attractive forces act between the PE chain and the substrate (e.g., van der Waals and hydration). These non-electrostatic forces may be quite important, as evidenced by adsorption of neutral polymers. For PEs, however, the forces responsible for the adsorption weaken substantially beyond the salt threshold. Therefore, one observes a wider maximum with respect to the one expected from electrostatic forces alone. Under these conditions, the adsorption process may no longer be irreversible, and the simple RSA model is expected to fail. Alternative models capable of describing this situation are discussed below.

**Morphology of adsorbed PE films.** The electrostatic RSA model suggests that PE chains adsorb to the substrate individually. Since the spacing between the chains is mainly dictated by the electrostatic repulsion between the adsorbing chains, the film remains laterally heterogeneous. Moreover, strong attractive electrostatic forces acting between the adsorbing PE and the substrate are expected to flatten the adsorbed chains. Therefore, an adsorbed PE layer will be typically thin and laterally heterogeneous. For more weakly charged PEs, and especially at higher salt levels, more homogeneous layers may form. Let us now discuss the experimental evidence supporting these claims.

Fig. 5 summarizes layer thickness measurements of adsorbed PE films with two different techniques.<sup>28,32</sup> The first technique is based on dynamic light scattering (DLS) in a colloidal particle suspension, where the layer thickness is inferred from the difference between the hydrodynamic radii of the particles in the presence and in the absence of the PE; see Fig. 5a.<sup>32,128</sup> The second technique relies on a combination of optical reflectivity and quartz crystal microbalance measurements on planar substrates; see Fig. 5b.<sup>28,129</sup> Both techniques yield comparable results. PE layers adsorbed on oppositely charged substrates are extremely thin, merely a few nm. Considering the fact that the diameter of PE chains in solution typically is 20–100 nm, the PEs are strongly flattened in the adsorbed state. Based on these thickness measurements, one further concludes that these films are rather compact and contain only 20–60% of water.<sup>28,32</sup> At higher salt levels, however, these films become more swollen and porous. Few additional reports confirm that PE films adsorbed on oppositely charged substrates are very thin indeed.<sup>18,111,130</sup> One also finds that the layer thickness increases with increasing salt levels and with increasing molar mass, especially at high salt concentrations.<sup>28</sup> An increase in thickness was also reported with the decreasing charge of the PE, and this quantity also passes through a maximum at very low charge densities.<sup>111</sup>

While data shown in Fig. 5 clearly support the picture of flat adsorbed PE films, one observes that DLS measurements yield a larger thickness than the ones measured by the surface sensitive techniques. Moreover, the latter data suggest a more gradual swelling of the film. While the differences in the substrates used may lead to these differences, they might also be related to the two sub-layer structure of an adsorbed PE film.<sup>94</sup> The thickness of these sub-layers may vary upon solution conditions and lead to the different salt dependencies observed with the two different techniques. One should also realize that thickness measurements for such extremely thin films are difficult and prone to systematic errors. Some of the available results in the literature should be thus considered with caution.

The lateral heterogeneity of adsorbed PE films can be best confirmed by AFM imaging. Such non-uniformities are particularly pronounced for highly charged PEs and low salt levels. Fig. 6 shows such images of adsorbed PEs recorded in the dry state. Fig. 6a shows adsorbed dendritic PAMAM, and the individual molecules can be clearly distinguished. Note that this layer is saturated, and no further adsorption will occur, in spite

dc\_1931\_21

of the unoccupied surface in between individual molecules. This low coverage results from the strong electrostatic repulsion between the adsorbing dendrimers. The other images show linear PEs adsorbed to different substrates. Fig. 6b refers to a saturated layer of PSS on amidine latex particles.<sup>131</sup> Fig. 6c and d show unsaturated layers of poly(vinyl pyridine) (PVP) on mica.<sup>132</sup>

While such imaging techniques provide strong evidence that adsorbed PE layers are laterally heterogeneous, quantitative characterization of these heterogeneities is mostly lacking. Exceptions are layers formed with dendritic PAMAM, whereby the individual molecules can be resolved with AFM. They can be described as dilute monolayers and they feature a liquid-like order as indicated by a structural peak in the radial distribution function.<sup>34,133</sup> The statistical properties of individual adsorbed linear polyelectrolytes and of nucleic acids were successfully determined with the AFM.<sup>74,132,134–136</sup> However, little is known about the detailed structure of saturated layers of adsorbed linear polyelectrolytes and the characteristic distances involved. Direct force measurements have confirmed that adsorbed layers of dendritic PAMAM and linear PSS are heterogeneous.<sup>107,131</sup> These techniques have also demonstrated that similar layers formed with LPEI are homogeneous down to about 10 nm, but probably heterogeneous on smaller length scales.<sup>48</sup> Weakly charged hydrophobic PEs have been reported to form more homogeneous layers, resembling disordered lamellar phases.<sup>74</sup> Similar structures were also predicted on theoretical grounds and were also referred to as the semi-dilute 2-d Wigner regime.<sup>88,126</sup>

An alternative interpretation of the small layer thicknesses shown in Fig. 5 could be related to the lateral heterogeneity of the films. Typically, surface sensitive and scattering techniques yield a laterally averaged thickness, and dilute, heterogeneous layers would lead to a smaller thickness than the gyration radius of an individual PE even if the adsorption process did not lead to a deformation in the normal direction. However, height measurements of adsorbed dendritic PAMAM with the AFM indicate that even these molecules flatten substantially.<sup>67,133</sup> These highly branched molecules have rather compact structures, and therefore linear PEs will flatten much more.

**Modeling of PE adsorption.** The electrostatic RSA model was introduced above to understand some basic features of PE adsorption. However, various alternative models of the adsorption process of PEs to oppositely charged substrates have been proposed.<sup>35–41</sup> The majority of the existing models are based on the assumption of reversible adsorption equilibrium. While this assumption is at odds with the irreversible nature of the adsorption process discussed in Section 2.1, such models may still provide useful insights.

An important class of analytical models is based on density functional theories. These theories normally assume that the adsorbed film is laterally homogeneous, and they attempt to estimate self-consistently the profiles of the concentrations and of the electric potential in the normal direction. Such a self-consistent field (SCF) approach was implemented within a numerical scheme by Fleer and co-workers.<sup>29,35,137</sup> Based on a similar formulation, simple scaling laws could be derived.<sup>138</sup> These approaches are capable of reproducing the frequently

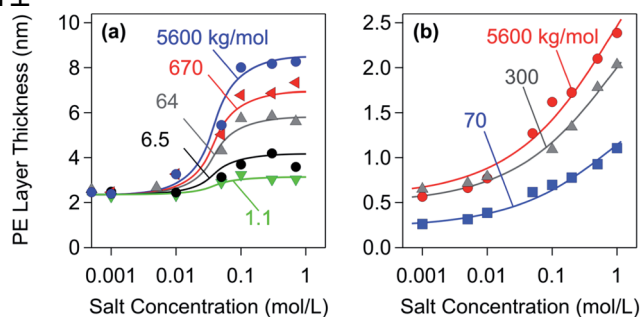


Fig. 5 Layer thickness of saturated PSS layers versus salt concentration adsorbed on oppositely charged substrates for different molecular masses of the sodium salt. (a) Amidine latex particles probed with DLS.<sup>32</sup> (b) Planar amino-functionalized silica probed with reflectivity and quartz crystal microbalance.<sup>28</sup>

observed increase of the adsorbed amount with increasing salt concentration, increasing charge density of the substrate, and decreasing charge of the PEs. The SCF approach was also able to provide information concerning the distribution of loops, tails, and trains, to rationalize experimentally observed adsorbed amounts, and to reproduce the maxima in the adsorbed amount for weakly charged PEs.<sup>137,139</sup> Since the adsorbed PE layers are laterally heterogeneous, results obtained from SCF models that assume laterally homogeneous layers must be interpreted with caution. These models are probably most useful to describe the adsorption of weakly charged PEs, which probably form more homogeneous layers.

Computer simulations have also been used to investigate the adsorption of PEs.<sup>39–41</sup> The conformation of a single adsorbed PE chain was studied by considering screened Coulombic interactions only.<sup>39</sup> These authors have found that the adsorbed chain is strongly flattened at low salt concentrations, while it swells at higher salt levels. The simulated normal extensions of the adsorbed PE chain show very similar trends to the measured layer thickness shown in Fig. 5b. This finding strongly supports the view that the layer thickness is determined by the dimensions of individual adsorbed PE chains that are well separated at the surface, leading to a laterally heterogeneous layer. When interactions are governed by electrostatic forces only, this study also confirms that PEs do not adsorb at oppositely charged surfaces above a critical salt concentration.<sup>39,127</sup>

Adsorption of PEs to spherical particles in the presence of salt was recently studied with computer simulations and density functional theories.<sup>40</sup> This approach explains the experimentally observed large accumulation of opposite charge to the particle surface. However, these simulations also predict a maximum in the adsorbed amount at very low salt concentrations, which is at odds with the experiment. All Coulombic interactions were explicitly taken into account in another recent computer simulation study of PE adsorption, whereby effects of short-range hydrophobic attractions were also investigated.<sup>41</sup> This study confirms the view that adsorbed PEs are strongly flattened and that the adsorbed layer is laterally heterogeneous. Unfortunately, the latter study was carried out in the absence of salt, and these conditions are difficult to realize experimentally.



dc\_1931\_21

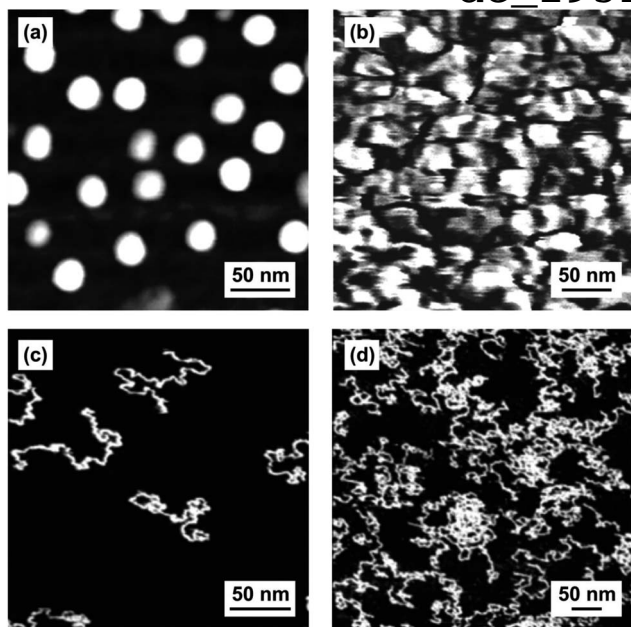


Fig. 6 AFM images of various PEs adsorbed on oppositely charged substrates recorded in air. Saturated layers formed with (a) dendritic PAMAM on mica in pH 4.0 solution without added salt and (b) PSS on amidine latex particles in 1 mM electrolyte solution.<sup>47</sup> Reprinted with permission from *J. Phys. Chem. B*, **113**, 8458. Copyright (2009) American Chemical Society. Unsaturated layers of PVP on mica with (c) small (d) and larger adsorbed amounts.<sup>132</sup> Reprinted with permission from *J. Phys. Chem. B*, **111**, 8597. Copyright (2007) American Chemical Society.

### 2.3 Charge balance in adsorbed polyelectrolyte layers

Let us now discuss the charge reversal phenomenon and the charge distribution within the adsorbed PE film.

**Charge reversal.** A most characteristic phenomenon in the adsorption of PEs to oppositely charged substrates is the charge reversal, which is also referred to as overcharging. An adsorbed saturated PE layer has practically always the opposite charge of that of the substrate.<sup>30,31,33,48,93,118,140–147</sup> Exceptions to this rule occur, but only for very weakly charged PEs.<sup>143,144,148</sup> The charge reversal may seem counterintuitive. One might suspect that the PE should be repelled from the substrate, when it attains the same charge as the PE. Since adsorbed PE layers are laterally heterogeneous, only the properties of the surface in the neighbourhood of the adsorption event are important. Therefore, provided an empty spot for adsorption exists, a PE molecule will adsorb. The saturation point of the adsorption is determined through the local environment of the adsorbing chain rather than the overall charge of the surface. Moreover, additional attractive interactions between the PE and the surface exist, for example, hydrophobic or van der Waals forces, and these forces are not influenced by the charge of the substrate.

The overall charge of adsorbed PE layers can be best addressed by electrokinetic techniques. Electrophoresis is the method of choice for colloidal particles, whereby the electrophoretic mobility can be converted into the surface potential ( $\zeta$ -potential) with appropriate models.<sup>30,48,140–142,148</sup> For planar substrates, streaming potential or streaming current techniques are being used.<sup>33,93</sup> In

many situations, this surface potential approximates the diffuse layer potential  $\psi_D$  well. When the surface potential is known, the surface charge density  $\sigma$  can be estimated with the Gouy-Chapman relationship<sup>54</sup>

$$\sigma = \frac{2k_B T \epsilon_0 \epsilon \kappa}{q} \sinh\left(\frac{q\psi_D}{2k_B T}\right) \quad (13)$$

where the symbols are defined in Section 2.2. Direct force measurements, which will be discussed in Section 3, can be also used to measure surface potentials of colloidal particles and substrates. However, the disadvantage of the latter technique is that in the normally used symmetric situation one can only determine the absolute value of the potential. The sign of the potential must be inferred independently.

The charge reversal upon PE adsorption is illustrated in Fig. 7a and b, where the surface potentials of bare amidine latex particles are compared to those with a saturated adsorbed PSS layer.<sup>131</sup> The data are consistent with the Gouy-Chapman eqn (13) with constant surface charge densities of  $+5.9 \text{ mC m}^{-2}$  for bare particles and  $-2.6 \text{ mC m}^{-2}$  for the coated ones. Besides the different signs, however, the particle coated with the PE behaves very similarly to a bare particle. This observation is not surprising given the fact that the adsorbed PE layer is very thin. The adsorbed PEs are indeed capable of reversing the positive charge of the bare particle and even accumulating substantial additional negative charge at the surface. A good agreement between surface potentials estimated from electrophoresis and direct force measurements is frequently found.<sup>48,107,131,147</sup> In some cases, however, these results disagree, probably due to surface charge heterogeneities.<sup>48</sup>

Fig. 8a illustrates the build-up of this negative charge upon addition of PSS in a suspension of positively charged latex particles.<sup>131</sup> At low PE doses, the particles are positively charged. At a particular dose, the surface charge is neutralized by the PE, and no diffuse layer forms. Upon further PE addition, the negative charge continues to accumulate, until one reaches the saturation point. Before that point is reached, the surface is unsaturated and no PE is dissolved in solution. For doses beyond the saturation point, the adsorbed amount remains constant and the excess PE dissolves in solution.

For unsaturated layers, no free PE is dissolved in solution. This fact can be confirmed in colloidal particle suspensions with electrophoresis experiments at different particle concentrations. Results of such experiments are illustrated in Fig. 8c with carboxylated latex particles and LPEI.<sup>149,150</sup> These particles are negatively charged and adsorbing LPEI leads to a pronounced charge reversal. The collapse of the plots of the electrophoretic mobility *versus* the PE dose for different particle concentrations confirms that the adsorption is quantitative. If this were not the case, there would be a shift of the corresponding curves due to partitioning between adsorbed and dissolved PEs.<sup>151</sup> Adsorbed PSS and PVA on oppositely charged latex particles were shown to behave analogously.<sup>31,140</sup>

The charge reversal of planar charged surfaces induced by adsorption of PEs can be also followed by streaming potential measurements.<sup>33,93,152</sup> These results are illustrated with the adsorption of poly(allyl amine) to mica in Fig. 8d.<sup>152</sup> Bare mica is

dc\_1931\_21

negatively charged. At high PE doses, the surface reverses its sign, and the saturation plateau is reached. To avoid the saturation of the surface, the PE solution was in contact with the surface for only 20 min. At lower polymer doses, the surface is unsaturated and passes through the charge reversal.

**Charge distribution within the adsorbed film.** The normal profiles of the charge density and of the electric potential are depicted in Fig. 7c and d. For a positively charged interface, they are shown in Fig. 7c and they are characterized by a localized layer of charged surface groups. This positive charge is compensated by an accumulation of anions and a depletion of cations in the diffuse layer. For a saturated adsorbed layer of an oppositely charged anionic PE shown in Fig. 7d, the positive charge of the surface is now overcompensated, resulting in a negatively charged surface. This negative charge is neutralized by a diffuse layer where cations are accumulated and anions are depleted.

The charge reversal phenomenon can be captured with a very simple model. One has to assume that the surface charge density of the substrate originates from two additive contributions<sup>107,153</sup>

$$\sigma = \sigma_0 + qZ_{\text{eff}}\Gamma \quad (14)$$

where  $\sigma_0$  is the surface charge density of the bare substrate and  $Z_{\text{eff}}$  is the effective charge of the adsorbed PE. The model predictions of the surface potential shown in Fig. 8b reflect the observed trends rather well. The validity of this linear superposition relationship was confirmed in some systems, but disagreement has been reported in others.<sup>30,33,93,152,153</sup>

Adamczyk and coworkers have proposed that this transition is more gradual, which would reflect a decrease of the effective charge with the surface coverage.<sup>33</sup> On the other hand, a sharper transition was observed for latex particles with adsorbed PSS and dendritic PAMAM.<sup>131,153</sup> In the two latter systems,  $Z_{\text{eff}}$  appears to be constant at first, then increases in magnitude near the charge neutralization point, and again remains constant after this point. Unfortunately, we currently lack a general picture concerning eventual variations of the effective charge of PEs upon changes in the adsorbed amount.

Let us now discuss to what extent the simplified picture shown in Fig. 7d actually reflects the actual charge distribution between the different adsorbed components.<sup>31,109,154</sup> At the charge reversal point, the interface is neutral, and thus the substrate, PE, and the adsorbed salt ions neutralize each other precisely. In some cases, the PE neutralizes the surface exactly, and one refers to stoichiometric adsorption. For other PEs, especially for highly branched ones or for weakly charged surfaces, the counterions of the PEs contribute substantially to the charge balance, and the adsorption is super-stoichiometric. In the case of adsorbed BPEI and PAMAM,<sup>31,155</sup> the counterions may be responsible for the neutralization of up to 90% of the charge originating from the adsorbed PE. In saturated layers, the situation is similar, since the overall surface charge that is neutralized by the diffuse layer is normally just a small fraction of the total charge carried by the adsorbed PE. Furthermore, the lateral heterogeneity will lead to lateral undulations of the

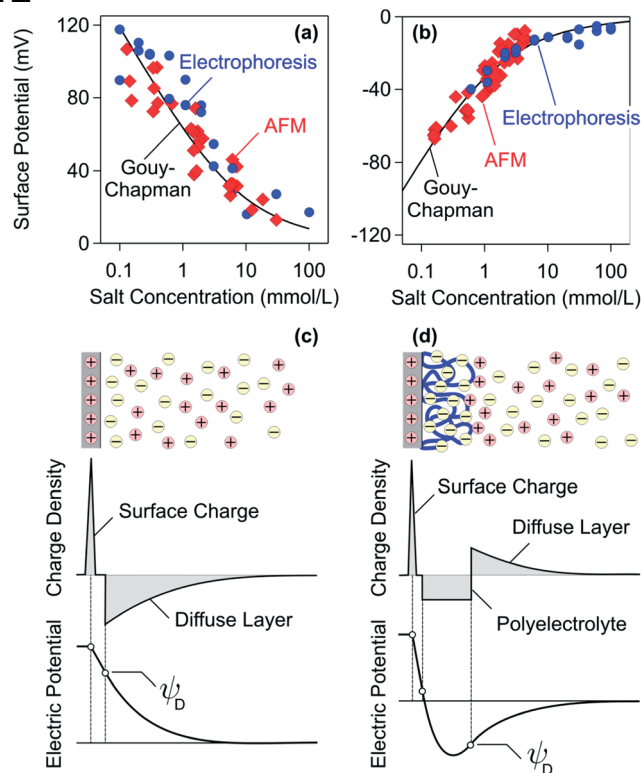


Fig. 7 Comparison of surface potentials for amidine latex particles determined by electrophoresis and direct force measurements by AFM. The solid line is the best fit with the Gouy–Chapman equation. (a) Bare particles and (b) coated with a saturated layer of PSS.<sup>153</sup> Schematic representation of the charge density and the electric potential profiles where the diffuse layer potential  $\psi_D$  is indicated. (c) Bare charged interface and (d) charged interface with an adsorbed PE of opposite charge.

diffuse layer. These effects might be responsible for the observed variations of the effective charge with the adsorbed amount of the PE.<sup>153</sup>

A fixed charge stoichiometry of the adsorption process can often be used to rationalize shifts of the charge reversal point. This principle explains why a higher dose of a more weakly charged PE is needed to neutralize the charge of a given surface.<sup>31,50</sup> This trend is also reflected in Fig. 8b. Similarly, a lesser amount of a given PE is needed to neutralize a surface of a smaller surface charge.<sup>150</sup> Dependencies on the solution pH involving weak PEs can be understood similarly. The charge of a weak cationic PE increases with decreasing pH. For a surface with a fixed charge density, the charge reversal point thus shifts towards a higher pH with an increasing amount of adsorbed PE.<sup>143</sup> The same trend is observed for a negatively charged surface with weak acid or amphoteric groups (e.g., silica) in the presence of strong cationic PEs.<sup>110,120</sup> Reverse trends are observed for weak anionic PEs adsorbed on a cationic surface of fixed charge density or for strong anionic PEs adsorbed on a positively charged surface with weak bases or amphoteric groups.<sup>144,148</sup> More complex phenomena are observed when the charges of the PE and of the surfaces are both pH dependent.<sup>4,120,156</sup>

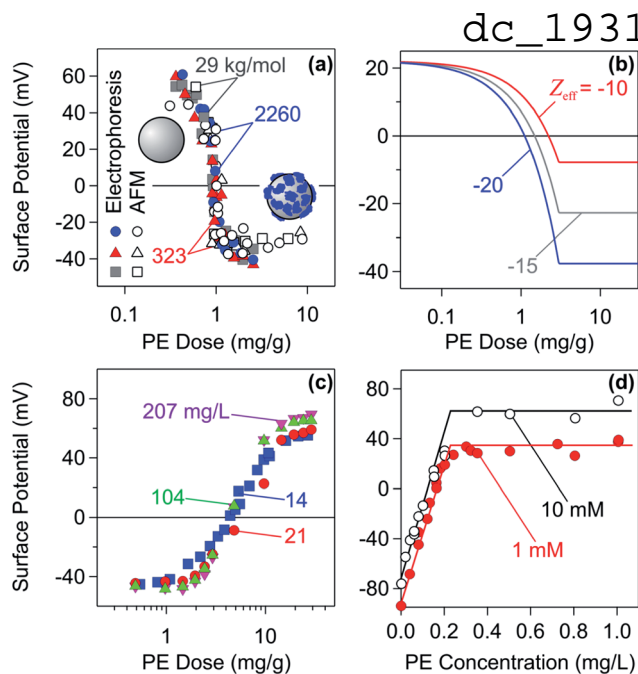


Fig. 8 Charge reversal by adsorbed PEs to oppositely charged substrates in the unsaturated regime as illustrated by surface potential measurements. (a) Amidine latex particles in the presence of PSS of different molecular masses of the sodium salt by electrophoresis and direct force measurements.<sup>47</sup> (b) Calculation of the charge reversal with linear superposition relationship. (c) Electrophoresis measurements of carboxylated latex particles in the presence of LPEI at different particle concentrations.<sup>149,150</sup> (d) Streaming potential measurements of mica in contact with poly(allyl amine) solutions at different electrolyte concentrations indicated for 20 min.<sup>152</sup> Reprinted from *J. Colloid Interface Sci.*, 303, Z. Adamczyk, A. Zembala and A. Michna, PE adsorption layers studied by streaming potential and particle deposition, 353, Copyright (2006), with permission from Elsevier.

The shift of the charge neutralization point for dendritic PAMAM with the molecular mass can be rationalized in a similar way.<sup>155</sup> Due to the compact architecture of these PEs, an increasing number of charged groups will be neutralized by their counterions the higher their molecular mass. Therefore, the effective charge increases more slowly than the molecular mass, thus the charge neutralization point shifts toward higher PE doses. However, this effect is absent for linear PEs. They adsorb in a much flatter configuration, and therefore the charge stoichiometry is independent of the molecular mass.

### 3 Forces induced by polyelectrolytes

In this section, we will discuss measured force profiles between charged surfaces or between particles with adsorbed polyelectrolytes (PEs) of opposite charge. An important observation will be that the classical DLVO theory describes forces in such systems reasonably well. Additional attractive non-DLVO forces have been identified and can be important under certain conditions, especially for PEs of high charge density and high molecular mass. These additional forces are largely of electrostatic origin and result from the laterally heterogeneous

patch-charge distribution within the adsorbed PE film. Additional attractive forces may occur due to bridging of PE chains or due to depletion at higher PE concentrations.

**DVLA forces.** The force  $F$  acting between two charged objects across an aqueous electrolyte solution is assumed to have two main contributions<sup>54,157</sup>

$$F = F_{vdw} + F_{dl} \quad (15)$$

namely, the attractive van der Waals force  $F_{vdw}$  and the repulsive electric double layer force  $F_{dl}$ . The van der Waals force originates from dispersive interactions between permanent and fluctuating dipoles of the constituent molecules. For a pair of particles of radius  $R$  this force can be approximated as

$$F_{vdw} = -\frac{RH}{12h^2} \quad (16)$$

whereby the Hamaker constant  $H$  characterizes its strength. This expression is valid when the surface separation  $h$  is small with respect to the particle radius  $R$ . This assumption is applicable when retardation effects are negligible and when the Derjaguin approximation is invoked. The double layer force can be viewed to originate from the osmotic pressure resulting from the overlap of the diffuse part of the double layers. Within the Derjaguin approximation, the force acting between two identical particles can be expressed at larger distances as

$$F_{dl} = 2\pi R\epsilon_0\epsilon\kappa\psi_{eff}^2 e^{-\kappa h} \quad (17)$$

where  $\psi_{eff}$  is the effective electric potential. For a weakly charged surface, this quantity is equal to the surface potential. For a highly charged surface, the Poisson–Boltzmann theory suggests that it converges to a constant value given by  $\psi_{eff} = 4k_B T/q$ .<sup>158</sup> This relationship is analogous to the previously mentioned relationship between the effective charge  $Z_{eff}$  and bare charge  $Z$ . The expression for the double layer force invokes the superposition approximation, which stipulates that the diffuse layer does not deform upon approach. At shorter distances, charge regulation or non-linearities may become important, but in many cases eqn (17) remains a good approximation. More accurate treatment on the mean-field Poisson–Boltzmann level normally relies on numerical solutions of the corresponding differential equation.

#### 3.1 Bare surfaces and surfaces with saturated PE layers

As discussed in Section 2.1, saturated layers form when the adsorbing PE is added in sufficiently large quantities. Such layers are normally thin and highly charged. Therefore, forces between these layers mainly originate from double layer interactions. In the following, we will discuss forces between bare surfaces first, and then between surfaces coated with saturated PE layers.

**Bare surfaces.** Fig. 9a shows typical force profiles between negatively charged sulfate latex particles measured with the colloidal probe technique at low salt concentrations.<sup>48</sup> The double layer interaction follows an exponential force law. The



dc\_1931\_21

range of this force corresponds to the thickness of the diffuse layer, which is given by the Debye length,  $\kappa^{-1}$ . This length decreases with increasing salt levels, as predicted by eqn (11). The intercept reflects the strength of the interaction and is related to the surface potential. The experimentally measured forces are perfectly consistent with DLVO theory, which is represented by the solid lines in Fig. 9. Similar double layer forces have been observed between other types of charged particles, such as positively charged latex, silica, or other materials.<sup>131,159,160</sup> Electrostatic potentials determined from the force profiles typically agree well with  $\zeta$ -potentials obtained from electrophoresis, especially for weakly charged surfaces, while for highly charged particles the magnitude of the observed  $\zeta$ -potentials tends to be higher.<sup>48,131,161</sup>

The forces become attractive at shorter distances, but this attraction cannot be well resolved due to the inherent mechanical jump-in instability.<sup>162</sup> During this instability, deviations from DLVO theory are mainly caused by hydrodynamic drag. This drag creates additional repulsive forces, which mask the attractive forces at short distances. The force measurements shown were carried out at relatively low salt levels, where double layer forces dominate. Similar force measurements at higher salt levels or for weakly charged particles have been reported more recently, and they reveal the expected attractive van der Waals forces.<sup>163</sup> These results confirm that the DLVO theory also correctly describes the transition between attractive and repulsive forces in such systems.

Similar force measurements between charged solid interfaces across aqueous solutions of monovalent electrolytes have been carried out with the SFA and the colloidal probe in the sphere–plate geometry.<sup>161,164–166</sup> In the latter case, the symmetry of the system remains difficult to ascertain. Nevertheless, these studies confirm that forces in such systems are consistent with the simple DLVO picture, at least down to distances of few nm.

**Surfaces coated with saturated PE layers.** When a charged substrate is incubated in a sufficiently concentrated solution of oppositely charged PEs, a saturated PE layer will form. This layer is thin and highly charged, and thus forces acting between such coated surfaces will be dominated by electrical double layer interactions. Fig. 9b illustrates this situation by reporting force profiles between sulfate latex particles coated with a saturated layer of cationic LPEI.<sup>48</sup> The forces resemble the ones acting between the corresponding bare charged surfaces shown in Fig. 9a. At low salt levels, these profiles are again strongly repulsive and can be well described by DLVO theory. Thereby, a Hamaker constant of  $4.0 \times 10^{-21}$  J has been used to model interactions between latex particles across aqueous electrolyte solutions and the same value will be used subsequently. The only difference is that the bare surfaces are negatively charged, while the coated ones are positively charged. Since the square of the surface potential enters eqn (17), these forces do not depend on the sign of the surface potential. The fact that interaction forces between bare particles and between PE-coated particles are similar is not surprising given the fact that PEs adsorb in a thin layer. PE-coated surfaces simply behave as any other charged interface. For surfaces coated with PEs, force and electrophoresis measurements typically yield very similar

electric surface potentials.<sup>48,131</sup> The congruence between these two techniques is also illustrated in Fig. 8a.

Numerous other studies confirm that interactions between surfaces coated with saturated PE films are governed by repulsive double layer forces. Such a behaviour was observed for positively charged amidine particles coated with the anionic PSS<sup>131</sup> and for negatively charged sulfate latex particles in the presence of cationic LPEI and dendritic PAMAM.<sup>48,107</sup> Double layer forces were observed between silica, mica, or functionalized surfaces in the presence of various oppositely charged PEs.<sup>72,109,167–175</sup> The strength of double layer forces could also be varied through solution pH.<sup>72,147,176</sup> This dependence originates from the resulting variation of the dissociation degree of the PE. In some cases, deviations from DLVO theory have been reported at short distances, and they were either attributed to steric repulsion<sup>168,169,177,178</sup> or to patch–charge attraction.<sup>48,107,131</sup> However, these contributions are rather weak and one can conclude that double layer forces dominate the interactions between charged substrates with saturated PE layers of opposite charge.

Bridging polymer chains are known to induce additional attractive forces, and this mechanism was suggested to be important for PEs as well.<sup>43,179,180</sup> Such bridging processes can be probed directly with the AFM, and this approach is referred to as single molecule force spectroscopy.<sup>109,181–183</sup> The principle is illustrated in Fig. 10. The force profiles are normally measured through a repeated approach and retraction cycles of the probe with respect to the surface, and the surfaces remain in contact for short periods of time. When the surfaces are in proximity, some of the PE chains adsorbed to one of the surfaces may adsorb to the other surface and thereby bridge both surfaces. The existence of such bridging PE chains is easily detected during the retraction of the probe, since these chains are being stretched and detached from the surfaces. These processes lead to characteristic spikes or plateaus in the retraction force curves.

Bridging events were investigated in detail for saturated layers of adsorbed PVA on silica by force measurements with AFM.<sup>109,182</sup> Representative examples are shown in Fig. 10. When the PE chain is anchored strongly to both surfaces, the chain is

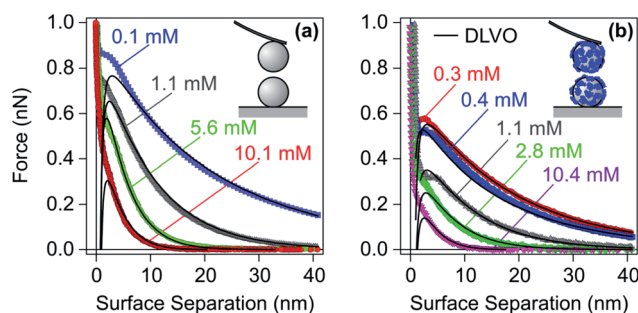


Fig. 9 Experimental force profiles for sulfate latex particles in monovalent electrolyte solutions adjusted to pH 4.0 compared with their best fits by DLVO theory. (a) Bare negatively charged particles and (b) the same particles at a LPEI dose of  $1.1 \text{ mg g}^{-1}$ , which results in a saturated adsorbed PE layer of positive charge.<sup>48</sup>



dc\_1931\_21

stretched, which leads to a characteristic spike. This situation is referred to as pulling and is shown in Fig. 10a. When the anchoring to one of the surfaces is weaker, the chain will detach continuously, which will lead to a plateau in the force curve. Here we refer to peeling, which is shown in Fig. 10b. More complex events equally occur and they are illustrated in Fig. 10c and d. Similar experiments were equally used to obtain information about the loop distribution of the adsorbed PEs.<sup>184</sup>

While such bridging processes are rare at low salt levels, they become rather frequent at higher salt concentrations and for weakly charged PEs.<sup>109</sup> Similar observations could be made for saturated BPEI films.<sup>169</sup> This trend can be rationalized since the adsorbed layers were thin under low salt conditions, and the PE chains are strongly bound to the substrate by attractive electrostatic forces. As the salt level increases, these attractive forces are screened, thus allowing PE chains to explore the regions further away from the surface. In this case, bridging becomes more frequent. Under these conditions, however, the forces are often completely attractive, and the presence of additional attractive bridging forces may not modify the picture substantially.

### 3.2 Surfaces coated with unsaturated layers

At lower PE doses, one obtains unsaturated layers, which feature lower adsorbed amounts than the saturated ones. As discussed in Section 2.2, adsorbed unsaturated layers are often laterally heterogeneous, but they can also be more homogeneous in some situations. Nevertheless, the principal contributions to the force can be again understood within DLVO theory. Let us first discuss the forces in the simpler case of laterally homogeneous layers, and later address the more complex situation of heterogeneously adsorbed layers.

**Homogeneous polyelectrolyte layers.** Fig. 11 shows the interaction forces between negatively charged sulfate latex particles at pH 4.0 for different doses of cationic LPEI.<sup>48</sup> Solid lines are best fits with DLVO theory. When no PE is added, the forces are dominated by double layer repulsion. As the PE dose increases, the surface charge is progressively neutralized, and the repulsive forces weaken. The charge reversal point is located near a dose of  $0.28 \text{ mg g}^{-1}$  ( $0.15 \text{ mg m}^{-2}$ ), where one observes attractive van der Waals forces only. As the dose is increased further, a positive charge builds up, and the forces become repulsive again. At doses above  $1.0 \text{ mg g}^{-1}$  ( $0.55 \text{ mg m}^{-2}$ ), the surface becomes saturated and the repulsive forces do no longer increase. The effect of an adsorbing PE results from the modification of the surface charge, and the forces can be well described by DLVO theory across the entire range of the PE dose. As shown in Fig. 11, theoretical DLVO predictions follow the experimental data accurately. Since DLVO theory is applicable, we suspect that the adsorbed LPEI layers are rather homogeneous. These layers are likely to be homogeneous on length scales exceeding the Debye length, which is about 10 nm in this case. In the repulsive force profiles, the short-range attractive part cannot be well resolved due to the jump-in instability.

Heterogeneously charged layers would show additional attractive non-DLVO forces.

Force measurements for unsaturated PE layers near the charge neutralization point are difficult to perform, and therefore only few such reports are available.<sup>48,107,131,176,185</sup> The main obstacle is that charge neutralization can be only achieved in a narrow range of PE doses, and this condition is difficult to realize for the small surface areas available in the currently used force measurement protocols. From this point of view, the SFA or its variants are more advantageous, since the surface area is few  $\text{cm}^2$ . The surface area of a single particle used in the colloidal probe experiment is only few  $\mu\text{m}^2$ , whereby the necessary PE doses are minute and they cannot be properly controlled. The recently described multi-particle colloidal probe technique circumvents this problem by depositing a larger number of particles to a substrate.<sup>48,107,131</sup> In this fashion, one may again reach surface areas of several  $\text{cm}^2$ , for which the necessary dose is simpler to control. Another possibility is to work with low PE concentration and to monitor the force profiles with time.<sup>185</sup> In such an experiment, the system initially passes through the charge neutralization point, while the saturated layer forms later.

Another possibility is to prepare a saturated layer with a weak PE and to neutralize the charge by adjusting the solution pH. With this technique, adsorbed PVP layers were shown to interact by pure van der Waals interactions at their charge neutralization point.<sup>176</sup> This finding suggests that these PVP films are also laterally homogeneous, similar to the ones formed with LPEI.<sup>48</sup> One may hypothesise that partially protonated LPEI and PVP form homogeneous adsorbed layers due to lowering of the PE charge by deprotonation and the presence of additional hydrophobic interactions.

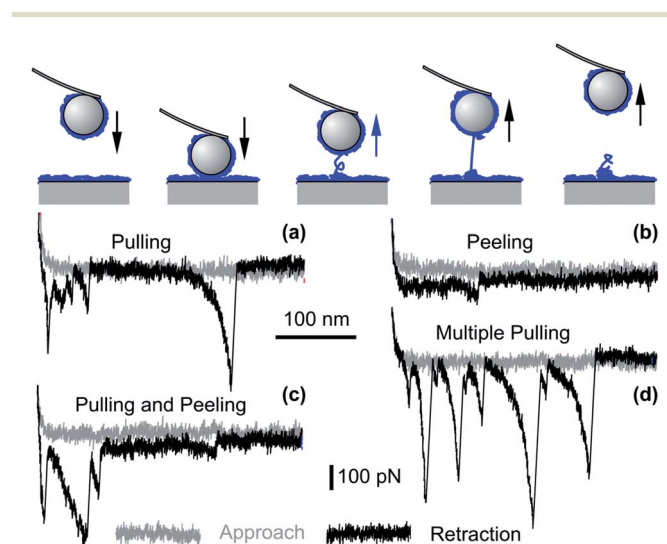


Fig. 10 Bridging events as probed by colloidal probe AFM force measurements for saturated PVA layers of molecular mass of  $520 \text{ kg mol}^{-1}$  adsorbed to silica in 100 mM electrolyte solution of pH 4.0. Single molecule (a) pulling and (b) peeling events. More complex events involving several molecules may show (c) a combination of pulling and peeling events and (d) multiple pulling events.<sup>109</sup>

dc\_1931\_21

**Heterogeneous polyelectrolyte layers.** Most experiments conducted on adsorbed PE layers indicate that forces involve additional attractive interactions. We suspect that such an attraction principally originates from the lateral heterogeneity of the adsorbed PE layers and the resulting patchy charge distributions. In this case, the interaction force can be approximated as<sup>186,187</sup>

$$F = F_{\text{vdW}} + F_{\text{dl}} + F_{\text{pc}} \quad (18)$$

Besides the two first terms, which correspond to the DLVO contribution, the additional term  $F_{\text{pc}}$  reflects the attractive non-DLVO force due to patch-charge attraction.

Fig. 12 shows interaction forces between amidine latex particles neutralized with PSS at a dose of  $1.0 \text{ mg g}^{-1}$  ( $0.58 \text{ mg m}^{-2}$ ).<sup>131</sup> One observes that the attractive forces are substantially stronger than the van der Waals force expected from DLVO theory, especially for high molecular mass and at low salt levels. Experimental force profiles can be well fitted when this additional non-DLVO force is assumed to be exponential

$$F_{\text{pc}} = -Ae^{-qh} \quad (19)$$

This exponential dependence was also found theoretically by analysing interactions between surfaces with a periodic charge distribution.<sup>186,187</sup> This analysis indeed yields an additional attractive interaction. This attraction results from the preferential orientation of the positively charged patches such that they face the negatively charged ones. Such patch-charge attractive forces are the strongest when the surface charge heterogeneities form a regular lattice, but these forces are also expected to be operational when the patches are arranged in a liquid-like fashion. The theoretical analysis relates the decay length  $q^{-1}$  of this interaction to the Debye length by the simple expression<sup>186</sup>

$$q^2 = \kappa^2 + \left(\frac{2\pi}{b}\right)^2 \quad (20)$$

where  $b$  is the lattice spacing. At low salt levels, the range of this force is governed by the lattice spacing, while at higher salt

levels, the force is screened as a regular double layer force. The data shown in Fig. 12a can be described by  $b = 15 \text{ nm}$ . This number agrees roughly with the size of the structures revealed by AFM imaging shown in Fig. 6b. With increasing salt concentrations, the patch-charge attraction is screened and at higher salt levels the forces are again described by DLVO theory. In that case, a Hamaker constant of  $9.0 \times 10^{-21} \text{ J}$  was used but the plane of origin was shifted to account for effects of roughness. Fig. 12b illustrates that the size of the surface heterogeneities also plays an important role. Their size decreases with decreasing molecular mass, and the additional non-DLVO force disappears.

Very similar results were obtained by direct force measurements between negatively charged sulfate latex particles in the presence of dendritic PAMAM.<sup>107,188</sup> Near the charge neutralization point, forces are attractive, and they are again much stronger than the van der Waals force, especially for high molecular mass and low salt levels. The additional attraction can be again rationalized with the exponential relationship given in eqn (19). The measured corresponding lattice spacing of this particular system is about  $b = 16 \text{ nm}$ , but this value is substantially smaller than the nearest neighbour spacing of the dendrimers at the surface, which is about  $50 \text{ nm}$ . This discrepancy probably originates from the assumption of a square lattice inherent to the patch-charge model, while the actual surface structure is irregular.

Additional attractive forces near the charge neutralization point were reported in other systems with the SFA or related techniques.<sup>185</sup> By exploiting the kinetics of the adsorption process, attractive forces near this point could be observed for PVA films at low salt levels.<sup>185</sup> These forces were equally reported to be exponential and substantially more attractive than the van der Waals forces. We suspect that these forces also originate from patch-charge attraction. Similar non-DLVO attractive forces were reported between layers of adsorbed poly((3-methacrylamido)-propyl)trimethylammonium chloride on mica.<sup>42</sup>

Polymer bridging might also lead to additional attractive forces. As discussed above, bridging events can be detected with the AFM in the retraction part of the force curves, as shown in Fig. 10. The occurrence of such bridging events was analyzed near the charge neutralization point for the LPEI and PSS systems.<sup>47,48</sup> While such events could be observed, they occurred at low salt concentrations very rarely. Moreover, forces observed in the PSS and PAMAM systems are similar, in spite of the fact that the PE architectures are very different. If bridging would be important, one expects substantial differences between the forces in these two systems.

At higher salt levels, where bridging forces are expected to be operational, the DLVO theory also predicts attractive forces. Therefore, additional attractive bridging forces may not alter the scenario much. At intermediate salt levels, however, where the strength of double layer forces and van der Waals forces are comparable, additional bridging forces may influence the picture considerably. Similarly, when the charge of the PEs is low, bridging forces might become important in analogy to neutral polymers.<sup>189</sup> This suggestion is supported by more frequent occurrences of single molecule bridging events

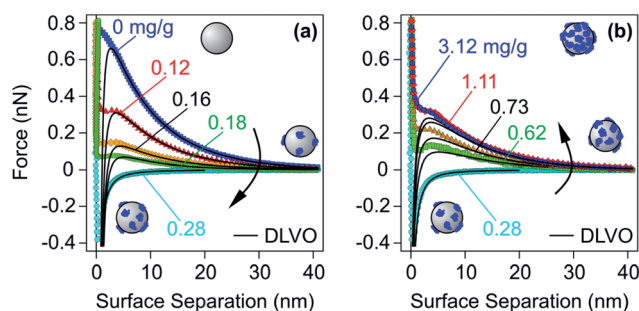


Fig. 11 Experimental force profiles for sulfate latex particles for different doses of LPEI at an ionic strength of  $1.1 \text{ mM}$  adjusted with a monovalent salt at  $\text{pH } 4.0$  compared with their best fits by DLVO theory.<sup>48</sup> PE doses (a) below and at the charge reversal point and (b) at the charge reversal point and above.

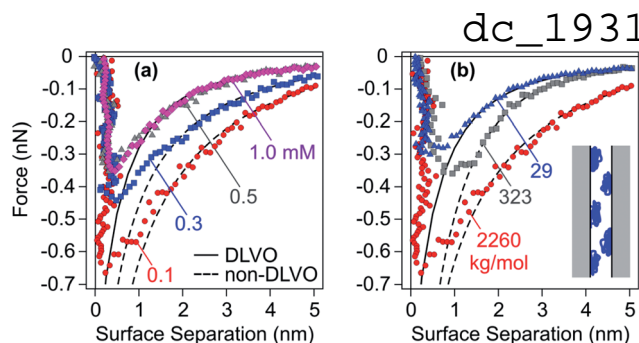


Fig. 12 Attractive force profiles for amidine latex particles neutralized with adsorbed PSS in monovalent salt solutions at pH 4.0 together with best fits by DLVO theory (solid lines) and additional patch-charge attraction (dashed lines).<sup>47</sup> The force curves might be inaccurate close to contact due to eventual jump-in instability. (a) Molecular mass of 2260 kg mol<sup>-1</sup> at different ionic strengths and (b) different molecular masses at an ionic strength of 0.1 mM. The scheme illustrates the patch-charge attraction mechanism.

observed with the AFM under these conditions.<sup>178,190</sup> However, the precise conditions where bridging forces become important remain unclear to us.

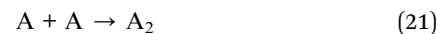
Interactions between surfaces in the presence of PEs were investigated theoretically in detail by density functional theories and computer simulations.<sup>191,192</sup> Density functional theories suggest that interactions can be indeed described by DLVO theory at larger distances. Computer simulations were used to model forces between surfaces by approximating the PEs as charged spheres that interact by means of screened Coulombic interactions. These simulations confirmed the importance of DLVO forces, but also suggested additional short-range interactions originating from ordered arrangements of the PEs at the surface.<sup>188</sup> A similar study with flexible PE chains, which included all Coulombic interactions explicitly, found similar additional attractive forces, but the range of the forces did strongly depend on the chain flexibility.<sup>193</sup> Attractive forces close to charge neutralization and repulsive forces away from this point were also reported.<sup>194</sup> These studies demonstrate the importance of additional attractive forces. Other computer simulation studies suggest that bridging forces might also be important.<sup>195–198</sup> However, these studies refer to bridging even when PEs are not adsorbed at both surfaces and these simulations are carried out under equilibrium conditions. The irreversible nature of the adsorption process and the resulting slow dynamics of the adsorbed chains may modify the nature of the bridging contributions substantially. On the other hand, the adsorbed PE chains may maintain some lateral mobility and equilibrate laterally to some extent.

**Depletion forces.** At higher PE concentrations, typically above few g L<sup>-1</sup>, and for non-adsorbing or weakly charged polymers, depletion forces become important.<sup>44,45,196,199–204</sup> Such forces result from the mismatch in the osmotic pressure within the gap between two approaching particles and the bulk solution. When the gap is small compared to the size of the PE coil, the PE concentration in the gap is smaller, leading to an attractive force between the particles. At higher PE

concentration, these forces may become oscillatory, as they reflect the structuring of the PE bulk solution. Depletion forces are well documented in PE solutions involving non-adsorbing surfaces.<sup>44,200–202</sup> As expected, depletion forces increase in strength with decreasing salt levels and increasing molecular mass of the PE. Depletion forces acting between surfaces saturated with oppositely charged PEs were reported as well.<sup>45,203</sup> These forces were suggested to set in already at moderate PE concentrations, and no oscillatory forces were observed in this case. The latter effect might be related to the presence of lateral surface heterogeneities of the adsorbed PE layers and may reflect similar modifications of depletion forces as induced by substrate roughness in particle suspensions.<sup>205</sup>

## 4 Particle aggregation induced by polyelectrolytes

Aggregation of colloidal particles is governed by the interaction forces acting between the particles. Simplistically, attractive forces lead to rapid particle aggregation, while this process is slowed down by repulsive forces. The elementary step of the aggregation process can be viewed as a chemical reaction



whereby a particle dimer is being formed from two monomeric particles. The formation rate of the dimers is given by<sup>54,206,207</sup>

$$\frac{dN_2}{dt} = \frac{k}{2} N_1^2 \quad (22)$$

where  $N_1$  and  $N_2$  are the number concentrations of the monomers and dimers, respectively, and  $k$  is the aggregation rate coefficient. The aggregation process does not stop with the formation of dimers, but continues through higher order aggregates.<sup>54,206,207</sup> These aggregates have an irregular, ramified structure and can be characterized as mass fractals. These aggregates may interlink such that finally only one large aggregate spans the entire container. In that case, one refers to the formation of a colloidal gel.<sup>208–210</sup>

**Aggregation rates from DLVO theory.** The key contribution of DLVO theory was to derive the aggregation rate coefficient in terms of the interaction potential between colloidal particles. From the steady-state solution of the forced diffusion equation one finds that the rate coefficient is given by<sup>52–54,206</sup>

$$k = \frac{4k_B T}{3\eta R} \left[ \int_0^\infty \frac{\beta(h/R)}{(2R+h)^2} \exp[V(h)/(k_B T)] dh \right]^{-1} \quad (23)$$

where  $\eta$  is the viscosity of the solution,  $V(h)$  is the interaction potential energy, and  $\beta(x)$  is the hydrodynamic resistance function at  $x = h/R$ . The interaction potential can be obtained by integrating the force profile

$$V(h) = \int_h^\infty F(h') dh' \quad (24)$$

while the resistance function can be approximated as<sup>206,211</sup>

dc\_1931\_21

$$\beta(x) = \frac{6x^2 + 13x + 2}{6x^2 + 4x} \quad (25)$$

DLVO theory predicts two regimes for the aggregation processes.<sup>54,206</sup> The first regime, referred to as the fast or diffusion controlled aggregation, typically occurs for high salt concentrations or small surface charge densities. In this situation, the aggregation rate coefficient is approximately given by the Smoluchowski value for hard spheres<sup>54,206</sup>

$$k = \frac{8k_B T}{3\eta} \approx 1.2 \times 10^{-17} \text{ m}^3 \text{ s}^{-1} \quad (26)$$

where the numerical value refers to water at room temperature. This expression can be obtained from eqn (23) by setting the exponential factor and the resistance function to unity. Experimentally observed aggregation rates in the fast regime are normally comparable to the Smoluchowski value, but they are often somewhat smaller.<sup>211–215</sup>

The second regime, referred to as the slow or reaction controlled aggregation, occurs at lower salt concentrations and higher surface charge densities. In this case, the interaction potential develops a barrier, which leads to a small aggregation rate coefficient. The relatively sharp transition between these two regimes is referred to as the critical coagulation concentration (CCC). This transition has been observed in numerous systems, for example, as a function of the salt concentration,<sup>215,216</sup> or when the surface charge density was varied by adjusting the solution pH.<sup>212–214</sup> The DLVO theory is capable of describing the aggregation rates accurately provided that the surface charge density is not too high.<sup>212</sup> At higher surface charge densities, important deviations may occur.

The aggregation rate coefficients are normally reported as the stability ratio defined as<sup>54,212</sup>

$$W = \frac{k_{\text{fast}}}{k} \quad (27)$$

where  $k_{\text{fast}}$  is the aggregation rate coefficient in the fast regime of a reference system, typically at high electrolyte concentrations, and  $k$  is the rate coefficient under the conditions in question. Therefore, the stability ratio is close to unity in the fast aggregation regime, and it increases as the aggregation slows down.

#### 4.1 Bare particles and particles with saturated PE layers

Aggregation rate coefficients of colloidal particles can be accurately measured with time-resolved light scattering, turbidity, or single particle counting.<sup>207,217,218</sup> In many situations, the trends observed can be well rationalized by DLVO theory. In the following, we will discuss aggregation rates in suspensions of bare particles first and then in suspensions with particles coated with saturated PE layers.

**Bare particles.** Aggregation rate coefficients of bare colloidal particles were reported in numerous studies.<sup>207,212–214,216,219–222</sup> The characteristic dependence of the stability ratio for charged sulfate and amidine latex particles on the concentration of monovalent salt is shown in Fig. 13a. The solid line represents the stability ratio calculated with DLVO theory whereby the

electrical surface potentials were estimated by electrophoresis. Experimental and calculated stability ratios show the regimes of slow and fast aggregation, and they feature a similar dependence on the salt concentration. In the fast aggregation regime that is encountered at high salt concentrations, the stability ratio is close to unity and constant. In the slow aggregation regime, the stability ratio increases rapidly with decreasing electrolyte concentration. The CCC is located at the transition between these two regimes and lies near 0.2–0.3 M, which is typical for highly charged particles in a monovalent salt solution.

A common difficulty with DLVO theory is that it predicts a substantially stronger dependence of the stability ratio on the salt concentration than that observed experimentally. In this example, this discrepancy is apparent in the slow aggregation regime by the different slopes of experimental data and of the DLVO calculations. A similar behaviour and analogous discrepancies with theoretical predictions have been reported in other systems containing charged particles in the presence of monovalent salts.<sup>216,219–223</sup> The origin of this discrepancy is probably related to lateral patch-charge heterogeneities.<sup>214,220,223–225</sup> These patch-charge heterogeneities that are also likely present on the bare particles have a different origin than the ones discussed above, which originate from the lateral heterogeneity of the adsorbed PE films. The patch-charge heterogeneities of the bare particles may originate from the discreteness of the charged groups or an uneven distribution of these groups at the surface that result from the synthesis process. Their presence was also evidenced by differential electrophoresis techniques.<sup>226</sup> These heterogeneities will equally induce additional attractive forces. Such attractions are expected to be stronger between particles suspended in solution than those measured with the colloidal probe AFM. Suspended particles can rotate freely and they will eventually find a configuration of the patches on the two particles involved that lead to an approach pathway of the lowest free energy.

In the fast regime, DLVO theory predicts an absolute rate constant of  $7.1 \times 10^{-18} \text{ m}^3 \text{ s}^{-1}$ . The fact that this value is smaller than Smoluchowski's value given in eqn (26) originates from the interplay between van der Waals forces and hydrodynamic interactions. The experimentally measured aggregation rate coefficient is  $3.5 \times 10^{-18} \text{ m}^3 \text{ s}^{-1}$  for the sulfate latex particles and  $4.4 \times 10^{-18} \text{ m}^3 \text{ s}^{-1}$  for the amidine latex. These values are smaller than the ones predicted by DLVO theory, and the remaining discrepancies probably originate from inaccuracies of the hydrodynamic resistance function at small separations.

**Particles coated with saturated polyelectrolyte layers.** Trends concerning the stability of particles coated with a saturated polyelectrolyte (PE) film are very similar to bare particles, suggesting that the principal interactions are governed by DLVO forces too.<sup>141,142</sup> Fig. 13b shows data of negatively charged sulfate latex particles coated with cationic PDDA and of positively charged amidine latex particles coated with anionic PSS. They are compared with DLVO calculations whereby surface potentials were estimated from electrophoresis. The characteristic regimes of slow and fast aggregation can be identified as well. Again, the DLVO theory predicts a stronger dependence of



dc 1931 21

the stability ratio on the salt concentration in the slow regime. This dependence seems even weaker than for the bare particles, suggesting that the patch-charge heterogeneities are more pronounced for the saturated PE layers than for the bare particles. For the particles coated with PEs, the CCC is shifted to higher salt concentrations and the stability ratio exceeds unity in the fast regime. This small increase in the stability ratio is probably due to additional contributions from repulsive steric forces originating from overlapping PE layers. Such additional forces may also lead to higher CCCs, but the more likely origin of this shift is the high surface charge density of saturated PE layers.

The similarity between bare colloidal particles and particles coated with a saturated PE layer was observed for various other systems, including negatively charged sulfate latex particles in the presence of LPEI, positively charged amidine latex particles in the presence of PSS or PAA, and hematite particles with alginate.<sup>142,227</sup> A similar behaviour was also reported for latex particles with poly(methacrylic acid) grafted to their surface.<sup>228</sup> This similarity is further supported by direct force measurements, which indicates that interactions between surfaces coated with saturated PE layers are well described by DLVO theory as illustrated in Fig. 9b. These findings clearly demonstrate that forces acting between the charged surfaces and those coated with a saturated PE layer are similar and that they can be understood within DLVO theory. This similarity is due to the very thin and compact nature of the adsorbed PE films.

Particles with an adsorbed saturated PE layer often have higher CCCs.<sup>141,142</sup> Particles with grafted PEs on their surface have CCCs in monovalent salts even above 1 M.<sup>228,229</sup> Saturated adsorbed PE films typically feature high surface charge densities, which will cause the CCC to shift to high salt concentrations. However, the systems shown in Fig. 13b are characterized by stability ratios larger than unity in the fast aggregation regime, pointing to a more stable suspension than the one predicted theoretically, even at high ionic strengths. Stabilization at high salt levels was also observed in the presence of neutral polymers or for grafted PE brushes.<sup>221,228,229</sup> This effect is

sometimes referred to as electrosteric stabilization.<sup>199,221,228</sup> This additional stabilization cannot be rationalized within DLVO theory, but reflects additional repulsive steric forces. However, such effects are not very important in charged particle suspensions in the presence of oppositely charged PEs.<sup>141,142,230</sup>

#### 4.2 Aggregation involving unsaturated polyelectrolyte layers

Stability ratios pass through a characteristic minimum with increasing PE doses. Since unsaturated PE layers undergo a charge reversal with increasing the mass of adsorbed PE, this dependence can be rationalized by DLVO theory. Adsorbed unsaturated layers are often laterally heterogeneous, but sometimes they can be more homogeneous. Let us now discuss the aggregation rates of particles in suspension in such situations. We will first focus on the simpler case of homogeneous layers and discuss heterogeneous layers later.

**Homogeneous polyelectrolyte layers.** The characteristic dependence of the stability ratio on the PE dose and the influence of the added monovalent salt are illustrated in Fig. 14. The example shown refers to negatively charged sulfate latex particles in the presence of LPEI in an electrolyte solution at pH 4.0.<sup>150</sup> Under these conditions, the ionization degree of LPEI is about 65%.<sup>231</sup> At low salt concentrations, one observes the characteristic U-shaped stability plot. The suspension is stable at low PE doses. With increasing doses, the stability ratio decreases, until it reaches unity near the charge neutralization point. This point is located near  $0.8 \text{ mg g}^{-1}$  ( $0.04 \text{ mg m}^{-2}$ ). When the PE dose is increased further, the suspension is stabilized again. At higher salt concentrations, one observes plateaus in the stability ratio at both low and high PE doses. These plateau values diminish rapidly with increasing salt concentrations, and for high salt concentrations the fast aggregation regime is reached for any PE dose. The salt dependence of these plateaus is better reflected in the stability plots *versus* the salt concentration for the bare and PE-coated particles, while the onset of fast aggregation is defined by the corresponding CCCs. This situation was discussed above and is illustrated in Fig. 13.

Let us compare these results with predictions of DLVO theory, whereby the surface potentials were estimated from electrophoresis. At low salt concentrations, DLVO theory reproduces the experimental data well. The likely reason why DLVO theory works in this case is that the adsorbed LPEI film is laterally homogeneous. Force measurements shown in Fig. 11 also suggest that the film is homogeneous on length scales of at least 10 nm. This number is in agreement with the present stability data, since DLVO predictions break down for salt concentrations near and above 10 mM. While the minimum is described reasonably well, the plateau at high LPEI doses is no longer located properly. While the DLVO theory is capable of predicting the overall shape of the stability curve at higher salt concentrations qualitatively, it fails to do so quantitatively. The predicted widths of the instability region and the values of the stability plateaus do not agree with experiments. At higher salt levels, the system is more stable than what is predicted by DLVO theory, possibly due to steric forces.

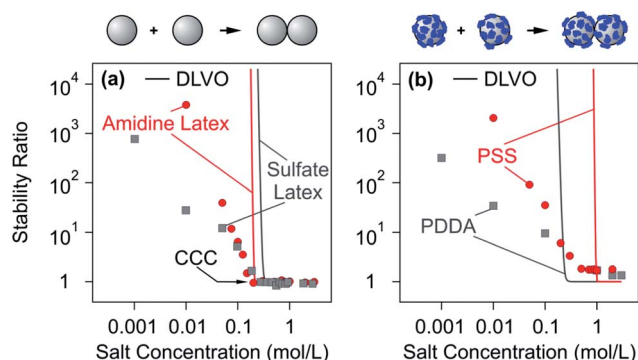


Fig. 13 Dependence of experimentally measured stability ratios of latex particles on monovalent salt concentration at pH 4.0 and comparison with DLVO theory. (a) Bare amidine latex and sulfate latex particles and (b) the same particles coated with a saturated layer of PSS and PDDA, respectively.<sup>140,142</sup> Schemes on the top illustrate the dimer formation without and in the presence of PEs.

dc\_1931\_21

Another experimental finding confirming the homogeneity of adsorbed LPEI layers is presented in Fig. 15a. This graph shows experimental stability data for different molecular masses.<sup>150</sup> No significant trend with the molecular mass can be established and a good agreement with DLVO theory is observed.

There are numerous other reports confirming that the aggregation near the charge reversal is rapid and that it slows down away from this point. They involve a wide range of PEs together with positively<sup>49,140,144,148,232</sup> and negatively charged particles.<sup>31,49,50,56,110,142,145,155</sup> However, the plateaus in the stability ratios at high and low PE dose are difficult to observe experimentally, and therefore they are often missing. Nevertheless, the existence of these plateaus has been clearly demonstrated in some systems.<sup>141,142,148,150</sup>

With increasing salt concentration, the fast aggregation regime widens and the dependence of the rate coefficient on the PE dose weakens in the slow regime. This salt dependence is generic and was reported for negatively charged latex and silica particles in the presence of cationic PEs<sup>31,49,110,142,155</sup> and for positively charged latex particles with PSS or PAA.<sup>140,148</sup>

**Heterogeneous polyelectrolyte layers.** Adsorbed PE films are often laterally heterogeneous, and in this situation the aggregation is faster due to the attractive patch-charge interactions.

Fig. 15b shows aggregation rates of sulfate latex particles in the presence of dendritic PAMAM of different molecular masses.<sup>155</sup> When the molecular mass is small, the dependence of the stability ratio on the PE dose is relatively well described by DLVO theory. For large molecular masses, however, the experimentally observed stability ratios are substantially smaller than the predicted ones. Attractive patch-charge interactions between heterogeneous surfaces are likely to be responsible for this reduction. When one approximates these interactions with eqn (19), the experimentally observed trend can be captured relatively well. The higher the molecular mass, the larger the size of the patches, and this increase leads to a larger range of attractive non-DLVO forces; see eqn (20). The stability measurements were carried out at a salt concentration of 1 mM, which corresponds to a Debye length of 10 nm. The nearest-neighbour distances between the dendrimers are below this value for the molecular mass of 3.3 kg mol<sup>-1</sup>, and thus the film should be considered homogeneous. The shift of the minimum in the stability plot shown in Fig. 15b reflects the shift in the charge neutralization point. This effect is discussed in Section 2.3 and is related to the compact architecture of dendritic PAMAM.

The role of patch-charge heterogeneities is typically manifested in the stability plots by widening of the fast regime and weaker dependence in the slow regime. These trends could also be well predicted by Monte Carlo simulations, where the dendritic PAMAM were modelled as charged hard spheres interacting with screened Coulomb potential.<sup>233</sup>

Similar dependencies on the molecular mass were observed for amidine latex particles in the presence of PSS or PAA,<sup>140,148</sup> for cationic PEs and sulfate latex,<sup>56</sup> or silica particles.<sup>234,235</sup> However, no dependence of the stability ratio on the molecular mass is observed for LPEI, as illustrated in Fig. 15a.<sup>150</sup> This

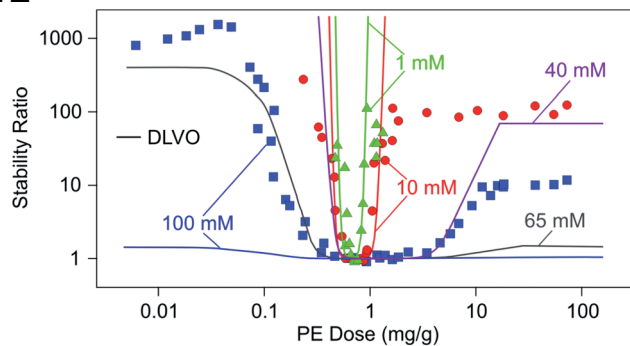


Fig. 14 Stability ratios of sulfate latex particles *versus* the dose of LPEI at different ionic strengths adjusted by a monovalent electrolyte and at pH 4. Solid lines are calculations with DLVO theory.<sup>150</sup> Note that only calculated curves are shown for 40 mM and 65 mM. These calculations illustrate that DLVO theory reproduces the overall dependence correctly, albeit not at the appropriate salt concentration.

observation reflects the homogeneity of the adsorbed film at length scales above 10 nm.

Another characteristic effect of patch-charge heterogeneities can be observed in the fast aggregation regime near the charge neutralization point. Fig. 16a shows stability ratios *versus* salt concentration at the charge neutralization point for dendritic PAMAM of different molecular masses. One observes that the stability ratio decreases with decreasing salt concentration and that this effect becomes increasingly pronounced with increasing molecular mass. This trend can be interpreted with the increasing strength of the patch-charge interactions. Calculations of the stability ratio by including the non-DLVO patch-charge contribution given in eqn (19) capture the salt dependence rather well. Therefore, we interpret this enhancement as originating from patch-charge attractions. Due to their electrostatic nature, these interactions are screened at higher salt concentrations. Since these patches increase in size with increasing molecular mass, this effect also becomes more important under these conditions. Fig. 16b illustrates that this enhancement in the stability ratio at the charge neutralization point can be also observed for different linear PEs. This trend was reported for sulfate latex particles neutralized with PVA, BPEI, or poly(aminoethyl methacrylate)<sup>49,56,143</sup> or amidine particles with PSS or PAA.<sup>140,148</sup> Adsorbed LPEI layers do not show this enhancement due to their lateral homogeneity.<sup>150</sup>

The question to what extent bridging forces are relevant in the aggregation process of charged particles involving oppositely charged PEs still remains open. The observed trends in the available experimental data are qualitatively consistent with DLVO theory and patch-charge attractions. While the effect of patch-charge attractions can be modelled with an exponential force profile, this treatment is approximate due to inherent lateral heterogeneity of the surface. At this point, no quantitative theory is capable of predicting aggregation rate constants from the respective surface charge distributions. Direct force measurements discussed in Section 3 confirm that bridging events are rare at low salt concentrations, and under these conditions bridging forces will be unimportant. At higher salt concentrations, however, bridging events can be frequently

dc\_1931\_21

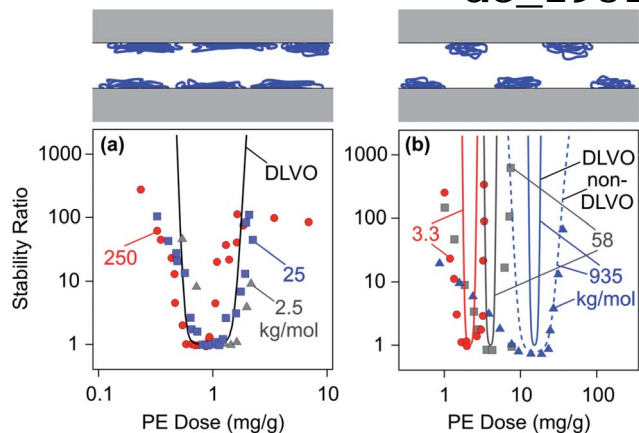


Fig. 15 Dependence of stability ratios of sulfate latex particles on the PE dose for different molecular masses in monovalent electrolyte solutions at pH 4.0 and comparison with DLVO theory. (a) LPEI in an electrolyte of 10 mM<sup>150</sup> and (b) dendritic PAMAM dendrimers at 1 mM.<sup>155</sup> The dashed line illustrates the effect of additional non-DLVO patch-charge attractions. The schemes on the top illustrate the homogeneous LPEI and heterogeneous PAMAM layers.

observed with the AFM, and therefore bridging forces could play a more important role. In this regime, however, the prevailing attractive interactions induce fast aggregation, and the corresponding rate depends only weakly on the strength of the attractive forces. In some systems, enhanced aggregation rates in the fast regime in the presence of alginate and multivalent cations were interpreted in terms of gelation, but they might also represent a signature of bridging.<sup>236,237</sup> However, analogous effects were not reported for other PEs so far.

**Depletion destabilization.** At higher polymer concentrations, typically around few g L<sup>-1</sup>, neutral polymers were shown to destabilize colloidal suspensions through depletion forces.<sup>208,238</sup> A similar destabilization could be achieved by PEs and nano-sized charged particles having the same charge as the particles.<sup>239–241</sup> The addition of neutral polymers to suspensions of charged particles does initially enhance the aggregation processes, but leads to phase separation and gelation at later times.<sup>208</sup> Similar phenomena are expected in charged colloidal suspensions in the presence of higher concentrations of oppositely charged PEs, but we are unaware of any systematic studies of the aggregation phenomena in such systems.

## 5 Outlook

Polyelectrolytes (PEs) adsorb irreversibly to oppositely charged substrates until saturation, which results in thin monolayers, which have the opposite charge than the substrate. Due to the irreversible nature of the adsorption process, the addition of PEs to colloidal suspensions at smaller doses leads to the formation of unsaturated layers, and thereby charge reversal can be induced.

The principal forces acting between saturated layers are repulsive due to double layer forces and the corresponding particle suspensions are stable. For unsaturated layers near the charge reversal point, the interaction forces are attractive and

the suspensions become unstable. Both phenomena are in agreement with DLVO theory, which can even describe interactions between homogeneous films quantitatively. For laterally heterogeneous films, attractive patch-charge interactions induce additional attractive forces leading to faster aggregation than predicted by DLVO theory.<sup>47</sup>

In spite of this reasonable level of understanding, we are still far away from being able to quantitatively predict interaction forces and colloidal stability solely from properties of the PEs and of the substrates. The charge reversal point for unsaturated layers can be estimated by assuming stoichiometric charge neutralization, even though numerous PEs adsorb in a superstoichiometric way due to counterion co-adsorption.<sup>31</sup> However, a proper way to address the extent of this co-adsorption process is currently unknown. Similarly, there are a number of uncertainties as to how to reliably estimate electric surface potentials of surfaces with adsorbed PEs.

Better characterization of the lateral surface structure of PE-coated surfaces and of the resulting surface charge heterogeneities represents an important need to progress further. At this point, we have little knowledge concerning the type of surface charge heterogeneities, the respective length scales, and when such layers might be considered as homogeneous. Most promising are AFM imaging techniques,<sup>134</sup> but obtaining high-resolution maps of surface potentials represents a challenge. Such maps can be interpreted in terms of radial distribution functions, as recently carried out with computer simulation results,<sup>41</sup> but corresponding experimental results are only available for dendritic PAMAM.<sup>34,133</sup> We further lack reliable models to estimate the interaction forces involving heterogeneously charged surfaces. In particular, such models must go beyond the current simplistic regular lattice arrangements,<sup>186,242</sup> and the question of random, liquid-like structures must be addressed.

The relevance of forces that are well established for neutral polymers, such as steric repulsion, bridging attraction, and depletion interactions, should be revisited for PEs in more detail. Based on the above discussion, bridging forces appear irrelevant at low salt levels and for highly charged PEs. With

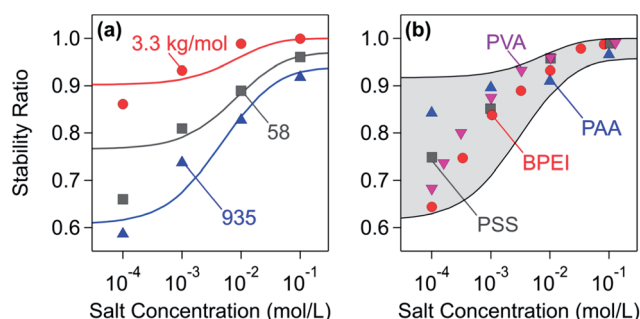


Fig. 16 The dependence of the stability ratios on the salt concentration at the charge neutralization point. Solid lines are calculations including non-DLVO contributions from patch-charge interactions. (a) Sulfate latex particles at pH 4.0 in the presence of dendritic PAMAM<sup>155</sup> and (b) amidine particles in the presence of linear PSS and PAA and sulfate latex in the presence of BPEI and PVA.<sup>49,140,143,148</sup>

dc\_1931\_21

increasing salt levels and decreasing charge densities, the PEs start to resemble neutral polymers, and thus steric and bridging forces will start to play a more important role.<sup>109,178</sup> However, it is unclear to us under what conditions this transition happens and what the respective mechanisms are.

On the other hand, depletion interactions have been established to play an important role at elevated PE concentrations. While depletion forces induced by non-adsorbing PEs have been studied in detail,<sup>44,201</sup> we have little information concerning such forces for PEs in the presence of oppositely charged substrates. An adsorbed saturated PE layer will make the surface effectively non-adsorbing for additional PE molecules, and thus the depletion interactions in these systems might well resemble the non-adsorbing case.

We hope that these questions will be addressed in the future by combining experimental techniques, computer simulations, and theory. These efforts are expected to lead to a more detailed picture of PE adsorption processes and the resulting interaction forces between substrates, and finally should give rise to reliable predictive tools that could be used to design optimal systems of PEs and substrates for the processes in question.

## List of abbreviations

The corresponding structural formulae of all PEs discussed are given in Fig. 1.

AFM	Atomic force microscope
BPEI	Branched poly(ethylene imine)
CCC	Critical coagulation concentration
DLS	Dynamic light scattering
DLVO	Derjaguin, Landau, Verwey, and Overbeek
LPEI	Linear poly(ethylene imine)
PAA	Poly(acrylic acid)
PAMAM	Poly(amido amine)
PDDA	Poly(diallyldimethyl ammonium)
PE	Polyelectrolyte
PLL	Poly(L-lysine)
PSS	Poly(styrene sulfonate)
PVA	Poly(vinyl amine)
PVP	Poly(vinyl pyridine)
RSA	Random sequential adsorption
SFA	Surface forces apparatus
SCF	Self-consistent field.

## Acknowledgements

We acknowledge useful discussions with Zbigniew Adamczyk, Vincent Ball, Lars Forsmann, Bo Jönsson, Christophe Labbez, Ger Koper, Robert Meszaros, Raffaele Mezzenga, Georg Papatavrou, Ionel Popa, Maria Santore, Imre Varga, and Corinne Vebert. We further thank Sergiy Minko for providing the high-resolution images appearing in Fig. 6c and d and Zbigniew Adamczyk for his permission to reproduce the data in Fig. 8d. This research was supported by the Swiss National Science Foundation, University of Geneva, State Secretariat for

Education, Research and Innovation within the COST Action D43, and the EU Framework Program.

## References

- 1 B. Bolto and J. Gregory, *Water Res.*, 2007, **41**, 2301–2324.
- 2 D. Horn and F. Linhart, *Retention aids*, Blackie Academic and Professional, London, 2nd edn, 1996.
- 3 N. Tabori and T. Amari, *Colloids Surf., A*, 2003, **215**, 163–171.
- 4 A. M. Howe, R. D. Wesley, M. Bertrand, M. Cote and J. Leroy, *Langmuir*, 2006, **22**, 4518–4525.
- 5 X. N. Chen, R. X. Huang and R. Pelton, *Ind. Eng. Chem. Res.*, 2005, **44**, 2078–2085.
- 6 I. Pochard, C. Labbez, A. Nonat, H. Vija and B. Jonsson, *Cem. Concr. Res.*, 2010, **40**, 1488–1494.
- 7 T. Phenrat, N. Saleh, K. Sirk, H. J. Kim, R. D. Tilton and G. V. Lowry, *J. Nanopart. Res.*, 2008, **10**, 795–814.
- 8 E. J. Bishop, D. E. Fowler, J. M. Skluzacek, E. Seibel and T. E. Mallouk, *Environ. Sci. Technol.*, 2010, **44**, 9069–9074.
- 9 S. Kim, J. H. So, D. J. Lee and S. M. Yang, *J. Colloid Interface Sci.*, 2008, **319**, 48–52.
- 10 E. Matijevic and S. V. Babu, *J. Colloid Interface Sci.*, 2008, **320**, 219–237.
- 11 A. S. Hoffman, *Adv. Drug Delivery Rev.*, 2012, **64**, 18–23.
- 12 V. Salgueirino-Maceira, F. Caruso and L. M. Liz-Marzan, *J. Phys. Chem. B*, 2003, **107**, 10990–10994.
- 13 S. Schwarz, J. E. Wong, J. Bornemann, M. Hødenius, U. Himmelreich, W. Richtering, M. Hoehn, M. Zenke and T. Hieronymus, *Nanomed. Nanotechnol. Biol. Med.*, 2012, **8**, 682–691.
- 14 R. Mezzenga, P. Schurtenberger, A. Burbidge and M. Michel, *Nat. Mater.*, 2005, **4**, 729–740.
- 15 G. Decher, *Science*, 1997, **277**, 1232–1237.
- 16 D. G. Shchukin, G. B. Sukhorukov and H. Möhwald, *Angew. Chem., Int. Ed.*, 2003, **42**, 4472–4475.
- 17 A. Fery, F. Dubreuil and H. Möhwald, *New J. Phys.*, 2004, **6**, 18.
- 18 T. Radeva and M. Grozeva, *J. Colloid Interface Sci.*, 2005, **287**, 415–421.
- 19 J. Ruhe, M. Ballauff, M. Biesalski, P. Dziezok, F. Grohn, D. Johannsmann, N. Houbenov, N. Hugenberg, R. Konradi, S. Minko, M. Motornov, R. R. Netz, M. Schmidt, C. Seidel, M. Stamm, T. Stephan, D. Usov and H. N. Zhang, *Adv. Polym. Sci.*, 2004, **165**, 79–150.
- 20 M. Ballauff and O. Borisov, *Curr. Opin. Colloid Interface Sci.*, 2006, **11**, 316–323.
- 21 S. Moya, O. Azzaroni, T. Farhan, V. L. Osborne and W. T. S. Huck, *Angew. Chem., Int. Ed.*, 2005, **44**, 4578–4581.
- 22 J. L. Dalsin, L. Lin, S. Tosatti, J. Voros, M. Textor and P. B. Messersmith, *Langmuir*, 2005, **21**, 640–646.
- 23 M. Elzbieciak-Wodka, M. Kolasinska-Sojka, D. Wodka, P. Nowak and P. Warszynski, *J. Electroanal. Chem.*, 2011, **661**, 162–170.
- 24 M. A. Cohen Stuart, W. T. S. Huck, J. Genzer, M. Muller, C. Ober, M. Stamm, G. B. Sukhorukov, I. Szleifer, V. V. Tsukruk, M. Urban, F. Winnik, S. Zauscher, I. Luzinov and S. Minko, *Nat. Mater.*, 2010, **9**, 101–113.



dc 1931\_21

- 25 N. T. Qazvini, S. Bolisetty, J. Adamcik and R. Mezzenga, *Biomacromolecules*, 2012, **13**, 2136–2147.
- 26 N. G. Hoogeveen, M. A. Cohen Stuart and G. J. Fleer, *J. Colloid Interface Sci.*, 1996, **182**, 133–145.
- 27 N. G. Hoogeveen, M. A. Cohen Stuart and G. J. Fleer, *J. Colloid Interface Sci.*, 1996, **182**, 146–157.
- 28 M. Porus, P. Maroni and M. Borkovec, *Langmuir*, 2012, **28**, 5642–5651.
- 29 J. Blaakmeer, M. R. Bohmer, M. A. Cohen Stuart and G. J. Fleer, *Macromolecules*, 1990, **23**, 2301–2309.
- 30 R. Rehmet and E. Killmann, *Colloids Surf., A*, 1999, **149**, 323–328.
- 31 J. Kleimann, C. Gehin-Delval, H. Auweter and M. Borkovec, *Langmuir*, 2005, **21**, 3688–3698.
- 32 E. Seyrek, J. Hierrezuelo, A. Sadeghpour, I. Szilagyí and M. Borkovec, *Phys. Chem. Chem. Phys.*, 2011, **13**, 12716–12719.
- 33 Z. Adamczyk, K. Sadlej, E. Wajnryb, M. Nattich, M. L. Ekiel-Jezewska and J. Blawdziewicz, *Adv. Colloid Interface Sci.*, 2010, **153**, 1–29.
- 34 B. P. Cahill, G. Papastavrou, G. J. M. Koper and M. Borkovec, *Langmuir*, 2008, **24**, 465–473.
- 35 G. J. Fleer, M. A. Cohen Stuart, J. M. H. M. Scheutjens, T. Cosgrove and B. Vincent, *Polymers at Interfaces*, Chapman and Hall, London, 1993.
- 36 C. Holm, J. F. Joanny, K. Kremer, R. R. Netz, P. Reineker, C. Seidel, T. A. Vilgis and R. G. Winkler, *Adv. Polym. Sci.*, 2004, **166**, 67–111.
- 37 R. R. Netz and D. Andelman, *Phys. Rep.*, 2003, **380**, 1–95.
- 38 A. V. Dobrynin, *Curr. Opin. Colloid Interface Sci.*, 2008, **13**, 376–388.
- 39 C. Y. Kong and M. Muthukumar, *J. Chem. Phys.*, 1998, **109**, 1522–1527.
- 40 J. Forsman, *Langmuir*, 2012, **28**, 5138–5150.
- 41 J. Y. Carrillo and A. V. Dobrynin, *Langmuir*, 2007, **23**, 2472–2482.
- 42 M. A. G. Dahlgren, A. Waltermo, E. Blomberg, P. M. Claesson, L. Sjostrom, T. Akesson and B. Jonsson, *J. Phys. Chem.*, 1993, **97**, 11769–11775.
- 43 P. M. Claesson, E. Poptoshev, E. Blomberg and A. Dedinaite, *Adv. Colloid Interface Sci.*, 2005, **114**, 173–187.
- 44 S. Biggs, D. C. Prieve and R. R. Dagastine, *Langmuir*, 2005, **21**, 5421–5428.
- 45 E. S. Pagac, R. D. Tilton and D. C. Prieve, *Langmuir*, 1998, **14**, 5106–5112.
- 46 X. C. Xing, G. Q. Sun, Z. F. Li and T. Ngai, *Langmuir*, 2012, **28**, 16022–16028.
- 47 I. Popa, G. Gillies, G. Papastavrou and M. Borkovec, *J. Phys. Chem. B*, 2009, **113**, 8458–8461.
- 48 M. Finessi, P. Sinha, I. Szilagyí, I. Popa, P. Maroni and M. Borkovec, *J. Phys. Chem. B*, 2011, **115**, 9098–9105.
- 49 F. Bouyer, A. Robben, W. L. Yu and M. Borkovec, *Langmuir*, 2001, **17**, 5225–5231.
- 50 M. Ashmore, J. Hearn and F. Karpowicz, *Langmuir*, 2001, **17**, 1069–1073.
- 51 Y. K. Leong, P. J. Scales, T. W. Healy and D. V. Boger, *Colloids Surf., A*, 1995, **95**, 43–52.
- 52 B. Derjaguin and L. D. Landau, *Acta Physicochim. URSS*, 1941, **14**, 633–662.
- 53 E. J. W. Verwey and J. T. G. Overbeek, *Theory of Stability of Lyophobic Colloids*, Elsevier, Amsterdam, 1948.
- 54 W. B. Russel, D. A. Saville and W. R. Schowalter, *Colloidal Dispersions*, Cambridge University Press, Cambridge, 1989.
- 55 V. K. La Mer and T. W. Healy, *Rev. Pure Appl. Chem.*, 1963, **13**, 112–133.
- 56 J. Gregory, *J. Colloid Interface Sci.*, 1973, **42**, 448–456.
- 57 G. Olanya, J. Iruthayaraj, E. Poptoshev, R. Makuska, A. Vareikis and P. M. Claesson, *Langmuir*, 2008, **24**, 5341–5349.
- 58 A. Naderi, G. Olanya, R. Makuska and P. M. Claesson, *J. Colloid Interface Sci.*, 2008, **323**, 223–228.
- 59 Y. Guo, J. van Beek, B. Zhang, M. Colussi, P. Walde, A. Zhang, M. Kröger, A. Halperin and A. D. Schlüter, *J. Am. Chem. Soc.*, 2009, **131**, 11841–11854.
- 60 J. J. Ramsden, *Chem. Soc. Rev.*, 1995, **24**, 73–78.
- 61 J. R. Lu, X. B. Zhao and M. Yaseen, *Curr. Opin. Colloid Interface Sci.*, 2007, **12**, 9–16.
- 62 Z. Adamczyk, *Curr. Opin. Colloid Interface Sci.*, 2012, **17**, 173–186.
- 63 V. Ball, A. Bentaleb, J. Hemmerle, J. C. Voegel and P. Schaaf, *Langmuir*, 1996, **12**, 1614–1621.
- 64 P. M. Claesson, E. Blomberg, J. C. Froberg, T. Nylander and T. Arnebrant, *Adv. Colloid Interface Sci.*, 1995, **57**, 161–227.
- 65 R. A. Silva, M. D. Urzua, D. F. S. Petri and P. L. Dubin, *Langmuir*, 2010, **26**, 14032–14038.
- 66 Z. Adamczyk, J. Barbasz and M. Ciesla, *Langmuir*, 2011, **27**, 6868–6878.
- 67 A. Mecke, I. Lee, J. R. Baker, M. M. B. Holl and B. G. Orr, *Eur. Phys. J. E*, 2004, **14**, 7–16.
- 68 S. Block and C. A. Helm, *Phys. Rev. E: Stat., Nonlinear, Soft Matter Phys.*, 2007, **76**, 030801.
- 69 L. Muresan, P. Maroni, I. Popa, M. Porus, R. Longtin, G. Papastavrou and M. Borkovec, *Macromolecules*, 2011, **44**, 5069–5071.
- 70 M. Porus, P. Maroni and M. Borkovec, *Langmuir*, 2012, **28**, 17506–17516.
- 71 Y. Samoshina, T. Nylander, V. Shubin, R. Bauer and K. Eskilsson, *Langmuir*, 2005, **21**, 5872–5881.
- 72 S. M. Notley, S. Biggs, V. S. J. Craig and L. Wagberg, *Phys. Chem. Chem. Phys.*, 2004, **6**, 2379–2386.
- 73 H. G. Pedersen and L. Bergstrom, *J. Am. Ceram. Soc.*, 1999, **82**, 1137–1145.
- 74 A. Gromer, M. Rawiso and M. Maaloum, *Langmuir*, 2008, **24**, 8950–8953.
- 75 T. Abraham, *Polymer*, 2002, **43**, 849–855.
- 76 J. Gregory and S. Barany, *Adv. Colloid Interface Sci.*, 2011, **169**, 1–12.
- 77 C. Porcel, P. Lavalle, V. Ball, G. Decher, B. Senger, J. C. Voegel and P. Schaaf, *Langmuir*, 2006, **22**, 4376–4383.
- 78 E. Laarz, A. Meurk, J. A. Yanez and L. Bergstrom, *J. Am. Ceram. Soc.*, 2001, **84**, 1675–1682.
- 79 A. P. Ngankam and P. R. Van Tassel, *Proc. Natl. Acad. Sci. U. S. A.*, 2007, **104**, 1140–1145.

dc 1931\_21

- 80 J. Penfold, I. Tucker, R. K. Thomas, D. J. F. Taylor, X. L. Zhang, C. Bell, C. Breward and P. Howell, *Langmuir*, 2007, **23**, 3128–3136.
- 81 L. Muresan, P. Sinha, P. Maroni and M. Borkovec, *Colloids Surf., A*, 2011, **390**, 225–230.
- 82 H. Walter, C. Harrats, P. Muller-Buschbaum, R. Jerome and M. Stamm, *Langmuir*, 1999, **15**, 1260–1267.
- 83 Z. Adamczyk, M. Nattich and J. Barbasz, *Adv. Colloid Interface Sci.*, 2009, **147–148**, 2–17.
- 84 N. Kozlova and M. M. Santore, *Langmuir*, 2006, **22**, 1135–1142.
- 85 K. L. Chen and M. Elimelech, *Environ. Sci. Technol.*, 2008, **42**, 7607–7614.
- 86 S. Abalde-Cela, S. Ho, B. Rodriguez-Gonzalez, M. A. Correa-Duarte, R. A. Alvarez-Puebla, L. M. Liz-Marzan and N. A. Kotov, *Angew. Chem., Int. Ed.*, 2009, **48**, 5326–5329.
- 87 D. Sebok, T. Szabo and I. Dekany, *Appl. Surf. Sci.*, 2009, **255**, 6953–6962.
- 88 R. R. Netz and J. F. Joanny, *Macromolecules*, 1999, **32**, 9013–9025.
- 89 G. J. M. Koper and M. Borkovec, *Polymer*, 2010, **51**, 5649–5662.
- 90 N. Volk, D. Vollmer, M. Schmidt, W. Oppermann and K. Huber, *Adv. Polym. Sci.*, 2004, **166**, 29–65.
- 91 I. Popa, B. P. Cahill, P. Maroni, G. Papastavrou and M. Borkovec, *J. Colloid Interface Sci.*, 2007, **309**, 28–35.
- 92 N. P. Huang, R. Michel, J. Voros, M. Textor, R. Hofer, A. Rossi, D. L. Elbert, J. A. Hubbell and N. D. Spencer, *Langmuir*, 2001, **17**, 489–498.
- 93 Z. Adamczyk, A. Michna, M. Szaraniec, A. Bratek and J. Barbasz, *J. Colloid Interface Sci.*, 2007, **313**, 86–96.
- 94 I. Varga, A. Mezei, R. Meszaros and P. M. Claesson, *Soft Matter*, 2011, **7**, 10701–10712.
- 95 R. Longtin, P. Maroni and M. Borkovec, *Langmuir*, 2009, **25**, 2928–2934.
- 96 R. Kargl, T. Mohan, M. Bracic, M. Kulterer, A. Doliska, K. Stana-Kleinschek and V. Ribitsch, *Langmuir*, 2012, **28**, 11440–11447.
- 97 M. Jiang, I. Popa, P. Maroni and M. Borkovec, *Colloids Surf., A*, 2010, **360**, 20–25.
- 98 L. E. Enarsson and L. Wagberg, *Langmuir*, 2008, **24**, 7329–7337.
- 99 R. Meszaros, I. Varga and T. Gilanyi, *Langmuir*, 2004, **20**, 5026–5029.
- 100 R. C. van Duijvenbode, I. B. Rietveld and G. J. M. Koper, *Langmuir*, 2000, **16**, 7720–7725.
- 101 Z. Adamczyk, L. Szyk and P. Warszynski, *J. Colloid Interface Sci.*, 1999, **209**, 350–361.
- 102 H. Dautzenberg, E. Gornitz and W. Jaeger, *Macromol. Chem. Phys.*, 1998, **199**, 1561–1571.
- 103 Y. Tie, C. Calonder and P. R. Van Tassel, *J. Colloid Interface Sci.*, 2003, **268**, 1–11.
- 104 J. W. Evans, *Rev. Mod. Phys.*, 1993, **65**, 1281–1329.
- 105 Z. Adamczyk, B. Senger, J. C. Voegel and P. Schaaf, *J. Chem. Phys.*, 1999, **110**, 3118–3128.
- 106 B. Senger, J. C. Voegel and P. Schaaf, *Colloids Surf., A*, 2000, **165**, 255–285.
- 107 I. Popa, G. Papastavrou and M. Borkovec, *Phys. Chem. Chem. Phys.*, 2010, **12**, 4863–4871.
- 108 M. Finessi, PhD, University of Geneva, 2013.
- 109 L. J. Kirwan, P. Maroni, S. H. Behrens, G. Papastavrou and M. Borkovec, *J. Phys. Chem. B*, 2008, **112**, 14609–14619.
- 110 D. Bauer, H. Buchhammer, A. Fuchs, W. Jaeger, E. Killmann, K. Lunckwitz, R. Rehmet and S. Schwarz, *Colloids Surf., A*, 1999, **156**, 291–305.
- 111 M. R. Bohmer, W. H. A. Heesterbeek, A. Deratani and E. Renard, *Colloids Surf., A*, 1995, **99**, 53–64.
- 112 S. A. Sukhishvili and S. Granick, *J. Chem. Phys.*, 1998, **109**, 6861–6868.
- 113 K. Esumi and M. Gojino, *Langmuir*, 1998, **14**, 4466–4470.
- 114 R. C. van Duijvenbode, G. J. M. Koper and M. R. Bohmer, *Langmuir*, 2000, **16**, 7713–7719.
- 115 T. Sennerfors, D. Solberg and F. Tiberg, *J. Colloid Interface Sci.*, 2002, **254**, 222–226.
- 116 T. J. Barnes, I. Ametov and C. A. Prestidge, *Langmuir*, 2008, **24**, 12398–12404.
- 117 V. Shubin, *J. Colloid Interface Sci.*, 1997, **191**, 372–377.
- 118 J. Lyklema and L. Deschenes, *Adv. Colloid Interface Sci.*, 2011, **168**, 135–148.
- 119 N. Hansupalak and M. M. Santore, *Langmuir*, 2003, **19**, 7423–7426.
- 120 D. Cakara, C. Chassagne, C. Gehin-Delval and M. Borkovec, *Colloids Surf., A*, 2007, **294**, 174–180.
- 121 E. Illes and E. Tombacz, *Colloids Surf., A*, 2003, **230**, 99–109.
- 122 B. Cabot, A. Deratani and A. Foissy, *Colloids Surf., A*, 1998, **139**, 287–297.
- 123 Z. Adamczyk and P. Warszynski, *Adv. Colloid Interface Sci.*, 1996, **63**, 41–149.
- 124 M. Semmler, E. K. Mann, J. Ricka and M. Borkovec, *Langmuir*, 1998, **14**, 5127–5132.
- 125 Z. Adamczyk, *Adv. Colloid Interface Sci.*, 2003, **100**, 267–347.
- 126 A. V. Dobrynin, A. Deshkovski and M. Rubinstein, *Macromolecules*, 2001, **34**, 3421–3436.
- 127 M. Muthukumar, *J. Chem. Phys.*, 1987, **86**, 7230–7235.
- 128 J. Hierrezuelo, I. Szilagyi, A. Vaccaro and M. Borkovec, *Macromolecules*, 2010, **43**, 9108–9116.
- 129 F. Hook, B. Kasemo, T. Nylander, C. Fant, K. Sott and H. Elwing, *Anal. Chem.*, 2001, **73**, 5796–5804.
- 130 A. Vaccaro, J. Hierrezuelo, M. Skarba, P. Galletto, J. Kleimann and M. Borkovec, *Langmuir*, 2009, **25**, 4864–4867.
- 131 I. Popa, G. Gillies, G. Papastavrou and M. Borkovec, *J. Phys. Chem. B*, 2010, **114**, 3170–3177.
- 132 Y. Roiter and S. Minko, *J. Phys. Chem. B*, 2007, **111**, 8597–8604.
- 133 R. Pericet-Camara, G. Papastavrou and M. Borkovec, *Langmuir*, 2004, **20**, 3264–3270.
- 134 S. Minko and Y. Roiter, *Curr. Opin. Colloid Interface Sci.*, 2005, **10**, 9–15.
- 135 L. J. Kirwan, G. Papastavrou, M. Borkovec and S. H. Behrens, *Nano Lett.*, 2004, **4**, 149–152.
- 136 F. Valle, M. Favre, P. de los Rios, A. Rosa and G. Dietler, *Phys. Rev. Lett.*, 2005, **95**, 158105.

dc 1931 21

- 137 H. G. M. van de Steeg, M. A. Cohen Stuart, A. de Keizer and B. H. Bijsterbosch, *Langmuir*, 1992, **8**, 2538–2546.
- 138 I. Borukhov, D. Andelman and H. Orland, *Macromolecules*, 1998, **31**, 1665–1671.
- 139 P. Linse, *Macromolecules*, 1996, **29**, 326–336.
- 140 G. Gillies, W. Lin and M. Borkovec, *J. Phys. Chem. B*, 2007, **111**, 8626–8633.
- 141 J. Hierrezuelo, A. Sadeghpour, I. Szilagy, A. Vaccaro and M. Borkovec, *Langmuir*, 2010, **26**, 15109–15111.
- 142 J. Hierrezuelo, A. Vaccaro and M. Borkovec, *J. Colloid Interface Sci.*, 2010, **347**, 202–208.
- 143 W. L. Yu, F. Bouyer and M. Borkovec, *J. Colloid Interface Sci.*, 2001, **241**, 392–399.
- 144 E. Illes and E. Tombacz, *J. Colloid Interface Sci.*, 2006, **295**, 115–123.
- 145 S. Sennato, D. Truzzolillo, F. Bordi, F. Sciortino and C. Cametti, *Colloids Surf., A*, 2009, **343**, 34–42.
- 146 F. Quemeneur, M. Rinaudo, G. Maret and B. Pepin-Donat, *Soft Matter*, 2010, **6**, 4471–4481.
- 147 A. Feiler, P. Jenkins and J. Ralston, *Phys. Chem. Chem. Phys.*, 2000, **2**, 5678–5683.
- 148 A. Sadeghpour, E. Seyrek, I. Szilagy, J. Hierrezuelo and M. Borkovec, *Langmuir*, 2011, **27**, 9270–9276.
- 149 I. Szilagy, A. Sadeghpour and M. Borkovec, *Langmuir*, 2012, **28**, 6211–6215.
- 150 I. Szilagy, D. Rosicka, J. Hierrezuelo and M. Borkovec, *J. Colloid Interface Sci.*, 2011, **360**, 580–585.
- 151 A. Mezei and R. Meszaros, *Langmuir*, 2006, **22**, 7148–7151.
- 152 Z. Adamczyk, A. Zembala and A. Michna, *J. Colloid Interface Sci.*, 2006, **303**, 353–364.
- 153 I. Popa, G. Papastavrou and M. Borkovec, *Macromolecules*, 2010, **43**, 1129–1136.
- 154 J. Dejeu, L. Buisson, M. C. Guth, C. Roidor, F. Membrey, D. Charrat and A. Foissy, *Colloids Surf., A*, 2006, **288**, 26–35.
- 155 W. Lin, P. Galletto and M. Borkovec, *Langmuir*, 2004, **20**, 7465–7473.
- 156 J. Sabin, C. Vazquez-Vazquez, G. Prieto, F. Bordi and F. Sarmiento, *Langmuir*, 2012, **28**, 10534–10542.
- 157 J. Israelachvili, *Intermolecular and Surface Forces*, Academic Press, London, 3rd edn, 2011.
- 158 S. H. Behrens and M. Borkovec, *J. Phys. Chem. B*, 1999, **103**, 2918–2928.
- 159 G. Toikka, R. A. Hayes and J. Ralston, *Langmuir*, 1996, **12**, 3783–3788.
- 160 C. Gutsche, U. F. Keyser, K. Kegler and F. Kremer, *Phys. Rev. E: Stat., Nonlinear, Soft Matter Phys.*, 2007, **76**, 031403.
- 161 P. G. Hartley, I. Larson and P. J. Scales, *Langmuir*, 1997, **13**, 2207–2214.
- 162 J. Israelachvili, *Intermolecular and Surface Forces*, Academic Press, London, 2nd edn, 1992.
- 163 P. Sinha, I. Szilagy, F. J. Montes Ruiz-Cabello, P. Maroni and M. Borkovec, *J. Phys. Chem. Lett.*, 2013, **4**, 648–652.
- 164 R. M. Pashley, *J. Colloid Interface Sci.*, 1981, **83**, 531–546.
- 165 G. Toikka and R. A. Hayes, *J. Colloid Interface Sci.*, 1997, **191**, 102–109.
- 166 G. Vigil, Z. H. Xu, S. Steinberg and J. Israelachvili, *J. Colloid Interface Sci.*, 1994, **165**, 367–385.
- 167 P. F. Luckham and J. Klein, *J. Chem. Soc., Faraday Trans. 1*, 1984, **80**, 865–878.
- 168 P. Berndt, K. Kurihara and T. Kunitake, *Langmuir*, 1992, **8**, 2486–2490.
- 169 R. Pericet-Camara, G. Papastavrou, S. H. Behrens, C. A. Helm and M. Borkovec, *J. Colloid Interface Sci.*, 2006, **296**, 496–506.
- 170 E. Poptoshev and P. M. Claesson, *Langmuir*, 2002, **18**, 2590–2594.
- 171 E. Poptoshev, M. W. Rutland and P. M. Claesson, *Langmuir*, 2000, **16**, 1987–1992.
- 172 P. M. Claesson and B. W. Ninham, *Langmuir*, 1992, **8**, 1406–1412.
- 173 G. Maurdev, L. Meagher, J. Ennis and M. L. Gee, *Langmuir*, 2001, **34**, 4151–4158.
- 174 C. E. McNamee, M. Matsumoto, P. G. Hartley, P. Mulvaney, Y. Tsujii and M. Nakahara, *Langmuir*, 2001, **17**, 6220–6227.
- 175 A. Szucs, T. Haraszti, I. Dekany and J. H. Fendler, *J. Phys. Chem. B*, 2001, **105**, 10579–10587.
- 176 P. G. Hartley and P. J. Scales, *Langmuir*, 1998, **14**, 6948–6955.
- 177 V. Bosio, F. Dubreuil, G. Bogdanovic and A. Fery, *Colloids Surf., A*, 2004, **243**, 147–155.
- 178 T. Abraham, D. Christendat, Z. Xu, J. Masliyah, J. F. Gohy and R. Jerome, *AIChE J.*, 2004, **50**, 2613–2626.
- 179 R. Podgornik and M. Licer, *Curr. Opin. Colloid Interface Sci.*, 2006, **11**, 273–279.
- 180 H. H. Huang and E. Ruckenstein, *Langmuir*, 2012, **28**, 16300–16305.
- 181 M. Rief, F. Oesterhelt, B. Heymann and H. E. Gaub, *Science*, 1997, **275**, 1295–1297.
- 182 T. Hugel, M. Grosholz, H. Clausen-Schaumann, A. Pfau, H. Gaub and M. Seitz, *Macromolecules*, 2001, **34**, 1039–1047.
- 183 X. Chatellier, T. J. Senden, J. F. Joanny and J. M. di Meglio, *Europhys. Lett.*, 1998, **41**, 303–308.
- 184 G. Papastavrou, L. J. Kirwan and M. Borkovec, *Langmuir*, 2006, **22**, 10880–10884.
- 185 E. Poptoshev, M. W. Rutland and P. M. Claesson, *Langmuir*, 1999, **15**, 7789–7794.
- 186 S. J. Miklavic, D. Y. C. Chan, L. R. White and T. W. Healy, *J. Phys. Chem.*, 1994, **98**, 9022–9032.
- 187 P. Richmond, *J. Chem. Soc., Faraday Trans. 2*, 1975, **71**, 1154–1163.
- 188 I. Popa, G. Papastavrou, M. Borkovec, M. Trulsson and B. Jonsson, *Langmuir*, 2009, **25**, 12435–12438.
- 189 J. Swenson, M. V. Smalley and H. L. M. Hatharasinghe, *Phys. Rev. Lett.*, 1998, **81**, 5840–5843.
- 190 Y. Zhou, Y. Gan, E. J. Wanless, G. J. Jameson and G. V. Franks, *Langmuir*, 2008, **24**, 10920–10928.
- 191 I. Borukhov, D. Andelman and H. Orland, *J. Phys. Chem. B*, 1999, **103**, 5042–5057.
- 192 J. Forsman and S. Nordholm, *Langmuir*, 2012, **28**, 4069–4079.
- 193 M. Turesson, J. Forsman and T. Akesson, *Langmuir*, 2006, **22**, 5734–5741.

dc 1931\_21

- 194 D. Truzzolillo, F. Bordi, F. Sciortino and S. Sennato, *J. Chem. Phys.*, 2010, **133**, 024901.
- 195 C. E. Woodward, T. Akesson and B. Jonsson, *J. Chem. Phys.*, 1994, **101**, 2569–2576.
- 196 A. Broukhno, B. Jonsson, T. Akesson and P. N. Vorontsov-Velyaminov, *J. Chem. Phys.*, 2000, **113**, 5493–5501.
- 197 R. Podgornik, P. Akesson and B. Jonsson, *J. Chem. Phys.*, 1995, **102**, 9423–9434.
- 198 R. Podgornik, *J. Chem. Phys.*, 2003, **118**, 11286–11296.
- 199 S. Biggs and T. W. Healy, *J. Chem. Soc., Faraday Trans.*, 1994, **90**, 3415–3421.
- 200 S. Biggs, J. L. Burns, Y. D. Yan, G. J. Jameson and P. Jenkins, *Langmuir*, 2000, **16**, 9242–9248.
- 201 A. Sharma, S. N. Tan and J. Y. Walz, *J. Colloid Interface Sci.*, 1997, **191**, 236–246.
- 202 A. J. Milling, *J. Phys. Chem.*, 1996, **100**, 8986–8993.
- 203 X. J. Gong and T. Ngai, *Langmuir*, 2013, **29**, 5974–5981.
- 204 D. Kleshchanok, R. Tuinier and P. R. Lang, *J. Phys.: Condens. Matter*, 2008, **20**, 073101.
- 205 Y. Zeng and R. von Klitzing, *Langmuir*, 2012, **28**, 6313–6321.
- 206 M. Elimelech, J. Gregory, X. Jia and R. A. Williams, *Particle Deposition and Aggregation: Measurement, Modeling, and Simulation*, Butterworth-Heinemann Ltd., Oxford, 1995.
- 207 P. Sandkuhler, M. Lattuada, H. Wu, J. Sefcik and M. Morbidelli, *Adv. Colloid Interface Sci.*, 2005, **113**, 65–83.
- 208 C. Gogelein, G. Nagele, J. Buitenhuis, R. Tuinier and J. K. G. Dhont, *J. Chem. Phys.*, 2009, **130**, 204905.
- 209 M. Lattuada, H. Wu and M. Morbidelli, *Langmuir*, 2004, **20**, 4355–4362.
- 210 K. Masschaele, J. Fransaer and J. Vermant, *Soft Matter*, 2011, **7**, 7717–7726.
- 211 E. P. Honig, G. J. Roeberson and P. H. Wiersema, *J. Colloid Interface Sci.*, 1971, **36**, 97–102.
- 212 S. H. Behrens, M. Borkovec and P. Schurtenberger, *Langmuir*, 1998, **14**, 1951–1954.
- 213 M. Kobayashi, M. Skarba, P. Galletto, D. Cakara and M. Borkovec, *J. Colloid Interface Sci.*, 2005, **292**, 139–147.
- 214 M. Schudel, S. H. Behrens, H. Holthoff, R. Kretschmar and M. Borkovec, *J. Colloid Interface Sci.*, 1997, **196**, 241–253.
- 215 H. Holthoff, S. U. Egelhaaf, M. Borkovec, P. Schurtenberger and H. Sticher, *Langmuir*, 1996, **12**, 5541–5549.
- 216 W. Lin, M. Kobayashi, M. Skarba, C. Mu, P. Galletto and M. Borkovec, *Langmuir*, 2006, **22**, 1038–1047.
- 217 H. Holthoff, A. Schmitt, A. Fernandez-Barbero, M. Borkovec, M. A. Cabrerizo-Vilchez, P. Schurtenberger and R. Hidalgo-Alvarez, *J. Colloid Interface Sci.*, 1997, **192**, 463–470.
- 218 S. H. Xu and Z. W. Sun, *Soft Matter*, 2011, **7**, 11298–11308.
- 219 D. R. E. Snoswell, J. M. Duan, D. Fornasiero and J. Ralston, *J. Colloid Interface Sci.*, 2005, **286**, 526–535.
- 220 H. Kihira, N. Ryde and E. Matijevic, *J. Chem. Soc., Faraday Trans.*, 1992, **88**, 2379–2386.
- 221 M. B. Einarson and J. C. Berg, *J. Colloid Interface Sci.*, 1993, **155**, 165–172.
- 222 C. Schneider, M. Hanisch, B. Wedel, A. Jusufi and M. Ballauff, *J. Colloid Interface Sci.*, 2011, **358**, 62–67.
- 223 S. H. Behrens, D. I. Christl, R. Emmerzael, P. Schurtenberger and M. Borkovec, *Langmuir*, 2000, **16**, 2566–2575.
- 224 T. Hiemstra and W. H. van Riemsdijk, *Langmuir*, 1999, **15**, 8045–8051.
- 225 S. Y. Shulepov and G. Frens, *J. Colloid Interface Sci.*, 1996, **182**, 388–394.
- 226 J. D. Feick and D. Velegol, *Langmuir*, 2002, **18**, 3454–3458.
- 227 K. L. Chen, S. E. Mylon and M. Elimelech, *Environ. Sci. Technol.*, 2006, **40**, 1516–1523.
- 228 G. Fritz, V. Schadler, N. Willenbacher and N. J. Wagner, *Langmuir*, 2002, **18**, 6381–6390.
- 229 X. Guo and M. Ballauff, *Langmuir*, 2000, **16**, 8719–8726.
- 230 C. N. Likos, K. A. Vaynberg, H. Lowen and N. J. Wagner, *Langmuir*, 2000, **16**, 4100–4108.
- 231 R. G. Smits, G. J. M. Koper and M. Mandel, *J. Phys. Chem.*, 1993, **97**, 5745–5751.
- 232 H. W. Walker and S. B. Grant, *Colloids Surf., A*, 1996, **119**, 229–239.
- 233 M. Trulsson, J. Forsman, T. Akesson and B. Jonsson, *Langmuir*, 2009, **25**, 6106–6112.
- 234 S. Schwarz, K. Lunkwitz, B. Kessler, U. Spiegler, E. Killmann and W. Jaeger, *Colloids Surf., A*, 2000, **163**, 17–27.
- 235 S. Schwarz, W. Jaeger, B. R. Paulke, S. Bratskaya, N. Smolka and J. Bohrisch, *J. Phys. Chem. B*, 2007, **111**, 8649–8654.
- 236 T. Abe, S. Kobayashi and M. Kobayashi, *Colloids Surf., A*, 2011, **379**, 21–26.
- 237 K. L. Chen, S. E. Mylon and M. Elimelech, *Langmuir*, 2007, **23**, 5920–5928.
- 238 J. E. Seebergh and J. C. Berg, *Langmuir*, 1994, **10**, 454–463.
- 239 A. Sharma, S. N. Tan and J. Y. Walz, *J. Colloid Interface Sci.*, 1997, **190**, 392–407.
- 240 M. J. Snowden, S. M. Clegg, P. A. Williams and I. D. Robb, *J. Chem. Soc., Faraday Trans.*, 1991, **87**, 2201–2207.
- 241 S. Rawson, K. Ryan and B. Vincent, *Colloids Surf.*, 1988, **34**, 89–93.
- 242 P. Richmond, *J. Chem. Soc., Faraday Trans. 2*, 1974, **70**, 1066–1073.





Cite this: *Nanoscale*, 2017, 9, 369

## Synthesis and formulation of functional bionanomaterials with superoxide dismutase activity†

Marko Pavlovic, Paul Rouster and Istvan Szilagyi\*

Layered double hydroxide (LDH) nanoparticles were prepared and used as solid support for superoxide dismutase (SOD) enzymes. Structural features were studied by XRD, spectroscopic methods (IR, UV-Vis and fluorescence) and TEM, while colloidal stability of the obtained materials was investigated by electrophoresis and light scattering in aqueous dispersions. The SOD quantitatively adsorbed on the LDH by electrostatic and hydrophobic interactions and kept its structural integrity upon immobilization. The composite material showed moderate resistance against salt-induced aggregation in dispersions, therefore, heparin polyelectrolyte was used to improve the colloidal stability of the system. Heparin of highly negative line charge density strongly adsorbed on the oppositely charged hybrid particles leading to charge neutralization and overcharging at appropriate polyelectrolyte loading. Full coverage of the composite platelets with heparin resulted in highly stable dispersions, which contained only primary particles even at elevated ionic strengths. Our results indicate that the developed bionanocomposite of considerable enzymatic function is a suitable candidate for applications, wherever stable dispersions of antioxidant activity are required for instance in biomedical treatments or in chemical manufacturing processes.

Received 28th September 2016,

Accepted 30th November 2016

DOI: 10.1039/c6nr07672f

www.rsc.org/nanoscale

## Introduction

Immobilization of native enzymes attracts widespread contemporary interest as indicated by the considerable number of reviews released recently in this topic in the chemical literature.<sup>1–5</sup> Enzymes attached to solid supports are widely used in catalysis,<sup>6</sup> analytical chemistry,<sup>7</sup> biotechnology,<sup>8</sup> water treatment<sup>9</sup> and in numerous chemical manufacturing processes.<sup>10,11</sup> Several immobilization techniques have been described, where carrier substances included insoluble inorganic particles (*e.g.*, silica,<sup>12</sup> carbon derivatives,<sup>13</sup> iron oxide,<sup>14</sup> metal–organic frameworks,<sup>4</sup> zirconium phosphate,<sup>15</sup> titania<sup>16</sup> and clays<sup>17,18</sup>), polymers<sup>19–21</sup> or hybrid materials.<sup>22</sup> The attachments were carried out by various forces (electrostatic interaction, physical adsorption, covalent linkage, *etc.*). One of the most important conclusions was that the matrix has to provide an environment, which is biocompatible and chemically inert. Consequently, the interaction with the solid support should not change the protein structure responsible for the enzymatic activity, but should be able to defend it from

environmental effects, which can lead to denaturation and loss of activity.<sup>23</sup>

Lamellar clay materials possess several advantageous properties, which make them popular solid supports in enzyme immobilization processes usually taking place through electrostatic interactions.<sup>7,24,25</sup> Accordingly, the protein loading is often high due to the significant ion exchange capacity of the clays, the electrostatic attraction provides a strong attachment, the distance between the lamellae can be tuned and pillared materials can be obtained, delamination into unilamellar nanosheets results in dispersions of high surface area and clays are available in large amount in nature or their preparation is relatively uncomplicated.

Among them, layered double hydroxides (LDHs) are one of the most popular enzyme carriers.<sup>7,18,25</sup> LDHs are hydroxylated-type anionic (*i.e.*, with anion exchange capacity) clays containing lamellar mixed hydroxides with exchangeable anions and water between the layers.<sup>26</sup> Although LDHs are less frequent than the cationic clays in nature, their synthesis is simple even in large amount and various methods are available.<sup>27–32</sup> The structure of the LDHs is based on Mg(OH)<sub>2</sub> (brucite) of octahedral coordination around the metal ions. The Mg<sup>2+</sup> can be substituted with trivalent cations (*e.g.*, Al<sup>3+</sup> and Fe<sup>3+</sup>) of similar coordination properties. This isomorphous substitution results in positively charged layers neutralized electrically by anions, which can be exchanged to other negatively

Department of Inorganic and Analytical Chemistry, University of Geneva,  
30 Quai Ernest-Ansermet, CH-1205 Geneva, Switzerland.

E-mail: istvan.szilagyi@unige.ch; Tel: +41223796031

†Electronic supplementary information (ESI) available. See DOI: 10.1039/c6nr07672f

dc\_1931\_21

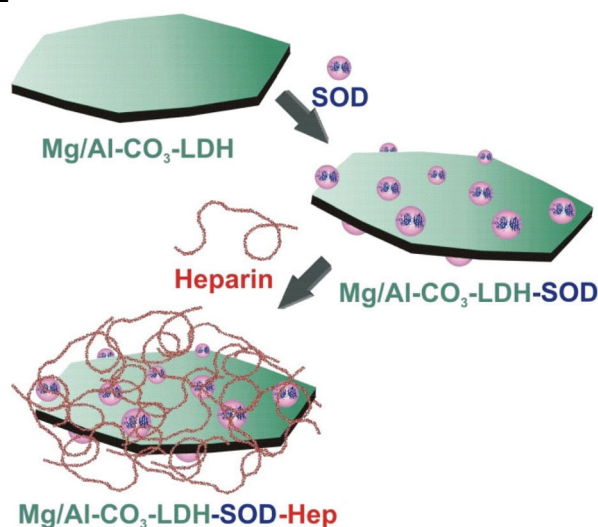
charged substances. The  $Mg^{2+}$  can also be replaced by other divalent metal ions ( $Fe^{2+}$ ,  $Zn^{2+}$ ,  $Ca^{2+}$ , *etc.*) leading to high compositional diversity of the LDH materials.

Amylase enzyme was adsorbed on  $Mg/Al-CO_3-LDH$  (*i.e.*, composed of  $Mg^{2+}$  and  $Al^{3+}$  layer forming metal ions and  $CO_3^{2-}$  charge compensating anions) resulting in a biohybrid, which showed excellent activity in hydrolyzing starch.<sup>33</sup> LDH-enzyme composites were also prepared for the development of biosensors. For example,  $Zn/Al$ -alginate-LDH was used to entrap polyphenol oxidase and the obtained composite material showed high sensitivity in catechol detection.<sup>34</sup> In another system, the conformation of pancreatic lipase upon adsorption on lactate-intercalated LDH was tuned by optimizing the enzyme-to-LDH ratio in the reaction mixture.<sup>35</sup> Urease enzyme was immobilized in/on  $Zn/Al-Cl-LDH$  in different ways. Namely, physically adsorbed on the outer surface and intercalated into the interlamellar space by the delamination-restacking method or during the coprecipitation process.<sup>36</sup> The latter method resulted in the highest amount of enzyme in the composite and the developed materials showed sufficient activity in urea hydrolysis. Such a coprecipitation method was also used to intercalate papain in an LDH containing  $Mg^{2+}$  and  $Al^{3+}$  metal ions in the lamellae.<sup>37</sup> The structure and the activity of the enzyme was the same after de-intercalation from the hybrid material indicating that the solid support is suitable to provide time-controlled release of papain.

Antioxidant enzymes including superoxide dismutase (SOD) are an important class of proteins for therapeutic applications and in various industrial manufacturing processes due to their high efficiency in decomposition of reactive oxygen species (ROS).<sup>38</sup> Immobilization of SOD on suitable solid supports has been performed to improve its formulation, reusability and resistance against the environmental effects (*e.g.*, change in pH, temperature or ionic strength).

Accordingly, SOD was physically adsorbed and covalently grafted to functionalized silica microspheres and the obtained composites showed excellent activity in decomposition of superoxide radicals.<sup>39</sup> Titania nanosheet-SOD hybrid material was found to be more active in enzymatic assays than the native protein.<sup>40</sup> SOD was covalently attached to carbon nanotubes and the highly dispersible composites successfully decreased the oxidative stress caused by ROS in living systems.<sup>41</sup> Other carbon derivatives were also used to immobilize the natural enzyme on electrode surfaces to develop biosensors in order to determine the concentration of superoxide radicals in biological samples.<sup>42,43</sup> Moreover, hydrogel vehicles were synthesized and SOD was encapsulated inside the nanoparticles to get protected from antibodies and degradation.<sup>44</sup> The immobilization process did not affect the catalytic activity and the developed system was proposed as a promising tool for enzymatic therapy.

Besides, to replace the sensitive and hardly manageable native SOD, artificial enzymes composed of transition metal complexes or other inorganic substances of sufficient SOD-like activity were prepared and immobilized in/on silica,<sup>45,46</sup> montmorillonite,<sup>47,48</sup> carbon nanotube<sup>49</sup> and polymer<sup>50</sup> particles.



**Scheme 1** Schematic representation of the SOD immobilization and heparin coating processes.

In the above examples, the researchers focused on the synthesis, solid state characterization and enzymatic activity tests of the hybrid materials. In spite of the fact that the majority of the applications takes place in heterogeneous systems, mostly in aqueous dispersions, no systematic studies dealing with the colloidal stability of the carrier-enzyme composites have been reported yet. This topic is extremely important, since aggregation of the carrier particles may result in inefficient catalytic activity and failure in enzyme delivery. For instance, immobilization of SOD on suitable solid supports may protect the enzyme during parenteral supplementation into human body, nevertheless, formation of irregularly shaped clusters upon particle aggregation may prevent the successful delivery and may block the veins and cause thrombosis.<sup>51</sup>

In the present study, we aimed at the design of stable dispersions consisting of SOD enzyme immobilized on  $Mg/Al-CO_3-LDH$  particles. The colloidal stability of the obtained biohybrid was tuned by surface functionalization with heparin polyelectrolyte (Scheme 1). The structure of the composite materials was investigated by microscopic and spectroscopic techniques, while charging and aggregation were probed by electrophoresis and light scattering. The bionanocomposites were applied in enzymatic assays, where they showed excellent superoxide radical scavenging activity. The results shed light on the importance of polyelectrolyte coating in order to obtain highly stable dispersions of antioxidant activity, which are suitable candidates for enzyme-based therapies in living systems for instance.

## Experimental

### Materials

The chemicals were of high purity level and commercially available substances purchased from Sigma-Aldrich with the

dc\_1931\_21

exception of sodium heparin, which was bought from Acros Organics. Enzymes, Cu<sup>2+</sup>-Zn<sup>2+</sup> superoxide dismutase from bovine erythrocytes (SOD, EC 1.15.1.1) and xanthine oxidase from bovine milk (EC 1.17.3.2.), were purchased in the form of lyophilized powder, which was dissolved in water for the measurements. Ultrapure water (Millipore) was used for sample preparation and the experiments were carried out at 25.0 ± 0.2 °C and at pH 7.5 ± 0.2, unless otherwise specified. To prepare phosphate buffer, precisely calculated amounts of sodium phosphate dibasic and sodium phosphate monobasic salt solutions were mixed together.

### Synthesis of Mg/Al-CO<sub>3</sub>-LDH

The LDH material (Mg/Al-CO<sub>3</sub>-LDH) was prepared by the flash coprecipitation method<sup>31,52,53</sup> followed by a hydrothermal treatment in order to improve the particle size distribution.<sup>30</sup> Briefly, 2.564 g of Mg(NO<sub>3</sub>)<sub>2</sub>·6H<sub>2</sub>O and 1.876 g of Al(NO<sub>3</sub>)<sub>3</sub>·9H<sub>2</sub>O were mixed together and dissolved in 100 mL of water under magnetic agitation. Then 1.060 g of Na<sub>2</sub>CO<sub>3</sub> was dissolved in 20 mL of 1 M NaOH solution and added to the previous sample. The obtained solution was stirred for 24 hours and the pH was kept at 9.0 ± 0.5. The solid precipitate was filtered (Nalgene Nylon Membrane Filter of 0.2 μm pore size) and washed extensively with water. After the washing step, the powder was dried overnight in an oven at 60 °C. The synthesized dried powder was dispersed in water to obtain a 4 wt% dispersion. The sample was then transferred in a teflon-lined autoclave (Col-Int Tech), which was sealed and a hydrothermal treatment was performed at 120 °C for 24 hours. After this procedure, the autoclave was removed from the oven and allowed to cool down at ambient temperature. The obtained product was washed several times with water during centrifugation and it was finally dispersed in water to get a 10 wt% stock dispersion and stored in the fridge. Before usage, this stock was diluted and treated in an ultrasonic bath for 5 min.

### Synthesis of Mg/Al-CO<sub>3</sub>-LDH-SOD composite

The composite material consisting of Mg/Al-CO<sub>3</sub>-LDH and SOD at a dose of 1 mg of SOD per 1 g of particle was prepared as follows. 0.1 mL of Mg/Al-CO<sub>3</sub>-LDH dispersion at 10 000 mg L<sup>-1</sup> concentration was mixed with 0.1 mL of SOD solution (10 mg L<sup>-1</sup>) and 4.8 mL water. The reaction took place during 6 hours to allow the SOD to adsorb on the surface of the LDH particles. Finally, 5 mL of 2 mM phosphate buffer solution was added to set the concentration of the composite material at 100 mg L<sup>-1</sup> and the total phosphate concentration at 1 mM. This stock dispersion was used for all of the further experiments.

### X-ray diffraction

In order to confirm the formation of the Mg/Al-CO<sub>3</sub>-LDH particles, X-ray diffraction (XRD) measurements were performed on an Empyrean diffractometer (Panalytical) using the CuKα<sub>1</sub> radiation (wavelength of 0.15406 nm). The LDH powder was placed on an 8 mm glass capillary and the data were collected in the 2θ range of 5–65°. The diffractogram of

the glass capillary was also recorded and subtracted from the XRD pattern of the material.

### Electrophoresis and light scattering

Electrophoretic mobilities were determined with a ZetaNano ZS (Malvern) instrument, while dynamic light scattering (DLS) measurements were performed with a CGS-3 goniometer system (ALV) at a scattering angle of 90°. In the time-resolved DLS experiments, the correlation functions were collected during 10–100 min depending on the speed of particle aggregation. For both experimental techniques, the samples were prepared in a similar manner. Dispersions prepared for electrophoretic mobility measurements were equilibrated overnight, while colloidal stability was probed immediately after sample preparation, in which aqueous solutions of calculated amount of polyelectrolyte and salt were mixed with stable dispersions resulting in 10 mg L<sup>-1</sup> final particle concentration. The colloidal stability was expressed in terms of stability ratio.<sup>53–55</sup> It should be noted here that stability ratios close to one indicate rapid particle aggregation and unstable systems, while higher values refer to slower aggregation and more stable dispersions.

### Spectroscopy

Infrared (IR) spectra were measured in the attenuated total reflectance (ATR) mode with a Spectrum 100 FT-IR spectrometer (PerkinElmer). The ATR crystal was made of diamond. Prior to the IR measurements, the internal reflection unit was washed with ethanol and dried. The solid material was placed on the ATR crystal and the spectrum was recorded in the wavenumber range of 4000 and 400 cm<sup>-1</sup> at a resolution of 4 cm<sup>-1</sup>.

UV-Vis absorption spectra were measured at wavelengths between 350 and 800 nm on a Lambda 35 spectrophotometer (PerkinElmer) using glass cuvettes (Hellma) cleaned with a 2 wt% Hellmanex solution (Hellma).

The fluorescence spectra of the bare and immobilized SOD were measured as follows. The enzyme was excited at a wavelength of 283 nm and the emission wavelength was recorded from 293 to 500 nm. A slit of 4 nm and 3 nm was used for the excitation and emission wavelength, respectively. All the spectra were recorded with a Fluorolog spectrometer (Horiba Jobin Yvon) using a 450 W xenon lamp.

### Microscopy

The morphology of the materials was studied by transmission electron microscopy (TEM) and by scanning electron microscopy (SEM). The TEM images were recorded on a Tecnai G2 Sphera microscope (FEI) at an acceleration voltage of 120 kV using a LaB6 cathode. The samples were prepared by placing 5 μL of solution on the plasma treated carbon mesh and by removing the excess liquid after 2 min. The obtained mesh with the material was installed on the sample holder and placed in the microscope.

For SEM imaging, 20 μL dispersion was deposited on the surface of an adhesive tape previously placed on the sample holder. After the evaporation of the solution, the sample

dc\_1931\_21

holder with the remaining material was gold coated. All the SEM images were obtained on a JSM-6510LV microscope (Jeol) with an acceleration voltage of 20 kV.

### Determination of the SOD concentration

The SOD content that remained in the solution after the adsorption process was measured by the Bradford test.<sup>56</sup> A stock solution of Coomassie Brilliant Blue dye was prepared by dissolving 100 mg in 50 mL of 95% ethanol and by adding 100 mL of 85% phosphoric acid. The solution was then completed with water to 1000 mL in a volumetric flask. Standard solutions of SOD ranging from 1 mg L<sup>-1</sup> to 20 mg L<sup>-1</sup> were prepared and the UV-Vis spectra were recorded after the addition of the dye.

### SOD assay

To determine the enzymatic activity of the bare and immobilized SOD, the classical Fridovich method was used.<sup>57</sup> Accordingly, the system contained xanthine and xanthine oxidase to produce superoxide radicals and nitroblue tetrazolium (NBT) as a scavenger indicator. For a typical test reaction, 0.1 mL of 3 mM xanthine, 0.1 mL of 3 mM NBT and 0.3 mL of 3 mg mL<sup>-1</sup> xanthine oxidase solution were mixed together followed by the addition of 0.1–2.5 mL of the enzyme containing samples. The above listed solutions were all prepared in phosphate buffer at pH 7.5 applying a total phosphate concentration of 1 mM. Upon the reduction of the NBT by the superoxide radicals, it changes its color from yellow to blue and the appearance of an absorption peak at 565 nm was followed with a spectrophotometer (Fig. S1†). Therefore, the absence or only slight formation of the reduced NBT evidences a strong SOD activity, *i.e.*, the efficient capture of the superoxide radicals. The inhibition (*I*) of the NBT-superoxide radical reaction was calculated by the following equation:

$$I = \frac{\Delta A_S - \Delta A_0}{\Delta A_0} \times 100 \quad (1)$$

where  $\Delta A_S$  and  $\Delta A_0$  correspond to the increase in absorbance at 565 nm during 5 min, as a consequence of the formation of the reduced form of NBT in the sample with SOD activity and without any SOD activity, respectively. The inhibition is given in percentage and the so-called IC<sub>50</sub> value represents the concentration of the enzyme corresponding to 50% inhibition.

## Results and discussion

The structure of the bare Mg/Al-CO<sub>3</sub>-LDH was characterized in solid state and its size and charge in aqueous dispersions. SOD adsorption was quantified and the obtained biohybrid was studied by TEM, SEM and by fluorescence and IR spectroscopy. Particle aggregation<sup>53–55,58,59</sup> was followed by DLS, where the colloidal stability as a function of salt and poly-electrolyte concentration was investigated, while electrophoresis was used to probe the charging behavior of the bare and coated particles. These characterizations were performed in two types of media, namely in NaCl solutions and in phos-

phate buffer to test the ion specific effects on the dispersion properties. The enzymatic function of the obtained hybrid materials was finally tested.

### Characterization of Mg/Al-CO<sub>3</sub>-LDH nanoparticles

The XRD pattern of the synthesized Mg/Al-CO<sub>3</sub>-LDH was recorded and the peaks were assigned to the respective diffraction planes (Fig. S2†). It was found that all the characteristic bands reported for hydroxalite-like materials<sup>26</sup> are present indicating the successful synthesis of the lamellar compound. The LDH lattice parameters such as the thickness of the layer with interlayer space (*d*), the height of the platelets (*ν*) with the number of sheets assembling in one platelet (*n*) and the average distance between the metal cations in the sheets (*a*) were calculated. The *ν* value was obtained by employing the Scherrer equation<sup>26</sup> and it was found to be 15.92 nm. By dividing the parameter *ν* with *d*, the *n* value was determined and showed that approximately 21 lamellae construct one platelet. Eventually, twice the position of the (110) reflection gave us an average *a* value of 0.30 nm. Such dimensions are typical for LDH materials.<sup>26,53,60</sup> TEM experiments were performed to characterize the morphology of the Mg/Al-CO<sub>3</sub>-LDH material (Fig. S3†). Platelets of distorted cylindrical shape were observed in the images.

DLS measurements carried out in stable dispersions yielded a hydrodynamic radius of 110 nm and a polydispersity index of 0.30 indicating a relatively narrow particle size distribution of the Mg/Al-CO<sub>3</sub>-LDH. The charging and aggregation properties were investigated in NaCl and phosphate buffer solutions (Fig. 1).

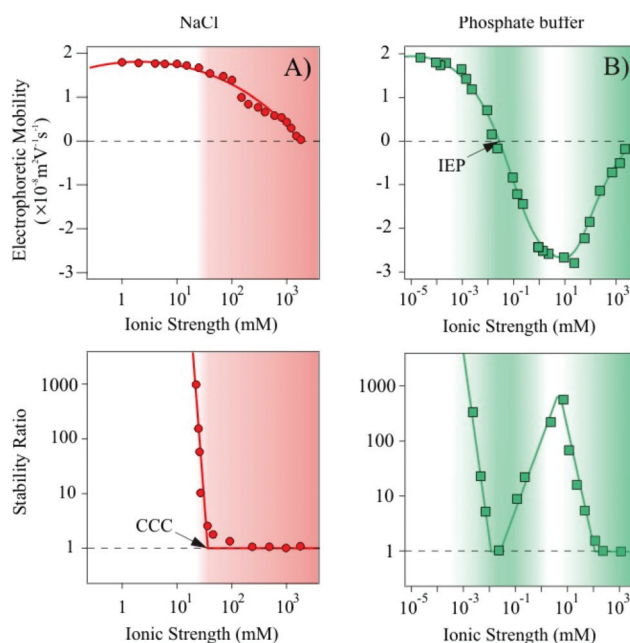


**Fig. 1** Top: electrophoretic mobilities of Mg/Al-CO<sub>3</sub>-LDH particles at different ionic strength set by NaCl (A) or phosphate buffer (B). Bottom: corresponding stability ratio values measured in the same systems. The lines are to guide the eyes and the shaded fields indicate the ionic strength range, where aggregation of the particles takes place.



dc\_1931\_21

Let us first discuss the situation, where the ionic strength was set by NaCl (Fig. 1A). At low ionic strength, the measurements yielded positive electrophoretic mobilities. By increasing the salt level, and therefore, the counterion concentration, screening of the particle charge occurred leading to a progressive decrease in the mobility values. The trend in the stability ratios measured under similar experimental conditions shows a decrease (*i.e.*, increasing aggregation rates) with increasing the NaCl concentration, while the values remained close to one at higher ionic strengths. The break point is referred to as the critical coagulation concentration (CCC).<sup>61</sup> Note that stability ratios close to unity indicate rapid (diffusion limited) particle aggregation, while higher values are signals for slow (reaction limited) aggregation processes.

However, when the ionic strength is set by phosphate buffer the situation is more complex (Fig. 1B). At low salt concentrations, the particles exhibit very similar electrophoretic mobilities compared to the ones determined for the NaCl system, nevertheless, the mobilities rapidly decrease by further addition of salt. Charge neutralization occurred at the isoelectric point (IEP) due to the adsorption of the phosphate species on the oppositely charged particles. Moreover, further adsorption resulted in a significant overcharging leading to Mg/Al-CO<sub>3</sub>-LDH of highly negative charge. An increase in the electrophoretic mobilities was observed at high ionic strength due to the screening effect of the Na<sup>+</sup> counterions on the negatively charged surface.

High stability ratios indicated stable dispersions at low phosphate concentrations, while the values decreased with the salt level until reaching the CCC. The CCC value was found to be in the same range of ionic strength as the IEP obtained from the mobility measurements. However, after a narrow instability region, where the stability ratios were found to be equal to unity within the experimental error, the aggregation slowed down and a maximum was observed in the stability ratios. This maximum appeared at similar phosphate concentrations, where the overcharging maximum occurred. Further increase in the phosphate level led to an acceleration of the aggregation and to unstable systems at higher ionic strengths.

Such charging and aggregation behaviors can fairly be explained by the theory of Derjaguin, Landau, Verwey and Overbeek (DLVO).<sup>61</sup> Accordingly, particles of sufficiently high charge possess an electrical double layer around them leading to an interparticle repulsion upon approach towards another particle. This electrical double layer can either be screened away by salts or can vanish due to charge neutralization by counterion adsorption. In the absence of the electrical double layer repulsion, attractive van der Waals forces predominate and hence, the particles rapidly aggregate.

In our systems, destabilization occurred by charge screening in the NaCl samples. For the phosphate buffer, the first fast aggregation regime is clearly owing to the charge neutralization upon phosphate adsorption, while the second destabilization at high concentration is caused by the screening effect of the Na<sup>+</sup> ions. In addition, the intermediate restabilization maximum is due to the remarkable overcharging and subsequent re-establishment of the repulsive electrical double

layer forces. Similar trends in the colloidal stability have already been reported for LDH particles in the presence of mono or multivalent anions.<sup>52,60</sup>

### Adsorption of SOD on the Mg/Al-CO<sub>3</sub>-LDH platelets

SOD was adsorbed on the Mg/Al-CO<sub>3</sub>-LDH platelets. Since the enzyme and the platelets are oppositely charged at the pH used, we have first followed the charging and aggregation behavior of the particles at different SOD doses at 1 mM ionic strength. This allowed us to determine the protein loadings, which do not destabilize the colloidal dispersion of Mg/Al-CO<sub>3</sub>-LDH. We found that the surface charges were not affected by the SOD adsorption up to an enzyme dose of 10 mg g<sup>-1</sup> (meaning 10 mg of SOD per 1 g of Mg/Al-CO<sub>3</sub>-LDH) resulting in stable dispersions under these experimental conditions (Fig. S4†). However, addition of higher amount of enzyme gave rise to charge neutralization and overcharging leading to unstable dispersions near the IEP and to restabilization of the samples at higher loading. The tendency in the aggregation processes can be explained similarly to the case discussed above for the Mg/Al-CO<sub>3</sub>-LDH platelets in phosphate buffer.

To further prove the adsorption of the enzyme on the surface of the inorganic nanoparticles, the IR spectrum of the Mg/Al-CO<sub>3</sub>-LDH-SOD composite was measured and compared to the spectra of the native enzyme and bare platelet (Fig. 2). The full assignments of the vibrational bands are shown in Table S1.†

From the IR spectrum of the hybrid material, the characteristic peaks of both the SOD and the Mg/Al-CO<sub>3</sub>-LDH components could be identified confirming the immobilization of the enzyme on the surface of the particle. Indeed, several peaks corresponding to the inorganic platelets were found in the range of 450–1400 cm<sup>-1</sup>, in addition to the two absorption bands referring to the bending mode of the CONH amide bond and to the C=C stretching vibration at 1522 cm<sup>-1</sup> and 1633 cm<sup>-1</sup>, respect-

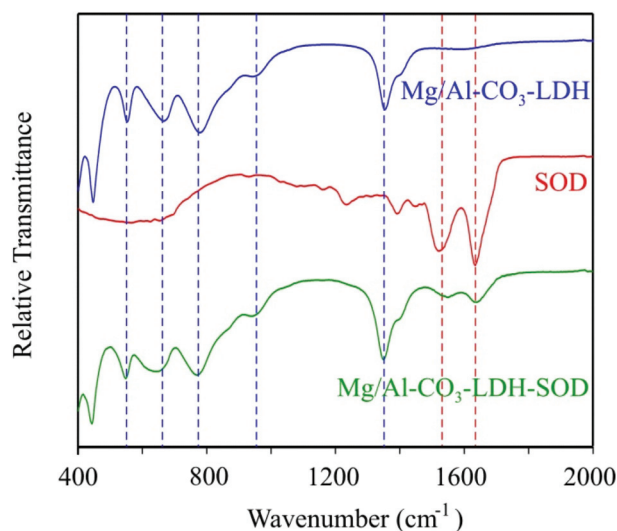


Fig. 2 IR spectra of bare Mg/Al-CO<sub>3</sub>-LDH, native SOD and the hybrid Mg/Al-CO<sub>3</sub>-LDH-SOD materials.

dc\_1931\_21

ively, of the enzyme.<sup>62</sup> This implies that the adsorption of the SOD did occur on the Mg/Al-CO<sub>3</sub>-LDH platelets resulting in the formation of the desired composite material.

Besides, the XRD pattern of the Mg/Al-CO<sub>3</sub>-LDH-SOD was recorded (Fig. S2†). The position of the (003) peak remained unchanged upon addition of SOD indicating no enzyme intercalation between the layers, but rather adsorption on the outer surface. Potential intercalation would increase the interlayer spacing and it would lead to a shift in the location of the (003) diffraction plane.<sup>26</sup>

The adsorption process was also quantified using the Bradford method to determine the SOD concentration in the solutions.<sup>56</sup> In this experiment, 0.1 mL of 10 000 mg L<sup>-1</sup> of particles and 0.1 mL of 100 mg L<sup>-1</sup> of enzyme (corresponding to a SOD dose of 10 mg g<sup>-1</sup>) were mixed together and diluted with 0.3 mL water. The solid material was then filtered off and the Bradford reagent was added to the filtrate. The UV-Vis absorption spectrum was recorded thereafter. The obtained results together with three reference measurements containing different amount of native SOD are shown in Fig. 3.

The absorbance decreases at 465 nm and increases at 595 nm by increasing the enzyme concentration. These shifts of the absorption maximum are based on the binding of the dye to the SOD. The UV-Vis spectrum of the filtrate was identical to the one of the reference sample, which contained no SOD molecules. This finding clearly shows that the enzyme quantitatively adsorbed on the Mg/Al-CO<sub>3</sub>-LDH and that no partitioning between the bulk and surface took place. We assume that the strong attractive forces between the enzyme and the solid support were achieved through electrostatic and hydrophobic interactions as well as by hydrogen bonding. Similarly high affinity has already been reported earlier for polyelectrolytes adsorbing on oppositely charged surfaces.<sup>53,55,60,63,64</sup> It should also be noted that these results

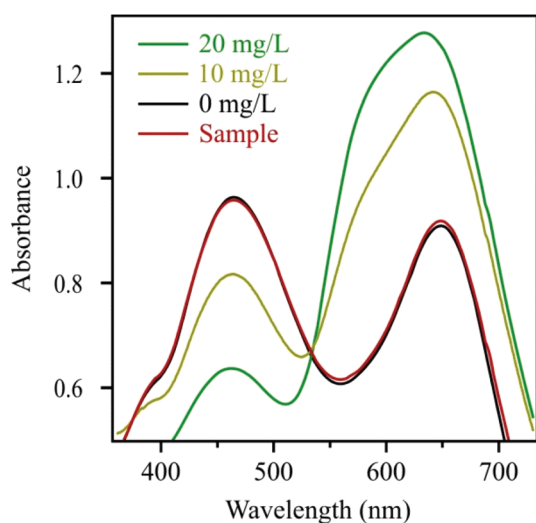


Fig. 3 Bradford tests for standard solutions of SOD of 10 mg L<sup>-1</sup> and 20 mg L<sup>-1</sup> concentrations and for the reference system without enzyme (0 mg L<sup>-1</sup>) as well as for the filtrate after the SOD adsorption process (sample).

indicate quantitative adsorption at SOD doses lower than 10 mg g<sup>-1</sup> too.

### Polyelectrolyte coating

Although SOD was successfully immobilized on the Mg/Al-CO<sub>3</sub>-LDH without significantly changing the colloidal stability of the dispersions, this stability is limited and the particles already aggregated at moderate ionic strengths, as discussed earlier. In order to improve their resistance against salt-induced aggregation, the Mg/Al-CO<sub>3</sub>-LDH-SOD was coated with heparin, which is a biocompatible anticoagulant possessing one of the highest negative line charge density within the natural polyelectrolytes.<sup>65,66</sup> Its effect on colloidal stability of LDH platelets has already been reported.<sup>53</sup>

First, the charging and the aggregation processes in the Mg/Al-CO<sub>3</sub>-LDH-SOD dispersions were investigated by electrophoresis and DLS, respectively. The measurements were carried out at different heparin doses to probe the effect of its adsorption on the colloidal stability and to determine the experimental conditions where highly stable dispersions can be obtained. The recorded electrophoretic mobilities and stability ratios are shown in Fig. 4.

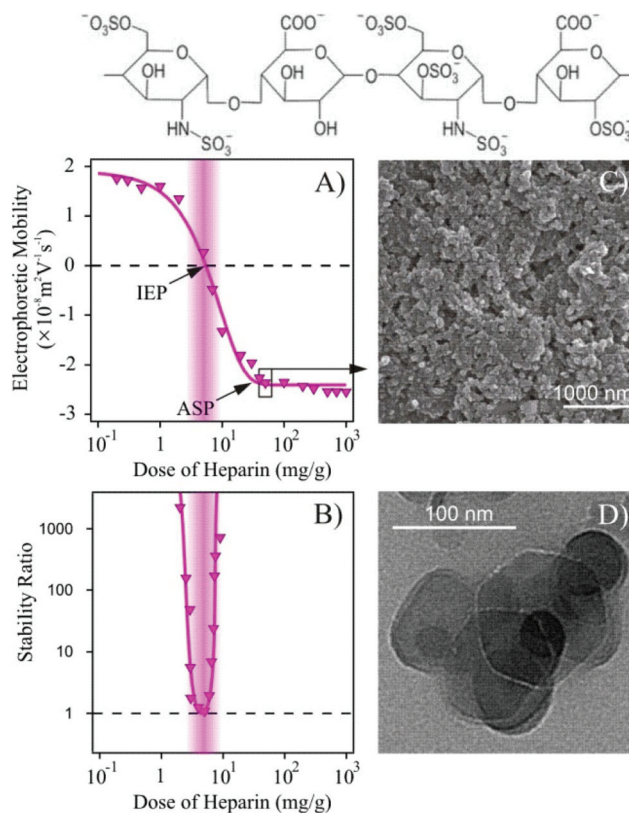


Fig. 4 Electrophoretic mobilities (A) and stability ratios (B) of Mg/Al-CO<sub>3</sub>-LDH-SOD (1 mg g<sup>-1</sup> enzyme load) as a function of the heparin concentration. The measurements were performed at 1 mM NaCl and at 10 mg L<sup>-1</sup> particle concentration. SEM (C) and TEM (D) images of Mg/Al-CO<sub>3</sub>-LDH-SOD obtained with a 50 mg g<sup>-1</sup> heparin coverage. The dose of heparin indicates mg of polyelectrolyte per 1 g of particle. The schematic representation of the heparin structure is shown on the top.

dc\_1931\_21

Increasing the dose of heparin initially led to a decrease in the mobilities, which reached the IEP due to the adsorption of the polyelectrolyte on the oppositely charged platelets (Fig. 4A). Further addition of heparin gave rise to overcharging and the mobilities decreased until the appearance of an adsorption saturation plateau (ASP). The onset of the ASP (around  $20 \text{ mg g}^{-1}$ ) corresponds to the highest possible dose of heparin that can be adsorbed on the particle surface leading to fully coated platelets (Mg/Al-CO<sub>3</sub>-LDH-SOD-Hep). Above this value, no more heparin adsorption is possible on the particles. These phenomena have already been reported in similar LDH-heparin systems<sup>53</sup> and also for other polyelectrolytes in the presence of oppositely charged particles.<sup>58,63,64</sup>

The stability ratios show an extremely narrow curve (Fig. 4B). The particles are unstable around the IEP due to the lack of stabilizing electrical double layers. The partially coated Mg/Al-CO<sub>3</sub>-LDH-SOD of positive charge as well as the negatively charged fully coated ones form stable dispersions at this low ionic strength. As predicted by the DLVO theory, the aggregation is hindered by the repulsive electrical double layer forces, whenever the particles possess sufficiently high surface charge.

The hydrodynamic radii of the Mg/Al-CO<sub>3</sub>-LDH, Mg/Al-CO<sub>3</sub>-LDH-SOD and Mg/Al-CO<sub>3</sub>-LDH-SOD-Hep particles were determined in stable dispersions at 1 mM ionic strength and they were found to be 110 nm, 106 nm and 111 nm, respectively. These values are within the experimental error of the DLS method ( $\pm 5 \text{ nm}$ ) and hence, one can realize that the SOD adsorption and heparin coating did not change the hydrodynamic radius of the bare Mg/Al-CO<sub>3</sub>-LDH significantly. This finding is in good agreement with hydrodynamic layer thickness data of polyelectrolyte chains adsorbed on colloidal particles.<sup>67</sup> Accordingly, thicknesses of up to 3 nm were reported at low ionic strengths and hence, considerable increase in the size of the Mg/Al-CO<sub>3</sub>-LDH platelets cannot be expected upon adsorption of SOD and heparin.

XRD pattern of the Mg/Al-CO<sub>3</sub>-LDH-SOD-Hep composite was measured to check the possible intercalation of the polyelectrolyte between the lamellae (Fig. S2†). The location of the characteristic (003) peak, which is related to the interlayer distance,<sup>26</sup> did not change significantly upon addition of the polyelectrolyte. This fact indicates that heparin intercalation did not take place and that it adsorbed on the outer surface of the particles. Similar observation was reported with other LDH platelets in the presence of heparin.<sup>53</sup>

The IR spectrum of the Mg/Al-CO<sub>3</sub>-LDH-SOD-Hep material was found to be very similar to the one measured for the Mg/Al-CO<sub>3</sub>-LDH-SOD (Fig. S5†) indicating that such a low amount of heparin cannot be detected by this technique.

Fig. 4C and D show the SEM and TEM images, respectively, at doses, where the Mg/Al-CO<sub>3</sub>-LDH-SOD platelets are fully coated with heparin. The TEM image confirms the above mentioned stability. Accordingly, primary particles can be observed on the picture indicating stable dispersions of the Mg/Al-CO<sub>3</sub>-LDH-SOD-Hep composites. Their shape was found to be very similar to the ones observed for the bare Mg/Al-CO<sub>3</sub>-LDH plate-

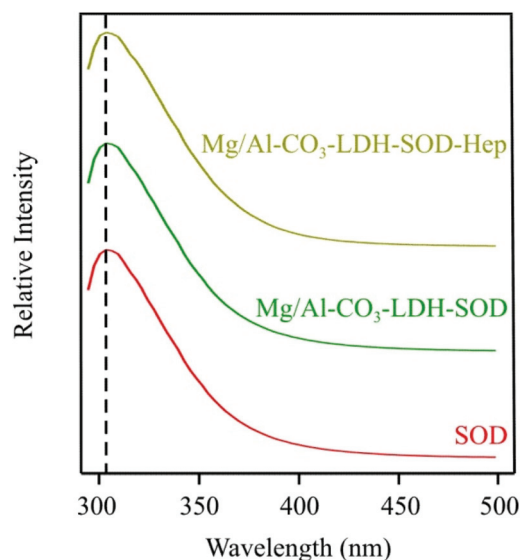


Fig. 5 Emission fluorescence spectra of SOD, Mg/Al-CO<sub>3</sub>-LDH-SOD and Mg/Al-CO<sub>3</sub>-LDH-SOD-Hep. The dashed line indicates the intensities at 306 nm wavelength.

lets (Fig. S3†). It should also be noted that the presence of a few aggregates may originate from the drying process during the sample preparation. Additionally, it was observed from the SEM image that the morphology of the material did not undergo any significant changes upon the SOD doping or heparin coating and exhibits typical LDH-type structure.

Fluorescence spectroscopy has been applied to probe the possible conformational changes in the SOD structure that can occur upon its adsorption on the Mg/Al-CO<sub>3</sub>-LDH surface and during the coating procedure with heparin (Fig. 5).

The 4-hydroxyphenyl side chain groups of the two tyrosine amino acids present in the protein were excited at a wavelength of 283 nm and the fluorescence intensities were followed in the emission wavelength range of 293–500 nm. The intensities at 306 nm wavelength and the recorded emission spectra were found to be similar for all the materials. This finding indicated that the microenvironment of the tyrosine side chains did not change upon their adsorption or coating. This information is crucial, because it indicates that the structural integrity of the SOD enzyme appears preserved meaning that it should lead to similar enzymatic activity in its bare, immobilized and coated forms. This issue will be further discussed later.

### Resistance against salt induced aggregation

In the previous sections, we have found that the dispersions of both Mg/Al-CO<sub>3</sub>-LDH-SOD and Mg/Al-CO<sub>3</sub>-LDH-SOD-Hep particles were stable at 1 mM ionic strength. However, the ionic strength is usually much higher in bioapplications, e.g., 160 mM in blood.<sup>68</sup> Therefore, we have further investigated the charging and aggregation of the bare and heparin-coated hybrid materials of immobilized SOD in a wide range of ionic strengths set either by NaCl or phosphate buffer solutions.



dc\_1931\_21

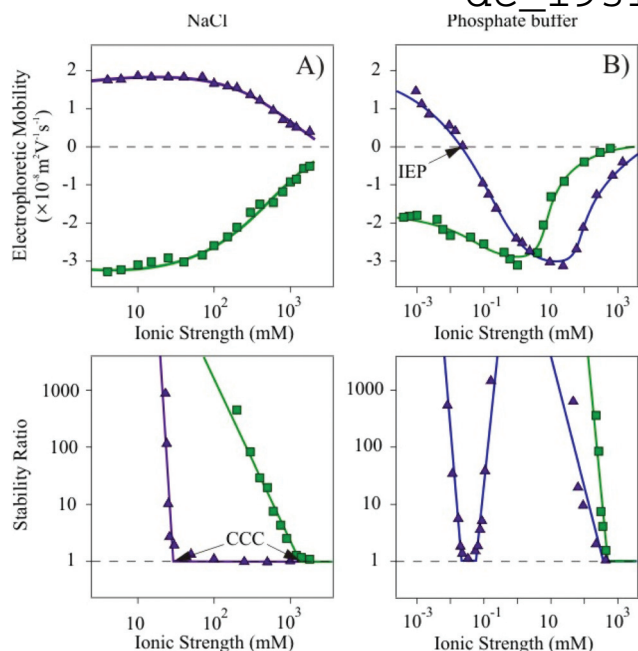


**Fig. 6** Electrophoretic mobilities (top) and stability ratios (bottom) of Mg/Al-CO<sub>3</sub>-LDH-SOD (triangles) and Mg/Al-CO<sub>3</sub>-LDH-SOD-Hep (squares) in NaCl (A) and phosphate buffer (B) solutions at different ionic strengths.

In the NaCl series (Fig. 6A), the Mg/Al-CO<sub>3</sub>-LDH-SOD particles are positively charged, while the Mg/Al-CO<sub>3</sub>-LDH-SOD-Hep ones are negative in the entire ionic strength range due to the overcharging phenomenon induced by the heparin adsorption, as discussed earlier. By comparing the magnitude of the mobility values at low ionic strengths, it is observed that the heparin-coated particles exhibit a higher surface charge, compared to both the bare and SOD modified nanoplatelets (Fig. 1 and 6A). By increasing the NaCl concentration, the surface charges of the Mg/Al-CO<sub>3</sub>-LDH-SOD and the Mg/Al-CO<sub>3</sub>-LDH-SOD-Hep particles are progressively screened by the counterions resulting in a decrease in the magnitude of the electrophoretic mobilities.

In addition, an enormous difference was observed in the CCC values, which were found to be equal to 29 mM and 989 mM for Mg/Al-CO<sub>3</sub>-LDH-SOD and Mg/Al-CO<sub>3</sub>-LDH-SOD-Hep, respectively. This 34 times increase induced by the polyelectrolyte coating probably originates from the establishment of two types of repulsive forces. Accordingly, electrical double layer forces are stronger for the Mg/Al-CO<sub>3</sub>-LDH-SOD-Hep due to their higher surface charge density compared to the bare platelets. Moreover, the adsorbed heparin molecules change their conformation especially at high ionic strengths<sup>67</sup> and hence, polyelectrolyte tails and loops form on the surface leading to steric repulsion between the molecules on the surface, once two coated particles approach each other. Such a powerful electro-steric repulsion has been reported in several polyelectrolyte-particle systems.<sup>53,60,69</sup>

To probe the specific effect of the ionic environment, similar set of experiments was carried out using phosphate

buffer instead of NaCl to set the ionic strength. Indeed, significant variations in the charging and aggregation behavior of the particles could be observed by changing the type of anions in the salts (Fig. 6B).

The tendency in the electrophoretic mobilities of the Mg/Al-CO<sub>3</sub>-LDH-SOD was found to be similar to the one of the Mg/Al-CO<sub>3</sub>-LDH particles shown in Fig. 1B. Accordingly, the charge neutralization at the IEP as well as the overcharging of Mg/Al-CO<sub>3</sub>-LDH-SOD occurred by varying the total phosphate concentration.

The colloidal stability was also analogous to the bare nanoplatelets. The stability ratios were high at low salt levels and in the intermediate phosphate concentration regime, while unstable dispersions were observed near the IEP at 0.035 mM and above 500 mM ionic strength due to the vanishing of the electrical double layer forces. The difference between the tendencies in the stability ratios of the Mg/Al-CO<sub>3</sub>-LDH-SOD particles dispersed in Cl<sup>-</sup> or in phosphate medium is striking due to the significant ion specific effects (*i.e.*, due to the dissimilar affinity of these anions to the oppositely charged surface) on the charging and on the corresponding aggregation behavior. In good agreement with our previous study,<sup>52</sup> our present results clearly show that HPO<sub>4</sub><sup>2-</sup> or H<sub>2</sub>PO<sub>4</sub><sup>-</sup> counterions adsorb strongly, while Cl<sup>-</sup> behaves as an indifferent ion and mainly remains in the bulk.

For the polyelectrolyte-coated Mg/Al-CO<sub>3</sub>-LDH-SOD-Hep, the mobilities follow different tendencies in phosphate buffer. At lower ionic strengths, the materials have high negative surface charge (Fig. 6B). The mobilities show a minimum at 1 mM likely owing to the additional phosphate adsorption on the heparin-coated platelets. The increased Na<sup>+</sup> concentration led to charge screening and to an increase in the electrophoretic mobilities at high ionic strengths, but the values remained negative in the entire concentration range investigated.

The dispersions were highly stable until elevated phosphate concentrations due to the above mentioned electro-steric stabilization mechanism and the CCC was located at a very high ionic strength (Fig. 6B). The fact that we found extremely high CCCs for the Mg/Al-CO<sub>3</sub>-LDH-SOD-Hep platelets in both NaCl and phosphate buffer indicates that the destabilization occurs mainly by the screening effect of the Na<sup>+</sup> ions, which are the bulk-forming counterions of the negatively charged particles, and the type of coions (*i.e.*, Cl<sup>-</sup>, HPO<sub>4</sub><sup>2-</sup> or H<sub>2</sub>PO<sub>4</sub><sup>-</sup>) has no or little influence on the colloidal stability.

Therefore, the advantage of the polyelectrolyte coating is clear. The bare particles aggregate at low ionic strengths in both NaCl and phosphate buffer solutions, whereas the Mg/Al-CO<sub>3</sub>-LDH-SOD-Hep ones form stable dispersions up to high salt levels. Thus, the latter ones are recommended for biomedical or other industrial applications, where the immobilized enzymes can be dispersed in a mixture of different salts at higher ionic strengths.

#### Enzymatic function

Although we have designed highly stable Mg/Al-CO<sub>3</sub>-LDH-SOD-Hep dispersions in the previous section, their ability to



dc\_1931\_21

capture superoxide radicals has to be verified in order to use them as antioxidants in any future applications. The enzymatic activity of the hybrid materials was determined by the Fridovich method<sup>57</sup> and compared to the one of native SOD. This assay is based on superoxide radical production from the xanthine-xanthine oxidase system and the inhibition of NBT reduction by the radicals is followed by measuring the color change in the solutions. The activities were quantified with the IC<sub>50</sub> values, which are the SOD concentrations necessary for the decomposition of half of the superoxide radicals forming in the test reaction.<sup>47,48,50</sup>

Prior to the enzymatic activity measurements with the SOD and its immobilized forms, we have tested the influence of the carrier particles and the coating agent on the probe reaction. The Mg/Al-CO<sub>3</sub>-LDH did not show any superoxide radical capturing ability in the particle concentration range used in our experiments. The role of the heparin in the assay is especially important to probe, since it can inhibit the xanthine-xanthine oxidase reaction by binding to the xanthine oxidase enzyme, which would lead to a smaller amount of superoxide radicals forming in the solution and to a false IC<sub>50</sub> value.<sup>70</sup> However, we found that inhibition of the xanthine oxidase takes place only at heparin concentrations above 20 mg L<sup>-1</sup> (Fig. S6†), which is higher than the maximum polyelectrolyte loading (5 mg L<sup>-1</sup>) applied in our experiments. Therefore, the heparin content in the Mg/Al-CO<sub>3</sub>-LDH-SOD-Hep does not affect the superoxide production in the assay.

Moreover, we found that the immobilization and the heparin coating did not change the activity of the SOD enzyme significantly. Very similar IC<sub>50</sub> values were determined (IC<sub>50</sub>(SOD) = 0.069 mg L<sup>-1</sup>; IC<sub>50</sub>(Mg/Al-CO<sub>3</sub>-LDH-SOD) = 0.056 mg L<sup>-1</sup> and IC<sub>50</sub>(Mg/Al-CO<sub>3</sub>-LDH-SOD-Hep) = 0.096 mg L<sup>-1</sup>) indicating an excellent superoxide radical scavenging activity for all materials. However, the shape of the inhibition *versus* SOD concentration curve is somewhat different for the Mg/Al-CO<sub>3</sub>-LDH-SOD material (Fig. S7†). We believe that this deviation originates from the fact that the Mg/Al-CO<sub>3</sub>-LDH-SOD composite is positively charged and thus, the negatively charged superoxide radicals are attracted electrostatically. This interaction may change the entire dismutation mechanism giving rise to differently shaped inhibition curves.

The fact that the IC<sub>50</sub> value determined for the Mg/Al-CO<sub>3</sub>-LDH-SOD-Hep platelets is similar to the one for the native enzyme means that we have successfully developed a colloidal system containing homogeneously dispersed hybrid particles of significant SOD activity. This novel bionanocomposite holds enormous promises for future biomedical applications and industrial manufacturing processes, wherever stable dispersions are required to decompose ROS including superoxide radicals.

## Conclusions

We report here on the immobilization of SOD enzyme on a nanoparticulate support and the formulation of the hybrid

materials. Mg/Al-CO<sub>3</sub>-LDH were synthesized by the coprecipitation method and successfully modified with the protein owing to its strong affinity to the surface through electrostatic, hydrophobic and hydrogen bonding interactions. No evidence was found for intercalation of SOD in the interlayer space indicating that the adsorption took place on the outer surface of the particles. The Mg/Al-CO<sub>3</sub>-LDH-SOD platelets showed moderate colloidal stability, which were sensitive to the ionic environment in the dispersions. Therefore, the resistance against salt-induced aggregation was improved by surface functionalization with heparin. Its adsorption led to charge neutralization and to overcharging at appropriate polyelectrolyte loadings. The presence of the saturated heparin layer on the particle surface resulted in an enormous stabilization effect for the Mg/Al-CO<sub>3</sub>-LDH-SOD-Hep materials in aqueous dispersions, which were stable up to high ionic strength irrespective of the type of salt dissolved in the samples. The immobilization did not change the structure of the enzyme and very similar enzymatic activities were determined for the native SOD, Mg/Al-CO<sub>3</sub>-LDH-SOD and Mg/Al-CO<sub>3</sub>-LDH-SOD-Hep. To summarize, highly stable dispersions of excellent superoxide radical scavenging activity were developed during the present work. Such systems possess huge potential in applications demanding bionanocatalysts of antioxidant activity used in heterogeneous samples.

## Acknowledgements

This work was supported by the Swiss National Science Foundation (150162), Swiss Secretariat for Education, Research and Innovation (C15.0024), COST Action CM1303 and the University of Geneva. The authors are thankful to Michal Borkovec for providing access to the light scattering instruments in his laboratory. The technical help of Celine Besnard in the XRD measurements is gratefully acknowledged.

## References

- 1 R. A. Sheldon and S. van Pelt, *Chem. Soc. Rev.*, 2013, **42**, 6223–6235.
- 2 Y. H. Lin, Z. W. Chen and X. Y. Liu, *Trends Biotechnol.*, 2016, **34**, 303–315.
- 3 V. E. Bosio, G. A. Islan, Y. N. Martinez, N. Duran and G. R. Castro, *Crit. Rev. Biotechnol.*, 2016, **36**, 447–464.
- 4 J. Mehta, N. Bhardwaj, S. K. Bhardwaj, K. H. Kim and A. Deep, *Coord. Chem. Rev.*, 2016, **322**, 30–40.
- 5 A. Popat, S. B. Hartono, F. Stahr, J. Liu, S. Z. Qiao and G. Q. Lu, *Nanoscale*, 2011, **3**, 2801–2818.
- 6 M. Pita, D. M. Mate, D. Gonzalez-Perez, S. Shleev, V. M. Fernandez, M. Alcalde and A. L. De Lacey, *J. Am. Chem. Soc.*, 2014, **136**, 5892–5895.
- 7 C. Mousty and V. Prevot, *Anal. Bioanal. Chem.*, 2013, **405**, 3513–3523.
- 8 A. Idris and A. Bukhari, *Biotechnol. Adv.*, 2012, **30**, 550–563.

dc\_1931\_21

- 9 N. Loncar and Z. Vujcic, *J. Hazard. Mater.*, 2011, **196**, 73–78.
- 10 A. Liese and L. Hilterhaus, *Chem. Soc. Rev.*, 2013, **42**, 6236–6249.
- 11 R. DiCosimo, J. McAuliffe, A. J. Poulouse and G. Bohlmann, *Chem. Soc. Rev.*, 2013, **42**, 6437–6474.
- 12 P. Santos-Moriano, L. Monsalve-Ledesma, M. Ortega-Munoz, L. Fernandez-Arrojo, A. O. Ballesteros, F. Santoyo-Gonzalez and F. J. Plou, *RSC Adv.*, 2016, **6**, 64175–64181.
- 13 J. H. Bartha-Vari, M. I. Tosa, F. D. Irimie, D. Weiser, Z. Boros, B. G. Vertessy, C. Paizs and L. Poppe, *ChemCatChem*, 2015, **7**, 1122–1128.
- 14 A. Salic, K. Pindric, G. H. Podrepsek, M. Leitgeb and B. Zelic, *Green Process. Synth.*, 2013, **2**, 569–578.
- 15 I. K. Deshapriya, C. S. Kim, M. J. Novak and C. V. Kumar, *ACS Appl. Mater. Interfaces*, 2014, **6**, 9643–9653.
- 16 H. Wu, C. H. Zhang, Y. P. Liang, J. F. Shi, X. L. Wang and Z. Y. Jiang, *J. Mol. Catal. B: Enzym.*, 2013, **92**, 44–50.
- 17 U. Andjelkovic, A. Milutinovic-Nikolic, N. Jovic-Jovicic, P. Bankovic, T. Bajt, Z. Mojovic, Z. Vujcic and D. Jovanovic, *Food Chem.*, 2015, **168**, 262–269.
- 18 E. Geraud, V. Prevot, C. Forano and C. Mousty, *Chem. Commun.*, 2008, 1554–1556.
- 19 A. Cerdobbel, T. Desmet, K. De Winter, J. Maertens and W. Soetaert, *J. Biotechnol.*, 2010, **150**, 125–130.
- 20 A. Fishman, I. Levy, U. Cogan and O. Shoseyov, *J. Mol. Catal. B: Enzym.*, 2002, **18**, 121–131.
- 21 D. Alsafadi and F. Paradisi, *Mol. Biotechnol.*, 2014, **56**, 240–247.
- 22 O. Kudina, A. Zakharchenko, O. Trotsenko, A. Tokarev, L. Ionov, G. Stoychev, N. Puretskiy, S. W. Pryor, A. Voronov and S. Minko, *Angew. Chem., Int. Ed.*, 2014, **53**, 483–487.
- 23 R. C. Rodrigues, C. Ortiz, A. Berenguer-Murcia, R. Torres and R. Fernandez-Lafuente, *Chem. Soc. Rev.*, 2013, **42**, 6290–6307.
- 24 A. J. Patil and S. Mann, *J. Mater. Chem.*, 2008, **18**, 4605–4615.
- 25 C. Mousty, *Appl. Clay Sci.*, 2004, **27**, 159–177.
- 26 D. G. Evans and R. C. T. Slade, in *Layered Double Hydroxides*, ed. X. Duan and D. G. Evans, 2006, vol. 119, pp. 1–87.
- 27 Q. Wang, S. V. Y. Tang, E. Lester and D. O'Hare, *Nanoscale*, 2013, **5**, 114–117.
- 28 Z. Ferencz, A. Kukovecz, Z. Konya, P. Sipos and I. Palinko, *Appl. Clay Sci.*, 2015, **112**, 94–99.
- 29 I. Dekany, F. Berger, K. Imrik and G. Lagaly, *Colloid Polym. Sci.*, 1997, **275**, 681–688.
- 30 Z. P. Xu, G. Stevenson, C. Q. Lu and G. Q. Lu, *J. Phys. Chem. B*, 2006, **110**, 16923–16929.
- 31 J. He, M. Wei, B. Li, Y. Kang, D. G. Evans and X. Duan, in *Layered Double Hydroxides*, ed. X. Duan and D. G. Evans, 2006, vol. 119, pp. 89–119.
- 32 H. F. Bao, J. P. Yang, Y. Huang, Z. P. Xu, N. Hao, Z. X. Wu, G. Q. Lu and D. Y. Zhao, *Nanoscale*, 2011, **3**, 4069–4073.
- 33 F. Bruna, M. G. Pereira, M. Polizeli and J. B. Valim, *ACS Appl. Mater. Interfaces*, 2015, **7**, 18832–18842.
- 34 M. S. P. Lopez, F. Leroux and C. Mousty, *Sens. Actuators, B*, 2010, **150**, 36–42.
- 35 Z. An, S. Lu, J. He and Y. Wang, *Langmuir*, 2009, **25**, 10704–10710.
- 36 S. Vial, V. Prevot, F. Leroux and C. Forano, *Microporous Mesoporous Mater.*, 2008, **107**, 190–201.
- 37 N. Zou and J. Plank, *J. Phys. Chem. Solids*, 2012, **73**, 1127–1130.
- 38 A. Bafana, S. Dutt, S. Kumar and P. S. Ahuja, *Crit. Rev. Biotechnol.*, 2011, **31**, 65–76.
- 39 Y. M. Fan, X. D. Cao, T. Hu, X. G. Lin, H. Dong and X. N. Zou, *J. Phys. Chem. C*, 2016, **120**, 3955–3963.
- 40 K. Kamada, A. Yamada and N. Soh, *RSC Adv.*, 2015, **5**, 85511–85516.
- 41 S. Singh and V. K. Dubey, *Int. J. Pept. Res. Ther.*, 2016, **22**, 171–177.
- 42 J. Tang, X. Zhu, X. H. Niu, T. T. Liu, H. L. Zhao and M. B. Lan, *Talanta*, 2015, **137**, 18–24.
- 43 X. Zhu, X. H. Niu, H. L. Zhao, J. Tang and M. B. Lan, *Biosens. Bioelectron.*, 2015, **67**, 79–85.
- 44 S. Bobone, E. Miele, B. Cerroni, D. Roversi, A. Bocedi, E. Nicolai, A. Di Venere, E. Placidi, G. Ricci, N. Rosato and L. Stella, *Langmuir*, 2015, **31**, 7572–7580.
- 45 Y. C. Fang, H. C. Lin, I. J. Hsu, T. S. Lin and C. Y. Mou, *J. Phys. Chem. C*, 2011, **115**, 20639–20652.
- 46 Z. Csendes, C. Dudas, G. Varga, E. G. Bajnoczi, S. E. Canton, P. Sipos and I. Palinko, *J. Mol. Struct.*, 2013, **1044**, 39–45.
- 47 I. Szilagyi, I. Labadi, K. Hernadi, I. Palinko, I. Fekete, L. Korecz, A. Rockenbauer and T. Kiss, *New J. Chem.*, 2005, **29**, 740–745.
- 48 I. Szilagyi, I. Labadi, K. Hernadi, T. Kiss and I. Palinko, in *Molecular Sieves: From Basic Research to Industrial Applications, Pts a and B*, ed. J. Cejka, N. Zilkova and P. Nachtigall, 2005, vol. 158, pp. 1011–1018.
- 49 L. Yuan, S. L. Liu, W. W. Tu, Z. S. Zhang, J. C. Bao and Z. H. Dai, *Anal. Chem.*, 2014, **86**, 4783–4790.
- 50 I. Szilagyi, O. Berkesi, M. Sipiczki, L. Korecz, A. Rockenbauer and I. Palinko, *Catal. Lett.*, 2009, **127**, 239–247.
- 51 T. L. Moore, L. Rodriguez-Lorenzo, V. Hirsch, S. Balog, D. Urban, C. Jud, B. Rothen-Rutishauser, M. Lattuada and A. Petri-Fink, *Chem. Soc. Rev.*, 2015, **44**, 6287–6305.
- 52 M. Pavlovic, R. Huber, M. Adok-Sipiczki, C. Nardin and I. Szilagyi, *Soft Matter*, 2016, **12**, 4024–4033.
- 53 M. Pavlovic, L. Li, F. Dits, Z. Gu, M. Adok-Sipiczki and I. Szilagyi, *RSC Adv.*, 2016, **6**, 16159–16167.
- 54 M. Schudel, S. H. Behrens, H. Holthoff, R. Kretzschmar and M. Borkovec, *J. Colloid Interface Sci.*, 1997, **196**, 241–253.
- 55 K. L. Chen, S. E. Mylon and M. Elimelech, *Langmuir*, 2007, **23**, 5920–5928.
- 56 M. M. Bradford, *Anal. Biochem.*, 1976, **72**, 248–254.
- 57 C. Beaucham and I. Fridovich, *Anal. Biochem.*, 1971, **44**, 276–287.

dc 1931\_21

- 58 A. Tiraferri and M. Borkovec, *Sci. Total Environ.*, 2015, **535**, 131–140.
- 59 J. Smith, G. B. Webber, G. G. Warr and R. Atkin, *Langmuir*, 2014, **40**, 1506–1513.
- 60 M. Pavlovic, P. Rouster, T. Oncsik and I. Szilagyi, *ChemPlusChem*, 2016, DOI: 10.1002/cplu.201600295.
- 61 D. F. Evans and H. Wennerstrom, *The Colloidal Domain*, John Wiley, New York, 1999.
- 62 J. T. Klopogge and R. L. Frost, *Appl. Catal., A*, 1999, **184**, 61–71.
- 63 I. Popa, G. Gillies, G. Papastavrou and M. Borkovec, *J. Phys. Chem. B*, 2010, **114**, 3170–3177.
- 64 I. Szilagyi, G. Trefalt, A. Tiraferri, P. Maroni and M. Borkovec, *Soft Matter*, 2014, **10**, 2479–2502.
- 65 G. A. Crespo, M. G. Afshar and E. Bakker, *Angew. Chem., Int. Ed.*, 2012, **51**, 12575–12578.
- 66 B. Casu, A. Naggi and G. Torri, *Carbohydr. Res.*, 2015, **403**, 60–68.
- 67 E. Seyrek, J. Hierrezuelo, A. Sadeghpour, I. Szilagyi and M. Borkovec, *Phys. Chem. Chem. Phys.*, 2011, **13**, 12716–12719.
- 68 I. Bertini, H. B. Gray, S. J. Lippard and J. S. Valentine, *Bioinorganic chemistry*, University Science Books, Mill Valley, 1994.
- 69 E. Illes and E. Tombacz, *J. Colloid Interface Sci.*, 2006, **295**, 115–123.
- 70 R. Radi, H. Rubbo, K. Bush and B. A. Freeman, *Arch. Biochem. Biophys.*, 1997, **339**, 125–135.

**SPECIAL ISSUE**  
**Immobilization of Superoxide Dismutase on Polyelectrolyte-Functionalized Titania Nanosheets**Paul Rouster,<sup>[a]</sup> Marko Pavlovic,<sup>[a]</sup> and Istvan Szilagyi<sup>\*[a, b]</sup>

The superoxide dismutase (SOD) enzyme was successfully immobilized on titania nanosheets (TNS) functionalized with the poly(diallyldimethylammonium chloride) (PDADMAC) polyelectrolyte. The TNS–PDADMAC solid support was prepared by hydrothermal synthesis followed by self-assembled polyelectrolyte layer formation. It was found that SOD strongly adsorbed onto oppositely charged TNS–PDADMAC through electrostatic and hydrophobic interactions. The TNS–PDADMAC–SOD material was characterized by light scattering and microscopy tech-

niques. Colloidal stability studies revealed that the obtained nanocomposites possessed good resistance against salt-induced aggregation in aqueous suspensions. The enzyme kept its functional integrity upon immobilization; therefore, TNS–PDADMAC–SOD showed excellent superoxide radical anion scavenging activity. The developed system is a promising candidate for applications in which suspensions of antioxidant activity are required in the manufacturing processes.

**Introduction**

The superoxide radical anion is known as the primary reactive oxygen species (ROS), as it can be spontaneously transformed into other ROS. The most-efficient defenders against these radicals are the superoxide dismutase (SOD) enzymes, which may contain different redox-active metal ions in their active centres.<sup>[1–3]</sup> Among them, the copper(II)–zinc(II) SOD is present in the plasma and in extracellular spaces, and it decomposes superoxide radicals into molecular oxygen and hydrogen peroxide.<sup>[4–6]</sup> The latter molecules are subsequently removed by the catalase enzyme.<sup>[7]</sup> However, supplementation of SOD is difficult owing to its high sensitivity to environmental conditions (e.g., temperature, pH, and complex nature in biofluids). Therefore, significant efforts have been made to prepare metal complexes,<sup>[8–12]</sup> nanoparticles or colloidal particles,<sup>[13]</sup> or their combinations<sup>[14–18]</sup> to obtain artificial SOD materials of similar activity, but with improved sensitivity relative to that of the native enzyme.

Besides, a promising way to improve the sensitivity and recyclability of SOD is to immobilize it on solid supports, such as inorganic particles,<sup>[19–23]</sup> polymers,<sup>[24,25]</sup> or other hybrid mate-


rials.<sup>[26]</sup> In addition, enzyme cascades containing SOD, catalase, or other peroxidase enzymes have been prepared, for which these natural biocatalysts were confined in silica nanoparticles,<sup>[27,28]</sup> polymeric vesicles,<sup>[29–31]</sup> or nanocontainers<sup>[32]</sup> to mimic the cellular environment and to achieve complete decomposition of ROS into molecular oxygen and water. Antioxidant enzymes have also been covalently linked to polymeric chains to obtain such antioxidant cascades.<sup>[33,34]</sup>


Titania materials are of great potential in enzyme immobilization owing to their advantageous surface properties as well as their chemical and thermal stability. Titania is an important class of materials that are widely used in many different fields including photocatalysis<sup>[35]</sup> and biomedical treatment.<sup>[36]</sup> In addition, immobilization of different enzymes on titanium-oxide supports has been achieved in various ways, and such nanocomposites were tested in enzymatic assays.<sup>[20,23,37–39]</sup> For instance, SOD was attached to titania-modified electrodes by physical adsorption to develop biosensors for detection of the superoxide radical anion.<sup>[20]</sup> It was found that the pH of the solution significantly influenced the nature of the interactions owing to the pH-dependent charging behaviour of the enzyme and titania and, hence, the efficiency of electron transfer of the SOD immobilized on the electrode surface. Titania nanosheets (TNS) of a few nanometers in the lateral dimension and SOD were mixed in aqueous suspensions, and the superoxide radical scavenging activity was tested.<sup>[23]</sup> Relative to the activity of the native enzyme, the addition of the TNS remarkably increased the SOD-like activity of the system.

However, less attention has been paid to the colloidal stability of the investigated titania–enzyme suspensions. This issue is critical in the design of suspensions of enzyme-like function, as aggregation and subsequent sedimentation of the carrier particles lead to lower enzyme-like activity and may prevent the application of such biocatalysts in liquid media. No systematic

[a] Dr. P. Rouster, M. Pavlovic, Dr. I. Szilagyi  
Department of Inorganic and Analytical Chemistry, University of Geneva  
30 Quai Ernest-Ansermet, 1205 Geneva (Switzerland)  
E-mail: istvan.szilagyi@unige.ch

[b] Dr. I. Szilagyi  
MTA-SZTE Lendület Biocolloids Research Group  
Department of Physical Chemistry and Materials Science  
University of Szeged  
1 Aradi vértanúk tere, 6720 Szeged (Hungary)  
E-mail: szistvan@chem.u-szeged.hu

 The ORCID identification numbers for the authors of this article can be found under <https://doi.org/10.1002/cbic.201700502>.

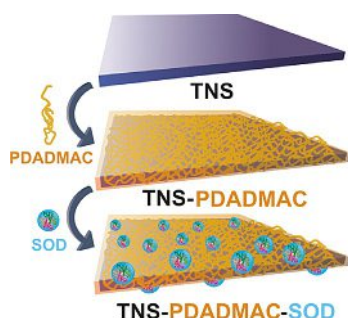
 This article is part of a Special Issue on Biocatalysis, which commemorates the BioTrans2017 Symposium in Budapest, Hungary.



studies on the aggregation of nanocomposites composed of SOD and titania have been published yet.

Nevertheless, significant effort has been made to improve the colloidal stability of bare titania particles of different shapes. Polyelectrolytes were found to be the most-effective stabilizing agents. Accordingly, poly(diallyldimethylammonium chloride) (PDADMAC) was used to coat the surface of titanium oxide nanosheets<sup>[40]</sup> and nanowires<sup>[41]</sup> to give rise to suspensions that were more stable than the bare materials. Charging and aggregation studies on protamine-functionalized particles shed light on the fact that the shape of the titania nanostructures did not affect the suspension stability.<sup>[42]</sup> An enormous stabilization effect against salt-induced aggregation was found for titanate nanowires once their surfaces were saturated with poly(styrene sulfonate)<sup>[43]</sup> or poly(amido amine) dendrimers.<sup>[44,45]</sup> In these studies, the polyelectrolytes were always useful to improve the colloidal stability of the titanium-oxide nanostructures; however, no information is available in the literature about the effect of the functionalizing polyelectrolyte of titania–enzyme hybrids.

The present study deals with the stability of TNS in the presence of the PDADMAC polyelectrolyte and on the immobilization of the SOD enzyme on the TNS–PDADMAC composite materials (Scheme 1). In addition, the superoxide radical anion scavenging activity of the obtained catalysts was tested and compared to that of the native enzyme.



**Scheme 1.** Schematic representation of SOD immobilization on PDADMAC-functionalized TNS.

## Results and Discussion

The effect of the PDADMAC dose on the charging and aggregation of the TNS was explored first by electrophoresis and dynamic light scattering (DLS), respectively. The main goal of this part of the study was to find the experimental conditions (i.e., the polyelectrolyte dose) under which stable particle suspensions could be obtained and used for the ensuing immobilization of the SOD enzyme. The pH of the suspensions was always kept at 7 with phosphate buffer, and the samples contained 4.5 mM NaCl to adjust the ionic strength.

The electrophoretic mobilities recorded at different PDADMAC loadings are presented in Figure 1A. The negative mobility values at low polyelectrolyte doses reflect the negative charge of the bare TNS at this pH,<sup>[40]</sup> and as a result of the low amount of oppositely charged PDADMAC, the surface charge

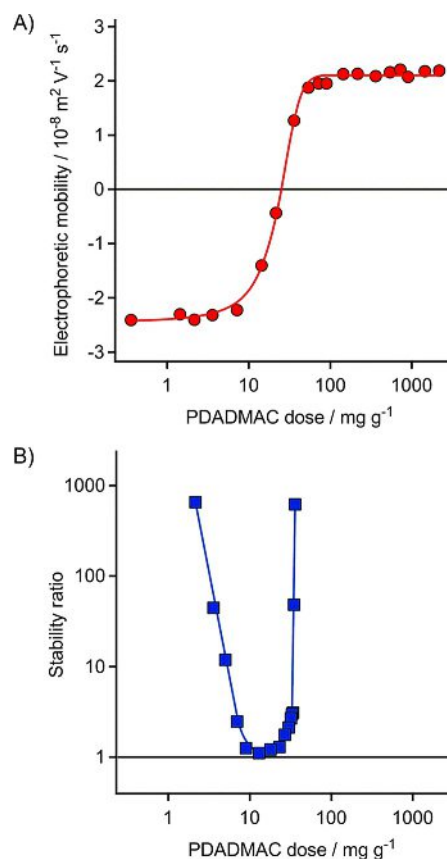


**Figure 1.** A) Electrophoretic mobility and B) stability ratio values of TNS in the presence of PDADMAC at pH 7. The samples contained 1 mM phosphate buffer and 4.5 mM NaCl to adjust the pH and the background electrolyte level, respectively. The mg g<sup>-1</sup> unit on the x axes indicates mg of polyelectrolyte per gram of particle. The lines are just to guide the eyes. Note that stability ratios close to unity refer to rapid particle aggregation and unstable suspensions, whereas higher values indicate more stable samples.

was compensated only to a small extent by the adsorbed polyelectrolytes. Such an adsorption process is clearly indicated by an increase in the mobility upon increasing the PDADMAC concentration, leading to charge neutralization at intermediate doses. Furthermore, the adsorption process continued after the charge neutralization point, and charge reversal of the TNS particles occurred. Such an inversion of the original charge is typical for charged surfaces in the presence of oppositely charged polyelectrolytes.<sup>[46–51]</sup> At high doses, the surface became saturated with adsorbed PDADMAC, and hence, the electrophoretic mobilities reached a plateau. Further added polyelectrolytes remained dissolved in the solution. These dissolved PDADMAC molecules do not affect the mobilities in this regime owing to their low scattered intensities (0.8 kcps at 0.14 mg L<sup>-1</sup> PDADMAC concentration) relative to those of the PDADMAC-coated TNS (120.6 kcps at 144 mg g<sup>-1</sup> polyelectrolyte dose).

The stability ratio values were measured by time-resolved DLS measurements by using the standard technique, which compares the aggregation rate constants with that determined in rapidly aggregating suspensions at high salt levels, as detailed elsewhere.<sup>[52]</sup> Note that stability ratios close to 1 indicate

unstable suspensions and fast aggregation, whereas higher values refer to more stable suspensions. The inverse of the stability ratio is equal to the fraction of successful (i.e., results in dimer formation) particle collisions in the system.<sup>[53]</sup> For instance, a stability ratio value of 10 means that 10% of the particle collisions leads to the formation of a particle dimer.

The particles were stable at low and high PDADMAC doses, as indicated by very high or not even measurable stability ratios (Figure 1B). In the intermediate regime, however, the stability ratios formed a U-shaped curve with a minimum near the polyelectrolyte dose corresponding to the charge-neutralization point in the electrophoretic measurements. The stability ratios were within the experimental error at this minimum, indicating rapid particle aggregation and unstable suspensions. This behaviour can be explained by the theory developed by Derjaguin, Landau, Verwey, and Overbeek,<sup>[49]</sup> and it is similar to that experienced earlier in systems containing charged colloidal particles and oppositely charged polyelectrolytes.<sup>[19,40–45,48,49]</sup> Accordingly, the nanosheets possessed sufficient charge at low and high doses, as indicated by the electrophoretic mobilities (Figure 1A), and the repulsive electrical double-layer forces stabilized the samples. At the charge-reversal point, the overall charge of the particles was close to zero, the electrical double layers vanished, and thus the attractive van der Waals forces destabilized the suspensions.

In the next step, SOD was immobilized on PDADMAC-functionalized TNS (TNS–PDADMAC) by applying a polyelectrolyte dose of 144 mg g<sup>-1</sup>. Under these conditions, PDADMAC formed a saturated layer on the surface of the TNS to give rise to positively charged particles. Owing to the fact that the enzyme has a negative net charge at the corresponding pH,<sup>[54]</sup> immobilization was expected to occur through electrostatic attraction between SOD and the TNS–PDADMAC hybrid.

The electrophoretic mobilities of the TNS–PDADMAC particles were measured at different SOD loadings (Figure 2), and the values decreased at higher doses, which indicated adsorption of the enzyme. However, the mobilities were high and constant up to a dose of 10 mg g<sup>-1</sup> SOD, as the adsorbed enzymes did not change the surface charge behaviour of TNS–PDADMAC at such low concentrations. An enzyme dose of 1 mg g<sup>-1</sup> was chosen for subsequent experiments, because it was found that at this dose the TNS–PDADMAC–SOD nanocomposite formed a stable suspension owing to repulsion by

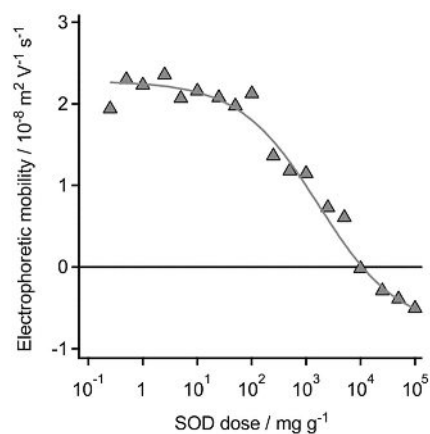


**Figure 2.** Electrophoretic mobility of TNS–PDADMAC particles at different SOD doses at pH 7. The mg g<sup>-1</sup> unit on the x-axis indicates mg of SOD per gram of particle. The lines serve to guide the eyes.

the electrical double layers and the enzyme quantitatively adsorbed on the surface of the hybrid materials. The latter result was obtained on the basis of the colorimetric determination<sup>[55]</sup> of SOD in the surrounding solution, which showed that more than 98% of the added enzyme molecules adsorbed on the TNS–PDADMAC surface and that only a negligible amount remained in solution. A similarly strong interaction between SOD and the clay particles was recently reported,<sup>[19]</sup> and it was suspected that the adsorption took place not only through electrostatic interactions, but also through hydrophobic forces and hydrogen bonding.

Transmission electron microscopy (TEM) imaging was performed to explore the morphology of bare TNS, PDADMAC-functionalized TNS, and PDADMAC and SOD-functionalized TNS (Figure 3). The suspensions were dried prior to imaging; therefore, some particle dimers can be seen in the pictures. However, it is evident from Figure 3 that the morphology of the nanosheets did not change upon polyelectrolyte functionalization and subsequent modification with the enzyme.

Given the fact that immobilized enzymes are often used in liquid environments containing electrolytes, the resistance of the TNS–PDADMAC and TNS–PDADMAC–SOD materials against salt-induced aggregation was tested. Accordingly, charging and aggregation at different ionic strengths adjusted with

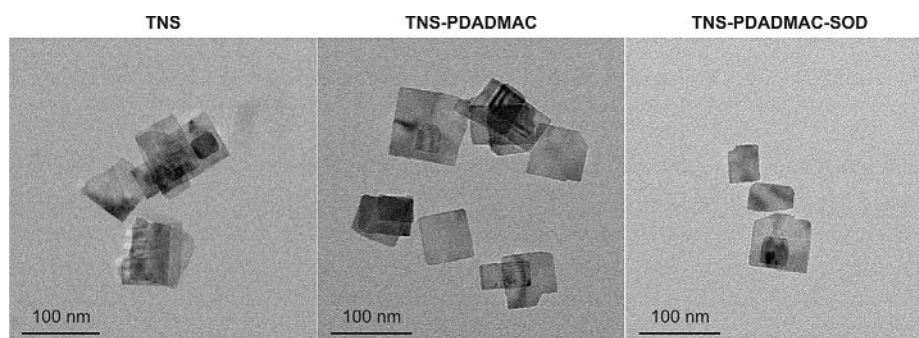


**Figure 3.** TEM images of bare TNS, TNS–PDADMAC, and TNS–PDADMAC–SOD recorded after drying stable suspensions.

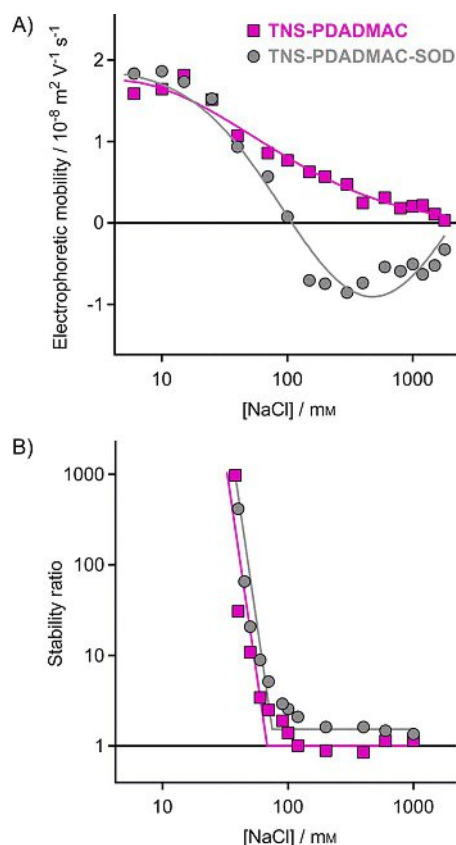


**Figure 4.** A) Electrophoretic mobilities and B) stability ratios of the TNS-PDADMAC and TNS-PDADMAC-SOD materials as a function of NaCl concentration at pH 7. The solid lines are just to guide the eyes.

NaCl were investigated by electrophoresis and DLS, respectively.

The electrophoretic mobilities decreased with the NaCl concentration in both cases owing to the screening effect of the electrolyte on the surface charge (Figure 4A). However, one striking difference was found between the two plots. The mobilities of TNS-PDADMAC remained positive over the entire ionic-strength range investigated, whereas for TNS-PDADMAC-SOD a charge inversion occurred at high NaCl concentrations indicated by slightly negative mobility values. It is suspected that this charge reversal is due to the specific affinity of the chloride anions to the enzyme, and this adsorption process turns the surface charge of TNS-PDADMAC-SOD negative at elevated salt levels. Similar behaviour of polyelectrolyte-coated particles was previously reported in the presence of monovalent anions of high concentration.<sup>[40,56]</sup> In addition, ion condensation and subsequent change in the effective charge was previously reported with synthetic and natural polyelectrolytes.<sup>[49]</sup> Such a phenomenon may lead to slight charge reversal of the polyelectrolyte-coated colloidal particles at high electrolyte concentrations.

Nevertheless, the different charging behaviour was not reflected in the aggregation processes followed under identical experimental conditions. As shown in Figure 4B, very similar stability ratios were measured for both TNS-PDADMAC and TNS-PDADMAC-SOD. Slow aggregation was observed at low

salt levels, and unstable suspensions were detected at high ionic strengths. These regimes were separated by the critical coagulation concentration (CCC), which indicates the NaCl concentration corresponding to the onset of the fast aggregation region.

The lack of restabilization due to charge reversal in the case of TNS-PDADMAC-SOD is a result of the low surface charge, that is, weak electrical double-layer forces, at high NaCl concentrations. Such a weak repulsion could not predominate over the attractive van der Waals forces acting between the particles. However, one small difference can be observed between the two curves. Accordingly, the stability ratios of TNS-PDADMAC-SOD are systematically slightly higher than one in the fast aggregation regime after the CCC, which implies that an additional weak repulsive force is present in the system. The force is most likely of steric<sup>[57-59]</sup> origin because of the overlap of the adsorbed SOD molecules upon the approach of two particles. This type of force is usually stronger if it is induced by adsorbed polyelectrolytes of higher molecular weight and/or lower line charge density.<sup>[19,40,44]</sup>

Finally, the superoxide radical anion scavenging activities of the native and immobilized SOD enzyme were tested in the Fridovich assay.<sup>[60]</sup> In brief, the radicals were produced by the reaction between xanthine and xanthine oxidase under aerobic conditions, by which they reacted with nitroblue tetrazolium (NBT) indicator molecules and changed their colour from yellow to blue upon reduction by the radicals. Such a colour change was followed spectrophotometrically, and the inhibition of the NBT-superoxide anion reaction was calculated on the basis of the development of the blue colour and was plotted against the SOD concentration (Figure 5). The SOD activities were expressed as  $IC_{50}$  values, which correspond to the SOD concentration needed to decompose 50% of the superoxide radical anions formed in the reaction mixture.

As shown in Figure 5, the inhibition curves are very similar for both SOD and TNS-PDADMAC-SOD, indicating that the enzyme kept its structural and functional integrity upon immobilization on the PDADMAC-modified TNS. Note that enzyme-free TNS-PDADMAC did not show any SOD-like activity in this

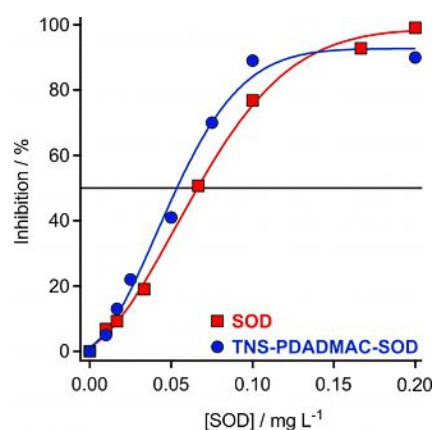


**Figure 5.** Superoxide radical anion scavenging activity of the native (SOD) and immobilized (TNS-PDADMAC-SOD) enzymes measured by the Fridovich assay.<sup>[60]</sup>



concentration regime. The IC<sub>50</sub> value was found to be slightly smaller for TNS-PDADMAC-SOD (0.057 mg L<sup>-1</sup>) than for native SOD (0.069 mg L<sup>-1</sup>). This increase in activity is most likely due to the positive surface charge of TNS-PDADMAC-SOD, which attracts the oppositely charged substrate and, thus, brings the superoxide radical anions to SOD immobilized on the surface.

On the basis of these results, one can conclude that highly stable suspensions of immobilized SOD were obtained, and the prepared TNS-PDADMAC-SOD materials exhibited high superoxide radical anion scavenging activity in the test reactions. The TNS-PDADMAC-SOD nanocomposite is of great potential in both biomedical treatments and chemical manufacturing processes in the food, textile, and cosmetic industries, or wherever the aim is to decompose ROS in aqueous suspensions; however, the suitability of the materials needs to be further investigated prior to their use in such applied processes.

## Conclusion

Stable suspensions of immobilized superoxide dismutase (SOD) enzyme were developed to scavenge superoxide radical anions. As the nanoparticulate support, poly(diallyldimethylammonium chloride) (PDADMAC)-functionalized titania nanosheets (TNS) were prepared by electrostatic adsorption of the oppositely charged polyelectrolyte on the nanosheet surface. Such adsorption led to charge neutralization at intermediate doses, and the suspensions were unstable in this regime. However, the samples were highly stable at doses for which a saturated PDADMAC layer formed on the TNS surface. SOD immobilization occurred through electrostatic and hydrophobic forces, which led to strong adsorption of the enzyme on the solid support. The morphology of the particles remained unaffected upon PDADMAC coating and SOD immobilization, and the obtained TNS-PDADMAC-SOD nanocomposite showed good resistance against salt-induced aggregation. The immobilized enzyme was found to be slightly more active in scavenging superoxide radical anions than the native one, most probably due to electrostatic attraction of the substrate to the particle surface. The developed stable suspensions of SOD can be recommended as antioxidants in liquid media applications, for which the level of superoxide radical anions has to be decreased.

## Experimental Section

**Materials:** The TNS were synthesized according to a procedure described elsewhere.<sup>[40]</sup> Briefly, tetrabutyl titanate was treated with hydrofluoric acid in an autoclave at an elevated temperature, and the resulted precursor material was filtered and thoroughly washed with water and ethanol. The obtained powder was washed with NaOH and water several times, and then, the obtained TNS were allowed to dry in an oven.

SOD (from bovine erythrocytes); PDADMAC (100–200 kDa molecular weight); Coomassie Brilliant Blue G; NBT; xanthine oxidase (from bovine milk); xanthine, and analytical-grade NaCl, NaOH, NaH<sub>2</sub>PO<sub>4</sub>·H<sub>2</sub>O, and Na<sub>2</sub>HPO<sub>4</sub>·2H<sub>2</sub>O were purchased from Sigma-Aldrich. Ethanol of reagent grade was bought from Fisher Scientific.

High-purity water (Millipore) was used for the preparation of all samples.

Prior to the PDADMAC coating of the TNS, the nanosheets were dispersed in pH 7 phosphate buffer solution. TNS-PDADMAC suspensions were prepared by mixing calculated amounts of PDADMAC and TNS under magnetic agitation for 2 h to allow the polyelectrolyte to fully coat the particles. The solution was then centrifuged at 10000 rpm for 20 min. The supernatant was removed, and the slurry was redispersed in 5 mM NaCl solution. Freshly prepared TNS-PDADMAC suspensions were made prior to SOD adsorption on the particles.

**Light scattering:** DLS experiments were performed in the time-resolved mode with a compact goniometer (CGS-3, ALV) at a scattering angle of 90°. The correlation function was acquired during 50–300 runs of 20 s each, depending on the speed of aggregation. By using a second-order cumulant fit, the hydrodynamic radius was obtained. The colloidal stability of the system was expressed in terms of stability ratio.<sup>[53]</sup> Unstable suspensions resulted in stability ratios close to unity, whereas more-stable suspensions were observed for higher stability ratio values. For the DLS experiments, 2 mL samples were prepared, for which the final particle concentration was set to 1 mg L<sup>-1</sup>. The ionic strength, polyelectrolyte, and enzyme doses were adjusted by mixing the appropriate amounts of NaCl solutions with stock solutions of PDADMAC and/or SOD.

**Electrophoresis:** Electrophoretic mobilities were measured with a Zetasizer Nano ZS (Malvern) instrument. The samples were prepared in a manner similar to that used for the DLS experiments, but differed in the final total volume. Accordingly, 5 mL suspensions were prepared for the electrophoretic measurements, and the samples were left to rest overnight before measuring their electrophoretic mobilities.

**Electron microscopy:** The samples were imaged by TEM (Tecnai G2 Sphera microscope, FEI). The device was equipped with a LaB6 cathode, and a voltage of 120 kV was applied for image recording. Prior to deposition of the colloidal dispersions on carbon hexagonal meshes (CF200H-CU-UL, Electron Microscopy Sciences), these meshes were treated by plasma for 20 s to increase their hydrophilicity. After an adsorption time of 2 min, the excess solution was removed from the mesh with a filter paper. The samples were then mounted on the specimen and placed in the microscope for imaging.

**Bradford test:** A stock solution of Coomassie Brilliant Blue dye was prepared by dissolving Coomassie Brilliant Blue (100 mg) in 95% ethanol (50 mL) and 85% phosphoric acid (100 mL). The solution was then completed to 1 L with ultrapure water in a volumetric flask. Standard SOD solutions of known concentrations ranging from 0.1 to 100 mg L<sup>-1</sup> were prepared. A calibration curve was measured by mixing SOD solution (0.4 mL) at a given concentration with the dye solution (1.6 mL). These samples were mixed together for 5 min, and the UV/Vis spectrum of the obtained solution was recorded with a Lambda 35 spectrophotometer (PerkinElmer). The absorbance bands at  $\lambda = 465$  and 594 nm corresponding to the free dye and both the enzyme-dye complex and free dye, respectively, were monitored. By measuring the ratio or difference in these absorbance bands, the total amount of enzyme remaining in the solution was determined.

**SOD activity:** To determine the SOD activity of the obtained material (TNS-PDADMAC-SOD), the Fridovich method was employed. However, the enzymatic assay protocol had to be slightly modified to adapt to the high scattering of the samples resulting from the



suspended TNS. Each sample was composed of xanthine (3 mM, 0.1 mL), NBT (3 mM, 0.1 mL), xanthine oxidase (3 mg mL<sup>-1</sup>, 0.3 mL), and suspension containing the catalyst (bare or immobilized SOD, 0–2.5 mL) with phosphate buffer and completed to a final volume of 3 mL. The phosphate buffer concentration in the samples was 1 mM and the pH was 7. Once all the reagents were mixed together, the samples were left to equilibrate for 1 min prior to monitoring the increase in the absorbance band at  $\lambda = 565$  nm for 5 min. The increase in the absorbance was determined for several SOD concentrations in the sample. Furthermore, due to the scattering of the TNS particles, the corresponding TNS-PDADMAC samples without SOD were used as references. The inhibition of the superoxide radical-NBT reaction was then calculated, and the superoxide radical anion scavenging activities were expressed as IC<sub>50</sub> values, which correspond to the SOD concentration needed to dismutase 50% of the radicals formed in the probe reaction.

## Acknowledgement

This research was supported by the Swiss Secretariat for Education, Research and Innovation (C15.0024) and COST Action CM1303. Special thanks to Prof. Michal Borkovec for access to the light-scattering instruments in his laboratory. I.S. is grateful to the Hungarian Academy of Sciences for the support through the Lendület program (LP2017-21/2017).

## Conflict of Interest

The authors declare no conflict of interest.

**Keywords:** antioxidants • enzymes • nanostructures • polyelectrolytes • titanium

- [1] J. A. Tainer, E. D. Getzoff, J. S. Richardson, D. C. Richardson, *Nature* **1983**, 306, 284–287.
- [2] T. J. Drake, C. D. Medley, A. Sen, R. J. Rogers, W. H. Tan, *ChemBioChem* **2005**, 6, 2041–2047.
- [3] A. Bafana, S. Dutt, S. Kumar, P. S. Ahuja, *Crit. Rev. Biotechnol.* **2011**, 31, 65–76.
- [4] I. Bertini, I. C. Felli, C. Luchinat, G. Parigi, R. Pierattelli, *ChemBioChem* **2007**, 8, 1422–1429.
- [5] J. S. Richardson, K. A. Thomas, B. H. Rubin, D. C. Richardson, *Proc. Natl. Acad. Sci. USA* **1975**, 72, 1349–1353.
- [6] S. M. Chen, X. H. Li, H. M. Ma, *ChemBioChem* **2009**, 10, 1200–1207.
- [7] I. Fita, M. G. Rossmann, *J. Mol. Biol.* **1985**, 185, 21–37.
- [8] M. Muresanu, M. Puscasu, S. Somacescu, G. Carja, *Catal. Lett.* **2015**, 145, 1529–1540.
- [9] I. N. Jakab, O. Lorincz, A. Jancso, T. Gajda, B. Gyurcsik, *Dalton Trans.* **2008**, 6987–6995.
- [10] J. Kalmár, B. Biri, G. Lente, I. Banyai, A. Budimir, M. Birus, I. Batinic-Haberle, I. Fabian, *Dalton Trans.* **2012**, 41, 11875–11884.
- [11] I. Szilágyi, I. Labadi, K. Hernadi, I. Palinko, N. V. Nagy, L. Korecz, A. Rockenbauer, Z. Kele, T. Kiss, *J. Inorg. Biochem.* **2005**, 99, 1619–1629.
- [12] W. S. Terra, S. S. Ferreira, R. O. Costa, L. L. Mendes, R. W. A. Franco, A. J. Bortoluzzi, J. Resende, C. Fernandes, A. Horn, *Inorg. Chim. Acta* **2016**, 450, 353–363.
- [13] Y. H. Lin, J. S. Ren, X. G. Qu, *Adv. Mater.* **2014**, 26, 4200–4217.
- [14] Z. Csendes, C. Dudas, G. Varga, E. G. Bajnoczi, S. E. Canton, P. Sipos, I. Palinko, *J. Mol. Struct.* **2013**, 1044, 39–45.
- [15] Y. C. Fang, H. C. Lin, I. J. Hsu, T. S. Lin, C. Y. Mou, *J. Phys. Chem. C* **2011**, 115, 20639–20652.
- [16] I. Szilágyi, O. Berkesi, M. Sipiczki, L. Korecz, A. Rockenbauer, I. Palinko, *Catal. Lett.* **2009**, 127, 239–247.
- [17] I. Szilágyi, I. Labadi, K. Hernadi, T. Kiss, I. Palinko in *Molecular Sieves: From Basic Research to Industrial Applications, Parts A and B, Vol. 158* (Eds.: J. Cejka, N. Zilkova, P. Nachtigall), Elsevier, Amsterdam, **2005**, pp. 1011–1018.
- [18] I. Szilágyi, I. Labadi, K. Hernadi, I. Palinko, I. Fekete, L. Korecz, A. Rockenbauer, T. Kiss, *New J. Chem.* **2005**, 29, 740–745.
- [19] M. Pavlovic, P. Rouster, I. Szilágyi, *Nanoscale* **2017**, 9, 369–379.
- [20] Y. P. Luo, Y. Tian, A. W. Zhu, H. Q. Liu, J. Q. Zhou, *J. Electroanal. Chem.* **2010**, 642, 109–114.
- [21] Y. P. Chen, C. T. Chen, Y. Hung, C. M. Chou, T. P. Liu, M. R. Liang, C. Y. Mou, *J. Am. Chem. Soc.* **2013**, 135, 1516–1523.
- [22] S. Singh, V. K. Dubey, *Int. J. Pept. Res. Ther.* **2016**, 22, 171–177.
- [23] K. Kamada, A. Yamada, N. Soh, *RSC Adv.* **2015**, 5, 85511–85516.
- [24] L. H. Xu, X. H. Ji, N. Zhao, C. X. Song, F. S. Wang, C. H. Liu, *Polym. Chem.* **2016**, 7, 1826–1835.
- [25] S. Bobone, E. Miele, B. Cerroni, D. Roversi, A. Bocedi, E. Nicolai, A. Di Venere, E. Placidi, G. Ricci, N. Rosato, L. Stella, *Langmuir* **2015**, 31, 7572–7580.
- [26] Y. M. Fan, X. D. Cao, T. Hu, X. G. Lin, H. Dong, X. N. Zou, *J. Phys. Chem. C* **2016**, 120, 3955–3963.
- [27] Y. H. Lin, Y. P. Chen, T. P. Liu, F. C. Chien, C. M. Chou, C. T. Chen, C. Y. Mou, *ACS Appl. Mater. Interfaces* **2016**, 8, 17944–17954.
- [28] F. P. Chang, Y. P. Chen, C. Y. Mou, *Small* **2014**, 10, 4785–4795.
- [29] I. Louzao, J. C. M. van Hest, *Biomacromolecules* **2013**, 14, 2364–2372.
- [30] P. Tanner, V. Balasubramanian, C. G. Palivan, *Nano Lett.* **2013**, 13, 2875–2883.
- [31] A. Grotzky, E. Atamura, J. Adamcik, P. Carrara, P. Stano, F. Mavelli, T. Nauser, R. Mezzenga, A. D. Schluter, P. Walde, *Langmuir* **2013**, 29, 10831–10840.
- [32] P. Tanner, O. Onaca, V. Balasubramanian, W. Meier, C. G. Palivan, *Chem. Eur. J.* **2011**, 17, 4552–4560.
- [33] A. Grotzky, T. Nauser, H. Erdogan, A. D. Schluter, P. Walde, *J. Am. Chem. Soc.* **2012**, 134, 11392–11395.
- [34] F. Y. Mahlici, Y. Sen, M. Mutlu, S. A. Altinkaya, *J. Membr. Sci.* **2015**, 479, 175–189.
- [35] R. Kun, M. Balazs, I. Dekany, *Colloids Surf. A* **2005**, 265, 155–162.
- [36] V. B. Damodaran, D. Bhatnagar, V. Leszczak, K. C. Papat, *RSC Adv.* **2015**, 5, 37149–37171.
- [37] H. Ren, Y. H. Zhang, J. R. Su, P. Lin, B. Wang, B. S. Fang, S. Z. Wang, *J. Biotechnol.* **2017**, 241, 33–41.
- [38] H. Wu, C. H. Zhang, Y. P. Liang, J. F. Shi, X. L. Wang, Z. Y. Jiang, *J. Mol. Catal. B* **2013**, 92, 44–50.
- [39] N. R. Haase, S. Shian, K. H. Sandhage, N. Kroger, *Adv. Funct. Mater.* **2011**, 21, 4243–4251.
- [40] P. Rouster, M. Pavlovic, I. Szilágyi, *RSC Adv.* **2016**, 6, 97322–97330.
- [41] T. Szabó, V. Toth, E. Horvath, L. Forro, I. Szilágyi, *Langmuir* **2015**, 31, 42–49.
- [42] P. Rouster, M. Pavlovic, E. Horvath, L. Forro, S. K. Dey, I. Szilágyi, *Langmuir* **2017**, 33, 9750–9758.
- [43] E. Horváth, L. Grebikova, P. Maroni, T. Szabo, A. Magrez, L. Forro, I. Szilágyi, *ChemPlusChem* **2014**, 79, 592–600.
- [44] M. Pavlovic, M. Adok-Sipiczki, E. Horvath, T. Szabo, L. Forro, I. Szilágyi, *J. Phys. Chem. C* **2015**, 119, 24919–24926.
- [45] T. Szabo, V. Toth, E. Horvath, I. Szilágyi, *Chimia* **2014**, 68, 454–454.
- [46] L. Avadiar, Y. K. Leong, *Colloid Polym. Sci.* **2011**, 289, 237–245.
- [47] J. Faraudo, A. Martin-Molina, *Curr. Opin. Colloid Interface Sci.* **2013**, 18, 517–523.
- [48] M. Pavlovic, P. Rouster, T. Oncsik, I. Szilágyi, *ChemPlusChem* **2017**, 82, 121–131.
- [49] I. Szilágyi, G. Trefalt, A. Tiraferri, P. Maroni, M. Borkovec, *Soft Matter* **2014**, 10, 2479–2502.
- [50] T. T. M. Ho, K. E. Bremmell, M. Krasowska, S. V. MacWilliams, C. J. E. Richard, D. N. Stringer, D. A. Beattie, *Langmuir* **2015**, 31, 11249–11259.
- [51] A. G. Cherstvy, R. G. Winkler, *J. Phys. Chem. B* **2005**, 109, 2962–2969.
- [52] G. Trefalt, I. Szilágyi, T. Oncsik, A. Sadeghpour, M. Borkovec, *Chimia* **2013**, 67, 772–776.
- [53] H. Holthoff, S. U. Egelhaaf, M. Borkovec, P. Schurtenberger, H. Sticher, *Langmuir* **1996**, 12, 5541–5549.
- [54] J. H. Bloor, D. Holtz, J. Kaars, D. J. Kosman, *Biochem. Genet.* **1983**, 21, 349–364.
- [55] M. M. Bradford, *Anal. Biochem.* **1976**, 72, 248–254.

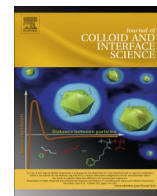
- [56] T. López-León, A. B. Jodar-Reyes, J. L. Ortega-Vinuesa, D. Bastos-Gonzalez, *J. Colloid Interface Sci.* **2005**, *284*, 139–148.
- [57] F. Iselau, T. P. Xuan, G. Trefalt, A. Matic, K. Holmberg, R. Bordes, *Soft Matter* **2016**, *12*, 9509–9519.
- [58] V. V. Arkhipova, V. V. Apyari, S. G. Dmitrienko, *Spectrochim. Acta Part A* **2015**, *139*, 335–341.
- [59] G. Fritz, V. Schadler, N. Willenbacher, N. J. Wagner, *Langmuir* **2002**, *18*, 6381–6390.
- [60] C. Beauchamp, I. Fridovich, *Anal. Biochem.* **1971**, *44*, 276–287.

---

Manuscript received: September 14, 2017

Accepted manuscript online: November 16, 2017

Version of record online: December 18, 2017

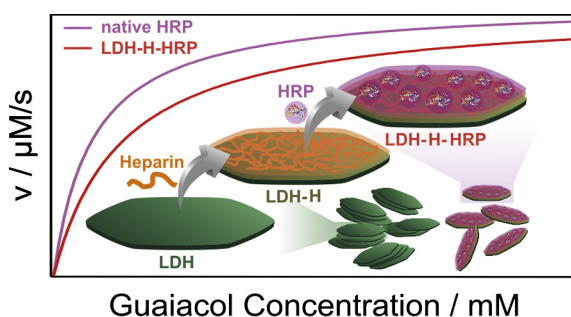


## Regular Article

## Horseradish peroxidase-nanoclay hybrid particles of high functional and colloidal stability

Marko Pavlovic<sup>a</sup>, Paul Rouster<sup>b</sup>, Zoltan Somosi<sup>c</sup>, Istvan Szilagyi<sup>c,d,\*</sup><sup>a</sup> Department of Inorganic and Analytical Chemistry, University of Geneva, CH-1205 Geneva, Switzerland<sup>b</sup> Institute of Condensed Matter and Nanosciences - Bio and Soft Matter, Université Catholique de Louvain, B-1348 Louvain-la-Neuve, Belgium<sup>c</sup> MTA-SZTE Lendület Biocolloids Research Group, University of Szeged, H-6720 Szeged, Hungary<sup>d</sup> Department of Physical Chemistry and Materials Science, University of Szeged, H-6720 Szeged, Hungary

## GRAPHICAL ABSTRACT



## ARTICLE INFO

## Article history:

Received 21 February 2018

Revised 29 March 2018

Accepted 2 April 2018

Available online 3 April 2018

## Keywords:

Layered double hydroxide

HRP enzyme

Immobilization

Colloidal stability

Hybrid material

## ABSTRACT

Highly stable dispersions of enzyme-clay nanohybrids of excellent horseradish peroxidase activity were developed. Layered double hydroxide nanoclay was synthesized and functionalized with heparin polyelectrolyte to immobilize the horseradish peroxidase enzyme. The formation of a saturated heparin layer on the platelets led to charge inversion of the positively charged bare nanoclay and to highly stable aqueous dispersions. Great affinity of the enzyme to the surface modified platelets resulted in strong horseradish peroxidase adsorption through electrostatic and hydrophobic interactions as well as hydrogen bonding network and prevented enzyme leakage from the obtained material. The enzyme kept its functional integrity upon immobilization and showed excellent activity in decomposition of hydrogen peroxide and oxidation of an aromatic compound in the test reactions. In addition, remarkable long term functional stability of the enzyme-nanoclay hybrid was observed making the developed colloidal system a promising antioxidant candidate in biomedical treatments and industrial processes.

© 2018 Elsevier Inc. All rights reserved.

## 1. Introduction

Enzymes are important natural biocatalysts in various catalytic processes as they exhibit high efficiency and substrate specificity

as well as provide green and sustainable manufacturing processes [1,2]. On the other hand, their high sensitivity to the environmental conditions (e.g., temperature [3], pressure [4] and pH [5]) and difficult separation from the reaction mixture [6] prevent their widespread use. The most efficient way to overcome these challenges is the enzyme immobilization, which became one of the most important fields in bio-relevant catalysis in the past decade [7].

\* Corresponding author at: Department of Physical Chemistry and Materials Science, University of Szeged, H-6720 Szeged, Hungary.

E-mail address: [szistvan@chem.u-szeged.hu](mailto:szistvan@chem.u-szeged.hu) (I. Szilagyi).

Immobilization techniques include binding to surfaces [8,9], catalyst entrapment [10] and cross-linking [11]. The first method relies on the affinity of the enzymes to the surface of the carrier particles and the attachment may take place through electrostatic and hydrophobic interactions or through primary and secondary chemical bonds [12,13]. The most commonly used supports for enzyme immobilization involve inorganic particles [14–16], synthetic or natural polymers [17] and various hybrid materials [18,19].

Among the first ones, clay materials including layered double hydroxides (LDHs) of dimensions in the nanoscale range represent a resourceful type of solid support to immobilize enzymes on their surface by physical adsorption or between the lamellae by intercalation [20–22]. Given the fact that the majority of the enzymes and other biomolecules are negatively charged at physiological pH, the anion exchange capacity of the LDHs has been widely utilized during the immobilization processes [23,24]. Other advantages in using LDHs as solid supports include high enzyme loading due to large surface area, which can even be further improved by delamination into unilamellar nanosheets, and their ease of synthesis as well as high compositional diversity [25,26]. Moreover, it has been shown that LDHs are biocompatible providing the opportunity to use them in biomedical applications [27–29]. Functionalization of LDHs with polymeric substances is a versatile tool to further extend the range of possible biomolecules that can be used to prepare LDH-based hybrid nanomaterials [30,31]. In biomedical applications, one of the aims is to obtain dispersions of stable functionalized particles, since their aggregation may lead to thrombosis [32].

Horseradish peroxidase (HRP) is a member of the vast group of peroxidases that can use hydrogen peroxide as an electron acceptor and further oxidize organic molecules [33]. HRP contains a heme group with an iron cation in its active center that can interact with hydrogen peroxide and form an intermediate state of enzyme that can oxidize organic molecules like guaiacol in the most typical HRP assay [34]. Immobilization of HRP has been in the focus of numerous research groups to develop hybrid materials for various applications including water treatment [35], sensing [36] and catalysis [37]. A wide range of solid supports was applied in the immobilization procedures. Accordingly, physical adsorption of HRP on quantum dots [16], titania [38] and nanocomposites [39] has been reported. Intercalation between oxide layers was also investigated to improve the enzyme sensitivity [40]. Another advantageous method to achieve strong enzyme binding to the carrier is the covalent linkage, which was achieved in the case of mesoporous silica [37] and polymer beads [41]. Coprecipitation of copper(II) salts and HRP resulted in nanoparticles of high surface area with enhanced catalytic activity and increased functional stability [42]. HRP containing hybrid materials were developed by preparing LDH-carbon nanodot composites first and by co-adsorbing them with the enzyme on an electrode to obtain selective and reproducible biosensor for hydrogen peroxide detection [18]. In addition, certain nanoparticles also showed significant HRP-like activity even without additional catalysts immobilized on their surface [43–45].

The previously mentioned studies mainly focused on the structural characterization, electrochemical properties and enzymatic activity of the hybrid materials, however, limited attention has been paid to the colloidal stability of the enzyme-particle systems. Given the fact that the majority of the applications take place in dispersions, aggregation processes and their effect on the efficiency in peroxide decomposition reactions are critical issues for obtaining highly active biohybrids. Therefore, in order to achieve stable composite dispersions having significant enzymatic function, the charging and aggregation processes under the application conditions have to be investigated in detail. The main goal of such inves-

tigations must be to develop fine colloidal dispersions of primary nanocomposite particles of high specific surface area.

In the present work, HRP enzyme was immobilized on the surface of LDH particles previously modified by adsorption of heparin (HEP) polyelectrolyte (Scheme 1). The enzyme loading was determined and optimized, in addition, the surface charge properties and aggregation processes were followed in the systems to obtain highly stable colloids. The efficiencies of the bionanohybrids were tested and compared to the bare enzyme. Finally, the long term functional and colloidal stability of the dispersions and the hydrogen peroxide consuming ability were assessed.

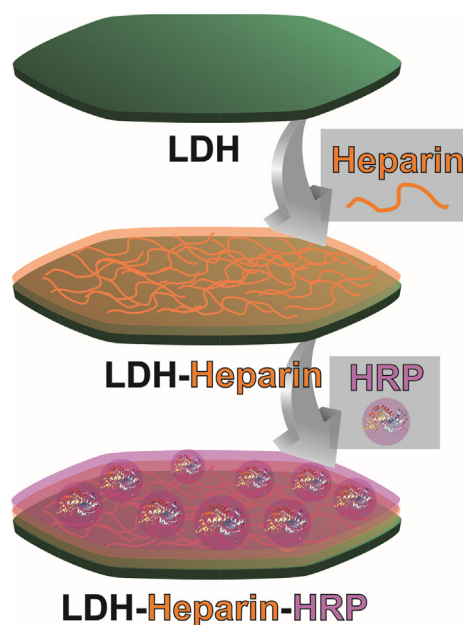
## 2. Materials and methods

### 2.1. Chemicals

Sodium heparin of low molecular weight (12–15 kg/mol) was obtained from Acros Organics. HRP (type VI, EC 1.11.1.7) was bought from Sigma-Aldrich (P8375) in the form of salt-free lyophilized powder (250 units/mg solid, Reinheitszahl value is 2.5–4.0) and used without further purification.  $\text{H}_3\text{PO}_4$  (99.99%), HCl (99%), NaOH (97%), NaCl (99.5%),  $\text{Na}_2\text{CO}_3$  (99.5%),  $\text{Al}(\text{NO}_3)_3 \cdot 9\text{H}_2\text{O}$  (98%),  $\text{Mg}(\text{NO}_3)_2 \cdot 6\text{H}_2\text{O}$  (99.99%),  $\text{NaH}_2\text{PO}_4$  (99%),  $\text{Na}_2\text{HPO}_4$  (99%) and Guaiacol (98%) were purchased from Sigma-Aldrich. The experiments were performed at 25 °C in aqueous medium using ultrapure Milli-Q water (Millipore) at pH (7.0 ± 0.5).

### 2.2. LDH synthesis

LDH nanoparticles composed of  $\text{Mg}^{2+}$  and  $\text{Al}^{3+}$  layer forming metal ions and  $\text{CO}_3^{2-}$  intercalated anions were synthesized by the “flash” coprecipitation method and their particle size distribution was improved by hydrothermal treatment, as described earlier [46]. In brief,  $\text{Mg}(\text{NO}_3)_2 \cdot 6\text{H}_2\text{O}$  and  $\text{Al}(\text{NO}_3)_3 \cdot 9\text{H}_2\text{O}$  salts were dissolved together in a stoichiometric ratio of 2:1 in 100 mL ultrapure water. A second solution composed of 20 mL of 1 M NaOH and  $\text{Na}_2\text{CO}_3$  in a stoichiometric ratio to  $\text{Mg}(\text{NO}_3)_2 \cdot 6\text{H}_2\text{O}$  of 1:1 was prepared. These two solutions were rapidly mixed together and the



**Scheme 1.** Representation of the heparin functionalization of LDH particles and the HRP immobilization process.



mixture was stirred during 24 h. The pH of the obtained solution was monitored and kept around 9. The solid precipitate was filtered (Nalgene Nylon Membrane Filter of 0.2  $\mu\text{m}$  pore size) and washed several times with ultrapure water. The particles were dried overnight in an oven at 60  $^{\circ}\text{C}$  prior to dispersing them in water to get 4 wt% dispersions. These samples were submitted to hydrothermal treatment for 24 h at 120  $^{\circ}\text{C}$ . The final product was washed several times with ultrapure water and eventually re-dispersed as 1 wt% dispersion that served as stock. Prior to their use, the particle dispersion was diluted to the desired concentration and treated in ultrasonic bath for a few minutes. The formation of LDH was confirmed with X-ray diffraction (XRD) measurement. The specific surface area of the obtained LDH material was determined to be 52.6  $\text{m}^2/\text{g}$  by the BET method. More details about the solid state characterization including the XRD spectrum of the particles are given in our earlier study [22].

### 2.3. Preparation of LDH-HEP-HRP

The final hybrid material was composed of 50 mg of heparin per 1 g of LDH and 10 mg of HRP to achieve high colloidal stability and optimal enzyme loading. Briefly, 0.5 mL of 10000 mg/L LDH dispersion, 0.25 mL of 1000 mg/L heparin and 0.5 mL of 10 mM NaCl were added to 3.7 mL of water and stirred during one hour in order to obtain a saturated polyelectrolyte layer on the LDH particles at a heparin dose of 50 mg/g. Finally, 50  $\mu\text{L}$  of 1000 mg/L HRP solution was added under vigorous stirring, which was maintained during one hour. The final product contained thus 10 mg of HRP per 1 g of LDH. In the above procedure, the pH of the stock solutions was set to pH (7.0  $\pm$  0.5) by NaOH or HCl prior to their mixing.

### 2.4. Electrophoresis

A Zetasizer Nano ZS (Malvern) instrument was used to determine the electrophoretic mobilities. The device applies the phase analysis light scattering technique and uses a He/Ne laser of 632 nm wavelength. Each sample was composed of 500  $\mu\text{L}$  of particle dispersion at 100 mg/L concentration, 500  $\mu\text{L}$  of 10 mM NaCl solution, desired volume of heparin stock solution and ultrapure water. The latter component was used to complete the sample to 5 mL. In the case of investigating the influence of the ionic strength on the electrophoretic mobilities of the particles, calculated volumes of salt solutions were added to 500  $\mu\text{L}$  of particle dispersion of 100 mg/L concentration and the samples were filled to 5 mL with water. This type of sample preparation always gave a final particle concentration of 10 mg/L with varying polyelectrolyte or salt concentration. Experiments were performed in capillary cells (Malvern) and the average value of 5 measurements was always reported.

### 2.5. Light scattering

Dynamic light scattering (DLS) experiments were carried out with a CGS-3 goniometer system (ALV) in round borosilicate glass cuvettes (Kimble Chase). The second cumulant fit was applied to the correlation function to determine the hydrodynamic radius ( $R_h$ ). In the time-resolved experiments, the correlation function was collected during 20 s and the measurements were run for 10–60 min depending on the speed of aggregation in the sample. The colloidal stability was described as stability ratio ( $W$ ) as follows [47–50].

$$W = \frac{k_{app}^{fast}}{k_{app}} \quad (1)$$

where  $k_{app}$  is the apparent aggregation rate constant, which can be calculated from the increase in  $R_h$  in the time-resolve measurements as shown below.

$$k_{app} = \frac{1}{R_h(0)} \frac{dR_h(t)}{dt} \quad (2)$$

The reference value of  $k_{app}^{fast}$  of the LDH was determined in 1 M NaCl solution, where the surface charges are screened and the aggregation of the platelets was controlled solely by the diffusion of the particles. Therefore, stability ratio of one corresponds to the fast particle aggregation and hence, it indicates unstable dispersions. The aggregation experiments with heparin coating were initiated by adding 200  $\mu\text{L}$  of 100 mg/L particle dispersion to 1800  $\mu\text{L}$  solution obtained by adding 200  $\mu\text{L}$  of 10 mM NaCl in 1600  $\mu\text{L}$  solution of heparin of calculated concentration. For colloidal stability assessment at different ionic strengths, 200  $\mu\text{L}$  of 100 mg/L particle or coated particle dispersion were added to 1800  $\mu\text{L}$  of NaCl solution of different concentration. In each DLS experiments, the final sample volume was always kept to 2 mL leading to a particle concentration of 10 mg/L, which is the same as the one applied in the electrophoretic mobility measurements. This particle concentration was a compromise between avoiding the formation of higher ranked aggregates and to obtain sufficiently high scattered intensities in the experiments.

### 2.6. Bradford test

The adsorbed amount of HRP on the LDH-HEP support was measured by determining the HRP concentration in the supernatant after centrifugation of the final material at 5824g during 5 min. The supernatants were further filtered using a 0.1  $\mu\text{m}$  pore size filter (Millipore) to eliminate the remaining platelets from the samples. The quantification was carried out by the Bradford test [51]. Accordingly, the Bradford reagent was prepared by dissolving Coomassie Brilliant Blue (ThermoFisher, 98%) dye in a mixture of water, ethanol (Fisher Chemicals, 99.8%) and  $\text{H}_3\text{PO}_4$ . After addition of 400  $\mu\text{L}$  of enzyme containing solution to 1600  $\mu\text{L}$  of the reagent and waiting 10 min to achieve equilibration, absorption spectra in the range of 350–800 nm were recorded with a Lambda 35 spectrophotometer (PerkinElmer). In this regime, two absorption bands appear, namely at 465 nm (from the free dye) and at 595 nm (from the dye-protein complex and free dye). In addition, the absorption of a blank sample that had 1600  $\mu\text{L}$  of reagent and 400  $\mu\text{L}$  of ultrapure water was also measured. For all of the previously mentioned samples, the difference between the absorbance at 465 nm and 595 nm was calculated and plotted as a function of the enzyme concentration. A calibration curve was determined first by applying the Bradford test to standard HRP solutions with a final enzyme concentration between 1 and 20 mg/L. Thereafter, the enzyme concentrations in unknown supernatant (without any particles) samples originated from the filtration processes above were measured. The LDH concentration was kept at 200 mg/L in these experiments.

### 2.7. Microscopy

Material morphology was investigated by transmission electron microscopy (TEM) imaging, which was performed on a Tecnai G2 Sphera microscope (FEI) utilizing a LaB6 cathode at an acceleration voltage of 120 kV. A sample volume of 5  $\mu\text{L}$  containing 100 mg/L of LDH or hybrid particles was dropcasted on plasma treated carbon meshes. After 2 min adsorption time, the excess of liquid was removed with a small piece of filter paper. Finally, the coated carbon mesh was placed on the sample holder of the microscope and representative micrographs of the particle samples were acquired.

### 2.8. HRP assay

HRP activity of the materials was performed by employing the guaiacol assay [34]. Samples for this assay were prepared by mixing 240  $\mu\text{L}$  of enzyme or material possessing enzymatic activity at a concentration of 5 mg/L, 1.872 mL of 12.9 mM phosphate buffer at pH 7 and 240  $\mu\text{L}$  of guaiacol at different concentrations (the final concentrations of guaiacol were varied between 2 mM and 40 mM). The dispersions or solutions were thoroughly mixed by vortex and 48  $\mu\text{L}$  of 135 mM hydrogen peroxide (Reactolab, 30%) solution was added. The samples were immediately introduced into the UV-Vis spectrophotometer and the increase in the absorbance at 470 nm wavelength, as a consequence of the formation of guaiacol degradation products, was followed. The absorbance values were plotted as a function of the reaction time and the linear part of the graph was fitted in order to obtain the reaction rate ( $\nu$ ) at the substrate ( $S$ ) concentration applied. Finally, the reaction rates were plotted as a function of the guaiacol concentration and fitted with the Michaelis-Menten model developed to study enzyme kinetics according to the following relation [52].

$$\nu = \frac{\nu_{\max}[S]}{K_m + [S]} \quad (3)$$

where  $K_m$  is the Michaelis-Menten constant and  $\nu_{\max}$  is the maximum reaction rate for the investigated system.

## 3. Results

### 3.1. Heparin functionalization of the LDH platelets

It is well-known that pristine LDH particles exhibit rather low colloidal stability preventing their application in a liquid medium, where the resistance against salt-induced aggregation is a key parameter [53]. However, it was shown earlier in several systems that polyelectrolyte coating improves the stability of the LDH dispersions significantly and also enhances the adsorption capacity in biomolecule immobilization [22,54,55]. In general, polyelectrolytes adsorb strongly on oppositely charged surfaces through electrostatic and hydrophobic interactions [56–59]. In our study, heparin, a biocompatible polyelectrolyte presenting one of the highest negative line charge density among the known macromolecules, was adsorbed on the platelets in different doses to tune the charging and aggregation processes in the LDH dispersions.

Fig. 1a shows the dependence of the electrophoretic mobilities on the heparin dose, which follows the typical tendency for oppositely charged polyelectrolyte-particle systems [22,49,54,56,57]. At very low heparin doses, the particles exhibit positive electrophoretic mobilities similar to the bare ones due to the positive structural charge of LDH materials. By increasing the dose of heparin, the mobilities decreased and reached the charge neutralization point at 3.5 mg/g, where the positive charge of the particles is neutralized by the adsorbed polyelectrolyte. By further addition of heparin into the system, the adsorption continues after the neutralization point and charge reversal occurs. The magnitude of the electrophoretic mobilities increases until reaching the onset of the adsorption saturation plateau, which indicates the heparin dose necessary to form a saturated polyelectrolyte layer on the platelets. Such saturation occurred at 50 mg/g polyelectrolyte dose. Further added heparin remained dissolved in the bulk and neither adsorbed on the particles surface nor influenced the electrophoretic mobility values. The magnitude of the mobilities at saturation is significantly higher in comparison to the one of the bare particles. This result predicts higher colloidal stability for the heparin coated platelets.

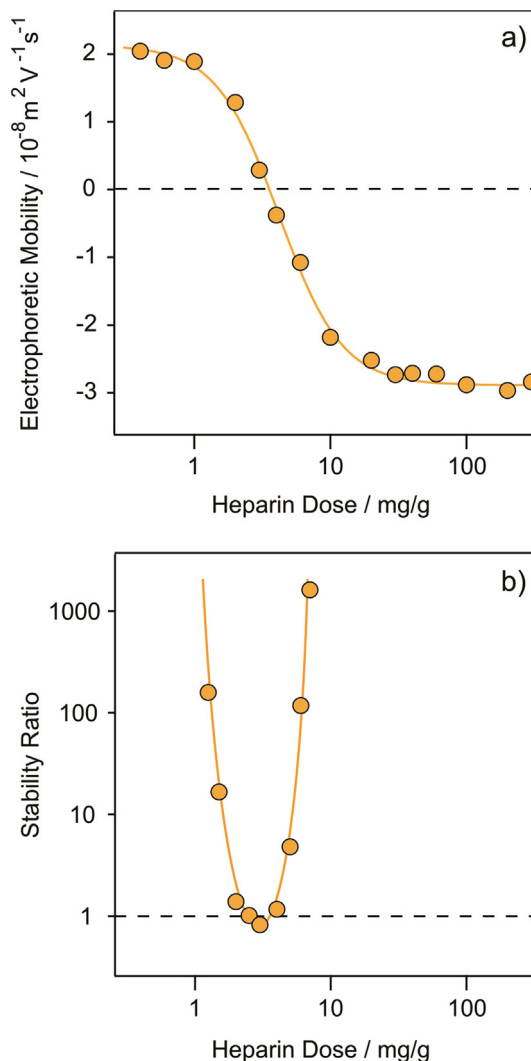


**Fig. 1.** Electrophoretic mobilities (a) and stability ratio values (b) of LDH particles in the presence of heparin. The background ionic strength was set to 1 mM by NaCl. The mg/g unit indicates mg of heparin per gram of LDH. Note that the accuracy of the electrophoretic measurements is about 10%, while 5% for the stability ratio data. The lines serve as eye guides.

The changes in the surface charge behavior clearly influenced the aggregation processes in the same samples. DLS has proved to be a suitable tool to investigate the stability of colloidal dispersions [22,50,60]. Therefore, the aggregation processes were followed by this method. The speed of aggregation is expressed in terms of stability ratio, its value is close to one for unstable, rapidly aggregating platelets, while high stability ratios indicate stable dispersions. As shown in Fig. 1b, the stability ratios are equal to one within the experimental error at doses in the close surrounding of the charge neutralization point indicating unstable LDH particles. Partially neutralized positive platelets and fully coated LDHs of negative charge below and above the neutralization point, respectively, demonstrate good colloidal stability, as indicated by high or not even measurable stability ratio values.

Such a trend in the aggregation processes is in line with the one predicted by the theory developed by Derjaguin, Landau, Verwey and Overbeek (DLVO) [61]. It is also similar to other heparin systems containing LDHs [22,49]. Accordingly, the particle interactions are mostly governed by van der Waals attractions once the charges of the functionalized platelets are low and thus, they

rapidly aggregate. On the other hand, repulsive electrical double layer forces are predominant in the systems of particles of sufficiently high surface charge at low and high heparin doses leading to stable dispersions.

### 3.2. Immobilization of HRP

From the previous experiments, one can conclude that the formation of a saturated heparin layer on the LDH particles led to highly stable dispersions of negatively charged particles. The HRP possesses a net positive charge under the experimental conditions applied due to its relatively high isoelectric point of 8.8 [33,62]. Therefore, electrostatic attraction is expected to occur between the heparin coated LDH platelets (LDH-HEP, 50 mg/g heparin dose) and the HRP molecules. The main goal was to immobilize the optimal amount of enzyme on the hybrid material, which leads to the formation of bionanocomposites of sufficient HRP activity. No buffer solutions were used to maintain the pH in order to avoid the competition between the enzyme and buffer constituents for the adsorption sites.

Moreover, it was very important to optimize the enzyme concentration in the hybrid materials. Indeed, the loading has to be high enough for a remarkable HRP activity and low enough to maintain the sufficiently high surface charge and hence, the strong interparticle repulsion by the electrical double layers. First, the mobility of the LDH-HEP was recorded in a wide range of HRP concentration (Fig. 2). At lower doses, up to 100 mg/g, no significant change can be detected in the electrophoretic mobilities due to the weak charge of the enzyme. At elevated loadings, above 100 mg/g, the mobilities slightly increased, i.e., the adsorption of the enzyme on the oppositely charged LDH-HEP led to a detectable change in the charge of the surface. Note that a decrease in the magnitude of surface charge may have a negative influence on the colloidal stability giving rise to unstable systems. Taking this fact into account, doses lower than 100 mg/g HRP were considered in the further immobilization studies.

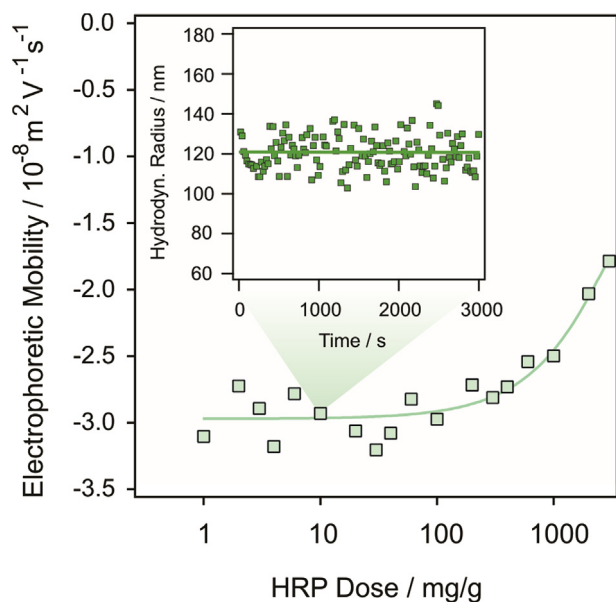


**Fig. 2.** Electrophoretic mobilities of LDH-HEP hybrid particles for different loadings of HRP. The inset graph represents the evolution of the hydrodynamic radius of LDH-HEP platelets functionalized with 10 mg/g of HRP during a period of 3000 s in a 1 mM NaCl solution. Note that the individual hydrodynamic radii were determined with an average error of  $\pm 5$  nm. The line acts as an eye guide.

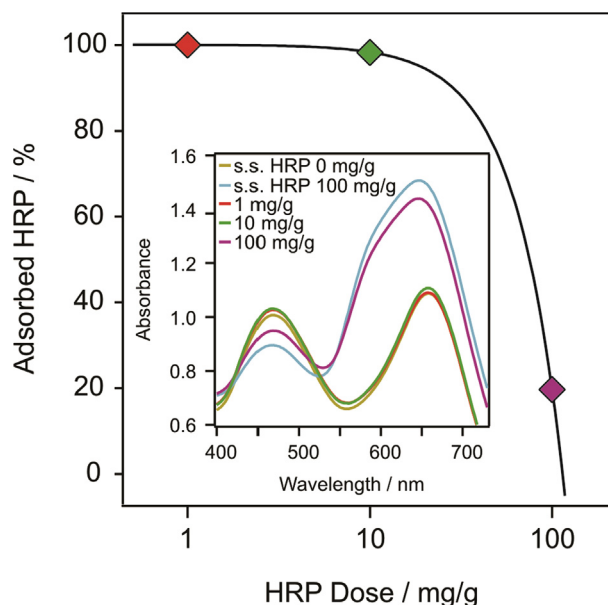


**Fig. 3.** Fraction of HRP adsorbed on the surface of LDH-HEP platelets as a function of the HRP dose determined by the Bradford test. Spectra of two standard solution of HRP together with three samples of different loadings are shown in the inset graph (s.s. HRP stands for standard solution of HRP).

To determine the adsorbed amount of HRP on the LDH-HEP platelets, i.e., to quantify the enzyme partitioning between surface and bulk solution, the Bradford test was employed [51]. In brief, the platelets were separated by filtration from the dispersions containing LDH-HEP and HRP and the concentration of the enzyme was determined in the filtrate. Three different HRP loadings (1 mg/g, 10 mg/g and 100 mg/g) were investigated (Fig. 3). It is evident that at 1 mg/g and 10 mg/g HRP dose, the adsorption process was quantitative within the experimental error ( $\pm 2\%$ ). Accordingly, the enzyme is of high affinity to the surface and no HRP remains dissolved in the bulk solution at these lower loadings. Such a strong attachment was also observed with another enzyme immobilized on polyelectrolyte functionalized particles [14,22]. At 100 mg/g dose, however, only 20% of the total amount of HRP present in the system adsorbs and 80% stays in the bulk. As a result, focus was made and further studies were carried out on the system that contained 10 mg of HRP per 1 g of LDH (LDH-HEP-HRP, 1 g of LDH particles modified with 50 mg of heparin and 10 mg of HRP).

Such a load provides sufficiently high enzyme concentration on the surface and excellent colloidal stability for the dispersions. The latter issue was further pursued by recording the time evolution of the hydrodynamic radius of the LDH-HEP-HRP hybrid (Fig. 2 inset). It was concluded that the composite material exhibits extraordinary stability as demonstrated by the constant hydrodynamic radius of about 120 nm during 3000 s under the experimental conditions applied.

Besides colloidal stability, the morphology of the obtained material was investigated by TEM imaging. Both bare LDH (Fig. 4a) and LDH-HEP-HRP hybrid (Fig. 4b) samples were prepared at low ionic strength of 1 mM, therefore, slight overlapping of the particles is only due to drying of the samples during the preparation of the microscopic grids for the TEM measurements. Nevertheless, the heparin functionalization and the enzyme immobilization processes did not cause any morphological changes. Both bare LDH and LDH-HEP-HRP exhibit the same round shape with similar dimensions.

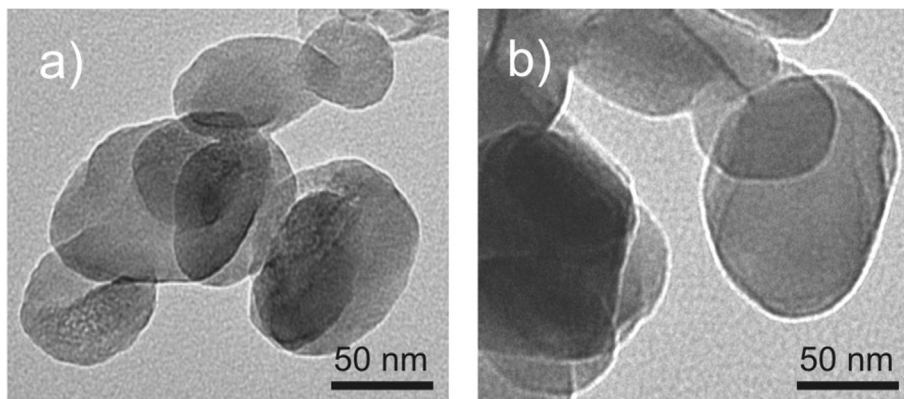


Fig. 4. TEM images of bare LDH platelets (a) and LDH-HEP-HRP hybrid material (b).

### 3.3. Resistance against salt-induced aggregation

As mentioned earlier, enzyme-particle hybrids are dispersed in a liquid in most of the applications. In these samples, the concentration of the ionic species is often high and they can induce aggregation of the composite materials [7,16]. Such an aggregation of the hybrid particles may lead to lower surface area, phase separation and loss of enzymatic activity [63,64]. Therefore, the successful enzyme-particle hybrid must possess high resistance against salt-induced aggregation. In the present work, this topic was investigated in electrophoretic and DLS measurements.

Electrophoretic mobilities of the bare LDH and the LDH-HEP-HRP hybrid were measured in a wide range of ionic strength (Fig. 5a). Obviously, the sign of the electrophoretic mobilities are the opposite due to the above discussed charge reversal phenomenon with LDH-HEP-HRP. Increasing the salt concentration gave rise to a decrease in the magnitude of the mobilities in both cases. The reason is the screened surface charge of both types of materials by the salt constituent ions [22,54]. At elevated ionic strength, the charge of the particles was almost completely screened leading to mobilities close to zero. Another important observation is that the absolute value of the electrophoretic mobility of the LDH-HEP-HRP is about twice higher than the bare LDH at low ionic strengths. This fact clearly predicts higher resistance against salt-induced aggregation for the hybrid material.

Indeed, the ionic strength dependence of the stability ratios measured under identical experimental conditions as the mobilities above was rather different (Fig. 5b). In general at low NaCl concentrations, both materials showed good stability due to their sufficiently high positive (LDH) or negative (LDH-HEP-HRP) surface charge and subsequent establishment of strong repulsive forces by the overlapping electrical double layers. However, the LDH particles exhibited moderate positive charge, while LDH-HEP-HRP hybrids possessed greater charge in magnitude as discussed in the mobility study. Therefore, by increasing the ionic strength, the LDH started to aggregate at lower salt levels compared to the composite material. As a consequence, the fast aggregation regime of stability ratios around unity was reached at lower NaCl concentrations for the bare platelets.

An important parameter that describes the colloidal stability of the systems is the critical coagulation ionic strength (CCIS, which is equal to the critical coagulation concentration in case of monovalent electrolytes) corresponding to the ionic strength, where the transition from stable to unstable dispersions occurs [22,56,57]. For the bare LDH platelets, the CCIS was found to be around 25 mM, while it was 1000 mM for the LDH-HEP-HRP. This information indicates a tremendous increase in the particle resistance against salt-induced aggregation. The tendency, i.e., stable dispersions at

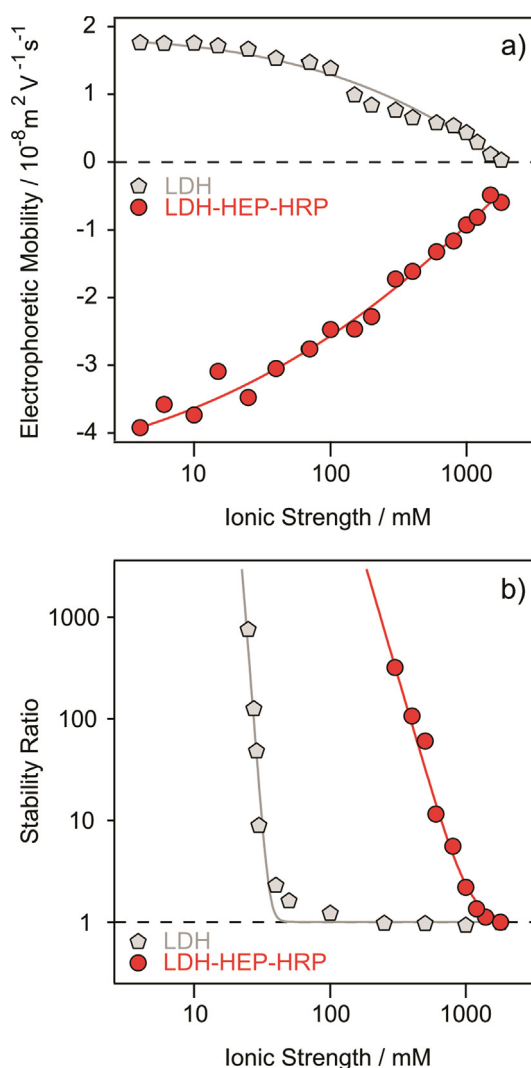


Fig. 5. Electrophoretic mobilities (a) and stability ratio values (b) of LDH and LDH-HEP-HRP materials as a function of the ionic strength set by NaCl. Solid lines are just to guide the eyes.

low and unstable ones at high ionic strength, is in line with the prediction by the DLVO theory [61]. Accordingly, repulsive electrical double layer forces predominate at low NaCl concentration, while these forces vanish due to charge screening and the attractive van der Waals forces act between the platelets above the CCIS.



However, the extremely high CCIS and smaller slope in the stability ratio versus ionic strength plot in the slow aggregation regime are signals for the presence of interparticle forces of non-DLVO origin for the LDH-HEP-HRP. It is suspected that steric repulsion [48,49,65] also takes place between the particles and stabilizes the colloidal dispersion. Such a steric stabilization originates from the overlap of the adsorbed polyelectrolyte chains and the subsequent rise of the osmotic pressure once two particles of saturated heparin layer approach each other. One can conclude that coating of LDH platelets with heparin and adsorption of enzyme influenced the colloidal stability in an extraordinary way and made these particles stable at ionic strengths exceeding the ones used in biomedical or industrial applications.

### 3.4. Enzymatic activity

It is essential to understand the effect of HRP adsorption on its enzymatic activity, i.e., whether the HRP kept its functional integrity upon immobilization or not. Therefore, we probed the activity of the LDH-HEP-HRP material and compared it to the activity of the native HRP enzyme in the guaiacol assay [34]. In brief, the increase of the absorbance at 470 nm is proportional to the increase in the concentration of the degradation products of guaiacol. The degradation of guaiacol occurs only if catalyzed by HRP in the presence of hydrogen peroxide. The increase in absorbance is used to calculate the reaction rate, which saturates at high guaiacol concentrations ( $v_{max}$ ). The reaction follows the Michaelis-Menten mechanism [52] and thus, the binding affinity of the substrate to the enzyme ( $K_m$ ) can be determined, as detailed in the experimental section.

The measured values and the calculations using the Michaelis-Menten kinetic model for the activity of the native enzyme (HRP) and the final material (LDH-HEP-HRP) are displayed in Fig. 6. Both of the compounds exhibit very similar activity, the  $v_{max}$  values agree within the experimental error ( $v_{max}^{HRP} = 2.80 \mu\text{M/s}$  and  $v_{max}^{LDH-HEP-HRP} = 2.72 \mu\text{M/s}$ ), while at the same time, the  $K_m$  values increased from 3.23 mM (HRP) to 5.25 mM (LDH-HEP-HRP) upon immobilization. Almost identical  $v_{max}$  values together with a slight increase of the  $K_m$  represent strong evidence that the forces driving the adsorption process were not sufficient to overcome the protein rigidity and to influence the native structure of the enzyme. In other words, immobilized HRP exhibits similar affinity towards the substrate with most of its active sites remaining available after the adsorption process.

The above mentioned activities were measured immediately after preparation of the LDH-HEP-HRP samples. To assess the

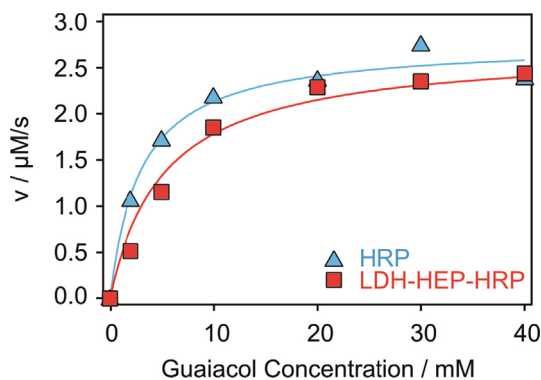


**Fig. 6.** Enzymatic activity of the native HRP enzyme and the LDH-HEP-HRP hybrid measured with the guaiacol assay. The solid lines are the fits obtained by using the Michaelis-Menten kinetic model. The results of the enzymatic assays were obtained with an average error of 10%.

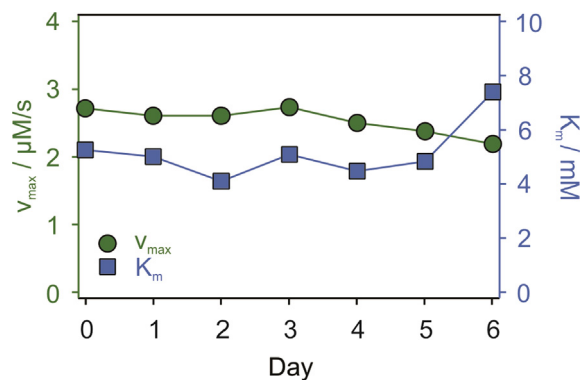


**Fig. 7.** Evolution of the maximum reaction rate ( $v_{max}$ ) and Michaelis-Menten constant ( $K_m$ ) for the LDH-HEP-HRP hybrid measured during a period of 6 days. The measurement error is about 10%.

long-term functional stability of the immobilized enzyme, the enzymatic activity of the hybrid materials was tested over several days. The determined  $v_{max}$  and  $K_m$  values are shown in Fig. 7. The tendency in  $v_{max}$  indicates that during the first four days of the experiment, the enzyme on the surface remained unharmed, but a 20% decrease of the initial value was observed after this period. Besides, no significant change was detected in the  $K_m$  values during five days for the LDH-HEP-HRP, however, a slight increase occurred in the sixth day. This is probably caused by small modifications in the native structure of the enzyme over this time period due to the interaction with the adsorbed heparin and LDH particles.

Nevertheless, it is important to emphasize that the hybrid material maintained a strong enzymatic activity over six days and this result is especially important and makes the LDH-HEP-HRP a promising applicant for any future applications, wherever the aim is to decompose hydrogen peroxide or to oxidize aromatic compounds in heterogeneous systems containing biocatalysts immobilized on particles and dispersed in liquid phase. Moreover in biomedical applications, these functionalized particles must form stable dispersions resistant against aggregation during the treatment.

## 4. Conclusions

A composite of HRP enzyme immobilized on heparin functionalized LDH platelets was synthesized to develop antioxidant hybrid materials. Biocompatible LDH nanoclay was prepared, used as solid support and coated with heparin polyelectrolyte to improve the colloidal stability and enzyme affinity to the surface. It was found that a saturated heparin layer is necessary to be adsorbed on the particles to achieve high resistance against salt-induced aggregation, while lower doses gave rise to charge neutralization of the LDH and subsequent rapid aggregation of the platelets. HRP adsorbed strongly and irreversibly on the polyelectrolyte coated LDH through hydrogen bonding, electrostatic and hydrophobic interactions. The obtained LDH-HEP-HRP hybrid could be aggregated only at extremely high ionic strengths and forms primary particles at salt levels used in the majority of the applications.

The enzymatic activities of the native HRP and the one in the hybrid material were very similar indicating the fact that the enzyme kept its structural and functional integrity during the immobilization process. The LDH-HEP-HRP material showed excellent long-term stability in the probe reaction and its ability in hydrogen peroxide decomposition and simultaneous oxidation of guaiacol was similar within the experimental error over several days.

The key improvement of the present study compared to previous works dealing with immobilized HRP enzymes [36,38,42] is clearly the excellent colloidal stability, which makes the system a promising antioxidant candidate in biomedical treatments to reduce the level of reactive oxygen species. In addition, the obtained high resistance against salt-induced aggregation can also be utilized in applications of environmental (e.g., water treatment) or industrial (e.g., formulation of cosmetic products) relevance, wherever the aim is to decompose hydrogen peroxide or to oxidize aromatic compounds.

### Acknowledgements

Financial supports by the Lendület program of the Hungarian Academy of Sciences (96130) and the Swiss National Science Foundation (150162) are gratefully acknowledged. The authors thank Tímea Simon for performing the specific surface area measurements.

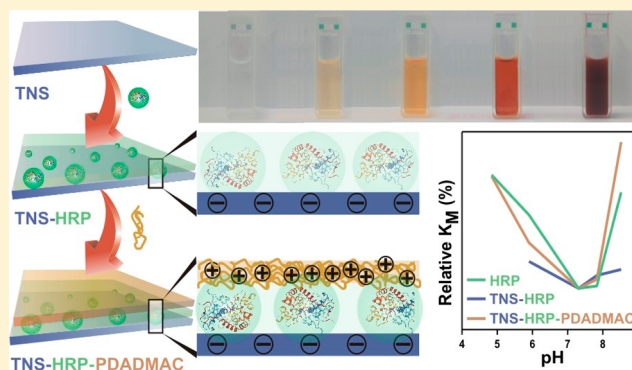
### References

- [1] U.T. Bornscheuer, G.W. Huisman, R.J. Kazlauskas, S. Lutz, J.C. Moore, K. Robins, *Nature* 485 (2012) 185–194.
- [2] X. Ma, A.C. Hortelao, T. Patino, S. Sanchez, *ACS Nano* 10 (2016) 9111–9122.
- [3] R.M. Daniel, M. Dines, H.H. Petach, *Biochem. J.* 317 (1996) 1–11.
- [4] S. Chakraborty, N. Kaushik, P.S. Rao, H.N. Mishra, *Compr. Rev. Food Sci. Food Saf.* 13 (2014) 578–596.
- [5] A.S. Yang, B. Honig, *J. Mol. Biol.* 237 (1994) 602–614.
- [6] D.J. Cole-Hamilton, *Science* 299 (2003) 1702–1706.
- [7] U. Hanefeld, L.Q. Cao, E. Magner, *Chem. Soc. Rev.* 42 (2013) 6211–6212.
- [8] O. Kudina, A. Zakharchenko, O. Trotsenko, A. Tokarev, L. Ionov, G. Stoychev, N. Pureskiy, S.W. Pryor, A. Voronov, S. Minko, *Angew. Chem.–Int. Ed.* 53 (2014) 483–487.
- [9] R.A. Sheldon, S. van Pelt, *Chem. Soc. Rev.* 42 (2013) 6223–6235.
- [10] A. Grotzky, E. Atamura, J. Adamcik, P. Carrara, P. Stano, F. Mavelli, T. Nausser, R. Mezzenga, A.D. Schluter, P. Walde, *Langmuir* 29 (2013) 10831–10840.
- [11] R.A. Sheldon, *Org. Process Res. Dev.* 15 (2011) 213–223.
- [12] I.K. Deshapriya, C.S. Kim, M.J. Novak, C.V. Kumar, *ACS Appl. Mater. Interf.* 6 (2014) 9643–9653.
- [13] M. Planchestainer, M.L. Contente, J. Cassidy, F. Molinari, L. Tamborini, F. Paradisi, *Green Chem.* 19 (2017) 372–375.
- [14] P. Rouster, M. Pavlovic, I. Szilagyi, *ChemBiochem* 19 (2018) 404–410.
- [15] J.H. Bartha-Vari, M.I. Tosa, F.D. Irimie, D. Weiser, Z. Boros, B.G. Vertessy, C. Paizs, L. Poppe, *ChemCatChem* 7 (2015) 1122–1128.
- [16] I. Inarritu, E. Torres, A. Topete, J. Campos-Teran, *J. Colloid Interface Sci.* 506 (2017) 36–45.
- [17] J. Kobayashi, Y. Mori, S. Kobayashi, *Chem. Commun.* (2006) 4227–4229.
- [18] Y.L. Wang, Z.C. Wang, Y.P. Rui, M.G. Li, *Biosens. Bioelectron.* 64 (2015) 57–62.
- [19] Y.M. Fan, X.D. Cao, T. Hu, X.G. Lin, H. Dong, X.N. Zou, *J. Phys. Chem. C* 120 (2016) 3955–3963.
- [20] G. Ali, T. Moreau, C. Forano, C. Mousty, V. Prevot, F. Charmantray, L. Lecquet, *ChemCatChem* 7 (2015) 3163–3170.
- [21] S. Vial, V. Prevot, F. Leroux, C. Forano, *Microporous Mesoporous Mat.* 107 (2008) 190–201.
- [22] M. Pavlovic, P. Rouster, I. Szilagyi, *Nanoscale* 9 (2017) 369–379.
- [23] Y.S. Gao, T.W. Teoh, Q. Wang, G.R. Williams, *J. Mat. Chem. B* 5 (2017) 9165–9174.
- [24] X. Mei, R.Z. Liang, L.Q. Peng, T.Y. Hu, M. Wei, *J. Mat. Chem. B* 5 (2017) 3212–3216.
- [25] S. Livi, V. Bugatti, L. Estevez, J. Duchet-Rumeau, E.P. Giannelis, *J. Colloid Interface Sci.* 388 (2012) 123–129.
- [26] Q. Wang, D. O'Hare, *Chem. Rev.* 112 (2012) 4124–4155.
- [27] S.J. Choi, J.M. Oh, J.H. Choy, *J. Mater. Chem.* 18 (2008) 615–620.
- [28] V.R.R. Cunha, R.B. de Souza, A. Martins, I.H.J. Koh, V.R.L. Constantino, *Sci. Rep.* 6 (2016).
- [29] M. Adok-Sipiczki, I. Szilagyi, I. Palinko, M. Pavlovic, P. Sipos, C. Nardin, *Colloid Polym. Sci.* 295 (2017) 1463–1473.
- [30] C. Mousty, V. Prevot, *Anal. Bioanal. Chem.* 405 (2013) 3513–3523.
- [31] G. Choi, H. Piao, M.H. Kim, J.H. Choy, *Ind. Eng. Chem. Res.* 55 (2016) 11211–11224.
- [32] A.M.E. Abdalla, L. Xiao, C.X. Ouyang, G. Yang, *Nanoscale* 6 (2014) 14141–14152.
- [33] M. Gajhede, D.J. Schuller, A. Henriksen, A.T. Smith, T.L. Poulos, *Nat. Struct. Biol.* 4 (1997) 1032–1038.
- [34] A.C. Maehly, B. Chance, *Methods Biochem. Anal.* 1 (1954) 357–424.
- [35] N. Duran, E. Esposito, *Appl. Catal. B* 28 (2000) 83–99.
- [36] A.T.E. Vilian, K. Giribabu, S.R. Choe, R. Muruganantham, H. Lee, C. Roh, Y.S. Huh, Y.K. Han, *Sens. Actuators, B* 251 (2017) 804–812.
- [37] Y.C. Lin, M.R. Liang, C.T. Chen, *Chem.–Eur. J.* 17 (2011) 13059–13067.
- [38] K. Kamada, A. Yamada, N. Soh, *RSC Adv.* 5 (2015) 85511–85516.
- [39] Y. Zhang, P.L. He, N.F. Hu, *Electrochim. Acta* 49 (2004) 1981–1988.
- [40] K. Kamada, T. Nakamura, S. Tsukahara, *Chem. Mat.* 23 (2011) 2968–2972.
- [41] A. Fishman, I. Levy, U. Cogan, O. Shoseyov, *J. Mol. Catal. B–Enzym.* 18 (2002) 121–131.
- [42] X.Y. Lang, L.L. Zhu, Y.N. Gao, I. Wheelodon, *Langmuir* 33 (2017) 9073–9080.
- [43] H. Wei, E.K. Wang, *Chem. Soc. Rev.* 42 (2013) 6060–6093.
- [44] M. Vazquez-Gonzalez, W.C. Liao, R. Gazelles, S. Wang, X. Yu, V. Gutkin, I. Willner, *ACS Nano* 11 (2017) 3247–3253.
- [45] R. Cai, D. Yang, S.J. Peng, X.G. Chen, Y. Huang, Y. Liu, W.J. Hou, S.Y. Yang, Z.B. Liu, W.H. Tan, *J. Am. Chem. Soc.* 137 (2015) 13957–13963.
- [46] Z.P. Xu, G. Stevenson, C.Q. Lu, G.Q. Lu, *J. Phys. Chem. B* 110 (2006) 16923–16929.
- [47] K.L. Chen, S.E. Mylon, M. Elimelech, *Langmuir* 23 (2007) 5920–5928.
- [48] F. Iselau, T.P. Xuan, G. Trefalt, A. Matic, K. Holmberg, R. Bordes, *Soft Matter* 12 (2016) 9509–9519.
- [49] M. Pavlovic, L. Li, F. Dits, Z. Gu, M. Adok-Sipiczki, I. Szilagyi, *RSC Adv.* 6 (2016) 16159–16167.
- [50] M. Kobayashi, S. Yuki, Y. Adachi, *Colloid Surf. A* 510 (2016) 190–197.
- [51] M.M. Bradford, *Anal. Biochem.* 72 (1976) 248–254.
- [52] K.A. Johnson, R.S. Goody, *Biochemistry* 50 (2011) 8264–8269.
- [53] M. Pavlovic, R. Huber, M. Adok-Sipiczki, C. Nardin, I. Szilagyi, *Soft Matter* 12 (2016) 4024–4033.
- [54] C. Vasti, A. Borgiallo, C.E. Giacomelli, R. Rojas, *Colloid Surf. A* 533 (2017) 316–322.
- [55] Z. Gu, H.L. Zuo, L. Li, A.H. Wu, Z.P. Xu, *J. Mater. Chem. B* 3 (2015) 3331–3339.
- [56] M. Pavlovic, P. Rouster, T. Oncsik, I. Szilagyi, *ChemPlusChem* 82 (2017) 121–131.
- [57] I. Popa, G. Gillies, G. Papastavrou, M. Borkovec, *J. Phys. Chem. B* 114 (2010) 3170–3177.
- [58] J.A. Lopez-Berganza, R.M. Espinosa-Marzal, *Cryst. Growth Des.* 16 (2016) 6186–6198.
- [59] M. Pavlovic, M. Adok-Sipiczki, C. Nardin, S. Pearson, E. Bourgeat-Lami, V. Prevot, I. Szilagyi, *Langmuir* 31 (2015) 12609–12617.
- [60] A. Kumar, S. Aerry, D.V. Goia, *J. Colloid Interface Sci.* 470 (2016) 196–203.
- [61] G. Trefalt, I. Szilagyi, M. Borkovec, *J. Colloid Interface Sci.* 406 (2013) 111–120.
- [62] C.B. Lavery, M.C. MacInnis, M.J. MacDonald, J.B. Williams, C.A. Spencer, A.A. Burke, D.J.G. Irwin, G.B. D'Cunha, *J. Agric. Food Chem.* 58 (2010) 8471–8476.
- [63] M. Elimelech, J. Gregory, X. Jia, R.A. Williams, *Particle Deposition and Aggregation: Measurement, Modeling, and Simulation*, Butterworth-Heinemann Ltd., Oxford, 1995.
- [64] R.C. Rodrigues, C. Ortiz, A. Berenguer-Murcia, R. Torres, R. Fernandez-Lafuente, *Chem. Soc. Rev.* 42 (2013) 6290–6307.
- [65] A. Tiraferri, L.A.S. Hernandez, C. Bianco, T. Tosco, R. Sethi, *J. Nanopart. Res.* 19 (2017).

## Functionalized Titania Nanosheet Dispersions of Peroxidase Activity

Paul Rouster,<sup>†</sup> Marko Pavlovic,<sup>‡</sup> Szilárd Sáringer,<sup>§,||</sup> and Istvan Szilagyi<sup>\*,§,||</sup><sup>†</sup>Institute of Condensed Matter and Nanosciences - Bio and Soft Matter, Université Catholique de Louvain, Louvain-la-neuve, Belgium<sup>‡</sup>Department of Inorganic and Analytical Chemistry, University of Geneva, Geneva, Switzerland<sup>§</sup>MTA-SZTE Lendület Biocolloids Research Group, University of Szeged, Szeged, Hungary<sup>||</sup>Department of Physical Chemistry and Materials Science, University of Szeged, Szeged, Hungary

**ABSTRACT:** Nanocomposites of titania nanosheets (TNS), horseradish peroxidase (HRP), and poly-(diallyldimethylammonium chloride) (PDADMAC) were prepared, and their colloidal and functional stabilities were assessed. HRP quantitatively adsorbed on bare TNS, and the adsorption process did not affect the charging and aggregation behavior of the colloidal system. The obtained TNS–HRP composite was functionalized by PDADMAC to stabilize the enzyme on the surface and to maintain good colloidal stability. Depending on the PDADMAC dose applied, its adsorption on TNS–HRP led to charge reversal of the particles from negative to positive. The formation of a saturated polyelectrolyte layer on the TNS–HRP (TNS–HRP–PDADMAC) gave rise to highly stable colloids, and especially the resistance against salt-induced aggregation was excellent. The enzymatic activity of different systems was investigated as a function of the pH of the medium and over time. The results indicated that HRP remained enzymatically active upon immobilization, and in addition, the pH range of application broadened compared to its native form. The developed TNS–HRP–PDADMAC system can thus be used in a wider pH range and possesses the advantages of a heterogeneous catalyst compared to the bare enzyme.



## INTRODUCTION

Titania nanoparticles of spherical or elongated structures have been extensively studied in the past decades due to their advantageous chemical properties utilized in various applications.<sup>1–3</sup> Among them, bioapplications, e.g., in medical devices,<sup>4</sup> as biosensors<sup>5</sup> or biomimetic materials<sup>6</sup> to improve the biocompatibility of polymeric scaffolds,<sup>7</sup> and in drug delivery,<sup>8</sup> became especially important. Indeed, these materials take advantage of the biocompatibility of titania and also of the suitability of its surface for the deposition of various types of coating agents to obtain improved surface properties.<sup>9–11</sup> In addition, preparation of 2-dimensional titania and other materials of sheet-like structure was the focus of several research groups.<sup>12–16</sup>

Enzymes, on the other hand, are sensitive biocatalysts that can partially or totally lose their enzymatic activity as a consequence of any changes occurring in their surrounding environment (e.g., pH, temperature, pressure, or ionic strength).<sup>17,18</sup> This major drawback of their environmental response can be overcome by immobilization on solid supports.<sup>17,19–21</sup> However, depending on the enzymes and the supports used, contradictory results were reported.<sup>17,22–24</sup> In some cases, immobilized enzymes performed better in harsher conditions compared to their native form in solution,

whereas in some situations, immobilization resulted in denaturation over time.

Among all the different classes of enzymes, oxidoreductase enzymes are of special importance for the removal of reactive oxygen species (ROS) like superoxide radical anions and hydrogen peroxide ( $H_2O_2$ ).<sup>25–27</sup> The superoxide dismutase enzyme is known for the efficient dismutation of superoxide radical anions by converting them to peroxide, which in turn is decomposed by catalase or horseradish peroxidase (HRP). When both types of enzymes are used together, they perform a cascade reaction leading to the complete decomposition of ROS. However, in some cases, when dealing only with  $H_2O_2$ , only one type of enzyme is needed. By mixing HRP with  $H_2O_2$ , the heme group of the HRP reacts with  $H_2O_2$ , and this intermediate compound behaves as an oxidizing agent toward aromatic substances.<sup>28,29</sup> This reaction has been used to develop biosensors in order to detect the presence of  $H_2O_2$  in solutions and to monitor its concentration and/or to decompose aromatic compounds.<sup>30–33</sup> Even though both HRP forms, native and immobilized, are highly efficient, the later one

Received: April 6, 2018

Revised: May 7, 2018

Published: May 8, 2018



is more favorable due to its possibility to be recycled and reused.<sup>29</sup>

Adsorption of HRP or other enzymes on solid supports (e.g., titania nanostructures, clay platelets, or silica nanoparticles) occurs through one or several types of interactions like covalent linkage, electrostatic attraction, hydrogen bonding, and hydrophobic interaction.<sup>11,34–36</sup> In general, these enzyme-functionalized surfaces possess enzymatic activity as emphasized in the case of HRP by the reduction of the H<sub>2</sub>O<sub>2</sub> content in solutions.<sup>22,37</sup> Moreover, HRP enzymes deposited in multilayered films retain their enzymatic function. During the buildup of such thin films, one can play on the location and amount of deposited enzymes, which in turn will affect their efficiency in catalyzing the removal of H<sub>2</sub>O<sub>2</sub>.<sup>38,39</sup> Similarly, core–shell structures or capsules were also investigated, where HRP enzymes were encapsulated either in their center or in their surrounding polyelectrolyte multilayer.<sup>40–42</sup> These materials possessed the advantage of further protecting the enzymes toward the external medium due to the presence of the polyelectrolyte multilayer coating.<sup>43</sup> Moreover, the enzymatic activity studies performed revealed that the enzymes were still efficient and possessed an improved lifespan compared to their free (non-immobilized) form.

In general, the structure of the enzyme–nanoparticle composites is characterized in detail, while little attention is paid to the colloidal stability of these systems. However, this is a critical issue since many applications, especially the biorelated ones, occur in dispersions. Indeed, aggregation of the nanocarriers leads to their unsuccessful use in delivery processes due to the formation of irregularly shaped clusters giving rise to a loss of their enzymatic activity.<sup>44</sup> Despite the importance of aggregation and charging of these colloids, only a limited number of studies reported systematic investigations in this field.

Here, we aim to design stable dispersions containing HRP immobilized on TNS acting as a nanocarrier. The colloidal behavior of the nanocomposites was tuned by functionalization with poly(diallyldimethylammonium chloride) (PDADMAC) polyelectrolyte. The charging and aggregation features of the different systems upon their surface functionalization were investigated at each step of the preparation in order to determine the conditions, under which the colloids were stable or tend to aggregate. The enzymatic activity of the nanocomposites was determined in biochemical assays to assess the influence of HRP immobilization on the activity, and the results were compared to its native form.

## EXPERIMENTAL SECTION

**Materials.** HRP (type VI, EC number 1.11.1.7), PDADMAC (20 wt % in water,  $M_w = 100–200$  kg/mol), Coomassie Brilliant Blue G, 2-methoxyphenol (guaiacol), phosphoric acid (85 v/v %), and analytical grade salts including sodium chloride (NaCl), sodium phosphate monobasic monohydrate (NaH<sub>2</sub>PO<sub>4</sub>·H<sub>2</sub>O), and sodium phosphate dibasic dihydrate (Na<sub>2</sub>HPO<sub>4</sub>·2H<sub>2</sub>O) were purchased from Sigma-Aldrich and used without further purification. Ethanol of reagent grade was acquired from Fisher Scientific. H<sub>2</sub>O<sub>2</sub> (30%) was purchased from Reactolab SA. TNS were synthesized according to a procedure described elsewhere.<sup>45</sup> Ultrapure water (Millipore) was used directly after production for all the sample preparations. The measurements were carried out at pH 7 and 25 °C.

Prior to their use, the TNS were dispersed in ultrapure water. A pH 7 phosphate buffer, at a concentration of 1 M, was prepared by mixing an appropriate amount of Na<sub>2</sub>HPO<sub>4</sub> and NaH<sub>2</sub>PO<sub>4</sub> solutions. Samples containing PDADMAC in a concentration range of 0.01–1000 mg/L were prepared by dissolving the polyelectrolyte in a 5 mM NaCl solution. HRP was dissolved in ultrapure water, and solutions with a concentration range of 0.01–1000 mg/L were prepared. TNS–HRP–PDADMAC dispersions were prepared by mixing TNS–HRP with PDADMAC to obtain a solution, where the particle concentration was 1 mg/mL and the final NaCl concentration was 4.5 mM. After 2 h of PDADMAC adsorption time, the solution was centrifuged at 10 000 rpm for 20 min. The supernatant was removed, and the slurry was redispersed in a 5 mM NaCl solution. More details concerning the sample preparation protocols are given later.

**Characterization Methods.** Electrophoretic mobility (EM) measurements were performed on a Zetasizer Nano ZS (Malvern Instruments) device. For the EM experiments, 5 mL solutions were prepared, where the final particle concentration was 1 mg/L. In general, 0.5 mL of the particles was added to 4.5 mL of solution containing a calculated amount of salt and/or coating material (HRP, PDADMAC). The sample was then allowed to rest overnight prior to the EM experiments. The reported results were the average of 5 independent measurements made under the same experimental conditions.

Dynamic light scattering (DLS) experiments were carried out on a CGS-3 goniometer system (ALV) at a scattering angle of 90°. To follow the aggregation processes, time-resolved DLS experiments were performed, where the correlation function was collected for 20 s and the measurements lasted for typically 10–120 min depending on the speed of aggregation. A second-order cumulant fit was used to determine the diffusion coefficient, which was then introduced in the Stokes–Einstein equation to calculate the hydrodynamic radius.<sup>46</sup> The stability of the colloidal dispersions was expressed in terms of stability ratio.<sup>45–47</sup> The sample preparation for DLS experiments was similar to the one applied for the EM measurements but differed in the fact that the aggregation rate of the particles was probed immediately after sample preparation.

Infrared (IR) spectra were recorded in the attenuated total reflectance mode (ATR) using a Spectrum 100 FT-IR spectrometer (PerkinElmer). The ATR crystal was made of diamond. Prior to the measurements, the internal reflectance unit was washed with ethanol and dried. The obtained spectrum is an average of 48 scans acquired at a resolution of 4 cm<sup>-1</sup>.

Transmission electron microscopy (TEM, Tecnai G2 Sphera microscope, FEI) images of the bare and coated TNS were recorded at each stage of their surface functionalization. The device was equipped with a LaB6 cathode and operated at a voltage of 120 kV. The colloidal suspension was deposited on a plasma-activated carbon hexagonal mesh (CF200H-CU-UL, Electron Microscopy Sciences). After 2 min adsorption time, the excess solution was removed with a filter paper. The mesh was then placed on the specimen and mounted in the microscope for imaging.

**Quantification of the HRP Amount in Solution.** The amount of HRP that did not adsorb on the TNS, i.e., remained dissolved in the bulk, was determined by the Bradford test.<sup>48,49</sup> A stock solution of Coomassie Brilliant Blue dye was prepared as follows. An amount of 100 mg of the dye was dissolved in 50 mL of 95 v/v % ethanol, and 100 mL of 85 v/v % phosphoric



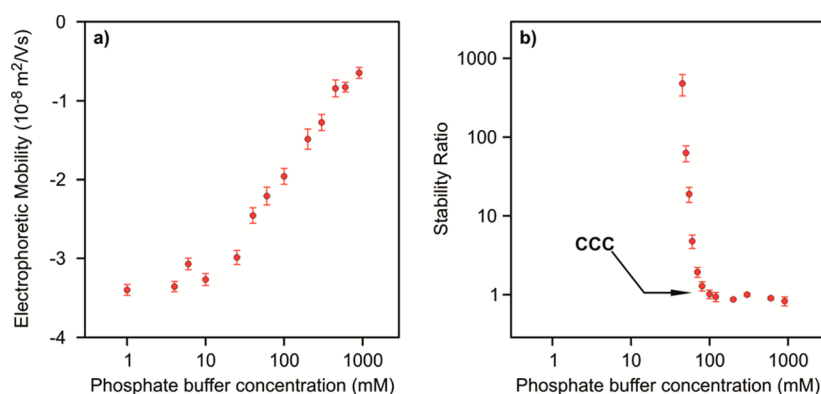


**Figure 1.** Influence of the phosphate buffer concentration on (a) the EM values and (b) stability ratios of the bare TNS at pH 7.

acid was added. The solution was completed to 1 L with ultrapure water. Thereafter, standard solutions of HRP with a concentration range of 0–100 mg/L were prepared by dilution. After mixing 400  $\mu$ L of the HRP standard solution with 1.6 mL of the dye solution, the UV–vis spectrum of the solution, after 5 min equilibration time, was recorded on a Lambda 35 spectrophotometer (Perkin Elmer). The change in the absorbance bands at 464 nm (free dye) and at 594 nm (enzyme dye and free dye) was monitored. The ratio in the intensity between these two peaks indicated the amount of HRP that did not adsorb on the surface of the TNS.

**Enzymatic Assay.** The determination of the HRP activity was performed by using the guaiacol assay.<sup>22,50,51</sup> In brief, 240  $\mu$ L of a HRP solution at a concentration of 5 mg/L was mixed with 1.872 mL of phosphate buffer at a concentration of 12.9 mM followed by the addition of 240  $\mu$ L of guaiacol at a given concentration. The cuvette was then sealed and vortexed for a few seconds. Finally, 48  $\mu$ L of H<sub>2</sub>O<sub>2</sub> at 135 mM was added in the cuvette, which was vortexed again and immediately introduced into the UV–vis spectrophotometer to follow the formation of the guaiacol degradation products at 470 nm wavelength (see abstract graphic for the color changes).<sup>52,53</sup> The increase in the absorbance at 470 nm was monitored as a function of the reaction time, where the linear part of the curve was fitted in order to obtain the reaction rate of the system. The results were analyzed with the Michaelis–Menten model as<sup>54</sup>

$$v = \frac{v_{\max}[S]}{K_m + [S]} \quad (1)$$

where  $v$  is the reaction rate;  $K_m$  is the Michaelis–Menten constant;  $v_{\max}$  is the maximum reaction rate for the investigated system; and  $[S]$  refers to the substrate concentration. For the time-dependent measurements, the HRP-containing samples were rested at room temperature. Appropriate amounts of aliquots were taken each day, and the enzymatic activities were tested in the above-described probe reaction.

## RESULTS AND DISCUSSION

**TNS Aggregation in Phosphate Buffer.** Bare titania, like other inorganic (e.g., clay, silica, and gold) nano-objects, often possesses a limited stability in the presence of monovalent salt solutions.<sup>45,55,56</sup> Therefore, a convenient way to increase the colloidal stability of such particles is to functionalize them with polyelectrolytes<sup>45,57</sup> or dendrimers.<sup>58</sup> In some cases, multivalent ions can be used to improve the stability of the bare

particles.<sup>56,59</sup> Indeed, in the presence of such ions, the particles first undergo fast aggregation above the first critical coagulation concentration (CCC) value, which marks the transition between stable and unstable dispersions. A further increase in the ionic strength above the first CCC value can lead to a restabilization of the particles marked by a second CCC value. This is due to further ion adsorption on the surfaces, which either leads to charge reversal or an increase in the magnitude of the electrokinetic potential.<sup>56</sup> Therefore, the influence of the phosphate buffer concentration at pH 7 on the charging and aggregation behavior of the bare TNS was investigated (Figure 1) in this study first in order to optimize the conditions for the further enzyme immobilization step.

The particles are negatively charged in the phosphate buffer concentration range investigated (Figure 1a) due to the fact that their point of zero charge was reported to be 5.2 earlier.<sup>56</sup> In this case, the phosphate ions are the co-ions; i.e., they possess the same sign of charge as the nanosheets. Furthermore, above a concentration of about 20 mM the magnitude of the EM decreases due to the increase of the surface charge screening by the sodium counterions.

The colloidal stability was assessed in time-resolved DLS experiments and expressed in terms of stability ratio, which is calculated from the initial increase of the hydrodynamic radius in aggregating samples.<sup>34,46,56</sup> Note that stability ratios close to unity indicate rapidly aggregating unstable colloids; however, in the case of higher values, the aggregation slows down, and the samples are more stable. In other words, a stability ratio of 10 means that 1/10 fraction of the particle collisions leads to dimer formation for instance.

The trend in the stability ratios of the system shows that the samples are stable up to a phosphate buffer concentration of 78 mM (Figure 1b). Above this value, TNS undergo fast aggregation as indicated by stability ratios close to one. These results are in line with the theory developed by Derjaguin, Landau, Verwey, and Overbeek (DLVO).<sup>60,61</sup> Indeed, the DLVO theory states that the overall interparticle force is the sum of the repulsive electrical double-layer force and the attractive van der Waals force. By increasing the ionic strength, the surface charges of the TNS are screened by the ions in the phosphate buffer leading to a thinning of the electrical double layer around the particles. Above the CCC, the repulsive electrical double-layer forces no longer prevail, and the attractive van der Waals forces predominate, giving rise to rapid aggregation of the particles and thus to unstable dispersions. It is obvious from these results that the particles are highly stable and negatively charged at a phosphate buffer

concentration of 10 mM. Therefore, this condition was chosen in order to obtain stable TNS dispersions for further enzyme immobilization.

**Immobilization of HRP.** The isoelectric point of HRP ranges from 5 to 9 depending on its origin and purification process.<sup>28,33</sup> In our case, however, the enzyme was positively charged at pH 7, and thus, it was expected to adsorb on the oppositely charged nanosheets by electrostatic attraction. It is also important to avoid the significant decrease in the magnitude of the surface charge upon HRP adsorption because it may lead to unwanted particle aggregation. Therefore, EM was recorded at different HRP doses to follow the charging properties (Figure 2). It was found that for an enzyme dose less

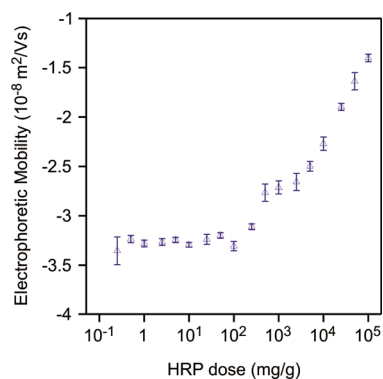


**Figure 2.** Evolution of the EM data of TNS as a function of the applied dose of HRP. The mg/g unit refers to mg of enzyme per gram of TNS.

than 100 mg/g the EM values were not affected by the amount of HRP in solution. Above this loading, the magnitude of the EM decreases. No stability ratio values could be determined in the HRP concentration regime investigated due to the high stability, i.e., the lack of aggregation processes, of the colloidal suspension.

However, applying a high amount of HRP dose to functionalize the particles does not necessarily result in a quantitative adsorption of the enzyme on the TNS. As a matter of fact, it is primordial to determine an HRP dose, which does not affect the colloidal behavior of the TNS and, on the other hand, also results in quantitative adsorption on the TNS, i.e., no HRP partitioning between the surface and the bulk. The quantification of the amount of adsorbed HRP on the TNS was performed by the Bradford test,<sup>48</sup> which determines the amount of HRP present in the bulk solution after enzyme adsorption. For HRP doses lower than 10 mg/g, it was found that after 2 h of adsorption time 99.9% of the enzyme adsorbed on the TNS. Such a strong adsorption is most likely due to the combined effects of electrostatic attraction, hydrogen bonding, and hydrophobic interaction between the enzyme and the nanosheet surface. Accordingly, 10 mg/g HRP dose was applied in the further studies, since no HRP is present apart from the one on the surface and the obtained TNS–HRP hybrid is of high colloidal stability.

Moreover, the adsorption of the enzyme on the TNS was also confirmed by IR spectroscopy. In Figure 3, the IR spectra of the native enzyme and TNS are shown along with the TNS–HRP hybrid. In the wavenumber region 800–1800 cm<sup>-1</sup>, the TNS possess no characteristic peaks, whereas several vibrational bands can be assigned to the HRP in this regime. The peaks at 1645 and 1525 cm<sup>-1</sup> are attributed to the amide I and amide II

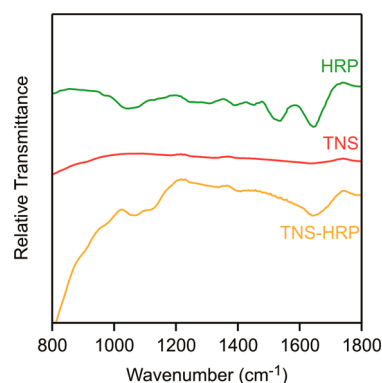


**Figure 3.** IR spectra of TNS, HRP, and TNS–HRP hybrid at an enzyme dose of 10 mg/g.

functions, respectively.<sup>62–64</sup> Upon immobilization of HRP on the TNS, the IR spectrum of TNS–HRP shows the appearance of the amide I function meaning that the enzyme was successfully adsorbed on the TNS. Thus, the combination of the Bradford test results with the IR spectrum of the TNS–HRP system unambiguously confirms that the HRP is quantitatively adsorbed on the TNS, once a dose of 10 mg/g is applied. Note that the TNS–HRP abbreviation refers to a 10 mg/g HRP coating of 1 g of TNS in the following.

#### Surface Functionalization by PDADMAC Adsorption.

Although HRP was successfully immobilized on TNS, the leakage of the enzyme from the nanoparticulate support may occur over time or during the operational use.<sup>65,66</sup> Therefore, the surface of TNS–HRP was functionalized by PDADMAC polyelectrolyte in order to prevent or minimize any leakage of the enzyme and also to reverse the surface charge of the nanocarrier from negative to positive in order to match the positive net charge of the native enzyme. PDADMAC is a strong polyelectrolyte, whose charge density is pH independent, meaning that any variation of the pH in the solution does not affect the surface charge of the functionalized TNS. To optimize the polyelectrolyte dose for the functionalization, the charging and aggregation behavior of the particles were initially investigated. The effect of HRP adsorbed on the TNS on the surface charge properties and colloidal stability was also probed, and the EM values of both TNS and TNS–HRP measured at different PDADMAC doses were determined and compared.

Let us first discuss the influence of the PDADMAC dose on the EM values in both TNS and TNS–HRP systems (Figure 4a). It was reported several times earlier that polyelectrolytes tend to strongly adsorb on oppositely charged surfaces.<sup>45,55,57,67,68</sup> For both systems at low PDADMAC dose, the EM values are similar to the ones of the bare particles. By increasing the amount of PDADMAC adsorbing on the surface, the EM values increase until reaching the charge neutralization point. Further addition of PDADMAC leads to charge reversal of the system and to the appearance of an adsorption saturation plateau. Beyond the dose corresponding to the onset of this plateau, no more polyelectrolyte can adsorb on the surface of the particles, and the remaining PDADMAC stays dissolved in the bulk. Such a trend in the EM data for oppositely charged polyelectrolyte–particle systems is typical and was reported previously for different types of dispersions.<sup>34,45,47,58,67</sup> It was observed that the charging behavior of both systems was very similar giving rise to similar charge neutralization points, and their surface saturates more or less at the same PDADMAC

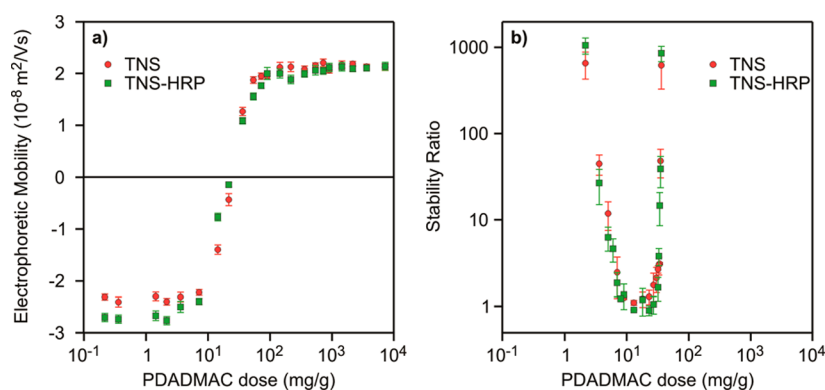


**Figure 4.** (a) EM data and (b) stability ratios of TNS and TNS–HRP as a function of the applied PDADMAC dose used to functionalize the materials.

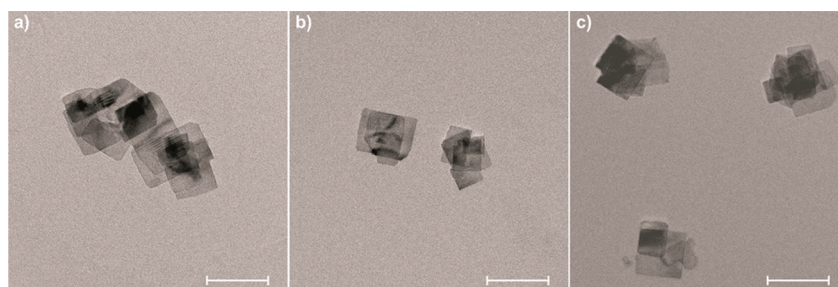


**Figure 5.** TEM images of (a) TNS, (b) TNS–HRP, and (c) TNS–HRP–PDADMAC. The scale bars are equal to 100 nm.

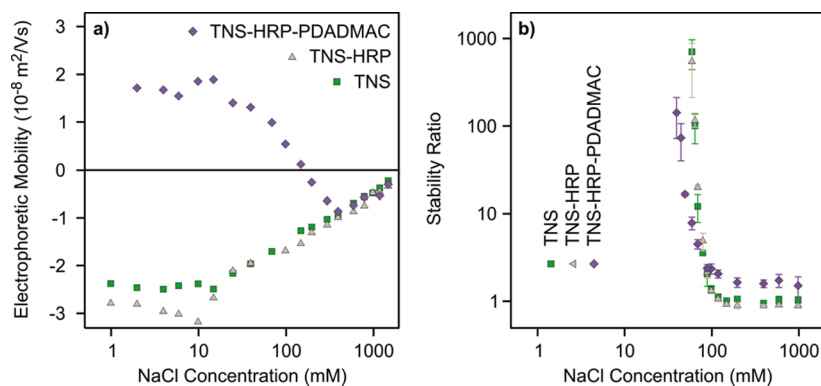


**Figure 6.** (a) EM and (b) stability ratio measurements of TNS, TNS–HRP, and TNS–HRP–PDADMAC as a function of the NaCl concentration.

loadings. Note that TNS–HRP–PDADMAC refers to PDADMAC coating of the TNS–HRP particles at the onset value for the saturation plateau (144 mg/g).

The colloidal stability of the TNS and TNS–HRP was also investigated (Figure 4b) under exactly the same experimental conditions as applied in the EM study. At low and high PDADMAC doses, the systems are highly stable, whereas aggregation occurs around the neutralization point, as indicated by stability ratio values close to unity at the minima of the plots. As for the electrophoresis measurements for both types of particles, similar aggregation results were obtained meaning that the applied dose of 10 mg/g of HRP used to functionalize the TNS did not affect the overall colloidal behavior of the particles. In addition, the TNS–HRP–PDADMAC hybrid material of saturated polyelectrolyte layer on the surface forms stable dispersion under the experimental conditions investigated.

Furthermore, the tendency of the stability ratios upon the PDADMAC coating of the particles is in line with the DLVO theory. Indeed, at low PDADMAC dose, the repulsive electrical double-layer forces of the particles overcome the attractive van der Waals forces leading to stable dispersions. Increasing the PDADMAC dose, the electrical double-layer forces weakened due to the surface charge compensation of the nanoparticles by the PDADMAC adsorption. Around the charge neutralization point, the particles are close to an electrostatically neutral state, and thus, aggregation occurs due to the predominance of the attractive van der Waals forces. Further adsorption of PDADMAC above the neutralization point leads to a restabilization of the systems, where aggregation is hindered by the generation of a positive electrical double layer around the particles upon PDADMAC adsorption. Similar tendency in the stability ratios was previously published in particle–oppositely charged polyelectrolyte systems.<sup>34,47,55</sup>



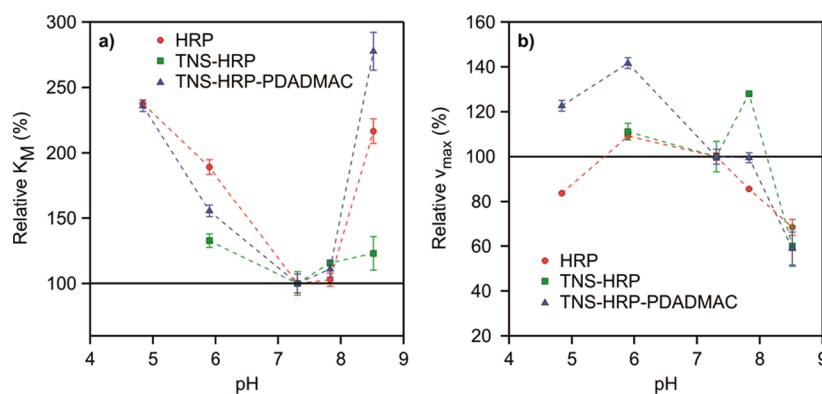


**Figure 7.** Relative (a)  $K_m$  and (b)  $v_{max}$  values of HRP in native (HRP), immobilized (TNS–HRP), and embedded (TNS–HRP–PDADMAC) forms as a function of the pH in a 10 mM phosphate buffer. The lines are just to guide the eyes.

Under the applied coating conditions, all the different systems (TNS, TNS–HRP, and TNS–HRP–PDADMAC) appear to be stable as indicated by the aggregation studies. This statement was further investigated by recording TEM images of the samples. When dispersed in a 10 mM phosphate buffer at pH 7, the TNS are stable, and low order of aggregates can be seen due to the drying process during the sample preparation for TEM imaging (Figure 5a). Similar observations were made, when recording TNS–HRP (Figure 5b) dispersions. Thus, the 10 mg/g dose of HRP used to functionalize the TNS does not affect the colloidal behavior of the system as already observed previously. The TEM images of the TNS–HRP–PDADMAC sample (Figure 5c) showed that upon charge reversal of the TNS–HRP by PDADMAC coating at the onset of the saturation plateau does not lead to any destabilization of the dispersion. Moreover, these TEM images clearly indicate that the morphology of the bare, enzyme-functionalized, and polyelectrolyte-coated nanosheets is the same.

**Resistance Against Salt-Induced Aggregation.** In the next step, the charging and aggregation processes of TNS, TNS–HRP, and TNS–HRP–PDADMAC materials were studied at different ionic strengths. The main idea was to investigate the influence of the successive coatings on the colloidal stability of the particles and whether it has been improved or not. For comparison, note that the CCC of the bare TNS dispersed in ultrapure water (without phosphate buffer) was found to be 19 mM.<sup>45</sup> Figure 6 shows the effect of the NaCl concentration on the EM and stability ratio values for the different systems.

From the charging behavior of the different materials (Figure 6a), it was observed that the TNS and TNS–HRP are negatively charged, whereas the TNS–HRP–PDADMAC is of positive charge in almost the entire salt concentration regime studied. This is in line with the results of the mobility studies discussed in the earlier sections. Moreover, from the salt-dependent electrophoresis experiments, the surface charge density of the materials was determined by converting the EM values at different salt concentrations to electrokinetic potentials by using the Smoluchowski equation followed by the fitting of the potentials at different ionic strength by the Debye–Hückel model.<sup>69</sup> The calculated surface charge densities were  $-15$  mC/m<sup>2</sup>,  $-16$  mC/m<sup>2</sup>, and  $+7.5$  mC/m<sup>2</sup> for TNS, TNS–HRP, and TNS–HRP–PDADMAC, respectively. Accordingly, the 10 mg/g of HRP deposited on the TNS did not affect the surface charge density of the material, whereas

the PDADMAC coating led to a decrease in the magnitude of the surface charge density.

Stability ratios were measured in the same systems to assess the colloidal stability (Figure 6b). The first observation was that the presence of 10 mM phosphate buffer increased the CCC from 19 to 78 mM compared to the bare TNS dispersed in water,<sup>45</sup> meaning that the stability of TNS raised 4 times. This is due to the specific phosphate adsorption and subsequent increase of the negatively charged group on the TNS surface.<sup>56,70</sup> The influence of the 10 mg/g HRP adsorbed on the TNS followed by the PDADMAC coating of the TNS was also studied. The calculated CCCs were found to be 82.4 and 78.6 mM in NaCl salt solutions for the TNS–HRP and TNS–HRP–PDADMAC, respectively. These results indicate that upon the successive adsorption of the enzyme and the polyelectrolyte no destabilization of the system occurred and that no extra stabilization of the TNS could be observed. However, the PDADMAC coating of the nanoparticulate support led to a positively charged nanocarrier of similar charge compared to the utilized native enzyme.

In addition, the Bradford test<sup>48</sup> was performed on the supernatant of the TNS–HRP–PDADMAC sample in order to check whether the HRP remained immobilized on the TNS surface upon the PDADMAC functionalization or desorbed from it. The results indicated that 99.7% of the enzyme was adsorbed on the TNS surface; i.e., no desorption of the enzyme took place during the coating process. Therefore, two types of stable nanocarriers (TNS–HRP and TNS–HRP–PDADMAC) were successfully developed.

**Enzymatic Activity Tests.** Although stable nanocarriers were obtained, their efficiency in the decomposition of H<sub>2</sub>O<sub>2</sub> had to be verified. The enzymatic activity of the native and immobilized enzymes was determined by using the guaiacol assay.<sup>22,50,51</sup> This biochemical test reaction consists of measuring the formation of the degradation products of guaiacol under the combined effect of HRP and H<sub>2</sub>O<sub>2</sub>. In brief, the HRP reacts with H<sub>2</sub>O<sub>2</sub> to form an oxidizing agent toward aromatic compounds,<sup>28,29</sup> like guaiacol for example. The formation of the guaiacol degradation products can then be monitored by following the color change of the solution over time.<sup>22,51</sup> Prior to the determination of the enzymatic activity of the native and immobilized form of HRP, the influence of the bare TNS and TNS–PDADMAC (without any HRP added) was tested by the guaiacol assay. Both types of materials exhibited no enzymatic activity; i.e., these materials alone were unable to degrade guaiacol. Hence, if an enzyme-like function is



observed during the further assays, it originates solely from the enzymes in the samples and not from the nanoparticulate supports.

As mentioned in the **Experimental Section**, the Michaelis–Menten model<sup>54</sup> was used to analyze the results of the assays. Accordingly, the Michaelis constants ( $K_m$ ) and the maximum reaction rate ( $v_{max}$ ) were calculated from the reaction rate versus substrate concentration plots (eq 1). The  $K_m$  value corresponds to the affinity of the enzyme toward the substrate. For example, a decrease in the  $K_m$  value refers to a higher affinity of the enzyme to guaiacol. The  $v_{max}$  is the maximum reaction rate that can be achieved by the system once the active site of the enzymes is completely saturated by the substrate.

The activities of the native (HRP), immobilized (TNS–HRP), and embedded (TNS–HRP–PDADMAC) forms of the enzyme were then probed as a function of the pH. The relative  $K_m$  (Figure 7a) and  $v_{max}$  (Figure 7b) data are plotted and correspond to the normalized  $K_m$  and  $v_{max}$  values for each sample at the optimum pH conditions, which is pH 7.3 in these systems. One can conclude from Figure 7a that all the systems possess an optimum pH range of application around 7.3–7.8, where the relative  $K_m$  is the lowest. Interestingly, the optimum relative  $v_{max}$  (Figure 7b) appears to be slightly different for all three systems. Indeed, the optimum pH range for HRP, TNS–HRP, and TNS–HRP–PDADMAC is around pH 5.9–7.3, 5.9–7.8, and 4.8–7.8, respectively. Interpreting the relative  $K_m$  and  $v_{max}$  values together, it can be observed that the immobilized and embedded forms of the HRP exhibit a broader pH range of application, where their relative enzymatic activity is higher compared to the native enzyme. These systems appear particularly interesting, whenever HRP needs to be used in a broad pH range or in slightly acidic conditions.

Knowing the optimum pH of application of these materials, the time-dependent activity was also probed. Indeed, upon immobilization, it is known that the enzymes may change their conformation resulting in a loss of activity due to denaturation.<sup>17</sup> Here, we probed the relative enzymatic activities for all three systems (HRP, TNS–HRP, and TNS–HRP–PDADMAC) at pH 7.3 over several days. In Figure 8, only the relative  $v_{max}$  values are given as no significant information from the relative  $K_m$  values could be obtained.

Compared to the native HRP, which appears to be stable over time by maintaining its initial activity, the immobilized and embedded forms of the HRP both lose their activity over time. After 1 day, the relative  $v_{max}$  decreased by 91% and 65% for

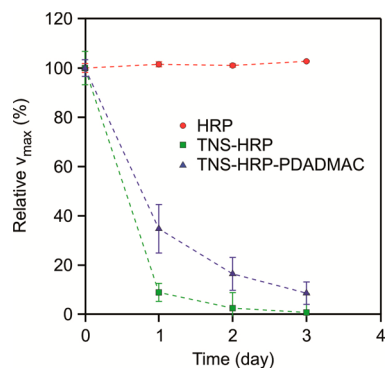


**Figure 8.** Time dependence of the relative  $v_{max}$  values of the native, immobilized, and embedded form of HRP in a 10 mM phosphate buffer at pH 7.3. The lines serve to guide the eye.

TNS–HRP and TNS–HRP–PDADMAC, respectively. After 3 days, TNS–HRP exhibited no more activity, whereas TNS–HRP–PDADMAC only retained 9% of its initial activity. To explain the decrease in the enzymatic activity of the HRP-coated nanocarriers, two assumptions were made: the first one being that the enzyme was desorbing over time from the nanocarrier and the second one that the HRP was being denaturated leading to a decrease in its activity. To check the first assumption, Bradford tests on the supernatant were performed to determine if any enzymes were present in it. The results indicated that no HRP leaked from the surface of the nanocarriers and that they were still immobilized or embedded. Thus, we could rule out the first assumption. Hence, the loss of enzymatic activity of the HRP-functionalized nanocarriers should be due to the denaturation of the enzyme over time. This process appeared to occur faster for TNS–HRP compared to TNS–HRP–PDADMAC.

Indeed, for TNS–HRP–PDADMAC, the HRP is trapped under the PDADMAC layer, and its denaturation was slower due to a blocking effect of the PDADMAC on the enzyme denaturation. For TNS–HRP, the enzyme is not trapped under a polyelectrolyte layer, and the loss in activity due to denaturation of HRP cannot be slowed down or hindered. Although the enzymatic activity of the nanocomposites decreases over time, the TNS–HRP–PDADMAC maintains considerable activity for 1 day. In addition, it possesses a broader pH range of application compared to the native enzyme. Considering these facts and also the advantages gained by the immobilization (e.g., better separation from the reaction mixture) the obtained TNS–HRP–PDADMAC hybrid is a promising approach for future applications in manufacturing processes for the removal of  $H_2O_2$  or oxidation of organic contaminants.

## CONCLUSIONS

We report here on the preparation and colloidal behavior of TNS and its HRP-modified and PDADMAC-coated derivatives. HRP quantitatively adsorbed on the TNS through electrostatic forces, hydrogen bonding, and hydrophobic interactions. PDADMAC adsorption on the TNS–HRP particles resulted in charge neutralization at lower and charge reversal at higher polyelectrolyte doses. Formation of a saturated polyelectrolyte layer on the nanosheets prevented enzyme leakage and aggregation of the particles. The TNS, TNS–HRP, and TNS–HRP–PDADMAC materials possessed similar behavior once dispersed in salt solutions of different concentrations. The relative enzymatic activity of HRP under its native, immobilized (TNS–HRP), and embedded (TNS–HRP–PDADMAC) forms was also probed. The results showed that upon adsorption of the enzyme the particles exhibited a broader pH range of application, where the relative enzymatic activity of HRP appeared to be higher compared to the native HRP in solution. However, the time-dependent study pointed out that the immobilized enzyme was being denaturated, especially in the case of TNS–HRP. Nevertheless, the obtained TNS–HRP–PDADMAC hybrid material can be used in a broader pH range and possess the advantages of a heterogeneous catalyst such as an easier separation from the reaction mixture.

## AUTHOR INFORMATION

### Corresponding Author

\*E-mail: [szistvan@chem.u-szeged.hu](mailto:szistvan@chem.u-szeged.hu)

ORCID 

Istvan Szilagyi: 0000-0001-7289-0979

## Author Contributions

The manuscript was written through contributions of all authors. All authors have given approval to the final version of the manuscript.

## Notes

The authors declare no competing financial interest.

## ACKNOWLEDGMENTS

This research was financially supported by the Lendület program of the Hungarian Academy of Sciences (96130) and the Swiss National Science Foundation (150162).

## REFERENCES

- (1) Asahi, R.; Morikawa, T.; Ohwaki, T.; Aoki, K.; Taga, Y. Visible-light photocatalysis in nitrogen-doped titanium oxides. *Science* **2001**, *293*, 269–271.
- (2) Rodriguez, E. F.; Chen, D. H.; Hollenkamp, A. F.; Cao, L.; Caruso, R. A. Monodisperse mesoporous anatase beads as high performance and safer anodes for lithium ion batteries. *Nanoscale* **2015**, *7*, 17947–17956.
- (3) Yu, Y. L.; Zhang, P.; Guo, L. M.; Chen, Z. D.; Wu, Q.; Ding, Y. H.; Zheng, W. J.; Cao, Y. The design of TiO<sub>2</sub> nanostructures (nanoparticle, nanotube, and nanosheet) and their photocatalytic activity. *J. Phys. Chem. C* **2014**, *118*, 12727–12733.
- (4) Gallo, J.; Panacek, A.; Prucek, R.; Kriegova, E.; Hradilova, S.; Hobza, M.; Holinka, M. Silver nanocoating technology in the prevention of prosthetic joint infection. *Materials* **2016**, *9*, 337.
- (5) Zhang, Y. H.; Xiao, P.; Zhou, X. Y.; Liu, D. W.; Garcia, B. B.; Cao, G. Z. Carbon monoxide annealed TiO<sub>2</sub> nanotube array electrodes for efficient biosensor applications. *J. Mater. Chem.* **2009**, *19*, 948–953.
- (6) Haase, N. R.; Shian, S.; Sandhage, K. H.; Kroger, N. Biocatalytic nanoscale coatings through biomimetic layer-by-layer mineralization. *Adv. Funct. Mater.* **2011**, *21*, 4243–4251.
- (7) Bolbasov, E. N.; Antonova, L. V.; Stankevich, K. S.; Ashrafov, A.; Matveeva, V. G.; Velikanova, E. A.; Khodyrevskaya, Y. I.; Kudryavtseva, Y. A.; Anissimov, Y. G.; Tverdokhlebov, S. I.; et al. The use of magnetron sputtering for the deposition of thin titanium coatings on the surface of bioresorbable electrospun fibrous scaffolds for vascular tissue engineering: A pilot study. *Appl. Surf. Sci.* **2017**, *398*, 63–72.
- (8) Khoshnood, N.; Zamanian, A.; Massoudi, A. Mussel-inspired surface modification of titania nanotubes as a novel drug delivery system. *Mater. Sci. Eng., C* **2017**, *77*, 748–754.
- (9) Damodaran, V. B.; Bhatnagar, D.; Leszczak, V.; Papat, K. C. Titania nanostructures: a biomedical perspective. *RSC Adv.* **2015**, *5*, 37149–37171.
- (10) Papat, K. C.; Eltgroth, M.; La Tempa, T. J.; Grimes, C. A.; Desai, T. A. Titania nanotubes: A novel platform for drug-eluting coatings for medical implants? *Small* **2007**, *3*, 1878–1881.
- (11) Wu, H.; Zhang, C. H.; Liang, Y. P.; Shi, J. F.; Wang, X. L.; Jiang, Z. Y. Catechol modification and covalent immobilization of catalase on titania submicrospheres. *J. Mol. Catal. B: Enzym.* **2013**, *92*, 44–50.
- (12) Wang, L. Z.; Sasaki, T. Titanium oxide nanosheets: Graphene analogues with versatile functionalities. *Chem. Rev.* **2014**, *114*, 9455–9486.
- (13) Zhang, N.; Yang, M. Q.; Liu, S. Q.; Sun, Y. G.; Xu, Y. J. Waltzing with the versatile platform of graphene to synthesize composite photocatalysts. *Chem. Rev.* **2015**, *115*, 10307–10377.
- (14) Han, C.; Zhang, N.; Xu, Y. J. Structural diversity of graphene materials and their multifarious roles in heterogeneous photocatalysis. *Nano Today* **2016**, *11*, 351–372.
- (15) Nicolosi, V.; Chhowalla, M.; Kanatzidis, M. G.; Strano, M. S.; Coleman, J. N. Liquid exfoliation of layered materials. *Science* **2013**, *340*, 1420.
- (16) Kordás, K.; Mohl, M.; Kónya, Z.; Kukovecz, A. Layered titanate nanostructures: perspectives for industrial exploitation. *Transl. Mater. Res.* **2015**, *2*, 015003–015020.
- (17) Krajewska, B. Application of chitin- and chitosan-based materials for enzyme immobilizations: a review. *Enzyme Microb. Technol.* **2004**, *35*, 126–139.
- (18) Wang, B.; Wang, Y. J.; Gao, X. F.; Li, Y. S. Utilization of parameters developed in layer-by-layer fabrication of protein-containing films for enzyme immobilization. *J. Biomater. Sci., Polym. Ed.* **2015**, *26*, 1312–1326.
- (19) Ansari, S. A.; Husain, Q. Potential applications of enzymes immobilized on/in nano materials: A review. *Biotechnol. Adv.* **2012**, *30*, 512–523.
- (20) Kudina, O.; Zakharchenko, A.; Trotsenko, O.; Tokarev, A.; Ionov, L.; Stoychev, G.; Pureskiy, N.; Pryor, S. W.; Voronov, A.; Minko, S. Highly efficient phase boundary biocatalysis with enzymogel nanoparticles. *Angew. Chem., Int. Ed.* **2014**, *53*, 483–487.
- (21) Planchestainer, M.; Contente, M. L.; Cassidy, J.; Molinari, F.; Tamborini, L.; Paradisi, F. Continuous flow biocatalysis: production and in-line purification of amines by immobilised transaminase from *Halomonas elongata*. *Green Chem.* **2017**, *19*, 372–375.
- (22) Kamada, K.; Yamada, A.; Soh, N. Enhanced catalytic activity of enzymes interacting with nanometric titanate nanosheets. *RSC Adv.* **2015**, *5*, 85511–85516.
- (23) DiCosimo, R.; McAuliffe, J.; Poulouse, A. J.; Bohlmann, G. Industrial use of immobilized enzymes. *Chem. Soc. Rev.* **2013**, *42*, 6437–6474.
- (24) Yincan, Z.; Yan, L.; Xueyong, G.; Qiao, W.; Xiaoping, X. Decolorization of color index acid orange 20 buffer solution using horseradish peroxidase immobilized on modified PAN-beads. *RSC Adv.* **2017**, *7*, 18976–18986.
- (25) Louzao, I.; van Hest, J. C. M. Permeability effects on the efficiency of antioxidant nanoreactors. *Biomacromolecules* **2013**, *14*, 2364–2372.
- (26) Chang, F. P.; Chen, Y. P.; Mou, C. Y. Intracellular implantation of enzymes in hollow silica nanospheres for protein therapy: Cascade system of superoxide dismutase and catalase. *Small* **2014**, *10*, 4785–4795.
- (27) Grotzky, A.; Nauser, T.; Erdogan, H.; Schluter, A. D.; Walde, P. A Fluorescently labeled dendronized polymer-enzyme conjugate carrying multiple copies of two different types of active enzymes. *J. Am. Chem. Soc.* **2012**, *134*, 11392–11395.
- (28) Zhang, Y.; He, P. L.; Hu, N. F. Horseradish peroxidase immobilized in TiO<sub>2</sub> nanoparticle films on pyrolytic graphite electrodes: Direct electrochemistry and bioelectrocatalysis. *Electrochim. Acta* **2004**, *49*, 1981–1988.
- (29) Soh, N.; Kaneko, S.; Uozumi, K.; Ueda, T.; Kamada, K. Preparation of an enzyme/inorganic nanosheet/magnetic bead complex and its enzymatic activity. *J. Mater. Sci.* **2014**, *49*, 8010–8015.
- (30) Duran, N.; Esposito, E. Potential applications of oxidative enzymes and phenoloxidase-like compounds in wastewater and soil treatment: A review. *Appl. Catal., B* **2000**, *28*, 83–99.
- (31) Yang, X. S.; Chen, X.; Zhang, X.; Yang, W. S.; Evans, D. G. Intercalation of methylene blue into layered manganese oxide and application of the resulting material in a reagentless hydrogen peroxide biosensor. *Sens. Actuators, B* **2008**, *129*, 784–789.
- (32) Magyar, M.; Hajdu, K.; Szabo, T.; Endrodi, B.; Hernadi, K.; Horvath, E.; Magrez, A.; Forro, L.; Visy, C.; Nagy, L. Sensing hydrogen peroxide by carbon nanotube/horseradish peroxidase biocomposite. *Phys. Status Solidi B* **2013**, *250*, 2559–2563.
- (33) Lavery, C. B.; MacInnis, M. C.; MacDonald, M. J.; Williams, J. B.; Spencer, C. A.; Burke, A. A.; Irwin, D. J. G.; D’Cunha, G. B. Purification of peroxidase from horseradish (*Armoracia rusticana*) roots. *J. Agric. Food Chem.* **2010**, *58*, 8471–8476.
- (34) Pavlovic, M.; Rouster, P.; Szilagyi, I. Synthesis and formulation of functional bionanomaterials with superoxide dismutase activity. *Nanoscale* **2017**, *9*, 369–379.

- (35) Franssen, M. C. R.; Steunenberg, P.; Scott, E. L.; Zuilhof, H.; Sanders, J. P. M. Immobilised enzymes in biorenewables production. *Chem. Soc. Rev.* **2013**, *42*, 6491–6533.
- (36) Fan, Y. M.; Cao, X. D.; Hu, T.; Lin, X. G.; Dong, H.; Zou, X. N. Enhancement of enzymatic activity using microfabricated poly-(epsilon-caprolactone)/silica hybrid microspheres with hierarchically porous architecture. *J. Phys. Chem. C* **2016**, *120*, 3955–3963.
- (37) Saladino, R.; Guazzaroni, M.; Crestini, C.; Crucianelli, M. Dye Degradation by layer-by-layer immobilised peroxidase/redox mediator systems. *ChemCatChem* **2013**, *5*, 1407–1415.
- (38) Rao, S. V.; Anderson, K. W.; Bachas, L. G. Controlled layer-by-layer immobilization of horseradish peroxidase. *Biotechnol. Bioeng.* **1999**, *65*, 389–396.
- (39) Caruso, F.; Schuler, C. Enzyme multilayers on colloid particles: Assembly, stability, and enzymatic activity. *Langmuir* **2000**, *16*, 9595–9603.
- (40) Gao, C. Y.; Liu, X. Y.; Shen, J. C.; Mohwald, H. Spontaneous deposition of horseradish peroxidase into polyelectrolyte multilayer capsules to improve its activity and stability. *Chem. Commun.* **2002**, 1928–1929.
- (41) Perazzini, R.; Saladino, R.; Guazzaroni, M.; Crestini, C. A novel and efficient oxidative functionalization of lignin by layer-by-layer immobilised Horseradish peroxidase. *Bioorg. Med. Chem.* **2011**, *19*, 440–447.
- (42) Balabushevich, N. G.; Tiourina, O. P.; Volodkin, D. V.; Larionova, N. I.; Sukhorukov, G. B. Loading the multilayer dextran sulfate/protamine microzised capsules with peroxidase. *Biomacromolecules* **2003**, *4*, 1191–1197.
- (43) Peyratout, C. S.; Dahne, L. Tailor-made polyelectrolyte microcapsules: From multilayers to smart containers. *Angew. Chem., Int. Ed.* **2004**, *43*, 3762–3783.
- (44) Moore, T. L.; Rodriguez-Lorenzo, L.; Hirsch, V.; Balog, S.; Urban, D.; Jud, C.; Rothen-Rutishauser, B.; Lattuada, M.; Petri-Fink, A. Nanoparticle colloidal stability in cell culture media and impact on cellular interactions. *Chem. Soc. Rev.* **2015**, *44*, 6287–6305.
- (45) Rouster, P.; Pavlovic, M.; Szilagy, I. Improving the stability of titania nanosheets by functionalization with polyelectrolytes. *RSC Adv.* **2016**, *6*, 97322–97330.
- (46) Holthoff, H.; Egelhaaf, S. U.; Borkovec, M.; Schurtenberger, P.; Sticher, H. Coagulation rate measurements of colloidal particles by simultaneous static and dynamic light scattering. *Langmuir* **1996**, *12*, 5541–5549.
- (47) Iselau, F.; Xuan, T. P.; Trefalt, G.; Matic, A.; Holmberg, K.; Bordes, R. Formation and relaxation kinetics of starch-particle complexes. *Soft Matter* **2016**, *12*, 9509–9519.
- (48) Bradford, M. M. Rapid and sensitive method for quantitation of microgram quantities of protein utilizing principle of protein-dye binding. *Anal. Biochem.* **1976**, *72*, 248–254.
- (49) Zor, T.; Selinger, Z. Linearization of the Bradford protein assay increases its sensitivity: theoretical and experimental studies. *Anal. Biochem.* **1996**, *236*, 302–308.
- (50) Kamada, K.; Nakamura, T.; Tsukahara, S. Photoswitching of enzyme activity of horseradish peroxidase intercalated into semi-conducting layers. *Chem. Mater.* **2011**, *23*, 2968–2972.
- (51) Zhang, L. H.; Gu, C.; Xiong, J.; Yang, M.; Guo, Y. Hemin-histamine-montmorillonite clay conjugate as a model biocatalyst to mimic natural peroxidase. *Sci. China: Chem.* **2015**, *58*, 731–737.
- (52) Doerge, D. R.; Divi, R. L.; Churchwell, M. I. Identification of the colored guaiacol oxidation product produced by peroxidases. *Anal. Biochem.* **1997**, *250*, 10–17.
- (53) Hwang, S.; Lee, C. H.; Ahn, I. S. Product identification of guaiacol oxidation catalyzed by manganese peroxidase. *J. Ind. Eng. Chem.* **2008**, *14*, 487–492.
- (54) Johnson, K. A.; Goody, R. S. The original Michaelis constant: translation of the 1913 Michaelis-Menten paper. *Biochemistry* **2011**, *50*, 8264–8269.
- (55) Szabo, T.; Toth, V.; Horvath, E.; Forro, L.; Szilagy, I. Tuning the aggregation of titanate nanowires in aqueous dispersions. *Langmuir* **2015**, *31*, 42–49.
- (56) Rouster, P.; Pavlovic, M.; Szilagy, I. Destabilization of titania nanosheet suspensions by inorganic salts: Hofmeister series and Schulze-Hardy rule. *J. Phys. Chem. B* **2017**, *121*, 6749–6758.
- (57) Pavlovic, M.; Li, L.; Dits, F.; Gu, Z.; Adok-Sipiczki, M.; Szilagy, I. Aggregation of layered double hydroxide nanoparticles in the presence of heparin: Towards highly stable delivery systems. *RSC Adv.* **2016**, *6*, 16159–16167.
- (58) Pavlovic, M.; Adok-Sipiczki, M.; Horvath, E.; Szabo, T.; Forro, L.; Szilagy, I. Dendrimer-stabilized titanate nanowire dispersions as potential nanocarriers. *J. Phys. Chem. C* **2015**, *119*, 24919–24926.
- (59) Pavlovic, M.; Huber, R.; Adok-Sipiczki, M.; Nardin, C.; Szilagy, I. Ion specific effects on the stability of layered double hydroxide colloids. *Soft Matter* **2016**, *12*, 4024–4033.
- (60) Verwey, E. J. W.; Overbeek, J. T. G. *Theory of stability of lyophobic colloids*; Elsevier: Amsterdam, 1948.
- (61) Derjaguin, B. On the repulsive forces between charged colloid particles and on the theory of slow coagulation and stability of lyophobic sols. *Trans. Faraday Soc.* **1940**, *35*, 203–214.
- (62) Kaposi, A. D.; Fidy, J.; Manas, E. S.; Vanderkooi, J. M.; Wright, W. W. Horseradish peroxidase monitored by infrared spectroscopy: effect of temperature, substrate and calcium. *Biochim. Biophys. Acta, Protein Struct. Mol. Enzymol.* **1999**, *1435*, 41–50.
- (63) Martin, M.; Salazar, P.; Campuzano, S.; Villalonga, R.; Pingarron, J. M.; Gonzalez-Mora, J. L. Amperometric magnetobiosensors using poly(dopamine)-modified Fe<sub>3</sub>O<sub>4</sub> magnetic nanoparticles for the detection of phenolic compounds. *Anal. Methods* **2015**, *7*, 8801–8808.
- (64) Moyo, M.; Okonkwo, J. O.; Agyei, N. M. A Novel hydrogen peroxide biosensor based on adsorption of Horseradish Peroxidase onto a nanobiomaterial composite modified glassy carbon electrode. *Electroanalysis* **2013**, *25*, 1946–1954.
- (65) Gilani, S. L.; Najafpour, G. D.; Moghadamnia, A.; Kamaruddin, A. H. Stability of immobilized porcine pancreas lipase on mesoporous chitosan beads: A comparative study. *J. Mol. Catal. B: Enzym.* **2016**, *133*, 144–153.
- (66) Long, J.; Li, X. F.; Zhan, X. B.; Xu, X. M.; Tian, Y. Q.; Xie, Z. J.; Jin, Z. Y. Sol-gel encapsulation of pullulanase in the presence of hybrid magnetic (Fe<sub>3</sub>O<sub>4</sub>-chitosan) nanoparticles improves thermal and operational stability. *Bioprocess Biosyst. Eng.* **2017**, *40*, 821–831.
- (67) Popa, I.; Gillies, G.; Papastavrou, G.; Borkovec, M. Attractive and repulsive electrostatic forces between positively charged latex particles in the presence of anionic linear polyelectrolytes. *J. Phys. Chem. B* **2010**, *114*, 3170–3177.
- (68) Ho, T. T. M.; Bremmell, K. E.; Krasowska, M.; MacWilliams, S. V.; Richard, C. J. E.; Stringer, D. N.; Beattie, D. A. In Situ ATR FTIR spectroscopic study of the formation and hydration of a fucoidan/chitosan polyelectrolyte multilayer. *Langmuir* **2015**, *31*, 11249–11259.
- (69) Delgado, A. V.; Gonzalez-Caballero, F.; Hunter, R. J.; Koopal, L. K.; Lyklema, J. Measurement and interpretation of electrokinetic phenomena. *J. Colloid Interface Sci.* **2007**, *309*, 194–224.
- (70) Rosenholm, J. B.; Kosmulski, M. Peculiar charging effects on titania in aqueous 1:1, 2:1, 1:2 and mixed electrolyte suspensions. *Adv. Colloid Interface Sci.* **2012**, *179*, 51–67.

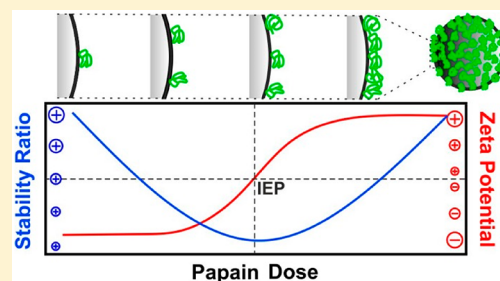


# Papain Adsorption on Latex Particles: Charging, Aggregation, and Enzymatic Activity

Szilárd Sáringer, Rita Achieng Akula, Adél Szerlauth, and Istvan Szilagyi\*

MTA-SZTE Lendület Biocolloids Research Group, Interdisciplinary Excellence Center, Department of Physical Chemistry and Materials Science, University of Szeged, 1 Rerrich Béla tér, H-6720 Szeged, Hungary

**ABSTRACT:** The effect of papain adsorption on the surface charge properties and aggregation mechanism of sulfate-functionalized polystyrene latex particles was studied. The positively charged enzyme possessed a high affinity to the oppositely charged particles, giving rise to charge neutralization and charge reversal at appropriate papain concentrations. The tendency in the particle aggregation rates at different enzyme doses revealed that the colloidal stability of the samples is governed by interparticle forces of electrostatic origin. The aggregation mechanism was qualitatively described within the classical DLVO theory, and unstable dispersions were detected near the charge neutralization point, while particle aggregation was not observed at low and elevated papain concentrations. The relatively high dispersion stability of the bare latex particles was maintained upon the formation of an enzyme layer on the surface, and the obtained latex–papain composite showed notable resistance against salt-induced aggregation. Remarkable hydrolytic and antioxidant activities of the immobilized enzyme were observed in probe reactions; therefore, the obtained hybrid can be considered as a multifunctional biocatalytic system with great promise in applications in industrial manufacturing processes.



## INTRODUCTION

Enzyme immobilization attracts widespread contemporary interest due to the progressively growing number of applications, where biocatalytic systems are involved in maintaining green and sustainable chemical manufacturing processes.<sup>1–3</sup> Various immobilization techniques including covalent grafting, physical adsorption, and enzyme entrapment were developed in the past to attach the proteins to the solid supports in order to achieve a high yield, long functional stability, and good selectivity.<sup>4</sup> Considerable effort was made to design and synthesize solid supports of advantageous chemical and physical properties; therefore, silica,<sup>5</sup> clays,<sup>6</sup> carbon derivatives,<sup>7,8</sup> polymeric substances,<sup>9,10</sup> titania,<sup>11</sup> and organic–inorganic hybrid materials<sup>12,13</sup> were applied to immobilize enzymes.

Among the enzyme families involved in immobilization processes, proteases represent an important class due to their widespread applications in the food, detergent, and pharmaceutical industries.<sup>14</sup> They hydrolyze amide bonds and, hence, convert long-chain proteins to peptides and subsequently to amino acids. This process is highly utilized in meat tenderization, beer clarification, and softening of cheese. As a prominent representative of the group proteases, the papain enzyme is widely used in the above applications.<sup>15</sup> Its main advantage over other proteases includes good hydrolytic activity against a broad range of protein substrates and that it can be produced in a considerable amount from the fruit of the papaya tree.<sup>16</sup> Apart from acting as a protease, papain showed remarkable antioxidant activity;<sup>17</sup> therefore, its utilization in chemical manufacturing processes in the food

industry is highly advantageous. Nevertheless, the use of native papain is often complicated, and thus, immobilization is highly recommended to improve stability, to achieve better recyclability, and to separate the enzyme from the reaction mixture after the catalytic process is terminated.

Accordingly, papain was immobilized on magnetic nanoparticles prepared by polymerization of methacrylate containing monomers in the presence of iron oxide powder.<sup>18</sup> To enhance the enzymatic affinity, the surface of the support was decorated by dye ligands, giving rise to remarkable enzyme loading into the nanoparticles. The immobilized papain showed excellent activity and stability in the hydrolytic decomposition of various proteins. In another system, papain was intercalated into layered double hydroxide nanoparticles in a coprecipitation synthesis carried out in the presence of the enzyme.<sup>19</sup> The papain attained a compressed conformation in the interlayer space; however, the original structure was recovered after releasing the enzyme from the host material, indicating a promising papain delivery system. Attachment of the enzyme to a hydrogel composite consisting of a cellulose derivative, polyalcohol, and silica particles led to a remarkable increment in the long term stability compared to the free enzyme.<sup>20</sup> Similar improvement was achieved in the functional stability once papain was covalently grafted to nanocomposites of gold, magnetite, and cellulose.<sup>21</sup> This material was used for the development of electrochemical sensors for peptide

Received: September 16, 2019

Revised: October 26, 2019

Published: October 31, 2019



detection. In addition, papain was embedded within poly-electrolyte–clay layers using the sequential adsorption method. However, the layered structure possessed limited stability, and enzyme leakage was detected.<sup>22</sup>

The above-discussed host–guest materials and also other papain–solid support hybrids are mainly used in heterogeneous systems; i.e., the hybrid materials are dispersed in liquid media. To achieve good catalytic performance, stable dispersions containing homogeneously distributed primary particles of high surface area are required, while the catalysts can be removed from the reaction mixture by particle aggregation and subsequent sedimentation or filtration. These facts highlight the importance of the colloidal stability of such systems. Indeed, it was pointed out earlier that protein adsorption on nanoparticles significantly changes the surface charge behavior of the solid supports, leading to a notable variation in the speed of particle aggregation.<sup>23–25</sup> For instance, the size of gold nanoparticle aggregates can be controlled by protein adsorption.<sup>26</sup> In addition, similar gold nanoparticles were prepared with a lysozyme monolayer on their surface, giving rise to the development of a biocompatible nanocomposite of excellent colloidal stability.<sup>27</sup> However, to the best of our knowledge, no studies on the influence of papain functionalization on the stability of the dispersions of particle supports were reported in the past.

Therefore, the aim of the present work was to investigate the effect of papain adsorption on the colloidal stability of polystyrene latex particles in oppositely charged systems; i.e., positively charged enzyme and negatively charged particles were present in the experiments due to the careful adjustment of the experimental conditions. The charging behavior and the aggregation processes were explored at different papain concentrations and ionic strengths with light scattering techniques. The possible change in the enzymatic activity upon immobilization was investigated in biochemical test reactions.

## EXPERIMENTAL SECTION

**Materials.** Spherical polystyrene latex particles were purchased from Thermo Fischer Scientific. The size was 430 nm in diameter with a coefficient of variation of 1.8%, as determined by the manufacturer using transmission electron microscopy (TEM) in the dried stage. The surface of the particles was functionalized with negatively charged sulfate groups, leading to a surface charge density of  $-12$  mC/m<sup>2</sup> provided on the basis of potentiometric titration by the company. Papain from *Carica papaya* was purchased from Sigma-Aldrich in powder form with  $\geq 3$  U/mg. Hydrogen chloride (HCl), sodium chloride (NaCl), sodium acetate, sodium carbonate anhydrous, calcium acetate, sodium phosphate monobasic anhydrous, disodium hydrogen phosphate anhydrous, dipotassium hydrogen orthophosphate trihydrate, casein, trichloroacetic acid (TCA), and methanol were purchased from VWR, while Folin & Ciocalteu's reagent was bought from Sigma-Aldrich. The 2,2-diphenyl-1-picrylhydrazyl (DPPH) was purchased from Alfa Aesar. These chemicals were analytical grade and used as received. All solutions were diluted using ultrapure water obtained from the VWR purity TU+ machine. The water and the salt solutions were filtered with a 0.1  $\mu$ m syringe filter (Millex).

**Light Scattering.** Dynamic light scattering (DLS) experiments were performed in time-resolved mode on an ALV-NIBS High-Performance Particle Sizer equipped with a 3 mW

He–Ne laser with a 633 nm wavelength. The correlation function was acquired during 20 s, and 100–250 runs were performed in the measurements depending on the speed of aggregation. To determine the particle size, a second cumulant fit was applied to the correlation function, and the Stokes–Einstein equation was used for the conversion of the diffusion coefficient to the hydrodynamic radius ( $R_h$ ).<sup>28,29</sup> During sample preparation, 2 mL dispersions were prepared. The particle concentration, ionic strength, and enzyme dose were adjusted by mixing appropriate amounts of stock solutions. The time-resolved measurements were initiated by adding the latex sample to the electrolyte–enzyme mixture. The experiments were carried out at 25 °C.

To study the early stages of particle aggregation, where mainly dimers form and no higher ranked aggregates are present in the samples, the experimental conditions were optimized by performing time-resolved DLS experiments in 1 M NaCl solutions at different particle concentrations (Figure

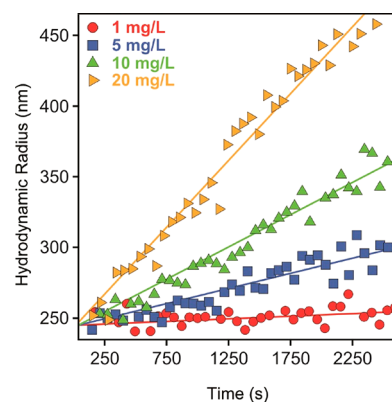


**Figure 1.** Particle concentration dependence (sulfate latex particles in 1 M NaCl) on the slopes of the hydrodynamic radius versus time plots. The solid lines are linear fits used to calculate the apparent aggregation rates in eq 1.

1). The apparent aggregation rates ( $k_{app}$ ) were calculated from these measurements as

$$k_{app} = \left. \frac{1}{R_h^0} \frac{dR_h}{dt} \right|_{t \rightarrow 0} \quad (1)$$

where  $R_h^0$  is the hydrodynamic radius of the monomers, which was measured by DLS as 236 nm in stable dispersions. This value is somewhat higher than the geometrical radius determined by TEM (215 nm) due to the finite polydispersity of the particles and to the different environments during the DLS and TEM measurements. At such a high salt level, the aggregation is driven solely by the diffusion of the particles. On the basis of the  $k_{app}$  data, a particle concentration of 10 mg/L was chosen for further experiments. This value gives a good compromise that the aggregation is in its early stage, the measurement time is reasonable, and the scattered intensity is high enough to perform accurate DLS measurements.

The absolute aggregation rate coefficient of dimer formation ( $k$ ) was determined at the above particle concentration in 1 M NaCl solution as<sup>30</sup>

$$k = \frac{k_{\text{app}}}{\left(1 + \frac{\sin(2qR)}{2qR}\right) \left(1 - \frac{R_{h1}}{R_{h2}}\right) N_0} \quad (2)$$

where  $R$  is the geometrical radius of the particles,  $N_0$  is the initial particle concentration,  $q$  is the scattering vector,<sup>29</sup> and  $R_{h1}$  and  $R_{h2}$  are the hydrodynamic radius of the monomer and dimer, respectively. The  $R_{h2}/R_{h1}$  ratio was reported to be 1.38.<sup>31</sup> Equation 2 assumes the validity of the Rayleigh–Gans–Debye approximation for the form factor, as it was demonstrated to be applicable to similarly sized latex particles.<sup>30–34</sup> The fast aggregation rate coefficient ( $k^{\text{fast}}$ ), which refers to the aggregation rate in unstable dispersions, was determined to be  $3.08 \times 10^{-18} \text{ m}^3/\text{s}$  at a high salt concentration.

The colloidal stability was expressed in terms of stability ratio ( $W$ ), which was calculated from the aggregation rate values as follows:

$$W = \frac{k^{\text{fast}}}{k} \quad (3)$$

One can realize that  $W = 1$  is associated with unstable dispersions, where all particle collisions result in dimer formation.

**Electrophoresis.** Electrophoretic mobilities were measured on a Litesizer 500 instrument (Anton Paar) equipped with a 40 mW semiconductor laser of 658 nm wavelength operating in the backscattering mode at a scattering angle of 175°. For the determination of the electrophoretic mobilities, 5 mL samples were prepared. In brief, a 0.5 mL particle dispersion of 100 mg/L concentration was added to 4.5 mL of solution composed of the enzyme and/or NaCl at appropriate concentrations. The samples were allowed to rest 2 h at room temperature before measuring the electrophoretic mobilities, which occurred after 1 min equilibration time in the device. The reported values were the average of five individual measurements. The experiments were performed in 350  $\mu\text{L}$  volume  $\Omega$ -shaped plastic cuvettes (Anton Paar). The electrophoretic mobilities ( $u$ ) were converted to  $\zeta$  potential by Smoluchowski's equation as<sup>35</sup>

$$\zeta = \frac{u\eta}{\epsilon_0\epsilon} \quad (4)$$

where  $\epsilon$  is the relative permittivity of water,  $\epsilon_0$  is the permittivity of the vacuum, and  $\eta$  is the viscosity of the water. These values are 78.5,  $8.9 \times 10^{-12} \text{ F/m}$ , and  $8.9 \times 10^{-4} \text{ Pas}$ , respectively, in water and at the temperature used.

**Hydrolytic Activity Measurements.** For the determination of the protease-like activity, the “Universal Protease Activity Assay” protocol (Sigma-Aldrich) based on the Lowry method was used.<sup>36</sup> Accordingly, a calibration curve was measured by adding a different amount of 1.1 mM standard tyrosine solution in several samples and completing a final volume of 2 mL with ultrapure water. Tyrosine serves as the product of the hydrolysis in the test reaction, and its concentration range was 0.055–0.550  $\mu\text{M}$  during calibration. After 30 min incubation at 37 °C, the solutions had a gradation of color correlating with the amount of tyrosine added. The UV–visible spectra of the obtained solutions were recorded on a Thermo Fischer Genesys 10S spectrophotometer. The absorbances at 660 nm were read and used to determine the tyrosine concentration. The protease-like activity experiments were carried out at 37 °C, and phosphate or acetate buffers

were used to adjust the pH to 7.5 or 4.0, respectively, as detailed below.

During the measurements, 5 mL of 0.65 wv% casein as a substrate was diluted with 50 mM phosphate buffer solution first. A mixture consisting of 10 mM sodium acetate buffer and 5 mM calcium(II) was used to dilute the free or the immobilized enzyme solutions to reach an enzyme concentration of 0.1 U/mL. The volume of the free or the immobilized enzyme added to a 5 mL casein solution was varied to run the probe at different papain concentrations. The reaction was stopped after 10 min by adding 5 mL of 110 mM TCA solution, and then, an appropriate volume of enzyme solution was added to each tube to reach 1 mL of the final volume for the enzyme solutions in each tube. After 30 min of incubation, 2 mL of samples were filtered with a 0.45  $\mu\text{m}$  syringe filter (Millex), and 5 mL of 500 mM sodium carbonate and 1 mL of 0.5 M Folin & Ciocalteu's reagent were added. The samples were then incubated again for 30 min. Thereafter, 2 mL of aliquots were filtered, and the absorbance was recorded. One unit of protease activity was equivalent to the amount of enzyme that required releasing 1  $\mu\text{g}$  of tyrosine/mL/min under standard assay conditions described above.

**Radical Scavenging Activity.** The DPPH radical scavenging activity was determined as reported earlier,<sup>37</sup> with a slight modification. In the stock solutions of the free or immobilized enzymes, the concentration of the papain was 1000 ppm. The varying volume of enzyme stock was added to 1 mL of 12 mg/L DPPH solution dissolved in methanol and completed with water to a final volume of 2 mL. The enzyme content of the samples was ranged between 50 and 500 ppm. After short, vigorous stirring, the absorbance of the mixture was measured at 517 nm, which is the wavelength of the characteristic visible band of the DPPH. The absorbance values were followed for 1 h to detect the decrease in the initial DPPH concentration upon its reduction by the papain. In the case of the immobilized papain, after the 1 h reaction time, the samples were centrifuged for 10 min at 10 000 rpm to remove the particles from the samples in order to avoid any light scattering events during the spectrophotometric measurement. The decrease in the DPPH concentration was expressed as follows:

$$\text{DPPH (\%)} = \frac{A}{A_0} 100 \quad (5)$$

where  $A$  is the absorbance measured after 1 h and  $A_0$  is the absorbance value at the beginning of the test reaction.

## RESULTS AND DISCUSSION

**Papain Adsorption.** Charging and aggregation properties of the sulfate latex particles were explored by electrophoresis and time-resolved DLS at different papain doses. The main goal was to find the optimal experimental conditions, where stable dispersions of enzyme–latex hybrid particles can be obtained. The pH of the samples was always kept at 4.0, and the dispersions contained 1 mM NaCl as a background electrolyte. The pH is below the pI of the enzyme;<sup>38</sup> therefore, papain was oppositely charged than that of latex due to the ionization of the sulfate groups present on the particle surface. Besides, these experimental conditions were selected due to the fact that the papain enzyme is used particularly in food and beer processing at a low pH.<sup>14</sup> The  $\zeta$  potentials recorded at various papain concentrations are shown in Figure 2a.

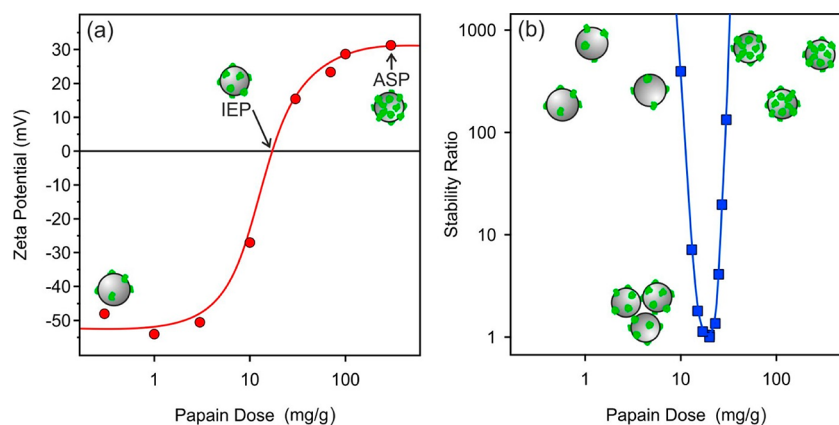


**Figure 2.** (a)  $\zeta$  potential and (b) stability ratio data of the sulfate latex particles as a function of the papain dose used to functionalize the particles. The measurements were carried out at pH 4.0 and 1 mM ionic strength adjusted by NaCl. The mg/g unit refers to mg of papain per 1 g of latex. The solid lines serve to guide the eyes.

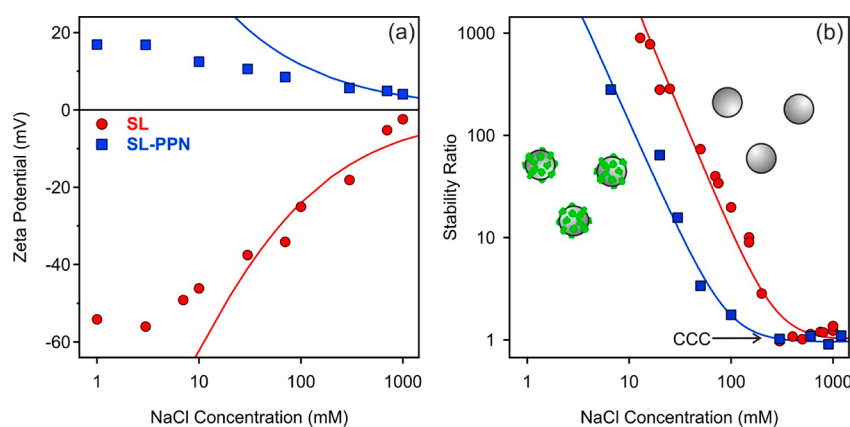


**Figure 3.** (a)  $\zeta$  potential and (b) stability ratio values of the SL and SL-PPN (400 mg of enzyme adsorbed on 1 g of latex) particles as a function of the ionic strength adjusted by NaCl. The solid lines are data calculated with eqs 6 and 8 in panels a and b, respectively.

In general, the  $\zeta$  potentials changed from negative to positive by increasing the added amount of papain, indicating its strong affinity to the oppositely charged particle surface. The potentials were negative at low doses, since the small amount of added enzyme compensated the surface charge of the particles only to a small extent. A further increase in the papain concentration led to charge neutralization at intermediate doses at the isoelectric point (IEP). The IEP is located at 20 mg/g. The adsorption process continued at doses higher than the IEP, and charge reversal of the particles occurred. At the highest doses applied, the  $\zeta$  potentials reached a plateau with an onset at around a 400 mg/g dose. The potentials were close to +30 mV at this plateau. Accordingly, the coated latex possesses a significantly lower magnitude of  $\zeta$  potential than the one for the bare particles (−55 mV), indicating a lower surface charge density for the former one. Papain added after the onset of the plateau remained dissolved in the solution. Such a charging behavior resembles the data determined earlier in oppositely charged particle–polyelectrolyte systems.<sup>39–42</sup> The driving forces causing the reversal in the sign of the surface charge in the adsorption process were identified as entropy gain due to solvent release upon adsorption, hydrophobic, and electrostatic interactions.<sup>42–45</sup>

Time-resolved DLS measurements were carried to determine stability ratio values under identical experimental conditions (i.e., particle concentration, pH, ionic strength,

and papain dose range were the same) as in the electrophoretic study discussed above. The dependence of the stability ratios on the papain concentration is shown in Figure 2b.

The particles were stable, and no aggregation was detected at low and high enzyme doses, as indicated by high or not even measurable stability ratios. In the intermediate regime, however, the stability ratios formed a U-shaped curve with a minimum near the polyelectrolyte dose corresponding to the IEP determined in the  $\zeta$  potential measurements. The stability ratios were unity within the experimental error at this minimum, indicating rapid particle aggregation and unstable dispersions. This behavior can be qualitatively explained by the theory developed by Derjaguin, Landau, Verwey, and Overbeek (DLVO),<sup>46–48</sup> and it is similar to that experienced earlier in systems containing colloidal particles and oppositely charged species such as multivalent ions<sup>32,49,50</sup> and polyelectrolytes.<sup>11,33,40,45</sup> The latex particles possessed sufficient charge at low and high doses, as indicated by the relatively high magnitude of the  $\zeta$  potentials, and the repulsive electrical double-layer forces stabilized the dispersions. At the IEP, where the adsorbed papain neutralized the charge of the sulfate latex, the electrical double layers vanished due to the lack of surface charge, and thus, the attractive van der Waals forces destabilized the dispersions. The presence of other types of interparticle forces, such as patch-charge,<sup>51</sup> steric,<sup>52</sup> or bridging interactions,<sup>53</sup> which may be present in particle–polymer

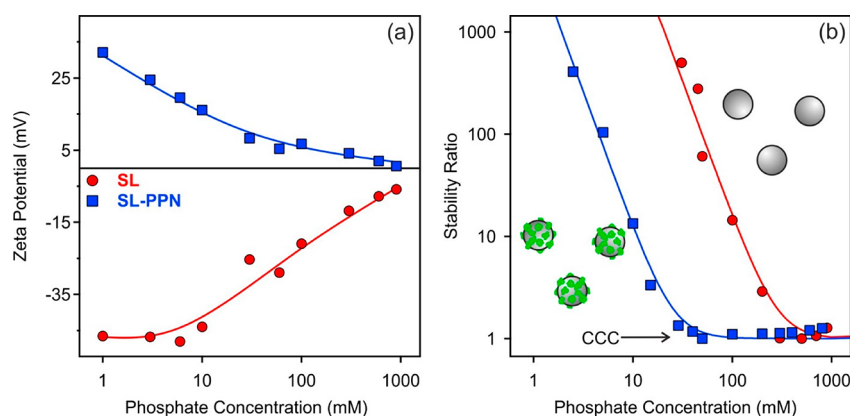


**Figure 4.** (a)  $\zeta$  potential and (b) stability ratio values of the SL and SL-PPN (400 mg of enzyme adsorbed on 1 g of latex) particles as a function of the phosphate concentration at pH 4.0. The solid lines are eye guides in panel a and calculated by eq 8 in panel b.

systems,<sup>54–56</sup> could not be detected on the basis of the above experimental results.

From these findings, one can conclude that papain adsorption at a dose of 400 mg/g gave rise to the formation of an enzyme layer on the latex surface (these particles will be denoted as SL-PPN later). Moreover, the obtained SL-PPN hybrid possessed excellent colloidal stability; i.e., highly stable dispersions of primary particles were present in the samples at the experimental conditions applied.

**Resistance against Salt-Induced Aggregation.** Given the fact that immobilized enzymes are often used in liquid environments containing electrolytes or even their mixtures, the resistance of the SL-PPN hybrid against salt-induced aggregation was tested and compared with the bare sulfate latex particles (SL). Prior to the aggregation study, the charging characteristics were assessed by determining the  $\zeta$  potentials at different ionic strengths (Figure 3a).

The magnitude of the potentials decreased with the NaCl concentration in both cases, owing to the screening effect of the electrolyte on the surface charge. However, the decrease was higher for the SL particles due to their elevated  $\zeta$  potentials at low ionic strengths, as discussed earlier. The potentials did not change the sign in the entire ionic strength range investigated. To determine the charge density ( $\sigma$ ), the Grahame equation was used:<sup>48</sup>

$$\sigma = \frac{2k_B T \epsilon_0 \epsilon \kappa}{e} \sinh \left[ \frac{e\zeta}{2k_B T} \right] \quad (6)$$

where  $k_B$  is the Boltzmann constant,  $T$  is the temperature,  $e$  is the elementary charge, and  $\kappa$  is the inverse Debye length, which can be calculated from the ionic strength ( $I$ ) as<sup>35</sup>

$$\kappa = \left( \frac{2N_A e^2 I}{\epsilon \epsilon_0 k_B T} \right)^{1/2} \quad (7)$$

where  $N_A$  is the Avogadro number. Due to the fact that  $\zeta$  potential is applied in eq 6, the surface charge at the slip plane was estimated by this model. The determined surface charge densities were 8 mC/m<sup>2</sup> and -18 mC/m<sup>2</sup> for the SL-PPN and SL, respectively. Such a lower magnitude of the charge density for the enzyme-coated latex most likely originates from counterion condensation phenomenon, which takes place for charged macromolecules in the electrolyte medium, leading to lower effective charges.<sup>57</sup>

The absolute aggregation rates of the SL and SL-PPN particles were determined at a high salt concentration, where the double-layer forces are screened and the particles rapidly aggregate. The values were found to be  $3.3 \times 10^{-18}$  m<sup>3</sup>/s and  $3.1 \times 10^{-18}$  m<sup>3</sup>/s for SL-PPN and SL, respectively. These data indicate that the nature of the attractive forces are very similar for both particles, and they originate most probably from van der Waals interactions, similar to other polyelectrolyte-coated latexes.<sup>34</sup> Figure 3b shows the stability ratios determined for SL and SL-PPN at different salt levels using eq 3.

Slow aggregation was observed at low ionic strengths, and unstable suspensions were detected at high NaCl concentrations in line with the prediction by the DLVO theory, i.e., the electrical double-layer forces disappear above the critical coagulation concentration (CCC), which was determined as<sup>58</sup>

$$W = 1 + \left[ \frac{\text{CCC}}{c} \right]^\beta \quad (8)$$

where  $c$  is the salt concentration and  $\beta$  was obtained from the change in the stability ratios in the slow aggregation regime before the CCC as

$$\beta = \frac{d \log 1/W}{d \log c} \quad (9)$$

Note that the above equations are empirical formulas to fit the stability ratio data at different NaCl concentrations and to obtain the CCC values. The different surface charge densities were reflected in the CCCs, and the bare SL possesses a higher CCC value of 270 mM compared to the 90 mM for SL-PPN. These data were calculated with eq 8. This decrease upon papain adsorption can be explained by the lower charge density and, hence, by the weaker double-layer forces acting between the SL-PPN particles.

Due to the fact that phosphate ions are often present during the applications of the papain enzyme, the colloidal stability of SL and SL-PPN particles was investigated in the presence of phosphate ions too. Similar conditions were used like in the case of NaCl-induced aggregation, and the phosphate ions are present 99% in the dihydrogen phosphate form; i.e., they are monovalent ions, at pH 4.0.<sup>59</sup> The magnitude of the  $\zeta$  potentials decreased with the phosphate concentration for both particles due to the progressive charge screening by the ionic environment and the possible specific adsorption of the phosphate ions in the case of the positively charged SL-PPN (Figure 4a).<sup>32</sup>



The aggregation behaviors in the presence of phosphate resemble the ones with NaCl discussed above. Slow and fast aggregation regimes are separated by well-defined CCC, which is similar (280 mM) to the CCC of the bare SL measured in the presence of NaCl. However, the CCC values varied for the SL-PPN in a different ionic environment, and 25 mM was determined with phosphate ions, which is significantly lower than the one determined in NaCl solutions. This decrease may come from the specific adsorption of phosphate ions<sup>32</sup> and subsequent weakening of the double-layer forces. Since the stability ratios were in unity within the experimental error above the CCC, the presence of additional (non-DLVO) forces, such as bridging through adsorbed phosphate ions, was excluded.

Besides, another important fact is that in the case of SL-PPN, the  $\zeta$  potentials are very low even before the CCC, where stable dispersions were detected. This result clearly indicates that the stabilizing forces are not only of electrostatic origin for the enzyme-coated particles. Since the bare SL behave as predicted by the DLVO theory, this additional stabilizing effect must come from the adsorbed papain chains, which overlap upon the approach of two particles, and an osmotic pressure arises, leading to repulsive forces. This so-called steric stabilization was reported earlier with polymer-functionalized colloidal particles;<sup>6,24,52</sup> nevertheless, one can observe them only with latex particles of a papain monolayer on the surface and not at partial coverage in the present system.

**Protease-like Function.** The hydrolytic activity of the free and immobilized papain was estimated on the basis of the hydrolysis of the casein substrate, as detailed in the [Experimental Section](#). The time-dependent enzymatic assay was investigated by recording the characteristic absorbance of the tyrosine product at a 660 nm wavelength. As shown in [Figure 5a](#) and [b](#), the absorbance values increased with the

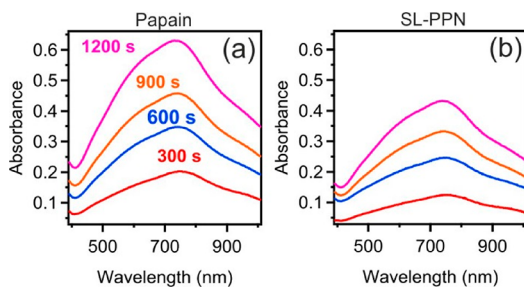


**Figure 5.** Time-dependent UV–visible spectra recorded during protease-like activity measurements with the (a) free papain and (b) SL-PPN. The applied papain dose was 3 ppm for both the free and immobilized enzymes.

reaction time for both the free and the immobilized enzyme. However, the increase was more pronounced for the free papain. By calculating the normalized activities, 0.28 U/mL and 0.19 U/mL were obtained for the papain and SL-PPN, respectively. These numbers indicate that the enzyme lost from its activity upon immobilization, most likely due to some conformational changes, which occurred once it was attached to the surface of the latex. Indeed, it was also reported earlier that enzymes may change their conformation, resulting in a loss of activity.<sup>60</sup> Such a change may result in decreased activity due to the hindered interaction between the active center and the substrate. Another reason for this decrease can be the relatively high absorbed amount (400 mg/g) of the enzyme.

Accordingly, the papain absorbed on the surface in more than one layer and the blocking effect of the outer layers, i.e., the limited accessibility of substrate molecules to the inner layers, decrease the efficiency. The third reason is in connection with the free enzyme in solution, where the free movement of the papain eases the collision with the substrate, while the immobilized one diffuses slower, and thus, it approaches fewer target molecules.

Although the enzymatic activity in the SL-PPN decreased compared to the native enzyme in homogeneous solution, the hybrid maintains significant protease-like activity. Considering these facts and also the advantages gained by the immobilization (e.g., better separation from the reaction mixture), the obtained SL-PPN hybrid is a promising candidate as a biocatalyst in hydrolytic processes.

**Radical Scavenging Activity.** The antioxidant activity of the papain enzyme has been reported in the literature;<sup>17</sup> however, no results on the antioxidant activity of the immobilized papain have been published yet. The DPPH radical scavenging assay has been widely used to evaluate the antioxidant properties of various antioxidants.<sup>37</sup> The DPPH content of the samples was followed by a spectrophotometer, and the decrease in % was calculated with [eq 5](#). These values were plotted versus the enzyme concentration, and the  $EC_{50}$  values were determined ([Figure 6](#)).

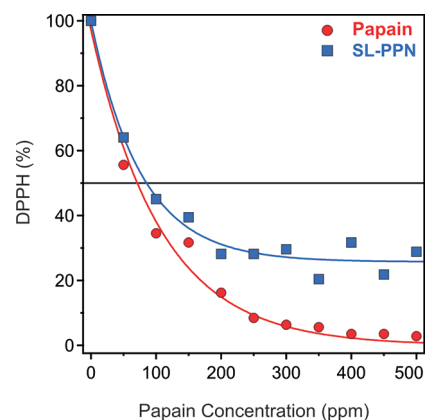


**Figure 6.** DPPH scavenging activity of the free papain and the SL-PPN expressed by the change in the substrate concentrations as a function of the enzyme dose. The lines are eye guides.

The  $EC_{50}$  represents the enzyme concentration, at which the initial DPPH concentration decreased to half; i.e., 50% of the radicals are scavenged by the antioxidant materials. The activity of the SL-PPN was determined as 85.4 ppm compared to the free enzyme, whose  $EC_{50}$  was 71.1 ppm. Accordingly, a decrease was experienced in the activity upon immobilization of the enzyme due to most likely the same reasons discussed above for the protease-like activity. Nevertheless, these results clearly indicate that the SL-PPN possesses remarkable antioxidant activity.

Considering the values reported above to quantify the different functions of the free enzyme and SL-PPN, one can conclude that the hydrolytic and antioxidant activities of papain decreased by 32% and 20%, respectively, upon immobilization. However, the enzymatic tests all together shed light on the fact that the hybrid materials is an excellent candidate in applications, where biocatalysts of hydrolytic and antioxidant activities are required in heterogeneous systems.

## CONCLUSIONS

The colloidal behavior of sulfate latex and its papain modified forms was studied through assessment of the charging and aggregation properties in a wide range of experimental conditions. The papain enzyme strongly adsorbed on the oppositely charged sulfate latex surface, mainly through electrostatic forces. The adsorption process resulted in charge neutralization at the intermediate and charge reversal at higher papain doses. The formation of an enzyme monolayer on the surface resulted in stable papain–latex dispersions, while unstable samples were observed at enzyme doses close to the charge neutralization point. The major interparticle forces were described within the DLVO theory; however, steric interactions between adsorbed enzyme chains and subsequent stabilization of the particles occurred at high papain coverage. The hydrolytic and antioxidant activity of the papain-coated latex was estimated, and they were slightly lower for the immobilized enzyme than for the free papain. Nevertheless, the obtained papain–latex hybrid material possesses the advantages of a heterogeneous catalyst such as easier separation from the reaction mixture, and thus, it can be used as a multifunctional material, for instance, in the food industry, where joint protease-like and antioxidant functions are welcome in several processes.

## AUTHOR INFORMATION

### Corresponding Author

\*E-mail: szistvan@chem.u-szeged.hu.

### ORCID

Istvan Szilagyi: 0000-0001-7289-0979

### Notes

The authors declare no competing financial interest.

## ACKNOWLEDGMENTS

Financial support by the Lendület program of the Hungarian Academy of Sciences (96130) and by the Ministry of Human Capacities Hungary (20391-3/2018/FEKUSTRAT) is gratefully acknowledged.

## REFERENCES

- (1) DiCosimo, R.; McAuliffe, J.; Poulouse, A. J.; Bohlmann, G. Industrial use of immobilized enzymes. *Chem. Soc. Rev.* **2013**, *42*, 6437–6474.
- (2) Papat, A.; Hartono, S. B.; Stahr, F.; Liu, J.; Qiao, S. Z.; Lu, G. Q. Mesoporous silica nanoparticles for bioadsorption, enzyme immobilization, and delivery carriers. *Nanoscale* **2011**, *3*, 2801–2818.
- (3) Bosio, V. E.; Islan, G. A.; Martinez, Y. N.; Duran, N.; Castro, G. R. Nanodevices for the immobilization of therapeutic enzymes. *Crit. Rev. Biotechnol.* **2016**, *36*, 1–18.
- (4) Sheldon, R. A.; van Pelt, S. Enzyme immobilisation in biocatalysis: Why, what and how. *Chem. Soc. Rev.* **2013**, *42*, 6223–6235.
- (5) Chang, F. P.; Chen, Y. P.; Mou, C. Y. Intracellular implantation of enzymes in hollow silica nanospheres for protein therapy: Cascade system of Superoxide Dismutase and Catalase. *Small* **2014**, *10*, 4785–4795.
- (6) Pavlovic, M.; Rouster, P.; Szilagyi, I. Synthesis and formulation of functional bionanomaterials with superoxide dismutase activity. *Nanoscale* **2017**, *9*, 369–379.
- (7) Demeter, E. L.; Hilburg, S. L.; Washburn, N. R.; Collins, T. J.; Kitchin, J. R. Electrocatalytic oxygen evolution with an immobilized TAML activator. *J. Am. Chem. Soc.* **2014**, *136*, 5603–5606.
- (8) Bartha-Vari, J. H.; Tosa, M. I.; Irimie, F. D.; Weiser, D.; Boros, Z.; Vertessy, B. G.; Paizs, C.; Poppe, L. Immobilization of phenylalanine ammonia-lyase on single-walled carbon nanotubes for stereoselective biotransformations in batch and continuous-flow modes. *ChemCatChem* **2015**, *7*, 1122–1128.
- (9) Planchestainer, M.; Contente, M. L.; Cassidy, J.; Molinari, F.; Tamborini, L.; Paradisi, F. Continuous flow biocatalysis: production and in-line purification of amines by immobilised transaminase from *Halomonas elongata*. *Green Chem.* **2017**, *19*, 372–375.
- (10) Welsch, N.; Wittemann, A.; Ballauff, M. Enhanced activity of enzymes immobilized in thermoresponsive core-shell microgels. *J. Phys. Chem. B* **2009**, *113*, 16039–16045.
- (11) Rouster, P.; Pavlovic, M.; Saringer, S.; Szilagyi, I. Functionalized titania nanosheet dispersions of peroxidase activity. *J. Phys. Chem. C* **2018**, *122*, 11455–11463.
- (12) Fan, Y. M.; Cao, X. D.; Hu, T.; Lin, X. G.; Dong, H.; Zou, X. N. Enhancement of enzymatic activity using microfabricated poly-(epsilon-caprolactone)/silica hybrid microspheres with hierarchically porous architecture. *J. Phys. Chem. C* **2016**, *120*, 3955–3963.
- (13) Kudina, O.; Zakharchenko, A.; Trotsenko, O.; Tokarev, A.; Ionov, L.; Stoychev, G.; Pureskiy, N.; Pryor, S. W.; Voronov, A.; Minko, S. Highly efficient phase boundary biocatalysis with enzymogel nanoparticles. *Angew. Chem., Int. Ed.* **2014**, *53*, 483–487.
- (14) Fernandez-Lucas, J.; Castaneda, D.; Hormigo, D. New trends for a classical enzyme: Papain, a biotechnological success story in the food industry. *Trends Food Sci. Technol.* **2017**, *68*, 91–101.
- (15) Drenth, J.; Jansonius, J. N.; Koekoek, R.; Swen, H. M.; Wolthers, B. G. Structure of papain. *Nature* **1968**, *218*, 929–932.
- (16) Kamphuis, I. G.; Kalk, K. H.; Swarte, M. B. A.; Drenth, J. Structure of papain refined at 1.65 Å resolution. *J. Mol. Biol.* **1984**, *179*, 233–256.
- (17) Liu, M. C.; Yang, S. J.; Hong, D.; Yang, J. P.; Liu, M.; Lin, Y.; Huang, C. H.; Wang, C. J. A simple and convenient method for the preparation of antioxidant peptides from walnut (*Juglans regia* L.) protein hydrolysates. *Chem. Cent. J.* **2016**, *10*, 39.
- (18) Alpay, P.; Uygun, D. A. Usage of immobilized papain for enzymatic hydrolysis of proteins. *J. Mol. Catal. B: Enzym.* **2015**, *111*, 56–63.
- (19) Zou, N.; Plank, J. Intercalation of papain enzyme into hydrotalcite type layered double hydroxide. *J. Phys. Chem. Solids* **2012**, *73*, 1127–1130.
- (20) Dai, H. J.; Ou, S. Y.; Liu, Z. J.; Huang, H. H. Pineapple peel carboxymethyl cellulose/polyvinyl alcohol/mesoporous silica SBA-15 hydrogel composites for papain immobilization. *Carbohydr. Polym.* **2017**, *169*, 504–514.
- (21) Mahmoud, K. A.; Lam, E.; Hrapovic, S.; Luong, J. H. T. Preparation of well-dispersed gold/magnetite nanoparticles embedded on cellulose nanocrystals for efficient immobilization of papain enzyme. *ACS Appl. Mater. Interfaces* **2013**, *5*, 4978–4985.
- (22) Szabo, T.; Szekeres, M.; Dekany, I.; Jackers, C.; De Feyter, S.; Johnston, C. T.; Schoonheydt, R. A. Layer-by-layer construction of ultrathin hybrid films with proteins and clay minerals. *J. Phys. Chem. C* **2007**, *111*, 12730–12740.
- (23) Lopez-Leon, T.; Santander-Ortega, M. J.; Ortega-Vinuesa, J. L.; Bastos-Gonzalez, D. Hofmeister effects in colloidal systems: Influence of the surface nature. *J. Phys. Chem. C* **2008**, *112*, 16060–16069.
- (24) Vasti, C.; Bedoya, D. A.; Rojas, R.; Giacomelli, C. E. Effect of the protein corona on the colloidal stability and reactivity of LDH-based nanocarriers. *J. Mater. Chem. B* **2016**, *4*, 2008–2016.
- (25) Moore, T. L.; Rodriguez-Lorenzo, L.; Hirsch, V.; Balog, S.; Urban, D.; Jud, C.; Rothen-Rutishauser, B.; Lattuada, M.; Petri-Fink, A. Nanoparticle colloidal stability in cell culture media and impact on cellular interactions. *Chem. Soc. Rev.* **2015**, *44*, 6287–6305.
- (26) Cobbe, S.; Connolly, S.; Ryan, D.; Nagle, L.; Eritja, R.; Fitzmaurice, D. DNA-controlled assembly of protein-modified gold nanocrystals. *J. Phys. Chem. B* **2003**, *107*, 470–477.
- (27) Yang, T.; Li, Z.; Wang, L.; Guo, C. L.; Sun, Y. J. Synthesis, characterization, and self-assembly of protein lysozyme monolayer-stabilized gold nanoparticles. *Langmuir* **2007**, *23*, 10533–10538.

- (28) Hassan, P. A.; Rana, S.; Verma, G. Making sense of Brownian motion: Colloid characterization by dynamic light scattering. *Langmuir* **2015**, *31*, 3–12.
- (29) Berne, B. J.; Pecora, R. *Dynamic light scattering*; Robert E. Krieger Publishing: Malabar, 1990.
- (30) Trefalt, G.; Szilagy, I.; Oncsik, T.; Sadeghpour, A.; Borkovec, M. Probing colloidal particle aggregation by light scattering. *Chimia* **2013**, *67*, 772–776.
- (31) Holthoff, H.; Egelhaaf, S. U.; Borkovec, M.; Schurtenberger, P.; Sticher, H. Coagulation rate measurements of colloidal particles by simultaneous static and dynamic light scattering. *Langmuir* **1996**, *12*, 5541–5549.
- (32) Sugimoto, T.; Cao, T. C.; Szilagy, I.; Borkovec, M.; Trefalt, G. Aggregation and charging of sulfate and amidine latex particles in the presence of oxyanions. *J. Colloid Interface Sci.* **2018**, *524*, 456–464.
- (33) Hierrezuelo, J.; Vaccaro, A.; Borkovec, M. Stability of negatively charged latex particles in the presence of a strong cationic polyelectrolyte at elevated ionic strengths. *J. Colloid Interface Sci.* **2010**, *347*, 202–208.
- (34) Hierrezuelo, J.; Sadeghpour, A.; Szilagy, I.; Vaccaro, A.; Borkovec, M. Electrostatic Stabilization of Charged Colloidal Particles with Adsorbed Polyelectrolytes of Opposite Charge. *Langmuir* **2010**, *26*, 15109–15111.
- (35) Delgado, A. V.; Gonzalez-Caballero, F.; Hunter, R. J.; Koopal, L. K.; Lyklema, J. Measurement and interpretation of electrokinetic phenomena. *J. Colloid Interface Sci.* **2007**, *309*, 194–224.
- (36) Cupp-Enyard, C. Sigma's non-specific protease activity assay - Casein as a substrate. *J. Visualized Exp.* **2008**, *19*, e899.
- (37) Brand-Williams, W.; Cuvelier, M. E.; Berset, C. Use of a free-radical method to evaluate antioxidant activity. *Food Sci. Technol.-Lebensm.-Wiss. Technol.* **1995**, *28*, 25–30.
- (38) Sahoo, B.; Sahu, S. K.; Bhattacharya, D.; Dhara, D.; Pramanik, P. A novel approach for efficient immobilization and stabilization of papain on magnetic gold nanocomposites. *Colloids Surf., B* **2013**, *101*, 280–289.
- (39) Hyde, E. D. E.; Moreno-Atanasio, R.; Millner, P. A.; Neville, F. Surface charge control through the reversible adsorption of a biomimetic polymer on silica particles. *J. Phys. Chem. B* **2015**, *119*, 1726–1735.
- (40) Iselau, F.; Xuan, T. P.; Trefalt, G.; Matic, A.; Holmberg, K.; Bordes, R. Formation and relaxation kinetics of starch-particle complexes. *Soft Matter* **2016**, *12*, 9509–9519.
- (41) Cherstvy, A. G.; Winkler, R. G. Simple model for overcharging of a sphere by a wrapped oppositely charged asymmetrically neutralized polyelectrolyte: Possible effects of helical charge distribution. *J. Phys. Chem. B* **2005**, *109*, 2962–2969.
- (42) Borkovec, M.; Papastavrou, G. Interactions between solid surfaces with adsorbed polyelectrolytes of opposite charge. *Curr. Opin. Colloid Interface Sci.* **2008**, *13*, 429–437.
- (43) Quesada-Perez, M.; Gonzalez-Tovar, E.; Martin-Molina, A.; Lozada-Cassou, M.; Hidalgo-Alvarez, R. Overcharging in colloids: Beyond the Poisson-Boltzmann approach. *ChemPhysChem* **2003**, *4*, 234–248.
- (44) Carrillo, J. Y.; Dobrynin, A. V. Molecular dynamics simulations of polyelectrolyte adsorption. *Langmuir* **2007**, *23*, 2472–2482.
- (45) Szilagy, I.; Trefalt, G.; Tiraferri, A.; Maroni, P.; Borkovec, M. Polyelectrolyte adsorption, interparticle forces, and colloidal aggregation. *Soft Matter* **2014**, *10*, 2479–2502.
- (46) Derjaguin, B.; Landau, L. D. Theory of the stability of strongly charged lyophobic sols and of the adhesion of strongly charged particles in solutions of electrolytes. *Acta Phys. Chim.* **1941**, *14*, 633–662.
- (47) Verwey, E. J. W.; Overbeek, J. T. G. *Theory of stability of lyophobic colloids*; Elsevier: Amsterdam, 1948.
- (48) Israelachvili, J. *Intermolecular and surface forces*, 3rd ed.; Academic Press: London, 2011.
- (49) Cao, T. C.; Sugimoto, T.; Szilagy, I.; Trefalt, G.; Borkovec, M. Heteroaggregation of oppositely charged particles in the presence of multivalent ions. *Phys. Chem. Chem. Phys.* **2017**, *19*, 15160–15171.
- (50) Sinha, P.; Szilagy, I.; Ruiz-Cabello, F. J. M.; Maroni, P.; Borkovec, M. Attractive forces between charged colloidal particles induced by multivalent ions revealed by confronting aggregation and direct force measurements. *J. Phys. Chem. Lett.* **2013**, *4*, 648–652.
- (51) Leong, Y. K. Interparticle forces arising from an adsorbed strong polyelectrolyte in colloidal dispersions: charged patch attraction. *Colloid Polym. Sci.* **1999**, *277*, 299–305.
- (52) Fritz, G.; Schadler, V.; Willenbacher, N.; Wagner, N. J. Electrosteric stabilization of colloidal dispersions. *Langmuir* **2002**, *18*, 6381–6390.
- (53) Brunel, F.; Pochard, I.; Gauffinet, S.; Turesson, M.; Labbez, C. Structure and yielding of colloidal silica gels varying the range of interparticle interactions. *J. Phys. Chem. B* **2016**, *120*, 5777–5785.
- (54) Feng, L. L.; Stuart, M. C.; Adachi, Y. Dynamics of polyelectrolyte adsorption and colloidal flocculation upon mixing studied using mono-dispersed polystyrene latex particles. *Adv. Colloid Interface Sci.* **2015**, *226*, 101–114.
- (55) Meng, Z. Y.; Hashmi, S. M.; Elimelech, M. Aggregation rate and fractal dimension of fullerene nanoparticles via simultaneous multiangle static and dynamic light scattering measurement. *J. Colloid Interface Sci.* **2013**, *392*, 27–33.
- (56) Saringer, S.; Rouster, P.; Szilagy, I. Regulation of the stability of titania nanosheet dispersions with oppositely and like-charged polyelectrolytes. *Langmuir* **2019**, *35*, 4986–4994.
- (57) Manning, G. S. Limiting laws and counterion condensation in polyelectrolyte solutions I. Colligative properties. *J. Chem. Phys.* **1969**, *51*, 924–933.
- (58) Grolimund, D.; Elimelech, M.; Borkovec, M. Aggregation and deposition kinetics of mobile colloidal particles in natural porous media. *Colloids Surf., A* **2001**, *191*, 179–188.
- (59) May, P. M.; Rowland, D.; Konigsberger, E.; Hefter, G. JESS, a Joint Expert Speciation System - IV: A large database of aqueous solution physicochemical properties with an automatic means of achieving thermodynamic consistency. *Talanta* **2010**, *81*, 142–148.
- (60) Krajewska, B. Application of chitin- and chitosan-based materials for enzyme immobilizations: a review. *Enzyme Microb. Technol.* **2004**, *35*, 126–139.



dc\_1931\_21



OPEN

# Nanocomposite-based dual enzyme system for broad-spectrum scavenging of reactive oxygen species

Marko Pavlovic<sup>1</sup>, Szabolcs Muráth<sup>2</sup>, Xénia Katona<sup>3</sup>, Nizar B. Alsharif<sup>2</sup>, Paul Rouster<sup>4</sup>, József Maléth<sup>3</sup> & Istvan Szilagy<sup>2</sup>✉

A broad-spectrum reactive oxygen species (ROS)-scavenging hybrid material (CASCADE) was developed by sequential adsorption of heparin (HEP) and poly(L-lysine) (PLL) polyelectrolytes together with superoxide dismutase (SOD) and horseradish peroxidase (HRP) antioxidant enzymes on layered double hydroxide (LDH) nanoclay support. The synthetic conditions were optimized so that CASCADE possessed remarkable structural (no enzyme leakage) and colloidal (excellent resistance against salt-induced aggregation) stability. The obtained composite was active in decomposition of both superoxide radical anions and hydrogen peroxide in biochemical assays revealing that the strong electrostatic interaction with the functionalized support led to high enzyme loadings, nevertheless, it did not interfere with the native enzyme conformation. In vitro tests demonstrated that ROS generated in human cervical adenocarcinoma cells were successfully consumed by the hybrid material. The cellular uptake was not accompanied with any toxicity effects, which makes the developed CASCADE a promising candidate for treatment of oxidative stress-related diseases.

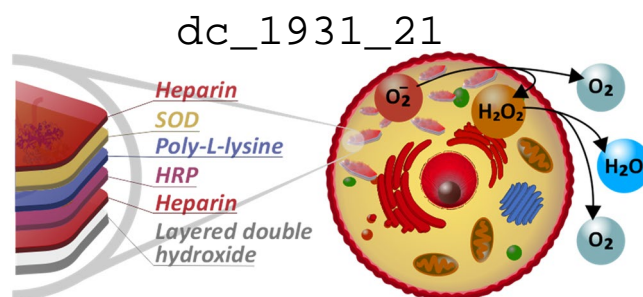
Hybrid materials containing enzymes confined in nano-sized objects or other self-assembled structures have attracted widespread contemporary interest due to their great potential as efficient biocatalytic systems in biomedical and industrial processes<sup>1–3</sup>. Natural enzymes inherently suffer from structural and functional sensitivity to environmental effects leading to a narrow window of operational conditions such as pH and temperature. To counter such drawbacks, enzyme immobilization has been a major focus of several research bodies in the past decades<sup>4–6</sup>. A more recent emphasis has been on co-immobilization to prepare confined enzyme cascades owing to the numerous possible cascade combinations. Among them, antioxidant enzyme cascades immobilized in/on various substrates represent an important class of materials that help combatting oxidative stress<sup>7</sup> caused by the extensive production of reactive oxygen species (ROS)<sup>8–10</sup>.

ROS are by-products of oxygen metabolism inducing irreversible functional alterations or even complete destruction of vital cell constituents such as lipids, nucleic acids and proteins leading to the development of various diseases<sup>11–13</sup>. One of the most common ROS that are produced in the mitochondrial respiratory chain is superoxide radical anion. Superoxide dismutase (SOD) is a naturally occurring enzyme and it is the primary defense line against these radicals<sup>14</sup>. However, decomposition of superoxide radicals by SOD generates hydrogen peroxide (together with molecular oxygen), another harmful ROS. In a living cellular environment, hydrogen peroxide is consumed by catalase (CAT)<sup>15</sup> and peroxidases<sup>16</sup> (e.g., horseradish peroxidase (HRP), chloroperoxidase (CPO) or lactoperoxidase (LPO)) enzymes. Therefore, the eventual combination of SOD with these enzymes gives a promising hybrid system and the cascade reaction can effectively reduce oxidative stress.

In this way, antioxidant enzymes were co-immobilized and cascade systems based on various solid supports were developed. Simultaneous encapsulation of polyelectrolyte-grafted SOD and CAT into hollow silica nanospheres prepared by a microemulsion-based sol–gel templating process was achieved<sup>17</sup>. The obtained hybrid material showed remarkable activity in the decomposition of superoxide radicals and hydrogen peroxide both in

<sup>1</sup>Department of Colloid Chemistry, Max Planck Institute of Colloids and Interfaces, 14476 Potsdam, Germany. <sup>2</sup>MTA-SZTE Lendület Biocolloids Research Group, Interdisciplinary Excellence Centre, Department of Physical Chemistry and Materials Science, University of Szeged, 6720 Szeged, Hungary. <sup>3</sup>MTA-SZTE Lendület Epithelial Cell Signaling and Secretion Research Group, Interdisciplinary Excellence Centre, University of Szeged, 6720 Szeged, Hungary. <sup>4</sup>Institute of Condensed Matter and Nanosciences-Bio and Soft Matter, Université Catholique de Louvain, 1348 Louvain-la-Neuve, Belgium. ✉email: szistvan@chem.u-szeged.hu





**Scheme 1.** Illustration of the structure of the developed CASCADE nanocomposite and its ROS scavenging ability.

test tube reaction and cellular environment. In another contribution, polymeric vesicles were loaded with SOD and CAT leading to cascade decomposition of superoxide radicals<sup>8</sup>. However, diffusion of hydrogen peroxide into these vesicles was limited. In addition, an artificial peroxisome composed of SOD and CAT in a polymeric nanocompartment was developed to combat oxidative stress in cells with significant success<sup>18</sup>.

Concerning the co-immobilization of SOD and peroxidase enzymes, a novel anticancer hydrogel containing SOD and CPO was prepared and converted ROS in tumor cells to singlet oxygen to achieve antiproliferation<sup>10</sup>. In this manner, it is possible to increase the enzyme and substrate concentration inspired by the nature of living cells. A catalytic system was formed by encapsulating SOD and LPO in the cavities of polymeric nanovesicles, which effectively transformed superoxide radicals to water and molecular oxygen<sup>9</sup>. Furthermore, SOD and HRP enzymes were covalently grafted to synthetic dendronized polymer chains and it was confirmed that both enzymes remained active upon immobilization<sup>19</sup>. In a follow-up research, the effect of size of the dendronized polymers on the catalytic activity of the enzyme cascade was assessed<sup>20</sup>.

These examples show that the co-attachment of antioxidant enzymes to the same carrier is possible and remarkable activities can be achieved in decomposition of both superoxide radical anions and hydrogen peroxide with the same material. However, the synthetic methods often involved complicated reactions and hardly accessible building blocks, which may impede the potential mass production of the biocatalytic systems. A facile and economic method is proposed here to co-immobilize SOD and HRP enzymes between polyelectrolyte layers built-up on layered double hydroxide (LDH) nanoparticles (Scheme 1). LDHs are versatile clay materials<sup>21–24</sup> of several advantages such as cytocompatibility, sufficient anion-exchange capacity and ease of synthesis even in larger amounts, which make LDHs to be very efficient delivery agents in biomedical applications<sup>25–27</sup>. The structural, colloidal and functional stability were investigated by various techniques and the ability to reduce intracellular oxidative stress was assessed. The expected role of the nanoparticulate support was to achieve high stability, to confine the enzymes similar to the intracellular environment and to enhance enzyme penetration through the cell wall.

## Results

**Design of the antioxidant composite.** The polyelectrolyte-based sequential adsorption method<sup>28</sup> on LDH nanoclay support was applied to co-immobilize SOD and HRP enzymes for tandem decomposition of superoxide radical anions and hydrogen peroxide (Fig. 1A). First, the LDH carrier was prepared by the coprecipitation technique and subsequent hydrothermal treatment<sup>29</sup> to improve the size distribution and polydispersity of the particles. The synthetic protocol is given in the Supplementary Information (SI). The formation of LDH was proven by X-ray diffraction (XRD) and Infrared (IR) spectroscopy. The assignment of the Miller indices, shown in Fig. S1A (in the SI), unambiguously confirms the existence of the lamellar structure, while the IR spectrum (Fig. S1B) of the obtained material contained the characteristic vibrations of the intralamellar metal hydroxide groups (552, 777 and 941  $\text{cm}^{-1}$ ) and the interlamellar carbonate anions (665 and 1351  $\text{cm}^{-1}$ ). More details about the structural characterization of the LDH are given elsewhere<sup>30</sup>.

Based on previous experiences with LDH-polyelectrolyte systems<sup>30–32</sup>, the surface charge and particle aggregation were tuned in each step of the sequential adsorption process to obtain stable particle dispersions. This issue was rarely addressed in earlier reports dealing with the co-immobilization of antioxidant enzymes. However, lack of sufficient colloidal stability, i.e., formation of particle aggregates, during preparation leads to several disadvantageous features in the final material such as decreased surface area, limited diffusion of the substrates to the active centers and phase separation due to formation of higher sized clusters.

The tendencies in surface charges in the individual steps were followed in electrophoretic mobility measurements (Fig. 1B). Accordingly, heparin (HEP) adsorption on the oppositely charged LDH significantly altered the surface charge, which was neutralized at the isoelectric point (IEP) and reversed at appropriately high HEP doses. Such a charge reversal was also reported in other LDH-polyelectrolyte systems<sup>30,32,33</sup> and originate mainly from entropy gain<sup>34</sup>, hydrophobic interactions<sup>35</sup> and ion correlations forces<sup>36</sup>. The surface saturation was indicated by a plateau (ASP) in the mobilities at high doses. As it was pointed out earlier<sup>30</sup>, intercalation of HEP between the LDH layers is not possible due to the limited interlayer space. Adsorption of HRP of positive overall charge did not change the charge of LDH-HEP (HEP dose was set at the ASP) significantly due its limited amount and low charge density. To optimize the conditions for SOD immobilization, the negatively charged LDH-HEP-HRP surface was modified with poly(L-lysine) (PLL), which possesses positive charge and thus, charge neutralization and reversal occurred similar to the first step involving LDH and HEP. Characteristic IEP and ASP values

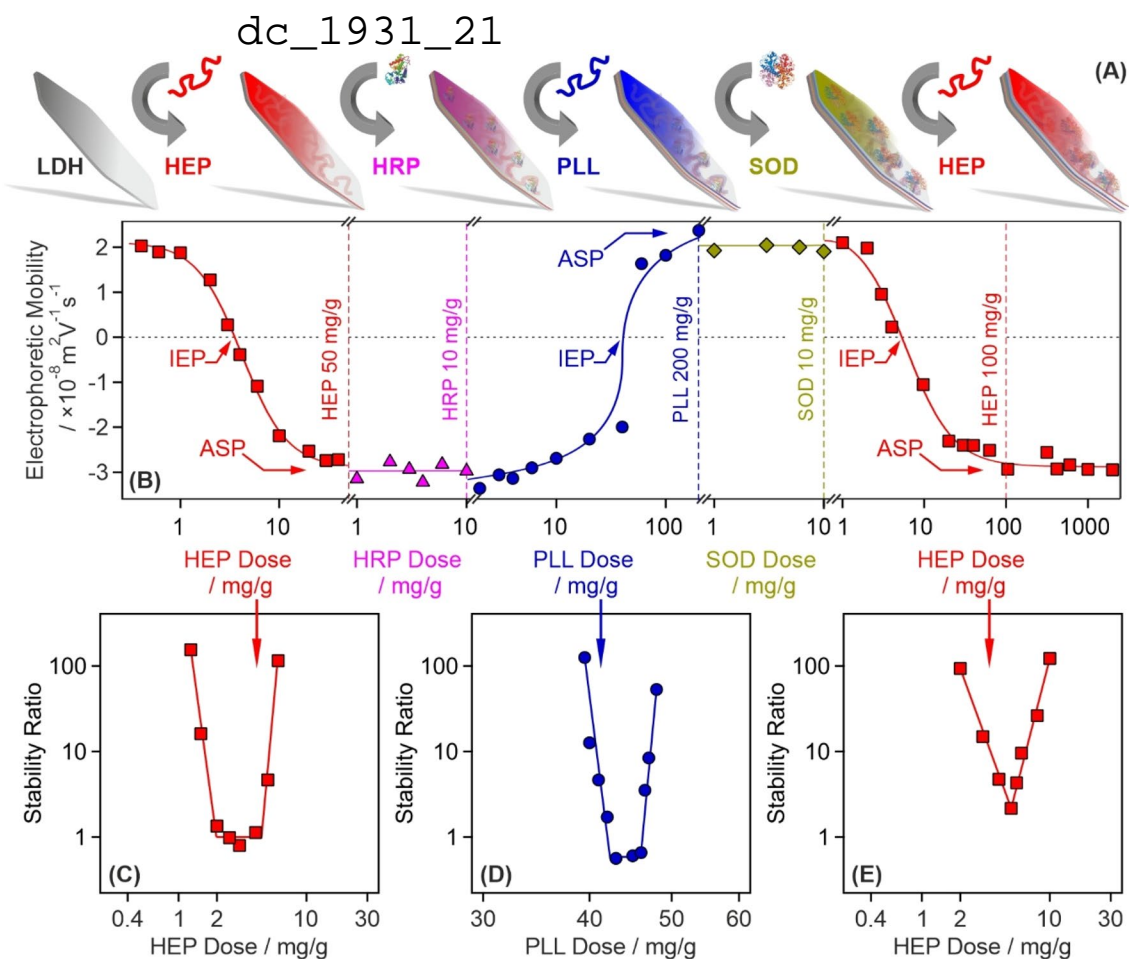


**Figure 1.** Illustration of the sequential adsorption process and tendencies in the charging and aggregation properties during the build-up of the polyelectrolyte-enzyme layers on the LDH particles. **(A)** Schematic representation of the preparation of the final CASCADE composite. **(B)** Changes in electrophoretic mobilities during the sequential adsorption procedure illustrated in **(A)**. The dashed vertical lines show the doses used in the synthesis of CASCADE. **(C)** Stability ratio of LDH particles as a function of the HEP dose. **(D)** Stability ratio of LDH-HEP-HRP particles as a function of the PLL dose. **(E)** Stability ratio of LDH-HEP-HRP-PLL-SOD particles as a function of the HEP dose. Note that the mg/g unit refers to mg of polyelectrolyte or enzyme per one gram of LDH particles. The solid lines are just to guide the eyes. IEP and ASP are abbreviations of doses corresponding to the isoelectric point and to the onset of the adsorption saturation plateau, respectively. The electrophoretic mobilities were determined with  $\pm 10^{-9} \text{ m}^2 \text{ V}^{-1} \text{ s}^{-1}$  precision, while the average error of the stability ratios is 10%.

were observed with the PLL too. The LDH-HEP-HRP-PLL was then decorated with SOD, nevertheless, the electrophoretic mobilities were the same within the experimental error at the enzyme dose range investigated. Finally, the LDH-HEP-HRP-PLL-SOD composite was coated with a terminating HEP layer making the final LDH-HEP-HRP-PLL-SOD-HEP (henceforth denoted as CASCADE) material negatively charged. The negative sign of charge is usually beneficial to hinder protein corona formation in biofluids<sup>37</sup> and does not prevent the nanoparticle penetration through the like-charged cell wall<sup>38</sup>. In CASCADE, the polyelectrolyte doses were set at the ASP (HEP1: 50 mg/g, PLL: 200 mg/g and HEP2: 100 mg/g) and the doses of both SOD and HRP were adjusted to 10 mg/g. These conditions resulted in a hydrodynamic radius of  $(121.8 \pm 3.5) \text{ nm}$ , polydispersity index of  $(0.35 \pm 0.08)$  and electrophoretic mobility of  $(-2.9 \pm 0.1) \times 10^{-8} \text{ m}^2 \text{ V}^{-1} \text{ s}^{-1}$  determined for CASCADE in stable dispersions at 10 mg/g particle concentration.

As mentioned above, remarkable colloidal stability of the sub-systems during the sequential adsorption process is crucial to obtain stable dispersions of primary CASCADE particles. Therefore, stability ratios were measured by dynamic light scattering (DLS) in the individual systems to probe possible particle aggregation. Note that stability ratios of unity refer to rapid aggregation and unstable dispersions, while higher values indicate slower aggregation and more stable samples<sup>39,40</sup>. The theoretical and technical backgrounds of the stability ratio measurements are given in the SI.

Using the same experimental conditions as in the mobility study, the effect of polyelectrolyte or enzyme adsorption on the stability ratios was determined. In the LDH-HEP system, stability ratios close to one indicated rapid particle aggregation and unstable dispersions near the IEP, while highly stable colloids were obtained at low and high HEP doses (Fig. 1C). No measurable particle aggregation was detected at the dose applied in CASCADE.

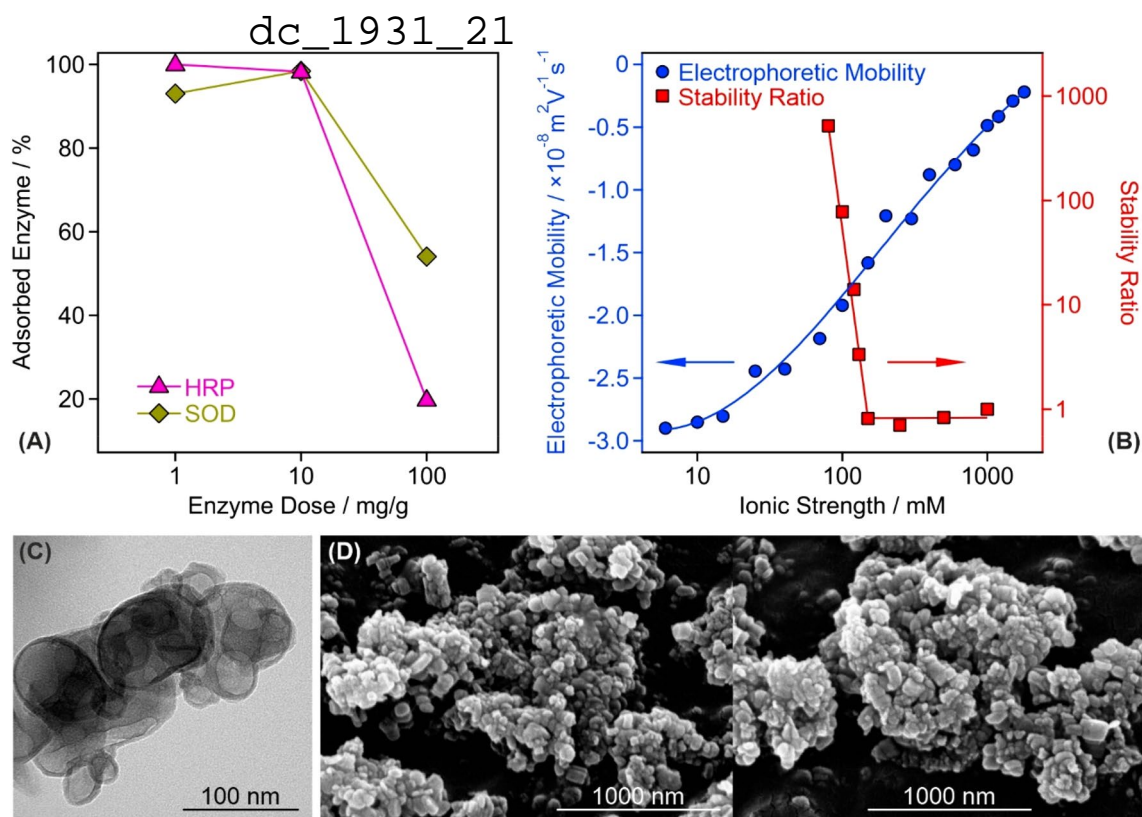


**Figure 2.** Structural and colloidal features of the CASCADE composite. **(A)** Partitioning of HRP and SOD enzymes between the bulk and the surface at different enzyme doses. The data indicate that the majority of the added enzyme molecules is adsorbed on the particle surfaces at 10 mg/g dose. **(B)** Influence of the ionic strength (adjusted by NaCl) on the electrophoretic mobility and stability ratio values of the CASCADE particles. For the latter, the critical coagulation concentration, the threshold value, which separates fast and slow aggregation regimes, was found to be 150 mM. **(C)** TEM and **(D)** SEM images of the obtained hybrid material. In **(A,B)** the solid lines serve to guide the eyes.

Similar U-shaped stability ratio curves were measured with PLL (Fig. 1D) and the second HEP (Fig. 1E) layer, i.e., the particles rapidly aggregated close to the IEP, while saturated polyelectrolyte layers formed at the ASP stabilized the dispersions. Such charge-aggregation patterns have been reported earlier with LDH-polyelectrolyte systems<sup>32,33</sup> and qualitatively agree well with the classical theory developed by Derjaguin, Landau, Verwey and Overbeek (DLVO)<sup>41</sup>.

Concerning the influence of enzyme adsorption on the colloidal stability of the samples, the electrophoretic mobilities of LDH-HEP did not change significantly in the 1–100 mg/g HRP concentration range (Fig. S2A). They increased at higher doses, however, this regime is out of the scope of the present investigation. The same conclusions can be made based on the mobility data recorded for LDH-HEP-HRP-PLL in the presence of SOD (Fig. S2B). In addition, the hydrodynamic radii of the particles did not change with time at 10 mg/g enzyme doses (Fig. S2 insets) indicating a highly stable dispersion under these experimental conditions.

On the basis of the results of the above electrophoretic and light scattering measurements one can conclude that both CASCADE and its sub-systems form highly stable dispersions, once the optimized doses (HEP1: 50 mg/g, HRP: 10 mg/g, PLL: 200 mg/g, SOD: 10 mg/g and HEP2: 100 mg/g) are applied during the sequential adsorption process. This information is particularly important for the successful application of the composite to combat ROS.

**Structural and colloidal characterization of CASCADE.** The enzyme doses were selected on the basis of charging and aggregation behavior of the composite particles, however, the nature of enzyme immobilization, i.e., whether their adsorption is quantitative or partitioning takes place between the surface and the bulk solution, must be studied in order to assess the structural stability of CASCADE. This issue was addressed by performing the Bradford test as a typical spectrophotometric method that can detect enzymes in a solution (see SI for further details of this Bradford test)<sup>42,43</sup>. Three different doses (1, 10 and 100 mg/g) were probed for both SOD and HRP enzymes. It was found that  $93.0 \pm 2.8\%$ ,  $98.4 \pm 3.0\%$  and  $54.1 \pm 1.6\%$  of the total added amount of SOD enzyme was immobilized in CASCADE at 1, 10 and 100 mg/g enzyme doses, respectively. For HRP, these numbers were  $99.9 \pm 3.0\%$ ,  $98.3 \pm 2.9\%$  and  $19.8 \pm 0.6\%$  (Fig. 2A). These results clearly indicate that complete adsorption occurred at the lower doses, i.e., no enzyme was found in the surrounding solution at 1 and 10 mg/g loadings. For the 100 mg/g loading, in contrast, about 46 and 80% of the total SOD and HRP, respectively, remained in the bulk confirming the partitioning of the enzymes between the surface and the solution.

dc\_1931\_21

Therefore, these results unambiguously support that the total amounts of added enzymes are embedded in the CASCADE hybrid at 10 mg/g enzyme doses.

Ionic strength is an important parameter in potential applications of antioxidant nanoparticles, since the presence of high level of electrolytes is one of the most frequent reasons for particle aggregation for materials including LDHs<sup>32,44</sup>. This may lead to significant loss in the ROS-scavenging activity. Therefore, the resistance against salt-induced aggregation was studied in electrophoretic and DLS measurements. In general, the colloidal stability of the CASCADE particles in salt solutions of different concentrations can be described by the DLVO theory<sup>40,41,44</sup>. Accordingly, stability ratios decreased by increasing the ionic strength (Fig. 2B) due to the weakening of the repulsive double layer forces, which vanish at high salt levels and thus, attractive van der Waals interactions predominate giving rise to rapid particle aggregation. This hypothesis is supported by the tendency in the mobility values, whose magnitude decreased with increasing the ionic strength due to the shrinking of the electrical double layer by progressive salt screening.

The sudden transition between the fast and slow aggregation regimes occurred at the so-called critical coagulation concentration, which was determined to be 150 mM for CASCADE. This value is 6-times higher than the one reported for the bare LDH nanoclay<sup>31</sup> indicating an enormous stabilizing effect of the polyelectrolyte-enzyme layer formed on the LDH surface.

The morphology of the CASCADE material was also investigated by recording transmission (TEM, Fig. 2C) and scanning (SEM, Fig. 2D) electron microscopy images. For comparison, the TEM and SEM images of the bare LDH support are shown in Fig. S3A and S3B-C, respectively. It can be concluded that the polyelectrolyte and enzyme coating had no impact on the sample morphology. The particles possessed disc-like shape, which is typical for LDH nanoclays prepared by the co-precipitation method and treated hydrothermally thereafter<sup>29</sup>. Note that CASCADE aggregates are present in the TEM/SEM images due to the sample preparation process during imaging. This includes dispersion drying leading to the formation of clusters of particles upon evaporation of the solvent.

**Enzymatic activity of CASCADE.** The obtained composite was first tested in biochemical test reactions to assess the SOD and HRP activities. The SOD assay<sup>45</sup> is based on the enzymatic production of superoxide radicals, whose presence can be detected upon reaction with NBT (nitroblue tetrazolium). This reaction is inhibited by the SOD enzyme and its concentration necessary to achieve 50% inhibition is called  $IC_{50}$  value, which can be read from the inhibition versus enzyme concentration plots (Fig. 3A). Detailed descriptions of the SOD assay are given in the SI. The  $IC_{50}$  data are listed for CASCADE together with the values measured for native SOD and HRP in Table 1. Two main conclusions can be drawn from these experimental data. First, the activity of CASCADE and SOD are very similar, which is a strong proof for the preservation of the enzyme structural integrity upon immobilization. Second, HRP does not show significant SOD activity, i.e., the  $IC_{50}$  value could not be determined, in the concentration regime investigated.

The HRP assay<sup>46</sup> is based on the catalytic oxidation of guaiacol, being the substrate, in the presence of hydrogen peroxide (see SI for more details). Comparing the kinetic data shown in Fig. 3B, it is evident that native SOD did not show any activity in the assay. In the case of CASCADE and HRP, the maximum reaction rate of the guaiacol oxidation ( $v_{max}$ ) was lower for CASCADE, although the substrate concentration at half of the maximum reaction rate ( $K_M$ ) remained comparable. The turnover number ( $k_{cat}$ ) was also calculated enabling the determination of the catalytic efficiency ( $k_{cat}/K_M$ ). This is an important parameter that gives information about the initial rate of reaction at substrate concentrations that are significantly lower than  $K_M$ , similar to the physiological conditions. A twofold drop in the catalytic efficiency occurred upon HRP immobilization and coating, nevertheless, the efficiency remained reasonably high making CASCADE suitable for hydrogen peroxide consumption.

The above results clearly show that both SOD and HRP enzymes remained highly active upon immobilization. Since enzyme immobilization may result in complete or significant loss in the activity, the unchanged performances are great achievements of the present work.

**Cellular enzymatic activity and cytocompatibility.** The above discussed enzymatic activity of CASCADE was also assessed in cellular environment. The uptake by HeLa cells was proved by a guaiacol assay-inspired method after lysis, which is detailed in the SI. After incubating the cells with CASCADE at 5 mg/L concentration, the colored product from guaiacol was not detectable, possibly due to the low total concentration of CASCADE taken-up by the cells (Fig. S4). However, at 10 and 20 mg/L loadings, the formation of the oxidized guaiacol was clearly detected by the increase in the absorbances, which was proportional to the CASCADE content. It was shown earlier that no enzyme leakage occurs at the dose applied in the timeframe of the experiment (Fig. 2A), therefore, one can claim that the CASCADE system successfully enters the cells after 60 min incubation.

Besides, fluorescent measurements were carried out using 2',7'-dichlorodihydrofluorescein diacetate ( $H_2DCFDA$ ) dye to quantify the intracellular ROS-scavenging activity of CASCADE. The  $H_2DCFDA$  is indirectly oxidized by ROS and the developed product generates the fluorescence signal (more details are given in the SI). The ROS production was artificially increased by adding 50  $\mu M$  menadione to the samples that generates ROS through redox cycling and triggers cell death at high concentrations. This method has been proven as sufficient tool to assess oxidative stress reducing ability of antioxidant compounds<sup>47,48</sup>. For comparison, a control experiment was performed without adding any biocatalytic compounds. After the 2 min initial perfusion with HEPES buffer only, the increase of intracellular oxidative stress was apparent via perfusion with HEPES mixed with menadione (Fig. 3C). The experiment was repeated with the cells incubated with CASCADE at 5, 10 and 20 mg/L concentrations for 60 min. While at 5 mg/L a slight decrease in the intracellular oxidative stress was already observable, the effect became more pronounced at 10 and 20 mg/L, where significant decrease in the



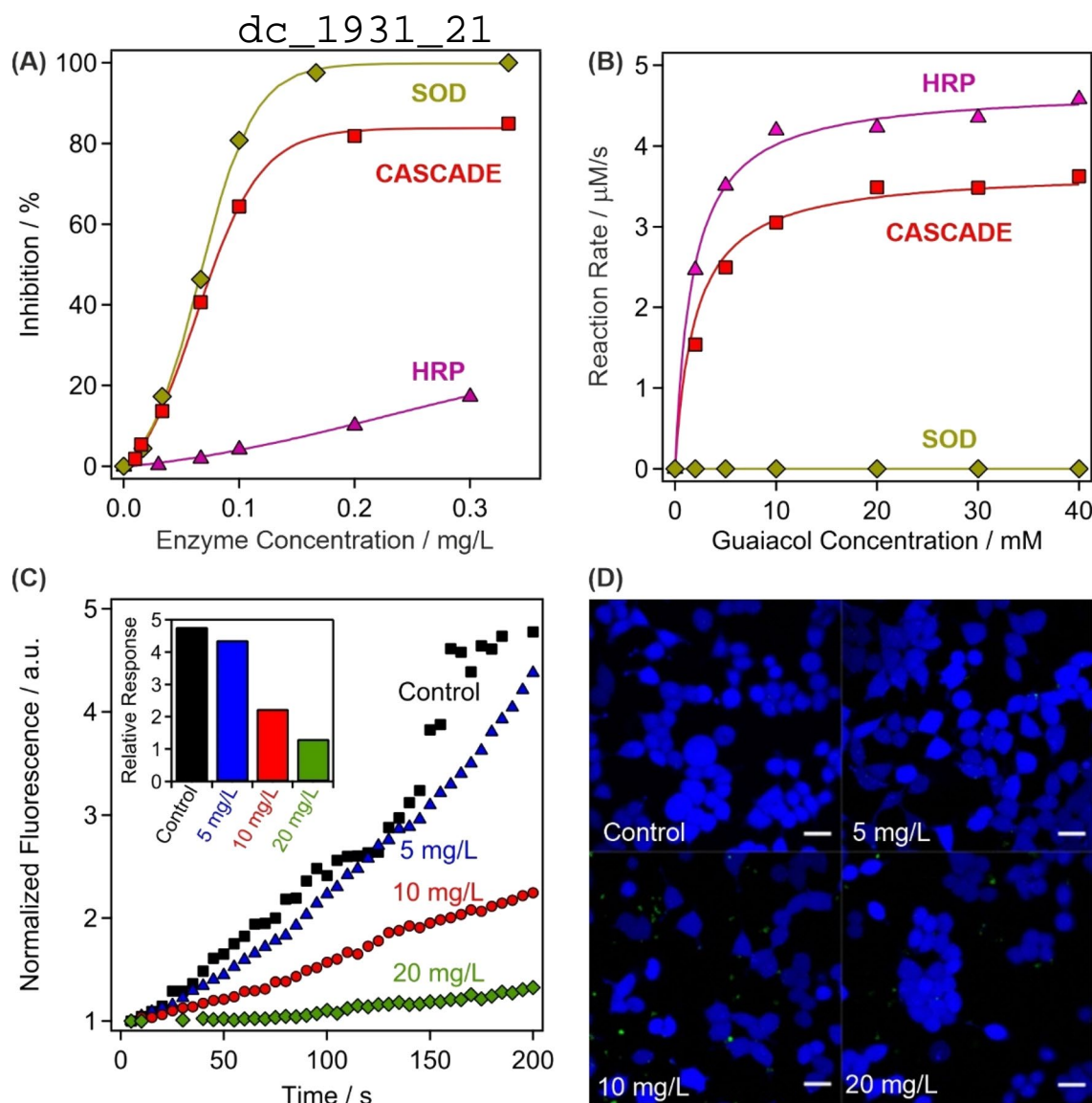


**Figure 3.** Assessment of the antioxidant activity of CASCADE. **(A)** SOD-like activity expressed by the inhibition of the NBT-superoxide radical reaction. The lines are mathematical functions used to interpolate the  $IC_{50}$  values. **(B)** HRP-like activity measured in the guaiacol-hydrogen peroxide reaction, where CASCADE acts as a catalyst. The solid lines represent the fits using the Michaelis–Menten model. **(C)** The fluorescent intensity of  $H_2DCFDA$  dye over time at different CASCADE loadings into HeLa cells. The maximal relative response of the detected fluorescent intensity is shown in the inset and in Table S1. **(D)** Live (blue fluorescent) HeLa cells were observed during the control experiments and at 5, 10 and 20 mg/L CASCADE doses. Scale bars represent 20  $\mu m$  dimension.

Sample	SOD activity	HRP activity		
	$IC_{50}$ (mg/L)	$v_{max}$ (mM/s)	$K_M$ (mM)	$k_{cat}/K_M$ (1/Ms)
SOD (native)	$0.069 \pm 0.003$	N/A <sup>a</sup>	N/A <sup>a</sup>	N/A <sup>a</sup>
HRP (native)	N/A <sup>a</sup>	$0.0046 \pm 0.0002$	$1.56 \pm 0.08$	$(2.59 \pm 0.13) \times 10^5$
CASCADE	$0.078 \pm 0.004$	$0.0038 \pm 0.0002$	$2.64 \pm 0.13$	$(1.27 \pm 0.06) \times 10^5$

**Table 1.** Enzymatic activity and kinetic parameters of CASCADE and the native enzymes. The average error of the assay measurements is about 5%. <sup>a</sup>The enzyme was inactive, i.e., the enzymatic activity could not be determined.

dc\_1931\_21

fluorescent intensity was apparent. Note that CASCADE and the dye molecules were incubated for 20 min prior to the experiments (i.e., before menadione was added) and no fluorescence signal was detected.

The data were analyzed with the statistical Mann–Whitney U-test (Fig. 3C inset). Applying a significance level (p value) of 5% for the test, the intensity of ROS production in 5 mg/L CASCADE incubated cells is not significantly different from the control group. However, at 10 and 20 mg/L loadings, the signals are remarkably lower compared to the control measurement with a p value under 0.01%. The full set of data is shown in Table S1. One can conclude that at 5 mg/L dose, even with proper enzymatic activity, the amount of immobilized enzymes taken-up was not sufficient to prevent intracellular oxidative stress. In contrast, at higher incubation doses, the antioxidant effect was expressed. Note that fluorescent intensity is already observable in the initial period without added menadione, since ROS are self-generated by the cells when removed from their feeding media. However, this initial fluorescence is also reduced at 10 and 20 mg/L CASCADE content, indicating the antioxidant effectiveness of the material.

On the one hand, the reduced amount of ROS in the cells originated from the preserved catalytic activity of the immobilized enzymes. However, ROS are not generated if cellular respiration ceases, i.e., if the cell death occurs by apoptosis or necrosis. Therefore, apoptosis/necrosis kit tests (see SI for details) were performed to measure the cell viability at different CASCADE doses (Fig. 3D). Note that the healthy cells are blue, while apoptosis and necrosis cause color change to green and red, respectively. However, cell death was not detected up to 20 mg/L CASCADE loading proving the remarkable activity of the immobilized HRP and SOD enzymes. Extensive apoptosis was observed at higher dose, as shown for 40 mg/g loading in Fig. S5. These results demonstrate the cellular uptake and cytocompatibility of the developed antioxidant material, while also maintaining its outstanding enzymatic activity in scavenging of biologically induced ROS in HeLa cells.

In conclusion, LDH nanoclays were synthesized and used as solid support for enzyme immobilization. The sequential adsorption method was suitable to build polyelectrolyte-enzyme layers on the LDH particles, however, the colloidal stability of the sub-systems prepared in the synthetic steps had to be optimized by tuning the surface charge and aggregation processes. HEP and PLL polyelectrolytes have proven to be appropriate building blocks, by strongly interacting with the oppositely charged particle surfaces leading to the formation of saturated polyelectrolyte layers and to an improved colloidal stability of the hybrid material. HRP and SOD enzymes were successfully embedded between the polyelectrolyte layers, since their strong interaction with the HEP and PLL chains prevented their desorption from the surface and provided an excellent structural stability. Remarkable enzymatic activity was observed in standard assays in dismutation of superoxide radical anions and in consumption of hydrogen peroxide. The preserved enzymatic activity was also confirmed by *in vitro* experiments. The CASCADE material was taken up by HeLa cells within reasonable incubation time. They showed sufficient cytocompatibility and remarkably decomposed the artificially generated ROS, when the CASCADE loading was appropriately high. Summarily, a facile synthetic route was demonstrated to obtain an effective antioxidant bionanomaterial composed of naturally occurring and easily accessible building-blocks. The obtained CASCADE hybrid possessed excellent structural, colloidal and functional stability, which makes it a promising candidate in antioxidant treatments of inflammatory bowel diseases via rectal injection.

## Methods

**Materials.** The quality and the source of all the chemicals are listed in the SI and they were used as received, unless stated otherwise.

**Electrophoresis.** The electrophoretic mobilities were determined on a ZetaSizer Nano ZS instrument (Malvern) that utilizes a He–Ne laser of 632 nm wavelength and applies the phase analysis light scattering technique. All samples were prepared the day prior to the measurement in order to equilibrate overnight. The final LDH concentration in the dispersions was set to 10 mg/L, while the final volume was 5 mL. Measurements were carried out in plastic capillary cells (Malvern) and the average value of five separate measurements was reported. This protocol led to a mean error of 5%.

**Light scattering.** The hydrodynamic radii were measured by DLS using a CGS-3 goniometer system (ALV) at 90° scattering angle. The correlation function was collected for 20 s and the cumulant fit was used to obtain the diffusion coefficient, which was applied in the Stokes–Einstein equation to calculate the hydrodynamic radius<sup>49</sup>. All aggregation tests were performed in round borosilicate test tubes (Kimble Chase), with a final sample volume of 2 mL and particle concentration of 10 mg/L.

**Structural analysis.** Morphological studies were carried out on a Hitachi S-4700 SEM and TEM at various magnifications using 10 kV (SEM) and 200 kV accelerating voltage (TEM). Before SEM measurements, the samples were sputter coated with gold. XRD and IR spectroscopy measurements were performed with an Empyrean diffractometer (Panalytical) and a Spectrum 100 FT-IR spectrometer (PerkinElmer), respectively.

**Determination of the enzyme content and enzymatic assays.** The concentration of the enzymes in solution was measured with the standard Bradford test<sup>42</sup>. The SOD and HRP activities were determined by the Fridovich<sup>45</sup> and guaiacol<sup>46</sup> assays with an average error of 10% and 5%, respectively. Detailed descriptions of these protocols are given in the SI.

**Cellular uptake.** The CASCADE material was added to HeLa cells in a culture flask of 70% confluency covered with 1 mL feeding media in various concentrations and the mixtures were incubated for 60 min (37 °C, 5 v%

dc\_1931\_21

CO<sub>2</sub> in air). After that, the liquid was removed, the cells were washed with Dulbecco's PBS (phosphate buffered saline, 9.5 mM phosphate content) twice to remove any residual CASCADE and the cells were lysed with RIPA (radioimmunoprecipitation assay, tenfold dilution) lysis buffer for 30 min. Each 10 mL of lysis buffer contained one mini cOmplete ULTRA tablet, a protease inhibitor. Cellular debris were removed via centrifugation at 4 °C (13,000 rpm, 10 min) and the supernatant liquid obtained was investigated by a guaiacol assay as described in the SI.

**Cellular ROS detection.** After the incubation step described above, a ROS sensitive dye (H<sub>2</sub>DCFDA, 5 μM concentration) in HEPES buffer solution was added to the cells. Microscopic analyses were carried out by following the increase in the drift corrected green fluorescence response of the ROS-sensitive dye on an LSM 880 confocal microscope (Zeiss) with a standard ROS detecting procedure detailed in the SI. Menadione in HEPES buffer (see SI for exact composition) was used to generate intracellular ROS. For further data evaluation, the Mann–Whitney U-test was performed in GraphPad Prism software package version 8.0.0 for Windows (Graph-Pad).

**Cell viability study.** Apoptosis/necrosis assay kit (blue, green and red) was used to monitor the live (blue), apoptotic (green) and necrotic cells (red) after 60 min incubation (HeLa cells fixed on cover glass with 70% confluency under 1 mL feeding media, 37 °C, 5 v% CO<sub>2</sub> in air) with the composite material at various concentrations. The measurements were carried out on the same microscope as the ROS experiments according to a standard procedure detailed in the SI. An average error of 10% must be considered for all data obtained from the above activity and viability measurements.

### Data availability

The data that support the findings of this study are available from the corresponding author upon reasonable request.

Received: 1 November 2020; Accepted: 8 February 2021

Published online: 22 February 2021

### References

- Vazquez-Gonzalez, M., Wang, C. & Willner, I. Biocatalytic cascades operating on macromolecular scaffolds and in confined environments. *Nat. Catal.* **3**, 256–273 (2020).
- Hwang, E. T. & Lee, S. Multienzymatic cascade reactions via enzyme complex by immobilization. *ACS Catal.* **9**, 4402–4425 (2019).
- Kazenwadel, F., Franzreb, M. & Rapp, B. E. Synthetic enzyme supercomplexes: co-immobilization of enzyme cascades. *Anal. Methods* **7**, 4030–4037 (2015).
- Kudina, O. *et al.* Highly efficient phase boundary biocatalysis with enzymogel nanoparticles. *Angew. Chem.-Int. Ed.* **53**, 483–487 (2014).
- Geraud, E., Prevot, V., Forano, C. & Mousty, C. Spongy gel-like layered double hydroxide-alkaline phosphatase nanohybrid as a biosensing material. *Chem. Commun.* 1554–1556 (2008).
- Parthasarathy, R. V. & Martin, C. R. Synthesis of polymeric microcapsule arrays and their use for enzyme immobilization. *Nature* **369**, 298–301 (1994).
- Lin, M. T. & Beal, M. F. Mitochondrial dysfunction and oxidative stress in neurodegenerative diseases. *Nature* **443**, 787–795 (2006).
- Louzao, I. & van Hest, J. C. M. Permeability effects on the efficiency of antioxidant nanoreactors. *Biomacromol* **14**, 2364–2372 (2013).
- Tanner, P., Onaca, O., Balasubramanian, V., Meier, W. & Palivan, C. G. Enzymatic cascade reactions inside polymeric nanocontainers: A means to combat oxidative stress. *Chem.-Eur. J.* **17**, 4552–4560 (2011).
- Wu, Q. *et al.* Cascade enzymes within self-assembled hybrid nanogel mimicked neutrophil lysosomes for singlet oxygen elevated cancer therapy. *Nat. Commun.* **10**, 240 (2019).
- Winterbourn, C. C. Reconciling the chemistry and biology of reactive oxygen species. *Nat. Chem. Biol.* **4**, 278–286 (2008).
- Pisoschi, A. M. & Pop, A. The role of antioxidants in the chemistry of oxidative stress: A review. *Eur. J. Med. Chem.* **97**, 55–74 (2015).
- Sohal, R. S. & Weindruch, R. Oxidative stress, caloric restriction, and aging. *Science* **273**, 59–63 (1996).
- Tainer, J. A., Getzoff, E. D., Richardson, J. S. & Richardson, D. C. Structure and mechanism of copper, zinc superoxide-dismutase. *Nature* **306**, 284–287 (1983).
- Fita, I. & Rossmann, M. G. The active-center of catalase. *J. Mol. Biol.* **185**, 21–37 (1985).
- Gajhede, M., Schuller, D. J., Henriksen, A., Smith, A. T. & Poulos, T. L. Crystal structure of horseradish peroxidase C at 2.15 angstrom resolution. *Nat. Struct. Biol.* **4**, 1032–1038 (1997).
- Chang, F. P., Chen, Y. P. & Mou, C. Y. Intracellular implantation of enzymes in hollow silica nanospheres for protein therapy: Cascade system of superoxide dismutase and catalase. *Small* **10**, 4785–4795 (2014).
- Tanner, P., Balasubramanian, V. & Palivan, C. G. Aiding nature's organelles: Artificial peroxisomes play their role. *Nano Lett.* **13**, 2875–2883 (2013).
- Grotzky, A., Nauser, T., Erdogan, H., Schluter, A. D. & Walde, P. A fluorescently labeled dendronized polymer-enzyme conjugate carrying multiple copies of two different types of active enzymes. *J. Am. Chem. Soc.* **134**, 11392–11395 (2012).
- Grotzky, A. *et al.* Structure and enzymatic properties of molecular dendronized polymer-enzyme conjugates and their entrapment inside giant vesicles. *Langmuir* **29**, 10831–10840 (2013).
- Fan, G. L., Li, F., Evans, D. G. & Duan, X. Catalytic applications of layered double hydroxides: recent advances and perspectives. *Chem. Soc. Rev.* **43**, 7040–7066 (2014).
- Yu, J. F., Wang, Q., O'Hare, D. & Sun, L. Y. Preparation of two dimensional layered double hydroxide nanosheets and their applications. *Chem. Soc. Rev.* **46**, 5950–5974 (2017).
- Taviot-Gueho, C. *et al.* Tailoring hybrid layered double hydroxides for the development of innovative applications. *Adv. Funct. Mater.* **28**, 1703868 (2018).
- Deak, A. *et al.* Spherical LDH-Ag<sup>0</sup>-montmorillonite heterocoagulated system with a pH-dependent sol-gel structure for controlled accessibility of AgNPs immobilized on the clay lamellae. *Langmuir* **31**, 2019–2027 (2015).
- Cao, Z. B., *et al.* 2D layered double hydroxide nanoparticles: Recent progress toward preclinical/clinical nanomedicine. *Small Methods* 1900343 (2019).

26. Ishihara, S. & Iyi, N. Controlled release of H<sub>2</sub>S and NO gases through CO<sub>2</sub>-stimulated anion exchange. *Nat. Commun.* **11**, 453 (2020).
27. Choi, G., Piao, H., Kim, M. H. & Choy, J. H. Enabling nanohybrid drug discovery through the soft chemistry telescope. *Ind. Eng. Chem. Res.* **55**, 11211–11224 (2016).
28. Decher, G. Fuzzy nanoassemblies: Toward layered polymeric multicomposites. *Science* **277**, 1232–1237 (1997).
29. Xu, Z. P. *et al.* Stable suspension of layered double hydroxide nanoparticles in aqueous solution. *J. Am. Chem. Soc.* **128**, 36–37 (2006).
30. Pavlovic, M., Rouster, P. & Szilagyi, I. Synthesis and formulation of functional bionanomaterials with superoxide dismutase activity. *Nanoscale* **9**, 369–379 (2017).
31. Pavlovic, M., Rouster, P., Somosi, Z. & Szilagyi, I. Horseradish peroxidase-nanoclay hybrid particles of high functional and colloidal stability. *J. Colloid Interface Sci.* **524**, 114–121 (2018).
32. Pavlovic, M., Rouster, P., Oncsik, T. & Szilagyi, I. Tuning colloidal stability of layered double hydroxides: from monovalent ions to polyelectrolytes. *ChemPlusChem* **82**, 121–131 (2017).
33. Vasti, C., Borgiallo, A., Giacomelli, C. E. & Rojas, R. Layered double hydroxide nanoparticles customization by polyelectrolyte adsorption: mechanism and effect on particle aggregation. *Colloid Surf. A* **533**, 316–322 (2017).
34. Dobrynin, A. V., Deshkovski, A. & Rubinstein, M. Adsorption of polyelectrolytes at oppositely charged surfaces. *Macromolecules* **34**, 3421–3436 (2001).
35. Carrillo, J. Y. & Dobrynin, A. V. Molecular dynamics simulations of polyelectrolyte adsorption. *Langmuir* **23**, 2472–2482 (2007).
36. Brunel, F., Pochard, I., Gauffine, S., Turesson, M. & Labbez, C. Structure and yielding of colloidal silica gels varying the range of interparticle interactions. *J. Phys. Chem. B* **120**, 5777–5785 (2016).
37. Vasti, C., Bedoya, D. A., Rojas, R. & Giacomelli, C. E. Effect of the protein corona on the colloidal stability and reactivity of LDH-based nanocarriers. *J. Mater. Chem. B* **4**, 2008–2016 (2016).
38. Marin, E. *et al.* Encapsulation of manganese dioxide nanoparticles into layer-by-layer polymer capsules for the fabrication of antioxidant microreactors. *Mater. Sci. Eng. C-Mater. Biol. Appl.* **117**, 111349 (2020).
39. Holthoff, H., Egelhaaf, S. U., Borkovec, M., Schurtenberger, P. & Sticher, H. Coagulation rate measurements of colloidal particles by simultaneous static and dynamic light scattering. *Langmuir* **12**, 5541–5549 (1996).
40. Kobayashi, M., Yuki, S. & Adachi, Y. Effect of anionic surfactants on the stability ratio and electrophoretic mobility of colloidal hematite particles. *Colloid Surf. A* **510**, 190–197 (2016).
41. Derjaguin, B. & Landau, L. D. Theory of the stability of strongly charged lyophobic sols and of the adhesion of strongly charged particles in solutions of electrolytes. *Acta Phys. Chim.* **14**, 633–662 (1941).
42. Bradford, M. M. Rapid and sensitive method for quantitation of microgram quantities of protein utilizing principle of protein-dye binding. *Anal. Biochem.* **72**, 248–254 (1976).
43. Zor, T. & Seliger, Z. Linearization of the Bradford protein assay increases its sensitivity: Theoretical and experimental studies. *Anal. Biochem.* **236**, 302–308 (1996).
44. Yu, W. Y., Du, N., Gu, Y. T., Yan, J. G. & Hou, W. G. Specific ion effects on the colloidal stability of layered double hydroxide single-layer nanosheets. *Langmuir* **36**, 6557–6568 (2020).
45. Beaucham, C. & Fridovich, I. Superoxide dismutase - improved assays and an assay applicable to acrylamide gels. *Anal. Biochem.* **44**, 276–287 (1971).
46. Doerge, D. R., Divi, R. L. & Churchwell, M. I. Identification of the colored guaiacol oxidation product produced by peroxidases. *Anal. Biochem.* **250**, 10–17 (1997).
47. Chen, C. A., *et al.* Legumain promotes tubular ferroptosis by facilitating chaperone-mediated autophagy of GPX4 in AKI. *Cell Death Dis.* **12**, 65–65 (2021).
48. Loor, G. *et al.* Menadione triggers cell death through ROS-dependent mechanisms involving PARP activation without requiring apoptosis. *Free Radic. Biol. Med.* **49**, 1925–1936 (2010).
49. Hassan, P. A., Rana, S. & Verma, G. Making sense of Brownian motion: Colloid characterization by dynamic light scattering. *Langmuir* **31**, 3–12 (2015).

## Acknowledgements

This research was financially supported by the Hungarian Academy of Sciences (96130, 95026 and LP2017-18/2017), by the National Excellence Programme (20391-3/2018/FEKUSTRAT), by the Ministry of Human Capacities (EFOP 3.6.2-16-2017-00006) and by the Albert Szent-Györgyi Research Grant (to JM by the Faculty of Medicine, University of Szeged). The project has also received funding from the EU's Horizon 2020 research and innovation program under grant agreement No. 739593. The support from the University of Szeged Open Access Fund (5129) is gratefully acknowledged.

## Author contributions

All authors have given approval to the final version of the manuscript. M.P. performed experiments and wrote the first draft of the manuscript, S.M. performed experiments, analyzed data and contributed to manuscript writing, X.K. performed experiments, N.B.A. performed experiments, P.R. performed experiments, J.M. designed the research and acquired funding, I.S. wrote the final manuscript, acquired funding and supervised the research.

## Competing interests

The authors declare no competing interests.

## Additional information

**Supplementary Information** The online version contains supplementary material available at <https://doi.org/10.1038/s41598-021-83819-4>.

**Correspondence** and requests for materials should be addressed to I.S.

**Reprints and permissions information** is available at [www.nature.com/reprints](http://www.nature.com/reprints).

**Publisher's note** Springer Nature remains neutral with regard to jurisdictional claims in published maps and institutional affiliations.



dc\_1931\_21



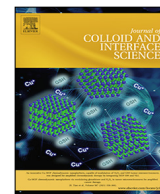
**Open Access** This article is licensed under a Creative Commons Attribution 4.0 International License, which permits use, sharing, adaptation, distribution and reproduction in any medium or format, as long as you give appropriate credit to the original author(s) and the source, provide a link to the Creative Commons licence, and indicate if changes were made. The images or other third party material in this article are included in the article's Creative Commons licence, unless indicated otherwise in a credit line to the material. If material is not included in the article's Creative Commons licence and your intended use is not permitted by statutory regulation or exceeds the permitted use, you will need to obtain permission directly from the copyright holder. To view a copy of this licence, visit <http://creativecommons.org/licenses/by/4.0/>.

© The Author(s) 2021



Contents lists available at ScienceDirect

## Journal of Colloid and Interface Science

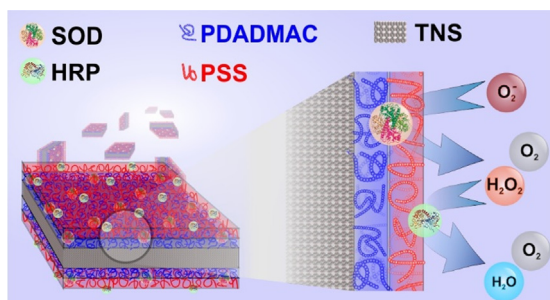
journal homepage: [www.elsevier.com/locate/jcis](http://www.elsevier.com/locate/jcis)

## Regular Article

## Co-immobilization of antioxidant enzymes on titania nanosheets for reduction of oxidative stress in colloid systems

Szilárd Sáringer<sup>a</sup>, Paul Rouster<sup>b</sup>, Istvan Szilagyi<sup>a,\*</sup><sup>a</sup> MTA-SZTE Lendület Biocolloids Research Group, Interdisciplinary Excellence Center, Department of Physical Chemistry and Materials Science, University of Szeged, H-6720 Szeged, Hungary<sup>b</sup> Institute of Condensed Matter and Nanosciences-Bio and Soft Matter, Université Catholique de Louvain, Louvain-la-Neuve B-1348, Belgium

## G R A P H I C A L A B S T R A C T



## A R T I C L E I N F O

## Article history:

Received 16 November 2020

Revised 4 January 2021

Accepted 5 January 2021

Available online 16 January 2021

## Keywords:

Enzyme cascade

Immobilization

Titania nanosheets

Antioxidant composite

Sequential adsorption

## A B S T R A C T

Immobilization of single antioxidant enzyme systems was frequently studied in the past, however, there is a lack of reliable reports on the co-immobilization of such enzymes. Here, an antioxidant enzyme cascade involving superoxide dismutase (SOD) and horseradish peroxidase (HRP) was successfully immobilized on titania nanosheets (TNS) by the sequential adsorption method using poly(diallyldimethylammonium chloride) (PDADMAC) and poly(styrene sulfonate) (PSS) polyelectrolyte building blocks. The development of the cascade system was based on a colloid approach, in which the charging and aggregation processes were optimized in each synthetic step. The polyelectrolyte and enzyme multilayers were built up in two different sequences at the particle interface, namely, TNS-PDADMAC-SOD-PSS-HRP and TNS-HRP-PDADMAC-SOD-PSS. The formation of the polyelectrolyte layers led to charge reversal of the carrier and the saturated PDADMAC and PSS layers stabilized the dispersions, in particular, their resistance against salt-induced aggregation was especially excellent. The results of enzymatic assays revealed that the SOD and HRP-like activities of the composites depended on the location of the enzymes in the hybrid material. The obtained compounds showed remarkable antioxidant effect and were able to simultaneously decompose superoxide radical anions and hydrogen peroxide. The cascade systems are of great promise in industrial manufacturing processes during the preparation of high-quality products without any damages by reactive oxygen species.

© 2021 The Author(s). Published by Elsevier Inc. This is an open access article under the CC BY license (<http://creativecommons.org/licenses/by/4.0/>).

## 1. Introduction

Normal biochemical reactions exposed to environmental effects and higher levels of dietary xenobiotics result in increased

\* Corresponding author.

E-mail address: [szistvan@chem.u-szeged.hu](mailto:szistvan@chem.u-szeged.hu) (I. Szilagyi).

generation of reactive oxygen species (ROS) such as superoxide ( $O_2^-$ ), hydroxyl free radicals ( $OH^\cdot$ ) or hydrogen peroxide ( $H_2O_2$ ) [1]. Extended ROS production induces oxidative stress leading to damage of cellular components such as DNA, proteins and lipids and also causes significant loss in the quality of industrial products [2–5]. The oxidative stress can be effectively neutralized by molecular and enzymatic antioxidants [6]. The latter ones, including superoxide dismutase (SOD) [7] and horseradish peroxidase (HRP) [8], are the most effective substances to combat oxidative stress, i.e., SOD dismutates  $O_2^-$  to molecular oxygen and  $H_2O_2$ , while HRP consumes  $H_2O_2$  in oxidation reactions. They act together as an enzyme cascade in the cellular environments [9].

However, native enzymes are sensitive to the environmental conditions giving rise to limited stability, which impedes efficient delivery and supplementation of these proteins. The complex environment of the biological systems (e.g., high electrolyte concentration and presence of enzyme inhibitors) and the harsh environmental conditions (e.g., elevated temperature and pressure) in the industrial applications usually lead to enzyme denaturation and loss of enzymatic activity [10,11]. To overcome these limitations and broaden their applicability, considerable research activity was performed in the past decades to immobilize native enzymes in/on solid supports to improve their performances in organic solvents and their heat tolerances [12–14]. Furthermore, immobilization may enhance the structural stability and selectivity of the proteins providing long-term stabilization of the enzymes, which prevents dissociation-related inactivation [15]. Another advantage in the industrial applications is that the immobilized enzymes can be easily separated and removed from the reaction mixtures [16].

Concerning the antioxidant enzymes, immobilization of single proteins including SOD [17–19] and HRP [20–22] on various substrates was frequently reported in the past. However, co-immobilization of such enzymes could be an appropriate mimic of the cellular environment, where ROS are decomposed to molecular oxygen and water in tandem reactions catalyzed by the enzymes. To the best of our knowledge, only one system has been published, in which SOD and HRP were co-immobilized via covalent grafting to dendronized polymer chains [23,24]. Excellent antioxidant activity was achieved, however, the supporting polymer is hardly available and the grafting requires a complicated reaction. To achieve cost-effective and facile preparation of an immobilized antioxidant enzyme cascade, the solid support and the procedure have to be simplified.

Concerning the carrier, titania particles are promising candidates for the co-immobilization of SOD and HRP enzymes. Titania and its composites are versatile materials [25–28] and they are of great potential in enzyme immobilization owing to their advantageous surface properties as well as their chemical and thermal stability. Among them, titania nanosheets (TNS) possess well-defined layered or unilamellar structures associated with high surface area, good thermal stability, pH tunable properties and biocompatibility [29–31]. Although single antioxidant enzymes were immobilized on TNS structures using polyelectrolytes as stabilizing agents for instance [18–20,32,33], immobilized enzyme cascades were not reported so far. The use of polyelectrolytes allows the use of the sequential adsorption method [34] as a possible enzyme immobilization technique, which has already been applied on planar surfaces to embed proteins between polyelectrolyte layers [35–37]. However, there is a lack of studies dealing with the co-immobilization of enzymes on nanoparticulate supports applying the polyelectrolyte-based sequential adsorption technique.

The present study aims at the design of stable dispersions of nanoparticle-supported antioxidant enzyme cascade involving polyelectrolytes as building blocks. The co-immobilization of HRP and SOD was carried out by the sequential adsorption of oppositely

charged polyelectrolytes (poly(diallyldimethylammonium chloride) (PDADMAC) and sodium poly(styrene sulfonate) (PSS)) on TNS particles through electrostatic forces. TNS was chosen as a solid support on the basis of our previous experiences in immobilization of single SOD [18] and HRP [20] enzymes, where it was observed that (i) the antioxidant activity remains similar upon enzyme adsorption on TNS, (ii) application of polyelectrolytes leads to improved colloidal stability and (iii) the obtained composites containing single enzymes possess all the advantages of a heterogeneous catalyst compared to the homogeneous counterpart. In addition, the use of catalase enzyme was also considered, but it lost its activity upon immobilization and hence, HRP was chosen as  $H_2O_2$  consuming center in the hybrid material. Light scattering techniques were used to optimize the charging and aggregation features of the sub-systems during the preparation process to determine the conditions, under which the colloids are stable in order to obtain fine particle dispersions of high surface area. The enzymatic activity of the nanocomposites was determined in biochemical assays for different ROS substrates to assess the antioxidant activity.

## 2. Materials and method

### 2.1. Chemicals

Titania nanosheets (TNS) were synthesized by an established protocol detailed elsewhere [38]. Superoxide dismutase (SOD, from bovine liver), positively charged poly(diallyldimethylammonium chloride) (PDADMAC, 20 wt%, average molecular mass of 275 kg/mol), negatively charged poly(styrene sulfonate) (PSS, sodium salt, molecular mass of 10.6 kg/mol), xanthine oxidase (lyophilized powder, 0.4–1.0 units/mg protein) were purchased from Sigma-Aldrich (Budapest, Hungary). Horseradish peroxidase (HRP), NaCl,  $H_2O_2$ ,  $NaH_2PO_4$  (anhydrous) and  $Na_2HPO_4$  (anhydrous) were purchased from VWR (Debrecen, Hungary). Xanthine (99%) was bought from Alfa Aesar (Karlsruhe, Germany). Nitro blue tetrazolium (NBT) chloride monohydrate and guaiacol (99%) were acquired from Acros (Debrecen, Hungary). Ultrapure water was produced with a VWR Puranility TU+ device for all the sample preparations. Salt solutions were filtered with a 0.1  $\mu$ m PVDF syringe filter purchased from Millex (Budapest, Hungary). The measurements were carried out at pH 7 and 25 °C, unless stated otherwise. Prior to use, TNS were dispersed in ultrapure water. Samples containing PDADMAC and PSS in a concentration range of 0.001–100 mg/L were obtained by dissolving the polyelectrolytes in ultrapure water. SOD and HRP enzymes were dissolved in ultrapure water and solutions with a concentration range of 0.001–40 mg/L were prepared.

### 2.2. Electrophoretic mobility

Electrophoretic mobilities were determined by electrophoretic light scattering with a Litesizer 500 instrument (Anton Paar, Graz, Austria) equipped with a 40 mW semiconductor laser operating at 658 nm wavelength. For all the measurements, 1 mL solutions were prepared. Accordingly, 0.1 mL of the TNS dispersions of 10 mg/L concentration was added to 0.9 mL solution composed of the calculated amount of polyelectrolyte, enzyme and NaCl, the latter one is to set the ionic strength. The samples were allowed to rest 2 h at room temperature before measuring the electrophoretic mobilities after 1 min equilibration time in the device. The reported values are the average of five individual measurements. The experiments were performed in 350  $\mu$ L volume omega-shaped plastic cuvettes (Anton Paar). The average error of the method is 5%.

### 2.3. Dynamic light scattering

To determine the hydrodynamic radius ( $R_h$ ) of the particles, dynamic light scattering (DLS) experiments were carried out with the same Litesizer 500 instrument as used in the mobility study. The cumulant fit [39] was used to fit the correlation function, which was collected for 20 s at 175° scattering angle. Time-resolved DLS measurements were performed to determine the apparent aggregation rate coefficient ( $k_{app}$ ) of particle dimer formation as [40]

$$k_{app} = \frac{1}{R_h(0)} \frac{dR_h(t)}{dt} \quad (1)$$

where  $t$  is the time of the experiment and  $R_h(0)$  is the hydrodynamic radius of the TNS determined in a stable dispersion. Examples for time-resolved DLS measurements are shown for the different systems in the [Supplementary material](#) in Fig. S1a–d.

The measurements were run for 40–120 min depending on the speed of aggregation. The same particle concentration (1 mg/L) was used in all of the time-resolved measurements. To compare the tendencies, the sample preparation for the DLS was done in a similar manner as the one described above for electrophoresis. The only difference was that the total volume was 2 mL for DLS and that the measurements were started directly after adding the particles to the solutions of polyelectrolyte, enzyme and NaCl. The samples were stirred with a Vortex before starting the time-resolved experiments. The colloidal stability was expressed in terms of stability ratio ( $W$ ), which was calculated from the  $k_{app}$  values as follows [18,40,41]

$$W = \frac{k_{app}^{fast}}{k_{app}} \quad (2)$$

where the fast condition corresponds to the diffusion-controlled aggregation of the particles achieved in 1 M NaCl solution. One can realize that a stability ratio of unity is associated to unstable dispersions, where all the particle collisions result in dimer formation. Note that the above protocol leads to a mean error of 10%.

### 2.4. Transmission electron microscopy

The morphology of the materials was explored by transmission electron microscopy (TEM). The TEM images were recorded on a Tecnai G2 Sphera microscope (FEI, Hillsboro, USA) at an acceleration voltage of 120 kV using a LaB6 cathode. The samples were prepared by placing 5  $\mu$ L of solution on a plasma-treated carbon mesh and by removing the excess liquid after 2 min. The obtained mesh with the material was installed on the sample holder and placed in the electron microscope. The drying process induced the formation of some particle aggregates.

### 2.5. Enzymatic assays

To determine the SOD-like activity of the obtained materials, the Fridovich method was employed [42]. However, the enzymatic assay protocol had to be slightly modified to adapt to the high scattering from the suspended TNS. Each sample was composed of xanthine (3 mM, 0.1 mL), NBT (3 mM, 0.1 mL), xanthine oxidase (3 mg/mL, 0.3 mL) and dispersion containing the catalyst (bare or immobilized SOD, 0–2.5 mL) in phosphate buffer and completed to a final volume of 3 mL. The phosphate buffer concentration in the samples was 2.7 mM and the pH was set at 7. Once all the reagents were mixed, the increase in the absorbance band at 565 nm was monitored for 6 min. The increase in the absorbance ( $\Delta A_s$ ) was determined for several SOD concentrations. Due to the scattering of the TNS particles, the corresponding samples without SOD were

used as references ( $\Delta A_0$ ). The inhibition ( $I$ ) of the superoxide radical anion ( $O_2^-$ )-NBT reaction was then calculated as

$$I = \frac{\Delta A_0 - \Delta A_s}{\Delta A_0} \cdot 100 \quad (3)$$

The  $O_2^-$  scavenging activities were expressed as  $IC_{50}$  values, which correspond to the SOD concentration needed to dismutate 50% of the  $O_2^-$  formed in the probe reaction.

The determination of the HRP activity was performed using the guaiacol assay [19,43,44]. In brief, 240  $\mu$ L of the bare or immobilized HRP sample containing 10 mg/L enzyme was mixed with 240  $\mu$ L of phosphate buffer (100 mM) followed by the addition of appropriate amount of guaiacol solution of 100 mM concentration and completed to a volume of 1680  $\mu$ L with ultrapure water. Finally, 720  $\mu$ L of  $H_2O_2$  (9 mM) was added into the cuvette, which was vortexed again and immediately introduced into the UV-vis spectrophotometer to follow the formation of the guaiacol degradation products at 470 nm wavelength [45]. The increase in the absorbance was monitored as a function of the reaction time and the linear part of the curve was fitted to calculate the reaction rate ( $v$ ). The Michaelis constant ( $K_m$ ) and the maximum reaction rate ( $v_{max}$ ) were calculated by the Lineweaver-Burk equation as follows [46]

$$\frac{1}{v} = \frac{K_m}{v_{max}} \frac{1}{[S]} + \frac{1}{v_{max}} \quad (4)$$

where  $[S]$  refers to the guaiacol concentration.

## 3. Results and discussion

The development of the enzyme cascade by the sequential adsorption technique requires stable dispersions of functionalized TNS in each steps of the process. Therefore, the colloidal stability of the sub-systems was optimized by investigating the surface charge and aggregation of the particles at different concentrations of the polyelectrolytes and enzymes. The resistance against salt-induced aggregation of the obtained cascade was also studied to assess the colloidal stability. Finally, the antioxidant activity was measured in dismutation of  $O_2^-$  and in the consumption of  $H_2O_2$ . Note that the immobilization of single SOD [18] and HRP [20] on TNS has been reported earlier, while the present study focuses on their co-immobilization.

### 3.1. Build-up of PDADMAC/PSS bilayer on TNS

Given the negative surface charge of TNS under the conditions investigated [38], the effect of the oppositely charged PDADMAC on the charging and aggregation of bare TNS was first studied by electrophoresis and DLS. The electrophoretic mobilities recorded at different PDADMAC loadings are presented in Fig. 1.

Strong adsorption of PDADMAC on oppositely charged surfaces was reported in the past [38,47–49], which was also observed in the present system. The adsorption process was clearly indicated by the progressive increase in the mobility values by increasing the PDADMAC concentration. Such an adsorption led to charge neutralization at the isoelectric point (IEP). Furthermore, the adsorption process continued after the charge neutralization point and charge reversal of the TNS particles occurred. Such an inversion of the original charge is typical for colloidal particles in the presence of oppositely charged polyelectrolytes [38,47,49–53]. At high doses, the surface became saturated with the adsorbed PDADMAC and hence, the electrophoretic mobilities reached a plateau at 150 mg/g. Note that the onset of this plateau is given by the intersection of the linear fits applied on the mobility data of the increasing region and of the plateau. For the latter one, a zero slope was



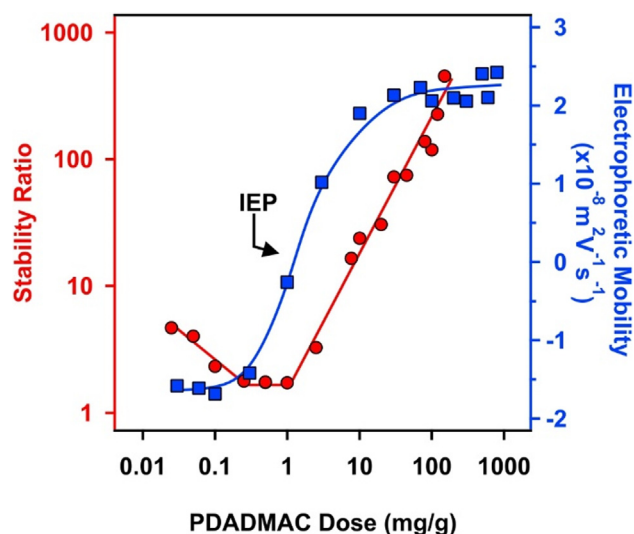


**Fig. 1.** Stability ratio (red circle) and electrophoretic mobility (blue square) of the TNS versus the PDADMAC dose. The ionic strength and the TNS concentration were 1 mM and 1 mg/L, respectively. The unit in the x-axis indicates mg of PDADMAC per 1 g of TNS. The lines serve to guide the eyes. The average error of the stability ratio and the mobility values are 10 and 5% respectively. (For interpretation of the references to colour in this figure legend, the reader is referred to the web version of this article.)

applied. One can notice that the charge reversal gave rise to a higher magnitude of charge, when comparing the mobilities measured at the lowest and highest PDADMAC doses.

DLS represents an excellent tool to determine the size of the colloidal particles in dispersions [41,54] and subsequently, to measure the rate of particle aggregation processes [40,41,52]. Therefore, stability ratio values were calculated from the rate constants determined at different PDADMAC doses in time-resolved DLS experiments (Fig. 1). The stability ratios close to unity indicated unstable dispersions at the IEP, while they steeply increased beyond the IEP giving rise to stable dispersions at high doses, after the adsorption saturation point discussed in the mobility studies. At low doses, however, a limited stability and low stability ratios were obtained.

The aggregation features of TNS at different PDADMAC doses resembles to the one predicted by the classical theory developed by Derjaguin, Landau, Verwey, and Overbeek (DLVO) [55]. Indeed, the nanosheets rapidly aggregate once the surface charges are neutralized at the IEP, where the repulsive electrical double layer interaction is absent and the attractive van der Waals force predominates. When the nanosheets possessed sufficient charge at high doses, the repulsive electrical double-layer forces stabilized the samples in conjunction with the DLVO theory. On the other hand at low polyelectrolyte doses, limited stability was achieved, which originates from the low charge of the bare particles and to the additional non-DLVO attractive forces, which is related to the so called patch charge effect due to polyelectrolyte adsorption at lower surface coverage [38,49,50].

Based on these results, a PDADMAC dose of 150 mg/g (denoted as TNS-PDADMAC in the following) was selected for the further steps of the sequential adsorption process. Under this condition, PDADMAC formed a saturated layer on the surface of the TNS giving rise to a stable dispersion of positively charged particles. In addition, the obtained TNS-PDADMAC possess higher colloidal stability than the bare particles. The net positive surface charge allows the immobilization of the negatively charged SOD enzyme through electrostatic interactions.

In the next step, the conditions were optimized to build-up a PSS layer on the TNS-PDADMAC. A major requirement was to

achieve high colloidal stability after the bilayer formation on the TNS particles. Accordingly, negatively charged PSS was adsorbed on the TNS-PDADMAC hybrid. Although, the PDADMAC/PSS multilayer formation was frequently reported on planar substrates [56–58], very limited information is available with nanoparticles acting as carrier for the multilayer [59]. Electrophoretic mobilities were first determined to probe the influence of the PSS concentration on the charging behavior of the TNS-PDADMAC (Fig. 2).

Considering the change in the magnitude of the electrophoretic mobilities, very similar tendencies were observed as in the systems containing only TNS and PDADMAC. PSS adsorption was clearly indicated by the decrease of the mobilities by increasing the PSS concentration. Such an adsorption process led to charge neutralization at the IEP and charge reversal at higher doses. The adsorption continued until the mobilities reached a plateau at 300 mg/g.

Stability ratio measurements revealed that the particles were stable at low and high polyelectrolyte doses. In the intermediate regime, the stability ratios formed a V-shape curve with a minimum near the IEP. This behavior is again in line with the DLVO theory, i.e., the acting interparticle forces are of electrostatic origin [55]. A major difference from the above system is that, the fast aggregation regime is extremely narrow. These results ensure that at 300 mg/g dose the TNS-PDADMAC-PSS particles are negatively charged and form highly stable colloids.

Note that the minimum of the stability ratio values was around 3 instead of 1 (the prediction of the DLVO theory), which indicates the presence of additional stabilizing forces. Since the fast aggregation rate of the TNS was used to calculate the stability ratios by equation (2), such a stabilizing effect must originate from the adsorbed polyelectrolyte layers. It was assumed that repulsive steric interactions are responsible for this phenomenon, however, this assumption deserves further discussion.

Accordingly, around the IEP, the overall charge of the particles is close to zero, which leads to a limited stability of the particles due to the absence of the electrostatic double layers and the sole presence of attractive van der Waals forces. Under these conditions, DLVO theory states that each particle collision must result in the formation of a dimer and the stability ratio values must be around unity in case of diffusion-controlled aggregation. However, when PSS is adsorbed on the PDADMAC layer of the particles, intrinsic

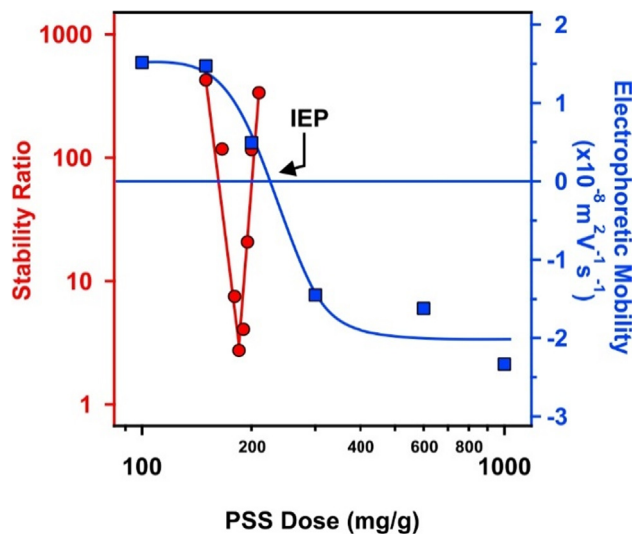


**Fig. 2.** Stability ratio (red circle) and electrophoretic mobility (blue square) of the TNS-PDADMAC as a function of the PSS dose at 1 mg/L TNS concentration and 1 mM ionic strength. The average error of the stability ratio and the mobility values are 10 and 5% respectively. (For interpretation of the references to colour in this figure legend, the reader is referred to the web version of this article.)

polymer-polymer and extrinsic polymer-ion charge compensations occur [60]. The ion compensated PSS charges on the polymer backbone form tails and loops dangling in the solution [61], which leads to the generation of a steric repulsion between the particles due to the raising osmotic pressure upon approach of the polyelectrolyte coated surfaces [62]. This effect, together with the electrostatic stabilization by the double layers leads to electrosteric stabilization [54], which was reported in various particle-polyelectrolyte systems [38,52,59]. Nevertheless, such an electrosteric repulsion is not sufficient to completely prevent particle aggregation here, as the stability ratio value is around 3 at the minimum.

### 3.2. Co-immobilization of the enzymes

The SOD and the HRP enzymes are negatively and positively charged at pH 7, since their pI values are 4.95 [63] and 8.80 [64], respectively. Therefore these enzymes are expected to adsorb on oppositely charged particles mainly by electrostatic attraction [18,20]. However, hydrophobic interactions and hydrogen bonding may play a role in the adsorption mechanism too. It was unambiguously confirmed before that positively charged TNS-PDADMAC forms highly stable colloids and hence, it is a suitable support for SOD. Moreover, extensive SOD adsorption may affect the charging and aggregation properties of TNS-PDADMAC. In other words, it is important to avoid a significant decrease in the magnitude of the surface charge upon enzyme adsorption because it may lead to a weakening of the double layer repulsion and subsequently, to unwanted particle aggregation. Therefore, the influence of SOD adsorption on the electrophoretic mobilities was first probed by recording the mobilities at different SOD concentrations (Fig. 3).

The results revealed that for an enzyme dose lower than 100 mg/g the mobility values of TNS-PDADMAC were not affected by the added amount of SOD. Above this loading, the magnitude of the mobilities slightly decreased. Note that no stability ratio values

could be determined in the SOD concentration range investigated due to the high stability, i.e., the lack of aggregation processes, of the colloidal dispersion. Therefore, a SOD dose of 10 mg/g was selected for the further steps. Earlier studies on a slightly different system [18] revealed that at this concentration the enzyme was quantitatively adsorbed and does not desorb from the particle surface. The obtained TNS-PDADMAC-SOD material (150 mg/g PDADMAC and 10 mg/g SOD) was then used to build up the PSS layer applying a 300 mg/g PSS loading (denoted as TNS-PDADMAC-SOD-PSS later), as discussed in the previous section.

The same requirements apply for the HRP adsorption on TNS-PDADMAC-SOD-PSS, therefore, the electrophoretic mobilities were measured at different enzyme loadings (Fig. 3). As a matter of fact, it is primordial to determine an HRP dose, which does not affect the colloidal behavior of the TNS. The mobility values were not changed significantly and no stability ratios could be determined in the enzyme dose regime studied. Based on the results of an earlier study [20], 10 mg/g concentration was selected for the HRP. At this dose, HRP adsorption does not significantly alter the charging and aggregation behavior of TNS-PDADMAC-SOD-PSS, and on the other hand, quantitative enzyme adsorption is expected. Accordingly, 10 mg/g dose was applied for both SOD and HRP embedded in the TNS-PDADMAC-SOD-PSS-HRP composite.

An overview of the electrophoretic mobilities and the hydrodynamic size of the sub-systems during the sequential adsorption process is shown in Fig. 4. The electrophoretic mobility of the bare particles is around  $-1.5 \times 10^{-8} \text{ m}^2/\text{Vs}$ . This slight negative charge led to a moderate stability and to higher hydrodynamic radius value due to the presence of particle aggregates. Nevertheless, the formation of the saturated PDADMAC layer provided an improved stability and thus, the radius of the positively charged TNS-PDADMAC decreased from 145 nm (bare TNS) to about 100 nm. The immobilization of SOD at 10 mg/g did not change the mobility significantly and slightly decreased the size. After the functionalization with the saturated PSS layer, the TNS-PDADMAC-SOD-PSS system possesses a negative charge with a mobility about  $-1.9 \times 10^{-8} \text{ m}^2/\text{Vs}$ . Note that very similar value for the TNS led to limited stability and formation of particle aggregates. However, the radius of TNS-PDADMAC-SOD-PSS was much lower compared to bare TNS. This result again sheds light on the

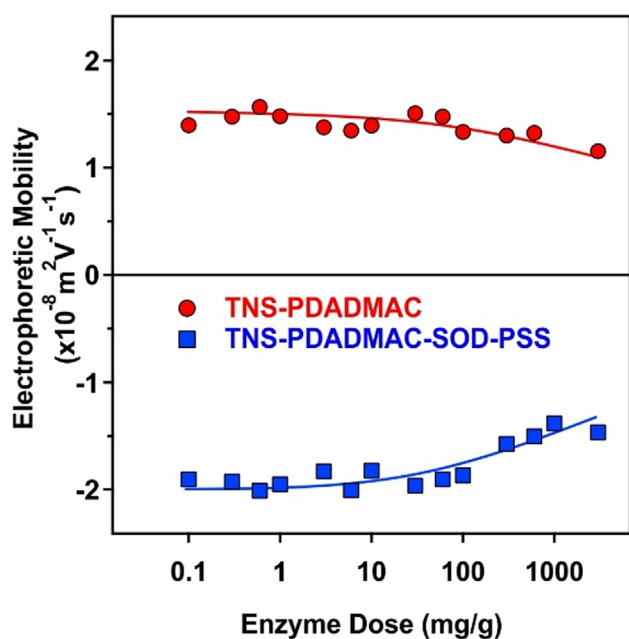


**Fig. 3.** Electrophoretic mobility of the TNS-PDADMAC (red circles) and the TNS-PDADMAC-SOD-PSS (blue squares) hybrid materials as a function of the enzyme (SOD and HRP, respectively) dose at pH 7, 1 mM ionic strength and 1 mg/L TNS concentration. The average error of the mobility values is 5%. (For interpretation of the references to colour in this figure legend, the reader is referred to the web version of this article.)

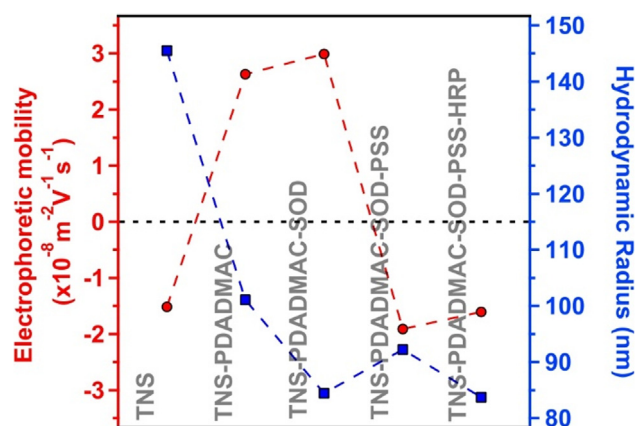


**Fig. 4.** Electrophoretic mobility (red circle) and hydrodynamic radius (blue square) at different steps during the sequential adsorption process. The ionic strength and the TNS concentration were set to 1 mM and 1 mg/L, respectively. The used PDADMAC and PSS doses were 150 and 300 mg/g, respectively, while 10 mg/g loadings were applied for both SOD and HRP enzymes. The connective dashed lines are to guide the eyes and the horizontal one indicates the zero electrophoretic mobility. The measurement error for both size and mobility is 5%. (For interpretation of the references to colour in this figure legend, the reader is referred to the web version of this article.)

importance of steric forces (see in the previous chapter) in the stabilization mechanism, since sole electrostatic repulsion fails to stabilize the colloids at this low mobility. The surface charge and hydrodynamic size did not change upon HRP immobilization in the last step of the sequential adsorption procedure.

TEM images recorded with the TNS-PDADMAC-SOD-PSS-HRP (Fig. 5) show the rectangular shape of the TNS. The morphology of the particles remained unaffected during the layer formations indicated by very similar images compared to the ones of the bare TNS without surface functionalization [38]. However, some low order aggregates of the particles can be observed. This is due to the drying of the samples, which could not be avoided during the TEM measurements.

### 3.3. Salt-induced aggregation

Given the fact that immobilized enzymes are often used in liquid environments containing electrolytes [16], the resistance of the fabricated hybrid material against salt-induced aggregation was tested. Accordingly, the ionic strength was systematically changed in the dispersions of the bare TNS and the TNS-PDADMAC-SOD-PSS-HRP material. Electrophoretic mobilities and stability ratios are presented in Fig. 6.

At low ionic strength, the mobility values of the bare TNS and the TNS-PDADMAC-SOD-PSS-HRP were about  $-1.5 \times 10^{-8}$  m<sup>2</sup>/Vs and  $-2.4 \times 10^{-8}$  m<sup>2</sup>/Vs, respectively (Fig. 6a). This difference indicates the development of higher surface charge upon multilayer formation. By increasing the ionic strength, the mobilities increased in both systems owing to the screening effect of the dissolved salt constituents on the surface charges.

The aggregation behavior at different ionic strengths were investigated by time-resolved DLS technique and the obtained stability ratios are shown in Fig. 6b. The slow and fast aggregation regimes, separated by the critical coagulation concentration (CCC) values, were observed in each case. The stability of the TNS was very limited even at low ionic strengths due to the low charge of the particles. The difference in the CCC values is striking, 10 and 300 mM were determined for TNS and TNS-PDADMAC-SOD-PSS-HRP, respectively. The stabilizing effect is twofold. On the one hand, higher surface charge indicated by higher magnitude of the mobilities led to stronger repulsion by the overlapping electrical double layers, in line with the DLVO theory. However, DLVO usually predicts CCC values around 100 mM and thus, additional repulsive forces are most likely present in the composite system. Similar to the TNS-polyelectrolyte sub-systems, this repulsion originates from steric interactions [52,54,59,62] between the loosely adsorbed polyelectrolyte chains extending towards the solution phase from the multilayered structure. The overlap of

polyelectrolyte tails and loops lead to the raise of an osmotic pressure upon the approach of two particles and subsequently, to the development of repulsive interparticle forces.

### 3.4. Enzymatic activity

The O<sub>2</sub><sup>-</sup> scavenging activities of the native and immobilized SOD enzyme were tested in the Fridovich assay [42], as detailed in the experimental part. The inhibition versus enzyme concentration graph (Fig. 7a) indicates a maximum inhibition of about 65% for TNS-PDADMAC-SOD-PSS-HRP material indicating a limited accessibility towards O<sub>2</sub><sup>-</sup> for the immobilized SOD.

An IC<sub>50</sub> value of 1.3 mg/L was obtained, which is significantly higher than the one determined for the TNS-PDADMAC-SOD sub-system (Table 1). Note that the higher IC<sub>50</sub> value means lower SOD activity and that the TNS-PDADMAC-PSS-HRP did not show any SOD-like activity in this concentration range. These data indicate that the building of the PSS-HRP layers on the TNS-PDADMAC-SOD led to a significant loss in the SOD-like activity. This may be due to some conformational changes of the enzyme upon immobilization and/or to some blocking effects of the outer polyelectrolyte layer, i.e., the hindered diffusion of the O<sub>2</sub><sup>-</sup> to the active site of the SOD.

The HRP-like activities were determined by the guaiacol assay [45]. Briefly, the HRP-active compound catalyzes the oxidation of the guaiacol substrate in the presence of H<sub>2</sub>O<sub>2</sub> and the formation of the brownish guaiacol degradation products can be monitored with a spectrophotometer. No enzymatic activity was observed for materials without the HRP component (Table 1), so the enzyme-like function originated solely from this enzyme embedded in the composites.

The Lineweaver–Burk plot (see equation (4)) was used to analyze the results of the HRP assay and the Michaelis constant (K<sub>m</sub>) together with the maximum reaction rate (v<sub>max</sub>) were calculated from the double reciprocal reaction rate versus the substrate concentration plot as shown in (Fig. 7b). The K<sub>m</sub> value corresponds to the affinity of the enzyme towards the substrate. For example, a decrease in the K<sub>m</sub> value refers to a higher affinity of the enzyme to guaiacol. The v<sub>max</sub> is the maximum reaction rate that can be achieved by the system once the active site of the enzymes is completely saturated by the substrate.

The determined K<sub>m</sub> and v<sub>max</sub> values for the TNS-PDADMAC-SOD-PSS-HRP were 23.50 mM and 0.10 mM/s, respectively. These data indicate a lower activity compared to the native enzyme, however, it can still be considered as a highly active material. A possible explanation may lie in the fact that HRP is located on the outer surface of the TNS-PDADMAC-SOD-PSS-HRP particles and thus, interacting strongly with PSS upon immobilization,

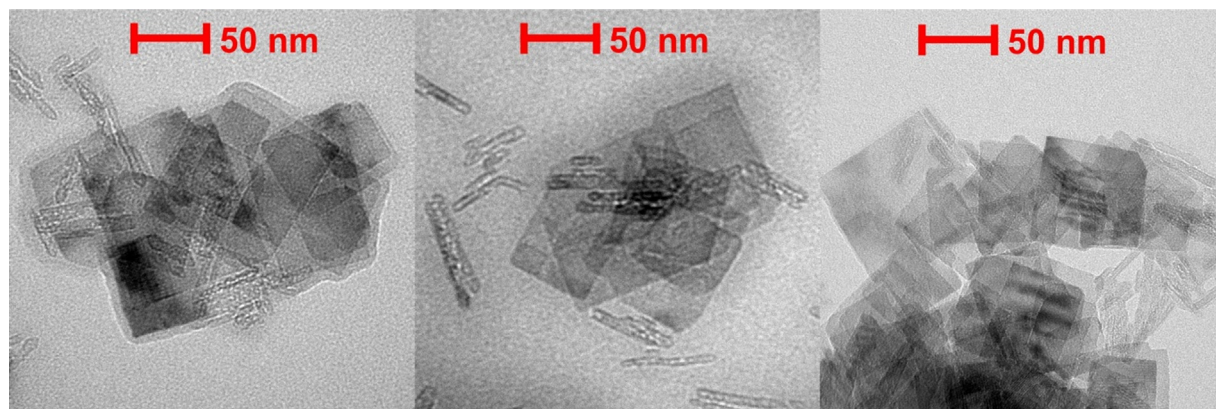
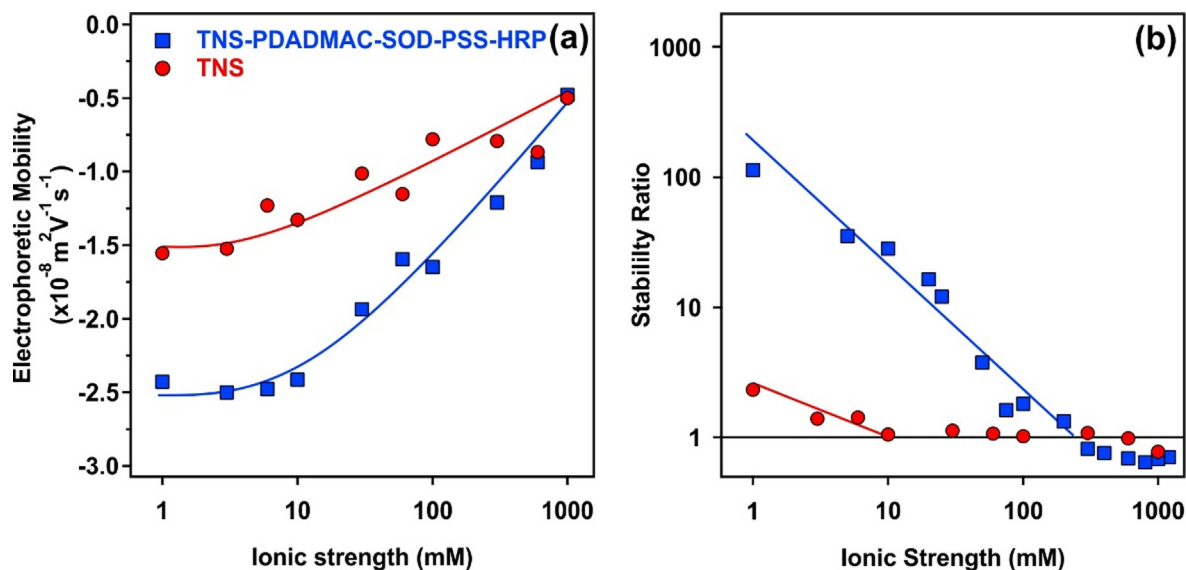
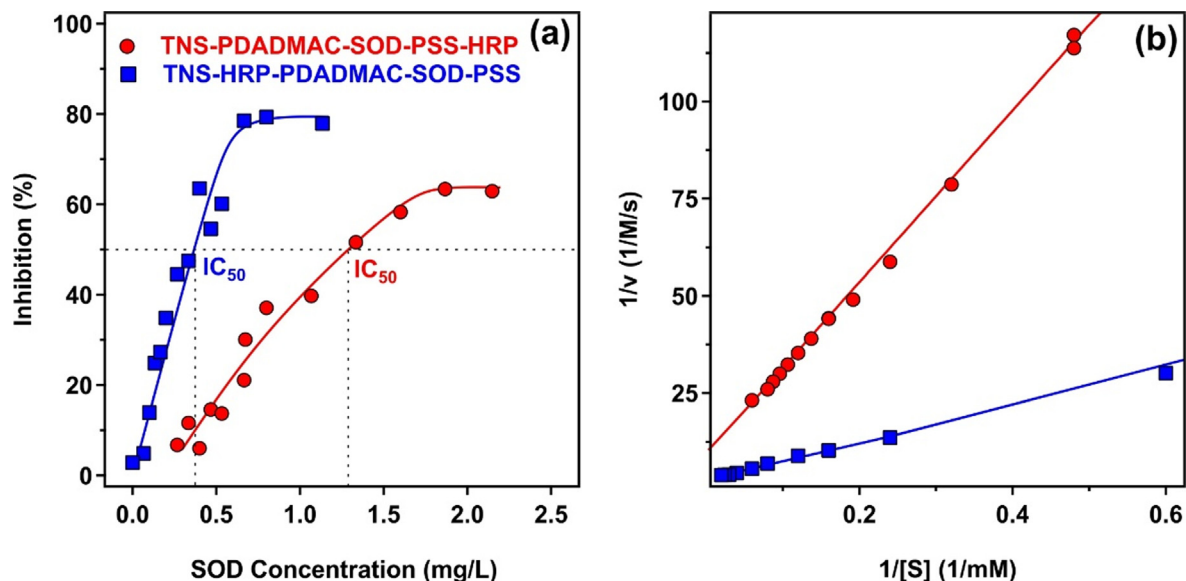


Fig. 5. Dried-stage TEM images of the TNS-PDADMAC-SOD-PSS-HRP cascade material.





**Fig. 6.** Electrophoretic mobility (a) and stability ratio (b) of the bare TNS (red circles) and the TNS-PDADMAC-SOD-PSS-HRP (blue squares) hybrid material as a function of the ionic strength adjusted with NaCl. The TNS concentration was set to 1 mg/L. The lines serve to guide the eyes. The mean error of the stability ratio and the mobility values are 10 and 5% respectively. (For interpretation of the references to colour in this figure legend, the reader is referred to the web version of this article.)



**Fig. 7.** (a) Inhibition of the NBT-O<sub>2</sub> reaction by the TNS-PDADMAC-SOD-PSS-HRP (red circles) and the TNS-HRP-PDADMAC-SOD-PSS (blue squares) hybrid particles. The inhibition values were obtained using equation (3). The solid line is a mathematical function used for the interpolation of the IC<sub>50</sub> value. (b) Lineweaver-Burk plot for the peroxidase activity of the TNS-PDADMAC-SOD-PSS-HRP and the TNS-HRP-PDADMAC-SOD-PSS hybrid particles. The solid line was obtained using equation (4). The average error of the measurements is within 5%. (For interpretation of the references to colour in this figure legend, the reader is referred to the web version of this article.)

**Table 1**

Parameters determined in the SOD and HRP assays.

Material	IC <sub>50</sub> (mg/L)	Maximum inhibition (%)	K <sub>m</sub> (mM)	v <sub>max</sub> (mM/s)
SOD	0.10 ± 0.01	90 ± 5	N/A <sup>a</sup>	N/A <sup>a</sup>
HRP	N/A <sup>a</sup>	N/A <sup>a</sup>	3.41 ± 0.15	0.59 ± 0.02
TNS-PDADMAC-SOD	0.22 ± 0.01	70 ± 4	N/A <sup>a</sup>	N/A <sup>a</sup>
TNS-PDADMAC-SOD-PSS-HRP	1.30 ± 0.04	65 ± 4	23.50 ± 2.27	0.10 ± 0.01
TNS-HRP	N/A <sup>a</sup>	N/A <sup>a</sup>	13.13 ± 1.17	0.41 ± 0.02
TNS-HRP-PDADMAC-SOD	0.15 ± 0.01	90 ± 5	3.91 ± 0.64	0.31 ± 0.04
TNS-HRP-PDADMAC-SOD-PSS	0.38 ± 0.03	80 ± 4	15.50 ± 1.19	0.34 ± 0.01

<sup>a</sup> N/A means that no measurable activity was detected.



which may have led to a distortion of the structure of its active center giving rise to a lower activity of the developed system compared to the native enzyme dissolved in solution.

### 3.5. Variation of the TNS coating architecture in the sequential adsorption method

To probe the influence of the location of the enzymes on their activities, the order of the building blocks was changed during the preparation of the enzyme cascade. In an earlier study, HRP was immobilized directly on the TNS particles without the use of any intermediate polyelectrolyte layer [20]. Therefore the multilayered architecture was built on the TNS-HRP hybrid following the TNS-HRP-PDADMAC-SOD-PSS order. The same polyelectrolyte and enzyme doses were used as in the TNS-PDADMAC-SOD-PSS-HRP system and the obtained mobility and size data measured for the system at each building steps are displayed in Fig. 8. The changes in the electrophoretic mobilities and the particle sizes during the sequential adsorption steps clearly indicated that the immobilization of HRP did not significantly influence the charging behavior of the bare TNS particles (Fig. 8). However, addition of HRP somehow increased the size, i.e., about 400 nm hydrodynamic radius was determined for TNS-HRP. Like for the previous systems, adsorption of a saturated PDADMAC layer gave rise to charge reversal and to a significant decrease in the particle size due to electrosteric stabilization. The immobilized SOD had basically no effect on the colloidal stability of the dispersions, while the adsorption of the PSS layer resulted in charge reversal of the particles. It should be noted that the mobility values of TNS-HRP-PDADMAC-SOD-PSS was very similar to the bare TNS or TNS-HRP and the hydrodynamic radius remained small, around 100 nm. This result again underpins the presence of electrosteric repulsive forces, which predominate over the van der Waals attractions.

The enzymatic assays were performed with TNS-HRP-PDADMAC-SOD-PSS, TNS-HRP and TNS-HRP-PDADMAC-SOD subsystems. The inhibition curve in the SOD assay recorded for the TNS-HRP-PDADMAC-SOD-PSS (Fig. 7a) indicates an improved activity in  $O_2^-$  dismutation compared to TNS-PDADMAC-SOD-PSS-HRP. The  $IC_{50}$  and the maximum inhibition values measured with the second studied system were 0.38 mg/L and 80%, respectively (Table 1). These values are much closer to the one of the native SOD, therefore highlighting the importance of the localization of SOD in the cascade system. As a result, the activity of SOD has been

remarkably improved by locating it in the outer layer of the composite material.

The HRP activity of the TNS-HRP-PDADMAC-SOD-PSS material was also determined (Fig. 7b). The  $K_m$  value was found to be 15.50 mM, while the maximum reaction rate was 0.34 mM/s. These values are comparable to the sub-systems (Table 1). More importantly, they indicate lower HRP-like activity than for the native enzyme, but higher than the one measured for TNS-PDADMAC-SOD-PSS-HRP. These findings clearly emphasize the importance of both enzymes (SOD and HRP) location in the multilayered system.

Accordingly, antioxidant dual enzyme systems of remarkable activities were obtained by applying either orders in the sequential adsorption procedure. The functions of both SOD and HRP were maintained during immobilization, however, no evidence was shown for their combined action. This can be further investigated for instance in cellular studies, while reducing ROS-induced oxidative stress.

The above results provide a research direction towards the development of dual enzyme-based antioxidant systems to be applied in industry or biomedical treatments. For instance, titania materials are used to protect skin against sunburn in cosmetics [65], while recovery treatment of UV radiation affected skin is possible with antioxidant enzymes [66] and also with their immobilized forms [67]. Therefore, the present composites containing the dual enzyme system are very promising candidates as additives in skin protecting products. Besides, the future application of the developed hybrid material in treatment of inflammatory bowel diseases is also possible [68]. In these treatments, rectal injection is applied as administering method. However, native antioxidant enzymes lose their activity during the process and thus, their functional stabilization by immobilization offers a solution for this problem.

## 4. Conclusions

In conclusion, SOD and HRP enzymes were successfully co-immobilized on TNS particles using PDADMAC and PSS polyelectrolytes in the sequential adsorption method, in which the order of the components was optimized to achieve the best enzyme activities. The obtained composite possessed high colloidal stability, i.e., excellent resistance against salt-induced aggregation was achieved, and showed remarkable ROS scavenging ability confirmed in dismutation of superoxide radicals and in consumption of hydrogen peroxide. These results shed light on the fact that co-immobilization of antioxidant enzymes is possible on nanoparticulate support without significant loss of the enzymatic activities. Although single SOD and HRP enzymes have already been embedded in composite materials [13,18,20,22], their joint confinement in the present nanostructure gives rise to a wider spectrum for scavenging of ROS including simultaneous decomposition of  $O_2^-$  and  $H_2O_2$ . Based on these results, the developed cascade systems are potential candidates to reduce the ROS level, i.e., to combat oxidative stress, in liquid medium, where colloidal stability is an important parameter. Potential applications involve cosmetic products for skin protection against sunburn and related treatment of UV radiation damage for skin cells as well as therapy for inflammatory bowel diseases applying rectal injection as administration method.

## CRedit authorship contribution statement

**Szilárd Sáringer:** Investigation, Formal analysis, Visualization, Writing - original draft. **Paul Rouster:** Investigation, Conceptualization. **Istvan Szilagy:** Conceptualization, Funding acquisition, Writing - review & editing.

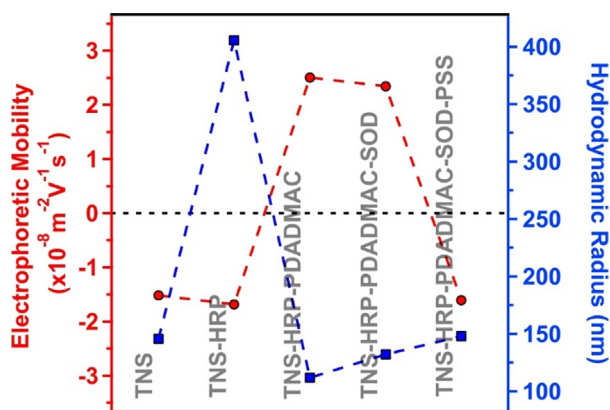


**Fig. 8.** Electrophoretic mobility (red circle) and hydrodynamic radius (blue square) data during the different steps of the sequential adsorption method. The ionic strength and the TNS concentration were set to 1 mM and 1 mg/L, respectively. The measurement error for both size and mobility is 5%. (For interpretation of the references to colour in this figure legend, the reader is referred to the web version of this article.)

## Declaration of Competing Interest

The authors declare that they have no known competing financial interests or personal relationships that could have appeared to influence the work reported in this paper.

## Acknowledgements

This research was supported by the Lendület program of the Hungarian Academy of Sciences (96130) and by the Ministry of Human Capacities, Hungary through the project 20391-3/2018/FEKUSTRAT. The support from the University of Szeged Open Access Fund (5139) is gratefully acknowledged.

## Appendix A. Supplementary material

Supplementary data to this article can be found online at <https://doi.org/10.1016/j.jcis.2021.01.012>.

## References

- [1] C.C. Winterbourn, Reconciling the chemistry and biology of reactive oxygen species, *Nat. Chem. Biol.* 4 (2008) 278–286.
- [2] C. Nirmala, M.S. Bisht, H.K. Bajwa, O. Santosh, Bamboo: A rich source of natural antioxidants and its applications in the food and pharmaceutical industry, *Trends Food Sci. Technol.* 77 (2018) 91–99.
- [3] J.W. Finley, A.N. Kong, K.J. Hintze, E.H. Jeffery, L.L. Ji, X.G. Lei, Antioxidants in foods: State of the science important to the food industry, *J. Agric. Food Chem.* 59 (2011) 6837–6846.
- [4] A. Bafana, S. Dutt, S. Kumar, P.S. Ahuja, Superoxide dismutase: an industrial perspective, *Crit. Rev. Biotechnol.* 31 (2011) 65–76.
- [5] L. Wang, Y. Li, L. Zhao, Z. Qi, J. Gou, S. Zhang, J.Z. Zhang, Recent advances in ultrathin two-dimensional materials and biomedical applications for reactive oxygen species generation and scavenging, *Nanoscale* 12 (2020) 19516–19535.
- [6] B.N. Ames, M.K. Shigenaga, T.M. Hagen, Oxidants, antioxidants, and the degenerative diseases of aging, *Proc. Natl. Acad. Sci. U. S. A.* 90 (1993) 7915–7922.
- [7] J. Richardson, K.A. Thomas, B.H. Rubin, D.C. Richardson, Crystal structure of bovine Cu, Zn superoxide dismutase at 3Å resolution – Chain tracing and metal ligands, *Proc. Natl. Acad. Sci. U. S. A.* 72 (1975) 1349–1353.
- [8] M. Gajhede, D.J. Schuller, A. Henriksen, A.T. Smith, T.L. Poulos, Crystal structure of horseradish peroxidase C at 2.15 angstrom resolution, *Nat. Struct. Biol.* 4 (1997) 1032–1038.
- [9] H. Sies, Oxidative stress: Oxidants and antioxidants, *Exp. Physiol.* 82 (1997) 291–295.
- [10] R.M. Daniel, M. Dines, H.H. Petach, The denaturation and degradation of stable enzymes at high temperatures, *Biochem. J.* 317 (1996) 1–11.
- [11] D. Constantinescu, H. Weingartner, C. Herrmann, Protein denaturation by ionic liquids and the Hofmeister series: A case study of aqueous solutions of ribonuclease A, *Angew. Chem.-Int. Edit.* 46 (2007) 8887–8889.
- [12] R.A. Sheldon, S. van Pelt, Enzyme immobilisation in biocatalysis: why, what and how, *Chem. Soc. Rev.* 42 (2013) 6223–6235.
- [13] M. Pavlovic, P. Rouster, I. Szilágyi, Synthesis and formulation of functional bionanomaterials with superoxide dismutase activity, *Nanoscale* 9 (2017) 369–379.
- [14] A. Popat, S.B. Hartono, F. Stahr, J. Liu, S.Z. Qiao, G. Qing (Max) Lu, Mesoporous silica nanoparticles for bioadsorption, enzyme immobilisation, and delivery carriers, *Nanoscale* 3 (2011) 2801, <https://doi.org/10.1039/c1nr10224a>.
- [15] R.C. Rodrigues, C. Ortiz, Á. Berenguer-Murcia, R. Torres, R. Fernández-Lafuente, Modifying enzyme activity and selectivity by immobilization, *Chem. Soc. Rev.* 42 (2013) 6290–6307.
- [16] U. Hanefeld, L.Q. Cao, E. Magner, Enzyme immobilisation: fundamentals and application, *Chem. Soc. Rev.* 42 (2013) 6211–6212.
- [17] B. Katana, P. Rouster, G. Varga, S. Muráth, K. Glinel, A.M. Jonas, I. Szilágyi, Self-assembly of protamine biomacromolecule on halloysite nanotubes for immobilization of superoxide dismutase enzyme, *ACS Appl. Bio Mater.* 3 (2020) 522–530.
- [18] P. Rouster, M. Pavlovic, I. Szilágyi, Immobilization of Superoxide Dismutase on polyelectrolyte functionalized titania nanosheets, *ChemBioChem* 19 (2018) 404–410.
- [19] K. Kamada, A. Yamada, N. Soh, Enhanced catalytic activity of enzymes interacting with nanometric titanate nanosheets, *RSC Adv.* 5 (2015) 85511–85516.
- [20] P. Rouster, M. Pavlovic, S. Sáringér, I. Szilágyi, Functionalized titania nanosheet dispersions of peroxidase activity, *J. Phys. Chem. C* 122 (2018) 11455–11463.
- [21] X. Lang, L. Zhu, Y. Gao, I. Wheelton, Enhancing enzyme activity and immobilization in nanostructured inorganic-enzyme complexes, *Langmuir* 33 (2017) 9073–9080.
- [22] M. Pavlovic, P. Rouster, Z. Somosi, I. Szilágyi, Horseradish peroxidase-nanoclay hybrid particles of high functional and colloidal stability, *J. Colloid Interface Sci.* 524 (2018) 114–121.
- [23] A. Grotzky, E. Altamura, J. Adamcik, P. Carrara, P. Stano, F. Mavelli, T. Nauser, R. Mezzenga, A.D. Schlüter, P. Walde, Structure and enzymatic properties of molecular dendronized polymer-enzyme conjugates and their entrapment inside giant vesicles, *Langmuir* 29 (2013) 10831–10840.
- [24] A. Grotzky, T. Nauser, H. Erdogan, A.D. Schlüter, P. Walde, A fluorescently labeled dendronized polymer-enzyme conjugate carrying multiple copies of two different types of active enzymes, *J. Am. Chem. Soc.* 134 (2012) 11392–11395.
- [25] A. Niecikowska, M. Krasowska, J. Ralston, K. Malysa, Role of surface charge and hydrophobicity in the three-phase contact formation and wetting film stability under dynamic conditions, *J. Phys. Chem. C* 116 (2012) 3071–3078.
- [26] S. Kment, F. Riboni, S. Pausova, L. Wang, L.Y. Wang, H. Han, Z. Hubicka, J. Krysa, P. Schmuki, R. Zboril, Photoanodes based on TiO<sub>2</sub> and alpha-Fe<sub>2</sub>O<sub>3</sub> for solar water splitting - superior role of 1D nanoarchitectures and of combined heterostructures, *Chem. Soc. Rev.* 46 (2017) 3716–3769.
- [27] Á. Veres, J. Ménesi, C. Janáky, G.F. Samu, M.K. Scheyer, Q. Xu, F. Salahioglu, M.V. Garland, I. Dékány, Z. Zhong, New insights into the relationship between structure and photocatalytic properties of TiO<sub>2</sub> catalysts, *RSC Adv.* 5 (2015) 2421–2428.
- [28] R. Kun, M. Balázs, I. Dékány, Photooxidation of organic dye molecules on TiO<sub>2</sub> and zinc-aluminum layered double hydroxide ultrathin multilayers, *Colloid Surf. A* 265 (2005) 155–162.
- [29] L.Z. Wang, T. Sasaki, Titanium oxide nanosheets: Graphene analogues with versatile functionalities, *Chem. Rev.* 114 (2014) 9455–9486.
- [30] D.V. Bavykin, F.C. Walsh, Elongated titanate nanostructures and their applications, *Eur. J. Inorg. Chem.* 2009 (2009) 977–997.
- [31] F.U. Rehman, C. Zhao, H. Jiang, X. Wang, Biomedical applications of nano-titania in theranostics and photodynamic therapy, *Biomater. Sci.* 4 (2016) 40–54.
- [32] K. Kamada, Intense emissions from photoproteins interacting with titanate nanosheets, *RSC Adv.* 4 (2014) 43052–43056.
- [33] L. Zhang, Q. Zhang, J. Li, Layered titanate nanosheets intercalated with myoglobin for direct electrochemistry, *Adv. Funct. Mater.* 17 (2007) 1958–1965.
- [34] G. Decher, J.B. Schlenoff, *Multilayer Thin Films*, Wiley-VCH, Weinheim, 2002.
- [35] P. Rouster, M. Dondelinger, M. Galleni, B. Nysten, A.M. Jonas, K. Glinel, Layer-by-layer assembly of enzyme-loaded halloysite nanotubes for the fabrication of highly active coatings, *Colloid Surf. B* 178 (2019) 508–514.
- [36] R.F. de Oliveira, M.L. de Moraes, O.N. Oliveira, M. Ferreira, Exploiting cascade reactions in bienzyme layer-by-layer films, *J. Phys. Chem. C* 115 (39) (2011) 19136–19140.
- [37] D.G. Ramírez-Wong, C. Bonhomme, S. Demoustier-Champagne, A.M. Jonas, Layer-by-layer assembly of brushes of vertically-standing enzymatic nanotubes, *J. Colloid Interface Sci.* 514 (2018) 592–598.
- [38] P. Rouster, M. Pavlovic, I. Szilágyi, Improving the stability of titania nanosheets by functionalization with polyelectrolytes, *RSC Adv.* 6 (2016) 97322–97330.
- [39] P.N. Pusey, Dynamic light scattering, in: P. Lindner, T. Zemb (Eds.), *Neutrons, X-Rays and Light*, Elsevier Science B.V., Amsterdam, 2002, pp. 203–220.
- [40] G. Trefalt, I. Szilágyi, T. Oncsik, A. Sadeghpour, M. Borkovec, Probing colloidal particle aggregation by light scattering, *Chimia* 67 (2013) 772–776.
- [41] A. Zaccone, H. Wu, M. Lattuada, M. Morbidelli, Correlation between colloidal stability and surfactant adsorption/association phenomena studied by light scattering, *J. Phys. Chem. B* 112 (2008) 1976–1986.
- [42] C. Beauchamp, I. Fridovich, Superoxide dismutase – improved assays and an assay applicable to acrylamide gels, *Anal. Biochem.* 44 (1971) 276–287.
- [43] K. Kamada, T. Nakamura, S. Tsukahara, Photoswitching of enzyme activity of horseradish peroxidase intercalated into semiconducting layers, *Chem. Mat.* 23 (2011) 2968–2972.
- [44] LiHui Zhang, C. Gu, J. Xiong, M. Yang, Y. Guo, Hemin-histamine-montmorillonite clay conjugate as a model biocatalyst to mimic natural peroxidase, *Sci. China-Chem.* 58 (2015) 731–737.
- [45] D.R. Doerge, R.L. Divi, M.I. Churchwell, Identification of the colored guaiacol oxidation product produced by peroxidases, *Anal. Biochem.* 250 (1997) 10–17.
- [46] K.A. Johnson, R.S. Goody, The original Michaelis constant: translation of the 1913 Michaelis-Menten paper, *Biochemistry* 50 (2011) 8264–8269.
- [47] I. Popa, G. Gillies, G. Papastavrou, M. Borkovec, Attractive and repulsive electrostatic forces between positively charged latex particles in the presence of anionic linear polyelectrolytes, *J. Phys. Chem. B* 114 (2010) 3170–3177.
- [48] T.T.M. Ho, K.E. Bremell, M. Krasowska, S.V. MacWilliams, C.J.E. Richard, D.N. Stringer, D.A. Beattie, In situ ATR FTIR spectroscopic study of the formation and hydration of a fucoidan/chitosan polyelectrolyte multilayer, *Langmuir* 31 (2015) 11249–11259.
- [49] S. Sáringér, P. Rouster, I. Szilágyi, Regulation of the stability of titania nanosheet dispersions with oppositely and like-charged polyelectrolytes, *Langmuir* 35 (2019) 4986–4994.
- [50] Y.K. Leong, Interparticle forces arising from an adsorbed strong polyelectrolyte in colloidal dispersions: charged patch attraction, *Colloid Polym. Sci.* 277 (1999) 299–305.
- [51] S. Muráth, S. Sáringér, Z. Somosi, I. Szilágyi, Effect of ionic compounds of different valences on the stability of titanium oxide colloids, *Colloids Interfaces* 2 (2018) 32.
- [52] F. Iselau, T. Phan Xuan, G. Trefalt, A. Matic, K. Holmberg, R. Bordes, Formation and relaxation kinetics of starch-particle complexes, *Soft Matter* 12 (2016) 9509–9519.

- [53] T. Klačič, A. Sadžak, J. Jukić, T. Preočanin, D. Kovačević, Surface potential study of ceria/poly(sodium 4-styrenesulfonate) aqueous solution interface, *Colloid Surf. A-Physicochem. Eng. Asp.* 570 (2019) 32–38.
- [54] G. Fritz, V. Schädler, N. Willenbacher, N.J. Wagner, Electrosteric stabilization of colloidal dispersions, *Langmuir* 18 (2002) 6381–6390.
- [55] D.F. Evans, H. Wennerstrom, *The Colloidal Domain*, John Wiley, New York, 1999.
- [56] E. Piccinini, S. Alberti, G.S. Longo, T. Berninger, J. Breu, J. Dostalek, O. Azzaroni, W. Knoll, Pushing the boundaries of interfacial sensitivity in graphene FET sensors: Polyelectrolyte multilayers strongly increase the debye screening length, *J. Phys. Chem. C* 122 (2018) 10181–10188.
- [57] O. Löhmann, M. Zerball, R. von Klitzing, Water uptake of polyelectrolyte multilayers including water condensation in voids, *Langmuir* 34 (2018) 11518–11525.
- [58] W. Cheng, C.H. Liu, T.Z. Tong, R. Epsztein, M. Sun, R. Verduzco, J. Ma, M. Elimelech, Selective removal of divalent cations by polyelectrolyte multilayer nanofiltration membrane: Role of polyelectrolyte charge, ion size, and ionic strength, *J. Membr. Sci.* 559 (2018) 98–106.
- [59] Z. Somosi, M. Pavlovic, I. Palinko, I. Szilágyi, Effect of polyelectrolyte mono- and bilayer formation on the colloidal stability of layered double hydroxide nanoparticles, *Nanomaterials* 8 (2018) 986.
- [60] R.A. Ghostine, M.Z. Markarian, J.B. Schlenoff, Asymmetric growth in polyelectrolyte multilayers, *J. Am. Chem. Soc.* 135 (2013) 7636–7646.
- [61] E. Seyrek, J. Hierrezuelo, A. Sadeghpour, I. Szilágyi, M. Borkovec, Molecular mass dependence of adsorbed amount and hydrodynamic thickness of polyelectrolyte layers, *Phys. Chem. Chem. Phys.* 13 (2011) 12716, <https://doi.org/10.1039/c1cp20654k>.
- [62] A. Fuchs, E. Killmann, Adsorption of polyelectrolytes on colloidal latex particles, electrostatic interactions and stability behaviour, *Colloid Polym. Sci.* 279 (2001) 53–60.
- [63] J. Bannister, W. Bannister, E. WOOD, Bovine erythrocyte cupro-zinc protein 1. Isolation and general characterization, *Eur. J. Biochem.* 18 (1971) 178–186.
- [64] C.B. Lavery, M.C. MacInnis, M.J. MacDonald, J.B. Williams, C.A. Spencer, A.A. Burke, D.J.G. Irwin, G.B. D' Cunha, Purification of peroxidase from horseradish (*Armoracia rusticana*) roots, *J. Agric. Food Chem.* 58 (2010) 8471–8476.
- [65] M. Morsella, N. d'Alessandro, A.E. Lanterna, J.C. Scaiano, Improving the sunscreen properties of TiO<sub>2</sub> through an understanding of its catalytic properties, *ACS Omega* 1 (2016) 464–469.
- [66] H.R. Rezvani, C. Ged, B. Bouadjar, H. de Verneuil, A. Taïeb, Catalase overexpression reduces UVB-induced apoptosis in a human xeroderma pigmentosum reconstructed epidermis, *Cancer Gene Ther.* 15 (2008) 241–251.
- [67] A.M. Pudlacz, E. Czechowska, M.S. Karbownik, K. Ranoszek-Soliwoda, E. Tomaszewska, G. Celichowski, J. Grobelny, E. Chabielska, A. Gromotowicz-Poplawska, J. Szemraj, The effect of immobilized antioxidant enzymes on the oxidative stress in UV-irradiated rat skin, *Nanomedicine* 15 (2020) 23–39.
- [68] F.A. Moura, K.Q. de Andrade, J.C.F. dos Santos, O.R.P. Araújo, M.O.F. Goulart, Antioxidant therapy for treatment of inflammatory bowel disease: Does it work?, *Redox Biol.* 6 (2015) 617–639.

## PAPER



Cite this: *J. Mater. Chem. B*, 2022, 10, 2523

## Development of polymer-based multifunctional composite particles of protease and peroxidase activities†

Szilárd Sáringer,<sup>a</sup> Tamás Valtner,<sup>a</sup> Árpád Varga,<sup>b</sup> József Maléth<sup>b</sup> and István Szilágyi<sup>b</sup> \*<sup>a</sup>

A hybrid material (SL–PPN–HEP–HRP) of dual enzyme function was prepared by co-immobilization of papain (PPN) and horseradish peroxidase (HRP) on sulphate latex (SL) microspheres using heparin (HEP) polyelectrolyte as a building block in the sequential adsorption method. The doses of PPN, HEP and HRP were optimized in each step of the preparation process to achieve high functional and colloidal stability. The enzymes and the polyelectrolyte strongly adsorbed on the oppositely charged surfaces via electrostatic forces, and enzyme leakage was not observed from the hybrid material, as confirmed by colorimetric protein tests and microscopy measurements. It was found that the polyelectrolyte acted as a separator between PPN and HRP to prevent hydrolytic attack on the latter enzyme, which otherwise prevents the joint use of these important biocatalysts. Excellent colloidal stability was obtained for the SL–PPN–HEP–HRP composite and the embedded PPN and HRP showed remarkable protease and peroxidase activities, respectively, at least until five days after preparation. The present results offer a promising approach to develop biocatalytic systems of dual function, which are often required in manufacturing processes in the food industry, where the colloidal stability of such multifunctional materials is a key parameter to achieve remarkable efficiency.

Received 26th August 2021,  
Accepted 27th October 2021

DOI: 10.1039/d1tb01861b

rsc.li/materials-b

## Introduction

Enzymes are highly efficient biocatalysts applied for industrial-scale catalysis because of several distinct advantages.<sup>1</sup> As such, their lower energy requirements, mitigation of waste generation, and simplified production routes have been partially realized in the pharmaceutical and food industries.<sup>2,3</sup> In nature, almost all of the intracellular reactions are catalysed by the cooperation of various enzymes.<sup>4</sup> The application of biocatalysts of multi-enzymatic functions is an important technology to produce many valuable chemicals in the industry, which integrates several biocatalytic transformations and thus, bridging the gap between single-enzyme catalysis and whole-cell catalysis.<sup>3</sup>

By the inspiration from multi-enzymatic reactions in nature, researchers have attempted to construct multifunctional

biocatalytic systems to produce desired chemicals or to decompose hazardous contents.<sup>5–7</sup> In industrial and biomedical applications, it is necessary to immobilize the enzymes to prolong their catalytic activities and to provide enhanced stability and resistance against severe conditions, including extreme pH, temperature and presence of enzyme inhibitors, and to protect them against proteolysis and to achieve reduced susceptibility to contamination.<sup>8–10</sup> Besides, immobilization of enzymes also offers several technical advantages, such as easier product recovery and purification.<sup>11</sup> As a solid support for enzymes, nano or colloidal particles provide ideal characteristics for maintaining efficient biocatalytic activity for the enzymes leading to remarkable advantages over conventional supports. As summarized in recent reviews,<sup>5,12–14</sup> various materials, such as graphene, carbon nanotubes, metal–organic frameworks, DNA nanostructures, polymers and metal oxides, have been applied for multi-enzyme immobilization. Different preparation strategies have been reported, which include fusion of enzymes, enzyme–scaffold complexes and parallel attachment of enzymes to solid supports.<sup>8,10</sup> Among such systems, biocatalysts of hydrolytic and antioxidant properties have attracted considerable attention due to their widespread use in various industrial processes.

Accordingly, plant proteases, such as papain (PPN),<sup>15</sup> are widely applied in the food industry for various purposes including

<sup>a</sup> MTA-SZTE Lendület Biocolloids Research Group, Interdisciplinary Excellence Center, Department of Physical Chemistry and Materials Science, University of Szeged, H-6720 Szeged, Hungary. E-mail: szisztvan@chem.u-szeged.hu

<sup>b</sup> HAS-USZ Momentum Epithelial Cell Signaling and Secretion Research Group and HCEMM-SZTE Molecular Gastroenterology Research Group, Department of Medicine, University of Szeged, H-6720 Szeged, Hungary

† Electronic supplementary information (ESI) available: Electrophoretic mobilities, stability ratios, data of Bradford, protease and peroxidase tests. See DOI: 10.1039/d1tb01861b



dc\_1931\_21

brewing, tenderization of meat, coagulation of milk and as a digestive aid.<sup>16</sup> Due to their hydrolytic attack on the peptide bonds and subsequent decomposition of proteins, proteases are also used to improve the flavour, nutritional value, solubility and digestibility of food proteins as well as to modify functional properties including coagulation and emulsification. Recently, several nanomaterials have been used as a matrix for PPN immobilization including magnetic nanoparticles,<sup>17</sup> carbon nanotubes<sup>18</sup> as well as polymeric micro- and nanoparticles.<sup>19,20</sup>

Besides, horseradish peroxidase (HRP)<sup>21</sup> is one of the most extensively studied peroxidase enzymes because of its widespread applications. It catalyses the oxidation of various substrates using hydrogen peroxide or other peroxide derivatives. HRP has been applied for the removal of phenols from wastewater,<sup>22</sup> organic compound syntheses<sup>23</sup> and development of biosensors.<sup>24</sup> Moreover, it is also being used in the food industry for improving nutritional quality of food. Removal of residual amount of hydrogen peroxide after cold sterilization of beer, rinsing and dairy treatment processes is carried out by HRP.<sup>2</sup> Its advantages include high activity, simple detection of products, relatively good stability and ease of immobilization.<sup>24</sup> The immobilization of HRP was performed with various solid supports such as silica nanoparticles,<sup>25</sup> polysaccharide derivatives,<sup>26</sup> chitosan,<sup>27</sup> graphene<sup>28</sup> or iron oxide.<sup>29</sup>

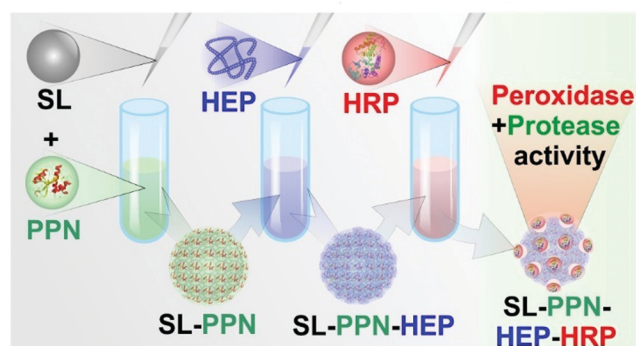
The above-mentioned examples clearly show that the combined use of PPN and HRP enzymes is desirable in certain industrial areas. On the one hand, the successful application requires separation of the enzymes to protect HRP from the proteolytic activity of PPN. This can be achieved by co-immobilization of the two enzymes. On the other hand, colloidal stability of these systems is a critical issue in the above applications. Indeed, aggregation of the carrier particles would lead to unsuccessful enzyme delivery processes due to the formation of irregularly shaped clusters giving rise to significant loss in enzymatic activity.<sup>30</sup> The joint immobilization of HRP and PPN with the sequential adsorption method<sup>31</sup> is a self-evident way to separate the enzymes in space on solid supports and to ensure sufficiently high colloidal stability of the composite suspension, as demonstrated earlier for immobilization of dual enzyme systems or enzyme mimicking compounds.<sup>32,33</sup> Moreover, an intermediate polyelectrolyte layer may provide enhanced protection for HRP against PPN.

Therefore, the aim of the present study is to design stable dispersions of a latex particle (SL)-supported multi-enzymatic system involving heparin (HEP) polyelectrolyte in the sequential adsorption process (Scheme 1). Scattering techniques were used to optimize the charging and aggregation features as well as to gain information on the structure of the SL-PPN-HEP-HRP composites, while the proteolytic and peroxidase activities were assessed in biochemical test reactions.

## Experimental section

### Materials

Spherical polystyrene latex (SL) particles functionalized with negatively charged sulphate groups and fluorophore conjugated



Scheme 1 Schematic illustration of the synthesis and enzymatic activity of the SL-PPN-HEP-HRP composite.

secondary antibody (Donkey anti-mouse Alexa 647) were purchased from Thermo Fischer Scientific. The radius of the SL particles was  $(215 \pm 4)$  nm, as determined by the manufacturer using transmission electron microscopy in the dried stage. The surface charge density of the particles was reported to be  $-12$  mC m<sup>-2</sup>. Papain (PPN) from *Carica papaya* ( $3$  U mg<sup>-1</sup>), heparin (HEP) sodium salt from porcine intestinal mucosa, Folin & Ciocalteu reagent, anti-HRP primary antibody, glucose oxidase, catalase, phosphate buffered saline (PBS), glucose and cysteamine hydrochloride were purchased from Sigma-Aldrich. Horseradish peroxidase (HRP), Coomassie brilliant blue, hydrogen peroxide, NaCl, NaH<sub>2</sub>PO<sub>4</sub> (anhydrous), Na<sub>2</sub>HPO<sub>4</sub> (anhydrous), orthophosphoric acid (85 w/w%), ethanol, trichloroacetic acid (TCA) and sodium carbonate were bought from WVR, while tyrosine and guaiacol were from Acros Organics. Paraformaldehyde (PFA) was acquired from Alfa Aesar and bovine serum albumin (BSA) was from PanBiotech. These chemicals were of analytical grade and were used as received. All solutions were diluted using ultrapure water obtained from a VWR Purity TU+ machine. The water and the salt solutions were filtered with a  $0.1$   $\mu$ m syringe filter (Millex).

### Composite preparation

The SL-PPN-HEP-HRP composite material was built up based on the sequential adsorption method (Scheme 1). Accordingly, SL particles were added to a solution containing a calculated amount of PPN at pH 4. The sample was stirred for 1.5 h on a rotational stirrer and HEP solution of appropriate concentration was added to the dispersion. After 1.5 h additional stirring, HRP was added to the samples followed by continuous stirring for 1.5 h. The doses of PPN, HEP and HRP were 400, 200 and 10 mg g<sup>-1</sup> SL, respectively, in the final composite.

### Electrophoretic mobility

Electrophoretic light scattering was used to determine the electrophoretic mobility of the particles with a Litesizer 500 instrument (Anton Paar) equipped with a 40 mW semiconductor laser operating at 658 nm wavelength. For all the measurements 1.5 mL samples were prepared, during which 0.15 mL of 100 mg L<sup>-1</sup> particle stock dispersion was added to a 1.35 mL solution composed of a calculated amount of polyelectrolyte

and/or enzyme as well as NaCl to set the ionic strength to 1 mM. The samples were allowed to rest for 2 h at room temperature before measuring the electrophoretic mobility after a 1 min equilibrating time in the device. The reported values were the average of 5 individual measurements, which were performed in omega shaped plastic cuvettes (Anton Paar). The standard deviation of the data was always within 5 mV.

### Dynamic light scattering

The hydrodynamic radius ( $r_h$ ) of the particles was determined by dynamic light scattering (DLS) with an ALV-NIBS High Performance Particle Sizer instrument. The cumulant fit was used to fit the correlation function, which was collected for 20 s at 173.5° scattering angle.<sup>34</sup> To determine the aggregation rate coefficient ( $k$ ) of the particle dimer formation, time-resolved DLS measurements were performed and the calculations were carried out as follows:<sup>35</sup>

$$\frac{1}{r_{h,0}} \left. \frac{dr_h}{dt} \right|_{t \rightarrow 0} = \left[ 1 + \frac{\sin(2qr)}{2qr} \right] \left( 1 - \frac{r_{h,1}}{r_{h,2}} \right) k n_0 \quad (1)$$

where  $n_0$  is the initial particle number concentration ( $2.27 \times 10^{14} \text{ m}^{-3}$ ),  $t$  is the time of the experiment,  $r_{h,0}$  is the initial hydrodynamic radius,  $q$  is the magnitude of the scattering vector,  $r$  is the geometrical radius and  $r_{h,1}/r_{h,2}$  is the ratio of the hydrodynamic radii of the monomer and the dimer. The measurements were run for 30 min to collect enough experimental points for the linear fits of the  $r_h$  versus  $t$  data. The sample preparations for DLS measurements were done in a similar manner to the ones described above for electrophoresis. The only difference was that the total volume was 2 mL for DLS, and the measurements were started directly after adding the particles to the solutions containing polyelectrolyte, enzyme and NaCl. The samples were stirred with a vortex mixer before the time-resolved experiments. The stability ratio<sup>36–38</sup> ( $W$ ) was calculated to express the colloidal stability of the particles as

$$W = \frac{k^{\text{fast}}}{k} \quad (2)$$

where the fast condition corresponds to the diffusion-controlled aggregation of the particles achieved in 1 M NaCl solutions. Stability ratio values close to unity are associated to unstable dispersions, where all the particle collisions result in dimer formation. The mean error of the stability ratio data was within 10%.

The critical coagulation concentration (CCC) values were calculated with the formula described as<sup>39</sup>

$$W = 1 + \left[ \frac{\text{CCC}}{c} \right]^\beta \quad (3)$$

where  $c$  is the molar salt concentration and  $\beta$  was obtained from the change in the stability ratios in the slow aggregation regime before the CCC as

$$\beta = \frac{d \log 1/W}{d \log c} \quad (4)$$

### Determination of enzyme content

The amount of PPN enzyme in solution was determined by the Bradford protein test.<sup>40</sup> Coomassie Brilliant Blue dye stock solution was prepared as follows. 100 mg of the dye was dissolved in the mixture of 50 mL of 95% ethanol and 100 mL of 85% phosphoric acid. The solution was then made up to 1000 mL with ultrapure water. Thereafter, standard solutions of PPN in the 1–100 mg L<sup>-1</sup> range and SL-PPN at 1000 mg L<sup>-1</sup> particle concentration were prepared. After mixing 0.4 mL of the test solution with 1.6 mL of the dye solution, the UV-Vis spectra of the samples were recorded after a 5 min equilibration time on a Thermo Fischer Genesys 10s spectrophotometer. The changes in the absorbance at 464 nm and 594 nm wavelength were monitored. The amount of PPN in the samples was calculated from the ratio of these absorbance values.

### Immunofluorescent labelling and dSTORM imaging

The immobilization of HRP on SL-PPN-HEP was confirmed by direct stochastic optical reconstruction microscopy (dSTORM). The particle suspensions were placed on cover glass (VWR). The samples were incubated for 20 min to promote adhesion. After 5 min long fixation with 4% PFA in PBS, specific binding sites were blocked by applying 10% BSA in PBS for 2 h at 37 °C. Anti-HRP primary antibody was used during a 2 h incubation step at room temperature. The sample was washed three times for 10 min with PBS. Fluorophore conjugated (Alexa 647) secondary antibody was applied prior to another washing step (three times for 10 min). For dSTORM imaging, cover glasses were placed on cavity slides filled with blinking buffer and sealed with a two component adhesive. The blinking buffer contained 100 U glucose oxidase, 2000 U catalase, 55.6 mM glucose and 100 mM cysteamine hydrochloride in 1 mL final volume completed with sterile PBS. dSTORM images were captured using Nanoimager S (Oxford Nanoimaging ONI Ltd).

### Hydrolytic activity measurements

The universal protease activity assay protocol based on the Lowry method<sup>41</sup> with some modifications was used for determination of the protease-like function. Accordingly, a calibration curve was prepared by adding different amounts of 1.1 mM standard tyrosine solution to several samples and completed to a final volume of 2 mL with ultrapure water. The final tyrosine concentrations in the samples were between 0.01 and 1 μM. Note that tyrosine is the product of the hydrolysis in the test reaction. After 30 min incubation at 37 °C, the colour change in the samples was measured with a spectrophotometer at 660 nm. The absorbance recorded at this wavelength was used to determine the tyrosine concentration in the samples. For the estimation of protease-like activity, the concentration of the bare and immobilized PPN was 2500 mg L<sup>-1</sup> in the stock solutions. For the measurements, 0.4 mL was added to 3.6 mL of 10 mM phosphate and 5 mM acetate buffer at pH 7. Thus, the PPN concentration was 250 mg L<sup>-1</sup> in the buffered solution. During the measurements, 0.65 w/v% casein, as a substrate, was diluted with 50 mM phosphate buffer solution first. Thereafter, 0.1 mL of free or immobilized enzymes was added

dc\_1931\_21

to 0.5 mL casein solution. The reaction was terminated after 20 min by adding 0.5 mL of 110 mM TCA solution and then, an appropriate volume of PPN solution or SL-PPN-HEP-HRP dispersion was added to the blank sample to reach the 1 mL final volume. After 30 min incubation at 37 °C, the samples were centrifuged at 10000 rpm for 10 min. Then, 0.75 mL of 500 mM sodium carbonate and 0.1 mL of Folin & Ciocalteus reagent were added to 3 mL of the supernatant. After 30 min incubation at 37 °C, the absorbance of the samples was recorded in the 400–800 nm range. The protease activity was determined from the absorbance values measured at 660 nm. One unit of protease activity was equivalent to the amount of enzyme that was required to release 1 µg of tyrosine per mL per min under the standard assay conditions described above. For the time dependent measurements, the stock solutions of 2500 mg L<sup>-1</sup> concentration were stored under room temperature and the activities of the samples were measured each day for a week applying the above-mentioned steps.

### Peroxidase activity measurements

The guaiacol assay was used to determine the HRP activity of the samples.<sup>42</sup> In brief, 0.125 mL of 25 mg L<sup>-1</sup> stock solution containing immobilized or bare enzymes was added to the mixture of 0.125 mL of 100 mM phosphate buffer and an appropriate volume of 100 mM guaiacol solution. The samples were completed to a volume of 0.85 mL with water. Finally, 0.35 mL of 9 mM hydrogen peroxide was added into the cuvette and introduced into the UV-Vis spectrophotometer to follow the formation of the guaiacol degradation products at 470 nm wavelength. The reaction rate ( $v$ ) was determined by linear regression of absorbance *versus* reaction time data. The Michaelis-Menten constant ( $K_m$ ) and the maximum reaction rate ( $v_{max}$ ) were calculated with the Lineweaver-Burk equations as follows:<sup>42</sup>

$$\frac{1}{v} = \frac{K_m}{v_{max}} \frac{1}{[S]} + \frac{1}{v_{max}} \quad (5)$$

where  $S$  refers to the guaiacol concentration. For the time dependent measurements, the stock solutions were incubated for 20 min at 37 °C prior to the measurements. Otherwise, the samples were stored in a refrigerator for 5 days and the above-mentioned measurement steps were carried out each day to determine the long-term HRP activity for the native and immobilized enzymes.

## Results and discussion

### PPN adsorption on SL

As the first step in the preparation of the SL-PPN-HEP-HRP composite, the adsorption of PPN on SL particles was studied in an earlier work of our group.<sup>43</sup> It was found that PPN strongly adsorbed on the oppositely charged SL surface through electrostatic forces at pH 4, which is below the pI of the PPN enzyme.<sup>44</sup> The charging and aggregation properties of the SL particles were explored by electrophoresis and time-resolved DLS measurements. The electrophoretic mobility of the latex particles

changed from negative to positive on increasing the amount of enzyme added (Fig. S1, ESI<sup>†</sup>) indicating strong affinity to the oppositely charged particle surface. The stability ratio values were high at low and elevated enzyme doses referring to stable dispersions under these conditions. A U-shaped curve was formed in the intermediate regime with a minimum corresponding to the isoelectric point (IEP) determined in the electrophoretic mobility measurements. At this minimum, the stability ratios were unity within the experimental error indicating unstable dispersions, *i.e.*, rapid particle aggregation. The theory developed by Derjaguin, Landau, Verwey and Overbeek (DLVO)<sup>45,46</sup> may qualitatively explain this behaviour of the particles since they possessed sufficient charge at high and low PPN doses, *i.e.*, strong repulsive forces were present due to the overlap of the electrical double layers. At the IEP, however, such a repulsive electrical double layer force was absent, and the suspensions were destabilized by the attractive van der Waals forces.

It is important to note that the SL surface saturated with the adsorbed enzyme around 400 mg g<sup>-1</sup> dose, as indicated by a plateau in the mobility above this PPN concentration. Moreover, the SL-PPN particles obtained at this dose formed a stable dispersion; therefore, these particles were chosen for the further steps in the sequential adsorption method to obtain the SL-PPN-HEP-HRP composite.

Our previous work<sup>43</sup> on PPN adsorption was extended by quantifying this process with the Bradford method, an excellent tool to determine the PPN concentration in solutions.<sup>40,47</sup> Accordingly, the SL-PPN dispersion (at 400 mg g<sup>-1</sup> PPN dose) was filtered to remove the particles and the filtrate was analysed with the Bradford test. The obtained results including the ones from the reference measurements with different amounts of native PPN are shown in Fig. S2a (ESI<sup>†</sup>) and the absorbance ratios are presented in Fig. S2b (ESI<sup>†</sup>). The absorbance decreased at 465 nm and increased at 595 nm on increasing PPN concentration. These changes in the absorption maxima are based on the binding of the applied dye to the PPN molecules. The enzyme concentration in the filtrate was found to be 2.1 mg L<sup>-1</sup>, which is 0.5% of the total amount of PPN. This value is within the experimental error of the test and clearly shows that more than 99% of the enzyme adsorbed on the SL and that no significant PPN partitioning between the bulk and the surface took place.

Considering the above results, the surface coverage can be estimated. Given the diameter of SL (430 nm) and PPN (7.2 nm),<sup>48</sup> calculations yielded 12.45 mg of enzyme adsorbed on 1 g of particles in the case of monolayer formation. Therefore, the 400 mg g<sup>-1</sup> dose at saturation indicates the development of PPN multilayers on the surface, which has been already assumed in our previous study<sup>43</sup> to explain loss in the enzymatic activity. Note that, however, this calculation was based on a smooth latex surface and possible conformational changes of PPN were not considered upon adsorption on SL.

### Functionalization with HEP

The net positive surface charge of SL-PPN allows the adsorption of the negatively charged HEP polyelectrolyte through

dc\_1931\_21

electrostatic interactions.<sup>49</sup> High colloidal stability was the major requirement to be achieved after the bilayer formation. Although polyelectrolyte multilayer formation was frequently reported on particles and planar surfaces as well,<sup>33,50–52</sup> very limited information is available on sequential adsorption processes involving saturated enzyme layers on colloidal particles.<sup>32,53</sup>

The electrophoretic mobility was first determined to probe the influence of the HEP concentration on the charging behaviour of the SL-PPN. Considering the change in the magnitude of the electrophoretic mobility on increasing the HEP dose, similar tendencies were observed as in the system containing SL and PPN. At low HEP doses, the SL-PPN possesses a positive net charge, while on increasing the HEP dose, the polyelectrolyte adsorption was clearly indicated by the decrease of mobility (Fig. 1).

Such an adsorption process led to charge neutralization at the IEP, which is located at 20 mg g<sup>-1</sup> dose. Above the IEP, charge reversal occurred at higher doses. The adsorption continued until the mobility reached a plateau at 200 mg g<sup>-1</sup> and further added polyelectrolytes remained dissolved in the bulk solution.

Stability ratio measurements revealed that the particles were stable at low and high polyelectrolyte doses. Like the dispersions containing SL and PPN (Fig. S1, ESI†), the stability ratios went through a minimum near the IEP. This behaviour is again in line with the DLVO theory, *i.e.*, the acting interparticle forces are of electrostatic origin, and similar to findings reported earlier with other polyelectrolyte-particle systems.<sup>38,49,52,54,55</sup> The minimum value of the stability ratios was around unity, which is indeed in agreement with the prediction of DLVO theory. On the other hand, there is a remarkable difference in the slopes of the stability ratios before and after the minimum value. At low polyelectrolyte doses, a smaller slope was observed, which indicates the occurrence of the non-DLVO

destabilizing effect, which may originate from the adsorbed PPN-HEP layers. It is assumed that the patch-charge effect<sup>56,57</sup> is responsible for this phenomenon as follows. At low polyelectrolyte doses, HEP adsorbed on the SL-PPN particles in islands or in so-called patches, while empty positively charged places (charges) were still available on the SL-PPN surface. The patches are electrostatically attracted by the opposite charges giving rise to the evolution of an attractive non-DLVO interaction in addition to the already existing van der Waals forces. The patch-charge interaction leads to faster aggregation of the particles and thus to lower stability ratios.

Overall, the above mobility and stability ratio data ensure that at 200 mg g<sup>-1</sup> polyelectrolyte dose the SL-PPN-HEP particles are negatively charged and form a highly stable colloid.

### Immobilization of HRP

The HRP enzyme is positively charged at pH 4 since its pI value is 8.8.<sup>21</sup> Therefore, HRP is expected to adsorb on the negatively charged SL-PPN-HEP surface at least by electrostatic attraction. However, hydrophobic interactions and hydrogen bonding may also play a role in the adsorption process. One should note that extensive HRP adsorption may affect the charging and aggregation properties of the SL-PPN-HEP particles. It is important to avoid a significant decrease in the magnitude of surface charge upon enzyme immobilization, because it may lead to a weakening of the double layer repulsion and to particle aggregation.

To explore the charging behaviour, the influence of HRP adsorption on the electrophoretic mobility of SL-PPN-HEP was probed by measuring the mobility at different HRP concentrations (Fig. S3, ESI†). One can observe that increasing the HRP dose did not lead to significant changes in the mobility, unlike PPN and HEP adsorption in the previous steps, due to its low charge density. The results revealed that for an enzyme dose lower than 100 mg g<sup>-1</sup>, the mobility values of SL-PPN-HEP were not affected by the added amount of HRP indicating a colloidal stability similar to that of the SL-PPN-HEP particles. Above this loading, the mobility slightly increased, which indicates weaker electrical double layer repulsion and consequently, an undesired decrease in colloidal stability. Considering these results, 10 mg g<sup>-1</sup> dose was selected (SL-PPN-HEP-HRP). Note also that this dose was applied in our previous immobilization studies<sup>55,58</sup> and this condition gave rise to remarkable peroxidase activities of the obtained composites.

The immobilization of HRP on the surface of the oppositely charged SL-PPN-HEP hybrid was confirmed by the dSTORM technique. The transmitted light image (Fig. 2a) showed several well-concentrated foci in the distant red range of light indicating the presence of HRP in the SL-PPN-HEP-HRP particles. After data acquisition (Fig. 2b), dSTORM revealed the spatial extent of the blinking events in Fig. 2c and the blinking frequency of the fluorophores along the white dashed line drawn in Fig. 2b as a function of distance (Fig. 2d). The dimension of the flashes shown in Fig. 2c and d is about 400 nm, which is in good agreement with the diameter of the SL nanoparticle used. These results provide unambiguous evidence for the adsorption of HRP on the SL-PPN-HEP

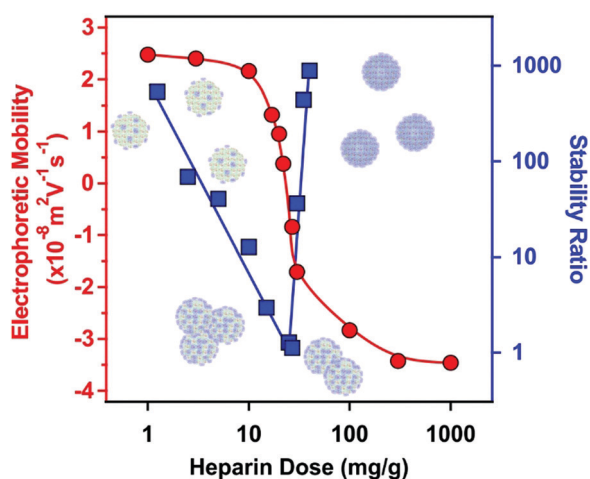


Fig. 1 Electrophoretic mobility (red circles) and stability ratio (blue squares) data of the SL-PPN particles as a function of the HEP dose. The measurements were carried out at pH 4 and 1 mM ionic strength adjusted by NaCl. The mg g<sup>-1</sup> unit refers to mg of HEP per 1 g of the particles. The solid lines serve to guide the eyes.



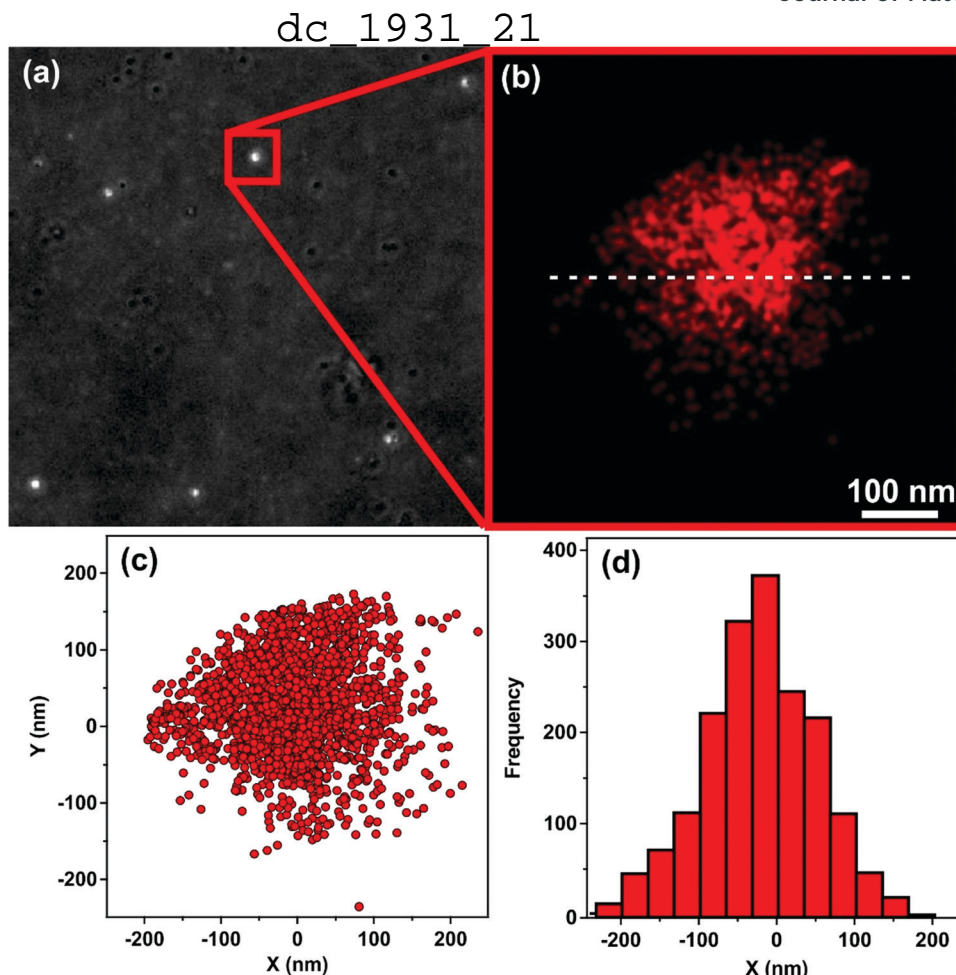


Fig. 2 Transmitted light image of the particles on a glass surface (a) and dSTORM picture of the marked focal point (b). Blinking events of the fluorophores were plotted along the X and Y axes (c) and the frequency of blinking events was plotted as a function of the distance (d) from the white dashed line shown in (b).

composite and that the enzyme is strongly attached to the particulate support.

An overview of the electrophoretic mobility, stability ratio and hydrodynamic radius data during the sequential adsorption process used for SL-PPN-HEP-HRP is shown in Fig. 3.

The mobility of the SL particles at low PPN doses was around  $(-3.81 \pm 0.06) \times 10^{-8} \text{ m}^2 \text{ V}^{-1} \text{ s}^{-1}$ . This negative charge resulted in stable colloids. The formation of a saturated PPN layer at  $400 \text{ mg g}^{-1}$  provided again stable dispersions and the magnitude of the mobility was  $(2.44 \pm 0.03) \times 10^{-8} \text{ m}^2 \text{ V}^{-1} \text{ s}^{-1}$ . After functionalization with HEP at  $200 \text{ mg g}^{-1}$ , the mobility was  $(-3.46 \pm 0.04) \times 10^{-8} \text{ m}^2 \text{ V}^{-1} \text{ s}^{-1}$  due to the high charge density of the polyelectrolyte. This saturated HEP layer provided high colloidal stability for the particles. Finally, the immobilization of HRP slightly decreased the mobility values to  $(-2.77 \pm 0.08) \times 10^{-8} \text{ m}^2 \text{ V}^{-1} \text{ s}^{-1}$ . The hydrodynamic radius of the SL-PPN-HEP-HRP composite was  $(280 \pm 6) \text{ nm}$ . As shown by the time-resolved data, no aggregation was detected for the final hybrid particles.

#### Resistance against salt-induced aggregation

Ionic strength is an important factor in the preparation, stability and applications of biocatalytic systems.<sup>30,59,60</sup> Therefore, the

charging and aggregation features of the obtained particles were tested in a wide range of salt concentration. The ionic strength was systematically changed in the dispersion of SL, SL-PPN and SL-PPN-HEP-HRP and the electrophoretic mobility values as well as stability ratios were determined, and the tendencies were compared (Fig. 4).

On increasing the ionic strength, the magnitude of the mobility decreased for all the systems owing to the screening effect of the dissolved salt constituents on the surface charges (Fig. 4a). The mobility was close to zero at high salt concentrations, but no charge reversal was observed in the ionic strength regime investigated.

Time-resolved DLS measurements were carried out to investigate the aggregation behaviour at different electrolyte levels. The obtained stability ratios are shown in Fig. 4b. The tendency in the data followed the prediction of the DLVO theory.<sup>46</sup> Accordingly, high stability ratios indicated stable dispersions at low salt concentrations, while they decreased by increasing the ionic strength. Rapid particle aggregation occurred after the critical coagulation concentration (CCC) values. The relatively high CCC data shed light on the remarkable colloidal stability of the particle systems. Similar results

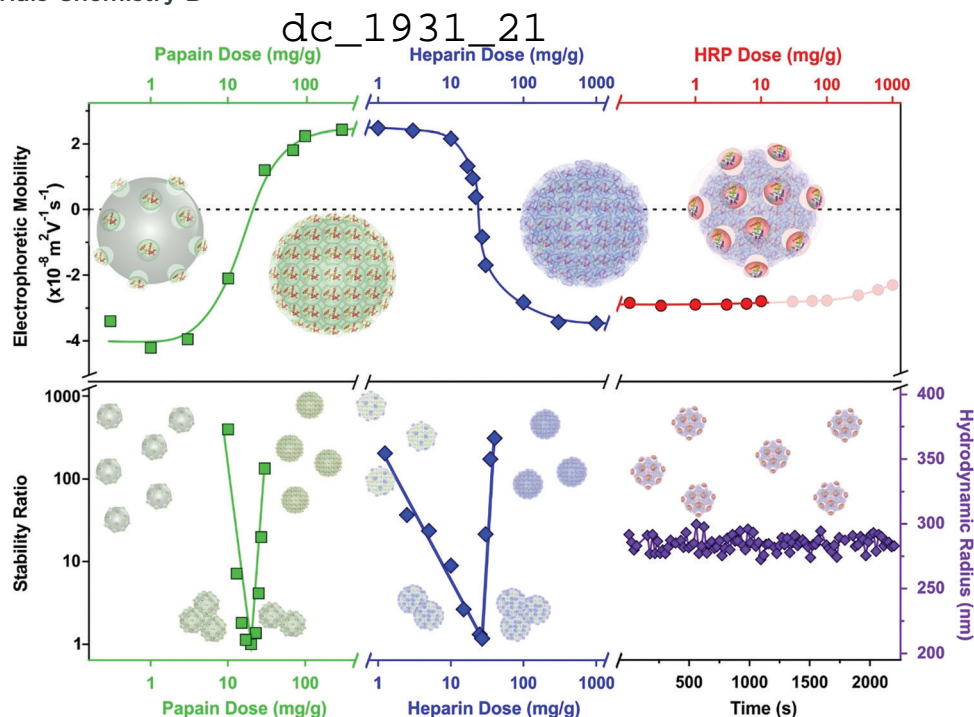


Fig. 3 Schematic illustration of the charging and aggregation tendencies during preparation of the SL-PPN-HEP-HRP composite by the sequential adsorption method. The evolution of the electrophoretic mobility (top) and stability ratios (bottom) as a function of the enzymes and polyelectrolytes is shown. The constant hydrodynamic radii of the SL-PPN-HEP-HRP composite confirm the absence of particle aggregation (bottom right corner). The particle concentration was  $10 \text{ mg L}^{-1}$  and the measurements were carried out at pH 4 and 1 mM ionic strength.

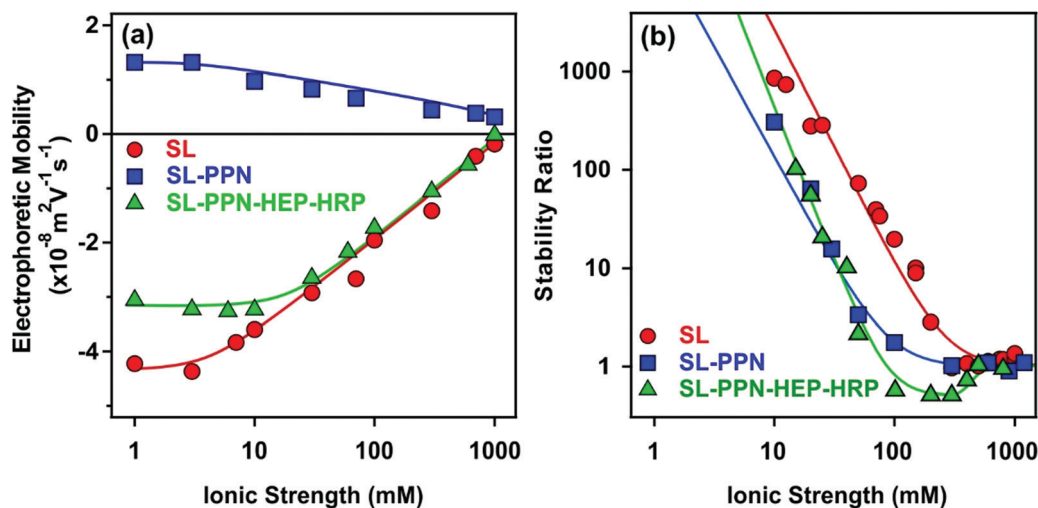


Fig. 4 (a) Electrophoretic mobility and (b) stability ratio of SL, SL-PPN, and SL-PPN-HEP-HRP particles as a function of the ionic strength adjusted with NaCl. The measurements were carried out at pH 4 and the particle concentration was  $10 \text{ mg L}^{-1}$ .

were reported earlier on polyelectrolyte-coated particle dispersions.<sup>49,52,54,58,61</sup>

The aggregation rates determined above the CCC values were  $3.1 \times 10^{-18} \text{ m}^3 \text{ s}^{-1}$ ,  $3.3 \times 10^{-18} \text{ m}^3 \text{ s}^{-1}$  and  $3.4 \times 10^{-18} \text{ m}^3 \text{ s}^{-1}$  for SL, SL-PPN and SL-PPN-HEP-HRP, respectively. This reasonable agreement between the data indicates that the nature of the attractive forces was very similar for all particles and such forces originate most probably from van der Waals attractions. Nevertheless, for the SL-PPN-HEP-HRP system, stability ratio values

lower than unity were observed in the fast aggregation regime after the CCC and the slope in the slow aggregation regime was also different from the other particle systems. This difference may originate from additional non-DLVO forces. First, such an acceleration in the aggregation is the result of the above discussed patch-charge interactions, which were frequently reported for highly charged polyelectrolytes adsorbing on oppositely charged surfaces.<sup>54,56,57</sup> Second, steric hindrance between adsorbed polyelectrolyte chains may evolve upon approach of

dc\_1931\_21

two particles, which leads to a non-electrostatic repulsion.<sup>38,52,57</sup> This effect is more pronounced at lower ionic strength and hence, should be responsible for the different slope in the slow aggregation regime of the SL-PPN-HEP-HRP composite.

### Protease activity

The hydrolytic activity of the immobilized and free PPN was determined on the basis of the hydrolysis of the casein substrate.<sup>41</sup> The assay was carried out daily during five days for SL-PPN-HEP-HRP to probe its functional stability over time. The quantitative analysis was based on the characteristic absorbance values of the tyrosine product appearing at 660 nm wavelength (Fig. S4, ESI<sup>†</sup>), from which the normalized activities were calculated (see the Experimental section for details). The determined activity on the first day was  $(0.62 \pm 0.01) \text{ U mL}^{-1}$  for the composite and  $(0.71 \pm 0.03) \text{ U mL}^{-1}$  for the native PPN. Thus, the immobilized PPN possessed 85% activity compared to the free PPN on the first day, while this value was only 67% for the SL-PPN system.

The decrease in the activity upon immobilization can be explained as follows. On the one hand, it is caused by the conformational changes of PPN, which occurred once attachment to the surface of the latex took place. Such a change may result in decreased activity due to the hindered interaction between the active centre and the substrate. On the other hand, a relatively high amount of PPN is adsorbed on SL, probably in more than one layer, and the blocking effect of the outer layers, *i.e.*, the limited accessibility of substrate molecules to the inner enzymes, decreased the efficiency.

However, it was observed in several studies<sup>62–64</sup> that PPN exhibited a high binding affinity to HEP and this binding is mediated mainly by electrostatic interactions. The presence of HEP may significantly change the PPN structure by increasing the  $\alpha$ -helix content of the enzyme. This binding can result in an increase in the affinity of the enzyme for the substrate. It was also shown that the interaction between HEP and PPN is specific, since other sulphated glycosaminoglycans, namely dermatan sulphate and chondroitin sulphate, were able to neither increase the affinity of PPN to the substrate, nor change the  $\alpha$ -helix content in PPN.<sup>65</sup> To explore the PPN-HEP interaction and its effect on the protease activity, PPN assays were carried out in the presence of HEP, *i.e.*, with PPN-HEP solution. The hydrolytic activity of the PPN-HEP system was about the same as the one determined for the native PPN enzyme. This result clearly indicates that possible interactions between PPN and HEP do not affect the protease function significantly.

Fig. 5 shows the change in the relative enzyme activities determined at different days. Although the enzymatic activity of the immobilized PPN decreases as a function of time, the hybrid material maintained significant protease-like activity even after 5 days. The decrease in the activity can be explained by the partial denaturation of the enzyme, the presence of PPN aggregates on the particles or by the accumulation of the products on the SL-PPN-HEP-HRP surface, which sterically hinders the interaction between the enzyme and the substrate. However, we do not have direct experimental proof for the exact

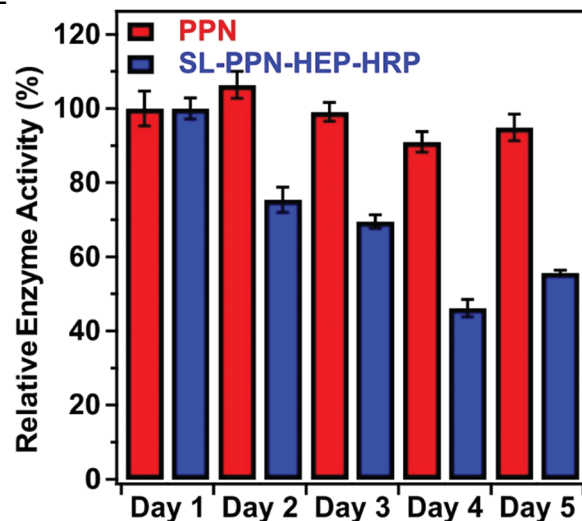


Fig. 5 Relative protease-like activity of the PPN enzyme and the SL-PPN-HEP-HRP composite as a function of time. The applied PPN concentration was  $22.7 \text{ mg L}^{-1}$  in all measurements.

reason of this loss in protease activity. Some decrease was also observed for the free PPN, but it was not significant, and the enzyme retained 95% of its activity even after 5 days.

The hydrolytic activities of the native and immobilized PPN were also assessed at  $50^\circ\text{C}$  and  $70^\circ\text{C}$  after a 1 hour incubation time (Fig. S5, ESI<sup>†</sup>). At the former temperature, the activities did not change significantly compared to the value measured without heat treatment, while at  $70^\circ\text{C}$ , the hydrolytic efficiency decreased by 45% and 60% for PPN and SL-PPN, respectively.

### Peroxidase activity

The peroxidase-like activity of the SL-PPN-HEP-HRP composite was tested in the guaiacol assay.<sup>42</sup> This biochemical test is based on the detection of the degradation products of guaiacol under the combined effect of HRP and hydrogen peroxide. The formation of the tetra-guaiacol product was monitored by following the colour change of the solution over time. As mentioned in the Experimental section, the Lineweaver-Burk plot was used to analyse the result and from the double reciprocal reaction rate *versus* substrate concentration plot, the Michaelis-Menten constant ( $K_m$ ) and the maximum reaction rate ( $v_{\text{max}}$ ) were calculated (Fig. S6, ESI<sup>†</sup>). The  $K_m$  value corresponds to the affinity of the enzyme towards the substrate. For example, a decrease in the  $K_m$  value refers to a higher affinity of the enzyme to guaiacol.  $v_{\text{max}}$  is the maximum reaction rate that can be achieved by the system once the active sites of the enzymes are completely saturated with the substrate.

The determined  $v_{\text{max}}$  values for the PPN-HRP mixed solution and for the SL-PPN-HEP-HRP composite were  $(0.125 \pm 0.070) \text{ mM s}^{-1}$  and  $(0.069 \pm 0.020) \text{ mM s}^{-1}$ , respectively, on the first day with freshly prepared samples. For these systems, the  $K_m$  values were  $(3.52 \pm 0.26) \text{ mM}$  and  $(29.16 \pm 9.71) \text{ mM}$ , respectively. The lower activity of the immobilized HRP might originate from the interaction with HEP on the surface.

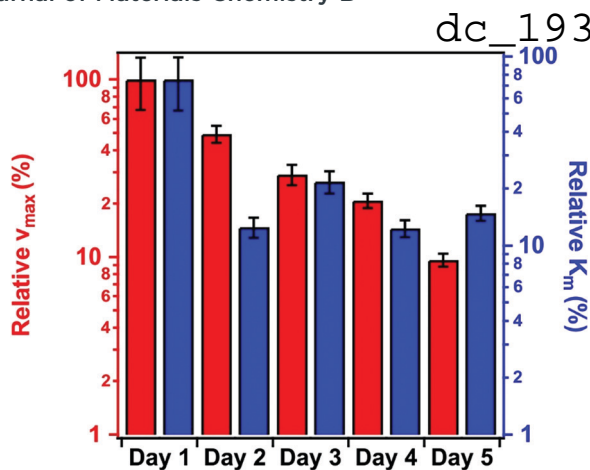


Fig. 6 Relative maximum reaction rate (red bars, left axis) and the Michaelis–Menten constant ( $K_m$ , blue bars, right axis) values of the SL–PPN–HEP–HRP composite as a function of time. The applied HRP concentration was  $2.6 \text{ mg L}^{-1}$ .

In the time dependent measurements, the activity of the immobilized enzymes decreased (Fig. 6); however, significant peroxidase-like activity was still detected after 5 days. In contrast, the PPN–HRP solution (*i.e.*, mixing HRP and PPN without SL and HEP) lost its activity after 3 days due to the hydrolysis of HRP by the PPN enzyme.

To further support our conclusions on the decrease of enzymatic activities of both PPN and HRP with time and upon immobilization, attempts were made to follow potential structural changes of the enzymes in the experiments. Nevertheless, neither scattering (SAXS) nor spectroscopy (FT-IR) techniques were useful due to the relatively large size of the carrier particles and their strong light scattering signal as well as their intense vibrational peaks in the fingerprint region.

Besides, the above results clearly indicate that the polyelectrolyte layer in the SL–PPN–HEP–HRP composite can protect HRP from proteolytic degradation by the PPN enzyme. Accordingly, the immobilized HRP exhibited good resistance to proteolysis by PPN. Such process usually takes place in the PPN–HRP mixed homogeneous solution. Similarly, it was reported earlier that the dissolved peroxidases were more easily inactivated in the presence of protease enzymes compared to their immobilized counterparts.<sup>66</sup>

The findings obtained with the enzymatic tests unambiguously pointed out that the SL–PPN–HEP–HRP composite containing the co-immobilized enzymes possesses significant protease and peroxidase activities, which are maintained at least for 5 days. This is a longer time than the one usually applied for PPN<sup>67</sup> and HRP<sup>68</sup> in industrial applications. Moreover, such a dual enzyme activity is accompanied with excellent colloidal stability making the developed hybrid a promising candidate for application in heterogeneous systems.

## Conclusions

In conclusion, PPN and HRP enzymes were successfully co-immobilized on SL microspheres by the sequential adsorption

method using HEP polyelectrolyte as a building block and a separator between the two enzymes. The polyelectrolyte and the enzyme doses were optimized to achieve high colloidal stability of the SL–PPN–HEP–HRP composite, as confirmed by the remarkable resistance achieved against salt-induced aggregation. The successful immobilization of the enzymes was proved by protein tests and by super-resolution microscopy and no enzyme leakage was detected. The protease and peroxidase activities of the immobilized enzymes were tested in biochemical assays. It was found that the enzymes lost some of their activities upon immobilization; however, the obtained SL–PPN–HEP–HRP composite was still very active, *i.e.*, it possessed significant PPN and HRP activities. Time-dependent peroxidase activity measurements revealed that such a dual activity is maintained at least for 5 days, while in the mixed solution of the native enzymes, HRP lost its activity after 3 days due to hydrolysis by the PPN enzyme. These results indicate that the applied HEP layer successfully protected HRP from the protease-like action of PPN. Therefore, the obtained SL–PPN–HEP–HRP hybrid material acts as an immobilized multi-enzymatic system with protease and peroxidase activities and possesses the advantages of a heterogeneous catalyst such as easier separation from the reaction mixture. The appreciable colloidal and functional stability, which is a crucial requirement for biocatalysts to be applied in industrial manufacturing processes, also promotes the application of the developed composite.

## Conflicts of interest

There are no conflicts to declare.

## Acknowledgements

The authors are thankful for the financial assistance of the Eötvös Lóránd Research Network (96130 and 95026), the Hungarian Academy of Sciences (LP2017–18/2017) and the National Excellence Programme (20391-3/2018/FEKUSTRAT, TUDFO/47138-1/2019/ITM and TKP2020). The project has received funding from the EU's Horizon 2020 research and innovation program under grant agreement No. 739593. The support from the University of Szeged Open Access Fund (5541) is gratefully acknowledged.

## References

- 1 S. J. Benkovic and S. Hammes-Schiffer, *Science*, 2003, **301**, 1196–1202.
- 2 S. Raveendran, B. Parameswaran, S. B. Ummalyma, A. Abraham, A. K. Mathew, A. Madhavan, S. Rebello and A. Pandey, *Food Technol. Biotechnol.*, 2018, **56**, 16–30.
- 3 J. Britton, S. Majumdar and G. A. Weiss, *Chem. Soc. Rev.*, 2018, **47**, 5891–5918.
- 4 E. Ricca, B. Brucher and J. H. Schrittwieser, *Adv. Synth. Catal.*, 2011, **353**, 2239–2262.
- 5 K. L. Xu, X. X. Chen, R. C. Zheng and Y. G. Zheng, *Front. Bioeng. Biotechnol.*, 2020, **8**, 660.



dc 1931 21

- 6 M. Vazquez-Gonzalez, C. Wang and I. Willner, *Nat. Catal.*, 2020, **3**, 256–273.
- 7 A. Grotzky, E. Atamura, J. Adamcik, P. Carrara, P. Stano, F. Mavelli, T. Nauser, R. Mezzenga, A. D. Schluter and P. Walde, *Langmuir*, 2013, **29**, 10831–10840.
- 8 R. A. Sheldon and S. van Pelt, *Chem. Soc. Rev.*, 2013, **42**, 6223–6235.
- 9 X. L. Wang, J. F. Shi, S. H. Zhang, H. Wu, Z. Y. Jiang, C. Yang, Y. X. Wang, L. Tang and A. F. Yan, *J. Mater. Chem. B*, 2015, **3**, 6587–6598.
- 10 E. T. Hwang and S. Lee, *ACS Catal.*, 2019, **9**, 4402–4425.
- 11 Y. Kulshrestha and Q. Husain, *Enzyme Microb. Technol.*, 2006, **38**, 470–477.
- 12 M. Bilal, M. Asgher, H. R. Cheng, Y. J. Yan and H. M. N. Iqbal, *Crit. Rev. Biotechnol.*, 2019, **39**, 202–219.
- 13 M. Massaro, G. Lazzara, S. Milioto, R. Noto and S. Riela, *J. Mater. Chem. B*, 2017, **5**, 2867–2882.
- 14 F. Kazenwadel, M. Franzreb and B. E. Rapp, *Anal. Methods*, 2015, **7**, 4030–4037.
- 15 J. Drenth, J. N. Jansonius, R. Koekoek, H. M. Swen and B. G. Wolthers, *Nature*, 1968, **218**, 929–932.
- 16 J. Fernandez-Lucas, D. Castaneda and D. Hormigo, *Trends Food Sci. Technol.*, 2017, **68**, 91–101.
- 17 T. G. Hu, J. H. Cheng, B. B. Zhang, W. Y. Lou and M. H. Zong, *Ind. Eng. Chem. Res.*, 2015, **54**, 4689–4698.
- 18 Q. Wang, L. Y. Zhou, Y. J. Jiang and J. Gao, *Enzyme Microb. Technol.*, 2011, **49**, 11–16.
- 19 F. C. Vasconcellos, G. A. S. Goulart and M. M. Beppu, *Powder Technol.*, 2011, **205**, 65–70.
- 20 C. Chankhampan, J. Manosroi, H. Yamamoto, K. Tahara, W. Manosroi, Y. Kawashima and A. Manosroi, *J. Exp. Nanosci.*, 2014, **9**, 138–151.
- 21 M. Gajhede, D. J. Schuller, A. Henriksen, A. T. Smith and T. L. Poulos, *Nat. Struct. Biol.*, 1997, **4**, 1032–1038.
- 22 J. Cheng, S. M. Yu and P. Zuo, *Water Res.*, 2006, **40**, 283–290.
- 23 M. J. H. Van Haandel, F. C. E. Saraber, M. G. Boersma, C. Laane, Y. Fleming, H. Weenen and I. Rietjens, *J. Agric. Food Chem.*, 2000, **48**, 1949–1954.
- 24 V. Vojinovic, R. H. Carvalho, F. Lemos, J. M. S. Cabral, L. P. Fonseca and B. S. Ferreira, *Biochem. Eng. J.*, 2007, **35**, 126–135.
- 25 M. S. Sadjadi, N. Farhadyar and K. Zare, *J. Nanosci. Nanotechnol.*, 2011, **11**, 9304–9309.
- 26 T. Mohan, R. Rathner, D. Reishofer, M. Koller, T. Elschner, S. Spirk, T. Heinze, K. Stana-Kleinschek and R. Kargl, *Biomacromolecules*, 2015, **16**, 2403–2411.
- 27 M. Monier, D. M. Ayad, Y. Wei and A. A. Sarhan, *Int. J. Biol. Macromol.*, 2010, **46**, 324–330.
- 28 M. B. Vineh, A. A. Saboury, A. A. Poostchi, A. M. Rashidi and K. Parivar, *Int. J. Biol. Macromol.*, 2018, **106**, 1314–1322.
- 29 S. A. Mohamed, M. H. Al-Harbi, Y. Q. Almulaiky, I. H. Ibrahim and R. M. El-Shishtawy, *Electron. J. Biotechnol.*, 2017, **27**, 84–90.
- 30 T. L. Moore, L. Rodriguez-Lorenzo, V. Hirsch, S. Balog, D. Urban, C. Jud, B. Rothen-Rutishauser, M. Lattuada and A. Petri-Fink, *Chem. Soc. Rev.*, 2015, **44**, 6287–6305.
- 31 G. Decher, *Science*, 1997, **277**, 1232–1237.
- 32 S. Saringer, P. Rouster and I. Szilagyi, *J. Colloid Interface Sci.*, 2021, **590**, 28–37.
- 33 Z. Somosi, N. V. May, D. Sebok, I. Palinko and I. Szilagyi, *Dalton Trans.*, 2021, **50**, 2426–2435.
- 34 H. Holthoff, S. U. Egelhaaf, M. Borkovec, P. Schurtenberger and H. Sticher, *Langmuir*, 1996, **12**, 5541–5549.
- 35 G. Trefalt, I. Szilagyi, T. Oncsik, A. Sadeghpour and M. Borkovec, *Chimia*, 2013, **67**, 772–776.
- 36 L. Ehrl, Z. Jia, H. Wu, M. Lattuada, M. Soos and M. Morbidelli, *Langmuir*, 2009, **25**, 2696–2702.
- 37 M. Kobayashi, S. Yuki and Y. Adachi, *Colloids Surf., A*, 2016, **510**, 190–197.
- 38 F. Iselau, T. P. Xuan, G. Trefalt, A. Matic, K. Holmberg and R. Bordes, *Soft Matter*, 2016, **12**, 9509–9519.
- 39 D. Grolimund, M. Elimelech and M. Borkovec, *Colloids Surf., A*, 2001, **191**, 179–188.
- 40 M. M. Bradford, *Anal. Biochem.*, 1976, **72**, 248–254.
- 41 C. Cupp-Enyard, *J. Visualized Exp.*, 2008, **19**, e899.
- 42 D. R. Doerge, R. L. Divi and M. I. Churchwell, *Anal. Biochem.*, 1997, **250**, 10–17.
- 43 S. Saringer, R. A. Akula, A. Szerlauth and I. Szilagyi, *J. Phys. Chem. B*, 2019, **123**, 9984–9991.
- 44 P. Alpay and D. A. Uygun, *J. Mol. Catal. B: Enzym.*, 2015, **111**, 56–63.
- 45 S. H. Behrens, D. I. Christl, R. Emmerzael, P. Schurtenberger and M. Borkovec, *Langmuir*, 2000, **16**, 2566–2575.
- 46 B. Derjaguin and L. D. Landau, *Acta Phys. Chim.*, 1941, **14**, 633–662.
- 47 T. Zor and Z. Seliger, *Anal. Biochem.*, 1996, **236**, 302–308.
- 48 N. Zou and J. Plank, *J. Phys. Chem. Solids*, 2012, **73**, 1127–1130.
- 49 M. Pavlovic, P. Rouster and I. Szilagyi, *Nanoscale*, 2017, **9**, 369–379.
- 50 R. F. de Oliveira, M. L. de Moraes, O. N. Oliveira and M. Ferreira, *J. Phys. Chem. C*, 2011, **115**, 19136–19140.
- 51 D. G. Ramirez-Wong, C. Bonhomme, S. Demoustier-Champagne and A. M. Jonas, *J. Colloid Interface Sci.*, 2018, **514**, 592–598.
- 52 Z. Somosi, M. Pavlovic, I. Palinko and I. Szilagyi, *Nanomaterials*, 2018, **8**, 986.
- 53 M. Pavlovic, S. Murath, X. Katona, N. B. Alsharif, P. Rouster, J. Maleth and I. Szilagyi, *Sci. Rep.*, 2021, **11**, 4321.
- 54 S. Saringer, P. Rouster and I. Szilagyi, *Langmuir*, 2019, **35**, 4986–4994.
- 55 P. Rouster, M. Pavlovic, S. Saringer and I. Szilagyi, *J. Phys. Chem. C*, 2018, **122**, 11455–11463.
- 56 Y. K. Leong, *Colloid Polym. Sci.*, 1999, **277**, 299–305.
- 57 I. Popa, G. Papastavrou and M. Borkovec, *Phys. Chem. Chem. Phys.*, 2010, **12**, 4863–4871.
- 58 M. Pavlovic, P. Rouster, Z. Somosi and I. Szilagyi, *J. Colloid Interface Sci.*, 2018, **524**, 114–121.
- 59 A. vander Straeten, A. Bratek-Skicki, A. M. Jonas, C. A. Fustin and C. Dupont-Gillain, *ACS Nano*, 2018, **12**, 8372–8381.
- 60 H. J. Kim, Y. Suma, S. H. Lee, J. A. Kim and H. S. Kim, *J. Mol. Catal. B: Enzym.*, 2012, **83**, 8–15.
- 61 J. Hierrezuelo, A. Sadeghpour, I. Szilagyi, A. Vaccaro and M. Borkovec, *Langmuir*, 2010, **26**, 15109–15111.

dc 1931\_21

- 62 P. C. Almeida, I. L. Nantes, C. C. A. Rizzi, W. A. S. Judice, J. R. Chagas, L. Juliano, H. B. Nader and I. L. S. Tersariol, *J. Biol. Chem.*, 1999, **274**, 30433–30438.
- 63 X. X. Zhang, X. Y. Liu, G. W. Su, M. M. Li, J. Liu, C. Y. Wang and D. Xu, *Commun. Biol.*, 2021, **4**, 198.
- 64 P. C. Almeida, I. L. Nantes, J. R. Chagas, C. C. A. Rizzi, A. Faljoni-Alario, E. Carmona, L. Juliano, H. B. Nader and I. L. S. Tersariol, *J. Biol. Chem.*, 2001, **276**, 944–951.
- 65 J. L. S. Tersariol, D. C. Pimenta, J. R. Chagas and P. C. Almeida, *Braz. J. Med. Biol. Res.*, 2002, **35**, 135–144.
- 66 S. Akhtar, A. A. Khan and Q. Husain, *J. Chem. Technol. Biotechnol.*, 2005, **80**, 198–205.
- 67 K. Liburdi, C. Boselli, G. Giangolini, S. Amatiste and M. Esti, *Foods*, 2019, **8**, 600.
- 68 S. E. Gilliland, *J. Dairy Sci.*, 1969, **52**, 321–324.

Review

# Antioxidant Materials Based on 2D Nanostructures: A Review on Recent Progresses

Szabolcs Muráth <sup>\*</sup>, Nizar B. Alsharif, Szilárd Sáringer, Bojana Katana, Zoltán Somosi and Istvan Szilagyí <sup>\*</sup>

MTA-SZTE Lendület Biocolloids Research Group, Interdisciplinary Excellence Centre, Department of Physical Chemistry and Materials Science, University of Szeged, 1 Rerrich Béla tér, H-6720 Szeged, Hungary; nizar.alsharif@chem.u-szeged.hu (N.B.A.); saringer.szilard@chem.u-szeged.hu (S.S.); bkatana@chem.u-szeged.hu (B.K.); somosiz@chem.u-szeged.hu (Z.S.)

\* Correspondence: murathsz@chem.u-szeged.hu (S.M.); szistvan@chem.u-szeged.hu (I.S.); Tel.: +36-62-343255 (I.S.)

Received: 31 January 2020; Accepted: 21 February 2020; Published: 26 February 2020



**Abstract:** Counteracting reactive oxygen species (ROS, e.g., superoxide radical ion, H<sub>2</sub>O<sub>2</sub> and hydroxyl radical) is an important task in fighting against oxidative stress-related illnesses and in improving product quality in industrial manufacturing processes. This review focuses on the recent advances on two-dimensional (2D) nanomaterials of antioxidant activity, which are designed for effective decomposition of ROS and thus, for reduction of oxidative stress. Some materials featured in this paper are of uni- or multi-lamellar structures modified with small molecular or enzymatic antioxidants. Others are enzyme-mimicking synthetic compounds (the so-called nanozymes) prepared without antioxidant additives. However, carbon-based materials will not be included, as they were extensively reviewed in the recent past from similar aspects. Given the landmark development around the 2D materials used in various bio-applications, sheet-like antioxidant compounds are of great interest in the scientific and technological communities. Therefore, the authors hope that this review on the recent progresses will be helpful especially for researchers working on novel developments to substantially reduce oxidative stress either in biological systems or industrial liquors.

**Keywords:** antioxidant activity; 2D nanomaterial; nanozyme; clay; enzyme; chalcogenide; metal organic framework; oxidative stress; reactive oxygen species; radical scavenge

## 1. Introduction

Nanomaterials with two-dimensional (2D) structure have attracted notable scientific interest due to their high surface area and intriguing properties arising from their large variety of composition [1–5]. Starting with their light element-based representatives (e.g., graphene, graphite, graphite oxides, carbon nitride, boron nitride and covalent organic frameworks), through metal chalcogenide sheets, layered double hydroxides (LDHs), montmorillonites (MMTs), metal organic frameworks (MOFs) to thin noble metal platelets, one of the main advantages is that their composition is tunable for specific applications. In addition, 2D materials possess unusual electronic, mechanical and optical properties and hence, they can be used as building blocks in a wide range of composites. Concerning the contemporary applications of 2D compounds, they serve as efficient catalysts for water splitting [6–15] or organic reactions [16–21], drug carriers [22–31], sensors [32–39], materials for energy production and storage [2,15,21,40–49] or adsorbers [50–55].

Biocompatible 2D materials gained considerable popularity in the biochemical community, as indicated by the rapidly growing number of their bio-medical applications [56–58]. Among them, 2D antioxidant composites were developed [59–61] and used in decomposition of reactive oxygen species

(ROS) [62] and subsequently, to reduce oxidative stress in living and industrial systems. Tremendous improvement has been accomplished in the number and variety of antioxidant materials obtained over this period and the following approaches were reported (Figure 1): (i) immobilized natural and artificial enzymes, (ii) 2D materials loaded with molecular antioxidants and (iii) 2D composites of radical scavenging activities (nanozymes). In the present contribution, the antioxidant characteristics of such 2D materials are summarized emphasizing metal-based nano-objects. The carbonaceous materials of 2D structure were greatly investigated in the recent past and collective reviews were published on their applications [57,63–79]. Therefore, carbon-based 2D materials will not be discussed here.

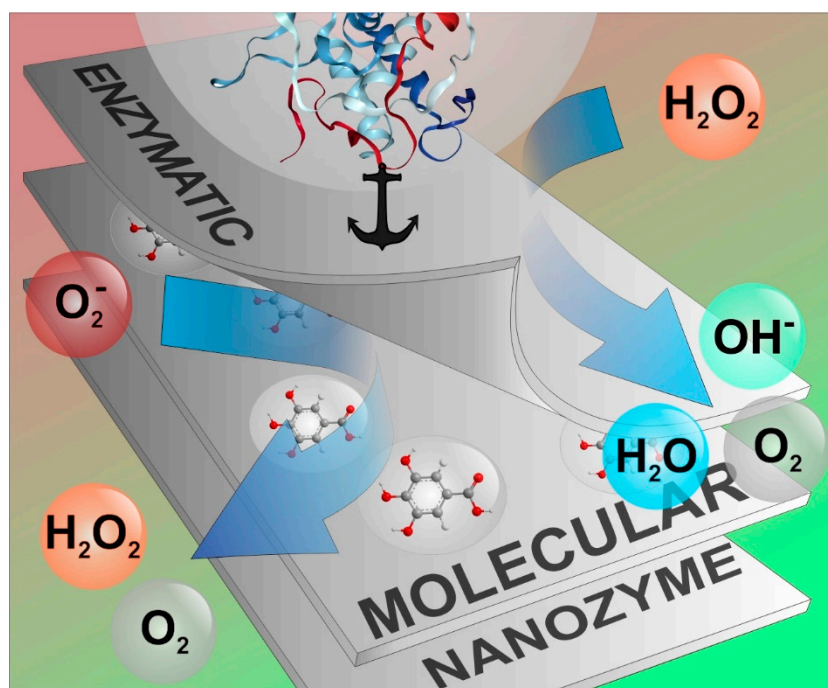


**Figure 1.** Illustration of molecular and enzymatic antioxidants immobilized in/on layered 2D materials. Schematic representation of superoxide radical anions and  $\text{H}_2\text{O}_2$  is also presented.

## 2. Natural Defense Systems versus Oxidative Stress

The most effective defense systems against reactive oxygen species (ROS), which induce oxidative stress at higher concentrations, are the antioxidant enzymes [80]. ROS include, for instance, superoxide radical anion,  $\text{H}_2\text{O}_2$ , hydroxyl and alkoxy radicals of short life time, but of extremely high reactivity [62]. They damage cell constituents leading to the development of various diseases such as chronic inflammation, neurological disorders and cancer [81]. On the other hand, efficient defense against ROS is also required in industrial manufacturing processes (e.g., food, cosmetic and textile industry) to improve the quality of the products [82,83].

Superoxide anion is one of the most notable ROS, since its decomposition by the superoxide dismutase (SOD) enzyme leads to the formation of molecular oxygen and  $\text{H}_2\text{O}_2$ . Therefore, the dismutation reaction is also a ROS source. Enzymatic assays were developed to estimate the SOD activity. In the most popular tests, radicals are produced in enzymatic ways and indicator molecules change their color upon reduction by the superoxide anions [84]. Inhibition of the radical-indicator reaction by the enzyme is the measure to assess the dismutation ability.

The two common enzyme groups that can break up  $\text{H}_2\text{O}_2$  are catalases and peroxidases [85,86]. During neutralization of harmful peroxides, catalases generate  $\text{O}_2$  gas and  $\text{H}_2\text{O}$ , while peroxidases perform homolytic bond cleavage on  $\text{H}_2\text{O}_2$  (Figure 1). The as-obtained hydroxyl radicals ( $\text{OH}\cdot$ ) either are consumed by an appropriate substrate near the active site or converted to water. The antioxidant



enzymes decompose ROS in tandem reactions in the intracellular environment, e.g.,  $\text{H}_2\text{O}_2$  produced by SOD is subsequently decomposed by catalase (see graphical abstract).

Besides antioxidant enzymes, molecular antioxidants also play an important role in reducing oxidative stress. They involve vitamins, carotenoids and flavonoids, for instance [87]. Supplementation from certain foods is feasible, however, their activity in ROS decomposition lags behind the enzymatic antioxidants. Non-enzymatic routes are also established to estimate antioxidant capacity. Methods based on free radicals involve 2,2-diphenyl-1-picrylhydrazyl (DPPH) [88], nitrogen monoxide (NO) [89], radical form of 2,2'-azino-bis(3-ethylbenzthiazoline-6-sulfonic acid) ( $\text{ABTS}^+$ ) [90] and peroxy nitrite ion ( $\text{ONOO}^-$ , prepared by the direct, cold peroxidation of nitrite salts) [91], which are relatively stable and can be reduced by the antioxidant of choice.

In addition, Fenton reaction, which is a catalytic route to decompose  $\text{H}_2\text{O}_2$  in the presence of metal ions, especially  $\text{Fe}^{2+}$  or  $\text{Fe}^{3+}$ , generating aggressive  $\text{OH}\cdot$  and  $\text{OOH}\cdot$  radicals, therefore used for strong oxidations and thus, it is a radical source to probe enzymatic antioxidant compounds [92]. Two indirect radical-based tests include thiobarbituric acid (TBA) as substrate [93]. The degradation of 2-deoxyribose by Fenton reaction [94] and egg lipid peroxidation [95] produces small dialdehydes, mainly malondialdehyde that gives a colored condensation product with TBA. If  $\text{OH}\cdot$  radicals in Fenton kinetics or the lipid damaging radicals are consumed by antioxidants, the color in the reactions with TBA are less profound. Further, two assays take oxidative metal complexes as reagents with  $\text{Fe}^{3+}$  (Ferric reducing antioxidant power assay (FRAP) [96], with 2,4,6-tris(2-pyridyl)-s-triazine ligand) and  $\text{Cu}^{2+}$  (cupric reducing antioxidant capacity (CUPRAC) assay [97], with 2,9-dimethyl-1,10-phenanthroline ligand) central ions. The latter test has a kinetic advantage as the  $\text{Cu}^{2+}$  complex is easier to reduce. For detailed antioxidant effect of various materials, the reader is referred to the works of Nimse and Pal [98] and Valgimigli et al. [99].

Due to the increased harmful environmental effects such as air pollution, food additives and radiations, the ROS level increased and thus, oxidative stress became an important issue nowadays. The supplementation of the above natural antioxidants is complicated due to their high sensitivity to the environmental conditions (enzymatic) or limited water solubility (molecular). Therefore, their heterogenization in composite materials, which provides sufficient protection and solubilization of the antioxidants, is a promising research direction.

### 3. Metal Oxide Structures

#### 3.1. Cobalt-Based 2D Oxides

The intrinsic peroxidase and catalase activity of  $\text{Co}_3\text{O}_4$  was first described in 2012 for cubic nanoparticles [100] (NPs) and was proven at several occasions for spherical NPs [101] and architectures consisting of  $\text{Co}_3\text{O}_4$  nanorods [102]. Morphology-dependent study was also conducted, revealing an order of nanocubes < nanorods < nanoplates (Figure 2) in catalytic activity, pointing out that the efficiency depends on the most exposed crystal plane [103]. The same correlation was found by Zhang et al. who were able to produce polyhedrons of  $\text{Co}_3\text{O}_4$ , possessing approximately 55% of peroxidase and 70–80% of catalase activity, compared to the 2D platelets [104]. Data of the quantitative assessment of the activity, together with other 2D antioxidant systems discussed in this feature article, are given in Table 1.

**Table 1.** Two-dimensional 2D nanomaterials of antioxidant properties and the quantitative assessment of their activities in test reactions.

Materials	Mimicked Enzymes		Activity Assessment <sup>a</sup>		Ref.
Cu(4-hydroxythiophenol) Nanosheets	Peroxidase	H <sub>2</sub> O <sub>2</sub> TMB	K <sub>m</sub> (mM) 0.716 0.431		[19]
MoS <sub>2</sub> Nanosheets	Peroxidase	H <sub>2</sub> O <sub>2</sub>	K <sub>m</sub> (mM) 0.003	v <sub>max</sub> (10 <sup>-6</sup> mol/min) 3.4	[39]
Mg/Al-CO <sub>3</sub> -LDH-SOD Mg/Al-CO <sub>3</sub> -LDH-SOD-Hep	SOD	Fridovich method <sup>b</sup>	IC <sub>50</sub> (mg/L) <sup>c</sup> 0.056 0.096		[60]
SOD-PDADMAC-TNS	SOD	Fridovich method <sup>b</sup>	IC <sub>50</sub> (mg/L) 0.057		[61]
Co <sub>3</sub> O <sub>4</sub> Sisal-like Structures	Peroxidase	H <sub>2</sub> O <sub>2</sub> TMB	K <sub>m</sub> (mM) 0.827 0.015		[102]
Co <sub>3</sub> O <sub>4</sub> Nanoplates	Peroxidase	H <sub>2</sub> O <sub>2</sub> TMB	K <sub>m</sub> (mM) 284 0.090	v <sub>max</sub> (10 <sup>-8</sup> M/s) 48.1 9.9	[103]
Co <sub>3</sub> O <sub>4</sub> Nanoplates	Peroxidase	Fixed TMB and H <sub>2</sub> O <sub>2</sub>	v 0.038 a.u./s		[104]
Co <sub>3</sub> O <sub>4</sub> Microbelts	Peroxidase	H <sub>2</sub> O <sub>2</sub> TMB	K <sub>m</sub> (mM) 0.0262 0.012		[105]
Co <sub>3</sub> O <sub>4</sub> -CeO <sub>2</sub> Nanosheets	Peroxidase	H <sub>2</sub> O <sub>2</sub> TMB	K <sub>m</sub> (mM) 132.2 0.36	v <sub>max</sub> (10 <sup>-8</sup> M/s) 4.3 16.7	[106]
Co <sub>3</sub> O <sub>4</sub> Nanosheets	Peroxidase	H <sub>2</sub> O <sub>2</sub> TMB	K <sub>m</sub> (mM) 2.22 0.082	v <sub>max</sub> (10 <sup>-8</sup> M/s) 11.8 6.6	[107]
V <sub>2</sub> O <sub>5</sub> nanosheets	Glutathione Peroxidase	GSH H <sub>2</sub> O <sub>2</sub>	K <sub>m</sub> (mM) 3.425 0.0573	v <sub>max</sub> (10 <sup>-8</sup> M/s) 778.8 388.5	[108]
VO <sub>2</sub> Nanosheets	Peroxidase	H <sub>2</sub> O <sub>2</sub> TMB	K <sub>m</sub> (mM) 2.924 0.111	V <sub>max</sub> (10 <sup>-8</sup> M/s) 97300 16800	[109]
HRP-Titanate Nanosheets	HRP	Guaiacol	K <sub>m</sub> (mM) 2.06	v <sub>max</sub> (10 <sup>-8</sup> M/s) 176	[110]
SOD-Titanate Nanosheets	SOD	Hypoxanthine/XO Cytochrome c	IC <sub>50</sub> (U) 0.036		
HPR-TiO <sub>x</sub> nanosheets-magnetic beads	HRP	Guaiacol	K <sub>m</sub> (mM) 1.8	v <sub>max</sub> (10 <sup>-8</sup> M/s) 330	[111]
Au-MoS <sub>2</sub> Nanoribbons	Peroxidase	H <sub>2</sub> O <sub>2</sub> TMB	K <sub>m</sub> (mM) 10 0.015	v <sub>max</sub> (10 <sup>-8</sup> M/s) 1170 670	[112]
MoS <sub>x</sub> -Co(OH) <sub>2</sub> Nanoflakes	Peroxidase	H <sub>2</sub> O <sub>2</sub> TMB	K <sub>m</sub> (mM) 0.127 0.236	v <sub>max</sub> (10 <sup>-8</sup> M/s) 8.73 5.69	[113]
MoSe <sub>2</sub> Nanosheets	Peroxidase	H <sub>2</sub> O <sub>2</sub> TMB	K <sub>m</sub> (mM) 0.155 0.014	v <sub>max</sub> (10 <sup>-8</sup> M/s) 0.99 0.56	[114]
VS <sub>2</sub> Nanosheets	Peroxidase	H <sub>2</sub> O <sub>2</sub> TMB	K <sub>m</sub> (mM) 3.49 0.28	v <sub>max</sub> (10 <sup>-8</sup> M/s) 55.7 41.6	[115]
Cu-Boron Nitride Nanosheets	Peroxidase	H <sub>2</sub> O <sub>2</sub> TMB	K <sub>m</sub> (mM) 25 0.175	v <sub>max</sub> (10 <sup>-8</sup> M/s) 12.5 3.76	[116]
Ni-MOF Nanosheets	HRP	H <sub>2</sub> O <sub>2</sub> TMB	K <sub>m</sub> (mM) 2.49 0.365	v <sub>max</sub> (10 <sup>-8</sup> M/s) 130 6.53	[117]

Table 1. Cont.

Materials	Mimicked Enzymes	Activity Assessment <sup>a</sup>			Ref.
HRP-Hep-LDH	HRP	Guaiacol	K <sub>m</sub> (mM) 5.25	v <sub>max</sub> (10 <sup>-8</sup> M/s) 272	[118]
Carnosine-MgAl-LDH Gallic acid-MgAl-LDH	– <sup>d</sup>	DPPH	Scavenging activity 95.9% 83.9%		[119]
Gallic acid-Zn <sub>2</sub> Al-NO <sub>3</sub> -LDH	– <sup>d</sup>	DPPH	Scavenging activity 93%		[120]
Organic solvent treated EA-LDH	– <sup>d</sup>	DPPH CUPRAC assay	Scavenging activity up to 80–90% TEAC value >1		[121]
IrganoxCOOH-MgAl-LDH Trolox-MgAl-LDH	– <sup>d</sup>	DPPH	EC <sub>50</sub> 0.13 0.24		[122]
Olanzapine-CaAl-LDH Olanzapine-NiAl-LDH	– <sup>d</sup>	DPPH ABTS NO	EC <sub>50</sub> (µg/mL) <sup>e</sup> 8.541 11.630 0.681 1.117 8.574 22.970		[123]
SOD-Hep-LDH Cu(Hsm) <sub>2</sub> -PVPMAA-LDH	SOD	Fridovich Method	IC <sub>50</sub> (nM) 2.9 97		[124]
DNA-CoAl-LDH	Peroxidase	H <sub>2</sub> O <sub>2</sub> TMB	K <sub>m</sub> (mM) 10.24 1.775	v <sub>max</sub> (10 <sup>-8</sup> M/s) 2.3 4.09	[125]
(Bael oil proteins)-MgAl-LDH	– <sup>d</sup>	DPPH	Scavenging activity 42–50%		[126]
CoAl-LDH	Peroxidase	H <sub>2</sub> O <sub>2</sub> TMB	K <sub>m</sub> (mM) 22.13 0.372	v <sub>max</sub> (s <sup>-1</sup> ) 0.598 0.101	[127]
NiFe-LDH	Peroxidase	H <sub>2</sub> O <sub>2</sub> TMB	K <sub>m</sub> (mM) 2.4 0.5		[128]
Polyethylene Glycol-Fe-LDH	Peroxidase	H <sub>2</sub> O <sub>2</sub>	K <sub>m</sub> (mM) 0.09	v <sub>max</sub> (10 <sup>-8</sup> M/s) 176	[129]
AEA-GSH- MMT	– <sup>d</sup>	ABTS	Scavenging activity 59.88%		[130]
Blue Berry Extract-MMT	– <sup>d</sup>	DPPH	Scavenging activity 38%		[131]
PHB-TPS/eugenol-MMT	– <sup>d</sup>	DPPH	Scavenging activity 92%		[132]
Hemin-Hsm-MMT	HRP	Guaiacol	Rate constant (A/min) 0.107		[133]
TOC-CSNPs/CS/MMT <sup>§</sup>	– <sup>d</sup>	DPPH	Scavenging activity 46.5%		[134]
ZnS-MMT	Peroxidase	H <sub>2</sub> O <sub>2</sub> TMB	K <sub>m</sub> (mM) 0.0254 0.055	v <sub>max</sub> (10 <sup>-8</sup> M/s) 0.750 7.993	[135]
CuS-MMT	Peroxidase	H <sub>2</sub> O <sub>2</sub> TMB	K <sub>m</sub> (mM) 2.27 0.0212	v <sub>max</sub> (10 <sup>-8</sup> M/s) 0.971 2.814	[136]
Ag <sub>2</sub> S-MMT	Peroxidase	H <sub>2</sub> O <sub>2</sub> TMB	K <sub>m</sub> (mM) 1.874 0.00412	v <sub>max</sub> (10 <sup>-8</sup> M/s) 2.286 5.27	[137]
CoNiS-3/MMT	Peroxidase	H <sub>2</sub> O <sub>2</sub> TMB	K <sub>m</sub> (mM) 1.247 0.821	v <sub>max</sub> (10 <sup>-8</sup> M/s) 6.92 68.31	[138]

Table 1. Cont.

Materials	Mimicked Enzymes	Activity Assessment <sup>a</sup>			Ref.
		Substrate/Assay	$K_m$ (mM)	$v_{max}$ ( $10^{-8}$ M/s)	
HRP-MMT	HRP	Phenol	12.96	7150	[139]
Cu-Zn complex-MMT	SOD	Fridovich method <sup>b</sup>		IC <sub>50</sub> ( $\mu$ M) 91.0	[140]
Cu-histidine-MMT	SOD	Fridovich method <sup>b</sup>		IC <sub>50</sub> ( $\mu$ M) 251	[141]
Ni Foam-CoP Nanosheets	Peroxidase	H <sub>2</sub> O <sub>2</sub> TMB	4.90 0.54		[142]
Co <sub>2</sub> (OH) <sub>2</sub> CO <sub>3</sub> -CeO <sub>2</sub> Nanosheets	Peroxidase	H <sub>2</sub> O <sub>2</sub> TMB	10.01 0.14	10.21 20.14	[143]
Fe <sub>3</sub> (PO <sub>4</sub> ) <sub>2</sub> ·8 H <sub>2</sub> O Nanoflowers	Peroxidase	H <sub>2</sub> O <sub>2</sub> TMB	0.11 0.36	5.58 1.58	[144]
Porous Iron Oxide Nanoflakes	Peroxidase	H <sub>2</sub> O <sub>2</sub> TMB	150.47 0.24	3.12 3.07	[145]

<sup>a</sup> The columns contain the applied substrate or assay and the quantitative measure of the activity; <sup>b</sup> The method is described in reference [84]; <sup>c</sup> Concentration of enzyme or enzyme mimic necessary to decompose 50% of the radicals forming in the test reaction; <sup>d</sup> General radical scavenging activity was assessed, no enzymatic assays was applied; <sup>e</sup> Top values belong to olanzapine-CaAl-LDH and the bottom ones to olanzapine-NiAl-LDH. Abbreviation list: TMB: 3,3',5,5'-tetramethylbenzidine, SOD: superoxide dismutase, GSH: glutathione, HRP: horseradish peroxidase, XO: xanthine oxidase, DPPH: 2,2-diphenyl-1-picrylhydrazyl, CUPRAC: cupric reducing antioxidant capacity, ABTS: 2,2'-azino-bis(3-ethylbenzthiazoline-6-sulfonic acid).

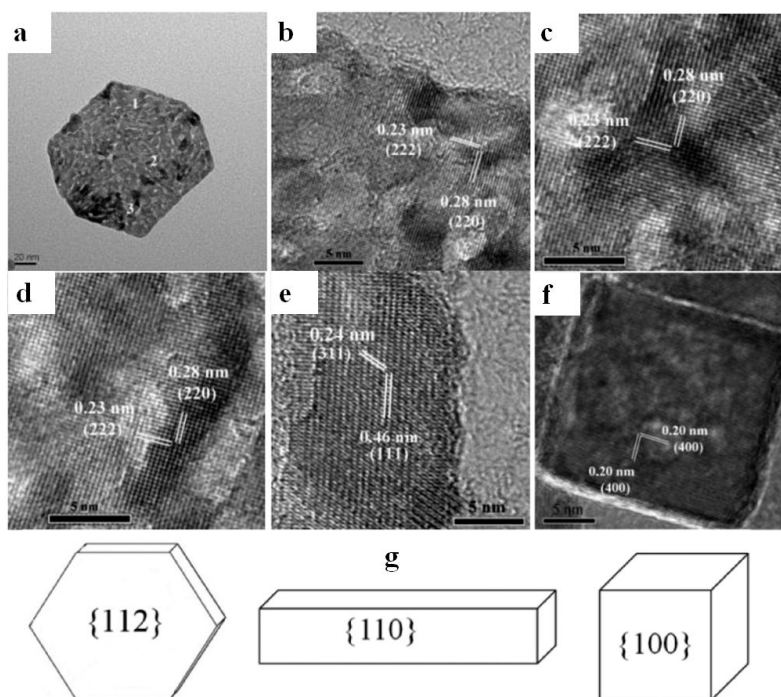


**Figure 2.** TEM image of a typical Co<sub>3</sub>O<sub>4</sub> nanoplate (a), high-resolution transmission electron microscopy (HRTEM) images of site 1 (b), site 2 (c) and site 3 (d) of Co<sub>3</sub>O<sub>4</sub> nanoplate, a HRTEM image of a Co<sub>3</sub>O<sub>4</sub> nanorod (e), a HRTEM image of a Co<sub>3</sub>O<sub>4</sub> nanocube (f) and exposed crystal planes on the nanoplate, nanorod and nanocube of Co<sub>3</sub>O<sub>4</sub> (g). Reproduced from Reference [103] with permission from the PCCP Owner Societies.

Elongated 2D Co<sub>3</sub>O<sub>4</sub> belts were obtained by electrospinning technique from Co(NO<sub>3</sub>)<sub>2</sub> containing polyvinylpyrrolidone gel with superior affinity compared to the native horseradish peroxidase (HRP)



enzyme and up to 100-fold higher activity was calculated from the Michaelis constants ( $K_m$ ) determined in the test reactions involving  $H_2O_2$  and TMB (3,3',5,5'-tetramethylbenzidine). Besides, the belts were found to be stable at significantly higher temperature than HRP [105]. The high-resolution transmission electron microscopy (HRTEM) images of the belts obtained reflect characteristic basal distances of 0.24 and 0.29 nm assigned to (311) and (220) interplanar spacings in  $Co_3O_4$ , respectively.

Platelets of  $Co_3O_4$  were combined with  $CeO_2$  sheets to a nanocomposite of relatively low affinity towards  $H_2O_2$ , as indicated by higher  $K_m$  values, but excellent maximum reaction rate ( $v_{max}$ ) was observed in the diffusion controlled regime [106]. Separately, both oxides are considered as peroxidase nanozymes that was reinforced in the composite, which was later used as a paper based analytical glucose sensor with smartphone software quantification.

In a recent finding, porous  $Co_3O_4$  nanoplates of pH-switchable peroxidase-like (acidic medium) or catalase-like (basic medium) properties was synthesized [107]. Overall, the porous flakes possessed remarkable kinetic parameters and were used as a glucose sensor enabled by glucose oxidase (GOx)-glucose selective reaction (Figure 3).

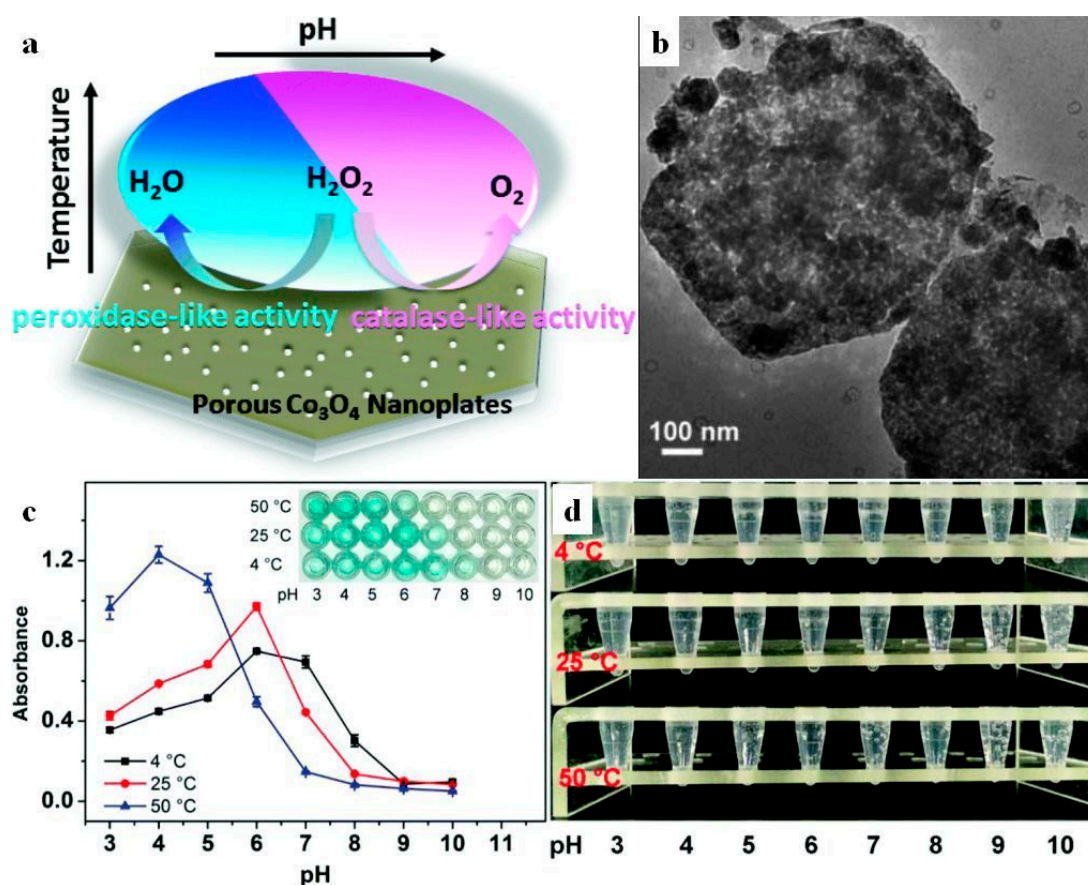


**Figure 3.** Schematic representation of the multienzymatic activity of porous  $Co_3O_4$  flakes (a) captured on TEM micrograph (b), the peroxidase activity of the nanoflakes in TMB assay with visual representation as inset photograph (c) and its  $O_2$  evolution through catalase activity (d). Reproduced from Reference [107] with permission from the Royal Society of Chemistry.

Finally, a mixed-valance state lamellar cobalt oxide with non-stoichiometric composition was also used as a nanozyme to oxidize TMB substrate with molecular  $O_2$  [146]. This structure was synthesized by partial oxidation of Co(II)-trimesate and was applied as a glutathione (GSH) sensor.

## 3.2. Vanadium-Based Oxides

Ghosh et al. extensively examined the morphology-activity correlation of orthorhombic  $V_2O_5$  structures of peroxidase activity [108]. Unlike  $Co_3O_4$  [104], they found that surface area is not a main factor in activity, but it is the accessibility of active sites on the dominant crystal faces. The GSH-mediated peroxidase activity and surface area of the nanomaterials obtained are depicted in Figure 4 (with  $V_2O_5$  abbreviated as V), showing that  $V_2O_5$  spheres reached the highest maximum rate, followed by flowers, sheets and wires, out of which only wires and 2D sheets are saturated at the lowest  $H_2O_2$  concentration.

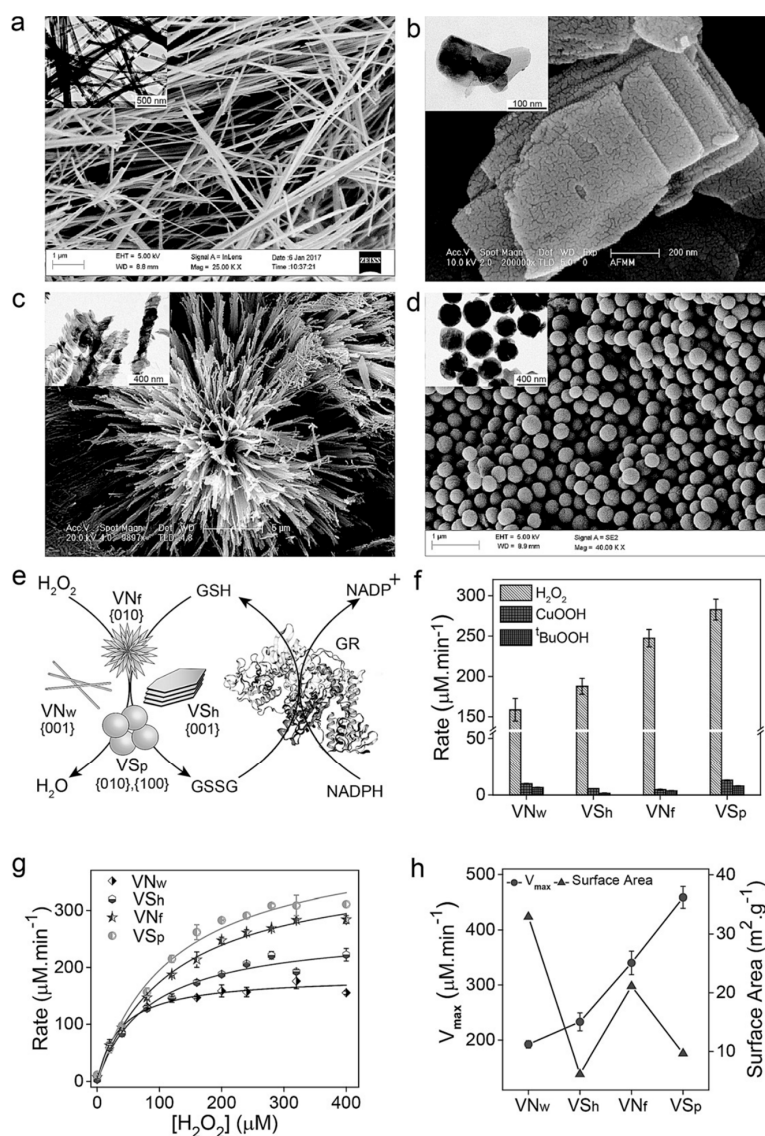


**Figure 4.** SEM and TEM (inset) images of  $V_2O_5$  nanowires ( $V_{Nw}$ ) (a),  $V_2O_5$  sheets ( $V_{Sh}$ ) (b),  $V_2O_5$  nanoflowers ( $V_{Nf}$ ) (c) and  $V_2O_5$  spheres ( $V_{Sp}$ ) (d). Reduction of  $H_2O_2$  by GSH in the presence of nanomaterials, glutathione reductase (GR) and NADPH (e). The GSH peroxidase-like activity using  $H_2O_2$ , tert-butyl hydroperoxide (t-BuOOH) and cumene hydroperoxide (CuOOH) (f). Michaelis–Menten plot for the nanozymes (g). Trends in  $v_{max}$  and surface area (h). Copyright (2020) Wiley. Used with permission from (Ghosh, S.; Roy, P.; Karmodak, N.; Jemmis, E.D.; Mugesh, G. Nanozymes: Crystal-facet-dependent enzyme-mimetic activity of  $V_2O_5$  nanomaterials. *Angew. Chem. Int. Ed.* **2018**, *57*, 4510–4515) Reference [108].

Aside from its peroxidase mimic, a layered  $V_2O_5$  2D structure was also used to detect GSH via an oxidase-type mechanism [147]. Lower valence state vanadium oxide,  $VO_2$  was investigated in various morphologies [109]. Fibrillar, lamellar and elongated NPs were tested against TMB substrate and it was pointed out that  $VO_2$  sheets exhibited the best kinetic overall parameters in regard of  $K_m$  and  $v_{max}$ . Additionally, the aforementioned  $VO_2$  particles were applied as  $H_2O_2$  sensors with the nanosheets providing linear range up to 62.5 mM  $H_2O_2$ , four times higher than the second best performing nanorods.

### 3.3. Titania-Based Composites

The prominent photocatalytic activity of pure and doped  $TiO_2$  is known for decades [4]. Despite Ti(IV) is moderately redox active,  $TiO_2$  is not an antioxidant nanozyme. However, its negative surface charge in a broad range of pH makes it a suitable vehicle for HRP immobilization, for instance. Xie et al., constructed hollow titania spheres based on sheets as building blocks, capable storing 20 mass% HRP owing to the porous structure [148]. This highly loaded material was used for electrochemical  $H_2O_2$  sensing with linearity over three orders of magnitudes.

Moreover, titania materials were proved as excellent solid supports for other antioxidant enzymes due to their biocompatibility, high abundance of surface functionalities and chemical inertness. Surface modifications with polyelectrolytes resulted in stable structures capable of hosting various enzymes. Accordingly, lamellar titania nanosheet (TNS)-based nanocomposite with this setup had peroxidase activity nearly identical to the bare HRP (Figure 5) [149]. An adsorbed positively charged poly(diallyldimethylammonium chloride) (PDADMAC) polyelectrolyte layer improved the enzyme's structural integrity over longer timeframes and maintained a good colloidal stability for the platelets.

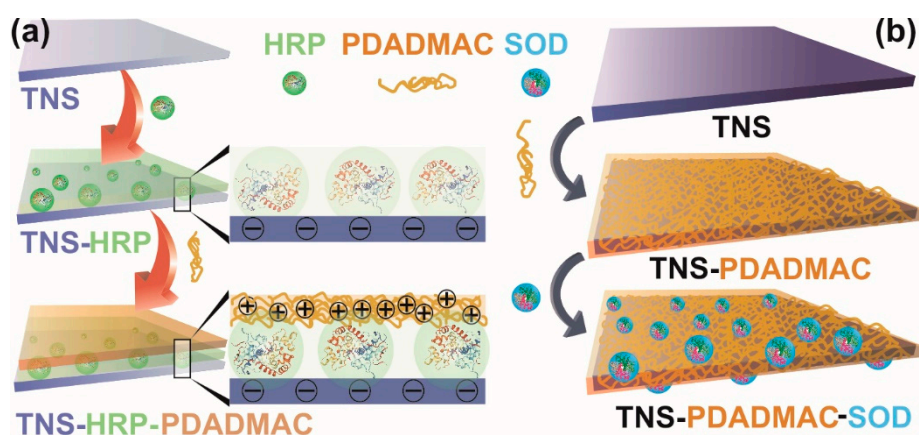


**Figure 5.** Illustration of HRP (a) and SOD (b) immobilization on titania nanosheet (TNS) of saturated poly(diallyldimethylammonium chloride (PDADMAC) polyelectrolyte layer on the surface. Reprinted with permission from (Rouster, P.; Pavlovic, M.; Saringer, S.; Szilagyi, I. Functionalized titania nanosheet dispersions of peroxidase activity. *J. Phys. Chem. C* **2018**, *122*, 11455–11463) Reference [149]. Copyright (2020) American Chemical Society (a). Copyright (2020) Wiley. Used with permission from (Rouster, P.; Pavlovic, M.; Szilagyi, I. Immobilization of superoxide dismutase on polyelectrolyte functionalized titania nanosheets. *ChemBiochem* **2018**, *19*, 404–410) Reference [61] (b).

The same TNS was used to immobilize SOD enzyme [61]. Surface functionalization was carried out first with PDADMAC to obtain positively charged sheets and the enzyme was attached through electrostatic and hydrophobic interactions. The same superoxide anion radical scavenging activity of the free and attached SOD indicated that the enzyme kept its structural integrity upon immobilization.

Kamada et al. demonstrated that nanometric titanate nanosheets enhanced the catalytic properties of aqueous HRP and SOD [110]. It was claimed that TNS served as a surfactant and helped to decrease the number of HRP and SOD aggregates in the solution, exposing more catalytic centers for the



reactions to occur. This was possible due to electrostatic attraction, thus immobilization of the enzymes on TNS particles, as indicated by dynamic light scattering measurements.

Stable suspensions were obtained by immobilizing HRP and magnetic beads on positively charged layered titania in slightly acidic samples [111]. Although steric hindrance and possibly slight conformational changes led to reduced HRP activity, the magnetic composite was separable with strong magnets at the end of catalytic cycles. Furthermore, the reused material maintained 80% of its original activity after 5 repetitions.

#### 4. Chalcogenide Structures

Among the other lamellar chalcogenides, molybdenum compounds were inspected thoroughly. Pure MoS<sub>2</sub> has multienzymatic activity under physiological conditions. It was reported to have the ability to scavenge superoxide radicals generated by the xanthine/xanthine oxidase system and to degrade H<sub>2</sub>O<sub>2</sub> in catalase and peroxidase-type manners [59]. Although the generation of OH· radicals was evident by using DMPO (5,5-dimethyl-pyrroline N-oxide) as a radical trap for electron paramagnetic resonance (EPR) spectroscopy measurements, the OH· radical products were transformed to H<sub>2</sub>O, proven by the scavenging of Fenton-type developed radicals. Furthermore, the 2D MoS<sub>2</sub> was used as a scavenger for other reactive species, e.g., NO and DPPH radicals, meaning that the nanozyme was an excellent oppressor of oxidative stress during in vitro measurements (Figure 6). Moreover, in vivo experiments revealed that MoS<sub>2</sub> sheets protected *E. coli* and *S. aureus* bacteria from H<sub>2</sub>O<sub>2</sub>-induced oxidative stress. While the nanozyme was fully biocompatible with *E. coli*, it expressed a moderate toxicity on *S. aureus*.

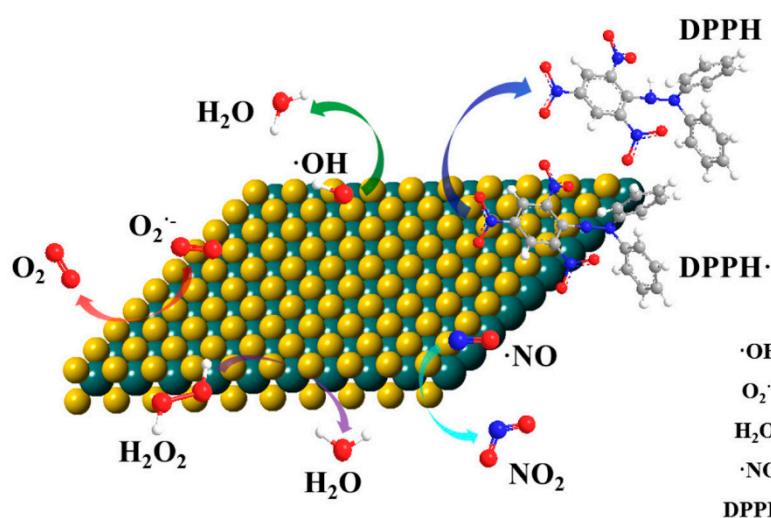


**Figure 6.** Illustration of the multi-fold antioxidant activity of MoS<sub>2</sub> nanosheets. Reprinted with permission from (Chen, T.M.; Zou, H.; Wu, X.J.; Liu, C.C.; Situ, B.; Zheng, L.; Yang, G.W. Nanozymatic antioxidant system based on MoS<sub>2</sub> nanosheets. *ACS Appl. Mater. Interfaces* **2018**, *10*, 12453–12462) Reference [59]. Copyright (2020) American Chemical Society.

Later, Nandu et al. showed that out of many proteins, lipase selectively masked the peroxidase activity of 2D MoS<sub>2</sub> [39], as indicated by the increasing  $K_m$  values, i.e., decreasing affinity towards H<sub>2</sub>O<sub>2</sub>. The  $v_{max}$  value was also decreased by more than 94% in the presence of lipase. Based on this principle, the MoS<sub>2</sub> NPs were used as a colorimetric lipase sensor.

The peroxidase activity of MoS<sub>2</sub> sheets can be improved by depositing Au NPs on the surface to drastically increase reaction rate (100-fold increment in  $v_{max}$ ) and the affinity to TMB substrate (350-fold decrease in  $K_m$ ) [112]. This system was also used as a probe in detection of free cholesterol.

In another study, 2D Co(OH)<sub>2</sub> flakes were combined with MoS<sub>4</sub><sup>2-</sup> ions and treated hydrothermally to get a mainly amorphous CoMo(OH)<sub>x</sub>S<sub>y</sub> or simply CoMo hybrid, perceived as MoS<sub>x</sub> doped



$\text{Co}(\text{OH})_2$  [113]. This novel material acted as a tri-enzymatic mimic with catalase, peroxidase and oxidase activity (Figure 7).

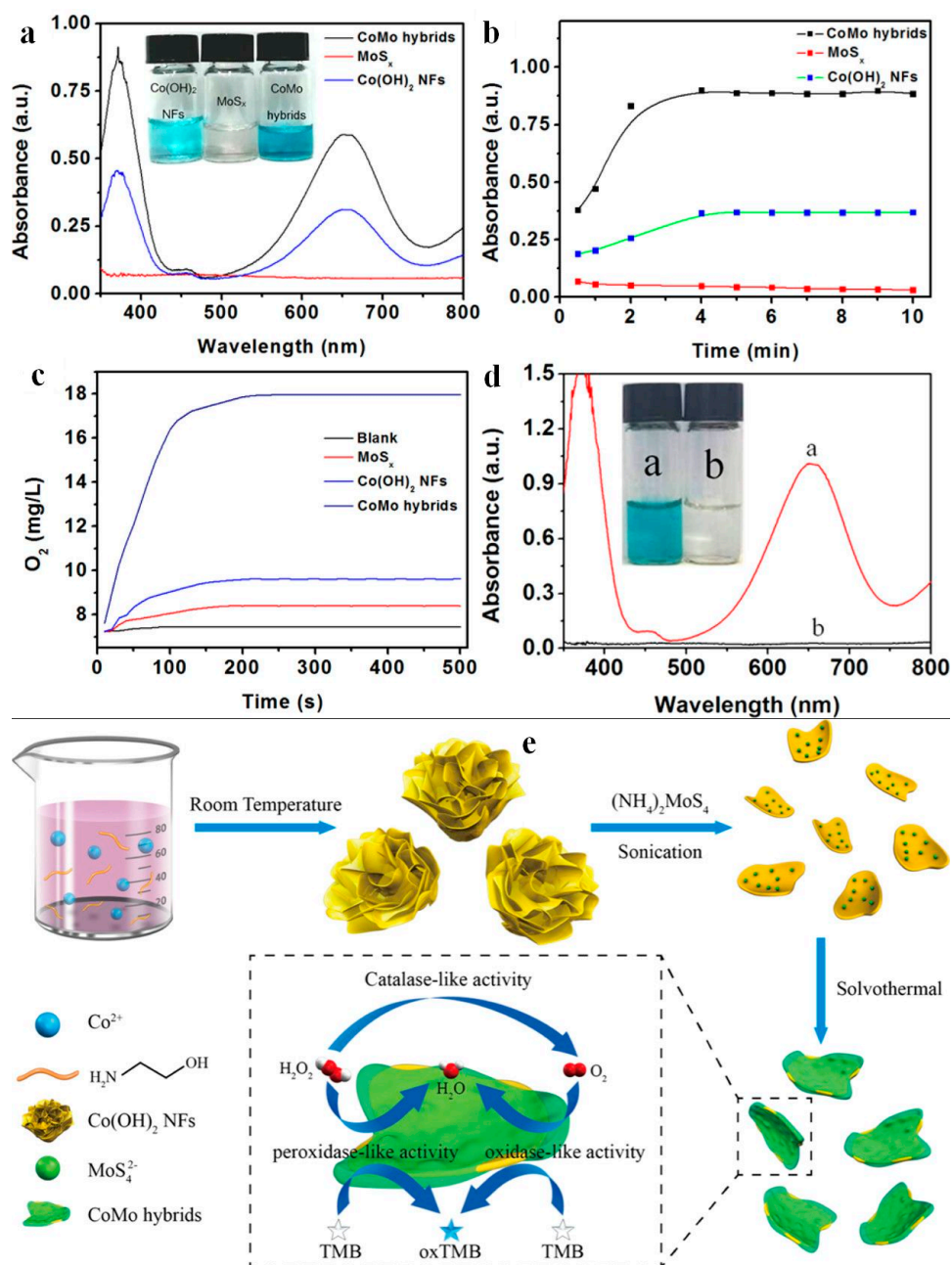


**Figure 7.** Absorbance intensity of TMB and 50 mM  $\text{H}_2\text{O}_2$  upon the addition of different materials (a). Time-dependent absorbance of TMB at 652 nm varied with different catalysts used (b).  $\text{O}_2$  generation from  $\text{H}_2\text{O}_2$  decomposition with different catalysts (c). Catalytic activity comparison of CoMo hybrids and the supernatant coexisting with the CoMo hybrids (d). Visualized reaction scheme to obtain the CoMo hybrids (e). Reprinted with permission from (Ding, Y.Q.; Wang, G.; Sun, F.Z.; Lin, Y.Q. Heterogeneous nanostructure design based on the epitaxial growth of spongy  $\text{MoS}_x$  on 2D  $\text{Co}(\text{OH})_2$  nanoflakes for triple-enzyme mimetic activity: Experimental and density functional theory studies on the dramatic activation mechanism. *ACS Appl. Mater. Interfaces* **2018**, *10*, 32567–32578) Reference [113]. Copyright (2020) American Chemical Society.

The molybdenous modification improved the Michaelis–Menten parameters of lamellar  $\text{Co}(\text{OH})_2$ . Exfoliated  $\text{MoSe}_2$  sheets with few hundreds nm lateral size also possessed superb peroxidase mimicking properties [114]. Although this structure's maximum rate in  $\text{H}_2\text{O}_2$  decomposition with TMB as chromogen is lower than that of native HRP's, the  $K_m$  values observed are outstanding, making the material an effective sensor for xanthine and  $\text{H}_2\text{O}_2$  detection (Table 1).

Huang et al. proved that  $\text{VS}_2$  sheets catalyzes homolytic cleavage of  $\text{H}_2\text{O}_2$  in a faster reaction than HRP and the nanozyme also possesses higher affinity to both  $\text{H}_2\text{O}_2$  and TMB compared to the native enzyme [115]. The same mechanism was implied for a  $\text{BN@CuS}$  composite [116], suitable for detection of cholesterol and for an  $\text{HRP@WS}_2$  hybrid [150], evidently. Several different sulfides were used as a composite building block with montmorillonites, which are detailed later.

## 5. Metal Organic Frameworks (MOFs)

MOFs are a subgroup of coordination polymers built up by metal ions coordinated and interlinked by multidentate bridging organic ligands [48]. In MOFs, the coordination network contains voids leading to enlarged surface area. Utilizing their favorable surface properties, Huang et al. constructed ca. 4 nm thick Cu-based MOFs with Fe or Co complexes of a porphyrin ligand (tetrakis(4-carboxyphenyl)porphyrin, TCPP) decorated with 2 nm spherical Au NPs [151]. While the bare MOF was attested to be a peroxidase mimic (in acidic buffers near pH 3–4, similar for all MOFs with peroxidase activity), Au deposition turned the material into a GOx mimic, after which the concentration of gluconic acid was measured by a photometric assay. Similarly, Qin et al. used the same Fe-TCPP in Zn, Co and Cu-MOFs as peroxidases with altered activity in the presence of numerous phosphates of biological relevance [152]. Based on their activity change, the peroxidase probe reaction was utilized to detect the biomolecules mixed with the MOFs. Ultrathin (2 nm) variants of the same Cu and Co-MOFs, alongside a Ni-containing one, were also synthesized and used as a modifier on glassy carbon electrodes fused with carbon nanotubes or graphene oxide [49].

Although MOFs are noteworthy peroxidase nanozymes under pH 5, this value makes it hard for researchers to utilize them during in vivo experiments. Bridging this gap, a cascade system was fabricated using the well-known Cu-MOF applying Fe-TCPP in the synthesis [153]. In the first step, GOx was immobilized on the framework that oxidized glucose in the presence of molecular  $\text{O}_2$ . During this reaction, the pH dropped (Figure 8), therefore the generated  $\text{H}_2\text{O}_2$  was decomposed by a self-activated peroxidase mechanism. The resulting  $\text{OH}\cdot$  radicals are strong potent antibacterial agents, decimating *S. aureus* bacteria after injecting onto mice wound using a band-aid containing the biocompatible  $\text{GOx@MOF}$  and glucose.

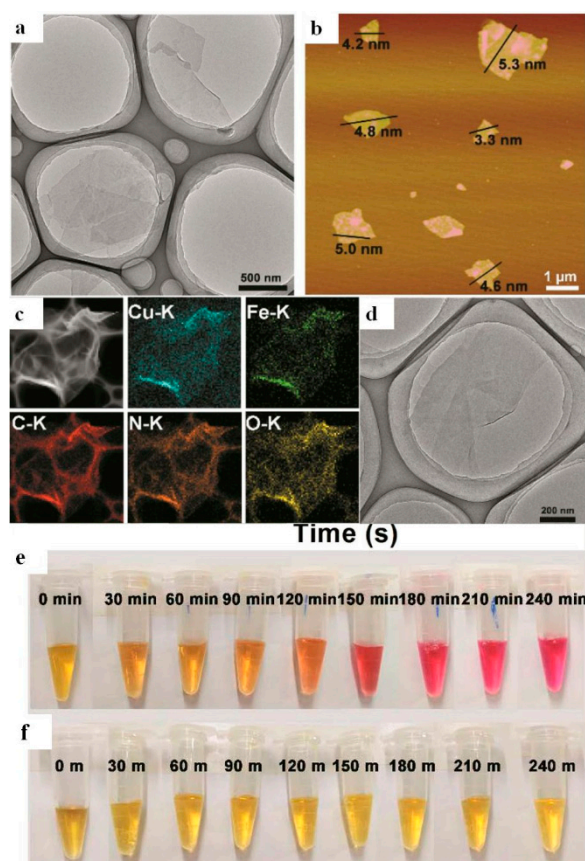


**Figure 8.** TEM micrograph of Cu-TCPP(Fe) 2D MOF nanosheets (a). AFM image of Cu-TCPP(Fe) 2D MOF nanosheets and their thickness distribution (b). Darkfield TEM image of typical Cu-TCPP(Fe) 2D MOF nanosheets and the corresponding TEM element mappings (c). TEM image of Cu-TCPP(Fe) 2D MOF/GOx (d). Time-dependent color changes of TMB reaction solutions catalyzed by the Cu-TCPP(Fe) 2D MOF/GOx every 30 min in pH 7.4 PBS buffer (0–240 min, e) or pH 7.4 PBS buffer (0–240 m, f). Methyl red pH indicator (0.001%) was used to signal the developing acidic conditions. Reprinted with permission from (Liu, X.P.; Yan, Z.Q.; Zhang, Y.; Liu, Z.W.; Sun, Y.H.; Ren, J.S.; Qu, X.G. Two-dimensional metal-organic framework/enzyme hybrid nanocatalyst as a benign and self-activated cascade reagent for in vivo wound healing. *ACS Nano* **2019**, *13*, 5222–5230) Reference [153]. Copyright (2020) American Chemical Society.

Chen et al. obtained Ni-MOF with *p*-benzenedicarboxylate ligands [117]. In acidic acetate buffer, TMB was oxidized via the peroxidase intrinsic activity of the material. The nanosheets had impeccable affinity towards the substrates, while maintaining high maximum rate. Since the selectivity of the catalyst was high, it was applied in the detection of H<sub>2</sub>O<sub>2</sub> in human serum samples with good accuracy. Furthermore, the material possessed remarkably low limit of detection.

## 6. Layered Double Hydroxides (LDHs)

The main structural motifs of LDHs are the positively charged metallic lamellae containing metal ions coordinated by hydroxide ions [5]. Generally, they are based on divalent and trivalent cations, although many exceptions are known. Since the surplus layer charge is neutralized by interlamellar (or intercalated) anions, the family of LDHs is suitable for immobilization of enzymatic [118,154] and molecular [119,155,156] antioxidants. Alternatively, large antioxidants may be anchored to the outer surface of LDHs through electrostatic attraction [60]. In this section, LDHs modified with simpler, then more complex drugs via intercalation will be introduced first. Thereafter, surface modified LDHs of antioxidant effect will be discussed, followed by some details about LDH nanozymes.

Among antioxidant drugs, the main target molecules for intercalation are phenolic compounds, e.g., ascorbic acid, ferulic acid and gallic acid. Gallate, the anionic form of gallic acid, preserved its antioxidant character in MgAl-LDH [119] and ZnAl-LDH [120]. Release kinetics were also scoped and for ZnAl-LDH, parabolic model (governed by intraparticle diffusion) provided the best fit, while for MgAl-LDH, a fast, diffusion-controlled stage (Freundlich model) was followed by the slow parabolic release. The antioxidant capacity was evaluated in DPPH assays. MgAl(gallate)-LDH scavenged 83.9% of initial DPPH radicals and the same method yielded a maximal 95% scavenging for ZnAl(gallate)-LDH. A plausible reason of the difference may arise from the synthetic procedure: the ZnAl variant was obtained from the delamination-reconstruction process, which can lead to LDHs of higher surface area, contrary to the coprecipitation method used for the synthesis of MgAl(gallate)-LDH.

Beside the gallate-containing MgAl-LDH, Kong et al. also crafted carnosine-intercalated MgAl-LDH through ion-exchange, which provided nearly complete scavenging (95.9%) of DPPH radicals [119]. Interestingly, although gallic acid is a strong antioxidant [87,157], it can act as a prooxidant [157], especially without oxidants present. This effect was exploited by Arratia-Quijada et al., who prepared ZnAl(gallate)-LDH that was used as cytotoxic agent against lung cancer cells [158]. Lima et al. modified ZnAl-LDH with ferulate anions [159]. The intercalant is known for its high antioxidant effect as a pure substance, but the authors proved that ferulate keeps its advantageous scavenging properties in the LDH as well and thus, successfully preventing H<sub>2</sub>O<sub>2</sub>-induced oxidative damage generation in fibroblast cultures. The prolonged release (10 h) from the carrier meant that the protective effect could be maintained for longer time frames. Similar multi-hour release kinetics was measured for two of the most known antioxidant, ascorbic acid (from MgAl-, MgFe- [160] and CaAl-LDH host [161]) and epigallocatechin gallate (from CaAl-LDH [162]).

Recently, polyphenolic ellagic acid (EA) was used to prepare an antioxidant LDH hybrid. Although the cleavage of lactone bonds in EA occurred, the material preserved its antioxidant activity after intercalation. Additionally, the LDH shell served as a tool to drastically improve the dispersibility of the originally hydrophobic EA. It was also proved that the release of EA from the mixed material is minimal. Organic solvents were also used to modify the surface properties of the hybrids and the originally ca. 60% DPPH scavenging activity of untreated EA-LDH increased to ca. 90% after treatment with ethanol and acetonitrile [121]. The materials also showed high TEAC (trolox equivalent antioxidant capacity) values. Trolox is the common name of 6-hydroxy-2,5,7,8-tetramethylchroman-2-carboxylic acid.

Regarding larger, but still molecular antioxidants, the most common target molecules are polyphenols. In this family, BHPPA (3-(3, 5-di-tert-butyl-4-hydroxy-phenyl)-propionic acid) is a model compound with good antioxidant effect, expressed in DPPH assay after intercalation in various LDHs [156,163,164]. The DPPH scavenging capability of such LDHs ranged from ca. 50% to 70%, which are comparable to the 60–70% effectivity of pure BHPPA, depending on the reaction conditions. Even though the values obtained are well below 100%, the nanocomposites were excellent polypropylene (PP) stabilizers against accelerated oxidation (Figure 9) [163], which probably arose from i) the BHPPA-protective effect of the LDH structure and ii) the general polymer stabilizing characteristics of LDHs originated from endothermic water loss at higher temperatures [165] and the reduced gas permeability through plastic [166]. The BHPPA-LDH hybrid surpassed Irganox 1010 [164], a frequent polymer antioxidant used in the industry.



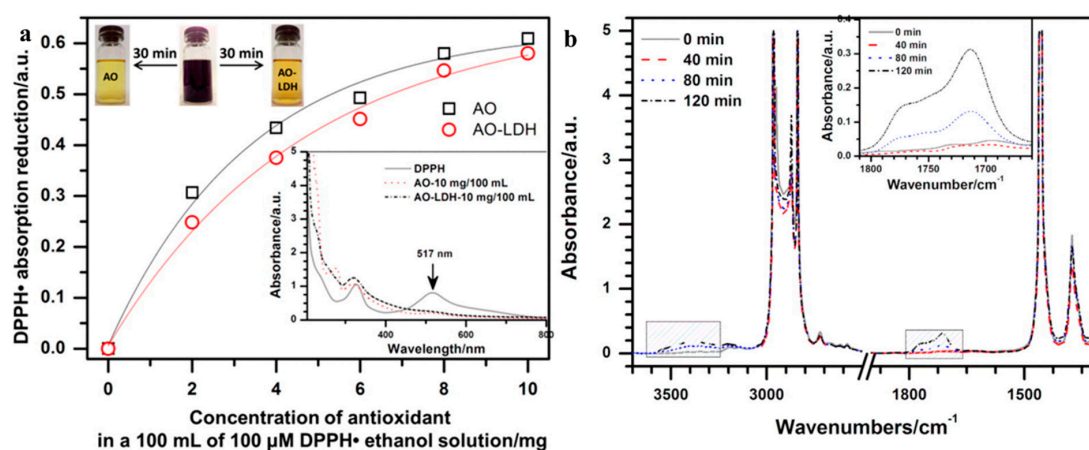


**Figure 9.** Radical-scavenging activity of BHPHA (denoted as AO) and BHPHA-LDH in a 100 mL of 100 μM DPPH ethanolic solution. The top inset represents the color change and the bottom inset shows UV-Vis absorption curves after radical scavenging for 30 min in a dark box (a). FT-IR absorbance spectra of pure PP in the range of 3700–1250 cm<sup>-1</sup> as a function of accelerated thermal aging time at 150 °C. Inset shows a magnified region of the FT-IR spectra in the wavenumber range of 1810–1660 cm<sup>-1</sup>, thus the carbonyl region indicating oxidation of the plastic (b). Reprinted with permission from (Feng, Y.J.; Jiang, Y.; Huang, Q.; Chen, S.T.; Zhang, F.B.; Tang, P.G.; Li, D.Q. High antioxidative performance of layered double hydroxides/polypropylene composite with intercalation of low-molecular-weight phenolic antioxidant. *Ind. Eng. Chem. Res.* **2014**, *53*, 2287–2292) Reference [163]. Copyright (2020) American Chemical Society. BHPHA: (3-(3, 5-di-tert-butyl-4-hydroxy-phenyl)-propionic acid; LDH: layered double hydroxides

In 2013, Lonkar et al. also reported the improved thermal behavior of PP containing BHPHA-LDH as a filler [167]. Gomez Amaro et al. investigated BHPHA and Trolox in intercalated from [122], revealing up to 90% DPPH scavenging for both antioxidant-modified LDHs with 14 and 13 mass% organic content, respectively. Irganox 1425, an ionic antioxidant consisting of a benzylphosphonate-type anion in Ca<sup>2+</sup> salt, a common building block in the LDH structures, was used as precursors to prepare CaAl-LDH intercalated with its anion [155]. The polymer additive kept its DPPH scavenging activity after intercalation with ca. 55% maximum effect, which is very similar, if not slightly higher than bare Irganox 1425. The LDH hybrid of olanzapine (2-methyl-4-(4-methylpiperazin-1-yl)-10H-thieno [2,3-b][1,5]-benzodiazepine) was also developed to overcompensate its low water solubility [123]. This drug molecule is a popular antipsychotic agent and due to the correlation between oxidative stress and brain damage [168], its antioxidant potential may be a reason for its pharmaceutical efficacy. It was demonstrated that the LDH hosts (CaAl- and NiAl-LDH) did not have negative effects in the assays investigated, e.g., DPPH assay, ABTS assay, NO scavenging and TBARS (TBA reactive substances) test. Moreover, the LDHs had synergistic effects with the olanzapine molecules. This was more pronounced for CaAl-LDH, which was often significantly more active than NiAl-LDH, as a carrier for olanzapine.

As mentioned earlier, larger, or more importantly, positively charged agents can be immobilized only via surface modifications. These examples tend to find enzymatic applications, e.g., the histamine (Hsm) containing Cu(Hsm)<sub>2</sub><sup>2+</sup> complex fixed on a polymer modified MgAl-LDH surface [124]. Poly(vinylpyridine-*b*-methacrylic acid (PVPMAA) copolymer of negative charge was used to reverse the originally positive surface charge of LDH enabling the adsorption of the positively charged Cu<sup>2+</sup> complex. Charge reversal also achieved higher colloidal stability, i.e., the LDH precipitated at higher background electrolyte concentrations. The complex-LDH composite was then used as a SOD mimic with comparable activity to bare SOD or a SOD-coated MgAl-LDH [60]. The latter material was obtained by modifying the surface of SOD-MgAl-LDH composite by heparin (Hep) polyelectrolyte giving rise to highly stable antioxidant dispersions. It was apparent that both SOD functioning LDHs

were highly active, but unlike natural enzymes,  $\text{Cu}(\text{Hsm})_2^{2+}$  was not heat sensitive and kept 90% of its activity at 80 °C, while SOD quickly denatured at higher temperatures (Figure 10).

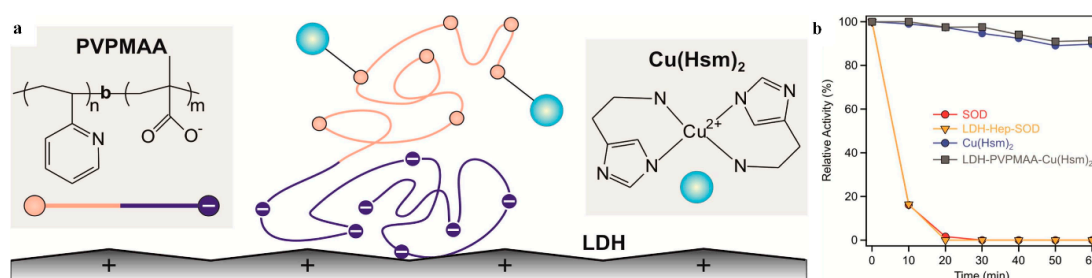


**Figure 10.** Schematic representation of formation of  $\text{Cu}(\text{Hsm})_2^{2+}$  on PVPMAA-coated LDH (a) and its activity in SOD assay compared to bare SOD, LDH-Hep-SOD and  $\text{Cu}(\text{Hsm})_2^{2+}$  at 80 °C as a function of reaction time (b). Reprinted from (Highly stable enzyme-mimicking nanocomposite of antioxidant activity, 543, Pavlovic, M.; Nafradi, M.; Rouster, P.; Murath, S.; Szilagy, I., *J. Colloid Interface Sci.* **2019**, 543, 174–182) Reference [124] Copyright (2020), with permission from Elsevier.

The intrinsic peroxidase activity was enhanced using deoxyribonucleic acid (DNA) from herring sperm [125]. The hybrids were constructed by surface electrostatic force between the building blocks. Furthermore, DNA-induced delamination of the carrier LDH (proved by X-ray powder diffraction and light scattering) facilitated the antioxidant reaction in the TMB test reaction, which showed best activity at 35–45 °C and at pH 3–4 with sudden decrease afterwards. Combined with GOx-glucose pair, Chen et al. used their DNA-LDH hybrid as a colorimetric glucose sensor.

Natural HRP bears gross positive charge in its active form, thus a Hep coating was used on the surface of MgAl-LDH before its immobilization [118]. The kinetic parameters in the guaiacol assay of the as-prepared composite LDH were slightly different compared to the free enzyme, representing that adsorption forces were insufficient to overcome the protein rigidity and to considerably influence the native structure of the enzyme. Beforehand, HRP-containing LDHs were synthesized using transition metal LDHs that were applied in the electrochemical detection of  $\text{H}_2\text{O}_2$  [154,169].

Mimicking the active site of HRP, hemin was immobilized in/on FeNi- and CuAl-LDH by Zhang et al. [170] and Qiao et al. [171], respectively. Despite its size, hemin is a good target for intercalation owing to the planar structure and negative charge through the carboxylic groups. It was demonstrated that FeNi(hemin)-LDH was an excellent peroxidase, surpassing free hemin. This is attributed to the dimerization of hemin outside the layered material, while in intercalated form, the hemin rings are mostly found as monomers. Finally, Zhang et al. developed an electrochemical sensor based on this material [170]. The CuAl(hemin)-LDH designed by Qiao et al. was tested as a scavenger of  $\text{ONOO}^-$  ions [171] (Figure 11). They also found that the composite was more active than hemin alone, which is interpreted by the electrostatic attraction between the anionic  $\text{ONOO}^-$  and the LDH particles, and also due to the  $\pi$  donor property of LDHs to the Fe center of hemin, as stated by the authors. The composite also inhibited the reaction between tyrosine and  $\text{ONOO}^-$  up to 80%.

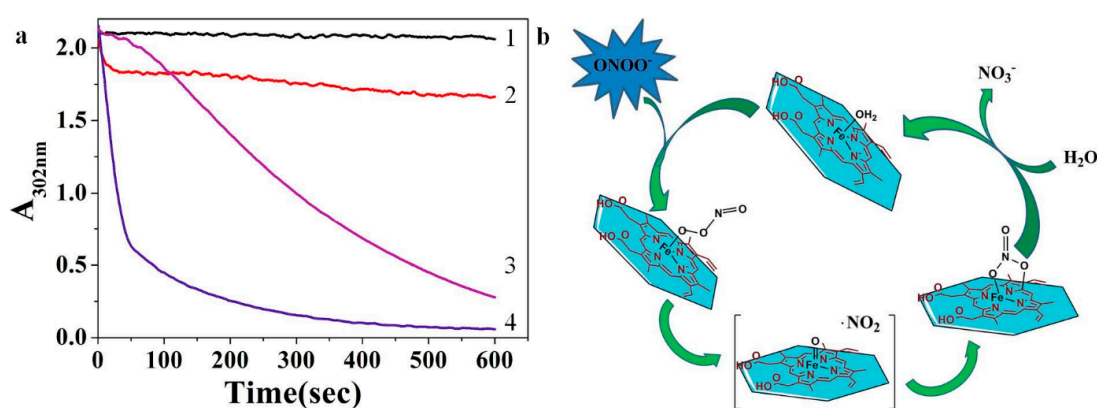


**Figure 11.** Peroxynitrite decomposition without (1) and with equivalent weight of LDHs (2), hemin (3) and hemin-LDHs (4). Peroxynitrite was mixed with scavengers at 25 °C and the reaction was followed at 302 nm (a). Proposed mechanism for the isomerization and reduction of  $\text{ONOO}^-$  and scavenging of  $\text{NO}_2^-$  by hemin-LDH hybrid nanosheets (b). Reproduced from Reference [171] with permission from the Royal Society of Chemistry.

A novel protein-LDH interaction was recently revealed when protein extracted from bael (*Aegle marmelos*) were anchored to the outer surface of MgAl-LDH [126]. The natural antioxidant proteins were scavengers of DPPH radicals on the LDHs (ca. 50% effectivity) and possessed antimicrobial effect towards *S. coliform*. In addition, the composite adsorbed  $\text{Pb}^{2+}$  ions according to Freundlich model.

The earliest report on LDHs with intrinsic nanozyme activity was published by Zheng et al. [172]. For this purpose, like for all the others, redox active metal ions are represented in the lamellae. In this instance, CoFe-LDH was used as a peroxidase mimic. The characteristics of the nanozyme were like those of HRP, regarding optimal pH and temperature dependence, but the platelets were active in a larger  $\text{H}_2\text{O}_2$  concentration regime. Thus,  $\text{H}_2\text{O}_2$  detection is possible in a range of reaction conditions. The obtained LDH was also used in the GOx mediated selective sensing of glucose via TMB test reaction. Afterwards, CoAl-LDH sheets exfoliated in L-asparagine solution were proven to have peroxidase mimic with pH optimum at 6 [127]. A similar approach with L-asparagine was applied to get exfoliated 2D NiFe-LDH with 2 nm thickness [128]. Both asparagine exfoliated LDHs showed Tyndall effect in aqueous suspension, indicating the formation of stable colloids. While the nanosheets of CoAl-LDH showed relatively lower affinity to  $\text{H}_2\text{O}_2$  ( $K_m = 22.1$  mM), NiFe-LDH and bare HRP had similar values with 2.4 and 3.7 mM, respectively (Table 1). The detection limit of NiFe-LDH was estimated to be 4.4 mM  $\text{H}_2\text{O}_2$ . The peroxidase-like activity of NiCo-LDH was described by Su et al. using homovanillic acid as a fluorescent dye upon reacting with  $\text{H}_2\text{O}_2$  [173]. It was found that the catalysis was strongly pH dependent and reached optimum above pH 8.3 with a linear response at pH between 8.4 and 8.9, before plateauing at 9.6. Another peroxidase mimic, CuAl-LDH was grown onto carbon fibers (Figure 12) after atomic layer deposition of  $\text{Al}_2\text{O}_3$  and hydrothermal conversion to the end-product [174]. Interestingly, the optimum temperature for this material was 70 °C, but at 60 and 80 °C, it showed similar efficiency. Activity also grew when using more catalyst, indicating that the reaction was not diffusion controlled. It was also shown that radical scavengers inhibit the catalytic reaction in a great manner. Peroxidase nanozyme CoFe-LDH was used as catalyst to obtain fluorescent polydopamine (PDA) from its monomer [175]. This procedure avoided using concentrated  $\text{H}_2\text{O}_2$  and yielded shorter reaction times. PDA is strongly fluorescent in aqueous solutions which is quenched by  $\text{Fe}^{3+}$  ions through coordination. However, intensity is restored when strong iron complexing pyrophosphate is introduced, with good linearity and selectivity. Another detection is possible through the addition of pyrophosphatase, which decomplexes the quenching  $\text{Fe}^{3+}$  ions and lower fluorescent signal is observed.

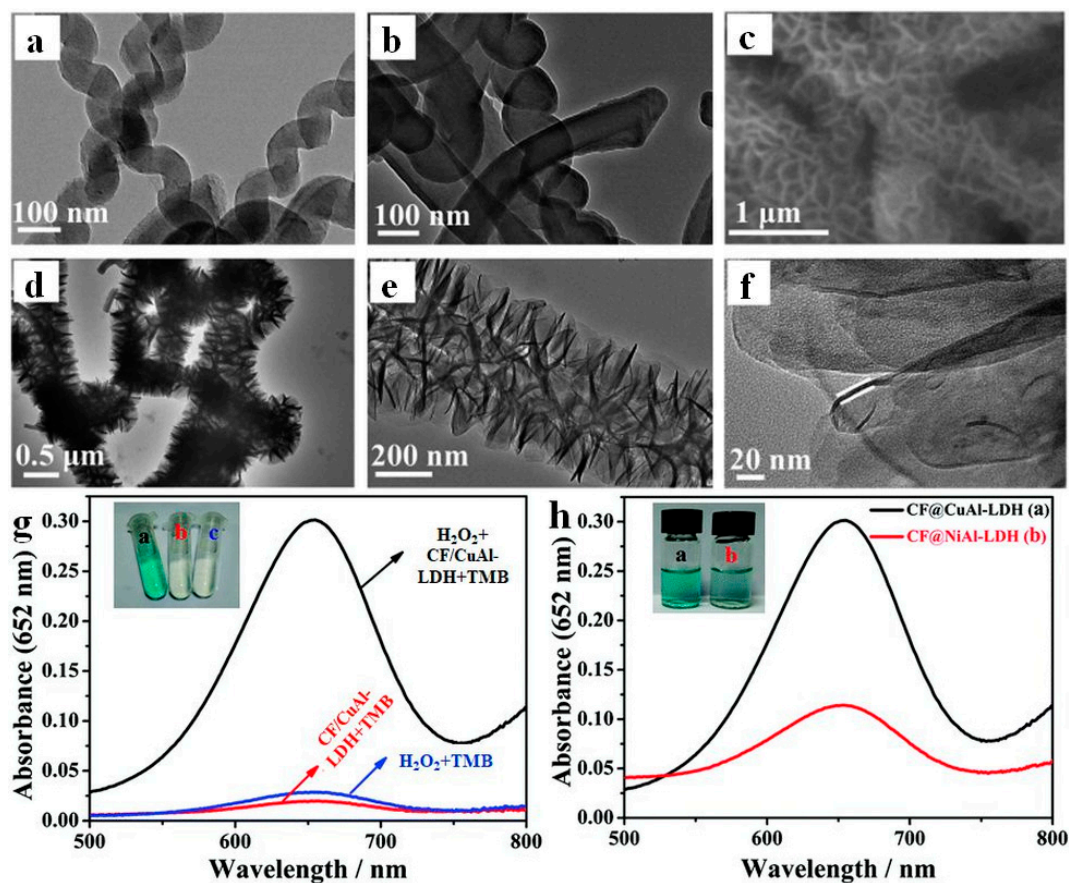


**Figure 12.** TEM micrograph of carbon fiber (CF) (a) and CF/Al<sub>2</sub>O<sub>3</sub> (b). SEM micrograph of CF/CuAl-LDH (c). TEM and HRTEM images of CF/CuAl-LDH (d–f). Absorbance in different reaction systems (g) and in different types of LDHs (h). Reproduced from Reference [174] with permission from the Centre National de la Recherche Scientifique (CNRS) and the Royal Society of Chemistry.

Recently reported MnFe-LDH possessed catalase mimicking activity and exhibited photothermal effect [176]. Methylene blue loading enhanced the efficacy of O<sub>2</sub>-dependent photothermal phenomenon. This way, the phototherapeutic effect in hypoxia cancer cells were gapped, as demonstrated in human cells and mice, in which the relative size of tumor was also reduced. We mention that even though it was not used as an antioxidant, rather a prooxidant, but Fe<sup>2+</sup> bearing FeAl-LDH was used to decompose H<sub>2</sub>O<sub>2</sub> with a Fenton-type mechanism inducing apoptosis in cancer cells through the generated OH· and OOH· radicals [129].

## 7. Montmorillonites (MMTs)

Montmorillonites are sheet-like silicate minerals with anionic layers and feasible, water-exchangeable cations between the individual sheets [31,130,177]. Their charging features, therefore, are the reverse of the already discussed LDHs. Hence, MMTs may possess antioxidant capacity by their own through fixing antioxidant compounds in their structures (e.g., intercalation or physical adsorption) or by the preparation of composite materials with synergistic nanomaterials.

Regarding intercalated MMTs, Baek et al. constructed GSH-containing MMT, coated with poly(vinylacetal diethylaminoacetate) (AEA) [130]. GSH is the most common antioxidant material in the body, but with low bioavailability, in case it is taken in orally. Carriers can overcome this barrier and it was found that GSH and GSH-MMT had an ABTS radical scavenging activity of ca. 60%. Diethyl aminoacetate coating was also introduced as a protective layer, which did not interfere with the antioxidant effect. After oral administration for mice, the concentration of GSH significantly



grew in liver, to which delivery of free GSH is minimal. Naturally occurring ionic species may also be intercalated from plant extracts, e.g., antioxidants from blueberry (*Vaccinium corymbosum*) that provided an intelligent potential food packaging nanomaterial, which is color-sensitive to pH [131]. Compared to the negligible DPPH scavenging activity of pure MMT (which probably arose from adsorption), the blueberry extract-modified clay showed exceptional activity with ca. 40% scavenging.

An antioxidant activity, close to the one of ascorbic acid, was assigned to the eugenol-MMT hybrid that was used as a filler in poly(3-hydroxybutyrate)-thermoplastic (PHB-TPS) starch composite that resulted in a functional material with evolved heat resistance and mechanical properties that also possessed antioxidant and antifungal properties [132]. The peroxidase nanozyme activity of hemin was demonstrated after adsorbing its highly active monomeric form in 7 mg/g dose on MMT [133]. Earlier, it was demonstrated that histidine amino acid residues activate the catalytic activity of HRP [178], which was substituted with intercalated Hsm in the case of hemin-MTT. This way, the relative catalytic activity of the MMT composite jumped to over 350% at 60 °C, where the performance of natural HRP decreased.

A chitosan (CS) coated MMT@(Ca-alginate) nanoparticle synthesis was recently reported with covalently bonded HRP enzyme on its outer surface to degrade aflatoxin B1 [179], a dangerous poison produced by molds. The role of negatively charged MMT in this structure was to promote aflatoxin adsorption and to attract more chitosan chains. Multiple chitosan/MMT composites were prepared in Fernando's group as a biocompatible substitute of classic polymer food wrappers [177,180,181]. These materials had adequate physical characteristics (tensile strength, optical properties, etc.) and were incorporated with rosemary (*Rosmarinus officinalis*) and ginger (*Zingiber officinale*) essential oils. This incorporation provided the composite with good antimicrobial activity and antioxidative protection for applications in poultry packaging. Yan et al. used  $\alpha$ -tocopherol (TOC) in a chitosan-MMT matrix as preservative for wrapping sliced ham with film of the material [134]. The film coating showed good antioxidant activity in DPPH assay even after 16-day storage, while in lipid oxidation tests, the remarkable antioxidant effect was expressed after 120 days.

Regarding MMT composites with other inorganic materials of overall antioxidant capacity, sulfide-MMT structures were under investigation previously. A facile way was worked out to construct ZnS/MMT composite via coprecipitation [135]. This material acted as a peroxidase mimic in a rapid fashion with merely a few minutes to form oxidized TMB. The activity measured was similar in the pH range 4–7 and from 20 to 70 °C. Besides, outstanding substrate affinity was achieved, compared to bare HRP (148-fold and 8-fold increase towards H<sub>2</sub>O<sub>2</sub> and TMB, respectively). A CuS/MMT composite was also considered as a peroxidase mimic with short timeframe (< 1 min) to reach colorimetric visualization with poorer kinetic parameters [136] (Table 1). Reaction kinetics for ZnS/MMT were also proved by EPR, trapping and detecting the OH· radicals formed from H<sub>2</sub>O<sub>2</sub> by DMPO spin trap. A very similar coprecipitation method, starting from thioacetamide, was used to obtain Ag<sub>2</sub>S/MMT composite [137]. The pH and temperature dependence profiles were fairly similar to other MMT systems and it was found that pure MMT also possessed peroxidase activity. In this case, terephthalic acid was used as fluorescent OH· radical trap to confirm the mechanism. Recently, the composite of MMT and CoNiS<sub>x</sub> was prepared, and remarkable peroxidase activity was observed [138]. It exhibited good affinity towards H<sub>2</sub>O<sub>2</sub> and TMB substrates, often surpassing bare HRP. Contrary to other MMT composites, elevated temperatures had negative impact on its activity above 35 °C, but at ambient temperatures showed linear response to H<sub>2</sub>O<sub>2</sub>.

MMT was also found to be the ideal clay mineral for soil organic matter modification linked with HRP adsorption [139]. Furthermore, MMT retained 91.3% activity of bare HRP and was reusable for phenol removal, tested for six cycles with slight activity loss.

Heterobinuclear [140] and mononuclear [141] Cu<sup>2+</sup> complexes containing amine and amino acid ligands were intercalated between the layers of MMT to obtain a heterogeneous catalysts for dismutation of superoxide radicals. The composites showed significant SOD-like function in the test reactions, in which the superoxide radical anions were generated by a photochemical reaction.

Finally, montmorillonite-intercalated  $\text{Cu}^{2+}$ -tris(2-aminoethyl) amine complexes were highly active in decomposition of  $\text{H}_2\text{O}_2$ , i.e., they acted as an excellent catalase mimicking antioxidant composite [182].

## 8. Miscellaneous Structures

Structures listed in this paragraph either did not fall under the categories listed before or were borderline (e.g.,  $\text{CeO}_2@\text{CO}_2(\text{OH})_2\text{CO}_3$ ) or were the only example of the material (see  $\text{Fe}_2\text{O}_3$ ).

He et al. published the synthesis of flaky CoP 2D particles on Ni foam substrate [142]. First,  $\text{Co}(\text{OH})_2$  was built on the metal carrier, which was phosphorylated with  $\text{NaH}_2\text{PO}_2$  in a hydrothermal manner. The precursor  $\text{Co}(\text{OH})_2$  had mediocre activity in the peroxidase test reaction, the end product possessed outstanding performance, while Ni foam (NF) was completely inert. More importantly, the same piece of catalyst showed the same activity for 12 cycles, which was unaffected by pH (2–14) and temperature (0–95 °C). The material was successfully used to detect uric acid in serum samples (with overall 5% error compared to clinical method) and in real urine samples as well with good selectivity to the substrate (Figure 13).

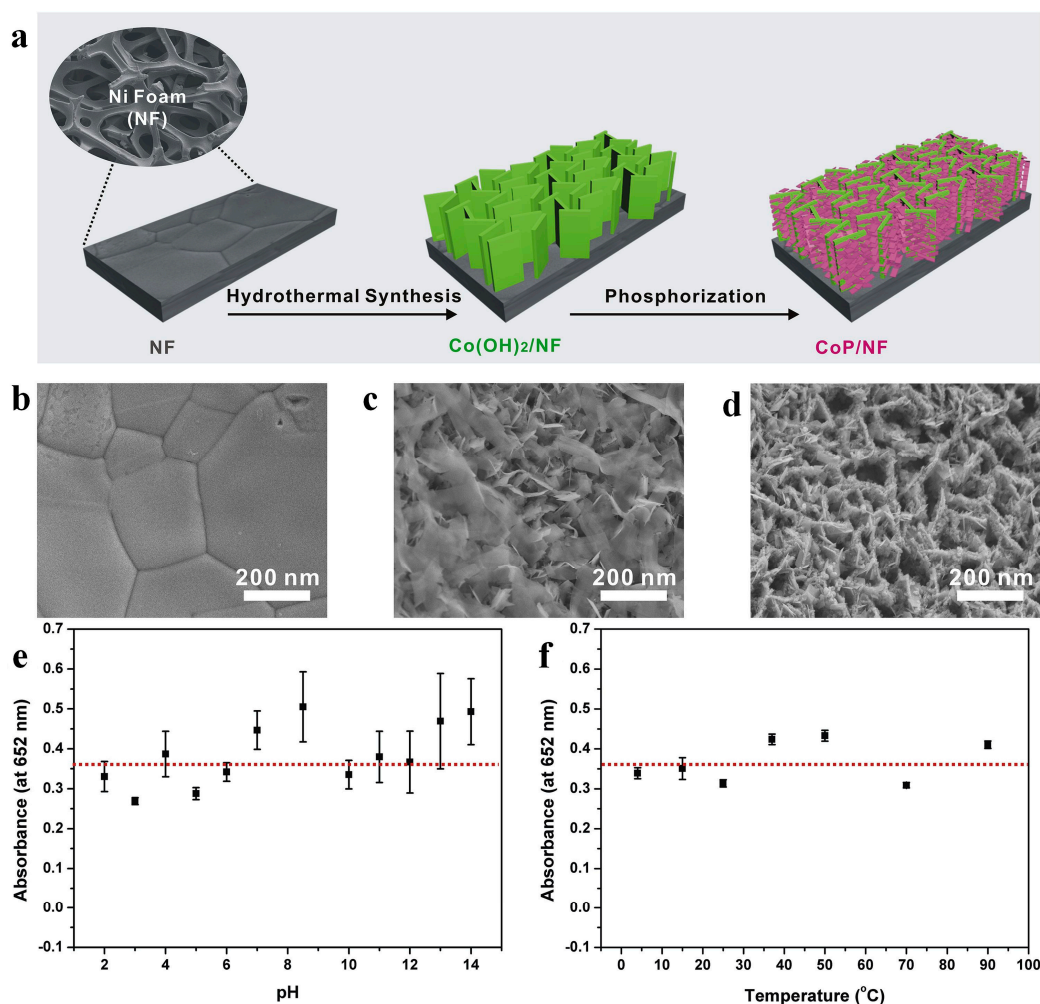


**Figure 13.** Illustration of the fabrication procedure of CoP/NF (a); SEM micrographs of NF (b);  $\text{Co}(\text{OH})_2/\text{NF}$  (c) and CoP/NF (d); the robustness and versatility of the CoP/NF nanozyme against harsh pH (e) and temperature (f). Reprinted from (Uricase-free on-demand colorimetric biosensing of uric acid enabled by integrated CoP nanosheet arrays as a monolithic peroxidase mimic. 1021, He, Y. F.; Qi, F.; Niu, X. H.; Zhang, W. C.; Zhang, X. F.; Pan, J. M., *Anal. Chim. Acta* **2018**, 1021, 113–120) Reference [142]. Copyright (2020), with permission from Elsevier.

A facile detection method based on CeO<sub>2</sub> nanoparticles on 2D CO<sub>2</sub>(OH)<sub>2</sub>CO<sub>3</sub> was introduced by Alizadeh et al [143]. After the material was characterized as an excellent peroxidase mimic with higher maximum rate than HRP's, a paper based colorimetric immunoassay method was developed with smartphone image analysis selective to carcinoembryonic antigen.

Deshapriya et al. used aminated and artificially cationized BSA (bovine serum albumin) as an overcharging agent on negatively charged, exfoliated ZrP (standing for -Zr(HPO<sub>4</sub>)<sub>2</sub>) sheets [183]. This led to the possible immobilization of numerous enzymes, including catalase. For GOx and tyrosinase, loading up to 640 and 380 mass% was achieved, respectively. Moreover, the bound enzymes kept their native structure and at least 80% of their activity, excluding tyrosinase with a value of ca. 40%.

Iron containing simple compounds were also tested as peroxidases. Fe<sub>3</sub>(PO<sub>4</sub>)<sub>2</sub> × 8 H<sub>2</sub>O sheets in a flower-like array were utilized as a potent nanozyme to detect H<sub>2</sub>O<sub>2</sub> with over 30 ionic and non-ionic abundant substances tested as an interfering agent, but the detection was considerably not distorted [144]. Glucose sensing was also achieved through the glucose-GOx reaction with good selectivity amongst other bioactive compounds. Tanaka et al. started from Fe<sup>3+</sup>-glycerate precursor and applied thermal treatment to obtain porous Fe<sub>2</sub>O<sub>3</sub> flakes [145]. It was found that lower pyrolysis temperatures resulted in better Fenton-type activity for the synthesized Fe<sub>2</sub>O<sub>3</sub>, since those products had higher surface area and higher hexagonal α-Fe<sub>2</sub>O<sub>3</sub> content with more active sites compared to cubic γ-Fe<sub>2</sub>O<sub>3</sub> (Table 1).

## 9. Summary and Outlook

As discussed above, antioxidant compounds of 2D structure has attracted widespread contemporary interest in the scientific and technological communities, wherever the goal is to decrease oxidative stress or to develop ROS sensing devices. The main advantages of the 2D structures are the high specific surface area and that processable samples for homogeneous film formation (e.g., for electrode modifications) can be easily prepared. Given the fact that these compounds are excellent candidates as building blocks of sensing materials, the ease of synthesis even in larger amount will definitely help in the commercialization of sensors and detectors.

Enzyme-loaded 2D NPs represent a very efficient ROS consuming class, however, the high sensitivity of the proteins to the environmental conditions often remains upon immobilization. Such a low resistance against pH, pressure and temperature can be improved by applying enzyme mimicking metal complexes as catalytic center in the 2D NP-based hybrids, but their efficiencies usually lag behind the one of the native enzymes. A returning problem in case of many molecular antioxidants is their low water solubility and thus, low bioavailability. The insufficient solubility may be increased by loading the 2D particles of high specific surface area with the antioxidant molecules, provided the carrier can be dispersed in liquid media. The new wave in the field of 2D antioxidants are the so-called nanozymes, which are able to decompose ROS without embedding enzymatic or molecular antioxidants in their structure. Metal-containing compounds hold great promise towards development of such 2D nanozymes.

Apart from the 2D antioxidant materials reported to date, novel hybrid materials are continuously being developed in the academic and industrial laboratories. Achieving excellent radical scavenging activity is the main priority, however, other important issues must also be considered. These include the physiological effect on living organisms, i.e., cell toxicity assessment is a must prior to the biomedical application. In addition, dispersions of antioxidant 2D particles are applied in most of the systems, therefore, the stability of the dispersions has to be precisely controlled. Unwanted particle aggregation processes lead to significant loss in the antioxidant activity and to non-processable samples. The stability issue can be solved by choosing appropriate stabilizing agents. Comprehensive studies in this topic are missing in the relevant literature.

**Author Contributions:** All authors participated in the manuscript preparation. All authors have read and agreed to the published version of the manuscript.

**Funding:** Financial support by the Hungarian Academy of Sciences (Lendület 96130), the National Research, Development and Innovation Office (SNN\_131558) and the Ministry of Human Capacities of Hungary (20391-3/2018/FEKUSTRAT) is gratefully acknowledged.

**Conflicts of Interest:** The authors declare no conflict of interest.

## References

1. Sasikala, S.P.; Lim, J.; Kim, I.H.; Jung, H.J.; Yun, T.; Han, T.H.; Kim, S.O. Graphene oxide liquid crystals: A frontier 2D soft material for graphene-based functional materials. *Chem. Soc. Rev.* **2018**, *47*, 6013–6045. [[CrossRef](#)]
2. Anasori, B.; Lukatskaya, M.R.; Gogotsi, Y. 2D metal carbides and nitrides (MXenes) for energy storage. *Nat. Rev. Mater.* **2017**, *2*, 16098. [[CrossRef](#)]
3. Yu, J.F.; Wang, Q.; O'Hare, D.; Sun, L.Y. Preparation of two dimensional layered double hydroxide nanosheets and their applications. *Chem. Soc. Rev.* **2017**, *46*, 5950–5974. [[CrossRef](#)] [[PubMed](#)]
4. Wang, L.Z.; Sasaki, T. Titanium oxide nanosheets: Graphene analogues with versatile functionalities. *Chem. Rev.* **2014**, *114*, 9455–9486. [[CrossRef](#)] [[PubMed](#)]
5. Gu, Z.; Atherton, J.J.; Xu, Z.P. Hierarchical layered double hydroxide nanocomposites: Structure, synthesis and applications. *Chem. Commun.* **2015**, *51*, 3024–3036. [[CrossRef](#)]
6. Rahman, M.Z.; Kwong, C.W.; Davey, K.; Qiao, S.Z. 2D phosphorene as a water splitting photocatalyst: Fundamentals to applications. *Energy Environ. Sci.* **2016**, *9*, 709–728. [[CrossRef](#)]
7. She, X.J.; Wu, J.J.; Xu, H.; Zhong, J.; Wang, Y.; Song, Y.H.; Nie, K.Q.; Liu, Y.; Yang, Y.C.; Rodrigues, M.T.F.; et al. High efficiency photocatalytic water splitting using 2D alpha-Fe<sub>2</sub>O<sub>3</sub>/g-C<sub>3</sub>N<sub>4</sub> Z-scheme catalysts. *Adv. Energy Mater.* **2017**, *7*, 1700025. [[CrossRef](#)]
8. Gao, G.P.; O'Mullane, A.P.; Du, A.J. 2D MXenes: A new family of promising catalysts for the hydrogen evolution reaction. *ACS Catal.* **2017**, *7*, 494–500. [[CrossRef](#)]
9. Zhu, M.S.; Sun, Z.C.; Fujitsuka, M.; Majima, T. Z-scheme photocatalytic water splitting on a 2D heterostructure of black phosphorus/bismuth vanadate using visible light. *Angew. Chem. Int. Ed.* **2018**, *57*, 2160–2164. [[CrossRef](#)]
10. Jiang, X.; Wang, P.; Zhao, J.J. 2D covalent triazine framework: A new class of organic photocatalyst for water splitting. *J. Mater. Chem. A* **2015**, *3*, 7750–7758. [[CrossRef](#)]
11. Li, Y.G.; Li, Y.L.; Sa, B.S.; Ahuja, R. Review of two-dimensional materials for photocatalytic water splitting from a theoretical perspective. *Catal. Sci. Technol.* **2017**, *7*, 545–559. [[CrossRef](#)]
12. Yang, L.; Guo, Z.L.; Huang, J.; Xi, Y.N.; Gao, R.J.; Su, G.; Wang, W.; Cao, L.X.; Dong, B.H. Vertical growth of 2D amorphous FePO<sub>4</sub> nanosheet on Ni foam: Outer and inner structural design for superior water splitting. *Adv. Mater.* **2017**, *29*, 1704574. [[CrossRef](#)] [[PubMed](#)]
13. Ida, S.; Ishihara, T. Recent progress in two-dimensional oxide photocatalysts for water splitting. *J. Phys. Chem. Lett.* **2014**, *5*, 2533–2542. [[CrossRef](#)] [[PubMed](#)]
14. Chen, B.; Zhang, Z.; Kim, S.; Baek, M.; Kim, D.; Yong, K. A biomimetic nanoleaf electrocatalyst for robust oxygen evolution reaction. *Appl. Catal. B Environ.* **2019**, *259*, 118017. [[CrossRef](#)]
15. Hussain, N.; Yang, W.J.; Dou, J.M.; Chen, Y.N.; Qian, Y.T.; Xu, L.Q. Ultrathin mesoporous F-doped -Ni(OH)<sub>2</sub> nanosheets as an efficient electrode material for water splitting and supercapacitors. *J. Mater. Chem. A* **2019**, *7*, 9656–9664. [[CrossRef](#)]
16. Sipiczki, M.; Adam, A.A.; Anitics, T.; Csendes, Z.; Peintler, G.; Kukovecz, A.; Konya, Z.; Sipos, P.; Palinko, I. The catalytic epoxidation of 2-cyclohexen-1-one over uncalcined layered double hydroxides using various solvents. *Catal. Today* **2015**, *241*, 231–236. [[CrossRef](#)]
17. Wang, X.R.; Han, X.; Zhang, J.; Wu, X.W.; Liu, Y.; Cui, Y. Homochiral 2D porous covalent organic frameworks for heterogeneous asymmetric catalysis. *J. Am. Chem. Soc.* **2016**, *138*, 12332–12335. [[CrossRef](#)]
18. Cao, L.Y.; Lin, Z.K.; Peng, F.; Wang, W.W.; Huang, R.Y.; Wang, C.; Yan, J.W.; Liang, J.; Zhang, Z.M.; Zhang, T.; et al. Self-supporting metal-organic layers as single-site solid catalysts. *Angew. Chem. Int. Ed.* **2016**, *55*, 4962–4966. [[CrossRef](#)]
19. Li, Y.Z.; Shu, J.; Huang, Q.Q.; Chiranjeevulu, K.; Kumar, P.N.; Wang, G.E.; Deng, W.H.; Tang, D.P.; Xu, G. 2D metal chalcogenides with surfaces fully covered with an organic “promoter” for high-performance biomimetic catalysis. *Chem. Commun.* **2019**, *55*, 10444–10447. [[CrossRef](#)]



20. Xiao, Y.W.; Guo, W.X.; Chen, H.H.; Li, H.F.; Xu, X.J.; Wu, P.; Shen, Y.; Zheng, B.; Huo, F.W.; Wei, W.D. Ultrathin 2D Cu-porphyrin MOF nanosheets as a heterogeneous catalyst for styrene oxidation. *Mater. Chem. Front.* **2019**, *3*, 1580–1585. [[CrossRef](#)]
21. Reyna-Villanueva, L.R.; Dias, J.M.; Medellin-Castillo, N.A.; Ocampo-Perez, R.; Martinez-Rosales, J.M.; Penaflor-Galindo, T.; Fuentes, G.A. Biodiesel production using layered double hydroxides and derived mixed oxides: The role of the synthesis conditions and the catalysts properties on biodiesel conversion. *Fuel* **2019**, *251*, 285–292. [[CrossRef](#)]
22. Mei, X.; Xu, S.M.; Hu, T.Y.; Peng, L.Q.; Gao, R.; Liang, R.Z.; Wei, M.; Evans, D.; Duan, X. Layered double hydroxide monolayers for controlled loading and targeted delivery of anticancer drugs. *Nano Res.* **2018**, *11*, 195–205. [[CrossRef](#)]
23. Li, X.Q.; Gong, P.W.; Li, Y.Z.; Yu, J.F.; Wang, F.; Li, X.A.; Fan, Z.J.; Wang, Z.F. Double-carrier drug delivery system based on polyurethane-polyvinyl alcohol/layered double hydroxide nanocomposite hydrogel. *Mater. Lett.* **2019**, *243*, 1–4. [[CrossRef](#)]
24. Li, Q.L.; Wang, J.P.; Liu, W.C.; Zhuang, X.Y.; Liu, J.Q.; Fan, G.L.; Li, B.H.; Lin, W.N.; Man, J.H. A new (4,8)-connected topological MOF as potential drug delivery. *Inorg. Chem. Commun.* **2015**, *55*, 8–10. [[CrossRef](#)]
25. Sun, X.M.; Liu, Z.; Welsher, K.; Robinson, J.T.; Goodwin, A.; Zaric, S.; Dai, H.J. Nano-graphene oxide for cellular imaging and drug delivery. *Nano Res.* **2008**, *1*, 203–212. [[CrossRef](#)]
26. An, J.Y.; Geib, S.J.; Rosi, N.L. Cation-triggered drug release from a porous zinc-adeninate metal-organic framework. *J. Am. Chem. Soc.* **2009**, *131*, 8376–8377. [[CrossRef](#)] [[PubMed](#)]
27. Reddy, A.B.; Manjula, B.; Jayaramudu, T.; Sadiku, E.R.; Babu, P.A.; Selvam, S.P. 5-Fluorouracil Loaded Chitosan-PVA/Na<sup>+</sup>MMT Nanocomposite Films for Drug Release and Antimicrobial Activity. *Nano Micro Lett.* **2016**, *8*, 260–269. [[CrossRef](#)]
28. Yang, J.H.; Lee, J.H.; Ryu, H.J.; Elzatahry, A.A.; Allothman, Z.A.; Choy, J.H. Drug-clay nanohybrids as sustained delivery systems. *Appl. Clay Sci.* **2016**, *130*, 20–32. [[CrossRef](#)]
29. Garcia-Villen, F.; Faccendini, A.; Aguzzi, C.; Cerezo, P.; Bonferoni, M.C.; Rossi, S.; Grisoli, P.; Ruggeri, M.; Ferrari, F.; Sandri, G.; et al. Montmorillonite-norfloxacin nanocomposite intended for healing of infected wounds. *Int. J. Nanomed.* **2019**, *14*, 5051–5060. [[CrossRef](#)]
30. Cui, Z.K.; Kim, S.; Baljon, J.J.; Wu, B.M.; Aghaloo, T.; Lee, M. Microporous methacrylated glycol chitosan-montmorillonite nanocomposite hydrogel for bone tissue engineering. *Nat. Commun.* **2019**, *10*, 3523. [[CrossRef](#)]
31. Dong, Y.C.; Feng, S.S. Poly(D,L-lactide-co-glycolide)/montmorillonite nanoparticles for oral delivery of anticancer drugs. *Biomaterials* **2005**, *26*, 6068–6076. [[CrossRef](#)] [[PubMed](#)]
32. Kou, L.Z.; Frauenheim, T.; Chen, C.F. Phosphorene as a Superior Gas Sensor: Selective Adsorption and Distinct I-V Response. *J. Phys. Chem. Lett.* **2014**, *5*, 2675–2681. [[CrossRef](#)] [[PubMed](#)]
33. Campbell, M.G.; Liu, S.F.; Swager, T.M.; Dinca, M. Chemiresistive Sensor Arrays from Conductive 2D Metal-Organic Frameworks. *J. Am. Chem. Soc.* **2015**, *137*, 13780–13783. [[CrossRef](#)] [[PubMed](#)]
34. Late, D.J.; Doneux, T.; Bougouma, M. Single-layer MoSe<sub>2</sub> based NH<sub>3</sub> gas sensor. *Appl. Phys. Lett.* **2014**, *105*, 233103. [[CrossRef](#)]
35. Yang, S.X.; Jiang, C.B.; Wei, S.H. Gas sensing in 2D materials. *Appl. Phys. Rev.* **2017**, *4*, 021304. [[CrossRef](#)]
36. Wang, G.Y.; Yang, L.L.; Li, Y.; Song, H.; Ruan, W.J.; Chang, Z.; Bu, X.H. A luminescent 2D coordination polymer for selective sensing of nitrobenzene. *Dalton Trans.* **2013**, *42*, 12865–12868. [[CrossRef](#)]
37. Huang, Y.X.; Guo, J.H.; Kang, Y.J.; Ai, Y.; Li, C.M. Two dimensional atomically thin MoS<sub>2</sub> nanosheets and their sensing applications. *Nanoscale* **2015**, *7*, 19358–19376. [[CrossRef](#)]
38. Xu, J.; Yan, D.P.; Li, S.D.; Lu, J. Controllable luminescence and electrochemical detection of Pb<sup>2+</sup> ion based on the 2,2'-Azino-bis(3-ethylbenzothiazoline-6-sulfonate) dye and dodecanesulfonate co-intercalated layered double hydroxide. *Dyes Pigment.* **2012**, *94*, 74–80. [[CrossRef](#)]
39. Nandu, N.; Hizir, M.S.; Roberston, N.M.; Ozturk, B.; Yigit, M.V. Masking the peroxidase-like activity of the molybdenum disulfide nanozyme enables label-free lipase detection. *ChemBioChem* **2019**, *20*, 1861–1867. [[CrossRef](#)]
40. Liao, H.P.; Wang, H.M.; Ding, H.M.; Meng, X.S.; Xu, H.; Wang, B.S.; Ai, X.P.; Wang, C. A 2D porous porphyrin-based covalent organic framework for sulfur storage in lithium sulfur batteries. *J. Mater. Chem. A* **2016**, *4*, 7416–7421. [[CrossRef](#)]

41. Hu, H.W.; Xin, J.H.; Hu, H.; Wang, X.W.; Miao, D.G.; Liu, Y. Synthesis and stabilization of metal nanocatalysts for reduction reactions—A review. *J. Mater. Chem. A* **2015**, *3*, 11157–11182. [[CrossRef](#)]
42. Rehman, J.; Fan, X.F.; Zheng, W.T. Computational insight of monolayer SnS<sub>2</sub> as anode material for potassium ion batteries. *Appl. Surf. Sci.* **2019**, *496*, 143625. [[CrossRef](#)]
43. Ramli, A.; Abu Bakar, M.N.; Osman, N.; Ismail, W.; Sepeai, S. Characterization of novel nitrogen-less derived 2D hybrid perovskite of C<sub>6</sub>H<sub>8</sub>N<sub>2</sub>PbBr<sub>3</sub> as a light-harvesting material for perovskite solar cell application. *Mater. Lett.* **2018**, *227*, 62–65. [[CrossRef](#)]
44. Sun, Z.Y.; Ma, T.; Tao, H.C.; Fan, Q.; Han, B.X. Fundamentals and challenges of electrochemical CO<sub>2</sub> reduction using two-dimensional materials. *Chem* **2017**, *3*, 560–587. [[CrossRef](#)]
45. Jagadale, A.D.; Guan, G.Q.; Li, X.M.; Du, X.; Ma, X.L.; Hao, X.G.; Abudula, A. Ultrathin nanoflakes of cobalt-manganese layered double hydroxide with high reversibility for asymmetric supercapacitor. *J. Power Sour.* **2016**, *306*, 526–534. [[CrossRef](#)]
46. Ahmed, N.; Morikawa, M.; Izumi, Y. Photocatalytic conversion of carbon dioxide into methanol using optimized layered double hydroxide catalysts. *Catal. Today* **2012**, *185*, 263–269. [[CrossRef](#)]
47. Sumboja, A.; Chen, J.W.; Zong, Y.; Lee, P.S.; Liu, Z.L. NiMn layered double hydroxides as efficient electrocatalysts for the oxygen evolution reaction and their application in rechargeable Zn-air batteries. *Nanoscale* **2017**, *9*, 774–780. [[CrossRef](#)]
48. Zheng, W.R.; Tsang, C.S.; Lee, L.Y.S.; Wong, K.Y. Two-dimensional metal-organic framework and covalent-organic framework: Synthesis and their energy-related applications. *Mater. Today Chem.* **2019**, *12*, 34–60. [[CrossRef](#)]
49. Bai, W.S.; Li, S.J.; Ma, J.P.; Cao, W.; Zheng, J.B. Ultrathin 2D metal—organic framework (nanosheets and nanofilms)—based xD-2D hybrid nanostructures as biomimetic enzymes and supercapacitors. *J. Mater. Chem. A* **2019**, *7*, 9086–9098. [[CrossRef](#)]
50. Chandra, D.; Das, S.K.; Bhaumik, A. A fluorophore grafted 2D-hexagonal mesoporous organosilica: Excellent ion-exchanger for the removal of heavy metal ions from wastewater. *Microporous Mesoporous Mater.* **2010**, *128*, 34–40. [[CrossRef](#)]
51. Mashtalir, O.; Cook, K.M.; Mochalin, V.N.; Crowe, M.; Barsoum, M.W.; Gogotsi, Y. Dye adsorption and decomposition on two-dimensional titanium carbide in aqueous media. *J. Mater. Chem. A* **2014**, *2*, 14334–14338. [[CrossRef](#)]
52. Cho, S.Y.; Kim, S.J.; Lee, Y.; Kim, J.S.; Jung, W.B.; Yoo, H.W.; Kim, J.; Jung, H.T. Highly enhanced gas adsorption properties in vertically aligned MoS<sub>2</sub> layers. *ACS Nano* **2015**, *9*, 9314–9321. [[CrossRef](#)] [[PubMed](#)]
53. Barnabas, M.J.; Parambadath, S.; Mathew, A.; Park, S.S.; Vinu, A.; Ha, C.S. Highly efficient and selective adsorption of Ln<sup>3+</sup> on pristine Zn/Al layered double hydroxide (Zn/Al-LDH) from aqueous solutions. *J. Solid State Chem.* **2016**, *233*, 133–142. [[CrossRef](#)]
54. Gu, P.C.; Xing, J.L.; Wen, T.; Zhang, R.; Wang, J.; Zhao, G.X.; Hayat, T.; Ai, Y.J.; Lin, Z.; Wang, X.K. Experimental and theoretical calculation investigation on efficient Pb(II) adsorption on etched Ti<sub>3</sub>AlC<sub>2</sub> nanofibers and nanosheets. *Environ. Sci. Nano* **2018**, *5*, 946–955. [[CrossRef](#)]
55. Li, Y.; Bi, H.Y.; Jin, Y.S. Facile preparation of rhamnolipid-layered double hydroxide nanocomposite for simultaneous adsorption of p-cresol and copper ions from water. *Chem. Eng. J.* **2017**, *308*, 78–88. [[CrossRef](#)]
56. Yan, L.; Zhou, M.J.; Zhang, X.J.; Huang, L.B.; Chen, W.; Roy, V.A.L.; Zhang, W.J.; Chen, X.F. A novel type of aqueous dispersible ultrathin-layered double hydroxide nanosheets for in vivo bioimaging and drug delivery. *ACS Appl. Mater. Interfaces* **2017**, *9*, 34185–34193. [[CrossRef](#)]
57. Chen, Y.; Tan, C.; Zhang, H.; Wang, L. Two-dimensional graphene analogues for biomedical applications. *Chem. Soc. Rev.* **2015**, *44*, 2681–2701. [[CrossRef](#)]
58. Darabdhara, G.; Bordoloi, J.; Manna, P.; Das, M.R. Biocompatible bimetallic Au-Ni doped graphitic carbon nitride sheets: A novel peroxidase-mimicking artificial enzyme for rapid and highly sensitive colorimetric detection of glucose. *Sens. Actuator B Chem.* **2019**, *285*, 277–290. [[CrossRef](#)]
59. Chen, T.M.; Zou, H.; Wu, X.J.; Liu, C.C.; Situ, B.; Zheng, L.; Yang, G.W. Nanozymatic antioxidant system based on MoS<sub>2</sub> nanosheets. *ACS Appl. Mater. Interfaces* **2018**, *10*, 12453–12462. [[CrossRef](#)]
60. Pavlovic, M.; Rouster, P.; Szilagyi, I. Synthesis and formulation of functional bionanomaterials with superoxide dismutase activity. *Nanoscale* **2017**, *9*, 369–379. [[CrossRef](#)]
61. Rouster, P.; Pavlovic, M.; Szilagyi, I. Immobilization of Superoxide Dismutase on polyelectrolyte functionalized titania nanosheets. *ChemBiochem* **2018**, *19*, 404–410. [[CrossRef](#)] [[PubMed](#)]

62. Winterbourn, C.C. Reconciling the chemistry and biology of reactive oxygen species. *Nat. Chem. Biol.* **2008**, *4*, 278–286. [[CrossRef](#)] [[PubMed](#)]
63. Hu, K.S.; Kulkarni, D.D.; Choi, I.; Tsukruk, V.V. Graphene-polymer nanocomposites for structural and functional applications. *Prog. Polym. Sci.* **2014**, *39*, 1934–1972. [[CrossRef](#)]
64. Wang, J.; Xu, F.; Jin, H.Y.; Chen, Y.Q.; Wang, Y. Non-noble metal-based carbon composites in hydrogen evolution reaction: Fundamentals to applications. *Adv. Mater.* **2017**, *29*, 1605838. [[CrossRef](#)] [[PubMed](#)]
65. Borenstein, A.; Hanna, O.; Attias, R.; Luski, S.; Brousse, T.; Aurbach, D. Carbon-based composite materials for supercapacitor electrodes: A review. *J. Mater. Chem. A* **2017**, *5*, 12653–12672. [[CrossRef](#)]
66. Jiang, L.B.; Yuan, X.Z.; Pan, Y.; Liang, J.; Zeng, G.M.; Wu, Z.B.; Wang, H. Doping of graphitic carbon nitride for photocatalysis: A review. *Appl. Catal. B Environ.* **2017**, *217*, 388–406. [[CrossRef](#)]
67. Li, X.M.; Tao, L.; Chen, Z.F.; Fang, H.; Li, X.S.; Wang, X.R.; Xu, J.B.; Zhu, H.W. Graphene and related two-dimensional materials: Structure-property relationships for electronics and optoelectronics. *Appl. Phys. Rev.* **2017**, *4*, 021306. [[CrossRef](#)]
68. Machado, B.F.; Serp, P. Graphene-based materials for catalysis. *Catal. Sci. Technol.* **2012**, *2*, 54–75. [[CrossRef](#)]
69. Kong, X.K.; Chen, C.L.; Chen, Q.W. Doped graphene for metal-free catalysis. *Chem. Soc. Rev.* **2014**, *43*, 2841–2857. [[CrossRef](#)]
70. Dreyer, D.R.; Todd, A.D.; Bielawski, C.W. Harnessing the chemistry of graphene oxide. *Chem. Soc. Rev.* **2014**, *43*, 5288–5301. [[CrossRef](#)]
71. Gadipelli, S.; Guo, Z.X. Graphene-based materials: Synthesis and gas sorption, storage and separation. *Prog. Mater. Sci.* **2015**, *69*, 1–60. [[CrossRef](#)]
72. Yang, K.; Feng, L.Z.; Shi, X.Z.; Liu, Z. Nano-graphene in biomedicine: Theranostic applications. *Chem. Soc. Rev.* **2013**, *42*, 530–547. [[CrossRef](#)] [[PubMed](#)]
73. Georgakilas, V.; Tiwari, J.N.; Kemp, K.C.; Perman, J.A.; Bourlinos, A.B.; Kim, K.S.; Zboril, R. Noncovalent functionalization of graphene and graphene oxide for energy materials, biosensing, catalytic, and biomedical applications. *Chem. Rev.* **2016**, *116*, 5464–5519. [[CrossRef](#)] [[PubMed](#)]
74. Li, X.; Yu, J.G.; Wageh, S.; Al-Ghamdi, A.A.; Xie, J. Graphene in Photocatalysis: A Review. *Small* **2016**, *12*, 6640–6696. [[CrossRef](#)] [[PubMed](#)]
75. Liu, J.Q.; Cui, L.; Losic, D. Graphene and graphene oxide as new nanocarriers for drug delivery applications. *Acta Biomater.* **2013**, *9*, 9243–9257. [[CrossRef](#)] [[PubMed](#)]
76. Zou, X.F.; Zhang, L.; Wang, Z.J.; Luo, Y. Mechanisms of the antimicrobial activities of graphene materials. *J. Am. Chem. Soc.* **2016**, *138*, 2064–2077. [[CrossRef](#)] [[PubMed](#)]
77. Yang, K.; Feng, L.Z.; Liu, Z. Stimuli responsive drug delivery systems based on nano-graphene for cancer therapy. *Adv. Drug Deliv. Rev.* **2016**, *105*, 228–241. [[CrossRef](#)]
78. Vesel, A.; Zaplotnik, R.; Primc, G.; Mozetic, M. Synthesis of vertically oriented graphene sheets or carbon nanowalls—review and challenges. *Materials* **2019**, *12*, 2968. [[CrossRef](#)]
79. Sun, Y.Q.; Wu, Q.O.; Shi, G.Q. Graphene based new energy materials. *Energy Environ. Sci.* **2011**, *4*, 1113–1132. [[CrossRef](#)]
80. El-Missiry, M.A. *Antioxidant Enzyme*; InTech: Rijeka, Croatia, 2012.
81. Brieger, K.; Schiavone, S.; Miller, F.J.; Krause, K.H. Reactive oxygen species: From health to disease. *Swiss Med. Wkly.* **2012**, *142*, 13659. [[CrossRef](#)]
82. Nirmala, C.; Bisht, M.S.; Bajwa, H.K.; Santosh, O. Bamboo: A rich source of natural antioxidants and its applications in the food and pharmaceutical industry. *Trends Food Sci. Technol.* **2018**, *77*, 91–99. [[CrossRef](#)]
83. Finley, J.W.; Kong, A.N.; Hintze, K.J.; Jeffery, E.H.; Ji, L.L.; Lei, X.G. Antioxidants in foods: State of the science important to the food industry. *J. Agric. Food Chem.* **2011**, *59*, 6837–6846. [[CrossRef](#)]
84. Beaucham, C.; Fridovich, I. Superoxide dismutase—improved assays and an assay applicable to acrylamide gels. *Anal. Biochem.* **1971**, *44*, 276–287. [[CrossRef](#)]
85. Fita, I.; Rossmann, M.G. The active-center of catalase. *J. Mol. Biol.* **1985**, *185*, 21–37. [[CrossRef](#)]
86. Gajhede, M.; Schuller, D.J.; Henriksen, A.; Smith, A.T.; Poulos, T.L. Crystal structure of horseradish peroxidase C at 2.15 angstrom resolution. *Nat. Struct. Biol.* **1997**, *4*, 1032–1038. [[CrossRef](#)] [[PubMed](#)]
87. Rice-Evans, C.A.; Miller, N.J.; Paganga, G. Structure-antioxidant activity relationships of flavonoids and phenolic acids. *Free Radic. Biol. Med.* **1996**, *20*, 933–956. [[CrossRef](#)]
88. Brand-Williams, W.; Cuvelier, M.E.; Berset, C. Use of a free-radical method to evaluate antioxidant activity. *Food Sci. Technol. Lebensm. Wiss. Technol.* **1995**, *28*, 25–30. [[CrossRef](#)]

89. Fox, J.B. Kinetics and mechanisms of the Griess reaction. *Anal. Chem.* **1979**, *51*, 1493–1502. [[CrossRef](#)]
90. Re, R.; Pellegrini, N.; Proteggente, A.; Pannala, A.; Yang, M.; Rice-Evans, C. Antioxidant activity applying an improved ABTS radical cation decolorization assay. *Free Radic. Biol. Med.* **1999**, *26*, 1231–1237. [[CrossRef](#)]
91. Beckman, J.S.; Beckman, T.W.; Chen, J.; Marshall, P.A.; Freeman, B.A. Apparent hydroxyl radical production by peroxynitrite—Implications for endothelial injury from nitric-oxide and superoxide. *Proc. Natl. Acad. Sci. USA* **1990**, *87*, 1620–1624. [[CrossRef](#)]
92. Koppenol, W.H. The centennial of the Fenton reaction. *Free Radic. Biol. Med.* **1993**, *15*, 645–651. [[CrossRef](#)]
93. Ohkawa, H.; Ohishi, N.; Yagi, K. Assay for lipid peroxides in animal-tissues by thiobarbituric acid reaction. *Anal. Biochem.* **1979**, *95*, 351–358. [[CrossRef](#)]
94. Fenton, H.J.H.; Healy, T.W. Oxidation of tartaric acid in presence of iron. *J. Chem. Soc. Trans.* **1894**, *65*, 899–910. [[CrossRef](#)]
95. Valko, M.; Rhodes, C.J.; Moncol, J.; Izakovic, M.; Mazur, M. Free radicals, metals and antioxidants in oxidative stress-induced cancer. *Chem. Biol. Interact.* **2006**, *160*, 1–40. [[CrossRef](#)]
96. Benzie, I.F.F.; Strain, J.J. The ferric reducing ability of plasma (FRAP) as a measure of antioxidant power: The FRAP assay. *Anal. Biochem.* **1996**, *239*, 70–76. [[CrossRef](#)]
97. Apak, R.; Guclu, K.; Ozyurek, M.; Karademir, S.E. Novel total antioxidant capacity index for dietary polyphenols and vitamins C and E, using their cupric ion reducing capability in the presence of neocuproine: CUPRAC method. *J. Agric. Food Chem.* **2004**, *52*, 7970–7981. [[CrossRef](#)]
98. Nimse, S.B.; Pal, D. Free radicals, natural antioxidants, and their reaction mechanisms. *RSC Adv.* **2015**, *5*, 27986–28006. [[CrossRef](#)]
99. Valgimigli, L.; Baschieri, A.; Amorati, R. Antioxidant activity of nanomaterials. *J. Mat. Chem. B* **2018**, *6*, 2036–2051. [[CrossRef](#)]
100. Mu, J.S.; Wang, Y.; Zhao, M.; Zhang, L. Intrinsic peroxidase-like activity and catalase-like activity of Co<sub>3</sub>O<sub>4</sub> nanoparticles. *Chem. Commun.* **2012**, *48*, 2540–2542. [[CrossRef](#)]
101. Dong, J.L.; Song, L.N.; Yin, J.J.; He, W.W.; Wu, Y.H.; Gu, N.; Zhang, Y. Co<sub>3</sub>O<sub>4</sub> nanoparticles with multi-enzyme activities and their application in immunohistochemical assay. *ACS Appl. Mater. Interfaces* **2014**, *6*, 1959–1970. [[CrossRef](#)]
102. Wang, Q.; Liu, S.W.; Sun, H.Y.; Lu, Q.F. Synthesis and intrinsic peroxidase-like activity of sisal-like cobalt oxide architectures. *Ind. Eng. Chem. Res.* **2014**, *53*, 7917–7922. [[CrossRef](#)]
103. Mu, J.S.; Zhang, L.; Zhao, G.Y.; Wang, Y. The crystal plane effect on the peroxidase-like catalytic properties of Co<sub>3</sub>O<sub>4</sub> nanomaterials. *Phys. Chem. Chem. Phys.* **2014**, *16*, 15709–15716. [[CrossRef](#)] [[PubMed](#)]
104. Zhang, W.; Dong, J.L.; Wu, Y.; Cao, P.; Song, L.N.; Ma, M.; Gu, N.; Zhang, Y. Shape-dependent enzyme-like activity of Co<sub>3</sub>O<sub>4</sub> nanoparticles and their conjugation with his-tagged EGFR single-domain antibody. *Colloid Surf. B Biointerfaces* **2017**, *154*, 55–62. [[CrossRef](#)] [[PubMed](#)]
105. Sun, H.Y.; Zhu, W.Y. Co<sub>3</sub>O<sub>4</sub> mirobelts: Preparation with the electrospinning technique and its investigation in peroxidase-like activity. *Appl. Surf. Sci.* **2017**, *399*, 298–304. [[CrossRef](#)]
106. Alizadeh, N.; Salimi, A.; Hallaj, R. Mimicking peroxidase-like activity of Co<sub>3</sub>O<sub>4</sub>-CeO<sub>2</sub> nanosheets integrated paper-based analytical devices for detection of glucose with smartphone. *Sens. Actuator B-Chem.* **2019**, *288*, 44–52. [[CrossRef](#)]
107. Wang, Q.Q.; Chen, J.X.; Zhang, H.; Wu, W.W.; Zhang, Z.Q.; Dong, S.J. Porous Co<sub>3</sub>O<sub>4</sub> nanoplates with pH-switchable peroxidase- and catalase-like activity. *Nanoscale* **2018**, *10*, 19140–19146. [[CrossRef](#)]
108. Ghosh, S.; Roy, P.; Karmodak, N.; Jemmis, E.D.; Mughesh, G. Nanoisozymes: Crystal-facet-dependent enzyme-mimetic activity of V<sub>2</sub>O<sub>5</sub> nanomaterials. *Angew. Chem. Int. Edit.* **2018**, *57*, 4510–4515. [[CrossRef](#)]
109. Tian, R.; Sun, J.H.; Qi, Y.F.; Zhang, B.Y.; Guo, S.L.; Zhao, M.M. Influence of VO<sub>2</sub> nanoparticle morphology on the colorimetric assay of H<sub>2</sub>O<sub>2</sub> and glucose. *Nanomaterials* **2017**, *7*, 347. [[CrossRef](#)]
110. Kamada, K.; Yamada, A.; Soh, N. Enhanced catalytic activity of enzymes interacting with nanometric titanate nanosheets. *RSC Adv.* **2015**, *5*, 85511–85516. [[CrossRef](#)]
111. Soh, N.; Kaneko, S.; Uozumi, K.; Ueda, T.; Kamada, K. Preparation of an enzyme/inorganic nanosheet/magnetic bead complex and its enzymatic activity. *J. Mater. Sci.* **2014**, *49*, 8010–8015. [[CrossRef](#)]
112. Nirala, N.R.; Pandey, S.; Bansal, A.; Singh, V.K.; Mukherjee, B.; Saxena, P.S.; Srivastava, A. Different shades of cholesterol: Gold nanoparticles supported on MOS<sub>2</sub> nanoribbons for enhanced colorimetric sensing of free cholesterol. *Biosens. Bioelectron.* **2015**, *74*, 207–213. [[CrossRef](#)] [[PubMed](#)]



113. Ding, Y.Q.; Wang, G.; Sun, F.Z.; Lin, Y.Q. Heterogeneous nanostructure design based on the epitaxial growth of spongy MoS<sub>x</sub> on 2D Co(OH)(2) nanoflakes for triple-enzyme mimetic activity: Experimental and density functional theory studies on the dramatic activation mechanism. *ACS Appl. Mater. Interfaces* **2018**, *10*, 32567–32578. [[CrossRef](#)]
114. Wu, X.J.; Chen, T.M.; Wang, J.X.; Yang, G.W. Few-layered MoSe<sub>2</sub> nanosheets as an efficient peroxidase nanozyme for highly sensitive colorimetric detection of H<sub>2</sub>O<sub>2</sub> and xanthine. *J. Mater. Chem. B* **2018**, *6*, 105–111. [[CrossRef](#)]
115. Huang, L.J.; Zhu, W.X.; Zhang, W.T.; Chen, K.; Wang, J.; Wang, R.; Yang, Q.F.; Hu, N.; Suo, Y.R.; Wang, J.L. Layered vanadium(IV) disulfide nanosheets as a peroxidase-like nanozyme for colorimetric detection of glucose. *Microchim. Acta* **2018**, *185*, 7. [[CrossRef](#)] [[PubMed](#)]
116. Zhang, Y.; Wang, Y.N.; Sun, X.T.; Chen, L.; Xu, Z.R. Boron nitride nanosheet/CuS nanocomposites as mimetic peroxidase for sensitive colorimetric detection of cholesterol. *Sens. Actuator B Chem.* **2017**, *246*, 118–126. [[CrossRef](#)]
117. Chen, J.Y.; Shu, Y.; Li, H.L.; Xu, Q.; Hu, X.Y. Nickel metal-organic framework 2D nanosheets with enhanced peroxidase nanozyme activity for colorimetric detection of H<sub>2</sub>O<sub>2</sub>. *Talanta* **2018**, *189*, 254–261. [[CrossRef](#)]
118. Pavlovic, M.; Rouster, P.; Somosi, Z.; Szilagyi, I. Horseradish peroxidase-nanoclay hybrid particles of high functional and colloidal stability. *J. Colloid Interface Sci.* **2018**, *524*, 114–121. [[CrossRef](#)]
119. Kong, X.G.; Jin, L.; Wei, M.; Duan, X. Antioxidant drugs intercalated into layered double hydroxide: Structure and in vitro release. *Appl. Clay Sci.* **2010**, *49*, 324–329. [[CrossRef](#)]
120. Ansy, K.M.; Lee, J.H.; Piao, H.; Choi, G.; Choy, J.H. Stabilization of antioxidant gallate in layered double hydroxide by exfoliation and reassembling reaction. *Solid State Sci.* **2018**, *80*, 65–71. [[CrossRef](#)]
121. Murath, S.; Szerlauth, S.; Sebok, D.; Szilagyi, I. Layered double hydroxide nanoparticles to overcome the hydrophobicity of ellagic acid: An antioxidant hybrid material. *Antioxidants* **2020**, *9*, 153. [[CrossRef](#)]
122. Amaro, L.P.; Cicogna, F.; Passaglia, E.; Morici, E.; Oberhauser, W.; Al-Malaika, S.; Dintcheva, N.T.; Coiai, S. Thermo-oxidative stabilization of poly(lactic acid) with antioxidant intercalated layered double hydroxides. *Polym. Degrad. Stabil.* **2016**, *133*, 92–100. [[CrossRef](#)]
123. Pontes-Neto, J.G.; Fontes, D.A.F.; de Lyra, M.A.M.; de Brito, M.D.M.; Chaves, L.L.; Rolim-Neto, P.J.; Soares, M.F.D.; Quintans, L.J.; de Freitas, R.M.; Soares-Sobrinho, J.L. Evaluation of antioxidant potential of novel CaAl and NiAl layered double hydroxides loaded with olanzapine. *Life Sci.* **2018**, *207*, 246–252. [[CrossRef](#)] [[PubMed](#)]
124. Pavlovic, M.; Nafradi, M.; Rouster, P.; Murath, S.; Szilagyi, I. Highly stable enzyme-mimicking nanocomposite of antioxidant activity. *J. Colloid Interface Sci.* **2019**, *543*, 174–182. [[CrossRef](#)] [[PubMed](#)]
125. Chen, L.J.; Sun, K.F.; Li, P.P.; Fan, X.Z.; Sun, J.C.; Ai, S.Y. DNA-enhanced peroxidase-like activity of layered double hydroxide nanosheets and applications in H<sub>2</sub>O<sub>2</sub> and glucose sensing. *Nanoscale* **2013**, *5*, 10982–10988. [[CrossRef](#)]
126. Olivera, S.; Hu, C.; Nagananda, G.S.; Reddy, N.; Venkatesh, K.; Muralidhara, H.B. Multipurpose composite for heavy metal sorption, antimicrobial, and antioxidant applications. *Int. J. Environ. Sci. Technol.* **2019**, *16*, 2017–2030. [[CrossRef](#)]
127. Chen, L.J.; Sun, B.; Wang, X.D.; Qiao, F.M.; Ai, S.Y. 2D ultrathin nanosheets of Co-Al layered double hydroxides prepared in L-asparagine solution: Enhanced peroxidase-like activity and colorimetric detection of glucose. *J. Mater. Chem. B* **2013**, *1*, 2268–2274. [[CrossRef](#)]
128. Zhan, T.R.; Kang, J.X.; Li, X.J.; Pan, L.; Li, G.J.; Hou, W.G. NiFe layered double hydroxide nanosheets as an efficiently mimic enzyme for colorimetric determination of glucose and H<sub>2</sub>O<sub>2</sub>. *Sens. Actuator B Chem.* **2018**, *255*, 2635–2642. [[CrossRef](#)]
129. Cao, Z.B.; Zhang, L.; Liang, K.; Cheong, S.S.; Boyer, C.; Gooding, J.J.; Chen, Y.; Gu, Z. Biodegradable 2D Fe-Al hydroxide for nanocatalytic tumor-dynamic therapy with tumor specificity. *Adv. Sci.* **2018**, *5*, 1801155. [[CrossRef](#)]
130. Baek, M.; Choy, J.H.; Choi, S.J. Montmorillonite intercalated with glutathione for antioxidant delivery: Synthesis, characterization, and bioavailability evaluation. *Int. J. Pharm.* **2012**, *425*, 29–34. [[CrossRef](#)]
131. Gutierrez, T.J.; Ponce, A.G.; Alvarez, V.A. Nano-clays from natural and modified montmorillonite with and without added blueberry extract for active and intelligent food nanopackaging materials. *Mater. Chem. Phys.* **2017**, *194*, 283–292. [[CrossRef](#)]

132. Garrido-Miranda, K.A.; Rivas, B.L.; Perez-Rivera, M.A.; Sanfuentes, E.A.; Pena-Farfal, C. Antioxidant and antifungal effects of eugenol incorporated in bionanocomposites of poly(3-hydroxybutyrate)-thermoplastic starch. *LWT Food Sci. Technol.* **2018**, *98*, 260–267. [[CrossRef](#)]
133. Zhang, L.H.; Gu, C.; Xiong, J.; Yang, M.; Guo, Y. Hemin-histamine-montmorillonite clay conjugate as a model biocatalyst to mimic natural peroxidase. *Sci. China Chem.* **2015**, *58*, 731–737. [[CrossRef](#)]
134. Yan, W.J.; Chen, W.B.; Muhammad, U.; Zhang, J.H.; Zhuang, H.; Zhou, G.H. Preparation of alpha-tocopherol-chitosan nanoparticles/chitosan/montmorillonite film and the antioxidant efficiency on sliced dry-cured ham. *Food Control* **2019**, *104*, 132–138. [[CrossRef](#)]
135. Ding, Y.Y.; Sun, L.F.; Jiang, Y.L.; Liu, S.X.; Chen, M.X.; Chen, M.M.; Ding, Y.N.; Liu, Q.Y. A facile strategy for the preparation of ZnS nanoparticles deposited on montmorillonite and their higher catalytic activity for rapidly colorimetric detection of H<sub>2</sub>O<sub>2</sub>. *Mater. Sci. Eng. C Mater. Biol. Appl.* **2016**, *67*, 188–194. [[CrossRef](#)]
136. Zhang, L.Y.; Chen, M.X.; Jiang, Y.L.; Chen, M.M.; Ding, Y.A.; Liu, Q.Y. A facile preparation of montmorillonite-supported copper sulfide nanocomposites and their application in the detection of H<sub>2</sub>O<sub>2</sub>. *Sens. Actuator B Chem.* **2017**, *239*, 28–35. [[CrossRef](#)]
137. Liu, Q.Y.; Jiang, Y.L.; Zhang, L.Y.; Zhou, X.P.; Lv, X.T.; Ding, Y.Y.; Sun, L.F.; Chen, P.P.; Yin, H.L. The catalytic activity of Ag<sub>2</sub>S-montmorillonites as peroxidase mimetic toward colorimetric detection of H<sub>2</sub>O<sub>2</sub>. *Mater. Sci. Eng. C Mater. Biol. Appl.* **2016**, *65*, 109–115. [[CrossRef](#)]
138. Wu, K.L.; Yang, B.C.; Zhu, X.X.; Chen, W.; Luo, X.L.; Liu, Z.X.; Zhang, X.; Liu, Q.Y. Cobalt and nickel bimetallic sulfide nanoparticles immobilized on montmorillonite demonstrating peroxidase-like activity for H<sub>2</sub>O<sub>2</sub> detection. *New J. Chem.* **2018**, *42*, 18749–18758. [[CrossRef](#)]
139. Kim, H.J.; Suma, Y.; Lee, S.H.; Kim, J.A.; Kim, H.S. Immobilization of horseradish peroxidase onto clay minerals using soil organic matter for phenol removal. *J. Mol. Catal. B Enzym.* **2012**, *83*, 8–15. [[CrossRef](#)]
140. Szilagyi, I.; Labadi, I.; Hernadi, K.; Palinko, I.; Fekete, I.; Korecz, L.; Rockenbauer, A.; Kiss, T. Superoxide dismutase activity of a Cu-Zn complex—bare and immobilised. *New J. Chem.* **2005**, *29*, 740–745. [[CrossRef](#)]
141. Szilagyi, I.; Labadi, I.; Hernadi, K.; Kiss, T.; Palinko, I. Montmorillonite intercalated Cu(II)-histidine complex—synthesis, characterisation and superoxide dismutase activity. In *Molecular Sieves: From Basic Research to Industrial Applications, Pts a and B*; Cejka, J., Zilkova, N., Nachtigall, P., Eds.; Elsevier: Amsterdam, The Netherlands, 2005; Volume 158, pp. 1011–1018.
142. He, Y.F.; Qi, F.; Niu, X.H.; Zhang, W.C.; Zhang, X.F.; Pan, J.M. Uricase-free on-demand colorimetric biosensing of uric acid enabled by integrated CoP nanosheet arrays as a monolithic peroxidase mimic. *Anal. Chim. Acta* **2018**, *1021*, 113–120. [[CrossRef](#)]
143. Alizadeh, N.; Salimi, A.; Hallaj, R. Mimicking peroxidase activity of Co-2(OH)(2)CO<sub>3</sub>-CeO<sub>2</sub> nanocomposite for smartphone based detection of tumor marker using paper-based microfluidic immunodevice. *Talanta* **2018**, *189*, 100–110. [[CrossRef](#)] [[PubMed](#)]
144. Guo, J.L.; Wang, Y.; Zhao, M. 3D flower-like ferrous(II) phosphate nanostructures as peroxidase mimetics for sensitive colorimetric detection of hydrogen peroxide and glucose at nanomolar level. *Talanta* **2018**, *182*, 230–240. [[CrossRef](#)] [[PubMed](#)]
145. Tanaka, S.; Masud, M.K.; Kaneti, Y.V.; Shiddiky, M.J.A.; Fatehmulla, A.; Aldhafiri, A.M.; Farooq, W.A.; Bando, Y.; Hossain, M.S.A.; Yamauchi, Y. Enhanced peroxidase mimetic activity of porous iron oxide nanoflakes. *ChemNanoMat* **2019**, *5*, 506–513. [[CrossRef](#)]
146. Wang, T.; Su, P.; Lin, F.Y.; Yang, Y. Self-sacrificial template synthesis of mixed-valence-state cobalt nanomaterials with high catalytic activities for colorimetric detection of glutathione. *Sens. Actuator B Chem.* **2018**, *254*, 329–336. [[CrossRef](#)]
147. Ganganboina, A.B.; Doong, R.A. The biomimic oxidase activity of layered V<sub>2</sub>O<sub>5</sub> nanozyme for rapid and sensitive nanomolar detection of glutathione. *Sens. Actuator B Chem.* **2018**, *273*, 1179–1186. [[CrossRef](#)]
148. Xie, Q.; Zhao, Y.Y.; Chen, X.; Liu, H.M.; Evans, D.G.; Yang, W.S. Nanosheet-based titania microspheres with hollow core-shell structure encapsulating horseradish peroxidase for a mediator-free biosensor. *Biomaterials* **2011**, *32*, 6588–6594. [[CrossRef](#)]
149. Rouster, P.; Pavlovic, M.; Saringer, S.; Szilagyi, I. Functionalized titania nanosheet dispersions of peroxidase activity. *J. Phys. Chem. C* **2018**, *122*, 11455–11463. [[CrossRef](#)]
150. Niu, Y.Y.; Zou, R.Y.; Yones, H.A.; Li, X.B.; Li, X.Y.; Niu, X.L.; Chen, Y.; Li, P.; Sun, W. Electrochemical behavior of horseradish peroxidase on WS<sub>2</sub> nanosheet-modified electrode and electrocatalytic investigation. *J. Chin. Chem. Soc.* **2018**, *65*, 1127–1135. [[CrossRef](#)]

151. Huang, Y.; Zhao, M.T.; Han, S.K.; Lai, Z.C.; Yang, J.; Tan, C.L.; Ma, Q.L.; Lu, Q.P.; Chen, J.Z.; Zhang, X.; et al. Growth of Au nanoparticles on 2D metalloporphyrinic metal-organic framework nanosheets used as biomimetic catalysts for cascade reactions. *Adv. Mater.* **2017**, *29*, 1700102. [[CrossRef](#)]
152. Qin, L.; Wang, X.Y.; Liu, Y.F.; Wei, H. 2D-metal-organic-framework-nanozyme sensor arrays for probing phosphates and their enzymatic hydrolysis. *Anal. Chem.* **2018**, *90*, 9983–9989. [[CrossRef](#)]
153. Liu, X.P.; Yan, Z.Q.; Zhang, Y.; Liu, Z.W.; Sun, Y.H.; Ren, J.S.; Qu, X.G. Two-dimensional metal-organic framework/enzyme hybrid nanocatalyst as a benign and self-activated cascade reagent for in vivo wound healing. *ACS Nano* **2019**, *13*, 5222–5230. [[CrossRef](#)] [[PubMed](#)]
154. Wang, Y.L.; Wang, Z.C.; Rui, Y.P.; Li, M.G. Horseradish peroxidase immobilization on carbon nanodots/CoFe layered double hydroxides: Direct electrochemistry and hydrogen peroxide sensing. *Biosens. Bioelectron.* **2015**, *64*, 57–62. [[CrossRef](#)] [[PubMed](#)]
155. Zhang, Q.; Jiao, Q.; Leroux, F.; Tang, P.G.; Li, D.Q.; Feng, Y.J. Antioxidant intercalated hydrocalumite as multifunction nanofiller for Poly(propylene): Synthesis, thermal stability, light stability, and anti-migration property. *Polym. Degrad. Stabil.* **2017**, *140*, 9–16. [[CrossRef](#)]
156. Lonkar, S.P.; Kutlu, B.; Leuteritz, A.; Heinrich, G. Nanohybrids of phenolic antioxidant intercalated into MgAl-layered double hydroxide clay. *Appl. Clay Sci.* **2013**, *71*, 8–14. [[CrossRef](#)]
157. Badhani, B.; Sharma, N.; Kakkar, R. Gallic acid: A versatile antioxidant with promising therapeutic and industrial applications. *RSC Adv.* **2015**, *5*, 27540–27557. [[CrossRef](#)]
158. Arratia-Quijada, J.; Rivas-Fuentes, S.; Saavedra, K.J.P.; Lamas, A.M.M.; Arizaga, G.G.C. Layered double hydroxide as a vehicle to increase toxicity of gallate ions against Adenocarcinoma cells. *Molecules* **2016**, *21*, 928. [[CrossRef](#)] [[PubMed](#)]
159. Lima, E.; Flores, J.; Cruz, A.S.; Leyva-Gomez, G.; Krotzsch, E. Controlled release of ferulic acid from a hybrid hydrotalcite and its application as an antioxidant for human fibroblasts. *Microporous Mesoporous Mater.* **2013**, *181*, 1–7. [[CrossRef](#)]
160. Gao, X.R.; Lei, L.X.; O'Hare, D.; Xie, J.; Gao, P.R.; Chang, T. Intercalation and controlled release properties of vitamin C intercalated layered double hydroxide. *J. Solid State Chem.* **2013**, *203*, 174–180. [[CrossRef](#)]
161. Gao, X.R.; Chen, L.; Xie, J.; Yin, Y.B.; Chang, T.; Duan, Y.C.; Jiang, N. In vitro controlled release of vitamin C from Ca/Al layered double hydroxide drug delivery system. *Mater. Sci. Eng. C Mater. Biol. Appl.* **2014**, *39*, 56–60. [[CrossRef](#)] [[PubMed](#)]
162. Shafiei, S.S.; Solati-Hashjin, M.; Samadikuchaksaraei, A.; Kalantarinejad, R.; Asadi-Eydivand, M.; Abu Osman, N.A. Epigallocatechin gallate/layered double hydroxide nanohybrids: Preparation, characterization, and in vitro anti-tumor study. *PLoS ONE* **2015**, *10*, e0136530. [[CrossRef](#)]
163. Feng, Y.J.; Jiang, Y.; Huang, Q.; Chen, S.T.; Zhang, F.B.; Tang, P.G.; Li, D.Q. High antioxidative performance of layered double hydroxides/polypropylene composite with intercalation of low-molecular-weight phenolic antioxidant. *Ind. Eng. Chem. Res.* **2014**, *53*, 2287–2292. [[CrossRef](#)]
164. Zhang, Q.; Jiao, Q.; Leroux, F.; Tang, P.G.; Li, D.Q.; Feng, Y.J. Antioxidant intercalated Zn-containing layered double hydroxides: Preparation, performance and migration properties. *New J. Chem.* **2017**, *41*, 2364–2371. [[CrossRef](#)]
165. Camino, G.; Maffezzoli, A.; Braglia, M.; De Lazzaro, M.; Zammarano, M. Effect of hydroxides and hydroxycarbonate structure on fire retardant effectiveness and mechanical properties in ethylene-vinyl acetate copolymer. *Polym. Degrad. Stabil.* **2001**, *74*, 457–464. [[CrossRef](#)]
166. Yu, J.F.; Liu, J.J.; Clearfield, A.; Sims, J.E.; Speigle, M.T.; Suib, S.L.; Sun, L.Y. Synthesis of layered double hydroxide single-layer nanosheets in formamide. *Inorg. Chem.* **2016**, *55*, 12036–12041. [[CrossRef](#)] [[PubMed](#)]
167. Lonkar, S.P.; Leuteritz, A.; Heinrich, G. Antioxidant intercalated layered double hydroxides: A new multifunctional nanofiller for polymers. *RSC Adv.* **2013**, *3*, 1495–1501. [[CrossRef](#)]
168. Ranjekar, P.K.; Hinge, A.; Hegde, M.V.; Ghate, M.; Kale, A.; Sitasawad, S.; Wagh, U.V.; Debsikdar, V.B.; Mahadik, S.P. Decreased antioxidant enzymes and membrane essential polyunsaturated fatty acids in schizophrenic and bipolar mood disorder patients. *Psychiatry Res.* **2003**, *121*, 109–122. [[CrossRef](#)]
169. Fernandez, L.; Ledezma, I.; Borrás, C.; Martínez, L.A.; Carrero, H. Horseradish peroxidase modified electrode based on a film of Co-Al layered double hydroxide modified with sodium dodecylbenzenesulfonate for determination of 2-chlorophenol. *Sens. Actuator B Chem.* **2013**, *182*, 625–632. [[CrossRef](#)]

170. Zhang, F.T.; Long, X.; Zhang, D.W.; Sun, Y.L.; Zhou, Y.L.; Ma, Y.R.; Qi, L.M.; Zhang, X.X. Layered double hydroxide-hemin nanocomposite as mimetic peroxidase and its application in sensing. *Sens. Actuator B-Chem.* **2014**, *192*, 150–156. [[CrossRef](#)]
171. Qiao, F.M.; Shi, W.J.; Dong, J.; Lv, W.; Ai, S.Y. Functional hybrids of layered double hydroxides with hemin: Synergistic effect for peroxynitrite-scavenging activity. *RSC Adv.* **2014**, *4*, 44614–44620. [[CrossRef](#)]
172. Zhang, Y.W.; Tian, J.Q.; Liu, S.; Wang, L.; Qin, X.Y.; Lu, W.B.; Chang, G.H.; Luo, Y.L.; Asiri, A.M.; Al-Youbi, A.O.; et al. Novel application of CoFe layered double hydroxide nanoplates for colorimetric detection of H<sub>2</sub>O<sub>2</sub> and glucose. *Analyst* **2012**, *137*, 1325–1328. [[CrossRef](#)]
173. Su, L.; Yu, X.A.; Miao, Y.Q.; Mao, G.J.; Dong, W.P.; Feng, S.L.; Liu, S.M.; Yang, L.K.; Zhang, K.G.; Zhang, H. Alkaline-promoted regulation of the peroxidase-like activity of Ni/Co LDHs and development bioassays. *Talanta* **2019**, *197*, 181–188. [[CrossRef](#)] [[PubMed](#)]
174. Wu, L.H.; Wan, G.P.; Shi, S.H.; He, Z.Y.; Xu, X.F.; Tang, Y.L.; Hao, C.C.; Wang, G.Z. Atomic layer deposition-assisted growth of CuAl LDH on carbon fiber as a peroxidase mimic for colorimetric determination of H<sub>2</sub>O<sub>2</sub> and glucose. *New J. Chem.* **2019**, *43*, 5826–5832. [[CrossRef](#)]
175. Xu, X.C.; Zou, X.B.; Wu, S.W.; Wang, L.J.; Niu, X.H.; Li, X.; Pan, J.M.; Zhao, H.L.; Lan, M.B. In situ formation of fluorescent polydopamine catalyzed by peroxidase-mimicking FeCo-LDH for pyrophosphate ion and pyrophosphatase activity detection. *Anal. Chim. Acta* **2019**, *1053*, 89–97. [[CrossRef](#)] [[PubMed](#)]
176. Ruan, Y.D.; Jia, X.D.; Wang, C.; Zhen, W.Y.; Jiang, X. Mn-Fe layered double hydroxide nanosheets: A new photothermal nanocarrier for O<sub>2</sub>-evolving phototherapy. *Chem. Commun.* **2018**, *54*, 11729–11732. [[CrossRef](#)] [[PubMed](#)]
177. Souza, V.G.L.; Pires, J.R.A.; Vieira, E.T.; Coelho, I.M.; Duarte, M.P.; Fernando, A.L. Activity of chitosan-montmorillonite bionanocomposites incorporated with rosemary essential oil: From in vitro assays to application in fresh poultry meat. *Food Hydrocoll.* **2019**, *89*, 241–252. [[CrossRef](#)]
178. Bhattacharyya, D.K.; Bandyopadhyay, U.; Banerjee, R.K. Chemical and kinetic evidence for an essential histidine in horseradish-peroxidase for iodide oxidation. *J. Biol. Chem.* **1992**, *267*, 9800–9804. [[PubMed](#)]
179. Zhou, F.F.; Luo, J.Q.; Qi, B.K.; Chen, X.R.; Wan, Y.H. Horseradish peroxidase immobilized on multifunctional hybrid microspheres for aflatoxin B1 removal: Will enzymatic reaction be enhanced by adsorption? *Ind. Eng. Chem. Res.* **2019**, *58*, 11710–11719. [[CrossRef](#)]
180. Pires, J.R.A.; de Souza, V.G.L.; Fernando, A.L. Chitosan/montmorillonite bionanocomposites incorporated with rosemary and ginger essential oil as packaging for fresh poultry meat. *Food Packag. Shelf Life* **2018**, *17*, 142–149. [[CrossRef](#)]
181. Souza, V.G.L.; Pires, J.R.A.; Rodrigues, P.F.; Lopes, A.A.S.; Fernandes, F.M.B.; Duarte, M.P.; Coelho, I.M.; Fernando, A.L. Bionanocomposites of chitosan/montmorillonite incorporated with Rosmarinus officinalis essential oil: Development and physical characterization. *Food Packag. Shelf Life* **2018**, *16*, 148–156. [[CrossRef](#)]
182. Szilagyi, I.; Horvath, L.; Labadi, I.; Hernadi, K.; Palinko, I.; Kiss, T. Mimicking catalase and catecholase enzymes by copper(II)-containing complexes. *Cent. Eur. J. Chem.* **2006**, *4*, 118–134. [[CrossRef](#)]
183. Deshpriya, I.K.; Kim, C.S.; Novak, M.J.; Kumar, C.V. Biofunctionalization of alpha-Zirconium Phosphate Nanosheets: Toward Rational Control of Enzyme Loading, Affinities, Activities and Structure Retention. *ACS Appl. Mater. Interfaces* **2014**, *6*, 9643–9653. [[CrossRef](#)] [[PubMed](#)]







## Research article

## Radical scavenging activity of plant extracts from improved processing

Adél Szerlauth<sup>a</sup>, Szabolcs Muráth<sup>a,b,\*\*</sup>, Sándor Viski<sup>c</sup>, Istvan Szilagyi<sup>a,b,\*</sup><sup>a</sup> MTA-SZTE Lendület Biocolloids Research Group, Department of Physical Chemistry and Materials Science, University of Szeged, Szeged, H-6720, Hungary<sup>b</sup> Interdisciplinary Excellence Center, Department of Physical Chemistry and Materials Science, University of Szeged, Szeged, H-6720, Hungary<sup>c</sup> HerbaPharm Europe Ltd., Battonya, H-5830, Hungary

## ARTICLE INFO

## Keywords:

Natural product chemistry  
Physical chemistry  
Food science  
Herbal extracts  
Antioxidant activity  
Plant processing  
DPPH assay  
Radical scavenge

## ABSTRACT

Radical scavenging activity of extracts obtained from 16 plants harvested in South Hungary was assessed and compared to the activity of ascorbic acid standard. During extraction, a novel technique involving an ethanolic treatment at ambient temperature was used for advanced active component release. Although the procedure is time consuming, it serves as an efficient and harmless route to extract valuable antioxidant compounds from their natural sources. The as-prepared extracts consist of two phases (except *Allium sativum*), a clear solution and a thick suspension containing solid plant parts that separates in about 2 h. The samples were analysed by the antioxidant assay based on the scavenging of 1,1-diphenyl-2-picrylhydrazyl (DPPH) free radicals. For most of the species, the solid phase retained considerable amount of available antioxidant agents, while the solution parts showed significant radical scavenging activity. The main exceptions were *Nigella sativa*, *Hippophae rhamnoides* and *Linum usitatissimum*, where the solid parts were less active. Overall, the extracts possessed remarkable antioxidant activity that were compared to published literature data and were found to be superior.

## 1. Introduction

One of the main achievements of modern health conscious lifestyle is the growing interest towards medicine, dietary supplements and food additives of natural origin, such as herbal extracts, which contain high amount of antioxidants or vitamins, depending on the source of plant organs (van der Goot et al., 2016). Antioxidants mainly help maintaining the ideal balance of radicals in cells, preventing oxidative stress related illnesses (Lin and Beal, 2006). Certain vitamins can also assist this goal (e.g., ascorbic acid and tocopherols), while serving other purposes in the body (sight, bone growth, metabolism, blood coagulation, biosynthesis of molecules, etc.). The lack or surplus of antioxidants and vitamins may equally lead to health problems that should be avoided, but herbal extracts are common tools to provide the recommended doses of these vital compounds.

In the past, the antioxidant potency of numerous plants, herbs and spices was reported. One of the most effective representatives is common walnut (*Juglans regia*). It was shown that both its green hull (Schott, 2013) and the nut possess significant activity (Fukuda et al., 2003; Liu et al., 2016) and the hull has antibacterial properties as well. The most important compounds responsible for the antioxidant effect are peptides

and polyphenols including tannins. Besides, the leaves of maidenhair tree (*Ginkgo biloba*) are also excellent sources of antioxidants, although the extract from the tree is more known for its remedial effects in treatment of dementia (LeBars et al., 1997).

The seeds of medicinal herbs are also concentrated sources of beneficial components. These plants include milk thistle (*Silybum marianum* (Wojdylo et al., 2007)), mustard (*Brassica juncea* (Katsube et al., 2004)), anise (*Pimpinella anisum* (Hinneburg et al., 2006)), guava (*Psidium guajava*, with flesh (Lim et al., 2007)), caraway (*Carum carvi*), coriander (*Coriandrum sativum* (Zheng and Wang, 2001)), etc. Edible fruits also contain large amount of antioxidants in combination with vitamins (mainly vitamin C) and polyphenols. Some of the most active ones are papaya (*Carica papaya*), guava (*Psidium guajava* (Lim et al., 2007)), sea-buckthorn (*Hippophae rhamnoides* (Wei et al., 2019)), fig (*Ficus carica*), persimmon (*Diospyros kaki* (Katsube et al., 2004)) and various berries (Hakkinen et al., 1999).

Moreover, fragrant herbs are often valuable resources of antioxidant compounds. They can be divided into subgroups such as culinary green herbs, e.g., rosemary (*Rosmarinus officinalis* (Visentin et al., 2012)), lemon balm (*Melissa officinalis* (Wojdylo et al., 2007)), parsley (*Petroselinum crispum* (Hinneburg et al., 2006)), mints (*Mentha* (Zheng and Wang,

\* Corresponding author.

\*\* Corresponding author.

E-mail addresses: [murathsz@chem.u-szeged.hu](mailto:murathsz@chem.u-szeged.hu) (S. Muráth), [szistvan@chem.u-szeged.hu](mailto:szistvan@chem.u-szeged.hu) (I. Szilagyi).

**Table 1**

The plants and their parts used for the extract preparation and the corresponding EC<sub>50</sub> (normalized to dried plant mass) and AAEQ values.

Plant	Part used	EC <sub>50</sub> (µg)/AAEQ (upper phase)	EC <sub>50</sub> (µg)/AAEQ (mixed)
Common walnut <i>Juglans regia</i>	Nut	0.27/38.31	0.24/44.18
Sea-buckthorn <i>Hippophae rhamnoides</i>	Seed	0.72/14.46	0.85/12.30
Maidenhair tree <i>Ginkgo biloba</i>	Leaf	2.52/4.13	1.46/7.12
Black caraway <i>Nigella sativa</i>	Seed	1.52/6.83	1.55/6.72
Horse-chestnut <i>Aesculus hippocastanum</i>	Nut	4.94/2.10	2.26/4.60
Milk thistle <i>Silybum marianum</i>	Seed	3.77/2.76	2.84/3.66
Common marigold <i>Calendula officinalis</i>	Petal	3.78/2.75	2.89/3.60
Ginger <i>Zingiber officinale</i>	Rhizome	4.62/2.25	3.91/2.66
Hemp <i>Cannabis sativa</i>	Seed	5.19/2.00	4.51/2.31
Caraway <i>Carum carvi</i>	Seed	5.85/1.78	4.86/2.14
Sweet wormwood <i>Artemisia annua</i>	Leaf	6.60/1.58	5.13/2.03
Linseed <i>Linum usitatissimum</i>	Seed	5.46/1.90	7.40/1.40
Bitter melon <i>Momordica charantia</i>	Seed	17.13/0.61	10.06/1.03
Garlic <i>Allium sativum</i>	Bulb	23.69/0.44	23.69/0.44
Soybean <i>Glycine max</i>	Bean	–	–
Summer squash <i>Cucurbita pepo</i>	Seed	–	–

2001)), roots, e.g., turmeric (*Curcuma longa*) and ginger (*Zingiber officinale* (Katsube et al., 2004)) and the onion genus, e.g., Chinese leek (*Allium tuberosum* (Katsube et al., 2004)) and garlic (*Allium sativum* (Amagase et al., 2001)). The members of the last group are unique, as they contain notable amount of sulphur compounds that are responsible for their joint antioxidant and antimicrobial character. Furthermore, the antioxidant property of chocolates with high cocoa content was also demonstrated (Medeiros et al., 2015).

In our contribution, 16 plants (Table 1), grown in South Hungary were harvested, dried and treated with a novel type extraction method to achieve high degree extraction of antioxidants of long shelf-life. The obtained extracts were characterized by means of probe reactions to assess their radical scavenging activity.

## 2. Experimental

### 2.1. Herbal extract preparation

The herbal extracts were prepared from 1000 g of dried plant parts milled to 50 µm grain size. The dried materials were hydrated with 200 mL of filtered water and these slurries were completed to 4000 mL with 96% ethanol solution. After 1 month soaking and extraction period, the larger insoluble parts were separated by centrifugation and the samples were portioned to 100 mL glass vials after vigorous mixing.

### 2.2. DPPH activity tests

The antioxidant activity of the extracts was evaluated by the DPPH (1,1-diphenyl-2-picrylhydrazyl) assay (Brand-Williams et al., 1995). Given the fact that the majority of natural antioxidants possess reactive hydrogen atoms, which serve as the reductants, the DPPH assay is a good

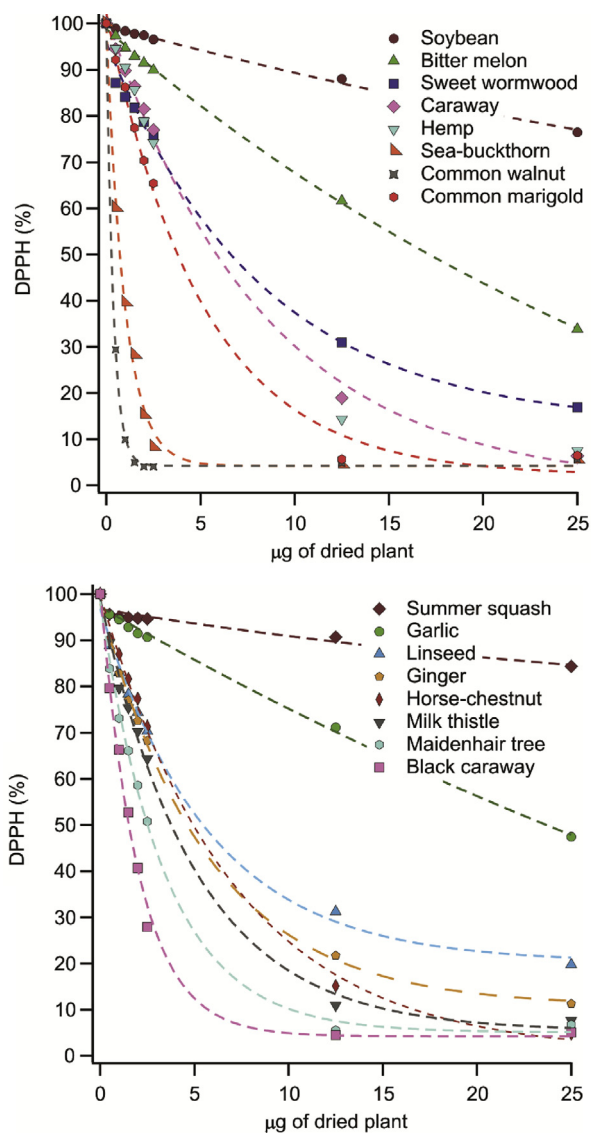


**Fig. 1.** Antioxidant activity expressed by the decrease of DPPH content as a function of the dried plant mass in the solution (upper) phases of the herb extracts investigated.

measure of the standard antioxidant profile. In a typical experiment, 3500 µL of 60 µM methanolic DPPH solution was mixed with 100 µL herbal extract of various concentrations. The transformation between the oxidized (initial, violet) and reduced (end-product, yellow) form of DPPH was followed by recording the absorbance decrease at 517 nm with a Thermo Scientific Genesys S10 spectrophotometer using 10 mm polystyrene cuvettes. The final absorbance values at steady-state were recorded. The remainder of DPPH is the ratio of final (A) and initial absorbance (A<sub>0</sub>) (DPPH% = A/A<sub>0</sub>). The effective concentration (EC<sub>50</sub>), i.e., the mass of the herbal extract needed to decompose 50% of the initial DPPH, was calculated using the DPPH% versus antioxidant concentration curves. For reference, ascorbic acid (AA) was used and the ascorbic acid equivalent (AAEQ) data were calculated from the obtained EC<sub>50</sub> numbers (AAEQ = EC<sub>50,AA</sub>/EC<sub>50,plant</sub>). The EC<sub>50,AA</sub> was determined to be 10.4 µg. All chemicals were from VWR International and used in analytical purity. The accuracy of the method is 5%.

## 3. Results and discussion

The mixed extracts possessed a dark colour and the liquor separated into two fractions in 120 min, excepting garlic extract, which appeared as

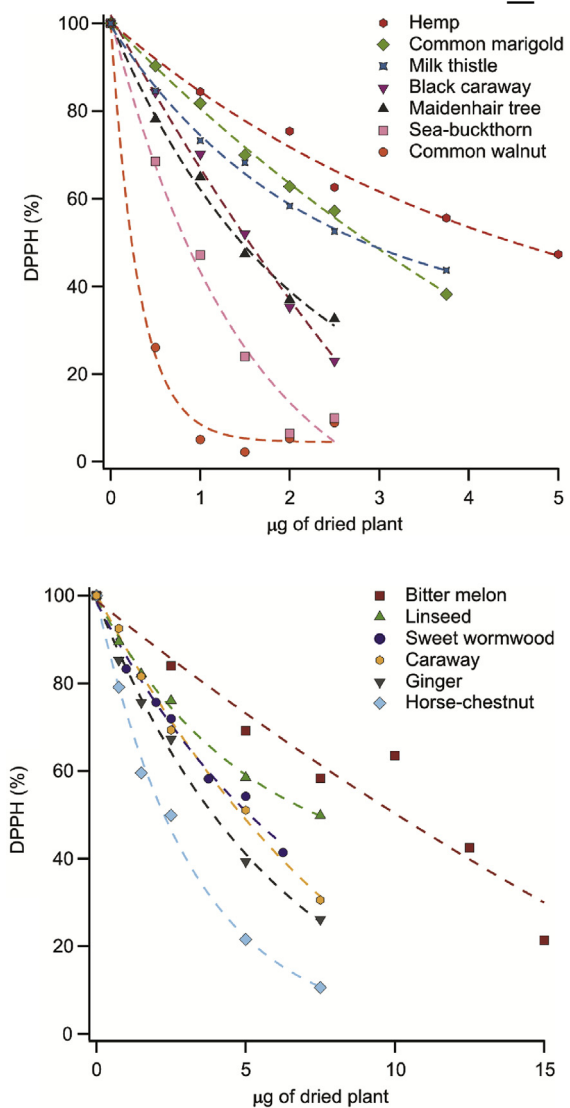


Fig. 2. Antioxidant activity expressed by the decrease of DPPH content as a function of the dried plant mass in the mixed herb extracts. Note that garlic consisted of only one clear solution phase, thus mixed extract could not be measured and the mixed extract of soybean and summer squash showed technical difficulties (strong colour) to measure.

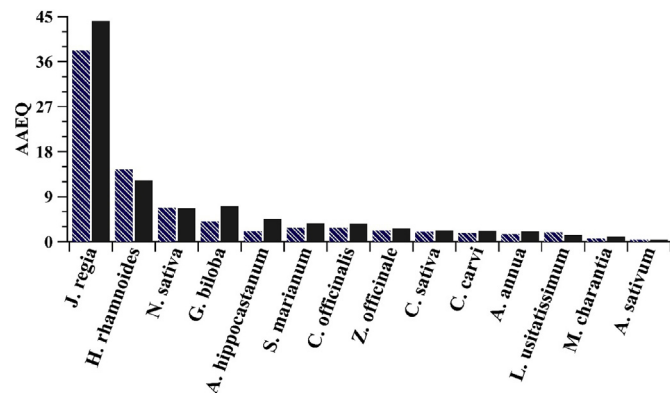


Fig. 3. Calculated AAEQ values of the extracts investigated (striped bars belong to the upper phase and full bars refer to the activity of mixed extract).

a homogeneous solution. The upper fraction is a clear ethanolic solution, while the lower phase contains small, aggregated plant parts. Both the upper and lower phases were analysed in the radical scavenging reactions.

The plant extracts required different time frames to achieve chemical equilibrium in the DPPH test, these periods were between 10 and 60 min. Since the reactivity of the antioxidant molecules is not uniform, this is a predictable characteristic. First, the upper phases, i.e., clear solutions, were investigated. After the equilibrium was reached at several doses of the extracts, the final DPPH content was expressed in mole percent and plotted against the mass of dried plant (i.e., the theoretical mass of dried plant required to make the volume of extract used for a measurement) in the cuvette. This mass ranged from 0 to 25 µg and was calculated from the extraction process, i.e., the volume of the extract pipetted for a measurement point and the density of the extracts, proven to be about 1 g/mL.

The DPPH scavenging activity of the plants varied and very poor, poor, mediocre and good scavengers were found, once comparing them together. The decreases of the DPPH concentration for all samples are shown in Fig. 1.

Overall, common walnut was the most effective antioxidant with 0.27 µg EC<sub>50</sub> value, followed by sea-buckthorn (0.72 µg). The activity of summer squash and soybean was insufficient to calculate the EC<sub>50</sub> values.

The experiments were repeated using shaken extracts to access information on the antioxidant activity of the slurry, i.e., the bottom phase, which sediments in long term. If the activity of the two phases combined is higher than the clear supernatants' one, the undissolved plant parts contain considerable amount of antioxidants that require longer time to express their effect. In the other case, the quantity of remaining antioxidants in the plant parts is low or insignificant. The activity curves of these mixed samples are shown in Fig. 2, while the EC<sub>50</sub> values together with the AAEQ data for all plants studied are tabulated in Table 1. In

Table 2  
Antioxidant compounds responsible for the radical scavenging activity of the plants investigated.

Plant	Main antioxidant components (Reference)
Common walnut <i>Juglans regia</i>	Polyphenols, peptides (Anderson et al., 2001; Fukuda et al., 2003; Liu et al., 2016)
Sea-buckthorn	Unsaturated fatty acids (Dubey et al., 2018)
<i>Hippophae rhamnoides</i>	Flavonoids, glycosides (van Beek, 2002)
Maidenhair tree <i>Ginkgo biloba</i>	Flavonoids, glycosides (van Beek, 2002)
Black caraway <i>Nigella sativa</i>	Terpenoids, tocopherols (Burits and Bucar, 2000; Trela and Szymanska, 2019)
Horse-chestnut <i>Aesculus hippocastanum</i>	Polyphenols (Margina et al., 2015)
Milk thistle <i>Silybum marianum</i>	Fatty acids, phenols (Mhamdi et al., 2016)
Common marigold <i>Calendula officinalis</i>	Terpenoids (Hamburger et al., 2003)
Ginger <i>Zingiber officinale</i>	Phenols (Jolad et al., 2004)
Hemp <i>Cannabis sativa</i>	Fatty acids, tocopherols (Oomah et al., 2002)
Caraway <i>Carum carvi</i>	Fatty acids, phenols (Ramadan et al., 2003)
Sweet wormwood <i>Artemisia annua</i>	Terpenoids (Cavar et al., 2012)
Linseed <i>Linum usitatissimum</i>	Tocopherols, polysaccharides (Fedeniuk and Biliaderis, 1994; Trela and Szymanska, 2019)
Bitter melon <i>Momordica charantia</i>	Dihydrocarveol (Braca et al., 2008)
Garlic <i>Allium sativum</i>	Sulphur compounds, phenols (Lawson and Gardner, 2005; Mnayer et al., 2014)
Soybean <i>Glycine max</i>	Isoflavones (Wang and Murphy, 1994)
Summer squash <i>Cucurbita pepo</i>	Tocopherols, fatty acids, phenols (Pericin et al., 2009; Rabrenovic et al., 2014)

addition, the AAEQ values are represented by scale bars in Fig. 3.

The main antioxidant composition of the plants investigated in the present study has been reported before and is detailed in Table 2. The more active plants are known for their widespread antioxidant content. On the other hand, the less active ones may worth a deeper look.

The bitter melon seeds contain various terpenes, possibly with low antioxidant, but good antimicrobial effect (Braca et al., 2008). The pungent sulphur compounds in garlic are also better known for their antimicrobial activity (Lawson and Gardner, 2005), but their DPPH scavenging ability has also been demonstrated earlier (Mnayer et al., 2014). Soybean, a sample with relatively low antioxidant activity, as indicated by its high EC<sub>50</sub> value, contains isoflavones, but only up to 5 mg in 1 g of bean (Wang and Murphy, 1994). Furthermore, flavones often react slowly with DPPH radicals, therefore, slow, but longer term activity is foreseen. On the other hand, the highly active extracts such as from common walnuts can be recommended as antioxidant dietary supplement to reduce oxidative stress.

#### 4. Conclusions

In the present research, an effective and antioxidant preserving method was developed to obtain highly active antioxidant extracts as ethanolic solutions from plants. The products separated into two phases over time, the radical scavenging activity of both phases was measured. Overall, the plant extracts exhibit remarkable antioxidant properties, from 0.44 (*Allium sativum*) to 44.18 (*Juglans regia*) AAEQ values. Based on their outstanding DPPH scavenging effect and other, already proven benefits, the extracts are promising candidates as commercial food supplements.

#### Declarations

##### Author contribution statement

Adél Szerlauth: Performed the experiments; Analyzed and interpreted the data.

Szabolcs Muráth: Conceived and designed the experiments; Analyzed and interpreted the data.

Sándor Viski: Contributed reagents, materials, analysis tools or data.

István Szilágyi: Conceived and designed the experiments; Wrote the paper.

##### Funding statement

This work was supported by the Hungarian Academy of Sciences (Lendület/96130) and the Ministry of Human Capacities of Hungary (20391-3/2018/FEKUSZTRAT).

##### Competing interest statement

The authors declare no conflict of interest.

##### Additional information

No additional information is available for this paper.

#### Acknowledgements

The authors are grateful to Mr. Deján Drágyi for the practical help during the antioxidant test reactions. Special thanks to Ildikó Masa and Árpád Mákos from HerbaPharm Europe Ltd for the professional preparation and delivery of the samples.

#### References

- Amagase, H., Petesch, B.L., Matsuura, H., Kasuga, S., Itakura, Y., 2001. Intake of garlic and its bioactive components. *J. Nutr.* 131 (3), 955–962.
- Anderson, K.J., Teuber, S.S., Gobeille, A., Cremin, P., Waterhouse, A.L., Steinberg, F.M., 2001. Walnut polyphenolics inhibit in vitro human plasma and LDL oxidation. *J. Nutr.* 131 (11), 2837–2842.
- Braca, A., Siciliano, T., D'Arrigo, M., Gennano, M.P., 2008. Chemical composition and antimicrobial activity of *Momordica charantia* seed essential oil. *Fitoterapia* 79 (2), 123–125.
- Brand-Williams, W., Cuvelier, M.E., Berset, C., 1995. Use of a free-radical method to evaluate antioxidant activity. *Food Sci. Technol.-Lebensm.-Wiss. Technol.* 28 (1), 25–30.
- Burits, M., Bucar, F., 2000. Antioxidant activity of *Nigella sativa* essential oil. *Phytother. Res.* 14 (5), 323–328.
- Cavar, S., Maksimovic, M., Vidic, D., Paric, A., 2012. Chemical composition and antioxidant and antimicrobial activity of essential oil of *Artemisia annua* L. from Bosnia. *Ind. Crops Prod.* 37 (1), 479–485.
- Dubey, S., Ramana, M.V., Mishra, A., Gupta, P.S., Awasthi, H., 2018. Seabuckthorn (*Hippophae rhamnoides* and *Hippophae salicifolia*) seed oil in combating inflammation: a mechanistic approach. *Pharmacogn. Res.* 10 (4), 404–407.
- Fedeniuk, R.W., Biliaderis, C.G., 1994. Composition and physicochemical properties of linseed (*linum usitatissimum* L) mucilage. *J. Agric. Food Chem.* 42 (2), 240–247.
- Fukuda, T., Ito, H., Yoshida, T., 2003. Antioxidative polyphenols from walnuts (*Juglans regia* L.). *Phytochemistry* 63 (7), 795–801.
- Hakkinen, S., Heinonen, M., Karenlampi, S., Mykkanen, H., Ruuskanen, J., Torronen, R., 1999. Screening of selected flavonoids and phenolic acids in 19 berries. *Food Res. Int.* 32 (5), 345–353.
- Hamburger, M., Adler, S., Baumann, D., Forg, A., Weinreich, B., 2003. Preparative purification of the major anti-inflammatory triterpenoid esters from marigold (*Calendula officinalis*). *Fitoterapia* 74 (4), 328–338.
- Hinneburg, I., Dorman, H.J.D., Hiltunen, R., 2006. Antioxidant activities of extracts from selected culinary herbs and spices. *Food Chem.* 97 (1), 122–129.
- Jolad, S.D., Lantz, R.C., Solyom, A.M., Chen, G.J., Bates, R.B., Timmermann, B.N., 2004. Fresh organically grown ginger (*Zingiber officinale*): composition and effects on LPS-induced PGE(2) production. *Phytochemistry* 65 (13), 1937–1954.
- Katsube, T., Tabata, H., Ohta, Y., Yamasaki, Y., Anurad, E., Shiwaku, K., Yamane, Y., 2004. Screening for antioxidant activity in edible plant products: comparison of low-density lipoprotein oxidation assay, DPPH radical scavenging assay, and Folin-Ciocalteu assay. *J. Agric. Food Chem.* 52 (8), 2391–2396.
- Lawson, L.D., Gardner, C.D., 2005. Composition, stability, and bioavailability of garlic products used in a clinical trial. *J. Agric. Food Chem.* 53 (16), 6254–6261.
- LeBars, P.L., Katz, M.M., Berman, N., Itil, T.M., Freedman, A.M., Schatzberg, A.F., 1997. A placebo-controlled, double-blind, randomized trial of an extract of *Ginkgo biloba* for dementia. *JAMA, J. Am. Med. Assoc.* 278 (16), 1327–1332.
- Lim, Y.Y., Lim, T.T., Tee, J.J., 2007. Antioxidant properties of several tropical fruits: a comparative study. *Food Chem.* 103 (3), 1003–1008.
- Lin, M.T., Beal, M.F., 2006. Mitochondrial dysfunction and oxidative stress in neurodegenerative diseases. *Nature* 443 (7113), 787–795.
- Liu, M.C., Yang, S.J., Hong, D., Yang, J.P., Liu, M., Lin, Y., Huang, C.H., Wang, C.J., 2016. A simple and convenient method for the preparation of antioxidant peptides from walnut (*Juglans regia* L.) protein hydrolysates. *Chem. Cent. J.* 10, 39.
- Margina, D., Olaru, O.T., Ilie, M., Gradinaru, D., Gutu, C., Voicu, S., Dinischiotu, A., Spandidos, D.A., Tsatsakis, A.M., 2015. Assessment of the potential health benefits of certain total extracts from *Vitis vinifera*, *Aesculus hippocastanum* and *Curcuma longa*. *Exp. Ther. Med.* 10 (5), 1681–1688.
- Medeiros, N.D., Marder, R.K., Wohlenberg, M.F., Funchal, C., Dani, C., 2015. Total phenolic content and antioxidant activity of different types of chocolate, milk, semisweet, dark, and soy, in cerebral cortex, hippocampus, and cerebellum of wistar rats. *Biochem. Res. Int.* 294659.
- Mhamdi, B., Abbassi, F., Smaoui, A., Abdelly, C., Marzouk, B., 2016. Fatty acids, essential oil and phenolics composition of *Silybum marianum* seeds and their antioxidant activities. *Pak. J. Pharm. Sci.* 29 (3), 953–959.
- Mnayer, D., Fabiano-Tixier, A.S., Petitcolas, E., Hamieh, T., Nehme, N., Ferrant, C., Fernandez, X., Chemat, F., 2014. Chemical composition, antibacterial and antioxidant activities of six essential oils from the Alliaceae family. *Molecules* 19 (12), 20034–20053.
- Oomah, B.D., Busson, M., Godfrey, D.V., Drover, J.C.G., 2002. Characteristics of hemp (*Cannabis sativa* L.) seed oil. *Food Chem.* 76 (1), 33–43.
- Pericin, D., Krimer, V., Trivic, S., Radulovic, L., 2009. The distribution of phenolic acids in pumpkin's hull-less seed, skin, oil cake meal, dehulled kernel and hull. *Food Chem.* 113 (2), 450–456.
- Rabrenovic, B.B., Dimic, E.B., Novakovic, M.M., Tesevic, V.V., Basic, Z.N., 2014. The most important bioactive components of cold pressed oil from different pumpkin (*Cucurbita pepo* L.) seeds. *LWT - Food Sci. Technol. (Lebensmittel-Wissenschaft -Technol.)* 55 (2), 521–527.
- Ramadan, M.F., Kroh, L.W., Morsel, J.T., 2003. Radical scavenging activity of black cumin (*Nigella sativa* L.), coriander (*Coriandrum sativum* L.), and Niger (*Guizotia abyssinica* Cass.) crude seed oils and oil fractions. *J. Agric. Food Chem.* 51 (24), 6961–6969.
- Schott, H., 2013. In vitro antibacterial and free radical scavenging activity of green hull of *Juglans regia*. *J. Pharm. Anal.* 3 (4), 298–302.
- Trela, A., Szymanska, R., 2019. Less widespread plant oils as a good source of vitamin E. *Food Chem.* 296, 160–166.
- van Beek, T.A., 2002. Chemical analysis of *Ginkgo biloba* leaves and extracts. *J. Chromatogr. A* 967 (1), 21–55.



- van der Goot, A.J., Pelgrom, P.J.M., Berghout, J.A.M., Geerts, M.E.J., Jankowiak, L., Hardt, N.A., Keijer, J., Schutyser, M.A.I., Nikiforidis, C.V., Boom, R.M., 2016. Concepts for further sustainable production of foods. *J. Food Eng.* 168, 42–51.
- Visentin, A., Rodriguez-Rojo, S., Navarrete, A., Maestri, D., Cocero, M.J., 2012. Precipitation and encapsulation of rosemary antioxidants by supercritical antisolvent process. *J. Food Eng.* 109 (1), 9–15.
- Wang, H.J., Murphy, P.A., 1994. Isoflavone composition of american and Japanese soybeans in Iowa - effects of variety, crop year, and location. *J. Agric. Food Chem.* 42 (8), 1674–1677.
- Wei, E.W., Yang, R., Zhao, H.P., Wang, P.H., Zhao, S.Q., Zhai, W.C., Zhang, Y., Zhou, H.L., 2019. Microwave-assisted extraction releases the antioxidant polysaccharides from seabuckthorn (*Hippophae rhamnoides* L.) berries. *Int. J. Biol. Macromol.* 123, 280–290.
- Wojdylo, A., Oszmianski, J., Czemerys, R., 2007. Antioxidant activity and phenolic compounds in 32 selected herbs. *Food Chem.* 105 (3), 940–949.
- Zheng, W., Wang, S.Y., 2001. Antioxidant activity and phenolic compounds in selected herbs. *J. Agric. Food Chem.* 49 (11), 5165–5170.



Article

# Layered Double Hydroxide Nanoparticles to Overcome the Hydrophobicity of Ellagic Acid: An Antioxidant Hybrid Material

Szabolcs Muráth <sup>1,2</sup>, Adél Szerlauth <sup>1</sup>, Dániel Sebők <sup>3</sup> and István Szilágyi <sup>1,2,\*</sup>

<sup>1</sup> MTA-SZTE Lendület Biocolloids Research Group, University of Szeged, H-6720 Szeged, Hungary; murathsz@chem.u-szeged.hu (S.M.); szerlauth.adel@gmail.com (A.S.)

<sup>2</sup> Department of Physical Chemistry and Materials Science, Interdisciplinary Excellence Center, University of Szeged, H-6720 Szeged, Hungary

<sup>3</sup> Department of Applied and Environmental Chemistry, Interdisciplinary Excellence Center, University of Szeged, H-6720 Szeged, Hungary; sebokd@chem.u-szeged.hu

\* Correspondence: szistvan@chem.u-szeged.hu; Tel: +36-62-343255

Received: 7 January 2020; Accepted: 11 February 2020; Published: 13 February 2020

**Abstract:** Ellagic acid (EA), a polyphenolic antioxidant of poor water solubility, was intercalated into biocompatible layered double hydroxide (LDH) nanoparticles by the coprecipitation method. Structural investigation of the composite revealed that the lactone bonds split under the synthetic experimental conditions, and EA was transformed to 4,4',5,5',6,6'-hexahydroxydiphenic acid during intercalation. To improve the surface properties of the EA-LDH composite, the samples were treated with different organic solvents. The antioxidant activity of the LDH hybrids was assessed in test reactions. Most of the obtained hybrids showed antioxidant activity comparable to the one of the free EA indicating that the spontaneous structural transformation upon immobilization did not change the efficiency in radical scavenging. Treatments with organic solvents influenced the activities of the materials remarkably. The main advantage of the immobilization procedure is that the products can be applied in aqueous samples in high concentrations overcoming the problem related to the low solubility of EA in water. The developed composites of high antioxidant content can be applied as efficient reactive oxygen species scavenging materials during biomedical treatments or industrial manufacturing processes.

**Keywords:** 2D antioxidant biomaterial; ellagic acid; layered double hydroxide; immobilization; radical scavenging

## 1. Introduction

Layered double hydroxides (LDH) represent the only inorganic layered materials with anion-exchange capacity found in nature. Their lamellae typically consist of divalent and trivalent metal ions, theoretically derived from isomorphous replacement of Mg(II) with Al(III) ions in the structure of layered Mg(OH)<sub>2</sub>, although a wide range of metallic compositions may be achieved [1]. The incorporation of cations of higher charge (Al(III), for instance) leads to the formation of positively charged layers. The general formula is stated as [M(II)<sub>1-x</sub>M(III)<sub>x</sub>(OH)<sub>2</sub>][A<sup>n-</sup>·mH<sub>2</sub>O], where M(II) and M(III) are divalent and trivalent metal ions and A<sup>n-</sup>·mH<sub>2</sub>O is the interlamellar (i.e., intercalated), charge-neutralizing anion in hydrated state [2]. Through tuning the composition of LDH and their composites with other materials [3], they can be used in a variety of applications including adsorbents for water purification [4,5], light emitters [6], corrosion-resistant coating material [7], contrast agents [8], solid support for bioactive substances [9,10], catalyst carriers [11] and catalysts in organic reactions [12,13], or in water splitting [14,15].

Intercalation of larger anions, such as biomolecules of various activities, gives rise to the development of hybrid materials with potential applications in biomedical processes. There are established ways to produce pillared LDH with non-steroidal drugs, such as diclofenac or ketoprofen [16] and indometacin or flurbiprofen [17], while the controlled release of the immobilized anticancer agent methotrexate was also demonstrated [18]. More profound effects were achieved with combined intercalation of anticancer drugs, e.g., fluorouracil and dactolisib [19]. Folic acid was incorporated in the structure of doxorubicin-modified LDH, and the presence of this targeting molecule improved the uptake in cancer cells, as shown in *in vitro* tests [20]. Furthermore, carborane-containing hybrids have potential applications in boron neutron capture therapy of cancer [21].

Antioxidant materials attract widespread contemporary interest due to the growing demand in biomedical as well as industrial processes, where reactive oxygen and nitrogen species cause significant damage [22–27]. Molecular (or non-enzymatic) anionic antioxidants, such as polyphenols and carboxylic acid derivatives, may also be encapsulated in LDH. Electrostatic interactions lead to stable composites. Thus, the intercalated organic materials, e.g., carnosine, gallic acid [20], and 3-(3,5-di-*tert*-butyl-4-hydroxy-phenyl)-propionic acid [28] maintain their radical scavenging activity. Among polyphenols, ellagic acid (EA) has generated notable research interest due to its high antioxidant activity and potential human applications, e.g., treatment of liver diseases [29]. EA commonly occurs in nature and shares from 2–10% (blueberry and currant) up to 75–90% (cloudberry and raspberry) of total polyphenol amount in various edible fruits [30]. Its content peaks in cloudberry with 0.2% of total mass and is also relevant in the antioxidant property of pomegranate [31].

It was demonstrated that EA plays a role in the chemoprevention of rat colon carcinogenesis, especially in combination with other anticancer drugs [32]. In addition, a synergistic effect between EA and quercetin was shown to induce apoptosis in human leukemia cells [33]. Recently, its protective feature was demonstrated against acrylamide, a compound with dangerous exposure symptoms related to peripheral neurotoxicity [34].

Despite the numerous positive effects, the main drawback of EA applications is the poor water solubility [35], which has also been an issue in soda pulping of eucalyptus, where greenish deposits (EA and its salts with divalent cations) clog the pipes [36]. Taken orally, the precipitation in gastric juice and relatively fast disposition of EA was shown, and the better uptake of its more soluble derivatives has been reported [37]. The bioavailability of EA was improved by encapsulation, successfully using zinc hydroxide carrier [38], collagen-chitosan matrix [39], and hydrophilic dendrimers [40] to overcompensate the solubility barrier. However, no comprehensive studies have been reported yet, where it was unambiguously confirmed that the antioxidant activity of EA-nanoparticle composites can be preserved. Using such bioactive hybrid materials, high antioxidant content can be provided in aqueous samples, e.g., in medical treatments or formulation procedures in the food and cosmetic industry.

In this research, for the first time, Mg<sub>2</sub>Al-LDH (denoted simply as LDH in the text), an inexpensive and biocompatible host [41], was used to mask the highly lipophilic property of EA. The structure of the novel EA-LDH composite material was also modified with organic solvents after synthesis, and the antioxidant activity of the different products was compared in two assays.

## 2. Materials and Methods

### 2.1. Materials

Magnesium(II) nitrate hexahydrate (Mg(NO<sub>3</sub>)<sub>2</sub>·6H<sub>2</sub>O), aluminum(III) nitrate nonahydrate (Al(NO<sub>3</sub>)<sub>3</sub>·9H<sub>2</sub>O), ellagic acid (EA), 4 M sodium hydroxide solution (NaOH), 1 M hydrochloric acid (HCl), ammonium acetate (NH<sub>4</sub>OAc), 2,2-diphenyl-1-picrylhydrazyl radical (DPPH), copper(II) chloride dihydrate (CuCl<sub>2</sub>·2H<sub>2</sub>O), neocuproine (Nc), Trolox (6-hydroxy-2,5,7,8-tetramethylchroman-2-carboxylic acid), methanol (MeOH), ethanol (EtOH), acetone (AC), acetonitrile (ACN), formamide (FA), *N,N*-dimethylformamide (DMF) and dimethyl sulfoxide (DMSO) were all purchased from VWR International (Radnor, Pennsylvania, USA) in analytical purity and were used as received.

Purified water was produced by reverse osmosis and UV irradiation (VWR Purity TU 3+ UV/UF system from VWR International).

## 2.2. Preparation of Hydrotalcite Intercalated with EA

The intercalation of the organic material was accomplished by coprecipitation [2]. A mixed metal nitrate solution was prepared by dissolving the salts in water with  $c(\text{Mg(II)}) = 0.2 \text{ M}$  and  $c(\text{Al(III)}) = 0.1 \text{ M}$ . This solution was thereafter added to the mixture of EA ( $625 \mu\text{mol}$ , structure is displayed in Figure 1) with  $4 \text{ M NaOH}$ . The EA-to-Al(III) molar ratio was 0.25, and a final pH of 13 was maintained during the reaction. Under these conditions, complete intercalation of the added EA was observed. The core structure of EA remains the same in the presence of a strong base. However, double deprotonation at pH above 12 and lactone ring opening may occur [42]. The slurry obtained was vigorously stirred at room temperature for 24 h, and the precipitate was separated by centrifugation at 4200 rpm (2090 rcf) for 10 min using an Orto Alresa (Madrid, Spain) Unicen 21 device. The solid material was washed three times with water and then dried at  $50 \text{ }^\circ\text{C}$  overnight. Hydrothermal treatment (HT) was also applied for the EA-LDH obtained. During this method, stirring was stopped after 1 h, and the slurry was transferred to an autoclave with Teflon lining (Col-Int Tech, Irmo, S.C., USA) and was treated at  $120 \text{ }^\circ\text{C}$  for 24 h in an oven. After cooling to ambient temperature, the sample was separated and purified as detailed earlier. Reference LDH was prepared using the same method, but without introducing EA or HT.

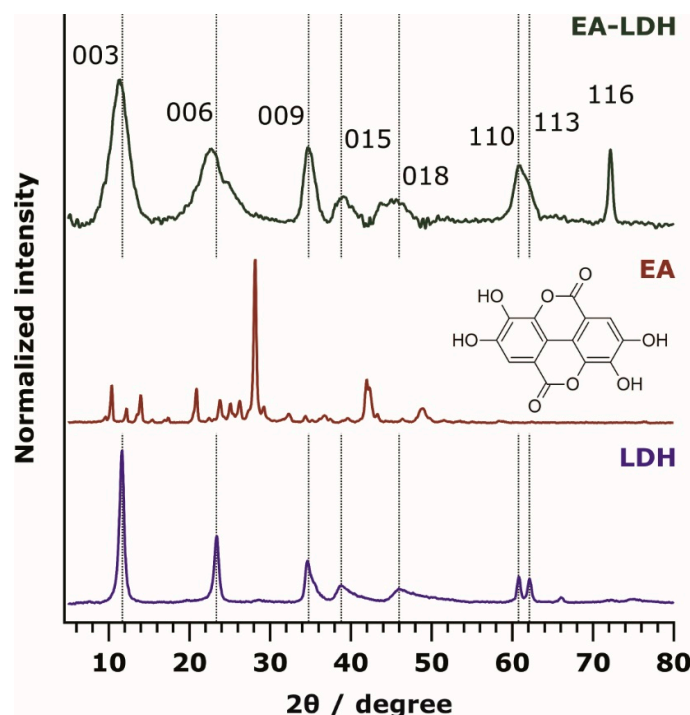


**Figure 1.** Powder XRD pattern of ellagic acid-layered double hydroxide (EA-LDH), EA, and LDH. The chemical structure of EA is shown in the inset. The Miller indices are indicated.

## 2.3. Aqueous Miscible Organic Solvent Treatment (AMOS-T) of the EA-LDH

Six solvents (MeOH, EtOH, AC, ACN, FA, and DMF) were applied to modify the surface properties of the organic-modified LDH [43]. In a typical method, the EA-LDH was synthesized as detailed before, and the aqueous washing was followed by a two-step stirring in 25–25 mL of the respective solvent for 2 h and 1 h each. Between the disjoint steps, the slurry was separated by centrifugation (4200 rpm, 2090 rcf, 20 min), and a fresh solvent aliquot was used. Finally, the modified EA-LDH composites were obtained after centrifugation (4200 rpm, 2090 rcf, 20 min) and drying at  $50 \text{ }^\circ\text{C}$  overnight. Overall, 9 materials were prepared, 8 of which contained EA (Table 1).



**Table 1.** Antioxidant activity values of the materials investigated.

Sample	EC <sub>50</sub> /10 <sup>-5</sup> M <sup>a</sup>	N <sub>DPPH</sub> <sup>b</sup>	ε/10 <sup>3</sup> M <sup>-1</sup> cm <sup>-1c</sup>	TEAC <sup>d</sup>
EA	0.25	11.78	71.0	4.61
EA-LDH	8.73	0.34	4.5	0.29
HT-EA-LDH <sup>e</sup>	-	-	2.4	0.15
MeOH-EA-LDH	4.19	0.70	14.7	0.96
EtOH-EA-LDH	1.98	1.48	17.7	1.15
AC-EA-LDH	2.17	1.35	17.8	1.16
ACN-EA-LDH	1.61	1.82	15.7	1.02
FA-EA-LDH <sup>e</sup>	-	-	1.5	0.10
DMF-EA-LDH	3.01	0.97	17.4	1.13

<sup>a</sup>EA concentration needed to decompose 50% of the DPPH radicals. <sup>b</sup>Number of DPPH decomposed by 1 EA. <sup>c</sup>Molar extinction coefficient of the materials in the CuPRAC assay. <sup>d</sup>Molar extinction coefficient of the materials compared to reference molecule Trolox in the CuPRAC assay. <sup>e</sup>The composite was not able to decrease the DPPH concentration below 50% in a reasonable time frame.

#### 2.4. Instrumental Characterization of the LDH

The X-ray diffractometry (XRD) measurements of the finely ground samples were performed on a Bruker (Billerica, MA, USA) D8 Advanced diffractometer with CuK<sub>α</sub> (λ = 0.1542 nm) as the radiation source at ambient temperature in the 5–80° (2θ, where θ is the incidence angle of the beam) range applying 0.02° step size. The basal spacing of the LDH was calculated by the Bragg's relation (Equation S1).

Morphological analyses were conducted using a Hitachi (Tokyo, Japan) S-4700 scanning electron microscope (SEM) at various magnifications with 10 kV accelerating voltage after gold deposition on the surface.

The Fourier transformed infrared (FT-IR) spectra of the solids were acquired using a JASCO (Easton, MD, USA) FTIR-4700 spectrometer with a DTGS (deuterated triglycine sulfate) detector in attenuated total reflectance (ATR, ZnSe accessory) mode. The spectral resolution was 1 cm<sup>-1</sup>, and a total number of 128 scans were collected for a spectrum. The noise of carbon-dioxide was removed by the built-in software package, and the spectra were baseline-corrected and smoothed.

UV-visible concentration measurements were conducted on a Thermo Fischer Genesys (Waltham, MA, USA) 10S dual beam spectrophotometer, equipped with a xenon flash lamp and a silicon photodiode detector.

The specific surface area of the LDH samples was determined using the BET (Brunauer–Emmett–Teller) method by measuring N<sub>2</sub> adsorption isotherms at 77 ± 0.5 K with a Micromeritics

Gemini (Norcross, GA, USA) 2375 Surface Area Analyzer instrument. Before measurements, the samples were evacuated at  $10^{-5}$  mm Hg and  $100\text{ }^{\circ}\text{C}$  overnight.

Dynamic light scattering measurements were performed to measure the size of the LDH and the hybrid particles in dispersions. The experiments were performed on a LiteSizer 500 device (Anton Paar, Graz, Austria) at a  $175^{\circ}$  scattering angle, applying the second cumulant fit to the correlation function. The hydrodynamic radii were calculated using the Stokes–Einstein equation [44].

### 2.5. Determining the EA content of the EA-LDH

The visible absorbance of EA at  $\lambda = 350\text{ nm}$  was measured after reacting a portion of the LDH obtained with 1 M HCl. Upon complete dissolution, the sample was diluted with a 50 V% aqueous MeOH solution, and the measurements were carried out at  $\text{pH} = 2.5$ . The calibration curve was acquired using a 30 mg/L EA stock solution in 50 V% MeOH solution at the same pH. The effect of the protonation state of EA to its UV-Vis spectrum was investigated by setting a pH of about 13 and 2 in a stirred cuvette. At these pH values, EA is present in an opened, deprotonated form (above pH 12) and in a fully protonated, lactone form (below pH 3). For the concentration measurements, 1 M NaOH (for basic pH) and 1 M HCl (for acidic pH) was added to a methanolic solution of EA to screen the UV-Vis spectra at different pH values.

### 2.6. Antioxidant Activity of the Hybrid Materials

The antioxidant property of the EA-LDH was monitored in the DPPH (2,2-diphenyl-1-picrylhydrazyl free radical) test reaction and the CuPRAC (cupric reducing antioxidant capacity) assay. The former one relies on the scavenging of commercially available DPPH free radicals [45], while the latter is based on the reducing potential of the material in question against neocuproine-chelated Cu(II) ions [46].

For the DPPH test, 3500  $\mu\text{L}$  of 60  $\mu\text{M}$  DPPH solution (in methanol, freshly prepared daily) was completed to 3600  $\mu\text{L}$  with water and with the aqueous suspension (5 g/L) of the LDH. The reference measurement was executed with EA dissolved in DMSO ( $c = 4.32\text{ mM}$ ) due to the poor water solubility. The absorbance decrease was followed at  $\lambda = 517\text{ nm}$ , the absorption maximum of DPPH, at various EA-to-DPPH molar ratios. The measurement time was 45 min for EA and 60 min for the EA-LDH hybrids. The Beer–Lambert equation was used for quantifying the remainder of DPPH from the initial absorbance (Equation S2).

For the CuPRAC method, 500  $\mu\text{L}$  solution of  $\text{CuCl}_2$  (10 mM), Nc (7.5 mM in ethanol), and  $\text{NH}_4\text{OAc}$  buffer ( $\text{pH} = 7$ , 1 M) were mixed in a cuvette. The reaction mixture was completed with 550  $\mu\text{L}$ , 1 mM aqueous EA-LDH suspensions, and with water. For reference, the DMSO solution of EA was used in 1 mM concentration as well. The cuvettes were set aside for 30 min (until the reaction finished), and the absorbance was measured at  $\lambda = 450\text{ nm}$ , the absorption maximum of the  $\text{Cu(I)Nc}_2$  complex formed.

For both methods, the absorbance values recorded at each point were corrected by the absorbance of the dispersed LDH, as they had a slight contribution due to light scattering phenomena. Measurement errors were assessed for both methods by triple repetition at 5 different concentrations, using EA-LDH. For data evaluation, Microsoft (Redmond, WA, USA) Excel 365 software was used to fit exponential (DPPH assay) and linear correlations (CuPRAC assay).

### 2.7. Release of EA from the Composites

The possible leakage of the intercalated substance was followed via UV-Vis spectrophotometry. The LDH hybrids were vigorously stirred in the simulated medium of the antioxidant assays (50 V% MeOH in water) in 5 g/L concentration for 60 min. At five different time intervals, 6 mL aliquots were sampled and filtered by a syringe filter (100 nm pore size) to remove the floating solid particles. Thereafter, the pH of the solution was set with 1 M HCl, and the EA content was measured as detailed in Section 2.5.

## 3. Results and Discussion

### 3.1. Structural Features

To prove the successful synthesis of the LDH and EA-LDH materials, XRD measurements were performed. The distinctive XRD pattern of the pristine LDH is shown in Figure 1 with the pattern of EA and EA-LDH.

The diffractogram of EA-LDH indicates that only 1 phase material was formed, and it contained the characteristic peaks reported earlier for LDH-based material [2]. It is obvious from the results that co-crystallization of EA and LDH did not occur during the synthesis, as only the peaks of LDH are present. Higher peak widths of the EA-LDH in comparison to the reference LDH indicate the formation of materials with somewhat poorer crystallinity. The intercalation of larger anions often leads to significantly increased layer distances [47–50], which may be reflected by the shift of the (003) peak towards lower  $2\theta$  values. A similar shift was present only to a small extent in the EA-LDH diffractogram. Therefore, it is likely that the guest EA ion is situated in a planar configuration between the layers without forming a pillared LDH. Considering the usual interlayer distance reported for  $Mg_2Al$ -LDH materials [51], a maximum space of 2.8 Å remains for the intercalants, which is large enough for anions with planar or nearly planar shape, such as EA in the present case. Such a flat conformation of the intercalated substances was also recommended earlier [52–54]. Such a conformation is expected due to its high-degree of conjugation. Apart from intercalation, EA adsorption on the outer LDH surface may have occurred during the syntheses.

As shown in Figure S1 and Table S1, the main structural features remained very similar in the XRD patterns after AMOS treatments (aqueous miscible organic solvent treatment, AMOS-T) of the EA-LDH. A basal spacing close to 7.5–7.9 Å was registered for all LDH, indicating slight increases after intercalation. These data shed light on the fact that washing the EA-LDH with AMOS did not significantly affect the lamellar structure of the materials.

The presence of organic matter in the LDH was proved by FT-IR spectroscopy by detecting and assigning the characteristic vibration bands of the individual substances in the composites. The spectra of the LDH support, EA, and EA-LDH hybrid material are shown in Figure 2.

While the spectrum of pure LDH and EA differed, the detail-rich region of EA from 1800 to 1000  $cm^{-1}$  was represented on the spectrum of EA-LDH confirming the presence of EA in the composite. The sharp band of C=O stretching (typical for esters) vibration at 1719  $cm^{-1}$  disappeared during the intercalation reaction in highly alkaline solution, implying spontaneous ring openings at the lactone bonds. Therefore, the intercalated ion is probably the deprotonated form of the opened EA, 4,4',5,5',6,6'-hexahydroxydiphenic acid (Figure 3) with close to planar geometry. Since this opened form exists only in highly alkaline samples, the data were only comparable with the one obtained for EA.

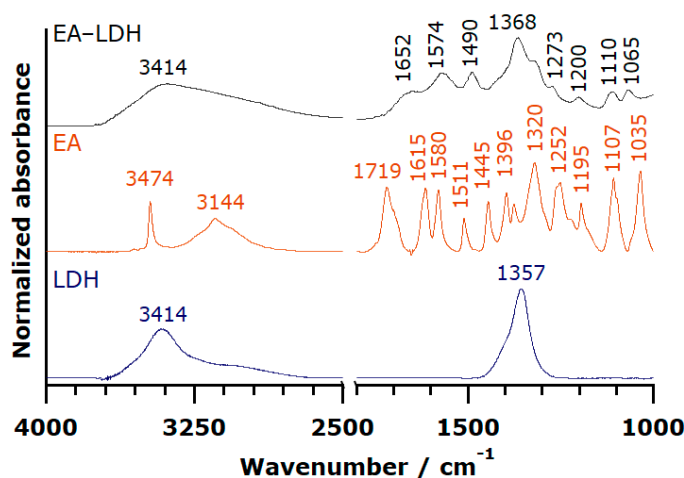
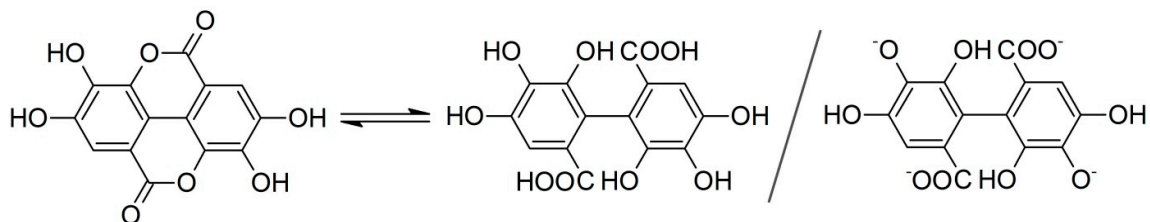


Figure 2. FT-IR spectra of EA-LD, EA, and LDH.



**Figure 3.** Chemical equilibrium between EA and its opened form, 4,4',5,5',6,6'-hexahydroxydiphenic acid, and its potential intercalated form.

The whole set of spectra, including the ones after AMOS treatments, are presented in Figure S2, and the full assignment of the FT-IR bands is tabulated in Table S2. The IR spectra of AMOS-T EA-LDH were identical to the original EA-LDH, indicating that the structure of the intercalated molecules did not change significantly upon washing with organic substances. Note that the incorporation of the solvent molecules is possible into the composites materials. However, the bands of the intercalated or adsorbed EA were indistinguishable from the ones corresponding to the AMOS. The above results, together with the XRD studies, clearly show that the AMOS-T changed neither the lamellar structure of the host nor the nature of the guest molecule. Signals for the presence of carbonate traces could be observed in the spectra. However, these molecules did not affect the EA intercalation and adsorption processes significantly.

To probe the possible effect of the washing steps on the morphology of the obtained hybrid materials, SEM micrographs were recorded. In Figure 4, the images of the LDH and EA-LDH are depicted, and the other modified LDH is shown in Figure S3.

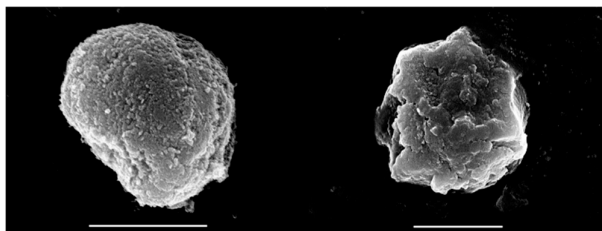


**Figure 4.** SEM micrograph of LDH (left) and EA-LDH (right) at 25,000 $\times$  and 18,000 $\times$  magnification, respectively. Scale bars represent 2  $\mu$ m.

Based on the SEM experiments, one can conclude that the synthesized materials present similar features irrespective of the intercalation process or the AMOS treatments. In each case, the samples consisted of similar aggregates in solid-state, built up from smaller, irregular grains. These morphological properties are common amongst LDH containing Mg(II) and Al(III) metal ions in the layers [55,56].

To determine the size of the individual LDH particles and of the EA intercalated derivatives after AMOS treatments, dynamic light scattering experiments were performed in aqueous dispersions. The obtained data (Table S1) indicated that the hydrodynamic radius of the as-prepared LDH was about 96 nm, while the radii of the EA containing samples were between 282 nm and 559 nm. These primary particles build up the aggregates observed by SEM in solid-state.

### 3.2. Determination of Antioxidant Content

After the acidic dissolution of the composites and appropriate dilution, the EA content of the LDH was evaluated by quantitative absorbance measurements. First, the reversibility of the lactone ring opening and closure was explored. Although the IR spectrum of EA undergoes changes that indicated the hydrolysis of the lactone bond, it reformed within seconds after the addition of HCl. This was proved by UV-Vis measurements, as the spectra of the two forms differed (Figure S4). Due



to the dynamic equilibrium, the antioxidant content of EA-LDH could be measured in an acidic medium.

Using the appropriately recorded calibration curve of EA (Figure S5), the antioxidant contents of the samples were calculated, and most of them fluctuated in a narrow window between 16.4 and 17.2 mass% (Table S3). However, the HT-EA-LDH and FA-EA-LDH contained relatively higher (18.9 mass%) and lower (14.7 mass%) amounts of immobilized EA, respectively. For HT-EA-LDH, the source of the higher EA content is attributed to the more effective adsorption at elevated temperatures. On the other hand, formamide is known as a potential delaminating agent of LDH [57–59], and thus, a temporary structural disruption might lead to lower EA loading.

The overall high EA content clearly indicates that intercalation was more prominent than adsorption on the outer surface. This fact is further confirmed by the comparison of the EA and Al(III) content of the LDH since one can deduce that approximately 50% of the anion exchanging positions were occupied by EA or 4,4',5,5',6,6'-hexahydroxydiphenic acid after the ring opening reaction (Figure 3). This fraction would be significantly lower if EA adsorbs solely on the outer surface. The estimate that 50% of anion exchange positions were occupied by the organic anions is the result of the quantity of Al(III) ions (responsible for anion exchange) and the intercalated species, assumed to form anions with four negative charges.

### 3.3. Antioxidant Activity of EA-LDH and Leakage of EA

To assess the radical scavenging activity of the composites, the redox reaction between the antioxidant compounds and DPPH radicals was tested (Figure S6). First, the reaction rate between bare or immobilized EA and DPPH had to be uncovered. The unmodified LDH showed no activity (not shown). Accordingly, purple colored DPPH reacts with the –OH groups of EA to transform into a light-yellow solution of DPPH-H, which does not contain radical. While bare EA in DMSO neutralized the free radicals in a moderate to fast manner depending on the concentration applied, the reaction reached a steady-state with a moderate rate using EA-LDH as aqueous colloids (Figure 5). The time difference until reaction completion for the free and the immobilized EA probably emerged from the poorer availability of EA anions between the lamellae.

Plotting the remainder of DPPH (Equation S2) at steady-state versus the concentration of EA at the start of the reaction (calculated from the EA content of LDH, as described earlier), the antioxidant materials behaved differently, and the activities depended strongly on the solvents used in the AMOS treatments. Accordingly, EA, ACN-EA-LDH, and EtOH-EA-LDH showed high activity, AC-EA-LDH, DMF-EA-LDH, and MeOH-EA-LDH showed mediocre activity, while low activity was assigned to EA-LDH. In addition, HT-EA-LDH and FA-EA-LDH showed very low ability in scavenging DPPH radicals (Figures 6 and S7). The very low scavenging of HT-EA-LDH and FA-EA-LDH means that they did not decompose half of the DPPH radicals within a reasonable timeframe, resulting in no  $EC_{50}$  and  $N_{DPPH}$  value.

Scavenging efficacy can be quantified with the effective concentration ( $EC_{50}$ ) of EA, which correlates with an initial concentration of EA to react with half of the DPPH. This value can be given in a dimensionless form (proportionate to initial DPPH concentration) to estimate the number of reduced DPPH radicals by one antioxidant moiety ( $N_{DPPH}$ , detailed in Equation S3) [45]. The entire data measured are displayed in Table 1 and Figure 7.

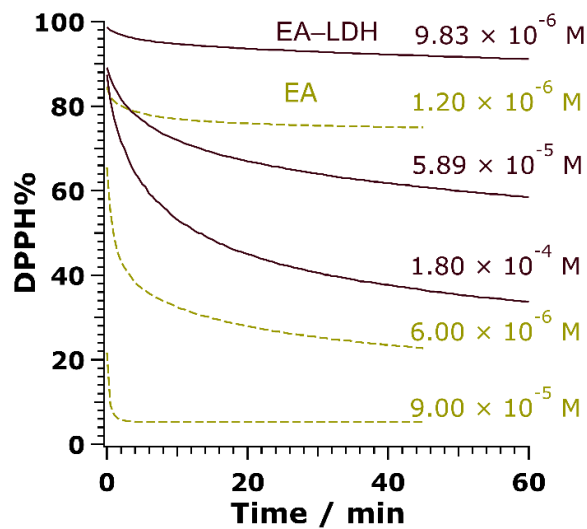


**Figure 5.** Changes in DPPH concentration in the presence of EA (dashed lines) and EA-LDH (full lines) as a function of the reaction time at 3 different initial antioxidant doses.

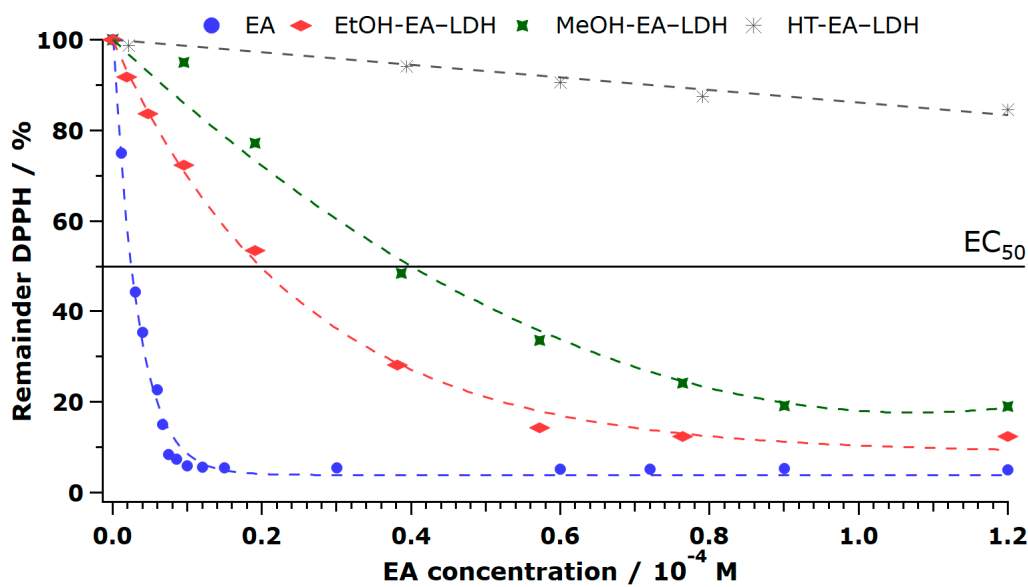


**Figure 6.** Percentage of remaining (non-reacted) 2,2-diphenyl-1-picrylhydrazyl radical (DPPH) at steady-state as a function of the EA concentration applied. EC<sub>50</sub> indicates the EA concentration necessary to decompose 50% of DPPH. Measurements have an error of about 3%.

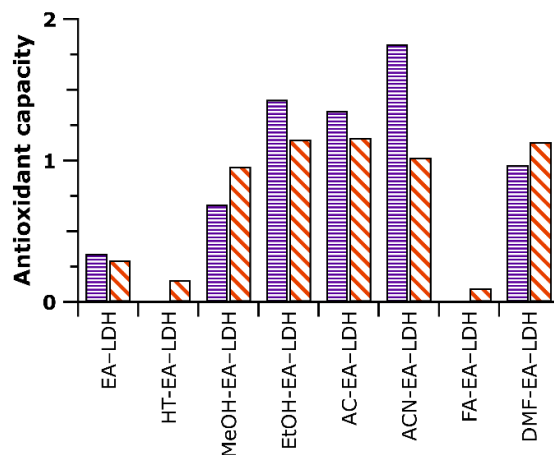


**Figure 7.** Antioxidant activity data determined in the DPPH and cupric reducing antioxidant capacity (CuPRAC) assays. The purple bars indicate  $N_{DPPH}$  values (with 3% error), while the orange striped ones belong to TEAC (with 4% error). Note that HT-EA-LDH and FA-EA-LDH did not decompose 50% of the DPPH radicals. Therefore, no  $N_{DPPH}$  values were calculated.

The values testify that even though the lactone form of EA was opened upon intercalation, the antioxidant activity was greatly preserved. Amongst LDH treated with AMOS, the ACN-EA-LDH and EtOH-EA-LDH showed the highest potential. Another remarkable result is that while EA had low solubility in water about 10 mg/L [60], the carrier LDH acted as a shield to form hydrophilic materials, applicable in much higher, nearly 100-fold (since 5 g/L EA-LDH suspensions may be used) doses, while still capable of effective DPPH scavenging. Note that the reaction between the saturated aqueous solution of EA and DPPH radicals was undetectable owing to the minimal change in the absorbance.

Although the  $N_{DPPH}$  values serve as a rough guide, one anionic EA moiety in the active EA-LDH hybrids typically react with 1–2 DPPH radicals via the intact phenolic –OH groups (Figure S6). The outstanding value for bare EA may be multifold. While the molecule only contains 4 –OH groups, nearly 12 molecules of DPPH is neutralized. This type of high activity of polyphenols is already known [45], the recombination of DPPH and a stabilized EA radical is possible.

The CuPRAC method [46] was also utilized to evaluate the antioxidant property of the materials in an aqueous medium. As detailed earlier, the  $Nc$  chelate of Cu(II) was formed in the cuvettes, and the antioxidant materials were added to reduce the central metal ions. The light blue complex turned into the orange-colored Cu(I) $Nc_2$  upon reaction, whose scheme is shown in Figure S6. The antioxidant activity corresponds to the reducing capability of EA, i.e., the more potent materials generate more Cu(I) complex.

After registering the final absorbance of Cu(I) $Nc_2$  after 30 min of reaction time using the bare and immobilized EA, it was concluded that the materials possessed different efficiency in the redox reactions, similar to the previously discussed DPPH test results. The unmodified LDH showed no activity (not shown). The final absorbances were plotted against the initial concentration of EA to unfold a linear correlation (Figures 8 and S8), from which the slopes give the molar extinction coefficient ( $\epsilon$ ), given the path length was the same. Note that higher  $\epsilon$  indicates higher antioxidant activity.

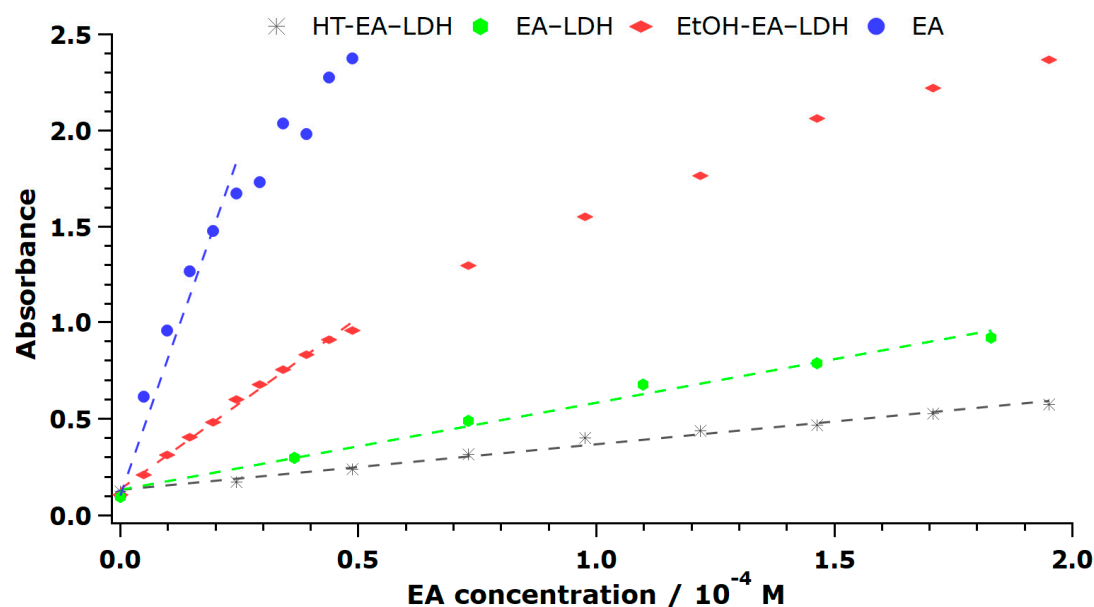


**Figure 8.** Formation of Cu(I)Nc<sub>2</sub> complex, followed by the EA concentration dependence of the absorbance values. The measurements have an error of about 4%.

The tendencies in the data show that EA (as DMSO solution) had high activity, ACN-EA-LDH, MeOH-EA-LDH, EtOH-EA-LDH, AC-EA-LDH, and DMF-EA-LDH also showed good activity, while FA-EA-LDH and HT-EA-LDH had low activity in the assay indicating poor antioxidant features.

Generally, the obtained  $\varepsilon$  values are compared to the one reported for Trolox (a water-soluble analog of vitamin E,  $\varepsilon = 15400 \text{ M}^{-1} \text{ cm}^{-1}$  under the experimental conditions applied in the present study) [46]. Thus, Trolox served as a reference material within the CuPRAC assay (Figure S9). This value is called TEAC (Trolox equivalent antioxidant capacity), and the corresponding values are shown in Table 1 and Figure 7.

Similarly to the DPPH test, the solution of EA showed the best results with the TEAC value almost 5. Although intercalation decreased the reducing potential, the majority of AMOS-T EA-LDH was more active than the reference material Trolox. One plausible explanation is that the positively-charged Cu(II)Nc<sub>2</sub> complex had a lower driving force to enter the interlamellar space due to electrostatic repulsion with the brucite-like layers. This repulsion might also lead to a reaction, in which the organic anions closer to the crystallite edges react more readily with the Cu(II) complex.

The potential desorption of the EA from the carrier LDH was assessed under test reaction conditions. It was concluded that typically 1–3 mass% of immobilized EA leaked from the LDH, with the exception of AC-EA-LDH, which released up to 6 mass% of its EA content (Table S4). The desorption was followed for 60 min, and the materials showed different characteristics, namely, continuous release (FA-EA-LDH, DMF-EA-LDH), sudden release (HT-EA-LDH, MeOH-EA-LDH, and EtOH-EA-LDH), and continuous release followed by re-adsorption (EA-EA-LDH, AC-EA-LDH, and ACN-EA-LDH). In accordance with the antioxidant capacity of bare EA, it was shown that the leaked EA contributed to the reduction in the antioxidant probes below 0.1%.

The BET surface areas of the LDH are collected in Table S3. The value of  $73 \text{ m}^2 \text{ g}^{-1}$  was typical for pristine LDH, while the effect of AMOS was striking. Accordingly, the samples with high activity also possessed a higher specific surface area (generally above  $150 \text{ m}^2 \text{ g}^{-1}$ ), resulting in better availability of the immobilized antioxidants. Washing with formamide and the hydrothermal treatment caused major collapse in the porous structure with  $< 10 \text{ m}^2 \text{ g}^{-1}$  specific surface area, and hence, these LDH were the least active in the test reactions, i.e., they possessed poorer antioxidant activities in those cases. On the other hand, the direct correlation between EA release and surface area was not found. The changes in the surface properties of AMOS-LDH most likely occurred due to the partial exchange of interlamellar water molecules to organic ones leading to materials of different



hydrogen bonding structures as well as with porosity alterations or partial exfoliation then restacking processes in certain solvents.

These above results clearly pointed out that the heterogenized EA kept its functional integrity. However, the extent of the scavenging ability depends on the structural features, such as porosity. The overall findings concluded from the structural and functional characterization of the samples revealed that the most effective materials are EtOH-EA-LDH, AC-EA-LDH, and ACN-EA-LDH. In general, the obtained composites are able to act as an efficient antioxidant in aqueous media, where the effectiveness of the free EA is impeded by its low solubility in water.

#### 4. Conclusion

The coprecipitation method was successfully used as an intercalation route to incorporate polyphenolic EA into LDH containing Mg(II) and Al(III) metal ions. The structural features of the novel EA-LDH hybrid were tuned by subsequent washing with organic solvents. The intercalated ions were those of the opened forms of EA, as revealed in IR and UV-Vis measurements. The obtained hybrids kept their lamellar structures and contained a significant amount of EA irrespective of the treatment with organic solvents. The materials were capable of scavenging DPPH radicals and of reducing Cu(II)Nc<sub>2</sub> complexes, indicating their high antioxidant activities. Upon intercalation, the modified LDH still acted as strong agents in the DPPH scavenging test reaction with 60 min reaction time to reach steady-state conditions. The active hybrids had an effective concentration, and the intercalated EA neutralized a significant amount of DPPH radicals. While in intercalated form, the reducing potential of EA decreased in CuPRAC assay, most of the modified LDH had higher activity than the typical reference molecule. Since EA is a phenolic compound with very poor water solubility, the hydrophilic LDH shell served as a protective environment to use this antioxidant without significant chemical modifications in aqueous media in higher concentrations. Therefore, the hybrids developed are promising candidates as *in vitro* and *in vivo* test materials against oxidative stress and in industrial manufacturing processes or product formulation, where the aim is to decrease the concentration of reactive oxygen species in aqueous medium.

**Supplementary Materials:** The following are available online at [www.mdpi.com/xxx/s1](http://www.mdpi.com/xxx/s1), **Figure S1:** XRD pattern of the LDH, and its composites prepared. The Miller indices are indicated, **Figure S2:** FT-IR spectra of LDH, its EA-intercalated form, and the hybrids modified with AMOS treatment, **Figure S3:** SEM micrograph of the LDH prepared: (A) LDH, (B) EA-LDH, (C) HT-EA-LDH, (D) MeOH-EA-LDH, (E) EtOH-EA-LDH, (F) AC-EA-LDH, (G) ACN-EA-LDH, (H) DMF-EA-LDH, (I) FA-EA-LDH. Scale bars represent 1  $\mu\text{m}$ , **Figure S4:** UV-Vis spectra of EA at different protonated states, **Figure S5:** UV-Vis calibration curve of EA in 50 V% aqueous MeOH solution. The absorbance values were recorded at 350 nm, **Figure S6:** Reaction scheme between EA and DPPH (upper, purple border) and between EA and Cu(II)Nc<sub>2</sub> (bottom, orange border) involving 2 –OH groups, **Figure S7:** Percentage of remaining (non-reacted) DPPH at steady-state as a function of the EA concentration applied. Data measured for all of the composites are shown. Measurements have an error of about 3%, **Figure S8:** The activity of the materials investigated in CuPRAC assay, as expressed in concentration-dependent absorbance values measured at 450 nm. Measurements have an error of about 4%, **Figure S9:** The reference activity of Trolox in CuPRAC assay expressed by the concentration-dependent absorbance values, **Table S1:** The position of the (003) diffraction peak and the corresponding basal spacing ( $d_0$ ) of the LDH prepared. The latter values were calculated with Equation S1. Hydrodynamic radii in water ( $R_h$ , at 10 mg/L particle concentration) are also shown, **Table S2:** Characteristic IR bands of the solids investigated, **Table S3:** EA content and specific surface area of the organic-modified LDH, **Table S4:** Released amount of EA (immobilized mass%) from the obtained EA-LDH hybrids at different desorption periods.

**Author Contributions:** S.M., A.S. and D.S. performed the experiments and analyzed the data. I.S. conceived the experiments and supervised the project. All authors participated in the manuscript preparation as well as have read and agreed to the published version of the manuscript.

**Acknowledgments:** This research was financially supported by the Lendület program of the Hungarian Academy of Sciences (96130) and by the Ministry of Human Capacities of Hungary through grant 20391-3/2018/FEKUSTRAT. D. S. is supported by the János Bolyai Research Scholarship of the Hungarian Academy of Sciences. The authors thank Zsuzsanna Hórits for the specific surface area measurements. The support from the University of Szeged Open Access Fund (4562) is gratefully acknowledged.

**Conflicts of Interest:** The authors declare no conflict of interest.

## References

1. Sideris, P.J.; Nielsen, U.G.; Gan, Z.H.; Grey, C.P. Mg/Al ordering in layered double hydroxides revealed by multinuclear NMR spectroscopy. *Science* **2008**, *321*, 113–117.
2. Evans, D.G.; Slade, R.C.T. Structural aspects of layered double hydroxides. In *Layered Double Hydroxides*; Duan, X., Evans, D.G., Eds.; Springer: Berlin, Heidelberg, Germany, 2006; Volume 119, pp. 1–87.
3. Taviot-Gueho, C.; Prevot, V.; Forano, C.; Renaudin, G.; Mousty, C.; Leroux, F. Tailoring hybrid layered double hydroxides for the development of innovative applications. *Adv. Funct. Mater.* **2018**, *28*, 1703868.
4. Zhou, J.Z.; Xu, Z.P.; Qiao, S.Z.; Liu, J.Y.; Liu, Q.; Xu, Y.F.; Zhang, J.; Qian, G.R. Triphosphate removal processes over ternary CaMgAl-layered double hydroxides. *Appl. Clay Sci.* **2011**, *54*, 196–201.
5. Pahalagedara, M.N.; Samaraweera, M.; Dharmarathna, S.; Kuo, C.H.; Pahalagedara, L.R.; Gascon, J.A.; Suib, S.L. Removal of azo dyes: Intercalation into sonochemically synthesized NiAl layered double hydroxide. *J. Phys. Chem. C* **2014**, *118*, 17801–17809.
6. Chen, Y.F.; Zhang, K.L.; Wang, X.Q.; Zheng, F.L. Study on a novel binary Zn<sub>n</sub>Eu layered double hydroxide with excellent fluorescence. *J. Fluoresc.* **2018**, *28*, 259–268.
7. Zhang, G.; Wu, L.; Tang, A.T.; Zhang, S.; Yuan, B.; Zheng, Z.C.; Pan, F.S. A novel approach to fabricate protective layered double hydroxide films on the surface of anodized Mg-Al alloy. *Adv. Mater. Interfaces* **2017**, *4*, 1700163.
8. Xie, W.S.; Guo, Z.H.; Cao, Z.B.; Gao, Q.; Wang, D.; Boyer, C.; Kavallaris, M.; Sun, X.D.; Wang, X.M.; Zhao, L.Y.; et al. Manganese-based magnetic layered double hydroxide nanoparticle: A pH-sensitive and concurrently enhanced T-1/T-2-weighted dual-mode magnetic resonance imaging contrast agent. *ACS Biomater. Sci. Eng.* **2019**, *5*, 2555–2562.
9. Li, S.D.; Li, J.H.; Wang, C.J.; Wang, Q.; Cader, M.Z.; Lu, J.; Evans, D.G.; Duan, X.; O'Hare, D. Cellular uptake and gene delivery using layered double hydroxide nanoparticles. *J. Mater. Chem. B* **2013**, *1*, 61–68.
10. Ma, R.; Wang, Z.G.; Yan, L.; Chen, X.F.; Zhu, G.Y. Novel Pt-loaded layered double hydroxide nanoparticles for efficient and cancer-cell specific delivery of a cisplatin prodrug. *J. Mater. Chem. B* **2014**, *2*, 4868–4875.
11. Kun, R.; Balazs, M.; Dekany, I. Photooxidation of organic dye molecules on TiO<sub>2</sub> and zinc-aluminum layered double hydroxide ultrathin multilayers. *Colloid Surf. A* **2005**, *265*, 155–162.
12. Yamaguchi, K.; Mori, K.; Mizugaki, T.; Ebitani, K.; Kaneda, K. Epoxidation of alpha,beta-unsaturated ketones using hydrogen peroxide in the presence of basic hydrotalcite catalysts. *J. Org. Chem.* **2000**, *65*, 6897–6903.
13. Tokudome, Y.; Morimoto, T.; Tarutani, N.; Vaz, P.D.; Nunes, C.D.; Prevot, V.; Stenning, G.B.G.; Takahashi, M. Layered double hydroxide nanoclusters: Aqueous, concentrated, stable, and catalytically active colloids toward green chemistry. *ACS Nano* **2016**, *10*, 5550–5559.
14. Zhou, P.; Wang, Y.Y.; Xie, C.; Chen, C.; Liu, H.W.; Chen, R.; Huo, J.; Wang, S.Y. Acid-etched layered double hydroxides with rich defects for enhancing the oxygen evolution reaction. *Chem. Commun.* **2017**, *53*, 11778–11781.
15. Sumboja, A.; Chen, J.W.; Zong, Y.; Lee, P.S.; Liu, Z.L. NiMn layered double hydroxides as efficient electrocatalysts for the oxygen evolution reaction and their application in rechargeable Zn-air batteries. *Nanoscale* **2017**, *9*, 774–780.
16. San Roman, M.S.; Holgado, M.J.; Salinas, B.; Rives, V. Characterisation of diclofenac, ketoprofen or chloramphenicol succinate encapsulated in layered double hydroxides with the hydrotalcite-type structure. *Appl. Clay Sci.* **2012**, *55*, 158–163.
17. Conterposito, E.; Van Beek, W.; Palin, L.; Croce, G.; Perioli, L.; Viterbo, D.; Gatti, G.; Milanesio, M. Development of a fast and clean intercalation method for organic molecules into layered double hydroxides. *Cryst. Growth Des.* **2013**, *13*, 1162–1169.
18. Qi, F.L.; Zhang, X.Q.; Li, S.P. A novel method to get methotrexatum/layered double hydroxides intercalation compounds and their release properties. *J. Phys. Chem. Solids* **2013**, *74*, 1101–1108.
19. Chen, J.Z.; Shao, R.F.; Li, L.; Xu, Z.P.; Gu, W.Y. Effective inhibition of colon cancer cell growth with MgAl-layered double hydroxide (LDH) loaded 5-FU and PI3K/mTOR dual inhibitor BEZ-235 through apoptotic pathways. *Int. J. Nanomed.* **2014**, *9*, 3403–3411.

20. Mei, X.; Xu, S.M.; Hu, T.Y.; Peng, L.Q.; Gao, R.; Liang, R.Z.; Wei, M.; Evans, D.; Duan, X. Layered double hydroxide monolayers for controlled loading and targeted delivery of anticancer drugs. *Nano Res.* **2018**, *11*, 195–205.
21. Ay, A.N.; Akar, H.; Zaulet, A.; Vinas, C.; Teixidor, F.; Zumreoglu-Karan, B. Carborane-layered double hydroxide nanohybrids for potential targeted- and magnetically targeted-BNCT applications. *Dalton Trans.* **2017**, *46*, 3303–3310.
22. Brenneisen, P.; Reichert, A.S. Nanotherapy and reactive oxygen species (ROS) in cancer: A novel perspective. *Antioxidants* **2018**, *7*, 31.
23. Pratsinis, A.; Kelesidis, G.A.; Zuercher, S.; Krumeich, F.; Bolisetty, S.; Mezzenga, R.; Leroux, J.C.; Sotiriou, G.A. Enzyme-mimetic antioxidant luminescent nanoparticles for highly sensitive hydrogen peroxide biosensing. *ACS Nano* **2017**, *11*, 12210–12218.
24. Huang, Y.Y.; Liu, C.Q.; Pu, F.; Liu, Z.; Ren, J.S.; Qu, X.G. A GO-Se nanocomposite as an antioxidant nanozyme for cytoprotection. *Chem. Commun.* **2017**, *53*, 3082–3085.
25. Vernekar, A.A.; Sinha, D.; Srivastava, S.; Paramasivam, P.U.; D'Silva, P.; Mughesh, G. An antioxidant nanozyme that uncovers the cytoprotective potential of vanadia nanowires. *Nat. Commun.* **2014**, *5*, 1–13.
26. Pavlovic, M.; Nafradi, M.; Rouster, P.; Murath, S.; Szilagyi, I. Highly stable enzyme-mimicking nanocomposite of antioxidant activity. *J. Colloid Interface Sci.* **2019**, *543*, 174–182.
27. Ha, E.S.; Sim, W.Y.; Lee, S.K.; Jeong, J.S.; Kim, J.S.; Baek, I.H.; Choi, D.; Park, H.; Hwang, S.J.; Kim, M.S. Preparation and evaluation of resveratrol-loaded composite nanoparticles using a supercritical fluid technology for enhanced oral and skin delivery. *Antioxidants* **2019**, *8*, 554.
28. Lonkar, S.P.; Kutlu, B.; Leuteritz, A.; Heinrich, G. Nanohybrids of phenolic antioxidant intercalated into MgAl-layered double hydroxide clay. *Appl. Clay Sci.* **2013**, *71*, 8–14.
29. Vargas-Mendoza, N.; Vazquez-Velasco, M.; Gonzalez-Torres, L.; Benedi, J.; Sanchez-Muniz, F.J.; Morales-Gonzalez, J.A.; Jaramillo-Morales, O.A.; Valadez-Vega, C.; Bautista, M. Effect of extract and ellagic acid from *Geranium schiedeanum* on the antioxidant defense system in an induced-necrosis model. *Antioxidants* **2018**, *7*, 178.
30. Hakkinen, S.; Heinonen, M.; Karenlampi, S.; Mykkanen, H.; Ruuskanen, J.; Torronen, R. Screening of selected flavonoids and phenolic acids in 19 berries. *Food Res. Int.* **1999**, *32*, 345–353.
31. Gil, M.I.; Tomas-Barberan, F.A.; Hess-Pierce, B.; Holcroft, D.M.; Kader, A.A. Antioxidant activity of pomegranate juice and its relationship with phenolic composition and processing. *J. Agric. Food Chem.* **2000**, *48*, 4581–4589.
32. Rao, C.V.; Tokumo, K.; Rigotty, J.; Zang, E.; Kelloff, G.; Reddy, B.S. Chemoprevention of colon carcinogenesis by dietary administration of piroxicam, alpha-difluoromethylornithine, 16-alpha-fluoro-5-androsten-17-one, and ellagic acid individually and in combination. *Cancer Res.* **1991**, *51*, 4528–4534.
33. Mertens-Talcott, S.U.; Percival, S.S. Ellagic acid and quercetin interact synergistically with resveratrol in the induction of apoptosis and cause transient cell cycle arrest in human leukemia cells. *Cancer Lett.* **2005**, *218*, 141–151.
34. Goudarzi, M.; Mombeini, M.A.; Fatemi, I.; Aminzadeh, A.; Kalantari, H.; Nesari, A.; Najafzadehvarzi, H.; Mehrzadi, S. Neuroprotective effects of ellagic acid against acrylamide-induced neurotoxicity in rats. *Neurol. Res.* **2019**, *41*, 419–428.
35. Przewloka, S.R.; Shearer, B.J. The further chemistry of ellagic acid II. Ellagic acid and water-soluble ellagates as metal precipitants. *Holzforschung* **2002**, *56*, 13–19.
36. Hewitt, D.G.; Nelson, P.F. Ellagic acid and the pulping of eucalypts. Part I. Some aspects of the chemistry of ellagic acid. *Holzforschung* **1965**, *9*, 97–111.
37. Smart, R.C.; Huang, M.T.; Chang, R.L.; Sayer, J.M.; Jerina, D.M.; Conney, A.H. Disposition of the naturally-occurring antimutagenic plant phenol, ellagic acid, and its synthetic derivatives, 3-o-decylellagic acid and 3,3'-di-o-methylallegic acid in mice. *Carcinogenesis* **1986**, *7*, 1663–1667.
38. Hussein, M.Z.; Al Ali, S.H.; Zainal, Z.; Hakim, M.N. Development of antiproliferative nanohybrid compound with controlled release property using ellagic acid as the active agent. *Int. J. Nanomed.* **2011**, *6*, 1373–1383.
39. Shaik, M.M.; Kowshik, M. Ellagic acid containing collagen-chitosan scaffolds as potential antioxidative biomaterials for tissue engineering applications. *Int. J. Polym. Mater. Polym. Biomat.* **2019**, *68*, 208–215.
40. Alfei, S.; Turrini, F.; Catena, S.; Zunin, P.; Parodi, B.; Zuccari, G.; Pittaluga, A.M.; Boggia, R. Preparation of ellagic acid micro and nano formulations with amazingly increased water solubility by its entrapment in pectin or non-PAMAM dendrimers suitable for clinical applications. *New J. Chem.* **2019**, *43*, 2438–2448.

41. Choi, S.J.; Choy, J.H. Layered double hydroxide nanoparticles as target-specific delivery carriers: Uptake mechanism and toxicity. *Nanomedicine* **2011**, *6*, 803–814.
42. Hasegawa, M.; Terauchi, M.; Kikuchi, Y.; Nakao, A.; Okubo, J.; Yoshinaga, T.; Hiratsuka, H.; Kobayashi, M.; Hoshi, T. Deprotonation processes of ellagic acid in solution and solid states. *Mon. Chem.* **2003**, *134*, 811–821.
43. Yang, M.S.; McDermott, O.; Buffet, J.C.; O'Hare, D. Synthesis and characterisation of layered double hydroxide dispersions in organic solvents. *RSC Adv.* **2014**, *4*, 51676–51682.
44. Hassan, P.A.; Rana, S.; Verma, G. Making sense of Brownian motion: Colloid characterization by dynamic light scattering. *Langmuir* **2015**, *31*, 3–12.
45. Brand-Williams, W.; Cuvelier, M.E.; Berset, C. Use of a free-radical method to evaluate antioxidant activity. *Food Sci. Technol. Lebensm. Wiss. Technol.* **1995**, *28*, 25–30.
46. Apak, R.; Guclu, K.; Ozyurek, M.; Karademir, S.E. Novel total antioxidant capacity index for dietary polyphenols and vitamins C and E, using their cupric ion reducing capability in the presence of neocuproine: CUPRAC method. *J. Agric. Food Chem.* **2004**, *52*, 7970–7981.
47. Kwon, T.; Tsigdinos, G.A.; Pinnavaia, T.J. Pillaring of layered double hydroxides (LDHs) by polyoxometalate anions. *J. Am. Chem. Soc.* **1988**, *110*, 3653–3654.
48. Beres, A.; Palinko, I.; Kiricsi, I.; Nagy, J.B.; Yoshimichi, K.; Mizukami, F. Layered double hydroxides and their pillared derivatives-materials for solid base catalysis; synthesis and characterization. *Appl. Catal. A* **1999**, *182*, 237–247.
49. Poznyak, S.K.; Tedim, J.; Rodrigues, L.M.; Salak, A.N.; Zheludkevich, M.L.; Dick, L.F.P.; Ferreira, M.G.S. Novel inorganic host layered double hydroxides intercalated with guest organic inhibitors for anticorrosion applications. *ACS Appl. Mater. Interfaces* **2009**, *1*, 2353–2362.
50. Huang, N.H.; Wang, J.Q. A new route to prepare nanocomposites based on polyvinyl chloride and MgAl layered double hydroxide intercalated with lauryl ether phosphate. *Express Polym. Lett.* **2009**, *3*, 595–604.
51. Miyata, S. Synthesis of hydrotalcite-like compounds and their structures and physicochemical properties 1. Systems  $Mg^{2+}-Al^{3+}-NO_3^-$ ,  $Mg^{2+}-Al^{3+}-Cl^-$ ,  $Mg^{2+}-Al^{3+}-ClO_4^-$ ,  $Ni^{2+}-Al^{3+}-Cl^-$  and  $Zn^{2+}-Al^{3+}-Cl^-$ . *Clay Clay Min.* **1975**, *23*, 369–375.
52. Vijaikumar, S.; Dhakshinamoorthy, A.; Pitchumani, K. L-proline anchored hydrotalcite clays: An efficient catalyst for asymmetric Michael addition. *Appl. Catal. A Gen.* **2008**, *340*, 25–32.
53. An, Z.; Zhang, W.H.; Shi, H.M.; He, J. An effective heterogeneous L-proline catalyst for the asymmetric aldol reaction using anionic clays as intercalated support. *J. Catal.* **2006**, *241*, 319–327.
54. Gu, Z.; Thomas, A.C.; Xu, Z.P.; Campbell, J.H.; Lu, G.Q. In vitro sustained release of LMWH from MgAl-layered double hydroxide nanohybrids. *Chem. Mat.* **2008**, *20*, 3715–3722.
55. Peng, C.; Yu, J.Y.; Zhao, Z.J.; Fu, J.Y.; Zhao, M.L.; Wang, W.; Dai, J. Preparation and properties of a layered double hydroxide deicing additive for asphalt mixture. *Cold Reg. Sci. Tech.* **2015**, *110*, 70–76.
56. Parida, K.; Satpathy, M.; Mohapatra, L. Incorporation of  $Fe^{3+}$  into Mg/Al layered double hydroxide framework: Effects on textural properties and photocatalytic activity for  $H_2$  generation. *J. Mater. Chem.* **2012**, *22*, 7350–7357.
57. Wu, Q.L.; Sjastad, A.O.; Vistad, O.B.; Knudsen, K.D.; Roots, J.; Pedersen, J.S.; Norby, P. Characterization of exfoliated layered double hydroxide (LDH, Mg/Al=3) nanosheets at high concentrations in formamide. *J. Mater. Chem.* **2007**, *17*, 965–971.
58. Murath, S.; Somosi, Z.; Toth, I.Y.; Tombacz, E.; Sipos, P.; Palinko, I. Delaminating and restacking MgAl-layered double hydroxide monitored and characterized by a range of instrumental methods. *J. Mol. Struct.* **2017**, *1140*, 77–82.
59. Yu, J.F.; Liu, J.J.; Clearfield, A.; Sims, J.E.; Speigle, M.T.; Suib, S.L.; Sun, L.Y. Synthesis of layered double hydroxide single-layer nanosheets in formamide. *Inorg. Chem.* **2016**, *55*, 12036–12041.
60. Bala, I.; Bhardwaj, V.; Hariharan, S.; Kumar, M. Analytical methods for assay of ellagic acid and its solubility studies. *J. Pharm. Biomed. Anal.* **2006**, *40*, 206–210.






## PAPER



Cite this: *Soft Matter*, 2020, 16, 10518

## Layered double hydroxide-based antioxidant dispersions with high colloidal and functional stability†

Adél Szerlauth, Szabolcs Muráth  and Istvan Szilagyí \*

Highly stable antioxidant dispersions were designed on the basis of ring-opened ellagic acid (EA) intercalated into MgAl-layered double hydroxide (LDH) nanoparticles. The morphology of the composite was delicately modified with ethanolic washing to obtain EtOH-EA-LDH with a high specific surface area. The colloidal stability was optimized by surface functionalization with positively charged polyelectrolytes. Polyethyleneimine (PEI), protamine sulfate (PS) and poly(acrylamide-co-diallyl dimethyl ammonium chloride) (PAAm-co-DADMAC) was adsorbed onto the surface of the oppositely charged EtOH-EA-LDH leading to charge neutralization and overcharging at appropriate doses. Formation of adsorbed polyelectrolyte layers provided remarkable colloidal stability for the EtOH-EA-LDH. Modification with PEI and PAAm-co-DADMAC outstandingly improved the resistance of the particles against salt-induced aggregation with a critical coagulation concentration value above 1 M, while only limited stability was achieved by covering the nanoparticles with PS. The high antioxidant activity of EtOH-EA-LDH was greatly preserved upon polyelectrolyte coating, which was proved in the scavenging of radicals in the test reaction applied. Hence, an active antioxidant nanocomposite of high drug dose and remarkable colloidal stability was obtained to combat oxidative stress in systems of high electrolyte concentrations.

Received 24th August 2020,  
Accepted 27th September 2020

DOI: 10.1039/d0sm01531h

rsc.li/soft-matter-journal

### 1. Introduction

Antioxidants are the cornerstone defence systems against naturally occurring oxidative species, which can induce a variety of illnesses that originate from oxidative stress.<sup>1,2</sup> In addition, it is important to prevent the unwanted oxidative degradation of foods,<sup>3,4</sup> paints<sup>5</sup> or cosmetics,<sup>6,7</sup> since it leads to lower quality and rapid expiration of these commercial products. Undoubtedly, antioxidant enzymes (*e.g.*, peroxidases, catalase and superoxide dismutase)<sup>8</sup> are the most effective tools to suppress such deterioration. Besides, numerous composites were developed by the combination of inorganic particles used as carriers and immobilized enzymatic or enzyme mimicking compounds to overcome the limitations of the native enzymes.<sup>9–11</sup>

Since the working conditions of enzymes are strictly regulated by multiple factors (temperature, pH, ionic strength, *etc.*), the use of non-enzymatic, with another term molecular antioxidants is also a popular choice.<sup>3,4,12,13</sup> However, the application of molecular antioxidants is often unfavoured due to their limited efficiency compared to the enzymes, low water

solubility and considerable chemical reactivity. To deal with these issues, the development of nanocomposites of antioxidant substances with solid supports were the focus of research groups in the past.<sup>14</sup> As solid carriers, various compounds have been considered, *e.g.*, titanium dioxide,<sup>15,16</sup> graphene oxide,<sup>17,18</sup> aluminosilicates<sup>19,20</sup> and layered double hydroxides (LDHs).<sup>21–23</sup>

The latter substances offer a large selection of materials that can be perceived as mixed metal hydroxides containing divalent and trivalent cations.<sup>24,25</sup> The positively charged LDH layers consist of hydroxide ions and coordinated metal cations, which most commonly are Mg<sup>2+</sup>, Ca<sup>2+</sup>, Ni<sup>2+</sup>, Cr<sup>3+</sup>, Al<sup>3+</sup> or Fe<sup>3+</sup>.<sup>26</sup> LDHs are excellent anion exchangers with anions situated (*i.e.*, intercalated) in the interlamellar space giving rise to practically countless possibilities of their composition.<sup>25,27</sup> In this way, molecular antioxidants were immobilized in the interlamellar space and/or on the outer surface of LDHs. LDH-based composite materials containing chlorogenic acid,<sup>22</sup> curcumin,<sup>23,28</sup> folic acid,<sup>29</sup> gallate<sup>30</sup> and phenolic compounds<sup>31</sup> of remarkable antioxidant activities were prepared and used to reduce oxidative stress in biomedical and industrial applications. Owing to the interchangeable anions, the surface charge of LDHs can be either negative (with anions of higher negative charge) or positive (with anions of lower charge), which is an important aspect of colloidal stability studies.

Despite the fact that nanoparticle-based antioxidants are usually used in heterogeneous systems, *i.e.*, the particles are

MTA-SZTE Lendület Biocolloids Research Group, Interdisciplinary Excellence Centre, Department of Physical Chemistry and Materials Science, University of Szeged, 1 Rerrich Béla tér, H-6720 Szeged, Hungary. E-mail: szisztvan@chem.u-szeged.hu

† Electronic supplementary information (ESI) available. See DOI: 10.1039/d0sm01531h

dc\_1931\_21

dispersed in a liquid, the colloidal stability of these systems have been rarely assessed. In turn, the activity of the materials strongly depends on the surface area, which can be improved by stabilization of the nanocomposites in the dispersions. Synthetic (e.g., polyacrylates,<sup>32</sup> polyamines<sup>33</sup> and polystyrenes<sup>34</sup>) and natural (e.g., polypeptides,<sup>35</sup> polysaccharides<sup>36</sup> and humic substances<sup>37</sup>) polyelectrolytes have been proven to be excellent stabilizing agents for nano- or colloidal particles in various applications including drug delivery,<sup>38</sup> wastewater treatment<sup>39</sup> and dye production.<sup>40</sup> Comprehensive studies carried out using surface sensitive techniques have revealed that their adsorption on oppositely charged surfaces is rather strong and irreversible.<sup>41–43</sup> These phenomena are accompanied by charge neutralization and overcharging in most of the cases.<sup>44</sup> The aggregation mechanisms in the dispersions are affected by the surface charge features and rapid particle aggregation was usually reported at doses close to the charge neutralization point, while highly charged particle–polyelectrolyte systems form more stable dispersions, *i.e.*, the rate of particle aggregation is slow or not even detectable due to the high colloidal stability.<sup>45,46</sup>

Similar observations were also made in LDH–polyelectrolyte systems.<sup>47</sup> Accordingly, highly stable polyacrylate–LDH composites were developed by applying the appropriate dose in the dispersions.<sup>48</sup> Surface charge properties and subsequent aggregation of LDH particles were extensively studied in the presence of biologically relevant media and the importance of protein corona formation was emphasized.<sup>49</sup> The colloidal stability and cellular uptake were improved by coating the LDH particles with albumin macromolecules, making the developed composite promising in drug delivery applications.<sup>50</sup> The dispersion stability of LDH–enzyme hybrids was remarkably improved by the formation of

polysaccharide layers leading to fine particle dispersions with excellent enzymatic activities.<sup>51,52</sup> Polyelectrolyte multilayers were built-up on the outer particle surfaces and used to design delivery systems with high colloidal stability.<sup>53,54</sup> Stabilization of LDH–molecular antioxidant composites by polyelectrolyte adsorption was not reported in the past, although this opportunity shows great promise towards the development of highly stable antioxidant dispersions.

In our earlier work,<sup>27</sup> we prepared MgAl-LDH intercalated with ellagic acid (EA, see Fig. 1a for the structure), a natural antioxidant with excellent radical scavenging activity.<sup>55</sup> The developed product proved to be an efficient antioxidant material of negative surface charge. In the present contribution, we have aimed to functionalize its surface with positively charged polyelectrolyte layers to tune the colloidal stability and thus, to improve the composite's applicability in aqueous systems, which are the most common media in the areas where antioxidant systems are required. Three cationic polyelectrolytes (polyethyleneimine (PEI), protamine sulfate (PS) and poly(acrylamide-*co*-diallyl dimethyl ammonium) (PAAm-*co*-DADMAC)) were considered as surface modifying agents. The colloidal behaviour and the antioxidant activity of the bare and coated composites were investigated using light scattering techniques and a spectrophotometric assay, respectively.

## 2. Experimental

### 2.1. Materials

For the synthesis of particles, analytical grade  $\text{Mg}(\text{NO}_3)_2 \cdot 6\text{H}_2\text{O}$ ,  $\text{Al}(\text{NO}_3)_3 \cdot 9\text{H}_2\text{O}$ , 4 M NaOH solution, anhydrous EtOH and ellagic acid (EA) were purchased from VWR International. For

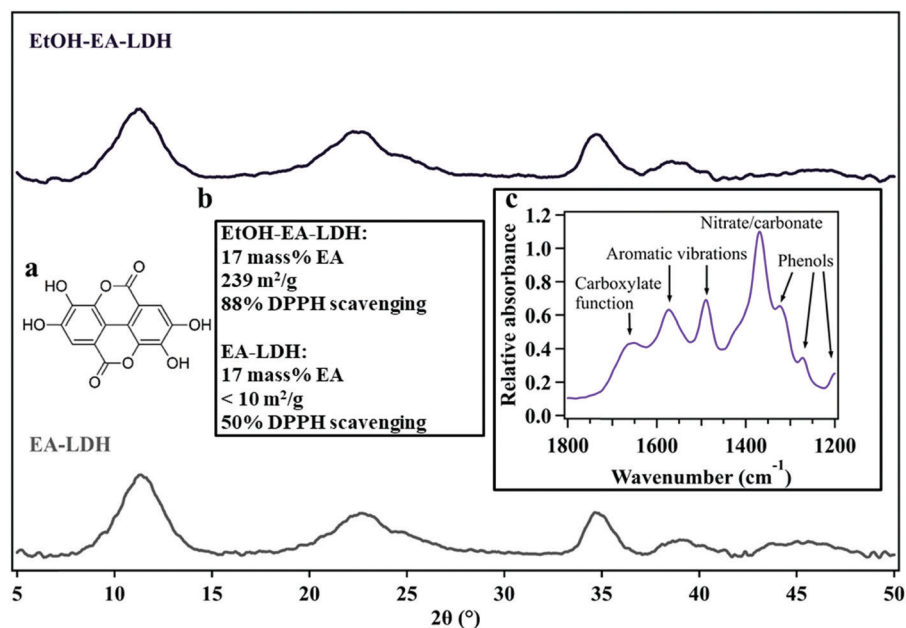


**Fig. 1** The powder X-ray diffraction patterns of EtOH–EA–LDH (upper) and EA–LDH (lower). Insets show (a) the molecular structure of EA, (b) composition, BET specific surface area and DPPH scavenging activity of the LDHs and (c) the snippet of a typical IR spectrum of EA–LDHs indicating the presence of ring-opened EA in the materials. The data are taken from ref. 27.

surface functionalization, PEI (*ca.* 30% w/v solution, branched, molecular weight of 70 000 g mol<sup>-1</sup>, catalogue no. 40529 from VWR International), PS (powdered, *ca.* 22.5% nitrogen content, from salmon, catalogue no. ICN19472905 from Fisher Scientific), and PAAm-*co*-DADMAC (*ca.* 10 wt% solution, molecular weight of 250 000 g mol<sup>-1</sup>, *ca.* 55% acrylamide content, catalogue no. 409081 from Sigma-Aldrich) were used. The molecular structure of the polyelectrolytes is shown in Fig. S1 (ESI<sup>†</sup>). The ionic strength was adjusted with NaCl (min. 99.8%, from VWR International). For the antioxidant assays, anhydrous MeOH and 2,2-diphenyl-1-picrylhydrazyl free radicals (DPPH) were acquired from VWR International. Water was purified with a Puranitu TU 3+ UV/UF system equipped with a UV irradiation unit (VWR). For the light scattering experiments, water was filtered through a hydrophilic syringe filter with 100 nm pore size (Millex). The pH of all solutions and dispersions used was adjusted to 9 with dilute NaOH solutions.

## 2.2. LDH synthesis

The preparation of the EA-loaded Mg<sub>2</sub>Al-LDH (simply EA-LDH) and its organic solvent modified variant (EtOH-EA-LDH) is described elsewhere.<sup>27</sup> Briefly, 25 mL solution of Mg(NO<sub>3</sub>)<sub>2</sub> and Al(NO<sub>3</sub>)<sub>3</sub> was added to the solution of EA in 4 M NaOH under vigorous stirring. The EA-to-Mg-to-Al molar ratio was 1:8:4 and a final pH value of 13 was reached. The precipitate was separated by centrifugation after 24 h at 4200 rpm (2090 rcf for 10 min in an Orto Alresa Unicen 21 centrifuge), followed by washing with water (3 × 15 mL) and drying at 50 °C overnight. Furthermore, EtOH treatment was applied to modify the surface properties of the material. For this, EA-LDH was prepared as detailed above. After the aqueous washing step, the wet product was stirred in 25–25 mL fresh EtOH for 120 and 60 min, respectively. The material was centrifuged between the two EtOH treatments and at the end of the synthetic procedure (4200 rpm (2090 rcf) for 20 min). The final drying was performed at 50 °C overnight.

## 2.3. Characterization methods

Electrophoretic mobility was measured on a LiteSizer 500 (Anton Paar) instrument equipped with a 40 mW laser source ( $\lambda = 658$  nm). The measurements were executed in  $\Omega$ -shaped plastic cuvettes (Anton Paar) with 400  $\mu$ L total volume. During sample preparation, calculated amounts of water, polyelectrolyte and NaCl solutions were mixed with the LDH stock suspensions to achieve the appropriate polyelectrolyte doses and ionic strengths. The samples were prepared 1 day before the electrophoretic measurements. The final particle concentration was set to 10 mg L<sup>-1</sup> in each experiment.

Dynamic light scattering (DLS) was used to determine the size of the dispersed LDH particles. The measurements were carried out in a LiteSizer 500 device in backscattering mode at a 175° angle. The cumulant method was used to fit the correlation functions, which were collected for 20 seconds to obtain the apparent hydrodynamic radius of the particles using the Stokes–Einstein equation (eqn (S1), see the ESI<sup>†</sup>).<sup>56</sup> The measurements were carried out using the same method as that used

for electrophoretic mobility determination with the exception that analyses were run immediately after mixing the components. Colloidal stability was expressed by means of stability ratio (eqn (S2), ESI<sup>†</sup>).<sup>57,58</sup> This value is unity if particle aggregation is diffusion controlled and greater than one if aggregation is slower, and thus the dispersion is more stable. We remark that the stability ratios of the EtOH-EA-LDH based samples at each ionic strength were obtained as the proportion of the appropriate aggregation rate and the fast aggregation rate of EtOH-EA-LDH, while for EA-LDH, the same principle was applied using the fast aggregation rate of EA-LDH for the normalization.

The morphology of the samples with saturated polyelectrolyte layers was examined in 10 mg L<sup>-1</sup> dispersions using transmission electron microscopy (TEM). The particles were fixed on a copper-coated carbon mesh TEM grid and were observed using a FEI TECNAI G<sup>2</sup> 20 X-TWIN instrument with 200 kV accelerating voltage.

## 2.4. Antioxidant capacity assays

The standard DPPH-based test reaction<sup>59</sup> was used to estimate the antioxidant activity of the materials. The general reaction route of the test is shown in Scheme S1 (ESI<sup>†</sup>). The DPPH-type activity was obtained after mixing 3500  $\mu$ L of 60  $\mu$ M methanolic DPPH solution with the dispersion containing the antioxidant material setting a range of DPPH-to-EA ratios. The decrease of absorbance at  $\lambda = 517$  nm corresponds to the reduction of DPPH radicals, which was observed for 120 min for the polyelectrolyte-coated composites on a Thermo Fisher Genesys 10S dual beam spectrophotometer. The remainder of the DPPH radicals was calculated by Lambert–Beer's law (eqn (S3), ESI<sup>†</sup>). The absorbance values at each concentration ratio were corrected by the absorbance of the dispersed particles, as they had a slight contribution due to light scattering phenomena. The efficient concentration (EC<sub>50</sub>) value is the antioxidant concentration at which half of the initial DPPH radicals decompose and was calculated from the fits performed on the remaining DPPH percentage data at different antioxidant concentrations.

# 3. Results and discussion

## 3.1. General remarks

The solid state characterization of the bare (uncoated) LDHs investigated in this study (EA-LDH and EtOH-EA-LDH) was carried out earlier, including their structural features and antioxidant content.<sup>27</sup> Briefly, the XRD patterns showed single phase materials bearing close resemblance to the other LDHs (Fig. 1)<sup>24</sup> indicating that no structural damage was observed after EA immobilization and high loading of the antioxidant.

Furthermore, the radical scavenging activity of these materials was also assessed. Both materials had a high antioxidant effect in the DPPH test with EtOH-EA-LDH having superior properties (Fig. 1b). It was correlated with the higher specific surface area of the EtOH-modified LDH that made it more facile for the solute DPPH compound to react with the immobilized EA.

Table 1 The characteristic size, charge, aggregation and scavenging activity parameters of the materials investigated

Sample	$R_h^a$ (nm)	$\sigma^b$ (mC m <sup>-2</sup> )	IEP <sup>c</sup> (mg g <sup>-1</sup> )	ASP <sup>c</sup> (mg g <sup>-1</sup> )	CCC <sup>d</sup> (mM)	EC <sub>50</sub> <sup>e</sup> (10 <sup>-5</sup> M)
EA-LDH	317	-5	—	—	21	8.73 <sup>f</sup>
EtOH-EA-LDH	120	-20	—	—	65	1.98 <sup>f</sup>
EtOH-EA-LDH/PEI	162	16	9	150	>1000	4.46
EtOH-EA-LDH/PS	142	6	30	200	10	—
EtOH-EA-LDH/PAAm-co-DADMAC	191	—	330	700	>1000	5.06

<sup>a</sup>  $R_h$  is the apparent hydrodynamic radius of the particles determined by DLS in stable dispersions. The measurement error was  $\pm 5$  nm. <sup>b</sup> Surface charge density ( $\sigma$ ) was calculated at the slip plane using eqn (1). <sup>c</sup> Isoelectric point (IEP) and adsorption saturation point (ASP) were determined from the zeta potential *versus* polyelectrolyte dose graphs. The dimension mg g<sup>-1</sup> corresponds to the mass ratio between the polyelectrolyte and the solid particle. These values were determined on the basis of electrokinetic measurements, in which the average error was 5%. <sup>d</sup> The critical coagulation concentration (CCC) was calculated using eqn (2). <sup>e</sup> The effective concentration (EC<sub>50</sub>) values were determined in the DPPH test with an average error of 3%. <sup>f</sup> These data were taken from ref. 27.

The underlying mechanism of these observations is a modified hydrogen-bonding system after ethanolic washing and probable low-degree exfoliation, which is a consequence of the partial replacement of structural water molecules by alcohols. The infrared spectra of EA-loaded LDHs attested the presence of organic moieties, although it was found that not EA, but its opened form (4,4',5,5',6,6'-hexahydroxydiphenic acid) was intercalated (Fig. 1c). For simplicity reasons, EA-LDH is used to abbreviate these composites.

Negligible release was detected from the carrier and the ethanolic treatment reduced the particle size (Table 1), which is beneficial for potential future applications. Combining the results, we chose EtOH-EA-LDH as a starting material for surface tuning to achieve high colloidal stability. Note that other organic solvents were also applied and EtOH was the most effective as a surface and textural modifier.

### 3.2. Functionalization of EtOH-EA-LDH with polyelectrolytes

As lamellar compounds consisting of positively charged layers, LDHs with simple anions bearing one negative charge generally possess positive overall surface charge.<sup>24</sup> However, intercalated EA has multiple negative charges that result in a gross negative surface charge for the EtOH-EA-LDHs. Hence, positively charged PEI, PS and PAAm-co-DADMAC were used as cationic polyelectrolytes to improve the colloidal stability of the EtOH-EA-LDH for the efficient decomposition of harmful radicals. Branched PEI has a high line charge density owing to its frequently abundant primary and secondary amino groups, which are partially protonated under the experimental conditions applied. PS is a small protein with numerous basic side chains of arginine amino acids. PAAm-co-DADMAC is a quaternary polyammonium salt and it also contains non-charged PAAm blocks in its chain possessing, therefore, the lowest line charge density. These polyelectrolytes have been proven as effective stabilizing or aggregating agents for colloidal particles;<sup>33,35,46,60,61</sup> however, no systematic colloidal stability studies were reported for LDHs. To assess the charging features at the slip plane, the electrophoretic mobilities were converted to zeta potentials using eqn (S4) ESI.†

Initially, the effect of polyelectrolyte dose on the zeta potential was considered (Fig. 2a). Particle concentration (10 mg L<sup>-1</sup>), pH (9) and the background electrolyte level (1 mM NaCl) was kept constant, *i.e.*, only the polyelectrolyte

dose was changed in the samples. At low polyelectrolyte doses, in general, the original zeta potential of EtOH-EA-LDH had a value of about -20 mV. Increasing the polyelectrolyte concentration led to higher potentials with a steep increase into the positive regime of the recorded curves. This sharp change indicated the adsorption of polyelectrolytes onto the EtOH-EA-LDH particles. Eventually, the negative charge of the support LDH was neutralized by the adsorbed polyelectrolytes, which is indicated as IEP (isoelectric point) in Fig. 2a. Further adsorption of the polyelectrolytes led to the formation of coated particles with gross positive charge. At high doses, the curves reached a plateau, which corresponds to a saturated polyelectrolyte layer on the EtOH-EA-LDH surface. This is indicated as ASP (adsorption saturation point) in Fig. 2a. Addition of further polyelectrolyte only increases its concentration in the bulk, as adsorption does not occur after ASP. Note that added polyelectrolytes below the ASP were strongly adsorbed on the oppositely charged particles, *i.e.*, no free polyelectrolyte could be found in the solution phase.<sup>46</sup> Similar charging behaviour has been reported earlier for oppositely charged particle-polyelectrolyte systems,<sup>32,35,45</sup> including LDH particles.<sup>10,47,48,51,52</sup>

Beside these generic findings in the tendency of the zeta potentials, system specific effects were also observed. Both IEP and ASP values increased in the PEI < PS < PAAm-co-DADMAC order (Table 1). Upon careful inspection it is observed that these numbers are not random, as polyelectrolytes with higher line charge density have lower IEP and ASP values. Indeed, it was reported earlier<sup>46,60</sup> that highly charged polyelectrolytes adsorb in smaller amounts due to the electrostatic repulsion between the adsorbed chains leading to the formation of polyelectrolyte islands on the surface. However, such a repulsion is much smaller for weakly charged polyelectrolytes giving rise to higher adsorbed amounts. Note that no experimental evidence was found for the influence of the structure of the polyelectrolytes (branched or linear) on the adsorption mechanism.

The aggregation of the polyelectrolyte-modified EtOH-EA-LDHs was followed at different doses by DLS. The time-dependent data of EtOH-EA-LDH coated with polyelectrolytes at three distinct doses (a small and high dose that resulted in slow or no aggregation and one intermediate that induced fast aggregation) are shown in Fig. S2 (ESI†). At the lowest dosages,



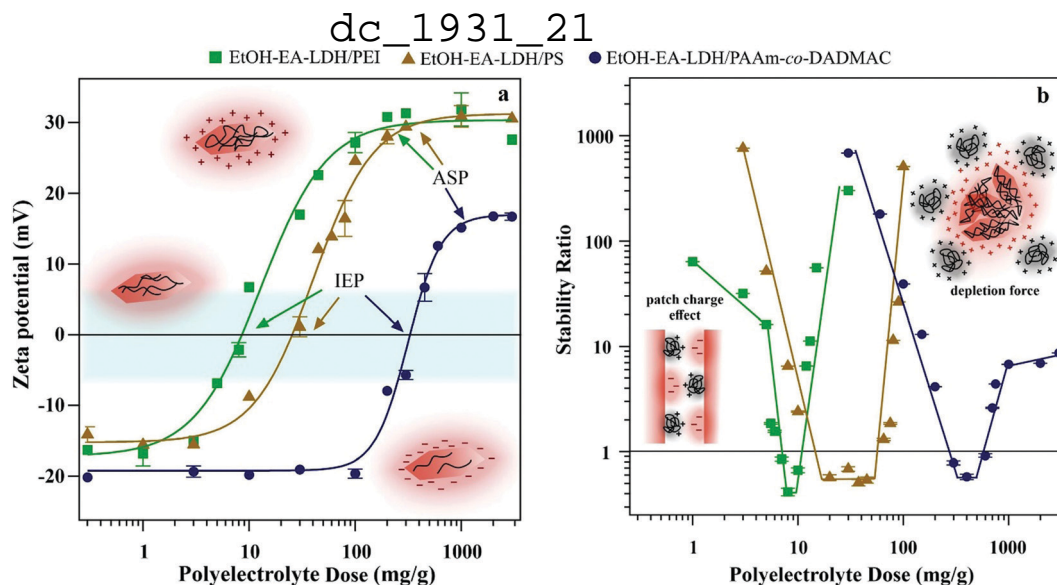


Fig. 2 (a) Zeta potential and (b) stability ratio of EtOH-EA-LDH as a function of the polyelectrolyte dose. Insets show (a) the charging properties of the LDH nanoparticles in different polyelectrolyte concentration regimes and (b) the schematic model of patch-charge effect and depletion force. Particle concentration was  $10 \text{ mg L}^{-1}$  at pH 9 and  $1 \text{ mM}$  ionic strength adjusted with NaCl. The  $\text{mg g}^{-1}$  unit means mg of polyelectrolyte per one gram of EtOH-EA-LDH. The solid lines are just a guide to the eye.

the particle size is constant within experimental error throughout the course of measurements. Increasing the dose leads to aggregation, which was detected from  $5 \text{ mg g}^{-1}$  (PEI),  $10 \text{ mg g}^{-1}$  (PS) and  $200 \text{ mg g}^{-1}$  (PAAm-co-DADMAC). This slower aggregation turned into a fast aggregation regime close to IEP values, where the dispersions were unstable. Increasing the dose resulted in stable suspensions through the overcharging characteristics of the polyelectrolytes; however, its extent was the most moderate for PAAm-co-DADMAC, which has the lowest line charge density.

Such behaviours lead to classical U-shaped curves of the stability ratios (see eqn (S2) in the ESI<sup>†</sup>), which were observed for the three polyelectrolytes (Fig. 2b). The DLVO theory (by Derjaguin, Landau, Verwey and Overbeek)<sup>44,46,62</sup> served as a qualitative tool to describe such systems. Before and after IEP, where surface charge is significant, repulsive electrical double layer forces prevent the aggregation of the particles and thus, stable dispersions are formed. However, at IEP, van der Waals attractive forces dominate, since repulsive forces of electrostatic origin do not exist at charge neutralization.

Certain deviations from DLVO theory were observed in our measurements. Under a  $5 \text{ mg g}^{-1}$  PEI dose, the slope of the stability curve is lower than expected by DLVO theory, which is due to the patch-charge effect (see Fig. 2b inset for schematic representation).<sup>44,46,61</sup> Accordingly, the absorbed PEI forms positive islands on the surface of the LDHs that can attract the bare surface of other partially covered LDH particles. Overall, these forces have a slight negative effect on colloidal stability since it acts as an additional attraction among van der Waals interactions. A similar patch-charge effect can explain that in the fast aggregation regime, the stability ratio is less than unity. Accordingly, aggregation is not merely diffusion limited under these conditions, since patch-charge attractive

forces accelerate dimer formation. Note that this non-DLVO force is present only at partial surface coverage. The assumption of the presence of patch-charge attraction is based on the tendency in the stability ratio data and on the comparison of results from other particle-polyelectrolyte systems. These forces were directly detected by the atomic force microscopy-based colloidal probe techniques earlier;<sup>44</sup> however, our system is not suitable for such measurements.

A non-DLVO destabilizing force appears also at a high dosage of PAAm-co-DADMAC. This is the so-called depletion force (see Fig. 2b inset for schematic representation), which can usually be observed at high polymer concentrations irrespective of the charge of the macromolecules and the particles.<sup>62</sup> These forces originate from the difference in the osmotic pressure within the gap between two approaching particles and the bulk solution. Once the particle separation distance is smaller than the size of the polymer, an attractive interparticle force will appear.<sup>46</sup>

The potential effect of polyelectrolyte adsorption at ASP on the particle morphology was investigated by TEM. All EtOH-EA-LDH particles shared the same motifs, independent of the presence or absence of polyelectrolytes. The materials consisted of particles with irregular shape that aggregated into a mass on the TEM grid. The example of EtOH-EA-LDH and EtOH-EA-LDH/PAAm-co-DADMAC is shown in Fig. 3, while the TEM micrographs from all materials are collected in Fig. S3 (ESI<sup>†</sup>).

### 3.3. Salt-induced aggregation of the polyelectrolyte-coated EtOH-EA-LDH

Since antioxidant efficiency is typically assessed in systems with dissolved electrolytes (*e.g.*, biofluids and industrial liquors), the resistance of the polyelectrolyte-functionalized particles against salt-induced aggregation was assessed. Polyelectrolyte doses were set to ASP equivalent values. First, we explored the surface

dc\_1931\_21

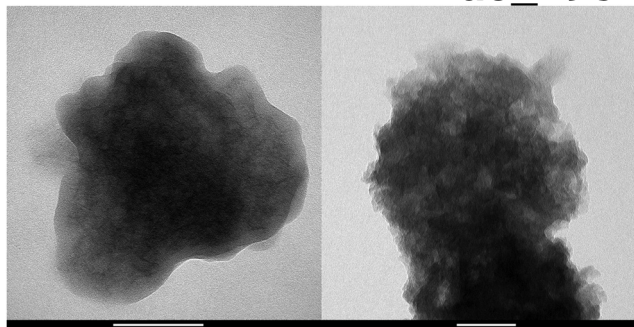


Fig. 3 TEM micrograph of EtOH-EA-LDH (left) and EtOH-EA-LDH/PAAm-co-DADMAC with 700 mg polyelectrolyte per 1 g of LDH dosage (right). Scale bars represent 100 nm.

charge characteristics of the composites at different ionic strengths (Fig. 4a).

One can see that the absolute value of zeta potentials decreased with the ionic strength, as the corresponding counterions from NaCl screen the charge of the dispersed particles, without causing charge inversion. The only exception was EtOH-EA-LDH/PAAm-co-DADMAC, which possessed close to zero charge at the slip plane in the regime of ionic strength screened. This is due to the abundant neutral acrylamide monomer units in the polymer chain. Note that these results imply that the surface charge is compensated at the slip plane by the neutral part of the copolymer, but the inner surface charge, which is not assessed in the electrokinetic measurements, can still be considerably high. The ionic strength–zeta potential correlation was fitted with the Gouy–Chapman equation to obtain the surface charge density ( $\sigma$ ) at the slip plane of the electrical double layer as<sup>46</sup>

$$\sigma = \frac{2k_B T \epsilon \epsilon_0 \kappa}{e} \sinh \frac{e\zeta}{2k_B T} \quad (1)$$

where  $k_B$  is the Boltzmann constant,  $T$  is the absolute temperature,  $\kappa$  is the inverse Debye length (detailed in eqn (S5), ESI†),  $\epsilon$  is the relative permittivity of water,  $\epsilon_0$  is the permittivity of the vacuum and  $e$  is the elementary charge.

Both bare LDHs are negatively charged and possess low charge ( $\sigma$  is  $-5$  and  $-16$   $\text{mC m}^{-2}$  for EA-LDH and EtOH-EA-LDH, respectively), which is typical for natural inorganic particles.<sup>35,47,60</sup> Similarly, relatively low magnitude of charge was determined for the EtOH-EA-LDH/PEI ( $+16$   $\text{mC m}^{-2}$ ) and EtOH-EA-LDH/PS ( $+6$   $\text{mC m}^{-2}$ ), while the former one is slightly higher due to the higher abundance of the protonated primary amino groups. Note that these charges were determined at the slip plane and that counterion condensation contributed to this low charge.<sup>63,64</sup> As detailed earlier, functionalization with PAAm-co-DADMAC yielded a material of a net charge close to neutral irrespective of the ionic strength applied.

The colloidal stability of the particles was studied and it was found that the velocity of aggregation increases with the NaCl concentration leading to a progressive decrease in the stability ratio values (Fig. 4b). The initial size of the particles was constant at low ionic strengths, meanwhile, high NaCl resulted in rapidly aggregating particles. Such a trend follows the predictions of the DLVO theory. The critical coagulation concentration (CCC), *i.e.*, the NaCl concentration, where electrical double layer forces disappear and van der Waals forces start dominating was defined as<sup>58</sup>

$$W = 1 + \left( \frac{\text{CCC}}{c_s} \right)^{-\beta} \quad (2)$$

where  $c_s$  is the salt (NaCl) concentration,  $\beta$  is the change of stability ratio in the slow aggregation regime as follows

$$\beta = \frac{d \log W}{d \log c_s} \quad (3)$$

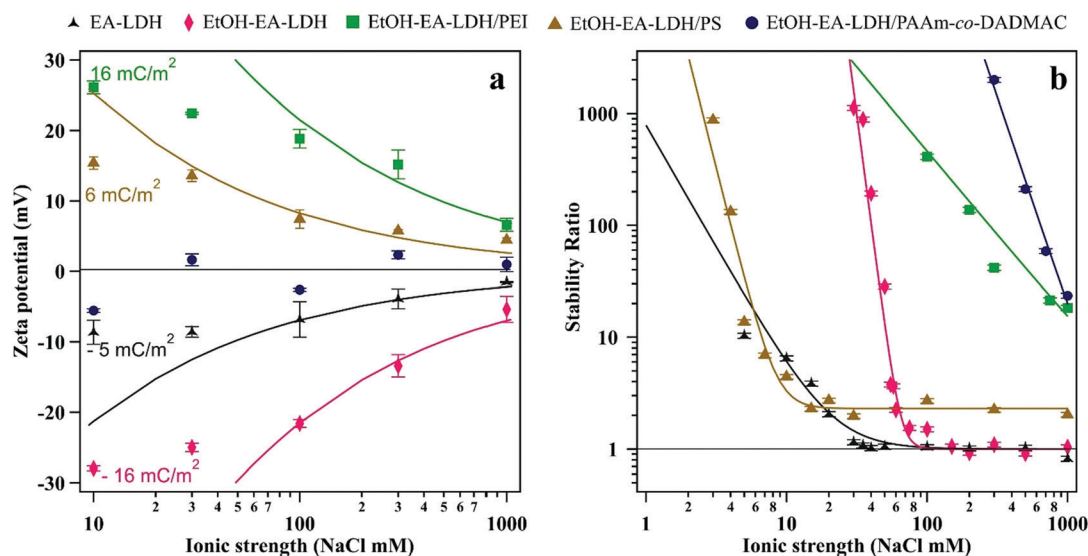


Fig. 4 (a) Zeta potential and (b) stability ratio of the bare and polyelectrolyte-coated LDH particles. Particle concentration was maintained at  $10 \text{ mg L}^{-1}$ . Particles carried polyelectrolyte at doses corresponding to the ASP (shown in Table 1). The solid lines were calculated using eqn (1) in (a) and eqn (2) in (b).

dc\_1931\_21

In general, the different surface charge density of the materials translated into significantly different CCC values (Table 1). Regarding the uncoated LDHs, it was observed that EtOH-EA-LDH (65 mM) had a higher CCC than EA-LDH (21 mM) due to its higher surface charge density. In addition, the slope of the slow aggregation regime of EA-LDH is smaller, which is correlated with its less pronounced negative surface charge and thus, weaker repulsion between the particles. However, these features are typical for bare LDH materials dispersed in monovalent electrolyte solutions.<sup>47,65,66</sup>

Out of the polyelectrolytes, PS lowered the CCC value of EtOH-EA-LDH to 10 mM. One can explain this using the structural property of PS being a flat-like molecule that forms a thin and weakly charged layer on the surface. The magnitude of the surface charge and hence, the strength of the double layer repulsion is smaller than for the bare particles. These facts give rise to a lower CCC value.

On the other hand, coating EtOH-EA-LDH with PEI and PAAm-co-DADMAC provided dispersions with superior resistance against salt-induced aggregation. The fast aggregation regime of these polyelectrolytes were not reached before 1 M NaCl concentration. The outstanding value of EtOH-EA-LDH/PEI was the consequence of joint repulsive steric and electrostatic forces. The former originates from the overlapping of the adsorbed polyelectrolyte chains and subsequent increase of osmotic pressure.<sup>67</sup> The latter is the double layer repulsion, discussed above. This so-called electrosteric stabilization provided extremely high colloid stability for the EtOH-EA-LDH/PEI. Although similar stabilization mechanisms were reported in other particle-polyelectrolyte systems,<sup>32,37,40</sup> such a high CCC was rarely reported. Concerning the EtOH-EA-LDH/PAAm-co-DADMAC particles, the fact that the zeta potentials were close to zero at all ionic strengths indicated the absence of double layer forces. They were reported as long-ranged forces in

direct force measurements,<sup>44,46</sup> and therefore, considerable charge should be detected in the electrokinetic measurements, if these forces are present. Considering this fact, it was assumed that the extremely high CCC of the EtOH-EA-LDH/PAAm-co-DADMAC is the consequence of strong steric repulsion between the coated particles. Such steric forces are usually more pronounced at higher ionic strengths, at which the adsorbed polyelectrolyte layer is swollen giving rise to the formation of polymeric tails and loops on the surface.<sup>68</sup>

The different modes of stabilization are represented in the apparent hydrodynamic radii (Table 1) data. Accordingly, among the ethanol-treated LDHs, the uncoated material possessed the lowest particle size (120 nm), while the radius was increased to 142 nm after PS adsorption, to 162 nm after PEI adsorption and to 191 nm after PAAm-co-DADMAC adsorption. These values indicate a thicker polyelectrolyte layer on the particles in this order, which enhances the steric repulsion due to the formation of polyelectrolyte tails and loops on the surface. As mentioned above, this effect can be even enhanced by increasing the ionic strength. Although the tendency in the apparent hydrodynamic radii clearly support the above assumption, note that the increment value in the radii is higher than the ones usually reported for thicknesses of adsorbed polyelectrolyte layers.<sup>46,68</sup> This is due to the fact that upon formation of the polyelectrolyte layer, the particles pass through the IEP for a very short time period, under which some aggregation may occur leading to higher apparent hydrodynamic radii for the coated particles and hence, to higher layer thickness values. This effect was earlier reported in other particle-polyelectrolyte systems, too.<sup>68</sup>

### 3.4. Radical-scavenging activity of the polyelectrolyte-coated LDHs

After assessing the colloidal properties of the materials, their DPPH scavenging activity was determined. The bare EA-LDH and EtOH-EA-LDH had 50 and 88% total scavenging activity with  $8.73 \times 10^{-5}$  and  $1.98 \times 10^{-5}$  M  $EC_{50}$  values determined in the assay, respectively. The  $EC_{50}$  (effective concentration) is the initial concentration of intercalated EA in the composites to decompose 50% of the DPPH radicals and is a common tool to quantify the material's antioxidant efficiency. In a typical test, the decrease in DPPH concentration was observed until steady state at various EA concentrations. These concentrations were calculated from the EA-content of the LDHs. The results of the antioxidant assays are shown in Fig. 5.

It was observed that in contrast to the uncoated LDHs that expressed their potential in 60 min (Fig. S4A, ESI<sup>†</sup>), *i.e.*, the steady state of the reaction was reached, the scavenging of DPPH radicals was not finished in this time period and hence, 120 min were allowed for the polyelectrolyte-functionalized EtOH-EA-LDHs to decompose a considerable amount of DPPH (Fig. S4B, ESI<sup>†</sup>) in the assays. A plausible explanation for this might be the hindrance of the intercalated EA molecules due to the polyelectrolyte layers on the surface of the particles that results in their reduced accessibility for the reacting DPPH radicals. However, this phenomenon provides a long-term radical scavenging activity for the material.

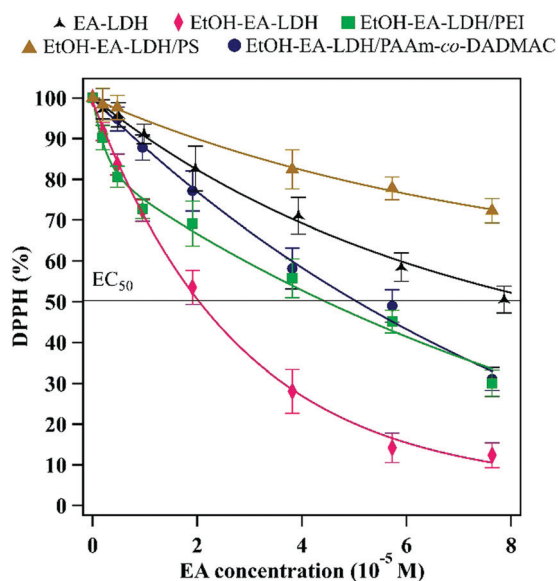


Fig. 5 DPPH scavenging activity of the bare and polyelectrolyte-coated LDH materials.

Besides the reaction time, the polyelectrolyte coatings also altered the DPPH scavenging effectiveness of the EtOH-EA-LDH (Table 1). Similar activity was assessed for EtOH-EA-LDH/PEI and EtOH-EA-LDH/PAAm-co-DADMAC with 70 and 69% total scavenging and  $4.46 \times 10^{-5}$  M and  $5.06 \times 10^{-5}$  M  $EC_{50}$  values, respectively. Although, the overall activity of the materials was below that of EtOH-EA-LDH, they showed high activity compared to the literature values of antioxidant-modified LDHs.<sup>69–71</sup> EtOH-EA-LDH/PS proved to be the least effective, underachieving untreated EA-LDH with less than 50% scavenging activity, thus no  $EC_{50}$  value could be determined. For reference, we assessed the DPPH scavenging activity of the free polyelectrolytes at ASP doses without any LDH added (Fig. S4C, ESI†). It was found that PS and PAAm-co-DADMAC showed negligible activity, thus their corresponding nanocomposites were efficient antioxidants owing to their EA content. On the other hand, PEI had sizeable contribution (ca. 42%) to the overall DPPH scavenging of its coated LDH. This is probably due to the numerous protonated amino groups of PEI. Interestingly, PS did not show the same effect, although possessing likewise protonated guanidine functions. These results show a clear correlation between the colloidal stability of the coated materials, since highly stable EtOH-EA-LDH/PEI and EtOH-EA-LDH/PAAm-co-DADMAC possessed higher radical scavenging activity than the EtOH-EA-LDH/PS of much lower colloidal stability and CCC, although the overall activity of EtOH-EA-LDH/PEI was partly from the adsorbed PEI.

## 4. Conclusions

The surface functionalization and colloidal tuning of an antioxidant LDH composite was explored. The EtOH-EA-LDH was prepared by the coprecipitation of EA and LDH followed by EtOH treatment to improve its structural properties, *i.e.*, to enlarge the specific surface area. The nanocomposite possessed negative surface charge, and thus, three cationic polyelectrolytes were chosen for surface functionalization, namely PEI, PS and PAAm-co-DADMAC. To optimize the experimental conditions for particle coating, the charging and aggregation of EtOH-EA-LDH were investigated by varying the polyelectrolyte dose. Stable dispersions were obtained at high doses, where the polyelectrolytes fully cover the surface of the LDH particles to form positively charged composites, meaning that overcharging occurred upon adsorption. However, a more important aspect is that colloidal stability of the particles is low without polyelectrolyte coating, in contrast to those with adsorbed polyelectrolyte layers. Thus, the salt-induced aggregation behaviour of the functionalized particles was also unravelled. While bare EA-LDH and EtOH-EA-LDH possessed lower CCC values, with PEI and PAAm-co-DADMAC on the surface, the dispersions were stable up to 1 M ionic strength. Interestingly, PS lowered the CCC of EtOH-EA-LDH, which was attributed to the flat-type adsorption and low line charge density of PS. On the other hand, it was shown that PAAm-co-DADMAC of neutral acrylamide units in the chain had significant steric effects on the colloidal stability, while joint steric and electrostatic repulsive

forces were responsible for the excellent resistance against salt-induced aggregation for the PEI-coated particles. The results of the radical scavenging activity assay revealed that the stable dispersions containing EtOH-EA-LDH/PEI (aided by the intrinsic scavenging property of PEI) and EtOH-EA-LDH/PAAm-co-DADMAC preserved the majority of the activity of EtOH-EA-LDH, scavenging 70%, 69% and 88% of the DPPH radicals, respectively. The polyelectrolyte layers on the surface somewhat reduced the availability of the intercalated antioxidants and the overall antioxidant capacity of the materials. Such a hindrance, however, provided a long-term activity for the hybrid materials. The long-term radical scavenging abilities, together with the extremely high colloidal stability, make EtOH-EA-LDH/PEI and EtOH-EA-LDH/PAAm-co-DADMAC promising candidates in applications, where antioxidant materials are used in liquid media containing high levels of electrolytes or their mixtures, *e.g.*, suppressing harmful oxidative agents under *in vivo* conditions.

## Conflicts of interest

There are no conflicts to declare.

## Acknowledgements

This research was financially supported by the Ministry of Human Capacities of Hungary (20391-3/2018/FEKUSTRAT), the Hungarian Academy of Sciences (96130) and by the National Research, Development and Innovation Office (SNN131558). The support from the University of Szeged Open Access Fund (4998) is gratefully acknowledged.

## References

- 1 R. S. Sohal and R. Weindruch, *Science*, 1996, **273**, 59–63.
- 2 S. Reuter, S. C. Gupta, M. M. Chaturvedi and B. B. Aggarwal, *Free Radical Biol. Med.*, 2010, **49**, 1603–1616.
- 3 J. W. Finley, A. N. Kong, K. J. Hintze, E. H. Jeffery, L. L. Ji and X. G. Lei, *J. Agric. Food Chem.*, 2011, **59**, 6837–6846.
- 4 R. Franco, G. Navarro and E. Martinez-Pinilla, *Antioxidants*, 2019, **8**, 542.
- 5 F. Rasti and G. Scott, *Eur. Polym. J.*, 1980, **16**, 1153–1158.
- 6 J. Couto, A. Figueirinha, M. T. Batista, A. Paranhos, C. Nunes, L. M. Goncalves, J. Marto, M. Fitas, P. Pinto, H. M. Ribeiro and M. E. Pina, *Antioxidants*, 2020, **9**, 154.
- 7 S. M. Lin, C. Y. Baek, J. H. Jung, W. S. Kim, H. Y. Song, J. H. Lee, H. J. Ji, Y. Zhi, B. S. Kang, Y. S. Bahn, H. S. Seo and S. Lim, *Sci. Rep.*, 2020, **10**, 55.
- 8 M. A. El-Missiry, *Antioxidant enzyme*, InTech, Rijeka, 2012.
- 9 J. J. Sun, R. Yendluri, K. Liu, Y. Guo, Y. R. Lvov and X. H. Yan, *Phys. Chem. Chem. Phys.*, 2017, **19**, 562–567.
- 10 M. Pavlovic, M. Nafradi, P. Rouster, S. Murath and I. Szilagyi, *J. Colloid Interface Sci.*, 2019, **543**, 174–182.



dc 1931\_21

- 11 G. F. D. del Castillo, M. Koenig, M. Muller, K. J. Eichhorn, M. Stamm, P. Uhlmann and A. Dahlin, *Langmuir*, 2019, **35**, 3479–3489.
- 12 O. O. Erejuwa, S. A. Sulaiman and M. S. Ab Wahab, *Molecules*, 2012, **17**, 4400–4423.
- 13 C. Nirmala, M. S. Bisht, H. K. Bajwa and O. Santosh, *Trends Food Sci. Technol.*, 2018, **77**, 91–99.
- 14 S. Murath, N. B. Alsharif, S. Saringer, B. Katana, Z. Somosi and I. Szilagyi, *Crystals*, 2020, **10**, 148.
- 15 K. C. Popat, M. Eltgroth, T. J. LaTempa, C. A. Grimes and T. A. Desai, *Biomaterials*, 2007, **28**, 4880–4888.
- 16 J. Karlsson, S. Atefyekta and M. Andersson, *Int. J. Nanomed.*, 2015, **10**, 4425–4436.
- 17 H. Hashemzadeh and H. Raissi, *Appl. Surf. Sci.*, 2020, **500**, 144220.
- 18 Z. Liu, J. T. Robinson, X. M. Sun and H. J. Dai, *J. Am. Chem. Soc.*, 2008, **130**, 10876–10877.
- 19 A. C. Santos, C. Ferreira, F. Veiga, A. J. Ribeiro, A. Panchal, Y. Lvov and A. Agarwal, *Adv. Colloid Interface Sci.*, 2018, **257**, 58–70.
- 20 X. Wen, F. Yang, Q. F. Ke, X. T. Xie and Y. P. Guo, *J. Mater. Chem. B*, 2017, **5**, 7866–7875.
- 21 X. Mei, S. M. Xu, T. Y. Hu, L. Q. Peng, R. Gao, R. Z. Liang, M. Wei, D. Evans and X. Duan, *Nano Res.*, 2018, **11**, 195–205.
- 22 F. Barahuie, M. Z. Hussein, P. Arulsevan, S. Fakurazi and Z. Zainal, *Sci. Adv. Mater.*, 2016, **8**, 501–513.
- 23 K. Khorsandi, R. Hosseinzadeh and M. Fateh, *RSC Adv.*, 2015, **5**, 93987–93994.
- 24 D. G. Evans and R. C. T. Slade, in *Layered Double Hydroxides*, ed. X. Duan and D. G. Evans, 2006, vol. 119, pp. 1–87.
- 25 Z. B. Cao, B. Li, L. Y. Sun, L. Li, Z. P. Xu and Z. Gu, *Small Methods*, 2019, 1900343, DOI: 10.1002/smt.201900343.
- 26 S. J. Mills, A. G. Christy, J. M. R. Genin, T. Kameda and F. Colombo, *Mineral. Mag.*, 2012, **76**, 1289–1336.
- 27 S. Murath, S. Szerlauth, D. Sebok and I. Szilagyi, *Antioxidants*, 2020, **9**, 153.
- 28 O. D. Pavel, A. Serban, R. Zavoianu, E. Bacalum and R. Birjega, *Crystals*, 2020, **10**, 244.
- 29 L. L. Qin, W. R. Wang, S. H. You, J. M. Dong, Y. H. Zhou and J. B. Wang, *Int. J. Nanomed.*, 2014, **9**, 5701–5710.
- 30 K. M. Ansy, J. H. Lee, H. Piao, G. Choi and J. H. Choy, *Solid State Sci.*, 2018, **80**, 65–71.
- 31 S. P. Lonkar, B. Kutlu, A. Leuteritz and G. Heinrich, *Appl. Clay Sci.*, 2013, **71**, 8–14.
- 32 A. Hajdu, M. Szekeres, I. Y. Toth, R. A. Bauer, J. Mihaly, I. Zupko and E. Tombacz, *Colloids Surf., B*, 2012, **94**, 242–249.
- 33 E. Koupanou, S. Ahualli, O. Glatte, A. Delgado, F. Krumeich and E. Leontidis, *Langmuir*, 2010, **26**, 16909–16920.
- 34 T. Klacic, A. Sadzak, J. Jukic, T. Preocanin and D. Kovacevic, *Colloids Surf., A*, 2019, **570**, 32–38.
- 35 B. Katana, P. Rouster, G. Varga, S. Muráth, K. Glinel, A. M. Jonas and I. Szilagyi, *ACS Appl. Bio Mater.*, 2020, **3**, 522–530.
- 36 M. X. Liu, R. He, J. Yang, Z. R. Long, B. Huang, Y. W. Liu and C. R. Zhou, *Clay Miner.*, 2016, **51**, 457–467.
- 37 A. Tiraferri, L. A. S. Hernandez, C. Bianco, T. Tosco and R. Sethi, *J. Nanopart. Res.*, 2017, **19**, 107.
- 38 L. L. Zhao, M. Skwarczynski and I. Toth, *ACS Biomater. Sci. Eng.*, 2019, **5**, 4937–4950.
- 39 B. Bolto and J. Gregory, *Water Res.*, 2007, **41**, 2301–2324.
- 40 S. Farrokhpay, *Adv. Colloid Interface Sci.*, 2009, **151**, 24–32.
- 41 F. Xie, T. Nylander, L. Piculell, S. Utsel, L. Wagberg, T. Akesson and J. Forsman, *Langmuir*, 2013, **29**, 12421–12431.
- 42 L. Muresan, P. Maroni, I. Popa, M. Porus, R. Longtin, G. Papastavrou and M. Borkovec, *Macromolecules*, 2011, **44**, 5069–5071.
- 43 R. Meszaros, I. Varga and T. Gilanyi, *Langmuir*, 2004, **20**, 5026–5029.
- 44 M. Borkovec, I. Szilagyi, I. Popa, M. Finessi, P. Sinha, P. Maroni and G. Papastavrou, *Adv. Colloid Interface Sci.*, 2012, **179**, 85–98.
- 45 L. L. Feng, M. C. Stuart and Y. Adachi, *Adv. Colloid Interface Sci.*, 2015, **226**, 101–114.
- 46 I. Szilagyi, G. Trefalt, A. Tiraferri, P. Maroni and M. Borkovec, *Soft Matter*, 2014, **10**, 2479–2502.
- 47 M. Pavlovic, P. Rouster, T. Oncsik and I. Szilagyi, *Chem-PlusChem*, 2017, **82**, 121–131.
- 48 C. Vasti, A. Borgiallo, C. E. Giacomelli and R. Rojas, *Colloids Surf., A*, 2017, **533**, 316–322.
- 49 C. Vasti, D. A. Bedoya, R. Rojas and C. E. Giacomelli, *J. Mater. Chem. B*, 2016, **4**, 2008–2016.
- 50 Z. Gu, H. L. Zuo, L. Li, A. H. Wu and Z. P. Xu, *J. Mater. Chem. B*, 2015, **3**, 3331–3339.
- 51 M. Pavlovic, P. Rouster, Z. Somosi and I. Szilagyi, *J. Colloid Interface Sci.*, 2018, **524**, 114–121.
- 52 M. Pavlovic, P. Rouster and I. Szilagyi, *Nanoscale*, 2017, **9**, 369–379.
- 53 Z. Somosi, M. Pavlovic, I. Palinko and I. Szilagyi, *Nanomaterials*, 2018, **8**, 986.
- 54 J. Carneiro, A. F. Caetano, A. Kuznetsova, F. Maia, A. N. Salak, J. Tedim, N. Scharnagl, M. L. Zheludkevich and M. G. S. Ferreira, *RSC Adv.*, 2015, **5**, 39916–39929.
- 55 N. Vargas-Mendoza, M. Vazquez-Velasco, L. Gonzalez-Torres, J. Benedi, F. J. Sanchez-Muniz, J. A. Morales-Gonzalez, O. A. Jaramillo-Morales, C. Valadez-Vega and M. Bautista, *Antioxidants*, 2018, **7**, 178.
- 56 P. A. Hassan, S. Rana and G. Verma, *Langmuir*, 2015, **31**, 3–12.
- 57 S. H. Behrens, M. Borkovec and P. Schurtenberger, *Langmuir*, 1998, **14**, 1951–1954.
- 58 D. Grolimund, M. Elimelech and M. Borkovec, *Colloids Surf., A*, 2001, **191**, 179–188.
- 59 W. Brand-Williams, M. E. Cuvelier and C. Berset, *Food Sci. Technol.*, 1995, **28**, 25–30.
- 60 P. Rouster, M. Pavlovic and I. Szilagyi, *RSC Adv.*, 2016, **6**, 97322–97330.
- 61 P. Rouster, M. Pavlovic, E. Horvath, L. Forro, S. K. Dey and I. Szilagyi, *Langmuir*, 2017, **33**, 9750–9758.
- 62 J. Israelachvili, *Intermolecular and surface forces*, Academic Press, London, 3rd edn, 2011.
- 63 M. Borkovec, G. J. M. Koper and C. Piguet, *Curr. Opin. Colloid Interface Sci.*, 2006, **11**, 280–289.
- 64 N. Malikova, A. L. Rollet, S. Cebasek, M. Tomsic and V. Vlachy, *Phys. Chem. Chem. Phys.*, 2015, **17**, 5650–5658.

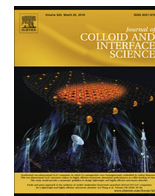
dc 1931 21

- 65 M. Pavlovic, P. Rouster, E. Bourgeat-Lami, V. Prevot and I. Szilagy, *Soft Matter*, 2017, **13**, 842–851.
- 66 M. Pavlovic, R. Huber, M. Adok-Sipiczki, C. Nardin and I. Szilagy, *Soft Matter*, 2016, **12**, 4024–4033.
- 67 G. Fritz, V. Schadler, N. Willenbacher and N. J. Wagner, *Langmuir*, 2002, **18**, 6381–6390.
- 68 J. Hierrezuelo, I. Szilagy, A. Vaccaro and M. Borkovec, *Macromolecules*, 2010, **43**, 9108–9116.
- 69 L. P. Amaro, F. Cicogna, E. Passaglia, E. Morici, W. Oberhauser, S. Al-Malaika, N. T. Dintcheva and S. Coiai, *Polym. Degrad. Stab.*, 2016, **133**, 92–100.
- 70 Q. Zhang, Q. Jiao, F. Leroux, P. G. Tang, D. Q. Li and Y. J. Feng, *Polym. Degrad. Stab.*, 2017, **140**, 9–16.
- 71 S. Olivera, C. Hu, G. S. Nagananda, N. Reddy, K. Venkatesh and H. B. Muralidhara, *Int. J. Environ. Sci. Technol.*, 2019, **16**, 2017–2030.



Contents lists available at ScienceDirect

Journal of Colloid and Interface Science

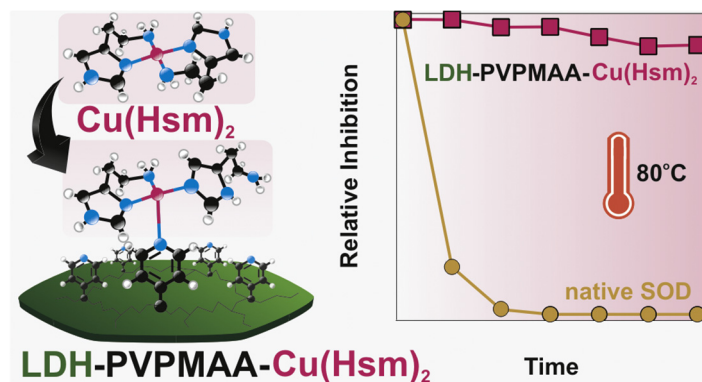
journal homepage: [www.elsevier.com/locate/jcis](http://www.elsevier.com/locate/jcis)

Regular Article

## Highly stable enzyme-mimicking nanocomposite of antioxidant activity

Marko Pavlovic<sup>a</sup>, Bálint Náfrádi<sup>b</sup>, Paul Rouster<sup>c</sup>, Szabolcs Muráth<sup>a,d</sup>, Istvan Szilagyi<sup>a,d,\*</sup><sup>a</sup> MTA-SZTE Lendület Biocolloids Research Group, University of Szeged, H-6720 Szeged, Hungary<sup>b</sup> Laboratory of Physics of Complex Matter, Ecole Polytechnique Fédérale de Lausanne, CH-1015 Lausanne, Switzerland<sup>c</sup> Institute of Condensed Matter and Nanosciences – Bio and Soft Matter, Université Catholique de Louvain, B-1348 Louvain-la-Neuve, Belgium<sup>d</sup> Interdisciplinary Excellence Center, Department of Physical Chemistry and Materials Science, University of Szeged, H-6720 Szeged, Hungary

## GRAPHICAL ABSTRACT



## ARTICLE INFO

## Article history:

Received 31 January 2019

Revised 15 February 2019

Accepted 16 February 2019

Available online 16 February 2019

## Keywords:

Antioxidant

Enzyme mimic

Nanoclay

Polymer functionalization

Dispersion stability

## ABSTRACT

A highly stable nanocomposite of antioxidant activity was developed by immobilization of a superoxide dismutase-mimicking metal complex on copolymer-functionalized nanoclay. The layered double hydroxide (LDH) nanoclays were synthesized and surface modification was performed by adsorbing poly(vinylpyridine-*b*-methacrylic acid) (PVPMAA). The effect of the adsorption on the charging and aggregation properties was investigated and the copolymer dose was optimized to obtain stable LDH dispersions. The LDH-PVPMAA hybrid particles showed high resistance against salt-induced destabilization in aqueous dispersions. Copper(II)-histamine ( $\text{Cu}(\text{Hsm})_2$ ) complexes were immobilized via the formation of dative bonds between the metal ions and the nitrogen atoms of the functional groups of the copolymer adsorbed on the particles. Changes in the coordination geometry of the complex upon immobilization led to higher superoxide radical anion scavenging activity than the one determined for the non-immobilized complex. Comparison of superoxide dismutase (SOD)-like activity of the obtained hybrid LDH-PVPMAA- $\text{Cu}(\text{Hsm})_2$  with the nanoclay-immobilized SOD enzyme revealed that the developed composite maintained its activity over several days and was able to function at elevated temperature, while the immobilized native enzyme lost its activity under these experimental conditions. The developed nanocomposite is a promising antioxidant candidate in applications, where high electrolyte concentration and elevated temperature are applied.

© 2019 Elsevier Inc. All rights reserved.

\* Corresponding author at: MTA-SZTE Lendület Biocolloids Research Group, University of Szeged, H-6720 Szeged, Hungary.

E-mail address: [szistvan@chem.u-szeged.hu](mailto:szistvan@chem.u-szeged.hu) (I. Szilagyi).

## 1. Introduction

Nanomaterials of enzyme-like features (so-called nanozymes) attracted considerable attention in the past decade to replace natural enzymes in order to overcome their high sensitivity to the environmental conditions such as pH, temperature and ionic strength [1]. In general, nanozymes consist of either bare nanoparticles or their functionalized derivatives [2]. In the first case, the materials themselves operate as a native enzyme, while in the latter case, metal complexes, which are able to mimic the structure and the function of natural metalloenzymes [3], are immobilized on nanoparticles to obtain enzyme-mimicking hybrid materials [4–6].

Nanozymes were also developed to replace antioxidant enzymes (e.g., superoxide dismutase (SOD), catalase (CAT), horseradish (HRP) and glutathione (GPx) peroxidases) [7], which are the primary defence systems against reactive oxygen species (ROS) such as superoxide, hydroxyl and peroxide radicals. Apart from their important roles in cell signalling [8], high ROS level leads to damage of biomolecules and causes various diseases including chronic inflammation and cancer [9]. Besides, the presence of ROS in formulation and chemical manufacturing processes in the food [10], pharmaceutical [11] and fuel [12] industry gives rise to lower quality products. The environmental conditions are especially harsh (e.g., elevated temperature or high ionic strength) in the industrial applications, therefore, antioxidant materials of high stability are required.

To develop efficient ROS scavenging systems, nanoparticles of various compositions were prepared. Among them, the most effective ones contained metal ions of redox activity, which mimic the function of the active centre of antioxidant enzymes and hence, they decompose ROS in redox reactions to molecular oxygen and/or water. For instance,  $Mn_3O_4$  nanozyme was reported as a material with multi-enzymatic activity, since it was able to mimic the function of SOD, CAT and GPx enzymes and thus, it protected living cells against oxidative stress [13]. Biocompatible platinum nanoparticles were synthesized and showed effective scavenging activity for intracellular ROS [14]. Such a multi-enzymatic antioxidant function was also found for Prussian blue [15] and  $Co_3O_4$  [16] nanoparticles, which were then applied as anti-inflammatory agent and in immunohistochemical assay, respectively. Bulk  $V_2O_5$  was reported as toxic, however,  $V_2O_5$  nanowires were found to be biocompatible and showed excellent GPx-mimicking properties [17].

Beside bare nanoparticle systems, composite nanomaterials were also reported as effective antioxidants. Self-assembly of  $V_2O_5$  and  $MnO_2$  nanoparticles through a dopamine linker led to high SOD, CAT and GPx-like activity and the obtained substance showed great promise in inflammation therapy [18]. The activity of some nanoparticle-based mimicking systems was even higher than the one determined for the native enzyme, like in the case of Pd-Ir core-shell HRP-mimicking nanoparticles [19]. It was shown that the peroxidase-like activity of nano-sized iron oxide can be tuned by surface functionalization due to the different affinity of the substrate to the coating molecules [20]. Appropriately chosen surface composition led to the development of a glucose sensor. In addition, triphenylphosphonium-conjugated ceria nanoparticles were prepared and used as antioxidant to reduce mitochondrial oxidative stress [21]. The role of the surface functional groups was to localize the mitochondria, while the ceria nanoparticles were responsible for the decomposition of ROS. Finally, SOD- and CAT-mimicking molecules were attached to cyclodextrin and the obtained hybrid compounds were processed into nanoparticle form, which significantly attenuated ROS-induced inflammation [22].

In the above examples, the antioxidant activity originated from the nanoparticles composed of metal ions with redox activity. In other systems, however, the nanoparticles were inactive in ROS scavenging and therefore, enzyme-mimetic activators were immobilized on their surface to achieve antioxidant activity. The most promising enzyme mimics contained transition metal ions [23,24] or their complexes [3,25,26] with structure similar to the one in the native enzymes. Such a structural mimic usually leads to a sufficient functional mimic too. The obtained nanoparticle-based hybrid composites were of similar ROS scavenging activity, but possessed a higher functional stability than the natural enzymes [27–29]. For instance, a copper(II)-zinc(II) heterobinuclear complex [30] of remarkable SOD activity [31] was immobilized on silica surface via either covalent bonds [32] or physical adsorption [33] and the obtained hybrid materials effectively mimicked the function of the native enzyme. Transition metal complexes of amino acids intercalated into clay materials [34] or covalently anchored to functionalized silica particles [35,36] were prepared and found to be efficient in dismutation of superoxide radical ions. Although the activity of these hybrids was lower than natural SOD, they exhibited the advantage of being less sensitive to the environmental conditions. In addition, hemin complexes were conjugated with montmorillonite [37] or to gold surfaces [38] to mimic peroxidase enzymes in oxidation reactions and hydrogen peroxide decomposition, respectively.

Apart from the enzymatic activity assessments and detailed structural characterization in solid state, these studies did not deal with the features of the obtained materials in dispersions. However, this is a critical point, since most of the applications took place in heterogeneous systems. Besides, there is a lack of information on the temperature-dependent functional stabilities, i.e., whether the antioxidant systems are able to act efficiently in ROS decomposition at higher temperatures or not. This issue is especially important in industrial applications of antioxidant materials, where elevated temperatures give rise to denaturation of the enzymes within short time intervals [39].

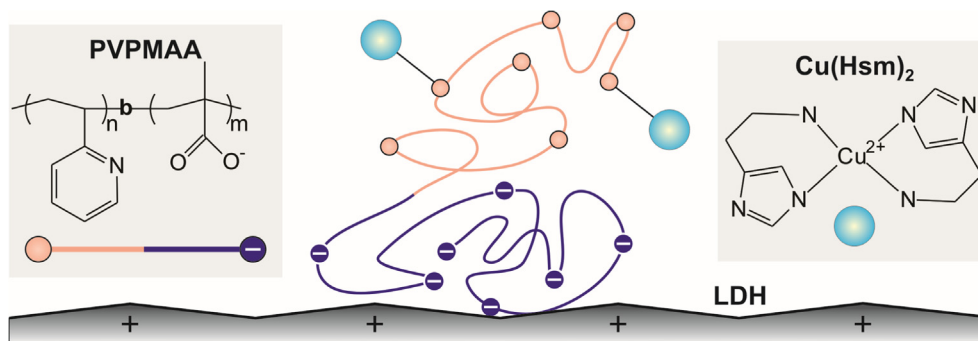
In the present work, SOD-mimicking nanozymes of high colloidal and functional stabilities were developed. Accordingly, copper(II)-histamine ( $Cu(Hsm)_2$ ) complexes were immobilized on poly(vinylpyridine-*b*-methacrylic acid) (PVPMAA) copolymer-functionalized layered double hydroxide (LDH) nanoclay particles (Scheme 1). Thorough characterization of the obtained hybrid material (LDH-PVPMAA- $Cu(Hsm)_2$ ) was carried out in dispersions and the long-term functional stability as well as the temperature resistance in dismutation of superoxide radical anions were assessed.

## 2. Materials and methods

### 2.1. Chemicals

Chemicals including  $Mg(NO_3)_2 \cdot 6H_2O$ ,  $Al(NO_3)_3 \cdot 9H_2O$ , NaOH, NaCl,  $NaH_2PO_4$ ,  $CuCl_2$ , nitro blue tetrazolium (NBT), histamine hydrochloride, xanthine oxidase (EC 1.17.3.2), xanthine, SOD (EC 1.15.1.1) were purchased from Sigma-Aldrich and used as received. The PVPMAA block copolymer was bought from Polymer Source and the number averaged molecular masses of the blocks were 10500 g/mol and 600 g/mol for PVP and MAA, respectively. For all experiments, ultrapure water produced by a Puranity TU3 UV/UF + water purification system (VWR) was used. Salt solutions and water applied in sample preparation for light scattering experiments were filtered with a syringe filter (Millex) of 0.1  $\mu m$  pore size. The measurements were carried out at 25 °C and at pH (7.0  $\pm$  0.5).





**Scheme 1.** Illustration of the composition of the LDH-PVPMAA-Cu(Hsm)<sub>2</sub> hybrid material.

## 2.2. Preparation and functionalization of LDH

The nanoclay was prepared by the flash co-precipitation method [40]. In the synthesis, nitrate solutions of magnesium(II) and aluminium(III) metal ions were mixed in a 2:1 M ratio and the pH of the solution was increased to 9 by quickly adding appropriate amount of NaOH. The obtained precipitate was aged, filtered and dried prior to hydrothermal treatment at 120 °C. The resulting material was filtered and washed with water. The solid compound was then redispersed in water and used as stock dispersion in the sample preparation processes. The more detailed preparation of the LDH is given elsewhere [41].

In the colloid stability experiments, the LDH particles were modified with different amount of PVPMAA to follow the charging and aggregation processes in the dispersions. In these measurements, calculated amount of stock nanoclay dispersions and copolymer solutions were mixed at the desired ionic strength to keep the LDH dose at 10 mg/L and to vary the PVPMAA dose in the 1–1000 mg/g range. Note that the mg/g unit refers to mg copolymer per one gram of particle.

## 2.3. Characterization techniques

Electrophoretic mobilities were measured with a LiteSizer 500 (Anton Paar) device equipped with a 40 mW laser source operating at 658 nm wavelength. The experiments were performed in omega-shaped capillary cuvettes (Anton Paar). The average of five individual measurements was reported.

Hydrodynamic radii were determined by dynamic light scattering (DLS) using a NIBS/HPPS particle size analyzer (ALV GmbH). This instrument contains a He-Ne laser of 3 mW power and 633 nm wavelength. The measurements were carried out at 173° scattering angle in disposable plastic cuvettes (VWR) and the correlation function was collected for 20 s.

Powder X-ray diffraction experiments were performed on an Empyrean (PANalytical) diffractometer in the reflection geometry using the CuK $\alpha$  radiation (Johansson type Ge monochromator). The data were collected for 2-Theta ranging from 5° to 70° with a step of 0.0131 and for an exposure time of either 298 s or 798 s per step.

Infrared (IR) spectra were measured in the attenuated total reflectance (ATR) mode with a Spectrum 100 FT-IR spectrometer (PerkinElmer). The ATR crystal was made of diamond. The solid material was placed on the ATR crystal and the spectrum was recorded in the wavenumber range from 4000 to 400 cm<sup>-1</sup> at a resolution of 4 cm<sup>-1</sup>. For the IR measurement, the solid materials were filtered from the dispersions, washed several times with water to remove weakly adsorbed copolymers and dried.

The electron paramagnetic resonance (EPR) spectroscopy measurements were carried out with a Bruker Elexsys E500 spectrometer operating at 9.4 GHz microwave frequency. The aqueous

solution used for the experiments was filled into 1.5 mm internal diameter Pyrex capillaries up to a height of 1 cm. The capillaries were arranged in a honeycomb structure inside a 4 mm outer diameter EPR capillary to minimize dielectric loss for an optimal signal-to-noise ratio. Care was taken to optimize the EPR accusation parameters to simultaneously obtain both broad and narrow spectral features without distortion. The analysis of the obtained spectra was performed with the EasySpin EPR spectrum simulation package [42].

Scanning electron microscopic (SEM) investigation was carried out using an S-4700 instrument (Hitachi) at various magnifications with 10 kV accelerating voltage. The sample was coated via physical noble metal vapour deposition to achieve electric conductivity.

The BET specific surface area was determined on the basis of N<sub>2</sub> adsorption-desorption isotherms with a NOVA 3000e device (Quantachrome Instruments).

## 2.4. Superoxide radical anion dismutation

The SOD-like activity was assessed in a standard biochemical assay [43]. Superoxide radical anions were produced by the reaction between xanthine and xanthine oxidase in the presence of NBT in phosphate buffer maintaining the pH at 7.5 during the reaction. Upon reduction by the radicals, NBT changes its colour from yellow to blue. The development of the absorption band at 565 nm was monitored with a Genesys 10S spectrophotometer (Thermo Scientific). The inhibition of the superoxide radical anion - NBT reaction by the scavenging compound was then calculated and the ability in dismutation of the superoxide radical anions was expressed in terms of IC<sub>50</sub> values, which correspond to the catalyst concentration necessary to decompose 50% of the radicals formed in the probe reaction. Moreover, long-term stability of the materials was measured and compared to the activity of the other catalysts (SOD, LDH-Hep-SOD (detailed characterization is given elsewhere [41]) and free Cu(Hsm)<sub>2</sub> complex). This was achieved by determining the IC<sub>50</sub> of the freshly prepared compounds and by comparing the initial 50% inhibition to the ones measured later. In that manner, the drop in the relative activity was followed during 4 days at room temperature or during 1 h at 80 °C.

The LDH-PVPMAA-Cu(Hsm)<sub>2</sub> material was prepared by mixing the nanoclay dispersion, the copolymer and the complex solutions at concentrations of 10 mg/L, 500 mg/g and 0.01 mM, respectively. The same samples were used in the EPR measurements. This condition was a compromise to obtain high colloidal and functional stability for the LDH-PVPMAA-Cu(Hsm)<sub>2</sub>, as detailed later.

## 3. Results and discussion

A SOD-mimicking LDH-PVPMAA-Cu(Hsm)<sub>2</sub> material was prepared and investigated. LDH is a lamellar anionic clay [44], i.e., it

possesses anion exchange capacity, and is widely used as carrier in biomedical delivery processes due to the ease of synthesis, biocompatibility and tuneable size [45–50]. PVPMAA was chosen, because the negatively charged MAA groups are expected to adsorb on the oppositely charged LDH surface by electrostatic forces, while the pyridine groups of the PVP part contains nitrogen atoms, which may be able to bind to the copper(II) centre of the  $\text{Cu}(\text{Hsm})_2$  complex through dative bonds leading to strong connection of the enzyme mimic to the copolymer-nanoclay carrier. The synthesis, characterization and SOD-like activity of the LDH-PVPMAA-Cu  $(\text{Hsm})_2$  are detailed as follows.

### 3.1. Characterization of the nanoclay

The formation of the layered structure was confirmed by XRD and the diffraction pattern (Fig. S1a) contained all the characteristic reflections previously reported for LDH of similar composition [40,44,46]. The specific surface area of the nanoclay was determined to be  $52.6 \text{ m}^2/\text{g}$  by the BET method. Morphologic analysis revealed that the material contains small grain-like platelets with rounded edges that form small aggregates in solid state. Such a hexagonal-based morphology is common among LDHs. The typical particle radius tends to be in the 50–100 nm range. DLS measurements yielded an average hydrodynamic radius of 110 nm and a polydispersity index of 0.3 in stable aqueous dispersions.

### 3.2. Adsorption of PVPMAA on LDH particles

The surface of the LDH particles was modified by adsorbing different amount of PVPMAA to tune its properties for further immobilization of the  $\text{Cu}(\text{Hsm})_2$  complex. Note that the nanoclay is positively charged, while the PVPMAA is negatively charged under the experimental conditions applied. The adsorption process was followed by electrophoretic measurements, where the PVPMAA dose was systematically varied and the charging behaviour was investigated at different copolymer concentrations (Fig. 1).

The mobilities were positive at low copolymer concentration due to the positive structural charge of the bare particles [51], however, they decrease by increasing the dose clearly indicating that the adsorption of PVPMAA took place on the LDH. Such an adsorption led to charge neutralization at about 50 mg/g

copolymer dose. By further increasing the concentration, charge reversal was observed and the particles became negatively charged. Similar charge reversal has already been reported with LDH particles in the presence of oppositely charged polymers [41,52,53] or copolymers [54] and it originates from electrostatic attraction between the polymer and the surface, entropic gain due to the release of the solvent molecules [55] and hydrophobic interactions [56]. At high PVPMAA doses, the mobilities reached a plateau and remained constant within the experimental error. The value of about  $-1.8 \times 10^{-8} \text{ m}^2/\text{Vs}$  corresponds to the electrophoretic mobility of the LDH-PVPMAA composite, which consists of the nanoclay and a self-assembled saturated copolymer surface layer at a dose of 500 mg/g.

The measurements were repeated at different ionic strengths (10 mM and 100 mM), however, the mobilities were very similar in the entire concentration range investigated (Fig. S2a). The doses needed for charge neutralization and surface saturation were significantly higher than the ones measured for pure poly(acrylic acid) (PAA) polyelectrolyte (Fig. S3a). This is due to the lower line charge density for the PVPMAA and thus, to the decreased repulsion between the negatively charged copolymer chains adsorbed on the surface.

Since the surface functionalized LDH will be used as carrier in dispersions, where highly stable primary particles are required, the colloidal stability was studied in the above systems. Accordingly, apparent aggregation rates (see Supporting Material (SM) for the details) were determined in the time-resolved DLS measurements. This technique has proven itself to be a powerful tool to investigate particle aggregation processes [51,57,58]. Thereafter, stability ratios [59] were calculated under the same experimental conditions as used in the above electrophoretic study (Fig. 1). Note that stability ratios close to unity correspond to rapidly aggregating samples and to unstable colloids, while higher values refer to more stable dispersions and to slower particle aggregation processes. In other words, the reciprocal of the stability ratios is equal to the fraction of particle collisions, which results in dimer formation. More details about the theoretical and practical backgrounds of the DLS measurements are given in the SM.

The measured U-shaped curve of the stability ratios at different copolymer doses resembles to the tendency reported for other systems containing LDH and oppositely charged polymers [51]. High stability ratios were obtained at low and high PVPMAA doses indicating stable dispersions. On the other hand, the samples were unstable in the intermediate concentration regime, where the stability ratios were one (deviations occurred only within the experimental error). Comparing the trends in the electrophoretic mobility and stability ratio data, one can realize that the unstable region is located at copolymer doses close to the charge neutralization point. The particles aggregate rapidly under these conditions and the aggregation process is controlled only by their diffusion.

The measurements were repeated at two more ionic strengths (Fig. S2b) to probe the effect of the salt concentration on the location of the slow and high aggregation regimes. No significant changes in the stability ratios were observed in the unstable region and at higher doses. However, the aggregation of the particles became rapid at low PVPMAA concentrations at 10 mM and 100 mM ionic strengths due to charge screening on the partially neutralized particles.

The stability ratio data measured at 1 mM ionic strength was compared to the ones determined with pure PAA (Fig. S3b). The unstable regime is located at lower polymer doses for PAA, since charge neutralization occurred at lower concentrations in that case. This fact also confirms that the fast aggregation regime is determined by the charge neutralization process of the particles.

The charging and aggregation behaviour of the particles at different PVPMAA doses are qualitatively in line with the theory

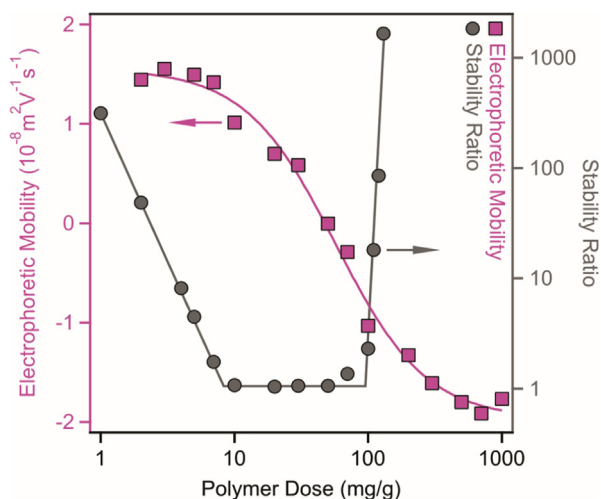


**Fig. 1.** Electrophoretic mobilities (squares) and stability ratios (circles) of the LDH particles in the presence of PVPMAA copolymer for different doses at 10 mg/L nanoclay concentration and 1 mM ionic strength adjusted by NaCl. The mg/g unit on the x-axis corresponds to mg of copolymer per one gram of LDH. The error in both mobility and stability ratio measurements is about 10%.

developed by Derjaguin, Landau, Verwey and Overbeek (DLVO) [60] to predict the colloidal stability of charged particles dispersed in electrolyte solutions. This theory states that such dispersions are stabilized by interparticle repulsions due to the presence of electrical double layers forming around the particles. At 1 mM ionic strength, this condition applies at low and high copolymer doses, where the functionalized LDH particles possess significantly high charges. However, attractive van der Waals forces are always present and the overall interparticle force is the sum of the attractive and repulsive forces. Once the charge of the particles is low or neutralized, the van der Waals forces overtake the repulsive ones and thus, the particles rapidly aggregate. In the dispersions containing LDH and PVPMAA, this condition applies at doses near the charge neutralization point.

The adsorption of the copolymer on the particles was also confirmed by IR spectroscopy by detecting the characteristic vibrations of both LDH and PVPMAA in the hybrid material. The spectra measured for the nanoclay particle, the copolymer and for its copolymer-functionalized derivative are shown in Fig. 2.

In the LDH-PVPMAA hybrid, a dose of 500 mg/g was applied, which corresponds to the PVPMAA concentration, where a saturated copolymer layer forms on the particle surface. Prior to the measurement, the LDH-PVPMAA material was filtered off, washed with water to remove the weakly adsorbed copolymer molecules and dried. The spectra clearly indicate that the adsorption process took place, since peaks originating from both LDH and PVPMAA could be detected in the spectrum of the composite material. Accordingly, 12 vibrational bands were observed for the LDH-PVPMAA, 6–6 corresponded to the carrier and the copolymer, respectively. For instance, the peaks at  $447\text{ cm}^{-1}$  and at  $781\text{ cm}^{-1}$  in the spectrum of LDH-PVPMAA are assigned to the Mg—O—H or

Al—O—H translations in the LDH [61]. The band at  $1433\text{ cm}^{-1}$  originate from the wagging of the C—H bond in the pyridine group [62]. The ring stretching mode was observed at  $1472\text{ cm}^{-1}$  confirming the successful adsorption of the PVPMAA on the LDH particles [63]. For the complete assignment of the IR peaks, see Table S1 in the SM.

### 3.3. Colloidal stability of the LDH-PVPMAA composite

The resistance of the LDH-PVPMAA material (LDH with a saturated copolymer surface layer) against salt-induced aggregation is an important issue in potential applications, where the nanocomposites are often dispersed in electrolyte solutions of high concentrations. Therefore, stability ratios of the hybrid were measured and compared to the ones determined for the bare particles to assess the stabilizing effect of the PVPMAA layer (Fig. 3).

Very similar dependencies were observed for the bare and copolymer coated LDH. Slow aggregation indicated by high stability ratios was observed at low ionic strengths, while the aggregation became rapid after a threshold salt concentration, which is the so-called critical coagulation concentration (CCC). Such a tendency of the stability ratios with varying salt level is predicted by the DLVO theory [60] and was reported for various charged colloidal particles dispersed in electrolyte solutions [51,64,65]. Repulsive forces generated by the electrical double layers weakened by increasing the ionic strength due to salt screening and they vanish at the CCC. Above this electrolyte concentration, attractive van der Waals forces predominate leading to rapid aggregation of the particles. Stability ratios close to unity above the CCC indicate diffusion controlled aggregation for both LDH and LDH-PVPMAA, which remained the same by further increasing the ionic strength.

Two observations in the tendencies deserve further discussion. First, the slope in the slow aggregation regime is smaller for the LDH-PVPMAA particles. This is due to surface heterogeneities upon copolymer functionalization. PVPMAA adsorbs non-uniformly on the surface and hence, forms islands (or patches) of negative charge [66]. These islands are electrostatically attracted to the empty surface places of another particle and thus, such a patch-charge attraction leads to additional attractive forces and to faster aggregation, i.e., lower stability ratios, and to smaller slopes in the

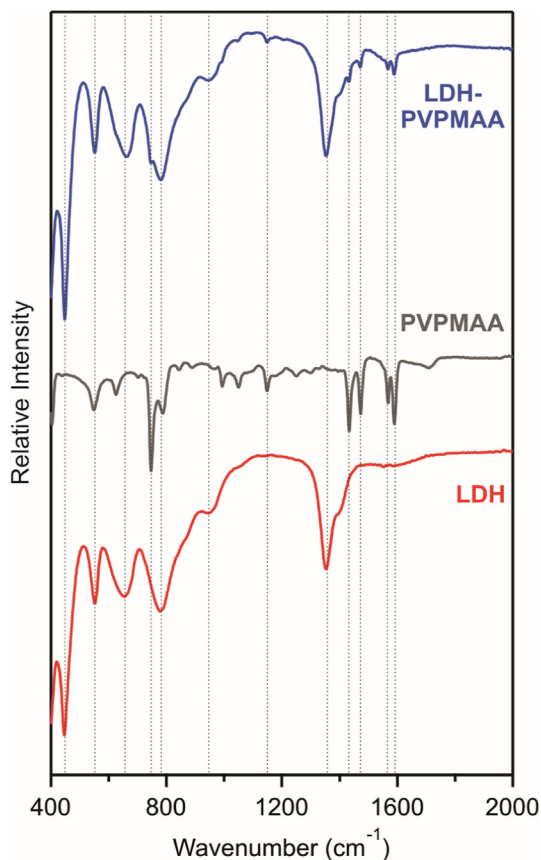


Fig. 2. IR spectra of the LDH, PVPMAA copolymer and the composite LDH-PVPMAA material. The latter one contains 500 mg of PVPMAA per one gram of LDH particle.

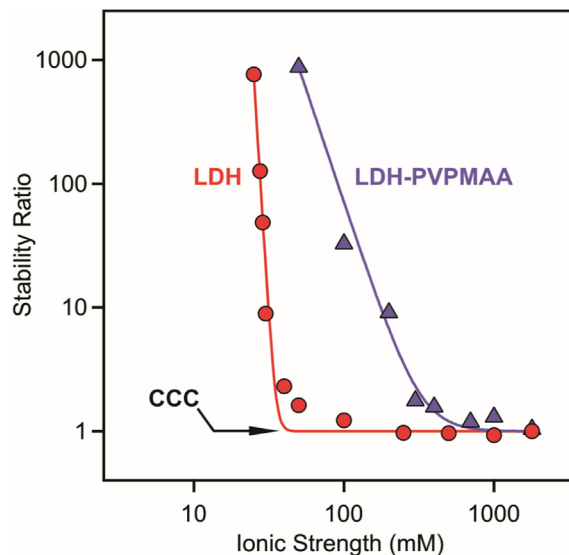


Fig. 3. Stability ratios of the LDH particles and LDH-PVPMAA composite material (500 mg of copolymer per gram of particles) as a function of the ionic strength adjusted by NaCl. The measurements were carried out at 10 mg/L particle concentration. The solid lines are fits obtained with equation S8.



slow aggregation regime [67]. The patch-charge interactions are absent in the case of the bare particles, since surface charge heterogeneities were formed upon the copolymer adsorption.

Second, the difference in the CCC values for LDH and LDH-PVPMAA is striking. A CCC of 40 mM was calculated for the bare and 610 mM for the copolymer coated particles. Such a large deviation in the CCC indicates the presence of strong repulsive forces. Electrophoretic mobility measurements carried out under the same experimental conditions (Fig. S4) revealed that the surface charge of the LDH and LDH-PVPMAA is comparable, therefore, the strong repulsive forces cannot originate only from the double layer repulsion in the latter case. Therefore, it was assumed that the particles are also stabilized by steric repulsion of the adsorbed copolymer chains. This type of interaction was found in several particle-polymer systems earlier [51,64,68,69]. The obtained high CCC for the LDH-PVPMAA indicates highly stable dispersions making the composite an excellent candidate for the further immobilization processes and for applications in samples of high ionic strength.

### 3.4. Immobilization of $\text{Cu}(\text{Hsm})_2$ on the LDH-PVPMAA particles

To mimic the function of the active centre of the SOD enzyme [70],  $\text{Cu}(\text{Hsm})_2$  complex of 1:2 metal-to-ligand ratio was prepared by mixing the copper(II) salt with the histamine solution in 1:2 stoichiometric ratio at neutral pH. It was previously reported that the 4 nitrogen atoms of the ligand molecules are symmetrically coordinated to the metal ions forming an equatorial plane [71]. Accordingly, the donor atoms of the functional groups (pyridine nitrogen or carboxylic oxygen) in the LDH-PVPMAA hybrid material are expected to occupy one or two coordination places around the metal ion.

To follow the immobilization of the complex on the nanoclay-copolymer composite, electrophoretic mobilities and stability ratios were measured at different  $\text{Cu}(\text{Hsm})_2$  concentrations (Fig. 4).

The tendencies in the mobilities and stability ratios were very similar to that observed for the LDH dispersions with systematic variation of the dose of the PVPMAA copolymer (Fig. 1). Obviously, the charge balance is opposite due to the negatively charged LDH-PVPMAA and  $\text{Cu}(\text{Hsm})_2$  of positive charge. The mobilities increased by increasing the complex concentration indicating adsorption on the composite. The affinity of the coordination compound was high to the surface leading to charge neutralization and reversal at

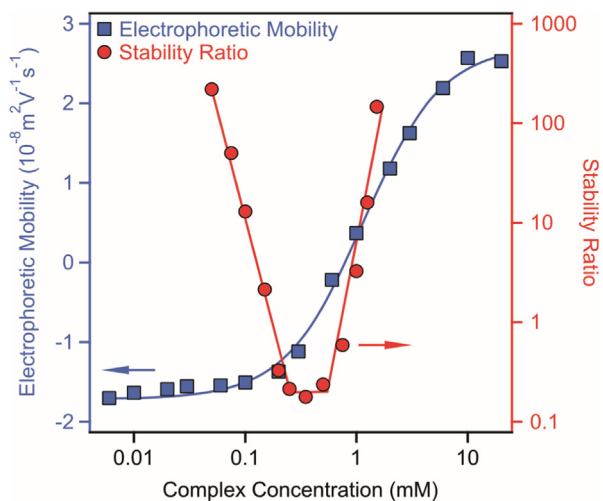


Fig. 4. Electrophoretic mobilities (squares) and stability ratios (circles) of the LDH-PVPMAA composite material as a function of the  $\text{Cu}(\text{Hsm})_2$  complex concentration measured at 10 mg/L particle concentration.

appropriate concentrations. The corresponding stability ratios can be adequately explained by the charging behaviour and the DLVO theory. The intermediate region in the U-shape curve is located near the charge neutralization point, where van der Waals attractions are predominant in the absence of repulsive double layer forces. Besides, at low and high  $\text{Cu}(\text{Hsm})_2$  concentrations, the dispersions are stable due to the presence of sufficiently charged particles and strong repulsive forces.

Although such a behaviour of charged colloidal particles in the presence of oppositely charged polyelectrolytes is common [51,64], it is rather atypical for divalent ions like the  $\text{Cu}(\text{Hsm})_2$  complex. Charging and aggregation of LDH was investigated in salt solutions of various valences [51,72,73], however, such a high extent of charge inversions has not been reported yet. The restabilization of the dispersions by charge reversal is also a non-expected behaviour in this system. These results clearly indicate that a specific interaction takes place between the LDH-PVPMAA and the  $\text{Cu}(\text{Hsm})_2$ .

Given the structure of the copolymer, the formation of dative bonds between the copper(II) centre and the pyridine nitrogen or carboxylic oxygen of the adsorbed copolymer chain is feasible. To investigate the possibility of this scenario, EPR spectroscopy experiments were performed. This method is sensitive to the changes in the coordination geometry around metal ions of unpaired electrons like copper(II) [31,33,34], therefore, the spectra of the  $\text{Cu}(\text{Hsm})_2$  in solution and on the LDH-PVPMAA surface were recorded (Fig. S5). A significant difference was found between the spectra indicating the different coordination geometry upon immobilization. The analysis of the measured spectrum for the LDH-PVPMAA- $\text{Cu}(\text{Hsm})_2$  material revealed that the EPR spectrum can be decomposed into two spectra of two independent copper(II) containing species (Fig. 5).

The fraction of the narrow component (A) is about 7% in both samples and it is unchanged upon immobilization on LDH-PVPMAA (Fig. S6) as confirmed by the same EPR parameters of  $g_x = g_y = g_z = 2.12$  and  $A = 210$  MHz. For species (A) the observed hyperfine interaction and the relatively narrow EPR linewidth indicate that the spin-spin interaction is weak and the species A are relatively rapidly moving.

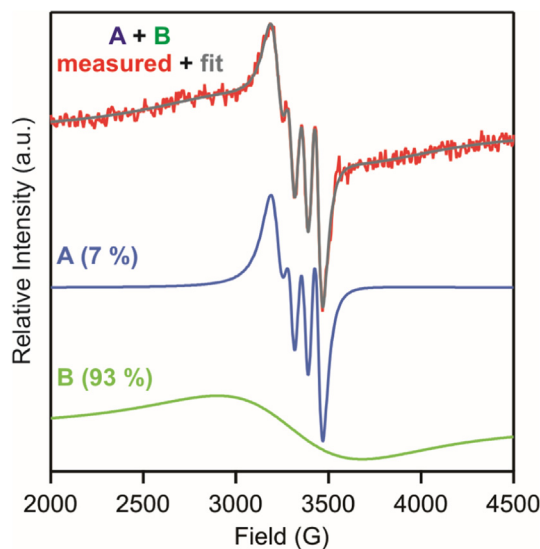


Fig. 5. Measured and fitted EPR spectra of the LDH-PVPMAA- $\text{Cu}(\text{Hsm})_2$  hybrid material (A + B, which contained about 7 mmol of  $\text{Cu}(\text{Hsm})_2$  per one gram of LDH-PVPMAA) together with the calculated spectra of the two copper(II) containing components (A and B) existing in the sample. Note that the majority (93%) of the copper(II) centres are in component B.



The broad component (**B**) is 93% in both the free and immobilized complex and the structure is significantly different for the  $\text{Cu}(\text{Hsm})_2$  in solution and on the surface. Spectrum analysis yielded  $g_x = g_y = 2.05$  and  $g_z = 2.25$  for the dissolved complex, while  $g_x = g_y = g_z = 2.14$  once the  $\text{Cu}(\text{Hsm})_2$  was attached to the LDH-PVPMAA. Hyperfine interaction was not resolved for the **B** species in neither configuration. These data shed light on that the coordination geometry around the metal centre in the **B** species is significantly different from the one in solution. Such a change in the arrangement of the donor atoms is most likely due to the coordination of the donor atoms of the functional groups of the LDH-PVPMAA composite to the metal centre of the complex.

Species with lower  $g_0$  value show stronger ligand field in the equatorial plane, therefore, the coordination of 4 nitrogen atom is suggested for the dissolved complex. The higher  $g_0$  value of the other isomer is probably produced by three equatorial nitrogen of the ligand and hence, one of the nitrogen of the  $\text{Cu}(\text{Hsm})_2$  attached to the LDH-PVPMAA is forced to occupy the axial position. The coordination of carboxylic group oxygens of the copolymer may also occur in the fourth equatorial position, however, this cannot be unambiguously confirmed by the present EPR data. Nevertheless, the remarkable change in the coordination geometry with species **B** clearly indicate the complexation of the functional groups of the adsorbed PVPMAA by the copper(II) centre.

### 3.5. SOD-like activity of the LDH-PVPMAA- $\text{Cu}(\text{Hsm})_2$

The superoxide radical anion scavenging activity of the obtained LDH-PVPMAA- $\text{Cu}(\text{Hsm})_2$  was probed in a biochemical test reaction [43] and compared to the activity of the non-immobilized  $\text{Cu}(\text{Hsm})_2$ , SOD and LDH-immobilized SOD enzyme (LDH-Hep-SOD) reported earlier [41]. In addition, the long-term stability and the temperature resistance of the SOD-like function were tested.

In the assay, the inhibition of the reaction between the NBT indicator compound and superoxide radical anions formed in situ was measured as a function of the copper(II) content of the enzyme or the mimicking complex (Fig. S7). The activities of the materials were expressed in terms of  $\text{IC}_{50}$  values, which is equal to the copper(II) concentration necessary to dismutate 50% of the radicals forming in the test reaction. These values were found to be  $2.6 \times 10^{-1} \mu\text{M}$ ,  $9.7 \times 10^{-2} \mu\text{M}$ ,  $2.1 \times 10^{-3} \mu\text{M}$  and  $2.9 \times 10^{-3} \mu\text{M}$  for  $\text{Cu}(\text{Hsm})_2$ , LDH-PVPMAA- $\text{Cu}(\text{Hsm})_2$ , SOD and LDH-Hep-SOD, respectively.

Although the  $\text{IC}_{50}$  determined for the native and immobilized enzymes were lower, the  $\text{Cu}(\text{Hsm})_2$  still showed significant SOD-like function. Besides, the activity of the complex increased upon immobilization, since a lower  $\text{IC}_{50}$  was measured for the LDH-PVPMAA- $\text{Cu}(\text{Hsm})_2$  compared to  $\text{Cu}(\text{Hsm})_2$ . Such an improved activity is due to the changes in the coordination geometry around the copper(II) ions (see the results of the EPR measurements in the previous chapter) once the donor atoms from the adsorbed copolymer is coordinated giving rise to an evolved structure allowing a more efficient scavenging of the superoxide radical anions. The  $\text{IC}_{50}$  of the LDH-PVPMAA- $\text{Cu}(\text{Hsm})_2$  is greater than those previously reported for SOD-mimicking metal complexes [30,31,34,74] and for the immobilized ones [32–34,75].

To probe the long-term stability of the hybrid material, the  $\text{IC}_{50}$  values were measured over 4 days for the above compounds and the relative activities, i.e., the data were normalized to the  $\text{IC}_{50}$  determined with the freshly prepared samples, were calculated. Fig. 6 shows the obtained tendencies in the long-term activities.

Although the native SOD kept its functional integrity, the immobilized derivative lost about 80% of its activity during the time period investigated. Such a decrease occurred most probably due to slow conformational changes on the surface, which led to a

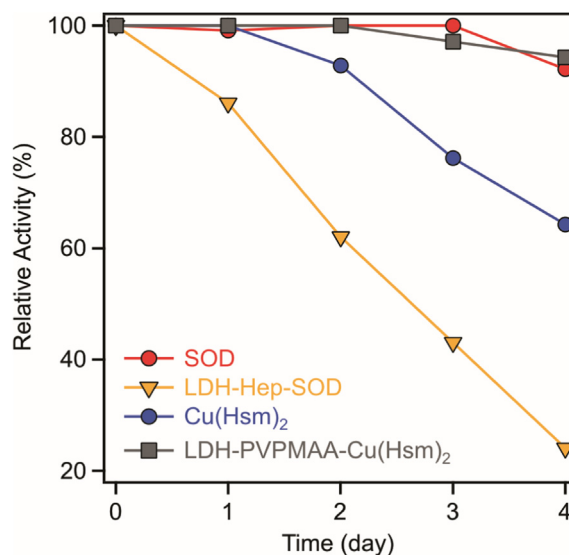


**Fig. 6.** Relative superoxide radical anion scavenging activity (related to the freshly prepared samples) of the native SOD (red circle), its immobilized form (LDH-Hep-SOD, yellow triangle), the  $\text{Cu}(\text{Hsm})_2$  complex (blue circle) and the LDH-PVPMAA- $\text{Cu}(\text{Hsm})_2$  hybrid material over 4 days measured at room temperature. Note that the error of the measurements is about 15%. (For interpretation of the references to colour in this figure legend, the reader is referred to the web version of this article.)

loss of the superoxide radical anion dismutation ability. Comparing the  $\text{Cu}(\text{Hsm})_2$  and LDH-PVPMAA- $\text{Cu}(\text{Hsm})_2$ , the relative activity of the complex in solution decreased significantly, however, the immobilized complex was of about the same efficiency after 4 days. This behaviour was similar to the one experienced by the native enzyme. Accordingly, the attachment of the  $\text{Cu}(\text{Hsm})_2$  to the copolymer-functionalized LDH gave rise to the formation of a hybrid material of high functional stability.

In the next step, the temperature resistance of the SOD-like function was investigated. The  $\text{IC}_{50}$  values were determined at  $80^\circ\text{C}$  periodically after 10 min for 1 h. The relative activities were again calculated as the obtained  $\text{IC}_{50}$  data normalized to the one

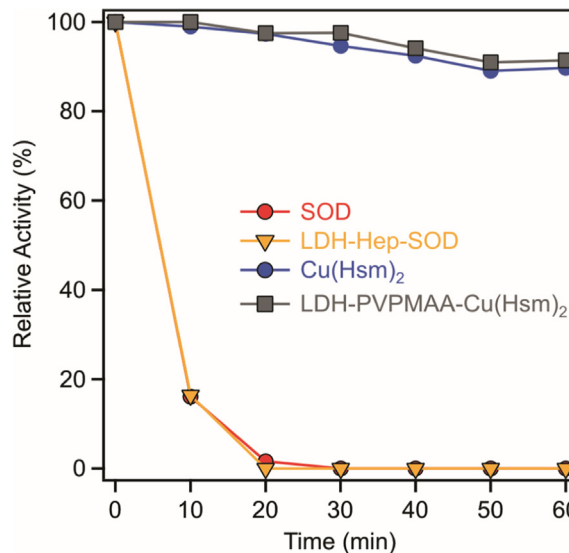


**Fig. 7.** Relative superoxide radical anion dismutating activities of the native SOD (red circle), its immobilized form (LDH-Hep-SOD, yellow triangle), the  $\text{Cu}(\text{Hsm})_2$  complex (blue circle) and the LDH-PVPMAA- $\text{Cu}(\text{Hsm})_2$  composite over 1 h at  $80^\circ\text{C}$ . (For interpretation of the references to colour in this figure legend, the reader is referred to the web version of this article.)

measured immediately after sample preparation and equilibration at 80 °C (Fig. 7).

Both native and immobilized SOD quickly lost their activities and denatured after about 20 min, while the Cu(Hsm)<sub>2</sub> and LDH-PVPMAA-Cu(Hsm)<sub>2</sub> kept 90% of their initial superoxide radical anion scavenging ability after 1 h. These results shed light on the fact that replacing the natural enzyme with the mimicking compounds led to the development of an antioxidant material of significant SOD-like activity even at elevated temperature.

Combining the results presented in Figs. 6 and 7, the following conclusions were taken. First, immobilization of the copper(II) complex significantly improved its long-term activity and the obtained LDH-PVPMAA-Cu(Hsm)<sub>2</sub> behaves in a similar manner as the native SOD. Second, the enzyme is not able to function at higher temperature, while the enzyme-mimicking composite is still highly active. In addition, the LDH-PVPMAA-Cu(Hsm)<sub>2</sub> forms highly stable colloid and the catalytic centres are linked with strong primary chemical bonds to the surface of the carrier particles. Accordingly, the obtained nanoclay-copolymer-complex hybrid material is an extremely promising candidate in applications, wherever longer term antioxidant effects are required in dispersions of high electrolyte concentrations or at elevated temperature.

#### 4. Conclusions

Antioxidant hybrid nanomaterial (LDH-PVPMAA-Cu(Hsm)<sub>2</sub>) composed of nanoclay carrier, copolymer stabilizer and copper(II) complex as catalytic centre was prepared, characterized and tested in dismutation of superoxide radical anions. The experimental conditions for the functionalization of the LDH with PVPMAA were optimized in order to obtain LDH-PVPMAA composite of high colloidal stability. The Cu(Hsm)<sub>2</sub> was successfully immobilized through dative bonds formed between the donor atoms of the adsorbed copolymer chains and the metal centre of the complex.

Structural changes in the coordination geometry around the copper(II) ions upon immobilization led to higher functional stability in dismutation of superoxide radical anions in comparison to the one determined for the complex in solution. The LDH-PVPMAA-Cu(Hsm)<sub>2</sub> kept its radical scavenging function for longer time period compared to the free Cu(Hsm)<sub>2</sub> and immobilized SOD. Moreover, the hybrid nanomaterial was highly active even at 80 °C, a condition, where the native or immobilized SOD enzyme quickly lost their antioxidant activity.

The obtained material is able to solve problems connected to ROS damage in the textile, food and cosmetic industry, where the manufacturing processes often take place in dispersions of high electrolyte concentration and/or at elevated temperature. Such an antioxidant effect is beneficial to produce good quality products of long term stability. Therefore, the LDH-PVPMAA-Cu(Hsm)<sub>2</sub> nanohybrid can be recommended as an efficient antioxidant.

#### Acknowledgements

The financial support by the Lendület program of the Hungarian Academy of Sciences (96130) and by the Ministry of Human Capacities, Hungary through grant 20391-3/2018/FEKUSTRAT is gratefully acknowledged. This work was also partially supported by the Swiss National Science Foundation (200021\_144419). The authors thank Professors Michal Borkovec and László Forró for the possibility to use the facilities in their laboratories.

#### Appendix A. Supplementary material

Supplementary data to this article can be found online at <https://doi.org/10.1016/j.jcis.2019.02.050>.

#### References

- [1] H. Wei, E.K. Wang, *Chem. Soc. Rev.* 42 (2013) 6060–6093.
- [2] Y.H. Lin, J.S. Ren, X.G. Qu, *Adv. Mater.* 26 (2014) 4200–4217.
- [3] R. Breslow, *Chem. Rec.* 1 (2001) 3–11.
- [4] G.Y. Tonga, Y.D. Jeong, B. Duncan, T. Mizuhara, R. Mout, R. Das, S.T. Kim, Y.C. Yeh, B. Yan, S. Hou, V.M. Rotello, *Nat. Chem.* 7 (2015) 597–603.
- [5] K. Kirkorian, A. Ellis, L.J. Twyman, *Chem. Soc. Rev.* 41 (2012) 6138–6159.
- [6] O. Kudina, A. Zakharchenko, O. Trotsenko, A. Tokarev, L. Ionov, G. Stoychev, N. Puretskiy, S.W. Pryor, A. Voronov, S. Minko, *Angew. Chem.-Int. Edit.* 53 (2014) 483–487.
- [7] M.A. El-Missiry, *Antioxidant Enzyme*, InTech, Rijeka, 2012.
- [8] B. D'Autreaux, M.B. Toledano, *Nat. Rev. Mol. Cell Biol.* 8 (2007) 813–824.
- [9] S. Reuter, S.C. Gupta, M.M. Chaturvedi, B.B. Aggarwal, *Free Radic. Biol. Med.* 49 (2010) 1603–1616.
- [10] J.W. Finley, A.N. Kong, K.J. Hintze, E.H. Jeffery, L.L. Ji, X.G. Lei, *J. Agric. Food Chem.* 59 (2011) 6837–6846.
- [11] C. Nirmala, M.S. Bisht, H.K. Bajwa, O. Santosh, *Trends Food Sci. Technol.* 77 (2018) 91–99.
- [12] D.F. Grishin, *Pet. Chem.* 57 (2017) 813–825.
- [13] N. Singh, M.A. Savanur, S. Srivastava, P. D'Silva, G. Mugesh, *Angew. Chem.-Int. Edit.* 56 (2017) 14267–14271.
- [14] M. Moglianetti, E. De Luca, P.A. Deborah, R. Marotta, T. Catelani, B. Sartori, H. Amenitsch, S.F. Retta, P.P. Pompa, *Nanoscale* 8 (2016) 3739–3752.
- [15] W. Zhang, S.L. Hu, J.J. Yin, W.W. He, W. Lu, M. Ma, N. Gu, Y. Zhang, *J. Am. Chem. Soc.* 138 (2016) 5860–5865.
- [16] J.L. Dong, L.N. Song, J.J. Yin, W.W. He, Y.H. Wu, N. Gu, Y. Zhang, *A.C.S. Appl. Mater. Interf.* 6 (2014) 1959–1970.
- [17] A.A. Vernekar, D. Sinha, S. Srivastava, P.U. Paramasivam, P. D'Silva, G. Mugesh, *Nat. Commun.* 5 (2014).
- [18] Y.Y. Huang, Z. Liu, C.Q. Liu, E.G. Ju, Y. Zhang, J.S. Ren, X.G. Qu, *Angew. Chem.-Int. Edit.* 55 (2016) 6646–6650.
- [19] X.H. Xia, J.T. Zhang, N. Lu, M.J. Kim, K. Ghale, Y. Xu, E. McKenzie, J.B. Liu, H.H. Yet, *ACS Nano* 9 (2015) 9994–10004.
- [20] F.Q. Yu, Y.Z. Huang, A.J. Cole, V.C. Yang, *Biomaterials* 30 (2009) 4716–4722.
- [21] H.J. Kwon, M.Y. Cha, D. Kim, D.K. Kim, M. Soh, K. Shin, T. Hyeon, I. Mook-Jung, *ACS Nano* 10 (2016) 2860–2870.
- [22] Y.Q. Wang, L.L. Li, W.B. Zhao, Y. Dou, H.J. An, H. Tao, X.Q. Xu, Y. Jia, S. Lu, J.X. Zhang, H.Y. Hu, *ACS Nano* 12 (2018) 8943–8960.
- [23] M. Vazquez-Gonzalez, W.C. Liao, R. Gazelles, S. Wang, X. Yu, V. Gutkin, I. Willner, *ACS Nano* 11 (2017) 3247–3253.
- [24] A. Pratsinis, G.A. Kelesidis, S. Zuercher, F. Krumeich, S. Bolisetty, R. Mezzenga, J. C. Leroux, G.A. Sotiriou, *ACS Nano* 11 (2017) 12210–12218.
- [25] C. Belle, J.L. Pierre, *Eur. J. Inorg. Chem.* (2003) 4137–4146.
- [26] A.J. Wu, J.E. Penner-Hahn, V.L. Pecoraro, *Chem. Rev.* 104 (2004) 903–938.
- [27] B. Sels, D. De Vos, M. Buntinx, F. Pierard, A. Kirsch-De Mesmaeker, P. Jacobs, *Nature* 400 (1999) 855–857.
- [28] P. Vanelderden, J. Vancauwenbergh, B.F. Sels, R.A. Schoonheydt, *Coord. Chem. Rev.* 257 (2013) 483–494.
- [29] M.R. Maurya, A. Kumar, J.C. Pessoa, *Coord. Chem. Rev.* 255 (2011) 2315–2344.
- [30] H. Ohtsu, Y. Shimazaki, A. Odani, O. Yamauchi, W. Mori, S. Itoh, S. Fukuzumi, *J. Am. Chem. Soc.* 122 (2000) 5733–5741.
- [31] I. Szilagyí, I. Labadi, K. Hernadi, I. Palinko, N.V. Nagy, L. Korecz, A. Rockenbauer, Z. Kele, T. Kiss, *J. Inorg. Biochem.* 99 (2005) 1619–1629.
- [32] Y.C. Fang, H.C. Lin, I.J. Hsu, T.S. Lin, C.Y. Mou, *J. Phys. Chem. C* 115 (2011) 20639–20652.
- [33] I. Szilagyí, I. Labadi, K. Hernadi, I. Palinko, I. Fekete, L. Korecz, A. Rockenbauer, T. Kiss, *New J. Chem.* 29 (2005) 740–745.
- [34] I. Szilagyí, I. Labadi, K. Hernadi, T. Kiss, I. Palinko, *Molecular Sieves: From Basic Research to Industrial Applications*, Pts a and b, 2005, pp. 1011–1018.
- [35] Z. Csendes, C. Dudas, G. Varga, E.G. Bajnóczi, S.E. Canton, P. Sipos, I. Palinko, *J. Mol. Struct.* 1044 (2013) 39–45.
- [36] M. Yang, W. Jiang, Z.Q. Pan, H. Zhou, *J. Inorg. Organomet. Polym. Mater.* 25 (2015) 1289–1297.
- [37] L.H. Zhang, C. Gu, J. Xiong, M. Yang, Y. Guo, *Sci. China-Chem.* 58 (2015) 731–737.
- [38] K. Sengupta, S. Chatterjee, A. Dey, *ACS Catal.* 6 (2016) 1382–1388.
- [39] R.M. Daniel, M. Dines, H.H. Petach, *Biochem. J.* 317 (1996) 1–11.
- [40] Z.P. Xu, G.S. Stevenson, C.Q. Lu, G.Q.M. Lu, P.F. Bartlett, P.P. Gray, *J. Am. Chem. Soc.* 128 (2006) 36–37.
- [41] M. Pavlovic, P. Rouster, I. Szilagyí, *Nanoscale* 9 (2017) 369–379.
- [42] S. Stoll, A. Schweiger, *J. Magn. Reson.* 178 (2006) 42–55.
- [43] C. Beaucham, I. Fridovich, *Anal. Biochem.* 44 (1971) 276–287.
- [44] Q. Wang, D. O'Hare, *Chem. Rev.* 112 (2012) 4124–4155.
- [45] G. Choi, H. Piao, M.H. Kim, J.H. Choy, *Ind. Eng. Chem. Res.* 55 (2016) 11211–11224.
- [46] C. Forano, F. Bruna, C. Mousty, V. Prevot, *Chem. Rec.* 18 (2018) 1150–1166.
- [47] Z. Gu, J.J. Atherton, Z.P. Xu, *Chem. Commun.* 51 (2015) 3024–3036.
- [48] S. Vial, V. Prevot, F. Leroux, C. Forano, *Micropor. Mesopor. Mat.* 107 (2008) 190–201.
- [49] V.J. Nagaraj, X. Sun, J. Mehta, M. Martin, T. Ngo, S.K. Dey, *J. Nanotech.* 2015 (2015) 350370.
- [50] N.K. Singh, Q.V. Nguyen, B.S. Kim, D.S. Lee, *Nanoscale* 7 (2015) 3043–3054.
- [51] M. Pavlovic, P. Rouster, T. Oncsik, I. Szilagyí, *ChemPlusChem* 82 (2017) 121–131.

- [52] C. Vasti, A. Borgiallo, C.E. Giacomelli, R. Rojas, *Coll. Surf. A* 533 (2017) 316–322.
- [53] V. Hornok, A. Erdohelyi, I. Dekany, *Coll. Polym. Sci.* 283 (2005) 1050–1055.
- [54] M. Pavlovic, M. Adok-Sipiczki, C. Nardin, S. Pearson, E. Bourgeat-Lami, V. Prevot, I. Szilagy, *Langmuir* 31 (2015) 12609–12617.
- [55] S.Y. Park, R.F. Bruinsma, W.M. Gelbart, *Europhys. Lett.* 46 (1999) 454–460.
- [56] J.Y. Carrillo, A.V. Dobrynin, *Langmuir* 23 (2007) 2472–2482.
- [57] J.A. Smith, O. Werzer, G.B. Webber, G.G. Warr, R. Atkin, *J. Phys. Chem. Lett.* 1 (2010) 64–68.
- [58] M. Kobayashi, M. Skarba, P. Galletto, D. Cakara, M. Borkovec, *J. Coll. Interf. Sci.* 292 (2005) 139–147.
- [59] M. Elimelech, J. Gregory, X. Jia, R.A. Williams, *Particle Deposition and Aggregation: Measurement, Modeling, and Simulation*, Butterworth-Heinemann Ltd., Oxford, 1995.
- [60] D.F. Evans, H. Wennerstrom, *The Colloidal Domain*, John Wiley, New York, 1999.
- [61] J.H. Lee, S.W. Rhee, D.Y. Jung, *Bull. Korean Chem. Soc.* 26 (2005) 248–252.
- [62] C.Y. Wang, M.H. Cui, *J. Appl. Polym. Sci.* 88 (2003) 1632–1636.
- [63] B.L. Li, X.L. Lu, Y.H. Ma, Z. Chen, *Eur. Polym. J.* 60 (2014) 255–261.
- [64] S. Muráth, S. Sáringer, Z. Somosi, I. Szilagy, *Coll. Interf.* 2 (2018) 32.
- [65] C. Schneider, M. Hanisch, B. Wedel, A. Jusufi, M. Ballauff, *J. Coll. Interf. Sci.* 358 (2011) 62–67.
- [66] I. Popa, G. Papastavrou, M. Borkovec, *Phys. Chem. Chem. Phys.* 12 (2010) 4863–4871.
- [67] Y.K. Leong, *Coll. Polym. Sci.* 277 (1999) 299–305.
- [68] E. Illes, E. Tombacz, *J. Coll. Interf. Sci.* 295 (2006) 115–123.
- [69] A. Tiraferri, L.A.S. Hernandez, C. Bianco, T. Tosco, R. Sethi, *J. Nanopart. Res.* 19 (2017).
- [70] J.S. Richardson, K.A. Thomas, B.H. Rubin, D.C. Richardson, *Proc. Natl. Acad. Sci. USA.* 72 (1975) 1349–1353.
- [71] C.G. Zhang, C.Y. Duan, Q. Hu, D.Y. Yan, *J. Chem. Crystallogr.* 29 (1999) 1153–1155.
- [72] G. Lagaly, O. Mecking, D. Penner, *Coll. Polym. Sci.* 279 (2001) 1090–1096.
- [73] M. Pavlovic, R. Huber, M. Adok-Sipiczki, C. Nardin, I. Szilagy, *Soft Matter* 12 (2016) 4024–4033.
- [74] W.S. Terra, S.S. Ferreira, R.O. Costa, L.L. Mendes, R.W.A. Franco, A.J. Bortoluzzi, J. Resende, C. Fernandes, A. Horn, *Inorg. Chim. Acta* 450 (2016) 353–363.
- [75] M. Mureseanu, M. Puscasu, S. Somacescu, G. Carja, *Catal. Lett.* 145 (2015) 1529–1540.

## PAPER



Cite this: *Dalton Trans.*, 2021, **50**, 2426

# Catalytic antioxidant nanocomposites based on sequential adsorption of redox active metal complexes and polyelectrolytes on nanoclay particles†

Zoltán Somosi,<sup>a</sup> Nóra V. May,<sup>b</sup> Dániel Sebők,<sup>c</sup> István Pálinkó <sup>d</sup> and István Szilágyi \*<sup>a</sup>

An antioxidant nanocomposite was prepared by successive adsorption of redox active metal complexes (copper(II)–bipyridyl and iron(III)–citrate) and polyelectrolytes (poly(styrene sulfonate) and poly(diallyldimethyl ammonium)) on layered double hydroxide nanoclay. The experimental conditions were optimized in each preparation step and thus, the final composite formed highly stable colloids, *i.e.*, excellent resistance against salt-induced aggregation was achieved. Due to the synergistic effect of the metal complexes, the developed composite showed remarkable activity in the dismutation of superoxide radicals, close to the one determined for the native superoxide dismutase enzyme. The obtained composite is highly selective for superoxide radical dismutation, while its activity in other antioxidant tests was close to negligible. Structural characterization of the composite revealed that the excellent superoxide radical scavenging ability originated from the advantageous coordination geometry around the copper(II) center formed upon immobilization. The structure formed around the metal centers led to optimal redox features and consequently, to an improved superoxide dismutase-like activity. The catalytic antioxidant composite is a promising candidate to reduce oxidative stress in industrial manufacturing processes, where natural enzymes quickly lose their activity due to the harsh environmental conditions.

Received 8th December 2020,  
Accepted 21st January 2021

DOI: 10.1039/d0dt04186f

rsc.li/dalton

## 1. Introduction

Combating oxidative stress *via* decomposition of reactive oxygen species (ROS) attracts widespread contemporary interest due to its importance in both health-related and industrial processes.<sup>1</sup> Accordingly, an elevated ROS level is responsible for the development of numerous diseases including cancer,<sup>2,3</sup> while their presence in manufacturing processes leads to reduced-quality commercial products in the food, textile and cosmetics industries.<sup>4–6</sup> The decomposition of ROS is naturally carried out by enzymatic (*e.g.*, superoxide dismutase, catalase

and various peroxidases) and molecular (*e.g.*, flavonoids, vitamins and tannins) antioxidants.<sup>7</sup> The most efficient ones are the enzymes, but their high sensitivity to temperature, pH, ionic strength and other factors makes them complicated to combat oxidative stress under harsh environmental conditions. This fact especially prevents their industrial application.

Natural enzymes may be replaced with artificial ones with improved resistance against the above-mentioned effects. Two major directions exist to develop enzyme mimicking compounds. First, nanomaterials with antioxidant activity attract widespread interest in the scientific and technological communities.<sup>8–11</sup> These nanomaterials, the so-called nanozymes, usually contain redox active metals such as iron,<sup>12</sup> cerium<sup>13</sup> or manganese,<sup>14</sup> which are responsible for the reaction with ROS. Second, transition metal complexes with structures similar to the active centers of antioxidant enzymes can be synthesized and used as antioxidant agents.<sup>15–17</sup> Literature data shed light on the fact that appropriate structural mimicking usually gave rise to considerable functional mimicking too, *i.e.*, once the active center was modelled adequately, the complexes possessed high ROS scavenging ability.<sup>18–22</sup>

<sup>a</sup>MTA-SZTE Lendület Biocolloids Research Group, Interdisciplinary Research Center, Department of Physical Chemistry and Materials Science, University of Szeged, H-6720 Szeged, Hungary. E-mail: szisztvan@chem.u-szeged.hu

<sup>b</sup>Centre for Structural Science, Research Centre for Natural Sciences, Hungarian Academy of Sciences, H-1117 Budapest, Hungary

<sup>c</sup>Department of Applied and Environmental Chemistry, University of Szeged, H-6720 Szeged, Hungary

<sup>d</sup>Department of Organic Chemistry, University of Szeged, H-6720 Szeged, Hungary

† Electronic supplementary information (ESI) available: Preparation method of samples for EPR measurements; XRD diffractogram; IR spectrum; measured and simulated EPR spectra. See DOI: 10.1039/d0dt04186f



Although promising antioxidant nanomaterials and metal complexes have been reported in the past, various drawbacks (*e.g.*, tendency for aggregation or considerable toxicity for nanoparticles and difficult separation or metal ion leakage for complexes) indicated that these research directions should be combined to develop efficient radical scavenging systems through immobilization of redox active coordination compounds on suitable nanoparticulate supports. Accordingly, considerable catalase mimicking activity was achieved by a manganese(II)-poly-L-histidine complex anchored to carboxylate modified multi-walled carbon nanotubes.<sup>23</sup> Due to their biocompatibility and advantageous surface properties, silica particles were proven to be suitable solid supports for enzyme mimicking complexes; therefore, various copper(II) complexes were attached to their surfaces.<sup>24–29</sup> Polymer-based latex particles were decorated with amino acids *via* covalent bonds and copper(II) complexes of considerable superoxide dismutase-like activity were prepared by adding metal salts to latex-amino acid hybrids.<sup>30</sup> Lamellar cationic clays were also used to immobilize metal complexes through electrostatic interactions due to their considerable cation exchange capacity.<sup>31,32</sup> However, the intercalation of the complexes between the lamellae hindered the diffusion of ROS to the catalytic centers and the elimination of the products, especially upon gas formation. Although a considerable amount of metal complexes could be immobilized with the above methods, their application in liquid environments was limited due to the tendency of the antioxidant composite particles for aggregation and subsequent sedimentation, which leads to significant loss of the enzyme-like activity.

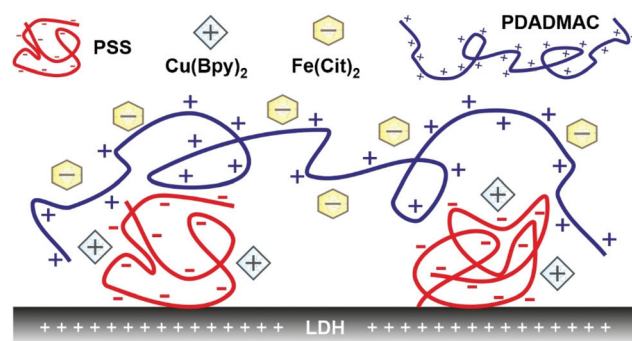
One of the ways to immobilize metal complexes and to maintain colloidal stability of the resulting material is the use of polyelectrolytes for surface functionalization of the enzyme mimicking composites. Polyelectrolytes are applied as efficient stabilizing agents for particle dispersions through repulsive electrostatic and intermolecular steric interactions arising upon their adsorption on oppositely charged surfaces.<sup>33–38</sup> For instance, in a recent contribution,<sup>39</sup> a poly(vinylpyridine-*b*-methacrylic acid) block co-polyelectrolyte was used to functionalize layered double hydroxide (LDH) nanoclay particles. The poly(methacrylic acid) part was responsible for the strong attachment to the particle surface, while copper(II)-histamine complexes were anchored *via* coordination bonds between the metal ions and the nitrogen donor atoms of the poly(vinylpyridine) part. In this way, the polyelectrolyte part provided not only remarkable colloidal stability but also excellent structural (no metal ion leakage) and functional (the composite was able to scavenge superoxide radicals even at high temperatures, where the natural antioxidant enzymes quickly lost the activity) stabilities. These literature data prompted the idea to use polyelectrolytes for immobilization of metal complexes on nanoparticle supports *via* surface functionalization. Besides, to widen the spectrum of the antioxidant activity, attachment of complexes of various metal ions to the same particle support is desired.

Therefore, the aim of the present study was to develop nanocomposites by sequential adsorption of polyelectrolytes and metal complexes onto the surface of LDH particles. Such self-assembled multilayers of polyelectrolytes have been widely used to immobilize various ROS scavenging or other bioactive molecules, but mostly on planar surfaces.<sup>40–43</sup> Only a few studies reported immobilization of enzymatic<sup>44,45</sup> or molecular<sup>46</sup> antioxidants on nanoparticles with this technique and no ROS scavenging complexes have been embedded into polyelectrolyte layers to date. It was demonstrated earlier in our group that building oppositely charged polyelectrolyte layers on LDH particles is feasible, once the appropriate dose of the polyelectrolytes is used in the steps of the sequential adsorption procedure.<sup>47</sup> This strategy was accompanied by the optimization of colloidal stability to obtain homogeneously distributed composite particles. Here, LDH particles were also used as the substrate due to their many positive aspects such as variable composition, biocompatibility, tuneability of size down to the nanoscale with low polydispersity, and relatively easy and cheap synthesis.<sup>34,48–50</sup> Two types of polyelectrolytes (poly(styrene sulfonate) (PSS) and poly(diallyldimethyl ammonium) (PDADMAC)) and metal complexes (copper(II)-bipyridyl ( $\text{Cu}(\text{Bpy})_2$ ) and iron(III)-citrate ( $\text{Fe}(\text{Cit})_2$ )) were applied in the sequential adsorption process to build the hybrid catalytic material (denoted as **COMP** hereafter; see Scheme 1). The structural features were investigated by X-ray diffraction (XRD), scanning electron microscopy (SEM), and electron paramagnetic resonance (EPR) and infrared (IR) spectroscopy; the colloidal stability was probed by light scattering methods, while the antioxidant activity was assessed by colorimetric assays based on UV-Visible (UV-Vis) spectroscopy measurements. To the best of our knowledge, this is the first study reporting co-immobilization of catalytic metal complexes by the sequential adsorption method on LDH particles to combat oxidative stress.

## 2. Experimental

### 2.1. Materials

Magnesium(II) chloride hexahydrate, iron(III) chloride hexahydrate, copper(II) chloride dihydrate, 4 M sodium hydroxide



**Scheme 1** Illustration of the schematic structure of the **COMP** hybrid material composed of PSS,  $\text{Cu}(\text{Bpy})_2$ ,  $\text{Fe}(\text{Cit})_2$  and PDADMAC immobilized on LDH nanoparticles.

(NaOH) stock solution, sodium chloride (NaCl), trisodium citrate dihydrate, ammonium acetate, methanol and the 2,2-diphenyl-1-picrylhydrazyl (DPPH) radical were all purchased from VWR International (Radnor, USA) with analytical purity and were used as received. Aluminum(III) chloride hexahydrate and xanthine were acquired in analytical grade from Alfa Aesar (Karlsruhe, Germany). 2,2'-Bipyridyl (99%) and nitro blue tetrazolium (90%, NBT) chloride monohydrate were purchased from Acros Organics (Geel, Belgium). Xanthine oxidase from bovine milk was purchased from Sigma-Aldrich. The sodium salt of poly(styrene sulfonate) (PSS, molecular mass of 10 kg mol<sup>-1</sup>) and 20 weight% aqueous poly(diallyldimethyl ammonium) chloride (PDADMAC, average molecular mass of 275 kg mol<sup>-1</sup>) solution were purchased from Sigma-Aldrich (Budapest, Hungary). Ultrapure water was produced by reverse osmosis and UV irradiation using a Puranity TU 3 + UV/UF system (VWR International).

## 2.2. Synthesis of LDH particles

The LDH particles were composed of magnesium(II) and aluminum(III) ions at a 2 : 1 molar ratio and chloride ions were the interlayer anions. The synthetic method was flash co-precipitation followed by hydrothermal post treatment to optimize the size distribution.<sup>51</sup> Accordingly, 15 mL of a mixed salt solution of magnesium(II) (3.0 mmol) and aluminum(III) (1.5 mmol) chloride was poured into 60 mL of vigorously stirred NaOH solution (0.15 M), which was stirred for an additional 30 min under a N<sub>2</sub> atmosphere to avoid carbonation. The freshly formed LDH precipitate was centrifuged to separate from the supernatant and washed five times with water. The obtained slurry was diluted with 50 mL water and was sonicated for 10 min in an ultrasonic bath, and then transferred to a stainless steel autoclave with a Teflon lining (Col-Int Tech, Irmo, USA), which was sealed and placed in a pre-heated oven at 120 °C for 24 h for hydrothermal post treatment. After the procedure was terminated, the autoclave was allowed to cool to room temperature, and the obtained material was centrifuged and washed with water several times. The final LDH material was dried and redispersed into a stock dispersion of 10 g L<sup>-1</sup> particle concentration. The successful formation of LDH was confirmed by XRD (Fig. S1a†) and IR spectroscopy (Fig. S1b†). As shown in the ESI,† the diffractogram and the spectrum showed the characteristic peaks reported for LDH materials earlier.<sup>34,48,49,51,52</sup>

## 2.3. XRD

The XRD measurements were carried out using a PW 1830 diffractometer (Philips, Amsterdam, The Netherlands), which applies Cu-K radiation and operates in Bragg-Brentano geometry with a Ni filter at a voltage of 40 kV and a current of 30 mA. The diffractograms were recorded in the 4–80°2-θ range with a step size of 0.02°. The powder samples were placed on a glass zero background holder for the acquisition of the XRD patterns.

## 2.4. Spectroscopy

The IR spectra were measured on a Bio-Rad Digilab Division FTS-65A/896 apparatus, equipped with a diffuse reflectance spectroscopy accessory. In a typical measurement, 256 scans were collected with 4 cm<sup>-1</sup> resolution in the 4000–600 cm<sup>-1</sup> wavenumber range.

The antioxidant assays were carried out by recording the UV-Vis spectra with a Genesys 10S spectrophotometer (Thermo Scientific, Waltham, USA). The wavelength range used was 190–1100 nm with 0.1 nm scaling.

EPR spectra were recorded with a Bruker EleXsys E500 spectrometer (microwave frequency 9.54 GHz, microwave power 13 mW, modulation amplitude 5 G, modulation frequency 100 kHz). The details of the sample preparation used in the EPR measurements are presented in Table S1 (in the ESI†). To record frozen solution spectra, 0.20 mL samples were mixed with 0.05 mL of methanol (to avoid crystallization of water) and transferred into quartz EPR tubes, and the spectra were recorded in a Dewar flask containing liquid nitrogen (77 K). The spectra were simulated using the “epr” program.<sup>53</sup> The spectra of Fe(Cit)<sub>2</sub> were measured separately and for the iron-containing samples, this broad singlet background signal was eliminated in order to be able to simulate the copper(II) spectrum components. The anisotropic EPR spectra were analyzed considering axial or rhombic *g*-tensors (*g<sub>x</sub>*, *g<sub>y</sub>*, *g<sub>z</sub>*) and copper hyperfine tensors (*A<sub>x</sub>*, *A<sub>y</sub>*, *A<sub>z</sub>*). The nitrogen superhyperfine structure was determined taking into account a rhombic hyperfine tensor (*a<sub>x</sub><sup>N</sup>*, *a<sub>y</sub><sup>N</sup>*, *a<sub>z</sub><sup>N</sup>*) in which the *x*, *y*, *z* directions referred to the *g*-tensor orientations. Orientation-dependent linewidth parameters (*α*, *β*, and *γ*) were used to fit the linewidths through the equation  $\sigma M_1 = \alpha + \beta M_1 + \gamma M_1^2$ , where *M*<sub>1</sub> denotes the magnetic quantum number of the copper(II) ion. Since natural copper(II) chloride was used for the measurements, the spectra were calculated by the summation of the <sup>63</sup>Cu and <sup>65</sup>Cu spectra weighed by their natural abundances. The hyperfine and superhyperfine coupling constants and the relaxation parameters were obtained in field units (Gauss = 10<sup>-4</sup> T).

## 2.5. Light scattering

Electrophoretic mobility values were measured by the phase analysis-based electrophoretic light scattering technique using a LiteSizer 500 (Anton Paar, Graz, Austria) device. Omega-shaped plastic capillary cuvettes (Anton Paar) were used for the measurements. The sample preparation process involved the mixing of a calculated amount of water, the polyelectrolyte and NaCl stock solutions to adjust the polyelectrolyte concentration and the ionic strength. The total volume of these mixtures was always 1.8 mL. The process was completed by adding 0.2 mL of 100 mg L<sup>-1</sup> LDH stock dispersion. The samples were then allowed to rest for 2 h at room temperature. The capillary cuvettes were flushed with the majority of the dispersions and the last 0.35 mL was used for the actual experiment. The reported electrophoretic mobility values were the average of

five individual measurements and their mean error was about 5%.

The time-resolved dynamic light scattering (DLS) technique was used to study the aggregation processes under different experimental conditions. The measurements were carried out with a Litesizer 500 instrument (Anton Paar) equipped with a 40 mW semiconductor laser operating at 658 nm wavelength in the backscattering mode at a scattering angle of 175°. The hydrodynamic radii were calculated with the Stokes–Einstein equation from the diffusion coefficients, which were determined by applying the cumulant method to fit the correlation function.<sup>54</sup> In an aggregating dispersion, the slopes obtained by the linear fits on the hydrodynamic radius *versus* time data were used to calculate the apparent aggregation rates.<sup>55</sup> The colloidal stability of the particles was expressed in terms of the stability ratio,<sup>56</sup> which is 1 by definition for unstable and quickly aggregating dispersions. Higher stability ratios refer to slower aggregation and more stable systems. The sample preparation procedures in the time-resolved DLS study were the same as in the electrophoretic mobility measurements, with the exception that the experiments were commenced immediately after the addition of the LDH stock dispersion followed by quick vortexing.

## 2.6. Microscopy

The morphology of the solids was characterized by using a Hitachi S-4700 scanning electron microscope. The surface of the samples was covered with gold *via* physical vapor deposition before the measurements which were conducted with 10 kV accelerating voltage. The samples were pre-emptively sonicated for 10 min prior to the experiments to eliminate particle aggregates. The dispersions were dried in the instrument.

## 2.7. Dismutation of superoxide radicals

For determining the superoxide radical scavenging activity of the adsorbed complexes, the Fridovich method was used.<sup>57</sup> The test systems contained xanthine and xanthine oxidase to produce superoxide radicals and NBT as a scavenger indicator. To carry out a probe reaction, 0.1 mL of 3 mM xanthine, 0.1 mL of 3 mM NBT and 0.3 mL of 3 mg mL<sup>-1</sup> xanthine oxidase solutions were mixed together followed by the addition of 0.1–2.5 mL of the composite stock dispersion. The above solutions were all prepared in phosphate buffer at pH 7.5 applying a total phosphate concentration of 1 mM. Upon the reduction of the NBT by superoxide radicals, its color changed from yellow to blue and the appearance of an absorption peak at 565 nm was followed with a spectrophotometer. Blank (without added catalyst) measurements were carried out and changes in the absorbance in these reference experiments were used to calculate the inhibition of the NBT–superoxide radical reaction at several concentrations of the antioxidant material.

## 2.8. Scavenging of DPPH radicals

The DPPH scavenging activity of the catalytic composites was evaluated by a standard assay.<sup>58</sup> Accordingly, in a typical test,

60 μM of DPPH was dissolved in 3500 μL of methanol and 100 μL of the catalytic material was added into the system followed by quick homogenization. During the reaction, the change in the concentration of violet-colored DPPH was followed by measuring the absorbances at 517 nm wavelength with a spectrophotometer, *i.e.*, decreases in the absorbances corresponded to the decrease in the radical concentration. The remaining DPPH percentage was then calculated to quantify the activity of the composite material.

# 3. Results and discussion

## 3.1. Assessment of charging and aggregation features during sequential adsorption

For the preparation of **COMP**, the sequential adsorption process, which included PSS, Cu(Byp)<sub>2</sub>, PDADMAC and Fe(Cit)<sub>2</sub> immobilization on the LDH surface, was applied. To optimize the experimental conditions in each step, electrophoretic mobilities and stability ratios were measured at different concentrations of the adsorbing substance (Fig. 1). The results were crucial to determine the dose of the polyelectrolytes and the concentration of the metal complexes to obtain stable particle dispersions in the individual steps.

First, PSS was adsorbed on the LDH support; the corresponding electrophoretic mobility and stability ratio data are shown in Fig. 1a. The LDH particles possess positive structural charge,<sup>34</sup> which is reflected in positive electrophoretic mobilities at low PSS doses. On increasing the polyelectrolyte loading, the mobility data showed a decrease due to the adsorption of PSS on the oppositely charged surface. The surface charge was neutralized around 10 mg g<sup>-1</sup> and further increase in the PSS dose gave rise to charge reversal. The adsorption process continued until surface saturation, which occurred after 100 mg g<sup>-1</sup>. Beyond this dose, there was no significant change in electrophoretic mobility values indicating that the further added PSS remained dissolved in the solution.

The speed of aggregation was investigated at different PSS doses in time-resolved DLS experiments, in which the stability ratios were determined.<sup>55</sup> Their values were close to unity in the case of fast (or diffusion controlled) aggregation, while high stability ratios refer to slower aggregation. In other words, the inverse of the stability ratio equals to the fraction of particle collisions, which results in dimer formation. The data shown in Fig. 1a indicate fast particle aggregation at doses close to the charge neutralization point, while the stability ratios increased away from this region, either at the low or high PSS dose sides. These results can be interpreted well within the DLVO (Derjaguin, Landau, Verwey and Overbeek) theory.<sup>33–35</sup> Accordingly, the presence of appropriately high surface charges leads to particle stabilization through electrical double layer forces, while attractive van der Waals forces predominate once the surface charges and thus the electrical double layer vanish, like the conditions at the charge neutralization point in the present system. These surface charge and aggregation features are typical for systems containing par-

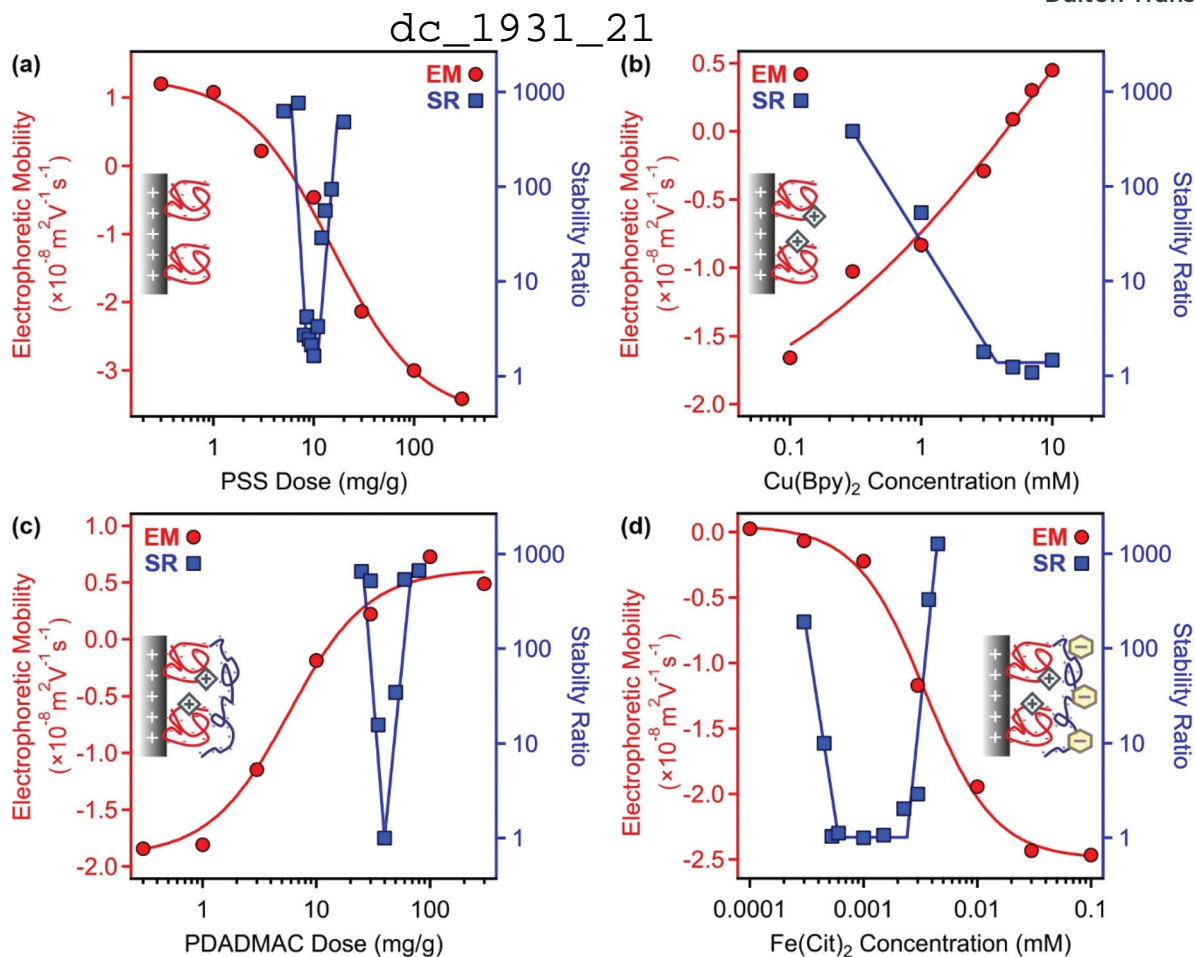


**Fig. 1** Electrophoretic mobilities (EM, circles) and stability ratios (SR, squares) determined in the LDH–PSS (a), LDH–PSS–Cu(Bpy)<sub>2</sub> (b), LDH–PSS–Cu(Bpy)<sub>2</sub>–PDADMAC (c) and LDH–PSS–Cu(Bpy)<sub>2</sub>–PDADMAC–Fe(Cit)<sub>2</sub> (COMP) (d) systems. The particle concentration was always 10 mg L<sup>-1</sup> and the solid lines are just eye guides. The mg g<sup>-1</sup> unit on the x-axis of (a) and (c) indicates mg polyelectrolyte per 1 gram of particle.

ticles and oppositely charged polyelectrolytes.<sup>33–35,38,39,47</sup> For further experiments, a PSS dose of 100 mg g<sup>-1</sup> was chosen (denoted as LDH–PSS thereafter), since these particles possess high negative charge and form stable dispersions under these experimental conditions.

Second, adsorption of Cu(Bpy)<sub>2</sub> was followed on the LDH–PSS particles. To prepare the complex, the metal ions and the ligands were dissolved and mixed in a 1:2 molar ratio. Literature data<sup>59–61</sup> suggest that in Cu(Bpy)<sub>2</sub>, the copper(II) ions are coordinated by four nitrogen atoms of the ligands in solutions. Besides, Cu(Bpy) complexes may also be present in a smaller extent. Therefore, the overall charge of the complexes is considered to be positive. Indeed, the electrophoretic mobility values increased with progressive addition of the complexes due to their adsorption on the oppositely charged LDH–PSS (Fig. 1b). Charge neutralization and slight charge reversal were observed at high complex concentrations, which were close to the solubility limit of the ligand. The stability ratios decreased by increasing the Cu(Bpy)<sub>2</sub> concentration and became unity after a threshold value, which resembles the critical coagulation concentration (CCC) reported for charged particles dispersed in salt solutions.<sup>33,34,56</sup> Since the goal of

this study was to identify the conditions in which the Cu(Bpy)<sub>2</sub>-decorated LDH–PSS forms a stable dispersion, 0.1 mM complex concentration was applied in further experiments. The obtained composite was named LDH–PSS–Cu(Bpy)<sub>2</sub>. Note that this substance has a net negative charge.

Third, PDADMAC was adsorbed on the LDH–PSS–Cu(Bpy)<sub>2</sub> particles. In general, very similar tendencies were observed to the ones in Fig. 1a measured for PSS adsorption. Electrophoretic mobility data clearly indicate that PDADMAC strongly adsorbs on the oppositely charged surface (Fig. 1c). Charge neutralization and reversal occurred at appropriate PDADMAC doses and the adsorption process continued until surface saturation, which was indicated by a plateau in the mobility values. The onset of this plateau was defined at 100 mg g<sup>-1</sup> loading. Stability ratio measurements revealed that the dispersions were highly stable at this PDADMAC concentration, *i.e.*, their values were extremely high at 100 mg g<sup>-1</sup> dose. Therefore, this dose was chosen (LDH–PSS–Cu(Bpy)<sub>2</sub>–PDADMAC) for the final functionalization with the Fe(Cit)<sub>2</sub> complexes.

Fourth, electrophoretic mobilities and stability ratios were determined for the LDH–PSS–Cu(Bpy)<sub>2</sub>–PDADMAC particles at



dc\_1931\_21

different  $\text{Fe}(\text{Cit})_2$  concentrations (Fig. 1d). Speciation in aqueous solutions containing iron(III) and citrate ions was frequently investigated in the past. The published results indicate that mixed hydroxy-citrate complexes may also form in the system; however, the species are all negatively charged.<sup>62,63</sup> The mobility data underline this information, since they decreased with the complex concentration due to adsorption on the oppositely charged surface. Charge neutralization occurred already at very low  $\text{Fe}(\text{Cit})_2$  loadings indicating its very strong affinity to the LDH-PSS-Cu(Bpy)<sub>2</sub>-PDADMAC particles leading to charge neutralization and very pronounced charge reversal at certain complex concentrations. Such a strong adsorption originates from electrostatic and hydrogen bonding interactions. The trend of the stability ratios resembles the ones measured upon polyelectrolyte adsorption for PSS and PDADMAC in the first and third steps of the sequential adsorption process. Accordingly, once the charges were low, *i.e.*, close to the charge neutralization point, the dispersions were unstable and fast particle aggregation was observed indicated by stability ratios of about 1. On the other hand, stable dispersions formed at  $\text{Fe}(\text{Cit})_2$  concentrations away from the charge neutralization point. Such a trend is qualitatively in line with the DLVO theory, as discussed above. To form the final COMP hybrid particle, 0.1 mM  $\text{Fe}(\text{Cit})_2$  concentration was chosen, under which conditions the composite possesses significant negative charge (zeta potential is -31.6 mV) and forms a highly stable dispersion, *i.e.*, stability ratios could not be determined in its aqueous dispersion at low ionic strength. Therefore, COMP was used in further structural and antioxidant investigations.

### 3.2. Structural and colloidal characterization of COMP

The SEM images were taken after drying the COMP dispersions. The morphology of the hybrid is similar to LDH materials prepared by the combined co-precipitation-hydrothermal treatment method earlier.<sup>48,51</sup> Accordingly, platelets of rounded edges can be discovered in the images. The lateral size of COMP was in the 150–200 nm range (Fig. 2).

EPR spectroscopy was used to explore the coordination geometry around the iron(III) and copper(II) ions with the help of samples prepared with and without nanoparticulate support. The EPR spectra of  $\text{Fe}(\text{Cit})_2$  (Fig. S2†) was a broad singlet line at 77 K due to fast relaxation; therefore, this background signal was eliminated from the iron(III) containing spectra and

copper(II) spectra have only been simulated. The EPR spectra of  $\text{Cu}(\text{Byp})_2$  was measured in aqueous solution at pH ~ 7 and this spectrum could be simulated by the sum of 25% mono- and 75% bis-ligand complex spectra (Fig. 3a).

The spectra of the copper(II)-bipyridyl solution have already been measured by Garribba *et al.*,<sup>64</sup> and it was found that the mono-ligand  $\text{Cu}(\text{Bpy})$  complex possesses the usual *g*-tensor

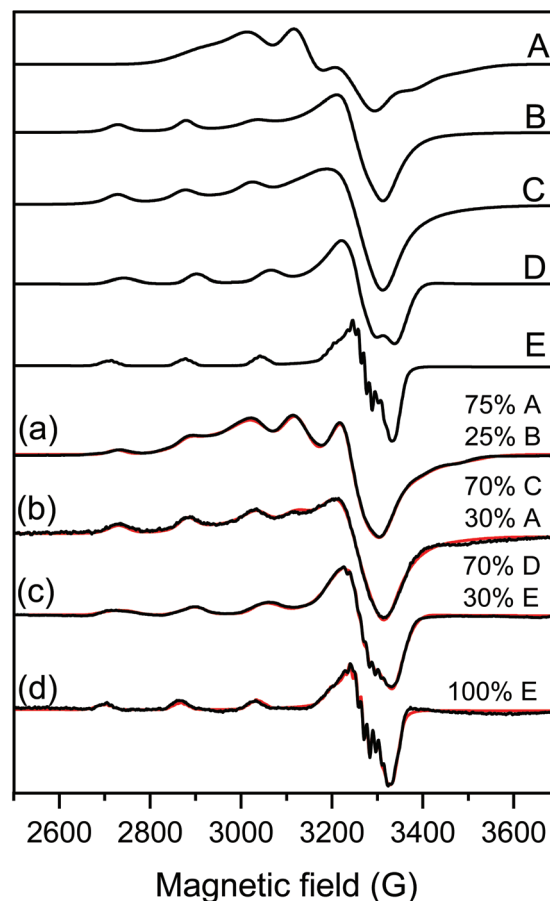


Fig. 3 Measured (black) and simulated (red) EPR spectra of samples containing (a)  $\text{Cu}(\text{Bpy})_2$  solution, (b) 100 ppm LDH-PSS-Cu(Bpy)<sub>2</sub>, (c)  $[\text{Cu}(\text{Bpy})_2]$  and  $[\text{Fe}(\text{Cit})_2]$  in aqueous solution and (d) 100 ppm COMP. For the details of sample preparation, see Table S1.† The spectra were simulated with the help of component spectra A:  $\text{Cu}(\text{Bpy})_2$ , B:  $\text{Cu}(\text{Bpy})$ , C: LDH-PSS-Cu(Bpy)<sub>2</sub>, D:  $\text{Cu}(\text{Bpy})_2(\text{Cit})$  and E:  $\text{Cu}(\text{Bpy})(\text{Cit})$  described with the EPR parameters listed in Table 1.

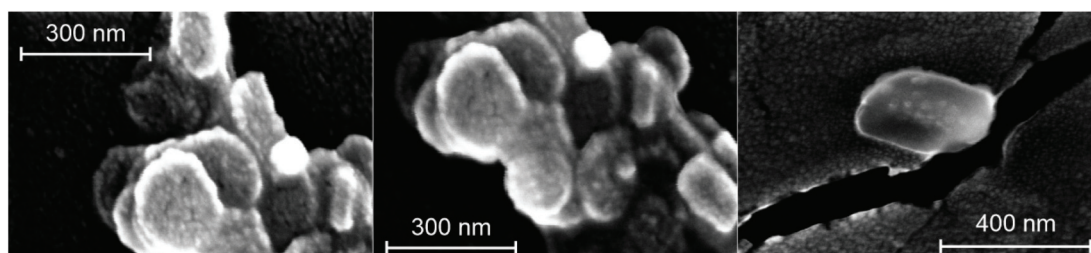


Fig. 2 SEM images of COMP. The measurements were performed after drying the dispersions.

dc\_1931\_21

Table 1 Anisotropic EPR parameters of components obtained in the simulation of the EPR spectra<sup>a</sup>

Coordination compound	$g_x$	$g_y$	$g_z$	$A_x$ (G)	$A_y$ (G)	$A_z$ (G)	$a_z^{N1}$ (G)	$a_z^{N2}$ (G)
							$a_{N1}^x$ (G)	$a_{N1}^y$ (G)
Cu(Bpy) <sub>2</sub>	2.177	2.177	2.017	83.7	83.7	75.8		
Cu(Bpy)	2.066	2.066	2.274	12.6	12.6	154.7		
LDH-PSS-Cu(Bpy) <sub>2</sub>	2.062	2.062	2.280	14.0	14.0	147.8		
Cu(Bpy) <sub>2</sub> (Cit)	2.063	2.063	2.259	23.5	23.5	157.0		
Cu(Bpy)(Cit)	2.065	2.051	2.283	4.8	14.6	163.8	11.4	12.7
							12.6	7.7
							10.6	13.8

<sup>a</sup>The experimental errors were  $\pm 0.001$  for  $g$  and  $\pm 1$  G for  $A$  and  $a_N$ .

values ( $g_x \sim g_y < g_z$ ) showing an elongated octahedral geometry, while the bis-ligand Cu(Bpy)<sub>2</sub> complex spectra show an opposite  $g$ -tensor trend ( $g_x \sim g_y > g_z$ ), which suggests trigonal bipyramidal geometry for this complex (Table 1).

This latter structure was found in the solid state where two Bpy coordinated in the equatorial-axial position and one water molecule occupied the third equatorial position in the single crystal structure of Cu(Bpy)<sub>2</sub>(H<sub>2</sub>O)·2PF<sub>6</sub>.<sup>65</sup> For LDH-PSS-Cu(Bpy)<sub>2</sub> (Fig. 3b), the obtained spectrum could be simulated with the sum of 30% Cu(Bpy)<sub>2</sub> and 70% of a new component with parameters close to the mono-complex (Table 1). Therefore, this new component is most likely the mono-complex Cu(Bpy). The EPR spectra of Cu(Bpy)<sub>2</sub> were recorded after adding Fe(Cit)<sub>2</sub> in solution without the nanoparticles (Fig. 3c) and it was found that the spectra were significantly different. These spectral changes can be due to the coordination of the Cit ligand to the copper(II)-bipyridyl complexes resulting in the mixed ligand complexes Cu(Bpy)(Cit) and Cu(Bpy)<sub>2</sub>(Cit), both with elongated octahedral geometries. For COMP (Fig. 3d), the EPR spectra could be fitted with the Cu(Bpy)(Cit) component spectra suggesting that adsorption on

COMP does not affect the EPR parameters significantly. However, it makes this mixed ligand complex exclusive in this complex system. The nitrogen superhyperfine structure clearly confirms the binding of two nitrogen donor atoms in the equatorial plane. The EPR spectra were also measured at 400 ppm COMP concentration (Fig. S2†) and dimerization or aggregation of paramagnetic centers on the COMP surface can be ruled out as the line broadening effect or the doublet or half field signal was not detected.

The resistance against salt-induced aggregation is an important parameter for catalytic materials applied in liquid environments, which is the case for most of the antioxidant compounds used in both medical treatments and industrial manufacturing processes. Therefore, this issue was addressed by determining the electrophoretic mobilities (Fig. 4a) and stability ratios (Fig. 4b) for the bare LDH and COMP at different ionic strengths adjusted with NaCl.

The magnitude of the mobilities followed the same tendency for both LDH and COMP. Accordingly, they decreased upon increasing the NaCl concentration, but no charge reversal was observed in the systems. This behavior is typical in dis-

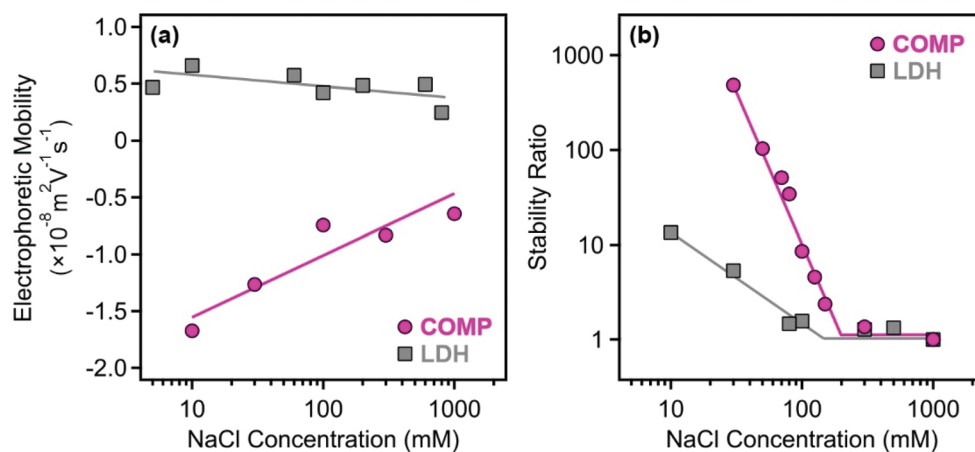


Fig. 4 Electrophoretic mobility (a) and stability ratio (b) values determined for the bare LDH (squares) and for COMP (circles) at different NaCl concentrations at 10 mg L<sup>-1</sup> particle concentration. The solid lines serve to guide the eyes and their breakpoint in (b) indicates the location of the CCC values.

persions containing charged particles and indifferent salts and can be explained by the screening effect of the salt constituents on the surface charges.<sup>34,39,56</sup> Comparing the data obtained for both materials, one can observe that the magnitude of the mobilities at low NaCl concentrations is about three times higher for **COMP** indicating that surface functionalization by sequential adsorption increased the surface charge significantly. This is also reflected in the stability ratio data, since only limited stability, *i.e.*, stability ratios were below 10 above 10 mM NaCl concentration, was observed for the bare LDH, while **COMP** formed highly stable dispersions at low ionic strengths. Besides, the shapes of the curves are somewhat similar and the stability ratios decreased by increasing the NaCl concentration until the CCC (the threshold salt concentration values, which separate fast and slow aggregation regimes) and remain unity thereafter. The onset of the fast aggregation is located at higher ionic strengths for **COMP** underlining the fact that it possesses significantly higher resistance against salt-induced aggregation.

Such a behavior can be described well by the DLVO theory, which states that higher charges lead to higher stability and elevated CCC values, since stronger electrical double layer forces can be screened at higher ionic strengths. An interesting discovery that deserves a short discussion is that the colloidal stability of **COMP** is somehow lower than the one reported earlier for the LDH-PSS-PDADMAC composite without immobilized metal complexes in the structure.<sup>47</sup> In that system, the fast aggregation regime at a stability ratio of 1 could not be reached due to the presence of extensive steric repulsion owing to the loosely adsorbed polyelectrolyte chains on the surface. These forces are most likely not present in **COMP** since the stability ratios are unity within the experimental error beyond the CCC indicating the presence of DLVO-type interactions (electrical double layer and van der Waals) only. The most sensible explanation is that the adsorption of the metal complexes on the polyelectrolyte layers gave rise to a more compact structure of the mixed complex-polyelectrolyte layer on the surface of the particles and thus, the formation of polyelectrolyte tails and loops, which are responsible for steric effects, is not preferred.

### 3.3. Antioxidant activity

Antioxidant enzymes contain redox active transition metal ions coordinated by donor atoms from the side chains of peptide-building amino acids and hence their active center can be considered as a metal complex.<sup>16,17</sup> Therefore, the Cu (Bpy)<sub>2</sub> and Fe(Cit)<sub>2</sub> complexes embedded in the **COMP** hybrid serve as the active centers in the present biocatalytic system. The polyelectrolyte environment may mimic the structure formation role of the peptide chains present in the native enzymes. Therefore, the superoxide dismutase-like activity was tested first (Fig. S3a†).

The superoxide radicals were produced from the oxidation of xanthine to uric acid with xanthine oxidase.<sup>57</sup> This colorimetric assay is based on the reduction of NBT to formazan by the forming superoxide radicals and consequently, the color

change from yellow to blue. Once the radicals formed are captured by the antioxidant material **COMP**, the reduction of NBT is inhibited and hence, no color change occurs. Such an inhibition was calculated from the spectrophotometric data recorded during the development of the blue color in the assays.

Based on the results, one can notice that the developed **COMP** hybrid exhibited excellent activity in the assay. The inhibition increased sharply with the concentration and reached 100% at about 0.050 mg L<sup>-1</sup>. The usual measure for the superoxide dismutase-like activity is the so-called IC<sub>50</sub> value, which gives the concentration of the catalyst necessary to dismutate 50% of the superoxide radicals forming in the assay. The IC<sub>50</sub> of **COMP** was found to be 0.026 mg L<sup>-1</sup> indicating remarkably high activity of the hybrid (Table 2).

For instance, the measured IC<sub>50</sub> is 63 times lower (meaning that the activity is 63 times higher) than the one reported earlier for Prussian blue antioxidant nanozymes.<sup>12</sup> More importantly, **COMP** has comparable superoxide radical scavenging activity to the native copper(II)-zinc(II) superoxide dismutase enzyme, whose IC<sub>50</sub> was determined to be 0.069 mg L<sup>-1</sup> earlier, in the same biochemical assay.<sup>52</sup> The maximum inhibitions (*I*<sub>max</sub>) of the native enzyme and **COMP** were very similar (100% and 95%, respectively, see Table 2). However, one must note that the concentration of the redox active metal ions is much higher in **COMP** than in the native enzyme due to the extensive structure-forming peptide part in the latter case. Applying equivalent concentrations of the stand-alone complexes to the IC<sub>50</sub> value of **COMP**, inhibition was observed neither for Cu(Bpy)<sub>2</sub> nor for Fe(Cit)<sub>2</sub>. The same result was obtained when the mixture of the two complexes was applied in solution. These data indicate that a synergistic effect between the coordination compounds takes place upon co-immobilization giving rise to remarkable improvement in the superoxide radical scavenging activity. Considering the EPR results discussed earlier, this excellent activity originates from the Cu(Bpy)(Cit) complexes formed upon co-immobilization of the metal complexes and hence, this active center is mostly responsible for the increased activity.

After the obtained excellent superoxide radical scavenging activity described above, the selectivity of the catalytic system was checked. The general radical scavenging activity of **COMP** was assessed in the standard DPPH test.<sup>58</sup> The reaction was followed through the color change from violet (DPPH radical) to yellow (reaction product), which was monitored by measuring the absorbance at 517 nm with a spectrophotometer. As shown in Fig. S3b,† some activity was observed; however, **COMP** was only able to decompose 55% of the initial DPPH

**Table 2** Activity of natural and artificial enzymes in dismutation of superoxide radicals

Compound	IC <sub>50</sub> (mg L <sup>-1</sup> )	<i>I</i> <sub>max</sub> (%)	Ref.
Superoxide dismutase	0.069	100	52
<b>COMP</b>	0.026	95	Present study

dc\_1931\_21

radicals within a reasonable timeframe, even at high catalyst concentrations. The effective concentration ( $EC_{50}$ ), which gives the **COMP** concentration needed to react with 50% of the DPPH radicals in the test, is  $49 \text{ mg L}^{-1}$ . These activity data, especially the low maximum percentage in the decomposition of the radicals, indicate moderate DPPH scavenging activity compared to other particle-based antioxidant materials.<sup>66–68</sup>

Applying the equivalent concentration (calculated from the  $EC_{50}$  value) of the lone complex of  $\text{Cu}(\text{Bpy})_2$  in solution led to only 5.9% scavenging activity, while for  $\text{Fe}(\text{Cit})_2$ , 9.7% was measured. In addition, the mixture of the two lone complexes resulted in 11.4% scavenged radicals. This result sheds light on the importance of the co-immobilization of the complexes; however, the DPPH decomposing activity of **COMP** is still moderate.

Moreover, the antioxidant abilities were tested in other probe reactions too, but the activities were detected neither in the guaiacol-based peroxidase assays<sup>69</sup> nor in the CUPRAC assays.<sup>70</sup> These assays were performed in purely aqueous solutions, where the solubility of the substrate is not a problem. The above results clearly indicate that **COMP** is exceptionally selective for superoxide radicals, while it fails in other antioxidant assays. Such a selectivity resembles the native enzyme, which is responsible solely for the decomposition of the superoxide radicals (and not other ROS) in living organisms.

## 4. Conclusions

An antioxidant nanocomposite was developed by the sequential adsorption technique involving 2 polyelectrolytes and 2 enzyme mimicking metal complexes immobilized successively on a LDH nanoclay support. The adsorption of the individual components occurred due to electrostatic interactions and their doses were optimized in order to obtain stable colloidal dispersions in the preparation steps. The obtained **COMP** hybrid possessed great resistance against salt-induced aggregation and the presence of all components was confirmed in the structure. The developed material showed remarkable activity in the dismutation of superoxide radicals; its mass normalized activity was close to the one reported for the native superoxide dismutase enzyme. Moreover, **COMP** represented negligible or zero activity in other antioxidant test reactions such as DPPH, peroxidase and CUPRAC assays indicating its selectivity towards superoxide radical dismutation. These facts make **COMP** a promising replacement of the superoxide dismutase enzyme, particularly in industrial processes, where native enzymes often denature and consequently, lose their antioxidant activity due to the harsh environmental conditions.

## Conflicts of interest

There are no conflicts to declare.

## Acknowledgements

This research was funded by the National Research, Development and Innovation Office (SNN131558) and by the Ministry of Human Capacities (20391-3/2018/FEKUSTRAT). The support from the University of Szeged Open Access Fund (5165) is gratefully acknowledged.

## References

- 1 C. C. Winterbourn, *Nat. Chem. Biol.*, 2008, **4**, 278–286.
- 2 A. A. Alfadda and R. M. Sallam, *J. Biomed. Biotechnol.*, 2012, 936486, DOI: 10.1155/2012/936486.
- 3 K. Brieger, S. Schiavone, F. J. Miller and K. H. Krause, *Swiss Med. Wkly.*, 2012, **142**, 13659.
- 4 K. M. Gupta, S. Das, P. S. Chow and C. Macbeath, *ACS Appl. Nano Mater.*, 2020, **3**, 5351–5361.
- 5 A. Bafana, S. Dutt, S. Kumar and P. S. Ahuja, *Crit. Rev. Biotechnol.*, 2011, **31**, 65–76.
- 6 J. W. Finley, A. N. Kong, K. J. Hintze, E. H. Jeffery, L. L. Ji and X. G. Lei, *J. Agric. Food Chem.*, 2011, **59**, 6837–6846.
- 7 B. N. Ames, M. K. Shigenaga and T. M. Hagen, *Proc. Natl. Acad. Sci. U. S. A.*, 1993, **90**, 7915–7922.
- 8 L. Valgimigli, A. Baschieri and R. Amorati, *J. Mater. Chem. B*, 2018, **6**, 2036–2051.
- 9 S. I. Tsekhmistrenko, V. S. Bityutskyy, O. S. Tsekhmistrenko, V. M. Polishchuk, S. A. Polishchuk, N. V. Ponomarenko, Y. O. Melnychenko and M. Y. Spivak, *Regul. Mech. Biosyst.*, 2018, **9**, 469–476.
- 10 S. Murath, N. B. Alsharif, S. Saringer, B. Katana, Z. Somosi and I. Szilagyi, *Crystals*, 2020, **10**, 148.
- 11 K. Takahashi and L. Takahashi, *Dalton Trans.*, 2016, **45**, 3244–3246.
- 12 N. B. Alsharif, G. F. Samu, S. Sáringer, S. Muráth and I. Szilagyi, *J. Mol. Liq.*, 2020, **309**, 113066.
- 13 A. Othman, L. Norton, A. S. Finny and S. Andreescu, *Talanta*, 2020, **208**, 120473.
- 14 N. Singh, M. A. Savanur, S. Srivastava, P. D'Silva and G. Mugesh, *Angew. Chem., Int. Ed.*, 2017, **56**, 14267–14271.
- 15 F. Yan, Y. Mu, G. L. Yan, J. Q. Liu, J. C. Shen and G. M. Luo, *Mini-Rev. Med. Chem.*, 2010, **10**, 342–356.
- 16 A. J. Wu, J. E. Penner-Hahn and V. L. Pecoraro, *Chem. Rev.*, 2004, **104**, 903–938.
- 17 D. P. Riley, *Chem. Rev.*, 1999, **99**, 2573–2587.
- 18 A. Horn, G. L. Parrilha, K. V. Melo, C. Fernandes, M. Horner, L. D. Visentin, J. A. S. Santos, M. S. Santos, E. C. A. Eleutherio and M. D. Pereira, *Inorg. Chem.*, 2010, **49**, 1274–1276.
- 19 I. N. Jakab, O. Lorincz, A. Jancso, T. Gajda and B. Gyurcsik, *Dalton Trans.*, 2008, 6987–6995, DOI: 10.1039/b811452h.
- 20 G. Tabbi, W. L. Driessen, J. Reedijk, R. P. Bonomo, N. Veldman and A. L. Spek, *Inorg. Chem.*, 1997, **36**, 1168–1175.
- 21 I. Labádi, M. Benko, M. Kata and I. Szilagyi, *React. Kinet. Catal. Lett.*, 2009, **96**, 327–333.



dc\_1931\_21

- 22 I. Szilagy, I. Labadi, K. Hernadi, I. Palinko, N. V. Nagy, L. Korecz, A. Rockenbauer, Z. Kele and T. Kiss, *J. Inorg. Biochem.*, 2005, **99**, 1619–1629.
- 23 J. X. Zhou, Y. Chen, L. T. Lan, C. Zhang, M. X. Pan, Y. Y. Wang, B. K. Han, Z. H. Wang, J. Jiao and Q. Chen, *Anal. Biochem.*, 2019, **567**, 51–62.
- 24 Y. C. Fang, Y. P. Chen, C. T. Chen, T. S. Lin and C. Y. Mou, *J. Mater. Chem. B*, 2013, **1**, 6042–6052.
- 25 I. Szilagy, L. Horvath, I. Labadi, K. Hernadi, I. Palinko and T. Kiss, *Cent. Eur. J. Chem.*, 2006, **4**, 118–134.
- 26 I. Szilagy, I. Labadi, K. Hernadi, I. Palinko and T. Kiss, *J. Mol. Struct.*, 2005, **744**, 495–500.
- 27 Z. Csendes, C. Dudas, G. Varga, E. G. Bajnoczi, S. E. Canton, P. Sipos and I. Palinko, *J. Mol. Struct.*, 2013, **1044**, 39–45.
- 28 Y. C. Fang, H. C. Lin, I. J. Hsu, T. S. Lin and C. Y. Mou, *J. Phys. Chem. C*, 2011, **115**, 20639–20652.
- 29 M. Yang, W. Jiang, Z. Q. Pan and H. Zhou, *J. Inorg. Organomet. Polym. Mater.*, 2015, **25**, 1289–1297.
- 30 I. Szilagy, O. Berkesi, M. Sipiczki, L. Korecz, A. Rockenbauer and I. Palinko, *Catal. Lett.*, 2009, **127**, 239–247.
- 31 I. Szilagy, I. Labadi, K. Hernadi, T. Kiss and I. Palinko, in *Molecular Sieves: From Basic Research to Industrial Applications, Pts a and B*, ed. J. Cejka, N. Zilkova and P. Nachtigall, 2005, vol. 158, pp. 1011–1018.
- 32 I. Labadi, I. Szilagy, N. I. Jakab, K. Hernadi and I. Palinko, *Mater. Sci.*, 2003, **21**, 235–244.
- 33 S. Muráth, S. Sáringer, Z. Somosi and I. Szilagy, *Colloids Interfaces*, 2018, **2**, 32.
- 34 M. Pavlovic, P. Rouster, T. Oncsik and I. Szilagy, *ChemPlusChem*, 2017, **82**, 121–131.
- 35 I. Szilagy, G. Trefalt, A. Tiraferri, P. Maroni and M. Borkovec, *Soft Matter*, 2014, **10**, 2479–2502.
- 36 R. Meszaros, I. Varga and T. Gilanyi, *Langmuir*, 2004, **20**, 5026–5029.
- 37 I. Safir, K. X. Ngo, J. N. Abraham, M. G. Afshar, E. Pavlova and C. Nardin, *Polymer*, 2015, **79**, 29–36.
- 38 A. Tiraferri and M. Borkovec, *Sci. Total Environ.*, 2015, **535**, 131–140.
- 39 M. Pavlovic, M. Nafradi, P. Rouster, S. Murath and I. Szilagy, *J. Colloid Interface Sci.*, 2019, **543**, 174–182.
- 40 O. S. Sakr and G. Borchard, *Biomacromolecules*, 2013, **14**, 2117–2135.
- 41 T. Szabo, M. Szekeres, I. Dekany, C. Jackers, S. De Feyter, C. T. Johnston and R. A. Schoonheydt, *J. Phys. Chem. C*, 2007, **111**, 12730–12740.
- 42 D. C. Kim, J. I. Sohn, D. J. Zhou, T. A. J. Duke and D. J. Kang, *ACS Nano*, 2010, **4**, 1580–1586.
- 43 B. Wang, Y. J. Wang, X. F. Gao and Y. S. Li, *J. Biomater. Sci., Polym. Ed.*, 2015, **26**, 1312–1326.
- 44 F. Caruso and C. Schuler, *Langmuir*, 2000, **16**, 9595–9603.
- 45 R. Saladino, M. Guazzaroni, C. Crestini and M. Crucianelli, *ChemCatChem*, 2013, **5**, 1407–1415.
- 46 V. Vergaro, Y. M. Lvov and S. Leporatti, *Macromol. Biosci.*, 2012, **12**, 1265–1271.
- 47 Z. Somosi, M. Pavlovic, I. Palinko and I. Szilagy, *Nanomaterials*, 2018, **8**, 986.
- 48 Z. B. Cao, B. Li, L. Y. Sun, L. Li, Z. P. Xu and Z. Gu, *Small Methods*, 2019, 1900343, DOI: 10.1002/smt.201900343.
- 49 G. Arrabito, A. Bonasera, G. Prestopino, A. Orsini, A. Mattoccia, E. Martinelli, B. Pignataro and P. G. Medaglia, *Crystals*, 2019, **9**, 361.
- 50 C. P. Chen, J. C. Buffet and D. O'Hare, *Dalton Trans.*, 2020, **49**, 8498–8503.
- 51 Z. P. Xu, G. Stevenson, C. Q. Lu and G. Q. Lu, *J. Phys. Chem. B*, 2006, **110**, 16923–16929.
- 52 M. Pavlovic, P. Rouster and I. Szilagy, *Nanoscale*, 2017, **9**, 369–379.
- 53 A. Rockenbauer and L. Korecz, *Appl. Magn. Reson.*, 1996, **10**, 29–43.
- 54 P. A. Hassan, S. Rana and G. Verma, *Langmuir*, 2015, **31**, 3–12.
- 55 H. Holthoff, S. U. Egelhaaf, M. Borkovec, P. Schurtenberger and H. Sticher, *Langmuir*, 1996, **12**, 5541–5549.
- 56 M. Kobayashi, M. Skarba, P. Galletto, D. Cakara and M. Borkovec, *J. Colloid Interface Sci.*, 2005, **292**, 139–147.
- 57 C. Beaucham and I. Fridovich, *Anal. Biochem.*, 1971, **44**, 276–287.
- 58 W. Brand-Williams, M. E. Cuvelier and C. Berset, *LWT-Food Sci. Technol.*, 1995, **28**, 25–30.
- 59 X. M. Zhang, M. L. Tong, M. L. Gong, H. K. Lee, L. Luo, K. F. Li, Y. X. Tong and X. M. Chen, *Chem. – Eur. J.*, 2002, **8**, 3187–3194.
- 60 T. Kohzuma, A. Odani, Y. Morita, M. Takani and O. Yamauchi, *Inorg. Chem.*, 1988, **27**, 3854–3858.
- 61 M. Juric, D. Pajic, D. Zilic, B. Rakvin, D. Milic and P. Planinic, *Polyhedron*, 2015, **98**, 26–34.
- 62 R. B. Martin, *J. Inorg. Biochem.*, 1986, **28**, 181–187.
- 63 I. Shweky, A. Bino, D. P. Goldberg and S. J. Lippard, *Inorg. Chem.*, 1994, **33**, 5161–5162.
- 64 E. Garribba, G. Micera, D. Sanna and L. Strinna-Erre, *Inorg. Chim. Acta*, 2000, **299**, 253–261.
- 65 Y. Shi, B. B. Toms, N. Dixit, N. Kumari, L. Mishra, J. Goodisman and J. C. Dabrowiak, *Chem. Res. Toxicol.*, 2010, **23**, 1417–1426.
- 66 S. Murath, S. Szerlauth, D. Sebok and I. Szilagy, *Antioxidants*, 2020, **9**, 153.
- 67 S. Saringer, R. A. Akula, A. Szerlauth and I. Szilagy, *J. Phys. Chem. B*, 2019, **123**, 9984–9991.
- 68 T. M. Chen, H. Zou, X. J. Wu, C. C. Liu, B. Situ, L. Zheng and G. W. Yang, *ACS Appl. Mater. Interfaces*, 2018, **10**, 12453–12462.
- 69 D. R. Doerge, R. L. Divi and M. I. Churchwell, *Anal. Biochem.*, 1997, **250**, 10–17.
- 70 M. Ozyurek, K. Guclu, E. Tutem, K. S. Baskan, E. Ercag, S. E. Celik, S. Baki, L. Yildiz, S. Karaman and R. Apak, *Anal. Methods*, 2011, **3**, 2439–2453.



# A colloid approach to decorate latex particles with Prussian blue nanozymes

Nizar B. Alsharif<sup>a</sup>, Gergely F. Samu<sup>b</sup>, Szilárd Sáringer<sup>a,b</sup>, Szabolcs Muráth<sup>a,b</sup>, Istvan Szilagyi<sup>a,b,\*</sup>

<sup>a</sup> MTA-SZTE Lendület Biocolloids Research Group, University of Szeged, H-6720 Szeged, Hungary

<sup>b</sup> Interdisciplinary Excellence Center, Department of Physical Chemistry and Materials Science, University of Szeged, H-6720 Szeged, Hungary

## ARTICLE INFO

### Article history:

Received 25 February 2020

Received in revised form 30 March 2020

Accepted 1 April 2020

Available online 18 April 2020

### Keywords:

Heteroaggregation

Enzyme mimic

Prussian blue

Latex

Colloidal stability

## ABSTRACT

Prussian blue (PB) nanoparticles of intrinsic peroxidase and superoxide dismutase-like activities were prepared by the co-precipitation method and immobilized on amidine functionalized polystyrene latex (AL) particles. The interaction between the AL and PB particles and the colloidal stability of the resulting AL-PB hybrid composites were assessed at different mass ratios via determination of the charging and aggregation characteristics in the samples. The negatively charged PB nanoparticles strongly adsorbed on the oppositely charged AL particles resulting in a range of AL-PB composites of positive, neutral and negative overall charge, once the PB dose was increased. The AL-PB composite of a saturated PB layer on the surface of the AL particles formed considerably stable dispersions. Further, the morphology, structural and functional features of the AL-PB composites were explored by electron microscopy and enzymatic assays. The results revealed that the immobilization of PB nanoparticles not only provided a sustained catalytic surface but did not compromise the enzyme-like activities. The obtained stable composite is a promising agent in antioxidant therapies and wherever the aim is to reduce oxidative stress at laboratory or larger scales.

© 2020 The Authors. Published by Elsevier B.V. This is an open access article under the CC BY license (<http://creativecommons.org/licenses/by/4.0/>).

## 1. Introduction

Although natural enzymes are remarkable catalysts under designated conditions, their production and purification is expensive and time-consuming [1]. More importantly, they suffer from inherent instability leading to a narrow window of operational conditions such as pH, pressure or temperature [2]. Under harsh conditions, protein structures denature, which causes a permanent loss of catalytic activity. Such drawbacks prompted the need for artificial enzymes, which are stable and low-cost materials possessing catalytic potential of the corresponding natural enzyme. Nanomaterials of enzymatic function (so-called nanozymes) have been heavily explored as alternatives for native proteins due to their large surface area, high reactivity and tunable physico-chemical properties [3]. These nanozymes comprise a vast variety of nanostructures and enzymatic activities [4–6].

Among them are nanozymes of antioxidant properties, which represent an important class of materials used for decomposition of reactive oxygen species (ROS) [7], whose presence gives rise to the evolution of various diseases in living organisms [8,9] and to lower quality products in industrial processes [10,11]. Accordingly, various nanoparticles have

been prepared and proved as efficient ROS scavenging catalysts, those include vanadium-pentoxide [12], copper [13], gold [14], platinum [15], molybdenum-disulfide [16], manganese oxide [17], cerium-oxide [18], carbonaceous [19], iron-cyanide [20] and hybrid [21] particles.

Prussian blue (PB), a mixed valence iron-cyanide complex, is a multifunctional material in both pure and composite forms. Apart from the utilization in ROS decomposition, PB was also used as a biomarker [22], a biomedical therapeutic agent [23] and a key part of electrochemical sensors [24]. Due to their low long-term toxicity [25] and that their presence in cells does not trigger production of hydroxyl radicals [26], application of PB nanostructures has attracted significant contemporary interest in the scientific community. They act as efficient functional mimic of superoxide dismutase (SOD), catalase and peroxidase enzymes due to their high affinity to oxygen-bearing radicals [20]. For instance, polymer-PB composites were prepared at different polymer molecular weights, whose optimal value had to be determined to obtain the most efficient ROS-scavenging activity in cells under stimulated oxidative stress [27]. A magnetic composite, which consists of iron-oxide core and PB shell was prepared and showed excellent peroxidase-like activity, i.e., H<sub>2</sub>O<sub>2</sub>-consuming ability, in laboratory test reactions [28]. Cubic PB nanoparticles were prepared in a polymer-assisted synthetic process and they sufficiently mimicked the function of a number of antioxidant enzymes under cellular environment [20]. Kinetic analysis of the test reactions revealed that such a multi-enzymatic activity

\* Corresponding author at: MTA-SZTE Lendület Biocolloids Research Group, University of Szeged, H-6720 Szeged, Hungary.

E-mail address: [szistvan@chem.u-szeged.hu](mailto:szistvan@chem.u-szeged.hu) (I. Szilagyi).

originates from the abundant redox potentials due to the different forms of iron in the material.

The stability of PB systems plays a key role in determining the suitability for a potential utilization. In most of the applications, PB nanoparticles are dispersed in liquid medium such as blood and cellular cytoplasm in living organisms as well as in industrial liquors during manufacturing processes. The colloidal stability of such systems is of special importance, since particle aggregation may lead to significant loss of the catalytic activity. Thus, surface modification of PB nanoparticles was performed with poly(ethylene glycol) [29], poly(diallyldimethylammonium chloride) [30], chitosan [31], native proteins [28] and poly(vinylpyrrolidone) [32] macromolecules to improve their dispersibility. Nevertheless, there is a lack of comprehensive studies on charging and aggregation of polymer functionalized PB particles. A deep understanding of colloidal stability and the factors that adversely affect it, is extremely important to obtain viable and robust colloidal PB systems.

In the present work, PB nanoparticles were prepared and immobilized on amidine functionalized polystyrene latex particles via controlled heteroaggregation. Such a procedure improved the colloidal stability of the PB nanoparticles as well as bound them to AL surface to increase their local concentration. The experimental conditions were optimized by following the charging and aggregation processes in the samples with microscopy, spectrophotometry and light scattering techniques, while the antioxidant property of the as-prepared and immobilized PB nanoparticles was assessed by enzymatic assays.

## 2. Experimental and methods

### 2.1. Materials

H<sub>2</sub>O<sub>2</sub> (30% m/m), HCl (37% m/m), KCl (≥99.5%), acetone (≥99.8%), K<sub>3</sub>[Fe(CN)<sub>6</sub>] (≥99.0%) and phosphate buffer were purchased from VWR™. Guaiacol (99%) and FeCl<sub>2</sub>·4H<sub>2</sub>O (≥99%) were acquired from Acros Organics. Amidine latex beads (AL in 4% w/v dispersions) were purchased from Invitrogen™. The AL particles are positively charged at low pH due to the protonation of the surface functional groups. Surface charge density of AL is +19.7 μC/cm<sup>2</sup>, the beads have a mean diameter of (0.51 ± 0.02) μm and a coefficient of size variation of 4.6%, as determined by the manufacturer with electron microscopy. Hellmanex® III cleaning agent was bought from Hellma. Xanthine (99%) was purchased from Alfa Aesar. Xanthine oxidase (lyophilized powder, 0.4–1.0 units/mg protein) was bought from Sigma-Aldrich. The pH was kept at (4.0 ± 0.2) throughout all experiments, except otherwise indicated. The VWR™ Puranility TU 3 UV/UF+ system was used to obtain ultrapure water, which was further filtered using PVDF-based 0.1 μm syringe filters purchased from MILLEX®V.

### 2.2. Preparation of PB particles and AL-PB hybrids

The PB nanoparticles were synthesized by the co-precipitation method [33]. The glasswares were carefully cleaned with Hellmanex® III and concentrated HCl solution. Under vigorous stirring, a 1.0 mM aqueous solution of K<sub>3</sub>[Fe(CN)<sub>6</sub>] (100 mL) was added dropwise to 100 mL of 1.0 mM FeCl<sub>2</sub>. After that, 400 mL of acetone was added to the resultant dark blue mixture. The solid materials were collected by centrifugation at a rate of 9000 rpm for 30 min and cleaned with acetone. The centrifugation process was repeated till all the PB was collected. Finally, the obtained PB nanoparticles were dispersed in a certain amount of ultrapure water to obtain a 10 g/L stock.

The immobilization of PB nanoparticles on the surface of AL to form AL-PB composites was achieved by simple mixing of proper volumes of PB and AL stocks, followed by the addition of a calculated volume of KCl solution to fix the ionic strength in the samples. The origin of the driving forces was electrostatic due to the oppositely charged PB and AL particles under the experimental conditions applied. The final AL-PB dispersions were homogenized by ultrasonication for 1 h. The concentration of

PB and AL particles in the composite dispersions was expressed as dose in milligrams of PB per one gram of AL (denoted as mg/g hereafter).

### 2.3. Electrophoretic light scattering

Electrophoretic mobility values were determined using an Anton Paar Litesizer™ 500 device equipped with a 658 nm wavelength laser source, with the applied voltage kept at 200 V throughout all electrophoretic light scattering measurements.

The pH-dependent surface charging of PB nanoparticles was studied with 100 ppm PB dispersions at different pH values. Concerning sample preparation, two 100 ppm stock PB dispersions were prepared and the pH was adjusted to 3 and 11, respectively. Then, a series of 8 mL PB dispersions was prepared by mixing different volumes of the two stocks, so that the pH in the series of dispersions gradually changed from 3 to 11. After each mixing, the resulting dispersion was homogenized by vortex and its pH value was unambiguously measured with a WTW pH benchtop meter (inoLab® pH 7310).

During the determination of the mobilities of the AL particles at different salt concentrations, a series of 25 ppm AL dispersions was prepared in the 1–1750 mM KCl concentration range. The effect of PB-to-AL mass ratio on the surface charge was determined in the 1–1000 mg/g PB dose regime at 1 mM ionic strength adjusted by addition of KCl. In each sample, the AL concentration was kept at 25 ppm, while the amount of PB particles was adjusted to the desired dose.

In general, the prepared dispersions were left to equilibrate for 2 h at room temperature. For the measurements, 350 μL samples were withdrawn from the dispersion of interest and were transferred to an omega cuvette (Anton Paar™). The electrophoretic mobility measurement was then performed at (25.0 ± 0.2) °C and reported as an average of 5 runs.

### 2.4. Dynamic light scattering

The hydrodynamic radius of the particles was determined by dynamic light scattering (DLS) using an ALV-NIBS/HPPS Particle sizer equipped with a 632.8 nm laser source. The scattered light was collected at 173° and data analysis was based on the cumulant fit [34].

The sample preparation protocols were identical to the ones described in the electrophoretic part above, with the exception that each measurement was started immediately after addition of the desired volume of AL or PB to the corresponding sample. The total volume of each sample was 2.0 mL and the experiments were carried out in disposable polystyrene cuvettes at (25.0 ± 0.2) °C.

In the time resolved setup, the hydrodynamic radius versus time curves contained 30–100 measurement points for each sample depending on the speed of the aggregation. The colloidal stability was expressed in terms of stability ratio (*W*), which was calculated using the following equation [34,35].

$$W = \frac{k_{app(fast)}}{k_{app}} \quad (1)$$

where *k<sub>app</sub>* is the apparent aggregation rate constant and *k<sub>app(fast)</sub>* is the apparent aggregation rate constant in a dispersion containing 1.0 M KCl. Under this condition, the aggregation is controlled solely by the diffusion of the particles, i.e., rapid particle aggregation occurs. The apparent aggregation rate constant was calculated from the hydrodynamic radius (*R<sub>h</sub>*) versus time (*t*) plots as follows.

$$k_{app} = \frac{1}{R_h(0)} \frac{dR_h(t)}{dt} \quad (2)$$

where *R<sub>h</sub>*(0) is the hydrodynamic radius of the monomer particles and  $\frac{dR_h(t)}{dt}$  is the slope of the linear fit of the *R<sub>h</sub>* versus *t* data points of the sample of interest. Note that stability ratios close to unity refer to

rapid or diffusion-controlled aggregation, while higher values indicate more stable samples.

### 2.5. Electron microscopy

The morphologies of the particles and their composites were analyzed by scanning (SEM, Hitachi S4700) and transmission electron microscopy (TEM, FEI Tecnai G2). Two 25 ppm dispersions of PB and AL as well as dispersions at PB doses of 1, 30 and 600 mg PB/g AL were imaged. For TEM, a volume of 5  $\mu\text{L}$  of each sample was introduced onto a copper-coated carbon mesh. Each aliquot was allowed to adsorb for 10 s, before removing the drop and introducing the next one. The sample grids were prepared 30 min before the measurements. For SEM, 5  $\mu\text{L}$  portions of all dispersions were introduced onto the SEM sample holder, a piece of silicon wafer on an aluminum disk. The samples were dried for a few minutes before being sputter coated with a thin gold film for 30 s. The sample holder was then introduced into the microscope for imaging.

### 2.6. X-ray photoelectron spectroscopy

The X-ray photoelectron spectroscopy (XPS) measurements were carried out with a SPECS<sup>TM</sup> instrument equipped with a PHOIBOS 150 MCD 9 hemispherical analyzer, under a main-chamber pressure in the  $10^{-9}$ – $10^{-10}$  mbar range. The analyzer was in fixed analyzer transmission mode with 40 eV pass energy for the survey scan and 20 eV pass energy for the high-resolution scans. The PB sample powder was pressed into an indium foil and loaded into the chamber on a gold-coated sample holder. Al K $\alpha$  X-ray source was used at 14 kV and at 150 W power. Charge referencing was done to the adventitious carbon (284.8 eV) on the surface of the sample. For spectrum evaluation, CasaXPS commercial software package was used.

### 2.7. UV–Vis spectrophotometry

The UV–Vis spectra were recorded with a GENESYS<sup>TM</sup> 10S UV–Vis spectrophotometer (Thermo Scientific) in the wavelength range of 300–900 nm. For PB analysis, 100 ppm dispersion was prepared in ultrapure water. The blank cuvette was filled with filtered water. After the sample was homogenized by ultrasonication for 10 min, the spectrum was recorded at a scan step of 0.5 nm.

### 2.8. Horseradish peroxidase assay

The following test was performed to confirm the horseradish peroxidase (HRP)-like activity of bare and immobilized PB nanoparticles. This assay relies on the oxidation of guaiacol substrate by  $\text{H}_2\text{O}_2$  in the presence of horseradish peroxidase or its mimic [36]. During the reaction, the color changes from colorless to a characteristic brown color, whose alteration was quantitatively analyzed by UV–Vis spectrophotometry. The guaiacol concentration was varied between 1 and 40 mM, while the concentrations of  $\text{H}_2\text{O}_2$  and the enzymatic material were kept constant. The pH of the medium was set at 7.0 using phosphate buffer for the adjustment. Therefore, in each of the 2400  $\mu\text{L}$  samples, a varied volume of 100 mM guaiacol stock solution was mixed with 240  $\mu\text{L}$  of 100 ppm PB dispersion (or a dispersion that is 100 ppm in PB and 167 ppm in AL to obtain 600 mg/g dose), 912  $\mu\text{L}$  of 131.6 mM phosphate buffer and a volume of ultrapure water to obtain a 2352  $\mu\text{L}$  sample. The cuvette was then vortexed for 10 s. Finally, 48  $\mu\text{L}$  of 135 mM  $\text{H}_2\text{O}_2$  were added and the cuvette was immediately introduced into the spectrophotometer and the linear absorbance versus time plot was recorded at 470 nm. The slopes of absorbance versus time graphs represent the corresponding reaction rates ( $v$ ) measured in absorbance unit per second. The reaction rate was converted to mM/s units by using the Beer-Lambert law. The optical light path is 1 cm and the molar extinction coefficient of the enzyme-catalyzed reaction product

tetraguaiacol is  $26.6 \text{ mM}^{-1} \text{ cm}^{-1}$ . Finally, the reaction rate was plotted as a function of the guaiacol concentration  $[S]$  in the corresponding sample. The horseradish peroxidase-like activity was assessed by fitting the plotted data with the Michaelis-Menten model of enzyme kinetics [37], as expressed in the following equation.

$$v = \frac{v_{\max}}{K_m + [S]} \quad (3)$$

where  $v_{\max}$  is the maximum possible rate regardless of the substrate concentration and  $K_m$  is the Michaelis-Menten constant.

### 2.9. Superoxide dismutase assay

To assess the ability of the nanozymes in dismutation of superoxide radical ions, the Fridovich assay was used [38], in which the radicals are generated by the oxidation of xanthine by xanthine oxidase. An indicator compound, nitroblue tetrazolium (NBT), helped to detect the antioxidant activity of the nanozyme of interest. The yellow colored NBT is reduced by the generated superoxide radical ions to form blue colored diformazan. In the presence of SOD or its mimicking materials, the generated radicals are totally or partially scavenged reducing the quantity of diformazan and thus, the intensity of blue color, which can be monitored spectrophotometrically.

In a typical measurement, a series of 3000  $\mu\text{L}$  samples were prepared, in which only the nanozyme concentration was changed. The concentration of the PB was varied between 1 and 4 ppm. Further, the concentration of phosphate buffer in the samples was kept at 10 mM. In each sample, 200  $\mu\text{L}$  of 3.0 mM xanthine and 100  $\mu\text{L}$  of 3.0 mM NBT were mixed followed by volumes of PB stock as well as phosphate buffer to obtain 2700  $\mu\text{L}$  sample. The cuvette was then vortexed for 10 s and 300  $\mu\text{L}$  of 1.5 g/L xanthine oxidase was added to the sample. Immediately after the addition of xanthine oxidase, the cuvette was vortexed for 5 s and introduced into the spectrophotometer, the absorbance versus time values were recorded at 565 nm wavelength for 6 min. Furthermore, eight blanks were also measured, each of which was prepared by adding all reagents mentioned except the nanozyme and an additional volume of phosphate buffer were added to maintain a final volume of 3000  $\mu\text{L}$ . The obtained data was interpreted by constructing the inhibition curve, a plot of the NBT reduction inhibition ( $I$ ) as a function of nanozyme concentration in the sample. The inhibition can be calculated as follows.

$$I = \frac{\Delta A_o - \Delta A_s}{\Delta A_o} \cdot 100 \quad (4)$$

where  $\Delta A_s$  is the change in absorbance during the 6 min measurement time for each sample and  $\Delta A_o$  is the averaged value of 6 min absorbance change for the eight blank samples. The concentration of the nanozyme that causes a 50% inhibition is the so-called  $\text{IC}_{50}$  value.

Note that light scattering by the particles has a contribution to the absolute absorbance values during the assays, however, this factor was eliminated by using only the relative increase in the absorbances in the individual experiments.

## 3. Results and discussions

### 3.1. Characterization of the PB particles

The PB particles were prepared by the co-precipitation method [33] and the structure was confirmed by XPS and spectrophotometry. Concerning the latter technique, Fig. S1 shows the characteristic UV–Vis absorption spectrum of the obtained PB. The spectrum is characterized by a broad absorption band located at 700 nm, which is attributed to the charge transfer between Fe(II) and Fe(III) along Fe(II)–CN–Fe(III) confirming the successful synthesis of the desired PB.



The chemical composition of PB was explored with XPS. The survey scan reveals the presence of Fe, C, N, O and Au elements (Fig. 1), where the latter one is from the gold plated sample holder. The high-resolution deconvoluted XP spectra of Fe 2p, C 1s, N 1s and O 1s regions are shown in Fig. S2. The peaks at 708.69 eV and 710.29 eV in Fig. S2a are assigned to Fe(II) 2p<sub>3/2</sub> and Fe(III) 2p<sub>3/2</sub>, respectively, which are in good accordance with literature values [39]. The presence of mixed-valence Fe indicates the formation of PB. The high resolution C 1s spectra was deconvoluted into four components, representing different chemical environments of the surface carbon moieties (Fig. S2b). The carbon in the ciano group of PB completely overlaps with the C-OH functionalities of the surface. Fig. S2c shows three major peaks for the N 1s region, the peak at 397.78 eV is assigned to nitrogen in the cyanide ligands [39,40] while the one at 399.35 eV is attributed to charge transfer processes between surface moieties [41]. The peak at 402.3 eV indicates the presence of positively charged nitrogen, most likely ammonium ions, which has been observed for PB compounds in other reports as well [39]. A possible source of the ammonium ions is the mild heat treatment during the sample drying process. Another indirect indication of the presence of ammonium ions is seen in Fig. S2a. The Fe(II) satellite peak at 712.68 eV is indicative that the majority of the surface Fe(II) exists in a high-spin state. In classical PB, however, Fe(II) should exist solely in a low-spin state, as the cyanide ligand is a strong field ligand. Weak ligand field in the PB lattice is only experienced at the Fe(III) sites. The Fe(II) can occupy these sites in the presence of monovalent cations (such as NH<sub>4</sub><sup>+</sup>), through the formation of an Everitt's salt type compounds (PB analogue) on the surface. The oxygen region in Fig. S2d can be fitted with one component centered at 532.76 eV, which corresponds to surface OH groups of the samples. The quantitative XPS composition analysis for all detected species resulted in the following composition (in atomic percentage, at.%) of the sample: 4.3% Fe, 53.1% C, 30.9% N and 11.7% O (Table S1).

The pH-dependence of PB particle size and charge was measured by DLS and electrophoresis, respectively (Fig. S3). The average hydrodynamic radius was found to be 42 nm at pH 4 and did not show any unambiguous trends by changing the pH. The electrophoretic mobility was determined to be  $-1.5 \cdot 10^{-8}$  m<sup>2</sup>/Vs and no clear pH-dependence was found in the pH regime 3–11. This mobility value corresponds to a zeta potential of around  $-19.7$  mV, once the Smoluchowski model is used for the conversion [42]. The negative charge originates from the deprotonated surface hydroxyl and carboxyl groups leading to an electrostatic repulsion between the individual particles and subsequently,

to hindered aggregation and stable particle stock dispersions under the storage conditions.

### 3.2. Homoaggregation of AL particles

To optimize the experimental conditions for aggregation rate measurements, the aggregation tendency of AL particles at different concentrations was studied via time resolved DLS. The background salt concentration, adjusted with KCl, was kept at 1.0 M KCl to ensure that all electrostatic repulsive interparticle forces are screened and thus, the particles undergo rapid aggregation, as suggested by the theory of Derjaguin, Landau, Verwey and Overbeek (DLVO) [43]. The results shown in Fig. S4 indicate that the slopes of the hydrodynamic radius versus time curves increase with the particle concentration. The apparent aggregation rate constants were calculated from these plots using Eq. (2). In addition, the half-time of aggregation ( $T_{1/2}$ ), i.e., the time interval, under which half of the primary particles form dimers, was calculated using the following equation.

$$T_{1/2} = \frac{2}{kC_0} \quad (5)$$

where  $C_0$  is the initial number concentration of the particles and  $k$  is the diffusion-controlled aggregation rate constant, as described by Smoluchowski [34]. The dependence of particle concentration on these values (Fig. S5) confirms that the apparent aggregation rate constant is larger in more concentrated dispersions and that the aggregation half-time decreases with the particle concentration. Based on these results, an AL concentration of 25 ppm was selected for further experiments. This value provides a good compromise as the early stage of the aggregation (i.e., no higher ranked aggregates form) can be followed, while the scattering intensity is high enough to perform reliable DLS measurements.

Using the selected experimental conditions above, the salt-induced aggregation of the AL particles was quantitatively assessed at different ionic strengths adjusted with KCl. The stability ratio value was calculated with Eq. (1) at each ionic strength value. The stability ratio significantly decreased as the KCl concentration was increased, until it reached unity indicating unstable dispersions and rapid particle aggregation (Fig. 2). Such a tendency is in line with the prediction by the DLVO theory. Accordingly, the background salt ions shrink the electric double layer around charged AL particles, therefore, the repulsive electrostatic forces weaken at higher salt concentrations. Until the threshold

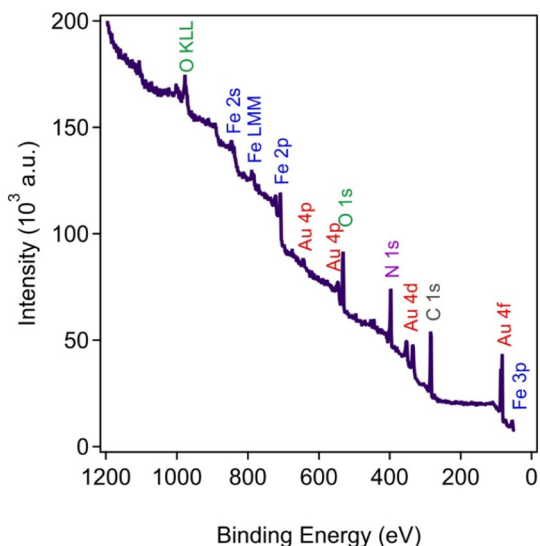


Fig. 1. XPS survey spectrum of the obtained PB nanoparticles in solid state. O KLL and Fe LMM are peaks of O and Fe for Auger transitions involving energy levels K, L and M.

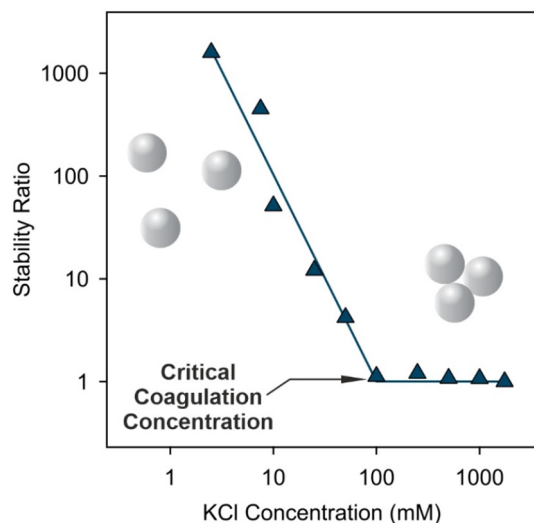


Fig. 2. Stability ratio values of 25 ppm AL dispersions as a function of the ionic strength adjusted by KCl at pH 4. The line serves to guide the eye.

concentration of 100 mM of KCl, so-called critical coagulation concentration, which separates slow and fast aggregation regimes, the double layer forces vanish and the particles undergo diffusion-controlled aggregation due to the predominance of the van der Waals attractive forces.

The ionic strength-dependent electrophoretic mobilities confirm the above explanation (Fig. 3). The values are positive at low salt levels due to the presence of the protonated amidine groups. As a result of the screening effect of the salt constituent ions on the surface charge, the mobilities decreased to almost zero by increasing the ionic strength. This clearly indicates the weakening of the electrostatic double layer repulsion, which is proportional to the charge of the particles [43]. Similar aggregation and charging properties were reported for latex particles in the presence of simple salts [34,44,45].

### 3.3. Heteroaggregation of AL and PB particles

Decoration of AL particles with oppositely charged PB nanoparticles occurred as a result of their controlled heteroaggregation. Their sizes are significantly different, the hydrodynamic radii were determined to be 249 nm for AL and 42 nm for PB (Table 1 and Fig. S6) in stable dispersions. This difference is also demonstrated by TEM images shown in Fig. S7. The DLS measurements carried out in stable dispersions indicated monomodal particle size distribution with good and moderate polydispersity for AL and PB, respectively. The scattered intensity of AL was higher at the same mass concentrations indicating that the AL particles scatter light much more and thus, they can be primarily detected by light scattering techniques, once both AL and PB particles are dispersed in the same sample. The magnitude of the electrophoretic mobility measured in stable dispersions was much higher for AL than for PB particles (Table 1). In the heteroaggregation experiments, i.e., particle collisions between AL and PB, the AL concentration was kept constant (25 ppm selected in the previous section), while the PB dose was systematically varied.

The charging properties were assessed with electrophoresis (Fig. 4). The electrophoretic mobilities gradually decreased as the PB dose increased with a characteristic range, where electrophoretic mobility values changed from positive to negative. At low PB doses, the electrophoretic mobilities are positive indicating an overall positive charge of the composites owing to the limited amount of adsorbed PB particles. As the PB dose increased, more negatively charged PB accumulated on the surface of the positively charged AL. When the amount of positive and negative charges was balanced, the AL-PB particles showed net

**Table 1**  
Characteristic size and charge parameters for AL and PB particles determined in stable dispersions at 25 ppm concentrations, 1 mM ionic strength and pH 4.

Material	$R_h^a$ (nm)	$I_s^a$ (kcps) <sup>a</sup>	PDI <sup>a</sup> (%)	EM <sup>a</sup> ( $10^{-8}$ m <sup>2</sup> /Vs)
AL	249	305	13.4	3.2
PB	42	168	23.5	-1.5

<sup>a</sup>  $R_h$  is the hydrodynamic radius,  $I_s$  is the scattering intensity, PDI is the polydispersity index, EM is the electrophoretic mobility and the unit kcps stands for to kilo counts per second.

zero charge, called isoelectric point (IEP). Further additions of PB generated AL-PB composites of an overall negative charge. Such a charge reversal was reported earlier for oppositely charged particle-polyelectrolyte systems [45–50] and also for latexes in the presence of clays [51,52]. The mobilities reached saturation at high PB doses, where the AL surface became saturated with adsorbed PB nanoparticles at the onset of the mobility plateau.

To assess the colloidal stability of the above dispersions, the stability ratios were measured under the same experimental conditions (Fig. 5). It is evident from the data that the gradual decrease in mobility values affected the stability of the AL-PB dispersions. Accordingly, at larger magnitude of the electrophoretic mobility values (both in the positive and negative regimes corresponding to low and high PB doses, respectively), the stability ratio values are large indicating rather stable dispersions. However, in the regions surrounding the IEP, the stability ratios drop to a value of one, which refers to rapid particle aggregation and to unstable dispersions. One significant observation, which is worthy of further discussion, is the presence of plateaus in the stability ratio values at low and high doses. The same trends were reported for polyelectrolyte-coated particles [53], which clearly indicate a similar origin of the interparticle forces for the bare and the PB-covered AL particles. Several studies have been reported for latex particle dispersions, in which the predominating interparticle forces were assigned to DLVO-type interaction [44,45,47], as discussed earlier in the previous section. Therefore, it is certain that the PB coating does not lead to the raise of additional interaction forces and the aggregation mechanism is driven by the balance between DLVO-type electrostatic double layer repulsion and van der Waals attraction. The latter one predominates around the IEP, where the overall charge of the AL-PB particles is zero and hence, the double layer forces vanish. Note that the agreement between the measured tendency in the stability ratios with the DLVO theory is purely

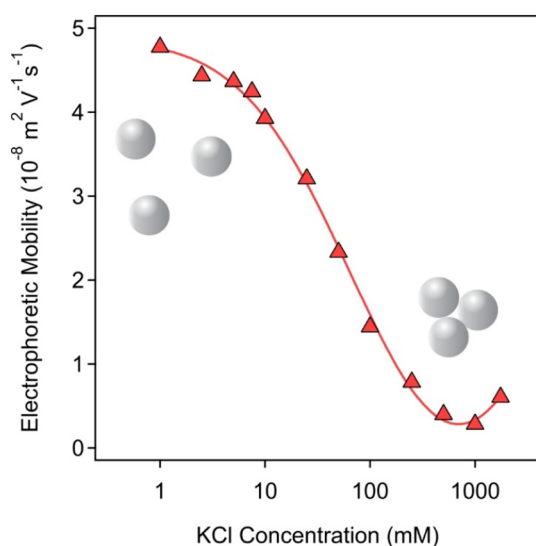


**Fig. 3.** Electrophoretic mobilities of 25 ppm AL dispersions as a function of ionic strength adjusted with KCl at pH 4. The lines serve to guide the eyes.

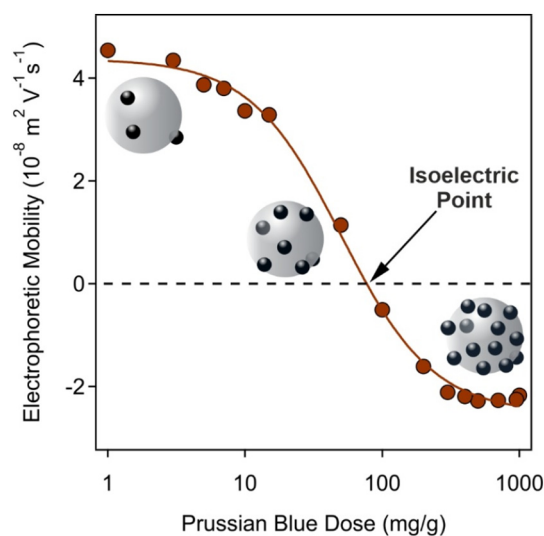


**Fig. 4.** Electrophoretic mobilities of AL particles at various PB concentrations at 1 mM ionic strength. The concentration of PB is expressed as dose, measured in mg/g (mg PB per one gram of AL). The lines serve to guide the eyes.

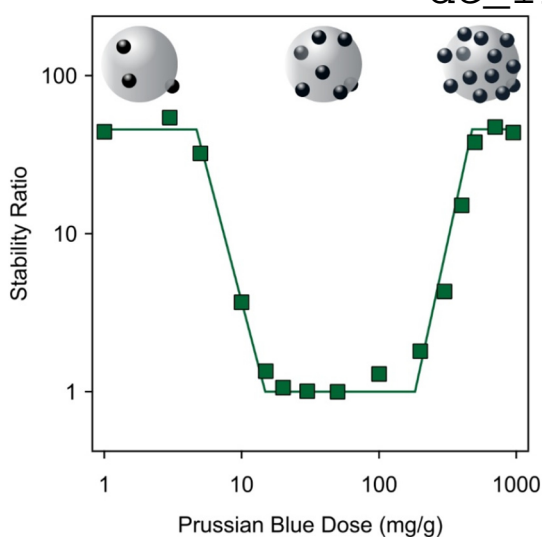


**Fig. 5.** Stability ratio values of AL-PB dispersions with different concentrations of PB. The concentration of PB is expressed as doses, measured in mg/g (mg PB per one gram of AL). The concentration of AL was kept at 25 ppm, while the ionic strength was 1 mM and the pH is 4. The solid line is to guide the eyes.

qualitative, since the extent of the interparticle forces cannot be calculated from the present results.

The coating process was also visualized by TEM/SEM images recorded at PB doses of 1, 30, and 600 mg/g (Fig. 6). In general, the particles were slightly agglomerated owing to the drying process during sample preparation. However, the images clearly show that more PB nanoparticles were immobilized as the dose increases. At the lowest dose, only a few PB nanoparticles could be detected on the AL surface, while at 30 mg/g, the AL particles are partially covered. The charge neutralization occurred around this dose, as pointed out in the electrophoretic mobility studies earlier. Finally, at 600 mg/g, the PB nanoparticles were uniformly distributed on the surface of AL. Note that the dispersions were found to be stable under the latter experimental condition.

This dose was used later to assess the antioxidant activity of the hybrid AL-PB composite, denoted as AL-PB-600 in the following sections.

### 3.4. Antioxidant activity

The HRP-like function of the PB and AL-PB-600 particles was assessed via the guaiacol assay, in which, guaiacol is oxidized by  $H_2O_2$  in the presence of the catalysts [36]. The obtained reaction rate data were plotted as a function of the substrate concentration (Fig. 7) and they fitted well to theoretical values determined by the Michaelis-Menten theory (Eq. (3)). The obtained  $v_{max}$  as well as  $K_m$  values are shown in Table 2. The  $v_{max}$  is the maximum reaction rate observed, where further increase in the substrate concentration does not increase the rate any further due to saturation of the catalytic sites of the enzyme or its mimics. The  $K_m$  is the guaiacol concentration that correspond to the rate half that of the  $v_{max}$ . The  $K_m$  value is a measure of the affinity between the enzyme or its mimics and the substrate, the lower the  $K_m$ , the higher the affinity between the enzymatic material and the substrate.

The obtained parameters for PB and AL-PB-600 were in the same range, i.e., the immobilization of the PB particles did not affect their HRP-like activity significantly. Similar values were reported also for the native enzyme [54], however, straight comparison is difficult due to the variation in added amount and the different chemical structure of the catalysts.

The ability of the PB and AL-PB-600 materials in dismutation of superoxide radical ions was tested by the Fridovich assay [38]. The inhibition of the NBT-radical reaction was calculated using Eq. (4) and presented as a function of the PB concentration in Fig. 8. A number of conclusions can be drawn based on the data. The PB did not lose the SOD activity upon immobilization on AL. However, because of inevitable hindrance of some catalytic sites on the surfaces of PB particles upon attachment to the AL latex surface, the maximum inhibition values decreased for AL-PB-600. Nevertheless, The  $IC_{50}$  values for PB and AL-PB-600 were very similar (Table 2), but significantly higher than the  $IC_{50}$  for native SOD. Because of the large difference in the nature of the materials, the direct comparison of the data is difficult. The retainment of SOD activity for AL-PB-600 is very promising in applications, where bare PB nanoparticles are likely to form an unstable colloid.

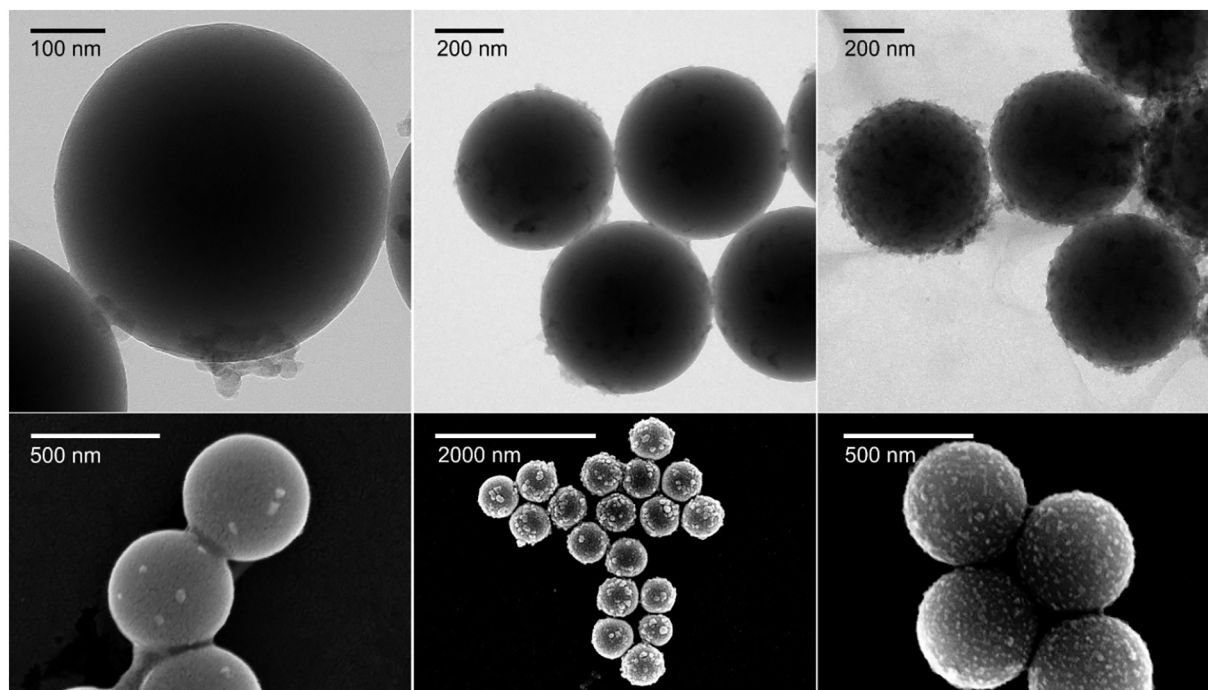


**Fig. 6.** Dried state TEM (upper row) and SEM (lower row) images of AL-PB systems at PB dose of 1 mg/g (left), 30 mg/g (middle) and 600 mg/g (right).

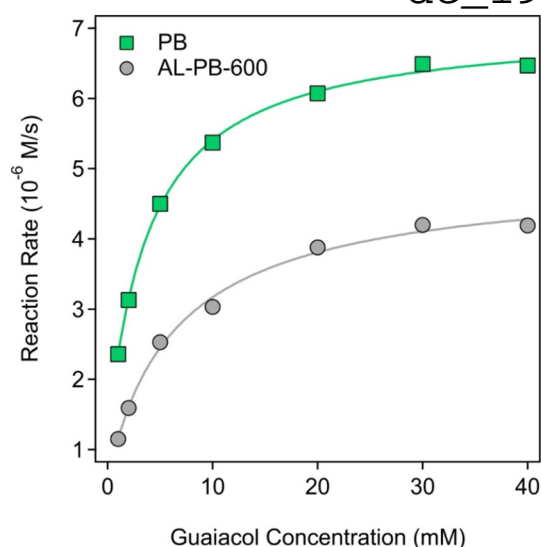


**Fig. 7.** HRP activity of PB (green squares) and AL-PB-600 (grey circles) particles. The solid lines are the Michaelis-Menten fits described by Eq. (3).

Note that the pH was different during the preparation of the AL-PB-600 (pH 4) and in the above assays (pH 7). However, neither AL nor PB particles change the sign of charge (positive and negative, respectively) during such a shift in the pH and thus, the AL-PB-600 structure remained stable in the enzymatic test reactions too.

#### 4. Conclusions

PB nanoparticles of antioxidant activity were synthesized and formulated by heteroaggregation with AL particles. This heteroaggregation can be also rationalized as an adsorption process of the PB nanoparticles on the AL surface due to their opposite charges. The structure of the bare PB was confirmed with UV-Vis spectrophotometry and XPS measurements, while the characteristic size and charge values of both particles were studied by electrophoretic and dynamic light scattering. The PB nanoparticles adsorbed strongly on the AL surface leading to charge neutralization and charge reversal at appropriate PB doses. The colloidal stability of the samples was assessed and confirmed that the aggregation of the PB-decorated AL particles is driven by DLVO-type forces. Accordingly, the electrostatic double layer repulsion stabilizes the dispersions at low and high PB doses, where the PB functionalized particles possess significant charge. At the IEP, however, the particles undergo diffusion-controlled aggregation due to the lack of charges, i.e., to the disappearance of the electrostatic double layers and predominance of attractive van der Waals forces. To test the antioxidant activity of the AL-PB composite, a PB dose of 600 mg/g, at which the overall charge was negative and a stable colloid is formed, was selected. The AL-PB-600 particles showed good antioxidant properties in two assays. Accordingly, HRP-like activity of PB was maintained upon immobilization on AL and the calculated Michaelis-Menten parameters were in

**Table 2**

Comparison of the results of HRP and SOD activity assays obtained for the PB, AL-PB-600 and native enzymes.

Material	$K_m$ (mM) <sup>a</sup>	$v_{max}$ (10 <sup>-6</sup> M/s) <sup>a</sup>	$IC_{50}$ (mg/L) <sup>b</sup>
PB	2.19 <sup>c</sup>	6.71 <sup>c</sup>	1.64
AL-PB-600	2.92 <sup>c</sup>	4.09 <sup>c</sup>	2.55
Native enzyme	3.23 <sup>d</sup>	2.80 <sup>d</sup>	0.07 <sup>e</sup>

<sup>a</sup> Calculated from the HRP assay data by Eq. (3) with an error of 1%.

<sup>b</sup> Determined in SOD activity assays with an average error of 5%.

<sup>c</sup> A PB concentration of 10 ppm was applied in the assays.

<sup>d</sup> The value is taken from Reference [54].

<sup>e</sup> Reference [55].

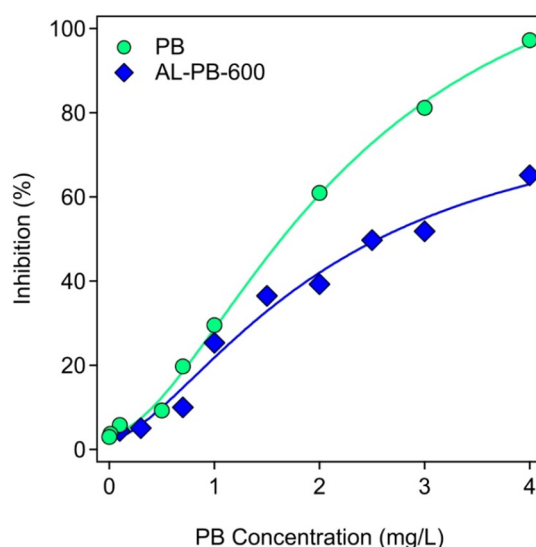


**Fig. 8.** Inhibition of the NBT-superoxide radical ion reaction by the PB (green circles) and AL-PB-600 (blue diamonds) particles. The inhibition values were obtained using Eq. (4). The solid lines are just to guide the eyes.

good agreement for PB and AL-PB-600. The results of the SOD-like activity study indicated that blocking the active sites of PB upon immobilization onto the AL surface led to a decrease in the ability to dismutate superoxide radical ions, however, the  $IC_{50}$  values were still in the range, where the AL-PB-600 hybrid can be considered as an efficient SOD mimic. These facts indicate that the obtained AL-PB-600 composites can be effectively used for superoxide radical ion dismutation as well as for  $H_2O_2$  consumption in heterogeneous systems, wherever the aim is to reduce the concentration of ROS.

#### CRedit authorship contribution statement

**Nizar B. Alsharif:** Investigation, Writing - original draft, Visualization. **Gergely F. Samu:** Investigation, Writing - original draft, Visualization. **Szilárd Sáringér:** Methodology, Software, Writing - review & editing. **Szabolcs Muráth:** Validation, Investigation, Writing - review & editing. **Istvan Szilagyi:** Conceptualization, Writing - original draft, Supervision, Funding acquisition, Writing - review & editing.

#### Declaration of competing interest

The authors declare that they have no known competing financial interests or personal relationships that could have appeared to influence the work reported in this paper.

#### Acknowledgments

This research was financially supported by the Lendület program of the Hungarian Academy of Sciences (96130) and by the Ministry of Human Capacities, Hungary (20391-3/2018/FEKUSTRAT). The authors are also thankful for the support of the University of Szeged Open Access Fund (4698).

#### Appendix A. Supplementary data

Supplementary data to this article can be found online at <https://doi.org/10.1016/j.molliq.2020.113066>.

#### References

- [1] S.J. Benkovic, S. Hammes-Schiffer, A perspective on enzyme catalysis, *Science* 301 (5637) (2003) 1196–1202.



- [2] X. Ma, A.C. Hortelao, T. Patino, S. Sanchez, Enzyme catalysis to power micro/nanomachines, *ACS Nano* 10 (10) (2016) 9111–9122.
- [3] H. Wei, E.K. Wang, Nanomaterials with enzyme-like characteristics (nanozymes): next-generation artificial enzymes, *Chem. Soc. Rev.* 42 (14) (2013) 6060–6093.
- [4] L. Qin, X.Y. Wang, Y.F. Liu, H. Wei, 2D-metal-organic-framework-nanozyme sensor arrays for probing phosphates and their enzymatic hydrolysis, *Anal. Chem.* 90 (16) (2018) 9983–9989.
- [5] F. Chen, M. Bai, K. Cao, Y. Zhao, J. Wei, Y.X. Zhao, Fabricating MnO<sub>2</sub> nanozymes as intracellular catalytic DNA circuit generators for versatile imaging of base-excision repair in living cells, *Adv. Funct. Mater.* 27 (45) (2017) 1702748.
- [6] Y.H. Lin, J.S. Ren, X.G. Qu, Catalytically active nanomaterials: a promising candidate for artificial enzymes, *Accounts Chem. Res.* 47 (4) (2014) 1097–1105.
- [7] L. Valgimigli, A. Baschieri, R. Amorati, Antioxidant activity of nanomaterials, *J. Mat. Chem. B* 6 (14) (2018) 2036–2051.
- [8] C.C. Winterbourn, Reconciling the chemistry and biology of reactive oxygen species, *Nat. Chem. Biol.* 4 (5) (2008) 278–286.
- [9] P. Brenneisen, A.S. Reichert, Nanotherapy and reactive oxygen species (ROS) in cancer: a novel perspective, *Antioxidants* 7 (2) (2018) 31.
- [10] C. Nirmala, M.S. Bisht, H.K. Bajwa, O. Santosh, Bamboo: a rich source of natural antioxidants and its applications in the food and pharmaceutical industry, *Trends Food Sci. Technol.* 77 (2018) 91–99.
- [11] J.W. Finley, A.N. Kong, K.J. Hintze, E.H. Jeffery, L.L. Ji, X.G. Lei, Antioxidants in foods: state of the science important to the food industry, *J. Agric. Food Chem.* 59 (13) (2011) 6837–6846.
- [12] A.A. Vernekar, D. Sinha, S. Srivastava, P.U. Paramasivam, P. D'Silva, G. Mughesh, An antioxidant nanozyme that uncovers the cytoprotective potential of vanadia nanowires, *Nat. Commun.* 5 (2014) 5301.
- [13] F. Dashtestani, H. Ghourchian, A. Najafi, Albumin coated copper-cysteine nanozyme for reducing oxidative stress induced during sperm cryopreservation, *Bioorg. Chem.* 80 (2018) 621–630.
- [14] F.M. Wang, E.G. Ju, Y.J. Guan, J.S. Ren, X.G. Qu, Light-mediated reversible modulation of ROS level in living cells by using an activity-controllable nanozyme, *Small* 13 (25) (2017) 1603051.
- [15] M. Moglianetti, E. De Luca, P.A. Deborah, R. Marotta, T. Catelani, B. Sartori, H. Amenitsch, S.F. Retta, P.P. Pompa, Platinum nanozymes recover cellular ROS homeostasis in an oxidative stress-mediated disease model, *Nanoscale* 8 (6) (2016) 3739–3752.
- [16] T.M. Chen, H. Zou, X.J. Wu, C.C. Liu, B. Situ, L. Zheng, G.W. Yang, Nanozymatic antioxidant system based on MoS<sub>2</sub> nanosheets, *ACS Appl. Mater. Interfaces* 10 (15) (2018) 12453–12462.
- [17] N. Singh, M.A. Savanur, S. Srivastava, P. D'Silva, G. Mughesh, A redox modulatory Mn<sub>3</sub>O<sub>4</sub> nanozyme with multi-enzyme activity provides efficient cytoprotection to human cells in a Parkinson's disease model, *Angew. Chem.-Int. Edit.* 56 (45) (2017) 14267–14271.
- [18] A. Pratsinis, G.A. Keesidis, S. Zuercher, F. Krumeich, S. Bolisetty, R. Mezzenga, J.C. Leroux, G.A. Sotiriou, Enzyme-mimetic antioxidant luminescent nanoparticles for highly sensitive hydrogen peroxide biosensing, *ACS Nano* 11 (12) (2017) 12210–12218.
- [19] Y.Y. Huang, C.Q. Liu, F. Pu, Z. Liu, J.S. Ren, X.G. Qu, A GO-Se nanocomposite as an antioxidant nanozyme for cytoprotection, *Chem. Commun.* 53 (21) (2017) 3082–3085.
- [20] W. Zhang, S.L. Hu, J.J. Yin, W.W. He, W. Lu, M. Ma, N. Gu, Y. Zhang, Prussian blue nanoparticles as multienzyme mimetics and reactive oxygen species scavengers, *J. Am. Chem. Soc.* 138 (18) (2016) 5860–5865.
- [21] Y.Y. Huang, Z. Liu, C.Q. Liu, E.G. Ju, Y. Zhang, J.S. Ren, X.G. Qu, Self-assembly of multienzymes to mimic an intracellular antioxidant defense system, *Angew. Chem.-Int. Edit.* 55 (23) (2016) 6646–6650.
- [22] M.K. Masud, J. Na, M. Younus, M.S.A. Hossain, Y. Bando, M.J.A. Shiddiky, Y. Yamauchi, Superparamagnetic nanoarchitectures for disease-specific biomarker detection, *Chem. Soc. Rev.* 48 (24) (2019) 5717–5751.
- [23] M.S. Moorthy, G. Hoang, B. Subramanian, N.Q. Bui, M. Panchanathan, S. Mondal, V.P.T. Tuong, H. Kim, J. Oh, Prussian blue decorated mesoporous silica hybrid nanocarriers for photoacoustic imaging-guided synergistic chemo-photothermal combination therapy, *J. Mat. Chem. B* 6 (32) (2018) 5220–5233.
- [24] G.W. Bishop, J.E. Satterwhite, S. Bhakta, K. Kadimisetty, K.M. Gillette, E. Chen, J.F. Rusling, 3D-printed fluidic devices for nanoparticle preparation and flow-injection amperometry using integrated Prussian blue nanoparticle-modified electrodes, *Anal. Chem.* 87 (10) (2015) 5437–5443.
- [25] Y. Chen, L. Wu, Q. Wang, M. Wu, B. Xu, X. Liu, J. Liu, Toxicological evaluation of Prussian blue nanoparticles after short exposure of mice, *Hum. Exp. Toxicol.* 35 (10) (2016) 1123–1132.
- [26] M. Shokouhimehr, E.S. Soehnlen, J.H. Hao, M. Griswold, C. Flask, X.D. Fan, J.P. Basilion, S. Basu, S.P.D. Huang, Dual purpose Prussian blue nanoparticles for cellular imaging and drug delivery: a new generation of T-1-weighted MRI contrast and small molecule delivery agents, *J. Mater. Chem.* 20 (25) (2010) 5251–5259.
- [27] H. Oh, J.S. Lee, D. Sung, J.H. Lee, S.H. Moh, J.M. Lim, W.I. Choi, Synergistic antioxidant activity of size controllable chitosan-templated Prussian blue nanoparticle, *Nanomedicine* 14 (19) (2019) 2567–2578.
- [28] X.Q. Zhang, S.W. Gong, Y. Zhang, T. Yang, C.Y. Wang, N. Gu, Prussian blue modified iron oxide magnetic nanoparticles and their high peroxidase-like activity, *J. Mater. Chem.* 20 (24) (2010) 5110–5116.
- [29] L. Cheng, H. Gong, W.W. Zhu, J.J. Liu, X.Y. Wang, G. Liu, Z. Liu, PEGylated Prussian blue nanocubes as a theranostic agent for simultaneous cancer imaging and photothermal therapy, *Biomaterials* 35 (37) (2014) 9844–9852.
- [30] W. Zhao, J.J. Xu, C.G. Shi, H.Y. Chen, Multilayer membranes via layer-by-layer deposition of organic polymer protected Prussian blue nanoparticles and glucose oxidase for glucose biosensing, *Langmuir* 21 (21) (2005) 9630–9634.
- [31] X.D. Li, X.L. Liang, F. Ma, L.J. Jing, L. Lin, Y.B. Yang, S.S. Feng, G.L. Fu, X.L. Yue, Z.F. Dai, Chitosan stabilized Prussian blue nanoparticles for photothermally enhanced gene delivery, *Colloid Surf. B-Biointerfaces* 123 (2014) 629–638.
- [32] T. Uemura, S. Kitagawa, Prussian blue nanoparticles protected by poly(vinylpyrrolidone), *J. Am. Chem. Soc.* 125 (26) (2003) 7814–7815.
- [33] W.M. Zhang, D. Ma, J.X. Du, Prussian blue nanoparticles as peroxidase mimetics for sensitive colorimetric detection of hydrogen peroxide and glucose, *Talanta* 120 (2014) 362–367.
- [34] H. Holthoff, S.U. Egelhaaf, M. Borkovec, P. Schurtenberger, H. Sticher, Coagulation rate measurements of colloidal particles by simultaneous static and dynamic light scattering, *Langmuir* 12 (23) (1996) 5541–5549.
- [35] F. Iselau, T.P. Xuan, G. Trefalt, A. Matic, K. Holmberg, R. Bordes, Formation and relaxation kinetics of starch-particle complexes, *Soft Matter* 12 (47) (2016) 9509–9519.
- [36] A.C. Maehly, B. Chance, The assay of catalases and peroxidases, *Methods Biochem. Anal.* 1 (1954) 357–424.
- [37] K.A. Johnson, R.S. Goody, The original Michaelis constant: translation of the 1913 Michaelis-Menten paper, *Biochemistry* 50 (39) (2011) 8264–8269.
- [38] C. Beaucham, I. Fridovich, Superoxide dismutase - improved assays and an assay applicable to acrylamide gels, *Anal. Biochem.* 44 (1) (1971) 276–287.
- [39] X.W. He, L.D. Tian, M.T. Qiao, J.Z. Zhang, W.C. Geng, Q.Y. Zhang, A novel highly crystalline Fe-4(Fe(CN)(6))<sub>3</sub> concave cube anode material for Li-ion batteries with high capacity and long life, *J. Mater. Chem. A* 7 (18) (2019) 11478–11486.
- [40] A. Forment-Aliaga, R.T. Weitz, A.S. Sagar, E.J.H. Lee, M. Konuma, M. Burghard, K. Kern, Strong p-type doping of individual carbon nanotubes by Prussian blue functionalization, *Small* 4 (10) (2008) 1671–1675.
- [41] E. Fluck, H. Inoue, S. Yanagisawa, Mossbauer and X-ray photoelectron spectroscopic studied of Prussian blue and its related compounds, *Z. Anorg. Allg. Chem.* 430 (3) (1977) 241–249.
- [42] A.V. Delgado, E. Gonzalez-Caballero, R.J. Hunter, L.K. Koopal, J. Lyklema, Measurement and interpretation of electrokinetic phenomena - (IUPAC technical report), *Pure Appl. Chem.* 77 (10) (2005) 1753–1805.
- [43] G. Trefalt, I. Szilagy, M. Borkovec, Poisson-Boltzmann description of interaction forces and aggregation rates involving charged colloidal particles in asymmetric electrolytes, *J. Colloid Interface Sci.* 406 (2013) 111–120.
- [44] F.J.M. Ruiz-Cabello, G. Trefalt, T. Oncsik, I. Szilagy, P. Maroni, M. Borkovec, Interaction forces and aggregation rates of colloidal latex particles in the presence of monovalent counterions, *J. Phys. Chem. B* 119 (25) (2015) 8184–8193.
- [45] S. Saringer, R.A. Akula, A. Szerlauth, I. Szilagy, Papain adsorption on latex particles: charging, aggregation, and enzymatic activity, *J. Phys. Chem. B* 123 (46) (2019) 9984–9991.
- [46] G. Gillies, W. Lin, M. Borkovec, Charging and aggregation of positively charged latex particles in the presence of anionic polyelectrolytes, *J. Phys. Chem. B* 111 (29) (2007) 8626–8633.
- [47] I. Szilagy, G. Trefalt, A. Tiraferri, P. Maroni, M. Borkovec, Polyelectrolyte adsorption, interparticle forces, and colloidal aggregation, *Soft Matter* 10 (15) (2014) 2479–2502.
- [48] I. Popa, G. Papastavrou, M. Borkovec, Charge regulation effects on electrostatic patch-charge attraction induced by adsorbed dendrimers, *Phys. Chem. Chem. Phys.* 12 (2010) 4863–4871.
- [49] L. Avadiar, Y.K. Leong, Interactions of PEI (polyethylenimine)-silica particles with citric acid in dispersions, *Colloid Polym. Sci.* 289 (3) (2011) 237–245.
- [50] T.D. Chaparro, R.D. Silva, I.S. Monteiro, A. Barros-Timmons, R. Giudici, A.M. dos Santos, E. Bourgeat-Lami, Interaction of cationic, anionic, and nonionic macroraft homo- and copolymers with laponite clay, *Langmuir* 35 (35) (2019) 11512–11523.
- [51] M. Pavlovic, P. Rouster, E. Bourgeat-Lami, V. Prevot, I. Szilagy, Design of latex-layered double hydroxide composites by tuning the aggregation in suspensions, *Soft Matter* 13 (4) (2017) 842–851.
- [52] M. Kobayashi, M. Nitani, N. Satta, Y. Adachi, Coagulation and charging of latex particles in the presence of imogolite, *Colloid Surf. A* 435 (2013) 139–146.
- [53] J. Hierrezuelo, A. Sadeghpour, I. Szilagy, A. Vaccaro, M. Borkovec, Electrostatic stabilization of charged colloidal particles with adsorbed polyelectrolytes of opposite charge, *Langmuir* 26 (19) (2010) 15109–15111.
- [54] M. Pavlovic, P. Rouster, Z. Somosi, I. Szilagy, Horseradish peroxidase-nanoclay hybrid particles of high functional and colloidal stability, *J. Colloid Interface Sci.* 524 (2018) 114–121.
- [55] M. Pavlovic, P. Rouster, I. Szilagy, Synthesis and formulation of functional bioanionomers with superoxide dismutase activity, *Nanoscale* 9 (1) (2017) 369–379.

## PAPER



Cite this: *J. Mater. Chem. B*, 2021,  
9, 4929

# Design of hybrid biocatalysts by controlled heteroaggregation of manganese oxide and sulfate latex particles to combat reactive oxygen species†

Nizar B. Alsharif,<sup>a</sup> Katalin Bere,<sup>a</sup> Szilárd Sáringer,<sup>ab</sup> Gergely F. Samu,<sup>ib</sup>  
Dóra Takács,<sup>a</sup> Viktória Hornok<sup>b</sup> and Istvan Szilagyi<sup>ib</sup>\*<sup>ab</sup>

The preparation of an antioxidant hybrid material by controlled heteroaggregation of manganese oxide nanoparticles (MnO<sub>2</sub> NPs) and sulfate-functionalized polystyrene latex (SL) beads was accomplished. Negatively charged MnO<sub>2</sub> NPs were prepared by precipitation and initially functionalized with poly(diallyldimethylammonium chloride) (PDADMAC) polyelectrolyte to induce charge reversal allowing decoration of oppositely charged SL surfaces *via* simple mixing. The PDADMAC-functionalized MnO<sub>2</sub> NPs (PMn) aggregated with the SL particles leading to the formation of negatively charged, neutral and positively charged (SPMn) composites. The charge neutralization resulted in rapidly aggregating dispersions, while stable samples were observed once the composites possessed sufficiently high negative and positive charge, below and above the charge neutralization point, respectively. The antioxidant assays revealed that SL served as a suitable substrate and that the PDADMAC functionalization and immobilization of MnO<sub>2</sub> NPs did not compromise their catalase (CAT) and superoxide dismutase (SOD)-like activities, which were also maintained within a wide temperature range. The obtained SPMn composite is expected to be an excellent candidate as an antioxidant material for the efficient scavenging of reactive oxygen species at both laboratory and larger scales, even under harsh conditions, where natural antioxidants do not function.

Received 9th March 2021,  
Accepted 2nd June 2021

DOI: 10.1039/d1tb00505g

rsc.li/materials-b

## Introduction

Despite being exceptional catalysts, natural enzymes suffer from significant sensitivity to such operational conditions as pH and temperature.<sup>1</sup> Under undesignated conditions, structures of proteins can denature and permanently lose their catalytic activity. Moreover, enzyme production and purification processes are time consuming and are often considerably expensive.<sup>2</sup> These drawbacks have paved the way to cost-effective and efficient artificial enzyme catalysts as alternatives to their natural counterparts. These enzyme mimics have diverse structures such as metal complexes, cyclodextrins, polymers, and more importantly nanomaterials.<sup>3–5</sup> Unlike natural enzymes, nanomaterial-based artificial enzymes (nanozymes) are easy and cheap to prepare and possess catalytic activity often well outside the operational

conditions of the mimicked natural biocatalysts, owing to their large surface area, structural stability and the possibility to tune the physico-chemical properties of such nanomaterials.<sup>4,6,7</sup>

In this way, nanomaterials possessing antioxidant activities have been widely explored in attempt to replace natural radical scavenging enzymes.<sup>8–11</sup> Since the early reports on superoxide dismutase (SOD) mimicry by fullerene derivatives,<sup>12,13</sup> extensive research has been reported in the literature on various antioxidant nanozymes of diverse structures and catalytic roles.<sup>4,6</sup> These include metallic nanoparticles such as Ag,<sup>14</sup> Au,<sup>15</sup> Pt,<sup>16</sup> and Pd;<sup>17</sup> metal oxides including Co<sub>3</sub>O<sub>4</sub>,<sup>18</sup> CeO<sub>2</sub>,<sup>9,19</sup> and CuO<sup>20</sup> nanospheres as well as V<sub>2</sub>O<sub>5</sub> nanowires;<sup>21</sup> metal chalcogenides such as FeS,<sup>22</sup> MoSe<sub>2</sub>,<sup>11</sup> MoS<sub>2</sub>,<sup>23</sup> and WS<sub>2</sub><sup>24</sup> nanosheets; carbon derivatives like fullerenes, carbon nanotubes, nanodots and metal-organic frameworks.<sup>6,10,25,26</sup>

Among these nanozymes, nanostructured MnO<sub>2</sub> has been reported to possess both SOD and catalase (CAT)-like activities.<sup>27,28</sup> Biocompatibility and biodegradability of MnO<sub>2</sub> materials have been confirmed as well.<sup>29–31</sup> They were applied in numerous fields such as energy storage,<sup>32,33</sup> chemotherapy,<sup>34</sup> sensing,<sup>35</sup> catalysis,<sup>36,37</sup> and drug delivery.<sup>38</sup> However, MnO<sub>2</sub> nanoparticles, as the case with most metal oxides, are water-insoluble materials with aqueous colloidal

<sup>a</sup> MTA-SZTE Lendület Biocolloids Research Group, University of Szeged, H-6720 Szeged, Hungary. E-mail: szistvan@chem.u-szeged.hu

<sup>b</sup> Interdisciplinary Excellence Center, Department of Physical Chemistry and Materials Science, University of Szeged, H-6720 Szeged, Hungary

† Electronic supplementary information (ESI) available: Material composition data, dispersions characteristics, deconvolution of XPS peaks as well as TEM and SEM images. See DOI: 10.1039/d1tb00505g

dc\_1931\_21

stability that is heavily dependent on the experimental conditions such as temperature, pH, ionic strength, and the presence of stabilizing agents (*e.g.*, surfactants or polymers).<sup>39</sup> Often, the industrial and biological applications of these nano-materials such as catalysis and drug delivery might normally be carried out at pH or ionic strength conditions where such particles are mostly unstable or too small to separate from the reaction mixture after the catalytic reaction is terminated. Thus, a versatile use of such materials necessitates a full understanding of their colloidal behavior.

Therefore, formulation of MnO<sub>2</sub> on larger support particles is desirable to improve their colloidal stability, to ease separation and to concentrate them in a smaller space to achieve efficient local catalytic activity. In our previous study, it was shown that anti-oxidant Prussian blue particles can be successfully immobilized on amidine latex particles of significantly larger size.<sup>39</sup> This prompted the idea to decorate supporting latex particles with manganese oxide nanoparticles, which are known as multifunctional materials in scavenging of reactive oxygen species. Heteroaggregation of differently sized particles in aqueous dispersions has been utilized to investigate fundamental processes and also to prepare various composite materials.<sup>40–43</sup> However, to the best of our knowledge, this is the first time, when broad-spectrum antioxidant MnO<sub>2</sub> NPs and latex particles are used for such a purpose.

Therefore, in the present work, polyelectrolyte functionalized MnO<sub>2</sub> NPs (PMn) were synthesized and their heteroaggregation with sulfate latex (SL) particles was investigated in a wide range of PMn-to-SL mass ratio. Charging and aggregation processes were explored by electrophoretic and dynamic light scattering to establish the colloidal stability regimes, while the structural features were studied with spectroscopy and electron microscopy methods. The SOD and CAT-like activities of the bare MnO<sub>2</sub> NPs and the obtained SPMn particles were extensively investigated at different temperatures. The preparation and catalytic activity assessment are illustrated in Scheme 1.

## Experimental section

### Materials

H<sub>2</sub>O<sub>2</sub> (30% m/m), HCl (37% m/m), NaCl (~99.5%), acetone (~99.8%), absolute ethanol (≥99.8%), NaOH (AnalaR

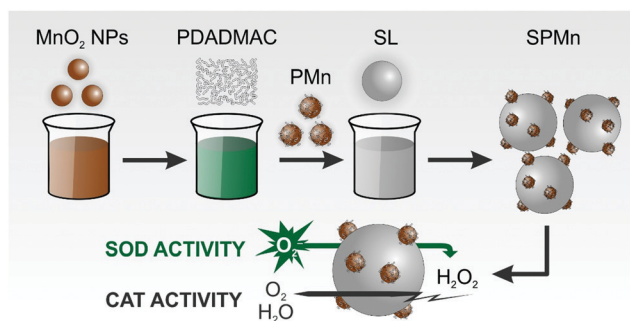
NORMAPUR<sup>®</sup>), and K<sub>2</sub>S<sub>2</sub>O<sub>8</sub> (98%, AnalaR NORMAPUR<sup>®</sup>) were purchased from VWR<sup>™</sup>, while KMnO<sub>4</sub> (reagent grade, 99%), nitro blue tetrazolium chloride (90%), styrene (99%), and polyvinylpyrrolidone (58 000 g mol<sup>-1</sup>) were bought from Acros Organics<sup>™</sup>. Oleic acid (90%, technical grade), PDADMAC (200 000–350 000 g mol<sup>-1</sup>, 20 wt%), and xanthine oxidase (lyophilized powder, 0.4–1.0 units per mg protein) were obtained from Sigma-Aldrich. Xanthine (99%) was purchased from Alfa Aesar. Phosphate buffer solution was prepared using NaH<sub>2</sub>PO<sub>4</sub> (99%, anhydrous) and Na<sub>2</sub>HPO<sub>4</sub> (≥99%, GPR RECTAPUR<sup>®</sup>), which were obtained from Acros Organics<sup>™</sup> and VWR<sup>™</sup>, respectively. Hellmanex<sup>®</sup> III cleaning agent was bought from Hellma while Spectra/Por<sup>®</sup> 6 dialysis membrane tubing was obtained from SpectrumLabs. The pH was kept at (9.0 ± 0.2) throughout all experiments, unless indicated otherwise. The VWR<sup>™</sup> Purity TU 3 UV/UF+ system was used to obtain ultrapure water, which was further filtered using PVDF-based 0.1 μm syringe filters purchased from MILLEX-VV. The ionic strength was adjusted by NaCl solutions.

### Preparation of MnO<sub>2</sub> NPs and SL

The glassware were carefully cleaned with Hellmanex<sup>®</sup> III and concentrated HCl solution. The MnO<sub>2</sub> NPs were prepared by following a reported procedure.<sup>28</sup> Briefly, 1.0 g of KMnO<sub>4</sub> was dissolved in 500 mL of ultrapure water and the resulting solution was vigorously stirred for 30 min. Then 10 mL of oleic acid was added, and the reaction mixture was left under vigorous stirring at 28 °C for 5 h. The formed black precipitate was then collected by centrifugation and washed with ultrapure water and ethanol to remove unreacted compounds. The obtained solid material was dried for 10 h at 80 °C. Finally, the nanoparticles were dispersed in ultrapure water to obtain a 10 g L<sup>-1</sup> stock. The SL particles were prepared by emulsifier-free emulsion polymerization using K<sub>2</sub>S<sub>2</sub>O<sub>8</sub> as an initiator.<sup>44</sup> In a typical synthesis, 12.1 g styrene and 60.5 mg polyvinylpyrrolidone (PVP) were added to 100 mL of deionized water at room temperature in a 250 mL three-neck round bottom flask, that is kept in an oil bath under N<sub>2</sub> atmosphere. The mixture was then stirred for 30 min at 400 rpm, and the temperature was increased progressively to 70 °C. Subsequently, 300 mg of K<sub>2</sub>S<sub>2</sub>O<sub>8</sub> were dissolved in 20 mL of deionized water, and the resulting solution was added to the reaction mixture that is then kept for 24 h at 70 °C. After the mixture was cooled to room temperature, the remnant styrene and PVP were removed by repeated washing, centrifugation, and redispersing. The product was washed by pure water and ethanol and dialyzed against water for one day. The final SL concentration was 50 g L<sup>-1</sup>, obtained by diluting the mother liquor.

### Preparation of PMn and SPMn particles

The immobilization of PDADMAC on the surface of MnO<sub>2</sub> NPs was achieved by simply mixing proper volumes of PDADMAC and MnO<sub>2</sub> NPs dispersions, followed by addition of NaCl solution to fix the ionic strength. The concentration of MnO<sub>2</sub> NPs was fixed, while the PDADMAC dose (in mg PDADMAC/g MnO<sub>2</sub> NPs) was altered until overall positively charged PMn



Scheme 1 Illustration of the synthesis and enzymatic activity of the SPMn hybrid composite.

particles were obtained. Similar procedure was followed during preparation of SPMn, where the concentration of SL was fixed as the dose of positively charged PMn (in mg PMn/g SL) was altered. After the addition of proper volumes of PMn and SL, the ionic strength was fixed by NaCl solution. In both cases, the origin of the driving forces was mainly electrostatic attraction between the oppositely charged PDADMAC and MnO<sub>2</sub> NPs as well as between PMn and SL under the applied experimental conditions. The final SPMn dispersions were homogenized by ultrasonication.

### Electrophoretic light scattering

Zeta potential values were determined using an Anton Paar Litesizer™ 500 device equipped with a 658 nm wavelength laser source, with the applied voltage kept at 200 V throughout all electrophoretic light scattering measurements. The initially measured electrophoretic mobilities were converted into zeta potentials by the Smoluchowski equation.<sup>45</sup> First, the pH-dependence of zeta potential of MnO<sub>2</sub> NPs and SL was studied in the pH range 3–11 at constant ionic strength of 1 mM. In a typical procedure, two 50 ppm stock MnO<sub>2</sub> NPs dispersions were prepared at pH 3 and 11, respectively. Then, a series of 8 mL MnO<sub>2</sub> NPs dispersions was prepared by mixing different portions of the two stocks, so that the pH in the series of dispersions gradually changed from 3 to 11. After each mixing, the resulting dispersion was homogenized by vortex and its pH value was unambiguously measured with a WTW pH benchtop meter (inoLab® pH 7310). The same procedure was followed for SL, except the concentration of two SL stocks was set at 125 ppm. For the determination of zeta potential of the SL at different salt concentrations, several 125 ppm SL dispersions were prepared with an ionic strength gradually varies between 1–1000 mM. In addition, the effect of PDADMAC dose on the charge of MnO<sub>2</sub> NPs was obtained in the 0.1–1000 mg PDADMAC/g MnO<sub>2</sub> NPs dose range at 1 mM ionic strength. In each sample, the MnO<sub>2</sub> NPs concentration was kept at 100 ppm, while the amount of polyelectrolyte was adjusted to the desired dose. The effect of PMn (where the dose of adsorbed PDADMAC on MnO<sub>2</sub> NPs results in positively charge PMn, as detailed later) on the charge of SL was studied in the dose range of 0.01–1000 mg PMn/g SL at 1 mM ionic strength. In all samples, the SL concentration was kept at 125 ppm, while the amount of PMn was adjusted to the desired dose. Generally, the prepared dispersions were left to equilibrate for 2 hours at room temperature. To measure the zeta potential, 700 μL were withdrawn from the dispersion of interest and were transferred to an omega cuvette (Anton Paar™). The zeta potential measurement was then performed at (25.0 ± 0.2) °C and reported as an average of 6 runs.

### Dynamic light scattering

The hydrodynamic radius of the particles was measured with dynamic light scattering (DLS) using an ALV-NIBS/HPPS Particle sizer equipped with a 632.8 nm laser source. The scattered light was collected at 173° and data analysis was based on the cumulant fit.<sup>46</sup> The DLS sample preparation is

identical to that followed in the electrophoretic part above, with the exception that each measurement was started immediately after addition of the desired volume of SL, MnO<sub>2</sub> NPs, or PMn to the corresponding samples. The total volume of each sample was 2.0 mL and the experiments were carried out in disposable polystyrene cuvettes at (25.0 ± 0.2) °C. Additionally, the pH-dependence of hydrodynamic radius of MnO<sub>2</sub> NPs and SL was studied in the pH range 3–11 at constant ionic strength of 1 mM. In all time-resolved DLS measurements, the hydrodynamic radius *versus* time curves contained 30–100 measurement points for each sample depending on the aggregation rate. The colloidal stability was expressed in terms of stability ratio (*W*) calculated with the following equation.<sup>47</sup>

$$W = \frac{k_{\text{app(fast)}}}{k_{\text{app}}} \quad (1)$$

where  $k_{\text{app}}$  is the apparent aggregation rate constant and  $k_{\text{app(fast)}}$  is the apparent aggregation rate constant at 1.0 M ionic strength, at which condition the aggregation process is solely controlled by the diffusion of the particles, *i.e.*, rapid particle aggregation occurs. The apparent aggregation rate constant was calculated from the hydrodynamic radius *versus* time plots as follows.<sup>46</sup>

$$k_{\text{app}} = \frac{1}{R_{\text{h}}(0)} \cdot \left( \frac{dR_{\text{h}}(t)}{dt} \right)_{t \rightarrow 0} \quad (2)$$

where  $R_{\text{h}}(0)$  is the hydrodynamic radius of the monomer particles and  $\frac{dR_{\text{h}}(t)}{dt}$  is the slope of the linear fit of the hydrodynamic radius *versus* time data points of the sample of interest. Stability ratio values close to unity indicate rapid or diffusion-controlled aggregation, while stable samples have high or not even measurable stability ratio values. In addition, the time during which half of the primary particles aggregate into dimers is called the aggregation half-time ( $T_{1/2}$ ), which was calculated using the following equation.<sup>48</sup>

$$T_{1/2} = \frac{2}{kN_0} \quad (3)$$

where  $N_0$  is the particle number concentration and  $k$  is Smoluchowski's diffusion-controlled aggregation rate constant.<sup>46</sup>

### Electron microscopy

The morphologies of the particles (SL, MnO<sub>2</sub> NPs, and SPMn) were analyzed by scanning (SEM, Hitachi S4700) and transmission electron microscopy (TEM, FEI Tecnai G2). In TEM sample preparation, 5 μL of the particle dispersion was introduced on a copper-coated carbon mesh. Each aliquot was left to adsorb for 10 seconds. The sample grids were prepared 30 min before the measurements. To prepare SEM samples, 5 μL volumes from each dispersion were introduced on the SEM sample holder, a piece of silicon wafer on an aluminum disk, and were left to dry for 10 min. The sample holder is coated with Au thin film *via* sputtering before it was introduced into the microscope.



dc\_1931\_21

### X-Ray photoelectron spectroscopy

The X-ray photoelectron spectroscopy (XPS) measurements were performed with a SPECS instrument equipped with a PHOIBOS 150 MCD 9 hemispherical analyzer, under a main-chamber pressure in the  $10^{-9}$ – $10^{-10}$  mbar range. The analyzer was in fixed transmission mode with 40 eV pass energy for the survey scan and 20 eV pass energy for the high-resolution scans. Al K $\alpha$  X-ray source was used at 14 kV and 150 W power. Charge referencing was done to the adventitious carbon (284.8 eV) on the surface of the sample. For spectrum evaluation, CasaXPS commercial software package was used.

### Atomic force microscopy

The SPMn composite were further investigated using a Multi-mode Nanoscope IIIa atomic force microscope (AFM, Digital Instruments, USA). The images were acquired in tapping mode in air at room temperature using a Si tip cantilever (Veeco Nanoprobe Tips RTESPA model) with a resonance frequency of 275–300 kHz. Height- and amplitude-mode images were recorded simultaneously with 1.0 Hz scan rate. Processing and analysis of the images were carried out using the off-line software Nanoscope V614r1. The sample for AFM was prepared by depositing a dilute dispersion on a freshly cleaved mica (Ted Pella, Highest Grade V1) and were left to dry at room temperature.

### Catalase assay

The catalase activity of MnO<sub>2</sub> NPs and SPMn was confirmed *via* the catalase assay reported elsewhere.<sup>28,49</sup> In the presence of catalase or its mimics, H<sub>2</sub>O<sub>2</sub> breaks down into water and molecular oxygen, and the reduction in the absorbance of H<sub>2</sub>O<sub>2</sub> at a wavelength of 240 nm is quantitatively observed with UV-Vis spectrophotometry (GENESYS™ 10S, Thermo Fischer Scientific). The concentration of MnO<sub>2</sub> NPs or SPMn was kept constant, while the concentration of H<sub>2</sub>O<sub>2</sub> was varied between 0 and 1 mM. The pH in the final samples was kept at (7.0 ± 0.1) using phosphate buffer. Thus, in each of the 2400  $\mu$ L samples, a varied volume of H<sub>2</sub>O<sub>2</sub> was mixed with 1000  $\mu$ L of 120 mM phosphate buffer followed by a volume of ultrapure water to obtain 2200  $\mu$ L sample. The cuvette was then vortexed for 10 seconds. Finally, 200  $\mu$ L of MnO<sub>2</sub> NPs dispersion (120 ppm) or SPMn dispersion (which is 120 ppm in MnO<sub>2</sub> NPs, at 200 mg PDADMAC/g Mn and 100 PMn/g SL) was added and the cuvette was vortexed for 3 seconds, and then immediately introduced into the spectrophotometer, where the linear absorbance *versus* time plot was recorded at 240 nm for 10 min. The slopes of absorbance *versus* time curve represent the corresponding reaction rates ( $\nu$ ) measured in absorbance unit per second. The reaction rate was converted to mM s<sup>-1</sup> units using the Beer–Lambert law. The optical light path is 1 cm and the molar extinction coefficient of H<sub>2</sub>O<sub>2</sub> is 39.4 M<sup>-1</sup> cm<sup>-1</sup>.<sup>28</sup> Finally, the reaction rate ( $\nu$ ) was plotted as a function of H<sub>2</sub>O<sub>2</sub> concentration ([S]) in the corresponding sample. The kinetics of enzymatic reaction was assessed by fitting the rate *versus* concentration data with

Michaelis–Menten model,<sup>50</sup> as expressed in the following equation.

$$\nu = \frac{\nu_{\max}}{K_m + [S]} \quad (4)$$

where  $\nu_{\max}$  is the maximum possible reaction rate that is independent of the substrate concentration and  $K_m$  is the Michaelis–Menten constant.

### Superoxide dismutase assay

The Fridovich assay<sup>51</sup> was used to probe the SOD activity of MnO<sub>2</sub> NPs or SPMn. The SOD enzyme catalyzes the dismutation of superoxide radical ions. Here, the xanthine oxidation reaction, catalyzed by xanthine oxidase, generates superoxide radical ions, which react with nitroblue tetrazolium (NBT) that turns from yellow to blue upon reaction with the radicals. In the presence of SOD or a mimicking material, the generated radical ions are scavenged reducing the amount of blue product as well as the intensity of blue color, which can be monitored by UV-Vis spectrophotometry. In a typical measurement, only the MnO<sub>2</sub> NPs or SPMn concentration was changed between 0 and 2 ppm. In the final sample, the phosphate buffer was kept at 10 mM to adjust pH (7.0 ± 0.1). Thus, in each of the 3000  $\mu$ L samples, 200  $\mu$ L xanthine (3.0 mM) and 100  $\mu$ L NBT (3.0 mM) were added to calculated volume of MnO<sub>2</sub> NPs or SPMn dispersion, followed by addition of a portion of phosphate buffer to obtain 2700  $\mu$ L sample. The cuvette was then vortexed for 5 seconds. Finally, 300  $\mu$ L xanthine oxidase (1.5 g L<sup>-1</sup>) was added to the sample before it was immediately vortexed for 5 seconds and introduced into the spectrophotometer. The change in absorbance with time was recorded for 6 min at 565 nm wavelength. Furthermore, eight blanks were also measured, each of which was prepared by adding all reagents mentioned except MnO<sub>2</sub> NPs or SPMn, with additional volume of phosphate buffer solution to keep the final concentrations identical. The inhibition curve is created by plotting the inhibition ( $I$ ) of the radical-NBT reaction for each sample against the final MnO<sub>2</sub> NPs or SPMn concentration in the corresponding sample. The inhibition can be calculated as follows.

$$I = \frac{\Delta A_0 - \Delta A_s}{\Delta A_0} \times 100 \quad (5)$$

where  $\Delta A_s$  is the change in absorbance during the 6 min measurement time and  $\Delta A_0$  is the averaged value of the absorbance change for the eight blank samples. The concentration of the nanozyme that causes 50% inhibition of is called the IC<sub>50</sub> value. During the assays, light scattering by the particles does contribute to the absolute value of absorbance, however, this factor was eliminated by taking the relative increase in the absorbance in the individual experiments.

## Results and discussion

### Characterization of the MnO<sub>2</sub> NPs and SL

The surface chemical composition of the prepared MnO<sub>2</sub> NPs was explored with XPS. The recorded survey scan, shown in

dc\_1931\_21

Fig. 1, reveals the presence of Mn, O, C, and K elements on the surface of the sample. The quantitative XPS composition analysis resulted in the following composition of the sample: 23.4 at% Mn, 19.5 at% C, 1.3 at% K and 55.8 at% O (Table S1, see ESI†). The large number of different oxidation states, the presence of mixed valence oxides, and the complex multiplet splitting makes the deconvolution of Mn 2p region rather complicated (Fig. S1a in the ESI†).<sup>52,53</sup> For our purposes, an initial assessment of the average oxidation state of Mn on the surface was carried out by determining the peak separation of the Mn 2s peaks shown in Fig. S1b (ESI†). The determined peak separation of 5.1 eV is slightly lower than values determined for common Mn(III) compounds (5.4 eV for MnOOH or 5.5 eV for Mn<sub>2</sub>O<sub>3</sub>). This signals that other compounds with different valence states are also present on the surface of the sample (e.g., Mn(IV) with 4.4 eV for MnO<sub>2</sub>). This value is in good agreement for the splitting of Na<sub>2</sub>MnO<sub>2</sub> type compounds.<sup>54</sup> Note, however, that care must be exercised with this approach, as it is not sufficient to reliably determine the chemical species present on the surface, and fitting of the Mn 2p peak must be carried out.<sup>53</sup> The high-resolution C 1s spectra in Fig. S1c (ESI†) can be attributed to the presence of adventitious carbon on the surface of the samples. The peaks 284.79 eV refer to C–C and C–H states while those at 288.09 eV and 286.14 eV indicate the presence of C–OH and O–C=O functionalities. The small amount of K<sup>+</sup> on the sample surface likely originates from the chemicals used during the synthesis procedure. The resolved high-resolution O 1s spectrum presented in Fig. S1d (ESI†) shows two components, one originating from the lattice oxide (529.73 eV) and the other originating from the presence of surface hydroxides (531.39 eV). Their position and comparable contribution suggest the prevalence of hydroxide species on the sample surface.<sup>53</sup> In a following step, the fitting of the Mn 2p

peak was carried considering the multiplet splitting of the species.<sup>52</sup> It was finally concluded that the surface primarily consists of MnO(OH) (64%) and MnO<sub>2</sub> (36%) species.

The pH-dependence of size and zeta potential of MnO<sub>2</sub> NPs is shown in Fig. 2a. In acidic and neutral pH, the MnO<sub>2</sub> NPs undergo excessive and rapid aggregation and the hydrodynamic radii of aggregates exceeded 1.5 μm. Thus, these conditions are not suitable to obtain monodisperse particle dispersions for further experiments. As the pH becomes basic, the particle size decreased significantly, reaching a radius of (83 ± 2) nm with a PDI of 11.9% at pH 9 and remained the same within the experimental error until pH 11.

These aggregation trends can be explained by observing the accompanying changes in zeta potentials.<sup>55</sup> Accordingly, the particles have low absolute zeta potential less than 20 mV up to pH 7, where the electrostatic forces are overcome by the van der Waals forces.<sup>56</sup> In basic medium, surface hydroxides are deprotonated, and at pH 9, MnO<sub>2</sub> NPs acquire a high negative zeta potential of (−37 ± 1) mV, which is high enough for electrostatic repulsion forces to dominate. In Fig. 2b, the SL zeta potential and size dependence on the pH is shown. Throughout the pH range of 3–11, the SL particles maintained an average hydrodynamic radius of (432 ± 16) nm, indicating high colloidal stability. The magnitude of the zeta potential increases gradually as the pH is increased owing to the increased deprotonation of the sulfate groups on the surface of SL. At pH 9, SL particles have a zeta potential of (−65 ± 1) mV and a hydrodynamic radius of (441 ± 33) nm with a PDI of 20.9%. The dispersion characteristics of the MnO<sub>2</sub> NPs and SL particles at pH 9 are summarized in Table S2 (ESI†).

The morphology of SL particles as well as MnO<sub>2</sub> NPs was visualized *via* electron microscopy. The SEM and TEM images of SL particles, shown in Fig. S2a and b (ESI†), respectively, feature the well-defined spherical morphology as well as the relatively low polydispersity of the prepared SL particles. On the other hand, MnO<sub>2</sub> NPs show flaky morphology as shown in the SEM image in Fig. S2c (ESI†). The aggregated state of the sample is attributed to drying process during SEM sample preparation. The TEM images of MnO<sub>2</sub> NPs, shown in Fig. S2d–f (ESI†), further feature the flaky nature of the MnO<sub>2</sub> NPs. Note that the hydrodynamic sizes measured by DLS are slightly higher than those of the individual particles observed in the SEM and TEM images due to the polydispersity of the particles and the presence of trace aggregates in the samples, whose effect is more pronounced in the light scattering measurements.

### Homoaggregation of SL and MnO<sub>2</sub> NPs

The aggregation tendency of SL at different SL concentrations and 1.0 M ionic strength was carried out to optimize the experimental conditions for later aggregation rate measurements. By setting the background salt concentration at 1.0 M, all electrostatic repulsive forces are screened and thus, SL are expected to undergo rapid aggregation according to the Derjaguin, Landau, Verwey and Overbeek (DLVO) theory.<sup>57,58</sup> As shown in Fig. 3a, the slopes of the linear fits of

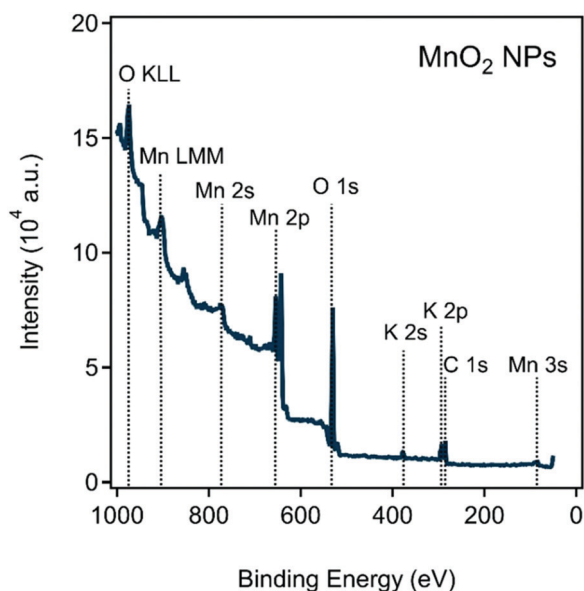


Fig. 1 XPS survey spectrum of the obtained MnO<sub>2</sub> NPs. The O KLL and Fe LMM represent Auger transitions involving energy levels K, L and M.

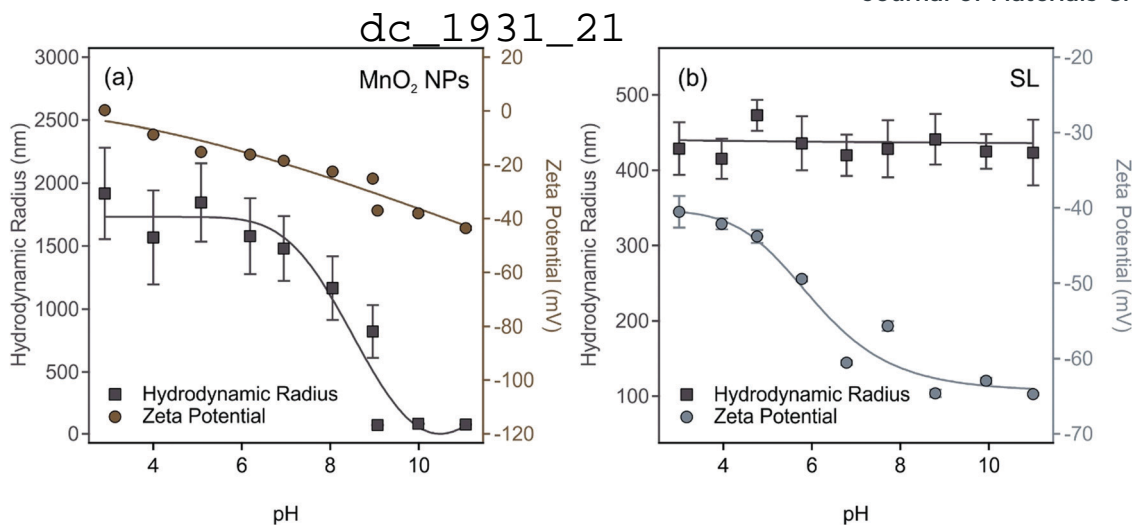


Fig. 2 The pH dependence of the hydrodynamic radius (squares) and zeta potential (circles) of (a) MnO<sub>2</sub> NPs and (b) SL particles. The concentration of the MnO<sub>2</sub> NPs and SL particles was 50 and 125 ppm, respectively, in the dispersions. The ionic strength was set to 1 mM. The lines are just to guide the eyes.

hydrodynamic radius *versus* time data increase when the concentration of SL was raised.

The apparent aggregation rate constants ( $k_{app}$ ) as well as the aggregation half-time ( $T_{1/2}$ ) for the corresponding samples were calculated using eqn (2) and (3), respectively, which are plotted in Fig. 3b as a function of the SL concentration. The data clearly show that  $k_{app}$  increases and  $T_{1/2}$  decreases with increasing particle concentration as a result of accelerated aggregation in concentrated samples. Moreover, in measurements such as those in Fig. 3a, the linear trends in the hydrodynamic radius–time data refer to early stage of aggregation and indicate the absence of higher ranked aggregates, which would cause deviation from linearity.<sup>46</sup> Accordingly, a compromised SL concentration of 125 ppm was used in further measurements, where early stage of aggregation can be followed, while the

scattering intensity is high enough for reliable DLS measurements.

The salt-induced aggregation of both particles was also assessed at different ionic strengths. Eqn (1) was used to obtain the stability ratio values at the corresponding NaCl concentrations. As shown in Fig. 4, the stability ratio of SL significantly decreased as the ionic strength was increased until it reached unity at the critical coagulation concentration (CCC) of 250 mM, the concentration that separates slow and fast aggregation regimes. The DLVO theory states that the salt constituent ions screen the surface charge resulting in shrinking of the electric double layer and weakening of the repulsive electrostatic forces around SL particles. Thus, when salt concentrations equal or exceed the CCC, the van der Waals attractive forces dominate, and particles undergo diffusion-controlled aggregation.

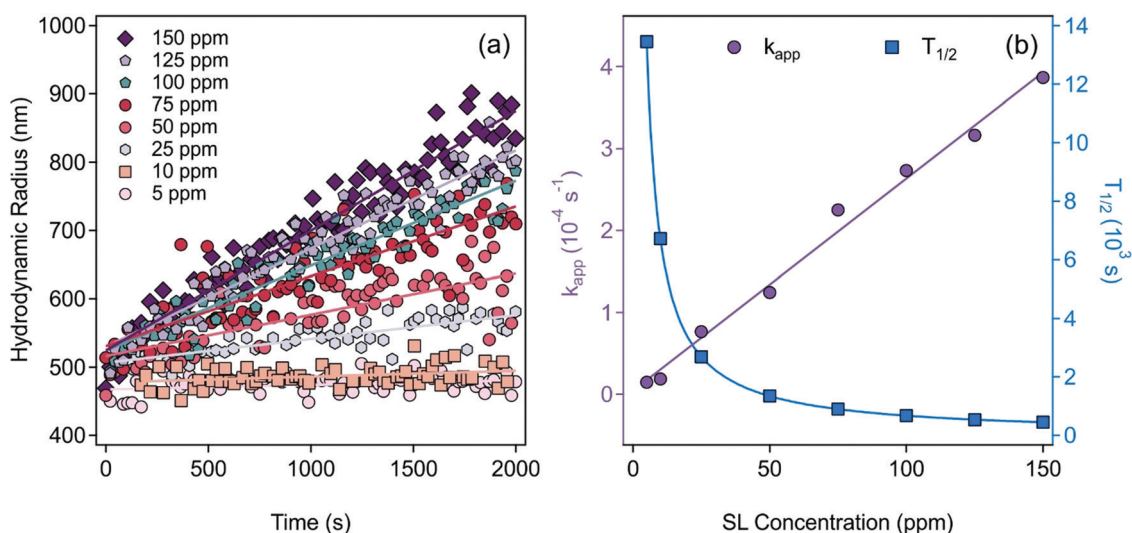


Fig. 3 (a) Time-resolved DLS measurements of SL at different concentrations at 1.0 M ionic strength. The straight lines represent the linear fits used to calculate the apparent aggregation rate constants with eqn (2). (b) The apparent aggregation rate constant ( $k_{app}$ ) as well as the aggregation half-time ( $T_{1/2}$ ) at different particle concentrations, obtained *via* eqn (2) and (3), respectively.

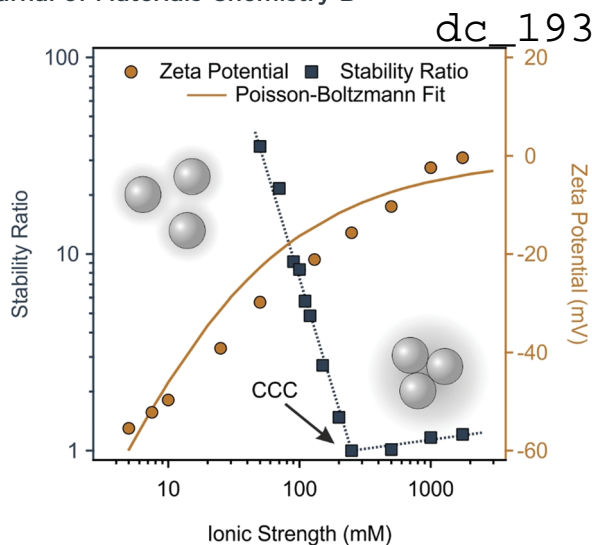


Fig. 4 Stability ratio (squares) and zeta potential (circles) values of SL particles as a function of the ionic strength. The pH was kept at 9 and the SL concentration was 125 ppm in all samples. The dotted blue line only serves as eye guidance. The continuous gold line is the Poisson–Boltzmann fit.

Similar findings are reached when the accompanying changes in SL zeta potentials at different ionic strengths are measured. SL possesses high zeta potential at low salt levels due to the presence of the deprotonated sulfate groups. As more salt is introduced, the zeta potential around SL drops owing to surface charge screening. The Poisson–Boltzmann theory<sup>59</sup> was used to fit the zeta potential data and a charge density of  $-15.0 \text{ mC m}^{-2}$  was determined at the slip plane (Table S2, ESI<sup>†</sup>).

Similar tendencies can be seen for  $\text{MnO}_2$  NPs in Fig. 5. The increase in the ionic strength gradually decreased the stability ratio as well as the magnitude of zeta potential because of charge screening, and the subsequent predominance of van

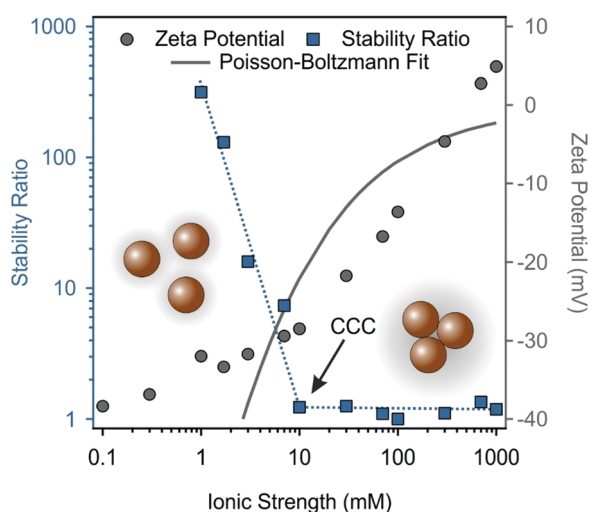


Fig. 5 Stability ratio (squares) and zeta potential (circles) values of 100 ppm  $\text{MnO}_2$  NPs dispersions as a function of the ionic strength. The pH was kept at 9 in all samples. The dotted blue line only serves as eye guidance. The continuous grey line is the Poisson–Boltzmann fit.

der Waals forces. The CCC occurred at 10 mM, which indicates rather low colloidal stability of the bare  $\text{MnO}_2$  NPs. Upon fitting the zeta potential data with the Poisson–Boltzmann model, the resulting surface charge density of  $\text{MnO}_2$  NPs was  $-5.2 \text{ mC m}^{-2}$ . In Fig. 5, the Poisson–Boltzmann fit somewhat deviates from the  $\text{MnO}_2$  NPs zeta potential data points at low salt concentrations, which is attributed to the electrokinetic effect reported earlier.<sup>60</sup> The surface charge density of the  $\text{MnO}_2$  NPs is significantly lower than the one determined for SL, which led to a higher CCC for SL in line with the prediction of the DLVO theory, since the resistance against salt-induced aggregation is stronger for particles of higher charge and thus, of stronger electrical double layer forces. Besides, the aggregation mechanism follows the prediction of the DLVO theory in both cases, similar to other charged colloidal particles dispersed in salt solutions.<sup>46,55,61–66</sup>

#### PDADMAC functionalization of $\text{MnO}_2$ NPs

Since the aim was to attach  $\text{MnO}_2$  NPs to the SL surfaces, the charge balance must be changed to achieve opposite charges on the interacting particles. Accordingly,  $\text{MnO}_2$  NPs were functionalized with PDADMAC polyelectrolyte. It is well known that polyelectrolytes adsorb strongly on oppositely charged surfaces and other molecules,<sup>67,68</sup> therefore, it was expected that the original negative sign of  $\text{MnO}_2$  NPs turns to positive after adding the appropriate amount of PDADMAC. Therefore, the precise dose was determined and fine-tuned so that the functionalized particles form stable dispersions. The zeta potential values of  $\text{MnO}_2$  NPs determined at different PDADMAC doses are shown in Fig. 6.

At low PDADMAC doses, the overall particle charge was negative, as indicated by the zeta potential values, which gradually increased as more PDADMAC was introduced. Around 20 mg PDADMAC/g  $\text{MnO}_2$  NPs, the zeta potential approached zero. At the isoelectric point (IEP), the amount of

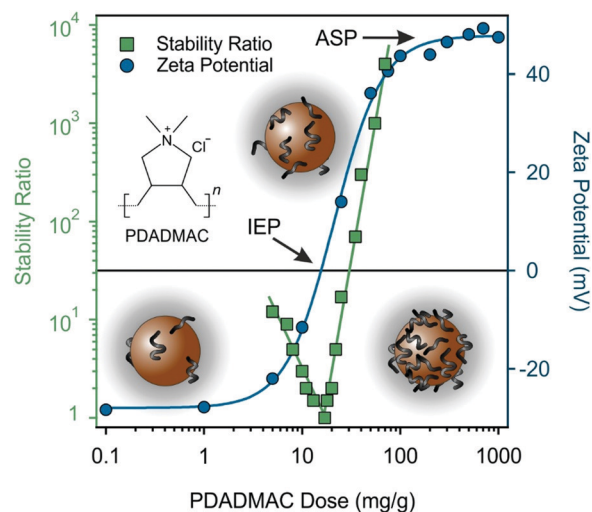


Fig. 6 Stability ratio (squares) and zeta potential (circles) values of  $\text{MnO}_2$  NPs at different PDADMAC doses. The ionic strength was 1 mM and the pH was 9. The concentration of  $\text{MnO}_2$  NPs was kept at 100 ppm. The solid lines serve as eye guidance. The polyelectrolyte concentration is expressed in mg PDADMAC per one gram of  $\text{MnO}_2$  NPs.



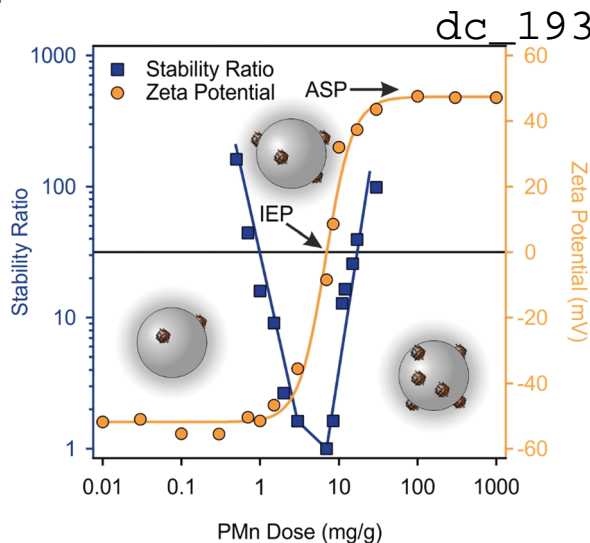


Fig. 7 Stability ratio (squares) and zeta potential (circles) values of SL particles in the presence of PMn at different concentrations. The concentration of SL was kept at 125 ppm, whereas the ionic strength was 1 mM and the pH was 9. The  $\text{mg g}^{-1}$  unit refers to mg PMn per one gram of SL. The solid lines serve as eye guidance only.

positive and negative charges are balanced and thus, the particles have zero net charge. Higher doses of PDADMAC resulted in charge reversal leading to positively charged particles. Similar charge reversal was reported earlier for oppositely charged particle–polyelectrolyte systems.<sup>64,66,69</sup> The zeta potential reached a maximum value at the onset of the adsorption saturation plateau (ASP) at  $100 \text{ mg g}^{-1}$  dose, where the  $\text{MnO}_2$  NPs surface became saturated with adsorbed PDADMAC and further added polyelectrolytes remain dissolved in the solution.<sup>70</sup>

Moreover, the stability ratios were measured under the same experimental conditions to assess the colloidal stability of the PDADMAC-functionalized  $\text{MnO}_2$  NPs dispersions. Fig. 6 shows that the gradual decrease in zeta potential values is paralleled with changes in the stability ratios. When the particles have high zeta potential (either positive or negative), the stability ratio values are large indicating stable dispersions. However, at PDADMAC doses around the IEP, the stability ratios drop to a value of one, which indicates rapid particle aggregation and unstable dispersions. Such a behavior is typical for oppositely charged particle–polyelectrolyte systems<sup>63,66,67</sup> and qualitatively agrees with the prediction of the DLVO theory.<sup>57,58</sup>

Lastly, since the  $\text{MnO}_2$  NPs surface became saturated with PDADMAC at doses that occur at or beyond the onset of the zeta

potential plateau, the particles prepared at  $200 \text{ mg g}^{-1}$  dose are denoted as PMn. At this experimental condition, the forming PMn possess high positive charge and high stability ratio and they are suitable for heteroaggregation with oppositely charged SL.

#### Heteroaggregation of PMn with SL

Based on the above results, oppositely charged PMn and SL particles were mixed in different ratios, while the concentration of negatively charged SL was kept at 125 ppm. In the resulting SPMn composite, the intensity of the scattered light originates mostly from SL particles rather than  $\text{MnO}_2$  NPs, as the magnitude of the intensity is proportional to the sixth power of the size of the scattering object,<sup>71</sup> which is also evident from the scattering intensity data of individual particles in Table S2 (ESI<sup>†</sup>). The zeta potential values at different PMn doses are shown in Fig. 7. At low doses, the overall charge of the particles is negative and slowly increased as more PMn were introduced into the system indicating their adsorption on the SL particles. The IEP occurred around a dose of  $10 \text{ mg g}^{-1}$ , where the zeta potential approaches zero. Higher doses of PMn led to positively charged particles. Such a charge inversion is common in polyelectrolyte–particle systems as discussed before, nevertheless, it was rarely reported in dispersions containing oppositely charged particles.<sup>72,73</sup> At and beyond  $30 \text{ mg g}^{-1}$ , the zeta potential reached a maximum value, where SL surface most likely became saturated with adsorbed PMn at dose values corresponding to the onset of the ASP.

Stability ratios were determined under the same experimental conditions. As Fig. 7 shows, large magnitude of zeta potential in both in the negative and positive regimes corresponds to large stability ratio values indicating stable dispersions. However, at PMn doses around the IEP, the stability ratios approach unity indicating unstable dispersions. Several studies on latex particles have attributed the predominant interparticle forces to DLVO-type interaction,<sup>65,67,74</sup> as discussed in the previous section. Thus, it is certain that the functionalization with PMn particles did not lead to the appearance of major additional interaction forces, and the aggregation mechanism is driven by the balance between DLVO type forces, namely, electrostatic double layer repulsion and van der Waals attraction. The latter one gradually predominates, when the overall charge of the particles approaches zero, *i.e.*, around the IEP, while the particles are stabilized by electrostatic repulsion at doses below or above this point. SPMn refers to a composite of 100 mg PMn per one gram of SL forming highly stable colloid.

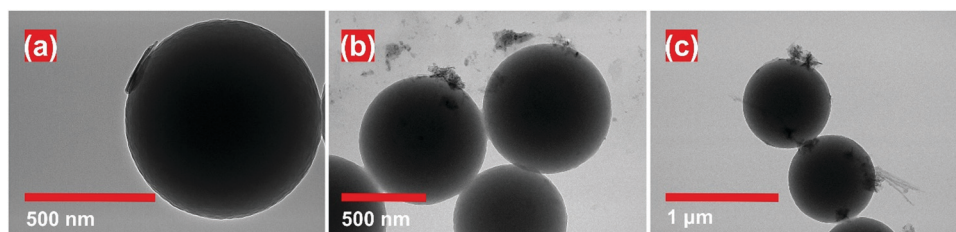


Fig. 8 TEM images of SPMn system at PMn doses of (a)  $0.1 \text{ mg g}^{-1}$ , (b)  $10 \text{ mg g}^{-1}$ , and (c)  $100 \text{ mg g}^{-1}$ .

dc\_1931\_21

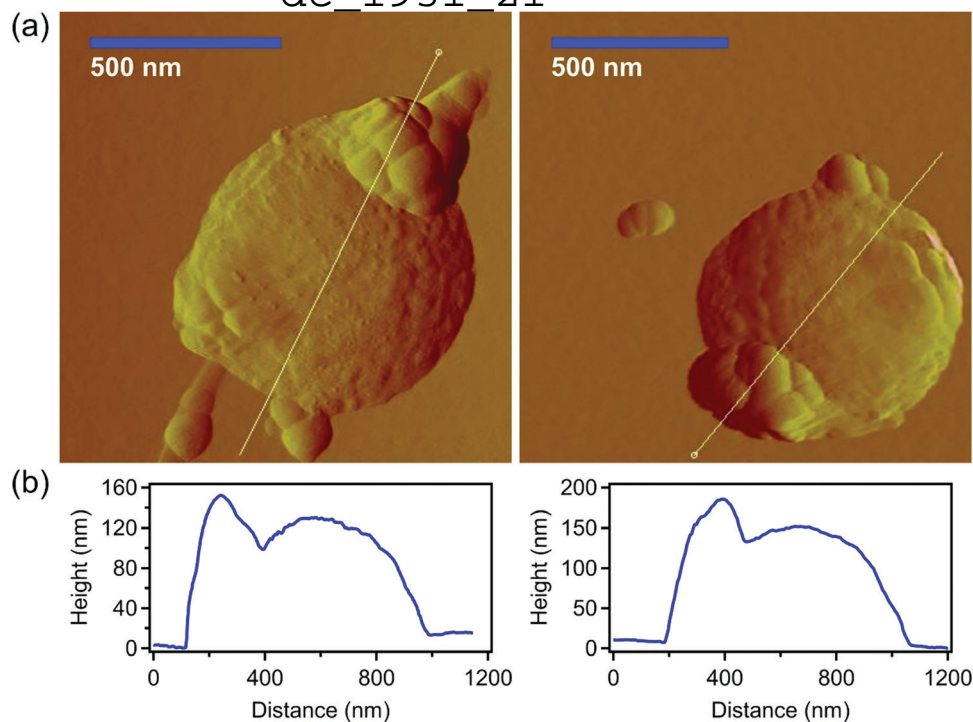


Fig. 9 (a) AFM amplitude images of SPMn deposited on a mica substrate as well as (b) the height profiles taken along the indicated white line.

The immobilization of PMn on SL was visualized by TEM images (Fig. 8), which were taken at PMn doses of 0.1, 10, and 100 mg g<sup>-1</sup>, corresponding to concentrations below, around, and above that at the IEP. The TEM sample preparation involves solvent removal, which typically leads to mild aggregation of the particles. However, the images clearly proved

the immobilization and increasing number of PMn can be observed on SL as the dose was increased in the samples.

In addition, the immobilization of PMn on SL was also visualized *via* AFM imaging. In these measurements, the SPMn sample was subjected to minimal changes due to simpler sample preparation, *e.g.*, neither vacuum drying, nor metal coating is required. Fig. 9 shows the AFM images of SPMn (100 mg PMn/g SL, as indicated above) along with the height profiles.

The functionalized MnO<sub>2</sub> NPs are clearly immobilized on the SL particles, forming antioxidant colloidal molecules. The height profile analysis also confirms the successful formation of the SPMn and indicates significantly different sizes for the component SL and PMn particles in accordance with the SEM and TEM images (Fig. S2, ESI<sup>†</sup>).

#### Antioxidant activity

The CAT-like activity of the MnO<sub>2</sub> NPs and SPMn particles was assessed *via* a standard assay,<sup>49</sup> in which H<sub>2</sub>O<sub>2</sub> breaks down in

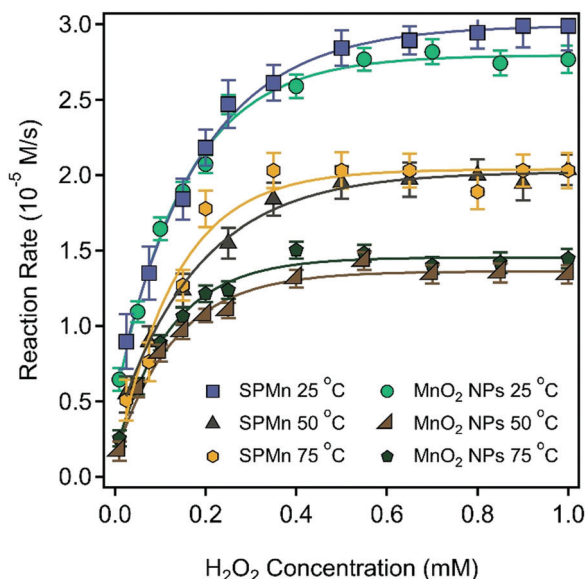


Fig. 10 CAT-like activity of MnO<sub>2</sub> NPs and SPMn at 25, 50, and 75 °C for both materials. The particle concentrations were 10 ppm and 100 ppm (in SL) for MnO<sub>2</sub> NPs and SPMn, respectively. The solid lines are the Michaelis–Menten fits described by eqn (4).

Table 1 Comparison of the results of CAT and SOD activity assays obtained for the MnO<sub>2</sub> NPs and SPMn particles

Material	$K_m^a$ (mM)	$v_{max}^a$ ( $10^{-5}$ M s <sup>-1</sup> )	IC <sub>50</sub> <sup>b</sup> (ppm)
MnO <sub>2</sub> NPs (25 °C)	0.083 ± 0.011	3.079 ± 0.101	0.274 ± 0.012
MnO <sub>2</sub> NPs (50 °C)	0.082 ± 0.008	1.517 ± 0.036	0.132 ± 0.005
MnO <sub>2</sub> NPs (75 °C)	0.074 ± 0.010	1.609 ± 0.049	0.192 ± 0.010
SPMn (25 °C)	0.099 ± 0.010	3.323 ± 0.079	0.311 ± 0.013
SPMn (50 °C)	0.118 ± 0.017	2.314 ± 0.085	0.271 ± 0.012
SPMn (75 °C)	0.106 ± 0.025	2.377 ± 0.139	0.417 ± 0.017

<sup>a</sup> Calculated by eqn (4). <sup>b</sup> Determined in SOD activity assays.

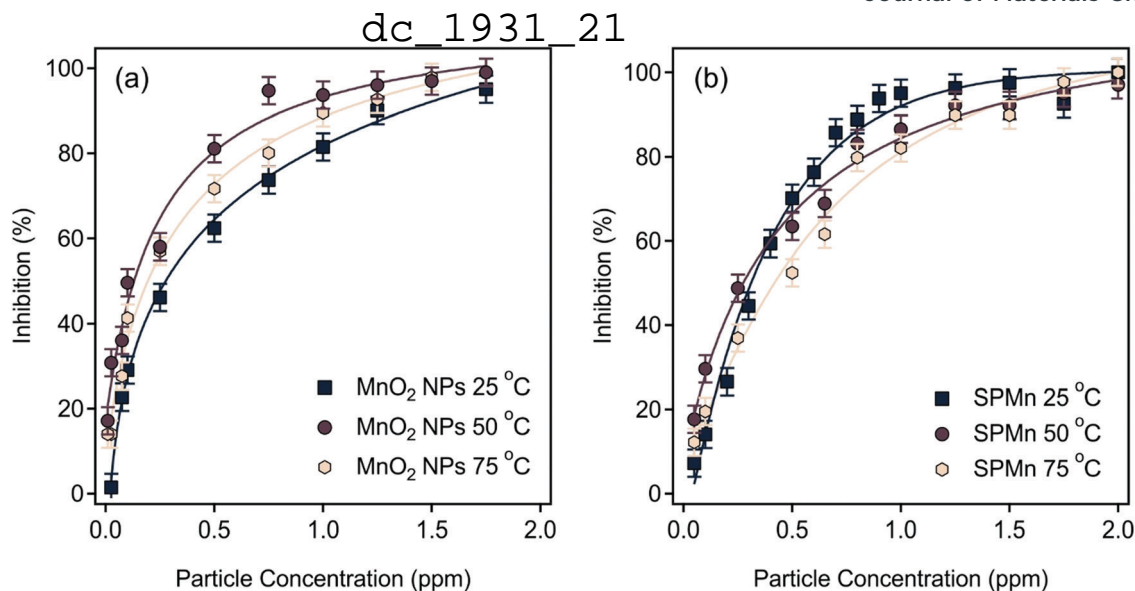


Fig. 11 Inhibition of the NBT-superoxide radical ion reaction by (a) MnO<sub>2</sub> NPs as well as (b) SPMn determined at 25 °C (squares), 50 °C (circles), and 75 °C (hexagons). The inhibition values were calculated using eqn (5). The solid lines are mathematical functions to interpolate the IC<sub>50</sub> values.

the presence of the enzyme or its mimic. The reaction rates *versus* concentration data points determined at different temperatures are plotted in Fig. 10.

One can notice that the experimental points can be well fitted with the Michaelis–Menten model (eqn (4))<sup>50</sup> and the  $K_m$  and  $v_{max}$  values were determined from the fits in all cases (Table 1). The  $v_{max}$  is the maximum reaction rate observed, where higher H<sub>2</sub>O<sub>2</sub> concentrations do not increase the rate any further, which can be attributed to the saturation of the catalytic sites. The  $K_m$  is the H<sub>2</sub>O<sub>2</sub> concentration that correspond to the rate half that of the  $v_{max}$ . The  $K_m$  value is a measure of the affinity between the catalyst and the substrate, where a lower  $K_m$  value indicates a higher affinity between the enzyme-like material and the substrate.

The results obtained revealed that the immobilization had no effect on the activity of MnO<sub>2</sub> NPs, as evident by the close  $K_m$  and  $v_{max}$  values of SPMn and MnO<sub>2</sub> NPs determined at 25 °C. In other words, neither the PDADMAC functionalization nor the attachment to SL altered the H<sub>2</sub>O<sub>2</sub> decomposition ability of MnO<sub>2</sub> NPs. Moreover, the CAT activity of both MnO<sub>2</sub> NPs and SPMn was obtained after the corresponding stock dispersions were thermally treated by immersion in a water bath at 50 °C and 75 °C for 90 min, and subsequent cooling to room temperature. As shown in Fig. 10, thermal treatment resulted in a decrease in the CAT activity of both MnO<sub>2</sub> NPs and SPMn compared to the untreated counterparts. The data indicate that the reduction of CAT activity was the same regardless of the temperature imposed, but the loss is more emphasized for MnO<sub>2</sub> NPs than for SPMn. However, no unambiguous explanation can be given for the reason of such decrease based on the present experimental data. Comparatively, the native CAT completely loses its activity at 70 °C after 30 min heating.<sup>75</sup> Although the thermal treatment also affected the activity of SPMn particles, they can still be considered as very active catalysts in H<sub>2</sub>O<sub>2</sub> decomposition, which shows that SPMn had

remarkable thermal and structural stability, making it a versatile candidate as antioxidant material in industrial processes for instance, where higher temperature is applied. The ability of the MnO<sub>2</sub> NPs and SPMn to dismutase superoxide radical ions was tested by the Fridovich assay.<sup>51</sup> The inhibition of the NBT-radical reaction was calculated using eqn (5) and plotted as a function of the MnO<sub>2</sub> NPs or SPMn concentration in Fig. 11.

The IC<sub>50</sub> values for MnO<sub>2</sub> NPs and SPMn were very similar at 25 °C (Table 1), but higher than the IC<sub>50</sub> for native SOD (0.07 ppm).<sup>63</sup> Thus, the functional integrity of MnO<sub>2</sub> NPs was kept upon polyelectrolyte functionalization and immobilization on SL. It is evident from the data of the heated samples that, unlike the CAT activity, there is no loss in SOD activity of either bare or immobilized MnO<sub>2</sub> NPs, even though the composite were thermally treated in a water bath at 50 °C and 75 °C for 90 min. The native SOD enzyme, however, was reported to lose its activity after 20 min at elevated temperatures.<sup>62</sup> These results clearly indicate that the MnO<sub>2</sub> NPs possess remarkable antioxidant potential, with preserved activity and excellent colloidal stability upon immobilization.

## Conclusions

MnO<sub>2</sub> NPs with antioxidant activity were synthesized, functionalized with PDADMAC, and immobilized on SL particles. Heteroaggregation was rationalized as an adsorption process of the PMn particles on the SL surface due to their opposite charges. The positively charged PMn particles adsorbed strongly on the SL leading to charge neutralization and charge reversal at the appropriate PMn doses. The colloidal stability of the samples was assessed, and the findings confirmed that the aggregation in the PMn–SL systems is driven by DLVO-type forces. Accordingly, the electrostatic double layer repulsion stabilizes the dispersions at low and high PMn doses, where

the particles possess significant charge. Near the IEP, however, the dispersions were unstable and diffusion-controlled aggregation occurred due to the lack of charges, *i.e.*, to the disappearance of the electrostatic double layers and predominance of attractive van der Waals forces. The SPMn hybrid showed excellent colloidal and functional stabilities. The CAT-like activity of MnO<sub>2</sub> NPs was maintained, although decreased, upon immobilization on SL and upon heating up to 75 °C, as indicated by the similarity of Michaelis–Menten parameters for both particles. The results of the SOD-like activity measurements implied no loss in MnO<sub>2</sub> NPs activity upon immobilization or heating, as similar IC<sub>50</sub> values were determined. These facts indicate that the obtained SPMn composites can be effectively used to combat reactive oxygen species in heterogeneous systems due to the excellent colloidal stability of the SPMn hybrid.

## Conflicts of interest

There are no conflicts to declare.

## Acknowledgements

Financial support from the Ministry of Human Capacities (20391-3/2018/FEKUSTRAT) and the Eötvös Lóránd Research Network (96130) is gratefully acknowledged. V. H. is supported by the Premium Postdoctoral Research Program (PPD-461042). The support from the University of Szeged Open Access Fund (5359) is gratefully acknowledged.

## References

- X. Ma, A. C. Hortelao, T. Patino and S. Sanchez, *ACS Nano*, 2016, **10**, 9111–9122.
- Y. H. Lin, J. S. Ren and X. G. Qu, *Acc. Chem. Res.*, 2014, **47**, 1097–1105.
- K. Kirkorian, A. Ellis and L. J. Twyman, *Chem. Soc. Rev.*, 2012, **41**, 6138–6159.
- H. Wei and E. K. Wang, *Chem. Soc. Rev.*, 2013, **42**, 6060–6093.
- J. S. Mu, L. Zhang, G. Y. Zhao and Y. Wang, *Phys. Chem. Chem. Phys.*, 2014, **16**, 15709–15716.
- J. J. X. Wu, X. Y. Wang, Q. Wang, Z. P. Lou, S. R. Li, Y. Y. Zhu, L. Qin and H. Wei, *Chem. Soc. Rev.*, 2019, **48**, 1004–1076.
- S. I. Tsekhmistrenko, V. S. Bituyutsky, O. S. Tsekhmistrenko, V. M. Polishchuk, S. A. Polishchuk, N. V. Ponomarenko, Y. O. Melnychenko and M. Y. Spivak, *Regul. Mech. Biosyst.*, 2018, **9**, 469–476.
- S. Murath, N. B. Alsharif, S. Saringer, B. Katana, Z. Somosi and I. Szilagyi, *Crystals*, 2020, **10**, 148.
- B. Bhushan and P. Gopinath, *J. Mater. Chem. B*, 2015, **3**, 4843–4852.
- D. Wang, X. L. Song, P. Li, X. J. J. Gao and X. F. Gao, *J. Mater. Chem. B*, 2020, **8**, 9028–9034.
- X. J. Wu, T. M. Chen, J. X. Wang and G. W. Yang, *J. Mater. Chem. B*, 2018, **6**, 105–111.
- H. Tokuyama, S. Yamago, E. Nakamura, T. Shiraki and Y. Sugiura, *J. Am. Chem. Soc.*, 1993, **115**, 7918–7919.
- L. L. Dugan, J. K. Gabrielsen, S. P. Yu, T. S. Lin and D. W. Choi, *Neurobiol. Dis.*, 1996, **3**, 129–135.
- H. Jiang, Z. H. Chen, H. Y. Cao and Y. M. Huang, *Analyst*, 2012, **137**, 5560–5564.
- W. W. He, Y. T. Zhou, W. G. Warner, X. N. Hu, X. C. Wu, Z. Zheng, M. D. Boudreau and J. J. Yin, *Biomaterials*, 2013, **34**, 765–773.
- M. Moglianetti, E. De Luca, P. A. Deborah, R. Marotta, T. Catelani, B. Sartori, H. Amenitsch, S. F. Retta and P. P. Pompa, *Nanoscale*, 2016, **8**, 3739–3752.
- L. Rastogi, D. Karunasagar, R. B. Sashidhar and A. Giri, *Sens. Actuators, B*, 2017, **240**, 1182–1188.
- J. S. Mu, L. Zhang, M. Zhao and Y. Wang, *ACS Appl. Mater. Interfaces*, 2014, **6**, 7090–7098.
- C. Murugan, N. Murugan, A. K. Sundramoorthy and A. Sundaramurthy, *Chem. Commun.*, 2019, **55**, 8017–8020.
- W. Chen, J. Chen, A. L. Liu, L. M. Wang, G. W. Li and X. H. Lin, *ChemCatChem*, 2011, **3**, 1151–1154.
- S. Ghosh, P. Roy, N. Karmodak, E. D. Jemmis and G. Mugesh, *Angew. Chem., Int. Ed.*, 2018, **57**, 4510–4515.
- Z. H. Dai, S. H. Liu, J. C. Bao and H. X. Jui, *Chem. – Eur. J.*, 2009, **15**, 4321–4326.
- T. M. Chen, H. Zou, X. J. Wu, C. C. Liu, B. Situ, L. Zheng and G. W. Yang, *ACS Appl. Mater. Interfaces*, 2018, **10**, 12453–12462.
- T. R. Lin, L. S. Zhong, Z. P. Song, L. Q. Guo, H. Y. Wu, Q. Q. Guo, Y. Chen, F. F. Fu and G. N. Chen, *Biosens. Bioelectron.*, 2014, **62**, 302–307.
- L. F. Wang, Y. Li, L. Zhao, Z. J. Qi, J. Y. Gou, S. Zhang and J. Z. Zhang, *Nanoscale*, 2020, **12**, 19516–19535.
- S. W. Wu, M. Qiu, B. C. Guo, L. Q. Zhang and Y. Lvov, *ACS Sustainable Chem. Eng.*, 2017, **5**, 1775–1783.
- W. Li, Z. Liu, C. Q. Liu, Y. J. Guan, J. S. Ren and X. G. Qu, *Angew. Chem., Int. Ed.*, 2017, **56**, 13661–13665.
- N. Singh, M. A. Savanur, S. Srivastava, P. D'Silva and G. Mugesh, *Angew. Chem., Int. Ed.*, 2017, **56**, 14267–14271.
- W. Chen, Y. Y. Yan, R. L. Han, J. Hu, Y. F. Hou and K. Q. Tang, *Photochem. Photobiol. Sci.*, 2021, **20**, 153–160.
- L. T. Yang, S. T. D. Chueng, Y. Li, M. Patel, C. Rathnam, G. Dey, L. Wang, L. Cai and K. B. Lee, *Nat. Commun.*, 2018, **9**, 3147.
- G. Dey, L. T. Yang, K. B. Lee and L. Wang, *J. Phys. Chem. C*, 2018, **122**, 29017–29027.
- M. Sawangphruk, P. Srimuk, P. Chiochan, A. Kittayavathananon, S. Luanwuthi and J. Limtrakul, *Carbon*, 2013, **60**, 109–116.
- K. G. Lee, J. M. Jeong, S. J. Lee, B. Yeom, M. K. Lee and B. G. Choi, *Ultrason. Sonochem.*, 2015, **22**, 422–428.
- D. R. Hu, L. J. Chen, Y. Qu, J. R. Peng, B. Y. Chu, K. Shi, Y. Hao, L. Zhong, M. Y. Wang and Z. Y. Qian, *Theranostics*, 2018, **8**, 1558–1574.
- S. J. Yao, S. Yuan, J. H. Xu, Y. Wang, J. L. Luo and S. S. Hu, *Appl. Clay Sci.*, 2006, **33**, 35–42.



dc 1931 21

- 36 D. Gu, J. C. Tseng, C. Weidenthaler, H. J. Bongard, B. Spliethoff, W. Schmidt, F. Soulimani, B. M. Weckhuysen and F. Schuth, *J. Am. Chem. Soc.*, 2016, **138**, 9572–9580.
- 37 T. Takashima, K. Hashimoto and R. Nakamura, *J. Am. Chem. Soc.*, 2012, **134**, 1519–1527.
- 38 M. Cheng, Y. Yu, W. D. Huang, M. Fang, Y. Chen, C. M. Wang, W. L. Cai, S. Y. Zhang, W. X. Wang and W. J. Yan, *ACS Biomater. Sci. Eng.*, 2020, **6**, 4985–4992.
- 39 T. Sasaki, *J. Ceram. Soc. Jpn.*, 2007, **115**, 9–16.
- 40 T. C. Cao, M. Borkovec and G. Trefalt, *Colloids Interfaces*, 2020, **4**, 52.
- 41 X. N. Wang, S. Wang, X. L. Pan and G. M. Gadd, *Chemosphere*, 2019, **221**, 486–492.
- 42 O. Ben Moussa, L. Tinat, X. J. Jin, W. Baaziz, O. Durupthy, C. Sayag and J. Blanchard, *ACS Catal.*, 2018, **8**, 6071–6078.
- 43 J. M. Lopez-Lopez, A. Schmitt, A. Moncho-Jorda and R. Hidalgo-Alvarez, *Adv. Colloid Interface Sci.*, 2009, **147**, 186–204.
- 44 X. Du and J. H. He, *J. Appl. Polym. Sci.*, 2008, **108**, 1755–1760.
- 45 A. V. Delgado, E. Gonzalez-Caballero, R. J. Hunter, L. K. Koopal and J. Lyklema, *Pure Appl. Chem.*, 2005, **77**, 1753–1805.
- 46 H. Holthoff, S. U. Egelhaaf, M. Borkovec, P. Schurtenberger and H. Sticher, *Langmuir*, 1996, **12**, 5541–5549.
- 47 G. Trefalt, I. Szilagyi, T. Oncsik, A. Sadeghpour and M. Borkovec, *Chimia*, 2013, **67**, 772–776.
- 48 M. Elimelech, J. Gregory, X. Jia and R. A. Williams, *Particle deposition and aggregation: measurement, modeling, and simulation*, Butterworth-Heinemann Ltd, Oxford, 1995.
- 49 A. C. Maehly and B. Chance, *Methods Biochem. Anal.*, 1954, **1**, 357–424.
- 50 K. A. Johnson and R. S. Goody, *Biochemistry*, 2011, **50**, 8264–8269.
- 51 C. Beaucham and I. Fridovich, *Anal. Biochem.*, 1971, **44**, 276–287.
- 52 M. C. Biesinger, B. P. Payne, A. P. Grosvenor, L. W. M. Lau, A. R. Gerson and R. S. Smart, *Appl. Surf. Sci.*, 2011, **257**, 2717–2730.
- 53 E. S. Ilton, J. E. Post, P. J. Heaney, F. T. Ling and S. N. Kerisit, *Appl. Surf. Sci.*, 2016, **366**, 475–485.
- 54 J. Y. Li, X. L. Wu, X. H. Zhang, H. Y. Lu, G. Wang, J. Z. Guo, F. Wan and R. S. Wang, *Chem. Commun.*, 2015, **51**, 14848–14851.
- 55 M. Galli, S. Saringer, I. Szilagyi and G. Trefalt, *Colloids Interfaces*, 2020, **4**, 20.
- 56 J. Israelachvili, *Intermolecular and surface forces*, Academic Press, London, 3rd edn, 2011.
- 57 E. J. W. Verwey and J. T. G. Overbeek, *Theory of stability of lyophobic colloids*, Elsevier, Amsterdam, 1948.
- 58 B. Derjaguin and L. D. Landau, *Acta Physicochim. URSS*, 1941, **14**, 633–662.
- 59 D. F. Evans and H. Wennerstrom, *The colloidal domain*, John Wiley, New York, 1999.
- 60 M. Borkovec, S. H. Behrens and M. Semmler, *Langmuir*, 2000, **16**, 5209–5212.
- 61 J. Hierrezuelo, A. Sadeghpour, I. Szilagyi, A. Vaccaro and M. Borkovec, *Langmuir*, 2010, **26**, 15109–15111.
- 62 M. Pavlovic, M. Nafradi, P. Rouster, S. Murath and I. Szilagyi, *J. Colloid Interface Sci.*, 2019, **543**, 174–182.
- 63 M. Pavlovic, P. Rouster and I. Szilagyi, *Nanoscale*, 2017, **9**, 369–379.
- 64 P. Rouster, M. Pavlovic, S. Saringer and I. Szilagyi, *J. Phys. Chem. C*, 2018, **122**, 11455–11463.
- 65 S. Saringer, R. A. Akula, A. Szerlauth and I. Szilagyi, *J. Phys. Chem. B*, 2019, **123**, 9984–9991.
- 66 S. Saringer, P. Rouster and I. Szilagyi, *Langmuir*, 2019, **35**, 4986–4994.
- 67 I. Szilagyi, G. Trefalt, A. Tiraferri, P. Maroni and M. Borkovec, *Soft Matter*, 2014, **10**, 2479–2502.
- 68 K. Kolman, O. Nechyporchuk, M. Persson, K. Holmberg and R. Bordes, *Colloids Surf., A*, 2017, **532**, 420–427.
- 69 L. Avadiar and Y. K. Leong, *Colloid Polym. Sci.*, 2011, **289**, 237–245.
- 70 E. Seyrek, J. Hierrezuelo, A. Sadeghpour, I. Szilagyi and M. Borkovec, *Phys. Chem. Chem. Phys.*, 2011, **13**, 12716–12719.
- 71 M. I. Mishchenko, L. D. Travis and A. A. Lacis, *Scattering, absorption, and emission of light by small particles*, University Press, Cambridge, 2002.
- 72 N. B. Alsharif, G. F. Samu, S. Saringer, S. Murath and I. Szilagyi, *J. Mol. Liq.*, 2020, **309**, 113066.
- 73 M. Pavlovic, P. Rouster, E. Bourgeat-Lami, V. Prevot and I. Szilagyi, *Soft Matter*, 2017, **13**, 842–851.
- 74 F. J. M. Ruiz-Cabello, G. Trefalt, T. Oncsik, I. Szilagyi, P. Maroni and M. Borkovec, *J. Phys. Chem. B*, 2015, **119**, 8184–8193.
- 75 A. Dincer and T. Aydemir, *J. Enzyme Inhib.*, 2001, **16**, 165–175.



Contents lists available at ScienceDirect

## Advances in Colloid and Interface Science

journal homepage: [www.elsevier.com/locate/cis](http://www.elsevier.com/locate/cis)

Historical Perspective

## Composite materials based on heteroaggregated particles: Fundamentals and applications



Nizar B. Alsharif, Szabolcs Muráth, Bojana Katana, Istvan Szilagyi \*

MTA-SZTE Lendület Biocolloids Research Group, Interdisciplinary Excellence Center, Department of Physical Chemistry and Materials Science, University of Szeged, 1 Rerich Béla tér, 6720 Szeged, Hungary

## ARTICLE INFO

## Keywords:

Heteroaggregation  
 Nanostructure  
 Composite  
 Colloidal stability  
 Self-assembly

## ABSTRACT

Homoaggregation of dispersed particles, i.e., aggregation of particles of the same shape, charge, size, and composition, is a well-studied field and various theoretical and experimental approaches exist to understand the major phenomena involved in such processes. Besides, heteroaggregation of particles, i.e., aggregation of particles of different shape, charge, size, or composition, has attracted widespread interest due to its relevance in various biomedical, industrial, and environmental systems. For instance, heteroaggregation of plastic contaminant particles with naturally occurring solid materials in waters (e.g., clays, silica and organic polymers) plays an important role in the decontamination technologies. Moreover, nanofabrication processes involving heteroaggregation of particles to prepare novel composite materials are widely implemented in fundamental science and in more applied disciplines. In such procedures, stable particle dispersions are mixed and the desired structure forms owing to the presence of interparticle forces of various origins, which can be tuned by performing appropriate surface functionalization as well as altering the experimental conditions. These composites are widely used in different fields from sensing through catalysis to biomedical delivery. The present review summarizes the recent progresses in the field including new findings regarding the basic principles in particle heteroaggregation, preparation strategies of heteroaggregated structures of different morphology, and the application of the obtained hybrid composites. Such information will be very helpful to those involved in the design of novel composites consisting of different nano or colloidal particles.

## 1. Introduction

Colloidal systems of nanostructured materials are constantly prone to dynamic changes such as aggregation, dissolution, sedimentation as well as chemical transformation [1–5]. While particles of stable colloids remain well separated and suspended, certain experimental conditions can induce homoaggregation (aggregation of the same particles), where particles approach each other and combine into large clusters leading to destabilization of the system [6]. Homoaggregation has been extensively studied and is now known to depend on numerous factors such as the pH, ionic strength, particle size, chemical composition, temperature, surface modification, the presence of naturally occurring organic matter or clays and the nature of the dispersion medium.

The Derjaguin-Landau-Verwey-Overbeek (DLVO) theory suggests that particle interactions and thus, the extent of homoaggregation is governed by relative contributions of two major interparticle forces, the attractive van der Waals as well as the repulsive electrostatic double

layer forces. Accordingly, when the overall effect of the interplay among factors affecting aggregation results in attractive forces such as high ionic strength and large particles, the colloidal system tends to aggregate giving rise to instability. On the other hand, when conditions result in repulsive overall effect, such as highly protonated or deprotonated metal oxide nanoparticles, the particles remain separated from each other resulting in a stable colloidal system. Such ability to control particle aggregation has enabled the implementation of colloidal systems in numerous applications including food items such as dairy products [7], drug emulsions [3,8,9], wastewater purification [10], rubber industry [11], leather tanning [12], paint industry [13], paper and retention aids [14].

In multi-component colloidal systems, however, homoaggregation may occur concurrently along with heteroaggregation (aggregation among dissimilar particles) [15–17]. Heteroaggregation is a fundamental phenomenon in colloidal dispersions and occurs between components of different chemical composition, surface potential, charge,

\* Corresponding author.

E-mail address: [szistvan@chem.u-szeged.hu](mailto:szistvan@chem.u-szeged.hu) (I. Szilagyi).<https://doi.org/10.1016/j.cis.2021.102456>

Received in revised form 27 May 2021;

Available online 31 May 2021

0001-8686/© 2021 The Author(s). Published by Elsevier B.V. This is an open access article under the CC BY license (<http://creativecommons.org/licenses/by/4.0/>).

shape, or size [15,16,18]. Not only multi-components colloidal systems occur more frequently in nature such as water sources, soil, and river deltas [19–24], but also in many industrial applications including mineral flotation and coating [25,26]. Most importantly, heteroaggregation between nanostructured materials (e.g., nanospheres, nanoplates, or nanotubes) has been used as a synthetic route to prepare nanocomposites with diverse structures for numerous applications such as catalysis, drug delivery, water purification, artificial enzymes, and energy storage, among others [27–31].

In general, hybrids of different nanoparticles are highly functional materials with great potential in various applications such as catalysis [32], energy storage [33,34], electronics [35], sensing [36], water purification [37], drug delivery [38], therapeutic agents [39], and spacecraft protective coating [40], to name a few. Although these hybrid materials have been prepared via both in situ (synthesis of one component in the presence of the other) or ex situ heteroaggregation (simple mixing of dispersions of pre-synthesized particles), the sole focus of this review article is to report the progresses made on the latter strategy regarding both fundamental studies as well as advances in functional hybrid materials formation. The ex situ heteroaggregation, illustrated in Fig. 1, is more advantageous and allows rapid, convenient, and cost-effective syntheses that circumvent harsh temperature and pH conditions as well as tedious functionalization and surface modification procedures.

## 2. The heteroaggregation process: fundamental studies

Colloidal systems of dissimilar nanoparticles cannot be fully described with the DLVO theory [41,42]. As the case with homoaggregation, nevertheless, the heteroaggregation process in binary systems is driven by the existent attractive forces as well as the tendency of particles to minimize their surface energy. Also, the extent of repulsive interactions of electrostatic and steric origin as well as attractive van der Waals forces is tuned by altering the experimental conditions such as the pH and surface functionalization [43]. In binary systems, while DLVO forces of van der Waals and electrostatic exist among similar particles, there exist certain experimental conditions where additional (non-DLVO) attractive forces act between the different particles (e.g., oppositely charged particles) that lead to favourable interactions and subsequent heteroaggregation into various heteroaggregates with promising potential as functional composites. Moreover, only does heteroaggregation occur among differently shaped nanoparticles (sphere-sphere, sphere-tube, sphere-plate, rod-plate, etc.), but also

between nanoparticles and naturally occurring inorganic, organic, biological colloids as well as viruses and bacteria [44–48]. The following subsections review the fundamental studies attempted to formulate an understanding of heteroaggregation based on the shape of the particles involved.

### 2.1. Sphere-sphere systems

During the heteroaggregation of spherical particles, the magnitude of the collective attractive (electrostatic and/or van der Waals) interparticle forces not only depends on the conditions in the medium such as the pH and the ionic strength, but also on the physicochemical properties of the particles themselves. Besides particle radius and interparticle distance, the van der Waals forces also depend on the Hamaker constant that manifests the inherent contribution of the nature, chemical composition, and the surface chemistry of the particles to the attractive forces. In addition, the particle size dependence tunes the aggregation regimes, where different types of interactions govern the aggregation process. For example, surface chemistry of particles similar in size significantly affect their homoaggregation, whereas in homoaggregation of differently sized particles, van der Waals forces play a major role, as their strength is proportional with the size of the particles [43]. On the other hand, heteroaggregation among either similarly or differently sized particles is governed by both the surface chemistry as well as DLVO type forces.

The fundamental features of heteroaggregation were explored in certain extent in the past due to the growing number of binary particle systems in various applications [48–52]. Extensive work has been carried out to fully understand heteroaggregation in multi-component dispersions, even though several aspects of heteroaggregation can be explained by DLVO. Hogg et al. presented the Hogg-Healy-Fuerstenau theory in 1965 to describe the kinetics of aggregation of binary colloidal systems. Using the Derjaguin and Debye-Hückel approximation for low surface potential, they derived a general expression that describes the potential energy of interaction between dissimilar particles and predicts the effect on system stability of parameters such as potential-determining ions, ionic strength, the particle size, and the relative presence of constituent particles [53]. Lopez-Lopez et al. reviewed the kinetic and structural aspects of theoretical and simulation advances on the heteroaggregation coupled with experimental work on the heteroaggregation of amidine and sulfate modified polystyrene latex (PS) particles in KBr electrolyte solutions [49]. In another review work, Lopez-Lopez et al. focused on electrostatically driven aggregation of

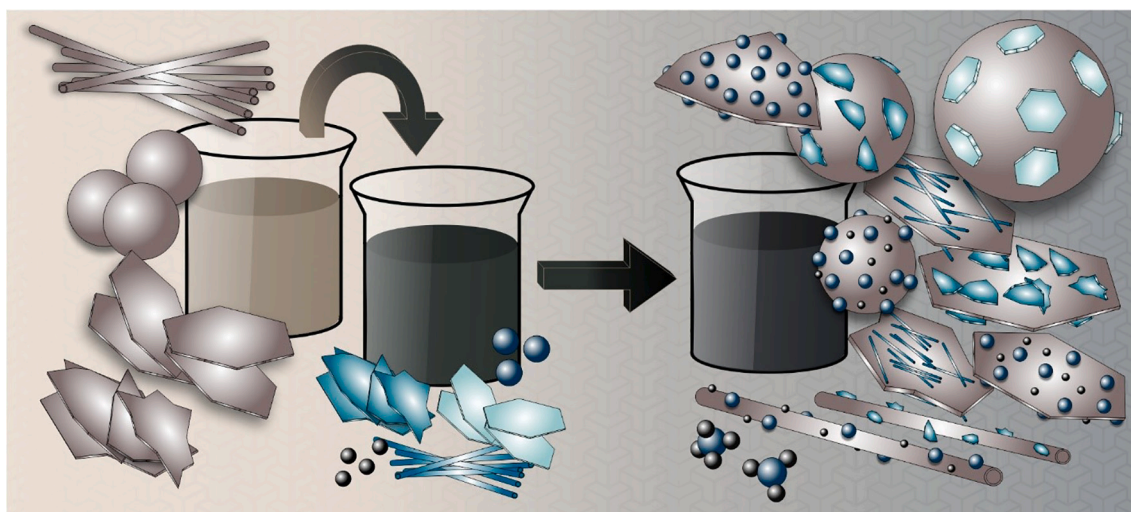


**Fig. 1.** Schematic illustration of ex situ heteroaggregation of particles of various sizes and shapes, where colloidal dispersions of pre-synthesized materials are simply mixed in the desired ratio.



binary systems of equally charged particles (symmetric system) using the same sulfate and amidine PS particles to carry out a detailed study on the heteroaggregation process and the colloidal stability over a wide range of electrolyte (KBr) concentration. The aggregation regimes as well as short and long-time aggregation kinetics were addressed from both experimental, theoretical and simulation point of view [16].

Studies were extended beyond simple symmetric systems. Trefalt et al. calculated the interaction forces and studied aggregation and deposition rates for asymmetric and symmetric systems as well as charged-neutral systems, based on the Poisson-Boltzmann model as well as the DLVO theory. The symmetry and charge regulation effects altered the heteroaggregation and deposition behaviour in such systems, but the dependence on the counter-ion valence for asymmetric systems was similar to that in systems of symmetrically charged particles [54]. The understanding of heteroaggregation processes in natural environments has been the focus of several studies. For example, Buffle et al. studied the colloidal interactions between inorganic colloids and natural organic matter (fulvic compounds as well as rigid and flexible biopolymers) to model the colloidal behaviour in natural aquatic systems. The colloidal interaction and stability depended on the size, electric charge, and conformation of the involved particles [19]. Also, Wang et al. reviewed the modelling and mechanism of heteroaggregation of nanoparticles and biocolloids (viruses, bacteria, proteins, DNA), geocolloids (clay minerals) and natural organic matter found in surface water, sediments, and soil [18].

Coupled experimental/simulation studies on heteroaggregation have been reported to gain more insight into the properties and behaviour of the resulting heteroaggregates. Cerbelaud et al. investigated the heteroaggregation of SiO<sub>2</sub> nanoparticles and Al<sub>2</sub>O<sub>3</sub> microparticles via Brownian dynamic simulations [55]. Parameters such as Debye length and surface potential were obtained experimentally for the commercial particles and the particle-particle interactions were interpreted in terms of the DLVO theory. Both experimental and simulation studies showed that very small amounts of added SiO<sub>2</sub> can destabilize the Al<sub>2</sub>O<sub>3</sub> suspensions by formation of aggregates, shown in Fig. 2, with good agreement between experimental and simulation results on the quantity of SiO<sub>2</sub> adsorbed on Al<sub>2</sub>O<sub>3</sub>.

Studies on heteroaggregation of different particles have also been reported in the presence of multivalent ions. Moazzami-Gudarzi et al. studied the interaction forces during homo and heteroaggregation between the oppositely charged sulfate latex and amidine latex particles in aqueous solutions containing monovalent salts or [Fe(CN)<sub>6</sub>]<sup>4-</sup> anions [56]. Quantitative interpretation of the force profiles suggested the existence of DLVO type particle-particle interactions with non-DLVO short-ranged attractive components. Moreover, Cao et al. studied heteroaggregation between oppositely charged amidine and sulfate latex particles in the presence of monovalent as well as SO<sub>4</sub><sup>2-</sup>, [Fe(CN)<sub>6</sub>]<sup>4-</sup>, and [Fe(CN)<sub>6</sub>]<sup>3-</sup> multivalent ions [51]. In monovalent salt solutions, the particles are oppositely charged, while one particle type reverses its charge upon addition of multivalent ions. Trefalt et al. systematically studied the homo and heteroaggregation of carboxylate, sulfate, and amidine latex particles at different KCl and polyamines concentrations. For carboxylate latex particles, charge reversal occurred at lower concentration for polyamines with higher number of amino groups, and for heteroaggregation between sulfate and amidine latex particles, stability ratio increased with increasing KCl concentration, but the effect is less pronounced compared to that for homoaggregation [57].

The experimental conditions such as pH, ionic strength, and component concentration profoundly affect the heteroaggregation rate and the properties of the resulting heteroaggregates, and thus, considerable number of studies have explored dependence patterns. For example, Voorn et al. studied the heteroaggregation kinetics between polystyrene-co-poly(isobutyl methacrylate) latex spheres and  $\gamma$ -Al(OH)<sub>3</sub> platelets as a function of the sphere/platelet number ratio, pH, and ionic strength [58]. Mixed dispersions of relevant constituents were analyzed via time resolved dynamic light scattering. High sphere/platelet number

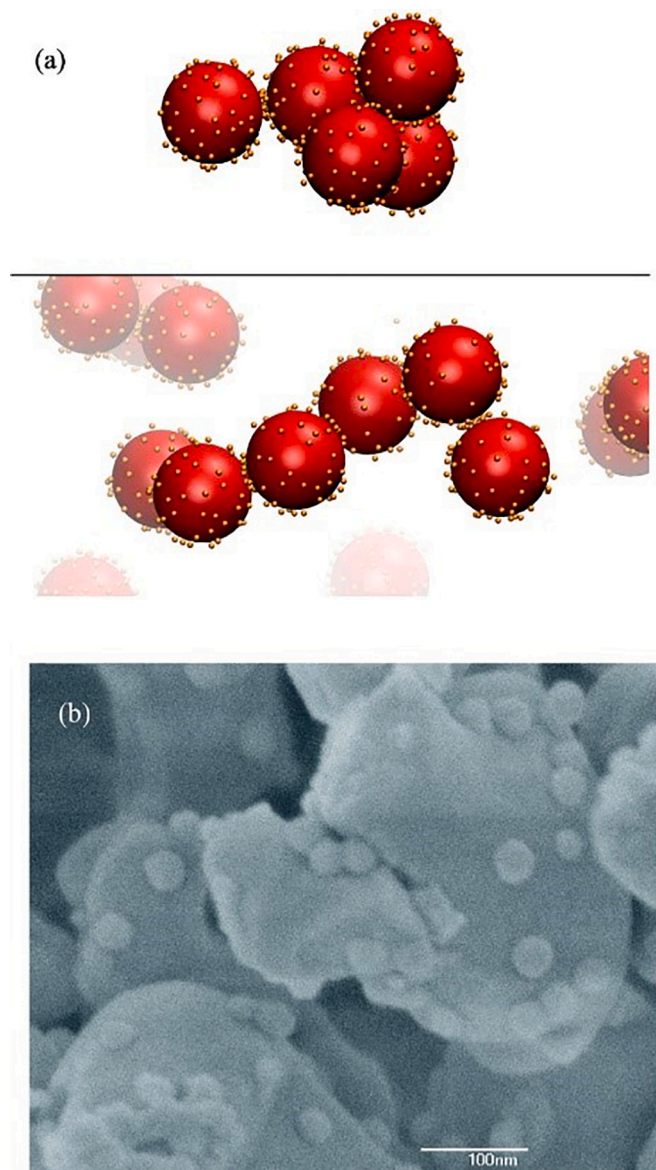


**Fig. 2.** (a) Snapshot of two agglomerates formed in the simulation and (b) Cryo-FEGSEM image of alumina particles surrounded by silica particles [55]. Reprinted (adapted) with permission from (Cerbelaud, A.; Videcoq, A.; Pagnoux, C.; Rossignol, F.; Ferrando, R., Heteroaggregation between Al<sub>2</sub>O<sub>3</sub> sub-micrometer particles and SiO<sub>2</sub> nanoparticles: Experiment and simulation. *Langmuir* 2008, 24 (7), 3001–3008). Copyright (2021) American Chemical Society.

ratio should be maintained to prevent the formation of multilayer aggregates and the heteroaggregated particles were stable within a pH range of 2–9 and up to different ionic strengths depending on the aggregate size. In another study, Lin et al. measured rate constants of heteroaggregation of commercial silica as well as amidine and sulfate latex over a wide range of ionic strength and different surface charge densities. The heteroaggregation rate constants increased slowly with decreasing ionic strength, and for highly charged surfaces, the rate constant was independent of the surface charge [59].

Also, Bansal et al. used commercial negatively charged silica and positively charged alumina-coated silica particles to study heteroaggregation in aqueous dispersions by following the pH-dependent surface charging as well as heteroaggregate size, structure, and flow properties [60]. Different phases formed upon mixing the oppositely charged particles with different positive particle ratio, such new phases



ranged from gel-like at high particle ratio, while clear, turbid, and sediment (with turbid and clear supernatant) phases formed at low particle ratio.

Parsai and Kumar probed the heteroaggregation of commercial ZnO and CuO nanoparticles in aqueous dispersions at different pH, ionic strength, and nanoparticle concentration by developing empirical equations to predict the difference in zeta potential as well as their aggregation and settling rate constants. The attractive van der Waals forces dominated in aggregation, and the nanoparticle concentration was found to be the major factor affecting settling rate constant, whereas the pH and ionic strength, and nanoparticle type affected the aggregation rate constant [61].

Nakamura et al. studied the interactions between a number of negatively charged PS with silica particles in the presence of the cationic surfactant cetylpyridinium chloride [62]. PS particles were either obtained commercially or synthesized by emulsifier-free polymerization, whereas silica particles were obtained from commercial sources. The negative charge on PS and silica particles decreased as more surfactant molecules were electrostatically adsorbed onto the particles, which became positively charged when surfactant concentration exceeded the isoelectric point (IEP). In the intermediate concentration regime, both particles were oppositely charged, and clustering of different particles was enabled. By selecting the proper surfactant dose, it is possible to dictate colloidal behaviour and the associations of different particles into heterogeneous colloidal clusters.

Lu et al. studied the interaction of aqueous graphene oxide (GO) colloidal particles with three clay particles under different solution chemistry conditions [63]. Both the GO and the three clay materials were obtained commercially. A solid sample of the relevant clay mineral was added to a dispersion of GO, and the mixture was shaken for a prolonged period of time. The affinity of clay particles towards GO was in the order of montmorillonite > kaolinite > diatomite under the same experimental conditions. Increasing the ionic strength or decreasing the pH improved the immobilization of GO nanoparticles onto clay minerals due to electrostatic interactions, while the addition of tartaric acid largely prevented the heteroaggregation of GO and the mineral particles.

Assembly of different particles has also been utilized to prepare thin films. Novel thin-film freeze-drying SEM was utilized by Harley et al. to study the heteroaggregation of oppositely charged amidine and smaller sulfate PS particles at different ionic strength conditions and in the presence and absence of pre-adsorbed layers of poly(vinyl alcohol-co-vinyl acetate) on both particles. The presence of the polymer affected the amount of immobilized sulfate latex particles, when electrolyte concentration exceeds a critical value, which indicates that the long-range interactions between the particles largely affected the heteroaggregation rate coefficient as well as the final amount of immobilized particles [64]. Fig. 3 shows the amidine-sulfate latex hybrid particles.

Heteroaggregation rates were measured even though it occurs simultaneously with homoaggregation. Yu and Borkovec studied the heteroaggregation of positively charged amidine and negatively charged sulfate PS by mixing appropriate concentrations in KCl solutions [15]. Absolute heteroaggregation rate constants between the two particles were determined with great accuracy. Both static and dynamic light scattering were used although the latter technique was more accurate and more sensitive. In another study from the same group, Yu et al. studied heteroaggregation kinetics of commercial amidine latex and carboxyl or sulfate latex particles and pointed out that the experimental conditions can be adjusted to exclude any significant homoaggregation [65]. By mixing appropriate volumes of the relevant dispersions, apparent aggregation rate constants were determined. The rate obtained from static light scattering measurements strongly decreased with increasing scattering angle, while rates from dynamic light scattering experiments showed more complex dependence, with values found within experimental error with both techniques. A formula was proposed to estimate the hydrodynamic radius of the asymmetric particle

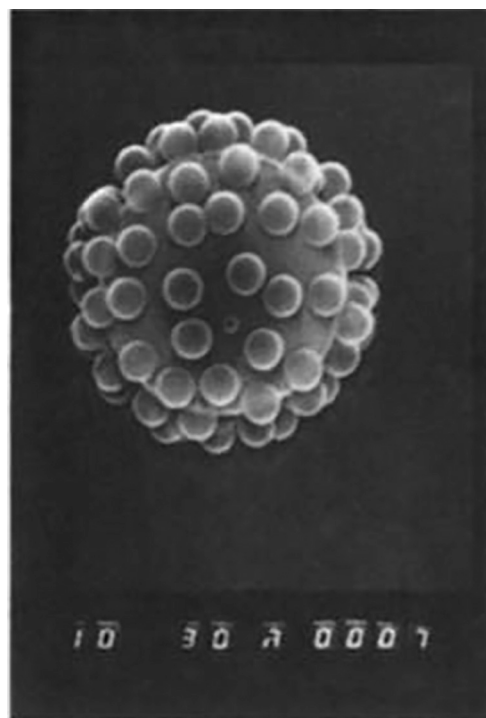


Fig. 3. Thin-film freeze-drying SEM image of amidine-sulfate latex hybrid [64]. Reprinted from (The adsorption of small particles onto larger particles of opposite charge. Direct electron microscope studies, 62 (1–2), Harley, S.; Thompson, D. W.; Vincent, B., *Colloids and Surfaces*, 1992, 163–176). Copyright (2021), with permission from Elsevier.

doublet agreed well with experimental data and theoretical predictions.

Aquatic systems such as sea and river water sources are colloidal in nature, and thus the heteroaggregation among the different particles in such systems was studied. Luo et al. investigated the heteroaggregation between positively charged CeO<sub>2</sub> and negatively charged TiO<sub>2</sub> nanoparticles in laboratory and natural water (rivers and reservoirs) [47]. In both water sources, the stability of the system generally increased with increasing CeO<sub>2</sub>/TiO<sub>2</sub> ratio. At the same CeO<sub>2</sub>/TiO<sub>2</sub> ratio, however, NaCl lowered the stability relative to a control sample by charge screening, while humic acid significantly increased the stability relative to the control sample by adsorbing onto the particles and preventing their approach due to steric hindrance. Fig. 4 illustrates the proposed mechanism for the competitive adsorption of humic acid onto CeO<sub>2</sub> and TiO<sub>2</sub> nanoparticles.

Also, Oriekhova and Stoll explored the heteroaggregation of positively charged polystyrene nanoplastics with negatively charged  $\alpha$ -Fe<sub>2</sub>O<sub>3</sub> and alginate particles by systematic mixing of their aqueous dispersions. The three materials were obtained commercially. Polystyrene nanoplastics were found to undergo heteroaggregation with  $\alpha$ -Fe<sub>2</sub>O<sub>3</sub> and alginate leading to charge neutralization and charge reversal. At 40 ppm nanoplastics, the IEP for nanoplastics-alginate occurred at 1 ppm, whereas in the nanoplastics- $\alpha$ -Fe<sub>2</sub>O<sub>3</sub> system, it occurred at 3 ppm nanoplastics dose, when the  $\alpha$ -Fe<sub>2</sub>O<sub>3</sub> concentration was fixed at 5 ppm. In the triple system of nanoplastics-alginate- $\alpha$ -Fe<sub>2</sub>O<sub>3</sub>, the presence of alginate led to a delay in the heteroaggregation due to a competitive interaction of alginate and  $\alpha$ -Fe<sub>2</sub>O<sub>3</sub> with nanoplastics particles. Also, when dispersed in Rhône river, polystyrene nanoplastics rapidly changed their surface charge from positive to negative possibly due to the adsorption of naturally existing components such as organic matter as well as inorganic and organic polyions [23].

Moreover, the environmental impact and the fate of nanoplastics particles in aquatic systems have been explored. For example, Singh et al. investigated the aggregation and stability of polystyrene

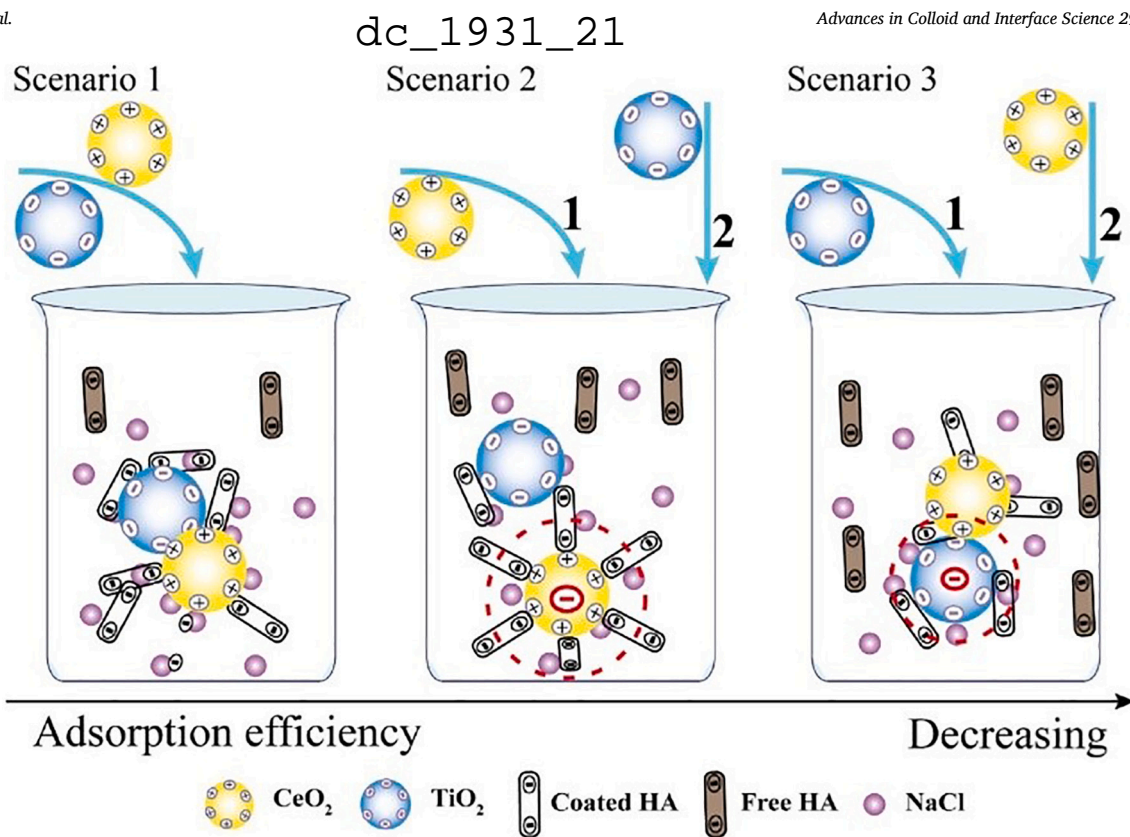


**Fig. 4.** Proposed mechanisms for the competitive adsorption of humic acid (HA) onto  $\text{CeO}_2$  and  $\text{TiO}_2$  nanoparticles [47]. Reprinted from (Heteroaggregation of  $\text{CeO}_2$  and  $\text{TiO}_2$  engineered nanoparticles in the aqueous phase: Application of turbiscan stability index and fluorescence excitation-emission matrix (EEM) spectra, 533, Luo, M. X.; Qi, X. J.; Ren, T. X.; Huang, Y. X.; Keller, A. A.; Wang, H. T.; Wu, B. R.; Jin, H. P.; Li, F. T., *Colloids Surf. A: Physicochem. Eng. Aspects*, 2017, 9–19). Copyright (2021), with permission from Elsevier.

nanoplastics in different aqueous environments (river water, seawater, and groundwater) under different ionic strengths and temperatures, and in the presence of dissolved organic matter (humic acid), inorganic soil colloids (bentonite clay particles), and heavy metal salts ( $\text{ZnCl}_2$ ,  $\text{CdCl}_2$ , and  $\text{HgCl}_2$ ). Lower critical coagulation concentration (CCC) values were obtained at higher temperature and in the presence of multivalent ions, whereas humic acid stabilized nanoplastics due to steric repulsion. The highest rate of aggregation was observed in seawater followed by river water and ground water, which can be attributed to the complex chemistry of these systems [66].

The aggregation tendency of particulate organic matter (POM) in soil was investigated to probe its effect on the performance of nanoparticles in remediation technologies. Wang et al. investigated the effect of POM on the potential of the Se nanoparticles (Se NPs) to capture toxic  $\text{Hg}^0$  in soil solution. The POM was extracted from black soil, while Se NPs were produced by reduction of  $\text{Na}_2\text{SeO}_3$  using the selenite-reducing bacterium *Citrobacter freundii* Y9. The soil solution was prepared by mixing black soil with Milli-Q water and the centrifuged supernatant was filtered and purified by dialysis. Low concentrations of POM (0–80 mg/L) inhibited heteroaggregation with Se NPs and led to enhanced stability of Se NPs, while POM particles underwent homoaggregation at higher POM concentration (80–100 mg/L). At neither concentration range was the Se NPs removal ability of  $\text{Hg}^0$  affected in the presence of POM [52].

Barton et al. assessed the relative affinity of several nanoparticles to undergo heteroaggregation with larger particles in activated sludge [67]. The relative affinity was found to be in the order of pristine  $\text{CeO}_2$  NPs,  $\text{TiO}_2$  NPs,  $\text{ZnO}$  NPs > poly(vinyl pyrrolidone) (PVP)-modified Ag NPs > citrate-functionalized  $\text{CeO}_2$  NPs > gum Arabic-modified Ag NPs. The trends in the removal of solids from sludge were similar to those of the affinity, indicating that higher affinity leads to more effective removal by the nanoparticles.

## 2.2. Sphere-plate systems

Tombácz et al. probed the heteroaggregation of magnetite ( $\text{Fe}_3\text{O}_4$ ) nanoparticles, obtained by co-precipitation, with commercial montmorillonite [68]. Fractal aggregates formed due to Coulombic interactions in suspensions of either particles as well as mixed suspensions. Potentiometric acid-base titration indicated that magnetite-montmorillonite hybrids occurred at low ionic strength and only in acidic pH conditions when the amphoteric sites develop a positive charge.

Guo et al. investigated the charge-dependent interactions of commercial  $\text{CeO}_2$  nanoparticles (NPs) with kaolinite via HRTEM and atomic force microscopy. The  $\text{CeO}_2$  NPs attached to kaolinite platelets via electrostatic interactions. The hybrid was prepared by dispersing a certain amount of kaolinite in an aqueous dispersion of  $\text{CeO}_2$  NPs. Neutral and positively charged  $\text{CeO}_2$  NPs showed a strong affinity to kaolinite surfaces, whereas negatively charged  $\text{CeO}_2$  NPs exhibited weak attachment to kaolinite. Such change in surface charge density in kaolinite might adversely affect the bioavailability of nutrients to plants, because of the interactions of kaolinite with its surrounding in soil pore water [69].

The heteroaggregation of three types of particulate zero-valence iron nanoparticles (nZVI) and two types of clay mineral particles (CMP) (kaolinite and montmorillonite) was studied by Wang et al. at different pHs (at 3.5, 6.5 and 9.5) and various nZVI-to-CMP mass ratios. Aqueous dispersions of the commercially obtained nZVI and CMP were mixed in the desired ratio. The pH was found to affect the dominant forces responsible for the formation of nZVI-CMP. Lewis acid-base (AB) interactions predominated in neutral or alkaline conditions, while electrostatic interactions dominated under acidic conditions. Both AB and van der Waals interactions could enhance the formation of nZVI-CMP heteroaggregates under neutral or alkaline conditions to overcome

electrostatic repulsion. The interaction behaviour of nZVIs with CMP might be extended to understand the interaction of nZVI with biocolloids such as proteins, DNA, viruses, and bacteria, where AB interactions are significant [44].

### 2.3. Miscellaneous systems

Khalil et al. utilized heteroaggregation to prepare thin films of nanofibrillated cellulose (NFC) and Ag NPs [70]. Both cellulose and Ag NPs were prepared and further coated with PVP as a stabilizing agent. The NFC-AgNPs composite was prepared by mixing aqueous suspensions of cellulose and AgNPs and subsequent homogenization. The NFC/PVP/AgNPs composite was used as a film material, which was prepared by introducing the composite suspension into Petri dishes followed by prolonged drying at elevated temperatures. The homogenous nanocomposite showed promising electrical conductivity and high tensile strength, a potential antistatic and static dissipative materials. The NFC/PVP/AgNPs mass ratio of 25/75/2 showed the highest electrical conductivity, which ranged from  $2.36 \times 10^{-10}$  S/cm to  $1.5 \times 10^{-6}$  S/cm at 30 °C.

In another study, Hassan et al. probed the effect of the addition of barium titanate (BT) nanoparticles into cellulose nanofibers (CNF) on the physicochemical properties of CNF/BT composite thin films [71]. The oxidized nanofibers were produced from bleached bagasse pulp, while BT nanoparticles were prepared from barium carbonate and titania. The nanocomposite was prepared by mixing the aqueous suspensions of CNF and BT at different mass ratios in a Teflon Petri dish along with a fixed ratio of glycerol. The resulting composites showed homogenous distribution of BT in the CNF matrix as well as good thermal stability. Also, the incorporation of BT nanoparticles to CNF decreased the tensile strength of the films but it increased the dielectric constant of the nanocomposites up to 5% (w/w) BT. In addition, the values of activation energy decreased as the doping level of BT nanoparticles increased, which indicates that the conductivity has an electronic and ionic nature.

Huynh et al. probed the effects of humic acid and the mass ratio of

negatively charged multi-walled carbon nanotubes (CNTs) and positively charged hematite nanoparticles on their heteroaggregation rates. Hematite nanoparticles were prepared by forced hydrolysis [72]. Certain volumes of hematite and CNTs dispersions were mixed at the required CNTs/hematite ratio. By altering the mass ratio, the heteroaggregation rates and information on the mechanism were obtained. At the optimal ratio, heteroaggregation rate was three times faster than the one measured for homoaggregation of hematite. Higher ratios caused a significant decrease in the heteroaggregation rate and the addition of humic acid had no effect on the tendencies in the heteroaggregation rates, but it reduced the maximum aggregate growth rate. Fig. 5 shows cryo-TEM images of CNT/hematite heteroaggregates at different ratios.

Jurado and Galvez used ex situ and in situ heteroaggregation to prepare organic-inorganic systems based on amyloid fibrils of both apoferritin (APO) and  $\beta$ -lactoglobulin (BLG), and inorganic nanoparticles [73]. Gold nanospheres (AuNSs) were obtained commercially while, maghemite and gold nanorods (AuNRs) were prepared by coprecipitation and seed-mediated growth method, respectively. The ex situ heteroaggregation was achieved by mixing aqueous suspensions of either APO or BLG amyloid fibrils with those of AuNs, AuNRs or maghemite and the resulting suspensions were then incubated for a prolonged period of time. The systems of APO fibrils with AuNRs, AuNSs, and PdNPs were also prepared in situ by preparing the relevant particles in the presence of APO fibrils. For the former approach, the assemblies showed improvement in magnetic anisotropy, probably due to fibril organisation and dipole-dipole interactions. For such organic-inorganic systems, the physical properties can be tuned by altering the nanoparticle composition, size, and shape while elastic and mechanical properties can be adjusted by altering the biological templates.

Liu et al. used GO, prepared by Hummer's method, to synthesize GO- $\text{Al}_2\text{O}_3$  hybrid in attempt to accurately understand the fate of the GO in the environment as well as the effect of GO size on its homo and heteroaggregation behaviour [74]. Aqueous dispersions of differently sized GO sheets were mixed with those of commercial  $\text{Al}_2\text{O}_3$  particles at different pH and ionic strength conditions. The heteroaggregation of GO- $\text{Al}_2\text{O}_3$  hybrid was attributed to the electrostatic attraction and

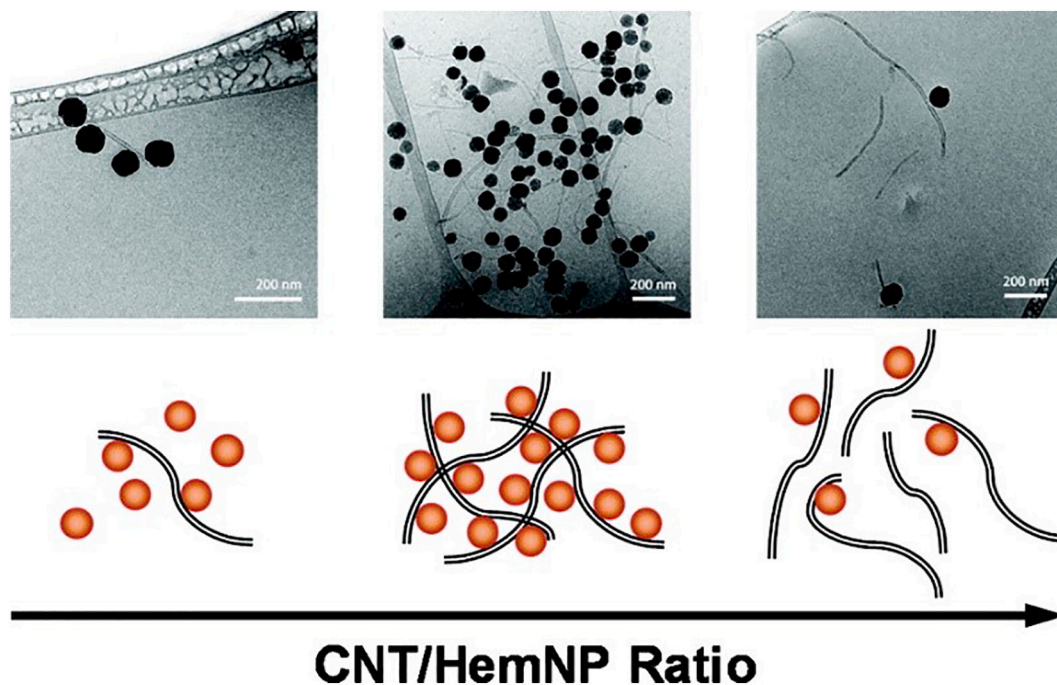


Fig. 5. Representative cryo-TEM images of heteroaggregates of CNT and hematite (HemNP) at (upper left) low, (upper center) optimal and (upper right) high CNT/HemNP ratios. Proposed heteroaggregation mechanisms at different nanoparticle distributions are shown at the bottom [72]. Reprinted (adapted) with permission from (Huynh, K. A.; McCaffery, J. M.; Chen, K. L., Heteroaggregation of multiwalled carbon nanotubes and hematite nanoparticles: rates and mechanisms. *Environ. Sci. Technol.* 2012, 46 (11), 5912–5920). Copyright (2021) American Chemical Society.



hydrogen bonding in aqueous media. The attachment capacity of large GO sheets onto  $\text{Al}_2\text{O}_3$  particles was greater than that of small GO, and the effect of the pH on the adsorption of  $\text{Al}_2\text{O}_3$  was different for different GO. The increase in the ionic strength facilitated the heteroaggregation between GO and  $\text{Al}_2\text{O}_3$ .

Besides, the effects of minerals on the adsorption process helps understand the fate of contaminants in natural water environments. For example, Jiang et al. found that the negatively charged  $\text{SiO}_2$  and positively charged  $\text{Al}_2\text{O}_3$  NPs largely prevented the adsorption of  $17\beta$ -estradiol onto GO and prolonged the adsorption equilibration time [45]. The oxide NPs were obtained commercially, while GO was prepared using the modified Hummers' method. Various amounts of NPs were added into a series of pre-dispersed GO suspensions, and the homogenized NPs-GO suspensions were then mixed with  $17\beta$ -estradiol solutions. The inhibition was more pronounced in the case of  $\text{Al}_2\text{O}_3$  than  $\text{SiO}_2$  due to the electrostatic attraction, which led to heteroaggregation between the oppositely charged  $\text{Al}_2\text{O}_3$  and GO lamellae. Moreover, GO tended to first homoaggregate and then heteroaggregate with  $\text{SiO}_2$ , as revealed by DLVO calculations.

Also, Chen et al. investigated the influence of particle size of minerals on the adsorption of pollutants such as sulfamethoxazole on multi-walled CNT in natural water in the presence of  $\text{SiO}_2$  or  $\text{Al}_2\text{O}_3$  nanoparticles of different sizes [75]. Both  $\text{SiO}_2$  and  $\text{Al}_2\text{O}_3$  inhibited the sulfamethoxazole adsorption on CNTs by competitive heteroaggregation of the latter with either nanoparticles. The extent of inhibition depended on the size and type of nanoparticles. The amount of sulfamethoxazole adsorbed on CNTs decreased with increasing  $\text{SiO}_2$  particle size but increased with increasing  $\text{Al}_2\text{O}_3$  particle size due to the different heteroaggregation patterns with CNTs. Electrostatic attraction between the oppositely charged CNTs and  $\text{Al}_2\text{O}_3$  favoured their heteroaggregation, while repulsive interactions between CNTs and  $\text{SiO}_2$  increased with

increasing  $\text{SiO}_2$  particle size. Fig. 6 shows TEM images of CNT-nanoparticle composite of different particle size.

#### 2.4. Conclusive remarks

As shown above, the introduction of inorganic nanostructured materials in aqueous media brings about different regimes of interactions not only among similar and dissimilar particles, but also between particles and the dispersion medium. The collective outcome of these interactions is the generation of surface charge responsible for the stability of colloidal systems of single-component composition. The nature and magnitude of the surface charge depend on the intrinsic properties of the material as well as the experimental conditions such as the pH and ionic strength. The DLVO theory emphasizes that the overall stability of such colloidal systems of particles in aqueous dispersions is dependent on the contribution of two major forces, attractive van der Waals and repulsive electrostatic forces. Conditions such as high ionic strength, low dielectric solvents, and pH near the isoelectric point significantly weaken the electrostatic repulsion, resulting in domination of van der Waals forces and subsequent aggregation. Moreover, the presence of oppositely charged particles spark the existence of non-DLVO type electrostatic attractive force that leads to heteroaggregation. Such observation presents a mechanism to deliberately and controllably trigger particle-particle heteroaggregation via manipulation of experimental conditions such as pH or surface functionalization with charged polyelectrolytes that cause particles to be oppositely charged. Heteroaggregation could also arise due to chemical interactions such as Lewis acid-base interactions as the case with nZVI and clay mineral particles and also via hydrogen bonding, when nanoparticles with abundant oxygen-containing groups are present, as we have seen with GO and  $\text{Al}_2\text{O}_3$ . In the following chapters, the implementation of these

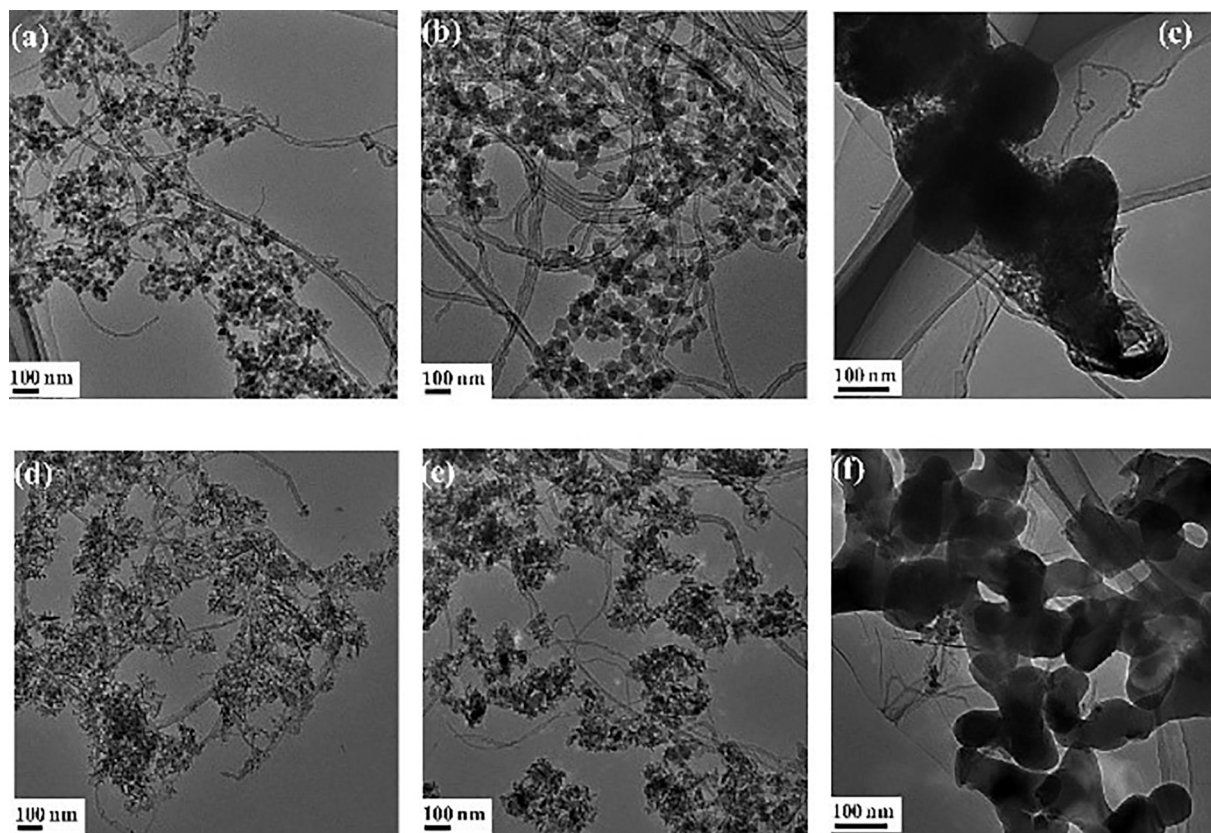


Fig. 6. TEM images of (a, b, c) CNTs- $\text{SiO}_2$  and (d, e, f) CNTs- $\text{Al}_2\text{O}_3$  composites ((a, b, c): 15 nm, 30 nm, and 100 nm  $\text{SiO}_2$ , (d, e, f): 20 nm, 50 nm, and 100 nm  $\text{Al}_2\text{O}_3$ , respectively) [75]. Reprinted from (Size-dependent impact of inorganic nanoparticles on sulfamethoxazole adsorption by carbon nanotubes, 316, Chen, B.; Sun, W. L.; Wang, C. H.; Guo, X. Y., *Chem. Eng. J.* 2017, 160–170). Copyright (2021), with permission from Elsevier.



heteroaggregation principles to fabricate novel and/or functional hybrid materials with promising physicochemical features in numerous applications is reviewed.

### 3. Novel heterostructures: heteroaggregation and characterization

In this section, various heterostructures of novel physicochemical features are discussed. They were prepared by heteroaggregation of particle dispersions and the observed new phenomenon is foreseen to be utilized in some fields, i.e., significant effort was made on structural characterization, however, applications only proposed based on the determined properties. We consider sphere-sphere, plate-plate, and sphere-plate geometries.

#### 3.1. Sphere-sphere systems

The photocatalytic potential of heteroaggregated structures of SnO<sub>2</sub> and TiO<sub>2</sub> particles has been explored by de Mendonça et al., who prepared TiO<sub>2</sub>-SnO<sub>2</sub> structures with semiconductor surface by microwave-assisted heteroaggregation of dispersions of TiO<sub>2</sub> and SnO<sub>2</sub> nanoparticles [76]. TiO<sub>2</sub> nanoparticles were synthesized by the decomposition of a peroxotitanium complex under hydrothermal conditions, while SnO<sub>2</sub> nanoparticles were obtained by hydrolysis. The TiO<sub>2</sub>-SnO<sub>2</sub> heterostructures were formed by mixing a TiO<sub>2</sub> dispersion of fixed concentration with differently concentrated SnO<sub>2</sub> dispersions followed by hydrothermal treatment at varying time and temperature in a microwave oven. The photocatalytic properties of TiO<sub>2</sub>-SnO<sub>2</sub> were attributed to the heterojunctions that were formed during the treatment step. When irradiated by UV light, TiO<sub>2</sub>-SnO<sub>2</sub> generates surface hydroxyl radicals that react with and transform terephthalic acid to a fluorescent product.

Siedl et al. explored the charge transfer processes in TiO<sub>2</sub>-SnO<sub>2</sub> hybrid by monitoring the changes in surface charge as well as its effect on the aggregation behaviour and photo-induced charge separation [29]. TiO<sub>2</sub> and SnO<sub>2</sub> nanoparticles were obtained by metal organic chemical vapor synthesis, and the TiO<sub>2</sub>-SnO<sub>2</sub> hybrid was formed by dispersing certain amounts of the nanoparticles in a solution of formic acid, that serves to adjust the surface charge on particles, followed by annealing at high temperature. The adjustment of surface charge and annealing enabled the formation of a blended hybrid that possesses high heterojunction concentration and exhibits enhanced cross section for charge separation due to effective interfacial charge transfer across the particle-particle interfaces. These interfacial phenomena make such hybrid systems excellent candidates for such applications as photocatalysis, water splitting, and solar energy conversion.

The effect of reaction conditions on the structural properties of gel network was evaluated by Martínez-Pedrero et al. via heteroaggregation of latex and carbon black particles. The gel was prepared by mixing particles of surfactant-functionalized carbon black and natural rubber latex, where the SDS surfactant served as a stabilizing surfactant that tunes the interaction between the two particles [11]. The gel elasticity was tuned by changing the concentration of SDS, ranging from a reversible weak gel state to an irreversible elastic solid state.

Duřak et al. showed that the nature of interaction forces responsible for the formation of heteroaggregates profoundly affects their properties. Spherical carboxyl-functionalized and silica-coated maghemite nanoparticles were heteroaggregated with larger amino-functionalized silica spherical nanoparticles [50]. Silica NPs were synthesized using a modified Stöber process, while its amino functionalization was achieved by grafting. On the other hand, maghemite was synthesized by the co-precipitation method and silica coating was carried out using the hydrolysis and polycondensation of tetraethoxysilane, while carboxyl coating was performed with covalent grafting. The electrostatically driven heteroaggregation was achieved by vigorous mixing of aqueous suspensions of silica and maghemite. The uniformity of the surface

coverage of maghemite depended on the type of interparticle interactions involved, chemical interactions resulted in more homogenous and greater coverage compared to electrostatic interaction. Fig. 7 shows TEM images of heteroaggregates at different conditions.

The aggregation pattern of metal oxides was found to depend on the pH conditions, Yi et al. used commercial CeO<sub>2</sub> nanoparticles with pyrogenic carbonaceous material (PCM) NPs to probe the effect of the pH on heteroaggregation behaviour by mixing the corresponding aqueous dispersions at the desired ratio and observing the changes in hydrodynamic radius and zeta potential [77]. At pH 5.3, heteroaggregation is favourable only at appropriate experimental conditions leading to charge neutralization and charge reversal, where repulsive electrostatic forces dominate at high and low PCM concentrations, whereas unstable systems were obtained at intermediate PCM concentrations. Around pH 7.1, CeO<sub>2</sub> particles are neutral and form unstable dispersion, while PCM is negatively charged and forms stable dispersions. Heteroaggregation occurred by charge-accumulation and core-shell stabilization mechanism, where PCM binds to and forms a negatively charged shell on the neutral surface of CeO<sub>2</sub> core.

Heteroaggregation of spherical particles of similar chemical composition, but with a significant difference in particle size has been reported by Zanini et al., who prepared heterostructures with various surface roughness of oppositely charged and differently sized silica particles, as shown in Fig. 8. The positive charge on smaller silica particles was achieved by surface functionalization with PDADMAC polyelectrolyte. Additionally, the heteroaggregation of PNIPAM-based microgels onto commercial PS microbeads was attributed to hydrophobic interactions. The size of adsorbed microgels changed with the pH conditions and the surface coverage of microgels was higher in acidic conditions [78].

#### 3.2. Sphere-plate systems

Veschambres et al. prepared nanocomposite films of particles of layered double hydroxides (LDH) and latex by heteroaggregation and solvent casting process [79]. The latex was synthesized by surfactant-free polymerization of methyl methacrylate (MMA) monomers and butyl acrylate (BA) co-monomers. MgAl-CO<sub>3</sub>-LDH, on the other hand, was prepared by flash co-precipitation followed by hydrothermal treatment. The electrostatic interactions led to the heteroaggregation between the oppositely charged LDH and latex particles upon mixing the corresponding dispersions, the formed LDH-latex hybrid was then transferred into a special chamber to form LDH-latex films. The microstructure could be controlled by varying the size of the latex beads and the LDH layers. Fig. 9 shows low and high magnification TEM images of composites at different LDH contents. The films showed a homogeneous cellular network of LDH layers, with higher LDH content resulting higher wall thickness. At high temperatures, the network is stiff enough to induce a mechanical percolation in the composites, when pure matrix shows a viscous behaviour.

Ji et al. prepared a porous nanomaterial by heteroaggregation between hematite and montmorillonite particles over a pH range of 2.5–7.5, under which they possess positive and negative charge, respectively [80]. Hematite was synthesized by forced hydrolysis while montmorillonite was obtained commercially. Dispersions of both particles were slowly mixed under intensive agitation, and the aggregate formation was monitored by turbidimetric titration, which showed that particle aggregate formation depends on the concentration of the particles added initially to the dispersions. Fig. 10 shows the possible heterostructures of montmorillonite sheets with differently sized hematite particles. The mass ratio affected the number of pores and the specific surface area of the composite. With increasing hematite content, the amount of the pores with an equivalent diameter of about 4 nm decreased, while those having a diameter of 10–20 nm increased.

Voorn et al. reported the formation of various sphere-platelet hybrids by simple mixing of aqueous dispersions of gibbsite with different silica

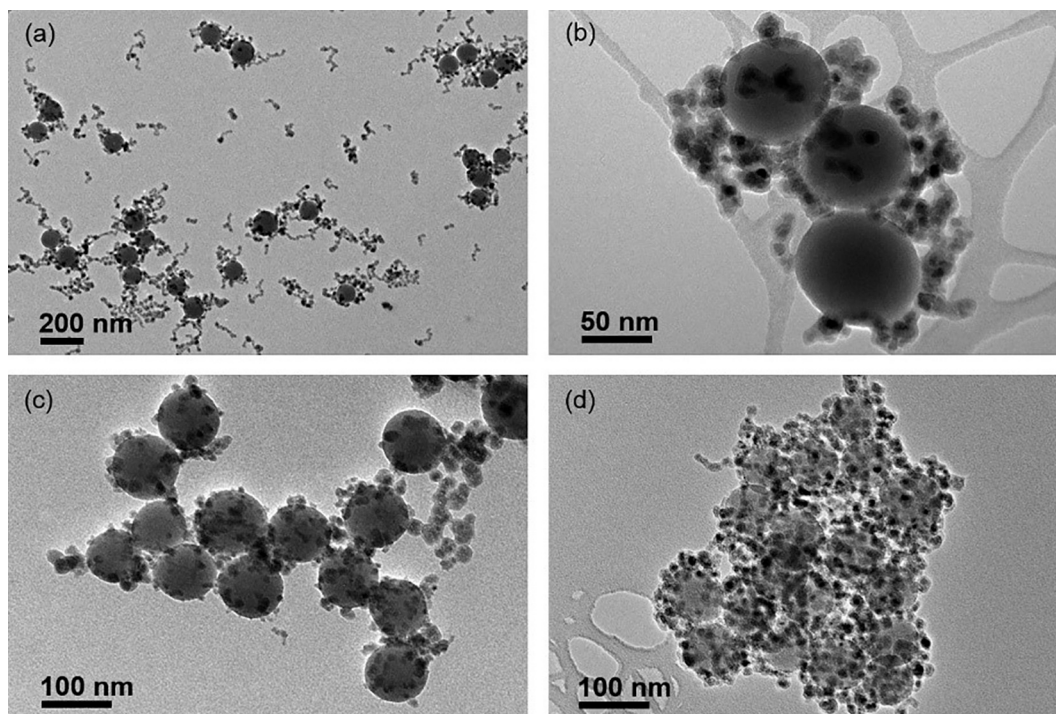


**Fig. 7.** TEM images of maghemite-silica heteroaggregates at (a, b) lower and (c) higher maghemite concentration, and at (d) lower maghemite concentration with increased ionic strength [50]. Reprinted from (Controlled heteroaggregation of two types of nanoparticles in an aqueous suspension, 438, Dusak, P.; Mertelj, A.; Kralj, S.; Makovec, D., *Journal of Colloid and Interface Science*, 2015, 235–243). Copyright (2021), with permission from Elsevier.

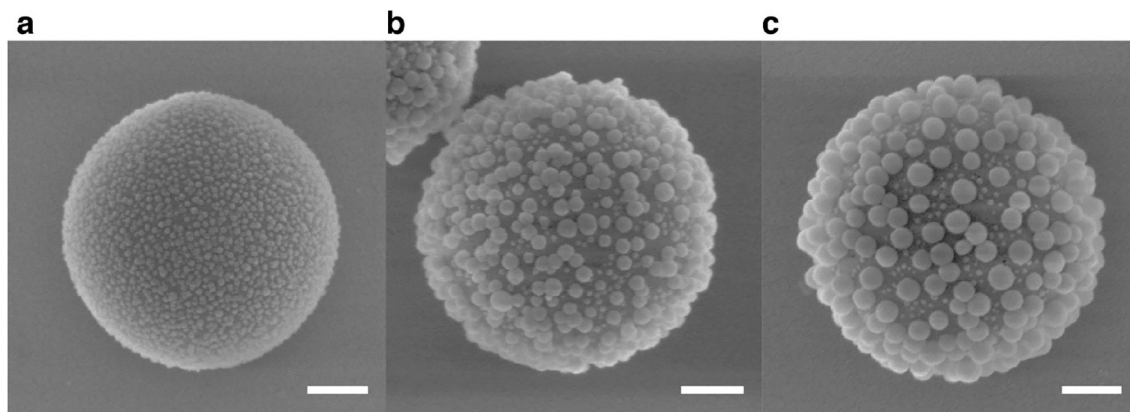


**Fig. 8.** Heterostructured silica (raspberry-like) particle. Silica particles of (a) 12 nm (b) 39 nm and 12 nm (c) and 72 nm and 12 nm silica particles adsorbed onto positively charged larger silica particles with average diameter of 1  $\mu\text{m}$ . The scale bars represent 200 nm [78]. Reprinted from (Fabrication of rough colloids by heteroaggregation, 532, Zanini, M.; Hsu, C. P.; Magrini, T.; Marini, E.; Isa, L., *Colloids and Surfaces A: Physicochemical and Engineering Aspects*, 2017, 116–124). Copyright (2021), with permission from Elsevier.

and latex particles including polystyrene, poly(isobutyl methacrylate), and poly(butyl methacrylate) (PBMA) [81]. The anionic latex particles were synthesized by feed emulsion polymerization and silica particles were obtained commercially. The heteroaggregated particles were annealed above the glass transition temperature of the polymer to ensure a thin polymer layer covering the gibbsite platelets is formed. The cryo-TEM images of gibbsite-PBMA composite are shown in Fig. 11. The colloiddally stable anisotropic hybrid particles possess a single layer of spheres on each side of the gibbsite platelets.

Yang et al. prepared a PS-LDH composite by heteroaggregation of the oppositely charged materials to probe the effect of different emulsifiers on the strength of interaction and polymeric properties [82]. The MgAl-LDH was prepared by the co-precipitation method, while PS was prepared by emulsion and soap-free emulsion polymerization using SDS,

CTAB, and HMPS as emulsifiers. The aqueous suspension of LDHs was slowly added to the PS emulsion, and the hybrid formation was driven by the electrostatic forces between anionic polymer particles and cationic LDHs platelets. A reactive emulsifier produced a stronger interaction and higher glass transition temperatures, and well-dispersed LDHs platelets resulted in composites of improved thermal stability.

Pavlovic et al. investigated the aggregation of polymer latex particles in the presence of LDH platelets of different compositions [83]. The MgAl-CO<sub>3</sub>-LDH and MgAl-NO<sub>3</sub>-LDH platelets were synthesized by flash co-precipitation followed by hydrothermal treatment, while P(MMA-co-BA) latex particles were prepared by surfactant-free emulsion polymerization. The oppositely charged species form the LDH-P(MMA-co-BA) hybrid upon mixing their aqueous dispersions due to the electrostatic attraction. Fig. 12 shows a schematic representation of the



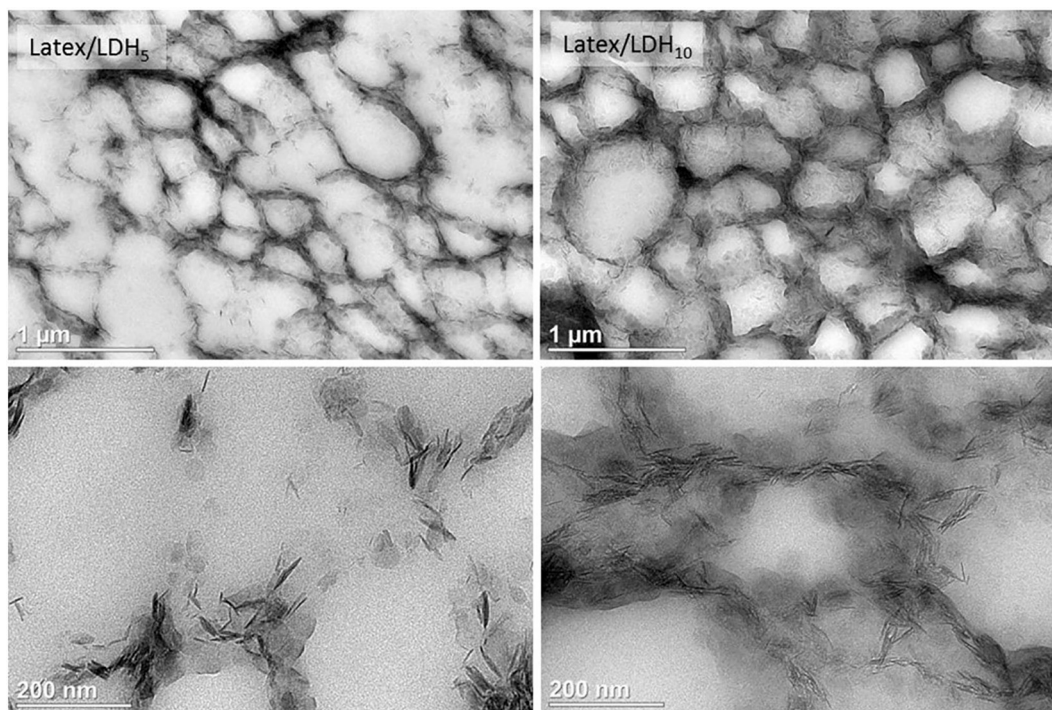


**Fig. 9.** TEM images of Latex/LDH<sub>5</sub> and Latex/LDH<sub>10</sub> samples (the subscript indicates the volume content of the LDH) at different magnifications [79]. The formed LDH network is well-visible on the pictures. Reprinted from (Layered double hydroxides: Efficient fillers for waterborne nanocomposite films, 130, Veschambres, C.; Halma, M.; Bourgeat-Lami, E.; Chazeau, L.; Dalmas, F.; Prevot, V., *Applied Clay Science*, 2016, 55–61). Copyright (2021), with permission from Elsevier.

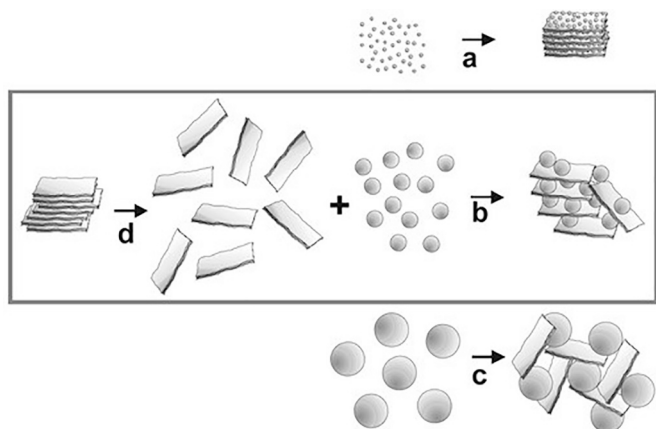


**Fig. 10.** Schematic illustration of (a) the preparation of organic-inorganic composites, (b) heteroaggregation with sol particles, and (c) emulsions, while synthesis of delaminated montmorillonite particles is shown in (d) [80]. Reprinted (adapted) with permission from (Ji, Y. Q.; Black, L.; Weidler, P. G.; Janek, M., Preparation of nanostructured materials by heterocoagulation-interaction of montmorillonite with synthetic hematite particles. *Langmuir* 2004, 20 (22), 9796–9806). Copyright (2021) American Chemical Society.

aggregation process of the P(MMA-co-BA) spheres with the adsorbed MgAl-CO<sub>3</sub>-LDH platelets on the surface. Electrostatic attraction between LDH and latex led to charge neutralization and reversal when the LDH dose was increased. The LDH-latex particles rapidly aggregated near the IEP but formed stable suspensions at LDH doses away from IEP.

### 3.3. Plate-plate systems

Li et al. fabricated NiFe-LDH/MnO<sub>2</sub> nanocomposite via layer-by-layer self-assembly and flocculation methods [84]. The SEM and TEM images in Fig. 13 highlight the structural features of nanocomposites

obtained by LBL method and flocculated methods. The MnO<sub>2</sub> nanosheets and NiFe-LDH were prepared separately via hydrothermal synthesis. For the flocculation process, the colloidal suspension of delaminated NiFe-LDH nanosheets was slowly added into the formamide suspension of MnO<sub>2</sub> nanosheets to form Ni<sup>2+</sup>-Fe<sup>3+</sup> LDH/MnO<sub>2</sub> with plate-like morphology. The precipitated flocculate was dried with nitrogen gas. Layered NiFe-LDH/MnO<sub>2</sub> was also prepared by sequential adsorption procedure. Cyclic voltammetry indicated good capacitance behaviour with an initial capacitance of 104 F/g for the material obtained by the aggregation process, which makes the nanocomposite a good potential candidate for use in lithium-ion batteries and supercapacitors.

Nethravathi et al. reported the preparation of co-stacked smectite clay/GO composites through delamination and re-stacking [85]. GO was prepared by the Hummers-Offeman method and its interlayers were intercalated with octylamine (OA) in the presence of small amounts of n-hexane. Commercial bentonite clay was modified by intercalating its interlayers with cetyltrimethyl ammonium (CTA) to give smectite-CTA. The GO-smectite composites were obtained by mixing and sonicating required volumes of the respective dispersions. The final composition is not uniform and has many smectite-rich and carbon-rich regions. Also, the clay component of the composites could be removed to obtain exfoliated and porous graphite.

Lagaly et al. probed the effect of mass ratio in composites of MgAl-LDH and sodium montmorillonite clay (extracted from Wyoming bentonite) on their mechanical properties. Composites were prepared by simple mixing of the corresponding dispersions [86]. The mass ratio as well as the presence of salts largely affected the mechanical stability as well as the aggregation pattern in the system. Heteroaggregation occurred when the LDH and clay mass fractions were 0.2 and 0.06, respectively. Maxima in the yield value and storage modulus was observed when the LDH mass ratio was 0.4–0.5. When the LDH was in excess, a steep decrease was observed in both the yield value and storage modulus, indicating a deterioration in mechanical properties, which can be utilized in future applications.

Huang et al. studied the effect of kaolinite and goethite associations

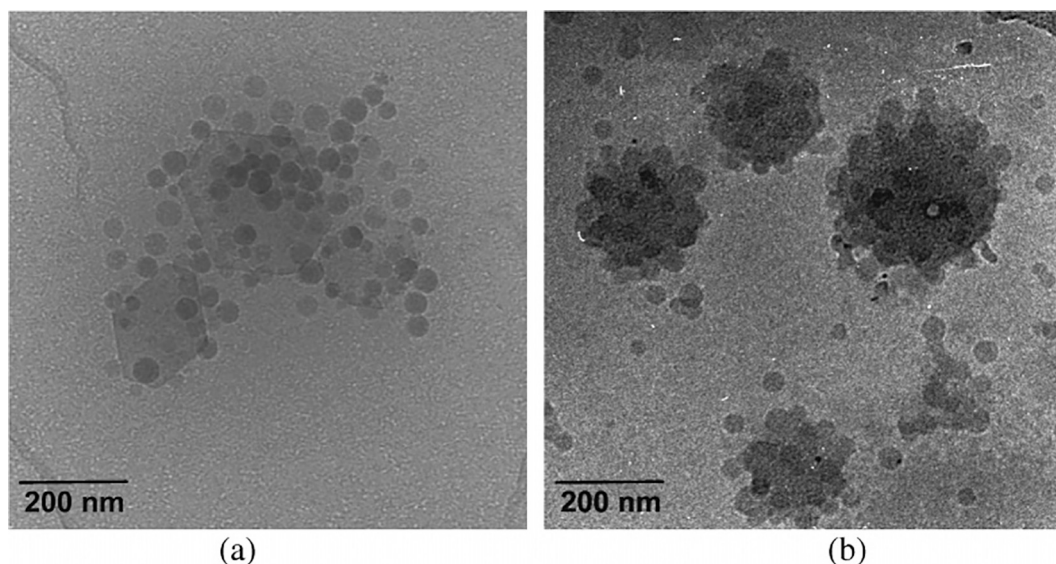


**Fig. 11.** Cryo-TEM images of cationic gibbsite with anionic PBMA particles at (a)  $\sim 0.3$  mM and (b)  $\sim 0.9$  mM NaCl [81]. Reprinted (adapted) with permission from (Voorn, D. J.; Ming, W.; van Herk, A. M.; Bomans, P. H. H.; Frederik, P. M.; Gasemjit, P.; Johansmann, D., Controlled heterocoagulation of platelets and spheres. *Langmuir*, 2005, 21 (15), 6950–6956). Copyright (2021) American Chemical Society.

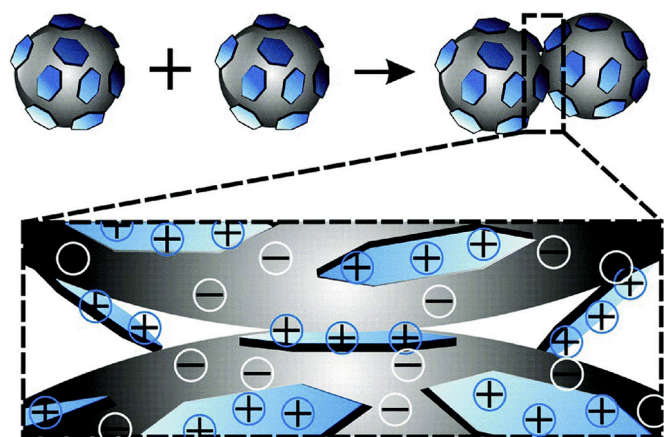


**Fig. 12.** Schematic representation of the aggregation process of the P(MMA-co-BA) spheres with the adsorbed MgAl-CO<sub>3</sub> platelets on the surface [83]. Reproduced from (Pavlovic, M.; Rouster, P.; Bourgeat-Lami, E.; Prevot, V.; Szilagyi, I., Design of latex-layered double hydroxide composites by tuning the aggregation in suspensions. *Soft Matter*, 2017, 13 (4), 842–851) with permission from The Royal Society of Chemistry.

(KGA) on the stability of GO in aquatic systems under different pH and ionic strength conditions as well as various GO concentrations by systematic introduction of clay minerals in GO dispersions [87]. The GO was prepared via improved Hummer's method. Heteroaggregation occurred when the pH was lower than 6 or 5, depending on the clay, and decreased with increasing GO concentration. The CCC of GO in the presence of KGA containing 10% goethite increased from less than 1 mM NaCl to 5 mM NaCl with the increase of pH from 5.5 to 9.

### 3.4. Miscellaneous systems

Heteroaggregation has been used to adsorb polysaccharide particles on fibrils. Jones et al. reported the formation of fibrils-polysaccharide complex by titrating  $\beta$ -lactoglobulin fibrils with the oppositely charged  $\kappa$ -carrageenan polysaccharide particles at low pH [88], which enabled studying the obtained morphology and mechanism of complex formation. The fibrils of  $\beta$ -lactoglobulin are formed by heating the

$\beta$ -lactoglobulin at low pH. The formation of aggregates occurred when the polysaccharide particles were attached along the protein fibrils. The attachment efficiency increased with the increase in the  $\kappa$ -carrageenan concentration, with maximum complexation efficiency occurred at a protein-to-polysaccharide weight ratio of 5:3. Fig. 14 shows a graphical representation of the fibrils-polysaccharide complex prepared by the heteroaggregation process.

CdSe-silica/Au nanowires and Au-silica/Au nanowires with drug delivery potential were reported by Pita et al. [89]. Au nanowires, prepared by soft solution phase synthesis, were coated with ultrathin silica layer via Stöber method. Then, differently sized nanoparticles of CdSe and Au were prepared and separately dispersed in toluene. The CdSe-silica/Au nanowires and Au-silica/Au nanowires, shown in Fig. 15, were prepared by mixing and subsequent sonicating of dispersion of silica/Au nanowires with the relevant dispersion of either CdSe or Au nanoparticles. The total coverage of Au nanowires increased with the particle size due to the presence of attractive van der Waals forces. Analysis of the recorded Raman peaks for bare and incorporated CdSe showed higher intensity for the latter owing to the generated surface plasmon propagation, which makes CdSe composite a potential candidate material for sensors development such as probe tips.

The heteroaggregation of GO with different minerals (montmorillonite, goethite, and kaolinite) in aqueous dispersions was investigated by Zhao et al. to gain an insight into the interactions of GO in aquatic systems, soil, and sediments [48]. Commercial graphite flakes were exfoliated via Hummers' method to obtain GO, and the commercial minerals were saturated with Ca<sup>2+</sup> and Na<sup>+</sup> by soaking in CaCl<sub>2</sub> and NaCl solutions. Mineral samples were introduced into GO dispersions, followed by prolonged shaking. In the pH range 4.0–8.5, GO and positively charged goethite formed heteroaggregates with multilayered structure, which resulted in enhanced dispersibility of the mineral due to electrostatic interactions. Also, the dissolved Fe<sup>3+</sup> ions of goethite did not destabilize GO suspension. On the other hand, GO showed no affinity towards montmorillonite or kaolinite.

## 4. Novel functional heterostructured materials

In this chapter, the main focus will be made on highly functional hybrid materials, which were prepared by heteroaggregation of individual particle systems, and they have proved as advantageous materials in certain applications. The latter point highlights the major difference



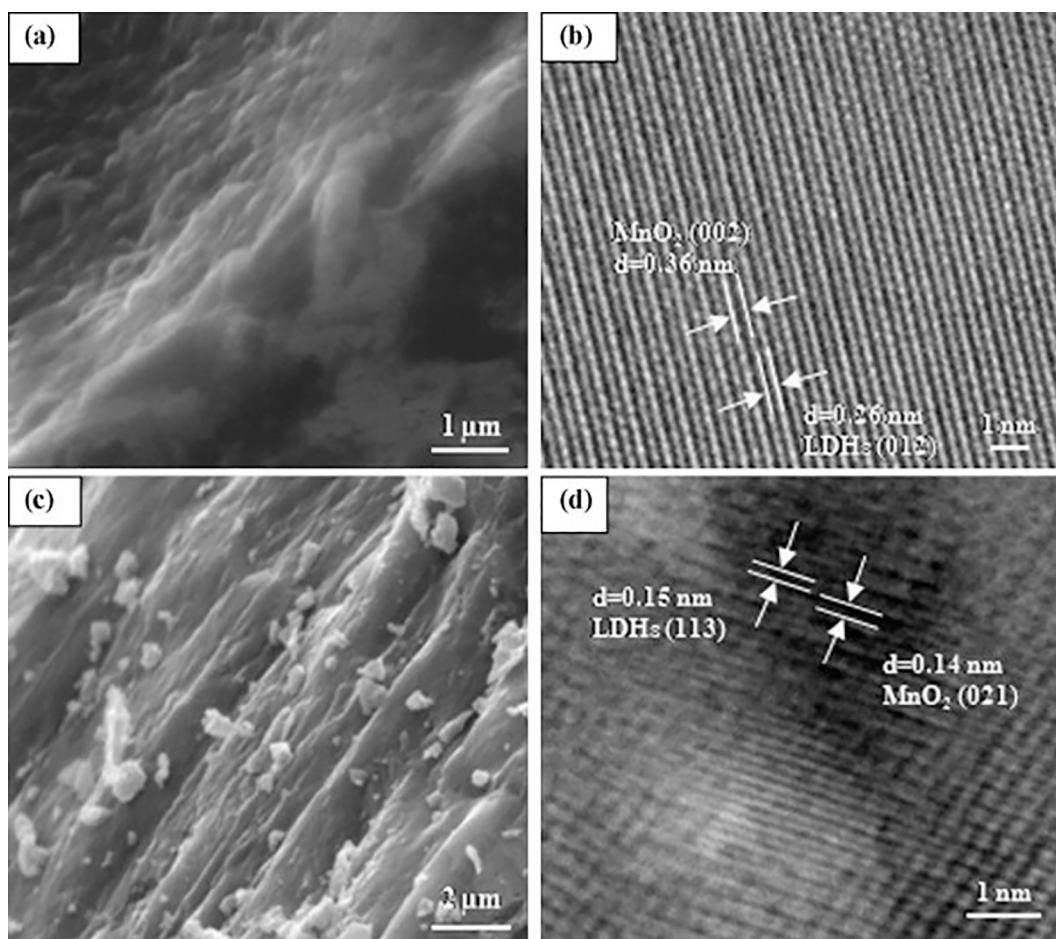


**Fig. 13.** SEM and high-resolution TEM images of nanocomposites obtained by (a, b) LBL method and (c, d) flocculated techniques [84]. Reprinted from (Fabrication and capacitance of NiFe-LDHs/MnO<sub>2</sub> layered nanocomposite via an exfoliation/reassembling process, 177 (1), Li, H.; Deng, L.; Zhu, G.; Kang, L.; Liu, Z.-H., *Mater. Sci. Eng. B*, 2012, 8–13). Copyright (2021), with permission from Elsevier.

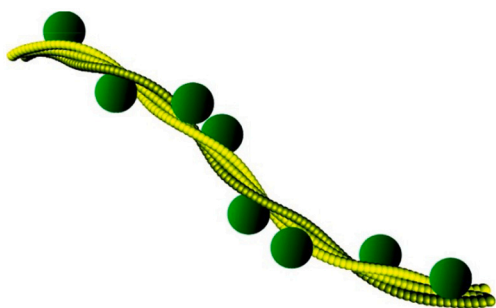


**Fig. 14.** Graphical representation of the fibril-polysaccharide complex prepared by heteroaggregation of  $\beta$ -lactoglobulin fibrils and globular clusters of  $\kappa$ -carrageenan (not to scale) [88]. Reprinted (adapted) with permission from (Jones, O. G.; Handschin, S.; Adamcik, J.; Harnau, L.; Bolisetty, S.; Mezzenga, R., Complexation of  $\beta$ -lactoglobulin fibrils and sulfated polysaccharides. *Biomacromolecules* 2011, 12 (8), 3056–3065). Copyright (2021) American Chemical Society.

between the present and previous chapters that the composites discussed below were used in real tests to assess their activity or performance.

#### 4.1. Coating and packaging

Yan et al. prepared antioxidant films as packaging wrapper that help

maintain the quality of food products and extend the shelf life without food preservatives [90]. The film material was prepared by adding different proportions of  $\alpha$ -tocopherol-chitosan nanoparticles to a dispersion of chitosan-montmorillonite and the films were prepared by pouring the resulting composite onto square PTFE plates, which were later dried. The films showed 46.5% DPPH radical scavenging activity after 16 days of storage. Also, by coating sliced ham with the film solution, measurement of peroxide and TBARs values showed that the film possesses enhanced antioxidant activity for 120 days.

#### 4.2. Antibacterial agents

Similar synthetic paths can be extended for preparing other functional materials such as antibacterial agents. For instance, Mallakpour and Hatami used Vitamin B9 (VB9) to prepare Ag@VB9-LDH composites as antibacterial agents [91]. The Ag nanoparticles were obtained by bio-friendly synthesis using *R. officinalis* leaves, while VB9-MgAl-LDH was prepared by co-precipitation of the metal salts in the presence of VB9. Then, the Ag@VB9-LDH composite was prepared by mixing homogeneous dispersions of Ag and VB9-MgAl-LDH. The resulting Ag@VB9-LDH composite was later incorporated in a chitosan biopolymeric matrix by mixing a water/acetic acid solution of chitosan with an aqueous dispersion of Ag@VB9-LDH to give chitosan/Ag@VB9-LDH composite. Both the Ag@VB9-LDH and the chitosan/Ag@VB9-LDH composites showed remarkable antibacterial activity against Gram-negative (*E. coli*) and Gram-positive (*S. aureus*), with the latter having greater inhibition zone diameter than with Ag@VB9-LDH. Fig. 16 shows FE-SEM images of

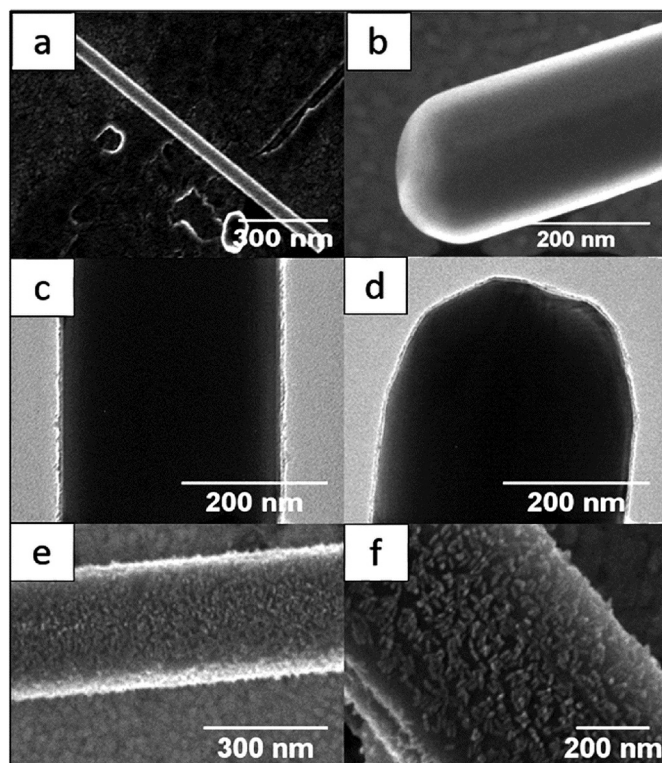


**Fig. 15.** Images of (a, b) Plain silver nanowires, (c, d) silver nanowires coated with silica, (e, f) silica coated silver nanowire coated with CdSe nanoparticles [89]. Reproduced from (Pita, I. A.; Singh, S.; Silien, C.; Ryan, K. M.; Liu, N., Heteroaggregation assisted wet synthesis of core-shell silver-silica-cadmium selenide nanowires. *Nanoscale*, 2016, 8 (2), 1200–1209) with permission from The Royal Society of Chemistry.

Ag@VB9-LDH and chitosan/Ag@VB9-LDH composite materials as well as pure LDH and chitosan.

Precillia et al. developed a GO/NiO composite that acted as an antibacterial agent against Methicillin Resistant *Staphylococcus aureus* and *A. baumannii* and as a potential fluorescent chemosensor for leucine. GO was prepared by the Hummers method and NiO NPs were synthesized via co-precipitation of the metal salt. The GO/NiO composite was prepared by prolonged mixing of well-dispersed aqueous dispersions of GO and NiO nanoparticles under reflux. The composite was more sensitive towards *A. baumannii* than *Staphylococcus aureus*, as indicated by the minimum inhibitory zone concentration (400  $\mu\text{g}/\text{mL}$  for *Staphylococcus aureus* and 200  $\mu\text{g}/\text{mL}$  for *A. baumannii*). Fluorescence analysis also indicated that the composite selectively detects leucine, even in the presence of other amino acids, through photo-induced electron transfer mechanism [92].

Almasi et al. fabricated an antimicrobial nanocomposite by impregnation of commercial CuO NPs into bacterial cellulose nanofibers (BCNF) as well as chitosan nanofibers (CHNF) [93]. The BCNF were produced by *Gluconacetobacter xylinus* culture, while CHNF obtained by the deacetylation of shrimp shell chitin through chemical treatments. The CuO-CHNF was prepared by mixing an aqueous CuO dispersion (contained 1% (v/v) acetic acid) with a dry base of CHNF followed by ultrasonic homogenization. The composite was obtained by filtration and subsequent drying. On the other hand, the CuO-BCNF composite was prepared similarly, but the CuO NPs were dispersed in water rather than 1% (v/v) acetic acid solution. The hybrid materials were formed via hydrogen bonds between organic and inorganic phases. While the crystalline structure of BCNF was preserved after CuO impregnation, CHNF underwent substantial changes in crystallinity with increased amorphous region. The CuO NPs antibacterial activity against both Gram-positive and Gram-negative bacteria decreased upon attachment

to BCNF, while CHNF was more effective than BCNF in release controlling of CuO NPs to water.

#### 4.3. Catalysis

Ben Moussa et al. prepared a bi-functional catalyst for selective n-heptane hydrocracking [46]. Two-domain  $\text{Al}_2\text{O}_3/\text{zeolite}$  composite was prepared by dropwise mixing of stable suspensions of  $\beta$ -zeolite and commercial boehmite ( $\gamma$ - $\text{AlOOH}$  nanoparticles) under vigorous stirring, and the obtained solid phase was calcined. The second composite of  $\text{Al}_2\text{O}_3/\text{zeolite}$ , characterized by larger zeolite domain, was prepared by wet mechanical mixing. Then, by adjusting the pH and Pt precursors, Pt nanoparticles were selectively deposited onto either  $\text{Al}_2\text{O}_3$  or zeolite domains, as shown in Fig. 17, with a soft thermo-reduction step was applied to obtain a composite Pt/ $\text{Al}_2\text{O}_3$ -zeolite with a well-dispersed Pt phase. The location of the Pt nanoparticles and the size of the zeolite domains did not significantly modify the conversion of n-heptane hydro isomerization. However, the location of Pt nanoparticles on zeolite/alumina aggregates impacted the selectivity of the resulting catalyst.

Li et al. synthesized a series of catalytic composites of NiAl-LDH decorated with captopril-capped  $\text{Au}_x\text{Pd}_y$  nanoclusters (NCs) with multiple Au/Pd ratios; the composites exhibited higher aerobic oxidation activity of 1-phenylethanol than monometallic NCs depending on the ratio [94]. The NiAl-LDH was prepared by the co-precipitation method, while bimetallic captopril-capped  $\text{Au}_x\text{Pd}_y$  NCs was synthesized by size-focusing synthetic strategy using  $\text{Na}_2\text{PdCl}_4$  and  $\text{HAuCl}_4 \cdot 4\text{H}_2\text{O}$ . The NiAl-LDH/ $\text{Au}_x\text{Pd}_y$  hybrid was prepared by the addition of captopril-capped  $\text{Au}_x\text{Pd}_y$  solid to an aqueous dispersion of NiAl-LDH under vigorous stirring (Fig. 18) followed by calcination. The catalytic activities increased and then decreased with decreasing the Au/Pd ratios from 24 to 1.56; the  $\text{Au}_{87}\text{Pd}_{13}/\text{NiAl-LDH}$  with a size of  $1.5 \pm 0.5$  nm showed the highest activity with a turnover frequency of  $6810 \text{ h}^{-1}$  and  $131,400 \text{ h}^{-1}$  in toluene and under solvent-free conditions, respectively. The catalyst showed high suitability to alcohol substrates and maintain 98% of the initial conversion of 1-phenylethanol after 10 cycles.

#### 4.4. Photocatalysis

Li et al. reported the synthesis of catalytic magnetite core/ $\text{W}_7\text{O}_{24}^{6-}$ -LDH shell nanocomposite [95]. Magnetite particles were synthesized using the solvent-thermal method and were further coated with silica via the sol-gel process. The silica-coated magnetic particles were further coated with 20 bilayers of  $\text{CO}_3^{2-}/\text{LDH}$  by alternate additions of the particles into aqueous solutions of  $\text{Na}_2\text{CO}_3$  and formamide-based suspensions of  $\text{W}_7\text{O}_{24}^{6-}$ -LDH nanosheets. The mixture was sonicated, and the solid particles were collected by centrifugation before introduction into the next solution/suspension. After that, the sample was ramp-heated under  $\text{N}_2$  atmosphere to remove water as well as  $\text{CO}_3^{2-}$  ions, and then was dispersed in water to recover the original LDH structure. The composite structure showed high anion loading capacity as well as catalytic activity towards the photodegradation of trace hexachlorocyclohexane in aqueous solutions and could effectively be recycled and reused up to six times without any apparent decrease in its catalytic activity.

Zhu et al. prepared a catalytic nanocomposite of black phosphorous (BP) nanosheets loaded with bismuth vanadate ( $\text{BiVO}_4$ ) nanosheets for water splitting applications [96]. BP nanoflakes were prepared through the exfoliation method in a *N*-methyl-2-pyrrolidone (NMP) solution, while  $\text{BiVO}_4$  nanosheets were synthesized using the hydrothermal method in the presence of sodium dodecylbenzenesulfonate. Then BP and  $\text{BiVO}_4$  nanosheets were easily hybridized by electrostatic interactions. The BP/ $\text{BiVO}_4$  heterostructures were prepared by adding  $\text{BiVO}_4$  solid sample into BP/NMP dispersion followed by prolonged sonication and stirring. The UV-Vis diffuse reflectance spectra and Mott-Schottky plots indicated that BP/ $\text{BiVO}_4$  heterostructures can be used as Z-scheme photocatalysts. Substantial amounts of  $\text{H}_2$  and  $\text{O}_2$  were



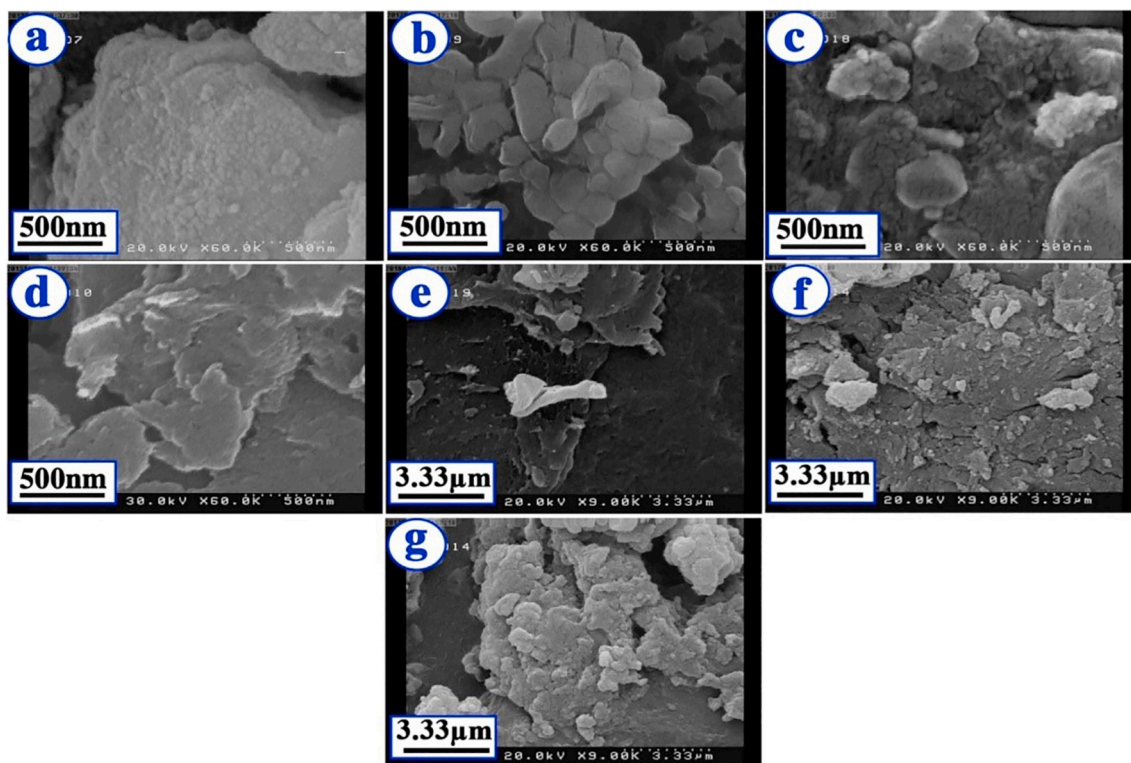


Fig. 16. FE-SEM images of (a) pure LDH (b) VB9-LDH and (c) Ag@VB9-LDH (d) pure chitosan and chitosan/Ag@VB9-LDH with (e) 3 wt% (f) 6 wt% and (g) 9 wt% of Ag@VB9-LDH [91]. Reprinted from (Green and eco-friendly route for the synthesis of Ag@Vitamin B9-LDH hybrid and its chitosan nanocomposites: Characterization and antibacterial activity, 154, Mallakpour, S.; Hatami, M., *Polymer*, 2018, 188–199). Copyright (2021), with permission from Elsevier.

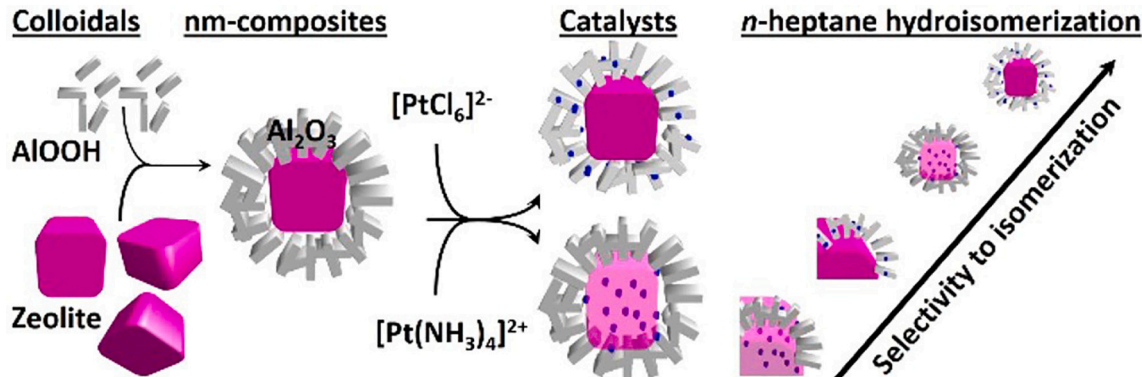


Fig. 17. Schematic representation of the synthesis and catalytic role of the two-domain  $\text{Al}_2\text{O}_3$ /zeolite composite [46]. Reprinted (adapted) with permission from (Ben Moussa, O.; Tinat, L.; Jin, X. J.; Baaziz, W.; Durupthy, O.; Sayag, C.; Blanchard, J., Heteroaggregation and selective deposition for the fine design of nano-architected bifunctional catalysts: Application to hydroisomerization. *ACS Catal.* 2018, 8 (7), 6071–6078). Copyright (2021) American Chemical Society.

detected under visible light irradiation in the presence of BP/ $\text{BiVO}_4$  without sacrificial agents, whereas neither BP nor  $\text{BiVO}_4$  alone could catalyze water-splitting reaction.

Gunjakar et al. reported the preparation of catalytic mesoporous nano-hybrid of co-stacked oppositely charged nanosheets of layered titanate and ZnCr-LDH [97]. The former was prepared by conventional solid-state reaction, while the latter was obtained by direct coprecipitation. The heterolayered nano-hybrid was synthesized by mixing the formamide suspensions of ZnCr-LDH and layered titanate under constant stirring. The restacked nano-hybrid was retrieved by centrifugation, washing, and vacuum-drying. The porosity could be controlled by changing the ratio of layered titanate/ZnCr-LDH, and the heterolayered nano-hybrid showed enhanced chemical stability as well as better catalytic activity in the visible light-induced  $\text{O}_2$  generation

compared to pristine ZnCr-LDH material.

Szabó et al. prepared  $\text{TiO}_2$ -GO composites with photocatalytic activity towards the decomposition of pollutants, and with accelerated sedimentation properties [98]. The GO was prepared from commercial graphite by Brodie method while  $\text{TiO}_2$  nanoparticles were obtained commercially. The  $\text{TiO}_2$ -GO composites were formed by addition of well-dispersed GO suspensions into aqueous dispersions of  $\text{TiO}_2$ , upon which the system is generated within seconds. The  $\text{TiO}_2$ -GO composite could catalyze the photo-oxidation of the phenols, as test pollutants, and possessed good recyclability that could be exploited in large scale treatment of wastewater. Compared to pure  $\text{TiO}_2$ , the presence of GO caused some loss of photocatalytic efficiency but induced an accelerated sedimentation leading to complete separation of the photocatalyst from the reaction mixture.

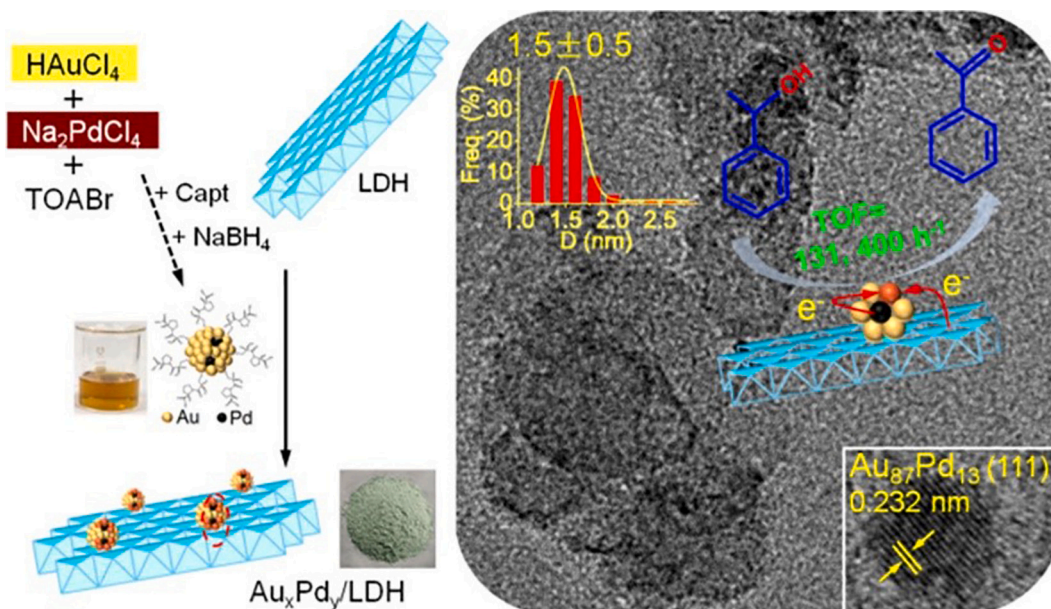


**Fig. 18.** (Left) Scheme of synthesis and structure of  $Au_xPd_y/LDH$ , (right) HRTEM image with the catalytic activity and size distribution of  $Au_{87}Pd_{13}/Ni_3Al-LDH$  [94]. Reprinted (adapted) with permission from (Li, J.; Xu, Y.; Wang, S.; Zhang, H., Ultrafine AuPd nanoclusters on layered double hydroxides by the capt-capped AuPd cluster precursor method: Synergistic effect for highly efficient aerobic oxidation of alcohols. *J. Phys. Chem. C*, 2019, 123 (25), 15,483–15,494). Copyright (2021) American Chemical Society.

In another work, Patzkó et al. prepared ZnO/ZnAl-LDH as a catalyst for phenol photo-oxidation [99]. Initially, the ZnAl-LDH was prepared from  $Zn(CH_3CO_2)_2 \cdot 2H_2O$  and  $Al(NO_3)_3$  while the  $Zn(OH)_2$  was prepared by hydrolysis. Then,  $Zn(OH)_2$  was intercalated into the LDH layers by mixing the corresponding dispersions, and the obtained solid was calcined at different temperatures to obtain the ZnO phase from  $Zn(OH)_2$ . The composite showed remarkable catalytic properties in phenol photo-oxidation in aqueous solutions. The calcination did not affect the catalytic activity significantly; however, the ratio of Zn/Al affected the phenol degradation rate, which peaked when a ratio of 4:1 was applied in the reaction mixture. Fig. 19 shows the heteroaggregation of LDH with ZnO nanoparticles and the structure of the ZnO/LDH nanocomposites after calcination.

Boppella et al. prepared reduced GO- $La_2Ti_2O_7/NiFe-LDH$  composite with remarkable photocatalytic activity towards  $H_2$  evolution under simulated light irradiation without expensive Pt co-catalyst [100]. The reduced GO (rGO), NiFe-LDH, and  $La_2Ti_2O_7$  (LTO) nanosheets were synthesized via modified Hummers method, co-precipitation method, and hydrothermal synthesis, respectively, while the rGO-LTO was prepared by dissolving the relevant solids in an aqueous medium followed by the thermal treatment in an autoclave. Finally, the rGO-LTO/NiFe-LDH was prepared by heteroaggregation of rGO-LTO and NiFe-LDH by mixing dispersions of the corresponding components in an ultrasonic bath. Fig. 20 shows TEM and HR-SEM images of the prepared composite as well as bare components. The  $H_2$  production rate of the novel rGO/LTO/NiFe heterostructure was 9 times higher than that of pure LTO, which can be attributed to the synergistic effect of rGO and NiFe-LDH. The composite also showed a minimal loss in activity after 4 runs, and the heterojunctions were stable under solar irradiation.

Mallakpour and Hatami reported the preparation of catalytic MgAl-LDH/Vitamin B9/ $TiO_2$  nanoparticles (LDH-VB9/ $TiO_2$ ) hybrid [101]. Commercially obtained VB9 was first intercalated into MgAl-LDH during the co-precipitation synthesis of the LDH. Aqueous dispersions of LDH-VB9 and commercial  $TiO_2$  nanoparticles were mixed and the resulting dispersion was then ultrasonicated, where the  $TiO_2$  nanoparticles were dispersed on the surface of the VB9-intercalated LDH layers. To enhance its physicochemical properties, the LDH-VB9/ $TiO_2$  composite was introduced as a filler into a matrix of crosslinked poly

(vinyl alcohol). The composites showed photodegradation potential of methylene blue (MB) dye under ultraviolet illumination. The rate constant of photodegradation by LDH-VB9- $TiO_2$  was higher than that catalysed by pure  $TiO_2$  as well as by the composite in poly(vinyl alcohol). The LDH-VB9- $TiO_2$  also showed a remarkable half-life for degradation of MB dye, compared to that without photocatalyst, and thus, can be utilized in many industrial applications such as water purification.

Evidently, owing to the complexity and requirements of the catalytic application processes, hybrid catalytic systems offer numerous advantages and are much more robust than their single-component counterparts. For example, heteroaggregated catalytic composites have better selectivity, higher activity due to sustained catalytic surface, and recyclability when incorporated with magnetic materials [102,103]. Polymer matrix composite catalysts have enhanced physicochemical properties such as electronic and thermomechanical features. The hybridization also influences the rate of adsorption/desorption and diffusion of molecules, and thus enables the control over the kinetics of the catalytic reactions [104]. Lastly, the incorporation of macropores into catalytic systems minimizes diffusion barriers and results in uniform distribution of active sites, it also increases light scattering and multiple internal reflections in photocatalytic materials resulting in improved photocatalytic efficiency [105].

#### 4.5. Removal of contaminant materials

Zong et al. prepared a hollow MgFe-layered double oxide (LDO) using carbon spheres (CSs) as cores. The hollow MgFe-LDO spheres were effective in the adsorption and removal of methylene blue [106]. The MgFe-LDO and CSs were prepared by co-precipitation and hydrothermal synthesis, respectively. Then, solid samples of CSs were added to aqueous dispersions of MgFe-LDO shell under ultrasonic irradiation, where the composite forms due to electrostatic heteroaggregation, and the obtained composites were then calcined to burn the carbon component and form hollow MgFe-LDO. Fig. 21 shows SEM and TEM images with the EDX elemental mapping of CSs, CSs@MgFe-LDHs and hollow MgFe-LDO. The efficient hollow material showed high adsorption capacity and rapid adsorption of methylene blue compared to ordinary LDO due to abundant and highly accessible active sites for



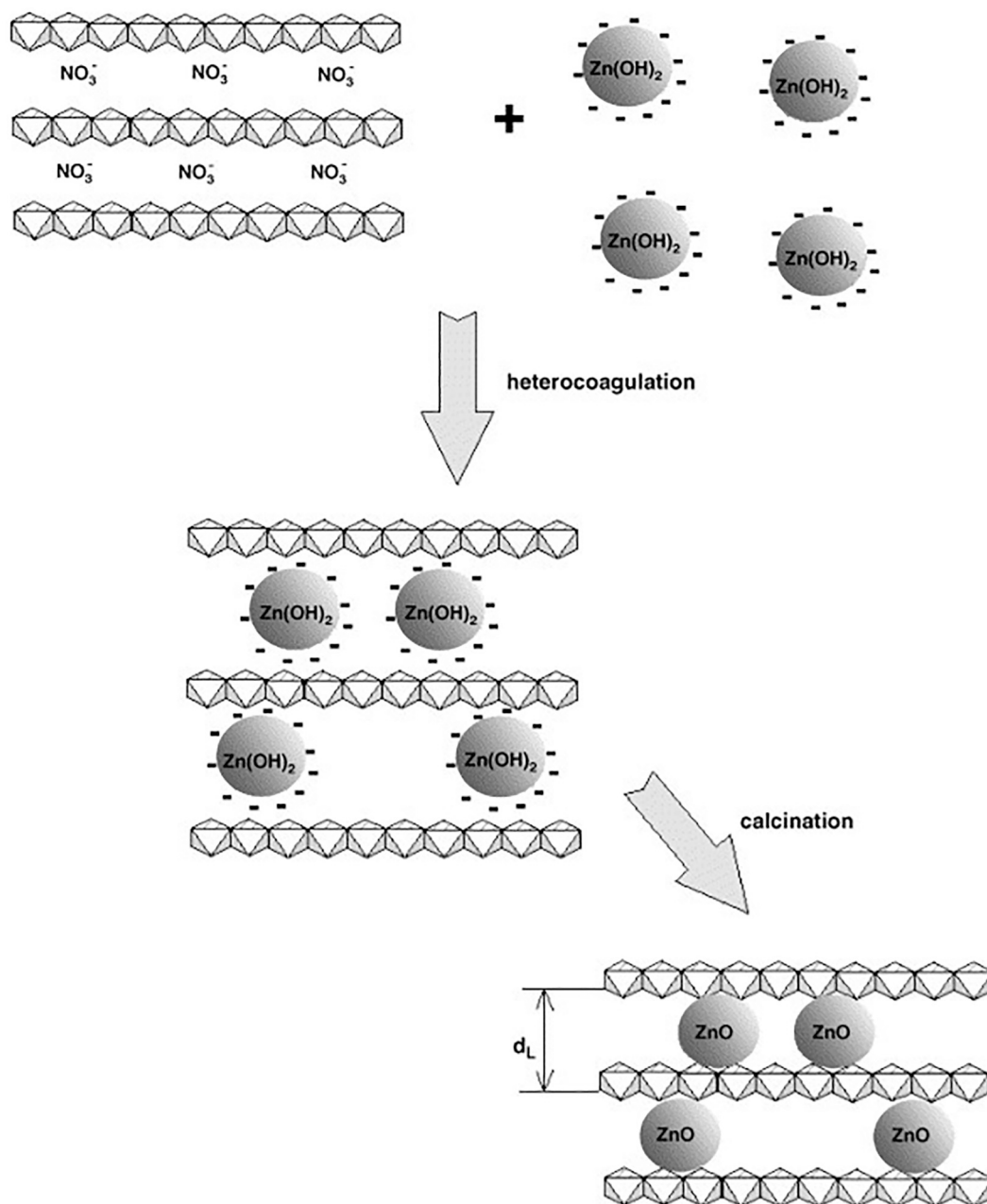


**Fig. 19.** Heterocoagulation of LDH with ZnO nanoparticles from stable dispersions and the structure of the ZnO/LDH nanocomposites after calcination [99]. Reprinted from (ZnAl-layer double hydroxides as photocatalysts for oxidation of phenol in aqueous solution, 265 (1–3), Patzko, A.; Kun, R.; Hornok, V.; Dekany, I.; Engelhardt, T.; Schall, N., *Colloids Surfaces A-Phys. Eng. Asp.*, 2005, 64–72). Copyright (2021), with permission from Elsevier.

adsorption, which occurred in a monolayered manner by chemical interactions. Additionally, the LDO was stable for at least five cycles and could be simply recycled via a magnet due to the presence of magnetic Fe.

Hu et al. reported the preparation of a novel nanocomposite for adsorption of RY2 dye from wastewater [107]. The composite was prepared by the heteroaggregation of MgAl-LDH nanoparticles and Na-modified bentonite sheets by mixing the relevant dispersions at different mass ratios, followed by calcination. The MgAl-LDH was prepared by coprecipitation under alkaline conditions, while bentonite was obtained commercially. The bentonite was further modified by soaking in 1 M NaCl solution to replace its exchangeable cations by  $\text{Na}^+$  cations. Fig. 22 shows SEM images of bentonite and LDH-bentonite hybrid. The dye uptake capacity increases with the increase in LDH loading in the hybrid, reaching 100% with a LDH/bentonite ratio of 2.3:1. For the

same ratio, the calcined sample showed better removal performance compared to uncalcined hybrids, and smaller LDH particles showed better removal ability owing to the larger surface area.

Gong et al. reported the preparation of a nanocomposite by attaching LDH nanocrystals onto carbon nanospheres (CNs) for removal of heavy metal ions such as  $\text{Cu}^{2+}$ ,  $\text{Cd}^{2+}$ , and  $\text{Pb}^{2+}$  from water [108]. The LDH was synthesized in pure methanol using  $\text{Mg}^{2+}$  and  $\text{Al}^{3+}$  salts, and the CNs was prepared through glucose carbonization under hydrothermal conditions in an aqueous media. The methanol-based suspensions of LDH and CNs were then mixed and ultrasonicated to obtain LDH@CNs nanocomposite, which was collected by centrifugation followed by drying. Fig. 23 shows TEM images of the LDH@CNs composite and its bare constituents. The heavy metal removal efficiency of LDH@CNs nanocomposite was much larger than that of any of its bare constituents. Removal efficiency of  $\text{Cu}^{2+}$ ,  $\text{Cd}^{2+}$ , and  $\text{Pb}^{2+}$  by LDH@CNs was 99.7%,

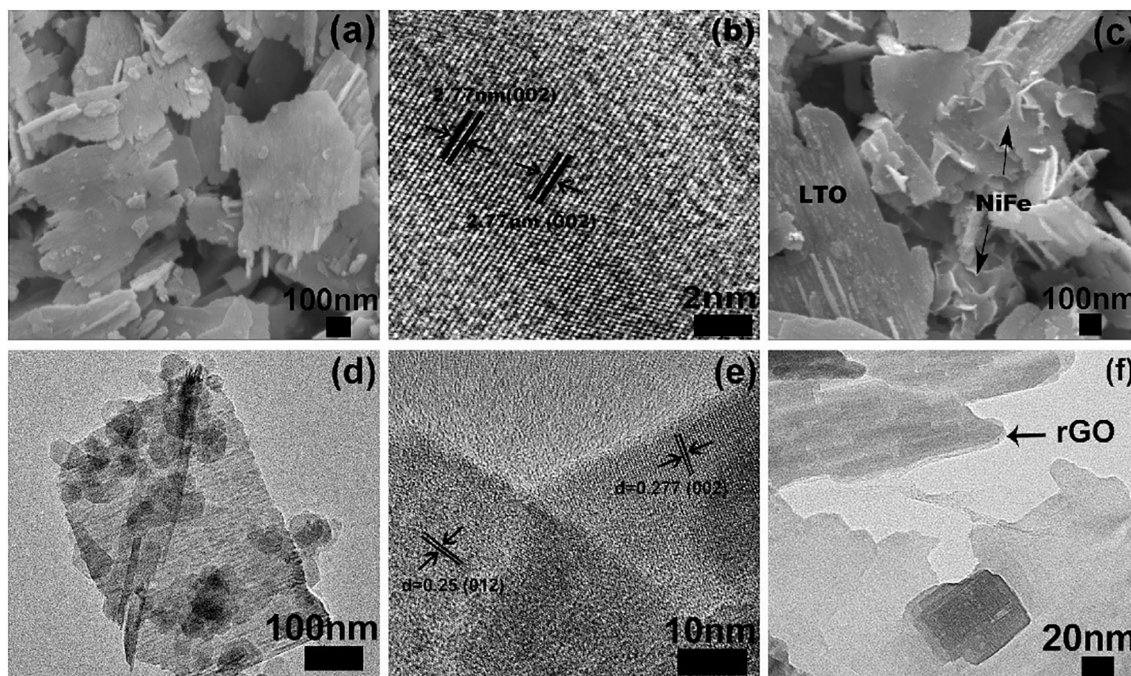


**Fig. 20.** Electron microscopy images. (a) HR-SEM image of LTO, (b) HR-TEM image of LTO, (c) HR-SEM image of LTO/NiFe-LDH, (d) TEM image of LTO/NiFe-LDH, (e) HR-TEM image of LTO/NiFe-LDH and (f) HR-TEM image of rGO/LTO. [100]. Reprinted from (Spatial charge separation on strongly coupled 2D-hybrid of rGO/La<sub>2</sub>Ti<sub>2</sub>O<sub>7</sub>/NiFe-LDH heterostructures for highly efficient noble metal free photocatalytic hydrogen generation, 239, Boppella, R.; Choi, C. H.; Moon, J.; Kim, D. H., *Appl. Catal. B-Environ.* 2018, 178–186). Copyright (2021), with permission from Elsevier.

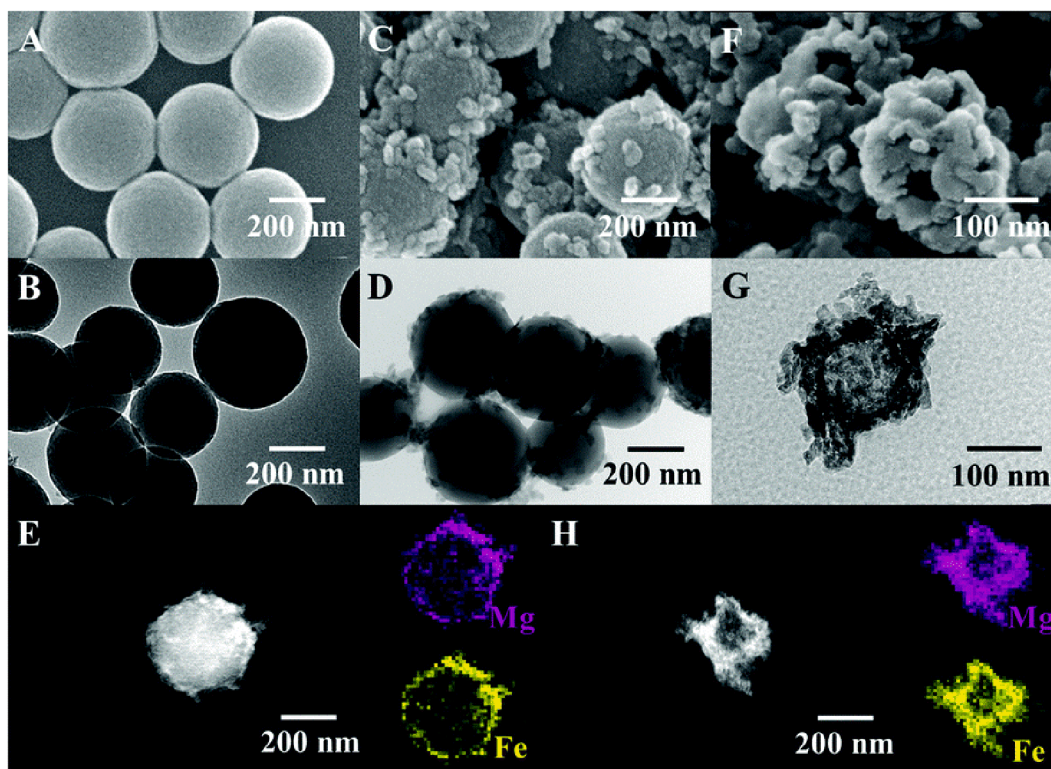


**Fig. 21.** SEM and TEM images of (A, B) CSs, (C, D) CSs@MgFe-LDHs and (F, G) hollow MgFe-LDO. The EDX elemental mapping results of (E) CSs@MgFe-LDHs and (H) hollow MgFe-LDO [106]. Reproduced from (Zong, Y. T.; Li, K. T.; Tian, R.; Lin, Y. J.; Lu, C., Highly dispersed layered double oxide hollow spheres with sufficient active sites for adsorption of methyl blue. *Nanoscale*, 2018, 10 (48), 23,191–23,197) with permission from The Royal Society of Chemistry.



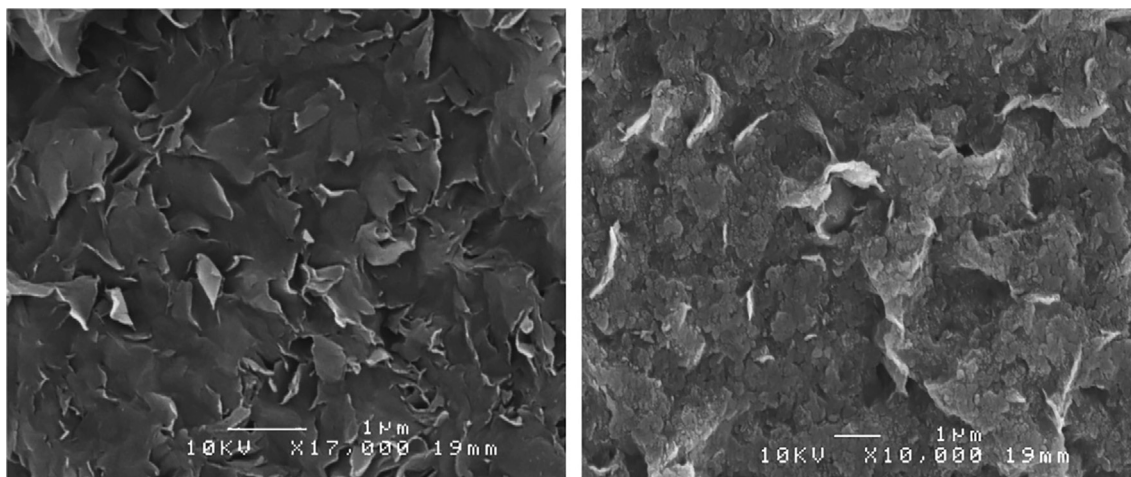


**Fig. 22.** SEM images of (left) bentonite and (right) LDH-bentonite hybrid [107]. Reprinted from (A novel colour removal adsorbent from heterocoagulation of cationic and anionic clays, 308 (1), Hu, Q. H.; Xu, Z. P.; Qiao, S. Z.; Haghseresht, F.; Wilson, M.; Lu, G. Q., *Journal of Colloid and Interface Science*, 2007, 191–199). Copyright (2021), with permission from Elsevier.

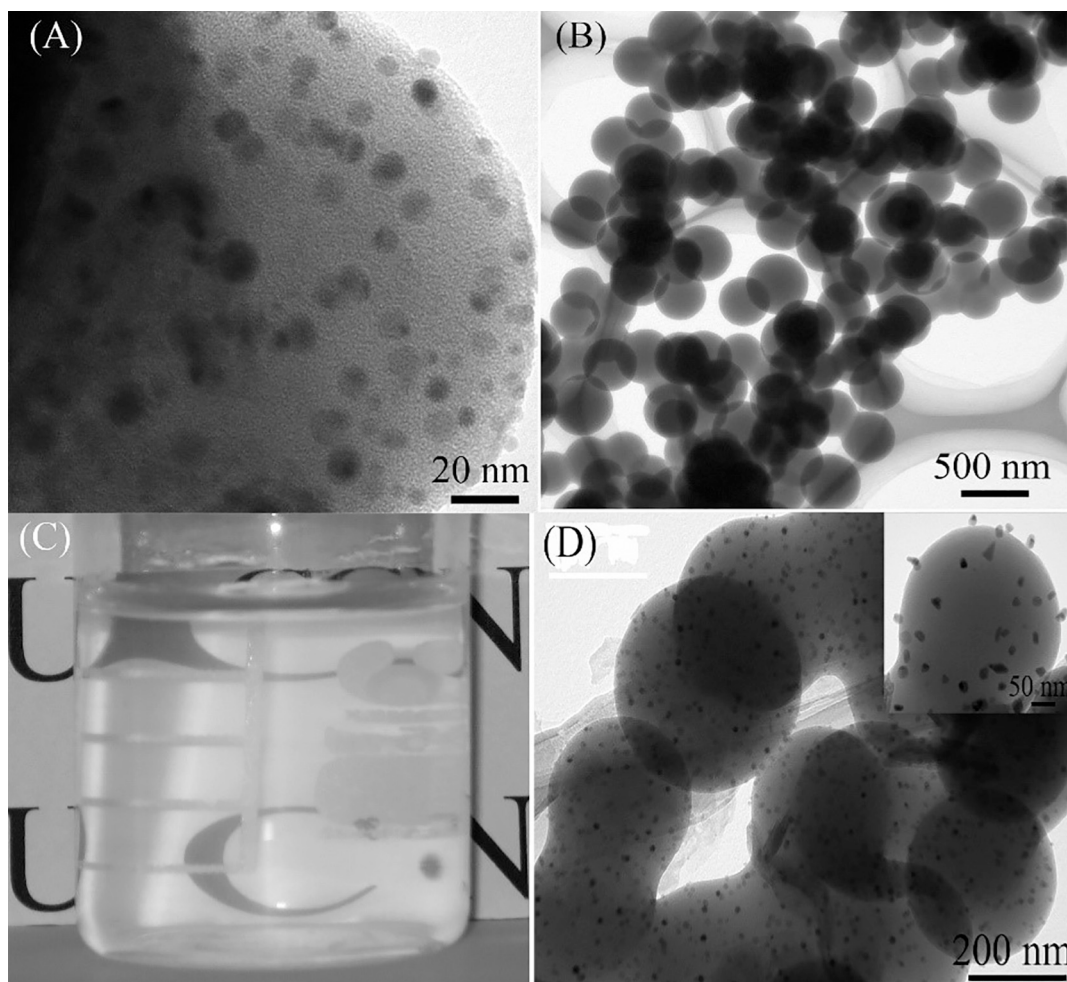


**Fig. 23.** TEM images of (A) LDH, (B) CNs, and (D) the assembly of LDH@CNs composites. (C) A translucent and stable suspension of LDH in methanol/water solvent [108]. Reprinted (adapted) with permission from (Gong, J. M.; Liu, T.; Wang, X. Q.; Hu, X. L.; Zhang, L. Z., Efficient removal of heavy metal ions from aqueous systems with the assembly of anisotropic layered double hydroxide nanocrystals@carbon nanosphere. *Environ. Sci. Technol.* 2011, 45 (14), 6181–6187). Copyright (2021) American Chemical Society.

89.3%, and 55.4%, respectively, and the maximum adsorption capacity was  $\sim 19.9$ ,  $\sim 17.5$ , and  $\sim 12.5$  mg/g, respectively, when the nanocomposite concentration was 10 mg/L. The order of removal  $\text{Cu}^{2+} > \text{Cd}^{2+} > \text{Pb}^{2+}$  can be attributed to closeness in atomic radii to the constituent ions of LDH.

Zhang et al. prepared a three-component composite by immobilizing magnetite ( $\text{Fe}_3\text{O}_4$ ) and MgAl-LDH particles onto GO sheets for removal of emulsified oils in water/oil systems [109]. The GO was synthesized by a modified Hummers and Offeman method, while magnetite-GO (MGO) hybrids were prepared by co-precipitating magnetite in the presence of GO. The MgAl-LDH precursor with a Mg/Al molar ratio of 3:1 was prepared by a co-precipitation method. The adsorbent composite MGO/MgAl-LDH was prepared by addition of LDH to a MGO suspension followed by sonication, the electrostatic attraction and hydrogen bonding enabled the heteroaggregation of LDH and MGO. Several composites with different LDH/MGO ratios were prepared. The hybrid materials retained oil removal efficiencies of 95.14%, 96.26%, and 97.88% for crude oil, white oil, and decane, respectively, after five cycles. The efficiency increased with the ionic strength and was also affected by the LDH/MGO ratio, where the highest removal potential was observed when the ratio was 1:1 for crude oil and 1:3 for white oil and decane. Fig. 24 shows the schematic preparation and structure of the composite as well as the removal action of MGO/MgAl-LDH hybrid.

Zubitur et al. studied the heteroaggregation between carbon black pigment particles with various polymeric particles, prepared by dispersion polymerization of poly(methyl methacrylate), polystyrene, poly(n-butyl acrylate), and other co-polymers [110]. Samples of 5% (w/w) dry pigment were added to methanol, ethanol, or water dispersions of the polymeric latex particles at different pigment ratios and were further sonicated to allow the pigment particles to be immobilized on the polymeric surface by heteroaggregation via acid-base interactions owing to the acidic and basic sites on carbon black. Carbon black adsorbs more uniformly in methanol and ethanol compared to water, and the adsorption was not affected by the different functional groups on the various polymeric particles.

#### 4.6. Optical materials

Lee et al. prepared a highly light scattering composite material by coating commercial PS particles with Au NPs and Ag nanocubes (NCs) [111]. The Au NPs and Ag NCs of various sizes were separately prepared and were further capped with PVP. Volumes of aqueous dispersions of latex and metal particles were mixed, followed by dropwise addition of tetrahydrofuran (THF) until the suspension has a THF concentration of 50% (v/v). By adjustments in the amount of added THF, not only homoaggregation could be avoided, but the coating morphology, metal coverage, and optical properties of the composite could be tuned. Smaller Au NPs resulted in continuous and close-packed metal coatings and possessed optical properties resembling those for complete shells. Larger Au NPs and Ag NCs, however, resulted in less dense coatings and higher scattering properties. Raman spectroscopy indicated the Au and Ag composites, especially Ag NCs-latex, exhibited highly enhanced Raman signals of PVP molecules and thus, can be used as effective SERS substrates. This result enables their use in biomedical imaging, sensors, photonics, and electronics. Fig. 25 shows SEM images of the obtained AuNP-Ps hybrid.

#### 4.7. Bioactive materials

Deák et al. heteroaggregated ZnMgAl-LDH and Ag NPs-loaded montmorillonite lamellae [112]. The former particles were prepared by the co-precipitation method, while the Ag NPs-montmorillonite lamellae were prepared by synthesis of Au NPs in the presence of montmorillonite. The LDH-Ag-montmorillonite composite was prepared by dissolving a sample of the prepared LDH solid in an aqueous dispersion of Ag NPs-montmorillonite. As shown in Fig. 26, the composite behaved like coherent gels at low pH ( $\leq 4.5$ ) and incoherent sols at higher pH ( $\geq 4.5$ ). The hybrid material was synthesized with composition that allows a sol-gel transition. The composite was suitable for the release of the immobilized antimicrobial Ag NPs via a pH-controlled gel-sol transition. The pH-responsive property in LDH-Ag-montmorillonite

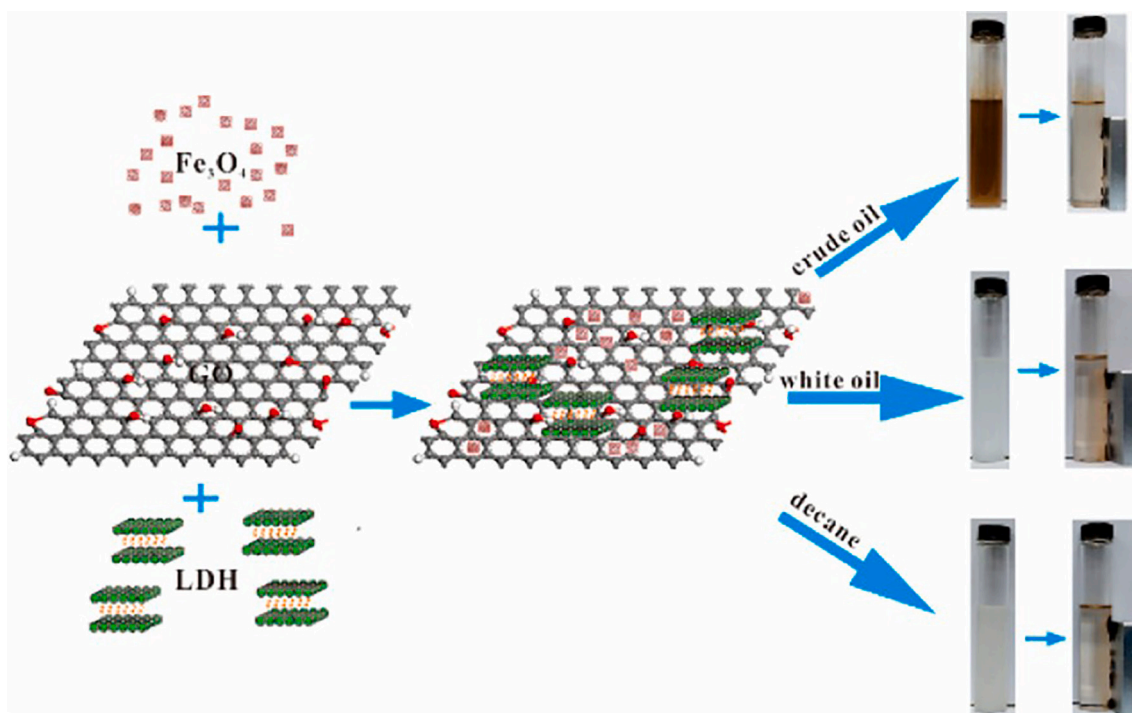
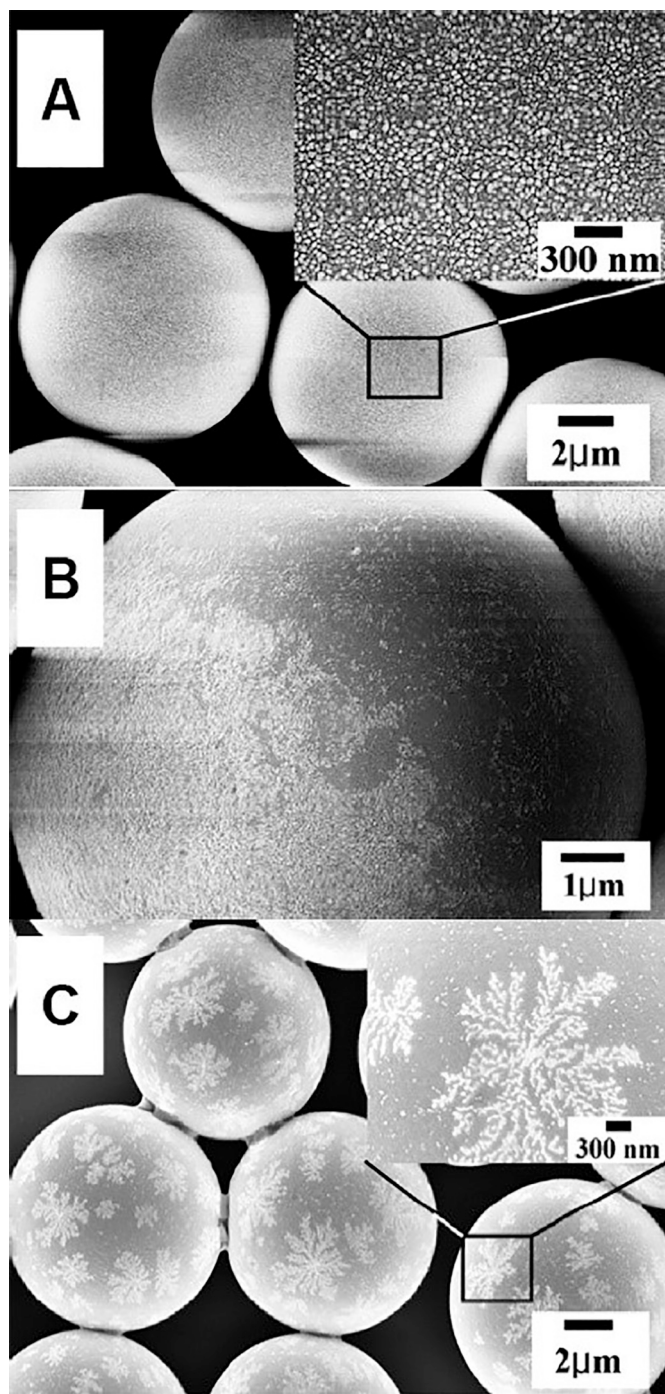


Fig. 24. Structure and removal activity of MGO/MgAl-LDH composites with crude oil, white oil and decane [109]. Reprinted (adapted) with permission from (Zhang, B.; Hu, R. T.; Sun, D. J.; Wu, T.; Li, Y. J., Fabrication of magnetite-graphene oxide/MgAl-layered double hydroxide composites for efficient removal of emulsified oils from various oil-in-water emulsions. *J. Chem. Eng. Data*, 2018, 63 (12), 4689–4702). Copyright (2021) American Chemical Society.





**Fig. 25.** SEM images of 30 nm AuNP-Ps hybrid obtained from (A) 50 vol% THF-water solution (B) 70 vol% THF-water solution (C) 50 vol% THF-water solution with fewer NPs compared to (A) [111]. Reprinted (adapted) with permission from (Lee, J. H.; Mahmoud, M. A.; Sitterle, V. B.; Sitterle, J. J.; Meredith, J. C., Highly scattering, surface-enhanced Raman scattering-active, metal nanoparticle-coated polymers prepared via combined swelling-heteroaggregation. *Chem. Mat.* 2009, 21 (23), 5654–5663). Copyright (2021) American Chemical Society.

enabled their application in biological systems that have acidic pH under normal conditions but become basic in case of abnormalities such as bacterial infection.

Lui et al. reported a novel  $\text{CeO}_2\text{-Fe}_3\text{O}_4\text{@LDH}$  bio-nanocomposite [113]. The polyacrylic acid (PAA)-stabilized  $\text{CeO}_2$  and  $\text{Fe}_3\text{O}_4$  NPs were prepared by precipitation and co-precipitation, respectively. The

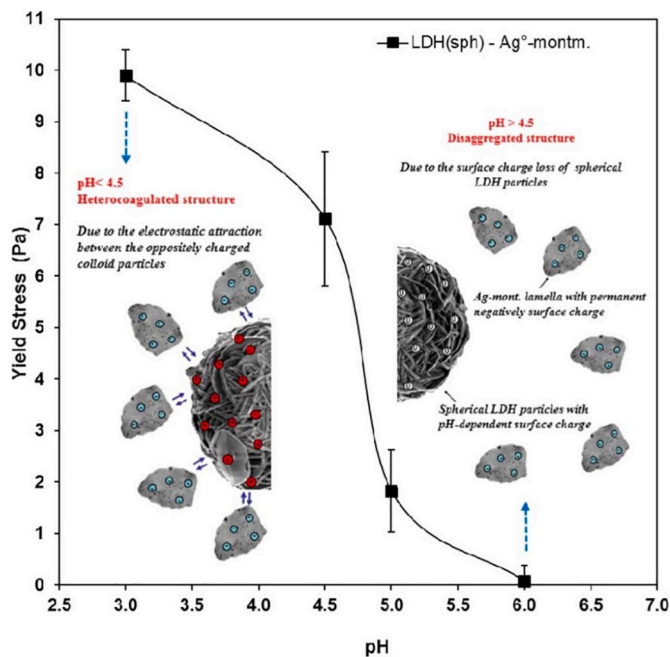


**Fig. 26.** The pH-dependent sol-gel transition of LDH-Ag-montmorillonite composite. Above pH 4.5, a disaggregated structure is observed due to loss of surface charge. At pH below 4.5, heteroaggregated structure was maintained due to electrostatic attraction between the building blocks [112]. Reprinted (adapted) with permission from (Deak, A.; Janovak, L.; Tallosy, S. P.; Bito, T.; Sebok, D.; Buzas, N.; Palinko, I.; Dekany, I., Spherical LDH-Ag<sup>0</sup>-montmorillonite heteroaggregated system with a pH-dependent sol-gel structure for controlled accessibility of AgNPs immobilized on the clay lamellae. *Langmuir*, 2015, 31 (6), 2019–2027). Copyright (2021) American Chemical Society.

MgAl-LDH was prepared by co-precipitation followed by hydrothermal treatment. The  $\text{CeO}_2\text{-Fe}_3\text{O}_4\text{@LDH}$  nanocomposite was prepared by adding a certain volume of the LDH suspension dropwise into an aqueous mixture of  $\text{CeO}_2$  and  $\text{Fe}_3\text{O}_4$  NPs under continuous stirring, where electrostatic forces between the NPs and LDH led to the composite formation. The novel biocompatible nanocomposite has shown great potential as an antioxidant for reactive oxygen species (ROS) scavenging in macrophages with no cytotoxicity to either macrophages or CHO cells at concentrations where ROS scavenging is significant. In MRI application, the composite exhibited a good magnetic resonance signal in the macrophages, making it a potential contrast agent for cell imaging processes. These functionalities are demonstrated in Fig. 27.

Darabdhara et al. prepared graphitic carbon nitride ( $\text{g-C}_3\text{N}_4$ ) nanosheets decorated with bimetallic Au-Ni NPs. The  $\text{g-C}_3\text{N}_4$  nanosheets were prepared by calcination of urea, and the resulting  $\text{g-C}_3\text{N}_4$  sample was dispersed in a mixture of ethanol/hexane by ultrasonication. The Au-Ni bimetallic nanoparticles were synthesized by solvothermal reduction technique using  $\text{Ni}(\text{acetylacetonate})_2$  and  $\text{HAuCl}_4 \cdot 3\text{H}_2\text{O}$  precursors, and the collected Au-Ni nanoparticles were dispersed in hexane. Then, dispersions of  $\text{g-C}_3\text{N}_4$  were mixed with the Au-Ni NPs dispersion to obtain the Au-Ni/ $\text{g-C}_3\text{N}_4$  nanocomposite, which showed intrinsic peroxidase activity towards a number of substrates such as 3,3',5,5'-tetramethylbenzidine (TMB) and 2,2'-azino-bis(3-ethylbenzthiazoline-6-sulphonic acid) (ABTS) in presence of  $\text{H}_2\text{O}_2$ , which enabled its incorporation into colorimetric glucose detection system with glucose oxidase with a detection limit of 1.7  $\mu\text{M}$  and a linear detection range of 0.5 to 30  $\mu\text{M}$  [114]. Monometallic Au/ $\text{g-C}_3\text{N}_4$  and Ni/ $\text{g-C}_3\text{N}_4$  nanocomposites, on the other hand, showed a detection limit of 3.55 and 6.23  $\mu\text{M}$ , respectively. The nanocomposites showed no cytotoxic towards HUVEC cell line, which rendered them biocompatible and suitable for biosensor applications.

Zhao developed a biosensor based on nanocomposite carrier and

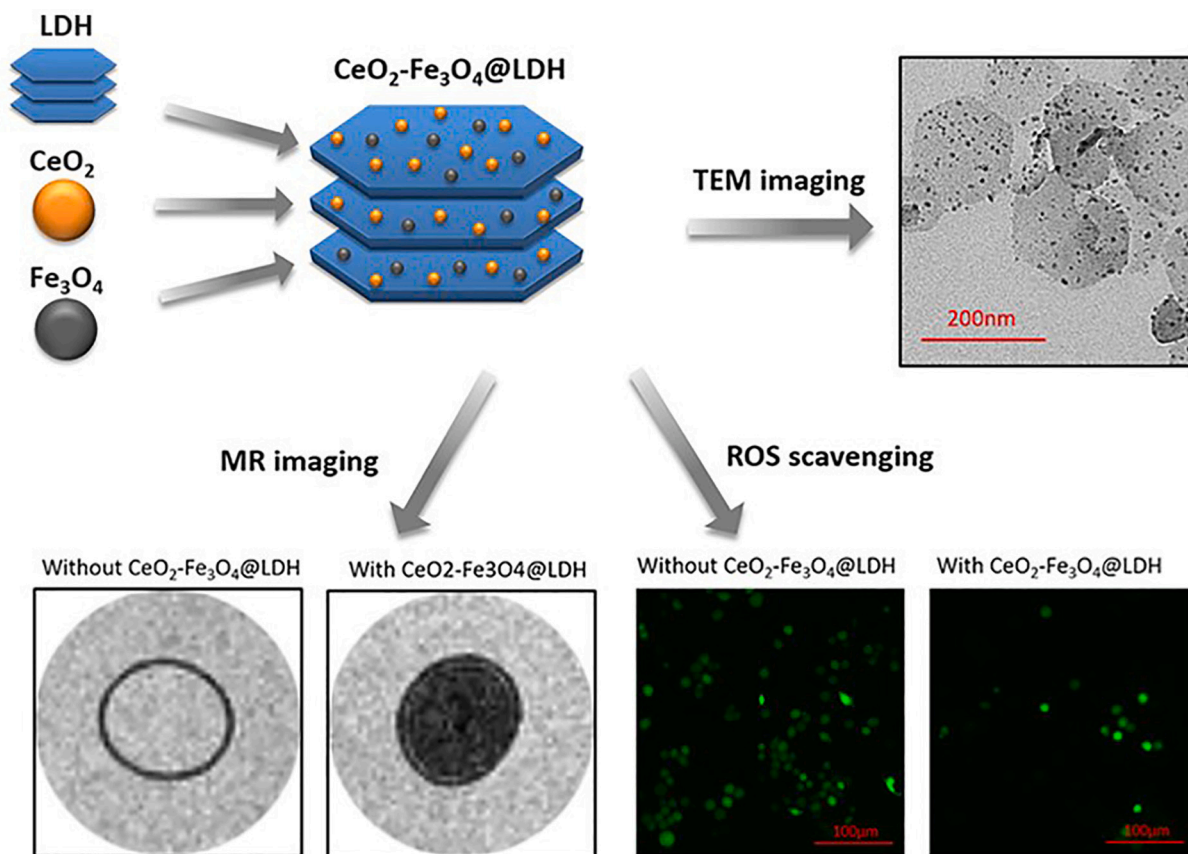


**Fig. 27.** Schematic representation of the expected structure of  $\text{CeO}_2\text{-Fe}_3\text{O}_4\text{@LDH}$  nanocomposite. TEM imaging confirms the immobilization of  $\text{CeO}_2$  and  $\text{Fe}_3\text{O}_4$  NPs onto the LDH platelets. The MRI signal, corresponding to darker colour, could be detected in presence of the nanocomposite. Macrophages, stimulated by  $\text{H}_2\text{O}_2$ , generate excessive ROS and exhibit green fluorescence signal, which was significantly reduced 1 day after treatment with  $\text{CeO}_2\text{-Fe}_3\text{O}_4\text{@LDH}$  nanocomposite [113]. Reprinted (adapted) with permission from (Liu, Y.; Wu, Y.; Zhang, R.; Lam, J.; Ng, J. C.; Xu, Z. P.; Li, L.; Ta, H. T., Investigating the use of layered double hydroxide nanoparticles as carriers of metal oxides for theranostics of ROS-related diseases. *ACS Appl. Bio Mater.* 2019, 2 (12), 5930–5940). Copyright (2021) American Chemical Society.

native horseradish peroxidase (HRP) enzyme. Chitosan-functionalized Au nanoparticles were heteroaggregated via electrostatic attraction with exfoliated montmorillonite nanoplates by simple mixing followed by sonication to give chitosan-Au/clay composite [115]. The positively charged chitosan-Au was prepared using the  $\text{HAuCl}_4$  precursor while negatively charged commercial montmorillonite was exfoliated by dispersing the clay in water with ultrasonication. Then, a glass carbon electrode (GCE) was coated with five layers of chitosan-Au/clay, where the native enzyme is intercalated between clay layers. The immobilized HRP showed two quasi-reversible redox peaks at  $-0.195$  V and the biosensor showed a rapid amperometric response to  $\text{H}_2\text{O}_2$  with a wide linear range of  $39 \mu\text{M} - 3.1$  mM and a detection limit of  $9.0 \mu\text{M}$ . The charge transfer coefficient, electron transfer rate constant, and Michaelis-Menten constant were evaluated to be 0.53,  $2.95 \text{ s}^{-1}$  and 23.15 mM, respectively.

Alsharif et al. prepared a composite of multi-enzymatic activity consisting of oppositely charged commercial amidine latex (AL) particles and Prussian blue ( $\text{Fe}^{\text{III}}_4[\text{Fe}^{\text{II}}(\text{CN})_6]_3$ ) nanoparticles (PB NPs) [30]. The latter was prepared via the co-precipitation of  $\text{K}_3[\text{Fe}(\text{CN})_6]$  and  $\text{FeCl}_2$ . The electrostatic attraction between the negatively charged PB and the positively charged AL enabled the formation of AL-PB composite. Aqueous dispersions of AL particles and PB NPs were mixed under magnetic stirring. The HRP and superoxide dismutase (SOD) activity of PB NPs was maintained upon immobilization onto AL surface. Fig. 28 shows SEM and TEM images of the AL-PB composite at different amounts of PB. The composite underwent an overall charge reversal as more negatively charged PB NPs were added to positively charged latex.

At high and low doses, the composite was highly negatively and positively charged, respectively, and was thus colloiddally stable. Around the IEP, however, charges were balanced, and the aggregation is facilitated. The developed hybrid has proven to be an efficient antioxidant of high functional and colloiddal stability.

Soh et al. reported a composite of HRP/single-layer titanate ( $\text{TiO}_x$ )/magnetic beads [116]. Single titanate layers were formed by hydrolysis of titanium (IV) tetraisopropoxide liquid with the tetrabutyl ammonium hydroxide solution. The excess salts in the resultant colloid were removed via dialysis with centrifugal filtration. The HRP enzyme as well as the amino-functionalized magnetic beads were obtained commercially. The nanocomposite was formed by mixing the  $\text{TiO}_x$ , HRP and the magnetic particles in slightly acidic solutions and the excess HRP was removed by centrifugation or magnetic separation. The HRP was intercalated into titanate nanosheet, and the composite is formed due to electrostatic interaction between the negatively charged titanate and positively charged magnetic beads and HRP. The immobilized HRP maintained enzymatic activity with *o*-phenylenediamine (OPD), guaiacol, and pyrogallol substrates. The complex was magnetically recoverable, enabling several cycles of use, with a residual activity of 80% after 5 cycles.

Gunawan and Xu developed hollow material by heteroaggregation of anisotropic LDH nanocrystals on carbon nanospheres (CNs) for drug release (Fig. 29) [117]. The LDH was synthesized in pure methanol solvent using mixed solution containing  $\text{Mg}(\text{NO}_3)_2 \cdot 6\text{H}_2\text{O}$  and  $\text{Al}(\text{NO}_3)_3 \cdot 9\text{H}_2\text{O}$  while CNs was prepared through carbonization of glucose under hydrothermal conditions. The LDH-CN hybrid was prepared by



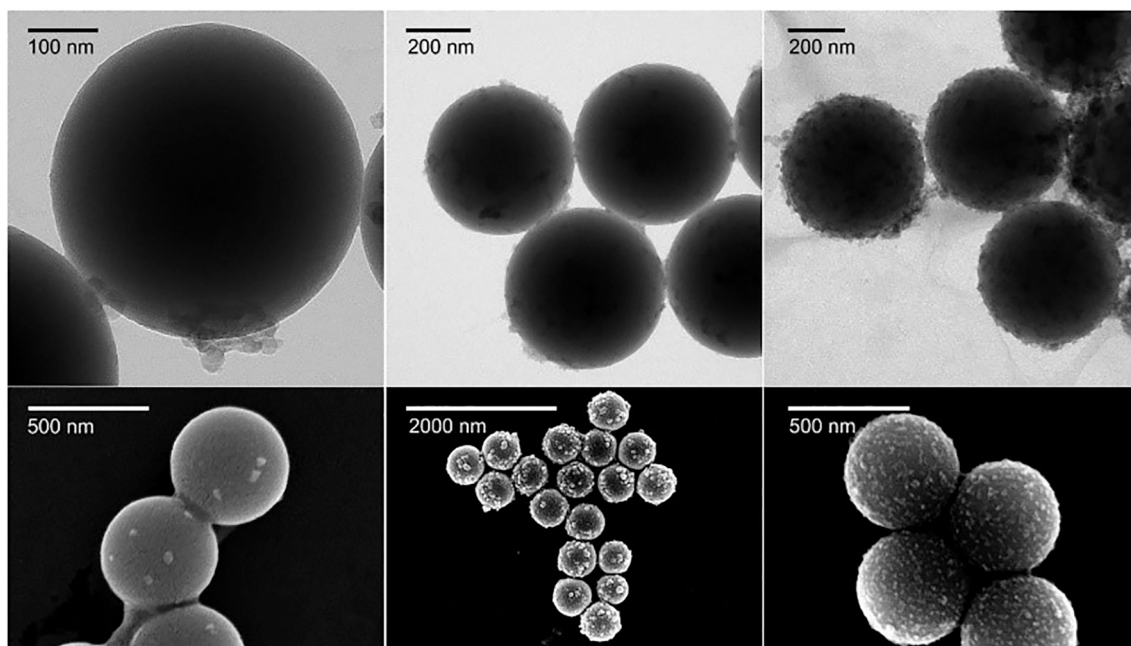


**Fig. 28.** TEM (upper) and SEM (lower) images of the AL-PB composite at 1 (left), 30, (middle), and 600 mg PB/g AL (right) [30]. Reproduced with permission from (Alsharif, N. B.; Samu, G. F.; Sáring, S.; Muráth, S.; Szilagy, I., A colloid approach to decorate latex particles with Prussian blue nanozymes. *J. Mol. Liq.* 2020, 309, 113,066). Copyright (2021), with permission from Elsevier. (For interpretation of the references to colour in this figure legend, the reader is referred to the web version of this article.)

mixing methanol-based dispersions of LDH and CNs. The obtained solid phase was calcined to remove the CNs core to give hollow MgAl oxides nanospheres, which were then used for *in vitro* drug release of ibuprofen. The hollow spheres had good structural integrity and were preserved during the transformation from LDH to oxide, even with a large volume contraction, which is attributed to the densely packed pristine LDH on CNs. Release profiles indicated no significant difference in ibuprofen release between hollow spheres and nanoplates, but hollow nanospheres exhibited lower density, less tendency towards aggregation, higher surface area compared to ibuprofen-LDH nanoplates, which can be utilized to encapsulate other molecules.

A biomedical nanocomposite of manganese ferrite nanoparticles (MFNPs) and oleylamine (OAM)-grafted GO (GO-g-OAM) was prepared by Peng et al. [118]. MFNPs were synthesized via thermolysis whereas GO was prepared through modified Hummer's method. The MFNPs/GO-g-OAM composites (MGONCs) were prepared via mini-emulsion process coupled with solvent evaporation, where  $\text{CH}_3\text{Cl}$ -based dispersions of GO-g-OAM and MFNPs were mixed, and the organic solvent was later evaporated. The MGONCs were further functionalized with polyethylene glycol (PEG) functional groups. The loading and size of composites were tailored by altering the GO/MFNPs ratio as well as sonication time. The obtained PEGylated MGONCs showed excellent colloidal stability and biocompatibility as well as excellent performance for hyperthermia and as MRI  $T_2$  contrast agents. For 14 nm MFNPs, a specific absorption rate of 1588.83 W/g and a  $T_2$  relaxivity value  $256.2 \text{ (mM Fe)}^{-1} \text{ s}^{-1}$  were obtained. Such hydrophobic NPs/GO nanocomposites have high potential for various biomedical applications.

#### 4.8. Electrochemical applications

Han et al. prepared a promising electrode material for supercapacitors based on NiAl-LDH and GO quantum dots (GOQDs) [119]. Homogenized formamide-based dispersions of NiAl-LDH sheets and GOQDs were mixed in 1:1, 3:1, 6:1, 9:1 volume ratios to give the GOQDs@NiAl-LDH composites. The NiAl-LDH was prepared by coprecipitation and then delaminated by ultrasonication, while GOQDs were prepared via ball milling. The GOQDs@NiAl-LDH composites

showed high specific capacitance, good current charge/discharge characteristics, and high cycle stability. The highest capacitance was obtained when the GOQDs content was 10%. Cyclic voltammetry curves indicated that the energy storage occurred by pseudocapacitance, and electrochemical impedance spectroscopy showed that the impedance of the composite decreased with increasing GOQDs content. The storage capacity of the composite was enabled due to enhanced conductivity and dispersivity of NiAl-LDH by GOQDs, which also prevented NiAl-LDH from restacking.

Bai et al. fabricated a functional material for photoanodes for high-efficiency dye-sensitized solar cells, which attract considerable attention worldwide [120]. The nanohybrid is formed via heteroaggregation of exfoliated titania ( $\text{Ti}_{0.91}\text{O}_2$ ) nanosheets and anatase  $\text{TiO}_2$  nanoparticles in an aqueous dispersion.  $\text{Ti}_{0.91}\text{O}_2$  nanosheets and  $\text{TiO}_2$  nanoparticles were prepared by Sasaki's method and hydrolysis, respectively. The electrode is formed by depositing nanohybrid on fluoride-doped tin oxide (FTO) substrate by doctor-blade method. The nanohybrid possesses high light-harvesting efficiency as well as mesoporous structure with slit-shaped pores and large surface area that enables high dye loading. The nanohybrid-based photoanode, illustrated in Fig. 30, demonstrated a higher overall conversion efficiency of 10.1% as well as low charge recombination.

Kim et al. fabricated functional composites with a promising performance as a Si anode material in Li-ion batteries [121]. Commercial Si nanoparticles were incorporated with TEMPO-oxidized cellulose nanofibers (TOCNF) that served as Si nanoparticles reinforcement as well as assistant additive to sodium carboxymethyl cellulose (CMC), which served as the Si anode binder. By mixing an aqueous suspension of TOCNF with Si nanoparticles dispersed in ethanol/water mixture, the Si-TOCNF composite was heteroaggregated and later retrieved via freeze-drying. The Si electrode was prepared by casting a slurry mixture containing the Si-TOCNF sample, conductive additive, and CMC binder with different weight ratios on a Cu foil with a doctor blade and dried in a vacuum oven. The effective interaction between TOCNF and Si nanoparticles was attributed to the hydrogen bonding, induced by the carboxylic groups of TOCNF. As a reinforcement fiber, the one-dimensional nature of TOCNF enhanced the mechanical properties such as hardness

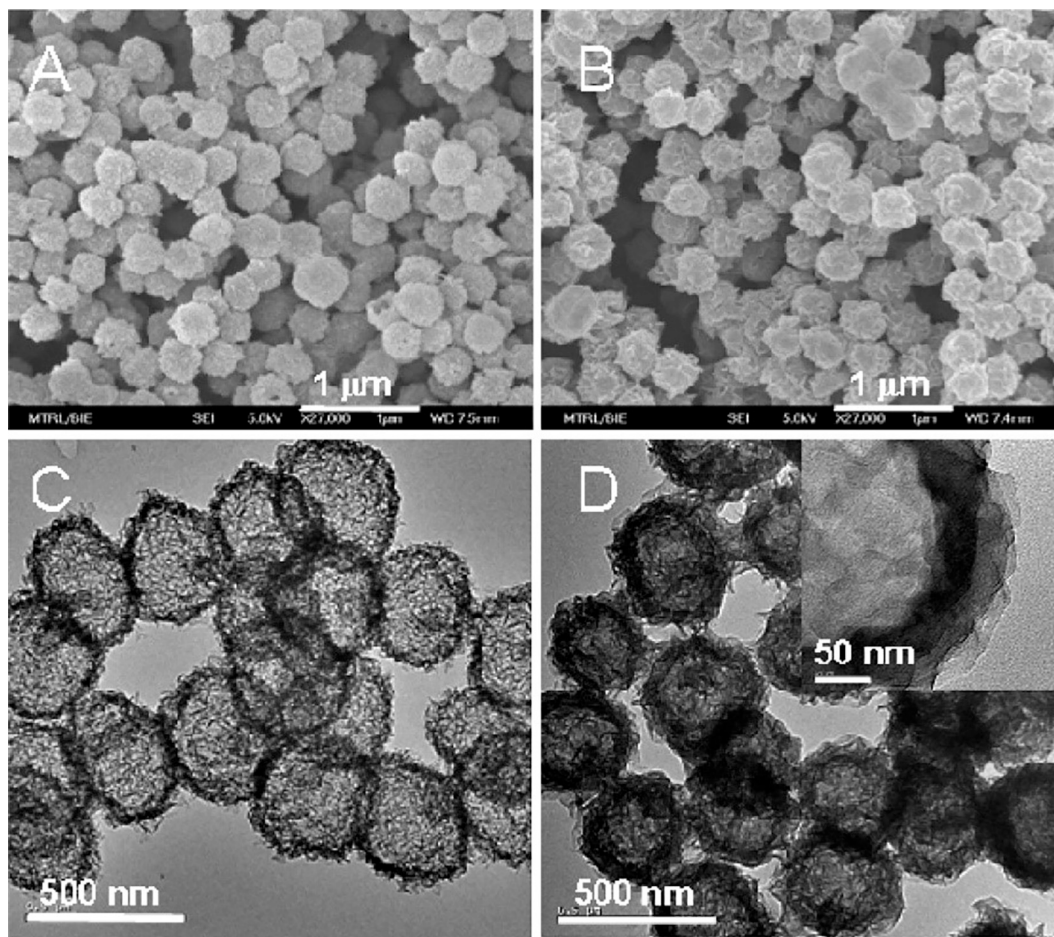


**Fig. 29.** (A) SEM and (C) TEM images of hollow MgAl oxide nanospheres obtained after calcination of LDH/CNs. (B) SEM and (D) TEM images of ibuprofen intercalated LDH hollow nanospheres after reconstruction [117]. Reprinted (adapted) with permission from (Gunawan, P.; Xu, R., Direct assembly of anisotropic layered double hydroxide (LDH) nanocrystals on spherical template for fabrication of drug-LDH hollow nanospheres. *Chem. Mat.* 2009, 21 (5), 781–783). Copyright (2021) American Chemical Society.

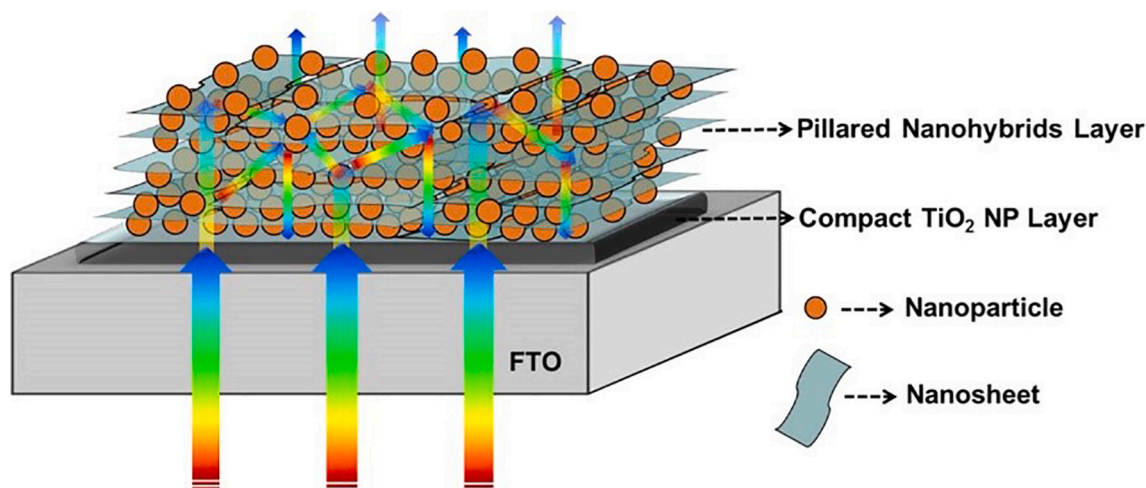


**Fig. 30.** Schematic diagram of layered nanohybrid-based photoanodes for solar cells [120]. Reprinted (adapted) with permission from (Bai, Y.; Xing, Z.; Yu, H.; Li, Z.; Amal, R.; Wang, L. Z., Porous Titania Nanosheet/Nanoparticle Hybrids as Photoanodes for Dye-Sensitized Solar Cells. *ACS Appl. Mater. Interfaces*, 2013, 5 (22), 12,058–12,065). Copyright (2021) American Chemical Society.

and reduced elastic modulus, better stress dissipation, and structural integrity to the Si electrode. TOCNF additive also significantly improved the CMC binder uniformity, which result in a better protected electrode surface.

#### 4.9. Sensor development

Wang et al. fabricated an HRP/CDS/LDH composite for hydrogen peroxide biosensing [122]. The highly pure CoFe-LDH platelets were



synthesized via co-precipitation, whereas carbon nanodots (CDs) were prepared by hydrothermal treatment. The HRP/CDs/LDH composite was prepared by mixing suspensions of CoFe-LDH and CDs followed by the addition of HRP suspension into the CDs/LDH mixture. The resulting suspension was cast on the pre-treated GCE surface. Cyclic voltammogram shows changes in the anodic and cathodic peak currents indicating an excellent electrocatalytic activity towards  $\text{H}_2\text{O}_2$ . Also, no significant changes in the current response were observed even when the concentrations of the interfering substances such as epinephrine, uric acid, and ascorbic acid were 10 times that of the  $\text{H}_2\text{O}_2$ . The biosensor maintained 87.6% of its original current response after one week of storage. Such outstanding properties of the HRP/CDs/LDH-based biosensor are attributed to the synergistic effect among the three constituents.

Amjadi et al. assembled a fluorescent probe for the detection of uric acid with satisfactory results upon analysis of human plasma and urine. The probe is based on a nanocomposite of nitrogen/sulfur co-doped carbon dots (S/N-CDs) and  $\text{MnO}_2$  nanosheets, which have rich redox chemistry and high extinction coefficient [123]. The S/N-CDs were synthesized via the hydrothermal method using citric acid and L-cysteine, while  $\text{MnO}_2$  nanosheets were prepared using  $\text{MnCl}_2 \cdot 4\text{H}_2\text{O}$  salt. The fluorescent composite S/N-CDs- $\text{MnO}_2$  was prepared by mixing aqueous dispersions of  $\text{MnO}_2$  and S/N-CDs in the presence of Britton-Robinson buffer. The addition of  $\text{MnO}_2$  nanosheets quenches the fluorescence due to the inner filter effect of the sheets; however, the addition of uric acid to the S/N-CDs- $\text{MnO}_2$  composite restores the fluorescence due to interaction with the  $\text{MnO}_2$  nanosheets. The low-cost probe showed environmental friendliness, good selectivity, and fast fluorescence response.

Dong et al. developed a fluorescent substrate by heteroaggregation of  $\text{MnO}_2$  nanosheets and polyethyleneimine-functionalized carbon dots (p-CDs), prepared by reduction and hydrothermal methods, respectively [124]. In the p-CDs@ $\text{MnO}_2$  composite,  $\text{MnO}_2$  nanosheets quenches the fluorescence of p-CDs via Förster resonance energy transfer, which can be restored by the addition of ascorbic acid due to reduction of  $\text{Mn}^{4+}$  in  $\text{MnO}_2$  to  $\text{Mn}^{2+}$ . Ascorbic acid is produced by hydrolysis of 2-phosphoascorbic acid by alkaline phosphatase, and thus the p-CDs@ $\text{MnO}_2$  composite was used as the fluorescence probe in a developed fluorescence enzyme-linked immunosorbent assay (ELISA), which showed good

accuracy, precision, and high specificity for the detection of amantadine. In chicken meat tissues, samples with amantadine concentrations as low as 0.6, 3.0 and 10.0 ng/mL were detected by fluorescent ELISA, making it a great candidate to be applied in detecting trace chemical contaminants in food.

In another work by He et al., a novel composite of nitrogen-doped quantum dot (CQDs) and the  $\text{MnO}_2$  nanosheets was developed as a turn-on fluorescence probe for detection of glutathione, as shown in Fig. 31. In the  $\text{MnO}_2$ -CQDs nanocomposite,  $\text{MnO}_2$  nanosheets were fluorescence quenchers, due to reduction of  $\text{Mn}^{4+}$  to  $\text{Mn}^{2+}$ , while CQDs served as fluorescence reporter. The oppositely charged CQDs and  $\text{MnO}_2$  nanosheets formed through electrostatic interaction. The low-cost composite showed excellent biocompatibility, high selectivity, and sensitivity with a detection limit of 10 nM glutathione, and thus it was used to detect glutathione level in living cells [125].

#### 4.10. Ceramics

Ceramic composites are very versatile materials with excellent physicochemical properties compared to their single-phase counterparts. The combination of matrix and reinforcement components have led to significant improvements in various properties such as thermal conductivity, mechanical strength, and hardness [126]. Among preparation strategies of these composites is heteroaggregation, where the components are mixed and homogenized before subjected to consolidation, a thermal treatment process such as sintering and hot pressing.

Madhavan et al. prepared porous ceramics from a Pickering emulsion of oppositely charged silica and alumina particles dispersed in decane/water mixture [127]. Equal volumes of decane and 1% (w/w) aqueous suspension of both particles are mixed and homogenized mechanically. The high stability of the emulsion is attributed to the electrostatic heteroaggregation between silica and alumina particles, and the subsequent adsorption of silica-alumina aggregates to the oil-water interface. By tuning the experimental conditions, gel-like Pickering emulsions serve as excellent templates for the fabrication of porous ceramics. By emulsion drying and sintering, the porous mullite ceramic structure had exceptional thermal and chemical resistance under harsh conditions.

In addition, Muñoz et al. utilized electrostatic heteroaggregation of

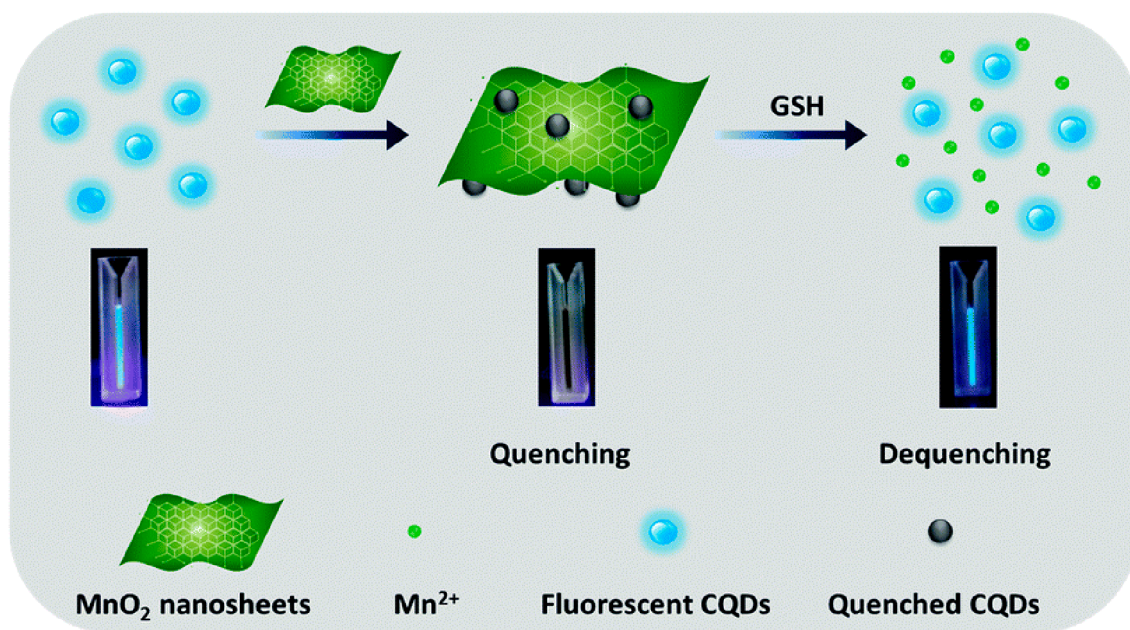


Fig. 31. The glutathione sensing mechanism through turn-on fluorescence using fluorescent CQDs quenched by  $\text{MnO}_2$  nanosheets [125]. Reproduced from (He, D. G.; Yang, X. X.; He, X. X.; Wang, K. M.; Yang, X.; He, X.; Zou, Z., A sensitive turn-on fluorescent probe for intracellular imaging of glutathione using single-layer  $\text{MnO}_2$  nanosheet-quenched fluorescent carbon quantum dots. *Chem. Commun.* 2015, 51 (79), 14,764–14,767) with permission from The Royal Society of Chemistry.

commercial and oppositely charged  $\text{Al}_2\text{O}_3$  platelets as well as silica and  $\alpha\text{-Al}_2\text{O}_3$  nanoparticles [128]. After mixing the relevant aqueous suspensions, the resulting three-component heteroaggregates were shaped into solid pellets via sedimentation and freeze-granulation methods. The solid pellets were obtained by drying and were later thermally treated using field assisted sintering to obtain nacre-like ceramic composites. Both shaping methods resulted in good component distribution as well as good alignment of alumina platelets in the sintered samples. The composite obtained by sedimentation had better flexural strength. However, samples obtained by freeze-casting had better mechanical properties despite a better alignment of platelets in sedimentation-prepared pellets as a result of the difference in the vitreous phase composition.

Fan et al. prepared several ceramic composites of multi-walled CNTs and alumina particles to probe the mechanical and electrical properties at different preparation conditions [129]. The CNTs/ $\text{Al}_2\text{O}_3$  composites were heteroaggregated by mixing separate aqueous suspensions of CNTs and  $\text{Al}_2\text{O}_3$  in the absence and presence of dispersants (SDS and AG). The resulting slurries were ball milled for a prolonged period of time and dried. The obtained solids were consolidated by hot pressing with uniaxial pressure under argon atmosphere to obtain ceramic CNTs/ $\text{Al}_2\text{O}_3$  composites. Compared to pure  $\text{Al}_2\text{O}_3$ , the SDS-dispersed CNTs resulted in 1.8 times increase in fracture toughness of ceramic CNTs/ $\text{Al}_2\text{O}_3$  composites that are 4% (w/w) in CNTs. When the CNTs and  $\text{Al}_2\text{O}_3$  were dispersed with SDS and AG, respectively, the resulting ceramics composite (2% (w/w) CNTs/ $\text{Al}_2\text{O}_3$ ) had 1.3 increase in fracture toughness and 14 orders of magnitude decrease in resistivity, compared to pure  $\text{Al}_2\text{O}_3$ .

Kaźmierczak-Bałata and Mazur probed the effect of carbon nanoparticles (graphene and GO) reinforcement on the mechanical and thermal properties of SiC ceramics, using different forms of commercially available SiC [130]. The SiC-carbon ceramic composites were prepared by first mixing the SiC power with an aqueous suspension of the relevant carbon nanoparticles that contain sintering additives (boron power and glucose). The resulting suspension was then heated until complete water evaporation, and the obtained sample was then thermally treated using the spark plasma sintering process to obtain ceramic composites. Incorporation of 2.5% (w/w) GO enhanced both the mechanical and thermal properties of the resulting composite, although it caused a slight decrease in the density. Besides, graphene had no effect on the mechanical and thermal properties. With GO reinforcement, the composite toughness as well as the thermal diffusivity increased from 1.21 to 1.75 MPa/m<sup>1/2</sup> and from 0.60 to 0.71 cm<sup>2</sup>/s, respectively, while the friction coefficient changed from 0.62 to 0.66. Thermal imaging revealed homogeneity of the local thermal properties of the products fabricated from the starting SiC powder.

## 5. Summary and outlook

The heteroaggregation process is a fundamental and complex phenomenon in multi-component colloidal systems and has been significantly explored both theoretically and experimentally. Such systems occur widely in nature as well as in numerous industrial applications. As seen before, the kinetics of heteroaggregation is heavily dependent on many factors such as the chemical composition, the particle size, the solvent, the pH, particle concentration, ionic strength, the surface charge, the presence of surface-active compounds, etc. By careful interplay of these factors, highly functional novel nanostructured composites have been prepared and utilized in several fields such as drug delivery, energy, catalysis, enzyme mimicking, etc.

Despite these successes, there has been no comprehensive view that completely explains the heteroaggregation process, and a full theoretical understanding still does not exist owing to the nature and the complexity of the phenomenon. Moreover, the extension of the DLVO theory to encompass heteroaggregation has also resulted in discrepancies between theoretical predictions and experimental findings, which can be

attributed to the numerous assumptions such as smoothness of the surface, constant charge, and potential as well as the negligence of particle-particle interactions. In addition, numerous experimental conditions such as non-aqueous media resulted in several non-DLVO type forces such as short-range attraction, depletion effect, hydrophobic interaction, and acid-base interactions, which could not be explained by the DLVO theory.

Finally, the heteroaggregation field in colloidal systems is still in its infancy owing to the numerous complications and involved variables, and a thorough understanding of the process and occurring interactions remains an unmet challenge with extensive work yet to be done. It is hoped that the present review helps to gain insight into the heteroaggregation processes and assists in designing more experiments to further improve our understanding in the colloidal domain.

## List of abbreviations

DLVO	Boris Derjaguin, Lev Landau, Evert Verwey and Theodoor Overbeek
SEM	Scanning electron microscopy
TEM	Transmission electron microscopy
HRTEM	High resolution transmission electron microscopy
HR-SEM	High resolution scanning electron microscopy
FE-SEM	Field emission scanning electron microscopy
cryo-FEGSEM	Cryogenic field emission gun scanning electron microscopy
cryo-TEM	Cryogenic transmission electron microscopy
EDX	Energy-dispersive X-ray spectroscopy
nZVI	Zero-valence iron nanoparticles
CMP	Clay mineral particles
POM	Particulate organic matter
PCM	Pyrogenic carbonaceous material
KGA	Kaolinite and goethite associations
GO	Graphene oxide
LDH	Layered double hydroxides
PDADMAC	Poly(diallyldimethylammonium chloride)
PNIPAM	Poly(N-isopropylacrylamide)
MMA	Methyl methacrylate
BA	Butyl acrylate
PBMA	Poly(butyl methacrylate)
HMPS	Sodium 2-hydroxyl-3-(methacryloxy)propane-1-sulfonate
SDS	Sodium dodecyl sulfate
CTAB	Cetrimonium bromide
CTA	Cetyltrimethyl ammonium
HA	Humic acid
OA	Octylamine
PTFE	Polytetrafluoroethylene
IEP	Isoelectric point
CCC	Critical coagulation concentration
LBL	Layer-by-layer assembly
PS	Polystyrene latex
CNTs	Carbon nanotubes
TBARs	Thiobarbituric acid reactive substances
VB9	Vitamin B9
NMP	N-methyl-2-pyrrolidone
Reduced GO	rGO
MB	Methylene blue
NCs	Nanoclusters/Nanocubes
LDO	Layered double oxides
CSs	Carbon spheres
CNs	Carbon nanospheres
PVP	Poly(vinyl pyrrolidone)
THF	Tetrahydrofuran
SERS	Surface enhanced Raman scattering
ROS	Reactive oxygen species
TMB	3,3',5,5'-tetramethylbenzidine
ABTS	2,2'-azino-bis(3-ethylbenzothiazoline-6-sulphonic acid)
OPD	O-phenylenediamine
HUVEC	Human umbilical vein endothelial cells
CHO	Chinese hamster ovary cells
MRI	Magnetic resonance imaging
HRP	Horseradish peroxidase
GCE	Glass carbon electrode
AL	Amidine latex
PB	Prussian blue
HemNP	Hematite nanoparticles

(continued on next page)

(continued)

SOD	Superoxide dismutase
DPPH	2,2-diphenyl-1-picrylhydrazyl
OAM	Oleylamine
PEG	Polyethylene glycol
PAA	Polyacrylic acid
GOQDs	Graphene oxide quantum dots
FTO	Fluoride-doped tin oxide
CDs	Carbon nanodots
ELISA	Enzyme linked immunosorbent assay
p-CDs	Polyethyleneimine-functionalized carbon dots
S/N-CDs	Nitrogen/sulfur co-doped carbon dots
CQDs	Nitrogen-doped quantum dots
AB	Lewis acid-base
NPs	Nanoparticles
MFNPs	Manganese ferrite nanoparticles
UV	Ultraviolet
AG	Arabic gum
NFC	Nanofibrillated cellulose
CNF	Cellulose nanofibers
BCNF	Bacterial cellulose nanofibers
TEMPO	2,2,6,6-Tetramethyl-1-piperidine oxyl
TOCNF	TEMPO-oxidized cellulose nanofibers
CHNF	Chitosan nanofibers
BT	Barium titanate
APO	Apoferitin
BLG	$\beta$ -lactoglobulin
CMC	Carboxymethyl cellulose

## Declaration of Competing Interest

The authors declare that they have no known competing financial interests or personal relationships that could have appeared to influence the work reported in this paper.

## Acknowledgment

Financial support from the Ministry of Human Capacities (20391-3/2018/FEKUSTRAT) and the Hungarian Academy of Sciences/Eötvös Lóránd Research Network (96130) is gratefully acknowledged. The support from the University of Szeged Open Access Fund (5267) is gratefully acknowledged.

## References

- [1] Dickinson E. Food colloids research: historical perspective and outlook. *Adv Colloid Interface Sci* 2011;165:7–13.
- [2] Feng LL, Stuart MC, Adachi Y. Dynamics of polyelectrolyte adsorption and colloidal flocculation upon mixing studied using mono-dispersed polystyrene latex particles. *Adv Colloid Interface Sci* 2015;226:101–14.
- [3] Moore TL, Rodriguez-Lorenzo L, Hirsch V, Balog S, Urban D, Jud C, et al. Nanoparticle colloidal stability in cell culture media and impact on cellular interactions. *Chem Soc Rev* 2015;44:6287–305.
- [4] Pavlovic M, Rouster P, Oncsik T, Szilagyí I. Tuning colloidal stability of layered double hydroxides: from monovalent ions to polyelectrolytes. *ChemPlusChem* 2017;82:121–31.
- [5] Muráth S, Sáringer S, Somosi Z, Szilagyí I. Effect of ionic compounds of different valences on the stability of titanium oxide colloids. *Coll Interf* 2018;2:32.
- [6] Shrestha S, Wang B, Dutta P. Nanoparticle processing: understanding and controlling aggregation. *Adv Colloid Interface Sci* 2020;279:102162.
- [7] Dickinson E. Structuring of colloidal particles at interfaces and the relationship to food emulsion and foam stability. *J Colloid Interface Sci* 2015;449:38–45.
- [8] Santos AC, Ferreira C, Veiga F, Ribeiro AJ, Panchal A, Lvov Y, et al. Halloysite clay nanotubes for life sciences applications: from drug encapsulation to bioscaffold. *Adv Colloid Interface Sci* 2018;257:58–70.
- [9] Cao ZB, Li B, Sun LY, Li L, Xu ZP, Gu Z. 2D layered double hydroxide nanoparticles: recent progress toward preclinical/clinical nanomedicine. *Small Methods* 2019;4:1900343.
- [10] Bolto B, Gregory J. Organic polyelectrolytes in water treatment. *Water Res* 2007;41:2301–24.
- [11] Martínez-Pedrero F, Alousque F, de Gaudemaris B, Berriot J, Gaboriaud F, Bremond N, et al. Making an elastomeric composite material via the heteroaggregation of a binary colloidal dispersion. *Soft Matter* 2012;8:8752–7.
- [12] Thomas AW, Foster SB. The colloidal content of vegetable tanning extracts. *J Ind Eng Chem* 1922;14:191–5.

- [13] Farrokhpay S. A review of polymeric dispersant stabilisation of titania pigment. *Adv Colloid Interface Sci* 2009;151:24–32.
- [14] Hubbe MA, Nanko H, McNeal MR. Retention aid polymer interactions with cellulosic surfaces and suspensions: a review. *BioResources* 2009;4:850–906.
- [15] Yu WL, Borkovec M. Distinguishing heteroaggregation from homoaggregation in mixed binary particle suspensions by multiangle static and dynamic light scattering. *J Phys Chem B* 2002;106:13106–10.
- [16] Lopez-Lopez JM, Schmitt A, Moncho-Jorda A, Hidalgo-Alvarez R. Electrostatic heteroaggregation regimes in colloidal suspensions. *Adv Colloid Interface Sci* 2009;147:186–204.
- [17] Cao TC, Borkovec M, Trefalt G. Heteroaggregation and homoaggregation of latex particles in the presence of alkyl sulfate surfactants. *Coll Interf* 2020;4:52.
- [18] Wang HT, Adeleye AS, Huang YX, Li FT, Keller AA. Heteroaggregation of nanoparticles with biocolloids and geocolloids. *Adv Colloid Interface Sci* 2015;226:24–36.
- [19] Buffle J, Wilkinson KJ, Stoll S, Filella M, Zhang JW. A generalized description of aquatic colloidal interactions: the three-colloidal component approach. *Environ Sci Technol* 1998;32:2887–99.
- [20] Jiang CL, Sequaris JM, Vereecken H, Klumpp E. Effects of inorganic and organic anions on the stability of illite and quartz soil colloids in Na-, Ca- and mixed Na-Ca systems. *Colloid Surf A* 2012;415:134–41.
- [21] Chanudet V, Filella M. The fate of inorganic colloidal particles in Lake Brienz. *Aquat Sci* 2007;69:199–211.
- [22] Missana T, Adell A. On the applicability of DLVO theory to the prediction of clay colloids stability. *J Colloid Interface Sci* 2000;230:150–6.
- [23] Oriekhova O, Stoll S. Heteroaggregation of nanoplastic particles in the presence of inorganic colloids and natural organic matter. *Environ Sci Nano* 2018;5:792–9.
- [24] Moore PS. Deltaic sedimentation. *Earth Sci Rev* 1966;1:87–104.
- [25] Xing YW, Xu MD, Gui XH, Cao YJ, Rudolph M, Butt HJ, et al. The role of surface forces in mineral flotation. *Curr Opin Colloid Interface Sci* 2019;44:143–52.
- [26] Dabros T, Vandeven TGM. Kinetics of coating by colloidal particles. *J Colloid Interface Sci* 1982;89:232–44.
- [27] Zubair M, Daud M, McKay G, Shehzad F, Al-Harathi MA. Recent progress in layered double hydroxides (LDH)-containing hybrids as adsorbents for water remediation. *Appl Clay Sci* 2017;143:279–92.
- [28] Wang J, Xu F, Jin HY, Chen YQ, Wang Y. Non-noble metal-based carbon composites in hydrogen evolution reaction: fundamentals to applications. *Adv Mater* 2017;29:1605838.
- [29] Siedl N, Baumann SO, Elser MJ, Diwald O. Particle networks from powder mixtures: generation of TiO<sub>2</sub>-SnO<sub>2</sub> heterojunctions via surface charge-induced heteroaggregation. *J Phys Chem C* 2012;116:22967–73.
- [30] Alsharif NB, Samu GF, Sáringer S, Muráth S, Szilagyí I. A colloid approach to decorate latex particles with Prussian blue nanozymes. *J Mol Liq* 2020;309:113066.
- [31] Patil AJ, Mann S. Self-assembly of bio-inorganic nanohybrids using organoclay building blocks. *J Mater Chem* 2008;18:4605–15.
- [32] Losch P, Huang WX, Goodman ED, Wrasman CJ, Holm A, Riscoe AR, et al. Colloidal nanocrystals for heterogeneous catalysis. *Nano Today* 2019;24:15–47.
- [33] Zhao Y, Zhao M, Ding X, Liu ZR, Tian H, Shen HH, et al. One-step colloid fabrication of nickel phosphides nanoplate/nickel foam hybrid electrode for high-performance asymmetric supercapacitors. *Chem Eng J* 2019;373:1132–43.
- [34] Guo C, Zhang Y, Yin M, Shi J, Zhang W, Wang X, et al. Co<sub>3</sub>O<sub>4</sub>@Co<sub>3</sub>S<sub>4</sub> core-shell neuroid network for high cycle-stability hybrid-supercapacitors. *J Power Sources* 2021;485:229315.
- [35] Zhai YC, Shen FZ, Zhang XT, Jing PT, Li D, Yang XD, et al. Synthesis of green emissive carbon dots@montmorillonite composites and their application for fabrication of light-emitting diodes and latent fingerprints markers. *J Colloid Interface Sci* 2019;554:344–52.
- [36] Bharadwaj S, Pandey A, Yagci B, Ozguz V, Qureshi A. Graphene nano-mesh-Ag-ZnO hybrid paper for sensitive SERS sensing and self-cleaning of organic pollutants. *Chem Eng J* 2018;336:445–55.
- [37] Yan LK, Zhang G, Zhang L, Zhang W, Gu JC, Huang YJ, et al. Robust construction of underwater superoleophobic CNTs/nanoparticles multifunctional hybrid membranes via interception effect for oily wastewater purification. *J Membr Sci* 2019;569:32–40.
- [38] Hernandez-Montelongo J, Fernandez-Fierro C, Benito-Gomez N, Romero-Saez M, Parodi J, Carmona ER, et al. Hybrid porous silicon/green synthesized Ag microparticles as potential carriers for Ag nanoparticles and drug delivery. *Mater Sci Eng C Mater Biol Appl* 2020;116:111183.
- [39] Ding Q, Liu DF, Guo DW, Yang F, Pang XY, Che BRE, et al. Shape-controlled fabrication of magnetite silver hybrid nanoparticles with high performance magnetic hyperthermia. *Biomaterials* 2017;124:35–46.
- [40] Li P, Guo W, Lu Z, Tian J, Li X, Wang H. UV-responsive single-microcapsule self-healing material with enhanced UV-shielding SiO<sub>2</sub>/ZnO hybrid shell for potential application in space coatings. *Prog Org Coat* 2021;151:106046.
- [41] Derjaguin B, Landau LD. Theory of the stability of strongly charged lyophobic sols and of the adhesion of strongly charged particles in solutions of electrolytes. *Acta Phys Chim* 1941;14:633–62.
- [42] Verwey EJW, Overbeek JTG. Theory of stability of lyophobic colloids. Amsterdam: Elsevier; 1948.
- [43] Israelachvili J. Intermolecular and surface forces. 3rd ed. London: Academic Press; 2011.
- [44] Wang YL, Yang K, Chefetz B, Xing BS, Lin DH. The pH and concentration dependent interfacial interaction and heteroaggregation between nanoparticulate zero-valent iron and clay mineral particles. *Environ Sci Nano* 2019;6:2129–40.



- [45] Jiang LH, Liu YG, Zeng GM, Liu SB, Que W, Li J, et al. Adsorption of 17 beta-estradiol by graphene oxide: effect of heteroaggregation with inorganic nanoparticles. *Chem Eng J* 2018;343:371–8.
- [46] Ben Moussa O, Tinat L, Jin XJ, Baaziz W, Durupthy O, Sayag C, et al. Heteroaggregation and selective deposition for the fine design of nanoarchitected bifunctional catalysts: application to hydroisomerization. *ACS Catal* 2018;8:6071–8.
- [47] Luo MX, Qi XJ, Ren TX, Huang YX, Keller AA, Wang HT, et al. Heteroaggregation of CeO<sub>2</sub> and TiO<sub>2</sub> engineered nanoparticles in the aqueous phase: application of turbiscan stability index and fluorescence excitation-emission matrix (EEM) spectra. *Colloid Surf A Physicochem Eng Asp* 2017;533:9–19.
- [48] Zhao J, Liu FF, Wang ZY, Cao XS, Xing BS. Heteroaggregation of graphene oxide with minerals in aqueous phase. *Environ Sci Technol* 2015;49:2849–57.
- [49] Lopez-Lopez JM, Schmitt A, Moncho-Jorda A, Hidalgo-Alvarez R. Stability of binary colloids: kinetic and structural aspects of heteroaggregation processes. *Soft Matter* 2006;2:1025–42.
- [50] Dusak P, Mertelj A, Kralj S, Makovec D. Controlled heteroaggregation of two types of nanoparticles in an aqueous suspension. *J Colloid Interface Sci* 2015;438:235–43.
- [51] Cao TC, Sugimoto T, Szilagyi I, Trefalt G, Borkovec M. Heteroaggregation of oppositely charged particles in the presence of multivalent ions. *Phys Chem Chem Phys* 2017;19:15160–71.
- [52] Wang XN, Wang S, Pan XL, Gadd GM. Heteroaggregation of soil particulate organic matter and biogenic selenium nanoparticles for remediation of elemental mercury contamination. *Chemosphere* 2019;221:486–92.
- [53] Hogg R, Healy TW, D.W. F. Mutual coagulation of colloidal dispersions. *Trans Faraday Soc* 1966;62:1638–51.
- [54] Trefalt G, Montes Ruiz-Cabello FJ, Borkovec M. Interaction forces, heteroaggregation and deposition involving charged colloidal particles. *J Phys Chem B* 2014;118:6346–55.
- [55] Cerbelaud A, Videcoq A, Pagnoux C, Rossignol F, Ferrando R. Heteroaggregation between Al<sub>2</sub>O<sub>3</sub> submicrometer particles and SiO<sub>2</sub> nanoparticles: experiment and simulation. *Langmuir* 2008;24:3001–8.
- [56] Moazzami-Gudarzi M, Adam P, Smith AM, Trefalt G, Szilagyi I, Maroni P, et al. Interactions between similar and dissimilar charged interfaces in the presence of multivalent anions. *Phys Chem Chem Phys* 2018;20:9436–48.
- [57] Trefalt G, Szilagyi I, Oncsik T, Sadeghpour A, Borkovec M. Probing colloidal particle aggregation by light scattering. *Chimia* 2013;67:772–6.
- [58] Voorn DJ, Ming W, Laven J, Meuldijk J, de With G, van Herk AM. Plate-sphere hybrid dispersions: Heterocoagulation kinetics and DLVO evaluation. *Colloid Surf A* 2007;294:236–46.
- [59] Lin W, Kobayashi M, Skarba M, Mu C, Galletto P, Borkovec M. Heteroaggregation in binary mixtures of oppositely charged colloidal particles. *Langmuir* 2006;22:1038–47.
- [60] Bansal P, Deshpande AP, Basavaraj MG. Hetero-aggregation of oppositely charged nanoparticles. *J Colloid Interface Sci* 2017;492:92–100.
- [61] Parsai T, Kumar A. Understanding effect of solution chemistry on heteroaggregation of zinc oxide and copper oxide nanoparticles. *Chemosphere* 2019;235:457–69.
- [62] Nakamura Y, Okachi M, Toyotama A, Okuzono T, Yamanaka J. Controlled clustering in binary charged colloids by adsorption of ionic surfactants. *Langmuir* 2015;31:13303–11.
- [63] Lu XY, Lu TT, Zhang HJ, Shang ZB, Chen JY, Wang Y, et al. Effects of solution chemistry on the attachment of graphene oxide onto clay minerals. *Environ Sci Process Impacts* 2019;21:506–13.
- [64] Harley S, Thompson DW, Vincent B. The adsorption of small particles onto larger particles of opposite charge. Direct electron microscope studies. *Colloids Surf* 1992;62:163–76.
- [65] Yu WL, Matijevic E, Borkovec M. Absolute heteroaggregation rate constants by multiple static and dynamic light scattering. *Langmuir* 2002;18:7853–60.
- [66] Singh N, Tiwari E, Khandelwal N, Darbha GK. Understanding the stability of nanoplastics in aqueous environments: effect of ionic strength, temperature, dissolved organic matter, clay, and heavy metals. *Environ Sci Nano* 2019;6:2968–76.
- [67] Barton LE, Therezien M, Auffan M, Bottero JY, Wiesner MR. Theory and methodology for determining nanoparticle affinity for heteroaggregation in environmental matrices using batch measurements. *Environ Eng Sci* 2014;31:421–7.
- [68] Tombacz E, Csanaky C, Illes E. Polydisperse fractal aggregate formation in clay mineral and iron oxide suspensions, pH and ionic strength dependence. *Colloid Polym Sci* 2001;279:484–92.
- [69] Guo BL, Jiang JC, Serem W, Sharma VK, Ma XM. Attachment of cerium oxide nanoparticles of different surface charges to kaolinite: molecular and atomic mechanisms. *Environ Res* 2019;177:108645.
- [70] Khalil AM, Hassan ML, Ward AA. Novel nanofibrillated cellulose/polyvinylpyrrolidone/silver nanoparticles films with electrical conductivity properties. *Carbohydr Polym* 2017;157:503–11.
- [71] Hassan ML, Ali AF, Salama AH, Abdel-Karim AM. Novel cellulose nanofibers/barium titanate nanoparticles nanocomposites and their electrical properties. *J Phys Org Chem* 2019;32:3897.
- [72] Huynh KA, McCaffery JM, Chen KL. Heteroaggregation of multiwalled carbon nanotubes and hematite nanoparticles: rates and mechanisms. *Environ Sci Technol* 2012;46:5912–20.
- [73] Jurado R, Galvez N. Apoferritin amyloid-fibril directed the in situ assembly and/or synthesis of optical and magnetic nanoparticles. *Nanomaterials* 2021;11:146.
- [74] Liu X, Xu XT, Sun J, Duan SX, Sun YB, Hayat T, et al. Interaction between Al<sub>2</sub>O<sub>3</sub> and different sizes of GO in aqueous environment. *Environ Pollut* 2018;243:1802–9.
- [75] Chen B, Sun WL, Wang CH, Guo XY. Size-dependent impact of inorganic nanoparticles on sulfamethoxazole adsorption by carbon nanotubes. *Chem Eng J* 2017;316:160–70.
- [76] de Mendonca VR, Dalmaschio CJ, Leite ER, Niederberger M, Ribeiro C. Heterostructure formation from hydrothermal annealing of preformed nanocrystals. *J Mater Chem A* 2015;3:2216–25.
- [77] Yi P, Pignatello JJ, Uchimiya M, White JC. Heteroaggregation of cerium oxide nanoparticles and nanoparticles of pyrolyzed biomass. *Environ Sci Technol* 2015;49:13294–303.
- [78] Zanini M, Hsu CP, Magrini T, Marini E, Isa L. Fabrication of rough colloids by heteroaggregation. *Colloid Surf A Physicochem Eng Asp* 2017;532:116–24.
- [79] Veschambres C, Halma M, Bourgeat-Lami E, Chazeau L, Dalmas F, Prevot V. Layered double hydroxides: efficient fillers for waterborne nanocomposite films. *Appl Clay Sci* 2016;130:55–61.
- [80] Ji YQ, Black L, Weidler PG, Janek M. Preparation of nanostructured materials by heteroaggregation-interaction of montmorillonite with synthetic hematite particles. *Langmuir* 2004;20:9796–806.
- [81] Voorn DJ, Ming W, van Herk AM, Bomans PHH, Frederik PM, Gsemjit P, et al. Controlled heterocoagulation of platelets and spheres. *Langmuir* 2005;21:6950–6.
- [82] Yang JT, Chen F, Ye YC, Fei ZD, Zhong MQ. Preparation and characterization of polystyrene (PS)/layered double hydroxides (LDHs) composite by a heterocoagulation method. *Colloid Polym Sci* 2010;288:761–7.
- [83] Pavlovic M, Rouster P, Bourgeat-Lami E, Prevot V, Szilagyi I. Design of latex-layered double hydroxide composites by tuning the aggregation in suspensions. *Soft Matter* 2017;13:842–51.
- [84] Li H, Deng L, Zhu G, Kang L, Liu Z-H. Fabrication and capacitance of Ni<sup>2+</sup>-Fe<sup>3+</sup> LDHs/MnO<sub>2</sub> layered nanocomposite via an exfoliation/reassembling process. *Mater Sci Eng B* 2012;177:8–13.
- [85] Nethravathi C, Viswanath B, Shivakumara C, Mahadevaiah N, Rajamathi M. The production of smectite clay/graphene composites through delamination and co-stacking. *Carbon* 2008;46:1773–81.
- [86] Lagaly G, Mecking O, Penner D. Colloidal magnesium aluminum hydroxide and heterocoagulation with a clay mineral. II. Heterocoagulation with sodium montmorillonite. *Colloid Polym Sci* 2001;279:1097–103.
- [87] Huang GX, Guo HY, Zhao J, Liu YH, Xing BS. Effect of co-existing kaolinite and goethite on the aggregation of graphene oxide in the aquatic environment. *Water Res* 2016;102:313–20.
- [88] Jones OG, Handschin S, Adamcik J, Harnau L, Bolisetty S, Mezzenga R. Complexation of b-lactoglobulin fibrils and sulfated polysaccharides. *Biomacromolecules* 2011;12:3056–65.
- [89] Pita IA, Singh S, Silien C, Ryan KM, Liu N. Heteroaggregation assisted wet synthesis of core-shell silver-silica-cadmium selenide nanowires. *Nanoscale* 2016;8:1200–9.
- [90] Yan WJ, Chen WB, Muhammad U, Zhang JH, Zhuang H, Zhou GH. Preparation of alpha-tocopherol-chitosan nanoparticles/chitosan/montmorillonite film and the antioxidant efficiency on sliced dry-cured ham. *Food Control* 2019;104:132–8.
- [91] Mallakpour S, Hatami M. Green and eco-friendly route for the synthesis of Ag@vitamin B9-LDH hybrid and its chitosan nanocomposites: characterization and antibacterial activity. *Polymer* 2018;154:188–99.
- [92] Pricilla RB, Bhuvanesh N, David CI, Murugan S, Nandhakumar R. GO/NiO nanocomposite: Chemosensor for L-Leucine and a potential antibacterial agent. *Mater Today Chem* 2021. <https://doi.org/10.1016/j.matpr.2020.11.466>.
- [93] Almasi H, Jafarzadeh P, Mehryar L. Fabrication of novel nanohybrids by impregnation of CuO nanoparticles into bacterial cellulose and chitosan nanofibers: characterization, antimicrobial and release properties. *Carbohydr Polym* 2018;186:273–81.
- [94] Li J, Xu Y, Wang S, Zhang H. Ultrafine AuPd nanoclusters on layered double hydroxides by the capt-capped AuPd cluster precursor method: synergistic effect for highly efficient aerobic oxidation of alcohols. *J Phys Chem C* 2019;123:15483–94.
- [95] Li L, Feng YJ, Li YS, Zhao WR, Shi JL. Fe<sub>3</sub>O<sub>4</sub> core/layered double hydroxide shell nanocomposite: versatile magnetic matrix for anionic functional materials. *Angew Chem Int Edit* 2009;48:5888–92.
- [96] Zhu MS, Sun ZC, Fujitsuka M, Majima T. Z-scheme photocatalytic water splitting on a 2D heterostructure of black phosphorus/bismuth vanadate using visible light. *Angew Chem Int Edit* 2018;57:2160–4.
- [97] Gunjakar JL, Kim TW, Kim HN, Kim IY, Hwang SJ. Mesoporous layer-by-layer ordered nanohybrids of layered double hydroxide and layered metal oxide: highly active visible light photocatalysts with improved chemical stability. *J Am Chem Soc* 2011;133:14998–5007.
- [98] Szabo T, Veres A, Cho E, Kim J, Varga N, Dekany I. Photocatalyst separation from aqueous dispersion using graphene oxide/TiO<sub>2</sub> nanocomposites. *Colloid Surf A* 2013;433:230–9.
- [99] Patzko A, Kun R, Hornok V, Dekany I, Engelhardt T, Schall N. ZnAl-layer double hydroxides as photocatalysts for oxidation of phenol in aqueous solution. *Colloid Surf A* 2005;265:64–72.
- [100] Boppella R, Choi CH, Moon J, Kim DH. Spatial charge separation on strongly coupled 2D-hybrid of rGO/La<sub>2</sub>Ti<sub>2</sub>O<sub>7</sub>/NiFe-LDH heterostructures for highly efficient noble metal free photocatalytic hydrogen generation. *Appl Catal B Environ* 2018;239:178–86.
- [101] Mallakpour S, Hatami M. LDH-VB9-TiO<sub>2</sub> and LDH-VB9-TiO<sub>2</sub>/crosslinked PVA nanocomposite prepared via facile and green technique and their photo-



- degradation application for methylene blue dye under ultraviolet illumination. *Appl Clay Sci* 2018;163:235–48.
- [102] Rossi LM, Costa NJS, Silva FP, Wojcieszak R. Magnetic nanomaterials in catalysis: advanced catalysts for magnetic separation and beyond. *Green Chem* 2014;16:2906–33.
- [103] Goodman ED, Zhou CS, Cargnello M. Design of organic/inorganic hybrid catalysts for energy and environmental applications. *ACS Central Sci* 2020;6:1916–37.
- [104] Xie ZK, Liu ZC, Wang YD, Yang QH, Xu LY, Ding WP. An overview of recent development in composite catalysts from porous materials for various reactions and processes. *Int J Mol Sci* 2010;11:2152–87.
- [105] Parlett CMA, Wilson K, Lee AF. Hierarchical porous materials: catalytic applications. *Chem Soc Rev* 2013;42:3876–93.
- [106] Zong YT, Li KT, Tian R, Lin YJ, Lu C. Highly dispersed layered double oxide hollow spheres with sufficient active sites for adsorption of methyl blue. *Nanoscale* 2018;10:23191–7.
- [107] Hu QH, Xu ZP, Qiao SZ, Haghseresht F, Wilson M, Lu GQ. A novel color removal adsorbent from heterocoagulation of cationic and anionic clays. *J Colloid Interface Sci* 2007;308:191–9.
- [108] Gong JM, Liu T, Wang XQ, Hu XL, Zhang LZ. Efficient removal of heavy metal ions from aqueous systems with the assembly of anisotropic layered double hydroxide nanocrystals@carbon nanosphere. *Environ Sci Technol* 2011;45:6181–7.
- [109] Zhang B, Hu RT, Sun DJ, Wu T, Li YJ. Fabrication of magnetite-graphene oxide/MgAl-layered double hydroxide composites for efficient removal of emulsified oils from various oil-in-water emulsions. *J Chem Eng Data* 2018;63:4689–702.
- [110] Zubitur MM, Sudol ED, Dimonie VL, El-Aasser MS. Monodisperse micron-size polymer core/nanoparticle pigment shell composite particles via heteroaggregation. *J Appl Polym Sci* 2009;114:264–74.
- [111] Lee JH, Mahmoud MA, Sitterle VB, Sitterle JJ, Meredith JC. Highly scattering, surface-enhanced Raman scattering-active, metal nanoparticle-coated polymers prepared via combined swelling-heteroaggregation. *Chem Mater* 2009;21:5654–63.
- [112] Deak A, Janovak L, Tallosy SP, Bito T, Sebok D, Buzas N, et al. Spherical LDH-Ag<sup>0</sup>-montmorillonite heterocoagulated system with a pH-dependent sol-gel structure for controlled accessibility of AgNPs immobilized on the clay lamellae. *Langmuir* 2015;31:2019–27.
- [113] Liu Y, Wu Y, Zhang R, Lam J, Ng JC, Xu ZP, et al. Investigating the use of layered double hydroxide nanoparticles as carriers of metal oxides for theranostics of ROS-related diseases. *ACS Appl Bio Mater* 2019;2:5930–40.
- [114] Darabdhara G, Bordoloi J, Manna P, Das MR. Biocompatible bimetallic au-Ni doped graphitic carbon nitride sheets: a novel peroxidase-mimicking artificial enzyme for rapid and highly sensitive colorimetric detection of glucose. *Sens Actuator B Chem* 2019;285:277–90.
- [115] Zhao XJ, Mai ZB, Kang XH, Zou XY. Direct electrochemistry and electrocatalysis of horseradish peroxidase based on clay-chitosan-gold nanoparticle nanocomposite. *Biosens Bioelectron* 2008;23:1032–8.
- [116] Soh N, Kaneko S, Uozumi K, Ueda T, Kamada K. Preparation of an enzyme/inorganic nanosheet/magnetic bead complex and its enzymatic activity. *J Mater Sci* 2014;49:8010–5.
- [117] Gunawan P, Xu R. Direct assembly of anisotropic layered double hydroxide (LDH) nanocrystals on spherical template for fabrication of drug-LDH hollow nanospheres. *Chem Mater* 2009;21:781–3.
- [118] Peng EW, Choo ESG, Chandrasekharan P, Yang CT, Ding J, Chuang KH, et al. Synthesis of manganese ferrite/graphene oxide nanocomposites for biomedical applications. *Small* 2012;8:3620–30.
- [119] Han YW, Liu N, Wang N, He ZH, Liu QC. Assembly of Ni-Al layered double hydroxide and oxide graphene quantum dots for supercapacitors. *J Mater Res* 2018;33:4215–23.
- [120] Bai Y, Xing Z, Yu H, Li Z, Amal R, Wang LZ. Porous titania nanosheet/nanoparticle hybrids as photoanodes for dye-sensitized solar cells. *ACS Appl Mater Interfaces* 2013;5:12058–65.
- [121] Kim JM, Cho Y, Guccini V, Hahn M, Yan BY, Salazar-Alvarez G, et al. TEMPO-oxidized cellulose nanofibers as versatile additives for highly stable silicon anode in lithium-ion batteries. *Electrochim Acta* 2021;369:137708.
- [122] Wang YL, Wang ZC, Rui YP, Li MG. Horseradish peroxidase immobilization on carbon nanodots/CoFe layered double hydroxides: direct electrochemistry and hydrogen peroxide sensing. *Biosens Bioelectron* 2015;64:57–62.
- [123] Amjadi M, Hallaj T, Kouhi Z. An enzyme-free fluorescent probe based on carbon dots - MnO<sub>2</sub> nanosheets for determination of uric acid. *J Photochem Photobiol A Chem* 2018;356:603–9.
- [124] Dong BL, Li HF, Sun JF, Mari GM, Yu XZ, Ke YB, et al. Development of a fluorescence immunoassay for highly sensitive detection of amantadine using the nanoassembly of carbon dots and MnO<sub>2</sub> nanosheets as the signal probe. *Sens Actuator B Chem* 2019;286:214–21.
- [125] He DG, Yang XX, He XX, Wang KM, Yang X, He X, et al. A sensitive turn-on fluorescent probe for intracellular imaging of glutathione using single-layer MnO<sub>2</sub> nanosheet-quenched fluorescent carbon quantum dots. *Chem Commun* 2015;51:14764–7.
- [126] Sternitzke M. Structural ceramic nanocomposites. *J Eur Ceram Soc* 1997;17:1061–82.
- [127] Madhavan N, Mukherjee M, Basavaraj MG. Porous ceramics via processable Pickering emulsion stabilized by oppositely charged colloids. *Langmuir* 2020;36:11645–54.
- [128] Munoz M, Cerbelaud M, Videcoq A, Saad H, Boule A, Meille S, et al. Nacre-like alumina composites based on heteroaggregation. *J Eur Ceram Soc* 2020;40:5773–8.
- [129] Fan JP, Zhao DQ, Xu ZN, Wu MS. Preparation of MWNTS/Al<sub>2</sub>O<sub>3</sub> composites and their mechanical and electrical properties. *Sci China Ser E Technol Sci* 2005;48:622–31.
- [130] Kazmierczak-Balata A, Mazur J. Effect of carbon nanoparticle reinforcement on mechanical and thermal properties of silicon carbide ceramics. *Ceram Int* 2018;44:10273–80.